META 2024 Toyama - Japan

The 14th International Conference on Metamaterials, Photonic Crystals and Plasmonics



July 16 – 19, 2024
Toyama - Japan

Proceedings

ISSN 2429-1390

metaconferences.org

META 2024 Toyama - Japan

The 14th International Conference on Metamaterials, Photonic Crystals and Plasmonics

Edited by

Junichi Takahara | Osaka University, Japan
Kotaro Kajikawa | Tokyo Institute of Technology, Japan
Said Zouhdi | Paris-Saclay University, France

TABLE OF CONTENT

ORGANIZATION I COMMITTEES 3

SPONSORS I EXHIBITORS 6

PLENARY SPEAKERS 8

KEYNOTE SPEAKERS 13

TUTORIALS 21

INDUSTRIAL WORKSHOPS 23

GUIDELINES FOR PRESENTERS I IN-PERSON 24

USEFUL INFORMATION 25

TECHNICAL PROGRAM 28

ORGANIZATION I COMMITTEES

Conference Chairs



Junichi Takahara
Osaka University
Japan



Kotaro Kajikawa
Tokyo Institute of Technology
Japan



Said Zouhdi
Paris–Saclay University
France

Organizing Committee

Andrea Fratalocchi (Saudi Arabia)
Hajime Ishihara (Japan)
Kentaro Iwami (Japan)
Satoshi Iwamoto (Japan)
Wakana Kubo (Japan)
Yu-Jung Lu (Taiwan)
Hiromi Okamoto (Japan)
Koichi Okamoto (Japan)
Junsuk Rho (Korea)
Pham Tien Thanh (Vietnam)
Takuo Tanaka (Japan)
Jeong Weon Wu (Korea)
Takaaki Yano (Japan)
Lei Zhou (China)

International Advisory Committee

Harry Atwater Harry (USA)
Federico Capasso (USA)
Nader Engheta (USA)
Teruya Ishihara (Japan)
Yuri Kivshar (Australia)
Graeme W. Milton (USA)
Manuel N.-Vesperinas (Spain)
Susumu Noda (Japan)
Franco Nori (Japan & USA)
Masaya Notomi (Japan)
Vladimir Shalaev (USA)
David R. Smith (USA)
Martin Wegener (Germany)
Xiang Zhang (Hong Kong)
Nikolay Zheludev (UK)

Technical Program Committee

Pierre-Michel Adam (France)
Ishwar Aggarwal (USA)
Antonio Ambrosio (Italy)
Benfeng Bai (China)
Xavier Begaud (France)
Maha Ben Rhouma (France)
Henri Benisty (France)
Jamal Berakdar (Germany)
Svetlana V. Boriskina (USA)
Che Ting Chan (Hong Kong)
Debashis Chanda (USA)
Pai-Yen Chen (USA)
Johan Christensen (Spain)
Alfredo De Rossi (France)
Alexander Dmitriev (Sweden)
Mohamed Farhat (Saudi Arabia)
Monika Fleischer (Germany)
Denis Garoli (Italy)
Alexander Govorov (USA)
Tatjana Gric (Lithuania)
Jean-Philippe Groby (France)
Ortwin Hess (UK)
Eugene Kamenetskii (Israel)
Howard (Ho Wai) Lee (USA)
Jensen Li (Hong Kong)
Qiang Li (China)
Yang Li (China)
Anatole Lupu (France)
Nicolò Maccaferri (Sweden)
Martin McCall (UK)
Marco Miniaci (France)
Taiichi Otsuji (Japan)
Willie Padilla (USA)
Dorota Pawlak (Poland)
Lucia Petti (Italy)
Virginie Ponsinet (France)
Giorgio Quaranta (Switzerland)
Jun Suk Rho (Korea)
Junichi Takahara (Japan)
Takuo Tanaka (Japan)
Hong Wei (China)
Chung-Tse Michael Wu (Taiwan)

Special Sessions Organizers

Guillermo Acuna (Switzerland)
Andrei Afanasev (USA)
Benfeng Bai (China)
Alessandro Belardini (Italy)
Maha Ben Rhouma (France)
Henri Benisty (France)
Jamal Berakdar (Germany)
Igal Brener (USA)
Debashis Chanda (USA)
Maria Chekhova (Germany)
Pai-Yen Chen (USA)
Hyuck Choo (Korea)
Diego Dalvit (USA)
Zi-Lan Deng (China)
Mohamed Farhat (Saudi Arabia)
Denis Garoli (Itlay)
Li Ge (USA)
Tatjana Gric (Lithuania)
Songyan Hou (China)
Hao Hu (China)
Kun Huang (China)
Kentaro Iwami (Japan)
Masanobu Iwanaga (Japan)
Baohua Jia (Australia)
Alina Karabchevsky (Israel)
Hui-Seon Kim (Korea)
Guixin Li (China)
Zhenfei Li (China)
Der-Hsien Lien (Taiwan)
Anatole Lupu (France)
Konstantinos Makris (Greece)
Shunsuke Murai (Japan)
Kazuteru Nonomura (Japan)
Willie Padilla (USA)
Dorota Pawlak (Poland)
Yu-Gui Peng (China)
Virginie Ponsinet (France)
Edik Rafailov (UK)
Takumi Sannomiya (Japan)
Sergey Saveliev (UK)
Radwanul H. Siddique (USA)
Hiroshi Sugimoto (Japan)
Junichi Takahara (Japan)
Mana Toma (Japan)
Shaojun Wang (China)
Hong Wei (China)
Oliver Wright (Japan)
Chung-Tse Michael Wu (Taiwan)
Fajun Xiao (China)
Alexandre Zagoskin (UK)
Weiren Zhu (China)
Xue-Feng Zhu (China)

Special Symposia Organizers



Jerome Plain
France



Alexander Govorov
USA



Davy Gérard
France



Pedro H. Martinez
Singapore



Junsuk Rho
Korea



Hakjoo Lee
Korea



Namkyoo Park
Korea



Seong Ok Han
Korea



Howard Lee
USA



Pin-Chieh Wu
Taiwan



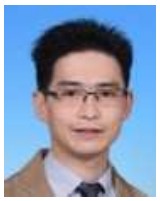
Qinghua Song
China



Eugene
Kamenetskii
Israel



Marco Miniaci
France



Jensen Li
Hong Kong



Vicente R. García
Spain



Vincent Pagneux
France



Noé Jiménez
Spain

SPONSORS I EXHIBITORS

Gold Sponsor

The Synopsys Optical Solutions Group provides design tools that model all aspects of light propagation. Our innovative software packages include CODE V® imaging design software, LightTools® illumination design software, the LucidShape® products for automotive lighting, and the RSoft™ Photonic Device Tools for passive and active photonic devices. And our optical measurement solutions give customers access to precision light scattering data for materials and media used in optical systems.

At META 2024, Synopsys will demonstrate MetaOptic Designer, an unprecedented inverse design tool that takes user-specified criteria and generates metalenses/metasurfaces for optimal design performance. Metalens design traditionally requires extensive physics knowledge and many hours of development. MetaOptic Designer removes these barriers with exclusive AI that automatically yields the best metalens designs as fast as possible.
Learn more about Synopsys Optical Solutions at:
https://www.synopsys.com/optical-solutions.html.

Silver Sponsor

Ansys Optics tools empower designers to expedite the development of groundbreaking optical products while improving performance, reliability, and yield. These solutions offer robust design, optimization, and verification simulation software backed by world-class support. With a suite of top-tier optical solvers, Ansys Optics provides user-friendly workflows for precise multiscale system design, from the nano to macro scale, enabling the design of diverse applications across various industries.

Ansys Optics enables photonics and optical design from meta-atoms to centimeter-scale metalenses by seamlessly leveraging the combination power of Lumerical FDTD, RCWA and Zemax OpticStudio.

Grants Program Sponsor

ACS Publications supports researchers through journals, eBooks, scientific programs, and the news magazine Chemical & Engineering News. With a comprehensive portfolio of 80+ journals, including 16 "gold" completely open access journals, ACS Publications has a home for every type of research. Journals include ACS Photonics, Nano Letters, ACS Nano, ACS Applied Materials & Interfaces, and JACS.

Other Partners

Osaka University is a national research university in Osaka, Japan. The university traces its roots back to Edo-era institutions Tekijuku (1838) and Kaitokudo (1724), and was officially established in 1931 as the sixth of the Imperial Universities in Japan, with two faculties: science and medicine. Following the post-war educational reform, it merged with three pre-war higher schools, reorganizing as a comprehensive university with five faculties: science, medicine, letters, law and economics, and engineering. After the merger with Osaka University of Foreign Studies in 2007, it became the largest national university in Japan by undergraduate enrollment.

Tokyo Institute of Technology Tokyo Tech is the top national university for science and technology in Japan with a history spanning more than 140 years. Of the approximately 10,500 students at the Ookayama, Suzukakedai, and Tamachi Campuses, half are in their bachelor's degree program while the other half are in master's and doctoral degree programs. International students number 1,800. There are 1,100 faculty and 600 administrative and technical staff members.

Université Paris-Saclay is a research university based in Paris, France. Université Paris-Saclay offers a comprehensive and varied range of Undergraduate, Master's and PhD degrees, renowned internationally thanks to the University's reputation for research excellence and the commitment of its academic staff. The University's constituent faculties, institutes and component institutions all contribute to the curricula with cutting-edge specialised courses in Science and Engineering, Life Sciences and Health, and Social Sciences and Humanities.
Université Paris-Saclayis ranked 1st in France and 13th in the world according to the Academic Ranking of World Universities (ARWU).

AEM - Advanced Electromagnetics is a peer-reviewed, Gold Open Access journal. It covers recent international research results in the general field of Electromagnetic Waves, Antennas and Propagation. Authors of articles published in Advanced Electromagnetics retain the copyright of their articles and are free to reproduce and disseminate their work (under a Creative Commons Attribution License). AEM is widely indexed and has a Scopus CiteScore of 2.2 (2021).

Nanophotonics (De Gruyter) covers recent international research results, specific developments in the field and novel applications. It publishes all article in a Gold Open Access model and belongs to the top journals in the field. Nanophotonics focuses on the interaction of photons with nano-structures, such as carbon nano-tubes, nano metal particles, nano crystals, semiconductor nano dots, photonic crystals, tissue and DNA.

PLENARY SPEAKERS



Harry Atwater

California Institute of Technology, USA

is the Otis Booth Leadership Chair of the Division of Engineering and Applied Science, and the Howard Hughes Professor of Applied Physics and Materials Science at the California Institute of Technology. Atwater's scientific effort focuses on nanophotonic light-matter interactions. His work spans fundamental nanophotonic phenomena and applications, including active wavefront shaping of light using metasurfaces, optical propulsion of lightsails, quantum and 2D nanophotonics as well as solar energy conversion, on earth and in space.

Atwater was an early pioneer in nanophotonics and plasmonics and gave a name to the field of plasmonics in 2001. He is Chair of the LightSail Committee for the Breakthrough Starshot program. Currently Atwater is also the Director for the Liquid Sunlight Alliance (LiSA), a Department of Energy Hub program for solar fuels, and was also the founding Editor in Chief of the journal ACS Photonics. Atwater is a Member of the US National Academy of Engineering, a Fellow of APS, MRS, SPIE and Optica, a Web of Science Highly Cited Researcher from 2014-2023, and is recipient of numerous awards, including the 2021 von Hippel Award of the Materials Research Society.



Hui Cao

Yale University, USA

Shaping light propagation in complex media

Hui Cao is the John C. Malone Professor of Applied Physics, a Professor of Physics, and a Professor of Electrical Engineering at Yale University. She received her Ph.D. degree in Applied Physics from Stanford University in 1997. Prior to joining the Yale faculty in 2008, she was on the faculty of Northwestern University for ten years. Her technical interests and activities are in the areas of mesoscopic physics, complex photonic materials and devices, nanophotonics, and biophotonics. Cao is a Fellow of IEEE, AAAS, APS and OSA, and an elected member of the National Academy of Sciences, and the American Academy of Arts and Sciences.

Shaping light propagation in complex media

By breaking the diffusion limit, we deliver optical energy into a target region of arbitrary size and shape anywhere inside a strong-scattering system. We further demonstrate an order of magnitude enhancement of remitted signals that carry information from deep inside a diffusive medium.



Franco Nori

Riken (Japan) and University of Michigan, USA

Topological dissipation in a time-multiplexed photonic resonator network and topological temporally mode-locked lasers

Franco Nori is a Chief Scientist at RIKEN, with a concurrent position at the University of Michigan. He received his PhD from the University of Illinois, and afterwards became a postdoc at the Institute for Theoretical Physics, University of California, Santa Barbara. His research group has done pioneering interdisciplinary studies at the interface between nanoscience, photonics, quantum optics, dissipative quantum open systems, quantum information processing, superconducting quantum circuitry, opto-mechanics, and condensed matter physics. He has been listed by the Web of Science as a "Highly Cited Researcher" (less than 0.1% are selected) in Physics for the past seven consecutive years: from 2017 to 2023. He is an Elected Fellow of the American Physics Society (APS), Institute of Physics (IoP), American Association for the Advancement of Science (AAAS), and Optical Society of America (OSA) [this last one "for fundamental contributions to quantum information science and optics, including circuit quantum electrodynamics, and the interface between quantum optics and quantum circuits"]. He received the 2014 Prize for Research in Physics, from the Matsuo Foundation, Japan; and the 2013 Prize for Science, by the Minister of Education, Culture, Sports, Science and Technology, Japan. Also, an "Excellence in Research Award" and an "Excellence in Education Award" from the University of Michigan. He is an Elected Member of the Academia Europaea, the Latin American Academy of Sciences, and a Foreign Member of the Swedish Royal Society of Arts and Sciences, in Gothenburg, Sweden. He won the 2023 W.E. Lamb Medal, and the 2024 Charles H. Townes Medal (from the OSA), both for research on Quantum Optics, Quantum Electronics and Quantum Information.

Topological dissipation in a time-multiplexed photonic resonator network and topological temporally mode-locked lasers

This talk provides an overview of recent results on topological dissipation in a time-multiplexed photonic resonator network, and topological temporally mode-locked lasers. A very brief summary will also be made of recent work on non-Abelian effects in dissipative photonic topological lattices.



Takashige Omatsu

Chiba University, Japan

Materials manipulation with structured light fields

Takashige Omatsu received his BS and PhD degrees in applied physics from the University of Tokyo in 1983 and 1992, and he has been a professor at Chiba University since 2007. He is currently working as a director of Molecular Chirality Research Center, Chiba University. He has been investigating the generation of structured light on a nano/ micron scale and pioneering nano/micro fabrications using structured light. He has already published 200+ journal papers, 250+ international conference papers, and 14 patents (including 2 US-patents), and he has performed 150+ invited presentations. Prof. Omatsu is working as the founding editor-in-chief of Optics Continuum (Optica), and he is also serving as a chair of the CLEO Pacific Rim Steering Committee. He was elected Optica, SPIE and JSAP fellow. Also, he was awarded Prize for Science and Technology, MEXT in 2016.

Materials manipulation with structured light fields

Structured light fields, such as optical vortex, has been currently growing up to a particle-like optical field (optical skyrmion). We review state-of-the-art structured materials fabrication and new materials manipulation with structured light fields.



Daria Smirnova

Australian National University, Australia

Localized states trapped by topological defects in photonic and hybrid metasurfaces

Daria Smirnova received her Ph.D. in Physics in 2016 from the Australian National University (ANU), followed by work experience in the USA, Russia, Japan, and Australia. Since 2019, she has consecutively held two prestigious fellowships supported by the Australian Research Council: the Discovery Early Career Researcher Award and, currently, the Future Fellowship at the ANU. In 2020, Daria was honoured as one of Australia's leading young researchers in The Australian's Special Report. Her research interests span over nonlinear physics, multipolar electrodynamics, nanophotonics, and topological photonics. The quality and impact of her works have been recognized through awards from international organizations, including the International Union of Pure and Applied Physics (IUPAP), MIT Technology Review, Elsevier, L'Oreal-UNESCO, the journal Nanophotonics, and the Australian and New Zealand Optical Society.

Localized states trapped by topological defects in photonic and hybrid metasurfaces
This talk will report novel phonon-polariton states trapped by topological defects in a silicon metasurface integrating hexagonal boron nitride (hBN). Spatially localized polaritonic modes originate from the coupling of electromagnetic fields with phonon vibrations in hBN.

KEYNOTE SPEAKERS



Gerrit Ernst Wilhem Bauer

University of the Chinese Academy of Science (China) & Tohoku University (Japan)

Gated Spin Communities

Gerrit Ernst Wilhem Bauer (*1956) was raised in the Gronau/Westfalen, Germany. He studied chemical engineering at Twente University in the Netherlands (M.Sc. 1980), experimental physics at the Hahn-Meitner Institute in Berlin (Ph.D. 1984) and theoretical physics as a JSPS Postdoctoral Fellow at the University of Tokyo. He spent 6 years at the corporate Philips Research Laboratories in Eindhoven (NL). He became professor in Theoretical Physics at Delft University of Technology in 1992, at the Tohoku University in Japan in 2011, and at the UCAS in China in 2022. He is presently Chair Professor at the Kavli Institute for Theoretical Science in Beijing as well as Professor and PI at the Advanced Institute of Material Science of Tohoku University on a shared basis. He is a Fellow of the American Physical Society and The Japan Society of Applied Physics. He received a.o. the Humboldt Research Award 2023. His published oeuvre in (mainly) theoretical condensed matter physics can be found under his Researcher ID F-8273-2010.

Gated Spin Communities
Conducting contacts modulate and control the magnetodipolar interaction that causes chirality of the magnetization and energy transport by spin waves at interfaces and in thin films. Metallic normal, ferromagnetic, and superconducting gates thereby generate new functionalities in magnonic circuits and devices.



Davide Bigoni

University of Trento (Italy)

Metamaterials with architected instabilities

Davide Bigoni has been holding a full professor position at the University of Trento (Italy) since 2001, where he is leading a very active group in the field of Solid ad Structural Mechanics. He was elected in 2009 Euromech Fellow (of the European Mechanics Society), received in 2012 the Ceramic Technology Transfer Day Award (of the ACIMAC and ISTEC-CNR), and in 2014 he was awarded the Doctor Honoris Causa degree at the Ovidius University of Constanta. He has received the Panetti and Ferrari Award for Applied Mechanics (from the Accademia delle Scienze di Torino), in 2018 he was Guest Lecturer for the Midwest Mechanics Seminars, in 2019 he was nominated Fellow of the Istituto Lombardo, Accademia di Scienze e Lettere, he was awarded a 60th Anniversary Issue of the Journal of the Mechanics and Physics of Solids. His research has been featured on 8 covers of International Journals. He has coordinated and has been involved in 3 European grants between academia and industry. He has been awarded 2 ERC advanced grants from the European Research Council, the first in 2013 and the second in 2021. He is co-editor of the Journal of Mechanics of Materials and Structures, is associate Editor of Mechanics Research Communications and member of the editorial boards of: Archives of Mechanics, International Journal of Solids and Structures, Journal of Elasticity, Journal of the Mechanical Behavior of Materials, Acta Mechanica Sinica, and International Journal of Applied Mechanics. He is reviewer for more than 150 international journals. He was vice chair of the panel PE8 for the European Research Council Starting Grants.

Metamaterials with architected instabilities
Homogenization is used for periodic elastic grids subject to axial prestress, to obtain equivalent elastic materials. The latter can be tailored to exhibit material instabilities driven by the microstructure of the grid and its level of prestress. Instabilities include shear band fromation and Hopf bifurcation, thus leading to odd elasticity.



Costantino De Angelis

Brescia University (Italy)

Analog computing with nonlinear flat optics

Costantino De Angelis received his PhD from the University of the Padova (1993) where he served as Assistant Professor of Electromagnetic Fields and Photonics. In 1998 he joined Brescia University where he is Full Professor of Electromagnetic Fields and Photonics since 2004. He is the head of the NORA group at the University of Brescia (https://nora.unibs.it/home) and his current research interest include nonlinear optics, nanophotonics, and optical metamaterials. He is a Fellow of OPTICA (the Optical Society of America).

Analog computing with nonlinear flat optics
Digital signal processing has revolutionized many fields of science and engineering, but it still shows critical limits; a long-sought solution is optical analog computing. We demonstrate here that nonlinear phenomena combined with engineered nonlocality in flat optics can be leveraged to synthesize Volterra kernels able to outperform linear devices.



Ortwin Hess

Trinity College Dublin (Ireland)

Nanoplasmonics as Enabler of Ultrafast Quantum Nanophotonics at Ambient Temperatures

Ortwin Hess currently holds the Chair Professorship of Quantum Nanophotonics and an SFI Research Professorship in the School of Physics and the CRANN Institute of Trinity College Dublin, The University of Dublin, Ireland. He is Editor-in-Chief of the gold open-access journal APL Quantum. Ortwin is a Fellow of the Institute of Physics (FInstP), a Fellow of Optica (formerly OSA) and a Professorial Fellow of Trinity College Dublin. Previously, Ortwin held the Leverhulme Chair in Metamaterials in the Blackett Laboratory at Imperial College London, UK. From 2003 to 2010 he was a full professor at the University of Surrey (Guildford, UK) and visiting professor at Stanford University, USA, and at the Ludwig-Maximilians University of Munich, Germany. Ortwin obtained the Dr.-rer-nat. (PhD) degree from the Technical University of Berlin, Germany in 1993 and the Habilitation (Dr.-habil.) at the University of Stuttgart, Germany in 1997. Ortwin's research interests bridge quantum nanophotonics with semiconductor and metamaterials physics, laser science and bio-medical photonics. He discovered the 'trapped-rainbow' principle, had the idea of stopped-light lasing and made defining contributions to the fields of spatio-temporal dynamics of semiconductor lasers, ultraslow light in metamaterials, complex quantum dot photonics and photonic crystals and strong coupling in nanoplasmonics. Ortwin pioneered active nanoplasmonics and optical metamaterials with quantum gain for which he has been awarded the Royal Society Rumford Medal.

Nanoplasmonics as Enabler of Ultrafast Quantum Nanophotonics at Ambient Temperatures
We discuss how nanoplasmonic-cavity strong coupling and ultrafast plasmonic near-field evolution can be exploited to achieve high-speed nanophotonic quantum operations at ambient temperatures, including dynamic multi-partite entanglement, and introduce a novel strategy for preparation and 'immortalization' of selected plasmon-exciton polariton states by means of quantum coherent perfect absorption



Malcolm Kadowala

University of Glasgow (UK)

Chiral Nanophotonics: Enabling Ultrasensitive Detection in Biophysical Measurements

Malcolm Kadowala is the Gardiner Chair of Chemistry at the University of Glasgow. He has pioneered the use of chiral plasmonic metamaterials for the study of biomaterials. His seminal paper on the demonstration of the application of chiral near fields for biomaterial characterisation (Nature Nano) has been cited >1100 times (Google Scholar). He was awarded a JSPS visiting Professorship at the Institute of Molecular Sciences, Japan in 2015, was a visiting Professor at the Dept of Physics, Osaka Metropolitan University, in 2018, and was awarded a Leverhulme research fellowship (2019-2021).

Chiral Nanophotonics: Enabling Ultrasensitive Detection in Biophysical Measurements
This talk will explore how the emerging field of chiral nanophotonics can overcome this barrier. By harnessing the unique properties of nanostructures, we can significantly enhance the interaction between light and chiral molecules. This allows for highly sensitive CD measurements, potentially reaching the single-molecule level.



Christoph Lienau

University of Oldenburg (Germany)

Two-dimensional electronic spectroscopy of many-body correlations in quantum materials

Christoph Lienau is a professor for experimental physics at the University of Oldenburg with an in interest in ultrafast dynamics of nanoscale systems. He studied physics in Göttingen and received a Ph.D. in Physical Chemistry in 1992. He then started postdoctoral work with Ahmed H. Zewail at Caltech as a Fellow of the German Science Foundation. In 1995 he accepted a position as senior member of the scientific staff at the newly founded Max Born Institute in Berlin in the department of Thomas Elsässer. Here, he founded a research activity in “Ultrafast nano-optics”. In 2006, he received a full professorship at the Institute of Physics in Oldenburg. He has published more than 250 articles in refereed journals and has given more than 150 invited and plenary talks at international conferences. Christoph served as head of the Semiconductor Physics Division of the German Physical Society and as Dean of the School of Mathematics and Natural Sciences in Oldenburg. He is a Fellow of the Optical Society of America and a Visiting Fellow of Chinese Academy of Sciences.

Two-dimensional electronic spectroscopy of many-body correlations in quantum materials
Two-dimensional electronic spectroscopy with few-femtosecond resolution is an emerging tool for probing quasi-particle interactions in quantum materials. The talk will discuss its use for exploring the quantum dynamics of strongly-coupled J-aggregate exciton/surface-plasmon hybrids, ultrafast intervalley couplings in atomically-thin semiconductors and for tailoring the nonlinearities of such semiconductors in plasmonic cavities.



Stefan Maier

Monash University (Australia) & Imperial College London (UK)

Silicon carbide as a platform for mid-IR metasurfaces

Stefan Maier is the Head of the School of Physics and Astronomy at Monash University and the Lee-Lucas Chair in Experimental Physics at Imperial College London. His main research interests lie in metasurfaces and nanophotonics for energy conversion, sensing, and optoelectronics. He is a Fellow of the Australian Institute of Physics, the Institute of Physics (UK) and Optica. He also currently serves as editor-in-chief for Nanophotonics. Stefan obtained his PhD in Applied Physics at Caltech, and held academic positions at the University of Bath and LMU Munich. He has been on the ICI Highly Cited list since 2017.

Silicon carbide as a platform for mid-IR metasurfaces
Silicon carbide enables strongly confined surface phonon-polaritons in the mid-infrared. We demonstrate the use of this materials platform for phonon-polariton metasurfaces supporting vortex and quasi bound-states-in-the-continuum resonances. Additionally we present results of active metasurfaces operating in the visible regime based on conductive polymers.



Agnès Maurel

Institute Langevin (France)

Acoustic grating with space-time modulation

Agnès Maurel is a research director at CNRS and conducts her research at the Langevin Institute in Paris. She studied physics at the École Normale Supérieure de Lyon and obtained her PhD in Paris, after which she completed postdoctoral fellowships at Stanford University and the Universidad de Chile. She studies wave propagation in complex media in the fields of acoustics, electromagnetism, elasticity, and water surface waves. She has been an associate editor for Wave Motion and the Journal of the Acoustical Society of America, and she is currently an associate editor for the Journal of Theoretical, Computational and Applied Mechanics. In recent years, her research has focused on the modeling of microstructured materials, including metamaterials and metasurfaces.

Acoustic grating with space-time modulation
We present a theoretical and numerical analysis of the diffraction of acoustic waves by space-time modulated gratings with rigid-type modulations. We report results exemplifying the non-reciprocal behavior of the grating, in relation with spatial and temporal harmonics.



Nam-Gyu Park

Sungkyunkwan University (Korea)

In the Quest for the Viable Perovskite Solar Cells

Nam-Gyu Park is a Distinguished Professor at the School of Chemical Engineering and Director of the SKKU Institute of Energy Science and Technology (SIEST), Sungkyunkwan University (SKKU). He received his B.S. degree in chemical education, and M.S. and Ph.D. degrees in chemistry from Seoul National University in 1988, 1992, and 1995, respectively. He worked as a postdoctoral researcher at ICMCB-CNRS, France, from 1996 to 1997 and at National Renewable Energy Laboratory, USA, from 1997 to 1999. He was director of the solar cell research center at the Korea Institute of Science and Technology (KIST) from 2005 to 2009 and senior researcher at the Electronics and Telecommunications Research Institute (ETRI) from 2000 to 2005 before joining SKKU as a full professor in 2009. He is a fellow of the Korean Academy of Science and Technology (KAST) since 2017. He has been working on photovoltaics since 1997. He was the first to report a long-term stable perovskite solar cell in 2012. This opened a new research area, so-called perovskite photovoltaics. He was selected as Citation Laureate (top 0.01% scientist); a New Class of Nobel Prize-Worthy Scientist on September 20, 2017, and included in highly cited researchers (HCR, top 1% scientists) from 2017 to 2023 by Clarivate Analytics. He received awards including the Scientist Award of the Month (2008), KIST Award of the Year (2009), Dupont Science and Technology Award (2010), SKKU fellowship (three times in 2013, 2018, and 2021), PVSEC Hamakawa Award (2015), Dukmyung KAST Engineering Award (2016), ACS-KCS Excellence Award (2018), Ho-Am Prize (Samsung, 2018) and Rank Prize (UK, 2022). Prof. Park has currently more than 390 refereed publications and more than 70 patents. He received an H-index of 116 from Google Scholar (105 from Web of Science and 108 from Scopus). He is the Senior Editor of ACS Energy Letters and serves on the Editorial Advisory Board for Chem. Rev., ChemSusChem, and Solar RRL.

In the Quest for the Viable Perovskite Solar Cells
Research endeavors focus on enhancing stability and exploring tandem structures for electricity generation in both terrestrial and space applications. The perovskite solar cell stands poised as the most promising energy solution, with its potential impact on sustainable energy surpassing current expectations once stability and lead immobilization challenges are effectively addressed.



Vladimir M. Shalaev

Purdue University, USA

Extreme Space-Time Optics & Quantum Meta-Photonics

Vladimir M. Shalaev, Scientific Director for Nanophotonics at Birck Nanotechnology Center and Distinguished Professor of Electrical and Computer Engineering at Purdue University, specializes in nanophotonics, plasmonics, and optical metamaterials. Vladimir M. Shalaev has received several awards for his research in the field of nanophotonics and metamaterials, including the Max Born Award of the Optical Society of America for his pioneering contributions to the field of optical metamaterials, the Willis E. Lamb Award for Laser Science and Quantum Optics, IEEE Photonics Society William Streifer Scientific Achievement Award, Rolf Landauer medal of the ETOPIM (Electrical, Transport and Optical Properties of Inhomogeneous Media) International Association, the UNESCO Medal for the development of nanosciences and nanotechnologies, OSA and SPIE Goodman Book Writing Award. He is a Fellow of the IEEE, APS, SPIE, MRS and OSA. Prof. Shalaev has authored three books, thirty invited book chapters and over 500 research publications.

Extreme Space-Time Optics & Quantum Meta-Photonics
We discuss all-optical modulation with single photons using electron avalanche, resulting in record-high nonlinearities. Then we show that transparent conducting oxides (TCOs) operating in the near-zero index regime can provide strong single-cycle modulation, enabling novel photonic time crystals. Finally, we discuss scalable quantum photonics with single-photon emitters in silicon nitride.



Kaoru Tamada

Kyushu University (Japan)

High Spatiotemporal Resolution Live Cell Imaging on a Plasmonic Metasurface

Kaoru Tamada is a Senior Vice President and Distinguished Professor in Kyushu University, Japan. After 7 years industrial experience, she moved to University of Wisconsin-Madison. After the experiences in RIKEN, AIST, MPIP and NUS, she became associate professor at Tokyo Tech in 2005. She moved to Research Institute of Electrical Communication (RIEC), Tohoku University, as a full professor in 2007 and Institute for Materials Chemistry and Engineering (IMCE), Kyushu University, in 2011. Her research interests include 2D self-assembly of organic molecules, metal and semiconductor nanocrystals, and their device applications. She obtained several awards for her achievement in nanoscience. She is a member of Science Council of Japan, Project Officer of JST SICORP e-ASIA program and Vice President of the Japan Society of Applied Physics. She is the associate editor of ACS Applied Nano Material sand advisory board member of several international journals.

High Spatiotemporal Resolution Live Cell Imaging on a Plasmonic Metasurface
Self-assembled monolayers composed of metal nanoparticles can be regarded as metasurfaces with high refractive index and extinction coefficient due to collective excitation of coupled localized surface plasmon resonance. This plasmonic metasurface confines light to the nanointerface and enhances fluorescence, thus enabling high-speed interfacial imaging with high axial and lateral resolution.



Mona Tréguer-Delapierre

University of Bordeaux (France)

Controlling nanomaterial properties using organization

Mona Tréguer-Delapierre is a Professor of Chemistry at the University of Bordeaux leading research in nanoparticle synthesis and assembly at the Institute of Chemistry of Condensed Matter of Bordeaux (ICMCB). She received her PhD from the University of Orsay (Paris-Saclay) and was a postdoctoral fellow at the University of Notre Dame (USA). She is the recipient of awards from the Chancellerie des Universités de Paris and H&M Zimmer of the University of Cincinnati. Her current research interests focus on how nanoparticles can be manipulated in 2D or 3D to engineer nanostructured materials with unusual optical effects.

Controlling nanomaterial properties using organization
We demonstrated a new concept for making nanostructures with unusual optical properties by organizing metal nanoparticles. In research and industry, molecules from drugs and polymers are made by combining high-yield chemical reactions in series. We have extended this approach to the nanoscale: we make metamolecules by combining high-yield colloidal reactions.



Din Ping Tsai

City University of Hong Kong (Hong Kong)

Intelligent Meta-lens for Imaging Underwater, Aerial and Land

Din Ping Tsai is currently Chair Professor of the Department of Electrical Engineering, City University of Hong Kong. He is an elected Fellow of AAAS, APAM, APS, AAIA, COS, EMA, IAE, IEEE, JSAP, NAI, OSA, SPIE, and TPS, respectively. He is the author and co-author of 372 SCI papers, 65 book chapters and conference papers, and 39 technical reports and articles. He was granted 69 patents for 45 innovations. He was invited as an invited speaker for international conferences or symposiums more than 340 times (30 Plenary Talks, 62 Keynote Talks). He received more than 40 prestigious recognitions and awards, including "Global Highly Cited Researchers," Web of Science Group (Clarivate Analytics) in 2020 and 2019, respectively; China's Top 10 Optical Breakthroughs in 2020 and 2018, respectively; "Mozi Award" from International Society for Optics and Photonics (SPIE) (2018); etc.

Intelligent Meta-lens for Imaging Underwater, Aerial and Land
We have developed a series of intelligent meta-lens systems for underwater, land, and aerial imaging and sensing. We reported the design, fabrication, characterization, and applications of the monocular, binocular, and multilocular meta-lens.



Anatoly V. Zayats

King's College London (UK)

Optical spin topologies in plasmonics and metamaterials

Anatoly V. Zayats is a Chair in Experimental Physics and the head of the Photonics & Nanotechnology at the Department of Physics, King's College London, where he also leads Nano-optics and Near-field Spectroscopy Laboratory (www.nano-optics.org.uk). He is a Co-Director of the London Centre for Nanotechnology and the London Institute of Advanced Light Technologies. His current research interests are in the areas of nanophotonics, plasmonics, metamaterials, optical spin-orbit coupling, plasmonically-derived hot carriers, scanning probe microscopy, nonlinear and ultrafast optics and spectroscopy, and optical properties of surfaces, thin films, semiconductors and low-dimensional structures. He is a founding co-editor-in-chief of Advanced Photonics journal. He is a Fellow of the Institute of Physics, the Optical Society of America, SPIE, the Royal Society of Chemistry and elected Member of Academia Europaea.

Optical spin topologies in plasmonics and metamaterials
We will discuss spin-orbit coupling in interaction of complex vector beams with plasmonic metamaterials. Spin-orbit coupling and topology of evanescent waves and vector beams propagating in free space and metamaterials in different dispersion regimes will be considered.



Jinfeng Zhao

Tongji University (China)

Elastic spin angular momentum in metamaterials and classical structures

Jinfeng Zhao received M.S. degree in solid mechanics from Tongji University and Ph.D. degree in physics from University Pierre and Marie Curie. He is currently working in Tongji University. Prof. Zhao has coauthored 60 journal articles, including Phys. Rev. Lett., Nat. Commun and J. Mech. Phys. Solids. He owns 20 Chinese patents. He has been selected as excellent young scholar by Shanghai Society of Theoretical and Applied Mechanics (2021). He has made over 10 invited and oral presentations in academic conferences. His research interests lie in chiral elasticity, metamaterials, phononic crystals and ultrasonic non-destructive evaluation. He has made significant experimental contribution to reveal the elastic spin angular momentum (SAM) in both classical structures and topological metamaterials. He has observed broadband super-diffraction wave focusing both inside and outside graded devices. He builds up graded Helmholtz resonators with IXPP films that lead to dual function, i.e. noise reduction and energy harvesting.

Elastic spin angular momentum in metamaterials and classical structures
Topological phenomena of bosonic-like waves have attracted wide interests during the last few years. Spin angular momentum (SAM) provides new insights from the local point of view. Here, we experimentally investigate SAM in metamaterials and classical structures. Multi-dimensional wave routing is achieved due to the SAM-wavenumber locking mechanism.

TUTORIALS



Prof. Franco Nori

Riken (Japan) and University of Michigan (USA)

Wednesday 17th July
14:00 - 15:00 — Main Hall

Topological Origin of Surface Maxwell Waves and Surface Acoustic Modes

Franco Nori is a Chief Scientist at RIKEN, with a concurrent position at the University of Michigan. He received his PhD from the University of Illinois, and afterwards became a postdoc at the Institute for Theoretical Physics, University of California, Santa Barbara. His research group has done pioneering interdisciplinary studies at the interface between nanoscience, photonics, quantum optics, dissipative quantum open systems, quantum information processing, superconducting quantum circuitry, opto-mechanics, and condensed matter physics. He has been listed by the Web of Science as a "Highly Cited Researcher" (less than 0.1% are selected) in Physics for the past seven consecutive years: from 2017 to 2023. He is an Elected Fellow of the American Physics Society (APS), Institute of Physics (IoP), American Association for the Advancement of Science (AAAS), and Optical Society of America (OSA) [this last one "for fundamental contributions to quantum information science and optics, including circuit quantum electrodynamics, and the interface between quantum optics and quantum circuits"]. He received the 2014 Prize for Research in Physics, from the Matsuo Foundation, Japan; and the 2013 Prize for Science, by the Minister of Education, Culture, Sports, Science and Technology, Japan. Also, an "Excellence in Research Award" and an "Excellence in Education Award" from the University of Michigan. He is an Elected Member of the Academia Europaea, the Latin American Academy of Sciences, and a Foreign Member of the Swedish Royal Society of Arts and Sciences, in Gothenburg, Sweden. He won the 2023 W.E. Lamb Medal, and the 2024 Charles H. Townes Medal (from the OSA), both for research on Quantum Optics, Quantum Electronics and Quantum Information.

Topological Origin of Surface Maxwell Waves and Surface Acoustic Modes
Interfaces between optical media (including dielectrics, metals, negative-index materials) can support surface electromagnetic waves, which now play crucial roles in plasmonics, metamaterials, and nanophotonics. We have shown [K. Y. Bliokh et al., Nat. Commun. 10, 580 (2019)] that surface Maxwell waves at interfaces between homogeneous isotropic media described by real permittivities and permeabilities have a topological origin explained by the bulk-boundary correspondence. This is explained by the nontrivial topology of the non-Hermitian photon helicity operator in the Weyl-like representation of Maxwell equations. The corresponding topological invariant, which determines the number of surface modes, describes the winding of the complex helicity spectrum across the interface. Our theory provides a new twist and insights for several areas of wave physics: Maxwell electromagnetism, topological quantum states, non-Hermitian wave physics, and metamaterials. We have also analyzed [K. Y. Bliokh et al., Phys. Rev. Lett. (2019)] another type of classical waves: longitudinal acoustic waves corresponding to spinless phonons. We show that surface acoustic waves, which appear at interfaces between media with opposite-sign densities, can be explained by similar topological features and the bulk-boundary correspondence. However, in contrast to photons, the topological properties of sound waves originate from the non-Hermitian four-momentum operator in the Klein-Gordon representation of acoustic fields.



Dr. Rachel Won

Nature Photonics, UK

Thursday 18th July
14:00 - 15:00 — Main Hall

Writing and Submitting Your Papers

Rachel Won is an International Editor of Nature Photonics. She joined the journal in June 2006 as one of four Founding Editors. Before that, Rachel worked for Aston University's Business Partnership Unit in Birmingham, UK, as a Medici Fellow commercializing research output of the university, particularly that of photonics research. She obtained her PhD in microwave photonics and nonlinear optics as a member of Aston's Photonics Research Group. She worked for Philips Optical Storage in Singapore as an Optics Engineer after completing her Master's degree study in Nanyang Technological University of Singapore doing research in optical fibre sensing. She holds a Bachelor's degree from the National University of Malaysia. She is a Fellow of OPTICA and the International Society of Optics and Photonics (SPIE).

Writing and Submitting Your Papers
This talk covers the detailed information and guidelines on scientific paper preparation and submission, including tips for writing an effective cover letter, an informative abstract, a comprehensive introduction and an attractive paper, and editorial and peer-review processes. You will also get to know how to choose a journal for submission, what editors seek, how your papers are reviewed and how to make an appeal.

INDUSTRIAL WORKSHOPS

SYNOPSYS®

16th & 17th July, 16:40 - 17:40 — Room 3

From Design to Manufacture - Complete Inverse Design Flow for MetaOptics

Chenglin Xu, Bryan Stone, JiSoo Park

Synopsys offers solutions to metalens design and manufacturing challenges, including tools for hybrid refractive metalens systems that consider manufacturing tolerances. This workshop is presented in two parts:

1. July 16: Introduction to MetaOptic Designer;
2. July 18: Demo of hybrid metalens system design and virtual fab simulation.

The workshop is free and open to all META conference attendees.

GUIDELINES FOR PRESENTERS I **IN-PERSON**

Oral Presentations

Each session room is equipped with a stationary computer connected to a LCD projector. Presenters must load their presentation files in advance onto the session computer. Technician personnel will be available to assist you.

Scheduled time slots for oral presentations are 15 mn for regular, 20 mn for invited presentations, 30 mn for keynote talks and 35 mn for plenary talks, including questions and discussions. Presenters are required to report to their session room and to their session Chair at least 15 minutes prior to the start of their session.

The session chair must be present in the session room at least 15 minutes before the start of the session and must strictly observe the starting time and time limit of each paper.

Poster Presentations

Presenters are requested to stand by their posters during their session. One poster board, A0 size (118.9 x 84.1 cm), in portrait orientation, will be available for each poster. Pins or thumbtacks are provided to mount your posters on the board. All presenters are required to mount their papers 30mn before the session and remove them at the end of their sessions. Posters must prepared using the standard AES poster template (available on the conference website).

USEFUL INFORMATION

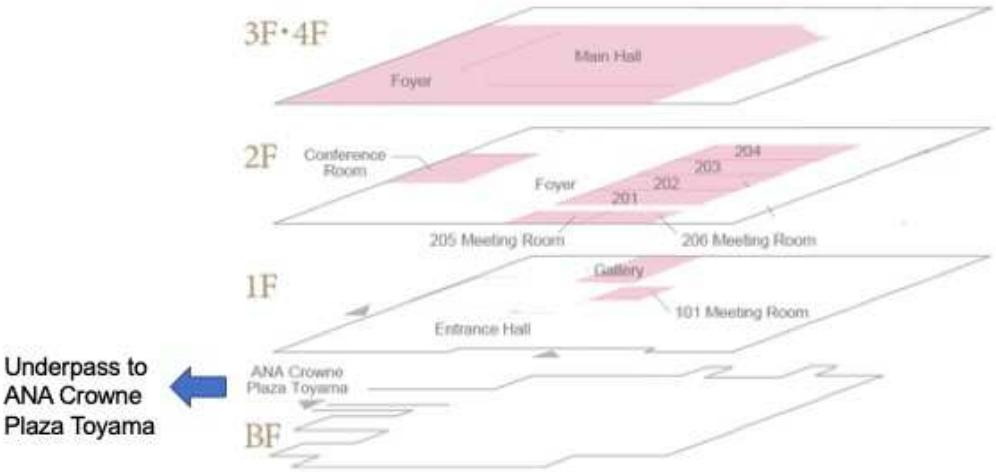
Venue

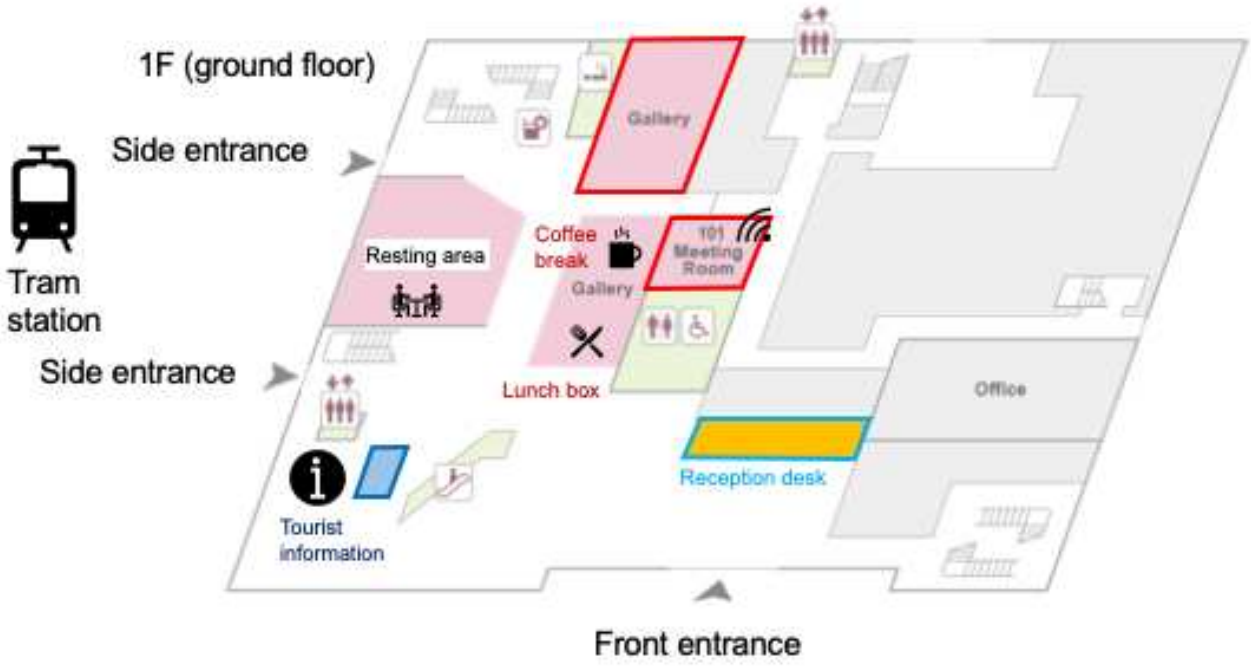
META 2024 will be held at
Toyama International Conference Center
1-2 Ote-machi, Toyama, Japan

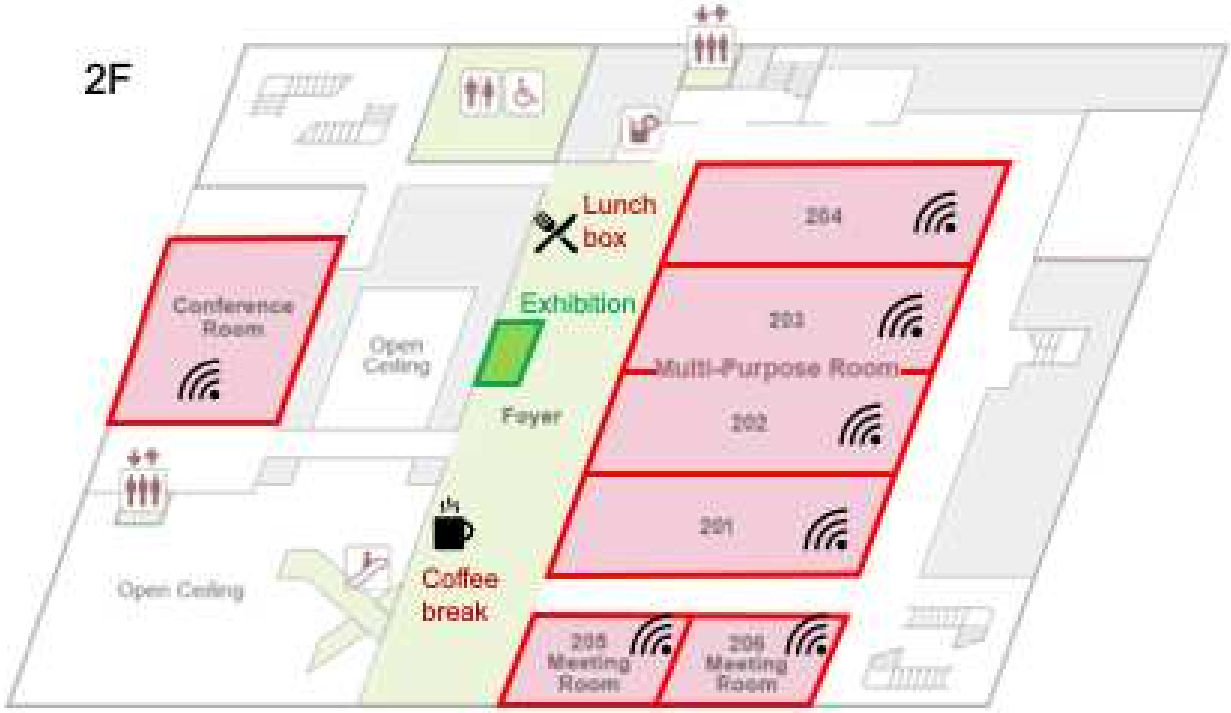
https://www.ticc.co.jp/english/

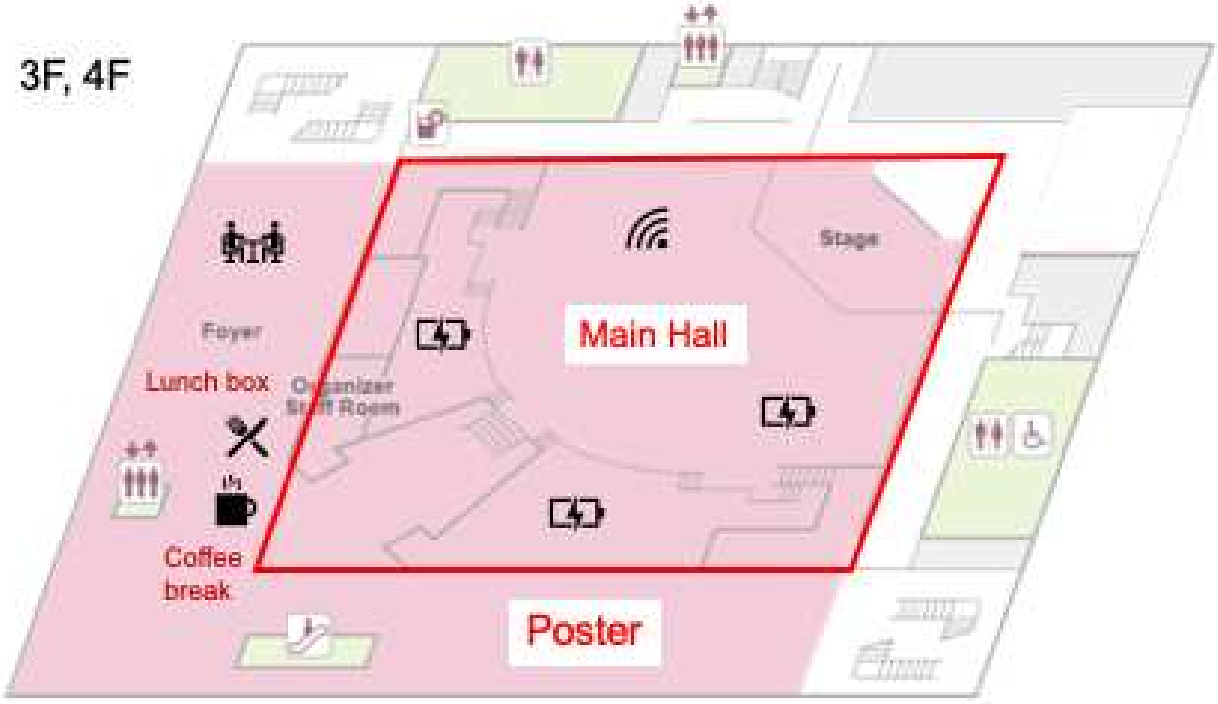


Floor Map of TICC




1F (ground floor)
Side entrance
Tram station
Side entrance
Resting area
Coffee break
Gallery
101 Meeting Room
Gallery
Lunch box
Office
Reception desk
Tourist information
Front entrance


2F
Lunch box
Conference Room
Exhibition
Open Ceiling
Foyer
Multi-Purpose Room
Open Ceiling
Coffee break
205 Meeting Room
206 Meeting Room



Getting to Venue

Toyama City is the largest city and capital of Toyama Prefecture in the Hokuriku Region of northern Chubu. The city is a former castle town and is historically a center of medicine. Due to its position on the Hokuriku Shinkansen (high speed “bullet train” rail line), Toyama is a popular stop for tourists on the way to other attractions in the area such as the Tateyama Kurobe Alpine Route.

Travel Information

Toyama is easily reachable from both within and outside Japan, positioned at an approximate equal distance from the country’s three major cities: Tokyo, Osaka, and Nagoya. It takes just 2 hours and 8 minutes from Tokyo via the Hokuriku Shinkansen (“bullet train"). Additionally, Toyama Airport offers connections from Tokyo and Sapporo, as well as direct flights from Shanghai, Taipei, Dalian, and Seoul.

For travelers arriving in Tokyo, there are two primary international airports: Haneda Airport and Narita Airport. Regardless of your arrival airport, you can take a train or bus to Tokyo Station and then catch the Hokuriku Shinkansen to Toyama Station, which typically takes about 2 hours and 30 minutes.

If you land at Haneda Airport, there’s another option available: transferring to a domestic flight bound for Toyama Airport, with three ANA flights available daily. Upon arrival at Toyama Airport, a convenient shuttle bus service can transport you to the city center in just 30 minutes.

- Getting to Toyama (Link to the Official Toyama City Travel Guide “Toyama Net”)
- Getting to Toyama (Link to the Official Toyama Travel Guide “Visit Toyama”)

TABLE OF CONTENTS

Plenary presentations

Materials manipulation with structured light fields (pp. 80)
Takashige Omatsu

Topological dissipation in a time-multiplexed photonic resonator network and topological temporally mode-locked lasers (pp. 82)
Franco Nori

Shaping light propagation in complex media (pp. 83)
Hui Cao

Localized states trapped by topological defects in photonic and hybrid metasurfaces (pp. 84)
Daria Smirnova

Active Metasurfaces in Space and Time (pp. 85)
Harry A. Atwater

Machine learning for metamaterials and metasurfaces

Elastic spin angular momentum in metamaterials and classical structures (pp. 87)
Jinfeng Zhao, Yao Huang, Yuxuan Zhang, Yongdong Pan

Metamaterials with architected instabilities (pp. 88)
Davide Bigoni

Silicon carbide as a platform for mid-IR metasurfaces (pp. 90)
Stefan Maier

In the Quest for the Viable Perovskite Solar Cells (pp. 91)
Nam-Gyu Park

Gated Spin Communities (pp. 92)
Tao Yu, Gerrit Bauer

Optical spin topologies in plasmonics and metamaterials (pp. 94)
Anatoly Zayats

Intelligent Meta-lens for Imaging Underwater, Aerial and Land (pp. 96)
X. Liu, M. K. Chen, T. Tanaka, Din Ping Tsai

Analog computing with nonlinear flat optics (pp. 98)
Costantino De Angelis, Domenico de Ceglia

Two-dimensional electronic spectroscopy of many-body correlations in quantum materials (pp. 100)
Christoph Lienau

High Spatiotemporal Resolution Live Cell Imaging on a Plasmonic Metasurface (pp. 102)
Kaoru Tamada

Chiral Nanophotonics: Enabling Ultrasensitive Detection in Biophysical Measurements (pp. 103)
Malcolm Kadodwala

Extreme Space-Time Optics & Quantum Meta-Photonics (pp. 104)
Vladimir M. Shalaev

Controlling nanomaterial properties using organization (pp. 105)
Mona Tréguer-Delapierre

Nanoplasmonics as Enabler of Ultrafast Quantum Nanophotonics at Ambient Temperatures (pp. 106)

Ortwin Hess

Spontaneous emergence of eyes in reinforcement learning agents (pp. 107)
Zongfu Yu, Boyuan Liu, Ming Zhou, Yurui Qu, Zhicheng Wu, Qingyi Zhou, Zongfu Yu

A universal infrared absorption analysis system using deep learning (pp. 108)
Eito Nakagawa, Hiroto Sasaki, Yoshiaki Nishijima

Deep learning-enabled metasurface design and autonomous meta-devices (pp. 110)
Chao Qian

Physics-informed inverse design of programmable metasurfaces (pp. 112)
Yucheng Xu, Jiq-Qi Yang, Sheng Wang, Jingbo Wu, Caihong Zhang, De-Chuan Zhan, Willie Padilla, Biaobin Jin, Kebin Fan

Effective machine-learning approaches with reduced dimensionality for design and knowledge discovery in large-scale nanophotonic structures (pp. 114)
Mahmoodreza Marzban, Mohammadreza Zandehshahvar, Mohammad R. Tavakol, Mohammad H. Javai, Ali Adibi

Design of Radiative Cooling Metamaterials by Generic Algorithm and Neural Network (pp. 115)
Kotaro Kajikawa

Wide Field-of-View and Broadband Metalens Imaging via Deep Learning (pp. 116)
Yunxi Dong, Bowen Zheng, Fan Yang, Hong Tang, Huan Zhao, Yi Huang, Tian Gu, Juejun Hu, Hualiang Zhang

Free-Form Inverse Design Driven by Machine Learning (pp. 118)
Timo Gahlmann, Philippe Tassin

Do we need machine learning to predict wave scattering in metasurface-programmable unknown complex media? (pp. 119)
Philipp del Hougne

Data-driven Inverse Design and Characterization of Metasurface (pp. 121)
Li Gao

Tutorials

Coupling theory of quasinormal mode for an efficient and intuitive modeling of optical-nanoresonator arrays with a large scale or varying arrangement (pp. 124)
Haitao Liu, Can Tao, Qiyong Tao, Zhe Qi, Ying Zhong

Disentangling Absorption and Radiation Decay in Optical Nanoresonators (pp. 126)
Kirill Koshelev

Efficient and tailored photon-pair generation from metasurfaces with quasi-normal modes (pp. 128)
Jihua Zhang, Jinyong Ma, Tongmao Fan, Yuxin Jiang, Andrey Sukhorukov

Anomalous acoustic tunneling effect with non-Hermitian Willis coupling (pp. 130)
Danwei Liao, Xinhua Wen, Xinghong Zhu, Jensen Li

Quasi-normal modes and transmission channels in non-Hermitian disordered media (pp. 132)
Valentin Freilikher

Exceptional points in a single dielectric nanoparticle (pp. 134)
Adria Canos Valero, Vjaceslavs Bobrovs, Thomas Weiss, Alexander S. Shalin, Yuri Kivshar

Photonics of topological transitions Disk - Ring - Split Ring (pp. 136)
M. E. Bochkarev, N. S. Solodovchenko, K. A. Bronnikov, K. B. Samusev, Mikhail Limonov

Response strength of general non-Hermitian systems at exceptional points (pp. 138)
Jan Wiersig

Scattering Singularities of Complex Non-Hermitian Systems Probed with Continuously Variable Metasurfaces (pp. 140)
Jared Erb, Thomas Antonsen, Steven Anlage

Frequency combs in dissipative Kerr cavities with non-Hermitian periodic potentials (pp. 141)
S. B. Ivars, M. Botey, K. Staliunas, Ramon Herrero

Nonperturbative effects in the eigenvalue sensitivity of non-Hermitian systems (pp. 143)
Henning Schomerus

Non-Hermitian mode-cleaning in linear and nonlinear optical waveguides (pp. 145)
Mohammad Nayeem Akhter, Ramon Herrero, Kestutis Staliunas, Muriel Botey

Non-Hermitian Systems with a Real Spectrum and Selective Skin Effect (pp. 147)
Li Ge

Pseudospectra and non-normality in non-Hermitian photonics (pp. 148)
Konstantinos Makris

Topological Origin of Surface Maxwell Waves and Surface Acoustic Modes (pp. 150)
Franco Nori

Writing and Submitting Your Papers (pp. 151)
Rachel Won

DNA nanotechnologies for photonics and sensing

A universal impedance-matching strategy towards ultrathin broadband perfect absorbers enabling efficient hot electron photodetection (pp. 153)
Cheng Zhang, Xiaofeng Li

Integrating functional inorganic nanomaterials for spatiotemporal modulation of full-polarized light emission (pp. 155)
Jiawei Lv, Jeong Hyun Han, Ki Tae Nam

Monolayer semiconductor superlattices for enhanced absorption with controlled interlayer interaction (pp. 156)
Sara Elrafei, Tom Sistermans, Lennart Heijnen, Rasmus Hjelmgart Godiksen, Alberto Curto

Infrared photoresponse in twisted bilayer graphene at a near-magic angle (pp. 158)
Dmitry Mylnikov, Ilya Mazurenko, Alexey Shupletsov, Aparna Parappurath, Saisab Bhowmik, Denis Bandurin, Arindam Ghosh, Alexander Chernov

Fabrication of vanadium dioxide micro- and nanostructures by laser-induced hydrothermal synthesis (pp. 160)
Christophe Pin, Hideki Fujiwara, Keiji Sasaki

Circularly polarized photoluminescence from light-emitting metasurfaces (pp. 162)
Vivian Ferry

Periodic Arrays of Single-Crystal Gold and Silver Nanoplates (pp. 163)
Svetlana Neretina, Z. R. Lawson, W. J. Tuff

Up- and Down-conversion Engineering with Surface Lattice Resonances (pp. 164)
Shunsuke Murai

Waveguiding and metasurface platforms for sensing (pp. 165)
Stefan Maier

Assymmetric electric fields induced on symmetric structure that yield chiral structured materials (pp. 166)
Hiromi Okamoto, Hyo-Yong Ahn, Tetsuya Narushima

Control of light emission of quantum emitters coupled to silicon nanoantenna (pp. 168)
Jean-Marie Poumirol, Martin Montagnac, Yoann Brûlé, Ana Estrada-Real, Ioannis Paradisanos, Aurellien Cuche, Sebastien Weber, Jonas Müller, Guilhem Larrieu, Vincent Larrey, Peter Wiecha, Frank Fournel, Olivier Boisron, Bruno Masenelli, Gerard Colas des

Francs, Bernhard Urbaszek, Gonzague Agez, Vincent Paillard

Ultrafast Optical Response of Plasmonic Doped-VO2 Metasurfaces (pp. 170)

Benedict Morris, Zahra Shayegan, Robin Reig, Baptiste San-Nicolas, Sébastien Frenkel, Joëlle Margot, Mohamed Chaker, Bruno Palpant

Publishing in Nature journals (pp. 171)

Rachel Won

Bound States in the Continuum: Advancements in Photonics from Enhanced Upconversion to Ultra-Sensitive Sensors (pp. 172)

Silvia Romano, Bruno Miranda, Aida Seifalinezhad, Adam Schwartzberg, Ivo Rendina, Vito Mocella, Gianluigi Zito

Scaling up Precision: Engineering Gold Nanoparticles for Optimal Performance in Advanced Production Platforms (pp. 174)

Kyoungweon Park, Eva Yazmin Santiago Santos Santos, Alexander Govorov, Richard A. Vaia

Development of new chiroptically active quantum nanostructures (pp. 176)

Yurii Gun'ko

DNA Origami Self-Assembled High-Index Dielectric Optical Antennas for Single-Molecule Fluorescence Manipulation (pp. 178)

M. Sanz Paz, N. Siegel, K. Kołątaj, F. Zhu, H. Hasebe, J. Gonzalez-Colsa, G. Serrera, H. Sugimoto, M. Fujii, P. Albella, Guillermo Acuna

Nonradiative Cooling (pp. 180)

Wakana Kubo

Proving non-thermal plasmon catalysis mechanisms through the overtone vibrational quantum states of reactants (pp. 182)

Zee Hwan Kim

Optoelectronic Physical Reservoir Computing with Digital Delayed Feedback featuring in situ Optimization (pp. 183)

Fyodor Morozko, Shadad Watad, Amir Naser, Antonio C. Lesina, Andrey Novitsky, Alina Karabchevsky

Innovative Deposition and Oxidation-Coupled Technique for Low-Temperature Fabrication of VO2, Thin Films and their Application to Photonic Devices (pp. 186)

Mohamed Chaker

Ultrafast Processes and Energy Dissipation in Hybrid Nanomaterials (pp. 187)

Gary Wiederrecht

Recent challenges in hybrid plasmonic nano-emitters (pp. 189)

Minyu Chen, Sylvie Marguet, Ali Issa, Safi Jradi, christophe Couteau, Celine Fiorini, Ludovic Douillard, Olivier Soppera, Jerome Plain, Tao Xu, Bin Wei, Renaud Bachelot

Tracing temporal plasmonics with direct field sampling (pp. 191)

Holger Lange, Kai-Fu Wong, Andreas Knorr, Francesca Calegari, Matthias Kling

Determining the orientation of gold nanorods by means of polarimetric spectroscopy (pp. 192)

P. Christian Simo, Annika Mildner, Dieter P. Kern, Monika Fleischer

Enhanced color down-shifting of colloidal quantum dots for high-resolution full-color displays (pp. 194)

Son Tung Ha, Ramon Paniagua-Dominguez, Hilmi Volkan Demir, Arseniy Kuznetsov

Fluorescence-based chiral sensing enhanced by silicon nanophotonics (pp. 196)

Tom Sistermans, Ershad Mohammadi, T. V. Raziman, Alberto Curto

Infrared Nanophotonics in Naturally-Hyperbolic Calcite Metamaterials (pp. 198)

Chase Ellis, Eric Seabron, Eric Jackson, Michael Meeker, Andrew Lang, Brandon Durant, Xitlali Juarez, Daniel Ratchford, Rhonda Stroud, Joseph Tischler

Mapping phonon polaritons with visible light (pp. 199)

Joseph Tischler, Kiernan Arledge, Chase Ellis, Nazli Rasouli Sarabi, Vincent Whiteside, Chul Soo Kim, Mijin Kim, Daniel Ratchford, Binbin Weng

Quasi-2D Colloidal Quantum Wells for High Optical Gain and High LED Efficiency (pp. 201)

Farzan Shabani, Furkan Isik, Savaş Delikanli, Hilmi Volkan Demir

Enhancing Infrared-to-Visible Photon Upconversion with Metasurfaces (pp. 203)

Mengfei Wu, Dileep Kottilil, Yuxiang Zhang, Kangning Yu, Sourav Adhikary, Jinal Tapar, Emmanuel Lassalle, Daniil Shilkin, Febiana Tjiptoharsono, Ramon Paniagua-Dominguez, Xiaogang Liu, Arseniy Kuznetsov

Nano antenna-assisted quantum dots emission into high-index planar waveguide (pp. 204)

X. Yu, J.-C. Weeber, L. Markey, J. Arocas, A. Bouhelier, A. Leray, Gérard Colas des Francs

Bioanalytics using plasmonic nanostructures (pp. 206)

F. Seier, L. Dubbert, M. Al-Maoush, A. Hoxha, A. Heewig, M. Urban, A. Csaki, Wolfgang Fritzsche

Hybrid Metamaterial Plasmonic Tweezers for Trapping and Manipulating Dielectric Particles and Biomolecules (pp. 208)

Viet Giang Truong, Domna G. Kotsifaki, German Suslin, Theodoros D, Bouloumis, Mirco Dindo, Paola Laurino, Síle Nic Chormaic

Polymerization of diazonium salts on gold nanoparticles: hot electron and heating effects (pp. 209)

Liudmila Trotsiuk, Aurelie Broussier, Anne-Laure Baudrion, Sylvie Marguet, Yun Luo, Claire Mangeney, Nordin Felidj, Pierre-Michel Adam, Renaud Bachelot

Designing lattices and interface modes in valley topological photonics (pp. 211)

Gaëtan Lévêque, Yan Pennec, Abdu Subahan Mohammed, Guillaume Durcournau, Pascal Szriftgiser, Alberto Amo

Controlling properties of collective plasmonic–diffractive excitations via dispersion engineering (pp. 213)

Jussi Kelavuori, Ali Panahpour, Mikko Huttunen

Nonlinear optical sensing in arrays of plasmonic nanoparticles (pp. 215)

Augustin Verneuil, A. Zilli, C. Vézy, J. Béal, M. Finazzi, M. Celebrano, Anne-Laure Baudrion

Rapid modulation of left- and right-handed optical vortices for precise measurements of helical dichroism (pp. 217)

Shun Hashiyada, Y. Y. Tanaka

Synthesis of tailored functional nanoparticles by polymerization induced by surface plasmons (pp. 219)

Olivier Soppera

DNA-assembled nanogaps for continuous single-molecule biosensing (pp. 221)

Livio Oliveira de Miranda, Abtin Saateh, Annelies Dillen, Mathias Dolci, Claudia Scarpellini, Khulan Sergelen, Hatice Altug, Jeroen Lammertyn, Peter Zijlstra

Anapole modes enabling linear and nonlinear chiral sensing in hybrid metasurfaces (pp. 222)

Guillermo Serrera, Javier Gonzalez-Colsa, Pablo Albella

DNA origami-based plasmonic nanoantennas for single-molecule SERS (pp. 224)

Yuya Kanehira, Amr Mostafa, Anushree Dutta, Sergio Kogikoski, Ilko Bald

Optical Modelling of DNA-Made Janus Nanoheaters (pp. 225)

Pablo Albella

Universal click-chemistry approach for the DNA functionalization of nanoparticles for the development of new optical nanoantennas (pp. 227)

Nicole Siegel, Hiroaki Hasebe, German Chiarelli, Denis Garoli, Hiroshi Sugimoto, Minoru Fujii, Guillermo Acuna, Karol Kołątaj

Optically active substrates through DNA-based lithography (pp. 229)

Veikko Linko

Broadband Circularly Polarized Thermal Emission enabled by Chiral Plasmonic Metamaterial (pp. 231)

René Iseli, Abraham De Jesus Aguilar Uribe, Bilel Abdennadher, Anne Nguyen, Viola Vogler-Neuling, Frank Scheffold, Jean-Jacques Greffet, Ullrich Steiner, Matthias Saba

Bio-Inspired Nanophotonics

Optical imaging based on metasurfaces (pp. 234)
Shuming Wang

Color arrestor pixels for high-fidelity, high-sensitivity imaging sensors (pp. 235)
Mingwan Cho, Joonkyo Jung, Myungjoon Kim, Jeong Yub Lee, Seokhwan Min, Jongwoo Hong, Shinho Lee, Minsung Heo, Jong Uk Kim, In-Sung Joe, Jonghwa Shin

Analysis of aliasing in phase gradient metasurfaces: Breaking efficiency limits of high-NA ultraviolet metasurface (pp. 237)
Kyungtae Kim, Junsuk Rho

Portable Hydrogen Sensing Enabled by Overlaid Holographic Metasurfaces andLiquid Crystal Integration (pp. 239)
Dohyun Kang, Younghwan Yang, Junsuk Rho

Control of Electric and Magnetic Dipole Emission by Purcell effect of Mie resonant Silicon nanosphere (pp. 240)
Hiroki Kasai, Hiroshi Sugimoto, Minoru Fujii

Exploring Wave Phenomena in Quasicrystal-Based Photonic Structures (pp. 242)
Mikhail Rybin

Polarization-selective metalens for varifocal imaging system (pp. 244)
Hyeonsu Heo, Gyeongtae Kim, Hongyoon Kim, Dongmin Jeon, Junsuk Rho

Artificial neural networks-based on-demand inverse design for 3D chiral metamaterials (pp. 246)
Jehyeon Shin, Jeonghoon Park, Jaebum Noh, Junsuk Rho

Inverse Design for wavelength and polarization multiplexing in optical metasurfaces (pp. 248)
Bo Xiong, Wei Ma

Generation of multi-channel overlapping perfect vortex beam on chip (pp. 249)
X. R. Zhao, Q. H. Wang, X. Z. Pei, C. Xu, Q. Kan, Yiyang Xie

Emission properties of plasmonic nanoshell lasers: Symmetric vs. antisymmetric lasing modes and gain-medium detuning effects (pp. 251)
Karen Caicedo, Melissa Infusino, Ashod Aradian, Alessandro Veltri

Robust gesture recognition based on millimeter-wave programmable metasurface (pp. 253)
Mingyi Li, Hongrui Zhang, Shengguo Hu, Jiawen Xu, Lianlin Li

Guided Domino Lithography: Enabling Uniform Fabrication of Single-Digit-Nanometer Plasmonic Nanoantenna Arrays (pp. 256)
Dong Kyo Oh, Jihae Lee, Huichang Yun, Junsuk Rho

Mass Production of Metalenses for Near-Infrared Imaging (pp. 258)
Seong-Won Moon, Joohoon Kim, Junsuk Rho

Negative index metamaterial using colloidal lithography for large-area and high productivity (pp. 260)
Youngsun Jeon, H. Cho, Junsuk Rho

A three-dimensional transformable metamaterial for programmable elastic waves control (pp. 262)
Zhou Hu, Rui Zhu, Zhibo Wei, Yan Chen

Advanced Heterostructures of Semiconductor Nanocrystals for Nanophotonics (pp. 264)
Hilmi Volkan Demir

Ultrasensitive Portable Surface-Enhanced Raman Spectroscopy for Clinical Applications (pp. 266)
Dehui Wan

Ultrafast electron dynamics at Fe(001)-Au(001) heterostructures (pp. 268)
M. Heckschen, Y. Beyazit, E. Shomali, F. Kühne, J. Jayabalan, P. Zhou, D. Diesing, M. E. Gruner, R. Pentcheva, B. Sothmann, Uwe

Bovensiepen

Sb2S3 phase change material for optical switching: the Brewster angle effect (pp. 270)
Gonzalo Santos, Diego Pérez-Francés, Josef Resl, María Losurdo, Yael Gutiérrez, Fernando Moreno

Modeling Photomolecular Effect Using Feibelman Parameters and Generalized Boundary Conditions for Maxwell Equations (pp. 272)
Gang Chen

Broadband Nonlinear Optical Waveguides Based On Conformal Transformation Optics (pp. 274)
Chunyu Huang, Yu Luo, Yule Zhao, Xiaofei Ma, Zhiwei Yan, Ziyi Liu, Chong Sheng, Shining Zhu, Hui Liu

Fano line shapes generated by excitonic nanoparticles (pp. 276)
Shinji Hayashi

Tunable Second Harmonic Generation from Lithium Niobate Metasurfaces (pp. 278)
Mengxin Ren, Lun Qu, Lu Bai, Zhengqing He, Wei Wu, Jingjun Xu

Chiral emission from perovskite metasurfaces and metacavities (pp. 279)
Young Chul Jun

Amorphous dielectric materials with complete photonic band-gaps in 3D (pp. 281)
Abraham de Jesus Aguilar Uribe, Marian Florescu, Frank Scheffold

Fundamental studies for new device applications in two-dimensional plasmonic crystals through analytical demonstrations in the submillimeter-wave band (pp. 283)
Go Itami, Osamu Sakai

Full-space Janus Metasurface for Direction-duplex Quad-channel Electromagnetic Wave Manipulation (pp. 285)
Weixu Yang, Shufang Dong, Ke Chen, Yijun Feng

Topological phase-supporting materials for nanophotonic sensing (pp. 287)
Gustavo Cruz, Sayan Roy, Arnab Banerjee, Peter Bermel

A polarization-tunable coloration with wide dynamic range using highly lossy material-based metal/dielectric/metal-subwavelength grating (pp. 289)
Yuusuke Takashima, Kentaro Nagamatsu, Masanobu Haraguchi, Yoshiki Naoi

In situ modification of the Quantum Hall effect with cavity vacuum fields (pp. 291)
Josefine Enkner, Lorenzo Graziotto, Felice Appugliese, Dalin Borici, Mattias Beck, Christian Reichl, Werner Wegscheider, Giacomo Scalari, Cristiano Ciuti, Jerome Faist

Nonlinear optics in low-index bulk media: past, present, and future (pp. 293)
Wallace Jaffray, Sven Stengel, Alexandra Boltasseva, Vladimir Shalaev, Andrea Di Falco, Marcello Ferrera

Ceramic metasurfaces for biophotonics applications in the visible range (pp. 295)
Mohammad Biabanifard, Tomasz Plaskocinski, Jianling Xiao, Andrea Di Falco

Magnetic control of electrically uncharged magneto-optical particles (pp. 297)
Manuel Marques, Shulamit Edelstein, Pedro A. Serena, Beatriz Castillo Lopez de Larrinzar, Antonio Garcia Martin

Development of Nonclassical Light Sources for Time-Resolved THz detection (pp. 299)
D. Adamou, L. Hirsh, T. Shields, S. Yoon, A. C. Dada, J. M. R. Weaver, D. Faccio, L. Caspani, M. Peccianti, Matteo Clerici

Mid-infrared topological edge modes in the symmetric and asymmetric photonic crystal slabs fabricated in SOI wafers (pp. 300)
Afshan Begum, Yuanzhao Yao, Takashi Kuroda, Yoshihiko Takeda, Naoki Ikeda, Takaaki Mano, Kazuaki Sakoda

The interplay of gain and loss in room-temperature planar polaritonic systems (pp. 302)
Anton Samusev

Continuous mechanical machining of asymmetric nanogratings with tailored period and shape by azimuthal

rotation-controlled nanoinscribing (pp. 304)
Jong G. Ok

Dynamic Thermoplasmonic Control of Colloids, Molecules and Liquids (pp. 306)
Martin Fränzl, Desmond Quinn, Diptabrata Paul, Frank Cichos

Recent progresses on quantum-enhanced nonlinear imaging (pp. 308)
Thomas Dickinson, Ivi Afxenti, Giedre Astrauskaite, Lennart Hirsch, Samuel Nerenberg, Ottavia Jedrkiewicz, Alessandra Gatti, Daniele Faccio, Caroline Müllenbroich, Matteo Clerici, Matteo Clerici, Lucia Caspani

Recent progress on chip-based Brillouin interactions (pp. 310)
Moritz Merklein

Topological transformations of vortex rings in paraxial laser beams (pp. 311)
Zhamila Kulchukova, Anton Desyatnikov

Artificial Neural Networks and Quantum Information Processing using Integrated Photonics (pp. 313)
Imtiaz Alamgir, Luigi Di Lauro, Stefania Sciara, Abdul Rahim Aadhi, Celine Mazoukh, Hao Yu, Bennet Fischer, Nicolas Perron, Nicola Montaut, Mario Chemnitz, Brent E. Little, Sai T. Chu, David J. Moss, Zhiming Wang, Roberto Morandotti

Scalable Chiral Photonic Architectures via Soft Nanoimprinting lithography (pp. 315)
Jose Mendoza-Carreño, Xiaoyu Qi, Isabel Alonso, Miquel Garriga, Luis Alberto Pérez, Agustín Mihi

Dynamically switchable phase contrast imaging with metaoptics (pp. 316)
Shaban Sulejman, Lincoln Clark, Haiwei Wang, Lukas Wesemann, Ann Roberts

Coherent Array of Superconducting Qubits as a Sensitive Microwave Antenna (pp. 318)
Patrick Navez, Alexander Balanov, Sergey Savel'ev, Alexandre Zagoskin

Graphene-based 2D Plasmonic Metamaterials for Terahertz Detectors (pp. 320)
Taiichi Otsuji, K. Tamura, Chao Tang, A. Satou, H. Fukidome, Y. Takida, H. Minamide, M. Ryzhii, V. Mitin, M. S. Shur, V. Ryzhii

Observation of off-Γ BIC in photonic crystals in both k- and real spaces (pp. 322)
Yuto Moritake, Taiki Yoda, Masaya Notomi

Dynamic plasmonics based on conducting polymers (pp. 324)
Shangzhi Chen, Magnus Jonsson

Integrated microlasers on a Bloch surface wave platform (pp. 325)
Yang-Chun Lee, Ya-Lun Ho, Bo-Wei Lin, M.-H. Chen, Di Xing, Hirofumi Daiguji, Jean-Jacques Delaunay

Tailoring the optical properties of 3D photonic crystals coated with Aluminum Zinc Oxide in the telecommunication wavelength (pp. 327)
Dimitra Ladika, Anna Theodosi, Odysseas Tsilipakos, Argyro Klini, Panagiotis Loukakos, Maria Kafesaki, Maria Farsari, David Gray

A Compact Silicon Photonic Crystal Spectrometer with Unprecedented Resolution (pp. 329)
Takasumi Tanabe, Junnosuke Kokubu, Ryo Sugano, Jinwei Zhang

Controlling the radiation space and wavelength with MIM metasurface in mid infrared wavelength (pp. 331)
Yoshiaki Nishijima, Tsuyoshi Kawaida, Megumi Tanaka, Kazuma Sekiya

Origin of high transmission via sharp bends of photonic-crystal waveguides with and without inversion symmetry (pp. 333)
Wei Dai, T. Yoda, Y. Moritake, Masaya Notomi

Attosecond Electron Microscopy (pp. 335)
Joel Kuttruff, David Nabben, Levin Stolz, Andrey Ryabov, Peter Baum

In-Operando Optical Spectroscopy of Field-Effect-Gated Transparent Conductive Oxides (pp. 337)
Michele Magnozzi, Maria Sygletou, Stefano Colace, Riccardo Magrin Maffei, Stefania Benedetti, Alessandro di Bona, Aleksandr Petrov, Piero Torelli, Emilio Bellingeri, Maurizio Canepa, Francesco Bisio

Ge-Sb-Te material for applications in photonics (pp. 339)
Mikhail Rybin

Field homogenization recipe for brain MRI (pp. 341)
Kyounsub Yoon, Sunkyu Yu, Namkyoo Park

Superoscillatory tweezer arrays for subwavelength trapping and manipulation of cold atoms (pp. 342)
Vincent Mancois, Kelvin Lim, Haijun Wu, Nikolay Zheludev, Yijie Shen, David Wilkowski

Epsilon-Near-Zero Regime in the Infrared for Ultrafast Switching (pp. 344)
Carl Davies, Andrei Kirilyuk

Advanced high contrast grating designs for biosensing applications (pp. 346)
Leonid Y. Beliaev, Giovanni Finco, Sungyeoung Kim, Larissa Vertchenko, Bjørn F. S. Nielsen, Mads V. Evensen, Ada-Ioana Bunea, Radu Malreanu, Lars René Lindvold, Osamu Takayama, Peter E. Andersen, Andrei V. Lavrinenko

Optoelectronic control of quantum optical phenomena with graphene (pp. 348)
Joel Cox

An electrically tunable polarization-selective photonic crystal based on a microcavity filled with a self-assembled uniformly lying helical liquid crystal (pp. 349)
Marcin Muszyński, Przemysław Oliwa, Pavel Kokhanchik, Piotr Kapuściński, Eva Oton, Rafał Mazur, Przemysław Morawiak, Wiktor Piecek, Przemysław Kula, Witold Bardyszewski, Barbara Piętka, Daniil Bobylev, Dmitry Solnyshkov, Guillaume Malpuech, Jacek Szczytko

Lasing of gain-doped plasmonic nanoshells: Threshold, emission linewidth and giant pull-out effects (pp. 351)
Ashod Aradian, Andres Cathey, Karen Caicedo, Milena Mora, Melissa Infusino, Alessandro Veltri

Manipulating the Exotic Quasi-Particles of van der Waals Correlated Antiferromagnet (pp. 353)
Han Htoon

Advanced Terahertz-Wave Phase and Polarization Control Devices Powered by Metasurfaces (pp. 355)
Yuehong Xu, Hiroaki Minamide

Manipulating Chemical Reactions with Light (pp. 357)
Z. Fusco, A. Edirisooriya, N. Lyu, C. David, Fiona Beck

Soft Metamaterials for Innovative Medical Devices (pp. 359)
Jianfeng Zang, Hanchuan Tang, Ye Tian, Zhangqi Pan

Design of Thin Film Metamaterial Absorber for IoT Application (pp. 361)
Tatsunosuke Matsui, Tomoki Narita, Sho Yoshikawa

Low-noise metamirrors for the visible spectral range (pp. 363)
Johannes Dickmann, Thomas Siefke, Jana Hartmann, Nico Wagner, Mika Gaedtke, Andreas Waag, Stefanie Kroker

Metamaterials based Pixelated Thermal Signature Control (pp. 365)
Zhuo Li, Xiu Liu, Yibai Zhong, Lin Wang, Tak Sing Wong, Han Wang, Jing Kong, Xu Zhang, Sheng Shen

Multipole coupling for control light propagation and trapping in dielectric and hybrid metasurfaces (pp. 367)
Andrey Evlyukhin, I. Allayarov, A. Calà Lesina, B. N. Chichkov

Structural Properties of Nanoporous Gold Metamaterial for Optical Applications (pp. 368)
Xinyan Wu, Fatemeh Ebrahimi, Maurice Pfeiffer, Nadiia Mameka, Manfred Eich, Alexander Petrov

Hot-electron induced chemistry using chiral and non-chiral plasmonic nanostructures (pp. 370)
Shashank Gahlaut, Christina Beresowski, Sergio Kogikoski Jr., Ilko Bald

Plasmon-enhanced nanospectroscopy for molecular sensing and control (pp. 371)
Taka-aki Yano

Ultrabroadband polarization-independent directional thermal emission (pp. 372)

Ziwei Fan, Taeseung Hwang, Sam Lin, Yixin Chen, Zi Jing Wong

Förster resonance energy transfer in absorbing environment (pp. 374)
Lyudvig Petrosyan, Mikhail Noginov, Tigran Shahbazyan

Resonances in doubly anisotropic, high-index nanoplatelets (pp. 376)
Bingying You, Tom Sistermans, Alberto Curto

Electromagnetic enhancement induced by subradiant plasmon resonance demonstrated by single plasmonic systems (pp. 378)
Tamitake Itoh, Yuko S. Yamamoto

Van Der Waals Polaritonic Crystals and Their Nanostructures (pp. 380)
Huanjun Chen, Zebo Zheng, Wuchao Huang, Shaozhi Deng

Scaling Challenges in Watts Level PCSELs (pp. 382)
Weidong Zhou, Chhabindra Gautam, Mingsen Pan

Integrated quantum photonic sources (pp. 383)
Xifeng Ren

Intracavity metasurfaces in fiber lasers for linear and nonlinear applications (pp. 384)
Lili Gui, Chuanshuo Wang, Hao Chen, Chao Meng, Xianglong Mei, Hailun Xie, Zhijin Chen, Fengbin Lin, Fei Ding, Sergey I. Bozhevolnyi, Kun Xu

High Q-factor coupled Fabry-Perot plasmonic nanoresonator (pp. 386)
Baptiste Fix

Multipolar description of the scattering of dense clusters of metallic nanoparticles (pp. 388)
Maeva Lafitte, Ranjeet Dwivedi, Philippe Barois, Alexandre Baron, Olivier Mondain-Monval, Virginie Ponsinet

Rayleigh surface waves of extremal elastic materials (pp. 390)
Yu Wei, Yi Chen, Wen Cheng, Xiaoning Liu, Gengkai Hu

Highly damped plasmonic and ferromagnetic metamaterials for wireless opto-magnetic actuation and detection (pp. 392)
Aritz Lafuente, Arnon Fluksman, Alejandro G. Roca, Ofra Benny, Josep Nogues, Mar Alvarez, Borja Sepulveda

Silicon-Nitride photonics for high-throughput biosensing applications (pp. 394)
Niels Verellen

Organic epsilon-near-zero and hyperbolic dispersion optical films (pp. 395)
Jeong Weon Wu

Deep ultraviolet meta-emitter boosted by bound states in the continuum (pp. 397)
Omar A. M. Abdelraouf, Aravind P. Anthur, Xiao Renshaw Wang, Qi Jie Wang, Hong Liu

Tailoring THz radiation pattern through intrapulse and interpulse difference-frequency generation at the nanoscale: modeling and perspectives (pp. 399)
Unai Arregui Leon, Luca Carletti, Davide Rocco, Costantino De Angelis, Giuseppe Della Valle

Versatile plasmonic colors with pixelated metasurface (pp. 401)
Maowen Song, Y. Lu, T. Xu

Efficient nonlinearities in metasurfaces enabled by bound states in the continuum (pp. 403)
Hayk Harutyunyan

Laser production of nanofibers (pp. 404)
Felix Quintero, Joaquin Penide, Raul Barciela, Monica Fernandez-Arias, Antonio Riveiro, Jesus del Val, Rafael Comesana, Fernando Lusquiños, Juan Pou

Silicon Nitride Platform for Quantum Photonics and Quantum Phononics (pp. 406)
Khaled Mnaymneh

Thermochromic thermal radiator based on angle selective thermal radiation applicable under direct solar irradiance (pp. 407)
Makoto Shimizu, Ryu Onozaki, Rihab Benlyas, Zhen Liu, Hiroo Yugami

High-performance Ultraviolet Metasurfaces based on Wide bandgap Dielectrics (pp. 408)
Cheng Zhang

Finite Difference Driven and Eigenmode Modelling of Polaritonic Systems (pp. 409)
Michele Tamagnone, Harsh Gupta, Tatiana Contino, Muhammad Atif Yaqub, Muhammad Waseem Ashraf

Strong Coupling with Different Photonic Modes within Single GaN Microstructure (pp. 410)
Yong-Hoon Cho

Engineered composites and plethora of on-demand functionalities and applications (pp. 411)
Dorota A. Pawlak, P. Piotrowski, M. Tomczyk, K. Sadecka, K. Bandopadhay, N. Aghad, K. Markus, A. Abbas, S. Saha, A. Materna, A. Bellardini, C. Sibilia

“Meta”-Optical Fibers (pp. 412)
Andrew Palmer, Yucheng Jin, Stuart Love, Yujin Zha, Beyonce Hu, Ho Wai Howard Lee

Tuning Nanoscale Photocurrent Direction and Terahertz Polarization State via Incident Light Polarization in Optoelectronic Metasurfaces (pp. 413)
Hou-Tong Chen, Jacob Pettine, Yunseok Choi, Chun-Chieh Chang

Control of non-hermitian degeneracy using intersubband polaritonic metasurfaces (pp. 414)
Hyeongju Chung, Beomjoon Kim, Gerhard Boehm, Mikhail A. Belkin, Jongwon Lee

Active layer morphology of organic and perovskite photovoltaics – a study based on grazing-incidence X-ray and neutron scattering (pp. 416)
Xinhui Lu

Optical spin waves (pp. 417)
Vage Karakhanyan, Roland Salut, Miguel Angel Suarez, Nicolas Martin, Thierry Grosjean

An ultra-low loss alumina waveguide platform for nonlinear photonics in the visible and UV (pp. 419)
Elissa McKay, Natale G. Pruiti, Matteo Clerici, Marc Sorel

Non-equilibrium light-matter interactions in photonic temporal crystals (pp. 420)
Bumki Min

Ultra-large Area Coherent Lasing Action through Hermitian/non-HermitianControl in Photonic Crystals (pp. 421)
Susumu Noda

Enhanced Optical Interactions in Nonlinear Topological Photonic Nanostructures (pp. 422)
Nicolae Panoiu

EM-Flow: A Conditional Reversible Flow-Based Deep Learning Model for Intelligent Electromagnetic Sensing by Reprogrammable Metamaterial (pp. 423)
Hongrui Zhang, Yanjin Chen, Mingyi Li, Hengxin Ruan, Lianlin Li

Bio-inspired metalens array for directional detection in 3D light imaging and ranging (pp. 428)
Clément Majorel, Amir Loucif, Emil Marinov, Renato Juliano Martins, Adelin Patoux, Virginie Brandli, Patrice Genevet

Symmetry Breaking in Bio-Inspired 2D Aluminum Networks probed by Electron Energy Loss Spectroscopy (pp. 429)
Jelena Wohlwend, Marcello Pozzi, Georg Haberfehlner, Ralph Spolenak, Henning Galinski

Investigating disorder in synthetic and biological 3D photonic structures with volume imaging (pp. 431)
Viola Bauernfeind, Kenza Djeghdi, Ullrich Steiner, Bodo D. Wilts

Controlling light and heat with Conducting Polymers and Cellulose (pp. 433)
Magnus Jonsson

Structural colors: toward AI-enabled design and solution-based fabrication (pp. 434)
Weijie Feng, Anwesha Saha, Taigao Ma, Haozhu Wang, L. Jay Guo

Self-Assembled Structural Color Colorimetric Sensor for Smart Phone based Bio-Chemical Sensing (pp. 436)
Pablo Cencillo, Mahdi Soudi, Debashis Chanda

Towards a machine learning approach for print parameter prediction in three-dimensional multiphoton laser lithography (pp. 438)
Sven Enns, Nicolas Lang, Julian Hering-Stratemeier, Georg von Freymann

High-performance optical diffuser inspired by Morpho butterfly's optical properties (pp. 440)
Akira Saito, Kazuma Yamashita, Kana Taniguchi, Shuta Sakamoto, Takuma Hattori, Yuji Kuwahara

Cross-reactive plasmonic arrays as artificial tastebud sensors (pp. 442)
Justin R. Sperling, Chad Sipperley, Rudi Schick, William J. Peveler, Alasdair W. Clark

Light-matter interaction on a chip

Deep Neural Networks for Prediction of Structure Parameters and Far-field Radiation Patterns of Nano-antenna (pp. 444)
Yi-Chiang Chang, Yung-Chiang Lan

Lithium niobate nanostructures: fabrication and nonlinear wavefront control (pp. 446)
Yunan Liu, Leyong Hu, Bo Wang, Junjie Li

Ultrathin Water-Immersion Metalens in the Visible (pp. 448)
Pei Ying Ho, Yu Chia Chung, Jia Hua Lee, Bo Ray Lee, Yao Wei Huang, Ray Hua Horng, Ming Lun Tseng

Lithium-plasmon-based low-powered dynamic color display (pp. 450)
Jie Liang, Yan Jin, Jia Zhu, Lin Zhou

Linearly Polarization-Sensitive Monolayer MoS2 Plasmonic Phototransistors (pp. 452)
Chen-Yu Wang, Shane Yeh, Jui-Han Fu, Cheng-Han Lin, Tzu-Yu Peng, Jia-Wern Chen, Feng-Yang Tsai, Vincent Tung, Yu-Jung Lu

Active Multitasking Metasurfaces: Simultaneous and Independent Steering of Frequency-Shifted Beams (pp. 454)
Prachi Thureja, Jared Sisler, Michael D. Kelzenberg, Ruzan Sokhoyan, Harry A. Atwater

Grayscale Electron Beam Lithography Direct Patterned Antimony Sulfide (pp. 456)
Wei Wang, Uwe Hübner, Tao Chen, Anne Gärtner, Joseph Köbel, Tanveer Ahmed Shaik, Astrid Bingel, Volker Deckert

Full-Stokes metasurface polarimetry based on multidimensional polarization conversion (pp. 458)
Chenglong Zheng, Huaping Zang, Peinan Ni

Impedance-matched zero-index metamaterials: from waveguide to antenna (pp. 460)
Yang Li

Reconfigurable Acoustic Metasurfaces for Controlling Disordered Sound Fields (pp. 462)
Guancong Ma

Enhanced Photogating Gain in Scalable MoS2 Plasmonic Photodetectors via Resonant Metasurfaces (pp. 463)
Yu-Jung Lu

Monocular metasurface camera for single-shot multi-dimensional imaging (pp. 464)
Yuanmu Yang

Active and Nonlinear Metasurfaces with the Generation and Relaxation of Plasmonically Induced Hot Carriers (pp. 465)
Wenshan Cai

Dirac Mass Gap Induced by Optical Gain and Loss (pp. 467)
Yidong Chong, Letian Yu, Haoran Xue, Yun Yong Terh, Ruixiang Guo, Eng Aik Chan, Cesare Soci, Baile Zhang

Third-harmonic generation in near-zero index heterogeneous nanostructures (pp. 469)

Matteo Silvestri, A. Sahoo, Luca Assogna, Paola Benassi, Carino Ferrante, Alessandro Ciattoni, Andrea Marini, Andrea Marini

Manipulation of Electron Beams by Laguerre-Gaussian Modes (pp. 471)
Yung-Chiang Lan, Ming-Chieh Lin

Methods for characterization of wafer scale SERS substrates (pp. 473)
Matthew Singer, Ryan Priore, Longfei Ye

Si Metasurfaces for DUV Plasmonics and Biomolecular Spectroscopy (pp. 475)
Bo Ray Lee, Mao Feng Jiang, Pei Ying Ho, Kuan-Heng Chen, Jia Hua Lee, Min-Hsiung Shih, Der-Hsien Lien, Tzu-En Lin, Ray-Hua Horng, Ming Lun Tseng

Compact depth sensing and facial recognition from integration of metasurface and photonic-crystal surface-emitting laser (pp. 477)
Yao-Wei Huang

Subradiant plasmonic cavities make bright polariton states dark (pp. 478)
J. E. Yim, Z. T. Brawley, Matthew T. Sheldon

Dynamic optical MEMS metasurfaces (pp. 480)
Fei Ding

Gap plasmon structures constructed by oligonucleotides and integrated with fluorophores (pp. 481)
Wan-Ping Chan, Yu-Long Lin, Shiuan-Yeh Chen

Three-dimensional co-axial double cylinder metasurface for high-sensitive gas molecular sensing (pp. 483)
Takuo Tanaka

Photoluminescent gratings and metasurfaces (pp. 484)
Pierre Berini

Electrochemically-tunable oxide materials for metasurfaces and large-area, additive patterning (pp. 486)
Vivian Ferry

Nonlinear all-dielectric metasurfaces driven by multipolar resonances and quasi-bound states in the continuum (pp. 488)
Hui-Hsin Hsiao

Metamaterial assisted super-resolution microscopy (pp. 490)
Zhaowei Liu

Multiparameter Sensing of On-Chip Infrared Photodetectors Enabled by Metasurfaces (pp. 491)
Mingjin Dai, Qi Jie Wang

Real-Time Multidimensional Imaging with an Encoding Metasurface (pp. 492)
Lidan Zhang, Chen Zhou, Hyunju Ahn, Shengyuan Chang, Md Tarek Rahman, Tunan Xia, Zhiwen Liu, Xingjie Ni

Introducing Circular Dichroism with Chiral Bound State in the Continuum (pp. 493)
Cheng-An Mao, Wen-Hui (Sophia) Cheng

Spherulite based Metasurfaces (pp. 494)
Jingbo Sun, Y. Liu, L. Zhou, Y. Shen, J. Zhou

Dispersion engineering of mid-IR polaritons in van der Waals crystals (pp. 496)
Sergey Menabde, Min Seok Jang

Experimental demonstration of ENZ-enhanced optical nonlinearity in ultrathin TiN epilayers (pp. 497)
F.-T. Tseng, I-H. Ho, S. Gwo, Hyeyoung Ahn

Absorption-Based Nanophotonic Quantum Sensing on Resonant Metasurfaces (pp. 499)
Laura Kim

Local high quality factor metasurfaces for extremely low threshold,nonlinear image filtering and efficient programmable

wave shaping (pp. 501)
Mark Lawrence, Lin Lin, Bo Zhao, Samuel Ameyaw

Nonlinear Mid-infrared Metasurfaces for Harmonic Generation and Deep-Subwavelength Nanomachining (pp. 502)
Maxim Shcherbakov

Near-field manipulation of angular momentum of light (pp. 504)
Haoran Ren

Controlling Far-Field Radiation with Photoluminescent and Incandescent Metasurfaces (pp. 506)
Anne Nguyen, Elise Bailly, Jean-Paul Hugonin, Jean-Jacques Greffet, Benjamin Vest

Nanoscale Extended Chirality Density Enhanced by Plasmonic Nanoresonator (pp. 508)
Hanwei Wang, Yulei Shen, Gayatri Chandran, Yang Zhao

Electrochemically Active Metasurface and Multispectral Light and Heat Management (pp. 510)
Po-Chun Hsu

Building Uncooled Infrared Camera based on One Atom Thick Graphene (pp. 512)
Debashis Chanda

Palladium Nanorods Overlayer Induced Electrostatic Contribution to Silicon Rib Waveguide Sensitivity (pp. 513)
Anastasia Novikova, A. Katiyi, A. Karabchevsky

Resonances Governed by Lattice Induced Multipole Coupling in Metasurfaces with Inversion Symmetry (pp. 515)
Izzatjon Allayarov, Andrey B. Evlyukhin, Antonio Calà Lesina

Vibrational Strong Coupling for Cavity catalysis of an Enantioselective Reaction (pp. 516)
Jaibir Singh, Pallavi Garg, Ramasamy Vijaya Anand, Jino George

Real time optical and mechanical environmental sensing based on nano-optomechanical disk resonators (pp. 518)
Elena Sentre-Arribas, Alicia Aparicio-Millan, Aristide Lemaître, Ivan Favero, Javier Tamayo, Montserrat Calleja, Eduardo Gil-Santos

Simulation of spatial rogue waves in a solid-state laser with transverse mode-locking (pp. 520)
Roza Navitskaya, Ihar Stashkevitch, Stanislav Derevyanko, Alina Karabchevsky

Novel Plasma Treatments for AlZnO Local Modulation and its Application on Fabrication of Planar Infrared Metasurfaces (pp. 522)
Kai Sun, Tom Howe, Cornelis H. de Groot, Otto Muskens

Inverse design for arbitrary optical materials and integrated nanophotonics (pp. 524)
Abhishek Nanda, Johannes Gedeon, Emadeldeen Hassan, Michael Kues, Antonio Calà Lesina

Photonics based non-invasive wearable devices for health monitoring. (pp. 526)
Edik Rafailov

Meta-optics for multi-dimensional manipulation of light

Crystallization of Induce Optical Vortex by Bessel Beams (pp. 528)
Sahil Sahoo, Yuri Gorodetski

Magnetoelectric effect in magnetic toroidal metal HoAgGe (pp. 530)
Akimitsu Kirikoshi, Satoru Hayami

Ultrafast Switching of Magnetization using Chiral Optical Phonons (pp. 532)
Carl Davies, F.G.N. Fennema, Arata Tsukamoto, Ilya Razdolski, Alexey V. Kimel, Andrei Kirilyuk

Realization of Wilson fermions in topolectrical circuits (pp. 534)
Huanhuan Yang, Lingling Song, Yunshan Cao, Peng Yan

Quantification of chirality based on electric toroidal monopole: Application to a twisted methane molecule (pp. 536)

Akane Inda, R. Oiwa, S. Hayami, H. M. Yamamoto, H. Kusunose

Gyromagnetic Double-zero-index Metamaterials Enable Ultrarobust Generation of Optical Spatiotemporal Vortices (pp. 538)
Xiaohan Cui, Ruo-Yang Zhang, Yuan-Song Zeng, Geng-Bo Wu, C. T. Chan

Control of Circularly Polarized Light Using Electron Beam (pp. 540)
Takumi Sannomiya

Classifying Topology in Open Photonic Systems (pp. 542)
Alexander Cerjan

Chiral and non-chiral magnetic texturing in antiferromagnetic Cr2O3 (pp. 543)
Oleksandr Pylypovskyi

Planar resonant metasurfaces with 3D intrinsic chirality (pp. 545)
Zi-Lan Deng, Meng-Xia Hu, Xin Li, Qian-Mei Deng, Feng-Jun Li, Xiangping Li

Generation of Ultra-compact Optical Vortex Through Photonic Spin-orbit Interactions in Nanostructures and Its Super-resolution Imaging (pp. 547)
Benfeng Bai

Chiral structures fabrication with structured light possessing orbital angular momentum (pp. 548)
Takashige Omatsu

Thermally induced dynamics of magnetic skyrmions and their device functions (pp. 550)
Masahito Mochizuki, Xichao Zhang, Junnosuke Matsuki

Topological magneto-optical effect induced by skyrmion lattice formation (pp. 552)
Yoshihiro Okamura, Y. D. Kato, M. Hirschberger, Y. Tokura, Y. Takahashi

Symmetry Breaking in Colloidal Metal Nanostructures by Circularly Polarized Light Directed Galvanic Replacement Reaction (pp. 553)
Monika Ghalawat, Daniel Feferman, Artur Movsesyan, Wanting He, Zhiming Wang, Dongling Ma, Alexander Govorov, Gil Markovich

Spin wave amplification through superradiance (pp. 554)
Xiangrong Wang, K. Y. Jing, X. Gong

Algebra of Optical Phase Dislocations (pp. 557)
Yuri Gorodetski

Peltier effect of phonons driven by electromagnetic waves (pp. 559)
Hiroaki Ishizuka, Masahiro Sato

Spatiotemporal Light Structuring (pp. 561)
Michael Almeida de Oliveira, Antonio Ambrosio

Orbital angular momentum of magnons in confined magnetodielectrics (pp. 562)
Eugene Kamenetskii

Exploring Strategies for Enhancing the Sensitivity of Chiroptical Spectroscopy with Aluminum Nanoplasmonics (pp. 563)
Bjoern Reinhard

A Scalar Product for Computing Fundamental Quantities in Matter (pp. 565)
Ivan Fernandez-Corbaton, Maxim Vavilin

Off-resonance Spin-locked Metasurfaces based on Quasi-Bound States in the Continuum and Nonreciprocal Chiral Splitters (pp. 567)
Zuojia Wang, Haochen Yang, Yujie Zhang, Guang Chen, Liqiao Jing

Detecting the symmetry breaking of the quantum vacuum in a QED system (pp. 569)
Tiefu Li

Si metasurface on a magneto-optical thin film for enhancing nonreciprocal polarization rotation (pp. 570)
Yasutomo Ota, Siyuan Gao, Tatsuya Kitai, Kota Taniguchi, Takeru Yambe, Satoshi Iwamoto

Manifestation of crystal chirality in quasiparticles (pp. 572)
Takehito Yokoyama

Pseudomagnetic fields in photonic crystals with synthetic strain: Observation of Landau levels and chiral edge states (pp. 573)
René Barczyk, L. Kuipers, Ewold Verhagen

Control of high harmonic generation and photo current in graphene by tuning laser polarization and combing two laser fields (pp. 575)
Masahiro Sato, Minoru Kanega

CP2 triple-Q state in the SU(3) Kondo lattice model (pp. 577)
Yutaka Akagi

Non-Hermitian Aharonov-Bohm effect under imaginary magnetic fields (pp. 579)
Tomoki Ozawa

Exploring magneto-optical and nonlinear processes using a polarimeter optical spectrum analyzer (pp. 580)
Eyal Buks

Deep-learning-based end-to-end metalens imaging (pp. 581)
Joonhyuk Seo, Jaegang Jo, Joohoon Kim, Joonho Kang, Chanik Kang, Seongwon Moon, Eunji Lee, Jehyeong Hong, Junsuk Rho, Haejun Chung

Cavity materials: Virtual Photons, Real Effects (pp. 583)
Qing-Dong Jiang

Dynamical control of topological solitons in ferroelectrics and dynamical multiferroicity via twisted light (pp. 584)
Lingyuan Gao, Sergei Prokhorenko, Yousra Nahas, Laurent Bellaiche

Exploring chiral nanogap structures using inverse topology design (pp. 586)
Atsushi Taguchi

Emergent One-Dimensional Helical State on the Surface Opposite to a Step Edge in Higher-Order Topological Insulators (pp. 588)
Akihiko Sekine, Manabu Ohtomo, Kenichi Kawaguchi, Mari Ohfuchi

Chirality-induced polarized phenomena in chiral inorganic materials (pp. 590)
Yoshihiko Togawa

Three-dimensional topological spin textures in chiral magnets (pp. 592)
Jiadong Zang

Nonreciprocal Optical Responses and Diode Effect in Superconductors: Quantum Geometry, Topological Superconductivity, and Exotic Pairing (pp. 593)
Hiroto Tanaka, Akito Daido, Hikaru Watanabe, Naratip Nunchot, Kyohei Nakamura, Shun Asano, Youichi Yanase

Toroidal-assisted Metasurface for High-performance Nanophotonics (pp. 595)
Pin Chieh Wu

Antiferromagnetic skyrmion lattice of the 4-sublattice tetrahedral order (pp. 596)
Tomoki Hirosawa, Maria Azhar, Alexander Mook

Chiral optical forces in integrated photonic waveguides for sorting enantiomers (pp. 597)
Iago Diez, Josep Martínez-Romeu, Sebastian Golat, Francisco Rodríguez-Fortuño, Alejandro Martínez

Surface Lattice Resonance for Enhanced Magnetoplasmonic Activity (pp. 599)
Terunori Kaihara, Pablo Rodriguez-Suarez, Paolo Vavassori

Correlation-enhanced interaction of a Bose-Einstein condensate with parametric magnon pairs and virtual magnons (pp. 601)
Oleksandr (Alexander) Serha (Serga)

Chirality in optical manipulation via electronically resonant light-matter interactions (pp. 603)
Hajime Ishihara

Twisted Cavity Resonators of Anyon Rotational Symmetry with Bulk Modes of Non-Zero Helicity (pp. 605)
Jeremy Bourhill, Emma Paterson, Maxim Goryachev, Michael Tobar

Polarization in inhomogeneous crystals and its relationship to quadrupole moments (pp. 607)
Nobuhiro Arai, Yang Gao, Di Xiao, Shuichi Murakami

Ultracompact, controllable circular polarization laser based on chiral metamaterials (pp. 608)
Ioannis Katsantonis, Anna Tasolamprou, Thomas Koschny, Maria Kafesaki

Thermal Hall effect from chiral magnon-magnon many-body scattering (pp. 610)
Dimos Chatzichrysafis, Alexander Mook

Giant electromagnetic nonreciprocity in magnetic epsilon-near-zero metamaterials (pp. 612)
Jun Qin, Yucong Yang, Shuang Xia, Lei Bi

Vorticity of Spin / Orbital Berry Curvature and Topological Charges in pseudo-nodal semimetals (pp. 614)
Peter Christian Schmitz, Dongwook Go, Yuriy Mokrousov

Photoacoustic spectroscopy and polarimetry spectroscopy for the chiro-optical characterization of nanostructures (pp. 615)
Alessandro Belardini, Emilija Petronijevic, Claudia Skubisz, Concita Sibilia

Screw dislocations in chiral magnets (pp. 616)
Maria Azhar, S. C. Shaju, V. P. Kravchuk, M. Garst, K. Everschor-Sitte

Making sense of the electron transport CISS effect properties and the spinterface model (pp. 618)
Amos Sharoni, Reut Bornovski, Seif Alwan, Yontant Dubi

Chiral Atoms and Helical Electrons (pp. 620)
Hiroshi Yamamoto

Photonic vortex lattice based on dielectric polarization textures (pp. 622)
Ramaz Khomeriki, Vakhtang Jandieri, Koki Watanabe, Daniel Erni, Douglas H. Werner, Marin Alexe, Jamal Berakdar

Hall Quantized Hall Effect (pp. 624)
Shun-Qing Shen

Optical forces of optical modes with helicity and angular momentum (pp. 626)
Gabriel Molina-Terriza

Nonlinear topological magnon spin Hall effect (pp. 628)
Peng Yan

Chiral coherent control of electronic population transfer with femtosecond pulses: towards all-optical and highly enantioselective photochemistry (pp. 630)
Andrés Ordóñez, Patricia Vindel-Zandbergen, David Ayuso

Valley-Hall Topological Waveguides for Integrated Quantum Photonics (pp. 632)
Nicholas J. Martin, Mahmoud J. Mehrabad, Luke Hallacy, Dominic Hallett, Xuchao Chen, René Dost, Eric Nussbaum, Andrew Foster, Edmund Clarke, Pallavi K. Patil, Stephen Hughes, Mohammad Hafezi, Mark Fox, Maurice S. Skolnick, Luke R. Wilson

Brillouin Light Scattering Study of Nonreciprocal Spin Dynamics in Artificial Chiral Magnets (pp. 634)
Mingran Xu, A. J. M. Deenen, H. Guo, D. Grundler

Satisfaction of circular polarized Laguerre-Gaussian mode generation requirements by mid-infrared thermal emission

metasurface (pp. 636)
Kazuma Sekiya, Yoshiaki Nishijima

Orbital angular momentum multiplexed metasurface for multi-wavelength holography (pp. 638)
Seong-Won Moon, Jaehyuck Jang, Junsuk Rho

Resonant exceptional points in terahertz metasurfaces (pp. 640)
Lei Wang, Caihong Zhang, Jingbo Wu, Kebin Fan, Biaobing Jin, Jian Chen, Peiheng Wu

Janus Bound States in the Continuum with Asymmetric Topological Charges and Intrinsic Chirality (pp. 642)
Meng Kang, Meng Xiao, C. T. Chan

Versatile Metaphotonic Singularities: Multidimensional, Optomechanical, and Topological Aspects (pp. 643)
Tianyue Li, Shuming Wang, Shining Zhu

Topological momentum gap in PT-symmetric photonic crystals (pp. 645)
Ming-Wei Li, Jian-Wei Liu, Wenjie Chen, Jian-Wen Dong

Evanescent Wave Manipulation Based on Non-Hermitian Physics (pp. 646)
Huanan Li

Unidirectional unpolarized photoluminescence emission via vortex excitation (pp. 648)
Jincheng Ni

Tunable metaoptics using phase change and van der Waals materials (pp. 649)
Kandammathe Valiyaveedu Sreekanth, Arash Nemati, Zeng Wang, Meng Zhao, Yuanda Liu, Jichao Fu, Jinghua Teng

Machine-learning aided optimization for metasurfaces (pp. 651)
Wei Ma

Multidimensional manipulation of LightFrom metasurfaces to liquid crystals (pp. 653)
T. Huang, Y. Xie, Z. Zhou, D. Zhang, Zile Li, G. Zheng

Metalens for Accelerated Optoelectronic Edge Detection under Ambient Illumination (pp. 654)
Shuai Wang

Strong light-matter interactions in plasmonic/dielectric metasurfaces

Observation of Projective Embedded Topology and Trijunction-Induced Topological State in Acoustic Lattices (pp. 657)
Hau Tian Teo, Yang Long, Kailin Song, Haoran Xue, Baile Zhang

Broadband sound attenuation under grazing flow via metamaterial-based acoustic liner (pp. 659)
Sibo Huang, Yong Li, Jie Zhu, Din Ping Tsai

Resonant enhancement of optoacoustic response in van der Waals materials (pp. 661)
Anton Samusev, Alex Carr, Claudia Ruppert, Giulia Magnabosco, Nicolas Vogel, Tetiana Linnik, Andrew Rushforth, Alexey Scherbakov, Manfred Bayer, Andrey Akimov

Subwavelength-Scale Variability Impact on Hypersonic 1-D Phononic and Photonic Crystals (pp. 663)
Omid Reza Ranjbar-Naeini, Gloria Conte, Jouni Ahopelto, Clivia Marfa Sotomayor Torres

Acoustic diffusers by phase-control acoustic metamaterials for reflected and transmitted waves (pp. 665)
Jia-Hong Sun, Yu-Wei Chen, Ching-Yun Chang

Non-Hermitian topological systems using nonreciprocal electroacoustic elements (pp. 667)
Anis Maddi, Guillaume Penelet, Vincent Pagneux, Vassos Achilleos

The role of elastic interfaces in a reduced relaxed micromorphic formulation of finite-size mechanical metamaterials (pp. 669)
Leonardo Andres Perez Ramirez, Jendrik Voss, Gianluca Rizzi, Svenja Hermann, Plastiras Demetriou, Angela Madeo

Unified model for multiple scattering problems in one-dimensional elastic waveguides (pp. 671)
Mario Lazaro, Vicente Romero-García, Luis M. García-Raffi, Richard V. Craster

Inverse Design of Broadband Acoustic Lens using Gradient-Based Optimization (pp. 673)
Feruza Amirkulova, Samer Gerges, Jovana Samaniego

Robustness evaluation of merged topological bound states in the continuum (pp. 675)
Jiamin Guo, Zhongming Gu, Jie Zhu

Observation of D-class topology in an acoustic metamaterial (pp. 677)
Shi-Qiao Wu, Wenting Cheng, Xiao-Yu Liu, Bing-Quan Wu, Emil Prodan, Camelia Prodan, Jian-Hua Jiang

3D printed polarizer for shear elastic waves (pp. 679)
Taeyul Choi, Yuqi Jinin, Teng Yang, Arup Neog, Arkadii Krokhin

Coherent excitation of torsional mechanical modes in coupled nanoantennas (pp. 681)
Jorge M. Garcia, Beatriz Castillo Lopez de Larrinar, Chushuang Xiang, N. Daniel Lanzillotti-Kimura, Antonio Garcia-Martin

Acoustic Realization of Multiple Topological Corner Modes in a Coupling-inverted Phononic Crystal (pp. 682)
Dongyi Wang, Guancong Ma

Single-pixel imaging based on time-modulated gratings and compressive sensing (pp. 684)
Pawel Packo, Daniel Torrent

Fast Quasiadiabatic Driving with 2D Optimization in Elastic Waveguides (pp. 686)
Dong Liu, Yiran Hao, Jensen Li

Dispersion relationship of weakly scattered media (pp. 688)
Mario Lazaro, Vicent Romero-García, Luis García-Raffi, Richard Craster

Braiding of Bloch eigenmodes in a non-Abelian topological phase with quaternion charge (pp. 690)
Xiaoming Wang, Guancong Ma

Tunable magnetic lattices as a platform for controlling sound waves (pp. 692)
Osama Bilal

Using Ping-Pong balls to reduce ambient noise (pp. 694)
Yan Pennec, Eric Cochin, Gaëtan Lévêque, Bahram Djafari-Rouhani

Modeling wave propagation and boundary effects in acoustic metamaterials by a relaxed micromorphic continuum (pp. 696)
Angela Madeo, Jendrik Voss, Svenja Hermann, Gianluca Rizzi, Felix Erel-Demore, Leonardo A. Perez Ramirez, Plastiras Demetriou, Patrizio Neff

Design strategies for amplitude and phase acoustic holograms in biomedical ultrasound (pp. 698)
Noé Jiménez, Diana Andrés, Alba Eroles-Simó, Alicia Carrión, Francisco Camarena

Topological Shear Band Engineering in Mechanical Metamaterials (pp. 700)
Jingyi Zhang, Jingran Liu, Anton Souslov, María Teresa Pérez Prado, Javier Segurado, Maciej Haranczyk, Johan Christensen

Viscous phononic supercrystal (pp. 701)
Arkadii Krokhin, Martin Ibarias, Jose Sanchez-Dehesa

Enhanced Understanding through Experimental Study: Disorderly Arrangement of Vertical GaN Nanowires in Polymer Materials (pp. 703)
F. Soldevila, A. Huynh, E. Charron, B. Bonello, B. Perrin, A. Chevillard, N. Gogneau, M. Tchernycheva, Olga Boyko

Control of FRET in radio frequencies with metasurfaces, in other words, dipole-dipole interactions in the near field of a metasurface (pp. 705)
Kseniia Lezhennikova, Kaizad Rustomji, Boris Kuhlmey, Tryfon Antonakakis, Pierre Jomin, Stanislav Glybovski, Martijn De Sterke, Jérôme Wenger, Redha Abdeddaim, Stefan Enoch

Non-resonant extraordinary acoustic transmission (pp. 707)
Oliver B. Wright, Eun Bok

Static Loading Challenges of Three-Dimensional Ultrawide Phononic Crystals and Elastic Metamaterials (pp. 708)
Cetin Yilmaz

Thermal rectification in graphite Tesla valve based on phonon hydrodynamics (pp. 710)
Masahiro Nomura

Exploring Tunable Poisson's Ratio in Origami Metamaterials (pp. 712)
Diego Misseroni

Twofold topological transition induced by third-nearest-neighbor hoppings in anartificial elastic polyacetylene (pp. 713)
Rafael Méndez-Sanchez, Yonatan Betancur-Ocampo, Bryan Manjarrez-Montañez, Angel Martínez-Argüello

Non-Hermitian Metasurfaces for Extraordinary Elastic-wave Manipulations of Higher-order Diffractions (pp. 715)
Bing Li, Jiali Cheng, Bochen Ren

Non-adiabatic phononic control of polariton Bose-Einstein condensates (pp. 717)
Alexander Kuznetsov, Klaus Biermann, Paulo Ventura Santos

Mechanical tuning of topological waveguiding in auxetic metamaterial (pp. 719)
Federico Bosia, Giorgio Carta, Maryam Morvaridi, Vinicius Fonseca Dal Poggetto, Antonio Gliozzi, Charles Croenne, Marco Miniaci, Nicola Pugno, Michele Brun

Tunable Topological Properties in Phononic Crystals via Photoresponsive Polymers (pp. 721)
Antonio Gliozzi, Federico Bosia, Bryn Davies, Gregory Chaplain, Marco Miniaci, Emiliano Descrovi, Richard Craster

Ultrasonic Hologram for Bi-directional Diffusion by Phase Controlling the Scattering Coefficients (pp. 723)
Eric Ballestero, Josep Rodríguez-Sendra, Jean-Philippe Groby, Noé Jiménez, Vicent Romero Garcia

Experimental study of sonic velocity modulations and time interfaces in a controllable piezoelectric phononic crystal (pp. 725)
Charles Croënne, Sarah Tessier Brothelande, Florian Allein, Jérôme O. Vasseur, Bertrand Dubus

On the role of phase in nonreciprocal vibration transmission in passive and active phononic lattices (pp. 727)
Ali Kogani, Jiuda Wu, Behrooz Yousefzadeh

Harnessing topology and nonlinearity for advanced elastic wave control (pp. 729)
Georgios Theocharis

Advancements in Vibration Energy Harvesting through Metamaterials: Insights from the MetaVEH Project (pp. 730)
Andrea Colombi, B. Zhao, R. Ardito, J. M. De Ponti, R. V. Craster

Topological states in periodic and disordered elastic metabeams (pp. 732)
Runcheng Cai, Yabin Jin, Yan Pennec, Laurent Carpentier, Xiaoying Zhuang, Bahram Djafari Rouhani

Diffusive Acoustic Metasurfaces for Single-element Photoacoustic Imaging (pp. 734)
Alejandro Cebrecos, Irene Pi-Martín, Roby Weeteling, Juan José García-Garrigós, Noé Jiménez

Broadband and low frequency acoustic absorber with frozen sound (pp. 736)
Anis Maddi, Come Olivier, Gaelle Poignand, Guillaume Penelet, Vincent Pagneux, Yves Aurégan

PT-latent symmetries (pp. 738)
Malte Röntgen, Xuelong Chen, Wenlong Gao, Vincent Pagneux, Vassos Achilleos

Physically Interpretable Data-Driven Modeling and Control of Wave Dynamics (pp. 740)
Tristan Shah, Feruza Amirkulova, Stas Tiomkin

Any Dispersion You Want - Demystifying Roton, Maxon, Saddle Point, and Higher-order van Hove Singularities via Nonlocal Phononic Crystals (pp. 741)

S. Paul, F. Chen, K. J. Deshmukh, B. Deng, A. Kazemi, X. Zhu, H. C. Fu, Pai Wang

Negative refraction in a single-phase flexural metamaterial with hyperbolic dispersion (pp. 743)
Kim Pham, Agnès Maurel, Jean-Jacques Marigo

Acoustic grating with space-time modulation (pp. 745)
Agnes Maurel, Kim Pham

Theoretical Bound of Symmetric Metasurfaces (pp. 747)
Chan Wook Park, Yoon Young Kim

AI-empowered acoustic metamaterials and their applications (pp. 749)
Bin Liang

Efficient electromechanical coupling to an optomechanical nanobeam (pp. 751)
Tapani Makkonen, Oili Ylivaara, Sara Pourjamal, Jouni Ahopelto

Acoustic and Optic drills by dynamic high-order Bessel beam mixing (pp. 753)
Kestutis Staliūnas, Gabrielius Kontenis, Noe Jimenéz

Superlattice nanowires: a versatile platform for phonon engineering (pp. 755)
Aswathi K. Sivan, Begoña Abad, Omer Arif, Johannes Trautvetter, Tommaso Albrigi, Alicia Ruiz Caridad, Chaitanya Arya, Diego de Matteis, Francesca Rossi, Valentina Zannier, Lucia Sorba, Riccardo Rurali, Ilaria Zardo

Optomechanical measurement of liquids in unconventional regimes (pp. 756)
Ivan Favero

Explorations with nonlinearity and coupled orbitals in mechanical andmagneto-mechanical topological crystalline insulators (pp. 757)
G. Liu, I. Grinberg, V. Workman, J. Noh, W. A. Benalcazar, M. Lin, Y. Ma, C. W. Peterson, J. Zhao, A. Mangu, C. Harris, T. L. Hughes, Gaurav Bahl

X-ray Transient Gratings: Access to Nanoscale Acoustics, Magnonics, and More (pp. 758)
Keith A. Nelson

Dielectric metasurfaces for nonlinear asymmetric imaging (pp. 759)
Davide Rocco, Andrea Locatelli, Luca Carletti, Maria Antonietta Vincenti, Costantino De Angelis

Effect of Thermal Annealing on Surface Plasmon Properties of Gold and Silver Nanodisk Structures for Live Cell Imaging (pp. 761)
Kota Yamasaki, Ryohei Hatsuoka, Tetsuya Matsuyama, Kenji Wada, Koichi Okamoto

Electromagnetic response of liquid crystal based tunable high refractive index dielectric rings metasurfaces (pp. 763)
Pratiksha Sakhare, Jayasri Dontabhaktuni

Self-Aligned Nanoring Doublet as a Single Particle Nanocavity for Strong Coupling (pp. 765)
Kyungwha Chung, Luke Lee

All-optical phase rotation in strongly coupled light-matter systems (pp. 766)
Fedor Benimetskiy, Paul Walker, Sylvain Ravets, Maurice Skolnick, Jacqueline Bloch, Dmitry Krizhanovskii

Long-range super-Planckian heat transfer between nano-emitters in a resonant cavity (pp. 768)
Kiryl Asheichyk, Philippe Ben-Abdallah, Matthias Krüger, Riccardo Messina

Weyl points and chiral states in correspondence of Bound States in Continuum connected by Fermi arc (pp. 770)
Vito Mocella, Fabrizio Sgrignuoli, Bryan Guilcapi Alulema, Silvia Romano, Gianluigi Zito, Bruno Miranda, Aida Seifalinezhad, Ivo Rendina

Embedding plasmonic gratings for enhanced polarized photodetection and imaging in the near-infrared (pp. 772)
Tong Yu, Cheng Zhang, Ying Luo, Xiaofeng Li

Strong coupling between surface plasmons and magnetic polaritons in a borophene-based hybrid system (pp. 774)

Ye Ming Qing

Condensation and Transport of Organic Exciton-Polaritons from Bound States in the Continuum (pp. 776)
Matthijs Berghuis, Jose Luis Pura, Gabriel Castellanos Gonzales, Mohammad Ramezani, Diego Romero Abujetas, Shunsuke Murai, Erik van Heist, José Sanchez Gil, Jaime Gómez Rivas

Engineering Light-Matter Interactions at the Nanoscale for Functional Devices (pp. 778)
Zhaogang Dong

Plasmonics and metamaterials for controlling optical properties and device applications through strong light-matter interactions (pp. 780)
Koichi Okamoto

Continuous wave-pumped second-harmonic generation and application from GaSe-assisted microfiber (pp. 782)
Biqiang Jiang, Zhen Hao, Yuxin Ma, Xuetao Gan, Jianlin Zhao

Light-matter strongly coupled states in optical microcavities using highly oriented organic molecular crystals (pp. 784)
Kenichi Yamashita

Infrared photodetectors based on 2D heterostructures modulated by photogating (pp. 786)
Jiong Yang, Chao Zhang, Bining Sheng, Xiaofeng Li

Significant loss suppression in metasurfaces via resonances coupling (pp. 788)
Guangyuan Li, Xiaoqing Luo, Xueqian Zhao

Integrated lithium niobate photonics: from communications to metrology (pp. 790)
Yang Li

Multi-wavelength single-mode plasmonic nanolasing in an H-shape cavity (pp. 792)
Fajun Xiao

Probing plasmonic light-matter interactions with Kelvin probe force microscope (pp. 794)
Satoshi Ishii, Min-Wen Yu, Kuo-Ping Chen

Optical Interplay between Triplet-Triplet Annihilation Upconversion Systems and Plasmons: Towards Upconverted Emission Enhancement (pp. 796)
Kosuke Sugawa, Shota Jin, Jotaro Honda

Silicon BIC metasurfaces for strong interactions with molecular vibrations (pp. 798)
Keisuke Watanabe, Hemam Rachna Devi, David Hernandez-Pinilla, Masanobu Iwanaga, Tadaaki Nagao

NanoOptoCraft: plasmonic MEMS, nanoscale patterning, and optical low-loss film (pp. 800)
Kenzo Yamaguchi

Robust quasi-BIC modes in a four cuboid cluster metasurface (pp. 802)
Jose Algorri, V. Dmitriev, H. E. Hernandez-Figueroa, L. Rodríguez-Cobo, F. Dell'Olio, A. Cusano, J. M. López-Higuera, D. C. Zografopoulos

Optical properties of chiral plasmonic nanostructures coupled with nanocavity (pp. 804)
Tomoya Oshikiri

Metamaterial Technology and Its Application Prospects

High-Density Carbon Nanotube Forest Metamaterials for Advanced Photonic Applications (pp. 807)
Hiroshi Furuta, Hinako Kimura, Hokuto Sakoda, Riko Matsuzaki, Saiful Islam, Kazuya Kobiro

Effective properties of self-assembled plasmonic clusters with spatial dispersion (pp. 809)
Ranjeet Dwivedi, Ashod Aradian, Kevin Vynck, Alexandre Baron

Optical properties and luminescence control of Ag/TiO2 stacked metasurfaces using out-of-plane quadrupole resonance (pp. 811)

TienYang Lo, S. Murai, K. Tanaka

Beyond Singularities: New Frontiers in Centrosymmetric Gain-Enhanced MetalNanoparticles and Their Applications (pp. 813)
Karen Caicedo, Milena Mora, Nicole Recalde, Maria Antonia Iatí, Rosalba Saija, Onofrio M. Maragò, Ashod Aradian, Melissa Infusino, Alessandro Veltri

Femtosecond pulse shaping with semiconductor Huygens' metasurfaces (pp. 815)
Katsuya Tanaka, D. Arslan, M. Weissflog, N. Geib, K. Gerold, A. Szeghalmi, M. Ziegler, F. Eilenberger, T. Pertsch, I. Staude

Bottom-up fabricated metasurfaces with correlated disorder for the light management in solar cells (pp. 817)
Prerak Dhawan, Maria Gaudig, Peter Piechulla, Alexander Sprafke, Ralf Wehrspohn, Carsten Rockstuhl

Creating Meta-Atoms Based on Gold Nanoparticle Assemblies on Polymer Microspheres (pp. 819)
Hiroshi Yabu

Aggregation of Core/Shell Quantum Rods in Composite Polymer Film for Polarization Conversion (pp. 821)
Yutaka Okazaki, Shusaku Kubota, Kan Hachiya, Takashi Sagawa

Development of Colloidal Silicon Nanoparticles and Composites for Photonic Applications (pp. 823)
Hiroshi Sugimoto, Minoru Fujii

Full-wafer fabrication of all-inorganic metalenses, waveguides and diffractive optics via direct nanoimprint lithography (pp. 825)
Dae Eon Jung, Vicent Einck, Alex Dawicki, Lucas Verrastro, Amir Arbabi, James Watkins

Transient dissipative structures in surface plasmon polaritons propagation (pp. 827)
Stanislav Derevyanko, Marat Spector

Optical to Terahertz Frequency Conversion using near Zero-index Nonlinear Hybrid Waveguides (pp. 829)
Chong Sheng, X. F. Ma, N. Y. Wang, R. Z. Cao, C. Sheng, S. N. Zhu, H. Liu

Low-frequency sound insulation and ventilation with spiral metastructure (pp. 831)
Shanjun Liang, Wenjian Kuang

Plasmonic Enhancement of the Performance of Integrated Phase-Change Memory and Computing Devices (pp. 833)
Junchao Song, Nikolaos Farmakidis, Ivonne Bente, Emanuele Gemo, June Sang Lee, Xuan Li, Samarth Aggarwal, Wen Zhou, Nathan Youngblood, Johannes Feldmann, Wolfram Pernice, Harish Bhaskaran, David Wright

Optical induced temperature change for ionic thermoelectric applications (pp. 835)
Dan Zhao, M. N. Liao, Magnus Jonsson

Picosecond dynamics of electromagnetically-induced transparency in infrared metamaterials (pp. 837)
The Linh Pham, Kacper Pilarczyk, Nils Deßmann, Fei Han, Joris Van de Vondel, Niels Verellen, Thanh Tung Nguyen, Ewald Janssens

Automated Design Flow for Hybrid Metalens System with Manufacturing Awareness (pp. 839)
Maryvonne Chalony, Yijun Ding, Larry Melvin, Bernd Kuechler, Bryan Stone, Evan Heller, Mayank Bahl, Rob Scarmozzino, Rob Scarmozzino, Chenglin Xu

The fabrication and application of 3D metamaterials (pp. 841)
Changzhi Gu, Yang Guo

Low-power Laser Coloration by Oxidation and Deformation of Self-assembled AL-PS Metamaterial (pp. 843)
Maxim Elizarov, Ning Li, Fei Xiang, Andrea Fratalocchi

Binocular Meta-lens for Computer Vision (pp. 845)
Xiaoyuan Liu, Mu Ku Chen, Takuo Tanaka, Din Ping Tsai

Plasmonic Nanoplatforms - A New Generation of Efficient Heat Generators for Thermoplasmonic Detection (pp. 847)
Andreea Campu, Simion Astilean, Monica Focsan

Hyperband Multi-functional Metasurface based on Double-walled Carbon Nanotubes (pp. 848)
Jin Zhang, Peng Liu, Zhipei Sun

Conducting polymer-cellulose devices for tunable infrared and THz optics (pp. 850)
Chaoyang Kuang, Shangzhi Chen, Magnus Jonsson

Boosting the tunability of Mid-infrared Metasurfaces based on graphene field-effect transistors (pp. 852)
Fei Han, The Linh Pham, Kacper Pilarczyk, Nguyen Thanh Tung, Dinh Hai Le, Guy A. E. Vandenbosch, Joris van de Vondel, Niels Verellen, Xuezhi Zheng, Ewald Janssens

Towards Plexcitonics: Direct Plasmonic Nanostructures Lithography on 2D Transition Metal Dichalcogenides (pp. 854)
Ermes Peci, Lorenzo Ramò, Michele Magnozzi, Emma Spotorno, Valentina Venturino, Maria Sygletou, Maria Caterina Giordano, Giorgio Zambito, Francesca Telesio, Maurizio Canepa, Francesco Bisio

Laser-based 3D printing of structures to control electromagnetic radiation: Bridging 2D, 2.5D, and 3D (pp. 856)
Gordon Zyla, Odysseas Tsilipakos, Dimitrios Zografopoulos, Savvas Papamakarios, Maria Farsari

Slime mold algorithm for topology optimization of photonics structure (pp. 858)
Kofi Edee, G. Granet, P. Bonnet

Tailoring gold plasmonic metasurfaces for efficient harmonic generation (pp. 860)
Shroddha Mukhopadhyay, Crina Maria Cojocaru, Maria Antonietta Vincenti, Kent Hallman, Agustin Mihi, Michael Scalora, Jose Trull

Synthesis and plasmonic properties of Fe3O4-Au-Pd hybrid nanoparticles (pp. 862)
Yukie Yokota, Mao Takeda

From synthesis to assembly: a Silicon based metasurface fabrication (pp. 864)
Juan Xin, Julien Proust, Jerome Plain

All-Garnet Magnetooptical Microcavity (pp. 866)
Taichi Goto

Microscale concave interfaces: a new reflective colorimetric platform (pp. 868)
Jacob Rada, Chi Zhou, Qiaoqiang Gan

Periodically nanostructured anisotropic coatings for spatial filtering and polarization control (pp. 870)
Julianija Nikitina, Matas Plukys, Darius Gailevičius, Kestutis Staliunas, Lina Grineviciute

Engineering spin-orbit coupling of light in weak and strong light-matter coupling regimes for topological photonics (pp. 872)
Jacek Szczytko, M. Muszyński, P. Oliwa, P. Kapuściński, P. Kokhanchik, M. Kędziora, K. Łempicka-Mirek, E. Oton, R. Mazur, P. Morawiak, W. Piecek, P. Kula, D. Bobylev, D. Solnyshkov, G. Malpuech, W. Bardyszewski, B. Piętka

Energy- and Time-resolved NIR to Visible Upconversion Luminescence from SingleNaYF4:Yb3+,Tm3+ Nanoparticles on Self-assembled Chiral Metasurfaces (pp. 874)
A. Ahmed, K. Y. Chiok, S. May, A. Baride, R. B. Anderson, S. Zhou, Steve Smith

Advanced Computational Electromagnetics for the Analysis and Design of Nanophotonic Devices

Refined Quantum Hydrodynamic Model for Deep Nanoscale Plasmonics with Noble Metal and Dielectrics (pp. 876)
Xue-Wen Chen

Innovative Approach: Inverse Design of 2D Slanted Gratings through the Fusion of Polynomial Modal Method, Neural Networks and Slime mold algorithm and/or Harris Hawkes optimizer, with Application in Augmented Reality (pp. 878)
Kofi Edee, G. Granet

Nanophotonic chirality transfer to dielectric Mie resonators (pp. 880)
Ershad Mohammadi, TV Raziman, Alberto G. Curto

Consensus ADMM for Photonic Design (pp. 882)
Hyeonhee Kim, Myungjoon Kim, Zeyu Kuang, Owen D. Miller, Jonghwa Shin

Optimizing Metasurface Design for Interference Lithography: Achieving Two-Dimensional Bravais Lattices with Arbitrary Motifs (pp. 884)
Myungjoon Kim, Nayoung Kim, Jonghwa Shin

Plasmonic semiconductor waveguides with tunable nonlinear optical response (pp. 886)
Gonzalo Alvarez-Perez, Huatian Hu, Cristian Ciraci

Adaptive Meshing Using A Posteriori Error Estimation (pp. 888)
Albin J. Svärdsby, Philippe Tassin

Hardware-Accelerated FDTD Simulation (pp. 889)
Zongfu Yu, Tyler Hughes, Shanhui Fan

Quasinormal mode expansion theory for mesoscale plasmonic nanoresonators with an analytical treatment of nonclassical electromagnetic boundary condition (pp. 890)
Haitao Liu, Can Tao, Ying Zhong

Effective Medium Theory for Photonic Parallel Universes (pp. 892)
Yun Lai

Space-time photonic metasurfaces (pp. 893)
Stefano Vezzoli, Anthony Harwood, Riccardo Sapienza

Topological transition from bound states in the continuum of plasmonic lattices (pp. 894)
Grazia Salerno, Rebecca Heilmann, Kristian Arjas, Kerttu Aronen, Jani-Petri Martikainen, Päivi Törmä

Singularity and topology in structured near fields (pp. 896)
Shubo Wang, Tong Fu, Shiqi Jia, Jie Peng, Ruo-Yang Zhang

Electron-tunneling-induced thermoelectric effects (pp. 898)
Mauricio Gómez Viloria, Riccardo Messina, Philippe Ben-Abdallah

High-Accuracy DDA (pp. 899)
Owen Miller

Thermal radiation at the nanoscale, electroluminescence, single and dual radiative heat engines (pp. 900)
J. Legendre, T. Châtelet, M. Thomas, O. Merchiers, P-Olivier Chapuis

Quantum Effects in Plasmonic/Nonlinear Meta-Surfaces: Development and Applications of Maxwell-TDDFT Method (pp. 902)
Takashi Takeuchi, Mitsuharu Uemoto, Kazuhiro Yabana

Computing free-electrons Kerr nonlinearities in semiconductor plasmonic systems (pp. 904)
Cristian Ciraci, Huatian Hu

Is photonic band topology rare or common? (pp. 905)
Thomas Christensen

THz Plasmonic Detectors Based on Field-Effect Transistors with Metallic Diffraction Grating Metasurfaces (pp. 906)
Akira Satou, T. Otsuji

Advancing Nano- and Quantum Photonics with Machine Learning (pp. 908)
B. Wilson, Y. Chen, V. Shalaev, A. Kildishev, Alexandra Boltasseva

Fast Multi-channel Full-wave Solver and Inverse Design with Augmented Partial Factorization (pp. 909)
Chia Wei Hsu

Physics-based design of dielectric particle accelerators (pp. 911)

Andrea Locatelli, Roberta Palmeri, Nunzio Salerno, Giorgio Mauro, Giuseppe Torrisi, Gino Sorbello, Davide Rocco

Quantifying Symmetry of Metasurfaces and Eigenmodes for Optimisation Design (pp. 913)
Matthew Parry, Andrey Sukhorukov, Dragomir Neshev

Efficient modelling and tailoring of nonlinear wavefront and enhanced third harmonic generation in dielectric metasurfaces (pp. 915)
Viktor Myroshnychenko

Modeling and Implementation of Asymmetric Angular Transmittance (pp. 917)
Mahmoud A. A. Abouelatta, Karim Achouri

Anamorphic meta-lenslet array for laser guide star wavefront sensing (pp. 919)
Josephine Munro, Sarah Dean, Neuton Li, Israel J. Vaughn, Andrew Kruse, Tony Travouillon, Dragomir Neshev, Robert Sharp, Andrey Sukhorukov

One-way excitation of normal incident light for a plasmonic grating coupler with trapezoidal dielectric gratings (pp. 921)
Jun Shibayama, Hinami Nakasaka, Kazuma Takeya

Machine-Learning Assisted Multi-User Frequency Selective Beam Steering with a Reconfigurable Intelligent Surface (pp. 923)
Alexander Wolff, Lukas Mueller, Steffen Klingel, Janis Krieger, Lars Franke, Ralf Stemler, Marco Rahm

Modelling and design of complex light matter interactions on the nanoscale (pp. 925)
Lora Ramunno

End-to-end Nanophotonic Inverse Design for Computational Imaging (pp. 926)
Zin Lin

On the different models of Graphene conductivity and its effects on Casimir forces and on radiative heat transfer in nanostructured systems (pp. 928)
Mauro Antezza

Low Dimensional Thermal Radiation (pp. 929)
Sebastian Volz

Duality Gaps in Photonic Inverse Design (pp. 931)
Sean Molesky

Existence of Friedrich-Wintgen bound states in the continuum in periodically perturbed slabs (pp. 932)
Amgad Abdrabou, Wangtao Lu, Ya Yan Lu

Design for quality: multifunctional flat optics using metasurfaces (pp. 934)
Hanyu Zheng, Fan Yang, Hung-I Lin, Yunxi Dong, Hualiang Zhang, Juejun Hu, Tian Gu

Second harmonic generation of optical beams with orbital angular momentum on dielectric films and metasurfaces (pp. 935)
Laure Coudrat, Domenico De Ceglia, Rana Tanos, Jean-Michel Gérard, Costantino De Angelis, Aloyse Degiron, Giuseppe Leo

Calculation of surface state spectra for topological photonic and acoustic crystals (pp. 936)
Y. X. Sha, Yi Yang

Modeling the Acousto-Plasmonic Coupling: Raman Energy Density Framework (pp. 938)
Nicolas Large, José Luis Montaño-Priede, A. Mlayah

Limits and opportunities for nonlinear nanophotonics (pp. 940)
Alejandro Rodriguez

Design and simulation of a metalens-based eye-tracking system (pp. 941)
Han-Hsiang (Michael) Cheng, Dan-Nha Huynh, Thibault Leportier, Jens Niegemann, Vlad Smagley, Erin Elliot, Allen Cheng

Chiro-optical and chiral-acoustic phenomena

TiO2 Nanoantenna Stickers for Fabricating Large-Area Twisted Metamaterials with Tunable Chiroptical Effects (pp. 946)
Jiayang He, Shunsuke Murai, Tienyang Lo, Katsuhisa Tanaka

Directional sources realized by toroidal dipoles (pp. 948)
Junho Jung, Yuqiong Cheng, Shubo Wang

Robust chiral optical force for small chiral molecules, inspired by a sea creature (pp. 949)
Robert P. Cameron, Duncan McArthur, Alison M. Yao

Acoustic Fullerene Metamaterials (pp. 950)
Danwei Liao, Jingyi Zhang, Shuochen Wang, Zhiwang Zhang, Alberto Cortijo, Maria A. H. Vozmediano, Francisco Guinea, Ying Cheng, Xiaojun Liu, Johan Christensen

Ultrafast topological phase switching of non-Hermitian photonic metasurfaces (pp. 951)
Sangha Lee, Donghak Oh, Junho Park, Soojeong Baek, Fabian Rotermund, Bumki Min

Directional manipulation of guided light by anisotropic chirality (pp. 952)
Yuqiong Cheng, Kayode Adedotun Oyesina, Bo Xue, Dangyuan Lei, Alex.M.H. Wong, Shubo Wang

Peculiar wave transports in elastic valley-chiral phononic crystal plates (pp. 953)
Weitao Yuan, Jinfeng Zhao

Chiral Plasmonic Structures as Acoustoplasmonic Transducers (pp. 954)
Beatriz Castillo López de Larrinzar, Chushuang Xiang, Edson R. Cardozo de Oliveira, N. Daniel Lanzillotti-Kimura, Antonio Garcia-Martin

Chiral phonon-originated nonreciprocal phenomena in magnets (pp. 955)
Yoichi Nii

Photonic and phononic characterization of twisted acoustoplasmonic nanostructures (pp. 956)
Beatriz Castillo López de Larrinzar, Jorge M. García Martínez, Chushuang Xiang, E. R. Cardozo de Oliveira, N. Daniel Lanzillotti Kimura, Antonio García Martín

How can planar become chiral? Maximum-chiral optics with flat metasurfaces (pp. 958)
Maxim Gorkunov, Alexander Antonov, Yuri Kivshar

Circularly-Polarized Light for Probing and Controlling Spins and Magnetization in Atomically-Thin Materials (pp. 960)
Marcos Guimaraes

Far-field and near-field chirality in plasmonic metamolecules (pp. 962)
T. Aoudjit, F. Lamaze, J. Béal, A. Hmima, W. d'Orsonnens, T. Maurer, J. Plain, J. Proust, Davy Gerard

1D and 2D Topological solitons in nanoelectromechanical resonator arrays (pp. 963)
Hiroshi Yamaguchi, Daiki Hatanaka, Motoki Asano, Samer Houri

Valley pseudospin polarized transports of ultrahigh frequency phonons in topological ring-waveguide coupled systems (pp. 964)
Daiki Hatanaka, Hiroaki Takeshita, Motoki Kataoka, Hajime Okamoto, Kenji Tsuruta, Hiroshi Yamaguchi

Non-reciprocal coupling between chiral phonons and magnons in ferromagnetic-semiconductor hybrid structures (pp. 965)
Alberto Hernandez-Mínguez, Ferran Macià, Joan Manel Hernàndez, Jens Herfort, Paulo Ventura Santos

Diffraction of OAM beams assisted by Bloch Surface Waves (pp. 967)
Niccolò Marcucci, Zongyuan Tang, Tianlong Guo, Matthieu Roussey, Yanjun Liu, Emiliano Descrovi

Angular momentum addition of flexural wave using transformation approach (pp. 969)
Pengfei Zhao, Xiaofan Wang, Liyou Luo, Jensen Li, Huanyang Chen

Topological boundary modes in a hexagonal flexural wave machine (pp. 971)
Motonobu Tomoda, Hayato Takeda, Ryoya Minami, Osamu Matsuda, Oliver B. Wright

Some three-dimensional acoustic flat bands (pp. 973)
Baile Zhang

Jet formation induced by sub-nanosecond optical vortex optical pulses (pp. 975)
Keisaku Yamane, Ryota Tamemoto, Kotaro Sato, Yasunori Toda, Takashige Omatsu, Ryuji Morita

Control of Circular Polarization Using Nonlinear Optical Effect in Dielectric Membrane Nanostructures (pp. 977)
Kuniaki Konishi

Three-dimensional Design of Acoustic/Elastic Waveguides based on Higher Order Topological Modes (pp. 978)
Kenji Tsuruta, Yusuke Hata, MD Anzan Uz Zaman

Fourier-based band structure computation for quasicrystalline media (pp. 979)
Marc Martí-Sabaté, Matheus I. N. Rosa, Sebastien Guenneau, Daniel Torrent

Acoustic Spin and Phonon Spin (pp. 981)
Jie Ren

Towards chiral phononic modes in silicon (pp. 983)
Clivia M. Sotomayor Torres, O. Florez

Tunable spiraling metamaterial as a platform for controlling sound waves, electromagnetic waves, and enhancing optomechanical coupling (pp. 984)
Osama Bilal

Acoustic Metasurface in a Nano-Opto-Electro-Mechanical Device for High Optomechanical Coupling Rate (pp. 986)
Abdellatif Gueddida, Yan Pennec, Laurent Carpentier, Gaëtan Lévêque, Bahram Djafari-Rouhani

Intrinsic Three-dimensional Spin Angular Momentum of Gigahertz Evanescent Acoustic Phonons (pp. 988)
Yi He, Hoon Sohn, Osamu Matsuda, Zhongqing Su

Quantum Metasurfaces

Quasi-BIC Mode Lasing in a Quadrumer Plasmonic Lattice (pp. 991)
Rebecca Heilmann, Grazia Salerno, Javier Cuerda, Tommi K Hakala, Päivi Törmä

Stable-to-unstable transition in quantum friction (pp. 993)
Daigo Oue, John Pendry, Mario Silveirinha

On-Chip Metaphotonics Empowered Single-Photon Emission (pp. 995)
Yinhui Kan, Xujing Liu, Sergey I. Bozhevolnyi

Dual-Band Control of Bound States in the Continuum with Pairwise Positioning of Singularities in Metasurfaces (pp. 997)
Chloe Doiron

Tailored generation of biphoton polarization Bell state from an InGaP metasurface (pp. 999)
Jinyong Ma, Tongmiao Fan, Tuomas Haggren, Jihua Zhang, Saniya Shinde, Frank Setzpfandt, Hark Hoe Tan, Chennupati Jagadish, Dragomir N. Neshev, Andrey A. Sukhorukov

Spontaneous Parametric Downconversion Facilitated by Intrinsic Nonlinear Response of Plasmonic Metal Nanoparticles (pp. 1001)
Andrei Piryatinski, Syed Shah, Michael Clark, Joseph Zyss, Maxim Sukharev

Quantum light-matter interfaces with arrays of trapped atoms (pp. 1003)
Efi Shahmoon

Lattice Resonances in Periodic Arrays with Multiparticle Unit Cells (pp. 1005)
Alejandro Manjavacas

Controlling quantum states and quantum noise with nonlinear photonics (pp. 1006)
Nicholas Rivera

Recent progress on photon pair generation in semiconductor metasurfaces (pp. 1007)
Tomas Santiago-Cruz, Jiho Noh, Vitaliy Sultanov, Sylvain D. Gennaro, Chloe F. Doiron, Hyunseung Jung, Maria V. Chekhova, Igal Brener

Applications of Spacetime Quantum Metasurfaces to Simulating Hawking Radiation (pp. 1009)
Patrick Brown, Wilton J. M. Kort-Kamp, Gerald Cleaver, Diego Dalvit

Space-Time Quantum Metasurfaces (pp. 1011)
Diego Alejandro Roberto Dalvit

Analog of Quantum Bit Empowered by A Novel Electromagnetic Metasurface (pp. 1012)
Long Chen, J. W. You, Z. Gu, Q. Ma, Tie Jun Cui

Integrated metasurfaces/metamaterials on photonic platform

Observation of momentum-gap topology of light (pp. 1017)
Yihao Yang

Approaching unity quantum coupling of free electrons and photons using nanophotonic structures (pp. 1018)
Yuval Adiv

Time Edge States Protected by Chiral Symmetry (pp. 1020)
Hao Hu

Thin film lithium niobate double notch filter (pp. 1021)
Songyan Hou

The Proposal of the Substrate-inverted Multi-Material Technology (SuMMIT) for Scalable Heterogeneously-Integrated Photonics (pp. 1023)
Jia Xu Brian Sia

Extending the bandwidth of nonlinear optics (pp. 1025)
Yu Luo, Chunyu Huang, Hui Liu

Spoof Plasmonic Skyrmions and Sensing Application (pp. 1027)
Liangliang Liu

Self-focusing beam in hyperbolic media (pp. 1028)
Yueqian Zhang, Chongwu Wang, Qian Wang, Qi Jie Wang, Yu Luo

Meta-optics for imaging, microscopy and information processing

The Multi-angle Beam Bender with Transformation Materials (pp. 1031)
Wen-Xiu Dong, Yun-Yun Lai, Jin Hu

Computer-generated holography and its applications to metasurfaces (pp. 1033)
Kexuan Liu, Yunhui Gao, Jiachen Wu, Zehao He, Liangcai Cao

Super-Resolution Exciton Imaging of Nanodefects in 2D Semiconductors (pp. 1034)
Jia-Tai Huang, Benfeng Bai

Manipulation of Electromagnetic field based on Plasmonic-ENZ Nonlinear Metasurface (pp. 1036)
Junhong Deng, Guixin Li

Metasurface array for single-shot spectroscopic ellipsometry (pp. 1037)
Shun Wen, Xinyuan Xue, Yuanmu Yang

Metasurface-enabled Wavefront Engineering for Advanced Imaging Technologies: 3D Sensing and Biomedical Imaging (pp. 1039)
Inki Kim

Monocular polarimetric metalens for ultracompact snapshot stereo-imaging (pp. 1040)
Shuming Wang

Towards thinner imaging systems with Huygens' spaceplates (pp. 1041)
Francisco J. Diaz-Fernandez, Luis M. Manez-Espina, Ana Diaz-Rubio, Viktar Asadchy

Varifocal Meta-lenses for Bio-imaging and 6G Communication (pp. 1043)
Mu Ku Chen, Jing Cheng Zhang, Xiaoyuan Liu, Yin Zhou, Jialuo Cheng, Takuo Tanaka, Din Ping Tsai

Subnanometer-matter's Farfield Optical Fingerprints and Metrology Applications (pp. 1045)
Xue-Wen Chen

Photothermal inspection of optoelectronic chips (pp. 1047)
Xiangping Li

Optical information processing on thin film lithium niobate (pp. 1048)
Mengjie Yu

Quantum metamaterials for artificial intelligence

Analyzing qubit arrays via a multiresolution approach (pp. 1050)
Mandana Bidarvand, Artur Sowa

Effects of Strong Capacitive Coupling Between Meta-Atoms in Three-Dimensional rf SQUID Superconducting Metamaterials (pp. 1052)
Jingnan Cai, Yilin Li, Steven Anlage

Point defect-based material solutions for quantum sensing and quantum reservoir computing (pp. 1053)
Viktor Ivady

An infinite array of boson sites - a rigorous approach (pp. 1055)
Artur Sowa, Jonas Fransson

Bloch transistor for quantum electronics (pp. 1056)
Ilya Antonov, Rais Shaikhaidarov, Kyung Ho Kim, Dmitry Golubev, Vladimir Antonov, Oleg Astafiev

Simultaneous AC bias and gate drive to control a SINIS turnstile (pp. 1058)
M. MarínSuárez, Yu. A. Pashkin, J. T. Peltonen, J. P. Pekola

Recent Advances in Metamaterials and their Applications

Optoelectronic metasurface based on photodiodes (pp. 1061)
Ya Lun Sun

Smart Electromagnetic Manipulation Based on Programmable Metasurfaces with Space Sensing (pp. 1063)
Yuanke Liu

Photonic topological states with auxiliary orbital degree of freedom in Kekulé modulation surface-wave metamaterials (pp. 1065)
Liyun Tao, Yahong Liu, Xin Zhou, Lianlian Du, Meize Li, Kun Song, Zhenfei Li, Xiaopeng Zhao

Particle Image Velocimetry Utilizing Binocular Polarization-independent Meta-lens (pp. 1067)
Xiaoyuan Liu, Zhou Zhao, Shengming Xu, Jingcheng Zhang, Yin Zhou, Yulun He, Takeshi Yamaguchi, Hua Ouyang, Takuo Tanaka, Mu Ku Chen, Shengxian Shi, Fei Qi, Din Ping Tsai

Reflective Moiré Metasurfaces: A Paradigm of Innovation and Challenge (pp. 1069)

Shuo Liu, Lei Zhang, Xiaoqing Chen

Metasurface-enabled light-to-microwave hybrid wireless communications (pp. 1071)
Xin Ge Zhang, Ya Lun Sun, Wei Xiang Jiang

Meta-lens Digital Image Correlation (pp. 1072)
Yu Ji, Zhou Zhao, Mu Ku Chen, Sheng Xian Shi, Din-Ping Tsai

Combinatorial Optimization of Electromagnetic Devices using metamaterial Function Units (pp. 1074)
Guoyan Dong

Phase Change Materials-based Metasurface Discs (pp. 1076)
Shuo Du, P. X. Liang, S. Hu, C. S. Li, C. Z. Gu, X. C. Chen

Chiral meta-coder for target camouflage and identification (pp. 1078)
Zhenfei Li, Weiren Zhu

Versatile and Flexible Membrane Metasurfaces for Optimal Optoelectronic Device Efficiency (pp. 1080)
Shaojun Wang

Plasmonic nanoparticle clusters with tiny gaps fabricated with self-assembly superlattices (pp. 1082)
Shao-Ding Liu, Lan-Qi Lian, Qiang Zhang

Optomechanical metasurfaces based on kirigami technology (pp. 1083)
Nanzhong Deng, Ashish Pandey, Gregory Roberts, Haogang Cai

Multiband and broadband acoustic topological metamaterial (pp. 1085)
Changlin Ding, Y. Sun, X. P. Zhao

The Design, Control and Optimization of Cavity-based Metamaterials for Miniature Spectrometer Application (pp. 1087)
Ruonan Ji, Qingquan Liu, Shaowei Wang

Overlapped Bandgap and Ultrabroadband Transmission in a Valley Photonic Insulator Based on Dendritic Structure (pp. 1089)
Yahong Liu, Meize Li, Peng Li, Liyun Tao, Lianlian Du

Perovskite Photovoltaics: Light-Matter Interaction

Subcell Characterization Platforms for Emerging Tandems (pp. 1092)
Jin Young Kim

Nano-photonics as a route to enhance the open circuit voltage from perovskite and organic photovoltaic cells (pp. 1094)
Jordi Martorell

Interface study for Sn-Pb mixed perovskite solar cells (pp. 1095)
Dong Hoe Kim

Crystal Growth and Composition Engineering for Reproducible Fabrication of High-Performance Perovskite Solar Cells (pp. 1096)
Jin-Wook Lee

Vacuum-Processed Additive: A Novel Approach for Controlling Growth of Perovskite Crystals in All Vacuum Processed Perovskite Solar Cells (pp. 1097)
K. Lee, Kyungkon Kim

Performance-limiting processes in lead-free Cs2AgBiBr6 double perovskite solar cells (pp. 1099)
Wolfgang Tress

Functions of Porous Carbon in Multi-Porous-Layered-Electrode Perovskite Solar Cells (MPLE-PSCs) (pp. 1101)
Seigo Ito

Halide Interfacial Layers for Perovskite Solar Cells (pp. 1103)
Jun Hong Noh

Surface Chemistry for Efficient Sn- and Pb-based Perovskite Photovoltaics (pp. 1104)
Atsushi Wakamiya, Minh Anh Truong, Noboru Ohashi, Tomoya Nakamura, Chien-Yu Chen, Richard Murdey

New Class of Semiconducting Organic-Inorganic Metal Halides for Photovoltaic Devices (pp. 1106)
Hyunjung Shin

Orientation control of perovskites using asymmetric amines (pp. 1107)
Yuko Takeoka, Hirona Kobayashi, Daizo Hishida, Masahiro Yoshizawa-Fujita, Masahiro Rikukawa

Improving efficiency and stability of hybrid perovskite devices (pp. 1109)
Yeng Ming Lam, Haixia Rao, Tze Chian Sum, Senyun Ye

Tailoring Charge Transport in Mixed-Valence Coordination Polymers for Emerging Molecular Devices (pp. 1110)
Marina Freitag

Plasmonics: Fundamentals and Applications

Plasmon-based chiroptical sensing (pp. 1114)
S. Liu, Rong-Yao Wang

Multifunctional Dynamic MEMS-based Optical Metasurfaces (pp. 1116)
Chao Meng, P. C. V. Thrane, Y. D. Deng, F. Ding, S. I. Bozhevonyi

Chiroptics of hybrid nanostructures : Strong coupling effect and interference effect (pp. 1118)
Wei Zhang

On-chip electrical detection of plasmon in the top-down fabricated plasmonic waveguides on SOI substrate (pp. 1120)
Xiangqian Li, Weikang Liu, Huijie Wang, Li Chen, Zhiqiang Guan, Hongxing Xu

Dynamic plasmonics with structured alkali metals (pp. 1122)
Jie Liang, Yan Jin, Jia Zhu, Lin Zhou

Nanometer-Scale Spatial and Spectral Mapping of Exciton Polaritons in Structured Plasmonic Cavities (pp. 1124)
David Masiello

Photoluminescence modulation of 2D semiconductors by individual plasmonic metal nanocrystals (pp. 1125)
Lei Shao

Plasmonic-assisted 2D hybrid broadband photodetectors (pp. 1127)
Ilya Goykhman

Tip-enhanced cavity-spectroscopy for quantum light-matter interactions at the nanoscale (pp. 1128)
Kyoung-Duck Park

White-nanolight-source through plasmon nanofocusing for nanoimaging, nanosensing, and nano-optical switching (pp. 1130)
Takayuki Umakoshi, Prabhat Verma

Nanocavity-dependent photon output from WSe2 single quantum emitter with broken valley symmetry (pp. 1132)
Xiulai Xu

Subnanometer Resolved Single-Molecule Optical Spectroscopy (pp. 1133)
Zhen-Chao Dong

Strong Coupling between Surface Plasmons and Excitons (pp. 1135)
Hong Wei

Chiral Response of plasmonic metasurface (pp. 1136)

Jinwei Shi

Statistical quantitative SERS beyond the single-molecule level and its physical foundations (pp. 1137)
Zhipeng Li, Longkun Yang, Hao Zhang, Hongxing Xu

Recent Developments in Optical Nanoantennas for Enhanced Light Matter Interaction

Dynamics of Thermal Asymmetry: Interfacial Thermal Conductance in Plasmonic Janus Nanostructures (pp. 1140)
Javier Gonzalez-Colsa, Fernando Bresme, Pablo Albella

Enhancement and Directional Control of Light Emission from Monolayer MoS2 by Silicon Nanosphere Antennas (pp. 1142)
Keisuke Ozawa, Daisuke Shima, Søren Raza, Keisuke Imaeda, Kosei Ueno, Hiroshi Sugimoto, Minoru Fujii

Optical Heating Triggered by Multipolar Mie Resonance of Silicon Nanoparticles (pp. 1144)
Mojtaba Karimi Habil, Kana Kondo, Hiroshi Sugimoto, Minoru Fujii

Plasmonic lightning-rod effect (pp. 1146)
Vlastimil Krapek, Rostislav Repa, Michael Foltyn, Tomas Sikola, Michal Horak

Controlled radiation modes of second harmonic generation from plasmonic nanoantennas (pp. 1148)
Yoshito Tanaka

Beam Engineering for Enhanced Light-Matter Interactions in Optical Nanostructures (pp. 1150)
Uttam Manna, Mahua Biswas

Spin-valley nanophotonics with atomically thin semiconductors (pp. 1152)
Alberto G. Curto

Multiplexed single-molecule plasmon sensing by spectral decomposition (pp. 1154)
Vincenzo Lamberti, Sjoerd Nooteboom, Tim Schellekens, Peter Zijlstra

Mie resonances in silicon nanospheres probed by pump-probe cathodoluminescence spectroscopy (pp. 1155)
Saskia Fiedler, Evelijn Akerboom, Patrick Spaeth, Hiroshi Sugimoto, Minoru Fujii, Albert Polman

Optical Metafluid Made from Silicon Nano-spheres (pp. 1157)
Minoru Fujii, Hiroshi Sugimoto

Solving Maxwell Equations from a Single Polarimetry Measurement (pp. 1159)
Jorge Olmos-Trigo

Probing the quantum tunneling in plasmonic gaps with magnetic plasmon resonances (pp. 1161)
Haisheng Luo, Ruizhao Yao, Helene Giesler, Sebastian Schlücker, Sheng Lan, Guangcan Li

Topology, Geometry, and Quantumness of Textured Light

Nonclassical states of light after high-harmonic generation in semiconductors:A Bloch-based perspective (pp. 1164)
Javier Rivera-Dean, Philipp Stammer, Andrew Maxwell, Th. Lamprou, Andrés Ordóñez, Emilio Pisanty, Paraskevas Tzallas, Maciej Lewenstein, Marcelo Ciappina

Lie Group Theory and Topology of Structured Light (pp. 1166)
Shinichi Saito

Selective Photoexcitation of Finite Momentum Excitons in 2D Materials by Using Structured Lights (pp. 1168)
Shun-Jen Cheng, Guan-Hao Peng, Ping-Yuan Lo, Wei-Hua Li, Oscar J. G. Sanchez, Jhen-Dong Lin, Kristan Bryan Simbulan, Ting-Hua Lu, Yann-Wen Lan

Propagation-Independent Polarization Features Near Phase Singularities of Electromagnetic Fields (pp. 1170)
Andrei Afanasev

Optical skyrmions (pp. 1172)

Jörg Götte, Zhujun Ye, Amy McWilliam, Fiona Speirits, Claire Cisowski, Sonja Franke-Arnold, Stephen Barnett

Generation and application of structured attosecond light pulses with controlled topology (pp. 1174)
Carlos Hernández-García

Interaction of structured light with a trapped ion (pp. 1176)
Anton A. Peshkov, R. Lange, Y. M. Bidasyuk, R. P. Schmidt, E. Jordan, M. Kromrey, K. K. Mehta, T. E. Mehlstäubler, N. Huntemann, E. Peik, A. Surzhykov

Non-Hermitian Photonics: Topological, Disordered and Quantum systems

Electrical tuning of exceptional points in microwave plasmonic structures (pp. 1179)
Hoon Yeub Jeong

Spontaneous disentanglement and thermalisation (pp. 1181)
Eyal Buks

Generation of orbital angular momentum by optical non-Hermitian skin effect in mirror-time symmetric media (pp. 1183)
Issei Takeda, Taiki Yoda, Yuto Moritake, Kenta Takata, Masaya Notomi

Non-Hermitian quasicrystals (pp. 1185)
Ananya Ghatak, I. Komis, Z. H. Musslimani, K. G. Makris

Extremely Narrow, Sharp-Peaked Resonances at the Edge of the Continuum (pp. 1187)
Ignas Lukosiunas, Lina Grineviciute, Julianija Nikitina, Darius Gailevicius, Kestutis Staliunas

Topological enhancement of non-normality in non-Hermitian systems (pp. 1189)
Masatoshi Sato

Bunching states and memory loss in noisy non-unitary dynamics of bosons (pp. 1190)
Ken Mochizuki, Ryusuke Hamazaki

Resonance energy transfer near PT-symmetric and non-Hermitian multilayer systems (pp. 1191)
Fiodar Marozka, Aliakasndr Arlouski, Alina Karabchevsky, Andrey Novitsky

Non-Bloch band theory of photonic crystals (pp. 1193)
Kazuki Yokomizo, Taiki Yoda, Yuto Ashida, Shuichi Murakami

Classifying topology in photonic crystal slabs despite their radiative environment (pp. 1195)
Stephan Wong, Terry A. Loring, Alexander Cerjan

Non-hermitian coupled modes controlled by the slot chirality in a parity-time symmetric waveguide pair (pp. 1197)
Alice De Corte, Bjorn Maes, Henri Benisty, Mondher Besbes

Dual symmetry classification of non-Hermitian systems and point-gap topology (pp. 1200)
Zhiyu Jiang, Geonhwi Hwang, Hideaki Obuse

Topological control of OAM in photonic lattices (pp. 1202)
Zhigang Chen

Sub-symmetry protected topological states (pp. 1203)
Ziteng Wang, Xiangdong Wang, Zhichan Hu, Domenico Bongiovanni, Dario Jukić, Liqin Tang, Daohong Song, Roberto Morandotti, Zhigang Chen, Hrvoje Buljan

Non-Hermitian Many-body Landau-Zener Systems: Quantum Dynamics and Correlations (pp. 1205)
Avadh Saxena, Rajesh K. Malla, Julia Cen, Wilton J. M. Kort-Kamp

2D Materials and Nanophotonics

Deep-Ultraviolet High-Quality-Factor Metasurfaces (pp. 1207)

Bo Ray Lee, Shang Jie Shen, Ting An Hsu, Mao Feng Jiang, Pei Ying Ho, Kuan-Heng Chen, Jia Hua Lee, Tzu-En Lin, Yao-Wei Huang, Ray-Hua Horng, Ming Lun Tseng

Electric Field driven Trion Drift in Suspended 2D Transition Metal Dichalcogenides (pp. 1209)

Woo Hun Choi, Seong Won Lee, Su-Hyun Gong

Tunable Transition Metal Dichalcogenide Based Metasurfaces in Liquid Crystal Medium (pp. 1211)

Anu Koviloor, Jayasri Dontabhaktuni

Photoluminescence and electroluminescence control of 2D semiconductors coupled to nanophotonic structures (pp. 1213)

Antti Moilanen, Takashi Taniguchi, Kenji Watanabe, Lukas Novotny

Strong nonlinear optical activities in the asymmetric 2D material with inversion-symmetry breaking (pp. 1214)

Song Zhu, Ruihuan Duan, Zheng Liu, Qi Jie Wang

Revealing the Local Band Structures of Sharp WS2/MoS2 Heterojunction and Graded WxMo1-xS2 Alloy by Near-Field Optical Imaging (pp. 1216)

Po-Wen Tang, He-Chun Chou, Shiue-Yuan Shiau, Xin-Quan Zhang, Yi-Hsien Lee, Chi Chen

Absorption Enhancement of Exciton of WS2 by Silicon Metasurface Based on Degenerate Critical Coupling (pp. 1218)

Dingwei Chen, Junichi Takahara

Hundred- to thousand-fold enhanced luminescence and the quantum nature manifested in continuous 2D materials coupled with metasurfaces (pp. 1220)

Masanobu Iwanaga, Xu Yang, Vasilios Karanikolas, Takashi Kuroda, Yoshiki Sakuma

Membrane Nanophotonic Platform for Enhanced Light-Matter Interaction of Transition Metal Dichalcogenide Monolayer (pp. 1222)

Ya-Lun Ho, Chee Fai Fong, Yen-Ju Wu, Kuniaki Konishi, Jui-Han Fu, Yuichiro Kato, Vincent Tung, Chun-Wei Chen

Nanoengineered Transition Metal Dichalcogenides Platform for Quantum Photonics: Generation and interference of single photons (pp. 1224)

A. Paralikis, C. Piccinini, P. Metuh, J. F. Neto, P. Wyborski, A. A. Madigawa, L. Vannucci, N. Gregersen, Battulga Munkhbat

Excitons in 2D TMDCs for metaoptics and photodetector applications (pp. 1226)

Zeng Wang, Jinghua Teng

Plasmonic photodetectors with superior optoelectronic performance demonstrated in MIR, NIR, visible and UV regions (pp. 1227)

Yu-Te Chu, Shyam Narayan Singh Yadav, Ching-Han Mao, Yu-Ping Kuang, Chang Hua Liu, Shangjr Gwo, Yu-Jung Lu, Pin-Chieh Wu, Ta-Jen Yen

Resonant exciton transfer in mixed-dimensional heterostructures for overcoming dimensional restrictions in optical processes (pp. 1229)

Nan Fang, Yih-Ren Chang, Daiki Yamashita, Shun Fujii, Mina Maruyama, Yanlin Gao, Chee Fai Fong, Keigo Otsuka, Kosuke Nagashio, Susumu Okada, Yuichiro K. Kato

Abundant optical properties of hexagonal boron nitride (pp. 1231)

Kenji Watanabe, Takashi Taniguchi

Plasmonic Strong Coupling and Tamm Plasmon Polaritons Photodetectors Enabled by 2D materials Hot Electrons (pp. 1233)

Kuo-Ping Chen

Unlocking the technology of wafer-scale layered atomic crystal growth on dielectric substrates for electronic and photonic applications (pp. 1235)

Xu Yang, Yoshiki Sakuma, Markus Pristovsek, Hiroshi Amano

Nano-optical imaging and spectroscopy

Dynamics and delocalized emissions of surface plasmon polaritons in one-dimensional plasmonic crystals (pp. 1238)

Izzah Machfuudzoh, Sotatsu Yanagimoto, Naoki Yamamoto, Takumi Sannomiya

Optical spin sorting in a plasmonic crystal waveguide (pp. 1240)
Kotaro Kihara, Midori Ikeuchi, Izzah Machfuudzoh, Takumi Sannomiya, H. Saito

Lifetime analysis of nitrogen-vacancy centers in nanodiamond particles using cathodoluminescence microscopy (pp. 1242)
Sotatsu Yanagimoto, Naoki Yamamoto, Akiba Keiichirou, Takumi Sannomiya

Theory for single molecule imaging with photo-induced force microscopy: A comparative study of phthalocyanine molecules (pp. 1244)
Mamoru Tamura, Hidemasa Yamane, Hajime Ishihara

Light-matter interaction probed by cathodoluminescence spectroscopy (pp. 1246)
Fatemeh Chahshouri, Masoud Taleb, Maximilian Black, Nahid Talebi

A plasmonic resonator array enhancing luminescence from a phosphor thin film studied by cathodoluminescence (pp. 1248)
Hikaru Saito, Yuichiro Kimura, Kentaro Matsuzaki, Kosuke Watanabe, Miki Inada, Takumi Sannomiya

Optical chiral fields and plasmon modes in gold nanostructures studied by apertured near-field spectroscopic imaging (pp. 1250)
Kohei Imura

New insights into optical property characterization of 2D semiconductor materials through time-correlated photon/electron spectroscopies (pp. 1252)
Florian Castioni, Yves Auad, Nadezda Varkentina, Alissa Freilinger, Steffi Woo, Noémie Bonnet, Jean-Denis Blazit, Xiaoyan Li, Marcel Tencé, Kenji Watanabe, Takashi Taniguchi, Odile Stéphan, Mathieu Kociak, Luiz Tizei

Femtosecond time-resolved microscopy for spatio-temporal characterization of structured surface plasmon polariton wave packets (pp. 1254)
Atsushi Kubo

Photon-STM study of exciton creation and annihilation processes in a single molecule (pp. 1256)
Miyabi Imai-Imada

Single-molecule photonics with scanning tunneling microscopy: nanospectroscopy and beyond (pp. 1258)
Hiroshi Imada

Meta and plasmonic materials for advanced biosensing and bioimaging

Deep subwavelength titanium nitride grating structures for mid-infrared vibrational absorption sensing (pp. 1261)
Leonid Beliaev, Evgeniy Shkondin, Andrei Lavrinenko, Osamu Takayama

Embryonic stem cell sensing with terahertz plasmonic exceptional points (pp. 1263)
Yang Guo, L. Y. Hu, C. Luo, W. Y. Chang, C. Z. Gu

Exceptional point sensing in planar terahertz metasurface (pp. 1265)
Bo Wang, Leyong Hu, Junjie Li

Topologically dark metamaterials for optical biosensing (pp. 1267)
Gleb Tselikov, Georgy Ermolaev, Aleksey Arsenin, Andrei Kabashin, Valentyn Volkov

Plasmon-enhanced fluorescence immunosensor using polymer-coated silver nanoparticles (pp. 1269)
Nahoko Okimi, Setsuko Yano, Yoshie Komatsu, Toshifumi Nanjyo, Mitsuhiro Uesugi, Ryo Kato, Takuo Tanaka, Fumihisa Kitawaki, Taka-aki Yano

Orthogonal chemical toolbox for antifouling biointerface on gold nanoparticle arrays serving in plasmonic biosensing applications (pp. 1271)
D. Cattozzo Mor, A. B. Plšek, V. T. Vu, G. Aktug, Z. Hubička, Chun-Jen Huang, Jackub Dostalek

Utilizing Flexible Polymer Linkers in a Continuous Monitoring Plasmonic Biosensor for Detecting Low Molecular Weight Analytes (pp. 1273)
Gizem Aktug, N. Asai, V. Van-Truc, C-J Huang, C. Monteiro da Santa, S. Park, K. Sergelen, Jackub Dostalek

Understanding on Light-matter Interaction in Chiral Plasmonics (pp. 1275)
Jeong Hyun Han, Ryeong Myeong Kim, Ki Tae Nam

Spectrometer-free colorimetric plasmonic biosensor for detection of food allergens (pp. 1276)
Daiki Hirabayashi, Kotaro Kajikawa, Mana Toma

High-speed near-field optical microscopy: super-resolution plasmonic imaging for biological studies (pp. 1277)
Takayuki Umakoshi

Recent advances in metasurface fluorescence biosensors for diverse targets (pp. 1279)
Masanobu Iwanaga

Polymeric Grating Prism-based Dual-mode Miniature Surface Plasmon Resonance Sensor (pp. 1281)
Akira Baba, Wisansaya Jaikeandee, Chutiparn Lertvachirapaiboon, Kazunari Shinbo, Keizo Kato, Sanong Ekgasit

Plasmonic biosensor platforms for digital single molecule assay readout (pp. 1282)
Katharina Schmidt, Naoto Asai, Gizem Aktug, Dario Cattozzo Mor, Prasanth Asokan, Stefan Fossati, Yevhenii Morozov, Andreas Weinhaeusel, Tomas Riedel, Andres de los Santos Pereira, Jakub Dostalek

Plasmonic Immunosensor Platform Composed of a Capture Interface Formed by Photochemical Reaction (pp. 1284)
Keiko Tawa

Recent Trends in Metaoptical and Plasmonic Systems

High Diffraction Efficiency Top-hat Beam Shaper Metasurface for Fluorescence Observation (pp. 1287)
Tomoki Shimatani, Jie Li, Ryota Yamada, Satoshi Ikezawa, Kentaro Iwami

High Transmittance 3D Metasurface Holograms Made of SiN for Multicolor Projection with Time-division-multiplexing Method (pp. 1289)
Tamaki Onozawa, Junpei Beppu, Masakazu Yamaguchi, Kentaro Iwami

Hyperspectral Imaging for Flat Optics enabled by Dielectric Metasurfaces (pp. 1291)
Marie Braasch, Thomas Pertsch, Phillip Manley, Sven Burger, Berthold Wegner, Paul Heimel, Tzenka Miteva

Development of Vapor Cells Based on Tri-functional Metasurface for Microfabricated Atomic Clock (pp. 1292)
Ryosei Ito, Ponrapee Prutphong, Katsuma Aoki, Satoshi Ikezawa, Motoaki Hara, Kentaro Iwami

All-optical spectral control by perfect absorber based on quadrupole resonance and photothermal effect (pp. 1294)
Seiya Shinkai, Junichi Takahara

Development of wide-angle metalenses capable of simultaneously capturing near and far-view images (pp. 1296)
Atsushi Hasegawa, Ryota Yamada, Keisuke Ozawa, Yuki Abe, Mineki Taoka, Takeshi Yamagishi, Kentaro Iwami

Enhancing the photo sensitivity of photo detector using nanophotonics approach (pp. 1298)
Soh Uenoyama

Enhancement of photothermal nonlinear scattering from Mie-resonant silicon nanostructures (pp. 1300)
Kentaro Nishida, Shi-Wei Chu

High-sensitivity image sensors based on dispersion-engineered metalenses (pp. 1302)
Masashi Miyata

Reconstructive Spectrometer Using Plasmonic Photodetector (pp. 1304)
Yuuki Kaneda, Eslam Abubakr, A. Abadi, Shun Yasunaga, Masaaki Oshita, Tetsuo Kan

Spatiotemporal Metamaterials and Metasurfaces

Physics-Driven Vector-Quantized Autoencoder for Space-Time-Coding Matrix (pp. 1307)
Xiao Qing Chen, Lei Zhang

Enhanced optical effects based on the bound states in the continuum (pp. 1309)
Haitao Jiang, Zhiwei Guo, Yong Sun

Down-conversion of terahertz wave frequencies by mode coupling at temporal boundaries in semiconductor waveguides (pp. 1310)
Keisuke Takano, Satoko Uchiyama, Shintaro Nagase, Yuka Tsuchimoto, Toshihiro Nakanishi, Yosuke Nakata, Joel Pérez-Urquizo, Julien Madéo, Keshav Dani, Fumiaki Miyamaru

Waveform-Selective Metasurfaces Varying in Time and Space at the Same Frequencies in Accordance with Pulse Width (pp. 1312)
Hiroki Wakatsuchi, Ashif Aminulloh Fathnan

Direction-of-arrival (DOA) estimation with a programmable space-time-modulated metamaterial receiver (pp. 1314)
Shaghayegh Vosoughitabar, Chung-Tse Michael Wu

Acoustic Fiber via Rotational Motion (pp. 1316)
Mohamed Farhat, Ying Wu

A Physical Unclonable Function Based on Time-Modulated Systems with Exceptional Points of Degeneracy (pp. 1317)
Pai-Yen Chen

Near-infrared metasurface with simultaneous control of dielectric and magnetic properties in the 100-THz band (pp. 1318)
Harumi Asada, Kumiko Ryu, Takehito Suzuki

Application of Deutsch-Jozsa Algorithm via an Inverse-Designed Polyimide Metamaterial (pp. 1320)
A. Blackwell, R. Yahiaoui, Y- H. Chen, P- Y. Chen, T. A. Searles, Zizwe A. Chase

Recent advances in non-Hermitian metamaterials

Realization of Geometry-Dependent Skin Effect in a Reciprocal Two-Dimensional (pp. 1323)
Mengying Hu, Kun Ding

Arbitrary Chern Vectors in Non-Reciprocal 3D Acoustic Crystals (pp. 1325)
Yan Meng, Linyun Yang, Xiang Xi, Yihao Yang, Gui-Geng Liu, Baile Zhang, Zhen Gao

Observation of Discrete-Light Temporal Refraction by a Quantized Moving Gauge Potential Barrier (pp. 1327)
Chengzhi Qin, Bing Wang, Stefano Longhi, Peixiang Lu

Heat circulation metadevices (pp. 1329)
Ran Ju, Pei-Chao Cao, Dong Wang, Minghong Qi, Liujun Xu, Shuihua Yang, Cheng-Wei Qiu, Hongsheng Chen, Ying Li

The Manipulation of Topological Modes and Anderson Localized Modes via non-Hermicity (pp. 1331)
Xulong Wang, Wei Wang, Guancong Ma

Acoustic orbital-related topological states and phase transitions (pp. 1333)
Feng Gao, Yu-Gui Peng, Xuefeng Zhu

Non-Hermitian skin effects in anisotropic metamaterials (pp. 1335)
Y. Tian, Xiujuan Zhang

Nanophotonics in Biomedical Applications

Ultrafast Photonic PCR with All-Solution Processed Perfect Absorber (pp. 1337)
Seho Lee, Abdulrahman Alsaadi, Inki Kim

Au film-porous anodic aluminum oxide-Al hybrid nanomaterial-based optical biosensor for detection of the VEGFA protein. (pp. 1338)

Uldis Malinovskis, Amanda Reke, Raimonds Poplausks, Aleksandrs Dutovs, Oskars Putans, Irina Oliseveca, Donats Erts, Indrikis Muiznieks, Juris Prikulis

Biomedical applications of laser reirradiated metallic nanoparticle (pp. 1340)

Ana María Vilas, Mohamed Boutinguiza, M. Fernández-Arias, Daniel Rodríguez, Oscar Barro, Felipe Arias-Gonzalez, Pablo Pou-Alvarez, Ramon Soto, Juan Pou

New materials for photonics

Demonstration of hybrid photonic crystal nanocavity using atomically thin van der Waals flakes (pp. 1343)

Chee Fai Fong, Daiki Yamashita, Nan Fang, Shun Fujii, Yih-Ren Chang, Takashi Taniguchi, Kenji Watanabe, Yuichiro Kato

The reduced loss of guided exciton-polariton modes in WS2 multilayers by hBN- encapsulation (pp. 1345)

Ho Seung Lee, Junghyun Sung, Dong-Jin Shin, Su-Hyun Gong

Titanium nitride as a an alternative metamaterial fabricated via gas nitridation (pp. 1347)

Liya Tony, I. Packia Selvam, Sankara Narayanan Potty

Super-resolution imaging of sulfur vacancies in 2D molybdenum disulfide using expansion microscopy and dSTORM (pp. 1350)

Pin-Jen Wang, Ting-Jui Ben Chang, Hui-Jen Lin, Shun-Min Yang, Mor Pal Vikram, Kai-Chun Huang, Tsung-Hsin Liu, Chih-Yang Huang, T. Tony Yang, Ann-Shyn Chiang, Yeu-Kuang Hwu, Chun-Wei Chen, Li-Chyong Chen, Han-Chun Wu, Shi-Wei Chu

Exciton-polaritons in van der Waals heterostructures coupled to optical bound state in the continuum (pp. 1352)

Dong-Jin Shin, HyunHee Cho, Woo Hun Choi, Ho Seung Lee, Su-Hyun Gong

All-Optical Excitation and Control of Ultrafast Lattice Dynamics in WSSe (pp. 1354)

Sergio Rey, Martin Cross, Malte Welsch, Frederik Schroeder, Binbin Zhou, Nicolas Stenger, Peter Jepsen, Edmund Kelleher

Metal-Insulator Transition in Vanadium Dioxide Inspected by Analytical Electron Microscopy (pp. 1356)

Jan Krpensky, Michal Horak, Jakub Planer, Peter Kepic, Jiri Kabat, Andrea Konecna, Vlastimil Krapek

TDBC microstructures made by local photo-bleaching in J-aggregate thin organic layers for photonics applications (pp. 1358)

Komlan Gadedjisso-Tossou, Antoine Bard, Kevin Chevrier, Clémentine Symonds, Jean-Michel Benoit, Joel Bellessa, Alban Gassenq

Ultrathin bismuth and antimony films as alternative materials towards versatile and sustainable metastructures (pp. 1360)

Fernando Chacon-Sanchez, Carlota Ruiz de Galarreta, Rosalia Serna

Harmonic enhancement via a time-varying Fabry-Perot resonator (pp. 1362)

Theodosios Karamanos, Stamatios Amanatiadis, Nikolaos Kantartzis, Fabrice Lemoult

Identify Defect and Strain of Monolayer WSe2 through Exciton Anisotropy (pp. 1364)

Shu-Hsien Chen, Sih-Wei Chang, Hsuen-Li Chen

Second optical harmonic generation in high-Q dielectric metasurfaces integrated with transition metal dichalcogenide films (pp. 1366)

Alena Nazarenko, Anna Chernyak, Alexander Musorin, Alexander Shorokhov, Andrey Fedyanin

Structured Light Generation Using Spherulite in Linear and Nonlinear Realm (pp. 1368)

Yuanfeng Liu, Le Zhou, Youcheng Xu, Yongzheng Wen, Natalia M. Litchinitser, Yang Shen, Jingbo Sun, Ji Zhou

Cost-Efficient Deterministic Engineering of Quantum Light Emission in Two-Dimensional Semiconductors (pp. 1370)

Snezana Lazic, Sanja Djurdjić Mijin, Ismael de Pedro Embid

Investigating the Optical Properties of Thin Films Coated with MWCNTs (pp. 1372)

Md Saiful Islam, Furuta Hiroshi

Optical antennas and plasmonics-based devices

Versatile Flexible Plasmonic Chip for Non-Invasive Dual Modal Glucose Detection (pp. 1375)
Andreea Campu, Simion Astilean, Monica Focsan

Developing Spatiotemporal Modulated Graphene-Based Waveguide to Integrate the whole Terahertz Transceiver Front-End in one Device (pp. 1376)
Mahsa Valizadeh, Leila Yousefi, MirFaez Miri

Vanadium dioxide for compensation of angle-dependent shifts in structural color filters (pp. 1378)
Katarína Rovenska, Filip Ligmajer, Peter Kepic, Beata Idesova, Jan Chochol, Jiří Liska, Tomas Sikola

Chiral spin-preserving reflection in helicoid-based plasmonic metamaterials (pp. 1380)
Eunji Im, Hyeohn Kim, Ji-hyeok Huh, Ki Tae Nam, Seungwoo Lee

Plasmon-enhanced photovoltaics, photocatalysis, and solar fuels

Noble Metal - Chalcopyrite Hybrid Nanostructures for Enhanced Plasmonic Photocatalysis (pp. 1383)
Bjoern Reinhard

Light-accelerated NiFe oxyhydroxides-alloy photoanode metasurfaces for efficient and stable solar water-splitting (pp. 1385)
Fei Xiang, Ning Li, Arturo Burguete-Lopez, Zhao He, Maxim Elizarov, Andrea Fratalocchi

Plasmonic-enhanced Fabry-Perot cavity for photocatalysis application (pp. 1387)
Ning Lyu, Anjalie Edirisooriya, Zelio Fusco, Fiona Beck, Christin David

Hot electron induced photoreduction of Fullerene C60 using coupled plasmonic - Fabry-Perot systems (pp. 1389)
Anjalie Edirisooriya, Ning Lyu, Zelio Fusco, Fiona Beck

MAPLE simulation for multilayer-layers solar cell based in ZnS- CZTSSe (pp. 1391)
Hala El-Khozondar, A. N. Sahmoud, R. J. El-Khozondar, Y. F. Nassar

Research on the enhancement of photocatalytic activity of bismuth-based materials by plasma effect (pp. 1393)
Derek Hao

Large-area self-organized plasmonic gold nanowire matrix for advanced photochemical applications (pp. 1395)
Giulio Ferrando, Matteo Gardella, Long Duy Pham, Hieu Si Nguyen, Chi Le Ha, The Hung Mai, Giorgio Zambito, Matteo Barelli, Maria Caterina Giordano, Francesco Buatier De Mongeot

Templated Self-Assembled Plasmonic Metasurfaces. From Lasing and Sensing to Photocatalysis (pp. 1397)
Tomas Tamulevičius, Klaudijus Midveris, Gvidas Klyvis, Tomas Klinavičius, Muhammad Haris, Nadzeya Khinevich, Asta Tamulevičienė, Mindaugas Juodėnas, Domantas Peckus, Joel Henzie, Sigitas Tamulevičius

Near Unity Index Meta-surface for Effective Reduction of CO2 to Methanol (pp. 1399)
Joel Yi Yang Loh

Plasmonics and nano-optics

A Direct Approach towards Nanoscale Mapping of Plasmonic Heat Generation in Nanostructures (pp. 1402)
Serene Pauly, Amit Kumar

Optimized Near-infrared Absorption of Reflective Aluminum Gratings: Theoretical and Experimental Investigation (pp. 1404)
Roy Avrahamy, Dror Cohen, Benny Milgrom, Ben Amir, Daniel Belker, Asi Solodar, Erez Golan, Oren Sadot, Amiel Avraham Ishaaya

Analyzing Absorption Mechanisms of Plasmonic and Dielectric Surface Lattice Resonance Embedded in Absorptive Medium (pp. 1406)
Joshua T. Y. Tse, Shunsuke Murai, Katsuhisa Tanaka

Spin angular momentum of enhanced electric fields around a plasmonic nanostructures excited by circularly polarized light (pp. 1408)
Naoki Ichiji, Takuya Ishida, Ikki Morichika, Tetsu Tatsuma, Satoshi Ashihara

On the quantization of non-Hermitian nanophotonic systems (pp. 1410)
Luke Hands, Angela Demetriadou, Ben Yuen

Lattice resonances in multipartite periodic arrays with electric and magnetic response (pp. 1412)
Juan R. Deop-Ruano, Juan J. Alvarez-Serrano, Luis Cerdan, Vincenzo Aglieri, Andrea Toma, Alejandro Manjavacas

Plasmonic anisotropy of metallic nanoparticles induced by uniaxially-stretched graphene substrates (pp. 1414)
Chihiro Yamano, Shin-nosuke Ozeki, Ryo Kato, Takuo Tanaka, Taka-Aki Yano

High-Q and Small Size Cavity with Mie Scattering Mirror (pp. 1415)
Bokyung Kim, Seokhyeon Hong, Youngsoo Kim, Seung Hyeon Hong, Juhan Lee, Soon-Hong Kwon

Mie-assisted photonic memories based on the phase change of silicon nanoparticles (pp. 1417)
Jhih-Jia Chen, Te-Hsin Yen, Kentaro Nishida, Junichi Takahara, Mihail Petrov, Shi-Wei Chu

Hybrid full-space metalens for ultraviolet light (pp. 1419)
Beata Idesova, Filip Ligmajer, Ondřej Červinka, Tomas Sikola

High NA multifocal array metalens (pp. 1421)
Hyemi Park, Yongjae Jo, Inki Kim

Lensless localized surface plasmon resonance sensor using porous anodic alumina based nanostructured metal-insulator-metal multilayers (pp. 1423)
Aleksandrs Dutovs, Amanda Reķe, Uldis Maļinovskis, Raimonds Popļausks, Donāts Erts, Juris Prikulis

Integrated Plasmo-Photonic Bimodal Interferometer for Temperature Sensing (pp. 1425)
Lamprini Damakoudi, Stelios Simos, Konstantinos Fotiadis, Dimosthenis Spasopoulos, Evangelia Chatzianagnostou, Omkar Bhalerao, Stephan Suckow, Max Lemme, Eleftherios Lidorikis, Nikos Pleros, Konstantinos Vyrsokinos

Self-referenced integrated plasmo-photonic sensor for temperature compensated refractive index sensing measurements (pp. 1427)
Stelios Simos, Lamprini Damakoudi, Evangelia Chatzianagnostou, Konstantinos Fotiadis, Dimosthenis Spasopoulos, Dimitris Bellas, Omkar Bhalerao, Stephan Suckow, Max Lemme, Nikos Pleros

Self-Assembled Plasmonic Nanoparticles for Photocatalysis (pp. 1429)
Asta Tamuleviciene, Klaudijus Midveris, Tomas Klinavicius, Muhammad Haris, Mindaugas Juodenas, Domantas Peckus, Sigitas Tamulevicius, Tomas Tamulevicius

Fluorescence enhancement of novel azulene-tetrazoles using metasurface structures (pp. 1430)
Veronica Anastasoaie, Iuliana Mihalache, Roxana Tomescu, Adrian Dinescu, Eleonora-Mihaela Ungureanu, Oana Brincoveanu, Dana Cristea

Manipulation of 2-Dimensional layers of plasmonic nanoparticles using a SAW device (pp. 1432)
Chandresh Sindal, Julien Reboud, Narayana M. S. Sirimuthu, Alasdair W. Clark, Jonathan M. Cooper

Optical response of Smooth and rough Mono and bilayers of plasmonic materials (pp. 1434)
Jorge Alberto Polito Lucas, Ana Lilia Gonzalez

Infrared Surface Lattice Resonances using Plasmonic Transition Metal Nitrides (pp. 1436)
Hsing-Yu Kuo, Tzu-Yu Peng, Jia-Wern Chen, Yu-Jung Lu

Highly-Sensitive Broadband Gap-Plasmon-Enhanced NbN Superconducting Single Photon Detectors (pp. 1438)
Feng-Yang Tsai, Jing-Wei Yang, Jia-Wern Chen, Li-Min Wang, Yu-Jung Lu

Revisable Tuning of Tamm Plasmon Polaritons (pp. 1440)
Ming-Jyun Ye, Kuo-Ping Chen

Large-area, two-dimensional single-crystal gold for low-loss nanoplasmonics (pp. 1442)

Chenxinyu Pan, Yuanbiao Tong, Anatoly V. Zayats, Limin Tong, Pan Wang

Chirality switchable molecular traps based on plasmonic metastructures with intertwined Fibonacci spirals (pp. 1443)
Chung-Kai Tseng, Tang-Chun Liu, Diksha Thakur, Chao-Yi Tai

Metal-dielectric gratings with broad geometric range for angle interrogation of surface plasmons (pp. 1445)
Shafeek Abdul Samad, Nityanand Kumawat, Priyamvada Venugopalan, Sunil Kumar

Modulable Chiral Plasmonic Activates via Stimulus Triggered Shape-Morphing (pp. 1447)
Yisheng He, Chunhong Ye

Utilizing a microcone array to control the distance between a microsphere and a SERS substrate for photonic nanojet-mediated SERS (pp. 1449)
Chen-Ting Hung, Yan-Ru Liu, Yih-Fan Chen

Investigating the charge carrier dynamics in an array of Split-H ladder (SHL) of Au on amorphous SiO2 (pp. 1451)
Nikita Vashistha, R. Sharma, T. N. Narayanan, R. S. Singh, Mahesh Kumar Sharma

Investigating Nonlinear Optical Switching via Nanosecond Z-scan: Coupling Saturable Absorption in Gold with Reverse Saturable Absorption in Strontium Titanate (pp. 1453)
Nikita Vashistha, Hitheshwar Prasad, N. Sri Ram Gopal, Rajiv K. Singh, Sandeep Singh, S. P. Singh, Mahesh Kumar

Hybrid Plasmonic Waveguide NFT for HAMR Heads (pp. 1455)
Will Lee, Andres Neira, Beverley McConnell, Robert Bowman

Titanium nitride (TiN) nano and microstructures as novel highly efficient SERS platform (pp. 1457)
Jan Krajczewski, Aleksandra Michałowska, Nozka Libor

Self-assembled silicon photonic cavities with atomic-scale confinement and self-aligned integration with photonic circuits (pp. 1459)
Ali Nawaz Babar, Thor August Schimmell Weis, Konstantinos Tsoukalas, Shima Kadkhodazadeh, Guillermo Arregui, Babak Vosoughi Lahijani, Søren Stobbe

Tamm Assisted Metasurfaces for classical and quantum photonics applications (pp. 1461)
Edmund Harbord, Huili Hou, Talal Alshammari, Mengxun Bai, David Dlaka, Angela Stephens, Jon Pugh, Ruth Oulton, Martin Cryan

Cd(Zn)O nanostructures for SEIRA sensing in de Mid-IR (pp. 1463)
Pablo Ibañez-Romero, Eduardo Martinez Castellano, Javier Yeste, Fernando Gonzalez-Posada, Thierry Taliercio, Vicente Muñoz-Sanjosé, Miguel Montes Bajo, Adrian Hierro

Plasmonic hydrogen sensor at the ppm level based on the plasmon-triggered switching (pp. 1465)
Pascal Giraud, Hugo Bruhier, Isabel Verrier, Salma Rajab Pacha, Christelle Varenne, Jérôme Brunet, Amadou Ndiaye, Yves Jourlin

Industrial WorkShop I: From Design to Manufacture - Complete Inverse Design (pp. 1467)
Chenglin Xu, Bryan Stone, JiSoo Park

Magnetically Controllable Multimode Interference in Topological Photonic Crystals (pp. 1468)
Weiyuan Tang, Mudi Wang, Shaojie Ma, C. T. Chan, Shuang Zhang

Coupled thermal and mechanical phenomena induced by the fluctuations of the electromagnetic field (pp. 1470)
Juan R. Deop-Ruano, Alejandro Manjavacas

Super-resolution elasticity imaging with nanobells (pp. 1472)
Rafael Fuentes Dominguez, Marina Paris Ogayar, Kerry Setchfield, Richard Smith, Daniel Jaque, Matt Clark

Super Resolution Imaging of Resonance Mode Inside Silicon Nitride Nanowire Based on Photothermal Nonlinearity (pp. 1474)
Yu-An Chen, Te-Hsin Yen, Kentaro Nishida, Chih-Wei Chang, Shi-Wei Chu

Acoustic and seismic metamaterials

Design of composite mufflers based on dissipative and reactive units (pp. 1477)
Yuzhen Yang, Han Jia, Quanquan Shi, Jun Yang

Frequency-selective valley edge waveguiding in topological phononic-crystal plates (pp. 1479)
Jin-Chen Hsu, Chun-Hao Wei, Che-Ting Huang

From Air to Water: Expanding Inverse-Design Applications in Ultrasonic OAM (pp. 1481)
Chuanxin Zhang, Xue Jiang, Dean Ta

Water-Air Acoustic Communication Based on Broadband Impedance Matching (pp. 1483)
Han Jia, Yuzhen Yang, Jun Yang

Tailoring acoustic complex media for optimal wave mode conversion (pp. 1485)
Hongkuan Zhang, Guancong Ma

Optimally designed ultra-thin underwater metamaterial absorber (pp. 1487)
Nan Gao, Sichao Qu, Alain Tinel, Bruno Morvan, Vicente Romero-García, Jean-Phillippe Groby, Ping Sheng

Fast-speed Ultrasonic Imaging Using a Single Sensor by Combining Disordered Metasurface and Artificial Intelligence (pp. 1489)
Wei Wang, Jie Hu, Jingjing Liu, Bin Liang, Jianchun Cheng

Chiral and hyperbolic metamaterials

Dielectric metasurface for wave-vector variant and circular polarization dependent transmission (pp. 1492)
Helene Wetter, Wenlong Gao, Falk Rehberg, Jan Wingenbach, Stefan Schumacher, Thomas Zentgraf

Photonic Modes in Gyrotropic-Hyperbolic Heterostructures (pp. 1494)
Daniele Battesimo Provenzano, Giuseppe Carlo la Rocca

Understanding The Reflective Footprint of Ghost and Leaky Hyperbolic Polaritons in Crystal Quartz (pp. 1496)
Mark Cunningham, Adam Lafferty, Mario Gonzalez Jimenez, Rair Macêdo

Enhanced chirality with Mie resonance-based multi-cylinder chiral metasurfaces (pp. 1498)
Seung Hyeon Hong, Seokhyeon Hong, Youngsoo Kim, Bo Kyung Kim, Juhan Lee, Soon-Hong Kwon

Unidirectional mode excitation due to magnetochiral effects (pp. 1500)
Hiroyuki Kurosawa, Keisuke Itoh, Tetsuya Ueda

Machine learning for metamaterial design

End-to-End Framework for Designing Broadband Achromatic Metalens in High-quality Long-infrared Imaging (pp. 1503)
Qizhou Wang, Daniele Veraldi, Arturo Burguete-Lopez, Maksim Makarenko, Andrea Fratalocchi

Free-form inverse design of dynamically tunable metamaterial absorber for Mid-Infrared applications (pp. 1505)
Ram Prakash Shanmugam, Aastha Jain, Rajesh Kumar, Anirban Mitra

Broadband large-scale photonics inverse design enabled by experimental machine learning (pp. 1507)
Maksim Makarenko, Sergey Rodionov, Qizhou Wang, Fedor Getman, Andrea Fratalocchi

Artificial intelligence optical hardware empowers real-time ultra-sensitive detection of dopamine at 10−11 mol/L (pp. 1509)
Ning Li, Qizhou Wang, Zhao He, Arturo Burguete-Lopez, Fei Xiang, Andrea Fratalocchi

Metamaterial-based devices

Fabrication of visible metalenses by thermal oxidation of silicon nanopillars (pp. 1512)
Taiyu Okatani, Rei Ando, Naoki Inomata, Yoshiaki Kanamori

Water sensors using soft films with metamaterials (pp. 1513)

Chia-Yi Huang, Harry Miyosi Silalahi

Polarization-Insensitive Ultra-Broadband Terahertz Metamaterials for 6G Applications (pp. 1514)
Bhagwat Singh Chouhan, Partha Pratim Barman, Bhumidhar Barman, Gagan Kumar

Bismuth-based color generation devices : from traditional optical cavities to gap-surface plasmon metastructures (pp. 1516)
Fernando Chacon-Sanchez, Carlota Ruiz de Galarreta, Rosalia Serna

Metasurface-Driven Hyperspectral Video Camera and Real-Time Spectral Analysis applications (pp. 1518)
Arturo Burguete Lopez, Qizhou Wang, Maksim Makarenko, Andrea Fratalocchi

MEMS-based double filter configuration for air gap sensing in tunable Fabry-Pérot filter (pp. 1520)
Pratyasha Sahani, S. Nabana, T. Okatani, N. Inomata, Y. Kanamori

Metamaterial Range Extended And Field localized Parity-Time Symmetrical Wireless Power Transfer System (pp. 1522)
Abdulrahman Mohammed Alsaadi, Inki Kim

Technology of auxetic-structured substrate for skin attachable conformal sensor (pp. 1524)
Jae-Hwan Lee, Tae-Gyong Kim, Jun-Sang Lee, Seung-Kyun Kang

Flexible Metasurface as an Efficient Resonator for 7T MRI (pp. 1526)
Santosh Maurya, Eiska Tegareh, Rita Schmidt

Fabrication of delay lines using spoof-surface-plasmon-polariton waveguides coupled with split-ring resonators for microwave integrated circuits (pp. 1528)
Minh Nguyen, Nobuaki Kikuchi, Toshiyuki Kodama, Taiyu Okatani, Naoki Inomata, Yoshiaki Kanamori

Numerical investigation of dielectric metasurfaces for refractive index-based sensing applications (pp. 1530)
Roxana Tomescu, Cristian Kusko, Veronica Anastasoaie, Dana Cristea

Advancements in polarization-sensitive metasurfaces (pp. 1532)
Ondřej Červinka, Martin Hrtoň, Jakub Lelek, Filip Ligmajer, Stěpan Vénos, Libor Ulehla, Tomas Sikola

Conductivity responsive effective permittivity control in GaAs tunable metamaterials (pp. 1534)
Minyeul Lee, Sungyoung Yoon, Jonghwa Shin

Real-time terahertz modulation with gold-MoS2 metasurface (pp. 1536)
Jianhong Zhang, Fangfang Ren, Jiandong Ye, Xiaoli Ji, Hai Lu

Realizing an acoustic T-shaped superscatterer with inverse design (pp. 1538)
Di Wang, Jie Zhu, Zhongming Gu

Design of a 3D Reconfigurable Intelligence Surface (pp. 1540)
Sung-Sil Cho, Biswarup Rana, Ic-Pyo Hong

Flexible metamaterial absorber on custom-engineered polymer nanocomposites as substrates (pp. 1542)
Kumaran Rengaswamy, Siva Bhagavathi L. G., Rahul Manohar O., Anjali Murugan, Vijayashri V., Chitti Venkata Krishnamurthy, Subramanian Venkatachalam

Dynamic medium based on tunable transmissive metasurfaces (pp. 1544)
Zhedong Wang, Chao Qian, Hongsheng Chen

An active Fabry-Pérot interferometer operated at terahertz frequencies based on pitch-variable subwavelength gratings (pp. 1546)
Ying Huang, Yangxun Liu, Taiyu Okatani, Naoki Inomata, Yoshiaki Kanamori

300-GHz-band transmission-type beamforming metasurface for an outdoor-to-indoor signal coverage extension for future wireless networks (pp. 1548)
Adam Pander, Hibiki Kagami, Daisuke Kitayama, Hiroyuki Takahashi

Giant Optical Anisotropy in Van der Waals Materials: Perspectives and Challenges (pp. 1550)

Valentyn Volkov, Georgy Ermolaev, Dmitry Grudinin, Kirill Voronin, Andrey Vyshnevyy, Arslan Mazitov, Gleb Tselikov, Ivan Kruglov, Davit Ghazaryan, Luis Martin-Moreno, Alexey Arsenin, Konstantin Novoselov

A Broadband Metamaterial-Based Electromagnetic Absorber with the Capability of being Fabricated by 3-D Printers (pp. 1552)

Mohammad Javadi, Leila Yousefi

Metamaterials and negative index materials

An Effective Medium Description for Cylinder- and Coated-cylinder- Multifunctional Metamaterials (pp. 1555)

Anna Tasolamprou, Charalampros Mavidis, Maria Kafesaki

Enhancing bandwidth in GHz metamaterials through superposed Lorentzian Resonances (pp. 1557)

Yun Hyeong, Hyeonjin Park, Jonghwa Shin

The Bandgap Characteristics of Wave Dispersion in Monocoupled Metamaterial (pp. 1559)

Abhigna Bhatt, Arnab Banerjee

Dissipative Triatomic Metamaterial for Broadband Asymmetric Elastic-wave Transmission (pp. 1561)

Sagr Alamri, Bing Li

The critical size of hybrid metal-dielectric nanoslits guide mode resonance optical filters by the spatial Fourier transform analysis (pp. 1563)

Rong He, Cheng Chen, Yuxiang Zheng, Liangyao Chen, Junpeng Guo

Bias-free optical metamaterial with nonreciprocal magnetoelectric response (pp. 1565)

Shadi Safaei Jazi, Ihar Faniayeu, Rafael Cichelero, Dimitrios C. Tzarouchis, Mohammad Mahdi Asgari, Alexandre Dmitriev, Shanhui Fan, Viktar Asadchy

First-principles prediction of nonlinear optical response in silicon nanostructures (pp. 1567)

Gosuke Matsuura, Shunsuke Yamada, Mitsuharu Uemoto

Electro-Optical Switching in Nonlinear Metasurfaces (pp. 1569)

Matthew Feinstein, Alexander Andronikides, Euclides Almeida

Metasurfaces and flat optics

Tunable filter based on the Brewster effect in metafilms: From all-pass filter to narrowband perfect absorber (pp. 1572)

Tomohiro Hoshino, Yasuhiro Tamayama

Robustness of Active Phase-Change Metasurfaces against High-Power Sources (pp. 1574)

George Braid, Carlota Ruiz de Galarreta, Joe Pady, Andrew Comley, Jacopo Bertolotti, C. David Wright

Centimeter-scale cylindrical metalens (pp. 1576)

Kyungtae Kim, Junsuk Rho

Diverse reconfigurability in far- and mid-infrared few-layer metasurfaces capable of polarization manipulation: case of phase-change materials (pp. 1578)

Andriy Serebryannikov, Akhlesh Lakhtakia

Polarization- and direction-multiplexed vector holography based on asymmetric transmission of bi-layer metasurfaces and its application (pp. 1580)

Joonkyo Jung, Hyeonhee Kim, Jonghwa Shin

Unified Metasurfaces for Dynamic Beam Steering (pp. 1582)

Hsiu-Ping Su, Po-Sheng Huang, Pin Chieh Wu

Large Field-of-View Near-Infrared Imaging based on Telecentric Metaoptics (pp. 1584)

Wei-Lun Hsu, Qiu-Chun Zeng, Chen-Yi Yu, Yen-Chun Chen, Yi-Fan Chen, Che-Chin Chen, Chih-Ming Wang

Flat optics light harvesting in large-area TMDs films for photoconversion and photochemical applications (pp. 1586)
Giulio Ferrando, Matteo Gardella, Giorgio Zambito, Francesco Bisio, Matteo Barelli, Maria Caterina Giordano, Francesco Buatier De Mongeot

Jones matrix holography with liquid crystal-integrated active metasurface (pp. 1588)
Hyeyoung Yoon, Hyounghan Kwon, Inki Kim

Photocurrent Enhancement induced by Fabry-Pérot quasi-Bound States in the Continuum in Silicon Nanodisk Hexagonal Array beyond 1400 nm in Wavelength (pp. 1590)
Keisuke Moriasa, Hiroaki Hasebe, Hiroshi Sugimoto, Minoru Fujii

Enhancement of Circular Dichroism by Engineered Absorption in Chiral Dielectric Metasurface (pp. 1592)
Anna Fitriana, Katsuya Tanaka, Lukas Raam Jaeger, Martin Hafermann, Thomas Pertsch, Carsten Ronning, Isabelle Staude

Tuneable Optical Edge Detection using Phase-Change Metasurfaces (pp. 1594)
Stuart Kendall, Carlota Ruiz de Galarreta, Joe Shields, Guoce Yang, Mengyun Wang, June Sang Lee, Nikolaos Farmakidis, Andy Moskalenko, Kairan Huang, Lou Deguzman, Andrea Alù, Jacopo Bertolotti, Harish Bhaskaran, C. David Wright

Inverse Design of microwave absorber based on adjoint topological optimization (pp. 1596)
Hyeonjin Park, Jonghwa Shin

Impact of Numerical Simulation Boundary-Decomposition Errors on Optical Performance of Meta-diffusors (pp. 1598)
Louis-Henri Fernandez-Mouron, Loumi Tremas, Mathys Legrand, Pascal Urard, Habib Mohamad, Lucie Dilhan, Enrico Giuseppe Carnemolla, Matteo Fissore, James Downing, Valérie Serradeil, Bruce Rae, Denis Rideau

Time-varying nonlinear effects in Q-boosted metasurfaces (pp. 1600)
Anna Chernyak, Alexander Musorin, Andrea Tognazzi, Paolo Franceschini, Costantino De Angelis, Andrey Fedyanin

Characterization of metasurface-based optical vortices using quadriwave lateral shearing interferometry (pp. 1602)
Yanel Tahmi, Samira Khadir, Matthieu Ansquer, Patrice Genevet, Benoit Wattellier

Reciprocal Lens: Imaging Based on Lateral Ray Shifting via Non-Local Metasurfaces (pp. 1604)
Jing Guang Chen, Wenzhe Liu, Lei Shi, Jian Zi, C. T. Chan

Fundamental limits to metalens critical dimensions (pp. 1606)
Nicolas Kossowski, Emil Marinov, Clément Majorel, Samira Khadir, Patrice Genevet

Mid-infrared achromatic metalens with large field-of-view based on standard i-line stepper (pp. 1608)
Yen-Chun Chen, Wei-Lun Hsu, Qiu-Chun Zeng, Chen-Yi Yu, Yu-Hsin Lin, Che-Chin Chen, Chih-Ming Wang

Robust nano-antenna metrology for metasurface design (pp. 1610)
Cecile Le Gall, Bastien Rouze, Cindy Bellanger, Jerome Primot, Julien Jaeck

Meta-lenses for second harmonic generation imaging on the tip of hair-thin optical fiber for advanced endoscopic imaging (pp. 1612)
Rafael Fuentes Dominguez, Diekolopemi Afuwape, Fei He, Richard Cousins, George Gordon

Optimized design strategy of polychromatic metasurfaces considering their fundamental dispersion limits (pp. 1614)
Adelin Patoux, Nicolas Kossowski, Clément Majorel, Samira Khadir, Patrice Genevet

Toroidal dipole bound states in the continuum in dielectric metasurfaces (pp. 1616)
Sheng-Wei Kao, Yi-Chi Kao, Ruey-Lin Chern

Holograms and wide-angle optics with hybrid supercell metasurfaces (pp. 1618)
Tatiana Contino, Harsh Gupta, Andrea Toma, Michele Tamagnone

Controlling Diffraction Efficiency Redistribution via Incomplete Phase Metagrating (pp. 1620)
Qiyao Liu, Zhengtong Liu, Xuezhi Ma, Jie Deng, Chen Zhang, Zhenmin Chen, Arash Nemati, Sui Kit Ng, Sergey Gorelik, Siew Lang Teo, Rong Ji, Meng Zhao, Leonard Verano Gonzaga, Hong Liu, Fuyong Yue, Shaohua Yu, Yu Luo, Qian Wang

Selective excitation of diverse subwavelength resonances in metasurfaces comprising volumetric resonators: a brief discussion (pp. 1622)

Andriy E. Serebryannikov

Designing a metasurface color router via photonic inverse design (pp. 1624)
Jeongwoo Son, Rishad Arfin, Mohamed H. Bakr, Jens Niegemann

Laser and cavities

Highly Efficient Stimulated Raman Conversion in SF6-filled Photonic Crystal Fiber (pp. 1627)
Roy Avrahamy, Daniel Belker, Aviran Halstuch, Amiel Avraham Ishaaya

Optical cavity based on reflective metasurfaces (pp. 1629)
Muhammad Waseem Ashraf, Muhammad Atif Yaqub, Tatiana Contino, Michele Tamagnone

Reconfigurable Tunable Integrated Optical Filter based on Nested Coupled Dual Ring Resonator (pp. 1631)
Pragya Mishra, Tushar Gaur, Talabattula Srinivas

Optical vortex generation using GaN nanopillars and metal nanostructures (pp. 1632)
Ryuji Kuruma, Masato Takiguchi, Peter Heidt, Yuto Moritake, Taiki Yoda, Adam Mock, Masaya Notomi

Photonic bandgap structures

3D Soft Photonic Crystal Photoswitch between Cubic Lattices (pp. 1635)
Eva Oton, Martin Cigl, Przemyslaw Morawiak, Sergei Mironov, Alexej Bubnov, Wiktor Piecek

Microlaser with topologically protected light distribution based on a 3D Soft-Matter-Based Photonic Crystal (pp. 1637)
Eva Oton, Marcin Muszyński, Przemysław Morawiak, Piotr Kapuściński, Przemysław Oliwa, Maria Popławska, Jacek Szczytko, Wiktor Piecek

Dirac bound states in the continuum in honeycomb photonic crystal slabs (pp. 1639)
Yi-Chi Kao, Sheng-Wei Kao, Ruey-Lin Chern

Enhancing photodetection and photoluminescence in low dimensional materials with photonic crystals (pp. 1641)
Muhammad Atif Yaqub, Harsh Gupta, Tatiana Contino, Muhammad Waseem Ashraf, Michele Tamagnone

High-bandwidth slow-light silicon modulators (pp. 1643)
Xingjun Wang, Changhao Han

Topological valley plasmons in twisted monolayer-double graphene moiré superlattices (pp. 1644)
Weiwei Luo, Jiang Fan, Alexey Kuzmenko, Wei Cai, Jingjun Xu

Design of inorganic photoelectrodes based on photonic crystals with incorporated Mo6 clusters. (pp. 1646)
Clement Lebastard, Adele Renaud, Stephane Cordier, Tetsuo Uchikoshi, Tohru Suzuki, Fabien Grasset

Emerging applications

Plasmonic Copper Nanorings for Building Energy Management (pp. 1649)
Xavier Baami Gonzalez, Jimmy Duc Tran, Duncan Sutherland

Reliability and remaining useful life of flexible silver nanowire-based transparent electrodes (pp. 1651)
Mikita Marus, Nikolay Lyapunov, Abel Wong, Tak-Lam Chan, Haibo Hu

Micro/Nano fabrication and characterization techniques

Fabricating High-Performance Metasurfaces via Direct Printing with Polymer Infused Titanium Dioxide Nanoparticles (pp. 1654)
Dong Kyo Oh, Joohoon Kim, Hyunjung Kang, Yujin Park, Junsuk Rho

Scanning Reflectance Anisotropy Microscopy: mapping of strained amorphous semiconductors and chiral metasurfaces (pp. 1656)

Fabian Haake, Henning Galinski, Ralph Spolenak

High-Index Atomic Layer-Nanoparticle Embedded-Resin Hybrid Metasurfaces for High-Performance Visible Metaphotonics (pp. 1658)
Dohyun Kang, Minseok Choi, Hyunjung Kang, Junsuk Rho

3D Inkjet Printing for the Manufacture of Micron-to-Millimeter-Scale Metamaterial Structures (pp. 1660)
Oliver Nelson Dummett, Lyudmila Turyanska, Richard Hague, Christopher Tuck

Nanopatterning of Nitride Nanostructures for Optoelectronic Applications (pp. 1662)
Sudarshana Patra, Amelia Korveziroska, Uttam Manna, Mahua Biswas

Post-synthesis band gap halide anion exchange tuning in CsPbBr3 nanocrystals and issues of light-induced phase segregation (pp. 1664)
Petr Liska, Tomas Musalek, Matous Kratochvíl, Tomas samořil, Petr Dvořak, Miroslav Kolíbal, Tomas Sikola

All-In-One Etching and Measurements of Silicon Metalens for Near-Infrared Focusing (pp. 1666)
Bingrui Lu, Søren Engelberth Hansen, Michael Juhl, Søren Stobbe

Evaporative Analysis of Lithium-Ion Battery Electrolytes Using Surface-Enhanced Raman Spectroscopy in a Controlled Microenvironment (pp. 1668)
Maziar Moussavi, Nadzeya Khinevich, Asta Tamulevičienė, Tomas Tamulevičius, Mindaugas Juodėnas, Sigitas Tamulevičius

Characterization of small microlens based on metasurface using Quadriwave Lateral Shearing Interferometry (pp. 1670)
Martin Lepers, Alain Ostrovsky, Jerôme Vaillant, Samira Khadir, Jean-Yves Duboz

Single- and multi-layer diffractive lens fabrication on fiber endoscope probes for advanced imaging technologies (pp. 1677)
Fei He, Rafael Fuentes-Dominguez, Richard Cousins, Christopher J. Mellor, Jennifer K. Barton, George S. D. Gordon

Fabrication of form birefringent 3D metastructures for visible wavelength range using 3D laser printing technique (pp. 1679)
Darius Gailevičius, Domas Paipulas, Saulius Juodkazis, Vygantas Mizeikis

Zeiss Crossbeam FIB-SEM for nanophotonic materials research and nanofabrication (pp. 1681)
Olena Vertsanova, Benjamin Tordoff, Feng Lin Ng

Modeling and computational techniques

Topology optimization for liquid crystal-based holograms (pp. 1684)
Peter Ropač, Yu-Tung Hsiao, Brecht Berteloot, Miha Ravnik, Jeroen Beeckman

Finite-difference frequency-domain calculations of chiral material composites (pp. 1686)
Takamichi Terao

Applications of a ray-based metalens design tool on freeform metasurfaces (pp. 1688)
Yijun Ding, Bryan Stone, Motoyuki Otake

Plenary presentations

Materials manipulation with structured light fields

Takashige Omatsu[1,2]

[1]Grasuate School of Engineering, Chiba University, Japan
[2]Molecular Chirality Research Center, Chiba University, Japan
[*]corresponding author: omatsu@faculty.chiba-u.jp

Abstract: Structured light fields, such as optical vortex, has been currently growing up to a particle-like optical field (optical skyrmion). We review state-of-the-art structured materials fabrication and new materials manipulation with structured light fields.

Structured light fields with designed spatial variations in amplitude or polarization, such as optical vortices and vector vortices, possess an annular spatial intensity profile and an orbital angular momentum (OAM) associated from a helical wavefront with an on-axis phase singularity. They have been intensely studied in a myriad of fundamentals and applications: for instance, optical trapping and manipulation, optical and quantum communications, super-resolution microscopy, and materials fabrication.
In particular, it has been discovered that the optical vortices enable the twist of irradiated materials at a nano- and micron-scale to form chiral structures, and thus, a variety of chiral structures, formed of metals, semiconductors, dielectrics, polymers, and crystals have been demonstrated. Such chiral structures will potentially pave the way towards the development of chiral meta-surfaces for detection and control of chiral chemical reaction at high time and cost efficiencies.

Magnetic skyrmions with topologically protected spin textures, assigned with the topological number, have been investigated as a new carrier for new generation magnetic data storages. A full Poincare beam possesses all polarization states on the Poincare sphere onto its cross section, and it is also attracting much attention in optical science and photonics as an analogous quasiparticle of light, termed optical skyrmions. Optical skyrmions, formed of the coherent superposition of orthogonally circularly polarized fundamental Gaussian and Laguerre-Gaussian modes with appropriate relative phase, exhibit topologically protected polarization textures. Going beyond conventional structured light fields such as optical vortices and vector vortices, optical skyrmions will offer new fundamental physics via exotic light matter interactions, however, they are still unmatured as a research topic. In fact, there are few reports of the interaction between optical skyrmions and materials.

In this paper, we review the state-of-the-art chiral nano/micro-structures with structured light fields, and we also address the demonstrations of new approaches to materials manipulation with quasi-particles of light, optical skyrmions.

References

1. Omatsu, T., Miyamoto, K., Toyoda, K., Morita, R., Arita, Y., Dholakia, K. “A new twist for materials science: the formation of chiral structures using the angular momentum of light,” Adv. Opt. Mater. Vol. 7, No. 14, 1801672 (2019).
2. Omatsu, T., Masuda, K., Miyamoto, K., Toyoda, K., Litchinitser, N. M., Arita, Y., Dholakia, K., “Twisted mass transport enabled by the angular momentum of light,” J. Nanophotonics Vol. 14, No. 1, 010901-010901 (2020).
3. Omatsu, T., Miyamoto, K., Yuyama, K. I., Yamane, K., Morita, R., “Laser-induced forward-transfer with light possessing orbital angular momentum,” J. Photochem. Photobiol. C Vol. 52, 100535 (2022).

4. Omatsu, T., “Can orbital angular momentum of light advance materials science?,” JSAP Review Vol. 2023, 230211 (2023).
5. Toyoda, K., Su, H. T., Miyamoto, K., Sugiyama, T., Omatsu, T., “Chiral crystallization manipulated by orbital angular momentum of light,” Optica Vol. 10, No. 3, 332-338 (2023).

Topological dissipation in a time-multiplexed photonic resonator network and topological temporally mode-locked lasers.

Franco Nori[1,2]

[1] RIKEN, Saitama, Japan
[2] University of Michigan, Ann Arbor, USA

Abstract: This talk provides an overview of recent results on topological dissipation in a time-multiplexed photonic resonator network [1], and topological temporally mode-locked lasers [2]. A very brief summary will also be made of recent work on non-Abelian effects in dissipative photonic topological lattices [3]. This work was done in collaboration with the group of Alireza Marandi at Caltech. More information is available in the references below [1-3].

[1] ***Topological dissipation in a time-multiplexed photonic resonator network*****,** C. Leefmans, A. Dutt, J. Williams, L. Yuan, M. Parto, F. Nori, S. Fan, A. Marandi, *Nature Physics* **18**, pp. 442–449 (2022). [PDF][Link_1][Link_2][arXiv][Suppl. Info.]. A nontechnical “News and Views” summary of this work is available here: [Link]

[2] ***Topological temporally mode-locked laser****,* C.R. Leefmans, M. Parto, J. Williams, G.H.Y. Li, A. Dutt, F. Nori, A. Marandi, *Nature Physics* (2024). [PDF][Link][arXiv] [Suppl. Info.]

[3] ***Non-Abelian effects in dissipative photonic topological lattices***, M. Parto, C. Leefmans, J. Williams, F. Nori, A. Marandi, *Nature Communications* **14**, 1440 (2023). [PDF][Link][arXiv][Suppl. Info.]

Shaping light propagation in complex media

Hui Cao

Department of Applied Physics, Yale University, New Haven, Connecticut06520, USA

hui.cao@yale.edu

Abstract:

Wave propagation in a random scattering medium has long been described by the diffusion equation. Recently, spatial wavefront shaping technique is utilized to overcome the diffusion in order to control coherent light propagation in random scattering media. By breaking the diffusion limit, we deliver optical energy into a target region of arbitrary size and shape anywhere inside a strong-scattering system. We further demonstrate an order of magnitude enhancement of remitted signals that carry information from deep inside a diffusive medium, illustrating the potential of coherent wavefront control for noninvasive diffuse-wave imaging applications.

Localized states trapped by topological defects in photonic and hybrid metasurfaces

Daria Smirnova

Research School of Physics, Australian National University, Canberra, ACT 2601, Australia
daria.smirnova@anu.edu.au

Abstract: The miniaturization of photonic technologies calls for a wise integration of photonic and material components for fully functional fast-speed integrated devices based on enhanced light-matter interactions. Topological photonic systems were recently proposed as a promising platform to couple structured modes of light on chip with solid-state matter excitations to establish resilient forms of polaritonic transport. This talk will report novel phonon-polariton states trapped by topological defects in a silicon metasurface integrating hexagonal boron nitride (hBN). Spatially localized polaritonic modes originate from the coupling of electromagnetic fields with phonon vibrations in hBN. The point defect mode is, in particular, identified to possess unique features stemming from its topological origin: a chiral polarization texture, a singular radiation leakage profile, and the possibility of being selectively excited through coupling to spin-polarized edge waves at heterogeneous topological interfaces.

Active Metasurfaces in Space and Time

Harry A. Atwater

California Institute of Technology, USA
*corresponding author: haa@caltech.edu

Abstract: Electro-optically tunable active metasurfaces that enable dynamic modulation of reflection and transmission amplitude, phase, and polarization using resonantly excited materials and phenomena are powerful design elements for meta-imaging and computation. As flat, low-profile optical elements, active metasurfaces have potential serve as cascadable, programmable components in optical meta-imaging systems, such as lens-less cameras and single-photon imaging systems. In this talk, I will discuss metasurfaces with high quality factor, local, resonant elements capable of two-dimensional phase gradient generation, in both passive and active metasurface designs. I will also describe active metasurfaces with both spatial and temporal phase gradients, and an active metasurface as a lens-less imaging system, and compare the characteristics to conventional lens-coupled image sensors.

Machine learning for metamaterials and metasurfaces

Elastic spin angular momentum in metamaterials and classical structures

Jinfeng Zhao[1*], Yao Huang[1], Yuxuan Zhang, and Yongdong Pan[1]

[1]School of Aerospace Engineering and Applied Mechanics, Tongji University, 100 Zhangwu Road, 200092, Shanghai, China

[*]corresponding author: jinfeng.zhao@tongji.edu.cn

Bosonic-like waves in topological metamaterials and/or phononic crystals have raised wide interest owing to their exotic features. The chirality of topological edge states (TES), known as pseudo-spin, is an important feature for performing robust wave manipulation. Unlike the mathematical concept of pseudo-spin, the spin angular momentum (SAM) of elastic waves describes their local but intrinsic chirality. The SAM of some guided modes locks to the wave direction, which leads to unidirectional routing in both metamaterials and classical structures.

Here, we successfully measure the elastic spin of acoustic Rayleigh and Lamb modes along different directions, and demonstrate spin-wavenumber locking over a broad frequency range [1]. Subwavelength chiral meta-sources are constructed thanks to a special design, and give rise to observed unidirectional routing of Rayleigh and Lamb modes. Moreover, by using one chiral source, simultaneous opposite routing is demonstrated for symmetric and antisymmetric Lamb modes in a single elastic plate [2].

Interestingly and importantly, we extend elastic SAM to valley metamaterials, and observe the previously overlooked elastic spin-valley locking mechanism [3]. Based on theoretical, numerical and experimental results, the SAM of valley chiral TES is found to relate both to spatial position and wavenumber. Putting a chiral source at a representative position on the metamaterial allows one to achieve unidirectional wave routing. The resulting wave direction agrees well with that expected according to the spin-wavenumber locking mechanism. This research shows that elastic SAM offers a new tool to explore valley metamaterials, and should be applicable other mode types in relevant topological metamaterials.

Acknowledgements

This work is supported by the National Natural Science Foundation of China (No. 12172256).

References

1. Yuan, W., Yang, C., Zhang, D., Long, Y., Pan, Y., Zhong, Z., Chen, H., Zhao, J., and Ren, J., “Observation of elastic spin with chiral meta-sources”, Nature Communications, Vol. 12, 6594, 2021.
2. Yang, C., Zhang, D., Zhao, J., Gao, W., Yuan, W., Long, Y., Pan, Y., Chen, H., Nori, F., Bliokh, K.Y., Zhong, Z., and Ren, J., “Hybrid spin and anomalous spin-momentum locking in chiral surface elastic waves”, Physical Review Letters, Vol. 131, No. 13, 136102, 2023.
3. Zhao, J., Yang, C., Yuan, W., Zhang, D., Long, Y., Pan, Y., Chen, H., Zhong, Z., and Ren, J., “Elastic valley spin controlled chiral coupling in topological valley phononic crystals”, Physical Review Letters, Vol. 129, No. 27, 275501, 2022.

Metamaterials with architected instabilities

Davide Bigoni[1*]

[1]Instabilities Lab, University of Trento, Via Mesiano 77, 38123 Italy
[*]Corresponding author: davide.bigoni@unitn.it

Abstract: Homogenization is used for periodic elastic grids subject to axial prestress, to obtain equivalent elastic materials. The latter can be tailored to exhibit material instabilities driven by the microstructure of the grid and its level of prestress. Instabilities include shear band fromation and Hopf bifurcation, thus leading to odd elasticity.

A design strategy is introduced for metamaterials displaying tailored instabilities. When the latter occur at the microscale, they are analyzed with a Floquet-Bloch wave technique, while analysis of macroinstabilities leads to the definition of an equivalent elastic material. This material can be obtained via homogenization theory for periodic elastic structures, subject to a state of axial prestress and incremental deformation involving axial and shear forces and bending moment [1]. Macroinstabilities in the form of shear bands usually occur only for compressive prestress, so that the stability domain for the equivalent material results unbounded in tension. We show that it is possible to design a material for which the stability domain is bounded, in other words, for which shear bands may form under tensile loads. The architecture of this structure is shown in Fig. 1 and the analysis of its dynamic behaviour leads to multiple band gaps, flat bands, and Dirac cones [2].

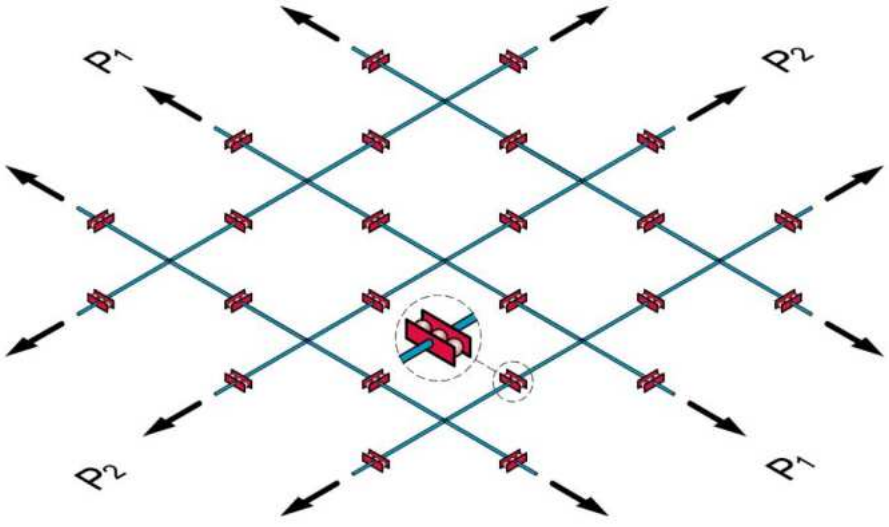


Fig. 1 - A grid of elastic and axially-preloaded rods, jointed through sliding constraints, provides an example of a metamaterial with a bounded (thus even including tension) stability domain. The fact that tensile preload may be applied precludes out-of-plane instabilities, so that the material can be used for structural membranes. In dynamics, the grid shows multiple band gaps, flat bands, and Dirac cones, while its equivalent homogeneous material provides an uncommon example of a material losing ellipticity at the parabolic boundary, thus evidencing ‘stress channelling’, corresponding to shear bands parallel (orthogonal) to the direction of the tensile (compressive) applied preload, P1 and P2.

The possibility of a Hopf bifurcation is introduced, as related to the presence of follower loads [3], or nonholonomic constraints [4], or discontinuity in the constraint curvature [5]. When this instability is implemented in a material [6], apparently work is produced in a closed strain cycle, so that conservation of energy is apparently violated. As mentioned, this violation is only apparent, as the material is able to "suck and release" energy from the environment. When a material is subject to a Hopf bifurcation, mechanical waves propagate through it without decaying, rather with amplification, because energy is extracted from the surroundings, Fig. 2.

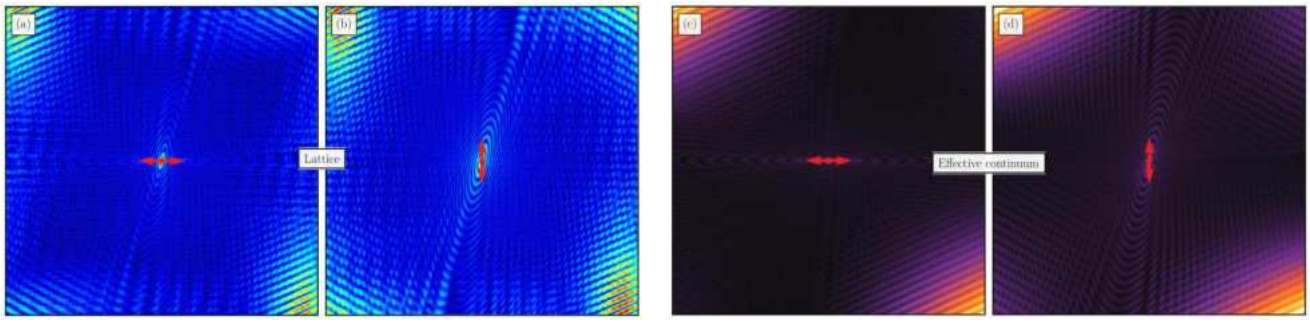


Fig. 2 - Time-harmonic forced response of an anisotropic lattice (a, b) and of the corresponding effective continuum (c, d), displaying flutter instability. The response is typical of the behavior of a dynamically unstable material, evidencing blowing-up waves traveling away from the forcing source but localized along two preferential directions.

The behaviour shown in the figure is typical of odd elasticity, violating hyperelasticity, and opens the way to new and unexpected applications in the field of metamaterials.

Acknowledgements: Financial support is gratefully acknowledged from the European Research Council (ERC) under the European Union's Horizon 2020 research and innovation programme (Grant agreement No. ERC-ADG-2021-101052956-BEYOND).

References

1. Bordiga G., Cabras L., Piccolroaz A. and D. Bigoni "Dynamics of prestressed elastic lattices: Homogenization, instabilities, and strain localization". J. Mech. Phys. Solids, Vol. 146, 104198, 2021.
2. Bordiga G., Bigoni D. and A. Piccolroaz "Tensile material instabilities in elastic beam lattices lead to a closed stability domain". Phil. Trans. Royal Soc. A, Vol. 380, 20210388, 2022.
3. Bigoni D., Kirillov O., Misseroni D., Noselli G. and M. Tommasini "Flutter and divergence instability in the Pfluger column: Experimental evidence of the Ziegler destabilization paradox". J. Mech. Phys. Solids Vol. 116, 99-116, 2018.
4. Cazzolli A., Dal Corso F. and D. Bigoni "Non-holonomic constraints inducing flutter instability in structures under conservative loadings". J. Mech. Phys. Solids, Vol. 138, 103919, 2020.
5. Rossi M., Piccolroaz A., and D. Bigoni "Fusion of two stable elastic structures resulting in an unstable system". J. Mech. Phys. Solids, Vol. 173, 105201, 2023.
6. Bordiga G., Piccolroaz A. and D. Bigoni "A way to hypo-elastic artificial materials without a strain potential and displaying flutter instability". J. Mech. Phys. Solids, Vol. 158, 104665, 2022.

Silicon carbide as a platform for mid-IR metasurfaces

Stefan A Maier[1,2]

[1]School of Physics and Astronomy, Monash University, Clayton, Victoria 3800, Australia
[2]Department of Physics, Imperial College London, London SW7 2AZ, UK
Stefan.Maier@monash.edu

Abstract: Silicon carbide enables strongly confined surface phonon-polaritons in the mid-infrared. We demonstrate the use of this materials platform for phonon-polariton metasurfaces supporting vortex and quasi bound-states-in-the-continuum resonances. Additionally we present results of active metasurfaces operating in the visible regime based on conductive polymers.

Surface-phonon polaritons, hybrid light/matter modes based on the coupling between the electromagnetic field and transverse optical phonons in the restrahlen band of polar dielectrics, are a promising route towards deep sub-wavelength mid-IR photonics. We examine the use of silicon carbide as a platform for surface phonon-polariton metasurfaces. Thin membranes of this material allow for the generation of even and odd surface phonon-polariton coupled modes, the dispersion of which we investigate using near-field optical microscopy [1]. Structuring of the sicilon carbide surface then enables the creation of functional mid-IR photonics structures, which we demonstrate for the cases of vortex modes and quasi bound-state-in-the-continuum resonances. We further present geometries based on out-of-plane symmetry breaking as a means for tailored surface enhanced infrared absorption (SEIRA) sensing [2] with a metallic metasurface.

The second part of the presentation focuses on the active tuning of metasurfaces enabled via switchable conductive polymers [3].

References

1. Mancini, A. *et al.* Near-Field Retrieval of the Surface Phonon Polariton Dispersion in Free-Standing Silicon Carbide Thin Films. *ACS Photonics* **9**, 3696–3704 (2022).
2. Aigner, A. *et al.* Plasmonic bound states in the continuum to tailor light-matter coupling. *Science Advances* 8, eadd4816 (2022).
3. Lu, W., Menezes, L. D. S., Tittl, A., Ren, H. & Maier, S. A. Active Huygens' metasurface based on *in-situ* grown conductive polymer. *Nanophotonics* **13**, 39–49 (2024).

In the Quest for the Viable Perovskite Solar Cells

Nam-Gyu Park

School of Chemical Engineering, SKKU Institute of Energy Science and Technology (SIEST), Sungkyunkwan University, Suwon 16419, Republic of Korea

(npark@skku.edu)

Meeting the escalating electricity demands of our advancing society, particularly at the terawatt scale, requires achieving high power conversion efficiency and low cost per peak watt in solar cell technology simultaneously. Prior to the introduction of perovskite solar cells, only a limited array of materials and technologies could meet both criteria. This presentation traces the evolution toward the development of practical solid-state perovskite solar cells. Beginning with an overview of initial technologies, the discussion progresses to the emergence of solid-state perovskite solar cells. Early efforts involved the use of quantum dot inorganic materials, such as nanocrystalline lead sulfide, as light harvesters. Despite their potential, these materials encountered significant challenges, primarily surface-defect-mediated recombination. Acknowledging these limitations, methylammonium lead triiodide ($MAPbI_3$) perovskite emerged as an alternative to inorganic quantum dots. However, initial implementations as sensitizers in liquid-electrolyte-contained structures yielded disappointing results, with efficiencies as low as 3-4% in 2009 and the dissolution of $MAPbI_3$. A breakthrough occurred in 2012 when a pioneering study demonstrated a 9.7% efficient and 500-hour-stable perovskite solar cell, leveraging $MAPbI_3$ and a solid hole transporting material. This pivotal advancement rendered perovskite solar cells a viable and durable technology. Subsequent years witnessed rapid growth in perovskite photovoltaic research, with efficiencies exceeding 26% using $FAPbI_3$, rivaling or surpassing existing technologies. Current research endeavors focus on enhancing stability and exploring tandem structures for electricity generation in both terrestrial and space applications. The perovskite solar cell stands poised as the most promising energy solution, with its potential impact on sustainable energy surpassing current expectations once stability and lead immobilization challenges are effectively addressed.

Gated Spin Communities

T. Yu[1] and G.E.W. Bauer[2,3,*]
[1]School of Physics, Huazhong University of Science and Technology, Wuhan 430074, China
[2]Kavli Institute for Theoretical Sciences, University of the Chinese Academy of Sciences, Beijing 100190, China
[3]WPI-AIMR and Institute for Materials Research and CSRN, Tohoku University, Sendai 980-8577, Japan
[*]corresponding author: g.e.w.bauer@gmail.com

Abstract: Conducting contacts modulate and control the magnetodipolar interaction that causes chirality of the magnetization and energy transport by spin waves at interfaces and in thin films. Metallic normal, ferromagnetic, and superconducting gates thereby generate new functionalities in magnonic circuits and devices.

Chiral spin waves [1]: Spin waves are the excitations of the magnetic order parameter in magnetic materials that are quantized into magnons. The energy spectrum of spin models with near-neighbor exchange interactions is parabolic for long wavelengths but it becomes strongly anisotropic in the presence of the magnetic dipole-dipole. The so-called Damon-Eshbach magnetostatic spin wave modes of bulk ferromagnets propagate with wave vector **k** normal to the magnetization **m** and are localized and locked at surfaces with normal **n** by the right-hand rule $\mathbf{k} \,||\, \mathbf{m} \times \mathbf{n}$, *i.e.* they are "chiral". This property is topologically protected in half-infinite ferromagnets. The propagation direction of the upper and lower surface modes of a magnetic slab is opposite. In ultrathin ferromagnets the surface modes on both sides morph into the lowest perpendicular standing spin wave modes with amplitudes that are constant over the film thickness. In that limit the spin waves are not chiral anymore. However, the magnetic stray fields on one side of the film are finite only when $\mathbf{k} \,||\, \mathbf{M} \times \mathbf{n}$, but vanish identically when $\mathbf{k} \,||\, -\mathbf{M} \times \mathbf{n}$. In the Damon Eschbach configuration inductive sources and detectors such as metallic strip lines on a given surface thereby interact only with spin waves that propagate in one direction. Magnon transport spectroscopy, Brillouin light-scattering, and diamond NV-center microscopy confirm the chirality of magnon transport in thin films of yttrium iron garnet (YIG). The chirality can be employed as microwave isolators in magnonic circuits.

Gating: The proximity of metallic gates affects a magnet by the diamagnetic eddy currents induced by the magnetic stray fields that are emitted by the spin waves. In normal metals they are dissipated according to Ohm's Law and thereby form an additional damping channel that increases the Gilbert damping constant on top of its intrinsic value. This effect can be distinguished from that of conventional spin-pumping by its wave number dependence or by inserting a thin insulating barrier that suppresses the short-range exchange but not the long long-range dipolar interaction. Moreover, the chirality of the stray field translates into non-local chiral damping, i.e. affects only spin waves that obey the right-hand rule. The induced eddy currents also generate Oersted magnetic fields that blue shift the magnon frequencies [2]. Superconducting gates therefore act as non-dissipative repulsive potential barriers for propagating spin waves [3].

The spin wave propagation and transport with chiral damping is a non-Hermitian Hamiltonian problem. Its numerical solution for finite systems leads to a chiral spin wave skin effect in which magnon accumulates at one edge. Three terminal thin film magnon "transistors" may consist of thin films of magnetic insulators gated by floating magnetic metal films. Here the angle between the thin film and gate magnetization controls the heat and spin currents between the source and drain, leading to a switchable spin wave Peltier effect [4]. When modelling the dissipative gate by a thermodynamic reservoir the two-terminal non-Hermitian problem becomes a three terminal Hermitian one. In the case of ballistic spin waves, the problem is equivalent to the integer quantum

Hall effect in the two-dimensional electron gas as sketched in Figure 1. The Landauer-Büttiker scattering theory of transport reveals that up to half of the source-drain currents may be diverted into the gate.

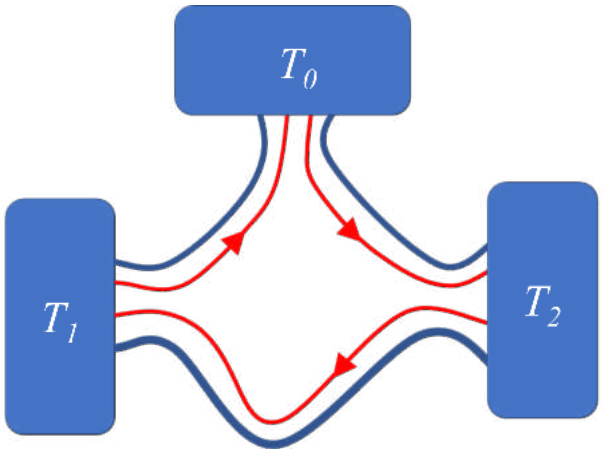


Figure 1: Two-terminal chiral spin wave transport in metal-gated thin magnetic films mapped onto the three-terminal contact configuration of the integer quantum Hall effect in the two-dimensional electron gas at filling factor 1. T_1 and T_2 are the temperatures of the source and drain, while the gate temperature T_0 is at the thermal equilibrium. Only the right moving spin waves generate eddy currents in the gate. This is equivalent to the electronic chiral edge channels of which only the upper one may flow into and out of the third reservoir.

Surprisingly, chiral damping also affects the scattering of spin waves by semi-transparent potential barriers [5]. With the right chirality they may profit from a sufficiently strong damping by an anomalous transmission probability that can be strongly enhanced from the intrinsic one up to unity. We analyze the numerical results by simple analytic model calculations for short-range scatterers.

We hope that our predictions will be useful for future spin-wave computing applications by enabling easy reprogramming and heat management of magnonic circuits.

We acknowledge support by the National Key Research and Development Program of China under Grant No. 2023YFA1406600, the National Natural Science Foundation of China under Grants No. 12374109 and No. 12088101, the startup grant of Huazhong University of Science and Technology, as well as JSPS KAKENHI Grants Nos. 19H00645 and 22H04965.

References

1. For a review with an extensive bibliography see: T. Yu, Z. C. Luo, and G. E. W. Bauer, “Chirality as generalized spin–orbit interaction in spintronics”, Phys. Rep., Vol. 1009, 1-115 (2023).
2. T. Yu and G. E. W. Bauer, “Efficient Gating of Magnons by Proximity Superconductors”, Phys. Rev. Lett., Vol. 129, 117201, 2022.
3. M. Borst, P. H. Vree, A. Lowther, A. Teepe, S. Kurdi, I. Bertelli, B. G. Simon, Y. M. Blanter, and T. van der Sar, “Observation and control of hybrid spin-wave–Meissner-current transport modes”, Science, Vol. 382, 430-434, 2023.
4. T. Yu, C. Cai, and G.E.W. Bauer, “Chirality Enables Thermal Magnon Transistors”, SCIENCE CHINA Physics, Mechanics & Astronomy, in press.
5. X. Ye, K. Xia, G. E. W. Bauer, and T. Yu, “Damping-Enhanced Magnon Transmission”, arXiv:2401.12022.

Optical spin topologies in plasmonics and metamaterials

Anatoly V. Zayats[1*]

[1]Department of Physics and London Centre for Nanotechnology, King's College London, Strand, London WC2R 2LS, United Kingdom

[*]corresponding author: anatoly.zayats@kcl.ac.uk

Abstract: We will discuss spin-orbit coupling in interaction of complex vector beams with plasmonic metamaterials. Spin-orbit coupling and topology of evanescent waves and vector beams propagating in free space and metamaterials in different dispersion regimes will be considered.

Light waves carry both spin and angular optical momenta and their interaction can be influenced by symmetry of the electromagnetic field and/or anisotropy of the medium where light propagates [1]. The ability to engineer and manipulate the properties of vector optical wavefronts and pulses with non-uniform polarisation is important in various applications including imaging, metrology, optical communications as well as biomedical and quantum technologies [2]. Spin-orbit coupling provides interesting applications in polarisation-enabled control of optical signals, or in reverse, controlling light polarisation. This coupling in evanescent fields is mediated by the transverse spin and results in complex topological field structures analogous to prototypical condensed matter phenomena, such as quantum spin-Hall effect, skyrmions, merons, and others [1,3-5]. At the same time, the interactions between propagating vector votes beams and the metamaterial strongly depends on the longitudinal field of the beam, which can be enhanced by the focusing, and whose morphology depends on the characteristics of the initial state of polarisation chosen [6,7]. These interactions may completely modify the initial polarisation state of the transmitted beam, in many cases resulting in its azimuthalisation or vortex modification [8,9]. The spin-orbit coupling is important for controlling waveguiding and for nonpolarized light [10-12].

In this talk, we will discuss spin-orbit coupling in guided waves and complex vector beams, both carrying longitudinal fields, their topological manifestations, interaction with anisotropic and epsilon-near-zero metamaterials, and the applications. Topologically protected states in guided and propagating beams, and polarisation structure stability and transformations will be considered. Strongly anisotropic metamaterials provide a flexible platform for tailoring complex vector beams and pulses for harvesting functionalities and applications of complex light beams with complex polarisation and phase distributions in numerous photonic and quantum technologies, imaging and metrology.

This work was supported by the ERC iCOMM project (789340).

References

1. Y. Shen, Q. Zhang, P. Shi, L. Du, X. Yuan, and A. V. Zayats, "Optical skyrmions and other topological quasiparticles of light," Nature Photonics, Vol. 18, 15-25, 2024.
2. K. Y. Bliokh et al, "Roadmap on structured waves," J. Opt., Vol. 25, 103001, 2023.
3. X. Lei, A. Yang, P. Shi, Z. Xie, L. Du, A. V. Zayats, and X.-C. Yuan, "Photonic spin lattices: symmetry constraints for

skyrmion and meron topologies," Phys. Rev. Lett., Vol. 127, 237403, 2021.

4. P. Shi, L. Du, C. Li, A. V. Zayats, and X.-C. Yuan, "Transverse spin dynamics in structured electromagnetic guided waves," Proc. Nat. Acad. Sci., Vol. 118, e2018816118, 2021.
5. X. Lei, L. Du, X. Yuan, and A. V. Zayats, "Optical spin–orbit coupling in the presence of magnetization: photonic skyrmion interaction with magnetic domains," Nanophotonics, Vol. 10, 3667, 2021.
6. A. Afanasev, J. J. Kingsley-Smith, F. J. Rodriguez-Fortuno, and A. V. Zayats, "Non-diffractive 3D polarisation features of optical vortex beams," Adv. Photon. Nexus, Vol. 2, 026001, 2023.
7. Y. Shen, B. Yu, H. Wu, C. Li, Z. Zhu, and A. V. Zayats, "Topological transformation and free-space transport of photonic hopfions," Adv. Photon., Vol. 5, 015001, 2023.
8. V. Aita and A. V. Zayats, "Enhancement of optical spin-orbit coupling in anisotropic ENZ metamaterials," IEEE Phot. Journ., Vol. 15, 0600108 (2023).
9. V. Aita, M. Shevchenko, Francisco J. Rodríguez-Fortuño, and A. V. Zayats, “Propagation of focused scalar and vector vortex beams in anisotropic media: A semianalytical approach,” Phys. Rev. B, Vol. 109, arXiv: 2402.04349, 2024.
10. M. F. Picardi, C. P. T. McPolin, J. J. Kingsley-Smith, X. Zhang, Sh. Xiao, F. J. Rodríguez-Fortuño, and A. V. Zayats, "Integrated Janus dipole source for selective coupling to silicon waveguide networks," Appl. Phys. Rev., Vol. 9, 021410, 2022.
11. A. V. Krasavin, P. Segovia, R. Dubrovka, N. Olivier, G. A. Wurtz, P. Ginzburg, and A. V. Zayats, "Generalization of optical theorem: experimental proof for radially polarized beams," Light: Sci. Appl., Vol. 7, 36, 2018.
12. J. S. Eismann, L. H. Nicholls, D. J. Roth, M. A. Alonso, P. Banzer, F. J. Rodríguez-Fortuño, A. V. Zayats, F. Nori, and K. Y. Bliokh, "Transverse spinning of unpolarized light," Nature Photonics, Vol. 15, 156, 2021.

Intelligent Meta-lens for Imaging Underwater, Aerial and Land

X. Liu[1,2], M. K. Chen[1,2,3], T. Tanaka[4,5,6] and D. P. Tsai[1,2,3]

[1]The State Key Laboratory of Terahertz and Millimeter Waves, City University of Hong Kong, Kowloon, Hong Kong 999077, China
[2]Department of Electrical Engineering, City University of Hong Kong, Kowloon, Hong Kong 999077, China
[3]Centre for Biosystems, Neuroscience, and Nanotechnology, City University of Hong Kong, Kowloon, Hong Kong 999077, China
[4]Innovative Photon Manipulation Research Team, RIKEN Center for Advanced Photonics, Saitama 351-0198, Japan
[5]Metamaterial Laboratory, RIKEN Cluster for Pioneering Research, Saitama 351-0198, Japan
[6]Institute of Post-LED Photonics, Tokushima University, Tokushima 770-8506, Japan
[*]Corresponding author: dptsai@cityu.edu.hk

Abstract: We have developed a series of intelligent meta-lens systems for underwater, land, and aerial imaging and sensing. We reported the design, fabrication, characterization, and applications of the monocular, binocular, and multilocular meta-lens.

Meta-lens is a planar optical device that can control the wavefronts of light via subwavelength nano-antennas. [1-4] Nano-antennas of various structures can provide all kinds of modulation of phase, amplitude, polarization, etc., for a wide range of applications. Traditional optical imaging systems usually consist of a group of lenses to correct spherical or chromatic aberration, which are bulky. When using more than one camera, there will be a set of complex data transformations to calibrate the whole imaging system. Meta-lenses are more flexible to match various scientific and technical application scenarios than the traditional optical lens, especially in space-constrained and fragile environments, such as drones, autonomous driving, and micro-submarines.

Due to the limited and specific light field information obtained by single-lens imaging, an intelligent and compact depth-sensing meta-device is proposed for autonomous land driving, as shown in Fig. 1(a). With the support of deep learning, the array of 3600 achromatic metalenses integrates the functions of light field imaging and structured light imaging, which is suitable for different scenes at all light levels. For the exploration of the aquatic environment, a novel GaN binocular meta-lens is specifically designed and fabricated to demonstrate underwater stereo vision (see Fig. 1(b)). Proposed underwater binocular meta-lens stereo vision can realize real-time depth imaging with neural networks. The intrinsic superhydrophobicity of nanostructured GaN meta-lens enables its anti-adhesion, stain-resistant, and self-cleaning functions. For the demands of compact, miniaturized, portable, lightweight, and low energy consumption, we demonstrate a GaN-based polarization-independent metalens camera on a drone, as shown in Fig. 1(c). The meta-lens can realize aerial photography and landing assistance for drones and reduce the weight burden to prolong flight time. Meta-lens will significantly benefit future imaging and sensing applications in aerial, land, and underwater environments.

Figure 2 presents the characterization and depth imaging results of the meta-lenses for aerial, land, and underwater imaging. The scanning electron microscope (SEM) images in Fig. 2(a,b,d) show the detailed nanostructures of the meta-lens, revealing the well-defined cylindrical nanostructures with various diameters that are arranged according to the focusing phase distribution. Fig. 2(c) displays an optical photograph of the GaN meta-lens on a sapphire substrate, which is easily recognizable by the naked eye. We process the captured image data using conventional neural networks to obtain fast and accurate depth map results. The depth imaging result in Fig. 2(e) demonstrates that our intelligent meta-device is equally effective for objects with gradually varying depths. Overall, our results indicate that the proposed meta-lenses hold significant

potential for imaging and sensing applications in aerial, land, and underwater environments.

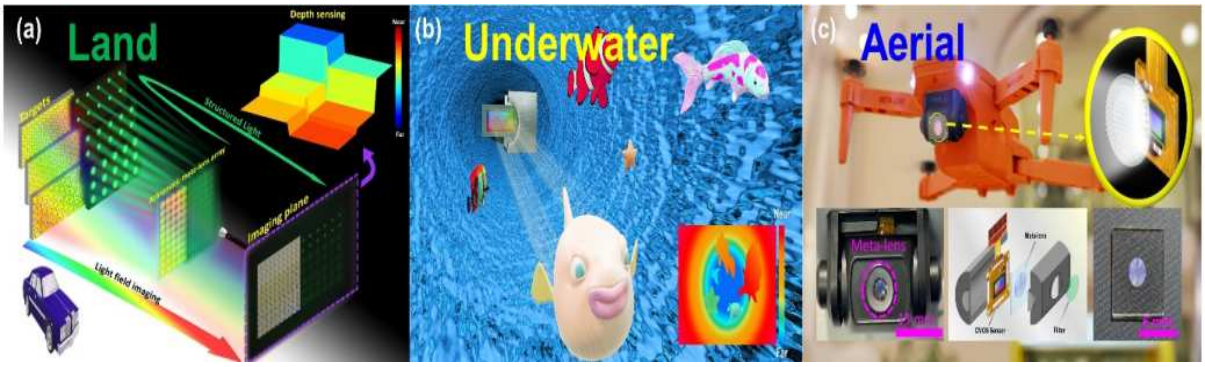


Fig. 1. Applications of meta-lenses. (a) Autonomous vehicles on land. (b) Submarine robot in the ocean. (c) Drone in the sky.

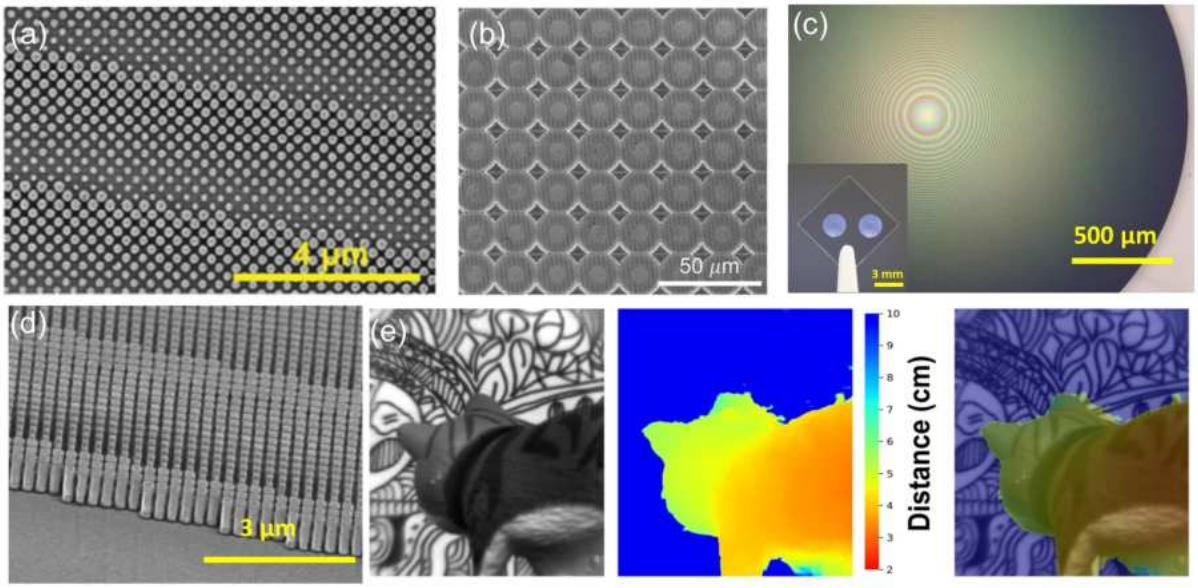


Fig. 2. Characterization and depth imaging results. (a) SEM image of monocular meta-lens on drone. (b) SEM image of achromatic meta-lens array for land imaging. (c) Optical image of binocular meta-lens. (d) SEM image of binocular meta-lens. (e) Depth image results with neural networks.

References

1. L. Li, Z. Liu, X. Ren, S. Wang, V.-C. Su, M.-K. Chen, C. H. Chu, H. Y. Kuo, B. Liu, W. Zang, G. Guo, L. Zhang, Z. Wang, S. Zhu, and D. P. Tsai, "Metalens-array-based high-dimensional and multi-photon quantum source," Science 368, 1487-1490 (2020).
2. M. K. Chen, X. Liu, Y. Sun, D. P. Tsai, "Artificial Intelligence in Meta-optics," Chem. Rev., 122(19), 15356-15413, (2022).
3. M. K. Chen, X. Liu, Y. Wu, J. Zhang, J. Yuan, Z. Zhang, D. P. Tsai, "A Meta-Device for Intelligent Depth Perception," Adv. Mater., 2107465 (2022).
4. X. Liu, M. K. Chen, C. H. Chu, J. Zhang, B. Leng, T. Yamaguchi, T. Tanaka, D. P. Tsai, "Underwater Binocular Meta-lens," ACS Photonics, 10(7), 2382–2389 (2023).
5. X. Liu, Z. Zhao, S. Xu, J. Zhang, Y. Zhou, Y. He, T. Yamaguchi, H. Ouyang, T. Tanaka, M. K. Chen, S. Shi, F. Qi, D. P. Tsai, "Meta-lens Particle Image Velocimetry," Adv. Mater., 2310134 (2023).
6. X. Liu, M. K. Chen, C. H. Chu, J. Zhang, B. Leng, T. Yamaguchi, T. Tanaka, D. P. Tsai, "Underwater Binocular Meta-lens," ACS Photonics 10 (7), 2382-2389 (2023).

Analog computing with nonlinear flat optics

C. De Angelis[1,2], **D. de Ceglia**[1,2]
[1]CNIT and Department of Information Engineering, University of Brescia, via Branze 38, Brescia, 25123, Italy.
[2]Istituto Nazionale di Ottica, Consiglio Nazionale delle Ricerche, via Branze 45, Brescia, 25123, Italy
[*]corresponding author: costantino.deangelis@unibs.it

Abstract: Digital signal processing has revolutionized many fields of science and engineering, but it still shows critical limits; a long-sought solution is optical analog computing. We demonstrate here that nonlinear phenomena combined with engineered nonlocality in flat optics can be leveraged to synthesize Volterra kernels able to outperform linear devices.

Flat-optics devices exhibiting a linear local (LL) response are defined by a position-dependent, linear transfer function $T_{LL}(\mathbf{r})$, which can be locally tailored by engineering metaatoms arranged within metasurfaces. An input signal, defined in real space as $I_\omega(\mathbf{r})$, is filtered linearly and locally, and transformed into an output $O_\omega(\mathbf{r})=T_{LL}(\mathbf{r})I_\omega(\mathbf{r})$. Wavefront engineering is arguably the most prominent application for LL systems [1]. Spatial dispersion, i.e., nonlocality, is usually regarded as a nonideality in LL flat-optics devices. However, the nonlocal response of metasurfaces has been recently indicated as an effective means to achieve advanced functionalities based on the independent control of spectral and angular selectivity [2].

To date, investigations into nonlocality have primarily focused on the linear-optics regime. The action of linear nonlocal (LN) systems is well described by a k-dependent transfer function $T_{NL}(\mathbf{k})$, which describes how the metasurface filters the angular spectrum of an input function, according to $O_\omega(\mathbf{k})=T_{NL}(\mathbf{k})I_\omega(\mathbf{k})$. Nonlocal metasurfaces are well suited for analog computing and image processing. For example, n-th order differentiation is easily achieved with transfer functions of type $(jk)^n$, while integration is obtained by synthesizing transfer functions of the type $(jk)^{1/n}$ [3].

Despite the advantages, linear approaches — both local and nonlocal — face limitations related to the restricted numerical aperture and frequency bandwidth, and the inherent linearity of the mathematical operations that one can engineer. Here we demonstrate that the combination of nonlinear and nonlocal effects in the same flat-optics device is a powerful strategy to achieve advanced image processing and analog computing functionalities with reduced structural complexity and increased efficiencies in terms of angular and frequency bandwidth [4]. The concept of nonlinear nonlocal (NN) flat-optics is illustrated in Fig. 1, highlighting the differences with respect to LL and LN approaches.

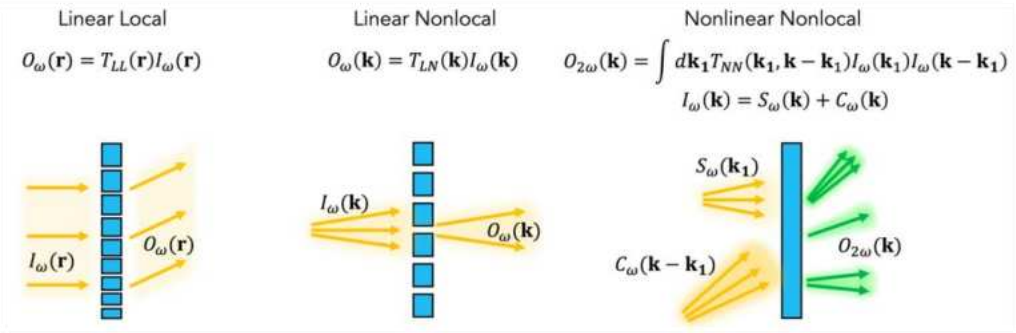


Fig. 1: Comparison between the transfer functions of flat-optics elements with LL, LN, and NN responses. Typical operation of the three systems. **a** Beam deflection (LL system). **b** Passive filtering of spatial-frequencies (LN system). **c** Nonlinear mixing of spatial frequencies (NN system)

We will provide illustrative examples that show the potential of NN flat-optics in analog computing. In the operation schematically illustrated in Fig. 2, we consider a gallium arsenide (GaAs) thin film. The film is excited by two coherent fields: a control field and a signal field. In a simple experimental setup, the control field (C_ω) may be for example a gaussian beam with very large cross section impinging at oblique incidence. The signal field (S_ω) is a small-divergent and normally-incident beam with transverse cross section defined by an arbitrary function.

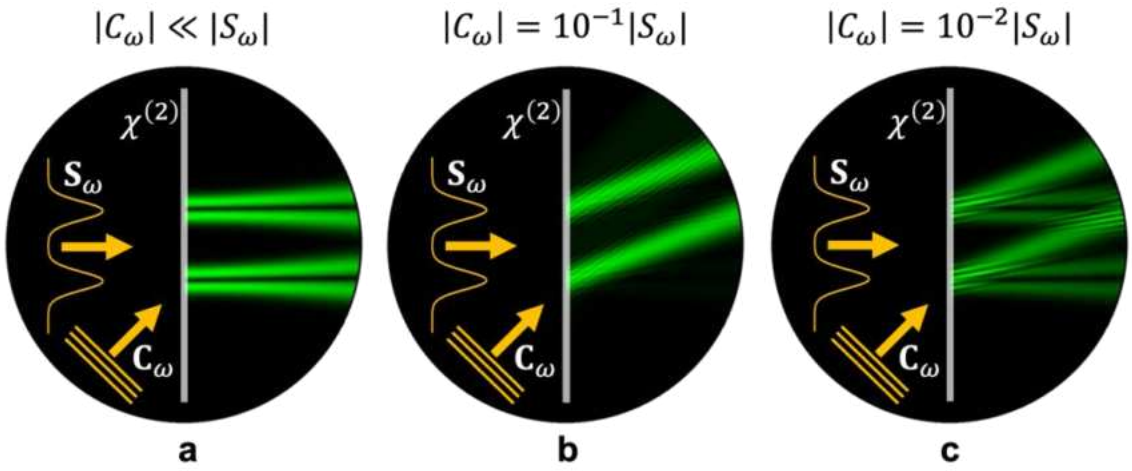


Fig. 2. Functionalities of a nonlinear nonlocal (NN) flat-optics element made of a thin film of gallium arsenide. The system is illuminated by two coherent beams: a control (C) and a signal (S), reported in orange. **a** When the amplitude of the control is much smaller than the amplitude of the signal, nonlinear edge detection is performed at the SH (the green beam transmitted is the "edge" of the signal, i.e., it is proportional to the derivative of the signal). **b** Nonlinear beam deflection is dominant. **c** SHG performs simultaneous nonlinear edge detection and nonlinear beam deflection of the signal. The deflection angle is determined by the angle of incidence of the control signal.

The example reported in Fig. 2 showcases the intriguing and unique capabilities of NN systems: (i) Analog computing and image processing functionalities that typically require patterned metasurfaces in the linear regime, such as beam deflection (or anomalous refraction) and edge detection, may be achieved by leveraging the nonlinear and nonlocal response of unpatterned thin films; (ii) The response of a NN system is intensity dependent, hence tunable; (iii) The filtering operations are inherently nonlinear; (iv) Since this approach does not rely on any electromagnetic resonance, it is also free from any fundamental constraint on the operational spectral bandwidth, as it happens instead for linear devices based on patterned metasurfaces; (v) Other input-output transformations may be foreseen by properly using the control function as a means to "write" other functionalities.

References

1. Hail, C.U., Foley, M., Sokhoyan, R. *et al.*, "High quality factor metasurfaces for two-dimensional wavefront manipulation" *Nat Commun* **14**, 8476 (2023).
2. Overvig, A. and Alù, A., "Diffractive nonlocal metasurfaces," *Laser Photonics Rev*. **16**, 2100633 (2022).
3. Kwon, H., Sounas, D., Cordaro, A., Polman, A. and Alù, A. "Nonlocal Metasurfaces for Optical Signal Processing," *Phys. Rev. Lett.*, 121, 173004 (2018).
4. de Ceglia, D., Alù, A., Neshev, D. N. and De Angelis, C., "Analog image processing with nonlinear nonlocal flat optics," *Opt. Mater. Express* 14, 92 (2024).

Two-dimensional electronic spectroscopy of many-body correlations in quantum materials

Christoph Lienau[1]

[1]Institut für Physik, Carl von Ossietzky Universität Oldenburg, 26111 Oldenburg, Germany
[*]corresponding author: Christoph.lienau@uni-oldenburg.de

Abstract: Two-dimensional electronic spectroscopy with few-femtosecond time resolution is an emerging tool for probing quasi-particle interactions in quantum materials. The talk will discuss its use for exploring the quantum dynamics of strongly coupled J-aggregate exciton/surface plasmon polariton hybrids, ultrafast manybody and intervalley couplings in atomically thin semiconductors and for tailoring the nonlinearities of such semiconductors in plasmonic cavities.

Many of the exciting properties of novel types of quantum materials, from polariton condensation to light-induced superconductivity arise from strong couplings among electrons, phonons, spins and photons in the material. These couplings give rise to the formation of new hybrid excitations, quasi-particles, with optical and electronic properties that can be vastly different from those of the uncoupled excitations. Two-dimensional electronic spectroscopies (2DES), replacing the excitation pulse in common pump-probe spectroscopies by a phase-locked pulse pair, can give unique insights into such couplings [1,2]. Cross peaks in the 2DES, oscillating as a function of time delay between pump pair probe, provide definite spectroscopic signatures for such couplings, making 2DES with few-femtosecond time resolution [3] a method of choice for unraveling the microscopic physical processes that govern quasi-particle formation in quantum materials.

In my talk, I will give an introduction into these multidimensional electronic spectroscopies and their applications to selected nanoscale materials. In a first example, I will use them to unravel the optical nonlinearities excitons in J-aggregated organic semiconductors [4,5] that are strongly to surface plasmon polaritons [1]. The data show how strong coupling transforms the usual diffusive hopping exciton transport in organics into a coherent transport of excitons over mesoscopic distances at room temperature. I will then discuss how 2DES can be employed to sensitively probe many-body interactions and intervalley couplings in atomically thin semiconductors, revealing the latter through ultrafast, 11-fs oscillations of exciton peaks. When coupling these excitons to plasmonic nanoresonators, new hybrid particles arise with optical nonlinearities that are vastly enhanced over those of both monolayer excitons and the plasmons. 2DES reveals how many-body correlations enhance the nonlinearities, opening up new pathways for tailoring optical nonlinearities in hybrid systems of atomically thin semiconductors that are coupled to external cavities. All these examples give strong indications that many-body interactions among two-quantum excitations are crucial for understanding the optical nonlinearities of such hybrid systems.

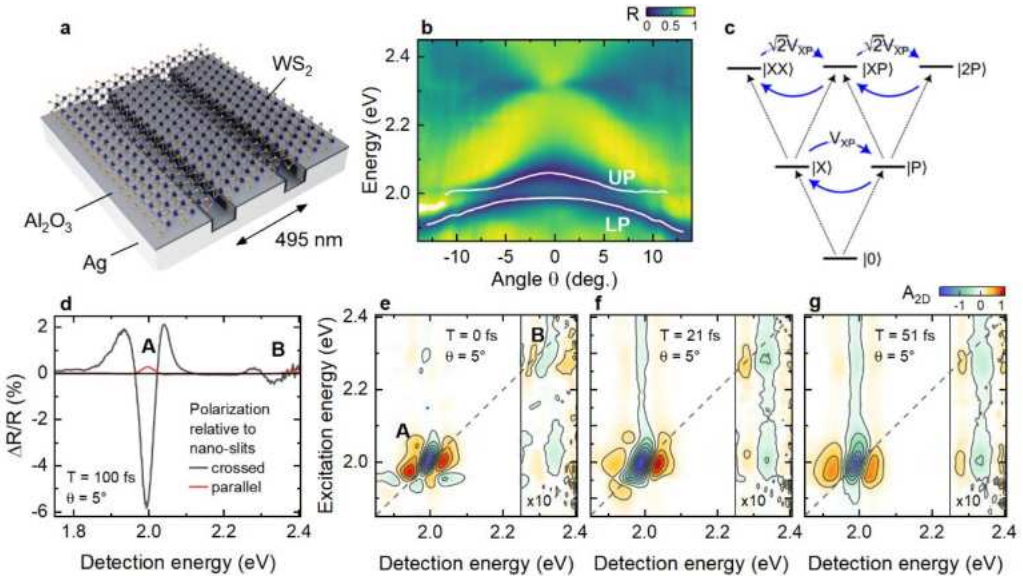


Fig. 1. a) Sketch of the hybrid sample comprising a periodic nano-slit array (20x50 µm²) milled into a silver film and coated with a 5-nm layer of Al_2O_3. The nanostructure is covered with an exfoliated monolayer of WS_2. b) Angle-dependent linear reflectivity showing an anti-crossing at an incidence angle of $\theta = \pm 5°$ forming upper (UP) and lower (LP) polariton branches with a coupling strength of $V_{XP} =$ 23 meV. c) Level scheme of strong coupling between the A exciton $|X\rangle$ and plasmon $|P\rangle$ including one- and two-quantum excitations. d) Differential reflectivity at $\theta = 5°$ and a waiting time of $T = 100$ fs for pulses polarized perpendicular to the nano-slits (black) and along the slits (red). A giant enhancement of the nonlinearity by a factor of ~20 is demonstrated, arising from the hybridization between $|X\rangle$ and $|P\rangle$. e)-g) 2DES maps for selected waiting times. Two polariton manifolds for the A and B exciton and cross-peaks are observed.

References

1. Timmer, D. et al., "Plasmon mediated coherent population oscillations in molecular aggregates", Nature Commun. 14, 8305 (2023).
2. Nguyen X. T. et al., "Phonon-driven intra-exciton Rabi oscillations in CsPbBr3 halide perovskites", Nature Commun. 14, 1047 (2023).
3. Timmer, D. et al., "Full visible range two-dimensional electronic spectroscopy with high time resolution", Optics Express 32, 835 (2024).
4. Quenzel T. et al., "Plasmon-Enhanced Exciton Delocalization in Squaraine-Type Molecular Aggregates", Acs Nano 16, 4693-4704 (2022).
5. Timmer, D. et al., "Charge Delocalization and Vibronic Couplings in Quadrupolar Squaraine Dyes", Journal of the American Chemical Society 144, 19150 (2022).

High Spatiotemporal Resolution Live Cell Imaging on a Plasmonic Metasurface

Kaoru Tamada

Kyushu University, Japan

Abstract: Self-assembled monolayers composed of metal nanoparticles can be regarded as metasurfaces with high refractive index and extinction coefficient due to collective excitation of coupled localized surface plasmon resonance (LSPR). This plasmonic metasurface confines light to the nanointerface and enhances fluorescence, thus enabling high-speed interfacial imaging with high axial and lateral resolution up to the theoretical limit even under wide-field microscopy. By using this imaging method, we were able to observe unique cell dynamics at the molecular level that have not been visualized before; such as a spider-web-like fibrous nascent adhesion spreading radially at the initial stage of cell adhesion and also asymmetrical motility of metastatic breast cancer cells discriminated from non-tumorous cells.

Chiral Nanophotonics: Enabling Ultrasensitive Detection in Biophysical Measurements

Malcolm Kadowala[1*]

[1] School of Chemistry, Joseph Black Building, University of Glasgow, Glasgow, G12 8QQ, UK
[*]corresponding author: malcolm.kadodwala@glasgow.ac.uk

Abstract: Spectroscopic techniques using circularly polarized light offer a powerful tool to analyze chirality, a crucial property in biomaterials. These techniques rely on the differential interaction of left- and right-handed circularly polarized light with chiral molecules. However, the inherently weak signal strength of circular dichroism (CD) limits their sensitivity. This talk will explore how the emerging field of chiral nanophotonics can overcome this barrier. By harnessing the unique properties of nanostructures, we can significantly enhance the interaction between light and chiral molecules. This allows for highly sensitive CD measurements, potentially reaching the single-molecule level.

Extreme Space-Time Optics & Quantum Meta-Photonics

Vladimir M. Shalaev

Purdue University
West Lafayette, Indiana, USA
corresponding author: shalaev@purdue.edu

Abstract: We first discuss all-optical modulation with single photons using electron avalanche, resulting in record-high nonlinearities. Then we show that transparent conducting oxides (TCOs) operating in the near-zero index (NZI) regime can provide strong single-cycle modulation, thus enabling novel photonic time crystals. Finally, we discuss scalable quantum photonics with single-photon emitters in silicon nitride that we recently discovered as well as the intriguing possibility to generate indistinguishable single photons by using plasmonic speedup that could enable important quantum photonics applications, including quantum communication and quantum computing.

Controlling nanomaterial properties using organization

M. Tréguer-Delapierre

ICMCB-CNRS UMR5026, U.Bordeaux, Pessac, France

mona.treguer@icmcb.cnrs.fr

We recently demonstrated a new concept for making nanostructures with unusual optical properties by organizing metal nanoparticles. In research and industry, molecules from drugs and polymers are made by combining high-yield chemical reactions in series. We have extended this approach to the nanoscale: we make metamolecules by combining high-yield colloidal reactions. Metamolecules are highly symmetric nanoclusters of metal and dielectric. They are needed for exotic optical materials like metafluids or for creating new light sources but they are notoriously difficult to make because of the precision required. We addressed this challenge by combining inorganic growth, polymerization and metal deposition. Though no individual reaction is new, the way we combine them is-much as the novelty in an organic synthesis scheme lies in determining what series of reactions will yield a target molecules. I will present the potential of this novel strategy. Through painstaking single-cluster spectroscopy measurement and comparison to simulation, I will show that the morphology is controlled to nanometer-scale precision. Previous approaches to making metamolecules fall into two classes: lithography, which offers control over morphology but limited throughput, and self-assembly, which offers high precision but limited control over yield. Our approach fits into neither category, et offers the best of both: high precision, high morphology yield, and bulk scale-up. It can be adapted to many other material systems. Moreover, I will present novel strategies regarding the organization of nanoparticles onto a substrate for mastering the visual appearance of an object at the macroscale (3). The coupling of nanoscale resonances and mesoscale interferences can be used to engineer spectrally and angularly the reflected light and lead to novel visual effects that are particularly impressive when changing viewing conditions (4). I will show how to use these studies to make useful materials and to gain a deeper understanding of the optics of materials at the nanoscale.

1.L.Roach, L.Lermusiaux, A.Baron, M.Tréguer-Delapierre in *Encyclopedia of Nanomaterials* edited by Y.Yadong, Y.Xia, (Elsevier, 1, ISBN 978-0-12-822425-0.000011-7) (2021)

2.L.Lermusiaux, L.Roach, A.Baron, M.Tréguer-Delapierre, *Nano Express,* 3, 2, 21003 (2022)

3.K.Vynck, R.Pacanowshi, A.Dufay, X.Granier, P.Lalanne, *Nature Materials*, 21, 1035, (2022)

4.A.Agreda, T.Wu, A.Hereu, M.Tréguer-Delapierre, G.Drisko, K.Vynck, P.Lalanne, *ACS Nano*, 17, 6362 (2023)

Nanoplasmonics as Enabler of Ultrafast Quantum Nanophotonics at Ambient Temperatures

Ortwin Hess[1]

[1]Trinity College Dublin, Dublin 2, Ireland
[*]corresponding author: ortwin.hess@tcd.ie

Abstract: We discuss how nanoplasmonic-cavity strong coupling and ultrafast plasmonic near-field evolution can be exploited to achieve high-speed nanophotonic quantum operations at ambient temperatures, including dynamic multi-partite entanglement, and introduce a novel strategy for preparation and 'immortalization' of selected plasmon-exciton polariton states by means of quantum coherent perfect absorption.

Spontaneous emergence of eyes in reinforcement learning agents

Dianjing Liu, Boyuan Liu, Ming Zhou, Yurui Qu, Zhicheng Wu, Qingyi Zhou, Zongfu Yu*

Department of Electrical and Computer Engineering, University of Wisconsin, Madison, Wisconsin 53706, U.S.A

A living animal exhibits remarkable ability to survive. It processes sensory input and takes actions to maximize the likelihood of survival. Researchers have been inspired to develop similar artificial agents powered by reinforcement learning—for instance, the DeepMind agent, which learns to play Atari arcade games. In the recent development, the ability to process raw sensory data such as the images, instead of handcrafted features, is one of the most important enablers, making it possible to train agents for different applications at scale. However, these agents are still different from fully autonomous agents such as living beings who not only process raw sensory data but also develop sensory function as part of their learning process. In this article, we show that an artificial agent powered by reinforcement learning can also spontaneously develop sensory functions. It can build its own bridge to connect the digital world to the physical one. This capability could be used to develop resilient agents that are adaptive in changing environments.

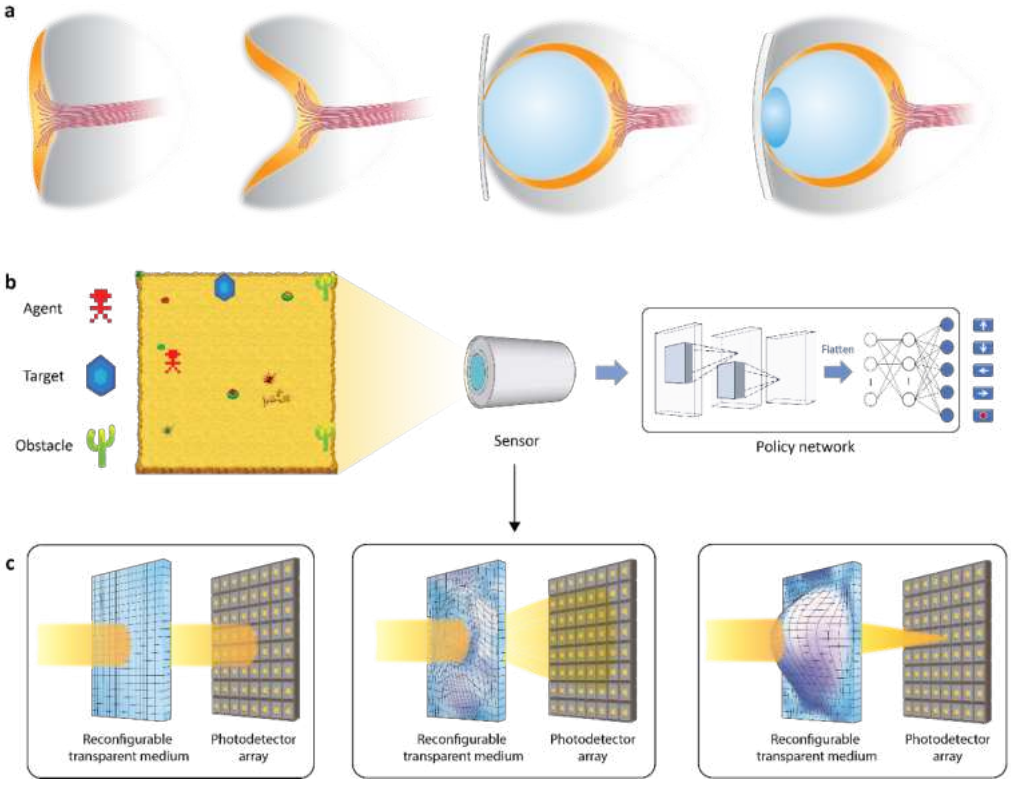


Figure 1. The evolution of ancient eyes and the spontaneous emergence of eyes in artificial agents. (a) Four evolutionary stages of eyes. (b) A simplified scenario to replicate the animal evolution process. On the left is a world with an agent, a target, and obstacles. The artificial agent is composed of a sensor and a neural network which function as the eyes and brain of an animal, respectively. It observes the world through the sensor and responds with action. (c) The sensor consists of a reconfigurable transparent medium and an array of light-sensitive detectors. The agent can adjust the shape of the transparent medium in the learning process. The three panels show the reconfigurable sensor at the beginning (left), intermediate (middle), and final (right) stages of the development.

A universal infrared absorption analysis system using deep learning

Eito Nakagawa[1], Hiroto Sasaki[1], and Yoshiaki Nishijima[1,2,3,4*]

[1]Department of Electrical and Computer Engineering, Graduate School of Engineering,
[2]Yokohama National University, 79-5 Tokiwadai, Hodogaya-ku
[3]Institute of Advanced SciencesYokohama National University, 79-5 Tokiwadai, Hodogaya-ku
[4]Institute for Multidisciplinary Sciences Yokohama National University, 79-5 Tokiwadai, Hodogaya-ku
[*]corresponding author: nishijima-yoshiaki-sp@ynu.ac.jp

Abstract: We focused on reducing the experimental cost of obtaining mid-infrared absorption spectra using machine learning techniques. The large amount of spectral data from HITRAN and quantum scientific calculations can be a useful method effective prediction to the experimental spectra.

1. Introduction

MIR absorption is focused in the field of molecular sensing using plasmon materials and metasurfaces. Mid-infrared spectroscopy is a sensing technique that utilizes the vibrational and rotational absorption of molecules. Its non-destructive nature and maintenance advantages are leading to increasing expectations in various environmental monitoring [1,2]. In the context of simultaneous detection of multiple molecules, the complex spectra due to inter and intra-molecular interference has prompted investigations into analysis methods using deep learning [3,4]. However, the significant amount of data required for training and the necessity for acquiring new data when using different measurement instruments pose challenges. Therefore, the aim of this study is to construct a generalized qualitative and quantitative gas analysis method resilient to the effects of different measurement instruments by training models using spectral data obtained from quantum chemical calculations.

2. Experiments

2-1. Qualitative analysis model

The model was trained using spectral data of nine different molecules calculated with Gaussian [5]. The structure of the model involves dividing the spectral data into frequency bins, inputting them into a Convolutional Neural Network (CNN), and combining the outputs to obtain the final output. Data augmentation was performed by shifting and scaling each spectral data peak and combining them to create training data consisting of 14,000 samples and test data consisting of 6,000 samples. After training the model, accuracy was measured using experimental data obtained from the infrared absorption spectral database HITRAN [6].

2-2. Quantitative analysis model

For quantitative analysis, actual spectral data of N2O and CH4 with concentration labels ranging from 0 to 1000 ppm, as well as actual spectral data equivalent to 1000 ppm of H2O, were obtained. Two training datasets were created: one containing actual spectral data of the target molecule (N2O) mixed with spectra of 10 molecules from HITRAN as noise, and the other containing actual spectra of CH4 and H2O as noise. Subsequently, a model focusing on image recognition was trained using the dataset based on HITRAN. Two types of datasets, one from HITRAN and the other from actual measurements, were used to assess both training prediction accuracy and generalization prediction accuracy.

3. Results and discussions

3-1. Qualitative analysis model

We obtain the accuracy measurement results for each molecular species. Additionally, the accuracy measurement results when using experimental data from HITRAN for training with a similar model are also obtained for comparison. Identification accuracy varies by molecule, reaching a maximum of 98%. However, the minimum accuracy is 53%, indicating impractical precision. Two main reasons account for the low accuracy: firstly, overlapping peaks between the peaks of the molecule in question and those of other molecules; secondly, discrepancies between the simulation data used for training and the experimental data. However, since identification is achieved when the domain of the training and test data is the same, it is believed that the latter factor has a more significant impact.

3-2. Quantitative analysis model

We constructed a total of nine models using three types of image classification models (RegNet, EfficientNet-V2, ConvNeXt) as the central learning models. These models were trained using three different patterns: normal learning, fine-tuning with pre-trained weights from ImageNet, and transfer learning where pre-trained weights were fixed. The top three models' training prediction accuracy and generalization prediction accuracy are analysed. Since the concentration labels in the dataset are incremented by 50 ppm, the target values for RMSE and MAE are 25. However, all models exceeded this value sufficiently in terms of training prediction accuracy. Additionally, predictions for the actual measurement dataset, which was not used for training, were below 25, demonstrating the models' robustness to real-world noise by leveraging the robustness against HITRAN noise.

4. Conclusions

We demonstrated the feasibility of qualitative and quantitative analysis of experimental spectra using data from HITRAN and quantum science calculations. However, the performance was inferior when using the same data for training and accuracy assessment, and identification was challenging for certain molecules. To address this issue, creating regression models to minimize discrepancies between simulation and experimental data is desired. In quantitative analysis, it is essential to appropriately select the 10 molecules introduced as noise. For future prospects, we aim to establish a method that adapts to a broader range of noise molecules by constructing multiple quantitative analysis models with different noise molecules and conducting ensemble predictions based on the results from qualitative analysis models.

5. Acknowledgement

YN is grateful for partial support from the Japan Society for the Promotion of Science (JSPS), Grants-in-Aid for Scientific Research, and JSPS Bilateral Joint Research Projects between Japan and Lithuania. This work was partially supported by PRESTO, Japan Science and Technology Agency (JST) (JPMJPR22B6).

6. References

[1] A. D' Arco, T. Mancini, M. C. Paolozzi, S. Macis, A. Marcelli, and et al, "High Sensitivity real-time VOCs monitoring in air through FTIR Spectroscopy using a Multipass Gas Cell Setup", *arXiv:2207.00340*, 2022

[2] G. Michel, "Multi-Gas analysis of ambient air using FTIR spectroscopy over Mexico City", *Atmosfera*, **16.1**, 1-13, 2003

[3] J. Acquarelli, T. van Laarhoven, J. Gerretzen, T. H. Tran, L. M. C. Buydens, E. Marchiori, "Convolutional neural networks for vibrational spectroscopic data analysis", *Analytica Chimica Acta*, **954**, 22–31, 2017.

[4] C. Yuanyuan, W. Zhibin, "Quantitative analysis modeling of infrared spectroscopy based on ensemble convolutional neural networks" *Chemometrics and Intelligent Laboratory Systems*, **181**, 1-10, 2018

[5] Gaussian 16, Revision C.01, M. J. Frisch, and et al, 2016.

[6] Gordon, I.E.; Rothman, L.S.; Hill, C.; Kochanov, R.V.; Tan,Y.; Bernath, P.F.; Birk, M.; Boudon, V.; Campargue, A.; Chance, K.V.;et al. "The HITRAN2016 molecular spectroscopic database". J. Quant. Spectrosc. Radiat. Transf 203 3-69(2017)

Deep learning-enabled metasurface design and autonomous meta-devices

Chao Qian

ZJU-UIUC Institute, Interdisciplinary Center for Quantum Information, State Key Laboratory of Extreme Photonics and Instrumentation, Zhejiang University, 310027 Hangzhou, China.

Email: chaoq@intl.zju.edu.cn

Abstract: Recent breakthroughs in deep learning have ushered in an essential tool for optics and photonics, recurring in various applications of material design, system optimization, and automation control. In this talk, we will share the recent advances in how to streamline metasurface design and develop self-driving meta-devices.

Summary: Deep learning-enabled on-demand metasurface design and adaptive meta-devices have been the subject of extensive expansion, as it can alleviate the time-consuming and low-efficiency shortcomings in conventional numerical simulations and dependent working manner. The unique advantages of deep learning lie in its data-driven signature to help the model discover useful information from a moderate amount of data with strong nonlinear fitting and generalization ability. Therefore, Deep learning has spawned new ways of gamifying conventional design procedure with case-by-case numerical simulations and bottom-up guidance strategy. In this talk, we will share the recent advances made in how to expedite three classes of metasurface design: forward prediction, inverse design, and spectral correlation. Furthermore, we will show how to develop automatic meta-devices that can automatically respond to external stimuli and dynamic environments without human intervention. Examples include chameleon-like self-adaptive invisibility cloak, wireless channel management, and optical illusion. At the same time, future challenges and perspectives are pinpointed, including data curation and knowledge migration, with the vision of free management of entire electromagnetic space.

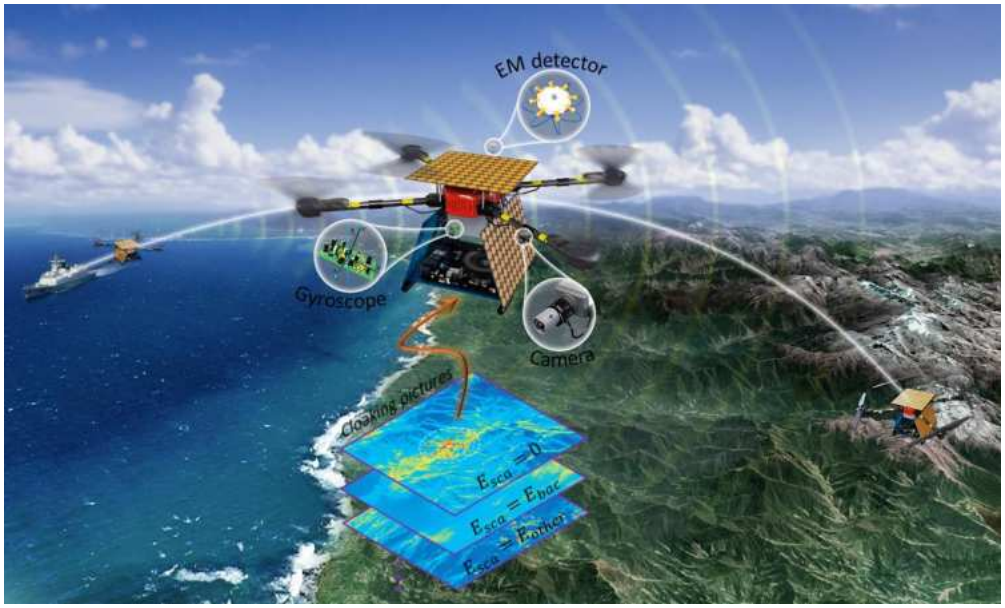


Figure 1. Deep learning enabled autonomous aeroamphibious invisibility cloak

References

1. C. Qian, B. Zheng, Y. Shen, L. Jing, E. Li, L. Shen, and H. Chen. *Nat. Photon.* **2020**, 14, 383-390.
2. C. Qian, Z. Wang, H. Qian, T. Cai, B. Zheng, X. Lin, Y. Shen, I. Kaminer, E. Li, and H. Chen. *Nat. Commun.* **2022**, 13, 2694.
3. C. Qian, Y. Yang, Y. Hua, C. Wang, X. Lin, T. Cai, D. Ye, E. Li, I. Kaminer, and H. Chen. *Nat. Commun.* **2022**, 13, 4383.
4. Z. Fan, C. Qian, Y. Jia, Z. Wang, Y. Ding, D. Wang, L. Tian, E. Li, T. Cai, B. Zheng, I. Kaminer, and H. Chen. *Sci. Adv.* **2022**, 8, eabn7905.
5. Y. Jia, C. Qian, Z. Fan, T. Cai, E. Li, and H. Chen. *Light. Sci. Appl.* **2023**, 12, 82.
6. T. Cai, B. Zheng, J. Lou, L. Shen, Y. Yang, S. Tang, E. Li, C. Qian, and H. Chen. *Adv. Mater.* **2022**, 2205053.
7. C. Qian, Y. Jia, Z. Wang, J. Chen, P. Lin, X. Zhu, E. Li, H. Chen, Autonomous aeroamphibious invisibility cloak with stochastic-evolution learning. *Adv. Photon.* 6, 016001 (2024).

Physics-informed inverse design of programmable metasurfaces

Yucheng Xu[1,2], Jia-Qi Yang[1], Sheng Wang[1], Jingbo Wu[1,2], Caihong Zhang[1,2], De-Chuan Zhan[1,2], Willie J. Padilla[3], Biaobing Jin[1,2], and Kebin Fan[1,2]

[1]Nanjing University, Nanjing, Jiangsu 210023, China

[2]Purple Mountain Laboratory, Nanjing, Jiangsu 210023, China

[3]Duke University, Durham, NC 27708,USA

Abstract: In this work, we proposed an efficient inverse design algorithm for a liquid-crystal based programmable metasurface through adding a physics layer, which is developed based on a modified coupled mode theory, into a residual neural work. We experimentally demonstrated an inversely designed programmable metasurface for beam steering application.

The electromagnetic response of metasurfaces is governed by Maxwell's equations and some other derivative physics-domain knowledge. Incorporating the physics-domain knowledge along with numerical methods has unlocked a myriad of routes to reshape the wavefront of electromagnetic waves at a subwavelength scale. Despite the significant progress, metasurfaces still suffer from constrained performance due to the limited design space and time-consuming forward design process. Recently, the rapidly developed data-driven deep learning algorithms have brought new vitality to the inverse design of metasurfaces, enabling the exploration of designs beyond regular shapes [1-3]. However, most of these design algorithms are statistically brute-force, treating the neural networks as "black-boxes". Therefore, these methods may be functional for designing but might not provide additional implicit physics laws or principles. [4-5] Here, we propose a novel physics-informed inverse design (PIID) method for precisely customizing a programmable LC-based terahertz steering metasurface. The physics domain knowledge, analytically developed based on a modified coupled mode theory (mCMT) with substrate effect included, is integrated into a residual multilayer perceptron (ResMLP) as a physical layer. The inverse design is based on the neural adjoint method [6]. We showed that without knowing the whole spectra information, our algorithm allows the inverse design only from three indicators: the required phase tuning $\Delta\varphi$ and reflection amplitude R at a specific frequency ω_D. The inclusion of an additional physics layer also facilitates the discovery of the correlation between geometries and resonant properties. Using this method, an inversely designed metasurface exhibits phase tuning of about 300° with a reflection amplitude over 0.9 at 465 GHz. Finally, we successfully demonstrated an inversely designed multi-bit programmable metasurface, which can be coded in 1-bit, 2-bit, and tri-state sequences arbitrarily, therefore able to steer the approximately normal incidence with deflected angles up to 65°. Our work underscores that incorporating physics domain knowledge can significantly streamline the inverse design process for highly performing metasurfaces, therefore opening up numerous avenues for various applications.

This work is supported by National Natural Science Foundation of China (62275118), the Fundamental Research Funds for the Central Universities, and Research fund for Jiangsu Key Laboratory of Advanced Techniques for Manipulating Electromagnetic Waves.

References

1. S. Molesky, Z. Lin, A. Y. Piggott, W. Jin, J. Vuckovi´c, and A. W. Rodriguez, Nature Photonics 12, 659 (2018).
2. Z. Li, R. Pestourie, Z. Lin, S. G. Johnson, and F. Capasso, ACS Photonics 9, 2178 (2022).
3. P. R. Wiecha, A. Arbouet, C. Girard, and O. L. Muskens, Photonics Research 9, B182 (2021).
4. R. Zhu, T. Qiu, J. Wang, S. Sui, C. Hao, T. Liu, Y. Li, M. Feng, A. Zhang, C.-W. Qiu, et al., Nature communications 12, 2974 (2021).
5. C.-H. Lin, Y.-S. Chen, J.-T. Lin, H. C. Wu, H.-T. Kuo, C.-F. Lin, P. Chen, and P. C. Wu, Nano letters 21, 4981 (2021)
6. Y. Deng, S. Ren, K. Fan, J. M. Malof, and W. J. Padilla, Optics Express 29, 7526 (2021).

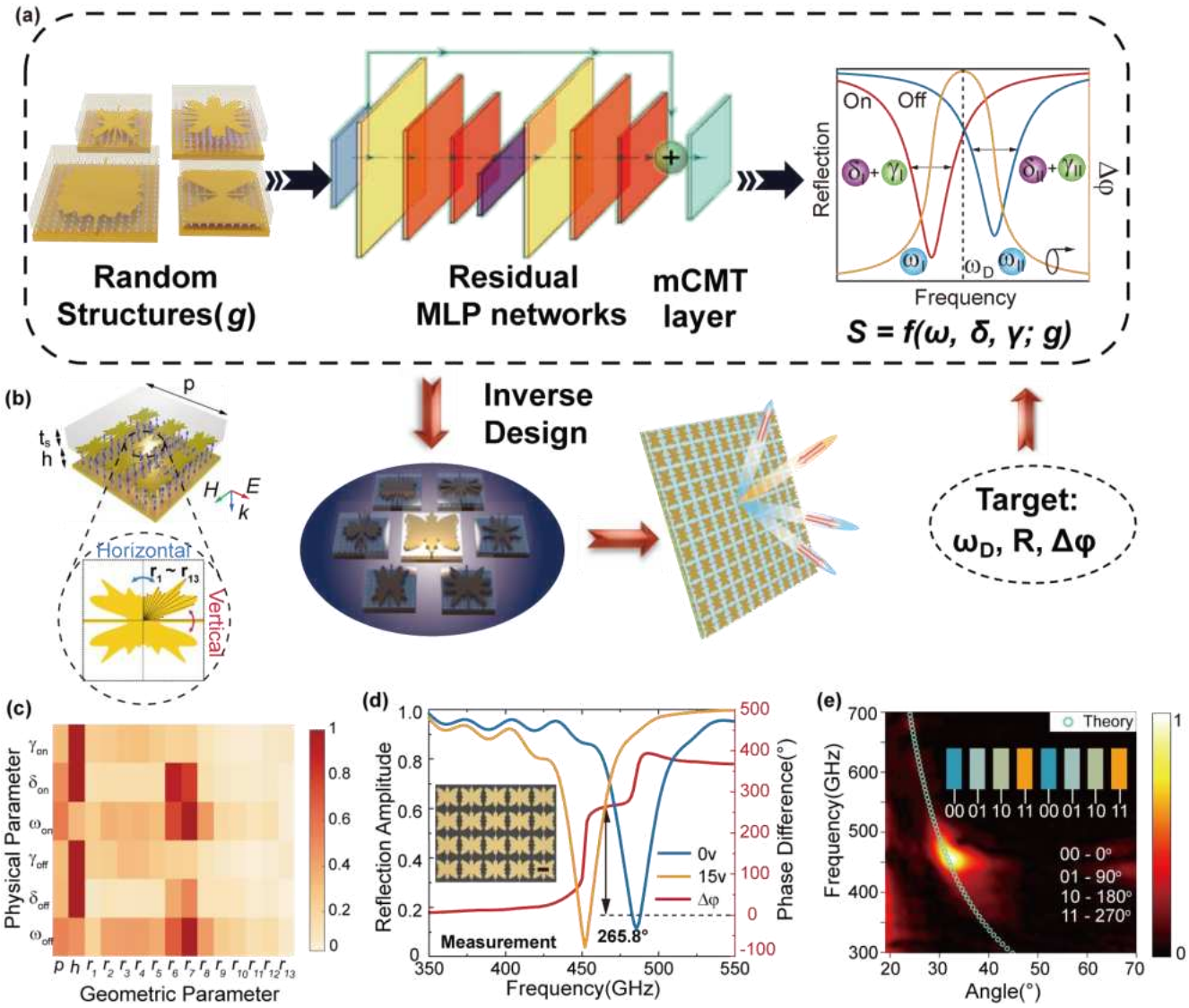


Figure 1 (a) Illustration of Inverse design procedure. The design targets include reflection amplitude *R* at the operating frequency ω_D and the phase change $\Delta\varphi$. A proposed ResMLP is used to train the data and inversely design the metasurface. (b) Illustration of the design includes total 15 geometric parameters. (c) Correlation between the physical parameters and geometries. (d) The experimental measurements of inversely designed liquid crystal based reconfigurable metasurface with phase change as large as 265°. (e) Experimentally demonstrated beam steering with encoding the phases close to 0, 90, 180 and 270 degrees in each supercell.

Effective machine-learning approaches with reduced dimensionality for design and knowledge discovery in large-scale nanophotonic structures

Mahmoodreza Marzban, Mohammadreza Zandehshahvar, Mohammad R. Tavakol, Mohammad H. Javai, and Ali Adibi
School of Electrical and Computer Engineering
Georgia Institute of Technology
Atlanta, GA 30332-0250
Phone: (404) 385-2738
Fax: (404) 894-4641
Email: adibi@ece.gatech.edu

Short Abstract:
This talk is focused on reducing the complexity of machine-learning (ML) approaches for the design and knowledge discovery in large-scale nanophotonic structures. The key aspects of this work are: 1) using manifold-learning approaches for minimizing the dimensionality of the response and design spaces, 2) working in a dimensionality-reduced design space to considerably increase the size of the supercell, and 3) pruning the resulting networks to highly reduce the complexity of the ML algorithms. Using these techniques, metaphotonic devices with 100's of features in their supercell can be analyzed and designed. Furthermore, the use of optimally defined metrics for ML algorithms for knowledge discovery and finding helpful information about the properties of photonic nanostructures will be discussed. Practical examples involving the design, fabrication, and characterization of metaphotonic structures using the ML techniques in this work will also be demonstrated.

Biography

Ali Adibi is the director of Bio and Environmental Sensing Technologies (BEST) and a professor and Joseph M. Pettit chair in the School of Electrical and Computer Engineering, Georgia Institute of Technology. His research group has pioneered several structures in the field of integrated nanophotonics for both information processing and sensing. He is the author of more than 220 journal papers and 520 conference papers. He is the editor-in-chief of the Journal of Nanophotonics, and the nanophotonic program track chair of the Photonics West meeting. He is the recipient of several awards including Presidential Early Career Award for Scientists and Engineers, Packard Fellowship, NSF CAREER Award, and the SPIE Technology Achievement Award. He is also a fellow of OSA, SPIE, and AAAS.

Design of Radiative Cooling Metamaterials by Generic Algorithm and Neural Network

Kotaro Kajikawa*

Tokyo Institute of Technology, Japan

*corresponding author: kajikawa@ee.e.titech.ac.jp

Abstract: Radiative cooling (RC) materials, cooling objects without electricity, are an essential research target for a sustainable society. The RC materials are required to have high transmittance in the visible and high emissivity in near-infrared regions. We study a genetic algorithm and neural network to design RC materials.

The development of radiative cooling (RC) materials, which can cool objects and buildings without electricity [1], is an important research topic for realizing a sustainable society. In particular, developing RC materials for solar cell cooling is an urgent task. The properties required for RC materials are high transmittance in the visible and near-infrared regions and high emissivity in the atmospheric window (ATW) region. ATW is a wavelength band with high atmospheric transmissivity, and heat can be released into the universe through this wavelength band. This phenomenon is responsible for the cold temperatures on sunny winter mornings.

One way to achieve these properties is to use a layered structure of oxide dielectrics. This is because the desired optical properties can be designed by superimposing the properties of each dielectric. This study used a genetic algorithm (GA) to design RC materials with multilayer layered films. GA is an evolutionary computation in which various parameters evolve toward a desired property using an algorithm miming biological heredity. In GA, emissivity calculation must be repeated many times, and the calculation must be fast. Although the optical properties of a multilayer structure can be obtained rigorously by analytical calculations, the amount of calculation increases as the number of layers increases. Therefore, using analytical calculations to calculate the optical properties of a 9-layer multilayer film is unrealistic, as this study did. Therefore, emissivity was predicted using neural networks (NNs) to speed up the process. NN takes time to prepare the dataset, but it is possible to predict the results quickly once it is prepared [2,3]. As a result, we achieved a speed that was more than 1000 times faster than the usual analytical emissivity calculation in the GA-based design of RC materials for the 9-layer multilayer laminate film.

References

1. Raman, A. P., Anoma, M. A., Zhu, L., Rephaeli, E., and Fan, S., “Passive radiative cooling below ambient air temperature under direct sunlight”, Nature, Vol. 515, 540-544, 2014.
2. Peurifoy, J., Shen, Y., Jing, L., Yang, Y., Cano-Renteria, F., DeLacy, B. G., Joannopoulos, J. D., Tegmark, M., Soljaciic, M., Science Adv. Vol. 4 eaar4206, 2018.
3. Akashi, N., Toma, M., Kajikawa, K., Appl. Phys. Express, Vol. 13, 042003, 2020.

Wide Field-of-View and Broadband Metalens Imaging via Deep Learning

Yunxi Dong[1], Bowen Zheng[1], Fan Yang[2], Hong Tang[1], Huan Zhao[1], Yi Huang[1], Tian Gu[2], and Juejun Hu[2], Hualiang Zhang[1*]

[1]ECE Dept., University of Massachusetts Lowell, Lowell, Massachusetts, USA
[2]Materials Science and Engineering Dept., Massachusetts Institute of Technology, Cambridge, Massachusetts, USA
*corresponding author, E-mail: hualiang_zhang@uml.edu

Abstract: We propose a deep learning (DL) strategy for reconstructing images captured with wide field-of-view (WFOV) metalenses. The DL employs a generative adversarial network (GAN) to correct chromatic aberration and image distortion in metalens imaging. Our image collection setup, combined with GAN model, significantly improves computational fidelity and metalens imaging performance.

1. Introduction

Metalenses offer a compact, flat form factor that enables precise control over wavefronts, positioning them as strong contenders to take over from bulky, traditional optical systems in cameras. [1], [2]. However, the inherent dispersive qualities of metalenses can result in considerable chromatic dispersion in sensor imaging. Designing metalenses with a WFOV poses additional challenges, including image distortion and reduced resolution at the edges.

In this paper, a WFOV metalens optical system utilizing commercial cameras and a deep learning (DL) image reconstruction approach was developed to tackle these issues. We implemented a novel GAN architecture in our DL model to rectify image distortion and recover the original resolution of the image. With this well-tuned network, the restored image's structural similarity (SSIM) increased 10dB on average compared with the raw image.

2. Wide Field-of-View Metalens Design

The general schematic of the designed wide field-of-view metametamelens is shown in Fig. 1. The targeted wavelength of the metalens is 525nm. It is consisted of a spacer, an adhesive layer, and a substrate (where meta-atoms reside on). Following the design process detailed in [3], the designed metalens can achieve 180-degree field of view with a lens diameter of 7mm, and a F-number of 1.8.

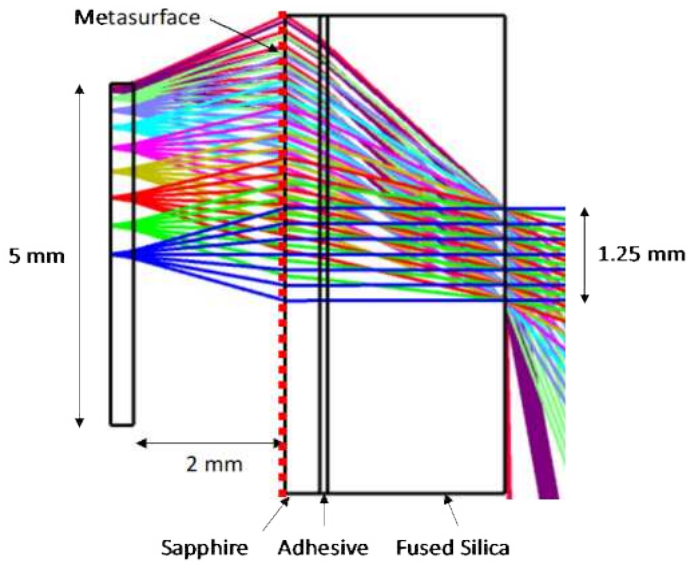


Fig. 1. General schematic of the designed metalens with 180-degree field-of-view.

3. MetaLens Imaging Reconstruction

To reconstruct the image, we designed our model based on the MIRUnet [4] model. In addition to the original model, a VGG-style discriminator was added to enhance image detail and suppress distortion. The detailed training data collection process is shown in Fig. 1a and the structure of MIRGAN is shown in Fig. 1b.

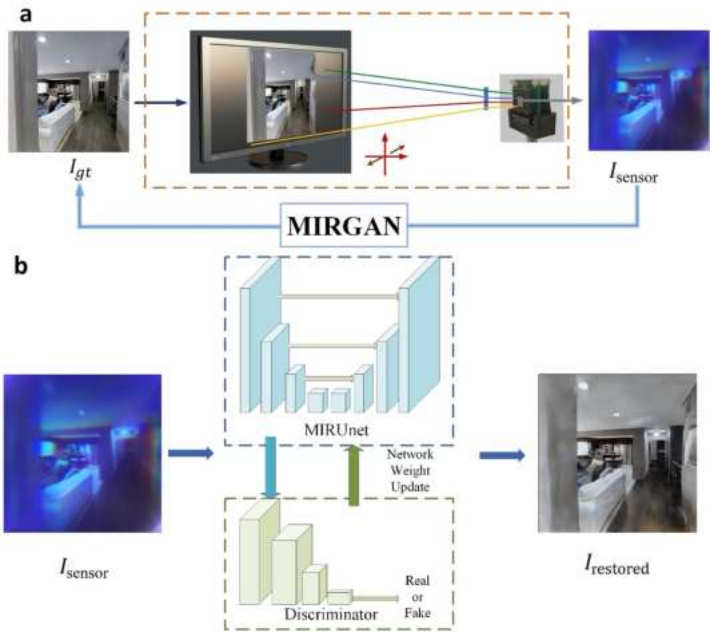


Fig. 2. (a) The training data collection setup: The experiment involves displaying the ground truth image (I_{gt}) on an LCD screen and then capturing it with a commercial camera equipped with a metalens (I_{sensor}). (b) Overview of MIRGAN: The structure of MIRGAN consists of the MIRUnet serving as the DL model generator and a VGG-style network acting as the discriminator.

Once fully trained, our DL model is capable of removing chromatic dispersion and geometric distortion in WFOV metalens imaging, while maintaining fine textures. Examples are shown in Fig. 2.



Fig. 3. Examples of image reconstruction using the proposed network.

Reference

[1] S. Wang *et al.*, "A broadband achromatic metalens in the visible," *Nature nanotechnology*, vol. 13, Mar. 2018, doi: 10.1038/s41565-017-0052-4.

[2] M. Khorasaninejad *et al.*, "Achromatic Metalens over 60 nm Bandwidth in the Visible and Metalens with Reverse Chromatic Dispersion," *Nano Lett.*, vol. 17, no. 3, pp. 1819–1824, Mar. 2017, doi: 10.1021/acs.nanolett.6b05137.

[3] F. Yang *et al.*, "Understanding wide field-of-view flat lenses: an analytical solution," *Chin. Opt. Lett.*, vol. 21, 023601, 2023.

[4] Y. Dong *et al.*, "High-fidelity achromatic metalens imaging via deep neural network," 2023, *arXiv:2308.00211* .

META 2024, TOYAMA - JAPAN, JULY 16 – 19, 2024

Free-Form Inverse Design Driven by Machine Learning

Timo Gahlmann and Philippe Tassin

Department of Physics, Chalmers University of Technology, 41296 Göteborg, Sweden

Abstract: We present an overview of our work on free-form inverse design of nanophotonic devices. We have developed a CGAN network that can provide lithographic masks for a meta-atom with desired transmission and reflection properties. We show examples of metasurfaces with refractive properties and even with meta-atoms with interdependent properties.

We will present a machine-learning approach to the inverse design of nanophotonic devices, i.e., optical devices with subwavelength patterning. Such devices allow us to control light at unprecedented levels, resulting in nontrivial scattering response, e.g., for holograms and retroreflectors. A nanophotonic device often consists of an array of scattering elements, each of which needs to have a specific transmission (or reflection) amplitude and phase. The challenge is, then, to find the shape and materials of meta-atoms with the desired scattering response. This engineering problem is called inverse design.

In this contribution, we will discuss a machine-learning approach [1,2] to inverse design. Our approach is based on a conditional generative adversarial network, as a way addressing the one-to-many problem in inverse design [3]. We discuss a range of machine-learning techniques that we have tested, including the use of expert models, noise in the input channels of the discriminator, and data augmentation, and how their use can—or cannot—improve or speed up neural networks for inverse design [4]. We will provide guidance for best practice and an overview of techniques that work.

Neural networks provide the big advantage that they can quickly generate a design for a meta-atom with desired transmission amplitude and phase once they are trained. The training of the neural networks still requires a large number of simulations of the nanophotonic device (with different geometries) to be used as training data, but they can be run in parallel on high-performance computer clusters. We will compare their time complexity with physics-informed gradient-descent topological optimization and conclude that machine learning is useful for systems described by large simulation models and/or when many similar designs need to be generated.

Finally, we will illustrate our machine-learning approach with several examples.

We acknowledge support from Chalmers' Excellence Initiative Nano and from the Swedish Research Council under Grant No. 2020-05284. The training data generation and ANN training were performed on resources provided by the Swedish National Infrastructure for Computing (NAISS), at the Chalmers/C3SE and KTH/PDC sites, partially funded by the Swedish Research Council under Grant No. 2022-06725.

References

1. Y. LeCun, Y. Bengio, and G. Hinton, "Deep learning," Nature 521, 436–444 (2015).
2. I. Goodfellow, Y. Bengio, and A. Courville, Deep Learning (MIT Press, 2016).
3. Gahlmann, T. and P. Tassin, "Deep neural networks for the prediction of the optical properties and the free-form inverse design of metamaterials," Phys. Rev. B, Vol. 106, 085408, 2022.
4. Gahlmann, T. and P. Tassin, "Evaluation of machine-learning techniques in the inverse design of optical devices," in press, 2004.

Do we need machine learning to predict wave scattering in metasurface-programmable unknown complex media?

Philipp del Hougne[1]

[1]Author Affiliation, Country
[*]corresponding author: philipp.del-hougne@univ-rennes.fr

Abstract: I discuss recent results on physics-compliant modeling of metasurface-programmable complex media, the estimation of these models' parameters (and associated ambiguities), and the relation of this area to optimal blind focusing on perturbation-inducing targets inside complex media. Physics-compliant models present 10X advantages over deep learning because of their naturally built-in constraints.

Across scales and wave phenomena, the massive tunability of complex scattering systems with programmable metasurfaces is emerging to tailor wave-matter interactions. The most prominent example are currently so-called smart radio environments. Solving the inverse-design problem of how to configure the metasurface for a desired functionality would strongly benefit from an accurate forward model. Given the unknown and overwhelmingly complex nature of the complex medium, a wide-spread belief is that only deep learning could approximate the forward mapping from metasurface configuration to scattered fields.

In this talk, I will discuss various principled learning-free approaches to the problem that rely on physics-compliant models and suitable parameter estimation. Compared to deep-learning benchmarks, these physics-compliant models present multiple 10X advantages [1]:

- Orders of magnitude better accuracy
- Orders of magnitude fewer parameters
- Orders of magnitude fewer required calibration examples

Moreover, the scaling of these performance indicators with the number of considered scattering coefficients is favorable. Most importantly, unlike physics-agnostic deep-learning approaches, physics-compliant models have naturally built-in constraints that enable the retrieval of the parameters under very frugal conditions, e.g., without ever measuring phase. This unlocks regimes of wave control that are – to the best of my knowledge – inaccessible with any other approaches, such as coherent control of metasurface-programmable complex media without ever measuring phase.

I will share recent results on parameter estimation of such physics-compliant models of metasurface-parametrized complex media [1], [2], and discuss the role of ambiguities in the parameter values.

Moreover, I will discuss other insights that can be derived from such models for seemingly unrelated problems, such as the optimal focusing of waves on a perturbation-inducing target inside a complex medium [3].

Finally, I will point out some areas for future work for which I do believe that deep learning may be necessary, notably in the context of dynamic complex media [4].

References

[1] J. Sol, H. Prod'homme, L. Le Magoarou, and P. del Hougne, "Experimentally realized physical-model-based wave control in metasurface-programmable complex media," *Nature Communications (in press), arXiv:2308.02349*, 2023.

[2] J. Tapie, H. Prod'homme, M. F. Imani, and P. del Hougne, "Systematic Physics-Compliant Analysis of Over-the-Air Channel Equalization in RIS-Parametrized Wireless Networks-on-Chip." *IEEE Journal on Selected Areas in Communications (in press), arXiv:2310.16195*, 2023.

[3] J. Sol, L. Le Magoarou, and P. del Hougne, "Optimal blind focusing on perturbation-inducing targets in sub-unitary complex media." *arXiv:2401.15415*, 2024.

[4] C. Saigre-Tardif and P. del Hougne, "Self-Adaptive RISs Beyond Free Space: Convergence of Localization, Sensing, and Communication Under Rich-Scattering Conditions," *IEEE Wireless Communications*, vol. 30, no. 1, pp. 24–30, 2023.

Data-driven Inverse Design and Characterization of Metasurface

Li Gao

[1] Nanjing University of Posts and Telecommunications, China
*corresponding author: iamlgao@njupt.edu.cn

Abstract: Deep neural network can capture the highly nonlinear, complex relationship between nanostructure geometry and its optical properties, and proves accurate inverse design of near-field enhancement, far-field spectrum and phase changes etc, which can be helpful for exploring subtle, complex multifunctional nanophotonics for sensing and energy conversion applications.

The electromagnetic response of nanophotonics is highly sensitive to their geometric parameters. In multi-dimensional parameter space, conventional full-wave simulation and numerical optimization can consume significant computation time and resources. It is also highly challenging to find the globally optimized result and perform inverse design for highly nonlinear data structure. In this talk, we demonstrate that deep neural network can capture the highly nonlinear, complex relationship between nanostructure geometry and its near- and far- field properties. Our deep learning approach proves accurate inverse design of near-field enhancement, far-field spectrum and phase changes etc, which can be helpful for exploring subtle, complex multifunctional nanophotonics for sensing and energy conversion applications (Figure 1a-d). We will also discuss the combined nanoimprinting lithography and reactive ion etching method to form large-area, low-cost nanophotonic devices and their facile optical sensing applications (Figure 1e,f).

The lateral geometry and material property of plasmonic nanostructures are critical parameters to tailor their optical resonance for sensing applications. While lateral geometry can be easily observed by scanning electron microscope or atomic force microscope, characterizing materials property of plasmonic device is not straightforward and requires delicate examination of material composition, cross-sectional thickness and refractive index. In this study, deep neural network is adopted to characterize these parameters of unknown plasmonic nanostructures through simple transmission spectra. The network architecture is established based on simulated data to achieve accurate identification of both geometric and material parameters. We then demonstrate the network training by a mixture of simulated and experimental data can result correct material property recognition. Our work may indicate a simple and intelligent characterization approach of plasmonic nanostructures by spectroscopic techniques (Figure 1g,h).

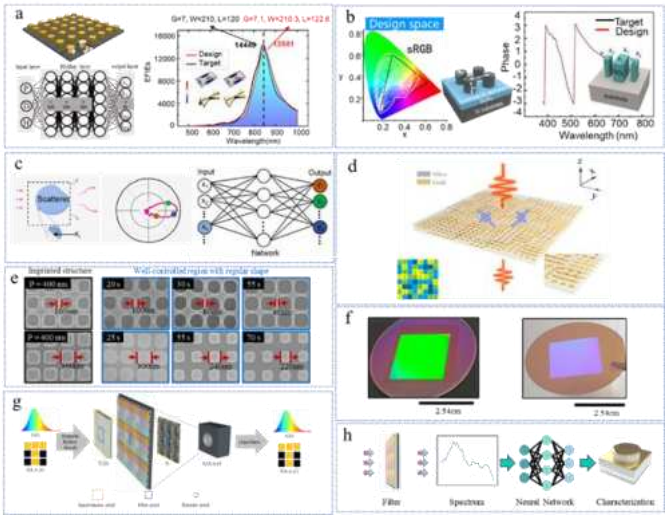


Figure 1-Summary of recent work on deep learning enabled inverse design(a-d), large-area fabrication of metasurface (e,f) and their computational characterization (g,h)

References

1. Lanfei Wang, Qiao Dong, Tianyi Zhou, Huijuan Zhao, Lianhui Wang, and Li Gao*, Multi-mode resonance of bound states in the continuum in dielectric metasurfaces. Optics Express 2024 (accepted).
2. Lanfei Wang, Wenqi Wang, Qiao Dong, Lianhui Wang, and Li Gao*, Deep learning enabled inverse design of bound states in the continuum with ultrahigh Q factor. Journal of the Optical Society of America B 41, A146-A151, 2024.
3. Zhixiao Zhang and Li Gao*, 2-bit Coding Metasurface with a Double Layer Random Flip Structure for Wide Band Diffuse Reflection and Reciprocity Protected Transmission. Optics Express 31(20), 32253-32262, 2023.
4. Huijuan Zhao, Xinyi Cao, Qiao Dong, Chunyuan Song, Lianhui Wang* and Li Gao*, Large-Area Silicon Photonic Crystal Supporting Bound States in the Continuum and Optical Sensing Formed by Nanoimprint Lithography. Nanoscale Advances 5, 1291-1298, 2023.
5. Qiao Dong, Wenqi Wang, Xinyi Cao, Yibo Xiao, Xiaohan Guo, Jingxuan Ma, Lianhui Wang* and Li Gao*, Plasmonic Nanostructure Characterized by Deep Neural Network Assisted Spectroscopy (invited). Chinese Optics Letter 21(1), 010004, 2023.
6. Li Gao*, Yurui Qu, Lianhui Wang* and Zongfu Yu*, Computational Spectrometers Enabled by nanophotonics and Deep Learning. Nanophotonics 11(11), 2507-2929, 2022.
7. Qingxin Wu, Xiaozhong Li, Li Jiang, Xiao Xu, Dong Fang, Jingjing Zhang, Chunyuan Song, Zongfu Yu, Lianhui Wang, and Li Gao*, Deep Neural Network for Designing Near- and Far-field Properties in Plasmonic Antennas. Optical Materials Express 11(7), 1907-1917, 2021.
8. Jinran Qie, Erfan Khoram, Dianjing Liu, Ming Zhou, and Li Gao*, Real-time Deep Learning Design Tool for Far-Field Radiation Profile. Photonics Research 9(4) B104-B108, 2021.
9. Li Jiang, Xiaozhong Li, Qingxin Wu, Lianhui Wang, and Li Gao*, Neural Network Enabled Metasurface Design for Phase Manipulation. Optics Express 29(2) 2521-2528, 2021.
10. Li Gao*, Xiaozhong Li, Dianjing Liu, Lianhui Wang, and Zongfu Yu, A Bidirectional Deep Neural Network for Accurate Silicon Color Design, Advanced Materials 31(51) 1905467, 2019.
11. Xiaozhong Li, Jing Shu, Wenhua Gu, and Li Gao*, Deep Neural Network for Plasmonic Sensor Modeling. Optical Materials Express 9(9), 3857-3862, 2019.

Tutorials

Coupling theory of quasinormal mode for an efficient and intuitive modeling of optical-nanoresonator arrays with a large scale or varying arrangement

Haitao Liu[1,2*], Can Tao[1,2,3], Qiyong Tao[1,2], Zhe Qi[1,2], and Ying Zhong[4]

[1]Institute of Modern Optics, College of Electronic Information and Optical Engineering, Nankai University, Tianjin, 300350, China
[2]Tianjin Key Laboratory of Micro-scale Optical Information Science and Technology, Tianjin, 300350, China
[3]The MOE Key Laboratory of Weak-Light Nonlinear Photonics, School of Physics and TEDA Applied Physics Institute, Nankai University, Tianjin 300457, China
[4]State Key Laboratory of Precision Measurement Technology and Instruments, Tianjin University, Tianjin 300072, China
[*]corresponding author: liuht@nankai.edu.cn

Abstract: Optical-nanoresonator arrays with a large scale or varying arrangement have important applications such as metasurfaces or optical-force manipulations, but their electromagnetic modeling using traditional full-wave numerical methods requires huge computational amount with poor physical intuitiveness. Here we report a coupling theory of quasinormal mode (QNM) to address such challenges.

Optical-nanoresonator arrays can simultaneously support localized resonance and mutual coupling between resonators, and have important applications such as periodic arrays supporting surface lattice resonance or non-periodic arrays forming metasurfaces [1]. For electromagnetic modeling of optical-nanoresonator arrays with a large scale (from tens to thousands of wavelengths) or varying arrangement (such as in the inverse design or optical-force manipulation), traditional full-wave numerical methods (such as finite element method) suffer from a huge computational load and poor physical intuitiveness. The recently developed coupling theories of QNM [2,3] could provide a recipe but still have limitations in rigorousness and application scope.

Here we report a QNM coupling theory for an efficient and intuitive modeling of optical-nanoresonator arrays with a large scale or varying arrangement [4-6]. In the theory [4], the scattered field $\mathbf{\Psi}^s(\mathbf{r},\omega)=[\mathbf{E}^s,\mathbf{H}^s]$ for P coupled nanoresonators is expressed as a superposition of the scattered fields of each individual resonator, $\mathbf{\Psi}^s(\mathbf{r},\omega)=\Sigma_{p=1}^{P}\mathbf{\Psi}_p^s(\mathbf{r},\omega)$, where ω denotes the excitation angular frequency. The scattered field $\mathbf{\Psi}_p^s$ of the p-th resonator is expanded upon the basis of its QNM field $\tilde{\mathbf{\Psi}}_{p,m}(\mathbf{r})=[\tilde{\mathbf{E}}_{p,m},\tilde{\mathbf{H}}_{p,m}]$,

$$\mathbf{\Psi}_p^s(\mathbf{r},\omega)=\sum_{m=1}^{M_p}\alpha_{p,m}(\omega)\tilde{\mathbf{\Psi}}_{p,m}(\mathbf{r}). \tag{1}$$

After obtaining the QNMs by solving the source-free Maxwell's equations, the QNM expansion coefficients $\alpha_{p,m}(\omega)$ in Eq. (1) can be determined by solving the following set of linear equations,

$$[\omega\mathbf{I}-\mathbf{K}(\omega)]\mathbf{a}(\omega)=\mathbf{b}(\omega). \tag{2}$$

In Eq. (2), $\mathbf{a}$ is a column vector with its (p,m)-th element being $\alpha_{p,m}$, $\mathbf{I}$ is the identity matrix, $\mathbf{K}$ is a matrix with its (p,m)-row and (q,n)-column element $\kappa_{(p,m),(q,n)}$ describing the coupling between the QNMs $\tilde{\mathbf{\Psi}}_{p,m}$ and $\tilde{\mathbf{\Psi}}_{q,n}$, and $\mathbf{b}$ is a column vector with its (p,m)-th element $\beta_{p,m}$ describing the excitation of $\tilde{\mathbf{\Psi}}_{p,m}$ by the background field $\mathbf{\Psi}^b$ as the excitation source. The total field is obtained as $\mathbf{\Psi}=\mathbf{\Psi}^s+\mathbf{\Psi}^b$.

For modeling optical-nanoresonator arrays with varying arrangement (i.e., varying relative positions or number of resonators), one can reuse the already solved QNMs of each individual resonator and only needs to recalculate the $\mathbf{K}$ and $\mathbf{b}$ and then solve Eq. (2), which requires much less computational amount than repeatedly

solving the Maxwell's equations of the array as done by traditional full-wave numerical methods. Such advantages can be shown in the calculation of optical force of multiple nanoparticles [5].

For modeling optical-nanoresonator arrays with a large scale, the QNM-coupling theory suffers from the far-field divergence of QNMs [2-4]. To address the issue, in the near-field region, far-field region, and their inbetween transition region, we propose to use the QNM field, the plane-wave expansion calculated by stationary-phase principle, and the scattered-field reconstruction, respectively, to achieve an accurate and efficient calculation of regularized QNM, which has no far-field divergence and are then used to replace the QNMs in Eqs. (1) and (2) [6]. Figure 1(b) shows that our theory can achieve an efficient modeling of optical-nanoresonator arrays with an overall size exceeding 50×50 wavelengths, which is challenging if using traditional full-wave numerical methods.

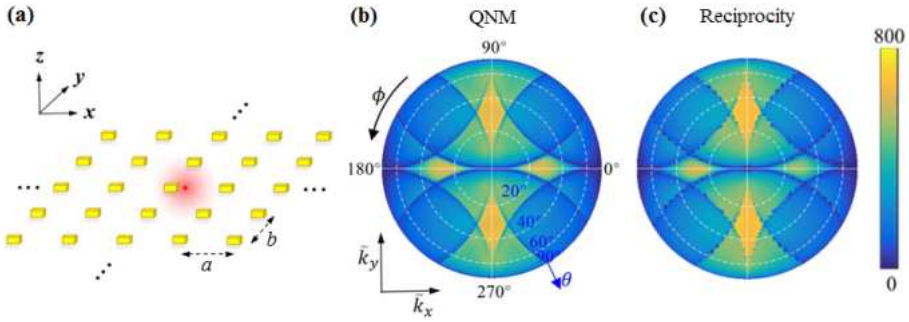


Fig. 1. (a) A periodic array of gold single-nanowire antennas in air (period a=b=1125 nm) excited by an x-polarized electric-current point source (red dot) of wavelength 1127 nm. Each antenna has a length 247 nm and a square cross-section of side length 40 nm. The source is located 20 nm away from the center of the right surface of the central antenna. (b) For an array size of 51×51, the far-field radiation-intensity angular distribution $P(\tilde{k}_x,\tilde{k}_y)$ calculated by the QNM-coupling theory (θ and ϕ being polar and azimuthal angles). (c) For an infinite periodic array, $P(\tilde{k}_x,\tilde{k}_y)$ calculated by the reciprocity method that relies on a full-wave Fourier modal method.

Acknowledgements: Financial support from the National Natural Science Foundation of China (62075104, 61775105) is acknowledged.

References

1. Zhang, S., H. Zhou, B. Liu, Z. Su and L. Huang, "Recent advances and prospects of optical metasurfaces," ACS Photonics, Vol. 10, No. 7, 2045-2063, 2023.
2. Kristensen, P. T., K. Herrmann, F. Intravaia and K. Busch, "Modeling electromagnetic resonators using quasinormal modes," Adv. Opt. Photonics, Vol. 12, No. 3, 612-708, 2020.
3. Cognée, K. G., "Hybridization of open photonic resonators," Ph.D. dissertation, Université de Bordeaux, Universiteit van Amsterdam, 2020.
4. Tao, C., J. Zhu, Y. Zhong and H. Liu, "Coupling theory of quasinormal modes for lossy and dispersive plasmonic nanoresonators," Phys. Rev. B, Vol. 102, No. 4, 045430, 2020.
5. Qi, Z., Y. Zhong and H. Liu, "Efficient method for the calculation of the optical force of multiple nanoparticles based on the coupling theory of quasinormal modes," Opt. Lett., Vol. 46, No. 18, 4610-4613, 2021.
6. Tao, Q., Y. Su, C. Tao, Y. Zhong and H. Liu, "Efficient method for modeling large-scale arrays of optical nanoresonators based on the coupling theory of quasinormal mode," Opt. Express, Vol. 32, No. 5, 7171-7184, 2024.

Disentangling Absorption and Radiation Decay in Optical Nanoresonators

K. Koshelev[1*]

[1]Nonlinear Physics Centre, Research School of Physics, Australian National University
[*]corresponding author: kirill.koshelev@anu.edu.au

Abstract: We derive exact expressions for the radiative and absorption decay rates of an individual quasi-normal mode of an optical resonator composed of highly dispersive and dissipative media, extending the time-averaged energy conservation theorem beyond the regime of weak losses. We confirm the theory with calculations for exactly solvable resonator geometries.

Optical resonators play an essential role in current developments in optics from optical metamaterials and integrated photonic circuits to sensing and strong light-matter coupling. In nanophotonics, optical resonators represent non-conservative systems with the radiative and non-radiative decay pathways, which complicates their mathematical description due to the non-applicability of standard Hermitian approaches. Recent studies outlined that quasi-normal modes (QNMs) represent the most natural way of description of such open resonators [1]. In the last years, there has been a substantial progress in resolving mathematical difficulties with the QNMs, including their normalization and spectrum incompleteness outside of the resonator volume for complex geometries [2].

The mode decay rate governs a variety of light-matter interaction effects in photonic structures, including spontaneous emission rate, Raman and nonlinear response enhancement, and lasing threshold value. For dispersive and absorptive photonic structures, the separation of decay rate into radiative and non-radiative contributions is of special importance, as their ratio could be detrimental for critical coupling, Purcell factor, or optical harmonic generation. To date, studies reporting on an accurate separation of radiative and non-radiative contributions are limited to complex multimodal approaches [3, 4] or weakly dispersive and weakly dissipative systems [5].

In this work, we derive the exact expression for the radiative and non-radiative decay rates for an individual QNM mode of a non-magnetic optical resonator with an arbitrary magnitude of permittivity dispersion and absorption, including highly dispersive and dissipative media, as schematically shown in Fig. 1(a).

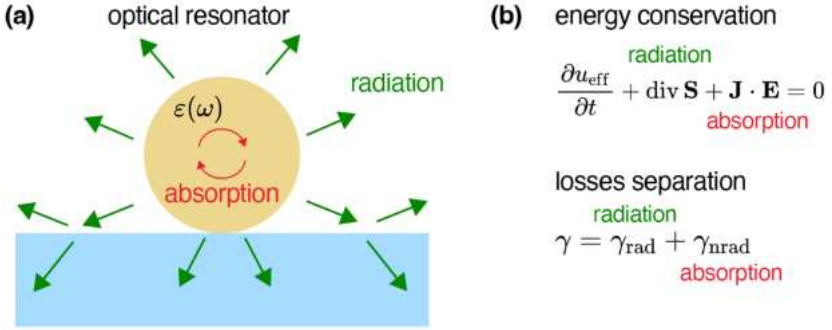


Figure 1. (a) Schematic of an optical resonator with permittivity dispersion and absorption losses. (b) Energy conservation theorem and exact decay rate separation into two independent pathways.

Using the divergence theorem, we show that for some m-th QNM mode with the complex frequency $\Omega_m = \omega_m - i\gamma_m$, an analogue of time-averaged energy conservation theorem can be written as [see Fig. 1(b)],

$$-\frac{\gamma_m}{8\pi}\int dV\left(\mathrm{R}_{\gamma_\mathrm{m}}[\varepsilon(\Omega_m)]|\mathbf{E}_m|^2 + |\mathbf{H}_m|^2\right) + \frac{c}{8\pi}\oint d\mathbf{S}\cdot\mathrm{Re}[\mathbf{E}_m\times\mathbf{H}_m^*] + \frac{\omega_m}{8\pi}\int dV\ \mathrm{I}_{\gamma_\mathrm{m}}[\varepsilon(\Omega_m)]|\mathbf{E}_m|^2 = 0. \quad (1)$$

Here, the permittivity is an analytic function in the complex frequency plane, evaluated at complex Ω_m, $\mathbf{E}_m$ and $\mathbf{H}_m$ are the electric and magnetic field of the QNM mode, and $\mathrm{R}_{\gamma_\mathrm{m}}[f(\Omega_m)]$ and $\mathrm{I}_{\gamma_\mathrm{m}}[f(\Omega_m)]$ are given by,

$$\mathrm{R}_{\gamma_\mathrm{m}}[f(\Omega_m)] = -\,\mathrm{Im}[\Omega_m f(\Omega_m) - \Omega_m^* f(\Omega_m^*)]\,/(2\gamma_m), \tag{2}$$

$$\mathrm{I}_{\gamma_\mathrm{m}}[f(\Omega_m)] = \mathrm{Im}\,[\Omega_m f(\Omega_m) + \Omega_m^* f(\Omega_m^*)]/(2\omega_m)\,. \tag{3}$$

We show that such definition of operators $\mathrm{R}_{\gamma_\mathrm{m}}[f(\Omega_m)]$ and $\mathrm{I}_{\gamma_\mathrm{m}}[f(\Omega_m)]$ allows to assign a specific physical meaning to the terms in Eq. (1), following the procedure in [5]. The left term corresponds to the total energy decay of the mode, the central term describes the mode energy transfer due to the radiative losses, and the right term represents mode ohmic losses; all terms averaged over the period $2\pi/\omega_m$. This can be confirmed by calculating the Taylor series of Eqs. (2,3) around the real frequency ω_m. The first two terms of expansion are given by,

$$\mathrm{R}_{\gamma_\mathrm{m}}[\varepsilon(\Omega_m)] = \frac{\partial}{\partial\omega_m}(\omega_m \mathrm{Re}\,[\varepsilon(\omega_m)]) - \frac{\gamma_m^2}{6}\frac{\partial^3}{\partial\omega_m^3}(\omega_m \mathrm{Re}\,[\varepsilon(\omega_m)]) + O\left[\left(\frac{\gamma_m}{\omega_m}\right)^4\right], \tag{5}$$

$$\mathrm{I}_{\gamma_\mathrm{m}}[\varepsilon(\Omega_m)] = \mathrm{Im}\,[\varepsilon(\omega_m)] - \frac{\gamma_m^2}{2\omega_m}\frac{\partial^2}{\partial\omega_m^2}(\omega_m \mathrm{Im}\,[\varepsilon(\omega_m)]) + O\left[\left(\frac{\gamma_m}{\omega_m}\right)^4\right]. \tag{6}$$

One can see that $\mathrm{R}_{\gamma_\mathrm{m}}[f]$ and $\mathrm{I}_{\gamma_\mathrm{m}}[f]$ generalize $\mathrm{Re}[f]$ and $\mathrm{Im}[f]$ for dispersive systems.

We apply the developed approach to resonators composed of materials that can be described with the generalized Drude-Lorentz form of permittivity and derive the exact form of $\mathrm{R}_{\gamma_\mathrm{m}}[\varepsilon(\Omega_m)]$ and $\mathrm{I}_{\gamma_\mathrm{m}}[\varepsilon(\Omega_m)]$. For the simplest case of Drude material with $\varepsilon(\omega) = \varepsilon_\infty - \omega_p^2/(w(w + i\gamma_0))$, we obtain the following expressions,

$$\mathrm{R}_{\gamma_\mathrm{m}}[\varepsilon(\Omega_m)] = \varepsilon_\infty + \frac{\omega_p^2(\omega_m^2+\gamma_m^2-\gamma_0^2)}{(\omega_m^2+\gamma_m^2-\gamma_0^2)^2+4\gamma_0^2\omega_m^2}, \tag{7}$$

$$\mathrm{I}_{\gamma_\mathrm{m}}[\varepsilon(\Omega_m)] = \frac{\gamma_0}{\omega_m}\frac{\omega_p^2(\omega_m^2-\gamma_m^2+\gamma_0^2)}{(\omega_m^2+\gamma_m^2-\gamma_0^2)^2+4\gamma_0^2\omega_m^2}. \tag{8}$$

Equations (7,8) show explicitly that only $\mathrm{I}_{\gamma_\mathrm{m}}$ is proportional to the non-radiative damping rate γ_0, as expected.

We further utilize the developed approach to calculate the exact values of radiative and non-radiative losses and their ratio for exactly solvable models, including a one-dimensional slab and three-dimensional spherical resonator. As an example, for the slab we show that in the limit of weak material dispersion and dissipation, the expressions for the radiative and non-radiative Q factor are reduced to $Q_{m,\mathrm{rad}} = (\pi m + \phi_r)/(2\ln[1/|r|])$ and $Q_{m,\mathrm{nrad}} = n/(2k)$, where n and k are the refractive index and extinction coefficient of the slab material, and $|r| = \sqrt{1-(4n)/(k^2+(1+n)^2)}$ is the slab material reflection coefficient with the reflection phase $\phi_r = \mathrm{atan}(-2k/(n^2+k^2-1))$. We believe our approach provides a novel platform for resonant nanophotonics.

The author acknowledges I. Toftul, M. Hamidi, A. C. Valero, and T. Weiss for useful discussions.

References

1. Both S. and Weiss T., "Resonant states and their role in nanophotonics", Semicond. Sci. Technol., Vol. 37, No. 1, 013002, 2021.
2. Sauvan C., Wu T., Zarouf R., Muljarov E.A. and Lalanne P., "Normalization, orthogonality, and completeness of quasinormal modes of open systems: the case of electromagnetism", Opt. Express, Vol. 30, No. 5, 6846-6885, 2022.
3. Sauvan C., Hugonin J.P., Maksymov I.S. and Lalanne P., "Theory of the spontaneous optical emission of nanosize photonic and plasmon resonators", Phys. Rev. Lett, Vol. 110, No. 23, 237401, 2013.
4. Rahimzadegan A. *et al.*, "Minimalist Mie coefficient model", Opt. Express, Vol. 28, No. 11, 16511-16525, 2020.
5. Lalanne P., Yan W., Vynck K., Sauvan C. and Hugonin J.P., "Light interaction with photonic and plasmonic resonances", Laser Photonics Rev., Vol. 12, No. 5, 1700113, 2018.

Efficient and tailored photon-pair generation from metasurfaces with quasi-normal modes

Jihua Zhang[1,2,*], Jinyong Ma[2], Tongmiao Fan[2], Yuxin Jiang[2], and Andrey A. Sukhorukov[2,*]

[1]Songshan Lake Materials Laboratory, Dongguan, Guangdong 523808, P. R. China
[2]ARC Centre of Excellence for Transformative Meta-Optical Systems, Department of Electronic Materials Engineering, Research School of Physics, The Australian National University, Canberra, ACT 2601, Australia
[*]corresponding author: zhangjihua@sslab.org.cn, andrey.sukhorukov@anu.edu.au

Abstract: We develop a general approach for modelling the spontaneous parametric down conversion in both infinite periodic and finite aperiodic metasurfaces via the quasi-normal modes. It is employed to investigate an aperiodic guided-mode-cavity metasurface and a periodic flatband metasurface, both show enhanced photon-pair generation with controllable two-photon states.

Metasurface comprising by artificial planar arrangement of nanostructures has recently drawn an increasing attention for the development of ultrathin quantum light sources through the spontaneous parametric down conversion (SPDC). By leveraging optical resonances in nanostructures, metasurfaces can boost the SPDC efficiency as well as engineer the generated two-photon states. However, modelling the complex and quantum SPDC process in different nanostructures has been a difficulty, preventing the tunability and versatility of metasurface SPDC sources. Recently, coupled mode theory and quasi-normal mode (QNM) theory have been applied for analyzing the SPDC in periodic metasurfaces [1] and single nanoantennaes [2], respectively. Here, we present a general approach to study the SPDC in both infinite periodic and finite aperiodic metasurfaces through the QNMs supported in the metasurfaces. Based on that, an aperiodic guided-mode-cavity metasurface and a periodic flatband metasurface are proposed and analyzed for photon pair generations. The results obtained by the proposed approach show excellent match with the ones obtained by the coupled mode theory.

Figure 1a shows the proposed aperiodic lithium niobate metasurface featuring a guided-mode cavity formed by two distributed Bragg reflectors sandwiching a truncated central grating. By optimizing the dimension of the cavity to match its resonance wavelength with the center grating, we obtained a QNM with a strong field confinement (Fig. 1b) and a high quality factor close to 1000. With the developed QNM approach, we theoretically study the SPDC process in the proposed metasurface, which predicts a SPDC rate up to 157 Hz/mW (Fig. 1c). This represents about 30 times enhancement of SPDC for a focused pump beam when compared to the previous periodic metasurface without a cavity, despite being half the transverse size.

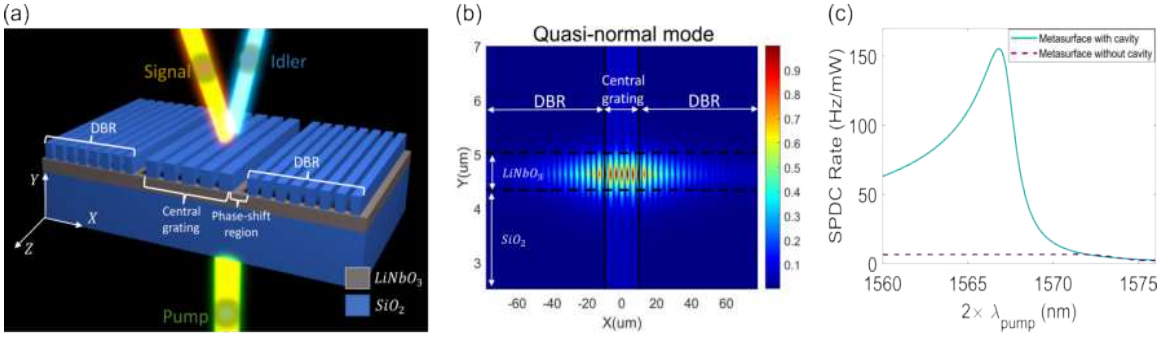


Figure 1. (a) Photon pair generation from a lithium niobate metasurface with a guided-mode cavity. (b) Electric field magnitude distribution of the dominant quasi-normal mode. (c) Simulated SPDC rate as a function of the pump wavelength.

Figure 2a depicts a flatband lithium niobate metasurface for a broad-angle SPDC source. By engineering the coupling between two QNMs with different natures, a nearly flatband dispersion is achieved within the angular range between -0.2 rad/μm and 0.2 rad/μm (Fig. 2b). When pumping for a degenerate SPDC wavelength near this resonant wavelength, the simulation suggests that photon pairs are uniformly emitted within a 6° field of view with a total emission rate up to 539 Hz/mW (Fig. 2c).

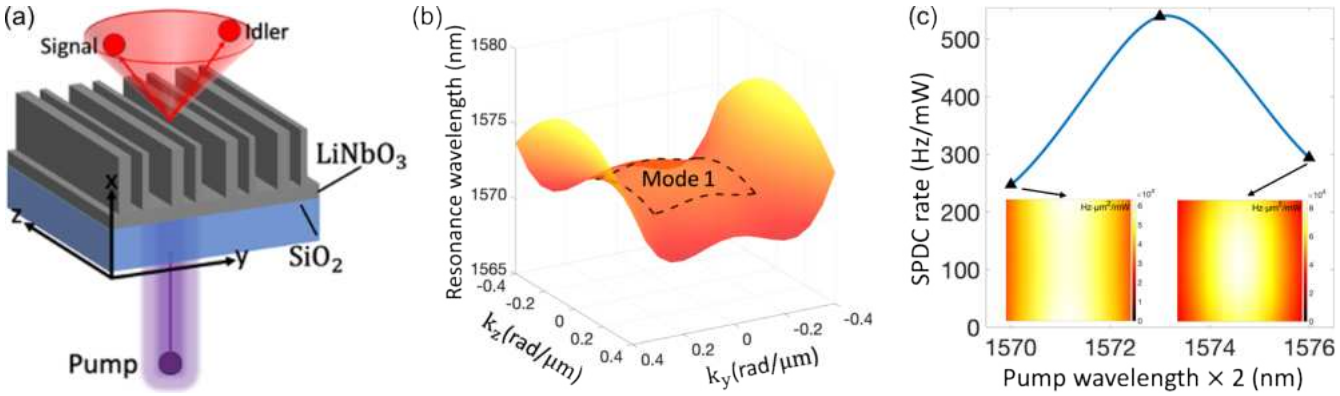


Figure 2. (a) Photon pair generation from a flatband lithium niobate metasurface. (b) Angular dispersion of the dominant quasi-normal mode. (c) Simulated SPDC rate as a function of the pump wavelength. Insets show two broad-angle emission patterns.

It is noteworthy that the QNM approach presented in this work is general to any nonlinear materials and any nanostructures. We anticipate that it will facilitate the investigation of flat-optics photon-pair sources with desired properties.

This work was supported by the Australian Research Council (CE200100010). Jihua Zhang was also supported by the Innovation Program for Quantum Science and Technology (2021ZD0302300) and Songshan Lake Materials Laboratory (XMYS2023002).

References

1. Zhang, J., Ma, J., Parry, M., Cai, M., Camacho-Morales, R., Xu, L., Neshev, D. N., Sukhorukov, A. A., "Spatially entangled photon pairs from lithium niobate nonlocal metasurfaces," Sci. Adv., Vol. 8, eabq4240, 2022.
2. Weissflog, M. A., Dezert, R., Vinel, V., Gigli, C., Leo, G., Pertsch, T., Setzpfandt, F., Borne, A., and Saravi, S., "Nonlinear nanoresonators for bell state generation," Appl. Phys. Rev., Vol. 11, 011403, 2024.

Anomalous acoustic tunneling effect with non-Hermitian Willis coupling

Danwei Liao[1], **Xinhua Wen**[1], **Xinghong Zhu**[1], **and Jensen Li**[1*]

[1]Department of Physics, The Hong Kong University of Science and Technology, Kowloon, Hong Kong, China.
[*]corresponding author: jensenli@ust.hk

Abstract: We extend anomalous tunneling phenomenon observed in reciprocal electromagnetic metamaterials to acoustic metamaterials via bianisotropy and Willis coupling, covering nonreciprocal regime. Digitally virtualized atoms are employed to generate the required non-Hermitian Willis coupling, which leads to decaying fields for both acoustic pressure and velocity within metamaterial.

Bianisotropy coupling the magnetic and the electric responses in EM wave as a key factor in creating Huygens metasurfaces, chiral metasurfaces, and nonreciprocal metasurfaces [1], has been used to perform optical tunneling due to its potential application value in optical filters, switches, and sensors. Anomalous tunneling effect, consisting of evanescent fields with opposite trends given by bianisotropy among multilayer metamaterials [2], can be extended to acoustics by introducing bianisotropy through coupling between sound pressure and velocity. This concept, also known as the Willis coupling, has been experimentally possible using acoustic metamaterials in airborne sound and elastics [3,4]. To supplement the current mechanism of classical tunneling effect, our work extends the condition of anomalous tunneling to include not only reciprocal but also nonreciprocal bianisotropy. By implementing nonreciprocal Willis coupling using programmable metamaterials through active atoms with a digital feedback circuit [5], anomalous acoustic tunneling effect is realized with both pressure and velocity decay to a minimal value in the middle of the device, while the decay ratio remains exponentially related to the size of bianisotropy and thickness of the effective media.

Here, we implement anomalous acoustic tunneling in a one-dimensional (1D) waveguide as two stacked layers with same length but opposite Willis coupling terms, by adjusting the constitutive matrix to obtain the decayed field in the middle while ideally total transmission for the whole device. The wave equation for the 1D acoustic system in an effective medium representation can be written as the following form under $e^{-i\omega t}$ convention

$$\partial_x \begin{pmatrix} v \\ p \end{pmatrix} = \frac{i\omega}{c} \begin{pmatrix} \beta & i\tau \\ i\tau' & \rho \end{pmatrix} \begin{pmatrix} p \\ v \end{pmatrix}, \tag{1}$$

where p is the pressure, v is the velocity multiplied by the acoustic impedance of the air, c is the sound speed in the air, β and ρ are the dimensionless compressibility and density, $\tau = -\tau_{\mathrm{r}} + \tau_{\mathrm{nr}}$ and $\tau' = \tau_{\mathrm{r}} + \tau_{\mathrm{nr}}$ represent the combination of reciprocal and nonreciprocal Willis couplings, respectively. As indicated in the schematic of the stacked layers in Fig. 1(a), for the left layer (green region) with width L from $x = 0$ to $x = L$, the Wills coupling is set as $\tau = -\tau_{\mathrm{r}} + \tau_{\mathrm{nr}}$, and the right layer (blue region) from $x = L$ to $x = 2L$ shares the same width and effective parameters β and ρ, but with flipped Willis coupling term of $-\tau = \tau_{\mathrm{r}} - \tau_{\mathrm{nr}}$. The pressure (purple lines) and velocity (orange lines) field profiles are obtained using the transfer matrix method, with the reciprocal case ($\tau_{\mathrm{r}} = 0.1$, $\tau_{\mathrm{nr}} = 0$, and $\beta = \rho = 0$) exhibiting a dip in the pressure field and a peak for the velocity field with full transmission. For the purely nonreciprocal case ($\tau_{\mathrm{r}} = 0$, $\tau_{\mathrm{nr}} = 0.1$, and $\beta = \rho = 1$), the pressure and velocity fields tunnel through stacked layers in the same trend, with a dip in the connecting interface of the two layers, acting as a fictitious potential barrier.

Based on analytical analysis of the transmittance diagram demonstrating that the purely nonreciprocal situation indicates superior robustness against the disturbance of effective parameters and Willis coupling term, we implement the experimental verification via active metaatoms realizing purely nonreciprocal Willis coupling. As depicted in Fig. 1(b), the effective medium layers in Fig. 1(a) are substituted by metaatoms positioned at the

top border (blue rectangles) of the waveguide with the detailed schematic presented in Fig. 1(c). Each atom consists of a PCB board with two pairs of microphones and speakers, and a microcontroller that can be programmed to do convolutions Y_{ij} $(i,j = 1,2)$ between the microphones and speakers as $S_i = \sum_{j=1,2} Y_{ij} D_j$ in time domain that behaves as secondary source generating specific scattering waves, allowing the realization of arbitrary constitutive parameters [5]. Four microphones (M_1 to M_4) are utilized to extract the scattering coefficients and additional microphone (D_M) in the middle for detecting the decay ratio of the field. Cascading four atoms with opposite sign of nonreciprocal Willis coupling on each side of the waveguide, the anomalous tunneling effect is achieved as indicated in Fig. 1(d), where the total transmission coefficient is approximately uniform and the decay ratio in the middle of the stacked layers could be minimized to rather small ratio.

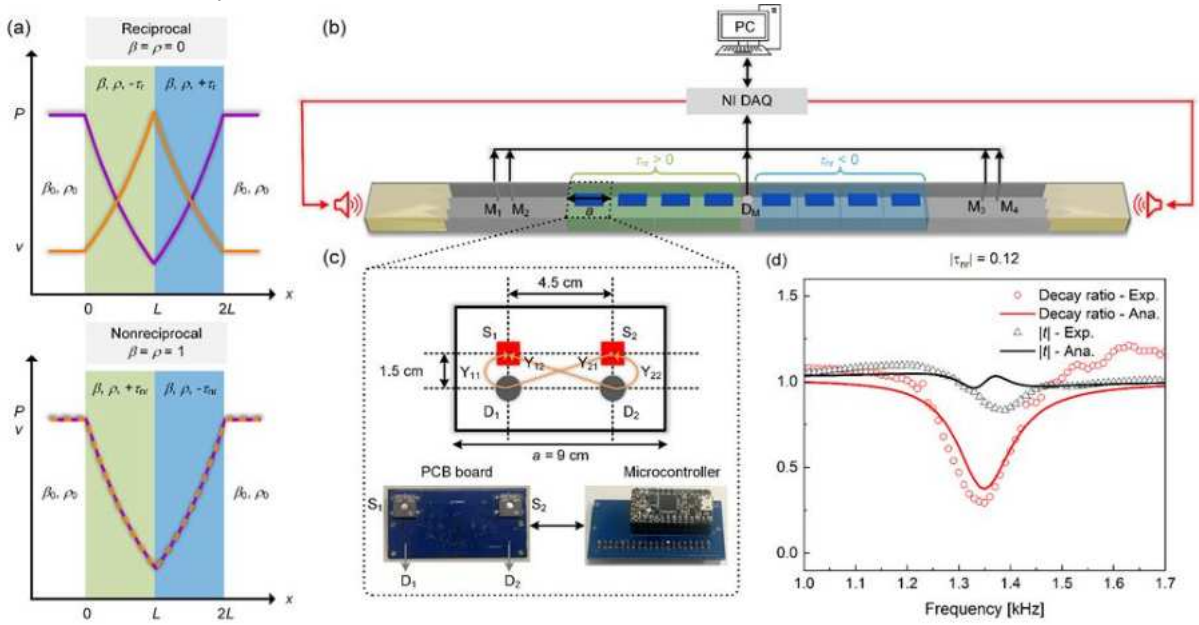


Figure 1. (a) Pressure (purple) and velocity (orange) field profiles for layers with phase elapse $\phi_L = \omega L/c = 8.9$ with purely reciprocal Willis coupling (upper panel) as a comparison to the purely nonreciprocal Willis coupling (lower panel). (b) Experimental setup consists of a 1D waveguide with active atoms. (c) Schematic and photograph of a single atom. (d) Measured (dots) and calculated (lines) results for the transmission coefficient and the decay ratio.

Acknowledgements: The work is supported by the Hong Kong RGC (16307522, AoE/P-502/20) and by Croucher Foundation (CAS20SC01, CF23SC01).

References

1. Asadchy, V. S., A. Díaz-Rubio, and S. A. Tretyakov, "Bianisotropic metasurfaces: physics and applications," Nanophotonics, Vol. 7, No. 6, 1069-1094, 2018.

2. Chen, M. L., Y. Bi, H.-C. Chan, Z. Lin, S. Ma, and S. Zhang, "Anomalous electromagnetic tunneling in bianisotropic ϵ−μ-zero media," Phys. Rev. Lett., Vol. 129, No. 12, 123901, 2022.

3. Muhlestein, M. B., C. F. Sieck, P. S. Wilson, and M. R. Haberman, "Experimental evidence of Willis coupling in a one-dimensional effective material element," Nat. Commun., Vol. 8, No. 1, 15625, 2017.

4. Chen, Y., X. Li, G. Hu, M. R. Haberman, and G. Huang, "An active mechanical Willis meta-layer with asymmetric polarizabilities," Nat. Commun., Vol. 11, No. 1, 3681, 2020.

5. Wen, X., H. K. Yip, C. Cho, J. Li, and N. Park, "Acoustic amplifying diode using nonreciprocal Willis coupling," Phys. Rev. Lett., Vol. 130, No. 17, 176101, 2023.

Quasi-normal modes and transmission channels in non-Hermitian disordered media

V. Freilikher

Department of Physics Bar-Ilan University, Israel
freiliv@biu.ac.il

Abstract: A review of quasi-normal modes (QNMs) studies in disordered open systems is presented. The existence of transmission resonances and hidden QNMs in weakly scattering media is demonstrated. The connection between QNMs and diffusive transmission channels is investigated. Algorithms of coherent control of wave transport in randomly scattering media are outlined.

Quasi-normal modes. The notion of QNMs is the natural extension of the classical concept of resonances in impenetrable cavities to open systems, in which stationary states do not exist because of the leakage to the outer space. QNMs can be found as the solutions of the corresponding differential equation with the outgoing boundary conditions. This problem is non-Hermitian, with complex-valued eigenvalues; however the set of the solutions is complete and bi-orthogonal [1], so that any field can be presented as a superposition of the QNMs. This approach is a powerful tool for investigating open systems, that do not conserve energy. QNMs also play an important role in a variety of inverse problems in target identification and non-destructive remote sensing [2]. In "clean" open resonators, quantum dotes and wires, to each QNM there corresponds a peak in the spectrum of the transmission coefficient, so-called transmission resonance (TR), whose frequency is equal to the real part of the QNM's eigenvalue. However, scattering on random fluctuations of material and geometrical parameters, that are ubiquitous in any real medium of propagation, can dramatically change the spectrum and the spatial structures of QNMs. One of the most striking manifestations of disorder is the violation of the one-to-one correspondence between the QNNs and TRs [3]. Due to the interference of multiply scattered fields in weakly disordered systems, some of the QNSs become invisible in transmission (hidden). The averaged ratio N_{res} /N_{mod} of the number of transmission peaks N_{res} to the total amount of QNMs N_{mod}, is a universal quantity, in the sense that it is independent of the physical nature of the random system, and in a given frequency interval is insensitive to the type and degree of disorder. It is close to the value $(2/5)^{1/2}$, which mathematically follows from the general statistical properties of random trigonometric polynomials. In contrast to TRs, the lifetime of a hidden mode (HM) does not rise with increasing fluctuations, rather remains unchanged or even decreases, depending on the strength of the coupling to the leads. The wave functions of HMs are also very unusual. The spatial profiles of their amplitudes are concentrated near one of the edges of the random sample, and exponentially decrease towards the other. As the scattering strength and/or the length of the system increase, HMs eventually become ordinary. Although they appear in the DOS in the same way as the ordinary modes do, HMs are non-conducting, i.e., do not contribute to the total transmission even in the ballistic regime [3].

Transmission channels. During almost a century, the diffusion approach was believed to be an adequate tool sufficient to interpret and explain theoretically the majority of transport phenomena in disordered media.

However, quite recently it became clear that the interference of multiply-scattered fields, which is neglected in the classical diffusion theory, dramatically affects all wave processes in systems with fluctuations. To account for the wave nature of the radiation it is expedient to describe the transport through a given disordered sample by a random transmission matrix (TM), which connects the set of orthogonal modes at the input to that at the output. It turns out that the eigenvectors and eigenvalues of TM, obtained by singular value decomposition bear significant physical meaning: they uniquely determine wave fronts and transmittances of the so-called transmission eigenchannels (TEs). Any incoming wave can be decomposed into a linear superposition of TEs, which propagate independently through the system with the transmittances equal to the corresponding eigenvalues τ. The shape of each channel is given by an eigenvector and is preserved all along the sample, including the output, meaning that signal does not spread in the transverse direction. At the same time, the longitudinal profile of the energy density distribution of TEs is universal [4, 5]. It is given by an analytical formula [4], where the details of the system, such as the geometry and the disorder parameters, enter only into the ratio L/l (L is the distance of propagation, l is the scattering mean free path). The important implication is that TEs can be harnessed to suppress reflection in favor of transmission, and vice versa. This is because the probability distribution of the transmission coefficients is bimodal: it is picked at $\tau = 1$ and $\tau = 0$, corresponding to highly transparent and reflecting channels respectively. The explicit form of this distribution can be the controlled by the reflectivities of the edges [6]. The adaptive wave front shaping technique and the on-chip coupling scheme enable access to all input modes. By selectively coupling the incident wave to the open or closed channels, it is possible not only vary the delivery of energy to the receiver, but also change its spatial density distribution inside the system [7]. Recently, original algorithms of output control by input front shaping in multimode fibers have been developed [8, 9].

References

1. P. Leung, S. Liu, K. Young, "Completeness and orthogonality of quasinormal modes ", P RA **49**, No. 4, 3057-3067, 1994.

2. F. Cakoni, H. Haddar *Editors*, "Transmission eigenvalues", Topical Issue, Journal of Inverse Problems **29**, 1 – 152, 2013.

3. Y. Bliokh, V. Freilikher, Z Shi, A. Genack, F. Nori, "Hidden modes in open disordered media: analytical, numerical, and experimental results", New J. Phys. **17**, 113009, 2015.

4. P. Fang, C. Tian, L. Zhao, Y. Bliokh, V.Freilikher, F. Nori, **"**Universality of eigenchannel structures in dimensional crossover"**,** PRB **99**, 094202, 2019.

5. H. Yılmaz, Chia Wei Hsu, A. Yamilov, H. Cao, "Transverse localization of transmission eigenchannels", Nature Photonics **352,** vol 13, 352–358, |2019.

6. L. Zhao, C. Tian, Y. Bliokh, V. Freilikher, "Controlling transmission eigenchannels in random media by edge reflection" PRB **92**, 094203, 2015

7. R. Sarma, A. Yamilov, S. Petrenko, Y Bromberg, H. Cao, "Control of energy density inside a disordered medium by coupling to open or closed channels", PRL **117**, 086803, 2016.

8. H. Cao, T. Cizmar, S. Turtaev, T. Tyc, S. Rotter, "Controlling light propagation in multimode fibers for imaging, spectroscopy, and beyond", Advances in Optics and Photonics **15**, 524 (2023).

9. Chun-Wei Chen, K. Wisal, M. Fink, A. Douglas Stone, H. Cao, "Exploiting space-time symmetry in dissipative nonlinear multimode amplifiers for output control", ArXiv:2402.10345v1 [physics.optics] 15 Feb 2024.

Exceptional points in a single dielectric nanoparticle

Adrià Canós Valero,[1*] Vjaceslavs Bobrovs,[2] Thomas Weiss,[1] Alexander S. Shalin,[3] and Yuri Kivshar[4]

[1]Institute of Physics, University of Graz, and NAWI Graz, 8010, Graz, Austria

[2]Riga Technical University, Institute of Telecommunications, Riga 1048, Latvia

[3]Center for Photonics and 2D Materials, Moscow Institute of Physics and Technology, Dolgoprudny 141700, Russia

[4]Nonlinear Physics Centre, Australian National University, Canberra ACT 2601, Australia

[*]corresponding author: adria.canos-valero@uni-graz.at

Abstract: Exceptional points are singularities of open systems, where eigenvalues and eigenvectors coalesce. They are being intensively studied in photonics, owing to their strong sensitivity to perturbations. However, most works are restricted to wavelength-scale structures. Here, we present rigorous criteria for the design of exceptional points in a single dielectric nanoparticle.

Open optical systems, i.e. systems interacting with an environment, are ubiquitous in nature. One of their most remarkable features is their ability to host spectral singularities where both eigenvalues and eigenvectors coalesce, known as exceptional points (EPs)[1]. While conventional eigenmodes shift linearly with a perturbation ϵ, at an nth-order EP, the shift is proportional to $\epsilon^{1/n}$, where n is the number of coalescing eigenmodes. This peculiarity renders EPs highly attractive for many applications, including biosensing schemes relying on resonance tracking [1]. This has triggered significant efforts for the realization of EPs at smaller scales, aiming at the detection of smaller analyte concentrations. However, the vast majority of studies are restricted to wavelength-scale systems based on waveguides, plasmonic metasurfaces and/or microresonators [1], [2].

Recently, all-dielectric nanoparticles have been shown to be a promising platform for applications in nanophotonics, owing to their negligible ohmic losses [3], [4]. Interestingly, a single dielectric nanoparticle can support a broad class of electric and magnetic resonances, giving rise to several exotic effects [3].

In this contribution, we will derive rigorous rules for the realization of EPs in a single dielectric nanoparticle in the visible range, successfully introducing EP physics to all-dielectric nanophotonics. We demonstrate that EPs are achievable through simple geometry tuning, making them possible in a broad class of dielectric materials, including silicon [5]. To demonstrate their existence, here we consider their formation from the electric (ED) and magnetic dipole (MD) eigenmodes of a nanocylinder with refractive index close to that of silicon (**Fig. 1a**).

Suppose that we perform a small perturbation in the shape of such particle. In particular, the perturbation must break the horizontal mirror symmetry, allowing the even and odd eigenmodes to hybridize (**Fig. 1a**, lower panel). We consider introducing a small conicity. Then, the eigenmodes of the perturbed particle (Modes 1,2 in **Fig.1b**) can be expressed as a linear combination of the original ones. Using the resonant state expansion method [6], this yields a generalized eigenvalue problem for the new eigenmodes. The hybrid magnetoelectric modes can coalesce at a pair of EPs upon changing two selected system parameters, the bottom radius and the conicity (**Fig. 1b**). Owing to the collapse of the eigenspace, the norms of the eigenmodes become the same and tend to zero at the EP (**Fig. 1c**). This poses interesting questions on the completeness of the eigenmode basis, which will be discussed.

We propose to utilize the new EPs to detect small local changes in the refractive index of the surrounding environment (**Fig.1d**). Specifically, we observe a larger spectral sensitivity of the frequency detuning in

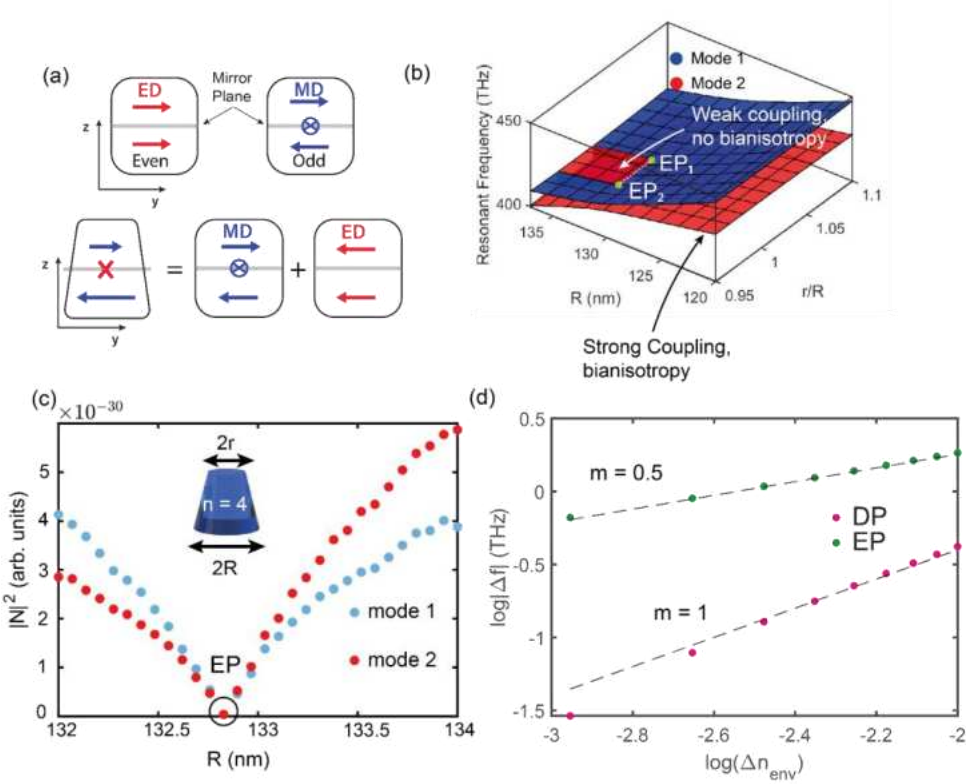


Figure 1. (a) Top: Scheme of the ED and MD modes of a dielectric nanocylinder with respect to a horizontal mirror plane. Bottom: effect of mirror symmetry breaking in the MD mode. (b) Evolution of the resonance frequencies of the single nanoparticle vs. bottom radius and the ratio of top to bottom radius. (c) Norm of the involved resonant states in the vicinity of the EP, for r/R = 0.972. Inset: investigated nanoparticle, with refractive index n=4. (d) Sensitivity of the investigated EP to changes in the environment refractive index, vs the ED and MD modes of the unperturbed nanoparticle (DP). Height: 100 nm.

comparison to the unperturbed eigenmodes of the nanocylinder, owing to the square-root asymptotic near the EP. This is clearly confirmed by a log-log plot of the detuning vs refractive index change, showing a slope of 1/2.

In conclusion, we have demonstrated that EPs can be achieved in single dielectric nanoparticles, paving the way for exciting applications and uncharted effects in all-dielectric nanophotonics.

References

[1] J. Wiersig, "Review of exceptional point-based sensors," *Photonics Res.*, vol. 8, no. 9, pp. 1457–1467, Sep. 2020, doi: 10.1364/PRJ.396115.

[2] J.-H. Park *et al.*, "Symmetry-breaking-induced plasmonic exceptional points and nanoscale sensing," *Nat. Phys.*, vol. 16, no. 4, pp. 462–468, Apr. 2020, doi: 10.1038/s41567-020-0796-x.

[3] Y. Kivshar, "All-dielectric meta-optics and non-linear nanophotonics," *Natl. Sci. Rev.*, vol. 5, no. 2, pp. 144–158, Mar. 2018, doi: 10.1093/nsr/nwy017.

[4] A. Canós Valero *et al.*, "Superscattering emerging from the physics of bound states in the continuum," *Nat. Commun.*, vol. 14, no. 1, p. 4689, Aug. 2023, doi: 10.1038/s41467-023-40382-y.

[5] A. Canós Valero, V. Bobrovs, T. Weiss, L. Gao, A. S. Shalin, and Y. Kivshar, "Bianisotropic exceptional points in an isolated dielectric nanoparticle," *Phys. Rev. Res.*, vol. 6, no. 1, p. 013053, Jan. 2024, doi: 10.1103/PhysRevResearch.6.013053.

[6] E. A. Muljarov and T. Weiss, "Resonant-state expansion for open optical systems: Generalization to magnetic, chiral, and bi-anisotropic materials," *Opt. Lett.*, vol. 43, no. 9, p. 1978, May 2018, doi: 10.1364/OL.43.001978.

Photonics of topological transitions Disk - Ring - Split Ring

M.E. Bochkarev[1], N.S. Solodovchenko[1], K.A. Bronnikov[1], K.B. Samusev[1,2], and M.F. Limonov[1,2*]

[1]Department of Physics and Engineering, ITMO University, St. Petersburg, 197101, Russia
[2]Ioffe Institute, St. Petersburg 194021, Russia
[*]corresponding author: m.limonov@metalab.ifmo.ru

Abstract: The chain of topological transitions disk – ring – split ring with a gradual change in structural parameters has been studied. We demonstrate that transitions between structures of different topologies are accompanied by impressive photonic effects.

This work consists of two parts connected by a common intermediate structure - a dielectric ring resonator of rectangular cross-section. The first part refers to the topological transition from a dielectric disk to a ring by introducing a coaxial hole. We carried out experimental and theoretical studies of the transformation of resonant scattering spectra, photonic eigenmodes and electromagnetic field distribution patterns with a gradual increase in the coaxial hole in the disk from zero to the ratio of the internal and external radii of 0.5. The hot spot at the center of the resonator flashes brightly immediately after the hole is formed, and then quickly decreases as the hole radius increases.

The hot spot can be explained using 2D Mie theory for an infinite dielectric cylinder with a coaxial hole, followed by a finite length case and numerical analysis using COMSOL Multiphysics. Considering the case of TE polarization for a ring resonator of infinite height, it is possible to express the radial and azimuthal components of the electric field in terms of the azimuthal number *m* and the Lorentz-Mie coefficients, which, in turn, are expressed in terms of Bessel functions. As is known, only the zero-order Bessel function J_0 is equal to unity at the center of coordinates ($r = 0$), and the remaining Bessel functions vanish, so we obtain that only the first azimuthal harmonic (corresponding to the electric dipole) has a local maximum at the center, generating a hot spot when a small hole is formed. Numerical calculations show that the hot spot goes out very quickly and disappears already at the ratio $R_{in}/R_{out} \sim 0.001$. Thus, a hot spot can be considered a hallmark of a dielectric disc $\rightarrow$ dielectric ring topological transition.

The second part of the work concerns the study of the topological transition from a dielectric ring of rectangular cross-section to a split ring [1]. As is known, the scattering spectra of a dielectric ring resonator are determined by a set of doubly degenerate CW and CCW modes and have a pronounced resonant character [2-4]. An important feature of our approach is that during all transformations of the structure we leave its length constant, changing only the curvature. As a result of theoretical and experimental studies, we discovered that at the transition the degeneracy of the CW-CCW ring modes is removed and two families of modes arise. The "ordinary" mode family does not undergo any changes, as do the "curved" strip modes [5,6]. The family of “topological” modes splits off from the “ordinary” modes with a monotonic phase change from 0 to π as the central angle in the split ring increases, reminiscent of the Berry phase in a Möbius strip [5,6]. We were able to establish in detail the unusual mechanism for the emergence of “ordinary” and “topological” modes. It turned out that “ordinary” modes arise when the field zero in the ring is oriented opposite the gap and therefore they practically do not change.

“Topological” modes arise when the antinode of the electric field of the ring mode is oriented towards the gap. In the process of topological transition and “cutting” one antinode into two, an additional phase is gradually added

from 0 to π, and the length of each topological wave monotonically decreases by half a period. Consequently, we obtain a Fabry-Pérot type resonator with an arbitrary resonant wavelength, that is, the resonator length is not a multiple of the resonant wavelength. Moreover, the phase and length of an ordinary wave does not change during the topological transition and can serve as an ideal reference in any research and various applications. Therefore, using a Fabry-Pérot topological resonator with variable curvature and fixed length, it is possible to realize resonant modes with an arbitrary non-integer number of waves, creating a new generation of resonators with unique classical and quantum applications [1].

This work was funded by the Russian Science Foundation (Project No. 23-12-00114).

References

1. Bochkarev, M., N. Solodovchenko, K Samusev, M Limonov, "Split ring versus Möbius strip: topology and curvature effects, " arXiv preprint arXiv:2312.04582.
2. Solodovechenko, N., M. Sidorenko, T. Seidov, I. Popov, E. Nenasheva, K. Samusev and M. Limonov, "Cascades of Fano resonances in light scattering by dielectric particles," Mater. Today, Vol. 60, 169-78, 2022.
3. A. P. Chetverikova, M. E. Bochkarev, N. S. Solodovchenko, K. B. Samusev, and M. F. Limonov, "Optical "fingerprints" of dielectric resonators, " J. Opt. Soc. Am. B, Vol. 40, 2146-2152 (2023).
4. A .P. Chetverikova, M. F. Limonov, M. S. Sidorenko, K. B. Samusev, N. S. Solodovchenko, "Radial and axial photonic galleries of dielectric rings," PNFA, 57, 101185 (2023).
5. J. Wang, S. Valligatla, Y. Yin, L. Schwarz, M. Medina-Sánchez, S. Baunack, C. H. Lee, R.Thomale, S. Li, V. M. Fomin, L. Ma, O. G. Schmidt, "Experimental observation of Berry phases in optical Möbius-strip microcavities, Nature Photonics," 17, 120 (2023).
6. B. Piccirillo, V. Vicuña-Hernández, "Tuning optical cavities by Möbius topology," Nature Photonics, 17, 13 (2023).

Response strength of general non-Hermitian systems at exceptional points

Jan Wiersig*

Institut für Physik, Otto-von-Guericke-Universität Magdeburg, D-39016 Magdeburg, Germany
*corresponding author: jan.wiersig@ovgu.de

Abstract: Non-Hermitian systems with exceptional points exhibit a strongly enhanced response to perturbations and excitations. We present the theory of the spectral response strength for the general case where the dimension of the Hilbert space can be larger than the order of the exceptional point.

Exceptional points (EPs) are spectral degeneracies in open wave systems which can produce a number of counterintuitive phenomena with potential applications in particular in optics and photonics [1]. At an EP of order n exactly n eigenvalues (eigenfrequencies) and the related eigenstates (modes) of a non-Hermitian Hamiltonian $\hat{H}_0$ coalesce [2]. When such a Hamiltonian is slightly perturbed, $\hat{H}_0 + \varepsilon\hat{H}_1$, the eigenvalues exhibit a strong spectral response $E_j - E_{\text{EP}} \propto \varepsilon^{1/n}$, where $\varepsilon > 0$ is the perturbation strength. These large splittings can be exploited for sensing applications [3]. For an $m \times m$ Hamiltonian $\hat{H}_0$ it was shown for the special case $m = n$, i.e. the Hilbert-space dimension equals the order of the EP, that the perturbation-induced splitting is bounded from above [4]

$$|E_j - E_{\text{EP}}|^n \le \varepsilon ||\hat{H}_1||_2 \, \xi \, , \tag{1}$$

where $||\cdot||_2$ is the spectral matrix norm, $\xi := ||\hat{N}^{n-1}||_2$ is the spectral response strength, and $\hat{N} := \hat{H}_0 - E_{\text{EP}}\mathbb{1}$ is the traceless part of the unperturbed Hamiltonian. For sensing applications EPs with large ξ are desirable.

For the generic case $m \ge n$ we use the expansion of the $m \times m$ Green's function of the unperturbed Hamiltonian $\hat{H}_0$ [5, 2]

$$\hat{G}(E) = \sum_l \left[\frac{\hat{P}_l}{E - E_l^{(0)}} + \sum_{k=2}^{n_l} \frac{\hat{N}_l^{k-1}}{(E - E_l^{(0)})^k} \right] \, . \tag{2}$$

The integer l labels the considered part of the point spectrum including isolated energy eigenvalues and EPs. The integer k labels additional terms for EPs only. Each operator $\hat{P}_l$ is a projector onto the generalized eigenspace of the eigenvalue $E_l^{(0)}$ with $\hat{P}_j\hat{P}_l = \delta_{jl}\hat{P}_l$ where δ_{jl} is the Kronecker-Delta. The operator $\hat{N}_l$ for a given EP of order n_l is a nilpotent operator of index n_l and defined by

$$\hat{N}_l := \left(\hat{H}_0 - E_l^{(0)}\mathbb{1}\right) \hat{P}_l \, . \tag{3}$$

It holds $\hat{P}_l\hat{N}_l = \hat{N}_l\hat{P}_l = \hat{N}_l$. To describe the situation near an EP of order n_l with eigenvalue $E_l^{(0)} = E_{\text{EP}}$ we consider the leading-order contribution in the Green's function (2)

$$\hat{G}(E) = \frac{\hat{N}_l^{n_l-1}}{(E - E_{\text{EP}})^{n_l}} \, , \tag{4}$$

Our analysis reveals that Eq. (1) is still valid with the spectral response strength

$$\xi = ||\hat{N}_l^{n_l-1}||_2 \, . \tag{5}$$

The right-hand side can be computed by hand in simple cases. In other cases, residue calculus can enable a numerical treatment. From the expansion in Eq. (2) one obtains

$$\hat{N}_l^{n_l-1} = \frac{1}{2\pi i} \oint_C dE \, (E - E_{\text{EP}})^{n_l-1} \hat{G}(E) \, , \tag{6}$$

with C being a simple closed path in the complex energy plane that contains only the eigenvalue E_{EP}. The function $\hat{G}(E)$ is calculated numerically for each energy E by matrix inversion and is integrated in Eq. (6). Finally, the spectral response strength ξ_{num} is numerically determined by Eq. (5).

We demonstrate the efficiency and accuracy of this scheme using the random-matrix approach introduced in Refs. [4, 6]. Consider the $n \times n$ matrix $\hat{H}_0$ having an EP with order n and eigenvalue E_{EP} created via a similarity transformation $\hat{H}_0 =$

$\hat{Q}\hat{J}\hat{Q}^{-1}$, where $\hat{J}$ is an $n \times n$ matrix with an EP of order n in Jordan normal form and $\hat{Q}$ is an $n \times n$ matrix whose elements are complex random numbers with real and imaginary parts being drawn from a uniform distribution on $[-1/2, 1/2]$. We calculate the associated response strength ξ from the former theory [4] for later comparison. Next, we create the $(m-n) \times (m-n)$-matrix $\hat{H}_{\mathrm{a}}$ with its elements to be complex random numbers with real and imaginary parts being drawn from a uniform distribution on $[-1/2, 1/2]$. Finally, we combine these two matrices to obtain the $m \times m$ Hamiltonian

$$\hat{H} = \hat{U} \begin{pmatrix} \hat{H}_0 & 0 \\ 0 & \hat{H}_{\mathrm{a}} \end{pmatrix} \hat{U}^{\dagger} \tag{7}$$

with the random unitary $m \times m$-matrix $\hat{U}$. The resulting Hamiltonian $\hat{H}$ has an EP with the same eigenvalue E_{EP}, the same spectral response strength ξ, and the same order n than the original lower-dimensional Hamiltonian $\hat{H}_0$. The construction of the Hamiltonian $\hat{H}$ in Eq. (7) is illustrated in Fig. 1. Figure 1(a) shows a realization of $\hat{H}$ before the unitary matrix $\hat{U}$ is applied and Fig. 1(b) shows $\hat{H}$ after the unitary transformation. The complex eigenvalues of this Hamiltonian are depicted in Fig. 1(c). It can be seen that the spectrum contains isolated eigenvalues and an EP of order 4.

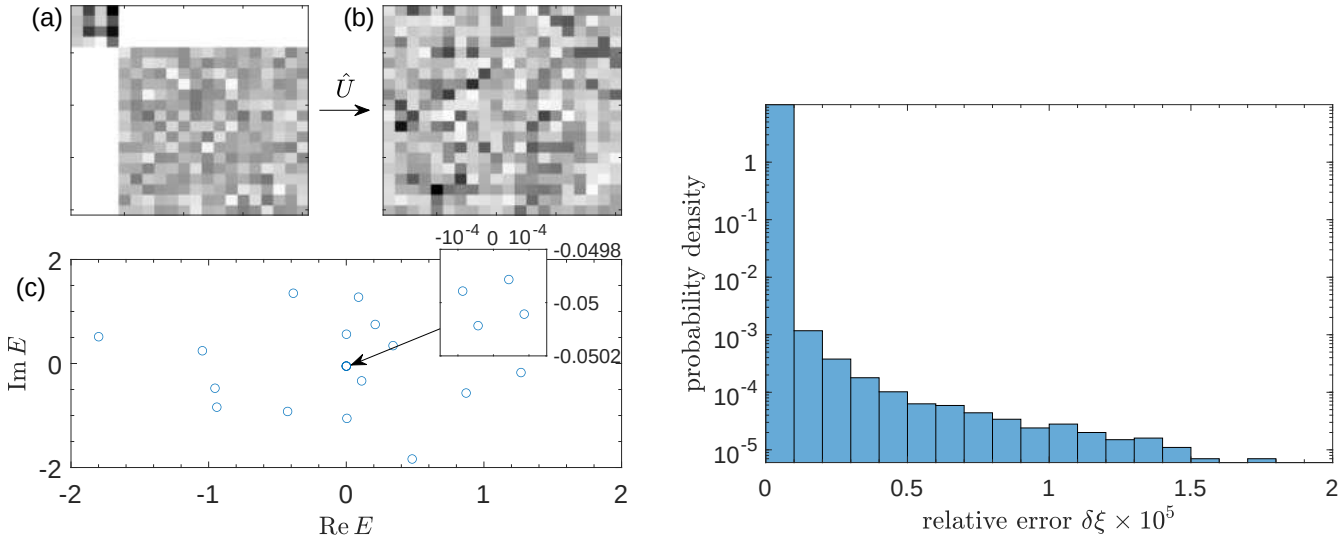


Figure 1: (Left) Illustration of the construction of a random 20×20-Hamiltonian exhibiting an EP of order 4 with eigenvalue $E_{\mathrm{EP}} = -i0.05$. A realization of the Hamiltonian (7) (a) without and (b) with the random unitary matrix $\hat{U}$, respectively. (c) Dimensionless complex eigenvalues of the Hamiltonian. The magnification in the inset reveals that the EP-eigenvalues are slightly split due to tiny rounding errors in the double-precision floating-point arithmetic. (Right) Probability density function of the relative error $\delta\xi := |\xi_{\mathrm{num}} - \xi|/\xi$ calculated from 10^7 realizations of random 20×20-Hamiltonians possessing an EP of order 4. The integration path C in Eq. (6) is a circle of radius 10^{-2} centered at $E_{\mathrm{EP}} = -i0.05$. About 10^{-5} of the data points have $\delta\xi > 2 \times 10^{-5}$ and are not shown.

The Hamiltonians $\hat{H}$ in Eq. (7) constitute a class of exemplary systems for the proposed scheme based on residue calculus in Eq. (6) to compute the spectral response strength ξ_{num} of EPs for the generic situation. The right subfigure of Fig. 1 shows a comparison for 10^7 realizations of 20×20-matrices $\hat{H}$ each with an EP of fourth order. It can be observed that the relative error of the spectral response strength is very small.

To summarize, we have presented the general theory of the spectral response strength for non-Hermitian systems with EPs of arbitrary order and to arbitrary Hilbert-space dimension. A numerical scheme based on residue calculus allows for an efficient and accurate calculation of the response strength. The theory is useful for the design of complex non-Hermitian systems in general but in particular for sensing applications.

References

1. M.-A. Miri and A. Alù, "Exceptional points in optics and photonics," *Science*, vol. 363, no. 6422, p. eaar7709, 2019.
2. T. Kato, *Perturbation Theory for Linear Operators*. New York: Springer, 1966.
3. W. Chen, Ş. K. Özdemir, G. Zhao, J. Wiersig, and L. Yang, "Exceptional points enhance sensing in an optical microcavity," *Nature (London)*, vol. 548, pp. 192–196, 2017.
4. J. Wiersig, "Response strengths of open systems at exceptional points," *Phys. Rev. Res.*, vol. 4, p. 023121, 2022.
5. J. Wiersig, "Moving along an exceptional surface towards a higher-order exceptional point," *Phys. Rev. A*, vol. 108, p. 033501, 2023.
6. J. Wiersig, "Petermann factors and phase rigidities near exceptional points," *Phys. Rev. Research*, vol. 5, p. 033042, 2023.

Scattering Singularities of Complex Non-Hermitian Systems Probed with Continuously Variable Metasurfaces

Jared Erb[1], **Thomas M. Antonsen**[1], **and Steven M. Anlage**[1*]

[1] Physics Department, University of Maryland, College Park, MD 20742-4111 USA
[*]corresponding author: anlage@umd.edu

Abstract: We utilize continuously tunable metasurfaces to establish coherent perfect absorption and exceptional point scattering singularities in generic microwave resonant systems in 1, 2, and 3-dimensions. We demonstrate CPA through 100% absorption of incident radiation, and examine the topological properties of multiple Exceptional Points in two- and three-dimensional parameter spaces.

We study the wave properties of complex enclosed non-Hermitian scattering systems in the limit where the wavelength is much smaller than the characteristic dimension of the enclosure. In this limit the scattering properties (S-matrix, impedance matrix, etc.) are extremely sensitive to variations in frequency or any property of the interior or perimeter structure of the cavity. We perform two-port S-matrix measurements of a variety of one-dimensional graphs, two-dimensional billiards, and three-dimensional enclosure scattering systems, all of which host two or more electronically tunable metasurfaces. The metasurfaces vary their reflection phase and amplitude as a function of dc voltage, and this has a strong impact on the scattering properties of the entire system. We focus on two scattering singularities generically present in non-Hermitian systems, namely coherent perfect absorption (CPA), and exceptional points (EP), as a function of experimental parameters. Our recent work utilizes multiple nonlinear and continuously tunable metasurfaces to achieve near-perfect absorption over a broad range of frequencies [1]. Placing multiple metasurfaces inside the cavity allows us to engineer desired scattering conditions, such as CPAs and EPs, by actively manipulating the poles and zeros of the scattering matrix through the application of multiple voltage biases [1]. We utilize complex time delay to identify the locations of potential CPA events in parameter space [2,3]. We find that both CPAs and EPs are a generic and common feature of all of the experimental systems studied. Both types of singularity can be created and destroyed through variations in metasurface configuration. This establishes continuous metasurface tuning as a means to exploit CPA and EP scattering singularities for applications.

We thank David Shrekenhamer, Timothy Sleasman of the Johns Hopkins Applied Physics Laboratory for assistance with the metasurfaces. This work is supported by ONR under Grant No. N000141912481, DARPA WARDEN under Grant No. HR00112120021, and NSF RINGS under Grant No. ECCS2148318.

References

1. Jared Erb, David Shrekenhamer, Timothy Sleasman, Thomas M. Antonsen, and Steven M. Anlage, "Control of the Scattering Properties of Complex Systems By Means of Tunable Metasurfaces," Acta Physica Polonica A **144** (6), 421-428 (2023).
2. Lei Chen, Steven M. Anlage, and Yan V. Fyodorov. Generalization of Wigner time delay to subunitary scattering systems. Phys. Rev. E, **103**, L050203, (2021).
3. Lei Chen and Steven M. Anlage, "Use of Transmission and Reflection Complex Time Delays to Reveal Scattering Matrix Poles and Zeros: Example of the Ring Graph," Phys. Rev. E **105**, 054210 (2022).

Frequency combs in dissipative Kerr cavities with non-Hermitian periodic potentials

S. B. Ivars [1], M. Botey [1], K. Staliunas[2], and R. Herrero[1]

[1] Departament de Fisica, Universitat Politecnica de Catalunya (UPC), Rambla Sant Nebridi 22, 08222, Terrassa, Barcelona, Catalonia, Spain

[2] Institucio Catalana de Recerca i Estudis Avancats (ICREA), Passeig Llus Companys 23, E-08010, Barcelona, Spain
*corresponding author: ramon.herrero@upc.edu

Abstract: We demonstrate stabilization of solitonic solutions and associated frequency combs in Kerr cavities with non-Hermitian periodic modulations. These potentials hybridize the two mechanisms of soliton formation, yielding new families of stable solitons and molecules and making them accessible. This scenario diversifies frequency combs, allowing real-time reshaping and broadening applications.

Solitonic solutions generated in nonlinear optical cavities and their spectrum, i.e. frequency combs, are a crucial tool for many applications as high precision spectroscopy, atomic clocks or optical communications and their real-time manipulation has been recently explored in different situations [1]. Here, we uncover a mechanism for a controlled reversible switching between different frequency combs corresponding to Localized States with different widths. Such control is based on the tilt of the snaking branch structures associated to different families of such solitonic solutions.

The proposed mechanism is based on the introduction of integrated electro-optical modulators and amplifiers inside dissipative Kerr cavities generating modulations of the refractive index and gain/losses in the form of a non-Hermitian periodic potential. Recently, nonlinear ring fiber or waveguide cavities have emerged as attractive options for generating frequency combs, see Fig. 1 a) [2]. Passive and dispersive cavities including third order Kerr nonlinearities and a complex spatial potential $V(x)$ follows the damped-driven Nonlinear Schrödinger Equation:

$$\frac{\partial A}{\partial t} = h - (1+i\delta)A + 2i|A|^2 A - i\frac{\partial^2 A}{\partial x^2} + V(x)A \qquad \text{with} \quad V(x) = me^{-i\phi}\cos(2\pi nx/L) \tag{1}$$

that includes the external energy injection h and the cavity detuning δ. The complex amplitude of the periodic potential is described m and ϕ, while n is the number of periods along the cavity with length L.

The Kerr nonlinearity induces bistability of homogeneous states and the formation of Pattern States (P) and Localized States (S) in a particular detuning interval. Dissipative Kerr cavities with normal/anomalous Group Velocity Dispersion (GVD) present P and S showing a branch structure with a collapsed/standard snaking shape, both inaccessible to be inside the bistable interval. As an example, Figure 1 b shows pattern branches for the unmodulated case with normal GVD and showing snaking branch structures collapsing to a particular detuning value inside the bistable interval (the Maxwell-Point) [3]. Each colored branch corresponds to a pattern composed by a different number of solitons inside the window. The periodic potential reduces the patterned structures while the number of periods in the cavity, n, determines the possible patterns and corresponding

localized structures, see Fig. 1 c) for n=7.

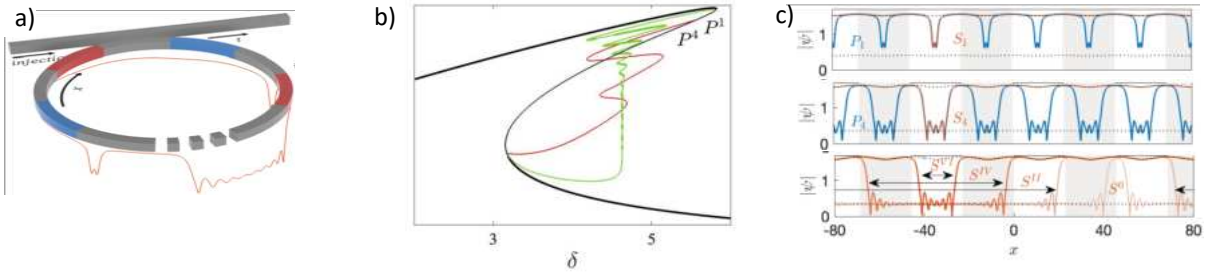


FIG. 1: a) Schematic representation of a modulated Kerr optical ring cavity. b) Homogeneous branches in black and pattern collapsed branches as a function of the detuning for solitons with 1 and 4 oscillations. c) Patterns in blue and corresponding localized states for a cavity with 7 oscillations of the potential.

The non-Hermitian potential hybridizes the two scenarios combining both collapsed and standard snaking branches, see Fig. 2 a). Collapsed branches correspond to solitons confined in one period of the potential modulation and with an increasing number of oscillations around the lower homogeneous state (upper and middle example of Fig. 1 c)), while standard snaking branches correspond to solitons spanning an increasing number of periods of the potential (lower example of Fig. 1 c)). Moreover, the non-Hermitian potential tilts the branch structures to the outside of the bistable interval (shaded in grey color) for a large enough m amplitude, see Fig. 2 b). This turns solitons accessible just scanning de detuning and allowing a controlled switching between different S states and corresponding frequency combs, see Fig. 2 c).

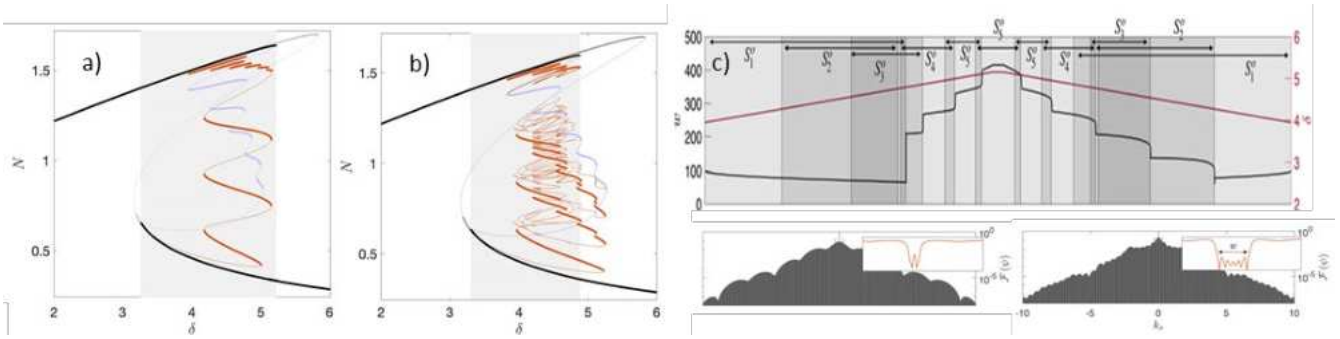


FIG. 2: Hybridised collapsed and standard snaking bifurcation structure of patterns (blue) and solitons and molecules (red) for a) m=0.1 and b) m=0.15. c) Consecutives switching between solitons and two corresponding frequency combs.

This work was supported by the Spanish government via PID2022-138321NB-C21 and Generalitat de Catalunya via 2021 SGR 00606.

References

1. Ivars, S. B., Kartashov, Y. V., de Córdoba, P. F., Conejero, J. A., Torner, L., and Milián, C., Nature Photonics pp. 1–8, 2023.
2. Wildi, T., Gaafar, M. A., Voumard, T., Ludwig, M., and Herr, T., Optica 10, 650, 2023.
3. Ma, Y.-P., Burke J., and Knobloch E., Physica D: Nonlinear Phenomena 239, 1867, 2010.

Nonperturbative effects in the eigenvalue sensitivity of non-Hermitian systems

H. Schomerus[1]

[1]Department of Physics, Lancaster Unversity, UK
[*]corresponding author: h.schomerus@lancaster.ac.uk

Abstract: Systems with an effectively non-Hermitian Hamiltonian display an enhanced sensitivity that arises from the nonorthogonality of their eigenstates. I derive an exact nonperturbative expression for this sensitivity that applies to arbitrary eigenvalue configurations. This reveals that states can have a sizable effect even if they are spectrally well separated.

Systems governed by an effectively non-Hermitian Hamiltonian exhibit heightened sensitivity to parametric and dynamic perturbations due to the nonorthogonality of their eigenstates [1-13]. This increased sensitivity is quantified by the Petermann factor [2], which originated from quantum noise theory, but turns out to the key characteristic for the general response of any non-Hermitian system. The Petermann factor diverges at exceptional points [3,4,5], which signals non-Hermitian phase transitions and results in significantly altered noise characteristics, such as a squared-Lorentzian line shape [6,7]. This enhanced sensitivity also leads to new design concepts for sensors [8]. Furthermore, in non-reciprocal settings, this effect provides insights into the dramatic difference between the spectral properties with open and periodic boundary conditions and leads to novel design concepts for directed sensing and amplification [9-11]. Because of these features, which are intimately tied to spectral degeneracies, very detailed theoretical descriptions now exist for the quasi-degenerate scenario, even for exceptional points of arbitrary order [12].

I present a precise nonperturbative expression for this sensitivity measure that is applicable across more general (indeed, arbitrary) eigenvalue configurations [13]. The expression disentangles spectral correlations from additional geometric data and maintains a straightforward asymptotic behavior near exceptional points of any order, while elucidating the impact of additional states within the system.

It then becomes evident that such states can significantly influence the system's sensitivity even when they are spectrally well separated. This is illustrated in Fig 1, which depicts how a related sensitivity measure changes when more and more eigenvalues are being incorporated into the description. Typically, a large number of eigenvalues is required before the true sensitivity can be established. The developed formalism reveals the origin and identifies the specific matrix elements responsible for this nonperturbative effect.

The algebraic method I use, which is based on the eigenvectors-from-eigenvalues idea [14], also reveals the shape of the states near an EP. Notably, they obey an equipartition principle governing the contributions from different directions in the quasidegenerate subspace of the system. This is illustrated in Fig 2.

Therefore, the presented formalism provides a systematic tool to determine and examine a key characteristic of non-Hermitian systems, their enhanced sensitivity dynamical and parametric to perturbations.

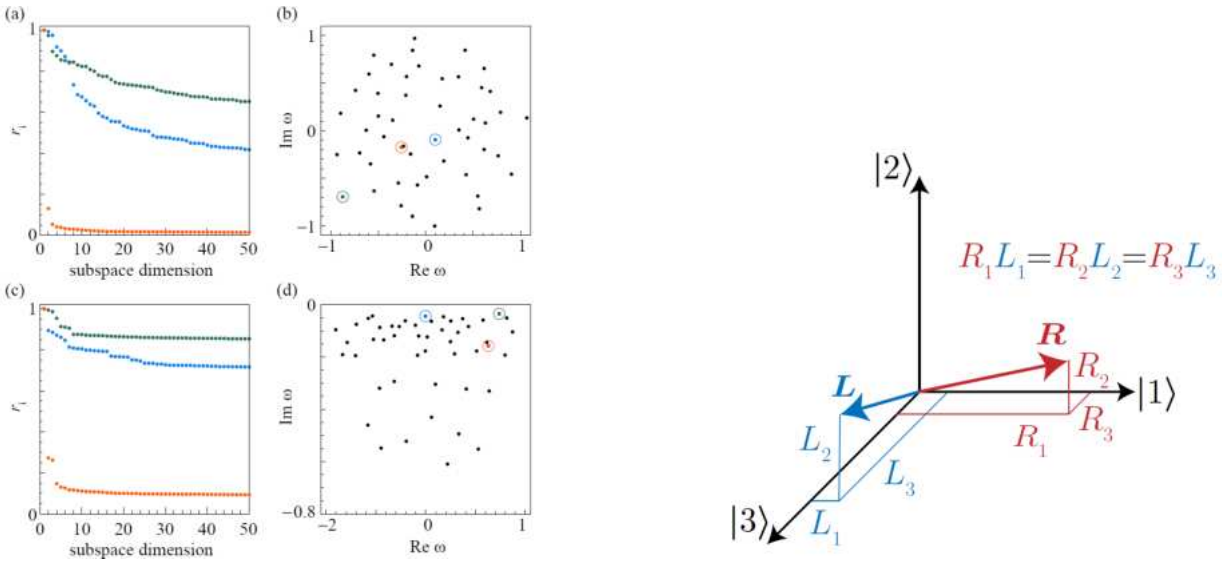


Figure 1 The systematic expansion presented here allows to detect how the spectral sensitivity is affected by well-separated eigenvalues. In the figure this illuminated by a systematic truncation of the system. Typically, the true value of the sensitivity (here represented by the phase rigidity $r \sim K^{-1/2}$) is only established when a large number of states are taken into account.

Figure 2 The formalism also reveals that within the quasidegenerate subspace, the contributions of the different directions are systematically linked to each other.

References

1. T. Kato, "Perturbation Theory for Linear Operators" (Springer, New York, 2013).
2. K. Petermann, IEEE J. Quantum Electron. 15, 566 (1979).
3. M. Patra, H. Schomerus, and C. W. J. Beenakker, Quantum-limited linewidth of a chaotic laser cavity, Phys. Rev. A 61, 023810 (2000).
4. W. D. Heiss, Exceptional points of non-Hermitian operators, Phys. Rev. E 61, 929 (2000).
5. M. V. Berry, Physics of nonhermitian degeneracies, Czech. J. Phys. 54, 1039 (2004).
6. G. Yoo, H.-S. Sim, and H. Schomerus, Quantum noise and mode nonorthogonality in non-Hermitian PT-symmetric optical resonators, Phys. Rev. A 84, 063833 (2011).
7. K. Takata et al, Observing exceptional point degeneracy of radiation with electrically pumped photonic crystal coupled-nanocavity lasers, Optica 8, 184 (2021).
8. J. Wiersig, Review of exceptional point-based sensors, Photon. Res. 8, 1457 (2020).
9. H. Schomerus, Nonreciprocal response theory of non-Hermitian mechanical metamaterials: Response phase transition from the skin effect of zero modes, Phys. Rev. Res. 2, 013058 (2020).
10. C. C. Wanjura, M. Brunelli, and A. Nunnenkamp, Topological framework for directional amplification in driven-dissipative cavity arrays, Nat. Commun. 11, 3149 (2020).
11. A. Hashemi, K. Busch, D. N. Christodoulides, S. K. Ozdemir, and R. El-Ganainy, Linear response theory of open systems with exceptional points, Nat. Commun. 13, 3281 (2022).
12. J. Wiersig, Petermann factors and phase rigidities near exceptional points, Phys. Rev. Res. 5, 033042 (2023).
13. H. Schomerus, Eigenvalue sensitivity from eigenstate geometry near and beyond arbitrary-order exceptional points, Phys. Rev. Research 6, 013044 (2024).
14. P. B. Denton, S. J. Parke, T. Tao, and X. Zhang, Bull. Am. Math. Soc. 59, 31 (2022).

Non-Hermitian mode-cleaning in linear and nonlinear optical waveguides

M. N. Akhter[1], R. Herrero[1], K. Staliunas[1, 2] and M. Botey[1]

[1] Departament de Física, Universitat Politècnica de Catalunya (UPC), Barcelona, Catalonia, Spain

[2] Institució Catalana de Recerca i Estudis Avancats (ICREA), Barcelona, Catalonia, Spain

*corresponding author: muriel.botey@upc.edu

Abstract: We present a novel all-optical mode-cleaning mechanism in waveguides triggered by an antisymmetric non-Hermitian potential. Unidirectional coupling among transverse modes enables light management, yielding ideally single-mode spatially coherent output. Analytical predictions based on a 1D linear and nonlinear mode coupling expansion are numerically validated.

Non-Hermitian systems in photonics hold unique properties such us controlling the flow of light, controlling stabilizing lasers or control optical turbulence, among others [1-5]. In guided wave optics, considerable efforts have been directed towards creating tailored gain and loss platforms to efficiently realize functionalities such as asymmetric mode transfer [6]. Just recently, non-Hermitian coupling induced by simultaneous longitudinal modulations of the propagation constant and of the gain/loss coefficient along graded was proposed for the control of the modes at the output, in parabolic multimode optical waveguides [7]

In this work, we propose the introduction of non-Hermitian potentials as a mode-cleaning mechanism in graded index waveguides, see Fig. 1a, which may represent an alternative to various attempts to address randomization [8,9,10]. We analytically predict and numerically demonstrate that non-Hermitian modulations lead to and effective control over all transverse modes eventually ideally resulting in single-mode spatially coherent output, irrespectively of the initial field distribution [11].

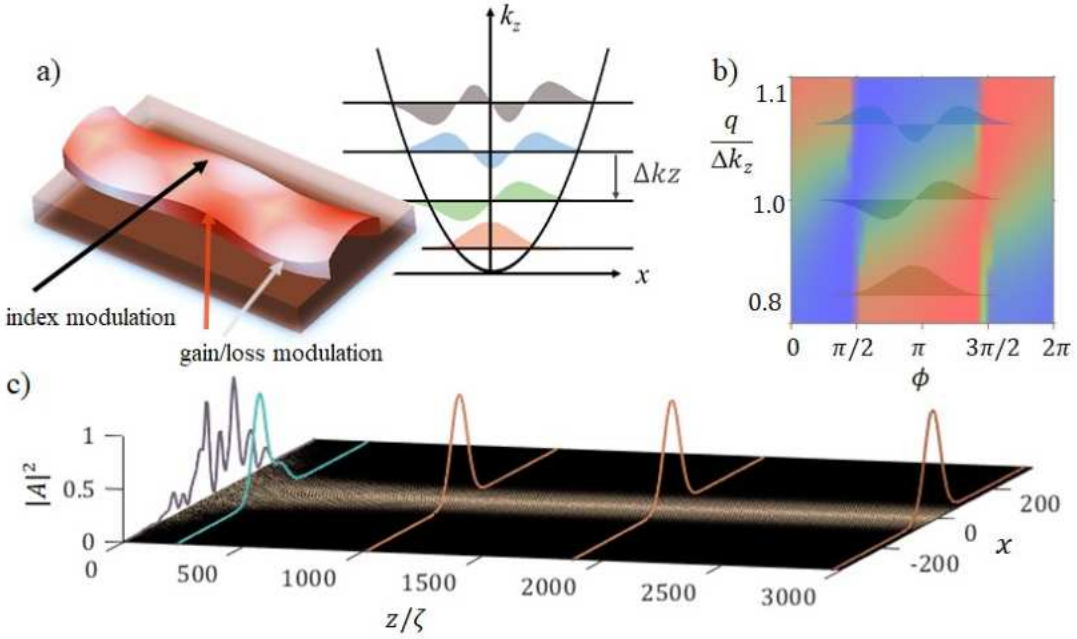


Figure 1. a) Periodically modulated non-Hermitian in a parabolic-index waveguide. Inset: spatial profile of the first equidistant transverse modes of the waveguide, with mode spacing Δk_z. b) Map of the participation of each mode into the final eigenmode of the modulated 1D waveguide, as a function of the gain/loss and index phase ϕ, and the wavenumber q of the non-Hermitian modulation. c) Evolution of a transverse noisy profile along the modulated

waveguide, distance normalized to the self-imaging period of the waveguide $\zeta=2\pi/\Delta k_z$.

The governing equation along linear multimode waveguides is the linear Schrödinger Equation (SE) while active multimode waveguides in quasi-CW regimes may be described by the Complex Ginzburg-Landau Equation (CGLE). We consider a non-Hermitian potential in the longitudinal direction with an antisymmetric transverse profile, which in the simplest from may be taken as:

$$V(x,z) = V(z)V(x) = \left[m_{re} cos(qz) + \mathrm{i} m_{im}\ cos(qz+\phi) \right]\ (x/x_0)\, \mathrm{e}^{-x^2/x_0^2} \tag{1}$$

being m_{re} and m_{im} the amplitude of the modulation, q the longitudinal wavenumber (assumed to be close to the mode spacing of the unmodulated waveguide, $q \approx \Delta k_z$), and ϕ the spatial delay between the index and gain/loss modulations. This potential is expected to stabilize the system while controlling the mode coupling. The analytical approach is based on the analysis of the eigenfunctions of the modulated system. We expect de system to evolve, after sufficient propagation along the wavelength, to an eigenmode of the coupling matrix. This allows mapping the mode cleaning-efficiency in terms of the parameters of the potential, namely the spatial delay between index and gain/loss modulations, ϕ in eq. (1), see Fig. 1b. By tuning the parameters, wide islands of mode cleaning are found indicating the robustness of the proposed mode-cleaning scheme. Finally, the predictions the prediction are numerically proven by direct integration of the SE or CLGE, for linear or nonlinear waveguides, respectively, see Fig 1c. The numerical results show how the resulting beam upon propagation in the non-Hermitian asymmetric waveguide resembles the locked mode state. For particular parameters of the potential a significant mode-cleaning is observed, as the beam acquires a bell-shaped profile in propagation along the waveguide by the non-Hermitian action. The study may be numerically extended to 2D waveguides -with different transverse profiles-, offering broad applicability.

To conclude, we propose and demonstrate an effective mode-cleaning for linear and nonlinear active waveguides, by introducing an asymmetric non-Hermitian potential.

References

1. A. Li, H. Wei, M. Cotrufo, M. Chen, S. Mann, X. Ni, B. Xu, J. Chen, J. Wang, S. Fan, C. Qiu, A. Alù, L. Chen, Nature Nanotechnology, vol. 18, no. 7, pp. 706-720, 2023.
2. R. El-Ganainy, M. Khajavikhan, D. N. Christodoulides and S. K. Ozdemir, Communications Physics, vol. 2, no. 1, pp. 37, 2019.
3. W. W. Ahmed, R. Herrero, M. Botey, Y. Wu and K. Staliunas, Physical Review Applied, vol. 14, no. 4, pp. 044010, 2020.
4. S.B. Ivars, M. Botey, R. Herrero, K. Staliunas, Physical Review A, 105(3), 033510, 2022
5. J. M. Pardell, R. Herrero, M. Botey and K. Staliunas, Optics express, vol. 29, no. 15, pp. 23997-24009, 2021.
6. S. Wu, W. Song, J. Sun, Z. Lin, H. Xin, S. Zhu and T. Li, Laser & Photonics Reviews, vol. 17, no. 8, pp. 2300306, 2023.
7. M. N. Akhter, S. B. Ivars, M. Botey, R. Herrero and K. Staliunas, Physical Review Letters, vol.131, no. 4, pp. 043604, 2023.
8. W. Ha, S. Lee, Y. Jung, J. K. Kim, and K. Oh, Optics express, vol. 17, no. 20, pp. 17536-17546, 2009.
9. A. Dudley, R. Vasilyeu, V. Belyi, N. Khilo, P. Ropot, and A. Forbes, Optics Communications, vol. 285, no. 1, pp. 5-12, 2012. K.
10. E. Deliancourt, M. Fabert, A. Tonello, et al., OSA Continuum, vol. 2, no. 4, pp. 1089-1096, 2019.
11. M. N., Akhter, M. Botey, R. Herrero, K. Staliunas, Nanophotonics, doi.org/10.1515/nanoph-2023-0713, 2024.

Non-Hermitian Systems with a Real Spectrum and Selective Skin Effect

Li Ge[1, 2*]

[1]Department of Physics and Astronomy, College of Staten Island, CUNY, Staten Island, NY, USA
[2]The Graduate Center, CUNY, New York, NY, USA
[*]corresponding author: li.ge@csi.cuny.edu

Abstract: We show a simple approach to constructing non-Hermitian Hamiltonians with a real spectrum, using the product of a Hermitian Hamiltonian H_0 and a positive semi-definite matrix A. When A is diagonal, we reveal a selective non-Hermitian skin effect where only the zero mode is a skin mode.

In this talk, we first introduce a simple approach that gives non-Hermitian Hamiltonians in their matrix forms with a real spectrum. We start with an arbitrary Hermitian Hamiltonian H_0, and we show that its product with a positive semi-definite matrix A leads to a non-Hermitian Hamiltonian H with a real spectrum. Because A is arbitrary itself and this procedure is not a similar transformation, the same H_0 can lead to an infinite set of H's with different real spectra. Depending on whether A has zero eigenvalue(s), the resulting H can possess an EP at zero energy. When A is only required to be Hermitian instead, the resulting H is pseudo-Hermitian that can have real and complex conjugate energy levels.

In the special case where A is diagonal, we compare our approach to an imaginary gauge transformation, and we show that our approach leads to a selective non-Hermitian skin effect, where only the zero mode is a skin mode and the non-zero modes reside in the bulk. Furthermore, we find that this selective non-Hermitian skin mode has a much lower lasing threshold than its counterpart in the standard non-Hermitian skin effect with the same spatial profile, when we pump at the boundary where they are localized. Finally, we show that the form of our construction can also be found, for example, in non-Hermitian dynamical matrices describing coupled frictionless harmonic oscillators with different masses.

This work is supported by the National Science Foundation (NSF) under Grants No. PHY-1847240 and No. DMR-2326698.

References

1. L. Ge, Innov. Discov. in press (2024).

Pseudospectra and non-normality in non-Hermitian photonics

K. G. Makris[1,2]

[1]*ITCP-Physics Department, University of Crete, Heraklion, 71003, Greece*

[2]*Institute of Electronic Structure and Laser (IESL) FORTH, Heraklion, 71110, Greece*

[*]corresponding author: makris@physics.uoc.gr

Abstract: In the context of non-Hermitian photonics we present recent results regarding sensitivity of non-normal optical waveguide lattices. We investigate dissipative optical lattices with gain/loss and asymmetric couplings and study their response in terms of their pseudospectra. The effect of disorder and optical nonlinearity will be also discussed.

Dissipation due to the inherent material losses has been always considered as an obstacle. However, based on the notion of parity-time (PT)-symmetry, that was recently introduced in the context of optical physics [1], such synthetic structures can utilize loss as an advantage in many applications [2,3]. Recently, in the context of non-Hermitian optics, the concept of non-Hermitian power eigenchannels was introduced [4] based on singular value decomposition of the associated propagator [5,6].

The first part of the talk is devoted to dissipative waveguide arrays with sparse gain with symmetric or not coupling coefficients. The sensitive to external perturbations in terms of pseudospectra will be presented in detail. In the second part of the talk, we will present recent results regarding the effect of uncorrelated disorder. Despite the Anderson localization of all eigenstates, the system exhibits counter-intuitive propagation by quantized jumps between states located around distant sites [7, 8]. The relevance of this type of transport to the corresponding asymmetry will be discussed.

Our pseudospectra approach can be applied to any non-Hermitian system that contains complex elements with loss-gain, or exhibits an asymmetry induced non-Hermiticity and thus exploits the meaning of wave transport in complex open systems.

Acknowledgements: This project was funded by the European Research Council (ERC- Consolidator) under the grant agreement No. 101045135 (Beyond Anderson).

References

1. K. G. Makris, R. El-Ganainy, D. N. Christodoulides, Z. H. Musslimani, ”Beam dynamics in PT symmetric optical lattices”, Phys. Rev. Lett. 100, 103904 (2008).

2. R. El-Ganainy, K. G. Makris, M. Khajavikhan, Z. H. Musslimani, S. Rotter and D. N. Christodoulides, "Non-Hermitian physics and PT symmetry", Nat. Phys. **14**, 11 (2018).
3. S. Xia, D. Kaltsas, D. Song, I. Komis, J. Xu, A. Szameit, H. Buljan, K.G. Makris, and Z. Chen, "Nonlinear tuning of PT symmetry and non-Hermitian topological states", Science **372** 72 (2021).
4. K.G. Makris and D. Psaltis, CLEO Conference, California, US, 2023.
5. K.G. Makris, L. Ge, and H.E. Türeci, "Anomalous transient amplification of waves in non-normal photonic media" Phys. Rev. X. **4**, 041044. (2014).
6. K. G. Makris, "Transient growth and dissipative exceptional points", Phys. Rev. E **104**, 054218 (2021).
7. A. Tzortzakakis, K. G. Makris, A. Szameit, and E. N. Economou, "Transport and spectral features in non-Hermitian open systems", Phys. Rev. Res. **3**, 013208 (2021).
8. A. Leventis, K. G. Makris, and E. N. Economou, "Non-Hermitian jumps in disordered lattices", Phys. Rev. B **106**, 064205 (2022).

Topological Origin of Surface Maxwell Waves and Surface Acoustic Modes

Franco Nori

Riken (Japan) and University of Michigan (USA)
fnori@riken.jp

Abstract: Interfaces between optical media (including dielectrics, metals, negative-index materials) can support surface electromagnetic waves, which now play crucial roles in plasmonics, metamaterials, and nano-photonics. We have shown [K. Y. Bliokh et al., Nat. Commun. 10, 580 (2019)] that surface Maxwell waves at interfaces between homogeneous isotropic media described by real permittivities and permeabilities have a topological origin explained by the bulk-boundary correspondence. This is explained by the nontrivial topology of the non-Hermitian photon helicity operator in the Weyl-like representation of Maxwell equations. The corresponding topological invariant, which determines the number of surface modes, describes the winding of the complex helicity spectrum across the interface. Our theory provides a new twist and insights for several areas of wave physics: Maxwell electromagnetism, topological quantum states, non-Hermitian wave physics, and metamaterials. We have also analyzed [K. Y. Bliokh et al., Phys. Rev. Lett. (2019)] another type of classical waves: longitudinal acoustic waves corresponding to spinless phonons. We show that surface acoustic waves, which appear at interfaces between media with opposite-sign densities, can be explained by similar topological features and the bulk-boundary correspondence. However, in contrast to photons, the topological properties of sound waves originate from the non-Hermitian four-momentum operator in the Klein-Gordon representation of acoustic fields.

Writing and Submitting Your Papers

Rachel Won

Nature Photonics, United Kingdom
r.won@nature.com

Abstract: This talk covers the detailed information and guidelines on scientific paper preparation and submission, including tips for writing an effective cover letter, an informative abstract, a comprehensive introduction and an attractive paper, and editorial and peer-review processes. You will also get to know how to choose a journal for submission, what editors seek, how your papers are reviewed and how to make an appeal.

DNA nanotechnologies for photonics and sensing

A universal impedance-matching strategy towards ultrathin broadband perfect absorbers enabling efficient hot electron photodetection

C. Zhang,[1,2,*] and X. Li[1,2,*]

[1]Country*School of Optoelectronic Science and Engineering & Collaborative Innovation Center of Suzhou Nano Science and Technology, Soochow University, Suzhou 215006, China*

[2]*Key Lab of Advanced Optical Manufacturing Technologies of Jiangsu Province & Key Lab of Modern Optical Technologies of Education Ministry of China, Soochow University, Suzhou 215006, China*

[*]corresponding author: zhangc@suda.edu.cn; xfli@suda.edu.cn (Prof. Li*)*

Abstract: We derive conditions for achieving impedance matching in ultrathin films with negligible/comparable thickness to the incident wavelength. We design and experimentally demonstrate broadband perfect absorbers operating across various spectral bands, with average absorption exceeding 90%. Integration with p-type silicon enables hot carrier photodetection, promising applications in telecommunication and near-infrared imaging.

Efficient light absorption is of significant importance for applications in optics and optoelectronics, such as structural colors, stray light elimination, optical switches, stealth technologies, photovoltaics and photodetection [1−3]. Optical reflection losses always exist due to the impedance mismatch at interfaces between air and absorbers. Typically, single and multilayer dielectric anti-reflection coatings with thickness of at least a quarter-wavelength of light are used to suppress reflection. The anti-reflection coatings based on destructive interference only works at specific incident wavelengths, angles and polarizations [4−6]. The thicknesses of anti-reflection coatings for the mid- and far-infrared are great, which can be a challenge and limitation for fabrication. Another approach involves the tapered nanostructures to realize the gradient effective refractive index, including nanocones, tapered gratings and nanopyramids, etc [7]. To achieve broadband anti-reflection effects, the lengths of the nanostructures are sufficiently long to eliminate optical resonances, which imposes similar thickness limitations. Another alternative way to achieve broadband optical absorption is to use plasmonic nanostructures, i.e., metamaterials. By precisely controlling the shape, size, and arrangement of the elements, the absorption bandwidth can be broadened by overlapping the multiple resonances, such as in nanocubes, nanodisks, nanocrosses, crossed trapezoids/gratings, multilayer grating stacks, and even resonators integrating the aforementioned nanostructures. Nevertheless, these plasmonic absorbers generally have delicately designed subwavelength nanopatterns that are fabricated through top-down lithography such as e-beam lithography (EBL), focused ion beam milling (FIB), and reactive ion etching (RIE), leading to high equipment cost, low fabrication throughput, and small footprint size that severely restrict the practical large-scale applications [8]. Therefore, there is significant benefit to achieve the ultrathin broadband perfect absorbers based on lithography-free planar multilayer structures.

In this work, we analytically derive the general solutions of film parameters for impedance matching using an absorbing film with thickness negligible or comparable to incident wavelength, or the case using a lossless dielectric film on any substrate. We present a detailed step-by-step process illustrating how to employ the strategy for designing multiple layers to achieve broadband perfect light absorption. We numerically and experimentally demonstrated the broadband and efficient absorbers working in different spectral bands, including the visible (0.4−0.8 μm), visible to short-wave infrared band (SWIR, 0.4−2.5 μm), middle-wave to long-wave infrared (MWIR−LWIR, 3−16 μm), and long to very long infrared (LWIR−VLIR, 16−32 μm and 8−32 μm) bands, respectively. The absorbers exhibit an average absorption ranging from 90% to 99.6% based on

multiple stacks comprising 2 to 9 layers, while also showcasing sustained high performance under large incident angles of up to 50° for unpolarized incidence and displaying excellent tolerance to film thickness errors of up to 30%. Furthermore, we achieve broadband perfect light absorption below the silicon bandgap by employing a planar absorber consisting of ultra-thin silicon (100 nm) and a transition metal film (20 nm), breaking the limitation of poor hot electron generation in thin metal films. The ultra-thin hot carrier photodetector shows a responsivity that is 3.5 to 45 times higher than that observed with a similar structure using a silicon substrate and transition metal film under backward incidence. As a proof of concept, the infrared communication and imaging are demonstrated, showing the great potential of the proposed device. The work presents a general solution for achieving broadband perfect absorption in ultrathin films under a planar configuration, paving the way for lithograph-free and large-area practical applications such as photodetector, photovoltaics, optical sensing, and stealth technology.

Acknowledgements: This work is supported by the National Natural Science Foundation of China (62120106001).

References

1. Knight M. W.; Sobhani H.; Nordlander P.; Halas N. J. Photodetection with active optical antennas. Science 2011, 332, 702–704.
2. Li W.; Valentine J. Metamaterial perfect absorber based hot electron photodetection. Nano Lett. 2014, 14, 3510–3514.
3. Chalabi H.; Schoen D.; Brongersma M. L. Hot-electron photodetection with a plasmonic nanostripe antenna. Nano Lett. 2014, 14, 1374–1380.
4. Arquer F. P. G. D.; Mihi A.; Konstantatos G. Large-area plasmonic-crystal hot-electron based photodetectors. ACS Photon. 2015, 2, 950–957.
5. Muehlbrandt S.; Melikyan A.; Harter T.; Köhnle K.; Muslija A.; Vincze P.; Wolf S.; Jakobs P.; Fedoryshyn Y.; Freude W.; Leuthold J.; Koos C.; Kohl M. Silicon-plasmonic internal-photoemission detector for 40 Gbit/s data reception. Optica 2016, 3, 741–747.
6. Sobhani A.; Knight M. W.; Wang Y.; Zheng B.; King N. S.; Brown L. V.; Fang Z.; Nordlander P.; Halas N. J. Narrowband photodetection in the near-infrared with a plasmon-induced hot electron device. Nat. Commun. 2013, 4, 1643.
7. Wang F.; Melosh N. A. Plasmonic energy collection through hot carrier extraction. Nano Lett. 2011, 11, 5426–5430.
8. Mubeen S.; Lee J.; Lee W.; Singh N.; Stucky G.; Moskovits M. On the plasmonic photovoltaic. ACS Nano 2014, 8, 6066–6073.

Integrating functional inorganic nanomaterials for spatiotemporal modulation of full-polarized light emission

J. Lv[1], J. H. Han[1], and K. T. Nam[1*]

[1]Seoul National University, Republic of Korea
[*]corresponding author: nkitae@snu.ac.kr

Abstract: Here we present a solid-state full-polarized controlling device by integrating the spatiotemporal modulation of the LED device, the precise control and efficient polarization emission through nanomaterial assembly, and the programmable patterning/positioning using 3D printing. We achieved an extremely high degree of polarization for both linearly and circularly polarized emission.

Solid-state polarized light-controlling devices made of (nano)materials without the conventional bulky polarization optics promise simpler device structure, miniaturization, and multi-functionality. While several design routes have been proposed for polarized light-controlling devices using organic or inorganic nanomaterials, they usually suffer from small degrees of polarization, limited polarization states, low light utilization efficiency, and the absence of spatiotemporal control. Herein, to address this challenge, we fabricated a six-polarized-elemental-pixels-based device by integrating the spatial-temporal modulation of LED device, the precise control of polarization by nanomaterial assembly and the programmable patterning/positioning by 3D printing. Our idea is scalable and form-factor-free, making it compatible with the state-of-the-art micro-LED display industry. We achieved a high degree of linearly polarized emission (DoP) over 0.8 through the templated alignment of quantum nanorods with ultrathin inorganic nanowires. Furtherly, by precisely controlling the phase retardation of the printed inorganic nanowire film, circularly polarized luminescence (CPL) with an anisotropic factor (glum) up to 1.1 was obtained. The linear combination of the on-off state of each pixel can generate enormous states of polarization. This concept is indeed a good platform for multiplexing spatiotemporal information with the aid of polarization freedom. As two examples, we demonstrated polarization-based encrypted communication and multichannel display using our device. The encrypted communication was enabled by the further integration of chiral plasmonic assemblies which add physical unclonable encryption on top of our device. As a result, dramatic modulation of the polarization states across the Poincare sphere that is difficult to be hacked by any other devices was achieved, enabling secured visible light communication (VLC). As for the multichannel display, we showed that 3D information can be transferred by one-shot 2D image, indicating the potential of our device in volumetric display and polarization-based hologram.

References

1. J. Lv. “Rational Design of All-Inorganic Assemblies with Bright Circularly Polarized Luminescence,” Advanced Materials, Vol. 35, No. 7, 2209539, 2023.
2. J. Lv., “Self-assembled inorganic chiral superstructures,” Nature Reviews Chemistry, Vol. 6, No. 2, 125–145, 2022.

Monolayer semiconductor superlattices for enhanced absorption with controlled interlayer interaction

S. A. Elrafei[1], T. T. C. Sistermans[1,2,3], L. M. Heijnen[1], R. H. Godiksen [1], A. G. Curto[1,2,3*]

[1] Department of Applied Physics and Eindhoven Hendrik Casimir Institute, Eindhoven University of Technology, Eindhoven, The Netherlands
[2] Photonics Research Group, Ghent University-imec, Ghent, Belgium
[3] Center for Nano- and Biophotonics, Ghent University, Ghent, Belgium

[*]Corresponding author: Alberto.Curto@UGent.be

Abstract: Strongly absorbing materials are needed for nanoscale optoelectronics and strong light-matter coupling applications. Here, we demonstrate that monolayer WS_2 superlattices provide higher absorption than natural monolayers and bilayers while preserving the exciton emission. The use of a molecular spacer allows us to control the interlayer coupling at sub-nanometric distances.

Strong light absorption in ultrathin materials plays a vital role in various applications, including light detection, waveguiding, and modulation. One relatively new class of strongly absorbing materials is that of atomically thin materials. Transition metal dichalcogenides (TMDs), such as tungsten disulfide (WS_2) and molybdenum diselenide ($MoSe_2$) possess unique optical properties. Bulk TMDs consist of weakly bound atomically thin layers, and stable monolayers can be easily prepared through exfoliation. Exfoliation provides the highest exciton quality for the strongest absorption and narrowest linewidth. Monolayer TMDs show an exceptionally strong absorption of light despite being less than one nanometer thick. The combination of strong absorption and the ability to tune the excitonic resonances through doping enables their use in nanoscale optical elements such as atomically thin photodetectors, modulators, and lenses. TMD monolayers can also be used to create atomically thin mirrors that are promising for spatial light modulators, active metasurfaces, and active cavity control. In addition, the high oscillator strengths and sharp resonances of excitons in these materials can enable reaching the regime of strong light-matter coupling and the manipulation of light via surface exciton-polaritons.[1,2]

Here, we create WS_2 monolayer-based structures to approach the fundamental thin-film absorption limit of 50%. We demonstrate three simple methods to obtain stronger absorption than monolayer WS_2. Different superlattice structures of WS_2 monolayers result in an increased light absorption, while also preserving the exciton emission and quality. We characterize these structures using transmission and photoluminescence spectroscopy. Additionally, we employ hyperspectral imaging to gain insight into the spatial variations of exciton properties. We start with simple structures containing two monolayers separated by a spacer to retain the optical properties of the individual monolayers. However, such structures prove to have coupling between layers that is difficult to control reliably and results in absorption reduction. Instead, we demonstrate the use of a molecular spacer to construct stable stacked bilayers. Finally, we fabricate higher-order superlattices with an increased number of layers using Al_2O_3 as a thin dielectric spacer to approach the thin-film absorption limit in a more scalable process.

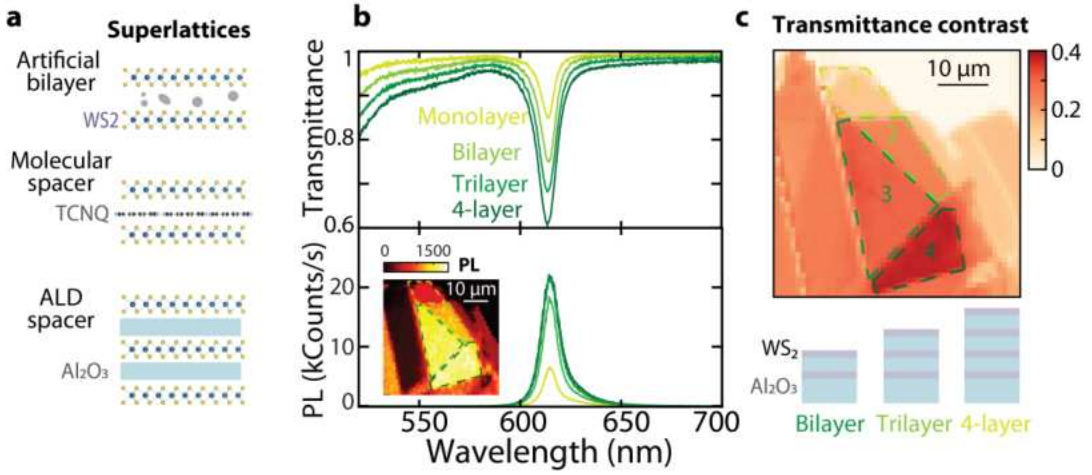


Figure 1. Stacking of WS_2 monolayers into superlattices for high absorption.

We have also investigated in detail the use of organic molecular spacers in WS_2 monolayer stacks to control the exciton properties through interlayer interactions. This approach enables finely tuning the interlayer coupling and modulates the interaction between WS_2 monolayers. Introducing molecular spacers addresses the limitations imposed by traditional spacer materials like hexagonal boron nitride and Al_2O_3 in achieving ultra-thin layers with controlled thickness and large area. The sub-nanometric control over the spacer thickness provides a substantial modulation of photoluminescence intensity and spectral shift. This method enables precise manipulation of the interaction strength between the monolayers, transitioning from strongly coupled layers at lower molecular concentrations to loosely coupled layers at higher concentrations. Additionally, we observe a considerable impact on the valence band splitting, evidenced by a change in the energy difference between A and B excitons.

Our work puts forward the potential of monolayer superlattices as a flexible platform for developing novel two-dimensional nanophotonic devices. As the superlattice fabrication process relies on simple methods, such superabsorbing materials are posed to have an impact on a variety of fields. By engineering the molecular spacers in monolayer stacks, we also unlock the potential to fine-tune excitonic properties and pave the way for nanoscale sensors and sub-nanometric rulers.

References

1. Wang, S. *et al.* Limits to Strong Coupling of Excitons in Multilayer WS 2 with Collective Plasmonic Resonances. *ACS Photonics* **6**, 286–293, 2019
2. Elrafei, S. A., Raziman, T. V., de Vega, S. García de Abajo, F. J., Curto, A. G. Guiding light with surface exciton-polaritons in atomically thin superlattices, arXiv preprint arXiv:2402.10180, 2024.
3. Elrafei, S. A., Heijnen, L. M., Godiksen, R. H., Curto A. G. Approaching the absorption limit with monolayer semiconductor superlattices arXiv:2402.10179, 2024.

Infrared photoresponse in twisted bilayer graphene at a near-magic angle

D. Mylnikov[1], I. Mazurenko[1], A. Shupletsov[2,3], A. Parappurath[4], S. Bhowmik[5], D. Bandurin[6], A. Ghosh[4], A. Chernov[1,2*]

[1] Center for Photonics and 2D Materials, MIPT, Dolgoprudny
[2] Russian Quantum Center, Skolkovo
[3] P.N.Lebedev Physical Institute, Moscow
[4] Department of Physics, Indian Institute of Science, Bangalore
[5] Department of Instrumentation and Applied Physics, Indian Institute of Science, Bangalore
[6] Department of Materials Science and Engineering, National University of Singapore
*corresponding author: chernov.ai@mipt.ru

Abstract: We have performed the transport and IR-photoresponse measurements in the twisted bilayer graphene. The structure demonstrates enhanced photothermoelectric response compared to the previous works. We demonstrate the gate-tunable biased photovoltage that strongly correlates with the peculiarities in transport measurements. The obtained results can be further used for tunable mid-infrared optoelectronics.

2D layers stacking of van der Waals materials enables various degrees of freedom for properties control [1]. Stacking of two monolayers leads to formation of a metamaterial with effective periodic potential due to the emerging moiré superlattice. Small-angle twisted bilayer graphene (tBLG) has attracted much attention since the breakthrough experimental work [2] due to appearance of low-energy flat bands. Strong electron-electron interactions within the bands lead to correlation-driven phenomena, realization of correlated phases, and result in new devices [3]. In particular, optoelectronic devices such as infrared and THz detectors have been recently demonstrated [4,5,6].

We investigated tBLG with mis-orientation angle close to 1° and lateral size ~3x1.25 μm^2 obtained by standard dry transfer technique. The Fermi level position was ruled by the back gate to the silicon substrate with 280 nm silicon oxide and 15 nm hBN flake as a gate insulator. Transport measurements were made using a standard 2-point scheme and lock-in amplifier at 111 Hz. The resistance dependence on gate voltage is shown in the Fig.1 by blue color. Central peak near -10V corresponds to the charge neutrality point (CNP), whereas side peaks at ±30 V (with respect to CNP) – to the full filling of the superlattice minizones, i.e., 4 electrons per moiré cell. The side peak positions correspond to ~0.95° moiré angle.

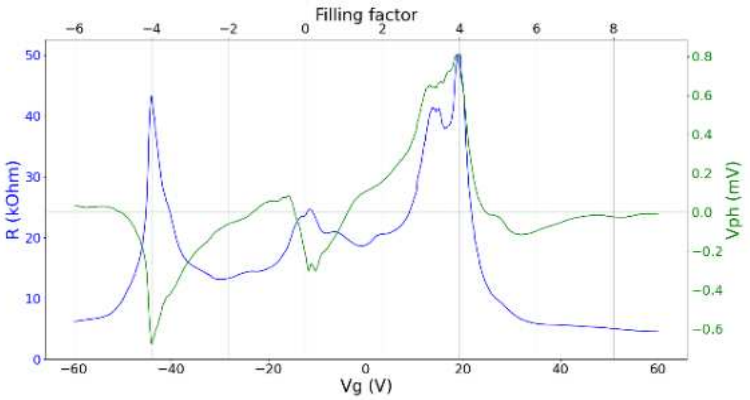


Figure 1. Resistance *R* (blue, left axis) and photovoltage *Vph* (green, right axis) versus the gate voltage *Vg*. T=8.6K, beam power on sample ~5uW

The IR-photoresponse in such structures was shown to have a bolometric nature [4,5] with the highest value ~30 mA/W though with the large bias current > 50μA [4]. We used 6 μm laser excitation in a regime of quasicontinuous wave with the frequency 11 Hz. The beam was focused by the lens on the substrate to the spot with the diameter ~40 μm. The voltage drop was measured by the synchronized lock-in amplifier. The maximum photocurrent observed was ~6 mA/W with no bias applied.

Also we preformed transport and IR-photoresponse measurements with applied bias DC current (see Fig.2). We observe strong *V(I)* non-linearity that has already been seen in graphene-based structures [7]. At current densities high enough Fermi distributions of electron and holes change. It is known as Schwinger mechanism of charge transport and it should affect photoresponse as well. The correlations between lower and upper panels in the Fig.2 are clearly seen. However, photoresponse of our sample has three different mechanisms that makes it difficult to explain the *Vph* behavior. The first one is photothermoelectric effect, i.e. Seeback effect due to the different radiation heating near the metal contacts of the sample. The second one is pure bolometric effect, i.e. the change of the sample resistivity due to radiation heating. Finally, due to nonlinear *V(I)* the rectification effect can lead to the origin of photovoltage.

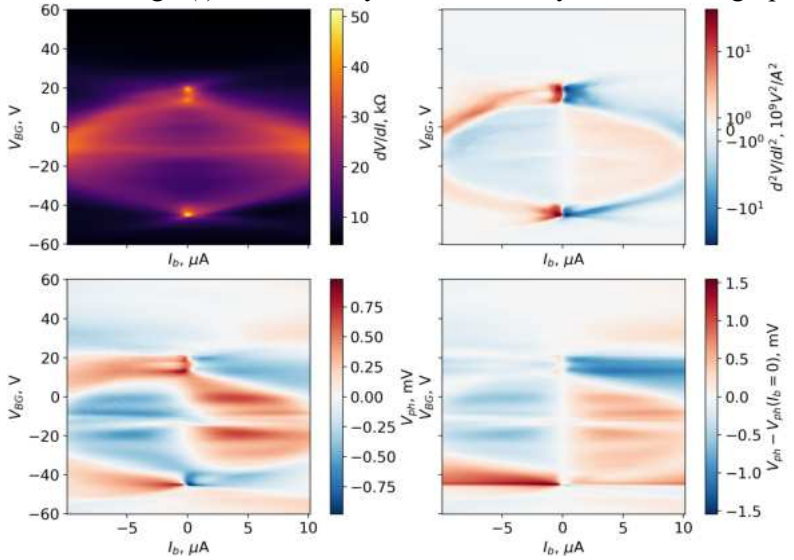


Figure 2. *dV/dI* (upper left), d^2V/dI^2 (upper right), *Vph* (lower left) and *Vph-Vph*(*Ib*=0) (lower right) maps with gate voltage *Vg* and bias current Ib changes. *dV/dI* and *Vph* were directly measured experimentally while d^2V/dI^2 is a numerical derivative of *dV/dI*.

To sum up, we performed transport and IR-photoresponse measurements on the tBLG with the mis-orientation angle 0.95° close to the magic one. We observed the signs of the transition to the Schwinger mechanism of charge carriers transport and measured photovoltage under IR irradiation in this regime. The correlation between photoresponse and transport maps was experimentally detected.

This work was supported by the RSF project 24-12-00370.

References

1. Kravtsov, V., Ivanova, T., Abramov, A. *et al.* "Valley polarization of trions in monolayer $MoSe_2$ interfaced with bismuth iron garnet" 2D Mater. **9**, 015019 (2022).
2. Dean, C., Wang, L., Maher, P. *et al.* "Hofstadter's butterfly and the fractal quantum Hall effect in moiré superlattices" Nature **497**, 598–602 (2013).
3. Cao, Y., Fatemi, V., Fang, S. et al. "Unconventional superconductivity in magic-angle graphene superlattices" Nature **556**, 43–50 (2018).
4. Bhowmik, S., Ghosh, A., and Chandni, U. "Emergent phases in graphene flat bands" arXiv:2309.08938.
5. Deng, B., Ma, C., Wang, Q. *et al.* "Strong mid-infrared photoresponse in small-twist-angle bilayer graphene" Nat. Photonics **14**, 549–553 (2020).
6. Hubmann, S., Di Battista, G., Dmitriev, I.A. *et al.* "Infrared photoresistance as a sensitive probe of electronic transport in twisted bilayer graphene" 2D Mater. **10,** 015005 (2023).
7. Mylnikov, D.A., Kashchenko, M.A., Kapralov, K.N. *et al.* "Infrared photodetection in graphene-based heterostructures: bolometric and thermoelectric effects at the tunneling barrier" arXiv:2312.05612.
8. Berdyugin, A.I., Xin, N., Gao, H. *et al.* "Out-of-equilibrium criticalities in graphene superlattices" Science **375**, 430–433 (2022).

Fabrication of vanadium dioxide micro- and nanostructures by laser-induced hydrothermal synthesis

C. Pin[1*], H. Fujiwara[2], and K. Sasaki[1]

[1]Research Institute for Electronic Science, Hokkaido University, Kita 20, Nishi 10, Kita-ku, Sapporo, Hokkaido, 001-0021, Japan
[2]Faculty of Engineering, Hokkai-Gakuen University, 1-1, Nishi 11, Minami 26, Chuo-ku, Sapporo, Hokkaido, 064-0926, Japan
[*]corresponding author: christophe.pin@es.hokudai.ac.jp

Abstract: Bottom-up synthesis of vanadium dioxide (VO_2) micro- and nanostructures is achieved by focusing an infrared laser beam on a gold film or on gold plasmonic nanoantennas immersed in a precursor solution. Site-selective VO_2 synthesis is demonstrated by controlling the excitation of localized surface plasmon resonances.

Vanadium dioxide (VO_2) has been thoroughly studied for its ultrafast solid-solid phase transition that occurs close to room temperature (about 60 ºC).[1,2] When the material switches from its semiconducting state to its metallic state, dramatic, nonlinear changes are observed not only in its electrical properties but also in its optical properties. For this reason, VO_2 is a material of particular interest for designing new electronic and photonic devices such as nanoscale switching devices with highly tunable electronic and optical responses.

The fabrication of integrated VO_2 micro- and nanostructures typically relies on conventional fabrication processes such as pulsed laser deposition, sputtering, and molecular beam epitaxy, or chemical solution deposition, followed by photo- or electron-beam lithography, and finally etching or lift-off steps.[2] However, those top-down fabrication techniques are costly and drastically limits the range of practically feasible nanostructure designs. On the contrary, cost-effective, bottom-up fabrication techniques often consist in the synthesis and assembly of particles in liquid dispersion. Solvothermal synthesis (including hydrothermal synthesis) of VO_2 nanoparticles, nanowires, and nanosheets has been reported.[2] However, the integration of dispersed nanomaterials in electronic and photonic devices is a quite challenging task.

In this work, we apply the recently demonstrated laser-induced hydrothermal synthesis method to directly grow VO_2 micro- and nanostructures on a substrate.[3,4] A precursor solution was prepared following a reported recipe.[5] After dropping a few microliters of the precursor solution on a sample (glass substrate with gold film/nanostructures), a 1064 nm infrared (IR) laser beam was focused onto the gold film/nanostructures at the surface of the glass substrate.

First, the fabrication of VO_2 microstructures was achieved by locally heating a 30nm-thick gold film covered with a 3nm-thick alumina layer. Figure 1(a) shows a SEM image of a well-crystalized, 1µm-large VO_2 structure with circular shape synthesized using a laser power of 18 mW. Despite the temperature threshold for the VO_2 synthesis reaction to happen and the aqueous environment, the local temperature elevation was large enough to enable the synthesis of crystallized VO_2 structures. The alumina layer was required to promote the adhesion of the synthesized VO_2 structures.

We then investigated the laser-induced hydrothermal synthesis of VO_2 at the surface of plasmonic nanostructures. Following a similar process, VO_2 nanostructures were successfully grown on gold nanodisks and nanorods. The excitation of localized surface plasmon resonances (LSPR) was found to enhance the photothermal heating of the gold nanostructures, enabling efficient VO_2 synthesis by plasmon-assisted

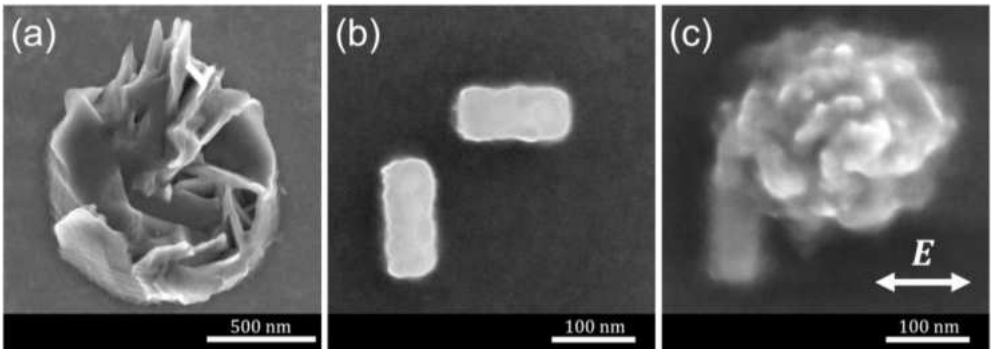


Figure 1. SEM images of (a) a 1µm-large VO_2 structure fabricated by focusing a 18 mW IR laser beam on an alumina-coated gold thin film, (b,c) gold dimer composed of two perpendicularly oriented, resonant plasmonic nanobars (b) before and (c) after irradiation of a 3.7 mW linearly polarized, focused laser beam with horizontal polarization orientation. A VO_2 shell was locally synthesized only on the horizontal nanobar.

hydrothermal synthesis.[4] Moreover, site-selective VO_2 synthesis was achieved by controlling the LSPR excitation of plasmonic nanostructures composed of nanobars with different orientations. As shown in Figure 1(b), by tuning the orientation of the linear polarization of the incident laser beam, VO_2 nanostructures were selectively grown on nanobars with similar orientation.

We believe that laser-induced hydrothermal synthesis and the plasmon-assisted hydrothermal synthesis techniques demonstrated in this work will enable the fabrication of highly tunable, hybrid micro- and nanodevices with novel designs and functionalities.

This work was supported by JSPS KAKENHI (JP20K15145, JP22H01923, JP19H04529, JP20K05290, JP18H05205, JP21H04657), the Cooperative Research Program of "Network Joint Research Center for Materials and Devices" (20211002), and the AMADA Foundation (AF-2021238-C2, AF-2021226-B3). The authors acknowledge the support from the Research Institute for Electronic Science and the Open Facility of Hokkaido University.

References

1. Shao, Z., X. Cao, H. Luo and P. Jin, "Recent progress in the phase-transition mechanism and modulation of vanadium dioxide materials," NPG Asia Mater., Vol. 10, 581–605, 2018.
2. Devthade, V. and S. Lee, "Synthesis of vanadium dioxide thin films and nanostructures," J. Appl. Phys., Vol. 128, 231101, 2020.
3. Fujiwara, H., T. Suzuki, R. Niyuki and K. Sasaki, "ZnO nanorod array random lasers fabricated by a laser-induced hydrothermal synthesis," New J. Phys., Vol. 18, 103046, 2016.
4. Fujiwara, H., T. Suzuki, C. Pin and K. Sasaki, "Localized ZnO growth on a gold nanoantenna by plasmon-assisted hydrothermal synthesis," Nano Lett., Vol. 20, 389–394, 2019.
5. Shi, R., J. Wang, X. Cai, L. Zhang, P. Chen, S. Liu, L. Zhang, W. Ouyang, N. Wang and C. Cheng, "Axial modulation of metal–insulator phase transition of VO_2 nanowires by graded doping engineering for optically readable thermometers," J. Phys. Chem. C, Vol. 121, 24877–24885, 2017.

Circularly polarized photoluminescence from light-emitting metasurfaces

V. E. Ferry[1*]

[1]University of Minnesota, USA
[*]corresponding author: veferry@umn.edu

Abstract: This talk will discuss recent results on semiconductor nanocrystal-based metasurfaces designed for circularly polarized photoluminescence. We will discuss two complementary fabrication routes, direct write electron beam lithography and large-area printing, and the design guidelines for incorporating chiral nanocrystals, chiral semiconductor patterns, and chiral plasmonic patterns to manipulate the optical response.

Chiral metasurfaces allow for the manipulation of circularly polarized light. This talk will discuss metasurfaces comprised of patterned, light-emitting semiconductor nanocrystals, where the light-emitting nanocrystals are patterned deterministically to form part of the metasurface.

This presentation will discuss several different implementations of these patterned, chiral structures. First, we study hybrid systems of plasmonic nanostructures and patterned, light-emitting nanocrystals. By strategically placing these nanopatterns, the polarization state, photoluminescence intensity, and angle of the emitted light can be controlled. The nanocrystal patterns are created using direct-write electron-beam lithography, where the nanocrystals serve as the resist. Exposure to the electron beam cross-links the ligands between the particles. We show how the spatial arrangement of these nanopatterns, shape, and chiral structures of either the quantum dot pattern or the nearby plasmonic structure influences the obsereved response. We will then discuss semiconductor metasurfaces made of chiral materials, and the design rules for amplifying circular dichroism with patterning. Finally, we will discuss an alternative fabrication route for large-area metamaterials that is both additive and roll-to-roll compatible. The method uses UV-based imprint lithography to produce a pattern with spatially modulated surface energy. When a functional ink is dragged over the surface it dewets and fills in the recesses. This method works for a variety of ink materials (metal, dielectric, semiconductor), can create multi-layer patterns, and offers flexibility in creating metamaterials on free-standing and flexible substrates.

Acknowledgements. This work was supported by the National Science Foundation under Award 2102835. Parts of this work were performed in the Characterization Facility at the University of Minnesota, which receives partial support from NSF through the MRSEC program. Portions of this work were also conducted in the Minnesota Nano Center, which is supported by NSF through the National Nano Coordinated Infrastructure (NNCI) under Award Number ECCS-2025124.

References

1. Ramamurthy, M., P. Pachidis, B. M. Cote, and V. E. Ferry, “Circularly polarized photoluminescence from nanostructured arrays of light emitters,” ACS Appl. Nano Mater., Vol. 1, No. 1, 491 - 499, 2023.
2. Donie, Y. J., M. Ramamurthy, R. D. Chakraborty, L. F. Francis, C. D. Frisbie, and V. E. Ferry, “Roll-to-roll compatible topochemical wetting control for metamaterial printing,” Adv. Opt. Mater., in press, 2024.

Periodic Arrays of Single-Crystal Gold and Silver Nanoplates

S. Neretina[1,2*], Z. R. Lawson[1], and W. J. Tuff[1]

[1]College of Engineering, University of Notre Dame, United States
[2]Department of Chemistry and Biochemistry, University of Notre Dame, United States
[*]corresponding author: sneretina@nd.edu

Abstract: In this presentation, we demonstrate the implementation of both plasmon-mediated and chemical reduction methods for generating large area arrays of single-crystal gold and silver hexagonal nanoplates, nanotriangles, and helical spirals on substrates.

Noble metal nanoplates represent a remarkable class of nanostructures that provide a highly compatible geometry for integration with wafer-based processing since the combination unites two systems that have an inherently two-dimensional character. In this presentation, we demonstrate the utility of using a crystalline substrate as the primary driver for forming substrate-based gold seeds with the internal defect structures and crystallographic alignment required for nanoplate growth. Using this capability along with other controls that are unique to substrate-based syntheses, we implement both plasmon-mediated and chemical reduction methods for generating arrays of hexagonal nanoplates, nanotriangles, and helical spirals.

References

1. R. D. Neal, Z. R. Lawson, W. J. Tuff, K. Xu, V. Kumar, M. T. Korsa, M. Zhukovskyi, M. R. Rosenberger, J. Adam, J. A. Hachtel, J. P. Camden, R. A. Hughes, S. Neretina, Large-area periodic arrays of atomically flat single-crystal gold nanotriangles formed directly on substrate surfaces. *Small* **2022**, 18, 2205780.
2. T. B. Demille, R. D. Neal, A. S. Preston, Z. Liang, A. G. Oliver, R. A. Hughes, S. Neretina, Epitaxially aligned single-crystal gold nanoplates formed in large-area arrays at high-yield. *Nano Res.* **2022**, 15, 296-303.
3. S. D. Golze, S. Porcu, C. Zhu, E. Sutter, P. C. Ricci, E. C. Kinzel, R. A. Hughes, S. Neretina, Sequential symmetry-breaking events as a synthetic pathway for chiral gold nanostructures with spiral geometries. *Nano Lett.* **2021**, 21, 2919−2925.

Up- and Down-conversion Engineering with Surface Lattice Resonances

S. Murai*

Department of Material Chemistry, Graduate School of Engineering, Kyoto University, Japan
*Corresponding author: murai@dipole7.kuic.kyoto-u.ac.jp

Abstract: We combined a luminescent layer or substrate with metallic or dielectric nanoantennae to harness the photoluminescence into a specific direction predefined by the antenna design. A notable (> 10 times) enhancement in radiation intensity into a designated direction is demonstrated. We describe the mechanism using a simple analytical model. We also fabricated "nanoantenna sticker" where the nanoantenna was embedded in a flexible polymer. The sticker can be stacked on any clean surfaces and act as nanoantenna.

Nanoantenna is a periodic array of scattering elements that can harness light into a specific direction. Combination of nanoantenna with phosphors enables spatial and spectral control over the luminescence (Fig. 1) [1-3]. In this presentation, we use several sets of nanoantennae (metallic or dielectric) and phosphors (organic or inorganic) to demonstrate the luminescence control. Typical nanoantenna consists of aluminum [1], silicon [2], and titanium dioxide [3]. We will discuss the difference of conversion efficiency from blue excitation to yellow-red luminescence for the metallic and dielectric nanoantenna.

We also introduce the nanoantenna stickers, which are the nanoantenna embedded in the flexible polymer [4]. We place this sticker on top of the luminescent layers to modulate their emission directionality. Because of its flexibility, the sticker gives control over luminescent directionality via stretching/compressing it.

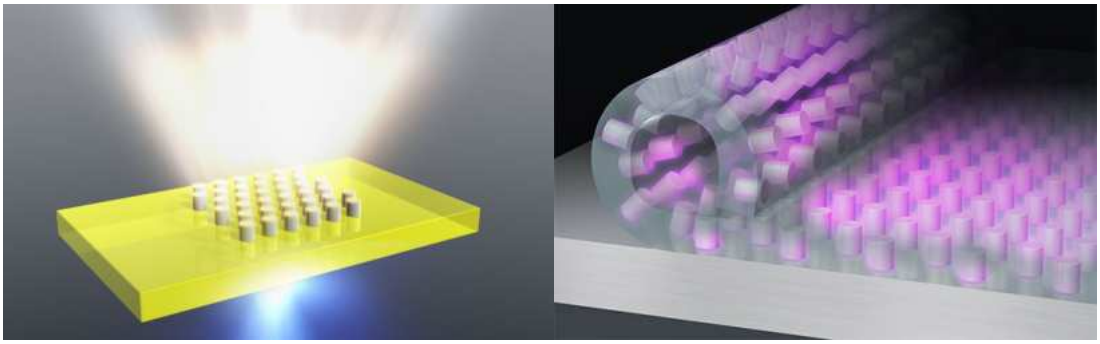


Fig. 1: (left) Sketch of the nanoantenna phosphor, converting a blue light into yellow photoluminescence with a directionality. (right) Sketch if the nanoantenna sticker, which is flexible and can be attached to any clean surfaces.

We acknowledge financial support from MEXT (Kekanhi 22K18884, 22H01776), Izumi Science and Technology Foundation, Casio Science Promotion Foundation and The Futaba Foundation.

References

1. Kamakura, R. et al., "Enhanced photoluminescence and directional white-light generation by plasmonic array," *J. Appl. Phys.* **124**, (2018) 213105
2. Liu, L. et al., "Loss Control with Annealing and Lattice Kerker Effect in Silicon Metasurfaces," *Adv. Photon. Res.*, (2021) 2100235
3. Murai, S. et al., "Photoluminescence engineering with nanoantenna phosphors," *J. Mater. Chem. C* **129**, (2023) 163101 11, 472-479
4. Agata, K. et al., "Stick-and-play metasurfaces for directional light outcoupling," *Appl. Phys. Lett*. **118**, (2021) 021110

Waveguiding and metasurface platforms for sensing

Stefan A Maier[1,2]

[1]School of Physics and Astronomy, Monash University, Clayton, Victoria 3800, Australia
[2]Department of Physics, Imperial College London, London SW7 2AZ, UK
Stefan.Maier@monash.edu

Abstract: Nanogap waveguides are demonstrated as a promising platform for the routing of Stokes emission in a context of surface-enhanced Raman scattering, or more generally for the decoupling of localised emission. Coupling of waveguides to metalenses provides additional opportunities for the creation of compact sensing devices.

The first part of the presentation introduces the concept of nanogap metallic waveguides and their utilization for the routing of localised emission [1, 2]. Focusing on surface-enhanced Raman scattering events, we demonstrate large coupling efficiencies near unity for Stokes emission, promising a novel avenue towards integrated, on-chip Raman sensors for biospectroscopy. Specifically we introduce the concept of a beta-factor, in analogy to laser physics, in order to quantify the coupling of Stokes scattering to waveguide modes.
The second part of the presentation will present our most recent works on metasurfaces for sensing, energy conversion, and routing of quantum emission [3].

References

1. Fu, M. *et al.* Near-unity Raman β-factor of surface-enhanced Raman scattering in a waveguide. *Nat. Nanotechnol.* **17**, 1251–1257 (2022).
2. Güsken, N. A. *et al.* Emission enhancement of erbium in a reverse nanofocusing waveguide. *Nat Commun* **14**, 2719 (2023).
3. Li, C. *et al.* Arbitrarily structured quantum emission with a multifunctional metalens. *eLight* **3**, 19 (2023).

Assymmetric electric fields induced on symmetric structure that yield chiral structured materials

H. Okamoto[1*], H.-Y. Ahn[1*], T. Narushima[1]

[1]Institute for Molecular Science, National Institutes of Natural Sciences, Japan
[*]corresponding authors: aho@ims.ac.jp, hyahn@ims.ac.jp

Abstract: Interference between an incident circularly polarized optical field and a scattered field by a plasmonic cuboid particle created a spiral-shaped optical field structure, which was replicated on a polymer relief through photo-polymerization.

Even when a symmetric nanostructure (typically plasmonic nanostructure) is illuminated with a linearly polarized optical field parallel to the symmetry axis, circularly polarized fields appear in the local sites near the nanostructure, and the spatial distribution of the handedness of the field is in an anti-symmetric manner (Figure 1).[1] Conversely, when a symmetric nanostructure is illuminated by circularly polarized light, assymmetric optical field distribution is induced, which has a potential to create materials with chiral assymmetry through photochemical reactions. This idea was actually reported to be achieved with metal nanocuboid, on which photoproduct was deposited at two of diagonal apexes.[2] The result was attributed to the plamonic mode structure induced on the cuboid when excited by circularly polarized light. In the present study, we report experimental results that an additional mechanism of chiral field generation due to interaction between the symmetric nanoparticle and circularly polarized light provides a further complex structure of the photoproduct.[3]

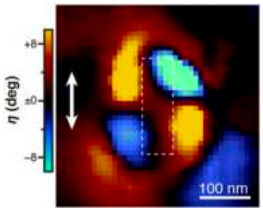


Fig. 1 Near-field ellipticity image (@ 800 nm) of a gold nanorod.[1]

We adopted a chemically synthesized Au@Ag nanocuboid particle as a plasmonic light scattering center to generate chiral optical field. The synthesized cuboid particle has dimensions of 60 × 60 × 120 nm^3, and shows transverse and longitudinal plasmon resonances at 470 and 700 nm, respectively, in a colloidal solution. The nanoparticles were dispersed on a fused-silica substrate using spin-coating of the colloidal solution. We investigated photopolymerization reaction in the periphery of the nanoparticle under circularly polarized illumination. For this purpose, the photopolymerizable mixture composed of the monomer divinylbenzene (DVB, 99 wt%) and the photoinitiator tetraphenylporphyrin (TPP, 1 wt%) was prepared. To start the polymerization reaction, a laser beam with a wavelength of 660 nm was irradiated to the substrate coated with Au@Ag nano-particles, which is immersed in the photopolymerizable mixture. Upon the irradiation, the excited state of TPP can initiate the polymerization reaction and immediately form polymer layers on the substrate.

Figures 2a and b show SEM images of the product on the Au@Ag cuboid nanoparticles after the exposure of a laser beam with left- and right-handed circular polarization (LCP and RCP), respectively. Depending on the handedness of circular polarization of the illumination, the S- or inverted S-shaped polymer layers that were oriented along the longitudinal axis of the nanoparticle were formed. In addition to it, if we look at the long-range area of the photo-treated sample, a spiral-shaped surface pattern was found, as shown in the AFM image (Figure 2c). The polymer structure formed on the surface by the LCP beam was formed in a circular area with a diameter of about 6 μm, which is matched with the area of the laser beam irradiation. The thickness of the polymer layer was about 200 nm in the central part, which corresponds to the thick polymer layer near the nanoparticle surface,

and it gradually decreased toward the outer edges. Radial groove patterns with periodic intervals (440 nm) were developed in the form of a double Archemedean spiral structure.

We discuss the origin of the created spiral photochemical product based on finite-difference time-domain (FDTD) simulation of the electric field near the nanoparticle. Figures 2d-g represent simulated optical field intensity in the periphery of the nanocuboid on the illumination of left- and right-handed circularly polarized light. In the close vicinity of the nanocuboid, assymmetric field distribution depending on the handedness of the circular polarization was generated, which well explains the created chiral polymer structures depicted in Figures 2a and b. In the wider area around the particle, we can find Archemedean-spiral-like structures of the field intensity, which reasonably resemble the created spiral structure observed in Figure 2c. The separated components of incident and scattered (by the particle) fields did not show any chiral feature (Figure 2h and i), which indicate that the double spiral structure might be originated from the interference between the incident (background) circularly polarized field and the scattered field by the plasmonic nanoparticle at the center.

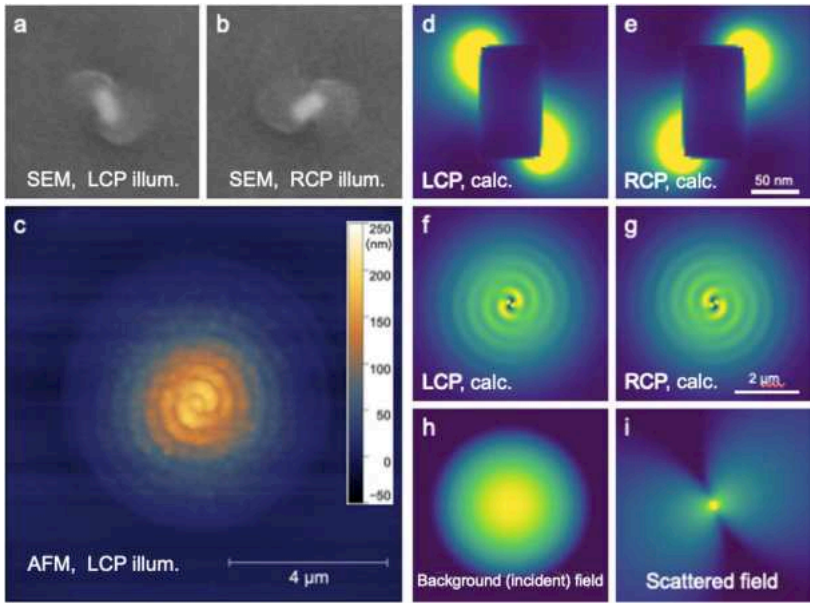


Fig. 2 (a,b) SEM images of photopolymerized structure formed around the cuboid nanoparticle under the (a) LCP and (b) RCP illumination. (c) AFM image of chiral double spiral structure. (d,e) Simulated electric field intensity near the cuboid nanoparticle under (d) LCP and (e) RCP illumination. (f,g) Simulated electric field intensity in several micrometer scales under (f) LCP and (g) RCP illumination. (h,i) Electric field distribution in log-scale of (h) background field of incident beam and (i) scattered field from the nanoparticle.

It is noteworthy that the chiral electromagnetic field scattered from the nanoparticle, although it is much weaker than the incident field in the far-field region, creates spiral-shaped intensity modulation over the several micrometer scale, and photopolymerization reaction condition used in this study is sufficiently sensitive to replicate the intensity profile of the generated interference pattern. We expect that further engineering of the geometry and the resonance of the central nanoparticle can yield the different chiral shapes of the interference patterns and the resulting chiral polymerized structures.

This work was supported in part by Grants-in-Aid for Scientific Research (Grant Nos. JP16H06505, JP21H04641, JP21K18884, and JP22H05135).

References

1. S, Hashiyada, T. Narushima, and H. Okamoto, “Imaging Chirality of Optical Fields near Achiral Metal Nanostructures Excited with Linearly Polarized Light,” ACS Photon., Vol. 5, 1486–1492, 2018.
2. K. Saito and T. Tatsuma, “Chiral Plasmonic Nanostructures Fabricated by Circularly Polarized Light,” Nano Lett., Vol. 18, 3209–3212, 2018.
3. H.-Y. Ahn, T. Narushima, and H. Okamoto, under revision.

Control of light emission of quantum emitters coupled to silicon nanoantenna

J-M. Poumirol[1, *], M. Montagnac[1], Y. Brûlé[2], A. Estrada-Real[6], I. Paradisanos[7], A. Cuche[1], S. J. Weber[1], J. Müller [3], G. Larrieu [3], V. Larrey[4], P. R. Wiecha[3], F. Fournel[4], O. Boisron[5], B Masenelli[5], G. Colas des Francs[2], B. Urbaszek[6], G. Agez[1] and V. Paillard[1]

[1] CEMES-CNRS, Université de Toulouse, Toulouse, France.
[2]ICB, Université de Bourgogne, CNRS, Dijon, France
[3]LAAS-CNRS, Université de Toulouse, Toulouse, France
[4]CEA-LETI, Université Grenoble-Alpes, Grenoble, France
[5]Université de Lyon, Université Lyon 1, CNRS UMR 5510, ILM, Villeurbanne, France.
[6]Institute of Condensed Matter Physics, Technische Universität Darmstadt, 64289 Darmstadt, Germany.
[7]Institute of Electronic Structure and Laser, Foundation of Research and Technology Hellas, 71110 Heraklion-Crete, Greece.

[*]corresponding author: jean-marie.poumirol@cemes.fr

Abstract: Optical Mie resonators based on silicon nanostructures allow tuning of light-matter interaction. Optically active materials such as transition-metal dichalcogenide monolayers or europium ions can be placed in the near-field region of such Mie resonators allowing control of both the excitation and the emission processes trough antenna design and cylindrical vector beams.

Enhancing and controlling the light emission of quantum emitters coupled to optically resonant nanostructures is essential for new light sources at the nanoscale. The photoluminescence (PL) intensity of a quantum emitter at a position r coupled to a nanoantenna is influenced by three parameters, as expressed in the following equation[1]:

$$I(\mathbf{r}, \omega_{exc}, \omega_{em}) = P_{exc}(\mathbf{r}, \omega_{exc}, \omega_{em}) \times \phi_{em}(\mathbf{r}, \omega_{em}) \times C_{coll}(\mathbf{r}, \omega_{em}) \quad (1)$$

where $P_{exc}(r, \omega_{exc})$ is the excitation rate, proportional to the excitation pump, $\phi_{em}(r,\omega_{em})$ is the quantum yield related to the local density of photon states (LDOS) at the emission angular frequency ω_{em}, and $C_{coll}(r,\omega_{em})$ is the collection efficiency, that depends on both the emission directivity and detection geometry.

Here we show that by placing an atomically thin semiconductor (TMD) directly in the near-field of individual dielectric nanoresonators, give us access to $\phi_{em}(\mathbf{r},\omega_{em})$[2, 3] without the use of complex near-field spectroscopy techniques. We compare the near-field resonance energies with far-field resonance energy measurements on the same resonators and observe a clear blue-shift of the near-field energies in our far field results. We show tuning of the optical absorption of the atomically thin semiconductor $MoSe_2$ through the interaction with the nanoresonator near-field.

In a second time, we investigated the photoluminescence mappings of Eu^{3+}-doped cluster-deposited films on Si nanorings using different cylindrical vector beams. We demonstrate that the polarization and shape of the excitation beam can also be used to manipulate light emission, as azimuthally or radially polarized cylindrical vector beam offers to spatially shape the electric and magnetic fields, in addition to the effect of silicon nanorings (Si-NRs) used as nanoantennas[4]. Now, in addition to the photon LDOS, we show that the excitation

beam shape and polarization have an important effect. Radial and azimuthal polarized beams exciting ring shape nanoantennas allow to tune the near-field hot spots, hence the local PL enhancement.

Our results show that it is possible to spatially shape the photoluminescence of quantum emitters coupled to dielectric nanoantennas by both the excitation and emission channels, offering important insights for the design of efficient TMD and Rare earth ions-based nano-devices.

We acknowledge partial funding from ANR HiLight, NanoX project 2DLight, the Institute of Quantum Technology in Occitanie IQO and a UPS excellence PhD grant.

References

1. Koenderink, A. F. Single-photon nanoantennas. ACS Photon. 4, 710–722 (2017).
2. Ana Estrada-Real *et. al,* "Probing the optical near-field interaction of Mie nanoresonators with atomically thin semiconductors," Communications physics (2023) 6:102
3. Jean-Marie Poumirol, *et. al.* , "Unveiling the Optical Emission Channels of Monolayer Semiconductors Coupled to Silicon Nanoantennas" *ACS Photonics* (2020), 7, 11, 3106–3115
4. M. Montagnac *et. al* . "Control of light emission of quantum emitters coupled to silicon nanoantenna using cylindrical vector beams," Light: Science & Applications (2023) 12:239

Ultrafast Optical Response of Plasmonic Doped-VO_2 Metasurfaces

B. Morris[1,2], Z. Shayegan[2], R. Reig[1,2], B. San-Nicolas[1,3], S. Frenkel[1,2], J. Margot[3], M. Chaker[2], and B. Palpant[1*]

[1]Laboratoire Lumière, Matière et Interfaces, CentraleSupélec, CNRS, ENS Paris-Saclay, Université Paris-Saclay, Gif-sur-Yvette, France
[2]Institut National de la Recherche Scientifique, Centre Énergie Matériaux et Télécommunications, Varennes, Québec, Canada
[3]Département de Physique, Université de Montréal, Montréal, Québec, Canada
[*]corresponding author: bruno.palpant@centralesupelec.fr

Abstract: Pure or tungsten-doped vanadium dioxide thin films are elaborated by pulsed laser deposition. Gold nanoparticle arrays are then deposited by e-beam lithography. The metasurface ultrafast optical response is determined. The influence of the localized plasmon resonance is analyzed in terms of photothermal conversion and near-field enhancement.

Thermochromic materials such as vanadium dioxide (VO_2) exhibit an insulator-metal phase transition (IMT) when their temperature exceeds a certain value or when they are illuminated by ultrashort light pulses. The phase transition occurs at the temperature T_{IMT}=68 °C for pure VO_2, and T_{IMT}=25 °C for VO_2 doped with tungsten ($W_{2\%}V_{98\%}O_2$). By combining plasmonic nanoparticles (NPs) and thermochromic materials, it is possible to obtain a metasurface with improved optical properties and faster dynamics compared with conventional VO_2.

We produced such metamaterials using various nanofabrication techniques. They consist of a thin layer of tungsten-doped VO_2 supporting, in a 2D lattice arrangement, gold nanodisks or nanorods produced by electron lithography. The temperature and thickness-dependent optical properties of VO_2 thin films were measured by spectroscopic ellipsometry. The results were analyzed alongside structural and electronic characterizations to elucidate the underlying physical origin of VO_2's distinctive properties. In addition, using ultrafast time-resolved pump-probe spectroscopy, we demonstrated a clear improvement in the optical properties of samples combining a doped-VO_2 thin film and gold NPs as compared with a configuration combining VO_2 and NPs, or simply with doped-VO_2 alone. These results highlight the contributions of the plasmonic effect and VO_2 doping on the energy threshold required to induce the phase transition. The mechanisms behind this threshold lowering will be discussed, involving photothermal conversion and amplification of the optical near-field by the NPs.

References

1. Otto, M. R., L. P. René de Cotret, D. A. Valverde-Chavez, K. L. Tiwari, N. Emond, M. Chaker, D. G. Cooke, and B. J. Siwick. "How optical excitation controls the structure and properties of vanadium dioxide," PNAS, Vol. 116, No. 2, 450–455, 2019.

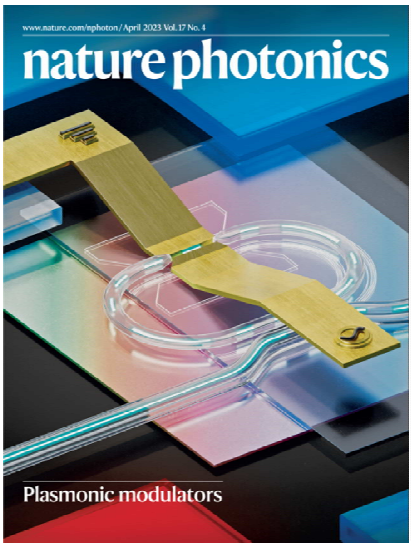
Publishing in *Nature* journals

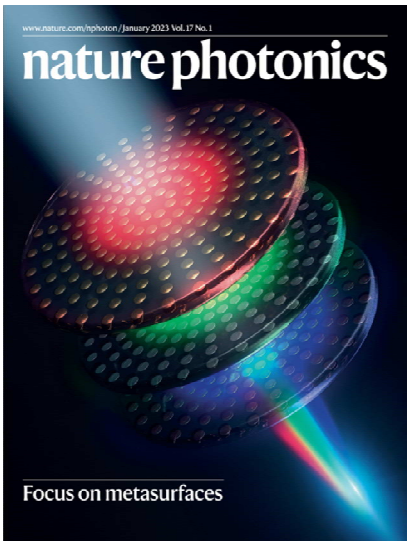
Rachel Won

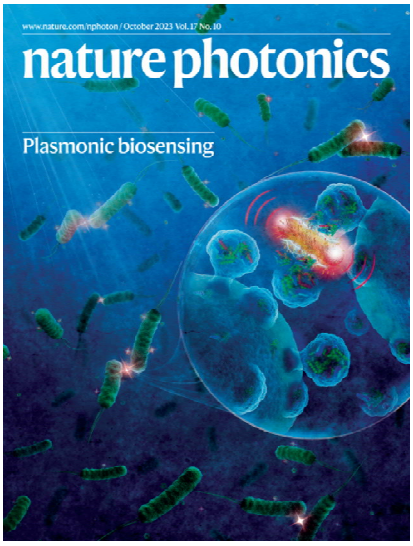
Nature Photonics, UK
r.won@nature.com

Abstract: In this talk, Rachel will tell you all you need to know about publishing your work in *Nature* journals, including an introduction to existing and new *Nature* journals, recent trends in publishing, options you have during your submission, and the editorial and peer review processes.

Biography: Rachel Won is an International Editor of *Nature Photonics*. She joined the journal in June 2006 as one of the four Founding Editors. Before that, Rachel worked for Aston University's Business Partnership Unit in Birmingham, UK, as a Medici Fellow, commercializing the research output of the university, particularly that of photonics research. She obtained her PhD in microwave photonics and nonlinear optics as a member of Aston's Photonics Research Group. She worked for Philips Optical Storage in Singapore as an Optics Engineer after completing her Master's degree study in Nanyang Technological University of Singapore doing research in optical fibre sensing. She holds a Bachelor's degree from the National University of Malaysia. She is a Fellow of OPTICA and SPIE (the International Society of Optics and Photonics).







Bound States in the Continuum: Advancements in Photonics from Enhanced Upconversion to Ultra-Sensitive Sensors

Silvia Romano[1], Bruno Miranda[1], Aida Seifalinezhad[1], Adam Schwartzberg[2], Ivo Rendina[1], Vito Mocella[1], Gianluigi Zito[1]

[1]Institute of Applied Sciences & Intelligent Systems, National Research Council, CNR-ISASI, Naples, Italy
[2]Molecular Foundry, Lawrence Berkeley National Laboratory, Berkeley, USA
Corresponding author: silvia.romano@cnr.it

Abstract:
Bound states in the continuum (BICs) refer to special electromagnetic modes that exist within the continuum of radiation modes but do not couple with them. Specifically, BICs are resonant states that possess infinitely high Q-factors due to their non-radiative nature [1, 2, 3]. Unlike typical resonant modes that radiate energy into the surrounding medium, BICs are characterized by their inability to couple with external radiation. This results in a divergence of the Q-factor, making them highly desirable for various applications in photonics and optical engineering. Our research group has showcased numerous applications of BICs, including biological and chemical sensing and imaging with the capacity to detect molecules of ultralow weight [4, 5, 6, 7], as well as surface amplification of fluorescence emission and Raman scattering [8].

Herein, we report remarkable recent results regarding two different applications. Firstly, we propose the concept of supercritical coupling in near-field coupled resonances close to the Friedrich–Wintgen condition applied to the giant enhancement of lanthanide nanoparticles upconversion [9]. Secondly, we present a pioneering sensor platform empowering the BIC sensing principle with a molecularly imprinted polymer (MIP) cladding layer suitably engineered for specific binding to transforming growth factor-beta (TGF-β), a multifunctional cytokine involved in regulating various cellular processes, including cell growth, differentiation, migration, apoptosis, and immune responses.

Both results highlight the growing significance of BICs and their role in advanced technologies through innovative coupling mechanisms.

References

1. C. Hsu et al., Bound states in the continuum. *Nat. Rev. Mater.* **1,** (2016)
2. J. Lee et al., Observation and Differentiation of Unique High-Q Optical Resonances Near Zero Wave Vector in Macroscopic Photonic Crystal Slabs. *Phys. Rev. Lett.* **109,** 67401 (2012)
3. V. Mocella and S. Romano, Giant field enhancement in photonic resonant lattices. *Phys. Rev. B - Condens. Matter Mater. Phys.* **92,** 1–5 (2015)
4. S. Romano et al., Label-Free Sensing of Ultralow-Weight Molecules with All-Dielectric Metasurfaces Supporting Bound States in the Continuum, Photon. Res. 6, 726 (2018)
5. G. Zito *et al.*, Label-Free DNA Biosensing by Topological Light Confinement, Nanophotonics-Berlin 10,

4279, (2021)
6. S. Romano et al., Ultrasensitive Surface Refractive Index Imaging Based on Quasi-Bound States in the Continuum, ACS Nano 14, 15417, (2020)
7. C Schiattarella et al. High-Q photonic aptasensor based on avoided crossing bound states in the continuum and trace detection of ochratoxin A." Biosensors and Bioelectronics: X 12, 100262 (2022)
8. S. Romano et al., Surface-Enhanced Raman and Fluorescence Spectroscopy with an All-Dielectric Metasurface. *J. Phys. Chem.* **122,** 19738–19745 (2018)
9. C. Schiattarella et al., Directive giant upconversion by supercritical bound states in the continuum, Nature (2024)

Scaling up Precision: Engineering Gold Nanoparticles for Optimal Performance in Advanced Production Platforms

Kyoungweon Park[1,2], Eva Yazmin Santiago Santos[3], Alexander Govorov[3], Richard A. Vaia[1]

Materials & Manufacturing Directorate, Air Force Research Laboratory, Wright-Patterson Air Force Base, Ohio 45433-7750

2 UES Inc., Dayton Ohio, 45432

3 Department of Physics and Astronomy, Ohio University, Athens OH USA

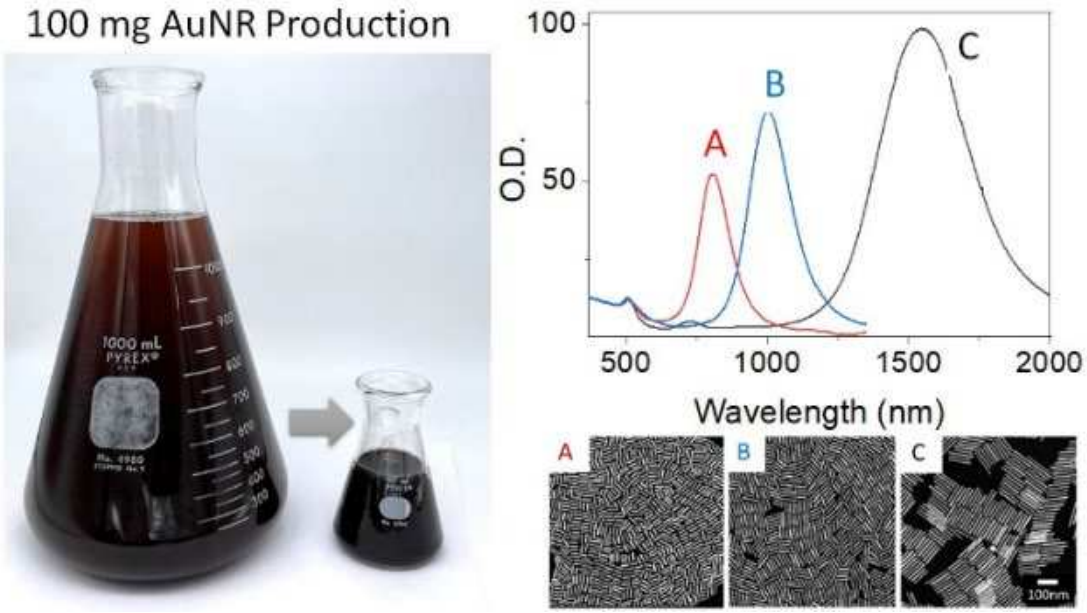
*corresponding author: Kyoungweon.park@eqlipsetechnologies.com

Abstract: We demonstrated the strategies for the synthesis of Gold NanoSpheres (AuNS), NanoRods (AuNR), and NanoWires (AuNW) that are both scalable and affordable. We explored how their properties can be tailored for optimal performance in specific applications. Implementing our approaches enables the realization of the full potential of gold nanoparticles and their assemblies, opening avenues for practical applications across various domains.

The intense light-matter interactions and large optical cross-section of metallic nanoparticles and their assemblies enable efficient focusing of optical fields at nanoscale. This unique capability is highly dependent on the shape and size of the nanoparticles enabling them to be a potential platform for a range of applications, including sensing, photo-detection, spectroscopy, and optical information processing. However, in order to realize the potential of these nanoparticles for practical use, it is crucial to develop scalable, reproducible, and cost-effective manufacturing processes that involve efficient synthesis with tunable structures, robust processing, and integration. Recent advancements, rooted in a deeper understanding of growth mechanisms, have transformed strategies along these lines for Gold NanoSpheres (AuNS), NanoRods (AuNR), and NanoWires (AuNW). Our synthetic strategies are designed to enable independent control of particle volume and dimensions while minimizing impurities and dispersity based on a refined understanding of the growth mechanism that governs the shape evolution of gold nanoparticles grown from single /penta twinned crystalline seeds.

These advancements have boosted production rates more than tenfold, while enhancing precise control over particle volume and dimensions, minimizing impurities, and reducing variation in particle size.1 As a result, solution dispersions exhibit absorption and scattering cross-sections nearing theoretical limits while displaying higher-order multipole plasmon resonances.2 As an example, we demonstrated films featuring voxelated structures

through the utilization of a highly concentrated solution (100+nM) tailored for specific applications.3 This involved combining techniques such as blade and spray coating, along with post-processing methods like laser reshaping. These films serve diverse functions as static and dynamic, multi-band filters, polarizers, and transparent conductors.



1. Park, K.; Ouweleen, M.; Vaia, R. A., Product Metrics for the Manufacturability of Single-Crystal Gold Nanorods via Reaction Engineering. ACS Applied Materials & Interfaces 2023, 15 (45), 52827-52842.

2. Miller, O.; Park, K.; Vaia, R. A., Towards maximum optical efficiency of ensembles of colloidal nanorods. Opt. Express 2022, 30 (14), 25061-25077.

3. Mahoney, C.; Park, K.; Jawaid, A.; Kowalski, B.; Gillman, A.; Tondiglia, V.; Treml, B.; White, T.; Vaia, R. A., Low-energy, nanoparticle reshaping for large-area, patterned, plasmonic nanocomposites. Journal of Materials Chemistry C 2018, 6 (26), 7157-7169.

Development of new chiroptically active quantum nanostructures

Y. K. Gun'ko*

School of Chemistry and CRANN, Trinity College Dublin, Dublin 2, Ireland
*corresponding author: igounko@tcd.ie

Abstract: This work is to develop new types of nanoparticulate materials possessing optical activity and chirality, study their properties, investigate their nature and explore their applications. Here report a range of new chiral nanomaterials including chiral semiconducting nanoparticles as well as chiral 2D nanostructures for potential enantioselective chemo-sensing applications.

Symmetry and chirality are properties commonly found throughout the natural world. Chirality is one of the most important factors in molecular recognition, with chiral compounds having a major role in chemistry, biology and medicine. Chirality has also been envisaged to play an important role in nanotechnology. Over the last years the area of chiral nanoparticles has received a great deal of attention due to the range of potential applications offered by these materials [1-4].

The main aim of our work is to develop new types of technologically important inorganic nanoparticulate materials possessing optical activity and chirality, study their properties, investigate their nature and explore their applications.

We have developed a range of new chiral nanomaterials including chiral ternary silver indium sulfide and selenide based semiconducting nanoparticles (quantum dots). In addition, we started to explore the properties of new anisotropic chiral 2D nanostructures. The new nanomaterials have shown a very interesting optical activity and unusual chiral morphologies which were confirmed by various instrumental techniques.

Several critical aspects on the nanocrystals growth and chemico-physical characterization, and the optimisation of the surface passivation by the chiral ligand in order to optimize the nanoparticle chirality are thoroughly investigated. Optical spectroscopy as circular dichroism and luminescence as well as nuclear magnetic resonance techniques are exploited to analyze the coordination processes leading to the formation of the ligand-nanocrystal chiral interface. The study highlights the dynamic nature of the interaction between the nanocrystals surface and the chiral ligand, and clarify some fundamental aspects for the transfer and optimization of the chiroptical activity. We have also explored potential applications of chiral quantum dots for chiral recognition and luminescent chemo- and bio- sensing.

Finally, we present an overview of chiral nanomaterials within the framework of synthesis-structure-property-application relationships and provide insights on how to leverage machine learning for the study of these highly complex relationships (see Figure 1 below).

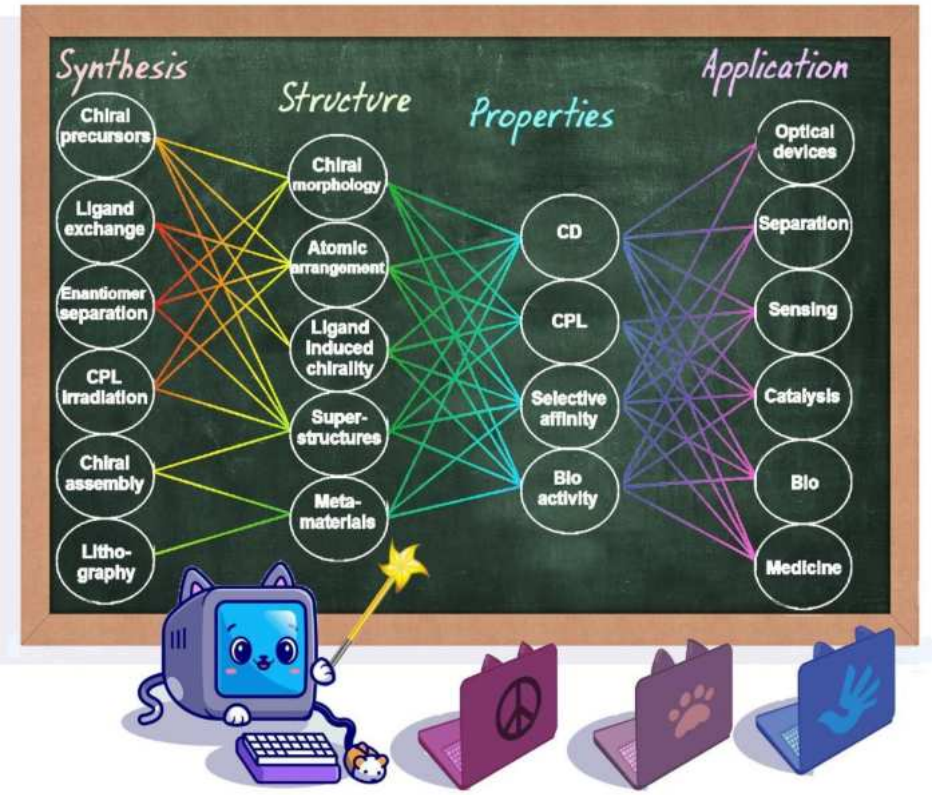


Figure 1. Schematic representation of the connectivity between synthesis, structure, properties, and applications of chiral nanomaterials [5].

Acknowledgements

The authors gratefully acknowledge financial support from the Science Foundation Ireland, SFI (project: SFI-20/FFP-A/8904).

References

1. Ben-Moshe, A., Maoz, B. M. , Govorov A. O. and Markovich G., “Chirality and chiroptical effects in inorganic nanocrystal systems with plasmon and exciton resonances”, Chem.Soc. Rev., Vol. 42, 7028-7041, 2013.
2. Milton, F. P., Govan, J., Mukhina, M. V. and Gun'ko, Y. K., “The chiral nano-world: chiroptically active quantum nanostructures”, Nanoscale Horizons, Vol. 1, 14-26, 2016.
3. Moloney, M. P., Govan, J., Loudon, A., Mukhina, M. and Gun'ko, Y. K., “Preparation of chiral quantum dots”, Nature Protocols, Vol. 10, 558-573, 2015.
4. J. Govan and Y. K. Gun'ko, “Recent progress in chiral inorganic nanostructures”, RSC Nanoscience & Nanotechnology ser., Nanoscience, Vol. 3, 1–30, 2016.
5. Kuznetsova, V., Coogan, Á., Botov, D., Gromova, Y., Ushakova E. V. and Gun’ko Y. K., “ Expanding the Horizons of Machine Learning in Nanomaterials to Chiral Nanostructures”, Advanced Materials, 2308912, 2024. https://doi.org/10.1002/adma.202308912.

DNA ORIGAMI SELF-ASSEMBLED HIGH-INDEX DIELECTRIC OPTICAL ANTENNAS FOR SINGLE-MOLECULE FLUORESCENCE MANIPULATION

M. Sanz Paz[1], N. Siegel[1], K. Kołątaj[1], F. Zhu[1], H. Hasebe[2], J. González-Colsa[3], G. Serrera[3], H. Sugimoto[2], M. Fujii[2], P. Albella[3] and G. P. Acuna[1,*]

[1]Department of Physics, University of Fribourg, Chemin du Musée 3, Fribourg CH-1700, Switzerland.

2 Department of Electrical and Electronic Engineering, Graduate School of Engineering, Kobe University, Kobe 657-8501, Japan.

3 Department of Applied Physics, University of Cantabria, 39005 Santander, Spain.
[*]corresponding author: Guillermo.acuna@unifr.ch

Abstract: We self-assemble optical antennas based on silicon nanoparticles using the DNA origami technique. We exploit these structures to manipulate the fluorescence properties of single fluorophores placed in their proximity. We focus on effects on the fluorescence lifetime, intensity and directivity.

Over the last decade, the DNA origami method[1] has established itself as one of the most versatile techniques for the bottom-up synthesis of hybrid species with tailored functionality[2]. This approach, which is based on the self-assembly of DNA strands into arbitrarily designed 3D structures, can be exploited to organize different entities, such as fluorophores, proteins, or NPs with nanometer precision and stoichiometric control. Consequently, it has been widely used to produce a variety of optical antennas for sensing and light manipulation at the single molecule level in controlled geometries. However, to date this approach has been constrained to Au, Ag and QD NPs with no works reported so far on combining DNA origami with high-index dielectric NPs. In this work, we develop a technique to functionalize high-index dielectric colloidal Si NPs[3] with DNA sequences using click-chemistry. To further demonstrate these findings, we self-assemble Si NP dimers using the DNA origami technique. Finally, we also exploit the DNA origami technique to position both Si NPs and organic fluorophores at controlled gaps to study the distance dependance energy transfer, the modification on the fluorescence rates (figure 1b) and the emission directivity. Our results show that in the vicinity of the Si NPs the radiate rate increases more than the non-radiative rate and that the Kerker condition can be exploited to obtain emission unidirectionality (figure 1c).

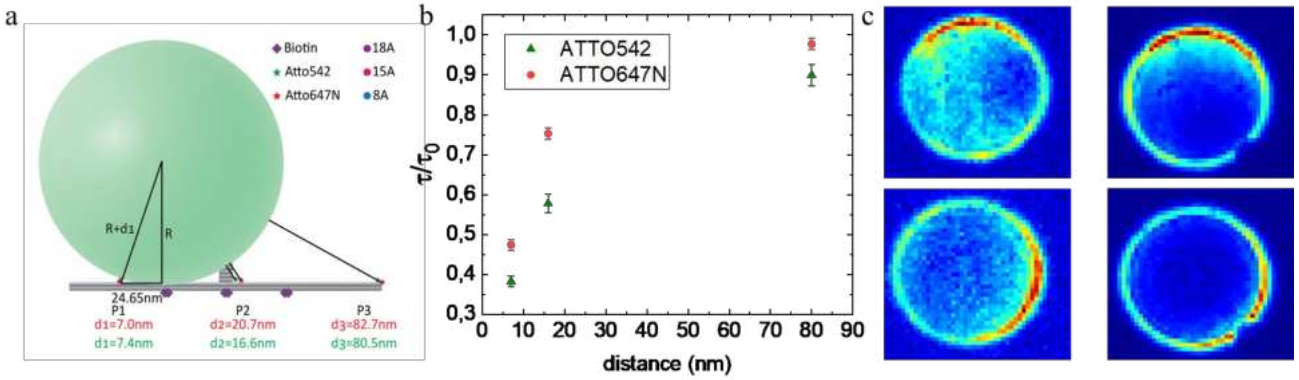


Figure 1. (a) Sketch of the DNA origami structure hosting a single Si NP and fluorophores at determined positions. (b) Fluorescence lifetime as a function of the distance to the nanoparticle. (c) Back-focal plane images

depicting the directivity induced by the presence of the Si NP.

References

1. P. W. K. Rothemund, Nature, **440**, 297–302 (2006)
2. A. Kuzyk, R. Jungmann, G. P. Acuna, N. Liu, ACS Photonics **5**, 1151 (2018)
3. H. Negoro, H. Sugimoto, M. Fujii, Nano Lett. **23**, 5101 (2023)

Nonradiative Cooling

Wakana KUBO*

Tokyo University of Agriculture and Technology, Japan

*corresponding author: w-kubo@cc.tuat.ac.jp

Abstract: We report a nonradiative cooling technology that can reduce the temperature of space surrounded by an opaque container. When a metamaterial-loaded thermoelectric device is placed in an opaque and sealed container, the metamaterial absorber absorbs the thermal radiation inside the container, resulting in a temperature reduction inside the container.

Radiative cooling is a key technology that reduces the temperature of sky-facing objects through radiative energy transfer between the objects and outer space at 3 K. An atmosphere has a transparent window ranging from 8 to 13 μm, which coincides with the thermal radiation of an object at ambient temperature, leading to thermal radiation from the object to the outer space. However, this technology is not applicable when cooling objects and spaces are surrounded by opaque absorbers. Here, we report a nonradiative cooling technology that can reduce the temperature of space surrounded by an opaque container.[1] When a metamaterial-loaded thermoelectric device is placed in an opaque and sealed container, the metamaterial absorber absorbs the thermal radiation inside the container, and the thermoelectric element converts the thermal energy to electric current. The generated current flows to the resister placed outside the container, releasing thermal energy to free space as Joule heating. To the best of our knowledge, there is no literature reporting the cooling technology combined with the thermal gathering acquired by the MA and thermoelectric conversion.[2] In this study, we demonstrate nonradiative cooling realized by metamaterial thermoelectric conversion and examine whether the non-radiative cooing occurs in an opaque and sealed container.

We used an MA consisting of a Ag film and Ag disk sandwiching a thin layer of calcium fluoride (Fig.1(a)). The MA-attached thermoelectric device (Fig.1(a)) was installed in an opaque container as shown in Fig. 1(b). Figure 1(c) shows the absorption spectra of the MA and control electrodes, and the blackbody radiation spectrum calculated at 311 K. The MA exhibited a sharp absorption around 9 μm. This unbalanced absorptivity difference between the MA and control electrodes can induce an additional thermal gradient

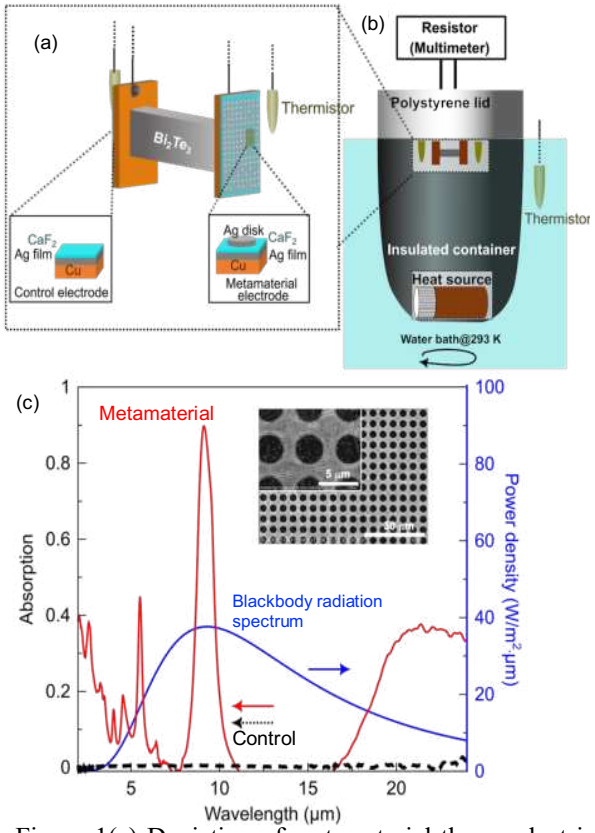


Figure 1(a) Depiction of metamaterial thermoelectric device and (b) schematic of a container soaked in a water bath at 293 K. (c) Comparison of absorption spectra of the metamaterial absorber (red line), a control electrode (dashed black line), and the blackbody radiation calculated at 311 K (blue line). The inset shows SEM images of the metamaterial absorber. The scale bars are 5 and 30 μm, respectively.

across the thermoelectric element, driving the thermoelectric conversion in an environment with uniform thermal radiation.

Figure 2(a) shows the time dependence of the environmental temperature difference of the containers loaded with MA or control devices. The container with the MA device showed a faster reduction in the environmental temperature than the container with the control device, indicating that the nonradiative cooling is demonstrated. The dashed lines in Figure 2(a) represent the effective output voltages generated by the MA and control devices. We repeated these experiments five times. Figure 2(b) shows the comparison of the averaged environmental temperature difference and effective output power generated on the MA and control devices. The environmental temperature difference in the container with the MA device was 6.2 ± 1.2 K (n = 5), while the container with the control device exhibited a difference of 5.9 ± 1.0 K (n = 5), resulting in a 0.4 K difference between the MA and control containers.

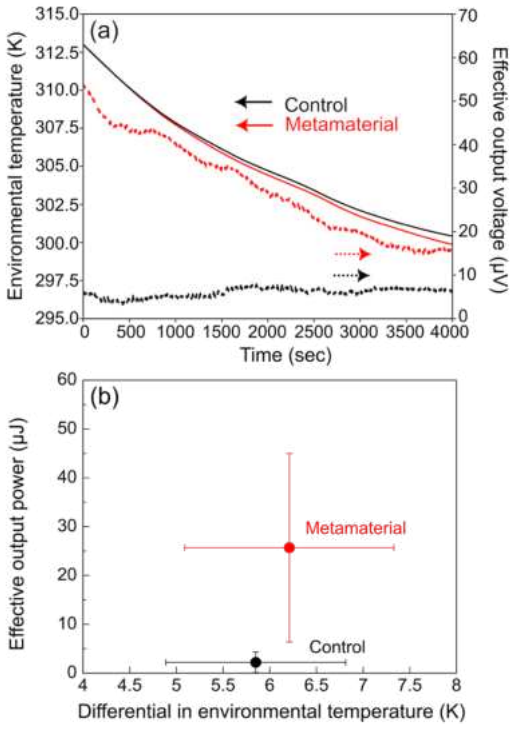


Figure 2(a) Time dependence of the environmental temperature difference within an opaque and sealed container loaded with the MA or control devices (solid lines) and the corresponding effective output voltages (dashed lines). (b) Comparison of the environmental temperature difference and the sum of output power generated on the MA and control devices observed for 1000 sec.

These results indicate that MA absorbs thermal radiation within the container and generates plasmonic local heat, creating a thermal gradient across a thermoelectric element and subsequent thermoelectric conversion. In addition, the electricity, which is a converted form of thermal energy through thermoelectric conversion, is transferred to the outside of the container, owing to the electrical bias generated on the thermoelectric device.

As proof of this concept, we evaluated the heat power extracted from the opaque and sealed container. If our experiment of nonradiative cooling is carried out ideally, the following equation is expected to hold,

$$Q_{cont} \cong Q_{MA} \cong \frac{Q_{TE}}{\eta}, \quad \text{Eq.(1)}$$

where, Q_{cont}, Q_{MA}, Q_{TE}, and η are the heat power extracted from the sealed container, the heat power absorbed by the MA, the heat power released through thermoelectric conversion, and the thermoelectric conversion efficiency, respectively. We evaluated these heat powers by analyzing five sets of measured data for comparison. Consequently, the calculated values of Q_{cont}, Q_{MA}, and Q_{TE} are (0.10 ± 0.05), 0.10, and (0.15 ± 0.05) J, meaning that these values fall within a very cloase range. These results support the fact that the temperature reduction inside the container with the MA is attributed to the thermal radiation absorption by the MA. We concluded that nonradiative cooling was successfully demonstrated. The nonradiative cooling gives an important insight that embedding arrays of metamaterial thermoelectric devices on the surfaces of roads and buildings suggests the potential for simultaneous environmental cooling and power generation through metamaterial thermoelectric conversion.

References

(1) Kawamura, N.; Tanaka, T.; Kubo, W. Nonradiative Cooling. *ACS Photonics* **2024**. DOI: 10.1021/acsphotonics.3c01757.

(2) Nakayama, R.; Saito, S.; Tanaka, T.; Kubo, W. Metasurface absorber enhanced thermoelectric conversion. *Nanophotonics* **2024**. DOI: doi:10.1515/nanoph-2023-0653 (acccessed 2024-02-09).

Proving non-thermal plasmon catalysis mechanism through the overtone vibrational quantum states

Zee Hwan Kim [1*]

[1]Department of Chemistry, Seoul National University, Seoul 08826, Korea
[*]corresponding author: zhkim@snu.ac.kr

Abstract: Employing SERS spectroscopy, we show that the plasmons activate the reactants to vibrational overtone states possessing > 0.5 eV of energy. We use the light intensity and wavelength dependences of the overtone population to quantify the non-thermal contribution to the activation and to validate the indirect hot electron transfer mechanism.

Plasmon-assisted chemical reactions, in which the chemical reactivity of surface-bound reactants is significantly enhanced and altered by the plasmon-excited metallic nanostructure, have attracted tremendous attention as a promising heterogeneous photocatalyst. One hypothesis for the mechanism is the non-thermal vibrational excitation (VE) of surface adsorbed reactants: the energetic electrons called the hot electrons (HEs), that are non-thermally excited during the decay of plasmons, transfer energy as a form of vibrational energy to the reactant. However, such a hypothesis has yet to be validated at the molecular quantum state level.

In this work, we study the steady-state distribution of overtone-excited reactants prepared by plasmon excitation. We find that the anti-Stokes peak of surface-enhanced Raman scattering (SERS) spectra of 4-nitrobenzene (NBT) reactant placed in a plasmon-excited metallic gap, obtained under the illumination of continuous-wave (cw) visible light, is asymmetrically broadened due to the overtone-excited reactants. From the lineshape analysis, we determine that at least 40 % of the vibrationally excited NBTs are in the overtone states under the light illumination of a few hundred kW/cm^2. We use the intensity and wavelength dependences of overtone-state distributions to clarify the thermal and non-thermal contributions to the activation and identify the physical origin of non-thermal activation.

Optoelectronic Physical Reservoir Computing with Digital Delayed Feedback featuring in situ Optimization

Fyodor Morozko, Shadad Watad, Amir Naser†
Antonio Cal`a Lesina[3], Andrey Novitsky[2] and Alina Karabchevsky[*]

[1]School of Electrical and Computer Engineering, Ben-Gurion University of the Negev, Beer-Sheva 8410501, Israel
[*]corresponding author: alinak@bgu.ac.il

[2]Belarusian State University, Minsk, Belarus.

[3]Hannover Centre for Optical Technologies, Institute for Transport and Automation Technology (Faculty of Mechanical Engineering), and Cluster of Excellence PhoenixD,Leibniz University Hannover, Hannover 30167, Germany.

Abstract: Reservoir computing (RC) is a neuromorphic approach mimicking biological neural systems by employing randomized and fixed internal connections. This simplifies training and facilitates straightforward implementation. Optoelectronic oscillators are among the most promising material platforms for physical RC, combining optics' high modulation bandwidth with electronics' robustness, flexibility, and tunability. We've developed a physical reservoir achieving state-of-the-art performance in tasks like pattern recognition and time-series prediction using delayed feedback. Notably, a single physical node utilizing FPGA-based delayed feedback, delivers impressive results. Incorporating digital delay provides adequate delay time within the reservoir's operational bandwidth, compatible with generic electronic hardware. This capability allows for tuning and in-situ optimization of delay time, achieving a normalized mean squared error (NMSE) below 0.6 in NARMA10 time series recovery task.

In the heart of reservoir computing (RC) is a nonlinear network of recurrent dynamical nodes called a reservoir featuring fixed rather than trained connections, allowing straightforward physical realizations. One of the most widely explored realizations of RC is in the delay system. The structure of a generic and delay-based RC is schematically shown in Figure 1.

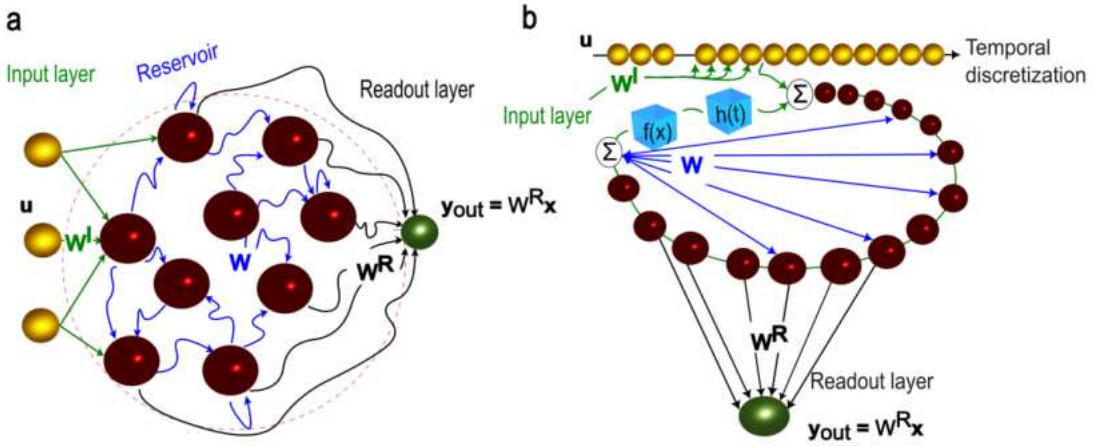


Figure 1: (a) Generic reservoir computing architecture. The depicted layout consists of distinct components: an input layer (bronze spheres) responsible for receiving external data, a reservoir (ruby spheres) featuring randomized fixed connections, and a linear readout layer (green spheres). (b) Delayed feedback-based reservoir

Figure 2 presents the experimental setup implementing RC in optoelectronic platform with delayed feedback.

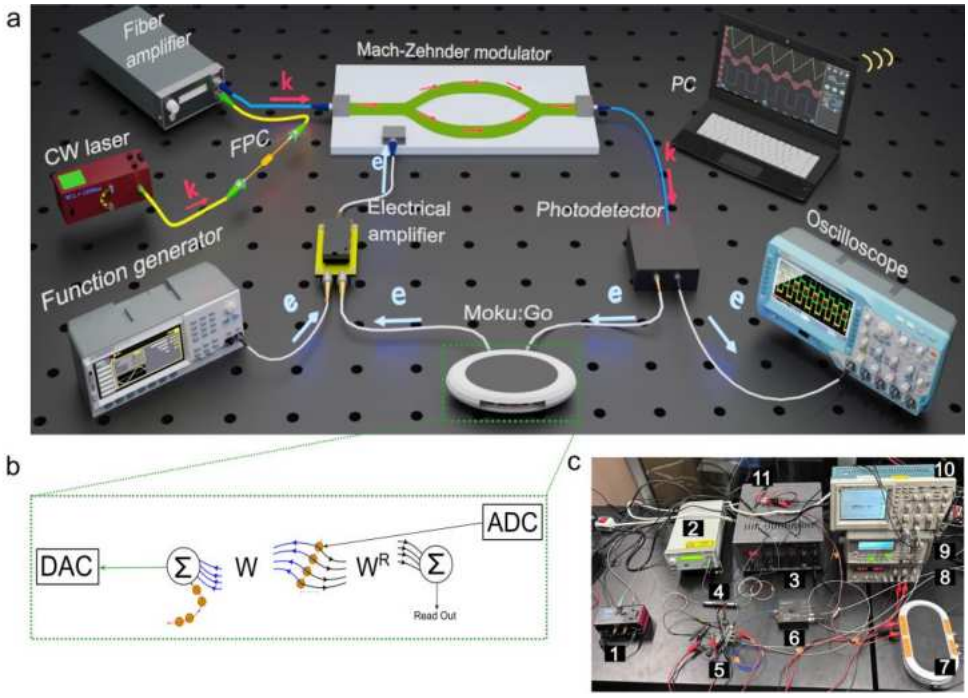


Figure 2: (a) Schematic of the experimental set-up. (b) Schematics of the digital delay and data digitizer combined with data digitizer: delayed feedback implements the reservoir's connectivity matrix W while the digitized reservoir states are weighted with the readout matrix W^R. (c) Photograph of the experimental setup, components are labeled as follows: 1. continuous-wave laser, 2. Erbium-doped fiber amplifier, 3. function generator producing trigger signal. 4. fiber polarization controller, 5. Mach-Zehnder modulator with electrical driver, 6. photodetector, 7. Moku:Go, 8. power supply for the electrical driver, 9. arbitrary waveform generator, 10. oscilloscope, 11. variable optical attenuator.

Figure 3 shows the results of *in-situ* optimization of our RC for NARMA10 time series recovery task.

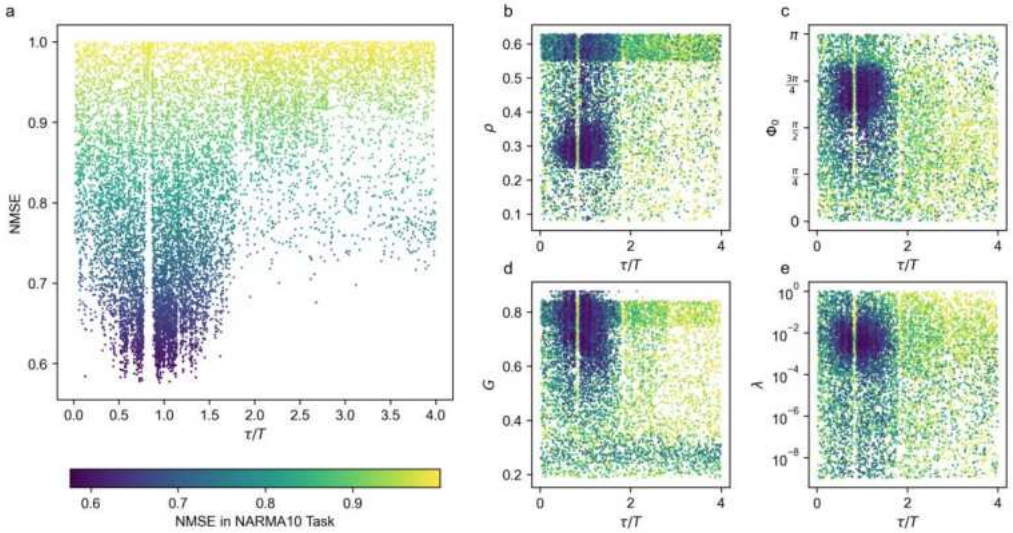


Figure 3 In-situ optimization results. Normalized mean square error (NMSE) in NARMA10 task as a function of (a) delay to clock cycle ratio τ /T and (b-e) τ /T together with another parameter of the reservoir: (b) τ /T and input scaling ρ, (c) τ /T and phase bias Φ0, (d) τ /T and net gain G, (e) τ /T and regularization parameter λ.

Funding: The research was supported by the EU ERA-NET DIEGO project Ministry of Energy, Grant No. 221-11-032, and the Lower Saxony's Minister of Science and Culture and the Volkswagen Foundation under the program "Zukunft.niedersachsen: Research Cooperation Lower Saxony – Israel".

References

1. J. Feldmann, N. Youngblood, M. Karpov, H. Gehring, X. Li, M. Stappers, M.Le Gallo, X.Fu, A.Lukashchuk, A. S.Raja, J. Liu, C. D. Wright, A. Sebastian, T. J. Kippenberg, W. H. P. Pernice, H. Bhaskaran, Nature 2021, 589, 7840 52.Y. LeCun, Y. Bengio, G. Hinton, Nature 2015, 521, 7553 436.
2. A. Rodan, P. Tino, IEEE Transactions on Neural Networks 2011, 22, 1 131.
3. L. Larger, M. C. Soriano, D. Brunner, L. Appeltant, J. M. Gutierrez, L. Pesquera, C. R. Mirasso, I. Fischer, Optics Express 2012, 20, 3 3241.
4. R. Martinenghi, S. Rybalko, M. Jacquot, Y. K. Chembo, L. Larger, Physical Review Letters 2012, 108, 24 244101.
5. Y. Paquot, F. Duport, A. Smerieri, J. Dambre, B. Schrauwen, M. Haelterman, S. Massar, Scientific Reports 2012, 2, 1 287.
6. P. Antonik, F. Duport, M. Hermans, A. Smerieri, M. Haelterman, S. Massar, IEEE Transactions on Neural Networks and Learning Systems 2017, 28, 11 2686.
7. L. Appeltant, M. Soriano, G. Van der Sande, J. Danckaert, S. Massar, J. Dambre, B. Schrauwen, C. Mirasso, I. Fischer, Nature Communications 2011, 2, 1 468.
8. F. T. Arecchi, G. Giacomelli, A. Lapucci, R. Meucci, Physical Review A 1992, 45, 7 R4225.
9. K. Ikeda, Optics Communications 1979, 30, 2 257.
10. T. H¨ulser, F. K¨oster, L. Jaurigue, K. L¨udge, Optical Materials Express 2022, 12, 3 1214.
11. N. Trouvain, L. Pedrelli, T. T. Dinh, X. Hinaut, In I. Farka˘s, P. Masulli, S. Wermter, editors, Artificial Neural Networks and Machine Learning ICANN 2020, volume 12397, 494–505. Springer International Publishing, Cham, ISBN 978-3-030-61615-1 978-3-030-61616-8, 2020.
12. A. Botchkarev, Interdisciplinary Journal of Information, Knowledge, and Management 2019, 14 045.
13. A. Lupo, E. Picco, M. Zajnulina, S. Massar, Optica 2023, 10, 11 1478.
14. J. Chen, Z. Zhou, B. J. Kim, Y. Zhou, Z. Wang, T. Wan, J. Yan, J. Kang, J.-H. Ahn, Y. Chai, Nature Nanotechnology 2023, 18, 8 882.
15. E. Picco, A. Lupo, S. Massar, Deep Photonic Reservoir Computer for Speech Recognition, 2023.
16. J. Wu, X. Lin, Y. Guo, J. Liu, L. Fang, S. Jiao, Q. Dai, Engineering 2022, 10 133.

Innovative Deposition and Oxidation-Coupled Technique for Low-Temperature Fabrication of VO_2 Thin Films and their Application to Photonic Devices

M. Chaker[1*]

[1]Institut National de la Recherche Scientifique, Centre Énergie Matériaux Télécommunications, Varennes, Qc, Canada
[*]corresponding author: mohamed.chaker@inrs.ca

Abstract: Vanadium dioxide is a "smart" material that exhibits a metal-to-insulator transition at a temperature of 68 °C. This property makes it of strong interest for many applications, including advanced photonic devices. An innovative deposition method is presented to achieve VO_2 thin films at low temperature on large area scale.

With the growing trend towards portable and adaptable devices in various fields, the demand for flexible electronics and coatings utilizing phase transition materials like vanadium dioxide (VO_2) as a functional layer is rising. VO_2 possesses a notably low transition temperature (T_c = 68°C) suitable for such applications. However, depositing high-quality crystalline VO_2 films directly onto polymer substrates remains challenging due to the thermosensitivity of such materials being barely compatible with usual VO_2 deposition methods. Two aspects were investigated in the present research. First, we introduced an improved deposition technique called sputtering oxidation coupling (SOC) using VN as intermediate material [1]. VN films are first deposited on quartz by magnetron sputtering. In a second step, a post-annealing process in oxygen is carried out to obtain VO_2. The lowest possible temperature for achieving VO_2 from VN with a significant electrical transition contrast is found to be 400°C, which makes the proposed method promising for growing VO_2 films directly on heat-sensitive polymer substrates such as Kapton. Second, we deposited VO_x films onto a Kapton substrate at room temperature using pulsed laser deposition (PLD) from a vanadium target and subsequently annealed it in an oxygen atmosphere at 390°C [2]. The electrical and optical properties of the VO_2/Kapton samples with different film thicknesses obtained by both techniques were investigated. The 200 nm-thick PLD vanadium dioxide films exhibit the best resistivity contrast with 3.1 orders of magnitude (OOM), while the 50 nm-thick PLD films show the best transmittance change of 54% at 2500 nm. The switching performances are comparable or even superior to those achieved previously using more complicated synthesis processes such as film transfer, introduction of buffer layers, and ink injection. Additionally, by coupling W elemental doping and thin film strain, we successfully tuned the VO_2 transition temperature to room temperature with a dopant concentration of only 1.1 at.% while maintaining a high electrical contrast (2 OOM). The impressive electrical and optical transition performance of the VO_2/Kapton samples, combined with their tunable transition temperature, makes them promising candidates for flexible electronic devices and photonic devices.

References

1. Xiang W, Le Drogoff B, Chaker M, "An Innovative Method to Achieve Large-Scale High-Quality VO_2 Thin Films: Oxidation of Vanadium Nitride Material Deposited by Sputtering", Applied Surface Science, Vol. 633, 157607, 2023.
2. Xiang W, Le Drogoff B, Koch D, Margot J, Chaker M, "High-quality VO_2 films synthesized on polymer substrates using room-temperature pulsed laser deposition and annealing", Ceramics International, Vol. 50, 838-846, 2024.

Ultrafast Processes and Energy Dissipation in Hybrid Nanomaterials

G. P. Wiederrecht[1]

[1]Center for Nanoscale Materials, Argonne National Laboratory, Lemont, IL, 60126, USA,

[*]corresponding author: wiederrecht@anl.gov

Abstract: Optically induced ultrafast processes are characterized to better understand energy flow and dissipation in nanostructured materials. The potential impacts on hybrid nanomaterials of interest for optoelectronics, energy conversion and sensing are described. Efforts to enhance the range of materials that can be explored by ultrafast spectroscopy are also described.

Nanostructured materials and their interaction with light produce many interesting and potentially useful properties. In many cases, the nanostructure size, shape, composition and local environment enable control of the magnitude of light-matter interactions at the nanoscale. This can produce important opportunities in widely varied fields such as quantum optics, optical energy conversion, nonlinear optics, sensing and many others. For example, in plasmonic materials, nanostructuring is known for producing large evanescent electromagnetic field enhancements near surfaces as compared to the bulk. This process is of strong interest for sensing given the fact that many plasmonic materials can be functionalized to selectively bind a wide range of molecular analytes. Another property of plasmonic nanostructures is that the enhanced electromagnetic fields at their surface can help produce a higher concentration of “hot” or “nonthermal” electrons that in principle can be used to perform work.[1] Hybrid systems, whereby the second material can interact with the enhanced field or enhanced concentration of hot electrons, can be designed to attempt to harness these enhanced photoprocesses for improved application efficiency. Electromagnetic coupling between closely spaced nanostructures, such as in many metamaterials, can also create enhanced and tunable light-matter interactions for varied applications.

These applications are impacted by ultrafast processes that frequently play a key role in the flow of energy and energy dissipation in nanoscale materials. For example, many nanomaterials undergo strong and ultrafast electron-phonon coupling (picoseconds or even faster) following the absorption of a photon, with optically excited electrons dissipating their energy into phonons as heat that can lead to poor optoelectronic performance or even melting. Time-resolved spectroscopy can be applied over varied spectral, temporal and spatial ranges to extract vibrational, electronic and structural changes resulting from photoexcitation and subsequent energy flow.[2] In this talk, ultrafast spectroscopy of novel nanomaterials are described, including high melting point refractory plasmonic metal nanostructures and colloidal nanoplatelets that can produce multi-exciton behavior upon photoexcitation. Hybridization of plasmonic and semiconductor materials, and the impact on ultrafast processes, are also described.

Ultrafast spectroscopy techniques that enable a wider range of materials to be studied are also described. In a nutshell, many interesting materials that are of interest for study cannot withstand ultrafast pulse illumination for a period long enough to characterize via standard spectroscopic techniques. We describe approaches, particularly ultrafast compressive sensing approaches, that can dramatically decrease the length of time needed to determine dynamical responses following optical excitation.[3]

Work performed at the Center for Nanoscale Materials, a U.S. Department of Energy Office of Science User Facility, was supported by the U.S. DOE, Office of Basic Energy Sciences, under Contract No. DE-AC02-06CH11357.

References

1. Besteiro, L. V., P. Yu, Z. Wang, A. W. Holleitner, G. V. Hartland, G. P. Wiederrecht, A. O. Govorov, “The fast and the furious: ultrafast hot electrons in plasmonic metastructures. Size and structure matter,” Nano Today, Vol. 27, 120-145, 2019.
2. Wiederrecht, G. P. *et al.*, “Nanomaterials and Sustainability,” ACS Energy Lett., Vol. 8, 3443–3449, 2023.
3. Adhikari, S., C. L. Cortes, X. Wen, S. Panuganti, D. J. Gosztola, R. D. Schaller, G. P. Wiederrecht, S. K. Gray, “Accelerating ultrafast spectroscopy with compressive sensing,” Phys. Rev. Appl. , Vol. 15, 024032, 2021.

Recent challenges in hybrid plasmonic nano-emitters

M. Chen[1,2], S. Marguet[3], A. Issa[1], S. Jradi[1], C. Couteau[1], C. Fiorini[4], L. Douillard[4], O. Soppera[5], J. Plain[1], T. Xu[2], B. Wei[2], and R. Bachelot[1,6]

[1]Light, nanomaterials, nanotechnologies (L2n) Laboratory, CNRS UMR 7076. University of Technology of Troyes, France
[2]School of mechatronic engineering and automation, key lab of advanced display and system application, Shanghai University, PR China
[3]Université Paris Saclay, CEA, CNRS, NIMBE F-91191 Gif sur Yvette, France
[4]Université Paris Saclay, CEA, CNRS, SPEC F-91191 Gif sur Yvette, France
[5]Université de Haute Alsace, CNRS, IS2M UMR 7361, F-68100 Mulhouse, France
[6]CNRS-International-NTU-Thales Research Alliance (CINTRA), IRL 3288, Singapore
[*]corresponding author: renaud.bachelot@utt.fr

Abstract: The development of hybrid plasmonic nanosources of light require the control of the spatial distribution of the active medium in the vicinity of metallic nanoparticles. An approach used to take up this challenge is based on plasmonic photopolymerization. In particular, the spatial symmetry can be controlled at the nanoscale.

Modern information and communication technologies request higher bandwidth and more efficient energy data communication to solve the challenge of increasing data traffic. In this context, optical data is the key: the fast development of integrated optics and nanophotonics has realized more and more optical functionality in a small chip [1]. Rapid growth of this nanophotonics area requires the development of advanced nanosources of light whose geometry must be scalable with nanophotonic devices and whose tunability must be simple and efficient. Over the past two decades, hybrid plasmonic nanosources based on energy transfer between metal nanoparticles and semiconductor quantum dots/nanocrystals (QDs) or organic dyes have turned out to constitute a promising solution of efficient optical nanosources [2].

We will discuss the different regimes of coupling between an active medium and a metallic nanoparticle that is seen as a nanocavity or a nanoantenna, and will stress the importance to control the nanoscale spatial distribution, and related symmetry, of the active medium.

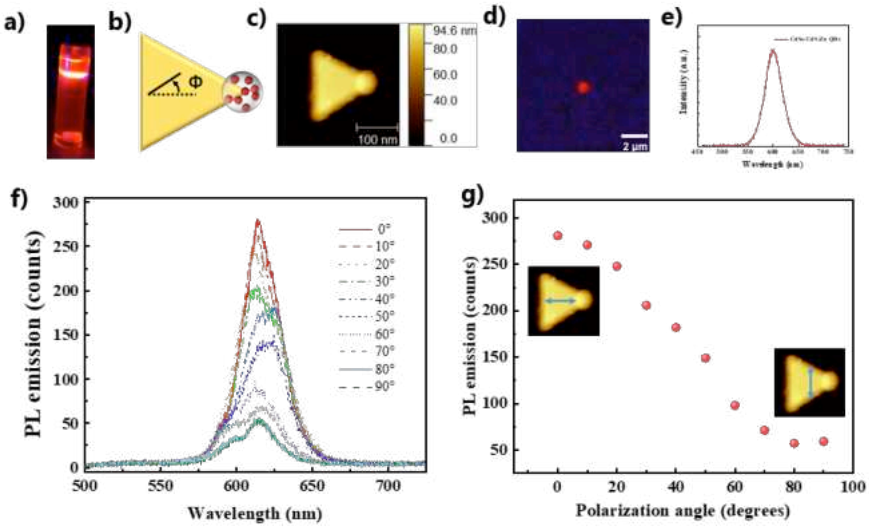
In microscale optoelectronics, the possibility to precisely control the spatial distribution of the active medium leads to optimization of systems and devices. At the nanoscale, this issue still constitutes a challenge.

We studied and exploited the controlled nanoscale spatial positioning of semiconductor quantum emitters in the close vicinity of metal nanostructures. This control relies on plasmon-assisted nano-polymerization [3,4] of a photosensitive formulation that hosts nano-emitters[5,6,7]. In addition to offering a promising platform for nanochemistry, this approach enables the design of the symmetry of the medium surrounding plasmonic nano-antenna.

Through selected examples, we will show that this approach has opened many new avenues and exciting concepts, such as

- Polarization-sensitive photoluminescence [8] (see Figure below as an illustration)
- Polarization-driven color selection [4]
- Life time engineering [9]
- Control of the local space symmetry group

- Rationalized plasmon-assisted donor-acceptor energy transfer [4]
- Single-photon switch that is driven by polarization [8]



Hybrid nanosource of light based on a gold nanotriangle. (a) Photoluminescence image of CdSe/CdS/Zn QD-containing photopolymerizable formulation illuminated by a UV lamp. (b) Illustration of the hybrid polymer/nanotriangle system obtained by plasmonic photopolymerization (c) its AFM image. (d) far-field PL image from the hybrid system and (e) corresponding PL spectrum. f) PL spectrum of the hybrid triangular nanosources for different polarization direction of the exciting field, (g) PL intensity as a function of the angle of polarization of the exciting laser.

Acknowledgements

This work is financially supported by the ANR (French Research Agency) through the projects STRONG-NANO, POPCORN, ADVANSPEC and NANO-PHOT (ANR-18-EURE-0013).

References

1. Coldren, L. A. et al. Diode Lasers and Photonic Integrated Circuits. Wiley, 2nd edition 2012.
2. e.g. V. Giannini et al., Chem. Rev. Vol. 11, 3888, 2011 ; Gonçalves, P. A. D et al., Nat. Commun., Vol. 11, 366, 2020
3. Ibn El Ahrach, H. et al., Phys. Rev. Lett., Vol. 98, 107402, 2007
4. Zhou, X et al., Nano Lett. Vol. 15, 7458, 2015
5. Ritacco, T. et al., ACS Appl. Nano Mater., Vol. 4, 6916, 2021
6. Issa, A. et al., ACS Appl. Mater. Interfaces, Vol. 13, 41846, 2021
7. Issa, A. et al., ACS Appl. Mater. Interfaces, Vol. 15, 21, 2023
8. Ge, D. et al., Nat. Commun., Vol. 11, 3414, 2020
9. Ge, D. et al., Photon. Res., Vol. 10, 1552, 2022

Tracing temporal plasmonics with direct field sampling

Holger Lange[1,2,*], Kai-Fu Wong[1,3], Andreas Knorr[4], Francesca Calegari[1,3], and Matthias F. Kling[5]

[1]The Hamburg Centre for Ultrafast Imaging, Hamburg, Germany
[2]Institute of Physics and Astronomy, Universität Potsdam, Potsdam, Germany
[3]Center for Free-Electron Laser Science, Hamburg, Germany
[4]Institut für theoretische Physik, TU Berlin, Berlin, Germany
[5]Stanford PULSE institute, SLAC National Accelerator Laboratory, Menlo Park, CA, USA

[*]corresponding author: holger.lange@uni-hamburg.de

Abstract: We present a direct sampling approach for localized surface plasmons in the petahertz domain, permitting to trace few-fs transient fields in the visible spectral region. The experiment can be accompanied by single-digit femtosecond optical pump-probe spectroscopy to correlate plasmon damping and electron dynamics in the time domain.

Determining the orientation of gold nanorods by means of polarimetric spectroscopy

P. C. Simo[1*], A. Mildner[1], D. P. Kern[1], and M. Fleischer[1*]

[1]Institute for Applied Physics and Center LISA+, 72076 Tübingen, Germany
[*]corresponding authors: christian.simo@uni-tuebingen.de, monika.fleischer@uni-tuebingen.de

Abstract: We present a technique to acquire the azimuthal orientation of gold nanorods of various aspect ratios within just four measurements. Dark-field spectroscopy enables the extraction of the eigenmode line shape and phase shift information, which can be used in tandem with an analytical dipole model to determine the azimuthal orientations.

Applications of chiroptical spectroscopy in biomedical and pharmaceutical research fields heavily depend on the knowledge of the azimuthal orientation of a structure, such as a gold nanorod (GNR), since the information on the polarization state is needed to investigate optically active hybrid compounds.[1] Similarly, angled meta-atom constituents of metasurfaces also need to stay within a low error margin to pass quality control and thus benefit from a reliable non-destructive method to extract their azimuthal orientation. When observing GNRs for simplicity, their azimuthal position naturally coincides with their plasmonic longitudinal resonance (LR) mode and can be determined with conventional excitation polarization sweep measurements.[2] Considering the high number of measurements per GNR, the throughput is limited and prone to errors originating from human precision. High-throughput single-shot methods could be achieved with an advanced optical setup and image analysis with deep-learning algorithms to eliminate the human error; however, the orientation predictions oftentimes depend on the aspect ratio (AR) <1.6 of the GNRs and on reaching standard deviations of below five degrees.[3,4]

In this work, we show an alternative spectroscopic method that gains angular information of a single GNR within four measurements with a regular dark-field setup, two polarizing filters, and a cross-shaped aperture, reaching a standard deviation of ±2.4°. Coherently fitting the measurements with the help of an analytical dipole model, the azimuthal angle of the LR is extracted by varying the planar orientation of the analyzing filter.[5] The additional elements, such as a piezo-electric rotational mount for the positioning of the analyzing polarizer filter, reduce the human error to a minimum while enhancing automation possibilities.

The analytical dipole model describes the intensity of the electric far-field radiation from dipoles excited by a plane wave with an arbitrary polarization angle Φ.[5] Each dipole with individual orientation and magnitude will express a phase shift φ relative to the polarized incident plane wave. If the electric far-field radiation is analyzed with a polarizing filter of angle Θ, the relative phase between the dipoles allows the extraction of the dipolar orientation. The phase shifts φ_1 and φ_2 of two dipoles with magnitudes $p_1(\omega)$ and $p_2(\omega)$ and respective orientations β and γ, which represent the orientations of transverse resonance (TR) and LR modes, can be calculated from a dark-field spectrum of a randomly spin-coated GNR under unpolarized excitation (see Figure 1a)). By keeping the excitation angle fixed at $\Phi = 45°$ and varying the analyzer angle to a set of random angles (here $\Theta = [9°, 106°, 155°]$), one can use the model to fit the data coherently and extract γ_{fit} (Figure 1b)). Comparing γ_{fit} to the SEM-extracted angle γ_{SEM} shows a standard deviation of only ±2.4° (see Figure 1c)). An SEM micrograph with the drawn-in γ_{fit} and γ_{SEM} can be seen in Figure 1d) and shows good concordance. This approach proves to be reliable with a low sensitivity to AR compared to the current state of the art.

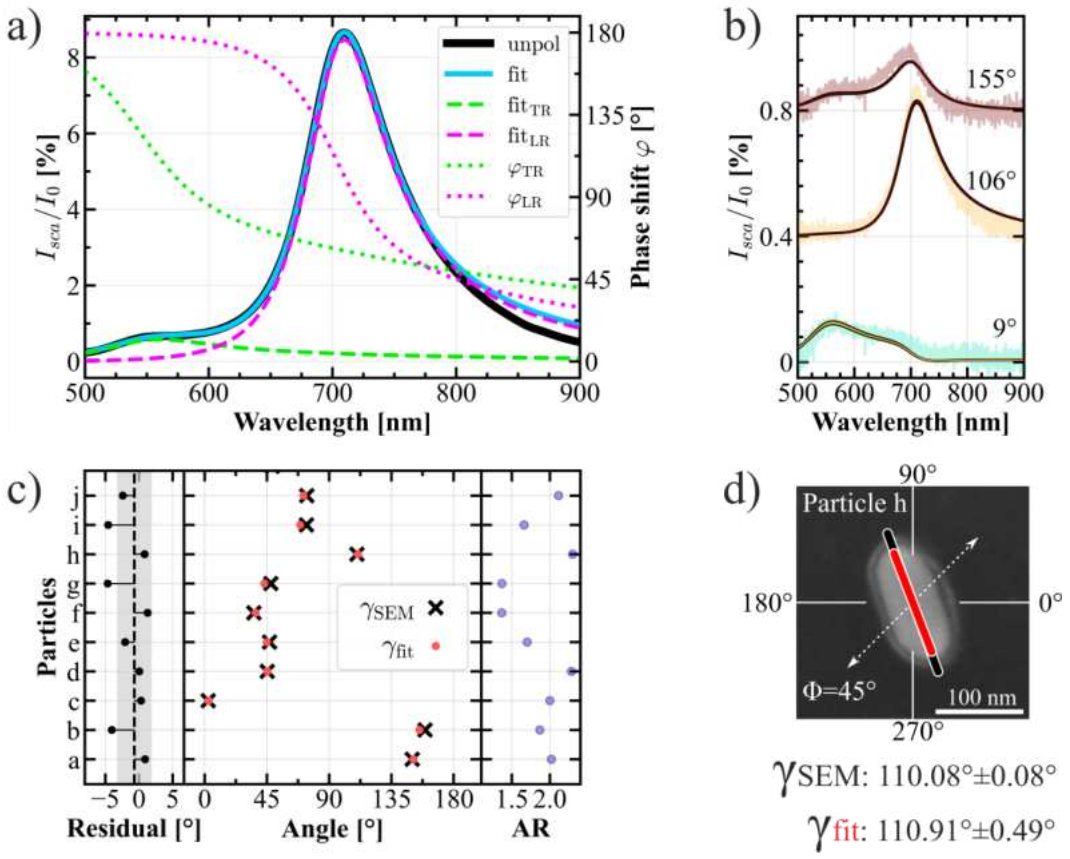


Figure 1. a) Spectrum under unpolarized excitation with fitting curve. The separate TR and LR modes were also plotted with the respective phase shift φ of the mode. **b)** Stacked polarimetric dark-field measurements with fixed excitation polarization and varied analyzer angle fitted coherently with the dipole model to extract the LR orientation γ_{fit}. **c)** Angles γ_{fit} from a collection of GNRs compared to their physical orientation γ_{SEM} extracted from SEM images. Residuals and the AR variation are also displayed to show the low standard deviation (gray band) and broad AR distribution (blue dots). **d)** SEM micrograph of particle "h" with superimposed axes and values of γ_{SEM} (black) and γ_{fit} (red).

References

1. Sachs, J., Günther, J.-P., Mark, A. G. and Fischer, P., "Chiroptical spectroscopy of a freely diffusing single nanoparticle", Nat. Commun, Vol. 11, No. 10, 4513, 2020.
2. Chang, W.-S., Ha, J. W., Slaughter, L. S. and Link, S., "Plasmonic nanorod absorbers as orientation sensors", PNAS, Vol. 107, No. 7, 2781-2786, 2010.
3. Bouchal, P., Dvořák, P., Hrtoň, M., Rovenská, K., Chmelík, R., Šikola, T., Bouchal, Z., "Single-Shot Aspect Ratio and Orientation Imaging of Nanoparticles", ACS Photonics, Vol. 10, Nr. 9, 3331-3341, 2023.
4. Hu, J., Liu, T., Choo, P., Wang, S., Reese, T., Sample, A. D., Odom, T. W., "Single-Nanoparticle Orientation Sensing by Deep Learning", ACS Cent. Sci., Vol. 6, Nr. 12, 2339-2346, 2020.
5. Mildner, A., Horrer, A., Weiss, P., Dickreuter, S., Simo, P. C., Gérard, D., Kern, D. P., Fleischer, M., "Decoding Polarization in a Single Achiral Gold Nanostructure from Emitted Far-Field Radiation", ACS Nano, Vol. 17, No. 24, 25656-25666, 2023.

Enhanced color down-shifting of colloidal quantum dots for high-resolution full-color displays

S. T. Ha[1], Hadi Kareem Shamkhi Alnaeemah[1], Ramon Paniagua-Dominguez[1], Hilmi Volkan Demir[2,3,4], and Arseniy Kuznetsov[1]

[1]Institute of Materials Research and Engineering, Agency for Science Technology and Research (A*STAR), 2 Fusionopolis Way, Singapore 138634

[2]LUMINOUS! Center of Excellence for Semiconductor Lighting and Displays, The Photonics Institute, School of Electrical and Electronic Engineering, Nanyang Technological University, 639798, Singapore

[3]Division of Physics and Applied Physics, School of Physical and Mathematical Sciences, Nanyang Technological University, 21 Nanyang Link, Singapore 637371

[4]UNAM—Institute of Materials Science and Nanotechnology, The National Nanotechnology Research Center, Department of Electrical and Electronics Engineering, Department of Physics, Bilkent University, Bilkent, Ankara, 06800, Turkey

[*]Corresponding author: ha_son_tung@imre.a-star.edu.sg, hvdemir@ntu.edu.sg and arseniy_kuznetsov@imre.a-star.edu.sg

Abstract: High volumetric optical cavity is essential for high performance light-emitting devices where absolute absorption is necessary. In this talk, I will present several design concepts of dielectric resonant nanostructures to enhance the fluorescent down-shifting proccess of colloidal quantum dots for applications in high-resolution full-color displays.

In the first design, we propose a resonant nanostructures based on the hybridisation of a waveguide mode within the quantum dot (QD) layer and a resonant “Bloch mode” originating from the high-index contrast grating made of TiO2 stripes on glass substrate as shown in Fig. 1a. The resonant structure has dual resonances at the blue wavelength (emission peak of microLEDs) and green wavelength (emission peak of green QDs) as shown in Fig. 1b,c, which can enhance both in-coupling (i.e., absorption) and out-coupling (i.e., emission) of the device. Most importantly, it has a large mode volume that results in the enhancement of a large number of QDs within the structure. Another design approach is to use a Gires-Tournois etalon cavity (aka the asymmetric Fabry-Perot etalon). This etalon is a standing-wave optical cavity that reflects light of all wavelengths of interest with a strong dispersion of the phase delay. Controlling the phase delay at the resonance wavelength for certain angle(s) allows maximum power transfer to the optical cavity. We modified the cavity by adding a metasurface layer made of SiO_2 and TiO_2 to further improve the optical confinement and thus, absorption in QD layer (Fig. 1d-f).

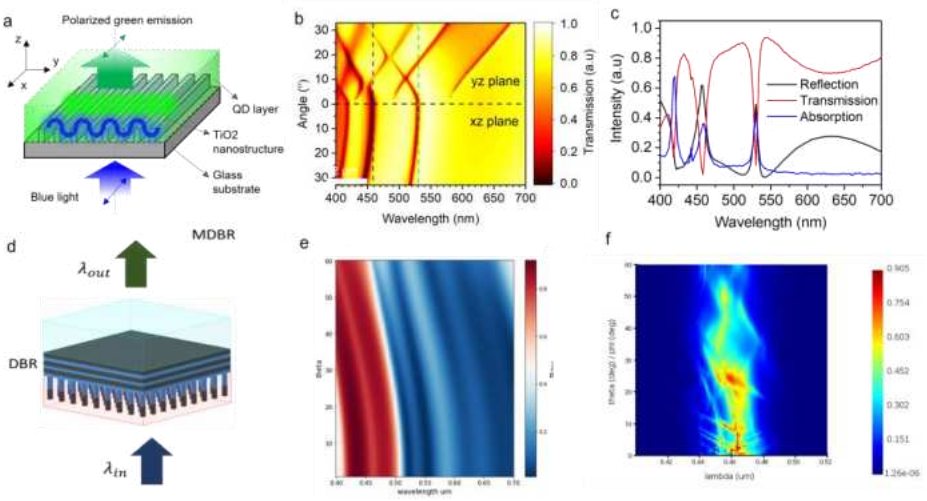


Figure 1. (a) Concept of nanoantenna-enhanced downconversion by high index grating. (b) Simulated angle-resolved transmission spectra. (c) Transmission, reflection and absorption of QDs in the grating cavity. (d) Concept of Gires-Tournois metasurface-DBR (GTMD) to enhance absorption. (e) Angle resolved reflection of the DBR mirror. (f) Absorption of the green QD as a function of angle of incidence and wavelength.

To pattern the QD on top of the pixelated nanostructures, we developed a direct deep-patterning technique for making fluorescent patterns with near-unity pixel yield, well-preserved quantum efficiency, precisely defined lateral sizes as well as uniform and desirable thickness for both green and red emitters with pixel sizes down to 300 nm as shown in Fig. 2a - d. A large mode volume can be created within a thin layer of the quantum dots (i.e., ~ 400 nm) by the interaction of the nanostructure resonances and the optical modes. This allows maximum mode overlapping between the resonance and the quantum dots, resulting in a large absorption and emission enhancement as can be seen in Fig. 2 e,f. We have achieved the maximum enhancement of ~ 141 times and a total emission enhancement of ~ 40 times within 0.55NA. The enhancement encompasses absorption enhancement, Purcell enhancement and directionality enhancement (i.e., outcoupling). We achieved total absorption of 35% for green quantum dots with a remarkably thin layer (i.e., ~ 400 nm).

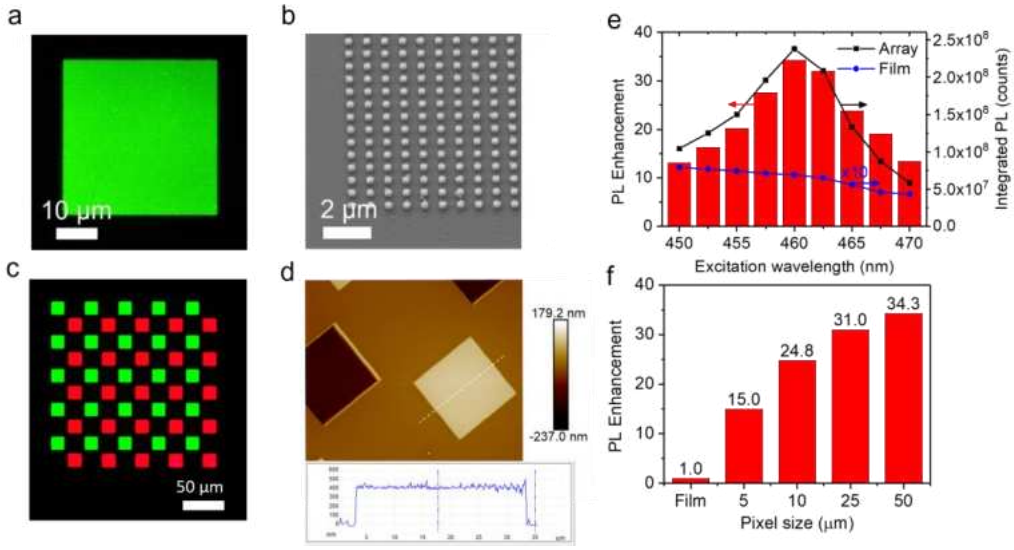


Figure 2. (a-b) Florescent microscopy images (a) and the corresponding SEM (b) of patterned green QDs with pixel size of 300 nm. (c) 2-layer patterning of green and red quantum dots with lateral accuracy of less than 100 nm. (d) AFM measurement of patterned QD layer on top of resonant nanostructure. (e-f) Fluorescence enhancement of QDs within the resonant nanostructure for different excitation wavelengths (e) and pixel sizes (f).

Acknowledgement The authors acknowledge the support from A*STAR MTC-Programmatic Fund (M21J9b0085).

References

1. Ha, S. T. et. al. “Dual-Resonance Nanostructures for Color Downconversion of Colloidal Quantum Emitters,” Nano Letters, Vol. 23, No. 24, 11802-11808, 2023.

Fluorescence-based chiral sensing enhanced by silicon nanophotonics

T. T. C. Sistermans[1,2], E. Mohammadi[3], T. V. Raziman[3], and A. G. Curto[1,2*]

[1] Photonics Research Group, Ghent University-imec, Ghent, Belgium

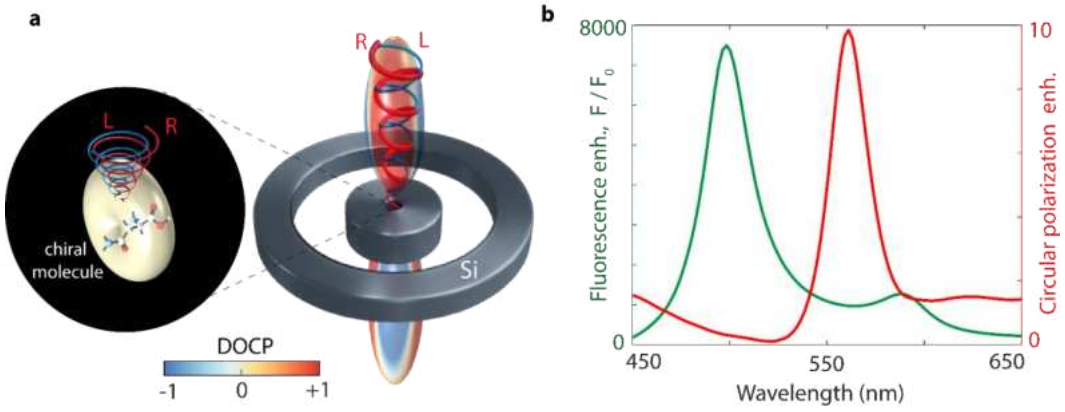
[2] Center for Nano- and Biophotonics, Ghent University, Ghent, Belgium

[3] Department of Applied Physics and Eindhoven Hendrik Casimir Institute, Eindhoven, The Netherlands

[*]Corresponding author: Alberto.Curto@UGent.be

Abstract: Chirality is omnipresent in biochemistry, where molecules with opposite handedness can have markedly different effects. Detecting molecular chirality is however plagued by low sensitivity, limiting it to high concentrations and volumes. We present nanophotonic structures and a polarization-modulation microscope to push the limits of chiral sensing using fluorescence.

Detecting the handedness of chiral molecules is critical in biomedicine, where the functionality of biomolecules such as proteins, amino acids, and carbohydrates can strongly differ between enantiomers. Circular dichroism (CD) is commonly used to distinguish enantiomers based on the differential absorption of right- and left-handed circular polarizations of light by chiral molecules. This transmission-based method requires measuring very small changes in absorption, which is inherently difficult at low concentrations due to the large background caused by the light source itself. As a result, the sensitivity is reduced, requiring a high density of molecules and long measurement times. Conventional methods are thus unsuitable for critical applications like detecting protein aggregates linked to various diseases.

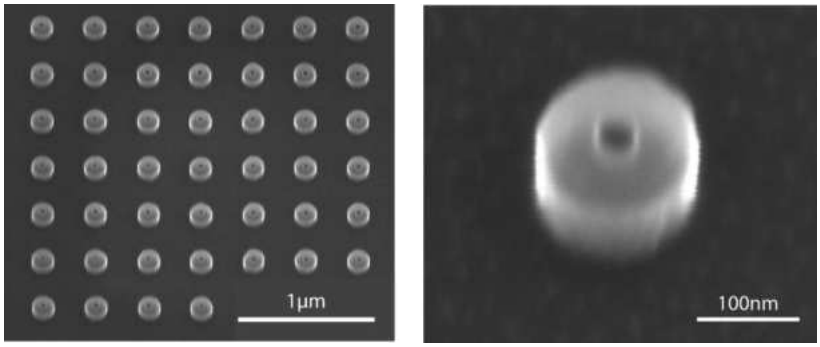


Silicon nanoantennas tailored to boost fluorescence-based chiral sensing.

Fluorescence-based chiral sensing bypasses some of the difficulties of CD by detecting light emitted at a different wavelength than the excitation source, allowing for the complete removal of the source background from the signal. In general, fluorescence-based chiral sensing can be split into two categories. Firstly, fluorescence detected circular dichroism (FDCD), where the differential absorption is measured as a difference in emitted fluorescence intensity. Secondly, circularly polarized luminescence (CPL), where molecules are excited by unpolarized light and the circular polarization of the emitted fluorescence is measured. Nanophotonics offers two routes to enhance the sensitivity of chirality detection [1], [2], [3], [4]. Super-chiral fields, offering a higher

chirality than circularly polarized plane waves, can exist within the near field of nanophotonic structures. Furthermore, nanophotonics can enhance the detected fluorescence intensity through excitation, Purcell, and collection enhancements. Our simulations using silicon nanostructures show a 10-fold polarization enhancement while simultaneously enhancing the fluorescence intensity 1000 times. This combination of enhancement is promising for probing molecular chirality at the single-molecule level, eliminating the impact of ensemble averaging.

We present our experimental progress, including fabrication methods for achieving such nanostructures using crystalline silicon for its high refractive index and lower losses than amorphous silicon. Furthermore, we introduce a custom-built microscope setup for measuring degrees of circular polarization below 1%. We use photoelastic modulation for precise polarization modulation and an avalanche diode for photon counting to enable lock-in detection with suppressed noise.



SEM images of fabricated nanophotonic structures for chiral sensing.

In conclusion, we combine advancements in silicon metasurfaces tailored for fluorescence-based chiral sensing and a novel polarization-resolved microscope to increase the sensitivity toward single-molecule chirality detection.

Acknowledgements. This work was financially supported by the European Research Council (ERC) under the European Union's Horizon 2020 research and innovation program (grant agreement 948804, CHANSON) and The Netherlands Organisation for Scientific Research (NWO) through an NWO START-UP Grant (740.018.009).

References

[1] S. Murai, G. W. Castellanos, T. V. Raziman, A. G. Curto, and J. G. Rivas, "Enhanced Light Emission by Magnetic and Electric Resonances in Dielectric Metasurfaces," *Adv Opt Mater*, vol. 8, no. 16, 2020.

[2] E. Mohammadi, A. Tittl, K. L. Tsakmakidis, T. V. Raziman, and A. G. Curto, "Dual Nanoresonators for Ultrasensitive Chiral Detection," *ACS Photonics*, vol. 8, no. 6, 2021.

[3] T. V. Raman, R. H. Godiksen, M. A. Müller, and A. G. Curto, "Conditions for Enhancing Chiral Nanophotonics near Achiral Nanoparticles," *ACS Photonics*, vol. 6, no. 10, 2019.

[4] E. Mohammadi, T. V. Raziman, and A. G. Curto, "Nanophotonic Chirality Transfer to Dielectric Mie Resonators," *Nano Lett*, vol. 23, no. 9, 2023.

Infrared Nanophotonics in Naturally-Hyperbolic Calcite Metamaterials

Chase T. Ellis[1*], Eric M. Seabron[2,3], Eric M. Jackson[1], Michael A. Meeker[2], Andrew C. Lang[2], Brandon K. Durant[2], Xitlali G. Juarez[2], Daniel Ratchford[1], Rhonda M. Stroud[4], and Joseph G. Tischler[1,5]

[1] *U.S. Naval Research Laboratory, 4555 Overlook Ave. SW, Washington, DC, USA*
[2] *NRC Postdoc residing at U.S. Naval Research Laboratory, 4555 Overlook Ave. SW, Washington, DC, USA*
[3] *Department of Electrical and Computer Engineering, Howard University, 2300 Sixth Street NW, Washington, DC*
[4] *Buseck Center for Meteorite Studies School of Earth and Space Exploration, Arizona State University, Tempe, AZ*
[5] *Department of Physics, University of Oklahoma, 440 W. Brooks St, Norman, OK, USA*
**corresponding author: chase.t.ellis.civ@us.navy.mil*

Abstract: Within this work, we investigate how mid-infrared can excite sub-diffractional, volume-confined hyperbolic modes within nanostructured surfaces of (100)-cut calcite crystals. We find that controlling the relative orientation of these nanostructures and the crystal anisotropy provides unique tuning of the spectral and energy propagation characteristics of these modes.

Calcite is the quintessential birefringent material – possessing different optical properties along its crystal axes. While small differences in the optical permittivity of calcite lead to interesting effects like double refraction in the visible spectral regime – in the infrared, this anisotropy becomes extreme, resulting in simultaneous dielectric and metallic optical behavior along different crystal axes. This extreme anisotropy occurs within the reststrahlen regions of calcite (w=870-888 cm-1 and 1400-1551 cm-1), which is the fundamental property required to support hyperbolic optical modes that are highly directional (depending only on the permittivity) and confined well-beyond the diffraction limit.

While hyperbolic modes have been well-studied in nanostructured materials with high degrees of symmetry – e.g., h-BN and (001)-oriented calcite with cylindrically-symmetric nanostructures and permittivities (isotropic in the sample plane) [1,2] – within this work, we investigate how such modes behave within a low-symmetry calcite system. To accomplish this, we fabricate a series of gratings on (100)-oriented calcite substrates that possess anisotropic optical behavior that lies within the sample plane. To investigate the optical properties of this metamaterial system, we perform polarization-dependent, infrared reflectance microscopy measurements and correlate the results to full-wave electromagnetic simulations performed within COMSOL. Overall, we find that these gratings support high-quality factor hyperbolic modes (Q > 200) that can be tuned throughout the entire reststrahlen region by only changing the relative orientation between the grating and the crystal axes – keeping the grating profile fixed. In addition to experimentally demonstrating this behavior, we have developed a semi-analytical model that predicts how the mode frequency and wave-directionality evolve with grating orientation, eliminating the need to perform full-wave electromagnetic simulations for each grating orientation.

[1] J.D. Caldwell et al. *Nature Communications* ***5****, 5221 (2015).*
[2] V. Breslin et al. *Optica* ***29****, 11760 (2021).*

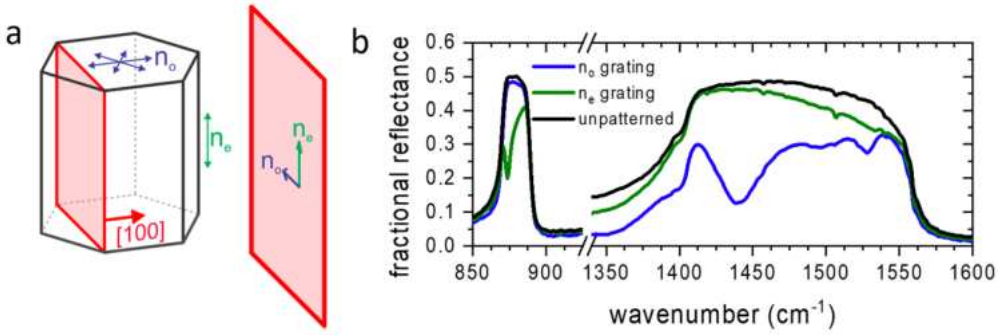


Figure 1 (a) [100] calcite crystal orientation with in-plane anisotropic optical properties along the extraordinary (n_e) and ordinary (n_o) crystal axes and (b) reflectance spectra from gratings aligned ~~n_e~~ perpendicular to the extraordinary (green curve) and ordinary ~~n_o~~ (blue curve) crystal axes.

Mapping phonon polaritons with visible light

Joseph G. Tischler[1*], Kiernan E. Arledge[1], Chase T. Ellis[2], Nazli Rasouli Sarabi[1], Vincent R. Whiteside[1], Chul Soo Kim[2], Mijin Kim[2], Daniel C. Ratchford[2], Michael A. Meeker[2,3], and Binbin Weng[1]

[,1] Homer L. Dodge Department of Physics and Astronomy, University of Oklahoma, Norman, 73019, USA
[2] U.S. Naval Research Laboratory, Washington D.C., 20375, USA
[3] Advanced Research Center, City University of New York, New York 10017, USA
[*]corresponding author: tischler@ou.edu

Abstract: Low-loss phonon polariton (PhP) modes are promising for mid-IR applications. Here, PhP eigenmodes in nanostructures of InP and 4H-SiC are spatially mapped using confocal Raman microscopy. We find that the polarizability selection rules surprisingly couple PhPs to bulk phonons, potentially providing a new approach to tune PhPs through phonon interactions.

Phonon polaritons (PhPs) are collective modes that emerge when photons couple with optical phonons in a polar dielectric material. PhPs have been shown to confine electromagnetic fields far below the diffraction limit just like surface plasmon polaritons (SPPs) can, notably without the high losses associated with SPP modes[1]. In addition, PhPs are widely tunable though nanostructure geometry, and coupling to free carriers[2]. These advantages have made PhP modes a promising platform for low-loss mid-infrared (mid-IR) photonics. Attention has also been drawn to the possibility of electrically pumped tunable mid-IR emitters based on PhPs, but efforts to demonstrate the viability of these devices has been frustrated by the presumed weak coupling between PhP and bulk phonon modes[2].

Assessing the promise of PhP modes as mid-IR emitters clearly requires a full investigation of the coupling between electrons, phonons, and PhP modes in dielectric nanostructures. This task is made more complicated by the fact that the coupling between electrons, phonons, and polaritons has high spatial dependence, further demanding a method that can spatially map these interactions. To date, investigating PhP eigenmodes has primarily been accomplished using near-field IR microscopy, such as near-field scanning optical microscopy (NSOM) and Nano-FTIR techniques. Recently, monochromatic electron energy loss spectroscopy (EELS) in scanning transmission electron microscope (STEM) setups has also been employed to visualize SPhP modes in nanostructured materials. In particular, tomographic EELS has enabled 3D measurements of Surface PhP (SPhP) modes in magnesium oxide nanocubes[3], demonstrating that specialized techniques can be employed to visualize the 3D distribution of PhP electromagnetic fields.

Increasingly, these efforts have been augmented with the techniques of Raman spectroscopy, leveraging its ability to provide abundant information on light-matter interactions. Raman techniques have particularly been used to probe PhPs in 2D materials. Initial works demonstrated resonant Raman spectroscopy as a valuable tool to probe PhP modes at Van der Waals (VdW) material interfaces. Furthermore, recent investigations have shown that conventional backscattering Raman can probe PhP modes in 2D GaSe, utilizing the polarizability selection rules[4]. Such techniques are not restricted to 2D materials, micro-Raman investigations of 4H-SiC nanopillars found that spatial dispersion of the permittivity in dielectric nanostructures can play a major role in the spectral behavior of PhPs[5]. This discovery highlights the fact that much of the physics related to the spatially dependent interactions of electrons, phonons, and SPhP modes in nanostructures remains uninvestigated. Therefore, efforts

to understand the physics governing PhPs in nanostructures, demand not only spectral probing of SPhP dispersion but also spatial mapping of light-matter interactions through the nanostructure volume with more sophisticated Raman techniques.

In this work, we report the full 3D mapping of SPhP electromagnetic fields in nanostructures of InP and 4H-SiC. We combined confocal Raman microscopy with an eigenmode reconstruction approach to provide a 3D view of localized polariton fields. Using this technique, we demonstrate that all Raman active bulk phonon modes in both InP and 4H-SiC do couple to the localized surface polariton modes, in contrast to the assumption that the longitudinal polarization field of the LO phonon is non-interacting with the transverse (and thus orthogonal) SPhP modes. Our Raman maps confirm that the polarizability selection rules form the dominant mechanism through which SPhPs couple to Raman phonons. For the specific case of the $A_1(LO)$ and $E_1(TO)$ phonon modes in 4H-SiC, electron-phonon coupling also plays a role, even for low-doped substrates. These results challenge the conventional understanding of SPhP-phonon coupling and indicate that electrically pumped SPhP mid-IR emitters might be achievable with dielectric nanostructures. Furthermore, our work provides a method for real-space mapping of SPhP eigenmodes in a manner analogous to tomographic EELS, but with no destructive sample preparation and not requiring the specialized equipment of highly-monochromatic EELS. Thus, Raman imaging can be a complimentary tool for the visualizing of SPhP modes which also provides a natural platform for investigating the interactions between electrons, phonons, and SPhPs.

B.W. acknowledges partial support from the Oklahoma Center for Advancement of Science and Technology's Research Grant No. AR21-052. C.T.E, C.S.K, M.K, D.C.R, and M.A.M acknowledge funding from the Office of Naval Research.

References

1. Hillenbrand, R., Taubner, T. & Keilmann, F. "Phonon-enhanced light–matter interaction at the nanometre scale," Nature, Vol. 418, No. 6894, 159-162, 2002.
2. Dunkelburger, A.M et. al, "Active tuning of surface phonon polariton resonances via carrier photoinjection," Nat. Photonics, Vol. 12, No. 1, 50-56, 2018.
3. Li, X et. al, "Three-dimensional vectorial imaging of surface phonon polaritons," Science, Vol. 371, No. 6536, 1364–1367, 2021.
4. Bergeron, A., Gradziel, C., Leonelli R., & Francoeur S. "Probing hyperbolic and surface phonon-polaritons in 2D materials using Raman spectroscopy," Nat. Communications, Vol. 14, No. 1, 4098, 2023.
5. Beechem, T. et al. "Influence of spatial dispersion on spectral tuning of phonon-polaritons," Physical Rev. B., Vol. 100, No. 20, 205419, 2019.

Quasi-2D Colloidal Quantum Wells for High Optical Gain and High LED Efficiency

F. Shabani[1], F. Işık[1], S. Delikanlı[1], and H. V. Demir*[1, 2]

[1]UNAM – Institute of Materials Science and Nanotechnology, Bilkent University, Turkey
[2]Luminous! Center of Excellence for Semiconductor Lighting and Displays, Nanyang Technological University, Singapore
*corresponding author: volkan@bilkent.edu.tr

Abstract: Colloidal quantum wells (CQWs) are shown to possess exceptionally high performance as the gain medium and active layer in the LEDs. The CQWs exhibit a record-breaking gain coefficient of 140,000 cm^{-1} with a lasing threshold of 8 μJ cm^{-2} and an ultra-high external quantum efficiency of 18.1% for CQWs-LEDs.

Colloidal semiconductor quantum wells (CQWs), also known as nanoplatelets, are among the most attractive groups of solution-processed nanocrystals, which provide a strong and versatile ground to engineer and tune the optical properties. The two-dimensional shape of these CQWs (Figure 1a) results in tight confinement in the vertical direction, which is the basis for many of their superior optical properties. Here, we report the advances in high-performance devices based on engineered CQWs

The CQWs were shown to possess an anisotropic emission behavior, which, by their collective assembly, an extremely high level of in-plane transition dipole moments of 92% was achieved (Figure 1b). The optical properties, including the absorption and PL were tuned by the design of the heterostructure and thickness of the CQWs covering a broad range of the visible spectrum (Figure 1b). We demonstrate that by careful design of the synthesis, complex heterostructures can be realized (Figures 1c and 1d), which possess tunable recombination pathways with a mixture of type-I and type-II natures. These excellent and distinct properties of the CQWs are the basis for fabricating devices with superior properties.

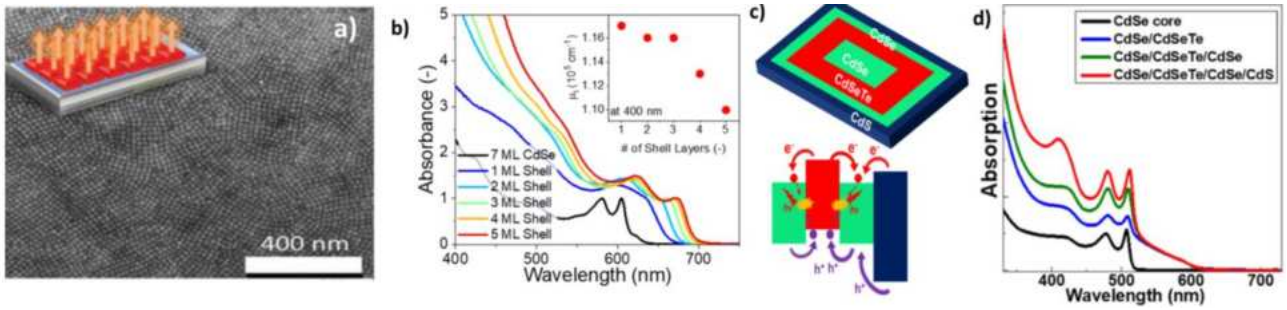


Figure 1. (a) TEM image of self-assembled CdSe/CdZnS core/shell CQWs. (b) Absorption spectra and absorption cross-section of CdSe/1-5 CdS core/shell CQWs. (c) Complex design of multi-crown CQWs and the possible recombination pathways, and (e) the resultant absorption spectra.

CdSe/CdSeTe/CdSe/CdS core/(multi)-crown type-II CQWs benefit from two type-II interfaces, yielding a photoluminescence quantum yield (PLQY) of ca. 90%. The terminating CdS crown layer enhances the in-solution and film stability, which is essential for the electroluminescence application. The LED device with these CQWs as the emissive layer (EML) exhibits an external quantum efficiency of 9.3% and a maximum luminance of 36,612 cd m^{-2}, the highest reported values for type-II CQWs.

CdSe/CdZnS core/alloyed shell CQWs exhibit a direct recombination PL with a near-unity PLQY. The all face-down self-assembled monolayer of these CQWs possesses an extra-high outcoupling efficiency of 34% in LED devices due to the high in-plane transition dipole moments, a step-wise hole transport layer (HTL) and Mg-doped ZnO electron transport layer (ETL), which prevents the exciton quenching (Figure 2a). While

self-assembly of the EML does not change the electroluminescence peak position (Figure 2b), it substantially enhances the EQE of the device from 9.5% for randomly-oriented EML to 16.3% (Figure 2c). The enhancement is due to the light-outcoupling, which can be further improved by exchanging the original bulky ligands with short ligands leading to an EQE of 18.1%.

The core/shell CQWs also provide a very interesting ground for optical gain performance. In a systematic study, giant CdSe/CdS core/shell CQWs with varying thickness demonstrate a gain coefficient of 140,000 cm^{-1} (Figure 2d), two orders of magnitude higher than the best reports for the colloidal nanocrystals, originating in the high density of states and suppressed Auger recombination. The whispering gallery mode (WGM) laser based on these CQWs (Figure 2e) resulted in an ultra-low lasing threshold of ca. 8 μJ cm^{-2} (Figure 2f), and further in-solution amplified spontaneous emission (ASE) was also observed.

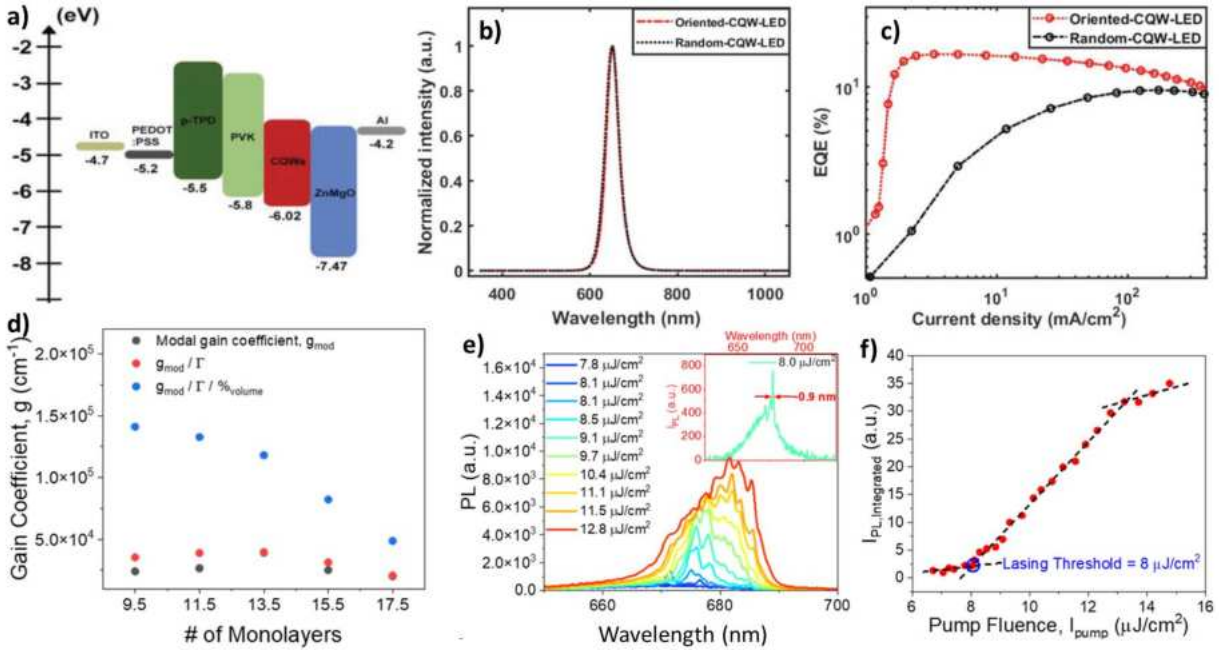


Figure 2. (a) Energy band diagram of the CQW-LEDs. (b) EL and (c) EQE of LEDs with random and self-assembled ELM. (d) Maximum modal gain coefficients with the shell thickness. (e) The lasing spectra of WGM-assisted CQWs. The inset shows the lasing spectrum at the threshold. (f) The lasing threshold measured via integrated PL intensity.

References

1. Shabani, F., Martinez, P.L.H., Shermet, N., Korkut, H., Sarpkaya, I., Dehghanpour Baruj, H., Delikanli, S., Isik, F., Durmusoglu, E.G., and Demir, H.V. ”Gradient Type-II CdSe/CdSeTe/CdTe Core/Crown/Crown Heteronanoplatelets with Asymmetric Shape and Disproportional Excitonic Properties,” Small, Vol 19, No. 11, p.2205729, 2023.
2. Delikanli, S., Canimkurbey, B., Hernández-Martínez, P.L., Shabani, F., Isik, A.T., Ozkan, I., Bozkaya, I., Bozkaya, T., Isik, F., Durmusoglu, E.G. and Izmir, M., Akgun, H., and Demir, H.V. “On the Rational Design of Core/(Multi)-Crown Type-II Heteronanoplatelets,” JACS, Vol 145, No. 22, p. 12033-12043, 2023.
3. Baruj, H.D., Bozkaya, I., Canimkurbey, B., Isik, A.T., Shabani, F., Delikanli, S., Shendre, S., Erdem, O., Isik, F. and Demir, H.V. “Highly-directional, Highly-Efficient Solution-Processed Light-Emitting Diodes of All-Face-Down Oriented Colloidal Quantum Well Self-Assembly,” Small, Vol. 19, No. 29, p.2206582, 2023.
4. Isik, F., Delikanli, S., Durmusoglu, E.G., Isik, A.T., Shabani, F., Baruj, H.D., and Demir, H.V. “Giant Colloidal Quantum Well Heterostructures of CdSe@CdS Core@Shell Nanoplatelets from 9.5 to 17.5 Monolayers in Thickness Enabling Ultra-High Gain Lasing” Small, in print.

Enhancing Infrared-to-Visible Photon Upconversion with Metasurfaces

Mengfei Wu[1,3*], Dileep Kottilil[1], Yuxiang Zhang[2], Kangning Yu[2], Sourav Adhikary[1], Jinal Tapar[1], Emmanuel Lassalle[1], Daniil Shilkin[1], Febiana Tjiptoharsono[1], Ramon Paniagua-Dominguez[1], Xiaogang Liu[2], and Arseniy Kuznetsov[1]

[1]Institute of Materials Research and Engineering, A*STAR, Singapore
[2]Department of Chemistry, National University of Singapore, Singapore
[3] Department of Materials Science and Engineering, National University of Singapore, Singapore
[*]corresponding author: wu_mengfei@imre.a-star.edu.sg

Abstract: Upconversion of infrared light into visible light has wide potential applications, but current efficiency is too low to be practical. Here, we present a variety of dielectric and plasmonic metasurfaces that enhance upconversion efficiency. We show that enhancement of several orders of magnitude may be achieved at low excitation flux.

Photon upconversion is a process that converts two or more low-energy photons into a higher-energy photon. Upconversion of infrared light into visible light is particularly interesting because of its potential to sensitize silicon to sub-bandgap photons, thereby benefiting a wide range of applications including deep-tissue imaging, telecommunications, sensing, and photovoltaics.

In our studies, we explore two types of upconversion, based on excitonic materials (specifically quantum dots and organics) and lanthanide-doped nanocrystals, respectively. Both types of upconversion have low external quantum efficiency in the solid state, owing to weak absorption of the incident infrared light.

Here, to improve infrared absorption, we design and implement a variety of dielectric and plasmonic metasurfaces with resonant wavelength at 980 nm or 1550 nm. For instance, we employ periodic arrays of resonant nanostructures to confine light efficiently in the upconversion nanomaterials. We also explore metasurface-integrated Fabry-Pérot cavities to allow greater tolerance of the cavity modes to fabrication variations.

With efficient integration of nanomaterials and metasurfaces, we show enhancement of upconversion luminescence by several orders of magnitude at low excitation flux, which saturates to about two orders at high excitation flux when the intermediate excited states reach a critically high population.

Finally, we discuss the feasibility, progress, and challenges of combining metasurface-enhanced upconversion with silicon photodetectors for sub-bandgap infrared detection.

The authors acknowledge funding support from the MTC Programmatic Fund (M21J9b0085), A*STAR Career Development Fund (C210112060), and MTC Young Individual Research Grant (M21K3c0129).

Nano antenna-assisted quantum dots emission into high-index planar waveguide

X. Yu, J.-C. Weeber, L. Markey, J. Arocas, A. Bouhelier, A. Leray, and G. Colas des Francs*

Laboratoire Interdisciplinaire Carnot de Bourgogne (ICB), CNRS UMR 6303, Université de Bourgogne, Dijon, France

*corresponding author: gcolas@u-bourgogne.fr

Abstract: We established directional quantum dot (QD) emission coupling to a planar TiO_2 waveguide assisted by a Yagi-Uda antenna. Antenna on waveguide is first designed by scaling radio frequency dimensions to nano-optics, taking into account the hybrid plasmonic/photonic platform. The optical characterization shows clear directional coupling originating from antenna effect.

In the past decades, strong efforts have been put towards convergence of integrated photonics and quantum technologies [1]. Recently, several groups have achieved direct on chip integration of single photon. Moreover, since quantum operation requires photons source presenting a long coherence time, Purcell-enhanced single photon sources are generally used so that the emission dephasing rate becomes negligible [2]. Most of on chip quantum circuits rely on single photon sources coupled to a micro-optical cavities of high quality. Another approach is to take benefit from the low mode volume of surface plasmon, pushing further integration capabilities. In this context, optical nano- antennas are promising candidates which provide both Purcell enhanced photon emission and directivity at the same time. Photonic waveguide decorated by optical antenna strongly focus guided mode onto a subwalength area compatible with single photon source excitation [3]. In this work, we investigate a reciprocal configuration, namely nano-antenna assisted quantum dot (QD) emission into high index (TiO_2) planar waveguide.

Design of Yagi-Uda antenna Yagi-Uda antenna consists of five gold nanorods: a reflector, a feed and three directors, as shown in Fig. 1. The lengths of the antenna elements (feed, directors and reflector) govern the antenna resonance whereas their spacing govern the antenna directivity. According to antenna theory, the feed length should be half the effective wavelength of the mode propagating along the rod to support a dipolar resonance. Therefore, we first estimate the effective wavelength $\lambda_{spp}=n_{spp}\ \lambda_0$ of the surface plasmon polariton (SPP) propagating along an infinite nanowire deposited on a TiO_2 planar waveguide at the QD emission wavelength λ_0 = 670 nm. Effective index n_{spp} = 3.64 so that Fabry-Perot like resonances for feed length $L_f \approx \lambda_0/(2n_{spp}) \approx 92$ nm. The length of reflector (L_r) and director (L_d) are deduced as $L_r = 1.25L_f \approx 115$ nm and $L_d = 0.9L_f \approx 83$ nm, respectively. For a directivity into the guided mode along the antenna y-axis spacings of feed to reflector (y_r) and feed to directors (y_d) are estimated from the RF rules as $y_r = \lambda_0/(4.4n_{wg}) = 89$ nm and $y_d = \lambda_0/(4n_{wg}) = 97$ nm where n_{wg} = 1.72 is the effective index of the TE guided mode, calculated for a 80 nm thick TiO_2 planar waveguide lying on a glass substrate. The thickness has been chosen to obtain a single mode waveguide. We completed this semi-analytical analysis with full electromagnetic numerical simulations based on finite element method (FEM).

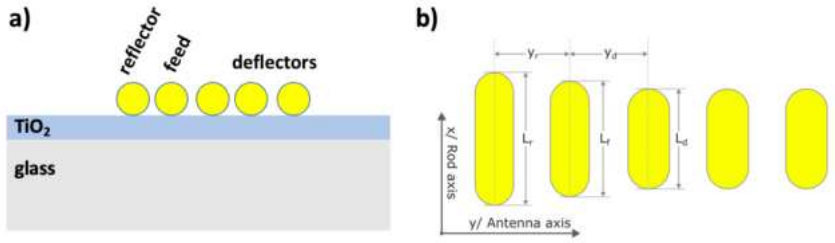


Fig 1: Scheme of the Yagi-Uda antenna on a TiO_2 planar waveguide. a) Side-view detailing of antenna elements. b) Top view with dimensions.

Directional QDs emission into planar waveguide We use 50 µm circular microdisk as planar waveguide so that the optical paths from its center to all directions are the same, see Fig. 2a. Antenna mediated QD emission coupled to TiO_2 waveguide is shown in Fig. 2b). Light coupled to microdisk propagates radially in the waveguide and scatters out at the edge. We observe directional scattering towards the right (0°) in agreement with the antenna effect but also unexpected directionality on the top left side (120°). We experimentally measured 39% coupling efficiency and 60% forward [4]. The efficiency of the device is very sensitive to the location of the quantum emitters. This hybrid platform based on plasmonic antenna assisted directive emission into photonic waveguide could also be used for lab-on-chip applications combining surface enhanced spectroscopies and photonics capabilities.

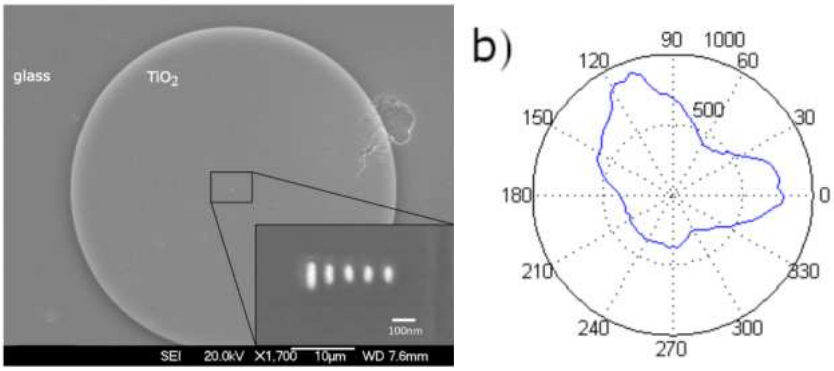


Fig. 2 : a) SEM image of Yagi-Uda gold nanoantenna centered on TiO_2 50 µm diameter microdisk planar waveguide. L_f =90 nm, L_d=85 nm, L_r=100 nm, y_r=85 nm and y_d=90 nm.b) Polar plot of the light scattered along the waveguide periphery with Yagi-Uda antenna assisted QD emission.

Acknowledgments Marie Sklodowska-Curie Grant Agreement No. 765075 (LIMQUET), FEDER-FSE 2021-2027 Bourgogne-Franche- Comté, French Investissements d'Avenir program EUR-EIPHI (17-EURE-0002). This work has benefited from the facilities of the platforms in Région Bourgogne Franche-Comté SMARTLIGHT (EQUIPEX+ contract ANR-21-ESRE-0040) and ARCEN Carnot (Renatech+ CNRS network)

References

[1] Couteau C. *et al*, Nature Review Physics **5** 326 (2023)

[2] Palstraa I M, Doelemana H M and Koenderink A F Nanophotonics **8** 1513 (2019)

[3] Bernal Arango F, Kwadrin A and Koenderink A F ACS Nano **6** 10156 1936 (2012)

[4] Yu X. *et al*, submitted (2024)

Bioanalytics using plasmonic nanostructures

F. Seier, L. Dubbert, M. Al-Maoush , A. Hoxha, A. Heewig, M. Urban, A. Csaki, W. Fritzsche*

Leibniz Institute of Photonic Technology (IPHT) Jena, Germany
*corresponding author: wolfgang.fritzsche@ipht-jena.de

Abstract: The effect of localized surface plasmon resonance (LSPR) on chemically synthesized gold nanoparticles is utilized to setup a biosensing platform with the potential for sensitive and specific detection of biomolecules of interest such as biomarkers. This principle is demonstrated both on a single particle level for DNA detection, then extended also to proteins, and to arrays of particles. In order to readout the arrays, imaging spectrometer were developed.

Detection of molecular interaction is an important analytical field with implications ranging from food or drinking water quality control over drug development to medical diagnostics. One approach for label-free detection of molecular targets is based on LSPR on metal nanostructures, which show a spectral change upon binding of molecules.

Imaging spectrometers allow for the spectrally resolved imaging of sample surfaces. In the case of a LSPR array, an array of spotted gold nanoparticles is utilized as sensors, and for specific identification of certain biomolecules, modified with receptor molecules which are specifically binding respective target molecules. In case of binding, the LSPR of the particles in this spot will change, when the refractive index on the surface of the nanosensors is changed. The LSPR shift (located in the visible range of light) is measured as sensor signal, and correlates with the surface concentration (also mass) of bound molecules.

In order to readout these spectral changes, imaging spectrometers are preferred compared to scanning approaches, as the measurement time does not directly scale with the number of spots. Moreover, already for medium integration (numbers of spots), scanning is hampering readout speed. Beside an imaging spectrometer based on Fourier transformation and a Michelson interferometer, less complex and faster approaches are studied, such as one based on Liquid Crystal Tunable Filter (LCTF) using electronically controlled liquid crystal (LC) elements to transmit only a selectable wavelength range of light. Here, the number and wavelength values are freely selectable. A faster but less flexible approach for imaging spectrometry has been realized using various LEDs with different wavelengths. The effect of the number of LEDs on the resulting detection capability of LSPR shift monitoring was studied. Moreover, various algorithms for peak shift detection were compared regarding their stability and reproducibility.

On the receptor side, beside DNA receptors for binding (sequence-complementary) DNA targets, also protein as well as small molecules and even heavy metal ions were studied as potential targets. Hereby the ease and reproducibility of surface functionalization plays an important role in the choice of suitable receptor molecules. Staying with the same class of molecules and an established immobilization chemistry but being able to detect various classes of molecules, such as DNA, proteins, small proteins and even metal ions, would provide an important advantage for LSPR sensing. Therefore, the use of DNA is preferred. DNA can bind by hybridization to complementary single-stranded DNA. However, DNA can also bind proteins, such as observed in cells for e.g. single-strand binding (SSB) proteins, or for transcription factors, which regulate the readout of DNA. Moreover, DNA can form quite defined 3D structures, which can act similarly to antibodies and selectively binding certain target structures. Such structures are called aptamers, which show a huge potential as

receptors in sensing approaches, as they overcome several problems connected with the established antibody receptors, such as reproducibility, ethical concerns (as antibodies are generated in animals), application conditions not limited to physiological conditions, etc.

Acknowledgements:
Funding by BMBF (01DS23017B and 13N15717) and TAB (2018 VF 0015; 2018 FE 9039).

Hybrid Metamaterial Plasmonic Tweezers for Trapping and Manipulating Dielectric Particles and Biomolecules

Viet Giang Truong,[1*] Domna G Kotsifaki,[2] German Suslin,[1] Theodoros D Bouloumis,[1]

Mirco Dindo,[3] Paola Laurino,[3,4] and Síle Nic Chormaic[1]

[1]Light-Matter Interactions for Quantum Technologies Unit

Okinawa Institute of Science and Technology Graduate University, Okinawa, 904-0495, Japan

[2]Photonics Lab, Division of Natural and Applied Sciences, Duke Kunshan University,
8 Duke Ave, Kunshan, Jiangsu Province 215316, China

[3]Protein Engineering and Evolution Unit,
Okinawa Institute of Science and Technology Graduate University, Okinawa, 904-0495, Japan

[4]Institute for Protein Research, Osaka University, Suita, Osaka 565-0871, Japan

[*]corresponding author: v.g.truong@oist.jp

Abstract: Precise manipulation and discrimination of particles on a scale smaller than the diffraction limit is a topic of enduring interest. This study provides an alternative approach for trapping and identifying dielectric and bioparticles using metamaterial plasmonic tweezers, while paving the way for label-free characterization of biomolecules at single-entity levels.

Summary: We introduce hybrid Fano-resonant metamaterial plasmonic tweezers (MPT) to exhibit stable nano-trapping. Although plasmonic tweezers can achieve manipulation on a scale smaller than the diffraction limit, direct trapping of sub-10 nm dielectric and bio-particles in an aqueous environment without modifications of surrounding mediums remains challenging.[1-3] Here, I will discuss on heat generations from photon-to-phonon conversion of a MPT system, and will review how to transfer this photothermal heating effect to rapidly trap single dielectric nanoparticles and enzymes, and follow the conformational changes of enzymes molecules in real-time. We observe that by analyzing the spatial probability distribution of trap particles under the increase of thermal gradients near the MPT′s surface, we are able to distinguish dielectric particles from biomolecules.[4]

We believe that this photothermal-assisted trapping approach will open a new set of opportunities for the development of ultrasensitive label-free detection and characterization of biomolecules at the single-particle level.

Key words: Metamaterials, plasmonic tweezers, single nanoparticle and enzyme trapping.

References

1. X. Han, V. G. Truong, P. Sunil Thomas, and S. Nic Chormaic, "Sequential trapping of single nanoparticles using a gold plasmonic nanohole array", *Photonics Research*, 6, 10, 981-986, (2018).
2. D. G. Kotsifaki, V. G Truong, and S. Nic Chormaic, "Fano-Resonant, Asymmetric, Metamaterial-Assisted Tweezers for Single Nanoparticle Trapping," *Nano Letter*, 20, 5, 3388-3395 (2020).
3. T. D Bouloumis, D. G Kotsifaki and S. Nic Chormaic "Enabling self-induced back-action trapping of gold nanoparticles in metamaterial plasmonic tweezers", *Nano Letter*, 23, 11 4723-4731 (2023).
4. D. G Kotsifaki, V. G Truong, M. Dindo, P. Laurino and S. Nic Chormaic, "Hybrid metamaterial optical tweezers for dielectric particles and biomolecules discrimination", arxiv.org/2402.12878 (2024)

Polymerization of diazonium salts on gold nanoparticles: hot electron and heating effects

L. Trotsiuk[1]*, A. Broussier[1], A.-L. Baudrion[1], S. Marguet[2], Y. Luo[3], C. Mangeney[3], N. Felidj[4], P.-M. Adam[1] and R. Bachelot[1]

[1] Light, nanomaterials, nanotechnologies (L2n), CNRS UMR 7076, Université de Technologie de Troyes, France
[2] Université Paris Saclay, France
[3] LCBPT, CNRS UMR 8601, Université Paris Cité, France
[4] ITODYS, CNRS UMR 7086, Université Paris Cité, France
* corresponding author: liudmila.trotsiuk@gmail.com

Abstract: In this work, we explored the polymerization of diazonium molecules on the surface of gold nanoparticles under CW- and pulsed laser irradiation. Two different polymerization mechanisms of diazonium salts can be induced by gold nanoparticles under irradiation through local heating and hot electron injection resulting in different polymer patterns.

Gold nanoparticles are considered a promising platform for nanochemistry and catalysis because they can boost chemical reactions by generating local heat and hot electrons under irradiation.[1] Nonetheless, the separation of hot electron and heating effects in the experiment is often challenging or even impossible, as these effects occur on the femto- or picosecond scale, whereas the reactions are typically performed within seconds or minutes. In this work, we investigate the polymerization of diazonium salts on the surface of gold nanoparticles, which can pass through two different mechanisms: cationic and radical ones. Diazonium molecules are highly reactive compounds, containing N_2^+-moiety, which can be eliminated under heating or by electron transfer.[2] We show that different excitation wavelengths as well as the regime of the excitation (CW or pulsed laser irradiation) result in different polymer patterns, which we associate with the dominance of heating-induced or hot electron-induced mechanisms of polymerization.

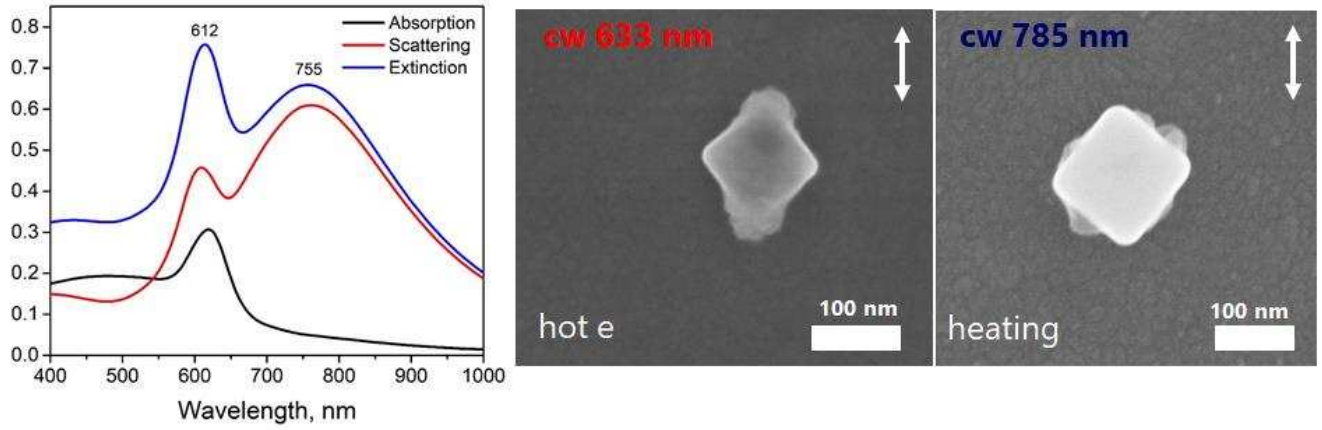


Figure 1. FDTD simulated optical spectra of a gold nanocube and experimental SEM images of gold nanocubes with polymerized diazonium structures under continuous-wave laser excitation.

The CW excitation of the quadrupolar plasmon resonance of gold nanocubes results in polymer growth on

the corners, with respect to the incident light polarization, and therefore can be assigned to a hot electron-induced process. The CW excitation of 785 nm that matches the dipolar mode of the gold nanocube leads to the chaotic polymer distribution, probably, caused by the thermal effects. Intriguingly that the excitation at the same wavelength of 785 nm but at the fs-pulsed regime also results in polarization-dependent polymerization on nanoparticle corners. Thus, by varying the excitation regime we can control the polymer growth and switch between thermal and electron-driven processes.

This study was financially supported by the French Research Agency (ANR) in the frame of the ADVANSPEC and POPCORN projects. Fabrication and characterization were made by the facilities of the Nano'mat platform and the French RENATECH+ network.

References

1. Cortés, E., Grzeschik, R., Maier, S.A. and Schlücker, S. “Experimental characterization techniques for plasmon-assisted chemistry”, Nat. Rev. Chem., Vol. 6, 259–274, 2022.
2. Mahouche-Chergui, S., Gam-Derouich, S., Mangeney, C., and Chehimi, M. M. “Aryl diazonium salts: a new class of coupling agents for bonding polymers, biomacromolecules and nanoparticles to surfaces”, Chem. Soc. Rev., Vol. 40, No. 7, 4143-4166, 2011.

Designing lattices and interface modes in valley topological photonics

Gaëtan Lévêque[1], Yan Pennec[1], Abdu Subahan Mohammed[1], Guillaume Durcournau[1], Pascal Szriftgiser[2], Alberto Amo[2]

[1]Institute of Electronics, de Microelectronics and Nanotechnology (IEMN, CNRS-8520), Cité Scientifique, Avenue Poincaré, 59652 Villeneuve d'Ascq, France.
[2]University of Lille, CNRS, UMR 8523-PhLAM-Physique des Lasers Atomes et Molécules, F-59000 Lille, France
[*]corresponding author: gaetan.leveque@univ-lille.fr

Abstract: Valley topological photonics allows designing devices whose performances strongly depend on the geometry of both unit cells and interfaces. We compare classical honeycomb crystals and a lattice consisting of three non-equivalent subsets of holes, whose richness brings insights in the relation between the interface geometry and the topological light conduction.

Topological photonics relies on mimicking quantum Hall effects in solid-sate physics to transport an electromagnetic signal in compact and low-loss devices[1]. In valley topological photonics, an interface is created between two mirror-image photonic crystals with broken inversion symmetry. Both are associated with Berry curvature confined close to K and K' high symmetry points and with opposite signs between both crystals. This allows exciting topologically protected edge-modes along the interface, which have been proven to sustain robust unidirectional propagation with low back-scattering at sharp bends and low sensitivity to lattice imperfections[2]. They are considered as choice systems for many applications in optical and terahertz telecommunications.

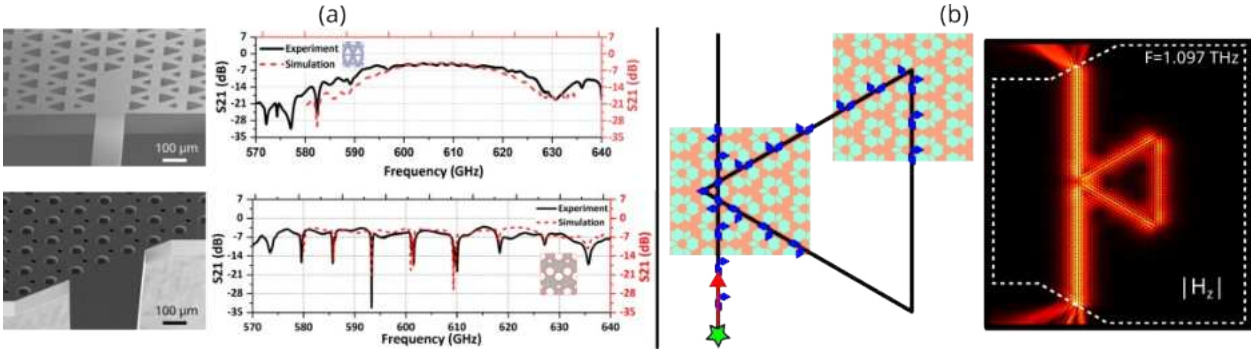


Figure 1: (a) Left: SEM images of triangular- and circular-holes-based topological devices. Right: experimental and numerical transmission through a ring resonator. (b) Left: ring resonator based on a three-diamonds lattice and with displacement interface. Right: typical magnetic field amplitude distribution at F = 1.097 GHz.

In order to build telecommunication devices based on valley topology, a silicon membrane is usually periodically structured with air holes. However, a careful choice of both the shape of holes and the geometry of interfaces between the two mirror-imaged lattices must be made. As illustrated on Fig. 1(a), the transmission through a topological ring cavity shows very different behavior depending on whether the holes are triangular and the interface zigzag (top), or the holes are circular and the interface bearded (bottom). In the former, the transmission is flat as immunity to back-scattering is high, while in the latter the occurrence of several regularly spaced resonances shows that the topological protection is lower[3], but that the device can be used as a filter. This

phenomenon is important to tailor the properties of passive functions for telecommunication technologies.

In order to expand this exploration of the effect the geometry of the interfaces on the waveguiding of light in valley photonic lattices, we propose a photonic crystal based on three non-equivalent subsets of diamond-shaped air holes. A total number of fourteen different bearded interfaces supporting edge modes can be built along a ΓK interface between two image lattices, instead of two bearded interfaces in the standard approach based on a honeycomb lattice with two-holes per unit cell. We show that, among them, six edge-modes can propagate along an interface between two lattices differing only by a translation. An example of such an interface is shown on Fig. 1(b), where the blue diamonds underline the edge. The lattices in contact are not mirror-symmetric, but differ only by a displacement. As a consequence, the two corresponding photonic crystals, despite having non-zero Berry curvature at their respective K and K' points, have strictly identical valley Chern number, which rules out the valley-topological origin of the corresponding edge modes. However, they show robust propagation at sharp corners and through ring resonators as illustrated on the magnetic field distribution of Fig. 1(b), raising new questions about the origin of the protection of the light propagation in circuits with sharp features, generally prohibited in devices based on trivial geometry.

G.L. and Y.P. are grateful for the Horizon-RIA action project Magnific (Project No. 101091968). A.A. is grateful to the European Research Council for support via the grant EmergenTopo (Grant No. 865151, the Labex CEMPI (Grant No. ANR-11-LABX-0007), and Region Hauts-de-France through the CPER Wavetech.

References

1. T. Ozawa et al., Rev. Mod. Phys. 91, 15006 (2019).
2. H. Xue, Y. Yang, and B. Zhang, Adv. Photonics Res. 2, 2100013 (2021).
3. G. Lévêque, Y. Pennec, P. Szriftgiser, A. Amo, and A. Martínez, Phys. Rev. A 108, 043505 (2023).

Controlling properties of collective plasmonic–diffractive excitations via dispersion engineering

J. Kelavuori[1], A. Panahpour[1], and M. J. Huttunen[1*]

[1]Tampere University, Finland
[*]corresponding author: mikko.huttunen@tuni.fi

Abstract: We show how strong dispersion can be used to control losses in diffractive–plasmonic resonances. Bragg-reflector waveguides are proposed as highly dispersive media for plasmonic metamaterials, allowing orders of magnitude reduction in array sizes, while still achieving ultra-high quality factors.

Collective plasmonic–diffractive resonances called surface lattice resonances (SLRs) combine the strong light–matter interactions of single particle plasmonics with the low losses of diffractive modes. The combination generates optical excitations with very strong local fields, which scale with diminished resonance losses. The losses are quantified using quality (*Q)* factor, linking energy loss per cycle to the total energy of the resonance. The high *Q*-factors and the strong light–matter interaction in SLRs make them attractive for applications in, for example, nonlinear optics and lasing. While *Q*-factor is one of the most important characteristics of the SLRs, the means to increase and control it are limited to some trivial methods. Namely, the radiative losses can be decreased by increasing array size and the spatial coherence of the light source,[1] and the material losses can be decreased by designing the diffractive mode far away from the single particle plasmonic resonance.[2] Furthermore, there has been research on utilizing out-of-plane resonances[3], and indirect excitation[2] to heighten *Q*-factors in SLRs. Also, active control over the SLR *Q*-factor can be achieved by induced symmetry breaking in the dielectric medium, causing reversible and controllable growth in radiative losses.[4]

Here, we propose a new method for increasing and controlling the *Q*-factors in SLRs. We show how utilizing strong refractive index dispersion in the medium surrounding the plasmonic nanoparticles can significantly decrease resonance losses. Previously, the effect has been demonstrated in microcavities using highly dispersive bulk materials as cavity medium.[5] We propose embedding plasmonic nanoparticles (NPs) to Bragg-reflector waveguides (BRWs), where extreme dispersion can be seen near the cutoff frequencies of the waveguide modes. Equivalently, the waveguide mode has a near flat band near its cutoff frequency, leading to almost divergent density of states. This highly enhanced Purcell factor leads to enhanced coupling between the NP scatterers. We show how the *Q*-factors in such structures are almost linearly dependent on the group index in the waveguide, and how, with the extreme dispersion in BRWs, the radiative losses can be diminished up to a hundred-fold. In plasmonic–diffractive resonances material losses quickly become dominant over radiative losses, lending the overall *Q*-factors less extreme. However, since the usual means for decreasing radiative losses in plasmonic NP arrays includes increasing the array size, this technique can be utilized to decrease array areas very efficiently. For example, a *Q*-factor traditionally achievable with an array size of 600×600 μm^2 can be obtained in just a 50×50 μm^2 area with a ten-fold increase in the group index. Such an increase is easily achievable in BRWs.

Figure 1 shows lattice-sum calculations for an array inside BRW with different dispersion properties. The group indices n_g for the excitations are calculated as:

$$n_g = n_{\mathrm{eff}} + \omega \frac{\mathrm{d}n_{\mathrm{eff}}}{\mathrm{d}\omega} \qquad (1)$$

where n_{eff} is the effective phase refractive index of a waveguide mode and ω is the angular frequency of the light. High group index values stem from extreme dispersion near the cutoff frequency. The frequency of the resonance was changed by varying the array period. The calculations were done for an empty-lattice approximation, and material losses were not included. Radiative losses are shown to decrease with increased number of particles, and with higher group indices. When the number of particles reaches a certain value, the Q-factors no longer grow, but are saturated to values close to 16 000 for our BRW. Further increase is halted by the losses in the BRW-mode inhibiting coupling between the far-away particles. This saturated particle count (N), especially, seems to be highly dependent on the used group index. Resonances at highly dispersive regions therefore need drastically less particles to achieve high Q-factors. The technique has potential to help plasmonic metasurface fabrication, and it allows the usage of SLRs in micrometer-scale pixels.

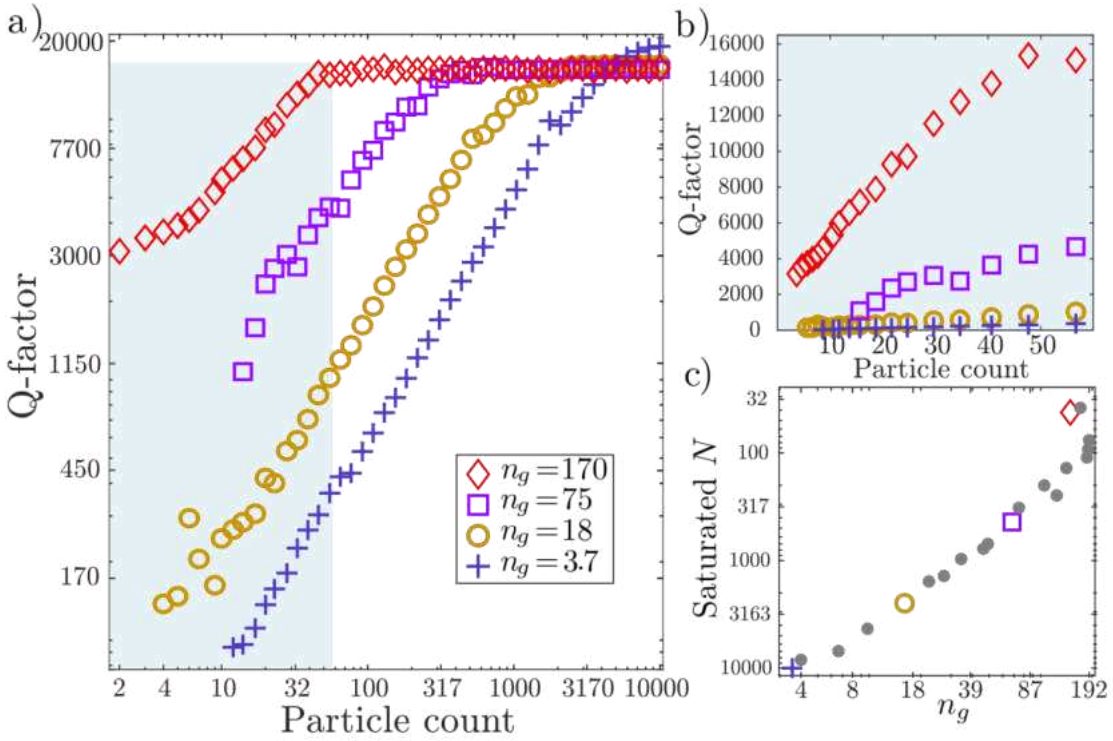


Figure 1. *Lattice-sum calculations for the diffractive mode for an array embedded in BRW. Each symbol corresponds to an excitation with certain group index. a,b) Q-factors of the resonances as a function of used particles in a) log-log -scale, b) linear scale. c) Loss-saturated number of particles as a function of group index in the BRW-SLR system in a log-log^{-1} -scale.*

References

1. Bin-Alam, M. S., et. al., "Ultra-high-Q resonances in plasmonic metasurfaces", Nat. Commun. Vol. 12, 974, 2021.
2. Kravets, V. G., et. al.," Plasmonic Surface Lattice Resonances: A Review of Properties and Applications", Chem. Rev. Vol. 118, No. 12, 5912–5951, 2018
3. Li, S. Q., et. al., "Ultra-sharp plasmonic resonances from monopole optical nanoantenna phased arrays" Appl. Phys. Lett. Vol. 104, 231101, 2014.
4. Kelavuori, J., et. al.,"Thermal Control of Plasmonic Surface Lattice Resonances", Nano Lett., Vol. 22, No. 10, 3879-3883, 2021.
5. Gao, G., et. al., "Air-mode photonic crystal ring resonator on silicon-on-insulator", Sci. Rep., Vol. 6, No. 1, 19999, 2016.

Nonlinear optical sensing in arrays of plasmonic nanoparticles

A. Verneuil[1,2], A. Zilli[2], C. Vézy[1], J. Béal[1], M. Finazzi[2], M. Celebrano[2] and A.-L. Baudrion[1]

[1]Light, Nanomaterials, Nanotechnologies, Université de Technologie de Troyes, Troyes, France
[2]Dipartimento di Fisica, Politecnico di Milano, Milan, Italy
*corresponding author: anne_laure.baudrion@utt.fr

Abstract: Second harmonic generation from plasmonic materials, originating mostly from the surface, is a promising platform for sensing applications. In this work, we investigate the performance of a sensor based on periodic and aperiodic metagratings of V-shaped nanoantennas, exploring both the intensity and angular variations of their nonlinear emission.

Second-harmonic generation (SHG), the optical process by which two photons at a fundamental wavelength (FW) are converted into one at twice the frequency, is well known to be forbidden in centrosymmetric crystal lattices,[1] such as those found in plasmonic materials. Thus, in this situation symmetry breaking is required for this phenomenon to be supported, which can be achieved in two ways: field gradients in the bulk of the material, or surface contributions.[2,3] This latter approach has received special attention due to its potential for sensing applications: indeed, a variation in the surface susceptibility tensor, mediated for instance by a biological binding event, could give rise to a large change in the observable SHG.

In a previous work from our group, Ghirardhini et al.[4] showed that using the SH signal in a refractometric experiment could provide a significantly enhanced sensitivity compared to the FW (up to one order of magnitude). However, her configuration was subject to significant damping of the emission due to the dense packing of the array, which suppressed all diffracted beams except the zero-order, and was moreover generating detrimental near-field coupling between the antennas.

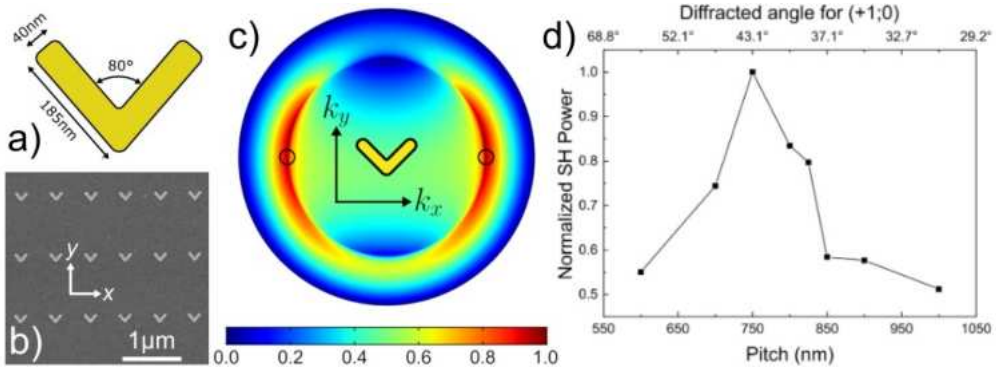


Figure 1: (a) Geometrical parameters of the nanoantennas. (b) Scanning electron microscope image of one of the gratings. The periods in x and y are 800 and 1025 nm, respectively. (c) EP in the Fourier plane of the substrate half-space associated with the antenna design given in (a), the black circles denoting the optimal position of the diffraction orders. (d) Optimization of the lattice parameters for SHG extraction, based on the lattice period in x.

In this context, we are working with a platform constituted by rectangular gratings of V-shaped gold nanoantennas, deposited on a glass substrate (see fig. 1a-b). The sample is pumped at a FW of 1550 nm, the SHG collected in epi configuration, ie. from the substrate side, and its Fourier plane is projected onto a camera, giving us insight into the angular behavior of the emission. Recently[5], we optimized the lattice arrangement to allow optimal extraction of SH signal, in an attempt to improve our signal-to-noise ratio. In particular, we achieved a doubling of the collected signal, by overlapping diffraction orders with the single particle emission

pattern (EP), as shown in fig. 1d. As the period in *x* is changed, so does the direction of the (±1;0) diffraction orders (or, equivalently, their lateral position in the Fourier plane). At 750 nm of pitch, the emission angle coincides with the emission lobes of the EP (see fig. 1c), leading to a significantly increased collected SH signal.

Interestingly, this optimization opens a new alleyway to improve the sensitivity: as the EP depends on the local refractive index (RI), but the diffraction pattern of our grating remains fixed (since we are collecting from the substrate side), the overlap provides a new way of probing the environment of the antennas. To explore this possibility, we first investigate several gratings of varying fixed period (fig. 2a-b), then move to a variably pitched lattice configuration (fig. 2c-d). In the first case, we find a maximum resolution (ie. minimal detectable refractive index variation) of 4×10^{-4} RIU (fig. 2b). In the second case, a broadening of the side (±1;0) diffraction orders is obtained by chirping the period in *x* (fig. 2c), within which we the shift of the angular emission as the RI changes can be observed (fig. 2d).

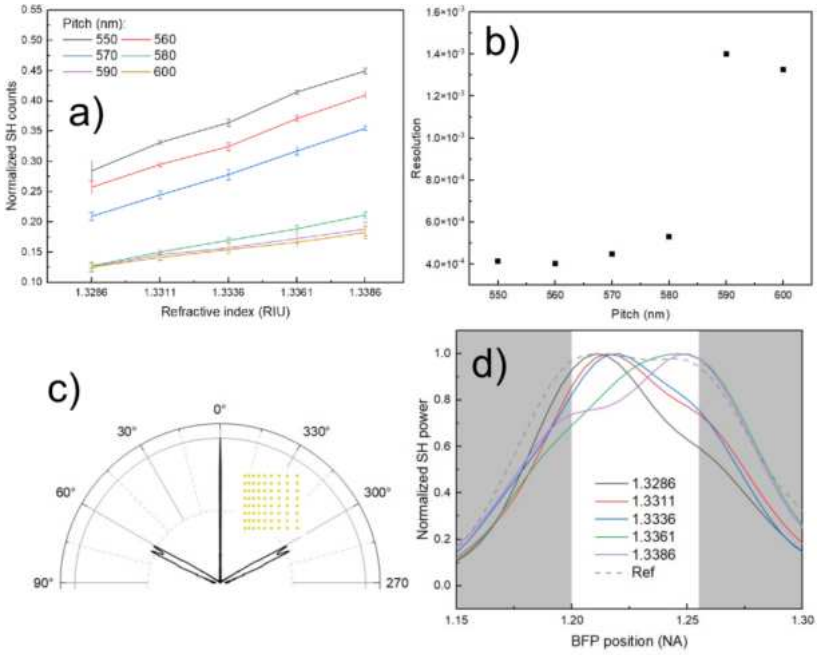


Figure 2: (a) Refractometric sensing experiment for different fixed pitch gratings. (b) The associated refractive index resolution for each configuration. (c) Calculated emission pattern of the variably pitched array (VPA) (inset: schematic of the lattice). (d) Cuts in the back focal plane of the VPA emission at the SH, for different RIs.

References

1. R. W. Boyd, Nonlinear optics, 3rd ed. Amsterdam; Boston: Academic Press, 2008.
2. D. De Ceglia, et al., "Role of antenna modes and field enhancement in second harmonic generation from dipole nanoantennas", Opt. Express, Vol. 23, No. 2, 1715, 2015.
3. G. Bachelier et al., "Origin of optical second-harmonic generation in spherical gold nanoparticles: Local surface and nonlocal bulk contributions", Phys. Rev. B, Vol. 82, No. 23, 235403, 2010.
4. L. Ghirardini et al., "Plasmon-Enhanced Second Harmonic Sensing", J. Phys. Chem. C, Vol. 122, No. 21, 11475-11481, 2018.
5. A. Verneuil et al., "Far-field mapping and efficient beaming of Second Harmonic by a plasmonic metagrating", Nanophotonics, *to be published*.

Rapid modulation of left- and right-handed optical vortices for precise measurements of helical dichroism

S. Hashiyada[1*], and Y. Y. Tanaka[1]

[1]Hokkaido University, Japan
[*]corresponding author: shun.hashiyada@es.hokudai.ac.jp

Abstract: We propose and experimentally demonstrate rapid modulation of the directions of handedness of optical vortices carrying orbital angular momentum (OAM) at around 50 kHz. This modulation is achieved through the rapid modulation of those of circularly polarized lights carrying spin angular momentum (SAM), coupled with the SAM-OAM conversion techniques.

Understanding chiral light-matter interactions in the context of angular momentum is crucial for both basic science and practical applications, including material chirality sensing and the development of chiral optical devices. An object in helical motion, i.e., a combination of translational and rotational motion, possesses angular momentum and exhibits chirality. A current in a chiral material, a circularly polarized light (CPL) and an optical vortex (OV) are chiral. CPL with spin angular momentum (SAM) of $s\hbar$ ($s = \pm 1$) per photon [1] is commonly employed to study the chiral-optical responses, such as circular dichroism (CD), defined as the difference in optical absorption for the left- and right-handed CPLs. Recent efforts to further understand how chiral matter interacts with the angular momentum of light have focused on exploring the chiral-optical response to an OV with quantized orbital angular momentum (OAM) of $l\hbar$ ($l = 0, \pm 1, \pm 2, \ldots$) [2]. An OV has a complex field characterized by $\exp(il\varphi)$, where φ is the azimuthal around the optical axis, and l is the topological charge (TC). Helical dichroism (HD) extends the concept of CD and denotes the difference in absorption that depends not only on the SAM but also on the OAM. In the previous study of the HD [3], generation of OVs with both positive and negative TC (l) is routinely achieved by using spatial light modulators (SLMs). While SLMs provide significant flexibility, they are limited by a slow response time. The switching of the left- (LH) and right-handed (RH) OVs occurs only below 100 Hz, a frequency comparable to low-frequency noise. This limitation poses a challenge for precise HD measurements.

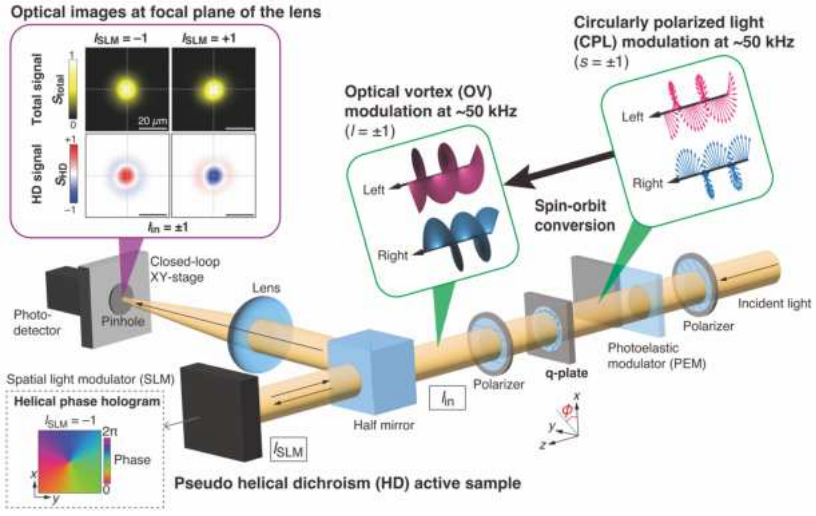


Figure 1. Optical system for the rapid modulation of OVs and the HD measurements using modulated OVs.

Here, we report a novel approach for the rapid modulation of the LH and RH OVs carrying OAM ($l = \pm 1$) at around 50 kHz. This is accomplished by employing a photoelastic modulator (PEM) to modulate the LH and RH CPLs carrying SAM ($s = \pm 1$) at around 50 kHz. Subsequently, these modulated CPLs are inserting into a q-plate [4] for SAM-OAM conversion (see Figure 1). To validate the capability of the proposed optical system for rapid modulation of OVs and HD measurement, we analyzed the light state using the Jones matrix method. The light transmitted through the polarizer and the PEM can be written as $\mathbf{E}_{\text{spin}} = \sqrt{\frac{1+\sin\delta}{2}}\mathbf{E}_{s=+1} + i\sqrt{\frac{1-\sin\delta}{2}}\mathbf{E}_{s=-1}$, where $\mathbf{E}_{s=+1}$ and $\mathbf{E}_{s=-1}$ are the vectors of the LH and RH CPLs, respectively. The parameter $\delta=\delta_0 \sin\Omega t$ describes the phase modulation induced by the PEM, where δ_0 is the amount of phase modulation, and Ω is the modulation frequency (around 50 kHz). This equation indicates sinusoidal modulation of the amplitudes of the left- and right-handed CPLs at Ω. After passing through the q-plate and the polarizer, modulated CPLs can be converted into modulated OVs as follows:

$$\mathbf{E}_{\text{orbit}} = \left(\sqrt{\frac{1+\sin\delta}{2}}\exp(+i\varphi) + i\sqrt{\frac{1-\sin\delta}{2}}\exp(-i\varphi)\right)\mathbf{E}_{\text{LP}}, \quad (1)$$

where $\mathbf{E}_{\text{LP}}$ is the vector of the linearly polarized light. Equation (1) is the main result of this study and indicates sinusoidal modulation of the amplitudes of the LH and RH OVs at Ω (around 50 kHz). When the modulated OVs interacts with a sample exhibiting HD, the complex amplitudes of the LH and RH OVs are further modulated by factors T_+ and T_-, respectively. The detected signal contains a frequency component of $n\Omega$ (where n is an integer). By demodulating the detected signal for the $n\Omega$-components with a lock-in detection technique, information for the total intensity ($S_{\text{sum}} = |T_+|^2 + |T_-|^2$) and the HD ($S_{\text{HD}} = |T_+|^2 - |T_-|^2$) of the sample for the left- and right-handed OVs are simultaneously obtained.

To experimentally demonstrate the proposed OV modulation, we utilized a SLM as a sample showing the HD (Fig. 1). Due to the interactions of the incident light ($l_{\text{in}} = \pm 1$) with SLM ($l_{\text{SLM}} = +1$), TC of the outgoing light should be $l_{\text{out}} = +2, 0$ according to the selection rule; $l_{\text{out}}=l_{\text{SLM}}+l_{\text{in}}$ [5]. For $l_{\text{out}} = +2, 0$, the beam intensity profiles of the focusing field should be donut-shaped and Gaussian, respectively, and the HD signal should have a negative maximum at the center of the beam. As shown in Figure 2(b-c), a negative and a positive HD signal peak were observed at the center of the beam for $l_{\text{SLM}} = +1, -1$, respectively, as expected. Therefore, we have successfully demonstrated the OV modulation. We demonstrated the OV modulation technique based on the rapid CPL modulation with a PEM and the SAM-OAM conversion with a q-plate. The method we have developed in this study is expected to establish the foundation for a high-precision HD measurement method.

References

1. Beth, R. A., "Mechanical detection and measurement of the angular momentum of light," Phys. Rev., Vol. 50, No. 2, 115–125, 1936.
2. Allen, L., Beijersbergen, M. W., Spreeuw, R. J. C. and Woerdman, J. P., "Orbital angular momentum of light and the transformation of Laguerre-Gaussian laser modes," Phys. Rev. A Vol. 45, No. 11, 8185–8189, 1992.
3. Brullot, W., Vanbel, M. K., Swusten, T. and Verbiest, T., "Resolving enantiomers using the optical angular momentum of twisted light," Sci. Adv. Vol. 2, No. 3, e1501349, 2016.
4. Marrucci, L., Manzo, C. and Paparo, D., "Optical spin-to-orbital angular momentum conversion in inhomogeneous anisotropic media," Phys. Rev. Lett. Vol. 96, No. 16, 163905, 2006.
5. Li, H., Phillips, D. B., Wang, X., Ho, Y. -L. D., Chen, L., Zhou, X., Zhu, J., Yu, S. and Cai, X., "Orbital angular momentum vertical-cavity surface-emitting lasers," Optica Vol. 2, No. 6, 547-552, 2015.

Synthesis of tailored functional nanoparticles by polymerization induced by surface plasmons

O. Soppera[1,2]

[1] Université de Haute-Alsace, CNRS, IS2M UMR 7361, F-68100 Mulhouse, France
[2] Université de Strasbourg, France
[*]corresponding author: olivier.soppera@uha.fr

Abstract: Polymerization induced by surface plasmon resonance was used to couple functional polymer on metal nanostructures. This approach is a method for investigating nanophotochemistry and opens the door towards new functional nanoobjects for applications in sensors or nanophotonics.

In this study, we describe an approach developed to carry out and characterize polymerization reactions triggered by the excitation of metal nanostructures. Nanoparticles prepared by chemical (colloidal synthesis) or physical (dewetting of gold films) methods are used. The particles are deposited on TEM grids, enabling nano-objects to be characterized at every stage of the experiments. Different configurations are used to irradiate the nanoparticles and induce polymerization reactions, with continuous or pulsed light, in the visible or near infrared, and different polarization states.

After irradiation, polymer patches are observed on the metal nanostructures. These patches are analyzed as a function of irradiation conditions, and compared with numerically calculated field maps.

Various chemistries were applied to this configuration. The main results were obtained by radical photochemistry induced by monophotonic or biphotonic absorption. On the basis of this chemistry, other polymerizations were induced, such as that of living photopolymerization systems, molecularly imprinted polymers or metal salt photoreductions.

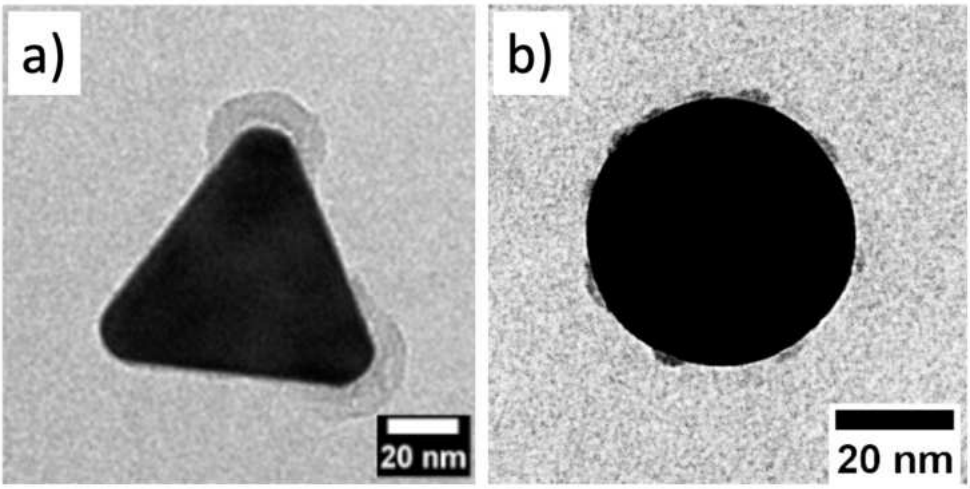


Figure : TEM images of metal nanoparticles with polymer nanopatches prepared by polymerization induced by surface plasmon resonance

This approach provides a platform for studying photopolymerization reactions at the nanoscale, highlighting novel phenomena linked to the confinement of light in nanovolumes and also to the extremely limited number of

reactive species excited in the volume corresponding to the optical near-field. Comparison of the different regimes also enables us to discriminate between the origins of chemical phenomena, between photochemistry, hot carriers and thermal effects. Finally, beyond these fundamental challenges, we demonstrate the interest of this route for the preparation of hybrid nanoparticles coupling functional materials to metallic nanostructures, with applications in the field of sensors and more generally nanophotonics.

References

1. Kameche, F.; Heni, W.; Telitel, S.; Vidal, L.; Marguet, S.; Douillard, L.; Fiorini-Debuisschert, C.; Bachelot, R.; Soppera, O. Probing Plasmon-Induced Chemical Mechanisms by Free-Radical Nanophotopolymerization. *J Phys Chem C* **2021**, *125* (16), 8719-8731. DOI: 10.1021/acs.jpcc.1c01693.
2. Khitous, A.; Lin, C. F.; Kameche, F.; Zan, H. W.; Malval, J. P.; Berling, D.; Soppera, O. Plasmonic Au Nanoparticle Arrays for Monitoring Photopolymerization at the Nanoscale. *ACS APPLIED NANO MATERIALS* **2021**, *4* (9), 8770-8780. DOI: 10.1021/acsanm.1c01377.
3. Khitous, A.; Molinaro, C.; Gree, S.; Haupt, K.; Soppera, O. Plasmon-Induced Photopolymerization of Molecularly Imprinted Polymers for Nanosensor Applications. *Advanced Materials Interfaces* **2023**, *10* (7), 2201651, https://doi.org/10.1002/admi.202201651. DOI: https://doi.org/10.1002/admi.202201651
4. Kameche, F.; Heni, W.; Telitel, S.; Ge, D.; Vidal, L.; Dumur, F.; Gigmes, D.; Lalevée, J.; Marguet, S.; Douillard, L.; et al. Plasmon-triggered living photopolymerization for elaboration of hybrid polymer/metal nanoparticles. *Materials Today* **2020**, *40*, 38-47. DOI: https://doi.org/10.1016/j.mattod.2020.03.023.
5. Yatsui, T.; Brandenburg, F.; Leuschel, B.; Soppera, O. Synthesis of silver nanostructure on gold nanoparticle using near field assisted second harmonic generation. *Scientific Reports* **2021**, *11* (1), 5642. DOI: 10.1038/s41598-021-84944-w.
6. Noel, L.; Khitous, A.; Molinaro, C.; Zan, H.-W.; Berling, D.; Grasset, F.; Soppera, O. Laser Direct Writing of Crystallized TiO2 by Photothermal Effect Induced by Gold Nanoparticles. *Advanced Materials Technologies* **2024**, *9* (1), 2300407. DOI: https://doi.org/10.1002/admt.202300407.
7. Khitous, A.; Noel, L.; Molinaro, C.; Vidal, L.; Grée, S.; Soppera, O. Sol–Gel TiO2 Thin Film on Au Nanoparticles for Heterogeneous Plasmonic Photocatalysis. *ACS Applied Materials & Interfaces* **2024**, *16* (8), 10856-10866. DOI: 10.1021/acsami.3c15866.

DNA-assembled nanogaps for continuous single-molecule biosensing

L. Oliveira de Miranda[1], A. Sateh[2], A. Dillen[3], M. Dolci[1], C. Scarpellini[3], K. Sergelen[4], H. Altug[2], J. Lammertyn[3], and P. Zijlstra[1*]

[1]Eindhoven University of Technology, Department of Applied Physics, Eindhoven, The Netherlands
[2]Ecole Polytechnique Federal de Lausanne, Lausanne, Switzerland
[3]KU Leuven, Departement Biosystemen, Leuven, Belgium
[4]Biomed X Institute, Heidelberg, Germany
[*]corresponding author: p.zijlstra@tue.nl

Abstract: We present a single-molecule plasmon sensor suitable for continuously monitoring analyte concentrations over time. We analyze the far-field optical properties of the sensor by single-particle spectroscopy. A reversible sandwich assay enables the monitoring of DNA markers a temporal resolution of minutes and a sub-picomolar limit-of-detection.

New biosensor technologies are of great interest for personalized health care, a sustainable food industry, and monitoring of our environment. There is an urgent need for sensing techniques that provide continuous information to enable autonomous sensors that operate at the point-of-interest. Here we present a DNA-assembled nanosensor based on a nanoparticle-on-film construct that is suitable for single-molecule and continuous biosensing. The sensor reports increases and decreases in analyte concentration with a temporal resolution of minutes and a sub-picomolar limit-of-detection.

The sensor operates by optically monitoring the binding and unbinding of single nanoparticles to the metal film. Particle-binding occurs through reversible single-molecule DNA interactions, providing a dynamic switching between bound and unbound states. Single-particle spectroscopy indicates that the far-field scattering spectrum in the bound state is an interplay between the propagating and localized plasmons and results in a strong reshaping of the spectrum. We develop a DNA sandwich assay where the frequency of binding events provides a readout for analyte concentration. The sensor has a sub-picomolar limit-of-detection and enables continuous monitoring of DNA in diluted serum with a temporal resolution of minutes. Analysis of the sensor dynamics further enables kinetic fingerprinting to distinguish mono- and multi-valent interactions. The presented sensor can be generalized to other analytes to serve as a continuous and autonomous biosensor for lowly concentrated analyte.

Anapole modes enabling linear and nonlinear chiral sensing in hybrid metasurfaces

G. Serrera[1], **J. González-Colsa**[1], **and P. Albella**[1]

[1] Department of Applied Physics, University of Cantabria, Avda. Los Castros, s/n, 39005 Santander, Spain

*pablo.albella@unican.es

Abstract: In this work, we present how anapole modes can be exploited in hybrid metasurfaces to significantly enhance circular dichroism (CD) up to 5 times. Our results demonstrate that this metasurface offers efficient generation of background-free nonlinear CD signals, up to a 10-fold enhancement, that complements linear CD measurements.

Chirality, denoting the lack of specular symmetry in any plane of an object and the resulting existence of two mirror images (enantiomers), is a key aspect for the understanding of the biological functionality of many molecules in the human body and pharmaceutical compounds [1]. This recognition has sparked a growing industrial interest in discriminating molecular chirality, given its implications for drug efficacy and safety.

One of the key challenges in finding new ways to enhance the intrinsically weak circular dichroism (CD) chiroptical effect, thus enabling an efficient chiral sensing. Over the past decade, the design and development of nanophotonic platforms tailored for this purpose have emerged as a significant area of research and innovation. Fundamentally, the CD effect is proportional to the local Optical Chirality Density (OCD) C [2], defined as

$$C = -\frac{\omega\varepsilon_0}{2}\Im\mathfrak{m}(\boldsymbol{E}^* \cdot \boldsymbol{B}) = -\frac{\omega}{2c^2}|\boldsymbol{E}||\boldsymbol{H}|\cos(\Phi) \quad (1)$$

where ω is the angular frequency, c the speed of light, ε_0 is the vacuum electric permittivity and Φ is the phase angle between $i\boldsymbol{E}$ and $\boldsymbol{H}$. In the case of plane waves in vacuum Φ is maximized when the polarization is circular. The overall nanophotonic enhancement of the CD effect comes from the ratio between the spatial average of this quantity over the sample volume and the OCD of circular light.

As can be seen in equation 1, OCD enhancement at a particular wavelength can be achieved by local field concentration in nanophotonic structures while the phase relation $\cos(\Phi)$ is preserved. Various approaches have been explored to address this challenge. For instance, proposals based on plasmonics have exploited the substantial electric field enhancement generated by Surface Plasmon Resonance (SPR) [3]. On the other hand, the use of High Refractive Index Dielectric (HRID) materials has gained attention due to their low-loss nature and mixed electric and magnetic resonances, which can enhance both fields [4]. Hybrid structures, combining synergistically metallic and dielectric features, have emerged as particularly promising candidates [5].

In particular, HRID structures exhibit the noteworthy capability to sustain anapole resonances, characterized by intense optical field confinement. In the context of chiral sensing, this feature is interesting for background-free OCD enhancement as the phase relation of circularly polarized light is preserved [6]. Complementarily, this field confinement in anapole resonances can be exploited to enhance nonlinear optical effects, notably Third Harmonic Generation (THG). For example, HRID materials, with high third-order susceptibilities, have been combined with metallic materials to enable highly efficient THG in hybrid systems [7].

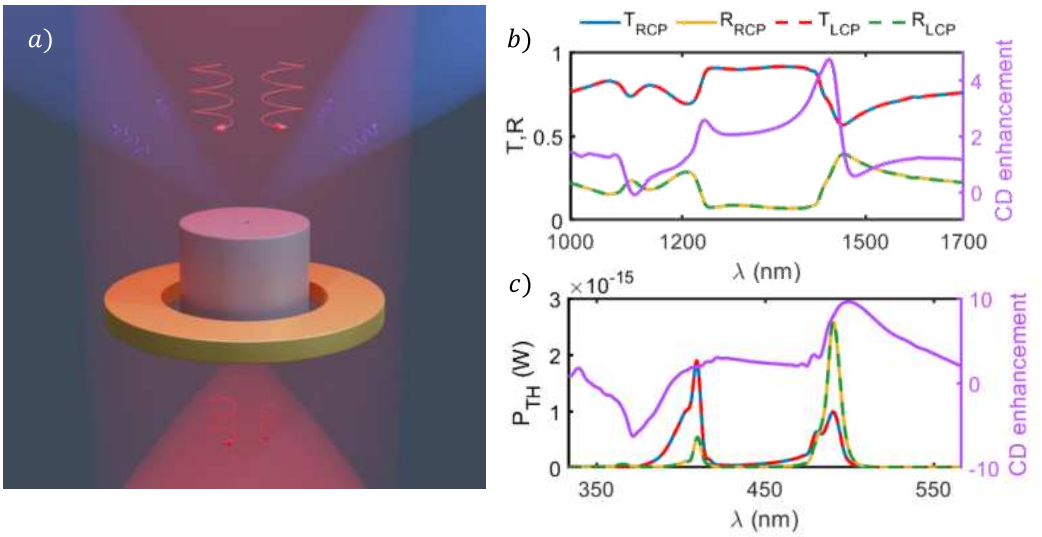


Figure 1. a) Depiction of the unit cell of the proposed metasurface. b) Linear reflectance and transmittance results of the proposed metasurface, together with linear CD enhancement up to 5 times. c) Third Harmonic Generation from the metasurface (reflection and transmission directions), with its associated CD signal, reaching a 10-fold enhancement at 490 nm.

In this study, we demonstrate numerically the efficacy of a hybrid structure (Figure 1a) consisting of a HRID (amorphous silicon) slotted nanodisk coupled to a gold ring as a promising platform for chiral sensing. This configuration yields a broadband, high average OCD value throughout a significant volume due to the confinement of electric and magnetic energy near anapole resonances. Additionally, we leverage these resonances to achieve a background-free, enhanced nonlinear third harmonic CD signal, with theoretical efficiencies up to 0.08%. Our results, summarized in Figure 1, show that CD enhancement can be 5-fold in the linear regime (Figure 1b) and up to 10 times in the third harmonic regime (Figure 1c).

G. S. and J. G.-C. acknowledge funding from the Spanish government for their predoctoral contract grants (FPU21/02296 and FPI/PRE2019-088809). This work was funded by the MOPHOSYS Project (PID2022-139560NB-I00) from Proyectos de Generación de Conocimiento provided by the Spanish Agencia Estatal de Investigación.

References

1. Zor, E., H. Bingol and M. Ersoz, “Chiral Sensors,” Trends Analyt. Chem., Vol. 121, 115662, 2019.
2. Tang, Y. and A. E. Cohen, “Optical Chirality and Its Interaction with Matter,” Phys. Rev. Lett., Vol. 104, 16390, 2010.
3. Hentschel, M., M. Schäferling, X. Duan, H. Giessen and N. Liu, “Chiral Plasmonics,” Sci. Adv., Vol. 3, 160273, 2017.
4. Tanaka, K. et al., “Chiral Bilayer All-Dielectric Metasurfaces,” ACS Nano, Vol. 14, No. 11, 15926–15935, 2020.
5. Mohammadi, E., A. Tittl, K. L. Tsakmakidis, T. V. Raziman and A. G. Curto, “Dual Nanoresonators for Ultrasensitive Chiral Detection”, ACS Phot., Vol. 8, No. 6, 1754-1762, 2021.
6. Du, K. et al., “Optical Chirality Enhancement in Hollow Silicon Disk by Dipolar Interference”, Adv. Opt. Mat., Vol. 9, No. 5, 2001771, 2021.
7. Shibanuma, T., G. Grinblat, P. Albella and S. A. Maier, “Efficient Third Harmonic Generation from Metal–Dielectric Hybrid Nanoantennas”, Nano Lett., Vol. 17, No. 4, 2647-2651, 2017.

DNA origami-based plasmonic nanoantennas for single-molecule SERS

Y. Kanehira[1], A. Mostafa[1], A. Dutta[1], S. Kogikoski[1] and I. Bald[1*]

[1] Institute of Chemistry, University of Potsdam, Germany
[*]corresponding author: bald@uni-potsdam.de

Abstract: DNA origami nanoforks are used to assemble versatile plasmonic nanoantennas optimized for single-molecule surface-enhanced Raman scattering (SERS). Here, we demonstrate the role of molecular orientation within the SERS hot spot on single-molecule spectra as well as a detailed analysis of single protein SERS spectra.

DNA origami nanostructures are ideally suited to arrange both plasmonic nanoparticles as well as receptors for analyte molecules with nanometer precision. In this way they can provide optimized substrates for surface-enhanced Raman scattering (SERS), where the strongest signal enhancement is localized in nanometric hot spots and where the DNA origami can be used to precisely position the molecules of interest. In recent years we have demonstrated the few- and single-molecule SERS detection in different nanoparticle arrangements.[1] We have created a dedicated DNA origami nanoantenna,[2] which was also used to study chemical changes in hemin,[3] and to detect single proteins.[2] Very recently, we have further optimized the plasmonic nanoantennas by comparing the SERS performance of dimers of different nanoparticle species from spherical Au and Ag nanoparticles to anisotropic gold nanoflowers and combinations thereof.[4] We could show that a combination of Au nanoflower and Ag nanosphere allows for a broadband SERS excitation and improved single-molecule detection.

In the present contribution recent unpublished single-molecule SERS results are presented focusing on the following aspects: i) We explore the influence of the orientation of molecules within the hot spot of DNA origami-assembled nanoparticle dimers on the single-molecules SERS spectra. ii) Single proteins are investigated in detail using SERS. Using cytochrome c as an example we demonstrate the occurrence and analysis of the amide III band as a structural marker band in single-molecule SERS spectra. Additionally, we studied the enzymatic activity of horseradish peroxidase (HRP) on the single-molecule level.

References

1. S. Kogikoski Jr, J. Ameixa, A. Mostafa and I. Bald, “Lab-on-a-DNA origami: nanoengineered single-molecule platforms,” Chem. Commun., 59, 4726–4741, 2023.
2. K. Tapio, A. Mostafa, Y. Kanehira, A. Suma, A. Dutta and I. Bald, “A Versatile DNA Origami-Based Plasmonic Nanoantenna for Label-Free Single-Molecule Surface-Enhanced Raman Spectroscopy” ACS Nano, 15, 7065, 2021.
3. A. Dutta, K. Tapio, A. Suma, A. Mostafa, Y. Kanehira, V. Carnevale, G. Bussi, I. Bald, “Molecular States and Spin Crossover of Hemin Studied by DNA Origami Enabled Single-Molecule Surface-Enhanced Raman Scattering” Nanoscale, 14, 16467-16478, 2022.
4. Y. Kanehira, K. Tapio, G. Wegner, S. Kogikoski Jr., S. Rüstig, C. Prietzel, K. Busch, and I. Bald, “The Effect of Nanoparticle Composition on the Surface-Enhanced Raman Scattering Performance of Plasmonic DNA Origami Nanoantennas” ACS Nano, 17, 21227-21239, 2023.

Optical Modelling of DNA-Made Janus Nanoheaters

Pablo Albella

Department of Applied Physics (Group of Optics), University of Cantabria, Faculty of Science, Santander, Spain

e-mail: pablo.albella@unican.es

Abstract: Nanostructures manufactured using DNA-based nanotechnology, especially DNA-origami, possess a DNA core that influences their thermoplasmonic performance. In this work, we identify key parameters that optimize its thermoplasmonic response by comparing them with their solid counterparts. We also explore the impact that random rotations have on their thermal performance.

The generation of Localized Surface Plasmon Resonances (LSPRs) is accompanied by a partial reemission of the incident electromagnetic energy (nanoantenna effect) but also by a partial absorption, which usually leads to substantial temperature increase. This behavior effectively converts the nanoparticles into both nanoantennae and miniaturized heat sources, commonly known in thermoplasmonics as nanoheaters [1].

Traditionally, researchers tried to minimize or avoid that absorptive nature of nanoantennae to reach strongly enhanced local fields and clean far field signals containing the information of the local targets [2]. However, plasmonic nanostructures (gold in particular), when acting as nanoheaters, have shown great potential in a wide range of applications such as drug delivery or photothermal therapies (PTTs). Hence, big efforts are being made to either find new nanoheaters or to improve the photoinduced thermal response of the existing metallic nanostructures [3-5].

Three factors are especially important when looking at designing nanoheaters for such applications: the biocompatibility of the nanostructure materials, the photothermal conversion efficiency of the applied agents and their stability under rotations with respect to the radiation source. These limiting factors provide a well-defined path for the design of nanoheaters oriented to PTTs. Firstly, nanoheaters must be made of biocompatible materials capable of providing a strong plasmonic response. Secondly, their geometry must support resonances within the so-called biological windows (NIR-I: 700-900 nm and NIR-II: 1000-1400 nm) where the penetration in the tissue and maximum permissible exposure (MPE) are maximum. Finally, they must present a reasonable tolerance to rotations [6]. It is well-known that anisotropic nanoheaters offer different thermal responses depending on their relative orientation with respect to the polarization of the incident beam [6-8]. This is of extreme importance in areas like PTT, where nanoheaters, either free in blood or attached to cells, present a random orientation distribution.

DNA-based nanotechnology, especially DNA origami techniques, provide feasible route to fabricate the aforementioned nanoheaters [9,10]. However, one of the main consequences of using DNA origami for the synthesis of metallic nanomaterials is that their structure is often not solid but has a core formed by DNA. This Janus-like composition can affect their optical behavior and have an impact in their thermoplasmonic response, which ultimately translates into practical variations of the photothermal efficiency.

Here, we present our most recent numerical results on the photothermal response of Janus nanoheaters based on DNA origami. We identify key parameters that optimize its thermoplasmonic response, comparing them with their solid counterparts, and exploring the impact that partial or complete metallic coatings have on their thermal performance. Finally, we study the behavior of these structures when they undergo random rotations and understand how this affects their averaged thermoplasmonic response.

This work was funded by the MOPHOSYS Project (PID2022-139560NB-I00) from Proyectos de Generación de Conocimiento provided by the Spanish Agencia Estatal de Investigación.

References

1. G. Baffou. Thermoplasmonics: Heating Metal Nanoparticles Using Light. Cambridge: Cambridge University Press, 2017
2. H. Wei, Stephanie K. Loeb, Naomi J. Halas, J. Kim. PNAS 117 (27) 15473, 2020.
3. J. J. Hu, Y. J. Cheng, X. Z. Zhang, *Nanoscale* **2018**, *10*, 22657.
4. B. Yang, C. Li, Z. Wang, Q. Dai, *Advanced Materials* **2022**, *34*, DOI 10.1002/adma.202107351.
5. J. González-Colsa, J. D. Olarte-Plata, F. Bresme, P. Albella, *Journal of Physical Chemistry Letters* **2022**, *13*, 6230.
6. J. González-Colsa, G. Serrera, J. M. Saiz, D. Ortiz, F. González, F. Bresme, F. Moreno, P. Albella, *Opt Express* **2022**, *30*, 125.
7. J. González-Colsa, A. Franco, F. Bresme, F. Moreno, P. Albella, *Sci Rep* **2022**, *12*, 14222.
8. F. Alali, I. H. Karampelas, Y. H. Kim, E. P. Furlani, *Journal of Physical Chemistry C* **2013**, *117*, 20178.
9. P. W. K. Rothemund, *Nature* **2006**, *440*, 297.
10. S. Dey, C. Fan, K. V. Gothelf, J. Li, C. Lin, L. Liu, N. Liu, M. A. D. Nijenhuis, B. Saccà, F. C. Simmel, H. Yan, P. Zhan, *Nature Reviews Methods Primers* **2021**, *1*

Universal click-chemistry approach for the DNA functionalization of nanoparticles for the development of new optical nanoantennas.

Nicole Siegel[1], Hiroaki Hasebe[2], Germán Chiarelli[1], Denis Garoli[3,4], Hiroshi Sugimoto[2], Minoru Fujii[2], Guillermo P. Acuna[1*], Karol Kołątaj[1*]

[1]Department of Physics, University of Fribourg, Chemin du Musée 3, Fribourg CH 1700, Switzerland

2 Department of Electrical and Electronic Engineering, Graduate School of Engineering, Kobe University, Kobe 657-8501, Japan.

3 Dipartimento di Scienze e Metodi dell'Ingegneria, Università di Modena e Reggio Emilia, Via Amendola 2 Padiglione Tamburini, 42122 Reggio Emilia, Italy.

4 Istituto Italiano di Tecnologia, Via Morego 30, 16163, Genova, Italy

[*]corresponding author: guillermo.acuna@unifr.ch, karol.kolataj@unifr.ch

Abstract: In this work, we present a new method to conjugate various nanoparticles with DNA by employing freezing-assisted SPAAC reaction, with a special focus on Si and SiO_2 NPs. Further, the developed method has been used for the fabrication of Si dimers using DNA origami structures.

Nanotechnology has revolutionized the fabrication of hybrid species with tailored functionalities. A milestone in this field is the DNA conjugation of nanoparticles, introduced almost 30 years ago by Mirkin's group via the deposition of thiol-modified DNA strands on Au NPs.[1] Since then, the reaction has been widely used, which has resulted in many modifications of the method. A particularly useful scheme is the freeze-thaw process, which results in both a shorter reaction time and a higher surface density of DNA.[2] In general, using thiolated-DNA provide a reliable way to functionalize only noble and coinage metals. Therefore, it is necessary to develop alternative techniques to address the DNA conjugation of NPs with surface compositions that are inert to thiols, including oxides, core-shell, polymeric NPs, and even NPs composed of active metals (Al, Ga) and metalloids (Si, Ge). Si NPs are an interesting example of such structures that cannot be functionalized using thiol chemistry. These high-index dielectric NPs have received growing attention in recent years, as theoretical and numerical studies have predicted novel properties including low heat losses and overlapping strong magnetic and electric modes in the visible range.[3] These features are key for applications in chiral sensing, unidirectional scattering, and the manipulation of magnetic dipole transitions, making Si NPs a convenient alternative to plasmonic NPs that exhibit relatively high losses and the absence of a magnetic response at optical frequencies.[3] However, in spite of the great potential of Si NPs, their stable conjugation with DNA strands has yet to be achieved.

Inspired by recent developments in the functionalization of Au NPs, we report here an approach to conjugate various nanomaterials with DNA by employing freezing-assisted SPAAC, with a special focus on Si and SiO_2 NPs (see Figure 1a). Impressively, this simple method of functionalization proved to tremendously improve the overall DNA deposition efficiency. When comparing with other approaches used for the DNA functionalization with SPAAC, we found that not only does freezing reduce the reaction time from about two days to only a few hours, but also that our method yields 2-10 times higher DNA density on the surface of the NPs, i.e., up to 0.2

molecules/nm^2 (see Figure 1b). The resultant DNA-Si NPs form highly stable colloids, which we incorporate into DNA origami structures via the formation of self-assembled NP dimers at pre-determined positions with an inter-particle gap of approximately 5-10 nm, as presented in Figure 1c. Our results show up to a 78% yield for the formation of NP dimers (i.e., versus unintended NPs monomers), thus representing the first step towards the synthesis of more complex geometries such as hybrid metal-dielectric antennas and the combination of high-index materials with other species in precise geometries. Finally, we demonstrate the versatility of this method by realizing the DNA functionalization of different NPs: oxide – TiO2, Au@SiO2, polymeric – PMMA and PS, as well as metallic Au NPs.

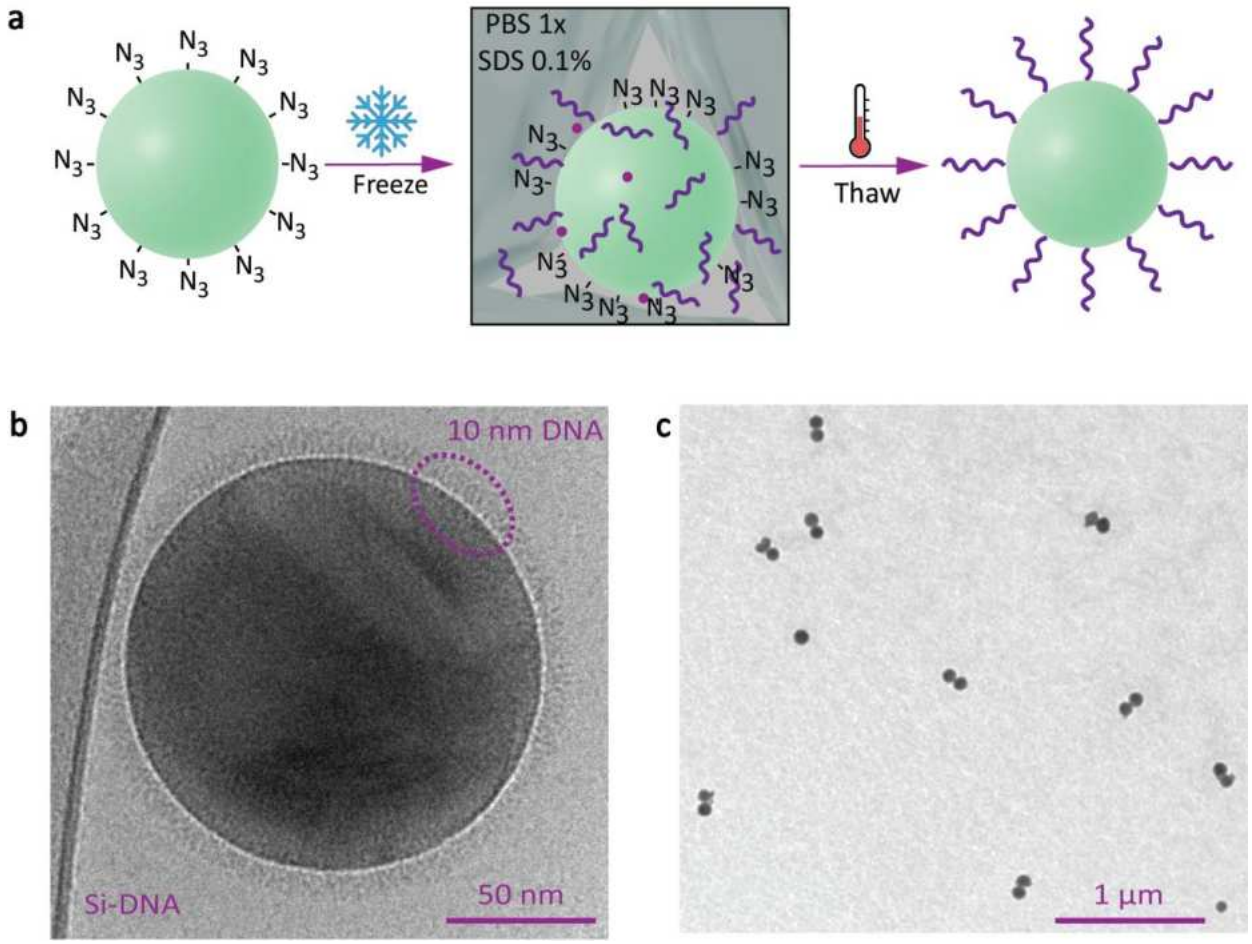


Figure 1. (a) General protocol of the functionalization of various nanoparticles through freezing-assisted DBCO-DNA deposition. (b) Cryo-EM image of a DNA-functionalized Si NP with visible DNA shell of 10 nm (purple circle). (c) TEM image of Si dimers connected through DNA origami.

References

1. Mirkin, C. A., Letsinger, R. L., Mucic, R. C. and Storhoff J. J., Nature, 382, 607, 1996
2. Liu, B. and J. Liu, J. Am. Chem. Soc., 139, 9471, 2017
3. Barreda, A. I., J. M. Saiz, F. González, F. Moreno, P. Albella, AIP Adv., 9, 040701, 2019

Optically active substrates through DNA-based lithography

V. Linko[1,2*]

[1] University of Tartu, Institute of Technology, Tartu, Estonia
[2] Aalto University School of Chemical Engineering, Espoo, Finland
[*]corresponding author: veikko.pentti.linko@ut.ee

Abstract: We show that by combining DNA origami with common top-down lithography methods, we can create versatile substrates that show superior properties in surface-enhanced Raman spectroscopy (SERS) applications.

Self-assembling biotemplates such as the versatile and rapidly folding DNA origami [1,2] provide an effective shortcut for fabricating nanoscale assemblies with intricate, sub-nanometer detail. Despite their convenience, then converting these biological constructs into equally accurate and small structures with more favorable physical properties is significantly more challenging. One recent approach attempting to overcome this is DNA-assisted lithography (DALI) [3]. DALI integrates DNA origami nanostructures as templates in negative-pattern lithographic masks and processes these with standard nanofabrication techniques (plasma etching, material evaporation, lift-off) to create metallic replicas of the template. Thus far, DALI has been used to pattern particles with sub-10 nm feature sizes from a limited selection of materials on silicon nitride and sapphire substrates [3].

Here, we present a remarkably more adaptable method that circumvents the material constraints of DALI with the incorporation of a sacrificial polymer layer into the process flow. The new technique, named the Biotemplated Lithography of Inorganic Nanostructures (BLIN) [4], enables the pattern transfer of engineered biotemplates into inorganic structures from a multitude of materials and on less restricted substrates. Due to its versatile and parallel nature, BLIN could provide an attractive alternative for patterning optically active devices and other nanopatterned surfaces. To demonstrate this, we fabricate Ag bowtie nanoantennas on common glass substrates and characterize their response in the near-infrared regime using optical transmission measurements and FDTD simulations. Further, we use the patterned substrates in surface-enhanced Raman spectroscopy (SERS) to augment the detection of Rhodamine 6G [5].

Moreover, we can create even more efficient SERS supporting substrates, which are based on DALI and a layered configuration of materials. In detail, we use DNA origami templates to form hybrid nanostructures consisting of aligned silver bowtie-shaped particles and apertures of similar shape in a silver film. It was shown that this particular geometry facilitated a four-fold advantage in Raman enhancement compared to common particle-based SERS substrates (experiments and FDTD). Our DALI-fabricated hybrid structures suppress the background emission, allow emission predominantly from the areas of high field enhancement, and support additional resonances associated with the nanoscopic apertures. Finally, these nanoapertures also enhance the fields associated with the resonances of the underlying bowtie particles [6,7]. The versatility and parallel nature of our fabrication scheme and all above-mentioned features make our optically resonant substrates attractive for various SERS-based applications.

References

1. Rothemund, P. W. K. “Folding DNA to create nanoscale shapes and patterns,” Nature, Vol. 440, No. 7082, 297–302, 2006.
2. Ijäs, H., T. Liedl, V. Linko and G. Posnjak, “A label-free light-scattering method to resolve assembly and disassembly of DNA nanostructures,” Biophys. J., Vol. 121, No. 24, 4800–4809, 2022.
3. Shen, B., V. Linko, K. Tapio, S. Pikker, T. Lemma, A. Gopinath, K. V. Gothelf, M. A. Kostiainen and J. J. Toppari, “Plasmonic nanostructures through DNA-assisted lithography,” Sci. Adv., Vol. 4, No. 2, eaap8978, 2018.
4. Piskunen, P., B. Shen, A. Keller, J. J. Toppari, M. A. Kostiainen and V. Linko, “Biotemplated Lithography of Inorganic Nanostructures (BLIN) for Versatile Patterning of Functional Materials,” ACS Appl. Nano Mater., Vol. 4, No. 1, 529–538, 2021.
5. Kabusure, K. M., P. Piskunen, J. Yang, M. Kataja, M. Chacha, S. Ojasalo, B. Shen, T. K. Hakala and V. Linko, “Optical characterization of DNA origami-shaped silver nanoparticles created through biotemplated lithography,” Nanoscale, Vol. 14, No. 27, 9648–9654, 2022.
6. Kabusure, K. M., P. Piskunen, J. Yang, V. Linko and T. K. Hakala, “Raman enhancement in bowtie-shaped aperture-particle hybrid nanostructures fabricated with DNA-assisted lithography,” Nanoscale, Vol. 15, No. 19, 8589–8596, 2023.
7. Kabusure, K.M., P. Piskunen, J. J. Saarinen, V. Linko and T. K. Hakala, in preparation, 2024.

Broadband Circularly Polarized Thermal Emission enabled by Chiral Plasmonic Metamaterial

René Iseli[1*], Abraham De Jesus Aguilar Uribe[2], Bilel Abdennadher[1], Anne Nguyen[3], Viola Vogler-Neuling[1], Frank Scheffold[2], Jean-Jacques Greffet[3], Ullrich Steiner[1], and Matthias Saba[1]

[1]Adolphe Merkle Institute, University of Fribourg, Chemin des Verdiers 4, 1700 Fribourg, Switzerland
[2]Department of Physics, Faculty of Sciences and Medicine, University of Fribourg, Ch. du Musée 3 (PER08), 1700 Fribourg, Switzerland
[3]Institut d'Optique Graduate School - Laboratoire Charles Fabry, 2 Av. Augustin Fresnel, 91120 Palaiseau, France
[*]corresponding author: rene.iseli@unifr.ch

Abstract: Using Nanoscribe IP-Dip technology on conductive substrates we create a metallic chiral woodpile for circular polarized thermal emission. The heated sample emits broadband circular polarized mid-infrared radiation in the optical transparency window of the atmosphere. Predicted on the basis of the local Kirchhoff law and theoretical studies considering fundamental evanescent Floquet states we show first experimental results.

Sensors and emitters in the mid-infrared (MIR) light regime have grown more popular with the possibility of sensing various distinctive molecules such as polymers, toxic or explosive agents and molecular gases [1] through targeting the fundamental vibrational resonance band of such materials. Furthermore, MIR sources designed in the atmospheric transparency window are useful for telecommunication. A variety of sources, predominantly based on semiconductor lasing, exist at these frequencies ([2–4]). However, some applications, such as chiral molecule detection, require a circularly polarized source, which currently depend on the narrow-banded accuracy of the polarizers. A broadband MIR emitter thus widens the field in which a sensor or telecommunication device can be used for.

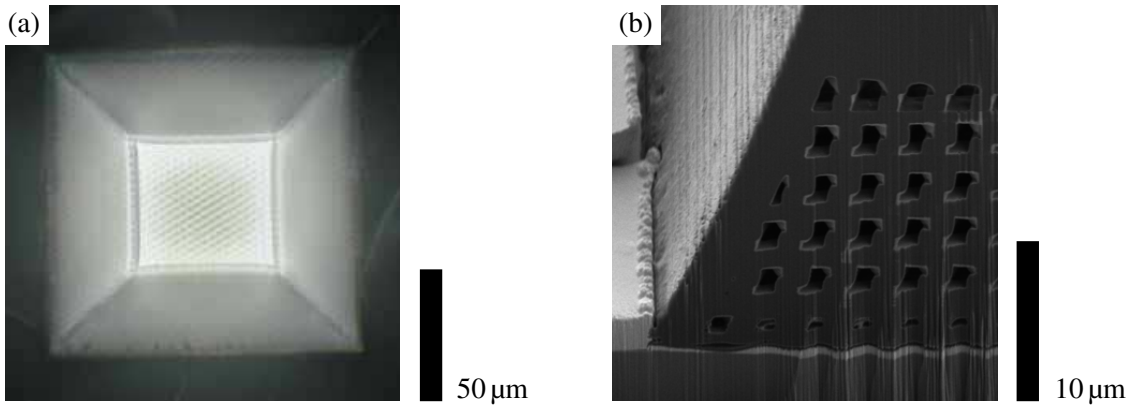


Figure 1: Cross polarization microscopy (a) of a chiral woodpile (100 µm^2) in a surrounding protective layer. The Woodpiles have a truncated pyramid shape to allow adjacent printing. Secondary electron microscopy image (b) of a cross section cut with a focused ion beam allow analysis of the printing quality inside the woodpile.

Here, we present a plasmonic chiral woodpile as a broadband circular polarized thermal emitter in the MIR regime. The chiral woodpile is a relatively simple design that can exhibit strong circular dichroism [5, 6]. According to the local Kirchoff law [7], a chiral woodpile of a lossy, plasmonic material is expected to have a strong, broandband CD between 3 µm and 4 µm insensitive to the precise geometrical details [8].

As two-photon-polymerization is a well-established fabrication technique for 3D MIR structures [9], we use the IP-Dip technology on Nanoscribe to design a pixel array of inverse woodpiles on a Cr/Au coated substrate. The conductive substrate allows the replication of the woodpile through elecrodeposition of platinum. Preliminary absorptivity measurements have been done on a Fourier-transform infrared spectroscopy setup. Step-by-step printing adaptations have been analyzed using a focused ion beam coupled with a secondary electron microscope as you can see in Fig.1.

References

[1] X. Tan, H. Zhang, J. Li, H. Wan, Q. Guo, H. Zhu, H. Liu, and F. Yi, "Non-dispersive infrared multi-gas sensing via nanoantenna integrated narrowband detectors," *Nature Communications*, vol. 11, no. 1, p. 5245, 2020. [Online]. Available: https://doi.org/10.1038/s41467-020-19085-1

[2] S. D. Jackson and R. K. Jain, "Fiber-based sources of coherent MIR radiation: key advances and future prospects (invited)," *Opt. Express*, vol. 28, no. 21, pp. 30 964–31 019, 2020. [Online]. Available: https://opg.optica.org/oe/abstract.cfm?URI=oe-28-21-30964

[3] X. Chen, X. Lu, B. Deng, O. Sinai, Y. Shao, C. Li, S. Yuan, V. Tran, K. Watanabe, T. Taniguchi, D. Naveh, L. Yang, and F. Xia, "Widely tunable black phosphorus mid-infrared photodetector," *Nature Communications*, vol. 8, no. 1, p. 1672, 2017. [Online]. Available: https://doi.org/10.1038/s41467-017-01978-3

[4] L. Tong, X. Huang, P. Wang, L. Ye, M. Peng, L. An, Q. Sun, Y. Zhang, G. Yang, Z. Li, F. Zhong, F. Wang, Y. Wang, M. Motlag, W. Wu, G. J. Cheng, and W. Hu, "Stable mid-infrared polarization imaging based on quasi-2D tellurium at room temperature," *Nature Communications*, vol. 11, no. 1, p. 2308, 2020. [Online]. Available: https://doi.org/10.1038/s41467-020-16125-8

[5] J.-H. Lee, J. C. W. Lee, W. Leung, M. Li, K. Constant, C. T. Chan, and K.-M. Ho, "Polarization Engineering of Thermal Radiation Using Metallic Photonic Crystals," *Advanced Materials*, vol. 20, no. 17, pp. 3244–3247, sep 2008. [Online]. Available: https://doi.org/10.1002/adma.200703160

[6] S. Takahashi, T. Tajiri, Y. Ota, J. Tatebayashi, S. Iwamoto, and Y. Arakawa, "Circular dichroism in a three-dimensional semiconductor chiral photonic crystal," *Applied Physics Letters*, vol. 105, no. 5, p. 51107, aug 2014. [Online]. Available: https://doi.org/10.1063/1.4892430

[7] J.-J. Greffet, P. Bouchon, G. Brucoli, and F. Marquier, "Light Emission by Nonequilibrium Bodies: Local Kirchhoff Law," *Physical Review X*, vol. 8, no. 2, p. 21008, apr 2018. [Online]. Available: https://link.aps.org/doi/10.1103/PhysRevX.8.021008

[8] B. Abdennadher, R. Iseli, U. Steiner, and M. Saba, "Broadband circular dichroism in chiral plasmonic woodpiles," *Applied Physics A*, vol. 129, no. 3, p. 229, 2023. [Online]. Available: https://doi.org/10.1007/s00339-023-06481-9

[9] S. Vaidya, J. Noh, A. Cerjan, and M. Rechtsman, *Observation of a charge-2 photonic Weyl point in the infrared*, feb 2020.

Bio-Inspired Nanophotonics

Optical imaging based on metasurfaces

Shuming Wang[1]

[1]National Laboratory of Solid State Microstructures, School of Physics, Nanjing University, Nanjing 210093, China

[*]corresponding author: wangshuming@nju.edu.cn

Abstract: The optical imaging has been demonstrated based on various metasurface devices, such as broadband achromatic metalens, ultracompact spectral light field imaging (SLIM) camera, and pixel-level metasurface-based Bayer-type colour router, etc.

Ideal imaging technique simultaneously requires the three-dimensional (3D) high spatial-resolution and the high spectral-resolution. To date, while compact 3D imaging technique and spectrometer have been individually developed, the combination of these techniques has only been realized in cumbersome systems, significantly limiting their practical applications. A long-standing and critical challenge is how to integrate the 3D spatial-resolution and the spectral-resolution into a single nanophotonic device. Herein, based on the precise wavefront control of metasurface and deep-leaning algorithm, we experimentally demonstrate the first ultracompact spectral light field imaging (SLIM) camera. The SLIM camera consists of TiO2 lens array on a CMOS camera. Owing to the high dispersion of metalens, both the 3D position information and the spectrum can be re-constructed without sacrificing the light throughput. The demonstrated spectral-resolution is as high as 4nm and the spatial-resolution reaches the diffraction limit, enabling the capability of SLIM in precise 3D imaging and material discrimination. By employing an inverse-design method, we demonstrate a pixel-level metasurface-based Bayer-type colour router, with the brightness twice as high as that of a commercial camera.

References

1. Wang, S. M., et al, “A broadband achromatic metalens in the visible”, Nature Nanotechnology 13, 227-232 (2018).
2. Lin, R. J., et al, “Achromatic metalens array for full-colour light-field imaging”, Nature Nanotechnology 14, 227-231 (2019).
3. Hua, Xia, et al, “Ultra-compact snapshot spectral light-field imaging”, Nature Communications 13, 2732 (2022).
4. Zou, Xiujuan, et al, “Pixel-level Bayer-type colour router based on metasurfaces”, Nature Communications 13, 3288 (2022).

Color arrestor pixels for high-fidelity, high-sensitivity imaging sensors

Mingwan Cho[1], Joonkyo Jung[1], Myungjoon Kim[1], Jeong-Yub Lee[2], Seokhwan Min[1], Jongwoo Hong[3], Shinho Lee[3], Minsung Heo[3], Jong Uk Kim[3], In-Sung Joe[3,*] and Jonghwa Shin[1,*]

[1] Department of Materials Science and Engineering, Korea Advanced Institute of Science and Technology (KAIST), Daejeon 34141, Republic of Korea.

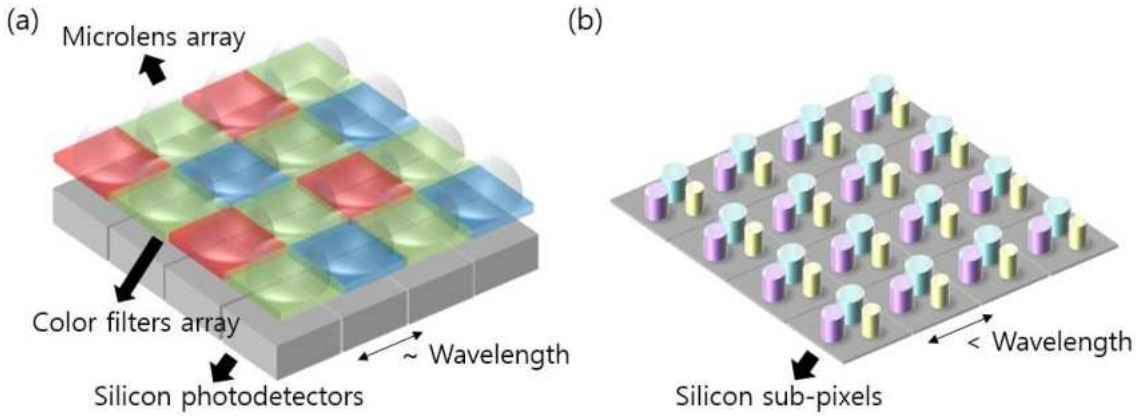
[2] Samsung Advanced Institute of Technology, 130, Samsung-ro, Yeongtong-gu, Suwon-si, Gyeonggi-do 16678, Republic of Korea.

[3] Semiconductor Research Center, Samsung Electronics, Samsungjeonja-ro 1, Hwaseong-si, Gyeonggi-do, 18448, Republic of Korea.

[*]corresponding author: qubit@kaist.ac.kr, insung.joe@samsung.com

Abstract: We introduce color arrestor pixels (CAPs), a breakthrough in CMOS sensor technology, offering unparalleled color accuracy and miniaturization. By mimicking human eye response with advanced metasurfaces, CAPs outperform traditional sensors, achieving high efficiency and angular tolerance with a small footprint. This innovation heralds a new era in high-fidelity imaging.

Silicon is the dominant material in complementary metal-oxide-semiconductor (CMOS) imaging devices because of its outstanding electrical and optical properties, well-established fabrication methods, and abundance in nature. However, with the ongoing trend toward electronic miniaturization, which demands smaller pixel sizes in CMOS image sensors, issues, such as crosstalk and reduced optical efficiency have become critical. These problems stem from the intrinsic properties of Si, particularly its low absorption in the long wavelength range of the visible spectrum, which makes it difficult to devise effective solutions unless the material itself is changed. Recent advances in optical metasurfaces have offered new possibilities for solving these problems. In this study, we propose color arrestor pixels (CAPs) as a new class of color image sensors whose composite spectral responses directly mimic those of the human eye. The key idea is to employ linearly independent combinations of standardized color matching functions. These new basis functions allow our device to reproduce colors more accurately than the currently available image sensors with red-green-blue filters or other metasurface-based sensors, demonstrating an average CIEDE2000 color difference value of only 2.88 when evaluating 24 colors from the Gretag-Macbeth chart under standard illuminant D65. Owing to their high fidelity to the human eye response, CAPs consistently exhibit exceptional color reproduction accuracy under various spectral illumination compositions. Simple schematic figure of CAPs is explained in Figure 1. With a small footprint of 855 nm height and 220 nm full-color pixel pitch, the CAPs demonstrated high absorption efficiencies of 80%, 82%, and 63% at wavelengths of 460 nm, 555 nm, and 596 nm, respectively, and good angular tolerance. With such a high density of pixels efficiently capturing accurate colors, CAPs present a new direction for optical image sensor research and their applications.



(c)

Light source	Perceiver		
	Human eye	RGB CF	CAP
D65		(14.9, 39%)	(2.59, 64%)
		(14.8, 41%)	(3.16, 58%)
		(12.3, 50%)	(2.26, 61%)
White LED		(9.17, 39%)	(2.35, 64%)
		(16.4, 41%)	(4.03, 58%)
		(9.55, 50%)	(2.83, 61%)

Figure 1: Comparison of conventional CIS with Bayer RGB color filters and CAPs. a) Schematic illustration of conventional CIS featuring a microlens array, Bayer RGB color filter array, and Si photodetectors. b) A diagram of the CAPs, with each supercell composed of three different sub-pixels. c) A visual comparison of colors among the naked human eye, CIS with Bayer RGB color filters, and CAPs when observed under standard illuminant D65 and white LED. The values represent efficiency and the average color difference values compared to the color captured by the human eye and the absorptance of the Si photodetector.

Acknowledgments: We would like to express our sincere gratitude to all the co-authors and the corresponding authors for their invaluable assistance and contributions to this research.
Research funding: This work was supported by the Samsung Electronics Co. Ltd(IO201214-08163-01).

References

1. J. S. T. Smalley, X. Ren, J. Y. Lee, et al., “Subwavelength pixelated CMOS color sensors based on anti-Hermitian metasurface,” *Nat. Commun.*, vol. 11, 2020, Art no. 3916.
2. J. Ho, Z. Dong, H. S. Leong, et al., “Miniaturizing color-sensitive photodetectors via hybrid nanoantennas towards sub-micron dimensions,” *Sci. Adv.*, vol. 8, no. 47, p. eadd3868, 2022.
3. S. Kim, C. Lee, S. Jeon, J. Park, and S. Kim. "Subwavelength sorting of full-color based on anti-Hermitian metasurfaces," *Nanophotonics*, vol. 10, no. 2, pp. 967-974, 2020.

Analysis of aliasing in phase gradient metasurfaces: Breaking efficiency limits of high-NA ultraviolet metasurface

K. Kim[1] **and J. Rho**[1,2,3,4*]

[1]Department of Mechanical Engineering, Pohang University of Science and Technology (POSTECH), Pohang 37673, Republic of Korea

[2]Department of Chemical Engineering, Pohang University of Science and Technology (POSTECH), Pohang 37673, Republic of Korea

[3]POSCO-POSTECH-RIST Convergence Research Center for Flat Optics and Metaphotonics, Pohang 37673, Republic of Korea

[4]National Institute of Nanomaterials Technology (NINT), Pohang 37673, Republic of Korea

[*]corresponding author: jsrho@postech.ac.kr

Abstract-

Designing phase gradient metasurfaces via phase sampling has been extensively investigated, as it enables manipulation of light intuitively. However, it causes unwanted aliasing which reduces the focusing efficiency and degrades imaging quality when the sampling level is insufficient. Here, we investigate aliasing patterns in metasurfaces and how to effectively address them, especially in case of large deflection angles and UV regime.

Metasurfaces have been garnered for several decades with their extraordinary electromagnetic properties by strategic arrangement of meta-atoms. The widely used method to design metasurfaces is phase sampling, mapping the desired phase map and allocating meta-atoms at corresponding phase [1]. This method has been successfully applied to such as lenses, holograms, beam steerers, and waveguides [2-3]. However, at large deflection angles, small periods, and short wavelengths, aliasing severely occurs, reducing efficiency and degrading imaging quality [4].

In this work, we investigate aliasing in gradient metasurfaces. One method to alleviate aliasing is to decreases the periodicity of the unit cell. However, it leads to increase fabrication difficulty and occurs unexpected nonlocal effect. We investigated aliasing in a beam steerer respect to the azimuthal angle of the sampling grid. We also analyzed the aliasing in metalenses with various NA and grid type. Finally, we demonstrate anti-aliasing ultraviolet metalens which has an NA of 0.9. By replacing the outer part of the metalens with an arrangement of asymmetric nanoantennas within a supercell, so-called metagrating, aliasing is effectively eliminated. This anti-aliasing metalens shows higher efficiency than phase sampling metalens. We believe that our findings will shed the light on the systems requiring high NA such as high-resolution imaging system, wide field-of-view in AR/VR devices and LIDAR systems, optical trapping systems and state of the art lithography technology [5].

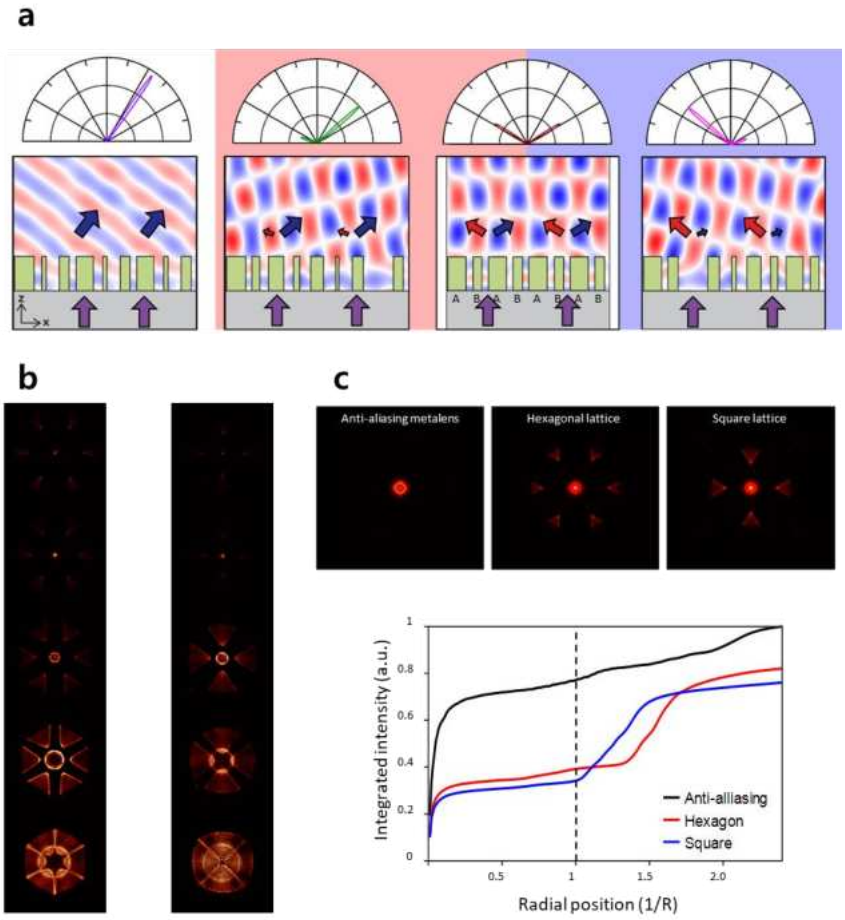


Figure 1. (a) Simulation results of various beam steerer with different deflection angle. Blue arrow represents desire order and red arrow represents aliasing order. (b) Results of Z-scan experiments. Right is hexagonal lattice metalens and square lattice metalens. The NA of both metalens is 0.95. (c) Simulated results of integrated intensity for Anti-alliasing metalens (black), Hexagonal lattice metalens (red), and Square lattice metalens (blue).

REFERENCES

1. Hu, Jie, et al., "A review on metasurface: from principle to smart metadevices.", Frontiers in Physics, Vol. 8, 586087, 2021.
2. Khorasaninejad, Mohammadreza, et al., "Metalenses at visible wavelengths: Diffraction-limited focusing and subwavelength resolution imaging.", Science, Vol. 352, Issue 6290, 1190-1194, 2016.
3. Wang, Qiu, et al., "Reflective chiral meta-holography: multiplexing holograms for circularly polarized waves.", Light: Science & Applications, Vol. 7, No.1, 2018.
4. Ra'di, Younes, Dimitrios L. Sounas, and Andrea Alù., "Metagratings: Beyond the limits of graded metasurfaces for wave front control.", Physical review letters, Vol. 119, No. 6, 067404, 2017.
5. Oh, Beomseok, et al., "Engineering metalenses for planar optics and acoustics.", Materials Today Physics, 101273, 2023.

Portable Hydrogen Sensing Enabled by Overlaid Holographic Metasurfaces and Liquid Crystal Integration

Dohyun Kang[1], Younghwan Yang1[1], and Junsuk Rho[1,2,3,4,5*]

[1]Department of Mechanical Engineering, Pohang University of Science and Technology (POSTECH), Pohang 37673, Republic of Korea

[2]Department of Chemical Engineering, Pohang University of Science and Technology (POSTECH), Pohang 37673, Republic of Korea

[3]Department of Electrical Engineering, Pohang University of Science and Technology (POSTECH), Pohang 37673, Republic of Korea

[4]POSCO-POSTECH-RIST Convergence Research Center for Flat Optics and Metaphotonics, Pohang 37673, Republic of Korea

[5]National Institute of Nanomaterials Technology (NINT), Pohang 37673, Republic of Korea
[*]corresponding author: jsrho@postech.ac.kr

Abstract: A commercially viable, portable hydrogen meta-sensor is introduced, integrating gas-responsive liquid crystal cells with two-by-two metasurface arrays. This innovation can identify hydrogen gas concentrations at four levels. Fabricated through cost-effective nanoimprinting methods, the metasurfaces make this gas meta-sensor promising for on-the-go sensing in diverse industrial applications.

Hydrogen has garnered attention as a sustainable alternative to traditional fossil fuels, fueled by the increasing need for long-distance energy transportation and the potential for high-energy storage density [1]. This highlights the necessity for portable and cost-effective concentration monitoring to mitigate potential hydrogen leakage [2]. In this study, we introduce a commercially viable, portable hydrogen meta-sensor achieved through the integration of gas-responsive liquid crystal cells with two-by-two metasurface arrays.

The hydrogen meta-sensor is structured in a sandwich-like arrangement involving an x-polarizer, liquid crystal, y-polarizer, and metasurfaces, incorporating well-defined optical modeling through overlaid holography. Within the hydrogen sensor, liquid crystal cells function as a crucial switch, facilitating real-time visual alarms based on gas concentration. Each metasurface within the arrays is embedded with diverse holographic images, aligning their visual content with the saturation level of metasurface-paired liquid crystals. Through practical experimentation, we showcase the capabilities of the multi-level gas meta-sensor, capable of identifying concentrations of hydrogen gas at four levels (50 ppm, 100 ppm, 150 ppm, and 200 ppm), presenting reconstructed holographic alarms in a visual format. Fabricated using cost-effective nanoimprinting methods, these metasurfaces position the multi-level gas meta-sensor as a promising on-the-go sensing platform for various industrial applications, holding significant potential for mass production.

References

1. Yue, M, et al. "Hydrogen energy systems: A critical review of technologies, applications, trends and challenges." Renewable and Sustainable Energy Reviews, 146, 111180, 2021.
2. Ramachandran, R. and Raghu K. M. "An overview of industrial uses of hydrogen." International journal of hydrogen energy, 23.7, 593-598, 1998.

Control of Electric and Magnetic Dipole Emission by Purcell effect of Mie resonant Silicon nanosphere

H. Kasai[1], H. Sugimoto[1*], and M. Fujii[1]

[1]Electrical and Electronic Engineering, Graduate School of Engineering, Kobe University, Japan

Abstract: The enhancement of magnetic dipole transition is a key factor for controlling light emission of rare-earth ions and facilitating spin-forbidden optical transition. In this study, we employ spherical silicon nanoparticles with magnetic-type Mie resonances for enhancing the magnetic dipole emission of Eu^{3+} ions.

In these days, in addition to the enhancement of electric dipole transition by the nanoantennas, the magnetic dipole transition enhancement have attracted attentions. This is expected to lead to the enhancement of magnetic dipole emission rate of rare earth ions[1,2] and spin-forbidden transition of molecules(e.g. $S_0 \rightarrow T_1$)[3, 4]. Several works have demonstrated the manipulation of magnetic dipole transitions by silicon (Si)-based Mie resonators. However, the observed magnetic emission rate enhancement was marginal. In this work, to achieve substantial magnetic Purcell enhancement, we employ silicon (Si) nanospheres (NSs) and try to enhance the electric and magnetic dipole emission of Eu^{3+} via Purcell effect originated from electric and magnetic Mie resonances.

Prior to the experimental study, we calculated the emission rate enhancement of electric and magnetic dipole emitters by a Si NS. Figure 1(a) shows calculated results of extinction efficiency of Si NP with 275 nm in diameter. The high-order Mie modes such as the magnetic quadrupole (MQ), electric quadrupole (EQ) exist in visible to near-infrared range. Figure 1(b) and (c) show the calculated results of radiative rate enhancement for electric and magnetic dipole emitters, respectively, by Si NS in 275 nm in diameter. At the resonance wavelength of the EQ (MQ), the radiative rate of electric (magnetic) dipole is largely enhanced. In particular, radiative rate for magnetic dipole is enhanced more than 50 times by the MQ resonance. There result indicates that it is possible to enhance electric and magnetic dipole emission of Eu^{3+} by tuning the resonance wavelength, *i.e*, Si NS size control.

Recently, our group have succeeded in producing highly spherical and crystalline Si NSs which have electric and magnetic Mie modes in visible to near-infrared range[4]. We attach Eu^{3+} complexes on the surface of Si NSs (see inset of Figure 2(a,c), Si NS:Eu). Figure 2(a) and (b) show the measured scattering and photoluminescence (PL) spectra of a

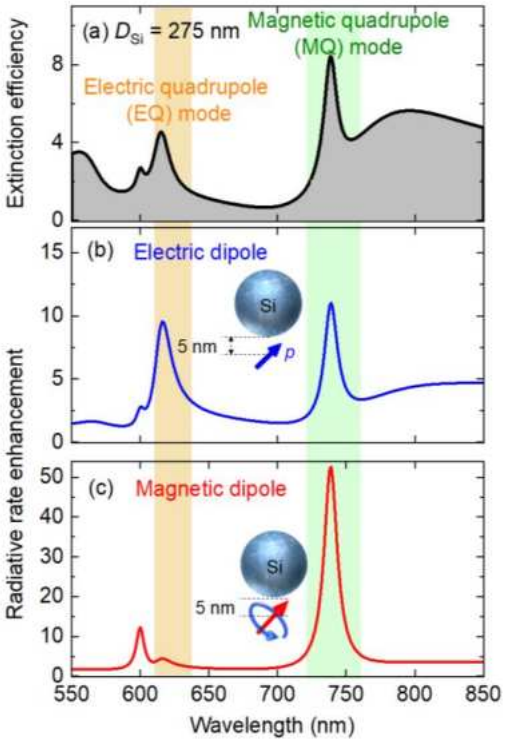


Figure 1: Calculated results of (a) Extinction efficiency and (b,c) radiative rate enhancement spectra for (b) electric and (c) magnetic dipole emitters by Si NS with 275 nm in diameter. Dipole emitters are placed at 5 nm from Si NP surface.

single Si NS: Eu (diameter: 205 nm), respectively. We can observe a MQ resonance at the wavelength of 590 nm in the scattering spectra. In the PL spectra, magnetic dipole emission ($^5D_0 \rightarrow {}^7F_1$) of Eu^{3+} is enhanced compared to reference spectra (blue shade) at the wavelength of 590 nm. As demonstrated in the calculated result, this is due to magnetic Purcell effect by Si NSs. Figure 2(c,d) shows the scattering and PL spectra of Si NS;Eu with 316 nm in diameter. At the wave- length of 690 nm, we can see an EQ resonance of a Si NS and enhancement of electric dipole emission of Eu^{3+}($^5D_0 \rightarrow {}^7F_4$). This is due to electric Purcell effect.

In the poster session, we demonstrate that the branching ratio of the $^5D_0 \rightarrow {}^7F_j$ (j = 0-4) transitions of Eu^{3+} ions can be controlled in a wide range by tuning the resonance wavelength and also discuss the result for selective enhancement of the transition to a specific Stark sublevel by precisely controlling the size of a Si NS.

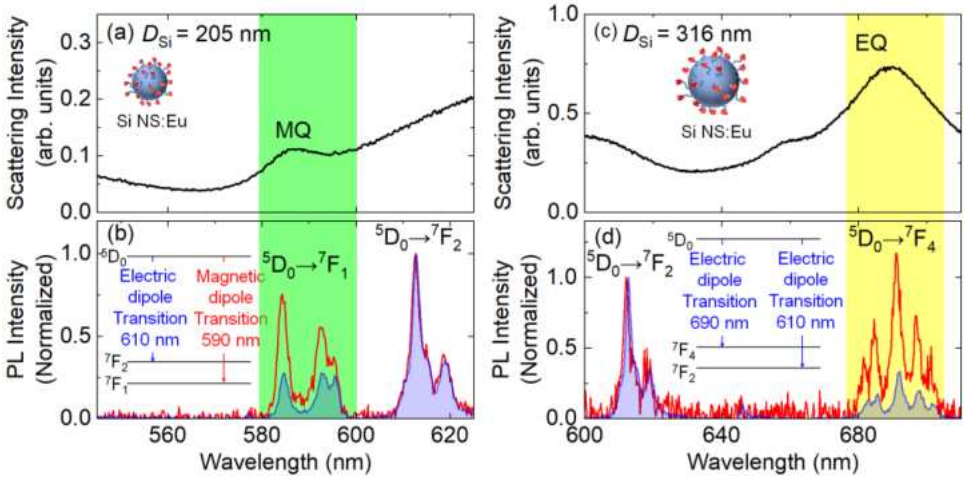


Figure 2: (a,c) Scattering and (b.d) PL spectra of single Si NS:Eu with the diameter of 205 nm(a,b) and 316 nm(c,d) (PL: red curve). PL is also shown as a blue shade.

References

1. Kasai, H. et al, "Selective Enhancement of Crystal-Field-Split Narrow f-f Emission Lines of Europium Ions by Electric and Magnetic Purcell Effect of Mie Resonant Silicon Nanosphere," Adv. Optical Materials., Vol. 12, Issue 1, 2301204, 2023.
2. Sugimoto, H. et al. "Mie Resonator Color Inks of Monodispersed and Perfectly Spherical Crystalline Silicon Nanoparticles" Adv. Optical Materials., Vol. 8, Issue 12, 2000033,2020.
3. Manjavacas, A. et al. "Magnetic Light and Forbidden Photochemistry: The Case of Singlet Oxygen" Journal of Materials Chemistry C. Vol. 5, Issue 45, 11824,2017.
4. Sugimoto, H. et al, "Direct Excitation of Triplet State of Molecule by Enhanced Magnetic Field of Dielectric Metasurfaces," Small, Vol. 17, Issue 47, 2104458, 2021.

Exploring Wave Phenomena in Quasicrystal-Based Photonic Structures

M. V. Rybin[1,2]

[1] School of Physics and Engineering, ITMO University, 197101 St. Petersburg, Russia

[2] Ioffe Institute, 194021 St. Petersburg, Russia
*corresponding author: m.rybin@metalab.ifmo.ru

Abstract: Quasicrystal-based photonic structures offer unique design flexibility due to their aperiodic nature, allowing for novel wave phenomena. This article reviews our recent reports on such structures, focusing on intrinsic light localization, photonic bandgap formation, and selective absorption of electromagnetic radiation, showcasing the potential of quasicrystals in photonics.

The recent decades witnessed significant advancements in artificial photonic media, e.g., photonic crystals and metamaterials. Fabrication techniques advanced, adapting theoretical concepts from condensed matter physics to the electromagnetic realm. Traditional treatments rely heavily on translational symmetry, simplifying analyses to single unit cells with Bloch solutions, yet limiting factors like crystallography rules or lack of intrinsic localization persist. Quasicrystals, though non-periodic, offer novel possibilities due to their ordered yet aperiodic nature. These structures hint at sustaining metamaterial properties, local density of photonic states modulation, and other unexplored effects. Our recent reports include intrinsic light wave localization in 3D icosahedral quasicrystals [1], polymer-based photonic structures with complete bandgaps [2], and systems with precise spectral and directional selectivity [3].

Understanding waves in periodic media is aided by the Bloch theorem, relating waves to a periodic function multiplied by a plane wave. Notably, periodic systems offer only localized modes near sample boundaries due to translation symmetry, contrasting quasicrystals where intrinsic wave localization is viable without such constraints. Recent numerical simulations [4] and experiments [1] on icosahedral quasicrystals confirmed this intrinsic wave localization effect, enhancing light-matter interactions and unveiling new possibilities for practical applications.

Aside from 3D structures, interlaced wire media with Penrose tiling patterns exhibit unique properties. These media consist of non-connected wire sublattices on parallel planes, enabling intriguing electromagnetic wave control. By exploiting the C5 rotational symmetry of Penrose tiling, these structures demonstrate diverse wave manipulation abilities, promising further advancements in photonics research and application development [5]. Numerical simulations on interlaced media based on the C5 Penrose tiling showed intrinsic localization of electromagnetic waves in a specific frequency range.

Quasicrystalline structures allow for the reduction of the material's refractive index to create a complete band gap. The overlap of stopbands related to Bragg scattering for all polarizations and directions in a frequency interval is crucial for this. Quasicrystals with a dense distribution of maxima in reciprocal space can have almost spherical Brillouin zones, reducing the requirements for dielectric index contrast for the complete photonic band gap to open up [2].

The modulation of the local density of photonic states was studied concerning translation symmetry. Quasicrystalline structures showed similar frequency modulation of the local density of photonic states as crystal structures, emphasizing the importance of structural ordering over translation symmetry [6]. Also, designing quasicrystalline structures by binarization of sine-type gratings enables manipulation of electromagnetic waves.

Recent designs have shown structures capable of absorbing waves incident at specific angles and frequencies while allowing other waves to pass through with minimal scattering [3].

Overall, quasicrystalline structures offer unique properties for controlling electromagnetic wave behaviors, especially in terms of creating complete photonic bandgaps and managing wave interactions based on specific design parameters.

This work was supported by the Russian Scientific Foundation (grant no. 20-79-10316).

References

1. Sinelnik, A. D. et al. “Experimental observation of intrinsic light localization in photonic icosahedral quasicrystals,” Adv. Opt. Mater., Vol. 8, 2001170, 2020.
2. Maiwald, L. et al. “Control over Light Emission in Low-Refractive-Index Artificial Materials Inspired by Reciprocal Design,” Adv. Opt. Mater., Vol. 10, 2100785, 2022.
3. Chistyakov V. A., Sidorenko M. S., Sayanskiy A. D. and Rybin M. V. “Quasicrystalline structures with narrow-band frequency–angular selectivity,” JETP Lett., Vol. 117, 742-746, 2023.
4. Jeon S. Y., Kwon H. and Hur K. “Intrinsic photonic wave localization in a three-dimensional icosahedral quasicrystal,” Nature Phys., Vol. 13, 363, 2017.
5. Koreshin E. A. and Rybin M. V. “Interlaced wire medium with quasicrystal lattice,” Phys.Rev. B, Vol. 105, 024307, 2022.
6. Chistyakov V. A., Sidorenko M. S., Sayanskiy A. D. and Rybin M. V. “Density of photonic states in aperiodic structures,” Phys. Rev. B, Vol. 107, 014205, 2023.

Polarization-selective metalens for varifocal imaging system

Hyeonsu Heo[1], Gyeongtae Kim[1], Hongyoon Kim[1], Dongmin Jeon[1], and Junsuk Rho [1, 2, 3,4,5*]

[1]Department of Mechanical Engineering, Pohang University of Science and Technology (POSTECH), Pohang 37673, Republic of Korea

[2]Department of Chemical Engineering, Pohang University of Science and Technology (POSTECH), Pohang 37673, Republic of Korea

[3]Department of Electrical Engineering, Pohang University of Science and Technology (POSTECH), Pohang 37673, Republic of Korea

[4]POSCO-POSTECH-RIST Convergence Research Center for Flat Optics and Metaphotonics, Pohang 37673, Republic of Korea

[5]National Institute of Nanomaterials Technology (NINT), Pohang 37673, Republic of Korea

[*]Corresponding author: jsrho@postech.ac.kr

Abstract: Achieving compact varifocal imaging system is significant topic for various practical applications. We introduce a multifocal metalens enabling focal length adjustment through incident polarization variation, targeting AR/VR applications. We analyze multifocal design platform with various lens parameters and explore alternative methods for increasing the focal points.

Metalens, thin and flat lens consisting of nanostructure arrays, have garnered considerable attention due to their potential to reduce the bulkiness of conventional optical imaging system [1]. However, conventional metalenses are limited in functionality, typically offering a single fixed focal length after fabrication. Previous works have aimed to introduce multiple focal lengths or multi-functionality within a single device [2]. Meanwhile, the exploration of varifocal imaging systems has gained prominence due to its applicability in addressing practical challenges, such as resolving the vergence-accommodation conflict (VAC) to enhance the usability of AR/VR systems. In this study, we present a multifocal metalens capable of shifting its focal length by varying the incident polarization and apply it to varifocal imaging system for AR/VR applications.

To achieve the selective imposition of phase profiles corresponding to lenses with two different focal length within a single metalens, we leverage both propagation phase and geometric phase modulation. We utilize the materials with high refractive index and low optical loss, such as SiN (532nm) and a-Si:H (635nm), to obtain enough options for structural parameter candidates. The versatility of fabricated metalens is demonstrated through its integration into varifocal imaging systems, including AR/VR imaging system capable of mitigating the VAC. Additionally, different metalens samples are designed with the various lens parameter and their impacts are analyzed, verified through extreme case of on-off metalens which multiplexed lens profile with zero-phase profile. To enhance the practicality of this platform, we also explore an alternative design method utilizing off-axis elements of Jones matrix to expand the number of focal points.

References

1. Moon, SW *et al*., "Recent progress on ultrathin metalenses for flat optics." *iScience.* Vol. 23, No. 12, 101877, 2020
2. Badloe, T *et al.,* "Electrically Tunable Bifocal Metalens with Diffraction-Limited Focusing and Imaging at Visible Wavelengths." *Adv. Sci.* Vol. 8, 2102646, 2021

Artificial neural networks-based on-demand inverse design for 3D chiral metamaterials

Jehyeon Shin[1], Jeonghoon Park[2], Jaebum Noh[2] and Junsuk Rho[2,3,4*]

[1] Graduate School of Artificial Intelligence, Pohang University of Science and Technology (POSTECH), Pohang 37673, Republic of Korea

[2]Department of Mechanical Engineering, Pohang University of Science and Technology (POSTECH), Pohang 37673, Republic of Korea

[3]Department of Chemical Engineering, Pohang University of Science and Technology (POSTECH), Pohang 37673, Republic of Korea

[4]Department of Electrical Engineering, Pohang University of Science and Technology (POSTECH), Pohang 37673, Republic of Korea

[*]corresponding author: jsrho@postech.ac.kr

Abstract: The bandgap properties of chiral metamaterials can be used to inhibit wave modes in physical beams. We use the inverse neural network to get chiral structures that have bandgap requirements by adjusting the range of maximal stress. This approach allows for building metamaterials while adjusting physical characteristics as intended.

With the advances in 3D printing technology, fabricating complex three-dimensional mechanical/elastic structures has become easier. Metamaterials are artificially designed materials with unique physical and mechanical properties not found in nature [1]. They possess distinctive physical features such as negative effective bulk modulus [2] and band gaps [3], making them suitable for use in numerous fields. By utilizing the band gap properties, we can suppress elastic waves in a physical beam, therefore decreasing the vibration of the structure. In particular, complete band gap to block elastic waves of all polarizations has been achieved through chiral mechanical metamaterials [4]. However, previous research lacked analysis regarding the stability of the structures. To design a stable metamaterial, it is essential to take into account both the band gap and stress analysis. However, simultaneously incorporating dynamic properties like as band gaps and static properties like stress creates a broad and intricate design domain, which results in constraints for traditional heuristic-based design approaches.

In this study, we propose a method for producing chiral mechanical metamaterials with desired characteristics through inverse design using artificial intelligence. The tandem architecture is used to address the non-uniqueness problem that could occur in the inverse design process. We develop a forward model for predicting bandgap frequencies and maximum Von Mises stress under compression, which was subsequently utilized for training in the inverse neural network (Fig. 1a). During the training of the inverse neural network, bias was assigned to minimize maximal stress. This makes it possible to design a structure with low stress while maintaining the bandgap distribution (Fig. 1b). Furthermore, the inverse neural network offers flexibility to precisely represent the bandgap criteria and alter the stress values based on the user's desire. Fig. 1c shows that the constructions of each row seem similar in appearance; however, the stress on the rods differs by more than three times. By using artificial intelligence for inverse design, we achieve metamaterial design that enhances stability while maintaining its physical properties.

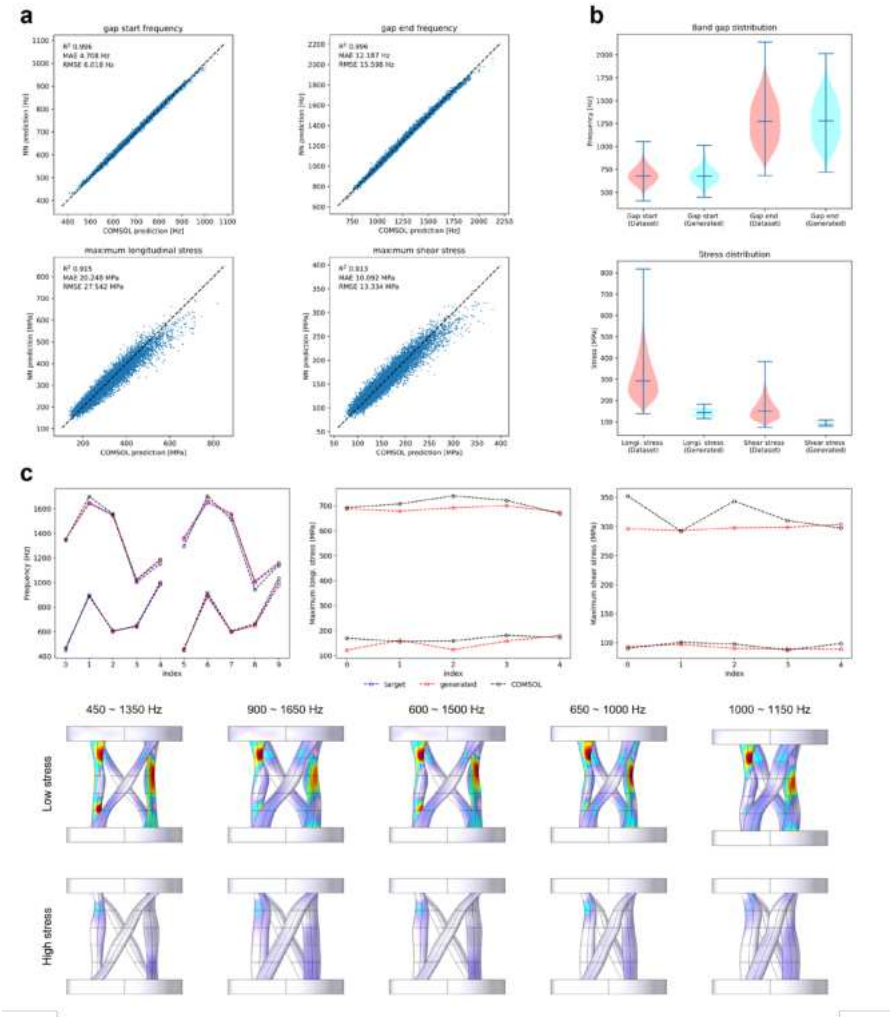


Figure 1. (a) The outputs estimated by neural networks (NN) are compared with the values of COMSOL, and the R-squared (R^2), root mean squared error (RMAE) and root mean squared error (RMSE) are calculated by comparing the NN. (b) Violin plots showing the distributions of the dataset (red) and generated set (blue) for bandgap frequencies and stresses. (c) Chiral metamaterials with low and high stress bias for five pairs of bandgaps. The stress distribution in each structure is analyzed using COMSOL. While the bandgaps are same, the stress on the rods differs by almost three times.

References

1. Bauer J., Meza L. R., Schaedler T. A., Schwaiger R., Zheng X., and Valdevit L., "Nanolattices: An Emerging Class of Mechanical Metamaterials," Advanced Materials, vol. 29, no. 40, p. 1701850, Oct. 2017.
2. Fang N. et al., "Ultrasonic metamaterials with negative modulus," Nature Mater, vol. 5, no. 6, pp. 452–456, Jun. 2006.
3. Park J., Lee D., Jang Y., Lee A., and Rho J., "Chiral trabeated metabeam for low-frequency multimode wave mitigation via dual-bandgap mechanism," Commun Phys, vol. 5, no. 1, p. 194, Jul. 2022.
4. Bergamini A. et al., "Tacticity in chiral phononic crystals," Nat Commun, vol. 10, no. 1, p. 4525, Oct. 2019.

Inverse Design for wavelength and polarization multiplexing in optical metasurfaces

Bo Xiong[1*], and Wei. Ma[1]

[1]Zhejiang University, China
[*]corresponding author: bo.xiong@zju.edu.cn

Abstract: By introducing the engineered noise to the precise solution of Jones matrix elements, we break the fundamental limit of polarization multiplexing capacity of metasurfaces. We experimentally demonstrate up to 11 independent holographic images using a single metasurface illuminated by different polarizations.

Near-infrared multi-spectral and multi-polarization imaging technology enhances target detection and recognition by distinguishing the spectral characteristics of various targets. However, traditional imaging systems heavily rely on complex optical filter designs that are often bulky and mechanically unstable, posing significant challenges for miniaturization and integration challenging. In this talk, we firstly designed a freeform dielectric metasurface with the wavelength-multiplexing focusing effect based on a deep learning model, which can separate the mixed near-infrared light into distinct wavelengths. To effectively modulate the complex amplitude of the transmitted light at three distinct near-infrared wavelengths (1150, 1350, and 1550 nm), high-index silicon freeform nanostructures supporting rich resonant modes were proposed. An inverse design model based on deep learning was utilized to generate individual freeform nanostructures pixel by pixel, satisfying the complex amplitude requirement for a multiplexed metalens design. Finally, a metasurface was employed to realize near-infrared multispectral imaging, which allowed for the distinct detection and decoding of images at the three target wavelengths. Moreover, we also designed a polarization multiplexing metasurfaces based on genetic algorithm, in which noise engineering has been introduced to break the polarization multiplexing capacity of metasurfaces that roots from the dimension constraints of the Jones matrix. Illuminated by the incidence with different linear polarization states, the metasurface can generate up to 11 independent holographic images at the corresponding channels. To the best of our knowledge, it is the highest capacity reported for polarization multiplexing. The proposed technology has a wide range of applications in clinical medicine, biological tissue imaging, and deep-space exploration.

References

1. **B Xiong**, Y Xu, W Li, W Ma[*], T Chu[*], Y Liu[*] "Deep Learning Design for Multiwavelength Infrared Image Sensors Based on Dielectric Freeform Metasurface", **Advanced Optical Materials** 2302200 (2024)
2. **B. Xiong**, Y. Liu, Y. H. Xu, L. Deng, C. W. Chen, J. N. Wang, R. W. Peng[*], Y. Lai, Y. M. Liu[*], and M. Wang[*], "Breaking the limitation of polarization multiplexing in optical metasurfaces with engineered noise," **Science**, Vol. 379, No. 6629, 294-299 (2023).
3. **B. Xiong**, Y. H. Xu, J. N. Wang, L. Li, L. Deng, F. Cheng, R. W. Peng[*], M. Wang[*] and Y. M. Liu[*], "Realizing colorful holographic mimicry by metasurfaces", **Advanced Materials** 33(21), 2005864 (2021).

Generation of multi-channel overlapping perfect vortex beam on chip

X. R. Zhao [1], Q. H. Wang [2], X.Z.Pei , C. Xu, Q. Kan[2] and Y. Y. Xie[1*]

[1] Key Laboratory of Optoelectronics Technology, Ministry of Education, Beijing University of Technology,Beijing, 100124, China

[2] Key Laboratory of Semiconductor Materials Science, Institute of Semiconductors, Chinese Academy of Sciences, Beijing, 100083, China

[*]corresponding author: xieyiyang@bjut.edu.cn

Abstract: This article endeavors to integrate a metasurface with a VCSEL to achieve a perfectly compact and miniaturized perfect vortex beams (PVB) integrated VCSEL chip. This concept is also applied to broaden the functionalities of PVB, including on-chip overlapping PVB and on-chip multi-channel overlapping PVB.

Introduction: Since the proposal of the PVB concept, its extensive application prospects have garnered swift attention, and methods for its generation have proliferated, such as through the application of spatial light modulators, interferometers, or conical lenses[1]. However, these traditional methods of generating PVBs involve a series of bulky optical components. In addition, Minor errors in alignment between individual optical components will affect the quality of the generated PVB. Some researchers utilize the two-dimensional structure of metasurfaces to combine the functions of axicons, vortex phase plates, and Fourier lenses in the same dimension to generate PVB. While this method significantly improves the efficiency of PVB generation, it still requires an independent feed source and imposes high requirements on the quality of the incident beam. Therefore, a more complete collimation system needs to be built, which hinders the further development of PVB. To reveal the full potential of PVB, people are committed to achieving miniaturization and integrated generation of PVB on different platforms. In this article, we present the generation and preparation of a chip that utilizes integrated metasurfaces to directly emit PVB. Unlike the traditional preparation of PVB, our method has the main advantage that we do not require independent feed sources or separate collimation systems[1,2]. We use metasurfaces as intermediaries to directly integrate the collimation function and the control function of vortex beams on the chip, further expanding the control function of the integrated chip on the beam, this provides more opportunities for the application of vortex beams with multiple topological charge value and stable spot diameters. At the same time, the generation of multi-channel overlapping PVB demonstrated here will pave the way for enhancing information capacity and security, as well as improving the number of particle capture and rotating target detection technologies. The proposed method has strong potential in new applications that traditional optics may not be able to achieve.

Results and Discussion: Fig.1a shows the intensity distribution of integrated metasurface PVB along the x-z plane, featuring different topological charge values of l=1, 3, and 5. Three PVBs with different topological charge values exhibit almost the same beam radius and beam divergence. Fig.1b records its intensity distribution at the identical measurement point. Additionally, Figure 1c shows the cross-section of the normalized intensity distribution extracted along the y-direction at a wavelength of 978nm. For three sets of PVB with different topological charge values of l=1, 3, and 5, the measured vortex diameters are 50.1, 50, and 50um, respectively, closely aligning with the theoretical value of 50μm. Besides the variations in topological charge value, the three metasurfaces characterized here share identical design parameters. Specifically, in this section, the period d of the prism is designed to be 39 um. The results suggest that, with the increase in topological charge value, the beam radius remains nearly constant. These findings robustly affirm the effectiveness of our method as a solution for developing PVB laser chips. Fig.2a displays the simulation and test results (left: l_1=2 and l_2=3;

middle:l_1=-2 and l_2=2; right:l_1=2 and l_2=3) of the superposition of PVB with different topological charge values. Fig. 2b illustrates the corresponding normalized intensity distribution.

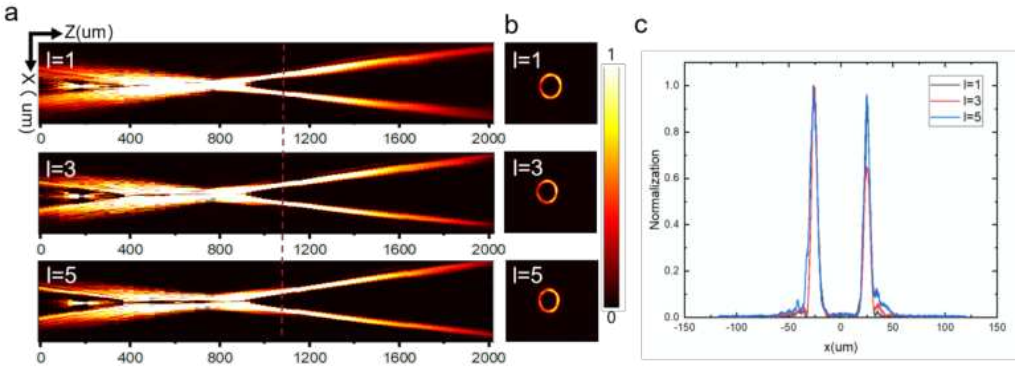


Fig. 1 Generation of the perfect vortex beams. a The measured beam intensity profile along the propagation direction. b The measured annular intensity profiles of the generated PVBs with topological charges of l = 1, 3, 5. c Normalized cross-sections of the annular intensity profiles of the PVBs

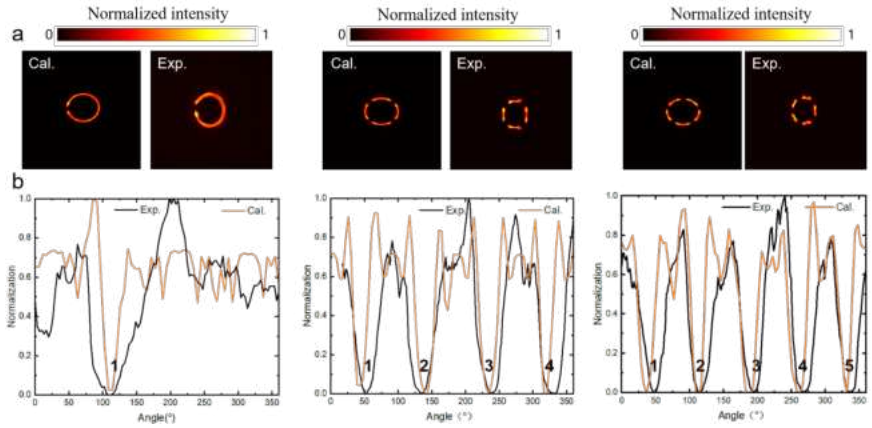


Fig.2 Characterization of overlapping perfect vortex beams. a The simulated and measured intensity distributions of the overlapping PVBs. b The relation between light intensity distribution and the azimuthal angle.

Conclusion: We have designed and demonstrated a series of all-dielectric metasurfaces with PVB, and integrated them on VCSEL chips to construct a complete system for generating structured beams with arbitrary engineering phase profiles on the chip. As a functional demonstration of this design, we further explored the generation of on-chip overlapping PVB and on-chip multi-channel overlapping PVB. Compared with traditional methods for generating and manipulating PVB, our work provides a compact integrated metasurface method to accomplish this complex task, which traditional optical design cannot achieve. This work helps to open up new opportunities for the application of PVB in the field of miniaturization.

References

1. Liu W, Yang Q, Xu Q, Jiang X, et al. “Multichannel terahertz quasi-perfect vortex beams generation enabled by multifunctional metasurfaces,” Nanophotonics, vol.11, No.16, 3631-3640, 2022.
2. Xie Y.Y, Ni P.N, Wang Q.H, et al. “Metasurface-integrated vertical cavity surface-emitting lasers for programmable directional lasing emissions,” Nature Nanotechnology, vol.15, No.2,125-130, 2020

Emission properties of plasmonic nanoshell lasers: Symmetric vs. antisymmetric lasing modes and gain-medium detuning effects

K. Caicedo[1*], M. Infusino[1], A. Aradian[2] and A. Veltri[1]

[1]Universidad San Francisco de Quito, Quito, Ecuador
[2]University of Bordeaux & CNRS, Bordeaux, France
*corresponding author: gcaicedo@asig.com.ec.

Abstract: This research explores the lasing dynamics of gain-doped metallic nanoshells, focusing on frequency pull-out effects and emission linewidth in relation to plasmonic resonances. By analyzing symmetric versus antisymmetric plasmonic modes and the impact of detuning the gain medium with respect to plasmonic resonances, we provide insights into optimizing nanoshell lasers.

Recent advances in nanophotonics have ushered in a new era of miniaturized light sources, leveraging the unique properties of metallic nanoshells (Figure 1). These structures, characterized by their distinct geometric configurations, have shown remarkable potential in enhancing light-matter interactions at the nanoscale. Central to this development is the concept of the gain-doped metallic nanoshells, which integrates optical gain materials in the core, surrounded by the plasmonic metal framework, offering a pathway to overcome intrinsic metallic losses and achieve lasing at the nanoscale (emission of coherent photons from the nanostructure)) [1]. This study delves into the comprehensive modeling and analysis of such gain-enhanced nanoshell systems, focusing on their lasing characteristics and the intricate interplay between their structural attributes and optical behaviors.

We will briefly introduce the theoretical framework we have used to describe the optical behavior of gain-enhanced metallic nanoshells [2-3]. It consists of a state-of-the-art time-dependent model that integrates the principles of optical Bloch equations, to describe the population dynamics in the embedded gain medium, as well as the free-electron motion for the metal, which are coupled together to describe the system behavior both below [21] and above the emission threshold [3]. This approached had already allowed to study the onset of the lasing instability at the threshold in another geometric configuration, i.e. a spherical nanoparticle immersed in gain medium [43]. In the case of the nanoshell geometry, due to fact that the lasing mode remains dipolar above the threshold (for a small enough particle), we were able to further study the lasing state itself [3], and we showed for the first time that unusually strong frequency pull-out effects dominate the dynamics and shape the emission spectrum – in striking contrast with the situation of conventional lasers.

The main goal of this study is to explore two avenues that have not been explored in our previous investigations. The first avenue is related to the fact that plasmonic nanoshells have two natural plasmon resonances (symmetric and antisymmetric), whose respective frequencies depend on the geometric aspect ratio. In the above work [32], as well as more generally in the literature, authors have considered the lasing of one of these resonances in a generic way, without going into the details of the respective benefits or specifics of choosing one or the other. This fact has motivated us to explore the similarities and differences of the lasing performance in both resonances above the gain threshold, starting with comparing and optimizing the amount of gain necessary for the system to start emitting. The optimization depends in particular on the aspect ratio

between the internal and external radii of the nanoshell.

The second avenue that we explored is about the implications of detuning between the gain frequency (transition frequency between the lower and upper energy states of the gain) and the plasmonic resonances of the nanoshell. In our previous work [32] and also in the literature, the gain medium emission spectrum is assumed to be centered exactly on the plasmonic resonance one wishes to bring to lasing. This is both because it simplifies theoretical considerations, and because this is the optimal positioning to minimize the necessary quantity of gain for lasings (since the peak emission is provided to the resonance). There is, however, no physical prerequisite to do so. We will therefore discuss the effect of detuning the gain with respect to the plasmonic resonance, in particular how the gain threshold, the lasing frequency, the emission width, and the above mentioned pull-out effects are affected. In particular, it is known from conventional lasers that gain detuning is a way to shift the laser's emission and hence make tunable lasers. We will discuss how this translates in the case of gain detuning in our nanolaser, making it tunable in a more flexible way than what is possible with centered gain situations.

(I think you can remove the two paragraphs below… this is not a real article, there is no need for a general conclusion, and this will save you some space!!!).

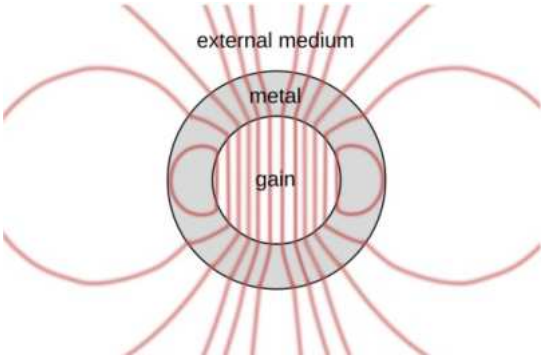


Figure 1. A spherical nanoshell particle, with a gain medium filling the core and a metallic shell, placed into an external medium.

References

1. Bergman, D. and Stockman, M. "Surface plasmon amplification by stimulated emission of radiation: quantum generation of coherent surface plasmons in nanosystems," Phys. Rev. Lett., Vol. 90, 027402, 2003.
2. Caicedo, K., Cathey, A., Infusino, M., Aradian, A., and Veltri, A. "Gain-driven singular resonances in active core-shell and nano-shell plasmonic particles," J. Opt. Soc. Am. B, Vol. 39, No. 1, 107–116, 2022.
3. Aradian, A., Cathey, A., Caicedo, K., Mora, M., Infusino, M., and Veltri, A (in preparation).
4. Veltri, A., Chipouline, A., and Aradian, A. "Multipolar, time-dynamical model for the loss compensation and lasing of a spherical plasmonic nanoparticle spaser immersed in an active gain medium," Sci Rep, Vol. 6, 2016.

Robust gesture recognition based on millimeter-wave programmable metasurface

Mingyi Li[1], Hongrui Zhang[1], Shengguo Hu[1], Jiawen Xu[1] and Lianlin Li[1*]

[1]School of Electronics, Peking University, Beijing 100871, China
*corresponding author, E-mail: lianlin.li@pku.edu.cn

Abstract

This paper proposes a novel approach to achieve robust gesture recognition by employing 26GHz millimeter-wave programmable metasurface. By leveraging beamforming for wavefront manipulation and deep learning for gesture classification, the proposed system aims to enhance accuracy and reliability for gesture recognition.

1. Introduction

Gesture recognition technology has garnered significant attention in recent years due to its potential for human-computer interaction. Among various technologies, radar-based millimeter-wave (mmWave) technology has emerged as a promising avenue for gesture recognition. Leveraging the unique properties of mmWave signals, such as high resolution and penetration capabilities, researchers have been able to develop sophisticated systems capable of accurately detecting hand movements. [1, 2, 3]

However, radar-based gesture recognition systems suffer from expensive prices and clutter interference, which limit the accuracy of recognition, whereas metasurface-based sensing can be a good solution to these problems. In recent years, the advent of programmable metasurfaces has sparked significant interest and exploration across various fields of research, particularly in wireless communication and sensing domains. These metasurfaces, composed of an array of subwavelength meta-atoms, offer unprecedented control over electromagnetic waves at subwavelength scales. Leveraging the concept of metasurfaces, researchers have begun to explore novel paradigms in wireless sensing, facilitated by the ability to dynamically manipulate the propagation and reflection of electromagnetic waves. For gesture recognition tasks, metasurfaces can be utilized to focus the beam on the hand region, thereby minimizing interference from surrounding objects or environmental clutter and enhancing the accuracy and robustness of recognition.

In this paper, we propose a 26 GHz programmable metasurface-based gesture recognition system, presenting the following contributions to enhance recognition robustness: (1)We design a large-scale focusing coding scheme to concentrate the beam on the region of interest, thereby increasing the amount of relevant information and reducing ambient scattering. (2)We implement a high frame rate data acquisition system, enabling the capture of subtle gesture variations with greater temporal resolution. This ensures that even rapid movements are accurately recorded, providing a richer dataset for subsequent analysis. (3)We develop an LSTM-based neural network for data processing. The network enhances the system's ability to distinguish between similar gestures by learning long-term dependencies and context within the gesture sequences.

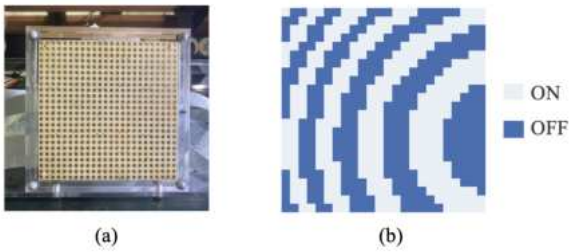


Figure 1: (a) The 26GHz programmable metasurface (b) A typical focusing coding pattern

2. System setup

As shown in Figure 1.(a), the programmable metasurface used in this paper operates at 26 GHz and is composed of an array of programmable metasurface units, each consisting of a PIN diode. By controlling the ON/OFF state of the PIN diode within each unit, the millimeter-wave beam can be focused on any spatial point (x, y, z) within a certain range. We use the so-called modified G-S (Gerchberg-Saxton) algorithm proposed in [4] to calculate the focusing coding pattern. A typical focused coding is illustrated in Figure 1.(b).

By predefined specification, we designate a 15cm × 15cm × 15cm cubic region in front of the metasurface as the gesture recognition area where the user performs gestures, as shown in Figure 2. In this study, we randomly selected 157 points within this area as focal points. Using the modified G-S algorithm, we calculate the corresponding 157 focusing coding patterns.

Our hardware system consists of a metasurface, a transmitting antenna, a receiving antenna, and a 26 GHz millimeter-wave transceiver module. During a single measurement, the transmitting antenna emits a 26 GHz single-frequency wave. The FPGA controls the metasurface to achieve code-switching for beam scanning. The receiving antenna collects the amplitude and phase of the echo signals corresponding to 157 different coding patterns. It is

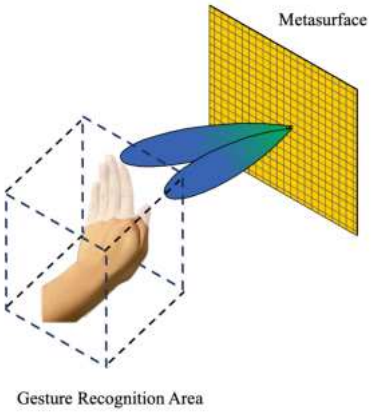


Figure 2: Schematic diagram of gesture recognition area.

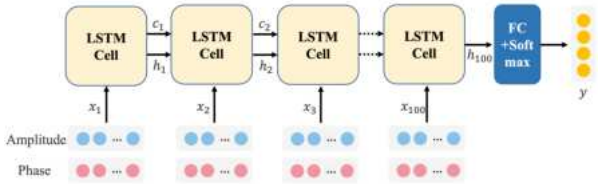


Figure 3: LSTM-based network.

noteworthy that the switching speed of the metasurface can reach 2.5 µs. Consequently, the coding switch time is only $2.5 \times 157 = 392.5$ µs. Including operations such as RF transmission and alignment, a single measurement can be completed in 30 ms, which allows the system to capture subtle gesture changes with higher temporal resolution.

3. Experimental Results

In this paper, we present an LSTM-based network designed for gesture recognition tasks, as depicted in Figure 3. The network processes 100 time samples, each comprising signal amplitudes and phases for 157 coding patterns. The LSTM network consists of 128 hidden units. The input dimension to the LSTM is 2×157, representing the combined amplitude and phase information for each time sample. The final output from the LSTM is fed into a fully connected layer to produce raw predictions across the specified gesture classes. These raw predictions are subsequently normalized using a softmax function to obtain class probabilities.

In this study, we collect data pertaining to four distinct gestures, designated as "fist," "left-to-right wave," "right-to-left wave," and "push." The corresponding microwave data for each gesture is illustrated in Figure 4. Approximately 100 samples are collected for each gesture, partitioned into 70% for training and 30% for validation.

In our implementation, the training is performed in a personal computer with Intel(R) Core (TM) i9-9980XE

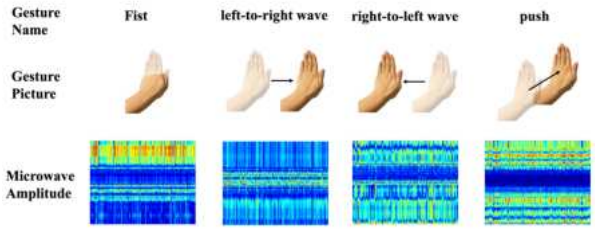


Figure 4: Gestures and corresponding microwave data.

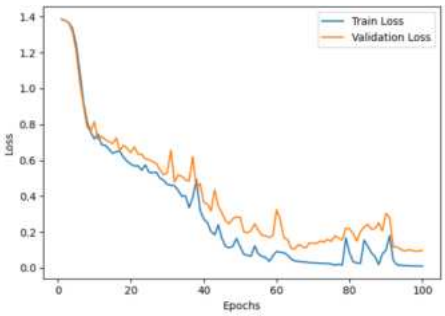


Figure 5: The training and validation losses.

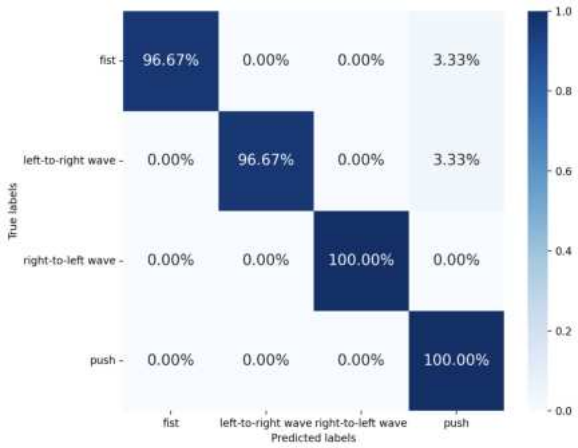


Figure 6: Confusion matrix of gesture classification.

CPU , 128GB RAM and NVIDIA GeForce RTX 2080 Ti GPU. The training is based on the Adam optimizer, with a batch size of 8 and 100 epochs. The learning rate is set to 0.0001. The training and validation losses are depicted in Figure 5.

After training, we collect a set of gesture data for testing, and the confusion matrix is shown in Figure 6. As can be seen, the recognition accuracy for all gestures exceeded 96%, with the "right-to-left wave" and "push" gestures achieving 100%. It is noteworthy that our test dataset includes gestures performed at different speeds, demonstrating the robustness of our method.

4. Conclusions

In conclusion, while radar-based gesture recognition technology has shown promise in recent years, it faces challenges such as high costs and interference. However, the emergence of metasurface-based sensing offers a potential solution to these issues. By leveraging programmable metasurfaces, which enable precise control over electromagnetic waves, we can enhance the accuracy and robustness of gesture recognition systems. In this paper, we propose a 26 GHz programmable metasurface-based system, which incorporates advanced features such as large-scale focusing coding, high frame rate data acquisition, and LSTM-based neural network processing to improve recognition performance. These contributions pave the way for more reliable and efficient human-computer interaction systems based on gesture recognition.

Acknowledgement

This work was supported by the National Key Research and Development Program of China under Grant Nos.2023YFB3811502, 2021YFA1401002.

References

[1] J.-T. Yu, L. Yen, and P.-H. Tseng, "mmWave radar-based hand gesture recognition using range-angle image," in *Proc. IEEE 91st Veh. Technol.* Conf. (VTC-Spring), 2020, pp. 1-5.

[2] H. Liu et al., "Real-time arm gesture recognition in smart home scenarios via millimeter wave sensing," *Proc. ACM Interact. Mobile Wearable Ubiquitous Technol.*, vol. 4, no. 4, pp. 1-28, 2020.

[3] L. O. Fhager et al., "Pulsed Millimeter Wave Radar for Hand Gesture Sensing and Classification," *IEEE Sens. Lett.*, vol. 3, no. 12, pp. 1-4, 2019.

[4] L. Li, T. J. Cui, W. Ji, S. Liu, J. Ding, X. Wan, Y. B. Li, M. Jiang, C.-W. Qiu, and S. Zhang, "Electromagnetic reprogrammable coding-metasurface holograms," *Nature Commun.*, vol. 8, no. 1, p. 197, 2017.

[5] S. Hochreiter and J. Schmidhuber, "Long short-term memory," *Neural computation*, vol. 9, no. 8, pp. 1735–1780, 1997

Guided Domino Lithography: Enabling Uniform Fabrication of Single-Digit-Nanometer Plasmonic Nanoantenna Arrays

Dong Kyo Oh[1], Jihae Lee[2], Huichang Yun[2], and Junsuk Rho[1,2,3,4,5*]

[1]Department of Mechanical Engineering, Pohang University of Science and Technology (POSTECH), Pohang 37673, Republic of Korea
[2]Department of Chemical Engineering, Pohang University of Science and Technology (POSTECH), Pohang 37673, Republic of Korea
[3]Department of Electrical Engineering, Pohang University of Science and Technology (POSTECH), Pohang 37673, Republic of Korea
[4]POSCO-POSTECH-RIST Convergence Research Center for Flat Optics and Metaphotonics, Pohang 37673, Republic of Korea
[5]National Institute of Nanomaterials Technology (NINT), Pohang 37673, Republic of Korea
[*]corresponding author: jsrho@postech.ac.kr

Abstract: Guided Domino Lithography (GDL) presents a novel solution for uniform fabrication of single-digit-nanometer plasmonic nanoantenna arrays. GDL leverages collapsing behavior of unstable photoresist nanostructures to achieve ultra-sharp bowtie masks. Experimental comparison with conventional lithography demonstrates superior yield and uniformity. GDL promises practical manufacturing for diverse quantum nanophotonic devices.

Plasmonic nanoantenna platforms have attracted significant attention for their wide-ranging applications in optical sensors, quantum plasmonics, and beyond. However, achieving uniform and reliable fabrication of nanoantennas at the single-digit-nanometer resolution remains a daunting challenge. In this study, we introduce guided domino lithography (GDL) as a novel solution for producing ultra-sharp nanoantenna arrays with remarkable uniformity [1].

GDL capitalizes on the collapsing behavior of unstable photoresist nanostructures, guided by a supporting structure, to ensure consistent fabrication of ultra-sharp bowtie photoresist masks. Through direct comparisons with conventional lithography methods under optimized electron beam exposure and development conditions (Fig. 1a), our experimental findings underscore GDL's superiority in terms of both yield and uniformity of nanoantenna shape across the fabrication area. Moreover, rigorous analyses are conducted to probe the electric field enhancement effects of ultra-sharp bowtie nanoantennas with diverse geometries (Fig. 1b). These analyses validate the substantial electric field enhancement achieved by the fabricated nanoantennas, further highlighting GDL's potential for practical manufacturing of single-digit-nanometer plasmonic nanoantennas.

In conclusion, GDL emerges as a promising solution for the uniform fabrication of ultra-sharp nanoantenna arrays at the single-digit nanometer scale. Our results not only demonstrate GDL's superior performance in process yield and uniformity compared to conventional lithography techniques but also underscore the significant electric field enhancement achieved by the fabricated nanoantennas. The GDL process thus holds tremendous potential as a practical manufacturing method, opening up new avenues for diverse quantum nanophotonic device applications [2,3].

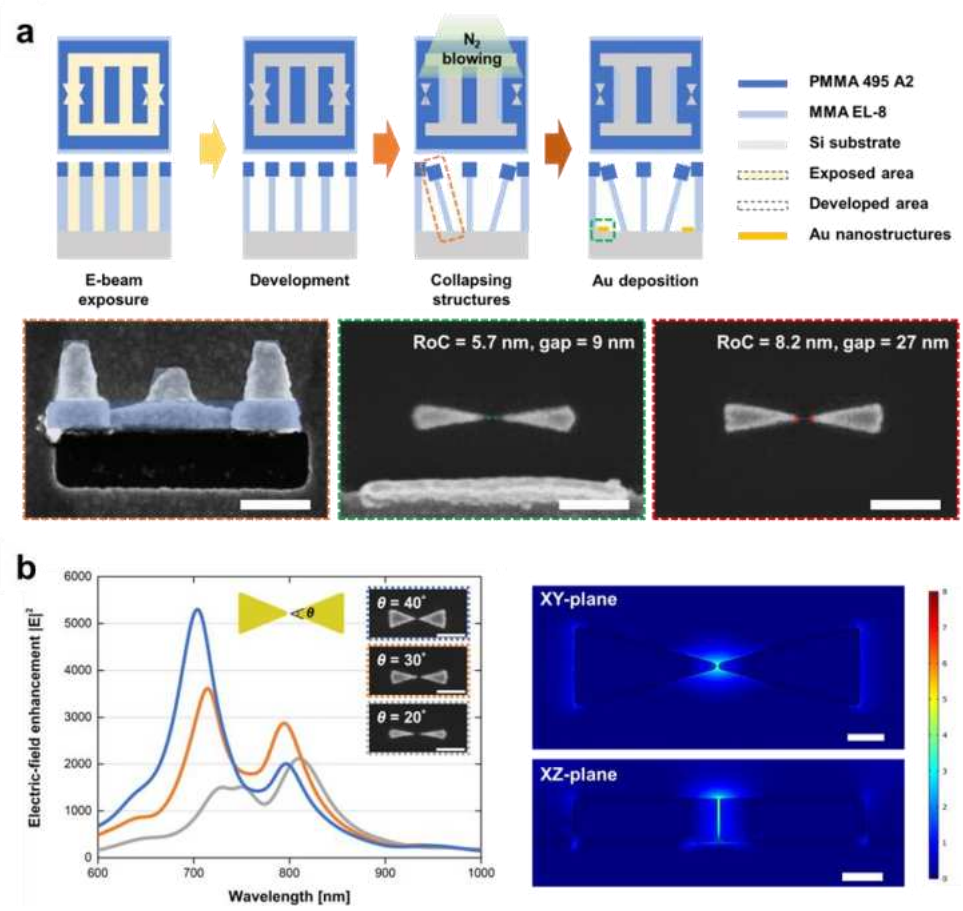


Figure 1. (a) Overview of the guided domino lithography (GDL) process and comparison of the ultra-sharp bowtie nanoantenna by GDL and electron beam lithography (EBL). All scale bars: 200 nm. (b) Electric field enhancement and field distribution of the ultra-sharp bowtie nanoantenna with various angles. Scale bars in (left): 200nm. Scale bars in (right): 50 nm.

References

1. Oh, D. K. *et al.*, "Guided Domino Lithography for Uniform Fabrication of Single-digit-nanometer Scale Plasmonic Nanoantenna," *Nanophotonics*, Vol. 12, No. 8, 1435-1441, 2023.
2. Kim, I. *et al.*, "Cascade Domino Lithography for Extreme Photon Squeezing," *Mater. Today*, Vol. 39, 89-97, 2020.
3. Kim, I. *et al.*, " Capillary-force-induced Collapse Lithography for Controlled Plasmonic Nanogap Structures," *Microsyst. Nanoeng.*, Vol. 6, 65, 2020.

Mass Production of Metalenses for Near-Infrared Imaging

S.-W. Moon[1], J. Kim[1], and J. Rho[1,2,3,4*]

[1] Department of Mechanical Engineering, Pohang University of Science and Technology (POSTECH), Pohang 37673, Republic of Korea
[2] Department of Chemical Engineering, Pohang University of Science and Technology (POSTECH), Pohang 37673, Republic of Korea
[3] Department of Electrical Engineering, Pohang University of Science and Technology (POSTECH), Pohang 37673, Republic of Korea
[4] POSCO-POSTECH-RIST Convergence Research Center for Flat Optics and Metaphotonics, Pohang 37673, Republic of Korea
[*]corresponding author: jsrho@postech.ac.kr

Abstract: This work presents scalable method for manufacturing near-infrared metalenses. we demonstrate a 1 cm diameter, 0.53 numerical aperture (NA) polarization-independent metalens composed of hydrogenated amorphous silicon. The proposed metalenses exhibit high-resolution imaging capabilities, making significant progress in metalens production and optical technology.

Metalenses are thin, flat surfaces engineered with nanostructures to manipulate light, offering alternatives to traditional bulky optical components[1]. These devices can precisely control the phase, amplitude, and polarization of light, making them highly efficient for various applications such as light-field imaging, augmented/virtual reality, and quantum source[2]. However, conventional metalens fabrication methods, requiring high-resolution nanopatterning techniques like electron beam lithography, are expensive, offer low throughput, and struggle with patterning large areas. In this work, we propose mass-production method for near-infrared metalenses at wafer-scale.

To focus incident light, the phase profile of metalens is expressed by

$$\varphi(r,\lambda) = \frac{2\pi}{\lambda}\left(f - \sqrt{r^2 + f^2}\right) \qquad (1)$$

where λ, f, and r represent wavelength of incident light, focal length, and radial coordinate on the metalens. Eq. (1) means the hyperbolic lens equation. The phase profile of metalens is implemented using cylinder-shape meta-atoms with various diameters.

Metalenses are fabricated using hydrogenated amorphous silicon (a-Si:H) on glass wafers through a direct photolithography process, as shown in Fig. 1(a)[3]. The process involves depositing a layer of a-Si:H, followed by patterning using an argon fluoride (ArF) excimer laser for high-resolution lithography. Fig. 1(b) shows cylindrical meta-atoms composed of a-Si:H. This method produces metalenses with a diameter of 1 cm and a numerical aperture (NA) of 0.53, capable of focusing light close to the diffraction limit (Fig. 1(c)). To evaluate imaging performance of metalenses, a 1951 USAF resolution target is captured by the proposed metalens, as shown in Fig. 1(d). The focusing efficiency of these metalenses at a 940 nm wavelength is measured to be 44%, demonstrating their high performance.

Furthermore, we demonstrate the application of these metalenses in bioimaging, using the example of imaging onion epidermal cells (Fig. 1(e)). The metalens-based imaging system provides superior resolution, which show the potential of metalenses in biological research and medical diagnostics.

In conclusion, we introduce an innovative method for fabricating high-performance, large-scale metalenses, highlighting their potential to revolutionize optical technologies. By offering solutions to the limitations of

traditional optics, such as size, weight, and flexibility in manipulating light, metalenses pave the way for the development of compact, efficient optical devices for a wide range of applications. This advancement is expected to accelerate the industrial adoption of metalens technology and expand its practical applications.

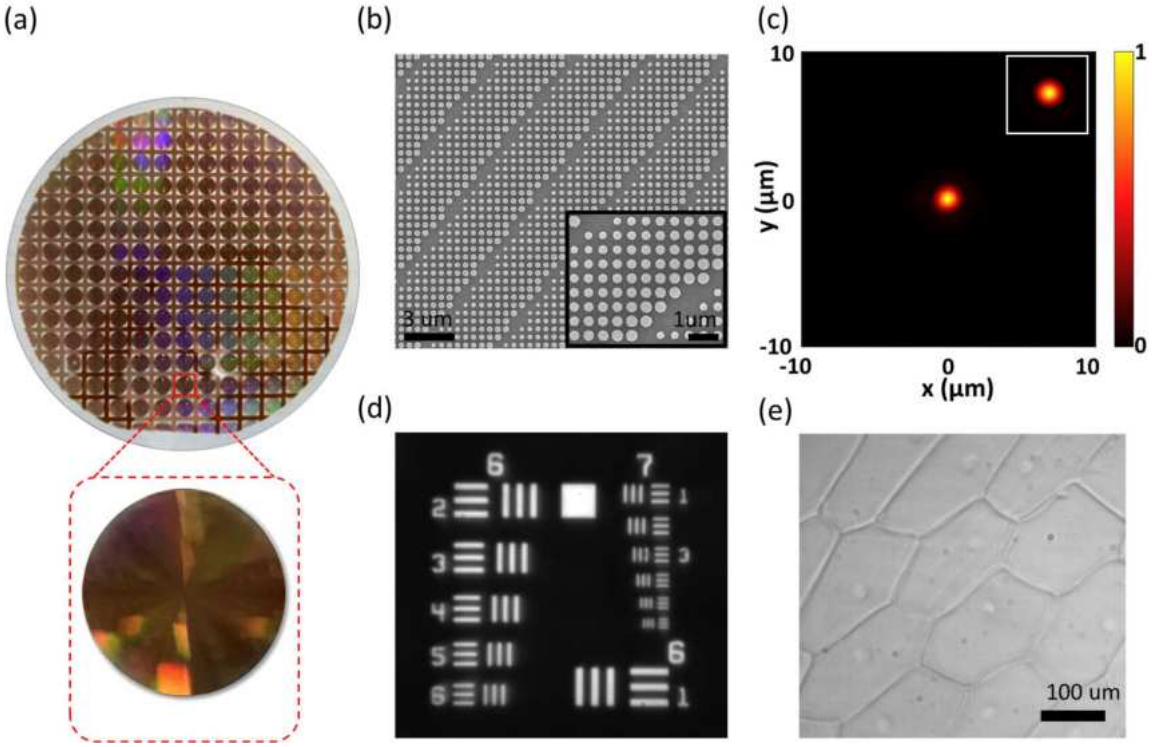


Figure 1 Near-infrared metalenses with a diameter of 1 cm and numerical aperture of 0.53. (a) Photography of metalenses in 8-in. wafer. (b) SEM image of metalens. Scale bar: 3 μm (Inset: 1 μm). (c) Measured intensity distribution on the focal plane (Inset: calculated intensity distribution). (d) Image of 1951 USAF resolution target obtained by metalens. (e) Microscopic image of the onion epidermal cells obtained by metalens-based imaging system.

References

1. Yu, N. and Capasso, F. “Flat optics with designer metasurfaces,” Nat. Mater. Vol. 13, 139–150, 2014.
2. Arbabi, A. and Faraon, A. “Advances in optical metalenses.” Nat. Photon. Vol. 17, 16–25, 2023.
3. Moon, S.-W. et al. “Wafer-Scale Manufacturing of Near-Infrared Metalenses.” Laser Photon. Rev. 2300929, 2024.

Negative index metamaterial using colloidal lithography for large-area and high productivity

Y. Jeon[1], H. Cho[1] and J. Rho[1,2,3,4,5*]

[1]Department of Mechanical Engineering, Pohang University of Science and Technology (POSTECH), Pohang 37673, Republic of Korea

[2]Department of Chemical Engineering, Pohang University of Science and Technology (POSTECH), Pohang 37673, Republic of Korea

[3]Department of Electrical Engineering, Pohang University of Science and Technology (POSTECH), Pohang 37673, Republic of Korea

[4]POSCO-POSTECH-RIST Convergence Research Center for Flat Optics and Metaphotonics, Pohang 37673, Republic of Korea

[5]National Institute of Nanomaterials Technology (NINT), Pohang 37673, Republic of Korea

[*]corresponding author: jsrho@postech.ac.kr

Abstract: Metamaterials are subwavelength structures designed to exhibit extraordinary phenomena such as negative refraction. A multilayer fishnet metamaterial fabricated using colloidal lithography offers large-area production. The material demonstrates negative refraction at 1550nm, promising sub-diffraction imaging, nanolithography and real-time biological imaging.

Metamaterials consist of artificially structured subwavelength components. Light perceives these structures as novel materials, exhibiting unusual optical properties not found in nature. With appropriate design, these subwavelength structures could be tailored to manipulate light. Negative refraction [1,2] is one of the optical phenomena that can be realized with these metamaterials. By controlling the effective permittivity and effective permeability as shown in the equation (1), a negative refractive index can be obtained when both signs are negative. This means that by controlling the nanostructure to have certain permittivity and permeability values, a negative refractive index can be achieved in a specific spectral range.

$$n = \sqrt{\varepsilon_{eff} \cdot \mu_{eff}} \tag{1}$$

Negative permittivity can be achieved by using metals such as gold and silver, or by adjusting the filling ratio of metal and dielectric according to the effective medium theory. Permeability can be negative at specific wavelengths via magnetic resonance. A representative design that satisfies both is a fishnet-structured metamaterial. This structure couples the magnetic strips ($\mu < 0$) with electric strips ($\varepsilon < 0$) in a broad spectral range to achieve negative refractive index. The spectral range may vary depending on the size of the structure. Design of negative index metamaterials faces certain demands such as high-precision, high-throughput and low-cost manufacturing. Although fishnet metamaterial could be fabricated through high-precision fabrications such as e-beam lithography and focused ion beam milling, low-throughput and high-cost are the bottleneck.

In this research, a multilayer fishnet metamaterial is fabricated through colloidal lithography, which can simply create large-area periodic structures (Fig. 1a). This method guarantees high productivity and low costs. The fabricated multilayer fishnet metamaterial (Fig. 1b), exhibits negative refraction near the optical communication wavelength (1550nm) in the NIR region, as confirmed through simulations (Fig. 1c). We expect that this multilayer

fishnet metamaterial will have applications in compact optical systems for sub-diffraction limit imaging, as well as in nanolithography and real-time biological imaging [3].

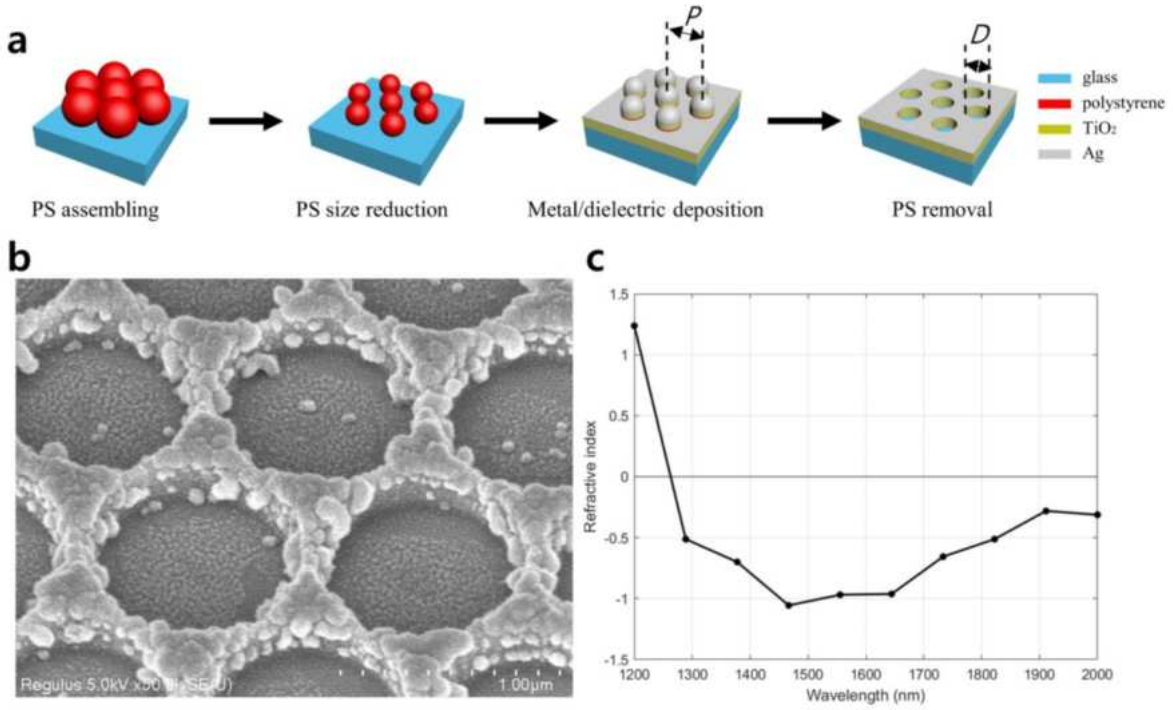


Figure 1. (a) Schematic of the large area multilayer fishnet metamaterials using colloidal lithography. (b) Scanning electron microscopy image of the fabricated multilayer fishnet metamaterials (×50K). (c) The calculated refractive index of multilayer fishnet metamaterials in near infrared (NIR).

References

1. Valentine, Jason, et al. "Three-dimensional optical metamaterial with a negative refractive index." *Nature,* Vol. 455, No.7211, 376-379, 2008.
2. Yang, Jianji, et al. "Theory of fishnet negative-index optical metamaterials." Phys. Rev. Lett., Vol. 107, No. 4, 043903, 2011.
3. Lee, Dasol, et al. "Realization of wafer-scale hyperlens device for sub-diffractional biomolecular imaging." ACS Photonics Vol. 5, No. 7, 2549-2554, 2017.

A three-dimensional transformable metamaterial for programmable elastic waves control

Zhou Hu[1], Rui Zhu[1*], Zhibo Wei[2] and Yan Chen[2,3]

[1] School of Aerospace Engineering, Beijing Institute of Technology, Beijing, China
[2] School of Mechanical Engineering, Tianjin University, Tianjin, China
[3] Key Laboratory of Mechanism Theory and Equipment Design of Ministry of Education, Tianjin University, Tianjin, China
[*]corresponding author: ruizhu@bit.edu.cn

Abstract: We propose a three-dimensional mechanical metamaterial which can transform its effective elasticity tensor and covers all seven types of extremal metamaterials. By engineering the zero modes in the proposed metamaterial, both the static and dynamic states of the 3D-printed prototype can be reconfigured. Moreover, reprogrammable wave functionalities are also demonstrated.

Mechanical metamaterials[1], comprising rationally designed microstructures, have moved from the stage of acquiring unconventional and programmable properties to the stage of tunability[2]. Generally, the tunable properties of mechanical metamaterials are due to zero modes that cost little to no elastic energy. In fact, the number of zero modes can alter the elasticity tensor among all seven extremal states, also known as extremal metamaterial[3], including null-, uni-, bi-, tri-, quadra-, penta- and hexa-mode, leading to extremal static properties and exotic wave phenomena[4,5]. Two marvelous applications of extremal metamaterials are the design of "invisible" acoustic and elastic cloaks with the penta-mode metamaterial[5,6] and the design of the shear wave polarizer with the quadra-mode metamaterial[7,8]. However, due to the lack of a blueprint for systematically designing the corresponding zero modes, extremal metamaterials with specific number of zero modes or with the ability to transform among all seven extremal states remain unimplemented. Here, we propose a methodology for the design of a mechanical metamaterial that can transform among all seven types of extremal metamaterials (Figure 1), leading to programmable wave functionalities, such as programmable elastic wave splitting and selective filtering. This work sheds lights on the design of new smart metamaterials, and offers the promise for the real-time manipulation of broadband low-frequency elastic waves.

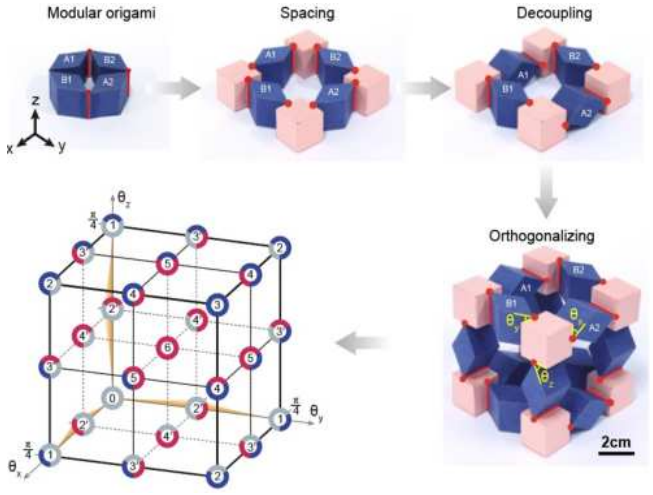


Figure 1. Constructing the unit cell of the 3D transformable extremal metamaterial via decoupled orthogonal design.

The authors greatly acknowledge the support of the National Natural Science Foundation of China (Projects 52035008, 51825503, 51721003, 11872112, U1837602, 11991033 and 11991030), the National Key Research and Development Program of China (2021YFE0110900), and the Tecent Foundation (Grant XPLORER-2020-1035).

References

1. Zadpoor A. A. Mater. Horiz., Vol. 3, 371-381, 2016.
2. Kadic M., Milton G. W., Van Hecke M., Wegener M. Nat. Rev. Phys., Vol. 1, 198-210, 2019
3. Milton G. W., Cherkaev A. V. J. Eng. Mater. Technol., Vol. 117, No. 4, 483-493, 1995.
4. Layman C. N., Naify C. J., Martin T. P., Calvo D. C., Orris G. J. Phys. Rev. Lett., Vol. 111, 024302, 2013.
5. Chen Y., Zheng M. Y., Liu X. N., Bi Y. F., Sun Z. Y., Xiang P., Yang J., Hu G. K. Phys. Rev. B, Vol. 95, 180104(R), 2017.
6. Buckmann T., Thiel M., Kadic M., Schittny R., Wegener M. Nat. Commun., Vol. 5, 4130, 2014.
7. Wei Y., Liu X. N., Hu G. K. Mater. Des., Vol. 210, 110031, 2021.
8. Groβ M. F., Schneider J. L. G., Wei Y., Chen Y., Kalt S., Kadic M., Liu X. N., Hu G. K., Wegener M. Adv. Mater., Vol. 35, 2211801, 2023.

Advanced Heterostructures of Semiconductor Nanocrystals for Nanophotonics

Hilmi Volkan Demir

NTU Singapore – Nanyang Technological University, School of Electrical and Electronic Engineering, School of Physical and Mathematical Sciences, School of Materials Science and Engineering, Singapore

Bilkent University UNAM, Department of Electrical and Electronics Engineering, Department of Physics, Institute of Materials Science and Nanotechnology, Ankara, Turkey

hvdemir@ntu.edu.sg, volkan@bilkent.edu.tr

Lighting and displays are integral parts of human activities and economic development. Semiconductor nanocrystals, now offering a market volume exceeding 1B Euros annually, have attracted great interest in quality lighting and displays. Such colloidal semiconductors enable enriched color conversion essential to superior lighting and displays. In this talk, we will introduce the emerging field of semiconductor nanocrystal optoelectronics. Here we will showcase most recent examples of advanced heterostructures of semiconductor nanocrystals along with their photonic structures and device architectures. Optical properties of these solution-processed nanostructures are conveniently controlled by tailoring their size, shape and composition to realize high-performance light generation and lasing. These colloids span different types and heterostructures of semiconductors in the forms of quantum dots and rods, most recently extending to the latest sub-family of nanocrystals, the colloidal quantum wells (CQWs).

In this talk, we will focus on atomically-flat, tightly-confined, quasi-2-dimensional CQWs, also popularly nick-named ‘nanoplatelets’, particularly for use in lighting and displays [1-6]. Also, we will present a powerful, large-area, orientation-controlled self-assembly technique for orienting these colloidal quantum wells either all face down or all edge up [7]. We will demonstrate three-dimensional constructs of their oriented self-assemblies with monolayer precision [8]. Among their extraordinary features important to applications in lighting and displays, we will show record high efficiency from their colloidal LEDs [9] and record high gain coefficients and record low lasing thresholds from their colloidal laser media [1,10-11] using heterostructures [2-6] and/or oriented assemblies [7,8] of the colloidal quantum wells.

Given their current accelerating progress, these solution-processed nanocrystals hold great promise to challenge their epitaxial thin-film counterparts in semiconductor optoelectronics.

References

[1] B. Guzelturk et al., HVD, Nano Letters 19, 277 (2019)
[2] Y. Altıntas et al., HVD, ACS Nano 13, 10662 (2019)
[3] N. Taghipour et al., HVD, Nature Communications 11, 3305 (2020)
[4] F. Shabani et al., HVD, Small 18, 2106115 (2022)
[5] E. G. Durmusoglu et al., HVD, ACS Nano 17, 7636 (2023)
[6] S. Delikanli et al., HVD, JACS 145, 12033 (2023)
[7] O. Erdem et al., HVD, Nano Letters 19, 4297 (2019)
[8] O. Erdem et al., HVD, Nano Letters 20, 6459 (2020)
[9] B. Liu et al., HVD, Advanced Materials 32, 1905824 (2020)
[10] J. Maskoun et al., HVD, Advanced Materials 33, 2007131 (2021)
[11] F. Isik et al., HVD, Small, in press (2024)

Ultrasensitive Portable Surface-Enhanced Raman Spectroscopy for Clinical Applications

D. Wan[1*]

[1]Institute of Biomedical Engineering, National Tsing Hua University, Hsinchu, Taiwan

[*]corresponding author: dhwan@mx.nthu.edu.tw

Abstract: This talk presents a facile, scalable fabrication strategy for developing an ultrasensitive SERS-based detection platform that serves as a rapid, label-free diagnosis device. Highly dense Au nanoparticle arrays with narrow gap distances is formed directly through physical vapor deposition on hydrophobic cellulose fibers to achieve excellent portable SERS performance.

Surface-enhanced Raman spectroscopy (SERS)-based biosensors have garnered significant attention for their label-free detection capabilities, ultrahigh sensitivity, and unique molecular fingerprinting. In this talk, I will illustrate an attractive development in SERS technology: a wafer-scale, ultrasensitive, highly uniform, and portable SERS detection platform (see Figure 1). This innovative platform is constructed on paper, featuring abundant and densely packed gold nanoparticles with narrow inter-particle gaps. These gold nanoparticles are deposited directly onto ultralow-surface-energy fluorosilane-modified cellulose fibers using a straightforward thermal evaporation process, with precise control over atom diffusion behavior.

Our paper-based SERS substrate stands out with an exceptionally high Raman enhancement factor, reaching an astounding 3.9×10^{11}. This platform exhibits remarkable detectability at sub-femtomolar concentrations, even achieving single-molecule-level sensitivity. It boasts excellent signal reproducibility, with a low relative standard deviation of 3.97%, making it highly reliable even when operated with a portable 785-nm Raman spectrometer. One of the most impressive aspects of this technology is its versatility. We employed this system for fingerprinting the identification of 12 diverse analytes, spanning clinical medicines (cefazolin, chloramphenicol, levetiracetam, nicotine), pesticides (thiram, paraquat, carbaryl, chlorpyrifos), environmental carcinogens (benzo[a]pyrene, benzo[g,h,i]perylene), and illegal drugs (methamphetamine, mephedrone). The lowest detection concentrations reached the sub-parts-per-billion (ppb) level, with a remarkable low of 16.2 parts per quadrillion (ppq) achieved for nicotine.

The potential applications of this novel technology are vast and impactful. It holds promise for clinical applications such as therapeutic drug monitoring for individualized medication adjustment and ultra-early diagnosis of pesticide intoxication. In addition, I will also illustrate a microneedle-assisted paper-based sensing platform for rapid, label-free, and ultrasensitive detection of molecules. The platform allows facile recovery of analytes and provides desirable recognition capacities through portable SERS. The sensing platform can be used for pain-free monitoring of drug levels in human interstitial fluid. In summary, the scalability, portability, and ultrasensitive nature of these fibrous SERS substrates open up new avenues for practical on-site detection in biofluid analysis, point-of-care diagnostics, and precision medicine.

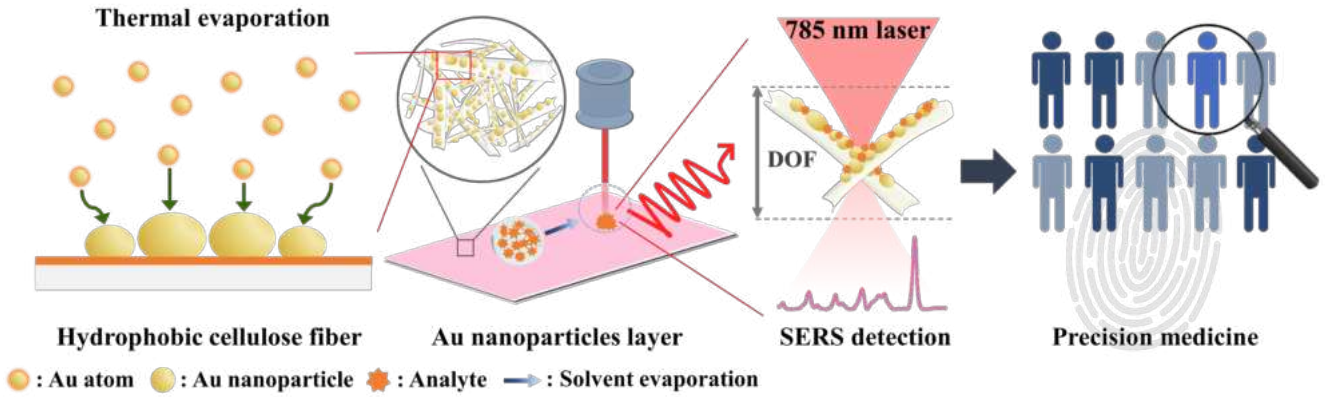


Figure 1. An ultrasensitive paper-based SERS detection platform for precision medicine.

References

1. H.-Y. Lin, W.-Ru Chen, L.-C. Lu, H.-L. Chen, Y.-H. Chen, M. Pan, C.-C. Chen, C. Chen*, T.-H. Yen*, D. Wan* "Direct Thermal Growth of Gold Nanopearls on 3D Interweaved Hydrophobic Fibers as Ultrasensitive Portable SERS Substrates for Clinical Applications", *Small*, 2023, 19, 2207404.
2. Y.-H. Chen, C.-C. Chen, L.-C. Lu, C.-Y. Lan, H.-L. Chen*, T.-H. Yen*, D. Wan* "Wafer-scale Fibrous SERS Substrates Allow Label-Free, Portable Detection of Food Adulteration and Diagnosis of Pesticide Poisoning", *Sensors and Actuators B: Chemical*, 2023, 391, 134035.
3. Y.-C. Hsieh, C.-Y. Lin, H.-Y. Lin, C.-T. Kuo, S.-Y. Yin, Y.-H. Hsu, H.-F. Yeh, J. Wang*, D. Wan* "Controllable-Swelling Microneedle–Assisted Ultrasensitive Paper Sensing Platforms for Personal Health Monitoring", *Advanced Healthcare Materials*, 2023, 12, 2300321.

Spatio-temporal propagation dynamics of optically excited electrons in Au/Fe/MgO(001) heterostructures

M. Heckschen[1], Y. Beyazit[1], E. Shomali[1], F. Kühne[1], J. Jayabalan[1], P. Zhou[1], D. Diesing[2], M. E. Gruner[1], R. Pentcheva[1], A. Lorke[1], B. Sothmann[1], U. Bovensiepen[1,3*]

[1]Faculty of Physics and CENIDE, University of Duisburg-Essen, Duisburg 47048, Germany
[2]Faculty of Chemistry and CENIDE, University of Duisburg-Essen, Essen 45711, Germany
[3]Institute for Solid State Physics, The University of Tokyo, Kashiwa, Chiba 277-8581, Japan
[*]corresponding author: uwe.bovensiepen@uni-due.de

Abstract: Understanding hot electron transport requires identification of diffusive or ballistic regimes. We determine the energy-dependent electron propagation time through Fe(001)-Au(001) heterostructures using femtosecond time-resolved photoelectron spectroscopy, electronic structure theory, and transport simulations. The electron velocity increases with growing Au layer thickness since the propagation aligns with the interface normal direction.

Optically excited processes are used in energy conversion applications. An essential aspect is that optical excitations lead to nonequilibrium phenomena which allow for carrier multiplication by carrier-carrier scattering, but also challenge our understanding of steady-state operation. The spatio-temporal dynamics of carrier-carrier scattering, in which transport of excited carriers and their interaction with other charge carriers proceed simultaneously, is highly relevant for improved energy-related applications. Properties like the ballistic mean free path of optically excited carriers can be measured in thin films by pump-probe experiments when the pump and the probe step are spatially separated [1,2]. A related problem occurs in photoinduced switching of magnetization in spin valves, by femtosecond laser pulses, that aims to reduce energy consumption in data storage technology [3]. The magnetic moment of a ferromagnet can be spatially redistributed in superdiffusive spin transport of optically excited carriers across interfaces inducing a spin-transfer torque [4], which may lead to magnetization reversal [3] at reduced energy compared to thermodynamic magnetization reversal. Furthermore, electronic excitation of layered systems has further potential regarding terahertz (THz) radiation generation [5]. In such systems, electronic excitations, which are induced optically in a ferromagnetic layer, the emitter, are transferred across an interface to another layer, the collector, which is electronically strongly interacting with the initially excited layer. For such phenomena, the energy-dependent scattering rate and length of optically excited carriers in heterosystems are essential because they determine the energy and momentum distribution.

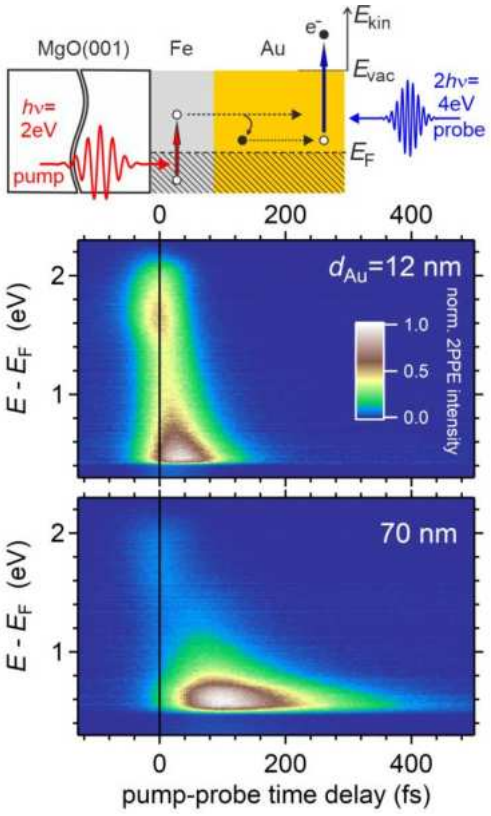


Fig. 1: Scheme of the back-side pump front-side probe geometry in time-resolved 2PPE spectroscopy (top). Time- and energy dependent photoelectron intensity for two thicknesses of the Au layer, as indicated, from [6].

As depicted in Fig. 1, we use a backside pump – frontside probe geometry to excite electron propagation across an epitaxial heterostructure Au/Fe/MgO(001) and detect the transport in a time-of-flight like approach in two-photon photoelectron emission (2PPE) on the Au surface. The photon energies used in femtosecond laser pulses are 2 eV for pumping and 4 eV for probing. With increasing Au layer thickness d_{Au} we observe an intensity drop in the 2PPE spectrum 1.7 eV above the Fermi energy E_F in combination with a shift of a second feature at 0.6 eV to later time delay, see Fig. 1. By real time time-dependent density functional theory calculations we assign the signal at 1.7 eV to electrons at their primary excitation and injection energy while the one at 0.6 eV represents electrons that have scattered inelastically with another electron, see [6] for details. By microscopic electron transport calculations, we quantify the inelastic scattering events occurring during the propagation time t^* through Au as a function of energy and compare it to the measured values, see Fig. 2. This comparison provides a determination of the number of scattering events of 1 to 4 which suggests a superdiffusive transport regime. For the high electron energies the measured t^* are shorter than the simulated ones indicating ballistic transport. With increasing d_{Au} the electron trajectories favor ballistic electron propagation along the interface normal direction which explains an experimentally observed increase in the effective electron propagation velocity with d_{Au}. This phenomenon facilitates electron momentum or energy selection by choice of the propagation layer thickness, as discussed in detail in [6].

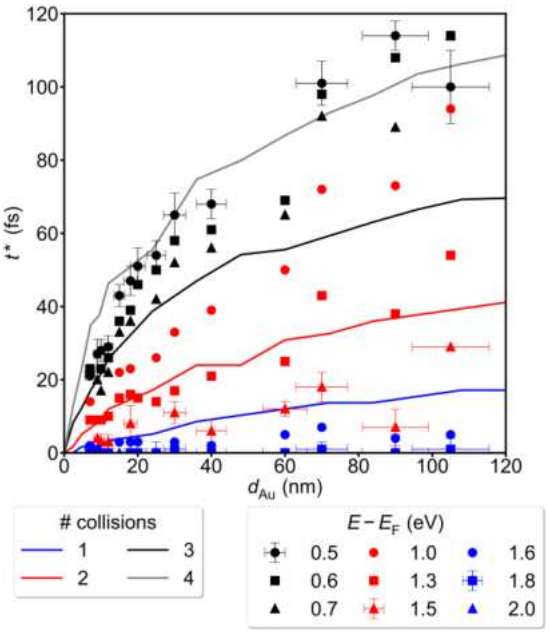


Fig. 2: Comparison of experimental and theoretical electron propagation time through the Au layer as a function of d_{Au}, from [6].

Funding by the German Research Foundation (DFG) within Project No. 278162697-SFB 1242 and through Project No. 043009-11 BO1823/12-FOR 5249 (QUAST) and computational time at magnitUDE (INST 20876/209-1 FUGG and INST 20876/243-1 FUGG), are gratefully acknowledged.

References

1. S. D. Brorson, J. G. Fujimoto and E. P. Ippen, “Femtosecond electronic heat-transport dynamics in thin gold films”, Phys. Rev. Lett., Vol. 59, 1962 (1987).
2. J. Sung et al., “Long-range ballistic propagation of carriers in methylammonium lead iodide perovskite thin films”, Nat. Phys., Vol. 16, 171 (2020).
3. J. Igarashi et al., , “Optically induced ultrafast magnetization switching in ferromagnetic spin valves”, Nat. Mater., Vol. 22, 725 (2023).
4. I. Razdolski et al., “Nanoscale interface confinement of ultrafast spin transfer torque driving non-uniform spin dynamics”, Nat. Commun., Vol. 8, 15007 (2017).
5. T. S. Seifert et al., Appl. Phys. Lett., Vol. 120, 180401 (2022).
6. M. Heckschen et al., “Spatio-Temporal Electron Propagation Dynamics in Au/Fe/MgO(001) in Nonequilibrium: Revealing Single Scattering Events and the Ballistic Limit”, PRX Energy, Vol. 2, 043009 (2023).

Sb_2S_3 phase change material for optical switching: the Brewster angle effect

G. Santos[1,†], D. Pérez-Francés[1,†], J. Resl[2], M. Losurdo[3], Y. Gutiérrez[1] and F. Moreno[1,*]

[1]Department of Applied Physics, Faculty of Sciences, University of Cantabria, 39005 Santander, Spain
[2]Center for Surface and Nanoanalytics (ZONA), Johannes Kepler Universität, A- 4040 Linz, Austria
[3]CNR ICMATE, Corso Stati Uniti 4, I- 35127 Padova, Italy
[†]Both authors contributed equally to this work.
[*]Corresponding author: morenof@unican.es

Abstract: Phase change materials in optical switching devices provides with tunable optical responses, ultrafast switching speeds, and low power consumption. In this contribution we will present a novel optical amplitude switch incorporating PCM antimony trisulfide (Sb_2S_3) based on the Brewster angle phenomenon.

The increasing importance of high-speed data processing with minimal energy consumption has spurred the utilization of light for signal transmission and processing. By employing nanostructures, the energy requirements and interaction timescales can be greatly reduced, enabling the integration of multiple devices that possess the ability to control, modulate, and process light signals with high speed and energy efficiency in the same chip [1]. The pursuit of more versatile nanophotonic devices has led to the exploration of phase-change materials (PCMs), offering the potential to create tunable and switchable nanophotonic systems through the modulation of their optical properties via external stimuli [2]. Reconfigurability offers significant advantages over conventional fixed-function devices by allowing dynamic adjustments in real-time, thus meeting the evolving demands of many photonic applications [3].

So far, reported optical switches are based on PCMs rely on $Ge_2Sb_2Te_5$ (GST). This is a consolidated technology for rewritable optical disk storage and non-volatile electronic memories due to its high thermal stability, fast switching speed, and ability to undergo numerous rewriting cycles. Most of GST based switches rely on absorption modulation because of the huge contrast in the extinction coefficient k at 1550 nm between crystalline ($k \simeq 1.49$) and amorphous ($k \simeq 0.12$) phases [4]. However, the high optical losses in GST make this material impractical for large-scale photonic integrated circuits (PICs) where light is guided through numerous phase change photonic routers. Additionally, the optical losses of GST limit its exploitation for applications where phase modulation is required without affecting the amplitude of the signal. Moreover, because of the increasing extinction coefficient k at shorter wavelengths for both phases, the integration of GST in photonic devices such as tunable metasurfaces operating in the visible or near infrared (near IR) becomes impractical [5].

Wide-bandgap PCMs are currently being investigated to overcome this limitation. They provide low-loss or even zero loss operation from the visible to mid IR range. Sb_2S_3 has been recently proposed as low-loss PCM. In its crystalline form, it has a band gap of 1.6 eV, while the amorphous phase 2.2 eV, enabling a low-losses spectra region (extinction coefficient $k = 0$) extending from 1.6 eV to the IR with an optical contrast $\Delta n \approx 0.5$. Sb_2S_3 has already been exploited in the design of reconfigurable structural color platforms, as well as amplitude and phase light modulation in all-dielectric metasurfaces and Mach-Zehnder interferometers (MZIs) operating in the C- and O- communication bands [6].

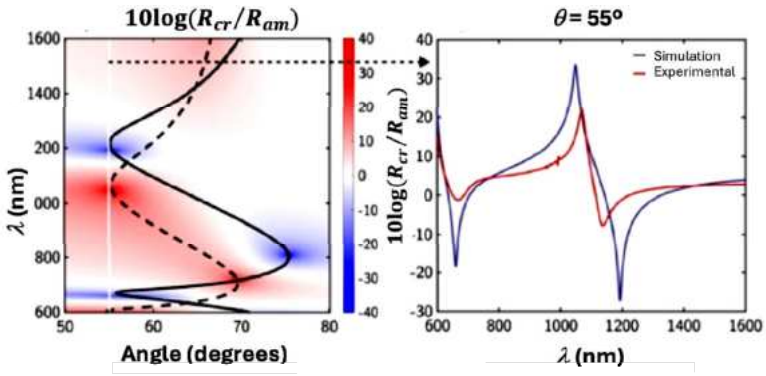


Fig. 1.- (*Left) Simulated optical contrast C in dB (C = 10log$_{10}$(R_{cr}/R_{am})) for p-polarization as a function of the angle of incidence and wavelength λ. (Right) Calculated and experimentally measured C spectra in dB for an incident angle of 55°. R_{cr} and R_{am} are the reflectivities of Sb_2S_3 in its crystalline and amorphous phases, respectively.*

In this work, amorphous and crystalline samples of Sb_2S_3 are optically and structurally characterized to explore their potential in the design of an optical amplitude switch based on the Brewster angle phenomenon [7]. The Brewster angle value depends on the refractive index of both materials at the reflective interface. Thus, the Brewster angle is strongly affected by the phase of the PCM. When the non-reflection condition is met for one of the Sb_2S_3 phases (i.e., at the Brewster angle), upon phase-change the Brewster condition is broken, leading to light reflection at the interface and producing an optical contrast in reflection that can be harnessed for optical switching applications. Sb_2S_3 is the alternative low-loss PCM with larger transparency window. i.e. spectral range beyond which neither of the material's phases experience optical losses. This is important for the optical switch based on Brewster angle, as this phenomenon only takes place if the material is transparent to light (negligeable extinction coefficient, $k \simeq 0$). With this optical switch configuration, we experimentally demonstrate an optical contrast of 22 dB (Fig. 1). Noteworthy, we theoretically predict that this contrast could be further enhanced by tailoring the incident angle and the wavelength of the beam. These findings highlight the potential of using the Brewster angle effect in developing efficient optical switch devices based on low-loss wide band gap PCMs such as Sb_2S_3.

Funding: H2020 Future and Emerging Technologies (899598 – PHEMTRONICS)

References

1. S. Zhu, P. Qiu, X. Shan, et al, "High-speed long-distance visible light communication based on multicolor series connection micro-leds and wavelength division multiplexing," Photonics Res. 10(8), 1892–1899, 2022.
2. M. Wuttig, H. Bhaskaran, and T. Taubner, "Phase-change materials for non-volatile photonic applications," Nat. Photonics 11(8), 465–476, 2017.
3. S. Abdollahramezani, O. Hemmatyar, H. Taghinejad, et al, "Tunable nanophotonics enabled by chalcogenide phase-change materials," Nanophotonics 9(5), 1189–1241 2020.
4. C. Ríos, M. Stegmaier, P. Hosseini, et al, "Integrated all-photonic non-volatile multi-level memory," Nat. Photonics 9(11), 725–732, 2015.
5. P. Moitra, Y. Wang, X. Liang, et al, "Programmable wavefront control in the visible spectrum using low–loss chalcogenide phase–change metasurfaces," Adv. Mater. 35(34), 2205367, 2023.
6. Y. Gutiérrez, A. P. Ovvyan, G. Santos, et al, "Interlaboratory study on Sb_2S_3 interplay between structure, dielectric function, and amorphous-to-crystalline phase change for photonics," iScience 25(6), 104377, 2022.
7. R. M. A. Azzam, "Fresnel's interface reflection coefficients for the parallel and perpendicular polarizations: global properties and facts not found in your textbook," in Polarization Analysis and Measurement II, vol. 2265 D. H. Goldstein and D. B. Chenault, eds., International Society for Optics and Photonics (SPIE, 1994), pp. 120–140.

Modeling Photomolecular Effect Using Feibelman Parameters and Generalized Boundary Conditions for Maxwell Equations

Gang Chen

Department of Mechanical Engineering
Massachusetts Institute of Technology
Cambridge, MA 02139, USA
gchen2@mit.edu

Abstract. Here, we re-derive a set of generalized boundary conditions for Maxwell equations using Feibelman parameters to describe the photomolecular effect: photons directly cleaving off water molecular clusters in the visible spectrum where bulk water has negligible absorption. We show that this approach can reasonably explain our experimental data.

Based on a series of experiments, we recently suggested that visible light can directly cleave off water molecular clusters from water-air interfaces, despite that bulk water absorbs very little in the visible spectrum, and we called this process the photomolecular effect(*1*, *2*). Our experimental observations were first made based on water evaporation from porous hydrogel and then from a single air-water interface under sunlight, light-emitting diodes (LEDs), and laser irradiation. The photomolecular effect was introduced to explain the super-thermal evaporation rates observed(*3*, *4*) in some solar interfacial-evaporation experiments: evaporation from porous materials floating on water surface subjected to sunlight irradiation(*5*, *6*). The photomolecular effect is surprising and poses challenges for modeling, from both microscopic and macroscopic perspectives. Microscopically, the details of water cluster cleavage processes remain unclear. Macroscopically, the question is how we can model the process based on the Maxwell equations. This paper focuses on answering the latter question, which is important for simulating absorption of clouds and hydrogels due to the photomolecular effect. We will show that the generalized boundary conditions for the Maxwell equations built on the Feibelman parameters, which were developed to describe responses of metal surfaces to light(*7*, *8*), can be used to capture the trends observed in photomolecular effect, hence lending confidence to the photomolecular effect in addition to establishing a foundation to simulate the effect.

Although all previous discussions of the Feibelman parameters were based on light interactions with electrons at a metal surface, the derivation of the generalized boundary conditions for the Maxwell equations requires no such background. As long as we recognize that the transition of the electrical field between the two sides of the interface occurs over a small distance, rather than change discontinuously, the generalized boundary conditions naturally emerge when one integrates over a spill-box spanning the transition region. (*9*, *10*)

$$[\![\boldsymbol{H}_{\parallel}]\!] = i\omega d_{\parallel}[\![\boldsymbol{D}_{\parallel}]\!] \times \boldsymbol{n} \quad (1)$$

$$[\![\boldsymbol{D}_{\perp}]\!] = d_{\parallel}\nabla_{\parallel} \cdot [\![\boldsymbol{D}_{\parallel}]\!] \quad (2)$$

$$[\![\boldsymbol{E}_{\parallel}]\!] = -d_{\perp}\nabla_{\parallel}[\![\boldsymbol{E}_{\perp}]\!] \quad (3)$$

$$[\![\boldsymbol{B}_{\perp}]\!] = 0 \quad (4)$$

where the operator $[\![\ \ ]\!]$ means the difference across the interface for the quantity inside the bracket, i.e., $[\![D_z]\!] =$

$D_z(0^+) - D_z(0^-)$, with z representing the coordinate perpendicular to the interface. The subscript "$\parallel$" means parallel to the interface (in x or y directions), while "$\perp$ " means in the z-direction. The gradient operator $\nabla_\parallel = \left(\hat{x}\frac{\partial}{\partial x} + \hat{y}\frac{\partial}{\partial y}\right) = \hat{x}ik_x$. The Feibelman parameters $d_\parallel$ and $d_\perp$ are $d_\perp = \frac{\int_{z_1}^{z_2} z\frac{dE_z}{dz}dz}{\int_{z_1}^{z_2}\frac{dE_z}{dz}dz}$ and $d_\parallel = \frac{\int_{z_1}^{z_2} z\frac{dD_x}{dz}dz}{\int_{z_1}^{z_2}\frac{dD_x}{dz}dz}$. The real part of $d_\perp$ measures the spatial deviation of the induced surface charge from z=0, and the real part of $d_\parallel$ is a measure of the location of the gradient of induced polarization parallel to the surface, i.e., the Feibelman parameters are the surface response functions. The imaginary part is related to dissipation, i.e., surface absorption.

Using the above boundary conditions, we can derive expressions for the surface absorptance for TM and TE-polarized incident light as

$$A_p = -\frac{4(n_2^2-n_1^2)}{(n_1\cos\theta_2+n_2\cos\theta_1)^2}\frac{2\pi n_1}{\lambda_o}\cos\theta_1(d_{\parallel i}\cos^2\theta_2 + d_{\perp i}\sin^2\theta_1) \quad (5)$$

$$\mathrm{A_s} \approx \frac{-4(n_2^2-n_1^2)}{[n_1\cos\theta_1+n_2\cos\theta_2]^2}\frac{2\pi n_1}{\lambda_o}\cos\theta_1 \mathrm{d_{\parallel i}} \quad (6)$$

where n_1 =1 is the refractive index of air and n2 the the refractive index water. These two expressions can be used to reasonably explain experimental data we observed in the photomolecular effect. We have used the above expressions to fit experimental data and found that the agreements were reasonable.

Acknowledgements, I would like to thank Dr. Guangxin Lyu for the experiments data used to compare with the model and the support of the MIT Bose Award.

References

1. Y. Tu, J. Zhou, S. Lin, M. Alshrah, X. Zhao, G. Chen, Plausible photomolecular effect leading to water evaporation exceeding the thermal limit. *Proc Natl Acad Sci U S A* **120** (2023).
2. G. Lv, Y. Tu, J. H. Zhang, G. Chen, "Photomolecular Effect: Visible Light Interaction with Air-Water Interface."
3. F. Zhao, X. Zhou, Y. Shi, X. Qian, M. Alexander, X. Zhao, S. Mendez, R. Yang, L. Qu, G. Yu, Highly efficient solar vapour generation via hierarchically nanostructured gels. *Nat Nanotechnol* **13**, 489–495 (2018).
4. X. Zhou, F. Zhao, Y. Guo, Y. Zhang, G. Yu, A hydrogel-based antifouling solar evaporator for highly efficient water desalination. *Energy Environ Sci* **11**, 1985–1992 (2018).
5. H. Ghasemi, G. Ni, A. M. Marconnet, J. Loomis, S. Yerci, N. Miljkovic, G. Chen, Solar steam generation by heat localization. *Nat Commun* **5**, 1–7 (2014).
6. P. Tao, G. Ni, C. Song, W. Shang, J. Wu, J. Zhu, G. Chen, T. Deng, Solar-driven interfacial evaporation. *Nat Energy* **3**, 1031–1041 (2018).
7. P. J. Feibelman, Surface electromagnetic fields. *Prog Surf Sci* **12**, 287–407 (1982).
8. A. Liebsch, *Electronic Excitations at Metal Surfaces* (1997).
9. Y. Yang et al., A general theoretical and experimental framework for nanoscale electromagnetism. *Nature* **576**, 248–252 (2019).
10. W. L. Schaich, W. Chen, Nonlocal corrections to Fresnel optics: How to extend d-parameter theory beyond jellium models. *Phys Rev B* **39**, 10714–10724 (1989).

Broadband Nonlinear Optical Waveguides Based On Conformal Transformation Optics

Chunyu Huang[1], Yu Luo[2], Yule Zhao[1], Xiaofei Ma[1], Zhiwei Yan[1], Ziyi Liu[1], Chong Sheng[1], Shining Zhu[1], Hui Liu[1,*]

[1]Collaborative Innovation Center of Advanced Microstructures National Laboratory of Solid State Microstructures, School of Physics Nanjing University, Nanjing, China
[2]School of Electrical and Electronic Engineering, Nanyang Technological University, Singapore
[*]corresponding author: liuhui@nju.edu.cn

Abstract: Integrated nonlinear optical devices are important in modern optical communications. However, a universal method for designing such devices on chip still lacking. We proposed a general strategy based on transformation optics to design curved accelerating waveguides with spatially gradient curvatures able to achieve broadband nonlinear frequency conversion on chip.

To achieve broadband quality in nonlinear optical devices, many approaches have been proposed, such as group-velocity dispersion engineering, zero-index waveguides, or microcavity [1-2]. However, these approaches strictly depend on material or are not strictly continuous.

Transformation optics (TO) is a novel optical designing method that provides additional degrees of freedom to manipulate electromagnetic waves by engineering the permittivity and permeability across space and time [3, 4]. Specifically, conformal transformation optics (CTO) eliminate the extreme anisotropy that hampers the experimental realization of TO, demonstrating its application in many interesting phenomena. However, most of applications of TO are limited to linear optics.

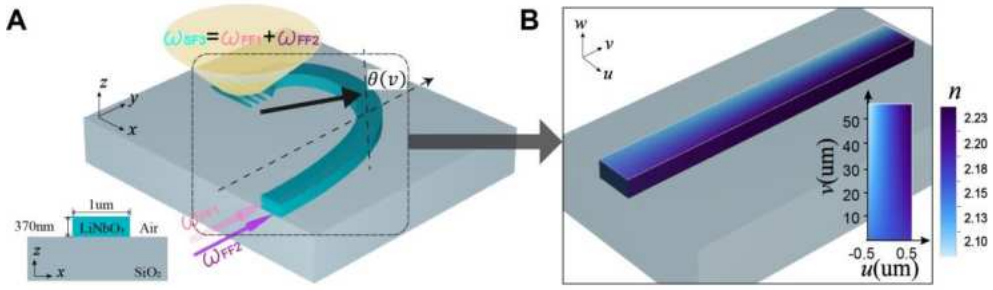


Fig.1 A. Depiction of a CAW of LNOI in the physical space (x, y, z), with the spatially gradient radius $r(v)$. The inset shows the material and the structure of CAWs in out work. **B**. The refractive index distribution of the transformed straight waveguide in the virtual space (u, v, w).

In this work, we present a general strategy utilizing TO to design curved accelerating waveguides (CAWs) with spatially gradient curvatures able to achieve broadband nonlinear frequency conversion on chip (Fig.1A). The CAW's radius is expressed by $r(v)$, where v denotes the imaginary axis after the transformation (Fig.1B). To transform it from the physical space $\xi = x + iy$ to a straight waveguide in virtual space $\zeta = u + iv$, we search a conformal mapping $\xi = f(\zeta)$, requiring the total length remain unchanged under the transformation, i.e. $|d\xi| = r(v)d\theta = dv$, where $\theta(v) = \int_0^v dv'/r(v')$ denotes the angle between the tangential direction of the curved waveguide and the vertical axis of the physical coordinate. The conformal mapping is then obtained through the integration of $\theta(-i\zeta')$ in terms of $\xi = \int_0^{-i\zeta} e^{i\theta(-i\zeta')}\, d\zeta'$. The theory of CTO enables us to calculate the refractive index of the straight waveguide

$$n = n_0 \left|\frac{d\xi}{d\zeta}\right| = n_0 \left|e^{i\theta(-i\zeta)}\right| \tag{1}$$

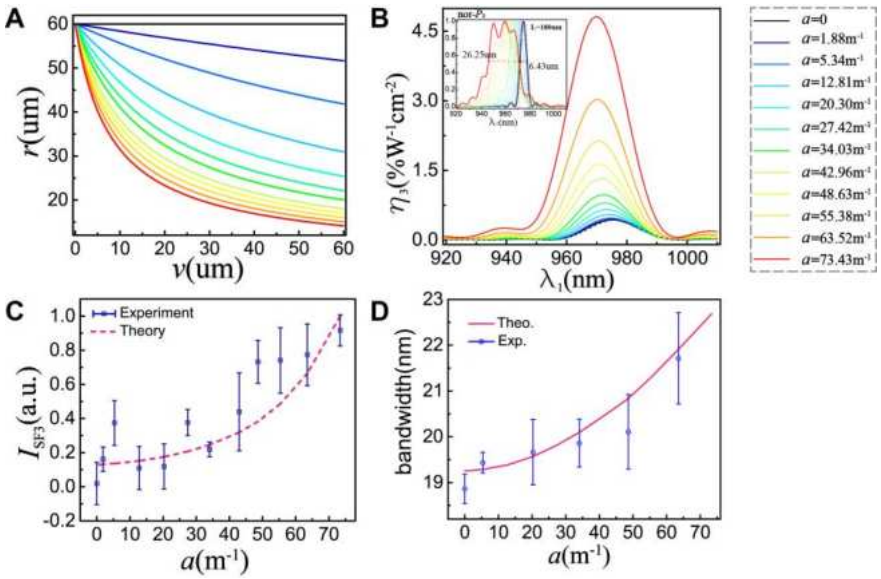


Fig.1 A. The radii of 11 CAWs as functions of v. The legend on the far right gives the exact values of accelerations. **B**. The normalized frequency conversion efficiency $\eta_3 = P_3/(P_1P_2L^2)$ as a function of the fundamental wavelength λ_1. The inset theoretically demonstrate that the normalized bandwidth of a CAW can be 4 times higher than $a = 0$ if the length of the waveguide increased to 180um. **C**. The dependence relation between the SFG output intensity with the acceleration a (for $\lambda_1 = 960nm$). **D**. The experimental results of SFG bandwidth for different CAWs.

To design CAWs in Fig.2A, we consider a spatially gradient radius given by $r(v) = r_0'/\left[\ln\left(n_0'\sqrt{1-av} - n_1'\right)\right]$, where $r_0' = 25.56um$, $n_0' = 1847.7$, and $n_1' = 1849.2$ are constants that will be determined through initial conditions. The mode index in such a CAW then be resulted to a simple function as $n_{\text{eff}}(v,\omega) = n_{\text{eff}}(0,\omega)\sqrt{1-a(\omega)v}$. Hence the wave equation governing the electric field in the CAW is given by,

$$\nabla^2 E - \frac{n_{\text{eff}}^2(0,\omega)(1-av)}{c^2}\frac{\partial^2 E}{\partial t^2} = 0 \tag{2}$$

The propagation solution of equation (2) takes the form of $E \sim (1-av)^{-1/4}\exp[i\phi(v,\omega)]$ since we interested in the case where the refractive index $n_{\text{eff}}(v,\omega)$ varies slowly along v, where the phase is $\phi(v,\omega) = n_{\text{eff}}(0,\omega)k_0(v - av^2/4)$. Then considering the sum-frequency generation (SFG) process $\omega_1 + \omega_2 = \omega_3$, we derive the transformed nonlinear SFG coupling equations by substituting the approximated solution to polarization equation $\boldsymbol{P} = \epsilon_0\chi^{(2)}\boldsymbol{E}^2$. The theoretical and experimental results are shown in Fig.2. We can see that both the conversion efficiency and the nonlinear conversion spectrum are boosted by the acceleration.

In conclusion, this approach offers a universal strategy to design broadband nonlinear optical devices on chip without the limitation of materials and the limitation of $\chi^{(2)}$ or $\chi^{(3)}$, and is applicable to various nonlinear optical processes. The experimental results validate the effectiveness of LNOI chip design, indicating its potential for practical applications.

References

1. M. A. Foster, A. C. Turner, J. E. Sharping, B. S. Schmidt, M. Lipson, and A. L. Gaeta, "Broad-band optical parametric gain on a silicon photonic chip," Nature, vol. 441, no. 7096, pp. 960-3, Jun 22 2006, doi: 10.1038/nature04932.
2. Y. Hu et al., "High-efficiency and broadband on-chip electro-optic frequency comb generators," Nature Photonics, 2022/08/29 2022, doi: 10.1038/s41566-022-01059-y.
3. J. B. Pendry, D. Schurig, and D. R. Smith, "Controlling Electromagnetic Fields," Science, vol. 312, no. 5781, pp. 1780-1782, 2006, doi: doi:10.1126/science.1125907.
4. U. Leonhardt, "Optical Conformal Mapping," Science, vol. 312, no. 5781, pp. 1777-1780, 2006, doi: doi:10.1126/science.1126493.

Fano line shapes generated by excitonic nanoparticles

S. Hayashi[1,2]

[1]Graduate School of Engineering, Kobe University, Japan
[2]Morrocan Foundation of Advanced Science, Innovation and Research, University Mohammed VI Polytechnic, Morocco
*corresponding author: s.hayashi@dragon.kobe-u.ac.jp

Abstract: Based on the Mie theory and its electrostatics approximation, we analyze analytically and numerically optical responses and resonant behaviors of internal fields in spherical excitonic nanoparticles and show that Fano line shapes can easily be generated in the scattering spectra and spectra of internal fields.

Dielectric nanoparticles not showing distinct Mie resonances have been discarded as useful elements of resonant nanophotonics. However, the incorporation of the excitonic transition into such nanoparticles may allow us to generate sharp resonances, in particular, Fano resonances, thereby enhancing the utility of such nanoparticles. As schematically shown in Fig. 1, we consider an excitonic sphere of radius R characterized by a dielectric function $\varepsilon(\omega)$ placed in a surrounding material with a dielectric constant ε_{m}. The dielectric function of the excitonic particle is assumed to take the following form:

$$\varepsilon(\omega) = \varepsilon_{\mathrm{b}} - \frac{f\omega_{\mathrm{exc}}^2}{\omega^2 - \omega_{\mathrm{exc}}^2 + i\gamma_{\mathrm{exc}}\omega_{\mathrm{exc}}},$$

with the background dielectric constant $\varepsilon_{\mathrm{b}} = 2.2$, the energy of exciton transition $\hbar\omega_{\mathrm{exc}} = 2.0664$ eV (600nm), $\hbar\gamma_{\mathrm{exc}} = 103.32$ meV and the oscillator strength $f = 0.13$; the parameter values were chosen to reproduce well optical spectra of the PVA film doped with J-aggregates of TDBC molecules[1,2], which is one of the typical excitonic materials.

The findings of this work are summarized as follows[3]:

I. Small particle limit

For a sufficiently small excitonic nanoparticle (small particle limit), calculations based on the electrostatics approximation show that scattering and extinction spectra exhibit the Fano line shape (external Fano resonances), caused by the interference between a broad background (Rayleigh scattering) and a sharp excitonic response. It is also shown analytically that the line shapes can be expressed by the generalized Fano function with a q factor expressed in terms of the system parameters.

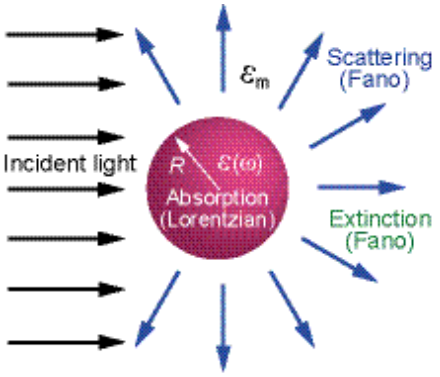


Fig. 1 Excitonic nanoparticle illuminated by incident light.

Figure 2(a) and 2(b) show spectra of efficiencies of scattering Q_{sca} and absorption Q_{abs}, respectively, of a spherical particle of TDBC-doped PVA with R =20 nm. Figure 2(c) shows the scattering efficiency of a pure PVA sphere (f = 0) without excitonic transition, called background scattering Q_{back}, which obeys the $(\hbar\omega)^4$- law of Rayleigh scattering. In Fig. 2(a) we see clearly an asymmetric line shape superposed on the Rayleigh background. As shown in Fig. 2(d), the spectrum of F_{sca} obtained by normalizing Q_{sca} to Q_{back} exhibits Fano line shape which is well reproduced by the generalized Fano function $F_{\mathrm{sca}}^{\mathrm{ap}}$ derived analytically within the electrostatics approximation. On the other hand, the normalized absorption spectrum F_{abs} exhibit the Lorentzian line shape as can be seen in Fig. 2(e).

II. Beyond the small particle limit

Calculations based on the exact Mie theory show that the Fano line shapes are preserved and can be well fitted by the generalized Fano function, provided that R is smaller than an upper bound value (results not shown here).

III. Internal electric fields

Behaviors similar to those of Q_{sca} are found for the enhancement factor FE of the internal fields averaged over the spherical particle (internal Fano resonances).

In Fig. 3(a), a spectrum of FE of the doped sphere is shown together with FE_{back} of undoped sphere, obtained within the electrostatics approximation. The spectrum of F_{int} obtained by normalizing FE to FE_{back} again shows the Fano line shape that can be well reproduced by the generalized Fano function F_{sca}^{ap} derived analytically.

The results of the present work provide a firm basis for discussing the external and internal Fano resonances in excitonic nanoparticles

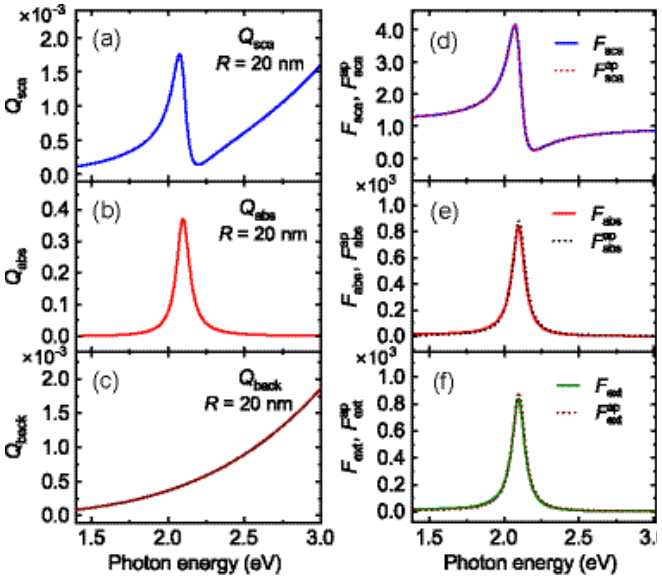


Fig. 2 Spectra of efficiencies of scattering Q_{sca} (a), absorption Q_{abs} (b) and background scattering Q_{back} (c) for an excitonic sphere. Comparison of the scattering (d), absorption (e) and extinction (f) spectra normalized the background scattering with those obtained by analytical expression of the generalized Fano function.

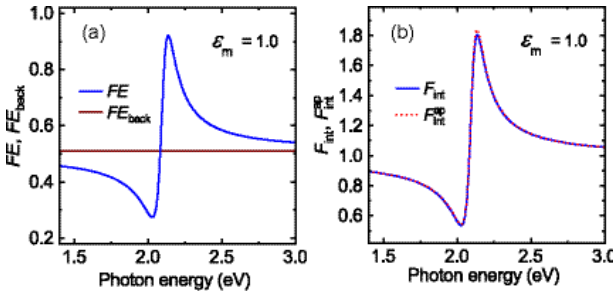


Fig. 3 (a) Spectrum of FE of doped sphere, field enhancement factor averaged over the sphere, and that of FE_{back} of undoped sphere. (b) Spectrum of F_{int} obtained by normalizing FE to FE_{back} and that of F_{sca}^{ap} obtained from the analytical expression of the generalized Fano function.

References

1. Gentile, M. J. S. Sánchez, N. and Barnes, W. L. Optical field-enhancement and subwavelength field-confinement using excitonic nanostructures, Nano Lett. Vol. 14, 2339, 2014.

2. Hayashi, S. Ishigaki, Y. and Fujii, M. "Plasmonic effects on strong exciton-photon coupling in metal-insulator-metal cavities," Phys. Rev. B, Vol. 86, 045408, 2012.

3. Hayashi, S. Sugimoto, H. Fujii, M. Nesterenko, D. V. Sekkat, Z. "Formation of Fano line shapes in optical responses and spectra of internal fields of excitonic nanospheres," Phys. Rev. B, Vol. 108,125408, 2023.

Tunable Second Harmonic Generation from Lithium Niobate Metasurfaces

Mengxin Ren[*], Lun Qu, Lu Bai, Zhengqing He, Wei Wu, and Jingjun Xu[†]
The Key Laboratory of Weak-Light Nonlinear Photonics, Ministry of Education, School of Physics and TEDA Applied Physics Institute, Nankai University, Tianjin, China
[*]corresponding author: ren_mengxin@nankai.edu.cn
[†]corresponding author: jjxu@nankai.edu.cn

Abstract: Metasurfaces have demonstrated themselves as a promising platform for enhanced second harmonic generation (SHG) to achieve ultracompact nonlinear light sources. Lithium niobate (LN), particularly the crystalline LN thin film on insulators (LNOI) has emerged recently as a promising platform to manufacture metasurfaces. In this talk, we will present our recent works about tunable SHG from lithium niobate metasurfaces.

Second harmonic generation (SHG), which converts the frequency of a laser ω to twice its frequency 2ω, plays a key role in extending spectral coverage of laser sources to wavelengths that are difficult to access by standard laser gain media. As we enter the Nano-era, the SHG at nanoscales with controllable performance is highly desired. Nonlinear metasurfaces have provided us with a revolutionary concept to engineer nonlinear responses from nanoscale. In addition, it also acts as a new platform to realize novel nanoscale SHG light sources. Recently, crystalline lithium niobate thin film on insulators (LNOI) has emerged as an excellent solution for the novel SHG metasurfaces and nonlinear light sources [1-4]. An SHG conversion efficiency higher than 0.1% has been achieved from LN metasurface framework [5]. How to further tune the SHG performance dynamically has become an urgent problem to address. In this talk, we will present our recent results on the topic of tunable SHG from lithium niobate metasurfaces. Our works offer insights for the development of tunable SHG sources in integrated photonics and nanoscale optical devices.

References

1. Bofeng Gao, Mengxin Ren, Wei Wu, Hui Hu, Wei Cai, Jingjun Xu. “Lithium niobate metasurfaces,” Laser Photonics Rev., 13, 1800312, 2019.
2. Junjun Ma, Jiaxin Chen, Mengxin Ren, Wei Wu, Wei Cai, Jingjun Xu. “Second harmonic generation and its nonlinear depolarization from lithium niobate thin films,” Opt. Lett., 45, 145, 2020.
3. Junjun Ma, Fei Xie, Weijin Chen, Jiaxin Chen, Wei Wu, Wei Liu, Yuntian Chen, Wei Cai, Mengxin Ren, Jingjun Xu. “Nonlinear lithium niobate metasurfaces for second harmonic generation,” Laser Photonics Rev., 15, 2000521, 2021.
4. Lun Qu, Lu Bai, Chunyan Jin, Qiang Liu, Wei Wu, Bofeng Gao, Juntao Li, Wei Cai, Mengxin Ren, Jingjun Xu. “Giant Second Harmonic Generation from Membrane Metasurfaces,” Nano Lett. 22, 9652, 2022.
5. Lun Qu, Zhidong Gu, Chenyang Li, Yuan Qin, Yiting Zhang, Di Zhang, Jiaxian Zhao, Qiang Liu, Chunyan Jin, Lishuan Wang, Wei Wu, Wei Cai, Huasong Liu, Mengxin Ren, Jingjun Xu, “Bright second harmonic emission from photonic crystal vertical cavity,” Adv. Funct., Mater., 33, 2308484, 2023.

Chiral emission from perovskite metasurfaces and metacavities

Young Chul Jun[1,*]

[1]Ulsan National Institute of Science and Technology (UNIST), Republic of Korea
[*]corresponding author: ycjun@unist.ac.kr

Abstract: In this talk, we discuss two recent experiments on chiral emission from resonant optical nanostructures. First, maximally chiral emission from perovskite metasurfaces is demonstrated using chiral quasi-bound states in the continuum. Second, chiral electroluminescence is achieved at room temperature with a substantial degree of circular polarization using thin-film-based chiral metacavities.

Chiral optical objects exhibit different optical responses under left circularly polarized (LCP) and right circularly polarized (RCP) light incidences. Chiral responses, such as circular dichroism and optical activity, are present in numerous natural materials; however, they are typically very weak. To overcome these limitations, various optical nanostructures, including three-dimensional chiral structures and two-dimensional planar chiral structures, have been widely studied. Chiral nanophotonic structures can significantly enhance the chiral optical responses and provide unprecedented design flexibility. Because chiral light sources are desirable for various applications, such as displays, optical recording, optical communication, bioimaging, and biomedical diagnosis, chiral emission is also attracting considerable attention. Highly enhanced chiral light–matter interactions are desirable to realize chiral light sources in compact device platforms.

In this invited talk, we introduce our recent experimental demonstrations on chiral emission from perovskite metasurfaces and metacavities [1-5]. Chiral light sources based on perovskite materials are attracting considerable attention to fully exploit their exceptional optoelectronic properties. Recently, there has been extensive research for achieving chiral photoluminescence from perovskite materials. However, it remains challenging to obtain chiral emission with a large degree of circular polarization (DCP) at room temperature. Moreover, there was no demonstration of chiral electroluminescence yet with a substantial DCP, although it represents a critical step toward practical device applications. Here, we mainly discuss two recent experiments from our group: (i) maximally chiral emission from perovskite metasurfaces and (ii) chiral electroluminescence from perovskite metacavities.

First, chiral quasi-bound states in the continuum are realized in the visible range by controlling the etching depths in the substrate and inducing out-of-plane symmetry breaking. An organic-inorganic hybrid perovskite film is spin-coated on a patterned glass substrate. Grayscale lithography is employed to control the etching depths in the substrate and induce out-of-plane symmetry breaking. An extremely high level of chiral emission from the perovskite metasurface is experimentally achieved in the normal direction at room temperature. Chiral emission is maximally enhanced for one helicity via critical coupling while strongly suppressed for the other helicity.

Second, chiral electroluminescence is experimentally achieved at room temperature with a substantial DCP (~0.38) using thin-film-based chiral metacavities. In our design, a periodic lattice of inversion-symmetry-broken polycrystalline silicon (poly-Si) patterns is integrated with an inorganic perovskite electroluminescence device. The bottom dielectric metasurface (poly-Si layer) and top metal layer forms a chiral metacavity, which supports

photonic eigenstates with close-to-maximum chiral response. Chiral Fabry–Pérot modes supported by the metacavity determine asymmetry of electroluminescence, and pairs of LCP and RCP waves of equal powers are generated in the opposite oblique directions. By optimizing the pattern geometry and dimension, we can enhance and tailor the chiral emission from the metacavity. Detailed theoretical analyses based on chiral coupled-mode theory have also been conducted.

References

1. I. C. Seo, Y. Lim, S.-C. An, B. H. Woo, S. Kim, J. G. Son, S. Yoo, Q-H. Park, J. Y. Kim, and Y. C. Jun, "Circularly polarized emission from organic-inorganic hybrid perovskites via chiral Fano resonances," ACS Nano 15, 13781 (2021).
2. S. Kim, B. H. Woo, S.-C. An, Y. Lim, I. C. Seo, D.-S. Kim, S. J. Yoo, Q-H. Park, and Y. C. Jun, "Topological control of 2D perovskite emission in the strong coupling regime," Nano Letters 21, 10076 (2021).
3. Y. Lim, I. C. Seo, S.-C. An, Y. Kim, C. Park, B. H. Woo, S. Kim, H.-R. Park, and Y. C. Jun, "Maximally chiral emission via chiral quasi-bound states in the continuum," Laser & Photonics Reviews, 17, 2200611 (2023).
4. Y. Lim, I. C. Seo, and Y. C. Jun, "Polarization distortion and compensation of circularly polarized emission from chiral metasurfaces," Curr. Opt. Photon. 7, 147 (2023).
5. S. Kim, S.-C. An, Y. Kim, Y. S. Shin, A. A. Antonov, I. C. Seo, B. H. Woo, Y. Lim, M. V. Gorkunov, Y. S. Kivshar, J. Y. Kim, and Y. C. Jun, "Chiral electroluminescence from thin-film perovskite metacavities," Science Advances 9, eadh0414 (2023).

Amorphous dielectric materials with complete photonic band-gaps in 3D.

Abraham Aguilar[1*], **Marian Florescu** [2], **and Frank Scheffold** [1]

[1]Department of Physics, University of Fribourg, Switzerland.

[2]Advanced Technology Institute and Department of Physics, University of Surrey, U.K.

[*]corresponding author: abraham.aguilaruribe@unifr.ch

Abstract: In a recent paper, our research group proposed a comprehensive framework that unifies the description of light transmission through three-dimensional amorphous dielectric materials **[1]**. In our model we address the role of both light localization and the photonic bandgap. Here, we present experimental results on light transmission and reflection in amorphous dielectric networks, providing empirical support for the theoretical framework.

Over the past decade, it has been demonstrated that amorphous photonic dielectric materials can exist in two and three dimensions, displaying a complete photonic bandgap that inhibits the propagation of electromagnetic waves within a specific frequency range [1]. These materials show great promise in both fundamental physics and various technological applications.

In a recent paper, our research group proposed a comprehensive framework that unifies the description of light transmission through three-dimensional amorphous dielectric materials. In our model we address the role of both light localization and the photonic bandgap [2]. Here, we present experimental results on light transmission and reflection in amorphous dielectric networks, providing empirical support for the theoretical framework [2].

Our findings include compelling evidence of complete photonic bandgaps in dielectric networks made of silicon. To fabricate these network structures, we employed direct laser writing of polymer templates followed by subsequent thermal shrinkage [3]. The polymer structures were then converted into high refractive index silicon through chemical vapor deposition.

Of particular importance in our investigation is the specific examination of the role of direct coherence reflection or single scattering in the proximity of the photonic bandgap, necessary to interpret the experimental data.

Acknowledgements: A.A and F. S. acknowledge the Swiss National Science Foundation through the National Centre of Competence in Research Bio-Inspired Materials (No. 205603) and projects No. 188494 and No. 169074.

References

1. Scheffold, F., Haberko, J., Magkiriadou, S., & Froufe-Pérez, L. S. (2022). "Transport through Amorphous Photonic Materials with Localization and Bandgap Regimes." *Phys. Rev. Lett.,* 129, 157402.

2. Florescu, M., Torquato, S., & Steinhardt, P. J. (2009). "Designer disordered materials with large, complete photonic band gaps." *Proceedings of the National Academy of Sciences,* 106(49), 20658-20663.
3. A. A. Uribe, Yazhgur, P., & Scheffold, F. (2023). "Experimental realization of Weaire–Phelan foams as photonic crystals." *APL Photonics,* 8(11), 111301.

Fundamental studies for new device applications in two-dimensional plasmonic crystals through analytical demonstrations in the submillimeter-wave band

G. Itami[1*] and O. Sakai[1]

[1]The University of Shiga Prefecture, Japan
[*]corresponding author: ot68gitami@ec.usp.ac.jp

Abstract: Plasmonics is attracting renewed attention as the demand for optical integrated circuits increases. In particular, localization and near-field enhancement of light by surface plasmon and plasmonic band design are important for device applications. A control method of plasmonic skin depth and band structures using periodic structures are introduced.

A metal hole array (MHA) is a representative structure of two-dimensional plasmonic crystal [1]. And its complemental structure, metal plate array (MPA) can also be used for surface wave generation, if the conductive part in MPAs is thick enough to act as a boundary [2]. The structures used in this study are MPA and the structure with holes in MPA, which is called a ring dipole array (RDA) shown in Figure 1(a) [3]. By widening holes in the RDA, the propagation state is changed to a differential mode from conventional surface wave modes. In this case, the resonant frequency of extraordinary transmission (EOT) is maintained, but the bandwidth gradually narrows and the Q-factor increases. This is a conversion process to a quasi-BIC mode following the toroidal dipole model. Here, the skin depth on the RDA can be expressed as follows.

$$L = \frac{c}{\sqrt{\omega^2 - {\omega_\mathrm{p}}^2}} \tag{1}$$

Here, ω is the angular frequency and ω_p is the cut-off frequency. As Fig. 1 (b) shows, the skin depth in the RDA can be controlled by using the size of holes (p), because the cut-off frequency is varied in the process while resonant frequency is kept. Next, the band structure in the two-layered model of the RDAs in Fig. 1(c) is discussed [4]. If an equivalent circuit model is used, the ideal propagation modes can be expressed as CRLH transmission lines and the dispersion relation shows a Dirac cone (ω'_r and ω_r: the upper and lower frequencies of Γ point), shown in Fig. 1(d). Varying the interval between the layers changes the resonance frequencies of the upper and lower bands, thus creating a band gap. In practice, the dispersion relation is expected to be similar to that of a Dirac cone due to the inclusion of multi-wave interference effects between surface wave modes, suggesting the possibility of modulating the surface wave propagation in the structure by changing the interval.

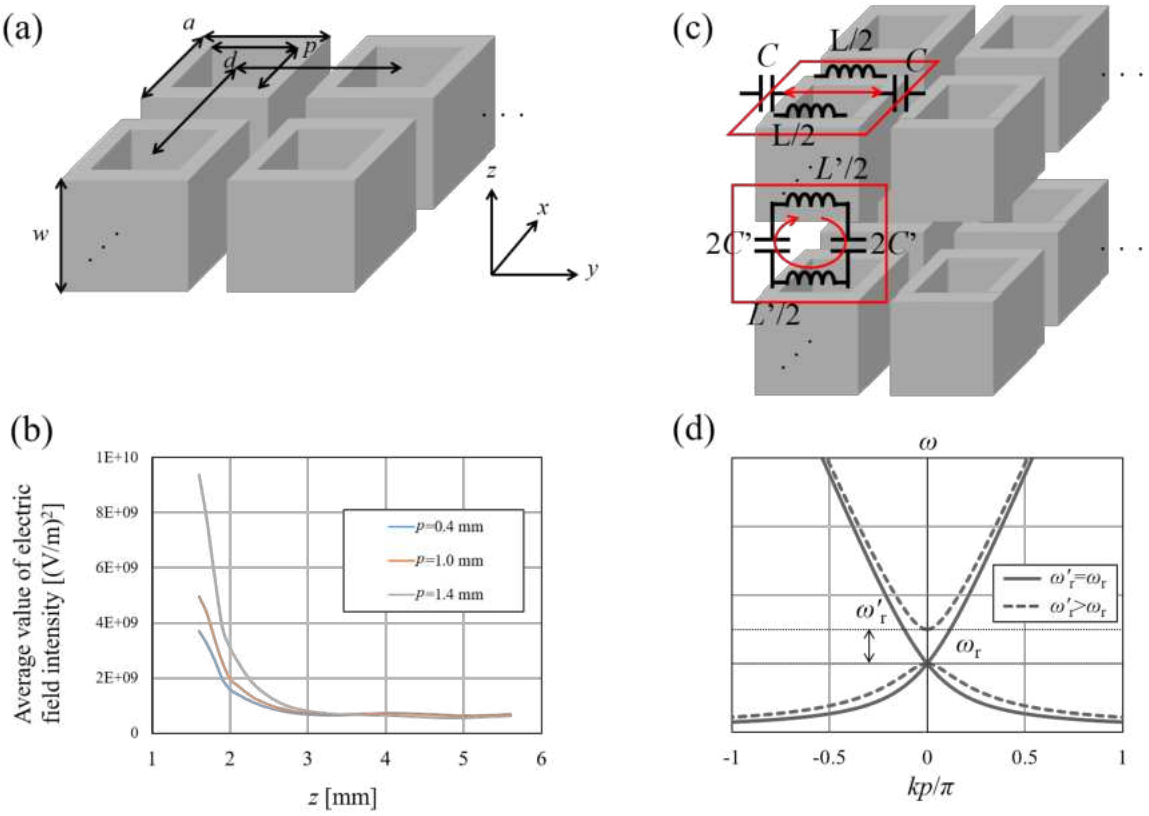


Figure. 1: (a)The structure of the ring dipole arrays, (b)one-dimensional spatial distribution of electric fields on surface modes in the RDA, (c) the structure of the two-layered ring dipole arrays, (d)the dispersion relation of Dirac cone in the two-layered ring dipole arrays.

References

1. J. B. Pendry, L. M. Moreno, and F. J. G. Vidal, "Mimicking Surface Plasmons with Structured Surfaces," Science, Vol. 305, 847–848, 2004.
2. G. Itami and O. Sakai, "Analysis and observation of the breakdown of Babinet's principle in complementary spoof surface plasmon polariton structures," Sci. Rep., Vol. 10, 11027, 2020.
3. G. Itami and O. Sakai, "Independent control method for plasmonic skin depth based on transformation from spoof surface plasmon polaritons to bound states in the continuum," Phys. Rev. B, Vol. 106, 245406, 2022.
4. G. Itami and O. Sakai, "Formation of a Dirac Cone and Dynamic Control of its Half-Metallic Properties Using Double-Layer Ring Dipole Arrays," Phys. Rev. Applied, Vol. 20, 034012, 2023.

Full-space Janus Metasurface for Direction-duplex Quad-channel Electromagnetic Wave Manipulation

Weixu Yang, Shufang Dong, Ke Chen and Yijun Feng*
School of Electronic Science and Engineering, Nanjing University, Nanjing, China
*corresponding author: yjfeng@nju.edu.cn

Abstract: This article presents a full-space Janus metasurface that enables asymmetric transmission-reflection-integrated electromagnetic wave functionalities for the right-handed circularly-polarized incidence propagating along opposite directions. As a proof of concept, direction-duplex quad-channel holographic images are demonstrated in microwave region using the fabricated metasurface.

Janus metasurfaces is a category of two-faced devices utilized for achieving distinct functions selectively excited by choosing the propagation directions [1]-[3]. Recently, full-space metasurfaces have gained much attention due to their coverage extension and function integration [4]. Although numerous Janus metasurfaces have been proposed to achieve asymmetric transmission functionalities, their reflection channels still keep unexploited, thus supporting only two channels.

As shown in Figure 1, here we propose a design strategy to extend the function of Janus metasurface from asymmetric transmission channels to direction-duplex full-space channels. As a result, when the metasurface is illuminated by a forward (+z) right-handed circularly-polarized (RCP) incidence, independent images of letters "F" and "R" are generated in the transmission and reflection regions, respectively. While for the backward (−z) RCP incidence, another two distinct images of letters "T" and "B" are achieved, thus yielding asymmetric full-space wave functionalities and integrating four independent channels in a single Janus metasurface.

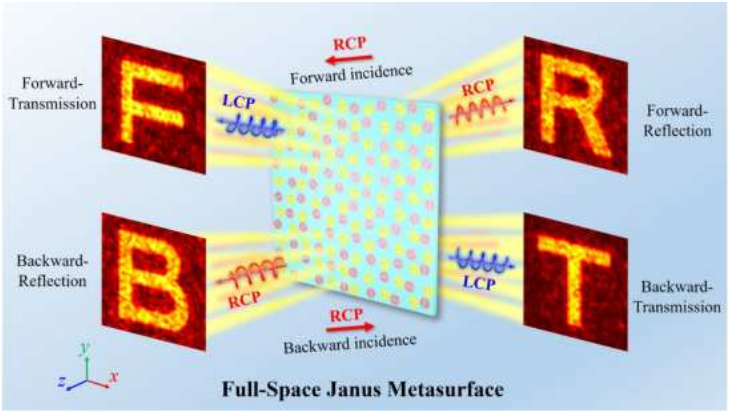


Figure 1. Conceptual illustration of the proposed full-space Janus metasurface.

To achieve this goal, two kinds of meta-atoms with direction-selective scattering properties, respectively denoted as yellow and red cells in Figure 1, are ingeniously designed and then interleaved in the Janus metasurface. The receiver-transmitter structure is adopted in each meta-atom, which is composed of left-handed circularly-polarized (LCP) and RCP patches with opposite chirality. Therefore, when the same incident wave illuminates the metasurface from two sides, the meta-atom will operate in transmission and reflection modes, respectively. By rotating the orientation angles of the receiver and transmitter patches, decoupled phase delays can be generated in such full-space channels. It is worth noting that the two kinds of meta-atoms can be

converted with each other by swapping their constituent receiver and transmitter, thus providing four degrees of freedom to independently manipulate four phase patterns for RCP incidence with opposite directions.

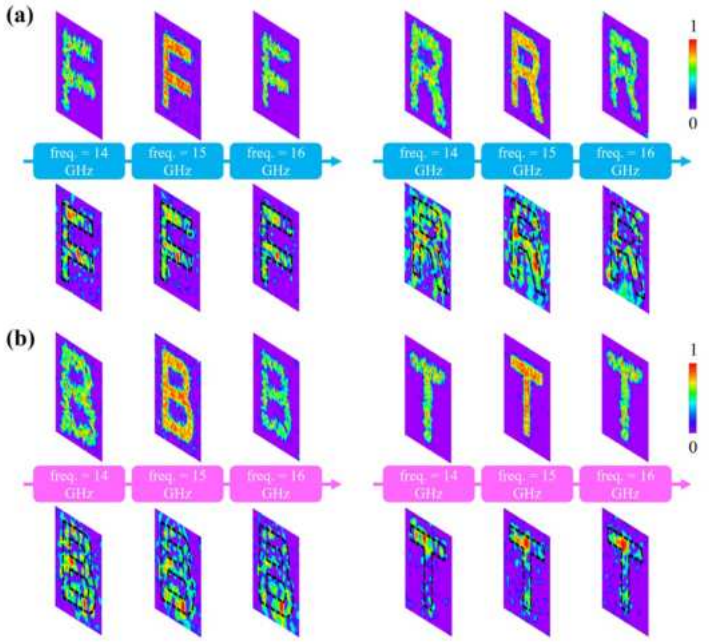


Figure 2. Direction-duplex full-space meta-holography for the (a) forward and (b) backward RCP incidence.

The theoretically calculated and experimentally measured results of direction-duplex full-space holographic images at three distinct frequencies are shown in Figure 2. The center frequency is 15 GHz. The fabricated metasurface consists of 40×40 pixels, occupying a size of 380×380 mm^2. Defining the imaging efficiency as the ratio of the energy concentrated in the holographic pattern to all energies on the imaging plane, the measured imaging efficiencies of four holographic images "F", "R", "B", and "T" are 81.5, 68.8, 70.1, and 78.2%, respectively at 15 GHz. The full-space Janus metasurface proposed here may open new possibilities toward sophisticated multifunctional meta-devices ranging from microwaves to optical systems.

Acknowledgements: This work was supported by National Natural Science Foundation of China (NSFC) (62271243, 62071215, 91963128), the Joint Fund of Ministry of Education for Equipment Pre-research (8091B032112), and the Key Research and Development Program of Jiangsu Province (BE2023084).

References

1. K. Chen et al., "Directional Janus metasurface," *Adv. Mater.*, Vol. 32, No. 2, 1906352, 2020.
2. G. Shang et al., "Transmission-reflection-integrated multiplexed Janus metasurface," *ACS Appl. Electron. Mater.*, Vol. 3, No. 6, 2637-6113, 2021.
3. M. A. Naveed et al., "Optical spin-symmetry breaking for high-efficiency directional helicity-multiplexed metaholograms," *Microsyst. Nanoeng.*, Vol. 7, No. 1, 34567723, 2021.
4. W. Yang, K. Chen, J. Zhao, T. Jiang, and Y. Feng, "A wideband high-efficiency transmit-reflect-array antenna for bidirectional radiations with distinct circular polarizations based on a metasurface," *IEEE Trans. Antennas Propag.*, Vol. 71, No. 4, 3695–3700, 2023.

Topological phase-supporting materials for nanophotonic sensing

G. Cruz[1], S. Roy[2], A. Banerjee[1], and P. Bermel[2,*]

[1]Department of Physics, Purdue University, West Lafayette, IN 47907, USA
[2]Birck Nanotechnology Center, Purdue University, West Lafayette, IN 47907, USA
[*]corresponding author: pbermel@purdue.edu

Abstract: Dimensionality affects topological phases in materials such as bismuth selenide telluride (BST), and applications to nanophotonic sensing. Understanding how to adjust the phase transition point of these materials allows us to put our sensor near the phase transition line, to substantially heighten its sensitivity to the local environment.

Recent papers have shown the potential of BST and related materials to form topological phases [1,2]. In the overarching thesis of our quantum sensing work, understanding how to adjust the phase transition point of these materials between topological insulator (TI) and topologically trivial states allows us to carefully position our sensor near the phase transition line, to substantially heighten its sensitivity to the local environment. Specifically, the abrupt change in an order parameter and topological invariants is highly sensitive to fluctuations which we aim to leverage. Work to date in our project has clearly shown that density functional theory (DFT) methods can be effectively implemented to calculate topological phase material band structures in bulk materials, along with Chern numbers, as well as other signatures of topological phases. They also provide the ability to predict the role of impurity of defect states in topological phase formation [3].

An example of the results obtained are shown in Fig. 1, below. They were calculated using standard Generalized Gradient Approximation (GGA) for the exchange and correlation energy in the parameterization of Perdew, Burke, and Ernzerhof (PBE-96), in the Full Potential Local Orbital Code (FPLO). A K-mesh subdivision of 12 × 12 × 4 was employed for a full 3D electronic band structure calculation.

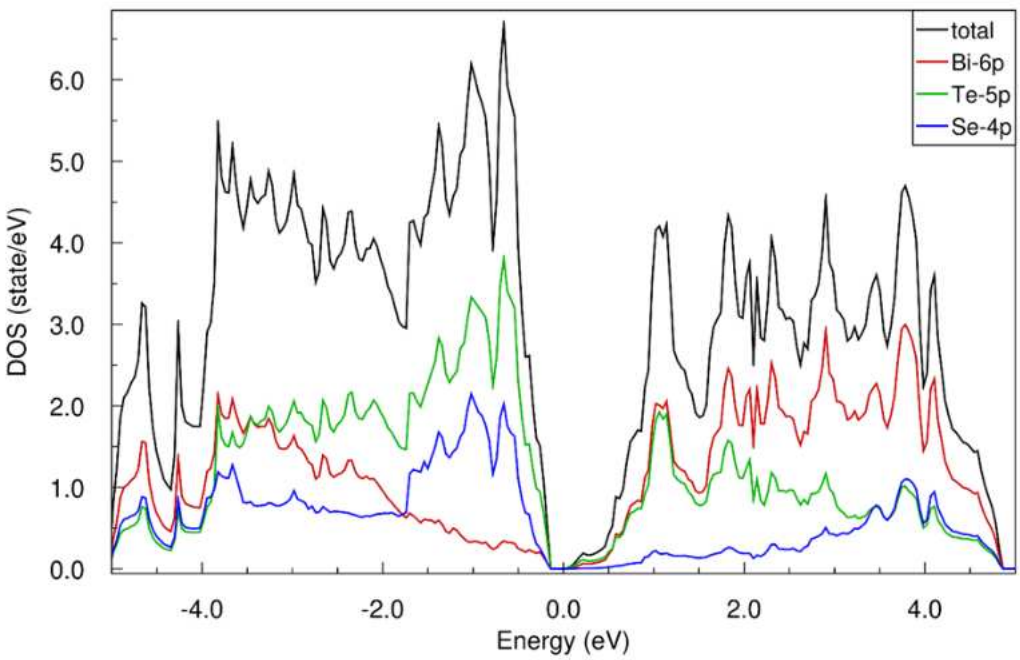


Fig. 1: DFT calculation of the electron density of states in bismuth selenide telluride (BST), including the specific orbitals most relevant to the topological state calculation. The bandgap is found to be approximately 0.14 eV, similar to experiment.

We are also completing analogous calculations for 2D and 1D quantum-confined versions of the same baseline material, to understand the role of reduced dimensionality in the ability to support topological phases.

Planned work in this area that should be completed by the time of this presentation aims to predict the potential of BST materials for enhanced quantum sensing. Using DFT calculations of one or more alloys of bismuth selenide telluride (or related compounds) formed into nanowires and nanosheets, to calculate the response of topological phase to mechanical strain and external electromagnetic fields (for sensing). Also, we will calculate key coupling parameters in a phenomenological Hamiltonian capturing the strength of coupling to strain, electric, and magnetic fields.

It will also be important to characterize BST and BST-like material band structures in reduced-dimensionality samples. In this work, we will perform Angle-Resolved PhotoEmission Spectroscopy (ARPES) on BST samples with reduced dimensionalities, provided by collaborators from Indiana University. This will be compared to both a control 3D bulk sample of BST, along with a measurement of the role that nanosheets and nanotubes play in topological phase in a relaxed state. If instrumentation supports, we will also measure the effects of mechanical strain, external electric fields, and external magnetic fields on the topological phase, and compare to theoretical predictions.

The ultimate goal of this work will be to combine state-of-the-art device and nanowire fabrication informed by prompt inputs from DFT, spin-orbit coupling (SOC), and computational modeling of magneto-chiral anisotropy in TI sensors to build a platform sensitive to amplitudes and phases of tiny electrical and magnetic signals.

We acknowledge support from the Center for Quantum Materials, an I/UCRC funded by a combination of National Science Foundation, industry, and other government sponsors.

References

1. Taskin, A. A., Satoshi Sasaki, Kouji Segawa, and Yoichi Ando. "Manifestation of topological protection in transport properties of epitaxial Bi 2 Se 3 thin films." *Physical review letters* 109, no. 6 (2012): 066803.
2. Zhang, Yi, Ke He, Cui-Zu Chang, Can-Li Song, Li-Li Wang, Xi Chen, Jin-Feng Jia et al. "Crossover of the three-dimensional topological insulator Bi2Se3 to the two-dimensional limit." Nature Physics 6, no. 8 (2010): 584-588.
3. Scanlon, David O., P. D. C. King, Ravi P. Singh, Alberto De La Torre, S. McKeown Walker, G. Balakrishnan, Félix Baumberger, and C. R. A. Catlow. "Controlling bulk conductivity in topological insulators: key role of anti-site defects." *Advanced Materials* 24, no. 16 (2012): 2154-2158.

A polarization-tunable coloration with wide dynamic range using highly lossy material-based metal/dielectric/metal-subwavelength grating

Y. Takashima[1,2*], K. Nagamatsu[1,2], M. Haraguchi[1,2], and Y. Naoi[1,2]

[1]Faculty of Science and Technology, Tokushima University, Japan
[2]Institute of Post-LED Photonics, Tokushima University, Japan
[*]corresponding author: takashima@tokushima-u.ac.jp

Abstract: A polarization-tunable coloration with wide dynamic range was demonstrated using the highly lossy metal-based metal/dielectric/metal-subwavelength grating structure. By using the spectrally broadened resonant reflections and phase retardations in the designed structure, we achieved the multi colors generation across entire visible region by simply rotating the polarization of light.

Color generation is important for enormous applications, for example displays, imaging, security, communication. Structural coloration via subwavelength resonant structures is one of the most interesting approaches because its optical characteristics, such as resonant wavelength, efficiency, and spectral shape can be artificially designed by adjusting the structural parameters [1]. In particular, the dynamic controlling of the structural color provides not only one static color but also multi colors, and it is very attractive for the applications mentioned above. Many reports have demonstrated the dynamic control of the structural color using polarization states [2, 3], mechanical stretch [4, 5], electro-chemical deposition [6], phase-change material [7] and metal hydrides [8]. However, the realization of wide tunable range of the coloration still be challenging.

This presentation introduces new strategy for the wide dynamic range color generation by using highly lossy metal-based metal/dielectric/metal-subwavelength grating (SWG) structure. In general, the design of the structural color avoids to the lossy materials because the optical loss causes broad resonant spectral shape and degradants the color performance. In contrast, we positively utilized the spectrally broadened resonant reflection for wide dynamic range of coloration rather than avoiding loss. The designed highly lossy metal/dielectric/SWG shows the relatively broadened resonant reflection spectra in visible region and the independent phase retardation for the orthogonal polarizations. The resonances generate the multi reflection colors across entire visible region by simply rotating polarization of the incident and the reflected lights. Our strategy realizes the wide dynamic range of structural color and opens new design and material selection concept for coloration.

References

1. Wang, D., Z. Liu, H. Wang, M. Li, L. Guo and C. Zhang, “Structural color generation: From layered thin films to optical metasurfaces,” Nanophotonics, Vol. 12, No. 6, 1019–1081, 2023.
2. Duempelmann, L. A. Luu-Dinh, B. Gallinet and L. Novotny, “Four-fold color filter based on plasmonic phase retarder,” ACS Photonics, Vol. 3, No. 2, 190–196, 2016.
3. Wang, H. and O. Martin, “Polarization-controlled chromo-encryption,” Adv. Opt. Mater., Vol. 11, Issue 7, 2202165, 2023.
4. Zhu, L., J. Kapraun, J. Ferrara and C. J. Chang-Hasnain, “Flexible photonic metastructures for tunable coloration,” Optica, Vol. 2, No. 3, 255–258, 2015.

5. Honma, H., K. Takahashi, M. Ishida and K. Sawada, “Continuous control of surface-plasmon excitation wavelengths using nanomechanically stretched subwavelength grating,” Appl. Phys. Express, Vol. 9, No. 2, 027201, 2016.
6. Moon, C, Y. Kim and J. Hyun, “Active electrochemical high-contrast gratings as on/off switchable and color tunable pixels,” Nat. Commun. Vol. 13, Issue 1, 3391, 2022.
7. Shu, F., F. Yu, R. Peng, Y. Zhu, B. Xiong, R. Fan, Z. Wang, Y. Liu and M. Wang, “Dynamic plasmonic color generation based on phase transition of vanadium dioxide,” Adv. Opt. Mater., Vol. 6, Issue. 7, 1700939, 2018.
8. Duan, X., S. Kamin and N. Liu, “Dynamic plasmonic colour display,” Nat. Commun. Vol. 8, 14606, 2017.

In situ modification of the Quantum Hall effect with cavity vacuum fields

J. Enkner[1], L. Graziotto[1], F. Appugliese[1] , D. Boriçi[3], M. Beck[1], C. Reichl[2], W. Wegscheider[2], G. Scalari[1], C. Ciuti[3], and J. Faist [1*]

[1]Institute of Quantum Electronics, ETH Zürich, Zürich 8093, Switzerland
[2]Laboratory for Solid State Physics, ETH Zürich, Zürich 8093, Switzerland
[3]CNRS, Laboratoire Matériaux et Phénomènes Quantiques, Université Paris Cité, F-75013 Paris, France
[*]corresponding author: jerome.faist@phys.ethz.ch

Abstract: Cavity vacuum fields can break the topological protection of edge states in the integer Quantum Hall effect. With the ability to in situ tune the light-matter coupling of this system, we observe a reduction of the g-factor and a hardening of the gap of fractional states while increasing the coupling.

Even in the absence of external illumination, a resonator exhibits modes populated with virtual photons, known as cavity vacuum fields. Placing a complementary split ring resonator (CSRR) around a GaAs-based heterostructure Hall bar, effectively immersing it in cavity vacuum fields, introduces a long-range perturbation that manifests itself effectively in opening a scattering channel for electrons in both bulk and edge states. Using this platform, previous investigations have demonstrated a breakdown of the topological protection of edge states within the integer quantum Hall regime [1]. Instead of the expected quantized Hall resistance and associated zero longitudinal resistance, quantization in Hall plateaus is lost paired with a finite longitudinal resistance. The theoretical interpretation of this effect, termed "cavity-mediated electron hopping" by C. Ciuti [2], describes the anti-resonant interaction between cavity vacuum fields and electrons in neighboring Landau levels, enabling electrons to scatter in and out of topologically protected edge states. This anti-resonant effect decays exponentially in magnetic field, with a decay rate associated to the system's Rabi frequency.

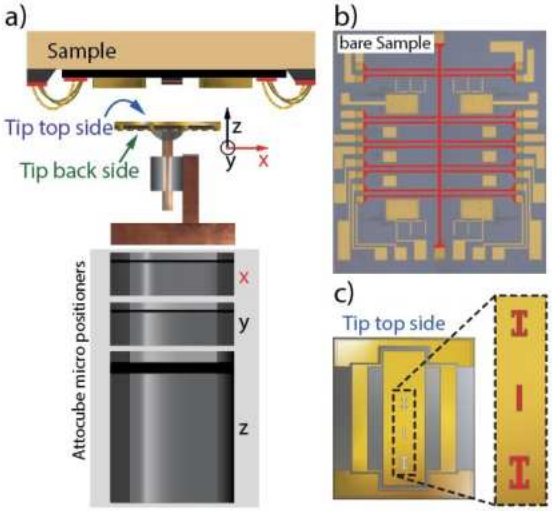


Figure 1: Sketch of the setup: The Atto cubes in 1a) enable the alignment of the cavity relative to the Hall bar, and therefore allows for in situ tuning of the coupling. The z axis can be used to alter the distance between the cavity plane 1c) and the sample with the Hall bar (in red) 1b).

In a recent experiment, we improved the experimental platform by introducing an in situ technique to vary the coupling between the cavity and the electrons inside the Hall bar [Fig. 1]. Utilizing three Atto cube micro-positioners, we can dynamically align and adjust the position of the 2D cavity plane relative to the Hall bar, enabling selective coupling with the extruding fringing fields of the cavity. This configuration allows for real-time tuning of the coupling as a function of the distance between the cavity plane and the Hall bar sample.

As the resonator is brought closer to the Hall bar, thus increasing the coupling, we observe intriguing phenomena such as the reduction of the g factor and the hardening of the gap for fractional Laughlin states 7/5, 5/3, and 4/3 [Fig. 2].

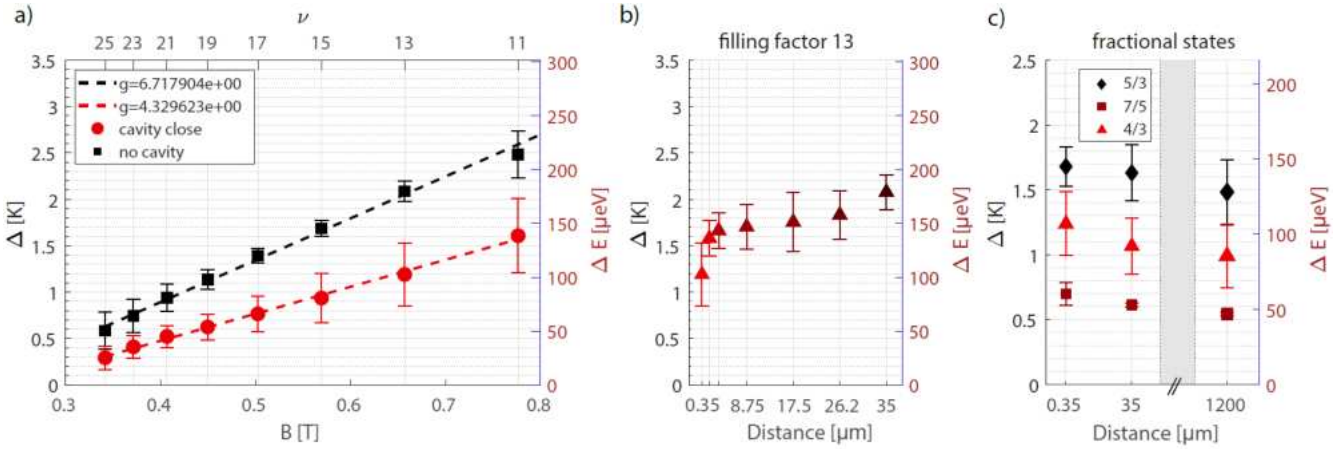


Figure 2: Figure 2a) shows the energy gap of the Zeeman-split states as a function of the magnetic field. From the corresponding linear fit, we infer the g-factor of the system indicated in the legend; 2b) shows the evolution of the activation energy for filling factor 13 as a function of the distance of the cavity from the sample surface; in 2c) we show the activation energy for the fractional states.

The distinct nature of models describing the physics of fractional and integer quantum Hall states necessitates different interpretations of the cavity's effect in these regimes. While the effect on the g-factor in the integer quantum Hall regime aligns with the theoretical framework of "cavity-mediated electron hopping", which can also be seen as an effective renormalization of the Zeeman splitting arising due to a cavity-induced long-range pertubation, for fractional states, the increased energy gap proportional to the coupling instead implies a modification of the short-range interaction between electrons.

These experimental findings offer exciting perspectives and hint at the potential emergence of a novel phenomenon within the field of cavity-engineered quantum materials.

References

1. F. Appugliese, et.al. Breakdown of topological protection by cavity vacuum fields in the integer quantum hall effect. Science, 375(6584):1030–1034, 2022.
2. C. Ciuti. Cavity-mediated electron hopping in disordered quantum hall systems. Physical Review B, 104(15):155307, 2021.

Nonlinear optics in low-index bulk media: past, present, and future

W. Jaffray[1], S. Stengel[1], A. Boltasseva[2], V. M. Shalaev[2], A. Di Falco[3], and M. Ferrera[1*]

[1]Heriot-Watt University, Institute of Photonics and Quantum Sciences, SUPA, Edinburgh EH14 4AS, UK

[2]Purdue University, School of Electrical and Computer Engineering, West Lafayette, Indiana 47907, USA

[3]University of St. Andrews, School of Physics and Astronomy, Fife, KY16 9SS, UK

*Corresponding author e-mail address: m.ferrera@hw.ac.uk

Abstract: Transparent conducting oxides have evolved from an industrial platform to a new playground for photonic scientists. Within this context, I will provide a quick overview of past results while also giving relevance to our most recent achievements and future perspectives around nonlinear integrated photonics and light acceleration in time-varying media.

During the last decade, the optics and photonics community have renewed their interest in transparent conducting oxides (TCOs), a class of materials that for more than two decades has been extensively utilized in the manufacture of transparent electrodes for photovoltaic and touchscreen applications. This resurgence of focus on TCOs is motivated by their potential as low-loss alternative to noble metals in the fabrication of ultra-compact plasmonic devices, and their remarkable optical nonlinearities in proximity to their crossover point — the wavelength at which the real component of the dielectric permittivity transitions in sign [1].

Furthermore, TCOs are epsilon-near-zero (ENZ) materials across an extensive near-infrared window, inclusive of the entire telecommunications bandwidth. Within this operational domain, they allow a host of novel electromagnetic phenomena, including supercoupling, wavefront freezing, photon doping, etc. [2]. A unique property of TCOs, when compared to other ENZ systems, is their extremely low real index ($n<0.2$) near the ENZ wavelength. This feature has been linked to a slow-light effect that significantly amplifies the materials' nonlinear properties [3-7].

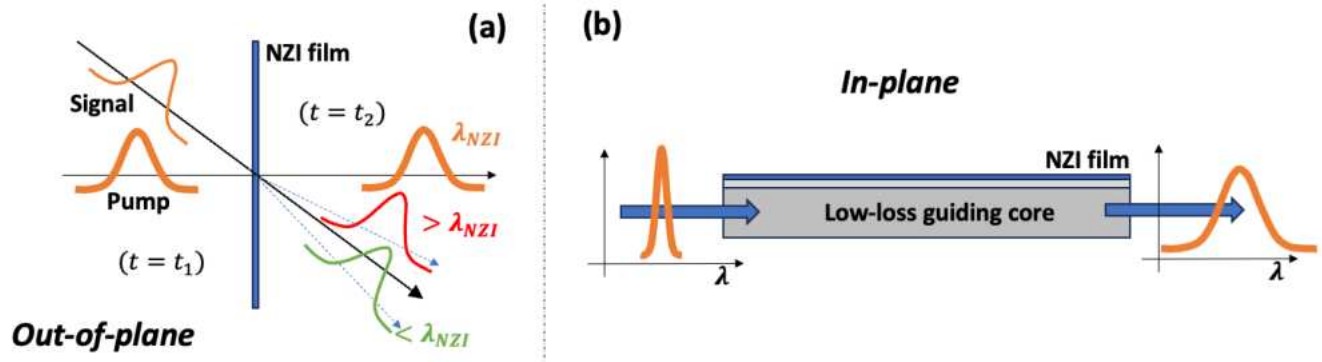


Figure 1 – Extreme nonlinear effects in TCO-based systems. a) Spatio-spectral fission in time-varying films. b) Nonlinear spectral broadening in NZI-coupled silicon nanowires.

The swift advancement of nonlinear optics in conductive oxides is motivated by a plethora of experimental results documenting unprecedented optical effects, such as unitary index change, bandwidth-large frequency shift, efficient on-chip nonlinear frequency conversion, etc. [8-10]. Along this talk, an evolving narrative about TCOs will be provided, from their initial industrial application as transparent electrodes, through their role as a

novel solution for low loss plasmonics, until their most recent connotation as driving force for the development of novel integrated nonlinear systems. More specifically to our most recent research achievements, I will discuss how the extreme optical modulation of the complex index in a low-index thin film can lead to a full spatio-spectral fission of a trespassing pulse (see Fig. 1-a), and also how by exploiting evanescent coupling between a low-loss optical channel and an upper layer of indium tin oxide, it is possible to attain novel nonlinear waveguides with unparallel nonlinear figure of merit over hundreds of microns of propagation length (see Fig. 1-b).

Conclusions:

Over the past thirty years, the perspective of scientists and technologists on transparent conducting oxides (TCOs) has undergone a significant transformation. Initially regarded as industrial materials for the mass production of transparent electrodes, TCOs have evolved into potential substitutes for metals in plasmonic applications and further into low-index nonlinear systems. In their latest role, these compounds have demonstrated unparalleled figures of merit for the creation of ultra-compact nonlinear devices. This trajectory suggests that the forthcoming phase of development for TCOs may well extend into quantum applications [11].

Acknowledgements

MF acknowledges support from AFOSR/EOARD (Award Num.: FA8655-23-1-7254), and EPSRC (Award Ref.: EP/X035158/1). This work is also supported (Purdue team) by the U.S. Department of Energy, Office of Basic Energy Sciences, Division of Materials Sciences and Engineering under Award DE-SC0017717 (sample preparation).

References

1. W. Jaffray, et al., “Transparent conducting oxides: from plasmonics integrated photonics” Adv. Opt. Phot. 14 (2), 148-208 (2022)
2. I. Liberal, N Engheta “Near-zero refractive index photonics” Nat. Photonics 11 (3), 149-158 (2017)
3. N Kinsey, et al., “Near-zero-index materials for photonics” Nat. Rev. Mater. 4 (12), 742-760 (2019)
4. O. Reshef, et al. “Beyond the perturbative description of nonlinear response of low-index materials” Opt. Lett. 42, 16, 3225-3228 (2017)
5. M. Clerici, et al. “Controlling hybrid nonlinearities in conducting oxides via two-colour excitation” Nat. Commun. 8 (1), 1-7 (2017)
6. W. Jaffray, et al. “Near-zero-index ultra-fast pulse characterization” Nature Commun. 13 (1), 1-8 (2022)
7. W. Jaffray, et al., “Nonlinear Loss Engineering in Near‐Zero‐Index Bulk Materials” Adv. Opt. Mater. 12 (1), 2301232 (2023)
8. M. Z. Alam, et al., “Large optical nonlinearity of nanoantennas coupled to an epsilon-near-zero material” Nature Photonics 12 (2), 79-83 (2018)
9. J.B. Khurgin, et al. “Adiabatic frequency shifting in epsilon-near-zero materials: the role of group velocity” Optica 7 (3), 226-231 (2020)
10. E. G. Carnemolla, et al., “Visible photon generation via four-wave mixing in near-infrared near-zero-index thin films” Optics Letters 46 (21), 5433-5436 (2021)
11. I. Liberal, A. Alù, N. Engheta “Zero-index metamaterials for classical and quantum light” Appl. Phys. Lett. 120, 260401 (2022)

Ceramic metasurfaces for biophotonics applications in the visible range

M. Biabanifard[1], T. Plaskocinski[1], J. Xiao[1], and A. Di Falco[1*]

[1]University of St Andrews, School of Physics and Astronomy, North Haugh, KY16 9SS, St Andrews, UK
[*]corresponding author: adf10@st-andrews.ac.uk

Abstract: We introduce ZrO_2 as a reliable material platform for photonic metasurfaces for on-chip optical trapping and imaging applications in the visible range. We demonstrate devices for optical trapping with a high numerical aperture at a wavelength as low as 488 nm, validating the use of the platform for biophotonics applications.

This work presents a new metasurface platform for the visible light range based on ceramic materials. ZrO2 has recently caught the attention of the nanophotonics community for its extended operational wavelength, and moderately high refractive index, with a flat dispersion across the visible range and negligible optical absorption, down to the UV region [1].

ZrO_2-based metasurfaces have the unique potential to revolutionize lab-on-chip applications in the green and blue regions of the visible spectrum, where light structuring is a pivotal paradigm for imaging and optical manipulation experiments.

To demonstrate this capability, we designed metasurfaces with high NA=1.2 operating at 532 nm and 488 nm and used them to create optical traps with high trap stiffness.

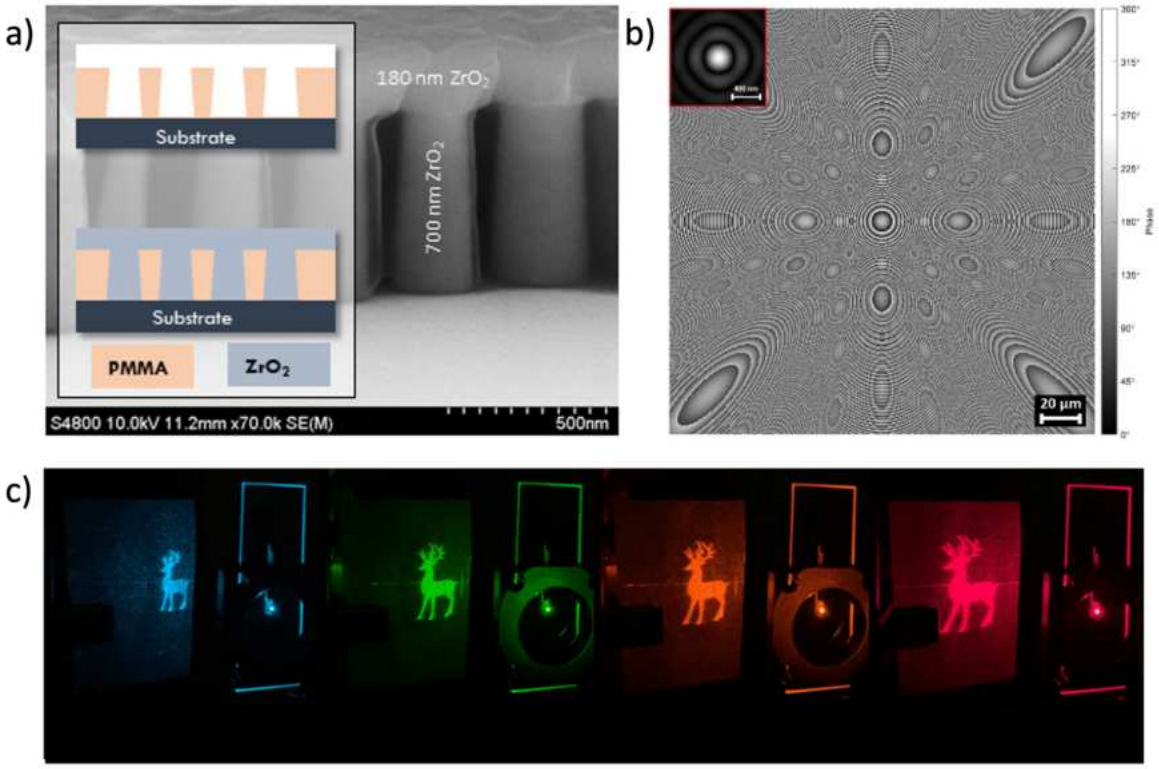


Figure 1 a) Scanning Electron Microscope image of a section of the metasurface (inset: sketch of the

fabrication process). b) Calculated phase profile for a metasurface focusing light with NA=1.2 (inset: experimental image of the focused spot). c) Collection of holographic images created by ceramic metasurfaces, covering the visible range.

The metasurfaces were fabricated (see Figure 1) using via Electron Beam Lithography, using PMMA as a positive-tone resist. After development, the air holes were filled with ZrO_2, using atomic layer deposition, which guarantees a complete filling of the holes. At variance with standard similar fabrication processes, we designed the meta-atoms to include the ZrO2 uniform cap. This choice simplifies the fabrication procedure and creates a natural protection layer which insulates the metasurface from the surrounding environment. This feature is particularly useful in biophotonic applications, where the metasurface is in contact with a not homogeneous medium, with variable refractive index.

For the optical trapping experiments, we used a custom setup. The ceramic metasurfaces were realized on the top slide of a microfluidic chamber, facing the liquid environment. The metasurfaces were illuminated with a collimated trapping beam from the top and a focused spot was formed in the middle of the chamber, at several tens of microns from the metasurface. Systematic trapping experiments with SiO_2 beads with a diameter of 2 μm showed an optical trapping stiffness greater than 200 pN/μm/W, at a wavelength of 488 nm. To the best of our knowledge, this is the first demonstration of on-chip optical trapping at wavelengths below 500 nm [2].

This demonstration unequivocally confirms the quality of the optical landscape created by the metasurfaces and candidates ZrO_2 to become a reference material platform for integrated biophotonics applications, in the visible region and beyond.

The project was supported by the European Research Council (ERC) under the European Union Horizon 2020 Research and Innovation Program (Grant Agreement No. 819346).

References

1. Kim, J., Kim, W., Oh, D.K., Kang, H., Kim, H., Badloe, T., Kim, S., Park, C., Choi, H., Lee, H. and Rho, J., “One-step printable platform for high-efficiency metasurfaces down to the deep-ultraviolet region,” Light: Science & Applications, Vol. 12, No. 1, 68 (2023).
2. Biabanifard, M., Plaskocinski, T., Xiao, J. and Di Falco, A. “ZrO2 Holographic Metasurfaces for Efficient Optical Trapping in The Visible Range,”, Adv. Opt. Mat., accepted for publication.

Magnetic control of electrically uncharged magneto-optical particles

M. I. Marqués[1*], S. Edelstein[2], P.A.Serena [2,] B. Castillo López de Larrinzar [3]and A. García-Martín[3]

[1]Departamento de Física de Materiales, IFIMAC and Instituto de Física de Materiales

Nicolás Cabrera" Universidad Autónoma de Madrid, 28049 Madrid, Spain

[2]Instituto de Ciencia de Materiales de Madrid (ICMM-CSIC), Campus de Cantoblanco, 28049 Madrid, Spain

[3]Instituto de Micro y Nanotecnología IMN-CNM, CSIC,CEI UAM+CSIC, Isaac Newton 8, Tres Cantos, 28760 Madrid, Spain

[*]corresponding author: manuel.marques@uam.es

Abstract: In this work we present a method to perform magnetic control of electrically uncharged particles based on magneto-optical materials illuminated by a spinning monochromatic light field. We analyze the behavior of these particles under different isotropic optical configurations, and we calculate the value of the induced magnetic charge.

Constant magnetic fields are known to interact with electrically charged particles inducing Lorentz forces that point in a direction perpendicular to the field. However, if the particle is electrically discharged, it is impossible to induce a force using a constant magnetic field. An exotic option is to mimic a magnetic charge on a neutral particle. This false magnetic monopole will interact with the magnetic field just as an electric charge would do with an electric field through the Coulomb interaction. Attempts to generate this magnetic charge have mainly relied on quasiparticles generated using condensed matter spin ice networks [1-3]. In this work we present another option based on neutral magneto-optical particles illuminated by a spinning monochromatic light field [4]. We will analyze the behavior of these particles under different fluctuating isotropic optical configurations [5,6], and we will calculate the value of the induced magnetic charge. We will prove that this is a purely non-reciprocal effect as the reciprocal equivalent (a chiral dipole) despite presenting a dichroic response, does not experience any force when illuminated by the spinning field. The magnetic charge induced by impinging radiation on the magneto-optical dipole is found to depend linearly on the helicity of the field. In addition, this artificial monopole experiences a dichroic permanent optical torque and does not interact with an external electric field.

We acknowledge financial support from the Spanish Ministry of Science and Innovation (MCIN), AEI and FEDER (UE) through projects PID2022-137569NB-C43, PID2022-137569NB-C41 and TED2021-131417B-I00 and the María de Maeztu (CEX2018-000805-M) Program for Centers of Excellence.

References

1. S. T. Bramwell, S. R. Giblin, S. Calder, R. Aldus, D. Prabhakaran, and T. Fennell, Measurement of the charge and current of magnetic monopoles in spin ice, Nature 461, 956 (2009).
2. S. J. Blundell, Monopoles, magnetricity, and the stray field from spin ice, Phys. Rev. Lett. 108, 147601 (2012).
3. C. Castelnovo, R. Moessner, and S. L. Sondhi, Magnetic monopoles in spin ice, Nature 451, 42 (2008).

4. S. Edelstein, R. M. Abraham-Ekeroth, P. A. Serena, J. J.Saenz, A. Garcia-Martin, and M. I. Marques, Magnetooptical stern-gerlach forces and nonreciprocal torques on small particles, Phys. Rev. Res. 1, 013005 (2019).
5. J. Luis-Hita, M. I. Marques, R. Delgado-Buscalioni, N. de Sousa, L. S. Froufe-Perez, F. Scheold, and J. J.Saenz, Light induced inverse-square law interactions between nanoparticles: “mock gravity" at the nanoscale, Phys. Rev. Lett. 123, 143201 (2019).
6. J. Luis-Hita, J. J. Saenz, and M. I. Marques, Active motion induced by random electromagnetic fields, ACS Photonics 9, 1008 (2022).

Development of Nonclassical Light Sources for Time-Resolved THz detection

D. Adamou[1], L. Hirsh[1], T. Shields[1], S. Yoon[1], A. C. Dada[2], J. M. R. Weaver[1], D. Faccio[2], L. Caspani[3], M. Peccianti[4], and M. Clerici[1,5,*]

[1]James Watt School of Engineering, University of Glasgow, Glasgow G12 8QQ, UK
[2]School of Physics and Astronomy, University of Glasgow, Glasgow G12 8QQ, UK
[3]Institute of Photonics, Department of Physics, University of Strathclyde, Glasgow G1 1RD, UK
[4]Emergent Photonics Research Centre, Department of Physics, Loughborough University, Loughborough LE11 3TU, UK
[5]Dipartimento di Scienza e Alta Tecnologia, Università degli Studi dell'Insubria, Via Valleggio 11, 22100, Como, Italy
[*]corresponding author: matteo.clerici@uninsubria.itu

Abstract: THz time-domain spectroscopy is a widespread technology. It is pump-and-probe-based and delivers a large dynamic range, currently limited by the probe shot noise. Therefore, quantum metrology tools, such as squeezed states, can enhance its sensitivity. We shall present our first attempts in this direction, including discrete and continuous variable approaches.

Time-domain spectroscopy in THz and infrared spectral ranges utilises constant carrier-envelope offset sources and ultrashort probe pulses, shorter than the half period of the highest frequency to be sampled. This method enables recording the electric field, providing spectrum and time-of-flight information. Limited by probe pulse shot noise, quantum metrology can enhance the sensitivity of THz time-domain spectroscopy (THz-TDS) [1]. Here, we discuss ongoing efforts towards developing a quantum-enhanced THz-TDS technique.

Quantum metrology offers potential improvements, like utilising NOON states for Heisenberg-limited phase estimation. We present experiments employing weak squeezed vacuum fields as probes in THz electro-optic sampling, detected with single-photon detectors. Our method achieves sensitivity limited by probe state statistics, using phase-locked single-photon detectors [2], opening avenues for quantum-enhanced THz sensing.

Classical approaches outperform discrete variable quantum enhancements for real-world THz-TDS applications due to the large probe pulse photon numbers. We aim to enhance THz-TDS sensitivity by employing macroscopic squeezed pulses. We explore the generation and detection of <200fs intensity correlated twin beams via parametric down-conversion for ultrafast quantum-enhanced sensing. Our setup involves a 40W, 1030 nm laser with a pulse duration of 245 fs. Quantum-correlated radiation is measured by high-efficiency, low-noise balanced photodetectors. Compared to a coherent source, we observe ~3dB noise reduction below the standard quantum limit with >500 nW average power pulses. This represents the highest noise suppression measured with <200 fs duration twin beams at 1030 nm. We discuss our results and design choices enabling significant noise reduction using sub-shot-noise correlations among ultrafast pulses.

The authors acknowledge support from UKRI (Fellowship "In-Tempo" EP/S001573/1), Innovate UK, Application Number PN 10001572 (HiQuED), and from the Defence Science and Technology Laboratory (DSTL, DSTLX-1000144632).

References

1. S. Virally et al., "Enhanced electro-optic sampling with quantum probes", *Phys. Rev. Lett.* 127, 270504 (2021).
2. T. Shields et al., "Electro-Optical Sampling of Single-Cycle THz Fields with Single-Photon Detectors", Sensors 22, 9432 (2022).

Mid-infrared topological edge modes in the symmetric and asymmetric photonic crystal slabs fabricated in SOI wafers

A. Begum[1], Y. Yao[1†], T. Kuroda[1], Y. Takeda[2], N. Ikeda[3], T. Mano[1], and K. Sakoda[1*]

[1]Research Center for Functional Materials, National Institute for Materials Science, Japan
[2]Center for Green Research on Energy and Environmental Materials, National Institute for Materials Science, Japan
[3]Research Network and Facility Service Division, National Institute for Materials Science, Japan
[†]Present affiliation: Department of Applied Physics, University of Tsukuba, Japan
[*]Corresponding author: sakoda.kazuaki@nims.go.jp

Abstract: We present the design, fabrication, and detection of topological bandgaps and edge modes of photonic crystal slabs fabricated in the top Si layer of SOI wafers. We show their polarization properties in addition to their dispersion relation based on high-resolution angle-resolved reflection measurements.

Topological photonic crystals (PhCs) have been attracting a great interest mainly because they can materialize helical one-way edge modes on the boundary between trivial and non-trivial PhCs (PhC-t and PhC-n). The PhC design for the helical edge modes was given by Wu and Hu[1)] for two-dimensional PhCs. Their recipe was modified by Barik et al.[2)] to apply to PhC slabs.

In this presentation, we would like to introduce our recent sample fabrications to materialize topological bandgaps and edge modes, and their confirmation by high-resolution reflection spectroscopy in the mid infrared range. We fabricated two types of specimens in the top Si layer of SOI (silicon on insulator) wafers with and without mirror symmetry about the mid horizontal plane of the PhC slab.

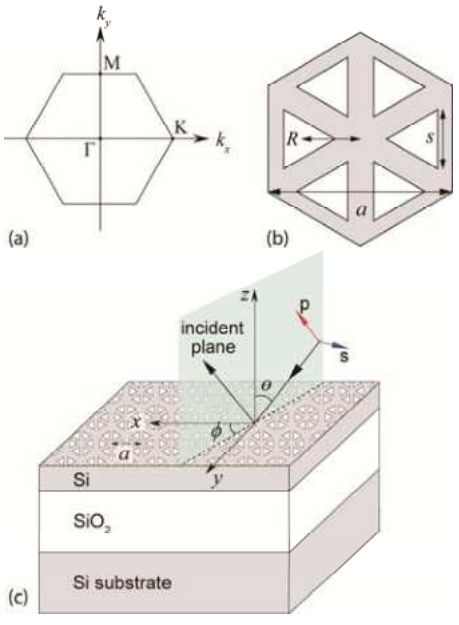


Fig. 1 (a) The first Brillouin zone of the PhC specimens of the C_{6v} symmetry and (b) the top view of the unit cell. (c) Configuration of the incident plane wave for the angle-resolved reflection measurement on the illustration of the asymmetric PhC structure.

Figure 1 shows the sample structure and the configuration of the angle-resolved reflection measurements.[3)] For the symmetric PhC specimens, we further capped the top Si layer with SiO_2 by plasma-enhanced CVD.[4)] Figure 2 shows SEM images of our specimens fabricated by electron-beam lithography.

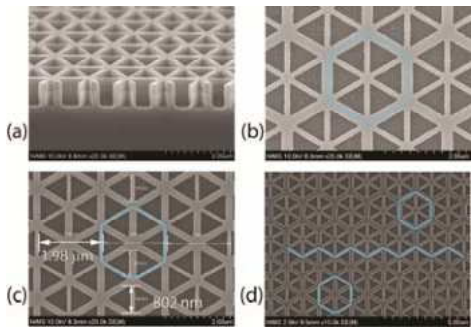


Fig. 2 SEM images of fabricated specimens. (a) Crosssectional view after etching. Top view of (b) PhC-t and (c) PhC-n. (d) Top view of the combination specimen.

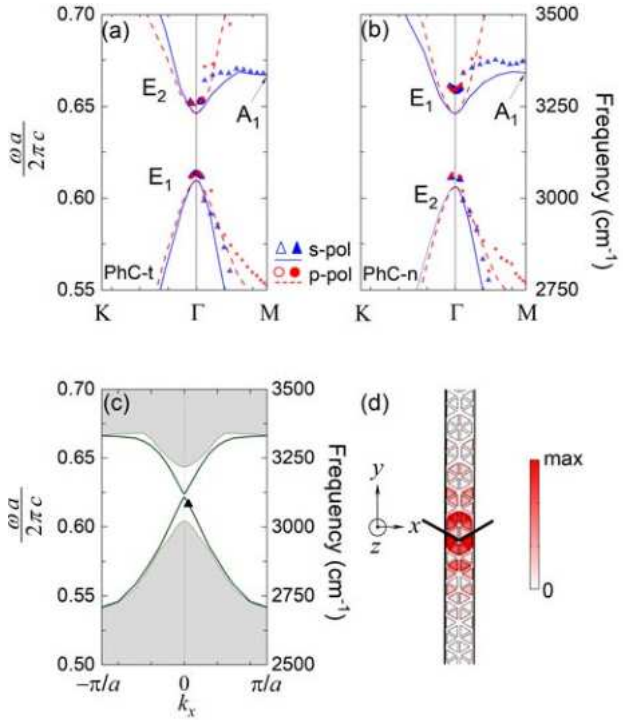


Fig. 3 (a) Dispersion relation of TE-like modes for asymmetric PhC-t and (b) PhC-n. Blue solid line and red broken line show calculated dispersion curves for s- and p-active modes, respectively. Blue open circle and red open triangle show data points measured for s and p polarizations, respectively. (c) The calculated dispersion relation of edge modes (dark green line) and the spectral range of bulk modes (gray color). (d) The time average of the square of the z component of the magnetic field.

By adjusting R in Fig. 2(b), we can materialize PhCs with topologically trivial (PhC-t) and non-trivial (PhC-n) bandgaps. Figure 3(a) and (b) show both the calculated and measured dispersion curves for the asymmetric PhCs. We used COMSOL Multiphysics for the calculation and a home-made high-resolution angle-resolved reflection setup[5] for the measurement around the Γ point. The dispersion relation of the edge mode materialized on the boundary between the PhC-t and PhC-n and its field distribution are shown in Fig. 3(c) and (d).

The dispersion relation of the edge modes was also measured by the angle-resolved reflection. As expected from the numerical calculations, the edge modes at the Γ point are linearly polarized whereas they are basically circularly polarized. The former feature was brought about by the 1:1 mixture of the upper and lower edge-mode branches due the absence of inversion symmetry around the boundary between the two PhCs.

We did the same calculations and measurements for the symmetric PhCs, for which the topological bandgaps are more rigorously defined, and confirmed the presence of the edge modes.

This work was supported by the Innovative Science and Technology Initiative for Security, Grant Number JPJ004596, ATLA, Japan.

References

1. L. H. Wu and X. Hu, “Scheme for achieving a topological photonic crystal by using dielectric material,” Phys. Rev. Lett., Vol. 114, No. 22, 223901, 2015.
2. S. Barik, A. Karasahin, C. Flower, T. Cai, H. Miyake, W. D. Gottardi, M. Hafezi and E. Waks, “A topological quantum optics interface,” Science, Vol. 359, No. 6376, 666–668, 2018.
3. A. Begum, Y. Yao, T. Kuroda, Y. Takeda, N. Ikeda, Y. Sugimoto, T. Mano and K. Sakoda, “Topological band gaps and edge modes materialized by symmetric silicon-on-insulator photonic crystal slabs in the mid-IR range,” Phys. Rev. A, Vol. 107, No. 4, 043507, 2023.
4. A. Begum, Y. Yao, T. Kuroda, Y. Takeda, N. Ikeda, Y. Sugimoto, T. Mano and K. Sakoda, “Design and observation of topological band gaps and edge modes of SOI photonic crystal slabs in the mid-infrared range,” J. Phys. Soc. Jpn., Vol. 92, No. 11, 114402, 2023.
5. T. Kuroda, S. Chalimah, Y. Yao, N. Ikeda, Y. Sugimoto and K. Sakoda, “Apparatus for high-precision angle-resolved reflection spectroscopy in mid-infrared region,” Appl. Spectrosc., Vol. 75, No. 3, 259–264, 2021.

The interplay of gain and loss in room-temperature planar polaritonic systems

Anton K. Samusev[1*]

[1]Experimentelle Physik 2, Technische Universität Dortmund, 44227 Dortmund, Germany
[*]corresponding author: anton.samusev@tu-dortmund.de

Abstract: Strong exciton-photon coupling in systems based on halide perovskites and 2D semiconductors at room temperature is demanded in tunable and nonlinear on-chip photonics. Here, we demonstrate a weak-to-strong coupling transition accompanied by the onset of polariton motional narrowing, polariton lasing enhanced by exceptional points, and an ultrafast high-contrast polariton modulator.

Tunable, highly nonlinear planar optical systems operating at room temperature are of great interest due to their potential applications in on-chip photonics. Contemporary quantum materials, such as perovskites and transition metal dichalcogenides (TMDs), offer stable excitons at ambient conditions. These can form exciton-polaritons by coupling to high-Q optical states in solid and nanostructured slabs with the on-demand design, enabling exceptionally large optical nonlinearity.

In the first part of the talk, I will employ an experimental approach to retrieve the full complex dispersion of both leaky and evanescent waves in arbitrary planar structures [1]. The method is based on back focal plane microspectroscopy combined with a solid immersion lens (SIL) separated from the sample by a precisely controlled nanoscale air gap (Otto geometry). Varying the gap allows for extracting both real and imaginary parts of the wavenumber of surface and guided waves propagating in an arbitrary in-plane direction. Using this approach, we directly probe and control guided exciton–polaritons in a planar TMD-based waveguide [2]. Careful measurement of angle-resolved reflectance maps as a function of the SIL-sample air gap enables reversible control of the waveguide and exciton-polariton dispersions. For a single-layer WS_2 deposited on an unpatterned dielectric slab waveguide, we retrieve the complete set of parameters of the system, which include radiative and nonradiative decay rates of the exciton resonance as well as the dependence of corresponding rates for the optical mode on the SIL-sample distance. Additionally, we demonstrate for the first time control of exciton-polariton coupling strength via SIL-induced rearrangement of the local electromagnetic field in the polaritonic waveguide. Utilizing the transition from weak to strong coupling regime, we experimentally observe the onset of the motional narrowing effect and demonstrate control over the inhomogeneous broadening of polaritons. Using a similar approach for a thin, unpatterned $MAPbBr_3$ perovskite film, we study how in-situ variation of radiative losses enables control over the spectrum and threshold of polariton-driven amplified spontaneous (ASE) and stimulated emission [3].

In the second part of the talk, we will discuss the engineering of polariton dispersion and regimes of polariton lasing in 1D photonic crystal slabs (PCSs) based on halide perovskites [4-6]. For the first time, we employ the mechanical scanning probe lithography (m-SPL) method to realize planar room-temperature exciton-polariton systems based on 2D perovskites [4]. The fabricated PCSs support the long-living polariton modes with a Q-factor up to 100. Thanks to the flexibility of the m-SPL method, it is possible to vary the modulation of the structures with a few tens of nanometers precision. This way, we achieve broad control over the dispersion, optical radiative losses, and the Rabi splitting of the exciton-polariton states in the planar photon

cavity based on (PEA)2PbI4. Our recent studies confirm that the demonstrated method can be introduced for other halide perovskites.

For a 1D PCS realized by nanopatterning of a thin (sub-100-nm) $MAPbBr_3$, we demonstrate room-temperature high-Q (up to Q≈2300) polariton lasing mediated by the exceptional points (EPs) in the exciton-polariton dispersion [5]. We reveal that the ASE in the studied samples originates from the accumulation of polaritons in the spectral region with the excitonic fraction in polariton of around 0.3. With further increase of the carrier concentration, the ASE broadens towards the red region due to the polariton relaxation, and EPs appear when the PCS modes' crossing falls in the gain spectral range. These results explain the fundamental origin of the lasing in lead-bromide perovskite PCSs and open new ways to realize room-temperature planar polariton lasers based on a wide variety of halide perovskites.

Finally, we demonstrate that such a MAPbBr3 perovskite PCS provides strong and ultrafast optical modulation based on the polariton condensation mediated by exceptional points at room temperature [6]. The modulation of transmission filtered spectrally and angularly exceeds 25 times the pristine values thanks to the accumulation of boson exciton-polaritons in a condensed state. The modulation time is 440 fs with a minimum control pump fluence of approximately 40 $\mu J/cm^2$. The combination of the relatively short modulation time and high transmission modulation depth is achieved thanks to the benefit features of EPs. Compared to existing systems, our optical modulator currently sets a record for the highest transmission modulation depth in the visible spectral range while exhibiting comparable time modulation values and control pump power consumption. Crucially, the modulation duration and its delay with respect to the pump pulse can be tailored by adjusting the pulse power and wavelength, providing multiple degrees of freedom for various applications.

This work was partially supported by Deutsche Forschungsgemeinschaft - project #529710370 and TU Dortmund core funds.

References

1. Permyakov, D., Kondratiev, V., Pidgayko, D., Sinev, I., and Samusev, A., "Probing optical losses and dispersion of fully guided waves through critical evanescent coupling," *JETP Letters*, Vol. 113, No. 12, 780– 786, 2021.
2. Kondratyev, V., Permyakov, D., Ivanova, T., Iorsh, I., Krizhanovskii, D., Skolnick, M., Kravtsov, V., and Samusev, A., "Probing and control of guided exciton-polaritons in a 2D semiconductor-integrated slab waveguide," *Nano Letters*, Vol. 23, No. 17, 7876–7882, 2023
3. Masharin, M., Khmelevskaia, D., Kondratiev, V., Markina, D., Utyushev, A., Dolgintsev, D., Dmitriev, A., Shahnazaryan, V., Pushkarev, A., Isik, F., Iorsh I., Shelykh, I., Demir, H., Samusev, A., Makarov, S., "Polariton lasing in Mie-resonant perovskite nanocavity," *Opto-Electronic Advances* (Accepted), 2024, arXiv:2305.12973.
4. Glebov, N., Masharin, M., Borodin, B., Alekseev, P., Benimetskiy, F., Makarov, S., and Samusev, A., "Mechanical scanning probe lithography of perovskites for fabrication of high-Q planar polaritonic cavities," *Applied Physics Letters*, Vol. 122, No. 14, 141103, 2023.
5. Masharin, M., Samusev, A., Bogdanov, A., Iorsh, I., Demir, H., and Makarov, S., "Room-temperature exceptional-point-driven polariton lasing from perovskite metasurface," *Advanced Functional Materials*, Vol. 33, No. 22, 2215007, 2023.
6. Masharin, M., Oskolkova, T., Isik, F., Demir, H., Samusev, A., Makarov, S., "Giant Ultrafast All-Optical Modulation Based on Exceptional Points in Exciton−Polariton Perovskite Metasurfaces," *ACS Nano*, Vol. 18, No. 4, 3447, 2023

Continuous mechanical machining of asymmetric nanogratings with tailored period and shape by azimuthal rotation-controlled nanoinscribing

Jong G. Ok[1*]

[1]Seoul National University of Science and Technology, Seoul, Republic of Korea
[*]corresponding author: jgok@seoultech.ac.kr

Abstract: We demonstrate the high-throughput mechanical patterning of period- and shape-tunable asymmetric nanogratings via azimuthal rotation-controlled nanoinscribing (ARC-DNI) which utilizes continuous inscription of a nanograting tool edge on viscoelastic polymers. ARC-DNI enables scalable fabrication of diverse asymmetric nanogratings with trapezoidal, triangular, and parallelogrammatic profiles for various photonic and diffractive optical elements.

This talk presents an azimuthal rotation-controlled dynamic nanoinscribing (ARC-DNI) process for the continuous and scalable fabrication of asymmetric nanograting structures with tunable periods and shape profiles. A sliced edge of a nanograting mold typically having a rectangular grating profile slides over a polymeric substrate to induce its burr-free plastic deformation into a linear nanopattern (Figure 1). During this continuous nanoinscribing process, the 'azimuth', which is the angle between the inscription stroke direction and the mold's grating line direction, can be rotated to tailor the period, geometrical shape and profile of the resultant nanogratings. By controlling the azimuth along with other important ARC-DNI parameters, specifically the temperature, force, and inscribing speed, we demonstrate that the azimuth-dependent change in the nanograting mold's opening profile and modulation of the temperature- and time-dependent viscoelastic polymer reflow can enable the continuous patterning of asymmetric, blazed, and slanted nanogratings having diverse geometrical profiles, such as trapezoids, triangles, and parallelograms. ARC-DNI can be utilized in many practical applications exemplified by diffractive optical elements and potentially in AR/VR devices.

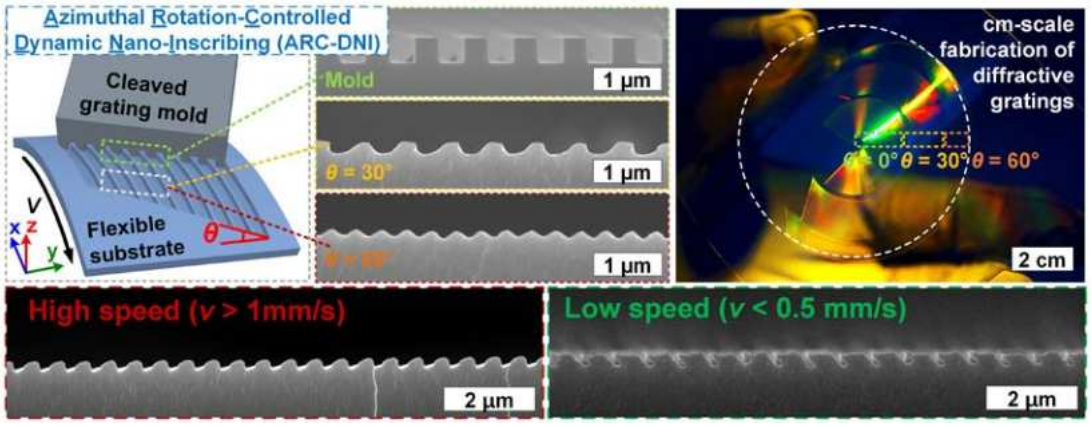


Figure 1. Scheme and components of the ARC-DNI process (left), results of controlled periods and shapes of ARC-DNI-ed asymmetric nanogratings (middle), and diffractive nanograting lens fabricated by performing ARC-DNI along a circular route (right). Inscribing speed-dependent change in the geometric shape of asymmetric nanogratings is demonstrated at the bottom.

Acknowledgements

This research was supported by grants from the National Research Foundation of Korea (NRF-2021M3H4A3A02099204, NRF-2022M3C1A3081178 (Ministry of Science and ICT), and NRF-2022R1I1A2073224 (Ministry of Education)) and the Korea Industrial Technology Association (KOITA-RND3-2022-04) funded by the Korean Government.

References

1. U. Lee, H. Kim, D. K. Oh, N. Lee, J. (Jonggab) Park, J. (Jaewon) Park, H. Son, H. Noh, J. Rho, and J. G. Ok, "Azimuthal rotation-controlled nanoinscribing for continuous patterning of period- and shape-tunable asymmetric nanogratings", Microsystems & Nanoengineering, in press, 2024.

Dynamic Thermoplasmonic Control of Colloids, Molecules and Fluids

M. Fränzl[1], D. Quinn[1], D. Paul[1], and F. Cichos[1*]

[1]Molecular Nanophotonics Group, Leipzig University, Linnéstr. 5, 04103 Leipzig, Germany
[*]corresponding author: cichos@physik.uni-leipzig.de

Abstract: Optically pumped plasmonic nanostructures allow a dynamic release of heat for an unprecedented control of objects like colloids and macromolecules in microfluidic environments. We report on experiments that assemble photonic and molecular structures with the help of local hydrodynamic flow and pressure fields that are the result of thermoplasmonic heating.

In microfluidics, the manipulation of liquids and suspended objects in small channels has diverse applications, including triggering chemical reactions, creating new materials, analyzing single cells at high throughput, and simulating organs on a chip [1]. Efficient mass and heat transport at small scales, along with experimental accessibility and control, drive innovation in fields like biology, chemistry, drug design, and medicine. Most microfluid manipulation methods thereby rely on external pressure differentials in complex channel systems where local control is difficult.

In recent years, new techniques have emerged for manipulating nano-objects and flows in a fluidic environment using remote control through light. These methods go beyond the force generation capabilities of optical tweezers and employ plasmonic structures. By generating temperature gradients with plasmonic structures at the boundaries between liquids and solid surfaces in simple fluidic slit pores, local flow patterns can be created to guide, manipulate, and separate suspended objects without the need for external pressure differences [2]. This new field is termed thermofluidics and comprises new rapid developments.

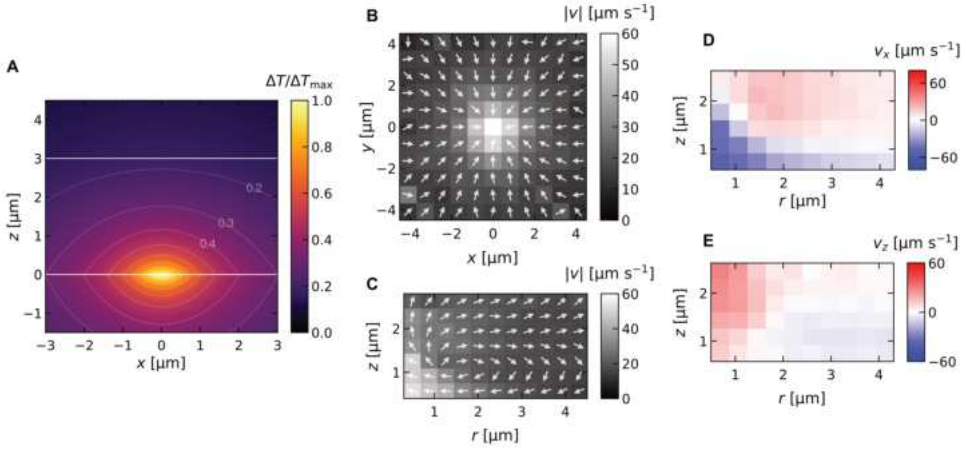


Figure 1. (**A**) Temperature field generated in a thin liquid film above a thin gold film by a focused laser. (**B**) Experimentally measured flow field generated by the temperature field in **A** directly at a gold water interface. (**C**) Flow field measured across the film thickness. (**D-E**) Magnitude of the flow vector components measured as a function of distance from the hot spot.

We show in this contribution how optically heated plasmonic nanostructures can induce complex hydrodynamic flow fields. These flow fields arise from forces generated in an ultrathin boundary layer of a few

nanometer thickness at the liquid-solid interface and are termed thermo-osmotic flows [2]. Such thermo-osmotic flows can be combined with van der Waals and electrostatic forces to dynamically generate controlled plasmonic structures using gold nanoparticles. The large thermal diffusivity at these length scales further ensures that complex temperature fields may be generated by multiplexing in time and space, which allows additional control on the cluster formation. We present the spectroscopic signatures of these clusters that can be formed and reformed on demand and dynamically.

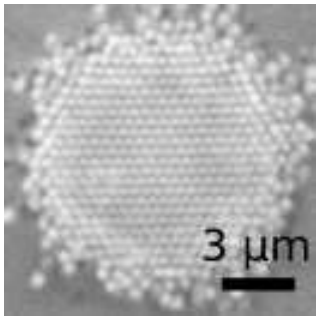


Figure 2. *Photonic crystallite grown from 300 nm polymer beads by thermoplasmonic actions.*

We further show how molecular compounds in the solution allow the non-equilibrium growth of photonic crystallite structures. The colloidal crystals are thereby formed with the help of osmotic pressure gradients that are the results of the interaction of the molecules with the plasmonic temperature fields. These functional photonic crystallites which exhibit clear signs of stop bands do not need any attractive interaction between the colloids to grow but are solely the result of the local pressure fields and hydrodynamic flow fields and cease if these are switched off. The thermal non-equilibrium nature thereby provides new dynamic control to form even mixed crystals which can be combined with real-time spectroscopy of the structures

The applied thermoplasmonic actions that involve thermophoresis, thermo-osmosis, thermo-viscous effects, or other secondary effects can be dynamically modified at high speeds due to fast thermal diffusion on the micrometer scale [2]. In addition to the manipulation of colloids [3], these techniques enable precise control over single and multiple macromolecules [4]. They facilitate the study of protein aggregation [5] and show promise for integration with advanced plasmonic sensing techniques creating feedback loops with the help of machine learning controlled feedback loops [6].

We acknowledge support from the SFB TRR102 “Polymers under multiple constraints: restricted and controlled molecular order and mobility” (DFG project number 189853844).

References

1. Galan E. A., Zhao H, Wang X., Dai Q., Huck W. T. S., & Ma S. “Intelligent Microfluidics: The Convergence of Machine Learning and Microfluidics in Materials Science and Biomedicine”, Matter, Vol. 3, No. 6, 1893-1922, 2020.

2. Fränzl M. & Cichos F. “Hydrodynamic manipulation of nano-objects by optically induced thermo-osmotic flows”, Nat Comm, Vol. 13, (656), 2022.

3. Lin L., Peng X., Mao Z., Wei X., Xie C., & Zheng Y. “Interfacial-entropy-driven thermophoretic tweezers”, Lab Chip, Vol. 17, 3061-3070, 2017.

4. Braun M., Bregulla A. P., Günther K., Mertig M., & Cichos, F. (2015). “Single Molecules Trapped by Dynamic Inhomogeneous Temperature Fields”, Nano Lett, Vol. 15, 5499-5505, 2015.

5. Fränzl, M., Thalheim T., Adler J., Huster D., Posseckardt J., Mertig M., & Cichos F. “Thermophoretic trap for single amyloid fibril and protein aggregation studies”, Nat Methods, Vol. 16, 611-614, 2019.

6. Fränzl, M. & Cichos, F. “Active particle feedback control with a single-shot detection convolutional neural network”, Sci Rep, Vol. 10, 12571, 2020.

Recent progresses on quantum-enhanced nonlinear imaging

T. Dickinson,[1] I. Afxenti,[2] G. Astrauskaite,[3] L. Hirsch,[2] S. Nerenberg,[3] O. Jedrkiewicz,[4,5] A. Gatti,[4] D. Faccio,[3] C. Müllenbroich,[3] M. Clerici,[2,5] and L. Caspani[1,*]

[1]Institute of Photonics, Department of Physics, University of Strathclyde, Glasgow G1 1RD, United Kingdom
[2]James Watt School of Engineering, University of Glasgow, Glasgow G12 8QQ, United Kingdom
[3]School of Physics and Astronomy, University of Glasgow, Glasgow G12 8QQ, United Kingdom
[4]Istituto di Fotonica e Nanotecnologie del CNR, Piazza Leonardo da Vinci 32, 20133 Milano, Italy
[5]Dipartimento di Scienze e Alta Tecnologia, Università dell'Insubria, Via Valleggio 11, 22100 Como, Italy

[*]corresponding author: lucia.caspani@strath.ac.uk

Abstract: We investigated the quantum nature of non-linear processes driven by non-classical light. We studied second-harmonic generation pumped by parametric down-conversion (PDC), and we observed a quantum effect for high-flux PDC, beyond the photon pairs regime.

Recent years have witnessed a renewed focus on exploring quantum effects in nonlinear light-matter interactions, specifically two-photon absorption (TPA) [1,2] and second-harmonic generation (SHG) [3], driven by nonclassical light sources. Ongoing debates surround the nature of the observed enhanced nonlinear signal, with doubts raised about its validity (see e.g. [4]). Additionally, scepticism persists regarding the applicability of quantum effects in two-photon interactions due to the low signals typically generated [5]. To contribute to this topic, our investigation delves into the SHG of parametric down-conversion, spanning both the spontaneous (photon pairs) regime and higher photon fluxes.

A 40 W, 500 kHz, 1030 nm, 245 fs pulsed laser (Light Conversion Carbide) undergoes frequency doubling to a central wavelength of 515 nm, serving as the pump for parametric down-conversion (PDC) in a 2 mm BBO crystal. After appropriate pump filtering, the resulting PDC is imaged onto a second identical crystal using a pair of 90-degree off-axis parabolic mirrors in a 4-f configuration to achieve second harmonic generation (eSHG). The eSHG signal was detected with a photomultiplier tube connected to a time-to-digital converter.

The eSHG signal, measured as a function of PDC energy in the low-gain, spontaneous regime, conforms to the expected linear scaling (inset of Fig. 1). To authenticate this as a genuine quantum effect, losses were introduced to the PDC beam, resulting in a decrease in the eSHG signal, a phenomenon absent in standard SHG driven by a classical beam. Notably,

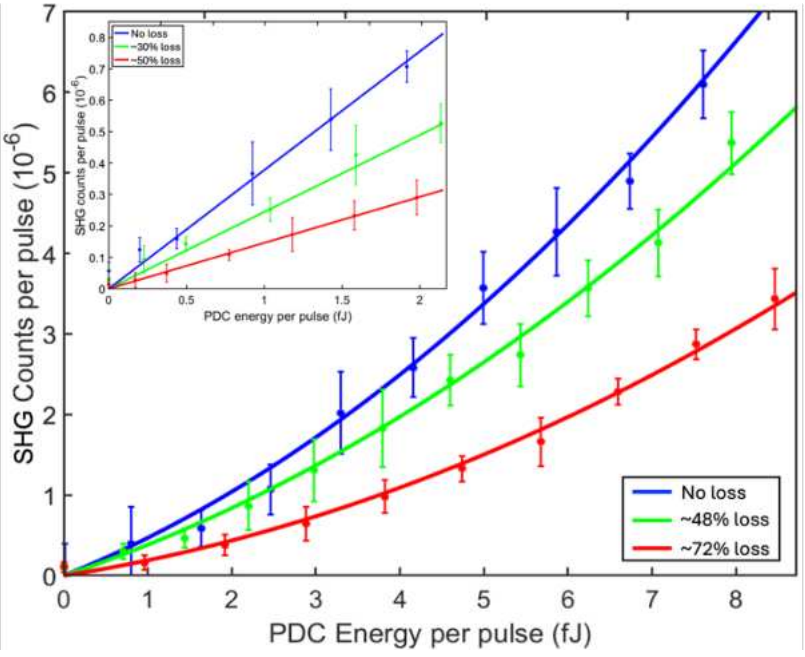


Fig. 1. SFG counts per pulse as a function of the PDC pulse energy in the spontaneous (inset) and stimulated regimes.

this effect persisted at higher PDC fluxes in the stimulated regime (Fig. 1 - main), confirmed by the nonlinear scaling of PDC versus pump energy. The observation of quantum effects beyond conventional quantum advantage regimes in eSHG or eTPA suggests potential avenues for leveraging quantum two-photon interactions in imaging and metrology.

The authors acknowledge support from EPSRC and UKRI (EP/V062492/1 and QuantIC ADF).

References

1. Lee et al., "Entangled photon absorption in an organic porphyrin dendrimer", J. Phys. Chem. B. **110**, 25582 (2006).
2. Tabakaev et al., "Spatial properties of entangled two-photon absorption", Phys. Rev. Lett. **129**, 10 (2022).
3. Dayan et al., "Nonlinear interactions with an ultra high flux of broadband entangled photons", Phys. Rev. Lett. **94**, 043602 (2005).
4. Mikhaylov et al., "Hot-Band Absorption Can Mimic Entangled Two-Photon Absorption", Phys. Chem. Lett. **13**, 1489 (2022).
5. Raymer et al., "How large is the quantum enhancement of two-photon absorption by time-frequency entanglement of photon pairs?" Optica **8**, 757 (2021).

Recent progress on chip-based Brillouin interactions

Moritz Merklein

The University of Sydney, Australia
*corresponding author: moritz.merklein@sydney.edu.au

Abstract: On-chip stimulated Brillouin scattering (SBS) is a powerful nonlinear effect for optical signal processing due to its narrow linewidth and tunability via an optical pump. Here, I present our recent discovery of surface acoustic wave SBS and our progress of integrating Brillouin active waveguides with electro-optic interfaces.

Topological transformations of vortex rings in paraxial laser beams

Zhamila Kulchukova* **and Anton S. Desyatnikov**

Department of Physics, School of Sciences and Humanities, Nazarbayev University, Astana, Kazakhstan
*corresponding author: zhamila.kulchukova@nu.edu.kz

Abstract: Vortex rings are generated by the interference of Gaussian beams and a plane wave. We describe non-trivial topological events controlled by relative amplitude and phase: birth and death of isolated vortex rings as well as reconnections of two or more vortex rings, including transformations which change the number of rings.

Historically, the term vortex ring is associated with the study of smoke rings by Helmholtz [1], while in optics, the first appearance of vortex rings is linked to the study of Airy rings [2,3]. The basic topological reactions associated with the rings include their birth and death at isolated points and reconnection of vortex lines [3,4].

We investigate whether vortex rings can be generated in linear paraxial systems and if asymmetries in the beam shape affect the topological structure. We explore an accessible model that generates vortex rings as a result of the superposition of a Gaussian beam and a co-propagating plane wave, which can be replicated using readily available laboratory equipment. The results are presented in more detail in Refs. [5,6].

Propagation of laser beams in free space is governed by the Schrödinger paraxial wave equation for slowly varying envelope of electric field E:

$$4i\frac{\partial E}{\partial t}+\frac{\partial^2 E}{\partial x^2}+\frac{\partial^2 E}{\partial y^2}=0, \tag{1}$$

here we use dimensionless coordinates x and y, measured in units of beam width w_0, and the "time" t is normalized by the diffraction length $z_R=\pi w_0^2/\lambda$. We use the fundamental solution to Eq. (1), the 1D Gaussian beam:

$$E_1(x,t;w_0,t_0)=\frac{w_0}{\sqrt{w_0^2+i(t-t_0)}}\exp\left(-\frac{x^2}{w_0^2+i(t-t_0)}\right), \tag{2}$$

to construct 2D Gaussian beams with elliptic transverse profile: $E(x,y,t)=E_1(x,t;w_x,d/2)E_1\left(y,t;w_y,-d/2\right)$. We reduce the parameter domain by introducing the ellipticity parameter ϵ, such that $w_x/w_y=\tan\epsilon$, and the beam is astigmatic for $d\neq 0$.

In case of the radially symmetric fundamental Gaussian mode [5] $(\epsilon=\pi/4, d=0)$, we look for the nodal (vortex) lines, $E=0$, of the superposition $E=E_2+Pe^{i\phi}$, here P is the relative intensity of the plane wave and ϕ is the relative phase difference. The vortices lie on the intersection of two surfaces: iso-surfaces for beam envelope intensity $|E(x,y,t)|=P$ and phase level surfaces, $\mathrm{Arg}\,E=\phi+2n\pi$. Two topological mechanisms are identified in this case: the nucleation of a single ring on the optical axis, when the phase ϕ passes through the endpoints of the intensity iso-surfaces, and a nucleation of a pair of counter-propagating rings.

The radial symmetry forces the rings to exhibit a flat configuration, oriented perpendicular to the axis of propagation [5], while in elliptic beam cases $(\epsilon\neq\pi/4)$ the rings deform in 3D space [6]. This introduces two additional topological transformations: nucleation of a pair off-axis rings and ring reconnections. The birth of an off-axis pair is the product of elliptic asymmetry: the rings are no longer flat; thus, they cannot annihilate with each other as it was possible in the radially symmetric beam. The underlying mechanism for the birth of a pair off-axis remains consistent across all three non-radial scenarios, although the nature of reconnections varies.

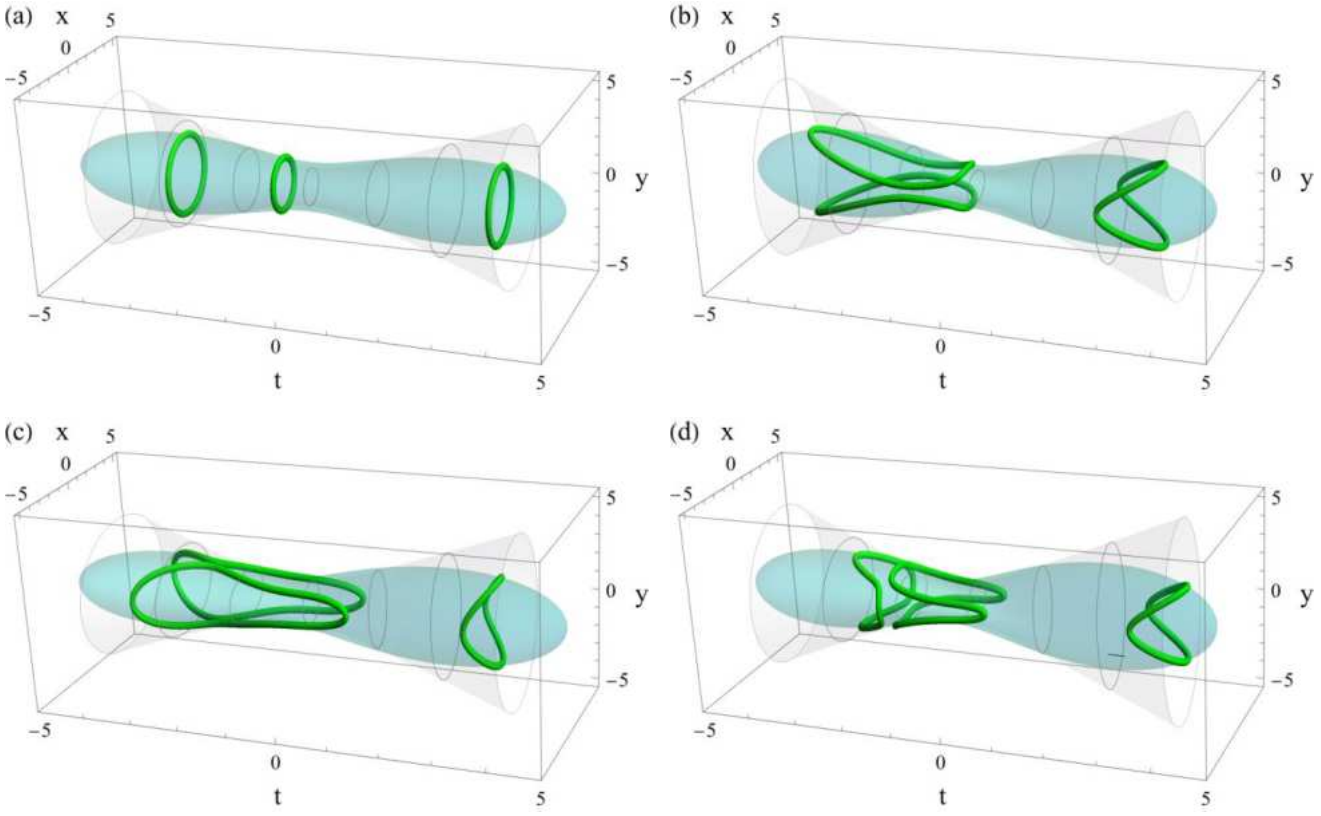


Figure 1. Beam shapes (grey surface), spheroids of intensity $P = 1/5$ (cyan surface), and vortex rings (thick green lines) for: (a) radially symmetric beam $(\phi = -0.1\pi)$, (b) elliptic beam $(\phi = -0.05\pi)$, (c) astigmatic beam $(\phi = -0.05\pi)$ and (d) elliptic-astigmatic beam $(\phi = -0.17\pi)$.

We identified the generic $2 \to 2$ reconnections, where two rings touch on a point and form two separate rings, that is present in all cases. However, at certain cases, i.e. ϕ passing through the point in the beam shape with the round transverse profile, $3 \to 3$ and $2 \to 4$ reconnection cases become possible, which is attributed to the elliptic symmetries and cannot be generic in nature.

References

1. H. Helmholtz, "LXIII. On Integrals of the hydrodynamical equations, which express vortex-motion," The London, Edinburgh, Dublin Philosophical Magazine and Journal of Science, Vol. 33, No. 226, 485–512, 1867.
2. A. Boivin and E. Wolf, "Electromagnetic field in the neighborhood of the focus of a coherent beam," Phys. Rev. Vol. 138(6B), B1561–B1565, 1965.
3. G. P. Karman, M. W. Beijersbergen, A. van Duijl, and J. P. Woerdman, "Creation and annihilation of phase singularities in a focal field," Optics Letters, Vol. 22, 1503–1505, 1997.
4. M. V. Berry and M. R. Dennis, "Topological events on wave dislocation lines: birth and death of loops, and reconnection," Journal of Physics A: Mathematical and Theoretical, Vol. 40, 65-64, 2007.
5. A. Desyatnikov, "Vortex rings in paraxial laser beams," Optics Express, Vol. 31, Art. No. 31955, 2023.
6. Z. Kulchukova and A. Desyatnikov, "Vortex ring reconnections in elliptic Gaussian beams," Optics Letters, Vol. 49, No. 4, 915-918, 2024

Artificial Neural Networks and Quantum Information Processing using Integrated Photonics

Imtiaz Alamgir[1], Luigi Di Lauro[1], Stefania Sciara[1], Abdul Rahim Aadhi[1], Celine Mazoukh[1], Hao Yu[1,2] Bennet Fischer[1], Nicolas Perron[1], Nicola Montaut[1], Mario Chemnitz[1], Brent E. Little[3], Sai T. Chu[4], David J. Moss[5], Zhiming Wang[2] and Roberto Morandotti[1*]

[1]Institut national de la recherche scientifique (INRS-EMT), Varennes J3X 1S2, Canada

[2]Institute of Fundamental and Frontier Sciences, University of Electronic Science and Technology of China, China

[3]QXP Technology, Inc, China

[4]City University of Hong Kong, China

[5]Optical Sciences Centre, Swinburne University of Technology, Australia

[*]corresponding author: Roberto.Morandotti@inrs.ca

Abstract: Integrated photonics advances emerging artificial intelligence and quantum information processing technologies. This work employs on-chip, reconfigurable devices for highly efficient, intelligent, and secure classical and quantum signal processing. We demonstrate simultaneous operations with high speed, low power consumption, and small footprints, paving the way for next generation telecommunication solutions.

Artificial intelligence and quantum information science provide innovative tools for advanced signal processing toward emerging smart technologies in the fields of, e.g., communication and optical computing [1,2]. For instance, software/electronic-based artificial neural networks have been used to optimize telecom data transmission [3]. Yet, current implementations are inefficient to process real-time signals due to high latency and low processing speeds. Similarly, quantum signal processing has been pivotal to implement quantum communication in fiber networks to guarantee unbreakable data security [4]. However, fiber-based quantum communication suffers from limited distances and low transmission speeds, due to photons scattering and losses.

We develop integrated, reconfigurable all-optical neural networks (ONNs) to process and recover nonlinearly distorted telecom signals at ultrafast speeds. In parallel, we use on-chip photonics for the generation and processing of complex entangled photon states toward high-speed quantum key distribution (QKD). These implementations are realized by utilizing a single all-integrated photonic platform, which comprises a nonlinear source (spiral waveguide or microring resonator) [5] and an on-chip programmable interferometry system [6].

Our proposed ONNs feature a recurrent network topology [1], where the encoded information density is enhanced via the use of a microcomb [3] and manipulated by means of wavelength division multiplexing techniques. We apply our ONNs for nonlinear channel equalization to regenerate the temporal waveform of the transmitted signal, which undergoes dispersive and nonlinear impairments due to propagation in the fiber channel. In general, this complex task demands the implementation of rigorous digital signal processing e.g., digital back propagation, requiring extensive computational power and a detailed understanding of the transmission system. Our objective is to develop highly versatile and easily integrable ONN platforms that are capable of processing telecom signals at ultra-high speeds and with reduced latency. Preliminary results suggest that our tunable ONN devices can process and accurately reconstruct nonlinearly distorted telecom waveforms, achieving processing speeds exceeding GHz/s with nanosecond-level latency.

The spiral waveguide and the cascade of on-chip interferometers can also be exploited for the generation of high-dimensional (qudit) time-entangled photon states at telecom wavelengths. The interferometers generate

pulse burst that subsequently induce spontaneous four-wave mixing and thus generate time-entangled photon pairs in the spiral waveguide. The programmable interferometers, combined with external fiber-based GHz speed phase modulation, are used for quantum state processing i.e., for quantum interference and quantum state tomography measurements, as well as telecom-compatible secure QKD. The use of entangled photons provides robustness against eavesdropping attacks, as they allow the exchange of a device-independent secret key. The use of qudits guarantees an increase in the secret key rate, noise resilience, and information capacity. From preliminary tests, we estimate a record high secret key rate of several hundred kbit/s and a quantum bit error rate below 12%. These results show the high robustness of the cryptography key generated via our photonic qudits against eavesdropping attacks.

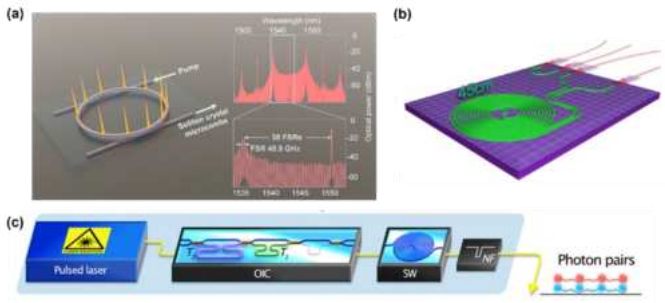


Fig. 1. (a) Schematic representation of an integrated microring resonator employed to generate a soliton crystals comb at C-band. Adapted from [7]. (b) Schematic representation of a spiral waveguide. Adapted from [5]. (c) Schematic representation of the scheme used for photon state generation. OIC: on-chip interferometer cascade; T1, T2: transmission ratios of the interferometers; SW: spiral waveguide; NF: notch filter.

Our platform provides compact and CMOS compatible solutions that enable significant scaling of information through time or frequency multiplexing, establishing it as a highly suitable candidate for signal processing applications. Moreover, the high nonlinearity and low heat dissipation profiles of our devices, will position our research in line with the needs for energy efficiency required by next-generation ONN, while also boosting quantum state processing, and the security of quantum optical signals in fiber telecom networks.

References

1. Shastri, B.J., Tait, A.N., Ferreira de Lima, T., Pernice, W.H.P., Bhaskaran, H., Wright, C.D., Prucnal, P.R., “Photonics for artificial intelligence and neuromorphic computing”, Nature Photonics, Vol. 15, 102-114, 2021.
2. Flamini, F., Spagnolo, N., Sciarrino, F., “Photonic quantum information processing: a review”, Reports on Progress in Physics, Vol. 2, No. 1, 016001, 1-32, 2019.
3. Xu, X., Tan, M., Corcoran, B., Wu, J., Boes, A., Nguyen, T.G., Chu, S.T., Little, B.E., Hicks, D.G., Morandotti, R., Mitchell, A., Moss, D.J., “11 TOPS photonic convolutional accelarator for optical neural networks”, Nature, Vol. 589, 44-51, 2021.
4. Wen, W., Chen, Z., Lu, L., Yan, W., Xue, W., Zhang, P., Lu, Y., Zhu, S., Ma, X., “Realizing an entanglement-based multiuser quantum network with integrated photonics”, Physical Review Applied, Vol. 18, No. 2, 024059, 1-4, 2022.
5. Moss, D.J., Morandotti, R., Gaeta, A.L., and Lipson, M., “New CMOS-compatible platforms based on silicon nitride and Hydex for nonlinear optics”, Nature Photonics, Vol. 7, 597-607, 2013.
6. Wetzel, B., Kues, M., Roztocki, P., Reimer, C., Godin, P.L., Rowley, M., Little, B.E., Chu, S.T., Viktorov, E., Moss, D., Pasquazii, A., Peccianti, M., and Morandotti, R., “Customizing supercontinuum generation via on-chip adaptive temporal pulse-splitting”, Nature Communications, Vol. 9, No. 4884, 1-10, 2018.
7. Xu, X., Tan, M., Corcoran, B., Wu, J., Nguyen, T.G., Boes, A., Chu, S.T., Little, B.E., Morandotti, R., Mitchell, A., Hicks, D.G., and Moss, D.J., “Photonic perceptron based on a Kerr microcomb for high-speed, scalable, optical neural networks”, Laser & Photonics Reviews, Vol. 14, No. 2000070, 1-10, 2020.

Scalable Chiral Photonic Architectures via Soft Nanoimprinting lithography

J. Mendoza-Carreño, X. Qi, I. Alonso, M. Garriga, L. A. Pérez and A. Mihi*

Institute of Materials Science of Barcelona (ICMAB-CSIC),
Campus de la UAB, 08193 Bellaterra, Spain
corresponding author: amihi@icmab.es
https://nanophotonics.icmab.es/

Abstract: Template-assisted self-assembly is a scalable nanofabrication technique in which elastomeric pre-patterned stamps are used to induce long range order from a colloidal dispersion used as ink. Metal colloids or perovskite nanocrystals are used to fabricate high quality and large area 2D photonic crystals supporting narrow lattice resonances and chiroptical properties.

Photonic architectures offer a promising avenue for optimizing the performance of various optoelectronic devices. Nevertheless, the future of optoelectronic devices hinges on cost-effective and large-scale manufacturing techniques that can reduce expenses and boost production efficiency. To harness the remarkable attributes of photonic structures for enhancing these devices, they must undergo a processing approach akin to that of the devices themselves.

Soft nanoimprinting lithography is a versatile, rapid, and cost-efficient method for crafting nanostructures from a diverse variety of materials. In soft nanoimprinting, we make use of pre-patterned elastomeric stamps to corrugate materials such as resists, biopolymers, colloids and nanomaterials in general. In all cases, the resulting photonic architectures can exhibit a resolution below 100 nm while covering areas up to 1 cm^2. During this presentation, I will explain how we use pre-patterned stamps to induce the long-range alignment into 2D lattices of different colloids, including gold and silver colloids and perovskite nanocrystals, to attain distinct optical properties, such as lattice resonances with high Q-factors.[1,2] Moreover, I will showcase how elastomeric molds featuring chiral 2D arrays can lead to chiral metasurfaces[3] exhibiting strong circular dichroism using traditional gold and silver colloids (g-factors of 0.4) and intense circularly polarized photoluminescence (CPL), making them seamlessly applicable in various practical applications.

References

1. X. Qi, L. A. Pérez, M. I. Alonso, and A. Mihi. ”High Q-Factor Plasmonic Surface Lattice Resonances in Colloidal Nanoparticle Arrays” ACS Applied Materials and Interfaces, 2024, 16, 1, 1259–1267
2. Molet, P.; Passarelli, N.; Pérez, L. A.; Scarabelli, L.; Mihi, A. “Engineering Plasmonic Colloidal Meta-Molecules for Tunable Photonic Supercrystals”. Advanced Optical Materials 2021, 9 (20).
3. Mendoza-Carreño, J.; Molet, P.; Otero-Martínez, C.; Alonso, M. I.; Polavarapu, L.; Mihi, A. “Nanoimprinted 2D-Chiral Perovskite Nanocrystal Metasurfaces for Circularly Polarized Photoluminescence. Advanced Materials 2023, 35, 2210477

Dynamically switchable phase contrast imaging with metaoptics

S. B. Sulejman[1], L. Clark[1], H. Wang[1], L. Wesemann[1], and A. Roberts[1*]

[1] ARC Centre of Excellence for Transformative Meta-Optical Systems, School of Physics, University of Melbourne, Victoria 3010, Australia

[*]Corresponding author: ann.roberts@unimelb.edu.au

Abstract: Metasurfaces can all-optically manipulate images in the object or image plane leading to an orders-of-magnitude reduction in size compared to Fourier plane approaches. Here approaches to dynamically modifying the response of a device, essential for multifunctional imaging, using polarization and phase change materials is discussed.

Although the use of optical systems to perform image processing in the Fourier plane has been well-known since the 1950s, most commonly applied operations (such as edge detection or enhancement) are more widely performed digitally. Information carried in an optical wavefield introduced by, for example, propagation through transparent objects or turbulence is, however, lost on acquisition with a camera. Although sophisticated computational strategies for extracting phase from intensity images exist, these can be relatively slow and computationally demanding. Conventional all-optical approaches for image processing and phase contrast imaging, on the other hand, typically require relatively bulky, and sometimes expensive, optics but the drive for miniaturization of optical components, and advances in nanoscience have underpinned a renewed interest in all-optical image processing.

An optical wavefield carrying an image can be decomposed into a superposition of plane waves each with a characteristic amplitude and phase travelling in a given direction with respect to the optical axis. There is a one-to-one correspondence between the direction of a plane wave contribution and the transverse components of the spatial frequency (k_x,k_y). Traditional spatial frequency filtering involves introducing an amplitude and/or phase mask into the focal plane of a lens taking advantage of its Fourier transforming property. This places constraints on the positioning of the filter as well as requiring bulky lenses and the inclusion of propagation distances from the object to the Fourier plane. It is also possible to directly manipulate the spatial frequency content via a device that has a reflection or transmission that depends on the angle of incidence of a plane wave performing a direct modification of the amplitude and/or phase of a given plane wave component. In addition to providing a more compact all-optical system, there is considerable flexibility in the positioning of the device within an optical system since the angular spectrum is manipulated directly [1]. Concepts from nanophotonics can be used to produce compact devices with a tailored angular dispersion and, hence, expanded capacity to manipulate images and, more generally, perform analogue computing [2,3]. Specifically, there is considerable scope for the development of compact devices that can, all-optically, generate enhanced contrast images of transparent, phase objects. We have previously shown that a commercially available notch filter can performs edge detection in transmission at the bandstop wavelength [4] and that a planar metal-insulator-metal Salisbury screen also can be used to enhance phase variations introduced by biological specimens and microlenses in reflection at the resonant wavelength [5]. We also demonstrated that a resonant waveguide grating in transmission [6] can be used to generate phase contrast images of unstained HeLa cells. A particular focus has been on the necessity of introducing an asymmetry into the system to produce pseudo-3D phase contrast images

similar to those seen using Differential Interference Contrast images [6-9].

Many implementations of phase contrast imaging would benefit from the capacity to switch the modality of the imaging process. For example, being able to simply change from a bright field to a phase contrast image or to extract phase gradient images along different directions in a sample provides a means to, not only visualize additional information, but also to perform quantitative phase imaging and wavefront recovery. This presentation will discuss recent progress in the use of various strategies including polarization, wavelength multiplexing and the use of phase change materials [10] to demonstrate a variety of different phase contrast images using a single, fixed meta-optic.

This research was funded by the Australian Government through the Australian Research Council Centre of Excellence grant (CE200100010). S.B.S., H.W. and L.C. also gratefully acknowledge the support of the Australian Government Research Training Program Scholarship and S.B.S. the Ernst & Grace Matthaei Scholarship.

References

1. Case, S.K. “Fourier processing in the object plane”, Opt. Lett. Vol. 4, No. 9, 286-288, 1979.
2. Zangeneh-Nejad, Sounas, D.L., Alù, A. and Fleury, R, “Analogue computing with metamaterials,”, Nature Reviews Materials, Vol. 6, 207-225, 2021
3. Wesemann, L., Davis, T. J. and Roberts, A. “Meta-optical and thin film devices for all-optical information processing,” Applied Physics Reviews, Vol. 8 No. 3, 031309, 2021.
4. S.B. Sulejman, N. Priscilla, L. Wesemann, W. S. L. Lee, J. Lou, E. Hinde, T. J. Davis and A. Roberts, “Thin film notch filters as platforms for biological image processing,” Sci. Rep., Vol. 13, 4494, 2023.
5. Wesemann, L., Panchenko, E., Singh, K. Della Gaspera, E., Gómez, D.E., Davis, T.J. and Roberts, A. “Selective near-perfect absorbing mirror as a spatial frequency filter for optical image processing,” APL Photonics, Vol. 4, 100801, 2019.
6. Wesemann, L., Rickett, J., Song, J., Lou, J., Hinde, E., Davis, T.J. and Roberts, A. "Nanophotonics enhanced coverslip for phase imaging in biology" Light Sci. Appl., Vol. 10, No. 1, 98, 2021.
7. Roberts, A., Gómez, D.E. and Davis, T.J., “Optical image processing with metasurface dark modes,” J. Opt. Soc. Am. A, Vol. 35, No. 9, 1575-1584, 2018
8. Davis, T.J., Eftekhari, F., Gómez, D.E. and Roberts, A. “Metasurfaces with asymmetric optical transfer functions for optical signal processing,” Phys. Rev. Lett. Vol. 123, 013901, 2019.
9. Wesemann, L., Rickett, J., Davis, T.J. and Roberts, A., “Real-time phase imaging with an asymmetric transfer function metasurface,”, ACS Photonics, Vol. 9, No. 5, 1803-1807, 2022.
10. Cotrufo, M., Sulejman, S. B., Wesemann, L., Rahman, Md. A., Bhaskaran, M., Roberts, A. and Alù, A., “Reconfigurable image processing metasurfaces with phase-change materials”, arXiv e-prints, 2023. doi:10.48550/arXiv.2311.13109.

Coherent Array of Superconducting Qubits as a Sensitive Microwave Antenna

P. Navez[1], A. G. Balanov[2], S. E. Savel'ev[2], and A. M. Zagoskin[2*]

[1]Université de Montpellier, France
[2]Loughborough University, United Kingdom
[*]corresponding author: a.zagoskin@lboro.ac.uk

Abstract: Progress in the creation of large-scale, artificial quantum coherent structures comprised of superconducting qubits opens new possibilities for their applications. Our analysis shows that such structures, in particular, an array of qubits in a resonator, can serve as sensitive antennas of microwave radiation, and that the signal-to-noise ratio under certain condition can exceed the Standard Quantum Limit and approach the Heisenberg limit of sensitivity.

Superconducting quantum bits keep playing the central role in the progress of quantum technologies due to their versatility of designs, relative facility of fabrication and robustness against decoherence [1]. They can serve as quantum analogues of both nondissipative and dissipative circuit elements, as building blocks of quantum metamaterials, or as artificial atoms; small driven arrays of superconducting qubits are predicted to demonstrate complex (chaotic or hyperchaotic) behaviour [2].

Superconducting qubits operate in the MW frequency range, which makes them attractive as unit elements of MW quantum antennas. Operating in quantum nondemolition regime, such antennas would be able to reach the standard quantum limit of sensitivity [3,4] or exceed it approaching the Heisenberg limit [5], at a single-photon level.

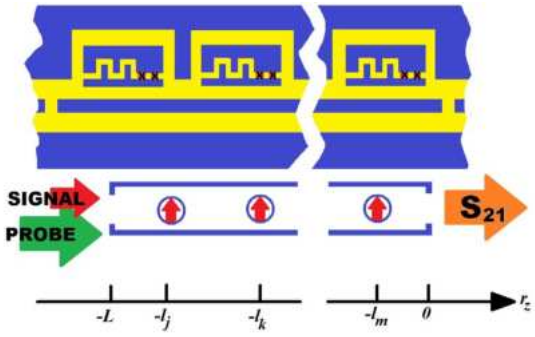


Figure 1. Array of transmon qubits in a cavity resonator (from [4]). The off-resonance interaction of the qubits with the signal in the presence of the probe produces detectable variations of the transmitted sigal.

This opens the road to a number of applications, such as open-air quantum communications in MW range, or an attempt to detect galactic axions [6].

This work was supported by the HORIZON EUROPE projects SUPERGALAX (Grant agreement ID:863313) and QRC-4-ESP (Grant agreement ID:101129663), and the Horizon Europe guarantee scheme – UKRI (UK).

References

1. Wendin, G. “Quantum information processing with superconducting circuits: a review,” Rep. Prog. Phys., Vol. 80, 106001, 2017.
2. Andreev, A. V., Balanov, A. G., Fromhold, T. M., Greenaway, M. T., Hramov, A.. E., Li, Weibin, Makarov, V. V., and A. M. Zagoskin, “Emergence and control of complex behaviors in driven systems of interacting qubits with dissipation,” npj Quantum Information, Vol. 7, 1, 2021.
3. Zagoskin, A. M., Wilson, R. D., Everitt, M., Savel'ev, S., Gulevich, D. R., Allen, J., Dubrovich, V. K., and E. Il'Ichev, “Spatially resolved single photon detection with a quantum sensor array,” Sci. Rep., Vol. 3, 3464, 2013.
4. Navez, P., Balanov, A. G., Savel’ev, S. E. and A. M. Zagoskin, “Quantum electrodynamics of non-demolition detection of single microwave photon by superconducting qubit array,” J. Appl. Phys., Vol. 133, 104401, 2023.
5. Navez, P., Balanov, A. G., Savel’ev, S. E. and A. M. Zagoskin, “Towards the Heisenberg limit in microwave photon detection by a qubit array,” Phys. Rev. B, Vol. 103, 064503, 2021.
6. Gatti, C. et al., “Coherent Quantum Network of Superconducting Qubits as a Highly Sensitive Detector of Microwave Photons for Searching of Galactic Axions,” IEEE Trans. Appl. Supercond., Vol. 33, 1501705, 2023.

Graphene-based 2D Plasmonic Metamaterials for Terahertz Detectors

T. Otsuji[1], K. Tamura[1], Chao Tang[1,2], A. Satou[1], H. Fukidome[1], Y. Takida[3], H. Minamide[3], M. Ryzhii[4], V. Mitin[5], M.S. Shur[6], and V. Ryzhii[1]

[1]Research Institute of Electrical Communication, Tohoku University, Japan
[2] Frontier Research Institute for Interdisciplinary, Tohoku University, Japan
[3]Center for Advanced Photonics, RIKEN, Japan
[4]University of Aizu, Japan
[5]University at Buffalo, SUNY, USA
[6]Rensselaer Polytechnic Institute, USA
[*]corresponding author: otsuji@riec.tohoku.ac.jp

Abstract: This paper reviews recent advances in the research and development of graphene-based 2D plasmonic metamaterials for terahertz detectors and reports on achieving responsivities.

Two-dimensional (2D) plasmons in graphene-channel FETs (GFETs) have attracted increasing attention as a promising mechanism for highly sensitive, fast-response, terahertz (THz) detection operating at room and elevated temperatures [1]. In addition, fast photothermoelectric (PTE) THz detection, as well as sensitive bolometric detection by graphene layer (GL) based van der Waals (vdW) 2D heterostructure devices has been enabled by superior carrier transport properties of graphene [2].

First, we investigated the plasmonic and photothermoelectric detection mechanisms for a single graphene FET (GFET). A few-layered, non-Bernal-stacked epitaxial graphene synthesized by thermal decomposition of a SiC substrate was utilized as the channel layer material. The gate stack included a plasma-enhanced chemical vapor-deposited SiN insulation layer. The Ti/Pd/Au asymmetric dual-grating-gate (ADGG) electrodes were fabricated by e-beam evaporation and lift-off (Fig. 1). The carrier density in the channel was periodically modulated by altering the ADGG bias and formed the plasmonic cavities underneath the highly biased gate fingers. Plasmonic rectification under zero drain bias resulted in fast and sensitive THz detection. The drain bias induced a DC potential slope along the channel heating carriers. The hot carriers absorbed the THz radiation and thermo-diffused towards the cold source and drain electrodes, unequally due to their drift/diffusion induced by the potential slope. This detection mechanism resulted in fast and more sensitive detection supported both by the photothermoelectric (majority) and plasmonic (minority) detection (Fig. 1). Such a detector had a 100-ps class fast detection response with 1-mA/W class modestly high responsivity as a GFET at room temperature (Fig. 1) [3].

Second, we investigated the vertical GL and b-As_xP_{1-x} heterostructures (Fig. 1) which can enhance the GL-based THz photodetector performance [4,5]. The intersubband transitions of graphene Dirac fermions in the GL (with extremely high transport properties) followed by the carrier propagation across the b-As_xP_{1-x} layers with much lower transport properties (Fig. 1) [4,5]. This carrier velocity modulation in a GL-bP-FET (GPFET) mediated the injection of extra carriers from the emitter contact providing the photoconductive gain, which can enable enormously high values of the detector responsivity [4,5]. The bias voltage V_{ds} and the signal voltage δV_{ω} were applied between the GPFET source and drain, whereas the signal voltage was produced by an antenna receiving the impinging THz radiation with frequency ω. The spectral dependences of the responsivity, R_{ω}^{V}, of the GPFET detectors were calculated for different scattering frequencies ν and different parameters of the structure (Fig. 2) [6-8]. An increase in the collision frequency ν smeared the resonant peak. In a wider frequency range, the

responsivity of the detectors under consideration was an oscillatory function of the radiation signal frequency ω with a set of the maxima at the plasmonic resonances $\omega = n\Omega$ (n being the resonance index). The dependences R_ω^V vs. $\omega/2\pi$ exhibit the alternating sharp maxima and relatively deep minima. The device characteristics of GPFETs with relatively low energy barrier layers (BLs) were optimized by choosing the barriers containing a number of the b-As_xP_{1-x} atomic layers. The resulting room temperature responsivities exceeded 5 kV/W and 10^3 A/W (Fig. 2) [8]. Furthermore, we analyzed the effect of the lateral thermal conductivity of the 2DEG and its Peltier cooling on the GPFET responsivity and its characteristics [9]. To confirm the significance of the electron thermal transfer in the GPFETs, we calculated the frequency dependences of the responsivity disregarding the electron thermal conductivity, i.e., neglecting the electron heat transfer to the side contacts [9]. The results indicate that the electron viscosity naturally weakens the plasmonic resonances [9]. The obtained results are an important contribution to terahertz devices in general and especially to plasmonic enhancement of the detector performance.

In summary, graphene-based 2D plasmonic metamaterials for terahertz (THz) detectors are promising for the realization of next-generation 6G and even 7G THz wireless communication services.

Acknowledgments: The JSPS KAKENHI (Grants # 20K20349 and # 21H04546), Japan; RIEC Nation-Wide Collaborative Research Project # R04/A10, Japan; and by AFOSR (contract number FA9550-19-1-0355, USA.

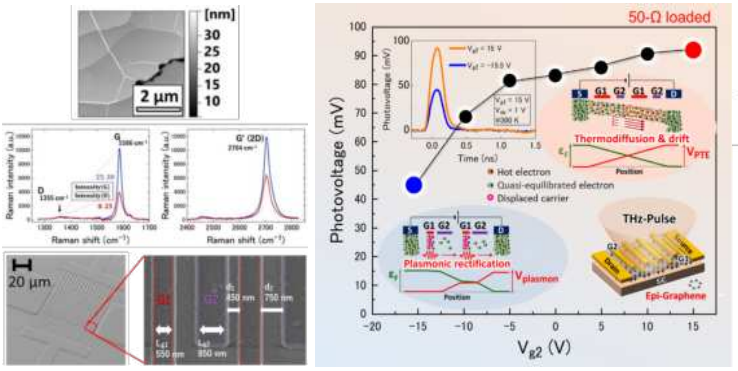


Fig.1. ADGG-GFET THz detector, structure (left) and measured performances (right) [3].

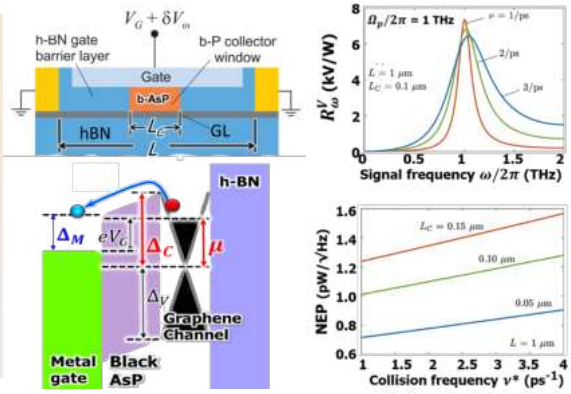


Fig. 2. A GPFET THz detector, structure (left) and simulated performances (right) [6-8].

References

1. Koppens, F.H.L, Mueller, T., Avouris, Ph., Ferrari, A.C., Vitiello, M.S., Polini, M. "Photodetectors based on graphene, other two-dimensional materials and hybrid systems," Nature Nanotechnol., Vol. 9, 780-793, 2014.
2. Cai, X., Sushkov, A.B., Suess, R.J., Adidi, M.N., Jenkins, G.S. et al., Fuhrer, M.S. "Sensitive room-temperature terahertz detection via the photothermoelectric effect in graphene," Nature Nanotech., Vol. 9, 814-819, 2014.
3. Tamura, K., Tang, C., Ogiura, D., Suwa, K., Fukidome, H., Takida, Y., Minamide, H., Suemitsu, T., Otsuji, T., Satou, A. "Fast and sensitive terahertz detection in a current-driven epitaxial-graphene asymmetric dual-grating-gate FET structure," APL Photonics, Vol. 7, Issue 7, 16101, 2022.
4. Ryzhii, V., Ryzhii, M., Mitin, V., Shur, M.S., and Otsuji, T. "Far-infrared photodetectors based on graphene/black-AsP heterostructures," Opt. Exp., Vol. 28, 2480-2489, 2020.
5. Ryzhii, M., Ryzhii, V., Maltsev, P.P., Ponomarev, D.S., Leiman, V.G., Karasik, V.E., Mitin, V., Shur, M.S., Otsuji T. "Far-infrared photodetection in graphene nanoribbon heterostructures with black-phosphorus base layers," Opt. Eng. SPIE, Vol. 60, 082002, 2020.
6. Ryzhii, V., Tang, C., Otsuji, T., Ryzhii, M., Mitin, V., Shur, M.S. "Hot-electron resonant terahertz bolometric detection in the graphene/black-AsP field-effect transistors with a floating gate," J. Appl. Phys., Vol. 133, 174501, 2023.
7. Ryzhii, M., Ryzhii, V., Shur, M.S., Mitin, V., Tang, C., Otsuji, T. "Terahertz bolometric detectors based on graphene field-effect transistors with the composite h-BN/black-P/h-BN gate layers using plasmonic resonances," J. Appl. Phys., Vol. 134, 084501, 2023.
8. Ryzhii, V., Tang, C., Otsuji, T., Ryzhii, M., Mitin, V., Shur, M.S. "Resonant plasmonic detection of terahertz radiation in field-effect transistors with the graphene channel and the black-As_xP_{1-x} gate layers," Sci. Rep., Vol. 13, 9665, 2023.
9. Ryzhii, V., Tang, C., Otsuji, T., Ryzhii, M., Mitin, V., Shur, M.S. "Effect of electron thermal conductivity on resonant plasmonic detection in the metal/black-AsP/graphene FET terahertz hot-electron bolometers," Phys. Rev. Applied, Vol. 19, 064033, 2023.

Observation of off-Γ BIC in photonic crystals in both k- and real spaces

Yuto Moritake[1*], Taiki Yoda[1,2], and Masaya Notomi[1,2]

[1]Department of Physics, Tokyo Institute of Technology, Japan
[2]NTT Basic Research Laboratories, NTT Corporation, Japan
[*]corresponding author: moritake@phys.titech.ac.jp

Abstract: Bound states in the continuum (BICs), which are localized states above the light, is actively studied due to their high Q-factor and topological nature. In this presentation, we introduce observation of photonic BIC with off-Γ wavenumbers not only in k- but also real spaces using light propagation imaging.

Bound states in the continuum (BICs) in photonics are exotic localized modes that are confined in the structures although they are above the light cone in k-space. Photonic BICs can be observed in various photonic systems including photonic crystals, metamaterials, and so on [1]. Since the BICs have no radiation loss, the Q-factor is infinite in principle, which makes the BICs very useful for application to lasers, and sensors, and so on. The photonic BICs can be categorized into two types: one is at-Γ BICs (symmetry protected BICs), and the other is off-Γ BICs (topologically protected BICs) which are observed at non-symmetric points in k-space. While a study on at-Γ BIC has long history, off-Γ BICs have been found recently and are attracting lot of attentions from researchers due to its intriguing features such as topological protection and steering ability [2,3]. In this presentation, we introduce our resent experimental demonstration about observation of off-Γ BIC in k- and real spaces.

In many papers, the off-Γ BIC was termed as “accidental” BIC because this kind of BIC is observed at a specific parameter of the structure, and we need to systematic parameter sweep to design it. However, recently, we found the “deterministic way” to generate off-Γ BIC by using structural symmetry and its topological nature [3]. This methodology enables us to design off-Γ BIC in any substrate with any thickness, which dramatically expand the capability of the off-Γ BIC. We start from traditional triangular lattice photonic crystal with C6 symmetry. In this structure, the at-Γ BIC with topological charge of 2 is achieved. Important point here is the topo. charge is not 1, but 2, which enables the “splitting” of the charge. When we introduce the perturbation breaking C_6 symmetry, the at-Γ BIC with topological charge of 2 split into two off-Γ BICs with charge of 1. Depending on the perturbation direction, we can control the split direction (k_x or k_y) in k-space. To observe “deterministic BIC,” photonic band was directly measured using Fourier plane imaging spectroscopy. We clearly observe the signal disappearance at off-Γ BIC due to extremely small radiation coupling of BICs. Our clear measurement allows to evaluate the Q-factors precisely and revealed the high Q-factors up to 1000 at around the off-Γ BICs.

Since off-Γ BICs have a finite in-plane wave number (different from the symmetry points), off-Γ BICs have a finite group velocity and thus can propagate in the slab. Although many papers observed off-Γ BIC using photonic band measurement (Fig. 1(a)), long-range propagation of the off- BIC has not been reported so far. To observe the off-Γ BIC propagation in real space, we utilize one-dimensional gratings supporting the off-Γ BIC [4]. The laser was injected from the side of the gratings, and we acquired the light scattering image from the upper side of the structures. At the BIC wavelength, propagation was clearly visualized and long-range propagation in millimeter scale was observed (Fig. 1(b)). The wavelength dependence of transmitted light intensity shows high transmission at around BIC wavelength. Interestingly, we observed unique self-collimation

behavior in the BIC propagation, which can be explained by localized Q-factor in k-space. Due to this feature, even when we tilt the incident angle, the direction of the propagation is unchanged.

In summary, we directly observed the off-Γ BIC in photonic crystals by using the photonic band measurements and propagation imaging. Fourier space imaging spectroscopy is a powerful to visualize the photonic band and observe the BICs. Moreover, light propagation measurements offer complementary information about off-Γ BICs. The observed unique long-range propagation by off-Γ BIC open the new opportunity to design photonic waveguides and integrated circuits.

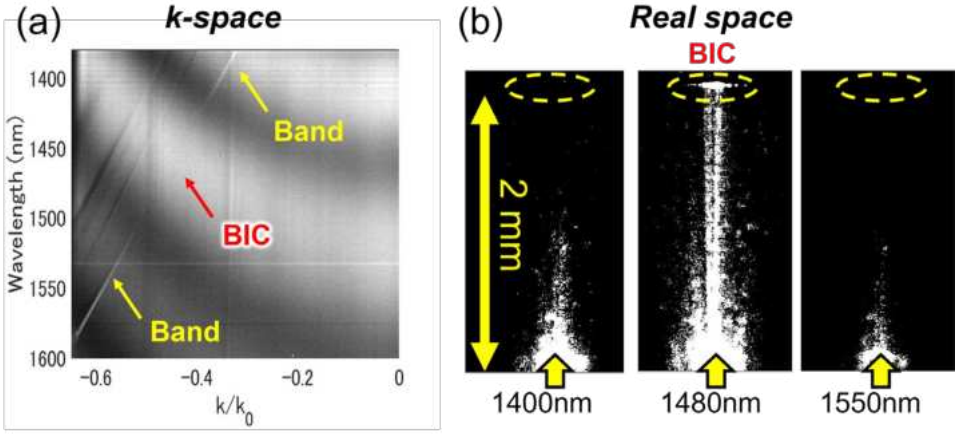


Fig.1 (a) k- and (b) real space observation of off- BICs. The BIC is observed using Fourier plane imaging spectroscopy in (a). The light propagation at the BIC wavelength clearly visualized in light propagation imaging measurements.

Acknowledgement

This work was supported by KAKENHI JP20H05641 and JP21K14551.

References

1. Hsu, C. W. et al. “Bound states in the continuum,” Nat. Rev. Matter., Vol. 1, 16048, 2016.
2. Zhen, B. et al., “Topological Nature of Optical Bound States in the Continuum,” Phys. Rev. Lett., Vol. 113, 257401, 2014.
3. Yoda, T. et al., “Generation and Annihilation of Topologically Protected Bound States in the Continuum and Circularly Polarized States by Symmetry Breaking,” Phys. Rev. Lett., Vol. 125, 053902, 2020.
4. Hamaya, K. et al., “Experimental observation of propagation of off-Γ BIC in 1D grating structures,” CLEO2024.

Dynamic plasmonics based on conducting polymers

Shangzhi Chen[1*], and Magnus P. Jonsson[1]

[1]Laboratory of Organic Electronics, Department of Science and Technology (ITN), Linkoping University, Norrkoping SE-601 74, Sweden

[*]corresponding author: shangzhi.chen@liu.se

Abstract: Conducting polymer nanoantennas with redox tunability form an emerging approach towards dynamic plasmonics. In this talk, the progress and future prospects of active plasmonics based on conducting polymers will be briefly reviewed.

Plasmonics based on conventional metals are broadly used for biosensing and optoelectronic devices, but suffer from limited optical tunability. We recently demonstrated conducting polymers as a new category of plasmonic materials exhibiting excellent optical tunability. In this talk, I will briefly introduce the emergence, current status, and future prospects of using conducting polymers for dynamic plasmonics.

Metal nanostructures are key elements in nano-optics due to their intense resonant interaction with light via plasmonic charge oscillation. However, they suffer from limited tunability due to the fixed optical properties of metals. By contrast, conducting polymers, a new category of organic conductors, exhibit excellent tunability and were recently introduced for dynamic plasmonic antennas. We revealed that nanoantennas based on conducting polymers show clear dipolar plasmonic resonance and sustain reversible tuning via chemical and electrical approaches[1,2]. In this talk, I will present our latest progress of conducting polymer nanoantennas made through colloidal lithography and their applications for dynamic optical systems[3].

Acknowledgements: financial support from Kunt and Alice Wallenberg Foundation, the Swedish Research Council (VR, No. 2020-00287 and 2022-00211), the Swedish Foundation for Strategic Research (SSF), and the Swedish Government Strategic Research Area in Materials Science on Functional Materials at Linkoping University (Faculty Grant SFO-Mat-LiU No. 2009 00971).

References

1. Chen, S., Kang, E. S. H., Shiran Chaharsoughi, M., Stanishev, V., Kuhne, P., Sun, H., Wang, C., Fahlman, M., Fabiano, S., Darakchieva, V., and Jonson, M. P. “Conductive polymer nanoantennas for dynamic organic plasmonics”, Nat. Nanotechnol., Vol. 15, No. 1, 35-40, 2020.
2. Karki, A., Cincotti, G., Chen, S., Stanishev, V., Darakchieva, V., Wang, C., Fahlman, M., and Jonsson, M. P., “Electrical tuning of plasmonic conducting polymer nanoantennas”, Adv. Mater., Vol. 34, No. 13, 2107272, 2022.
3. Chen, S. and Jonsson, M. P., “Dynamic conducting polymer plasmonics and metasurfaces”, ACS Photonics, Vol. 10, No. 3, 571-581, 2023.

Integrated microlasers on a Bloch surface wave platform

Y.-C. Lee[1], Y.-L. Ho[1], B.-W. Lin[1], M.-H. Chen[1], D. Xing[1], H. Daiguji[1], J.-J. Delaunay[1]

[1]School of Engineering, The University of Tokyo, Japan
*corresponding author: jean@mech.t.u-tokyo.ac.jp

Abstract: We report the stimulated emission of a quasi-Bloch surface wave mode guided in a ring made of a gain material. The ring is patterned by UV lithography on a 1D photonic crystal using a dye-doped resist. The reported microlasers exhibit narrow line widths of approximately 0.02 nm.

Integrating coherent light sources on existing surface wave platforms offers tremendous opportunities in the areas of sensing and data processing. Here, we demonstrate a microfabricated coherent light source based on the stimulated emission of a guided Bloch surface wave mode [1].

The proposed Bloch surface wave (BSW) ring laser consists of a thin ring structure made of the gain material on a truncated 1-D photonic crystal. The presented results are shown for a ring (diameter = 100 µm and thickness = 140 nm) made of a SU8 resist doped with the dye rhodamine 6G fabricated by UV lithography on the top of a truncated 1-D photonic crystal consisting of a SiO_2/TiO_2 multilayer. The lasing mode is investigated using mode analysis. Fig 1 (left) shows a typical electric field distribution for a BSW mode (maximum at the layer interfaces between the low and high refractive indices) with an effective refractive index of the mode n_{eff} = 1.38. This structure was optically pumped using a ns pulse laser (532 nm) and lasing was achieved above a pump threshold of 30 µJ/mm^2. Fig 1 (center) exhibits a typical lasing peak series obtained for ring structures sustaining whispering gallery modes. The lasing behavior is confirmed by examining the very narrow full width at half maximum of the emission peaks (0.02 nm) and the pump threshold for lasing. To confirm that this experimental lasing mode corresponds to the simulated BSW mode shown in the left figure, the radiation leaked by the lasing structure is collected from its bottom and analyzed using a back focal plane configuration (Fig. 1 (right) showing both below and above lasing threshold angular distribution). The direction of the light in the mode is analyzed via radiation leakage and corresponds to a numerical aperture 1.32~1.4 (i.e., 1.32 < n_{eff} < 1.4), as seen in the ring position for the case above the lasing threshold. This confirms that the observed lasing mode corresponds to the BSW mode having n_{eff} = 1.38 and validates the presented BSW ring laser principle.

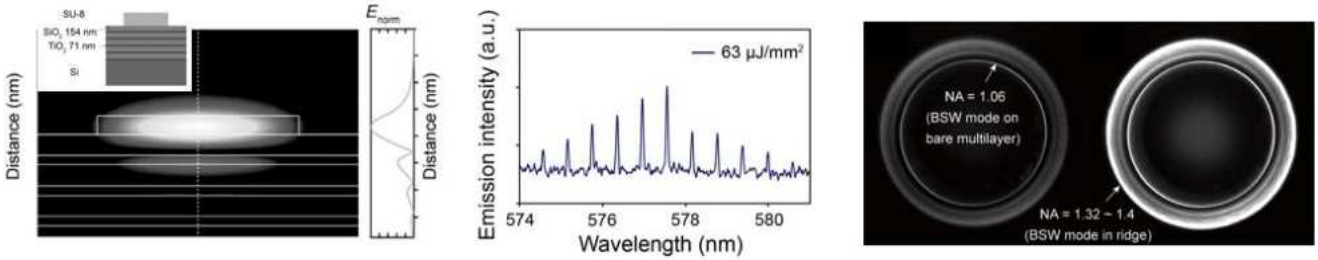


Figure 1 (left) Analysis of the lasing mode. (center) Lasing results exhibiting whispering gallery mode behavior. (right) Leakage radiation pattern in the back focal plane below and above the lasing threshold confirming the effective index of the lasing mode.

Detailed discussion about the quality factor of the employed mode as well as potential applications of these microlasers will be presented.

Acknowledgments: Supported by JSPS KAKENHI (JP20F40045, JP21H01383, JP20H02197) and Advanced Characterization Nanotechnology Platform of the University of Tokyo (JPMXP09F-21-UT-0021).

Reference

1. Y.-C. Lee, Y.-L. Ho, B.-W. Lin, M.-H. Chen, D. Xing, H. Daiguji, J.-J. Delaunay “High-Q lasing via all-dielectric Bloch-surface-wave platform,” Nature Communications, Vol. 14, 64458, 2023.

Tailoring the optical properties of 3D photonic crystals coated with Aluminum Zinc Oxide in the telecommunication wavelength

D. Ladika[1*], A. Theodosi[1,2], O. Tsilipakos[3], A. Klini[1], P.A. Loukakos[1] , M. Kafesaki[1,2], M. Farsari[1], D. Gray[1]

[1] Institute of Electronic Structure and Laser, Foundation for Research and Technology-Hellas, Heraklion, Crete, Greece

[2] Department of Materials Science and Technology, University of Crete, Greece

[3] Theoretical and Physical Chemistry Institute, National Hellenic Research Foundation, GR-11635 Athens, Greece

[*]Corresponding author: dladika@iesl.forth.gr

Abstract: Introducing a novel approach to customize the optical properties of a transparent conductive oxide that exhibits epsilon-near-zero (ENZ) behavior in three dimensions. The combination of 3D photonic crystals with the ENZ material yields a promising 3D device with static optical properties suitable for telecommunication applications.

The emerging photonic materials, have gained significant attention the last decades (i.e., Transparent Conductive Oxides-TCOs), which possess unique properties such as tailorability, large damage thresholds and epsilon-near- zero behavior[1]. In optical device design, tailoring the optical and especially the ENZ behavior by manipulating the properties of such materials plays a crucial role in achieving the desired functionalities. In general, ENZ materials, with their ability to increase light-matter interaction and effectively confine light within sub-wavelength structures, offer substantial advantages for optoelectronic devices[2].

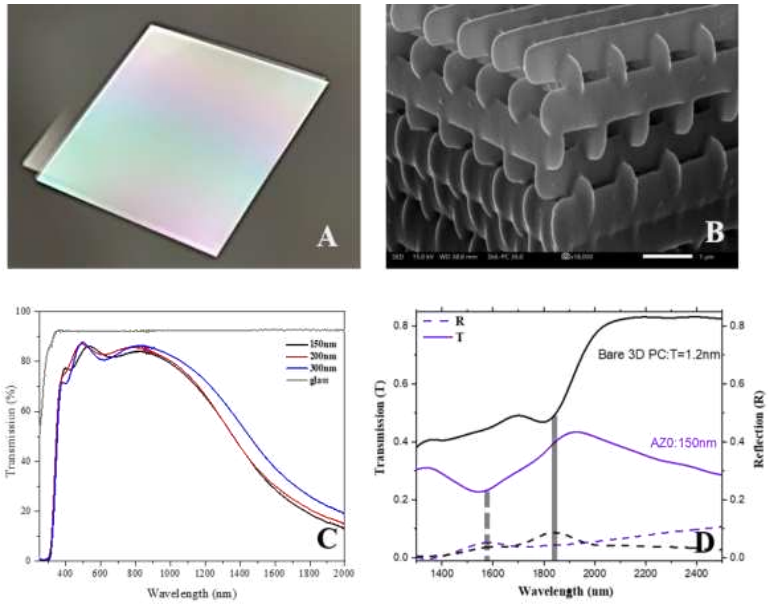


Figure 1 A. AZO thin film, **B**. SEM image of 3D PC coated with AZO thin film, **C**. Transmission spectra of the AZO thin films with 150,200,300nm and **D**. Transmission (solid line) and reflection (dashed line) measurements of the 1.2μμm inlayer periodicity 3D PC without(black) and with 150nm AZO thin film(purple) coating

Aluminum Zinc Oxide (AZO) is one of the preferable TCOs studied for its ENZ behavior, showing promise in nonlinear optics, and tunable nanophotonic devices, among others[3][4]. Until recently, AZO has mainly been studied as thin films or coatings in one- or two-dimensional structures. These studies revealed that altering AZO's thickness, carrier concentration, doping, or substrates can enhance different properties, both linear and nonlinear.

Another widely studied way of light-matter interaction is the photonic crystal environment. Photonic crystals (PCs) are divided in one-, two- and three-dimensional structures. Specifically, PCs are consisting of different dielectrics with different refractive indices that are periodically arranged to provide a photonic bandgap[5].

In this work, a novel approach is introduced to customize the ENZ behavior of AZO in a three-dimensional environment. The method involves developing 3D photonic crystals (PCs), through Multiphoton Lithography (Figure 1B), and subsequently coating them with AZO thin films (Fig. 1B), using the Pulsed Laser Deposition method. The shift observed in the bandgap of the AZO-coated 3D PCs (Fig. 1D) demonstrates the tailored static optical properties of AZO in three dimensions. This successful development of 3D PCs coated with AZO further underscores the synergy between the extraordinary optical properties of well-investigated 3D PCs and the morphological, structural, and optical characteristics of AZO thin films (Fig.1A, C) within the ENZ regime. This outcome is new promising platform for applications in photonics and tunable photonics, especially in the telecommunication band.

References

[1] S. Saha *et al.*, "Tailoring the Thickness-Dependent Optical Properties of Conducting Nitrides and Oxides for Epsilon-Near-Zero-Enhanced Photonic Applications," *Adv. Mater.*, 2022, doi: 10.1002/adma.202109546.

[2] E. G. Carnemolla *et al.*, "Degenerate optical nonlinear enhancement in epsilon-near-zero transparent conducting oxides," *Opt. Mater. Express*, vol. 8, no. 11, p. 3392, 2018, doi: 10.1364/ome.8.003392.

[3] A. Anopchenko, "Atomic layer deposition of ultra-thin and smooth Al-doped ZnO for zero-index photonics," *Mater. Res. Express*, vol. 5, no. 1, 2018, doi: 10.1088/2053-1591/aaa653.

[4] M. Ferrera, "Transparent conducting oxides: from all-dielectric plasmonics to a new paradigm in integrated photonics," *Adv. Opt. Photonics, Vol. 14, Issue 2, pp. 148-208*, vol. 14, no. 2, pp. 148–208, Jun. 2022, doi: 10.1364/AOP.448391.

[5] I. Sakellari *et al.*, "Quantum dot based 3D printed woodpile photonic crystals tuned for the visible," *Nanoscale Adv.*, vol. 1, no. 9, pp. 3413–3423, 2019, doi: 10.1039/c9na00357f.

A Compact Silicon Photonic Crystal Spectrometer with Unprecedented Resolution

Takasumi Tanabe*, Junnosuke Kokubu, Ryo Sugano, and Jinwei Zhang

Department of Electronics and Electrical Engineering, Faculty of Science and Technology, Keio University, Japan
*corresponding author: takasumi@elec.keio.ac.jp

Abstract: We introduce a compact, cost-effective silicon photonic crystal spectrometer with unparalleled resolution (0.01 nm for single, <0.03 nm for multiple wavelengths), leveraging a chirped waveguide for enhanced precision.

Advancements in photonic nanostructures have led to more efficient devices. We have developed a small (740×9 μm^2) silicon (Si) photonic crystal spectrometer that greatly exceeds traditional resolution limits by employing a chirped waveguide that enhances resolution through light scattering and random localization. The need for such compact, cost-effective, high-resolution spectrometers is growing, particularly in optical communications and smart manufacturing. Traditional, larger spectrometers face a size versus resolution trade-off that our approach overcomes. By capitalizing on nanophotonic technologies and the inherent randomness in photonic crystal structures, we bypass common fabrication precision issues, offering a significantly miniaturized spectrometer without sacrificing performance, thus providing a novel solution to a longstanding challenge in photonics.

The core of our spectrometer design is a chirped Si photonic crystal (PhC) waveguide, which narrows as light moves through it, with a total size of 740×9 μm^2. The PhC has a constant lattice spacing of 420 nm and a hole diameter of 262.3 nm. The Si slab is 220 nm thick and clad by SiO_2. This waveguide begins wider than standard (W1.05) and tapers slightly narrower (W0.99), creating a chirped structure. This design causes light of certain wavelengths to scatter at specific locations, determined by the waveguide's narrowing mode gap frequencies. However, due to fabrication limits, this tapering happens in 2 nm increments, leading to an essential design resolution of 1.6 nm at telecom wavelengths, which may not meet all application needs.

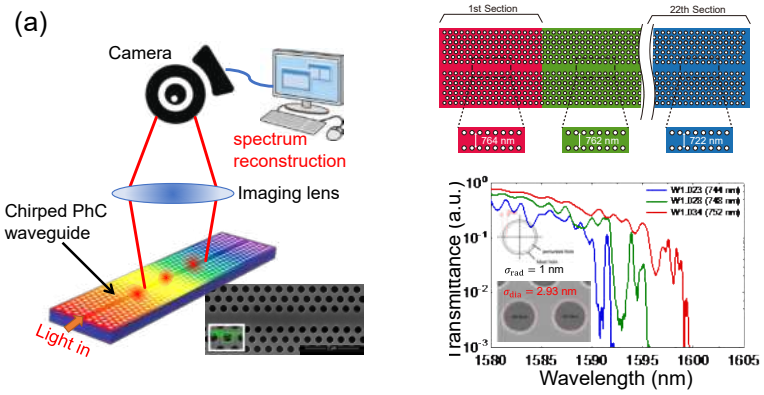


Fig. 1: (a) Experimental setup. (b) Device structure (chirped PhC waveguide). (c) Transmittance spectrum of PhC waveguides with different widths containing randomness.

To overcome this, we leverage natural randomness in the fabrication process, where slight variations in the air holes' positions, diameters, and shapes induce random light trapping (Anderson localization). This randomness produces high-quality (Q) resonances, allowing us to detect slight wavelength differences. We use

this inherent structural variability to enhance resolution beyond the 2 nm design limit, effectively using randomness as a tool rather than a hindrance. Calibration is crucial due to the variability introduced by this randomness, necessitating a detailed database of localization patterns for different wavelengths. This calibration process is similar to that of conventional spectrometers but exploits the unique properties of our design to achieve superior resolution.

Our experimental setup involved designing and fabricating a device using standard Si photonics processes. We first measured the transmittance spectrum across various waveguide widths, confirming the expected mode gap shifts and observing resonant peaks with quality factors ranging from 10^4 to 10^5. We captured light localization patterns at different single wavelengths using an IR camera, showcasing the device's ability to resolve wavelengths with high precision.

We developed a calibration process for single wavelength reconstruction by scanning across a wavelength range and recording IR camera images. It generated a calibration matrix to reconstruct the input spectrum from observed light patterns. Employing a cost minimization algorithm, including the Fast Iterative Shrinkage-Thresholding Algorithm (FISTA), allowed us to achieve a wavelength accuracy of ±0.01 nm, surpassing the design resolution of 1.6 nm. Our results demonstrate high precision over a broad bandwidth, with a significant portion of measurements falling within this narrow error margin.

We also explored multi-wavelength reconstruction, assuming the superposition of intensity patterns for inputs of different wavelengths. We confirmed through experimental and simulation validations that our device and reconstruction algorithms can accurately decipher multi-wavelength information, even distinguishing wavelengths separated by as little as 0.01 nm with a modest error. This capability extends to reconstructing continuous spectra, highlighting the device's versatility and high resolution in practical applications.

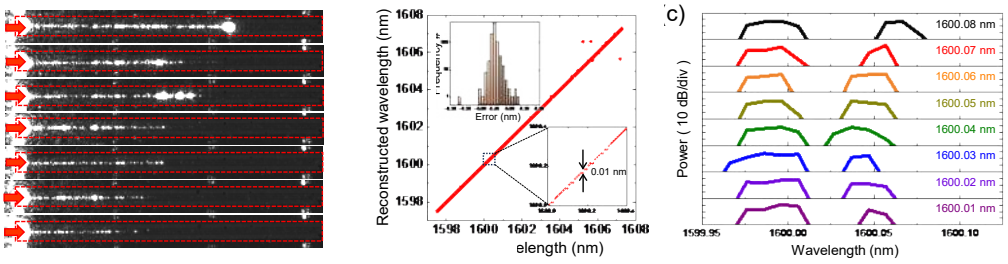


Fig. 2: (a) IR camera image taken from the top of the slab when a single wavelength laser is input from the left. (b) Reconstructed wavelength for single input wavelength with our device. The wavelength accuracy is 0.01 nm. (c) Reconstructed spectra for multi-wavelength input. One wavelength is fixed at 1600.00 nm, and the other is scanned from 1600.01 to 1600.08 nm.

In summary, our compact spectrometer demonstrates exceptional wavelength accuracy of ±0.01 nm for single-wavelength inputs and a resolution of 0.03 nm for multi-wavelength inputs within a minimal footprint. The innovation of leveraging inherent structural randomness and a precisely engineered chirped structure surpasses the anticipated resolution limit of 1.6 nm. This approach challenges the traditional view of fabrication errors as obstacles and showcases a method to exploit these variances to enhance device performance. This breakthrough offers promising directions for advancing nanophotonic devices, suggesting new strategies for improving precision and efficiency in photonics technology.

Controlling the radiation space and wavelength with MIM metasurface in mid infrared wavelength

Y. Nishijima[1,2,3,4,*], T. Kawaida[1], M. Tanaka[1], K. Sekiya[1]

1. *Department of Electrical and Computer Engineering, Graduate School of Engineering,*
2. *Yokohama National University, 79-5 Tokiwadai, Hodogaya-ku*
3. *Institute of Advanced SciencesYokohama National University, 79-5 Tokiwadai, Hodogaya-ku*
4. *Institute for Multidisciplinary Sciences Yokohama National University, 79-5 Tokiwadai, Hodogaya-ku*
5. *PRESTO, JST*

**nishijima-yoshiaki-sp@ynu.ac.jp*

Abstract: We have realized the thermal radiation control of MIM metasurface using the concept of metalens. The reflection phase was obtained FDTD simulation and fabricated the metasurface by electron beam lithography. The focal spot of thermal radiation can be seen with desired focal point.

1. Introduction

The absorption metasurface, consisting of Metal – Insulator – Metal nanostructures (MIM), has a unique optical property. The bottom metal film layer prohibits light transmission; The incident light is strongly localized in the insulator layer and absorbed by the MIM metasurface. At the same time, due to Kirchhoff's law of thermal radiation, which indicates the equivalence of absorption and emission efficiency, the absorption metasurface became the thermal radiation metasurface. We have developed MIM metasurfaces as mid-infrared light sources and other sensing applications [1-7]. Due to these optical properties, MIM metasurface is focused as the mid-infrared light source for infrared optical sensors. However, the thermal radiation pattern for far-field from the conventional radiative metasurface is spread out over approximately 120 degrees. This will lose the amount of light that is taken into the detectors. To resolve this problem, we tried to realize the thermal radiation control without a lens and the other optical components, based on the metalen technology.

2. Experiments

2-1. FDTD simulations for design of metasurface

The design of the metasurface was optimized using FDTD (Finite differential time domain) simulation with commercial software (Ansys Lumerical FDTD solver). The components of MIM structures were set with gold-SiO2-gold nanodisk; all permittivity was set to Palik's data. The thickness of the gold film was 200 nm, SiO2 was 150 nm, and a gold nanodisk thickness was 50 nm. In addition, The radius of the gold nanodisk was adjusted from 0.5 μm to 1.3 μm, and the period of the simulation region was set to 3 μm with periodic boundary conditions. The phase of optical reflection at the desired wavelength was monitored with a power monitor, which was put above the plane wave light source. There is no way to calculate thermal radiation directly using the FDTD method. Therefore, in this study, we have designed a total metasurface based on the phase of reflection light.

2-2. Fabrication of metasurface

Metasurface fabrication using electron beam lithography was performed as described elsewhere in more detail based on a previous report. In short, 5 nm Cr and 200 nm Au were thermal deposited on a silicon substrate first. After depositing 5 nm Cr, a set of samples with SiO2 layers from 100 nm to 500 nm (with a 100 nm step)
were deposited by electron-beam (EB) evaporation. After, an electron beam lithography (EBL) resist was spin-coated, and EBL exposure was performed to define the top-layer metallic nanostructures. After

development, Cr 5 nm and various metals were deposited, and lift-off followed.

2-3. Experimental setup for thermal radiation pattern

Micro spectroscopy was used for spectral characterization of meta-surface MIM structures, which had a footprint with a 300 mm cross-section. A Fourier transform infrared (FT-IR) spectrometer and a microscope unit (FTIR-6000 and IRT-1000, JASCCO) were used to measure the reflection spectra in the mid-infrared region. Film of Au of 350 nm thickness was used for the reflection reference, with 98% reflectance in the entire mid-infrared area. Thermal radiation was measured using the FTIR system. Compact FTIR (ARCOptix) was connected to collimation mirrors and reflection objective lenses. The sample was set on the piezo heater and in the x, y, and z tri-axial stages.

3. Results and discussions

The metasurface was fabricated with the uniform disk, f = 5 mm, f = 7.5 mm, and f = 10 mm setting with a 5 mm total disk area. From the reflection spectra, absorption peaks have appeared around 5 mm. The uniform metasurface was set to minimize the reflection at 5 mm. Due to the different sizes of disks, the focusing metasurface has lower absorption compared to the uniform disk metasurface. The thermal radiation results show apparently focusing features in the designed focal length except for the uniform wavelength.

4. Conclusions

We first reported controlling the thermal radiation of the MIM metasurface using the metalens concept. The FDTD simulation results successfully controlled the focal spot. This means that the reflection phase should have a high correlation with that of the phase of thermal radiation. The performance of the metasurface is not completely optimized, but the directional control radiation should be applied to the mid-infrared sensors, energy harvesting, radiation cooling, and so on.

5. Acknowledgement

YN is grateful for partial support from the Japan Society for the Promotion of Science (JSPS), Grants-in-Aid for Scientific Research, and JSPS Bilateral Joint Research Projects between Japan and Lithuania. This work was partially supported by PRESTO, Japan Science and Technology Agency (JST) (JPMJPR22B6).

6. References

[1] Y. Nishijima, A. Balčytis, S. Naganuma, G. Seniutinas, S. Juodkazis, “Kirchhoff’s metasurfaces towards efficient photo-thermal energy conversion,” *Scientific reports*, **9**, 8284, 2019

[2] N. To, S. Juodkazis, Y. Nishijima, “Detailed Experiment-Theory Comparison of Mid-Infrared Metasurface Perfect Absorbers,” *Micromachines*, **11**, 409, 2020

[3] Y. Nishijima, S. Morimoto, A. Balcytis, T. Hashizume, R. Matsubara, A. Kubono, N. To, R. Meguya, J. Morikawa, S. Juodkazis, “Coupling of molecular vibration and metasurface modes for efficient mid-infrared emission,” *Journal of Materials Chemistry C*, **10**, 451-462, 2022.

[4] Y. Nishijima, N. To, A. Balcytis, and S. Juodkazis, “Absorption and scattering in perfect thermal radiation absorber-emitter metasurfaces,” *Optics Express*, **30**, 4058-4070, 2022.

[5] Y. Nisijima, S. Judkazis, “The tunable coupling between metasurface and molecular vibration towards the platform of spectral analysis”, *Bulletin of the Chemical Society of Japan*, **95**, 1318–1324, 2022.

[6] Y. Nishijima, S. Kimura, Y. Takeshima, and S. Jodkazis, “Metasurfaces as energy valves for sustainable energy management,” *Micromachines*, **13**, 1769, 2022

[7] Y. Nishijima, S. Judkazis, “Control of vibration-metasurface coupling at mid-infrared spectral window for inorganic thermal emitters”, *Bulletin of the Chemical Society of Japan,* **95**, 1411–1418, 2022.

Origin of high transmission via sharp bends of photonic-crystal waveguides with and without inversion symmetry

W. Dai[1,2], T. Yoda[1,2], Y. Moritake[1], and M. Notomi[1,2*]

[1]Department of Physics, Tokyo Institute of Technology, Japan
[2]NTT Basic Research Laboratories, NTT Corporation, Japan
[*]corresponding author: notomi@phys.titech.ac.jp

Abstract: We investigate transmission properties via sharp bends of various triangular- and square-lattice photonic-crystal waveguides including valley-photonic waveguides, and have found that high transmission appears for some type of bands and interface configurations, irrespective of the inversion symmetry. This phenomenon is governed by bright circularly-polarized singular points around the bending interface.

The bending loss is one of the troublesome issues for nanophotonic integrated circuits, especially for photonic crystal waveguides. Concerning this issue, valley photonics has attracted much attention because many reports showed that one can achieve broad-band high transmission via sharp bends in valley-photonic waveguides without any local modification around the bending corners. Since the back reflection would be suppressed in valley-photonic waveguides when the valley spin is preserved, this property has been regarded as the result of the valley properties. However, it is not clear whether the valley spin could be really preserved at the bending corners.

In this study, we investigate a systematic model structure for 120-degree bends based on a triangular-lattice air-hole photonic crystal slab shown in Fig. 1, which covers various types of interfaces with and without the inversion symmetry by varying the shifting parameter *S* and the hole shape. This model represents various valley-photonic waveguides with broken inversion symmetry and their counter-parts having the inversion symmetry. We confirmed that this model structure shows nontrivial Berry curvature when the inversion symmetry is broken, and thus should have valley properties. As a result of numerical electromagnetic simulations, we found that broad-band high bend transmission appears for a certain value of *S*. An important finding is that the appearance of the high bend transmission is solely determined by the shifting parameter S and does NOT depend on the existence of the inversion symmetry.

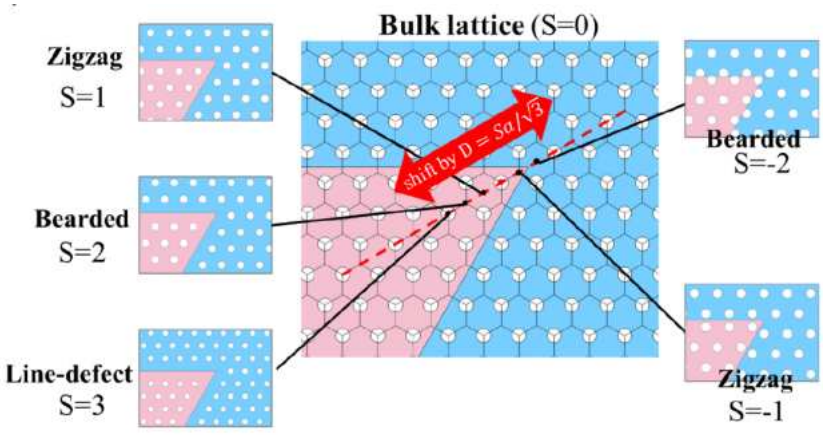


Fig. 1. Structure model for 120-degree bends in triangular-lattice photonic crystal waveguides.

Previously, it has been reported that glide-symmetric valley photonic waveguides show sharp bend transmission contrast across the degeneracy

point at the Brillouin zone boundary, which was argued as the valley property of each band[1]. In our simulation, we have observed similar high transmission contrast in our model structures when the structure has a glide-symmetry. Interestingly, this property also does NOT depend on the existence of the inversion symmetry. Since the essence of the valley properties arises from the existence of the inversion symmetry, the present result indicates that high transmission does not originate from the valley properties. We performed optical transmission measurements for the proposed model with various parameter S fabricated in Si photonic crystal slabs, and confirmed that the experiment shows essentially the same results.

Next, we investigate 90-degree bends of square-lattice photonic crystal waveguides with a glide symmetry shown in Fig. 2. Similar to the cases of glide-symmetric triangular lattices, the existence of the degeneracy point in square lattices is protected by the glide symmetry. Our numerical studies have shown that this structure shows a very similar high bending transmission contrast across the degeneracy point. It would be worth noting that this square-lattice waveguide posses the inversion symmetry and does not have valley properties at all.

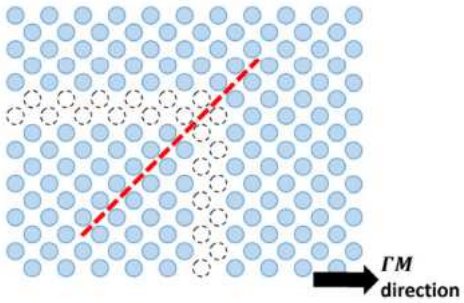


Fig. 2. Structure model for 90-degree bends in square-lattice photonic crystals.

In summary, we have theoretically and experimentally confirmed that broad-band high bend transmission, including interesting transmission contrast across the degeneracy point, appears in a wide range of configurations, irrespective to the existence of the inversion symmetry[2,3]. Concerning the physical mechanism of the high transmission, we found that the bending transmission is highly affected by the circularly-polarized topological singular points. In both cases for triangular- and square-lattice photonic crystal waveguides, we found that high bend transmission appears when the bright circularly-polarized topological singular points exist around the bending interface. We discuss more in detail about the effect of circularly-polarized singular points in the conference.

References

1. H. Yoshimi, T. Yamaguchi, and Y. Ota et al., “Slow light waveguides in topological valley photonic crystals,” Opt. Lett. 45, 2648–2651 (2020).
2. Wei Dai, Taiki Yoda, Yuto Moritake, and Masaya Notomi, “Large transmittance contrast via 90-degree sharp bends in square lattice glide-symmetric photonic crystal waveguides”, Optics Express, Vol. 32, pp. 3946-3958 (2024).
3. W. Dai, T. Yoda, and Y. Moritake et al., “High transmission in 120-degree sharp bends of inversion-symmetric and inversion-asymmetric photonic crystal waveguides,” arXiv:2310.17487

Attosecond Electron Microscopy

Joel Kuttruff, David Nabben, Levin Stolz, Andrey Ryabov, Peter Baum

Department of Physics, University of Konstanz, Universitaetsstrasse 10, 78464 Konstanz, Germany
corresponding author: peter.baum@uni-konstanz.de

Abstract: We introduce attosecond transmission electron microscopy as a method to probe the electromagnetic near-fields of nanostructures in space and time.

Introduction. When light strikes a material, the initial interaction involves the reaction of the material's bound or free electrons to the light wave's rapidly changing electric field cycles. This movement is influenced by the material's atomic and nanoscale structure and properties, which act as a restoring force. Consequently, the behavior of materials on extremely small and fast spatial and temporal scales plays a crucial role in determining their macroscopic properties. Gaining insights into and manipulating the motion of electrons at scales smaller than a light cycle period and wavelength—specifically, attoseconds and nanometers—are critical for advancements in modern optics and nanophotonics. However, progress in these areas significantly depends on our capacity to observe and quantify the electromagnetic aspect of material responses over space and time.

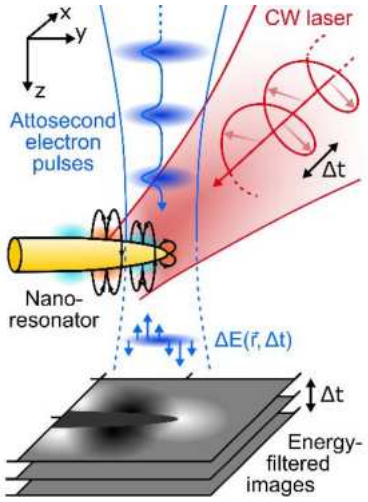


Fig. 1. Attosecond electron microscopy. A continuous-wave laser (red) with tailored polarization excites a nanophotonic material (yellow). Attosecond electron pulses (blue) probe the time-frozen electric fields as a function of space ($\vec{r}$) and delay time (Δt). Light-cycle contrast appears via spatiotemporal electron energy changes $\Delta E(\vec{r}, \Delta t)$.

Methods. Here we present the advancement of transmission electron microscopy to achieve attosecond temporal resolution, thus enabling the visualization of optical field oscillations on their fundamental dimensions [1]. We use a continuous-wave laser with 1064 nm wavelength to periodically speed up and slow down the electron beam in a transmission electron microscope. This process creates high-contrast attosecond pulses (Figure 1, illustrated in blue). The sample under investigation, such as a nanophotonic resonator (depicted in yellow), is excited by the same continuous-wave laser (shown in red). The electron pulses used for probing (blue), which are synchronized with the laser phase and have sub-cycle duration, allow the local electromagnetic fields within and around the sample (shown in orange/cyan) to seem virtually static. Depending on the spatial location $\vec{r}$ and arrival time Δt with respect to the light cycle, the electron wave packets experience a gain or loss of kinetic energy $\Delta E(\vec{r}, t)$ by travelling through the electric fields around the nanoresonator. The energy change is captured by a CMOS-based camera system equipped with a post-column energy filter. By varying the time delay Δt we can create a dynamic, spatio-temporal movie that showcases the near-field response of the sample in both real space and time, at the attosecond and nanometer scale.

Results. We explored using helical light to influence the spatiotemporal chirality of near fields around a plasmonic needle tip, modified with a slit at the apex using a focused ion beam (Fig. 2a). The circularly polarized laser targeted the needle asymmetrically at 45° angles, generating distinct plasmonic field cycles along the needle. As

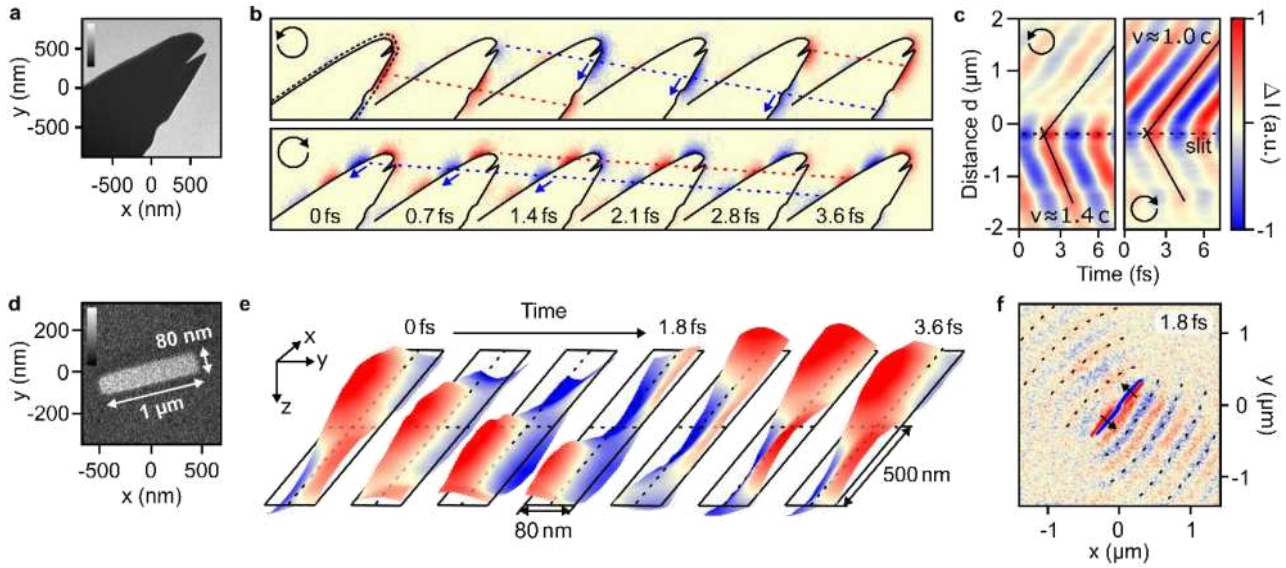


Fig. 2. Dynamics of the electric fields in nanoresonators. a, Image of the modified tungsten nanotip. **b,** Time-resolved electron energy changes for left-circular (upper panel) and right-circular excitation light (lower panel). The dashed lines and arrows visualize the propagation dynamics of the positive (red) and negative (blue) field cycles. **c,** Measured electron energy gain along the surface of the nanotip (dashed black line of Fig. 2b) as a function of time and distance from the tip. Dashed line, location of the nanoslit; black lines, phase velocities. **d,** Image of the slit resonator, milled into a freestanding 200-nm thick silicon membrane. **e,** Measured electron energy changes as a function of space and time. **f,** A snapshot at t = 1.8 fs shows the re-radiation of the nanoresonator into the membrane material. The black dashed lines highlight the propagating wave front of the buried field cycles.

shown in the dynamic snapshots (Fig. 2b), the plasmonic fields move from the needle's cut to its shaft with varying periodicity and phase velocity, depending on the circular polarization direction. The dynamics were directional, favoring the needle's upper side for left-handed polarization and the lower side for right-handed polarization, which we ascribe to a dynamic electron-surfing effect. Analysis of electron energy changes around the needle (Fig. 2c) revealed phase velocities of (1.4±0.1) c on the right/lower side and (1.0±0.1) c on the left/upper side, attributable to the interplay between the needle's plasmon polariton wave and the excitation wave. The interaction creates a superluminal phase velocity on the laser-facing side and a subluminal velocity on the opposite side. In a second experiment, we examined the spatiotemporal behavior of dielectric nanoresonators in a 200-nm thick silicon membrane (Fig. 2d) with dimensions tailored to the laser wavelength, allowing for formation of higher-order modes. The laser's 45° azimuthal angle and parallel polarization to the resonator's short axis allowed us to observe temporal shifts between quadrupolar and dipolar field distributions, indicating the interaction of phase-shifted modes (Fig. 2e). Notably, the guided waves' complex re-radiation pattern, trapped by silicon's high refractive index, was visualized using light-cycle contrast microscopy (Fig. 2f), highlighting its capability to also reveal internal field dynamics within materials.

Summary. In summary, our experiments demonstrate that attosecond transmission electron microscopy offers a powerful and non-invasive technique for capturing the intricate dynamics of light-matter interactions on a fundamental spatial and temporal scale, holding significant promise for pushing the boundaries of modern optics and nanophotonics into new areas of application.

References

1. Nabben, D., Kuttruff, J., Stolz, L., Ryabov, A., Baum, P. Attosecond electron microscopy of sub-cycle optical dynamics. Nature 619, 63–67 (2023).

In-Operando Optical Spectroscopy of Field-Effect-Gated Transparent Conductive Oxides

M. Magnozzi[1,*], M. Sygletou[1], S. Colace[1], R. Magrin Maffei[2,3], S. Benedetti[3], A. di Bona[3], A. Petrov[4], P. Torelli[4], E. Bellingeri[5], M. Canepa[1] and F. Bisio[5]

[1]OptMatLab, Dipartimento di Fisica, Università di Genova, via Dodecaneso 33, 16146 Genova, Italy
[2] Dipartimento di Scienze Fisiche Informatiche Matematiche, Università di Modena e Reggio Emilia, via Campi 213/a, 41125 Modena, Italy
[3] CNR-NANO, via Campi 213/a, 41125 Modena, Italy
[4] CNR-IOM, Laboratorio TASC, AREA Science Park, Basovizza, 34149 Trieste, Italy
[5] CNR-SPIN, C.so Perrone 24, 16152 Genova, Italy
[*]corresponding author: magnozzi@fisica.unige.it

Abstract: Transparent conductive oxides (TCOs) are often exploited as active optical materials in field-effect configuration. Voltage-driven charge accumulation/ depletion in TCOs allows to tune their optical response. We report an in-operando investigation of TCOs under field effect, exploiting spectroscopic ellipsometry and optical modelling to reconstruct the charge-density profile within the materials.

Active photonics materials are capable of changing their optical properties in response to an external stimulus. In this category, transparent conductive oxides (TCOs) are active optical materials often exploited within field-effect devices, where the voltage-induced charge accumulation or depletion is the physical effect leading to the desired modification of the optical response. In order to understand the role of active photonic materials within devices, it is paramount to assess the microscopic characteristics of the charge-injection/depletion spatial profile. This allows, in turn, to reconstruct the spatial gradients of dielectric function and, ultimately, model and predict the optical response of the active photonic devices.

In this contribution we report an in-operando spectroscopic-ellipsometry (SE) investigation of various active photonic devices under variable applied voltage. The devices under scrutiny are in the form of planar capacitors, with the TCO acting as one of the electrodes. Thanks to a careful modelling of the spatial grading of the optical response of the systems under applied bias, we are able to reconstruct the charge injection/depletion profile within the TCO at the TCO/dielectric interface, and model the corresponding spatial gradient of the dielectric functions.

In Figure 1 we report the data relative to a system based on Al-doped ZnO (AZO). AZO films ≈70 nm thick were grown on STO (110) substrates with the aim of obtaining a large charge modulation. AZO thin films were deposited by pulsed laser ablation (PLD) on 110-oriented 500 μm thick STO. The aluminum content was nominally 0.1%. The STO substrate is an insulating centrosymmetric paraelectric material with a perovskite structure. It exhibits a very large DC permittivity constant, reading ~22000 at 4.2 K. An Ag backgate was realized at the back of the STO. Spectroscopic ellipsometry (SE) experiments were conducted by means of a J.A. Woollam V-VASE ellipsometer. The AZO/STO was mounted in a cryostat with optical viewports (Oxford Instruments Optistat CF-V) at a temperature of 4.2 K (spectral range 0.7−3.2 Ev). The variations of the optical response of the AZO films were investigated by applying an electric field of 2 kV/cm across the STO substrate. The top left and bottom left panels report the ellipsometry spectra $\Psi(\lambda)$ and $\Delta(\lambda)$ (lines) and the respective variations upon applied voltage (symbols).

Upon application of the external voltage, charge is accumulated in the TCO, with areal density:

$$\sigma_e = \frac{\varepsilon_r \varepsilon_0 V_g}{d} \qquad (1)$$

and decay constant λ_D. Here ε_r is the DC dielectric constant of STO, V_g is the applied voltage and d is the STO thickness. In the bottom right panel of Figure 1, we show the experimental data related to the voltage-induced Ψ variation (symbols), along with theoretically-calculated spectra (lines). The theoretical values correspond to different values of spatial decay constants λ_D for the injected/depleted charge inside the TCO, starting from the TCO/dielectric interface. The black line corresponds to uniform charge distribution within the TCO, and clearly does not agree with the experimental data. Varying λ_D (coloured lines) it is possible to optimize the agreement with the experimental data, finding the best value for λ_D =2 nm (green line), that corresponds to the physical decay constant of the injected/depleted charge profile within the TCO [1].

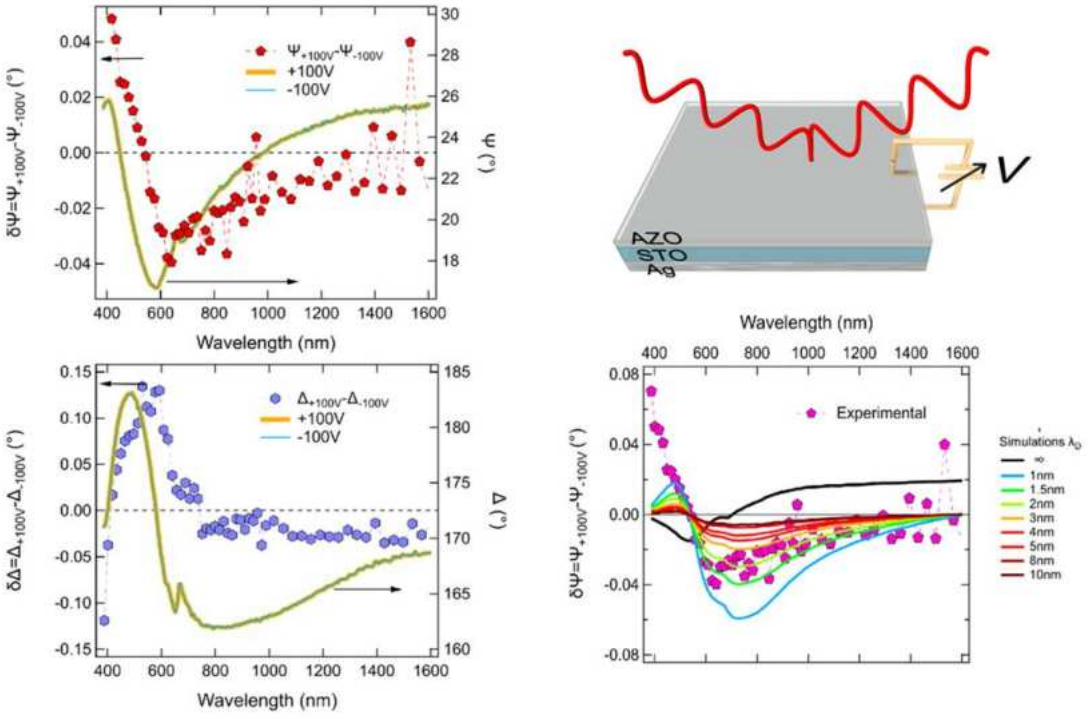


Figure 1: spectroscopic ellipsometry characterization of the AZO/STO/Ag system.

This analysis shows that it is possible to reconstruct the spatial charge profile at buried TCO/dielectric interfaces within active-photonic devices modulated by field effect. This result paves the way for the optimization of the optical response of TCOs in active materials and metamaterials.

References

1. M. Sygletou et al., “In-Operando Optical Spectroscopy of Field-Effect-Gated Al-Doped ZnO” ACS Applied Materials & Interfaces 15 (2), 3112-3118, 2023

Ge-Sb-Te material for applications in photonics

M. V. Rybin[1,2]

[1] School of Physics and Engineering, ITMO University, 197101 St. Petersburg, Russia

[2] Ioffe Institute, 194021 St. Petersburg, Russia
*corresponding author: m.rybin@metalab.ifmo.ru

Abstract: Phase change materials including Ge-Sb-Te (GST) are under extensive studies for applications in photonics. Here is a brief review of recent works reported by our team in this topic: modification of radiation properties, fabrication of GST samples by lithography and other techniques, and study of single GST particle resonators.

During the last decades an intensive research was focused to artificial photonic media, starting from photonic crystals to metamaterial and metasurface-based structures. Advanced photonics exhibited many novel phenomena and photonic-based devices that promise application of the unique properties. One of the important functionality is a reversible post-fabrication modification of the optical response. To this end, nonlinear techniques allow going to the ultrafast but tiny modification of the refractive index [1]. Stronger effects can be achieved by using thermal heating of materials with a phase transition for example vanadium dioxide. However for both of these approaches, the photonic structure retreats to its initial state right almost after the external treatment ceasing.

Recently non-volatile phase change materials (PCM) attracted a remarkable attention of photonic community, because PCM have two metastable phases, which coexist at the normal conditions, but their optical and electric properties are dramatically changed [2]. The three-component Ge, Sb, Te material (GST) is one of the most studied PCM in the context of its application regarding to the electronic devices such as the solid-state memory. The integration of novel materials into photonic structures demands a bunch of conceptual, technological and engineering problems to be solved, i.e. we have to deliver answers to the questions including: Where to place PCM in the photonic structure? How to fabricate the samples? Which additional opportunities do provide the using of PCM? Here I report on our recent research on reversible non-volatile switched photonic based on GST material.

The stoichiometric composition $Ge_2Sb_2Te_5$ has a notably high dielectric index, which is about 15 in visible range and over 35 in the near-infrared telecommunication bands for the crystalline state. The phase change leads to modification of dielectric environment of an emitting center located nearby. So the GST provides unique opportunity to change the photoluminescent properties of a quantum emitter through Purcell effect. We studied the modification of halide perovskite photoluminescence affected by a sublayer of GST, which state was changed by optical means [3]. Another interesting point is the generation of the high-order harmonics by GST itself and its peculiarities on the crystalline and amorphous state [4]. The physics of high-harmonics is completely different from the second and third harmonic generation one. Unlike the latter appearing due to non-harmonic perturbation of the atomic potential, the former is caused by the Bloch currents of carriers in the conductive bands. The fundamental question whether high-harmonics are possible in GST had no evident answer in general and our experimental studies shed the light on it.

Next problem was to fabricate metasurfaces made of GST by a lithography method. We designed an array of

GST rods with rectangular cross-section supporting magnetic dipole mode. This structure has a strong reflection modulation in the telecommunication bands. Then we fabricated the metasurface and examined its properties in experiment, which shows a good agreement with the prediction of the numerical simulation [5].

2.5D metasurfaces has additional degree of freedom in the third dimension. They provide more flexibility for design and adjusting resonance spectral positions. However, they are hardly to be produce by lithography. We used two-photon polymerization to fabricate two lattices of low-index posts with different height. On the second step GST was electro dispersed onto the polymer matrix forming 2.5D metasurface comprising GST nanoparticles at the top of the posts. We examined the response of the metasurface in dependence on GST state by varying the post height difference. In the amorphous GST state, a Mie-type resonance in nanoparticles was tuned to the lattice resonance leading to the electromagnetically induced transparency effect. For the crystalline state of GST, the lattice resonance position was kept, while the Mie resonances were detuned. As a result, we observed an on/off switching in the response of the 2.5D metasurface [6].

Photonic systems including optical antennas require single elements. So we aimed to fabricate and study single GST nanoparticle. We used laser-induced forward transfer technique to produce GST nanospheres by an ablation from the GST thin film on the donor substrate and the nanoparticles were received on the acceptor substrate. The properties of GST nanoparticle were examined by TEM imaging, Raman spectroscopy, and second harmonic generation methods. Also we demonstrated several cycles of reversible GST state switching in single nanoparticles by optical means. The response was controlled by dark-field scattering measurements [7].

To sum up, the integration of GST into meta-optical structures has a great potential for discovering novel fundamental effects. Also, GST has many interesting applications in photonics.

This work was supported by the Russian Scientific Foundation (grant no. 24-12-00170).

References

1. Makarov, S. V. et al. “Light‐Induced Tuning and Reconfiguration of Nanophotonic Structures,” Laser & Photon. Rev., Vol. 11, No. 5, 1700108, 2017.
2. Wuttig, M., Bhaskaran, H. and Taubner, T., “Phase-change materials for non-volatile photonic applications,” Nature Photon., Vol. 11, No. 8, 465–476, 2017.
3. Kushchenko, O.M. et al, “All optically switchable active photonics based on the halide perovskite GST platform,” Laser & Photon. Rev., Vol. 17, No. 8, 2200836, 2023.
4. Korolev, V. et al, “Tunable high-order harmonic generation in GeSbTe nano-films ” (in press).
5. Solomonov, A.I. et al. “Ge-Sb-Te based metasurface with angle-tunable switchable response in the telecom bands,” Phys. Rev. B, Vol. 108, No. 8, 085127, 2023.
6. Solomonov, A.I. et al. “2.5 D switchable metasurfaces,” Opt. & Laser. Tech., Vol. 161, 109122, 2023.
7. Rybin, M.V. et al. “Optically Reconfigurable Spherical Ge-Sb-Te Nanoparticles with Reversible Switching,” Laser & Photon. Rev., Vol. 16, No. 2, 2100253, 2022.

Field homogenization recipe for brain MRI

Kyoungsub Yoon[1], Sunkyu Yu[2], and Namkyoo Park[1*]

[1]Photonic Systems Lab., Dept. of ECE, Seoul National University, Seoul 08826, Korea
[2]Intelligent Wave Systems Lab., Dept. of ECE, Seoul National University, Seoul 08826, Korea
[*]corresponding author: nkpark@snu.ac.kr

Abstract: We present the systematic design of cylindrical metasurfaces that provide the designer wavefront for the ultrahigh field brain MRI. We achieve substantially improved B_1^+ whole brain homogeneity, implying the solution for the issue which has persisted in the past 20 years.

The ultrahigh field (UHF) brain MRI with static magnetic field B_0 over 7T is widely used in the diagnostics of Alzheimer, Parkinson disease, and multiple sclerosis lesions [1]. However, in the UHF MRI regime, the wavelength of the B_1^+ field in the tissue becomes smaller than the human head, leading to the B_1^+ inhomogeneity arising from the modal interference. As B_1^+ field homogenization is essential for high signal-to-noise ratio and uniform imaging contrast, the active parallel RF transmission approach [2] and the passive method based on high permittivity materials [3] have been suggested for the mitigation of B_1^+ inhomogeneity. However, the mesoscopic nature of the participating elements in UHF MRI hindered sufficient *volume* homogenization so far [2-4]. Here, we tackle this problem by systematically controlling the scattering patterns. The solution is confirmed with the full-wave analysis utilizing realistic human models. Our technique constitutes the successful solid approach for the homogenization problem, which has been persistent in the past 20 years. In the talk, the application of metasurfaces will be discussed.

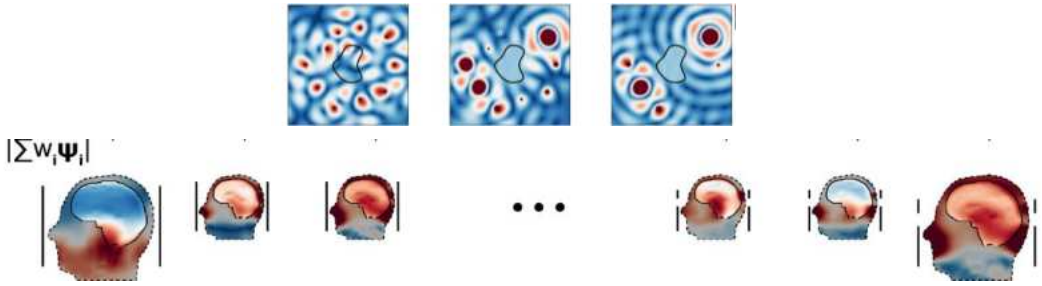


Figure 1. Top. The proposed concept, showing the evolution of scatterer-based field homogenization. Bottom: The B_1^+ field evolution in the brain, obtained from the optimization process.

References

1. Van der Kolk, A. G., Hendrikse, J., Zwanenburg, J. J., Visser, F., and Luijten, P. R. “Clinical applications of 7 T MRI in the brain,” Eur J Radiol, Vol. 82, Iss. 5, 708–718, 2013.
2. Deniz, C. M. “Parallel transmission for ultrahigh field MRI.” Top Magn Reson Imaging, Vol. 28, No. 3, 159-171, 2019.
3. Van Gemert, J., Brink, W., Webb, A., and Remis, R., “High-permittivity pad design tool for 7T neuroimaging and 3T body imaging.”, Magn Reson Med, Vol. 81, Iss. 5, 3370-3378, 2019.
4. Park, M., Noh, H., and Park, N. “Mitigation of B_1^+ inhomogeneity for ultra-high-field magnetic resonance imaging: hybrid mode shaping with auxiliary EM potential.” Sci. Rep., Vol. 10, No. 11752, 2020.

Superoscillatory tweezer arrays for subwavelength trapping and manipulation of cold atoms.

V. Mancois[1*], K. Lim[1], H.J. Wu[2], N.I. Zheludev[3], Y.J. Chen[1] and D. Wilkowski[1,4,5]

[1]Centre for Disruptive Photonic Technologies, Nanyang Technological University, Singapore 637371, Singapore
[2]Wang Da-Heng Center, HLJ Key Laboratory of Quantum Control, Harbin University of Science and Technology, Harbin, China
[3]Optoelectronics Research Centre, University of Southampton, Southampton, UK
[4]Centre for Quantum Technologies, National University of Singapore, 117543 Singapore, Singapore.
[5]MajuLab, International Joint Research Unit IRL 3654, CNRS, Université Côte d'Azur, Sorbonne Université, National University of Singapore, Nanyang Technological University, Singapore, Singapore.

[*]Corresponding author: vincent.mancois@ntu.edu.sg

Abstract: Spatial control of atoms with subwavelength accuracy is a crucial tool for quantum computing and quantum simulations. Using superoscillatory structured light we plan on extending the recent work on single atom subwavelength trapping to few atoms superoscillatory tweezer arrays, where trap sizes and interdistances is dynamically tuned below diffraction limit.

Tweezer arrays of neutral atoms are a strong candidate for making a viable quantum computer. They however require the loading and rearrangement of individual atoms in the register at the beginning of each computing cycle. After rearranging the atoms in the array, the individual qubits -encoded into the atom electronic state- can be addressed selectively via shining a laser onto them to perform the different gates required. The duration of a single computing cycle is then limited by 1) the initial random loading, 2) the rearrangement and 3) the sequence of quantum gates. State-of-the art neutral atoms arrays use high numerical aperture lenses in vacuum to minimize the lattice parameter [1], effectively reducing the time for rearranging and increasing the qubit-qubit coupling, i.e. reducing the laser power and duration required for the gates. It is thus important to continue looking for smaller lattice parameters to relief constraints on the laser system during the rearrangement and computing steps. This idea is also present in quantum simulation with neutral atoms, where one wishes to control the relative strength between tunneling and interaction in a generic Hamiltonian. Having a dynamically tunable lattice parameter for such a system is also very exciting and promise to reveal more of the phase diagram.

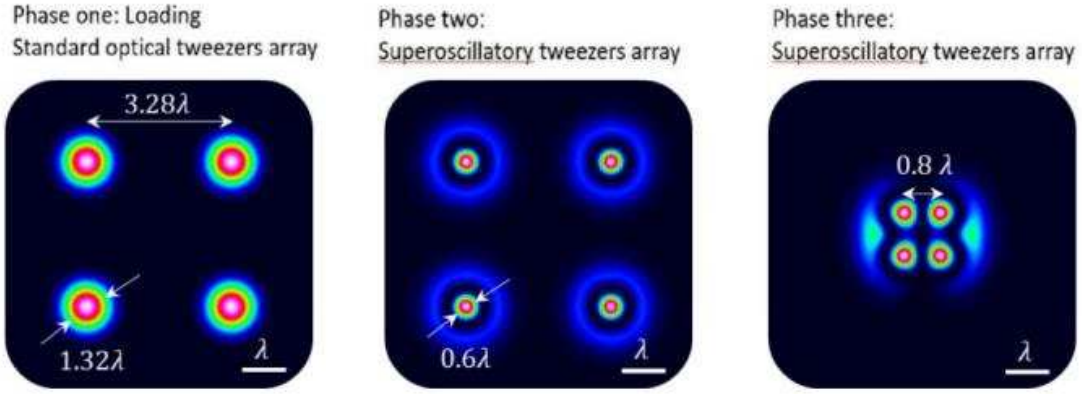


Figure 1 Three-steps loading of four site tweezer array and subsequent transfer to subwavelength trap size and interdistances. Steps are quasi-adiabatically connected using spatial light modulators.

We have previously demonstrated the trapping of a single atom in a sub-wavelength superoscillatory tweezer [2]. Our next objective is to extend this concept to few atoms (2 to 4) and demonstrate the loading and deterministic rearrangement of a superoscillatory tweezer array of a few sub-Doppler cooled thermal atoms. Fig.1 shows such the loading sequence, where initially 4 atoms are loaded in a standard tweezer array then transferred *in situ* in the superoscillatory array and finally brought closer to each other at subwavelength distances. By controlling the relative intensity of the tweezers and lowering the central potential barrier, we can classically, *i.e.* thermally rearrange the atoms.

Another level of control is eventually attainable by cooling the atoms to the fundamental state of the tweezer potential and control dynamically the tunneling between tweezers. This requires a precise control of the relative intensity and relative distance between individual sites to fulfil the resonant tunneling condition.

References

1. Henriet, L., Beguin, L., Signoles, A., Lahaye, T., Browaeys, A., Reymond, G., and Jurczak, C. “Quantum computing with neutral atoms”. Quantum, Vol. 4, page 327, 2020.
2. Rivy, H.M., Aljunied, S.A., Lassalle, E., Zheludev, N.I., Wilkowski, D, “Single atom in a superoscillatory trap,” Commun. Phys., Vol. 6, No. 155, 2023.

Epsilon-Near-Zero Regime in the Infrared for Ultrafast Switching

C. S. Davies[1*] and A. Kirilyuk[1]

[1] HFML-FELIX, Radboud University, Nijmegen, The Netherlands
[*]corresponding author: carl.davies@ru.nl

Abstract: Using narrow-band infrared pulses tailored to entirely fit the epsilon-near-zero regime, we experimentally find that the magnetization in iron-garnet films and the polarization in ferroelectric barium titanate can be permanently reversed. This offers a novel strategy for the ultrafast switching of spontaneous magnetization and polarization.

Ultrashort pulses of light can serve as fascinating multi-faceted instruments for the coherent and efficient manipulation of spontaneous order parameters. By sculpting the many attributes of light-wave pulses, such as their frequency, polarization, duration, peak amplitude and so on, and also the optical properties of the irradiated medium, it is possible to substantially strengthen the coupling between light and matter. Groundbreaking works in the research field of non-linear phononics have, across the last two decades, powerfully demonstrated that high-frequency lattice vibrations, when driven to high amplitude by mid- to far-infrared (IR) optical pulses, can temporarily modify a variety of spontaneous orderings [1]. This approach revolves around the excitation of IR-active transverse optical (TO) phonon modes, which are marked by poles in the imaginary part of the permittivity.

Here, we discuss an alternative strategy in which the optical pulses are instead tailored to match the frequency of longitudinal optical (LO) phonons, i.e., the frequency at which the real part of the medium's permittivity goes to zero. Specifically, using narrow-band IR optical pulses delivered by the free-electron laser facility FELIX with frequency ranging between 6 THz and 30 THz (wavelength 10-50 μm) [2], we irradiate ferrimagnetic iron-garnet films [3], antiferromagnetic nickel-oxide films [4] and ferroelectric crystals of barium titanate [5]. We consistently find that the strongest impact is obtained when the frequency of the optical pulse matches not that of the strongly-absorbing TO phonon modes but rather that of the LO phonon modes (Fig. 1). We note that these materials have very dissimilar crystal symmetries, causing the phonon modes in all these systems to have very different character. Moreover, the LO phonon modes are equivalent to longitudinal electromagnetic waves, so they cannot even be directly excited by the impinging light.

To therefore explain these results, we draw attention to the fact that the spectral position of the LO phonon mode actually corresponds to the frequency at which the material's permittivity goes to zero [6]-[7]. In this so-called epsilon-near-zero (ENZ) regime, the attributes of light-matter interaction become highly counter-intuitive. For example, in barium titanate, we estimate that the wavelength of the penetrating optical pulse stretches by a factor of two, and its group velocity diminishes by almost a factor of forty. Moreover, the light-matter interaction becomes strongly amplified. Our results highlight the importance of the ENZ regime for ultrafast switching of spontaneous order parameters [8]. Moreover, the fact that ENZ conditions often organically emerge in the infrared spectral range suggests that the demonstrated mechanism could be truly universal, capable of strengthening light-matter interaction and permanently switching order parameters in a wide variety of systems.

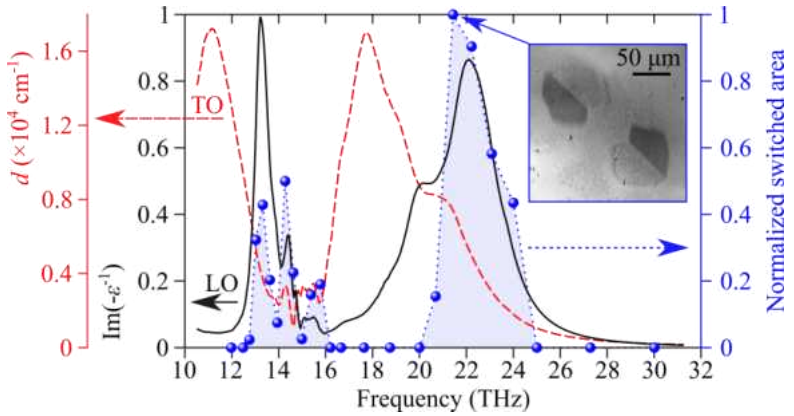


Fig. I Spectral dependence of the magnetic switching (blue dotted curve), and the longitudinal (LO, black solid curve) and transverse (TO, red dashed curve) optical phonon modes respectively measured in Co:YIG. Adapted from Ref. [3].

We thank A. V. Kimel, M. Kwaaitaal, D. Lourens and A. Stupakiewicz for fruitful discussions. We gratefully acknowledge the Nederlandse Organisatie voor Wetenschappelijk Onderzoek (NWO-I) for their financial contribution, including the support of the FELIX Laboratory. C.S.D. acknowledges support from the European Research Council ERC Grant Agreement No. 101115234 (HandShake).

References

1. Disa, A.S., Nova, T.F. and Cavalleri, A. "Engineering crystal structures with light," Nature Phys., Vol 17, 1087 (2021).
2. Knippels, G.M.H. et al, "Generation and complete electric-field characterization of intense ultrashort tunable far-infrared laser pulses," Phys. Rev. Lett., Vol. 83, 1578–1581 (1999).
3. Stupakiewicz, A. et al, "Ultrafast phononic switching of magnetization," Nature Phys. Vol. 17, 489–492 (2021).
4. Stremoukhov, P. et al. "Phononic manipulation of antiferromagnetic domains in NiO," New. J. Phys., Vol. 24, 023009 (2022).
5. Kwaaitaal, M., Lourens, D.G., Davies, C.S. and Kirilyuk, A. "Epsilon-near-zero regime enables permanent ultrafast all-optical reversal of ferroelectric polarization," Nat. Photon. (in press, 2024).
6. Kinsey, N., DeVault, C., Boltasseva, A. and Shalaev, V.M. "Near-zero-index materials for photonics," Nat. Rev. Mater., Vol. 4, 742–760 (2019).
7. Reshef, O., De Leon, I., Alam, M. Z. and Boyd, R. W. "Nonlinear optical effects in epsilon-near-zero media." Nat Rev Mater., 4, 535–551 (2019).
8. Davies, C.S. and Kirilyuk, A. "Epsilon-near-zero regime for ultrafast opto-spintronics," (submitted, 2024).

Advanced high contrast grating designs for biosensing applications

L. Yu. Beliaev[1], G. Finco[2], S. Kim[3], L. Vertchenko[4], B. F. S. Nielsen1[1], M. V. Evensen[1], A.-I. Bunea[5], R. Malureanu[1], L. R. Lindvold[1], O. Takayama[*1], P. E. Andersen[3], A. V. Lavrinenko[1]

[1]DTU Electro – Department of Electrical and Photonics Engineering,

Technical University of Denmark, Ørsteds Plads 343, DK-2800 Kgs. Lyngby, Denmark

[2]ETH Zurich, Institute for Quantum Electronics, Department of Physics, Optical Nanomaterial Group, Zurich, Switzerland

[3]DTU Health Tech, Department of Health Technology, Technical University of Denmark,

Ørsteds Plads, Building 345C, DK-2800 Kongens Lyngby, Denmark

[4]Sparrow Quantum Ltd, Copenhagen, Denmark

[5]DTU Nanolab - National Center for Micro- and Nanofabrication,

Technical University of Denmark, Ørsteds Plads 347, DK-2800 Kgs. Lyngby, Denmark

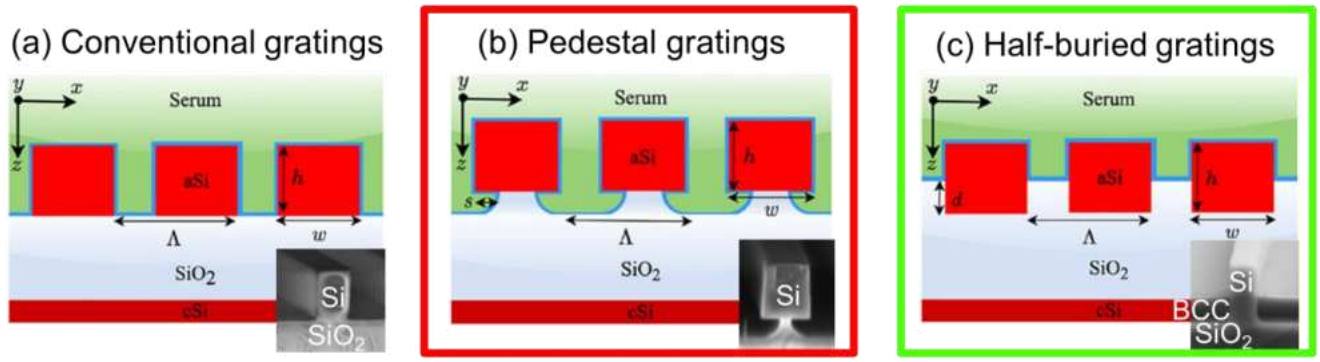
[*]corresponding author: otak@dtu.dk

Abstract: We propose two novel designs of high contrast gratings (HCGs) composed of silicon grating bars: pedestal and half-buried HCG designs, and demonstrate that these designs exhibit improved bulk refractive index sensitivity and limit of detection (LoD) for myoglobin, in a concentration range relevant for clinical diagnostic applications.

Refractometric sensing has been used widely among other optical read-outs schemes for biosensing applications. High contrast gratings (HCGs) [1] or non-local metasurfaces [2,3] are grating structures made of high refractive index material like Si surrounded by a low refractive index matrix and they support guided-mode resonances localized around grating bars. HCGs have been used for biosensing applications by detecting resonance shifts induced by local refractive index change, which in turn is caused by the presence of the analyte in solution and by the binding of analyte molecules to the sensor surface [1].

Here, we report two novel HCG designs and their realization for biosensing applications, named ”pedestal” and ”half-buried” HCGs (Fig. 1(a)-(c)) [4-6]. The two HCG designs aim at increasing the overlap between hot spots of electric fields and analyte around the Si gratings as means to increase the wavelength shift of resonance. These HCG structures were fabricated by the combination of deep ultraviolet lithography and dry etch techniques. Pedestal HCGs were realized by controlled etching of silicon dioxide substrate below silicon grating bars with hydrogen fluoride in the vapor phase [5]. Half-buried HCGs were fabricated with a benzocyclobutene (BCB) polymer layer that partially fills the gaps between the silicon grating bars [6]. We performed optical characterization of sensing performance of the two designs to compare them to conventional HCG structures.

The bulk refractive index sensitivity of each type of grating is 409 nm/RIU, 482 nm/RIU, and 536 nm/RIU for the half-buried, conventional, and pedestal HCGs, respectively (Fig. 1(d)). To examine surface sensitivity, the conventional and pedestal HCGs were utilized for detection of the model analyte avidin with a limit of detection (LoD) of 3.2 ng/ml and 2.1 ng/ml. Finally, half-buried and pedestal HCGs were tested for myoglobin detection, yielding LoDs of 34.6 ng/ml and 37.3 ng/ml, respectively. This shows that the half-buried and pedestal HCGs exhibit gives enhanced sensitivity over conventional ones, being a potential platform for biosensing applications.



(d) Sensing platform	Q-factor	FOM [RIU^{-1}]	BRIS [nm/RIU]	Avidin detection LoD [ng/mL]	Avidin detection LoQ [ng/mL]	Myoglobin detection LoD [ng/mL]	Myoglobin detection LoQ [ng/mL]
Conventional HCG	1.3×10^3	438	482	3.2	213	-	-
Pedestal HCG	1.5×10^3	564	536	2.1	85	37.3	138
Half-buried HCG	1.1×10^3	293	409	-	-	34.6	102

Figure 1: Schematic illustration of (a) conventional, (b) pedestal, and (c) half-buried high contrast grating (HCG) structures. The insets are scanning electron microscope (SEM) images of fabricated HCG structures. (d) Summary table of sensing performance of each HCG structure. BRIS stands for bulk refractive index sensitivity.

This research was funded by Independent Research Fund Denmark, DFF Research Project 2 ”PhotoHub” (8022-00387B). The authors would like to acknowledge the support from the Danish National Center for Micro- and Nanofabrication (DTU Nanolab).

References

1. Sun, T., S. Kan, G. Marriott, C. Chang-Hasnain, “High-contrast grating resonators for label-free detection of disease biomarkers,” Scientific Reports Vol. 6, 27482, 2016.
2. Franceschini, P., A. Tognazzi, G. Finco, L. Carletti, I. Alessandri, A. C. Cino, C. De Angelis, O. Takayama, R. Malureanu, A. V. Lavrinenko, D. de Ceglia, “Nonlocal resonances in pedestal high-index-contrast metasurfaces based on a silicon-on-insulator platform,” Applied Physics Letters Vol. 123, No. 7, 071701, 2023.
3. Tognazzi, A., P. Franceschini, O. Sergaeva, L. Carletti, I. Alessandri, G. Finco, O. Takayama, R. Malureanu, A. V. Lavrinenko, A. C. Cino, D. de Ceglia, C. De Angelis, “Giant photoinduced reflectivity modulation of nonlocal resonances in silicon metasurfaces,” Advanced Photonics Vol. 5, No. 6, 066006, 2023.
4. Finco, G., M. Z. Bideskan, L Vertchenko, L. Y. Beliaev, R Malureanu, L. René Lindvold, O. Takayama, P. E. Andersen, A. V. Lavrinenko, “Guided-mode resonance on pedestal and half-buried high-contrast gratings for biosensing applications,” Nanophotonics Vol. 10, No. 17, 4289–4296, 2021.
5. Beliaev, L. Y., P. G. Stounbjerg, G. Finco, A. I. Bunea, R. Malureanu, L. R. Lindvold, O. Takayama, P. E Andersen, A. V. Lavrinenko “Pedestal High-Contrast Gratings for Biosensing,” Nanomaterials Vol. 12, No. 10, 1748, 2022.
6. Beliaev, L. Y., S. Kim, B. F. S. Nielsen, M. V. Evensen, A. I. Bunea, R. Malureanu, L. R. Lindvold, “Optical Biosensors Based on Nanostructured Silicon High-Contrast Gratings for Myoglobin Detection,” ACS Applied Nano Materials Vol. 6, No 13, 12364–12371, 2023.

Optoelectronic control of quantum optical phenomena with graphene

Mikkel Have Eriksen[1] **and Joel D. Cox**[1,2]

[1]POLIMA—Center for Polariton-driven Light-Matter Interactions, University of Southern Denmark, Campusvej 55, DK-5230 Odense M, Denmark
[2]Danish Institute for Advanced Study, University of Southern Denmark, Campusvej 55, DK-5230 Odense M, Denmark
[*]corresponding author: cox@mci.sdu.dk

Abstract: We explore strategies to harness the polariton-assisted nonlinear response and optoelectronic tunability of graphene to actively control quantum light emission and manipulate the quantum states of atomic systems.

Coherent control of light and atomic systems enables fundamental explorations of quantum physics while promising disruptive applications in diverse fields, ranging from information and communications technologies to optical sensing and metrology. In this context, the intrinsically strong and actively tunable light-matter interactions available in atomically thin materials such as graphene offer unique opportunities to trigger nonlinear and quantum optical phenomena on the nanoscale by invoking their supported polaritons and near field interaction with proximal quantum light emitters [1,2]. Here we propose to harness the optoelectronic properties of graphene to electrically control the coupling of light to nearby atoms. In particular, we investigate optically-driven two-level atomic systems exhibiting controllable bistability due to the self-interaction mediated by the graphene sheet. Our results indicate that the electro-optical bistability and hysteresis exhibited by the atom manifest in the intensity, spectrum, and quantum statistics of the light emitted by the atomic system. The optically-driven atom-graphene system thus constitutes a platform for active and *in situ* control over driven quantum optical systems for explorations in coherent quantum control and atomic physics.

References

1. Cox, J. D. and García de Abajo, F. J., "Nonlinear graphene nanoplasmonics," Acc. Chem. Res. 52, 2536 (2019).
2. Rasmussen, T. P., Gonçalves, P. A. D., Xiao, S., Hofferberth, S., Mortensen, N. A. and Cox, J. D., "Polaritons in two-dimensional parabolic waveguides," ACS Photonics 8, 1840 (2021).
3. Eriksen, M. H., Olsen, J. E., Wolff, C. and Cox, J. D., "Optoelectronic control of atomic bistability with graphene," Phys. Rev. Lett. 129, 253602 (2022).

An electrically tunable polarization-selective photonic crystal based on a microcavity filled with a self-assembled uniformly lying helical liquid crystal

Marcin Muszyński[1], Przemysław Oliwa[1], Pavel Kokhanchik[2], Piotr Kapuściński[1], Eva Oton[3], Rafał Mazur[3], Przemysław Morawiak[3], Wiktor Piecek[3], Przemysław Kula[4], Witold Bardyszewski[5], Barbara Piętka[1], Daniil Bobylev[2*], Dmitry Solnyshkov[2,6], Guillaume Malpuech[2], and Jacek Szczytko[1]

[1]Institute of Experimental Physics, Faculty of Physics, University of Warsaw, Poland
[2]Université Clermont Auvergne, Clermont Auvergne INP, CNRS, Institut Pascal, F-63000 Clermont-Ferrand, France
[3]Institute of Applied Physics, Military University of Technology, Warsaw, Poland
[4]Institute of Chemistry, Military University of Technology, Warsaw, Poland
[5]Institute of Theoretical Physics, Faculty of Physics, University of Warsaw, Poland
[6]Institut Universitaire de France (IUF), 75231 Paris, France
[*]corresponding author: daniil.bobylev@uca.fr

Abstract: We study a microcavity-based photonic crystal formed by self-assembled uniformly lying helices of the embedded cholesteric liquid crystal. Applying an external voltage breaks the system's mirror symmetry inducing optical activity due to the inter-band interaction. This suggests a dynamically tunable way of controlling light polarization at the nanoscale.

Intrinsic properties of soft matter provide an accessible and versatile toolkit for photonic systems engineering [1]. In particular, tunability, self-assembly and remarkable optical characteristics of liquid crystals enriched the functionality of such optical devices as microcavities [2], giving rise to tunable photonic spin-orbit coupling [3], photonic persistent spin helix [4] and topological transitions [5].

Here, we study a planar optical microcavity filled with a cholesteric liquid crystal twisted around the axis parallel to the microcavity planes forming the so-called uniform lying helix (ULH) [6]. The ULH formation relies on the self-organization of liquid crystal molecules, which can be easily tuned by applying an external voltage. The cavity transforms photons into effective 2D free massive quasi-particles [7, 8]. In turn, the embedded ULH creates a polarization-dependent periodic potential felt by these quasi-particles resulting in the emergence of band gaps in the dispersion relation for one of the two possible linear polarizations. In this regime, the strong optical activity due to the cholesteric liquid crystal twist is suppressed inside the microcavity because of the mirrors restoring the inversion symmetry. However, if the molecules are tilted by applying an external voltage, the modes of different linear polarization couple, resulting in the emergence of optical activity. Strong anisotropy of liquid crystals promotes remarkable dynamic control over multiple parameters of the band structures, including the optical activity strength, band energies, and the width of the photonic band gap. Such tunability is challenging to achieve by alternative methods. Additionally, by introducing a dye within the microcavity, we demonstrate the capability of our platform to achieve the spin-polarized lasing. This level of control over band structure and spin-orbit coupling opens new avenues for light-matter interactions.

This work was supported by the National Science Centre grants 2019/35/B/ST3/04147, 2019/33/B/ST5/02658 and 2017/27/B/ST3/00271, and the Ministry of National Defense Republic of Poland Program -- Research Grant MUT Project 13-995 and MUT University grant (UGB) for the Laboratory of Crystals Physics and Technology for the year 2021 and the European Union's Horizon 2020 program, through a

FET Open research and innovation action under the grant agreements No. 964770 (TopoLight). Additional support was provided by the ANR Labex GaNext (ANR-11-LABX-0014), the ANR program "Investissements d'Avenir" through the IDEX-ISITE initiative 16-IDEX-0001 (CAP 20-25), and the ANR project "NEWAVE" (ANR-21-CE24-0019).

References

1. Kléman, M. and Lavrentovich, O. D, “Soft matter physics: an introduction,” New York: Springer, 2003.
2. Ma, L.L., Li, C.Y., Pan, J.T. et al., “Self-assembled liquid crystal architectures for soft matter photonics,” Light Sci. Appl., Vol. 11, 270, 2022.
3. Rechcińska, K., Król, M., Mazur, R. et al., “Engineering spin-orbit synthetic Hamiltonians in liquid-crystal optical cavities,” Science, Vol. 366, 727, 2019.
4. Król, M., Rechcińska, K., Sigurdsson, H., et al., “Realizing optical persistent spin helix and Stern-Gerlach deflection in an anisotropic liquid crystal microcavity,” Phys. Rev. Lett., Vol. 127, 190401, 2021.
5. Król, M., Septembre, I., Oliwa, P., et al., “Annihilation of exceptional points from different Dirac valleys in a 2D photonic system,” Nat. Comm., Vol. 13, 5340, 2022.
6. Bisoyi, H.K., Bunning, T.J., and Li, Q., “Stimuli-driven control of the helical axis of self-organized soft helical superstructures,” Adv. Mater., Vol. 30, 1706512, 2018.
7. Kavokin, G.M.A., “Cavity Polaritons” Elsevier, 2003.
8. Kavokin, G.M.A., “Exciton Polaritons in Microcavities: New Frontiers” Springer-Verlag, 2012.

Lasing of gain-doped plasmonic nanoshells: Threshold, emission linewidth and giant pull-out effects

A. Aradian[1*], A. Cathey[2], K. Caicedo[3], M. Mora[3], M. Infusino[3], and A. Veltri[3]

[1]University of Bordeaux & CNRS, Bordeaux, France
[2]Max Planck Institute for Plasma Physics, Garching, Germany
[3]Universidad San Francisco de Quito, Quito, Ecuador
[*]corresponding author: ashod.aradian@crpp.cnrs.

Abstract: We present a model describing the lasing / spasing properties of a nanoshell made of a plasmonic metal, whose core is filled with a gain medium. We calculate the nonlinear lasing state above the threshold, demonstrating that the emission linewidth is dictated by unusually strong frequency pull-out effects.

Nanoscale structures combining together optical gain with plasmonic (or other) resonators have formed a thriving topic of research over the last two decades, starting with the 2003 hallmark article by Bergman and Stockman [1] on spasers. In particular, when the provided gain exceeds loss sources in the structure, a coupled phenomenon of "spasing" (coherent generation of plasmons) and "nanolasing" (emission of coherent photons from the nanostructure) emerges. Numerous experimental and theoretical works have followed on all flavors of nanolasers based on combinations of metals, semi-conductors, doped dielectrics made into various geometries (see for example the following review of the literature [2]).

One promising class of nanolasers are hybrid spherical nanoparticles, e.g. core-shell particles where the core is made of a metal and the shell is made of a gain medium, or nanoshell particles where, oppositely, the gain medium is in the core and the metal in the outside shell. We studied the optical response of both geometries using a simplified approach based on the quasi-static polarizability of the nanoparticle [3]. This allowed us to describe in a compact manner the behavior of the nanolaser under the lasing threshold (where it behaves like an optical amplifier of the probe field), and also to obtain the value of the lasing threshold. However, the lasing behavior itself could not be described using this approach, since it was a static one, hence intrinsically unable to treat the nonlinear time dynamics at play above the threshold. (This is, by the way, true as well for many spaser-related works in the literature, which rely on static dielectric permittivities).

In a different work [4], we studied the situation of a homogeneous metal nanosphere plunged into an unbounded gain medium (like a dye solution), this time using a much more realistic model, allowing both for temporal and spatial variations of the fields, where the population dynamics within the levels of the gain medium was described and coupled to the fields in the nanoparticle. This allowed to demonstrate analytically that when the gain in the system (provided by some external pumping) was sufficiently increased, the system underwent a *self-oscillation instability*, i.e., the nanoparticle would produce a non-zero field even if it was not excited by any probe field – which is one way to define the lasing threshold. We also showed that, as the instability grows, the system in this geometry inevitably triggers a cascade of multiple lasing modes. This cascade dramatically complexified the theoretical description and made the detailed study of the long-term lasing state of the system out of reach.

In the present work, we aimed at bridging these gaps by applying the same time-dependent model to the nanoshell geometry shown in Fig. 1(a). We show that the nanoshell system does *not* enter into a mode cascade

above the threshold, so that the dipolar lasing mode is the only one active above the threshold. We use optical Bloch equations to describe the dynamics of the gain medium within a two-level effective framework. This provides differential equations for the population inversion and the polarization inside the gain medium. The metal is described using a free-electron equation of motion. Taking into account the single-mode operation of the lasing state, boundary conditions are implemented accordingly at interfaces, with the caution that electrical permittivities cannot be used above the threshold due to the dynamical nature of the lasing state.

Similarly to the previously studied geometry of a homogeneous particle in a gain medium, we find the condition for the lasing threshold within our model as a self-oscillation, and show that it exactly matches the more intuitive approach used in [3]. Then, we solve the model equations above the threshold and find that, after a transient, the nanolaser reaches a steady state of emission where the intensity of the emitted field is kept constant, but the complex field amplitude is submitted to slow rotations in time, as shown in Figure 1(b). Such behavior is commonly known as a "frequency pull-out" effect in the field of classical lasers.

However, while pull-out effects are responsible for delicate shifts of laser frequencies in macroscopic lasers, we find that in the nanoshell laser, these effects are comparatively huge, so much so that they reshape the spectrum of emission [see Fig. 1(c)] and are ultimately responsible for defining the emission linewidth of the nanolaser. This novel finding is a strikingly different paradigm as compared to standard laser physics.

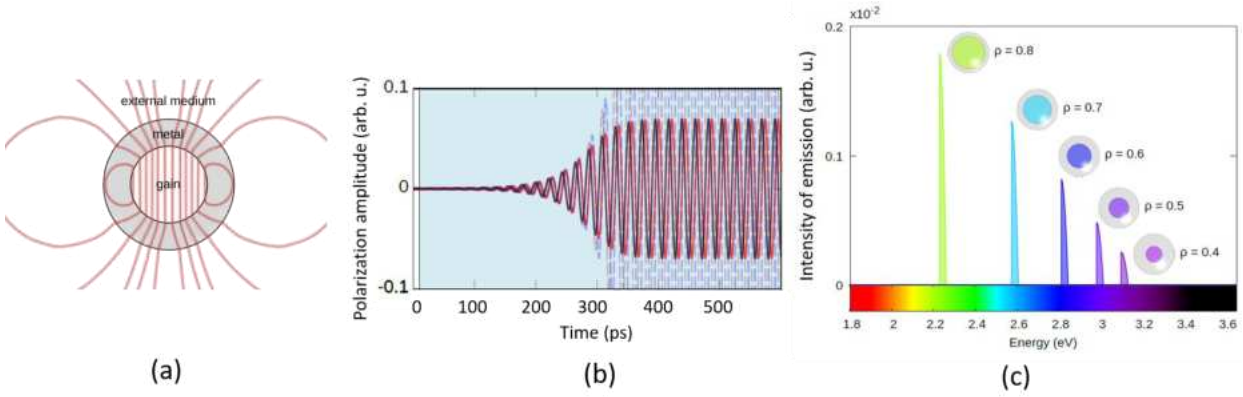


Figure 1. (a) Nanoshell schematics. (b) Transient growth and steady state (lasing) of a component of the polarization inside the gain medium. (c) Nanolaser emission spectrum for various aspect ratios of the nanoshell (left to right, from thinner to thicker shell).

References

1. Bergman, D. and M. Stockman, "Surface Plasmon Amplification by Stimulated Emission of Radiation: Quantum Generation of Coherent Surface Plasmons in Nanosystems," Phys. Rev. Lett., Vol. 90, 027402, 2003.
2. Azzam, S. I. *et al*., "Ten years of spasers and plasmonic nanolasers,", Light: Science & Applications, Vol. 9, 90, 2020.
3. Caicedo, K., A. Cathey, M. Infusino, A. Aradian, and A. Veltri, "Gain-driven singular resonances in active core-shell and nano-shell plasmonic particles," J. Opt. Soc. Am. B, Vol. 39, No. 1, 107–116, 2021.
4. Veltri, A., A. Chipouline and A. Aradian, "Multipolar, time-dynamical model for the loss compensation and lasing of a spherical plasmonic nanoparticle spaser immersed in an active gain medium," Sci. Reports, Vol. 6, 33018, 2016.

Manipulating the Exotic Quasi-Particles of van der Waals Correlated Antiferromagnet

Han Htoon

Center for Integrated Nanotechnologies, Materials Physics and Applications Division,
Los Alamos National Laboratory, Los Alamos, NM 87547, USA
htoon@lanl.gov

Abstract: We report influences of material composition and lateral dimension on spin-correlated exciton and magnons of van der Waal correlated antiferromagnets MPX_3 (M = Mn, Fe, Ni; X = S, Se)

A Van der Waals correlated antiferromagnet, metal phosphorus trichalcogenides (MPX_3, M = Mn, Fe, Ni; X = S, Se), have emerged as promising candidates for next generation spintronics, and quantum information technologies. Nickel phosphorus trisulfide ($NiPS_3$) is a most notable member of this family and has been extensively studied for its unique properties, including the emergence of an ultra-sharp photoluminescence (PL) peak at ~1.476 eV below Néel temperature of 150 Kelvin. While the highly anisotropic, linearly polarized emission of this PL peak has been shown to be directly correlated to the long-range spin order of $NiPS_3$, its ultra-narrow linewidth of a few hundred μeV has led to the speculation that it is originated from a coherent many-body exciton state. Observations of multiple phonon bounds states and formation of exciton-polaritons also creates more excitement as they present new possibilities for design and control of correlated electron systems.

Aiming to achieve understanding and control of this spin-correlated exciton, we first conduct temperature dependent, polarization resolved, PL and Raman spectroscopy studies on compounds of $NiPS_3$ doped with different concentration of Mn ($Ni_{1-x}Mn_xPS_3$). We observed systematic variation in characteristics of the spin-correlated exciton revealing their sensitive dependence on disturbance in the magnetic order of $NiPS_3$. Notably, the sharp peak disappeared beyond x of 0.2 (Fig. 1a). Furthermore, we analyzed the polarization-resolved PL of $Ni_{1-x}Mn_xPS_3$ alloys. At 5 K, increase of Mn concentration leads to decrease in degree linear polarization. In parallel, Raman spectroscopy of $Ni_{1-x}Mn_xPS_3$ revealed the two magnon scattering peak, a key indicator of correlated antiferromagnetism in $NiPS_3$, exhibited a shift towards lower energies and suppression when x is increased from 0 to 0.2 (Fig. 1b). This correlates with our findings in the PL spectrum further underscores the pivotal role of Mn impurities in disrupting the AFM order of $NiPS_3$ system. This study unveils the interplay between impurity-induced disruption in spin structures and PL and Raman characteristics in $NiPS_3$, shedding light on their potential for future application.

Next to understand how the reduction in lateral size influence the spin-correlated exciton, we conducted single nano-flake PL spectroscopy on individual crystalline nanoflakes (NFs) of $NiPS_3$ that prepared by wet-chemical synthesis. Our study revealed that by reducing the lateral dimension of correlated antiferromagnet $NiPS_3$ flakes to tens of nanometers and thickness (Fig. 2a) to less than ten nanometers, we can switch-off the bulk spin-correlated exciton in at 1.47 eV and activate new, ultra sharp optical transition in visible-range (1.8 – 2.2 eV) (Fig.2 c). These ultra-sharp lines display resolution limited lineweidth of <120 μeV at 4.2 K share the spin-correlated nature of the bulk exciton by displaying a strong linear polarization below Néel temperature. Furthermore, exciton photoluminescence lineshape analysis reveals a polaronic character via coupling with at-least 3 phonon

modes and a comb-like Stark effect through discretization of charges in each layer. These findings augment the knowledge on the many-body nature of excitonic quasi-particles in correlated antiferromagnets and also establish the nanoscale correlated antiferromagnets as a promising platform for integrated magneto-optic devices.

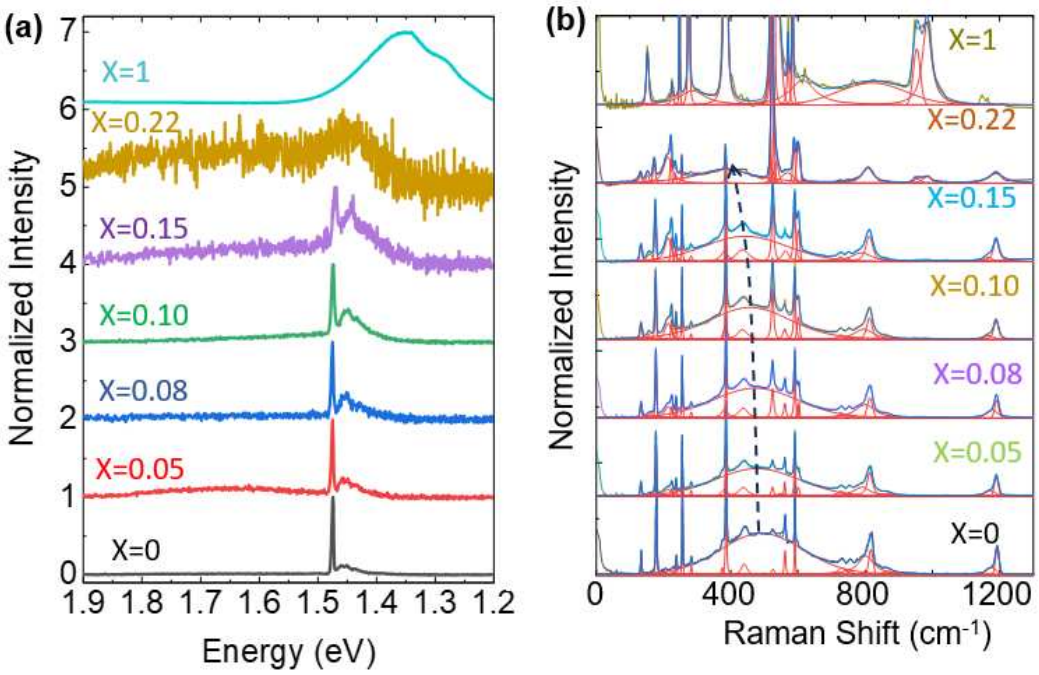


Fig. 1(a) Low T (4K) PL spectra of bulk $Ni_{1-x}Mn_xPS_3$ showing the disappearance of spin correlated exciton emission. Low T Raman spectra of bulk $Ni_{1-x}Mn_xPS_3$ showing the weaking of 2 magnon scattering peak.

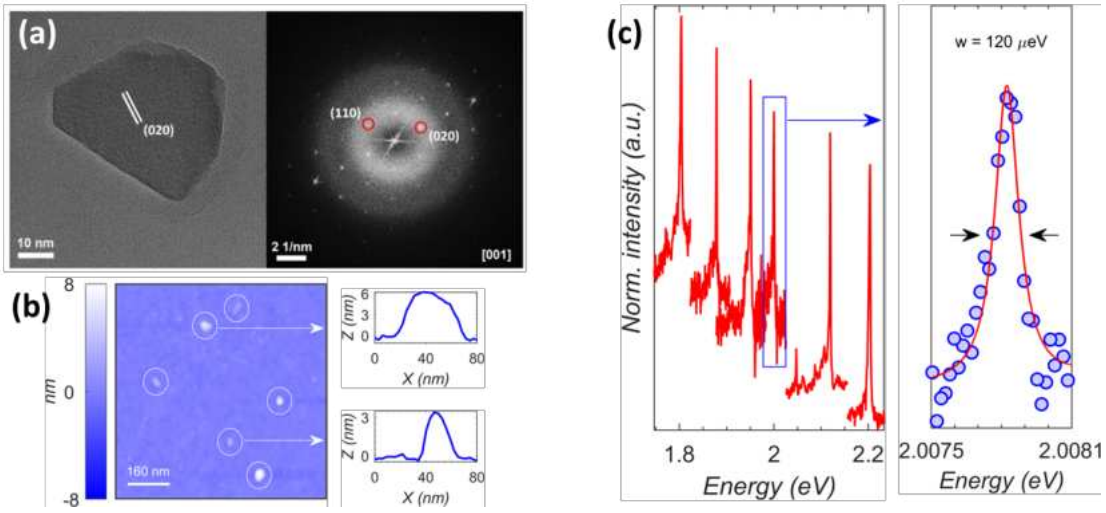


Fig. 2 (a) High-Res TEM image and diffraction pattern of $NiPS_3$ nanoflakes.(b) AFM image of $NiPS_3$ nanoflakes. (c) Low T (4K) PL spectra and zoom in view showing ultra-sharp PL emission.

Advanced Terahertz-Wave Phase and Polarization Control Devices Powered by Metasurfaces

Yuehong Xu[1*], **Hiroaki Minamide**[1]

[1]RIKEN Centre for Advanced Photonics, RIKEN, Japan

[*]corresponding author: yuehong.xu@riken.jp

Abstract: This work introduces several advanced terahertz-wave phase and polarization control devices powered by metasurfaces, integrating dynamic and geometric phase control. This spin-decoupled phase control method offers robust and flexible solutions for beam steering and polarization multiplexing.

Terahertz (THz) waves, nestled between microwaves and infrared, are prized for their unique electromagnetic properties, offering deep penetration and safe application across various fields such as non-destructive testing and communications. However, traditional THz phase and polarization control devices are bulky and limited in function, driving the need for innovative, lightweight, and versatile solutions. Advances in metasurface technology, particularly through the Pancharatnam-Berry (PB) phase control for circular polarization, have significantly improved phase modulation. Federico Capasso's team further revolutionized this field in 2017 by introducing a spin-decoupled phase modulation technique into metasurface in optical regime, enabling separate phase control for different circular polarizations and paving the way for more sophisticated meta-devices. Subsequent THz domain research has built upon this spin-decoupled phase modulation approach, spearheading a series of developments.

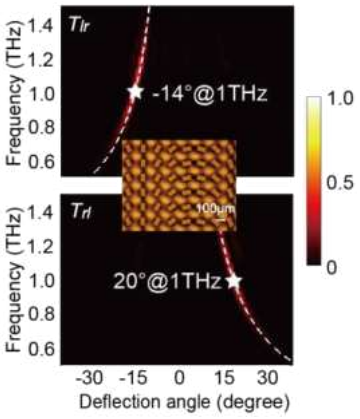


Figure 1. Experimental results of the THz asymmetric angle anomalous deflection device.

In 2019, Yuehong Xu et al leveraged the high efficiency and adaptable phase tuning of all-dielectric metasurfaces, in conjunction with the PB phase and dynamic phase, to unveil a spin-decoupled phase modulation technique in THz regime. The design method skillfully integrates both dynamic phase (φ_f) and PB phase ($\pm 2\alpha$) into a single structure, which consists of a high-resistance silicon pillar with half-wave plate property. This spin-decoupled phase control method enables independent control of the phase of left-handed (LCP) ($\varphi_{lr}=\varphi_f-2\alpha$) and right-handed (RCP) ($\varphi_{rl}=\varphi_f+2\alpha$) circularly polarized THz waves. Both the PB phase control and dynamic phase control can be achieved by rotating the pillar and altering its geometric parameters, respectively. This method breakouts the spin phase lock limitations inherent in PB phase-only control, facilitating the creation of several spin-dependent asymmetric angle anomalous deflection devices as shown in figure 1, as well as a suite of linear polarization (LP) -dependent dual-channel polarization converters. This design methodology offers insights for the generation of polarization beams and systems for polarization multiplexing in THz regime.

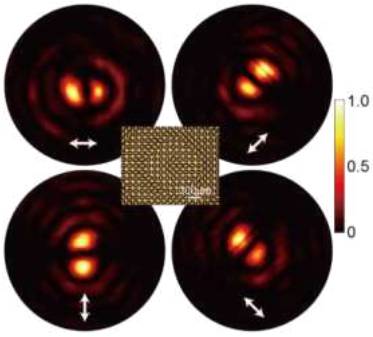


Figure 2. Experimental results of the radial polarization Bessel beam generator: Under *x*-linearly polarized incidence, the electric field distribution maps are detected in four linearly polarization directions.

In 2020, leveraging the same phase control strategy, Yuehong Xu et al achieved development in independently manipulating the emission phase distributions of THz waves for two circular polarization channels. By harmonizing with the principles of polarization superposition, they pioneered a method for generating LP-related THz vector beams, successfully realizing

generators for LP-related THz vector vortex and Bessel beams in experiments, as shown in figure 2. This achievement enabled the acquisition of radial and azimuthal THz vector polarization distributions under orthogonal linear polarizations, facilitating advancements in THz multi-channel communication and super-resolution imaging.

Recently, we focused on exploring and developing THz multi-beam polarization control meta-devices based on spin-decoupled phase control strategy. Leveraging the principle of phase discontinuities, by integrating two rows (columns) of meta-gratings with opposing phase gradients along the *x* (*y*) direction and adeptly managing the initial phase difference between these two rows (columns) of meta-gratings, it is feasible to generate four beams from a single incident light beam, as shown in the formulas.

$$\Psi^x_{rl_odd} = \frac{2\pi x}{nP},\ \Psi^x_{rl_even} = -\frac{2\pi x}{nP} + \Psi^x_{rl},\ \Psi^y_{rl_odd} = \frac{2\pi y}{nP},\ \Psi^y_{rl_even} = -\frac{2\pi y}{nP} + \Psi^y_{rl} \quad (1)$$

$$\Psi^x_{lr_odd} = \frac{2\pi x}{nP},\ \Psi^x_{lr_even} = -\frac{2\pi x}{nP} + \Psi^x_{lr},\ \Psi^y_{lr_odd} = \frac{2\pi y}{nP},\ \Psi^y_{lr_even} = -\frac{2\pi y}{nP} + \Psi^y_{lr} \quad (2)$$

Moreover, this approach enables the manipulation of the polarization states of the four emitted beams. Specifically, with $\Psi^x_{rl} = \pi,\ \Psi^y_{rl} = \pi/2,\ \Psi^x_{lr} = 0,\ \Psi^y_{lr} = 0$, a THz four-beam polarization rotator is designed. In this case, when the incident wave is a 0° LP wave, the orientation angles of the LP output for the four beams are respectively 0°, 45°, 90° and -45 °, as shown in figure 3. This device will increase the versatility of THz wave manipulation, contributing to advancements in THz communication, multi-polarization imaging, biomedical sensing, and more.

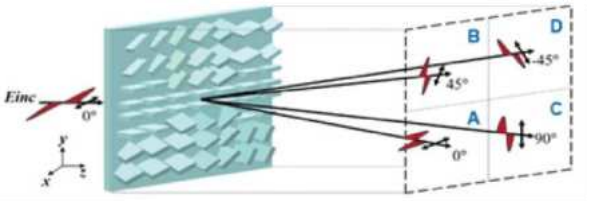


Figure 3. Function diagram of the THz four-beam polarization rotator

In summary, this work primarily focuses on the wavefront control of THz waves through orthogonal polarization (circular polarization) parameter multiplexing. Utilizing all-dielectric metasurfaces, we introduce several advanced multifunctional THz wavefront control devices developed via the spin-decoupled phase control method. These include asymmetric THz anomalous deflection devices with unique deflection angles, THz vector vortex and Bessel beam generators, and THz multi-beam polarization control devices. These contributions are poised to offer novel solutions for THz applications, potentially propelling further advancements in the field of THz technology and its interdisciplinary applications.

Acknowledgements: This work was supported (in part) by Innovative Science and Technology Initiative for Security Grant Number JPJ004596, ATLA, Japan.

References

1. Berry M. “The Adiabatic phase and Pancharatnam’s phase for polarized light,” J. Mod. Opt., Vol. 34, No. 11, 1401–1407, 1987.
2. Balthasar M, Rubin N, Devlin R, et al. “Metasurface polarization optics: independent phase control of arbitrary orthogonal states of polarization,” Phys. Rev. Lett., Vol. 118, No. 11, 113901, 2017.
3. Xu Y, Li Q, Zhang X, et al. “Spin-decoupled multifunctional metasurface for asymmetric polarization generation,” ACS Photonics, Vol. 6, No. 11, 2933-2941, 2019.
4. Xu Y, Zhang H, Li Q, et al. “Generation of terahertz vector beams using dielectric metasurfaces via spin-decoupled phase control,” Nanophotonics, Vol. 9, No. 10, 3393–3402, 2020.
5. Yu N, Genevet P, Kats M A, et al. “Light propagation with phase discontinuities: generalized laws of reflection and refraction,” Science, Vol. 334, No. 6054, 333–337, 2011.

Manipulating Chemical Reactions with Light

Z. Fusco[1], A. Edirisooriya[1], N. Lyu[1,2], C. David[2], F. J. Beck[1]

[1]School of Engineering, College of Engineering, Computing and Cybernetics, Australian National University, Australia

[2]Institute of Condensed Matter Theory and Optics, Abbe Center of Photonics, Friedrich Schiller University of Jena, Max-Wien-Platz 1, 7743 Jena, Germany

*corresponding author: fiona.beck@anu.edu.edu

Abstract: Light-matter coupling mediated by plasmonic resonances could allow the manipulation of chemical reactions. Resonant energy transfer between plasmonic modes and molecular energy levels can activate molecular bonds, inducing bond breaking or triggering transformation which can enhance or suppress a particular chemical reaction pathway, and ultimately determine the final product distribution.

While there have been extensive reports of using plasmons to enhance photocatalytic (PC) and photo-electrochemical (PEC) reactions over the last decades [1], the concept of *controlling chemical reaction pathways with resonant light-matter coupling* has only recently been explored [2]. Plasmons allow efficient light-matter coupling via optically-driven, collective oscillations of the conduction electrons in metals. They can be induced and sensitively controlled by modifying the geometry of metal nanostructures. At energies around the resonance, plasmons produce strong, optical near-fields confined to sub-wavelength volumes, and can excite electrons to energy levels well above the Fermi level, leading to a population of energetic 'hot' carriers. Nearby molecules can then resonantly couple with plasmonic modes, through either electron or photon transfer. Resonant transfer of electrons between plasmonic metal structures and molecular energy levels can produce transient negative ions, accessing new potential energy surfaces and changing preferred reaction pathways. Additionally, reversible exchange of either electrons or photons can leave the metal–adsorbate molecule complex in a vibrationally excited state, which can activate chemical bonds, triggering dissociation or transformation reactions. Experimental demonstrations are only just beginning to provide indirect evidence of these mechanisms [1, 3]. As the final product distribution depends on the reaction pathway, selectively activating particular intermediate reaction steps by plasmonic light-matter coupling could be used to target high value products. Seminal work by Prof Jain's group in 2018 confirmed that plasmonic nanoparticles can photoreduce CO_2 to C_{2+} products [4].

In this talk, I will give an overview of our investigations into plasmonic light-matter coupling, and how this can be used to modify photocatalytic (PC) and photo-electrochemical (PEC) reactions. Our approach is to combine insights from a combination of time dependent density functional theory simulations (TD-DFT) (Fig. 1b and c), nano-scale characterization and modelling (BEM, FEM) of plasmonic resonances, and in-situ monitoring of chemical reactions using surface enhanced Raman spectroscopy (Fig. 2) to probe underlying mechanisms [5, 6]. In addition, I will discuss how insights from atomistic studies and model molecule-nanoparticle systems can be leveraged to design practical photoelectrodes and photocatalysts for large scale CO_2 reduction based on self-assembled dendritic structures [7],[8].

The authors acknowledge the financial support of the International Research Training Group META-ACTIVE.

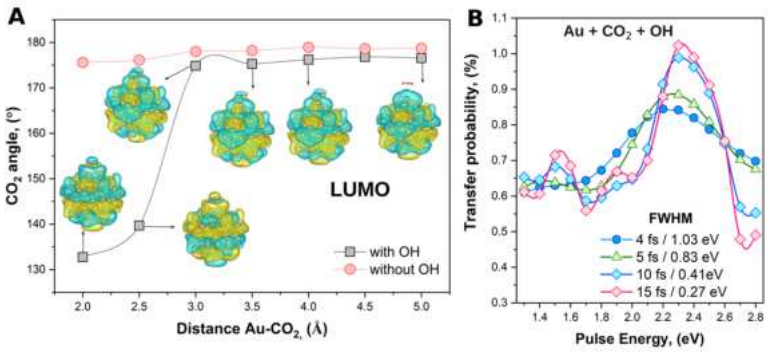


Figure 1 A) DFT calculations of Au nanoclusters as a CO_2 molecule is adsorbed. CO_2 bond angle as a function of the distance is shown with (red line) and without (black line) a hydroxide molecule (+OH) present. The LUMO of the systems are also shown. B) Results from TD-DFT showing the fraction of carriers that are directly transferred to the adsorbed CO_2 molecule as a as a function of the excitation frequency for different pulse widths. From ref [5]

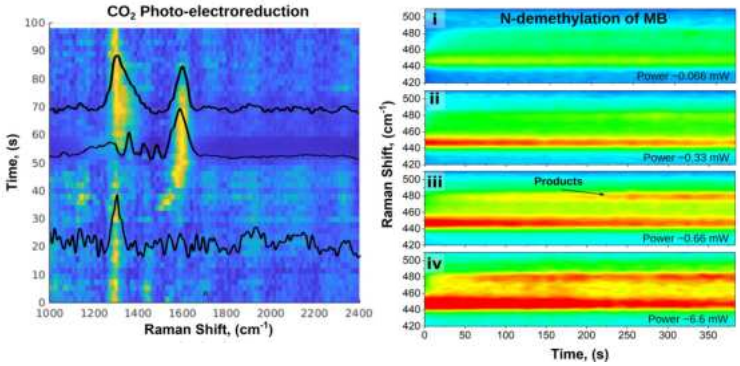


Figure 2. (Left) Time resolved surface enhanced Raman spectra of the CO_2 photo-electroreduction on large-scale plasmonic Au dendritic substrates, showing the appearance of reaction intermediates. (Right) Time resolved surface enhanced Raman spectra of the N-demethylation of Methylene Blue (MB) as a function of incident illumination power, showing the evolution of the product peak [6].

References

[1] S. Ezendam, M. Herran, L. Nan, C. Gruber, Y. Kang, F. Grobmeyer, R. Lin, J. Gargiulo, A. Sousa-Castillo, E. Cortes, ACS Energy Lett 2022, 7, 778.

[2] D. Devasia, A. Das, V. Mohan, P. K. Jain, Annu Rev Phys Chem 2021, 72, 423.

[3] Z. Fusco, F. J. Beck, Nanophotonics 2024.

[4] S. Yu, A. J. Wilson, J. Heo, P. K. Jain, Nano Letters 2018, 18, 2189.

[5] Z. Fusco, D. Koenig, S. C. Smith, F. J. Beck, Pre-print 2024, https://doi.org/10.48550/arXiv.2402.11726

[6] Z. Fusco, K. Catchpole, F. J. Beck, Journal of Materials Chemistry C 2022.

[7] Zelio Fusco, Rufus Turner, Anjalie Edirisooriya, Asim Riaz, Fiona J Beck, In Preperation.

[8] Z. Fusco, A. Riaz, C. David, F. J. Beck, Advanced Materials Interfaces 2022, 2202236.

Soft Metamaterials for Innovative Medical Devices

Jianfeng Zang[1,*], Hanchang Tang[1], Ye Tian[1], Zhangqi Pan[1]

[1] School of Integrated Circuits and Wuhan National Laboratory for Optoelectronics, Huazhong University of Science and Technology, Wuhan 430074, China

[*]Corresponding author: jfzang@hust.edu.cn

Abstract: Soft metamaterials can generate mechanical deformation when subjected to external stimuli like optics, acoustics, mechanics, electric field, magnetic field, etc., resulting in new properties or functions. This talk will summarize our recent works on soft acoustics metamaterials [1-3], and their medical applications including bioinspired cochlear [4], implantable sensors.

Soft metamaterials have the advantages of flexibility, ductility, and biocompatibility, and can be designed on-demand to precisely regulate the physical field and endow with exotic characteristics, which can realize great innovations in complex medical scenarios, difficult medical tasks and better functionality compared with traditional medical devices. A fundamental starting point for the design of soft metamaterials lies in the fact that the very small modulus and low density of the soft substrate need to be considered as this is both an excellent medium for elastic wave transmission and a key parameter affecting elastic wave transmission. Thus, the structural primitives and ordering modes of the soft metamaterials are the basis for the functional design. Based on the principle of local resonance and the translational acoustic method, the structural paradigms of soft metamaterials, including skeletonized hypersurfaces, topological arrangement, disordered hyperuniform distribution, gradient index, and periodical arrangement, are investigated holistically.

First, we have fabricated a porous network metasurface of soft polymer fiber/rigid beads that are physically equivalent to crosslinked spring-mass resonators based on the electrostatic spinning process. And the traditional paper-cutting art to carve the ultrathin metasurface into hollow-out patterns is incorporated, resulting in a variety of remarkable functions, including acoustic vortex, focusing, and super-resolution.

The above mentioned metasurfaces fall under the category of 2D materials, while soft material takes on a more pronounced role in 3D devices. We study topological states in soft metamaterials. The on-demand reversible switch in topological phase has been achieved by changing filling ratio, tension, and/or compression of the elastic metamaterials with the topological arrangement based on hexagonal lattice. By combining two elastic metamaterials with distinct topological invariants, we further demonstrate the formation and dynamic tunability of topological interface states by mechanical deformation, and the manipulation of elastic wave propagation. Our approaches to dynamically control interface states in soft materials paves the way for the precise regulation and utilization of acoustic waves on the surface of the human body.

Soft metamaterials are capable of not only controlling the fundamental properties of waves, but also the energy concentration of waves. Based on the disordered hyperuniform distribution, we constructed an acoustic black hole achieving a remarkable concentration of vibrations in broad frequency bands by a maximum enhancement factor of ~4000 at 1930 Hz. The disordered hyperuniform elastic metamaterials (DHEM), with

rational sizes from ~1 cm to ~1000 cm, covers a broad range of frequencies from ~10 Hz to ~10 kHz. Moreover, the soft DHEM enabling conformal attachments on uneven object. This demonstrates the promise of the application of elastic waves in the human body, such as elastic wave lithotripsy, surgery, and signal transmission.

The acoustic rainbow trap effect is realized by gradient index metamaterials, deduced by transformation acoustic theory. Based on this, a bioinspired soft elastic metamaterial that reproduces the shape and key functions of the human cochlea is reported. Inspired by human cochlea, the metamaterials are designed to possess graded microstructures with high effective refractive index distributed on a spiral shape to implement position-related frequency demultiplexing, passive sound enhancements of 10 times, and high-speed parallel processing of 168-channel sound/piezoelectric signals. Besides, it is demonstrated that natural hearing artificial cochlea has fine frequency resolution up to 30 Hz, a wide audible range from 150–12 000 Hz, and a considerable output voltage that can activate the auditory pathway in mice. This work blazes a promising trail for reconstruction of natural hearing in patients with severe hearing loss.

The phononic crystal is the most fundamental acoustic metamaterial and have been extensively and intensively studied. When it is combined with soft materials, such as hydrogels, additional advantages will be integrated. We present an implantable, bioresorbable, and wireless metastructured hydrogel (metagel) sensor for continuously monitoring of in vivo signals. The metagel sensors are encompassing biodegradable and stimulus-responsive hydrogels as well as periodically aligned air columns with a specific acoustic reflection spectrum. Implanted into animal bodies (rat, pig), the metagel can sensitively detect physiological environment signals including strain, pressure, temperature, and pH. The metagel sensor provides promising multiparametric sensing performances on par with conventional non-resorbable wired clinical benchmarks.

In summary, we have revealed new applications for different structural paradigms, especially in the biomedical field, which greatly expand the idea and direction of novel medical device design and are expected to play a disruptive role in the diagnosis and treatment of difficult and complicated diseases.

References

1. Shuaifeng Li, Degang Zhao, Hao Niu, Xuefeng Zhu, Jianfeng Zang*, Observation of elastic topological states in soft materials, Nature Communications, 2018, 9, 1370.
2. Hanchuan Tang, Zesi Chen, Ni Tang, Shuaifeng Li, Yaxi Shen, Yugui Peng, Xuefeng Zhu*, and Jianfeng Zang*, Hollow-out patterning ultrathin acoustic metasurfaces for multi-functionalities using soft fiber/rigid bead networks, Advanced Functional Materials, 2018, 1801127.
3. Hanchuan Tang, Zhuoqun Hao, Ying Liu, Ye Tian, Hao Niu, Jianfeng Zang*, Soft and disordered hyperuniform elastic metamaterials for highly efficient vibration concentration, National Science Review, 2022, 9, nwab133.
4. Hanchuan Tang, Shujie Zhang, Ye Tian, Tianyu Kang, Cheng Zhou, Shuaikang Yang, Ying Liu, Xurui Liu, Qicai Chen, Hongjun Xiao*, Wei Chen*, Jianfeng Zang*, Bioinspired Soft Elastic Metamaterials for Reconstruction of Natural Hearing, Advanced Science, 2023,10, 2207273.

Design of Thin Film Metamaterial Absorber for IoT Application

T. Matsui[1*], T. Narita, S. Yoshikawa

[1] Department of Electrical and Electronic Engineering, Graduate School of Engineering, Mie University, Japan
*corresponding author: matsui@elec.mie-u.ac.jp

Abstract: We show numerical designs of the thin film metamaterial absorber. We designed a subwavelength-thick ground plane-less and reflection-less metamaterial absorber that shows frequency-selective narrow-band near-perfect absorption, and also designed polymer thin film metamaterial absorber that can be fabricated by printing technology, both work at 2.4 GHz for IoT application.

With the advent of metamaterials, a rich variety of novel concepts such as negative index, super- and hyper-lens, and optical cloaks that cannot be obtained from natural materials have been demonstrated in recent years. Many studies have been devoted to invent metamaterials with optical effects for more practical device applications, and among these, metamaterial perfect absorbers (MPAs) [1–4] are promising. We have so far developed metamaterial absorber that shows frequency-selective absorption working at the Wi-Fi band of 2.4 GHz and low reflection in a wide spectral range [5]. The absorber does not have a ground plane and is constructed with a square array of pairs of C-shaped split-ring resonators (SRRs) orthogonally arranged in such a way that induced electric and magnetic dipoles destructively interfere and no reradiation of electromagnetic (EM) waves is observed. The SRRs are made of nichrome with high ohmic loss so that EM energy dissipates as heat. In the optimum design, absorption of 97% is achieved at 2.4 GHz. The thickness of the absorber is 20 mm, which correspond to 1/6 of the wavelength of the EM field [5]. We are aiming at developing more thinner, plate or film type of metamaterial absorber, and here, we demonstrate (1) subwavelength-thick ground plane-less and reflection-less metamaterial absorber that shows frequency-selective narrow-band near-perfect absorption and (2) polymer thin film metamaterial absorber that can be fabricated by printing technology. In this study, the design of the devices and analysis of their microwave responses were performed using 3D EM field

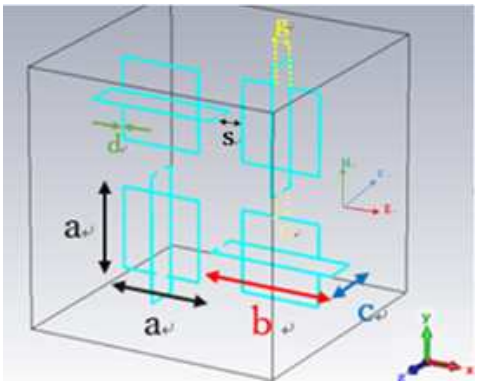


Figure 1. The schematic of the designed reflection-less frequency-selective metamaterial absorber consist of square and rectangular shaped SRRs. The supporting PDMS matrix is omitted for clarity.

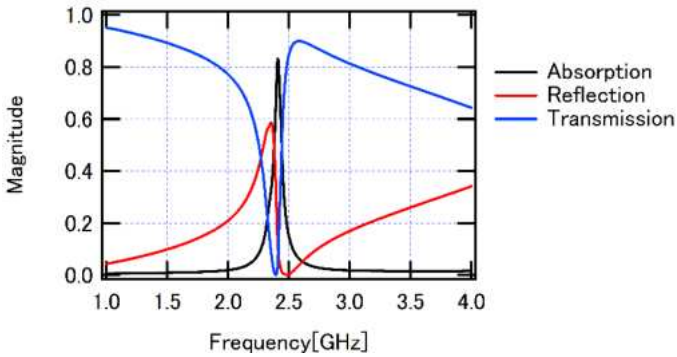


Figure 2. Absorption, reflection, and transmission spectra of the designed metamaterial absorber.

analysis software, CST Studio.

In the first approach, we tried to compress C-shaped SRRs into rectangular shape to make the device thinner as schematically shown in Fig. 1. We assumed to use cupper ($\sigma = 5.8\times10^7$ S/m) for SRRs and PDMS as a supporting material and achieved high absorption of 83% at 2.41 GHz as shown in Fig. 2. The thickness was made down to 7 mm, which correspond to 1/18 of the wavelength of the EM field. In the second approach, we assumed to use one of the most promising π-conjugated polymers, poly(3,4-ethylenedioxythiophene):poly(styrene sulfonate) (PEDOT:PSS) [6] as a ink and fabricate the absorber by screen printing [7]. Details will be presented at the conference. Our basic concept can be extended to higher frequency ranges and may be utilized for next-generation wireless communications, the IoT, and so forth.

Acknowledgements: This project was supported by the Telecommunications Advancement Foundation.

References

1. Landy, N. I., S. Sajuyigbe, J. J. Mock, D. R. Smith, and W. J. Padilla, "Perfect metamaterial absorber," Phys. Rev. Lett., Vol. 100, No. 20, 207402, 2008.
2. Watts, C. M., X. Liu, and W. J. Padilla, "Metamaterial electromagnetic wave absorbers," Adv. Mater., Vol. 24, OP98–OP120, 2012.
3. Cui, Y., Y. He, Y. Jin, F. Ding, L. Yang, Y. Ye, S. Zhong, Y. Lin, and S. He, "Plasmonic and metamaterial structures as electromagnetic absorbers," Laser Photonics Rev., Vol. 8, No. 4, 495–520, 2014.
4. Wang, B.-X., C. Xu, G. Duan, W. Xu, and F. Pi, "Review of Broadband Metamaterial Absorbers: From Principles, Design Strategies, and Tunable Properties to Functional Applications", Adv. Funct. Mater., Vol. 33, 2213818, 2023.
5. Matsui, T., S. Taniguchi, K. Yoshida and H. Murata, "Reflection-less frequency-selective microwave metamaterial absorber", OSA Continuum, Vol. 4, No. 8, 2351–2363, 2021.
6. Zhang, X., W. Yang, H. Zhang, M. Xie and X. Duan, "PEDOT:PSS: From conductive polymers to sensors", Nano. Prec. Eng., Vol. 4, 045004, 2021.
7. Li, Z., S. K. Sinha, G. M. Treich, Y. Wang, Q. Yang, A. A. Deshmukh, G. A. Sotzing and Yang Cao, "All-organic flexible fabric antenna for wearable electronics", J. Mater. Chem. C, Vol. 8, 5662–5667, 2020.

Low-noise metamirrors for the visible spectral range

J. Dickmann[1,2,*], T. Siefke[3,4], J. Hartmann[1,2], N. Wagner[1,2], M. Gaedtke[1,2], A. Waag[1,2], and S. Kroker[1,2,5]

[1]Technische Universität Braunschweig, Institute of Semiconductor Technology, Hans-Sommer-Str. 66, 38106 Braunschweig, Germany.
[2]LENA (Laboratory for Emerging Nanometrology), Langer Kamp 6a/b, 38106 Braunschweig, Germany.
[3]Friedrich Schiller University Jena, Institute of Applied Physics, Albert-Einstein-Strasse 15, 07745 Jena, Germany.
[4]Fraunhofer Institute of Applied Optics and Precision Engineering, Albert-Einstein-Str. 7, 07745 Jena, Germany.
[5]Physikalisch-Technische Bundesanstalt, Bundesallee 100, 38116 Braunschweig, Germany.
[*]corresponding author: j.dickmann@tu-braunschweig.de

Abstract: Explore recent developments in metamirrors, utilizing sub-wavelength micro- and nanostructures. These mirrors offer advantages such as high reflectivity and focusing in a single, thin layer. This talk reviews low-noise meta mirrors for precision applications, tracking progress from infrared to visible spectra, providing insights into the ongoing advancements in this field.

Optical frequency stabilization is integral to modern experiments, essential for applications like interferometric gravitational wave detectors in the infrared [1] and optical atomic clocks in the visible spectrum [2]. Existing laser frequency stabilization systems, relying on Bragg mirrors within optical cavities, face limitations from thermal noise [3]. An innovative solution lies in metamirrors—micro- or nanostructured layers of highly refractive material on a low-refractive substrate (see Fig. 1) [4]. Calculations indicate their potential to reduce thermal noise by over an order of magnitude [5,6]. Recent experiments at 1550 nm demonstrate promising results with cavity finesses reaching 12,000 [4].

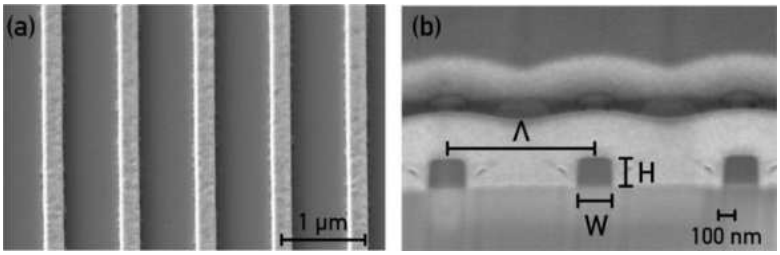


Figure 1: Scanning electron microscope images of a fabricated low-noise meta mirror for a working wavelength of 1550 nm consisting of a structured silicon layer on top of a silica substrate. (a) top view, (b) side view. [4]

Future research aims to explore alternative materials for metamirror fabrication, extending their application wavelength to the visible spectrum. Figure 2 illustrates thermal noise calculations for various metamirror materials such as silicon, diamond, titania, and gallium nitride (GaN), along with their respective working wavelengths. Diamond, with its high Young's modulus, stands out for superior noise performance, surpassing silicon and competitors at the application wavelength. Although titania and GaN exhibit slightly inferior noise performance, likely due to higher mechanical losses, these metamirrors theoretically reduce Bragg mirror thermal noise by over an order of magnitude, translating to a more than 100-fold reduction in noise power density. Moreover, the application wavelength ranges of titania and GaN extend seamlessly into the visible spectrum. With AlGaN, the application wavelengths can even be shifted into the UV, down to 250 nm.

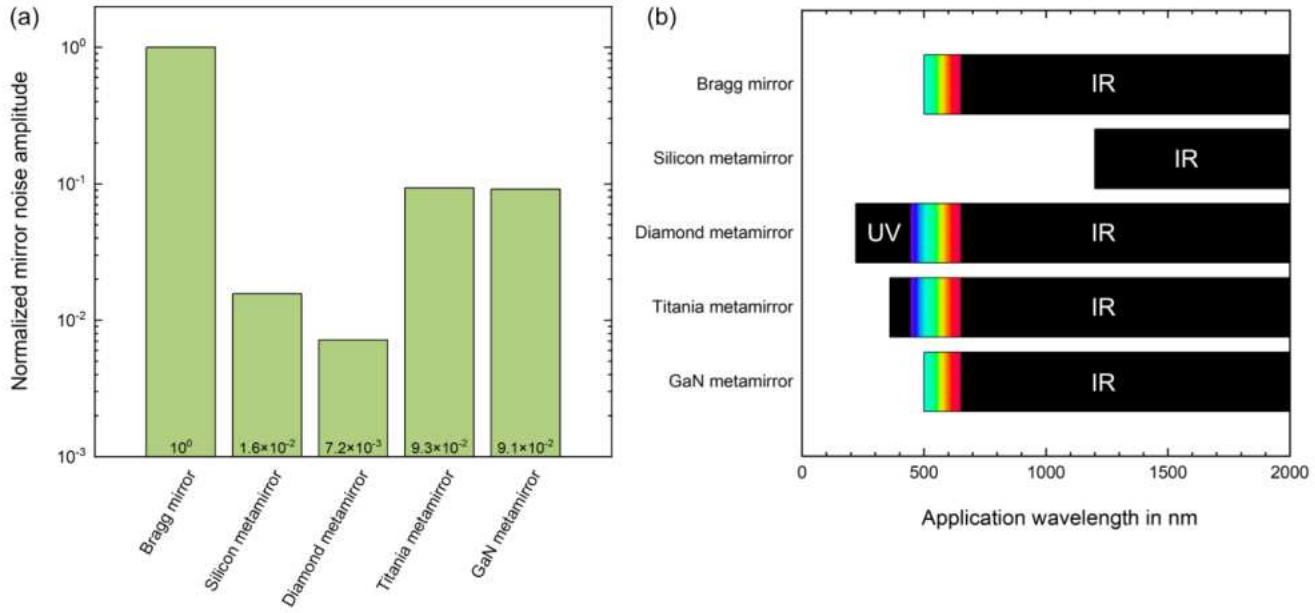


Figure 2: (a) Calculated thermal noise of metamirrors based on different materials, normalized to the thermal noise of a dielectric Bragg mirror consisting of 52 layers made from silica and tantala (wavelength 1.55 µm). (b) Application wavelengths of the different mirrors based on the absorption coefficient (IR – infrared, UV – ultraviolet).

In this talk, we will delve into the latest advancements in low-noise metamirrors, specifically focusing on their applications in the visible spectral range.

Acknowledgements: Funded by the Deutsche Forschungsgemeinschaft (DFG, German Research Foundation) under Germany's Excellence Strategy—EXC-2123 QuantumFrontiers—390837967. J.D. and S.K. also acknowledge partial support by European Association of National Metrology Institutes. This project (20FUN08 NEXTLASERS) has received funding from the EMPIR programme co-financed by the Participating States and from the European Union's Horizon 2020 research and innovation programme.

References

1. The LIGO Scientific Collaboration "Advanced LIGO," Class. Quantum Grav., Vol. 32, 074001, 2015.
2. Ludlow, A. D., et al., "Optical atomic clocks," Rev. Mod. Phys., Vol. 87, No. 2, 637, 2015.
3. Kessler, T., et al., "A sub-40-mHz-linewidth laser based on a silicon single-crystal optical cavity," Nat. Photonics, Vol. 6, No. 10, 687-692, 2012.
4. Dickmann, J., et al., "Experimental realization of a 12,000-finesse laser cavity based on a low-noise microstructured mirror," Commun. Phys., Vol. 6, No. 1, 16, 2023.
5. Dickmann, J., et al., "Influence of polarization and material on Brownian thermal noise of binary grating reflectors," Phys. Lett. A, Vol. 382, No. 33, 2275-2281, 2018.
6. Dickmann, J. and Kroker, S., "Highly reflective low-noise etalon-based meta-mirror," Phys. Rev. D, Vol. 98, No. 8, 082003, 2018.

Metamaterials based Pixelated Thermal Signature Control

Zhuo Li[1], Xiu Liu[1], Yibai Zhong[1], Lin Wang[2], Tak Sing Wong[2], Han Wang[3], Jing Kong[4], Xu Zhang[1] and Sheng Shen[1*]

[1]Carnegie Mellon University, USA
[2]Pennsylvania State University, USA
[3]University of Hong Kong, Hong Kong
[4]Massachusetts Institute of Technology, USA
[*]corresponding author: sshen1@cmu.edu

Abstract: We will present two examples about metamaterials based pixelated thermal signature control. Inspired by leafhopper-generated brochosomes, we designed binary metastructures functioning as pixel twins to achieve pixelated thermal signature control at the microscale. We also experimentally demonstrated dynamic, pixelated modulation of coherent emission based on an electrically programmable plasmonic metasurface.

Inspired by leafhopper-produced brochosomes, here we introduce an infrared signature management solution by pixelating surfaces with a spatial resolution down to the micrometer level with a pair of micro-sized pixel twins [1]. Brochosomes are hollow spherical structures with distributed open pores interconnected by a hollow cavity. Based on the brochosome-inspired pixel twins, we demonstrate a dual effect of concealing binary information/images in the visible range but displaying them in the infrared range via thermal excitation, without relying on external light sources such as lasers. To mimic the binary states in digital electronics, these brochosome-like pixel (BLP) twins are engineered with either open pores (op-BLPs) or closed pores (cp-BLPs) and perform as the building blocks for spatial emissivity manipulation. BLP twins show distinct emissivities when thermally excited, which form infrared counterparts of the binary states 0 and 1. Therefore, images can be encoded using a 'bitmap' consisting of the pixel twins, which can then be visualized using infrared imaging systems. This pixel-by-pixel approach employs unique brochosome geometries, instead of specific material property for emissivity control, and thus is compatible with different substrates. Remarkably, the two types of BLPs share similar appearances when observed under visible imaging systems. This similarity allows the stored patterns formed by one type of BLPs to blend with the background formed by the other. This effect resembles 'background matching', a common camouflage strategy in nature. To the best of our knowledge, this is the first time that a pair of microscopic structures has been designed to be distinguishable in the infrared range, while remaining indistinguishable in the shorter visible range, despite the fact that the shorter wavelength typically provides a finer spatial resolution, according to the Rayleigh criterion.

To date, various methods have been employed to actively excite thermal infrared metasurfaces, such as thermal hot plate, mechanical actuation, and optical laser pulse. However, the realization of electrically programmable on-chip integration for large-area pixelated 2D arrays remains a significant challenge. Single-pixel active metasurfaces, by electrically modulated refractive indices of materials like graphene and transparent conductive oxides, typically yields limited infrared emissivity contrast. Joule heating in an incandescent metasurface with a fixed resistance restricts the pixel modulation to binary on/off states and imposes constraints on the available design parameters for coherent characteristics due to the overlap of electrodes with the optically active region. Although state-of-the-art research has predominantly featured with

in-plane fan-out writing designs for 1D arrays, the electrically driven 2D pixelated metasurfaces have rarely been demonstrated due to the complexities of electrical addressing.

In this work, we experimentally demonstrate the pixelated modulation of coherent thermal emission from an electrical-programmable plasmonic metasurface integrated with a graphene field effect transistor (Gr-FET) [2]. The exceptionally broadband transparency of single-layer graphene enables the free-form control over plasmonic meta-atoms fulfilling the design space for controlling mid-infrared coherent states across a wide range of wavelengths and polarizations. The spatial temperature modulation generated by the Gr-FET is effectively synergized with the emissivity control by the localized surface plasmon polaritons (LSPPs) from gold nanoantennas. This integrated temperature-emissivity modulation is systematically extended to form a pixelated 2D array, signifying a new approach toward scalable 2D electrical wiring for densely packed, individually addressable pixels. Specifically, a 3×3 sweeping pixel array demonstrates diverse alphanumeric displays, supported by an explicit analytical model detailing the control mechanism. Our method offers superior potential in large-area scalability: to independently control N×N pixel arrays, but only 2N+1 electrical pins rather than N^2 pins are required. The extremely small thermal mass from the ultrathin graphene film further enables rapid modulation, achieving a 3-dB bandwidth of 146 kHz in a total 95 μm×95 μm device. In conjunction with the CMOS-compatible fabrication and outstanding high-temperature resilience of the large-area chemical vapor deposited (CVD) graphene, our device represents a significant stride in the development of next-generation mid-infrared active metadevices.

Acknowledgements: We acknowledge the contributions from Jiayu Li, Hyeong Seok Yun, Zexiao Wang Tianyi Huang, Sen Lin, Jingyi Zou, Haozhe Wang, Zhien Wang, Xiao Luo, Rui Cheng for this work. This work is funded by the Office of Navy Research (Awards #N00014-20-1-2095, #N00014-21-1-2337, and #N00014-23-1-2173), National Science Foundation (Grant No. CBET-1931964) and Defense Threat Reduction Agency (Grant No. HDTRA1-19-1-0028). J. K. acknowledges the support from the Semiconductor Research Corporation Center 7 in JUMP 2.0 (Grant No. 145105-21913) and the U.S. Army DEVCOM ARL Army Research Office through the MIT Institute for Soldier Nanotechnologies under Cooperative Agreement number W911NF-23-2-0121. Z.L. acknowledges the support from the Liang Ji-Dian Graduate Fellowship.

References

1. Li, Z., Wang, L., Liu, X., Li, J., Yun, H., Wang, Z., Zhang, X., Wong, T.-S. and Shen, S. “Brochosome-inspired binary metastructures for pixel-by-pixel thermal signature control,” *Science Advances*, in press, 2024.
2. Liu, X., Zhong, Y., Wang, Z., Huang, T., Lin, S., Zou, J., Wang, H., Wang, Z., Li, Z., Luo, X., Cheng, R., Li, J., Yun, H., Wang, H., Kong, J., Zhang, X. and Shen, S., submitted, 2024.

Multipole coupling for control light propagation and trapping in dielectric and hybrid metasurfaces

A. B. Evlyukhin[1,2*], I. Allayarov[2,3,4], A. Calà Lesina[2,3,4], and B. N. Chichkov[1,2]

[1]Institute of Quantum Optics, Leibniz University Hannover, Welfengarten 1, Hannover 30167, Germany

[2]Cluster of Excellence PhoenixD, Leibniz University Hannover, Hannover 30167, Germany

[3]Hannover Centre for Optical Technologies, Leibniz University Hannover, Hannover 30167, Germany

[4]Institute of Transport and Automation Technology, Leibniz University Hannover, Garbsen 30823, Germany

[*]corresponding author: evlyukhin@iqo.uni-hannover.de

Abstract: A general concept of multipole coupling is discussed to explain the control of light propagation and trapping in dielectric and hybrid metasurfaces. Several examples with important application perspectives are presented.

We demonstrate and discuss multipole mechanisms for controlling light propagation and the trapping effect in structures composed of dielectric nanoparticles supporting electric and magnetic multipole resonances. First, the concept of multipole coupling is introduced to explain what type of multipoles can be coupled and why in periodic nanoparticle structures (metasurfaces). Then, a realization of such coupling for light trapping, which does not require special conditions of irradiation with incident light or geometric distortion of the symmetry of periodic structures, is presented. It is shown that the trapping effect can arise due to energy exchange between multipole moments of the same parity symmetry excited in different nanoparticles of a symmetrical structure. As an example, we consider how multipole coupling in a metasurface consisting of particles with high refractive index leads to the excitation of a dark electric octupole mode with strong energy storage in the plane of the metasurface [1]. The realization of a multiresonance response [2] and accidental quasi bound states in the continuum (BICs) associated with multipole interactions in symmetric metasurfaces is demonstrated. We further demonstrate the effects of magneto-electric multipole coupling in metasurfaces and individual structures consisting of particles with bianisotropic electromagnetic response. A general strategy for the realization of the resonant absorption band in metasurfaces consisting of bianisotropic hybrid (dielectric/metal) particles is also discussed [3]. The presented mechanisms have a general character and can be realized in many structures, which opens new perspectives for their application.

References

1. Prokhorov A. V., M. Yu. Gubin, A. V. Shesterikov, A. V. Arsenin, V.S. Volkov, A. B. Evlyukhin. Nano Letters, “Lasing effect in symmetrical van der Waals heterostructured metasurfaces due to lattice-induced multipole coupling,” Vol. 23, 11105−11111, 2023.
2. Allayarov I, A. B. Evlyukhin, A. Calà Lesina, “Multiresonant all-dielectric metasurfaces based on high-order multipole coupling in the visible,” Opt. Express, Vol. 32, 5641-5658, 2024.
3. Ma H., A. B. Evlyukhin, A. E. Miroshnichenko, F. Zhu, S. Duan, J. Wu, C. Zhang, J. Chen, B. Jin, W. J. Padilla, K. Fan. “Extremely thin perfect absorber by generalized multipole bianisotropic effect,” Adv. Opt. Matt. 2301968, 2023.

Structural Properties of Nanoporous Gold Metamaterial for Optical Applications

Xinyan Wu[1*], Fatemeh Ebrahimi[1,2], Maurice Pfeiffer[1], Nadiia Mameka[3], Manfred Eich[1,2], and Alexander Petrov[1,2]

[1] Hamburg University of Technology, Institute of Optical and Electronic Materials, Hamburg, Germany

[2] Helmholtz-Zentrum Hereon, Institute of Functional Materials for Sustainability, Geesthacht, Germany

[3] Helmholtz-Zentrum Hereon, Institute of Materials Mechanics, Geesthacht, Germany
[*]corresponding author: xinyan.wu@tuhh.de

Abstract: Nanoporous gold (npAu), known for its adjustable large surface-to-volume ratio and broadband light absorption, exhibits potential for advanced optical applications. Our study investigates the npAu structural properties and its impact on absorption, electron collision frequency and photoemission efficiency. Optimizing npAu feature sizes enhanced performance in photocatalysis processes is demonstrated.

In this study, we investigate the fabrication of high quality npAu thin film with adjustable feature sizes, and apply it as model material for a comprehensive study of surface effects on absorption, photoemission efficiency and electron collision frequency. Electrochemical dealloying was employed to provide a precise control of the selective dissolution of the less noble metal (Ag) from a AuAg leaf precursor to produce npAu thin film (around 140 nm thick). NpAu gold thin film with small ligament sizes can be obtained from dealloying at high potentials, which induce a fast removal of Ag atom and less diffusion of Au atom to coarsen. The smallest ligament can reach down to about 6.5 nm, as shown in Fig 1, and the overall average ligament size is around 8 nm.

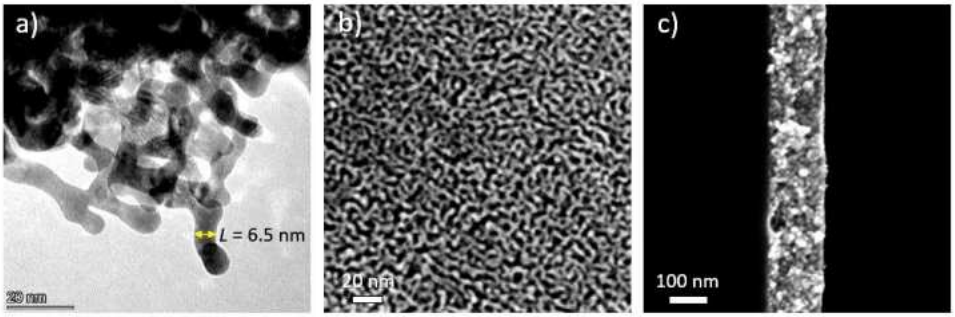


Figure 1. a) the microstructure of top view from Transmission Electron Microscope, b) microstructure of top view from Scanning Electron Microscope, c) the microstructure of side view from Scanning Electron Microscope

Then we conducted photoelectron injection from npAu into the electrolyte under UV illumination to investigate electron transfer processes. Simultaneously, cyclic voltammetry scans from a potentiostat were applied to coarsen npAu thin films from a small initial ligament sizes (below 10nm), allowing for an *in-situ* study of the influence of npAu ligament size on photocurrent. The resulting variations in ligament size were verified using Scanning Electron Microscopy (SEM). By strategically limiting the upper scan potential, subtle changes in ligament size were obtained, providing a means to modify the surface-to-volume ratio of npAu at the lower limit of the nanoscale.

Our results, as shown in Fig 2, demonstrate that the internal quantum efficiency of the npAu network photoelectrode is significantly influenced by ligaments of npAu thin film. We observed a notable trend: as the ligament size increased from ~8 to ~16 nm, the quantum efficiency exhibited a corresponding decrease, following with high precision the inverse square relationship to the ligament size. In contrast to prior findings [1] that suggested efficiency would level

off with decreasing ligament size, we did not find any saturation effect within this range of ligament sizes. The parabolic dependence on the inverse ligament size shows the dominant role of surface photoemission in the observed photocurrent with a smaller contribution of volume photoemission.

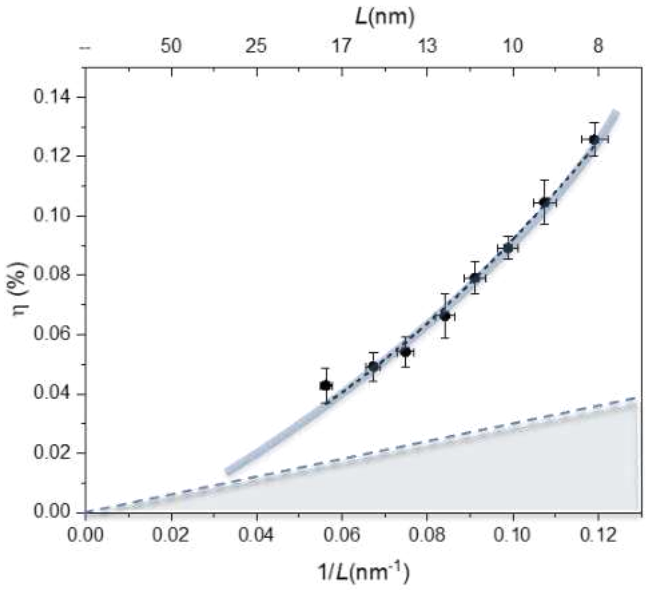


Figure 2. Size dependence of the internal quantum efficiency η of photoemission at a wavelength λ = 291 nm measured at 0.33 V vs. RHE. The dashed line represents a parabolic fit with linear and quadratic terms versus inverse ligament size L^{-1}. The shaded area under dashed curve shows the volume contribution.

In the study of absorption of npAu, we integrated an electrochemical cell on a spectroscopic ellipsometer, enabling in-situ measurements of optical properties during electrochemical processes, such as surface oxidation and reduction. The oxidized surface with large surface to volume ratio is believed to cause an enhanced effective electron collision frequency of metal [2,3]. Previous research on gold nanoparticles demonstrated an increased damping rate at the plasmon resonance [4]. Our results on flat gold also exhibited a similar effect, holding promise for observing more pronounced effects on npAu gold with a much larger surface area.

References

1. Graf, Matthias, et al. "Surface-to-volume ratio drives photoelelectron injection from nanoscale gold into electrolyte." ACS catalysis 9.4 (2019): 3366-3374.
2. Graf, Matthias, Gregor B. Vonbun-Feldbauer, and Marc TM Koper. "Direct and broadband plasmonic charge transfer to enhance water oxidation on a gold electrode." ACS nano 15.2 (2021): 3188-3200.
3. Khurgin, Jacob, et al., “Direct Plasmonic Excitation of the Hybridized Surface States in Metal Nanoparticles,” ACS Photonics 8 (2021): 2041–2049.
4. Foerster, Benjamin, et al. "Interfacial states cause equal decay of plasmons and hot electrons at gold–metal oxide interfaces." Nano Letters 20.5 (2020): 3338-3343.

Hot-electron induced chemistry using chiral and non-chiral plasmonic nanostructures

S. Gahlaut[1], C. Beresowski[1], S. Kogikoski[1] and I. Bald[1*]

[1] Institute of Chemistry, University of Potsdam, Germany
[2]Author Affiliation, Country
[*]corresponding author: bald@uni-potsdam.de

Abstract: We investigate the influence of nanoparticle structure and excitation condition on the rate of plasmon-induced chemical reactions using surface-enhanced Raman scattering (SERS). In particular, we focus on the size of Au and Ag nanoparticles, as well as chiral Au nanocubes using excitation with circularly polarized light.

One of the most intriguing applications of plasmonic nanoparticles is based on their ability to transform the energy of light into chemical energy. A broad range of chemical transformations have been demonstrated already to be triggered directly by excitation of the nanoparticle's surface plasmon resonance. It is still debated whether hot electrons or heat are driving the plasmon-induced chemical reactions, but the details depend on the respective chemical systems and the nanoparticle species. We have recently established the plasmon-induced transformation of 8-bromoadenine into adenine as a model system, in which the carbon-bromine bond is cleaved by an irreversible transfer of a hot electron from the light-excited nanoparticle to the 8-bromoadenine molecule.[1,2] We have characterized the kinetics of the plasmon-induced dissociation of 8-bromoadenine by surface-enhanced Raman scattering (SERS) on Au and Ag nanoparticles, and with 8-bromoadenine incorporated into DNA. [1,2]

The plasmon-induced molecular transformations can be controlled by the choice of nanoparticle species. In this contribution we systematically explore two aspects of nanoparticle structure: i) The influence of nanoparticle size on the rate of bromoadenine decomposition is studied using SERS. ii) The possibility to control the reactivity of molecular transformations by polarization is explored using chiral Au nanocubes, which are excited with either left- or right-handed circularly polarized light. We demonstrate that reaction rates are increasing with the size of nanoparticles within nanoparticle clusters. With chiral Au nanocubes the reaction rates depend on the polarization of the excitation light and the photochemical g factor can exceed the optical g factor and can be boosted by choosing proper excitation conditions. This allows for precise control of plasmonic reactivity by the choice of nanostructure and excitation condition.

References

1. A. Dutta, R. Schürmann, S. Kogikoski Jr., N. S. Mueller, S. Reich and I. Bald "Kinetics and Mechanism of Plasmon-Driven Dehalogenation Reaction of Brominated Purine Nucleobases on Ag and Au," ACS Catal., 11, 8370-8381, 2021.
2. S. Kogikoski Jr., A. Dutta and I. Bald, "Spatial Separation of Plasmonic Hot-Electron Generation and a Hydrodehalogenation Reaction Center Using a DNA Wire", ACS Nano, 15, 20562, 2021.

Plasmon-enhanced nanospectroscopy for molecular sensing and control

Taka-aki Yano[1,2]

[1] Tokushima University, 2-1 Minami-Josanjima, Tokushima 770-8506, Japan
[2] RIKEN, Wako, Saitama 351-0109, Japan

*corresponding author: yano.takaaki@tokushima-u.ac.jp

Abstract: We present plasmon-enhanced nanospectroscopy using a sharp metallic tip which enables us to demonstrate not only nanoscale sensing but also nanoscale control of molecular reactions.

We have been developing a variety of laser-based nanospectroscopic methods in combination with plasmonics and metamaterials where optical nanostructures play a crucial role in enhancing various optical signals (visible absorption/reflection, Raman scattering, fluorescence, infrared absorption) from targeting molecules. Here in this talk, we focus on active plasmon-enhanced Raman microscopy using a plasmonic tip which enables us to demonstrate not only nanoscale observation but also nanoscale control of molecular reactions.

Tip-enhanced Raman scattering (TERS) microscopy is a powerful surface analytical tool with single molecule sensitivity and nanoscale spatial resolution. A sharp metallic probe tip plays important roles in plasmonically enhancing Raman scattering from sample molecules in the vicinity of tip. We demonstrated TERS spectroscopy of a single gold-binding peptides (GBP) which exhibit specific binding affinity to gold surface, as schematically shown in Fig. 1(a). The time-dependent TERS spectra in Fig. 1(b) show temporal fluctuations of both TERS intensity and frequency, enabling us to spectroscopically elucidate the binding sites and mechanisms.

Recently, we have developed a new type of TERS microscopy in combination with local application of external stimuli such as pressure and voltage to sample molecules through the tip apex (Fig. 2), enabling us to induce various chemical reactions in the vicinity of the tip. The chemical reactions were spectroscopically probed by detecting tip-enhanced Raman scattering in response to the external stimuli.

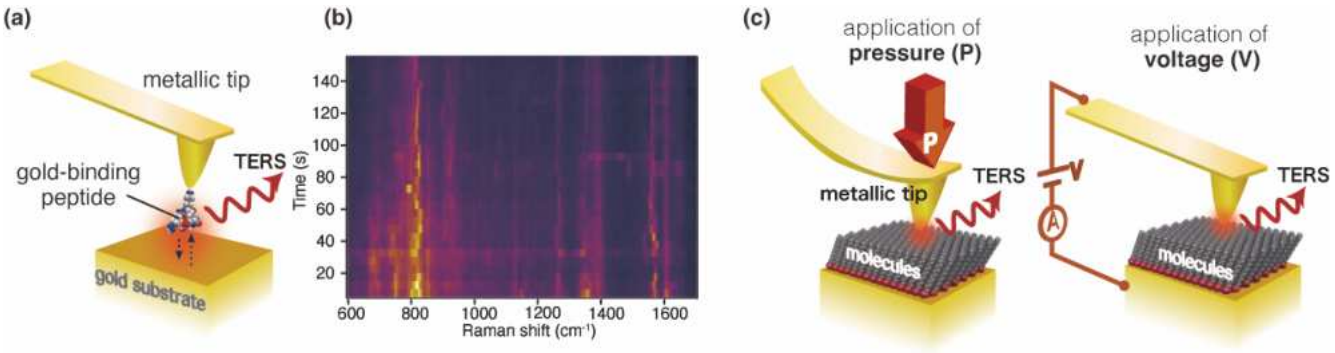


Figure 1 (a) Schematic of TERS measurement of a single gold-binding peptide (GBP) adsorbed on the gold substrate. (b) Time-dependent TERS spectra of GPB. (c) Advanced TERS microscopies in combination with tip-applied external stimuli.

Ultrabroadband polarization-independent directional thermal emission

Ziwei Fan[1,3], Taeseung Hwang[2], Sam Lin[2], Yixin Chen[2], Zi Jing Wong[1,2,3]*

[1] Department of Aerospace Engineering, Texas A&M University, College Station, USA.
[2] Department of Materials Science and Engineering, Texas A&M University, College Station, USA.
[3] School of Electronic Science and Technology, Eastern Institute of Technology, Ningbo, China.
*corresponding author: zijing@tamu.edu

Abstract: By leveraging non-imaging optical principles, a pixelated micro-emitter is experimentally demonstrated for ultrabroadband, polarization-independent directional control of thermal radiation. This design enables high emissivity contrasts at different view angles. By exploiting the tunable angular range of the pixelated micro-emitter, we create an infrared display with directionally encoded information.

The intrinsic quasi-isotropy of thermal radiation hinders potential advancements in radiative cooling, thermal sensing, thermal photovoltaic and incandescent infrared lighting. Thus, directional thermal radiation is highly sought after and has been realized within narrow spectral ranges with phonon polariton gratings[1], plasmonic metasurfaces[2], nanoantenna[3], and bull's eye structures[4]. However, these works only realized directional control of thermal emission over a narrow wavelength range with reduced radiative efficiency. Recent efforts have been made to remove the bandwidth limitation by utilizing the Brewster effect[5], impedance engineering[6], and gradient epsilon-near-zero (ENZ) metamaterials[7]. Nevertheless, these approaches only controlled p-polarized thermal emission over an insufficiently wide spectral range. A novel design with polarization-independence and ultrabroad bandwidth is therefore desired.

Here we design a three-dimensional (3D) pixelated directional micro-emitter (PDME) whose pixel structure is composed of parabolic reflectors on a thermal emitter. Our design centers on the concept of etendue conservation, where etendue is proportional to both areal and angular spread of light. By mapping thermal emission from a small area A_0 to a large area A_1 (Figure 1a), the angular range of thermal emission will be reduced at A_1 owing to the conservation of etendue. Figure 1b inset shows an SEM image of the fabricated PDME with 15° acceptance angle (15°-PDME), demonstrating high structural quality. We characterize the angular-resolved thermal emissivity of the 15°-PDME through radiometric measurements over the range of 7.5 – 14 μm. In Figure 1b, an angular width of ±16° is identified, with the maximal emissivity over 0.8, well matching the design and simulated results. The emissivity for different polarizations matches each other, proving the polarization-independent feature of the PDME. Spectral characterization was performed with a Fourier-transform infrared spectrometer (FTIR), showing abrupt emissivity drop over a large spectral range (5-20 μm) when the angle increases (Figure 1c).

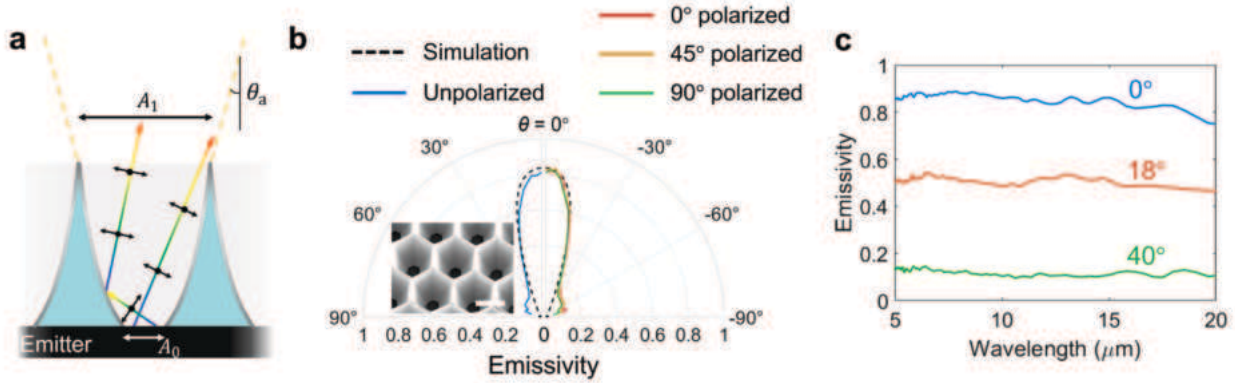


Figure 1 | a, 2D illustration of the PDME. **b**, Angular-resolved thermal emissivity for unpolarized and polarized thermal emission from the 15°-PDME. The inset shows an SEM image of the 3D hexagonal pixels, scale bar: 50 μm. **c**, Measured emissivity spectra of the 15°-PDME from different angles.

Next, we explore the tunability of our directional micro-emitter to create a pixelated display that directionally encodes infrared information and achieves thermal camouflage. By integrating pixels with varying acceptance angles (Figure 2a), we produce IR messages visible only from certain directions, effectively camouflaging them in the background. For example, the "TAMU" pattern was visible at approximately 30°, but obscured at other angles (Figure 2b).

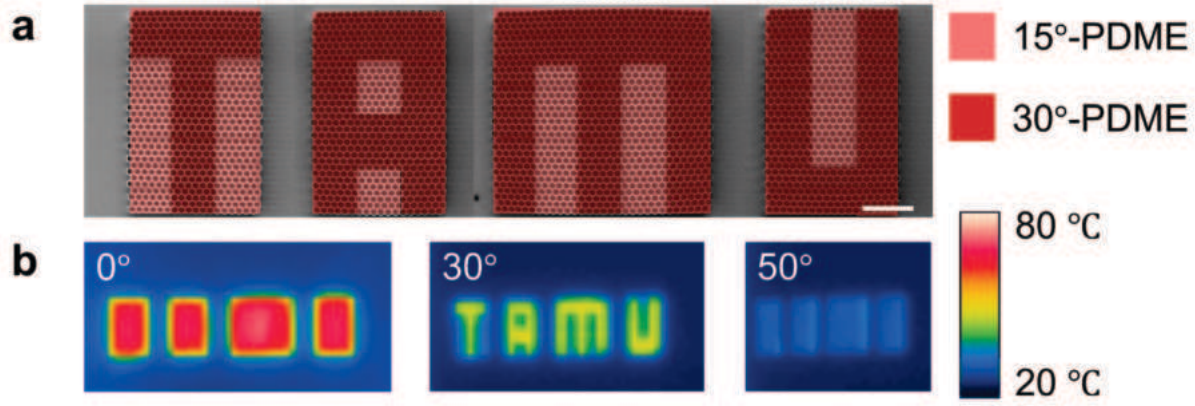


Figure 2 | a, SEM image (scale bar: 500 μm) and **b,** thermal images of a pixelated PDME camouflage composed of 30° and 15°-PDME pixels.

In summary, we have created a compact pixelated directional micro-emitter exhibiting performance superior to previous works, including polarization-independence, high emissivity (> 0.8), narrow angular range (down to ±16°) and an ultrabroad spectral range (5 – 20 μm). We further demonstrate the PDME's ability to encode information into the viewing angle of infrared displays.

References

1 Greffet, J.-J. *et al.* "Coherent emission of light by thermal sources". Nature Vol. 416, 61-64, 2002.

2 Costantini, D. *et al.* "Plasmonic Metasurface for Directional and Frequency-Selective Thermal Emission". Phys. Rev. Appl. Vol. 4, 014023, 2015.

3 Centini, M. *et al.* "Hybrid thermal Yagi-Uda nanoantennas for directional and narrow band long-wavelength IR radiation sources". Opt. Express Vol. 28, 19334-19348, 2020.

4 Han, S. E. & Norris, D. J. "Beaming thermal emission from hot metallic bull's eyes". Opt. Express Vol. 18, 4829-4837, 2010.

5 Qu, Y., Pan, M. & Qiu, M. "Directional and Spectral Control of Thermal Emission and Its Application in Radiative Cooling and Infrared Light Sources". Phys. Rev. Appl. Vol. 13, 064052, 2020.

6 Argyropoulos, C., Le, K. Q., Mattiucci, N., D'Aguanno, G. & Alù, A. "Broadband absorbers and selective emitters based on plasmonic Brewster metasurfaces". Phys. Rev. B Vol. 87, 205112, 2013.

7 Xu, J., Mandal, J. & Raman, A. P. "Broadband directional control of thermal emission". Science Vol. 372, 393-397, 2021.

Förster resonance energy transfer in absorbing environment

L. S. Petrosyan[1], M. N. Noginov[2], and T. V. Shahbazyan[1*]

[1]Department of Physics, Jackson State University, Jackson, MS 39217 USA
[2]Center for Materials Research, Norfolk State University, Norfolk, VA 23504, USA
*corresponding author: shahbazyan@jsums.edu

Abstract: We present an analytical model for Förster resonance energy transfer between donors and acceptors in the presence of a metal surface. We find that energy transfer to the metal results in a reduction of the Förster radius, leading to a suppression of concentration quenching for high molecule concentrations.

In this paper, we develop an analytical theory to Förster resonance energy transfer (FRET) between donor and acceptor molecules in the presence of an inhomogeneous absorbing environment such as metallic structures characterized by a complex dielectric function. Specifically, we show that energy transfer to the environment, which accompanies FRET, results in a reduction of the Förster radius R_F characterizing FRET efficiency between the molecules. For large concentration of molecules situated near a metal surface, this leads to a suppression of fluorescence concentration quenching for small average molecule separations from the metal and to a reduction of the effective fluorescence decay rate relative to that in homogeneous environment. Our numerical calculations of the effective fluorescence decay rate for molecules embedded in a dielectric slab on top of a metal surface reveal a characteristic minimum at intermediate slab thicknesses for high molecule concentrations, consistent with the experiment [1-2].

We start with the probability rate of acceptor excitation by the donor's electric field [3]

$$W_a(R_{ad},t)=\frac{3c\kappa_{ad}^2}{2\pi\hbar\omega R_{ad}^6}\sigma_a(\omega)|\boldsymbol{p}_d(t)|^2$$

where $\sigma_a(\omega)$ is acceptor's absorption cross-section at the transition frequency ω, R_{ad} is the donor-acceptor separation, $\boldsymbol{p}_d$ is the excited donor's dipole moment causing the transition, and κ_{ad}^2 characterizes molecules' mutual polarization. In the presence of metal surface, the donor's dipole moment is time dependent, $\boldsymbol{p}_d(t)=\boldsymbol{p}_d e^{-\Gamma_d t/2}$, where $\Gamma_d=\gamma_d+\gamma_s$ is the donor's full decay rate comprised of the fluorescence rate γ_d and the energy transfer rate to the metal $\gamma_s \gg \gamma_d$. In this case, to properly define the Förster radius, the FRET probability rate should be averaged over the fluorescence time as

$$W_a'=\tau_d^{-1}\int W_a(t)dt=\left(\frac{\gamma_d}{\Gamma_d}\right)W_a$$

The modified Förster radius R_F' is determined from the condition $\tau_d W_a'(R_{ad})=1$, where τ_d is the free donor's fluorescence decay time, and we obtain

$$\frac{R_F'^6}{R_F^6}=\frac{\gamma_d}{\Gamma_d}$$

indicating that in an absorbing environment the effective Förster radius is reduced.

The emission kinetics is obtained in a standard way by averaging out over random position of the acceptors [3] and we obtain the time-dependent fluorescence intensity as

$$I_d(t)\sim e^{-\Gamma_d t-N_A'\sqrt{\pi\gamma_d t}}$$

where $N_A'=n_A V_F'$ is the acceptor number within modified Förster volume $V'_F=4\pi R_F'^3/3$ and n_A is the acceptor concentration. Thus, in the absorbing environment, the number of acceptors that can be efficiently

excited by the donor is effectively reduced by the factor $\sqrt{\gamma_d/\Gamma_d}$, leading to an interplay between the metal quenching and concentration quenching at intermediate distances to the metal surface.

In Fig. 1a, we show the calculated effective fluorescence decay rate from dielectric film doped by HITS:PMMA die molecules on top of Ag surface versus the film thickness at various die concentrations. These calculations are compared with the experimental data taken on a similar system shown in Fig. 1b [2]. A clear minimum of the effective decay rate is observed for high molecule concentrations indicating that, for intermediate average molecule distances to the metal surface, the metal quenching is weakened while the concentration quenching is still suppressed. The mechanism of this suppression is a reduction of the effective Förster radius in an absorbing environment due to competition between two energy transfer channels.

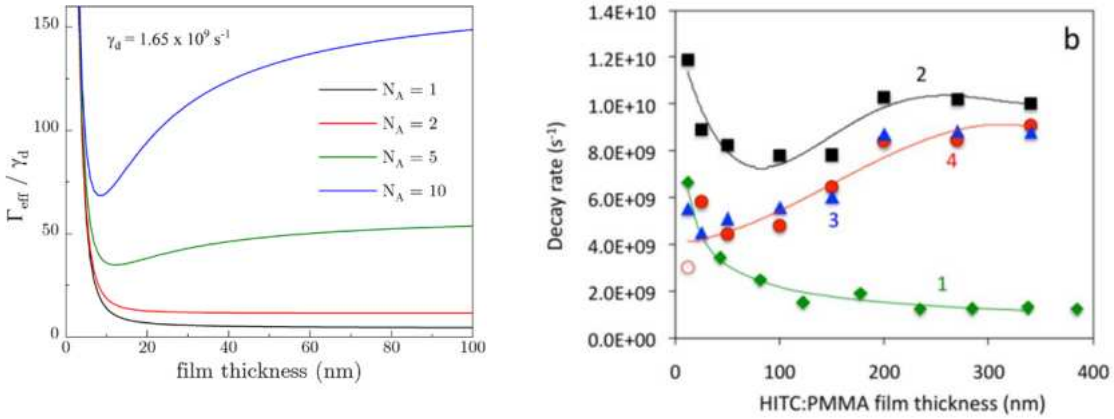


Figure 1. (a) Calculated effective decay rate from dielectric film doped by HITS:PMMA die molecules on top of Ag surface vs. film thickness for various molecule concentrations. (b) Experimental data for the effective decay rate taken on a similar system [2].

References

1. S. Rout *et al*., Nanomaterials 10, 2135 (2020).
2. S. Koutsares *et al*., JOSA B 38, 88 (2021).
3. V. M. Agranovich, M. D. Galanin, *Electronic Excitation Energy Transfer in Condensed Matter* (North-Holland, Amsterdam, 1983)

Resonances in doubly anisotropic, high-index nanoplatelets

Bingying You[1,2], Tom T. C. Sistermans[1,2*], and Alberto G. Curto[1,2*]

[1] Photonics Research Group, Ghent University-imec, Ghent, Belgium
[2] Center for Nano- and Biophotonics, Ghent University, Ghent, Belgium

[*]Corresponding author: Alberto.Curto@UGent.be

Abstract: Optical anisotropy plays a crucial role in the manipulation of light. Its strength is, however, limited to low values in conventional materials. Transition metal dichalcogenides possess both high refractive index and high birefringence. Here, we investigate optical resonances in nanoplatelets with both geometrical and refractive index anisotropies to control light scattering and emission.

Anisotropy plays a crucial role in manipulating light as the basis for optical components such as polarizers, waveplates, or modulators and phenomena like phase matching in nonlinear optics. The functionality of these devices hinges primarily on the retardance between two orthogonal linear polarizations, which is proportional to both the thickness and the birefringence (Δn) of the material. A large birefringence is thus beneficial for the performance and compactness of such components. Birefringence is a tuning degree of freedom for nanophotonics, for example, in electro-optic modulators, waveguides with reduced cross-talk, and electro-optic polarization conversion. Beyond natural materials, metasurfaces and metamaterials can be constructed to achieve high anisotropy but suffer from losses and fabrication challenges. As a result, natural materials with higher anisotropy than conventional dielectrics or metals are in demand.

Transition metal dichalcogenides are promising birefringent materials due to their layered van der Waals structure, which naturally leads to a large intrinsic birefringence above unity. In particular, molybdenum disulfide (MoS_2) possesses the highest birefringence of all natural materials in the near infrared. Such a high birefringence is possible thanks to the presence of strong excitons. They endow MoS_2 with a high in-plane refractive index above 4.5 while making it possible to have higher out-of-plane index contrast than lower index dielectrics. A high refractive index also enables the existence of Mie-type resonances in MoS_2 nanostructures for enhancing and controlling light-matter interaction.

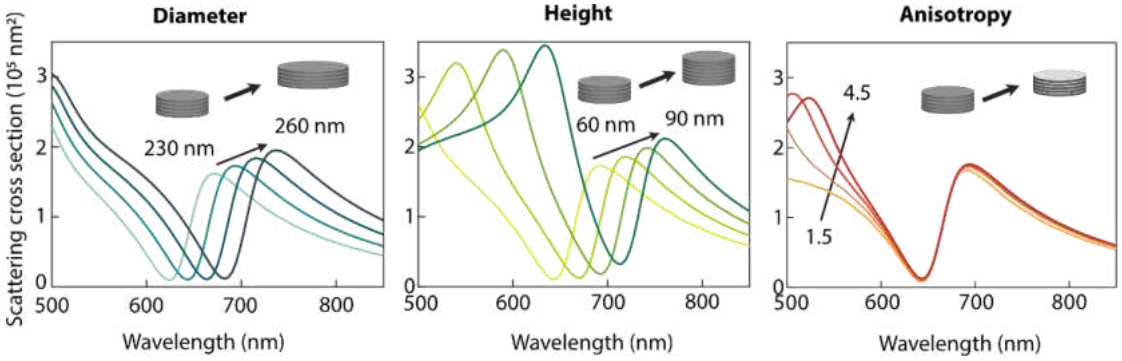


Figure 1. Different dependence of electric and magnetic dipole resonances on geometrical and optical anisotropy.

Here, we study the optical resonances sustained by nanoplatelets made of high refractive index material with high optical anisotropy. Nanoplatelets have both geometrical and refractive index anisotropies. Their high refractive index enables them to sustain electric and magnetic resonances. We find a distinct impact of changing geometric and birefringence on the tunability of electric and magnetic resonances, which we explain using multipolar expansion. Due to their double anisotropy, the optical response of nanoplatelets strongly depends on the direction of illumination, as different illumination conditions can lead to in-plane or out-of plane electric and magnetic multipoles. We also show that nanoplatelets can control the polarization and directionality of the scattering radiation patterns. Finally, we show preliminary experimental results using MoS_2 nanoplatelets.

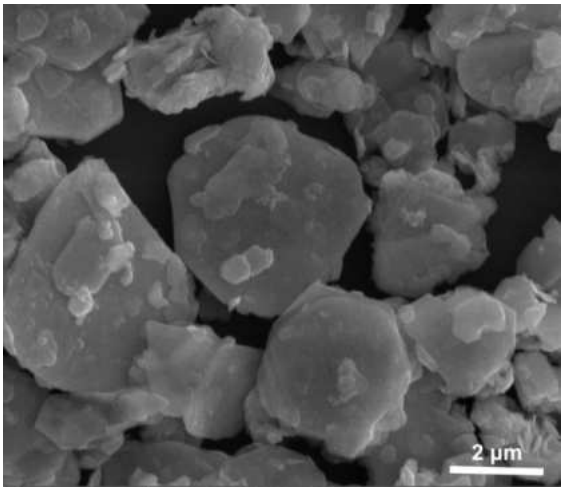


Figure 2. SEM image of MoS_2 nanoplatelets.

In summary, high-refractive-index nanoplatelets with intrinsic out-of-plane anisotropy and large birefringence exhibit a wealth of electric and magnetic multipolar resonances that are sensitive to geometry and anisotropy in distinct manners. We envision that nanoplatelets could be used to enhance and direct light scattering and light emission, with applications in light-emitting devices and lasers.

References

1. Ermolaev, G. A., D. V. Grudinin, Y. V. Stebunov, *et al.*, "Giant optical anisotropy in transition metal dichalcogenides for next-generation photonics," *Nature Communications*, Vol. 12, No. 854, 2021.
2. Verre, R., D. G. Baranov, B. Munkhbat, J. Cuadra, M. Käll, and T. Shegai, "Transition metal dichalcogenide nanodisks as high-index dielectric Mie nanoresonators," *Nature Nanotechnology*, Vol. 14, 679-683, 2019.
3. Hinamoto, T., and Fujii, M., "MENP: an open-source MATLAB implementation of multipole expansion for nanophotonics," *Optics Express*, Vol. 4, No. 5, 1640–1648, 2021.

Electromagnetic enhancement induced by subradiant plasmon resonance demonstrated using single plasmonic systems

T. Itoh[1*], and Y. S. Yamamoto[2]

[1] National Institute of Advanced Industrial Science and Technology (AIST), Japan
[2] Japan Advanced Institute of Science and Technology (JAIST), Japan
[*]corresponding author: tamitake-itou@aist.go.jp

Abstract: Plasmon resonance has been used for exploring the mechanism of surface enhanced Raman scattering (SERS) of single plasmonic systems. We here investigated the relationships between SERS, electromagnetic enhancement factor, and plasmon resonance Rayleigh scattering spectra of single nanoparticle dimers. The numerical analysis revealed that the SERS is mainly caused by dipole-quadrupole coupled resonance, which is subradiant, for asymmetric dimers.

Surface enhanced Raman scattering (SERS) has opened a variety of exciting research fields [1]. Plasmon resonance is a key for the large Raman enhancement based on electromagnetic (EM) mechanism [2]. Dipole-dipole (DD) coupled plasmon resonance coupled with molecular exciton resonance have been focused for reproducing surface enhanced Raman scattering (SERS) with SEF spectra using single plasmonic dimers [3]. However, when the sizes of the NPs of a dimer differ significantly, the largest EM enhancement factor F_R is not generated by the DD-coupled plasmon but by dipole–quadrupole (DQ)-coupled plasmon, which is a subradiant mode [4-6]. In such a situation, the DD-coupled plasmon contributes to transfer the excitation light energy to the DQ-coupled plasmon, and emits SERS with SEF by receiving energy from the DQ-coupled plasmon through near-field interactions. In this case, the DD-coupled plasmon resonance Rayleigh scattering $C_{sca}(\omega)$ spectra obtained by dark-field spectroscopy are not identical to the F_R spectra. This contribution of DQ-coupled plasmon resonance may look the breakdown of EM mechanism; thus, is needed to be carefully examined.

The relationships between SERS with SEF spectra and DD-coupled plasmon resonance $C_{sca}(\omega)$ are systematically

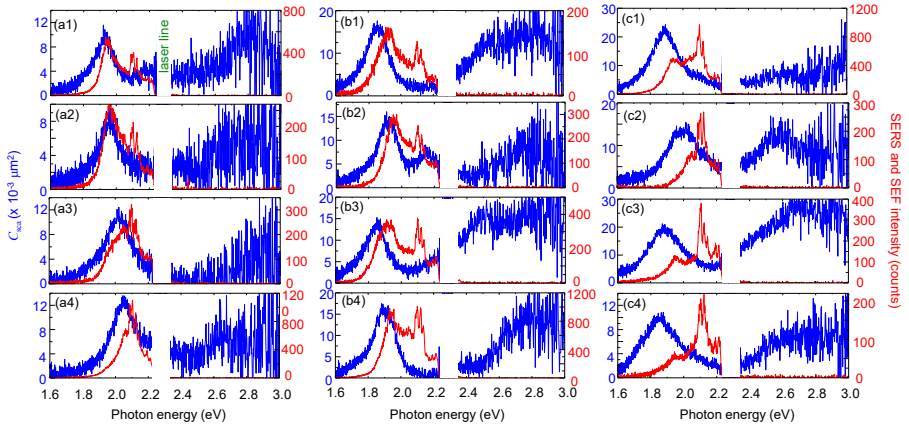


Fig. 1 (a1)–(a4) $C_{sca}(\omega)$ spectra (blue lines) and spectra of SERS and SEF (red lines) of single dimers exhibiting similar spectral shapes (Type I). (b1)–(b4) $C_{sca}(\omega)$ spectra and spectra of SERS and SEF for single dimers exhibiting spectral deviation with respect to each other (intermediate type). (c1)–(c4) $C_{sca}(\omega)$ spectra and spectra of SERS and SEF with maxima that are close to spectral dips in the $C_{sca}(\omega)$ (Type II).

examined for single silver NP dimers to clarify the contribution of DQ-coupled plasmon resonance to SERS with SEF as shown in Fig. 1. The spectral envelopes of the SERS with SEF were mostly similar to those of the plasmon resonance spectra. However, some dimers showed their spectral envelopes that shifted to higher-energy regions from the DD-coupled plasmon resonance maxima. In short, there are two types of relationships: Type I, in which the envelopes of the SERS with SEF are similar to the plasmon resonance maxima, and Type II, in which the envelopes shift to the higher-energy side from the maxima. The relationships indicated that the SERS with SEF, which spectral envelope is similar to the plasmon resonance $C_{sca}(\omega)$ spectra, is mainly caused by DD coupled plasmon resonance in symmetric dimers. The SERS with SEF, which spectral envelopes shift to higher energies, may be mainly caused by DQ-coupled plasmon resonance in asymmetric dimers. The experimental spectra for both $C_{sca}(\omega)$ and SERS with SEF were successfully reproduced in FDTD calculation by changing the degree of morphological asymmetry in the dimers. This analysis of the calculations revealed that Types I and II are caused by DD and DQ coupled resonance, respectively. DQ coupled resonance is subradiant; thus, The DQ coupled resonance receives excitation light and emits SERS and SEF light through near-field interaction with DD-coupled resonance. Furthermore, $F_R(\omega)$ obtained by absorption spectroscopy showed the spectral correlation between $F_R(\omega)$ and plasmon resonance absorption, because both origins are common in quantum optics, namely, AP term [6]. The absorption spectroscopic method of single dimers are described elsewhere [8]. This analysis method has applied to plasmonic nanowire dimers and successfully exhibit the contribution of DQ coupled resonance to SERS and SEF [7].

References

1. Itoh, T., M. Procházka, Z. C. Dong, W. Ji, Y.S. Yamamoto, Y. Zhang and Y. Ozaki, “Toward a New Era of SERS and TERS at the Nanometer Scale: From Fundamentals to Innovative Applications,” Chem. Rev. Vol. 123, 1552–1634, 2023.
2. Itoh, T., Y. S. Yamamoto and Y. Ozaki, “Plasmon-enhanced spectroscopy of absorption and spontaneous emissions explained using cavity quantum optics,” Chem. Soc. Rev. Vol. 46, 3904-3921, 2017.
3. Itoh, T. and Y. S. Yamamoto, “Reproduction of surface-enhanced resonant Raman scattering, and fluorescence spectra of a strong coupling system composed of a single silver nanoparticle dimer and a few dye molecules,” J. Chem. Phys. Vol. 149, No. 244701, 2018.
4. Itoh, T., and Y. S. Yamamoto, “Contribution of subradiant plasmon resonance to electromagnetic enhancement in resonant Raman with fluorescence examined by single silver nanoparticle dimers,” J. Phys. Chem. C Vol. 127, 5886–5897, 2023.
5. Itoh, T., and Y. S. Yamamoto, “Correlated polarization dependences between surface-enhanced resonant Raman scattering and plasmon resonance elastic scattering showing spectral uncorrelation to each other,” J. Phys. Chem. B Vol. 127, 4666–4675, 2023.
6. Itoh, T., and Y. S. Yamamoto, “Demonstration of electromagnetic enhancement correlated to optical absorption of single plasmonic system coupled with molecular excitons using ultrafast surface-enhanced fluorescence,” J. Chem. Phys. Vol. 159, No. 034709, 2023.
7. Itoh, T., and Y. S. Yamamoto, “Electromagnetic enhancement spectra of one-dimensional plasmonic hotspots along silver nanowire dimer derived via surface-enhanced fluorescence,” J. Chem. Phys. Vol. 160, No. 024703, 2023.
8. T. Itoh, Y. S. Yamamoto, and T. Okamoto, “Absorption cross-section spectroscopy of a single strong-coupling system between plasmon and molecular exciton resonance using a single silver nanoparticle dimer generating surface-enhanced resonant Raman scattering,” Phys. Rev. B, Vol. 99, No. 235409, 2019.

Van Der Waals Polaritonic Crystals and Their Nanostructures

H. J. Chen*, Z. B. Zheng, W. C. Huang, and S. Z. Deng

State Key Laboratory of Optoelectronic Materials and Technologies, Guangdong Province Key Laboratory of Display Materials and Technologies, School of Electronics and Information Technology, Sun Yat-sen University, Guangzhou 510275, China

*corresponding author: chenhj8@mail.sysu.edu.cn

Abstract: Recent studies have unveiled the capability of van der Waals (vdW) two-dimensional atomic crystals and their nanostructures to sustain diverse polaritonic modes across the mid-infrared to THz spectral range. In this presentation, we will share our latest research progress in the exploration of polaritons within nanostructures of vdW crystals. Additionally, we will delve into the optoelectronic and photonic applications that emerge from these investigations.

Polaritons are hybrid modes formed through the coupling of the electromagnetic field with the charged collective excitations in materials[1]. They exhibit a remarkable ability to confine the electromagnetic field within or at the surface of a material, thereby significantly enhancing the interaction between electromagnetic fields and matter at the nanoscale. This unique property positions polaritons as highly advantageous for the development of nanophotonic and optoelectronic devices. Noble metals, doped semiconductors, and their nanostructures excel at supporting polaritons in the visible and near-infrared regime. However, their field confinement capabilities degrade significantly as the operational frequency shifts into the mid-infrared and terahertz region. This limitation makes them unsuitable for developing high-performance and miniaturized photonic and optoelectronic devices in the specified frequency domain. Recent studies have uncovered the remarkable capability of van der Waals (vdW) two-dimensional atomic crystals and their nanostructures to sustain diverse polaritonic modes across the mid-infrared to terahertz spectral range[2,3]. In this presentation, we will briefly review the roadmap of polaritonic van der Waals crystals. Subsequently, we will introduce our recent work on the plasmon polariton properties of graphene and its nanostructures. Following that, we will share our discovery of hyperbolic phonon polaritons in a type of semiconducting van der Waals crystal, specifically, the α-MoO_3[4,5]. We will demonstrate that, owing to the in-plane anisotropic dielectric function of α-MoO_3, phonon polaritons can propagate within the basal plane with a hyperbolic wavefront, leading to strong electromagnetic field confinement in the mid-infrared region. Exploiting this exotic characteristic, we have developed a type of polariton tuners with frequency and polarization selection capabilities in the far-field. Furthermore, we utilize these tuners to create polarization notch filters, showcasing distinctive features including high-Q (300) resonance and extinction ratios up to 6.5 dB at a remarkably thin sub-wavelength thickness of 200 nm[6].

Acknowledgements: H.C. and S.D. acknowledge support from the National Key Basic Research Program of China (grant nos. 2019YFA0210200 and 2019YFA0210203) and the National Natural Science Foundation of China (grant no. 91963205).

References

1. Huang, K. Lattice Vibrations and Optical Waves in Ionic Crystals. *Nature* **1951**, *167*, 779–780.
2. Basov, D. N., Fogler, M. M., García de Abajo F. J. Polaritons in Van Der Waals Materials. *Science* **2016**, *354*, aag1992.
3. Low, T., Chaves, A., Caldwell, J. D., Kumar, A., Fang, N. X., Avouris P., Heinz, T. F., Guinea, F., Martin-Moreno, L.

and Koppens F. Polaritons in Layered Two-Dimensional Materials. *Nat. Mater.* **2017**, *16*, 182–194.

4. Zheng, Z. B., Chen, J. N., Wang, Y., Wang, X. M., Chen, X. B., Liu, P. Y., Xu, J. B., Xie, W. G., Chen, H. J., Deng, S. Z. and Xu, N. S. Highly Confined and Tunable Hyperbolic Phonon Polaritons in Van Der Waals Semiconducting Transition Metal Oxides. *Adv. Mater.* **2018**, *30*, 1705318.
5. Zheng, Z. B., Xu, N. S., Oscurato, S. L., Tamagnone, M., Sun, F. S., Jiang, Y. Z., Ke, Y. L., Chen, J. N., Huang, W. C., Wilson, W. L., Ambrosio, A., Deng, S. Z., Chen, H. J. A Mid-Infrared Biaxial Hyperbolic Van Der Waals Crystal. *Sci. Adv.* **2019**, *5*, eaav8690.
6. Huang, W. C., Folland, T. G., Sun F. S., Zheng, Z. B., Xu, N. S., Xing, Q. X., Jiang, J. Y., Caldwell, J. D., Yan, H. G., Chen, H. J. and Deng, S. Z. In-Plane Hyperbolic Polariton Tuners in Terahertz and Long-Wave Infrared Regimes. *Nat. Commun.* **2023**, *14*, 2716.

Scaling Challenges in Watts Level PCSELs

Weidong Zhou[1], Chhabindra Gautam[1], and Mingsen Pan[1,2]

[1]Department of Electrical Engineering, University of Texas at Arlington, Arlington, Texas 76019, USA.

[2]Semergytech, Inc., Fort Worth, TX 76104, USA

Email: wzhou@uta.edu

Abstract: Photonic Crystal Surface Emitting Lasers (PCSELs) have emerged as a third-generation diode laser technology for high power high brightness high speed lasers with applications in LiDAR and 3D sensing, datacom and lasercom, photonic and quantum integrated circuits. In this talk, we report PCSEL performance trade-offs and challenges in power scaling, modal competition, and charge injection control. We will report the impact of charge injection control, the design towards high speed high power lasers, and coherent coupled PCSEL arrays. Perspectives on the future directions will also be discussed.

References:

1. W. Zhou and M. Pan, “The Future of Photonic Crystal Surface Emitting Lasers (Perspective)”, Appl. Phys. Lett. 123, 140501 (2023). (Editors Pick)
2. A. Kalapala, A. Song, M. Pan, C. Gautam, L. Overman, K. Reilly, T. Rotter, G. Balakrishnan, R. Gibson, R. Bedford, J. Coleman, S. Fan, and W. Zhou, "Scaling Challenges in High Power Photonic Crystal Surface-Emitting Lasers," IEEE Journal of Quantum Electronics, Vol. 58, 2400409 (2022), doi: 10.1109/JQE.2022.3165314.

Integrated quantum photonic sources

Xifeng Ren

[1] CAS key laboratory of quantum information, University of science and technology of China, Hefei, China, 230026

[*]corresponding author: renxf@ustc.edu.cn

Abstract: I will introduce our recent works about quantum photonic sources based on nanophotonic structures, such as 2D materials, metalens array, microcavity, nanowaveguide, etc.

Integrated quantum photonics has attracted intensive attention due to the compactness, scalability, and stability. Quantum photonic source, especially an on-chip entangled photon source, is a basic device for realizing quantum photonic integrated circuits (QPICs). I will introduce our recent works about quantum photonic sources based on nanophotonic structures and materials, such as 2D materials [1], metalens array [2], microcavity [3], nanowaveguide, etc.

References

1. Lin Li, Zexuan Liu, Xifeng Ren, Shuming Wang, Vin-Cent Su, Mu-Ku Chen, Cheng Hung Chu, Hsin Yu Kuo, Biheng Liu, Wenbo Zang, Guangcan Guo, Lijian Zhang, Zhenlin Wang, Shining Zhu, and Din Ping Tsai, Metalens-array-based high-dimensional and multi-photon quantum source, Science 368, 1487-1490 (2020).
2. Qiangbing Guo, Xiao-Zhuo Qi, Lishu Zhang, Meng Gao, Sanlue Hu, Wenju Zhou, Wenjie Zang, Xiaoxu Zhao, Junyong Wang, Bingmin Yan, Mingquan Xu, Yun-Kun Wu, Goki Eda, Zewen Xiao, Shengyuan A. Yang, Huiyang Gou, Yuan Ping Feng, Guang-Can Guo, Wu Zhou, Xi-Feng Ren, Cheng-Wei Qiu, Stephen J. Pennycook & Andrew T. S. Wee, Ultrathin quantum light source with van der Waals NbOCl2 crystal, Nature 613, 53–59 (2023).
3. Bo-Yu Xu, Li-Kun Chen, Jin-Tian Lin, Lan-Tian Feng, Rui Niu, Zhi-Yuan Zhou, Ren-Hong Gao, Chun-Hua Dong, Guang-Can Guo, Qi-Huang Gong, Ya Cheng, Yun-Feng Xiao & Xi-Feng Ren，Spectrally multiplexed and bright entangled photon pairs in a lithium niobate microresonator, Science China Physics, Mechanics & Astronomy 65, 294262 (2022).

Intracavity metasurfaces in fiber lasers for linear and nonlinear applications

Lili Gui[1*], Chuanshuo Wang[1], Hao Chen[1], Chao Meng[2], Xianglong Mei[1], Hailun Xie[1], Zhijin Chen[1], Fengbin Lin[1], Fei Ding[2], Sergey I. Bozhevolnyi[2], and Kun Xu[1]

[1]State Key Laboratory of Information Photonics and Optical Communications, Beijing University of Posts and Telecommunications, Beijing, 100876, China
[2]SDU Nano Optics, University of Southern Denmark, Campusvej 55, DK-5230 Odense, Denmark
[*]corresponding author: liligui@bupt.edu.cn

Abstract: Intracavity metasurfaces are explored for spatially or temporally modulating light wave inside fiber lasers. First we harness static and dynamic metasurfaces for building orbital-angular-momentum (OAM) laser sources. Secondly, resonant metasurfaces are used for Q-switched or mode-locked fiber lasers. They open new perspectives in structured optics, ultrafast optics and neuromorphic photonics.

Ultrathin plasmonic and dielectric metasurfaces enable flexible manipulation of the interacted optical wave in magnitude, phase, polarization etc. in both linear and nonlinear regime. Here we show applications of metasurfaces integrated in fiber lasers. In comparison with single-pass strategies, our strategies making use of combination with fiber lasers could provide efficient gain together with filtering mechanisms that ensure desired light-matter interactions with high efficiency and high purity. For this purpose we demonstrate two examples. The first example is to utilize the phase-control degree of freedom of metasurfaces in order to generate structured beams directly from a laser [1-4]. With this strategy loss issues of metasurfaces can be compensated and relaxed. We will show how to design both linear, V-shaped and circular fiber cavities in order to fully exploit the phase manipulation capabilities of both metallic and dielectric metasurfaces, including both static and dynamic functionality. The second example is to employ the nonlinear absorption properties of metasurfaces by virtue of local-field enhancement (the magnitude-control degree of freedom) [5-8] in order to tailor and enhance the pulsing building processes in fiber lasers, the typical nonlinear operation ranges in lasers. In this case the design principles of nonlinear metasurfaces for optical frequency generation that have been extensively studied before can be easily extended to investigations of intracavity nonlinear dynamics, and hence it provides exciting and versatile avenues for designing new saturable absorbers and reaching related applications such as optical neuromorphic computing, spiking neural networks, and so on. All these trials open new doors for integrated laser technologies, structured beam generation, ultrafast nonlinear nanophotonics, and intelligent optical information processing, etc.

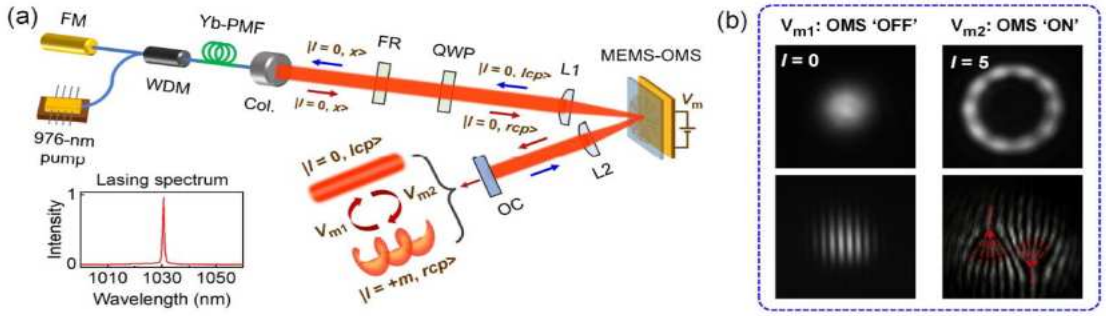


Figure 1. MEMS-metasurface enabled mode-switchable vortex laser. (a) Schematic of the V-shaped fiber laser. Inset graph: lasing spectrum. (b) Measured intensity distribution (first row) and self-interference patterns (second row) of the emitted Gaussian (topological charge $l = 0$) and OAM ($l = 5$) beams.

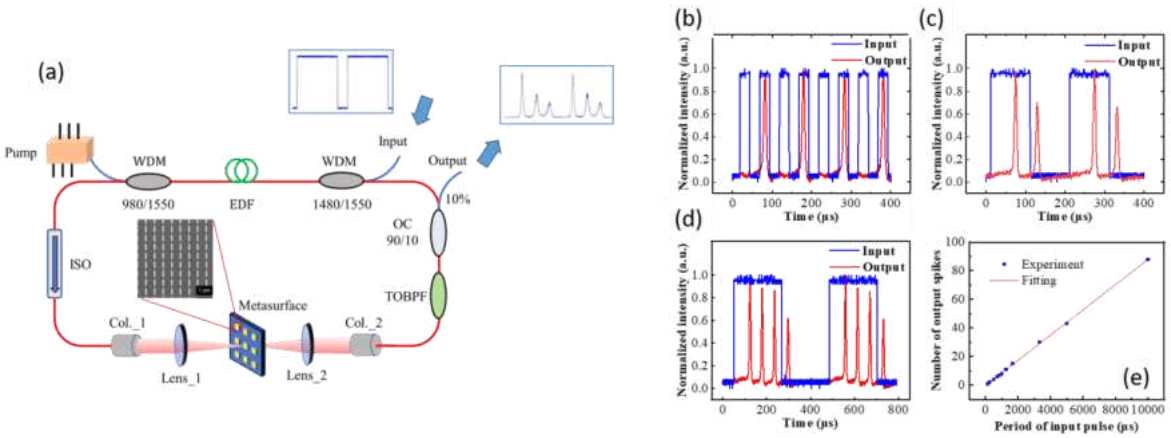


Figure 2. Nonlinear metasurface enabled excitable fiber laser mimicking dynamics of a biological neuron. (a) Schematic of the fiber laser. Inset graph: SEM image of the gold saturable absorber metasurface. (b-e) Typical input-output relationship exhibiting pulse encoding ability of the optical spiking neuron.

This work was supported by National Natural Science Foundation of China (61905018), Fundamental Research Funds for the Central Universities (ZDYY202102-1), Fund of State Key Laboratory of Information Photonics and Optical Communications (Beijing University of Posts and Telecommunications) of China (IPOC2021ZR02), the Villum Fonden (Award in Technical and Natural Sciences 2019, Grant No. 37372 and 50343).

References

1. Gui, L., C. Wang, F. Ding, H. Chen, X. Xiao, S. I. Bozhevolnyi, X. Zhang and K. Xu, “60 nm Span Wavelength-Tunable Vortex Fiber Laser with Intracavity Plasmon Metasurfaces,” ACS Photonics, Vol. 10, No. 3, 623-631, 2023.
2. Wang, C., L. Gui, X. Mei, H. Chen, F. Ding, C. Meng, S. I Bozhevolnyi and K. Xu, “Intracavity spatially modulated metasurfaces for a wavelength-tunable figure-9 vortex fiber laser,” Opt. Express, Vol. 32, No. 4, 6423-6431, 2024.
3. Wang, C., C. Meng, X. Mei, P. C. V. Thrane, L. Gui, H. Chen, F. Ding, K. Xu and S. I. Bozhevolnyi, "MEMS-metasurfaces enabled mode-switchable vortex lasers," in preparation for submission to Nature Communications, 2024.
4. Chen, H., L. Gui, C. Wang, Y. Xu, X. Mei and K. Xu, "Intracavity polarization-multiplexing metasurfaces for efficiency and topological charge controllable vortex fiber laser," in preparation for submission to Laser & Photonics Reviews, 2024.
5. Chen, Z., L. Gui, C. Wang, X. Xiao, C. Meng, S. I. Bozhevolnyi, T. Zhang , X. Zhang and K. Xu, "Gold metasurfaces as saturable absorbers for all-normal-dispersion ytterbium-doped mode-locked fiber laser," IEEE Photon. J., Vol. 14, No. 3, 1530406, 2022.
6. Xie, H., L. Gui, Y. Liu, F. Lin, Z. Zhang and K. Xu, “Giant two-photon absorption response from a silicon quasi-BIC metasurface,” Appl. Phys. Lett., Vol. 123, No. 21, 211704, 2023.
7. Xie, H., L. Gui, X. Zhou, Y. Zhou and K. Xu, "Aluminum metasurface saturable absorber for wavelength-tunable Q-switching Yb-doped fiber laser, " in preparation for submission to APL Photonics, 2024.
8. Gui, L., F. Lin, Y. Wei, Z. Lu, Z. Zhang, X. Sun, Y. Lan and K. Xu, "Gold saturable metasurface for building a wavelength-tunable optical spiking neuron, " Submitted to Optics Express, 2024.

High Q-factor coupled Fabry-Perot plasmonic nanoresonator

B. Fix[1*]

[1] DOTA,ONERA,Université Paris Saclay F-91123 Palaiseau - France

[*]corresponding author: baptiste.fix@onera.fr

Abstract: Multi Fabry-Perot (FP) nanoresonators have been widely described as independent cavities. However, we evidence the coupling of FP nano-cavities leading to perfectly absorbing high quality factor plasmonic resonators through an analytical model and experimental demonstration on several architecture. Applications for nonlinear optics and infrared photodetection will be presented.

The Fabry-Perot (FP) interferometer was invented in 1899, and consisted of two parallel highly reflecting mirrors, the resonance behavior being characterized by peaks or dips in the transmission and reflection spectra [1]. It has been used in a variety of devices among which optical cavities for lasers or filters [2]. In the past two decades, the development of nanophotonics has given birth to FP-like resonators [3], in which a guided mode in a metallic cavity has a behavior that is well described by the FP formalism. The advantages of these nanoresonators are their compactness, and the possibility to combine them to design broadband or multiband resonances. It is well accepted that, since these metallic cavities are the siege of localized resonances, they have negligible influences on each other when they are combined [7]–[6]. The two most common plasmonic nanostructures with a FP behavior are the metal-insulator-metal patch nanoantennas (horizontal resonance), and the high aspect ratio nanogrooves (vertical resonance). Both of these resonators are promising for applications ranging from thermal emission [7], or infrared detection [8] to biosensing [9]. Yet, they suffer from their low quality factor.

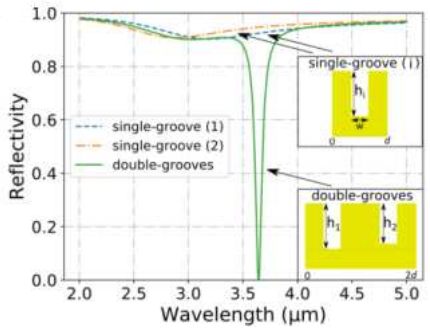


Figure 1 Comparison between the reflectivity of two under-coupled single-nanogroove resonators and the reflectivity of a critically coupled resonator composed of the two aforementioned cavities. The geometrical parameters of the

In this letter, we introduce double cavity Fabry-Perot like nanoresonator in both vertical and horizontal configurations. It departs from the previous work on multimirror FP resonators, as the mirrors are in an hybrid configuration between series and parallel. It gives birth to a spectacular effect where critical coupling (a zero of reflectivity) is obtained while, independently, each of the two cavities is loosely-coupled to free space. Moreover, the quality factor of the double cavity resonators is increased from 11 to 50, well beyond the limit for FP plasmonic nanoresonator [4]. We developed an analytical model that confirms the multimirror FP behavior Then we experimentally demonstrate the coupled Fabry-Perot resonance on a horizontal nanoresonator.

First, we study a periodic double-groove resonator whose period contains two grooves of different heights. While the reflectivity of the periodic single-groove resonators does not go below 85%, the resonance of the double-groove presents a zero of reflectivity and a quality factor of 50 (See Figure 1). We demonstrate thanks to a simple analytical

model that this coupling can be ascribed to a double FP cavity resonance, with the unique feature that the cavities are coupled to one another through a common mirror.

For the experimental demonstration, we consider horizontal nano FP cavities which are analogue to the nanogrooves providing a simple geometry transformation. The resulting horizontal coupled FP nanostructures studied in this letter are made of three layers as illustrated in the inset of the figure 4.b. A top periodic nanostructure composed of one or several gold ribbons of the same height (t=50 nm) but different width denoted by capital letters (W_A= 400 nm and W_B= 495 nm) is deposed on two continuous layers, a SiC insulating layer of 280 nm thickness and a gold mirror.

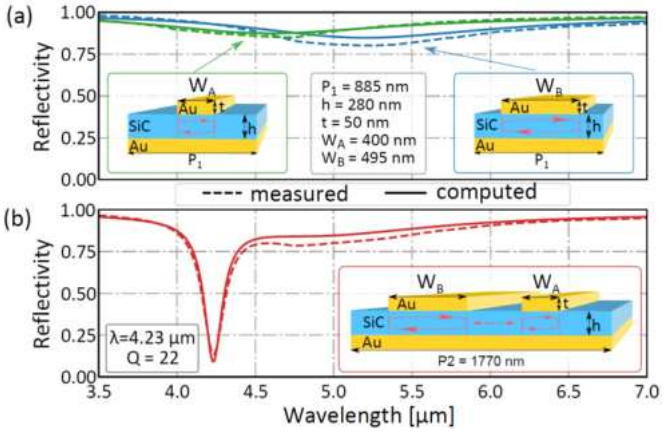


Figure 2: *Measured (dotted) and computed (plain) reflection spectra of (a) single-FP structures and (b) the coupled nano FP structure. Due to the thickness of the SiC layer, the two single FP resonators are under-coupled and their reflectivities do not go below 80%. Due to the coupling between the two FP, the new coupled FP resonance is visible at λ= 4.23 µm with a minimum of reflectivity of 14% and a high Q-factor of 22. The insets represent the different structures*

Finaly, we discuss how the new properties of this coupled FP resonator can be used in multiple domain such as the non-linear optics [11] or infrared photodetection [12]

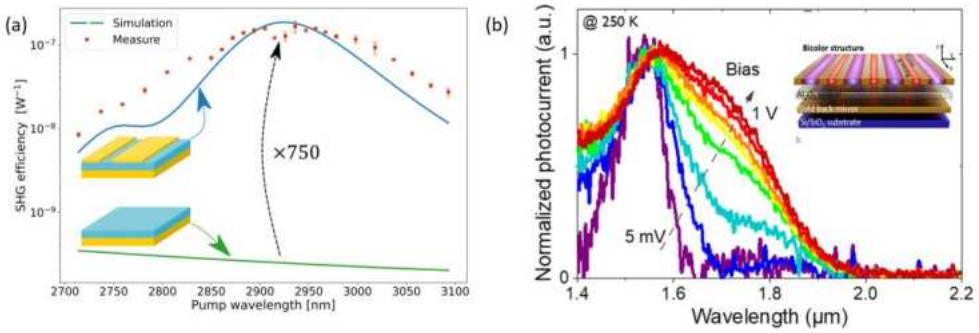


Figure 3: (a) Efficiency of the second harmonic generation enhanced in an horizontal coupled nano-FP structure.[11]

(b) Evidence of the bias reconfigural photoresponse of a quantum-dot on vertical coupled nano-FP structure. [12]

In conclusion, the description of the double-groove resonator paves the way to the manipulation and the engineering of the equivalent mirror coupling the two nanocavities, in order to reach multimirror interferences predictions. This structure is also very promising for many practical applications such as non-linear optics, infrared photodetection, gaz sensing, etc.

References

[1] C. Fabry and A. Perot, Ann Chim Phys, 16,7, 1899.

[2] E. Schubert et al., Science, vol. 265, no. 5174, 1994.

[3] J. Dorfmüller et al., Nano Lett., vol. 9, no. 6, 2009.

[4] P. Bouchon et al., Opt. Lett., vol. 37, no. 6, 2012

[5] X. Liu et al., Phys. Rev. Lett., vol. 104, no. 20, 2010.

[6] Y. Cui et al., Laser Photonics Rev., vol. 8, 4, 2014.

[7] M. Makhsiyan et al., Appl. Phys. Lett., 107, 25, 2015.

[8] H. T. Miyazaki et al., Appl. Phys. Lett., vol. 92, 2008.

[9] M. W. Knight et al., Science, 332, 6030, May 2011.

[10] A. Cattoni et al., Nano Lett., vol. 11, no. 9, 2011.

[11] T. Matthia, et al. Opt. Lett. 47, 4415-4418 (2022)

[12] T. H. Dang et al. *ACS Photonics* 5, 1601–1607 (2023)

Multipolar description of the scattering of dense clusters of metallic nanoparticles

M. Lafitte[1], R. Dwivedi[2], P. Barois[1], A. Baron[1,3], O. Mondain-Monval[1], and V. Ponsinet[1*]

[1]Centre de Recherche Paul Pascal, CNRS UMR 5031 and Univ. Bordeaux, Pessac F-33600, France
[2]ENSEMBLE3 Centre of Excellence, Warsaw 01-919, Poland
[3]Institut Universitaire de France, 1 rue Descartes, 75231 Paris Cedex 05, France
[*]corresponding author: virginie.ponsinet@crpp.cnrs.fr

Abstract: Optical metasurfaces are two-dimensional assemblies of optical nanoresonators and could constitute next generation ultrathin optical components. We propose an emulsion-based scalable fabrication approach both for the fabrication of colloidal resonators, presenting a strong interaction with light with simultaneous magnetic and electric modes of resonance, and for their deposition in homogeneous films.

The emergence of optical metamaterials is intertwined with that of artificial materials designed to present a significant degree of magnetic polarization under light. Self-assembly methods have typically contributed to this endeavor by fabricating subwavelength structured particles and materials that harbor strong optical magnetism [1]. This specific property can give access to so-called Huygens scatterers. For Huygens scatterers under plane wave illumination, the scattering is dominated by a mode of even parity (such as the electric dipolar mode with Mie coefficient a_1) and a mode of odd parity (such as the magnetic dipolar mode of Mie coefficient b_1) having equal magnitudes and phases, so that they interfere constructively in the forward direction and destructively in the backward direction, leading to forward scattering. Strong forward scattering is important for metasurface applications because it ensures that backscattering is canceled, or minimized, which results in high transmissivity for low-loss all-dielectric metasurfaces and potential near perfect absorption for lossy Huygens scatterers.

Densely-packed spherical colloidal clusters of metallic nanoparticles (NPs) have been proposed theoretically as efficient Huygens scatterers [2]. More generally, they have garnered a lot of interest recently, because they involve localized resonant inclusions that are assembled into a Mie resonator and present structural degrees of freedom as required for resonance engineering. We have used an emulsion route to assemble plasmonic clusters with Au NPs [3] and Ag NPs [4], and have studied their optical properties in liquid suspensions. Furthermore, we have proposed a new method to directly assemble metasurfaces covered with such clusters. This method implements a two-in-one hierarchical process: the fabrication of the clusters and their simultaneous deposition on a surface.

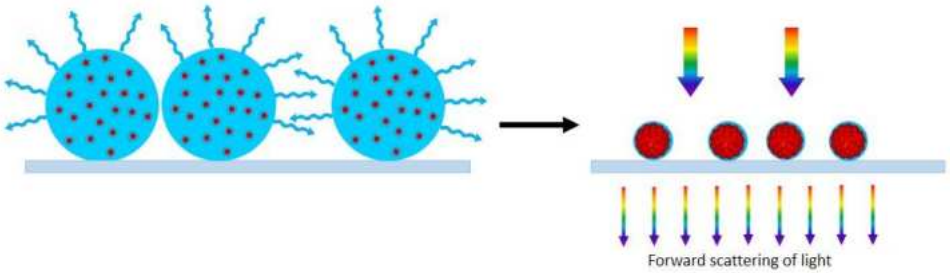


Figure 1. Schematics of emulsion route for simultaneous fabrication and deposition of the Huygens nanoresonators on a surface

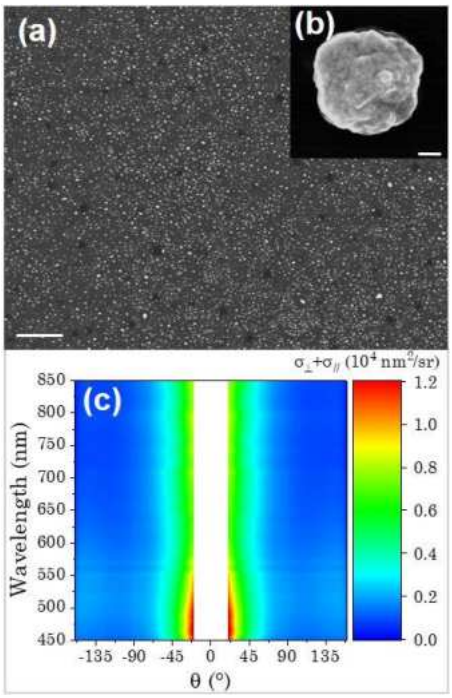


Figure2. Metasurface and meta-atoms. Scanning electron microscopy image of (a) a metasurface (bar = 10 µm), (b) a meta-atom (bar = 100 nm), (c) wavelength- and angle-resolved measurement of the differential scattering cross-section (in nm²/steradian) for a suspension of meta-atoms in a solvent.

Clusters of controlled sizes (in the range 80-200 nm) and metal fraction (between 15 and 55 vol%) with gold NPs (r = 6.7 nm) [3] or silver NPs (r = 11.2 nm) [4] were produced and deposited on a glass substrate. We measured the reflection and transmission spectra of the metasurface as well as the spectral and angular polarization-resolved differential scattering cross-section of the nanoresonators after re-dispersion in a solvent. The clusters exhibit different resonant modes, with strong electric and magnetic dipolar resonances as well as quadrupolar electric resonances, and present strong forward scattering. Comparing our measurements with numerical results reveal that this forward scattering is the result of multipolar interferences and highlight the role of the electric quadrupole in the blue-end of the spectrum and that of the magnetic dipole at the red-end. The scattering cross sections reach values as large as 4 times the geometrical cross section of the clusters, and we show that this figure is an increasing function of the volume fraction of silver NPs inside the clusters. The measured surface absorbances are as high as 50%, while the layer of adsorbed objects is only 100−200 nm thick. This demonstrates the strong interaction of the deposited resonators with incoming light.

Here, we demonstrate that an emulsion drying route can provide control of the structure, and therefore properties, of colloidal clusters both in the volume of a continuous phase or at the surface of a substrate. This “two-in-one” process opens a new route for the fabrication of metasurfaces with enhanced and targeted optical properties that is both simple and scalable.

Acknowledgements. We thank F. Lagugné-Labarthet for his help with the analysis of the nanoparticle ligands by Raman spectroscopy.

References

1. Aradian, A., P. Barois, O. Mondain-Monval, V. Ponsinet and A. Baron, “The bottom-up approach toward artificial optical magnetism in metastructures”, in Hybrid Flatland Metastructures, Caputo, R.; Lio, G. E., Eds. AIP Publishing LLCMelville, New York, 2021, DOI: 10.1063/9780735422902.
2. Dezert, R., P. Richetti, and A. Baron. “Isotropic Huygens dipoles and multipoles with colloidal particles” Phys. Rev. B, Vol. 96, No. 18, 180201, 2017.
3. Elanchelyian, R., R. Dézert, S. Castano, A. Bentaleb, E. Nativ-Roth, O. Regev, P. Barois, A. Baron, O. Mondain-Monval and V. Ponsinet, “Tailored self-assembled nanocolloidal Huygens scatterers in the visible” Nanoscale Vol. 12, No. 47, 24177-24187, 2020.
4. Lafitte, M., R. Dwivedi, R. Elancheliyan, F. Lagugné-Labarthet, L. Buisson, I. Ly, P. Barois, A. Baron, O. Mondain-Monval and V. Ponsinet, “Colloidal Self-Assembly of Silver Nanoparticle Clusters for Optical Metasurfaces” Langmuir Vol. 40, No. 5, 2601–2615, 2024.

Rayleigh surface waves of extremal elastic materials

Y. Wei[1], Y. Chen[1], W. Cheng[1], X. N. Liu[1], G. K. Hu[1*]

[1]School of Aerospace Engineering, Beijing Institute of Technology, Beijing 100081, China
[*]corresponding author: hugeng@bit.edu.cn

Abstract: We theoretically investigate the propagation of Rayleigh waves in extremal materials based on continuum theory and verify our findings with designed metamaterials. Dispersion relations and polarizations of Rayleigh waves in extremal materials are derived, and the impact of higher order gradient effects is also investigated using strain gradient theory.

The characteristics of Rayleigh waves (as shown in Fig. 1) in traditional elastic solids are well known, while their natures in extremal elastic materials have largely remained unexplored. Extremal elastic materials can exhibit highly different bulk wave properties compared to classical elastic materials [1-2]. Mathematically, they are defined as elastic materials whose 6×6 elastic matrixes have $N \geqslant 1$ zero eigenvalue [3]. Depending on N, we refer them as unimode materials ($N = 1$), bimode materials ($N = 2$), trimode materials ($N = 3$), quadramode materials ($N = 4$), or pentamode materials ($N = 5$) [3]. Each of the zero eigenvalues is attributed to a soft deformation mode of the material in the sense that the deformation requires conceptually zero energy. Classical elastic solids correspond to $N = 0$ with no soft modes. The presence of soft modes in extremal elastic materials can drastically change their bulk wave properties, allowing to design interesting wave devices. For example, pentamode-based acoustic cloak [4], metasurface [5], quadramode-based phonon polarizer [6-7], triplemode-based zero-refractive-index [1], just name a few. However, investigations on Rayleigh surface waves, closely linked to bulk wave properties, in extremal elastic materials have been relatively scarce.

In this talk, we focus on the study of Rayleigh surface waves of two-dimensional (2D) extremal elastic materials, whose elasticity matrixes are 3×3. In such case, we have two types of extremal elastic materials, i.e., the unimode material ($N = 1$) and the bimode material ($N = 2$). By directly solving the constraint equations [8],

$$\mathbf{u} = \left(A_1 \begin{bmatrix} 1 \\ \chi_1 \end{bmatrix} e^{k\xi_1 x_2} + A_2 \begin{bmatrix} 1 \\ \chi_2 \end{bmatrix} e^{k\xi_2 x_2} + A_3 \begin{bmatrix} 1 \\ \chi_3 \end{bmatrix} e^{k\xi_3 x_2} + A_4 \begin{bmatrix} 1 \\ \chi_4 \end{bmatrix} e^{k\xi_4 x_2} \right) e^{\mathrm{i}k(x_1 - ct)}, \tag{1.1}$$

as well as governing equations for Cauchy elasticity and second gradient elasticity

$$\begin{aligned} &\left(\sigma_{ij} - M_{ijk,k}\right)_{,j} = \rho \frac{\partial^2 u_i}{\partial t^2}, \\ &\sigma_{ij} = C_{ijkl} u_{k,l} + E_{ijklp} u_{k,lp}, \\ &M_{ijk} = E_{lpijk} u_{l,p} + D_{ijklpq} u_{l,pq}, \\ &f_i = \left[C_{ijkl} u_{k,l} - \left(2\delta_{pr} - m_p m_r\right) D_{ijpklq} u_{k,lqr} \right] m_j = 0, \\ &R_i = D_{ijpklq} m_j m_p u_{k,lq} = 0, \end{aligned} \tag{1.2}$$

(A_3, A_4, E_{ijklp} and D_{ijpklq} simultaneous equal to 0 for Cauchy elasticity, otherwise for second gradient elasticity) it is demonstrated that Rayleigh wave cannot propagate in 2D extremal Cauchy elastic materials when the principal axes of materials are parallel to the free planar surface, including the well-known fact that water (an isotropic 2D bimode extremal material) are not able to support Rayleigh waves as a special case. In Eq. (1.1), c denotes phase velocity, k is the wave number and the imaginary unit i. The ξ = b/k , and the real part of b is

supposed to be positive so that the displacements tend to zero when x_2 decreases from the free surface. The amplitude A and ratio χ are independent of x_i and t. In Eq. (1.2), M_{ijk} is the hyperstress tensor, C_{ijkl} is the fourth-order Cauchy elasticity tensor, D_{ijklpq} and E_{ijklp} respectively denotes the sixth-order elasticity tensor and the fifth-order coupling elasticity tensor. The f_i and R_i are respectively the surface force and surface double-force.

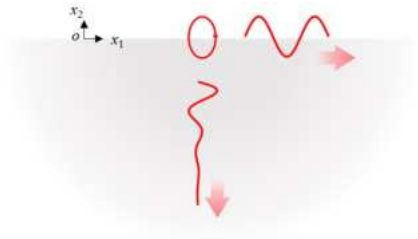


Fig. 1. Scheme of Rayleigh wave.

However, when the microstructural effect is pronounced, we showed that Rayleigh waves can propagate at finite frequencies if second gradient terms of displacement are properly introduced, i.e., the Rayleigh waves can propagate with a dispersive nature when second gradient effects are considered. The characteristics of Rayleigh waves of some isotropic second gradient elasticity have been analyzed in detail. To validate our findings obtained from continuum perspectives, we propose to construct the corresponding discrete models with pantographic microstructures, and to examine their band structures. It is found that for certain isotropic pure second gradient elasticity, the polarization of particles on surface can be either linearly or elliptically polarized, and the Rayleigh waves may not be unique. The results predicted by the discrete models agree quite well with their continuum counterparts. This work provides the first systematic study on Rayleigh waves in extremal elastic materials, and pure second gradient materials as well, and offers a new prospective to control Rayleigh waves in extremal elastic metamaterials.

Acknowledgements:

We acknowledge the support from National Natural Science Foundation of China (Grants No. 11632003, No. 11972083, No. 11991030).

References

1. Wei, Y. and G. K. Hu, "Wave characteristics of extremal elastic materials," Extreme Mech. Lett. Vol. 55, 101789, 2022.
2. Norris, A.N., "Acoustic cloaking theory," Pro. R. Soc. A, Vol. 464, 2411, 2008.
3. Milton, G.W. and A.V. Cherkaev, "Which elasticity tensors are realizable?," J. Eng. Mater. Technol. Vol. 117, 483, 1995.
4. Chen, Y., X. N. Liu, G. K. Hu, "Latticed pentamode acoustic cloak,". Sci. Rep.-UK Vol. 5, 15745, 2015.
5. Chen, Y. And G. K. Hu, "Broadband and High-Transmission Metasurface for Converting Underwater Cylindrical Waves to Plane Waves," Phys. Rev. Applied 12, 044046, 2019.
6. Wei, Y., X. N. Liu and G. K. Hu, "Quadramode materials: Their design method and wave property," Mater. Des. Vol. 210, 110031, 2021.
7. Groß, M. F., J. L. G. Schneider, Y. Wei, Y. Chen, S. Kalt, M. Kadic, X. N. Liu, G. K. Hu, M. Wegener, "Tetramode Metamaterials as Phonon Polarizers," Adv. Mater. Vol. 35, 2211801, 2023.
8. Achenbach, J., " Wave propagation in elastic solids," Elsevier, 2012.

Highly damped plasmonic and ferromagnetic metamaterials for wireless opto-magnetic actuation and detection

A. Lafuente[1], A. Flucksman[2], A.G. Roca[1], O. Benny[2], J. Nogues[1], M. Alvarez[3] and B. Sepúlveda[3*]

[1]Catalan Institute of Nanoscience and Nanotechnology (ICN2), Bellaterra, Spain

[2]Institute for Drug Research, The Hebrew University of Jerusalem, Jerusalem, Israel

[3]Instituto de Microelectrónica de Barcelona (IMB-CNM, CSIC). Bellaterra, Spain

[*]corresponding author: borja.sepulveda@csic.es

Abstract: Highly damped plasmonic and ferromagnetic metamaterials exhibit highly efficient broadband light absorption, minimal scattering and strong magnetic actuation capabilities. Here we show how this combination can be applied to develop: (i) wirelessly soft opto-magnetic actuators and detectors and (ii) locally amplified nanotherapies enabling tumor eradication at ultra-low drug concentrations.

Nanostructures of typical plasmonic materials (e.g., Au, Ag) exhibit vivid colors and narrow band resonances, resulting from their negative real part of the dielectric constant and low values of the imaginary part. In contrast, highly damped plasmonic (HDP) materials show negative real part of the dielectric constant, but they present large values of the imaginary part, thus drastically changing their optical response. As a result, HDP nanostructures exhibit deeper light penetration, intense broadband absorption and highly reduced scattering. These features are ideal for generating highly efficient photothermal actuation. Typical HDP materials include many transition metals, such as Cr, Mn, Fe, Ni, or Co. Therefore, in several of these transition metals it is possible to combine strong ferromagnetism at room temperature and HDP behavior. Here, we show how this combination can be exploited, in the case of metallic iron, as multifunctional metamaterials to develop: (i) soft opto-magnetic actuators and detectors, and (ii) locally amplified nanotherapies enabling tumor eradication at ultra-low drug concentrations (Figure 1).

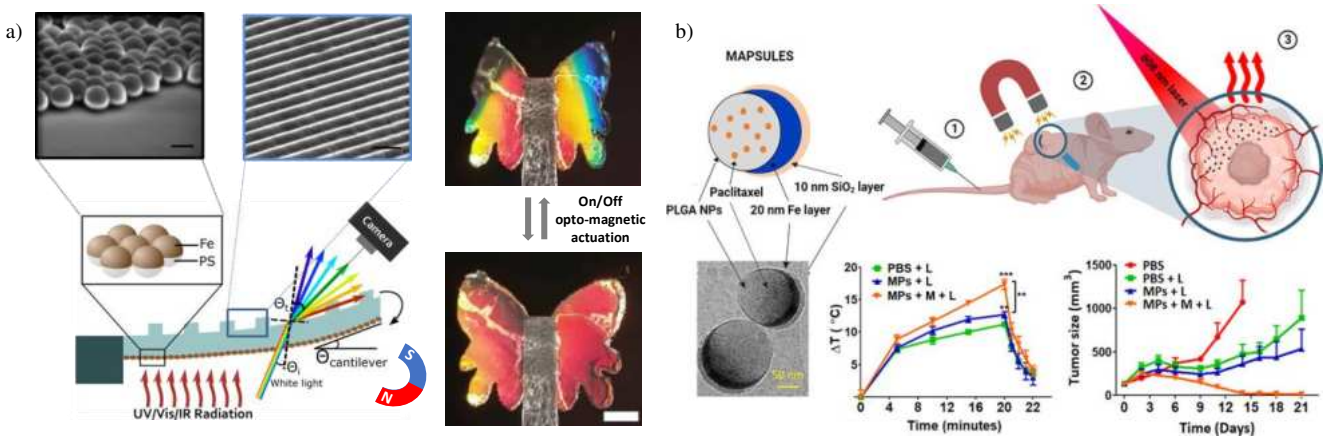


Figure 1: a) Pictures and schematic of the wireless soft opto-magnetic actuators and detectors. b) Schematic representation of the efficient tumor eradication at ultralow drug concentration via externally magnetic concentration and photothermal actuation.

In the first application, we show soft dual opto-magnetic actuators with integrated mechanochromic self-sensing, supporting synergistic untethered optical and magnetic actuation, and self-report of the mechanical state by changing its structural coloration with the bending curvature [1-4]. The actuators are composed of an iron metamaterial layer that is mechanically coupled to thin free-standing soft silicone films whose back-side is periodically corrugated, to act as a light bendable diffraction grating. The opto-magnetic actuator exhibits light absorption in an ultrabroadband spectral range (at least from 0.3 μm to 18 μm), and powerful multimode magnetic actuation by torque or magnetophoretic force. An imaging algorithm accurately quantifies and 2D-maps in real-time the colour changes with a conventional RGB camera, such as a smartphone camera, thereby enabling simple and cost-effective wireless control of the actuation strength.

In the second application, we demonstrate metallic iron-based and drug loaded magnetoplasmonic nanocapsules (MAPSULES) for wirelessly controlled cancer nanotherapies [5,7]. The MAPSULES are composed of a magnetoplasmonic Fe/SiO_2 semishell deposited on 100-200 nm diameter Poly(lactic-co-glycolic acid) (PLGA) beads loaded with paclitaxel. The intense broadband absorption of the MAPSULES in the near-infrared is used for local optical heating, with efficiency similar to the best plasmonic nanoheaters. The MAPSULES exhibit a magnetic vortex configuration, which due to its vanishing remanent magnetization results in virtually no dipolar interactions between particles, leading to an outstanding colloidal stability despite their magnetic strength. Importantly, the strong magnetic character allows remote manipulation of the MAPSULES to easily concentrate them at the site of action and to amplify the photothermal effects. The MAPSULES have enabled complete eradication of the tumors in vivo in mice by combining magnetic concentration in the tumor and local photothermal actuation, using a drug concentration between 200 and 500-fold lower than the therapeutic window of the free drug.

The HDP metamaterial concept can be extended to other metals, polymers with different size, shape, stiffness, and for other drugs. The cost-effective fabrication of the multifunctional HDP metamaterials and their wireless actuation can be applied to a wide range of biomedical, sensing and thermal applications.

Acknowledgements

The authors thank the PDC2022-133036-I00, PID2022-138588OB-C31 and PID2022-138588OB-C32 projects funded by MICIU/AEI/10.13039/501100011033.

References

1. Güell-Grau P., *"*Mechanochromic detection for soft opto-magnetic actuators" ACS Appl. Mater. Interfaces, Vol. 13, 47871-47881, 2021
2. Güell-Grau P., *"*Ultrabroadband light absorbing Fe/polymer flexible metamaterial for soft opto-mechanical devices"**,** Appl. Mater. Today, Vol. 23, 101052, 2021
3. Güell-Grau P., "Elastic plasmonic-enhanced Fabry-Perot cavities with ultrasensitive stretching tunability", Adv. Mater., Vol. 34, 2106731, 2021
4. Pujol-Vila F., "Soft optomechanical systems for sensing, modulation, and actuation", Adv. Funct. Mater. Vol. 33, 2213109, 2023
5. Li, Z., "Simultaneous local heating/thermometry based on plasmonic magnetochromic nanoheaters", Small, Vol. 14, 1800868, 2018
6. Flucksman, A., "Efficient tumor eradication at ultralow drug concentration via externally controlled and boosted metallic iron magnetoplasmonic nanocapsules", ACS Nano, Vol. 17, 1946-1958, 2023.
7. Flucksman, A., "Modular drug-loaded nanocapsules with metal dome layers as a platform for obtaining synergistic therapeutic biological activities", ACS Appl. Mater. Interfaces Vol. 15, 50330-50343, 2023

Silicon-Nitride Photonics for High-throughput Biosensing Applications

Niels Verellen[1*]

[1]imec, Kapeldreef 75, B-3001 Leuven, Belgium
[*]corresponding author: niels.verellen@imec.be

Abstract: Silicon nitride nanophotonics offers a platform that is ideally suited for visible-light bio applications. Allowing to integrate complex optical functionality on a small footprint, including on-chip routing and manipulation of free-space radiation.
We will review our recent applications of the platform in high-throughput molecular sensing, cytometry, optogenetics, and microscopy.

Silicon nitride nanophotonics offers a platform that is ideally suited for visible-light bio applications. Allowing to integrate complex optical functionality on a small footprint, including on-chip routing and manipulation of free-space radiation.
We will review our recent applications of the platform in high-throughput molecular sensing [1], cytometry, optogenetics [2,3], and microscopy [4].

References

1. Neutens P. *et al*, Journal of Biophotonics (2023)
2. Mahanty *et al*, News and Views, Nature electronics 6, 939 (2023)
3. Neutens P. *et al*, IEDM proceedings, (2023)
4. Arisev O. *et al*, Proceedings Optica Advanced Photonics Congress (2022)

Organic epsilon-near-zero and hyperbolic dispersion optical films

Jeong Weon Wu

Department of Physics, Ewha Womans University, Seoul 03760, South Korea
jwwu@ewha.ac.kr

Abstract— Organic thin films presenting a lamellar structure exhibit a hyperbolic dispersion with epsilon-near-zero (ENZ) crossing taking place. Polymethine character of excited-state of donor-acceptor-donor structure is associated with the ENZ behavior of organic molecular films. Linear optical properties such as directive emission and photoluminescence lifetime of fluorescent polymer are controlled by organic ENZ film. Both nonlinear refractive index and nonlinear absorption coefficient of a polymethine thin film are strongly enhanced in the ENZ spectral region, as an example of a third-order nonlinear optical process in organic ENZ films.

Epsilon-near-zero (ENZ) takes place when the real part of dielectric permittivity crosses the zero-point in the spectrum of dielectric permittivity. Owing to the dielectric permittivity being near zero, there are a variety of important linear optical applications such as directive emissions, electric field enhancement in ENZ mode, perfect absorption, and a deep direct writing lithography, to name a few. Furthermore, the nonlinear optical processes, both quadratic and cubic, have been found to be enhanced in ENZ spectral range.

Regarding organic thin film, an organic monolithic $QQT(CN)_4$ molecular film showed a transverse negative hyperbolic dispersion possessing a transverse ENZ. [1,2] Furthermore, regioregular poly (3-alkylthiophenes) (rr-P3AT) organic film is reported to show a similar transverse negative hyperbolic dispersion possessing a transverse epsilon-near-pole (ENP). [3] That is, $QQT(CN)_4$ and rr-P3AT films possess ENZ and ENP, respectively, at the parallel component of dielectric constant, i.e., $\epsilon_{\|}$. Hyperbolic dispersion of these organic thin films is attributed to a spontaneously aligned lamellar alternating-sublayers structure. Polymethine character of excited-state of donor-acceptor-donor structure is associated with the ENZ behavior of organic molecular films. [4]

Using [2,4-bis[8-hydroxy-1,1,7,7-tetramethyljulolidin-9-yl] squaraine] organic thin films, ENZ responses between 450 and 620 nm are demonstrated. Both nonlinear refractive index and nonlinear absorption coefficient are enhanced by more than two orders of magnitude in the ENZ spectral region. These optical effects in the visible spectral range come from the strongly dispersive permittivity of molecular aggregates resulting from the coupling of excitonic transition dipoles. [5]

We introduced an organic ENZ film placed on top of a polymeric fluorophore film to demonstrate a directive emission. By taking advantage of the structural coherence in the P3HT film and the ENZ

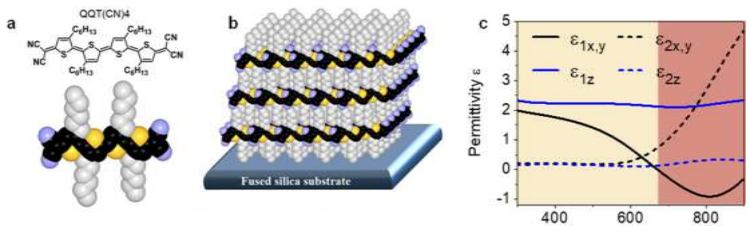


Figure 1: (a) Molecular structure and space-filling representation of $QQT(CN)_4$ (insulating alkyl side chains are represented in gray). (b) Schematic representation of the layered molecular packing structure in spin-coated polycrystalline $QQT(CN)_4$ thin films. (c) x,y component and z component of the real and imaginary parts of the complex permittivity of $QQT(CN)_4$. [1]

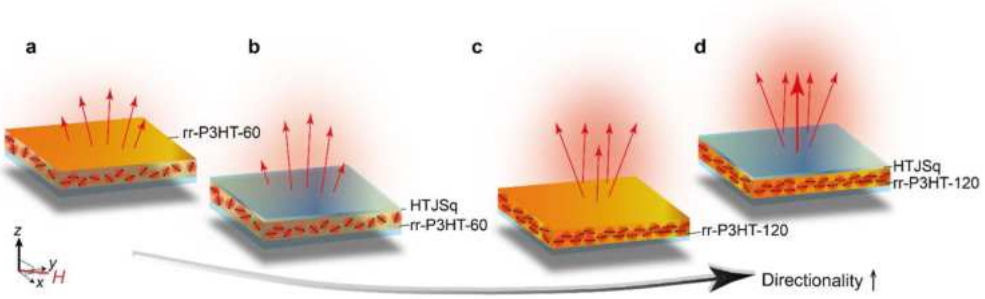


Figure 2: Schematics of directional emission from (a) rr-P3HT-60 bare film, (b) rr-P3HT-60 film with HTJSq film on top, (c) rr-P3HT-120 bare film, and (d) rr-P3HT-120 film with HTJSq film on top. [6]

response in the squaraine molecular film, 42% increase in directive emission is achieved. Spatial coherence of optical wave originating from the ENZ response in squaraine film is responsible for the directive emission of photoluminescence. Notably, HTJSq ENZ film offers wavelength tunability for controlling the directive emission at optical frequency. Based on purely organic compositions, the emission directionality is increased at visible wavelength spectral range by taking advantage of the spatial coherence in squaraine film and structural coherence in polymeric fluorophore film. Capability to control directive emission with organic ENZ films is highly useful in applications requiring bio-compatibility of a fluorophore-embedding medium. [6]

Also, we demonstrated a simple approach to achieve a wavelength-dependent photoluminescence (PL) lifetime modification using monolithic organic molecular aggregates films. These single monolithic organic films are designed to have a Lorentzian dispersion, including epsilon-near-zero (ENZ) and epsilon-near-pole (ENP) spectral regions with increased and decreased photonic density of states, respectively. This dispersion leads to enhanced and depressed PL decay rates at different wavelengths. [7]

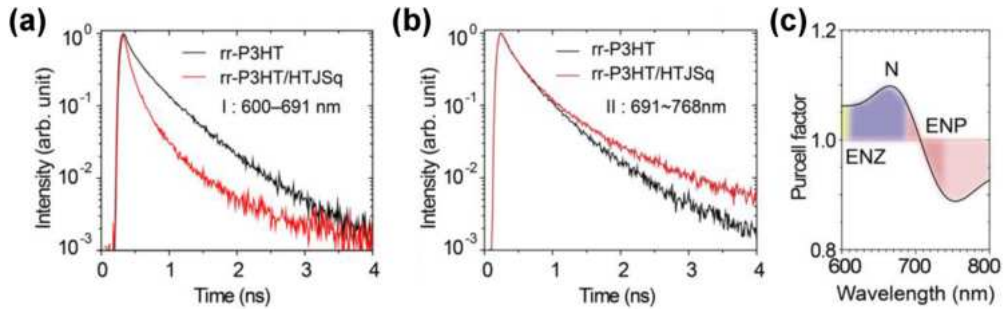


Figure 3: Spectrally resolved PL decay curves in the spectral ranges of (a) 600–691 nm and (b) 691–768 nm. (c) Calculated wavelength-dependent Purcell factor. [7]

REFERENCES

1. Y. U. Lee, O. P. Gaudin, K. Lee, E. Choi, V. Placide, K. Takaishi, T. Muto, P. André, A. Muranaka, M. Uchiyama, et al., *ACS Photonics* **2019**, *6*, 7 1681.
2. M. Kim, K. R. Choi, Y. U. Lee, B. Heinrich, S. Y. Ko, F. Mathevet, J.-C. Ribierre, A. D'Aleo, J. W. Wu, V. Placide, *Advanced Optical Materials* **2021**, *9*, 22 2101091.
3. Y. U. Lee, K. Yim, S. E. Bopp, J. Zhao, Z. Liu, *Advanced Materials* **2020**, 2002387.
4. K.-R. Choi, D. H. Kim, Y. U. Lee, V. Placide, S. Huynh, D. Yao, G. Canard, E. Zaborova, F. Mathevet, L. Mager, et al., *RSC Advances* **2021**, *11*, 60 38247.
5. Y. U. Lee, E. Garoni, H. Kita, K. Kamada, B. H. Woo, Y. C. Jun, S. M. Chae, H. J. Kim, K. J. Lee, S. Yoon, et al., *Advanced Optical Materials* **2018**, *6*, 14 1701400.
6. K.-R. Choi, M. Kim, J. W. Wu, A. D'Aléo, Y. U. Lee, *Nanophotonics* **2023**, *12*, 13 2471.
7. K.-R. Choi, S. Li, D. H. Park, B. C. Joo, H. Lee, E. S. Kang, S. Nic Chormaic, J. W. Wu, A. D'Aléo, Y. U. Lee, *Nanophotonics* **2024** (*in press*).

Deep ultraviolet meta-emitter boosted by bound states in the continuum

Omar A. M. Abdelraouf [1, 2*], Aravind P. Anthur[2], Xiao Renshaw Wang*[1, 3], Qi Jie Wang*[1, 3], Hong Liu*[2]

[1] School of Physical and Mathematical Sciences, Nanyang Technological University, Singapore 637371, Singapore

[2] Institute of Materials Research and Engineering, A*STAR, 2 Fusionopolis Way, #08-03, Innovis, Singapore 138634, Singapore

[3] School of Electrical and Electronic Engineering, 50 Nanyang Avenue, Nanyang Technological University, Singapore 639798, Singapore

*omar_abdelrahman@imre.a-star.edu.sg, renshaw@ntu.edu.sg, qjwang@ntu.edu.sg, h-liu@imre.a-star.edu.sg

Abstract: We demonstrated a crystalline silicon (c-Si) metasurface simultaneously exciting bound states in the continuum (BICs) resonance at the near-infrared wavelength and a plasmonic resonance at the DUV regime to enhance third harmonic generation (THG). We achieved a THG power of 14.5 nW under a peak power density of 15 GW/cm^2.

1. Introduction

Recently, bound states in the continuum (BIC) have emerged to get extremely high Q-factor cavity that theoretically reaches infinity [1]. Ultracompact deep ultraviolet (DUV) coherent light sources can find applications in bioimaging [2], nanolithography [3], and medical inspection [4]. Although conventional nonlinear crystals exhibit relatively high conversion efficiency, their optical losses in DUV hinder their operating regime. Metasurfaces consisting of low-loss nonlinear materials, such as crystal silicon (-Si), would enhance the nonlinear conversion efficiency [5].

2. Results and discussion

We have demonstrated a BIC resonance inside the c-Si metasurface and its unit cell consists of two resonators as shown in Fig. 1a. The structural parameters for the metasurface include the width of top and bottom sides denoted by L_1 and L_2, respectively. The cross-section of the two resonators is a right trapezoid. In the case of L_1=L_2, the BIC resonance is confined so that it cannot be coupled to the radiation spectrum. We only observed a BIC resonance after inducing lattice symmetry breaking by reducing the top side width L_1 of both right trapezoids as shown in Fig. 1b. The theoretical Q-factor was up to 900 for $\Delta L = L_2 - L1 = 20$ nm.

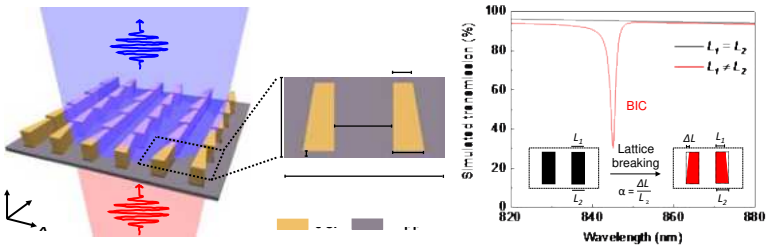


Figure. 1 Metasurface design of c-Si metasurface supporting BIC resonance. (a) 3D schematic of c-Si metasurface on sapphire with a pump fs-laser at wavelength 840 nm, denoted by E_ω, and the collected THG in DUV range at a wavelength 280 nm, denoted by $E_{3\omega}$. (b) Simulated transmission before and after lattice symmetry breaking showing BIC near 840 nm.

The fabrication steps of our metasurface started with electron beam lithography using a negative e-beam resist

hydrogen silsesquioxane (HSQ) of thickness 100 nm. Then, we performed a reactive ion etching using chlorine gas to transfer the HSQ pattern to c-Si, as shown in the inset of Fig. 2a. The experimental Q-factor obtained was more than 180. We pumped the fabricated c-Si metasurface using a linearly polarized fs-laser with the polarization in the horizontal direction. The DUV-THG was measured by using a photomultiplier tube (PMT) after filtering the pump laser.

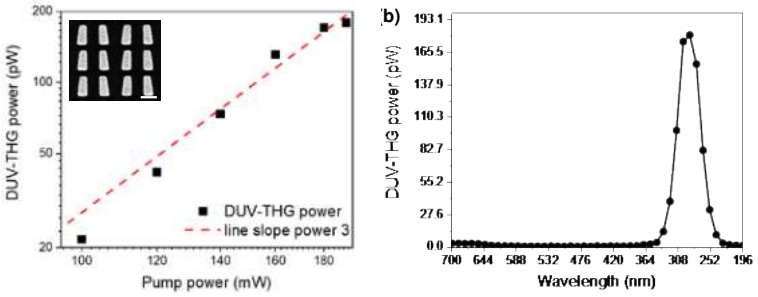


Figure. 2 DUV-THG measurement of c-Si BIC metasurface. (a) The measured DUV-THG versus pump power at a wavelength around 280 nm. (inset) the SEM image of the fabricated c-Si metasurface, with a scale bar of 200 nm. (b) The measured DUV-THG spectrum versus wavelength.

We plotted the DUV-THG power as a function of the pump power in Fig. 2a. The maximum DUV-THG power was up to 200 pW at a pump power of 200 mW. In addition, we measured the DUV-THG spectrum by rotating the resolving prism before the PMT and the results are plotted in Fig. 2b. Our finding will help in obtaining efficient silicon photonic devices operating in the DUV regime.

3. Acknowledgements

LH and QJW acknowledge support from A*STAR AME programmatic grant (grant no. A18A7b0058).
XRW and QJW acknowledge support from Academic Research Fund (AcRF) Tier 2 (Grant No. MOE-T2EP50220-0005 and MOE-T2EP50120-0009, respectively) and Tier 3 (Grant No. MOE2018-T3-1-002) from Singapore Ministry of Education and the Agency for Science, Technology and Research (A*STAR) under its AME IRG grant (Project No. A20E5c0094). APA acknowledges support from A*STAR Strategic Programme Funds (C210917001). Authors acknowledge Dr. DENG Jie for his discussion on SEM images.

4. References

[1] Hsu, C. W.; Zhen, B.; Stone, A. D.; Joannopoulos, J. D.; Soljačić, M., Bound states in the continuum. *Nat. Reviews Materials* 2016, 1 (9), 1-13.

[2] Weigelin, B.; Bakker, G.-J.; Friedl, P., Third harmonic generation microscopy of cells and tissue organization. *Journal of Cell Science* 2016, 129 (2), 245-255.

[3] Wu, B.; Kumar, A., Extreme ultraviolet lithography: A review. *Journal of Vacuum Science & Technology B: Microelectronics and Nanometer Structures Processing, Measurement, and Phenomena* 2007, 25 (6), 1743-1761.

[4] Ager III, J. W.; Nalla, R. K.; Breeden, K. L.; Ritchie, R. O., Deep-ultraviolet Raman spectroscopy study of the effect of aging on human cortical bone. *Journal of biomedical optics* 2005, 10 (3), 034012.

[5] Abdelraouf, Omar AM, Aravind P. Anthur, Zhaogang Dong, Hailong Liu, Qian Wang, Leonid Krivitsky, Xiao Renshaw Wang, Qi Jie Wang, and Hong Liu. "Multistate Tuning of Third Harmonic Generation in Fano-Resonant Hybrid Dielectric Metasurfaces." *Advanced Functional Materials* 31, no. 48 (2021): 2104627.

Tailoring THz radiation pattern through intrapulse and interpulse difference-frequency generation at the nanoscale: modeling and perspectives

U. Arregui Leon[1*], L. Carletti[2], D. Rocco[2], C. De Angelis[2] and G. Della Valle[1*]

[1]Department of Physics, Politecnico di Milano, Piazza Leonardo da Vinci 32, 20133, Milano, Italy
[2]Department of Information Engineering, University of Brescia, Via Branze 38, 25123, Brescia, Italy
[*]corresponding authors: unai.arregui@polimi.it; giuseppe.dellavalle@polimi.it

Abstract: All-dielectric nanoantennas and metasurfaces unlock the possibility to engineer the directionality of electromagnetic fields owing to the interference between multipolar resonances. We exploit this concept in the framework of NIR-to-THz conversion from flat-optics elements and analyze the role of pump's degrees of freedom in the intrapulse and interpulse schemes for difference-frequency generation.

The terahertz (THz) region of the electromagnetic spectrum (1 – 30 THz) enables to address physical mechanisms that are of great interest not only for fundamental research (e.g. materials science, optics...) but also for applications in telecommunications, biology and industry [1]. Such a variety of disciplines, in which powerful and compact THz devices are required, fairly explains the wide range of methods that have been developed for THz generation: photoconduction, spintronics, laser-induced plasma, or wave-mixing in $\chi^{(2)}$ media [2]. Each of these processes invokes different characteristics of the generated light in terms of bandwidth, efficiency or tunability. Among all, difference-frequency generation (DFG) mediated by the effective $\chi^{(2)}$ of nanophotonic platforms has gained attention owing to the breakthrough in their modeling and fabrication techniques. Particularly, all-dielectric nanoantennas have been proved to be a competitive alternative to plasmonic structures in the near-infrared (NIR) [3] as well as in the THz regime [4], owing to their ability to harness Mie resonances, exploit bulk nonlinearities and circumvent intrinsic ohmic losses in metals. In this work, we present their potential to tailor the emission pattern of THz radiation generated from AlGaAs and $LiNbO_3$ nanocylinders, paving the way to functionalities such as nonlinear routing and sensing.

The concept for rectifying a femtosecond pulse to a THz signal is presented in Figure 1(a) below. A laser pulse polarized along the *x* axis of the laboratory frame excites a magnetic dipolar mode, thereby localizing and enhancing the fields at the laser fundamental within the nanostructure. Considering the NIR fields at an angular frequency ω_1 and at $\omega_2 = \omega_1 - \omega_{THz}$ that fall within the bandwidth of the resonance, the local $\chi^{(2)}(\omega_{THz}, \omega_1, -\omega_2)$ will induce a nonlinear/DFG polarization current density (left panels in Figs. 1(b)-(e)) operating as a sub-wavelength THz source.

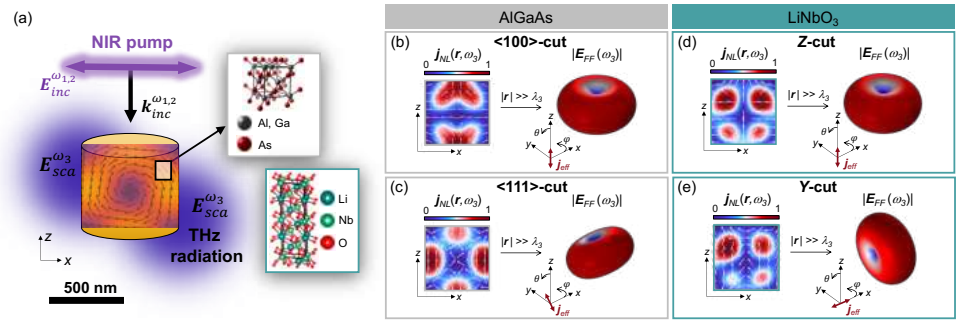


Figure 1. (a) Intrapulse DFG (optical rectification) in high-index dielectric nanopillars, pumped at the magnetic dipole resonance. Nonlinear THz radiation is shown in (b)-(c) for AlGaAs and in (d)-(e) for $LiNbO_3$ nanoantennas [4].

Interestingly, the possibility to grow the nanopillars along different crystallographic directions of the medium results in a reconfiguration of the spatial distribution of nonlinear currents, since the projection of the NIR internal fields on the crystallographic frame (in which $\chi^{(2)}(\omega_{THz}, \omega_1, -\omega_2)$ is defined) will correspondingly change. Figures 1(b)-(e) show that both AlGaAs and $LiNbO_3$ nanoantennas can be designed to remove the radiation null from the forward/backward directions [4].

The same strategy can be followed in the presence of not one but two NIR pulses: the DFG process takes now place between two different pump spectra separated by a THz distance. Such a two-beam scheme, despite the increased set-up complexity, might be preferred for spectroscopy applications requiring high-power, narrowband and tunable THz waves [1]. Figure 2(a) shows the optical-to-THz conversion efficiency obtained with the interpulse DFG in the $LiNbO_3$ nanopillar, when the linearly polarized pumps are mutually orthogonal. The decomposition of the nonlinear THz fields into a spherical multipolar basis elucidates the transition from a purely *z*-directed electric dipole emission (intrapulse case, with degenerate pump polarization) to a superposition of in-quadrature electric dipoles and a magnetic dipole moment. In this spirit, the angle between the two pumps can be used as a knob to control all-optically the THz emission characteristics at an almost constant efficiency (Fig. 2(b)).

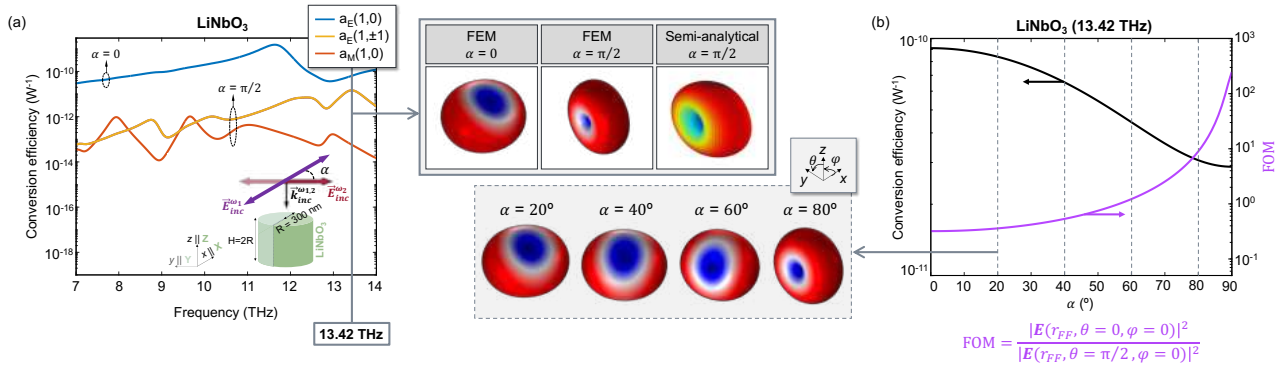


Figure 2. (a) Contribution of electric, $a_E(l,m)$, and magnetic, $a_M(l,m)$, multipolar coefficients to the conversion efficiency of the $LiNbO_3$ nanopillar. (b) Evolution of the efficiency and emission pattern for a varying interpulse polarization angle (α).

These degrees of freedom (crystal orientation, pump configuration and polarization) can be exploited even better in a metasurface configuration, constituted by a two-dimensional periodic arrangement of the proposed nanopillars. Actually, the metasurface could exhibit unprecedented flexibility to steer the THz generated beam analogous to the case of negative index media, but in the nonlinear regime of optical rectification.

This work is part of the METAFAST project (no. 899673) funded by the EU H2020 programme.

References

1. Leitenstorfer, A. et al., "The 2023 terahertz science and technology roadmap", Journal of Physics D: Applied Physics, Vol. 56, No. 22, p. 223001, 2023.
2. Fülöp, J. A., Tzortzakis, S. and Kampfrath, T., "Laser-driven strong-field terahertz sources", Advanced Optical Materials, Vol. 8, No. 3, p. 1900681, 2020.
3. Carletti, L. et al., "Controlling second-harmonic generation at the nanoscale with monolithic AlGaAs-on-AlOx antennas", Nanotechnology, Vol. 28, No. 11, p. 114005, 2017.
4. Arregui Leon, U. et al., "THz Generation via Optical Rectification in Nanomaterials: Universal Modeling Approach and Effective χ^(2) Description", Laser & Photonics Reviews, p. 2300669, 2023.

Versatile plasmonic colors with pixelated metasurface

M. Song, Y. Lu*, and T. Xu*

National Laboratory of Solid-State Microstructures, Collaborative Innovation Center of Advanced Microstructures, Nanjing University, Nanjing 210093, China

*corresponding author: yqlu@nju.edu.cn, xuting@nju.edu.cn

Abstract: Here, we design and experimentally demonstrate surface-relief plasmonic metasurfaces that realize high-performance colors and high-density data storage. The plasmonic resonances could be engineered to provide extraordinary capabilities in realizing ultra-high saturated colors or encode various information states into a single subwavelength pixel.

The ever-growing interest of developing modern digital displays and color printing industries drives the urgent need for advanced structural color techniques to realize remarkable color performances. Currently, metasurface-based structural coloration shows unprecedented advantages in chiaroscuro presentation, wide-gamut palette, high-saturation and dynamic tunability. However, most previous approaches are incapable of simultaneously achieving all the above merits [1]. Here, we design and experimentally demonstrate a surface-relief plasmonic metasurface that combines those advantages in one [2]. The color pixel consists of ultra-shallow nanoapertures placed at the centers of hexagonal unit cells, enabling independent manipulation of color hue, saturation and brightness by individually varying geometric dimensions and orientation of the nanoapertures. The plasmonic resonances provide extraordinary capabilities in realizing ultra-high saturated colors and the resonant positions of individual pixels are linearly varied with the lateral size of the nanoapertures, establishing a one-to-one relationship between spectral and spatial information. By uniting differently oriented nanoapertures to modulate color properties and mimicking the conventional sketch drawing & oil-painting techniques, the experimentally photographed microscale images vividly showcase photorealistic and stereoscopic impressions as depicted in Fig. 1a. The reproduced artworks present strikingly clear and subtle renderings of texture details of the original paintings. Moreover, another all-aluminum metasurface is proposed to enhance data-storage density [3]. Localized surface plasmon resonance ensures small unit size approaching diffraction limit with at least 8 different color states encoded in each individual pixel. Distinct information states can be encoded and revealed from the patterned metasurface when the unique polarizer-analyzer combination is provided, thus exhibiting significant potentials in steganography and anticounterfeiting techniques as shown in Fig. 1b. We believe our findings open up avenues for high-fidelity color printing, novel display technique, high-density data storage as well as advanced optical steganography.

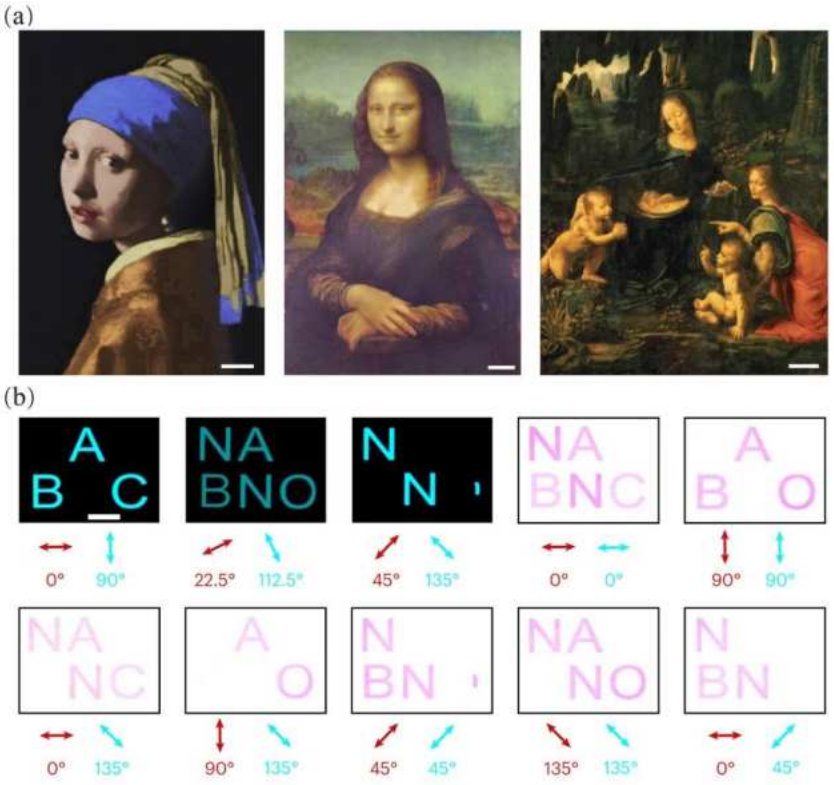


Figure 1 (a) Experimentally captured optical photographs of the metasurface based artworks. The images show ultra-smooth transitions between the different color hues and brightness by using our plasmonic coloring approach. All the white scale bars represent 200 μm. (b) Experimentally captured optical micrographs of the steganographic information display. Different information states can be clearly decrypted under special combinations of polarizer and analyzer angles. Scale bar: 40 μm.

Acknowledgement

The authors would like to acknowledge the support by the National Natural Science Foundation of China (No. 62322507).

References

1. Song, M. Wang, D., Peana, S., Choudhury, S., Nyga, P., Kudyshev, Z., Yu, H., Boltasseva, A., Shalaev, V. and Kildishev, A., "Colors with plasmonic nanostructures: a full-spectrum review," Appl. Phys. Rev. Vol.6, 041308, 2019.
2. Song, M., Feng, L., Huo, P., Liu, M., Huang, C., Yan, F., Lu, Y. and Xu, T., "Versatile full-color nanopainting enabled by pixelated plasmonic metasurface," Nat. Nanotechnol. Vol.18, 71–78, 2023.
3. Song, M., Wang, D., Kudyshev, Z., Xuan, Y., Wang, Z., Boltasseva, A., Shalaev, V. and Kildishev, A., "Enabling optical steganography, data storage, and encryption with plasmonic colors," Laser & Photon. Rev., Vol.15, 2000343, 2021.

Efficient nonlinearities in metasurfaces enabled by bound states in the continuum

H. Harutyunyan[1*]

[1]Dpartment of Physics, Emory University, Atlanta, GA 30322, USA

[*]corresponding author: hharuty@emory.edu

Abstract: We present a novel approach to designing high-quality bound states in the continuum (BIC) in dielectric metasurfaces using magnetic dipole resonances coupled to a mirror, enabling strong light–matter interaction without the need for asymmetric geometry or polarization dependence. This simplifies fabrication and enhances practical applications, demonstrated by a record-breaking third harmonic generation efficiency. Additionally, we showcase superior modulation characteristics with a pulsewidth-limited switching time of 100 fs and a remarkably low energy consumption, facilitated by the narrow photonic resonance of our metasurface. Our findings offer significant potential for optical sensing, quantum photonics, and nonlinear devices.

References

1. G. Yang, M. S. Allen, J. W. Allen, and H. Harutyunyan, Nano Lett., 24, 1679–1686, (2024)
2. G. Yang, S. U. Dev, M. S. Allen, J. W. Allen, and H. Harutyunyan, Nano Lett., 22, 2001–2008, (2022)

Laser production of nanofibers

F. Quintero[1], J. Penide[2], R. Barciela[1], M. Fernández-Arias[1], A. Riveiro[1,3], J. del Val[4], R. Comesaña[1,3], F. Lusquiños[1], J. Pou[1*]

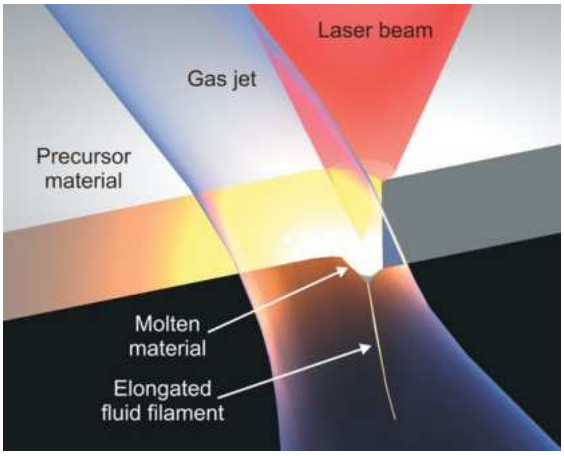
[1]LaserON Research Group, CINTECX, School of Engineering, University of Vigo, Vigo, Spain
[2] Medical & Engineering Technologies, GMIT, H91 T8NW, Galway, Ireland
[3] Materials Engineering, Applied Mechanics and Const. Dept. University of Vigo, Vigo, Spain
[4] Defense University Center, Spanish Naval Academy, Marín, Spain
[*]corresponding author: jpou@uvigo.es

Abstract: Nanofibers are novel materials with very special properties, different from their bulk counterparts, due to the very reduced size and consequent microstructural differences. In this presentation two novel laser-assisted technologies, specific developed for the production of nanofibers, will be introduced: Laser Spinning and COFIBLAS.

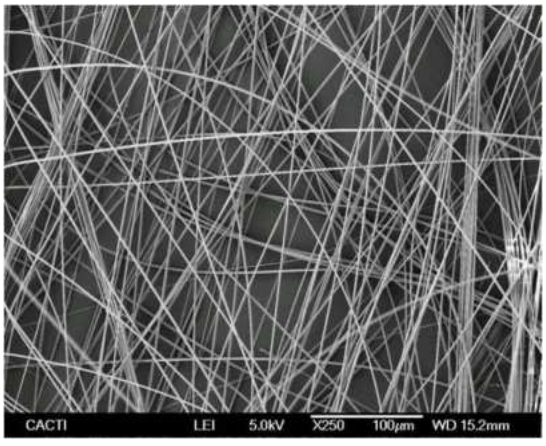
Introduction & main results

The search for materials with improved mechanical properties and functionalities has boost the development of advanced continuous nanofibers. The development of nanofibers and nanotubes predicted the production of new nano-composites with exceptional mechanical properties. However, the breakthrough predictions haven't been achieved yet, in part due to the reduced length of the nanofibers or nanotubes, which restrained the mechanical reinforcement and manufacturing. Consequently, there is an enormous interest in the development of advanced continuous nanofibers, but conventional methods for fiber spinning cannot produce fibers thinner than some micrometers robustly. Here, we present two laser-assisted methods to produce glass nanofibers.

On one hand we have Laser Spinning. This technique involves melting and elongation of a precursor material with tailored composition using a high power laser and a supersonic gas jet. Laser Spinning can quickly produce a big quantity of glass nanofibers. Figure 1a shows the schematic idea of this technique. The type of product obtained by this technique is shown in figure 1b.



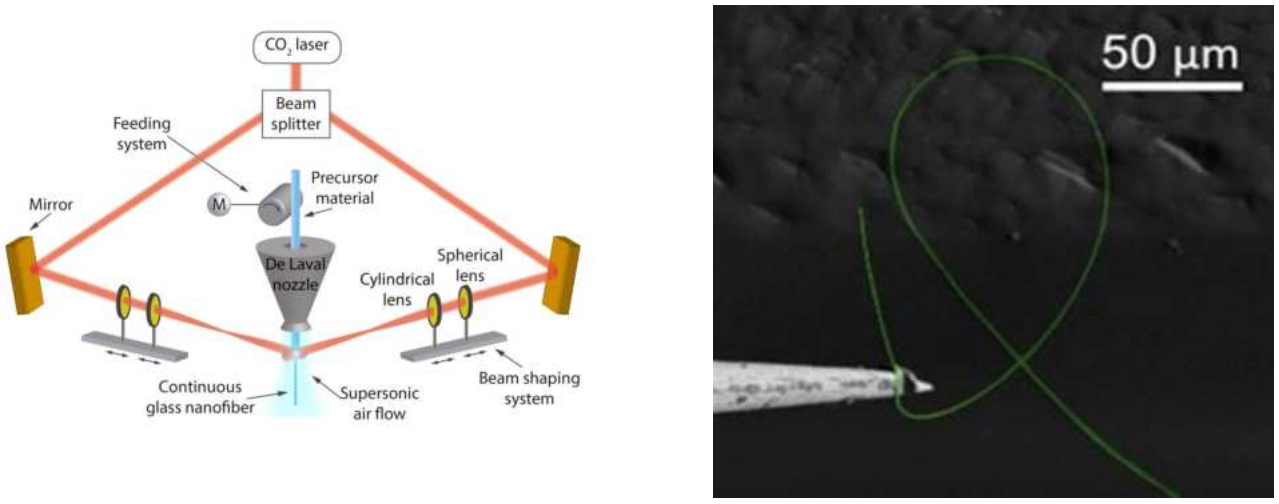
a)



b)

Figure 1. *a) Schematic illustration of the Laser Spinning technique. b) Example of the nanofibers produced by Laser Spinning. [1].*

On the other hand, Continuous Fiberizing by Laser melting and Supersonic dragging (Cofiblas) is a new process that basically consists on irradiating the precursor material uniformly, therefore heating it extremely fast using a high power laser while, at the same time, the molten material is rapidly drawn and cooled by the action of a supersonic air jet. A laser beam shaping system was specifically developed for this method. This beam shaping system allows a precise control of the temperature distribution in the filament. A de Laval nozzle was designed to provide a coaxial gas jet that exerts a high tension localized at the molten segment of the to-be-formed nanofiber.



a) b)

Figure 2. *a) Schematic illustration of the COFIBLAS technique. b) Example of the extraordinary flexibility of the nanofibers produced by COFIBLAS [2].*

Figure 2a shows the schematic configuration of the COFIBLAS experimental system. Figure 2b shows an image taken by scanning electron microscopy of one nanofiber produced by the COFIBLAS process. It is quite remarkable its extraordinary flexibility.

This innovative method produces glass nanofibers with lengths that are, effectively, unlimited by the process. This method enabled the production of virtually unlimited long, solid, and nonporous glass nanofibers that display outstanding flexibility and could be separately arranged and weaved.

Both techniques will be explained as well as the potential applications of the nanofibers so produced in the biomedical field, textile field, composite manufacturing, etc.

Acknowledgements

This work was partially supported by the Government of Spain [PID2020-117900RB-I00 (MCI/AEI/FEDER, UE)], and by Xunta de Galicia (ED431C 2023/25).

References

1. Quintero, F., Pou, J., Comesaña, R., Lusquiños, F., Riveiro, A., Mann, A.B., Hill, R.G., Wu, Z.Y., Jones, J.R. (2009) Laser spinning of bioactive glass nanofibers. Advanced Functional Materials 19, 3084-3090.
2. Quintero F, Penide J, Riveiro A, del Val J, Comesaña R, Lusquiños F, et al. Continuous fiberizing by laser melting (Cofiblas): Production of highly flexible glass nanofibers with effectively unlimited length. Science Advances.(2020) 6:eaax7210. https://doi.org/10.1126/sciadv.aax7210.6.

Silicon Nitride Platform for Quantum Photonics and Quantum Phononics

K. Mnaymneh[1*], A. M. Tareki[1,2] and C. Kupchak[2]

[1] National Research Council of Canada, 1200 Montreal Road, Ottawa, Canada K1A 0R6
[2] Department of Electronics, Carleton University, 1125 Colonel By Drive, Ottawa, Canada K1S 5B6
[*]corresponding author: khaled.mnaymneh@nrc-cnrc.gc.ca

Abstract: We present our work for producing high quality silicon nitride films for integrated quantum optics and quantum phononics. Our main findings are related to refractive index and its dependence on the film stress and surface roughness. Furthermore, photon and phonon dispersion relations, particle group velocities and the nonlinear index depends very much on the material quality. Here we show how we can use fabrication steps and tools to ensure the reliable realization of next-generation devices targeting applications in quantum technologies.

Thermochromic thermal radiator based on angle selective thermal radiation applicable under direct solar irradiance

M. Shimizu[1*], R. Onozaki[1], R. Benlyas[1], Z. Liu[1], and H. Yugami[1]

[1]Graduate School of Engineering, Tohoku University, Japan
[*]corresponding author: makoto.shimizu.a3@tohoku.ac.jp

Abstract: In this study, a thermochromic thermal radiator is proposed that can dissipate heat at high temperature but insulate heat at low temperature. In addition, thanks to the angular selective thermal radiation property at high temperature, it is applicable under solar irradiance due to its angular selective emission (absorption) property.

In this study, a novel heat dissipating device based on radiative heat transfer with the ability to release heat at high temperatures and insulate it at low temperatures is realized, thus realizing a device whose thermal radiation properties change with ambient temperature. This property is realized by using vanadium dioxide, which undergoes a temperature-dependent metal-insulator phase transition, in a metamaterial structure as shown in Fig. 1. We have previously reported that by reducing the thickness of the dielectric layer in a metal-dielectric-metal metamaterial structure, angle-selective thermal radiation at a grazing angle can be achieved[1]. It is also seen when thin films of polaritonic material are formed on a reflective substrate and is called Berreman mode[2]. This device is applicable to realize a device that can dissipate heat based on radiative heat transfer even in an environment where direct sunlight is incident from the vertical direction.

These characteristics would be applied to spacecraft heat dissipation control. For example, in an environment with direct sunlight, the device can reflect sunlight and promote thermal radiation from the spacecraft, while in an environment without sunlight, the device can suppress radiation as much as possible and insulate heat. In this way, the heat dissipation characteristics can be passively controlled according to the environment to reduce the temperature difference. More detail will be explained in the presentation.

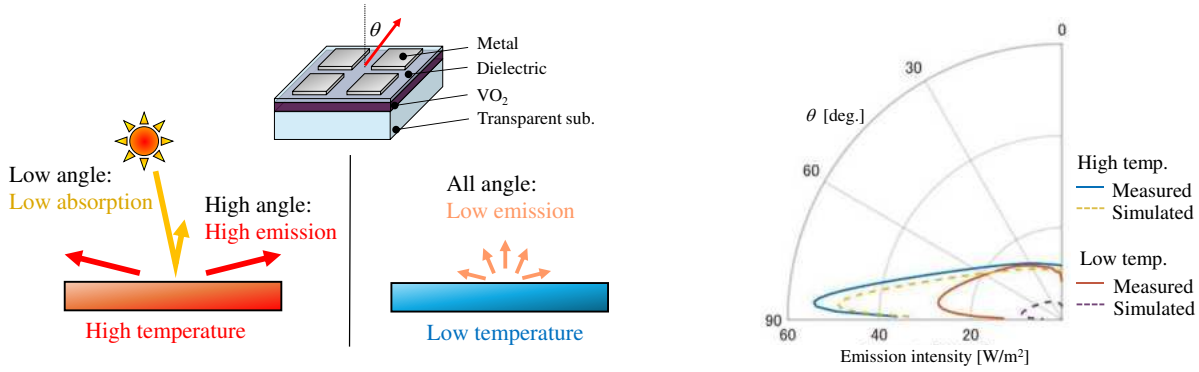


Fig. 1 Schematic image of the proposed thermochromic device and its emission property changing with surrounding temperature (Left). Angle dependence of emission property of the device is shown where the solid lines are the measured ones and dashed lines are the simulated ones (Right).

References

1. R. Benlyas et al., “Multiband infrared emissions limited in the grazing angle from metal-dielectric-metal metamaterials”, Opt. Express, Vol. 30, No. 6, 9380-9388, 2022.
2. S. Vassant et al., “Berreman mode and epsilon near zero mode”, Opt. Express, Vol. 20, No. 21, 23971-23977, 2012.

High-performance Ultraviolet Metasurfaces based on Wide bandgap Dielectrics

Cheng Zhang

School of Optical and Electronic Information & Wuhan National Laboratory for Optoelectronics, Huazhong University of Science and Technology, Wuhan, Hubei 430074, China

cheng.zhang@hust.edu.cn

Abstract: I will present our recent work on employing wide bandgap dielectrics to implement an array of high-performance metasurface optics in the ultraviolet, including down to the deep-ultraviolet region.

In this talk, I will show how low-loss, all-dielectric metasurfaces operating at ultraviolet (UV) wavelengths down to the deep-UV range can be implemented using wide-bandgap dielectric materials[1,2]. The exploited materials in this study include Tantalum Pentoxide (Ta_2O_5) and Hafnium Oxide (HfO_2). For the Ta_2O_5-based metasurfaces, we develop a reactive sputtering process which produces loss-less Ta_2O_5 films for the entire near-UV region, and a fluorine-based reactive ion etching (RIE) process which produces Ta_2O_5 nanostructures with decent sidewall profiles. We demonstrate high-NA metalenses and broadband metaholograms operating across the near-UV regime. For the HfO_2-based metasurfaces, we develop a unique Damascene fabrication process, involving both low-temperature atomic layer deposition (ALD) of HfO_2 onto patterned resist and back etching with Argon (Ar) ion milling, to achieve high-aspect-ratio HfO_2 nanostructures with straight and smooth sidewall profiles. We demonstrate a variety of polarization-independent and polarization-multiplexed UV metasurface devices having representative wave-front shaping functionalities, namely diffraction-limited focusing, hologram projection and self-accelerating beam generation, operating at distinct UV wavelengths down to the deep-UV region.

References

1. C. Zhang, et al., “Low-loss metasurface optics down to the deep ultraviolet region,” Light Sci. Appl. 9, 55, 2020.

2. C. Zhang, et al., “Tantalum pentoxide: a new material platform for high-performance dielectric metausrface optics in the ultraviolet and visible region,” Light Sci. Appl. 13, 23, 2024.

Finite Difference Driven and Eigenmode Modelling of Polaritonic Systems

M. Tamagnone[1*], H. Gupta[1,2], T. Contino[1,2], M. A. Yaqub[1,2], and M. W. Ashraf[1]
[1]Istituto Italiano di Tecnologia, via Morego 30, 16163 Genova, Italy
[2]Dipartimento di Chimica e Chimica Industriale, Università degli Studi di Genova, Genova, Italy
[*] michele.tamagnone@iit.it

Abstract: We present a new numerical finite difference numerical package capable of handling periodic driven or eigenvalue linear problems in an arbitrary number of dimensions and with user-defined physical laws (e.g. Maxwell's or Schrodinger's equations). We then illustrate the applications to experimental nanophotonic devices and highly confined polaritons in 2D materials.

This project has received funding from the European Research Council (ERC) under the European Union's Horizon 2020 research and innovation programme (Grant agreement No. 948250).

Strong Coupling with Different Photonic Modes within Single GaN Microstructure

Yong-Hoon Cho
Department of Physics and KI for the NanoCentury,
Korea Advanced Institute of Science and Technology (KAIST), Daejeon, Republic of Korea
*corresponding author: yhc@kaist.ac.kr

Abstract:
Exciton-polaritons are quasi-particles that are half-light and half-matter, which can form single-ground-state polariton condensates in microcavities. In particular, since GaN has large exciton binding energy and high oscillator strength, a GaN hexagonal microrod has been utilized for the generation and condensation of exciton-polaritons at room temperature. Firstly, we observed whispering gallery polariton condensation in GaN hexagonal microrod structures at room temperature [1, 2]. When it is excited by a laser, various photonic and polariton modes such as whispering gallery modes (WGMs) and Fabry-Perot modes can be generated. Optical properties of the WGMs and the Fabry-Perot modes generated in a hexagonal GaN microrod are systematically compared and an experimental technique for selecting a specific mode is investigated among the various photonic modes in the microrod. In particular, angle-resolved micro-photoluminescence (μPL) experiments are performed with varying excitation beam spot sizes to study the tendency of photonic and polaritonic modes. The emission and interference characteristics are analyzed and compared in both real and momentum spaces. Second, we successfully fabricated triangular GaN structures by using the selective area growth method with metal-organic chemical vapor deposition and could observe polariton condensation coupled with WGMs and superscar modes (SSM). The SSM is an optical cavity mode found in polygonal structures that has a longer optical path and higher quality factors compared to the WGM. We could adjust the dominant mode between WGM and SSM for the condensation by changing the opening shape on the GaN template for the selective area growth. To elucidate the processes of polariton formation and condensation in a triangular structure, angle-resolved μPL experiments are carried out with varying excitation power.

References

1. H. G. Song, S. Choi, C. H. Park, S. H. Gong, C. Lee, M. S. Kwon, D. G. Choi, K. Y. Woo, and Y. H. Cho*, “Tailoring the potential landscape of room-temperature single-mode whispering gallery polariton condensate,” Optica Vol. 6, 1313, 2019.
2. H. G. Song, M. Choi, K. Y. Woo, C. H. Park, and Y. H. Cho*, “Room-temperature polaritonic non-Hermitian system with single microcavity,” Nature Photonics Vol. 15, 582, 2021.

Engineered composites and plethora of on-demand functionalities and applications

D. A. Pawlak[1,2], P. Piotrowski[1,2], M. Tomczyk[1], K. Sadecka[1], K. Bandopadhay[1], N. Aghad[1], K. Markus[1], A. Abbas[1], S. Saha[1], A. Materna[1], A. Bellardini[3], C. Sibilia[3]

[1]ENSEMBLE3 Centre of Excellence, Warsaw, Poland
[2]Chemistry Dept., University of Warsaw, Poland
[3]Sapienza Univ. of Rome, Italy
[*]corresponding author: dorota.anna.pawlak@ensemble3.eu

Abstract: New composite materials and their properties will be shown including various potential applications. The studied materials belong to two types of composites: (i) eutectic composites where two or more crystalline phases can be combined to enable particular functionality, (ii) glass composites where various nanoparticles can be embedded in glass matrices.

"Meta"-Optical Fibers

Andrew Palmer, [1,2] Yucheng Jin, [1,2] Stuart Love, [1,2], Yujin Zha, [1,2] Beyonce Hu, [1,2] **Ho Wai Howard Lee**[1,2,3,*]

[1] *Department of Physics & Astronomy, University of California, Irvine, United States*

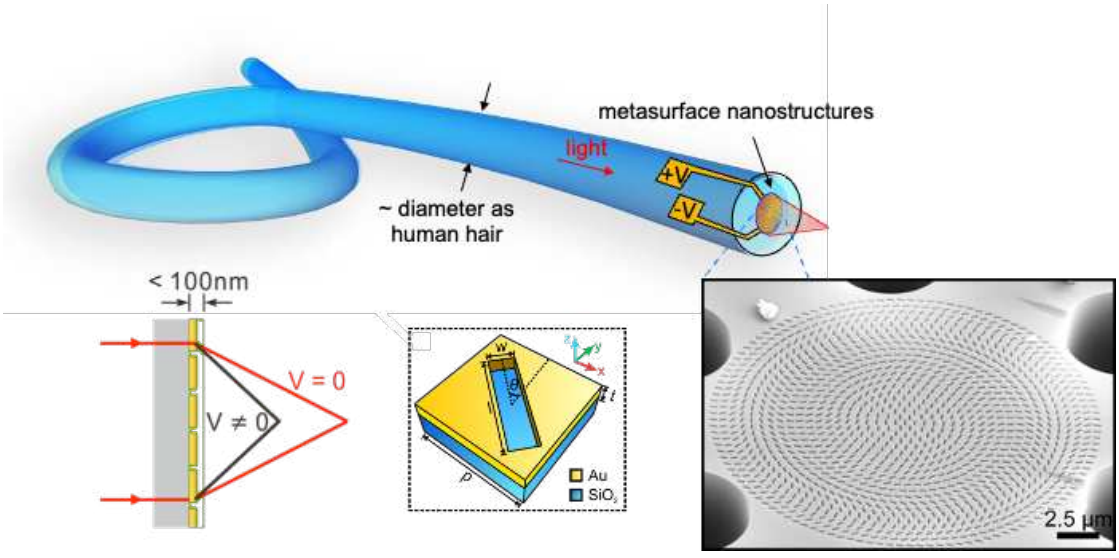
[2] *Beckman Laser Institute and Medical Clinic, University of California, Irvine, United States*

[3] *Eddleman Quantum Institute, University of California, Irvine, United States*

Howardhw.lee@uci.edu

Abstract: Optical fiber is a well-established and efficient light-guiding medium. Although optical fiber is efficient for transmitting light, its functionality is limited by the dielectric material of the core, which has poor optoelectronic, magneto-optical, and nonlinear-optical responses and has a dielectric diffraction limit. Therefore, the optical properties of the optical fiber such as phase, amplitude, polarization, and mode profile, cannot be altered after the fiber drawing fabrication, thus limiting the development of novel in-fiber devices. Integration of new materials and nanostructures into fiber will enhance processing/transmission capabilities and novel functionalities.

In this talk, I will present our recent development of "Meta"-optical fiber, an advanced optical fiber integrated with emerging nanophotonic concepts such as optical metasurfaces, plasmonic nanowires, and zero-index photonics. I will present the development of ultrathin optical metalens which is cascaded on the facet of a photonic crystal fiber that enables light focusing. I will also discuss the ability to develop tunable meta-optical fiber for advanced beam steering and dynamic focusing. These advanced "meta"-optical fibers open a pathway to revolutionary in-fiber optical imaging/endoscopy, lasers/spectroscopies, and optical communication devices.



This work was supported in part by Air Force Office of Scientific Research (FA9550-21-1-02204) and National Science Foundation (Award Number: 2345825)

META 2024, TOYAMA - JAPAN, JULY 16 – 19, 2024

Tuning Nanoscale Photocurrent Direction and Terahertz Polarization State via Incident Light Polarization in Optoelectronic Metasurfaces

Hou-Tong Chen[1*], Jacob Pettine[1], Yunseok Choi[1] and Chun-Chieh Chang[1]

[1] Center for Integrated Nanotechnologies, Los Alamos National Laboratory, Los Alamos, NM 87545, USA

[*]corresponding author: chenht@lanl.gov

Abstract: Nanoscale vectorial photocurrents were observed in symmetry-broken optoelectronic metasurfaces. Nanoantennas with three-fold rotation symmetry enable the continuous rotation of the photocurrent direction and the linear polarization of the emitted terahertz radiation by 360°, and the switching of terahertz vector beams between radial and azimuthal directions, via the incident light polarization.

Control of non-hermitian degeneracy using intersubband polaritonic metasurfaces

Hyeongju Chung[1], Beomjoon Kim[1], Gerhard Boehm[2], Mikhail A. Belkin[2] and Jongwon Lee[1*]

[1] Department of Electrical Engineering, Ulsan National Institute of Science and Technology (UNIST), Ulsan 44919, Korea
[2] Walter Schottky Institute, Technical University of Munich, Carching 85748, Germany
[*]corresponding author: jongwonlee@unist.ac.kr

Abstract: We suggest the control of non-Hermitian degeneracies in the mid-infrared spectrum using two electrically tunable plasmonic split-ring resonators. These resonators interface with intersubband transitions within multiple-quantum-wells and can be independently manipulated via two bias voltages. At a wavelength of 8.97μm, we achieve the convergence of eigen polarization states.

In the past decade, metasurfaces have garnered significant attention for their ability to manipulate the phase, amplitude, and polarization of scattered light locally. Moreover, ongoing research has focused on developing reconfigurable metasurfaces capable of dynamically adjusting their functionalities. Recent efforts in the mid-infrared spectrum have showcased reflection and phase modulation using electrically reconfigurable polaritonic metasurfaces. These metasurfaces integrate plasmonic ridge-resonators with the remarkable electro-optic properties of Stark-tunable intersubband transitions (IST) in multiple quantum wells (MQWs) [1].

From a foundational standpoint, a metasurface functions as an open system, engaged in continual interaction with the incident field and resonant nanostructures, either absorbing or exchanging energy. These open systems undergo parity-time symmetry breaking at exceptional points (EPs), leading to intricate scattering phenomena linked with optical singularities. While EPs have primarily been observed experimentally in passive settings, they are profoundly sensitive to structural fabrication and prone to fabrication errors, necessitating repetitive manufacturing. To tackle these challenges, a recent study employed a graphene-based device, showcasing EP emergence in an electrically modulated interaction between light and a cluster of organic molecules in the terahertz range [2]. Additionally, an experimental demonstration revealing a missing dimension within a reduced polarization eigenspace at a chiral EP has been achieved using a graphene-metal hybrid metasurface [3].

In this study, we propose the creation of non-Hermitian degeneracies, specifically EPs, employing an electrically reconfigurable intersubband polaritonic metasurface. This metasurface is engineered to merge the electromagnetic modes of two orthogonal plasmonic split-ring resonators and Stark tuning of intersubband transitions by applying bias voltages independently to the MQW layer for each split-ring resonator.

We devised a 300nm-thick MQW layer comprising 16 repetitions of double quantum wells, constructed with $In_{0.52}Al_{0.48}As$ and $In_{0.53}Ga_{0.47}As$ materials, as depicted in Fig. 1(a). The absorption energy of IST between the 1st and 2nd states in the conduction band of the MQW is 122 meV at 0V bias. By applying bias voltages ranging from +1.5V to -1.5V, the IST energy can be adjusted from 105meV to 141meV, respectively. In the presence of IST absorption, the dielectric constant of the MQW layer undergoes modification, albeit solely in the surface normal direction (z-direction). Figure 1(b) displays the calculated imaginary part of the dielectric constant for bias voltages ranging from -1.5V to +1.5V. The unit cell structure depicted in Figure 1(c) comprises left x-directional and right y-directional split-ring resonators, along with two vertical load lines featuring bridges for independent bias voltage application. Each x- and y-split ring resonator can initiate plasmonic resonances for x- (left) and y- (right) polarized incident light, respectively, thereby generating enhanced E_z fields within the MQW layer that can interact with the IST. The coupled mode with the IST can be manipulated by applying bias voltage to each split-ring resonator independently, leading to spectral and phase modulation of x- and

y-polarized reflected light. Figure 1(d) illustrates the reflection spectra of r_{xx}, r_{xy}, r_{yx}, and r_{yy} (where the subscript [yx] denotes reflected linear polarization conversion from x- to y-linear polarization) at a constant V_x of +0.9V while V_y varies from -1.5V to +1.5V in increments of 0.3V. By applying bias voltages to the unit cell structure, several EPs are discovered. One of these EPs is depicted in Figure 2. To attain EPs (non-Hermitian degeneracy), the magnitude and phase of eigenvalues are extracted from the reflection matrix of Figure 1(d) around the wavelength of 8.97μm, as illustrated in Figures 2(a) and 2(b). Specifically, the EP is achieved when both V_x and V_y are set to +0.9V, indicated by the yellow sphere in Figures 2(a) and (b), respectively. Furthermore, the eigenpolarization states are derived from the reflection matrix of Figure 1(d) and plotted on the Poincaré sphere as depicted in Figure 2(c), spanning the wavelength range from 8.75μm to 9.55μm. When V_x is held constant at +0.9V and V_y varies from -1.5V to +0.9V, the eigenpolarization states transition from vertical and horizontal linear polarization to left circularly polarized (LCP) states. Beyond V_y = +1.5V, the eigenpolarization states segregate once more. Figure 2(d) illustrates the eigenpolarization states of the EP, with the LCP states converging at the wavelength of 8.97μm and applied voltages of V_x and V_y set to +0.9V.

This work was supported by a National Research Foundation of Korea (NRF) grant funded by the Korea government (MSIT) (No. 2022R1A2C301189812 and 2022M3H4A1A04096465)

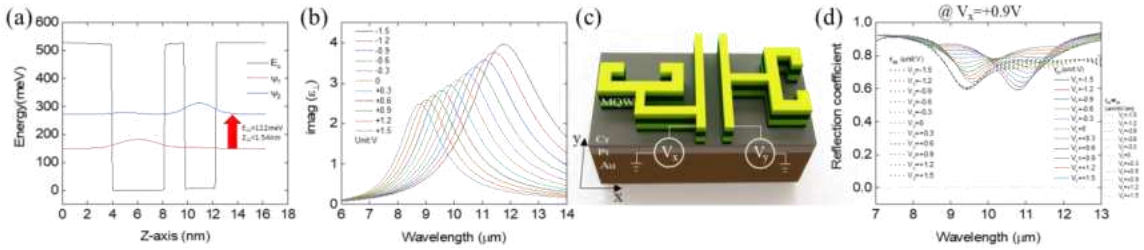


Fig. 1. (a) Conduction band diagram of an one period of MQWs at 0V. The layer sequence (in nm) is 4/**4.2**/1.6/**2.5**/4 where InGaAs wells are shown in bold. The red arrow shows the IST energy of 122 meV and transition dipole moment is 1.54nm. (b) Calculated imaginary part of the normal permittivity from -1.5V to +1.5V. (c) Schematic of one unit cell of the metasurface. (d) Simulated reflection coefficient spectra of the unit-cell structure at a fixed V_x=+0.9V and varying V_y from -1.5 V to +1.5 V.

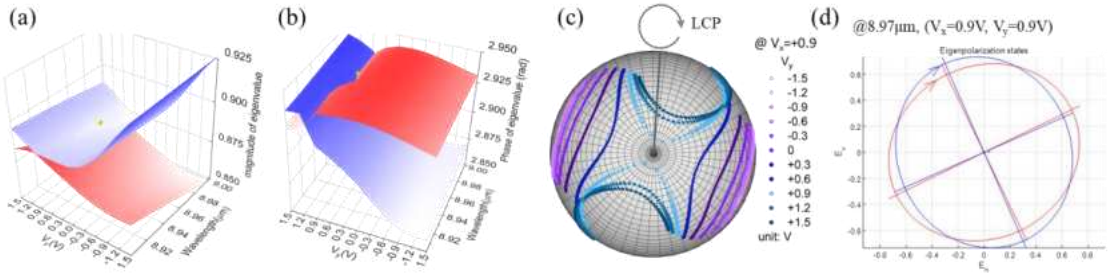


Fig. 2. (a) Magnitude and (b) phase of eigenvalue spectra extracted from reflection matrix of Fig. 1(d) by applying a fixed bias voltage of V_x=+0.9V and varying V_y from -1.5V to +1.5V with interval of 0.3V. (c) Calculated eigen polarization states plotted on Poincaré sphere and the wavelength range from 9.55μm to 8.75μm. (d) Coalesced eigen polarization states of exceptional point (LCP) obtained by applying bias voltage V_x=+0.9V and V_y=+0.9V at a wavelength of 8.97μm.

References

1. H. Chung et al., Advanced Science, 10, 2207520 (2023).

2. M. S. Ergoktas et al., Science, 376, 184-188 (2022).

3. S. Baek et al., Light: Science & Applications 12, 87 (2023).

Active layer morphology of organic and perovskite photovoltaics – a study based on grazing-incidence X-ray and neutron scattering

Xinhui Lu[1*]

[1] Department of Physics, The Chinese University of Hong Kong, Shatin, Hong Kong, 999077, China,

[*]corresponding author: xinhui.lu@cuhk.edu.hk

Abstract: Nowadays, solar industry becomes the fastest growing industry due to the rising demands to solve the energy crisis and environmental problems. Third-generation solar cells, especially organic and perovskite solar cells are all relying on a semiconducting thin-film active layer to harvest the solar energy. The bulk morphology of the active layer in terms of crystal structure, orientation and nanophase separation behaviors is known to be critical to the organic solar cell device performance. Here, we will present our recent studies on the process-structure-device correlation of organic and perovskite solar cells. In these studies, state-of-art grazing incidence scattering techniques using X-rays and neutrons were employed for various purposes, such as grazing incidence wide-angle/small-angle X-ray scattering (GIWAXS/GISAXS), grazing incidence transmission small-angle X-ray scattering (GTSAXS), grazing incidence neutron scattering (GISANS). These techniques can also be applied in material science, chemistry, biology and condensed matter physics studies. By modifying the wavelength of the probing beam and the experimental geometry, a variety of sample types, such as solutions, powders, surfaces and thin films, can be studied, covering wide length scales as well as versatile dynamic and kinetic behaviors.

References

1. G. Cai, Y. Li, Y. Fu, H. Yang, L. Mei, Z. Nie, T. Li, H. Liu, Y. Ke, X.-L. Wang, J.-L. Brédas, M-C Tang, X. Chen, X. Zhan, and X. Lu, Deuteration-enhanced neutron contrasts to probe amorphous domain sizes in organic photovoltaic bulk heterojunction films. *Nat. Commun.*, **15**, 2784, 2024.

2. X. Xia, L. Mei, R. Sun, S. Li, C-Y Chen, J-M Lin, J. Min*, H. Chen*, X.-K. Chen* and X. Lu*, Uncovering the Crystalline Packing Advantages of Asymmetric Y-series Acceptors for Efficient Additive-insensitive and Intrinsically Stable Organic Solar Cells. *Adv. Energy Mater,* 2303785, 2024.

3. M. Qin, Y. Li, Y. Yang, P. F. Chan, S. Li, Z. Qin, X. Guo, L. Shu, Y. Zhu, Z. Fan, C.-J. Su*, and X. Lu*, Regulating the Crystallization Kinetics and Lattice Strain of Lead-Eree Perovskites with Perovskite Quantum Dots. *ACS Energy Lett.*, 3251–3259, 2022.

4. X. Xia, T-K. Lau, X. Guo, Y. Li, M. Qin, K. Liu, Z. Chen, X. Zhan, Y. Xiao, P. F. Chan, H. Liu, L. Xu, G. Cai, N. Li, H. Zhu, G. Li, Y. Zhu, T. Zhu, X. Zhan, X-L. Wang and X. Lu, Uncovering the Out-of-plane Nanomorphology of Organic Photovoltaic Bulk Heterojunction by GTSAXS, *Nat. Commun.*, **12**, 6226, 2021.

Optical Spin Waves

V. Karakhanyan[1], R. Salut[1], M. A. Suarez[1], N. Martin[1], and T. Grosjean[1*]

[1]Optics department, FEMTO-ST Institute UMR 6174, University of Franche-Comté, CNRS, France
[*]corresponding author: thierry.grosjean@univ-fcomte.fr

Abstract: The precession of the magnetic moments in magnetic materials, forming spin waves, has many applications in magnetism and spintronics. We show that an optical analog of spin waves (OSW) can be generated in arrays of plasmonic nanohelices.

The concept of chirality is ubiquitous, impacting fields from biology and medicine to physics and materials science [1,2]. In optics, chiral effects is usually linked to helical waves carrying angular momentum. Recent research has explored the concept of photonic skyrmions by analogy to skyrmions in magnetic material [3,4]. Similarly, we investigate the possibility of generating a photonic counterpart to the spin waves propagating in ferromagnets.

Utilizing gold-coated carbon helices, we demonstrate that near-field coupling between adjacent homochiral helices results in optical waves with intrinsic angular momentum tied to the nanostructures' handedness. These waves propagate independently of the helix direction and are reflected at interfaces between enantiomeric nanohelices, forming heterochiral arrays (see Figure 1). Such a property mirrors the reflection of spin waves between two magnetic materials of opposite magnetization (i.e., of oppostite precession handedness). We fabricated chains of helical nanoantennas and observed energy transport indicative of optical spin waves. The ability of these waves to be guided and reflected within the nanoantenna arrays highlights their potential for integrated photonic applications. The experimental results confirm our theoretical predictions [5].

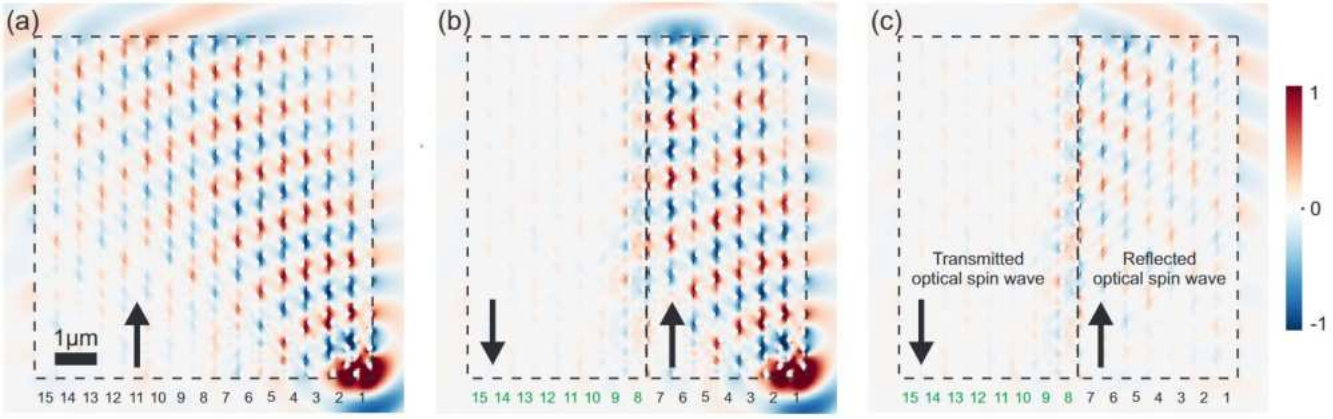


Figure 1: Reflection of a spin-wave at the interface between two homochiral helix chains of opposite handedness. (**a**) Real part of the x-component of the electric field in a homochiral array of fifteen 19-pitch helices. The array is excited with a y-polarized dipole source positioned at the bottom end of the rightmost helix

(λ = 1.55μm). (**b**) The handedness of 8-15 helices is inverted, leading to 2 helix arrays of opposite handedness. In (**a**) and (**b**), the homochiral helix arrays are delimited with dashed lines. The helix handedness in each domain is represented with an arrow. (**c**) Transmitted and reflected optical spin waves on either side of the interface.

The ability of OSW to be guided in a chain of subwavelength chiral structures and to be reflected at the interface between enantiomeric elements holds promise for angular momentum transfer and manipulation in compact integrated platforms. Spin-optical functionalities may arise from the combination of diverse operations on OSW including waveguiding, focusing, interference, steering and modulation, within metamaterials and metasurfaces possibly merging positive and negative refractive indices.

This work is funded by the French Agency of Research (ANR), the Region "Bourgogne Franche-Comté", the EIPHI Graduate School, the French RENATECH network.

References

1. A. Salam, J. Mol. Evol., vol. 33, pp. 105–113, 1991.
2. W. H Brooks et al. Curr. Top. Med. Chem., vol. 11, no. 7, pp. 760–770, 2011
3. S. Tsesses et al. Science, vol. 361, no. 6406, pp. 993–996, 2018.
4. L. Du et al. Nat. Phys., vol. 15, no. 7, pp. 650–654, 2019.
5. V. Karakhanyan et al. 2023. *Submitted*

META 2024, TOYAMA - JAPAN, JULY 16 – 19, 2024

An ultra-low loss alumina waveguide platform for nonlinear photonics in the visible and UV

E. McKay [1], N. G. Pruiti [1], M. Clerici [2], and M. Sorel [1,3,*]

[1] University of Glasgow, Glasgow, United Kingdom
[2] Università degli Studi dell'Insubria, Como, Italy
[3] Istituto di Tecnologie della Comunicazione, dell'Informazione e della Percezione (TeCIP), Pisa, Italy
[*]corresponding author: marc.sorel@glasgow.ac.uk

Abstract: We demonstrate ultra-low loss alumina waveguides for visible and UV photonics with sub-dB/cm loss at 450 nm through optimization of film deposition and lithography. Using this technology, we demonstrate the first octave spanning supercontinuum generation in dispersion engineered alumina waveguides spanning a range from the UV to near-IR.

Non-equilibrium light-matter interactions in photonic temporal crystals

Bumki Min[1]

[1]Department of Physics, KAIST, Republic of Korea
[*]corresponding author: bmin@kaist.ac.kr

Abstract: Using classical light-matter interaction theory and Floquet analysis, we demonstrate a significant increase in spontaneous emission decay rates at momentum gap frequencies in photonic temporal crystals. These crystals also facilitate the excitation of atoms from ground to excited states with photon emission.

Over the past several decades, the principal strategies for controlling spontaneous emission have primarily involved the utilization of resonant or space-periodic photonic structures. Initially proposed by Purcell [1] and subsequently elaborated by Yablonovitch [2] in relation to photonic crystals, this method capitalizes on the influence of spatial environments to control the spontaneous emission decay rates of atoms or quantum emitters. Recently, the emergence of time-varying photonics has necessitated a thorough reexamination of the spontaneous emission processes within dynamically evolving environments. This is particularly relevant in the photonic temporal crystals, where optical properties are subject to time-periodic modulations [3-5].

In this work, we employ classical light-matter interaction theory combined with Floquet analysis to uncover a significant enhancement in the spontaneous emission decay rate at the momentum gap frequency within photonic temporal crystals. This remarkable increase is primarily due to mechanisms of loss and gain induced by time-periodicity, along with the inherent non-orthogonality of Floquet eigenstates. Furthermore, our findings reveal that photonic temporal crystals not only enhance spontaneous emission decay rates but also facilitate the excitation of an atom from its ground state to an excited state. This transition is notably accompanied by the spontaneous emission of a photon, adding a new layer of functionality to these time-varying photonic structures.

References

1. E. M. Purcell, Spontaneous emission probabilities at radio frequencies, Phys. Rev. 69, 674 (1946).
2. E. Yablonovitch, Inhibited spontaneous emission in solidstate physics and electronics, Phys. Rev. Lett. 58, 2059 (1987).
3. N. Wang, Z.-Q. Zhang, and C. T. Chan, Photonic Floquet media with a complex time-periodic permittivity, Phys. Rev. B 98, 085142 (2018).
4. J. Park and B. Min, Spatiotemporal plane wave expansion method for arbitrary space–time periodic photonic media, Optics Letters 46, 484 (2021).
5. J. Park, H. Cho, S. Lee, K. Lee, K. Lee, H. C. Park, J.-W. Ryu, N. Park, S. Jeon, and B. Min, Revealing non-Hermitian band structure of photonic floquet media, Science Advances 8, eabo6220 (2022).

Ultra-large Area Coherent Lasing Action through Hermitian/non-Hermitian Control in Photonic Crystals

Susumu Noda*

Department of Electronic Science and Engineering, Kyoto University, Kyoto 615-8510, Japan

*corresponding author: snoda@kuee.kyoto-u.ac.jp

Abstract: Realizing large-scale high-power and high-beam-quality semiconductor lasers, which rival (or even replace) bulky gas and solid-state lasers, is one of the ultimate goals of photonics and laser physics. Conventional high-power semiconductor lasers, however, inevitably suffer from poor beam quality owing to the onset of oscillation in many modes, and moreover, the oscillation is destabilized by disruptive thermal effects under continuous-wave (CW) operation. Here, we surmount these challenges by scaling photonic-crystal surface-emitting lasers (PCSELs) [1-5] up to as large as 3mm in diameter while controlling Hermitian and non-Hermitian couplings [6] inside a double-lattice photonic crystal [4] and maintaining these couplings even under CW conditions. The obtained CW brightness, a figure of merit that encapsulates both the output power and the beam quality, reaches ~1 $GWcm^{-2}sr^{-1}$, [6] which rivals those of existing bulky lasers. Our work is an important milestone toward the advent of high-beam quality 1-kW-class semiconductor lasers and toward innovation in a wide variety of industrial applications, from smart material processing to even aerospace applications.

References:

[1] M. Imada, S. Noda, A. Chutinan, T. Tokuda, M. Murata, G. Sasaki, “Coherent two-dimensional lasing action in surface-emitting laser with triangular-lattice photonic crystal structure”, *Applied Physics Letters*, 1999, vol. 75, pp. 316–318.

[2] S. Noda, K. Kitamura, T. Okino, D. Yasuda, Y. Tanaka, “Photonic-crystal surface-emitting lasers: Review and introduction of modulated-photonic crystals”, *IEEE J. Sel. Top. Quantum Electron*. 2017, vol. 23, Article number: 4900107.

[3] K. Hirose, Y. Liang, Y. Kurosaka, A. Watanabe, T. Sugiyama, and S. Noda, “Watt-class high-power, high-beam-quality photonic-crystal lasers”, *Nature Photonics*, 2014, vol.8, pp. 406–411.

[4] M. Yoshida, M. De Zoysa, K. Ishizaki, Y. Tanaka, M. Kawasaki, R. Hatsuda, B.S.Song, J. Gelleta, and S. Noda, “Double-lattice photonic-crystal resonators enabling high-brightness semiconductor lasers with symmetric narrow-divergence beams”, *Nature Materials*, 2019, vol. 18, pp.121–128.

[5] S. Noda, T. Inoue, M. Yoshida, J. Gelleta, M. D. Zoysa, and K. Ishizaki, “High-power and high-beam-quality photonic-crystal surface-emitting lasers: a tutorial”, Adv. Opt. Photonics 15, (2023) pp. 977-1032.

[6] T. Inoue, M. Yoshida, J. Gelleta, K. Izumi, K. Yoshida, K. Ishizaki, M. De Zoysa and S. Noda, *Nature Comms*, 2022, vol.13, Article number: 3262.

[7] M. Yoshida, S. Katsuno, T. Inoue, J. Gelleta, K. Izumi, M. De Zoysa, “High-brightness scalable continuous-wave single-mode photonic-crystal laser”, Nature 618, (2023) pp. 727-732.

META 2024, TOYAMA - JAPAN, JULY 16 – 19, 2024

Enhanced Optical Interactions in Nonlinear Topological Photonic Nanostructures

N. C. Panoiu[1*]

[1]Department of Electronic and Electrical Engineering, University College London, Torrington Place, London WC1E 7JE, United Kingdom

[*]corresponding author: n.panoiu@ucl.ac.uk

Abstract: In this talk, I will review some recent results regarding nonlinear optical interactions in certain topological photonic systems. In particular, I will present a detailed analysis of the band topology of 2D photonic crystals (PhCs) with hexagonal symmetry and demonstrate that nonlinear optical processes can be readily implemented via one-way edge modes of this setup. In the second part of my talk, I will illustrate how bound states in the continuum (BICs) of certain PhC slabs, engineered to possess sharp resonances with high quality factors at both the fundamental frequency and second-harmonic, can be used to achieve an orders-of-magnitude enhancement of the SHG. This double-resonance phenomenon is used to significantly enhance the SHG from the PhC slabs.

"EM-Flow": A Conditional Reversible Flow-Based Deep Learning Model for Electromagnetic Inverse Problems

Hongrui Zhang[1], Yanjin Chen[1], Mingyi Li[1], Hengxin Ruan[1] and Lianlin Li[1*]

[1]School of Electronics, Peking University, Beijing 100871, China
*corresponding author, E-mail: lianlin.li@pku.edu.cn

Abstract

Deep learning (DL) is playing an increasingly important role in dealing with nonlinear electromagnetic (EM) problems. However, it is a fundamental but unresolved challenge that many DL predictions lack the reliability assessment and physical laws. Here, We present "EM-Flow", a novel deep learning approach for solving EM inverse problems employing a conditional flow-model-based reversible network architecture. The proposed model can learn EM scattering and inverse scattering processes simultaneously, and thus the physical constraint on DL solutions can be automatically imposed. Moreover, owing to the employment of the renormalization group, the interpretability of DL solutions can be ensured in the process of transformation between the target and its scattered field. Selected results have been provided to demonstrate the state-of-art performance of the proposed method in terms of its reconstruction quality and robustness. The proposed method could reveal a new perspective for solving the EM inverse problems including EM inverse scattering and EM imaging based on programmable metasurface with the reliability, interpretability and physical constraints.

1. Introduction

Deep learning (DL) has emerged as a powerful tool extensively utilized in electromagnetic (EM) applications such as EM inverse scattering and EM sensing based on the programmable metamaterial, particularly for dealing with the troublesome yet prevalent EM inverse problems. Compared with the traditional deterministic or stochastic methods such as the Born iteration method (BIM) [1] and the contrast source inversion (CSI) [2] which suffer from the problems of excessive computational complexity and low inversion efficiency. In order to promote its utilization in practical scenes, DL-based methods have obvious advantages in computational efficiency and imaging effect.

Recently, many excellent efforts have been made in this emerging direction in order to learn the mapping between the scattered fields and the scatterer model parameters. To introduce the physical constraints on the artificial networks thereby expect the improvement on the reconstruction quality, more and more hybrid inversion approaches have been proposed aiming at the combination of the conventional noniterative approaches and artificial neural networks [3]. Nonetheless, the current EM inversion methods based on deep learning are usually unidirectional mapping and regard the deep learning as a black box, which is obviously out of the physical law. What's more, most of the DL solutions are deterministic, and they are lack of the uncertainty. But it is usually not true in practical applications because of the unknown ground truth and the uncertainties in measurements and the inverse model.

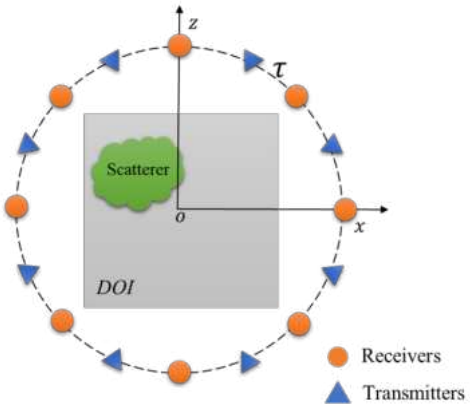


Figure 1: Full-wave 2D forward and inverse scattering model configuration.

In order to resolve above difficulties, here we propose a probabilistic reversible hierarchical deep neural network (DNN) called "EM-Flow", which is inspired by the idea of renormalization group (RG) [4] in physics and the flow-based model in generation model. As an important concept from theoretical physics, RG can help investigate the changes in physical systems at different scales and retrieve the targets on the small scale from that on the large scale through coarse-graining in a hierarchical structure. The random latent variables z in different level separated during this process allow us to quantify the uncertainty and statistical properties. Meanwhile, we introduce the flow-based generation model [5] to make the network reversible and realize the bidirectional mapping between the scattered field and the permittivity. Characterized by the conditional renormalization and generation-flow mechanism with a reversible hierarchical structure, EM-Flow excels in resolving both 2D and 3D EM imaging challenges.

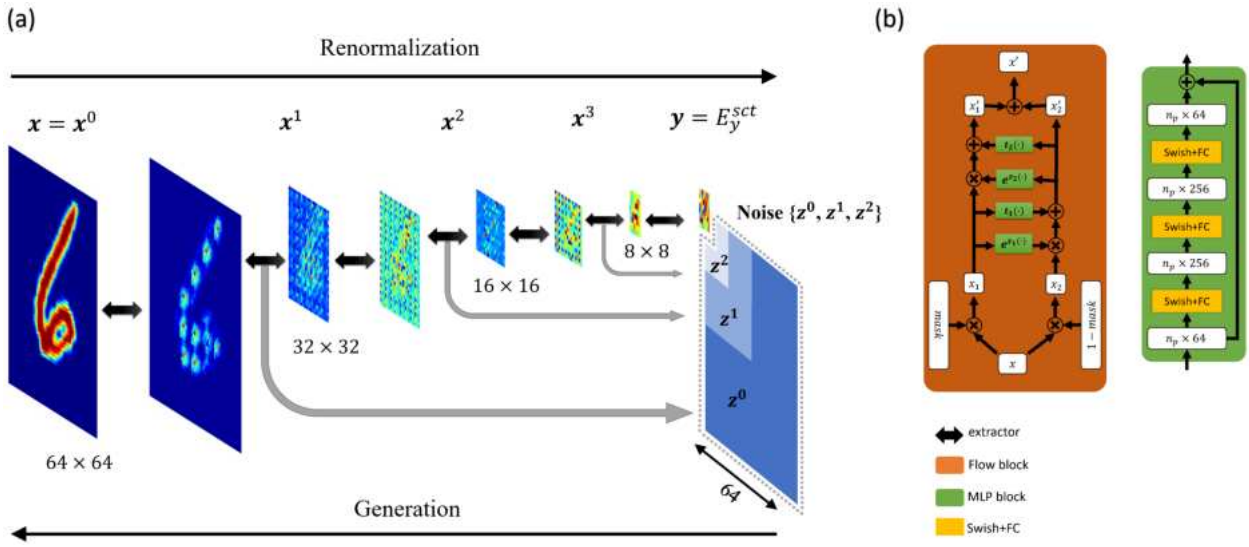


Figure 2: The architecture of cRG-Flow. (a) The schematic diagram of cRG-Flow. (b) The internal structure of the flow block with the composition of the MLP block it contains.

2. Methods

2.1. Forward and inverse models

Taking the 2D numerical experiment as an example, we show our experimental configuration in Fig. 1 for 2D full-wave forward and inverse scattering problems. The forward scattering and inverse scattering which are defined by the state and data equation can be respectively expressed as

$$E_y^{inc}(\boldsymbol{r}) = E_y^{tot}(\boldsymbol{r}) + \frac{jk_0^2}{4}\int_{DOI}\chi_\epsilon(\boldsymbol{r}')E_y^{tot}(\boldsymbol{r}')H_0^{(2)}(k_0|\boldsymbol{r}-\boldsymbol{r}'|)d\boldsymbol{r}', \tag{1}$$

$$E_y^{sct}(\boldsymbol{r}) = -\frac{jk_0^2}{4}\int_{DOI}\chi_\epsilon(\boldsymbol{r}')E_y^{tot}(\boldsymbol{r}')H_0^{(2)}(k_0|\boldsymbol{r}-\boldsymbol{r}'|)d\boldsymbol{r}', \tag{2}$$

where $\boldsymbol{r} \in domain\ of\ interest\ (DOI)$ in (1) and $\boldsymbol{r} \in \Gamma$ (receiving area) in (2), $\boldsymbol{r}'$ are the position vectors, k_0 is the wavenumber in free space and $H_0^{(2)}$ is the 0th-order Hankel function of the second kind. E_y^{inc} and E_y^{tot} are the incident electric and the total electric field, and $E_y^{sct} = E_y^{tot} - E_y^{inc}$ represents the scattered field. What's more, here we assume that the background medium in the DOI is air, so the contrast function χ_ϵ can be expressed as $\chi_\epsilon(\boldsymbol{r}) = \epsilon_r(\boldsymbol{r}) - 1$, where $\epsilon_r = \varepsilon_r + \frac{\sigma}{j\omega}$ is the complex relative permittivity. Here θ is the weights of this end-to-end reversible DNN.

2.2. Architecture of EM-Flow

The overall architecture of EM-Flow is shown in Fig. 2(a), which is an extension of the well-known RG-Flow [6]. It establishes the connection between the relative permittivity distribution $\boldsymbol{x}$ and the scattered fields $\boldsymbol{y}$ through a bidirectional hierarchical network structure, where we assume that $\boldsymbol{x}^h$ is the input of the hth layer of the EM-Flow and in particular $\boldsymbol{x}^1 = \boldsymbol{x}$ is the relative permittivity ϵ_r.

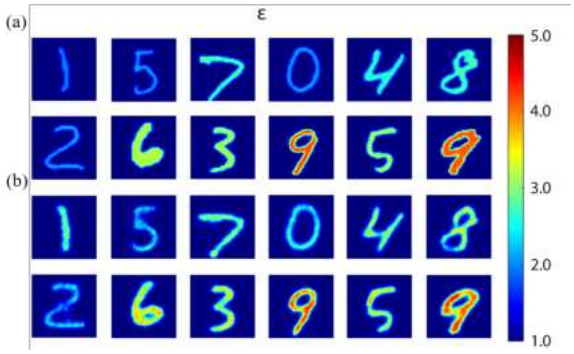


Figure 3: Some examples for the lossy targets. (a) Ground truths of ϵ. (b) Inversion results ϵ by EM-Flow.

The pipeline from left to right in Fig. 2(a) is defined as renormalization $(\boldsymbol{y}, \boldsymbol{z}) = R_\theta(\boldsymbol{x})$, which corresponds to the EM forward scattering process of calculating the scattered fields through dielectric parameters. And its inverse process $\boldsymbol{x} = R_\theta^{-1}(\boldsymbol{y}, \boldsymbol{z}) = G_\theta(\boldsymbol{y}, \boldsymbol{z})$ is called generation, which means the EM inverse scattering process of reconstructing dielectric parameters through scattered fields from right to left. The parameter θ is the weights of this end-to-end reversible DNN.

As a probabilistic DL model for the EM problems, our EM-Flow is a three-port network. To quantify the uncertainty of an output $\boldsymbol{x}$ given the input $\boldsymbol{y}$, we introduce a random latent variable $\boldsymbol{z}$ and $\boldsymbol{z}^h$ is the latent variable of the hth layer of EM-Flow, which represents the disturbance noise and incorporates uncertainty quantification into EM-Flow. In order to minimize the mutual information between the hidden variables and force the variables in each layer to be independent of each other, we choose independent and identically distributed (i.i.d) Gaussian random distributions for all $\boldsymbol{z}$. According to the change of variables theorem,

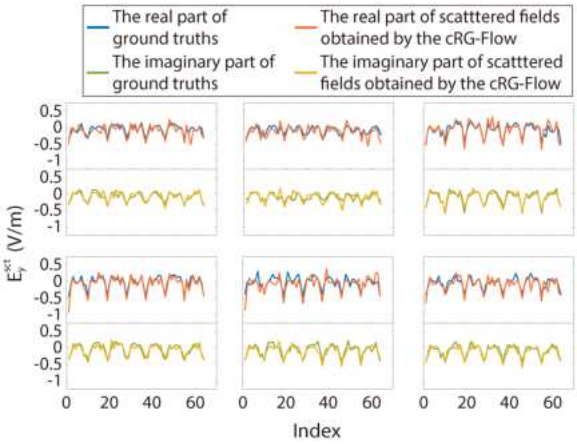


Figure 4: Test of EM-Flow for solving the scattering problems on lossy dataset.

we can model the conditional distribution $p(\boldsymbol{x}|\boldsymbol{y})$ through marginalization over all possible $\boldsymbol{z}$ as

$$\begin{aligned} p_\theta(\boldsymbol{x}|\boldsymbol{y}) &= \int p(\boldsymbol{x}|\boldsymbol{y},\boldsymbol{z})p(\boldsymbol{z})d\boldsymbol{z} \\ &= p(\boldsymbol{z})\left|\det\left(\frac{\partial(\boldsymbol{y},\boldsymbol{z})}{\partial G_\theta(\boldsymbol{y},\boldsymbol{z})}\right)\right|, \end{aligned} \tag{3}$$

where the prior distribution $p(\boldsymbol{z})$ describes the uncertainty of the DL model.

The EM-Flow extracts features layer by layer through a number of bijective cascaded flow blocks with the same internal structure built from the coupling layer [5] as illustrated in Fig. 2(b). Either $s(\cdot)$ or $t(\cdot)$ is just a completely symmetrical multi-layer perceptron (MLP) with a residual structure, composed of fully connected operations and nonlinear activation functions. According to the derivative chain rule, $\ln\left|\det\left(\frac{\partial R_\theta(\boldsymbol{x})}{\partial \boldsymbol{x}}\right)\right|$ in (3) can be easily calculated by the following formula

$$\ln\left|\det\left(\frac{\partial R_\theta(\boldsymbol{x})}{\partial \boldsymbol{x}}\right)\right| = \sum_{l=1}^{L}\left[s_2(\boldsymbol{x}_2') + s_1(\boldsymbol{x}_1)\right]_l, \tag{4}$$

where l indicates the lth flow block, and L is the total number of flow blocks in the network. Each step of the renormalization includes extracting coarse-scale information from $\boldsymbol{x}$ and then inputting it to the next layer, and splitting the remaining fine-grained information into the latent variable $\boldsymbol{z}$ until getting the coarse-grained variable $\boldsymbol{y}$ in the last layer. These separated eigenvectors can be regarded as potential variables at different scales. Conversely, we can directly generate fine-scale $\boldsymbol{x}$ from coarse-scale $\boldsymbol{y}$ in the reverse network. Once the potential variables $\boldsymbol{z}$ of all layers are given, we can recursively generate the fine-scale observation variable $\boldsymbol{x}$ from the input $\boldsymbol{y}$.

According to the maximum likelihood method, the total loss function contains three terms: flow-based model, renormalization and generation. They are defined as follows:

$$\begin{aligned} \mathcal{L}_{total} &= \mathcal{L}_{flow} + \mathcal{L}_{renormalization} + \mathcal{L}_{generation} \\ &= -\mathbb{E}_{\boldsymbol{x},\boldsymbol{y}}\left[\ln p_\theta(\boldsymbol{x}|\boldsymbol{y}) + \ln p_\theta(\boldsymbol{y}|\boldsymbol{x}) + \ln p_\theta(\boldsymbol{x}|\boldsymbol{y},\boldsymbol{z})\right] \\ &= \frac{1}{N}\sum_{n=1}^{N}\left(-\ln p(R_\theta^{\boldsymbol{z}}(\boldsymbol{x}_n)) - \ln\left|\det\left(\frac{\partial R_\theta(\boldsymbol{x}_n)}{\partial \boldsymbol{x}_n}\right)\right|\right) \\ &+ \frac{1}{N}\sum_{n=1}^{N}\left(\alpha\left\|\boldsymbol{y}_n - R_\theta^{\boldsymbol{y}}(\boldsymbol{x}_n)\right\|^2\right) \\ &+ \frac{1}{N}\sum_{n=1}^{N}\left(\beta\left\|\boldsymbol{x}_n - G_\theta(\boldsymbol{y}_n,\boldsymbol{z})\right\|^2\right), \end{aligned} \tag{5}$$

where N is the total number of the samples, and $\boldsymbol{y}_n$ and $\boldsymbol{x}_n$ are the nth scattered field and relative permittivity distribution, respectively. The parameters α and β which are heuristically set to be 1.0 in our experiments determine the variance of $p_\theta(\boldsymbol{y}|\boldsymbol{x})$ and $p_\theta(\boldsymbol{x}|\boldsymbol{y},\boldsymbol{z})$, respectively. $\mathcal{L}_{flow}$ grants the uncertainty to $\boldsymbol{x}$, while $\mathcal{L}_{renormalization}$ and $\mathcal{L}_{generation}$ encourage the certainty of $\boldsymbol{y}$ and $\boldsymbol{x}$.

2.3. Architecture adjustment for 3D objects

Here, we emphasize that the proposed EM-Flow is a highly versatile and flexible model, meaning its internal module structure can be freely adjusted according to our requirements and data formats. Based on the mesh-free modeling method for 3D objects based on the 3D point cloud [7], we adapt EM-Flow to the structure suitable for 3D targets. Compared to the model handling 2D EM inverse scattering above, we replace the primary operational units with 1D convolutional networks, and all operations such as masking, hierarchical extraction and separation are applied to different channels rather than pixels. This means that all points entirely share the same convolutional kernel and masking operations. The modified schematic structure and more details could be found in [7].

3. Results

3.1. 2D numerical results

3.1.1. Lossy handwritten digits

Considering that in practical imaging scenarios targets are generally lossy, we go straight to the lossy handwritten digits which will obviously make it more difficult. The relative permittivity of all the targets is randomly chosen in the range of [2.0, 5.0]. Fig. 3 demonstrates the good inversion performance of our trained network on lossy targets. Reversibility is another significant advantage of EM-Flow, so we directly test its performance in solving forward scattering problem by the network trained above. Fig. 4 shows the scattering results using the scatter shown in the first row of Fig. 3 as the input. It can be seen that although EM-Flow can solve EM scattering problem with a satisfactory accuracy, the results is not as good as its inversion performance. The reason is that we pay more attention to its inversion performance in training phase, so we can give a larger value of α in (5) to balance the two results.

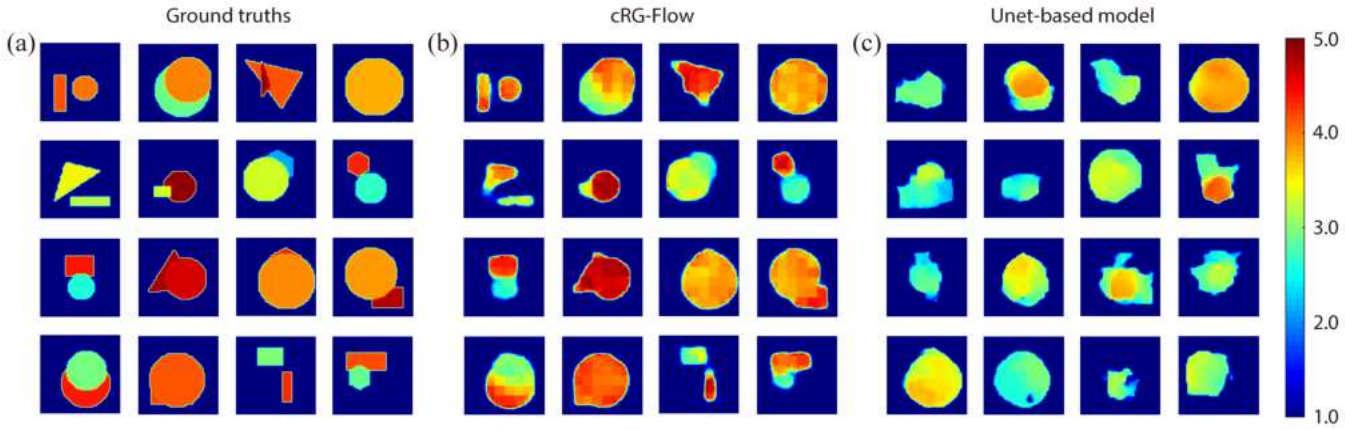


Figure 5: Sixteen representative examples over the nested polygons/circles dataset. (a) Ground truths of ϵ. (b) Inversion results ϵ by EM-Flow. (c) Inversion results ϵ by Unet-based model.

3.1.2. Nested geometries

In order to further verify the capability of our network, we selected targets with more complex shapes which increase the difficulty of inversion during the training and testing stage. At the same time, we used a common network with the U-net sturcture [8] to conduct the same experiment. For fair comparison, the EM-Flow has the almost same the number of trainable parameters as that of U-net.

A set of experiments are conducted over the nested polygon/circle dataset; where the scatterers are random combinations of triangles, circles, rectangles and hexagons, and the relative permittivity is randomly chosen in the range of [2.0, 5.0]. Corresponding results reported in Fig. 5 show that the EM-Flow significantly outperforms the U-net network. Moreover, the average SSIM of the inversion results of EM-Flow is around 0.91, while that of the inversion results of the U-net network is about 0.46. We also find that the U-net suffers from the severe overfitting, but the EM-Flow have not the overfitting. Two possible reasons are: (1) the EM-Flow learns the bidirectional mapping of the scattering fields and relative permittivity; (2) the introduction of a random variable z in EM-Flow makes the less prone to overfitting.

3.2. 3D numerical results

Using the EM-Flow designed for the 3D object based on the point cloud, we train and test the performance of the proposed model with the 3D-MNIST dataset and 3D-object dataset respectively. Fig. 6 show the ground truths of scatterer point clouds and the reconstructed results for the two datasets. We can see that both datasets yield good reconstruction results. Additionally, it is evident that the inversion results for 3D objects are slightly worse than those for digits. The reason for this is that the shapes of 3D objects are more complex than those of handwritten digits. More results could be found in [7], which proved that the proposed model performs very well in addressing the formidable challenge of 3D EM compressing imaging while substantially curtailing data and computational overhead compared to conventional 3D mesh-based models.

3.3. 2D EM compressing imaging

In this section, we validate the performance of our proposed model through challenging 2D EM compressive imaging experiments. Intelligent metasurfaces have been proven to be powerful tools for addressing EM inverse problems such as EM compressing imaging [9, 10, 11]. Based on the metasurface-empowered system described in [9], we demonstrate that our model can achieve high-precision 2D EM imaging and real-time indoor human activity sensing. Fig. 7 shows some results. As can be seen, the imaging accuracy is lower compared to 2D EM inverse scattering simulation experiments due to the significant noise and other interferences present in practical experiments.

4. Conclusions

In this paper, we propose a probabilistic reversible hierarchical neural network named EM-Flow to solve both EM forward and inverse scattering problems at the same time. We choose the representative 2D and 3D numerical examples together with the 2D EM compressing imaging experiment to verify the excellent performance of EM-Flow in reconstruction quality, feasibility, and robustness and show its advantages compared with the traditional DL inversion method. We believe that the proposed methodology holds promise for advancing EM imaging and sensing, with potential applications spanning smart homes, elderly care detection, security check and beyond.

Acknowledgement

This work was supported by the National Key Research and Development Program of China under Grant Nos. 2023YFB3811502, 2021YFA1401002.

References

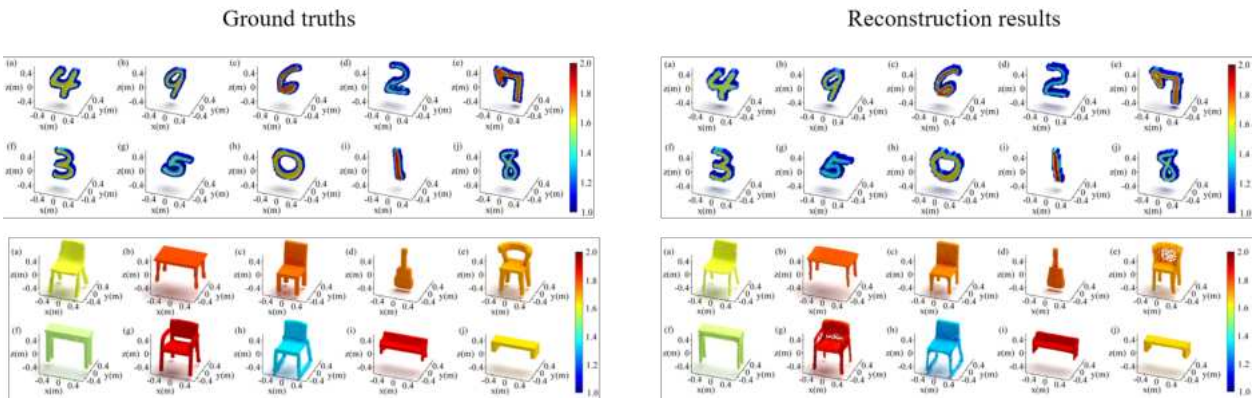


Figure 6: Some representative reconstruction results with corresponding ground truths for 3D EM inverse scattering.

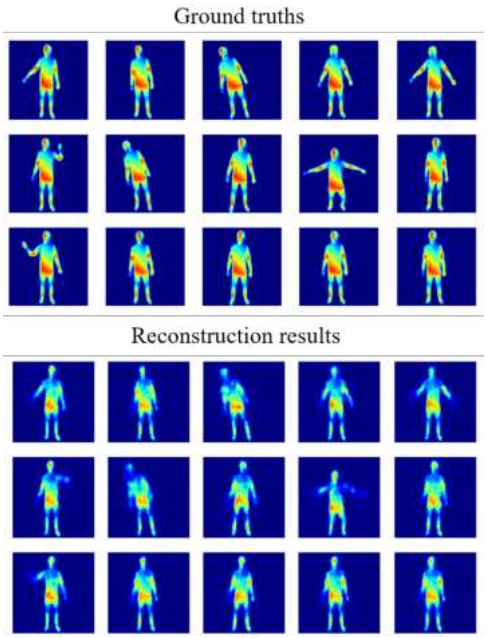


Figure 7: Some representative reconstruction results with corresponding ground truths for 2D EM compressing imaging.

[1] Y. M. Wang and W. C. Chew, "An iterative solution of the two-dimensional electromagnetic inverse scattering problem," *Int. J. Imaging Syst. Technol.*, vol. 1, no. 1, pp. 100–108, 1989.

[2] P. M. van den Berg and R. E. Kleinman, "A contrast source inversion method," *Inverse Probl.*, vol. 13, pp. 1607–1620, 1997.

[3] L. Li, L. G. Wang, F. L. Teixeira, C. Liu, A. Nehorai, and T. J. Cui, "Deepnis: Deep neural network for nonlinear electromagnetic inverse scattering," vol. 67, no. 3, pp. 1819–1825, 2019.

[4] K. G. Wilson, "Renormalization group and critical phenomena. i. renormalization group and the kadanoff scaling picture," *Physical Review B*, vol. 4, no. 9, pp. 3174–3183, 1971.

[5] L. Dinh, D. Krueger, and Y. Bengio, "Nice: Nonlinear independent components estimation," *Computer Science*, 2014.

[6] H. Y. Hu, D. Wu, Y. Z. You, B. Olshausen, and Y. Chen, "Rg-flow: A hierarchical and explainable flow model based on renormalization group and sparse prior," *arXiv preprint arXiv:2010.00029*, 2020.

[7] Y. Chen, H. Zhang, T. J. Cui, F. L. Teixeira, and L. Li, "A mesh-free 3-d deep learning electromagnetic inversion method based on point clouds," *IEEE Transactions on Microwave Theory and Techniques*, 2023.

[8] O. Ronneberger, P. Fischer, and T. Brox, "U-net: Convolutional networks for biomedical image segmentation," in *International Conference on Medical image computing and computer-assisted intervention*, 2015, pp. 234–241.

[9] Z. Wang, H. Zhang, H. Zhao, T. J. Cui, and L. Li, "Intelligent electromagnetic metasurface camera: system design and experimental results," *Nanophotonics*, vol. 11, no. 9, pp. 2011–2024, 2022.

[10] H. Zhang, Y. Chen, Z. Wang, T. J. Cui, P. Del Hougne, and L. Li, "Semantic regularization of electromagnetic inverse problems," *Nature Communications*, vol. 15, no. 1, p. 3869, 2024.

[11] H. Zhang, H. Ruan, H. Zhao, Z. Wang, S. Hu, T. J. Cui, P. Del Hougne, and L. Li, "Microwave speech recognizer empowered by a programmable metasurface," *Advanced Science*, p. 2309826, 2024.

Bio-inspired metalens array for directional detection in 3D light imaging and ranging

Clément Majorel[1, *], Amir Loucif[1], Emil Marinov[1], Renato Juliano Martins[1], Adelin Patoux[1], Virginie Brandli[1] and Patrice Genevet[1,2,†]

[1] Université Côte d'Azur, CNRS, CRHEA, rue B. Gregory, 06560 Valbonne, France
[2] Physics department, Colorado School of Mines, Coorstek 1523 Illinois Street, Golden, Colorado, 80401, USA
corresponding authors: [*] clement.majorel@crhea.cnrs.fr, [†] Patrice.genevet@mines.edu

Abstract: We present a bio-inspired metalens array designed to perform directional detection in a 3D light detection and ranging (LiDAR) experiment. Thanks to the high compactness of metasurfaces, our component can be easily integrated in front of any sensing device.

Over the last two decades, many optical components have been largely inspired by biological systems, and some of them are based on the operating principle of arthropod faceted eyes [1, 2, 3]. Each facet of the eye is an optical subsystem, named ommatidium. The curvature of the eye has specifically evolved so that each subsystem forming this compound imaging system can capture light originating from a very specific direction only. In order to mimic arthropod vision, some works show examples of microlens arrays fabricated on a thin flat layer of polymer [1, 2]. This polymer is bent into curved geometries by applying a stress, with the objective of obtaining shapes that are as close as possible of that of the arthropod eyes [1, 2, 3]. From our side, to imitate the eye of an arthropod, we designed a flat component consisting of an array of metalenses and a detection surface made up of a set of photosensitive pixels. Each pixel is associated with an off-axis metalens featuring a unique phase profile. By adjusting the phase profile of all the lenses, we reproduce the curvature of the eye while retaining a planar component. As a result, all the metalenses focus light at the same distance, facilitating on-chip integration.

This component can be used in various imaging systems, such as the plenoptic cameras, based on a lens assembly. As a proof of concept, we experimentally demonstrated the imaging capability of our metasurface in a scanning LiDAR experiment. We proved that by combining a laser source and this metasurface, we can perform angular time-of-flight detection of the objects making up a scene.

The aim of this presentation is to explain how this metasurface was conceived, how we characterized it and to present the results of the LiDAR experiment.

References

1. Z.-Y. Hu, Y.-L. Zhang, C. Pan, J.-Y. Dou, Z.-Z. Li, Z.-N. Tian, J.-W. Mao, Q.-D. Chen, and H.-B. Sun, "Miniature optoelectronic compound eye camera," Nature Communications, vol. 13, no. 1, p. 5634, 2022
2. D. Floreano, R. Pericet-Camara, S. Viollet, F. Ruffier, A. Br¨uckner, R. Leitel, W. Buss, M. Menouni, F. Expert, R. Juston, M. K. Dobrzynski, G. L'Eplattenier, F. Recktenwald, H. A. Mallot, and N. Franceschini, "Miniature curved artificial compound eyes," Proceedings of the National Academy of Sciences, vol. 110, no. 23, pp. 9267–9272, 2013
3. Y. M. Song, Y. Xie, V. Malyarchuk, J. Xiao, I. Jung, K.-J. Choi, Z. Liu, H. Park, C. Lu, R.-H. Kim, R. Li, K. B. Crozier, Y. Huang, and J. A. Rogers, "Digital cameras with designs inspired by the arthropod eye," Nature, vol. 497, no. 7447, pp. 95–99, 2013

Symmetry Breaking in Bio-Inspired 2D Aluminum Networks probed by Electron Energy Loss Spectroscopy

Jelena Wohlwend[1], Marcello Pozzi[1], Georg Haberfehlner[2], Ralph Spolenak[1] and Henning Galinski[1]

[1]ETH Zürich, Switzerland
[2]TU Graz, Austria

[*]corresponding author: jelena.wohlwend@mat.ethz.ch

Abstract: Natural networks such as lichen show intriguing properties for light absorption. Inspired by such natural networks, using energy electron loss spectroscopy, we analyze the plasmonic modes of different 2D aluminum networks. We resolve a multitude of different plasmonic modes and show the influence of size, connectivity, and symmetry.

Our daily lives are intertwined with a plethora of networks, ranging from urban transportation and social networks to power grids. Amidst, natural networks such as lichen, coral or algae are especially interesting as they have been optimized by natural selection to fulfill specific functions, e. g. the transport of nutrients or the absorption of light. This is especially evident in the brown algae, which use photonic structures for a dynamic color change. This dynamic color change in response to varying light conditions enables the manipulation of photosynthesis beyond the photochemical process [1].

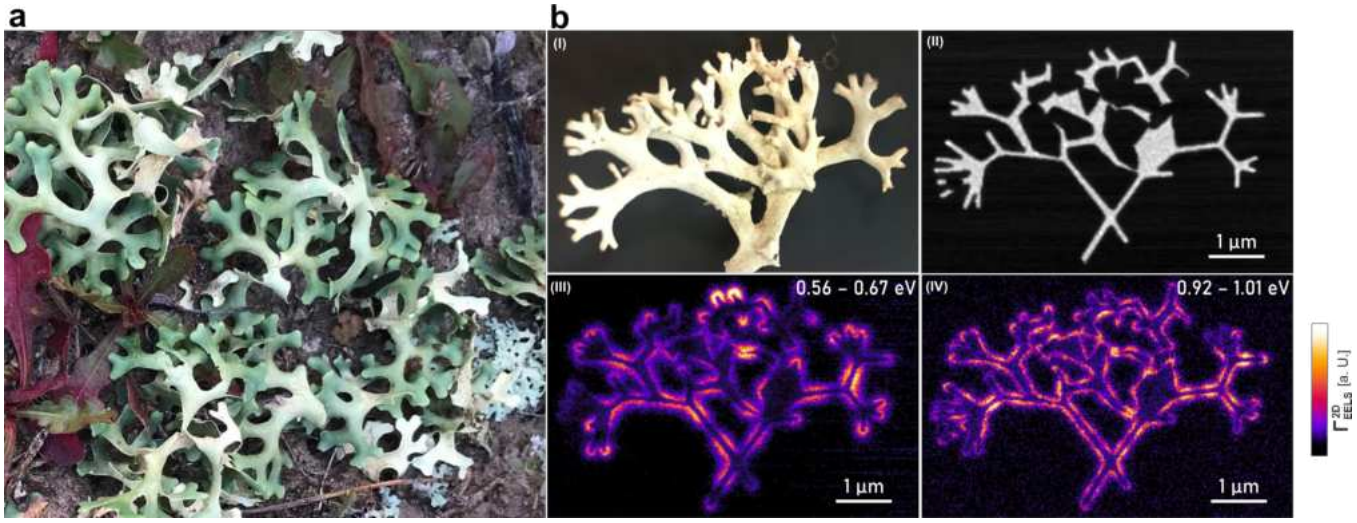


Figure 1: Plasmonic Modes in Lichen networks (a) Image of a common Lichen (b) HAADF image showing a nanoscale reproduction of the lichen network out of aluminum (c) Energy-filtered EELS images corresponding to different maxima in the EELS spectrum showing the excitation of multiple plasmonic resonances in the lichen network.

Inspired by such natural networks, we explore different 2D network metamaterials by electron energy loss spectroscopy (EELS). The different aluminum network nanostructures, ranging from nature inspired lichen and Voronoi networks to Cayley trees and random binomial graphs were fabricated by electron beam lithography and followed by electron beam evaporation. EELS allows to probe the local photonic local density of states (LDOS) with sub-nanometer resolution (Figure 1 and 2). Additionally, EELS spectra and maps of the network nanostructures were

simulated using a boundary element method (Figure 2 a & b). EELS analysis revealed plasmon resonances in the near-IR and visible regions of the electromagnetic spectrum, in good accordance with simulations of aluminum structures of comparable size.

Furthermore, we explore the influence of broken symmetries on the plasmonic modes of the 2D networks. Asymmetrical plasmonic nanostructures have shown extraordinary properties for sensing and biosensing applications [3]. By leveraging the effects of symmetry breaking, we find that it enables us to locally engineer the plasmonic resonances of the networks and thereby facilitates the precise tuning of the local field enhancements. This capability holds great promise for improving the sensitivity and selectivity of plasmonic sensors and opens up new avenues for the detection and characterization of analytes at the nanoscale.

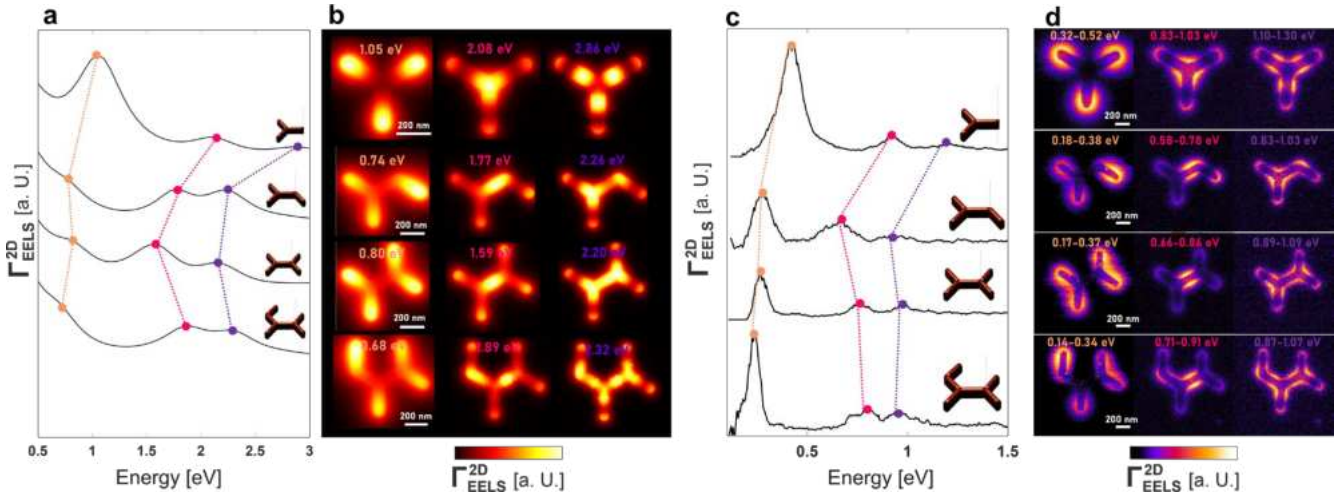


Figure 2: Symmetry breaking in 2D aluminum Cayley trees. (a) Simulated EEL spectra for different Cayley trees, computed in the point shown in the schematics and (b) the corresponding EELS maps at the energies highlighted in (a) [2]. (c) Experimental EEL spectra of different Caylee trees and (d) the corresponding EELS maps at the energies highlighted in (c). Similar modes profiles are observed in both the experimental and the simulated maps. Deviations in absolute energy values stem from the difference in size (smaller for the simulated ones) due to computational reasons.

Our work demonstrates the relation between topology, size and symmetry and plasmonic resonances of 2D network nanostructures. Thereby, EELS gives us direct insight into the LDOS, enabling us to analyze the local field enhancement and mapping the plasmonic resonances of the aluminum networks with ultra-high spatial resolution. The introduced symmetry breaking, along with subsequent mode engineering, holds great potential for site-specific sensing with our 2D network metamaterials.

References

1. Lopez-Garcia, M., N. Masters, H. E. O'Brien, J. Lennon, G. Atkinson, M. J. Cryan, R. Oulton, and Heather M. Whitney, "Light-induced dynamic structural color by intracellular 3D photoniccrystals in brown algae," Science Advances, Vol 4, Issue 4,2375-2548, 2018
2. Hohenester, U. and Trügler A, "MNPBEM – A Matlab toolbox for the simulation of plasmonic nanoparticles," Computer Physics Communications, Vol. 183, Issue 2, 370-381, 2012
3. Yang Chen, Jie Gao, and Xiaodong Yang, " Chiral Metamaterials of Plasmonic Slanted Nanoapertures with Symmetry Breaking, " *Nano Letters* 2018 *18* (1), 520-527

Investigating disorder in synthetic and biological 3D photonic structures with volume imaging

V. Bauernfeind[1,2*], Kenza Djeghdi[1,2], U. Steiner[1,2], and B. D. Wilts[2,3]

[1] Adolphe Merkle Institute, University of Fribourg, Switzerland
[2] National Centre of Competence in Research Bio-Inspired Materials, Switzerland
[3] Department Chemistry and Physics of Materials, Paris-Lodron University Salzburg, Austria
[*] corresponding author: viola.bauernfeind@unifr.ch

Abstract: Disorder in photonic structures often alters their optical signal. Complex photonic structures with varying extents of disorder have been found in many animals. In vitro, such structures are often achieved via self-assembly processes. Using volume imaging, we work towards a quantitative understanding of disorder in three-dimensional photonic structures.

Nanostructures on the length scale of visible light are the origin of many brilliant structural colors in nature (1). Complex three-dimensional nanostructures are commonly found in many vibrantly colored insect scales and bird feathers. The dimensions and extent of order in these structures govern the spectral profile and scattering behavior of the optical signal, which may be further altered by absorbing pigments.

Nanostructures smaller than the length scale of visible light are becoming increasingly popular due to their interesting optical properties as they can be exploited as metamaterials for optical computing, or as optical filters or medical devices (2). Our group obtains blueprints for complex nanostructures through block copolymer self-assembly. The fabrication steps induce network distortions, which may diminish the material's desired optical properties. Performing accurate ultrastructural analysis is thus an essential asset for block copolymer-based metamaterials.

The mechanisms governing the transport of electromagnetic waves through ordered three-dimensional structures are well described, but our understanding of how disorder influences optical signals is still limited. To relate optical signals to varying extents of disorder in photonic structures, a quantification of disorder is needed which often requires a volumetric description of the three-dimensional structure. Photonic structures with elements as small as 30 nm and total dimensions on the micrometer scale make high demands on the experimental techniques to obtain volumetric data. Furthermore, many photonic structures are porous, thus achieving high refractive index contrast and often good scattering contrast in scattering experiments (3). Porosity, however, poses another challenge for volume imaging in a slice-and-view approach because it comes with a finite depth of view.

We advanced the quantification of disorder in porous three-dimensional photonic structures and developed an efficient technique for contrast-enhanced volumetric imaging using focused ion beam tomography (4,5,6). Volumetric reconstructions allowed us to extract quantitative network characteristics from complex synthetic copolymer networks with diamond symmetry and biological structures in insect scales of various symmetry classes (Figure 1). Full-wave optical simulations provided simultaneous insight into the optical properties of the photonic structures. Upon comparison with optical measurements, we obtained a comprehensive understanding of the interplay of order and disorder in photonic structures.

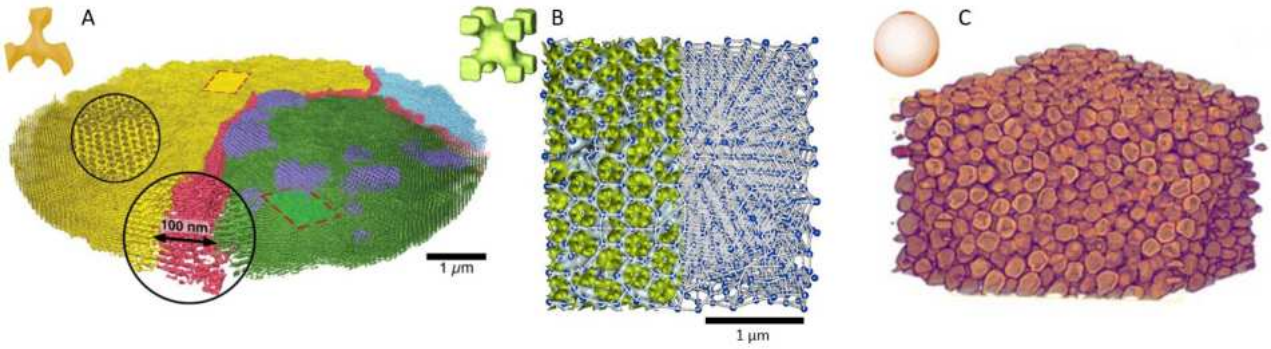


Figure 1. Volumetric analysis of complex networks using ptychography and FIB-SEM tomography. Insets illustrate subunits of the structure. **A** Synthetic block copolymer self-assembled diamond-type network. **B** I-WP-type photonic network in the longhorn beetle *Sternotomis amabilis* ssp. *sylvia*. **C** Photonic structure in the longhorn beetle *Anoplophora graafi* (diamond-like sphere assembly, V = 2805 × 3015 × 1905 nm^3).

The authors acknowledge generous funding from the Adolphe Merkle Foundation, the National Centre of Competence in Research Bio-Inspired Materials, and the European Research Council (ERC) through grant PrISMoID (833895).

References

1. Kinoshita, S., Yoshioka, S., & Miyazaki, J. (2008). Physics of structural colors. *Reports on Progress in Physics*, 71(7), 076401.
2. Dolan, J. A., Wilts, B. D., Vignolini, S., Baumberg, J. J., Steiner, U., & Wilkinson, T. D. (2015). Optical properties of gyroid structured materials: from photonic crystals to metamaterials. *Advanced Optical Materials*, 3(1), 12-32.
3. Saranathan, V., Seago, A. E., Sandy, A., Narayanan, S., Mochrie, S. G., Dufresne, E. R., ... & Prum, R. O. (2015). Structural diversity of arthropod biophotonic nanostructures spans amphiphilic phase-space. *Nano letters*, 15(6), 3735-3742.
4. Djeghdi, K. (2024). *Nanostructured self-assembled diamond-like morphologies in biological and polymeric materials. Thesis* [PhD thesis, University of Fribourg]
5. Djeghdi, K., Steiner, U., & Wilts, B. D. (2022). 3D Tomographic Analysis of the Order‐Disorder Interplay in the *Pachyrhynchus congestus mirabilis* Weevil. *Advanced Science*, 9(26), 2202145.
6. Bauernfeind, V., Djeghdi, K., Gunkel, I., Steiner, U., & Wilts, B. D. (2023). Photonic Amorphous I‐WP‐Like Networks Create Angle‐Independent Colors in *Sternotomis virescens* Longhorn Beetles. *Advanced Functional Materials*, 2302720.

Controlling light and heat with Conducting Polymers and Cellulose

Magnus Jonsson

Organic Photonics and Nanooptics group, Laboratory of Organic Electronics, Department of Science and Technology, Linköping University, Sweden

E-mail: magnus.jonsson@liu.se

My group studies novel ways to control light and heat using organic materials like redox-tunable conducting polymers and cellulose. Applications ranges from bioinspired reflective color displays[1,2] and radiative cooling[3-5] to dynamically tunable metasurfaces[6-9] and adaptive camouflage[10]. I plan to present our most recent work on those topics, including nanoantennas based on anisotropic conducting polymers[11] and switchable THz cellulose aerogels.[12]

1. *Dynamically tuneable reflective structural colouration with electroactive conducting polymer nanocavities.* S. Rossi et al. **Advanced Materials** 2021, 33, 40, 2105004
2. *Tunable structural color images by UV-patterned conducting polymer nanofilms on metal surfaces*. S. Chen et al. **Advanced Materials** 2021, 33, 33, 2102451
3. *Structurally Colored Cellulose Nanocrystal films as Trans-Reflective Radiative Coolers*. R. Shanker et al. **ACS Nano** 2022, 16, 7, 10156-10162
4. *Electrical Tuning of Radiative Cooling at Ambient Conditions*
   D. Banerjee et al. **Cell Reports Physical Science** 2023, 4, 101274
5. *Cellulose-based Radiative Cooling and Solar Heating Powers Ionic Thermoelectrics*
   M. Liao et al. **Advanced Science** 2023, 10, 2206510
6. *Conductive polymer nanoantennas for dynamic organic plasmonics*. S. Chen et al. **Nature Nanotechnology** 2020, 15, 35-40.
7. *Electrical Tuning of Plasmonic Conducting Polymer Nanoantennas*. A. Karki et al. **Advanced Materials** 2022, 34, 13, 2107172
8. *Doped Semiconducting Polymer Nanoantennas for Tunable Organic Plasmonics*. A. Karki et al. **Communications Materials** 2022*,* 2022, 3, 48
9. *Dynamic conducting polymer plasmonics and metasurfaces.* S. Chen and M. P. Jonsson. **ACS Photonics** 2023, 10, 3, 571–581
10. *Electrically tunable infrared optics based on ion-permeable conducting polymer paper*
    C. Kuang et al. submitted 2023
11. *Tuneable anisotropic plasmonics with shape-symmetric conducting polymer nanoantennas*
    Y. Duan et al. **Advanced Materials** 2023, 35, 51, 2303949
12. *Switchable Broadband Terahertz Absorbers based on Conducting Polymer-Cellulose Aerogels*
    C. Kuang et al. **Advanced Science** 2023, in press

Structural colors: toward AI-enabled design & solution-based fabrication

Weijie Feng[4], Anwesha Saha[2], Taigao Ma[3], Haozhu Wang[1] and L. Jay Guo[1,4*]
[1]Department of Electrical Engineering and Computer Sciences
[2]Applied Physics, [3]Department of Physics, [4]Macromolecular Science & Engineering
The University of Michigan, Ann Arbor, MI, USA
[*]Corresponding author: guo@umich.edu

Abstract: Structural colors in the form of layered structures can be mass-produced and have been applied in industrial applications. Such structures can now be designed by using machine learning algorithms. Environmental-friendly chrome-like coating can be designed this way and made by PVD process. Solution process was explored as low-cost alternative to make layered structures.

Structural colors made of inorganic elements contrasts the natural dye pigments, and they are environmental-friendly and offers long-term stability[1]. However, a large class of structural colors relies on precision patterning techniques, which limits their large-scale applications. Another category that is based on multilayer thin film structures are more scalable, but currently depends on vacuum deposition processes[1]. The design of such layered structures requires accumulated experience, thus creates high entry barriers to many. This talk will describe our efforts to address the above challenges.

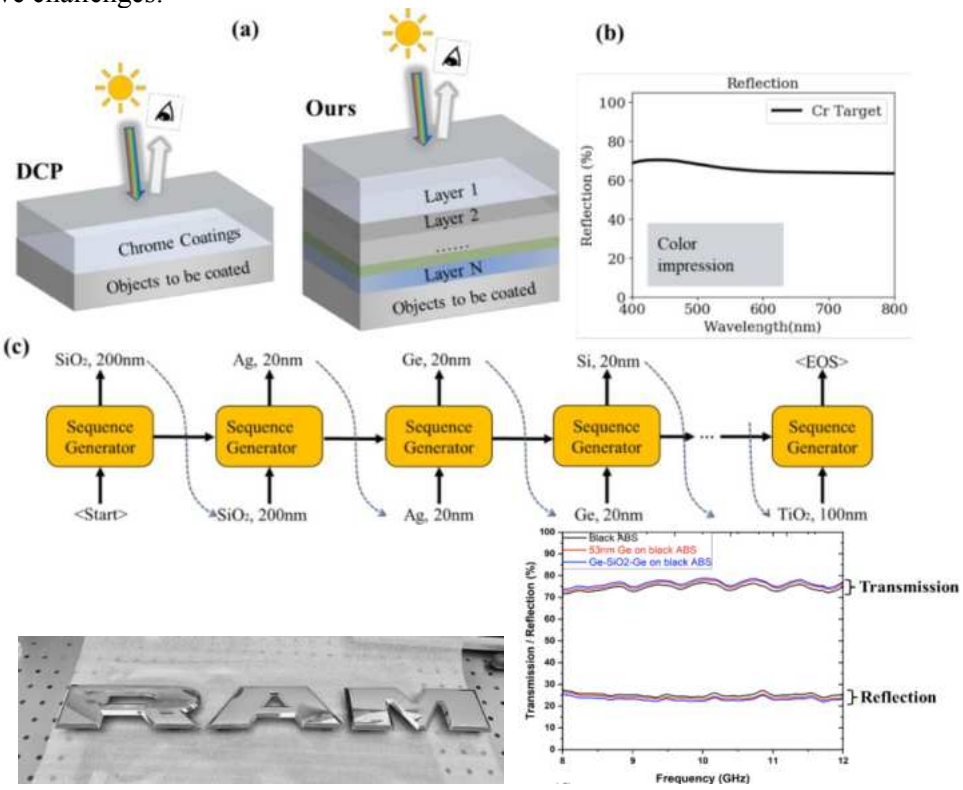


Figure 1. (a) Layered structure to mimic the Chrome reflection spectrum and excluding Cr from the material selection. (b) Reflection spectrum and visual appearance of a Cr layer. (c) Sequential design process used by Reinforcement learning algorithms. Photo of fabricated sample showing chrome-finishing appearance, which shows RF transparency measured in 8-12 GHz range.

To design a thin film structure that can produce the desired color, we formulate the task as an inverse design problem, *i.e.,* design multilayer structures to achieve a certain optical response, such as reflection spectrum of a target color. However, the design process can be non-trivial because for each layer both material selection and thickness need to be considered. To make this easier, many

optimization-based methods have been devised. But these methods are usually based on heuristic searching, which can lead to suboptimal performance. We applied Reinforcement Learning algorithm to treat the multilayer structures as a sequence generation process, and can automatically design the structures to satisfy the targe optical spectrum[2].

To illustrate, we design a structure to mimic the chrome-appearance. Decorative chrome plating is ubiquitous in creating highly appealing chrome-finish. However, the fabrication uses hazardous process with adverse health effects for the workers and causes significant environmental impact. To overcome these challenges, we employ reinforcement learning to generate multilayer structures to mimic chrome's reflection spectrum, which are then fabricated entirely with environmentally benign materials and deposited using PVD process on a variety of substrates. Furthermore, we show another unique functionality by making a chrome-look coating transparent to RF waves, which is not possible at all with traditional chrome coatings. This is achieved by removing metals from consideration during the design process using reinforcement learning algorithm[3].

To reduce the cost of making layered structural colors, we develop a full solution-based method to fabricate multilayer thin film structures, which contrasts with the conventional vacuum-based physical vapor deposition process. We chose copper/dioxide/copper as a model system due to its simple structure and wide color tunability, and carried out systematic investigation for each layer to ensure good film quality as well as its compatibility with all previous layers[4].

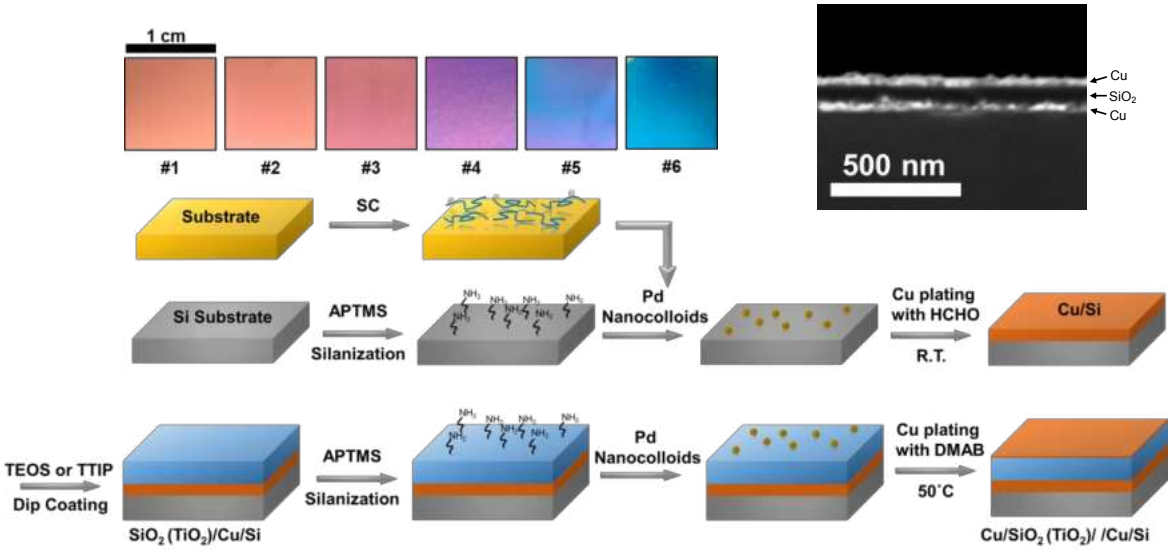


Figure 2. Pictures of solution processed colored samples and cross-section SEM of the cooper/SiO_2/cooper layer. Schematic of steps used in all-solution process to fabricate the individual layers, each compatible with the previous layer.

References

1. D. Wang, Z. Y. Liu, H. Wang, M. Li, L. J. Guo, C. Zhang, "Structural color generation: from layered thin films to optical metasurfaces," *Nanophotonics*, 12(6): 1019–1081, 2023.
2. H. Z. Wang, Z. Zheng, C. G. Ji, L. J. Guo, "Automated Optical Multi-layer Design via Deep Reinforcement Learning," *Mach. Learn.: Sci. Technol.* ***2,*** *025013,* 2020.
3. A. Saha, T. G. Ma, H. Z. Wang, L. J. Guo, "Environmentally Sustainable and Multifunctional Chrome-like Coatings Having No Chromium Designed with Reinforcement Learning," *ACS Appl. Mater. Interfaces* 23, 28772-28780, 2023.
4. W. J. Feng, C. G. Ji, L. J. Guo, "Primary and Secondary Reflective Color Realized by Full-Solution-Processed Multi-Layer Structures," *Adv. Opt. Mater*. 11, 2300456, 2023.

Self-Assembled Structural Color Colorimetric Sensor for Smart Phone based Bio-Chemical Sensing

P. Cencillo-Abad[1], M. Soudi[1, 2], D. Chanda[1,2,3*]

[1]NanoScience Technology Center, University of Central Florida, USA
[2]Department of Physics, University of Central Florida, USA
[3]CREOL, The College of Optics and Photonics, University of Central Florida, USA
[*]corresponding author: Debashis.Chanda@ucf.edu

Abstract: We present a self-assembly platform for low-cost, scalable nanoplasmonic colorimetric sensors, overcoming limitations of traditional fabrication methods. This versatile platform enables real-time detection of chemicals, biomarkers, and environmental conditions, integrating seamlessly with smartphones for portable, power-free diagnostic and sensing applications.

Summary: Colorimetric sensors provide real-time, cost-effective, and high-resolution detection, and are thus a crucial diagnostic tool in various fields. These sensors, which change color in response to specific physical or chemical conditions, offer versatility and adaptability. The interaction of light with the sensor material, which can be fine-tuned to respond to specific stimuli, facilitates this color change. The potential for miniaturization and integration with portable devices, along with their simplicity, makes colorimetric sensors a promising technology for the future. In particular, nanosensors, operating on the nanoscale, have received great attention in recent decades for their remarkable performance. Indeed, their small size allows for high sensitivity and specificity, enabling the detection of minute changes in the environment. These sensors exploit the unique properties of nanomaterials, such as their large surface area to volume ratio and quantum effects, to achieve superior performance. However, the complex and costly processes often involved in the fabrication of nanosensors can limit their widespread adoption.

Here, we present a self-assembly platform for the fabrication of nanoplasmonic colorimetric sensors, providing a solution for large-scale and low-cost nanosensors. This platform simplifies the fabrication process and reduces costs by leveraging the self-assembly of aluminium nanoparticles evaporated through a temperature and pressure-controlled process, making it compatible with current industrial standards[1,2]. Our approach to structural coloration exploits the plasmonic resonances arising naturally from the interaction of light with a random array of self-assembled metallic nanoislands. These nanoislands, grown using conventional thin film techniques, are placed near a mirror, creating a strong hybridization of localized plasmon and subwavelength cavity modes. This results in a single resonance with minimal angular and polarization dispersion and over 90% reflectance at certain wavelengths. The optical response of these nanostructures can be easily adjusted across the entire visible spectrum through simple changes in geometrical parameters, achieving a full color range. Through large-scale fabrication techniques, we produce stand-alone paints that are ready to be transferred onto any substrate. By fabricating the structures through large-scale techniques we produce stand-alone paints that are ready to be transferred onto any substrate.

Importantly, changes in the geometrical parameters or material properties of the structure, triggered by an external stimulus, directly impact its color[3]. We demonstrate how alterations in the morphology of the nanoparticles, resulting from the interaction of the self-assembled layer with an analyte, can be correlated to the

concentration of the target chemical for direct detection of ammonia in water. Alternatively, functionalizing the structure with a carefully selected array of ligands, aptamers, or antibodies, the color can selectively respond to the presence of targeted relevant biomarkers, such as IgG concentrations in blood. Furthermore, the hybridization of an active polymer layer provides readily available solutions for environmental sensing. This approach also allows for the creation of reusable, powerless tags for monitoring environmental conditions such as humidity or temperature, as well as tamper-proof labels for condensation. we demonstrate how a straightforward algorithm leveraging a smartphone camera and image recognition technology can replace traditional bulky and costly spectroscopic systems, streamlining the color-reading procedure. This makes the sensor viable for applications demanding affordability and portability.

References

1. Cencillo-Abad, P., Franklin, D., Mastranzo-Ortega, P., Sanchez-Mondragon, J. & Chanda, D. Ultralight plasmonic structural color paint. *Sci. Adv.* **9**, (2023).
2. Franklin, D. *et al.* Self-assembled plasmonics for angle-independent structural color displays with actively addressed black states. *Proc. Natl. Acad. Sci.* **117**, 13350–13358 (2020).
3. Cencillo-Abad, P. *et al.* Reusable Structural Colored Nanostructure for Powerless Temperature and Humidity Sensing. *Adv. Opt. Mater.* (2023).

Acknowledgements This work at University of Central Florida was supported by National Science Foundation Grant #ECCS-1920840. P.C.A. acknowledges the support from the UCF Preeminent Postdoctoral Fellowship Program (P3).

Towards a machine learning approach for print parameter prediction in three-dimensional multiphoton laser lithography

S. Enns[1], N. Lang[1], J. Hering-Stratemeier[1], and G. von Freymann[1,2*]

[1]Physics Department and Research Center OPTIMAS, RPTU Kaiserslautern-Landau, Kaiserslautern, Germany
[2]Fraunhofer Institute for Industrial Mathematics ITWM, Kaiserslautern, Germany
[*]corresponding author: georg.freymann@rptu.de

Abstract: Reducing deviations between design and 3D micro-printed samples without several test prints is difficult since important material properties depend on the process parameters. We present first results towards a detailed prediction of 3D printed structures based on a modeling approach combined with machine learning to adjust the corresponding process parameters.

3D micro-printing using multiphoton laser lithography is an established additive manufacturing technique for the fabrication of, e.g., bio-inspired photonic structures. Recently we could clarify the underlying mechanism of the brilliant whiteness of the cyphochilus beetles using a 3D printed model system [1]. However, deviations between the programmed target structure and the printed samples are inherent, as the material behavior strongly depends on the resulting cross-linking density, which influences the diffusion of the radicals, the overall stability during development and the shrinkage of the structure. Predictions of these interdependent parameters are in principle possible via solving the underlying coupled differential equations describing the photo-chemistry [2]. For extended samples this approach fails due to the numerical costs. Machine learning (ML) has proven to be able to predict parameters in complicated situations in which simulations based on physical models are not practical. The challenge is to provide enough meaningful training data to build the neuronal network.

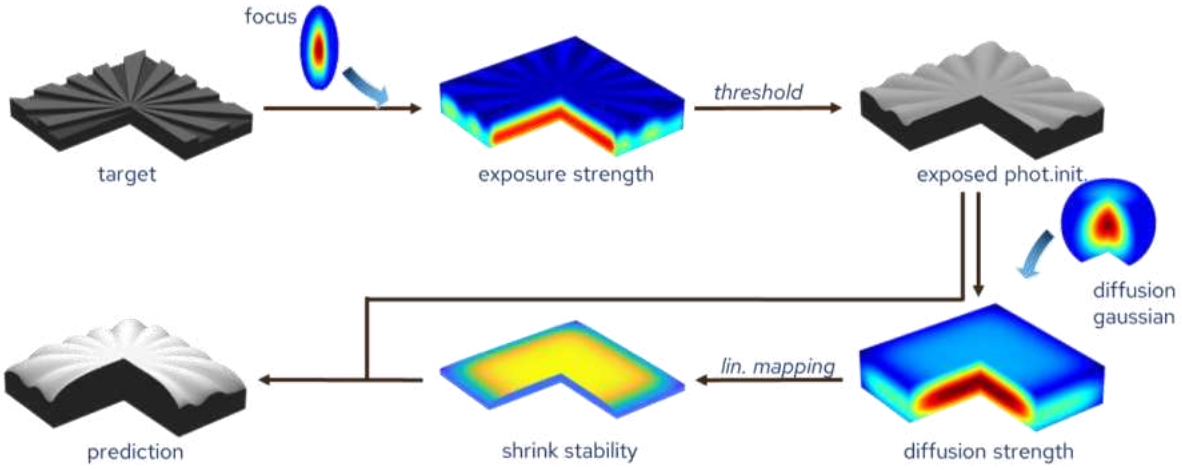


Fig. 1: Schematic representation of the print prediction algorithm: Starting with the target data, exposure dose, radical diffusion, shrinkage and final exposure threshold are calculated to predict the print result.

We use a print prediction algorithm (see Fig. 1) recently developed by us [3] to generate large training data sets, which allow in a first step to generate reliable prediction of the printed structure base solely on the desired target values used for programming the 3D micro-printing device. For ease of characterization, we limit our study

to 2.5D structures as their topography can be easily measured using confocal microscope techniques. Based on this prediction a set of corrected print parameters is calculated, which allows for printing structures which are very close to the designed structure. Fig. 2 presents one example: The target topography is shown on the left-hand side. The center picture shows the measured data if the original design is printed. Huge deviations are obvious. The target data are fed into the trained neuronal network to calculate the print outcome and to derive from these values a corrected set of print parameters. With this set of parameters, the structure has been printed whose measured topography is shown on the right-hand side. Fig. 2 (b) depicts the measured topography values for the cross-sections marked in Fig. 2 (a) showing very nice correspondence between the target structure (red) and the ML-corrected structure (blue). The strong deviations at the edges are due to the difficulty to measure steep edges with the confocal microscope.

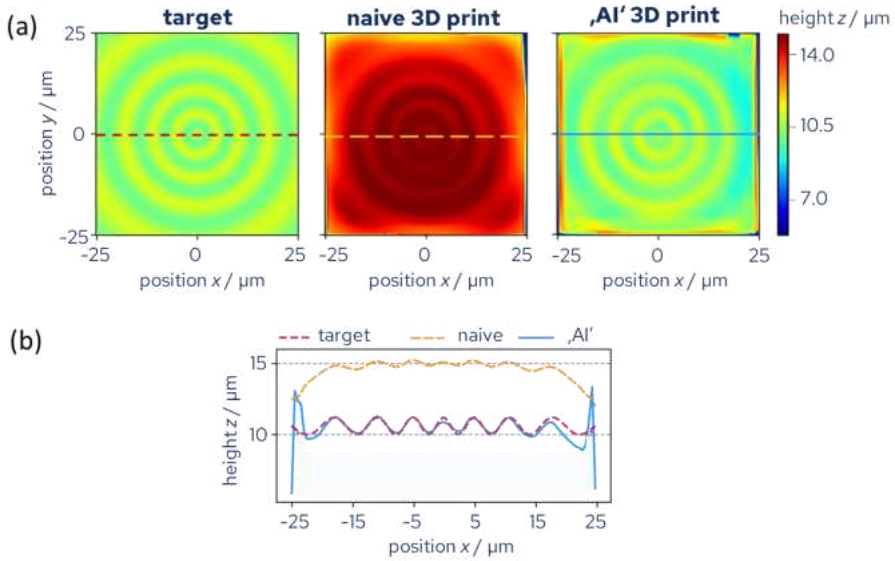


Fig. 2: (a) From left to right: Comparison between the target topography, the measured topography after the printing and the measured topography after printing with the machine-learning corrected parameter set. (b) Cross-section values along the lines in (a) showing the improvement after machine-learning correction.

In conclusion we present first steps towards a machine-learning based approach to predict a set of corrected print parameters allowing to reduce the amount of parameter sweeps in 3D micro-printing.

We acknowledge support by the Deutsche Forschungsgemeinschaft (DFG, German Research Foundation) – Project-ID 172116086 – SFB 926. The authors gratefully acknowledge the institute for measurement and sensor technology (MTS) at the University of Kaiserslautern-Landau for the opportunity of taking confocal measurements.

References

1. R. C. R. Pompe, D. T. Meiers, W. Pfeiffer, and G. von Freymann “Weak localisation enhanced ultrathin scattering media”, Advanced Optical Materials 10, 2200700 (2022).
2. Erik H. Waller and Georg von Freymann “Spatio-temporal proximity characteristics in 3D µ-printing via multi-photon-absorption”, Polymers 8, 297 (2016).
3. Nicolas Lang, Sven Enns, Julian Hering, and Georg von Freymann “Towards efficient structure prediction and pre-compensation in multi-photon lithography”, Optics Express 30, 28805 (2022).

High-performance optical diffuser inspired by *Morpho* butterfly's optical properties

A. Saito[1,2*], K. Yamashita[1], K. Taniguchi[1], S. Sakamoto[1], T. Hattori[1,2], and Y. Kuwahara[1,2]

[1] Department of Precision Engineering, Osaka University, Suita, Osaka 565-0871, Japan
[2] RIKEN SPring-8 Center, Sayo-gun, Hyogo 679-5148, Japan
[*]corresponding author: saito@prec.eng.osaka-u.ac.jp

Abstract: A novel type of diffraction-based optical diffuser was developed inspired by *Morpho* butterfly's optical properties and specific nanostructures. This diffuser can give simultaneously high transmittance, wide angular spread, low color dispersion, diffused-shape controllability, and anti-fouling. Such multi-functional property has been impossible by conventional diffusers that are based on scattering or refraction.

Optical diffusers are essential optical device because it can spread the incident light and create a uniform illumination. This function serves to various application such as daylight window, liquid crystal display, organic light emitting diodes (OLEDs), laser optics, photography lighting, medicine, etc. For these applications, optical diffusers are required to have multi-functions such as i) high transmittance, ii) wide-angle diffusion, iii) low color dispersion (Fig. 1). However, conventional diffusers can hardly achieve these conditions simultaneously. This is because their principles to diffuse the incident light are based on "multiple scattering" or "refraction", which makes the above properties fall into trade-off relationship. Then, we were inspired by the optical properties of *Morpho* butterflies [1].

Morpho butterfly's metallic blue is known as a representative of interferential structural colors, whereas its single color in wide angular range contradicts the interference. This mystery is attributed to specific nanostructures on their wing having both narrow width to produce the wide spread and disorder to prevent the color dispersion [1] (Fig. 2). To simultaneously satisfy the above-mentioned three conditions, we used these *Morpho*-principles, i.e. narrow width and nano-disorder. Also, the limited number of diffraction event that occurs only at an incident interface without multiple scattering can give high transmittance [2,3](Fig. 3). Although our first proposed nanostructure was difficult to fabricate (Fig. 3), we designed a feasible nanostructure using 2D-3D conversion principle obtained from our reflection studies [4].

Finally, a novel *Morpho*-type diffuser was successfully fabricated using nanoimprint technique, which was verified [5] in comparison with the articles on the market [6,7] (Fig. 4). Moreover, our diffuser could provide additional functions to control the diffused light-shape and anti-fouling [8].

References

1. A. Saito, in "Biomimetic Photonics", O. Karthaus, Ed., CRC press, p.96–115, p.226–242, 2012.
2. A. Saito, K. Yamashita et al., J. Opt. Soc. Am. B 38, 1532–1537, 2021.
3. A. Saito, K. Yamashita, T. Hattori, Y. Kuwahara: Jpn. J. Appl. Phys., 61, SD0801, 2022.
4. K. Yamashita, M. Fukihara, Y. Hirai, Y. Kuwahara, and A. Saito, Jpn. J. Appl. Phys. 59, 052009, 2020.
5. K. Yamashita, A. Saito et al., Opt. Express 29, 30927–30936, 2021.
6. Sumika Acryl Co. Ltd, "Properties of translucent acrylic sheet [in Japanese]".
7. Mitsubishi Engineering-Plastics Corporation, "Extrusion Diffusion Polycarbonate Resin", homepage.
8. K. Yamashita, K. Taniguchi, T. Hattori, Y. Kuwahara, A. Saito, Adv. Opt. Mater. 2301086, 2023.

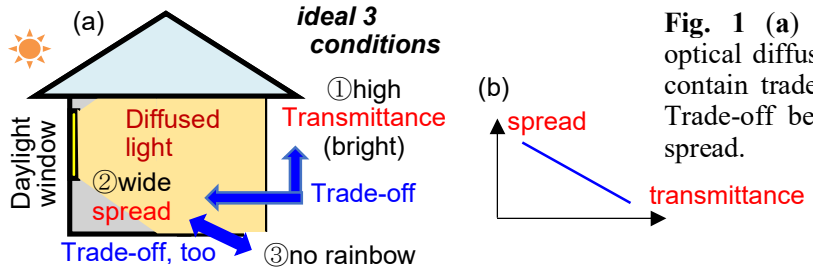


Fig. 1 (**a**) Conditions necessary for ideal optical diffuser (ex. Daylight window), which contain trade-off relationship in between. (**b**) Trade-off between transmittance and angular spread.

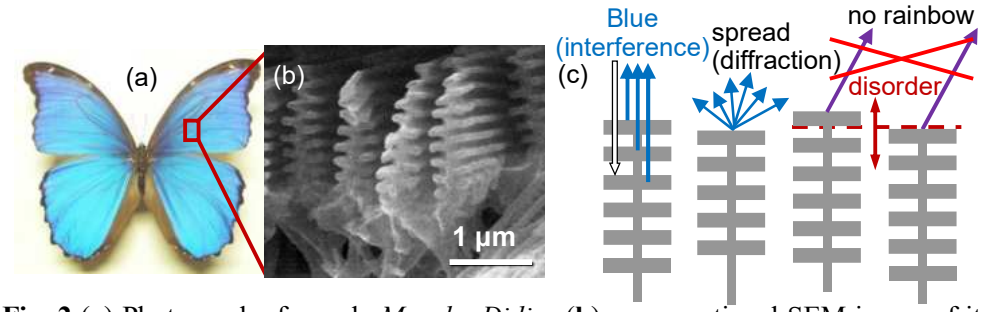


Fig. 2 (**a**) Photograph of a male *Morpho Didius* (**b**) cross-sectional SEM image of its wing scale's nanostructure. (**c**) Schematic of the principles of the *Morpho*-color that produce a single color in a wide-angular range in spite of the interference [1].

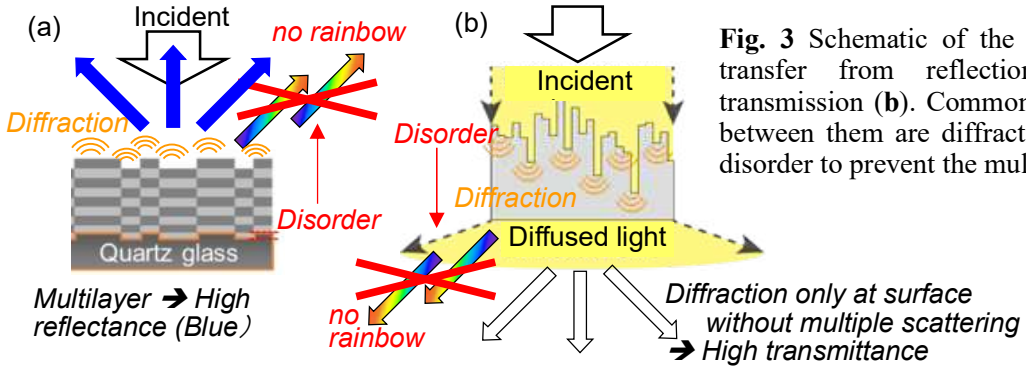


Fig. 3 Schematic of the concept of transfer from reflection (**a**) to transmission (**b**). Common principles between them are diffraction spread, disorder to prevent the multicolor [3].

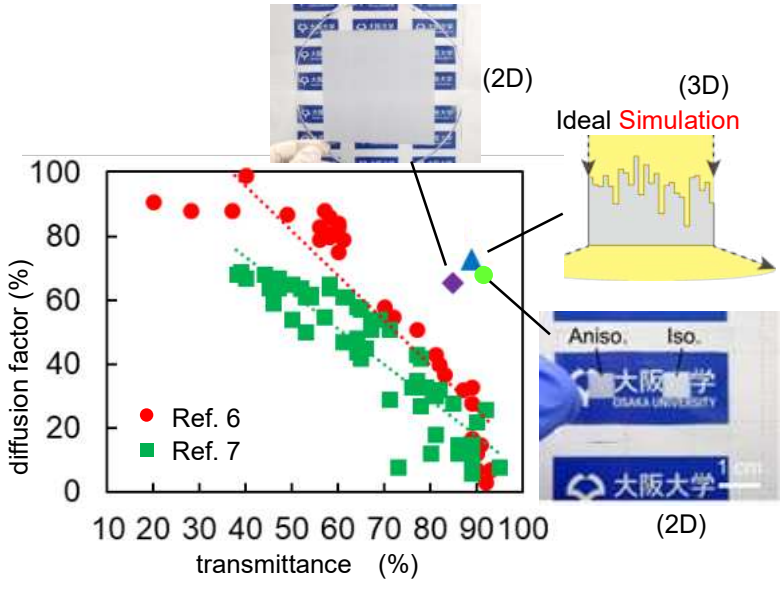


Fig. 4 Plots of diffusion factors vs. transmittance for different types of diffusers. Red circles and green squares represent the results for the market articles from a company [6] and another one [7], respectively. Other plots indicate our results: blue triangle for the simulation on the original 3D design, violet rhombus for the measurement on the 1st fabricated diffuser [5], and light green circle for the improved model [8].

Cross-reactive plasmonic arrays as artificial tastebud sensors

Justin R. Sperling [1], Chad Sipperley,[2] Rudi Schick,[2] William J. Peveler [3], Alasdair W. Clark* [1]
[1]James Watt School of Engineering, University of Glasgow, Glasgow, United Kingdom
[2] Spraying Systems Co., Glendale Heights, IL 60139, United States
[3] School of Chemistry, University of Glasgow, Glasgow, United Kingdom

*corresponding author: Alasdair.clark@glasgow.ac.uk

Abstract: We present a cross-reactive nanoplasmonic sensor system capable of identifying and classifying almost any complex liquid mixture. Analogous to biological tastebuds, our commercially available plasmonic sensor shows promise in a variety of industrial applications as a simple, rapid quality control measure.

There are a variety of analytical tools that are used in the beverage industry for quality control. Typically, these tools are large, expensive, and are not compatible with real-time, in-line monitoring (e.g. gas chromatography mass spectrometry). On the other end of the scale are human tasters who can be trained to recognize impurities within batches of product, but who, due to the nature of human taste, are prone to giving inconsistent scores. As such, there is the need for simple, real-time sensory tools that can be deployed within production facilities as quality control systems; tools designed specifically to be *non-specific* sensors that can analyse almost any complex liquid, and which, ideally, could also provide "taste" scores analogous to those provided by human testers. Here, we present a nano-scale optical tastebud system that fits these requirements. Our tool can be deployed as a small foot-print benchtop device, or in-line, for applications in industrial mixture production, counterfeit goods detection, quality testing at drinking water treatment sites, and environmental monitoring.

Light-matter interaction on a chip

Deep Neural Networks for Prediction of Structure Parameters and Far-field Radiation Patterns of Nano-antenna

Yi-Chiang Chang and Yung-Chiang Lan*

[1]Department of Photonics, National Cheng Kung University, Taiwan
*corresponding author: lanyc@mail.ncku.edu.tw

Abstract: The inverse neural network (INN) and forward neural network (FNN) are established for bi-directional prediction of structure parameters and far-field radiation patterns of nano-antennas. The INN with pre-trained VGG16 model has better predictive performance. The FNN can capture the main features of predicted radiation patterns.

Optical nano-antennas have tremendous potential in applications of optical communications. Traditionally, the nano-antennas are designed by simulation methods such as finite-difference time-domain (FDTD) method or finite element method (FEM). However, these simulations generally take a lot of time. Recently, deep neural network provides a new and effective scheme to design the nano-antennas. In this work, the inverse neural network (INN) and forward neural network (FNN) are established for bi-directional prediction of structure parameters and far-field radiation patterns of nano-antennas [1].

The INN model uses convolution layers and max pooling layers for feature extraction from radiation patterns and employs a fully connected layer for the classification prediction of structural parameters. Conversely, the FNN model takes structural parameters as input and utilizes transposed convolution layers to effectively reconstruct far-field radiation patterns (Fig. 1). Furthermore, in INN, the transfer learning scheme is used to enhance the accuracy of the model's predictions by employing pre-trained VGG16 model [2]. The studied structure of the nano-antenna is plotted in Fig. 2 with the structure parameters listed in Table 1. A total of 8,000 data (provided by FDTD simulations [3]) are used in INN and FNN for training (70 %), validating (15 %) and testing (15 %) (and adopting the random shuffle method). The INN model is evaluated using two different error assessment metrics which are relative error (Δy_{re}) and R^2 value. For FNN, root mean square error (RMSE) and mean absolute error (MAE) are utilized for evaluating the performance of the FNN model.

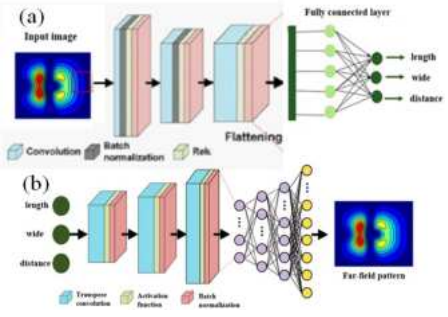


Fig. 1 Schematic diagrams of (a) INN model and (b) FNN model.

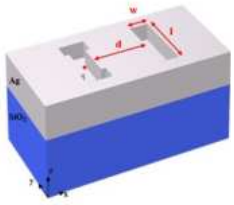


Fig. 2 Schematic diagram of nano-antenna structure. The x-polarized dipole source is placed in the middle of the I-shaped antenna with wavelength of 650 nm.

Table 1. Structural parameters

Structure	Minimum	Maximum	Increment
L	80 nm	270 nm	10 nm
W	20 nm	210 nm	10 nm
D	110 nm	300 nm	10 nm

The training results of the INN model are shown in Table 2. It can be observed that in the predictions of test

set, the INN model's predictions for the structural parameters of length and distance are more precise compared to its predictions for width. The lower predictive ability for structural parameters of width compared to other parameters may be due to the issue of “one-to-many mapping”. In deep learning, it means that the model is handling complex non-linear relationships between multiple outputs predicted from a single input. When the input features are not strongly associated with certain output labels it can lead to decreased predictive performance for the label. The training results of INN using VGG16 pre-trained model are shown in Table 3. Compared to the Table 2, it is evident that the VGG16 model improves predictive performance over the original INN model, particularly in predicting the structural parameters of length and width. This indicates that the VGG16 model is capable of capturing more complex and subtle features. Figure 3 plots the label and prediction with the smallest error in the test datasets of the FNN. Figure 3 shows that, despite of the predicted images being notably blurrier than the label images, FNN still captures the main features of radiation patterns.

Table 2. Prediction results of the INN model

	Train			Validation			Test		
Δy_{re}	L	W	D	L	W	D	L	W	D
<5%	43.1%	26.8%	79.9%	46.2%	25.3%	78.8%	43%	26.3%	80.3%
<10%	68.7%	48.1%	96.8%	70.6%	47.6%	96%	70%	46.9%	96.6%
R^2	0.781	0.504	0.94	0.80	0.492	0.936	0.808	0.489	0.96

Table 3. Prediction results of the VGG16 model

3str	Train			Validation			Test		
Δy_{re}	L	W	D	L	W	D	L	W	D
<5%	92.1%	88.5%	98.8%	93.3%	87.7%	98.6%	94.1%	89.7%	98.3%
<10%	95.6%	94.2%	99.3%	96.6%	93.5%	99.1%	96.1%	94.2%	99.2%
R^2	0.945	0.867	0.98	0.945	0.84	0.977	0.942	0.858	0.966

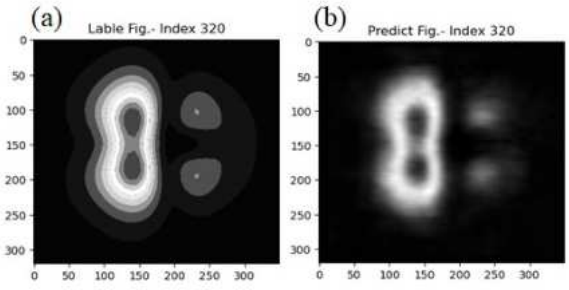


Fig. 3 Radiation patterns for (a) FDTD simulation and (b) predicted by FNN model.

This work was partially supported by the National Science and Technology Council of Taiwan (No. 112-2112-M-006-002-)

References

1. T. Ma, M. Tobah, H. Wang and L. J. Guo, “Benchmarking deep learning-based models on nanophotonic inverse design problems,” Opto-Electron Sci. 1, 210012 (2022).
2. K. Simonyan and A. Zisserman. "Very deep convolutional networks for large-scale image recognition." arXiv preprint arXiv:1409.1556 (2014).
3. https://meep.readthedocs.io/en/latest/

Lithium niobate nanostructures: fabrication and nonlinear wavefront control

Yunan Liu, Leyong Hu, Bo Wang*, and Junjie Li*

Beijing National Laboratory for Condensed Matter Physics,

Institute of Physics, Chinese Academy of Sciences, Beijing 100190, China

*Corresponding author:wangbo2014@iphy.ac.cn, jjli@iphy.ac.cn

Abstract: We have innovated a unique dry etching method for producing lithium niobate nanostructures with side-wall angles exceeding 85 degrees. Utilizing this technique, we have successfully created a second harmonic metalens boasting a remarkable numerical aperture of up to 0.7.

Lithium niobate (LN) has a large second-order nonlinear coefficients (d33=27 pm/V) and wide transparent window spanning from the ultraviolet to the mid-infrared spectral region (350nm-5 μm) [4]. These excellent properties of LN material make it as one of the most outstanding nonlinear optical material. Bulk LN crystals has long been used as intense terahertz or mid-infrared sources and optical modulators. However, optical devices made of high-quality nanostructured LN are still difficult to fabricate due to its strong physical and chemical stability [1,2], which has been a huge obstacle for the more advanced applications of LN.

We developed a novel dry etching method for LN metasurface, and successfully achieve high-quality LN nanostructures with sidewall angle close to 85° at the depth of 300 nm and the selection ratio as high as 8: 1. In our process technique, we choose inductively coupled plasma etching to ensure processing efficiency while achieving fine processing. We find that gas composition and flow rate are two most important parameters determining etching results. Figure 1 shows the fabricated LN nanostructures with various shapes: nanopillars (a), concentric cylinder (b), and nanoholes (c). We believe this etching process is accurate enough to improve LN-based optical devices.

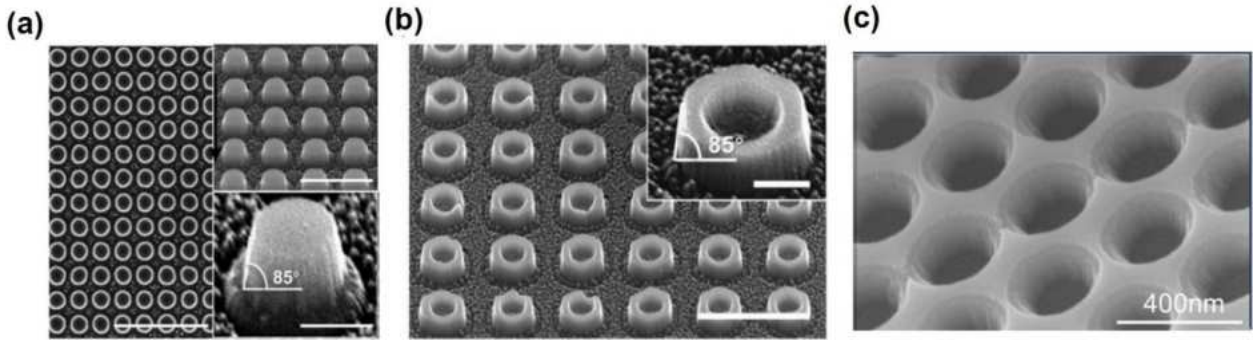


Figure 1: SEM image of various patterned LN nanostructure arrays by nanofabrication process.

We design and fabricate a second harmonic metalens to show the nonlinear wavefront control [3] captivity. The meta-atoms are elliptical holes. Figure 2(a) shows the arrangement of the elliptical holes. The local phase of the emitted second harmonic waves is controlled by tailoring the major and minor axis of the elliptical holes. Figure 2(b)

shows the fabricated LN metalens. Figure 2(c) and 2(d) shows the intensity distributions of the second harmonic waves in the focal plane and a line cross section through the focus, respectively. We observed symmetric focusing of the second harmonic waves with high quality and negligible stray light in the focal plane. The focus lens are 100 μ m and the numerical aperture is up to 0.7, which is among the most high value of nonlinear metalens.

This work was supported by the National Natural Science Foundation of China (1230446, 12074420 and U21A20140,)

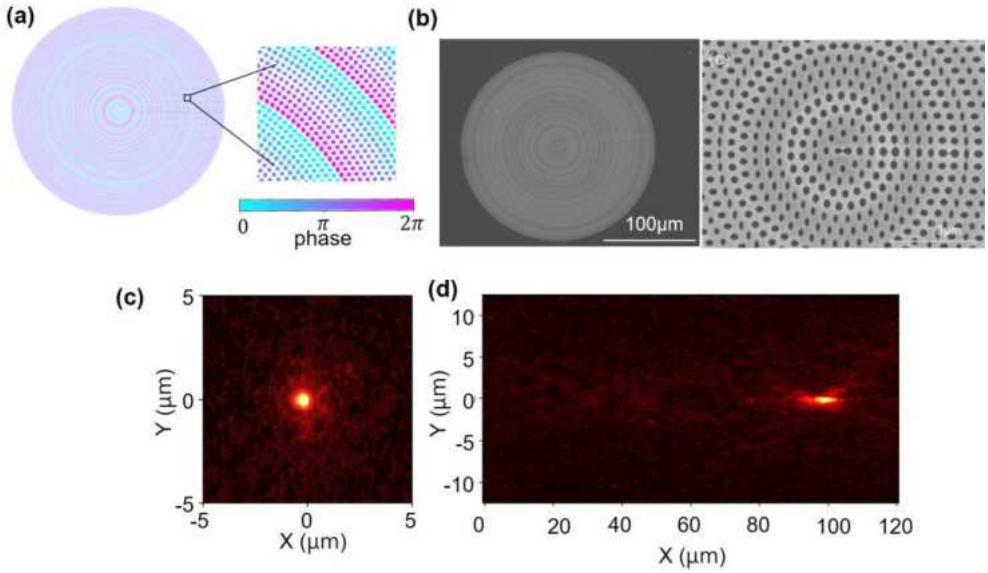


Figure 2: (a) The arrangement of the elliptical holes against the local phase of the emitted second harmonic waves. (b) SEM image of the fabricated metalens. (c,d) Second harmonic field intensity in the focus plane and line cross section.

References

1. Fedotova, Anna, et al. "Second-harmonic generation in resonant nonlinear metasurfaces based on lithium niobate." Nano letters 20.12 (2020): 8608-8614.
2. Ma, Junjun, et al. "Nonlinear lithium niobate metasurfaces for second harmonic generation." Laser & Photonics Reviews 15.5 (2021): 2000521.
3. Keren-Zur S, Avayu O, Michaeli L, et al. Nonlinear beam shaping with plasmonic metasurfaces[J]. Acs Photonics, 2016, 3(1): 117-123.
4. Gao, Bofeng, et al. "Lithium niobate metasurfaces." Laser & Photonics Reviews 13.5 (2019): 1800312.

Ultrathin Water-Immersion Metalens in the Visible

PEI YING HO,[1‡] YU CHIA CHUNG,[1‡] JIA HUA LEE, [1‡] BO RAY LEE,[1]
YAO WEI HUANG,[2] AND MING LUN TSENG[1*]
1The Institute of Electronics, National Yang Ming Chiao Tung University, Hsinchu, 30010, Taiwan
2Department of Photonics, College of Electrical and Computer Engineering, National Yang Ming Chiao Tung University, Hsinchu 30010, Taiwan
*mltseng@nycu.edu.tw

Abstract: Immersion metalenses are important to numerous applications. We report an ultrathin water-immersion metalens for the visible range. The metalens consists of GaP meta-atoms of various shapes that enable Huygens' resonance for wavefront control. This work provides a striking platform to realize nanophotonic components for bioimaging, sensing, and many other applications.

Immersion lenses play a critical role in many applications, including biomedical imaging, spectroscopy, and lithography. It is of great importance to realize miniaturized immersion lenses for further advancing these technological applications. Metasurfaces have attracted significant attention due to their great ability to manipulate light at nanoscale. To date, realizing efficient water-immersion metasurface-based lenses (metalenses [1]) in the visible range remains unsolved. Here, we report an ultrathin water-immersion metalens by combining a high-index material GaP(fig. 1b) and a group of well-tailored unit cells (meta-atoms). To design and analyze the optical properties of the meta-atoms and the metalens, we used commercial FDTD software ANASYS Lumerical with a combination of an optimization algorithm in the simulations. To design a group of meta-atoms that are feasible for their nanofabrication and show efficient wave control capability, we tuned the geometry of nanoparticles with different shapes We successfully designed eight meta-atoms of different shapes with a thickness of 85 nm, which is less than one-sixth of the operation wavelength (532 nm). The shapes of meta-atoms include disks, squares, and crosses. Overall, the meta-atoms show high transmittance (>80%) and cover complete 2π phase control (fig. 1c).

To gain further insight into the resonance of the meta-atoms, in figure 1d and 1e, we calculated multiple expansion [2], generalized Kerker coefficient [3], and the field distribution of the meta-atoms. The calculations show that the meta-atoms' unique properties are associated with Huygens' resonance[4], which results from the interference between electric and magnetic dipole modes in our meta-atoms. To showcase the utility of the meta-atoms for water-immersion meta-optics, we designed a metalens with a diameter of 14.4 μm and a focal length of 55 μm. Figure 1f shows the required phase distribution for realizing such a water-immersion metalens, which was encoded by carefully arranging the meta-atoms along the surface. The resulting metalens light focusing, with a focal width (FWHM) close to the diffraction limit (0.53λ/NA), is shown in Figure 1g. According to the results in this work, we expect that the reported water-immersion metasurface will lead to novel nanophotonic systems and foster innovative applications in the foreseeable future.

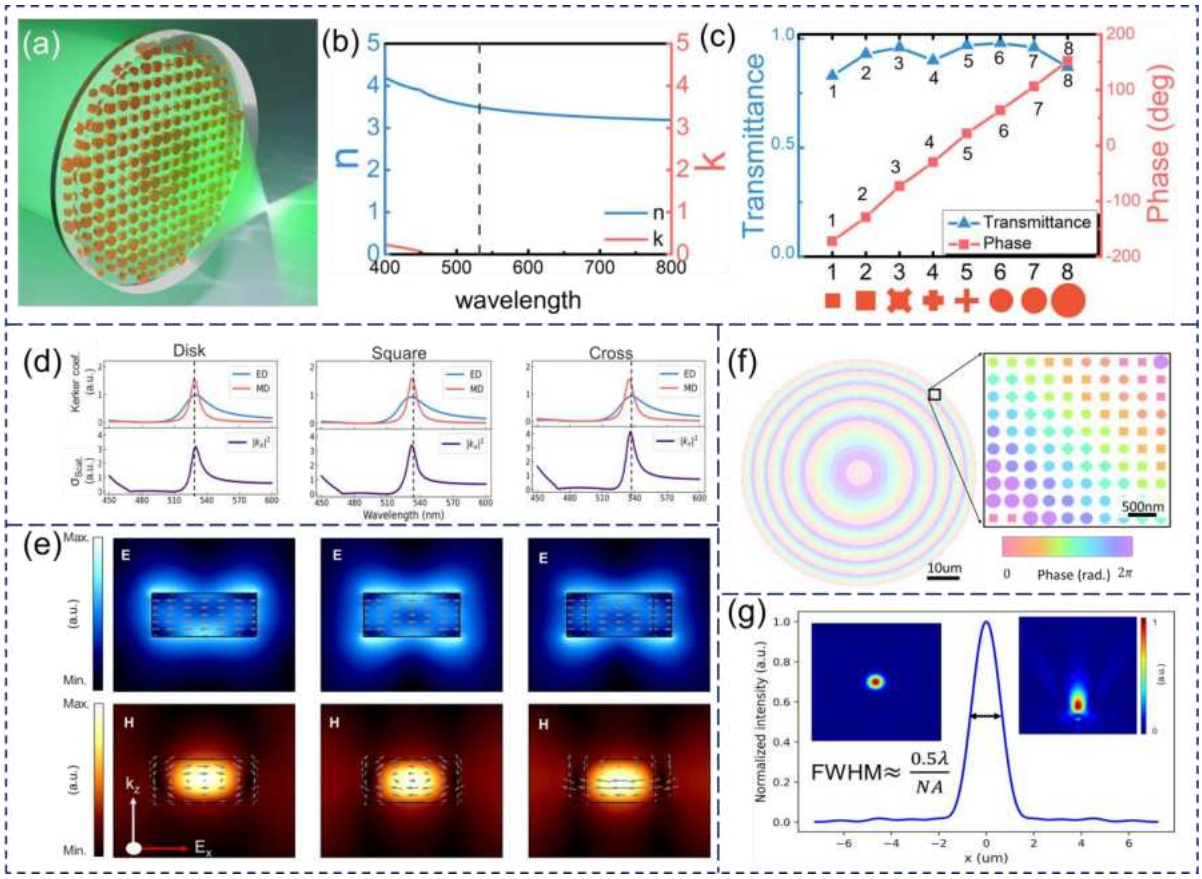


Fig. 1 (a) Schematic of metalens (b)The refractive index (n value) and extinction coefficient (k value) of GaP. (c) Transmittance and transmission phase of each structural unit within a supercell. (d) Calculated multiple expansion and generalized Kerker coefficient. (e) Field distribution of the meta-atoms. (f) Phase distribution for water-immersion metalens. (g) The focal width (FWHM) of the focal spots.

Acknowledgements. The authors acknowledge support from the National Science and Technology Council (NSTC 112-2636-M-A49-001) in Taiwan, the Ministry of Education in Taiwan under the Yushan Fellow Program, and the Center for Integrated Electronics-Optics Technologies and Systems, National Yang Ming Chiao Tung University. This work was also supported by the Higher Education Sprout Project of National Yang Ming Chiao Tung University and the Ministry of Education (MOE), Taiwan.

References

1. Tseng, M. L. et al. Metalenses: Advances and Applications. Advanced Optical Materials 6, 1800554 ,2018.
2. Hinamoto, T. & Fujii, M. MENP: an open-source MATLAB implementation of multipole expansion for nanophotonics. OSA Continuum 4 ,2021.
3. Hassanfiroozi, A. et al. Toroidal‐Assisted Generalized Huygens' Sources for Highly Transmissive Plasmonic Metasurfaces. Laser & Photonics Reviews 16 ,2022.
4. Decker, M. et al. High-Efficiency Dielectric Huygens' Surfaces. Advanced Optical Materials 3, 813-820 ,2015.
5. Chen, W. T. et al. Immersion Meta-Lenses at Visible Wavelengths for Nanoscale Imaging. Nano Lett 17, 3188-3194 ,2017.

Lithium-plasmon-based low-powered dynamic color display

Jie Liang[1], Yan Jin[1], Jia Zhu[1] and Lin Zhou[1*]

[1]College of Engineering and Applied Sciences, Nanjing University, China
[*]corresponding author: linzhou@nju.edu.cn

Abstract: In modern electronics, displays and power supplies stand as pivotal yet independent pillars. This report introduces a novel dual-function lithium-plasmon dynamic display, seamlessly blending dynamic color features with energy recycling to achieve both low energy consumption and high resolution.

Alkali metals are attracting significant attention at the intersection of plasmonics and energy storage. On the one hand, alkali metal is emerging as a low-loss and active plasmonic material. On the other hand, lithium (Li), as the lightest metal, has long been regarded as the holy grail of high-energy-density anode materials, with a high specific capacity (3860 mAh/g) and the lowest electrochemical potential (-3.04 V versus the standard hydrogen electrode).

Here, for the first time, we demonstrates a Li metal-based low-powered dynamic plasmonic color display, which is simultaneously a nanostructured anode of a Li metal battery, with the inherited advantages of dynamic tunability and extremely low energy consumption. During the charging process, Li metal nucleates and grows on a pre-patterned substrate, resulting in the generation and tuning of plasmonic colors. During the discharging process, Li metal strips off from the substrate, thus leading to the erasure of the color (as shown in Figure 1).

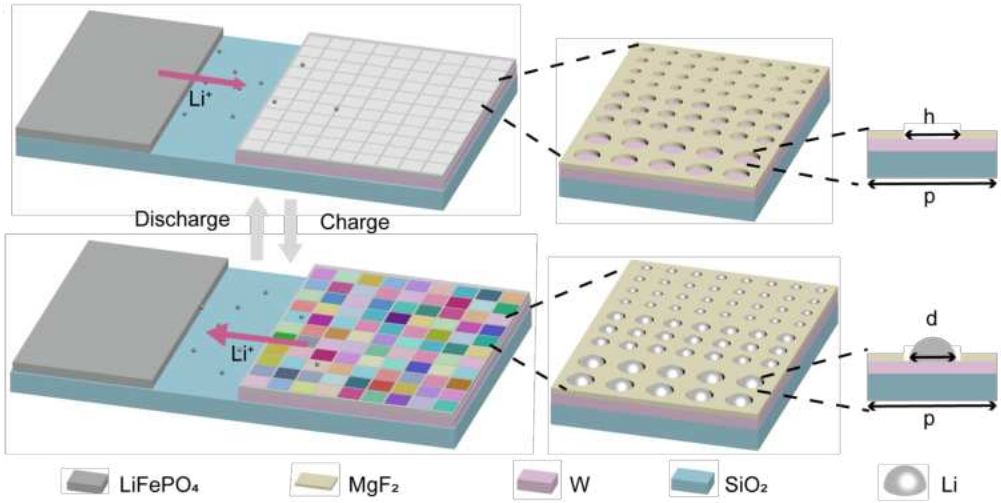


Figure 1. Schematic and illustration of the low-powered dynamic plasmonic color display. The display panel, which serves as the anode of the battery, is composed of silica (SiO_2) substrate, tungsten (W) conductive film (100 nm thick) and a magnesium fluoride (MgF_2) insulating layer (30 nm thick) with periodic holes under the colorless 'off' state. Each pixel is composed of periodic holes with a given lateral period (p) and diameter (h). During the charging (electrodeposition) process, Li nanoparticles with diameter (d) generate colors as the 'on' state. These colors can be erased during the discharging process once Li nanoparticles are stripped off.

The energy storage characteristics of lithium metal can effectively realize energy recovery and reuse during the charging and discharging process. Because of the dual functionality (plasmonic display and energy storage) of Li metal, each pixel is a micro-lithium battery in a display device, in which one charged pixel can power another one to release its energy, and vice versa, during repeated cycling. The energy storage feature of Li metal enables effective energy recycling and reduces the overall energy consumption to 0.390 mW cm^{-2} for the active coloration state and 0.105 mW cm^{-2} for the static coloration state of a proof-of-concept display/battery device, which is much lower than the energy consumption of LCD, LED, EPD display devices, vital for energy-efficient display technologies in the future.

In summary, benefiting from the light field manipulation beyond the diffraction limit and the energy storage battery of Li metals, this work shows much lower energy consumption, much higher spatial resolution, higher compactness, considerable modulation speed and good eye protection for the full-color display. Thus, this Li-metal-based plasmonic color display shows the best overall performance, opening up a promising direction for future high-performance display technology. Their results may offer a unique opportunity to develop a nano-scaled integrated platform for energy storage and information display.

We acknowledge the micro-fabrication center of National Laboratory of Solid State Microstructures (NLSSM) for technique supports, and these research works are supported by the National Key Research and Development Program of China (Nos. 2022YFA1404300, 2021YFA1400700); the National Natural Science Foundation of China (Nos. 12022403, 62375123) and the Excellent Research Program of Nanjing University (ZYJH005).

References

1. Jie Liang, Yan Jin, Huiling Yu, Xinjie Chen, Lin Zhou*, Pengcheng Huo, Ye Zhang, Haiyang Ma, Yi Jiang, Bin Zhu, Ting Xu, Hui Liu, Shining Zhu, Jia Zhu*. Lithium-plasmon-based low-powered dynamic color display, ***National Science Review*** nwac120, (2023)

Linearly Polarization-Sensitive Monolayer MoS_2 Plasmonic Phototransistors

Chen-Yu Wang[1,2*], Shane Yeh[1,2], Jui-Han Fu[3], Cheng-Han Lin[1,2], Tzu-Yu Peng[1,2], Jia-Wern Chen[1], Feng-Yang Tsai[1,2], Vincent Tung[3], and Yu-Jung Lu[1,2]

[1]Research Center for Applied Sciences, Academia Sinica, Taipei 11529, Taiwan

[2]Department of Physics, National Taiwan University, Taipei 10617, Taiwan

[3]Department of Chemical System Engineering, School of Engineering, The University of Tokyo, Tokyo 113-8656, Japan

[*]corresponding author: r11222046@ntu.edu.tw

Abstract: We demonstrate highly polarization-sensitive plasmonic phototransistors using a monolayer MoS_2 on an HfN-gated structure and integrated with plasmonic Au nanorod arrays. Through finite-difference time-domain (FDTD) calculations, we achieved a strong linear polarization selectivity of up to 90 % under illumination at 660 nm.

Accurate detection of polarized light is crucial for fields such as quantum communication and quantum information processing. However, the current technology indispensably requires multiple optical components, inevitably resulting in substantial losses and diminished efficiency in polarized light detection. In this study, we introduce polarization-sensitive phototransistors built upon a scalable monolayer of MoS_2 [1,2], utilizing a HfN back gate, and integrated with plasmonic gold (Au) nanorod arrays. The strength of the interaction between excitons and surface plasmon resonances is finely tuned using plasmonic nanostructures, as confirmed by Finite-difference time-domain (FDTD) simulations. Our simulations show that phototransistors with Au nanorod arrays (550 nm in length, 55 nm in width, and 30 nm in height) with periodicity of 620 nm/200 nm, demonstrate pronounced linear polarization selectivity when illuminated at 660 nm. These plasmonic devices exhibit a polarization-dependent absorption spectrum with a linear polarization ratio of 90.5%. This enhanced polarization sensitivity provided by the plasmonic nanostructures opens avenues for further exploration of efficient polarized-light sensitive phototransistors. Finally, we will explore the promising applications of these ultra-thin, high polarization-sensitive phototransistors.

Fig.1 shows the material properties of HfN film. Fig. 1(a) presents the AFM image of HfN film with rms of 0.5 nm. Fig. 1(b) reveals the Raman spectrum of the monolayer MoS_2 on the HfN-based gated structure (30 nm Al2O3 / 100 nm HfN). Fig. 1(c) shows the comparison of PL intensity from monolayer MoS_2 with and without the HfN plasmonic substrate. The results indicate that the PL intensity significantly increases around 660 nm for the one with the HfN back reflector. Fig.2 shows the simulation result of plasmonic Au nanorod arrays. Fig. 2(a) reveals the electric field distribution under illumination with an *x*-polarized light at 660 nm. A strong localized field can be observed. Fig. 2(b) illustrates the electric field distribution under illumination with a *y*-polarized light of 660 nm. It discloses barely any optical field confinement. Fig. 2(c) shows the effective absorbance in monolayer MoS_2 on a different substrate.

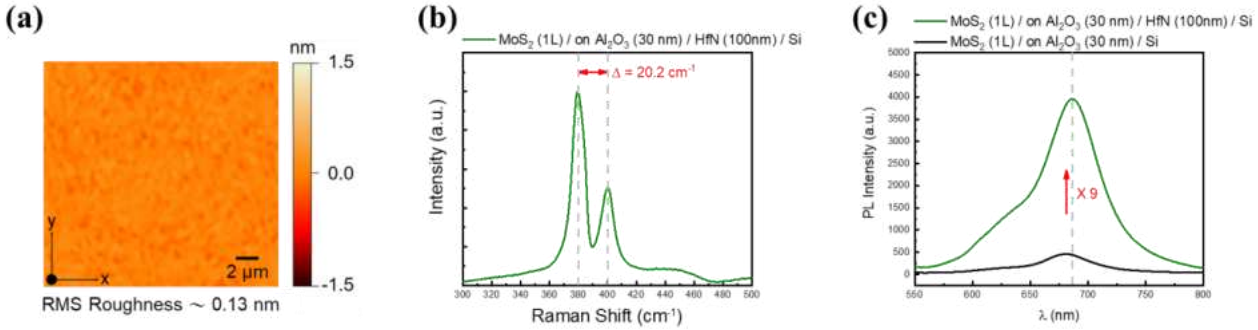


Figure 1. Material properties of monolayer MoS_2 on HfN film. (a)AFM image of HfN film. (b)Raman spectrum of monolayer MoS_2 on HfN. (c)PL spectra of Monolayer MoS_2 on different substrates.

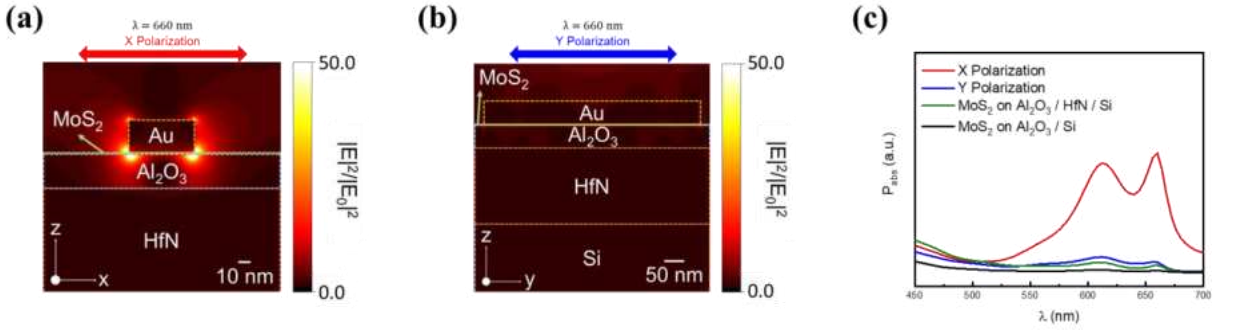


Figure 2. The simulation results of plasmonic Au nanorod arrays. (a) Electric field distribution under illuminated with an *x*-polarized light at 660 nm, (b) Electric field distribution under illuminated with a *y*-polarized light at 660 nm, (c) The power absorption per unit volume (P_{abs}) in monolayer MoS_2 on a different substrate.

References

1. Jui-Han Fu, Jiacheng Min, Che-Kang Chang, Chien-Chih Tseng, Qingxiao Wang, Hayato Sugisaki, Chenyang Li, Yu-Ming Chang, Ibrahim Alnami, Wei-Ren Syong, Ci Lin, Feier Fang, Lv Zhao, Chao-Sung Lai, Wei-Sheng Chiu, Wen-Hao Chang, **Yu-Jung Lu**, Kaimin Shih, Lain-Jong Li*, Yi Wan*, Yumeng Shi*, Vincent Tung*. Orientated Lateral Growth of Two-Dimensional Materials on C-plane Sapphire. *Nature Nanotech.* 18, 1289–1294 (2023)
2. Wei-Ren Syong, Jui-Han Fu, Yu-Hsin Kuo, Yu-Cheng Chu, Mariam Hakami, Tzu-Yu Peng, Jason Lynch, Deep Jariwala, Vincent Tung, and **Yu-Jung Lu***, Enhancing Photogating Gain in Scalable MoS_2 Plasmonic Photodetectors *via* Resonant Plasmonic Metasurfaces. *ACS Nano* (Accepted) (2024)

Active Multitasking Metasurfaces: Simultaneous and Independent Steering of Frequency-Shifted Beams

P. Thureja[1], J. Sisler[1], M. D. Kelzenberg[1], R. Sokhoyan[1] and H. A. Atwater[1*]

[1]Thomas J. Watson Laboratories of Applied Physics, California Institute of Technology, CA 91125 Pasadena, USA
[*]corresponding author: haa@caltech.edu

Abstract: We experimentally steer frequency-shifted light using an electrically tunable ITO-based metasurface operating at near-infrared wavelengths. By independently addressing metasurface elements, we superimpose MHz driving frequencies with nonresonant spatial phase offsets. This configuration creates a chip-scale platform for simultaneous and independent control of the frequency and wave vector of light.

Active metasurfaces comprising arrays of programmable nanoantennas have gained widespread interest due to their potential for versatile wavefront shaping. Until now, researchers have primarily focused on using active metasurfaces to dynamically control the amplitude, phase, and polarization of light at a fixed wavelength. Recently, there has been growing interest in high-frequency temporal modulation to generate beams at new output wavelengths using a single excitation wavelength. While experimental demonstrations at radio frequencies exhibited large modulations with intuitive antenna designs and fast response times [1], optical frequency demonstrations thus far have faced constraints in real-world applications with most demonstrations relying on all-optical pump-probe schemes [2, 3]. Addressing this gap, our group recently introduced an electrically tunable space-time metasurface operating at 1530 nm by modulating an indium tin oxide (ITO)-based metasurface with two interdigitated electrodes at MHz frequencies [4].

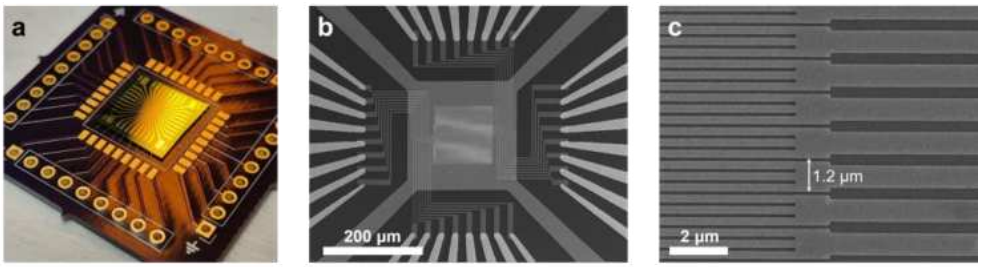


Figure 1. (a) 32-electrode metasurface wire bonded into PCB. (b) SEM of metasurface. (c) Each metasurface electrode is connected to three nanoantennas, corresponding to an effective period of 1.2 µm.

In this work, we build upon our previous proof-of-concept demonstration [4] and incorporate 32 independently addressable metasurface electrodes for versatile wavefront engineering (Fig. 1). The current ITO-based active metasurface exhibits a modulation in the amplitude and phase > 200° at ~1510 nm. In a first step, we collectively modulate all metasurface elements at frequencies up to 10 MHz and frequency-shift the reflected light by multiples of the driving frequency. The measured frequency spectrum is determined by the applied waveform and corresponds to a time-domain Fourier transform of the reflected field in space and time. We then introduce incremental phase offsets between the driving waveforms applied to each electrode to superimpose the temporally varying waveform with a spatially varying phase front. The traveling-wave-like modulation created through this configuration simultaneously shifts the frequency and tangential momentum of

the reflected light, enabling steering of frequency-shifted light up to angles of +/- 20°. Since the spatial variation of phase leverages nonresonant phase offsets that are introduced through an arbitrary waveform generator, we achieve highly directive steering of frequency-shifted light to target angles.

In a next step, we discuss the potential of the proposed space-time metasurface for multi-channel communication, achieved through spatial multiplexing of two subarrays with two distinct driving waveforms at different frequencies (Fig. 2a, 2b). A comparison of the frequency spectra obtained while only modulating one subarray in time *vs.* modulating both subarrays simultaneously shows that there is negligible crosstalk between the two driving frequencies (Fig. 2c). Independent control of phase offsets within each subarray enables simultaneous, independent, and deterministic steering of two frequency-shifted beams. We further discuss the incorporation of this control scheme into free-space laser communication systems, specifically in the realm of intersatellite optical communication. Here, we examine the potential impact of space-time modulation on the overall performance of the system. The methods outlined in this work lay the groundwork for active multitasking metasurfaces, promising increased channel capacity in next-generation optical technologies.

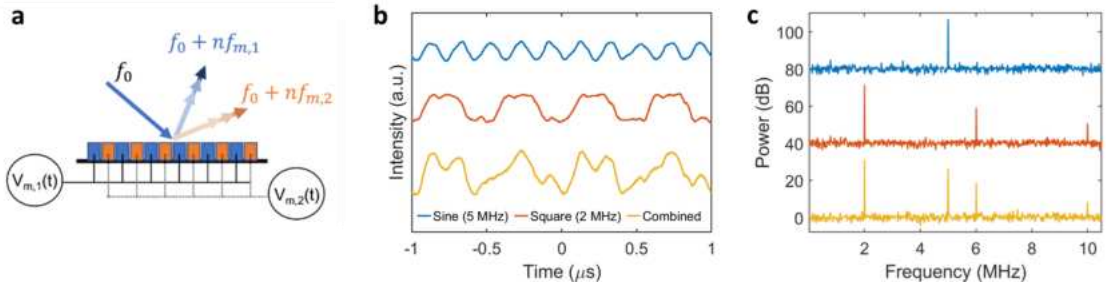


Figure 2. (a) Schematic of multi-frequency multi-beam steering with two independently modulated subarrays indicated in orange and blue, respectively [5]. (b) Time-domain reflection intensity and (c) frequency spectra for modulation of an individual subarray with a 5 MHz sine wave (blue), a 2 MHz square wave (orange) and both subarrays simultaneously with a 5 MHz sine wave and a 2 MHz square wave, respectively (yellow). The time-domain intensity and power spectra are offset for clarity. The incident laser wavelength was 1530 nm.

This work was supported by the Air Force Office of Scientific Research Meta-Imaging MURI grant #FA9550-21-1-0312.

References

1. Zhang, L., Chen, X. Q., Liu, S., Zhang, Q., Zhao, J., Dai. J. Y., Bai, G. D., Wan, X., Cheng, Q., Castaldi, G., Galdi, V. and Cui, T. J., "Space-time-coding digital metasurfaces," Nat. Commun., Vol. 9, No. 1, 4334, 2018.
2. Guo, X., Ding., Y., Duan, Y. and Ni, X., "Nonreciprocal metasurface with space-time phase modulation," Light Sci. Appl., Vol. 8, No. 1, 123, 2019.
3. Karimi, M., Alam, M. Z., Upham, J., Reshef, O., and Boyd, R. W., "Time-varying gradient metasurface with applications in all-optical beam steering," Nanophotonics, Vol. 12, No. 9, 1733–1740, 2023.
4. Sisler, J., Thureja, P., Grajower, M. Y., Sokhoyan, R., Huang, I., and Atwater, H. A., submitted, 2023.
5. Thureja, P., Sokhoyan, R., Hail, C. U., Sisler, J., Foley, M., Grajower, M. Y., and Atwater, H. A., "Toward a universal metasurface for optical imaging, communication, and computation," Nanophotonics, Vol. 11, No. 17, 3745-3768, 2022.

Grayscale Electron Beam Lithography Direct Patterned Antimony Sulfide

Wei Wang[1,2*], Uwe Hübner[1], Tao Chen[1,2], Anne Gärtner[3], Joseph Köbel[1,2], Tanveer Ahmed Shaik[1,2], Astrid Bingel[3], Volker Deckert[1,2,4, 5*]

[1]Leibniz Institute of Photonic Technology (IPHT), 07745 Jena, Germany.

[2]Institute of Physical Chemistry, Friedrich Schiller University Jena (FSU), 07743 Jena, Germany

[3]Fraunhofer Institute for Applied Optics and Precision Engineering (Fraunhofer IOF), 07745 Jena, Germany

[4]Abbe Center of Photonics and Faculty of Physics, FSU, 07745 Jena, Germany

[5]Jena Center for Soft Matter (JCSM), FSU, 07743 Jena, Germany

[*]corresponding author: w.wang@uni-jena.de, volker.deckert@uni-jena.de

Abstract: We present a combination of grayscale electron beam lithography (g-EBL) and direct forming methodology to fabricate free-form antimony sulfide structures. 4-level Fresnel Zone Plates (FZP) and metalenses were produced and characterized. The method can be used for the fabrication of 3D micro-optical elements in a single step manner.

The refractive index n=n+ik, is the most important parameter for the design and fabrication of diffractive optical elements (DOEs) and metasurfaces [1]. Recently, antimony trisulfide (Sb_2S_3) has attracted much attention as it is a promising candidate for the fabrication of micro-optical devices. Sb_2S_3 has high refractive index (n~2.5 and 4.5 at 633 nm vacuum wavelength for amorphous and crystalline Sb_2S_3, respectively) while still maintaining low losses, which renders Sb_2S_3 an ideal candidate for the fabrication of high performance DOEs and metasurfaces.

In the previous study [2], Wei Wang et al. demonstrated for the first time that the antimony-butyldithiocarbamic-complex can be used for the direct patterning of Sb_2S_3 nanostructures via various lithography methods, including EBL. In our recent [3] study, Sb_2S_3 nanostructures with controlled lateral and vertical profile were obtained through a single step g-EBL direct patterning scheme (Fig. 1(a)) for the first time. The refractive index of the electron beam patterned structure was calculated based on an optimization algorithm that is combined with genetic algorithm and transfer matrix method. Fig. 1(b) and 1(c) illustrate the schematic of as fabricated 4-level Sb_2S_3 FZP and metalens, respectively. Both FZP's and metalenses satisfy the 4-level approximated spatial variation of the phase as a parabolic lens:

$$\varphi(x,y) = \left[-\frac{2\pi n}{\lambda_0}\left(\sqrt{x^2+y^2+f_0^2}-f_0\right)\right]_{2\pi} \quad (1)$$

FZP is functionalized via height induced propagation phase modulation (delay) composed of a concentric ring staircase structure (Fig. 1(d)). The metalens is based on the phase delay imposed by meta-atoms arranged on 2D lattices (Fig. 1(e)). Both micro-lens exhibit diffraction limited performance and can be used for optical imaging [3].

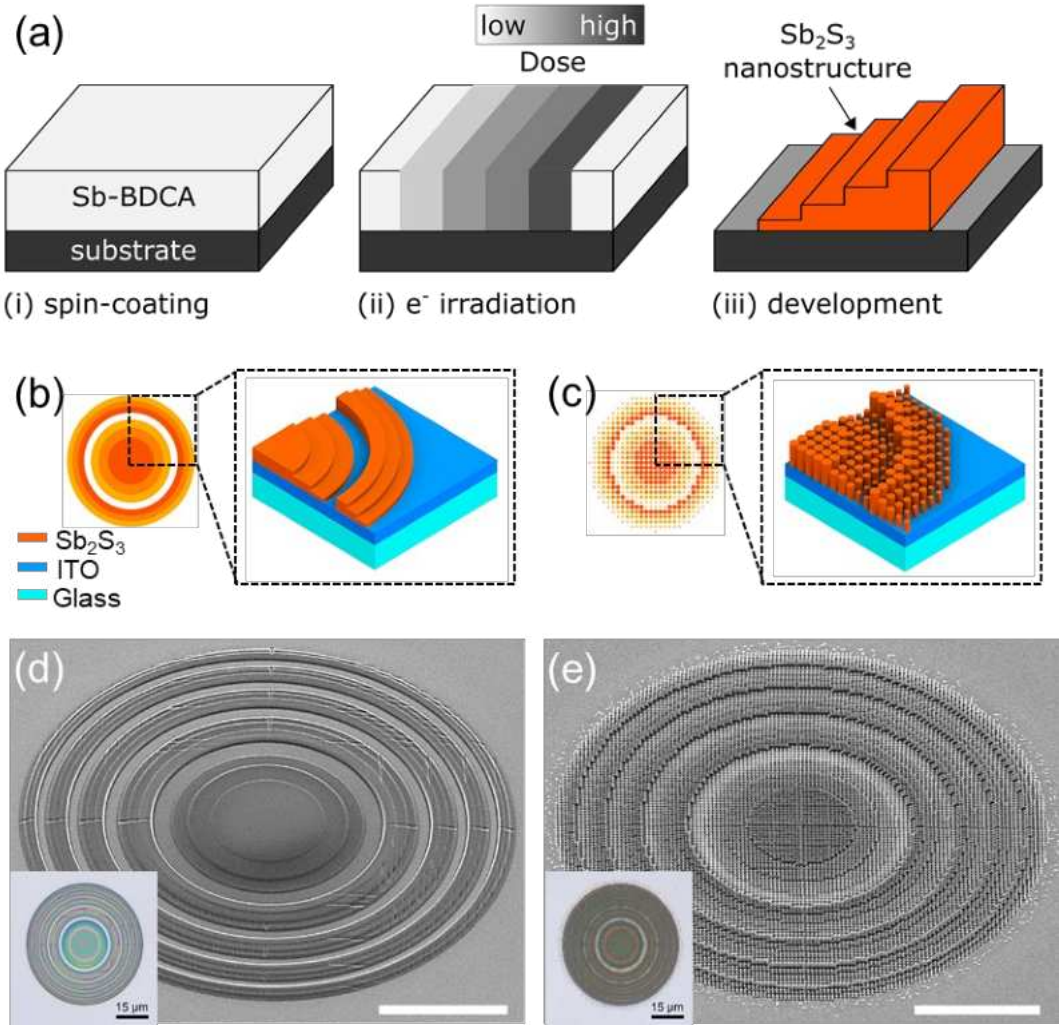


Figure 1. (a) Scheme of the grayscale EBL process and the constituent elements of 4-level Sb_2S_3 (b) FZPs and (c) metalenses. SEM and optical microscope images of a 4-level Sb_2S_3 (d) FZP and (e) metalens. All images are from [3]. Scale bar: 15 µm.

Acknowledgement: WW thanks for financial support through the IPHT Innovation Project 2021/2022 (690082), DFG, CRC-TRR 234 "CataLight" Project C04. VD appreciates financial support via the DFG Collaborative Research Center SFB 1375 (NOA) Project C02.

References

[1] E. Bayati, A. Zhan, S. Colburn, M.V. Zhelyeznyakov, A. Majumdar, Role of refractive index in metalens performance, Applied Optics 58 (2019) 1460-1466.

[2] W. Wang, P. Pfeiffer, L. Schmidt‐Mende, Direct patterning of metal chalcogenide semiconductor materials, Advanced Functional Materials 30 (2020) 2002685.

[3] W. Wang, U. Hübner, T. Chen, A. Gärtner, J. Köbel, F. Jahn, H. Schneidwind, A. Dellith, J. Dellith, T. Wieduwilt, Grayscale Electron Beam Lithography Direct Patterned Antimony Sulfide, arXiv preprint arXiv:2401.13427 (2024).

Full-Stokes metasurface polarimetry based on multidimensional polarization conversion

Chenglong Zheng[1], Huaping Zang[1], Peinan Ni[1,*]

[1]Zhengzhou University, China
[*]corresponding author: nipeinan@zzu.edu.cn

Abstract: We demonstrate a multi-focus metalens for terahertz polarization detection that requires only a single measurement to obtain complete polarization parameters and reconstruct the polarization state of the incident field. The proposed metasurface polarimetry may find applications in the fields of real-time terahertz detection and integrated optics.

Polarization, as important information carried by electromagnetic waves, is crucial in imaging, encryption, image processing, and other fields. How to generate specific polarization states and how to identify the polarization state of electromagnetic waves are both research hotspots. Combined with the wavefront modulation properties of metasurfaces, some polarization detection schemes based on polarization filtering and polarization splitting have been developed. However, existing polarization detection schemes in the terahertz band still face challenges such as narrow operating bandwidth and the requirement for multiple measurements.

Recently, we proposed a multi-focus metalens for polarization detection in the terahertz band. Unlike previously reported two-focus or six-focus metalenses used for polarization detection, or some other polarization detection schemes, the proposed metasurface converted all polarization components used to characterize Stokes parameters into the same polarization state, ensuring that only a single measurement is needed to obtain complete polarization parameters and reconstruct the polarization state of the incident field. This provided a new option for real-time polarization detection in the terahertz band and could be extended to visible light and other electromagnetic bands.

The proposed metasurface consisted of six subarrays (Fig. 1); each subarray sequentially focused x-polarized, y-polarized, 45°-polarized, 135°-polarized, left-handed circularly polarized (LCP), and right-handed circularly polarized (RCP) components in the incident wave and converted them into x-polarization. These subarrays only focused their corresponding polarization components onto the focal plane, excluding their orthogonal polarization states. The polarization state of the incident wave could be reconstructed using the intensities of the six foci.

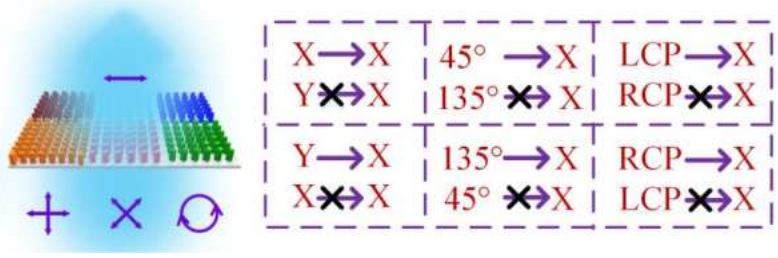


Fig. 1. Schematic of the proposed multi-focus metalens for polarization detection. For arbitrarily polarized wave incidence, this metalens converted each of the six polarized components of the incident wave into x polarization and focused them individually at six positions on the same focal plane.

Figures 2(a-f) illustrated the measured intensity distributions of the transmitted field when the incident waves

were x-polarized, y-polarized, 45°-polarized, 135°-polarized, LCP, and RCP, respectively. For x- and y-polarized wave incidence, the incident polarization states can be inferred from the large contrast between the first and second foci. The calculated parameters S_1 were close to 1 and −1, respectively. For the 45° and 135° polarizations, the parameter S_2 close to 1 and −1, respectively. When the incident waves were circularly polarized, the intensity differences were mainly reflected in the fifth and sixth foci. We compared the experimentally detected polarization states with the incident ones on the same Poincaré sphere, and these six polarization states were in each of the six directions of the three coordinate axes.

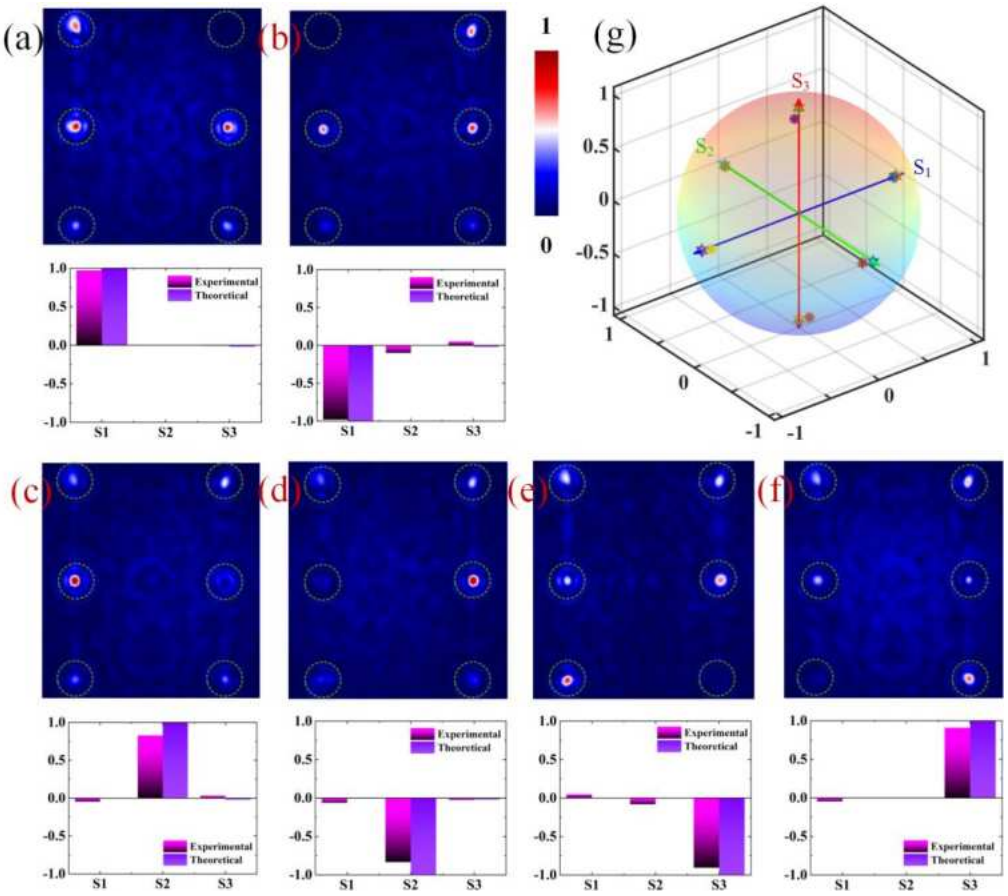


Fig. 2. Experimental characterization of the proposed multi-focus metalens for polarization detection. (a-f) measured intensity distributions of the transmitted x-polarized component, and full-Stokes parameters of the measured polarization states and the incident ones. (g) representation as points on the Poincaré sphere of the measured polarizations (*) and the incident ones (hexagrams).

In conclusion, we demonstrated a polarization detection scheme that requires only a single measurement. The implementation of the scheme was based on a six-focus metalens, which converted six polarization states used to characterize Stokes parameters into x polarization and focused them. Thus, the complete polarization parameters can be obtained by measuring only the transmitted x-polarized response. This efficient polarization detection scheme may find applications in fields such as integrated optics and polarized optics.

References

1. R. Wang, M. A. Ansari, H. Ahmed, et al. Light Sci. Appl. 12, 103 (2023).
2. Z. Jiang, J. Lu, J. Fan, et al. Laser Photon. Rev. 17, 2200484 (2023).
3. C. Zheng, H. Li, J. Liu, et al. Photonics Res. 12, 514-521 (2024).

Impedance-matched zero-index metamaterials: from waveguide to antenna

Y. Li[1*]

[1] State Key Laboratory of Precision Measurement Technology and Instruments, Department of Precision Instrument, Tsinghua University, Beijing 100084, China
[*]corresponding author: yli9003@mail.tsinghua.edu.cn

Abstract: Photonic-crystal-based zero-index metamaterials feature a uniform spatial phase distribution. Coupling between zero-index modes and plane wave induces in-plane and out-of-plane radiations. We close these radiation channels by forming zero-index modes with BICs, leading low propagation-loss zero-index waveguides. Alternatively, we also leverage out-of-plane radiations to achieve high-directivity small-aperture antennas.

Zero-refractive-index metamaterials show the unique feature of uniform spatial phase distributions, enabling the interaction of single optical mode with matter over an infinite area in an arbitrary shape[1]. This feature brings many novel optical physics and devices, such as cloak, supercoupler, large-area single-mode laser, and extended superradiance. Additionally, zero-index metamaterials have appealing applications in generation of entangled photon pairs via spontaneous four-wave mixing according to the phase-mismatch free characteristic.

Photonic crystal-based zero-index metamaterials realize zero-index behavior via the degeneracy of a transverse magnetic (TM) monopole mode and two TM dipole modes. The monopole mode and the transverse dipole mode correspond to the zero effective permittivity and permeability, respectively, leading to an impedance-matched zero index. The monopole mode and transverse dipole mode can induce in-plane and out-of-plane radiations, respectively.

When we use zero-index metamaterial as a waveguide, such radiations will induce a high propagation loss. To reduce this propagation loss, metals were utilized to hinder radiations by constructing a mirror reflector for the radiation channels. But metals result in high ohmic losses, leading to an overall loss up to 1000dB/mm. In dielectric materials, bound state in the continuum (BIC) has been applied to decrease the radiation losses via destructive interference between several radiation channels. Despite the effective suppression of radiations, the present BIC-based zero-index dielectric metamaterials are typically in a slab configuration which is boundless along the in-plane directions. Such a bulky structure has no lateral radiation by nature, but it is inflexible in realizing various integrated photonic devices such as mirroring and Mach-Zehra interferometer.

We achieved a 1D metawaveguide with zero refractive index along the propagation direction, featuring phase-advance free, high flexibility, and low propagation loss. This zero-index metawaveguide consists of several silicon bow-tie units arranged in a single row, leading to a corrugated metawaveguide. With the fine-tuned structure, a monopole mode and a transverse dipole mode are degenerated at the center of the Brillouin zone. This degeneracy state forms a Dirac-like cone at Γ point and 1550 nm. Simulation results show that effective permittivity and permeability linearly cross zero at 1550 nm. In measurement, on-chip interferometry is used to measure the effective refractive index, in which two counter-propagating coherent continuous waves are incident into the metawaveguide. We extracted the effective index according to the interference patterns via $n_{\mathrm{eff}} = \lambda_0/(2d)$, where λ_0 is the vacuum wavelength and d is the distance between two adjacent nodes or anti-nodes. The experimentally extracted absolute value of refractive index is consistent with the simulation results, both reaching zero near 1550 nm.

We canceled the in-plane radiation of monopole mode and out-of-plane radiation of transverse dipole mode via a quasi-BIC. This quasi-BIC leads to a measured propagation loss down to ~10 dB/mm in the metawaveguide without any extra confining structures such as photonic band gap structures, leading to a compact footprint and high flexibility [2].

By leveraging the out-of-plane radiations of zero-index metamaterials, we achieved a high-directivity small-aperture zero-index antenna. To achieve a zero-index metamaterial with deep-sub-wavelength unit cell, we synthesized a ceramic — $SrTiO_3$ — with a microwave relative permittivity as high as 290. Based on this ceramic, we fabricated a square array of $SrTiO_3$ pillars in a $BaTiO_3$ background matrix, leading to a highly homogeneous zero-index metamaterial whose lattice constant is one tenth of the free-space wavelength. By incorporating this metamaterial into an open rectangular metallic waveguide, we achieved a zero-index antenna[3]. When this antenna's aperture size varies from $0.5\lambda_0 \times 0.5\lambda_0$ to $1.2\lambda_0 \times 1.2\lambda_0$, this antenna can always approach the fundamental limit in the antenna directivity. Compared with dielectric antennas, our zero-index antenna shows comparable directivities with a better scalability.

References

[1] Y. Li, C. T. Chan, and E. Mazur, "Dirac-like cone-based electromagnetic zero-index metamaterials," *Light: Science & Applications,* vol. 10, no. 1, p. 203, 2021 2021.

[2] T. Dong *et al.*, "Low-loss nanoscale zero-index metawaveguides and metadevices," *Optica,* vol. 11, no. 6, pp. 799-805, 2024.

[3] Y. Liu *et al.*, "High-permittivity ceramics enabled highly homogeneous zero-index metamaterials for high-directivity antennas and beyond," *eLight,* vol. 4, no. 1, p. 4, 2024.

Reconfigurable Acoustic Metasurfaces for Controlling Disordered Sound Fields

Guancong Ma

Department of Physics, Hong Kong Baptist University, Kowloon Tong, Hong Kong, China

phgcma@hkbu.edu.hk

Abstract: Disordered sound fields are ubiquitous in our daily life – the sound in a room undergoes multiple scattering form such a sound field. Here, we show that reconfigurable acoustic metasurfaces can control the disordered sound for various advanced functionalities, including the generation of quiet zones, and the elimination of cross-talks.

Wavefield shaping in disordered systems has attracted significant interest in recent years. Reverberant environments are examples of such systems in acoustics that we experience every day. These sound fields are essentially random fields that are difficult to control. Here, we show that reconfigurable acoustic metasurfaces can effectively control reverberating sound fields by actively altering the reflective phases, thereby re-scaping the sound field. The acoustic metasurface we employed has 200 units of electrically adjustable Helmholtz resonator, each capable of producing reflected waves with two different choices of phase factors across a broad frequency range of 1000-1700 Hz. They are individually controlled by e a variety of feedback-driven optimization schemes. We will also discuss the limitations and possible paths for further improving the performance of metasurfaces. Our works show that acoustic metasurfaces can bring new solutions to room acoustics and open new directions for acoustic engineering.

Acknowledgments. This work was supported by the National Natural Science Foundation of China (11922416) and the Hong Kong Research Grants Council (RFS2223-2S01, 12302420, 12300419, 12301822).

Enhanced Photogating Gain in Scalable MoS_2 Plasmonic Photodetectors *via* Resonant Metasurfaces

Yu-Jung Lu[1,2*]
[1]Research Center for Applied Sciences, Academia Sinica, Taipei 11529, Taiwan
[2]Department of Physics, National Taiwan University, Taipei 10617, Taiwan

*E-mail: yujunglu@gate.sinica.edu.tw

Abstract

Monolayer transition metal dichalcogenides (TMDs) are promising materials for electronics and photonics at highly scaled lateral dimensions. Despite extensive research efforts, optimizing scalable monolayer devices has been an ongoing challenge. Their low photon absorption poses a challenge for high-performance optoelectronic devices. We present plasmonic phototransistors (photoFETs) that integrate monolayer molybdenum disulfide (MoS_2) with plasmonic metasurfaces [1-2], such as Ag, Bi, HfN, and TiN. These plasmonic photoFETs exhibit a significant enhancement in photocurrent compared to pristine 2D photoFETs, enabling high-performance devices with ultrahigh photoresponsivity. The enhancement is achieved through plasmonic nanostructures that enhance light absorption [1-4], photo-carrier generation, photo-gating, and hot-carrier transfer rates. Here, we introduce a novel demonstration of utilizing scalable nitride-based resonant plasmonic metasurfaces, with a work function of 4.7 eV, to dramatically augment the light-matter interaction in wafer-scale monolayer single-crystal MoS_2 photodetectors. Our pioneering approach has achieved not only excellent responsivity but also an impressive detectivity of 2.58×10^{12} Jones *via* the *plasmon-enhanced photogating effect*.

A salient feature of this work is the introduction of a novel concept: the giant photocurrent enhancement propelled by the local-electromagnetic-field enhanced photogating effect. This leads to a substantial 190-fold photocurrent boost compared to conventional MoS_2 photodetectors. Moreover, our uniquely designed plasmonic photodetectors consistently retain their performance with minimal degradation. Complementing our experimental results, we have incorporated comprehensive theoretical simulations that elucidate the foundational mechanisms behind scalable 2D plasmonic photodetectors. Perhaps most exciting is the broad applicability of our findings. The integration of 2D semiconductors with HfN plasmonic platforms is not only fully compatible with existing Si CMOS processes but is also scalable across wafer dimensions. This paves the way for an expansive range of applications, spanning imaging, sensing, and optical communications, heralding a new era for photodetection technology.

Reference

[1] Hao-Yu Lan, Yu-Hung Hsieh, Zong-Yi Chiao, Deep Jariwala, Min-Hsiung Shih, Ta-Jen Yen, Ortwin Hess, **Yu-Jung Lu***, Gate-Tunable Plasmon-Enhanced Photodetection in a Monolayer MoS_2 Phototransistor with Ultrahigh Photoresponsivity. *Nano Lett.* 21, 3083–3091 (2021)

[2] Ching-Han Mao, Chin-Chien Chung, Wei-Ren Syong, Yu-Chi Yao, Kai-Yuan Hsiao, Ming-Yen Lu, Mario Hofmann, Ya-Ping Hsieh, **Yu-Jung Lu**, and Ta-Jen Yen*. Bifunctional Semimetal as a Plasmonic Resonator and Ohmic Contact for an Ultrasensitive MoS_2 Photodetector. *ACS Photonics* 10, 1495–1503 (2023)

[3] Z-Y Chiao, Y-C Chen, J-W Chen, Y-C Chu, J-W Yang, T-Y Peng, W-R Syong, H W H. Lee, S-W Chu, and **Y-J Lu***, Full-Color Generation Enabled by Refractory Plasmonic Crystals. *Nanophotonics* 11, 2891-2899 (2022)

[4] Y-H Hsieh, B-W Hsu, K-N Peng, K-W Lee, C W Chu, S-W Chang, H-W Lin*, T-J Yen*, and **Y-J Lu***, Perovskite Quantum Dot Lasing in a Gap-Plasmon Nanocavity with Ultralow Threshold, *ACS Nano* 14, 11670 (2020).

Monocular metasurface camera for single-shot multi-dimensional imaging

Yuanmu Yang[1*]

[1] Department of Precision Instrument, Tsinghua University, China
[*]corresponding author: ymyang@tsinghua.edu.cn

Abstract: I will present our group's recent effort to replace conventional camera lenses with metalenses. We aim to build compact camera systems that can capture multi-dimensional light field information of a target scene in a single shot under ambient illumination conditions.

Conventional camera systems can only detect light intensity while losing important information about the target scene, including depth, polarization, and spectrum. In order to further obtain the multi-dimensional light-field information of the target object, it is often required to use bulky and expensive instruments. Metasurface is composed of an array of optical antennas that can manipulate the amplitude, phase, polarization, and spectrum of light at the subwavelength scale. By replacing conventional diffractive of refractive elements with metasurfaces in imaging systems, one may be able to build optical sensors for single-shot multi-dimensional imaging with low size, weight, power, and cost. Here, I will present our group's recent effort to replace conventional camera lenses with metalenses. By leveraging the unique capability of metasurface to tailor the vectorial field of light, in combination with an advanced image retrieval algorithm, we aim to build compact camera systems that can capture multi-dimensional light field information of a target scene in a single shot under ambient illumination conditions. Specifically, I will show how we use a polarization-multiplexed metalens for imaging through turbid water. Recently, we further extended such a concept to build a monocular camera that can capture a 4D image, including 2D all-in-focus intensity, depth, and polarization of a target scene in a single shot. The miniaturized 3D camera module may be seamlessly integrated with smartphones, AR/VR headsets, and robots for a variety of applications, including face and gesture recognition, spatial localization and mapping, and collision avoidance.

References

1. Z. Shen, F. Zhao, C. Jin, S. Wang, L. Cao, Y. Yang "Monocular metasurface camera for passive single-shot 4D imaging". Nature Communications 14, 1035 (2023)
2. L. Li, S. Wang, F. Zhao, Y. Zhang, S. Wen, H. Chai, Y. Gao, W. Wang, L. Cao, Y. Yang "Single-shot deterministic complex amplitude imaging with a single-layer metalens". Science Advances 10, eadl0501 (2024)

Active and Nonlinear Metasurfaces with the Generation and Relaxation of Plasmonically Induced Hot Carriers

W. Cai[1*]

[1]School of Electrical and Computer Engineering, Georgia Institute of Technology, 777 Atlantic Drive NW, Atlanta, GA 30332-0250, USA

[*]corresponding author: wcai@gatech.edu

Abstract: The generation, transport, and relaxation of hot electrons in plasmonic metasurfaces provide a novel route to active and nonlinear optical effects with ultrafast responses. Here, we present the exploitation of hot carrier dynamics for diverse applications in all-optical modulation, nonlinear optical signal generation, and photoinduced optical chirality.

Plasmonic metasurfaces consisting of nanostructured metals and electron-accepting materials serve as an enormously fruitful arena for the investigation and utilization of optically excited energetic carriers. The coherent coupling of electromagnetic radiations to plasmons creates a nonequilibrium distribution of electrons at an elevated temperature, known as hot electrons. The dynamics of such hot carriers has been wide employed for various applications, ranging from the detection of sub-bandgap photons in semiconductors to the production of hydrogen gas via photocatalytic processes.

The generation, transfer, and relaxation of hot carriers also provide a novel route to active nonlinear optical effects. For example, the optical Kerr nonlinearity of plasmonic metals provides enticing prospects for developing reconfigurable and ultracompact all-optical modulators. Although enhanced nonlinear responses of metals are known to enable the optical control of light, the intrinsically slow relaxation dynamics of photoexcited carriers, primarily governed by electron-phonon interactions, impedes sub-picosecond modulation speeds. In this talk, we present femtosecond all-optical modulation in plasmonic systems via the activation of relaxation pathways for hot-electrons at the interface of metals and electron acceptor materials. We show that the relaxation kinetics and the optical nonlinearity can be tuned by leveraging the spectral response of the plasmonic system in the linear regime. Our findings introduce a generic scheme for achieving sub-picosecond modulation speeds in plasmonic systems, suitable for the ultrafast control of the intensity, polarization, and phase of light upon exchange of energetic hot carriers.

The dynamics of hot carriers in plasmonic system is further exploited for the creation of optically induced second-order nonlinear materials. Second-order optical processes are pivotal to the active modulation and wave mixing of light waves. The inversion symmetry in most materials, however, prevents achieving a bulk chi-2 effect, thereby limiting the portfolio of second-order nonlinear materials. We propose and demonstrate ultrafast conversion of a statically-passive dielectric to a transient second-order nonlinear medium upon the generation and transfer of plasmonically induced hot electrons. Triggered by an optical switching signal, the amorphous dielectric with vanishing intrinsic chi-2 develops dynamically tunable second-order nonlinear responses, which can be leveraged to address the critical need for all-optical control of second-order nonlinearities in nanophotonic systems.

Ultrafast optical switching in plasmonic platforms relies on the third-order Kerr nonlinearity, which is tightly linked to the dynamics of hot carriers in nanostructured metals. Although extensively utilized, a fundamental understanding on the dependence of the switching dynamics upon optical resonances has often been overlooked. We employ all-optical control of resonance bands in a hybrid photonic-plasmonic crystal as an empowering technique for probing the resonance-dependent switching dynamics upon hot carrier formation. Differential optical spectral measurements reveal an enhanced switching performance near the anti-crossing point arising from strong coupling between local and nonlocal resonance modes. Furthermore, entangled with hot-carrier dynamics, the nonlinear correspondence between optical resonances and refractive index change results in tailorable dispersion of recovery speeds which can notably deviate from the characteristic lifetime of hot carriers.

We further exploit hot-carrier dynamics to facilitate the creation of handedness-selectable transient chirality in achiral optical metasurfaces. As much as chiral metasurfaces are significant in stereochemistry and polarization control, tunable chiroptical response is important for their dynamic counterparts. A single metasurface device with invertible chiral states can selectively harness or manipulate both handedness of circularly polarized light upon demand, where in fact chiral inversion in molecules is an active research field. Tactics for chirality switching can be classified into geometry modification and refractive index tuning. However, these generally confront slow modulation speed or restrained refractive index tuning effects in the visible regime with forbidden 'true' inversion. Here, we reconfigure the 'optical' geometry through inhomogeneous spatiotemporal distribution of hot carriers as a breakthrough, transforming a plasmonic achiral metasurface into an ultrafast transient chiral medium with near-perfectly-invertible handedness in the visible. The photoinduced chirality relaxes through the fast spatial diffusion process of electron temperature compared to electron-phonon relaxation, empowering hot-carrier-based devices to be particularly suitable for ultrafast chiroptics. Our comprehensive understanding provides new protocols for optically characterizing hot-carrier dynamics and optimizing all-optical light modulation and chirality manipulation for operations across the visible spectrum.

References

1. Taghinejad, M., H. Taghinejad, Z. Xu, K.-T. Lee, S. P. Rodrigues, J. Yan, A. Adibi, T. Lian and W. Cai, "Ultrafast control of phase and polarization of light expedited by hot-electron transfer," Nano Lett., Vol. 18, No. 9, 5544-5551, 2018.
2. Taghinejad, M., Z. Xu, K.-T. Lee, T. Lian and W. Cai, "Transient second-order nonlinear media: Breaking the spatial symmetry in the time domain via hot-electron transfer," Phys. Rev. Lett., Vol. 124, No. 1, 013901, 2020.
3. Kim, A. S., M. Taghinejad, A. Goswami, L. Raju, K.-T. Lee, and W. Cai, "Tailored dispersion of spectro-temporal dynamics in hot-carrier plasmonics," Adv. Sci., Vol. 10, No. 8, 2205434, 2023.
4. Kim, A. S., A. Goswami, M. Taghinejad, and W. Cai, "Phototransformation of achiral metasurfaces into handedness-selectable transient chiral media," in press, 2024.

Dirac Mass Gap Induced by Optical Gain and Loss

Y. D. Chong[1*], Letian Yu[1], Haoran Xue[2], Yun Yong Terh[1], Ruixiang Guo[1], Eng Aik Chan[1], Cesare Soci[1], and Baile Zhang[1]

[1]Nanyang Technological University, Singapore
[2]Chinese University of Hong Kong, Hong Kong
[*]corresponding author: yidong@ntu.edu.sg

Abstract: We introduce a non-Hermitian lattice model whose quasiparticle excitations are governed by the Dirac equation. Unusually, this non-Hermitian system has bands with real energies and orthogonal eigenstates. The physical implications of the gain/loss induced Dirac mass gap are explored using a synthetic lattice in a coupled fiber loop experiment.

The Dirac equation, which first formulated to describe relativistic quantum mechanical electrons, also governs quasiparticle excitations in certain periodic lattices[1]. Synthetic metamaterials are useful for exploring this area of physics, as they can be flexibly engineered with a variety of properties. For example, they can deliberately incorporate gain and/or loss in order to violate the Hermitian symmetry of the Hamiltonian, leading to interesting situations such as unbroken parity/time reversal (PT) symmetry, which allows for the existence of stable non-Hermitian quasiparticles that do not blow up or decay in time.[2]

In the context of the Dirac equation, non-Hermitian perturbations usually create exceptional points (EPs) or rings of EPs,[3] rather than opening a mass gap. Quasiparticles governed by EPs typically behave very differently from Dirac particles; for instance, the dynamics is usually unstable since the band energies are not real everywhere in the vicinity of an EP.

Recently, we have formulated a non-Hermitian lattice symmetry we call “semi-Hermiticity”, which allows non-Hermitian systems to retain key features of Dirac quasiparticles.[4] A semi-Hermitian Hamiltonian can host bands with real energies, with eigenstates that are pairwise orthogonal. Hence, the non-Hermitian bandstructure can be described by an effective Dirac Hamiltonian, with a *real* mass gap that can be tuned via gain/loss.

To explore this, we implemented a looped optical fiber experiment[5] (Fig. 1**a**) hosting a synthetic lattice with the semi-Hermitian symmetry (Fig. 1**b**). As the gain and loss are adjusted, the non-Hermitian quasiparticles acquire a Dirac mass (Fig. 1**c**), which is observed as a transition from conical to non-conical diffraction (Fig. 1**d**).

In Hermitian systems, it is well known that the sign of the Dirac mass affects the Chern topology of the participating bands. We show that the Dirac mass in our semi-Hermitian lattice plays a similar role, through the observation of a gain/loss-induced topological boundary state (Fig. 1**e**). We have also performed experiments to explore other aspects of these non-Hermtian Dirac quasiparticles. For instance, they can exhibit an anomalous variant of Klein tunneling,[6] whereby a quasiparticle incident on a potential step is strongly transmitted (as in conventional Klein tunneling), but with the transmitted flux amplified or damped by the interface itself (Fig. 1**d**).

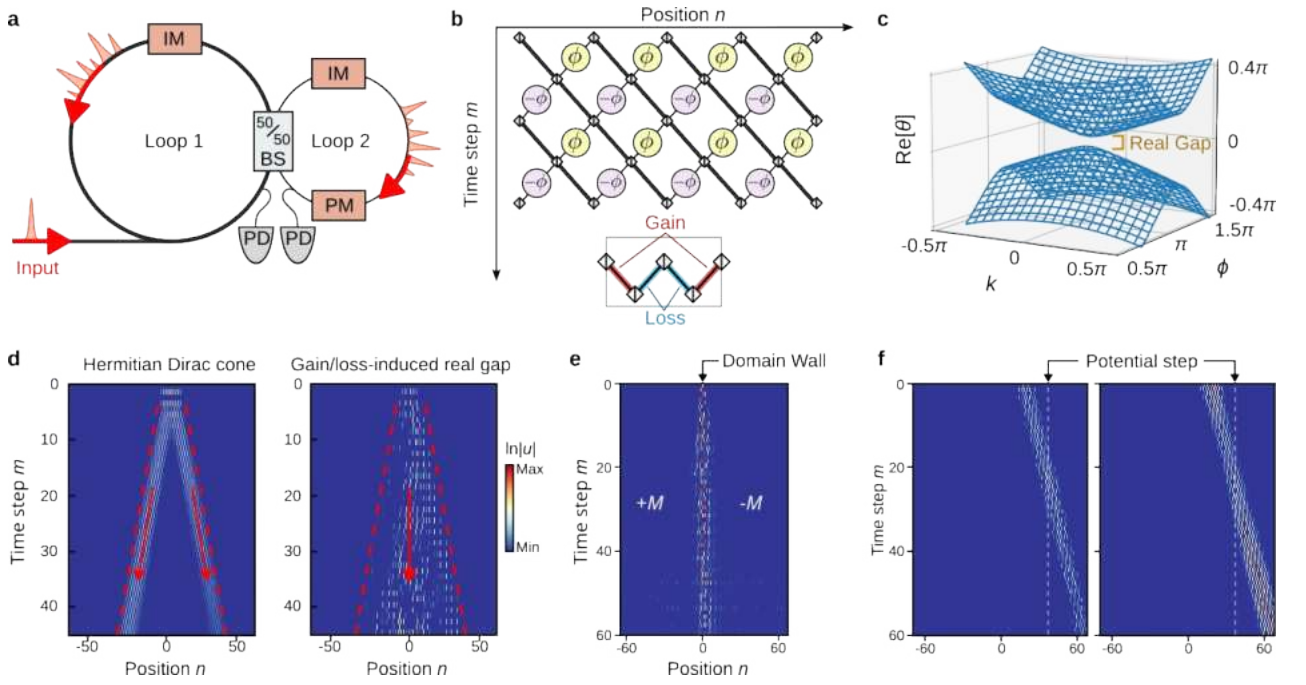


Figure 1. **a**, Schematic of the experiment. Two optical fiber loops are coupled by a 50/50 beamsplitter (BS). Each loop has an intensity modulator (IM), and the short loop also has a phase modulator (PM). The pulses are measured by photodetectors (PD). **b**, In the synthetic lattice, the index *n* in each pulse train maps to position, and the round trip number *m* maps to time. The pulses are modulated by a phase shift $\pm\phi$ and gain/loss. **c**, Floquet bandstructure featuring a real Dirac mass *M*. **d**, Observation of conical diffraction (left), and its disappearance when the gain/loss and hence the Dirac mass are nonzero (right). **e**, Observation of a topological boundary state between domains of opposite *M*. **f**, Observation of Klein tunneling at a potential step (left), and an anomalous variant that does not conserve flux at the boundary.

This work was supported by the Singapore Ministry of Education (MOE) Tier 1 Grant No. RG148/20, and by the National Research Foundation (NRF), Singapore under Competitive Research Programme NRF-CRP23-2019-0005 and NRF-CRP23-2019-0007, NRF Investigatorship NRF-NRFI08-2022-0001, and the Quantum Engineering Programme grant number NRF2021-QEP2-01-P01.

References

1. Bansil, A., Lin, H., and Das, T., "Colloquium: Topological band theory", Rev. Mod. Phys., Vol. 88, No. 2, 021004, 2016.
2. Bender, C. M., "Making sense of non-Hermitian Hamiltonians", Rep. Prog. Phys., Vol. 70, No. 6, 947-1018, 2007.
3. Cerjan, A., *et al.*, "Experimental realization of a Weyl exceptional ring", Nat. Photon., Vol. 13, 623-628, 2019.
4. Xue, H. and Wang, Q. and Zhang, B. and Chong, Y. D., "Non-Hermitian Dirac Cones", Phys. Rev. Lett., Vol. 124, No. 23, 236403 (2020).
5. Regensburger, A., *et al.*, "Photon Propagation in a Discrete Fiber Network: An Interplay of Coherence and Losses", Phys. Rev. Lett., Vol. 107, No. 23, 233902, 2011.
6. Terh, Y. Y., Banerjee, R., Xue, H., and Chong, Y. D., "Scattering dynamics and boundary states of a non-Hermitian Dirac equation", Phys. Rev. B, Vol. 108, No. 4, 045419, 2023.

Third-harmonic generation in near-zero index heterogeneous nanostructures

M. Silvestri[1], A. Sahoo[1], L. Assogna[1], P. Benassi[1,2], C. Ferrante[2], A. Ciattoni[2], and A. Marini[1,2*]

[1]Department of Physical and Chemical Sciences, University of L'Aquila, Via Vetoio, 67100 L'Aquila, Italy
[2]Consiglio Nazionale delle Ricerche, CNR-SPIN, Via Vetoio 10, 67100 L'Aquila, Italy
[*]corresponding author: andrea.marini@univaq.it

Abstract: We theoretically model third-harmonic generation produced by collision-driven nonlinear electron dynamics in near-zero index heterogeneous nanostructures. We focus on a sodium-aluminum bilayer and model the harmonic generation process to explore its potential for the development of compact extreme ultraviolet radiation sources and for integrated spectroscopy schemes.

Nonlinear (NL) radiation-matter interactions give rise to many physical phenomena particularly relevant to quantum mechanical processes and offer a promising platform to devise compact ultraviolet (UV) radiation sources [1]. Harmonic generation (HG) is one of the main nonlinear effects amplified by photonic materials with low dielectric permittivity, also known as epsilon near zero (ENZ) media. These materials enhance coherent NL radiation-matter interactions thanks to their natural ability to bypass phase-matching requirements, thus playing a crucial role in several NL phenomena, e.g., optical switching [2]. Currently, ENZ media are adopted to enhance NL optical effects, particularly in the near-infrared part of the spectrum, where doped semiconductors, oxides, and nitrides display this behavior. Poor materials show marked ENZ features in the UV that are promising for guidance [3] and for resonant third-harmonic generation (THG) in thin films, and for manipulation and guidance of extreme-UV (XUV) radiation.

Here, we investigate the potential of two different setups: the first one involves a sodium (Na) – based thin films [4], and the second one a sodium-aluminum (Na-Al) bilayer, both with nanometer-size thicknesses. We focus our discussion mainly on the latter configuration, studying THG produced by out-of-equilibrium (OOE) electron dynamics. To model NL electron dynamics in such heterogeneous nanostructures, we consider the Fokker-Planck-Landau (FPL) theoretical framework, obtaining a set of hydrodynamical equations (HDEs) by solving analytically the Landau collisional integral in the weak coupling limit [5]. Thanks to a perturbative approach, we derive an analytical expression for the dependence over the pump field angular frequency ω of the collision-driven THG NL-susceptibility $\chi_{\mathrm{coll}}^{(3\omega)}$. Moreover, by modelling the THG radiation process accounting multiple reflections of forward (FW) and backward (BW) waves, we obtain the pump field distribution within the thin films in the undepleted pump approximation. In Fig. 1a, where we depict the dependence of the FW intensity of the THG signal over the pump wavelength λ and incidence angle θ, one can see that the THG process exhibits a double resonance for transverse magnetic (TM) pump excitation $\lambda_{\mathrm{THG}} = \lambda/3$ in the ENZ regime due to the coupling of the pump field enhancement and the radiation of the microscopic dipoles. Conversely, for transverse electric (TE) pump excitation, see Fig. 1e, we observe THG enhancement due to the excitation of Fabry-Perot resonances. Finally, we note that for specific angle conditions, it is possible to excite surface plasmon polatitons (SPPs) at the Na-Al interface thanks to attenuated total internal reflection (ATIR), see Fig. 1a, obtaining a THG enhancement factor of 7 orders to magnitude, suggesting the potential of NZI heterogeneous nanostructure devices in the development of integrated XUV source.

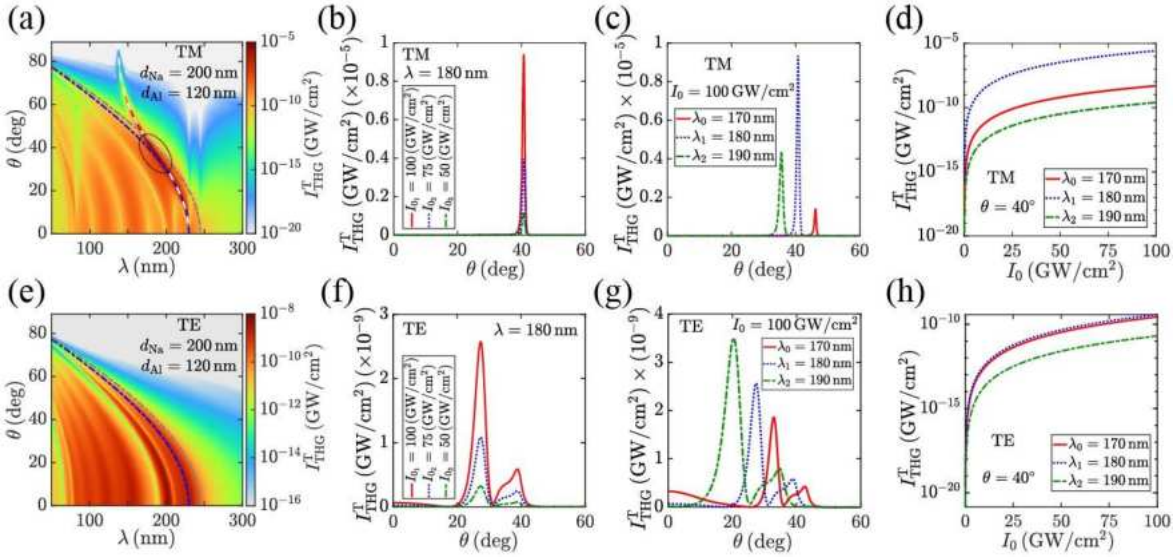


Fig. 1. **(a,e)** Dependence of the FW intensitiy of the THG signal I^T_{THG} over the pump wavelength λ and incidence angle θ for fixed pump intensity $I_0 = 100$ GW/cm^2. The dashed white curve in **(a)** indicates the SPP dispersion curve, while the dot-dashed grey and blue curves indicate the Al and Na NZI dispersion curves, respectively for λ_{THG} and λ. **(b,c,f,g)** Dependence of I^T_{THG} over the pump incidence angle for **(b,f)** fixed pump wavelength λ =180 nm and several intensities $I_0 = 50$, 75, 100 GW/cm^2, and **(c,g)** fixed pump intensities $I_0 = 100$ GW/cm^2 and several wavelengths λ = 170, 180, 190 nm [highlighted by the black circled area in (a)]. **(d,h)** Dependence of I^T_{THG} over the pump intensity I_0 for fixed incidence angle and several wavelengths λ = 170, 180, 190 nm. All plots are obtained for $d_{Na} = 200$ nm and $d_{Al} = 120$ nm and refer to either **(a-d)** TM or **(e-h)** TE polarisation of the impinging pump field.

References

1. Semmlinger, M., M. Zhang, M. L. Tseng, T.-T. Huang, J. Yang, D. P. Tsai, P. Nordlander, and N. J. Halas, "Generating Third Harmonic Vacuum Ultraviolet Ligth with a TiO2 Metasurface," Nano Lett., Vol. 19, No. 12, 8972-8978, 2019.
2. Agryropoulos, C., P.-Y. Chen, G. D'Aguanno, N. Engheta, and A. Alù, "Boosting optical nonlinearities in ε-near-zero plasmonic channels," Phys. Rev. B, Vol. 85, No. 4, 045129, 2012
3. Assogna, L., C. Ferrante, A. Ciattoni and A. Marini, "XUV plasmonic waveguides by near-zero index heterostructures," J. Phys. Photonics Vol. 5, 045001, 2023.
4. Silvestri, M., A. Sahoo, L. Assogna, P. Benassi, C. Ferrante, A. Ciattoni, and A. Marini, "Resonant third-harmonic generation driven by out-of-equilibrium electron dynamics in sodium-based near-zero index thin films," Nanophotonics, 0743, 2024. https://doi.org/10.1515/nanoph-2023-0743
5. Marini, A., A. Ciattoni, and C. Conti, "Out-of-equilibrium electron dynamics of silver driven by ultrafast electromagnetic fields – a novel hydrodynamical approach," Faraday Discuss., Vol. 214, 235-243, 2019.

Manipulation of Electron Beams by Laguerre-Gaussian Modes

Yung-Chiang Lan[1,*] and Ming-Chieh Lin[2]

[1] *Department of Photonics, National Cheng Kung University, Taiwan*
[2] *Department of Electrical and Biomedical Engineering, Hanyang University, Korea*
[*]corresponding author: lanyc@mail.ncku.edu.tw

Abstract: Manipulation of electron beam by Laguerre-Gaussian (LG) modes is investigated using finite-difference time-domain particle-in-cell (FDTD-PIC) simulations. The collective and individual behaviors of macro-electrons are examined. Dependence of electron beam size and current on electric field amplitude and gradient of LG modes are also explored.

Light can have spin angular momentum (SAM) and orbital angular momentum (OAM) [1]. SAM is associated with right- and left-circularly polarized lights. The light with OAM indicates that it has an azimuthal phase dependence of exp(-imφ) and independent of the polarized state (m is an integer number and its sign indicates the handedness with respect to light's propagation direction). The cylindrical Laguerre-Gaussian (LG) laser modes have an azimuthal phase dependence and carry OAM. Recently, microwave OAM beams are generated by using dielectric and metasurface antenna [2]. On the other hand, the electron pulse can obtain OAM to form electron vortices through OAM transfer from photons to electrons [3].

Acceleration of an electron pulse by an LG laser pulse was also proposed and investigated very recently [4]. In this work, modulation of electron beam by LG modes is investigated by particle-in-cell finite-difference time-domain simulations (PIC-FDTD) [5]. An electron beam is irradiated by focused circular-polarized LG modes with different OAMs at microwave regime (12 GHz). The collective and individual behaviors of macro-electrons will be investigated. Dependence of electron beam size and current on electric field amplitude and gradient of LG modes are also explored.

Figures 1(a) and 1(b) show the simulated E_z-field phase profiles of focused circular-polarized LG modes with OAM (m) equal to = +1 and +2, respectively. Here the handedness is defined along the direction of wave propagation (i.e. +x direction). Both Figs.1(a) and 1(b) agree with the typical phase patterns of LG modes in the literature. Furthermore, they have a phase singularity on the beam axis with zero field intensities.

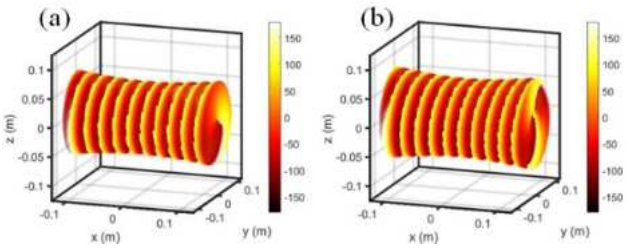


Fig. 1: Simulated E_z-field phase profiles of focused circular-polarized LG modes with m = +1 and +2.

The simulated azimuthal velocity profiles of macro-particles display 3-D spiral patterns with the number of strands equal to sum of state number of SAM (s) and OAM (m) of LG modes. These spiral patterns move with

the electron beams like a wave. The macro-particles also exhibit both orbit revolution and small rotation motion (Figs.2). The former is very similar to the gyromotion of electrons with applying an external magnetic field. The rotation motion has the same frequency as the LG mode while the orbit revolution frequency is far lower. Both the size and current of electron beams at the focal plane decrease with the increase of the electric field amplitude and gradient. This work can provide a new type of electron beams manipulated by LG waves only.

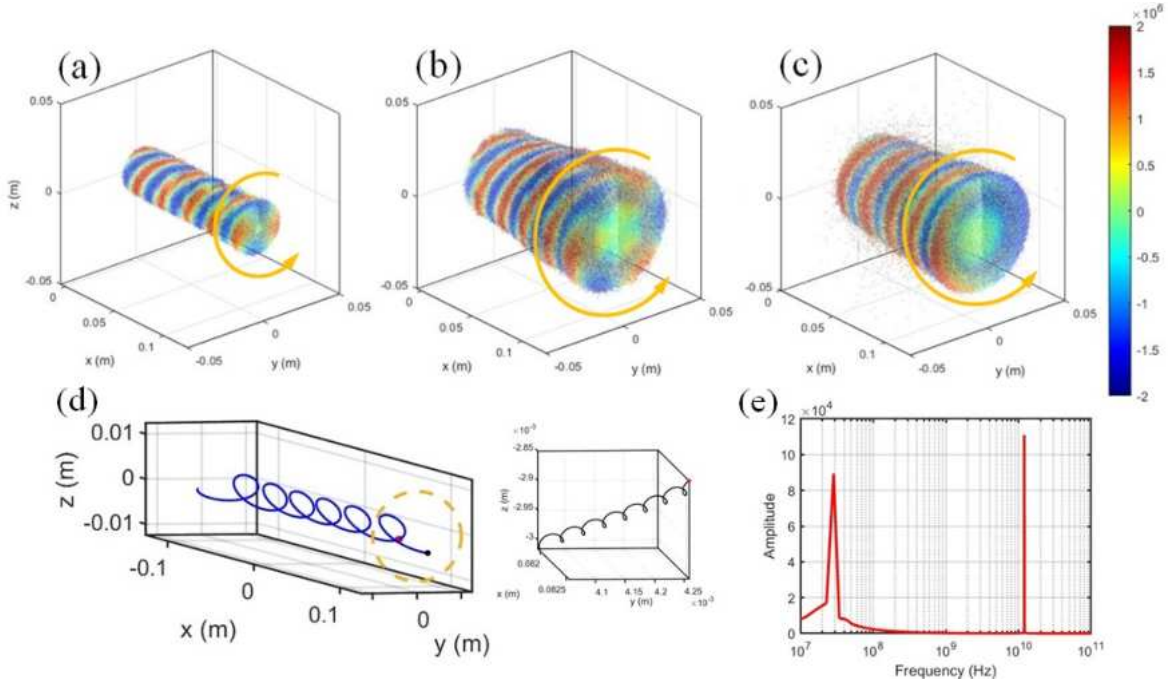


Fig. 2: (a)-(c) Simulated instant azimuthal-velocity profiles of macro-particles for LG modes with (*s*, *m*) equal to (1, 1), (1,2), and (-1, 2), respectively. (d) Simulated trajectory of a macro-particle. (e) FFT spectrum of velocity of the macro-particle.

This work was partially supported by the National Science and Technology Council of Taiwan (No. 112-2112-M-006-002-), the Hanyang University (No. HY-201400000002393), the National Research Foundation of Korea (No. 2015R1D1A1A01061017), and the Alexander von Humboldt Foundation of Germany.

References

1. M. Padgett, J. Courtial, and L. Allen, “Light’s Orbital Angular Momentum,” Phys. Today 57, 35–40 (2004).
2. J. Xu, Y. Hao, K. Bi, R. Zhang, S. Huang, and J. Zhou, “Microwave Orbital Angular Momentum Beam Generation Based on Circularly Polarized Metasurface Antenna Array,” Eng. Sci. 6, 30–35 (2019).
3. J. Verbeeck, H. Tian, and P. Schattschneider, “Production and application of electron vortex beams,” Nature 467, 301-304 (2010).
4. H. Song, K. H. Pae, J. W., J. Song, S. Lee, C. M. Kim, C. M. Ryu, W. Bang, and C. H. Nam, “Characteristics of electron beams accelerated by parallel and antiparallel circularly polarized Laguerre–Gaussian laser pulses,” Appl. Phys. B 129, 56 (2023).
5. C. Nieter and J. R. Cary, “VORPAL: a versatile plasma simulation code,” J. Comput. Phys. 196, 448-473 (2003). No. 10, 1064–1076, 1986.

Methods for characterization of wafer scale SERS substrates

M. Singer[1*], R. Priore[2], and L. Ye[2]

[1]Thorlabs Inc, USA
[2]Thorlabs Spectral Works, USA
[*]Corresponding author: msinger@thorlabs.com

Abstract: *In this work, we demonstrate a textured SiO_2 substrate with Au plasmonic layer that can be fabricated on a standard 4" wafer. The resulting SERS substrate is characterized at the wafer scale using automated tools, paving the way for mass produced and consistent SERS chips.*

Surface enhanced Raman spectroscopy (SERS) is an established method for biosensing of low concentration or fragile materials. However, some challenges remain with implementing SERS devices in commercial applications, such as chip-to-chip variability, batch-to-batch variability, and limited shelf life to name a few [1]. While some commercial SERS chips show promising attributes, such as low limit of detection (LOD) and ease of fabrication [2], we have yet to find a commercial SERS substrate that can simultaneously meet all requirements for a high performing commercial SERS substrate. Furthermore, the careful and automated characterization of the prerequisite specifications is an important step towards commercialization and widespread adoption of this technology.

In this work, we demonstrate the fabrication of a SERS substrate that simultaneously meets many of the aforementioned requirements for a high performing SERS chip. Importantly, we detail the characterization performed to provide this chip to the public. To achieve this result, we employ a lithography free, wafer-scale fabrication method designed to create nanopillars coated in Au (Fig 1a). The Au-coated pillars act like a metal insulator metal (MIM) absorbing structure in the vertical direction [3]. In this case, the incident light is absorbed by the Au and a surface plasmon polariton (SPP) propagates along the height of the pillar (Fig 1b). The varying width of the pillar allows for light trapping over a broad wavelength range. Specifically, at the Raman excitation wavelength of 785 nm, the field enhancement of trapped light is approximately 10^4. While this field enhancement value is modest and other architectures are capable of higher values [4], we believe that our low-cost batch fabrication process, and wafer-scale-compatible Relative Standard Deviation (RSD) characterization technique yields an acceptable tradeoff against ultimate performance.

To characterize our SERS substrates, we developed an automated system consisting of the Thorlabs laser driver, RSBR1 Raman spectrometer, and automated XY stage as shown in Fig 1c. This spectrometer uses a 785 nm excitation wavelength and a defocused beam of 1 mm diameter paired with a coded input aperture to increase throughput while maintaining spectral resolution [5]. For Raman measurements, we drop cast twelve, 2.5 µL droplets of 1,2-Di(4-pyridyl) ethylene (BPE) with a 100 mM concentration evenly across the 4" wafer. The automated stage acquires a measurement at 2 mm intervals across the entire wafer. Due to uneven drying effects, we see clear signs of overlapped droplets and coffee rings. However, these imperfections have a minor impact on the overall Raman signal as shown in Fig 1d. Additionally, upon comparing the brightfield image (Fig 1e) with the mapped Raman signature (Fig 1f), a correlation is evident between intensity of the Raman signature and the overlapping droplets. The measured RSD across the entire wafer is 16.7%. Further test results to be reported in the full publication include five wafers fabricated and tested for batch-to-batch RSD. Additionally, wafers were

fabricated and kept in an inert N_2 environment for six months and compared against wafers stored under ambient conditions. We observe minimal degradation in performance between the two sample sets. Finally, the limit of detection for the SERS substrate was found to be in the 100 nM range for an excitation intensity of 10 mW with a 5 s integration time. The presented research satisfies numerous requirements for a high performing SERS substrate including low cost, low RSD in chip-to-chip and batch-to-batch comparisons, long shelf life, and low LOD. Additionally, we demonstrate an automated and wafer-scale testing protocol, allowing for the consistent characterization of batch-fabricated SERS chips. This method will pave the way for commercial integration of low-cost elements for biosensing, security, and pharmaceutical applications.

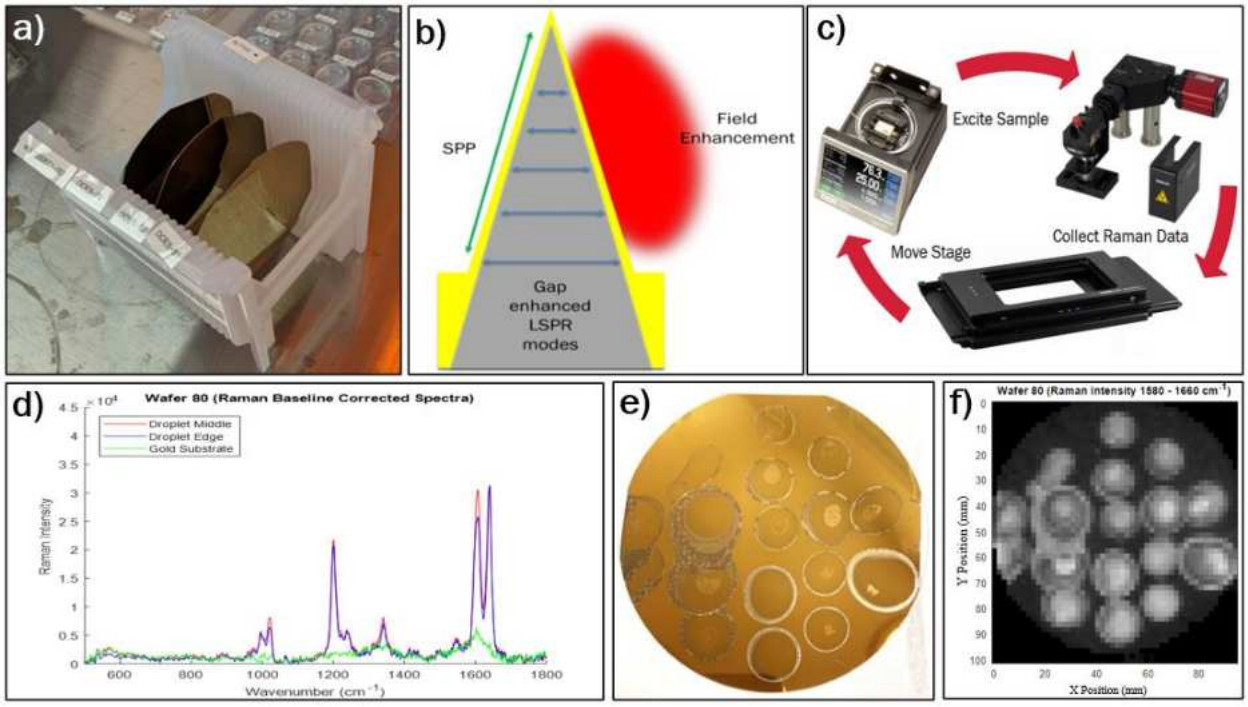


Figure 1. a) Image of a pilot run of 4" wafers post fabrication. b) Schematic of the physical mechanism for light absorption and field enhancement. c) Process flow of our automated Raman measurement system for wafer mapping. d) Raman spectra of BPE molecules at the center, edge, and off droplet. e) Brightfield image of a 4-inch wafer with 12 BPE droplets. f) Mapped Raman intensity of the same 4" wafer indicating the droplet placement.

This work has been funded by Thorlabs Inc. We disclose that the device described here will be released as a product on our website and Thorlabs and the authors stand to profit from its sale.

References

1. Natan, M. J. "Concluding Remarks Surface Enhanced Raman Scattering," Faraday Discuss, Vol. 132, 321–328, 2006.
2. Liu, Y. et al, "Evaluation of the Reliability of Six Commercial SERS Substrates," Plasmonics, Vol. 15, 743–752, 2020.
3. Zhang, N, "Ultrabroadband Metasurface for Efficient Light Trapping and Localization: A Universal Surface-Enhanced Raman Spectroscopy Substrate for "All" Excitation Wavelengths," Advanced Mat Interfaces, Vol. 2, No. 10, 2015
4. Srivastava, K. S. "Optimal Interparticle Gap for Ultrahigh Field Enhancement by LSP Excitation via ESPs and Confirmation Using SERS," The Journal of Physical Chemistry, Vol. 120, No. 50, 28735-28742, 2016
5. Gehm, E. M. "Static two-dimensional aperture coding for multimodal, multiplex spectroscopy," Applied Optics, Vol. 45, No. 13, 2965–2974, 2006.

Si Metasurfaces for DUV Plasmonics and Biomolecular Spectroscopy

Bo Ray Lee[1], Mao Feng Jiang[1], Pei Ying Ho[1], Kuan-Heng Chen[1], Jia Hua Lee[1], Min-Hsiung Shih[2], Der-Hsien Lien[1], Tzu-En Lin[3], Ray-Hua Horng[1,4], Ming Lun Tseng[1,4]*

[1]Institute of Electronics, National Yang Ming Chiao Tung University, Hsinchu 300, Taiwan
[2] Research Center for Applied Sciences, Academia Sinica, Taipei 11529, Taiwan
[3] Institute of Biomedical Engineering, National Yang Ming Chiao Tung University, Hsinchu 300, Taiwan
[4]Center for Integrated Electronics-Optics Technologies and Systems, National Yang Ming Chiao Tung University, Hsinchu 300, Taiwan
Corresponding author: mltseng@nycu.edu.tw

Abstract: We demonstrate plasmonic metasurfaces made of Si for DUV spectroscopy. Due to the photon-doping effect arising from the interband transition in the DUV, Si nanostructures show significant plasmonic resonance. The metasurface shows field enhancement at 266nm due to Fano-type resonance. Applications for enhancing fluorescence and Raman scattering will be discussed.

DUV light has been recently found to be very useful for advancing many critical techniques[1,2], including molecular spectroscopy, clinical imaging, and advanced nanolithography. Metasurfaces[3] can further improve those DUV applications by leveraging their capability to enhance electromagnetic fields at the nanoscale. Here, we demonstrate that Si can be used as a promising material platform for DUV plasmonics and metasurfaces. Under DUV illumination, a photon doping effect occurs in Si, inducing the transition of electrons into conduction bands and resulting in free electrons within the conduction band. This phenomenon enables plasmonic resonances in Si nanostructures. The transition of the Si's property from optically dielectric to optically metal can be observed in the spectrum of its dielectric constant. Figure la displays the real and imaginary parts of the dielectric constant (ε) of Si in the UV range. The real part of the dielectric constant turns to be negative below ~ 280nm, confirming its metal-like properties in the DUV. We introduced a tadpole-like unit cell in the metasurface design to enable strong field enhancement in Si metasurfaces. The field enhancement of the metasurface can be effectively tuned by tuning the expanding angle of the unit cell's tail. As a result, the metasurface shows a strong field enhancement up to 700-fold at 266 nm. To experimentally realize the metasurface, we performed electron beam lithography on Si chips. A 50-nm-thick resist PMMA layer coated on the Si chip was exposed by using an electron beam writer with an acceleration voltage of 50 keV. After development in MIBK/PA solvent, the pattern of the metasurface was transferred into the PMMA layer. The pattern was subsequently transferred into the Si chips by performing ICP-RIE to etch uncovered Si. Figure le shows the SEM image of the resulting sample. To characterize the sample's DUV properties, we built a micro-spectrometer consisting of a broadband UV-Vis light source for excitation and achromatic DUV objectives. Figure 1f shows the simulation and experimental spectra of the sample. The polarization direction Is shown in Figure Ic. The experimental spectrum shows a good agreement with the simulation sample. The discrepancy can be associated with the sample imperfection. The sample's robustness in various solvents commonly used in bioassays. The results confirm the metasurface's stability in those solvents. The possibility for using the reported metasurfaces for DUV Raman and fluorescence spectroscopy will be discussed.

In conclusion, we demonstrate a novel class of plasmonic metasurface in the DUV by leveraging the photo-doping effect of Si. The metasurface shows an ideal field enhancement in the DUV and proper robustness. This work paves a novel route toward novel nanophotonic devices and sensing chips in this critical range.

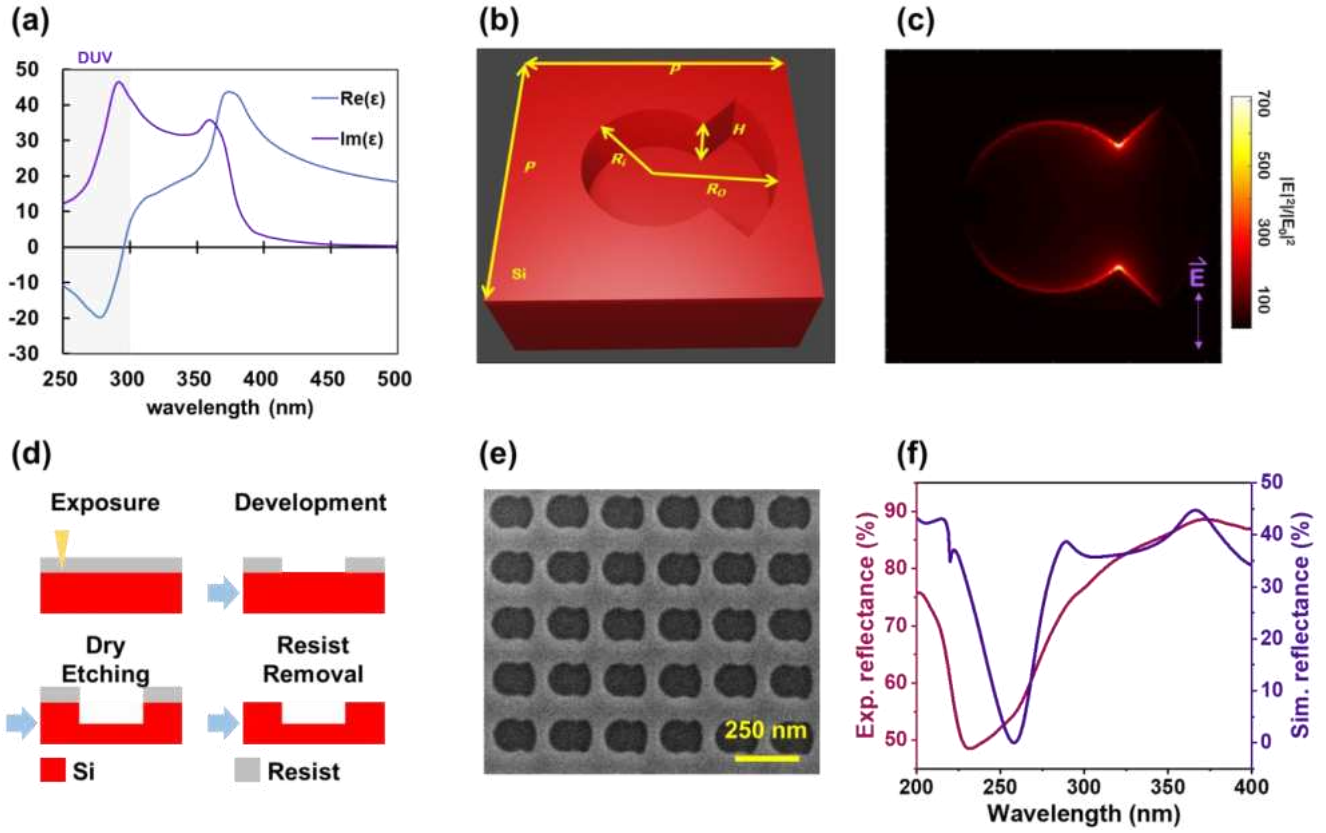


Figure 1. Si metasurface working in the DUV range. (a) dielectric constants (i.e., the relative permitivity) of Si. (b) Geometric parameters of the unit cell: inner radius (Ri): 50nm; outer radius (Ro): 100nm; structure angle (θ): 90°; thickness (H): 50nm. (c) Simulation of the electric enhancement profile at wavelength 266nm. (d) The fabrication process. (e) SEM image of the sample. (f) Simulation and experiment spectra of the metasurface.

Acknowledgements. The authors acknowledge support from the National Science and Technology Council ((NSTC 112-2636-M-A49-001)) in Taiwan, the Ministry of Education in Taiwan under the Yushan Fellow Program, and the Center for Integrated Electronics-Optics Technologies and Systems, National Yang Ming Chiao Tung University. This work was also supported by the Higher Education Sprout Project of National Yang Ming Chiao Tung University and the Ministry of Education (MOE), Taiwan.

References

1 Kumamoto, Y., Taguchi, A. & Kawata, S. Deep‐Ultraviolet Biomolecular Imaging and Analysis. *Advanced Optical Materials* **7**, 1801099, doi:10.1002/adom.201801099 (2018).

2 Bian, J. *et al.* Laser Transfer, Printing, and Assembly Techniques for Flexible Electronics. *Advanced Electronic Materials* **5**, doi:10.1002/aelm.201800900 (2019).

3 Tseng, M. L., Jahani, Y., Leitis, A. & Altug, H. Dielectric metasurfaces enabling advanced optical biosensors. *Acs Photonics* **8**, 47-60 (2020).

1.

Compact depth sensing and facial recognition from integration of metasurface and photonic-crystal surface-emitting laser

Yao-Wei Huang[1*]

[1] National Yang Ming Chiao Tung University, Taiwan
[*]corresponding author: ywh@nycu.edu.tw

Abstract: Our depth sensing and facial recognition technology leverages the innovative integration of metasurfaces and photonic-crystal surface-emitting lasers with structured light and monocular depth-sensing. Compared to existing approaches, our method projects a higher density of infrared dots across a wider field of view, offering substantial benefits for future spatial computing systems.

Structured light depth sensing technology employs dot projectors to generate pre-encoded spots onto objects. However, dot projectors based on vertical-cavity surface-emitting laser (VCSEL) arrays have several issues such as complex optical system, bulky diffractive optical elements (DOE) and collimator optics, and high-power consumption.

In this talk, I will report on our recent developments of novel depth sensing system that utilizes metasurface and photonic crystal surface-emitting laser (PCSEL), realizing facial recognition in monocular depth sensing [1,2]. Our single-shot system projects approximately 47,500 infrared spots from a compact 297-μm-dimention metasurface, which is lens-free and has an area 233 times smaller than the commercial DOE-based dot projector used in the Face ID on the iPhone. Our proposed system provides a measured field-of-view of 158°. Furthermore, the system reduces 5-10 times the amount of power compared to VCSEL-array based dot projectors.

Furthermore, we realize depth information and 3D point cloud by projecting light dots on statue *David* and calculating its depth map with the block matching algorithm. Our depth-sensing capabilities operate in real-time at approximately 15 frames per second. To quantitatively recognize the face is *David*, we train a facial recognition classifier by using OpenCV. As results, both of our approach and dop projection from iPhone yield accurate results in categorizing the facial features of *David* with similar score [2]. This demonstrates the potential of our approach for commercial applications, offering substantial benefits for future spatial computing systems.

References

1. Hsu, W.-C., Chang, C.-H., Hong, Y.-H., Kuo, H.-C., and Huang, Y.-W., “Compact structured light generation based on meta-hologram PCSEL integration,” Discover Nano, Vol. 18, 87, 2023.
2. Hsu, W.-C., Chang, C.-H., Hong, Y.-H., Kuo, H.-C., and Huang Y.-W., “Metasurface- and PCSEL-based structured light for monocular depth perception and facial recognition,” Nano Letters, Vol. 24, No. 5, 1808–1815, 2024.

Subradiant Plasmonic Cavities Facilitate Novel Polariton States for Vibrational Strong Coupling

J. E. Yim[1], Z. T. Brawley[1], and M. T. Sheldon[2*]

[1]Texas A&M University, College Station, Texas, USA
[2]University of California, Irvine, USA
[*]corresponding author: m.sheldon@uci.edu

Abstract: This study examines vibrational strong coupling (VSC) in subradiant plasmonic cavities, using polymethyl methacrylate to reveal unique spectral characteristics that contrast with the typical modal behavior. The findings demonstrate the manipulation of dark and bright states, enhancing understanding of polaritons.

Introduction- Vibrational strong coupling (VSC) involves the resonant exchange of energy between molecular vibrational modes and electromagnetic cavity modes, creating hybrid states known as polaritons. Traditional studies utilize bright cavities, which limit observation of non-radiative states [1,2]. We explore the use of subradiant, or "dark," plasmonic cavities which facilitate unique interactions due to their high quality factors and minimal interaction with free-space radiation.

Experimental Setup- Our experimental design employs nanostructured plasmonic surfaces capable of supporting subradiant modes, specifically designed to target the carbonyl stretch in polymethyl methacrylate (PMMA) films. The unique geometry of these surfaces allows for detailed study of both subradiant and radiant modes under varying conditions (Figure 1).

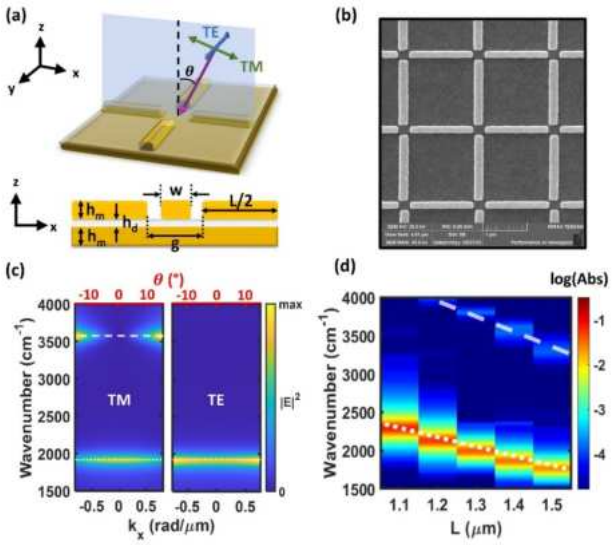
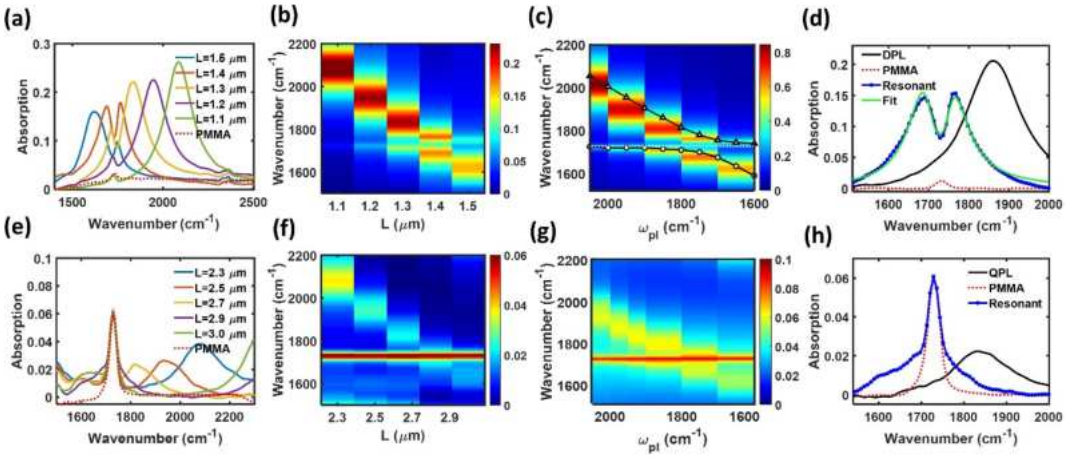


Fig. 1: Far-field behavior of Au nanorod arrays. (a) Schematic unit cell of the array composed of Au nanorods arranged with fourfold rotational symmetry. The electric field polarization of TE- and TM-polarized planewave as well as the corresponding wavevector are shown with blue, green, and pink arrows, respectively. The zenith angle (θ) of a non-normal planewave is also shown. The xz-cross section of the unit cell denoting the width (w), length (L), and height of Au rod (hm) is depicted below. The height of dielectric layer (hd) and gap width (g) are denoted. (b) Scanning Electron Microscope (SEM) image of an L = 1.4 μm array. (c) The calculated dispersion of the same array as a function of in-plane wavevector (kx) or angle of incidence (θ). The electric field intensity (|E|2) is normalized to the maximum value in the x- and y-axis range shown. (d) Experimental absorption with different lengths (L) of the rods. The absorption intensity is plotted on a log scale.

Results and Discussion - *Far-Field Observations* - Figure 1 illustrates the far-field properties of our designed Au nanorod arrays, showing the dispersion characteristics of dipolar and quadrupolar modes and their interaction with incident light. The subradiant modes display distinct behavior by remaining "dark" at normal incidence but gaining radiant character at oblique angles, which is pivotal for accessing and studying these



states.

Fig. 2: Far-field VSC behavior. (a, b) Experimental absorption measured when dipolar plasmons (DPL) were tuned pthrough the C=O stretching mode of PMMA. The red dotted trace is a control PMMA spectrum. (e, f) Experimental absorption measured when quadrupolar plasmons (QPL) were tuned to the molecular vibration frequency. (c, g) Simulated dispersion reproducing (b, f). In simulation, the quadrupolar resonances were excited off-axis (θ=17.5°). The fitted dispersion of the upper (triangle) and lower (circle) polariton branches and the uncoupled molecular vibration (white dotted) are also plotted on (c). (d, h) Experimental spectra for resonant cases (blue dots). For the DPL-molecular system, the experimental spectrum was fit to the two-coupled oscillator model (green). The substrate before deposition of PMMA (black), and the control PMMA spectrum (red dash) are also plotted.

Vibrational Strong Coupling Analysis - Significant findings were observed when these modes were tuned through the PMMA vibrational frequencies. In the case of dipolar modes, expected anti-crossing behavior was observed, indicative of strong coupling. However, the quadrupolar modes, due to their subradiant nature, did not exhibit typical VSC behavior in far-field measurements until probed at specific angles (Figure 2). This demonstrates the crucial role of mode symmetry in the emergence of polariton states. *Near-Field and Computational Insights* - Further computational analysis and near-field probing confirm the presence of dark polariton states under normal incidence, challenging conventional understanding of polariton visibility in spectroscopic measurements. These results are critical as they show the potential of subradiant cavities to control the visibility and properties of polariton states, offering a new tool for the experimental probing of molecular interactions within these states.

Conclusion - Our study confirms that subradiant plasmonic cavities can significantly alter the landscape of vibrational strong coupling. By manipulating the symmetry and radiative properties of cavity modes, we can selectively influence the visibility and behavior of polariton states. This insight opens new avenues for the study of polariton chemistry and the development of advanced materials and devices based on strong light-matter interactions.

Acknowledgements - Z.T.B., J.Y. and M.S. acknowledge the funding from the National Science Foundation, Grant. No. CHE-2108288 , Welch Foundation (A-1886)

References

[2] K. Hirai, R. Takeda, J.A. Hutchison and H. Uji-i, "Modulation of Prins Cyclization by Vibrational Strong Coupling," *Angew. Chem. Int. Ed.*, vol. 59, no. 13, pp. 5332-5335, 2020, https://doi.org/https://doi.org/10.1002/anie.201915632.

[2] M.S. Rider and W.L. Barnes, "Something from nothing: linking molecules with virtual light," *Contemp. Phys.*, vol. 62, no. 4, pp. 217-232, 2021, https://doi.org/10.1080/00107514.2022.2101749.

Dynamic optical MEMS metasurfaces

F. Ding

Centre for Nano Optics, University of Southern Denmark, Campusvej 55, DK-5230 Odense, Denmark
*corresponding author: feid@mci.sdu.dk

Abstract: We have demonstrated a micro-electro-mechanical (MEMS) mirror-integrated dynamic optical metasurface platform for dynamic wavefront control with high modulation efficiencies and fast speed by electrically controlling the air gap between the plasmonic metasurface and MEMS mirror.

Plasmonic metasurfaces have attracted increasing attention due to their unprecedented capabilities of manipulating optical fields at subwavelength spatial resolutions [1]. Despite significant progress, most metadevices demonstrated to date are passive and lack dynamic modulation post-fabrication. Therefore, it is highly desirable to realize tunable metasurfaces with functionalities actively controlled by external stimuli. In this talk, I will discuss a MEMS-integrated tunable metasurface platform for active wavefront shaping by integrating MEMS mirrors and optical metasurfaces (OMSs) with the mirror-OMS separation being electrically controlled. Recent experimental demonstrations of electrically controlled full-range phase retarders [2] and polarizers [3,4] are presented.

References

1. F. Ding, Y. Yang, R. Deshpande, and S. Bozhevolnyi, “A review of gap-surface plasmon metasurfaces: fundamentals and applications,” Nanophotonics 7, 1129 (2018).
2. C. Meng, P. C. V. Thrane, F. Ding, and S. I. Bozhevolnyi, “Full-range birefringence control with piezoelectric MEMS-based metasurfaces,” Nat. Commun. 13, 2071 (2022).
3. F. Ding, Y. Deng, C. Meng, P. C. V. Thrane, and S. I. Bozhevolnyi, “Electrically tunable topological phase transition in non-Hermitian optical MEMS metasurfaces,” Sci. Adv. 10, eadl4661 (2024)
4. Y. Deng, C. Meng, P. C. V. Thrane, S. im Sande, S. I. Bozhevolnyi, and F. Ding, “MEMS-Integrated metasurfaces for dynamic linear polarizers”, Optica 11, 326−332 (2024).

Gap plasmon structures constructed by oligonucleotides and integrated with fluorophores

W.-P. Chan[1], Y.-L. Lin[1], S.-Y. Chen[1*]

[1]Department of Photonics, National Cheng Kung University, Tainan City, Taiwan
[*]sychen72@ncku.edu.tw

Abstract: Structures supporting gap plasmon modes have been widely utilized in metasurfaces. Here, we show that the gap plasmon structures constructed by oligonucleotides (short DNA strands) and their interaction with embedded fluorophores. This configuration may extend the capability of active metasurfaces.

Gap plasmon supported by truncated MIM (metal-insulator-metal) structures is commonly used in the metasurface for modulating phase, amplitude, and polarization of electromagnetic waves. These structures mainly consist of a metal film and patterned metal disks separated by a dielectric gap which is normally optically passive. In this work, we use oligonucleotides (short DNA strands) to efficiently construct structures supporting gap plasmon and simultaneously integrate fluorophores into the structures.

The MIM configuration is composed of gold nanoparticles (NP) and a gold film which are glued by oligonucleotides. The surface of citrate stabilized gold nanoparticles are modified by oligonucleotides through salt aging method[1], Fig.1(A). These oligonucleotide-loaded gold nanoparticles are adsorbed on an ultra-flat gold film through the intrinsic affinity between DNA bases and gold atoms. The adsorption of oligonucleotide-modified gold NP to the gold film is efficient, which only takes 30s while the original gold NP cannot be attached to the gold film, Fig. 1(C)(D). The various gap modes[2] can be observed between this particle-on-film configuration, Fig. 1(B). Since this oligonucleotide driven method is highly efficient, it can be combined with e-beam lithography to generate periodic patterns, as shown in Fig. 1(E).

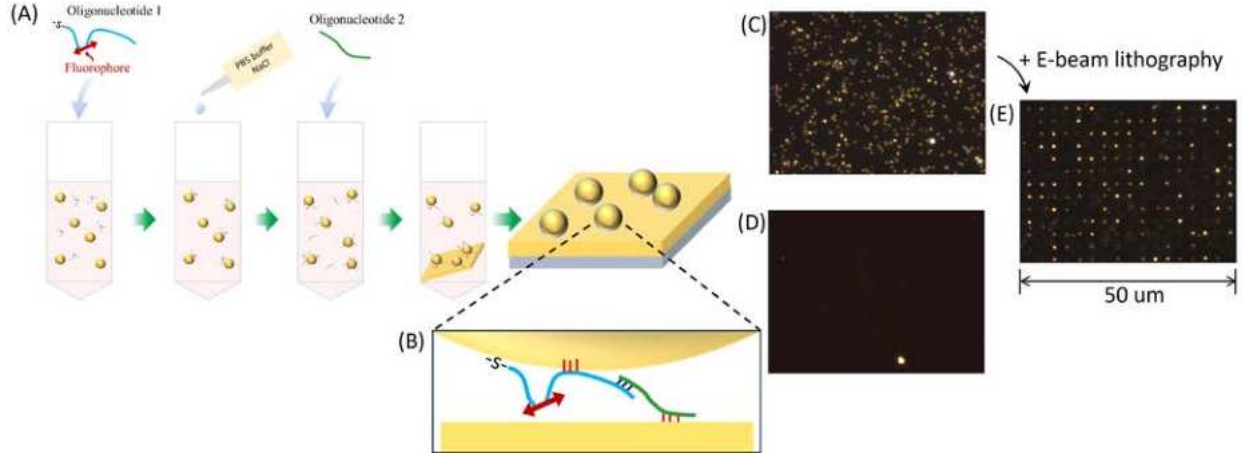


Fig. 1. (A) Salt aging method for modifying gold NP surface with oligonucleotides. (B) The gap region of particle-on-film configurations. Dark-field scattering images of oligonucletoide-modified gold NP (C) and Unmodified NP (D) on gold films. (E) Dark-field scattering image of periodic particle-on-film structures.

In a conventional structure supporting gap plasmon for the metasurface, the gap layer is usually an optically

passive material such as silica, aluminum oxide, etc. Here, the gap plasmon structure can further be integrated with fluorophores through fluorophore-modified oligonucleotides. The exciton of fluorophores can strongly interact with gap plasmon to form polariton at room temperature. We find that the polariton can be perturbed by laser illuminations. As shown in Fig. 2(A), the photoluminescence (PL) spectra under successive illuminations are changed probably because of the alternation of the coupling strength. On the other hand, the PL spectra of the configuration without fluorophores are stable, Fig 2(B).

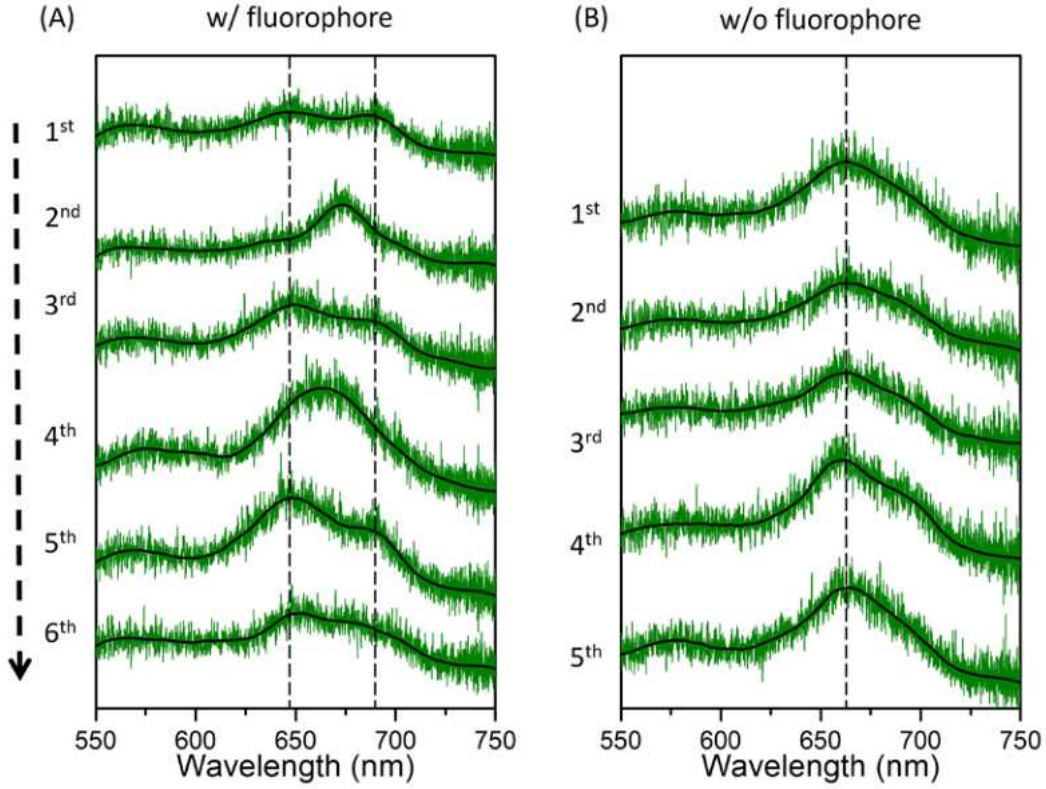


Fig. 2 PL spectra of NP-on-film structures with fluorophores (A) and without fluorophores (B).

Our oligonucleotide driven method can construct NP-on-film structures supporting gap plasmon which can interact with the exciton of the embedded fluorophores. This may provide tunability of the metasurfaces.

Acknowledgements. This project is supported by National Science and Technology Council of Taiwan (NSC NSTC 112-2628-E-006 -018 -MY3 and MOST 111-2221-E-006 -063 -MY3).

References

1. W.-P. Chan, J.-H. Chen, W.-L Chou, W.-Y. Chen, H.-Y. Liu, H.-C. Hu, C.-C. Jeng, J.-R. Li, C. Chen, S.-Y. Chen, “Efficient DNA-driven nanocavities for approaching quasi-deterministic strong coupling to a few fluorophores,” ACS nano, Vol. 15, No. 8, 13085–13093, 2021.
2. C.-Z. Huang, M.-J. Wu, S.-Y. Chen, “High Order Gap Modes of Film-Coupled Nanospheres,” J. Phys. Chem. C, Vol. 119, No. 24, 13799–13806, 2015.

Three-dimensional co-axial double cylinder metasurface for high-sensitive gas molecular sensing

Takuo Tanaka[1,2,3]

[1]RIKEN Center for Advanced Photonics, Japan
[2]RIKEN Cluster for Pioneering Research, Japan
[3] Institute of Post-LED Photonics, Tokushima University, Japan
[*]corresponding author: t-tanaka@riken.jp

Abstract: An ultra-sensitive infrared spectroscopic gas detection technique enhanced by a three-dimensional (3D) metasurface is proposed. A 3D co-axial double-cylinder structure is introduced as the unit structure of the metasurface. Owing to its strong resonant absorption, unwanted background in IR spectroscopy are suppressed, and the signal-to-background ratios has been improved.

Highly sensitive sensing techniques for biological and chemical materials are becoming imperative in our daily lives. Among the wide range of techniques available, infrared (IR) absorption spectroscopy stands out as one of the most promising analysis methods due to its intrinsic label-free and noninvasive detection characteristics. However, its practical applications are limited by weak signals caused by the inherently low IR absorption of natural substances and strong background noise from the surrounding environment.

Recently, we introduced metallic metasurface absorbers to enhance infrared spectroscopy, aiming to suppress unwanted background signals and improve sensitivity. By leveraging plasmonic enhanced electromagnetic fields and plasmon-molecular coupling in metasurface absorbers, we achieved attomolar (10^{-18} mol) level molecular sensitivity. This was demonstrated using self-organized molecular monolayers of 16-Mercaptohexadecanoic acid as solid samples covering the device's surface [1]. For liquid samples, we developed a metal-insulator-metal (MIM) metasurface absorber consisting of a nanofluidic channel with a depth of several tens of nanometers as an insulator layer [2]. For gas samples, we proposed the use of 3D vertically aligned MIM structures (Fig. 1(a)) [3]. In this paper, we propose a three-dimensional co-axial double cylinder metasurface shown in Fig.1 (b) for physically durable and optically effective enhancement of IR spectroscopic signals. Experimental result of the butane signal taken by this device is shown in Fig. 1(c).

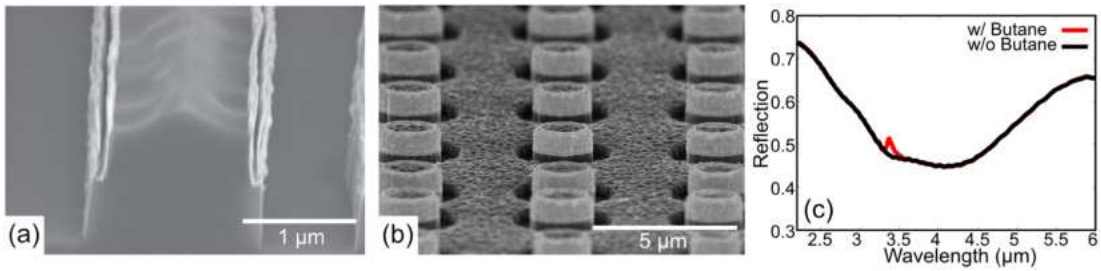


Figure 1 (a) and (b) metasurface absorbers, and (c) detected butane spectrum.

References

[1] A. Ishikawa and T. Tanaka, Scientific Reports **5**, 12570 (2015).
[2] T. H. H Le and T. Tanaka, ACS Nano **11**, 9780-9788 (2017).
[3] D.-S. Su, D. P. Tsai, T.-J. Yen, and T. Tanaka, ACS Sensors **4**, 2900-2907 (2019).

Photoluminescent gratings and metasurfaces

Pierre Berini

School of Electrical Engineering and Computer Science, University of Ottawa, Canada
Department of Physics, University of Ottawa, Canada
Nexus for Quantum Technologies Institute, University of Ottawa, Canada
pberini@uottawa.ca

Abstract: Carbonaceous residue is transformed into carbon quantum emitters on Ag gratings by hot carriers excited through surface plasmon decay thereon. Yellow photoluminescence emerges *in situ* as the carbon dots form in an O_2 depleted environment. The ability to form photoluminescent carbon dots through plasmonic excitation opens a novel pathway to photoluminescent metasurfaces.

SPPs propagating on metal waveguides or resonating on metal nanoparticles, nanoantennas or gratings are generally strongly absorbed by the metal, leading to the effective creation of energetic carriers - “hot electrons” and/or “hot holes” - also localized along the surface. These energetic carriers can be harvested and used for a broad range of applications, *e.g.*, to enhance the performance of optoelectronic and photovoltaic devices, or to open new reaction pathways in chemistry and electrochemistry [1].

Here we report the transformation of carbonaceous residue on Ag gratings into carbon quantum emitters when the gratings are excited by surface plasmons and placed in an O_2 depleted environment [2]. The carbonaceous residue originates from PMMA used in a He+ lithography process applied to create the gratings [3,4]. The surface plasmons excited on the Ag gratings at 532 nm decay partly by exciting hot carriers therein which then act to transform the residue into light-emitting carbon dots in the absence of O_2. Plasmon decay also serves to pump the carbon dots such that bright yellow photoluminescence (~575 nm) emerges *in situ* and in real-time.

The top panel of Fig. 1 shows a series of surface enhanced Raman scattering (SERS) spectra captured over time from a Ag grating supporting SPP excited at 532 nm and exposed to CO_2 in a gas flow cell [2]. The spectra indicate growth of photoluminescent graphitic carbon on the surface, as indicated by clear D and G peaks superimposed on a broad and intense photoluminescent band. The observed luminescence consists of yellow light and persists as long as CO_2 exposure is maintained (Fig. 1, bottom panel). Exposure to O_2 then reverses the process leading to the disappearance of photoluminescence. In some cases, the emission was also accompanied by carbon deposits on the gratings, observable under helium ion microscopy (Fig. 1, right panel), which may be formed by the decomposition of CO_2 [5].

The ability to form photoluminescent carbon dots through plasmonic excitation opens an exciting new pathway to photoluminescent structures and metasurfaces.

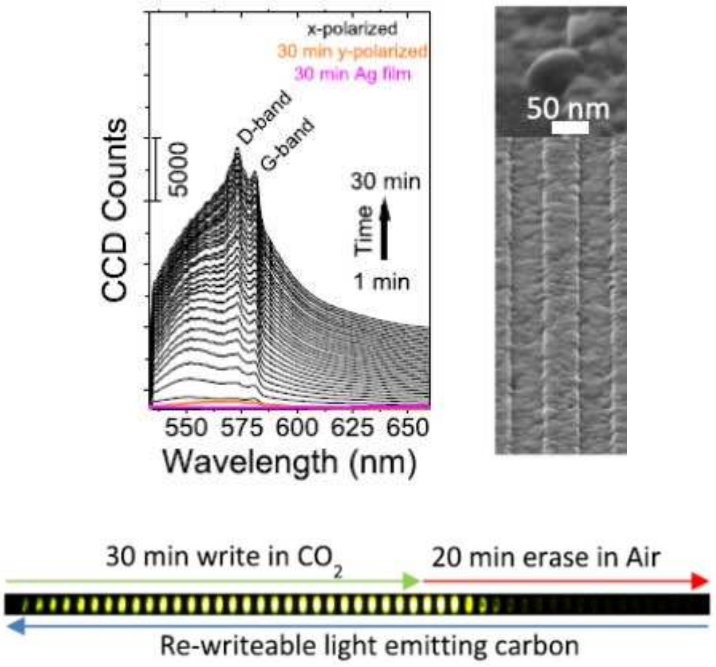


Fig. 1. Top left panel: SERS spectra evolving over time showing the emergence of photoluminescence (broad peak) and the formation of carbon dots (narrow D and G bands). Bottom panel: emergence and disappearance of yellow photoluminescence as carbon dots form in CO_2 then disappear in Air, as captured by a visible camera mounted to an optical microscope. Top right panel: helium ion microscope image of carbon deposits on a Ag grating.

References

1. Hirbodvash, Z., Krupin, O., Northfield, H., Olivieri, A., Baranova, E. A., Berini, P., "Infrared surface plasmons on a Au waveguide electrode open new redox channels associated with the transfer of energetic carriers," Science Advances, Vol. 8, eabm9303, 2022
2. Walia, J., Rashid, S., Killaire, G., Variola, F., Weck, A., Berini, P., "Reconfigurable carbon quantum emitters from CO_2 gas reduced via surface plasmons," Optica, Vol. 8, pp. 708-709, 2021
3. Rashid, S., Walia, J., Northfield, H., Hahn, C., Olivieri, A., Calà Lesina, A., Variola, F., Weck, A., Ramunno, L., Berini, P., "Helium ion beam lithography and liftoff," Nano Futures, Vol. 5, 025003, 2021
4. Walia, J., Rashid, S., Variola, F., Berini, P., "Focussed Helium Ion Beam Exposure of Polymethylmethacrylate: Creation of Negative Tone Images, Polyenes, and Fluorescent Carbon Layers," Advanced Engineering Materials, 2201707, 2023
5. Sandoval, M.G., Walia, J., Houache, M. S. E., Abu-Lebdeh, Y., Berini, P., Faccio, R., Weck, A., "CO_2 activation and dissociation over Ag(111) surfaces in the presence of surface charge density: A static gas phase DFT study," Applied Surface Science, Vol. 610, 155498, 2023

Electrochemically-tunable oxide materials for metasurfaces and large-area, additive patterning

V. E. Ferry[1*]

[1]University of Minnesota, USA
[*]corresponding author: veferry@umn.edu

Abstract: This talk will discuss two strategies for new, tunable metasurfaces. The first part of the talk will discuss the use of electrolyte gating to control the optical properties of materials, focusing on $La_{1-x}Sr_xCoO_{3-d}$ as an exemplary case. The second part will discuss large-area fabrication methods for multilayer, flexible devices.

Alternative materials for metasurfaces enable new properties and lay the foundation for advanced applications. Phase-change materials that change optical properties in response to an applied stimulus, such as voltage, are highly attractive for the development of tunable and switchable metamaterials. The first part of this talk will focus on new electrochemical materials that exhibit significant modulation in optical response under applied voltage.

$Sr_xCoO_{3-\delta}$ (SCO) has attracted considerable attention recently as a voltage-tunable materials system. $La_{1-x}Sr_xCoO_{3-\delta}$ (LSCO) offers similar advantages, but with additional advantages in stability. As deposited, LSCO has a perovskite structure. We focus here on ion-gated systems. Application of a positive gate voltage facilitates the formation and migration of oxygen vacancies. This is accompanied by substantial change in magnetic, electrical, thermal, and optical properties.

We fabricate electric double layer transistors consisting of thin-films of LSCO and an ion gel. We use spectroscopic ellipsometry to map the complex refractive index across the phase diagram of LSCO before and after gating. At $x < 0.18$, as-grown LSCO has a perovskite crystal structure and high refractive index. Upon application of a gate voltage, the LSCO films change to another lower-index, lower-loss insulating perovskite state with $\Delta n > 0.6$. At $x > 0.18$, as-grown LSCO has a perovskite structure and is a lossy metal. Application of the gate voltage transforms LSCO to an oxygen-vacancy-ordered brownmillerite crystal structure with high-index ($n > 2.5$) and low-loss. LSCO is therefore an interesting platform material for switchable metasurface applications, and can be used in either optical applications that require on-off switching (at $x > 0.18$) or resonance modulation (at $x < 0.18$).

The second part of the talk will discuss a new fabrication method for very large-area metasurfaces, which is both additive and roll-to-roll compatible. The method uses UV-based imprint lithography to produce a pattern with spatially modulated surface energy. When a functional ink is dragged over the surface it dewets and fills in the recesses. This method works for a variety of ink materials (metal, dielectric, semiconductor), can create multi-layer patterns, and offers flexibility in creating metamaterials on free-standing and flexible substrates.

Acknowledgements. The work on LSCO was supported primarily by the National Science Foundation through the University of Minnesota MRSEC under Award Number DMR-2011401. Parts of this work were performed in the Characterization Facility at the University of Minnesota, which receives partial support from NSF through the MRSEC program. Portions of this work were also conducted in the Minnesota Nano Center, which is supported by NSF through the National Nano Coordinated Infrastructure (NNCI) under Award Number

ECCS-2025124.

References

1. Chakraborty, R. D. , W. Postligione, S. Ghosh, K. A. Mkhoyan, C. Leighton, and V. E. Ferry, “Optical properties of electrochemically gated $La_{1-x}Sr_xCoO_{3-\delta}$ as a topotactic phase change material,” Adv. Opt. Mater., Vol. 11, No. 16, 2300098, 2023.
2. Ramamurthy, M., P. Pachidis, B. M. Cote, and V. E. Ferry, “Circularly polarized photoluminescence from nanostructured arrays of light emitters,” ACS Appl. Nano Mater., Vol. 1, No. 1, 491 - 499, 2023.
3. Donie, Y. J., M. Ramamurthy, R. D. Chakraborty, L. F. Francis, C. D. Frisbie, and V. E. Ferry, “Roll-to-roll compatible topochemical wetting control for metamaterial printing,” Adv. Opt. Mater., in press, 2024.

Nonlinear all-dielectric metasurfaces driven by multipolar resonances and quasi-bound states in the continuum

Hui-Hsin Hsiao[1*]

[1] Department of Engineering Science and Ocean Engineering, National Taiwan University, Taipei, Taiwan 11677

[*]corresponding author: hhhsiao@ntu.edu.tw

Abstract: The interaction of multipolar resonances in all-dielectric metasurfaces provides a unique platform for confining strong near-field enhancement inside nanocavities as well as tailoring far-field scattering properties. Here, we investigated third-harmonic generation of all-dielectric metasurfaces driven by the generalized Kerker condition and quasi-bound states in the continuum, respectively.

Recently, high-index dielectric metasurfaces that support Mie resonances have been extensively studied for efficient second- and third-harmonic generation (THG) owing to their advantages for a higher laser damage threshold and intrinsic low dissipative loss [1, 2]. In this study, we designed an amorphous silicon (*a*-Si) nanopillar array that sustains toroidal dipole (TD), electric dipole (ED), and magnetic dipole (MD) resonances in the near-infrared region (Figure 1a). By varying the diameter of nanopillars (*D*), the spectral positions of the MD and TD modes can be effectively tuned as shown in Figure 1b. A pronounced THG enhancement is observed when these two modes become spectrally overlapped, corresponding to the generalized Kerker condition where the constructive interference of the total electric dipole (TED, referring to the summation of ED and TD scattered field) and the MD mode takes place [3]. This leads to the suppression of backward scattering as well as the strong field enhancement inside the nanocavities. Our simulation (experimental) results show a 214-fold (17-fold) THG enhancement in the vicinity of the generalized Kerker condition compared with the THG signal of the TD resonance (Figures 1d and e).

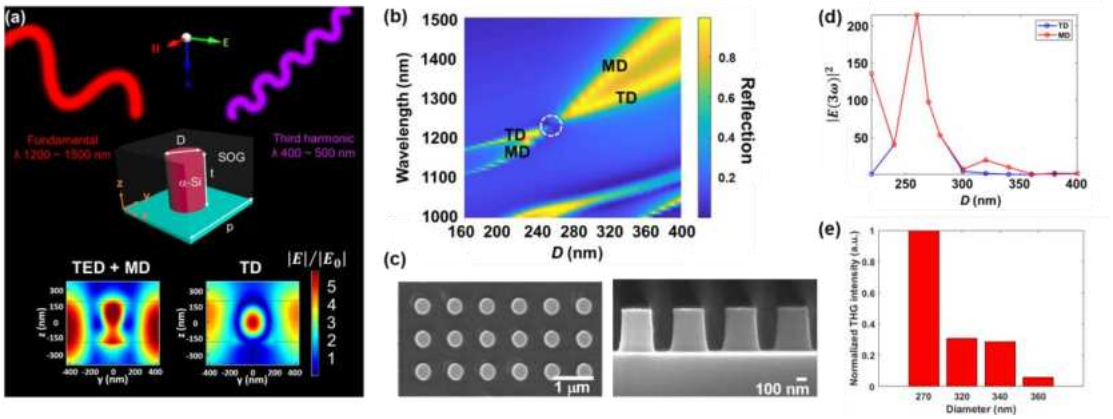


Figure 1. (a) Schematic view of nanopillar arrays. Insets: The electric field distributions at the reflection dip of *D* = 260 nm (left) and at the TD mode of *D* = 360 nm (right). (b) Simulated reflection spectra of nanopillar arrays as a function of *D*. The SEM images of the fabricated samples (d) at the top (left) and lateral (right) views, respectively. (d) Calculated and (e) measured THG peak intensities for samples with different diameters.

In addition, symmetry-protected quasi-bound states in the continuum (quasi-BIC) controlled by

metasurfaces with broken in-plane symmetry can generate sharp resonance with strong light concentration within the nanostructures [4]. Here, we developed a simple approach for designing high quality-factor (Q-factor) quasi-BICs using asymmetry kite-shaped *a*-Si nanopillar arrays and investigated their THG signals (Figure 2a). By breaking the in-plane symmetry of the kite-shaped nanopillars with different axial length difference (Δx) defined in Figure 2b, a quasi-BIC resonance was excited in the transmission spectra around the wavelength of 1325 nm for Δx = 15 nm (Figure 2d). The Q-factors of quasi-BICs exhibit the quadratic dependence on the geometry asymmetry (Figure 2e). In addition, the resonant spectral profile of quasi-BICs can be readily tuned between Fano and Lorentzian-lineshapes through the interplay between quasi-BIC resonances and the broadband MD mode. The high-Q quasi-BIC resonance exhibits an extremely intensive field enhancement confined within the nanocavities, thus resulting in four order of magnitude THG enhancement in calculation and 46.4-fold THG in experiment as shown in Figure 2f. These Si-based designs are compatible with the state-of-art complementary metal-oxide-semiconductor (CMOS) technology and provide a new platform to enhance the nonlinear conversion.

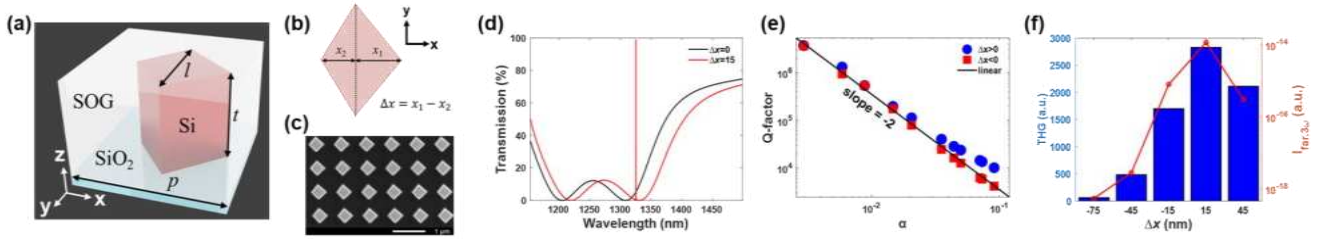


Figure 2. (a) The schematic and (b) the top views of the asymmetric kite-shaped nanopillars. (c) The SEM image of the fabricated sample. (d) Simulated transmission spectra for Δx = 0 (black curve) and 15 nm (red curve). (e) Dependence of Q-factors for quasi-BICs on the asymmetry parameter α for the asymmetric kite-shaped nanopillars. (e) Measured (blue bars) and calculated TH peak intensities (red curve) for asymmetric kite-shaped nanopillars with different axial length difference of Δx.

The authors acknowledge financial support from National Science and Technology Council (NSTC) of Taiwan under the grant NSTC 110-2112-M-002-048-MY3 and from National Taiwan University (NTU) under the grant NTU-113L7867.

References

1. M. R. Shcherbakov, D. N. Neshev, B. Hopkins, A. S. Shorokhov, I. Staude, E. V. Melik-Gaykazyan, M. Decker, A. A. Ezhov, A. E. Miroshnichenko, I. Brener, A. A. Fedyanin, and Y. S. Kivshar, "Enhanced Third-Harmonic Generation in Silicon Nanoparticles Driven by Magnetic Response," Nano Lett. **14**, 6488-6492 (2014).

2. A. S. Shorokhov, E. V. Melik-Gaykazyan, D. A. Smirnova, B. Hopkins, K. E. Chong, D.-Y. Choi, M. R. Shcherbakov, A. E. Miroshnichenko, D. N. Neshev, A. A. Fedyanin, and Y. S. Kivshar, "Multifold Enhancement of Third-Harmonic Generation in Dielectric Nanoparticles Driven by Magnetic Fano Resonances," Nano Lett. **16**, 4857-4861 (2016).

3. A.-Y. Liu, J.-C. Hsieh, K.-I. Lin, S. H. Tseng, and H.-H. Hsiao, "Third Harmonic Generation Enhanced by Generalized Kerker Condition in All-Dielectric Metasurfaces," Advanced Optical Materials **11**, 2300526 (2023).

4. K. Koshelev, S. Lepeshov, M. Liu, A. Bogdanov, and Y. Kivshar, "Asymmetric Metasurfaces with High-Q Resonances Governed by Bound States in the Continuum," Phys. Rev. Lett. **121**, 193903 (2018).

Metamaterial assisted super-resolution microscopy

Zhaowei Liu*
Department of Electrical and Computer Engineering, University of California, San Diego
9500 Gilman Drive, La Jolla, California, USA
*Corresponding author: zhaowei@ucsd.edu

Abstract: Metamaterial assisted illumination nanoscopy (MAIN) has recently been proved to be a promising approach for linear super-resolution microscopy with unprecedented resolution capability. In this talk, I will summarize some of our recent progresses in the field and showing biological imaging examples with resolution down to 20nm scales.

Super-resolution microscopy (SRM) techniques (STED, PALM, STORM, SIM) have been extensively explored in the last two decades with improved resolution beyond the diffraction limit. Especially, structured illumination microscopy (SIM) has attracted great attention due to its advantages to perform high spatial-temporal imaging with low photo-toxicity and wide field of view. However, traditional SIM can only improve the resolution by two-fold because both the illumination and detection optics are diffraction limited.

We developed a speckle metamaterial-assisted illumination nanoscopy (speckle-MAIN) technique, which extends the attainable resolution of SIM to deep subwavelength scales by utilizing high-resolution illumination patterns enabled by metamaterials. Our initial experiment has shown a >7-fold improvement in imaging resolution. With a recently developed stat-of-the-art optical hyperbolic metamaterials, including an Ag/MgO metamaterials at a nominal thickness of 2.5nm and a P3HT based organic hyperbolic material, we demonstrated speckle-MAIN with a >14-fold resolution improvement and achieving image at 20nm scale. We will showcase this recent advancement by showing some 2D and 3D bioimaging examples and also discuss future possibilities to improve imaging speed by more efficient deep-learning based image reconstruction algorithms. Similar SRM idea can be extended to label-free imaging with greatly improved resolution as well.

The MAIN represents a simple super-resolution imaging approach that offers distinct benefits such as low illumination power, high photostability, low cost, and a broad spectrum of selectable probes (or label-free), making it an appealing candidate for dynamic imaging of life science samples.

References

1. Lee, Y. U., et. al., “Hyperbolic material enhanced scattering nanoscopy for label-free super-resolution imaging,” Nat. Commun., Vol. 13, No. 1, 6631, 2022.

2. Lee, Y. U., et., al., “Ultrathin layerd hyperbolic metamaterial-assisten illumination nanoscopy,” Nano Lett. Vol. 22, No. 14, 5916-5921, 2022.

3. Lee, Y. U., et., al., “Organic hyperbolic material assisted illumination nanoscopy,” Adv. Sci. Vol. 8, No. 22, 2102230 2021.

4. Burns, Z. and Liu, Z., “Untrained, physics-informed neural networks for structured illumination microscopy,” Opt. Express, Vol. 31, No. 5, 8714-8724, 2023.

Multiparameter Sensing of On-Chip Infrared Photodetectors Enabled by Metasurfaces

Mingjin Dai[1], and Qi Jie Wang[1,2] *

[1]School of Electrical and Electronic Engineering, Nanyang Technological University, Singapore 639798, Singapore
[2]Centre for Disruptive Photonic Technologies, School of Physical and Mathematical Sciences, Nanyang Technological University, Singapore 637371, Singapore
*Corresponding author: qjwang@ntu.edu.sg

Abstract: On-chip multiparameter infrared photodetectors are highly desirable for the next-generation ultra-compact optical and optoelectronic systems[1,2]. Here, we proposed the on-chip infrared photodetectors to realize multiparameter detection such as intensity, polarization, chirality, and orbital angular momentum enabled by using the metasurface integrated with two-dimensional materials[3-5].

Acknowledgements

This work is partially supported by Singapore National Research Foundation Competitive Research Program (NRF-CRP29-2022-0003).

References

1. Martínez, A. “Polarimetry enabled by nanophotonics,” Science, 362, 750-751, 2018.
2. Ji, Z. et al. “Photocurrent detection of the orbital angular momentum of light,” Science, 368, 763-767, 2020.
3. Dai, M. et al. “On-chip mid-infrared photothermoelectric detectors for full-Stokes detection,” Nat. Commun. 13, 4560, 2022.
4. Dai, M. et al. “Long-wave infrared photothermoelectric detectors with ultrahigh polarization sensitivity,” Nat. Commun. 14, 3421, 2023.
5. Dai, M. et al. “High-Performance, Polarization-Sensitive, Long-Wave Infrared Photodetection via Photothermoelectric Effect with Asymmetric van der Waals Contacts,” ACS Nano 16, 295-305, 2022.

Real-Time Multidimensional Imaging with an Encoding Metasurface

Lidan Zhang, Chen Zhou, Hyunju Ahn, Shengyuan Chang, Md Tarek Rahman, Tunan Xia, Zhiwen Liu, and Xingjie Ni*

Department of Electrical Engineering, The Pennsylvania State University, University Park, PA, USA

*corresponding author: xingjie@psu.edu

Abstract: We present a metasurface capable of encoding light information across multiple dimensions – polarization, frequency, and time – via the distinct optical responses of its constituent meta-atoms, and consequently, the complete properties of the light field can be captured by a single snapshot. A deep learning-based recovery algorithm is employed to facilitate real-time retrieval of multidimensional images.

Light fields carry comprehensive channels of information, including intensity, spectrum, and polarization. Traditional cameras, however, are limited to capturing merely the intensity distribution, thus neglecting a wealth of additional valuable data. While specialized imaging systems exist – such as hyperspectral for spectral information and polarimetric for polarization data – these alternatives often suffer from drawbacks, being bulky, slow, and expensive. Addressing these limitations, we introduce an all-dielectric encoding metasurface designed to enable the acquisition of comprehensive hyperspectro-polarimetric imagery through a singular, efficient snapshot.

Our metasurface is engineered with unique spectral and polarization responses inherent in its constituent meta-atoms. Such design allows for the encoding of spectral and polarization information into an intensity pattern, which can be readily captured by conventional camera technology. In addition, we integrated a custom-tailored deep learning network, specifically developed to support real-time image recovery. This synergy empowers our system to precisely decode full-Stokes polarization information over an extensive spectral range (700 nm to 1150 nm), directly from a single captured snapshot. Notably, our system achieves a spectral resolution up to 0.23 nm.

Beyond static imagery, our system excels in dynamic capture, successfully recording full-Stokes hyperspectro-polarimetric video in real time, at a commendable rate of 28 frames per second. This performance metric is predominantly constrained only by the inherent readout rate of the camera used.

In summary, our development of the metasurface encoder, in concert with the deep learning-based decoder, presents a compact, rapid, and cost-effective solution for multidimensional imaging. This approach ensures the maximal exploitation of the rich information embedded within light fields. The technology developed could mark a significant leap forward in imaging capabilities and pave the way for diverse applications across various fields, from scientific research to commercial photography and beyond.

Introducing Circular Dichroism with Chiral Bound State in the Continuum

Cheng-An Mao, Wen-Hui (Sophia) Cheng*
National Cheng Kung University, Taiwan
*corresponding author: wcheng@gs.ncku.edu.tw

Abstract: A structure of all-dielectric metasurface with the concept of chiral BIC is introduced and studied. By break both in-plane and out-of-plane symmetry, intrinsic chiral metasurfaces with strong circular dichroism of around 0.9 at normal incidence can be realized.

Chirality is a property observed in natural molecules, which refers to the geometric nature of molecules that cannot overlap with their mirror-symmetric image without rotation. The strong optical chirality induced by artificial metamaterials has drawn much attention. Most of the proposed metamaterials exhibiting strong circular dichroism (CD) are three-dimensional chiral metamaterials, while their two-dimensional counterparts, known as chiral metasurfaces, need to be operated with oblique incident light (extrinsic chirality). However, three-dimensional metamaterials require a more sophisticated fabrication process. Here, we propose a tilted dielectric structure to overcome the weak chiro-optical responses of intrinsic chiral metasurfaces by inducing chiral bound states in the continuum. Our design strategy aims to break both in-plane and out-of-plane symmetry using two deformation parameters. Strong circular dichroism (∼0.9) and large polarization rotation (∼200,000°/mm) at normal incidence in the near-IR region are demonstrated with FDTD simulation. From multipole decomposition, we further interpret the results and reveal that higher-order multipoles play an important role in the observed large circular dichroism. We expect that this work could be applicable to future applications for chiral sensing, polarization optics, quantum optics, asymmetric photocatalysis and chiral light sources and detectors.

Keyword: chiral; dielectric; metasurface; intrinsic chirality; optical activity

The work is supported by National Science and Technology Council, Taiwan (2030 Cross-Generation Young Scholars Program, 112-2628-E-006-020), and Ministry of Education (Yushan Fellow Program), Taiwan, and in part from the Higher Education Sprout Project of the Ministry of Education to the Headquarters of University Advancement at National Cheng Kung University (NCKU).

Spherulite based metasurfaces

J. Sun[1]*, Y. Liu[1], L. Zhou[1], Y. Shen[1], J. Zhou[1]

[1]State Key Laboratory of New Ceramics and Fine Processing, School of Materials Science and Engineering, Tsinghua University, Beijing 100084, China
*corresponding author: jingbosun@tsinghua.edu.cn

Abstract: Spherulites are crystals with cylindrical crystalline structures and thus exhibit anisotropic optical properties with cylindrical symmetry. Here we proposed several way of generating and modulating cylindrical vector optical vortex beams by using spherulites. This strategy provides promising opportunities for the spherulite applications in structured light fields.

Usually, structured light beams refer to vector beams with cylindrical polarization states or optical vortex with spiral phase distribution or even cylindrical vector optical vortex, and thus provides more degrees of freedom in modern optical applications [1]. These types of beams with circular symmetry are seen as "inhomogeneity" in the frame of Cartesian coordinate (x, y, z). However, they are "homogeneous" and regular in a cylindrical coordinate (r, θ, z). Artificially engineered materials, known as metamaterials or metasurfaces are preferred in the generations or modulations of the structured light [2]. The structures of these metamaterials or metasurfaces are usually designed to be in circular symmetry, which can produce the desired cylindrical optical properties, but are always troubled by strong scattering, limited working bandwidth and the challenging fabrication for the unit cell sizes or numbers are not uniform and decrease along the radial direction towards the center [1-4]. On the other hand, spherulites are radially polycrystalline aggregates where needle-like crystals are aligned radially from the center of the spherulite to provide a perfectly central symmetrical shape and thus natural cylindrical anisotropy [5]. Here, by designing and constructing spherulite crystals with certain circular anisotropy in both linear and nonlinear levels, we demonstrate several spherulite based devices including a spin-orbital angular momentum convertor, a cylindrical vector beams splitter and a nonlinear vortex modulator.

The spin-orbital angular momentum convertor is based on a spherulite composed by a radially distributed structure, which is formed by the self-assembly of disk-like aromatic molecules, i.e., electron-rich "donor" and electron-poor "acceptor", in a condensational crystallization process [6]. The "donor" and "acceptor" molecules are alternatively packed at the radial direction to form a face-centered columnar structure. The charge-transfer absorbance effect occurs between the donor and the acceptor, which significantly enhances the absorption along the normal of the disks and finally enables a cylindrically anisotropic extinction between the radial and azimuthal directions of the assembled spherulite. A beam of circular polarization can be treated as a linear combination of a radially polarized optical vortex and an azimuthally polarized optical vortex with a topological charge of 1 while $\pi/2$ out of phase between each other. In our design, when a left circularly polarized beam transmits through the spherulite, the radially polarized component is filtered due to the strong absorption and the remained part is azimuthally polarized optical vortex with topological charge of 1, which realizes the generation of the orbital angular momentum (OAM) transformed from the spin angular momentum of the incidence.

The cylindrical vector beams splitter is based on the spherulite with cylindrically anisotropic refraction indices while with a wedge-shaped prism by using the nematic LC (4'-Pentyl[1,1'-biphenyl]-4-carbonitrile, 5CB). The

5CB molecule is intrinsically anisotropic with its refractive index (n_e) along the longer axis larger than that (n_o) along the short axis [7]. Once these molecules are constructed into a spherulite with the longitudinal axis along the azimuthal direction of the material, the formed spherulite may show cylindrically anisotropic indices with $n_A=n_e$ and $n_R=n_o$, which is mimicking the metamaterials consisted of concentric multi-layered structure. If such a spherulite is cut into a prism, cylindrical vector beams passing through the prism experience the cylindrical anisotropy and are thus refracted to two different directions. A left or right circularly polarized beam can be decomposed into radial and azimuthal components. After passing through the spherulite prism, the output beams contain topological charge of either +1 or -1 depending on the chirality of the input circular polarization.

The nonlinear optical vortex modulator is based on a spherulite with a ferroelectric nematic phase. The polar molecules are arranged in an azimuthal array, showing a vortex polarity. Such a vortex polarity exhibits anisotropic indices, second harmonic generation and a sum frequency effect, which can manifold vortex generation at different wavelengths, topological charges and polarization states.

This work was supported by the National Key R&D Program of China (Grant No. 2022YFB3806000).

References

1. Y. Shen, et al., “Optical vortices 30 years on: OAM manipulation from topological charge to multiple singularities,” Light. Sci. Appl. Vol. 8, 1-29, 2019.
2. C. Rosales-Guzmán, et al., “A review of complex vector light fields and their applications,” J. Opt. Vol. 20, 123001, 2018.
3. N. M. Litchinitser, “Structured light meets structured matter,” Science Vol. 337, 1054-1055, 2012.
4. R. C. Devlin, et al., “Arbitrary spin-to-orbital angular momentum conversion of light,” Science Vol. 358, 896-901, 2017.
5. A. G. Shtukenberg, et al., “Spherulites,” Chem. Rev. Vol. 112, 1805-1838, 2012.
6. M. Van Winkle, et al., “Laser rewritable dichroics through reconfigurable organic charge-transfer liquid crystals,” Adv. Mater. Vol. 30, 1706787, 2018.
7. Y. Liu, et. al. “Structuring light sorter
8. based on a cylindrically anisotropic spherulite prism,” EPJ Appl. Metamat., Vol. 11, 3, 2024.

Dispersion engineering of mid-IR polaritons in van der Waals crystals

S. G. Menabde[1] **and M. S. Jang**[1*]

[1]School of Electrical Engineering, Korea Advanced Institute of Science and Technology (KAIST), Korea
[*]corresponding author: jang.minseok@kaist.ac.kr

Abstract: In this talk, I discuss several experimental approaches that can be used to manipulate the dispersion of mid-IR polaritons and significantly reduce their damping at the same time: monocrystalline gold, ultra-high-index and low-loss topological insulators, and harmonically corrugated gold substrate.

Polaritons – hybrid light–matter waves emerging from the coupling of light to collective oscillations of charges – promise a deeply subdiffractional light manipulation. In particular, polaritons in low-dimensional van der Waals crystals boast extremely high field confinement. However, tightly confined polaritons are prone to severe scattering loss, making it challenging to fully exploit wave phenomena at the nanoscale. In this talk, I discuss several experimental approaches that can be used to manipulate the dispersion of mid-IR polaritons and significantly reduce their damping at the same time. First, I will highlight the effects of the monocrystalline gold substrate on the polaritonic dispersion. Second, I will introduce bismuth and antimony chalcogenides, which are topological insulators, as a new family of ultra-high-index and low-loss van der Waals dielectrics for polaritonic applications in mid-IR. Finally, dispersion engineering with a harmonically corrugated gold substrate will be discussed.

Experimental demonstration of ENZ-enhanced optical nonlinearity in ultrathin TiN epilayers

F.-T. Tseng[1], I-H. Ho[1], S. Gwo[2], and H. Ahn[1*]

[1]Department of Photonics, College of Electrical and Computer Engineering, National Yang Ming Chiao Tung University, Hsinchu 30010, Taiwan.
[2] Department of Physics, National Tsing Hua University, Hsinchu 300, Taiwan.
[*]corresponding author: hyahn@nycu.edu.tw

Abstract: Epsilon-near-zero (ENZ) effect for metals can be observed in the visible range, but only for ultrathin layers with nanoscale thickness. We report the first experimental realization of ENZ-enhanced ultrafast optical nonlinearity from refractory TiN ultrathin epilayers grown by MBE via the thickness and incidence-angle dependent z-scan and transient absorption measurements.

Recent advances of the epsilon-near-zero (ENZ) materials, whose real part of the permittivity vanishes in certain spectral ranges, offer a new route to achieve the subwavelength confinement and immense enhancement of field and optical nonlinearity.[1-3] The ENZ mode is a confined mode existing only for a given range of thickness (L) satisfying $L \lesssim \lambda_p/50$, where λ_p is the plasma wavelength of materials.[3] Therefore, the commonly used ENZ materials including transparent conductive oxides (TCOs) show their ENZ wavelengths (λ_{ENZ}) in the near-infrared band. Meanwhile, the ENZ wavelengths of metals are in the visible range and the ENZ effect for metals can be realized only for ultrathin films with nanoscale thickness. Typically, the ideal enhancement of field intensity due to the ENZ properties of the materials is known to follow an inverse-square dependence on L,[1] but the percolation threshold (for example, $\gtrsim$6 nm for gold) of metal layers limits the reduction of thickness to achieve an observable enhancement of nonlinearity.[4] Moreover, most metal ENZ materials show relatively high optical losses which causes significant optical attenuation. Therefore, the realization of ENZ effect from metals has been limitedly reported and it is important to search for ENZ materials with low optical losses and high ENZ effect operating in the visible spectral region. In addition, to be utilized in nonlinear optoelectronic devices, nonlinear optical materials need to be not only thermally stables, but also defect-free and high quality to avoid the local heating under intense optical excitation.

Titanium nitride (TiN) is a transition metal nitride possessing many excellent characteristics comparable or superior to noble metals. TiN is highly conductive and chemically stable, and moreover its bulk melting temperature is as high as 3000 ℃, allowing for large nonlinear responses under high intensity excitation and a good candidate for robust and low-cost metallic material that is compatible with complementary metal–oxide–semiconductor (CMOS) fabrication technologies. Besides, high quality ultrathin TiN epilayers exhibing <2 nm percolation threshold thickness could be successfully grown by molecular-beam epitaxy technique.

In this work, we report the ENZ-assisted enhancement of nonlinear optical properties of MBE-grown ultrathin TiN films ranging in thickness from 2 to 50 nm. Dielectric properties are investigated by spectroscopic ellipsometry[5] and the nonlinear optical responses of ultrathin TiN films are explored using nonlinear transmission z-scan technique and transient reflection spectroscopy. It is found that the third-order nonlinearity and carrier dynamics can be tuned by the thickness-dependent ENZ properties. Figure 1a exhibits a significant enhancement of nonlinear responses as the film thickness is reduced below approximately 10 nm and at wavelengths around λ_{ENZ} determined by ellipsometry. Further enhancement is observed for p-polarized beam incident at a specific

angle controlled by the film thickness. (Figure 1b) Additionally, Figure 1c shows that ultrathin TiN films have a sub-picosecond carrier response time, which is long enough to accumulate the nonlinear change and subsequent enhancement.[6]

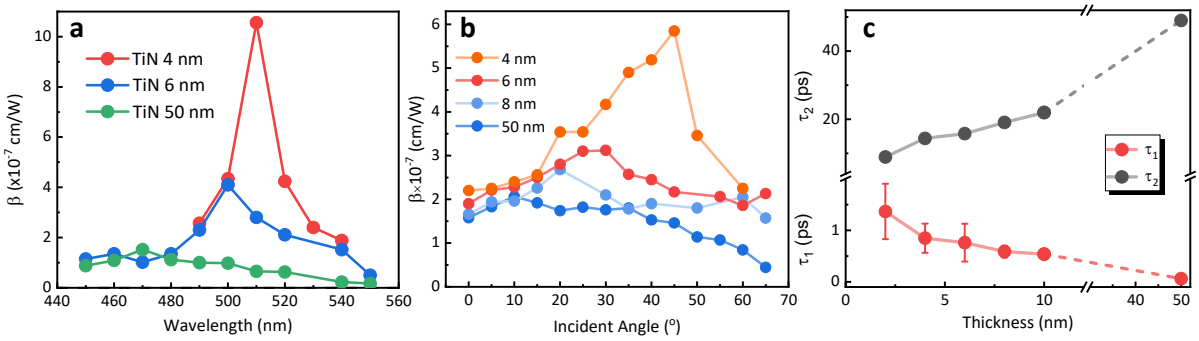


Figure1. (a)(b) Wavelength- and incidence angle-dependence of nonlinear absorption coefficient (β) for ultrathin and thick TiN films. (c) Thickness dependence of carrier lifetimes (τ_1, ultrashort, τ_2, long electron-phonon interaction time) of ultrathin and thick films.

Our results demonstrate that the significant ENZ-enhanced nonlinearity can be realized in ultrathin metal films which have been challenged by optical losses and ultrathin thickness. Combined with its refractory property, ultrathin TiN films can provide an ideal platform in applications of nonlinear ENZ nanodevices operating in the visible spectral range.

H.A. received funding from the National Science and Technology Council of Taiwan (NSTC 110-2124-M-A49-009-MY3 and NSTC 111-2112-M-A49-044), S.G. from the Ministry of Science and Technology of Taiwan (NSTC 111-2123-M-007-002).

References

1. Campione, S., Brener, I., Marquier, F. “Theory of epsilon-near-zero modes in ultrathin films,” Phys. Rev. B, vol. 19, 121408, 2015.
2. Luk, T. S., Ceglia, D., Liu, S., Keeler, G. A., Prasankumar, R. P., Vincenti, M. A., Scalora, M., Sinclair, M. B., Campione, S. “Enhanced third harmonic generation from the epsilon-near-zero modes of ultrathin films.” Appl. Phys. Lett. vol. 106, 151103, 2015.
3. Alam, M. Z., Leon, I. D. L., Boyd, R. W. “Large optical nonlinearity of indium tin oxide in its epsilon-near-zero region,” Science, vol. 352, 795−797, 2016.
4. Gurung, S., Anopchenko, A., Bej, S., Joyner, J., Myers, J. D., Frantz, J., Lee, H. W. H. “Atomic Llayer engineering of epsilon-near-zero ultrathin films with controllable field enhancement,” Adv. Mater. Interfaces, vol. 7, 2000844, 2020.
5. Ho, I H., Chang, C.-W., Chen, Y.-L., Chang, W.-Y., Kuo, T.-J., Lu, Y.-J., Gwo, S., Ahn, H. “Ultrathin TiN epitaxial films as transparent conductive electrodes,” ACS Appl. Mater. Interfaces. vol. 14, 16839–16845, 2022.
6. Ho, I H., Chang, C.-W., Lu, Y.-J., Gwo, S., Ahn, H. “Transient optical properties of titanium aluminum nitride ($Ti_{1-x}Al_xN$) epilayers. J. Phys. Chem. C, vol. 127, 13731–13739, 2023.

Absorption-Based Nanophotonic Quantum Sensing on Resonant Metasurfaces

Laura Kim[1*]

[1]University of California Los Angeles, USA
[*]lbkim@ucla.edu

Abstract: Optically addressable nitrogen vacancy (NV) centers in diamond have emerged as one of the leading quantum sensing platforms but suffer from suboptimal readout due to the inefficient spin-photon interface. I will discuss spin-coupled resonant metasurfaces that offer opportunities for near-unity readout fidelity within a nanoscopic sensing volume for wide-field sensing applications.

Nitrogen-vacancy (NV) centers in diamonds have become a leading solid-state quantum system for wide-field sensing applications, owing to their ability to optically measure quantities such as electric field, magnetic field, and temperature. Atom-sized quantum sensors constructed from this spin-based qubit system can, in principle, achieve a remarkable sensitivity on the order of nT for one-second integration, comparable to the size of a magnetic field generated by a single electron approximately 50 nm away. However, the inefficient transduction process of mapping spin information onto optical fields creates a suboptimal readout of the spin population. The conventional optical readout is done by collecting visible fluorescence. This method is significantly limited due to poor photon collection efficiency and slow radiative transition; as a result, the sensors relying on the conventional fluorescence method remain nearly 1000 times less sensitive than the spin-projection-noise-limited sensitivity. Efforts to gain photonic control of the visible transition have been made; still, the challenge, especially for ensemble-based sensing at ambient conditions, is that an improved rate of fluorescence comes at the cost of diminishing spin contrast [1]. I will discuss nanophotonic strategies for enhancing spin-optic coupling for the *infrared* (IR) metastable transition of NV centers, which allows for *absorption*-based spin readout [2]. Unlike florescence-based detection, this approach offers a straightforward path to significant sensitivity improvements.

First, I will report on a spin-coupled plasmonic metasurface, which relies on the Rayleigh-Wood anomaly mode. This resonant mode strikes the right balance of maximizing the spatial overlap with a given near-surface sub-micron-scale NV layer and enhancing the rate of spin-dependent IR optical transition. This resonant surface is designed to readily couple with external radiation, allowing for shot-noise-limited sensing with a standard camera and eliminating the need of single-photon detectors [3,4]. I theoretically predict that the diamond-spin plasmonic metasurface for IR absorption readout reaches a volume-normalized magnetic field sensitivity of 10 pT $Hz^{-½}$ $um^{3/2}$ with the present-day NV diamond samples and fabrication techniques, which is about three orders of magnitude improvement over what has been previously realized [3]. I highlight that plasmonic metasurfaces have a particular advantage: the metallic structures with a subwavelength spacing can create desired magnetic field or electric field gradients to address NV spin transitions site-specifically. This capability can be leveraged to achieve deep sub-pixel imaging capabilities, paving the way for a new type of quantum micro(nano)scopy. Additionally, I will discuss all-dielectric structures, including q-BIC spin-diamond metasurfaces and slow-light waveguides, as an alternative platform. They offer high-quality factors with no optical losses and are excellent candidates for phase-sensitive dispersive readout schemes. I will report on both recent theoretical and experimental progress concerning such spin-coupled resonant metasurfaces. I will demonstrate that the spin-coupled resonant metasurfaces coherently encode information about the local magnetic field on spin-dependent phase and amplitude

changes of near-telecom light.

The reported spin-coupled resonant metasurfaces are projected to bridge the significant gap between the best demonstrated ensemble-based bulk NV sensors and the inherent spin-projection-noise-limited sensitivity [5]. The projected performance makes these studied metasurfaces attractive for addressing long-standing questions about electromagnetic phenomena and dynamics in quantum materials that remained elusive with classical sensors. Ensemble sensors operating at room temperature hold particular significance for probing biological samples and devices under natural operating conditions. We anticipate targeting the most demanding applications, such as chip-scale spatially-resolved chemical shift NMR and MRI of individual cells and molecules, noninvasive imaging of the magnetic signals from neuronal circuits in animals, and imaging of integrated circuits.

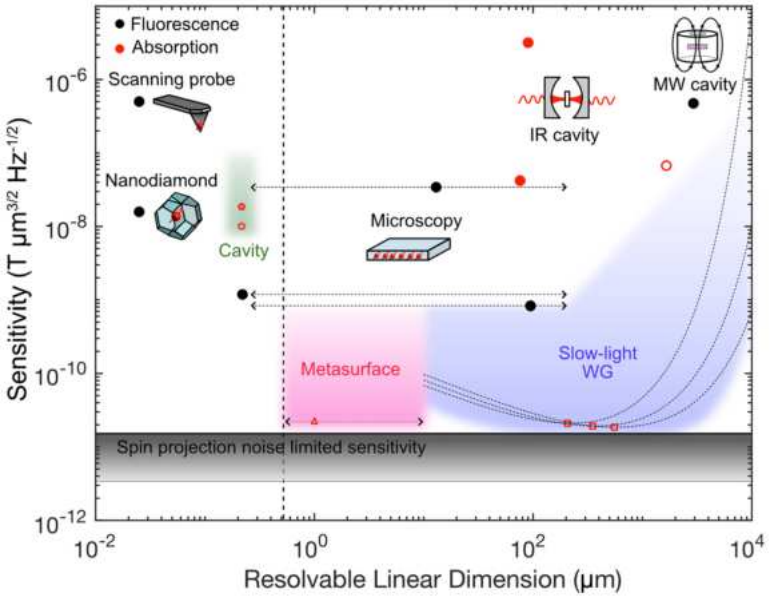


Figure 1. Resonantly enhanced nanophotonic quantum sensing based on absorption-based readout is projected to bridge the gap between the spin-projection-noise-limited sensitivity and the performances of current sensors [5].

References

1. S. Bogdanov, et al., "Electron spin contrast of Purcell-enhanced nitrogen-vacancy ensembles in nanodiamonds," PRB 96, 035146, 2017.
2. V. Acosta, et al., "Optical properties of the nitrogen-vacancy singlet levels in diamond," PRB 82, 201202(R), 2010.
3. L. Kim, et al., "Absorption-Based Diamond Spin Microscopy on a Plasmonic Quantum Metasurface," ACS Photonics 8(11), 3218-3225, 2021.
4. L. Kim, et. al., Patent US11585870B2, 2023.
5. L. Kim, et al., "Nanophotonic quantum sensing with engineered spin-optic coupling," Nanophotonics (2023): https://doi.org/10.1515/nanoph-2022-0682.

Local high quality factor metasurfaces for extremely low threshold nonlinear image filtering and efficient programmable wave shaping

Mark Lawrence, Lin Lin, Bo Zhao, and Samuel Ameyaw

Department of Electrical and Systems Engineering, Washington University in St. Louis, St. Louis, Missouri 63130, USA

Email: markl@wustl.edu

Abstract: The key benefits that metasurfaces offer image processing originate from the ability to almost arbitrarily manipulate light fields on a subwavelength scale. Unfortunately, the latest frontiers of efficient nonlinear and dynamic light shaping are at odds with the traditional metasurface paradigm as the demand for dramatically amplified light-matter coupling typically constrains dielectric meta-atoms to be much bigger than the wavelength. Here, we present a solution to this problem in the form of metasurfaces composed of dipolar guided mode resonators. Achieving meta-atom quality factors of over 1000 while maintaining subwavelength pixel pitch, we demonstrate nonlinear all-optical image processing with $<200\mu W/\mu m^2$, as well as fast, high contrast, spatial light modulation with sub-wavelength resolution driven by volt-level electrical biasing.

Nonlinear Mid-infrared Metasurfaces for Harmonic Generation and Deep-Subwavelength Nanomachining

Maxim R. Shcherbakov[1,2,3,*]
[1]Department of Electrical Engineering and Computer Science, University of California, Irvine, CA 92697, USA
[2]Beckman Laser Institute and Medical Clinic, University of California, Irvine, CA 92697, USA
[3]Department of Materials Science and Engineering, University of California, Irvine, CA 92697, USA
[*]corresponding author: maxim.shcherbakov@uci.edu

Abstract: We perform shot-controlled fifth harmonic generation measurements from a SiC meta-membrane with resonances in the mid-infrared. Back focal plane imaging reveals more than two orders of magnitude enhancement of the FHG from the meta-membrane, compared to the unstructured SiC film of the same thickness, along with an unusual Kerr-induced spectral behavior.

Nonlinear light-matter interactions can be strongly enhanced in photonic nanostructures [1] and metasurfaces [2], where the subwavelength thicknesses lifts the phase-matching requirement via resonant excitation. Free-standing metasurfaces–or meta-membranes–represent an attractive alternative to metasurfaces on substrates. In meta-membranes, the active layer of the device is its only layer. Exceptional linear-optical characteristics of free-standing metallic, dielectric and phonon-polaritonic metasurfaces, such as resonant reflectance, transmittance, absorbance, diffraction and polarization sensitivity, have been revealed. However, poor thermal dissipation has made the studies of freestanding metasurfaces under strong laser excitation challenging.

In this paper, we report on the nonlinear optical responses of meta-membranes. A SiC-based holey metasurface exhibits collective resonances in the mid-infrared frequency range (4000 nm) and produces bright fifth harmonic generation (FHG; 800 nm) in the back focal plane (BFP) of the imaging system. The sample of a meta-membrane was fabricated from a SiC free-standing film starting with a monocrystalline 4H-SiC on insulator (SiCOI) substrate fabricated as described in [3]. A typical SEM image of the membrane and its schematic is given in Fig. 1a. The unpatterned parts of the membrane were used for control measurements. The transmittance of the patterned membrane depends on location, with a typical example shown in Fig. 1b. For the design polarization of the sample (V, along the short sides of the rectangular holes), there are pronounced resonances with the Q-factor in the range of 22-31 across the membrane in the desired spectral region.

FHG BFP images show several orders of diffraction at 800 nm, as selected with a bandpass filter (see Figure 1c). The presence of the diffraction orders and the absence of incoherent emission filling the whole objective aperture signifies the absence of parasitic emission such as multiphoton photoluminescence. The FHG nature of the detected signal is additionally proven with single-shot measurements performed while increasing the pump intensity. Fitted with $y = ax^b$, the resulting slopes are $b_V = 5.0 \pm 0.4$ and $b_H = 4.9 \pm 0.7$, signifying the perturbative regime of harmonic generation. No single-shot FHG was observed for any pump intensity used in the experiment from an unstructured membrane. To estimate the maximum FHG enhancement enabled by nanostructuring, we have captured a single-shot FHG frame from the metasurface and an accumulated FHG signal from 1,000 shots measured at the unstructured part of the membrane, both at the same intensity of 300 GW/cm2. The resulting FHG counts are 16±2 for the metasurface using a single V-polarized shot and 40±2 for the unstructured membrane collected over 1,000 shots, signifying around FHG 400-fold enhancement in the metasurface.

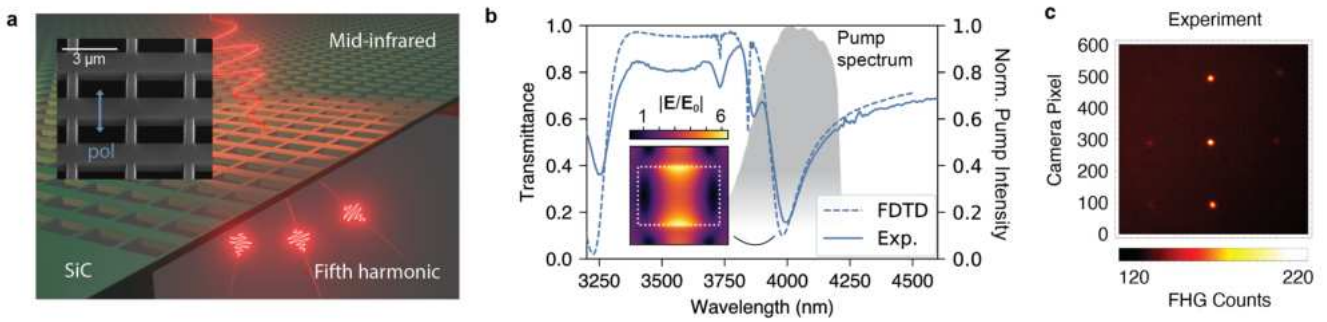


Figure 1. (a) SEM micrograph (left) and schematic (right) of the sample. (b) An experimental mid-IR transmittance spectrum of the sample for the design polarization (solid line) and the corresponding FDTD calculation (dashed line). The spectrum of the pump laser is superimposed (gray shaded area). The calculated local field distribution at a wavelength of 4000 nm in the middle section of the meta-membrane is shown to provide a substantial field enhancement at the pump wavelength. (c) Single-shot FHG from the free-standing SiC meta-membrane: BFP of the FHG emission from the metasurface for the horizontal (V, design) polarization.

We observed that several shots in the same position would permanently damage the metasurface, as the long-term laser damage tends to accumulate in resonant nanostructures [4]. To study the resonance-dependent behavior of FHG, sequences of single-shot measurements, each on a fresh spot of the sample, were performed going across it in places with differing thicknesses for the design polarization (V). The position of each shot was recorded, and its thickness derived by using a thickness map of the membrane obtained before it was. From the thickness, the resonance wavelength of the patterned membrane at each point can be reconstructed by comparison with numerical simulations. The FHG counts for the single-shot measurements are obtained for resonances with different wavelengths across the sample. The difference in the peak position for the FHG as a function of the resonance wavelength is attributed to the dynamic resonance red shift that we successfully explain in the context of a coupled-mode theory with a time-varying resonance frequency.

References

1. Aouani, H., et al., Third-harmonic-upconversion enhancement from a single semiconductor nanoparticle coupled to a plasmonic antenna. *Nature Nanotechnol.* **9**, 290–294 (2014).
2. Lee, J. *et al.* Giant nonlinear response from plasmonic metasurfaces coupled to intersubband transitions. *Nature* **511**, 65–69 (2014).
3. Lukin, D. M. *et al.* 4H-silicon-carbide-on-insulator for integrated quantum and nonlinear photonics. *Nature Photon.* **14**, 330–334 (2020).
4. Shcherbakov, M. R. *et al.* Nanoscale reshaping of resonant dielectric microstructures by light-driven explosions. *Nat. Commun.* **14**, 6688 (2023).

Near-field manipulation of angular momentum of light

Haoran Ren[1]

[1]School of Physics and Astronomy, Faculty of Science, Monash University, Australia

[*]corresponding author: Haoran.ren@monash.edu

Abstract: Nanophotonics opens the possibility of realising subwavelength optical vortices through coupling optical beams into subwavelength surface polaritons. I will highlight our recent work on hybrid nanophotonic circuits and nano-lasers used for angular-momentum-selective on-chip applications, as well as on dispersion control and multiplication of low-loss polaritonic vortices at mid-infrared frequencies.

Selective control of light is essential for optical science and technology with numerous applications. Nanophotonic waveguides and integrated couplers have been developed to achieve selective coupling and spatial control of multiple degrees of freedom of light [1-10]. Plasmonic nanostructures can enable compact multiplexing of the orbital angular momentum (OAM) of light [11-13]; however, strong dissipation of the highly localised OAM-distinct plasmonic fields in the near-field region hinders on-chip OAM transmission and processing. We demonstrated that incident OAM beams can selectively excite single-crystalline cadmium sulfide nanowires through coupling OAM-distinct plasmonic fields into nanowire waveguides for long-distance transportation [14]. This allowed us to build an OAM-controlled hybrid nanowire circuit for optical logic operations including AND and OR gates.

In addition to the demonstration of passive hybrid circuit, we recently demonstrated an active hybrid nanophotonic circuit that enables nonlinear optical selectivity based on the spin and OAM of light [15]. We designed active nanolaser circuits consisting of plasmonic metasurfaces and individual perovskite nanowires, allowing selective coupling of spin and OAM-distinctive plasmonic fields into nanowires that exhibit single-mode lasing. The optically selected nanolaser with nonlinear increase of light emission greatly enhances the baseline optical selectivity offered by the metasurface from about 0.4 up to near unity. Our demonstrated nonlinear optical selectivity may find important applications in all optical logic gates and nanowire networks, ultrafast optical switches, nanophotonic detectors, and on-chip optical and quantum information processing.

Optical vortices (OVs) with defined topological features are a ubiquitous phenomenon in optics. Owing to the diffraction limit of light, the minimum size of free-space OVs is fundamentally limited to the wavelength scale, while reduction of the physical size of OVs is required for photonic integration, on-chip information processing, and unveiling of new structured light-matter interactions. Nanophotonics opens the possibility of realizing subwavelength OVs via coupling optical beams into subwavelength confined surface states, such as surface plasmon polaritons [16-19] and surface phonon polaritons (SPhPs) [20-22]. However, the topological charge offered by the surface structure used for launching polaritonic OVs is always a fixed quantity. Here, we overcome this limitation via dispersion-driven topological charge multiplication [23]. We switch the topological charge of polaritonic OVs within a small ~3% frequency range by leveraging the strong sublinear dispersion of low-loss SPhPs on silicon carbide membranes. Our work paves the way for all-optical ultrafast switching of OVs and the exploration of OAM-based light-matter interactions at mid-infrared frequencies.

H.R. acknowledges funding support from the Australian Research Council (Projects DE220101085 and DP220102152).

References

1. H. G. Park et al., Nat. Photonics 2, 622-626 (2008).
2. A. Y. Piggott et al., Nat. Photonics 9, 374-377 (2015).
3. B. Shen, P. Wang, R. Polson, R. Menon, Nat. Photonics 9, 378-382 (2015).
4. J. Lin et al., Science 340, 331-334 (2013).
5. J. Petersen, J. Volz, A. Rauschenbeutel, Science 346, 67-71 (2014).
6. D. Pan, H. Wei, L. Gao, H. Xu, Phys. Rev.Lett. 117, 166803 (2016).
7. F. J. Rodríguez-Fortuño et al., Science 340, 328-330 (2013).
8. S. H. Gong, F. Alpeggiani, B. Sciacca, E. C. Garnett, L. Kuipers, Science 359, 443-447 (2018).
9. L. Sun et al., Nat. Photonics 13, 180-184 (2019).
10. Y. Chen et al., Nat. Nanotechnol. 17, 1178-1182 (2022).
11. H. Ren, X. Li, Q. Zhang, M. Gu, Science 352, 805-809 (2016).
12. Z. Yue, H. Ren, S. Wei, J. Lin, M. Gu, Nat. Commun. 9, 4413 (2018).
13. H. Ren, M. Gu, Laser Photonics Rev. 12, 1700255 (2018).
14. H. Ren et al., Nano Lett. 21, 6220-6227 (2021).
15. C. He et al., Nano Lett. 24, 1784-1791 (2023).
16. W. L. Barnes et al., Nature 424, 824-830 (2003).
17. H. Kim et al., Nano Lett. 10, 529-536 (2010).
18. A. David et al., Optica 2, 1045-1048 (2015).
19. G. Spektor et al., Science 355, 1187-1191 (2017).
20. J. D. Galdwell et al., Nanophotonics 4, 44-68 (2015).
21. L. Xiong et al., Nano Lett. 21, 9256-9261 (2021).
22. M. Wang et al, eLight 2, 12 (2022).
23. A. Mancini et al, Nat. Photonics https://doi.org/10.1038/s41566-024-01410-5 (2024).

Controlling Far-Field Radiation with Photoluminescent and Incandescent Metasurfaces

A. Nguyen[1], E. Bailly[1], J.-P. Hugonin[1], J.-J. Greffet[1] and B. Vest[1]

[1]Université Paris-Saclay, Institut d'Optique Graduate School, CNRS, Laboratoire Charles Fabry, 91127, Palaiseau, France.

[*]email: benjamin.vest@institutoptique.fr

Abstract: Intrinsically incoherent thermal or luminescent emitters can be coupled to metasurfaces to establish some coherence in emission and therefore to enable structuration of the emitted field. We present here light-emitting metasurfaces designed using a Kirchhoff's law approach demonstrating a controlled of the polarization state and angular radiation pattern.

Designing a light-emitting system means shaping light emission so that it matches requirements in terms of radiation pattern, polarization, or spectrum. However, non-lasing sources rely on spontaneous emission processes: the intrinsic randomness of emission prevents the structuration of a light beam by interference effects and most often results in isotropic and unpolarized emission. This has a straightforward solution: optical components. Lenses, irises, diaphragms, mirrors shape the angular spectrum; filters shape the temporal spectrum; Polarizers and waveplates can convert the polarization state, etc… Hence, the current optical engineering workflow is to first use a light emitting material matching a minimal number of requirements, and to eventually shape the emitted light with additional components external to the light source itself, mostly by filtering and rejecting some part of the energy. The addition of external components increases the bulkiness of light-emitting devices, affecting their total energy footprint and limiting integration, miniaturization and introducing losses.

Our work exploits the concept of **Light-Emitting Metasurfaces (LEMs):** devices that do integrate luminescent emitters consisting typically of a substrate covered with arrays of nanoresonators in interaction with luminescent emitters, distributed over the surface of the device. The LEM supports extended electromagnetic modes which play the role of a resonator. Although emitters are incoherent, their decay into the surface modes establishes a non-zero degree of coherence at long range. Besides, the surface modes can be coupled to the far-field (using grating effects for instance).

Light emission engineering is achieved by tailoring the properties of this leaky mode. At this end, we use a **Kirchhoff's approach**, extensively in the context of thermal emission. Here, the power emitted for a polarization (l) in a solid angle dΩ around the direction u at wavelength λ is given by [1]:

$$\mathrm{d}^2P_e^{(l)}(\mathbf{u},\lambda,\mu) = d\lambda d\Omega \int_V d^3\mathbf{r}'\alpha^{(l)}(-\mathbf{u},\mathbf{r}',\lambda,\mu)\frac{hc^2}{\lambda^5}\frac{1}{\exp(\frac{hc}{\lambda k_BT}-\frac{\mu}{k_BT})-1} \quad (1)$$

α is the local absorption rate within the resonator. The second factor is the blackbody radiance evaluated at $hc/\lambda - \mu$, where μ is the photon chemical potential which accounts for the pumping of the system. This relation shows that the local absorption rate α is the key to tailor quantitatively the spectral, angular, and polarization dependence of the emission. The integral is performed over the volume V of emitting material. This formulation

shows that emission in a mode is connected to emitting material placed in regions of high local absorption rate.

We use the Kirchhoff's approach to design and fabricate several LEMs. First, an **incandescent LEM** providing chiral emission in the MWIR (see Fig. 1) [2]. It consists of an array of thin metallic wires, heated by Joule effect on top of a transparent substrate. While the whole wire is heated at once, only the central fraction of the pattern, where inversion symmetry is broken, contributes to dichroism.

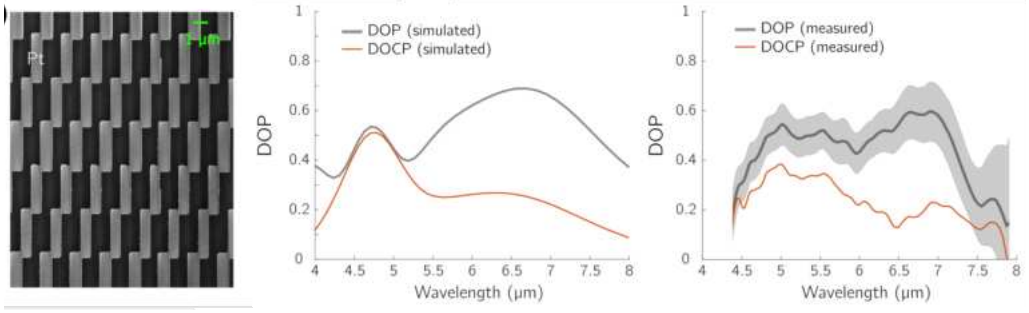


Fig. 1 Incandescent LEM for chiral emission [2] (a) SEM picture of the fabricated device. (b) Simulated and measured degree of polarization (DOP) and degree of circular polarization (DOCP). Shaded areas represent one-sigma error bars.

Second, **photoluminescent LEMs** consisting of metallic gratings covered with nanoplatelets provided by the LPEM [58]. Light occurs around 610 nm, within a 20° wide angular range (Fig. 2) [3], therefore establishing directional emission out of an ensemble of incoherent emitters.

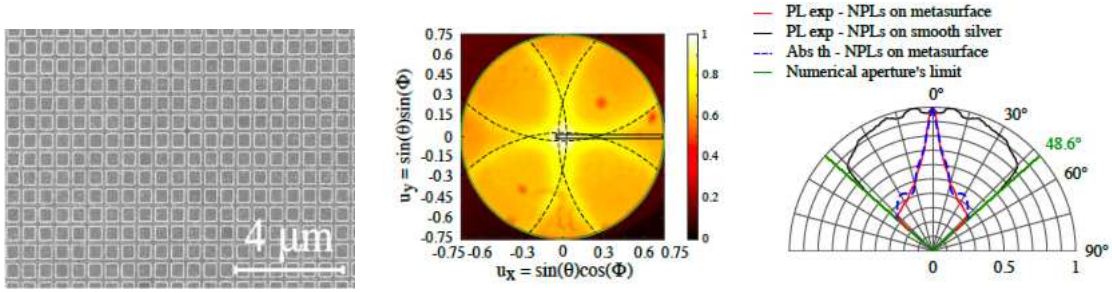


Fig. 2 2D Photoluminescent LEM for directional emission [3]. (Ledt) SEM image of the 2D silver grating forming the base of the LEM (Center) Fourier plane image of the photoluminescent emission **(**Right) Experimental angular radiation pattern (solid red) compared to simulated absorption using the Kirchhoff's formalism (blue dotted). Emission occurs within a 20° FWDH angular cone. Emission from unstructured emitter layer is isotropic (solid black)

Acknowledgements. This work is supported by the French National Agency (ANR) (ANR-17-CE24-0046 and ANR-17-CE24-016).

References

[1] J. J. Greffet, P. Bouchon, G. Brucoli, and F. Marquier, *Light Emission by Nonequilibrium Bodies: Local Kirchhoff Law*, Phys. Rev. X **8**, 21008 (2018).

[2] A. Nguyen, J.-P. Hugonin, A.-L. Coutrot, E. Garcia-Caurel, B. Vest, and J.-J. Greffet, *Large Circular Dichroism in the Emission from an Incandescent Metasurface*, Optica **10**, 232 (2023).

[3] E. Bailly, J.-P. Hugonin, J.-R. Coudevylle, C. Dabard, S. Ithurria, B. Vest, and J.-J. Greffet, *2D Silver-Nanoplatelets Metasurface for Bright Directional Photoluminescence, Designed with the Local Kirchhoff's Law*, ACS Nano **18**, 4903 (2024).

Nanoscale Extended Chirality Density

Hanwei Wang[1], Yulei Shen[1], Gayatri Chandran[1], and Yang Zhao[1,2,3*]

[1]Department of Electrical and Computer Engineering, University of Illinois Urbana Champaign, United States
[2]Holonyak Micro and Nanotechnology Laboratory, University of Illinois Urbana Champaign, United States
[3]Department of Bioengineering, University of Illinois Urbana Champaign, United States
[*]Corresponding author: yzhaoui@illinois.edu

Abstract: Chirality is essential in physical, chemical, and biological processes, playing a critical role in disease formation and drug synthesis. While metasurfaces enhance chirality detection, they often introduce significant background. This talk will address these challenges and introduce new design principles to improve the signal-to-noise ratio for more effective chirality detection.

Chirality describes molecules or structures that are not superimposable with their mirror counterparts, namely, enantiomers. Enantiomers may exhibit different biological, physical, or chemical properties, and therefore, have been widely studied. Enantioselective light-matter interactions such as absorption[1], fluorescence[2], and optical forces[3] have been applied to detect and separate enantiomers. Macroscopically, these interactions result in different responses to left- and right-handed circularly polarized light, which can be analyzed using circular dichroism (CD) spectroscopy. However, CD signals are typically weak at low molecule concentrations. To measure trace amounts of chiral molecules, high-quality factor dielectric nano-resonators or metamaterials have been used to detect the enantioselective shift of the resonance frequency[4]. Additionally, plasmonic nanostructures have been employed to enhance chiral absorption through an increased local optical chirality density[5]. Traditionally, such enhancement is modeled through an electric dipole-magnetic dipole (ED-MD) interaction, where the surface plasmon resonance enhances the local optical chirality, thus increasing the differential chiral absorption. However, this overlooks chiral absorption components that are from higher-order multipolar absorption, especially in the presence of plasmon-induced spatial non-homogeneity of the fields[6].

Macroscopic chiral molecules may support non-zero quadrupole moments if the molecules are not completely randomized. In a general gradient field, such an interaction can lead to chiral absorption. However, little is known about how this interaction contributes to the overall chiral absorption in spatially varying gradient fields, for example, those induced by resonant nanostructures. The molecular ED-EQ interaction is sensitive to the field gradient created by localized surface plasmon resonance, which could result in additional chiral absorption, while such an enhancement mechanism and the spectral features are expected to be distinct from the well-known ED-MD interaction[7].

We assume that the chiral medium facilitates an electric dipole-electric quadrupole (ED-EQ) interaction[8] characterized by $Q_{i,j}^{\pm} = \sum_k \gamma_{i,j,k} P_k^{\pm}$, where ± denotes the left- and right- handedness of light; $\gamma_{i,j,k}$ is the ED-EQ coupling coefficient [9]; i, j, k represent the Cartesian coordinates; and P is the polarization vector. For simplicity, we assume the chiral medium has a scalar ED-EQ coefficient, and Q has only non-zero diagonal terms. The polarization vector is associated with the ED-MD interaction through $P_k^{\pm} = \varepsilon_0 \chi E_k^{\pm} - i\frac{\kappa}{c} H_k^{\pm}$, where

χ is the linear susceptibility, κ is the Pasteur parameter that describes the ED-MD interaction, and c is the speed of light. Our analysis focuses on the absorptions associated with the electric dipole, magnetic dipole, and electric quadrupole. Notably, the absorption involving electric quadrupole contains a term analogous to the optical chirality density, $C = \mathrm{Im}\left(E^* \cdot B\right)$, as $C_k^{\ e} = \frac{\partial E_k^{\ *}}{\partial k} B_k$, which is main discussion of this presentation.

In this talk, we show that a chiral medium supporting both ED-MD and ED-EQ interactions can exhibit the extended chirality beyond the traditionally defined optical chirality density. We demonstrate numerically that the overall chiral absorption is associated with the ED-EQ interactions induced by the resonance of metal-insulator-metal nano-resonator. The resonator not only enhances the molecule's chiral absorption through an increased optical chirality density but also through an enhanced ED-EQ interaction via the field gradient.

References

1. Tang, Y. & Cohen, A.E. Optical chirality and its interaction with matter. *Physical review letters* **104**, 163901 (2010).
2. Solomon, M.L., Abendroth, J.M., Poulikakos, L.V., Hu, J. & Dionne, J.A. Fluorescence-detected circular dichroism of a chiral molecular monolayer with dielectric metasurfaces. *Journal of the American Chemical Society* **142**, 18304-18309 (2020).
3. Zhao, Y., Saleh, A.A. & Dionne, J.A. Enantioselective optical trapping of chiral nanoparticles with plasmonic tweezers. *Acs Photonics* **3**, 304-309 (2016).
4. Garcia-Guirado, J., Svedendahl, M., Puigdollers, J. & Quidant, R. Enhanced chiral sensing with dielectric nanoresonators. *Nano letters* **20**, 585-591 (2019).
5. Zhao, Y., Askarpour, A.N., Sun, L., Shi, J., Li, X. & Alù, A. Chirality detection of enantiomers using twisted optical metamaterials. *Nature Communications* **8**, 14180 (2017).
6. Yang, N. & Cohen, A.E. Local geometry of electromagnetic fields and its role in molecular multipole transitions. *The Journal of Physical Chemistry B* **115**, 5304-5311 (2011).
7. Govorov, A.O. Plasmon-induced circular dichroism of a chiral molecule in the vicinity of metal nanocrystals. Application to various geometries. *The Journal of Physical Chemistry C* **115**, 7914-7923 (2011).
8. Zhou, F., Li, Z.-Y., Liu, Y. & Xia, Y. Quantitative analysis of dipole and quadrupole excitation in the surface plasmon resonance of metal nanoparticles. *The Journal of Physical Chemistry C* **112**, 20233-20240 (2008).
9. Holt, A. & Karlström, G. Inclusion of the quadrupole moment when describing polarization. The effect of the dipole‐quadrupole polarizability. *Journal of computational chemistry* **29**, 2033-2038 (2008).

Electrochemically Active Metasurface and Multispectral Light and Heat Management

P. -C. Hsu[1*]

[1]Pritzker School of Molecular Engineering, University of Chicago, USA
[*]corresponding author: pochunhsu@uchicago.edu

Abstract: Electrochemistry is a powerful tool with gigantic refractive index changes. This talk includes three subjects: (i) Conjugated polymers for near-perfect dynamic thermal meta-emitter. (ii) Reversible metal electrodeposition for multispectral solar and mid-infrared control and dynamic beam steering. (iii) Spectrally selective hierarchical fabric for practical radiative cooling for the human body.

Electrochemistry is a powerful tuning knob for inducing drastic optical property changes. By applying an electrical bias while using counterions to maintain charge neutrality, electrochemistry can vary the carrier density or even trigger a phase transformation in an electrically addressable manner, which is particularly desirable in many applications where tunable range, scalability, or non-volatility is crucial. Meanwhile, metamaterials provide additional degrees of freedom to boost performance and achieve multifunctional control. However, electrochemically active metasurfaces are still largely underexplored, partly due to the lack of intrinsic property databases for newly developed materials. More co-development is needed among fundamental materials science, metasurface design, and electrochemical device engineering. In this talk, I will present two types of electrochemically active materials and one work dedicated to radiative cooling textiles: (i) Conducting polymers for near-perfect dynamic thermal emitter. We conducted infrared ellipsometry to measure the potential-dependent optical property and designed a tunable metal-dielectric-metal near-perfect absorber for wearable variable emittance (WeaVE) devices for personal thermoregulation. (ii) Reversible metal electrodeposition for multispectral solar and mid-infrared control. The potential, electrolyte, and interfacial properties dictate the metal morphology, allowing reversible switching between a solar adsorber and a radiative cooler for all-year-round renewable thermoregulation for net-zero-energy buildings. (iii) Spectrally selective hierarchical fabric for practical personal radiative cooling against urban heat island effect and surrounding thermal radiation. We use vibrational spectroscopy to down-select the textile material that has high and selective emissivity in the atmospheric transmission window. This special spectral property effectively blocks the radiative heat gain from the thermal radiation from the buildings and grounds, resulting in higher radiative cooling power than a broadband-emitting fabric. These research outcomes can lead toward energy-efficient thermoregulation for the human-energy-building nexus for net-zero goals.

Acknowledgements: We thank funding support from the National Science Foundation (ECCS Award No. 2145933), Sony Corporation, and the Pritzker School of Molecular Engineering at the University of Chicago.

References

1. Q Li, T.-H. Chen, P.-C. Hsu* “Use electrochemistry to charge the next dynamic thermal metamaterials” Next Energy (2024) DOI: 10.1016/j.nxener.2024.100108
2. T.-H. Chen†, Y. Hong†, C.-T. Fu, A. Nandi, W. Xie, J. Yin*, P.-C. Hsu* “A kirigami-enabled electrochromic wearable variable-emittance device for energy-efficient adaptive personal thermoregulation” PNAS Nexus (2023) DOI:

10.1093/pnasnexus/pgad165

3. C. Sui, J. Pu, T.-H. Chen, Y.-T. Lai, Y. Rao, R. Wu, Y. Han, K. Wang, X. Li, J. Liang, V. Viswanathan*, P.-C. Hsu* "Dynamic electrochromism for all-season radiative thermoregulation" Nature Sustainability (2023) DOI: 10.1038/s41893-022-01023-2
4. R. Wu†, C. Sui†, T.-H. Chen, Z. Zhou, Q. Li, G. Yan, Y. Han, J. Liang, P.-J. Hung, E. Luo, D. V. Talapin, P.-C. Hsu* "Spectrally engineered textile for radiative cooling against urban heat islands" In Revision, Science.
5. G. Higueros,†, K. Wang†, C. Sui, P.-C. Hsu* "Solution-Processed Metallic Nanowires Network for Wearable Transparent Thermal Radiation Shield" In Revision, ACS Nano.
6. Q Li, T.-H. Chen, P.-C. Hsu* "Use electrochemistry to charge the next dynamic thermal metamaterials" Next Energy (2024) DOI: 10.1016/j.nxener.2024.100108

Building Uncooled Infrared Camera based on One Atom Thick Graphene

Debashis Chanda

CREOL, College of Optics and Photonics, University of Central Florida, Florida, USA
*corresponding author: Debashis.Chanda@ucf.edu

Abstract: The talk will outline a novel strategy for uncooled, tunable, multispectral infrared detection. Due to the low photon energy, detection of infrared photons is challenging at room temperature. One atom thick graphene offers an alternative mechanism bypassing material bandgap restriction. Further, the ability of carrier concentration modulation on graphene via external voltage offers dynamic spectral selectivity for “color” night vision/sensing. The performance of preliminary demonstration compares favorably even with present cryogenically cooled detection schemes paving the path for commercial development of many applications from space exploration to healthcare.

Palladium Nanorods Overlayer Induced Electrostatic Contribution to Silicon Rib Waveguide Sensitivity

A. Novikova[1*], A. Katiyi[1] and A. Karabchevsky[1]

[1]School of Electrical and Computer Engineering, Ben-Gurion University of the Negev, Beer-Sheva 8410501, Israel
[*]corresponding author: novikoan@post.bgu.ac.il

Abstract: The methods to identifying fast-evaporating substances must be fast, easy to use and sensitive [1,2]. In our work, we modified the surface of rib waveguides with gold nanorods coated with palladium to adsorb the hexane and N-Methylaniline molecules to the waveguide surface. This led to the increased overlap of the evanescent fields with molecules under investigation. Our results on mixtures of hexane and N-methylaniline show absorption of 7.6 dB (amine group) and 6.8 dB (CH group). The absorption of hexane bonds in water is 5.5 dB, which is 100 times higher than those predicted by the numerical simulation.

We investigated the absorption spectrum of the N-methylaniline (NMA) in a hexane mixture and pure hexane on modified waveguides. The IR spectra of the mixtures are presented in Figure 1.

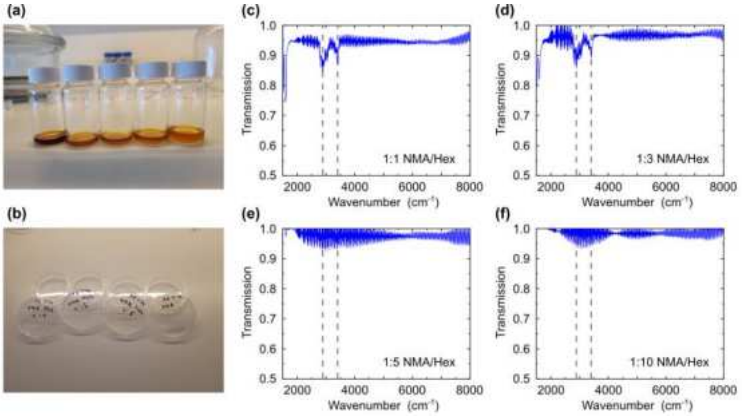


Figure 1. FTIR spectroscopy results. (a) Samples with different concentrations of NMA in hexane and (b) glass slides with palladium layer (concentration of 10 μg/ml in water) with the samples deposited on them. FTIR spectra of glass samples with a concentration of (c) 1:1 NMA to hexane, (d) 1:3 NMA to hexane, (e) 1:5 NMA hexane and (f) 1:10 NMA hexane.

The peaks appear at 3490 cm^{-1} and are associated with CH, methyl group. The peaks associated with N-methyl bond are located at 2812, 2801 cm^{-1} and 2855.65, 2879.45 cm^{-1}. Next, we characterized the gold nanorods with palladium and rib waveguides by means of optical spectroscopy. The clean surface of the waveguide shows strips with varying widths where the wider strip is 20 μm wide and the smaller is 9.9 μm wide, a strip height of 400 nm. The top of the waveguide has a layer of Ta_2O_5. We determined the concentration of palladium in water does not form conglomerates on the surface, but separate areas and amounted to 10 μg/ml.

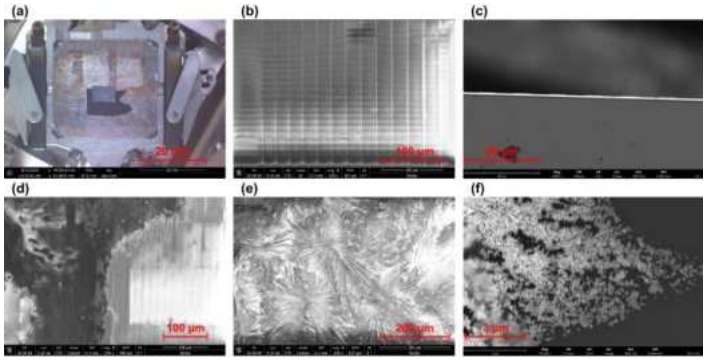


Figure 2. Scanning electron microscope (SEM) images. (a) a photograph of a rib waveguide with palladium positioned on the scanning electron microscope holder. (b) Top view and (c) side view of the surface of a clean rib waveguide. (d) Rib waveguide with palladium nanorods deposited on the top of the waveguide while the palladium nanorods in water had a 100 μg/ml concentration. (e) Zoomed-in image of rib waveguide with palladium. (f) Rib waveguide with palladium nanorods deposited on the top of the waveguide while the palladium nanorods in water had a concentration of 10 μg/ml.

To assess the performance of the modified rib waveguide in a molecular environment, we designed an experimental setup as shown in Fig. 3a. The transmittance of pure and nanorod-coated rib waveguides in air was measured to obtain a reference spectrum. Figure 3e shows the transmission of a pure rib waveguide (blue graph) and a modified rib waveguide with N-methylaniline with hexane (red curve) at a wavelength range of 1300-1600 nm. Absorption bands appear at wavelengths of 1379 nm, 1448 nm, and 1589 nm. The first two peaks are attributed to C-H bones and the last to N-H bonds. Figure 5f shows that in hexane in water, the absorption appears at a wavelength (red curve) of 1379 nm (CH_3) with a drop of 5.5 dB and the blue-shifted peak. There is a peak at 1448 nm (CH_2) with a drop of 1.5 dB. Both peaks are attributed to the C-H bonds of hexane.

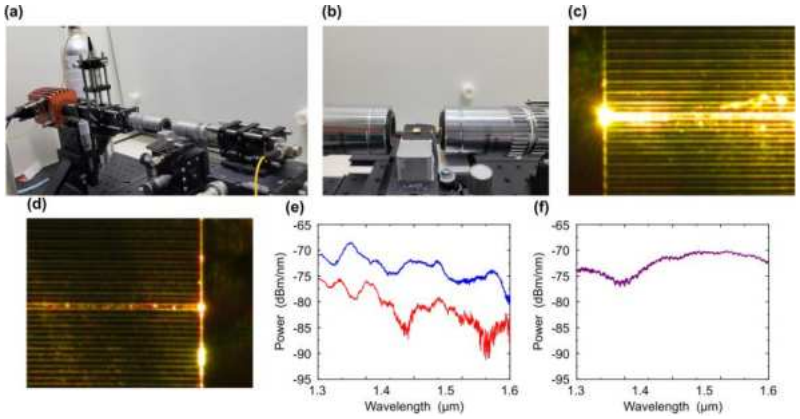


Figure 3. (a) The experimental setup and (b) zoom in on the modified rib waveguide with palladium nanorods. Microscope top view images of (c) the input and (d) output facets. (e) Measured transmission spectra at a wavelengths range of 1.3-1.6 μm modified rib waveguides with palladium nanorods with a mixture of N-methylaniline in hexane (red curve) with a concentration of 1:3 (NMA/hexane) and clean rib waveguide (blue curve). (f) Normalized transmission spectra at a wavelength range of 1.3-1.6μm of modified rib waveguide with hexane in water 1:1.

Funding: This research was supported by the Ministry of Science & Technology, Israel- Grant #0006276.

References

1. Novikova, A. and Karabchevsky, A. "Green Extraction of Graphene from Natural Mineral Shungite," Nanomaterials, No. 24, 4356, 2022.
2. Novikova A., Katiyi, A., Halstuch, A. and Karabchevsky, A. "Green-Graphene Protective Overlayer on Optical Microfibers: Prolongs the Device Lifetime," Nanomaterials, No 17, 2915, 2022.

Resonances Governed by Lattice Induced Multipole Coupling in Metasurfaces with Inversion Symmetry

I. Allayarov[1,2,*], A. B. Evlyukhin[2,3], and A. Calà Lesina[1,2]

[1]Institute for Transport and Automation Technology, Leibniz University Hannover, Garbsen, Germany

[2]Cluster of Excellence PhoenixD, Leibniz University Hannover, Hannover, Germany

[3]Institute of Quantum Optics, Leibniz University Hannover, Hannover, Germany

[*]corresponding author: izzatjon.allayarov@hot.uni-hannover.de

Abstract: We discuss multiresonant features of symmetric metasurfaces and the physical mechanism behind them, i.e., the lattice induced coupling between high-order Mie-type multipoles. Our analytical and numerical results provide important possibilities in the design of simple metasurfaces for structural color generation, optical sensing, and nonlinear processes.

Simple resonant nanostructures serve as a physical basis for many technological advances in modern nanophotonics. For instance, on the basis of dielectric metasurfaces [1] many optical effects have been realized and proposed [2]. In this context, the study of the relation between resonances and the structural parameters of such systems is important for pushing the limits of current technologies as well as for new applications.

To partially address this big issue, we have investigated a multiresonant response of symmetric metasurfaces. Because multiresonant metasurfaces can be used to have a compact device that operates in multiband regime and is desired for various applications e.g., in sensing, nonlinear optics, structural color generation. Based on our analytical and numerical calculations, we have designed multiresonant metasurfaces by exploiting lattice-induced electromagnetic coupling effect within the same parity multipoles [3]. The proposed metasurface that consists of a regularly arranged (i.e., periodic lattice) array of symmetric dielectric nanoparticles, has potential application in structural color generation (pixel) since it exhibits simultaneous resonances at almost red, green, and blue wavelengths.

Another important aspect of our investigation is that our results provide important possibilities in the design of simple and symmetric metasurfaces with high quality factor resonances that are crucial for optical sensing, lasing and nonlinear processes. Details of this case will be presented at the conference.

We acknowledge support from DFG (German Research Foundation) under Germany's Excellence Strategy within the Cluster of Excellence PhoenixD (EXC 2122, Project ID 390833453).

References

1. A. B. Evlyukhin, C. Reinhardt, A. Seidel, et al., "Optical response features of Si-nanoparticle arrays," Phys. Rev. B **82**, 045404 (2010).
2. W. Liu, Z. Li, H. Cheng, and S. Chen, "Dielectric resonance-based optical metasurfaces: From fundamentals to applications," Iscience, **23** (2020).
3. I. Allayarov, A. B. Evlyukhin, A. Calà Lesina, "Multiresonant all-dielectric metasurfaces based on high-order multipole coupling in the visible," Opt. Express **32**, 5641 (2024).

Vibrational Strong Coupling for Cavity Catalysis of an Enantioselective Reaction

J. Singh[1], P. Garg[1], R.V. Anand[1] and J. George[1*]

[1]Indian Institute of Science Education and Research Mohali, India
[*]Corresponding author: jgeorge@iisermohali.ac.in

Abstract: Vibrational strong coupling is applied, and Fabry-Perot cavity mode is coupled to the reactant vibration in an asymmetric aldol reaction. Increase in product formation is observed by NMR, but negligible changes in enantioselectivity are observed by chiral HPLC. Control experiments suggest the minimum involvement of enantioselectivity in the rate-determining step.

Summary: In the 1960s, when the laser was first invented, scientists tried to modify reactions by shining lasers, and they were partially successful, but the large dissipation in the molecular system hindered its vast applicability. In the last decade, strong light-matter interaction and its applications in the form of a new field, namely Vibrational Strong Coupling (VSC), have also proved to achieve the same goal even more fascinatingly. Since the latter does not require any outside photon but utilizes vacuum energy to induce the changes. In VSC, a molecular vibration of the interest is coupled to the cavity mode of the resonant frequency, forming the new and exotic hybrid polaritonic states separated by vacuum rabi splitting energy. It measures the strength of the interaction between light and matter. Mathematically, Rabi splitting depends on the following equation.

$$\hbar\Omega_R = 2V_n = 2\boldsymbol{d}\cdot\boldsymbol{E} = 2d\cdot\sqrt{\frac{\hbar\omega_c}{2\varepsilon_0\upsilon}}\times\sqrt{n_{ph}+1} \quad (1)$$

Here, V_n is the interaction energy in the absence of any type of dissipation, and it is the scalar product of the transition dipole moment (d) and the electric field strength (E). ω_c is the resonant frequency, E_0 is the vacuum permittivity, υ is the mode volume, and n_{ph} is the number of photons involved. Even if n_{ph} is zero, some splitting will still exist; therefore, it is called vacuum Rabi splitting energy.[1] VSC can modify the ground state chemical reactions,[2,3] crystallization process,[4], etc. It has also been proposed that chiral cavities can modify the enantioselective outcome of the ground-state chemical reaction.[5] But as of now, no experimental reports are presently dealing with an enantioselective reaction inside an achiral FP cavity.

For our experiment, we chose an asymmetric aldol reaction in which two reactants, namely 4-nitro benzaldehyde and acetone, react together in the presence of *L*-proline to form an enantioselective product. The reaction mixture was injected into a microfluidic cell, acting as a Fabry-Pérot cavity. Both the reactants contain a carbonyl vibration, which is coupled to the cavity mode of the resonant cavity. Coupling of the vibrational band of the reactants results in the formation of the polaritonic states with their own exotic properties and leads the system into the strong coupling. This reaction was allowed for a fixed amount of time before quenching and taking out the products for further analysis. The amount of the product in the reaction mixture is estimated by the ^{1}H Nuclear Magnetic Resonance (NMR) spectroscopy. The product formation is roughly 48(±5) % in the experiment without VSC.

On the other hand, in the VSC experiment, this product formation was boosted to a great extent and increased up to 90% at ON-resonance. This shows the reaction progress is greatly enhanced under VSC with the vacuum photon (Figure 1A). Next, we tested the enantioselectivity of the product using chiral High-Performance Liquid Chromatography (HPLC). The enantioselectivity calculated from the six measurements was 62 (±4) % of the R-enantiomer for the non-VSC experiment. For the VSC experiments, the enantioselectivity of the product at ON-

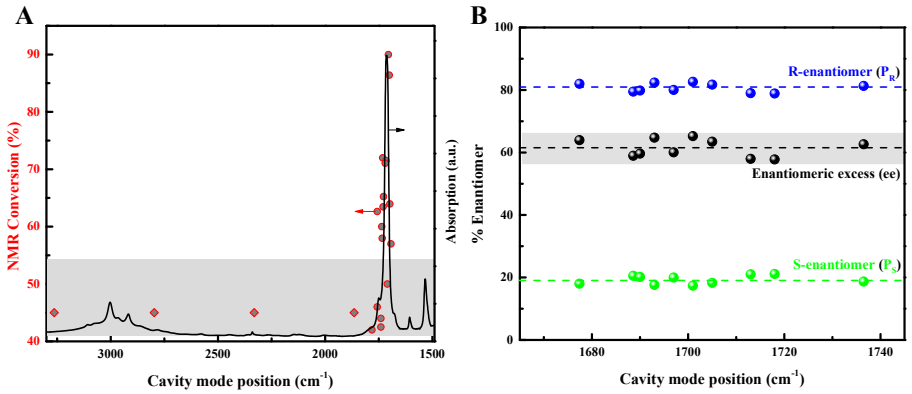


Figure.1 Effect of VSC on reaction yield and enantioselectivity. Variation in **(A)** %NMR conversion and **(B)** enantiomeric excess upon varying the cavity mode position (Gray shaded region shows the variation in enantiomeric excess in the non-cavity experiments).

resonance conditions were largely unaffected (Figure 1B). To investigate further, temperature-dependent experiments were carried out without the cavity since, in much of the literature, it is reported that VSC can modify the reaction rate similarly to temperature increase. Therefore, in non-cavity, if the rise in the temperature can cause an increase in the rate of product formation, enantioselectivity should vary. But, for the current system, negligible change in the enantioselectivity was observed with increased temperature.

Additionally, the literature suggests that this reaction proceeds in two major steps: (1) formation of the intermediate and (2) formation of the product by enantioselective attack of the aldehyde on the intermediate. The slowest step is the first step, where the intermediate is being formed, and therefore, we proposed that VSC can modify the reaction yield but not the product enantioselectivity in this system because the chiral step is not the slowest. Hence, systems with rate-determining and enantioselective steps that are more closely interlinked can be tested under VSC, and the product's enantioselectivity can be modified.[6]

Jaibir Singh and Pallavi Garg thank CSIR and UGC for the Shyama Prasad Mukherjee fellowship and UGC-SRF fellowship, respectively. MoE is acknowledged for the funding support and IISER Mohali for infrastructure facilities.

References

1. George, J. & Singh, J. Polaritonic Chemistry: Band-Selective Control of Chemical Reactions by Vibrational Strong Coupling. *ACS Catal.* **13**, 2631–2636 (2023).
2. Thomas, A. *et al.* Ground-state chemical reactivity under vibrational coupling to the vacuum electromagnetic field. *Angew. Chemie* **128**, 11634–11638 (2016).
3. Lather, J., Bhatt, P., Thomas, A., Ebbesen, T. W. & George, J. Cavity Catalysis by Cooperative Vibrational Strong Coupling of Reactant and Solvent Molecules. *Angew. Chemie* **131**, 10745–10748 (2019).
4. Hirai, K., Ishikawa, H., Chervy, T., Hutchison, J. A. & Uji-i, H. Selective crystallisation via vibrational strong coupling. *Chem. Sci.* **12**, 11986–11994 (2021).
5. Baranov, D. G., Schäfer, C. & Gorkunov, M. V. Toward Molecular Chiral Polaritons. *ACS Photonics* **10**, 2440–2455 (2023).
6. Singh, J., Garg, P., Anand, R. V. & George, J. Cavity Catalysis of an Enantioselective Reaction under Vibrational Strong Coupling. *Chem. - A Eur. J.* **e202400607**, 1–5 (2024).

Real time optical and mechanical environmental sensing based on nano-optomechanical disk resonators

E. Sentre-Arribas[1], A. Aparicio-Millán[1], A. Lemaître[2], I. Favero[3], J. Tamayo[4], M. Calleja, and E. Gil-Santos[1*]

[1] Optomechanical Sensors Lab, Instituto de Micro y Nanotecnología, IMN-CNM (CSIC), Spain
[2]Centre des Nanosciences et Nanotechnologies, CNRS, Université Paris-Saclay, France
[3]Matériaux et Phénomènes Quantiques, CNRS, Université Paris-Cité, France
[4] Bionanomechanics Lab, Instituto de Micro y Nanotecnología, IMN-CNM (CSIC), Spain
[*]eduardo.gil@csic.es

Abstract: In this work, we use nano-optomechanical disk resonators for environmental monitoring. We show that simultaneous tracking of both optical and mechanical modes enables to discriminate between temperature and humidity effects. We demonstrate that actively tracking the optical mode allows to directly obtain reliable mechanical signals, avoiding previous calibration and extra post-processing.

Optical and mechanical resonators have each been abundantly employed in sensing applications. Here we show that bringing together optical and mechanical resonances in a unique sensing platform significantly improves the sensor performance [1]. We employ nanoscale optomechanical disk resonators (Fig. 1.a) fabricated out of GaAs. They simultaneously support high quality optical and mechanical modes, which provide extraordinary sensitivities. Figure 1.b shows the relevance of actively tracking the optical mode when operating optomechanical sensors. It enables the obtention of direct reliable mechanical signals, which avoids previous calibrations and extra post-treatment. In addition, actively tracking the optical mode enlarges the sensing range and prevents degradation of the device sensitivity during the experiment.

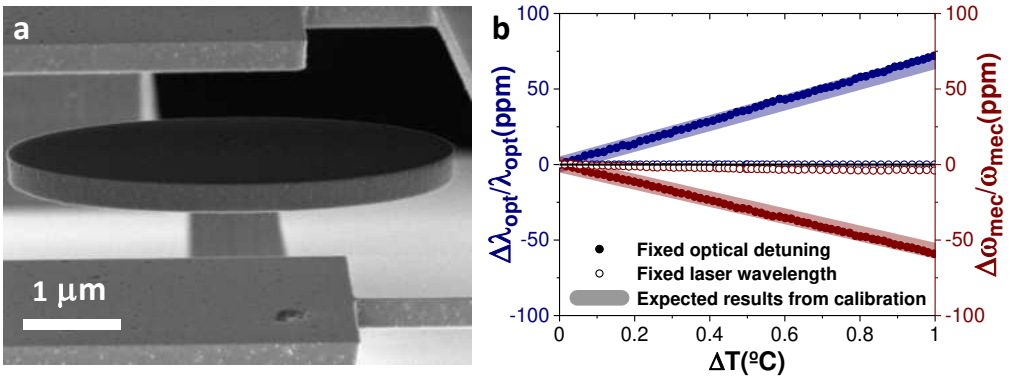


Figure 1. *(a) Scanning electron microscopy image of a GaAs optomechanical disk (r=2.5 um, t=320 nm) resting on an AlGaAs pedestal. (b) Optical (blue) and mechanical (red) resonance shifts as a function of temperature change, fixing the optical wavelength (open circles) and the optical detuning (full circles). Solid lines represent the expected responses.*

To demonstrate the capabilities of simultaneously tracking optical and mechanical signals, we perform environmental monitoring experiments (Fig. 2), in which we vary the temperature and the relative humidity and study the response of our device. By analyzing optical and mechanical signals, we are able to discern in between both temperature and relative humidity effects with a resolution of 1 mK and 0.1%, respectively, and, importantly, when both parameters change at the same time.

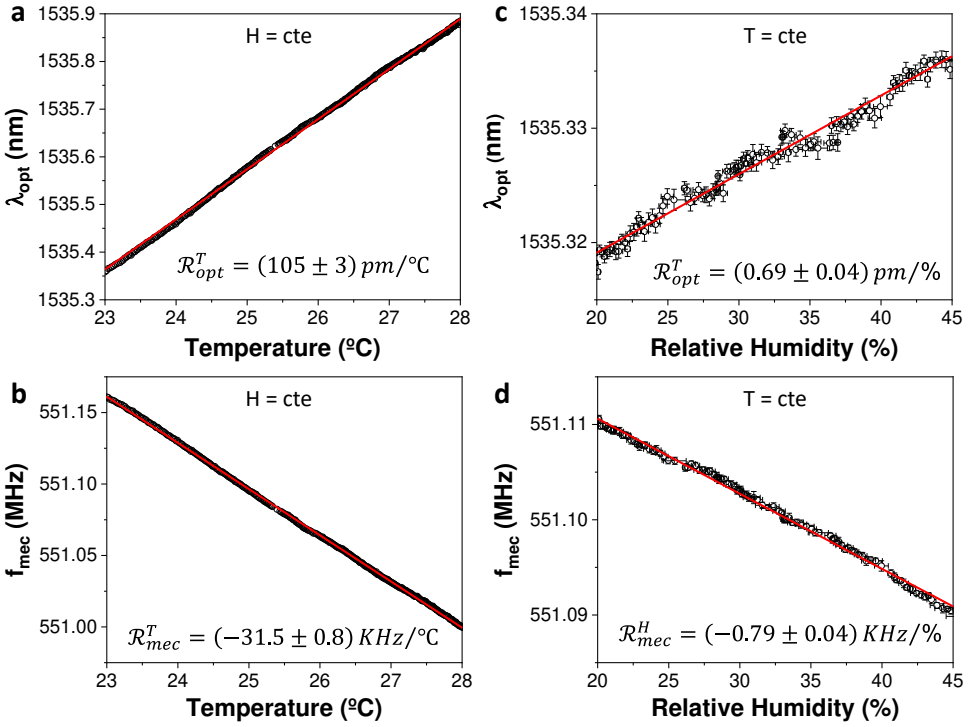


Figure 2. *Optical and mechanical responsivity to temperature and relative humidity changes. (a) Evolution of the disk WGM resonant wavelength and (b) the disk 1st RBM resonant frequency as a function of temperature, at constant relative humidity. (c) Evolution of the disk WGM resonant wavelength and (d) the disk 1st RBM resonant frequency as a function of the relative humidity, at a constant temperature.*

Although we perform environmental sensing, the conclusions of this work extend to other sensing applications. This work sets the basis for multi-mode sensing based on optomechanical disk resonators [2].

Acknowledgments: We acknowledge the service from the Micro and Nanofabrication Laboratory and the X-SEM laboratory at IMN-CNM funded by the "Comunidad de Madrid" (project S2018/NMT-4291 TEC2SPACE) and by MINECO (project CSIC13-4 × 10–1794 with support from FEDER, FSE). Work partially supported by the European Union's Horizon 2020 Research and Innovation Program under grant agreement no. 731868-VIRUSCAN, by the "Fundación BBVA" under the program "Beca Leonardo a Investigadores y Creadores Culturales 2021" through the project DISOM, and by the "Fundación Ramón Areces" under the project OPTOCAP. Also acknowledge the financial support by the Spanish Science and Innovation Ministry through Ramón y Cajal grant RYC-2019-026626-I, and through the projects "CELLBIOPHYS" and "ONCODEEPLASM"; the one by "Comunidad Autónoma de Madrid" through the project Y2020/BIO- 65194 scCANCER-CM. and from ERC NOMLI project (no 770933).

References

1. Sentre-Arribas, E., Aparicio-Millán, A., Lemaître, A., Favero, I., Tamayo, J., Calleja, M., and Gil-Santos, E. "Simultaneous optical and mechanical sensing based on optomechanical resonators", ACS Sensors, 2023. 10.1021/acssensors.3c02103.
2. O. Malvar, E. Gil-Santos, J. J. Ruz, E. Sentre-Arribas et al., "Multifrequency Nanomechanical Mass Spectrometer Prototype for Measuring Viral Particles Using Optomechanical Disk Resonators," 2023 IEEE 36th International Conference on Micro Electro Mechanical Systems (MEMS), Munich, Germany, pp. 153-156, 2023.

Simulation of spatial rogue waves in a solid-state laser with transverse mode-locking

R. Navitskaya[1,2], I. Stashkevitch[1], S. Derevyanko[2*], and A. Karabchevsky[2]

[1]Faculty of Physics, Belarusian State University, 4 Nezalezhnasti Avenue, 220030 Minsk, Belarus
[2]School of Electrical and Computer Engineering, Ben-Gurion University of the Negev, Beer Sheva, Israel
[*]corresponding author: stasd@bgu.ac.il

Abstract: We investigate theoretically the generation of spatial and spatio-temporal rogue waves in a multimode Q-switched Nd:YAG laser as a result of spontaneous transverse mode-locking. The statistics and temporal dynamics of rogue waves are defined by the frequency separation between the modes and spatial anisotropy of the mode configuration.

Spatial and spatio-temporal rogue waves (RWs) represent “hot spots” with extreme intensities that can emerge spontaneously in complex multimode optical systems. Their formation in lasers can be governed by different factors including nonlinearity, dispersion, gain, and spatial effects [1]. In the case of negligible nonlinear effects in the laser cavity, spatial rogue waves can be onset by spontaneous phase synchronization of transverse modes with close frequencies and assisted by spatially anisotropic mode configuration [2].

To investigate the spatio-temporal dynamics of a multimode laser, we represent the total field inside the cavity through the superposition of individual mode fields [3]:

$$E(x,y,z,t) = \sum_{q,m,n} A_{qmn}(t) U_{mn}(x,y,z) e^{2\pi i \nu_{qmn} t + i\varphi_{qmn}}, \quad (1)$$

where $A_{qmn}(t)$, ν_{qmn}, and φ_{qmn} describe the slowly varying amplitude, frequency, and phase of the mode with a longitudinal index q and transverse indices m,n; $U_{mn}(x,y,z)$ is the spatial field distribution of the mode.

Under the absence of nonlinear effects, the mode frequencies ν_{qmn} and field distributions $U_{mn}(x,y,z)$ are defined by the laser cavity configuration [4]. Typically, the transverse modes can be approximated by Laguerre-Gaussian (LG) or Hermite-Gaussian (HG) modes in the case of a cylindrical or rectangular geometry. The mode phases φ_{qmn} are assumed to be uncorrelated and randomly distributed in the range $[0, 2\pi]$. The time dependence of the mode field amplitudes $A_{qmn}(t)$ is defined by the laser generation regime. Here, we consider the actively Q-switched Nd:YAG laser with up to 15 transverse LG modes and one longitudinal mode (q=0) with parameters described in [2].

Two main factors defining the statistical properties and temporal dynamics of spatial rogue waves are the frequency difference between the transverse modes and spatial anisotropy in the laser mode configuration. The frequency spacing between modes, which corresponds to the inverse period of beating, determines the period of intensity oscillations in the transverse cross-section of the beam. In the case of small frequency separation between the modes (large period of beating), the beam spatial profile is almost unchanged during the entire Q-switched pulse duration, and spatial RWs can be formed for certain realization of initial mode phases φ_{qmn} as a result of the spontaneous mode-locking effect. For increased frequency spacing between modes (smaller period of beating), intensity over the beam profile exhibits periodic behavior during the Q-switched pulse length. At certain time moments, spatio-temporal RWs can be generated [2]. An example of the simulated spatio-temporal dynamics of the output laser beam is shown in Figure 1 for the frequency separation between modes equal to 5

MHz, which represents the limiting case of spatio-temporal RWs formation when the period of beating is comparable to the Q-switched pulse duration (200 ns). The generated spatio-temporal rogue wave with peak intensity larger than 20 mean intensity values is illustrated in Figure 1c.

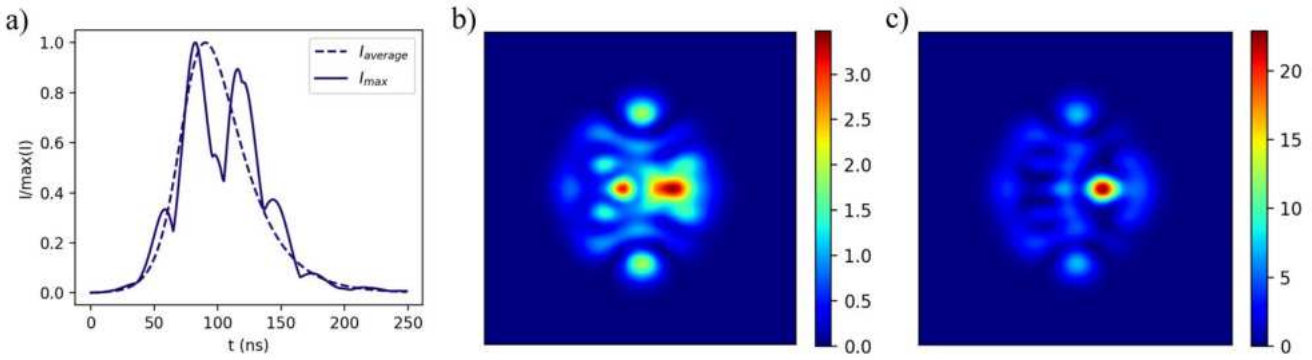


Figure 1. Example of the simulated spatio-temporal dynamics of the output laser beam: (a) temporal profiles of peak and spatially averaged intensity normalized to their maximal values; (b) transverse intensity profile averaged over the Q-switched pulse duration; (c) instantaneous transverse intensity profile corresponding to maximal peak intensity (t = 82 ns). The beam profiles in (b) and (c) are normalized to the same value of mean intensity.

Another important factor assisting the RWs generation is the spatial anisotropy of the mode configuration. This can be achieved by exciting a specific subset of transverse laser modes with close positions of the mode lobes in space, which leads to the increased probability of obtaining non-symmetrical beam patterns with intense "hot spots" formed as a result of the mode superposition. In the absence of nonlinear effects in the laser cavity, this effect is responsible for the L-shaped intensity statistics of spatial RWs, which was shown both theoretically [2] and experimentally [5].

References

1. Akhmediev, N. et al., "Roadmap on optical rogue waves and extreme events", J. Opt. 18, 063001, 2016.
2. Navitskaya, R., I. Stashkevich, S Derevyanko, and A. Karabchevsky, "Simulation of spatial rogue waves in actively Q-switched solid-state laser with transverse mode locking", Optics and Laser Technology, 171, 2024.
3. Schepers, F. et al., "Modal reconstruction of transverse mode-locked laser beams", Applied Physics B. 126, 168, 2022.
4. Kogelnik, H. and T. Li, "Laser beams and resonators", Applied Optics 5, 1550–1567, 1966.
5. Navitskaya, R., I. Stashkevich, S. Derevyanko, and A. Karabchevsky, "Spatial rogue waves in the actively Q-switched Nd:YAG laser under low Kerr nonlinearity", Opt. Express 30, 37076-37084, 2022.

Novel Plasma Treatments for Al:ZnO Local Modulation and its Application on Fabrication of Planar Infrared Metasurfaces

K. Sun[1*], T. Howe[1,2], C. H. de Groot[2], and O. L. Muskens[1]

[1]School of Physics and Astronomy, University of Southampton, Southampton, UK

[2]School of Electronics and Computer Science, University of Southampton, Southampton, UK

[*]corresponding author: k.sun@soton.ac.uk

Abstract: Al:ZnO (AZO) is very popular as a plasmonic infrared material. Here, we demonstrate a novel technique using O_2/H_2 plasma to modulate AZO optical responses and can be used to form AZO metasurfaces. Through s-NOM nearfield scanning, we demonstrate local optical property modulation in the AZO metasurface with sub-10 nm roughness.

In the past decade, optical metasurfaces have been researched for their potentials to tailor optical responses at different wavelength ranges. By defining sub-wavelength feature arrays, optical properties can be engineered to strongly enhance light-matter interactions and achieve electromagnetic control over amplitude, phase and polarization. To achieve infrared spectrum control, Al-doped ZnO (AZO) have been widely investigated in epsilon-near-zero (ENZ) response in infrared band and various optical metasurface applications [1].

Conventionally, the AZO metasurfaces are formed as sub-wavelength nanostructures through plasma etching, which selectively removes AZO and create property contrast. However, this non-planar structured surface provides further challenges when integrating with further functional coatings or another metasurface [2]. This work investigates a novel technique to locally and selectively modulate AZO optical property, and further demonstrates its implementation for planar optical metasurfaces. Figure 1a shows the schematic of the O_2/H_2 plasma treatment on AZO films at a lifted temperature. After the O_2 plasma treatment, refractive index can be significantly changed, and the AZO film becomes dielectric with a low k over the whole range from 0.2 to 40 µm from the metallic response in infrared (Figure 1b). For different Al:ZnO cycle ratios, the carrier density is seen to decrease with O_2 plasma to around 3×10^{19} cm^{-3} (the limit of optical response) and slightly increase with H_2 plasma. It is also noted that the pure ZnO is etched by the 20 min H_2 plasma but not AZO.

The AZO metasurface can be formed through a patterned SiN sacrificial layer for selective O_2 plasma exposure and the SiN can be selectively removed after the plasma treatment, leaving an AZO film with property contrast. Figure 1d shows topological mapping of the sample and square array can be clearly identified with unexposed (high carrier, H-AZO) and exposed (low carrier, L-AZO) in dimension of 1100 nm and 200 nm, respectively. However, the step height between exposed and unexposed AZO regions is less than 10 nm and therefore considered as topologically flat. The dot-like features are believed to be polymer or residue during the removal of masking layer, SiN and could be eliminated in further process optimization.

Figure 1e shows optical amplitude mapping of nearfield measurement at 8 µm wavelength. Unlike the little variation in topological mapping, the amplitude contrast unambiguously follows the AZO arrays made of exposed and unexposed regions as bright squares surrounded by dark frame. A higher amplitude is seen for the unexposed AZO whilst a lower amplitude is seen for the exposed AZO region. From the literature, the higher IR amplitude corresponds to high carrier concentration of zinc oxide, which is more metallic. Thus, the local AZO carrier reduction by O_2 plasma can be evidenced by the nearfield mapping. Figure 1f shows optical phase mapping at 8 µm wavelength. Higher phase rings are seen to surround the square-like unexposed AZO regions. Unlike optical amplitude corresponding to carrier density, the optical phase of ZnO peaks at carrier density

~10^{19} cm^{-3}, which well agrees with the locations as the interface between high carrier and low carrier AZO.

In summary, we present a novel O_2/H_2 plasma treatment technique to effectively modulate AZO optical property. Through an O_2 plasma diffusion barrier (SiN), AZO carrier density can be selectively and locally modulated and a planar AZO metasurface can be formed through the material optical contrast without physically removing AZO. The near-field mapping technique confirms the metasurface's flatness of sub-10 nm in roughness/step and further visualizes the local optical property modulation in term of magnitude and phase, with a spatial dimension of few ten nanometers. The formed planar AZO metasurface shows consistent response of AZO metasurface manufactured by selective etching and this technique offers broad potentials for new functional optical structures and devices.

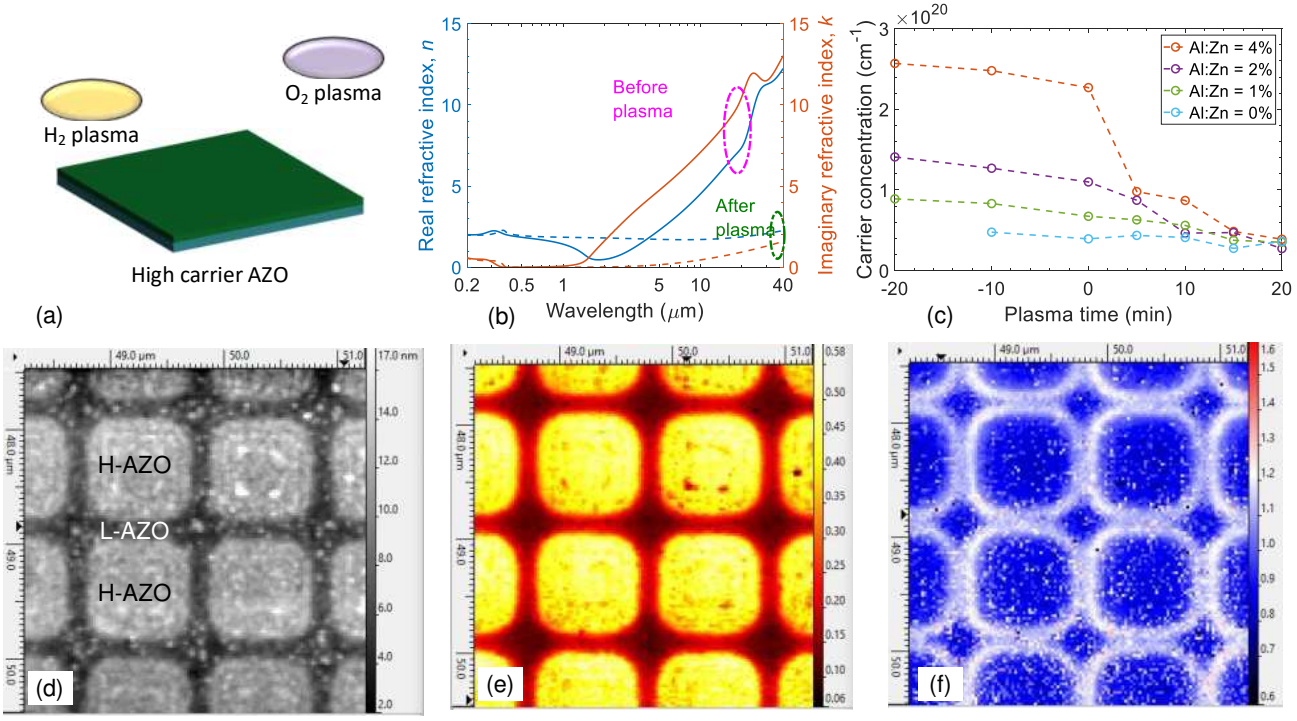


Figure 1 (a) schematic of H_2 and O_2 plasma on AZO film, (b) Ellipsometry extracted refractie index of AZO film before and after O_2 plasma treatment, (c) extracted carrier density of AZO films after different plasma treatments (O_2 plasma as positive and H_2 plasma as negative), (d) schematic of the AZO with features unexposed to O_2 plasma and gap exposed to O_2 plasma, (b) AFM image of the nearfield scanned region, (e) optical magnitude mapping of the AZO arrays and (f) optical phase mapping of the AZO arrays. The wavelength of laser for nearfield measurement is 8 μm.

Acknowledgements. The work is financially supported by DASA/Dstl. The authors would like to thank Dr Lars Mester from Attocube systems AG for supporting in characterizing the samples using s-SNOM.

References

1. Sun, K., E. Vassos, X. Yan, C. Wheeler, J. Churm, P. R. Wiecha, S. A. Gregory, A. Feresidis, C. H. de Groot and O. L. Muskens, "Wafer-Scale 200 mm Metal Oxide Infrared Metasurface with Tailored Differential Emissivity Response in the Atmospheric Windows", Adv. Optical Mater., 2200452, 2022.
2. Sun, K., W. Xiao, S. Ye, N. Kalfagiannis, K. S. Kiang, C. H. de Groot and O. L. Muskens, "Embedded Metal Oxide Plasmonics Using Local Plasma Oxidation of AZO for Planar Metasurfaces", Adv. Mater., 2001534, 2020.

Inverse design for arbitrary optical materials and integrated nanophotonics

Abhishek Nanda[1,2,3], Johannes Gedeon[1,2,3], Emadeldeen Hassan[4,5], Michael Kues[3,6], Antonio Calà Lesina[1,2,3,*]

[1] Hannover Centre for Optical Technologies, Leibniz University Hannover, 30167 Hannover, Germany

[2] Institute for Transport and Automation Technology, Faculty of Mechanical Engineering, 30823 Garbsen, Germany

[3] Cluster of Excellence PhoenixD, Leibniz University Hannover, 30167 Hannover, Germany

[4] Department of Applied Physics and Electronics, Umeå University, SE-901 87 Umeå, Sweden

[5] Department of Electronics and Electrical Communications, Menoufia University, Menouf 32952, Egypt

[6] Institute of Photonics, Leibniz University Hannover, 30167 Hannover, Germany

*Presenting author: antonio.calalesina@hot.uni-hannover.de

Abstract: We focus on time-domain topology optimization techniques for the inverse design of materials with arbitrary optical dispersion and anisotropy. This method enables 3D free-form nanostructures with broadband performance. We also present the frequency-domain inverse design of integrated beam splitters with desired phase at the output ports for quantum information processing.

Nanophotonics design is traditionally obtained by direct methods. In direct design, we start from a geometry suggested by prior knowledge or intuition and optimize a set of parameters until a satisfactory performance is achieved. In recent years, inverse design techniques have emerged as promising alternatives to direct design methods. In inverse design, the desired objective is predefined and algorithms based on numerical simulations and optimization methods are developed to find non-intuitive solutions. Topology optimization based on the adjoint method is a powerful technique for nanophotonics inverse design due to its computational efficiency. The method has already enabled devices with superior performance compared to traditional design approaches, along with unlocking new functionalities. Despite the tremendous progress in this field, there are still plenty of opportunities to advance the technique to handle, e.g., advanced optical materials and novel objective functions.

In this talk, I will present our recent works on the use of inverse design methods combined with parallel computing for applications in scattering engineering for broadband field confinement, and integrated nanophotonics. I will focus on the inverse design techniques we developed in-house to optimize media with any arbitrary optical dispersion and anisotropy, where the time-domain nature of the method allows us to achieve broadband performance with one run of the solver [1]. Inspired by the research interest on fundamental limits in electromagnetics, I will also present the inverse design of integrated beam splitters with arbitrary phase [2]. The phase of the signals at the output ports of a beam splitter is responsible, e.g., for the quantum interference between two photons, known as the Hong–Ou–Mandel effect. Therefore, we believe the inverse design of unconventional integrated optical devices may lead to novel experiments in quantum information processing.

Acknowledgements

We acknowledge the computing time granted by the Resource Allocation Board and provided on the supercomputer Lise and Emmy at NHR@ZIB and NHR@Göttingen as part of the NHR infrastructure (project nip00059). We acknowledge the central computing cluster operated by Leibniz University IT Services (LUIS), which is funded by the Deutsche Forschungsgemeinschaft (DFG, German Research Foundation), project number INST 187/742-1 FUGG. This research was funded by: European Research Council (QFreC project, Grant agreement ID 947603); DFG (EXC 2122, Project ID 390833453); DFG (Project CA 2763/2-1, Project ID 527470210).

References

[1] J. Gedeon, E. Hassan, and A. Calà Lesina, "Time-Domain Topology Optimization of Arbitrary Dispersive Materials for Broadband 3D Nanophotonics Inverse Design," *ACS Photonics*, vol. 10, no. 11, pp. 3875–3887, 2023, doi: 10.1021/acsphotonics.3c00572.

[2] A. Nanda, M. Kues, and A. Calà Lesina, "Exploring the fundamental limits of integrated beam splitters with arbitrary phase via topology optimization," *Opt Lett*, vol. 49, no. 5, p. 1125, 2024, doi: 10.1364/OL.512100.

Title: Photonics based non-invasive wearable devices for health monitoring.

Prof E.U. Rafailov

Optoelectronics and Biomedical Photonics Group, Aston Institute of Photonic Technologies, Aston University, Birmingham, B4 7ET, UK

Continuous monitoring of human health and activity using wearable devices will be a key technology in the sensor network society for years to come. Recent advances in the development of the miniaturised optoelectronics components with low energy consumption have opened a new perspective for the implementation of non-invasive wearable sensors for health monitoring and personalised medicine. In this paper we will review our recent development of wearable sensors based on Laser Doppler flowmetry and Fluorescence spectroscopy and demonstrate potential applications for such devices.

Meta-optics for multi-dimensional manipulation of light

Crystallization of Induce Optical Vortex by Bessel Beams

Sahil Sahoo and Yuri Gorodetski*
Electrical and Electronic Engineering department,
Ariel University, 407000, Ariel, Israel
* corresponding author: yurig@ariel.ac.il

Abstract

The process of optical vortex formation through interference patterns culminates in the creation of an optical vortex lattice. Our study illustrates the gradual emergence of optical vortices and their crystallization within the array, resulting in the formation of an optical vortex lattice. This phenomenon is exemplified through the implementation of a Bessel beams array on the plasmonic metasurface.

1 Introduction

Optically driven vortex lattices have opened up new and interesting applications in optics. These lattices have a pivotal function in the construction of the pseudo vortex structures in the ultra-cold atomic Bose-einstein condensates gas.[1] Furthermore, they are important in the creation process of photonic crystal fabrication.[2] The generation of these lattices is achieved through beam interference. Researchers have propelled the field forward by employing multi-beam interference techniques. This involves utilizing circularly polarized illumination through the metasurfaces with orthogonal nano-slit pairs, combined with spiral segments, contributing to the generation of optical vortex lattice fields.[3] These fields result from the combination of geometric and dynamic phases, creating intricate lattice patterns.[2,3]

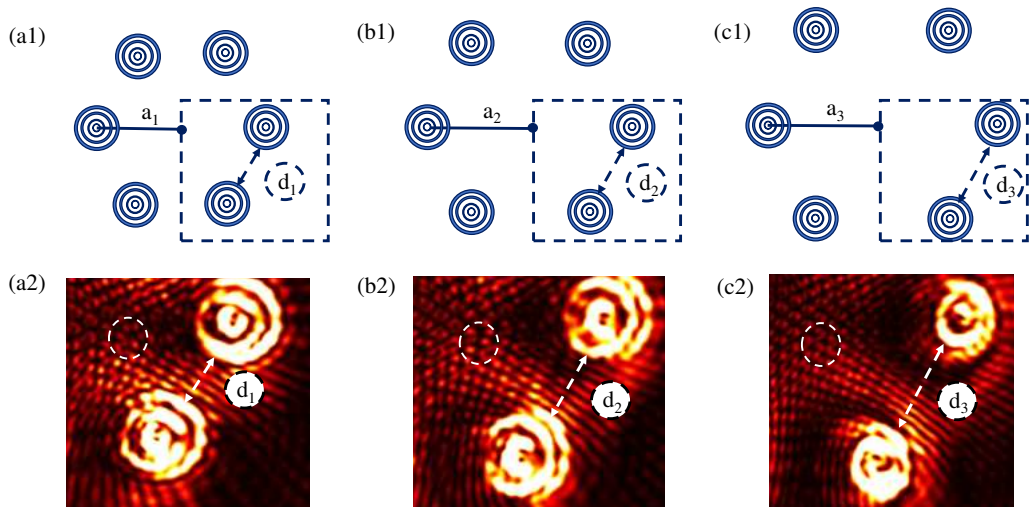


Figure 1: In Figures (a1), (b1), and (c1), we depict the hexagonal arrangement of Bessel beams with hexagonal radii of $8\lambda_{spp}$, $9\lambda_{spp}$, and $11\lambda_{spp}$ respectively. Consequently, the separation distance between the Bessel beams increases, as indicated by $d_1 < d_2 < d_3$. In Figures (a2), (b2), and (c2), we illustrate the evolution of vortices for different array sizes. As the intensity changes, these vortices eventually converge towards the center to form a crystalline structure of vortex lattice.

Advanced techniques, including spin-based plasmonic effects with different geometries, further enhance the formation of optical lattice structures by directing plasmonic waves towards the centre of the geometry, enabling superposition and intricate pattern creation.[4] Plasmonic waves arise from the interaction of an electromagnetic (EM) wave with a metallic subwavelength structure. This interaction entails coupling EM waves with confined electronic oscillations which are known as surface plasmon polaritons (SPPs). The near-field intensity distribution of SPPs is influenced by the polarization state of the incident beam. By designing a plasmonic cavity with a polarization-dependent geometric phase, a plasmonic vortex Bessel beam can be produced.[5] We have demonstrated how the core region of a hexagonal array of Bessel beams at each corner may exhibit intricate interference patterns caused by plasmonic waves. The emergence of an optical vortex lattice is governed by the intrinsic topological characteristics of this configuration and the modifications made to the hexagonal array size. The interference of plasmonic waves leads to the formation of vortices, and as the array size increases, these vortices appear to merge successively, ultimately forming the complete lattice of vortices as shown in Figure 1. The gradual formation of the vortex lattice mirrors offering an intriguing analogy to crystallization process. While researchers have studied vortices crystallization in the rotation of atomic-molecular Bose-Einstein by thermal quenching,[6,7] there is still a knowledge gap concerning the formation of vortex crystals through plasmonic wave interference, which we are studying by gradually increasing the array size. The sequential addition of vortices suggests that the vortex formation occurs during interference, however, it appears that changing the array size causes the initially generated vortices to move toward more stable energy state. Eventually, the energy reaches a point of maximum stability, culminating in the formation of a vortex crystal. Moreover, the vortex lattice demonstrates remarkable topological stability, it appears to be able to preserve its structure regardless of disturbances such as the blocking of a single Bessel beam from the array. This shows the lattice exhibits remarkable topological stability, making it resilient to the disturbance.

References

[1] J. R. Abo-Shaeer, C. Raman, J. M. Vogels, and W. Ketterle, "Observation of vortex lattices in bose-einstein condensates," *Science*, vol. 292, no. 5516, pp. 476–479, 2001.

[2] R. Zhang, Y. Zhang, L. Ma, X. Zeng, X. Li, Z. Zhan, X. Ren, C. He, C. Liu, and C. Cheng, "Nanoscale optical lattices of arbitrary orders manipulated by plasmonic metasurfaces combining geometrical and dynamic phases," *Nanoscale*, vol. 11, pp. 14024–14031, 2019.

[3] H. Gao, Y. Li, L. Chen, J. Jin, M. Pu, X. Li, P. Gao, C. Wang, X. Luo, and M. Hong, "Quasi-talbot effect of orbital angular momentum beams for generation of optical vortex arrays by multiplexing metasurface design," *Nanoscale*, vol. 10, pp. 666–671, 2018.

[4] S. Tsesses, R. Dahan, K. Wang, T. Bucher, K. Cohen, O. Reinhardt, G. Bartal, and I. Kaminer, "Tunable photon-induced spatial modulation of free electrons," *Nature Materials*, vol. 22, p. 345–352, Jan. 2023.

[5] Y. Gorodetski, A. Niv, V. Kleiner, and E. Hasman, "Observation of the spin-based plasmonic effect in nanoscale structures," *Phys. Rev. Lett.*, vol. 101, p. 043903, Jul 2008.

[6] S.-W. Su, C.-H. Hsueh, I.-K. Liu, T.-L. Horng, Y.-C. Tsai, S.-C. Gou, and W. M. Liu, "Spontaneous crystallization of skyrmions and fractional vortices in fast-rotating and rapidly quenched spin-1 bose-einstein condensates," *Phys. Rev. A*, vol. 84, p. 023601, Aug 2011.

[7] C.-F. Liu, H. Fan, S.-C. Gou, and W.-M. Liu, "Crystallized and amorphous vortices in rotating atomic-molecular bose-einstein condensates," *Scientific reports*, vol. 4, p. 4224, 02 2014.

Magnetoelectric effect in magnetic toroidal metal HoAgGe

A. Kirikoshi[1*] and S. Hayami[1]

[1]Department of Physics, Hokkaido University, Japan
[*]corresponding author: ak3@phys.sci.hokudai.ac.jp

Abstract: We theoretically study the magnetic states in HoAgGe. The two distinct ordered phases accompany the magnetic toroidal moment with a finite magnetic ordering wave vector. We construct a tight-binding model and discuss the differences in magnetoelectric effects under these phases based on the microscopic electronic degrees of freedom.

In a geometrically frustrated spin system, exotic magnetic phases such as a quantum spin liquid and a spin ice state are expected. In recent years, it has been reported that the two distinct kagome spin ice states are realized in the rare-earth compound HoAgGe at low temperatures, and its transport property has been investigated [1,2]. Meanwhile, the concept of augmented multipoles has been developed, and the complex magnetic structure can be classified by the multipole degrees of freedom [3,4]. In terms of the site-cluster type multipoles, the kagome spin ice states in HoAgGe are the ferri/antiferrotoroidal ordered phases with magnetic ordering wave vector (1/3,1/3,0). Since both spatial inversion and time-reversal symmetry are broken in the magnetic toroidal order, cross-correlated responses such as the linear magnetoelectric effect are expected, as found in the antiferromagnetic metal $UNiB_4$ with a ferrotoroidal moment [5,6]. However, the difference between the response phenomena and transport properties in the ferrotoroidal order and those in the toroidal ordered phase with a finite magnetic ordering wave vector has yet to be fully clarified.

Our research aims to show the differences in response phenomena and transport properties between these ordered phases. To achieve this, we have constructed a minimal tight-binding model consisting of multiorbital on a nine-sublattice distorted kagome structure. We found that different spin ice-ordered phases are characterized by the distribution of local imaginary orbital hybridization between orbitals with different parities, which can be examined through the magnitude of the magnetoelectric effect at each site. We will also discuss the contribution of electron hopping and lattice distortion to the magnetoelectric effect.

This work was supported by JSPS KAKENHI Grants Number JP21H01037 and JP23H04869.

References

1. Zhao, K., H. Deng, H. Chen, K. A. Ross, V. Petříček, G. Günther, M. Russina, V. Hutanu and P. Gegenward, “Realization of the kagome spin ice state in a frustrated intermetallic compound,” Science, Vol. 367, No. 6483, 1218–1223, 2020.
2. Li, N., Q. Huang, X. Y. Yue, S. K. Guang, K. Xia, Y. Y. Wang, Q. J. Li, X. Zhao, H. D. Zhou, and X. F. Sun, “Low-temperature transport properties of the intermetallic compound HoAgGe with a kagome spin-ice state,” Phys. Rev. B, Vol. 106, 014416, 2022.
3. Suzuki, M.-T., T. Nomoto, R. Arita, Y. Yanagi, S. Hayami, and H. Kusunose, “Multipole expansion for magnetic structures: A generation scheme for a symmetry-adapted orthonormal basis set in the crystallographic point group,” Phys. Rev. B, Vol. 99, 174407, 2019.
4. Yanagi, Y., H. Kusunose, T. Nomoto, R. Arita, and M.-T. Suzuki, “Generation of modulated magnetic structures based

on cluster multipole expansion: Application to α-Mn and CoM_3S_6," Phys. Rev. B, Vol. 107, 014407, 2023.

5. Ota, K., M. Shimozawa, T. Muroya, T. Miyamoto, S. Hosoi, A. Nakamura, Y. Homma, F. Honda, D. Aoki, and K. Izawa, "Zero-field current-induced Hall effect in ferrotoroidic metal," arXiv:2205.05555.
6. Saito, H., K. Uenishi, N. Miura, C. Tabata, H. Hidaka, T. Yanagisawa, and H. Amitsuka, "Evidence of a new current-induced magnetoelectric effect in a toroidal magnetic ordered state in $UNiB_4$," J. Phys. Soc. Jpn., Vol. 87, 033702, 2018.

Ultrafast Switching of Magnetization using Chiral Optical Phonons

C. S. Davies[1*], F. G. N. Fennema[1], A. Tsukamoto[2], I. Razdolski[1,3], A. V. Kimel[4] and A. Kirilyuk[1]
[1] HFML-FELIX, Radboud University, Nijmegen, The Netherlands
2 Radboud University, Institute for Molecules and Materials, Nijmegen, The Netherlands
3 Nihon University, Chiba, Japan
4 University of Bialystok, Bialystok, Poland
[*]corresponding author: carl.davies@ru.nl

Abstract: Using chiral optical phonons that are driven at resonance within a paramagnetic substrate, we demonstrate that magnetization can be non-locally switched in a magnetic overlayer. This application of the ultrafast Barnett effect offers a novel and potentially universal pathway for the ultrafast switching of magnetization.

Very recently, a series of pioneering experiments have revealed how ultrafast photo-induced demagnetization transfers angular momentum from the spins to the lattice via the Einstein-de Haas effect [1]-[2]. Here, we explore whether the ultrafast Barnett effect – by which mechanical rotations create magnetization [3] - can reciprocally channel angular momentum from rotating lattice vibrations to spins (Fig. 1a). Using ultrashort optical pulses delivered by the free-electron-laser facility FELIX [4], we coherently excite optical phonons at resonance in a paramagnetic substrate (Fig. 1b). Importantly, the optical pulses are circularly-polarized, thus enabling specific optical phonons to become similarly circularly-polarized. The orbital angular momentum of the phonons give rise to a magnetization $\mathbf{M}_{BE}$, pointing either parallel or antiparallel to the substrate's normal. This then switches the magnetization in the nearby magnetic GdFeCo nanolayer.

Typical results proving the feasibility of this switching approach are shown in Fig. 1c. In our experiments, we sweep 3.3-ps-long circularly-polarized pulses, with central wavelength $\lambda = 21$ μm, across the multilayered stack. Using magneto-optical imaging in equilibrium, we assess the impact on the magnetic domains of GdFeCo mounted on a sapphire substrate. We clearly see, depending on the combination of initial magnetic polarity and optical helicity, the switching (or lack thereof) of switched magnetization. By adjusting the duration of the pulses, we are able to distinguish this effect from exchange-driven switching of magnetization observed previously [5].

By tuning the central wavelength of the pumping pulses, we identify that the switching efficiency scales with the strength of the transverse optical phonons found in the sapphire substrate (Fig. 1d). Additional measurements of the same GdFeCo mounted on a fused-silica substrate reveals a different spectral dependence of switching efficiency, that again correlates with the transverse optical phonons in the fused-silica substrate. A control measurement, repeated for the same magnetic overlayer mounted instead on silicon, showed no helicity-dependent switching. The latter is explained by the lack of infrared-active optical phonons present in silicon.

We therefore conclude that we have discovered the ultrafast Barnett effect [6], which can be used to switch magnetization non-locally using coherent lattice vibrations excited within an underlying substrate. Our results represent a breakthrough that could potentially be used to switch magnetic order on a universal scale, since rotational vibrations of ions are found in a multitude of paramagnetic substrates.

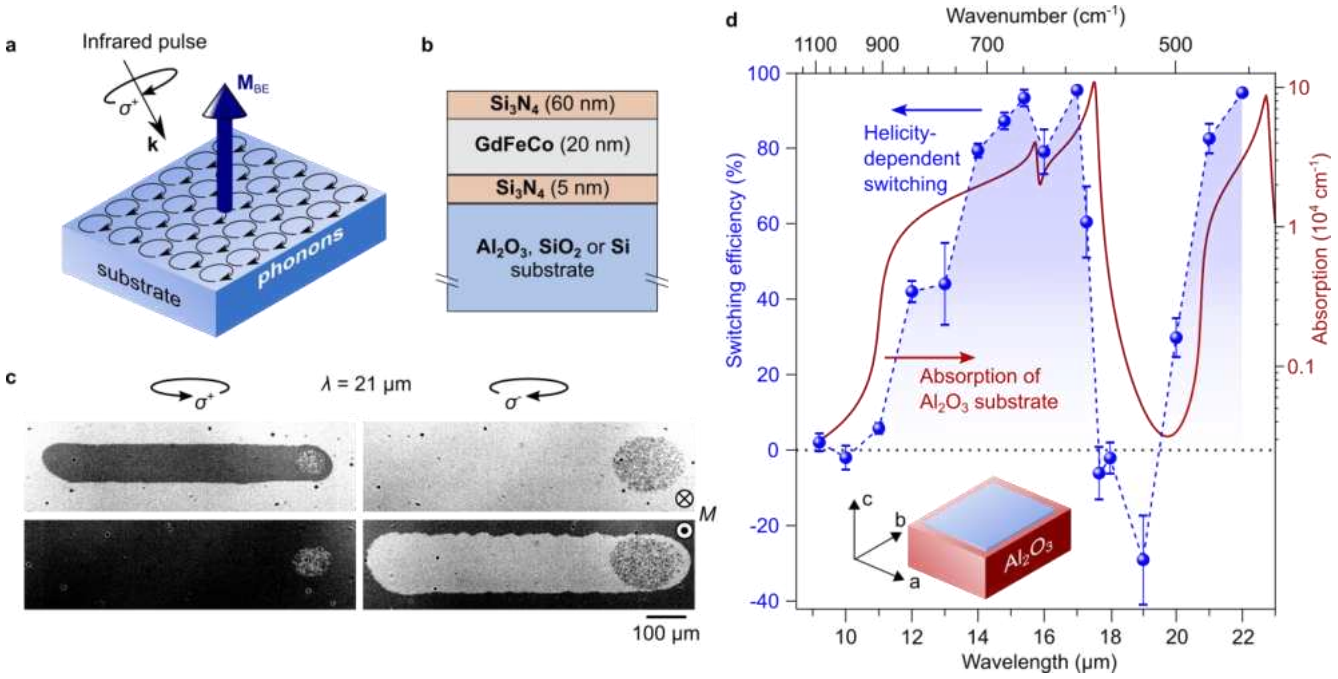


Figure I a Sketch of how circularly-polarized phonons vibrating in a paramagnetic substrate, coherently excited at resonance by circularly-polarized light with helicity $\sigma^{\pm}$, give rise to a magnetization $\mathbf{M}_{BE}$. **b** nanolayer structure used in our experiments. **c** Magneto-optical images of GdFeCo, mounted on a sapphire substrate, taken before and after exposure to circularly-polarized pulses (wavelength λ = 21 μm, duration τ ~3.3 ps) that are scanned from left to right. **d** Spectral dependence of the efficiency of helicity-dependent switching (blue dashed line) and the population of transverse optical phonons in the substrate (red solid line).

We thank all technical staff at FELIX for technical support. We gratefully acknowledge the Nederlandse Organisatie voor Wetenschappelijk Onderzoek (NWO-I) for their financial contribution, including the support of the FELIX Laboratory. C.S.D. acknowledges support from the European Research Council ERC Grant Agreement No. 101115234 (HandShake).

References

1. C. Dornes et al. “The ultrafast Einstein–de Haas effect.” Nature, Vol. 565, 209 (2019).
2. S. R. Tauchert et al. “Polarized phonons carry angular momentum in ultrafast demagnetization.” Nature, Vol. 602, 73 (2022).
3. S. J. Barnett, “Magnetization by Rotation.” Phys. Rev., Vol. 6, 239 (1915).
4. G. M. H. Knippels and A. F. G. van der Meer, “FEL diagnostics and user control.” Nucl. Instrum. Methods Phys. Res., Vol. 144, 32 (1998).
5. C. S. Davies et al. “Exchange-driven all-optical magnetic switching in compensated 3*d* ferrimagnets.” Phys. Rev. Res., Vol. 2, 032044(R) (2020).
6. C. S. Davies, F. G. N. Fennema, A. Tsukamoto, I. Razdolski, A. V. Kimel and A. Kirilyuk, “Phononic Switching of Magnetization by the Ultrafast Barnett Effect” Nature (in press, 2024).

Realization of Wilson fermions in topolectrical circuits

Huanhuan Yang, Lingling Song, Yunshan Cao, and Peng Yan
School of Physics and State Key Laboratory of Electronic Thin Films and Integrated Devices, University of Electronic Science and Technology of China, Chengdu 610054, China
*corresponding author: yan@uestc.edu.cn

Abstract: We realize the Wilson fermions (WFs) in momentum space with electrical circuits and find the structure of WFs manifest as topological spin textures analogous to the half skyrmion, half-skyrmion pair, and Néel skyrmion structures, depending on their mass. We further confirm their topological features in lattice space.

The Wilson fermion (WF) is a fundamental particle in the theory of quantum chromodynamics. Theoretical calculations have shown that the WF with a half skyrmion profile represents a quantum anomalous semimetal phase supporting a chiral edge current, but the experimental evidence is still lacking. We experimentally observed WFs in circuit systems. In addition, we mapped WFs with different masses or configurations to magnetic solitons with different skyrmion charges, which will enable us to study the properties of skyrmions, half skyrmions, and half-skyrmion pairs in electrical circuit platforms. We showed that the nontrivial spin-texture of WFs in momentum space is fully characterized by Chern numbers and winding number in 2D and 3D systems, respectively. The chiral edge current associated with the QASM state dictated by a fractional Chern number was directly detected. Our work presents the first circuit realization of WFs, which sets a paradigm for other platforms, such as cold atoms, photonic, and phononic metamaterials, to further explore these fascinating phenomena.

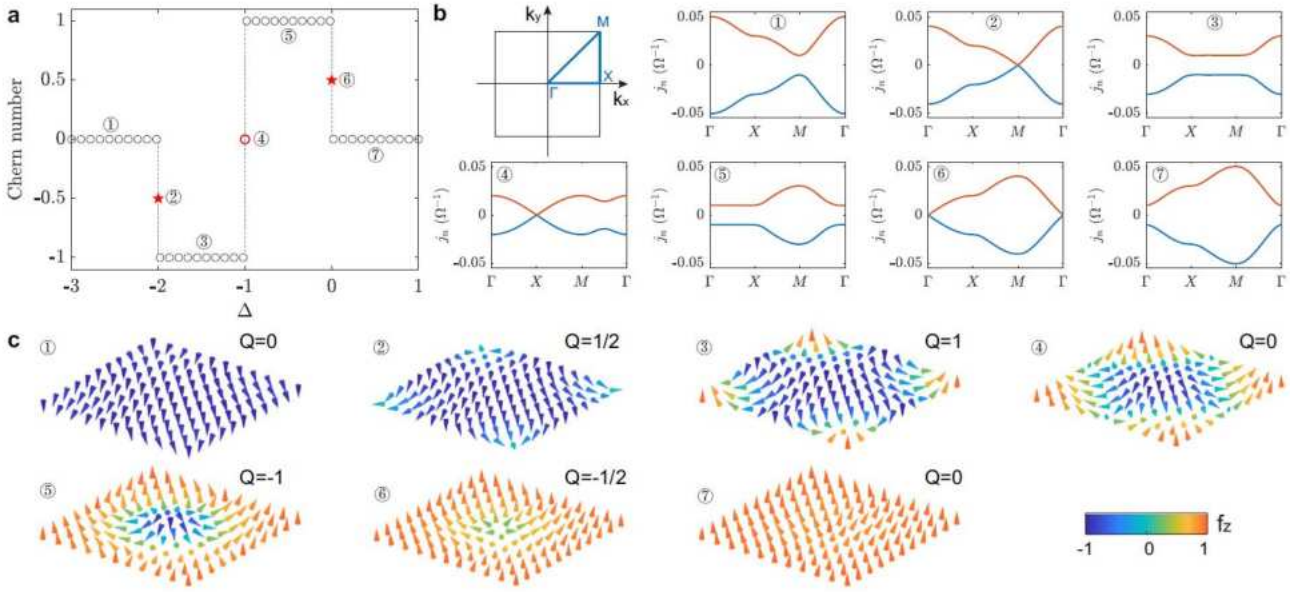


Figure 1 Topological indexes and Wilson fermions. **a**, The Chern number C steps as a function of the dispersionless mass Δ. The red stars and circle represent C=±1/2 and C= 0, corresponding to quantum anomalous semimetal and normal semimetal phases, respectively. **b**, The first Brillouin zone and the typical band structures for Δ = -2.5, -2, -1.5, 0, -0.5, 0, 0.5 respectively, corresponding to different parameter intervals in (a). The orange and blue curves indicate the two branches of band structures. **c**, The spin textures of Wilson fermions in the momentum space

Acknowledgements: This work was supported by the National Key Research Development Program under Contract No. 2022YFA1402802 and the National Natural Science Foundation of China (Grants No. 12074057, No. 11604041, and No. 11704060).

References

1. Huanhuan Yang, Lingling Song, Yunshan Cao, and Peng Yan, “Realization of Wilson fermions in topolectrical circuits”, Commun. Phys. **6**, 211, 2023.

Quantification of chirality based on electric toroidal monopole: Application to a twisted methane molecule

A. Inda[1*], R. Oiwa[2], S. Hayami[1], H. M. Yamamoto[3,4], and H. Kusunose[4,5]

[1] Graduate School of Science, Hokkaido University, Japan
[2] RIKEN Center for Emergent Matter Science (CEMS), Japan
[3] Institute for Molecular Science, Japan
[4] QuaRC, Institute for Molecular Science, Japan
[5] Department of Physics, Meiji University, Japan
[*]corresponding author: inda@phys.sci.hokudai.ac.jp

Abstract: We propose a way to quantitatively evaluate chirality in terms of the electric toroidal monopole, a time-reversal-even pseudo(parity-odd) scalar at the quantum-mechanical level. Applying the method to a twisted chiral methane molecule, we analyze the important model parameter for chirality beyond the symmetry analysis.

Chirality ubiquitously appears in condensed matter physics, chemistry, biochemistry, and so on. In terms of symmetry, a chiral object has neither spatial inversion symmetry nor mirror symmetry, while the time-reversal symmetry is preserved [1]. Barron defined the chirality as a "time-reversal-even pseudoscalar" object from the symmetry point of view [2]. Owing to the lack of the spatial inversion and mirror symmetries, the chiral object exhibits various chirality-induced phenomena, such as chirality-induced spin selectivity [3] and non-degenerate phonon excitations [4]. Nevertheless, the quantitative analysis has not been fully established because of the lack of the microscopic description. Thus, it remains unclear what microscopic key ingredients are important to induce the above chirality-induced phenomena.

Recently, the symmetry-adapted multipole basis (SAMB) has been established, which enables us to express arbitrary electronic degrees of freedom in the physical Hilbert space by a linear combination of four types of multipole basis with distinct spatial inversion and time-reversal parities [5, 6, 7]: electric, magnetic, magnetic toroidal, and electric toroidal multipoles. In the framework of the SAMB, the chirality is microscopically described by the electric toroidal monopole (ETM) [8]. We propose such an ETM as a quantitative indicator of the chirality at the quantum mechanical level [9]. We demonstrate our scenario in the simplest situation by exemplifying the achiral methane molecule model. First, we construct an effective tight-binding model based on the SAMB with the use of a symmetry-adapted Wannier method (SymClosestWannier [10]). Then, we consider a symmetry lowering of the methane molecule by twisting the hydrogen atoms around a two-fold rotational axis so that the molecular object acquires the chiral property. We clarify that the expectation values of the ETM become nonzero when the methane molecule is twisted. Furthermore, we clarify that the handedness of chirality corresponds to the sign of the expectation value of the ETM. We also show that the modulation of spin-dependent imaginary hopping between the hydrogen atoms is essential, while the relativistic spin-orbit coupling in the carbon atom has less effect on chirality.

This research was supported by JSPS KAKENHI Grants Numbers JP21H01037, JP22H04468, JP22H00101, JP22H01183, JP23H04869, JP23K03288, JP23H00091, and by JST PRESTO (JPMJPR20L8) and JST CREST (JP- MJCR23O4), and the grants of Special Project (IMS program 23IMS1101), and OML Project (NINS program No. OML012301) by the National Institutes of Natural Sciences.

References

1. Kelvin, W. T. B. “The molecular tactics of a crystal” (Clarendon Press, 1894).
2. Barron, L.D. “True and false chirality and parity violation,” Chem. Phys. Lett. Vol. 123, 423–427 (1986).
3. Göhler, B., V. Hamelbeck, T. Z. Markus, M. Kettner, G. F. Hanne, Z. Vager, R. Naaman, and H. Zacharias, “Spin Selectivity in Electron Transmission Through Self-Assembled Monolayers of Double-Stranded DNA,” Science Vol. 331, 894–897 (2011).
4. Pine, A., “Direct Observation of Acoustical Activity in α Quartz,” Phys. Rev. B, Vol. 2, 2049 (1970).
5. Hayami, S. and H. Kusunose, “Microscopic Description of Electric and Magnetic Toroidal Multipoles in Hybrid Orbitals,” J. Phys. Soc. Jpn. Vol. 87, 033709 (2018).
6. Hayami, S., M. Yatsushiro, Y. Yanagi, and H. Kusunose, “Classification of atomic-scale multipoles under crystallographic point groups and application to linear response tensors,” Phys. Rev. B Vol. 98, 165110 (2018).
7. Kusunose, H., R. Oiwa, and S. Hayami, “Symmetry-adapted modeling for molecules and crystals,” Phys. Rev. B Vol. 107, 195118 (2023).
8. Kishine, J.-i., H. Kusunose, and H. M. Yamamoto, “On the Definition of Chirality and Enantioselective Fields,” Isr. J. Chem. Vol. 62, e202200049 (2022).
9. Inda, A., R. Oiwa, S. Hayami, H. M. Yamamoto, and H. Kusunose, “Quantification of chirality based on electric toroidal monopole,” arXiv: 2402. 13611.
10. Oiwa, R., A. Inda, S. Hayami, T. Nomoto, R. Arita, and H. Kusunose, “SymClosestWannier,”.

Gyromagnetic double-zero-index metamaterials enable ultrarobust generation of optical spatiotemporal vortices

Xiaohan Cui[1], Ruo-Yang Zhang[1], Yuan-Song Zeng[2], Geng-Bo Wu[2], and C. T. Chan[1*]

[1]Department of Physics, Hong Kong University of Science and Technology, Clear Water Bay, Kowloon, Hong Kong, China

[2]State Key Laboratory of Terahertz and Millimeter Waves and Department of Electrical Engineering, City University of Hong Kong, Hong Kong, China

[*]corresponding author: phchan@ust.hk

Abstract: We expand the scope of conventional double-zero-index media by introducing non-reciprocity and experimentally realizing gyromagnetic double-zero-index metamaterials (GDZIMs). A homogeneous GDZIM slab displays an ultra-robust reflection phase vortex, unaffected by slab thickness adjustments. This discovery reveals a novel mechanism for generating robust optical spatiotemporal vortices by breaking time-reversal symmetry.

Electromagnetic zero-refractive-index (ZRI) media are an exemplary family of extreme parameter metamaterials, which exhibit extraordinary optical properties and have wide-ranging applications in wave manipulation and nonlinear optics. In this family of metamaterials, a special member is the media with both zero permittivity and permeability, $\epsilon = \mu = 0$, known as double-zero-index metamaterials (DZIMs). DZIMs are unique in that they not only present a ZRI but also show a conical band intersection at the double-zero-index frequency. This property unlocks a myriad of exclusive optical characteristics and functionalities, such as universal impedance matching and perfect transmission on-chip ZRI materials with ultralow loss, ZRI bound states in the continuum, and large-area single-mode lasing.

While an ordinary DZIM requires its scalar permittivity and permeability to be zero, our work show that by introducing non-reciprocity, the realm of ZRI metamaterials can be substantially expanded. In this work, we experimentally realize, for the first time, such a generalized DZIM, called gyromagnetic double-zero-index metamaterials (GDZIMs) and a nonzero gyromagnetic permeability tensor $\overleftrightarrow{\mu} = \begin{pmatrix} \mu_r & i\alpha \\ -i\alpha & \mu_r \end{pmatrix}$ with a determinant of zero $\det(\overleftrightarrow{\mu}) = \mu_r^2 - \alpha^2 = 0$. We theoretically and experimentally reveal that the GDZIMs not only carry the prominent features of conventional DZIMs, but also gain exotic nonreciprocal characteristics that allow us to observe new wave phenomena in ZRI photonics. In particular, we found that the GDZIMs can be realized by a photonic crystal composed of ferrite rods in the presence of an external magnetic field. By tuning the parameters of the photonic crystal to attain an accidental twofold Dirac cone degeneracy at the center of the Brillouin zone (as opposed to the triple Dirac-like cone degeneracy in ordinary DZIMs), we have observed that the effective permittivity and the determinant of the effective permeability of the homogenized medium both approach zero at the Dirac-point frequency ω_D, whereas the components of the permeability tensor maintain finite values.

The GDZIMs inherit the capability as usual DZIMs to match impedance with any medium, but they differ from the traditional DZIMs by virtue of the nonreciprocity that arises from the breaking of time reversal symmetry. The nonreciprocal nature of GDZIMs is primarily manifested in their extraordinary property of reflection and transmission. At the Dirac-point frequency ω_D, the impedance-matching guarantees that normally incident waves upon a GDZIM slab are perfectly transmitted, while the nonreciprocity causes the reflection phase of oblique incidence waves to be asymmetric about the $k_{\parallel} = 0$ axis. Taken together, these two properties result in the deterministic formation of a vortex singularity in the reflection phase of a GDZIM slab, which is fixed at the point of $(\omega, k_{\parallel}) = (\omega_D, 0)$ in the frequency-momentum plane. This further ensures that when a Gaussian pulse

normally impinges upon the slab, the reflected pulse carries a spatiotemporal (ST) vortex.

Optical ST vortices, which carry transverse orbital angular momentum (OAM), have attracted considerable attention due to their potential applications in optical tweezers, superresolution imaging, and optical information processing. The GDZIM offers a novel approach to generate ST vortices. Compared to other methods of synthesizing ST vortices, such as using a customized spatial light modulator, the current approach stems from the intrinsic Dirac cone band topology of a homogenous GDZIM and boasts exceptional robustness in that the central frequency of the generated spatiotemporal vortices is independent of both the thickness of the GDZIM slab and the refractive index of the background medium.

In summary, by constructing topological metamaterials at the critical transition point of photonic Chern insulator phases, we have experimentally materialized GDZIMs. Such materials represent a conceptual advancement over conventional DZIMs by integrating nonreciprocal and tensor-valued constitutive indices of null determinants. The realization of GDZIMs not only lays the foundation for achieving highly functional devices, such as unidirectional ZRI waveguides and scalable chiral single-mode lasers. It also builds a bridge that connects ZRI photonics, topological photonics, and singular optics, shedding new light on each domain and paving the way for unexplored interdisciplinary research directions.

Acknowledgements: We acknowledge support from Research Grants Council (RGC) Hong Kong and the Croucher Foundation.

Control of Circularly Polarized Light Using Electron Beam

T. Sannomiya[1*]

[1]Tokyo Institute of Technology, Japan
[*]corresponding author: sannomiya.t.aa@m.titech.ac.jp

Abstract: This study explores novel approaches to control circular polarization using electron beam excitation. Scanning transmission electron microscopy based cathodoluminescence technique reveals possibilities of circularly polarization light control by electron beam. The demonstrations include manipulating polarization in symmetric structures such as spherical nanoantennas and circular holes in a metal film.

Circular polarization of light is typically controlled using structures with geometric chirality. However, by breaking the symmetry of the entire observation system, including excitation and detection, "chiral" responses can also be obtained from achiral structures. We here demonstrate the control of circular polarization generation using fast electrons even from structures considered to be perfectly symmetric (without chirality), such as spheres or circular holes.[1,2] For the sphere, the circular polarization of light can be controlled by the phase difference between two orthogonal electric dipoles excited within the sphere by the fast electron beam.[1] This phase difference can be controlled by appropriately selecting the excitation position of the electron beam on the sphere, thus breaking the geometric symmetry of the system. In other words, the irradiation (excitation) position of the electron beam enables control of the rotation direction of the electric dipoles, i.e., the selection of right-handed or left-handed circular polarizations. Such achiral antennas allow obtaining equivalent responses of right-handed and left-handed circular polarization from a single antenna, and the ultra-fast switching by electron beams proves to be advantageous.

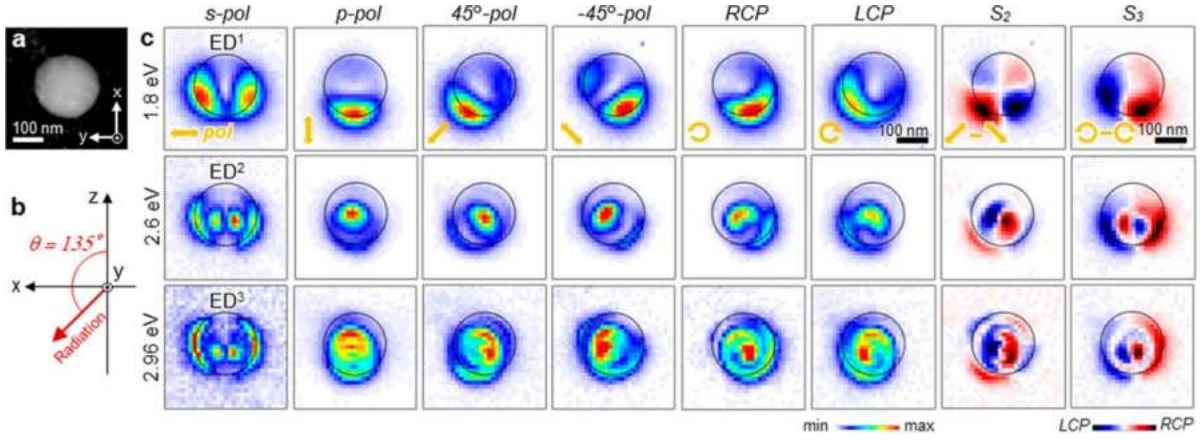


Figure 1. Circularly polarized light emission from a 250 nm Si sphere. [1] (a) STEM dark-field image of the probed Si nanosphere with a diameter of 250 nm (same particle as in Figure 2c). (b) Schematic illustration of the cathodoluminescence detection configuration. (c) Cathodoluminescence (CL) maps with different polarizations as well as representative Stokes maps at different energies. The CL signal is integrated over photon energy within a ± 0.1 eV interval at a detection angle θ = 135°. The edge of the Si nanosphere is indicated by black circles.

In addition to spheres, control of circular polarization in metallic films with circular apertures possessing surface plasmon polaritons (SPPs) — another achiral structure — is achievable using electron beam excitation via a different mechanism.[2] In this case, circular polarization is controlled by the interference of transition radiation (TR) emitted as high-speed electrons pass through the metallic film and the scattered waves from the apertures mediated by surface plasmon polaritons (SPPs).[3] When the electron beam is irradiated away from the aperture, SPPs are excited simultaneously with TR, propagating and exciting local modes of the metallic aperture to scatter light. As all processes of scattering via TR and SPPs are coherent, TR and scattered waves interfere. The polarization and phase difference of these waves can be controlled by the excitation position of the electron beam and the distance between the holes.

This presentation discusses these two approaches of circular polarization generation. The experiments are conducted using a scanning transmission electron microscope (STEM) to detect electron-beam-excited luminescence (cathodoluminescence, CL). An acceleration voltage of 80 kV and a current of 1 nA are utilized, forming an electron probe of approximately 1 nm. This STEM-CL instrument allows angle-resolved spectrum acquisition at each electron beam position. By scanning the electron beam, 4D data sets consisting of 1D angle, 1D wavelength, and 2D space are obtained, which allows analyzing interference of light from multiple coherent emission sources. To fully evaluate the polarization, Stokes parameters are calculated from polarimetric light measurements of six different polarizations.

Acknowledgements:
This work was supported by JSPS Kakenhi (20J14821, 21H01782, 22H05033), JST FOREST (JPMJFR213J), and JST PRESTO (JPMJPR17P8).

References

1. T. Matsukata, F. J. García de Abajo, and T. Sannomiya, “Chiral Light Emission from a Sphere Revealed by Nanoscale Relative-Phase Mapping”, ACS Nano, Vol. 15, No. 2, 2219–2228, 2021.
2. T. Sannomiya, T. Matsukata, and N. Yamamoto, “Controllable Chiral Light Generation and Vortex Field Investigation Using Plasmonic Holes Revealed by Cathodoluminescence”, Nano Letters, Vol 24, No. 3, 859–865, 2024.
3. T. Sannomiya, A. Konečná, T. Matsukata, Z. Thollar, T. Okamoto, F. J. García de Abajo, N. Yamamoto, “Cathodoluminescence Phase Extraction of the Coupling between Nanoparticles and Surface Plasmon Polaritons”, Nano Letters, Vol. 20, No. 1, 592-598, 2020.

Classifying Topology in Open Photonic Systems

A. Cerjan[1*]

[1]Center for Integrated Nanotechnologies, Sandia National Laboratories, Albuquerque, New Mexico 87185, USA
[*]corresponding author: awcerja@sandia.gov

Abstract: We develop a mathematical framework for determining the topology and associated measure of protection for photonic structures embedded in free space. This framework is both applicable to 2D systems with radiative environments along their edges, as well as 2.5D slab systems that radiate into free space from their surfaces.

Photonic topological insulators exhibit bulk-boundary correspondence, which requires that boundary-localized states appear at the interface formed between topologically distinct insulating materials. However, many topological photonic devices share a boundary with free space, either on their sides or their surfaces, which raises a subtle but critical problem as free space is gapless for photons above the light line. Thus, traditional definitions of topological invariants cannot be rigorously applied – in the absence of a global bulk bandgap common to all of the materials in the system, there is no clear definition of topological protection, nor can one calculate invariants based on integrating over completely occupied bands. Here, we use a local theory of topological materials to resolve bulk-boundary correspondence in heterostructures containing gapless materials and in radiative environments. In particular, we construct the heterostructure's spectral localizer, a composite operator based on the system's real-space description that provides a local marker for the system's topology and a corresponding local measure of its topological protection; both quantities are independent of the material's bulk band gap (or lack thereof). Using this framework, we demonstrate how to rigorously classify topology both in photonic systems whose edges are surrounded by air, as well as photonic crystal slabs whose surfaces radiate into the surrounding free space environment. Moreover, we show that approximating radiative outcoupling as material absorption overestimates a heterostructure's topological protection.

Acknowledgements: This work is part-funded by Sandia National Laboratories (SNL). SNL is managed and operated by NTESS under DOE NNSA contract DE-NA0003525.

References

1. A. Cerjan, L. Koekenbier, and H. Schulz-Baldes, "Spectral localizer for line-gapped non-Hermitian systems," *Journal of Mathematical Physics* **64**, 082102 (2023).
2. K. Y. Dixon, T. A. Loring, and A. Cerjan, "Classifying Topology in Photonic Heterostructures with Gapless Environments," *Physical Review Letters* **131**, 213801 (2023).
3. S. Wong, T. A. Loring, and A. Cerjan, "Classifying topology in photonic crystal slabs with radiative environments," in prep.

Chiral and non-chiral magnetic texturing in antiferromagnetic Cr_2O_3

O. V. Pylypovskyi[1*]

[1]Helmholtz-Zentrum Dresden-Rossendorf e.V., Institute of Ion Beam Physics and Materials Research, 01328 Dresden, Germany
[*]corresponding author: o.pylypovskyi@hzdr.de

Abstract: The spontaneous appearance of magnetic textures in the easy-axis antiferromagnets can be related to the grain boundaries and crystal interfaces. Here, we discuss the properties of domain walls in thin films and the surface-symmetry-driven Dzyaloshinskii-Moriya interaction using Cr_2O_3 as the case study.

The physics of antiferromagnetic (AFM) materials offers unique features for fundamental research and applications because of their reach material properties, high eigenfrequencies and robustness to external magnetic fields [1-3]. Challenging access to their magnetic state is facilitated by the development of surface-sensitive techniques, which include magnetotransport [4,5], magnetic circular dichroism [6], Nitrogen vacancy (NV) magnetometry [7,8] and others. The AFM Cr_2O_3 (chromia) with the easy axis of magnetic anisotropy and four spins in the unit cell is a special example of a room temperature magnetoelectric medium [2,9]. While the Dzyaloshinskii-Moriya interaction (DMI) is symmetry-allowed in bulk chromia, it links two AFM vectors and vanishes in the collinear ground state. This enables a search for chiral properties of chromia at textures and interfaces.

In contrast to the single crystals [8], the thin-film chromia samples usually possess the multidomain magnetic state associated with their granular structure, leading to the domain wall pinning. In particular, the NV magnetometry reveals the complex maze-like AFM domain pattern over large areas, which spontaneously appears during (zero) field-cooling procedure and can be quantified by means of the Minkovsky-Boulingand fractal dimension d_c. We model the grain boundaries by the modification of exchange bonds and anisotropy as a Gaussian distribution with the given mean and standard deviation σ. While the spatial variation of anisotropy has a very low influence on the magnetic texture, the experimentally observed d_c is reproduced when the average inter-grain exchange coupling is about 10-15% of its bulk value J_0. The standard deviation influences the distribution of domains by size, allowing us to conclude that for the samples under investigation $\sigma \gtrsim 0.2J_0$ which includes a small portion of ferromagnetic coupling between grains. We found that the domain walls mainly follow the grain boundaries, possessing a narrow width determined by the inter-grain coupling parameters, in contrast to the domain walls in single crystals, where it is determined by the competition between exchange and anisotropies [10].

The surface properties of AFMs are often interpolated from the behavior of their bulk, which may hide a broad range of phenomena. The magnetic symmetry group $\bar{3}'m'$ of bulk chromia determines two high-symmetry and thermodynamically stable crystallographic cuts with the in-plane easy axis of anisotropy, which renders them nominally compensated ones. These so-called *m*- and *a*-plane cuts have the magnetic symmetries of m' and 2, respectively. Therefore, both allow out-of-plane magnetic moment [11]. A change of the magnetic symmetry group from the sample's interior to the surface can be a reason for the change in magnetic ordering. Namely, the m' group allows the canted ferrimagnetic state, while for the *a* plane the rotation axis makes two pairs of magnetic

sublattices independent of each other. This is revealed in the surface-symmetry-driven DMI, which enables terms linking the magnetization and the Neel vector in the surface energy density [12].

The density functional theory (DFT) analysis of *m* and *a* planes shows that the minimal energy configuration corresponds to the canted spin state, with the canting angle to be about $0.5°$. The canting direction is determined by the Neel vector and is opposite for these surface cuts for the same bulk magnetic ordering. The specific feature of the *m*-plane cut is that the magnetic sublattices become inequivalent as in ferrimagnet and there is an additional uncompensated magnetization along the *c* axis of chromia. The theoretically predicted behavior of *m* and *a* planes is confirmed by magnetotransport measurements [12].

To summarize, while there is no clear evidence of chiral magnetic textures in bulk Cr_2O_3, the picture can be substantially different at the interfaces. The grain boundaries act as the strong pinning sites for the domain walls in chromia thin films. This leads to the complex maze-like domain patterns and stimulates further research of granular AFMs to determine the properties of these domain walls. The properties of single crystal boundaries depend on their magnetic symmetry. Certain symmetries, available at the nominally compensated chromia surfaces, enable the Dzyaloshinskii-Moria interaction and lead to the dependence of the surface magnetization on the antiferromagnetic order parameter. The emergent chiral properties of the crystal defects in AFMs open a possibility to explore the defect-driven physics and utilize it for spintronic applications.

References

1. Yan, H., Z. Feng, P. Qin et al, Adv. Mater. Vol. 32, 1905603, 2020
2. Shiratsuchi, Y., K. Toyoki and R. Nakatani, J. Phys.: Cond. Mater. Vol. 33, 243001, 2021
3. Hoffman, A. and W. Zhang, J. Magn. Magn. Mater. Vol. 553, 169216, 2022
4. Kosub, T., M. Kopte, F. Radu et al, Phys. Rev. Lett. Vol. 115, 097201, 2015
5. Mahmood, A., W. Echtenkamp, M. Street et al., Nat. Comm. Vol. 12, 1674, 2021
6. Du, K., X. Xu, C. Won et al., npj Quant. Mater., Vol. 8, 17, 2023
7. Casola, F., T. van der Sar and A. Yacoby, Nat. Rev. Mater., Vol. 3, 17088, 2018
8. Hedrich, N., K. Wagner, O. Pylypovskyi et al., Nat. Phys., Vol. 17, 574, 2021
9. Weber S. and N. Spaldin, Phys. Rev. Lett. Vol. 130, 146701, 2023
10. Pylypovskyi, O., N. Hedrich, A. Tomilo et al., Phys. Rev. Appl., Vol. 20, 014020, 2023
11. Weber, S., A. Urru, S. Bhowal et al., ArXiv:2306.06631, 2023
12. Pylypovskyi, O., S. Weber, P. Makushko et al., ArXiv:2023.13438, 2023

Planar resonant metasurfaces with 3D intrinsic chirality

Zi-Lan Deng*, Meng-Xia Hu, Xin Li, Qian-Mei Deng, Feng-Jun Li, Xiangping Li

Guangdong Provincial Key Laboratory of Optical Fiber Sensing and Communications, Institute of Photonics Technology, College of Physics & Optoelectronic Engineering, Jinan University, Guangzhou 510632, China
*Corresponding author: zilandeng@jnu.edu.cn

Abstract: This talk presents our recent studies on the chiral resonant metasurfaces with planar structures embedded in an asymmetric environment, 3D intrinsic chirality could be achieved with simultaneous tunable quality factor and emission circular dichroism, enabling new possibilities for circularly polarized light sources, chiral molecule detection, and chiral nonlinear optics.

Chirality refers to the property of an object that cannot coincide with its mirror image after rotation or translation. The study of chiral properties is significant in multiple disciplines. Particularly in the field of optics, the interaction between light and certain chiral geometric structures can stimulate chiroptical response that is manifested by the amplitude or phase differences between left-handed circular polarization (LCP) and right-handed circular polarization (RCP). On the other hand, resonant metasurfaces with high quality factor (Q factor), possessing excellent capabilities for strong light-matter interactions, have been extensively applied in cutting-edge areas like light emission(*1*), sensing(*2*), nonlinear optics(*3*), and quantum optics(*4*).

Recently, resonant metasurfaces with bound state of continuum (BIC) have been exploited to boost the optical chirality to its maximum(*5, 6*). Usually, three-dimensional (3D) geometries with broken symmetries in both in-plane and out-of-plane are required to achieve the 3D intrinsic optical chirality without polarization conversion under normal incidence. However, the precise manufacturing of such 3D chiral nano-structures are usually challenging, and existing technologies lack flexibility in adjusting chirality and Q factors simultaneously. Here, we introduce an effective strategy to achieve 3D intrinsic optical chirality by merely planarized structures using all-dielectric BIC metasurfaces. This structure, by design, breaks in-plane symmetry to achieve 3D intrinsic chirality within a planar structure in an asymmetric environment. Additionally, it allows flexible tuning of its chirality in terms of the degree of circular polarization and Q factors.

It is worth mentioning that this structure exhibits extremely high chiral emission capability. The circular dichroism of emission (CD) reaches unitary, suggesting that when the chiral metasurfaces is combined with active materials, various strong chiral emission devices with pure circular polarization generation could be constructed. This discovery opens new possibilities for applications requiring ultra-high Q factors and precise chirality control, such as circularly polarized light sources, chiral molecule detection, and chiral nonlinear optics.

In summary, our research paves a new path for controlling chirality and optimizing Q factors in the field of optics, expanding the application scope of optical metasurfaces.

Key words: metasurface, chirality, bound state in the continuum

References

1. Y. H. Lee *et al.*, Hierarchically manufactured chiral plasmonic nanostructures with gigantic chirality for polarized emission and information encryption. *Nature Communications* **14**, 7298 (2023).
2. Y. Zhao *et al.*, Chirality detection of enantiomers using twisted optical metamaterials. *Nature Communications* **8**, 14180 (2017).
3. J. T. Collins, D. C. Hooper, A. G. Mark, C. Kuppe, V. K. Valev, Second-Harmonic Generation Optical Rotation Solely Attributable to Chirality in Plasmonic Metasurfaces. *ACS Nano* **12**, 5445-5451 (2018).
4. K. Wang *et al.*, Quantum metasurface for multiphoton interference and state reconstruction. *Science* **361**, 1104-1108 (2018).
5. T. Shi *et al.*, Planar chiral metasurfaces with maximal and tunable chiroptical response driven by bound states in the continuum. *Nature Communications* **13**, 4111 (2022).
6. X. Zhang, Y. Liu, J. Han, Y. Kivshar, Q. Song, Chiral emission from resonant metasurfaces. *Science* **377**, 1215-1218 (2022).

Generation of Ultra-compact Optical Vortex Through Photonic Spin-orbit Interactions in Nanostructures and Its Super-resolution Imaging

Benfeng Bai*

Department of Precision Instrument, Tsinghua University, Beijing 100084, China
*corresponding author: baibenfeng@tsinghua.edu.cn

Abstract: With photonic spin-orbit interactions, efficient generation of ultra-compact optical vortices (OVs) in meta-devices are reported, which have a minimum radius of 1 μm and a signal-to-noise ratio larger than 6 dB. A spin-selective and phase-resolved scanning near-field optical microscopy (SSPR-SNOM) is established to probe and visualize the OV generation process.

The mutual interplay between different angular momenta of light, i.e., the so-called photonic spin-orbit interaction (SOI), has attracted much attention in recent years. Nanoscale optical vortices (OVs) carrying orbital angular momenta can be generated via photonic SOI in nanostructures and have important applications in many emerging fields such as quantum communication and optical manipulations.

In this talk, we first report our recent advances in the efficient generation of ultra-compact optical vortices (OVs) in meta-devices, including a geometric-phase metasurface and an achiral plasmonic annular nanoaperture (PAN).[1, 2] Especially, the PAN is shown to be the simplest nanostructure to generate the most compact OV with a radius down to only 1 μm and possesses a signal-to-noise ratio larger than 6 dB. With this method, the generation of a 3×3 OV array within a small area of 6×6 μm^2 is demonstrated experimentally. Then, we establish and employ a spin-selective and phase-resolved scanning near-field optical microscope (SNOM) to super-resolution image the photonic SOI and OV generation process in the spin basis. The dynamic evolution of the wavefront of the generated OV is directly probed from the near field to the intermediate field and to the far field with subwavelength resolution, which intuitively reveals the SOI process. The findings provide a simple and effective solution for large-scale, low-cost OV beam generation and offer a powerful tool for experimental exploration of the nanoscale photonic SOI.

References

1. T. Cui, L. Sun, B. Bai, and H.-B. Sun, “Probing and imaging photonic spin-orbit interactions in nanostructures,” Laser Photon. Rev., Vol. 15, 2100011, 2021.
2. T. Cui, M. Zhang, L. Sun, S. Zhang, J. Wang, B. Bai, and H.-B. Sun, “Spin-symmetry-selective generation of ultracompact optical vortices in nanoapertures without chirality,” Small Struct., Vol. 1, 2000008, 2020.

Chiral structures fabrication with structured light possessing orbital angular momentum

T. Omatsu[1,2]

[1]Graudate School of Engineering, Chiba University, Japan
[2]Molecular Chirality Research Center, Chiba University, Japan
[*]corresponding author: omatsu@faculty.chiba-u.jp

Abstract: We demonstrate the fabrication of chiral structured materials by utilizing structured light possessing orbital angular momentum (OAM), that is an optical vortex. Such chiral structures pave the way towards a myriad of innovative technologies: for instance, an optical vortex induced self-written helical fiber acts as a mode-convertor for OAM states.

Structured light with an orbital angular momentum (OAM), that is an optical vortex and its related family, possesses a ring-shaped spatial intensity profile arising from its helical wavefront with an on-axis phase singularity [1,2]. In recent years, it has been discovered that the OAM of optical vortex twists the irradiated materials, such as metals, semiconductors, polymers, and even crystals, thus resulting in the fabrication of nano/micro-scale chiral structured materials [3,4]. Optical vortex induced chiral structures will open the way towards exotic chiral engineered materials with physical properties beyond natural materials. Such chiral materials have never been fabricated with the illumination of a circular polarized planer light field only with a spin angular momentum (SAM).

In this presentation, we review the demonstration of optical vortex induced chiral structures. Also, we report on the optical vortex induced helical fiber, which enables the mode conversion between Gaussian and optical vortex modes [5,6]. This demonstration will offer advanced OAM communication devices, and it will give us new fundamental insights.

Also, today, beyond conventional optical vortices, particle-like structured light with topologically protected polarization textures, herein referred optical skyrmions [7], have been demonstrated. We also address advanced photo-induced topological engineered materials with optical skyrmions via exotic light matter interactions.

References

1. L. Allen, M. W. Beijersbergen, R. J. C. Spreeuw, J. P. Woerdman, "Orbital angular momentum of light and the transformation of Laguerre-Gaussian laser modes," Phys. Rev. A 45, 8185–8189 (1992).
2. J. Leach, M. J. Padgett, S. M. Barnett, S. Franke-Arnold, J. Courtial, "Measuring the Orbital Angular Momentum of a Single Photon," Phys. Rev. Lett. 88, 257901 (2002).
3. T. Omatsu, K. Miyamoto, K. Toyoda, R. Morita, Y. Arita, K. Dholakia, "A New Twist for Materials Science: The Formation of Chiral Structures Using the Angular Momentum of Light," Adv. Opt. Mater. 7, 1801672 (2019).
4. T. Omatsu, K. Masuda, K. Miyamoto, K. Toyoda, N. M. Litchinitser, Y. Arita, K. Dholakia, "Twisted mass transport enabled by the angular momentum of light," J. Nanophotonics 14, 1 (2020).
5. J. Lee, Y. Arita, S. Toyoshima, K. Miyamoto, P. Panagiotopoulos, E. M. Wright, K. Dholakia, T. Omatsu, ACS Photonics 5 (10), 4156-4163 (2019).

6. Y. Arita, J. H. Lee, H. Kawaguchi, R. Matsuo, K. Miyamoto, K. Dholakia, T. Omatsu, “Photopolymerization with high-order Bessel light beams,” Opt. Lett. 45, 4080-4083 (2020).
7. Y. Shen, Q. Zhang, P. Shi, L. Du, X. Yuan, A. V. Zayats, "Optical skyrmions and other topological quasiparticles of light,” Nat. Photon. 18, 15–25 (2024).

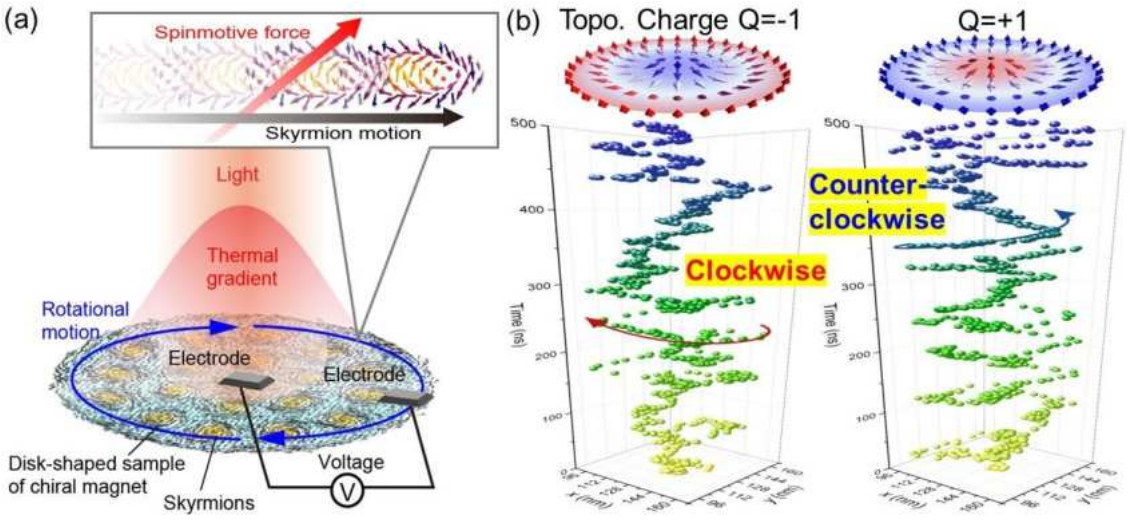
Thermally Induced Dynamics of Magnetic Skyrmions and Their Device Functions

Masahito Mochizuki[1*], Xichao Zhang[1], and Junnosuke Matsuki[2]

[1]Department of Applied Physics, Waseda University, Okubo, Shinjuku-ku, Tokyo 169-8555, Japan
[2]Department of Basic Science, The University of Tokyo, Komaba, Meguro, Tokyo 153-8902, Japan
[*]masa_mochizuki@waseda.jp

Abstract: Thermally induced dynamics of magnetic topology in magnets has turned out to host rich physical phenomena and device functions, which are subjects to intensive studies in the research of spintronics recently. Here we discuss two phenomena of magnetic skyrmions related with their thermal motion, i.e., the thermoelectric effect with DC-voltage generation and the active-matter like behavior called chiral swimmer, which were revealed in the recent theoretical studies.

We first discuss the heat-electricity conversion with skyrmions in the presence of thermal gradient [1,2]. A confined skyrmion crystal exhibits rotational motion when a radial temperature gradient is present due to an inverse effect of the topological magnon Hall effect [2]. We discuss that this thermally induced rotational motion of skyrmions can be exploited for the DC-voltage generation. A moving skyrmion texture generates a spinmotive force perpendicular to its moving direction. Consequently, the rotational motion of skyrmions confined in a circular disk generates DC electric voltage in the radial direction. The proposed phenomenon can be exploited as spintronic thermoelectric devices to realize the heat-electricity conversion.



(a) Schematics of the thermoelectric effect of magnetic skyrmions (b) Chiral Brownian motion of skyrmions as a source of active-matter-like behaviors.

Then we discuss the active-matter-like behaviors of magnetic skyrmions due to the chiral Brownian motion [3]. Skyrmions as chiral objects show chiral nature in interactions with nanostructures, which can lead to intriguing

phenomena. We discuss that the Brownian dynamics of skyrmions interacting with a chiral flower-like obstacle in a ferromagnet exhibits topology-dependent outcomes, which can be regarded as a spontaneous mesoscopic order-from-disorder phenomenon driven by thermal fluctuations. This phenomenon can be utilized to control the skyrmion position and distribution without any external driving force and can be exploited as a new way to design topology-sorting devices.

References

[1] J. Matsuki and M. Mochizuki, Phys. Rev. B **107**, L100408 (2023).

[2] M. Mochizuki, X. Z. Yu, S. Seki, N. Kanazawa, W. Koshibae, J. Zang, M. Mostovoy, Y. Tokura, and N. Nagaosa, Nature Materials 13, 241 (2014).

[3] X. Zhang, J. Xia, O. A. Tretiakov, M. Ezawa, G. Zhao, Y. Zhou, X. Liu, and M. Mochizuki, Nano Letters 23, 11793 (2023).

Topological magneto-optical effect induced by skyrmion lattice formation

Y. Okamura[1*], Y. D. Kato[1], M. Hirschberger[1,2], Y. Tokura[1,2,3], and Y. Takahashi[1,2]

[1]Department of Applied Physics and Quantum Phase Electronics Center, University of Tokyo, Japan

[2]RIKEN Center for Emergent Matter Science, Japan

[3]Tokyo College, University of Tokyo, Japan

[*]corresponding author: okamura@ap.t.u-tokyo.ac.jp

Abstract: We show the magneto-optical Kerr effect (MOKE) induced by the skyrmion formation, i.e., topological MOKE, in Gd_2PdSi_3. The magneto-optical rotation is significantly enhanced in the skyrmion phase, which demonstrates the topological MOKE ranging up to the sub-eV region. This finding exemplifies the light-skyrmion interaction arising from the emergent gauge field.

Magnetic skyrmions are nanometric whirlpools of spins, where the directions of the constituent spins wrap the unit sphere [1], attracting enormous attention as potential information carriers in next-generation memory/logic devices. Due to their non-coplanar spin arrangement, the resultant scalar spin chirality gives rise to the fictious magnetic field (emergent magnetic field) acting on the conduction electrons, which leads to unique transport phenomena through the coupling to low-energy quasi-particles, such as the topological Hall effect. However, the high-frequency or optical response of skyrmions has remained elusive so far.

In this presentation, we show the novel magneto-optical effect induced by the gauge field from skyrmion lattice in the centrosymmetric magnet Gd_2PdSi_3 [2,3]. Although it has been long believed that the magneto-optical Kerr effect (MOKE) is proportional to the magnetization, we reveal that the skyrmion lattice phase exhibits the marked enhancement of MOKE. This previously unobserved optical response directly manifests the emergence of the topological MOKE induced by the gauge field generated from skyrmions, which never requires the strong spin-orbit interaction in stark contrast to the conventional magnetization-induced MOKE. The topological MOKE is observed even up to sub-eV region in photon energy, which demonstrates the significant change in electronic structure even far from Fermi level. Such the change is also found to cause the topological Hall effect as a transport response through its accompanying Berry curvature, establishing the comprehensive understanding of the emergent electrodynamics ranging from DC to optical region. Our findings exemplify the existence of strong light-skyrmion interaction mediated by the gauge field in the optical region, potentially enabling the functional operation of skyrmion-based devices integrated with the versatile laser technology.

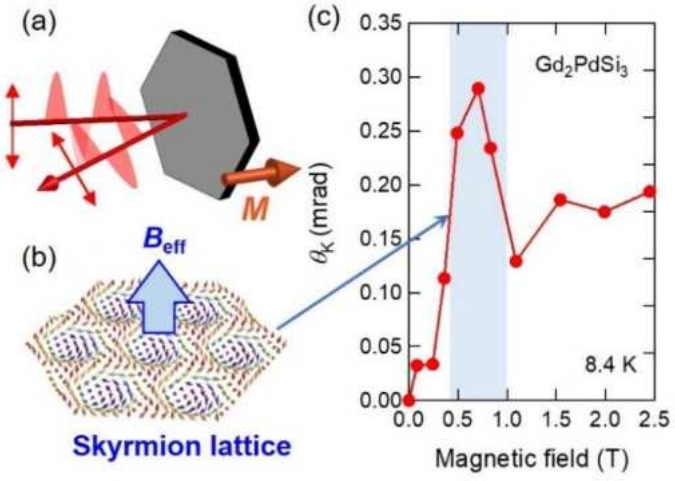


Fig. 1: (a,b) Schematic illustration of magneto-optical Kerr effect (MOKE) (a) and skyrmion lattice (b). (c) Magnetic-field dependence of the MOKE

References

[1] Back, C. *et al.,* J. Phys. D: Appl. Phys. **53**, 363001 (2020).

[2] Kurumaji, T. *et al.,* Science **365,** 914 (2019).

[3] Kato, Y. D., Okamura, Y. *et al.,* Nat. Commun. **14,** 5416 (2023).

Symmetry Breaking in Colloidal Metal Nanostructures by Circularly Polarized Light Directed Galvanic Replacement Reaction

M. Ghalawat[1], D. Feferman[1], A. Movsesyan[2,3], W. He[4], Z. Wang[3], D. Ma[4], A. O. Govorov[2], and G. Markovich[1*]

[1] School of Chemistry, Tel Aviv University, Tel Aviv 6977801, Israel
[2] Department of Physics and Astronomy and Nanoscale, and Quantum Phenomena Institute, Ohio University, Athens, OH, 45701 USA
[3] Institute of Fundamental and Frontier Sciences, University of Electronic Science and Technology of China, Chengdu, 610054 China
[4] Centre Énergie Materiaux et Telécommunications, Institut National de la Recherche Scientifique (INRS), Varennes, QC J3X 1P7, Canada
[*]corresponding author: gilmar@post.tau.ac.il

Abstract: Colloidal gold@silver nanocuboids were illuminated with circularly polarized light during partial galvanic replacement reaction of the silver shell with gold ions. This resulted in a small symmetry breaking manifested through appearance of circular dichroism, in spite of the random rotational averaging of the nanocuboids with respect to the illumination direction.

Illumination of elongated cuboidal gold@silver core-shell nanoparticles with circularly polarized light within the range of their plasmon resonance wavelengths during partial galvanic replacement reaction (GRR) with gold ions resulted in symmetry breaking of their shape and appearance of significant circular dichroism (CD) signals. This chiral symmetry breaking is probably related to asymmetric localized plasmonic “hot-spots” excited at opposite corners of the nanocuboids (NCs), which lead to oxidation and dissolution of surface silver atoms, followed by some silver re-deposition in parallel to deposition of gold atoms at corners of the nanocuboids. The shape changes of the nanocuboids post GRR under circularly polarized light illumination, analyzed by electron microscopy and electron tomography, were different from those occurring through GRR in dark or under linearly polarized light illumination. The slight chiral symmetry breaking occurs in spite of significant averaging of the effect due to the free rotation of the NCs with respect to the illumination direction, as predicted previously by Govorov and coworkers [1]. The effect becomes smaller in more symmetric geometrical shapes of silver nanoparticles such as triangular nanoprisms and nanocubes, down to zero CD in spherical Au@Ag nanoparticles, as predicted theoretically.

This work was supported by the United States-Israel Binational Science Foundation (BSF) grant no. 2018050.

References

1. A. Moveseyan, A. Muravitskaya, L. V. Besteiro, E. Y. Santiago, O. Ávalos-Ovando, M. A. Correa-Duarte, Z. M. Wang, G. Markovich and A. O. Govorov, “Creating Chiral Plasmonic Nanostructures Using Chiral Light in a Solution and on a Substrate: The Near-Field and Hot-Electron Routes” Adv. Opt. Mater., Vol. 11, 2300013, 2023.

Spin wave amplification through superradiance

X. R. Wang[1,2,*], K. Y. Jing[1], and X. Gong[1]

[1] Physics Department, The Hong Kong University of Science and Technology, Clear Water Bay, Kowloon, Hong Kong and HKUST Shenzhen Research Institute, Shenzhen 518057, China

[2] Chinese University of Hong Kong (Shenzhen), China

[*]corresponding author: phxwan@ust.hk

Abstract: Superradiance is a phenomenon of multiple facets that occurs in classical and quantum physics under the extreme conditions. A notion of supermirror made of energy-source powered medium with an inverted spectrum is proposed. Supermirrors resemble the Hawking radiation or the Dicke superradiance. The principle is demonstrated for spin waves.

Wave amplification is an important subject in wave physics. In wave applications, an indispensable component is to amplify a wave which will surely decay or attenuate during its propagation and transportation. Some waves have many efficient and effective ways of amplification. For example, electromagnetic waves in the visible light range can be amplified by the gain medium with population inversion. However, spin wave amplification is still an unsolved problem in magnonics.

Spin waves, the collective excitations of strongly correlated spins, have attracted much attention in the spintronic community due to their rich physics [1-3] and potential applications [4-7]. One challenge in spin-wave based applications is the strong spin wave damping such that it can only propagate a relatively short distance, order of millimeters even for the lowest known damping material of yttrium iron garnet [8,9]. Thus, an effective method for amplifying an arbitrary spin wave is demanded in order to realize the power of spin waves.

Many efforts have been made on spin wave amplification. The anti-damping nature of current-induced Slonczewski spin transfer torque (STT) [10-13] and spin orbit torque [14-16] was considered first. A straightforward analysis of the Landau-Lifshitz-Gilbert (LLG) equation suggests that STTs can exponentially amplify all spin waves. Unfortunately, experiments and micromagnetic simulations observed only the increase of spin wave propagation distance in a proper current, but no spin wave amplification despite many attempts [10-16]. People have also used parametric pumping to amplify spin waves. The idea is to resonate spin waves with external oscillating fields such as an electromagnetic or mechanic wave [18-23]. At resonance, energy from external fields can be transformed into the energy of a spin wave. However, parametric pumping requires specific resonant conditions that are only applicable to a particular wave frequency. The Klein paradox [24,25] has been proposed to amplify spin waves. The concept involves using STT to create a spin wave analogue of black and white holes [25] such that positive-energy and negative-energy spin wave modes can be coupled together in an inhomogeneous FM film. Experimental evidence of this proposal is yet to be provided. Nonlinear 3-magnon and 4-magnon process have also been proposed to amplify spin waves and to create spin wave combs [26]. This approach often requires stringent conditions and for a specific mode.

Reflection and refraction are general wave phenomena occurring at the interface of two homogeneous media. A general rule is that the intensities of both reflected and refracted waves are smaller than the in-coming

wave intensity due to the energy conservation law. A wave in normal media has a normal spectrum whose long wave frequency (energy) is a local minimum (at zero wave number) such that the group and phase velocities are in the same directions (for isotropic media). Under certain circumstances, the spectrum minimum could be away from zero wave number. The group and phase velocities in certain frequency window could be in the opposite directions. We term it as a pumped medium and corresponding spectrum to be inverted because it can only occur with an external energy source. In this talk, I will present a notion of super-mirrors which manifests superradiances under an easily realized condition. We show that an interface separating a normal medium from a pumped medium. The wave frequency in the normal medium increases with the wavenumber and is minimal at zero wavenumber while the wave frequency in the pumped medium is minimal at a negative wavenumber. There is a frequency window in which the phase velocity and group velocity are opposite. To demonstrate the working principle for spin waves, we show that the interface of a current-free (normal) ferromagnet (FM) and a current-flow (pumped) FM is such a supermirror. Surprisingly and interestingly, the reflection coefficient of a wave at the interface between a normal medium and a pumped medium can be greater than 1. The super-reflection is the consequence of current-induced spectrum inversion where spin wave hase and group velocities are in the opposite directions. The physics is that incident spin wave is refracted and activates a backward propagating spin wave inside pumped FM region. The refracted spin wave re-enter the normal FM region to constructively interfere with the reflected wave. It appears that the pumped FM region coherently emits reflected waves, leading to a super-reflection. The process resembles superradiance of a spinning black hole through the Hawking radiation, or the Dicke superradiance of cavity photons inside population inverted media. The physics is clearly revealed in a generic FM model and is confirmed by micromagnetic simulations.

This work is supported by the National Key Research and Development Program of China (No. 2020YFA0309600), the NSFC Grant (No. 11974296), and Hong Kong RGC Grants (No. 16300522, 16300523, and 16302321).

References

1. H. Y. Yuan, Y. S. Cao, A. Kamra, R. A. Duine and P. Yan, Quantum magnonics: When magnon spintronics meets quantum information science, Physics Reports, 965: 1-74 (2022).
2. X. S. Wang, P. Yan, Y. H. Shen, G. E. W. Bauer, and X. R. Wang, Domain wall Propagation through Spin Wave Emission, Phys. Rev. Lett. 109, 167209 (2012).
3. P. Yan, X. S. Wang, and X. R. Wang, All-Magnonic Spin-Transfer Torque and structure Wall Propagation, Phys. Rev. Lett. 107, 177207 (2011).
4. X. S. Wang, H. W. Zhang, and X. R. Wang, Topological Magnonics: A Paradigm for Spin-Wave Manipulation and Device Design, Phys. Rev. Applied 9, 024029 (2018).
5. A. V. Chumak, A. A. Serga, and B. Hillebrands, Magnon transistor for all-magnon data processing, Nat. Commun. 5, 4700 (2014).
6. G. Csaba, A. Papp, and W. Porod, Perspectives of using spin waves for computing and signal processing, Phys. Lett. A, 381, 1471 (2017).
7. A. Barman, G. Gubbiotti, S. Ladak, et al, The 2021 magnonics roadmap, J. Phys.: Condens. Matter, 33 413001 (2021).
8. I. Bertelli , J. J. Carmiggelt, T. Yu, et al., Magnetic resonance imaging of spin-wave transport and interference in a magnetic insulator, Sci. Adv. 6, 46 (2020).

9. C. Liu, J. Chen, T. Liu, F. Heimbach, H. Yu, Y. Xiao, J. Hu, M. Liu, H. Chang, T. Stueckler, S. Tu, Y. Zhang, Y. Zhang, P. Gao, Z. Liao, D. Yu, K. Xia, N. Lei, W. Zhao, and M. Wu, Long-distance propagation of short-wavelength spin waves, Nat. Commun. 9, 738 (2018).
10. E. Padron-Hernandez, A. Azevedo, and S. M. Rezende, Amplification of Spin Waves by Thermal Spin-Transfer Torque, Phys. Rev. Lett. 107, 197203 (2011).
11. S. M. Seo, K. J. Lee, H. Yang, and T. Ono, Current-Induced Control of Spin-Wave Attenuation, Phys. Rev. Lett. 102, 147202 (2009).
12. An, K., Birt, D. R., Pai, C. F., Olsson, K., Ralph, D. C., Buhrman, R. A., Li, X., Control of propagating spin waves via spin transfer torque in a metallic bilayer waveguide, Phys. Rev. B, 89, 140405 (2014).
13. S. Woo and G. S. D. Beach, Control of propagating spin-wave attenuation by the spin-Hall effect, J. Appl. Phys. 122, 093901 (2017).
14. B. Divinskiy, V. E. Demidov, S. Urazhdin, R. Freeman, A. B. Rinkevich, and S. O. Demokritov, Excitation and amplification of spin waves by spin-orbit torque, Adv. Mater. 30, 1802837 (2018).
15. V. E. Demidov, S. Urazhdin, A. Anane, V. Cros, and S. O. Demokritov, Spin-orbit-torque magnonics, J. Appl. Phys. 127, 170901 (2020).
16. A. I. Nikitchenko and N. A. Pertsev, Spin-orbit torque control of spin waves in a FM waveguide, Phys. Rev. B 104, 134422 (2021).
17. P. A. Kolodin, P. Kabos, C. E. Patton, B. A. Kalinikos, N. G. Kovshikov, and M. P. Kostylev, Amplification of microwave magnetic envelope solitons in thin yttrium iron garnet films by parallel pumping, Phys. Rev. Lett. 80, 1976 (1998).
18. T. Brächer, P. Pirro, and B. Hillebrands, Parallel pumping for magnon spintronics: Amplification and manipulation of magnon spin currents on the micron-scale, Phys. Rep. 699, 1 (2017).
19. B. Heinz ,M. Mohseni, A. Lentfert, R. Verba, M. Schneider, B. Lägel, K. Levchenko, T. Brächer, C. Dubs, A. V. Chumak, and P. Pirro, Parametric generation of spin waves in nanoscaled magnonic conduits, Phys. Rev. B 105, 144424 (2022).
20. P. Chowdhury, P. Dhagat, and A. Jander, Parametric amplifcation of spin waves using acoustic waves, IEEE Trans. Magnet. 51, 1300904 (2015).
21. P. Graczyk, M. Krawczyk, Coupled mode theory for the acoustic wave and spin wave interaction in the magphonic crystals: Propagating magnetoelastic waves, Phys. Rev. B 96, 024407 (2017).
22. R. Verba, V. Tiberkevich, I. Krivorotov, and A. Slavin, Parametric Excitation of Spin Waves by Voltage-Controlled Magnetic Anisotropy, Phys. Rev. Appl. 1, 044006 (2014).
23. O. Klein, Die Reflexion von Elektronen an einem Potentialsprungnach der relativistischen Dynamik von Dirac, Zeitschrift für Physik 53, 157 (1929).
24. R. Brito, V. Cardoso, P. Pani, Superradiance, Lect. Notes Phys. 906, 1–237 (2015).
25. Doornenbal R J, Roldán-Molina A, Nunez A S, and Duine R.A, Spin-wave amplification and lasering driven by inhomogeneous spin-transfer torques, Phys. Rev. Lett. 122, 037203 (2019).
26. Z. Y. Wang, H. Y. Yuan, Y. S. Cao, and P. Yan, Twisted Magnon Frequency Comb and Penrose Superradiance, Phys. Rev. Lett. 129, 107203 (2022).
27. X. R. Wang, X. Gong, and K. Y. Jing, Supermirrors and spin wave amplifications, Appl. Phys. Lett. (2024).

Algebra of Optical Phase Dislocations

Gorodetski Yuri*
Electrical and Electronic Engineering department,
Ariel University, 407000, Ariel, Israel
* corresponding author: yurig@ariel.ac.il

Abstract

We demonstrate that by combining a physical lattice dislocation with the Berry phase dislocation in one structure the manipulation with the topological charge of the emerging vortex beams can be controlled in an intriguing way. As a result, the plasmonic field in the near-field can be modified and selectively excited.

1 Introduction

The study of physical nature of electromagnetic fields often involves topological concepts and mathematical tools that are equivalently suitable for crystal lattice, especially when the dislocation is an object of investigation. Crystal lattice structures exhibit topological defects as line dislocations, disrupting atomic arrangements and affecting material properties.[1] The topological parameter defining the dislocation "strength" - the Burgers vector, has a global effect on a stress distribution in the material.[2] In analogy with solids, a dislocation in a diffractive optical element or a photonic crystal leads to phase singularities in electromagnetic fields. Around the phase singularity the wavefront forms a helical surface of the

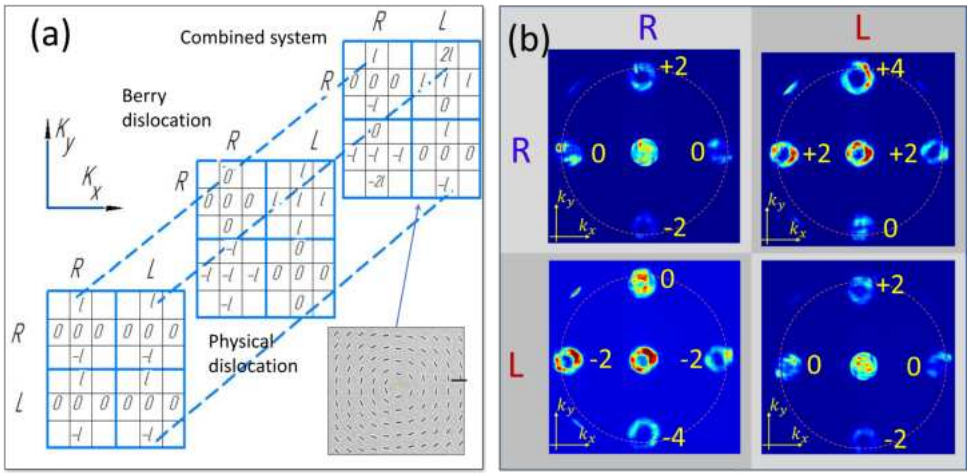


Figure 1: Algebra of dislocations. (a) – dislocation summation rules. Inset shows the combined structure with $l = 2$. The scale bar length is 1 μm. (b) – k - space patterns for all the possible combinations of the polarization states.

form $E \propto \exp(il\varphi)$ (with φ being an azimuthal angle), resulting in a phase shift of $l \times 2\pi$ upon circumvention. Such a wavefront dislocation – an optical vortex – is a unique phenomenon in optical fields widely investigated due to its intriguing topological properties, and a variety of technological applications. The singularity itself is a point of phase discontinuity where the modulus of the complex field

amplitude E vanishes.[3] Optical vortices are characterized by a topological charge - l denoting orbital angular momentum (OAM) per photon in units of $\overline{h}$.[4]

Regular optical waves containing a single screw dislocation or an array of dislocations were experimentally generated using diverse techniques. These methods included transmission or diffraction of laser beams from specially synthesized holographic phase masks, liquid crystal optics and helical transmission phase plates. Phase defects became evident in laser light scattered by a random phase diffuser or transmitted through a multi-mode fiber.[5] The experimental observation of optical vortices has been reported in the oscillation of ring cavities that housed a photo-refractive crystal as a gain medium, as well as in a linear cavity featuring a photo refractive phase-reversal mirror.[6] Recently, the phenomenon of the geometric Pancharatnam-Berry phase (PBPh) has attracted much interest as a means of manipulating the optical field in a polarization dependent manner.[7] The effect has been induced by a local manipulation with the field polarization, that leaded to a distinctive phase of circular states. In the following years the PBPh-based systems have been implemented in surface plasmons (SP) to excite polarization-dependent and unidirectional distributions in the near-field and in the far-field.[8] Moreover, it has been shown that the geometric phase could be algebraically added to the dynamic phase cused by the plasmon propagation and result in strongly asymmetric polarization-based behaviour. In particular, we have shown that in a periodic bi-structure comprising of periodically rotated nanoslits arranged in a square or hexagonal array the plasmon acquires a combined momentum addition due to the grating periodicity and the nanoslit rotation.[9]

In this work we examine the concept of "algebra of optical dislocations". We form a plasmonic structure with physical (fork-type) dislocation and a structure inducing helical Berry phase. We demonstrate the effects of these two types of dislocations alone and finally combine them into one system. The experimental investigation of these combined structures reveals a polarization and position-dependent vortex formation in the k-space. We derive the summation rules for the two types of the optical dislocations and verify them experimentally. The combined system extends the ability to control light matter interaction in the nanoscale and suggests a novel degree of freedom in nanophotonics and optics communication.

References

[1] J. F. Nye and M. V. Berry, "Dislocations in wave trains," *Proceedings of the Royal Society of London. A. Mathematical and Physical Sciences*, vol. 336, no. 1605, pp. 165–190, 1974.

[2] M. D. Williams, M. M. Coles, D. S. Bradshaw, and D. L. Andrews, "Direct generation of optical vortices," *Physical Review A*, vol. 89, no. 3, p. 033837, 2014.

[3] V. Y. Bazhenov, M. Vasnetsov, and M. Soskin, "Laser beams with screw dislocations in their wavefronts," *Jetp Lett*, vol. 52, no. 8, pp. 429–431, 1990.

[4] A. M. Yao and M. J. Padgett, "Orbital angular momentum: origins, behavior and applications," *Advances in optics and photonics*, vol. 3, no. 2, pp. 161–204, 2011.

[5] I. Basistiy, M. Soskin, and M. Vasnetsov, "Optical wavefront dislocations and their properties," *Optics Communications*, vol. 119, no. 5-6, pp. 604–612, 1995.

[6] G. Indebetouw and S. R. Liu, "Defect-mediated spatial complexity and chaos in a phase-conjugate resonator," *Optics communications*, vol. 91, no. 3-4, pp. 321–330, 1992.

[7] H. G. Berry, G. Gabrielse, and A. Livingston, "Measurement of the stokes parameters of light," *Applied optics*, vol. 16, no. 12, pp. 3200–3205, 1977.

[8] Y. Gorodetski, A. Drezet, C. Genet, and T. W. Ebbesen, "Generating far-field orbital angular momenta from near-field optical chirality," *Physical review letters*, vol. 110, no. 20, p. 203906, 2013.

[9] L. Singh, M. Fox, S. Sternklar, and Y. Gorodetski, "Topological diffraction from grating with space variant chirality," *ACS Photonics*, vol. 9, no. 4, pp. 1395–1399, 2022.

Peltier effect of phonons driven by electromagnetic waves

Hiroaki Ishizuka[1,*] **and Masahiro Sato**[2]

[1]Tokyo Institute of Technology, Japan
[2]Chiba University, Japan
[*]corresponding author: ishizuka@phys.titech.ac.jp

Abstract: We show that a phenomenon analogous to the Peltier effect occurs by phonon photocurrent in a material subject to a linearly polarized light. We derive a general formula for the nonlinear Peltier coefficient. An order-of-magnitude estimate using this theory predicts an experimentally observable energy current using available THz-infrared light sources.

In semiconductors, a steady electric current in material causes a temperature gradient, a phenomenon known as Peltier effect [Fig. 1(a)]. As the Peltier effect is caused by the energy carried by carriers in semiconductors, an analogous phenomenon can occur by a flow of other quasi-particles, such as magnons and phonons. A possible route to realize the Peltier effect of magnons and phonons is to use a nonlinear response. For instance, optical generation of spin current by controlling magnon [1-3] and spinon [4] flows using a nonlinear response similar to the bulk photovoltaic effect has been proposed recently. As magnons and spinons also carry energy, a flow of magnons and other low-energy excitations may induce a phenomenon similar to the Peltier effect. Among various candidates, phonons might be an interesting candidate for the optical control of heat flow, as the thermal properties of insulators are often dominated by phonons.

In this work, we show that a Peltier effect analog of phonons occurs in a material subject to linearly polarized light [5] [Fig. 1(b)]. Under light illumination, an energy current of phonons occurs through a nonlinear optical effect, similarly to the bulk photovoltaic effect [6]. We formulate the generic formula for the nonlinear Peltier coefficient of this nonlinear energy current carried by phonons using nonlinear response theory. Using the general formula, we show that the photogalvanic energy current occurs only in a non-centrosymmetric system with two or more optical phonon bands (three or more bands, including the acoustic mode). This is in contrast to the bulk photovoltaic effect and the nonlinear spin current, which occurs in two band models. We also find that the nonlinear Peltier effect is related to the shift vector of phonons, similar to that of shift current [7]. However, reflecting the difference in mechanism, the nonlinear Peltier effect is related to the position of a single phonon

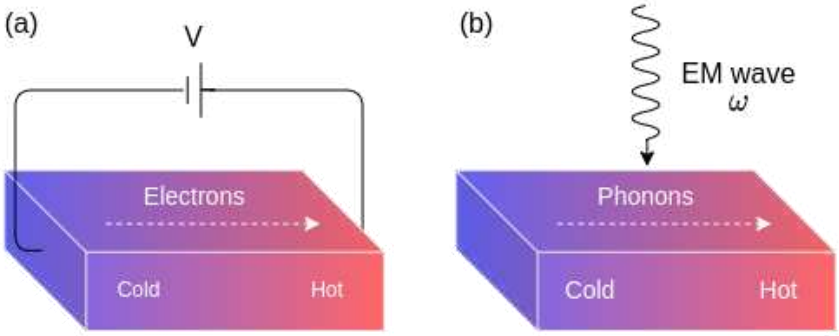


Fig. 1: Schematics of (a) the Peltier effect and (b) nonlinear Peltier effect of phonons.

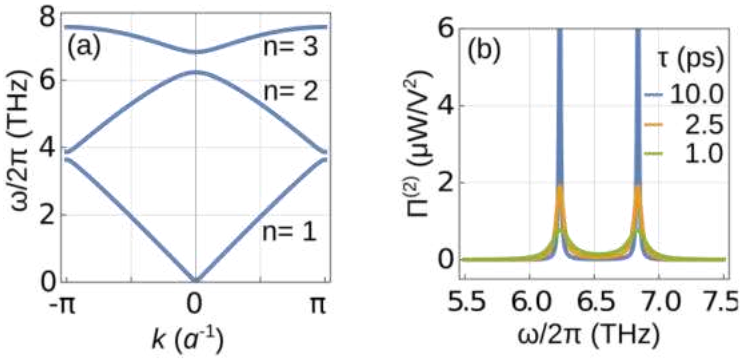


Fig. 2: Nonlinear Peltier effect of phonons in a simple three-band model. (a) The phonon dispersion of three sublattice model, and (b) the calculated nonlinear Peltier coefficient.

excited during the rectification process, whereas the shift current is related to the difference of valence and conduction electrons.

We demonstrate the generation of the photogalvanic energy current using a one-dimensional ion chain with three ions in a unit cell (Fig. 2), which predicts the generation of an experimentally observable energy current using THz-infrared light sources with $E \sim 10^5$ V/m. Recently, thermal imaging techniques have enabled spatial resolution of temperature in small devices [8]. As the nonlinear Peltier effect induces a temperature gradient in an isolated device, it should be observable using the thermal imaging method.

This work is supported by JSPS KAKENHI (Grant Numbers JP19K14649, JP23K03275, JP20H01830, and JP20H01849), and by a Grant-in-Aid for Scientific Research on Innovative Areas “Quantum Liquid Crystals” (Grant No. JP19H05825) and “Evolution of Chiral Materials Science using Helical Light Fields” (Grants No. JP22H05131 and No. JP23H04576) from JSPS of Japan.

References

1. Proskurin, I., Ovchinnikov, A. S., Kishine, J.-I. and Stamps, R. L. “Excitation of magnon spin photocurrents in antiferromagnetic insulators,” Phys. Rev. B Vol. 98, 134422, 2018.
2. Ishizuka, H. and Sato, M. “Theory for shift current of bosons: Photogalvanic spin current in ferrimagnetic and antiferromagnetic insulators,” Phys. Rev. B Vol. 100, 224411, 2019.
3. Ishizuka, H. and Sato, M. “Large photogalvanic spin current by magnetic resonance in bilayer Cr trihalides,” Phys. Rev. Lett. Vol. 129, 107201, 2022.
4. Ishizuka, H. and Sato, M. “Rectification of Spin Current in Inversion-Asymmetric Magnets with Linearly Polarized Electromagnetic Waves,” Phys. Rev. Lett. Vol. 122, 197702, 2019.
5. Ishizuka, H. and Sato, M. “Peltier effect of phonons driven by ac electromagnetic waves,” *preprint* (arXiv:2310.03271), 2023.
6. Sturman, B. I. and Fridkin, V. M. “The Photovoltaic and Photorefractive Effects in Noncentrosymmetric Materials” (Gordon and Breach, Philadelphia, 1992).
7. von Baltz, R. and Kraut, W. “Theory of the bulk photovoltaic effect in pure crystals,” Phys. Rev. B Vol. 23, 5590, 1981.
8. Uchida, K., Daimon, S., Iguchi, R. and Saitoh, E. “Observation of anisotropic magneto-Peltier effect in nickel,” Nature Vol. 558, 95, 2018.

Spatiotemporal Light Structuring

Michael de Oliveira[1], **A. Ambrosio**[1*]

[1]Istituto Italiano di Tecnologia, Via Rubattino 81, 20134 – Milano, Italy

[*]corresponding author: antonio.ambrosio@iit.it

Abstract: We show to coherently control both the spatial and temporal characteristics of laser beams by using a Fourier space-time shaper based on an axicon grating to disperse the frequencies of a pulsed beam into colinear rings which are then individually tailored with an azimuthal phase via a digital modulator.

We present a novel approach to tailor the OAM dependence of the spectrum of a pulsed laser to generate space-time wave packets that exhibit a unique spiralling trajectory through space-time. Our technique leverages a Fourier space-time shaper, innovatively designed around an axicon grating with circular geometry. This design choice is instrumental in mirroring the cylindrical symmetry inherent in vortex beams, enabling the separation of frequencies into co-linear radial rings that can be independently modulated with an azimuthal phase.
We demonstrate unprecedented control over the properties of the wave packet.

Orbital angular momentum of magnons in confined magnetodielectrics

E. O. Kamenetskii

School of Electrical and Computer Engineering, Ben Gurion University of the Negev, Israel

Corresponding author: kmntsk@bgu.ac.il

Abstract: Can magnon excitations have both spin and orbital angular momentum (OAM)? Whereas a single spin flip of magnon is $S = \pm\hbar$, the OAM L of such a magnon is unknown. An analysis of quantum confinement of magnetostatic magnons observed in a quasi-2D ferrite disk shows that an OAM in such a sample is a half-integer internal angular momentum related to a circulating flow of energy. Unique properties of quantum atmosphere in a vacuum vicinity zone of a ferrite disk are associated with symmetry broken patterns and magnetoelectric characteristics.

==========

Can magnon excitations have both spin and orbital angular momentum (OAM)? This question arises for more than a century, since the experiments of Einstein and de Hass [1] and the measurements of Barnett [2]. Whereas a single spin flip of magnon is $S = \pm\hbar$, the OAM L of such a magnon is unknown. Since the total angular momentum $J = S + L$ should be conserved, magnons in a confined magnetodielectric will be sensitive to external fields. In recent studies [3], quantum confinement of magnons has been observed in a quasi-2D ferrite disk placed inside a microwave structure. An analysis shows that an OAM of magnetostatic modes in a ferrite disk is a half-integer internal angular momentum related to a circulating flow of energy. The effect is associated with magnetoelectric characteristics. The symmetry broken patterns are observed by unique properties of quantum atmosphere in a vacuum vicinity zone of a ferrite disk. It is worth noting that we are talking about pseudoangular OAM. While the conservation of angular momentum follows from invariance under rotations of all the constituents of a solid, the conservation of pseudoangular momentum follows from invariance under rotations of fields while keeping the solid fixed [4].

References

[1] A. Einstein and W. J. de Hass, Experimental proof of the existence of Ampere's molecular currents, Verh. Dtsch. Phys. Ges. **17**, 152 (1915).

[2] S. J. Barnett, Magnetization by rotation, Phys. Rev. **6**, 239 (1915).

[3] E. O. Kamenetskii, Magnetic dipolar modes in magnonpolariton condensates, J. Mod. Opt. **68**, 1147 (2021).

[4] S. Streib, Difference between angular momentum and pseudoangular momentum, Phys. Rev. B **103**, L100409 (2021).

Exploring Strategies for Enhancing the Sensitivity of Chiroptical Spectroscopy with Aluminum Nanoplasmonics

B.M. Reinhard[1]

[1]Department of Chemistry and The Photonics Center, Boston University, Boston, MA 02215, United States

*corresponding author: bmr@bu.edu

Abstract: A scalable nanofabrication strategy for the generation of chiral or achiral aluminum nanoantennas that support plasmon resonances in the UV is evaluated, and design criteria for UV-resonant surfaces that enhance the sensitivity of molecular circular dichroism (CD) spectroscopy are discussed.

Circular dichroism (CD) is a spectroscopy that allows a rapid structural characterization of biomolecules and pharmaceutic compounds. It is of particular interest as an assay to characterize the chirality of molecules in solution or embedded in thin films. Fundamentally, the CD signal is determined by the difference in absorption of a sample under left and right circularly polarized light (r/l-CPL), $\Delta A = A_{\text{l-cpl}} - A_{\text{r-cpl}}$. The absorption rate for any molecule under l/r-CPL excitation is:[1,2]

$$A_{\text{l-CPL/r-CPL}} = \frac{\omega}{2}\alpha''|\mathbf{E}|^2 + \frac{\omega}{2}\mu_0^2\chi''|\mathbf{H}|^2 \pm \frac{\omega}{c^2\varepsilon_0}G''\text{Im}(\mathbf{E}^* \cdot \mathbf{H}) \quad (1)$$

In this expression α'', χ'', and G'' define the imaginary parts of the electric polarizability, the magnetic susceptibility and the chiral polarizability of the target molecule. The first two terms do not depend on the chirality of the molecule and do not contribute to the molecular CD signal, which only depends on the third G''-containing term.

As chiral light-matter interactions are generally weak, CD spectroscopy requires high concentrations and long acquisition times, and there is significant interest in implementing strategies that can boost molecular CD signals. G'' is a molecular constant that cannot be enhanced, so that the $\text{Im}(\mathbf{E}^* \cdot \mathbf{H})$ factor, which is directly related to the optical chirality density,[1,3,4] remains as only parameter to increase the difference in absorption rate for r/l-CPL according to equation 1. Enhancing CD through increased optical chirality density requires correct alignment of electric and magnetic fields in the UV for most molecules of interest. Another mechanism that can potentially enhance molecular CD signals is based on chirality transfer, which generates a chiral response at the plasmon resonance when chiral molecules are in contact with a plasmonic antenna.[5,6] In the case of conventional, discrete plasmonic antennas made of gold or silver, the weak overlap between plasmonic and molecular resonances is one factor that limits chirality transfer.

Plasmonic nanostructures fabricated from gold or silver provide strong electromagnetic field localization throughout the visible and into the near-infrared, which has been exploited for enhancing light-matter interactions and boosting signal intensities in surface-enhanced spectroscopies. Surface enhanced Raman spectroscopy (SERS) is one prominent example.[7] Conventional gold and silver nanostructures face, however, significant challenges to increase the sensitivity of molecular CD spectroscopy, especially, for those molecules whose resonances lie in the UV (which is the case for most biomolecules of interest). Aluminum nanostructures can support plasmon resonances in the UV spectral range,[8–10] and are thus of potential interest as building blocks for antennas that enhance the sensitivity of molecular CD spectroscopy. In this presentation, design criteria of plasmonic antennas that can increase the sensitivity of CD spectroscopy through enhanced optical chirality density[11] or chirality transfer[5] are outlined and evaluated.

A second challenge in addition to the design of appropriate antennas that can increase CD sensitivity in the UV is the need for a scalable fabrication of the antennas, ideally on a scale that makes them compatible with widely available CD spectrometers. In this presentation, a scalable nanofabrication strategy will be introduced that allows the fabrication of extended random arrays of aluminum nanoparticles with tunable plasmon resonances throughout the wavelength range between 180 – 500 nm. The fabrication strategy provides access to both chiral and achiral aluminum nanostructures depending on the details of the fabrication. The aluminum nanoparticle arrays, and their spectral response will be characterized and first applications to increase the sensitivity of molecular CD spectroscopy will be presented and discussed.

References

(1) Tang, Y.; Cohen, A. E. Optical Chirality and Its Interaction with Matter. *Phys. Rev. Lett.* **2010**, *104* (16), 163901. https://doi.org/10.1103/PhysRevLett.104.163901.

(2) Solomon, M. L.; Saleh, A. A. E.; Poulikakos, L. V.; Abendroth, J. M.; Tadesse, L. F.; Dionne, J. A. Nanophotonic Platforms for Chiral Sensing and Separation. *Acc. Chem. Res.* **2020**, *53* (3), 588–598. https://doi.org/10.1021/acs.accounts.9b00460.

(3) Tang, Y.; Cohen, A. E. Enhanced Enantioselectivity in Excitation of Chiral Molecules by Superchiral Light. *Science* **2011**, *332* (6027), 333–336. https://doi.org/10.1126/science.1202817.

(4) Schäferling, M.; Dregely, D.; Hentschel, M.; Giessen, H. Tailoring Enhanced Optical Chirality: Design Principles for Chiral Plasmonic Nanostructures. *Phys. Rev. X* **2012**, *2* (3), 031010. https://doi.org/10.1103/PhysRevX.2.031010.

(5) Govorov, A. O. Plasmon-Induced Circular Dichroism of a Chiral Molecule in the Vicinity of Metal Nanocrystals. Application to Various Geometries. *J. Phys. Chem. C* **2011**, *115* (16), 7914–7923. https://doi.org/10.1021/jp1121432.

(6) Govorov, A. O.; Fan, Z.; Hernandez, P.; Slocik, J. M.; Naik, R. R. Theory of Circular Dichroism of Nanomaterials Comprising Chiral Molecules and Nanocrystals: Plasmon Enhancement, Dipole Interactions, and Dielectric Effects. *Nano Lett.* **2010**, *10* (4), 1374–1382. https://doi.org/10.1021/nl100010v.

(7) Yan, B.; Thubagere, A.; Premasiri, W. R.; Ziegler, L. D.; Dal Negro, L.; Reinhard, B. M. Engineered SERS Substrates with Multiscale Signal Enhancement: Nanoparticle Cluster Arrays. *ACS Nano* **2009**, *3* (5), 1190–1202. https://doi.org/10.1021/nn800836f.

(8) Besteiro, L. V.; Zhang, H.; Plain, J.; Markovich, G.; Wang, Z.; Govorov, A. O. Aluminum Nanoparticles with Hot Spots for Plasmon-Induced Circular Dichroism of Chiral Molecules in the UV Spectral Interval. *Advanced Optical Materials* **2017**, *5* (16), 1700069. https://doi.org/10.1002/adom.201700069.

(9) Davis, M. S.; Zhu, W.; Strait, J.; Lee, J. K.; Lezec, H. J.; Blair, S.; Agrawal, A. Chiroptical Response of Aluminum Nanocrescents at Ultraviolet Wavelengths. *Nano Lett.* **2020**, *20* (5), 3656–3662. https://doi.org/10.1021/acs.nanolett.0c00586.

(10) Liu, J.; Yang, L.; Zhang, H.; Wang, J.; Huang, Z. Ultraviolet-Visible Chiroptical Activity of Aluminum Nanostructures. *Small* **2017**, *13* (39), 1701112. https://doi.org/10.1002/smll.201701112.

(11) Alizadeh, M. H.; Reinhard, B. M. Plasmonically Enhanced Chiral Optical Fields and Forces in Achiral Split Ring Resonators. *ACS Photonics* **2015**, *2* (3), 361–368. https://doi.org/10.1021/ph500399k.

A Scalar Product for Computing Fundamental Quantities in Matter

I. Fernandez-Corbaton[1] **and Maxim Vavilin**[2]

[1]Karlsruhe Institute of Technology, Institute of Nanotechnology, Germany
[2]Karlsruhe Institute of Technology, Institute of Theoretical Solid State Physics, Germany
ivan.fernandez-corbaton@kit.edu

Abstract: We introduce a systematic way to obtain expressions for computing the amount of fundamental quantities such as helicity and angular momentum contained in static matter, given its charge and magnetization densities. In an exemplary application, we compute the helicity and angular momentum squared stored in a magnetic Hopfion.

Research in light-matter interactions benefits from theoretical tools whose generality allows one to treat light and matter in similar ways. In classical electrodynamics, light and matter are treated in a rather similar way: As continuous fields such as the electric and magnetic fields $\mathbf{E}(\mathbf{r},t)$ and $\mathbf{B}(\mathbf{r},t)$ representing radiation, and the densities of charge $\rho(\mathbf{r},t)$, current $\mathbf{J}(\mathbf{r},t)$, polarization $\mathbf{P}(\mathbf{r},t)$, and magnetization $\mathbf{M}(\mathbf{r},t)$, representing matter. In the case of the radiation fields, there exists a convenient and general way to compute the amount of fundamental quantities such as linear and angular momentum contained in a given dynamic electromagnetic field [1]. This approach exploits the tools of Hilbert spaces. The quantities are computed "à la Dirac" as sandwiches:

$$\langle f|\Gamma|f\rangle, \tag{1}$$

where $|f\rangle$ is the ket representing the field and Γ the Hermitian operator representing the quantity of interest, e.g. an angular momentum operator. The expression of the scalar product for the free radiation fields, which is used in particular for obtaining explicit expressions from Eq. (1), reads:

$$\langle f|g\rangle = \int_{\mathbb{R}^3} \frac{\mathrm{d}^3\mathbf{k}}{\hbar \mathrm{c}_0|\mathbf{k}|} \begin{bmatrix}\mathbf{F}_+(\mathbf{k})\\ \mathbf{F}_-(\mathbf{k})\end{bmatrix}^\dagger \begin{bmatrix}\mathbf{G}_+(\mathbf{k})\\ \mathbf{G}_-(\mathbf{k})\end{bmatrix}, \tag{2}$$

where $\mathrm{c}_0 = 1/\sqrt{\varepsilon_0\mu_0}$, and the two kets $|f\rangle$ and $g\rangle$ are represented by their plane wave components of well-defined helicity $\lambda = 1$ and $\lambda = -1$, corresponding to left- and right-handed circular polarizations, respectively:

$$\mathbf{F}_\pm(\mathbf{r},t) = \sqrt{\frac{\varepsilon_0}{2}}\left[\mathbf{E}(\mathbf{r},t) \pm \mathrm{i}\mathrm{c}_0\mathbf{B}(\mathbf{r},t)\right] = \int_{\mathbb{R}^3} \frac{\mathrm{d}^3\mathbf{k}}{\sqrt{(2\pi)^3}}\, \mathbf{F}_\lambda(\mathbf{k}) \exp(\mathrm{i}\mathbf{k}\cdot\mathbf{r} - \mathrm{i}\mathrm{c}_0|\mathbf{k}|t), \tag{3}$$

with $\mathbf{k}\cdot\mathbf{F}_\lambda(\mathbf{k}) = 0$, and the angular frequency is restricted to positive values $\omega = \mathrm{c}_0|\mathbf{k}| > 0$.

Together, Eq. (1) and Eq. (2) are a general and convenient way of computing the amount of any fundamental quantity in the field. This motivates the following question: *Can this algebraic approach be used for material objects?* The answer is *yes* [3]. The algebraic approach can be extended towards the matter side, resulting in particular in a way to obtain expressions for computing the amount of fundamental quantities contained in static material objects from their *static* charge and magnetization densities, $\rho(\mathbf{r})$ and $\mathbf{M}(\mathbf{r})$, which are assumed to be spatially confined. The expressions are again obtained as

$$\langle \Phi_{\omega=0}|\Gamma|\Phi_{\omega=0}\rangle, \tag{4}$$

where $|\Phi_{\omega=0}\rangle$ represents now the static ($\omega = 0$) charge and magnetization densities of matter, or, equivalently, the following Fourier transforms:

$$\mathbf{M}(\mathbf{k}) = \int_{\mathrm{V}} \frac{\mathrm{d}^3\mathbf{r}}{\sqrt{(2\pi)^3}}\, \mathbf{M}(\mathbf{r}) \exp(-\mathrm{i}\mathbf{k}\cdot\mathbf{r}),\ \mathbf{E}(\mathbf{k}) = \frac{-\mathrm{i}\hat{\mathbf{k}}}{\varepsilon_0|\mathbf{k}|} \int_{\mathrm{V}} \frac{\mathrm{d}^3\mathbf{r}}{\sqrt{(2\pi)^3}}\, \rho(\mathbf{r}) \exp(-\mathrm{i}\mathbf{k}\cdot\mathbf{r}), \tag{5}$$

where V is the finite volume occupied by $\rho(\mathbf{r})$ and $\mathbf{M}(\mathbf{r})$, and the definition of $\mathbf{E}(\mathbf{k})$ follows from $\nabla\cdot\mathbf{E}(\mathbf{r}) = \rho(\mathbf{r})/\varepsilon_0$. Crucially, the appropriate scalar product can be written as:

$$\langle\Phi^1_{\omega=0}|\Phi^2_{\omega=0}\rangle = \int_{\mathbb{R}^3} \frac{\mathrm{d}^3\mathbf{k}}{\hbar c_0|\mathbf{k}|} \begin{bmatrix} \sqrt{\varepsilon_0}\,\mathbf{E}^1(\mathbf{k}) \\ \sqrt{\mu_0}\,\mathbf{M}^1(\mathbf{k}) \end{bmatrix}^\dagger \begin{bmatrix} \sqrt{\varepsilon_0}\,\mathbf{E}^2(\mathbf{k}) \\ \sqrt{\mu_0}\,\mathbf{M}^2(\mathbf{k}) \end{bmatrix}. \tag{6}$$

The defining property of the scalar product in Eq. (2) is that it is conformally invariant [6]. That is, the value of $\langle f|g\rangle$ is identical to the scalar product between $\mathrm{X}|f\rangle$ and $\mathrm{X}|g\rangle$, for any transformation X in the 15-parameter conformal group in 3+1 Minkowski spacetime. Such group is the largest group of invariance of Maxwell equations *including sources as spacetime densities when these have the appropriate transformation properties*. After removing the transformations that do not preserve the static $\omega = 0$ condition, the remaining transformations also form a group: The 10-parameter conformal group in three-dimensional Euclidean space. The expression in Eq. (6) is invariant under such group.

In particular, with $\rho(\mathbf{r})$ and $\mathbf{M}(\mathbf{r})$ at hand, the expression in Eq. (6) allows explicit numerical computations of $\langle\Phi|\Gamma|\Phi\rangle$ for any Γ. Table 1 contains the values for the helicity and angular momentum squared stored in a magnetic Hopfion. A magnetic Hopfion is a twisted configuration of magnetization that can be hosted by some chiral magnetic materials [5]. The charge density $\rho(\mathbf{r})$ is ignored in this exemplary application.

$\langle\mathrm{M}\|\Lambda\|\mathrm{M}\rangle$	$\langle\mathrm{M}\|\mathrm{J}^2\|\mathrm{M}\rangle$
-129.1 $\hbar$	$1.30\times10^3\ \hbar^2$

Table 1: Helicity Λ, and angular momentum squared J^2 stored in a magnetic Hopfion. An analytical approximation to the magnetization $\mathbf{M}(\mathbf{r})$ of the Hopfion in a chiral FeGe magnet of cylindrical shape [5] was used in the calculations.

In the case of the Hopfion, the value of its helicity, equal to -129.1$\hbar$, implies a lower bound for the number of circularly polarized photons that would be needed in a helicity-dependent all optical switching of the Hopfion onto its mirror image of opposite helicity: $\lceil 129.1\times 2\rceil = 259$. Additionally, -129.1$\hbar$ also bounds the helicity that can be radiated by the Hopfion as it loses its chirality, for example by the action of a large magnetic bias aligning its magnetization density vector along the same direction at all points.

References

[1] Bialynicki-Birula, I. "Photon wave function", *Progress in Optics*, Vol. 36, Elsevier, Amsterdam, 1996.

[2] Fernandez-Corbaton, I. and Vavilin, M. "A Scalar Product for Computing Fundamental Quantities in Matter". Symmetry 2023, 15, 1839.

[3] Ivan Fernandez-Corbaton, "Total helicity of electromagnetic fields and matter", *Phys. Rev. B* 103, 054406 (2021).

[4] P. Sutcliffe, "Hopfions in chiral magnets", *Journal of Physics A: Mathematical and Theoretical* 51, 375401 (2018).

[5] L. Gross, "Norm invariance of MassZero equations under the conformal group", *J. Math. Phys.* 5, 687 (1964).

Off-resonance Spin-locked Metasurfaces based on Quasi-Bound States in the Continuum and Nonreciprocal Chiral Splitters

Zuojia Wang[1*], Haochen Yang[1], Yujie Zhang[2], Guang Chen[3] and Liqiao Jing[1]

[1]Zhejiang University, China
[2]Shandong University, China
[3]Hangzhou City University, China
[*]corresponding author: zuojiawang@zju.edu.cn

Abstract: We demonstrate off-resonance spin-locked metasurfaces inspired by quasi-bound states in the continuum, to achieve hybridized analog computing in two domains. High-quality resonance is excited in a broadband spin-locked scattering spectrum, providing frequency fliting in meta-splitters and meta-deflectors. We also discuss how nonreciprocal chiral splitting can be controlled in gyromagnetic metasufaces.

Given the merits of robust resonance and high quality (Q) factor, the bound state in the continuum (BIC) is attracting growing interest and experiencing a research upsurge in metasurfaces studies. Due to its high-Q characteristic at resonance, symmetry-protected BIC becomes an alternative approach widely used for high-Q metasurfaces in practice. While the twofold rotational symmetry (C2) of the structure is destroyed, the bound state leaks and true BICs will gradually transform into quasi-BIC status.

We propose and demonstrate a class of quasi-BIC assisted off-resonance metasurfaces that combine high-Q resonance and phase-modulation together [1]. The structure of the meta-atoms is evolved from symmetric split-ring (SSR) by engineering two asymmetric degrees, the radian of the semi-ring and the radius of the added ring, so that the C2 symmetry is broken. A single resonance model based on CMT is developed to analyze the high-Q resonance in a broadband spin-locked spectrum in ASR with symmetry-protected BIC, which has high robustness against circularly polarized scattering interference from environment. A phase-only resonance of linear polarization leads to a high-Q resonance of circular polarization with broadband helicity-preserving. PB phase is introduced to achieve broadband beam splitting and deflection with the phase modulation over the full 2π range. Then, we have proposed the concept of hybridized analog computing based on such off-resonance metasurfaces. Scalar multiplication in frequency spectrum and convolution in angular spectrum have been realized simultaneously by designer quasi-BIC assisted meta-splitter and quasi-BIC assisted meta-deflector.

Next, we study the nonreciprocal coupling effect between the resonant modes in absorbers and discover a chiral absorption behavior under asymmetric phase coupling [2]. A coupled-mode theory is established to quantitatively analyze the inherent nonreciprocal chiro-optical effects. Theoretical calculation on gyromagnetic metasurfaces points out that nonreciprocal coupling between inherent resonant modes cannot offer linear dichroism in reflection, yet is capable of providing circular dichroism. When the coupling strengths are tuned to opposite phases and equal amplitudes, an ideal perfect absorption of one circular polarization can be reached.

Broadband non-reciprocal transmission via a low-biased gyromagnetic metasurface will be further discussed. A triple-stacked structure broadens the isolation bandwidth utilizing multiple dipole resonances where the metallic disks act as photonic dopants, enhancing the slab's gyromagnetic and gyroelectric responses. The sign of gyromagnetic activity flips at two chiral modes, and the equivalent switching of the external biased revealed. Microwave measurement demonstrates that the bandwidth for an isolation ratio exceeding 10 dB is over 3 GHz. The broadband nonreciprocal performance maintains relatively stable, exhibiting strong robustness

against the bias disturbance.

References

1. Yang, Haochen, Xuan Chen, Enzong Wu, Peng Tang, Liqiao Jing, Fei Gao, Hongsheng Chen, and Zuojia Wang. “Off‐Resonance Spin‐Locked Metasurfaces Empowered by Quasi‐Bound States in the Continuum for Optical Analog Computing.” Advanced Functional Materials 33, no. 47, 2305110, 2023
2. Wang, Zuojia, Haochen Yang, and Liqiao Jing. “Nonreciprocal coupling induced chiral absorption.” Journal of Optics 25, no. 7, 074002, 2023.

Detecting the symmetry breaking of the quantum vacuum in a QED system

Tiefu Li[1*]

[1]School of Integrated Circuits, Tsinghua University, China
[*]corresponding author: litf@tsinghua.edu.cn

Abstract: In ultrastrong coupling regime, a qubit–resonator system has an entangled quantum vacuum with a nonzero average photon number. We experimentally observe the vacuum by the induced symmetry breaking of a dispersively coupled probe qubit. This result opens a way to experimentally explore the novel quantum-vacuum effects.

Hybrid quantum systems in the ultrastrong, and even more in the deep-strong, coupling regimes can exhibit exotic physical phenomena and promise new applications in quantum technologies. In these nonperturbative regimes, a qubit–resonator system has an entangled quantum vacuum with a nonzero average photon number in the resonator, where the photons are virtual and cannot be directly detected. The vacuum field, however, can induce the symmetry breaking of a dispersively coupled probe qubit. We experimentally observe this Higgs-like quantum-vacuum symmetry breaking induced by the field of a lumped-element superconducting resonator deep-strongly coupled with a flux qubit. The violation of the Xmon parity selection rule comes from virtual paths enabled by its interaction with an electromagnetic resonator whose parity symmetry is significantly broken by the deepstrong light–matter interaction with a flux qubit. The experimental results are in very good agreement with our theoretical analysis. The proposed setting offers a novel way to explore quantum-vacuum effects emerging in the light–matter ultra-strong and deep-strong coupling regimes and can be used as a tool to explore the coherence properties of quantum vacua in this exotic hybrid quantum system, and the occurrence of superradiant phase transitions in Dicke-like systems.

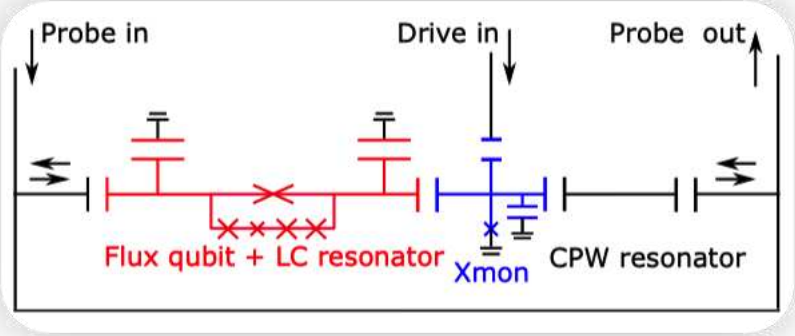


Fig. 1, Circuit diagram of the device.

References

1. Wang, S. P. “Probing the symmetry breaking of a light–matter system by an ancillary qubit,” Nature Communications, 14, 4397, 2023.
2. Wang, S. P. “Photon-dressed Bloch-Siegert shift in an ultrastrongly coupled circuit quantum electrodynamical system,” Phys. Rev. Appl., 13, 054063, 2020.

Si metasurface on a magneto-optical thin film for enhancing nonreciprocal polarization rotation

Y. Ota[1*], S. Gao[1], T. Kitai[1], K. Taniguchi[1], T. Yambe[1] and S. Iwamoto[2]

[1]Department of Applied Physics and Physico-Informatics, Keio University, Japan
[2]Research Center for Advanced Science and Technology, The University of Tokyo, Japan
[*]corresponding author: ota@appi.keio.ac.jp

Abstract: Magneto-optical interactions in transparent materials are generally weak, making the devices bulky. Here, we discuss the design of a Si metasurface placed on a magneto-optical thin film. A 45° nonreciprocal polarization rotation at 1.5 μm was achieved by loading a 140-nm-thick Si metasurface on a 513-nm-thick Bi:YIG membrane.

Magneto-optical (MO) interactions in the optical regime are of technological importance for diverse applications including optical data communications. However, MO interactions are known to be weak in transparent optical materials, hampering downsizing of MO devices. Indeed, a typical Faraday rotator for optical isolation at telecommunication wavelengths has a thickness of ~ 0.3 mm, even using a family of yttrium iron garnets (YIGs), which are known as one of the best transparent MO materials in the optical domain at room temperature. To enhance the MO effects and miniaturizing the Faraday rotator, nanostructuring of YIG will be a promising approach, since it will allow for the use of metasurfaces for enhancing light matter interactions through resonant wave trapping [1]. However, it is widely recognized that nanopatterning of YIG is extremely difficult and has not been succeeded even after many trials over the years. This suggests that enhancing MO effects without nanopatterning of YIG itself will be a key challenge in the realization of ultracompact Faraday rotators [2].

In this talk, we will discuss the design of Si metasurface loaded on a thin YIG membrane [3]. We found a significant enhancement of Faraday rotation under the resonance with guided modes in the Si and YIG layers. A Faraday rotation of 45° was achieved at a wavelength of 1.5 μm by loading a 140-nm-thick Si metasurface on a 513-nm-thick unpatterned YIG membrane.

Figure 1 shows a schematic of the investigated photonic structure. A Si metasurface is placed on a 513-nm-thick Bi:YIG membrane prepared on glass. Magnetic field is vertically applied so that the Bi:YIG layer induces MO Faraday rotation. The metasurface is consisted of a square lattice of air holes in a 140-nm-thick Si slab. There are two air holes in the unit cell as shown in Fig. 1. The shapes of the airholes are slightly elliptic so that quasi-BIC (bound states in the continuum) resonance modes can be excited by vertical optical access. We carefully controlled the ellipticity of the airholes to attain a desired Q factor of the resonance, enabling arbitrary control over the light-matter interaction at the resonance. Moreover, by controlling the thickness of the Bi:YIG layer, the system can support dual resonance in the spectral domain, which induces electromagnetically-induced transparency for high light transmission. Figure 2 shows a resulting spectral response of Faraday rotation and optical transmission. We obtained a 45° polarization rotation at the resonance at 1.5 μm while maintaining 70% light transmittance. The value of polarization rotation is 800 times higher than that attainable in a plane Bi:YIG of the same thickness. Our design can significantly downsize the Faraday rotator and thus is of technological importance.

The details of the design will be discussed in the talk, in which we will also discuss other scenarios to increase MO interactions [4] and our recent effort for mitigating the effect of fabrication imperfections of MO metasurfaces as a Faraday rotator [5] and for enhancing MO interactions in photonic nanostructures.

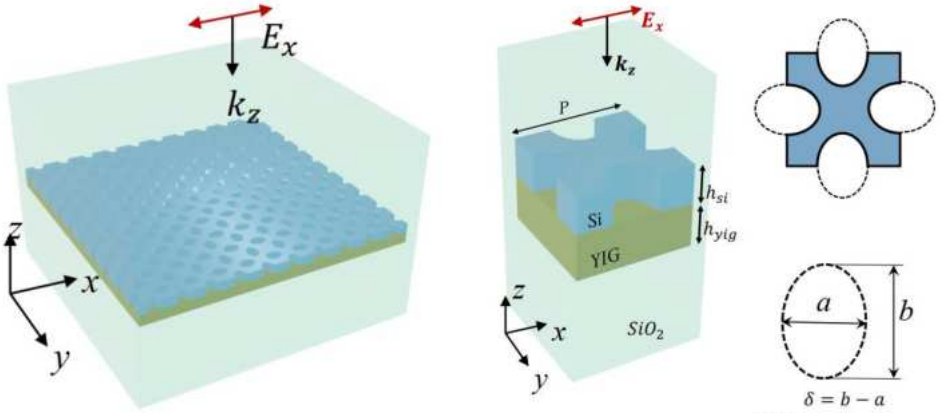


Figure 1. Investigated Si metasurface loaded on a Bi:YIG thin film

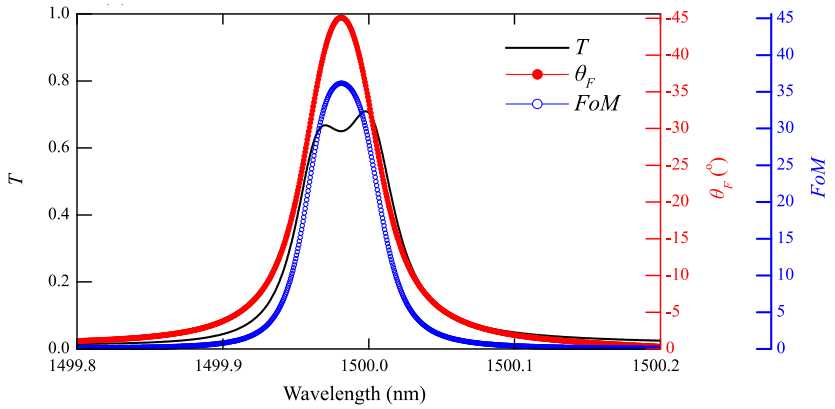


Figure 2. Optical response of the MO metasurface exhibiting a giant Faraday rotation of 45

Acknowledgements: We thank T. Liu, F. Tian, S. Ishida, H. Matsukiyo, H. Otsuki, Y. Narazaki, and Y. Tanimura for their technical support and fruitful discussions. This work was supported by KAKENHI (17H06138, 19K05300, 22H00298, 22H01994, 22K18989), JST CREST(JPMJCR19T1), JST FOREST Program (JPMJFR213F), Nippon Sheet Glass Foundation.

References

1. A. Christofi, Y. Kawaguchi, A. Alù and A. B. Khanikaev, Opt. Lett. **43**, 1838 (2018).
2. S. Xia, D. O. Ignatyeva, Q. Liu, J. Qin, T. Kang, W. Yang, Y. Chen, H. Duan, L. Deng, D. Long, M. Veis, V. I. Belotelov and L. Bi, ACS Photonics **9**, 1240 (2022).
3. S. Gao, Y. Ota, T. Liu, F. Tian and S. Iwamoto, Appl. Phys. Express **16** 072003 (2023)
4. S. Gao, Y. Ota and S. Iwamoto, The 13th International Symposium on Photonic and Electromagnetic Crystal Structures (PECS-XIII), 29-A-05, Tokyo, Japan (2023).
5. S. Gao, Y. Ota, F. Tian, T. Liu, and S. Iwamoto, Opt. Express **31**, 13672 (2023)

Manifestation of crystal chirality in quasiparticles

T. Yokoyama[1*]

[1]Tokyo Institute of Technology, Japan

[*]corresponding author: yokoyama@stat.phys.titech.ac.jp

Abstract: I will talk about how crystal chirality is manifested in quasiparticles: Bogoliubov quasiparticles in superconductors and magnons in ferromagnets in the presence of chiral crystal structures.

We propose a mechanism of spin current generation under an external electric field due to chiral phonons in a chiral-structure superconductor based on the Bogoliubov de Gennes and the Boltzmann equations. We show that the spin current carried by quasiparticles flows along the screw axis and shows a quadratic dependence on the electric field at the low-field range, leading to a nonreciprocal spin transport. The spin current also shows a nonmonotonic temperature dependence and has a maximum at around the superconducting transition temperature.

We also investigate magnons in ferromagnets with chiral structures. The chirality of the crystal is manifested in orbital angular momentum of magnons. We discuss possible experimental setup to verify our predictions.

References

1. D. Yao, M. Matsuo, and T. Yokoyama, arXiv:2401.04497

Pseudomagnetic fields in photonic crystals with synthetic strain: Observation of Landau levels and chiral edge states

R. Barczyk[1], L. Kuipers[2], and E. Verhagen[1*]

[1]Center for Nanophotonics, AMOLF, Amsterdam, The Netherlands
[2]Kavli Institute of Nanoscience, Delft University of Technology, Delft, The Netherlands
[*]corresponding author: verhagen@amolf.nl

Abstract: We experimentally demonstrate pseudomagnetic fields in photonic crystals with engineered synthetic strain, and investigate the resulting photonic Landau-levels and novel guided chiral edge states. This offers a design paradigm for optical confinement, radiation, and light-matter interaction.

Drawing inspiration from condensed matter physics has proven to be a rich resource for the emulation of topological phenomena in the photonic domain. It provides an especially interesting design paradigm for photonic crystals, which offer a versatile platform for control over on-chip routing and confinement of light, out-of-plane emission, and enhanced light-matter interactions. In contrast to electronic systems, photonic crystals allow for tailoring each unit cell individually, yielding enormous control over the properties of the states they host, and in particular over topological light confinement.

It is known for graphene that inhomogeneous *strain* of the crystal lattice can induce strong pseudomagnetic fields that lift the Dirac-point degeneracies and create discrete, highly degenerate Landau levels, analogous to those in quantum Hall systems subject to strong magnetic fields. As this mechanism does not require the breaking of time-reversal symmetry, it has high potential to be applied also to photons, which do not interact with real magnetic fields. It was recently predicted that engineered deformation in two-dimensional photonic crystals with Dirac-like dispersion acts as effective strain, and could generate synthetic pseudomagnetic fields for photons, leading to localization at flat bands, i.e., photonic Landau levels.[1] Realizing such states in photonic crystals is especially appealing because of the potential to enhance light-matter interactions due to high density of states of such flat bands. Moreover, the concept of synthetic strain engineering and pseudomagnetic fields provides a new design paradigm for on-chip photons with tailored spectral and spatial properties.

In this work, we experimentally demonstrate the realization of pseudomagnetic fields in photonic crystals through synthetic strain engineering.[2] We observe photonic Landau levels and characterize their spectral and localization properties. As an illustration of spatial tailoring of pseudomagnetic fields we create interfaces between opposing magnetic fields and observe novel chiral edge states that result.

We fabricate silicon photonic crystal membranes operating at telecom wavelengths with Dirac dispersion. We engineer synthetic strain that varies quadratically in one direction through perturbation of the unit cell (Fig. 1a). We probe the photonic crystal's modes in real- and momentum-space through Fourier spectroscopy. This reveals the formation of photonic Landau levels that are weakly coupled to the radiation continuum through an intentional breaking of unit cell symmetry. The states show characteristic square-root dependence of the mode spacing with the pseudomagnetic field strength (Fig. 1c-d). Interestingly, the Landau levels exhibit remarkably high quality factors. Moreover, we reveal that the states come in degenerate pairs with circular polarization linked to propagation direction, illustrating the relation to photonic spin-orbit coupling. Their localization properties are linked to long-range interactions, illustrating the difference between photonic and electronic

behaviour.

Finally, we fabricate a device that combines two domains of opposite pseudomagnetic field (Fig. 2). In analogy to the quantum Hall effect, domains of opposite magnetic field would have different topological order, meaning that chiral edge states are expected at their interface, connecting the bulk Landau levels.[3] We observe signatures of these novel photonic topological states in far-field spectroscopy (Fig. 2), and characterize their spatial and polarization properties. These states propagate within the radiation continuum, with theoretical quality factors approaching 10^7.

In conclusion, we have experimentally demonstrated synthetic strain engineering to induce pseudomagnetic fields in telecom-frequency photonic crystals. This provides intriguing prospects for the enhancement of light-matter interactions in highly degenerate flat bands, and the topological control of optical localization and radiation at the nanoscale.

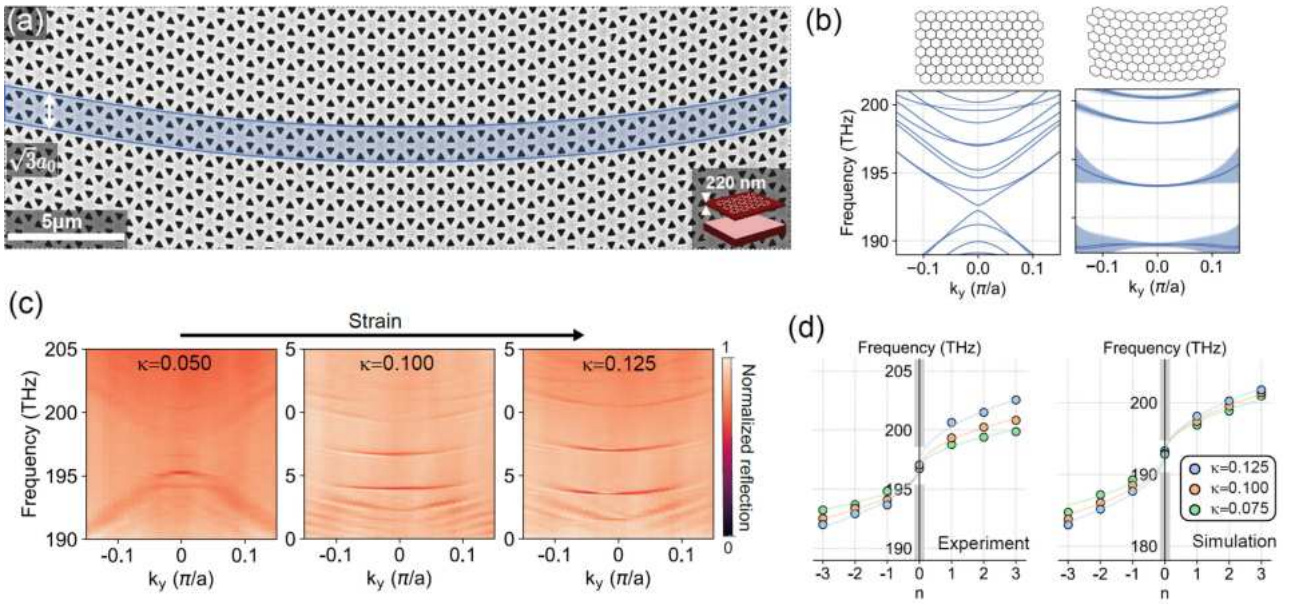


Figure 1. (a) SEM image of a strained photonic crystal membrane, with a_0 the lattice constant (b) Numerically retrieved dispersion for the supercell of a pristine and a strained photonic crystal. Straining opens a bandgap and induces flat Landau levels. (c) Evolution of the photonic Landau levels in lattices with increasing strain magnitude κ, observed through Fourier spectroscopy. (d) Frequencies of Landau-levels for various κ.

References

1. Guglielmon, J, Rechtsman, M. C., and Weinstein, M. I. "Landau levels in strained two-dimensional photonic crystals," Phys. Rev. A 103, 013505 (2021).
2. Barczyk, R., Kuipers, L., and Verhagen, E., "Observation of Landau levels and chiral edge states in photonic crystals through pseudomagnetic fields induced by synthetic strain," Nat. Photon., in press (2024). Preprint: arXiv:2306.03860
3. Huang, Z.-T., Hong, K.-B., Lee, R.-K., Pilozzi, L., Conti, C., Wu, J.-S., and Lu, T.-C. "Pattern-tunable synthetic gauge fields in topological photonic graphene," Nanophotonics 11, 1297 (2022).

Control of high harmonic generation and photo current in graphene by tuning laser polarization and combing two laser fields

Masahiro Sato[1*] **and Minoru Kanega**[1]

[1]Department of Physics, Chiba University, Inage, Chiba, Japan
[*]corresponding author: sato.phys@chiba-u.jp

Abstract: We theoretically study laser-driven high harmonic generation (HHG) and zeroth-order harmonics (photo-induced DC current) in graphene. It is shown that the HHG spectrum and photo current can be controlled by changing the laser polarization and the laser-field trajectory with two laser mixture.

Laser-driven high harmonic generation (HHG) is one of the simplest nonlinear optical response of materials. HHG refers to the optical phenomenon that when we apply an intense laser with frequency ω to a material, a radiated light including several waves with different frequencies $n\omega$ is generated (n is an arbitrary integer) through light-matter interaction [see Fig. 1(a)]. Over the last decade, HHG in solids [1] has been actively studied from both application and fundamental scientific viewpoints. In fact, second-order harmonic generation (SHG) with $n = 2$ has been often used as devices (such as laser pointer) and a probe of the inversion symmetry breaking in crystals. Moreover, the fundamental harmonics with $n = 1$, which corresponds to photo current (light induced rectification of electric current), is the basic optical phenomenon for solar cell [2].

In recent years, we have theoretically studied HHG in quantum many-body systems and developed the microscopic method of analyzing the HHG based on quantum master (GKSL) equation [3]. In this conference, we will report our recent theoretical result about HHG in graphene, honeycomb-lattice electron systems [see Fig. 1(b)] [4]. In particular, we consider what an effective way of controlling the HHG spectra (e.g., the presence or absence of nth-order harmonics generation) in solids is. We show that an application of DC current, tuning the polarization of incident light (from linear to circularly polarization) and use of two-color laser (mixture of two different light waves) provide powerful ways of controlling the HHG.

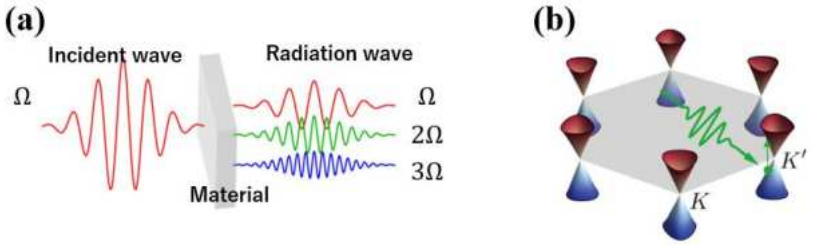


Figure 1: (a) Image of laser-driven HHG in solids. (b) Image of Dirac electron bands and laser irradiation in graphene.

Figure 2 shows the computed HHG spectra generated from laser-driven electric currents along the x and y directions, $J_x(\omega)$ and $J_y(\omega)$, in graphene models with different parameters. One finds from this figure that the spectra are drastically changed by tuning the laser polarization, the magnitude of applied DC current, and the staggered potential. We emphasize that the former two parameters of laser polarization and DC current can be accurately controlled in real experiments.

Figure 3 shows our numerical results of HHG spectra in graphene models under an irradiation of two-color laser, which consists of one laser with frequency Ω_1 and ellipticity ε_1 and another with Ω_2 and ε_2. Here we set $\Omega_2 = 2\Omega_1$ and $\varepsilon_1 = 0$ (± 1) corresponds to linear (circular) polarization. We find that the presence or

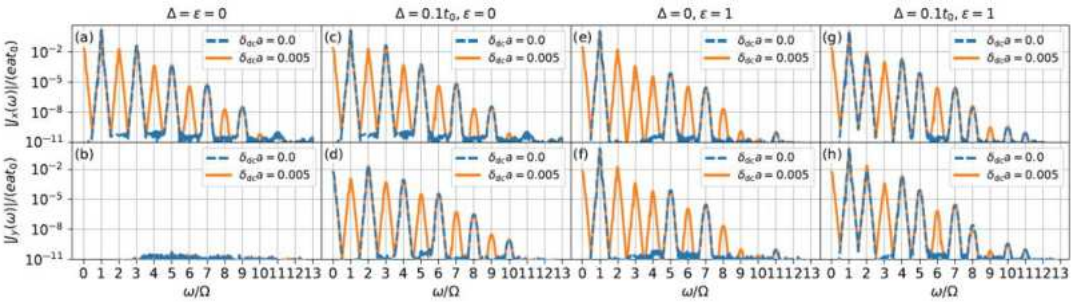


Figure 2: Computed HHG spectra of graphene models irradiated by laser pulses. Upper and lower panels respectively correspond to currents flowing along x and y directions. Parameters Δ, ε, and δ_{dc} are respectively a staggered potential, the ellipticity of laser ($\varepsilon = 0$ and $\varepsilon = 1$ are respectively linearly and circularly polarized lights) and an external DC electric field ($\propto$ external DC current).

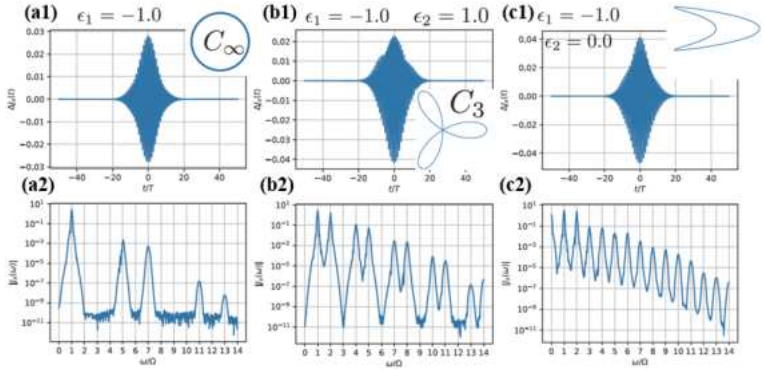


Figure 3: Calculated HHG spectra in graphene under the application of two-color laser. Upper and lower panels are respectively oscillating electric fields of applied laser pulses as a function of time and the corresponding HHG spectra. As a reference, we put the result of a single-color circularly polarized laser ($\varepsilon_1 = -1$) in panel (a). In Panels (b) and (c), the frequency is set to $\Omega_2 = 2\Omega_1$. Diagrams of circle (a1), mitsuba (b1), and boomerang (c1) represent the trajectories of the laser fields.

absence of nth-order harmonics strongly depends on the combination of $(\Omega_1, \varepsilon_1)$ and $(\Omega_2, \varepsilon_2)$. Namely, our result indicates that HHG spectra can be controlled by tuning parameters of two-color laser.

We show that the shapes of HHG spectra in Figs. 2 and 3 are well explained by the argument based on dynamical and static symmetries [3,4]. In addition, the numerical analysis based on the GKSL equation enables us to quantitatively estimate the HHG spectra in a broad parameter regime from a weak laser to an intense laser. In the conference, we would like to report the advantages of our analysis and it's results in more detail.

References

1. See for example, S. Ghimire, *et al*, Nature Phys. **7**, 138 (2011); O. Schubert, *et al*, Nature Photo. **8**, 119 (2014).
2. See for example, L. Z. Tan, *et al*, npj Comput. Mater. **2**, 16026 (2016); Y. Tokura and N. Nagaosa, Nat. Commun. **9**, 3740 (2018).
3. T. N. Ikeda and M. Sato, Phys. Rev. B**100**, 214424 (2019); M. Kanega, T. N. Ikeda, and M. Sato, Phys. Rev. Res. **3**, L032024 (2021).
4. M. Kanega and M. Sato, in preparation.

CP^2 triple-Q state in the SU(3) Kondo lattice model

Yutaka Akagi*

Department of Physics, University of Tokyo, Japan
*corresponding author: yutaka-akagi@g.ecc.u-tokyo.ac.jp

Abstract: This research details the CP^2 triple-Q state in the SU(3) ferromagnetic Kondo lattice model, highlighting its ground state phase diversity and topological magnetism at varying itinerant fermion filling and Kondo coupling strength.

Recent years have seen significant interest in quantum condensates with SU(N) symmetry (N≥3), such as SU(N) Mott insulator (SU(N) magnets), within cold atom frameworks [1,2]. Advances have also been made in the experimental realization of Kondo physics, where itinerant electrons and localized spins interact, using two "orbital" degrees of freedom in alkaline earth metal fermions [3,4]. The feasibility offered by cold atom systems has intensified the focus on SU(N) Kondo lattice systems. So far, their magnetism has been clarified, mainly in one dimension [5].

Ferromagnetic Kondo coupling is a natural occurrence when considering Kondo lattice systems with cold atoms. For instance, in the SU(3) ferromagnetic Kondo lattice model, itinerant fermions with three colors align their magnetic dipoles and quadrupoles with SU(3) localized moments at each lattice site. In this work, we investigate the SU(3) ferromagnetic Kondo lattice model on a triangular lattice, extending methods from Refs. [6, 7] to map out the ground state phase diagram as functions of itinerant fermion filling n (particle number density) and Kondo coupling strength J_K. We have identified that the smallest size CP^2 triple-Q state realizes at n = 1/4 [8], showcasing non-trivial topological magnetism with triple-Q peaks in both magnetic dipole and quadrupole structure factors [9]. Additional discovered phases include a CP^2 three-sublattice state at n = 1/3 and a CP^2 ferromagnetic state within areas of low-carrier density (refer to Ref. [5]). In this talk, we will discuss these phases in detail.

Acknowledgements

The works were supported by JSPS KAKENHI Grants No. JP20K14411, JSPS Grant-in-Aid for Scientific Research on Innovative Areas “Quantum Liquid Crystals” (KAKENHI Grant No. JP22H04469), and JST PRESTO Grant No. JPMJPR2251. Numerical calculations were carried out using HPC facilities provided by Okinawa Institute of Science and Technology.

References

1. S. Taie, R. Yamazaki, S. Sugawa, and Y. Takahashi,
“An SU(6) Mott insulator of an atomic Fermi gas realized by large-spin Pomeranchuk cooling,”
Nat. Phys. **8**, 825 (2012).
2. C. Hofrichter, L. Riegger, F. Scazza, M. Höfer, D. R. Fernandes, I. Bloch, and S. Fölling,
“Direct Probing of the Mott Crossover in the SU(N) Fermi-Hubbard Model,”
Phys. Rev. X **6**, 021030 (2016).
3. L. Riegger, N. D. Oppong, M. Höfer, D. R. Fernandes, I. Bloch, and S. Fölling,

"Localized Magnetic Moments with Tunable Spin Exchange in a Gas of Ultracold Fermions,"
Phys. Rev. Lett. **120**, 143601 (2018).

4. K. Ono, Y. Amano, T. Higomoto, Y. Saito, and Y. Takahashi.,
"Observation of spin-exchange dynamics between itinerant and localized ^{171}Yb atoms,"
Phys. Rev. A **103**, L041303 (2021).
5. K. Totsuka,
"Ferromagnetism in the SU(N) Kondo lattice model: SU(N) double exchange and supersymmetry,"
Phys. Rev. A **107**, 033317 (2023).
6. H. T. Ueda, Y. Akagi, and N. Shannon,
"Quantum solitons with emergent interactions in a model of cold atoms on the triangular lattice,"
Phys. Rev. A **93**, 021606(R) (2016).
7. K. Remund, R. Pohle, Y. Akagi, J. Romhányi, and N. Shannon,
"Semi-classical simulation of spin-1 magnets,"
Phys. Rev. Research **4**, 033106 (2022).
8. See the classical-spin case:
Y. Akagi and Y. Motome,
"Spin Chirality Ordering and Anomalous Hall Effect in the Ferromagnetic Kondo Lattice Model on a Triangular Lattice,"
J. Phys. Soc. Jpn. **79**, 083711 (2010).
9. See also CP^2 Skyrmion crystals in other systems:
Y. Amari, Y. Akagi, S. B. Gudnason, M. Nitta, and Y. Shnir,
"CP^2 skyrmion crystals in an SU(3) magnet with a generalized Dzyaloshinskii-Moriya interaction,"
Phys. Rev. B **106**, L100406 (2022).

Non-Hermitian Aharonov-Bohm effect under imaginary magnetic fields

Tomoki Ozawa[1*]

[1]Advanced Institute for Materials Research, Tohoku University, Japan
[*] tomoki.ozawa.d8@tohoku.ac.jp

Abstract: We discuss the Aharonov-Bohm effect under imaginary magnetic fields. We find that the Aharonov-Bohm effect appears as amplification and/or decay of the norm of the wavefunction, reflecting the enclosed imaginary flux inside the trajectory we consider. We consider both real and parameter space versions of this non-Hermitian Aharonov-Bohm effect.

Following the recent development of non-Hermitian quantum mechanics, it is now possible to consider the effects of magnetic fields which take imaginary values, i.e. imaginary magnetic fields. As a manifestation of physics of imaginary magnetic fields, we consider how Aharonov-Bohm effect appears under the imaginary magnetic fields.

Aharonov-Bohm effect is the effect where the particle going through two different trajectories acquires a relative phase which is proportional to the magnetic flux enclosed by the two trajectories. Whcn the magnetic field takes an imaginary value, the magnetic flux enclosed by trajectories becomes imaginary. Then the relative phase in the Aharonov-Bohm effect becomes a relative number whose magnitude is different from one. As a result, the wavefunction of a particle going through one path would have its magnitude different from that of a particle going through another path.

We consider this non-Hermitian version of the Aharonov-Bohm effect both in real and parameter spaces. In the real space setup, we consider a two-dimensional lattice model with a perpendicular imaginary magnetic field. By preparing a wavepacket and making it go through a closed trajectory, we see that the norm of the final wavefunction is different from the initial wavefunction, and the difference can be precisely explained by the imaginary Aharonov-Bohm phase factor [1].

In a parameter space, we consider a wavefunction to be in one eigenstate of some non-Hermitian Hamiltonian which depends on a set of parameters. By making the parameter change adiabatically and forming a closed trajectory in the parameter space, we see that the final state wavefunction and the initial state wavefunction have different norms. This difference is again explained by the Aharonov-Bohm phase factor, where the role of the imaginary magnetic field is played by the imaginary Berry curvature [2,3].

This work is supported by JSPS KAKENHI Grant No. JP20H01845, JST PRESTO Grant No. JPMJPR2353, and JST CREST Grant No. JPMJCR19T1.

References

1. Ozawa, T. and T. Hayata, “Two-dimensional lattice with an imaginary magnetic field,” Phys. Rev. B **109**, 085113 (2024).
2. Anandwade, R., Y. Singhal, S. N. M. Paladugu, E. Martello, M. Castle, S. Agrawal, E. Carlson, C. Battle-McDonald, T. Ozawa, H. M. Price, and B. Gadway, “Synthetic mechanical lattices with synthetic interactions,” Phys. Rev. A **108**, 012221 (2023).
3. Singhal, Y., E. Martello, S. Agrawal, T. Ozawa, H. Price, and B. Gadway, “Measuring the adiabatic non-Hermitian Berry phase in feedback-coupled oscillators,” Phys. Rev. Research **5**, L032026 (2023).

Exploring magneto-optical and nonlinear processes using a polarimeter optical spectrum analyzer

Eyal Buks[1]

[1]Technion, Israel
[*]corresponding author: eyal@ee.technion.ac.il

Abstract: Two recently-discovered effects are explored. The first is an unequally spaced optical comb that occurs in a fiber loop operated at low temperatures. The second effect under study is single sideband modulation that is observed in an optical modulator based on a ferrimagnet. Both effects are explored using polarization measurements.

We integrate a coherent optical spectrum analyzer with a rotating quarterwave plate polarimeter. The combined polarimeter optical spectrum analyzer (POSA) allows the extraction of the state of polarization with high spectral resolution. In this work, POSA is used to study two optical systems. The first is an optical modulator based on a ferrimagnetic sphere resonator [1]. We explore the underlying magneto-optical mechanism that breaks time reversal symmetry, and consequently enables modulation having sideband asymmetry. The second system under study is a cryogenic fiber loop laser, which produces an unequally spaced optical comb [2]. Polarization measurements provide insights on the nonlinear processes responsible for comb creation. Characterizations extracted from POSA data provide guidelines for performance optimization of applications based on these systems under study.

References

1. Banoj Kumar Nayak and EB, Journal of Applied Physics 132, 193905 (2022).
2. EB, Phys. Rev. Applied 19, L051001 (2023).

Deep-learning-based end-to-end metalens imaging

Joonhyuk Seo[1†], Jaegang Jo[2†], Joohoon Kim[3†], Joonho Kang[2], Chanik Kang[1], Seongwon Moon[3], Eunji Lee[4], Jehyeong Hong[2], Junsuk Rho[3,4,*], Haejun Chung[1,2,*]

[1]Department of Artificial Intelligence, Hanyang University, Seoul, 04763, Republic of Korea
[2]Department of Electronic Engineering, Hanyang University, Seoul, 04763, Republic of Korea
[3]Department of Mechanical Engineering, POSTECH, Pohang, 37673, Republic of Korea
[4]Department of Chemical Engineering, POSTECH, Pohang, 37673, Republic of Korea
[*]corresponding author: jsrho@postech.ac.kr, haejun@hanyang.ac.kr

Abstract: Metalens imaging suffers from a trade-off between broadband focusing efficiency and operating bandwidth of metalenses. We demonstrate a deep-learning-driven end-to-end image restoration framework to overcome the physical limitations of metalenses. The proposed framework achieves full-color imaging for a mass-produced 10-mm-diameter metalens and provides high image qualities comparable with ground truth images.

Metalenses, ultra-thin film lenses composed of subwavelength structures, have been spotlighted as a technology to overcome the limitations of conventional lenses, such as chromatic aberration, shadowing effect, bulky systems, and high manufacturing costs [1]. Consequently, they have been considered ideal replacements for conventional optical elements in optical sensors, smartphone cameras, unmanned aerial vehicle cameras and AR/VR devices. [1-2] However, recent studies suggest that the metalenses suffer from a fundamental trade-off between broadband focusing efficiency and operating bandwidth. [3-4] As a result, the large-area metalenses at present show chromatic aberration [10] or low focusing efficiency over a wide bandwidth [11-13], which hinders the commercialization of metalens-based compact imaging. In this study, we propose deep-learning-driven end-to-end metalens imaging (referred to as DRMI) to overcome the physical constraints of a mass-produced 10-mm-diameter metalens.

The metalens used in our imaging system is highly efficient but has strong chromatic aberration, which causes different types of image distortion than geometric lenses. The images captured from the metalens (referred to as 'metalens images') exhibit severe position-dependent distortion and high-frequency information loss. To restore the metalens images, we add two functionalities to a baseline image restoration model NAFNet: positional embedding and adversarial learning scheme in frequency domain. The positional embedding is applied to restore the position-dependent distortion of the images. Most image restoration models, including NAFNet, use randomly cropped patches of images for training to reduce computational complexities. However, these cropped patches have no information about the position-dependent distortions of images. Therefore, we embed the positional information of the pixels in the patches using a 1x1 convolution layer. Furthermore, to restore the high-frequency information, we apply the adversarial learning scheme, which comprises an auxiliary network that discriminates Fourier-transformed metalens images and ground truth images. [7-8]

Our results show the ground truth images, the metalens images, and the reconstructed images. The metalens images are severely blurred compared to the ground truth images, with more blur in the outer region than the inner region. On the other hand, the restored images show high image quality comparable with the ground truth images in both inner and outer regions.

Model	Image Quality Metric (Mean/Std)		
	PSNR	SSIM	LPIPS
Metalens Image	14.722/1.328	0.364/0.160	0.788/0.112
MIRNetV2	18.517/1.893	0.586/0.135	0.553/0.098
SFNet	18.231/1.727	0.597/0.129	0.520/0.095
HINet(Local)	21.300/2.333	0.674/0.117	0.449/0.097
NAFNet	21.731/2.382	0.676/0.116	0.436/0.097
DRMI	22.109/2.423	0.691/0.109	0.428/0.096

Table 1. Image quality metrics of DRMI and other image restoration models. (Best)

Table 1 shows quantitative comparisons of image quality metrics between DRMI and other restoration models. DRMI shows the greatest performance compared to those of metalens images.

Consequently, DRMI has significantly enhanced the resolution of metalens imaging systems, suggesting a potential to accelerate the commercialization of ultra-compact and ultra-light imaging systems.

References

1. Kim, J. et al. Scalable manufacturing of high-index atomic layer-polymer hybrid metasurfaces for metaphotonics in the visible. *Nature Materials* **22**, 4, 474-481 (2023)
2. Lee, G. et al. Metasurface eyepiece for augmented reality. *Nat Commun* **9**, 4562 (2018)
3. Kamli, S. M. et al. A review of dielectric optical metasurfaces for wavefront control. *Nanophotonics* **7**, 1041-1068 (2018)
4. Presutti, F. et al. Focusing on bandwidth: achromatic metalens limits. *Optica* **7**, 624-631 (2020)
5. Fan, C. et al. Ultrawide-angle and high-efficiency metalens in hexagonal arrangement. *Scientific Reports* **10**, 15677 (2020)
6. Wang, S. et al. A broadband achromatic metalens in the visible. *Nature nanotechnology* **13**, 227-232 (2018)
7. Goodfellow, I. et al. Generative adversarial nets. *Advances in neural information processing systems* **27** (2014)
8. Miyato T. et al. Spectral Normalization for Generative Adversarial Networks. *ICLR* (2018)

Cavity quantum materials: Virtue photons, Real effects.

Qing-Dong Jiang[1*]

[1]Shanghai Jiao Tong University, China
[*]corresponding author: qingdong.jiang@sjtu.edu.cn

Abstract: A material with symmetry breaking inside can transmit the symmetry breaking to its vicinity by vacuum fluctuations. The vacuum in proximate to a symmetry-broken material is referred as its quantum atmosphere[1]. Here, we show that a symmetry-broken quantum atmosphere can induce a significant modification of the material or molecular properties.

Summary: In recent years quantum optics and quantum materials start to emerge together, leading to the new direction called cavity quantum materials. In this talk, we show that cavity symmetry-broken quantum fluctuations lead to many interesting modifications of the material's properties, such as band structure, topology, and magnetism.

In this paper[2], we propose an entirely new route to select chirality by using quantum fluctuations near parity-symmetry-broken materials. In this paper[3], we propose a new way to achieve flat band in twisted bilayer graphene, an essential issue in the field. In this paper[4], we show that chiral cavity can induce an angular-momentum dependent Lamb shift.

The vacuum in proximate to a symmetry-broken material is referred as its quantum atmosphere[1,2,3]. Using quantum atmosphere to select chirality is efficient yet dramatically different from previous proposals where real fields are needed. We show that parity-symmetry breaking and quantum fluctuations can induce a chirality-dependent shift of the molecular ground-state energy, leading to a chemical reaction process that favors producing one chirality over the other. Besides analytical analysis, we further perform the first-principle calculation to find specific examples, showing that our proposal gives significant chirality selectivity.

Acknowledgements: The authors are sponsored by Pujiang Talent Program 21PJ1405400 and TDLI starting up grant and Jiaoda 2030.

References

1. Qing-Dong Jiang, and Frank Wilczek, Quantum atmospherics for materials diagnosis, Phys. Rev. B 99, 201104(R).
2. Yanzhe Ke, Zhigang Song, and Qing-Dong Jiang, Vacuum-Induced Symmetry Breaking of Chiral Enantiomer Formation in Chemical Reactions, Phys. Rev. Lett. 131, 223601 (2023);
3. Cunyuan Jiang, Matteo Baggioli, Qing-Dong Jiang, Engineering flat bands in twisted-bilayer graphene away from the magic angle with chiral optical cavities, arXiv:2306.05149.
4. Qing-Dong Jiang, Angular Momentum-Dependent Spectral Shift in Chiral Vacuum Cavities, arXiv:2307.14964
5. Qing-Dong Jiang and Frank Wilczek, Axial Casimir force, Phys. Rev. B 99, 165402 (2019).
6. Qing-Dong Jiang and Frank Wilczek, Chiral Casimir forces: Repulsive, enhanced, tunable, Phys. Rev. B 99, 125403 (2019).

Dynamical control of topological solitons in ferroelectrics and dynamical multiferroicity via twisted light

Lingyuan Gao[1], Sergei Prokhorenko[1], Yousra Nahas[1], and Laurent Bellaiche[1*]

[1] Physics Department and Institute for Nanoscience and Engineering, University of Arkansas, Fayetteville, Arkansas, USA
[*]corresponding author: laurent@uark.edu

Abstract: Via the use of first-principle-based atomistic simulations, it is demonstrated that twisted light can induce emergent electrodynamic phenomena in ferroelectric systems. These include: (1) dynamical evolution of topology in ferroelectric skyrmions, (2) effective gyration of dipolar vortex arrays, and (3) orbital magnetic moments of ions and composed magnetic topological textures.

Twisted light carries a nonzero orbital angular momentum (OAM), that can be transferred from light to electrons and particles ranging from nanometers to micrometers. Up to now, the interplay between twisted light with dipolar systems has scarcely been explored, though the latter bear abundant forms of topologies and embrace strong light-matter coupling. Here, using first-principle-based simulations, we show that twisted light can excite and drive dynamical topological polar states with novel features in ferroelectric ultrathin films. For OAM of light equal to 1, a polar skyrmion is successively created and annihilated alternately at two interfaces, as well as experiences a periodic transition from a markedly "Bloch" to "Néel" character, accompanied with the emergence of a "Bloch point" topological defect with vanishing polarization. The dynamical evolution of skyrmions is connected to a constant jump of topological number between "0" and "1" over time. For higher OAM of light, local electric dipoles self-order and form a vortex array distributed along azimuthal directions. Owing to its intrinsic symmetry, the evolution of vortex array with time can be viewed as an effective spinning around the central axis, while its rotation speed is also connected to the OAM value. These intriguing phenomena are found to have an electrostatic origin.

Furthermore, electric dipoles follow the evolving pattern of the optical field and circular motions of rotating dipoles create strong on-site orbital magnetic moments of ions. By characterizing topology of orbital magnetic moments in each 2D layer, we identify the vortex type of magnetic topological texture—magnetic merons with a one-half topological charge and robust stability. Our study thus demonstrates that and explains why this unique light-matter interaction can be very powerful in creating and manipulating topological solitons in functional materials as well as generating magnetic fields and dynamical multiferroicity in nominally nonmagnetic materials.

We acknowledge the support from the Grant MURI ETHOS W911NF-21-2-0162 from Army Research Office (ARO), the Vannevar Bush Faculty Fellowship (VBFF) Grant No. N00014-20-1-2834 from the Department of Defense and Award No. DMR-1906383 from the National Science Foundation Q-AMASE-i Program (MonArk NSF Quantum Foundry). We also acknowledge the computational support from the Arkansas High Performance Computing Center and HPCMP Pathfinder Award for computational resources.

References

1. Gao, Lingyuan, Sergei Prokhorenko, Yousra Nahas and Laurent Bellaiche, "Dynamical Multiferroicity and Magnetic Topological Structures Induced by the Orbital Angular Momentum of Light in a Nonmagnetic Material," Phys. Rev.

Lett., Vol. 131, No. 11, 086901, 2023.

2. Gao, Lingyuan, Sergei Prokhorenko, Yousra Nahas and Laurent Bellaiche, “Dynamical Control of Topology in Polar Skyrmions via Twisted Light,” Phys. Rev. Lett., Vol. 132, No. 2, 026902, 2024.
3. Gao, Lingyuan, Sergei Prokhorenko, Yousra Nahas and Laurent Bellaiche, “Effective Gyration of Polar Vortex Arrays Controlled by High Orbital Angular Momentum of Light,” Phys. Rev. B, in press, 2024.

Exploring chiral nanogap structures using inverse topology design

A. Taguchi[1*]

[1]Resaerch Institute for Electronic Science, Hokkaido University, Japan
[*]corresponding author: taguchi@es.hokudai.ac.jp

Abstract: Chiral nanostructures hold the potential for controlling chiral light-matter interactions at the nanoscale, yet the structure design poses challenges due to intricate near-field responses involving helically structured light. We present the inverse design of chiral nanostructures, demonstrating excellent chiroptical functionalities with a structural complexity that is unattainable by designing with human intuition.

Chiroptical light-matter interactions play a crucial role in various fields, such as circular dichroism (CD) spectroscopy, chiral chemistry, optical trapping and manipulation, spin quantum information technology, and so on. Extensive efforts have been devoted to enhancing chiroptical light-matter interaction using chiral metallic nanostructures and metamaterials [1]. However, the design of these structures has traditionally relied on heuristic approaches, largely dictated by a finite set of preassigned design parameters determined by humans. Considering the inherent complexity of chiral structured light, we explored crafting a high-performing chiral nanophotonic structure.

Topology optimization (TO), initially proposed for mechanical designs [2], uses gradient-based searches rooted in Maxwell's equations [3]. TO enables the handling of large-scale structure designs, comprising hundreds to potentially billions of dielectric values at each spatial point, offering a considerable degree of design freedom [4]. This allows for designing structures by passing through topologically discontinuous deformation, which is not possible using traditional design approaches that only optimize dimensional design parameters and the outer shape. Here, using TO, we show nanogap antennas with increased dissymmetry for improved CPL coupling [5].

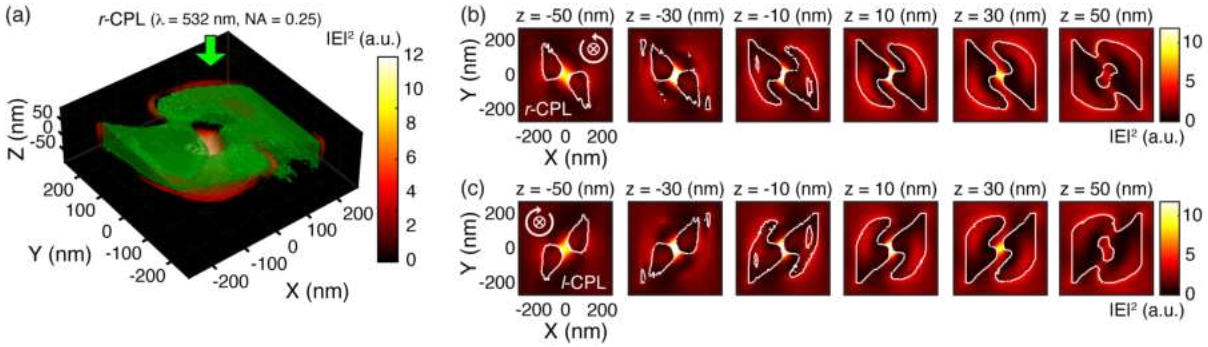


Fig. 1: Chiral gap antenna structure designed using topology optimization. (a) 3D rendering of the structure optimized for *r*-CPL and (b) the sectional view at various z positions. (c) Similar to (b) but optimized for incident *l*-CPL having reversed handedness.

A typical topology-optimized structure is represented in Figs. 1(a) and 1(b) along with the electric field intensity overlayed on the structure. The material is titanium dioxide (TiO_2) placed on a silicon dioxide (SiO_2) substrate. We configured TO to maximize the energy flow at the center of the TiO_2 slab, which had a size of 400 nm x 400 nm x 100 nm, upon being illuminated with right-handed circularly polarized light (*r*-CPL) at a

wavelength of 532 nm (Fig. 1(a)). As seen in the figure, the structure exhibits a spiral shape with an 8-nm-wide gap at the center of the body. Interestingly, the handedness of the spiral was reversed when we switched the handedness of the CPL from right to left (Fig. 1(c)). We calculated the field intensity enhancement for the structure optimized for *r*-CPL. The results are shown in Figs. 2(a) and 2(b) for both *r*-CPL and *l*-CPL excitations. The field intensities within the gap were much stronger when the excitation had the same handedness as the optimization (*r*-CPL). We evaluated the factor of enhancement as the electromagnetic field intensity within the gap divided by the value at the same position but calculated without the structure. The enhancement factors were 56 and 10 for *r*-CPL and *l*-CPL excitation, respectively. To evaluate the dissymmetry of the structure for the handedness of the circular polarization, we defined the dissymmetry factor $g = 2(I_R–I_L)/(I_R+I_L)$ and depicted in Fig. 2(c). The calculated value of the dissymmetry factor was –1.40 within the gap, which is sufficiently large [5].

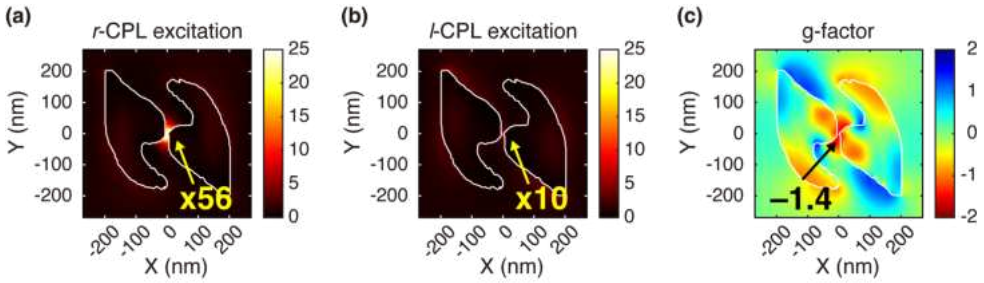


Fig. 2: (a,b) Distribution of the intensity enhancement factor for (a) *r*-CPL excitation (polarized co-circularly) and (b) *l*-CPL excitation (polarized cross-circularly), respectively. (c) Dissymmetry factor (g-factor) of the field intensity enhancement.

In the presentation, we show an in-depth analysis of the near-field polarization of the designed chiral nanogap structures. We then, based on the analysis, propose a CPL emission device using the chiral gap antenna. We also discuss how the structure impacts the spin angular momentum density of incoming light flowing inward the nanogap, which, we found, implies a profound design strategy of chiral nanostructures with enhanced optical chirality [6] at the nanoscale.

We thank the use of the AI-compatible advanced computer system at the Information Initiative Center, Hokkaido University, Sapporo, Japan, under the joint research program. This study is supported by a Grant-in-Aid for Transformative Research Areas, “Evolution of Chiral Materials Science using Helical Light Fields” (Grants No. JP22H05131, No. JP22H05137) from JSPS KAKENHI, Japan.

References

1. M. Hentschel, M. Schäferling, X. Duan, H. Giessen, and N. Liu, “Chiral plasmonics,” Sci. Adv. Vol. 3, e1602735, 2017.
2. M.P. Bendsøe, and N. Kikuchi, “Generating optimal topologies in structural design using a homogenization method,” Comput. Meth. Appl. Mech. Eng. Vol. 71, 197–224, 1988.
3. J.S. Jensen, J.S. and O. Sigmund, “Topology optimization for nano-photonics,” Laser Photon. Rev. Vol. 5, 308–321, 2011.
4. N. Aage, E. Andreassen, B.S. Lazarov, and O. Sigmund, “Giga-voxel computational morphogenesis for structural design,” Nature Vol. 550, 84–86, 2017.
5. A. Taguchi, Y. Fukui, and K. Sasaki, Submitted; arXiv:2402.10742 [physics.optics].
6. Y. Tang and A.E. Cohen, “Optical chirality and its interaction with matter,” Phys. Rev. Lett. Vol. 104, 163901, 2010.

Emergent One-Dimensional Helical State on the Surface Opposite to a Step Edge in Higher-Order Topological Insulators

Akihiko Sekine[1*], Manabu Ohtomo[1], Kenichi Kawaguchi[1], and Mari Ohfuchi[1]

[1]Fujitsu Research, Fujitsu Limited, Japan
[*]corresponding author: akihiko.sekine@fujitsu.com

Abstract: We show theoretically that a one-dimensional conducting state with a helical spin structure, which also has a linear dispersion near the zero energy, emerges at a step edge and on the surface opposite to the step edge in three-dimensional higher-order topological insulators such as few-layer Td-WTe_2.

The spin-momentum-locked helical conducting states appearing at the boundaries between a topologically nontrivial phase and a topologically trivial phase have been studied intensively and extensively, pursuing practical technological applications. For example, topological quantum computation utilizing Majorana zero modes has low error rate because the qubits are robust against noises due to the topological nature of Majorana fermions. Also, possible ways to manipulate and utilize the two-dimensional (2D) helical states on the surfaces of 3D topological insulators have been investigated actively in spintronics.

In this work, we study theoretically the electronic structure of 3D higher-order (second-order) topological insulators such as few-layer Td-$X$$Te_2$ (X = Mo, W), which host the 1D helical states called the hinge states at their 1D edges. By diagonalizing the tight-binding model [1, 2] in a 3D geometry with a step edge [Fig. 1(a)], we find that a 1D helical conducting state emerges at a step edge and on the surface opposite to the step edge [3]. We also find that the 1D helical conducting state on the surface opposite to a step edge emerges when the electron hopping in the direction perpendicular to the step is weak. Such an existence of the emergent 1D helical conducting state on the surface opposite to a step edge in the weak coupling regime can be understood by considering an addition of different-sized independent blocks of 3D higher-order topological insulators [Fig. 1(b)]. On the other hand, when the electron hopping in the direction perpendicular to the step is strong, we find that the location of the emergent 1D helical conducting state moves from the surface opposite to the step edge to the dip (270° edge) below the step edge. In this case, the existence of the 1D helical conducting state at the dip below the step edge can be explained by that a gapless topological boundary state generically appears where a sign change in the mass of surface Dirac fermions occurs, as in the case of ordinary 1D topological hinge states. These two physical pictures are connected continuously without the bulk bandgap closing [Fig. 1(c)].

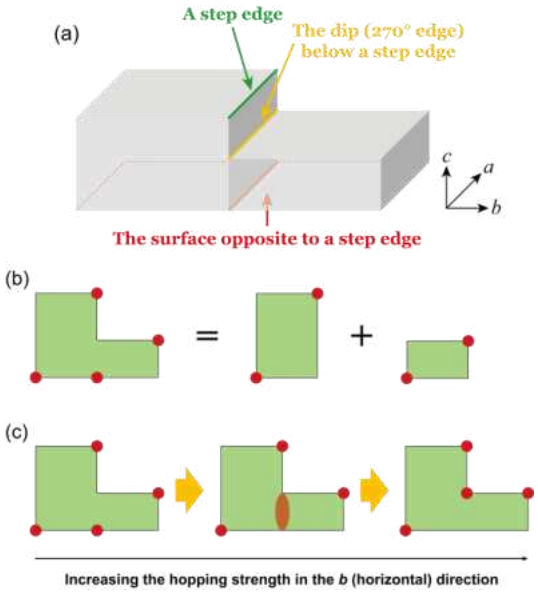


Fig. 1. Schematic illustration of (a) the geometry we consider, (b) the weak coupling regime in the b direction, and (c) the evolution of the location where the 1D helical conducting state emerges with respect to the decreasing hopping strength in the b direction. The filled red circles in (b) and (c) indicate the locations of 1D helical states.

Because one or more step edges can be created as desired by leveraging experimental processes commonly used in thin-film devices, our finding paves the way for on-demand creation of 1D helical conducting states from 3D higher-order topological insulators, which could lead to, e.g., a realization of high-density Majorana qubits.

References

1. Wang, Z., Wieder, B. J., Li, J., Yan, B., and Bernevig, B. A., "Higher-order topology, monopole nodal lines, and the origin of large fermi arcs in transition metal dichalcogenides $X\mathrm{Te}_2$ (X = Mo, W)" Phys. Rev. Lett. **123**, 186401 (2019).
2. Choi, Y.-B. *et al*., "Evidence of higher-order topology in multilayer WTe_2 from Josephson coupling through anisotropic hinge states," Nat. Mater. **19**, 974 (2020).
3. Sekine, A., Ohtomo, M., Kawaguchi, K., and Ohfuchi, M., "Emergent one-dimensional helical channel in higher-order topological insulators with step edges", J. Appl. Phys. **134**, 165707 (2023).

Chirality-Induced Polarized Phenomena in Chiral Inorganic Materials

Y. Togawa[1, 2*]

[1] Department of Physics and Electronics, Osaka Metropolitan University, Japan
[2] Quantum Research Center for Chirality, Okazaki, Japan
[*]corresponding author: ytogawa@omu.ac.jp

Abstract: A role of chirality in materials is discussed with an emphasis on the emergence of macroscopic polarization of spin angular momenta and angular momenta in chiral inorganic materials.

A role of chirality in materials is discussed in terms of an emergence of macroscopic polarization response, being inspired by recent studies on chirality-induced selectivity of spin angular momenta and angular momenta with chiral materials. These viewpoints will bring us to a new frontier of chiral material science.

In this talk, we discuss the significance of experimental findings that chiral inorganic materials exhibit a spin-polarized state when the charge current is injected into them [1-6]. A spin-polarized transport occurs in a linear regime of the current-voltage characteristics. Importantly, a robust protection of the spin polarization enables a nonlocal spin transport over micrometers or longer [7]. Namely, spin transport occurs macroscopically in chiral materials. A comprehensive understanding of these nontrivial spin response remains an important issue and may clarify the interplay between structural and dynamical chirality. In this connection, controlling chirality in inorganic materials remains an important issue [5]. The influence of dynamical fluctuations, which are characteristic of chiral materials and known as chiral phonon [8, 9], is also argued in the viewpoint of polarization phenomena [10].

References

1. Inui, A., R. Aoki, Y. Nishiue, K. Shiota, Y. Kousaka, H. Shishido, D. Hirobe, M. Suda, J. Ohe, J. Kishine, H. M. Yamamoto and Y. Togawa, “Chirality-Induced Spin-Polarized State of a Chiral Crystal $CrNb_3S_6$,” Physical Review Letters, Vol. 124, 166602, 2020.
2. Nabei, Y., D. Hirobe, Y. Shimamoto, K. Shiota, A. Inui, Y. Kousaka, Y. Togawa and H. M. Yamamoto, “Current-induced bulk magnetization of a chiral crystal $CrNb_3S_6$,” Applied Physics Letters, Vol. 117, 052408, 2020.
3. Shiota, K., A. Inui, Y. Hosaka, R. Amano, Y. Onuki, M. Hedo, T. Nakama, D. Hirobe, J. Ohe, J. Kishine, H. M. Yamamoto, H. Shishido and Y. Togawa, “Chirality-induced spin polarization over macroscopic distances in chiral disilicide crystals,” Physical Review Letters, Vol. 127, 126602, 2021. Featured in Physics 14, s113.
4. Shishido, H., R. Sakai, Y. Hosaka and Y. Togawa, “Detection of chirality-induced spin polarization over millimeters in polycrystalline bulk samples of chiral disilicides $NbSi_2$ and $TaSi_2$,” Applied Physics Letters, Vol. 119, 182403, 2021.
5. Kousaka, Y., T. Sayo, S. Iwasaki, R. Saki, C. Shimada, H. Shishido and Y. Togawa, “Chirality-selected crystal growth and spin polarization over centimeters of transition metal disilicide crystals,” Japanese Journal of Applied Physics, Vol. 62, 015506, 2023.
6. Shishido, H., Y. Hosaka, K. Monden, A. Inui, T. Sayo, Y. Kousaka and Y. Togawa, “Spin polarization gate device based on the chirality-induced spin selectivity and robust nonlocal spin polarization,” Journal of Chemical Physics, Vol. 159, 064502, 2023.

7. Togawa, Y., A. S. Ovchinnikov and J. Kishine, “Generalized Dzyaloshinskii-Moriya Interaction and Chirality-Induced Phenomena in Chiral Crystals,” Journal of the Physical Society of Japan, Vol. 92, 081006, 2023. Special Topics Dzyaloshinskii-Moriya Interactions: Physics of Inversion Symmetry Breaking.
8. Ishito, K., H. Mao, Y. Kousaka, Y. Togawa, S. Iwasaki, T. Zhang, S. Murakami, J. Kishine and T. Satoh, “Truly chiral phonons in α-HgS,” Nature Physics, Vol. 19, 35-39, 2023.
9. Ishito, K., H. Mao, K. Kobayashi, Y. Kousaka, Y. Togawa, H. Kusunose, J. Kishine and T. Satoh, “Chiral phonons: circularly polarized Raman spectroscopy and ab initio calculations in a chiral crystal tellurium,” Chirality, Vol. 35, 338-345, 2023.
10. Ohe, K., H. Shishido, M. Kato, H. Matsuura and Y. Togawa, “Chirality-Induced Selectivity of Phonon Angular Momenta in Chiral Quartz Crystals,” Physical Review Letters, Vol. 132, 056302, 2024.

Three-dimensional topological spin textures in chiral magnets

Jiadong Zang[1]

[1]University of New Hampshire, USA
[*]corresponding author: jiadong.zang@unh.edu

Abstract: In this talk, I will discuss our recent attempts of generalizing topological spin textures in two-dimensions to those in three-dimensions.

Chiral magnets are a series of magnets with broken inversion symmetry. A new type of spin interaction therein, the Dzyaloshinskii-Moriya interaction, stimulates the formation of many novel topological spin textures. One important example is the emergence of magnetic skyrmion, whose nontrivial topology enables unique dynamical property and thermal stability, and gives rise to promising applications in future spintronic devices. However, skyrmion is just a two-dimensional texture. Its three-dimensional (3D) counterparts are widely unexplored. In this talk, I will discuss realization of 3D skyrmionic textures, including target skyrmion, skyrmion bundle, and skyrmionic vortices. I will also discuss the magnetic hopfion, a rigorously defined 3D topological texture. We propose the presence of zero-field hopfion in synthetic chiral magnetic multilayers. All these 3D textures exhibit novel dynamical properties that can be formulated in terms of collective coordinates. These works could stimulate the development of 3D spintronics.

This work was supported by the U.S. Department of Energy (DOE), Office of Science, Basic Energy Sciences (BES) under Award No. DE-SC0020221.

References

1. F. Zheng, H. Li, S. Wang, D. Song, C. Jin, W. Wei, A. Kovacs, J. Zang, M. Tian, Y. Zhang, H. Du, and R. E. Dunin-Borkowski, Direct imaging of zero-field target skyrmion and its polarity switch in chiral magnetic nanodisk, Phys. Rev. Lett. 119, 197205 (2017)
2. J. Tang, Y. Wu, W. Wang, L. Kong, B. Lv, W. Wei, J. Zang, M. Tian, and H. Du, Magnetic Skyrmion Bundles and Their Current-Driven Dynamics, Nature Nanotechnology 16, 1086 (2021).
3. K. Niitsu, Y. Liu, A. C. Booth, X. Z. Yu, N. Mathur, M. J. Stolt, D. Shindo, S. Jin, J. Zang, N. Nagaosa, and Y. Tokura, Geometrically stabilized ground-state skyrmion in FeGe tetrahedral nanoparticle, Nature Materials 21, 305 (2022).
4. Y. Liu, R. K. Lake, J. Zang, Binding a hopfion in a chiral magnet nanodisk, Physical Review B 98, 174437 (2018)
5. Y. Liu, W. T. Hou, X. F. Han, and J. Zang, Three-dimensional dynamics of magnetic hopfion driven by spin transfer torque, Physical Review Letters 124, 127204 (2020).

META 2024, TOYAMA - JAPAN, JULY 16 – 19, 2024

Nonreciprocal Optical Responses and Diode Effect in Superconductors: Quantum Geometry, Topological Superconductivity, and Exotic Pairing

H. Tanaka[1], A. Daido[1*], H. Watanabe[2], N. Nunchot[1], K. Nakamura[1], S. Asano[1], and Y. Yanase[1]

[1]Department of Physics, Kyoto University, Japan
[2]Research Center for Advanced Science and Technology, University of Tokyo, Japan
[*]corresponding author: yanase@scphys.kyoto-u.ac.jp

Abstract: We present the theoretical framework of nonreciprocal transport and optical responses in superconductors. The optical second-harmonic generation, bulk photocurrent, superconducting diode effect, and nonreciprocal Meissner effect are discussed. Observation of exotic Cooper pairing and topological superconductivity is proposed.

First, we show that superconductors with the space-inversion symmetry breaking host unique nonreciprocal optical responses, such as the photocurrent generation and second-harmonic generation [1]. Unlike the normal state, the nonlinear optical conductivity shows divergence at low frequencies. The divergent behaviors are attributed to the nonreciprocal superfluid density and the Berry curvature derivative, characteristic of the space-inversion symmetry-breaking superconductors. These indicators quantify the performance of superconductors in nonlinear optics. We also formulate the shift current, injection current, and gyration current which show peaks around the superconducting gap frequency. The microscopic conditions for the nonreciprocal optical responses in noncentrosymmetric superconductors are clarified, and we find that the spin-triplet Cooper pairs are needed for the nonlinear optical responses in time-reversal symmetric single-band superconductors [2]. From this result, we propose the probe of spin-triplet Cooper pairs induced by the spin-orbit coupling in noncentrosymmetric superconductors, which was theoretically predicted but not yet verified experimentally. When the time-reversal symmetry is broken, conventional superconductors also show the nonreciprocal optical responses. We evaluate the nonlinear optical conductivity in noncentrosymmetric superconductors under the magnetic field and show that it is enhanced by quantum geometry in the band structure [3]. We also show the sign-reversal phenomenon associated with the emergence of topological superconductivity. Therefore, we propose the bulk probe of topological superconductivity, which has been awaited for a long time.

Second, stimulated by the recent discovery of the superconducting diode effect (SDE) [4], we propose an intrinsic mechanism to cause the SDE [5]. The SDE refers to the nonreciprocity of the critical current. We show that the SDE is caused by the nonreciprocity of the Landau critical momentum and propose that the crossover phenomenon in the helical superconducting state can be proved by the SDE. The intrinsic SDE unveils the rich phase diagram and functionalities of noncentrosymmetric superconductors.

The nonreciprocal correction to the superfluid density also leads to the nonreciprocal Meissner effect, namely, asymmetric screening of magnetic fields due to the nonreciprocal magnetic penetration depth. Performing a microscopic analysis of an exotic superconductor UTe_2, we show that the nonreciprocal Meissner effect is useful for probing parity-mixing properties and gap structures in superconductors [6].

References

1. Hikaru Watanabe, Akito Daido, Youichi Yanase, Phys. Rev. B **105**, 024308 (2022).
2. Hiroto Tanaka, Hikaru Watanabe, Youichi Yanase, Phys. Rev. B **107**, 024513 (2023).
3. Hiroto Tanaka, Hikaru Watanabe, Youichi Yanase, in preparation.
4. F. Ando, Y. Miyasaka, T. Li, J. Ishizuka, T. Arakawa, Y. Shiota, T. Moriyama, Y. Yanase, and T. Ono, Nature **584**, 373 (2020).
5. Akito Daido, Yuhei Ikeda, Youichi Yanase, Phys. Rev. Lett. **128**, 037001 (2022).
6. Hikaru Watanabe, Akito Daido, Youichi Yanase, Phys. Rev. B **105**, L100504 (2022).

Toroidal-assisted Metasurface for High-performance Nanophotonics

Pin Chieh Wu[1]

[1] Department of Photonics, National Cheng Kung University, Tainan 70101, Taiwan
*corresponding author: pcwu@gs.ncku.edu.tw

Abstract: We propose using toroidal-assisted responses to enhance the transmission efficiency of plasmonic metasurfaces. The Fano coupling between toroidal dipoles and quadrupoles enables a cross-polarization converter with 22.9% efficiency, and a hybrid meta-atom can achieve over 50% efficiency in the near-infrared region.

Plasmonic metasurfaces have been widely studied for their potential to create high-performance flat optical components and polarization converter devices[1-3]. However, these devices are often limited in efficiency due to the use of highly radiative electric and magnetic multipoles. As a result, they may not be suitable for real-world applications, especially when compared to dielectric metasurfaces which can have more limited interaction with incident light due to their high aspect ratio.

In this work, we propose a new strategy to enhance the transmission efficiency of plasmonic metasurfaces. We take advantage of the Fano coupling between toroidal dipoles and quadrupoles, which introduces minimal radiative loss and strong field confinement[4, 5]. By incorporating these low-loss toroidal multipoles, we have experimentally demonstrated a giant cross-polarization converter with a transmission efficiency of 22.9% in a single-layer plasmonic metasurface, which is close to the theoretical limit of 25%. Additionally, we have shown that a hybrid plasmonic meta-atom can achieve a transmission efficiency of over 50% in the near-infrared (NIR) region[6]. By integrating a solid nano-structure with its inverse complementary, we realized a plasmonic metasurface with a circular cross-polarization conversion efficiency higher than 50% in transmission at NIR wavelengths. Such high optical performance metasurface is achieved by simultaneously exciting the electric, magnetic, and toroidal multipolar modes, which satisfies the generalized Kerker condition and improves the transmission efficiency. These results open up new possibilities for the development of highly efficient plasmonic metasurface components and systems that could be used in real-world applications.

References

1. N. Meinzer, W. L. Barnes, and I. R. Hooper, *Nat. Photon.* **8**, 889-898 (2014).
2. P. Genevet, F. Capasso, F. Aieta, M. Khorasaninejad, and R. Devlin, *Optica* **4**, 139-152 (2017).
3. C. Hou-Tong, J. T. Antoinette, and Y. Nanfang, *Rep. Prog. Phys.* **79**, 076401 (2016).
4. A. Hassanfiroozi, P.-S. Huang, S.-H. Huang, K.-I. Lin, Y.-T. Lin, C.-F. Chien, Y. Shi, W.-J. Lee, and P. C. Wu, *Adv. Opt. Mater.* **9**, 2101007 (2021).
5. A. Hassanfiroozi, Z.-S. Yang, S.-H. Huang, W.-H. Cheng, Y. Shi, and P. C. Wu, *Adv. Opt. Mater.* **11**, 2202717 (2023).
6. A. Hassanfiroozi, Y.-C. Cheng, S.-H. Huang, Y.-T. Lin, P.-S. Huang, Y. Shi, and P. C. Wu, *Laser Photon. Rev.* **16**, 2100525 (2022).

Antiferromagnetic skyrmion lattice of the 4-sublattice tetrahedral order

T. Hirosawa[1*], M. Azhar[2], and A. Mook[3]

[1]Aoyama Gakuin University, Japan
[2]University of Duisburg-Essen, Germany
[3]Johannes Gutenberg University Mainz, Germany
[*]corresponding author: hirosawa@hosi.phys.s.u-tokyo.ac.jp

Abstract: The 4-sublattice tetrahedral order is the smallest topological spin texture with spatially uniform topological charge density. In this work, we study a minimal spin lattice model of the tetrahedral phase. We investigate the magnetic phase diagram when the Dzyaloshinskii–Moriya interaction is present.

Magnetic skyrmions exhibit topological spin structures in real space. Recently, nanosized skyrmions have been observed in various magnetic systems [1,2]. Ultrasmall skyrmions have a technological advantage for memory applications due to higher memory density. Furthermore, the discovery of ultrasmall skyrmions has stimulated many theoretical studies since a new mechanism is needed for stabilizing them. Itinerant electrons are now believed to play a fundamental role [3].

In this work, we consider the 4-sublattice tetrahedral order in triangular lattice. It consists of four spins pointing to the vertices of a tetrahedron. The positive biquadratic interaction stabilizes the tetrahedral order [4,5], which is a higher-order spin interaction beyond the Ruderman-Kittel-Kasuya-Yosida (RKKY) interaction. We study a minimal spin-lattice model, including the antiferromagnetic exchange, positive biquadratic interaction, and the Dzyaloshinskii–Moriya interaction. We find that the orientation of tetrahedral order is rotated in space when the Dzyaloshinskii–Moriya interaction is introduced. The twisted tetragonal order results in formation of multiple-Q states with a longer wavelength. Remarkably, we find that the antiferromagnetic skyrmion lattice (AFM-SkXs) is favored over the single-Q helical phase even without external fields. We discuss the magnetic excitations of AFM-SkXS and nontrivial magnon topology.

References

1. S. Heinze, K. von Bergmann, M. Menzel, J. Brede, A. Kubetzka, R. Wiesendanger, G. Bihlmayer, and S. Blügel, “Spontaneous atomic-scale magnetic skyrmion lattice in two dimensions”, Nat. Phys. 7, 713 (2011).
2. N. D. Khanh, T. Nakajima, X. Yu, S. Gao, K. Shibata, M. Hirschberger, Y. Yamasaki, H. Sagayama, H. Nakao, L. Peng, K. Nakajima, R. Takagi, T.-h. Arima, Y. Tokura, and S. Seki, “Nanometric square skyrmion lattice in a centrosymmetric tetragonal magnet”, Nat. Nanotech. 15, 444 (2020).
3. S. Hayami and Y. Motome, “Topological spin crystals by itinerant frustration”, J. Phys.: Condens. Matter 33, 443001 (2021).
4. I. Martin and C. D. Batista, “Itinerant Electron-Driven Chiral Magnetic Ordering and Spontaneous Quantum Hall Effect in Triangular Lattice Models”, Phys. Rev. Lett. 101, 156402 (2008).
5. Y. Akagi, M. Udagawa, and Y.Motome, “HiddenMultiple-Spin Interactions as an Origin of Spin Scalar Chiral Order in Frustrated Kondo Lattice Models”, Phys. Rev. Lett. 108, 096401 (2012).

Chiral optical forces in integrated photonic waveguides for sorting enantiomers

I. Diez[1*], **J. Martínez-Romeu**[1], **S. Golat**[2], **F. J. Rodríguez-Fortuño**[2], **and A. Martínez**[1]

[1]Nanophotonics Technology Center, Universitat Politècnica de Valencia, Camino de Vera, s/n Building 8F, 46022, Valencia, Spain

[2]Department of Physics, King's College London, Strand, London WC2R 2LS, United Kingdom
[*]corresponding author: iroddie@upv.edu.es

Abstract: Optical forces with opposite signs for enantiomeric versions of a molecule or nanoparticle can enable their separation, essential in chemistry and pharmaceutics. We analyze such forces in integrated dielectric waveguides with simulations, demonstrating separation within seconds for high and low chirality nanoparticles.

Enantiomeric separation, crucial in chemistry and pharmaceutics, conventionally relies on chemical methods like chiral High-Performance Liquid Chromatography, which are slow, expensive, and molecule-specific[1]. An alternative method using optical chiral forces[2] has recently gained attention. Recent theoretical works and experiments have explored optically-induced separation of microparticles, primarily with free-space beams[3]. However, using guided light in integrated waveguides presents a promising approach due to an enhanced chiroptical interaction, essential for sorting smaller particles, and due to the potential for large-scale integration. This study focuses on lossless dielectric waveguides, made of silicon Si or silicon nitride SiN, which offer low propagation loss and compatibility with telecom wavelengths[4]. By analyzing the chiral forces exerted by the optical field at different wavelengths on nanoparticles of various sizes, we show that integrated waveguides can effectively sort enantiomers, potentially enabling rapid enantiomeric separation in photonic integrated circuits.

From electromagnetic simulations we obtain the electric and magnetic fields of the mode supported in the waveguide cross-section for computing the optical force exerted by the mode on a nearby particle. The net optical force that the electromagnetic field ($\boldsymbol{E}$, $\boldsymbol{H}$) exerts on a dipolar particle is given by[2]:

$$\langle \boldsymbol{F} \rangle = \frac{1}{2}\Re\left[(\boldsymbol{\nabla}\otimes\boldsymbol{E})\boldsymbol{p}^* + \mu(\boldsymbol{\nabla}\otimes\boldsymbol{H})\boldsymbol{m}^* - \frac{k^4}{6\pi}\eta(\boldsymbol{p}^*\times\boldsymbol{m})\right] \quad (1)$$

where $\boldsymbol{p} = \alpha_e \varepsilon \boldsymbol{E} + i\alpha_c \boldsymbol{H}/c$ and $\boldsymbol{m} = \alpha_m \boldsymbol{H} - i\alpha_c \boldsymbol{E}/\eta$ are the electric and magnetic dipole moments obtained from the polarizabilities ($\alpha_e, \alpha_m, \alpha_c$) that model the particle's linear response to the electromagnetic field. The polarizability values are calculated with chiral Mie theory[5]. Further detail of each term of the different chiral and achiral forces arising from Equation 1 can be found in previous work[6,7]. Once the force field throughout the medium surrounding the waveguide is obtained, the trajectory of an individual particle is computed with a tracking algorithm that considers the stochastic nature of the Brownian motion of the particle in a fluid. We applied this algorithm to hundreds of particles, for both enantiomers, to do a statistical study on the probability of separation.

We explored different guided modes for separating both enantiomers of low or high chirality non-absorbing particles either transversally or longitudinally to the waveguide. We found that for high-chirality particles a quasi-TE mode at short wavelengths (λ=405 nm) can separate enantiomers transversally at each side of the waveguide due to a dominant magnetic-spin chiral force (see Figure 1(a)). At longer wavelengths (λ=1310 nm), a combination of quasi-TE and a 90º-delayed quasi-TM mode (with same mode index) generates a quasi-circularly polarized mode that enables an attractive/repulsive transversal sorting of smaller nanoparticles due to the transversal helicity

density gradient chiral force[7]. For low-chirality particles we found that a combination of a quasi-TE and a quasi-TM (with different mode index $\Delta n = n_{TE} - n_{TM}$, at λ=1310 nm) generates a beating pattern of alternating helicity, resulting in a longitudinal helicity density gradient along the waveguide that separates the enantiomers every $\lambda/(2\Delta n)$ distance (see Figure 1(b)). All the beforementioned sorting mechanisms successfully occur within seconds for nanoparticles suspended in fluid at room temperature. This study suggests that long Si and SiN waveguides present a viable path towards enantiomeric separation using guided light in photonic integrated circuits.

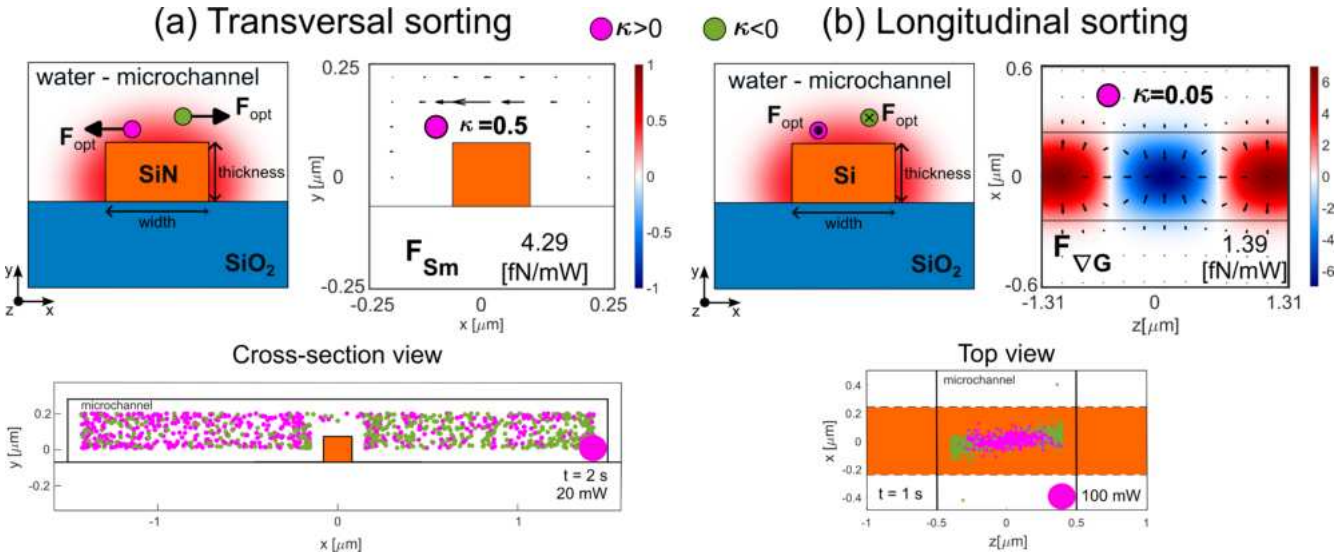


Figure 1 Schematic of each optical sorting configuration, together with the plot of the responsible chiral force, and results of the particle tracking simulations. **(a)** A quasi-TE guided mode in a SiN waveguide produces a dominant magnetic-spin chiral force ($\mathbf{F}_{Sm}$) responsible for the transversal sorting of high-chirality non-absorbing particles (radius = 80 nm, ε=2, μ=1, κ=0.5) at λ=405 nm. **(b)** A superposition of a quasi-TE and a quasi-TM mode (with different mode indices) in a Si waveguide produces a helicity density gradient chiral force ($\mathbf{F}_{\nabla G}$) responsible for the longitudinal sorting of low-chirality non-absorbing particles (radius = 100 nm, ε= 2, μ=1, κ=0.05) at λ=1310 nm.

The authors acknowledge funding from the European Commission under the CHIRALFORCE Pathfinder project (101046961) and Innovate UK Horizon Europe Guarantee (UKRI 10045438).

References

1. Jacques, J., Collet, A. & Wilen, S. H. *Enantiomers, Racemates, and Resolutions*. (Wiley, New York, 1981).
2. Genet, C. Chiral Light–Chiral Matter Interactions: an Optical Force Perspective. *ACS Photonics* **9**, 319–332 (2022).
3. Hayat, A., Mueller, J. P. B. & Capasso, F. Lateral chirality-sorting optical forces. *Proc. Natl. Acad. Sci.* **112**, 13190–13194 (2015).
4. Xiang, C., Jin, W. & Bowers, J. E. Silicon nitride passive and active photonic integrated circuits: trends and prospects. *Photonics Res.* **10**, A82–A96 (2022).
5. Bohren, C. F. Light scattering by an optically active sphere. *Chem. Phys. Lett.* **29**, 458–462 (1974).
6. Golat, S. *et al.* Optical chiral sorting forces and their manifestation in evanescent waves and nanofibres. Preprint at https://doi.org/10.48550/arXiv.2310.11272 (2023).
7. Martínez-Romeu, J., Diez, I., Golat, S., Rodríguez-Fortuño, F. J. & Martínez, A. Chiral forces in longitudinally invariant dielectric photonic waveguides. *Photonics Res.* **12**, 431 (2024).

Surface Lattice Resonance for Enhanced Magnetoplasmonic Activity

Terunori Kaihara[1*], Pablo Rodriguez-Suarez[1], and Paolo Vavassori[1,2]

[1]CIC nanoGUNE BRTA, Donostia–San Sebastian 20018, Spain
[2] IKERBASQUE, Basque Foundation for Science, Bilbao 48013, Spain
[*]corresponding author: t.kaihara@nanogune.eu

Abstract: We investigate the magneto-optical effect enhancement in magnetoplasmonic metacrystals. Utilizing surface lattice resonance in periodic arrangements and noble/ferromagnetic metal hybridization, we achieve a ~4-fold enhancement over film counterparts without the need for correction by the fill factor. This underscores the importance of far-field coupling via surface lattice modes.

Magneto-optical (MO) effects are widely used in magnetic/spin detection/characterization, magnetic storage, and optical telecommunications technologies, extending their active areas from X-rays to THz in the wavelength domain and down to subpicoseconds in the time domain.[1] The enhancement of MO effects by magnetoplasmonics is of great interest for active nanophotonics, sensing, magnetic/spintronic dynamics, etc.[2] The MO enhancement in a magnetoplasmonic nanocavity is based on the fact that the orthogonal polarization resulting from spin-orbit interactions under spin polarization undergoes dual plasmon resonances, where the electric field of the incident polarization is amplified by the quality factor Q at the localized plasmon resonance (LPR) and again amplified by Q at the LPR in the orthogonal direction[3] though this Q^2 enhancement is limited to Q by the presence of the Q-fold initial polarization unless simultaneous control of both polarizations is implemented.[4] To make the best of the Q-factor, the hybridization of noble and ferromagnetic metals has often been employed. In addition, when a ferromagnetic film in contact with a noble metal becomes as thin as a few monolayers, the film exhibits perpendicular magnetic anisotropy (PMA) that makes the magnetic active control of the polarization easier.[5] In this work, we demonstrate an enhancement of the Polar MO Kerr (PMOKE) effect in periodic magnetoplasmonic nanodisk arrays consisting of noble and ferromagnetic metal multilayers that outperforms its film counterpart in the MO activity (MOA) with a high Q factor.

Figure 1(a) shows a schematic of a layered Au/Co disk array. The disk is composed of N alternating layers of 3 nm Au and 1 nm Co and is arrayed in a square lattice with a period of P on a glass substrate. In such a periodic arrangement, a surface lattice resonance (SLR) occurs, which is a Fano resonance between an LPR of each disk and a diffracted incident light to the surface mode and is characterized by intense sharp peaks in the reflectance spectra (see Fig. 1(b)). Since the LPR can only couple with the diffracted waves in its transverse direction, for x-polarized light incidence in the figure, the SLR arises depending on the array pitch in the y-direction. Under magnetization in the z-direction, the MO-induced LPR in the y-direction also exhibits the SLR depending on the pitch in the x-direction.[6] Figure 1(b) shows the reflectance spectra of the disk arrays of different diameters with P=500 nm and N=7. The comparison of the periodic and random arrays of D=180 nm demonstrates a strong amplification in resonance due to the SLR at a wavelength of λ = 750 nm. The MOA for D=180 nm exceeds the film counterpart by a factor of ~4 at the maximum at λ=900 nm as a result of the SLR in Fig. 1(c) even without taking the fill factor into account. From an application point of view, a figure of merit can be defined as FoM = reflectance × MOA as seen in Fig. 1(d). Although the reflectance of the film sample is as high as ~80% close to a pure Au film (~98%) thanks to the high Au content, the FoM for D=180 nm at λ=900 nm is comparably large with a much higher Q factor, which cannot be achievable without the SLR.

As has been seen, a Au/Co multilayered system with PMA and SLR can be a promising building block for high-performance magnetoplasmonic metacrystals and sensing applications. We would also like to discuss the arbitrary control of SLR by introducing angled incidence and sublattices,[7,8] and the lattice effect between multipolar plasmon modes in ring/disk nanocavities.

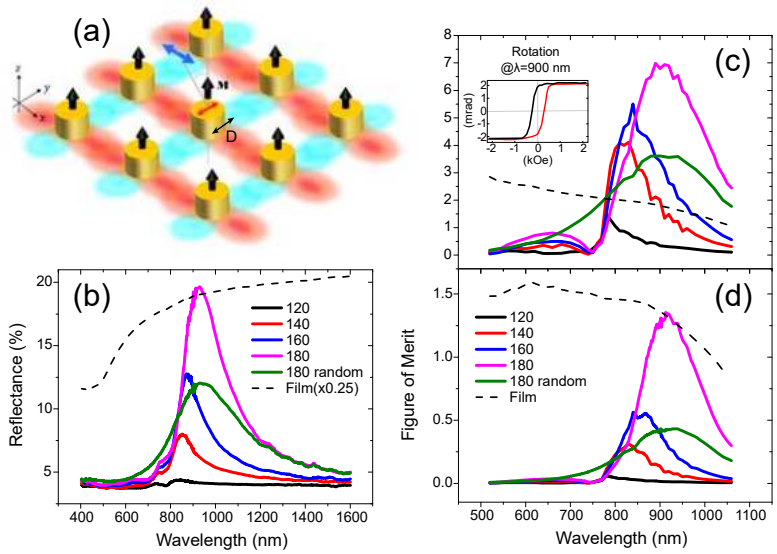


Figure 1. (a) A sketch of the Au/Co periodic multilayer array under study. (b)-(d) Experimentally observed reflectance, magneto-optical activity, and their figure of merit, respectively, measured in an index-matching liquid at normal incidence. The sample has P=500 nm, N=7, and diameters D given in the legend (nm). The inset in (c) is a representative hysteresis loop of the PMOKE rotation.

The authors acknowledge support from the Spanish Ministry of Science, Innovation and Universities under the Maria de Maeztu Units of Excellence Programme (grant n. CEX2020-001038-M) and the Spanish Ministry of Science and Innovation via the project n. PID2021-123943NB-I00 (MCIN/FEDER). T.K. acknowledges support via the European Union's Horizon 2020 Research and Innovation Programme under the Marie Słodowska-Curie Grant Agreement n. 101029928 (MANACOLIPO).

References

1. Kimel, A. *et al.* The 2022 magneto-optics roadmap. *J. Phys. D. Appl. Phys.* **55**, 463003 (2022).
2. Maccaferri, N. *et al.* Magnetoplasmonics in confined geometries: Current challenges and future opportunities. *Appl. Phys. Lett.* **122**, 120502 (2023).
3. Maccaferri, N. *et al.* Tuning the Magneto-Optical Response of Nanosize Ferromagnetic Ni Disks Using the Phase of Localized Plasmons. *Phys. Rev. Lett.* **111**, 167401 (2013).
4. López-Ortega, A. *et al.* Enhanced magnetic modulation of light polarization exploiting hybridization with multipolar dark plasmons in magnetoplasmonic nanocavities. *Light Sci. Appl.* **9**, 49 (2020).
5. Freire-Fernández, F., Mansell, R. & van Dijken, S. Magnetoplasmonic properties of perpendicularly magnetized $[Co/Pt]_N$ nanodots Francisco. *Phys. Rev. B* **101**, 054416 (2020).
6. Maccaferri, N. *et al.* Anisotropic Nanoantenna-Based Magnetoplasmonic Crystals for Highly Enhanced and Tunable Magneto-Optical Activity. *Nano Lett.* **16**, 2533–2542 (2016).
7. Baur, S., Sanders, S. & Manjavacas, A. Hybridization of Lattice Resonances. *ACS Nano* **12**, 1618–1629 (2018).
8. Zundel, L., May, A. & Manjavacas, A. Lattice Resonances Induced by Periodic Vacancies in Arrays of Nanoparticles. *ACS Photonics* **8**, 360–368 (2021).

Correlation-enhanced interaction of a Bose–Einstein condensate with parametric magnon pairs and virtual magnons

A. A. Serga[1*]

[1]Fachbereich Physik and Landesforschungszentrum OPTIMAS,
Rheinland-Pfälzische Technische Universität Kaiserslautern-Landau, 67663 Kaiserslautern, Germany
[*]corresponding author: serha@rptu.de

Abstract: Nonlinear interactions in a magnetic medium excited by parametric pumping lead to Bose–Einstein condensation of spin-wave quanta—magnons. Using Brillouin light scattering spectroscopy, we have discovered a correlation-enhanced four-wave interaction process of the magnon condensate with fully correlated parametric magnon pairs, which results in off-resonant spin-wave excitations—virtual magnons.

Nonlinear wave interactions govern the behavior of various systems in nature. In the field of magnetism, the use of nonlinear phenomena opens promising prospects for applications of magnonics and spintronics in neuro-morphic computing, microwave data processing, and nanoscale wave logic circuits [1–3].

Traditionally, nonlinear-wave interactions are investigated via observation of real quasiparticles—quanta of freely propagating waves, i.e., eigenmodes of the nonlinear medium. In our experiments with highly populated magnon gases in ferromagnetic yttrium iron garnet (YIG) films probed by means of Brillouin light scattering (BLS) spectroscopy (see Fig. 1), we found several types of virtual magnons—quanta of off-resonant spin waves—driven by real magnons through the appropriate nonlinearity [4, 5]. These virtual magnons appear upon parametric pumping (this process is shown by orange arrows in Fig. 1) with the participation of a Bose–Einstein condensate (BEC) [5, 6] formed at the bottom of the spin-wave spectrum.

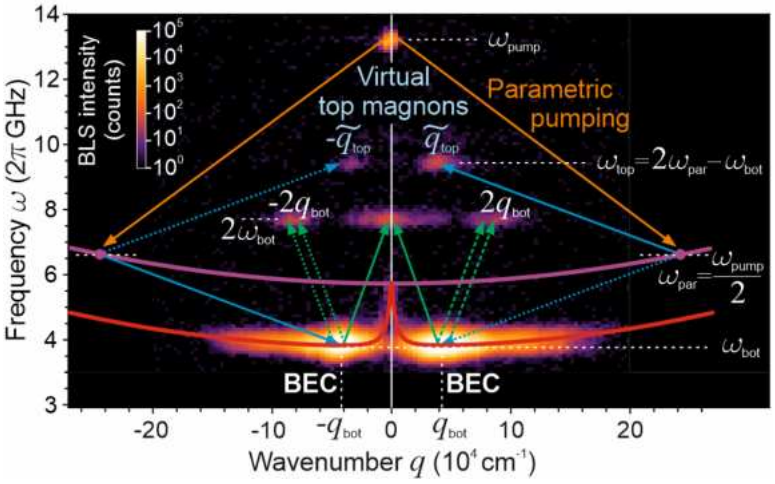


Figure 1: BLS intensity spectra of real and virtual magnons. The spectra were measured during the action of microwave pumping in the 6.7 μm-thick yttrium iron garnet (YIG, $Y_3Fe_5O_{12}$) film tangentially magnetized by the field of 1350 Oe. The experimental intensity spectra are shown together with the calculated magnon dispersion curves and diagrams representing the relevant quasiparticle scattering processes.

Some excitations outside the spin-wave dispersion range arise from the confluence of BEC magnons, as shown by the pairs of green arrows in Fig. 1. Others, named here as "virtual top magnons," are generated through four-magnon scattering processes involving the magnon condensate and parametric magnons (see the pairs of blue arrows). Theory shows that these scattering processes are correlation-enhanced due to the coherence of

parametrically generated magnon pairs, which have opposite wave vectors and fully correlated phases [7], and the coherence of BECs. This process is a classical analog of quantum mechanical correlation-enhanced scattering.

The study of interactions between virtual and real quasi-particles, both in the classical and quantum limits, is useful for their application in new information transfer and data processing technologies, including quantum magnonics and coherent quantum optics [8–12].

This research was funded by the Deutsche Forschungsgemeinschaft (DFG, German Research Foundation) within the Transregional Collaborative Research Center – TRR 173 – 268565370 “Spin+X” (project B04), by Grant No. ECCS-2138236 from the National Science Foundation of the United States, and by NSF-BSF Grant No. 2020765.

References

1. Pirro, P., V. I. Vasyuchka, A. A. Serga and B. Hillebrands, “Advances in coherent magnonics,” Nat. Rev. Mater., Vol. 6, 1114–1135, 2021.
2. Wang, Q., M. Kewenig, M. Schneider, R. Verba, F. Kohl, B. Heinz, M. Geilen, M. Mohseni, B. Lägel, F. Ciubotaru, C. Adelmann, C. Dubs, S. D. Cotofana, O. V. Dobrovolskiy, T. Brächer, P. Pirro and A. V. Chumak, “A magnonic directional coupler for integrated magnonic half-adders,” Nat. Electron., Vol. 3, No. , 765–774, 2020.
3. Koerner, C., R. Dreyer, M. Wagener, N. Liebing, H. G. Bauer and G. Woltersdorf, “Frequency multiplication by collective nanoscale spin-wave dynamics,” Science, Vol. 375, No. 6585, 1165–1169, 2022.
4. L’vov, V. S., A. Pomyalov, D. A. Bozhko, B. Hillebrands and A. A. Serga, “Correlation-enhanced interaction of a Bose–Einstein condensate with parametrically generated magnon pairs and virtual magnons,” Phys. Rev. Lett., Vol. 131, No. 15, 156705, 2023.
5. L’vov, V. S., A. Pomyalov, S. V. Nazarenko, D. A. Bozhko, A. J. E. Kreil, B. Hillebrands and A. A. Serga, “Bose–Einstein condensation in systems with flux equilibrium,” Phys. Rev. B, Vol. 109, No. 1, 014301, 2024.
6. Demokritov, S. O., V. E. Demidov, O. Dzyapko, G. A. Melkov, A. A. Serga, B. Hillebrands and A. N. Slavin, “Bose–Einstein condensation of quasi-equilibrium magnons at room temperature under pumping,” Nature, Vol. 443, No. 7110, 430–433, 2006.
7. Melkov, G. A., A. A. Serga, A. N. Slavin, V. S. Tiberkevich, A. N. Oleinik and A. V. Bagada, “Parametric interaction of magnetostatic waves with a nonstationary local pump,” J. Exp. Theor. Phys., Vol. 89, No. 6, 1189–1199, 1999.
8. Fukami, M., D. R. Candido, D. D. Awschalom and M. E. Flatté, “Opportunities for long-range magnon-mediated entanglement of spin qubits via on- and off-resonant coupling,” PRX Quantum, Vol. 2, No. 4, 040314, 2021.
9. Hetényi, B., A. Mook, J. Klinovaja and D. Loss, “Long-distance coupling of spin qubits via topological magnons,” Phys. Rev. B, Vol. 106, No. 23, 235409, 2022.
10. Silaev, M. “Ultrastrong magnon-photon coupling, squeezed vacuum, and entanglement in superconductor/ferromagnet nanostructures,” Phys. Rev. B, Vol. 107, No. 18, L180503, 2023.
11. Bailey, J., P. Sukhachov, K. Baumgaertl, S. Finizio, S. Wintz, C. Dubs, J. Raabe, D. Grundler, A. Balatsky and G. Aeppli, “Multi-band Bose–Einstein condensate at four-particle scattering resonance,” arXiv:2201.11043.
12. Bozhko, D. A., A. J. E. Kreil, H. Yu. Musiienko-Shmarova, A. A. Serga, A. Pomyalov, V. S. L'vov and B. Hillebrands, “Bogoliubov waves and distant transport of magnon condensate at room temperature,” Nat. Commun., Vol. 10, No. 1, 2460, 2019.

Chirality in optical manipulation via electronically resonant light-matter interactions

H. Ishihara

Department of Materials Engineering Science, Osaka University, Japan
*corresponding author: ishi@mp.es.osaka-u.ac.jp

Abstract: Particles ranging in size from the atomic scale to the micro scale can be mechanically manipulated by optical forces. This presentation delves into the effects of light-matter chiral interaction that appear in the optical force phenomena, which are discussed based on the electronically resonant linear and nonlinear optical response.

Photons carry momentum, and consequently, they exert force on matter systems when scattered or absorbed. This phenomenon serves as a mechanism for mechanically manipulating small materials ranging in size from the atomic scale to the micro scale. Optical manipulation of nanostructures poses particular challenges due to the extremely weak optical forces involved, in comparison to those acting on micro-particles, and the complex interactions with environmental materials such as solvents. Promising strategies involve the utilization of strongly localized and enhanced light electric fields resulting from localized surface plasmon resonance (LSPR) [1] and/or electronic resonance effects [2]. We have proposed the latter approaches employing both linear optical response [3] and nonlinear response [4], enabling not only the enhancement of force but also the selective manipulation based on the quantum mechanical characteristics of individual particles [5], along with the development of novel spectroscopies utilizing optical forces [6]. This presentation discusses following topics related to light-matter chiral interactions in resonance optical force phenomena.

< 1 > Peculiar physical effects arise when either light, targeted materials, or both exhibit chirality. Various schemes for chiral selective optical manipulations have been proposed [7]. However, studies based on the microscopic geometrical structures of targeted materials have been lacking. We have theoretically proposed chiral selective optical manipulation by utilizing resonant electronic resonance [8]. In this study, we calculated the chiral selective optical force exerted by circularly polarized light using a microscopic model of dimer molecules, specifically Tröger's base porphyrin, without resorting to any phenomenological parameters to represent chirality. We discussed the dynamics of molecules manipulated by counter-propagating beams to assess the feasibility of single molecular chiral selection. Recently, we have expanded these investigations to include chiral selective trapping of typical chiral molecules by LSPR [9]. In this work, calculations of optical force based on molecular electronic states obtained through first-principles calculations have revealed a variety of degrees of freedom for trapping single molecules, depending on the orientation of molecules and the sites of metallic structures sustaining LSPR.

< 2 > An optical vortex is known as a beam possessing orbital angular momentum, giving rise to rotational motion of particles. We have theoretically proposed some unique trapping mechanisms using optical vortices. For instance, the chiral formation of trapped nanoparticles can be achieved by employing counter-propagating optical vortices [10]. Furthermore, the resonant nonlinear response induced by optical vortices plays interesting roles in the formation of nanoparticles. As we proposed in Ref. [4], resonant nonlinearity can generate a stimulated recoil force, which acts as a negative dissipative force, pulling particles towards the light source. By

exploiting this mechanism, we can alter the direction of particle motion by pumping the excited states. Building upon this concept, we have suggested a super-resolution trapping method resembling stimulated emission depletion microscopy (STED) by combining Gaussian beams with vortex beams [11]. Moreover, it is noteworthy that by pumping rotating particles, the direction of rotation can be switched [12]. This implies that direction switching can occur not only for linear motion but also for rotational motion through induced stimulated emission. In this presentation, we will propose a theoretical scheme to achieve the switching of rotational direction using stimulated recoil force induced by optical vortices.

References

1. Y. Zhang et al., ***Light: Science & Applications*** **10**, 59 (2021).
2. H. Ishihara, ***Advances in Physics: X***, **6**, 1885991 (2021)
3. T. Iida and H. Ishihara, ***Phys. Rev. Lett***. **90**, 057403 (2003)
4. T. Kudo and H. Ishihara, ***Phys. Rev. Lett.*** **109**, 087402 (2012)
5. H. Fujiwara, et al., ***Sci Adv***. **7**:eabd9551 (2021)
6. T. Wada and H. Ishihara, ***Opt. Exp***. **30**, 17490 (2022)
7. A. Kakkanattu, et al., ***Opt. Exp***. **29**, 12543 (2021)
8. T. Horai, et al., ***Opt. Exp.*** **29**, 38824 (2021)
9. H. Yamane, et al., ***Opt. Exp.*** **31**, 13708 (2023)
10. T. Iida, T. Yoshimizu and H. Ishihara, ***phys. stat. sol***. (c) **6**, 69 (2009)
11. M. Hoshina, et al., ***ACS Photon***. **5**, 318 (2018)
12. M. Hoshina, N. Yokoshi and H. Ishihara, ***Opt. Exp***. **28**, 14980 (2020)

Twisted Cavity Resonators of Anyon Rotational Symmetry with Bulk Modes of Non-Zero Helicity

J. F. Bourhill[1], E. C. I. Paterson [1] , M. Goryachev and M. E. Tobar[1*]

[1]Quantum Technologies and Dark Matter Labs, Department of Physics, University of Western Australia, 35 Stirling Hwy, 6009 Crawley, Western Australia.
[*]corresponding author: michael.tobar@uwa.edu.au

Abstract: We present a new type of resonator through the formation of twisted hollow structures, which leads to the realization of a cavity with anyon rotational symmetry, and allows the existence of bulk resonant modes with non-zero electromagnetic helicity in vacuo. By constructing a stabilized oscillator from the resonator, we show that the modes couple to ultra-light dark matter axions by adding amplitude-modulated sidebands through the axion-photon chiral anomaly. This removes the typical requirement for an external magnetic field and therefore permits the use of superconducting materials to reduce surface losses and enhance sensitivity to axions.

Chirality is a fundamental property present in many physical systems, which exhibit asymmetry, ranging from particle physics, topological and quantum systems, complex molecules, and chiroptical phenomena. Many such systems that couple to electromagnetism occur as surface states, at high energy or frequency, or due to complex meta-structures or plasmonic systems, which inevitably add loss. In this work, we realize a new class of electromagnetic resonator, which we call the "anyon cavity resonator", based on twisted waveguide and "Möbius-like" structures [1]. Resonators based on Möbius strips have been shown to exhibit fermion rotational symmetry with respect to ring resonator with no twist, which in contrast exhibits boson rotational symmetry [2]. Here, our new type of resonators exhibits anyon rotational symmetry, realized through the formation of twisted hollow structures, optimized with an equilateral triangular cross-section (Fig. 1). Unlike other cavity resonators, resonant bulk modes reveal non-zero helicity [3-5], through a photonic magneto-electric coupling in vacuo. The normalized helicity in (1) can range between -1 and 1 and is tied to the conservation of Zilch [3], or photonic chirality [7] and is usually considered when photons interact with chiral molecules or materials. Here, $\mathbf{E}_p$ and $\mathbf{B}_p$ are the resonant modes electric and magnetic vector phasor amplitudes. Analogously, the axion is calculated to couple to photons through a chiral anomaly, whether in condensed matter physics or in quantum chromodynamics (QCD) and the introduction of the axion as a modification to Maxwell's equations introduces a non-zero Zilch to the equations of motion [1].

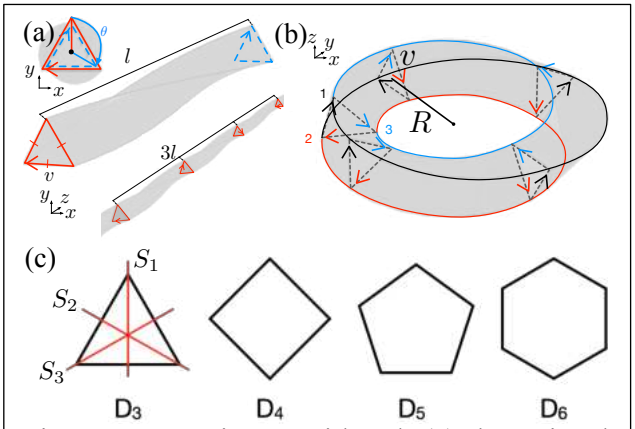


Fig 1. Geometries considered; (a) the twisted triangular waveguide resonator and (b) the triangular Möbius-like ring resonator. (c) The dihedral group of regular convex polygons, D_n, which have 2n symmetries, n rotational and n reflection.

$$\mathscr{H}_p = \frac{2\,\mathrm{Im}[\int \mathbf{E}_p(\vec{r}) \cdot \mathbf{B}_p^*(\vec{r})\ d\tau]}{\sqrt{\int \mathbf{E}_p(\vec{r}) \cdot \mathbf{E}_p^*(\vec{r})\ d\tau \int \mathbf{B}_p(\vec{r}) \cdot \mathbf{B}_p^*(\vec{r})\ d\tau}} \tag{1}$$

We show that the square of the magnitude of the helicity is equivalent to the form factor that couples low-mass axions to photons as an amplitude modulation of a single mode through a parametric interaction. Thus, we show the first sensitive ultra-light laboratory axion dark matter experiment through photon coupling may be realized by implementing such a resonator in an ultra-stable oscillator configuration and searching for signals in the Fourier spectrum of amplitude fluctuations. This removes the typical requirement for an external magnetic field and therefore permits the use of high-Q superconducting materials to reduce surface losses and enhance sensitivity to axions.

Acknowledgements

This work was funded by the Australian Research Council Centre of Excellence for Engineered Quantum Systems, CE170100009 and the Centre of Excellence for Dark Matter Particle Physics, CE200100008.

References

1. Bourhill, J. F., E. C. I. Paterson, M. Goryachev and M. E. Tobar, "Searching for ultralight axions with twisted cavity resonators of anyon rotational symmetry with bulk modes of nonzero helicity," PRD, 108:052014, 2023.
2. Ballon, D. J., H. U. Voss, "Classical Möbius-Ring Resonators Exhibit Fermion-Boson Rotational Symmetry," PRL, 101:247701, 2008.
3. Cameron, R. P., S. M. Barnett, A. M. Yao, "Optical helicity, optical spin and related quantities in electromagnetic theory," New Journal of Physics, 14(5):053050, 2012.
4. Bliokh, K. Y., A. Y. Bekshaev, F. Nori, "Dual electromagnetism: helicity, spin, momentum and angular momentum," New Journal of Physics, 15(3):033026, 2013.
5. Bliokh, K.Y., Y. S. Kivshar, F. Nori, "Magnetoelectric Effects in Local Light-Matter Interactions," PRL, 113:033601, Jul 2014.
6. Lipkin, D. M., "Existence of a New Conservation Law in Electromagnetic Theory," Journal of Mathematical Physics, 5(5):696–700, 1964.

Polarization in inhomogeneous crystals and its relationship to quadrupole moments

Nobuhiro Arai[1], Yang Gao[2], Di Xiao[3,4], Shuichi Murakami[1*]

[1] Department of Physics, Tokyo Institute of Technology, Ookayama, Meguro-ku, Tokyo 152-8551, Japan
[2] University of Science and Technology of China, Hefei, Anhui 230026, China
[3] Department of Materials Science & Engineering, University of Washington, Seattle WA 98915
[4] Department of Physics, University of Washington, Seattle WA 98915University of Science and Technology of China, Hefei, Anhui 230026, China
[*] corresponding author: murakami@stat.phys.titech.ac.jp

Abstract: We revisit the problem of a definition of the electric quadrupole moment as a bulk quantity. We calculate the polarization for inhomogeneous crystals, from which we derive the formula for the electric quadrupole moment. We show that the resulting formula cannot possess the property of bulk-boundary correspondence, i.e. it is not related to the quadrupole moment of a finite-sized crystal, but it is rather a hidden physical quantity which is manifest only when the crystal has inhomogeneity. Crystals under uniform electric or magnetic fields can be regarded as such example where the Hamiltonian is position dependent, and show that our result completely agree with previous works in such cases

The quantum formula of electric quadrupole moments has been previously discussed in previous literatures[1,2]. Nonetheless, unlike the quantum formula of polarization, which has been formulated as the modern theory of polarization, the definition of the electric quadrupole moment in crystals is still elusive. We revisit this problem by means of linear response theory[3]. We focus on an inhomogeneous crystal where the inhomogeneity is given by a perturbation linear in position. We calculate its polarization, and found that it consists of two contributions, one is due to the change of the local Hamiltonian, and the other is due to spatial inhomogeneity. The latter one should be related to the bulk quadrupole moment, since spatial variation of the quadrupole moment leads to polarization. We compare our results with the similar work[2] by the semiclassical theory. We also discuss the relationship with Ref. 1 where the quadrupole moment is calculated as a linear response to the spatial gradient of the electric field.

Y.G. acknowledges the support of the 363 Fundamental Research Funds for the Central Universities, 364 China (Grant No. WK2340000102). D.X. is supported by DOE Award No. DE-SC0012509. S. M is supported by JSPS KAKENHI Grant Numbers JP22K18687 and JP22H00108.

References

1. Daido, A., Shidade, A. and Yanase, A. Phys. Rev. B 102, 235149 (2020).
2. Zhao, Y., Gao, Y. and D. Xiao, Phys. Rev. B 104, 144203 (2021).
3. Arai, N., Y. Gao, D. Xiao, and S. Murakami, in preparation (2024).

Ultracompact, controllable circular polarization laser based on chiral metamaterials

I. Katsantonis[1,2], A. Tasolamprou[1,3], Th. Koschny[4], and M. Kafesaki[1,2*]

[1]Institute of Electronic Structure and Laser, Foundation for Research and Technology Hellas (FORTH), Heraklion, Crete, Greece
[2]Dept. of Materials Science and Technology, Univ. of Crete, Greece
[3]Dept. of Physics, National and Kapodistrian University of Athens, Athens, Greece
[4]Ames Lab and Dept. of Physics and Astronomy, Iowa State University, Ames, Iowa, US
[*]corresponding author: kafesaki@iesl.forth.gr

Abstract: We demonstrate (theoretically) an ultracompact lasing structure formed by combining a bi-isotropic chiral metamaterial with a gain medium. The structure provides dynamically controllable polarization emission, ranging from left-handed circularly polarized (CP) to right-handed CP. The dynamic polarization control is achieved by changing the polarization of a linearly polarized pump wave.

Circularly polarized emission lasers constitute a topic of increasing interest in recent years, due to their involvement and high potential impact in many different phenomena and applications. These range from sensing and spectroscopy, in particular molecular chirality sensing, chemistry and biophysics to even quantum optics [1-4].

The most obvious way to achieve a circularly polarized emission laser is to combine a gain material with a chiral response. Chiral metamaterials, due to their huge chiral response (compared to natural chiral materials), constitute one of the most promising choices for the chiral response [5-6]. Indeed, recent studies demonstrated promising ultra-compact elliptically polarizing lasing configurations. Their relevant structures though were not able to give pure circularly polarized laser light, and even more importantly, could not provide a controllable polarization response.

The present study aims to remedy both those inefficiencies. In particular, we demonstrate here, through detailed numerical simulations, a bi-isotropic chiral metasurface structure able to provide almost pure circularly polarized emission lasing, being in parallel dynamically tunable through the pump-wave polarization [8]. Changing the linearly polarized pump wave polarization the laser emission can be transformed from almost pure left-handed circularly polarized to right-handed. Besides, the laser polarization can be also engineerable through the structure geometry [8].

Our proposed structure is formed from pairs of mutually twisted metallic crosses embedded in a gain-bearing dielectric host (of thickness 100 nm). The structure design is shown in Fig. 1(a). Fig. 1(b) demonstrates the lasing emission for two different structure geometries. The emission is maximized when the gain material resonance overlaps with the magnetic resonance of the structure, at ~207 GHz.

Our structure and results demonstrate the possibility to achieve ultra-compact and controllable circularly polarized emission lasing structures employing chiral metamaterials and metasurfaces. Such a possibility can open a great prospect in all applications based or affected by the chiral light-matter interactions.

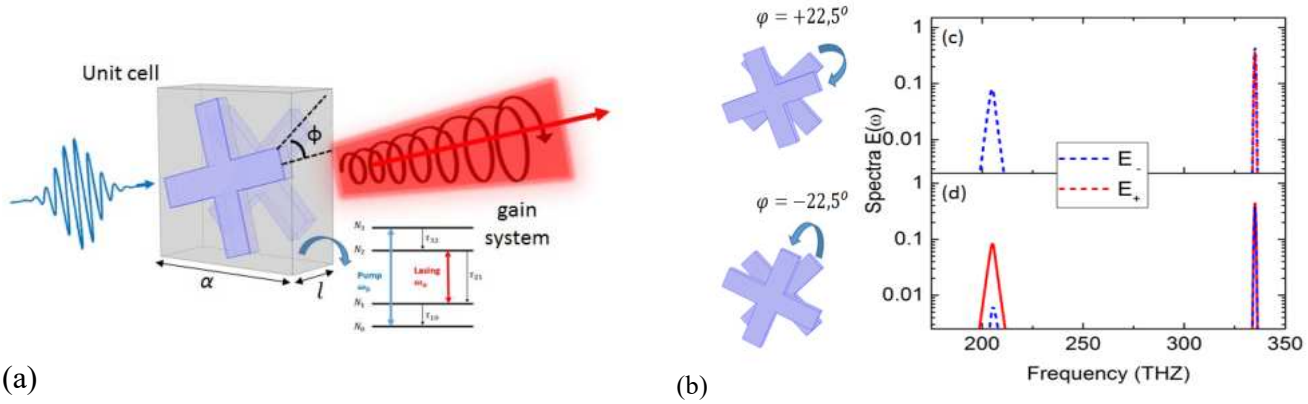


Figure 1: (a) The unit cell of the proposed structure: A pair of mutually twisted metallic crosses, embedded in a dielectric medium dopped with a gain material (dye molecules). The gain material is modelled as a 4-level atomic system [7], as shown also in the figure. The unit cell lateral size is α=300 nm and the thickness l=100 nm. (b) The spectral response of the structure for two opposite values of the twist angle, φ. The pump field (E) at ~330 THz is linearly polarized, while the output (laser) field is either left-handed circularly polarized (E_-; top case) or right-handed (E_+; bottom case).

Acknowledgments: The work is supported by the EU Project CHARTIST

References

1. T. J. Wenzel, Prasad I. Polavarapu (ed.), "Chiral analysis: advances in spectroscopy, chromatography, and emerging methods", 2nd ed, Analytical and bioanalytical chemistry, Vol. 410, 7261, 2018.
2. R. Naaman, Y. Paltiel, and D. H. Waldeck, "Chiral induced spin selectivity and its implications for biological functions", Annual Review of Biophysics, Vol. 51, 99, 2022.
3. I. Thanopoulos, E. Paspalakis, and Z. Kis, "Laser-driven coherent manipulation of molecular chirality", Chemical Physical Review, Vol. 390, 228, 2004.
4. H. Hubener, U. De Giovannini, C. Sch¨afer, J. Andberger, M. Ruggenthaler, J. Faist, and A. Rubio, "Engineering quantum materials with chiral optical cavities", Nature Materials, Vol. 20, 438, 2021.
5. K. Konishi, M. Nomura, N. Kumagai, S. Iwamoto, Y. Arakawa, M. Kuwata-Gonokami, "Circularly Polarized Light Emission from Semiconductor Planar Chiral Nanostructures". Phys. Rev. Lett., Vol. 106, 057402, 2011.
6. X. Zhang, Y. Liu, J. Han, Y. Kivshar, Q. Song, "Chiral emission from resonant metasurfaces". Science, Vol. 377, 1215, 2022.
7. A. Fang, T. Koschny, and C. M. Soukoulis, "Lasing in metamaterial nanostructures", Journal of Optics A: Pure and Applied Optics, Vol. 12, 024013, 2010.
8. I. Katsantonis, A. Tasolamprou, E.N. Economou, Th. Koschny, and M. Kafesaki, "Dynamically controllable circularly polarized emission lasing based on chiral metasurfaces", in preparation.

Thermal Hall effect from chiral magnon-magnon many-body scattering

D. Chatzichrysafis[1], **A. Mook**[1*]

[1]Johannes Gutenberg University Mainz, Germany
[*]corresponding author: amook@uni-mainz.de

Abstract: We present a theory of thermal Hall transport caused by magnon-magnon skew scattering. In field-polarized chiral magnets, the Dzyaloshinskii-Moriya interaction causes three-magnon scattering, which interferes with four-magnon scattering to break the microscopic detailed balance. The resulting skew scattering produces a thermal Hall conductivity even without a magnon Berry curvature.

The thermal Hall effect has emerged as a promising probe of charge-neutral collective excitations in insulating materials. It is well known that quasiparticles such as phonons, magnons and other magnetic excitations can contribute to the thermal Hall conductivity. Typical microscopic mechanisms are scattering [1] and the intrinsic Berry curvature of quasiparticles, which leads to an anomalous velocity [2,3]. There also is increasing evidence that many-body scattering between quasiparticles must be taken into account for quantitative modeling of heat transport [4], since predictions based on the harmonic (non-interacting) theory are not supported by experimental data [5].

We consider a chiral magnet with Dzyaloshinskii-Moriya interaction (DMI) on the square lattice. In the field-polarized phase, i.e. in a magnetic field strong enough to overcome the formation of spin spirals, there is only a single magnon band and hence the magnon Berry curvature is zero. We perform a nonlinear spin wave theory and truncate it beyond four-magnon scattering. The DMI gives rise to three-magnon interactions that break the time-reversal symmetry and a thermal Hall effect can be expected. We evaluate the thermal Hall conductivity within a semiclassical transport theory and show that it is related to a broken microscopic detailed balance of the scattering events in the collision integral, as it appears due to the interference between three- and four-magnon scattering. We evaluate the longitudinal and transverse thermal conductivities and discuss how they change as a function of temperature and magnetic field. We find Hall angles on the order of 10^{-3}, a typical value showing that many-body scattering can be as important as other contributions to thermal Hall transport.

This work was funded by the Deutsche Forschungsgemeinschaft (DFG, German Research Foundation) -- Project No. 504261060 (Emmy Noether Programme).

References

1. Strohm, C., G. L. J. A. Rikken, and P. Wyder, “Phenomenological Evidence for the Phonon Hall Effect”, Phys. Rev. Lett. 95, 155901, 2005.
2. Katsura, H., N. Nagaosa, and Patrick A. Lee, “Theory of the Thermal Hall Effect in Quantum Magnets”, Phys. Rev. Lett. 104, 066403, 2010.
3. Matsumoto, R., and S. Murakami, “Theoretical Prediction of a Rotating Magnon Wave Packet in Ferromagnets”, Phys. Rev. Lett. 106, 197202, 2011
4. Mangeolle, L., L. Balents, and L. Savary, “Phonon Thermal Hall Conductivity from Scattering with Collective Fluctuations”, Phys. Rev. X 12, 041031, 2022.

5. Suetsugu, S., T. Yokoi, K. Totsuka, T. Ono, I. Tanaka, S. Kasahara, Y. Kasahara, Z. Chengchao, H. Kageyama, and Y. Matsuda, “Intrinsic suppression of the topological thermal Hall effect in an exactly solvable quantum magnet”, Phys. Rev. B 105, 024415, 2022.

Giant electromagnetic nonreciprocity in magnetic epsilon-near-zero metamaterials

J. Qin[1], Y. Yang[1], S. Xia[1], L. Bi[1*]

[1]University of Electronic Science and Technology of China, China
[*]corresponding author: bilei@uestc.edu.cn

Abstract: Magnetic epsilon-near-zero (ENZ) metamaterials present unique advantages of improving the electromagnetic nonreciprocity. Here, we report our recent progress on nonreciprocal electromagnetic wave manipulations via magnetic ENZ metamaterials, demonstrating strong nonreciprocal thermal absorption using InAs ENZ films, and significantly enhanced Cotton-Mouton effect in magnetic zero-index metamaterials based on $Y_3Fe_5O_{12}$ photonic crystals.

Magneto-optical (MO) materials can break Lorentz reciprocity and play an important application for nonreciprocal photonics devices. However, conventional MO materials show weak MO response, limiting the performance of the photonics devices. At optical frequencies, the MO response of magnetic materials depends on the degree of asymmetry of the permittivity tensor, which can be characterized by $\gamma = |a/\varepsilon_c|$, where a and ε_c are the off-diagonal and diagonal components of the permittivity tensor. Previous works have mostly focused on how to enhance the a, with little effort carried out to reduce the ε_c. The electromagnetic nonreciprocity in these magnetic ENZ metamaterials remains elusive. In this work, we report our recent progress on nonreciprocal electromagnetic wave manipulations based on MO ENZ metamaterials. We first report the observed broadband nonreciprocal thermal absorption in InAs ENZ films. Then we report a zero-index metamaterial based on a $Y_3Fe_5O_{12}$ (YIG) photonic crystal, which exhibits significantly enhanced Cotton-Mouton effect and nonreciprocal phase shift.

Experimentally realizing strong infrared nonreciprocal absorption remains an open challenge, and existing proposals of nonreciprocal absorbers are restricted to a narrow working waveband. Here, we report that strong infrared nonreciprocal absorption can be realized around the ENZ frequency of InAs thin films with film thickness of only λ/40, owing to the excitation of asymmetric Berreman mode. The nonreciprocal bandwidths can be improved by adding dielectric gratings sitting on the InAs film and designing multilayer composed of gradient-doped InAs films, potentially useful in thermophotovoltaic devices. [1]

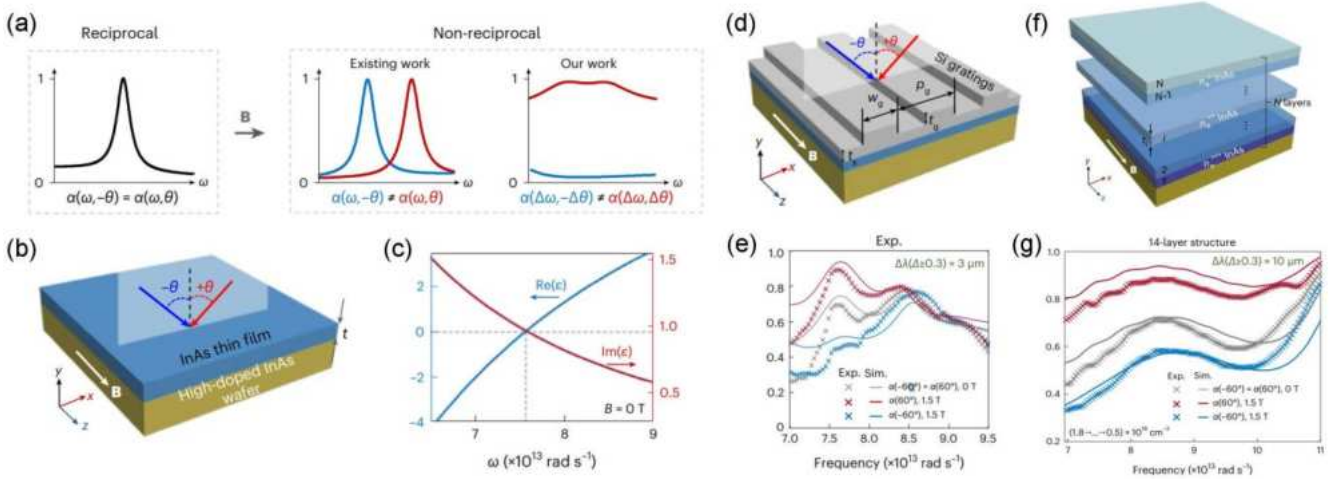


Fig. 1. Nonreciprocal thermal absorption based on MO ENZ materials. (a) Compared absorption spectra of reciprocal (left) and non-reciprocal (right two) absorbers. (b) Schematic of a single magnetized InAs thin film atop the reflective high-doped InAs substrate. (c)

Dielectric permittivity of the fabricated InAs film at B = 0 T. (d) Schematic of dielectric gratings on the previous single-layer structure. (e) Simulated angle-resolved non-reciprocal absorption spectra of the sample and the measured non-reciprocal spectra at θ = 60° and B = 1.5 T. (f) Schematic of a magnetized ENZ multilayer with gradient doping. (g) Measured and simulated asymmetric absorption spectra of the 14-layer sample at θ = 60°.

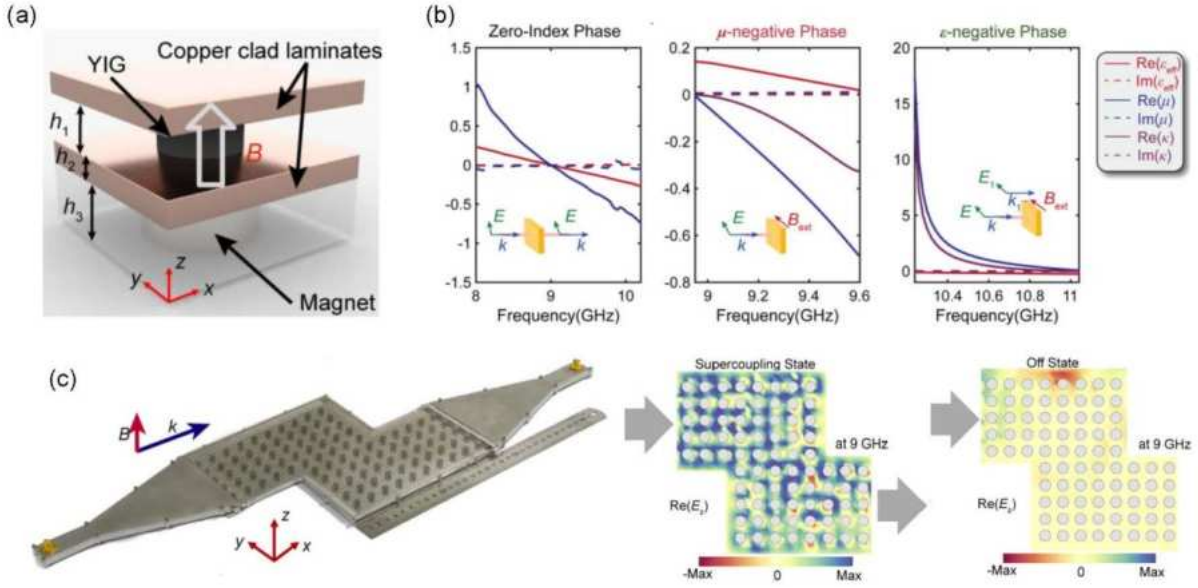


Fig. 2. Magnetically tunable zero-index metamaterial. (a) Schematic diagram of the active Dirac-like cone-based zero-index metamaterial. (b) Magnetic field-induced phase transition of active zero-index metamaterial. (c) Structure and characterization of a microwave switch based on active Dirac-like cone-based zero-index metamaterial.

Due to the large optical loss of InAs ENZ films, the materials are suitable only for reflection-based nonreciprocal systems. In a different work, we report a magnetic zero-index metamaterial (ZIM) based on low loss YIG photonic crystal, as shown in Fig. 2. The zero effective index is resulted from the Dirac-like cone dispersion formed by accidental degeneracy of two linear dispersion bands and a quadratic dispersion band. We observe significantly enhanced Cotton-Mouton effect and nonreciprocal phase shift in such metamaterials at the microwave frequency, realizing the magnetic field induced on-off switch of the supercoupling state. Based on this effect, we experimentally demonstrated a tunable microwave switch with a low intrinsic loss of 0.95 dB and a high extinction ratio of up to 30.63 dB at 9 GHz. [2] The ZIM metamaterials are attractive for applications such as compact nonreciprocal electromagnetic devices.

References

1. Liu, M. et al. “Broadband mid-infrared non-reciprocal absorption using magnetized gradient epsilon-near-zero thin films,” Nat. Mater., 22, 1196-1202, 2023.
2. Yang, Y. et al. “Magnetically tunable zero-index metamaterials,” Photon. Res., 11, 1613-1626, 2023.

Vorticity of Spin / Orbital Berry Curvature and Topological Charges in pseudo-nodal semimetals.

***Peter Schmitz[1], Dongwook Go[1,2] and Yuriy Mokrousov[1,2]**

[1] Peter Grünberg Institut 1, Forschungszentrum Jülich, 52425 Jülich, Germany
[2] Institute of Physics, Johannes Gutenberg University Mainz, 55099 Mainz, Germany
[*] peter.christian.schmitz@rwth-aachen.de

Abstract: We investigate the relationship between crossings in Spin-Orbital-texture and the Berry-curvature-flux, in terms of divergence and vorticity, on avoided-crossing-manifolds in the 3D-BZ of selected vdW-materials and TI/NI-superlattices. We identify hidden currents with topological charge and chirality in symmetry-subspaces, such as the inversion (anti)-symmetric states on adjacent sides of the interfaces.

While the topological classification of band structures has expanded rapidly, some of its foundations remained inconsistent: Could avoided crossings be the main sources of Berry curvature [1], rather than Dirac points ? Having a singularity at such, how do the textures of Spin/Orbital polarization translate to their Berry curvature counterpart ? And do these fields contain more than just scalar charges, possibly vorticity ?

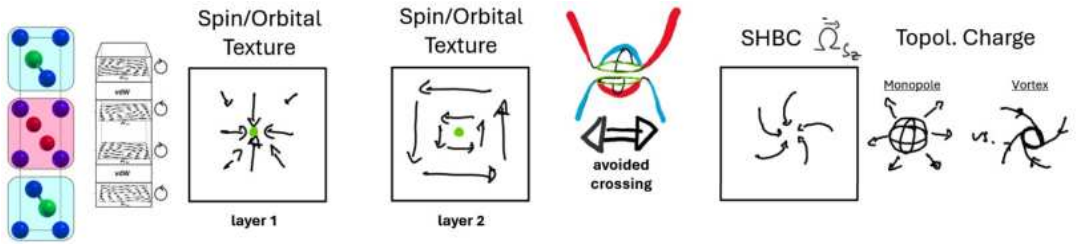


Figure 1. Left: Spin-Orbital texture. Middle: Band inversion from interface states. Right: BC texture and charges.

$$\Omega^{\mathrm{spin}\gamma}_{n,\alpha\beta}(\boldsymbol{k}) = \hbar^2 \sum_{m\neq n} \frac{-2\,\mathrm{Im}[\langle n\boldsymbol{k}|\frac{1}{2}\{\hat{\sigma}_\gamma, \hat{v}_\alpha\}|m\boldsymbol{k}\rangle\langle m\boldsymbol{k}|\hat{v}_\beta|n\boldsymbol{k}\rangle]}{(\epsilon_{n\boldsymbol{k}} - \epsilon_{m\boldsymbol{k}})^2 - (\hbar\omega + i\eta)^2} \qquad \text{(eq. 1)}$$

While the community has recognized Spin Weyl insulators (=3D Spin-Hall TIs) [2], in the broader study of pseudo-nodal line and -sphere semimetals [3] with segregated avoided crossing manifolds, it is necessary to employ Gauss+Stokes analysis of the fully vectorized BC around them and to account for the chiral spin texture with a modified gauge [4] of the perturbative spin current formula 1. As we pioneer such analysis for different materials, we observe via site-projection that hidden polarization textures and currents manifest in symmetry subspaces such as inversion (anti)symmetric bonds around vdW gaps, which can be understood as superposition of lower-dimensional semimetals, eg. Spin-Weyl states at the interfaces of TI+NI superlattices [5].

We acknowledge financial support by the DFG and FZ Jülich and computing resources from RWTH Aachen (CLAIX)

References

1. M.A. Wilde and C. Pfleiderer, “Large curvature near a small gap”, Nature Physics 18, 731–740 (2022)
2. R. González-Hernández and B. Uribe, “Spin Weyl Topological Insulators”, PRB, 109, 045126 (2024)
3. J. Wang, .. , W. Duan, F. Liu and B. Huang, “Pseudo Dirac nodal sphere semimetal”, PRB **98**, 201112 (2018)
4. F. Pientka, .., I. Mertig and B. L. Gyorffy, “Gauge Freedom for degenerate Bloch states”, PRB 86, 054413 (2012)
5. A.A. Burkov and L. Balents, “Weyl Semimetal in a Topological Insulator Multilayer”, PRL **107**, 127205 (2011)

Photoacoustic spectroscopy and polarimetry spectroscopy for the chiro-optical characterization of nanostructures

A. Belardini[1*], E. Petronijevic[1], C. Skubisz[1], C. Sibilia[1]

[1]Sapienza Università di Roma, SBAI Department, Italy
[*]corresponding author: alessandro.belardini@uniroma1.it

Abstract: Chiro-optical characterization at nanoscale can be performed by using different techniques. The most used ones are the spectral extinction measurements in transmission, or in reflection where samples on opaque substrate were used. In addition to these techniques, there are other less conventional ones such as photoacoustic spectroscopy and spectral polarimetry.

The importance of chirality is crucial in nature as well as in applications ranging from drug synthesis to single molecule detection. For this reason, many types of metasurfaces have been created to increase the sensitivity of light to chirality. At the same time, several techniques for the optical characterization of circular dichroism have been developed. Chiro-optical characterization at nanoscale can be performed by using different techniques. The most used ones are the spectral extinction measurements, were left-handed circular polarized light (LCP) and right-handed circular polarized light (RCP) impinge on samples and were recollected in transmission or in reflection (in case of samples on opaque substrate). In addition to these techniques, there are other less conventional ones such as photoacoustic spectroscopy which is able to evaluate the absorption even from scattering samples or powders, and spectral polarimetry where the Stokes parameters are explored as a function of the wavelength [1].

Here we compare results obtained by measuring different self-assembled intrinsic and extrinsic chiral nanostructures [2] with all these techniques and also with nonlinear techniques such as the Second Harmonic Generation Circular Dichroism (SHD-CD) and Photothermal deflection techniques. Applications on organic materials and molecules are also described.

Acknowledgements: This work was partially founded by European Union – Next Generation EU PRIN 2022 PNRR Project INSPIRE n. P2022LETN5 and by Sapienza Research Grant prot. n. RG1221816B6FA2E9.

References

1. Petronijevic, E., Belardini, A., Leahu, G., Li Voti, R., and Sibilia, C. ,“Nanostructured materials for circular dichroism and chirality at the nanoscale: towards unconventional characterization,” Opt. Mater. Express Vol. 12, 7 (2022).
2. Petronijevic, E., Belardini, A., Leahu, G. et al., “Broadband optical spin dependent reflection in self-assembled GaAs-based nanowires asymmetrically hybridized with Au,” Sci. Rep. Vol. 11, 4316 (2021).

Screw dislocations in chiral magnets

M. Azhar[1*], S. C. Shaju[1], V. P. Kravchuk[2,3] , M. Garst[4] and K. Everschor-Sitte[1]

[1]Faculty of Physics and Center for Nanointegration Duisburg-Essen (CENIDE), University of Duisburg-Essen, 47057 Duisburg, Germany
[2]Leibniz-Institut für Festkörper- und Werkstoffforschung Dresden (IFW), Germany
[3]Bogolubov Institute for Theoretical Physics, NAS of Ukraine
[4]Karlsruhe Institute of Technology, Germany
[*]corresponding author: maria.azhar@uni-due.de

Abstract: We report the micromagnetic structure of screw dislocation line defects, within the 1-dimensional periodic spiral magnetic order in cubic chiral magnets. Using analytical and numerical techniques we show that the far field of these dislocations has the universal form found in general for lamellar order, with a non-trivial core structure.

The micromagnetic energy for cubic chiral magnets at leading order in spin-orbit coupling is,

$$\mathcal{E} = A(\partial_i \boldsymbol{n})^2 + D\boldsymbol{n}(\boldsymbol{\nabla} \times \boldsymbol{n}) - M_s \mu_0 H n_z. \tag{1}$$

where $\boldsymbol{n}$ is a unit vector oriented along the magnetization direction, A is the ferromagnetic exchange constant, D is the Dzyaloshinskii-Moriya interaction (DMI) constant, and an external magnetic field is applied along the z direction. The DMI stabilizes a helimagnetic order for a large range of temperatures and applied magnetic field. In this helimagnetic phase the magnetization varies only along the helix axis, that is aligned with the applied field, giving rise to a one-dimensional periodic magnetic texture. This texture shares many similarities with generic lamellar order like cholesteric liquid crystals, for example, it possesses disclination and dislocation defects [1].

Here, we investigate both analytically and numerically screw dislocations of helimagnetic order, in which the far field is universally determined by a topological index ν that quantizes the Burgers vector characterizing the dislocation. Whereas the far-field of these defects is universal, we find that various core structures can be realized even for the same Burgers vector of the screw dislocation [2] (see Figure 1).

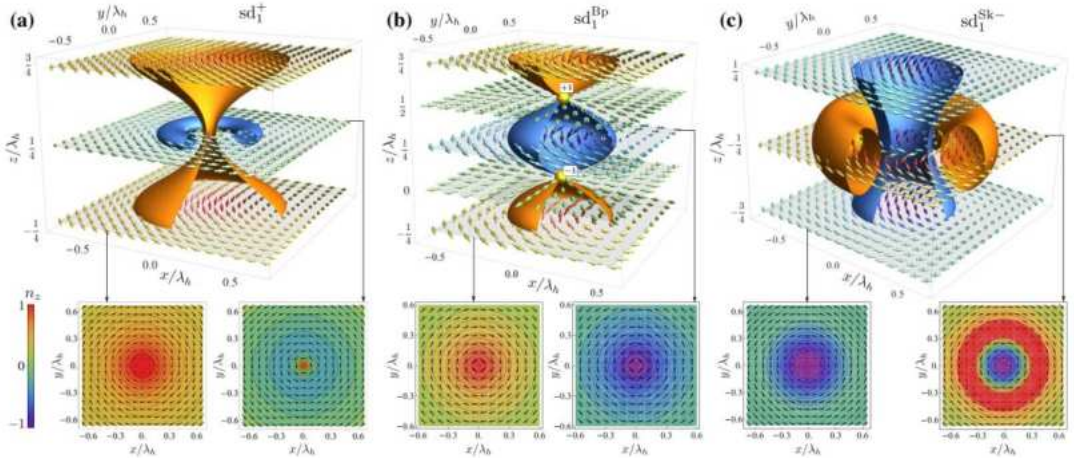


Figure 1 Micromagnetic texture of ν=+1 screw dislocation lines in chiral magnets.

Intriguingly, we identify screw dislocations with a smooth magnetic core and a simple screw structure ($\nu = +1$), that exist as vortex strings encircled by fractional Hopfion rings. The latter prediction has recently been experimentally confirmed by means of transmission electron microscopy [3]. Another astonishing spin structure that we predicted arise from a singular core comprising a chain of Bloch points with alternating topological charge.

Our findings enrich the portfolio of topological magnetic structures ubiquitously being present in bulk and thin-film helimagnets and will play a crucial role on the way to 3D nanomagnet and spintronics applications.

References

1. Schoenherr, P., et al, "Topological domain walls in helimagnets," Nature Physics, Vol. 14, 465, 2018.
2. Azhar, M., V. P. Kravchuk, and M. Garst, "Screw dislocations in chiral magnets," PRL, Vol. 128, 157204, 2022.
3. Zheng F., et al, "Hopfion rings in a cubic chiral magnet," Nature, Vol. 623, 718, 2023.

Making sense of the electron transport CISS effect properties and the spinterface model

A. Sharoni[1]*, R. Bornovski[1], S. Alwan[2] and Y. Dubi[2]

[1]Department of Physics & Institue of Nanosciene, Bar Ilan University, Ramat Gan 590002, Israel
[2]Department of Chemistry, Ben Gurion University of the Negev, Beer Sheva, Israel
*corresponding author: amos.sharoni@biu.ac.il

Abstract: Transport CISS effect is observed in metal-chiral-ferromagnet junctions, where current changes dramatically with magnetization of FM. Understanding different experimental findings and their origin is difficult. We show our spinterface model well explains effects such as magnitude of CISS signal and temperature dependence. We present recent experimental results supporting the model.

When electrons are injected through a chiral molecule, the resulting current may become spin polarized. This effect, known as the chirality-induced spin-selectivity (CISS) effect, has been suggested to emerge due to the interplay between spin–orbit interactions and the chirality within the molecule. However, such explanations require unrealistically large values for the molecular spin–orbit interaction without any physical justification. Put simply, to date, the physical origin of the CISS effect is unknown. Moreover, many of the reported results to date are surprising, and present a challenge for theory.

In this talk we will focus on the electron transport manifestation of the CISS effect, commonly observed in a metal - chiral molecule - ferromagnet junctions, where the total current is different when the ferromagnet is magnetized parallel or anti-parallel to the molecular chirality axis. This spin polarization (i.e., the percent difference between the two currents) may depend on different parameters, and was reported to show a variety of effects. These include such effects as: (1) The spin polarization measured to be close to 100% even though the polarization of the ferromagnetic (FM) detector electrode is much smaller. (2) The temperature dependence has been reported to decrease the magnitude of the CISS effect in some cases, while in other cases to increase it.

Here, we build upon the “spinterface” theory for the CISS effect[1] based on the interplay between spin–orbit interactions in the electrode, the chirality of the molecule (which induces a solenoid field), and spin-transfer torque at the molecule–electrode interface.

Using a mean-field calculation with simple models for the molecular junction, we show that our phenomenological theory can qualitatively account for all key experimental observations, most importantly the magnitude of the CISS with realistic parameters. We show analytically that experimental results indicate that the origin of the CISS effect must involve some interaction mechanism (as opposed to non-interacting electronic effects), since the observed CISS polarization can be much larger than the ferromagnetic electrode spin-polarization. Specifically, we show that a non-interacting single-level model cannot reproduce experimental data even if the molecular spin-filtering is perfect. On the other hand, we show that the spinterface mechanism can indeed lead to arbitrarily large CISS polarization.[2] We demonstrate this by showing excellent fit between the spinterface model and recent experiments where the effective magnetization of the ferromagnetic electrode was changed continuously. As a second example of the spinterface model we will show the temperature dependence of the CISS and the importance of correctly analyzing the experimental results. [3]

Finally, we will describe a set of experiments which can be used as a “smoking gun” for differentiating the

spinterface mechanisms from other theoretical explanations and show some of our recent experimental data that is aimed at testing these predictions.

References

1. Alwan, S. and Y. Dubi, *Spinterface Origin for the Chirality-Induced Spin-Selectivity Effect.* Journal of the American Chemical Society, **143,** 14235 (2021).
2. Alwan, S., A. Sharoni, and Y. Dubi, *The role of electrode polarization in the electron transport chirality-induced spin-selectivity effect.* Submitted to J. Chem Phys (2024).
3. Alwan, S., et al., *Temperature-dependence of the chirality-induced spin selectivity effect—Experiments and theory.* The Journal of Chemical Physics, **159** 014106 (2023).

Chiral Atoms and Helical Electrons

H. M. Yamamoto[1*, 2, 3]

[1]CIMoS, Institute for Molecular Science, Japan
[2] QuaRC, Institute for Molecular Science, Japan
[3] SOKENDAI, Japan
[*]corresponding author: yhiroshi@ims.ac.jp

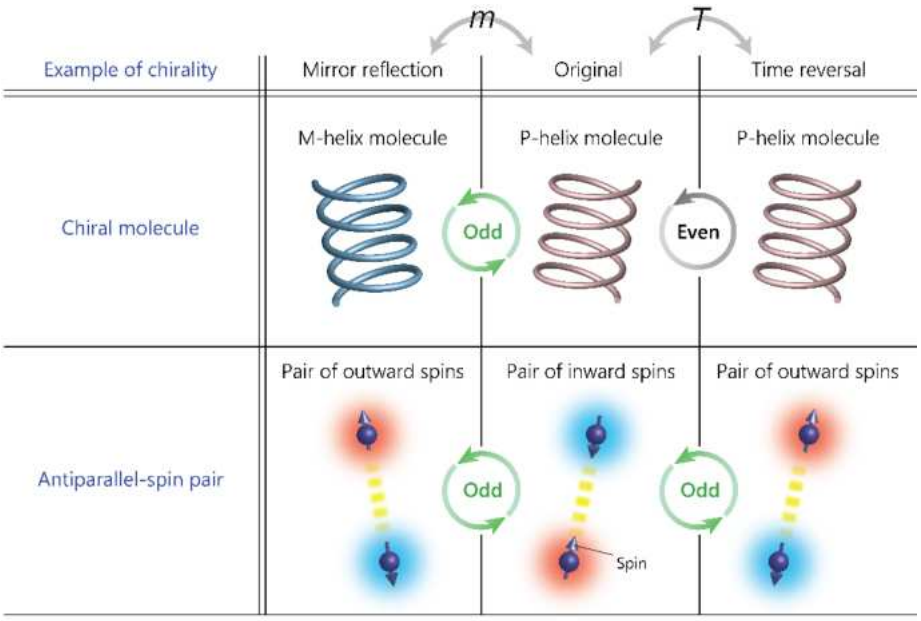
Abstract: An internal mechanism of Chirality-Induced Spin Selectivity (CISS) is discussed based on a symmetry consideration in which electron's helicity is connected to molecular chirality and spin accumulation with a language of electronic multipoles.

Chirality-Induced Spin Selectivity (CISS) is attracting recent attention as a new source of spin polarized current [1]. With this effect, an electron spin is aligned parallel to or antiparallel to its velocity after passing through a chiral molecule. Here the electron acquires either positive or negative helicity (= $\boldsymbol{p}\cdot\boldsymbol{s}$ where $\boldsymbol{p}$ and $\boldsymbol{s}$ are linear and spin angular momentum, respectively) depending on the handedness of the molecule. This is a chiral information imprinting from molecular handedness to electron's helicity, both of which are parity(P)-odd and time-reversal(T)-even. We are now trying to identify a common language to describe molecular chirality and electron's helicity in a simple and convenient manner. For this purpose, electrical toroidal monopole (G_0) is ideal so that we need to quantify the molecular chirality in this terminology [2, 3].

It is also interesting to point out that, in a hypothetical consideration, an enhancement of spin polarization is associated with anti-parallel spin pair accumulation at two opposite ends of a chiral molecule in CISS. Note that such an anti-parallel spin pair is T-odd state, while the chiral molecular structure is T-even. We think symmetry conversion from T-even to T-odd quantities gives an essential clue to understand CISS effect that can generate huge spin polarization in a non-equilibrium condition. We have made such a symmetry consideration based on multipole basis and found that a T-odd chirality can emerge from an accumulation of spin current (= electrical toroidal monopole G_0) at reservoirs. In addition, we have experimentally shown that chiral organic superconductor can exhibit spin accumulation at two opposite crystal edges whose directions are anti-parallel to one another [4]. This can be regarded as a macroscopic-size emulation of chiral molecules that has T-odd spin accumulations at their opposite ends. A connection to falsely chiral influence [5] will be also discussed.

References

1. B. Göhler, *et al., Science* **331**, 894 (2011)
2. J. Kishine, H. Kusunose, and HMY, *Isr. J. Chem*. **62**, e202200049 (2022)
3. A. Inda, R. Oiwa, S. Hayamai, HMY and H. Kusunose, *arXiv:*2402.13611 (2023)
4. R. Nakajima, HMY *et al*., *Nature* **613**, 479 (2023)
5. L. D. Barron *Chem. Soc. Rev*. **15**, 189 (1986)


m
T
Example of chirality
Mirror reflection
Original
Time reversal
M-helix molecule
P-helix molecule
P-helix molecule
Chiral molecule
Odd
Even
Pair of outward spins
Pair of inward spins
Pair of outward spins
Antiparallel-spin pair
Odd
Odd
Spin

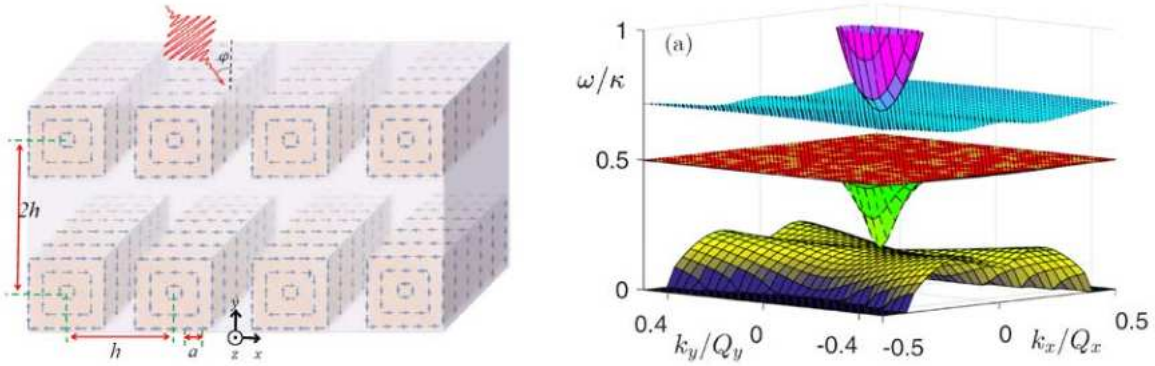
Photonic vortex lattice based on dielectric polarization textures

Ramaz Khomeriki[1], Vakhtang Jandieri[2,3], Koki Watanabe[4], Daniel Erni[3], Douglas H. Werner[5], Marin Alexe[6], and Jamal Berakdar[2,*]

[1]Physics Department, Tbilisi State University, 3 Chavchavadze, 0128 Tbilisi, Georgia
[2]Martin-Luther University, Halle-Wittenberg, 06099 Halle, Germany
[3]Faculty of Engineering, Center for Nanointegration Duisburg-Essen, 47048 Duisburg, Germany
[4]Department of Information and Communication Engineering, Fukuoka Institute of Technology, Fukuoka 811-0295, Japan
[5]Department of Electrical Engineering, The Pennsylvania State University, University Park, PA 16802, USA
[6]Department of Physics, University of Warwick, Coventry CV4 7AL, United Kingdom
[*]corresponding author: jamal.berakdar@physik.uni-halle.de

Abstract: The existence of polar vortex textures in strained nanoscale ferroelectric materials has been recently experimentally verified. As shown in this contribution, such materials offer a new route to study chiral, topological, and photonic systems. We show that, in the THz regime, the polar vortex lattice couples simultaneously to electric and magnetic field components leading to the formation of a photonic vortex lattice with particular dispersion. We discuss the spectral and mode properties of the formed photonic textures and discuss possible utilization in optoelectronics.

Materials with polar ordering are shown in [1]-[4] to exhibit chiral and vortex lattice textures (*e.g.*, as schematically depicted in Fig. 1a) that can be controlled by external stimuli, *e.g.*, by switching the underlying ferroelectric polarization [3]. We address in this contribution the characteristics of the photonic modes that are hosted in such dielectric structures. Analytical considerations, supported by rigorous self-contained material-specific numerical simulations [5] for the electromagnetic scattering, evidence the polarization-dependent optoelectronic modes and the emergence of photonic band-gaps (Fig.1b). In particular, we demonstrate how the ferroelectric vortex lattice enables a coupling to electric and magnetic fields simultaneously resulting in a novel type of photonic vortex lattice with particular dispersion that we analyze for a wide class of ferroelectric layered heterostructures. The proposed method based on the coupled differential equations presents an efficient numerical tool for the analysis of other types of structured ferroelectrics and gives a full picture of the coupling behavior of the electromagnetic waves with the vortex of electric dipole arrays.



(a) (b)

Figure 1: Schematics of ferroelectric vortex lattice which we use for the photonic simulations. The arrows show the local ferroelectric polarization direction that curl to form neighboring vortices with opposite chiralities. The equilibrium distances between the centers of the vortices along the *x*- and the *y*-axes are h and $2h$, respectively. The distribution of the local polarization along the *z* direction is uniform. The distance between the neighboring electric dipoles is a. We consider an electromagnetic wave incident with an inclined angle of φ. (b) Dispersion of the TM (H_z, E_x, E_y) modes calculated from the linear set of Bloch mode equations [5] where the wavevector is measured in units of $Q_x = 2\pi/h$ and $Q_y = \pi/h$. The frequency unit in this example is approximately $\kappa = 2\pi$ THz. More details can be found in [5].

References

1. Tang, Y. L., Zhu, Y. L., Ma, X. L., Borisevich, A. Y., Morozovska, A. N., Eliseev, E. A., Wang, W. Y., Wang, Y. J., Xu, Y. B., Zhang, Z. D., and Pennycook, S. J. Observation of a periodic array of flux-closure quadrants in strained ferroelectric PbTiO3 films, Science **348**, 547 (2015).
2. Rusu, D., Peters, J. J. P., Hase, T. P. A., Gott, J. A., Nisbet, G. A. A., Strempfer, J., Haskel, D., Seddon, S. D., Beanland, R., Sanchez, A. M., and Alexe, M. Ferroelectric incommensurate spin crystals, Nature (London) **602**, 240 (2022).
3. Behera, P., Parsonnet, E., Gómez-Ortiz, F., Srikrishna, V., Meisenheimer, P., Susarla, S., Kavle, P., Caretta, L., Wu, Y., Tian, Z., Fernandez, A., Martin, L. W., Das, S., Junquera, J., Hong, Z. and Ramesh, R. Emergent ferroelectric switching behavior from polar vortex lattice. Adv. Mater., **35**: 2208367 (2023).
4. Sánchez-Santolino, G., Rouco, V., Puebla, S. *et al.* A 2D ferroelectric vortex pattern in twisted BaTiO3 freestanding layers. Nature **626**, 529–534 (2024).
5. Khomeriki, R., Jandieri, V., Watanabe, K., Erni, D., Werner, D. H., Alexe, M., and Berakdar, J. Photonic ferroelectric vortex lattice. Phys. Rev. B **109**, 045428 (2024).

Half Quantized Hall Effect

Shun-Qing Shen*

Department of Physics, The University of Hong Kong, Pokfulam, Hong Kong
*sshen@hku.hk

Abstract: A single gapless Dirac cone of fermions on a lattice gives rise to one half quantum Hall conductance while a gapped Dirac cone of fermions always has zero or one quantum Hall conductance. This effect can be realized in a semi-magnetic topological insulator film.

The quantum Hall effects refer to a series of peculiar quantum states of matter in the two-dimensional electron system in a strong magnetic field at a very low temperature. Similar phenomena in quasi-two-dimensional materials in the absence of a magnetic field are named the quantum anomalous Hall effect. So far, all the quantum Hall effects occur in insulating phases and are characterized by the TKNN number or Chern number for the band structure as a topological invariant. The longitudinal conductivity is zero and either the Hall resistivity or conductivity is quantized. The bulk-edge correspondence illustrates that the number corresponds to the number of the localized edge modes around the system boundary, which carries the dissipationless chiral charge current. Here we report a half-quantized Hall effect in a semi-magnetic topological insulator. The Hall conductance is half quantized and the longitudinal conductance is nonzero, but the Hall resistivity is not quantized. This effect is attributed to the existence of a single gapless Dirac cone of fermions on a lattice. More general, the half quantization occurs when the Fermi surface is invariant under the parity symmetry or time reversal symmetry while the symmetry is broken in the whole system. [1] [2]

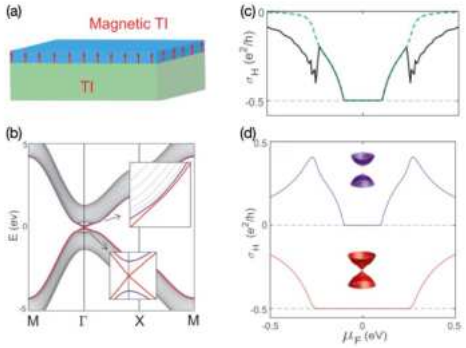


Figure 1: The Hall conductance for the gapless and gapped surface bands in a semi-magnetic topological insulator. (a). Schematic of a magnetic topological insulator film. (b) The band structure of a tight-binding model. (c) The total Hall conductance as a function of the chemical potential. (d) The Hall conductance of the gapped and gapless surface bands. (Adapted from Ref [3].)

We begin with a tight binding model for a three-dimensional topological insulator with finite thickness in the z-axis, incorporating the Zeeman field on the top layer to simulate magnetic ion doping. Periodic boundary conditions are performed in the x and y directions. The exact diagonalization method yields the energy dispersion and corresponding eigenstates explicitly, which are well defined the 2D first Brillouin zone. Numerical results corroborate the presence of gapped and gapless surface Dirac fermion cones in a semi-magnetic TI. The top surface Dirac cone is gapped due to the Zeeman field. However it is important to note the surface Dirac cones appear only near the Γ point, and are confined within the bulk gap Δ of the topological insulator, occupying only a small portion of the first Brillouin zone. Outside the regime, the wave functions of the energy eigenstates evolve into the bulk, and are no longer confined near the top and/or bottom surface. Using the TKNN formula, we calculated the Hall conductance for the bands associated with the top and bottom surface Dirac cones\. The Hall conductance for the gapless Dirac cone become half-quantized when the chemical potential is located within the bulk gap Δ while the

Hall conductance for the gapped Dirac cone exhibits a peak near the bulk band edge, which height is less than 0.5 and drops to zero when the chemical potential is located within the gap V of the top surface states. Consequently, the total Hall conductance is one half quantized when the chemical potential is situated within the gap V.

The observation of zero Hall conductance for the fully-filled top gapped Dirac cone aligns with the TKNN theorem and the Chern number. The gapped top surface states only arise within the bulk gap Δ of TI. While the nonzero Berry curvature of these states may contribute to a nonzero Hall conductance it is not expected to yield half-quantized value due to the finite ratio of V/Δ. A value of 0.5 can only be achieved when the ratio of V/Δ approaches zero. However, the first Brillouin zone is finite, and the remaining portion of the bands also contributes a nonzero Hall conductance, effectively cancelling out the contribution from the gapped surface states. This cancellation is dictated by the TKNN theorem in the presence of a nonzero V. In an open boundary condition, as there are no localized chiral edge states in the gapless and metallic system, we find that the chiral edge current is carried by the gapless surface states. The current density peaks at the edge and decays in a power law rather than the exponential decay as in the conventional quantum anomalous Hall effect [4]. We term the unexpected and nontrivial quantum phase as "parity anomalous semimetal" [1]. We also discovered a metallic quantum anomalous Hall effect without chiral edge states in a magnetic sandwich structure of topological insulators [5]. The set of works open the door to exploring novel topological states of matter with fractional topological invariants.

The half quantum Hall effect of a gapless Dirac cone is closely associated with the quantum anomaly in quantum field theory [1]. Quantum anomaly refers to the failure of a symmetry present in a theory's classical action to be a symmetry of any regulation of the fully quantum theory. Strictly speaking, there is no parity anomaly in a solid or on a lattice, as the lattice spacing in a solid crystal provides a natural cut-off for the wave vector, and both the first Brillouin zone and the band width are finite. In the case of the one-half quantum Hall conductance, it is believed to be closely related with the physics of parity anomaly. Near the Dirac crossing point or in the regime of the gapless surface states, electrons respect the parity symmetry, and the Berry curvature vanishes. However, the occupied electrons away from this regime break the symmetry, and contribute an exactly half-quantized Hall conductance.

This work was supported by the Research Grants Council, University Grants Committee, Hong Kong under Grant No. C7012-21G and No. 17301823.

References:

[1] B. Fu, J. Y. Zou, H. W. H. Z. A. Wang and S. Q. Shen, "Quantum anomalous semimetals," *npj Quantum Mater.,* vol. 7, no. 1, p. 94, 2023.

[2] Q. S. Shen, "Half quantized Hall effect," *Coshare Science,* vol. 02, no. v1, pp. 1-41, 2024.

[3] J. Y. Zou, R. Chen, B. Fu, H. W. Wang, Z. A. Hu and S. Q. Shen, "Half-quantized Hall effect at the parity-invariant Fermi surface.," *Phys. Rev. B,* vol. 107, no. 12, p. 125153, 2023.

[4] J. Y. Zou, B. Fu, H. W. Wang, Z. A. Hu and S. Q. Shen, "Half-quantized Hall effect and power law decay of edge-current distribution," *Phys. Rev. B,* vol. 105, no. 20, p. L201106, 2022.

[5] K. Z. Bai, B. Fu, Z. Y. Zhang and S. Q. Shen, "Metallic quantum anomalous Hall effect without chiral edge states," *Phys. Rev. B,* vol. 108, p. L241047, 2023.

Optical forces of optical modes with helicity and angular momentum

Gabriel Molina-Terriza[1,2,3*]

[1]Centro de Física de Materiales, UPV-EHU/CSIC, Paseo Manuel de Lardizabal 5, E-20018 San Sebastián, Spain

[2]Donostia International Physics Center, Paseo Manuel de Lardizabal 4, E-20018 San Sebastián, Spain

[3]Ikerbasque Foundation for Science, Maria Diaz de Haro 3, E-48013 Bilbao, Spain

[*]corresponding author: gabriel.molina.terriza@gmail.com

Abstract: I will show our latest results in the control of the scattering and optical forces using modes of light with well-defined angular momentum and helicity. Traditionally, the roles of helicity and angular momentum are mixed. I will present the differential features of angular momentum and helicity of optical beams.

The angular momentum of light is a property that has been studied thoroughly in the last three decades. The ability of controlling the angular momentum of light through its spatial properties opened up the field of structured light with multiple applications in communications, quantum optics, optical trapping and the scattering of light by small particles.

Traditionally, the angular momentum of light is separated into spin and orbital parts. The spin is related with the circular polarization of optical fields, while the orbital is related with the azimuthal phase of a cylindrically symmetric field. While this separation may have its applications in the paraxial regime, it has encountered many problems when applied to focused beams and non-paraxial fields in general. On the other hand, another quantity also related to the circular polarization of optical fields, the helicity of light, has allowed to better interpret the interaction of light and matter both in the paraxial and non-paraxial regimes, with classical and quatum states of light. The key element is that angular momentum modes of light have a distinct relationship with rotational symmetries, while modes of well-defined helicity have a relationship with the duality symmetry between electric and magnetic parts of an optical field.

We have exploited these relationships to better understand the role of the angular momentum and the helicity in scattering experiments and, more recently in optical forces. In particular, we have experimentally used optical modes with well-defined angular momentum and helicity to trap particles in the Mie regime and showed that these particles can be stably trapped in the center of the beam as shown in Fig. 1

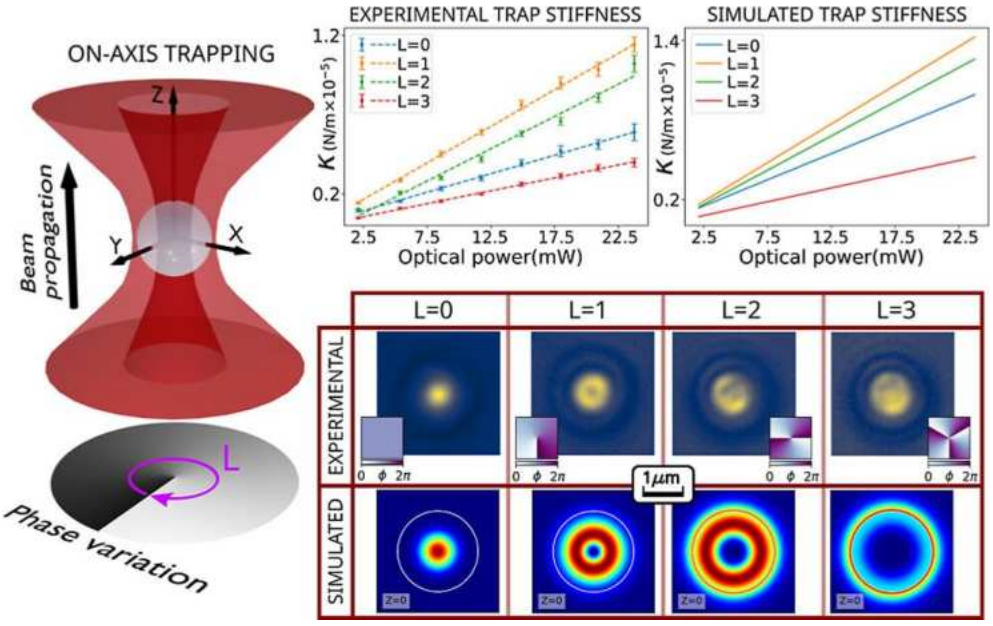


Figure 1: Comparison between experimental and experimental results of the optical trapping of silica particles in modes with well-defined angular momentum and helicity.

We have also developed numerical and theoretical techniques in order to elucidate the differential role of these quantities both in the scattering and the optical forces of optical beams.

We acknowledge funding through the CSIC Research Platform on Quantum Technologies PTI-001, from IKUR Strategy under the collaboration agreement between Ikerbasque Foundation and DIPC/MPC on behalf of the Department of Education of the Basque Government and from the projects EQC2018-004060-P, FIS-2017-87363-P, and PID2022-143268NB-I00 of Ministerio de Ciencia, Innovación y Universidades.

References

1. Fernandez-Corbaton, I. et al, “Electromagnetic Duality Symmetry and Helicity Conservation for the Macroscopic Maxwell's Equations,” Phys. Rev. Lett., Vol. 111, 060401, 2013.
2. Fernandez-Corbaton, I., et al, “Helicity and angular momentum: A symmetry-based framework for the study of light-matter interactions,” Phys. Rev. A, Vol. 86, 042103, 2012.
3. Gómez-Viloria, I. et al, “On-Axis Optical Trapping with Vortex Beams: The Role of the Multipolar Decomposition,” ACS photonics, Vol. 11, 626, 2024.
4. Molezuelas-Ferreras, M., et al, “Characterizing the Backscattered Spectrum of Mie Spheres”, Laser Photonics Rev., Vol. 18, 2300665, 2024

Nonlinear topological magnon spin Hall effect

Peng Yan*

School of Physics and State Key Laboratory of Electronic Thin Films and Integrated Devices, University of Electronic Science and Technology of China, Chengdu 610054, China

*corresponding author: yan@uestc.edu.cn

Abstract: Nonlinear scattering of magnons and skyrmions in antiferromagnets leads to a spin Hall effect that emerges from real-space topology.

When a magnon passes through two-dimensional magnetic textures, it will experience a fictitious magnetic field originating from the 3×3 skew-symmetric gauge fields. To date, only one of the three independent components of the gauge fields has been found to play a role in generating the fictitious magnetic field while the rest two are perfectly hidden. In this work, we show that they are concealed in the nonlinear magnon transport in magnetic textures. Without loss of generality, we theoretically study the nonlinear magnon-skyrmion interaction in antiferromagnets. By analyzing the scattering features of three-magnon processes between the circularly polarized incident magnon and breathing skyrmion, we predict a giant Hall angle of both the confluence and splitting modes. Furthermore, we find that the Hall angle reverses its sign when one switches the handedness of the incident magnons. We dub it nonlinear topological magnon spin Hall effect. Our findings are deeply rooted in the bosonic nature of magnons that the particle number is not conserved, which has no counterpart in low-energy fermionic systems and may open the door for probing gauge fields by nonlinear means.

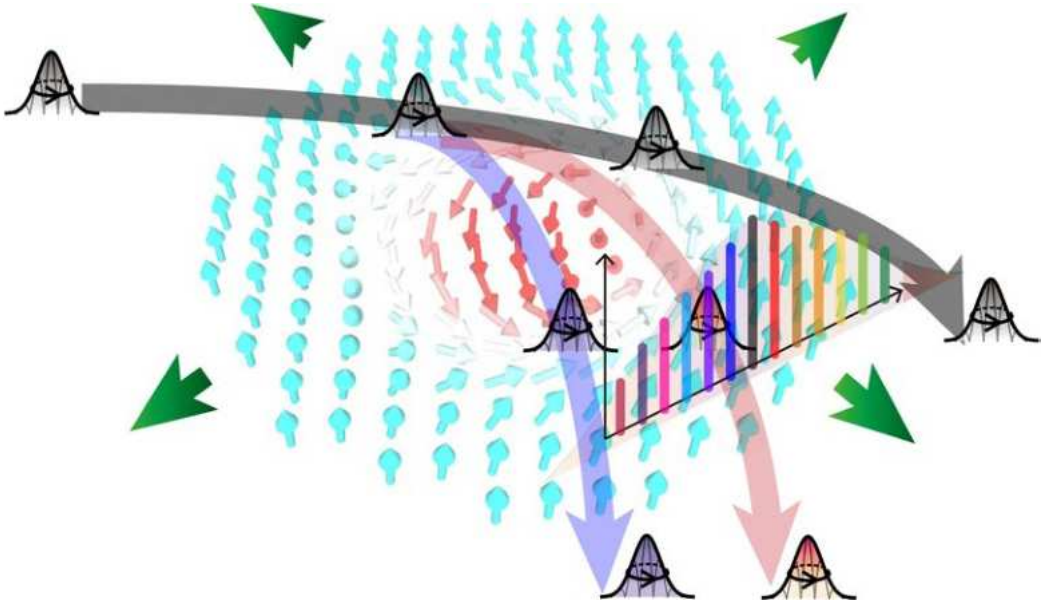


Fig. 1: Schematic of the giant spin Hall angle in the nonlinear scattering of magnons by skyrmion in antiferromagnets.

This work was funded by the National Key Research and Development Program under Contract No. 2022YFA1402802 and the National Natural Science Foundation of China (NSFC) (Grants No. 12074057 and No. 12374103).

References

1. Z. Jin, X. Yao, Z. Wang, H. Y. Yuan, Z. Zeng, W. Wang, Y. Cao, and P. Yan, “Nonlinear Topological Magnon Spin Hall Effect”, Phys. Rev. Lett. 131, 166704 (2023).
2. Z. Wang, H. Y. Yuan, Y. Cao, and P. Yan, “Twisted Magnon Frequency Comb and Penrose Superradiance”, Phys. Rev. Lett. 129, 107203 (2022).
3. Z. Wang, H. Y. Yuan, Y. Cao, Z.-X. Li, R. A. Duine, and P. Yan, “Magnonic Frequency Comb through Nonlinear Magnon-Skyrmion Scattering”, Phys. Rev. Lett. 127, 037202 (2021).
4. Y. Jiang, H. Y. Yuan, Z.-X. Li, Z. Wang, H. W. Zhang, Y. Cao, and P. Yan, “Twisted Magnon as a Magnetic Tweezer”, Phys. Rev. Lett. 124, 217204 (2020).

Chiral coherent control of electronic population transfer with femtosecond pulses: towards all-optical and highly enantioselective photochemistry

A. Ordóñez[1,2], P. Vindel-Zandbergen[3] and D. Ayuso[1,2,3*]

[1]School of Physical and Chemical Sciences, Queen Mary University of London, E1 4NS London, UK
[2]Department of Physics, Imperial College London, SW7 2AZ London, UK
[3]Department of Department of Chemistry, New York University, 10003 New York, USA
[4]Max-Born-Institut, 12089 Berlin, Germany
[*]corresponding author: d.ayuso@qmul.ac.uk

Abstract: We provide a route to achieve highly enantioselective photochemistry via interference between two quantum pathways leading to an electronic excitation. Our simulations reveal differences of up to 19% in the excited state populations of R and S carvone, a major improvement over what is possible with circularly polarized light (~0.01%)

Enantioselective photochemistry relies on the ability to induce different electronic transitions in left-handed and right-handed versions (enantiomers) of a chiral molecule using light. This is usually a very challenging task, as opposite enantiomers share the same energy spectrum, and photoexcitation with circularly polarized light is barely enantioselective. As a result, highly enantioselective photochemistry remains an important milestone of photochemistry, which could enable laser-driven alternatives to traditional chemical methods for enantio-purification and enantioselective synthesis. These are tasks of immense importance in the chemical industry, where producing samples with only one of the two enantiomers of a chiral molecule starting from racemic (50% R – 50% L) mixtures is required in numerous applications. Whereas great progress has been recently achieved in the context of coherent control over *rotational* excitations [1,2], extending these achievements to *electronic* excitations and shorter timescales is extremely challenging.

Here we show how we can tailor light to induce highly enantioselective population transfer between electronic states using intense femtosecond pulses, which can trigger highly enantioselective photochemistry, see Fig. 1a,b. Our approach relies on driving and controlling an enantioselective interference between two quantum pathways leading to an electronic excitation, and it is supported by analytical modelling and ab-initio simulations which take into account the molecular orientation distribution and the variation of the field across the sample [3].

In the case of one- vs. two-photon interference (Fig. 1c,d), one of the dimensions of the interaction region must remain on the same order or smaller than the longest of the wavelengths. Otherwise, the enantioselectivity is washed out. While this is relatively easy to achieve when dealing with microwaves, it is a rather restricting condition for optical wavelengths and requires taking special measures, such as using carefully oriented ultrathin liquid microjets. In contrast, we can achieve highly enantioselective population transfer using a two- vs. three-photon interference (Fig. 1e,d). This scheme allows for interaction regions much larger than the longest wavelength. Our simulations show that it can lead to a 19% difference between the excited state populations of R and S enantiomers of carvone. This massive improvement over what is possible with circularly polarized light (~0.01%) brings all-optical enantioselective photochemistry within range for practical applications.

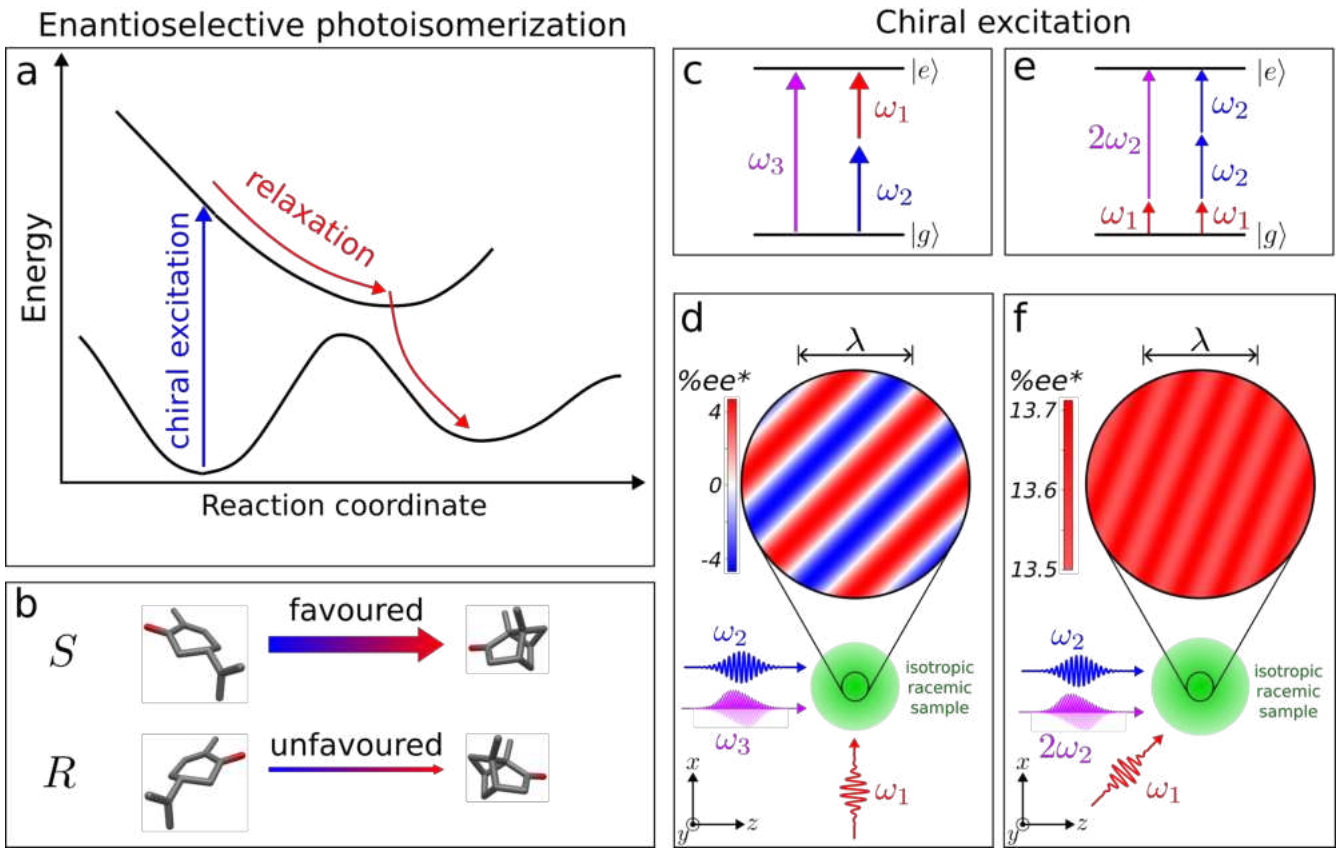


Fig. 1. a, Photochemistry is triggered by an electronic excitation, which often leads to chemical rearrangements (e.g. isomerization or dissociation). **b,** If the electronic excitation is driven by chiral light, the excitation becomes more likely in one of the two enantiomers. **c,** Enantioselective excitation can be achieved via coherent control. The microwave approach [1,2] relies on one-vs-two photon interference, and it leads to a subwavelength oscillation of the enantioselectivity across the interaction region. **d**, red and blue describe regions where more S and R enantiomers are excited, respectively, hindering applications in the optical domain. **e,f,** Such oscillations can be avoided by careful design in a two-vs-three photon interference scheme (**e**); note that the enantioselectivity is approximately constant (**f**).

References

1. S. Eibenberger, J. Doyle and D. Patterson. "Enantiomer-Specific State Transfer of Chiral Molecules", *Phys. Rev. Lett.* **118**, 123002 (2017)
2. J. Lee, J Bischoff, A. O. Hernandez-Castillo, B. Sartakov, G. Meijer and S. Eibenberger-Arias, "Quantitative Study of Enantiomer-Specific State Transfer", *Phys. Rev. Lett.* **128**, 173001 (2022)
3. A. Ordonez, P. Vindel-Zandbergen, D. Ayuso, "Chiral coherent control of electronic population transfer: towards all-optical and highly enantioselective photochemistry", ArXiv:2309.02392 (2023)

Valley-Hall Topological Waveguides for Integrated Quantum Photonics

N.J. Martin[1], M.J. Mehrabad[2], L. Hallacy[1], D. Hallett[1], X. Chen[1], R. Dost[1], E. Nussbaum[3], R. Dost[1], A. Foster[1], E. Clarke[4], P.K. Patil[4], S. Hughes[3], M. Hafezi[2], A.M Fox[1], M.S. Skolnick[1], and L.R. Wilson[1*]

[1]Department of Physics and Astronomy, University of Sheffield, Sheffield S3 7RH, UK
[2]Joint Quantum Institute, NIST/University of Maryland, College Park, Maryland 20742, USA
[3]Centre for Nanophotonics, Department of Physics, Engineering Physics and Astronomy, Queen's University, Kingston, Ontario, Canada K7L 3N6
[4]EPSRC National Epitaxy Facility, University of Sheffield, Sheffield S1 4DE, UK
[*]Corresponding author: luke.wilson@sheffield.ac.uk

Abstract: This study investigates chiral interactions and mode manipulation in quantum photonic circuits using topological photonic crystals and quantum dots. It features four pivotal advancements: tunable photon emission, efficient mode tapering, chiral multiport routing, and a comparative analysis of waveguides, with important implications for the design of efficient integrated quantum devices.

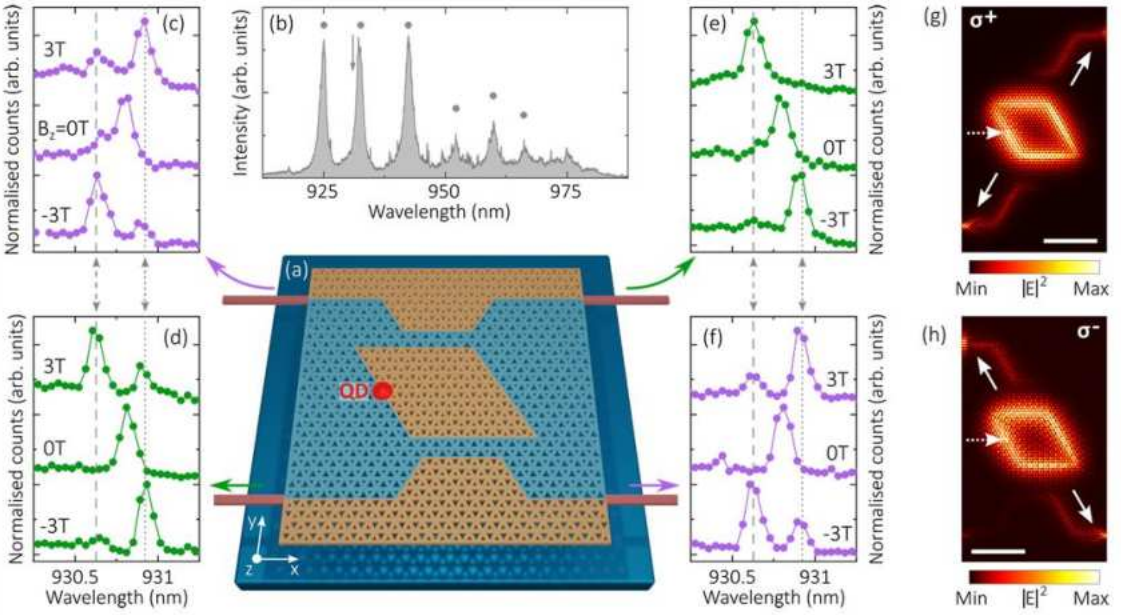


Figure 1: (a) Schematic of the topological photonic add-drop filter, with a quantum dot (QD) embedded at the resonator interface. Each of the four nanobeam waveguides is terminated with a grating out-coupler (OC), not shown. (b) PL spectrum acquired from an OC under high-power excitation of the resonator interface. The longitudinal resonator modes are marked by filled circles (c-f) Low power PL spectra for a single QD located at the resonator interface and with an optical transition near-resonant with a longitudinal mode (see arrow in (b)). The spectra are acquired from the OCs in the (c) top left, (d) lower left, (e) top right and (f) lower right of the device, respectively. Data is shown for three different magnetic field strengths, B_z =-3T, 0T and 3T, respectively. Dashed and dotted lines indicate the approximate wavelengths of the two QD transitions under non-zero magnetic field. (g-h) Simulated, time-averaged electric field intensity in the plane of the device, for a (g) σ^+ or (h) σ^- polarized dipole placed at a chiral point at the resonator interface (approximate location given by the dashed arrow). Solid arrows indicate the dominant coupling directions from of the resonator in each case. Scale bars 4μm.

Chiral Quantum Optical Interfaces: We experimentally integrate semiconductor quantum dots into a valley-Hall topological photonic crystal waveguide, forming a ring resonator that supports helical modes. We create an integrated topological add-drop filter within a valley-Hall photonic crystal membrane showcasing multiport chiral emission and wavelength-selective single photon routing, facilitated by resonator longitudinal modes. The device's inherent nonreciprocity at the single-photon level promotes advanced quantum optical devices like on-chip circulators and logic gates [1–2].

Comparative Study of Nano-Photonic Waveguides: Our analysis compares the chiral coupling of quantum emitters in topological versus conventional photonic waveguides, highlighting the current limitations of topological waveguides despite the potential advantages offered by state-of-the-art inverse design methods [3].

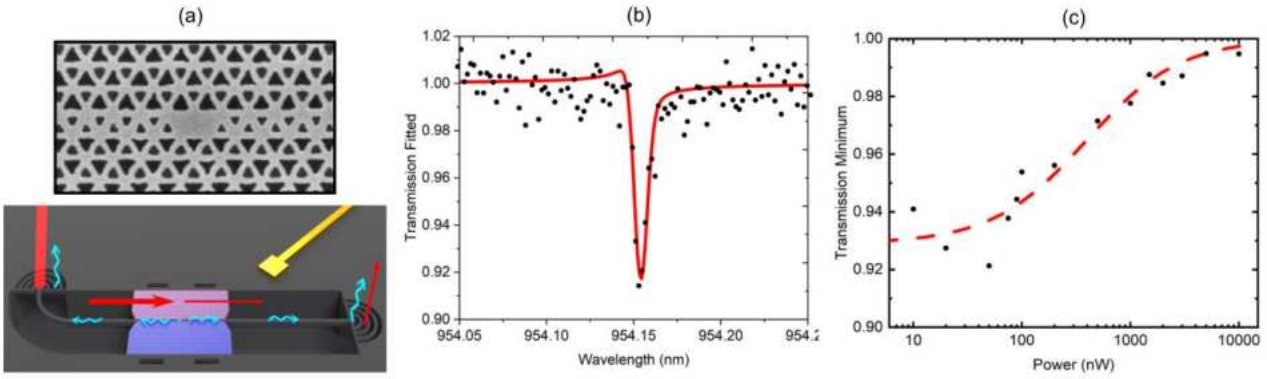


Figure 2: (a) SEM image of the valley-Hall waveguide defect, with a render of resonant transmission scheme positioning pump laser and far-field collection at separate out-couplers. (b) An example of transmission spectra observed at 50nW power at λ= 954.16nm with a fitted maximum dip of ~8%. (c) transmission dip from 10nW to 10μW, demonstrating non-linear power dependence. The dashed red line fits experimental data, showing saturation and plateau of transmission.

Non-Linear Quantum Optics at a Topological Interface: Addressing the integration challenges, we stabilize the charge environment for quantum dots within defects, achieving single-photon resonance fluorescence. We also develop an efficient interface for topological-conventional mode conversion, bridging the gap between novel topological designs and traditional photonics technologies. These collective works significantly advance the field of integrated quantum photonics, providing a robust framework for exploring non-linear optical phenomena and enhancing the design of next-generation photonic devices.

References

1. M. Jalali Mehrabad et al., "Chiral topological photonics with an embedded quantum emitter," Optica, vol. 7, no. 12. Optica Publishing Group, p. 1690, Nov. 30, 2020. doi: 10.1364/optica.393035.
2. M. Jalali Mehrabad et al., "Chiral topological add–drop filter for integrated quantum photonic circuits," Optica, vol. 10, no. 3. Optica Publishing Group, p. 415, Mar. 17, 2023. doi: 10.1364/optica.481684.
3. N. J. Martin et al., "Topological and conventional nano-photonic waveguides for chiral integrated quantum optics." arXiv, 2023. doi: 10.48550/ARXIV.2305.11082.

Brillouin Light Scattering Study of Nonreciprocal Spin Dynamics in Artificial Chiral Magnets

M. Xu[1*], A. J. M. Deenen[1], H. Guo[1], and D. Grundler[1, 2]

[1]Institute of Materials (IMX), Ecole Polytechnique Fédérale de Lausanne (EPFL), 1015 Lausanne, Switzerland,

[2]Institute of Electrical and Micro Engineering (IEM), EPFL, 1015 Lausanne, Switzerland,
[*]corresponding author: mingran.xu@epfl.ch

Abstract: Magnetic chirality, a material characteristic that originated from simultaneous time-reversal symmetry breaking and spatial inversion symmetry breaking. Here, we report an investigation on an artificially chiral magnet, which processes magnetic chirality and exhibits substantial magnon nonreciprocity at GHz frequencies at room temperatures.

Chirality, a characteristic of objects being nonsuperimposable mirror images of each other, plays a crucial role across various scientific disciplines and technology fields [1-2]. Magnetic chirality arises from broken spatial-inversion symmetry and time-reversal symmetry, which occur simultaneously in specific noncentrosymmetric crystals [3-4], and innately manifests nonreciprocal transmission of signal. Natural crystals possess the relevant magnetic ordering at low temperatures and require a complex fabrication process, consequently, leading to lack of room-temperature applications. In this study, we designed and created artificial chiral magnets (ACMs). By combining a mass production methodology, i.e., atomic layer deposition (ALD) of a ferromagnetic metal, and polymeric scaffolds produced by two-photon lithography (TPL) [5], we prepared screw-like tubular structures with left-handedness (LH) and right-handedness (RH) (Fig. 1a). The polymer (gray) had an outer diameter of 2 μm and was conformally coated with a 30 nm thick Nickel shell using ALD. The produced shell contains helical reliefs (helix regions) alongside a uniform tubular segment (tube region). When a magnetic field +H is applied parallel to ACMs, the magnetization in the tube region aligns longitudinally while aligning spirally in the helix region, forming screw-like (helical) spin textures. The handedness of the textures follows the corresponding structural chirality, generating opposite polarized toroidal moments $\mp\tau$ in LH and RH-ACMs, respectively (Fig. 1b). In the following we show that the different toroidal moments induce inverse nonreciprocities for magnons (Fig. 2).

The spin dynamics were investigated by μ-BLS with high spatial resolution. The samples were mounted on a piezostage and positive and negative external magnetic fields were applied in different orientations along the z-axis. The long axis of ACMs was positioned parallel to the z-axis. The green laser (wavelength: 532 nm) with a power of 3 mW was focused on the surface of the ACM using a 100x objective lens with a numerical aperture of 0.75. By analyzing Stokes and anti-Stokes scattering processes of thermal magnons with laser light, we identified asymmetries in resonance frequencies Δf and intensities of BLS peaks ΔI as shown in Fig. 2. In Fig. 2, the magnon spectrum obtained on the RH-ACM exhibits a stronger intensity of the Stokes peak compared to the anti-Stokes peak. The LH-ACM exhibits an opposite asymmetry. We attribute the observed nonreciprocity to asymmetric dispersion relations induced by the screw-like spin textures, which trigger mirrored nonreciprocities between LH and RH ACMs in Fig. 2.

We have successfully designed and synthesized ACMs. They showed asymmetric thermal magnon spectra attributed to the handedness-dependent magnon nonreciprocity. As evidenced in Fig. 2, by employing structures with mirrored handedness, a reversed asymmetric magnon spectrum is detected. We have observed that, in

spatial scanning spectra, the handedness and magnetic field polarity dependent asymmetries [6], which unveils the magnetic chirality of ACMs. The characteristics of the ACMs hence mimic reciprocities of intrinsic chiral magnets. The observed pronounced frequency shift (~ 1 GHz) and intensity difference (~ 50%), establishes its effectiveness for future high-frequency microwave electronics at room temperature and illuminates the potential of 3D assemblies of ferromagnetic materials.

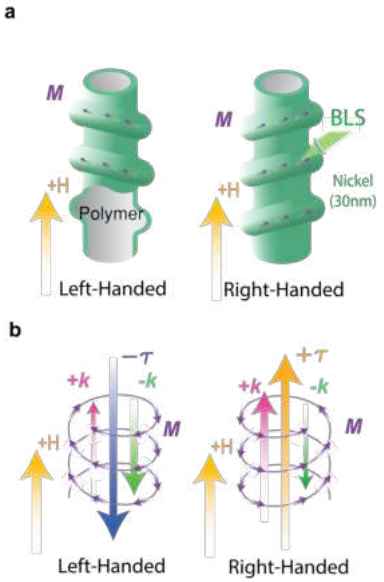


Fig. 1. (a) Schematics of left-handed and right-handed ACM. While applying a +H (right), the magnetic moments align following the structural handedness. (b) Conceptual illustration of toroidal moments ±τ induced by screw-like helical spin textures and its interplay with spin waves with wave vectors +k and -k.

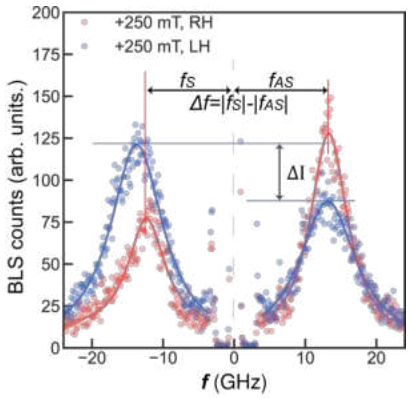


Fig. 2. Spectra of thermal magnons of an RH- (pink dots) and LH- (green dots) ACM collected by μ-BLS. The solid curves represent the Lorentzian fitting of the peaks

Acknowledgements

This research was supported by the SNSF via grant number 197360. The simulations and post-processing have been performed using the facilities of the ScientificIT and Application Support Center of EPFL. The authors thank the technique support from CMi at EPFL.

References

1. G. L. Rikken and E. Raupach, "Observation of magneto-chiral dichroism," Nature, vol. 390, no. 6659, pp. 493–494, 1997.
2. R. Nakajima, D. Hirobe, G. Kawaguchi, Y. Nabei, T. Sato, T. Narushima, H. Okamoto, and H. M. Yamamoto, "Giant spin polarization and a pair of antiparallel spins in a chiral superconductor," Nature, vol. 613, no. 7944, pp. 479–484, 2023.
3. S.-W. Cheong and X. Xu, "Magnetic chirality," npj Quantum Materials, vol. 7, no. 40, 2022.
4. Y. Tokura and N. Nagaosa, "Nonreciprocal responses from noncentrosymmetric quantum materials," Nature Communications, vol. 9, no. 3740, 2018.
5. H. Guo, A. J. Deenen, M. Xu, M. Hamdi, and D. Grundler, "Realization and control of bulk and surface modes in 3D nanomagnonic networks by additive manufacturing of ferromagnets," Advanced Materials, vol. 35, pp. 2303292 1–11, 2023.
6. M. Xu, A. J. Deenen, H. Guo, D Grundler - arXiv preprint arXiv:2404.19153, 2024.

Satisfaction of circular polarized Laguerre-Gaussian mode generation requirements by mid-infrared thermal emission metasurface

K. Sekiya[1*], and Y. Nishijima[1]

[1]Yokohama National University, Japan
[*]corresponding author: sekiya-kazuma-hx@ynu.jp

Abstract: We studied the design methodology for generating circularly polarized Laguerre-Gaussian beams using a metal-insulator-metal structured mid-infrared metasurface. As a result, it suggested that a two-layered meta-molecule with optimized three-dimensional chiral structure could control circular dichroism and geometric phase, indicating the potential realization of compact devices emitting ultra-narrowband mid-infrared radiation.

Introduction: The circularly polarized Laguerre-Gaussian (CP-LG) beam is a complex light mode that couples the orbital angular momentum (OAM) of a light vortex (or Laguerre-Gaussian beam) with the spin angular momentum (SAM). It has been demonstrated that due to the in-plane light-induced forces (IP-LIF) originating from the SAM spin direction, this light vortex exhibits circular dichroism and allows for velocity modulation of trapped particles[1]. The realization of a compact device emitting CP-LG beams is expected to bring significant progress in structural analysis and optical manipulation techniques.

The metal-insulator-metal nanostructures (MIM) multi layered mid infrared meta-surface we have proposed allows for microscale design and control of thermal radiation states by appropriately defining and adjusting the shape of meta-molecules placed on the meta-surface. To generate CP-LG beams, two requirements are necessary: spin selectivity and a 2π phase shift on the wavefront. It has been previously demonstrated that a three-dimensional chiral symmetric structure of meta-molecules exhibits circular dichroism[2]. Building upon this idea, we defined a chiral structure by stacking meta-molecules into two layers and applying orientation angles and aimed to improve circular dichroism and phase control through structural optimization.

FDTD Simulations: The two meta-molecules are designed both rectangular, and their shapes are determined by nine parameters (size of each meta-molecules, distance between meta-molecules, rotation angle of upper-layer meta-molecules relative to lower-layer meta-molecules, and meta-molecule periodicity). In the optimization process, we set the objective function to maximize extinction of right circularly polarized light (conversely, a maximized left circularly polarized metamolecule can be defined by taking the mirror symmetry of the optimized structure). This study was validated using electromagnetic field analysis simulations software based on the finite-difference time-domain (FDTD) method.

Results and discussions: As a result, the optimized meta-molecules exhibit different shape parameters between the upper and lower layers, demonstrating three-dimensional chirality. In wideband simulations, it achieved an absorption rate $\mathcal{A}$=0.86 and a circular dichroism absorbance CD=0.4 at wavelength λ=5.1 μm. This means the possibility of the emission of elliptically polarized light with an ellipticity of 0.4 and single-wavelength radiation. Additionally, π range rotation of meta-molecule about the radiation axis revealed a gradual 2π shift in radiation phase while maintaining the constant absorption wavelength. This result aligns with the theory of phase delay due to changes in polarization state indicated by the Pancharatnam-Berry (PB) phase[3]. By fitting the phase state to the rotation, it is practically feasible to achieve 100% phase coverage.

Conclusions: We designed meta-molecule structures that simultaneously satisfy the requirements of circular polarization and optical vortex properties, demonstrating the possibility of radiating CP-LG beams in the mid-infrared region by representing phase gradients based on geometric phase on the meta-surface. Future work will explore the feasibility of realizing CP-LG beams as small-scale devices through the observation of their topological charges and evaluation of physical prototypes.

References

1. M. Tamura, T. Omatsu, S. Tokonami, and T. Iida, "Interparticle-Interaction-Mediated Anomalous Acceleration of Nanoparticles under Light-Field with Coupled Orbital and Spin Angular Momentum," Nano Lett. Vol. 19, No. 8, 4873–4878, 2019.
2. H. S. Khaliq, A. Nauman, J.-W. Lee, and H.-R. Kim, "Recent Progress on Plasmonic and Dielectric Chiral Metasurfaces: Fundamentals, Design Strategies, and Implementation," Adv. Optical Mater., Vol. 11, 2300644, 2023.
3. M. V. Berry, "The Adiabatic Phase and Pancharatnam's Phase for Polarized Light," J. Mod. Opt., Vol. 34, No. 11, 1401-1407, 1987.

Orbital angular momentum multiplexed metasurface for multi-wavelength holography

S.-W. Moon[1], J. Jang[2], and J. Rho[1,2,3,4*]

[1] Department of Mechanical Engineering, Pohang University of Science and Technology (POSTECH), Pohang 37673, Republic of Korea
[2] Department of Chemical Engineering, Pohang University of Science and Technology (POSTECH), Pohang 37673, Republic of Korea
[3] Department of Electrical Engineering, Pohang University of Science and Technology (POSTECH), Pohang 37673, Republic of Korea
[4] POSCO-POSTECH-RIST Convergence Research Center for Flat Optics and Metaphotonics, Pohang 37673, Republic of Korea
[*]corresponding author: jsrho@postech.ac.kr

Abstract: This study introduces a wavelength-multiplexed orbital angular momentum holographic device capable of encoding and reconstructing multiple holographic images using light of specific wavelengths and topological charges. The device, demonstrating significant storage potential, successfully encoded and reconstructed nine distinct images under defined conditions.

Metasurface is an advanced optical component characterized by its structure, which is composed of one- or two-dimensional array of nanostructures[1]. Metasurface plays the role of an exceptional platform for various optical applications. In particular, metasurface-based holograms have attracted significant attention due to their subwavelength pixel pitch, complex amplitude manipulation, and multiplexablity.

In this work, we introduce an orbital angular momentum (OAM) metasurface that employs wavelength and OAM multiplexing for the creation of holograms capable of preserving OAM properties within the image plane. When an OAM beam illuminates the hologram, holographic image is reconstructed through the convolution of the original image and Fourier transform of a helical wavefront, which is characterized by a doughnut-shaped intensity distribution and a spiral phase profile. The intensity profiles of pixels in the holographic image depend on the topological charges of the incident OAM beam, leading to a distinctive doughnut-shaped pixel intensity distribution as topological charges increase.

To encode these OAM-conserving holographic images onto a metasurface, precise sampled images are achieved through multiplication of object images with 2D Dirac comb function [2]. This technique effectively prevents interference between neighboring pixels in reconstructed holographic images. The sampling parameters are specifically chosen according to the largest radius of the kernel in the image plane, ensuring each pixel preserves the properties of the incident OAM beam. Additionally, OAM selectivity is accomplished by combining the hologram with a spiral phase profile of an opposite topological charge to the incident beam, allowing for the reconstruction of holographic images with peak intensity for specific OAM modes, as shown in Fig. 1(a).

We further explore the design and implementation of an OAM-selective and multiplexing meta-hologram, as shown in Fig. 1(b). By employing a modified Gerchberg-Saxton algorithm, the phase profile of the meta-hologram is optimized to facilitate holographic images. Moreover, we demonstrate the feasibility of multiplexing holographic images for various OAM modes on a single metasurface, considering wavelength dependencies to ensure consistent image sizes across different wavelengths (Fig. 1(c)). The proposed metasurface achieves full-color OAM holographic display capabilities, showcasing the potential for advanced holographic displays and

optical data storage solutions.

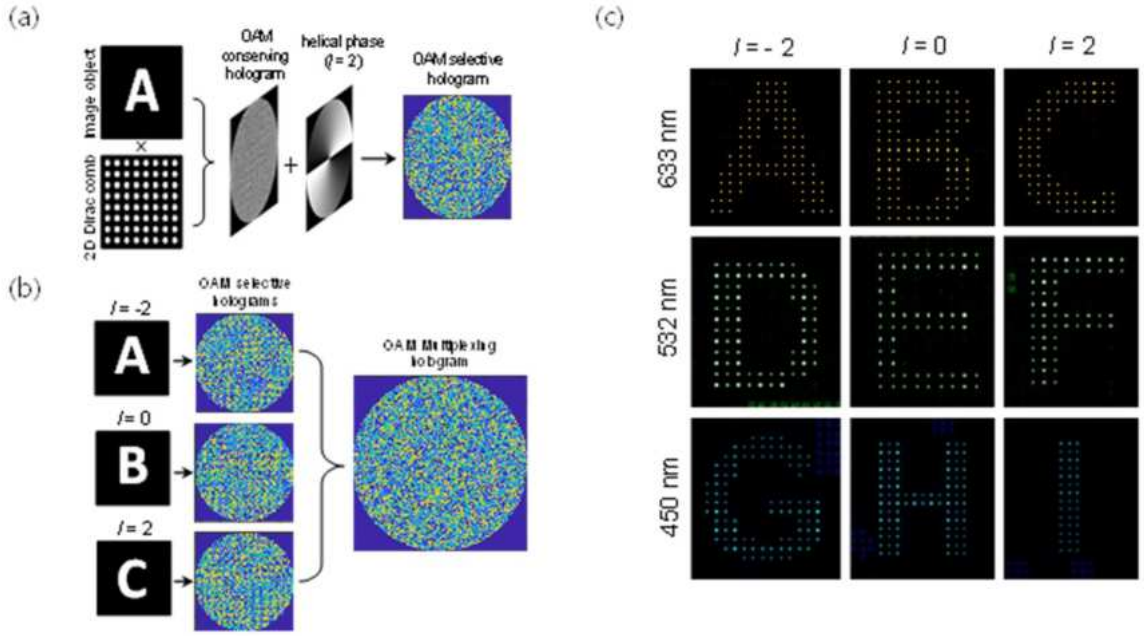


Figure 1 (a) Design method for orbital angular momentum selective hologram (b) Encoding orbital angular momentum multiplexing hologram (c) Holographic images for the wavelengths and topological charges of incident light.

References

1. Yu, N. and Capasso, F. "Flat optics with designer metasurfaces," Nat. Mater. Vol. 13, 139–150, 2014.
2. Fang, X. et al. "Orbital angular momentum holography for high-security encryption," Nat. Photonics Vol. 14, 102–108, 2020.

Resonant exceptional points in terahertz metasurfaces

Lei Wang[1], **Caihong Zhang**[1,2,*], **Jingbo Wu**[1,2], **Kebin Fan**[1,2], **Biaobing Jin**[1,2], **Jian Chen**[1,2] **and Peiheng Wu**[1]

[1]Nanjing University, China
[2]Purple Mountain Laboratories, China
[*]corresponding author: chzhang@nju.edu.cn

Abstract: In this study, we comprehensively investigate the resonant exceptional point (EP) in terahertz metasurfaces, which directly realize the singularity of complex frequency requiring one measurement only. Our approach not only provides a novel perspective to understanding EP in non-Hermitian terahertz metasurfaces but also offers alternative methods for terahertz high-sensitivity sensing.

Studies on EP in terahertz metasurfaces mostly focus on the scattering exceptional point (EP).[1] However, due to the highly sensitive characteristics of the EP itself, errors induced by multiple measurements are inevitable in practical sensing applications by this type of EP. Thus, our interest lies in exploring another form of EP in the terahertz region that requires one measurement only. As shown in Fig. 1, the resonant EP bilayer metasurface structure we designed consists of two layers of non-equal metal rods. Figure 1c and 1d visualize the variation of the Riemann surface consisting of the real and imaginary parts of the intrinsic complex frequency with respect to the longitudinal (*dy*) and transversal (*dx*) parameter space, and it can be clearly seen that the EP points at the crossings.

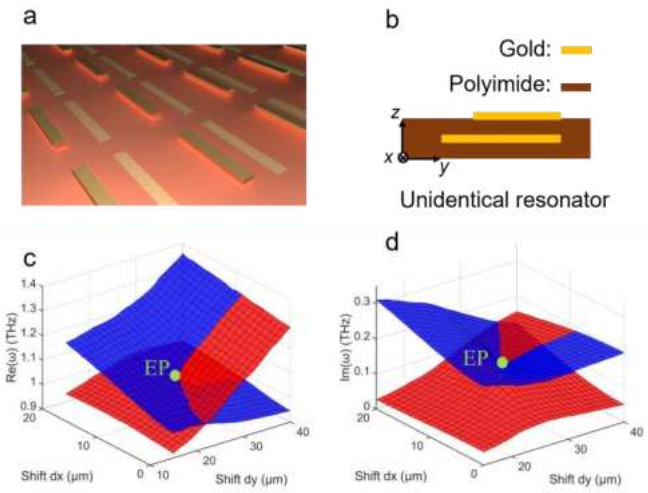


Fig. 1. (a) Schematic diagram of proposed bilayer metasurface structure with resonant EP. (b) Unit cell of unidentical resonators. (c) Real and (d) imaginary parts of the eigenmodes of the identical resonators.

In order to experimentally demonstrate the existence of EP, we characterized three groups of samples with four different values of *dy*. The frequency response spectral results of these metasurface samples were characterized by a fiber-based THz time-domain spectroscopy. Transmittance can be extracted from $T(\omega) = \left| E_{sam.} / E_{ref.} \right|^2$, in which $E_{sam.}$ and $E_{ref.}$ are the Fourier transforms of the time-domain electric field

measurements of the EP metasurface sample and reference, respectively.

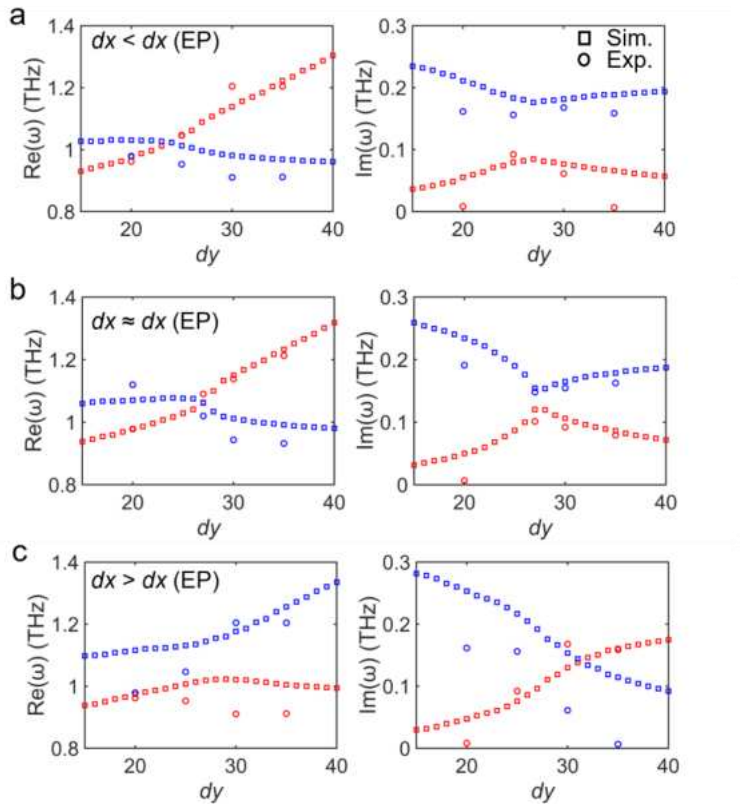


Fig. 2. Experimental observation of EP in metasurfaces. Experimental (circles) and simulated (squares) complex frequencies as a function of *dy* for (a) *dx* = 5 μm, (b) 9.5 μm, and (c) 15 μm. Blue and red distinguish two modes.

As shown in Fig. 2, the two-dimensional representation of the Riemann surface in Fig. 1 provides a more intuitive observation of the phase transition from PT symmetry to PT symmetry breaking. In Fig. 2a, we observe the intersection of real part of eigen-frequencies and the absence of intersection of imaginary part of eigen-frequencies at *dy* = 24 μm, indicating that the system is in the PT symmetry broken phase. In Fig. 2b, both real and imaginary part intersect at *dy* = 27 μm, indicating that the system is at EP. In Fig. 2c, we observe the absence of intersection of real part of eigen-frequencies and intersection of imaginary part of eigen-frequencies around *dy* = 32 μm, suggesting that the system is in the PT-symmetric phase. Thus, we demonstrate the ability to achieve a singularity of complex frequencies directly. Our EP proposal contributes to further understanding non-Hermitian physics in terahertz metamaterials/metasurfaces, as well as providing a novel approach for highly sensitive detection and biosensing and other functional devices.

This work was supported by the National Key Research and Development Program of China (Nos. 2021YFB2800701), the National Nature Science Foundation of China (NSFC) (Nos. 62222106, 92163216, 62071217, 62027807, and 62288101), and the Fundamental Research Funds for the Central Universities.

References

1. Wang, L., Liu H., Li T., Tian D., Zhang C. H., Wu J. B., Fan K. B., Jin B. B., Chen J., Wu P. H., "Resonant exceptional points sensing in terahertz metasurfaces" Appl. Phys. Lett. (Accepted, DOI: 10.1063/5.0193106)

Janus Bound States in the Continuum with Asymmetric Topological Charges and Intrinsic Chirality

Meng Kang[1], Meng Xiao[2,3*], and C. T. Chan[1*]

[1]Department of Physics, The Hong Kong University of Science and Technology, Hong Kong, China
[2]Key Laboratory of Artificial Micro- and Nano-structures of Ministry of Education and School of Physics and Technology, Wuhan University, Wuhan 430072, China
[3]Wuhan Institute of Quantum Technology, Wuhan 430206, China
[*]corresponding author: phmxiao@whu.edu.cn, phchan@ust.hk

Abstract: We propose Janus bound states in the continuum (BICs), a new topological defect with asymmetric topological charges for upward and downward radiation. Janus BICs enable the realization of chiral BICs and offer a novel approach to control momentum-space phase singularities and enhance direction- and spin-dependent asymmetric light-matter interactions.

We introduce the concept of Janus bound states in the continuum (BICs), which is a new type of topological defect featuring asymmetric topological charges in upward and downward radiation. By harnessing the unique topological property of Janus BICs, we achieve chiral BICs and gain additional freedom in controlling phase singularities. Specifically, Janus BICs are produced by introducing up-down mirror symmetry breaking to merge multiple circularly polarized states (C points) with the same topological charges into a symmetry-protected BIC on only the downward side. Consequently, the topological charge of the BIC on the downward side is modified, while the upward side remains unaffected, forming a Janus BIC. To achieve chiral BICs, we further introduce in-plane mirror symmetry breaking to tune two C points with the same topological charge and identical handedness on the upward side to the Janus BIC. This process ends in a Janus chiral BIC with large intrinsic chirality and an infinite Q factor. Janus BICs can induce distinct Pancharatnam–Berry phase singularities in momentum space for different incident channels, providing a new approach to control optical angular momentum. Janus chiral BICs hold promise in enhancing direction-dependent and spin-dependent asymmetric light-matter interaction, opening new pathways for improving chirality-dependent operation for on-chip devices.

Versatile Metaphotonic Singularities: Multidimensional, Optomechanical, and Topological Aspects

Tianyue Li[1], Shuming Wang[1], and Shining Zhu[1]
[1]National Laboratory of Solid-State Microstructures, Collaborative Innovation Center of Advanced Microstructures, School of Physics, Nanjing University, Nanjing, 210093, China
[*]corresponding author: leos4a@163.com

Abstract: This presentation highlights metaphotonic singularities in nanophotonics, emphasizing their multi-dimensional nature and optomechanics applications. Using spin-dependent metasurfaces and Jones matrix innovations, we show dynamic control and transformation of singular light beams, advancing nano-device development and on-chip optical manipulation in metaphotonic physics.

Photonic singularities refer to those undefined or discontinuous points in structured light fields or eigen-spectra in the periodic metastructures, and have been extensively studied across various nanophotonic systems. In the field of metaphotonics, investigating photonic singularities at sub-wavelength scales in localized near-fields or propagating into far-fields pave the way to enriched light-matter interactions, enabling multi-dimensional singular phenomena. This is further analyzed from a topological perspective and applied in the field of momentum transfer light-matter interactions, such as optomechanics. In this presentation, we will first discuss the multi-dimensional characteristics of phase singularities in the generalized spin-orbit conversion, caused by three-dimensional (3D) polarization field interference in non-paraxial light fields, as shown in Fig. 1a. This is dynamically observed through specially designed spin-dependent metasurfaces, enabling switchable Bessel beam generators[1]. Then, to further shape the form of singularities on metasurfaces, we not only developed the upper limit of the degrees of freedom of the Jones matrix but also proposed a local and global phase design method, theoretically and experimentally demonstrate the structural transformation of non-diffracting singular beams along optical trajectories, i.e., from circular Airy beam to Bessel beam, as depicted in Fig. 1b. Hence, we considered further methods for generating generalized singular beams, extracting and encoding the intensity profile of any figures onto the azimuthal phase gradient of a metasurface (Fig. 1c), creating a multifunctional generalized angular momentum plate for singular beam generation, representing a paradigm shift in phase singularity optical devices, extending beyond the conventional J-plate[2] and T-plate[3]. In its application in optomechanics, we focus on an integrated multifunctional optical tweezer-spanner, allowing for rotation and optical capture of nanoparticles, significantly reducing the volume through multi-dimensional characteristics. By combining the Mie scattering process with the birefringent properties of nanoantennas, we established a polarization multiplexing function capable of phase processing two independent dimensions of polarization, achieving simultaneous trapping and rotation of particles[4], as shown in Fig. 1d. This method is extended to generate programmable optical spanner and generalized vortex beams. Importantly, deformable metasurfaces can serve as artificial particles, enabling car-like motion or 'Metavehicles,' allowing arbitrary movement on a two-dimensional (2D) plane without the need for tightly focused structured light beams, anticipating to provide opportunities for developing on-chip optical manipulation (Fig. 1e)[5]. Meanwhile, the new ultrafast metavehicles reduce the need for additional incident fields, and their complete in-plane control heralds a new chapter in optical meta-manipulation. For singularities in the eigen-spectrum of metasurfaces, we focused on the Dirac singularity in 2D flat photonic structures, flexibly coupling six-folded rotation symmetric (C_6) honeycomb

lattices and C_3-symmetric triangular lattices with topological properties, as illustrated in Fig. 1f. These are combined into various domain wall photonic hybrid topological polycrystalline circuits, achieving multi-dimensional localized edge-corner modes at different frequencies and spins. These findings represent just the tip of the iceberg in the study of metamaterial photonic singularities. We believe that exploring the connections between photonic singularities will not only advance fundamental research in multi-dimensional light fields but also further promote the application of on-chip integrated optical devices and optical meta-manipulation.

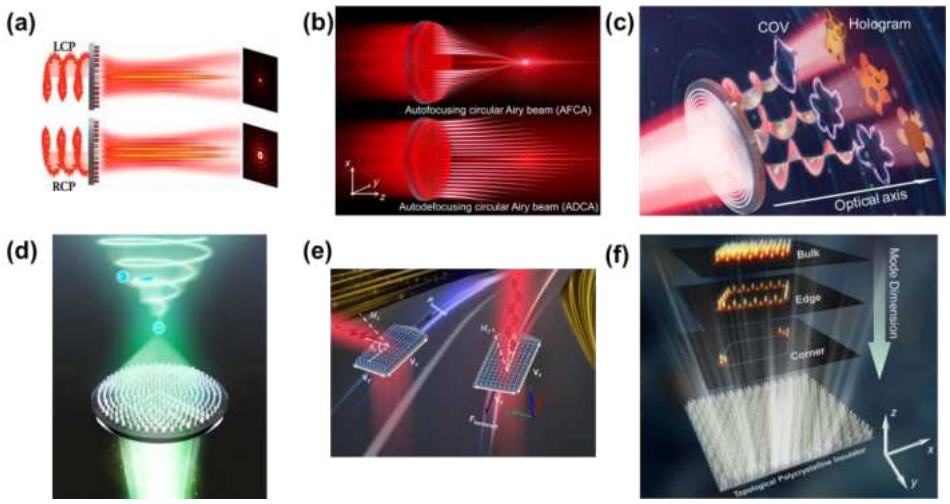


Figure 1. a. Spin-dependent higher-order Bessel beam generator. b. Structural deformation of singularity diffraction-free beams along the optical axis, with the top showing self-focusing circular Airy beams (CABs) and the bottom displaying self-defocusing CABs. c. Customized optical vortex with spin-selective metasurfaces. d. Integrated optical tweezers-spanners. e. Lateral force-reversible metavehicles. f. Photonic hybrid polycrystalline insulators.

Acknowledgements. This work was supported by the National Program on Key Basic Research Project of China (2022YFA1404300), National Natural Science Foundation of China (No. 12325411, 62288101, 11774162), The Open Research Fund of the State Key Laboratory of Transient Optics and Photonics, Chinese Academy of Sciences (SKLST202218), the Fundamental Research Funds for the Central Universities (020414380175). Postgraduate Research & Practice Innovation Program of Jiangsu Province (KYCX23_0096).

References

1. Li Tianyue et al., "Generation and Conversion Dynamics of Dual Bessel Beams with a Photonic Spin-Dependent Dielectric Metasurface," Phys. Rev. Appl., Vol. 15, 014059, 2021.
2. Devlin Robert C et al., "Arbitrary spin-to–orbital angular momentum conversion of light," Science, Vol. 358, 896–901 2017.
3. Dorrah Ahmed H et al., "Structuring total angular momentum of light along the propagation direction with polarization controlled meta-optics," Nat. Commun., Vol. 12, No. 34, 6249, 2021.
4. Li Tianyue et al., "Integrating the optical tweezers and spanner onto an individual single-layer metasurface," Photon. Res., Vol. 9, No. 6, 1062-1068, 2021.
5. Li Tianyue et al., "Reversible lateral optical force on phase-gradient metasurfaces for full control of metavehicles," Opt. Lett., Vol. 48, No. 2, 255-258, 2023.

Topological momentum gap in PT-symmetric photonic crystals

Ming-Wei Li[1], Jian-Wei Liu[1], Wen-Jie Chen[1*], and Jian-Wen Dong[1*]

[1]Author Affiliation, Country School of Physics & State Key Laboratory of Optoelectronic Materials and Technologies, Sun Yat-sen University, Guangzhou 510275, China

[*]corresponding author: chenwenj5@mail.sysu.edu.cn; dongjwen@mail.sysu.edu.cn

Abstract: We study the topological feature of the momentum bandgap (PT-broken regime) with a simple 1D binary photonic crystal. Our theory shows that its momentum band (PT-exact regime) can exhibit nontrivial band topology, guaranteeing the existence of a robust temporal boundary state localized in time but extended in space.

Recently, many topological concepts have been extended and rebuilt in non-Hermitian system. However, most previous works are concerned with the topologies of energy/frequency bands and the associated in-gap spatial boundary states. From another perspective, PT-broken regimes in non-Hermitian band structure can be viewed as a momentum bandgap if we take Bloch k as the eigenvalue instead of energy/frequency. Here, we study the topological feature of the momentum bandgap (PT-broken regime) with a simple 1D binary photonic crystal as an example. Our theory shows that its momentum band (PT-exact regime) can exhibit nontrivial band topology, manifested as a local geometric phase. This guarantees the existence of a topological temporal boundary state localized in time but extended in space. The robustness against defects or disorders is numerically demonstrated by full-wave simulations. Although our idea is demonstrated in a simple 1D PT-symmetric photonic system, it can in principle apply to any PT-symmetric or pseudo-Hermitian system. Our findings would extend and supplement the current understanding of topological spatial edge states and provide a new perspective on topological physics in non-Hermitian systems.

References

1. Li, M.-F., Liu, J.-W., Chen, W.-J. and Dong, J.-W., “Topological momentum gap in PT-symmetric photonic crystals,” arXiv: 2306.09627, 2023.

Evanescent Wave Manipulation Based on Non-Hermitian Physics

Huanan Li*

MOE Key Laboratory of Weak-Light Nonlinear Photonics, School of Physics, Nankai University, Tianjin 300071, China
*corresponding author: hli01@nankai.edu.cn

Abstract: We present the concept of parity-time (PT) symmetry and spectral singularities as applied to evanescent waves, along with the first experimental verification of PT symmetry for evanescent waves using an acoustic platform. Our study sheds light on the opportunity to manipulate evanescent waves through non-Hermitian physics.

In the broad context of non-Hermitian physics, the concept of parity-time (PT) symmetry has unlocked remarkable possibilities for novel wave manipulations that are not unattainable within the confines of Hermitian systems [1]. In unbounded scattering systems with PT symmetry, the system response is characterized by a scattering matrix S which satisfies the fundamental relation $PTSPT = S^{-1}$ [2]. Traditionally, PT symmetry in scattering settings has been applied to propagating wave manipulation, enabling novel wave manipulations such as laser-absorber modes and anisotropic transmission resonances (ATRs). PT-symmetric systems operating in laser-absorber mode can simultaneously act as lasers and coherent perfect absorbers (CPAs), with this dual functionality experimentally confirmed in both optical and radio-frequency domains.

First, we propose an intriguing pathway to PT symmetry that leverages the incidence of evanescent waves on anti-PT-symmetric structures, which interestingly does not necessarily require the presence of gain [3]. Utilizing two exemplary anti-PT symmetric configurations, one integrating coupled resonators and the other photonic heterostructures [Fig. 1(a)], we demonstrate that PT-symmetric responses can be revealed via evanescent wave excitations. These excitations enable the generalized S matrix to adhere to the same fundamental relationship that govern conventional PT symmetric systems with balanced gain and loss when excited by propagating waves [Fig. 1 (b)]. In the system of anti-PT symmetric coupled resonators, the detuning of resonance frequencies between the dimer defect resonators functions as an effective mechanism of gain and loss. Then we introduce a versatile coupled-resonator acoustic waveguide (CRAW) system to observe evanescent wave within a bandgap [Fig. 1(c)], and demonstrate the PT-symmetric scattering response from an engineered anti-PT symmetric dimer defect under stationary-state evanescent wave incidence [4]. By examining the generalized scattering matrix in the evanescent wave regime, we observe hallmark PT phenomena—including phase transitions at an exceptional point, ATRs, and laser-absorber modes—in systems without the customary balanced gain and loss.

Finally, based on parity-time symmetry, we introduce the concept of spectral singularities (SSs) for evanescent waves, and explore their exotic features [5]. SSs emerge at isolated real frequencies when the scattering coefficients of a system diverge, producing scattering anomalies in non-Hermitian systems. So far, the emergence of these exotic SSs has been restricted to propagating waves. Here, we extend them to evanescent waves and show that, due to the decoupling between energy transport and scattering strength for evanescent waves, an evanescent wave SS with diverging scattering coefficients can support arbitrary magnitude (infinite or finite) and reversible energy flow [Fig. 1(d)], depending on how the evanescent wave SS is approached in parameter space. Our results shed light on the opportunity to manipulate structured waves for extreme wave-matter interactions based on non-Hermitian physics, which may be extended to nanophotonics.

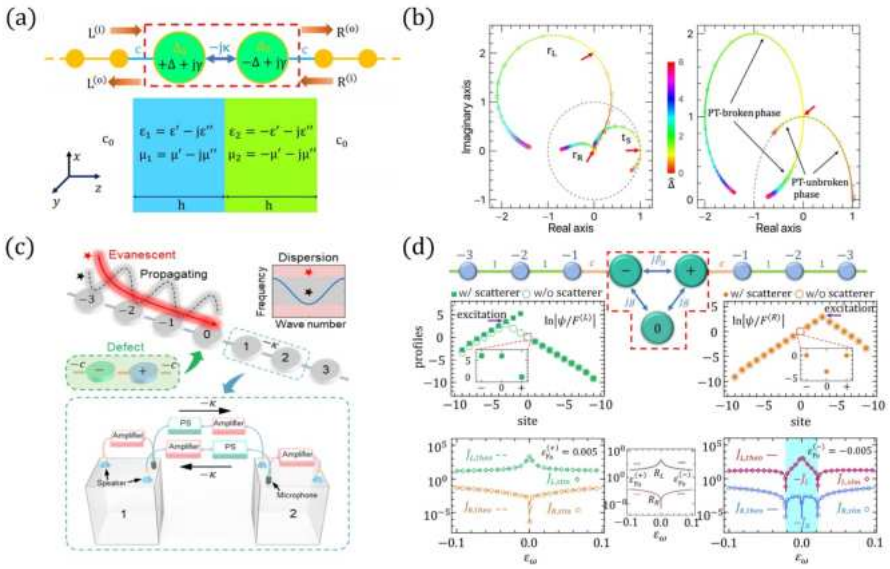


Figure 1: (a) Schematics of the anti-PT-symmetric coupled resonators (upper panel) and photonic heterostructures (lower panel). (b) Effective PT-symmetric response for evanescent waves: variations in the complex plane of scattering parameters (left panel) and eigenvalues (right panel), associated with the generalized S matrix. (c) CRAW system for observing evanescent-wave scattering. Upper panel: schematic of the uniform CRAW. The waveguide's dispersion relation (top right corner) illustrates that selecting a frequency at the bandgap (red star in the pink region) excites an evanescent wave, characterized by the exponentially decaying profile. Lower panel: schematic of the acoustic cavities with feedback circuits. (d) Upper panel: schematic of the geometry formed by a three-site defect (see the dashed red box) embedded in a coupled-resonator waveguide. Middle panels: logarithm of the (normalized) field profiles $\left|\psi/F^{(\alpha)}\right|$ in the scattering set-up, near a unidirectional SS. Lower panels: normalized energy flux J_α at the excitation port $\alpha = L, R$ as a function of the incident frequency detuning ε_ω when the damping coefficient detuning ε_{γ_0} switches from the value $\varepsilon_{\gamma_0}^{(+)} = 0.005$ (lower left panel) to $\varepsilon_{\gamma_0}^{(-)} = -0.005$ (lower right panel), with the associated left and right reflectance R_α, $\alpha = L, R$, in the lower middle panel. (a), (b) Adapted from ref [3]. (d) Adapted from ref [5].

References

1. D. Christodoulides and J. Yang, *Parity-Time Symmetry and Its Applications* (Springer, Berlin, 2018).
2. Y. D. Chong, L. Ge, and A. D. Stone, "PT-symmetry breaking and laser-absorber modes in optical scattering systems," Phys. Rev. Lett., Vol. 106, No. 9, 093902 (2011).
3. H. Li, A. Mekawy, and A. Alù, "Gain-free parity-time symmetry for evanescent fields," Phys. Rev. Lett., Vol. 127, No. 1, 014301 (2021).
4. Z. Chen, H. He, H. Li, M. Li, J. Kou, Y. Lu, J. Xu, and A. Alù, "Observation of Parity-Time Symmetry for Evanescent Waves," under review.
5. H. He, Z. Chen, H. Li, C.-H. Tu, J. Xu, and A. Alù, "Evanescent wave spectral singularities in non-Hermitian photonics," Phys. Rev. B, Vol. 109, No. 4, L041405 (2024).

Unidirectional unpolarized photoluminescence emission via vortex excitation

Jincheng Ni[1*]

[1] Department of Precision Machinery and Precision Instrumentation, University of Science and Technology of China, Hefei, Anhui 230027, China

[*]corresponding author: njc@ustc.edu.cn

Abstract: Directional light emission at subwavelength scale is key for quantum information processing and optical imaging in photonics and biology. Here, we present unidirectional emission of unpolarized luminescence in a spatially symmetric nanopillar lattice assisted by photonic orbital angular momenta (OAM), providing a tunable and large directional emission method for nanoscale optical control based on photonic OAM.

Directional light emission at subwavelength scale is key for quantum information processing and optical imaging in photonics and biology. Spin-orbit interaction of light is widely adopted for dynamically tuning the circularly polarized photoluminescence direction. However, the directional emission governed by spin mechanism is challenging for most luminescence materials, which typically generate unpolarized luminescence. Here, we present unidirectional emission of unpolarized luminescence in a spatially symmetric nanopillar lattice assisted by photonic OAM, providing a tunable and large directional emission method for nanoscale optical control based on photonic OAM as an additional degree of freedom.

Acknowledgements: This work was supported by the National Natural Science Foundation of China (Grant Nos. 61927814, 52122511, 52075516, and 61805230). J.N. acknowledges support from the start-up funding of the University of Science and Technology of China and the CAS Talents Program.

References

1. J. Ni, S. Ji, Z. Wang, S. Liu, Y. Hu, Y. Chen, J. Li, X. Li, J. Chu, D. Wu, and C.-W. Qiu, “Unidirectional unpolarized luminescence emission via vortex excitation,” Nature Photonics 17, 601-606 (2023).
2. J. Ni, S. Liu, Y. Chen, G. Hu, Y. Hu, W. Chen, J. Li, J. Chu, C.-W Qiu, and D. Wu, “Direct Observation of Spin–Orbit Interaction of Light via Chiroptical Responses,” Nano Letters 22, 9013-9019 (2022).

Tunable metaoptics using phase change and van der Waals materials

Kandammathe Valiyaveedu Sreekanth, Arash Nemati, Zeng Wang, Meng Zhao, Yuanda Liu, Jichao Fu, Jinghua Teng*

Institute of Materials Research and Engineering (IMRE), Agency for Science, Technology and Research (A*STAR), Singapore

*corresponding author: jh-teng@imre.a-star.edu.sg

Abstract: We introduce our recent works on chalcogenide phase change materials for tunable Tamm plasmonic response for bio-sensing, color coding, wide-angle perfect absorption and light beam switching, as well as van der Waals materials for electrically tuning of flat lens focusing, refractive index and near infrared plasmonic resonance.

Metaoptics constructed by sub-wavelength structures on a thin film has attracted tremendous interests for its great potentials over conventional refractive optics. Tunable metaoptics by employing active optical materials responding to external stimuli could further enhance the capability and adaptability of the optical system.[1] Chalcogenide alloys have phase changes between amorphous and crystalline with temperature changing across the phase transition temperature, which induce both refractive index and electrical conductivity changes and have been applied to diverse tunable micro-nano-optical devices across wide spectral range. [2-4] The unique properties of 2D materials such as the strong quantum confinement, bandgap tuning and flexible integration with different substrates bring many new opportunities to photonics and tunable metaoptics.[5] In this talk, I will give a brief review of tunable and reconfigurable metaoptics followed by introducing some of our recent works in this area using phase change and van der Waals materials.

We use low-loss Sb_2S_3 to construct a tunable Tamm plasmon polariton (TPP) cavity as a scalable sensing platform for surface enhanced resonance Raman spectroscopy (SERRS). By tuning the TPP resonance to match the laser excitation wavelength with the plasmonic resonance and the absorption peak of the biomolecules such as cardiac Troponin I protein, our SERRS is shown to be able to greatly reduce the detection limit.[6] Combining a broad-band and a narrow-band absorber made up of Sb_2S_3, we show tunable optical Fano resonance in the visible wavelength and a nano-optical coatings for optical steganography.[7] A wide-angle (0° to 70°) large spectral range tunable perfect absorption through critical coupling is achieved by utilizing a two-layer stack consisting of a high refractive index Sb_2S_3 on a reflecting silver layer. [8] We also demonstrate a transmission mode polarization-insensitive beam switching metasurface based on $Ge_2Sb_2Te_5$ at telecommunication wavelength with a switching angle of 15° and directivity of 82.4%. [9]

By manipulating the carrier density and interaction of excitons in 2D transition metal dichalcogenides, we show the large phase and refractive index tuning in a monolayer WS_2 assisted by optical cavity effect.[10] Electrostatically tunable near infrared plasmonic resonance around wavelength of ~1.67 μm in few-layer $NbSe_2$ is observed, which offers strong field confinement as compared to other near-IR plasmonic materials due to the atomic thickness.[11] A flat lens made of van der Waals ferroelectric material that can have its focusing been modulated by electrical bias through electro-optic effect will also be introduced.[12]

Authors thank the funding support by the National Research Foundation, Singapore under NRF-CRP (NRF-CRP26-2021-0004) and the Agency for Science, Technology and Research (A*STAR) under MTC Programmatic (M22L1b0110), IAF-PP program (H19H6a0025) and IRG program (A2083c0058).

References

1. Arash Nemati, Qian Wang, Minghui Hong, Jinghua Teng*, “Tunable and reconfigurable metasurfaces and metadevices,” Opto-Electron. Adv. Vol. 1, 180009, 2018.
2. Kandammathe Valiyaveedu Sreekanth, Sambhu Jana, Mohamed Elkabbash, Ranjan Singh and Teng Jinghua, “Phase change material-based tunable Fano resonant optical coatings and their applications,” Nanophoton. 2024. Doi: 10.1515/nanoph-2023-0723
3. Patinharekandy Prabhathan, Kandammathe Valiyaveedu Sreekanth, Jinghua Teng, et. al., “Roadmap for Phase Change Materials in Photonics and beyond,” iScience Vol. 26, 107946, 2023
4. Chunqi Zheng, Robert E Simpson, Kechao Tang, Yujie Ke, Arash Nemati, Qing Zhang, Guangwei Hu, Chengkuo Lee, Jinghua Teng, Joel K.W. Yang, Junqiao Wu, Cheng-Wei Qiu, “Enabling Active Nanotechnologies by Phase Transition_ From Electronics, Photonics to Thermotics,” Chem. Rev. Vol. 122, 15450–15500, 2022.
5. Ahmed Elbanna, Hao Jiang, Quandong Fu, Juan-Feng Zhu, Yuanda Liu, Meng Zhao, Dongjue Liu, Samuel Lai, Xian Wei Chua, Jisheng Pan, Ze Xiang Shen, Lin Wu, Zheng Liu, Cheng-Wei Qiu and Jinghua Teng, “2D Material Infrared Photonics and Plasmonics,” ACS Nano Vol. 17, 4134–4179, 2023.
6. Kandammathe Valiyaveedu Sreekanth, Patinharekandy Prabhathan, Ranjan Singh and Jinghua Teng, “Tunable Tamm plasmon cavity as a scalable sensing platform for surface enhanced resonance Raman spectroscopy,” Nature Commun. Vol.14, 7085, 2023
7. Patinharekandy Prabhathan, Kandammathe Valiyaveedu Sreekanth, Jinghua Teng and Ranjan Singh, “Electrically Tunable Steganographic Nano-Optical Coatings,” Nano Lett. Vol. 23, 5236-5241, 2023.
8. Kandammathe Valiyaveedu Sreekanth, Patinharekandy Prabhathan, Apoorva Chaturvedi, Yulia Lekina, Shen Zexiang, Jinghua Teng and Ranjan Singh, “Wide-angle tunable critical coupling in nanophotonic optical coatings with low-loss phase change material,” Small, Vo. 18, 2202005, 2022.
9. Arash Nemati, Guanghui Yuan, Jie Deng, Aihong Huang, Weide Wang, Toh Yeow Teck, Jinghua Teng and Qian Wang, “Controllable polarization insensitive and large-angle beam switching with phase-change metasurfaces,” Adv. Opt. Mater. Vol. 10, 2101847, 2022.
10. Zeng Wang, Matej Sebek, Xinan Liang, Ahmed Ramadan Abdelmontaleb Elbanna, Arash Nemati, Nan Zhang, Choon Hwa Ken Goh, Mengting Jiang, Jisheng Pan, Zexiang Shen, Xiaodi Su, Nguyen Thi Kim Thanh, Handong Sun, Jinghua Teng, “Greatly enhanced resonant exciton-trion conversion in electrically modulated atomically thin WS2 at room temperature,” Adv. Mater. Vol. 35, 2302248, 2023
11. Meng Zhao, Jing Li, Matej Sebek, Yanjun Liu, Michel Bosman, Qian Wang, Xinting Zheng, Le Yang, Jiong Lu, Jinghua Teng*, “Electrostatically Tunable Near-Infrared Plasmonic Resonance in Solution Processed Atomically Thin NbSe2,” Adv. Mater. Vol. 33, 2101950, 2021.
12. Yuanda Liu, Yaze Wu, Ruihuan Duan, Jichao Fu, and Jinghua Teng, et. al. “Linear electro-optic effect in 2D ferroelectric for electrically tunable metalens,” submitted

Machine-learning aided optimization for metasurfaces

Wei Ma[1*]

[1] College of Information Science and Electronic Engineering, Zhejiang University, Hangzhou, 310027, China.
[*]corresponding author: ma_wei@zju.edu.cn

Abstract: We present an algorithm-driven strategy to automatically design metasurfaces for multi-dimensional light manipulation. Our metasurface design pipeline comprises iterative optimization steps, integrating gradient-based optimization or heuristic algorithms enhanced by machine learning models. This approach has been experimentally validated using multi-channel holograms, focusing lenses, and guided light control.

Recently, with the aid of intelligent algorithms, the nanophotonic community has witnessed tremendous development in the design, measurement and application of nanophotonic devices and systems. The core impetus is the prevalence of inverse design methods, which convert a design problem into an optimization problem, and solve it with various algorithms automatically 1.

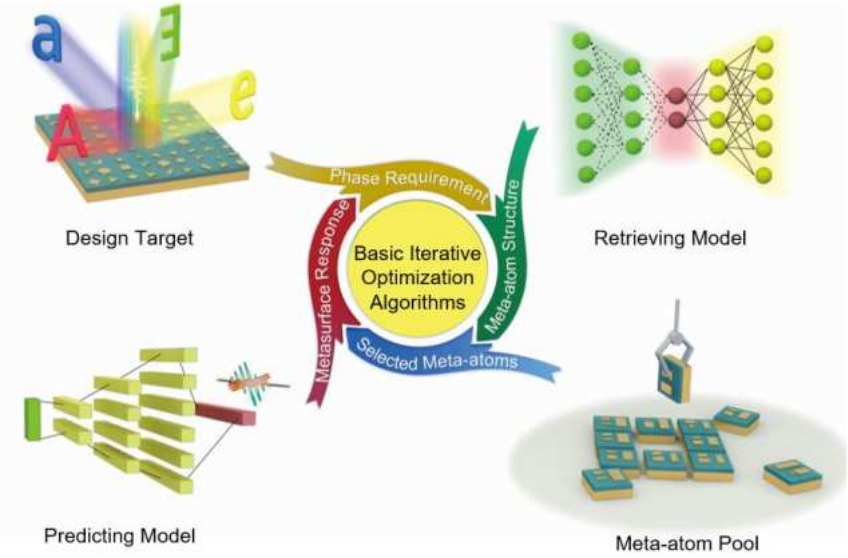


Figure 1 General end-to-end design pipeline for metasurface enhanced by machine learning

In this talk, we conceptually propose and experimentally demonstrate an end-to-end design pipeline with embedded statistical machine learning models for automatic design of metasurfaces. Instead of a two-step design routine including designing each meta-atom through a parameter sweep and then arrange them periodically, we resort to statistical machine learning as the bridge that directly links the structural parameters of each single meta-atom and the target metasurface performance. The machine learning model is composed of several probabilistic inverse retrieving models and a deterministic predicting model, which accurately capture and faithfully reproduce the statistical features of the high-dimensional joint distribution of meta-atom structures and their optical responses. Consequently, instead of artificially decoupling the complex optical response into independent sub-targets, a system-level multi-object optimization can be implemented to fully exploit the design space to push the design capacity to its physical limit. Under this design scheme, we experimentally demonstrated several design examples of metasurfaces including multi-channel holograms[2], wavelength-multiplexed light focusing[3], guided-wavefront manipulation[4], and ultra-compact fully etched grating

coupler.[5]

References

1. Yihao Xu, Bo Xiong, Wei Ma*, Yongmin Liu*, “Software-defined nanophotonic devices and systems empowered by machine learning”, Progress in Quantum Electronics, Vol. 89, 100469, 2023.
2. Wei Ma*, Yihao Xu, Bo Xiong, Lin Deng, Ruwen Peng*, Mu Wang, and Yongmin Liu*, “Pushing the Limits of Functionality-multiplexing Capability in Metasurface Design based on Statistical Machine Learning”, Advanced Materials, Vol. 34, No. 16, 2110022, 2022.
3. Bo Xiong, Yihao Xu, Wenwen Li, Wei Ma,* Tao Chu,* and Yongmin Liu*, “Deep Learning Design for Multiwavelength Infrared Image Sensors Based on Dielectric Freeform Metasurface”, Advanced Optical Materials, online, (2024). https://doi.org/10.1002/adom.202302200
4. Wei Ma*, Maojing Hou, Ruiqi Luo, Bo Xiong, Nan Liu, Guandong Liu, and Tao Chu, “Topologically-optimized on-chip metamaterials for ultra-short-range light focusing and mode-size conversion”, Nanophotonics, Vol. 12, No. 6, 1189-1197, 2023.
5. Qiao Wang, Ruiqi Luo, Nan Liu, Maojing Hou, Bo Xiong, Guandong Liu, and Wei Ma*, “Single-step-etched ultra-compact metamaterial grating coupler enabled by a hierarchical inverse design approach”, SCIENCE CHINA Physics, Mechanics & Astronomy, Vol. 67, No. 2, 224211, 2024.

Multidimensional manipulation of Light：From metasurfaces to liquid crystals

T. Huang[1], Y. Xie[1], Z. Zhou[1,2], D. Zhang[1], Z. Li[1*], and G. Zheng[1]

[1]Electronic Information School, Wuhan University, Wuhan, 430072 China
[2]NUS Graduate School, National University of Singapore, Singapore 119077, Singapore
[*]corresponding author: lizile@whu.edu.cn

Abstract: Metasurfaces exhibit exceptional abilities to manipulate the amplitude, phase, polarization, and spectral properties of light fields. These mechanisms for light field control can be extended to other material systems like liquid crystals, facilitating the creation of novel functionalities and devices.

Metasurfaces are artificial planar structural materials with subwavelength-scale features, enabling precise and flexible control over various parameters of incident electromagnetic waves such as amplitude, phase, polarization, and spectral characteristics at subwavelength scales.[1] This capability has garnered significant attention in recent years, and one notable advantage of metasurfaces over traditional optical elements is their ability to simultaneously manipulate multiple optical parameters, allowing for the design of more complex optical components.

Liquid crystals (LCs) possess unique optical properties, including polarization control and sensitivity to external stimuli, making them widely applicable in displays, optical communications, biosensing, and spatial light modulations. Through the manipulation of LC directors' orientations using an external electric field, LCs exhibit electro-optic effects, resulting in the formation of pixels with varying optical amplitudes/intensities. In addition to intensity modulation, phase modulation in LCs is typically achieved through optical path differences and depends on the thickness of the LC layer. Recently, continuous phase modulation in LCs has been achieved via the Pancharatnam–Berry (PB) phase, stemming from the spin–orbit interaction of light in inhomogeneous anisotropic media.[2]

Given their similarities in light field control properties, metasurfaces and liquid crystals enable the development of novel functional devices with similar yet distinctive characteristics[3,4]. This report will introduce multi-channel image display devices, all-optical multi-order multiplexing differentiation, and LC-based spectral singlet techniques.

References

1. Li, Z., S. Yu and G. Zheng, “Advances in exploiting the degrees of freedom in nanostructured metasurface design: from 1 to 3 to more,” Nanophotonics, Vol. 9, No. 12, 3699–3731, 2020.
2. Chen, P., B. Wei., and W. Hu, et.al., “Liquid-Crystal-Mediated Geometric Phase: From Transmissive to Broadband Reflective Planar Optics,” Adv. Mater., Vol. 32, No. 27, 1903665, 2020.
3. Deng, L., J. Deng and Z. Guan, et.al., “Malus-metasurface-assisted polarization multiplexing,” Light. Sci. Appl., Vol. 7, 58, 2020.
4. Chen, K., C. Xu., and Z. Zhou, et.al., “Multifunctional Liquid Crystal Device for Grayscale Pattern Display and Holography with Tunable Spectral-Response,” Laser Photonics Rev., Vol. 16, No. 3, 2100591, 2022.

Metalens for Accelerated Optoelectronic Edge Detection under Ambient Illumination

Shuai Wang

Qingdao Innovation and Development Center, Harbin Engineering University, Qingdao, China
*corresponding author: swang@hrbeu.edu.cn

Abstract: Analog optical edge detection systems usually rely on coherent laser sources for illumination, which significantly restricts their use in imaging tasks with ambient illumination. Here, we demonstrated a metalens-assisted imaging system that can allow optoelectronic edge detection under ambient illumination. It holds great potential for image processing under ambient illumination.

Compact optical systems for edge detection have been realized using a metasurface or multilayer films to mimic spatial differentiation[1-4]. Nonetheless, one of the major challenges of most demonstrated optical edge detection systems is that they typically require coherent laser light for illumination. For a spatially incoherent imaging system[5], the relationship between the output image $I_{out}(k)$ and input object $I_{in}(k)$ in the spatial frequency domain is described as,

$$I_{out}(k) = T(k)I_{in}(k), \quad (1)$$

where $T(k)$ is the optical transfer function, serving as the autocorrelation function of the amplitude transfer function. It is noteworthy that $T(k)$ always reaches maxima at $k = 0$. This contradicts the requirement of a vanishing transfer function at the center of the spatial frequency for image differentiation[5].

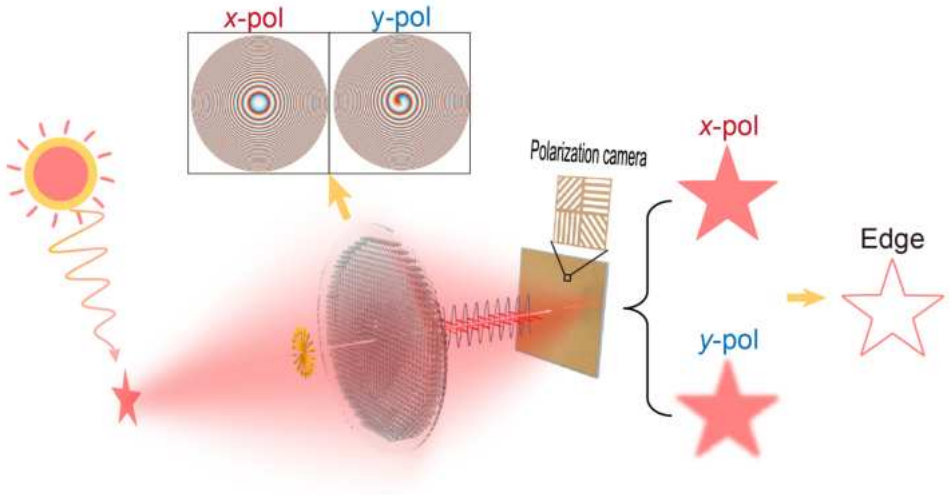


Figure 1. Schematic illustration of using polarization-multiplexed metalens for accelerated isotropic edge detection under ambient sunlight illumination.

Here, we proposed a polarization-multiplexed metalens for edge detection under ambient incoherent illumination shown in Fig.1. The metalens is designed to generate a pair of drastically different optical transfer functions (OTFs) for light with two orthogonal linear polarizations. Subsequently, an effective OTF can be synthesized via digital subtraction between the two OTFs, resulting in an isotropic high-pass filtering response. After multiplication between the polarization-dependent OTFs with the target object, the *x*- and *y*-polarized

images can be captured by a commercially available polarization camera in a single shot. For an image with $N\times N$ pixels, the computational complexity of the optoelectronic edge detection system with the point-by-point digital subtraction is $O(N^2)$. In contrast, for digital image processing using a convolution kernel with $a\times a$ pixels mimicking high-pass filtering response, it requires a point-by-point multiplication followed by a one-by-one summation, resulting in a computational complexity of $O(2a^2N^2)$. This reduction by a factor of $2a^2$ results in accelerated isotropic image differentiation. Therefore, the proposed system, while being extremely compact, can greatly reduce the computational complexity for edge detection under ambient incoherent illumination.

We integrated the polarization-multiplexed metalens with a polarization camera and experimentally demonstrated single-shot edge detection of indoor and outdoor scenes, including a flying airplane, under ambient sunlight illumination. The proposed system showcased the potential of using polarization multiplexing for the construction of complex optical convolution kernels towards accelerated machine vision tasks such as object detection and classification under ambient illumination.

This work was supported by the National Natural Science Foundation of China (62135008, 61975251) and the China Postdoctoral Science Foundation (2023M731911).

References

1. T. Zhu, Y. Zhou, Y. Lou, et al., Plasmonic computing of spatial differentiation. *Nat. Commun.*, 2017. **8**(1), 15391.
2. H. Kwon, D. Sounas, A. Cordaro, et al., Nonlocal Metasurfaces for Optical Signal Processing. *Phy. Rev. Lett.*, 2018. **121**(17), 173004.
3. Y. Zhou, H. Zheng, I.I. Kravchenko, and J. Valentine, Flat optics for image differentiation. *Nat. Photonics*, 2020. **14**(5), 316-323.
4. C. Jin and Y. Yang, Transmissive nonlocal multilayer thin film optical filter for image differentiation. *Nanophotonics*, 2021. **10**(13), 3519-3525.
5. H. Wang, C. Guo, Z. Zhao, and S. Fan, Compact Incoherent Image Differentiation with Nanophotonic Structures. *ACS Photonics*, 2020. **7**(2), 338-343.

Strong light-matter interactions in plasmonic/dielectric metasurfaces

Observation of Projective Embedded Topology and Trijunction-Induced Topological State in Acoustic Lattices

H. T. Teo[1], Y. Long[1*], K. Song[1], H. Xue[2], and B. Zhang[1, 3†]

[1]Division of Physics and Applied Physics, School of Physical and Mathematical Sciences, Nanyang Technological University, Singapore 637371, Singapore
[2]Department of Physics, The Chinese University of Hong Kong, Shatin, Hong Kong SAR, China
[3]Centre for Disruptive Photonic Technologies, Nanyang Technological University, Singapore 637371, Singapore
corresponding authors: *yang.long@ntu.edu.sg, †blzhang@ntu.edu.sg

Abstract: Contrary to dimension increment for weak topology, we demonstrate dimension reduction in insulators with projective crystal symmetry to construct embedded topology. Based on the one-dimensional strong topology at interfaces between two-dimensional trivial insulators, we realize a trijunction-induced topological state on tight-binding and acoustic platforms, thus enriching band topology in subdimensions.

Dimension plays a significant role in topological classifications [1]: varying dimension without changing symmetry conditions can result in distinct topology. For instance, dimension-increment-induced weak topology is constructed by stacking strong topological insulators from low dimensions. On the contrary, dimension reduction can also induce new topology by constructing (n-1)-dimensional strong topological insulators, even from an n-dimensional trivial insulator [see Fig. 1(a)]. This topology is called "embedded topology" [2]. However, symmetries that support embedded topology is still unclear.

Projective crystal symmetry, arising from the time-reversal-invariant gauge field, has contributed to new topological phenomena like Möbius-twisted edge bands [3]. Although dimension still plays a crucial role in characterizing the resultant novel topological phases, there is no theoretical and experimental work on the effect of dimension reduction under projective crystal symmetry, particularly from the perspective of embedded topology.

In 2D insulators, we demonstrate embedded topology via dimension-reduction-induced 1D strong topological insulators protected by projective crystal symmetry. By restricting to projective mirror symmetry and time-reversal symmetry, 2D insulators are trivial according to the topological classification [1]. We realize the dimension reduction through the formation of the interface between two insulators using the tight-binding model in Fig. 1(b). We begin with insulators A and B whose edge bands form a gapless Möbius twist under projective translation symmetry [2]. After the dimension reduction by connecting to insulator C, the projective translation symmetry is broken, thus gapping out the Möbius edge bands as shown in Fig. 2(a). These two isolated edge bands form a strong 1D insulator protected by projective mirror symmetry and time-reversal symmetry [1], leading to an embedded topological insulator. After connecting two 1D topologically

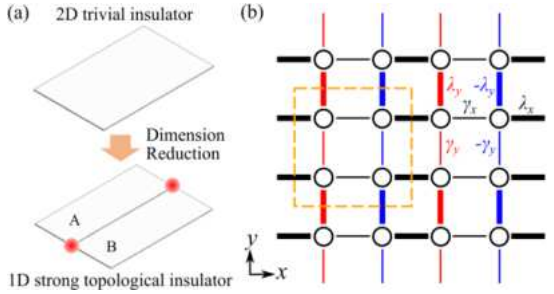


FIG. 1. (a) The effect of dimension reduction on the band topology at the interface. (b) Illustration of the lattice model. The colors and thickness of bonds indicate different real hopping strengths $\gamma_{x,y}$ and $\lambda_{x,y}$. The yellow dashed box denotes the unit cell. Insulators A, B, and C employ hoppings (γ_x, λ_x, γ_y, λ_y) = (1,1,1,10), (1,10,1,1), and (10,1,10,1), respectively.

distinct insulators based on dimension reduction, i.e., forming a trijunction [see Fig. 2(b)], a topological state emerges in the gap and localizes at the trijunction [see Figs. 2(c)-2(d)]. In acoustic lattices, we also perform the experimental observation of the trijunction-induced topological state with similar coupling distributions, as illustrated in Fig. 3.

Based on the projective crystal symmetry, similar constructions of embedded topology can be readily implemented in classical wave platforms and electric circuits. Furthermore, this novel idea can even be generalized to higher-dimensional systems, thus enriching topology in subdimensions.

This research is supported by Singapore National Research Foundation Competitive Research Program under Grant No. NRF-CRP23-2019-0007, and Singapore Ministry of Education Academic Research Fund Tier 3 under Grant No. MOE2016-T3-1-006 and Tier 2 under Grant No. MOE2018-T2-1-022 and Grant No. MOE2019-T2-2-085. H.X. acknowledges support from the startup fund of The Chinese University of Hong Kong. Y.L. acknowledges the support of the Eric and Wendy Schmidt AI in Science Postdoctoral Fellowship, a Schmidt Futures program.

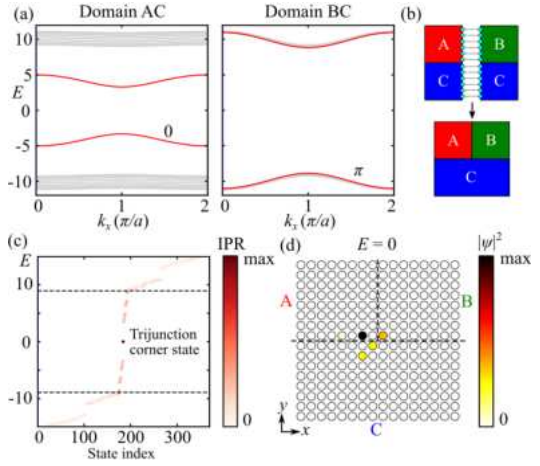


FIG. 2. (a) Edge dispersions of domains AC and BC, where the domains are periodic along x direction. The bulk (interface) bands are labelled in red (grey). The Berry phase of the interface bands is included. (b) Formation of trijunction by connecting two domains along x direction. Bonds are added between domains with distinct topology. (c) Eigenvalue spectrum of the finite 2D lattice with a trijunction, color-coded by the IPR of eigenstates. The dashed lines denote the common bandgap of insulators A, B, and C. (d) The eigenstate distribution of the trijunction-induced topological state. The domain walls are represented by the dashed lines.

References

1. Chiu C.-K., Teo J. C. Y., Schnyder A. P., and Ryu S., "Classification of topological quantum matter with symmetries", Rev. Mod. Phys., Vol. 88, No. 3, 035005 (2016).
2. Tuegel T. I., Chua V., and Hughes T. L., "Embedded topological insulators", Phys. Rev. B, Vol. 100, No. 11, 115126 (2019).
3. Zhao Y. X., Huang Y.-X., and Yang S. A., "Z_2-projective translational symmetry protected topological phases", Phys. Rev. B, Vol. 102, No. 16, 161117(R) (2020).

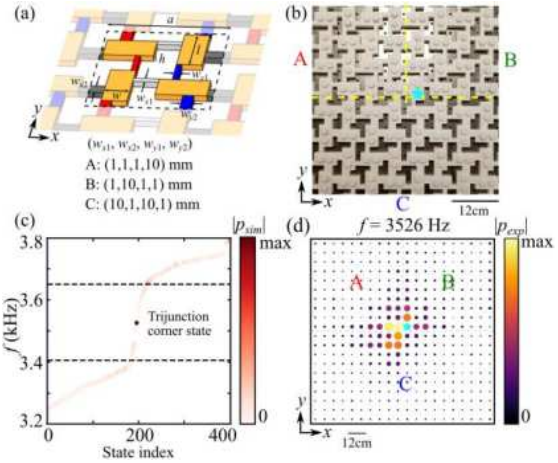


FIG. 3. (a) Schematics of the acoustic crystal consisting of acoustic resonators (orange) and coupling tubes. With the unit cell highlighted by the dotted rectangle, lattice constant a = 120 mm and the remaining parameters are labelled. (b) Partial view of the finite sample with 20 × 20 resonators and a trijunction at the center. (c) Simulated eigenfrequencies of the finite sample with the local pressure $|p_{sim}|$ (at the cyan star) scaled by the colorbar. The dashed lines enclose the simulated common bandgap of three insulators. (d) Excitation of the trijunction-induced topological state, where the colorbar characterizes the measured pressure $|p_{exp}|$. The cyan star and dashed lines in panels (b) and (d) indicate the position of speaker and domain walls, respectively.

Broadband sound attenuation under grazing flow via metamaterial-based acoustic liner

Sibo Huang[1], Yong Li[2], Jie Zhu[2], and Din Ping Tsai[1*]

[1]Department of Electrical Engineering, City University of Hong Kong, Hong Kong, China
[2]Institute of Acoustics, School of Physics Science and Engineering, Tongji University, Shanghai 200092, China
[*]corresponding author: dptsai@cityu.edu.hk

Abstract: This work presents a metamaterial-based acoustic liner consisting of a front perforated plate, an air interlayer, and an array of neck-embedded Helmholtz resonators. The presented liner experimentally achieves efficient sound attenuation within 800-3000 Hz in the presence of grazing flows with speeds from 10 m/s to 60 m/s.

Acoustic liners are widely used to attenuate the noise in aero-engines and exhaust mufflers [1-3]. Many conventional acoustic liners can effectively reduce noise for target modes in relatively narrow bands. However, on the one hand, broadband high-efficiency sound attenuation with thin structures remains challenging. On the other hand, in the presence of air flow, the acoustic impedances of the acoustic liners shift significantly along with the varying speeds of the flow, resulting in low tolerance to varying flow speeds and limiting the liners' overall performance in specific applications [1-3].

In this work, we present a metamaterial-based acoustic liner capable of effective broadband sound attenuation in the presence of grazing flow. The presented liner consists of a front perforated plate, an air interlayer, and an array of neck-embedded Helmholtz resonators (NEHRs) [4]. The NEHR array contributes to the thin thickness and provides the desired impedance condition in a wide frequency range. Besides, the front perforated plate maintains the aerodynamic flow smoother near the liner. With a suitable modulation of the acoustic impedance of the metamaterial-based liner in a broad frequency band, efficient broadband sound attenuation can be achieved under various speeds of grazing flows. In the experiment, we designed a sample having a thickness of 40.5 mm, and it can achieve remarkable sound attenuation within 800 Hz to 3000 Hz, both in the absence of air flow and in the presence of grazing flows with speeds from 10 m/s to 60 m/s [5].

Figure 1(a) depicts that the metamaterial-based acoustic liner is placed on one side of a rectangular flow duct to attenuate the sound energy. This situation is consistent with the most common practical application in aero-engines and exhaust mufflers. Figure 1(b) shows the sound-attenuation performance of the designed liner in the frequency band from 800 Hz to 3000 Hz under the condition of 130 dB of sound pressure level and without flow, where the peak value of transmission loss achieves 52.7 dB at 1600 Hz. Experiments were conducted in the flow duct test setup, as shown in Fig. 1(c).

Simulation results clearly demonstrate that the sound energy is strongly dissipated during the transmission along the designed liner. Based on the modulated impedance conditions, the sound-attenuation efficiency at 1600 Hz decreases as the flow speed increases but still remains at a high level, as shown in Fig. 2(a). The more comprehensive results of transmission losses are presented in Figs.2(b)-(c). On the whole, the thin meta-liner keeps high levels of transmission losses in a broad frequency range sustaining a relatively large variation of flow speeds.

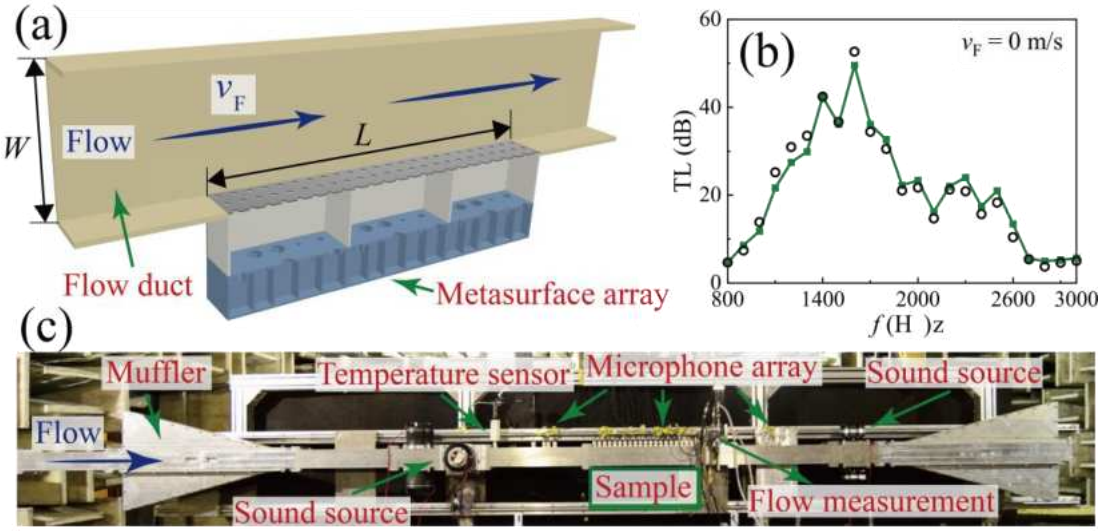


FIG. 1. (a) The cut-open view of a side-branched metamaterial-based acoustic liner in a flow duct. (b) The numerically calculated (the green line) and measured (black circles) transmission loss of the metamaterial-based acoustic liner without flow. (c) The aero-acoustic test setup.

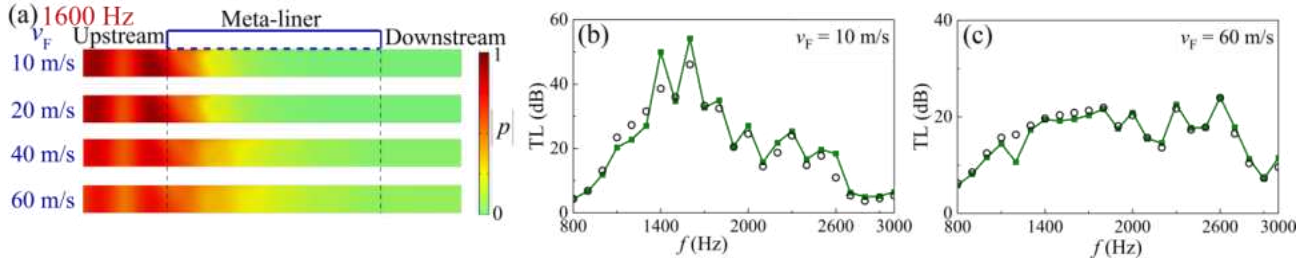


FIG. 2. (a) T Distributions of sound pressure amplitudes of the designed liner under various speeds of grazing flow at 1600 Hz. The numerically calculated (the green line) and measured (black circles) transmission loss of the metamaterial-based acoustic liner in the presence of grazing flow at speeds of 10 m/s (b) and 60m/s (c).

Acknowledgements

This work is supported by the Research Grants Council of Hong Kong SAR under Grant No. AoE/P-502/20, C1015-21E, C5031-22G, and CityU15303521, the National Natural Science Foundation of China under Grant Nos. 12074286 and 92263208, and the Shanghai Science and Technology Committee under Grant Nos. 21JC1405600 and 20ZR1460900.

References

1. S. Huang, Y. Li, J. Zhu, D.P. Tsai, “Sound-Absorbing Materials”. Phys. Rev. Appl., Vol. 20, 010501, 2023.
2. X. Ma and Z. Su, “Development of acoustic liner in aero engine: a review”, Sci. China Technol. Sci., Vol. 63, 2491, 2020.
3. H. Jiang and X. Huang, “Efficient Impedance Eductions for Liner Tests in Grazing Flow Incidence Tube”. J. Vib. Acoust., Vol. 139, 031002, 2017.
4. S. Huang, X. Fang, X. Wang, B. Assouar, Q. Cheng, Y. Li, “Acoustic perfect absorbers via Helmholtz resonators with embedded apertures”, J. Acoust. Soc. Am., Vol. 145, 254-262, 2019.
5. S. Huang, E. Zhou, Z. Huang, P. Lei, Z. Zhou, Y. Li, “Broadband sound attenuation by metaliner under grazing flow”, Appl. Phys. Lett., Vol. 118, 0635, 2021.

Resonant enhancement of optoacoustic response in van der Waals materials

Anton K. Samusev[1*], Alex D. Carr[2], Claudia Ruppert[1], Giulia Magnabosco[3], Nicolas Vogel[3], Tetiana L. Linnik[1,4], Andrew W. Rushforth[2], Alexey V. Scherbakov[1], Manfred Bayer[1], Andrey V. Akimov[2],

[1]Experimentelle Physik 2, Technische Universität Dortmund, 44227 Dortmund, Germany

[2]School of Physics and Astronomy, University of Nottingham, Nottingham NG7 2RD, United Kingdom

[3]Institute of Particle Technology, Friedrich-Alexander-Universität Erlangen-Nürnberg, 91058 Erlangen, Germany

[4]Department of Theoretical Physics, V.E. Lashkaryov Institute of Semiconductor Physics, 03028 Kyiv, Ukraine
[*]corresponding author: anton.samusev@tu-dortmund.de

Abstract: Acoustic nanocavities with high (above 10 GHz) resonance frequencies can be exploited in sensing and quantum devices. We demonstrate that for a sub-100-nm-thick van der Waals layer, the combination of exciton and Fabry-Pérot resonances, both tuned to the optical probe frequency, grants enhanced photoelastic response demanded in possible single-phonon applications.

Nanoacoustic devices, i.e., nanostructures supporting acoustic resonances, operating in the frequency range of 1-10 GHz, can serve as building blocks in quantum computing, optical cooling and sensing, filtering, and modulation of optical signals [1]. Along with Si-, GaAs-, and GaN-based systems, transition metal dichalcogenides (TMDs) represent a versatile platform for the realization of nanoacoustic devices with the resonances extended towards 0.01-1 THz frequency range characterized by high quality-factors above 10^3, see e.g. Ref. [2, 3]. Contrary to the previous studies, mainly aimed at the increase of acoustic mode eigenfrequency and lifetime, in this work, we focus on achieving highly efficient optical generation and detection of such high-frequency longitudinal acoustic (LA) phonons – breathing modes (BM) – in multilayer TMDs [4].

Here we study the optical generation and detection of high-frequency (10-200 GHz) coherent LA phonons in a WSe_2 nanolayer (Fig. 1a) as a function of its thickness. The sub-100-nm layers of TMD are deposited on top of an opal substrate, which acts as a firm mechanical insulator preventing the escape of high-frequency phonons from the TMDs into the substrate. We experimentally observe acoustically-induced relative changes in the relative reflectivity of more than 10^{-4}, an order of magnitude higher than previously reported in multilayer TMD-based systems [2, 3]. The comparison of the measured time-resolved pump-probe reflectivity signal with the one modeled theoretically reveals a strong dependence of the coherent signal amplitude on the complex photoelastic constant when probing with the wavelength in the vicinity of the exciton resonance in WSe_2. Moreover, bringing the thickness of the layer close to the lowest-order optical Bragg condition (thickness of 81 nm, Fig. 1(b, c)) grants an additional way to resonantly enhance the photoelastic response of such a nanoacoustic device. Our theoretical estimates show that such acoustic nanocavities combining exciton and Fabry-Pérot resonances, both tuned to the frequency of the optical probe, can be employed for operations with single phonons of high (above 10 GHz) frequencies at elevated temperatures.

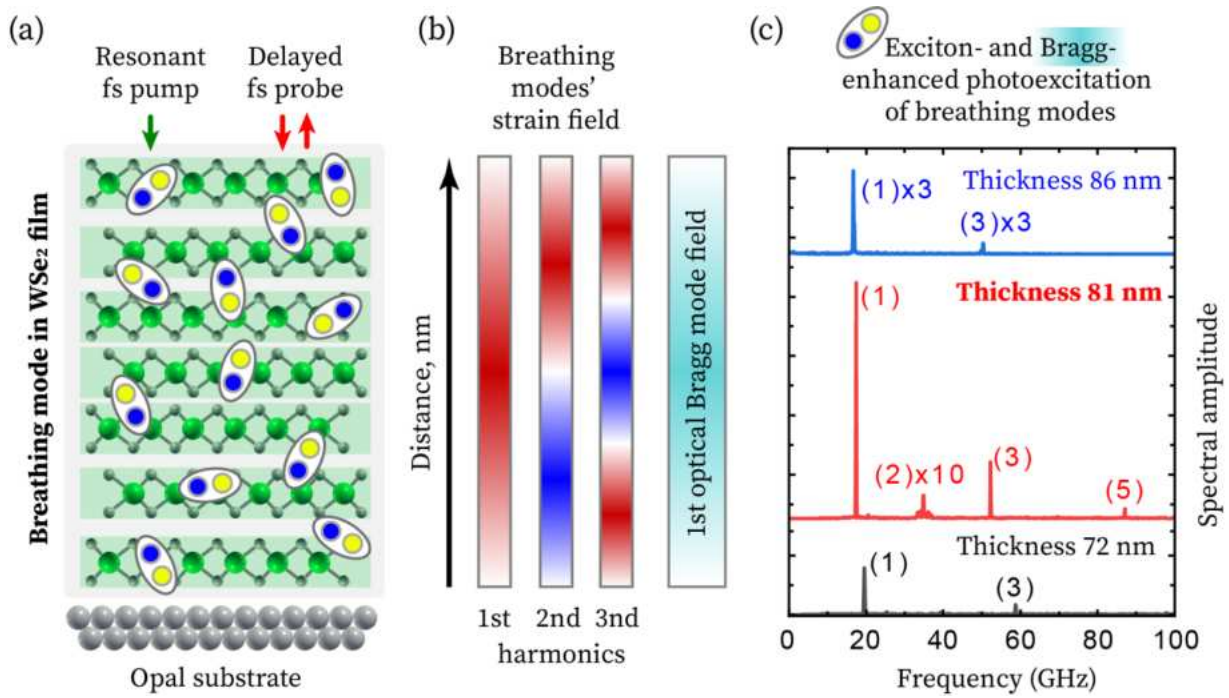


Figure 1. (a) Excitation and resonant detection of BMs in WSe2 film. (b) Distribution of strain field of the three lowest-order BMs. (c) Spectra of the optically detected coherent acoustic signals revealing BMs of the five lowest orders. The amplitudes of the spectral peaks get resonantly enhanced at the film thickness of 81 nm due to the lowest optical Fabry-Pérot mode, whose electric field is shown rightmost in panel (b).

This work was supported by the Engineering and Physical Sciences Research Council (Grant No.EP/V056557/1), the Mercur Foundation (Grant Pe-2019-0022), the Deutsche Forschungsgemeinschaft (TRR 142 projects A06 and A10) and the research centre "Future Energy Materials and Systems" of the Research Alliance Ruhr. A.K.S. acknowledges the support of the Deutsche Forschungsgemeinschaft through the Walter Benjamin Programme (project #529710370). T.L.L. acknowledges Alexander von Humboldt Foundation support through the Philipp Schwartz Initiative and TU Dortmund core funds. A.V.A. acknowledges the Alexander von Humboldt Foundation. The authors thank V. E. Gusev for the help in theoretical calculations.

References

1. Aspelmeyer, M., Kippenberg, T. J., Marquardt, F. "Cavity optomechanics," Review of Modern Physics, Vol. 86, No. 4, 1391-1452, 2014.
2. Soubelet, P., Reynoso, A. A., Fainstein, A., Nogajewski, K., Potemski, M., Faugeras, C., Bruchhausen, A. E., "The lifetime of interlayer breathing modes of few-layer 2H-MoSe2 membranes," Nanoscale, Vol. 11, No 21, 10446-10453, 2019.
3. Zalalutdinov, M. K., Robinson, J. T., Fonseca, J. J., LaGasse, S. W., Pandey, T., Lindsay, L. R., Reinecke, T. L., Photiadis, D. M., Culbertson, J. C., Cress, C. D. and Houston, B.H., "Acoustic cavities in 2D heterostructures. Nature Communications., Vol. 12, No. 1, 3267, 2021.
4. Carr, A.D., Ruppert, C., Samusev, A.K., Magnabosco, G., Vogel, N., Linnik, T. L., Rushforth, A. W., Scherbakov, A.V., Bayer, M., Akimov, A.V., "Enhanced photon-phonon interaction in WSe2 acoustic nanocavities," ACS Photonics (Accepted), 2024.

Subwavelength-Scale Variability Impact on Hypersonic 1-D Phononic and Photonic Crystals

O. R. Ranjbar-Naeini[1] *, G. Conte[1], J. Ahopelto[2] and C. M. Sotomayor Torres[1]

[1]International Iberian Nanotechnology Laboratory, Nanophononics Group, 4715-330 Braga, Portugal

[2]VTT Technical Research Centre of Finland Ltd., FI-02044 Espoo, Finland

*corresponding author: omid.ranjbar@inl.int

Abstract: Slight variations in the critical dimensions of fabricated nano-opto-electro-mechanical systems (NOEMS) impact their performance by affecting the band gaps and dispersion relation. We study the effect of variability, using COMSOL simulations, on 1-dimensional hypersonic phononic and photonic crystals at telecom wavelength designed to operate at a mechanical frequency of 2 GHz.

The development of a scalable NOEMS device, based on the optomechanical (OM) interaction of GHz phononic and THz photonic elements within extremely small volumes, has received significant attention in recent years due to RF-optical conversion, frequency combs generation and the potential use in quantum technologies [1-3].

The variability of critical dimensions (CDs) resulting from state-of-the-art semiconductor micro- and nano-fabrication process of NOEMS devices is probably inevitable due to its statistical nature below and around 10 nm. Despite rigorous fabrication protocols, slight variations in the CDs during the fabrication process could potentially impact the performance of NOEMS devices. This is of crucial importance since the photon-phonon interactions within the combined unit cells affect the dispersion relations, and any deviation from the expected behaviour based on the design often results in the emergence of dissipation channels for both phonons and photons [4].

We perform a parametric study of subwavelength variability in CDs of 1-D hypersonic phononic and photonic crystals in which the simultaneous confinement of phonons and photons is achieved in a OM nanobeam [5, 6]. The devices are fabricated in nanocrystalline silicon (nc-Si). For this purpose, an amorphous silicon (Si) layer is deposited by low pressure chemical vapour deposition (LPCVD). The thickness control is in the range of 2-5 nm. The amorphous Si film is transformed to nc-Si by annealing, which also leads to stress changes from compressive to tensile in a highly reproducible manner. The most demanding step is the fabrication of the OM nanobeam, based on electron beam lithography and dry etching. An example of a fabricated nanobeam is shown in Figure 1 (a). The most important CDs for the OM operation of the nanobeam include the width of the beam, the diameter of the holes, the alignment of the holes with respect to the stubs, the stubs dimension and shape. Moreover, the slope and smoothness of the sidewalls also affect the OM coupling since the mirror symmetry at the mid-plane is broken. Finally, the nanobeams are released by HF dip or in HF vapour; this is a reproducible process once removal of polymer residuals is under control.

The device in Figure 1 (a) was designed so that each unit cell features a single hole at the center and two symmetric stubs on the sides. These strategically designed air holes within the nc-Si structure are responsible for the photonic gaps. Likewise, the stubs in the waveguide control the phononic band gaps and stubs design aims at realization of a full phononic bad gap at all the k-values. The band structures for photonic and phononic modes in the cavities of the nanobeams are computed by Finite-Element Method (FEM) via the COMSOL Multiphysics software. To facilitate this analysis, Bloch-Floquet periodic boundary conditions are applied to the sides of the

unit cell to determine the band structures. Parameter ranges used to obtain the effect of variability are: air holes diameters from 250 nm to 320 nm, stubs lengths from 450 nm to 550 nm, stubs widths from 200 nm to 300 nm, air hole position with off-centre deviations from 0 to 7 nm and sidewall angles from 90° to 74° on the hypersonic and photonic band gap.

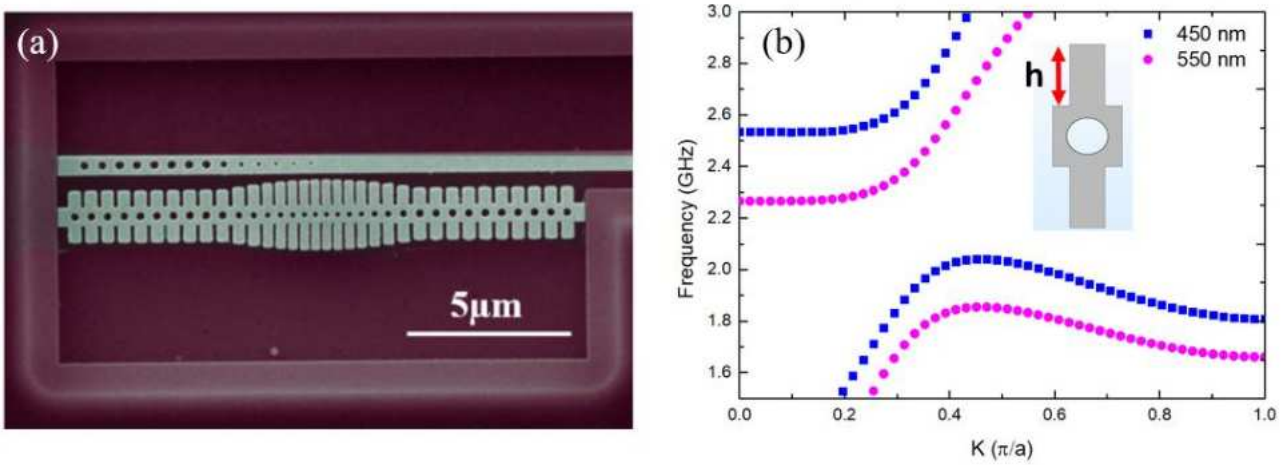


Figure 1: (a) SEM image of a nc-Si suspended optomechanical nanobeam and an integrated optical waveguide for 2 GHz operation. (b) Phononic band structure for stub lengths equal to 450 nm (blue squares (■)) and to 550 nm (magenta circles (●)). Inset: the unit cell with the red arrow showing the stub length.

We find that, for example,an increase of 100 nm in the stub length impacts the phononic band gap by shifting it to lower frequencies and reducing its width at the rate of -8.46×10^{-4} GHz/nm (Figure 1 (b)). Variations are also observed with respect to the sidewall angle; deviating it from 90°, the phononic band gap changes from 474 MHz to 566 MHz for sidewalls of 74°.

The authors acknowledge funding from the project CHIST-ERA-21- MUSICIAN – Multifunctional silicon integrated NOEMS for broadband access networks.

References:

[1] Ng RC, Nizet P, Navarro-Urrios D, Arregui G, Albrechtsen M, García PD, Stobbe S, Sotomayor-Torres CM, Madiot G. Intermodulation of optical frequency combs in a multimode optomechanical system. Physical Review Research. 2023 Aug 25;5(3):L032028.

[2] Barzanjeh S, Xuereb A, Gröblacher S, Paternostro M, Regal CA, Weig EM. Optomechanics for quantum technologies. Nature Physics. 2022 Jan;18(1):15-24.

[3] Arnold G, Wulf M, Barzanjeh S, Redchenko ES, Rueda A, Hease WJ, Hassani F, Fink JM. Converting microwave and telecom photons with a silicon photonic nanomechanical interface. Nature communications. 2020 Sep 8; 11(1):4460.

[4] García PD, Bericat-Vadell R, Arregui G, Navarro-Urrios D, Colombano M, Alzina F, Sotomayor-Torres CM. Optomechanical coupling in the Anderson-localization regime. Physical Review B. 2017 Mar 14; 95(11):115129.

[5] Pennec Y, Rouhani BD, Li C, Escalante JM, Martínez A, Benchabane S, Laude V, Papanikolaou N. Band gaps and cavity modes in dual phononic and photonic strip waveguides. AIP advances. 2011 Dec 1; 1(4).

[6] Oudich M, El-Jallal S, Pennec Y, Djafari-Rouhani B, Gomis-Bresco J, Navarro-Urrios D, Torres CM, Martinez A, Makhoute A. Optomechanic interaction in a corrugated phoxonic nanobeam cavity. Physical Review B. 2014 Jun 18; 89(24):245122.

Acoustic diffusers by phase-control acoustic metamaterials for reflected and transmitted waves

Jia-Hong Sun[1*], Yu-Wei Chen[2], and Ching-Yun Chang[1]

[1]Department of Mechanical Engineering, Chang Gung University, Taiwan
[2]Institute of Biomedical Engineering, Chang Gung University, Taiwan
[*] jhsun@mail.cgu.edu.tw

Abstract: This paper studied acoustic metamaterials that can control the phase of sound waves. Two types of microstructures were used to control proper phase delay for reflected and transmitted acoustic waves, respectively. By arranging the microstructures properly, thin-plane acoustic diffusers were designed, and specimens were fabricated to be tested in experiments.

Metamaterials are materials consisting of designed artificial microstructures that can manipulate waves, such as EM waves, elastic waves in solids, and acoustic waves in air. Acoustic metamaterials (AM) are currently studied to control the reflection, transmission, and absorption of sound[1-4]. In these studies, controlling the phase shift of sound by using metamaterials is a crucial topic. Controlling the phase shift of acoustic waves at each microstructure can be realized as rearranging the phase of point sources. Such AM can deflect the directions of the reflected or transmitted waves, and the corresponding sound field characteristics alter. For example, a Schroeder diffuser combines wells of different depths to have the non-uniform phases of the reflected wave[4]. Further, metamaterials that control the transmitted waves' phase were reported, but further applications are needed. Thus, in this paper, we report our studies on metamaterials for controlling phase shift of reflected and transmitted acoustic waves and their further application as diffusers.

Two types of microstructures were studied for control phase delay of reflected and transmitted acoustic waves, respectively. For the reflected waves, a Helmholtz-like cavity structure was proposed[2] to control the phase of reflected waves and was adapted in this study. On the transmitted waves, a channel is the fundamental part of the microstructure that allows sounds to pass through a solid structure. We used coiling channels introduced in reference 3 to control the phase delay. The finite-element method (COMSOL Multiphysics) was used to calculate the sound pressure fields of waves and study the designs of these microstructures. The geometric size of Helmholtz-like cavities affected the reconstruction of reflected waves and controlled the phase. The coil channels have different lengths, thus delaying the incident wave and shifting the output's relative phase. We used the finite-element method to calculate the sound pressure fields of waves reflected from a Helmholtz-like cavity and waves passing the coiling channel, respectively. Then, both the Helmholtz-like cavity and the coiling channel were designed to have a phase delay of 0, $\pi/8$, ..., and $15\pi/8$, respectively. These microstructures were used as the basic units for further applications.

Proper arrangments of the basic units constructed the functional metamaterials. For example, with different phase delays in space, an array of linear increasing phase delay units can steer the direction of the incident wave when it passes the metasurface. In this study, we designed acoustic diffusers based on the principle used in the Schroder diffusers to arrange the phase delay of units according to the quadratic residue sequences (QRS). Then, the sound pressure fields were simulated, and the diffusion coefficients of the diffusers were calculated. The AM diffusers for reflected and transmitted waves both showed that directional incident waves become diffusion. The

specimens of the AM diffuser were fabricated by 3D printing, and consistent results were obtained in experiments. These results showed that Helmholtz-like cavities controlled the reflective wave phases, and coiling channels controlled the transmitting wave phase efficiently. Functional AM diffusers can be easily applied to sound field control inside buildings and significantly contribute to architectural acoustics.

Acknowledgements： The authors gratefully thank the financial support from Ministry of Science and Technology, Taiwan (MOST 109-2221-E-182-018, MOST 110-2221-E-182-046).

References

1. B. Assouar, et al., “Acoustic metasurfaces,” Nature Reviews Materials, Vol. 3, 460-472, 2018.
2. Y. Zhu, et al., Ultrathin Acoustic Metasurface-Based Schroeder Diffuser. Physical Review X, 7(2), 2017
3. G. Memoli, et al., “Metamaterial bricks and quantization of meta-surfaces,” Nature Communications, Vol. 8(1), No. 14608, 2017.
4. M. R. Schroeder, “Diffuse sound reflection by maximum−length sequences,” The Journal of the Acoustical Society of America, Vol. 57, 149-150, 1975.

Non-Hermitian topological systems using nonreciprocal electroacoustic elements.

A. **Maddi**[1*], **G. Penelet**[1], **V. Pagneux**[1] **and V. Achilleos**[1]

[1] Laboratoire d'Acoustique de l'Université du Mans (LAUM), UMR 6613, Institut d'Acoustique - Graduate School (IA-GS), CNRS, Le Mans Université, France.
[*]corresponding author: anis.maddi@univ-lemans.fr

Abstract: In this work, we explore the use of active acoustic elements for the design of non-Hermitian topological systems. We experimentally observe the emergence of the non-Hermitian skin effect in a nonreciprocal acoustic network. Additionally, we discuss the transition from PBC to OBC and the associated boundary sensitivity.

Recently, we have witnessed a growing interest in the development of non-Hermitian topological systems. Such systems are characterized by complex eigenenergies resulting from the presence of losses/gains in the system, and offer promising new possibilities for wave control and the design of improved sensors [1-2]. A particularly striking effect of this type of system involves the emergence of the non-Hermitian skin effect, which occurs during the transition from a periodic boundary condition (PBC) to an open boundary condition (OBC). As a result of this transition, the eigenfrequencies can become real and the energy is exponentially localized at one edge of the system. These effects have been reported in many physical configurations, including acoustics and electronics [3-6].

Non-hermitian topological systems can be studied using simple models, such as the Hatano-Nelson or the Su-Schrieffer-Heeger, which are both among the most prominent in the field. The Hatano-Nelson model describes a one-dimensional lattice with an asymmetric coupling, whereas the Non-hermitian SSH describes a dimer with an asymmetric coupling. Both models can display complex eigenfrequencies for a periodic configuration, which becomes real when open boundaries are imposed. This transition leads to the localisation of all the eigenmodes of the Hatano-Nelson at one side of the system, whereas the Non-hermitian SSH can show different localisations depending on the parameter of the system.

In our work, we demonstrate theoretically that a transfer matrix approach can be used to map an acoustic problem to both the Hatano-Nelson model [6] and SSH. Our experimental setup consists of a series of cells. Each cell is made up of two coupling ducts and a cavity housing a loudspeaker. The loudspeaker is controlled through the use of a microphone facing the membrane which feeds back an amplified signal to the loudspeaker.
This allows a broadband nonreciprocal wave propagation. For the Hatano-Nelson model, we show that the acoustic system can be mapped using the transfer matrix M of a single cell following the expression,

$$u_{n+1} + t\,u_{n-1} = Eu_n \qquad \text{Eq. (1)}$$

where $t = det(M)$ and $E = Tr(M)$. This allows us to make a direct link between the eigenfrequencies of the HN model and the modes of the acoustic problem, in which the presence of losses enable us to obtain a stable system despite the complex closed loop spectrum.

Using a network of N=8 cells (see Fig.1), we experimentally demonstrate the emergence of the non-Hermitian skin effect in the acoustic equivalent of the Hatano-Nelson model. Moreover, by using diaphragm with different radii, we demonstrate the gradual transition from a looped to a line spectrum, highlighting the sensitivity of the system to variations in boundary conditions.

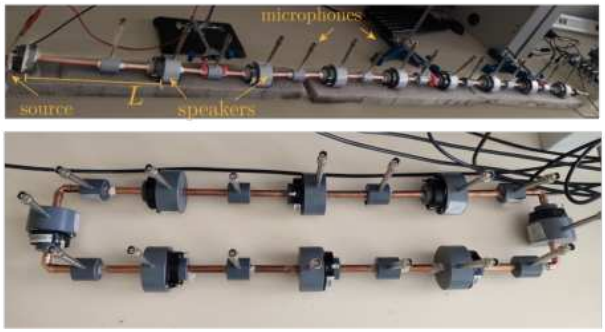


Figure 1 : Experimental setup for the Hatano-Nelson in OBC and PBC configuration .

References

1. Okuma, N., & Sato, M. (2023). Non-hermitian topological phenomena: A review. *Annual Review of Condensed Matter Physics*, *14*, 83-107.
2. Budich, J. C., & Bergholtz, E. J. (2020). Non-Hermitian topological sensors. *Physical Review Letters*, *125*(18), 180403.
3. Hofmann, T., Helbig, T., Schindler, F., Salgo, N., Brzezińska, M., Greiter, M., ... & Neupert, T. (2020). Reciprocal skin effect and its realization in a topolectrical circuit. *Physical Review Research*, *2*(2), 023265.
4. Helbig, T., Hofmann, T., Imhof, S., Abdelghany, M., Kiessling, T., Molenkamp, L. W., ... & Thomale, R. (2020). Generalized bulk–boundary correspondence in non-Hermitian topolectrical circuits. *Nature Physics*, *16*(7), 747-750.
5. Zhang, L., Yang, Y., Ge, Y., Guan, Y. J., Chen, Q., Yan, Q., ... & Zhang, B. (2021). Acoustic non-Hermitian skin effect from twisted winding topology. *Nature communications*, *12*(1), 6297.
6. Maddi, A., Auregan, Y., Penelet, G., Pagneux, V., & Achilleos, V. (2023). Exact analogue of the Hatano-Nelson model in 1D continuous nonreciprocal systems. *arXiv preprint arXiv:2306.12223*.

The role of elastic interfaces in a reduced relaxed micromorphic formulation of finite-size mechanical metamaterials

L. A. Perez Ramirez[1*], J. Voss[1], G. Rizzi[1], S. Hermann[1], P. Demetriou[1] and A. Madeo[2]

[1]Faculty of Architecture and Civil Engineering, TU Dortmund, Germany
[2]Head of Chair of Continuum Mechanics, Faculty of Architecture and Civil Engineering, TU Dortmund, Germany
[*]corresponding author: leonardo.perez@tu-dortmund.de

Abstract: The surfaces and interfaces found in finite-size metamaterials are likely to trigger boundary effects. Introducing elastic interfaces in the micromorphic formulation of the problem captures this boundary-driven response in the simplified framework of generalized continuum mechanics. Finite-size specimens, identical almost everywhere except at their boundaries, may show different responses.

The mechanical properties of traditional materials, both in small geometrical dimensions and in bulk, are known to be subject to size-effects that can be controlled by the interfaces and surfaces of its microstructure [1]. Moreover, these effects dominate the mechanical response when the external dimensions of the material specimen approach the characteristic length scale of its microstructure [2]. This suggests that the architected nature of metamaterials can enable a similar phenomenon when considering finite-size metamaterial specimens.

We show that boundary-driven responses are present in finite-size metamaterials by running direct simulations of the microstructured domain. The lattice of the metamaterial is translated so that different samples are generated, while keeping the same bulk material. These have the same macro-size and the same bulk properties, but different geometries at their boundaries. We also use the reduced relaxed micromorphic model to simulate an equivalent system in view of its capacity to capture the dispersion, anisotropy and band-gaps of metamaterials [3], at a lower computational cost. The kinetic and strain energy of this model are shown in equations (1) and (2), respectively.

$$K\left(\dot{u}, \nabla\dot{u}, \dot{P}\right) = \frac{1}{2}\rho\langle\dot{u},\dot{u}\rangle + \frac{1}{2}\langle\, \mathbb{J}_{\mathrm{m}}\mathrm{sym}\,\dot{P}, \mathrm{sym}\,\dot{P}\,\rangle + \frac{1}{2}\langle\, \mathbb{J}_{\mathrm{c}}\mathrm{skew}\,\dot{P}, \mathrm{skew}\,\dot{P}\,\rangle + \frac{1}{2}\langle\, \mathbb{T}_{\mathrm{e}}\mathrm{sym}\,\nabla\dot{u}, \mathrm{sym}\,\nabla\dot{u}\,\rangle + \frac{1}{2}\langle\, \mathbb{T}_{\mathrm{c}}\mathrm{skew}\,\nabla\dot{u}, \mathrm{skew}\,\nabla\dot{u}\,\rangle \tag{1}$$

$$\mathrm{W}(\nabla u, P) = \frac{1}{2}\langle\, \mathbb{C}_{\mathrm{e}}\mathrm{sym}\,(\nabla u - P), \mathrm{sym}\,(\nabla u - P)\,\rangle + \frac{1}{2}\langle\, \mathbb{C}_{\mathrm{c}}\mathrm{skew}\,(\nabla u - P), \mathrm{skew}\,(\nabla u - P)\,\rangle + \frac{1}{2}\langle\, \mathbb{C}_{\mathrm{micro}}\mathrm{sym}\,P, \mathrm{sym}\,P\,\rangle \tag{2}$$

The results of the microstructured simulations show a distinct response of the displacement field when the lattice is translated, and consequently, the corresponding boundaries are different, see Figure 1. This suggests a boundary-driven phenomenon. Even though the reduced relaxed micromorphic model has been shown to adequately capture the dynamic response of metamaterial plates [4], it has also been observed that it cannot account for boundary effects when using perfect interfaces [5]. However, when the interface of the micromorphic domain is considered elastic (the tractions have non-vanishing jumps at the considered interfaces), it is possible to account for the boundary-driven effects of the finite-size metamaterials [6]. Therefore, we use imperfect interfaces in the micromorphic formulation to introduce a differentiated response attuned to the structure at the boundary. A

correlation between the shape of the surface tractions at the interface is observed when comparing the micromorphic and microstructured results.

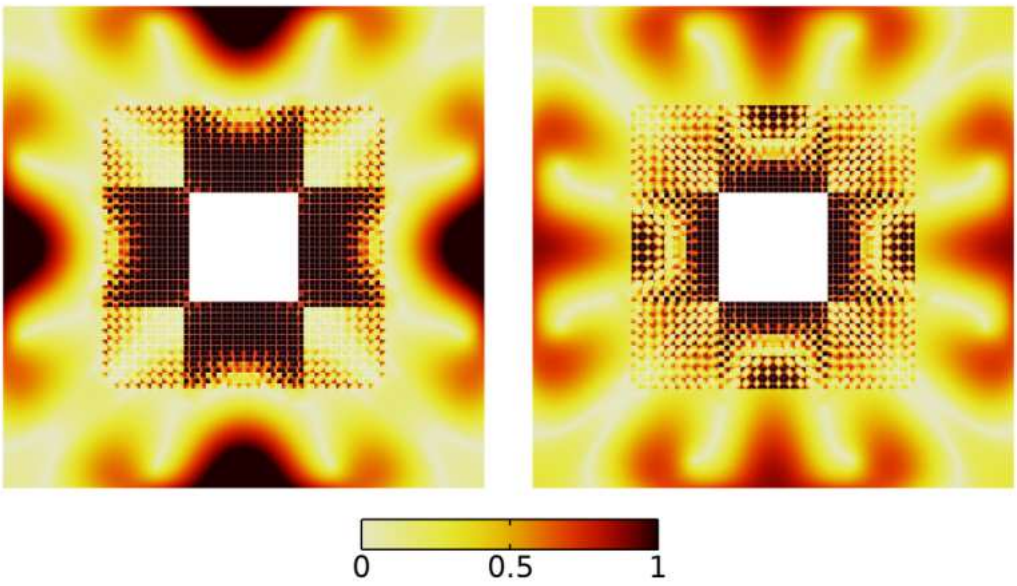


Figure 1. Normalized displacement field of a time-harmonic study at 1450 Hz of a plate subject to a radial expansion load. Two metamaterial cores are generated by the translation of its lattice while remaining surrounded by a classical linear elastic material.

Acknowledgments: Angela Madeo, Leonardo A. Perez Ramirez, Gianluca Rizzi, Svenja Hermann, and Plastiras Demetriou, acknowledge support from the European Commission through the funding of the ERC Consolidator Grant META-LEGO, N° 101001759.

References

1. Dehm, G., C. Motz, C. Scheu, H. Clemens, P. Mayrhofer and C. Mitterer, "Mechanical size-effects in miniaturized and bulk materials," Adv. Eng. Mater., Vol. 8, No. 11, 1033–1045, 2006.
2. Surjadi, J.U., L. Gao, H. Du, X. Li, X. Xiong, N.X. Fang and Y. Lu, "Mechanical metamaterials and their engineering applications," Adv. Eng. Mater., Vol. 21, No. 3, 1800864, 2019.
3. d'Agostino, M.V., G. Barbagallo, I.-D. Ghiba, B. Eidel, P. Neff and A. Madeo, "Effective description of anisotropic wave dispersion in mechanical band-gap metamaterials via the relaxed micromorphic model," J. Elasticity, Vol. 139, No. 2, 299–329, 2020.
4. Demore, F., G. Rizzi, M. Collet, P. Neff and A. Madeo, "Unfolding engineering metamaterials design: relaxed micromorphic modeling of large-scale acoustic meta-structures," J. Mech. Phys. Solids, Vol. 168, 104995, 2022.
5. Demetriou, P., G. Rizzi and A. Madeo, "Reduced relaxed micromorphic modeling of harmonically loaded metamaterial plates: investigating boundary effects in finite-size structures," Arch. Appl. Mech., Vol. 94, No. 1, 81–98, 2024.
6. Perez Ramirez, L. A., F. Erel-Demore, G. Rizzi, J. Voss, and A. Madeo, "Effective surface forces and non-coherent interfaces within the reduced relaxed micromorphic modeling of finite-size mechanical metamaterials," J. Mech. Phys. Solids, Vol. 186, 105558, 2024.

Unified model for multiple scattering problems in one-dimensional elastic waveguides

M. Lázaro[1,2], V. Romero-García[1], L.M. García-Raffi[1*], R. V. Craster[2],

[1]Universitat Politècnica de València, Spain

[2]Imperial College London, UK

[*]corresponding author: lmgarcia@mat.upv.es

Abstract:. In this paper, a new model for the wave response of waveguides with an arbitrary number of scatterers is proposed. We consider two types of scatterers: resonator-type and inclusion-type, these latter as small properties perturbations (material and cross section). A resulting unified mathematical model results for both type of scatterers.

Studies focused on the scattering of elastic waves, there has been considerable attention on the interaction among point defects within clusters. Notably, this encompasses the seminal contributions of Foldy [1] and Lax [2], which established the theoretical underpinnings for representing defects as sources, either isotropic or otherwise, with undetermined intensities. A thorough examination of scattering theories, along with their relation to integral equations, is presented by Martin [3].

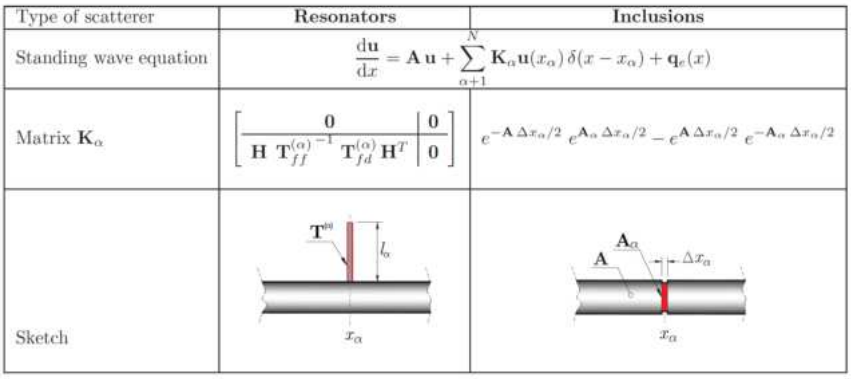


Figure 1. Sketch of the proposed unified model valid for all considered type of scatterers: resonator-type (left) and inclusion-type (right).

In the context of the present work, we consider as pointwise scatterers those substructures that are connected to a main elastic beam and have either internal resonances or local changes of properties (of material and/or section), in a very small length. In both cases, the propagating waves are affected in magnitude and phase by these obstacles. Furthermore, for the same number of scatterers, the correlation in the order of the scatterers positions also affects the wave response. The two situations are in essence different but produce wave effects of the same type. Our main objective is to unify the mathematical treatment of both scatterer models, something that is done in the current contribution in the context of elastic waves of any type (longitudinal, flexural, torsional or shear waves). The procedure is based on the multiple-scattering approach for 1D elastic waveguides. The wave field along the longitudinal direction verifies the equation of motion together with the kinematics relationships, gathered in the system of ordinary differential equations

$$\frac{d\boldsymbol{u}}{dx} = \boldsymbol{A}\,\boldsymbol{u} + \sum_{\alpha=1}^{N} \boldsymbol{K}_\alpha\,\boldsymbol{u}(x_\alpha)\cdot\delta(x-x_\alpha) + \boldsymbol{f}_e(x) \tag{1}$$

Where $\boldsymbol{u}(x)$ represents the state-vector (kinematics and generalized forces) of the waveguide. The matrix $\boldsymbol{A}$ includes all inertial and mechanical properties of the medium and $\boldsymbol{f}_e(x)$ stands the vector of external forces. We propose a common mathematical model based on the solution of Eq. (1) but with different scattering impedance matrices $\boldsymbol{K}_\alpha$ depending on the type of scatterer. The table shown in Fig. 1 summarizes the two approaches, depending on the type of scatterer: (1) resonator-type or (2) inclusion-type. The numerical results for resonator-type scatterer are considered exact since they are attached pointwise to the beam. On the other side, inclusion-type scatterer are modeled as simple pointwise source terms, which generates some error in the results. It is proved that the error depends on the wavelength and on the contrast of properties. In Fig. 2 some results for a rod with classical longitudinal waves are represented, showing the good agreement of the proposed model with the exact solution obtained with the Transfer Matrix Method.

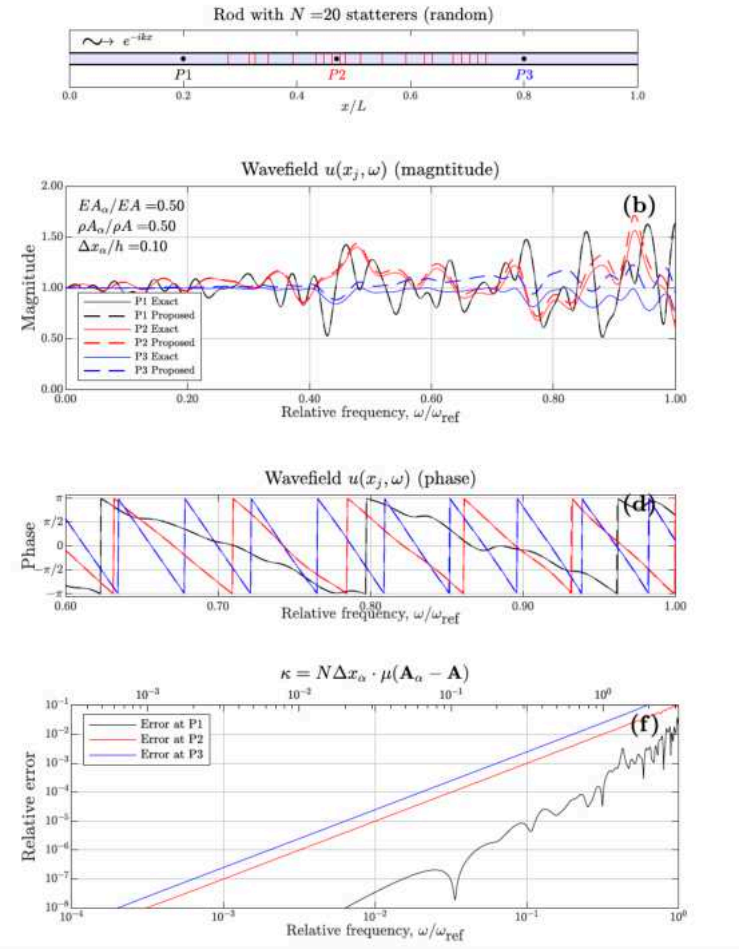


Figure 2. Numerical results of wave field of a rod. (b) and (d): magnitude and phase of wavefield. (f) relative error of the proposed method with relative frequency.

Acknowledgments

Authors are grateful for the partial support under Grant No. PID2020-112759GB-I00 funded by MCIN/AEI/10.13039/501100011033. L.M.G.-R. and V.R.-G. acknowledge support from Grant No. CIAICO/2022/052 of the "Programa para la promoción de la investigación científica, el desarrollo tecnológico y la innovación en la Comunitat Valenciana" funded by Generalitat Valenciana. M.L is grateful for support under the "Programa de Recualificación del Sistema Universitario Español para 2021-2023", (funded by "Instrumento Europeo de Recuperación (Next Generation EU) en el marco del Plan de Recuperación, Transformación y Resiliencia de España", a través del Ministerio de Universidades.

References

1. Foldy, L., "The multiple scattering of waves. i. general theory of isotropic scattering by randomly distributed scatterers", 393 Phys. Rev. 67 (1945) 107–119.
2. Lax, M., "Multiple scattering of waves" , Rev. Mod. Phys. 23 (1951) 287–310..
3. Martin, P., "Multiple Scattering. Interaction of Time-Harmonic Waves with N Obstacles", Cambridge University Press, 398 2006.

Inverse Design of Broadband Acoustic Lens using Gradient-Based Optimization

F. A. Amirkulova[1*], S. Gerges[1], and J. Samaniego[1]

[1]San José State University, USA
[*]corresponding author: feruza.amirkulova@sjsu.edu

Abstract: We design broadband acoustic lenses through gradient-based optimization. The root mean square of absolute pressure amplitudes at the focal point is maximized, considering a range of frequencies and incident angles amidst the nonuniform configuration of scatterers. We demonstrate how the analytical form of gradients enriches the modeling and solution accuracy.

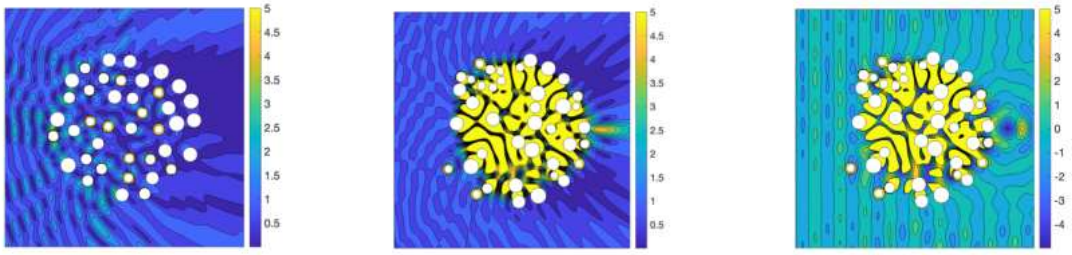
An acoustic Luneburg lens can focus the incident plane waves from any direction to a focal point on the opposite side of the lens configuration without aberrations [1, 2]. This work presents a semi-direct approach to broadband acoustic Luneburg lens design, employing gradient-based optimization algorithms and utilizing multiple scattering theory. Our method focuses on maximizing the absolute pressure amplitude at the focal point, achieved by incrementally adjusting the positions and radii of a set of cylinders so that they transform into an effective acoustic focusing apparatus. We obtained an analytical formula for the gradients of the absolute pressure amplitude at the focal point with respect to positions [3, 4] and radii [5] of a set of cylinders in closed form rather than relying on numerical evaluation of gradients through finite differences.

For a plane wave incidence, we define the objective function $|p_f(\{x_m\})|^{RMS}$ as the root mean square (RMS) of a set of the absolute pressure amplitudes $|p_f|$ at the focal point over some range of normalized wavenumbers $k_i a_{max}$ $(i = 1,2,\dots,N_k)$ and over a range of incident angles $\psi_l (l = 1,2,\dots,N_l)$ [3, 5]:

$$|p_f(\{x_m\})|^{RMS} = \left(\frac{1}{N_k}\frac{1}{N_\psi}\sum_{i=1}^{N_k}\sum_{l=1}^{N_\psi}|\,p_f(k_i a_{max},\psi_l,\{x_m\})|^2\right)^{1/2} \qquad (1)$$

where $\boldsymbol{x}_j = [\boldsymbol{r}, a_i]$, a_j and $\boldsymbol{r}_j$ are correspondingly the radius and position of the jth scatterer, $j = \overline{1,M}$, M is the total number of scatterers in the configuration, and $a_{max} = \max(a_i)$. The objective function is non-convex and highly non-linear, and has many local maxima and global maximum at infinity. Then, we define the broadband gradient vectors with respect to positions $\boldsymbol{r}_j$ and a_j [3, 5]:

$$[\boldsymbol{q}_j^{RMS}]_p = \frac{\partial |p_f(\{x_m\})|_p^{RMS}}{\partial \boldsymbol{x}_j}, j = 1,2,\dots M. \qquad (2)$$

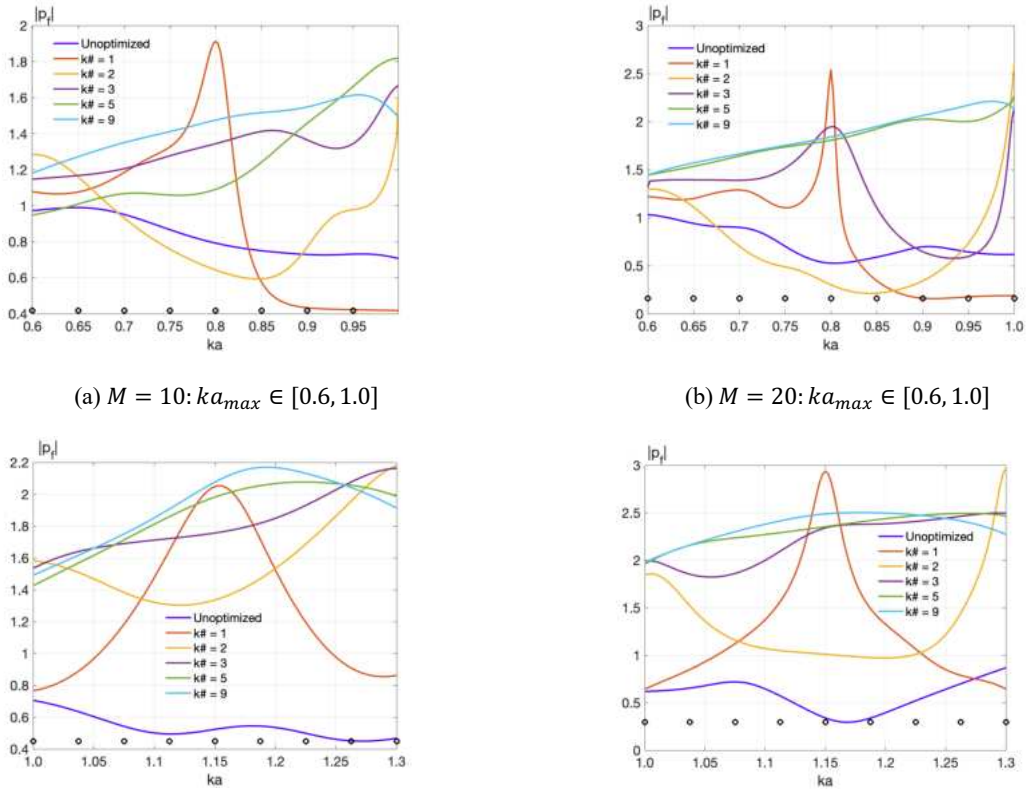


(a) non-optimized: $|\,p\,|$ (b) optimized: $|\,p\,|$ (c) optimized: $Re(p)$

Figure 1. The absolute value of the total acoustic pressure field $|p|$ at normal plane wave incidence on the optimized configurations of $M = 40$ rigid cylinders at normalized wavenumber $ka_{max} = 2$.

We solve the non-convex optimization problems with non-linear constraints. To prevent cylinder overlapping, the distances between their centers are constrained to be greater than the minimal allowable distance, which is selected to be greater than the diameter of the cylinders. In addition, the cylinders are constrained to move inside a fixed circular region. Computations are performed on MATLAB using sequential quadratic programming (SQP) algorithms, *MultiStart* optimization solver to supply the gradients of p_f and gradients of RMS of p_f with respect to $\boldsymbol{x}_j$ vectors over a range of wavenumbers. We start with an initial random planar configuration of non-uniformly sized cylinders and employ the MATLAB build function *fmincon* alongside *MultiStart*. This approach harnesses the efficient local solvers within *MultiStart*, enabling simultaneous exploration of a wide variety of starting points.

Supplying analytical gradients of the function p_f enhances the optimized solution accuracy, reduces computational time, and enables parallel computing with *MultiStart*. Figure 1 illustrates the total acoustic pressure field at normal plane wave incidence for configurations of $M = 40$ rigid cylinders at normalized wavenumber $ka_{max} = 2$. Figure 1 (a) shows the total absolute pressure $|p|$ for nonoptimized configuration of $M = 40$ cylinders. Figures 1(b) and 1(c) clearly demonstrate the focusing effect for plane wave incidence on a optimized core of $M = 40$ cylinders.



(a) $M = 10$: $ka_{max} \in [0.6, 1.0]$ (b) $M = 20$: $ka_{max} \in [0.6, 1.0]$

(c) $M = 10$: $ka_{max} \in [1.0, 1.3]$ (d) $M = 20$: $ka_{max} \in [1.0, 1.3]$

Figure 2. The absolute value of the total acoustic pressure field $|p|$ versus wavenumber at normal plane wave incidence on the non-optimized (blue curve) and optimized configuration of M=10 and 20 rigid cylinders for a range of normalized wavenumbers ka_{max}. The pressure amplitude $|p|$ is optimized at *1,2, 3, 5, and 9* equidistant values of wavenumbers $ka_{max} \in [0.6, 1.0]$ and $ka_{max} \in [1.0, 1.3]$.

Figure 2 depicts the variation of the absolute value of the total acoustic pressure $|p|$ with wavenumber at normal plane wave incidence on the optimized configuration of $M = 10$ and $M = 20$ rigid cylinders for a range of normalized wavenumbers ka_{max}: $ka_{max} \in [0.6, 1.0]$ and $ka_{max} \in [1.0, 1.3]$. The absolute pressure $|p|$ is optimized at *1,2, 3, 5,* and *9* equidistant values of wavenumbers. The trade-off between the increase of the frequency band and focusing efficiency leads to the shift of peak performance for broadband focusing. Numerical results indicate that significant sound pressure amplification can be achieved by optimal scatterer rearrangement using this analytical-numerical technique. The method can be extended to design 3D lenses.

References:

1. Yuan, B., Liu, J., Long, H., Cheng, Y. and Liu, X. “Sound focusing by a broadband acoustic Luneburg lens.” JASA 2022, Vol. 151, 2238–2244. https://doi.org/10.1121/10.0009909.
2. Kim, J.W., Hwang, G., Lee, S.J., Kim, S.H. and Wang, S. “Three-dimensional acoustic metamaterial Luneburg lenses for broadband and wide-angle underwater ultrasound imaging.” MSSP 2022, Vol. 179, 109374. https://doi.org/10.1016/j.ymssp.2022.109374.
3. Amirkulova, F., Gerges, S. and Norris, N. “Sound Localization Through Multi-scattering and Gradient-based Optimization.” Mathematics Vol. 9, No 22, 2862, 2021
4. Amirkulova, F., Gerges, S. and Norris, N., “Broadband acoustic lens design by reciprocity and optimization. JASA Express Lett.” Vol. 2, 024005, 2022, https://doi.org/10.1121/10.0009633
5. Amirkulova, F., Gerges, S. and Samaniego, J. “The gradient of absolute pressure and its application to sound localization.” (*In preparation, to be submitted to Applied Sciences MDPI*)

Robustness evaluation of merged topological bound states in the continuum

Jiamin Guo[1], Zhongming Gu[1,†], and Jie Zhu[1,‡]

[1] Institute of Acoustics, School of Physics Science and Engineering, Tongji University, Shanghai 200092, China

Abstract: We propose a theoretical model for realizing merged topological bound states in the continuum (TBICs), focusing on the investigations of system robustness through tight-binding calculations and numerical simulations. Our findings demonstrate that the topologically protected merged bound states exhibit remarkable robustness against various types of defects and perturbations.

Bound states in the continuum (BICs), a concept introduced by von Neumann and Wigner in 1929, represent unique bound states that exist within the bulk band without interacting with extended modes. Researches in BIC physics have surged due to its potential for advanced wave manipulation [1]. Apart from their topological notions [2], BICs also have been studied in the field of topological insulators, which are dubbed topological BICs (TBICs) [3]. The topological edge states in the continuum and topological corner states in the continuum have been successively verified by in many physical systems. Meanwhile, in recent years, there has been an increasing amount of research focusing on the robustness of TBICs. Yet, merging multiple TBICs remains an uncharted area.

In this work, we delve into this relatively unexplored domain, exploring the robustness of engineered merged topological corner states in the continuum. It is acknowledged that the robustness of a system can be inspected through various operations, including but not limited to the introduction of random perturbations, defect structures, or external sources of interference. Considering the random disorder of potential energy, for nontrivial systems, the eigenvalues and localized characteristics of trivial states will change, while nontrivial modes exhibit a certain degree of protection against perturbations [2].

To investigate this, we first perform calculations based on the tight-binding model, followed by full-wave simulations on the acoustic structure. In the tight-binding calculations, the disorder is introduced by changing the resonant frequencies, i.e., modifying the on-site terms in Hamiltonian. In the simulation, the disorder is introduced by placing a hard cylinder with random size inside the resonator. All numerical results indicate that for bulk disorder (perturbing cylinders on all sites except for corners), the merged topological corner states in the continuum remain stable, with the resonance peaks being unshifted. Conversely, under corner disorder, the corner states persist to exist but are no longer degenerate, with the resonance peaks still exist but shift to higher frequencies. These observations underscore the potential of merged topological bound states in the continuum in realizing devices with enhanced robustness, applicable across various wave systems.

Our conclusions highlight the successful realization of a bilayer lattice for merging TBICs in acoustics. This study not only paves the way for further exploration of merging BICs in higher-order topological materials but also opens avenues for the development of enhanced robust topological devices with minimal energy leakage. Through this research, we aim to inspire further investigations and applications leveraging the unique properties of merged TBICs to develop next-generation devices characterized by unprecedented performance metrics.

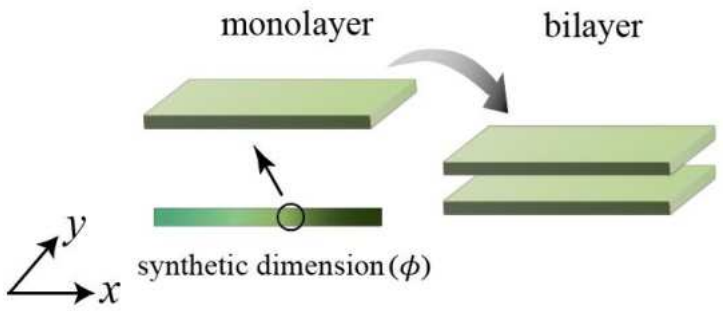


FIG.1. Schematic of constructing the merged topological bound states in the continuum. The symbol ϕ indicates a synthetic dimension in addition to the fundamental spatial dimensions (x and y directions).

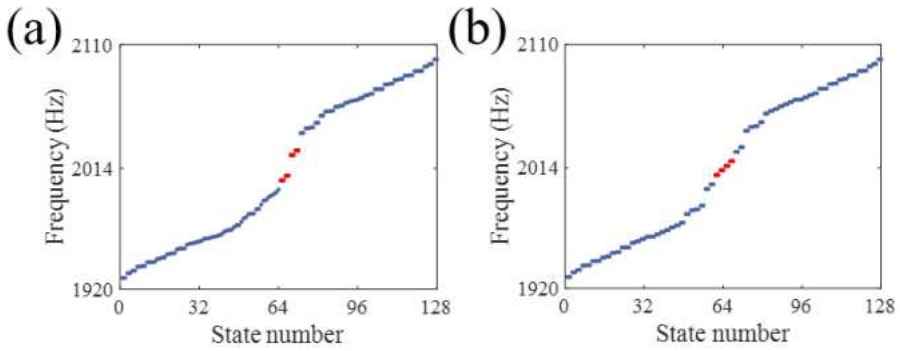


FIG.2. Numerical demonstrations of robustness. (a) Simulated eigenfrequencies for our nontrivial acoustic lattice with on-site disorder on all sites except the four corners (left) and (b) only on the four corners (right).

Acknowledgements

This work was supported by the National Key R&D Program of China (Grant Nos. 2022YFA1404400 and 2022YFA1404403), the National Natural Science Foundation of China (Grant No. 92263208 and 12304494), the Research Grants Council of Hong Kong SAR (Grant AoE/P-502/20), the Fundamental Research Funds for the Central Universities.

References

1. M. Kang, T. Liu, C. T. Chan and M. Xiao, “Applications of bound states in the continuum in photonics,” Nat. Rev. Phys., Vol. 5, No. 10, 659–678, 2023.
2. W. A. Benalcazar and A. Cerjan, “Bound states in the continuum of higher-order topological insulators,” Phys. Rev. B, Vol. 101, No. 16, 161116, 2020.
3. L. Liu, T. Li, Q. Zhang, M. Xiao and C. Qiu, “Universal Mirror-Stacking Approach for Constructing Topological Bound States in the Continuum,” Phys. Rev. Lett., Vol. 130, No. 10, 106301, 2023.

Observation of D-class topology in an acoustic metamaterial

Shi-Qiao Wu[1,2,3,#], Wenting Cheng[4,#], Xiao-Yu Liu[1], Bing-Quan Wu[1], Emil Prodan[5,†], Camelia Prodan[6,†], Jian-Hua Jiang[1,7,†]

[1]*School of Physical Science and Technology & Collaborative Innovation Center of Suzhou Nano Science and Technology, Soochow University, Suzhou 215006, China*

[2]*School of Physics and Optoelectronic Engineering, Foshan University, Foshan 528000, China*

[3]*Guangdong-Hong Kong-Macao Joint Laboratory for Intelligent Micro-Nano Optoelectronic Technology, Foshan University, Foshan 528000, China*

[4]*Department of Physics, University of Michigan, Ann Arbor MI48109, USA*

[5]*Department of Physics, Yeshiva University, New York NY10033, USA*

[6]*Department of Physics and Engineering Physics, Fordham University, New York NY10023, USA*

[7]*Suzhou Institute for advanced research, University of Science and Technology of China, Suzhou 215123, China*

[#]These authors contributed equally to this work.

[†]Correspondence should be addressed to: prodan@yu.edu (Emil Prodan), cprodan@fordham.edu (Camelia Prodan), or jianhuajiang@suda.edu.cn (Jian-Hua Jiang).

Abstract

Topological D-class phases (TDPs) are archetypes of the ten-fold classification of topological phases with particle-hole symmetry. Here, with a novel design scheme, we realize 2D TDPs in an acoustic crystal by synthesizing both the particle-hole and fermion-like time reversal symmetries for a wide range of frequencies.

Topological class	Time-reversal symmetry	Particle-hole symmetry	Chiral symmetry	Realization in 2D metamaterials
A	0	0	0	✓ [14,30]
D	0	+1	0	✗
DIII	-1	+1	1	✗
AII	-1	0	0	✓ [15,27]
C	0	-1	0	✗

[a]There are five nontrivial topological classes in 2D systems, characterized by combinations of time-reversal, particle-hole, and chiral symmetries. The number 0 in each column stands for absence of symmetry, while ± 1 indicate the presence of a symmetry together with the even or odd character of the symmetry operator relative to squaring. The check marks in the last column indicate whether the topological symmetry class has been realized in 2D metamaterials in the past, and citations to the relevant works are placed next to the marks.

References

[1] Kane CL, Mele EJ. Z_2 topological order and the quantum spin Hall effect. Phys Rev Lett 2005;95:146802.

[2] Bernevig BA, Hughes TL, Zhang SC. Quantum spin Hall effect and topological phase transition in HgTe quantum wells. Science 2006;314:1757-61.

[3] König M, Wiedmann S, Brüne C, et al. Quantum spin Hall insulator state in HgTe quantum wells. Science 2007;318:766–70.

[4] Hasan MZ, Kane CL. Colloquium: topological insulators. Rev Mod Phys 2010;82:3045–67.

[5] Qi XL, Zhang SC. Topological insulators and superconductors. Rev Mod Phys 2011;83: 1057–110.

[6] Schnyder AP, Ryu S, Furusaki A, et al. Classification of topological insulators and superconductors in three spatial dimensions. Phys Rev B 2008;78:195125.

[7] Ryu S, Schnyder AP, Furusaki A, et al. Topological insulators and superconductors: Tenfold way and dimensional hierarchy. New J Phys 2010;12:65010.

[8] Altland A, Zirnbauer MR. Nonstandard symmetry classes in mesoscopic normal-superconducting hybrid structures. Phys Rev B 1997;55:1142-61.

3D printed polarizer for shear elastic waves

Tae-Youl Choi[1*], Yuqi Jin[2], Teng Yang[2], Arup Neogi[3], and Arkadii Krokhin[4]

[1]Department of Mechanical Engineering, University of North Texas, Denton, Texas 76207, USA
[2]Center for Agile and Adaptive Additive Manufacturing, University of North Texas, Denton, Texas 76207, USA
[3]Institute of Fundamental and Frontier Sciences, University of Electronic Science and Technology of China, Chengdu 611731, People's Republic of China
[4]Department of Physics, University of North Texas, Denton, Texas 76203, USA
[*]corresponding author: tae-youl.choi@unt.edu

Abstract: Anisotropy of 3D printing process is explored for design of a polarization rotator of shear waves. Due to strong anisotropy of elastic modulus of 3D printed sample the polarization of shear wave rotates following the gradual change in the direction of the infilled lines. The fabricated 90° rotator demonstrates high performance.

Usually, the mechanical properties of materials produced using the current additive manufacturing process are inferior to conventionally manufactured products. At the same time, manipulation of the various process parameters and mechanisms can produce structures with a very wide range of prescribed mechanical and physical properties from the same printing tool. Here we report a layered design of acoustic polarization rotator that can be easily fabricated using additive manufacturing process. We were motivated by a metamaterial-based polarization rotator for linearly polarized electromagnetic waves of the terahertz region [1]. It contains a tri-layer metasurface of thin metal plates with parallel narrow slits separated by a dielectric. The slits result in a strong anisotropy in transmitting electromagnetic waves with parallel or perpendicular polarization. In solids, rotation of a shear elastic wave oscillation plane can be realized by applying phased array systems and complex metamaterials [2]. The fabrication of these metamaterial designs is quite complex, making their practical use cost prohibitive.

The line-by-line 3D printed process provides high anisotropy of the shear modulus. The axis of anisotropy gradually rotates from layer to layer by an adjustment of the printing direction. The proposed in Ref. [4] cylindrical-shaped transverse acoustic 90° rotator shown schematically in Fig. 1. A stack of layers printed with a small angular shift, as shown in Fig. 1(c). It is known that the shear modulus in a straight-line infill FDM printed product has the maximum (minimum) value over the deformation along (across) the infilled line direction [3].

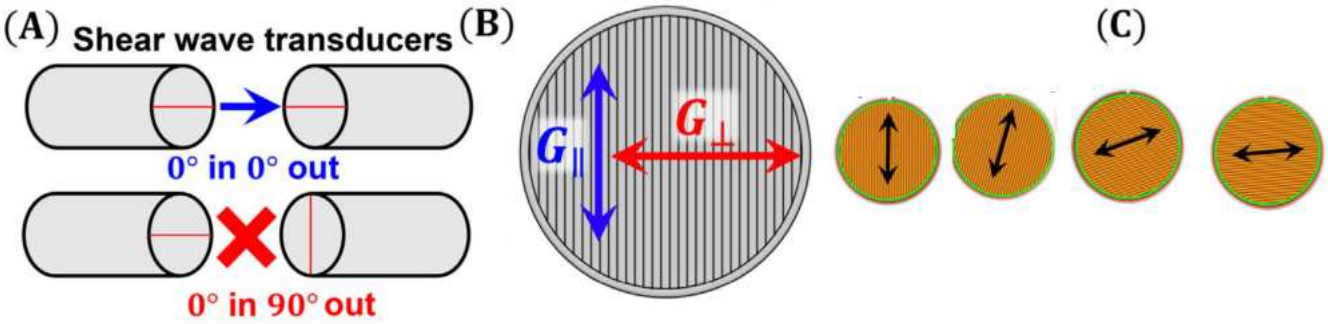


Figure 1. Principle scheme of polarization rotator. (A) Mutual orientation of emitting/detecting shear wave transducers. (B) Top view of the anisotropic pattern in a layer of 3D printed structure with line infill. The shear modulus is higher in the direction perpendicular to the infilled lines than in the parallel direction, $G_{\parallel} >> G_{\perp}$. (C) The infill line orientations were gradually rotated providing total rotation by 90°.

The performance of the FDM acoustic polarizer was characterized by measuring the transmission of the

shear wave propagating from left to right using a pair of shear-wave transducers shown in Fig 1(A). The polarizer samples were printed by PolyPrinter 229 single extruder FDM printer. We used black ABS (Acrylonitrile Butadiene Styrene) filament. The pattern of infilled straight lines is shown in Fig. 1(B). It corresponds to uniaxial anisotropy with significant contrast $G_{\parallel} >> G_{\perp}$ ($E_{\parallel} << E_{\perp}$).

In a bistatic configuration of two single-element shear transducers, an acoustic signal can hardly be detected when the emitting and receiving transducers are oriented mutually perpendicular. The transmission measurements through a practically uniform and isotropic molded ABS plastic slab are shown in Fig. 2(A) for parallel and perpendicular orientation of the transducers. The averaged over frequency amplitude ratio $A_{0°\to 90°}/A_{0°\to 0°}$ was as small as 0.008. The same transmission through polarization rotator with angle of rotation through a single layer $\alpha = 5°$ is shown in Fig. 2(B). A rotation of the anisotropy axis leads to about two orders of magnitude increase in the ratio $A_{0°\to 90°}/A_{0°\to 0°}$ = 0.66, as compared to a homogeneous plastic slab.

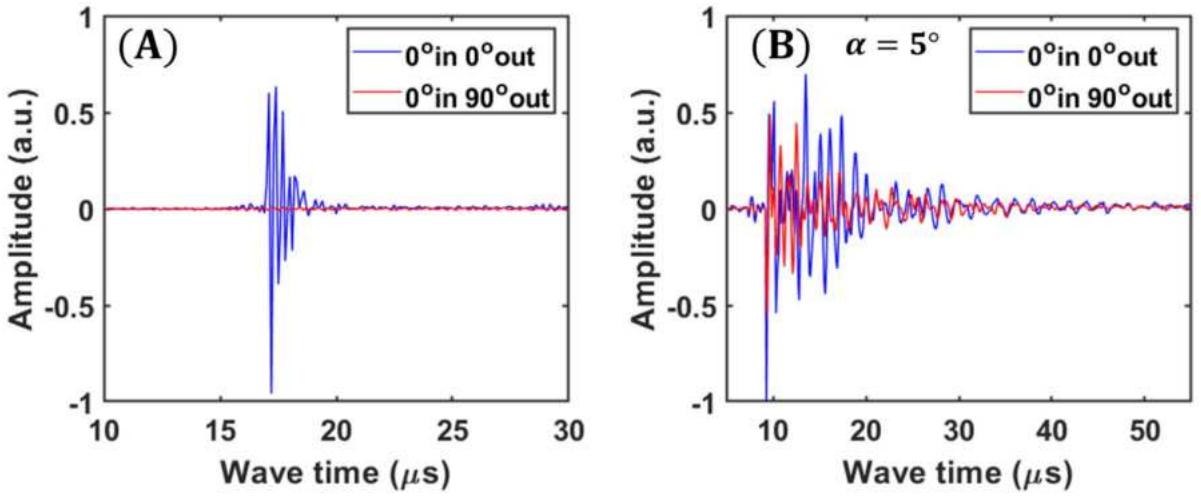


Figure 2. Transmission of shear wave pulses through different fabricated samples. (A) Transmissions through a uniform and isotropic ABS slab obtained by the molding process. (B) Transmissions through the printed PR with $\alpha = 5°$.

In our experiments we demonstrated even the higher efficiency of the proposed polarization rotator containing 90 printed layers, each rotated by 1°. Moreover, the efficiency can be improved by optimization with respect to the parameters of the 3D printing process.

This work was supported by EFRI Grant No. 1741677 from the USA National Science Foundation. The authors acknowledge the infrastructure and support of the Center for Agile Adaptive and Additive Manufacturing (CAAAM) funded through State of Texas Appropriation No. 190405-105-805008-220.

References

1. Cong, L., Cao, W., Zhang, X., Tian, Z., Gu, J., Singh, R., Han, J. and W. Zhang, "A perfect metamaterial polarization rotator," Appl. Phys. Lett. V. 103, 171107, 2013.
2. Li, Y., Jiang, X., Liang, B., Cheng, J.-C. and L. Zhang, "Metascreen-based acoustic passive phased array," Phys. Rev. Appl. V. 4, No. 2, 024003, 2015.
3. Jin, Y., Yang, T., Heo, H., Krokhin, A., Shi, S. Q., Dahotre, N., Choi, T.-Y. and A. Neogi, "Novel 2D dynamic elasticity maps for inspection of anisotropic properties in fused deposition modeling objects," Polymers V. 12, No. 9, 1966, 2020.
4. Jin, Y., Yang, T., Choi, T.-Y., Dahotre, N.B., Neogi, A. and A. Krokhin, "Polarization rotator for shear elastic waves," Appl. Phys. Lett. V. 121, 042201, 2022.

Coherent excitation of torsional mechanical modes in coupled nanoantennas

J.M. García[1]*, B. Castillo López de Larrinzar[1], C. Xiang[2], N.D. Lanzillotti-Kimura[2] and A. García-Martín[1]

[1]Instituto de Micro y Nanotecnología IMN-CNM, CSIC (CEI UAM+CSIC), Tres Cantos, Madrid, Spain
[2]Centre de Nanosciences et de Nanotechnologies, Université Paris-Saclay, Palaiseau, France
*corresponding author: jm.garcia@csic.es

Abstract: The study presents a theoretical analysis of the phononic and plasmonic modes of couples nanoantennas, their surface deformation field and electromagnetic field profiles.

Summary

Metallic nanoantennas have been studied as efficient coherent phonon generators and detectors, harnessing their characteristic optical absorption and polarization dependence of the optical modes [1-2]. The ability to control the excitation of phononic modes depends on the properties of the multiple optical resonances of the system. Lately, it has been made possible to optimally excite and detect phonon modes via plasmon resonances at the same optical frequency using chiral nanostructures and circularly polarized light [3]. However, torsional modes remain elusive in nanophononic studies. In this work we present a simple system composed of two coupled bars, where torsional mechanical modes can be excited using light with null angular momentum. The twisting of the phononic mode (Fig. 1) [4] is provided by the peculiar symmetry of the mechanical eigenmode due to the interaction of the bars via either the substrate or a central connector.

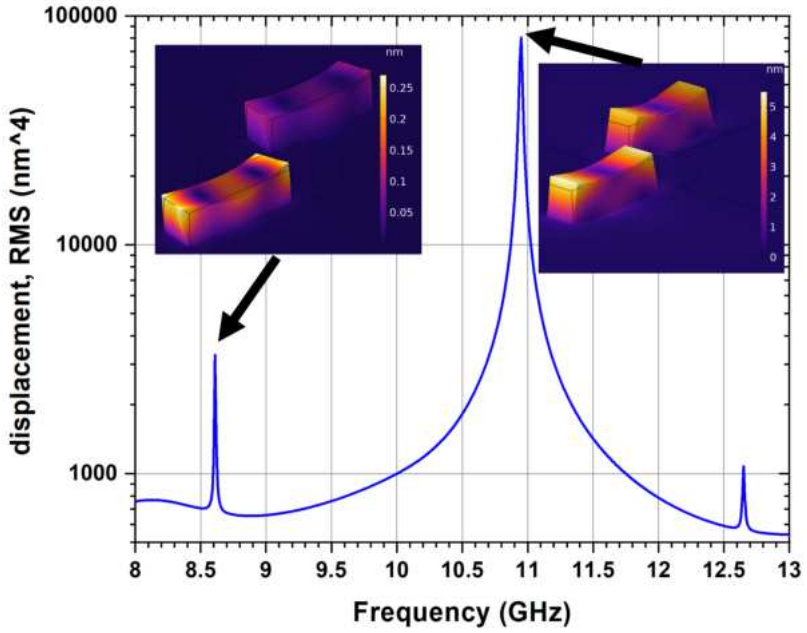


Figure 1: Vibrational modes of couples nanoantenna bars.

References

1. K. O'Brien, et al. Nature communications 5 (1), 4042, (2014).
2. N.D. Lanzillotti-Kimura, et al. Physical Review B 97 (23), 235403, (2018)
3. Castillo López de Larrinzar, B., et al., Nanophotonics 12, 1957 (2023)
4. B. Castillo López de Larrinzar, et al., to be submitted (2024)

Acoustic Realization of Multiple Topological Corner Modes in a Coupling-inverted Phononic Crystal

Dongyi Wang[1*], Guancong Ma[1]
[1]Department of Physics, Hong Kong Baptist University, Kowloon Tong, Hong Kong, China
[*]corresponding author: phwang@hkbu.edu.hk

Abstract: Here, an unprecedented higher-order topological phase safeguarded by a larger-than-unity multipole chiral number (MCN) is experimentally realized with coupling inversion, i.e., long-range couplings stronger than the nearest-neighbour ones, in acoustic crystal. Sixteen topological corner modes are observed in the mid-gap (4 at each corner), protected by an MCN=4 phase.

The field of quantum and classical topological phases has been enriched recently with the development of higher-order topological band theory, localized modes like topological corner modes (TCMs) are thus observed. Numerous novel applications, including topological lasers, quantum optics and energy confinement, are correspondingly inspired by these 0D bound states. Yet, the generation of multiple TCMs at a single corner, which holds great potential for both scientific investigations and modern applications, remains highly desired but unachievable.

With the introduction of appropriate long-range couplings (LRCs), a winding number of a standard one-dimensional Su-Schrieffer-Heeger model can be integers larger than one. Analogically, with LRCs greater than nearest-neighbor couplings (NNCs) in magnitude (regarded as coupling inversion), the unconventionally generalized winding number in higher dimensions can be modulated. The topological invariants characterizing such lattice are referred to as the "multipole chiral numbers" (MCNs) [1], built from sublattice multipole moment operators. Greater-than-unity MCNs safeguard multiple mid-gap localized states at each corner, yet the requirement of coupling inversion is unrealizable in natural materials where couplings generally decay with the increase of distance.

Here, an acoustic wave system is leveraged to overcome the difficulties of coupling inversion [2]. Employing coupled acoustic cavities, we design and experimentally realize a multiple chiral topological phase (MCTP) possessing an MCN of 4. Specifically, a tight-binding Hamiltonian is used to describe the square lattice composed of 4-site unit cells:

$$H(\boldsymbol{k}) = \begin{bmatrix} 0 & h(\boldsymbol{k}) + g(\boldsymbol{k}) \\ h^{\dagger}(\boldsymbol{k}) + g^{\dagger}(\boldsymbol{k}) & 0 \end{bmatrix}, \tag{1}$$

where

$$h(\boldsymbol{k}) = \begin{pmatrix} u + ve^{-ik_x} & -u - ve^{-ik_y} \\ -u - ve^{ik_y} & -u - ve^{ik_x} \end{pmatrix}, \quad g(\boldsymbol{k}) = \begin{pmatrix} we^{-2ik_x} & -we^{-2ik_y} \\ -we^{2ik_y} & -we^{2ik_x} \end{pmatrix}, \tag{2}$$

u, v, w denoting the magnitudes of intra/intercell NNCs and LRCs, respectively. The formed lattice is shown in Fig. 1 (a). An additional synthetic magnetic field with π-flux threads, each plaquette in the lattice, induced by LRCs. When $w > v$, the system becomes an MCTP with an MCN of 4. Thus, 16 near-degenerate modes are protected and observed in the bulk gap of the spectrum as shown in Fig. 1(b), which are bound states localized around the four corners (four per corner, each possessing a different configuration as shown in Fig. 1(c).)

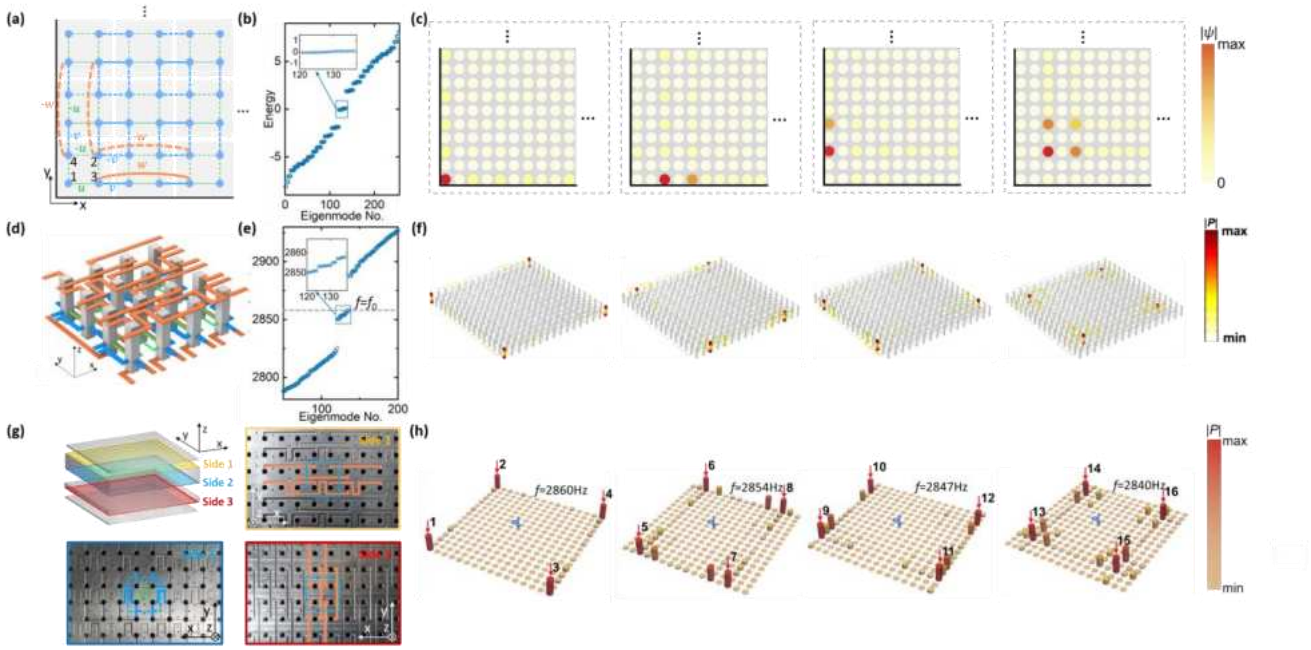


Figure. 1 Schematics, fabricated sample, and the corresponding TCM results obtained from the tight-binding model, simulation and experiment. Schematics of (a) the lattice model, (d) the acoustic lattice design, and (g) the fabricated acoustic lattice employed in experiments. Spectrums demonstrating 16 in-gap TCMs calculated by (b) TBM and (e) simulation. The amplitude distribution profiles of TCMs obtained from (c) TBM calculation, (f) simulation, and (h) experiment, categorized into four groups based on their spatial configurations.

Judiciously designing space-coiling air channels functioning as coupling terms by tuning their geometrical parameters, including channel length L_c, width D_c, and connecting position z_c on the cavity, NNC and LRC coefficients are precisely modulated and the coupling inversion is obtained. The acoustic crystal design is shown in Fig. 1 (d). Sixteen mid-gap TCMs can be identified in the corresponding finite-element simulation results illustrated in Fig. 1 (e,f), all of which are localized around corners and demonstrate four different kinds of intensity profiles compatible with a crystal in the MCN=4 phase. The fabricated sample is shown in Fig. 1 (g), and the experimentally measured spatial profiles of the TCMs are shown in Fig. 1 (h), well-consistent with their numerically calculated counterparts.

Overall, employing acoustic crystals, we experimentally demonstrate the existence of a chiral-symmetric higher-order topological phase with MCN>1 for the first time, and highlight the important role of LRCs in realizing novel topological phases. We also exemplify that classical-wave systems like the acoustic platform utilized in this work possess great potential for studying novel topological models. The proposed MCTP may benefit both further scientific research like investigation of non-Abelian physics, and realistic applications such as spatially multiplexed energy confinement and multi-mode corner-emitting topological lasers.

Acknowledgement: This work was funded by the National Key R&D Program of China No. 2022YFA1404400

References

1. Benalcazar, W. A. and Cerjan, A. “Chiral-Symmetric Higher-Order Topological Phases of Matter”, Phys. Rev. Lett. 128, 127601, 2022.
2. Wang, D. et al. “Realization of a Z-Classified Chiral-Symmetric Higher-Order Topological Insulator in a Coupling-Inverted Acoustic Crystal,” Phys. Rev. Lett. 131, 157201, 2023.

Single-pixel imaging based on time-modulated gratings and compressive sensing

P. Packo[1], **D. Torrent**[2]

[1]Department of Robotics and Mechatronics, AGH University of Krakow, Al. A. Mickiewicza 30, Kraków 30-059, Poland
[2]GROC, UJI, Institut de Noves Tecnologies de la Imatge (INIT), Universitat Jaume I, Castelló 12071, Spain
[*]corresponding author: pawel.packo@agh.edu.pl

Abstract: In this work, a single-pixel imaging system, made of a homogeneous slab of material with time-dependent transmission properties, is employed for image reconstruction. We use the compressive sensing theory to optimize the recovery process and limit the number of coding sequences of the grating.

Imaging methods suffer a limitation dictated by the theory of diffraction which implies that only details of the order of the wavelength of the field can be coupled to the free space. Finer details are lost since they are carried by evanescent waves that decay quickly with increasing the distance from the object. Consequently, these details can be captured only very close to the object, i.e. in the near field [1]. Various methods, based on spatial coupling of the near-field waves to the free space, have been proposed to overcome these limitations [2].

In this work we employ an alternative approach for alleviating the above issues of the image reconstruction process, through application of a time-modulated metamaterial surface that couples the near-field waves to the free space. Analogously to a spatial grating generating diffracted modes, the proposed time grating excites waves at different frequencies, each carrying information about the Fourier transform of the image. We show that the reconstruction process can be carried out through the analysis of the temporal spectrum at a single point in space, hence indicating that time gratings can be used for fast and single-pixel imaging.

The model equation, without the loss of generality, is given as the scalar wave equation [3],

$$\nabla^2\psi = \frac{1}{c_0^2}\partial_{tt}\psi, \tag{1}$$

with ψ being the wavefield and c_0 the wave speed. The grating is introduced as an impedance boundary, hence

$$\partial_z\psi^+ - \partial_z\psi^- = \xi(t)\,\psi, \tag{2}$$

where $\xi(t)$ is the time-modulated impedance of the screen located at $z = 0$. The function $\xi(t)$ can be designed in way it is useful for the imaging process, hence it will be also referred to as a coding sequence.

For a wavefield of frequency ω_0 and wavevector **k** in the plane of the screen (i.e. in the x-y plane), the field generated at the modulated screen will be composed of the fundamental wave and a number of waves at frequencies other than ω_0. Assuming that multiple waves comprise the wavefield after this interaction, it is possible to derive formulas for their amplitude coefficients, once the form of $\xi(t)$ is known, from Eq. (2).

Now, let's assume the image to be reconstructed is placed in the x-y plane at $z = 0$ and given via its Fourier transform coefficients, $A_0(\boldsymbol{k})$. We illuminate the image with a plane wave of frequency ω_0, hence waves propagating along the z axis (with amplitudes given by $A_0(\boldsymbol{k})$), form the representation of the object. We note, however, that for waves which wavenumber is greater than k_0, i.e. $k > k_0$, their wavenumber component along the z axis will be complex, hence such a wave will be evanescent and will vanish after a small distance from the screen. The idea of inducing modulation of the screen is to ensure that for all **k**, there will be always a propagating

wave along z and, as a consequence, all information contained in $A_0(\boldsymbol{k})$ will be transferred to the detector. In other words, in this process, the modulated screen couples the evanescent waves to the free space ensuring their detection at (virtually) any point behind the grating.

In what follows we assume that the modulation pattern is time-periodic with frequency ν, hence the waves generated at the grating propagate at $\Omega_n = \omega_0 + 2n\pi\nu$, with n being integers. The proposed imaging process, apart from generating a set of harmonics at the grating (located at the same coordinate as the object, i.e. $z = 0$), consists of a second, receiving, screen which transmittance is inhomogeneous and given by $T_S(\boldsymbol{r})$ (no modulation at the receiving screen). We assume that the total field collected at this screen is integrated, hence the output of the system is a single time-dependent signal containing harmonics at Ω_n. The latter will, of course, depend on the coding sequence $\xi(t)$. The spectral content of the acquired signal ψ_I is given as

$$\psi_I(\Omega_n) = \iint T_S^*(\boldsymbol{k}) T_n(k, \omega_0) e^{iq_n l} A_0(\boldsymbol{k}) d^2\boldsymbol{k}, \tag{3}$$

where T_n is the nth transmission coefficient, q_n is the wavenumber along z and l is the distance between the receiving and modulated screens. Equation (3) can be seen as a system of equations, with $\psi_I(\Omega_n)$ representing the image through the harmonics at the receiving screen and $A_0(\boldsymbol{k})$ being the actual image in the Fourier space. The remaining portion of the equation is the coefficient matrix that depends on the coding sequence. The reconstruction process consists mathematically of inverting the coefficient matrix to recover $A_0(\boldsymbol{k})$ from the measurements $\psi_I(\Omega_n)$. The number of rows in the coefficient matrix depends on the number of harmonics excited by a given coding sequence. This number does not need to be very high though, as the experiment may be repeated with a new coding sequence and new rows can be added to the matrix until it becomes square and invertible.

We illustrate the proposed imaging approach by studying an image illuminated by a wave of $f_0 = 1$ Hz and $c_0 = 1$ m/s and applying a real-valued random modulation signal to the grating. The coding sequence allows for exciting a total of 16 harmonics (including the fundamental frequency, i.e. the 0th harmonic). Such a measurement contributes to 31 rows of the coefficient matrix (amplitudes and phases). The image under investigation is represented through its Fourier spectrum of 129 x 129 coefficients, i.e. 8385 unique complex coefficients. Consequently, a total of 560 measurements is required for the coefficient matrix to be square and invertible. This process allows for lossless image reconstruction.

It is widely known that images exhibit sparse representation in the spectral domain. Typically, only a few percent of coefficients are required for satisfactory reconstruction. This observation opens new possibilities of applying compressive sensing strategies to limit the number of measurements in the image recovery process. By applying the compressive sensing theory [4], we reduced the number of data necessary for satisfactory image reconstruction to approximately 20 % of the initial data.

This research was supported by the DYNAMO project (101046489), funded by the European Union.

References

1. J. W. Goodman, Introduction to Fourier optics, Roberts and Company Publishers, 2005
2. C. Luo, S. G. Johnson, J. D. Joannopoulos, J. B. Pendry, Subwavelength imaging in photonic crystals, Phys. Rev. B 68, 045115, 2003
3. P. Packo, D. Torrent, Far-Field Perfect Imaging with Time-Modulated Gratings, Phys. Rev. Applied 17, 064040, 2022
4. Richard G. Baraniuk, Compressive sensing [lecture notes], IEEE Signal Process. Mag. 24, 118, 2007

Fast quasiadiabatic driving in controlling elastic wave propagations

Dong Liu[1], Yiran Hao[1] and Jensen Li[1*]

[1]Department of Physics, The Hong Kong University of Science and Technology, Kowloon, Hong Kong, China.
[*]corresponding author: jensenli@ust.hk

Abstract: Shortcuts to adiabaticity (STA) in quantum control allow fast evolving the state on the same band as if it is in the adiabatic regime. We simulate the fast quasiadiabatic driving (a STA) using a double elastic waveguide system, facilitating designs of metamaterials to manipulate elastic wave propagation with compact devices.

The adiabatic theorem [1] states that a quantum system follows an instantaneous eigenstate when the system is varied slowly enough in comparison with the energy scale between its eigenstates. In case the system is varied fast enough, adiabaticity is lifted and transitions between different eigenstates become much more favorable. This creates many difficulties in preparing quantum states, an increasingly important problem for quantum information processing, quantum computing and simulations. This problem has sparked recent interest in achieving shortcuts to adiabaticity (STA) [2], i.e., various algorithms to force a system to evolve to its final state as if it were undergoing adiabatic evolution, in a very short duration during which the adiabatic theorem breaks down in a conventional sense. There are several existing algorithms, including counterdiabatic driving, fast quasiadiabatic driving (FAQUAD), invariance-based engineering and non-Hermitian shortcuts.

The STA algorithms are closely related to the control of state evolution starting from a propagating equation, which implies that they can in practice be demonstrated using classical wave systems. This also indicates the feasibility of applications to other classical waves, providing a new mechanism to design more compact devices, especially in optics, such as polarization rotators, beam splitters, and other photonic integrated circuits. In this work, we establish a connection between STA algorithms and elastic systems. Compared with quantum or optical systems, which typically only permit the observation of the output state, the evolution of the state during the propagation of an elastic wave system can be readily probed with a laser scanning vibrometer, making the testing and development of STA algorithms much easier.

Here, we use flexural waves owing to their experimental convenience for field mapping and verification using a scanning laser vibrometer, where the experimental setup incorporates two waveguides coupled by bridges. In the propagation model, the "Hamiltonian" or propagation matrix is a 2-by-2 matrix,

$$\mathcal{H} = \begin{pmatrix} k_1 & \kappa \\ \kappa & k_2 \end{pmatrix}, \qquad (1)$$

where the diagonal elements represent the propagation constants of the two waveguides and the two off-diagonal terms represent the coupling between them. The thickness of waveguides can be used to tune the refractive indices, and hence the propagation constants k_1 and k_2, varying as $n \propto 1/h^{1/2}$ [3]; the cross-section of the bridges can be used to tune the coupling term κ. Then, as shown in Fig. $1(a)$, along the propagating direction of the flexural wave, we can construct position-dependent Hamiltonian from site to site and optimize possible k_1, k_2 and κ for intermediate sites (the first and last sites are fixed to predetermine the initial and final state) to change the character (relative amplitude between the two waveguides) of the state in an adiabatic process. We refer to this approach as FAQUAD, which is achieved by minimizing the so-called adiabaticity parameter. Without optimization (3D-printed resin sample in Fig. $1(a)$), the power flow cannot transfer from one waveguide to another (Fig. $1(b)$) but evenly distributed at the output (r.h.s.). In contrast, after optimization (another sample not shown), the power flow can adiabatically transfer from one waveguide to another, equivalently staying in the same band (Fig. $1(c)$). Our experimental results show that the FAQUAD successfully allows evolving the initial state to the final target state as if it were undergoing adiabatic evolution although the device length is very short (compact).

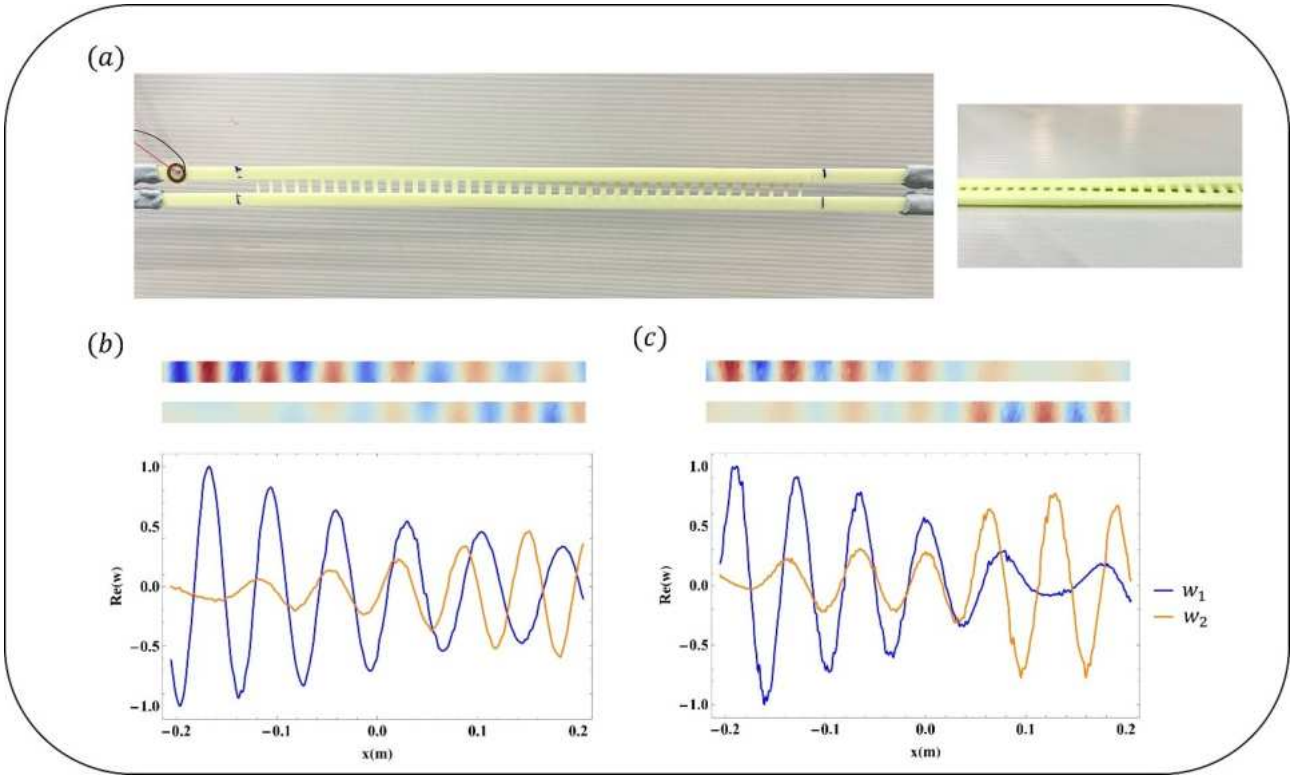


Figure. 1 (a) shows the experimental setup. The upper (lower) waveguide is waveguide 1 (2). (b) and (c) show the field pattern for the experimental results (real part of displacements) for the two samples before and after optimization. (b) is the result without optimization and the power transfers from waveguide 1 to both waveguides. (c) is the result after optimization (another sample) and the power transfers from waveguide 1 to 2 seemingly in the adiabatic regime.

Acknowledgements: The work is supported by the Hong Kong RGC (16307522, AoE/P-502/20) and by Croucher Foundation (CF23SC01).

References

1. Born, M., & V. Fock, "Beweis des adiabatensatzes," Zeitschrift für Physik, Vol. 51, No. 3-4, 165-180, 1928.

2. Guéry-Odelin, D., A. Ruschhaupt, A. Kiely, E. Torrontegui, S. Martínez-Garaot, & J. G. Muga, "Shortcuts to adiabaticity: Concepts, methods, and applications," Rev. Mod. Phys., Vol. 91, No. 4, 045001, 2019.

3. Lee, D., Y. Hao, J. Park, I. S. Kang, S. H. Kim, J. Li, & J. Rho, "Singular lenses for flexural waves on elastic thin curved plates," Phys. Rev. Appl., Vol. 15, No. 3, 034039, 2021.

Dispersion relationship of weakly scattered media

M. Lázaro[1,2*], V. Romero-García[1], L.M. García-Raffi[1], R. V. Craster[2],

[1]Universitat Politècnica de València, Spain

[2]Imperial College London, UK
[*]corresponding author: malana@upv.es

Abstract:. In this paper periodic media with an arbitrary number of scatterers in the unit cell are considered. Our goal is to know analytically the propagation conditions outside the forbidden bands. By applying perturbative techniques we are able to find analytical solutions and the mathematical conditions under which our technique converges.

Periodic structures, also known as Phononic Crystals for sound and vibrations, have been exploited during the last decade to develop acoustic filters and waveguides for sound or vibrations [1], among other applications.

The introduction of subwavelength perturbations of the medium has allowed to manipulate and design metamaterials under disordered but correlated distributions in the long wavelength (hyperuniform media) achieving special properties and finding surprising transparency or absorption results [2,3]. In addition, metamaterials with a quasi-periodic pattern pattern in the scatterer distribution exhibit especially highly predictable correlation properties [4,5]. Designs of transparent metamaterials such as those based on stealth distributions require ensuring that scattering induced by perturbations is weak. Thus, our main objective is to find analytical solutions that allow us to find the dispersion relation in those frequency bands where propagation is guaranteed: i.e. outside the band-gaps. We have developed a methodology that allows us to find analytical relations of the dispersion relation of a medium, either 1D or 2D. We use procedures based on asymptotic perturbation, introduced here in a rigorous way assuming in the context of weak scattering. The developments are carried out in the context of elastic waves for beams and plates such as those shown in Fig. 1. We also deduce the closed-forms of propagation modes, expressionas that in turn relate the geometrical distribution of points in the medium with the wave propagation properties.

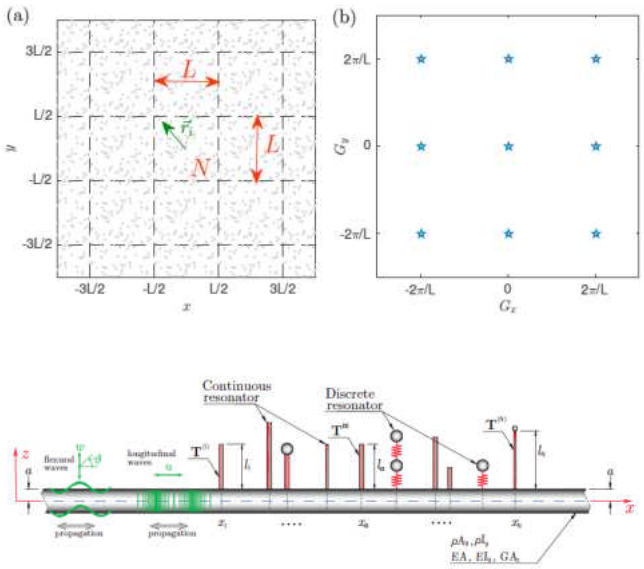


Figure 1. (a) and (b) direct and recirpocal space of a 2D distribution of points in 2D. Periodic replication of unit cello f size $L \times L$. (Bottom) Unit cell with N scatterers-resonators

We have obtained promising results for both beams and plates. Fig. 2 shows some results for a Timoshenko beam with multiple resonators at random positions within a unit cell. In both plots the dispersion relation with a set of scatterers is plotted in blue, computed using the exact approach of the Transfer Matrix Method (TMM).

In Fig. 2 (left) the red curve represents the dispersion relation of the homogeneous beam (without scatterers). This curve shows the typical classical relation predicting the occurrence of two modes from the shear frequency (bending and shear waves). Fig. 2 (right) shows in red the dispersion relation using the linear approximation of our method (first iteration). Closed analytical expression for this relation have been derived. It is remarkable how the wavenumbers are adjusted in those zones outside the bandgaps associated to the scatterer resonances in the whole frequency range.

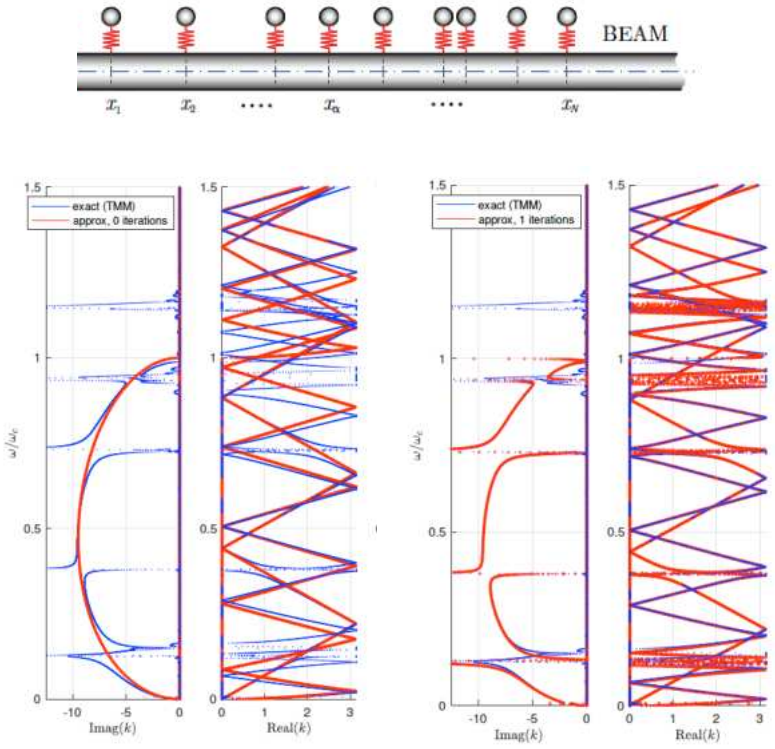


Figure 1. (**Top**) Timoshenko beam with multiple resonators distributed in the unit cell of the periodic medium. (**Bottom-left**) In blue: dispersion relation of the medium with resonators calculated with the transfer matrix method (exact). In red: dispersion relation of the Timoshenko beam without resonators (homogeneous). (**Bottom-right**) In blue: idem as above: exact solution. In red: dispersion relation approximated with a single iteration (linear approximation) using our perturbative method.

Acknowledgments

Authors are grateful for the partial support under Grant No. PID2020-112759GB-I00 funded by MCIN/AEI/10.13039/501100011033. L.M.G.-R. and V.R.-G. acknowledge support from Grant No. CIAICO/2022/052 of the "Programa para la promoción de la investigación científica, el desarrollo tecnológico y la innovación en la Comunitat Valenciana" funded by Generalitat Valenciana. M.L is grateful for support under the "Programa de Recualificación del Sistema Universitario Español para 2021-2023", (funded by "Instrumento Europeo de Recuperación (Next Generation EU) en el marco del Plan de Recuperación, Transformación y Resiliencia de España", a través del Ministerio de Universidades.

References

1. Deymier, P. A. "Acoustic Metamaterials and Phononic Crystals", Springer, 2013.
2. Romero-García, V., Chéron, É. and Kuznetsova, S., Groby, J., Félix, S., Pagneux, V. and Garcia-Raffi, L. "Wave transport in 1D stealthy hyperuniform phononic materials made of non-resonant and resonant scatterers," APL Materials, vol. 9, no. 10, p. 101101, 2021.
3. Romero-García, V., Lamothe, N., Theocharis, G., Richoux O. and L. M. García-Raffi, L.M. "Stealth acoustic materials," Phys. Rev. Applied, vol. 11, no. 054076, 2019.
4. Lázaro, L., Niemczynowicz, Siemaszko A., García-Raffi, L. "Elastodynamical properties of Sturmian structured media," J. Sound Vib., vol. 517, no. 116539, 2022.
5. Lázaro, L. and García-Raffi, L.M. "Hyperuniformity of quasiperiodic tilings generated by continued fractions," Physical Review B, vol. 109, no. 1, p. 014202, 2024.

META 2024, TOYAMA - JAPAN, JULY 16 – 19, 2024

Braiding of Bloch eigenmodes in a non-Abelian topological phase with quaternion charge

Xiaoming Wang[1,2*] Guancong Ma[1,2]

1 Department of Physics, Hong Kong Baptist University, Kowloon Tong, Hong Kong, China
2 Shenzhen Institute for Research and Continuing Education, Hong Kong Baptist University, China
Corresponding author: xmwangphy@hkbu.edu.hk

Abstract: In this work, we show that non-Abelian quaternion charges can be realized by braiding its Bloch eigenmodes. An acoustic system with built-in synthetic dimensions is proposed for the realization of the non-Abelian topological phase and for the observation of the non-Abelian braiding of its eigenmodes.

The concept of braiding groups in relation to elementary particles is an interesting topic in physics. In a quantum mechanical system, e.g., a system with two indistinguishable particles has state $\psi_1\psi_2$ in Dirac notation. If the particles are bosons (fermions), then the exchange of the two particles yields $|\psi_1\psi_2\rangle = e^{i\theta}|\psi_2\psi_1\rangle$, where θ = 0 (θ = π) . When θ take values other than θ = 0 nor θ = π, the particles are called anyons. Remarkably, θ can also be a set of non-communicative matrixes, which correspond to the non-Abelian anyons braiding. In other words, the intrinsic property of elementary particles are encoded in θ .

Recently, non-Abelian topological phase has been proposed as a novel multiband topological phase. Its band topology is classified by a non-Abelian group, the quaternion group $Q_8 = \{\pm i, \pm j, \pm k, -1, 1\}$. The eight group elements obey the following relations as $ij = k, jk = i, ki = j$ and $i^2 = j^2 = k^2 = -1$. Different from Abelian topological band insulators, non-Abelian topological phases involve multiple bulk bandgaps and support nontrivial edge states even winding number is zero. Here, we show that non-Abelian quaternion charge can be realized by unique braiding its Bloch eigenmodes.

We consider a parity-time symmetric three-band Hamiltonian with

$$h(k) = \begin{bmatrix} s_a + 2v_a\cos k & 2u\sin k & 2w\sin k \\ 2u\sin k & s_b + 2v_b\cos k & 2v\sin k \\ 2w\sin k & 2v\sin k & s_c + 2v_c\cos k \end{bmatrix} \quad (1)$$

All parameters are real. Its eigenvectors are purely real vectors. The topological space of the above Hamiltonian is given as $M = \frac{O(3)}{O(1)\times O(1)\times O(1)}$, and the fundamental group is $\pi_1(M) = Q_8$. Consider the adiabatic evolution of all three eigenvectors $|u_k^n\rangle$ with m and n label different bands. The end states of the evolution is given by $|\psi(1,2,3),t\rangle = \int_0^t A_{3\times3}(k)dk\,|\psi(1,2,3),t=0\rangle$, where $[A_{3\times3}(k)]_n^m = \langle u_k^m|\partial_k|u_k^n\rangle$, $|\psi(1,2,3)\rangle$ is matrix and compose of all three eigenvectors. The same as

k, t vary from 0 to 2π. We find that the phase factor $\int_0^{2\pi} A_{3\times3}(k)dk$ can be always written as the combinations of the representations of Artin braid group B_3. An example is illustrated in Figure 1(b), where we braid the first two eigenmodes twice to obtain non-Abelian charge $Q_8 = i$. Thus the eigenvectors evolution of non-Abelian charge $Q_8 = i$ is expressed as

$$|\psi(1,2,3), t=\pi\rangle = b_{12}\,|\psi(1,2,3), t=0\rangle$$
$$|\psi(1,2,3), t=2\pi\rangle = (b_{12})^2\,|\psi(1,2,3), t=0\rangle$$

Where b_{12}, b_{23} denote the representation of Artin braid group B_3. The mapping between non-Abelian quaternion charges and braiding protocols are listed in Figure 1(c)-(i). Moreover, we also find that parity-time symmetry and spectral reciprocity together also ensure single-band Berry phase to be quantized in half Brillouin zone (BZ). Such a property can be characterized by defining a new topological invariant, we call a Half-BZ winding number. It is defined as $\mathrm{W}_{1/2} = \int_p^{p+\pi} i\langle\psi(k)|\partial_k|\psi(k)\rangle dk$ (p denotes start point).

Model (1) and the braiding of the bands therein can be demonstrated using an acoustic cavity system as shown in Figure1(a). We will show that the non-Abelian braiding process can be directly probed by measuring the acoustic pressure.

In summary, we reveal the intrinsic relations between non-Abelian quaternion charge and braiding group for the first time. We design an acoustic system to illustrate the non-Abelian properties of non-Abelian quaternion charge experimentally. A new topological invariant Half-BZ winding number is defined to distinguish all eight non-Abelian quaternion topological phases, while traditional winding number failed to distinguish some of them. Moreover, the above results can be also generalized for more than 3 bands. Our findings can deepen the understanding of the non-Abelian origin of non-Abelian topological phases.

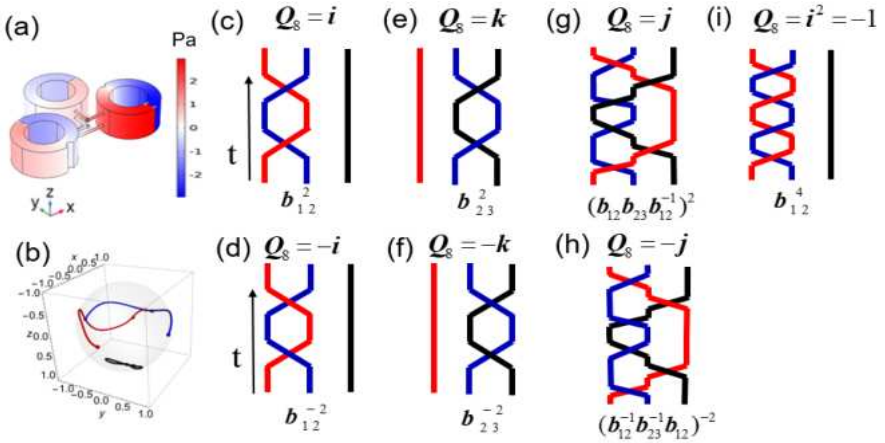


Figure 1. (a)Illustration of the structure of the acoustic cavities, color bar denotes acoustic pressure. (b)Eigenvectors evolution on a sphere. Three different colored trajectories represent the evolution of the three different eigenmodes. (c)-(i)Illustration of different braiding protocols to realize different non-Abelian charges. Those three different eigenmodes are marked with three different colors and considered as three strands. The braiding operations are represented by the crossing of the above colored strands.

Acknowledgement: The National Key R&D Program of China No. 2022YFA1404400

Tunable magnetic lattices as a platform for controlling sound waves

Osama R. Bilal[1*]

[1]Department of Mechanical, Aerospace, and Manufacturing engineering, University of Connecticut, Storrs, Connecticut 06269, USA Affiliation, Country
[*]corresponding author: Osama.bilal@uconn.edu

Abstract: In this work, we realize metamaterials with programmable dynamical characteristics by combining analytical, numerical, and experimental analyses, to utilize tunable nonlinear magnetic lattices for sound wave manipulation.

Metamaterials can be defined as repeating geometric patterns in space, creating artificial lattices. Such lattices can be utilized as platforms to realize peculiar static and dynamic behavior (such as negative effective mass density, negative effective dynamical stiffness, and negative effective Poisson's ratio). These geometric patterns are usually fixed once the metamaterials are fabricated. While many theoretical and numerical studies of tunable metamaterials exist, realization of experimental platforms remain limited because of challenges in manufacturability, the destructive nature of reprogramming, and inherent nonlinearities. A valid path for functional tunability of matter is external stimuli, e.g., either static or dynamic load, which can effectively induce an external field to tune the materials. This, however, can translate to large shape change in the material with the potential rise of instabilities, phase transitions, degradation, and geometric frustration. This can hinder our ability to utilize programmable materials [1,2].

In this line of work, we realize metamaterials with programmable dynamical characteristics by combining analytical, numerical, and experimental analyses, to utilize tunable nonlinear magnetic lattices [3-6]. We create our lattices by confining self-aligned, free-floating disks of embedded permanent magnets in a range of symmetries within a fixed boundary and a pre-engineered magnetic field. The magnetic repulsive forces between the boundary magnets and the free-floating disks cause the disks to self-align and rest within their surrounding magnetic potential wells. Each disk or group of disks can act as a single building block, or a unit cell, of the lattice. These unit cells repeat in space, forming a one-dimensional or two-dimensional metamaterial with unique wave propagation characteristics. We design the geometry of the confining boundary, disk symmetry, and number of embedded magnets within each disk such that the tuning of the boundary's magnetic field controls the assembly of the disks. The relative positions and orientation angles between the disks define the corresponding metamaterial phase (ordered, quasi-ordered or random) and its stability conditions (mono-stable or multi-stable) (Figure 1). By changing the boundary geometry, number of disks, their symmetry, and therefore the resulting magnetic couplings within the unit cell, the transmittable frequencies through the metamaterial can be programmed. Figure 2 shows a few examples of the possible ordered lattices (crystalline), semi-ordered lattices (quasi-crystalline) or random (amorphous) assemblies that can self-assemble within the different boundaries.

The proposed platform can be utilized to engineer self-assembled metamaterials capable of manipulating low-frequency waves, within a relatively small volume, while utilizing negligible mass. Moreover, the nonlinear potentials between the disks and their boundaries can be harnessed to demonstrate phenomena with no linear parallel such as amplitude dependent response, bifurcation, chaos, non-reciprocity, and solitons. In addition, the self-assembly nature of the disks can be key in creating re-programmable materials with exceptional properties.

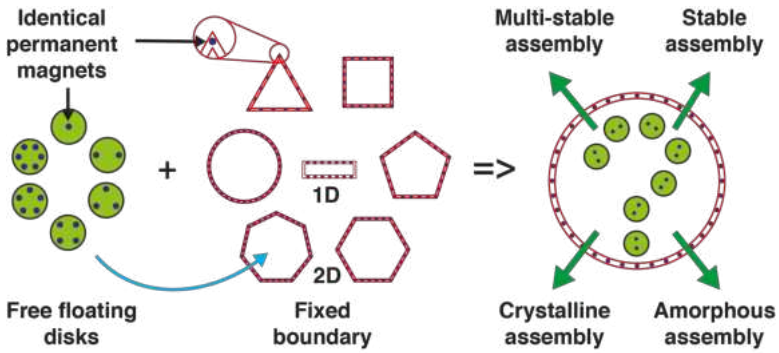


Figure 1: Schematic representation of the different symmetries of the disks confined within boundaries with embedded magnets of different shapes, resulting in a variety of lattice types and properties.

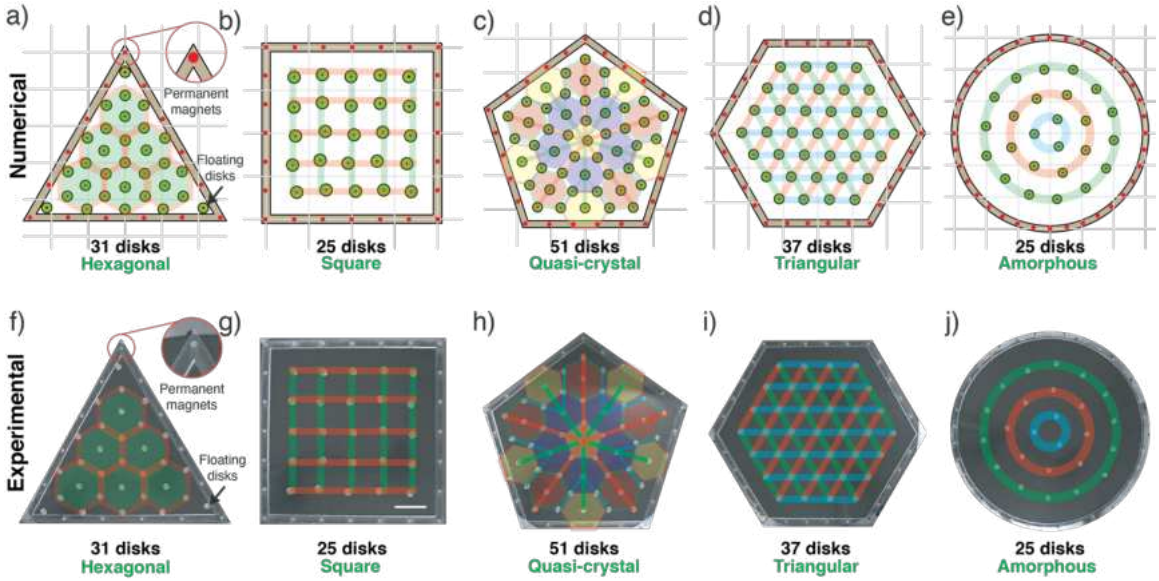


Figure 2: Example of numerical (top) and experimental (bottom) self-assembled lattices within two-dimensional magnetic boundaries with highly ordered, semi-ordered and random configurations.

References

1. Deng, Bolei, et al. "Characterization, stability, and application of domain walls in flexible mechanical metamaterials." *PNAS* 117.49 (2020): 31002-31009.
2. Li, Jian, Nitesh Arora, and Stephan Rudykh. "Elastic instabilities, microstructure transformations, and pattern formations in soft materials." *Current Opinion in Solid State and Materials Science* 25.2 (2021): 100898.
3. Watkins, Audrey A., and Osama R. Bilal. "Demultiplexing infrasound phonons with tunable magnetic lattices." *Frontiers in Materials* (2020): 410.
4. Watkins, Audrey A., Austin Eichelberg, and Osama R. Bilal. "Exploiting localized transition waves to tune sound propagation in soft materials." *Physical Review B* 104.14 (2021): L140101.
5. Norouzi, Ehsan, Audrey A. Watkins, and Osama R. Bilal. "Classification of emerging patterns in self-assembled two-dimensional magnetic lattices." *Physical Review E* 104.4 (2021): 044902.
6. Watkins, Audrey A., Austin Eichelberg, and Osama R. Bilal. "Harnessing Reprogrammable Phase Transitions to Control the Propagation of Sound Waves." *Physical Review Applied* 17.2 (2022): 024036.

Using Ping-Pong balls to reduce ambient noise

Y. Pennec[1*], E. Cochin[2], G. Lévêque[1] and B. Djafari-Rouhani[1]
[1]IEMN University of Lille, Cité Scientifique, 59650, Villeneuve d'Ascq, France
[2]UMET University of Lille, Cité Scientifique, 59650, Villeneuve d'Ascq, France
[*]corresponding author: yan.pennec@univ-lille.fr

Abstract:
We study an acoustic metasurface using interconnected ping-pong balls as Helmholtz resonators (HR) for broad low-frequency spectral responses. We demonstrate how inter-unit coupling alters low-frequency acoustic insulation and introduce additional attenuation modes. Both numerical and experimental methods are employed for analysis.

Controlling the attenuation of acoustic waves in the sonic range represents one of the major challenges in our urbanized societies for the well-being of human life. One principal issue remains the narrowband response of and the difficult question of covering a large frequency spectrum, keeping a simple geometric arrangement of the metasurface. The coupling between elementary Helmholtz Resonators (HR) units appears as a key factor to cover this objective. We propose to investigate the case of coupled HR and showed that the degeneracy of the low-frequency resonance can be raised, leading to many absorptions peaks. Through a combination of numerical analysis and experimentation, we demonstrate that a metasurface made of interconnecting HR units offers new opportunities with multiple local resonances. The interaction between HRs can be manipulated by adjusting geometrical parameters, such as the number of holes and their orientations, the number of resonators, or the separation distance between units [1, 2].

To demonstrate the coupling property, we studied a finite system made up of 9 ping-pong balls, connected to each other by drilling the balls with openings of radius 2 mm. Each ball has, therefore, been pierced with four holes, allowing the connection in both *y* and *z* directions. We performed the eigenmode calculation of the system and found, as expected, 9 eigenmodes, shown in Fig. 1(a). We found three sets of modes, namely, two dipolar modes degenerated two times [(ii), (iii) and (vii), (viii)], two others which change sign under a $\pi/2$ rotation [(iv) and (vi)], and finally three modes totally symmetric [(i), (v), and (ix)]. The resonance properties of the 9-balls resonator structure have been tested under the excitation of an acoustic plane wave launched in the direction of propagation *x*. For the sake of experimental facilities, the pressure has been detected in the central ball, as shown in the inset of Fig. 1(c). Figure 1(b) presents the numerical calculation of the SPL, considering the lossless (dashed lines) system. Three peaks appear in the frequency spectrum, which can easily be associated with the eigenmodes (i), (v), and (ix) for which the pressure in the central ball is different from zero. Indeed, among all the modes, only the totally symmetric ones (i), (v), and (ix) are compatible with the symmetry of a normal acoustic excitation.

To fit the experimental results, we have considered the air dissipation, using a thermoviscous acoustic model where the air motion is described based on the momentum, continuity, and energy equations,

$$\omega\rho_0\overrightarrow{v_t} = -\nabla P_t\vec{I} + \nabla.\left(\mu[\nabla\overrightarrow{v_t} + (\nabla\overrightarrow{v_t})^T] - \left[\frac{2}{3}\mu - \mu_B\right][\nabla.\overrightarrow{v_t}]\vec{I}\right.$$

$$i\omega\rho_t = -\rho_0\nabla\overrightarrow{v_t}$$

$$i\omega(\rho_0 C_p T_t - T_0 \alpha_p P_t) = \nabla.(\kappa \nabla T_t)$$

$$\rho_t = \rho_0(\beta_T P_t - \alpha_p T_t)$$

where ρ_0 is the air density (1.2 kg/m^3) at the ambient temperature T_0 = 293 K, and P_t, v_t, T_t, and ρ_t are the values of the pressure, velocity, temperature, and density at the considered position in space and for the given acoustic frequency. The bulk and dynamic viscosities employed in the simulations are those of air, namely, $\mu_B = 1.09\ 10^{-5}$ Pa.s and $\mu = 1.81\ 10^{-5}$ Pa.s. C_p, κ, β_T, and α_p are the heat capacity at constant pressure, the coefficient of thermal conduction, the isothermal compressibility, and the coefficient of thermal expansion. I is the identity vector.

When the thermoviscous losses are taken into consideration, we found that the three peaks are shifted toward the low frequencies with a decrease in amplitude (dashed lines in fig 1(b)). The experimental demonstration was carried out by gluing 9 balls together, positioning the microphone in the middle of the central resonator. The experimental data, presented in Fig. 1(c), capture the 3 peaks obtained in the numerical calculation with a good agreement.

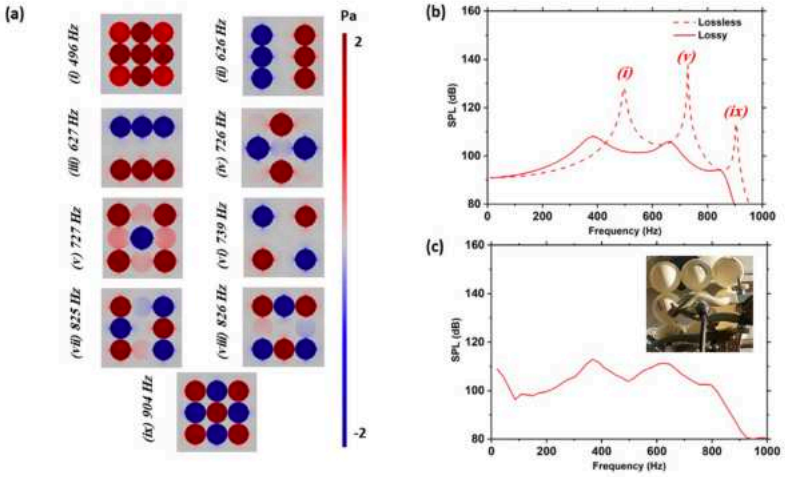


Figure 1 (a) Eigenmodes calculation of the nine-ball connected resonator. Numerical (b) and experimental (c) SPL recorded inside the central ball of a lossless (dashed lines) and lossy (solid line) system.

Acknowledgements

This result has received funding from the European Union's Horizon 2020 research and innovation program INSPIRE under the Marie Skłodowska Curie Grant Agreement No. 813424.

References

1. Sabat R., E Cochin, M Kalderon, G Lévêque, I Antoniadis, B Djafari-Rouhani, Yan Pennec, "Title of the journal paper," Journal of Applied Physics 134 (14), 2024.
2. R Sabat, Y Pennec, G Lévêque, D Torrent, C Ding, B Djafari-Rouhani, « Single and coupled Helmholtz resonators for low frequency sound manipulation" Journal of Applied Physics 132 (6), 2022.

Modeling wave propagation and boundary effects in acoustic metamaterials by a relaxed micromorphic continuum

Angela Madeo, Jendrik Voss, Svenja Hermann, Gianluca Rizzi, Felix Erel-Demore, Leonardo A. Perez Ramirez, Plastiras Demetriou and Patrizio Neff

TU Dortmund / Institute of Structural Mechanics and Dynamics /
jendrik.voss@tu-dortmund.de / August-Schmidt-Str. 8, 44227 Dortmund

Abstract: The relaxed micromorphic model (RMM) is employed to investigate the elastic wave propagation of mechanical metamaterials. This model adeptly captures band gaps, restricting wave propagation at specific frequencies. Addressing finite-size blocks, we enrich the RMM framework to incorporate essential boundary effects, exemplifying this through the concept of boundary forces.

Exploring the dynamical response of mechanical metamaterials in the framework of elastic propagation has gathered increasing attention in the last decades. In order to describe elastic wave propagation in metamaterials, i.e. solids with heterogeneities or microstructure, it is necessary to consider non-local or enriched models. The relaxed micromorphic model (RMM) [1, 2, 3] proposed here can describe these effects as a continuous material with enriched kinematics. One of the most important micro-mechanical effects is the appearance of *band gaps* for which waves at given frequencies cannot propagate through the material.

We have shown in previous papers [1, 2, 3] that the relaxed micromorphic model can describe the bulk behavior of mechanical metamaterials. Things become more complicated when considering finite-size metamaterial blocks for which boundary effects may play a major role, e.g. due to the reduced size of the block itself. In these cases, the relaxed micromorphic model framework must be enriched to account for these boundary effects. We will show how the concept of *boundary forces* can be used to address the modeling of finite-size metamaterial specimens in the context of micromorphic elasticity.

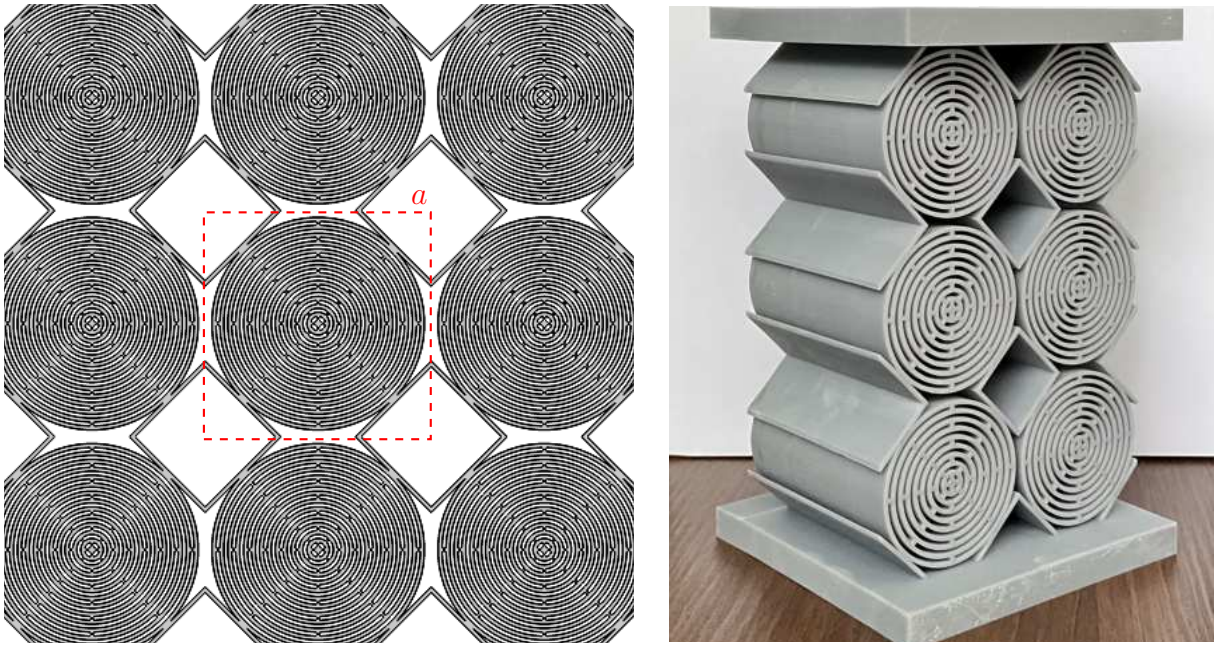


Figure 1: (Left) A 3x3 section of a metamaterial made up of a given unit cell marked by the red dashed square with size a. (Right) The experimental prototype of the metamaterial's structure.

References

[1] A. Madeo, P. Neff, I.-D. Ghiba, P. Placidi and G. Rosi, "Wave propagation in relaxed micromorphic continua: modeling metamaterials with frequency band-gaps". *Continuum Mechanics and Thermodynamics*, 27.4 (2015). Pp. 551–570.

[2] M.V. d'Agostino, G. Barbagallo, I.-D. Ghiba, B. Eidel, P. Neff and A. Madeo, "Effective description of anisotropic wave dispersion in mechanical band-gap metamaterials via the relaxed micromorphic model". *Journal of Elasticity*, 139.2 (2020). Pp. 299–329.

[3] J. Voss, G. Rizzi, P. Neff and A. Madeo, "Modeling a labyrinthine acoustic metamaterial through an inertia-augmented relaxed micromorphic approach". *Mathematics and Mechanics of Solids*, 28(10) (2023). Pp. 2177–2201.

Design strategies for amplitude and phase acoustic holograms in biomedical ultrasound

N. Jiménez[1*], D. Andrés[1], A. Eroles-Simó[1], A. Carrión[1], and F. Camarena[1]

[1]Instituto de Instrumentación para Imagen Molecular, Universitat Politècnica de València – CSIC, València, Spain
[*]corresponding author: nojigon@upv.es

Abstract: We present several topologies for phase-and-amplitude acoustic holograms based on metamaterial and phononic crystals. These approaches go beyond traditional phase holograms and produce sharper acoustic images for non-invasive and localized preclinical and clinical therapeutical applications like neuromodulation, drug delivery or surgery, or biomedical ultrasound imaging. Several application examples are provided.

Passive acoustic structures like metamaterials can be used to engineer wavefronts in many practical applications. By tuning its topology, the local refraction, scattering or inner resonances can be tailored for a particular functionality. Among them, acoustic holograms are emerging as a low-cost technology to focus therapeutic ultrasound beams [1-8]. These high-performance lenses can produce therapeutic acoustic images of arbitrary shape into biological tissues. In addition, by exploiting time-reversal symmetry of the wave equation acoustic holograms can encode complex wavefronts compensating the aberrations of stiff layers, enabling the focusing of ultrasound into the human brain. However, usually acoustic holograms are only designed to encode the phase of the beam, neglecting the amplitude information of the time-reversed wavefront. In addition, most of the design strategies for sound waves in air are not suitable for biomedical ultrasound applications, which are generally water-coupled.

In this work, we propose metasurfaces with internal resonances to encode the full-wave information in a 3D-printed structured material. In particular, we report the use of metasurfaces to synthesize wavefronts by tuning subwavelength 3D-printed elastic resonators for ultrasonic frequencies, as shown in Fig. 1. These structures are shown to be remarkably flexible for spatially-coding arbitrary phase-conjugated fields corresponding to the ones used for selected biomedical ultrasound applications.

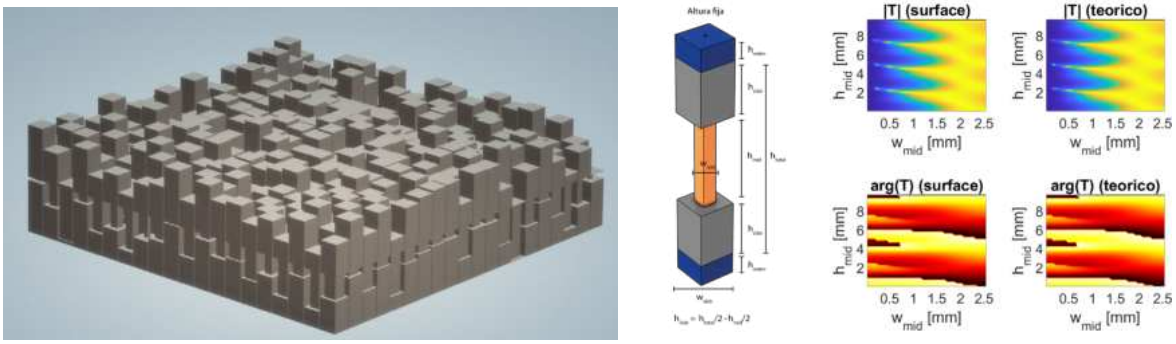


Figure 1. Topology of an acoustic hologram using a metamaterial as a building block. Phase and magnitude can be controlled locally to generate accurate acoustic images.

Then, by mimicking phase-and-amplitude information, these lenses can synthesize complex and arbitrary acoustic images with great accuracy. In this way, by tuning the hologram inner structure, we can synthesize

high-intensity acoustic images with unprecedent resolution, which are currently being applied to focus therapeutic ultrasound beams and treat several diseases in a non-invasive, non-ionizing, localized and low-cost manner. This approach improves the targeting of ultrasound and paves the road for low-cost biomedical ultrasound applications.

We acknowledge financial support from Ministerio Español de Ciencia e Innovación and the Ministerio de Universidades Grants “Ramón y Cajal” RYC2021-034920-I, and FPU19/00601, Agencia Estatal de Investigación PID2022-142719OB-C21 and CNS2023-145707 funded by MCIN/AEI/10.13039/501100011033 and to the Agencia Valenciana de la Innovació through grants INNVA1/2022/37, INNVA2/2022/11 and METASMART project INNEST/2022/345, and by Generalitat Valenciana through the programs Programa de Garantía Juvenil I+D EDGJID/2021/189, CIAICO/2023/052, and the program Equipamiento e Infraestructuras FEDER 2021-22 IDIFEDER/2021/004.

References

1. S. Jiménez-Gambín, et al. "Holograms to focus arbitrary ultrasonic fields through the skull." Physical Review Applied 12.1 (2019): 014016.
2. S. Jiménez-Gambín, et al. "Generating Bessel beams with broad depth-of-field by using phase-only acoustic holograms." Scientific reports 9.1 (2019): 20104.
3. S. Jiménez-Gambín, et al. "Transcranial focusing of ultrasonic vortices by acoustic holograms." Physical Review Applied 14.5 (2020): 054070.
4. D. Andrés, et al. "Thermal holographic patterns for ultrasound hyperthermia." Applied Physics Letters 120.8 (2022).
5. S. Jiménez-Gambín, et al. "Acoustic holograms for bilateral blood-brain barrier opening in a mouse model." IEEE Transactions on Biomedical Engineering 69.4 (2021): 1359-1368.
6. D. Andrés, et al. "Numerical study of acoustic holograms for deep-brain targeting through the temporal bone window." Ultrasound in Medicine & Biology 48.5 (2022): 872-886.
7. D. Andrés, et al. "Holographic Focused Ultrasound Hyperthermia System for Uniform Simultaneous Thermal Exposure of Multiple Tumor Spheroids." Cancers 15.9 (2023): 2540.
8. D. Andrés, et al. "Methods to design and evaluate transcranial ultrasonic lenses using acoustic holography." Physical Review Applied 20.4 (2023): 044071.

Topological Shear Band Engineering in Mechanical Metamaterials

Jingyi Zhang[1], Jingran Liu[1], Anton Souslov[2], María Teresa Pérez Prado[1], Javier Segurado[1], Maciej Haranczyk[1], and Johan Christensen[1*]

[1]IMDEA Materials Institute, Calle Eric Kandel, 2, 28906 Getafe, Madrid, Spain

[2]Department of Physics, Cavendish Laboratory, 19 J. J. Thomson Avenue, Cambridge CB3 0HE, United Kingdom

[*]Corresponding author: johan.christensen@imdea.org

Abstract: In this contribution we focus on mechanical metamaterials and discuss how the lattice topology can influence stress localizations when uniaxial compression is applied. We discuss a theoretical model that faithfully can predict the shape and orientation of stress localizations, which appear in good agreement with experimental measurements.

Viscous phononic supercrystal

A. A. Krokhin[1*], M. A. Ibarias[2], and J. Sánchez-Dehesa[2]

[1]University of North Texas, USA
[2] Universitat Politècnica de València, Spain
[*]corresponding author: arkady@unt.edu

Abstract: An effective medium theory and experimental study are proposed for a supercrystal of metallic rods in viscous background. Supercrystal (SC) is a combination of two phononic crystals with different periods imbedded in a viscous fluid. The decay coefficient of sound is calculated analytically at low frequencies when both lattices homogenize.

A monochromatic sound decays in a viscous fluid with the decay coefficient $\gamma_0 = \omega^2(\frac{4}{3}\eta_0 + \xi_0)/2\rho_0 c_0^3$, where ρ_0, c_0, η_0, and ξ_0 are the fluid density, speed of sound, and viscosity coefficients. If the wave meets a solid wall, dissipation is strongly enhanced due to formation of the boundary layer $\delta = \sqrt{2\eta_0/\omega\rho_0}$. A solid-fluid phononic crystal behaves in the low-frequency limit as a homogeneous medium. The effective elastic parameters of this medium, speed of sound c_{eff} and fluid density ρ_{eff}, are calculated using the homogenization procedures proposed in Ref. [1]. Dissipation in a phononic crystal occurs mainly within the boundary layers formed around each solid scatterer. Due to multiple scattering, the level of dissipation exceeds by orders of magnitude the viscous losses in the corresponding background fluid. The exact formula for the viscous decay coefficient in a 2D phononic crystal with arbitrary Bravais lattice was recently obtained in Ref. [2]

$$\gamma_{ph}(\hat{\mathbf{k}}) = \frac{L}{2A_c c_{eff}(\hat{\mathbf{k}})}\sqrt{\frac{\omega\eta_0}{2\rho_0}}N(\hat{\mathbf{k}}) \tag{1}$$

Here A_c is the area of the unit cell and $N(\hat{\boldsymbol{k}})$ is the direction-dependent numerical factor expressed through multiple series over reciprocal lattice vectors. This factor contains information about the microstructure of the lattice. It grows fast with the filling fraction reaching $\sim 10^3 - 10^5$ for the fillings near the close packing [2]. If the crystal lattice possesses the 3[d] or higher order axis of rotational symmetry, the effective medium is isotropic. Otherwise, it is an anisotropic metafluid where the effective parameters depend on the direction of propagation $\hat{\mathbf{k}}$. The effective viscosity for phononic crystal can be easily introduced from the equality $\gamma_{ph}(\hat{\mathbf{k}}) = \gamma_0$, that gives

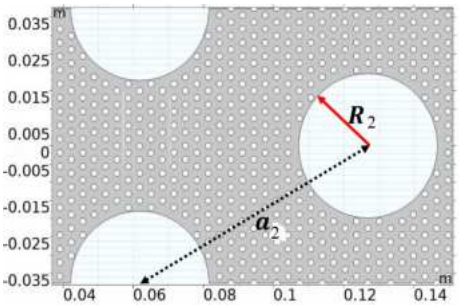


Figure 1. 2D phononic SC of solid cylinders in air. The cylinders of radii $R_1 = 0.88$ and $R_2 = 19.7$ mm are arranged in hexagonal lattices with periods $a_1 = 3.76$ mm and $a_2 = 20\,a_1 = 75.1$ mm. The filling fractions are $f_1 = 0.2$ and $f_2 = 0.25$.

$$\eta_{eff}(\hat{\mathbf{k}}) = \frac{3\rho_{eff}(\hat{\mathbf{k}})c_{eff}(\hat{\mathbf{k}})}{2\omega^2}\gamma_{ph}(\hat{\mathbf{k}}). \tag{2}$$

The effective viscosity is anisotropic in general case, and it scales as $\sim\omega^{-3/2}$ with frequency. For a phononic crystal of solid cylinders of radius $R_1 = 0.88$ mm arranged in a hexagonal lattice with period $a_1 = 3.76$ mm in air the effective viscosity calculated from Eq. (1) yields $\eta_{eff} = 0.365 \cdot 10^6/\omega^{3/2}$ g /s·cm. At frequency 1 kHz the effective viscosity is $3.2 \cdot 10^5$ times greater than the viscosity of air.

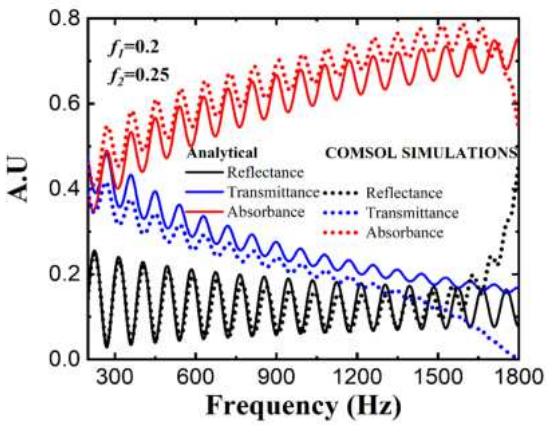


Figure 2. Transmission, reflection, and absorption spectra for SC slab of L=23a_2 length.

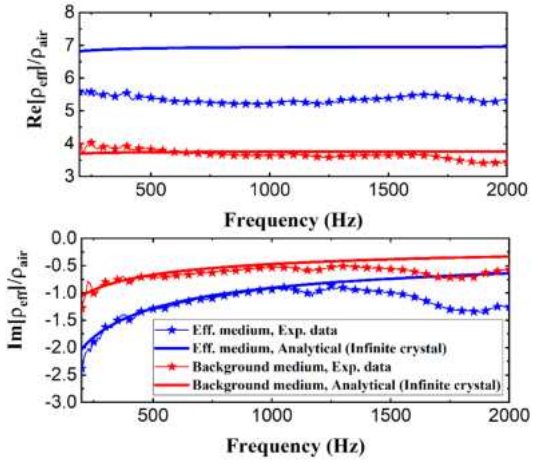


Figure 3. Normalized complex effective mass density.

Strongly enhanced effective viscosity of phononic crystal can serve as a viscous matrix for a phononic crystal with larger period. Such doubly periodic structure (Fig. 1) can be considered as strongly absorbing SC. Here we report analytical, numerical, and experimental results for sound transmission through a viscous SC. Note that it is assumed that sound wave weakly decays passing through a SC, i.e., $\gamma_{sc}^{-1} \gg \lambda \gg a_2$ and both lattices homogenize. Using the technique developed in Ref. [2], the decay coefficient γ_{sc} for 2D SC was calculated. For the SC shown in Fig. 1 the decay coefficient yields $\gamma_{sc} = 0.048\sqrt{\omega}$ m^{-1}. This leads to the effective viscosity $\eta_{sc} = \frac{0.51 \cdot 10^6}{\omega^{3/2}}$ $\frac{\text{g}}{\text{cm}\cdot\text{s}}$. To justify this result transmission through the SC slab of length $L = 23a_2 = 1.56$ was numerically modelled using COMSOL software. The spectra for the SC and for a homogeneous plate with the calculated effective parameters are shown in Fig. 2. There is a good agreement, which confirms the results of the homogenization theory for the viscous SC. All the spectra exhibit Fabry-Perot oscillations with period $2L/c_{sc} = 90$ Hz.

The experiment was performed with a 3D printed SC slab of ABS plastic placed in a standard ACUPRO impedance tube. The geometrical parameters of the SC are: $a_1 = 2.5$ mm, $R_1 = 1$ mm, $a_2 = 33.7$ mm, $R_2 = 9.7$ mm, and the length of the slab is $L = 30$ mm. Since the length of the slab fits only one row of big cylinders, the dispersive properties of the SC are not manifested well. At the same time, the slab contains enough periods a_1. Since the decay length of this SC is about 0.5 m, it is hard to measure it directly. Instead, the complex mass density was extracted experimentally [3] and compared to the analytical result $\rho_c = \lambda_{sc}/c_c^2$, where $\lambda_{sc} \approx \lambda_0/(1-f_1)(1-f_2) = 0.254$ Pa is the bulk modulus of the SC and $c_c = c_{sc}(1 - i\gamma_{sc}c_{sc}/\omega)^{-1}$ is the complex speed of sound. The plots in Fig. 3 demonstrate good agreement for the set of small cylinders with period a_1. For the SC the agreement is observed only for the $Im\,\rho_c$, which is responsible for viscous losses.

This work is supported by the NSF grant No. 1741677, by the AFOSR grant FA9550-23-1–0630, and by the RDI grant PID2020-112759GB-I00 funded by MCIN/AEI/10.13039/501100011033.

References

1. Krokhin, A. A., J. Arriaga and L.N. Gumen, “Speed of sound in periodic elastic composites,” Phys. Rev. Lett., Vol. 91, 264302, 2003; Torrent, D., A. Håkansson, F. Cervera and J. Sánchez-Dehesa, "Homogenization of two-dimensional clusters of rigid rods in air," Phys. Rev. Lett. Vol. 96, 204302 (2006).
2. Ibarias, M., Y. Zubov, J. Arriaga and A. A. Krokhin, “Phononic crystal as a homogeneous viscous metamaterial,” Phys. Rev. Res., Vol. 2, 022053(R), 2020.
3. Guild, M. D., V. M. Garcia-Chocano, W. Kan and J. Sánchez-Dehesa, “Enhanced inertia from lossy effective fluids using multi-scale sonic crystals,” AIP Advances, Vol 4, 124302, 2014.

Enhanced Understanding through Experimental Study: Disorderly Arrangement of Vertical GaN Nanowires in Polymer Materials

F. Soldevila[1], A. Huynh[1], E. Charron[1], B. Bonello[1], B. Perrin[1], A. Chevillard[2], N. Gogneau[2], M. Tchernycheva[2] and O. Boyko[1*]

[1]University Pierre et Marie Curie - Institut des NanoSciences de Paris, 4, place Jussieu 75252 Paris, France

[2]Centre de Nanosciences et de Nanotechnologies, UMR 9001 CNRS, Univ. Paris-Saclay, 8 Avenue de la Vauve, 91120 Palaiseau, France

[*]olga.boyko@insp.jussieu.fr

Abstract: Our study focuses on the elastic properties of gallium nitride (GaN) nanowires within a polymer matrix, vital for force sensor and artificial skin development. Utilizing picosecond acoustics, we investigate surface wave propagation, offering insight into the composite material's elasticity and resonant properties, crucial for advancing nanotechnology applications.

Here we present our work focusing on the study of the elastic properties of gallium nitride (GaN) nanowires integrated into a polymer matrix. This material is currently the most promising for the development of force sensors and is often cited in projects for creating artificial skin.

GaN nanowires exhibit exceptional elastic properties [1] and a very good piezoelectric response [2,3]. They have been studied individually, but their integration into a polymer matrix and the study of their properties as a whole pose a different experimental challenge from that of the previously used AFM technique.

In our work, we concentrate on studying the elasticity of this new composite material and examine the propagation of surface waves using picosecond acoustics technique. Picosecond acoustic technique enables the generation and detection of high-frequency elastic waves through ultrashort light pulses. Thanks to this non-destructive and contactless method, a picosecond acoustic pulse creates an acoustic wave on the surface of nanostructures. The behavior of the surface wave is studied in both time and space. Based on these elements, we analyze the elasticity of the entire ensemble of nanowires in the polymer layer. Drawing on our experience in the field of acoustic metamaterials, we compare these disordered structures with the latest ones by studying the resonant properties of the nanowires.

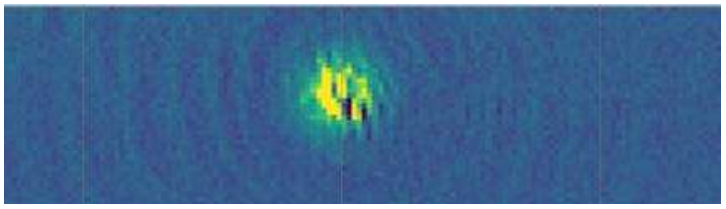


Figure 1. Spatial map (snapshot) of surface acoustic wave propagating on the surface of polymer including GaN nanowires.

References

1. Espinosa, H. D., Bernal, R. A., & Minary-Jolandan, M. (2012). A review of mechanical and electromechanical properties of piezoelectric nanowires. Advanced Materials, 24(34), 4656-4675. https://doi.org/10.1002/adma.201104810
2. Zhu, G., Yang, R., Wang, S., & Wang, Z. L. (2010). Flexible high-output nanogenerator based on lateral ZnO nanowire array. Nano letters, 10(8), 3151-3155. https://doi.org/10.1021/nl101973h
3. Xu, S., Qin, Y., Xu, C. et al. Self-powered nanowire devices. Nature Nanotech 5, 366–373 (2010). https://doi.org/10.1038/nnano.2010.46

Control of FRET in radio frequencies with metasurfaces, in other words, dipole-dipole interactions in the near field of a metasurface.

Kseniia Lezhennikova [1,2], Kaizad Rustomji[1], Boris T. Kuhlmey[3], Tryfon Antonakakis[2], Pierre Jomin[1], Stanislav Glybovski[4], C. Martijn de Sterke[3], Jerome Wenger[1], Redha Abdeddaim[1], Stefan Enoch[1]

[1] Aix Marseille Univ, CNRS, Centrale Med, Institut Fresnel, Institut Marseille Imaging, AMUTech, 13013 Marseille, France

[2] Multiwave Technologies AG, 3 Chemin du Pré Fleuri 1228, Geneva, Switzerland

[3] Institute for Photonics and Optical Sciences (IPOS), School of Physics, University of Sydney NSW 2006, Australia

[4] School of Physics and Engineering, ITMO University, St.Petersburg, Russia

[*]corresponding author: stefan.enoch@univ-amu.fr

Abstract: Energy transfer by Förster resonance (FRET) and the local density of states (LDOS) are both dependent on the electromagnetic environment. An analogy between direct measurements with a microwave antenna has been developed both theoretically and experimentally. A review of the work we have done on this subject will be presented.

FRET measurements in the optical regime are difficult because they require nanoscale control of the position and orientation of the molecules [1-5]. The idea of exploiting an analogy between optics and antenna measurements in the microwave domain has been used to measure the local density of photonic states [6,7]. Recently, we had proposed microwave antenna measurement analogy to improve spatial resolution and precise control of orientation [8-10]. However, the finite size of microwave antennas can affect energy transfer measurements, particularly over short distances. Thus, to obtain accurate results, the finite length of the antenna must be taken into account. In the presented work, we will take advantage of an analytical model that explicitly takes finite size of dipole antennas into account to get a more accurate understanding of dipole-dipole energy transfer in the microwave regime.

We compare our analytical model with experiments on energy transfer between antennas placed next to a perfect electrically conducting mirror. This allows us to establish criteria for the design of microwave experiments, distinguishing between regimes in which finite size effects can be neglected and those in which they must be taken into account.

In addition, present experiments carried out in the microwave domain which show that the excitation of surface waves on a dedicated metasurface can strongly modify near-field dipole-dipole interactions. While, it has been known for a long time that plasmonics can lead to a considerable modification of emission properties however, less is known about the role of surface modes such as surface plasmons on FRET. This makes it possible to envisage metasurfaces designed to control dipole-dipole energy transfer, with applications in many fields [11,12].

The work presented in the field of electromagnetism has natural extensions in acoustics and for mechanical waves in general, for instance for seismic waves.

This project was supported by the European Union's Horizon 2020 Research and Innovation program under grant agreement No 952106 (M-ONE project) and by the Excellence Initiative of Aix-Marseille International Associated Laboratory in Photonics between France and Australia ALPhFA+. Stanislav Glybovski acknowledges the support by the Ministry of Science and Higher Education of the Russian Federation (Project No. 075-15-2022-1120).

References

1. L. Novotny and B. Hecht, Principles of Nano-Optics (Cambridge University Press, 2012).
2. C. Blum, N. Zijlstra, A. Lagendijk, M. Wubs, A. P. Mosk, V. Subramaniam, and W. L. Vos, *Nanophotonic Control of the Förster Resonance Energy Transfer Efficiency*, Phys. Rev. Lett. **109**, 203601 (2012).
3. F. D. Lewis, L. Zhang, and X. Zuo, *Orientation Control of Fluorescence Resonance Energy Transfer Using DNA as a Helical Scaffold*, J Am Chem Soc **127**, 10002 (2005).
4. A. Iqbal, S. Arslan, B. Okumus, T. J. Wilson, G. Giraud, D. G. Norman, T. Ha, and D. M. J. Lilley, *Orientation Dependence in Fluorescent Energy Transfer between Cy3 and Cy5 Terminally Attached to Double-Stranded Nucleic Acids*, Proceedings of the National Academy of Sciences **105**, 11176 (2008).
5. B. Hellenkamp et al., *Precision and Accuracy of Single-Molecule FRET Measurements—a Multi-Laboratory Benchmark Study*, Nat Methods **15**, 669 (2018).
6. J.-J. Greffet, M. Laroche, and F. Marquier, Impedance of a Nanoantenna and a Single Quantum Emitter, Phys. Rev. Lett. 105, 117701 (2010).
7. A. E. Krasnok, A. P. Slobozhanyuk, C. R. Simovski, S. A. Tretyakov, A. N. Poddubny, A. E. Miroshnichenko, Y. S. Kivshar, and P. A. Belov, An Antenna Model for the Purcell Effect, Sci. Rep. 5, 12956 (2015).
8. K. Rustomji, M. Dubois, B. Kuhlmey, C. M. de Sterke, S. Enoch, R. Abdeddaim, and J. Wenger, *Direct Imaging of the Energy-Transfer Enhancement between Two Dipoles in a Photonic Cavity*, Phys Rev X **9**, 11041 (2019).
9. K. Rustomji, M. Dubois, P. Jomin, S. Enoch, J. Wenger, C. M. de Sterke, and R. Abdeddaim, *Complete Electromagnetic Dyadic Green Function Characterization in a Complex Environment–Resonant Dipole-Dipole Interaction and Cooperative Effects*, Phys Rev X **11**, 21004 (2021).
10. Lezhennikova, K., Rustomji, K., Kuhlmey, B.T. et al. Experimental evidence of Förster energy transfer enhancement in the near field through engineered metamaterial surface waves. *Commun Phys* **6**, 229 (2023). https://doi.org/10.1038/s42005-023-01347-1.
11. J. B. Pendry, L. Martín-Moreno, and F. J. Garcia-Vidal, *Mimicking Surface Plasmons with Structured Surfaces*, Science **305**, 847 (2004).
12. S. B. Glybovski, S. A. Tretyakov, P. A. Belov, Y. S. Kivshar, and C. R. Simovski, *Metasurfaces: From Microwaves to Visible*, Phys. Rep. **634**, 1 (2016).

Non-resonant extraordinary acoustic transmission

Oliver B. Wright[1] and Eun Bok[2]

[1]Graduate School of Engineering, Osaka University, Suita, Osaka 565-0871, Japan
[2]Department of Physics and Engineering Physics, Yonsei University, Wonju 26493, Korea
[*]corresponding author: olly@eng.hokudai.ac.jp

Abstract: Acoustic metamaterials, which are engineered structures composed of sub-wavelength resonators, are designed to control sound propagation in ways not found in natural materials. Here we discuss the curious case of enhanced transmission through bare holes without resonance using the language of metamaterials.

Electromagnetic metamaterials, consisting of sub-wavelength oscillators that show effective negative permeability or permittivity have led to many applications over the last 20 years. In parallel, acoustic metamaterials showing effective negative density or modulus were introduced [1,2]. Curious phenomena such as acoustic negative refraction, superlensing and cloaking were demonstrated.

Following progress in electromagnetism, in the domain of acoustics metamaterial-related giant extraordinary transmission of kHz airborne waves has also been reported [3], that is, greatly enhanced resonant acoustic transmission through membrane-covered holes. Similar observations were documented for surface or bulk acoustic waves in solids [4,5].

Here we present recent kHz experiments on the extraordinary transmission of airborne sound through bare holes without the occurrence of any resonance [6]. Although resonances are essential in electromagnetism to overcome poor transmission through bare holes, this is not so in fluid acoustics. A plate perforated with bare holes can transmit nearly all the sound normally incident on it, which has practical applications in sound transparent screens. However, this phenomenon has not previously been systematically interpreted in terms of extraordinary transmission. Here we present such an analysis, and hope to make you appreciate, for example, how sound-transparent screens with holes at bank service counters work, and how to optimize them. Because of the enhanced acoustic energy density in the holes, we also propose applications in acoustic energy harvesting.

[1] Z. Liu, X. Zhang, Y. Mao, Y. Zhu, Z. Yang, C. T. Chan, and P. Sheng, Science 289, 1734 (2000).
[2] S. H. Lee and O. B. Wright, Phys. Rev. B 93, 024302 (2016).
[3] J. J. Park, K. J. B. Lee, O. B. Wright, M. K. Jung, and S. H. Lee, Phys. Rev. Lett. 110, 244302 (2013).
[4] S. Mezil, K. Chonan, P. H. Otsuka, M.Tomoda, O. Matsuda, S. H. Lee, and O. B. Wright, Sci. Rep. 6, 33380 (2016).
[5] T. Devaux, H. Tozawa, P. H. Otsuka, S. Mezil, M. Tomoda, O. Matsuda, E. Bok, S. H. Lee, and O. B. Wright, Sci. Adv. 6, 8507 (2020).
[6] E. Bok, J. J. Park, A. A. Maznev, S. H. Lee, and O. B. Wright, Phys. Rev. B 108, 144111 (2023).

Static Loading Challenges of Three-Dimensional Ultrawide Phononic Crystals and Elastic Metamaterials

C. Yilmaz[1*]

[1] Department of Mechanical Engineering, Bogazici University, 34342 Bebek, Istanbul, Turkey
[*]corresponding author: cetin.yilmaz@bogazici.edu.tr

Abstract: Three-dimensional ultrawide phononic crystals and elastic metamaterials can ideally be applied for vibration isolation, elastic wave shielding and seismic protection. However, most designs in the literature are additively manufactured from polymers in small sizes. Challenges regarding production of these ultrawide designs in large sizes will be explained considering static loading.

When a periodic structure is excited within a vibration stop band or phononic band gap, transmission of vibrations or elastic waves can be eliminated. For broadband excitations, Bragg scattering [1,2] can be used by periodically varying mass (or density) and/or stiffness (or elastic modulus) values of the constituents of the structure. However, the lowest frequency Bragg gap is centered about the wave speed divided by the lattice constant. Hence, low elastic modulus and high density or large lattice constants are needed to generate band gaps at low frequencies, which are not practical for most engineering applications. If a structure is subject to narrowband excitation, then local resonance method [3-5] can be used by choosing local resonance frequency close to the excitation frequency. Local resonance method can generate band gaps below the Bragg limit. Yet, to obtain wide gaps at low frequencies heavy resonators are required [4,5]. Periodic structures that utilize Bragg scattering method are generally referred as phononic crystals, while the ones that use the local resonance method are usually referred as elastic metamaterials as band gaps can be generated below the Bragg limit. For elastic metamaterials and phononic crystals, obtaining wide band gaps at low frequencies is a major challenge.

Inertial amplification method was proposed [6-8] to circumvent the limitations of the Bragg scattering and local resonance methods for obtaining wide band gaps at low frequencies. In this method, effective mass of a periodic structure can be increased with embedded displacement amplification mechanisms so that band gaps below the Bragg limit can be obtained. Moreover, unlike the local resonance method, band gap formation does not rely on resonating substructures that are only effective around their resonance frequency. Instead, band gap forms due to inertial coupling, which yield broadband response [9]. Moreover, as another advantage over the local resonance method, periodic structures with wide low-frequency band gaps can be designed without necessitating large masses due to the increased effective inertia [6-7]. Since inertially amplified periodic structures can generate band gaps below the Bragg limit, they are considered as elastic metamaterials.

Three-dimensional (3D) ultrawide phononic crystals and elastic metamaterials can ideally be applied for vibration isolation, elastic wave shielding and seismic protection. However, 3D designs in the literature with arithmetic mean normalized bandwidth larger than 100% are generally produced from polymers via additive manufacturing in small sizes [10-16]. Furthermore, to achieve very large bandwidths, these designs involve thin ligaments or flexures joints. Consequently, their load carrying capacities are low. If these type of designs are scaled up to 1 meter or larger sizes, high stresses would be present on the ligaments and flexures due to large self-weight. Thus, additive manufacturing with polymers may not be feasible for large sizes. Although 3D ultrawide phononic crystals and elastic metamaterials are designed to function under dynamic excitations, their static load carrying capacities should also be critically evaluated (see for example [17]) if they are aimed to be used for load bearing applications such as vibration or seismic isolation.

In this invited talk, various 3D ultrawide phononic crystal and elastic metamaterial designs will be shown. Challenges regarding production of these designs in large sizes will be explained considering stress and deformation constraints under static loading. To overcome these challenges, a new design will be proposed.

Acknowledgement

Cetin Yilmaz acknowledges the support from the Turkish Academy of Sciences Distinguished Young Scientist Award (TUBA-GEBIP).

References

1. Sigalas, M. M. "Elastic and acoustic wave band structure", J. Sound Vib., Vol. 158, No. 2, 377–382, 1992.
2. Sigalas, M. M. and E. N. Economou, "Band structure of elastic waves in two dimensional systems", Solid State Commun., Vol. 86, No. 3, 141–143, 1993.
3. Liu, Z., X. Zhang, Y. Mao, Y. Y. Zhu, Z. Yang, C. T. Chan and P. Sheng, "Locally resonant sonic materials", Science, Vol. 289, No. 5485, 1734–1736, 2000.
4. Liu, Z., C.T. Chan and P. Sheng, "Three-component elastic wave band-gap material", Phys. Rev. B, Vol. 65, No. 16, 165116, 2002.
5. Goffaux, C. and J. Sanchez-Dehesa, "Two-dimensional phononic crystals studied using a variational method: Application to lattices of locally resonant materials", Phys. Rev. B, Vol. 67, No. 14, 144301, 2003.
6. Yilmaz, C., G.M. Hulbert and N. Kikuchi, "Phononic band gaps induced by inertial amplification in periodic media", Phys. Rev. B, Vol. 76, No. 5, 054309, 2007.
7. Yilmaz, C. and G.M. Hulbert, "Theory of phononic gaps induced by inertial amplification in finite structures", Phys. Lett. A, Vol. 374, No. 34, 3576–3584, 2010.
8. Yilmaz, C. and G.M. Hulbert, "Dynamics of locally resonant and inertially amplified lattice materials", In: A.S. Phani, M.I. Hussein, editors. Dynamics of lattice materials, 233–258, Wiley, USA, 2017.
9. Yilmaz, C. "Identifying different phononic band gap generation methods", In 5th International Conference on Phononic Crystals/Metamaterials, Phonon Transport and Topological Phononics, Tucson, Arizona, USA, 23-24, 2019.
10. Taniker, S. and C. Yilmaz, "Design, analysis and experimental investigation of three-dimensional structures with inertial amplification induced vibration stop bands", Int. J. Solids Struct., Vol. 72, 88–97, 2015.
11. Lucklum, F. and M.J. Vellekoop, "Bandgap engineering of three-dimensional phononic crystals in a simple cubic lattice", Appl. Phys. Lett., Vol. 113 No. 20, 201902, 2018.
12. D'Alessandro, L., R. Ardito, F. Braghin and A. Corigliano, "Low frequency 3D ultra-wide vibration attenuation via elastic metamaterial", Sci. Rep. Vol. 9, 8039, 2019.
13. D'Alessandro, L., A.O. Krushynska, R. Ardito, N.M. Pugno and A. Corigliano, "A design strategy to match the band gap of periodic and aperiodic metamaterials" Sci. Rep. Vol. 10, No. 1, 16403, 2020.
14. Muhammad and C.W. Lim, "Phononic metastructures with ultrawide low frequency three-dimensional bandgaps as broadband low frequency filter", Sci. Rep., Vol. 11, No. 1, 7137, 2021.
15. Muhammad, "Design and manufacturing of monolithic mechanical metastructures governing ultrawide low frequency three-dimensional bandgaps", Addit. Manuf. Vol. 47, 102231, 2021.
16. Martinez, J., J. Moughames, G. Ulliac, M. Kadic and V. Laude, "Three-dimensional phononic crystal with ultra-wide bandgap at megahertz frequencies", Appl. Phys. Lett. Vol. 118, 063507, 2021.
17. Otlu, S. N., B. Acar, Z.G. Tetik and C. Yilmaz, "Three-dimensional ultra-wide elastic metamaterial with inertial amplification mechanisms having optimized flexure hinges", Int. J. Solids Struct., Vol. 282, 112453, 2023.

META 2024, TOYAMA - JAPAN, JULY 16 – 19, 2024

Thermal rectification in graphite Tesla valve based on phonon hydrodynamics

Masahiro Nomura

Institute of Industrial Science, The University of Tokyo, Japan
corresponding author: nomura@iis.u-tokyo.ac.jp

Abstract: We demonstrate a phonon hydrodynamics approach to realize the rectification of heat conduction in isotopically enriched graphite crystals. We design a Tesla valve at the micrometer scale within a 90-nm-thick sample and experimentally observe a discernible 14% difference between the thermal conductivity in the opposite directions at 40 K.

The Tesla valve (TV) has found extensive application in the rectification of fluid flows without reliance on moving components [1]. The inherent asymmetry of the Tesla valve induces distinct fluid flow behaviors in opposing directions. In contrast to the rectification of fluid flows within microfluidic channels, the rectification of phonons presents a more formidable challenge, primarily attributable to the dearth of fluid-like phonon flows within the majority of microsolid systems. In this study, graphite was employed for thermal rectification, given its intrinsically robust hydrodynamic phonon behavior attributed to its strong lattice anharmonicity and elevated Debye temperature [2]. Asymmetric TV structures were fabricated within a 90-nm-thick graphite sample, as illustrated in Fig. 1(a-b). The graphite with a ^{12}C isotope content reaching 99.98% to minimize the defect scattering. The principal heat flow channel spanned a length of 26 μm and a width of 4.5 μm. Notably, the bend channel maintained an identical width to that of the main channel. The investigation of temperature-dependent thermal rectification effects was conducted utilizing microscale time-domain thermoreflectance (μ-TDTR). At 10 K, comparable thermal conductivity (κ) values were observed in both the forward and backward directions, suggesting that ballistic phonons exhibit a propensity to traverse the entire structures, primarily influenced by boundary scattering. Beyond 20 K, there was a discernible transition, with momentum-conserved normal scattering gradually assuming prominence. This transition is attributed to the collective flow of phonons through the graphite TV. In the forward case, as depicted in Fig. 1a, hydrodynamic phonons predominantly traverse from the heat source to the sink via the main channel. Conversely, in the backward case (Fig. 1b), two distinct hydrodynamic phonon flows diverge from the heat source. The convergence of these two flows leads to a loss of phonon momentum and introduces resistance to thermal transport. This phenomenon results in a notable disparity between κ_f and κ_b in the temperature range of 30 to 60 K, as illustrated in Fig. 1c. In Fig. 1d, we define the diodicity of the heat flow as the ratio of κ_f to κ_b. At 40 K, a pronounced establishment of phonon hydrodynamic flows occurs, with resistive Umklapp scattering remaining relatively scarce. Notably, the strongest rectification effect is observed, wherein κ_f surpasses κ_b by approximately 14%. This investigation elucidates thermal rectification in solid graphite TVs, thereby paving the way for novel approaches in thermal management leveraging phonon hydrodynamics.

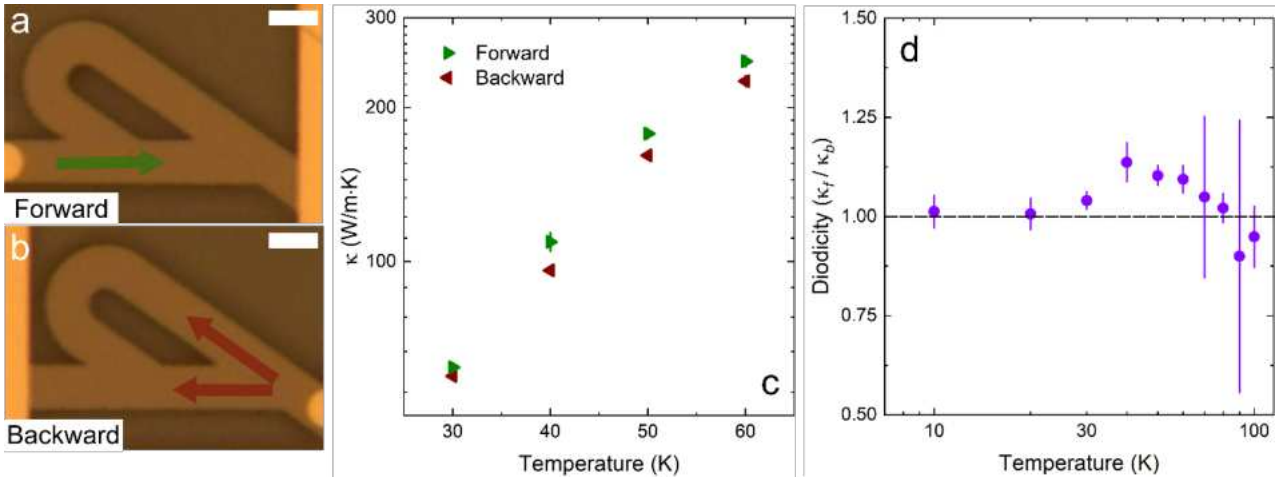


Figure 1 (a-b) Optical microscope images of graphite TVs in forward and backward directions. Arrows indicate heat flow directions. Scale bars: 5 μm. (c) Thermal conductivity (κ) and (d) diodicity as a function of temperature.

Acknowledgments This work is a collaboration with X. Huang, R. Anufriev, L. Jalabert, K. Watanabe, T. Taniguchi, Y. Guo, Y. Ni, and S. Volz, and is supported by CREST JST (JPMJCR19Q3), JSPS KAKENHI (21H04635, 20H00354, 21H05233, 23H02052), MEXT, Japan.

References

1. A. Purwidyantri and B. A. Prabowo, Chemosensors 11, 256 (2023).
2. X. Huang, Y. Guo, Y. Wu, S. Masubuchi, K. Watanabe, T. Taniguchi, Z. Zhang, S. Volz, T. Machida, and M. Nomura, “Observation of phonon Poiseuille flow in isotopically purified graphite ribbons”, Nat. Commun. 14, 2044 (2023).

Exploring Tunable Poisson's Ratio in Origami Metamaterials

D. Misseroni[1*]
[1]Department of Civil, Environmental and Mechanical Engineering, University of Trento, Trento, Italy

[*]corresponding author: diego.misseroni@unitn.it

Abstract: We present a triclinic metamaterial system of minimal symmetry derived from a Trimorph origami pattern. We investigate the Trimorph pattern through mathematical analyses, numerical simulations, and experimental validation. We developed a manufacturing technique and a testing device, named the Saint-Venant setup, to quantify its reversible auxeticity.

Testing origami metamaterials presents a challenge due to their high deployability in both transverse and longitudinal directions. Traditional uniaxial testing methods, which involve clamping the two ends of a sample to a testing machine, need to be revised since they lead to experimental inaccuracies. Moreover, the theoretical formulae describing the mechanical behavior of origami metamaterials are usually derived assuming two conflicting requirements: rigid and zero-thickness panels. To overcome these challenges, we developed a novel manufacturing process and a specific experimental platform, nicknamed Saint-Venant setup. This setup enables complete free deployment of the origami metamaterial, mimicking a proper periodic system in experiments without violating theoretical assumptions. The fabrication process, based on the use of a CNC milling machine, enables fine control of panels' stiffness and folding hinge properties. This manufacturing method is beneficial for creating multistable systems where each stable state is self-stressed, a feature difficult to achieve using paper models or 3D printing. This leads to programmable geometrically frustrated configurations. We demonstrated the effectiveness of our method by capturing the tunable auxeticity and tristable behavior of a triclinic metamaterial system with minimal symmetry originating from a Trimorph origami pattern. Our findings have important implications for designing and testing origami metamaterials with unique mechanical properties.

Acknowledgment
This research is funded by the European Union (ERC-2022-COG-101086644-SFOAM).

Twofold topological transition induced by third-nearest-neighbor hoppings in an artificial elastic polyacetylene

R. A. Méndez-Sánchez[1*], Y. Betancur-Ocampo[2], B. Manjarrez-Montañez[1], and A. M. Martínez-Argüello[3]

[1]Instituto de Ciencias Físicas, Universidad Nacional Autónoma de México, Cuernavaca, Mexico
[2]Instituto de Física, Universidad Nacional Autónoma de México, Ciudad de México, Mexico
[3]Instituto de Física, Benemérita Universidad Autónoma de Puebla, C. P. 72570 Puebla, Puebla, Mexico
[*]corresponding author: mendez@icf.unam.mx

Abstract: An artificial elastic molecule, which emulates the electronic properties of the cis-polyacetylene with third-nearest-neighbor hoppings is introduced. The tight-binding band structure shows a transition between two topological phases with different winding numbers. The low frequency excitations obey the modified Dirac equation. The finite element numerical simulations agree with the theory.

The coupled-resonator phononic waveguides (CRPW) [1] are the analog of the well-known coupled-resonator optical [2] and acoustical waveguides [3]. The CRPW are formed coupling defects in an otherwise periodic structure. When a resonant frequency of the defects falls within a bandgap of the periodic structure a tight-binding (TB) regime, that emulates the TB regime of condensed matter physics, emerges. Generalizations to coupled-resonator phononic molecules (CRPMo) and metamaterials (CRPM) are straightforward.

One of the differences between the optical/acoustical structures and the phononic ones is that in the latter the hoppings to higher neighbors can be engineered *ad-hoc*. This kind of studies allow to study a new variety of phenomena and are almost impossible to realize in photonic and acoustic systems. Here we present a CRPMo that resembles the cis-polyacetylene, with third-nearest-neighbor hoppings [4] (See Fig. 1).

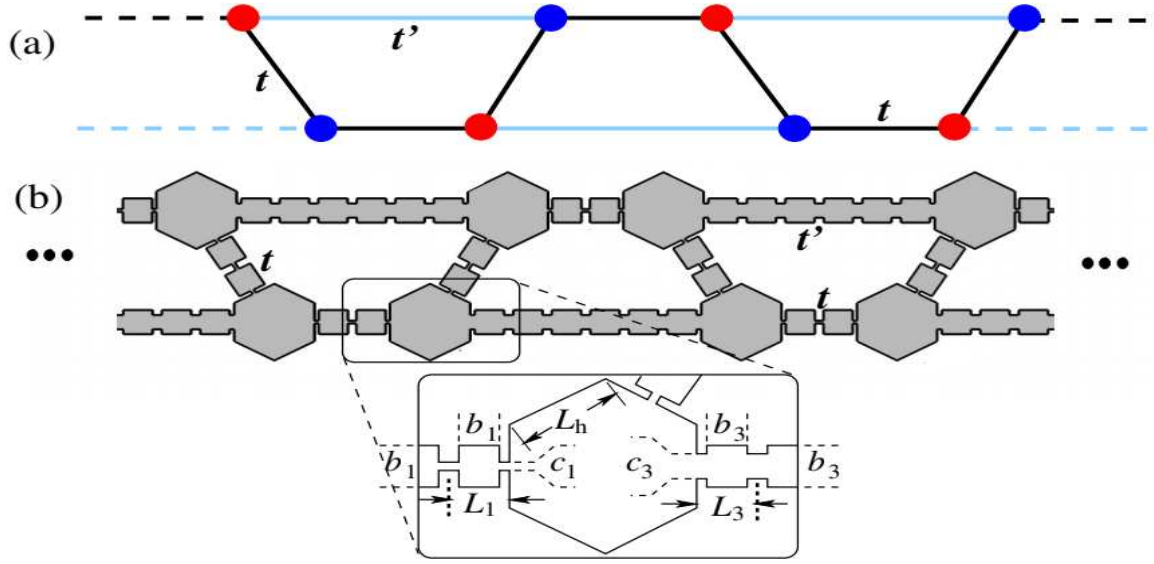


Figure 1: Cis-polyacetylene with first (t) and third (t') nearest-neighbor hopping: (a) tight-binding model, and (b) artificial elastic cis-polyacetylene molecule. The site frequency is governed by L_h and the hopping parameters by L_i and b_i, i=1,3.

The unit cell in the phononic cis-polyacetilene is composed by four meta-atoms; thus four bands are expected.

In Fig. 2 the band structures for the elastic structure of Fig. 2 (b), for different third nearest-neighbors hoppings (t'), and fixed nearest-neighbor hopping (t), are given. Those bands were obtained with finite elements. In case (a), when t'=0 a Dirac cone emerges. In case (b), when the t'<t, this cone disappears and a gap emerges. In case (c), when t'=t, two Dirac cones emerge. Finally, a new gap emerges when t'>t. Cases (b) and (d) correspond to topological phases with opposite winding numbers.

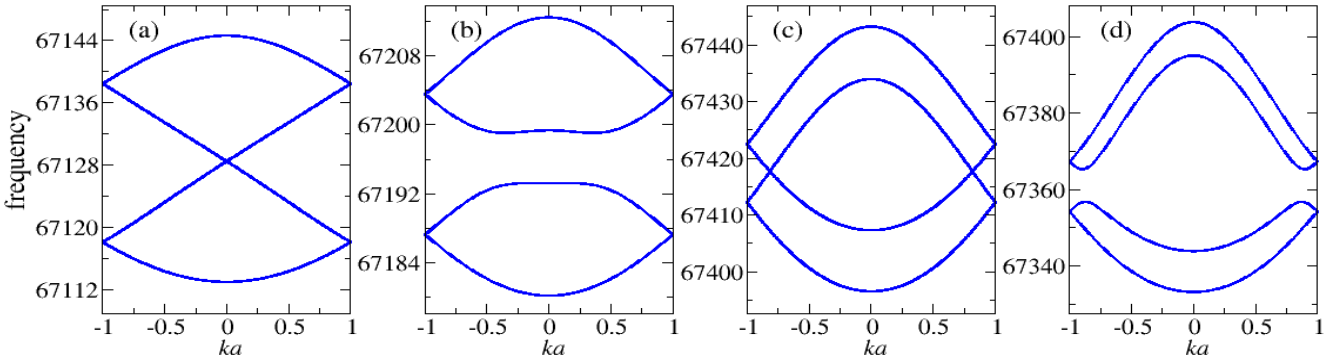


Figure 2: Band structures of the artificial elastic cis-poliacetilene of Fig. 1 L_h = 27 mm, L_1 = 22 mm, b_1 = 17 mm, c_1 = 2 mm, L_3 = 22.4608 mm, b_3 = 17 mm, and c_3 = 5, 7, 9, 10 mm for cases (a) to (d).

The TB Hamiltonian of the phononic cis-polyacetilene with third-nearest-neighbor hoppings is given by [4]

$$H = \begin{bmatrix} f_0 & g^*(k) & 0 & h^*(k) \\ g(k) & f_0 & h(k) & 0 \\ 0 & h^*(k) & f_0 & g^*(k) \\ h(k) & 0 & g(k) & f_0 \end{bmatrix},$$

where f_0 is the site frequency, $g(k) = t\exp(ika/6)$, $h(k) = t\exp(-ika/3) + t'\exp(2ika/3)$, with k the wave vector and a the lattice constant. The bands of the TB Hamiltonian agree with the FE simulations. Also, the low-energy excitations of the cys-polyacetylene TB-model with third-nearest-neighbor hoppings follow a modified Dirac equation instead of the common Dirac equation that satisfy the low-energy excitations in the trans-polyacetylene.

Y.B.-O. and R.A.M.-S. acknowledge financial support from UNAM-PAPIIT under projects IA106223 and IN111021, respectively. R.A.M.-S. A.M.M.-A. and B.M.-M. acknowledge financial support from CONAHCYT.

References

1. J. A. López-Toledo, G. Báez, and R. A. Méndez-Sánchez, "Tight-binding model for torsional and compressional waves in high-quality coupled-resonator phononic metamaterials", Mech. Adv. Mat. and Struc., Vol. 29, 6301, 2022.
2. A. Yariv, A., Y. Xu, R. K. Lee, and A. Scherer, "Coupled-resonator optical wave-guide: a proposal and analysis", Opt. Lett. Vol 24, No. 11, 711-713, 1999.
3. J. M. Escalante, A. Martínez, and V. Laude, Dispersion relation of coupled-resonator acoustic waveguides formed by defect cavities in a phononic crystal, J. Phys. D: Appl. Phys. Vol. 46, No. , 475301 (2013).
4. Y. Betancur-Ocampo, B. Manjarrez-Montañez, M. Martínez-Argüello, and Rafael A. Méndez-Sánchez, "Twofold topological phase transitions induced by third-nearest-neighbor hoppings in 1D chains", Phys. Rev. B, to appear.

Non-Hermitian Metasurfaces for Extraordinary Elastic-wave Manipulations of Higher-order Diffractions

Bing Li[1*], Jiali Cheng[1], and Bochen Ren[1]

[1] School of Aeronautics, Northwestern Polytechnical University, Xi'an, Shaanxi, 710072, China
[*]corresponding author: bingli@nwpu.edu.cn

Abstract: Beyond the traditional paradigm of Hermitian physics, the concept of non-Hermiticity has recently inspired a surge of nontrivial principles and applications. In this work, we propose several active and passive non-Hermitian metasurfaces that enable unprecedented elastic-wave manipulations, including skin-like effects, asymmetric wave propagation, and perfect absorption.

The past decades have witnessed the remarkable development and explosive implications of meta-structures in elastic-wave steering under the Hermitian systems that disregard material loss. However, the reality of practical applications is inevitably intertwined with loss, leading to the dissipation of elastic wave energy. Traditionally, such losses were viewed as detrimental, potentially compromising the performance of elastic wave devices. Yet, a paradigm shift has emerged from recent groundbreaking research, which has uncovered the potential of strategically engineered loss/gain within non-Hermitian systems to facilitate remarkable wave steering phenomena[1-3]. Through the meticulous design of loss and gain media, complex wave-matter interactions can be realized, encompassing unidirectional wave propagation, band merging, and enhanced sensing capabilities. This novel perspective paves the way for innovative applications in acoustics, seismology, and materials science, where the judicious use of loss and gain can be harnessed to achieve unprecedented control over elastic waves[2-4].

The advent of non-Hermitian metasurfaces has opened new frontiers for elastic wave control, offering a reduced structure footprint in low-dimensional designs. Despite their promise, metasurfaces face inherent limitations stemming from their gradient index characteristics, which can constrain their capabilities. Achieving highly efficient wave manipulation in advanced artificial materials, with a focus on ultra-compact dimensions and easy fabrication, remains an open challenge. This work proposes a design strategy that leverages non-Hermitian modulation to surmount these obstacles. The proposed non-Hermitian metagratings (NHMGs)[4], characterized by their subwavelength unit cells, enable a suite of extraordinary elastic-wave manipulations, including the skin-like effect, asymmetric propagation, and perfect absorption. Building upon these capabilities, we have further engineered a cloaking device based on NHMG, as depicted in Fig. 1, which can effectively shield arbitrary-shaped targets from detection[4]. Our research not only expands the repertoire of elastic wave manipulation techniques in non-Hermitian materials but also offers an ultra-compact solution for wave control, holding significant potential for engineering applications.

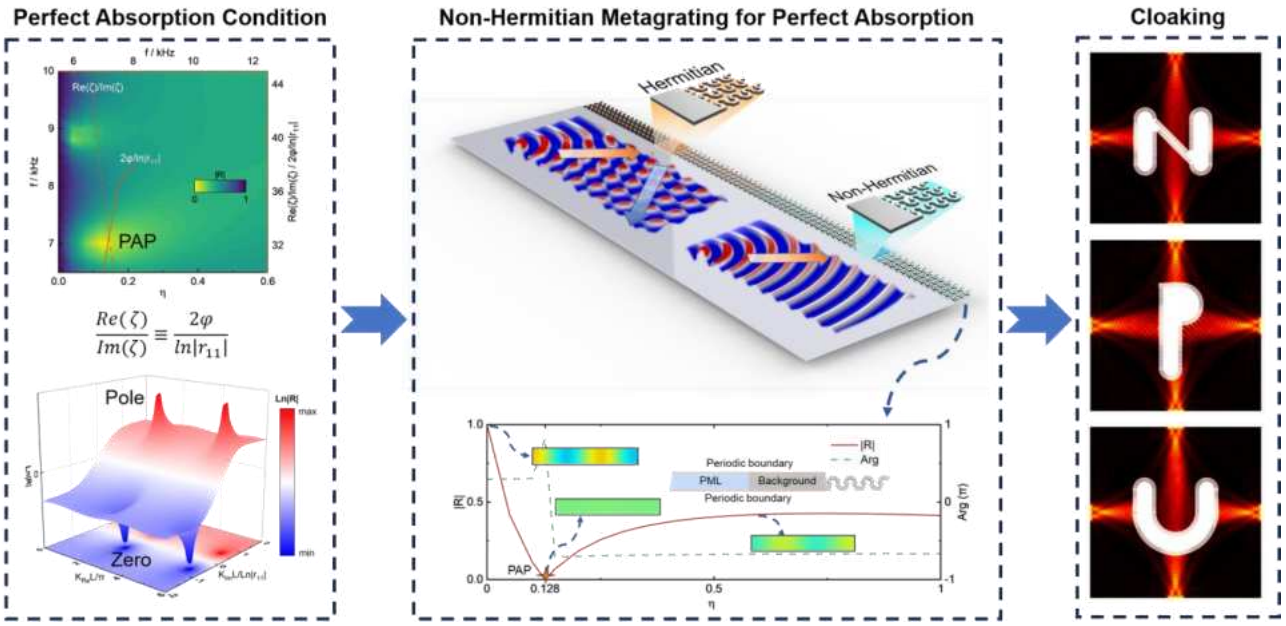


Fig.1 The proposed non-Hermitian metagrating for perfect absorption and arbitrary-shaped target cloaking

The authors acknowledge the financial support from the National Natural Science Foundation of China (NSFC) (Grant No. 12272298), the Natural Science Foundation of Chongqing (No. CSTB2023NSCQ-MSX0899).

References

1. Zhu, W., Fang, X., Li, D., Sun, Y., Li, Y., Jing, Y., & Chen, H. “Simultaneous observation of a topological edge state and exceptional point in an open and non-Hermitian acoustic system,” Physical Review Letters, 121(12), 124501, 2018.
2. Cao, L., Zhu, Y., Wan, S., Zeng, Y., & Assouar, B. “On the design of non-Hermitian elastic metamaterial for broadband perfect absorbers,” International Journal of Engineering Science, 181, 103768, 2022.
3. Li, B., Hu, Y., Chen, J., Su, G., Liu, Y., Zhao, M., & Li, Z. “Efficient asymmetric transmission of elastic waves in thin plates with lossless metasurfaces,” Physical Review Applied, 14(5), 054029, 2020.
4. Cheng, J., Hu, Y., Li, B. “Non-Hermitian metagrating for perfect absorption of elastic waves,” Materials Horizons, Advance Article, 2024.

Non-adiabatic phononic control of polariton Bose-Einstein condensates

A. S. Kuznetsov[1], K. Biermann[1], and P. V. Santos*[1]

[1]Paul-Drude-Institut für Festkörperelektronik, Leibniz-Institut im Forschungsverbund Berlin e.V., Hausvogteiplatz 5-7, 10117 Berlin, Germany

*corresponding author: santos@pdi-berlin.de

Abstract:

Exciton-polariton Bose-Einstein condensates (BECs) with their long coherence times and high sensitivity to strain fields are excellent candidates for mediating the coherent interaction between photons, phonons, and electronic excitations in the solid state. We have recently demonstrated that polariton BECs modulated by high-frequency (i.e., GHz) acoustic waves provide a solid-state platform for optomechanics in the non-adiabatic regime, i.e., with polariton acoustic frequencies exceeding the BEC coherence rate [1,2]. Here, we investigate the non-adiabatic behavior of BECs modulated by sub-GHz surface acoustic waves (SAWs) in the regime of acoustic energy modulation amplitudes χhf_{SAW} far exceeding the modulation energy quantum, hf_{SAW}., i.e., for modulation indices $\chi>>1$, where f_{SAW} is the SAW frequency. We show that the large energy modulation reveals a novel regime of temporal coherence that is controlled by the acoustic modulation amplitude rather than just by the ratio between the modulation quantum and the BEC coherence.

The experiments were carried out on a polariton BEC confined within a 4x4 μm^2 intracavity trap formed in an (Al,Ga)As microcavity. The photoluminescence (PL) spectrum of these non-resonantly excited BECs was probed using a etalon with a frequency resolution of 0.3 GHz. Such a spectrum, as is displayed by the blue curve in Fig. 1(b), yields a linewidth $\gamma \sim 0.5$ GHz, corresponding to coherence times approaching 2 ns. The trap is placed in a field antinode of a SAW resonator consisting of two interdigital transducers operating at f_{SAW}=0.384 GHz. The red curve in Fig. 1(b) displays the PL spectrum of the trap when a nominal radio-frequency power P_{rf} = 10 dBm is applied to the SAW transducers. The strain field of the SAW modulates the energy of the confined BEC, leading to the appearance of non-adiabatic sidebands around the undisturbed BEC emission. By varying the acoustic power, we could show that the maximum frequency shifts of the sidebands are proportional to $\sqrt{P_{rf}}$ and, thus, to amplitude of the SAW strain field.

The high energy modulations amplitudes are expected to induce temporal coherences at time scales much shorter than the SAW period, $1/f_{SAW}$. The BEC coherence under acoustic excitation was probed in the time domain using the interferometric setup sketched in Fig. 1c. Here, the autocorrelation delay τ is controlled by the shifting the position of mirror M_2. In the absence of a SAW, the autocorrelation is characterized by short oscillations with period π/ω_{PL}, where $\hbar\omega_{PL}$ is the BEC emission energy (cf. upper panel of Fig. 1(d)). The acoustic energy modulation with amplitude χhf_{SAW} introduces a modulation of the envelope of the short-period oscillations with a periodicity $\tau_{ac} = 1/(2\,\chi\, hf_{SAW})$ controlled by the modulation index, as illustrated in the main panel of Fig. 1(d). This periodicity $\tau_{ac} = 30$ ps for the modulation index $\chi=44$ in this figure is almost two orders of magnitude smaller than the SAW period of 2600 ps.

The individual non-adiabatic sidebands cannot be clearly distinguished in Fig. 1(b) for small frequency shifts Δf, since their linewidths γ is comparable to the energy spacing hf_{SAW}. For large shifts, in contrast, one observes pronounced oscillations at the extrema of the modulation with frequency spacing far exceeding the SAW frequency (cf. dashed rectangle). These oscillations result from the bunching of the sidebands to form beats with the frequency spacing $\gg f_{SAW}$: they provide evidence to a novel regime of temporal coherences at time scales much

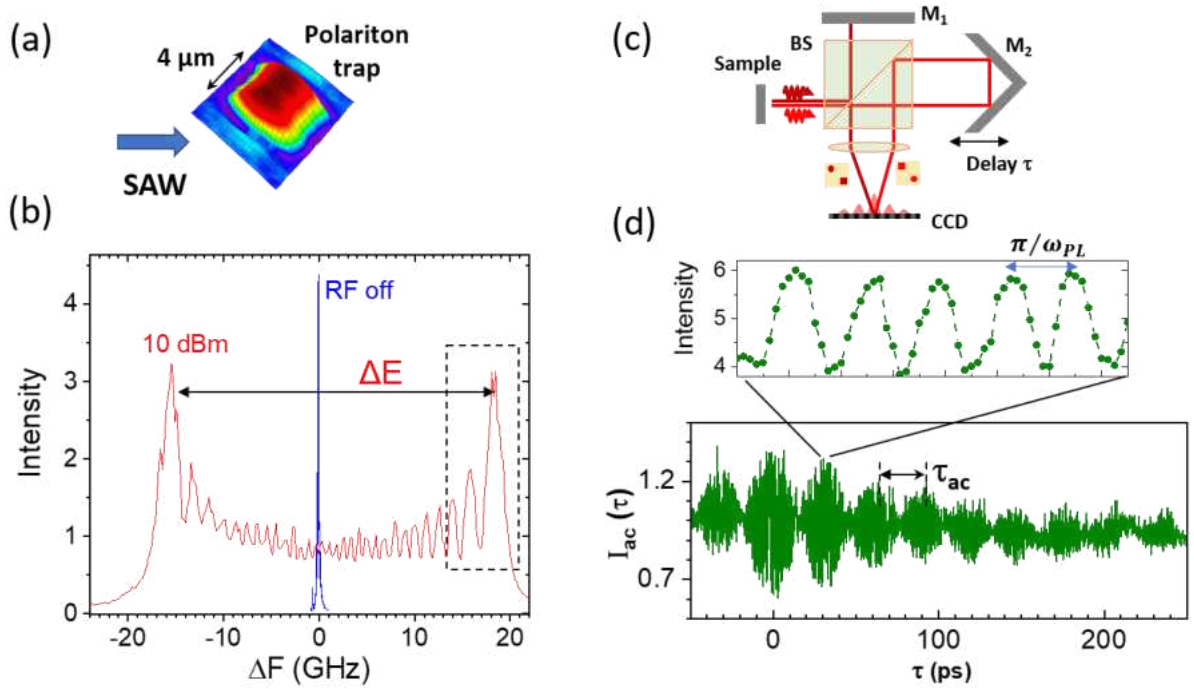


Figure 1. (a) Polariton BEC trap pumped by a surface acoustic wave (SAW). (b) (red curve) High-resolution photoluminescence (PL) spectra (spectral resolution of 0.3 GHz) displaying non-adiabatic sideband spectra recorded for a nominal rf-power Prf applied to the SAW transducer of 10 dBm (corresponding to χ=44). The blue curve shows the corresponding spectrum in the absence of acoustic excitation. The dashed rectangle indicates the region of acceleration beats. (c) Interferometric setup for temporal correlation measurements. (d) Autocorrelation traces of the PL emission under an energy modulation amplitude χhf_{SAW} with χ=44. The short-time autocorrelation oscillations associated with PL emission energy (with period π/ω_{PL}) is displayed in the inset. The acoustic modulation forms beats with time displaced by a period $\tau_{ac} = \pi/(\chi h\, f_{SAW})$ inversely proportional to the modulation amplitude χ.

shorter than the SAW period, which is induced at high amplitude modulation indices. In order to justify this assertion, we developed a model for the nonadiabatic modulation of the confined BECs, which reproduces very well the experimental spectral features in Fig. 1(b). The model shows that these spectral features, denoted as acceleration beats, arise from the bunching of the non-adiabatic sidebands induced by the accelerated energy changing rates close the extrema of the modulation [3]. The results presented here show that the strong interaction with vibrations together with the efficient optical and acousto-electrical control makes confined polariton BECs modulated by high-frequency acoustic waves excellent candidates for coherent information transfer between the GHz and near-infrared frequency domains..

References

1. D. L. Chafatinos *et al.*, "Polariton-driven phonon laser", Nat. Comm., Vol. 11, 4552, 2020.
2. A. S. Kuznetsov *et al.*, "Microcavity phonoritons: a coherent optical-to-microwave interface", Nat. Comm., Vol. 14, 5470, 2023.
3. A. S. Kuznetsov *et al.*, "Acceleration-induced spectral beats in strongly driven harmonic oscillators", In Research, https://doi.org/10.21203/rs.3.rs-3197243/v1, 2023.

Mechanical tuning of topological waveguiding in auxetic metamaterial

F. Bosia[1*], G.Carta[2], M. Morvaridi[1], V.F. Dal Poggetto[3], A. S. Gliozzi[1], C. Croenne[3], M.Miniaci[3], N. Pugno[4,5], M. Brun[2]

[1] Department of Applied Science and Technology, Politecnico di Torino, Corso Duca degli Abruzzi 24, Italy
[2] Department of Mechanical, Chemical and Materials Engineering, University of Cagliari, Piazza d'Armi, 09123 Cagliari, Italy
[3] Université Lille, CNRS, Centrale Lille, Junia, Université Polytechnique Hauts-de-France, UMR 8520—IEMN—Institut d'Electronique de Microélectronique et de Nanotechnologie, Lille F-59000, France
[4]Laboratory for Bioinspired, Bionic, Nano, Meta Materials and Mechanics, Department of Civil, Envi-ronmental and Mechanical Engineering, University of Trento, Trento, 38123, Italy
[5]School of Engineering and Materials Science, Queen Mary University of London, London, E1 4NS, UK.

[*]corresponding author: federico.bosia@polito.it

Abstract: We control topologically protected states applying uniaxial prestrain in an auxetic metasurface, realized in a thin slab applying oriented cuts in a hexagonal lattice, where degeneracy is removed and topological band gaps opened by reducing the cut lengths. Scatter-free propagation can then be manipulated with the application of prestrain.

So far, most of the investigations on the properties of auxetic materials and metamaterials have focused on their static behaviour, but there are indications that many attractive features also appear in their dynamic properties. In particular, auxeticity enables large volumetric deformations at relatively low values of stress due to the small bulk modulus, while maintaining the shear modulus significantly large (as is typical of a solid), since the ratio between the bulk and the shear moduli tends to zero as the Poisson's ratio ν tends to the lowest limit of -1 (for an isotropic medium). This also applies to topological protection, which has recently emerged as a as a unique means to propagate waves through sharp corners or bends, being robust with respect to structural disorder, defects or backscattering [1]. In this context, it would be particularly important to introduce dynamic tunability (i.e. a means to modify in time the operational frequency of a given the device) employing an external field such as prestrain.
To do this, we use a phononic lattice whose unit cell design is based on the introduction of oriented cuts arranged in a hexagonal pattern within a thin sheet of material. This structure exhibits auxetic behaviour with an extremely negative Poisson's ratio [2]; at the same time, the band structure for both in-plane and out-of-plane modes admits various Dirac cones, which can be exploited for the creation of topological valley modes. The breaking of C6-symmetry of the unit cells to remove degeneracy is obtained by changing the length of alternate cuts, generating topologically protected modes in two frequency ranges. For the considered structure, this feature only occurs in the presence of cell auxeticity. In these frequency ranges, there is good wave localization at the interface and propagation at sharp edges with negligible backscattering.
The scatter-free waveguiding properties can now be manipulated by the simple application of unidirectional quasi-static pre-strains (Fig.1a) of moderate amplitudes (typically below 10%), in which geometrical nonlinearity can be activated. This allows a controlled variation of the unit cell dispersion properties, with the removal of the topological band gaps (Fig.1b), thus enabling the reversible transition from localized waveguiding to nonlocalized propagation (Figs. 1c,d,e,f). This modification can also be generated in limited portions of the propagation domain,

by applying strain that is variable in space or time.

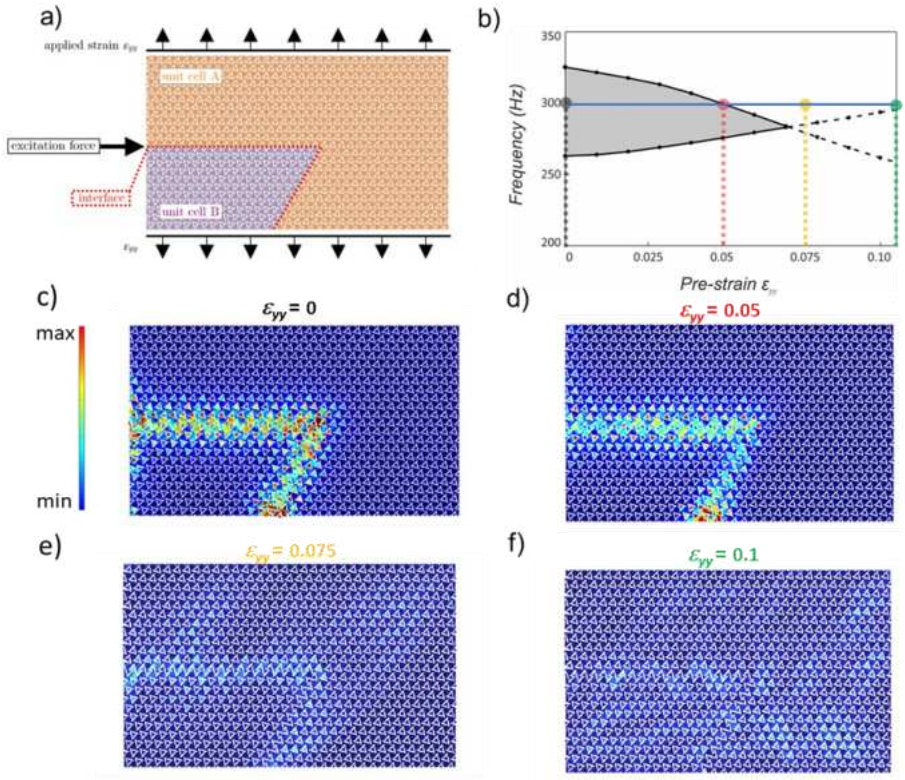


Figure 1: Tuning of waveguiding by applying an external pre-strain εyy. (a) Schematic of the FEM model for frequency domain simulations. b) Detail of the and gap as a function of pre-strain. Displacement fields for f=300 Hz and c) εyy =0, d) εyy =0.05, e) εyy =0.075, and f) ι yy =0.1, illustrating progressive loss of wave localization for increasing pre-strain.

Given the relative simplicity of the design, these auxetic tunable topological metamaterials should be amenable to fabrication in soft polymeric or elastomeric samples with standard techniques (e.g. molding and machining), and the required material/geometrical nonlinearity could be generated at relatively small applied pre-strain, allowing for an experimental realization of proof-of-concept experiments, and further extending the possibilities in the fast-growing field of tunable metamaterials.

References

1. S. D. Huber, Topological Mechanics, Nat Phys 12, 621 (2016).
2. M. Morvaridi, G. Carta, F. Bosia, A. S. Gliozzi, N. M. Pugno, D. Misseroni, and M. Brun, Hierarchical Auxetic and Isotropic Porous Medium with Extremely Negative Poisson's Ratio, Extreme Mech Lett 48, (2021).

Tunable Topological Properties in Phononic Crystals via Photoresponsive Polymers

A.S. Gliozzi[1*], F. Bosia[1], B. Davies[2], G. J. Chaplain[3], M. Miniaci[4], E. Descrovi[1], R.V. Craster[2]

[1] Department of Applied Science and Technology, Politecnico di Torino, Corso Duca degli Abruzzi 24, Italy
[2] Department of Mathematics, Imperial College London, South Kensington Campus, London SW7 2AZ, UK
[3] Department of Physics and Astronomy, University of Exeter, Exeter EX4 4QL, UK.
[4] Université Lille, CNRS, Centrale Lille, Junia, Université Polytechnique Hauts-de-France, UMR 8520—IEMN—Institut d'Electronique de Microélectronique et de Nanotechnologie, Lille F-59000, France

[*]corresponding author: antonio.gliozzi@polito.it

Abstract:
This study explores the tunability of phononic crystals' topological properties, using photoresponsive azo-polymers based on the Su-Schrieffer-Heeger model. It demonstrates dynamic adjustment of edge mode frequencies in a one-dimensional SSH chain and the ability to induce topological phase changes in a two-dimensional SSH lattice through illumination.

The exploration of phononic crystals and their topological properties has opened fascinating avenues for manipulating wave propagation in materials. This study employs photoresponsive polymers in constructing phononic crystal systems, enabling the dynamic control of their topological properties through laser illumination, which alters the polymers' elastic properties upon exposure to light [1], thus facilitating the modification of the systems' topological characteristics under investigation. Within this context, we describe two systems based on Su-Schriffer-Heeger model. The first system explores a one-dimensional SSH chain implemented by aligning pairs of elements with varying coupling strengths, achieved through alternating "long" and "short" distances between them [2]. The basic structural unit consists of a polymeric slab (thickness $t = 1.5\,mm$ and width $a = 7\,mm$) upon which elastic rods, each $20\,mm$ tall and $0.5\,mm$ in radius, are periodically positioned within a unit cell (see Fig. 1a). These rods are placed at a distance s_i from one another, symmetrically around the center of the cell. We design two types of cells characterized by differing separation distances, s_1 and s_2, with s_2 being defined as $a - s_1$. Both cell types exhibit identical dispersion curves and share a common bandgap, interconnected by a mere shift of s_2. Two periodic structures are created by replicating 10 times these unit cells, which are subsequently joined to create a singular configuration that introduces a discontinuity in periodicity at the interface between the arrays. This disruption acts as a "defect", effectively serving as an interface between Zak phases and supporting a topologically protected edge mode. The photo-responsive characteristics of the material is exploited to decrease its Young's modulus through stimulation by a laser beam with a wavelength of $\lambda = 405\,nm$, targeting the sample's central region (interface) from the side. This was exploited to examine the effects of altering the elastic constants on the topological edge mode confined at the interface. Indeed, by enhancing the laser power directed at the central defect region, the peak associated with the localized mode moves to lower frequency values, as depicted in Fig. 1(b), observing a maximum shift of around $300\,Hz$ at $250\,mW$ from the initial frequency. This frequency shift, triggered by targeted illumination on the sample, exhibits a linear dependency on the laser power and can extend up to the edge of the band gap. Importantly, this adjustment is completely reversible upon the cessation of illumination.

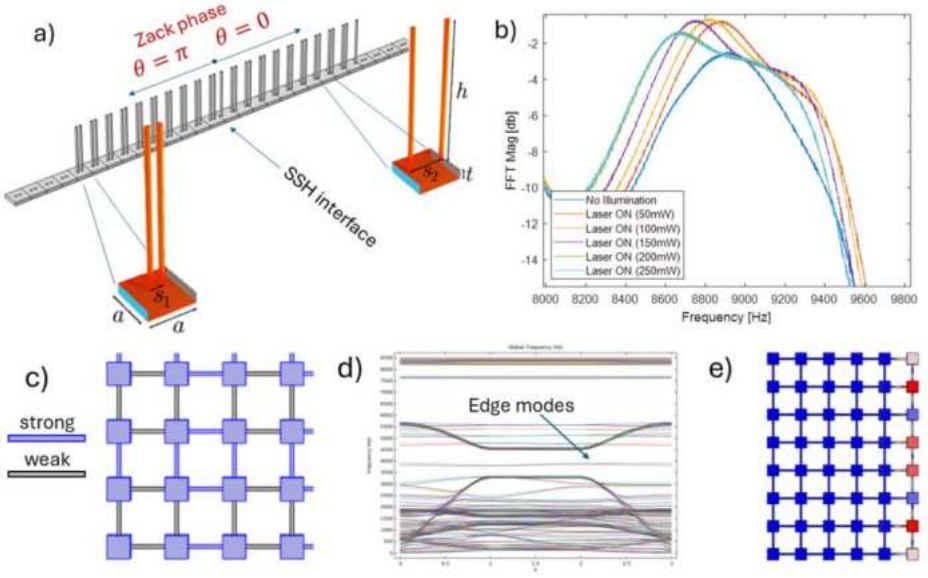


Figure 1:a) One-dimensional SSH based sample with zoom on the two unit cells of lateral dimension a and dstances between the pillars of s_i.b)Edge mode shift upon laser light illumination. c) Two-dimensional system with strong and weak bond depending on the young modulus value. d) Observation of the edge-mode in the band gap. e) Localized edge mode on the two-dimensional lattice

The second system extends these concepts to a two-dimensional lattice, composed of interconnected SSH chains. The SSH model's extension to 2D lattices has opened the door to a rich variety of topological states, including higher-order topological insulators, weak topological insulators, and Weyl semimetals [3].

Our investigation introduces a novel approach to engineering these topological phases by leveraging the unique properties of photoresponsive polymers. We commence with a uniformly connected 2D lattice, consisting of beams ($12\ mm$ in length and $1.25\ mm$ in square cross-section) linking mass nodes ($8\ mm$ cubes), fabricated from a photoresponsive polymer. This initial configuration represents a neutral state, with all links equivalent, thereby lacking any distinct topological character. The innovation lies in our method of inducing topological variation: by projecting a precise pattern of laser light onto the lattice, we selectively alter the mechanical properties of the polymer links. This selective illumination simulates the introduction of "strong" and "weak" bonds within the SSH model, thereby patterning the lattice into configurations that exhibit diverse topological phases. By changing the pattern of illumination, we can dynamically transition the lattice through various topological states, effectively “drawing” new topological properties onto the material with light.

Our work not only demonstrates a practical method for the manipulation of topological phases in 2D systems but also enriches our understanding of the interplay between material properties and topological physics, offering a versatile platform for the study and exploitation of topological phenomena.

References

1. Gliozzi, A.S., Miniaci, M., Chiappone, A. et al., Nat Commun 11, 2576 (2020).
2. G. C. Chaplain, A.S. Gliozzi et al., Appl. Phys. Lett. 122, 221703 (2023)
3. Hongyu Ma, Ze Zhang, Pei-Hao Fu, Jiansheng Wu, and Xiang-Long Yu, Phys. Rev. B 106, 245109 (2022)

Ultrasonic Hologram for Bi-directional Diffusion by Phase Controlling the Scattering Coefficients

E. Ballestero[1], J. Rodríguez-Sendra[2], J.-P. Groby[1], N. Jiménez[2] and V. Romero-García[3*]

[1]Laboratoire d'Acoustique de l'Université du Mans, LAUM - UMR 6613 CNRS, Le Mans Université, France
[2]Instituto de Instrumentación para Imagen Molecular, Consejo Superior de Investigaciones Científicas (CSIC), Universitat Politècnica de València, València, Spain.
[3]Instituto Universitario de Matemática Pura y Aplicada (IUMPA), Departamento de Matemática Aplicada, Universitat Politècnica de València, València, Spain.
[*]corresponding author: virogar1@mat.upv.es

Abstract: We report an ultrasonic hologram based on Quadratic Residue sequences encoded with resonant building blocks behaving as an ideal Lambertian scatterer from both sides, with spatial autocorrelation coefficients $\delta \approx 0.7$ each one, therefore diffusing waves in both transmission and reflection.

In this work, we present a bi-directional asymmetric ultrasonic hologram that can simultaneously control both the reflected and transmitted wave-fields. To do that we design a surface made of a discrete spatial distribution of monolithic elements with different properties than the surrounding medium. This allows to compress two identical or different wavefield scattering patterns (for transmission and reflection) into a single monolithic object. Depending on the applications, such hologram could be useful in situations where transmitted and reflected wavefields need to be controlled at the same time, such as a bi-directional diffusing system emitting and receiving equally in and from all directions (equivalent of perfect optical diffusers in optics [1]) or as a bi-directional beam directivity selector, e.g., focusing/collimating/decollimating beam switch. Such hologram could also be used directly in reflection situations for minimizing unwanted specular reflections, e.g., reflections from surgical instruments during ultrasound-guided medical procedures [2].

We consider the building block is made of a monolithic polymer block of length l surrounded by two water blocks of length d_1 and d_2 respectively (see Fig. 1(a)). The sound pressures, p, and normal particle velocities, v_z, at $z = 0$ and at $z = L$ can be modelled by means of the Transfer Matrix Method (TMM). We consider each building block is independent from each other in the structure and considered as an equivalent fluid. Such approximation can be made due to the low difference in impedance between the water and polymer media, with a polymer-to-water impedance ratio, coupled with the fact that shear waves can also be neglected due to the system being considered under normal incidence. Therefore, the scattering coefficients of each building block can be calculated

In order to design a lens that can behave as an ideal scatterer in both reflection and transmission directions, the latter must display a phase distribution coefficient at the surface, $\xi(x, y)$, such that the spatial Fourier transform of said distribution approximates a flat distribution. There are many number theoretic sequences that can help design such phase distribution, such as the maximum length or quadratic residue sequences [3]. Here, the quadratic residue (QR) sequence will be used. In order to determine the phase distribution coefficient at the surface, $\xi(x, y)$, we perform a data base of properties of the monolithic polymer block to produce the desired phase of the reflection and transmission coefficients.

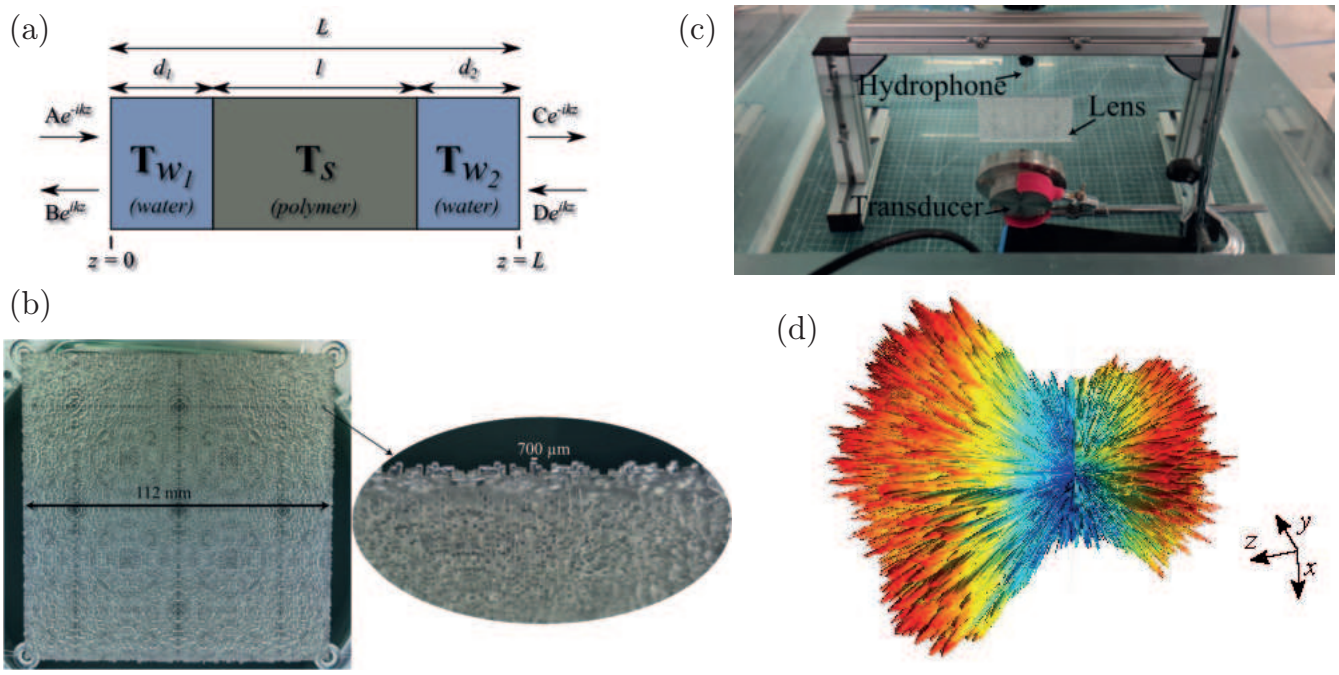


Figure 1. (a) Representative 1D Scattering Matrix diagram of a block of total length L composed of a polymer element and an exterior water medium. (b) Picture and detail of the fabricated sample. (c) Experimental setup. (d) 3D measured acoustic field at 1.1 MHz from both sides of the diffusing hologram.

A picture of the fabricated sample can be seen in Fig. 1(b). It has been experimentally tested for underwater acoustics in the water tank shown in Fig. 1(c). In this talk we will show the excellent agreement between the theoretical predictions and the experimental results, and we will discuss in details the main features of the system with a Physical insight of interest for the audience of the META conference.

The collaboration between the authors of this article was made possible thanks to Institut d'Acoustique -- Graduate School (IAGS) project (ANR-17-EURE-0014) from the Laboratoire d'Acoustique du l'Université du Mans (LAUM) for the support and mobility. The authors gratefully acknowledge the ANR-RGC METARoom (ANR-18-CE08-0021). Project. N. J. and V.R.-G. acknowledge financial support from Conselleria de Innovación, Universidades, Ciencia y Sociedad Digital de la Generalitat Valenciana through project CIAICO/2022/052 of the Programa para la promoción de la investigación científica, el desarrollo tecnológico y la innovación en la Comunitat Valenciana.

References

1. D. Arslan, A. Rahimzadegan, S. Fasold, M. Falkner, W. Zhou, M. Kroychuk, C. Rockstuhl, T. Pertsch, and I. Staude, Advanced Materials 34, 2105868 (2022),
2. J. Huang, P. Dupont, A. Undurti, J. Triedman, and R. Cleveland, Ultrasound in medicine & biology 32, 721 (2006).
3. T. Cox and P. D'Antonio, "Schroeder diffusers: A re- view," *Building Acoustics*, vol. 10, no. 1, pp. 1–32, 2003.

Experimental study of sonic velocity modulations and time interfaces in a controllable piezoelectric phononic crystal

C. Croënne[1*], S. Tessier Brothelande[1], F. Allein[1], J. O. Vasseur[1] and B. Dubus[1]

[1]Univ. Lille, CNRS, Centrale Lille, Univ. Polytechnique Hauts-de-France, Junia, UMR 8520-IEMN, F-59000 Lille, France
[*]corresponding author: charles.croenne@isen.fr

Abstract: This communication concerns the experimental study of elastic wave propagation in a piezoelectric phononic crystal with controllable electrical conditions. The two control laws under study are (a) non-stop shifting conditions in the so-called sonic regime of modulation, and (b) global abrupt changes of conditions, i.e. time interfaces.

Phononic crystals made of piezoelectric materials exhibit the remarkable property that their dispersion can be modified by means of changes in their electrical boundary conditions. For instance, a stack of identical piezoelectric rings separated by thin electrodes (Fig. 1) presents different dispersion characteristics if these electrodes are grounded or left in floating potential[1]. The essential difference lies in the presence of a Bragg band gap of electrical origin in the former case, which is absent in the latter.



Figure 1 – Picture of the piezoelectric phononic crystal with its electrodes connected to a dedicated control system which consists in a chain of printed circuit boards supporting electrical switches whose state evolutions can be programmed through a digital signal processor (DSP).

Since the frequency of this gap is directly related to the distance between two grounded electrodes, this effect supplies an easy route to the realization of a space-time modulated propagation medium. In practice, a periodic subset of electrodes can be grounded, while the rest is left floating, and this subset can be spatially shifted as a function of time, resulting in an equivalent space-time modulated medium[2]. An important advantage of this type of system lies in the easiness to reach modulation speeds equal or even significantly greater than sound wave velocity, since the modulation is realized through sets of electronic circuits controlling the electrical conditions. In this communication, experimental results for these regimes are presented, discussed and confronted with theoretical predictions. The so-called *sonic* case (i.e. modulation speed exactly equal to sound wave velocity) is of special interest since analytical developments show that it results in an overlap (degeneracy, see Fig. 1) of dispersion branches[3] and possibly broadband parametric amplification effects[4].

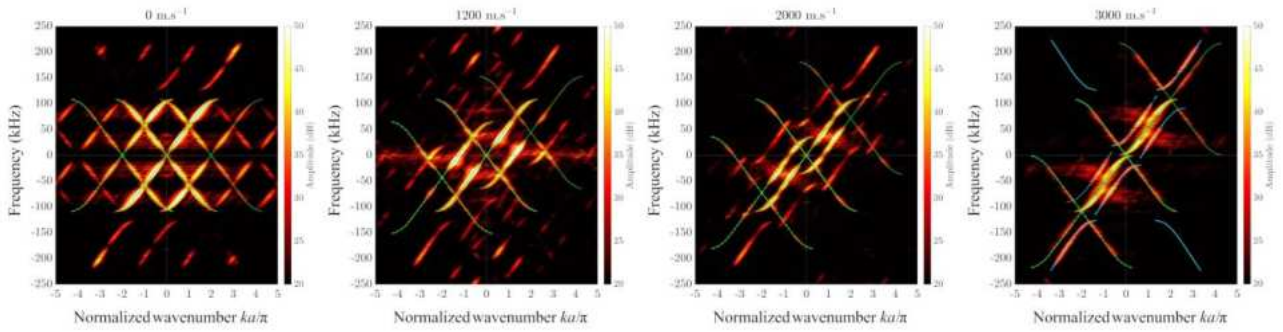


Figure 2 – Space-time Fourier transforms of measured electrical potentials inside the modulated phononic crystal for different modulation speeds c_m. Green and blue lines are guides for the eye, pointing out the general dispersion branch evolution as a function of c_m. The fourth case corresponds to the sonic regime, with branches in partial overlap.

In addition to modulation control laws (i.e. perpetually shifting electrical conditions), this type of device also enables the realization of time interfaces (i.e. global abrupt changes of conditions), turning them into members of the recently defined class of *Floquet metamaterials*[5]. Scattering of wave packets by one or several time interfaces of different types is experimentally investigated. In addition to the general effects related to time interfaces, piezoelectricity-related effects are discussed. In particular, the possibility of trapping elastic wave propagation-related electrical charges at each electrode is studied.

References

1. S. Degraeve et al., “Bragg band gaps tunability in an homogeneous piezoelectric rod with periodic electrical boundary conditions”, J. Appl. Phys. 115, 194508, 2014.
2. S. Tessier Brothelande et al., “Experimental evidence of nonreciprocal propagation in space-time modulated piezoelectric phononic crystals”, Appl. Phys. Lett. 123, 201701, 2023.
3. E. S. Cassedy, “Dispersion relations in time-space periodic media part II—Unstable interactions”, Proc. IEEE 55(7), 1154-1168, 1967.
4. E. Galiffi et al., “Broadband nonreciprocal amplification in luminal metamaterials”, Phys. Rev. Lett. 123, 206101, 2019.
5. S. Yin et al., “Floquet metamaterials”, eLight 2, 8, 2022.

On the role of phase in nonreciprocal vibration transmission in passive and active phononic lattices

A. Kogani[1], J. Wu[1], and B. Yousefzadeh[1*]

[1]Department of Mechanical, Industrial and Aerospace Engineering, Concordia University, Montreal, QC, Canada
[*]corresponding author: behrooz.yousefzadeh@concordia.ca

Abstract: We highlight the contribution of phase to nonreciprocal vibration transmission in nonlinear (passive) and spatiotemporally modulated (active) phononic lattices of finite length. We showcase nonreciprocal response regimes characterized by equal energies transmitted in opposite directions. A nonreciprocal phase shift is the only contributor to breaking of reciprocity in this scenario.

Nonreciprocity is an important problem from a fundamental perspective and in terms of additional functionalities that it enables in mechanical devices [1]. Common realizations of nonreciprocal response rely on implementation of nonlinearity or time-varying properties within the mechanical system. In most cases, the focus is on maximizing the nonreciprocal energy transfer: the difference in the transmitted energies or amplitudes when the locations of the source and receiver are interchanged. Here, we emphasize the role of phase in nonreciprocal vibration transmission in both nonlinear and time-varying phononic lattices. We focus on response regimes that are characterized by nonreciprocal phase shifts: the transmitted energies are equal for the left-to-right (LR) and right-to-left (RL) directions, but the transmitted phases are not.

Fig. 1 shows the systems we study to demonstrate nonreciprocal phase shifts. Panels (a) and (b) show, respectively the representative units used for the lattices with spatiotemporal modulation and nonlinear stiffness. In each case, the steady-state response of the system to a harmonic excitation is computed. Excitation is first applied to the left end of the system and the response at the right end is monitored (left-to-right transmission, LR). The locations of source and receiver are then interchanged and the procedure is repeated (right-to-left transmission, RL). The response is reciprocal if and only if the two outputs are identical.

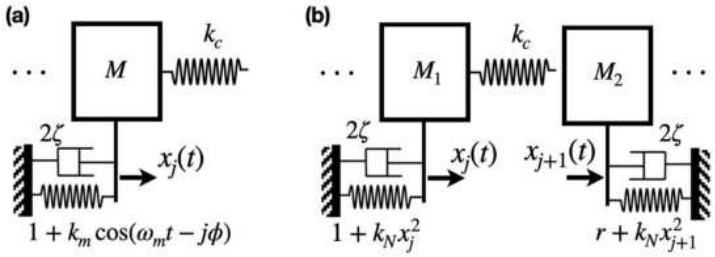


Figure 1: Representative units of the phononic lattice: (a) time-varying system, (b) nonlinear system.

In the nonlinear systems, nonreciprocal dynamics requires breaking the mirror symmetry of the system. This is enabled within the unit cell in Fig. 1(b) by the mass ratio (M_2/M_1) or stiffness ratio (r). Response regimes that exhibit nonreciprocal phase shifts ($\Delta\varphi$) can be computed for the unit cell or for the entire lattice using numerical continuation techniques [2,3]; see Fig. 2(a) for an example response. Computation of the nonreciprocal phase

shifts also allows obtaining reciprocal dynamic response in a nonlinear system with broken mirror symmetry [4].

In systems subject to spatiotemporal modulations, the definition of phase is not as straightforward because the response of the system is quasi-periodic. This is due to the presence of two incommensurate frequencies: external and parametric drive. The envelope of the response, however, remains periodic. It is therefore possible to search for nonreciprocal phase shifts in the modulated system by considering the response envelope instead. If the response envelope exhibits nonreciprocal phase shift, so does the original signal. Fig. 2(b) shows an example of a response computed in this manner that exhibits nonreciprocal phase shift [5].

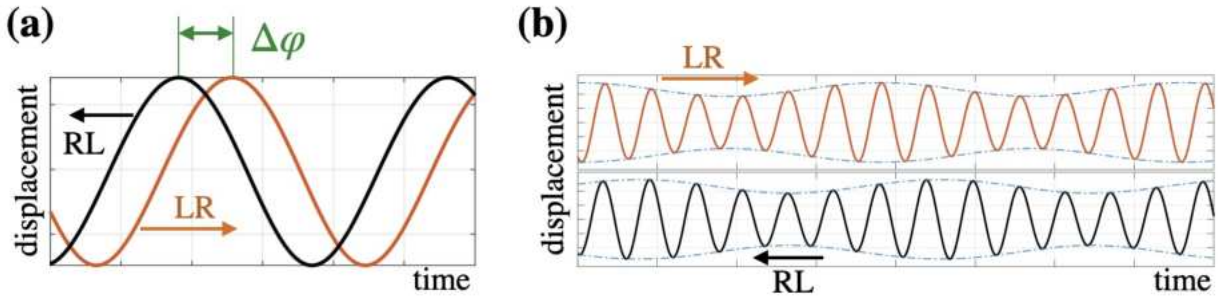


Figure 2: Response exhibiting nonreciprocal phase shift: (a) nonlinear system, (b) modulated system.

In summary, we showcased the contribution of nonreciprocal phase shifts in realizing nonreciprocal vibration transmission in short phononic lattices. To highlight the role of phase, we focused on nonreciprocal dynamics where the transmitted energies do not depend on the direction of travel but the transmitted phases do. For modulated systems, this became possible by formulating the response in terms of its response. We hope these findings contribute to enhancing the performance of devices that operate based on nonreciprocity.

We acknowledge financial support from the Natural Sciences and Engineering Research Council of Canada through the Discovery Grant program, and from Centre de Recherches Mathématiques, Quebec.

References

1. Nassar, H. et al, “Nonreciprocity in acoustic and elastic materials”, Nat. Rev. Mater., Vol. 5, No. 9, 667–685, 2020.
2. Yousefzadeh, B., “Computation of nonreciprocal dynamics in nonlinear materials”, J. Comp. Dyn. Vol. 9, No. 3, 451-464, 2022.
3. Kogani, A. and B. Yousefzadeh, “Nonreciprocal phase shifts in a nonlinear periodic waveguide,” arXiv preprint arXiv:2311.07737, 2023.
4. Giraldo, A. and B. Yousefzadeh, “Restoring the reciprocity invariance in nonlinear systems with broken mirror symmetry”, Extreme Mech. Lett., Vol. 61, 102008, 2023.
5. Wu, J. and B. Yousefzadeh, “Computation of response envelopes in a lattice material with spatiotemporal modulations,” Proceedings of the Canadian Society for Mechanical Engineering Int’l Congress, Sherbrooke, QC, 2023.

Harnessing topology and nonlinearity for advanced elastic wave control

G. Theocharis[1]

[1]Laboratoire d'Acoustique de l'Université du Mans (LAUM), UMR 6613, Institut d'Acoustique - Graduate School (IA-GS), CNRS, Le Mans Université, France
*corresponding author: georgios.theocharis@univ-lemans.fr

Abstract: In this talk we will investigate structures for advanced control of elastic waves using concepts and tools from topological materials and nonlinear dynamics. This line of research has practical applications in the design of robust elastic wave devices and reconfiguration of flexible elastic materials.

The first part of the talk will focus on topological mechanics. The recent discovery of topological materials in condensed matter physics has led to the emergence of a new notion of topology associated with the intrinsic wave dispersion of a structure. As a result, numerous mechanical designs have been developed that exhibit non-trivial and robust energy localisation. This talk will give a brief overview of the different classes of topological mechanical metamaterials, and then present a new family of finite-frequency mechanical metamaterials that we have recently introduced [1]. Here, robust topological properties appear in deformation coordinates, while topological edge waves appear for free boundaries.

The second part of the talk will focus on the nonlinear dynamics of flexible elastic metamaterials. Flexible elastic metamaterials (flexEMs) are defined as engineered structures that can deform substantially, repeatedly and reversibly [2]. Although recent advances have improved our understanding of the quasi-static mechanical properties of flexEMs, there are not many studies on their nonlinear dynamic response. In this talk, two types of flexEMs will be presented. One consisting of (i) rotating rigid units (particles of different shapes) coupled with soft elastic elements [3] and (ii) a lattice of coupled buckled beams, a bistable mechanical metamaterial [4]. Using various analytical and numerical techniques, we were able to find several nonlinear wave solutions, including solitons, breathers and wave extreme events, that can be supported by these types of flexEMs.

We acknowledge the support from ANR project ExFLEM ANR-21-CE30-0003-01. This presentation is based on several works that have been done in collaboration with: Antoine Demiquel, Apostolos Paliovaios, Vassos Achilleos, Vincent Tournat, Florian Allein, Adamantios Anastasiadis, Rajesh Chaunsali, Ian Frankel, Nicholas Boechler and Fotis Diakonos.

References

1. F. Allein, A. Anastasiadis, R. Chaunsali, I. Frankel, N. Boechler, F.K. Diakonos, G. Theocharis, Nat. Commun. 14 (1), 6633 (2023).
2. B. Deng, J. R. Raney, K. Bertoldi, and V. Tournat, Nonlinear waves in flexible mechanical metamaterials, J.Appl. Phys., 130, 040901 (2021).
3. A. Demiquel, V. Achilleos, G. Theocharis, and V. Tournat, Modulation instability in nonlinear flexible mechanical metamaterials, Phys. Rev. E , 107, 054212 (2023); A. Demiquel, V. Achilleos, G. Theocharis, and V. Tournat, Envelope vector solitons in flexible mechanical metamaterials, in preparation.
4. A. Paliovaios, G. Theocharis, V. Achilleos, V. Tournat, Transition waves in bistable systems generated by collision of moving breathers, submitted.

Advancements in Vibration Energy Harvesting through Metamaterials: Insights from the MetaVEH Project

A. Colombi[1*], B. Zhao[2], R. Ardito[3], JM De ponti [3], RV. Craster[4]

[1]Zürich University of Applied Sciences (ZHAW), Winterthur, 8401, Switzerland

[2]Department of Civil, Environmental, and Geomatic Engineering, ETH Zürich, Zürich, 8093, Switzerland

[3]Department of Civil and Environmental Engineering, Politecnico di Milano, 20133 Milano, Italy

[4]Dept. of Mathematics, Imperial College London, UK

[*]corresponding author: colo@zhaw.ch

Abstract: MetaVEH project, funded by the EU, pioneers in metamaterials for efficient vibration energy harvesting, enhancing frequency bandwidth and energy conversion. Achievements promise sustainable, battery-free solutions for autonomous devices, marking significant strides in self-powered electronics and sustainable energy solutions.

The EU-MetaVEH project represents a remarkable effort, to redefine the landscape of energy harvesting through the innovative application of metamaterials. This initiative has successfully designed, developed, and demonstrated novel metamaterials tailored for efficient vibration energy harvesting, targeting the broad frequency range of environmental vibrations. Our approach integrates cutting-edge research in resonant metamaterial structures with sophisticated energy conversion mechanisms, enabling the capture and conversion of vibrational energy from ambient sources into usable electrical energy.

The project's technical journey encompassed the exploration and optimization of multi-scale resonant structures, capable of enhancing energy harvesting from low-frequency vibrations, a challenging area for conventional materials. Through meticulous design and engineering, we achieved significant breakthroughs in increasing the bandwidth and efficiency of energy harvesters. These advancements were supported by rigorous computational modeling and experimental validation, leading to the development of prototypes with superior performance characteristics.

The insights gained from this project contribute significantly to the field of metamaterials, opening new avenues for research and application in energy harvesting and beyond. We believe our research will have profound implications for the future of autonomous sensors and devices, offering a sustainable alternative to battery-powered systems.

In this talk, I will present the most relevant results of the past 4 years of research and outline the challenges that still lies ahead.

The authors acknowledge support from the H2020 FET-proactive project METAVEH under the grant agreement 95203

References

1. J.M. De Ponti, L. Iorio, E. Riva, F. Braghin, A. Corigliano, R. Ardito, Enhanced Energy Harvesting of Flexural Waves in Elastic Beams by Bending Mode of Graded Resonators, Front. Mater., Vol. 8, pp. 1-7 (2021).

2. J.M. De Ponti, L. Iorio, G.J. Chaplain, A. Corigliano, R.V. Craster, R. Ardito, "Tailored Topological Edge Waves via Chiral Hierarchical Metamaterials", Phys. Rev. Applied 19, 034079 (2023).
3. B. Zhao, H. R. Thomsen, J. M. De Ponti, E. Riva, B. Van Damme, A. Bergamini, E. Chatzi, and A. Colombi, “A graded metamaterial for broadband and high-capability piezoelectric energy harvesting”, Energy Convers. Manag., vol. 269, p. 116056, (2022).

Topological states in periodic and disordered elastic metabeams

R. Cai[1,2], Y. Jin[3], Y. Pennec[1], L. Carpentier[1], X. Zhuang[2] and B. Djafari-Rouhani[1*]

[1]Institut d'Electronique, de Microélectonique et de Nanotechnologie, UMR CNRS 8520, Département de Physique, Université de Lille, 59650 Villeneuve d'Ascq, France
[2]Department of Geotechnical Engineering, College of Civil Engineering, Tongji University, 200092 Shanghai, China
[3]School of Aerospace Engineering and Applied Mechanics, Tongji University, 200092 Shanghai, China
[*]corresponding author: bahram.djafari-rouhani@univ-lille.fr

Abstract: We study theoretically topological interface states in periodic and disordered pillared elastic metabeams. Using band inversion symmetry, we obtain interface states and through their coupling achieve a robust Fano mechanical resonance. Then, we show multiple topological interface states in hyperuniform disordered pillared metabeams. Finally, we consider topological Anderson insulators.

The emergence of topological materials has opened many avenues in various wave problems including elastic media. We have devoted several works to topological phononics in pillared structures consisting of an array of pillars on a plate. We demonstrated the analogs of valley-Hall and spin-Hall crystals[1], robust edge modes at the interface of two topologically different structures and various refraction phenomena at the edges' outlet[1], the existence of corner modes[2] as well as a topological vortex mode[3].

In this presentation, we focus on the case of a beam supporting an array of pillars. First, we present our results on periodic structures where the pairing between the beams allows us to construct the analog of the Su-Schrieffer-Heeger (SSH) model[4]. Considering each of the four types of waves that propagate along the beam (respectively symmetrical or antisymmetrical with respect to a horizontal and a vertical plane), we showed the existence of interface states at the boundary of two topologically different phases. Then, we made the superposition of the gaps associated with two types of modes, namely the symmetric and antisymmetric shear modes as shown in Figure 1. The coupling between their respectively low Q (dark) and high Q (bright) interface modes allows to achieve a robust topological Fano resonance[4].

Furthermore, we present topological interface modes between two SSH-like hyperuniform pillared metabeams with different Zak phases[5]. We demonstrate that this structure could open new bandgaps at low frequencies, of which some are nontrivial and can support topological interface modes, as shown in Figure 2. We further show that the number of low-frequency bandgaps supporting the topological modes increases with the level of randomness, hence providing a high number of interface modes in the same structure[5].

To extend these investigations to topological Anderson insulators driven by disordered non-Hermitian modulation, we have built a SSH type model with non-Hermitian on-site disorder and found that the disorder would drive a system from trivial to nontrivial. Based on this model, we expect to construct a topological insulator in the elastic beam where the non-hermiticity originates from the utilization of piezoelectric patches.

Our work offers a reliable platform for studying topological properties in elastic waves and designing novel and robust wave control devices. These findings pave the way for future research on disordered and hyperuniform systems for novel wave manipulation.

Acknowledgments: This work is part of the project MAGNIFIC of the European Union's Horizon Europe research and innovation program under grant agreement No 101091968 and the CHIST-ERA Call 2021 under the grant agreement No CHIST-ERA-20-NOEMS-003.

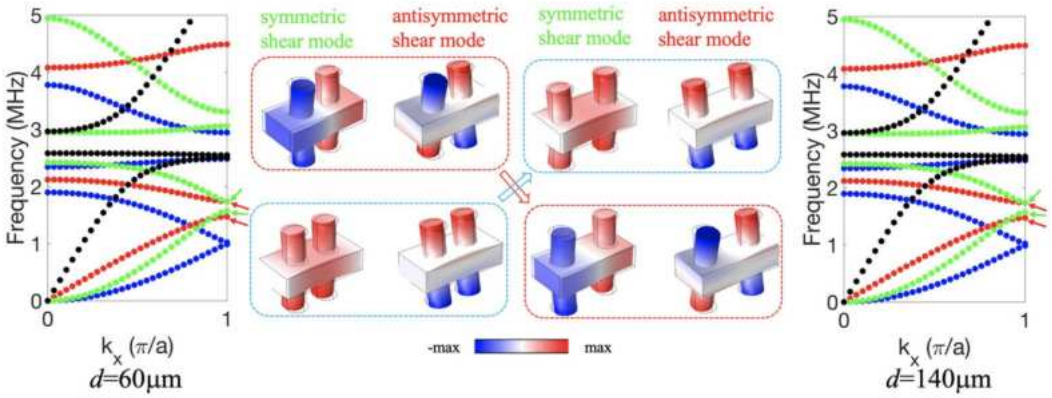


Figure 1. Band structures for the metabeam with a short interval (left-hand panel) between the pillars in the unit cell and a large interval (right-hand panel). The eigenstates of the symmetric and antisymmetric shear modes above and below the gap (shown as the green and red arrows) are presented beside the dispersion. The eigenstates shown in red and blue dotted boxes flip showing a band inversion symmetry.

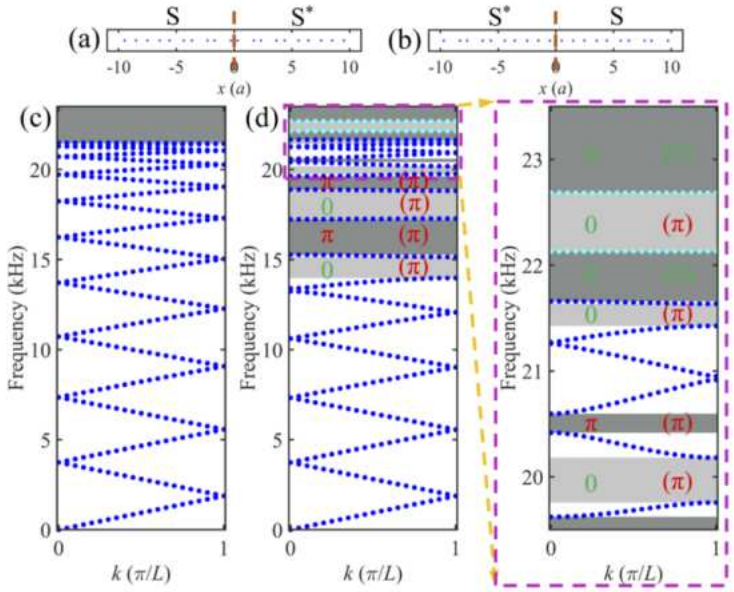


Figure 2. Pillar positions for hyperuniform SS* (a) and its SSH-like counterpart S*S (b). (c) Band structures of the supercell of 20 unit cells in the periodic case. (d) Band structures of the supercell SS* and S*S in the hyperuniform case. The left and right values represent the Zak phases of bandgaps of the metabeam SS* and S*S, respectively. The light and dark grey regions represent the nontrivial and trivial bandgaps, respectively.

References

1. Wang, W. et al, “Topologically valley, pseudospin and pseudospin-valley protected edge states in symmetric pillared phononic crystals”, Phys. Rev. B 100, 140101(R), 2019.
2. Yang, L. et al, “Robust Fano resonance between mechanical first and second order topological states”, International Journal of Mechanical Sciences, 236, 107768, 2022.
3. Wen, Z. et al, “Topological vortex mode for flexural waves in pillared plates”, Materials and Design, 233, 112209, 2023.
4. Wang, W. et al, “Robust Fano resonance in a topological beam”, Phys. Rev. B 101, 024101, 2020.
5. Cai, R. et al, “Topological elastic interface states in hyperuniform pillared metabeams”, APL Materials 12, 011121, 2024.

Diffusive Acoustic Metasurfaces for Single-element Photoacoustic Imaging

A. Cebrecos[1*], I. Pi-Martín[1], R. Weeteling[1], J. J. García-Garrigós[1], N. Jiménez[1]

[1]Instituto de Instrumentación para Imagen Molecular (i3M), CSIC – Universitat Politècnica de València, Camino de Vera S/N, 46022, Valencia, Spain

[*]corresponding author: alcebrui@upv.es

Abstract: We present a novel strategy to generate high-resolution photoacoustic images based on spatiotemporal encoding by combining a single-element detector and a reflecting cavity with attached acoustic metasurfaces designed to maximize sound diffusion in reflection. Numerical results demonstrate the potential of this concept to develop low-cost photoacoustic imaging systems.

Photoacoustic tomography is an emergent medical imaging modality that utilizes laser-generated ultrasonic waves to create images driven by optical absorption of tissues thanks to the photoacoustic effect [1]. It combines the high spatial resolution of ultrasound images with the high-contrast and spectroscopic character of optical imaging. Image reconstruction in photoacoustics is typically based on the time-of-flight reading of acoustic waves registered at multiple positions, normally via multi-element ultrasonic arrays distributed along a certain surface. Hence, spatial resolution is strongly dependent on the geometry and aperture of the acoustic detector. Generally, optimal resolution is achieved if all emitted photoacoustic waves are captured, i.e., if the sample is surrounded by the measurement surface. Typical ultrasound probe configurations (linear, planar, arc-shaped, etc.) do not fulfill such condition, affecting the resolution, as multiple angular components are lost. This is known as the "limited view problem" and implies that high resolution systems are generally associated to large multi-element detectors which require dedicated electronics per channel, resulting in high cost and complexity.

An alternative to spatial encoding consists in carrying out the reconstruction process by temporal encoding of the received data in a single waveform. Here, the lack of spatially variant data is compensated by enlarging the received angular spectrum through the generation of replicas of the original signal via scattering [2], randomized reflecting elements [3] or reflecting surfaces enclosing the imaging sample [4, 5]. Temporal encoding solves the limited view problem and suggests that the number of detectors could be drastically reduced, replacing multi-element arrays with smaller single-element detectors, paving the way for the realization of low-cost advanced imaging systems.

In this work, we propose a novel strategy to generate photoacoustic images based on temporal encoding. Our approach utilizes a single-element detector and an acoustically reflecting cavity enclosing the imaging sample. To obtain an efficient reconstruction with high spatial resolution, acoustic metasurfaces are designed to maximize sound diffusion and attached to the cavity walls.

Numerical simulations have been carried out using a pseudo-spectral time-domain method using the k-wave toolbox [6]. We consider three closed cavities (rectangular, chaotic and rectangular with metasurfaces), a single-element detector and a set of circular targets with an initial pressure distribution to solve the forward acoustic wave propagation problem. Image reconstruction is performed using time-reversal, i.e., the registered waveform at the detector is time-reversed and back-projected into the domain, where the reconstructed image corresponds to the pressure values at the last temporal sample. The designed acoustic metasurfaces are composed of a set of quarter-wavelength resonators whose depth is set to maximize sound diffusion in reflection. In this

way, we have chosen a quadratic residue sequence to define the depths, as it provides a flat response in the angular spectrum.

The lateral resolutions for increasing simulation times have been calculated for the three tested cavities, being averaged over the nine sources, as shown in Figure 1. The rectangular cavity incorporating diffusive acoustic metasurfaces outperforms both the rectangular and chaotic cavities in terms of lateral resolution values, but also showing a reduced standard deviation, indicating a high uniformity in the representation of the acoustic sources along the space, as shown in Figs. 1(c-e). Numerical results demonstrate a remarkable enhancement in the spatial resolution with respect to existing closed-cavity configurations based in rectangular and chaotic cavities, indicating the potential of diffusive acoustic metasurfaces to achieve a high-quality reconstruction using a simple and affordable photoacoustic imaging system.

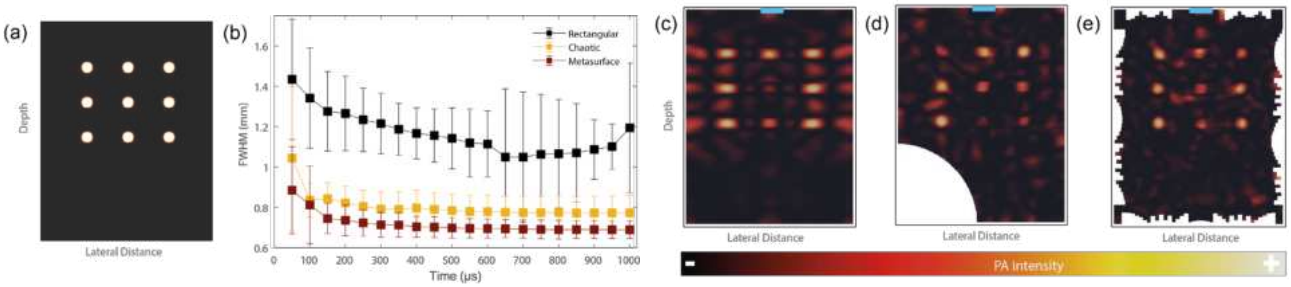


Figure 1. Photoacoustic image reconstruction scenarios: (a) Initial pressure distribution. (b) Lateral resolution for increasing simulation times. Reconstructed images for (c) rectangular, (d) chaotic and (e) rectangular cavity with metasurfaces.

Acknowledgments

We acknowledge financial support from Ministerio Español de Ciencia e Innovación grants "Ramón y Cajal" RYC2021-034920-I, Agencia Estatal de Investigación PID2022-142719OB-C21 and CNS2023-145707, to the Agencia Valenciana de la Innovació grants INNVA2/2022/11 and INNEST/2022/345, and by Generalitat Valenciana grant, CIAICO/2023/052, and IDIFEDER/2021/004.

References

1. Beard, P. "Biomedical photoacoustic imaging". Interface Focus, Vol. 1, 602, 2011.
2. Deán-Ben, X. L., et al. "Acoustic scattering mediated single detector optoacoustic tomography". PRL, Vol. 123, No. 17, 174301, 2019.
3. Zhao, Y., L. Wang. "Single-shot photoacoustic imaging with single-element transducer through a spatiotemporal encoder". JBO, Vol. 28, No 4, 046004, 2023.
4. Cox, B. T., S. R. Arridge and P. C. Beard, "Photoacoustic tomography with a limited-aperture planar sensor and a reverberant cavity". Inverse Problems, Vol. 23, No 6, S95, 2007
5. Cox, B., P.C. Beard, "Photoacoustic tomography with a single detector in a reverberant cavity". Journal of the Ac. Soc. Of Am., Vol. 125, No 3, 1426-1436, 2009.
6. Treeby, B. E., B. T. Cox. "K-wave: Matlab toolbox for the simulation and reconstruction of photoacoustic wavefields". J. Biomed. Opt. Vol. 15, 021314, 2010.

Broadband and low frequency acoustic absorber with frozen sound

A. Maddi,[1] C. Olivier,[2] G. Poignand,[1] G. Penelet,[1] V. Pagneux,[1*] and Y. Auregan[1]

[1]Laboratoire d'Acoustique de l'Université du Mans (LAUM), UMR 6613, Institut d'Acoustique - Graduate School (IA-GS), CNRS, Le Mans Université, France
[2]Centre de Transfert de Technologies du Mans (CTTM), 2 rue Thalès de Milet, 72000 Le Mans,France.
[*]corresponding author: vincent.pagneux@univ-lemans.fr

Abstract: We present the design of an ultra-broadband, low-frequency and non-reciprocal absorber based on thermoacoustic effects using liquid nitrogen. It is shown that the system can achieve an absorption of up to 95% in the very low frequency range (10 Hz), with a broadband absorption above 80% over 6.3 octaves.

Acoustic wave damping at low frequencies is widely regarded as one of the most difficult challenges in the field of wave control, due to the fact that most materials have low absorption rates in this range. This is especially true when the system in question is much smaller than the typical wavelength [1-2]. It is well established that in a transmission problem, the maximum amount of absorption that can be achieved by a symmetrical point scatterer is only half of the incident energy [3]. To improve the performance of compact absorbers, one approach is to break the geometrical symmetry of the system, which has been shown to significantly increase absorption levels in various experiments. Another potential solution to this problem is to break the reciprocity of the system, which would allow for greater absorption of waves coming from one direction.There are several mechanisms that can be used to break the reciprocity in acoustics, one of which is the thermoacoustic effect. This effect describes the conversion of thermal or mechanical energy that occurs when gas parcels interact with the solid frame of a porous medium that is subjected to a temperature gradient. The thermoacoustic effect has been the subject of extensive research for several decades as an alternative to traditional heat engines and refrigeration technologies [4-5].

The aim of this work is to show that when an acoustic wave strikes a compact porous medium at a normal angle from one side, it is possible to significantly increase the absorption rate beyond the intrinsic limit of 50% by cooling the opposite side of the medium. This results in an efficient, broadband, subwavelength absorber [6] that can achieve near-total absorption as long as the temperature of the cold spot is sufficiently low.

Figure 1(left) shows the experimental setup for the liquid nitrogen broadband absorber. The setup includes two long ducts, each equipped with a microphone, that are connected to the absorber. The cross-sectional area of the waveguide used in the setup is 5 cm by 1 cm. The absorber used in the experiment consists of either one or two cells in series, depending on the chosen configuration. Each cell is equipped with a regenerator made of stacked stainless steel wire meshes, with a length of 1.6 cm, an estimated porosity of 0.8 (pore radius of 72 μm). A cold and an ambient heat exchanger are attached to each side of the regenerator, both made of honeycombed aluminum material with a length of 1.5 cm, a porosity of 0.945, and a pore radius of 450 μm. Heat can be added or removed from the system through these heat exchangers. The cold source consists of a pair of insulated aluminum reservoirs with an inner volume of 52 cm3, filled with liquid nitrogen (see Figure 1). During operation, liquid nitrogen is regularly added to the reservoirs to maintain their fullness. The hot source consists of cartridge heaters inserted into solid aluminum blocks, placed at the heat exchanger location on either side of

the waveguide. A thermocouple is placed near the hot source on the external face of the duct to monitor the hot temperature T0 and ensure that it stays close to room temperature by adjusting the power P supplied to the heater. On the left of Figure 1 is shown the absorption obtained with this system, with an absorption of up to 95% in the very low frequency range (10 Hz) and a broadband absorption above 80% over 6.3 octaves.

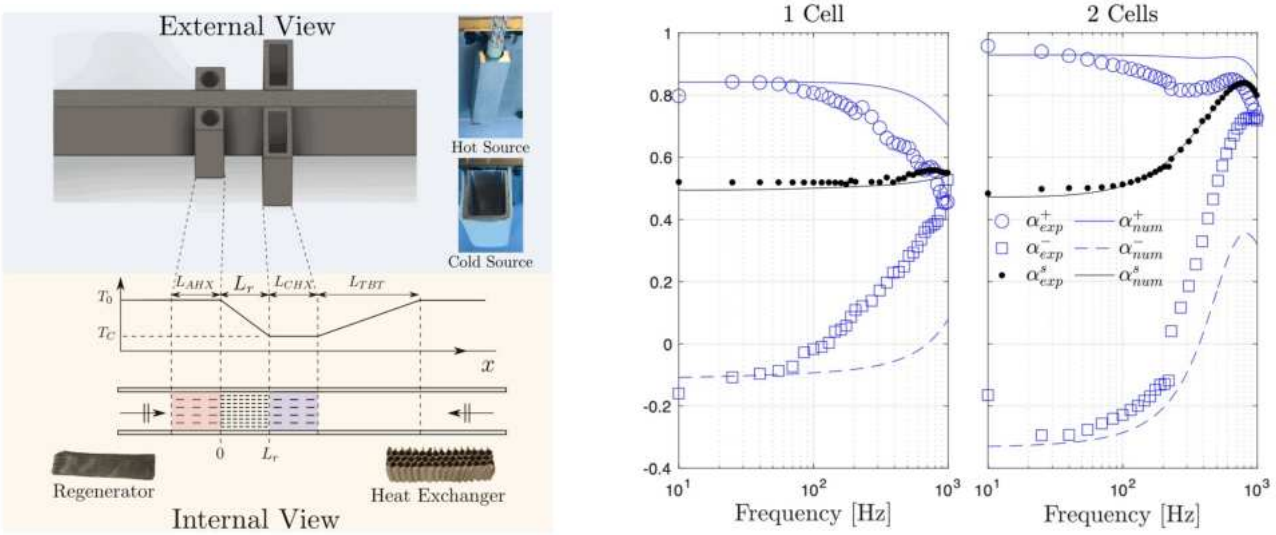


Figure 1: (**Left**): Sketch of the thermoacoustic cell used in the experiment The cell includes a regenerator surrounded by hot and cold heat exchangers and a thermal buffer tube. The regenerator is made up of a pile of ultrathin stainless steel mesh grids, and the heat exchangers are made of honeycombed aluminum material that is in thermal contact with heat sources placed outside the waveguide. The ambient heat source is an electric cartridge heater inserted into an aluminum block, while the cold heat source consists of a thermally insulated aluminum reservoir filled with liquid nitrogen. (**Right**): Absorption coefficients as a function of the frequency for one cell and two cells. Blue and black colors represent the configurations with and without the heat sources, respectively.

Acknowledgements: This work was supported by the French National Agency for Research (SelfiXs Project, ANR-18-CE92-0001).

References

1. Qu, S. & Sheng, P., “Microwave and acoustic absorption metamaterials,” Phys. Rev. Appl. 17, 047001, 2022.
2. Yang, M. & Sheng, P., “Sound absorption structures: From porous media to acoustic metamaterials,” Annu. Rev. Mater. Res. 47, 83–114, 2017.
3. Farooqui, M., Aurégan, Y. & Pagneux, V. ,“Ultrathin resistive sheets for broadband coherent absorption and symmetrization of acoustic waves,” Phys. Rev. Appl. 18, 014007, 2022.
4. Rott, N. “Thermoacoustics,” Adv. Appl. Mech. 20, 135–175, 1980.
5. Swift, G. W. “Thermoacoustic engines,” J. Acoust. Soc. Am. 84, 1145–1180, 1988.
6. Maddi, A., Olivier, C., Poignand, G., Penelet, G., Pagneux, V., & Aurégan, Y., “Frozen sound: An ultra-low frequency and ultra-broadband non-reciprocal acoustic absorber,” *Nature Communications*, *14*(1), 4028, 2023.

PT-latent symmetries

M. Röntgen[1], X. Chen[2], G. Gao[2], V Pagneux[1] and V. Achilleos[1*]

[1]Laboratoire d'Acoustique de l'Universit´e du Mans, Unite Mixte de Recherche 6613, Centre National de la Recherche Scientifique, Avenue O. Messiaen, F-72085 Le Mans Cedex 9, France
[2]EIT Institute for Advanced Study, Ningbo, China
[*]corresponding author: Achilleos.Vasssos@univ-lemans.fr

Abstract: In this work, we combine PT-symmetry with hidden symmetries, introducing the concept of latent PT -symmetry. We show how such systems can be designed, and experimentally confirm our theory. Moreover, we provide the means on how to keep the PT-unbroken phase of the system arbitrarily large.

Latent symmetries are those that aren't initially noticeable in the original system, but they emerge after a dimensional reduction process that is similar to an effective Hamiltonian [1,2]. These symmetries, initially rooted in graph theory, have been recently utilized in various physical configurations such as condensed matter systems, electric circuits[3], mechanical setups, and acoustic[4] and electromagnetic wave setups. In these applications, latent symmetries have been proven to significantly influence the underlying asymmetric system, leading to phenomena like spectral degeneracies or equireflectionality of the scattering matrix.

Here, we introduce the concept of latent symmetries into the domain of parity-time (PT) symmetry [3,4]. Specifically, we focus on the fundamental example of non-hermitian physics, the PT-symmetric dimer. Despite its simplicity, it encapsulates most of the intriguing phenomena of such systems, including the shift from real to complex spectra and the emergence of an exceptional point. This system has also been experimentally realized on various platforms, including photonics, acoustics, and electric circuits.

From a technical standpoint, a PT-symmetric dimer can be created by adding gain and loss, of equal strength, to a mirror-symmetric dimer. In this paper, we demonstrate how the original mirror-symmetric system can be replaced by an asymmetric one that possesses a latent mirror-symmetry. When gain and loss are introduced to this system, the result is a latently PT-symmetric system.

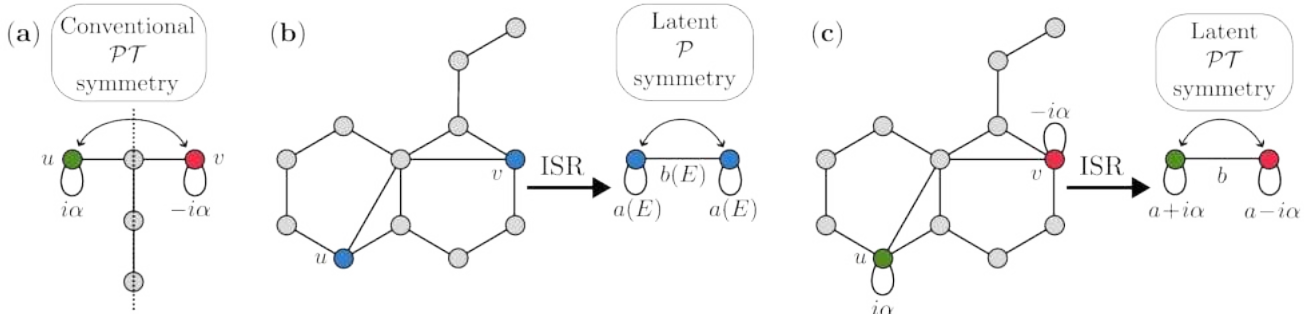


Figure 1. (a) A classic P T -symmetric system. (b) A latently reflection-symmetric system: Performing the isospectral reduction (ISR) over the two sites u, v yields a P-symmetric dimer (see text for details). (c) A latently P T -symmetric system (see text for details). In all three subfigures, a line between sites/nodes i, j corresponds to coupling of 1 between them. Loops correspond to diagonal terms in the underlying Hamiltonian.

The main idea is illustrated in Figure 1. The panel (a) shows a conventional discrete system composed of 5 coupled sites and two of them exhibit either loss (red circle) or gain (green circle). The system is clearly mirror symmetric around the axis denoted with dashed lines. This system was designed using the usual construction principle for PT-symmetry: Start from a reflection symmetric system and put complex on-site potentials ±iα (gain/loss) on one or more pairs of symmetric sites. However, while powerful, this principle is limited in the

sense of requiring a reflection-symmetric system as the starting point.
Our results drastically generalize this construction principle by using the concept of latent reflection symmetry. A latent symmetric setup is shown in Figure 1 (b), where although there is not clear symmetry in the system one can show that sites *u* and *v* are actually related with local mirror symmetry. As such combining the two concepts we can construct a system as the one shown in Figure 1 (c) which is non-Hermitian and at first look it has no symmetry, however we show that it is actually PT-symmetric. More specifically one can write an effective eigenvalue problem for this system of 12 sites in the form of a simple dimer which has an effective PT-symmetry as illustrated in the bottom right of Figure 1 (c).

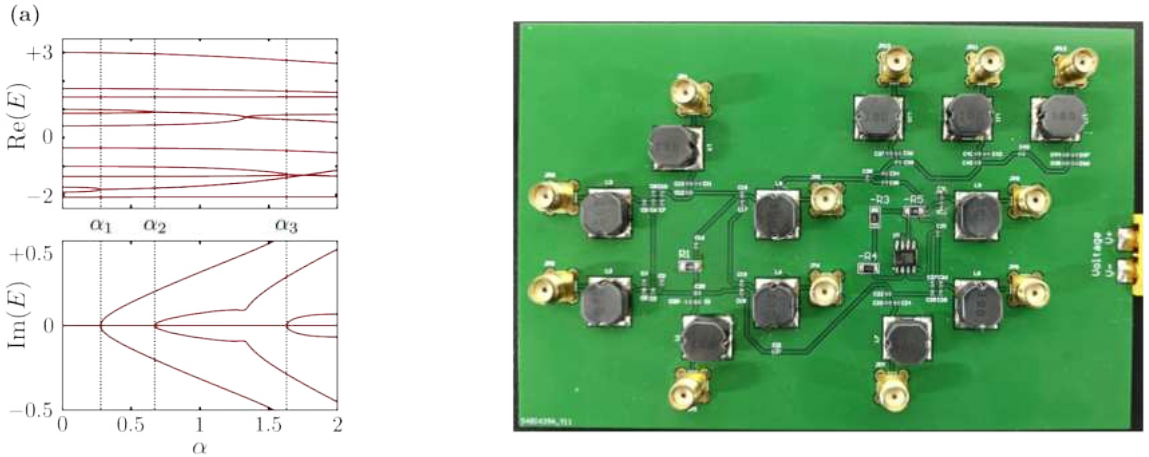


Figure 2. **Left**: Eigenvalue spectrum of the setup shown in Fig. 1(b), with the three exceptional point. **Right**: The electrical network used for experiments which simulates the same system as in Fig. 1(c).

To illustrate the fact that the proposed model shares the same properties as a typical PT-symmetric problem we plot the eigenvalues of the setup of Fig. 1 (c) as a function of the gain-loss parameter α which is shown in Fig 2 (a). Before the PT-symmetry breaking point the non-Hermitian problem has a fully stable (real) spectrum. However after a critical value of the gain/loss parameter, the eigenvalues collapse by pairs and unstable modes appear.

We note that such a setup could be realized in many different setups including acoustic waveguides [6] and optical fibers. Here as a prototype we performed experiments in an electric circuit shown in Fig 2 (b). Our results confirm the theoretical predictions and motivate further efforts on finding non-Hermitian systems with no obvious symmetries that share the same properties PT-symmetric ones.

Acknowledgements, V.A. is supported by the EU H2020 ERC StG "NASA" Grant Agreement No. 101077954. M.R. and V.A. acknowledge financial support from the NoHENA project funded under the program Etoiles Montantes of the Region Pays de la Loire.

References

1. L. Bunimovich and B. Webb, Isospectral Transformations: A New Approach to Analyzing Multidimensional Systems and Networks, 1st ed., Springer Monographs in Mathematics (Springer, New York, NY, United States, 2014).
2. D. Smith and B. Webb, "Hidden symmetries in real and theoretical networks", Physica A 514, 855 (2019).
3. M. Rontgen, *et al.* "Equireflectionality and customized unbalanced coherent perfect absorption in asymmetric waveguide networks", Phys. Rev. Appl. 20, 044082 (2023).
4. M. Rontgen, C. V. Morfonios, P. Schmelcher, and V. Pagneux, "Hidden symmetries in acoustic wave systems" , Phys. Rev. Lett. 130, 077201 (2023).
5. C. M. Bender and S. Boettcher, "Real spectra in non- hermitian Hamiltonians having PT symmetry", Phys. Rev. Lett. 80, 5243 (1998).
6. Y. Aurégan and V. Pagneux, Phys. Rev. Lett. 118, 174301 (2017).

Physically Interpretable Data-Driven Modeling and Control of Wave Dynamics

T. Shah[1], F. A. Amirkulova[1*], and S. Tiomkin[1]

[1]San José State University, USA

[*]corresponding author: feruza.amirkulova@sjsu.edu

Abstract: We present a novel machine learning method, based on deep neural networks, for efficiently learning the dynamics of an acoustic wave equation from samples. Our model is fully interpretable and maps physical constraints and intrinsic properties of the real acoustic environment into its latent representation of information.

In this talk, we present a novel machine learning method [1], based on deep neural networks and representation learning [2, 3], for efficiently learning the dynamics of an acoustic wave equation from samples and controlling the wave equation with Model Predictive Control. We have developed [1] an environment and algorithm that can serve as a basis for machine learning (ML) research in continuous dynamical systems governed by wave equations. Our environment is capable of simulating designs that can be manipulated in continuous time and influence complex PDE systems with physically realizable mechanisms. The novel algorithm we introduce operates on partial information from the environment and incorporates domain knowledge from acoustics to structure a latent representation of system dynamics. Our model is interpretable through physical properties; therefore, a level of meaning can be assigned to the evolution of its latent dynamics. With the interpretable structure of the latent space, we can apply a novel and trainable perfectly matched layer (PML) that actively dissipates energy. We discover that energy buildup in latent space is an important attribute and must be dissipated to allow the latent dynamics to maintain stability in the steady state. To our knowledge, a PML layer has not been incorporated into neural networks before. Furthermore, our work is the first to control acoustic waves in the time domain with ML enabling the efficient design of time-varying acoustic metamaterials. Time-varying metamaterials [4] can leverage the temporal dimension and drastically expand the range of degrees of freedom available for controlling wave dynamics.

We demonstrate the capabilities of our data-driven model on an important problem in acoustics, which is the minimization of total scattered energy. We consider a 2D planar motion and multiple scattering by fluid cylindrical structures embedded in acoustic media. Our environment and its implementation offer the technical tools required to further explore this area and establish stronger connections between acoustics and ML. We show that the prediction of scattered energy by our model generalizes in time and can be extended to long time horizons.

References

1. Shah, T., Amirkulova, F. and Tiomkin, S. “Taming Waves: A Physically-Interpretable Machine Learning Framework for Realizable Control of Wave Dynamics.” *arXiv preprint arXiv:2312.09460*, 2023.

2. Werner, S. and Peitz, S. *“*Learning a model is paramount for sample efficiency in reinforcement learning control of PDE*s.”* arXiv:2302.07160 *2023.*

3. Wu, T. , Maruyama, T. and Leskovec, J. *“*Learning to accelerate partial differential equations via latent global evolution*.”* arXiv:2206.07681 *2022.*

4. Engheta, N. “Four-dimensional optics using time-varying metamaterials.” Science, Vol. 379, No. 6638, pp. 1190–1191, Mar. 2023, doi:10.1126/ science.adf1094.

Any Dispersion You Want – Demystifying Roton, Maxon, Saddle Point, and Higher-order van Hove Singularities via Nonlocal Phononic Crystals

S. Paul[1], F. Chen[1], K. J. Deshmukh[2], B. Deng[3], A. Kazemi[1], X. Zhu[4], H. C. Fu[1], and P. Wang[1*]

[1]Department of Mechanical Engineering, University of Utah, Salt Lake City, USA
[1]Department of Mathematics, University of Utah, Salt Lake City, USA
[3]Guggenheim School of Aerospace Engineering, Georgia Institute of Technology, Atlanta, USA
[2]Department of Civil and Environmental Engineering, University of Utah, Salt Lake City, USA
[*]Corresponding author: pai.wang@utah.edu

Abstract: We first show precise inverse design of band structures via beyond-nearest-neighbor (BNN) interactions in discrete nonlocal phononic crystals of both 1D and 2D cases. Next, we focus on localized modes with vanishing group velocity and explain related concepts such as rotons, van Hove singularities, and bound states in continuum (BIC).

In this talk, we demonstrate the capability to completely and analytically customize the dispersion relations in phononic crystals by incorporating nonlocal springs [1]. We show dispersion curves with multiple critical points of the first (roton [2, 3] or maxon [4]) and second order (undulation point [1] – See Fig. 1) in one-dimensional case. We further study the wave packet dynamics at each of the critical points and illustrate how we can use them to create novel behaviors of localized modes. In addition, we investigate critical points such as the saddle point in 2D cases – See Fig. 2. Our studies enable future research on non-propagating elastic wave modes in terms of topology, scaling, and symmetry.

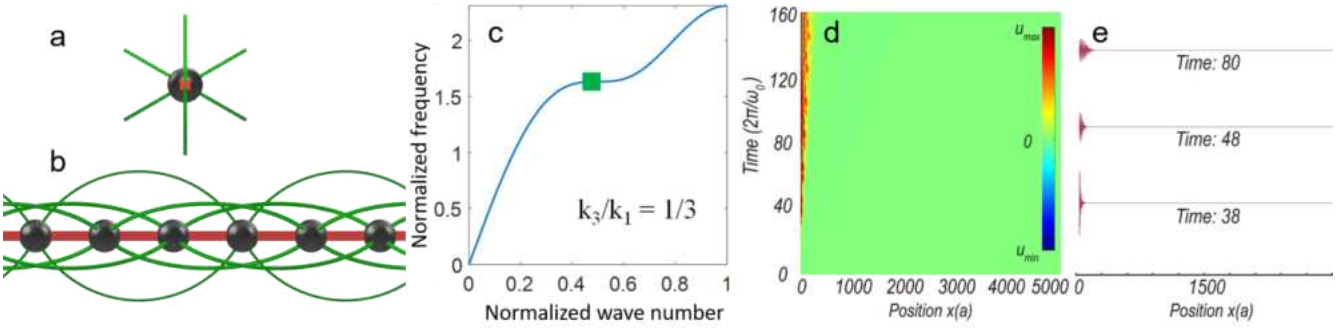


Figure 1: Non-local phononic crystals with second-order zero-group-velocity (ZGV) modes: (a)&(b) are the front and side views of the non-local 1D chain with stronger $k_3 = (1/3)\ k_1$. (c) shows the dispersion relations with a second-order ZGV mode at a stationary inflection point (undulation, green square). (d)&(e) show the time-domain simulation results on a finite chain of 5000 unit cells.

Next, we relate these phenomena to several popular concepts in condensed matter physics: (A) van Hove singularities in the density of states that arise directly from critical points of dispersion bands; and (B) Bound states in continuum, which are natural results of the strongly localized wave modes.

In addition, we also present experimental observations of two categories of van Hove singularities: The ordinary one with a vanishing group velocity and the high-order one with the simultaneous vanishing of both group velocity and spatial spreading rate.

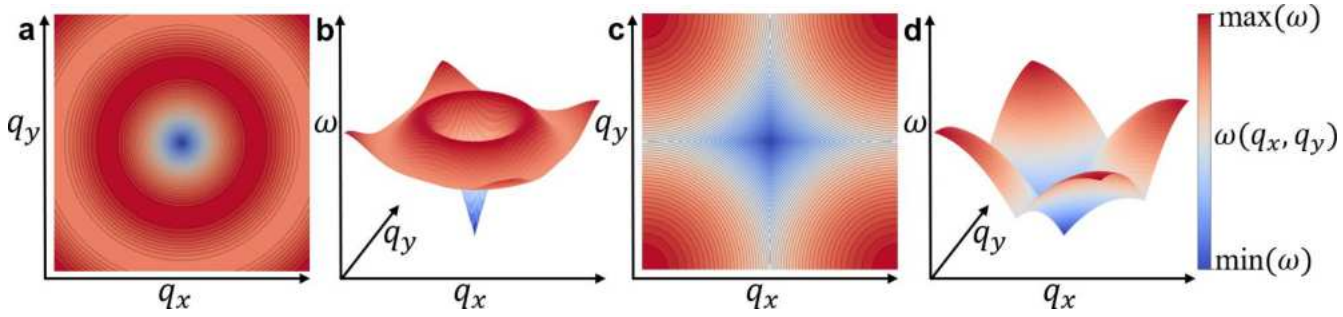


Figure 2: Dispersion contour plots of example 2D non-local phononic lattices.

This work was supported by the P.W.'s startup research funds of the Department of Mechanical Engineering at University of Utah. K.J.D. is grateful to the National Science Foundation for support through Grant No. DMS2107926. The support and resources from the Center for High Performance Computing at the University of Utah are gratefully acknowledged. The authors are grateful to Professor Graeme Milton at Utah, Professor Srikantha Phani at UBC, Professor Mahmoud Hussein at CU Boulder, and Professor Guancong Ma at HKBU for inspirational discussions.

References

1. Kazemi, A., Deshmukh, K. J., Chen, F., Liu, Y., Deng, B., Fu, H. C., & Wang, P. (2023). Drawing Dispersion Curves: Band Structure Customization via Nonlocal Phononic Crystals. Physical Review Letters, 131(17), 176101.
2. Chen, Y., Kadic, M., & Wegener, M. (2021). Roton-like acoustical dispersion relations in 3D metamaterials. Nature communications, 12(1), 3278.
3. Iglesias Martínez, J. A., Groß, M. F., Chen, Y., Frenzel, T., Laude, V., Kadic, M., & Wegener, M. (2021). Experimental observation of roton-like dispersion relations in metamaterials. Science advances, 7(49), eabm2189.
4. Samak, M. M., & Bilal, O. R. (2024). Evidence of zero group velocity at the lowest dispersion branch through local interactions. APL Materials, 12(1).

Negative refraction in a single-phase flexural metamaterial with hyperbolic dispersion

Kim Pham[1*], Agnès Maurel[2] and J.-J. Marigo[3]

[1] LMI, ENSTA Paris, Institut Polytechnique de Paris, 91120, Palaiseau, France
[2] Institut Langevin, ESPCI Paris, Université PSL, CNRS, 1 rue Jussieu, Paris 75005, France
[3] Sorbonne Univ., CNRS, Inst. Jean Le Rond d'Alembert, UMR 7190, 75005 Paris, France

[*]corresponding author: kim.pham@ensta-paris.fr

Abstract: This study examines the band structure of a single-phase elastic metamaterial based on flexural resonances, employing two-scale asymptotic homogenization and Bloch–Floquet analysis. It reveals two frequency-dependent mass densities governing symmetric/antisymmetric flexural resonances, leading to low-frequency band-gaps and negative refraction in hyperbolic regions of the dispersion diagram.

Negative refraction (NR) and band-gaps (BG) are commonly observed phenomena in the wave band structure of photonic/phononic crystals, offering significant potential for applications in perfect lens design across various fields such as electromagnetism, acoustics, and elastodynamics. While NR crystals aim to overcome diffraction limits, BG crystals act as efficient insulators or defect-immune wave propagators. However, their practical utility is often constrained to high frequencies, limiting widespread application due to the necessity for comparable wavelength and crystal periodicity.

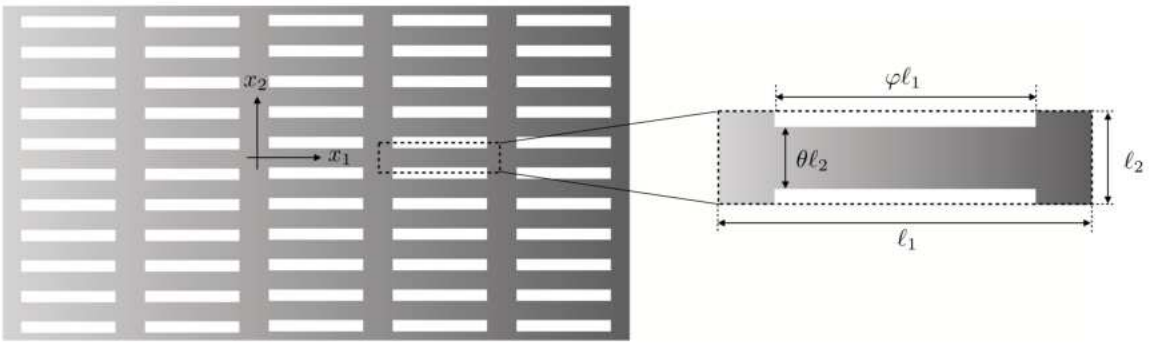


Figure 1: *Single-phase flexural metamaterial; the inset shows the unit cell containing a slender beam with flexural resonances*

Locally resonant metamaterials (LRM) have emerged as a solution to extend these properties to low frequencies over the past two decades. By incorporating subwavelength resonant mechanisms at the microstructural level, LRMs significantly impact macroscopic wave propagation. Despite their effectiveness in exhibiting BGs, achieving low-frequency NR remains challenging. Various strategies have been explored, including elastic LRMs based on single-phase materials, particularly elongated structures such as beams or plates with low bending stiffness, offering control over low-frequency flexural modes beneficial for seismic wave management.
The derivation of effective parameters for NR and BG materials from microstructures involves two primary approaches: discrete and homogenization methods. Discrete approaches model the system as discrete analogues of the continuous system, offering explicit dispersion relations through Bloch–Floquet analysis. However,

potential inadequacies between discrete and continuous systems pose risks. In contrast, homogenization approaches directly deal with the actual system, providing deductive effective parameters but are often limited to long wavelength regimes. This work proposes a combined approach leveraging the strengths of both methods.

This work deals with a a two-dimensional elastic structure made of a periodic collection of dumbbell-shaped specimens whose central elements consist in thin beams of length $\varphi\ell 1$ and thickness $\theta\ell 2$, see Figure 1(*Marigo et al. 2023*). By employing Bloch–Floquet analysis and two-scale asymptotics, the dispersion of elastic waves in flexural metamaterials is derived analytically,

$$(\rho_s - \rho_a)\omega^2 \sin^2 \frac{k_1 \ell_1}{2} + (1-\varphi)Ek_2^2 = \rho_s \omega^2$$

where (ρ_s, ρ_a) are frequency-dependent mass densities that can exhibit simultaneously negative values in some frequency range. Through exploration of the entire Brillouin zone, evidence of band-gaps due to resonances of symmetric and antisymmetric flexural modes is presented, each associated with a frequency-dependent effective mass density. The interplay between these densities yields elliptical or hyperbolic dispersion, facilitating the occurrence of negative refraction in the latter case, see Figure 2.

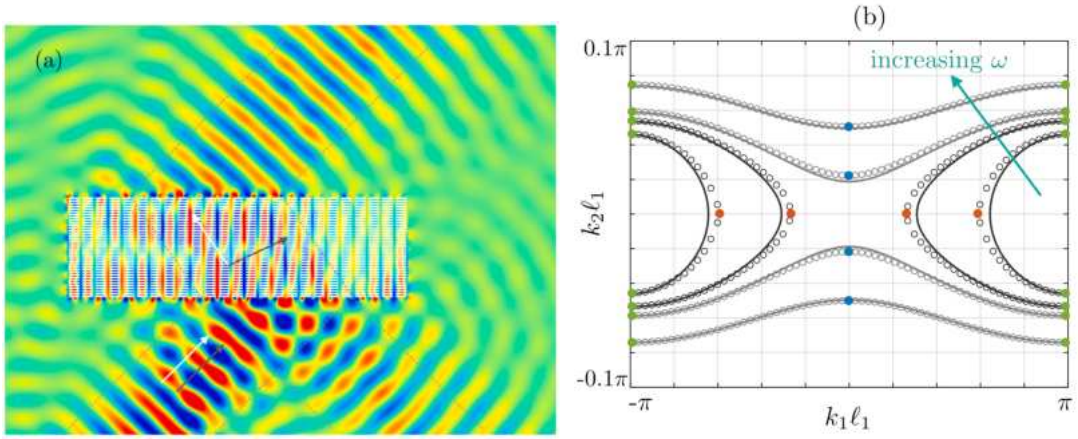


Figure 2: *(a) Negative refraction through a slab filled with our structure, (a) in the actual problem from direct numerics, (b) Iso-frequency contours with hyperbolic dispersion*

References

1. Marigo, J. J., Maurel, A., & Pham, K. (2023). Negative refraction in a single-phase flexural metamaterial with hyperbolic dispersion. *Journal of the Mechanics and Physics of Solids*, *170*, 105126.
2. Euvé, L. P., Pham, K., & Maurel, A. (2023). Negative refraction of water waves by hyperbolic metamaterials. *Journal of Fluid Mechanics*, *961*, A16.
3. Marigo, J. J., Pham, K., Maurel, A., & Guenneau, S. (2021). Effective model for elastic waves in a substrate supporting an array of plates/beams with flexural and longitudinal resonances. *Journal of Elasticity*, *146*, 143-177.
4. Marigo, J. J., Pham, K., Maurel, A., & Guenneau, S. (2020). Effective model for elastic waves propagating in a substrate supporting a dense array of plates/beams with flexural resonances. *Journal of the Mechanics and Physics of Solids*, *143*, 104029.

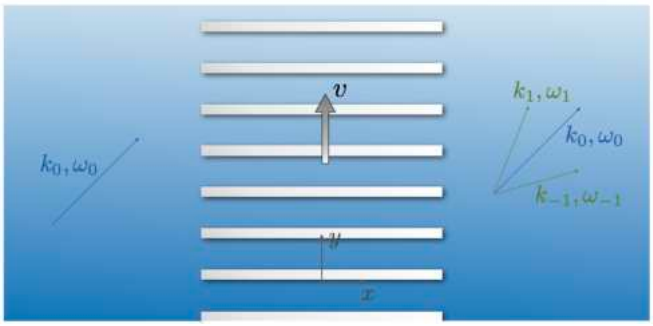
Acoustic grating with space-time modulation

A. Maurel[1]*, and K. Pham[2]

[1]Institut Langevin, ESPCI Paris, Université PSL, CNRS, 1 rue Jussieu, 75005 Paris, France
[2]LMI, ENSTA Paris, Institut Polytechnique de Paris, 828 Bd des Maréchaux, 91732 Palaiseau, France
*agnes.maurel@espci.fr

Abstract: We present a theoretical and numerical analysis of the diffraction of acoustic waves by space-time modulated gratings with rigid-type modulations. We report results exemplifying the non-reciprocal behavior of the grating, in relation with spatial and temporal harmonics.

Space-time metamaterials, refers to materials whose properties vary in the N + 1 dimensions, N in space and 1 in time. The term itself appeared around twenty years ago with the intuitive idea that the higher the dimensions, the more degrees of freedom we have to realize wave systems with the desired functionalities. There was pioneering work in the 1960s, mainly in electromagnetism, afterwards probably the most systematic description of these media was proposed by Lurie, who called them *dynamic materials*. Among these dynamic materials, he introduced the distinction between *kinetic material* when there is a mechanical movement of the material and *activated material* when the material does not move but its properties vary in space and time. In both cases, the most expected effects are non-reciprocity and the generation of temporal harmonics. Since then, there has been many theoretical and experimental studies for the two types of dynamic materials.



We have been interested in such activated material, namely a grating made of a periodic set of sound rigid blocks in a fluid, see figure 1.

Figure 1: Space-time modulated grating.

We consider the scattering problem leading to the solution, in reflection and transmission, of the form :

$$\varphi(x,y,t) = \begin{cases} e^{i(\alpha_0 x + \beta_0 y - \omega_0 t)} + \sum_n r_n e^{i(-\alpha_n x + \beta_n y + \omega_n t)}, \\ \sum_n t_n e^{i(\alpha_n x + \beta_n y - \omega_n t)}, \end{cases}$$

$$\omega_n = \omega_0 + \mathrm{M}\, c \frac{2n\pi}{h}, \quad k_n = \frac{\omega_n}{c}, \quad \beta_n = \beta_0 + \frac{2n\pi}{h}, \quad \alpha_n^2 + \beta_n^2 = k_n^2.$$

We shall discuss two particular behaviors of the modulated grating:

1) Perfect mode conversion and perfect transmission : Under specific condition, and when at least two modes are propagating (real value of αn), perfect transmission associated with perfect mode conversion

is observed, as illustrated in Figure 2. We stress that the non-reciprocity prevents in the reported case that the time reversed transmitted waves produces perfect mode conversion (unless the modulation is inverted).

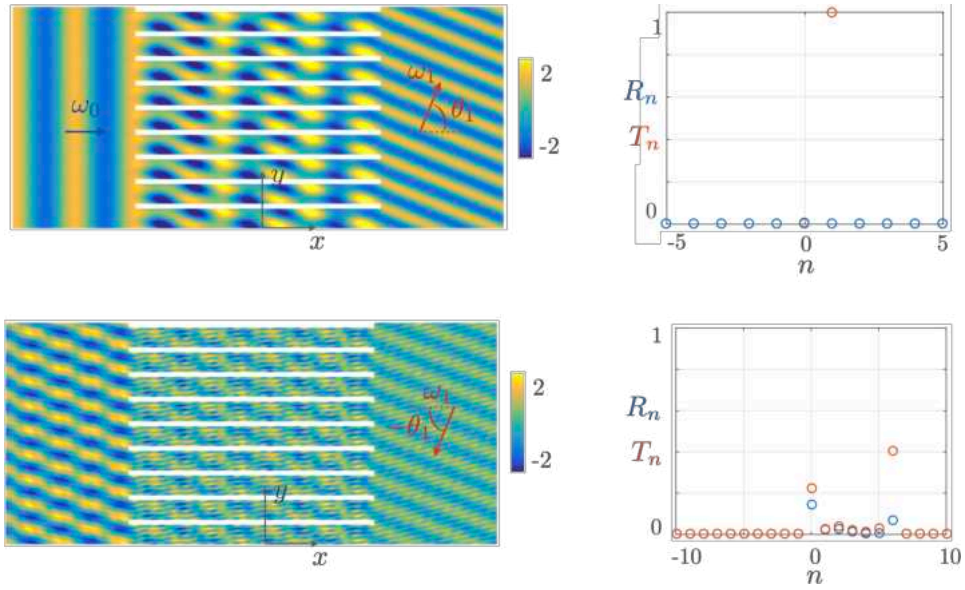


Figure 2: (top) Perfect transmission with perfect mode conversion for a wave at normal incidence , (bottom) evidence of non-reciprocal propagation.

2) Temporal Fano resonances associated with the excitation of the acoustic analog of quasi-spoof plasmons producing a succession of perfect transmission and perfect reflection, which is not possible at zero modulation due to symmetry.

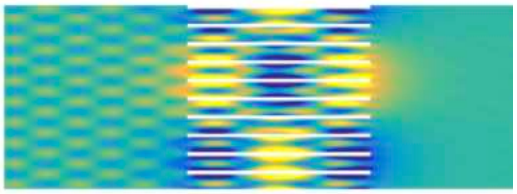


Figure 3: Quasi SPPs excitable through scattering and responsible of Fano resonance.

References

[1] Pham, K., & Maurel, A. « Diffraction grating with space-time modulation. » *Journal of Computational Physics*, *469*, 111528 (2022).

[2] Pham, K., & Maurel, A. « How space-time modulations modify spoof surface plasmons and scattering properties in acoustic metagratings, Physical Review B, 108(2), 024303 (2023).

Theoretical Bound of Symmetric Metasurfaces

C. W. Park[1] **and Y. Y. Kim**[1,2*]

[1]Institute of Advanced Machines and Design, Seoul National University, 1 Gwanak-ro, Gwanak-gu, Seoul 08826, South Korea
[2]Department of Mechanical Engineering, Seoul National University, 1 Gwanak-ro, Gwanak-gu, Seoul 08826, South Korea
[*]corresponding author: yykim@snu.ac.kr

Abstract: Symmetry may restrict the transmission and phase coverage of local scatterers of the metasurfaces. We investigate the theoretical limit of transmission coverage of the symmetric metasurface. We conduct numerical simulations of controlling acoustic wavefronts to validate our theoretical results.

We rigorously investigate the theoretical bound of a symmetric metasurface. Local responses of symmetric metasurfaces are identical, independent of incident direction. This condition can be written by the reflection coefficients as

$$\mathbf{r} = \mathbf{r}' \tag{1}$$

where the unprimed and primed symbols mean the forward and backward incident directions, respectively. Using Eq. (1) and assuming passive lossless metasurfaces, we derived two coupled equations of transmittance and phase information, which is expressed as For equations,

$$-\frac{1}{2}\sqrt{T}\left(\frac{1}{\sqrt{Z_r}}+\sqrt{Z_r}\right) \le \cos(\theta) \le \frac{1}{2}\sqrt{T}\left(\frac{1}{\sqrt{Z_r}}+\sqrt{Z_r}\right) \tag{2}$$

$$\frac{T^2\cos^2(\theta)}{\left[1/2T^{\frac{3}{2}}\left(1/\sqrt{Z_r}+\sqrt{Z_r}\right)\right]^2}+\frac{T^2\sin^2(\theta)}{\left(T^{\frac{3}{2}}\right)^2} \ge 1 \tag{3}$$

where, T is transmittance, θ is transmission phase, and Z_r is the impedance ratio of background medium.

Our theoretical analysis revealed that the maximum transmittance cannot be unity and also that only a finite number of phases can be selected to cover 2π phase change for the maximum efficiency, which is demonstrated by Fig. 1.

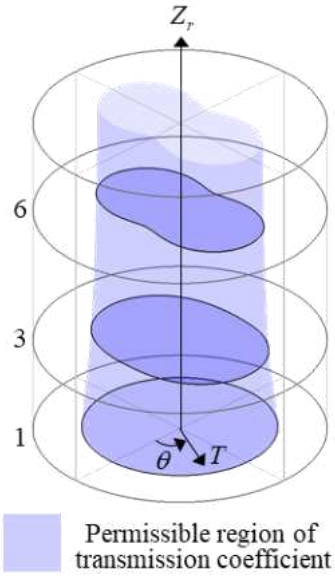


Figure 1. Permissible region of transmission coefficient for a symmetric metasurface.

To show the effect of limitations on transmission coefficients, we conduct numerical simulations of beam steering and focusing of acoustic waves by the symmetric metasurfaces. The transmission performance is significantly degraded due to the lack of possible transmission phases.

References

1. Park, C. W. and Kim, Y. Y. “Theoretical analysis of transmission and phase coverage by a symmetric metasurface across dissimilar media,” EML, 61, 102030, 2023.

AI-empowered acoustic metamaterials and their applications

B. Liang *

Key Laboratory of Modern Acoustics, MOE, Institute of Acoustics, Department of Physics, Nanjing University, Nanjing 210093, P. R. China
*corresponding author: liangbin@nju.edu.cn

Abstract: In this talk, I will discuss some of our recent advances obtained by coalescing artificial Intelligence and acoustic artificial structures with extraordinary acoustic properties. Furthermore, I will also mention the applications of acoustic metamaterials in several important scenarios such as architectural acoustics and acoustic communication.

Simple and precise sound manipulation is of fundamental interest and practical significance in acoustics and many related fields, but is challenging due to the limitation in the acoustical properties of naturally available materials. The recent emergence of acoustic metamaterials which comprises a large number of subwavelength unit cells and behaves like a homogeneous medium with special acoustical properties overcomes the limitations of acoustical properties of naturally available materials and enables novel wave-steering phenomena, which would also open new applications in many diverse scenarios. Meanwhile, artificial intelligence is already impacting many other scientific disciplines and research fields. In this talk I will first briefly review some of our recent advances that provides acoustic metamaterials allowing novel unconventional sound manipulation such as wavefront manipulation, asymmetric transmission and production of acoustic orbital angular momentum. Then I will discuss what we can obtain by combining acoustic metamaterial with artificial intelligence. To go beyond the limitation in current acoustic metamaterials that only form sound waves form the desired fields, we build an acoustic "neuromorphic system" based on artificial structures, and proved that an array of unit cells following deep-learning-assisted design of parameters is endowed with the 'intelligence' to solve complicated tasks in a simple, precise, fast and passive manner. On the other hand, based on the unconventional wave-steering functionality and high design flexibility, we propose to inversely design acoustic metamaterials with the aid of machine learning technique and realize a series of acoustic functional devices with superb performance, whose applications in various scenarios such as absorption and isolation of low-frequency sound is also demonstrated.

References

1. B. Liang, X. S. Guo, J. Tu, D. Zhang, and J. C. Cheng, An acoustic rectifier, Nat. Mater. 9, 989 (2010).
2. Y. Zhu, X. Fan, B. Liang, J. Cheng, and Y. Jing, Ultrathin Acoustic Metasurface-Based Schroeder Diffuser, Phys. Rev. X 7, 021034 (2017).
3. Y. Ding, Y. Peng, Y. Zhu, X. Fan, J. Yang, B. Liang, X. Zhu, X. Wan, and J. Cheng, Experimental Demonstration of Acoustic Chern Insulators, Phys Rev Lett 122, 014302 (2019).
4. K. Wu, J. J. Liu, Y. J. Ding, W. Wang, B. Liang, and J. C. Cheng, Metamaterial-based real-time communication with high information density by multipath twisting of acoustic wave, Nat. Commun. 13, 5171 (2022).
5. J. Weng, Y. Ding, C. Hu, X. F. Zhu, B. Liang, J. Yang, and J. Cheng, Meta-neural-network for real-time and passive deep-learning-based object recognition, Nat. Commun. 11, 6309 (2020).
6. H.-x. Li, J.-j. Liu, Z.-x. Chen, K. Wu, B. Liang, J. Yang, J.-c. Cheng, and J. Christensen, Superwavelength self-healing

of spoof surface sonic Airy-Talbot waves, Nat. Commun. 14, 7633 (2023)

META 2024, TOYAMA - JAPAN, JULY 16 – 19, 2024

Efficient electromechanical coupling to an optomechanical nanobeam

T. Makkonen[1], O. Ylivaara[1], S. Pourjamal[1], and J. Ahopelto[1*]

[1] VTT Technical Research Centre of Finland Ltd, Finland
[*]corresponding author: Jouni.ahopelto@vtt.fi

Abstract: We have developed a new approach for efficient electromechanical coupling into an optomechanical nanobeam. We exploit small bulk acoustic wave transducers integrated directly to the nanobeam. The transducers operate at GHz frequencies and at room temperature. Simulations suggest that in optimized structures, the conversion efficiency can approach 90 %.

Optomechanics provides an interesting alternative for low-power information technology[1]. Adding the possibility of electromechanical excitation in the system, further functionalities become available, including flexible modulation of the optical signal and direct readout. The most common way for electromechanical excitation is to use surface acoustic waves (SAW) generated by interdigitated transducers (IDT)[2]. The challenge of using IDTs is related to relatively low conversion efficiency of electrical signals to mechanical energy flow in the nanoscale beams[3], although high conversion efficiencies have been obtained by IDTs operating at low temperatures[4]. Another challenge is the typically large surface area required by the IDT electrodes. The latter can be tackled by using acoustic metasurfaces[5] to steer and focus the waves, but the coupling efficiency can still remain low.

In this work we have investigated the possibility to integrate small bulk acoustic wave (BAW) transducers directly in the optomechanical nanobeam to enhance the coupling efficiency and conversion of the electrical signal to the mechanical modes in the beam. The target is broadband operation at a few GHz range and at room temperature using a small footprint transducers. The simulated devices have transducers with a footprint of 10-30 μm^2, connected to a 220 nm thick and 800 nm wide silicon nanobeam. The main loss mechanisms include viscous losses and anchor losses, i.e., leakage into the substrate. By optimizing the anchoring, conversion efficiency approaching 90 % can be achieved, see Figure 1. In addition to simulations, we will tackle the challenges in fabrication and characterization of the devices.

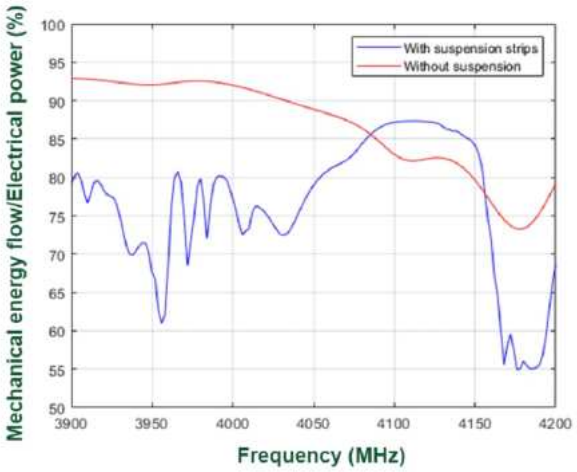


Figure 1. Simulated conversion efficiency of the electrical power fed to the device to mechanical energy flow in the nanobeam. Red: Ideal case with no connection from the transducer to the substrate (floating transducer). Blue: The transducer suspended by 1-dimensional phononic crystals with a band gap slightly above 4 GHz.

This work has been funded by the Academy of Finland through ERA-NET CHISTERA Program, project MUSICIAN, Grant # 357745 and by the European Commission, project MAGNIFIC, Grant # 101091968.

References

1. Mercadé L., L. L. Martín, A. Griol, D. Navarro-Urrios, and A. Martínez, "Microwave oscillator and frequency comb in a silicon optomechanical cavity with a full phononic bandgap," Nanophotonics, Vol. 9, 3535–3544, 2020.
2. Navarro-Urrios D., M. F. Colombano, G. Arregui, G. Madiot, A. Pitanti, A. Griol, T. Makkonen, J. Ahopelto, C. M. Sotomayor-Torres, and A. Martínez, "Room-Temperature Silicon Platform for GHz-Frequency Nanoelectro-Opto-Mechanical Systems," ACS Photonics, Vol. 9, 413−419, 2022.
3. Korovin A. V., Y. Pennec, M. Stocchi, D. Mencarelli, L. Pierantoni, T. Makkonen, J. Ahopelto, and B. Djafari Rouhani, "Conversion between surface acoustic waves and guided modes of a quasiperiodic structured nanobeam, " J. Phys. D: Appl. Phys., Vol. 52, 32LT01, 2019.
4. Mirhosseini M., A. Sipahigil, M. Kalaee, and O. Painter, "Superconducting qubit to optical photon transduction," Nature, Vol.588, 599-603, 2020.
5. Liu D., L. Hao, W. Zhu, X. Yang, X. Yan, C. Guan, Y. Xie, S. Pang, and Z. Chen, "Recent Progress in Resonant Acoustic Metasurfaces," Materials, Vol. 16, 7044, 2023.

Acoustic and Optic drills by dynamic high-order Bessel beam mixing

K. Staliūnas[1,2,*], G. Kontenis[3], N. Jimenéz[4]

[1]ICREA, Passeig Lluís Companys 23, 08010, Barcelona, Spain
[2]UPC, Dep. de Fisica, Rambla Sant Nebridi 22, 08222, Terrassa, Spain
[3]Laser Research Center, Vilnius University, Sauletekio 10, Vilnius, Lithuania
[4]Instituto de Instrumentación para Imagen Molecular, Centro Mixto CSIC—Universitat Politècnica de València, 46022, València, Spain
[*]corresponding author: kestutis.staliunas@icrea.cat

Abstract: We demonstrate experimentally dynamical acoustic and optical "drill" beams, presenting nonstationary intensity distributions that resemble the spinning mechanical drill. The drills appear as the spatiotemporal interference of two Bessel-vortex beams of different topological charges and different carrier frequencies. We explore material processing with such drills.

Exotic beams such acoustic vortices are emerging as tools for wave-matter interaction, including particle trapping and manipulation, mechanical torque transfer applications, or acoustic transceivers and underwater communications. Acoustic vortex beams are wave fields with phase singularities, and around these spots the phase of the beam rotates with the azimuthal coordinate. Therefore, in acoustic beams the phase is helical in the space. In this work we present acoustic drills, a new type of beam whose intensity distribution matches the shape of a helix, twisting around the beam axis. In addition, the intensity distribution rotates with time along the axis of the beam with a controlled direction and angular frequency, therefore resembling the shape of a rotating mechanical drill [1]. The acoustic drill which we present here is analogous to the recently demonstrated optical drill [2].

We synthesize two confocal and detuned Bessel beams of elongated focal spot and arbitrary topological charge using two concentric 3D-printed acoustic holograms. The outer beam is excited by a custom piezoelectric ring (84-mm external diameter, 50-mm internal diameter) and a concentric unfocused circular transducer (50-mm aperture). Each transducer is excited with a separate AWG and RF amplifier, with a pulsed burst of around 1 MHz central frequency. The frequency was slightly detuned, to about several Hertz. Field measurements were taken in water, k-space pseudospectral simulations were performed, and the field was calculated using the Rayleigh-Sommerfeld integral. Camera measurements were taken at the surface of the water.

We show that elongated drill beams are obtained using two high-order Bessel beams. Analytic, numeric, and experimental results are in good agreement, showing the helical structure of intensity distribution rotating with a controlled angular frequency. Acoustic drills emerge as the spatiotemporal interference of two confocal and detuned vortex beams. Analytical constraints for optimal beam overlapping were obtained. We show how the parameters of the helical beam are fully tuneable, their period, winding, rotation speed and direction, number of windings, and we link these parameters to the geometrical and detuning parameters of the primary vortex beams. This new wave structure opens novel avenues for wave-matter interaction, such as contactless particle manipulation, matter processing or biomedical applications.

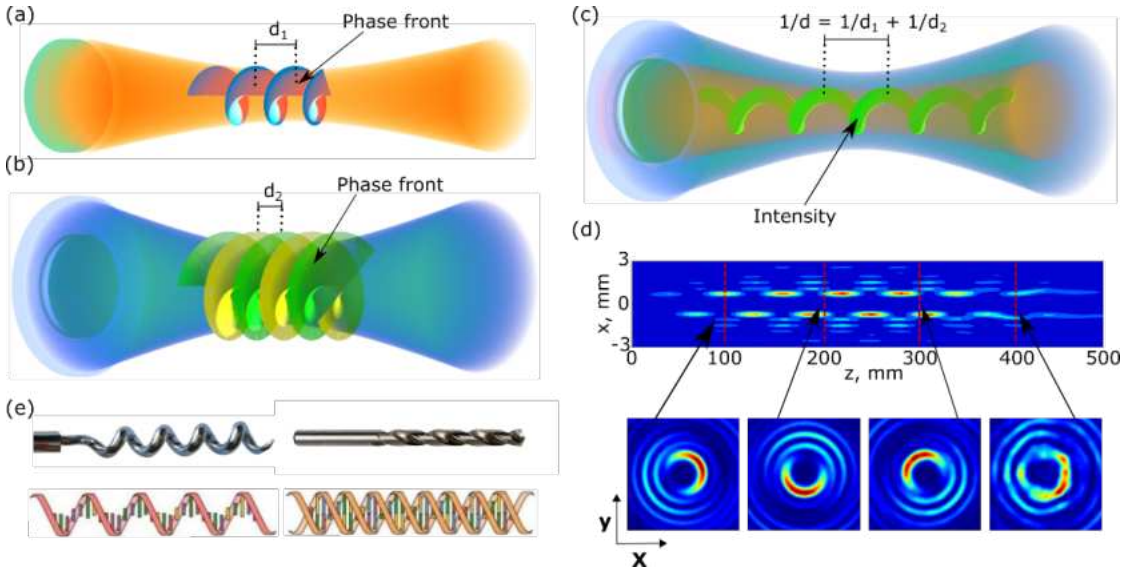


Fig.1. Acoustic drill beams. (a) phase helical Bessel beam with the single helicity m=1; (b) phase helical Bessel beam with the double helicity m=2; (c) Optical drill bit emerging from the interference of phase-helical beams (a) and (b); (d) axial x-z and transverse x-y cross-sections of the simulated intensity distribution; (e) mechanical and biological analogues of the same geometrical structure.

References

1. Jimenez, N., Staliunas, K., Camarena, F., Sistema y método de generación de haces acústicos confocales de vórtice con superposición espacio temporal, European Patent ES2811650, 2021.
2. Kontenis, G., Gailevicius, D., and Staliunas, K., Optical drills by dynamic high-order Bessel beam mixing, Phys. Rev. Applied, 17, 034059, 2022.

Superlattice nanowires: a versatile platform for phonon engineering

Aswathi K. Sivan[1], Begoña Abad[1], Omer Arif[2], Johannes Trautvetter[1], Tommaso Albrigi[3], Alicia Ruiz Caridad[1], Chaitanya Arya[1] , Diego de Matteis[1], Francesca Rossi[4], Valentina Zannier[2], Lucia Sorba[2] , Riccardo Rurali[3], and Ilaria Zardo[1]

[1]*Department of Physics, University of Basel, Switzerland*

[2]*NEST, Instituto Nanoscienze-CNR and Scuola Normale Superiore, Pisa, Italy*

[3]*Institut de Ciencia de Materials de Barcelona (ICMAB-CSIC), Spain*

[4]*IMEM—CNR, Parco Area delle Scienze 37/A, I-43124 Parma, Italy*

Phonons, the vibrations of an atomic lattice, are responsible for heat and sound transport within materials. The ability to control and manipulate phonons is essential for effective thermal management. Engineering materials at the nanoscale are key to achieving this, demanding advanced fabrication or growth techniques. [1] Superlattices (SLs), characterized by periodic heterostructures, offer a means to explore novel phononic properties. [2] Especially, SL structures with nanoscale periodicities serve as a model system for studying the transition from coherent to incoherent phonon transport. [3] However, achieving smooth interfaces between layers, relative to the characteristic phonon wavelengths, remains challenging during the growth process, hindering the fabrication of nanoscale SL structures for phonon engineering. Nanowires (NWs), on the other hand, are quasi-one-dimensional structures that allow the growth of axial and radial heterostructures otherwise difficult in planar structures. [4] SL NWs are, therefore, a powerful platform to manipulate heat transport using coherent phonon effects.

In this study, we aim to showcase the remarkable adaptability of NWs as a platform for effective phonon engineering. Specifically, we focus on the investigation of SL NWs composed of group III-V semiconductors, namely GaAs/GaP and InAs/InP. [2,5] Group III-V semiconductor NWs are ideal material systems to explore nano-photonic and electronic properties. [6] However, their phononic properties remain unexplored. Using inelastic light scattering techniques such as Raman spectroscopy and Brillouin interferometry, we show that the phononic and electronic properties of SL NWs can be tuned by controlling the SL periodicity. Our results are also corroborated with the help of ab initio calculations.

References

[1] Maldovan, M. Nature 503, 209–217 (2013)

[2] K. Sivan, A., Abad, B., et al., ACS Appl. Nano Mater 6, 18602–18613 (2023)

[3] Ravichandran, J., Yadav, A., Cheaito, R. et al. Nature Mater 13, 168–172 (2014)

[4] Jonas, J., K., A., Dick, CrystEngComm, 13, 7175-7184, (2011)

[5] Arif, O., Zannier, V., et al. Nanoscale 15, 1145-1153 (2022)

[6] Gudiksen, M., Lauhon, L., Wang, J. et al. Nature 415, 617–620 (2002)

Optomechanical measurement of liquids in unconventional regimes

Ivan Favero

Université Paris Cité, CNRS, Paris, France
*corresponding author: ivan.favero@u-paris.fr

We discuss our recent achievements using nano-optomechanical devices and concepts to measure liquid dynamics with increased temporal resolution and sensitivity. This has enabled access to previously unexplored temporal and spatial scales in the liquid state, leading to the observation of unconventional regimes. This is an example of the application of optomechanical technologies to probe complex matter.

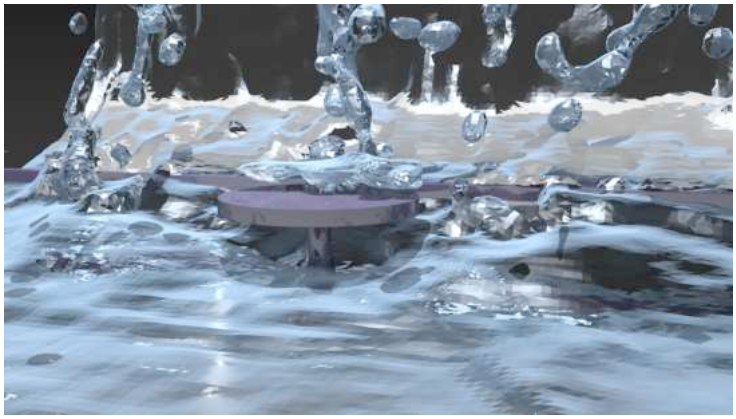


Illustration of an optomechanical disk interacting with a moving liquid

References

1. E. Gil-Santos et al, Nature Nanotechnology 10 (9), 810-816 (2015)
2. S. Sbarra et al, Nature Communications 13 (1), 6462 (2022)
3. H. Neshasteh et al, Physics of Fluids 35 (5) (2023)
4. H. Neshasteh et al, “Optomechanical micro-rheology of complex fluids at ultra-high frequency” (2024)

Explorations with nonlinearity and coupled orbitals in mechanical and magneto-mechanical topological crystalline insulators

G. Liu, I. Grinberg, V. Workman, J. Noh, W.A. Benalcazar, M. Lin, Y. Ma, C.W. Peterson, J. Zhao, A. Mangu, C. Harris, T.L. Hughes, and G. Bahl

University of Illinois at Urbana-Champaign, USA
*corresponding author: bahl@illinois.edu

Abstract: Mechanical and magneto-mechanical structures be engineered to generate a variety of nonlinear couplings and can even emulate orbital physics. In this talk I will discuss our team's experimental work to leverage such couplings for topological pumping, non-linearity induced spontaneous transitions, and new orbital-based topological states.

The coupling of mechanical resonators via magnetic fields is intrinsically nonlinear and can produce a variety of interesting coupling terms [1] that can also be dynamically modulated through non-contact means. Using this idea we have demonstrated [2] that it is possible to robustly transport states across 1-dimensional magneto-mechanical metamaterials using an analogue of the Thouless pump, even in the presence of severe spatial and temporal disorder. Such devices also readily enable the exploration of trapped states at dislocations in lattices [3].

We have also discovered that the amplitude-frequency nonlinearity intrinsic to magneto-mechanical materials can be used to self-tune the material locally based on excitation level. This has enabled our experimental research on self-induced boundary states, tunneling, and digitization effects [4] and could lead to smart responsive structures in the future.

Most recently, we are exploring how the parity representations of mechanical resonances can be considered as atomic orbitals. Using this new idea, we were able to demonstrate the first mono-atomic orbital-based 1D topological crystalline insulator [5].

We acknowledge support from the Office of Naval Research MURI grant N00014-20-1-2325, Emory University, and the US Department of Energy Office of Basic Energy Sciences. Division of Materials Sciences and Engineering.

References

1. I.H. Grinberg, A. Mangu, C. W. Peterson, E. Wilken-Resman, J. T. Bernhard, G. Bahl, "Magnetostatic spring softening and stiffening in magneto-mechanical resonator systems," IEEE Transactions on Magnetics 55(8), 4003505, 2019.
2. I. H. Grinberg, M. Lin, C. Harris, W. A. Benalcazar, C. W. Peterson, T. L. Hughes, G. Bahl, "Robust temporal pumping in a magneto-mechanical topological insulator," Nature Communications 11:974, 2020.
3. I.H. Grinberg, M. Lin, W.A. Benalcazar, T.L. Hughes, G. Bahl, "Trapped state at a dislocation in a weak magneto-mechanical topological insulator," Phys. Rev. Applied 14, 064042, 2020.
4. G. Liu, J. Noh, J. Zhao, G. Bahl, "Self-Induced Dirac Boundary State and Digitization in a Nonlinear Resonator Chain," Physical Review Letters, 129, 135501, 2022.
5. G. Liu, V. Workman, J. Noh, Y. Ma, T.L. Hughes, W.A. Benalcazar, G. Bahl, "A mono-atomic orbital-based 1D topological crystalline insulator," arXiv:2310.10403, 2023.

X-ray Transient Gratings: Access to Nanoscale Acoustics, Magnonics, and More

Keith A. Nelson

Dept. of Chemistry, MIT, Cambridge, MA 02139, USA
*corresponding author: kanelson@mit.edu

Abstract: Transient grating (TG) measurements exploit interference between crossed excitation pulses to define a spatial period, and corresponding wavevector, for thermoelastic and other time-dependent dynamics that are measured. The TG method has been extended to extreme UV and hard x-ray spectral ranges, accessing nanometer periods for acoustic waves, thermal transport, magnons, and other high-wavevector responses. Recent results will be reviewed. Nondestructive excitation of nonlinear acoustic/shock waves will also be discussed.

Dielectric metasurfaces for nonlinear asymmetric imaging

D. Rocco[1,2], A. Locatelli[1,2*], L. Carletti[1,2], M. A. Vincenti[1,2], and C. De Angelis[1,2]

[1]Department of Information Engineering, University of Brescia, Italy
[2]National Institute of Optics - National Research Council (INO-CNR), Brescia, Italy
[*]corresponding author: andrea.locatelli@unibs.it

Abstract: We report nonlinear asymmetric generation of light from a dielectric metasurface via second-harmonic generation. In this platform, conversion efficiency is dramatically different when the metasurface is pumped from air and substrate. We exploit these findings to demonstrate that we can generate different images at second-harmonic depending on the illumination direction.

Dielectric metasurfaces are a promising platform employed in various research domains including sensing, lasing, all-optical modulation, and nonlinear optics, to name a few. Indeed, it is well known that nonlinear interactions between light and matter in metasurfaces offer a viable avenue for achieving miniaturized control over light. In this framework, asymmetric nonlinear metasurfaces have recently garnered increased attention, with particular emphasis on their application as optical isolators [1-3].

In this study, we demonstrate nonlinear asymmetric generation of light in a dielectric metasurface through second harmonic generation. The unit cell of the proposed metasurface is reported in Fig. 1(a). By reversing the illumination direction of the pump, we observe a variation of the power of the nonlinear emitted signal of more than one order of magnitude, see Figs. 1(b) and (c). In particular, we can identify three different operating points named A, B and C. Point A corresponds to a metasurface associated with a strongly emitted SH for the case of backward incidence (pump launched from the substrate). Contrarily, point B is related to a metasurface generating strong SH signal when the incidence light is propagating in the forward direction (pump impinging from the air side). Instead, by working at point C the SH power is poorly emitted for both pump directions.

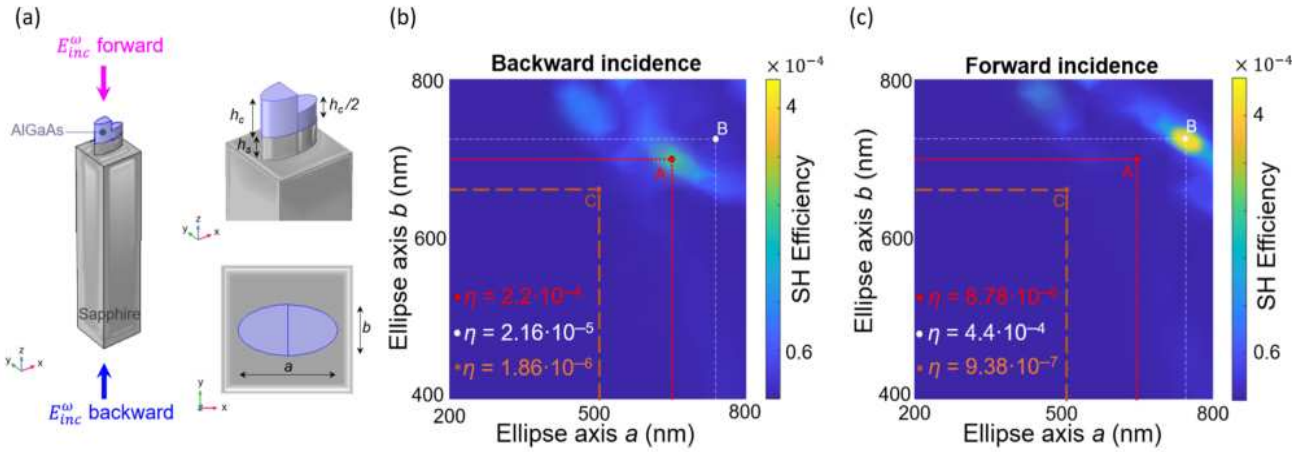


Figure 1. (a) Sketch of the proposed metasurface made of AlGaAs nano-chairs placed over a sapphire substrate with a sapphire pedestal in between them. Both nano-chair and pedestal are assumed to have an elliptical base with major and minor axes named *a* and *b*, respectively. The period is equal to 880 nm, the height of the pedestal is h_s = 250 nm and the

AlGaAs thickness is h_c = 400 nm. (b) Emitted SH efficiency as a function of the ellipse axes a and b for pump with backward or forward incidence, respectively.

Furthermore, we show how a properly designed metasurface composed of adjacent regions with geometrical parameters corresponding to points A, B and/or C can produce two distinct images at the second harmonic when the illumination direction is reversed, as displayed in Fig. 2. Notably, the conversion efficiency of the generated SH signal reaches 4.4×10^{-4} for a pump intensity of 1 GW/cm^2. We emphasize that our design does not need any external control bias and can be easily extended to different $\chi^{(2)}$ nonlinear phenomena.

As a matter of fact, dielectric metasurfaces characterized by a large asymmetric response based on nonlinear phenomena can find application in a plethora of research areas such as optical encryption, nonlinear multi-color imaging systems and QR code generation.

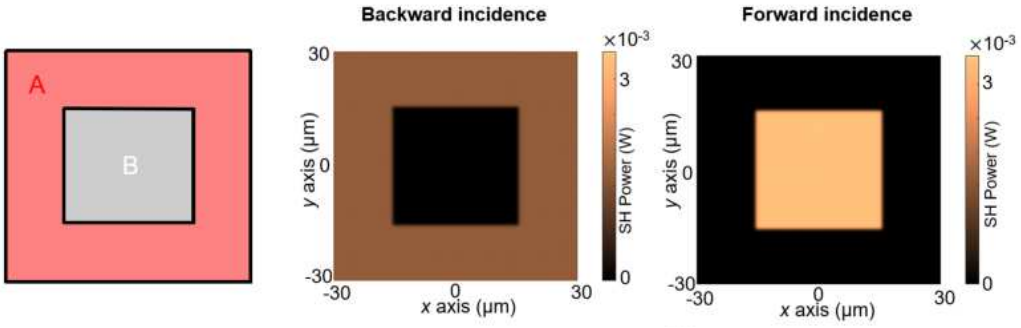


Figure 2. An example of generation of complementary SH images as a function of the pump direction when using regions with A and B geometry as building blocks.

The authors acknowledge financial support from NATO in the framework of SPS Grant no. G5984 – RESPONDER, and from the Italian Ministry for University and Research as part of the PRIN PNRR 2022 project FLAIRS (P2022RFF9K) - NextGenerationEU, PRIN 2022 project DOSE (2022MANFK5), PRIN 2022 project GRACE6G (2022H7RR4F), PRIN 2022 project NO LIMITHz (2022BC5BW5), PRIN 2022 project PILLARS (2022YJ5AZH), PRIN 2020 project METEOR (2020EY2LJT).

References

1. Cotrufo, M., A. Cordaro, D.L. Sounas, A. Polman, and A. Alù, “Passive bias-free non-reciprocal metasurfaces based on thermally nonlinear quasi-bound states in the continuum,” Nature Photon., Vol. 18, 1-10, 2023.
2. Kruk, S.S., L. Wang, B. Sain, Z. Dong, J. Yang, T. Zentgraf, and Y. Kivshar, “Asymmetric parametric generation of images with nonlinear dielectric metasurfaces,” Nature Photon., Vol. 16, 561-565, 2022.
3. Cotrufo, M., S.A. Mann, H. Moussa, A. Alù, “Nonlinearity-Induced nonreciprocity – Part I,” IEEE Trans. Microwave Theory Tech., Vol. 69, No. 8, 3569-3583, 2021.

Effect of Thermal Annealing on Surface Plasmon Properties of Gold and Silver Nanodisk Structures for Live Cell Imaging

K. Yamasaki[1], R. Hatsuoka[1], T. Matsuyama[1], K. Wada[1] and K. Okamoto[1*]

[1]Osaka Metropolitan University, Japan
[*]OkamoT@omu.ac.jp

Abstract: We investigate the effect of thermal annealing on Localized Surface Plasmon Resonance (LSPR) properties of gold and silver nanodisk structures. We found that gold structures showed blue-shifts and narrowing of peaks, while silver structures exhibited peak blue-shifts and reduction in intensity. These changes were analyzed using an electromagnetic field analysis.

Introduction

Blue light may potentially damage human bodies. However, assessing the impact of blue light on cells via fluorescence imaging is challenging due to the risk of damage by incident light. We aim to selectively enhance photoluminescence utilizing LSPR, thereby reducing cell damage from excitation light. In our previous study, we annealed nanodisk structures fabricated by Electron Beam Lithography to improve the plasmon properties [1]. In silver nanodisk structures, the LSPR peak shifted toward the short wavelength side while retaining its sharpness. Conversely, gold nanodisk structures exhibited peak narrowing accompanied by a blue-shift. In this research, we employed electromagnetic field analysis to accurately fit the LSPR peak shifts and to explore the differences in the annealing effects between silver and gold nanodisk structures.

Methods

Finite-Difference Time-Domain (FDTD) calculations were conducted using Fujitsu Poynting for Optics. We employed the dielectric function of the Drude model derived through fitting to that of the Lorentz Drude model [2] in a specific spectral region. The validity of the model was confirmed by simulating the LSPR peaks. Finally, we optimized the Oscillation Strength (OS) and the Damping Frequency (DF) to fit the LSPR peak shifts.

Results and discussions

Figure 1 (a) shows the dielectric function of silver approximated by the Lorentz Drude (LD) model and the Drude model. The relative instantaneous permittivity and the damping frequency in the Drude model were optimized in the visible spectrum region to fit the LD model. Figure 1 (b) and (c) respectively show the extinction spectra of silver nanodisk structures using the LD model and the Adjusted Drude model. The height of the disks was set to 30 nm with a radius of 50 to 90 nm. LSPR peaks calculated by using both the LD model and the adjusted Drude model exhibited remarkable similarity.

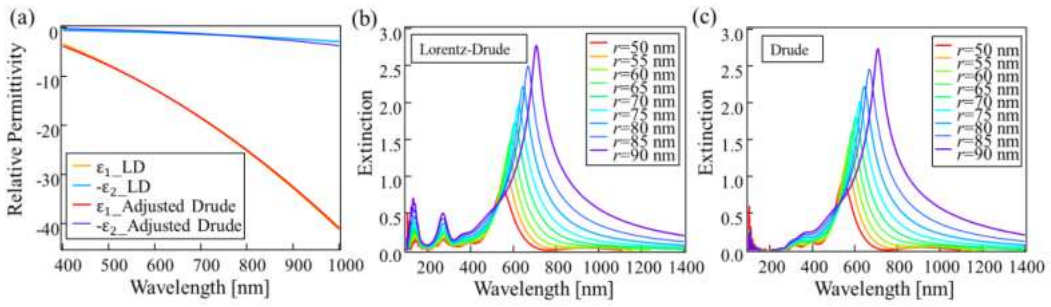


Figure 1. Dielectric function of silver and simulated spectra of silver nanodisk structures

Figure 2 shows the LSPR peak of silver nanodisk structures with a Ni height of 2nm and Ag height of 40 nm (a) in the experiment, (b) in the simulation by varying only the radius and (c) in the simulation by changing both the radius and the dielectric function. As shown in Figure 2 (a), the LSPR peak shifted while maintaining its intensity to some extent due to thermal annealing. While the radius decreased from 55 nm to 50 nm as the annealing temperature increased, this phenomenon was not reproducible in simulations that considered only the size or shape changes. Figure 2 (c) reveals an increase in OS due to thermal annealing. We posit that electrons trapped in the defects were enabled to oscillate due to thermal annealing.

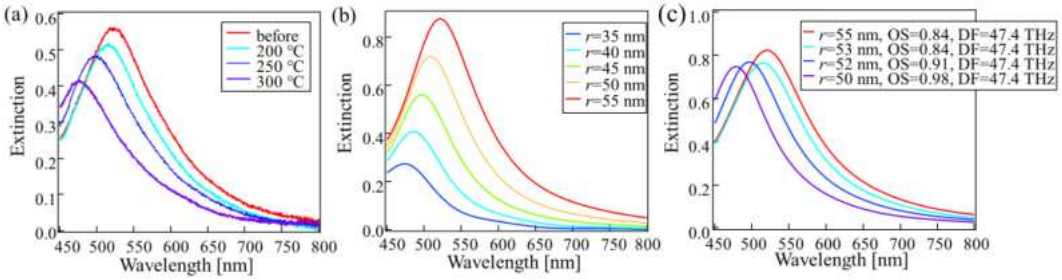


Figure 2. Extinction spectra of silver nanodisk structures

Figure 3 (a) and (b) respectively show the schematic diagram and extinction spectrum of silver nanodisk structures with ellipsoidal hemisphere. Extinction spectrum of silver nanodisk structures with height of 40 nm and radius of 50 nm is also included. The LSPR peak intensity decreases while the peak position and sharpness remained almost unchanged. The morphological changes account for the decrease in peak intensity in the experiment.

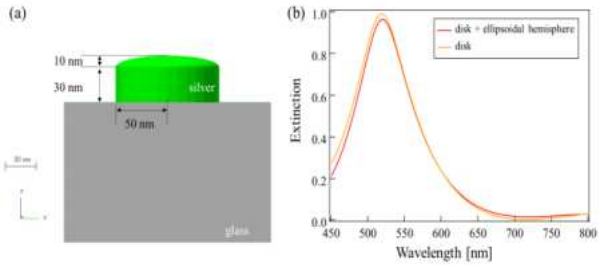


Figure 3. Silver nanodisk structures with ellipsoidal hemisphere

Figure 4 shows the LSPR peak of gold nanodisk structures with Ni height of 2 nm and Au height of 20 nm (a) in the experiment and (b) in the simulation by modifying the dielectric function. The radius of gold nanodisk structures was 83 nm and almost unchanged by thermal annealing. Figure 4 (b) demonstrates that OS increased as the annealing temperature increased. We attribute the decreased DF to an increase in mean free path due to the reduction of grain boundaries by thermal annealing.

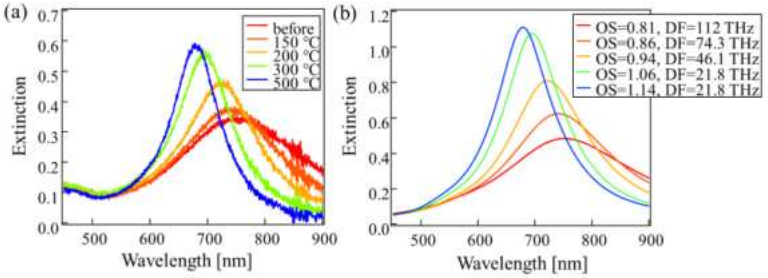


Figure 4. Extinction spectra of gold nanodisk structures

References

1. Osaka, N., M. Ozawa, T. Matsuyama, K. Wada, and K. Okamoto, "Flexible tuning of the peak wavelength and intensity of localized surface plasmon resonance by heat treatment of nanodisk structures fabricated by electron beam lithography," Optical Materials Express, Vol. 13, No. 5, 1504–1512, 2023
2. Rakić, A. D., A. B. Djurišsić, J. M. Elazar, M. L. Majewski, "Optical properties of metallic films for vertical-cavity optoelectronic devices," Applied Optics, Vol. 37, No. 22, 5271–5283, 1998

Electromagnetic response of liquid crystal based tunable high refractive index dielectric rings metasurfaces

Pratiksha Sakhare[1*] and Jayasri Dontabhaktuni[1]

[1] Department of Physics, Mahindra University, Hyderabad, India

*corresponding author : Pratiksha20pphy005@mahindrauniversity.edu.in

Abstract: In current work, we present detailed numerical investigation of high refractive index circular and square rings. We calculate scattering response, near-field, far-field radiation profiles of rings in infrared regime. We observe tunability, formation of certain modes as a function of thickness, liquid-crystal orientations with applications towards optically active metadevices, sensors.

Summary:

The control of light-matter interaction in metasurfaces offers an unprecedented potential for manipulation and tuning of light. Mie scattering occurs in dielectric structures made of high refractive index material. When metals are formed into specific geometries, such split-ring resonators (SRRs), they can generate magnetic resonant modes. However, displacement currents in the dielectric medium generate magnetic fields naturally for basic geometries like cubes and spherical particles, which excite the magnetic resonant modes [1-4]. All-dielectric metasurfaces have been gathering lot of interest in the recent years due to their intense localization of fields, excitation of magnetic modes as well as giving rise to novel resonant modes such as anapoles, quasi-BIC states, etc. [5-8]. Liquid crystals have attracted great attention due to the optical anisotropy and flexible control through optical, thermal, magnetic and electrical fields [9].

In this work, we investigate the effect of both the anisotropic properties of the medium and geometry of the dielectric structures on the electromagnetic response. A layer of periodic circular and square dielectric rings made of high refractive index materials such as Tellurium (Te, n~5.79) is taken in air as well as liquid crystal medium. The electromagnetic response of dielectric structures and electric and magnetic field profiles are studied in detail in near and far-field regions using numerical simulations based on CST. Further, we also investigate the effect of anisotropic medium on the electromagnetic response and exploit the tunability exhibited by the liquid crystals medium in which a surface of periodic high refractive index dielectric material is embedded. Electromagnetic waves of frequency in the range 10-70 THz are incident on the layer of Te rings of thickness 0.5um. The electromagnetic response of such dielectric structures and hence the electric and magnetic field profiles are studied in detail using FEM based numerical simulations. The circular and square dielectric structures are placed in the XY plane filled with air. Periodic boundary conditions are applied along X- and Y-directions. Plane electromagnetic wave is incident at one of the ports on the Z-axis with polarization along Y direction and magnetic field (H-field) is along X-direction. The periodicity of the unit cell is 2.5 um and the thickness of the cell along the Z-direction is 5um. The thickness of the rings is varied from 0.2um till 2.5um to

look at the effect of thickness on the field modes generated inside the materials. This rings when placed in birefringent liquid crystal medium orientation of liquid crystal molecules are observed to enhance certain modes over the other giving rise to tunable metasurfaces.

Conclusions:

In the present work, it is observed that effect of geometry and the refractive index of the dielectric rings play a significant role on the resonance characteristics. Typically square rings show sharper resonances (high Q-factors) and high field localization compared to the circular rings. Thinner rings support the electric modes predominantly while rings of thickness more than the radius exhibit only magnetic modes. Further, we also investigated the effect of anisotropic medium on the electromagnetic response and exploit the tunability exhibited by the liquid crystals medium. Te rings in liquid crystal medium give rise to novel toroidal-like magnetic modes and hybrid modes at certain frequencies. By carefully designing the dielectric rings in the liquid crystals one can find applications in optically active materials for opto-electronic devices and sensors.

Acknowledgements:

This work was funded by Government of India. PS and JD acknowledge financial support by DST-SERB EMR (CR) Grant EMR/2017/004045.We also grateful to Mahindra University, Hyderabad, for supporting and providing necessary resources to conduct our research.

References:

1. Butakov, N. A. and J. A. Schuller, “Designing Multipolar Resonances in Dielectric Metamaterials,” Sci. Rep., 6, 1, 38487, 2016.
2. Kapitanova, P. et. al.,“Giant field enhancement in high index dielectric subwavelength particles,” Sci. Rep., 7, 1, 731, 2017.
3. Zhao, Q., J. Zhou, F. Zhang and D. Lippens, “Mie resonance based dielectric metamaterials,” Materials today, 12, 12, 60-69, 2009.
4. Amanaganti, S., D. R. Chowdhury, M. Ravnik and J. Dontabhaktuni, “Electromagnetic response of dielectric nanostructures in liquid crystals,” Proc. SPIE Emerging Liquid Crystal Technologies XIII 105551F, 2018.
5. Sakhare, P. A. and J. Dontabhaktuni, “Tailoring the resonant modes in liquid crystal based all-dielectric metasurfaces,” Sci. Rep., 13, 1, 6780, 2023.
6. Koshelev, K., A. Bogdanov and Y Kivshar, “Meta-optics and bound states in the continuum,” Science Bulletin, 64, 12, 836-842, 2019.
7. Wang, Y. et al. “Efficient Excitation and Tuning of Multi-Fano Resonances with High Q-Factor in All-Dielectric Metasurfaces,” Nanomaterials, 12, 13, 2292, 2022.
8. Yang, Y. et al. “All-dielectric metasurface analogue of electromagnetically induced transparency,” Nature communications, 5, 1, 5753, 2014.
9. Santonocito A., B. Patrizi, and G. Toci, “Recent Advances in Tunable Metasurfaces and Their Application in Optics,” Nanomaterials, 13, 10, 1633, 2023.

Self-Aligned Nanoring Doublet as a Single Particle Nanocavity for Strong Coupling

Kyungwha Chung[1,2], Luke P. Lee[1,2,*]

[1]Institute of Quantum Biophysics, Sungkyunkwan University, Republic of Korea
[2] Harvard Medical School, Harvard University; Department of Medicine, Brigham and Women's Hospital, Boston, Massachusetts 02115, United States
[*]corresponding author: lplee@bwh.harvard.edu

Abstract: Au self-aligned nanoring doublets (SANDs) are introduced as a single-nanoparticle cavity at room temperature for strong coupling with randomly distributed chlorophyll-a molecules, without highly concentrated J-aggregates, mirrors, or any sophisticated effort to create dimers.

Achieving strong coupling in practical applications of cavity quantum electrodynamics often poses significant challenges due to the delicate conditions required. In particular, the realization of strong coupling with single nanoparticles has been predominantly demonstrated using J-aggregate dye molecules. In this work, we present a plasmonic cavity probe capable of transforming a nanocavity within a single nanoparticle. Our approach utilizes a plasmonic structure based on a gold self-aligned nanoring doublet (Au SAND) that incorporates an intraparticle nanogap (Fig. 1). Through dark-field scattering measurements on individual particles, we observe the emergence of exciton-plasmon polaritons, known as plexcitons, evidenced by the bifurcation of the scattering peak into two distinct resonances. Finite-element modeling is employed to elucidate the correlation between the Au SAND morphology and the cavity resonance wavelength relative to the exciton absorption, while temporal coupled-mode theory quantifies the strength of coupling. Verification of plexciton states is accomplished through photoluminescence measurements, which demonstrate light emission from the lower plexciton state. The proposed CQED nanocavity serves as a promising nanoprobe for the detection of small molecules within cells and offers a platform for groundbreaking biomolecular studies.

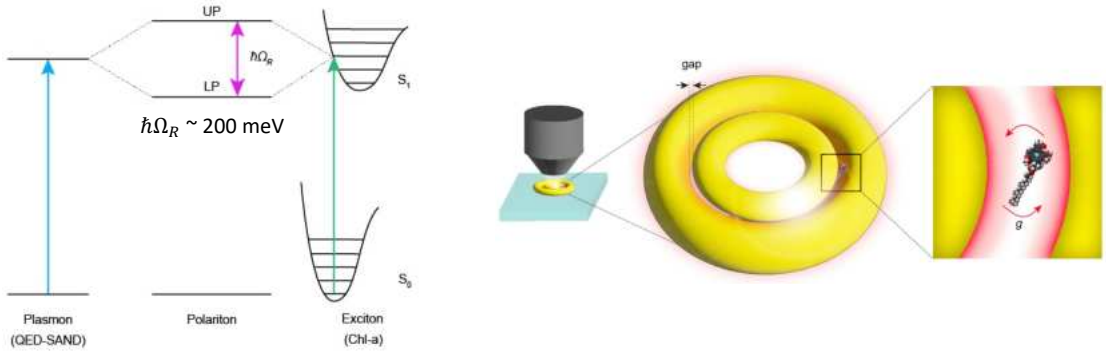


Figure 1. Schematic illustration of coupling between SAND and Chlorophyll-a (left) and experimental configuration.

This research was supported by the National Research Foundation of Korea (NRF) grant funded by the Korea government (MSIT) (NRF-2021R1C1C20034).

All-optical phase rotation in strongly coupled light-matter systems.

F. A. Benimetskiy[1]*, P. M. Walker[1], S. Ravets[2], Maurice S. Skolnick[1], J. Bloch[2], and D. N. Krizhanovskii[1]

[1]Department of Physics and Astronomy, University of Sheffield, UK
[2]Université Paris-Saclay, CNRS, Centre de Nanosciences et de Nanotechnologies (C2N), France
*corresponding author: f.benimetskiy@sheffield.ac.uk

Abstract: We demonstrate cross-phase modulation of up to 17.5 mrad per polariton using laser beams attenuated to the average intensity of single photons, the highest amount achieved without using atom-like emitters. This advance opens new possibilities for quantum information processing and nonlinear quantum optics using strongly coupled light-matter systems.

The rapid development of quantum technologies is driving the implementation of novel photonic systems and spurring active research into new physical aspects within well-known photonic platforms. A key aspect of quantum photonics is the interaction of photons through optical nonlinearities, such as cross-phase modulation. In this study, we demonstrate that exciton-polaritons in an open cavity with embedded quantum wells can provide the necessary nonlinearity for the experimental observation of cross-phase modulation.

Our device is a tunable microcavity containing a single InGaAs quantum well (QW) (see Fig.1 (a)). The strong coupling between cavity modes and exciton resonances in the QW gives rise to exciton-polaritons. This strong nonlinear optical response in polariton systems enables the observation of various optical nonlinear phenomena [1-3], including single-photon-level nonlinear phase shifts [4].

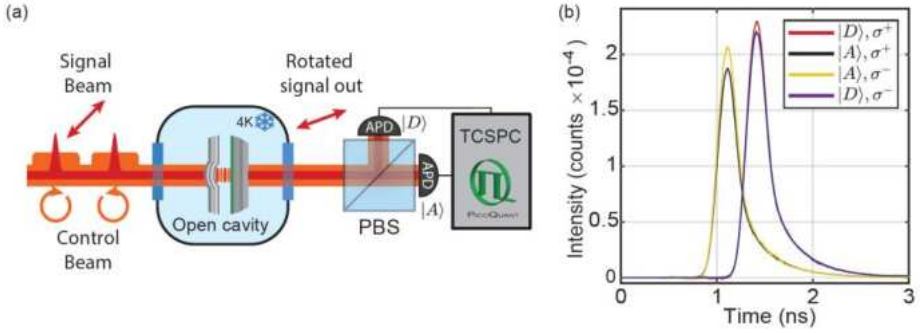


Fig.1 (a) Simplified schematic of the experimental setup. (b) Example of experimentally measured TCSPC curves for the signal beam after subtracting the background signal from the control beam.

To demonstrate the cross-phase shift, we resonantly excited the exciton-polariton state using a pulsed beam linearly polarized (signal beam) and a circularly polarized pulse beam with a longer duration (control beam). The linear polarization of the signal can be decomposed into two circularly polarized components. Polariton interactions strongly depend on the relative circular polarization [5]. As a result, the co-polarized signal component acquires a relative phase shift, leading to a rotation in the signal beam's linear polarization angle. Measuring this polarization change reveals the amount of the phase shift.

Examples of raw TCSPC curves recorded during a phase shift measurement are shown in Fig.1 (b). $|D\rangle$ and $|A\rangle$ denote the signals from avalanche photodiodes (APDs) measuring those polarization components while σ^+ and σ^- specify the control beam state. The phase shift ϕ is deduced from the difference in polarization degree with the

σ^+ and σ^- control beam, for relatively small nonlinear resonance shifts compared with the linewidth:

$$\phi \approx \frac{1}{2} \cdot \left(\frac{I_{|D\rangle}^{\sigma+} - I_{|A\rangle}^{\sigma+}}{I_{|D\rangle}^{\sigma+} + I_{|A\rangle}^{\sigma+}} \right) - \left(\frac{I_{|D\rangle}^{\sigma-} - I_{|A\rangle}^{\sigma-}}{I_{|D\rangle}^{\sigma-} + I_{|A\rangle}^{\sigma-}} \right)$$

Fig. 2 presents the relationship between the phase change and the number of polaritons $N_{Polaritons}$. These dependencies were measured for exciton-polariton states with an exciton fraction of approximately 35%. For the Sample A is 17.5 mrad per polariton, and for Sample B the phase shift is equal to 13 mrad per polariton. The main difference between the samples is the value of the observed Rabi splitting, which characterises the strong coupling between the excitons in a quantum well (QW) and the longitudinal mode LG_{00} in an open cavity. For Sample A, the Rabi splitting is equal to 2.66 meV, and for Sample B, it is 2.3 meV. One of the possible reasons for the observed difference is the lower oscillator strength of excitons in Sample B (as characterised in additional experiments). This not only affects the value of Rabi splitting but also can reduce the exciton nonlinearity, thereby reducing the observed optical phase shift.

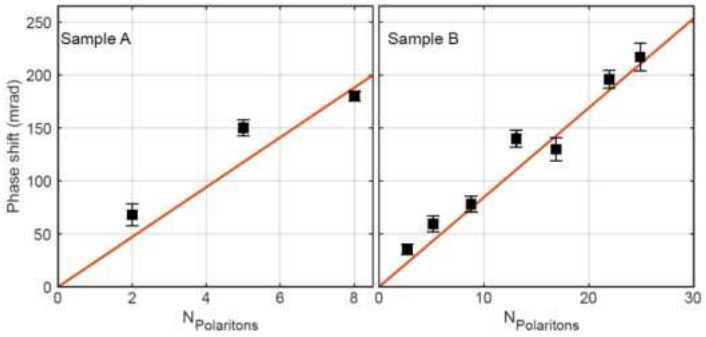


Fig.2 Phase shift measured on samples A and B as a function of the excited polariton number. The solid lines represent the best fits of straight lines passing through the origin to the data points.

For the first time, we have experimentally demonstrated an all-optical phase shift in a polariton system based on an open cavity, achieving a phase shift value of up to 17.5 mrad per polariton. In our experiment, we used laser beams that were synchronized in time and had the same wavelength. These beams were attenuated to an average intensity comparable to that of several photons. The optical phase shift demonstrated is five times larger than that observed in previous experiments with exciton-polaritons in semiconductor micropillars [4]. This marks the highest value achieved without the use of atom-like emitters, paving the way for new approaches in a wide class of nonlinear quantum optical phenomena and offering promising avenues for quantum information processing with polaritonic systems.

References

1. Delteil, A., Fink, T., et.al. “Towards polariton blockade of confined exciton–polaritons,” Nat. Mater., Vol. 18, No. 3, 219–222, 2019.

2. Muñoz-Matutano, G., Wood, A., et.al. “Emergence of quantum correlations from interacting fibre-cavity polaritons,” Nat. Mater., Vol. 18, No. 3, 213–218, 2019.

3. Amo, A., and Bloch, J. “Exciton-polaritons in lattices: A non-linear photonic simulator,” C. R. Phys., Vol. 17, No. 8, 934–945, 2016.

4. Kuriakose, T., Walker, P. M., et.al. “Few-photon all-optical phase rotation in a quantum-well micropillar cavity,” Nat. Photonics, Vol. 16, No. 8, 566–569, 2022.

5. Vladimirova, M., Cronenberger, S., et.al. “Polariton-polariton interaction constants in microcavities,” Phys. Rev. B, Vol. 82, No. 7, 075301, 2010

Long-range super-Planckian heat transfer between nano-emitters in a resonant cavity

K. Asheichyk[1], P. Ben-Abdallah[2], M. Krüger[3], and R. Messina[2*]

[1]Department of Theoretical Physics and Astrophysics, Belarusian State University, 5 Babruiskaya Street, 220006 Minsk, Belarus
[2]Laboratoire Charles Fabry, UMR 8501, Institut d'Optique, CNRS, Université Paris-Saclay, 2 Avenue Augustin Fresnel, 91127 Palaiseau Cedex, France
[3]Institute for Theoretical Physics, Georg-August-Universität Göttingen, 37073 Göttingen, Germany
[*]corresponding author: riccardo.messina@institutoptique.fr

Abstract: We study radiative heat transfer between two nano-emitters placed inside different types of closed cavities by means of a fluctuational-electrodynamics approach. We highlight a very sharp dependence of this transfer on cavity width and connect this to the matching between the material-induced resonance and the resonant modes of the cavity.

Two bodies kept at different temperatures and separated by vacuum exchange heat radiatively via the transfer of thermal photons. While this energy flux is limited at far separation distances by Stefan-Boltzmann's law, the pioneering works of Rytov [1] and Polder and Van Hove [2] showed that this limit can be overcome in the so-called near field, i.e., when the separation distance is small compared to the thermal wavelength (around 10 microns at ambient temperature). This amplification can be remarkable for materials supporting resonant modes of the electromagnetic field [3] (in particular polar materials supporting phonon-polaritonic resonances in the infrared region of the spectrum).

The possibility to transport this energy from a thermal source at distances larger than its thermal wavelength remains today a challenging problem which could find broad applications in a variety of the fields (e.g., thermal management and information transfer). With this respect, a remarkable attention has been paid during the past decade to the study of heat transport between two closely separated emitters or within a larger set of emitters, the main goal being to manipulate and tailor the radiative heat exchanges at the nanoscale. Some of these works have focused on the transfer between emitters in the proximity of a substrate or a cylindrical waveguide, showing how the two nano-emitters can couple through the surface resonance existing at the interface between this external body and vacuum and how this additional channel contributes to the transfer by amplifying or inhibiting it. More specifically, some works have considered the impact of confinement on the heat transfer between two nanoparticles, by placing them inside a planar cavity, revealing interesting effects [4–8]. However, they do not address at all the role played by the cavity width in the exchanged flux and especially how the presence of the cavity can make the heat transport strongly super-Planckian (far above the blackbody limit) at large separation distance between the emitters.

In this work we study the near-field radiative heat transfer between two nano-emitters placed inside a cavity (both planar and cylindrical) and highlight the crucial role played by the cavity width. More specifically, we unveil the major interplay between cavity resonant modes, whose frequencies are purely governed by the cavity width and material, and resonances existing at the interface between each nano-emitter and vacuum, giving the leading contribution to near-field radiative heat transfer in vacuum. We show that this interplay and the matching

of these resonances is at the origin of a very sharp dependence of heat transfer on cavity width, allowing for order-of-magnitude variations, as well as transitions from amplification to inhibition with respect to transfer in vacuum, with variations of the cavity width in the micron range. We also show that the characteristic distance at which the effect takes place depends on the geometry, providing a simple tool to choose the most convenient geometry depending on the desired distance. Our results pave the way to easier strategies to export and tune near-field super-Planckian radiative heat flux to distances larger than the thermal wavelength.

P.B.-A. and R.M. acknowledge financial support from Labex Nanosaclay, Grant No. ANR-10-LABX-0035 (Flagship project MaCaCQu). K.A. is supported by the Deutsche Forschungsgemeinschaft (DFG, German Research Foundation) through the Walter Benjamin fellowship (Project No. 453458207).

References

1. Rytov, S. M., "Theory of Electrical Fluctuations and Thermal Radiation" (Academy of Sciences Press of USSR, Moscow, 1953).
2. Polder, D. and van Hove, M., "Theory of Radiative Heat Transfer between Closely Spaced Bodies", Phys. Rev. B **4**, 10 (1971).
3. Joulain, K., Mulet, J.-P., Marquier, F., Carminati, R. and Greffet, J.-J., "Surface electromagnetic waves thermally excited: Radiative heat transfer, coherence properties and Casimir forces revisited in the near field", Surf. Sci. Rep. **57**, 59 (2005).
4. Sääskilahti, K., Oksanen, J. and Tulkki, J., "Quantum Langevin equation approach to electromagnetic energy transfer between dielectric bodies in an inhomogeneous environment", Phys. Rev. B **89**, 134301 (2014).
5. Asheichyk, K. and Krüger, M., "Heat radiation and transfer in confinement", Phys. Rev. B **98**, 195401 (2018).
6. Zhang, Y., Dong, J., Tang, G. and Yi, H.-L., "Many-particle radiative heat transfer in a nonreciprocal graphene plasmonic cavity", Phys. Rev. B **103**, 195433 (2021).
7. Chen, J., Wang, B. X. and Zhao, C. Y., "Near-field radiative heat transport between nanoparticles inside a cavity configuration", Int. J. Heat Mass Transf. **196**, 123213 (2022).
8. Zhang, Y.-J., Zhang, Y., Yang, S.-H. and Yi, H.-L., "Strain-induced control of radiative heat transfer between nanoparticles in a plasmonic cavity", Int. J. Heat Mass Transf. **202**, 123677 (2023).

Weyl points and chiral states in correspondence of Bound States in Continuum connected by Fermi arc

V. Mocella[1], F. Sgriguoli, B.Guilcapi Alulema, S.Romano, G. Zito, B. Miranda, A. Seifalinezhad, I.Rendina

[1] Institute of Applied Sciences and Intelligent Systems, National Research Council (CNR-ISASI), Via P. Castellino 111, Napoli, 80131, Italy
[2] Department of Engineering, Università degli Studi di Napoli Parthenope, Centro Direzionale di Napoli, Isola C4, 80143 Naples, Italy
*corresponding author: vito.mocella@cnr.it

Abstract: We establish a correlation between Bound States in the Continuum (BIC), Fermi arcs, Weyl points, and singularities in far-field in a theoretical model. Experiments prove that without chirality, in materials or in nanostructures, around the BIC condition the far-field exhibits chiral behavior, confirming the existence of a Weyl point.

In recent years has it been demonstrated that Bound states in continuum, are intrinsically topological phenomena, revealing that BICs are singularities located at the vortex center (V-point) in the direction of polarisation of the far-field radiation [1]. Although more complex topological charges can be found in PhC slab, V-points located in Γ are generally associated with an integer topological charge while C-points, obtained with symmetry breaking, exhibit a split of the integer topological charge into semi-integer charges [2]. In literature, C-points are distinguished from BICs as they are linked to resonances with a finite quality factor [3], [4], [5]. However, through theoretical modelling and experiments, we will demonstrate C-points can also be related to the BIC condition.
We show the experimental existence of states with opposite chirality (Fig.1). These correspond to Fermi arcs connecting C-points with opposite winding, as confirmed by numerical simulations, which also validate the theoretical model.

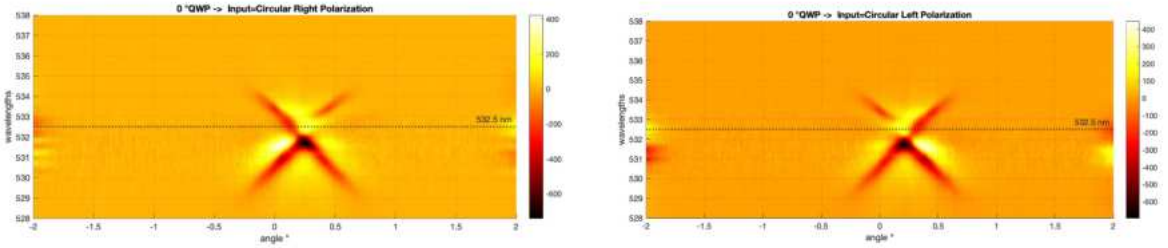


Figure 1: Opposite input circular polarisation experimental transmitted field

References

1. Zhen, B. et al. "Topological Nature of Optical Bound States in the Continuum" *Phys. Rev. Lett.* **113**, 465–5, 2014.
2. Zhang, Y. et al. "Observation of Polarization Vortices in Momentum Space" Phys. Rev. Lett. 120, 186103, 2018.

3. Yin, X., et al. “Observation of topologically enabled unidirectional guided resonances” Nature 580, 467–471, 2020.
4. Yoda, T. & Notomi, M. “Generation and Annihilation of Topologically Protected Bound States in the Continuum and Circularly Polarized States by Symmetry Breaking” Phys. Rev. Lett. 125, 053902, 2020.
5. Zhang, X. et al. “Chiral emission from resonant metasurfaces” Science **377**, 1215–1218, 2022.

Embedding plasmonic gratings for enhanced polarized photodetection and imaging in the near-infrared

T. Yu,[1,2] C. Zhang,[1,2,*] Y. Luo,[1,2] and X. Li[1,2,*]

[1]Country*School of Optoelectronic Science and Engineering & Collaborative Innovation Center of Suzhou Nano Science and Technology, Soochow University, Suzhou 215006, China*

[2]*Key Lab of Advanced Optical Manufacturing Technologies of Jiangsu Province & Key Lab of Modern Optical Technologies of Education Ministry of China, Soochow University, Suzhou 215006, China*

[*]corresponding author: zhangc@suda.edu.cn; xfli@suda.edu.cn (Prof. Li*)*

Abstract: We proposed and experimentally demonstrated embedded plasmonic gratings, boosting hot electron generation and extraction efficiency. We achieved a 1.7 mA/W responsivity at λ=1455 nm, three times higher than non-embedded setups. We integrated the photodetector into a near-IR light imaging system, showcasing impressive polarized imaging capabilities.

In contrast to conventional semiconductor photodetectors constrained by energy bandgaps, hot-electron photodetectors (HE-PDs) leverage metal-semiconductor Schottky barriers to convert hot electrons into photocurrents. These devices offer several advantages, including adjustable Schottky barriers, ease of fabrication, sub-bandgap photodetection, room-temperature operation, and flexibility in wavelength and polarization tuning. However, their practical application has been limited by a low quantum efficiency due to inefficient hot-electron generation and extraction. Thus, surface plasmons (SPs), which are a kind of coherent oscillations of free electrons in metals, attracted the attention of researchers, since it provides an efficient way of harvesting light with confined and enhanced electric filed in nanoscale volumes [1−3]. Nevertheless, a critical and pivotal step continues to impede the efficacy of hot electron photoelectric detection: the collection of hot electrons. Even when hot electrons are efficiently generated within the metallic layer and reach the Schottky interface, only those meeting specific injection criteria [4−6] can successfully traverse the Schottky barrier, entering the semiconductor and contributing to the formation of photocurrent.

To overcome this limitation, we have introduced an innovative approach: embedding a metallic grating structure within our HE-PD. Unlike traditional designs with the metal grating solely on the substrate's surface, our device fully integrates the metallic grating within the silicon substrate. This design creates 3D Schottky barriers along both the planar and vertical sides of the plasmonic element, significantly expanding the momentum space and improving hot-electron injection efficiency. We present a remarkable achievement in the form of a narrow-band, geometrically tunable, and polarization-sensitive fully embedded Au/Si grating photodetector (FEG-HE-PD) designed for near-infrared applications, boasting high responsivity. By exciting surface plasmons (SPs), we induce a localized electric field in the Au film, resulting in an impressive optical absorption efficiency of approximately 85% and efficient hot-electron generation. Moreover, the embedded Au grating extends the momentum space, further enhancing hot-electron injection efficiency. The FEG-HE-PD exhibits exceptional performance, with a high responsivity of 2.5 mA/W in simulation and 1.7 mA/W in experiments, outperforming planar HE-PDs relying on Tamm plasmons and microcavities. Additionally, our device excels in responsivity and high-resolution imaging compared to typical grating-based HE-PDs that lack full embedding.

To demonstrate its suitability for polarization-sensitive photodetection, we present a photocurrent mapping (PCM) image under TM/TE polarization at 1450 nm. This showcases the successful application of our device in

single-pixel imaging systems. The embedded Au/Si grating photodetector, offering tunable wavelength capabilities and high polarization sensitivity, holds significant promise across various applications, including wavelength-sensitive photodetection, polarization detection, sensing, and imaging. Its silicon-based structure further enhances its practicality and appeal for real-world implementations.

Acknowledgements: This work is supported by the National Natural Science Foundation of China (62120106001).

References

1. Narang P.; Sundararaman R.; Atwater H. A. Plasmonic hot carrier dynamics in solid-state and chemical systems for energy conversion. *Nanophotonics* **2016**, 5, 96–111.
2. Blandre E.; Jalas D.; Petrov A. Yu.; Eich M. Limit of efficiency of generation of hot electrons in metals and their injection inside a semiconductor using a semiclassical approach. *ACS Photonics* **2018**, 5, 3613–3620.
3. Zhang C.; Cao G.; Wu S.; Shao W.; Giannini V.; Maier S. A.; Li X. Thermodynamic loss mechanisms and strategies for efficient hot-electron photoconversion. *Nano Energy* **2019**, 55, 164–172
4. Li W.; Valentine J. G. Harvesting the loss: surface plasmon-based hot electron photodetection. *Nanophotonics* **2017**, 6, 177–191.
5. Sobhani A.; Knight M. W.; Wang Y.; Zheng B.; King N. S.; Brown L. V.; Fang Z.; Nordlander P.; Halas N. J. Narrowband photodetection in the near-infrared with a plasmon-induced hot electron device. *Nat. Commun.* **2013**, 4, 1643 – 1648.
6. Knight M. W.; Wang Y.; Urban A. S.; Sobhani A.; Zheng B. Y.; Nordlander P.; Halas N. J. Embedding Plasmonic Nanostructure Diodes Enhances Hot Electron Emission. *Nano Lett.* **2013**, 13, 1687 – 1692.

Strong coupling between surface plasmons and magnetic polaritons in a borophene-based hybrid system

Ye Ming Qing[1,2,*]

[1]College of Electronic and Optical Engineering & College of Flexible Electronics (Future Technology), Nanjing University of Posts and Telecommunications, Nanjing 210023, China
[2]State Key Laboratory of Millimeter Waves, Southeast University, Nanjing 210096, China
[*]Corresponding author: ymqing@njupt.edu.cn

Abstract: Borophene-based hybrid plasmonic structure enables strong coupling between surface plasmons and magnetic polaritons. This interaction leads to unique energy transfer, dual-band light trapping, and mode splitting characteristics, described by a coupled oscillator model. This innovative work offers a platform for light-matter studies and plasmonic device development.

The manipulation of light-matter interaction, particularly the strong coupling between incident waves and nanostructures, has garnered significant attention [1]. Two-dimensional (2D) materials hold promise for compact electronic and photonic devices due to their unique properties and thin dimensions. Compared to traditional metallic plasmonic systems, 2D materials like graphene and black phosphorus exhibit extreme field confinement, low dissipation, and easy controllability, enhancing light-matter interaction [2-8]. However, their low carrier densities (~ 10^{17} m^{-2}) limit plasmonic responses to infrared and terahertz bands. Finding 2D materials with higher carrier densities and plasmonic frequencies for optical manipulation beyond these regions is crucial. Monolayer borophene, a newly emerging 2D material, has attracted attention due to its high density of Dirac electrons (~ 10^{19} m^{-2}). It supports highly tunable confined plasmons in the visible and near-infrared regions, complementing other 2D materials. Recent studies have investigated borophene surface plasmons (BSP), exploring their plasmonic properties and coupling effects [9].

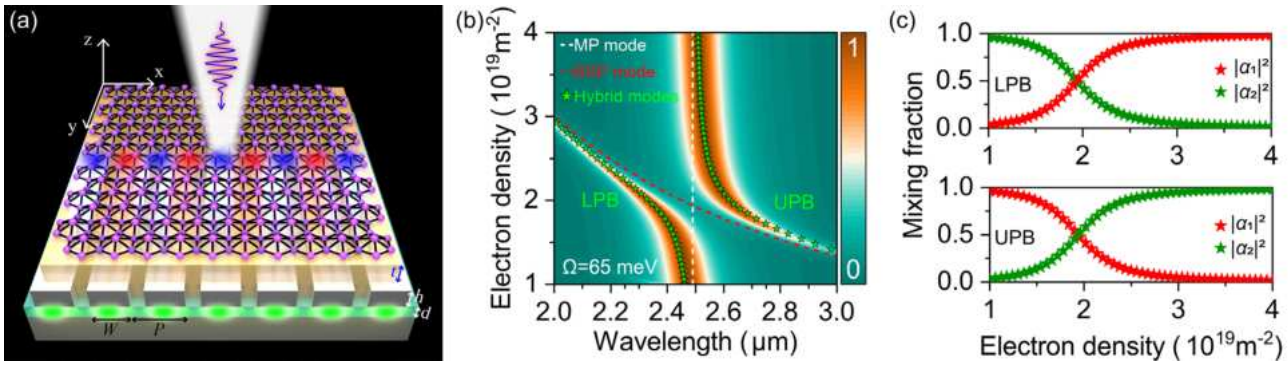


Fig. 1 (a) The schematic of the proposed hybrid borophene-based plasmonic system. (b) Absorption spectra of the proposed hybrid plasmonic system with varying borophene electron density. The red and white dashed lines are the theoretical dispersion relations of the BSP and MP modes, and the green stars are the analytical hybrid dispersion relations. (c) The mixing fractions of the BSP mode and MP mode in the polariton bands for the BSP-MP coupling.

Figure 1(a) depicts the proposed structure, composed of a continuous α-phase borophene monolayer, an insulator-covered subwavelength silver grating, a dielectric spacer, and a silver substrate. The structure's geometric parameters are: P = 100 nm, W =90 nm, t =20 nm, h =10 nm, d =8 nm. The insulator is Al_2O_3 (refractive index is 1.75), while the spacer is Si (refractive index is 3.42). The permittivity of Silver follows the

Drude model [3], and the monolayer borophene exhibits anisotropic conductivity, also described by a semiclassical Drude model [9]. As shown in Fig. 1(b), we investigate the strong coupling between BSP and localized resonance mode (MP) in the hybrid system. Using the inductor-capacitor circuit model and multilayer waveguide theory [3-5, 9-10], we predict MP and BSP resonant modes. Numerical simulations confirm the simultaneous excitation of both modes, enabling their coupling. The hybridization can be dynamically regulated by adjusting the borophene electron density, resulting in an anticrossing behavior with Rabi splitting of 65 meV and new hybrid polariton bands. This strong BSP-MP coupling behavior can be analyzed using the coupled oscillator model [3-6]. To gain a deeper understanding of the coupling process, we further retrieve the relative mixing fractions of the BSP mode and MP mode in the two polariton bands, which are shown in Fig. 1(c), which indicates the evolutionary behavior of BSP and MP in each hybrid band.

In summary, the coexistence of these two resonances fosters a coupling interaction that facilitates mode hybridization, energy-exchange channels, and enhanced light-absorption characteristics. Our innovative nanostructure exemplifies remarkable efficiency, charting a path for effective light modulation in terms of absorption or reflection. This breakthrough paves the way for potential applications in photonic and plasmonic technologies leveraging the unique properties of borophene.

The author acknowledges the support of the National Natural Science Foundation of China (62305173), the Natural Science Foundation of the Jiangsu Higher Education Institutions of China (23KJB140015), the Open Project of the State Key Laboratory of Millimeter Waves (K202433), and the Natural Science Research Start-up Foundation of Recruiting Talents of Nanjing University of Posts and Telecommunications (NY222080).

References

1. Qing, Y. M., Y. Ren, D. Lei, H. F. Ma and T. J. Cui, “Strong coupling in two-dimensional materials-based nanostructures: a review,” J. Opt., Vol. 24, 024009, 2022.
2. Qing, Y. M., H. F. Ma and T. J. Cui, “Multifunctional space-timecoding amplitude modulated graphene metasurfaces,” J. Opt. Soc. Am. B, Vol. 38, No. 10, 3206-3211, 2021.
3. Qing, Y. M., H. F. Ma and T. J. Cui, “Strong coupling between magnetic plasmons and surface plasmons in a black phosphorus-spacer-metallic grating hybrid system,” Opt. Lett., Vol. 43, No. 20, 4985-4988, 2018.
4. Qing, Y. M., H. F. Ma and T. J. Cui, “Theoretical analysis of tunable multimode coupling in a grating-assisted double-layer graphene plasmonic system,” ACS Photon., Vol. 6, No. 11, 2884-2893, 2019.
5. Qing, Y. M., H. F. Ma and T. J. Cui, “Investigation of strong multimode interaction in a graphene-based hybrid coupled plasmonic system,” Carbon, Vol. 145, 596-602, 2019.
6. Qing, Y. M., H. F. Ma and T. J. Cui, “Strong coupling between excitons and guided modes in WS_2-based nanostructures,” J. Opt. Soc. Am. B, Vol. 37, No. 5, 1447-1452, 2020.
7. Qing, Y. M., Z. Huang, H. Jiang and B. Li, “Polarization-dependent thermal-tunable graphene-based metamaterial exploiting critical coupling with guided mode resonances,” J. Opt. Soc. Am. B, Vol. 40, No. 2, 233-238, 2023.
8. Huang, Z., H. Jiang, Z. Wang, Y. M. Qing and B. Li, “Thermally-electrically tunable graphene-based guided-mode resonant perfect absorber,” IEEE Photon. Technol. Lett., Vol. 35, No. 4, 175-178, 2023.
9. Qing, Y. M., Y. Wang, Z. Yang, J. Wu and S. Yu, “Manipulating the interaction between propagating surface plasmons and localized magnetic polaritons in a borophene-based hybrid system,” Phys. Rev. A, Vol. 109, 013504, 2024.
10. Qing, Y. M., H. F. Ma and T. J. Cui, “Angle-insensitive dual-functional resonators combining cavity mode resonance and magnetic resonance,” Opt. Lett., Vol. 44, No. 12, 3118-3121, 2019.

Condensation and Transport of Organic Exciton-Polaritons from Bound States in the Continuum

A. M. Berghuis[1], J. L. Pura[2], G. W. Castellanos[1], M. Ramezani[1], D. R. Abujetas[3], S. Murai[4], E. van Heist[1], J. A. Sánchez-Gil[5] and J. Gómez Rivas[1]

[1] Eindhoven University of Technology, The Netherlands, [2] Universidad de Valladolid, Spain
[3] Fribourg University, Switzerland [4]Kyoto University, Japan, [5]Consejo Superior de Investigaciones Científicas, Spain
*corresponding author: a.m.berghuis@tue.nl

Abstract: We show the formation of a polariton condensate from molecules strongly coupled to a bound state in the continuum in a metasurface of Si nanoparticles. We find that the condensation threshold depends on the excitation spot size, due to ballistic transport of the polaritons in the plane of the metasurface.

Bound states in the Continuum (BICs) are symmetry protected optical modes with theoretically infinitely long lifetimes due to the absence of the radiation to the far field. We show that a periodic array of Si nanoparticles supports a BIC with a suppressed radiation leakage at normal incidence due to quadrupolar character of the mode. This character results in a vanishing of the overlap integral of the mode profile at the surface with the radiation continuum. Theses properties make BICs an interesting platform for the investigations of light matter interactions.

We apply a layer of perylene dye molecules on top of this cavity. Due to the overlap of the resonance energy of the cavity and the energy of the excitons in the molecules, this system reaches the strong light-matter coupling regime, supporting polaritons that are partially photonic and partially excitonic. The partially photonic properties, give the polaritons their very low effective mass, enabling non-equilibrium Bose-Einstein condensation at room temperature. Condensation is reached at sufficiently high polariton concentrations and has to compete with the radiative decay of the polaritons to the ground state. The extremely long lifetime of the BIC gives the reservoir excitons more time to relax to the polariton band and reach the critical density for condensation resulting in a low threshold at pump fluences of ~4μJ cm^{-2} for a spot size of 0.1 mm^2. The emission from the polaritons provides a convenient way to probe the distribution of polaritons in energy-momentum space (Fig. 1). However, the symmetry protected BIC at normal incidence prevents emission from the condensate at this angle. Instead, the emission escapes from two points in momentum and energy space at very small angles (See Fig. 1 and 2a).

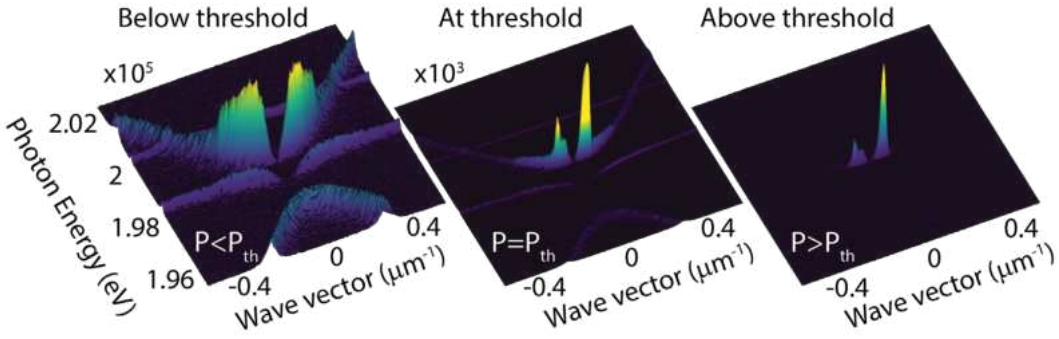


Figure 1 Emission in energy-momentum space from the molecules strongly coupled to the metasurface. (a) below condensation threshold, (b) at condensation threshold and (c) above condensation threshold.

We find that the required fluence for condensation is strongly dependent on the size of the excitation spot, where the threshold reduces for larges excitation spot sizes, while for very small excitation areas the molecules degrade before the condensation threshold is reached. We hypothesize that this effect is due to the transport of polaritons away from the excitation area. We model this observation by adding a term for the ballistic transport of polaritons to the rate equations for polariton condensation and numerically solve the equations for different initial excitation conditions. With this method, we explain both the spot size dependent threshold and the spatial distribution of the polariton condensate as measured above threshold (Fig 2 b and c).

These findings give a more complete understanding of the dynamics of polariton condensates and illustrate the importance of confining the polaritons when aiming for small scale and low threshold polariton condensates. The confinement could be achieved by designing a metasurface with a band structure with low group velocity or by creating a potential well to trap the polaritons.

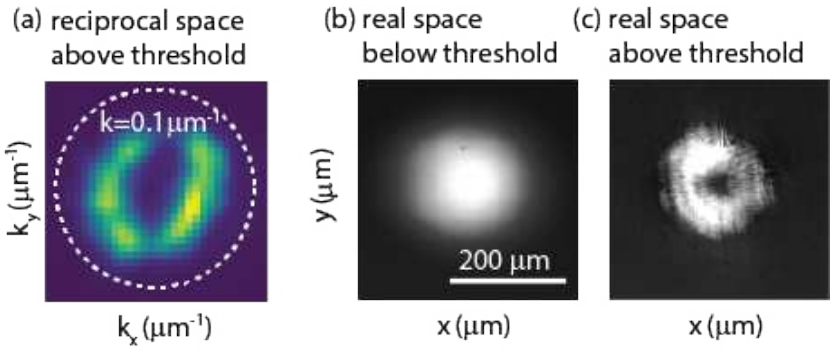


Figure 2 (a) Torus shaped emission profile in reciprocal space. (b) spatial distribution of the polaritons below threshold and (c) spatial distribution of the polaritons above threshold.

Acknowledgements

This research is funded by the Innovational Research Incentives Scheme of the Nederlandse Organisatie voor Wetenschappelijk Onderzoek (NWO) through the Gravitation grant "Research Centre for Integrated Nanophotonics" and through the Vici Grant (680-47-628). It is also funded by the Spanish Ministerio de Ciencia e Innovación through Grants MELODIA/PGC2018-095777-B-C21 and BICPLAN6G/TED2021-131417B-I00 (MCIN/AEI/10.13039/501100011033 and European Union NextGenerationEU/PRTR), and by the University of Valladolid, within the Margarita Salas program, grant number CONVREC-2021-23 and by the Ministry of Education, Culture, Sports, Science and Technology (MEXT), Japan (22H01776), JSPS collaborative work (JPJSBP120219920), and the Asahi Glass Foundation.

References

1. Berghuis, A.M., Castellanos G.W., Murai S., Pura J.L., Abujetas D.R., van Heijst, E, Ramezani,M., Sánchez-Gil J.A., and Gómez-Rivas,J "Room temperature exciton−polariton condensation in silicon metasurfaces emerging from bound states in the continuum" Nano Lett., 23, 5603–5609, 2023.

Engineering Light-Matter Interactions at the Nanoscale for Functional Devices

Zhaogang Dong[1,2,*]

[1]Institute of Materials Research and Engineering, A*STAR (Agency for Science, Technology and Research), 2 Fusionopolis Way, #08-03 Innovis, 138634 Singapore
[2]Department of Materials Science and Engineering, National University of Singapore, 9 Engineering Drive 1, 117575, Singapore
[*]corresponding author: dongz@imre.a-star.edu.sg

Abstract: In this talk, we will present our recent work on engineering light-matter interactions at the nanoscale for functional devices, such as highly saturated red color pixels, color-sensitive miniaturized detectors, imaging of bound-states-in-the-continuum (BIC) mode, quasi-BIC resonance for enhancing cathodoluminescence, tunable color pixels, Si UV plasmonics, and tunable perovskite emission wavelength.

Nanostructural optical antennas based on either metallic or dielectric nanostructures have enabled the strong light-matter interactions, where the structural resonances are based on plasmonic or Mie resonances. In this talk, we present our recent work on the development of miniaturized detector devices and light sources as enabled by optical nanoantennas with resonances, such as silicon nanoantenna array for fluorescence enhancements [1], imaging of the bound-states-in-the-continuum (BIC) mode [2], quasi-BIC resonance for enhancing cathodoluminescence (CL) emission [2], the highly saturated red color pixels [3], color-sensitive miniaturized Silicon-Al detectors [4], tunable color pixels [5, 6], the plasmonic resonances of Si nanostructures at ultra-violet (UV) [7] and emission wavelength engineering of perovskite quantum dots [8].

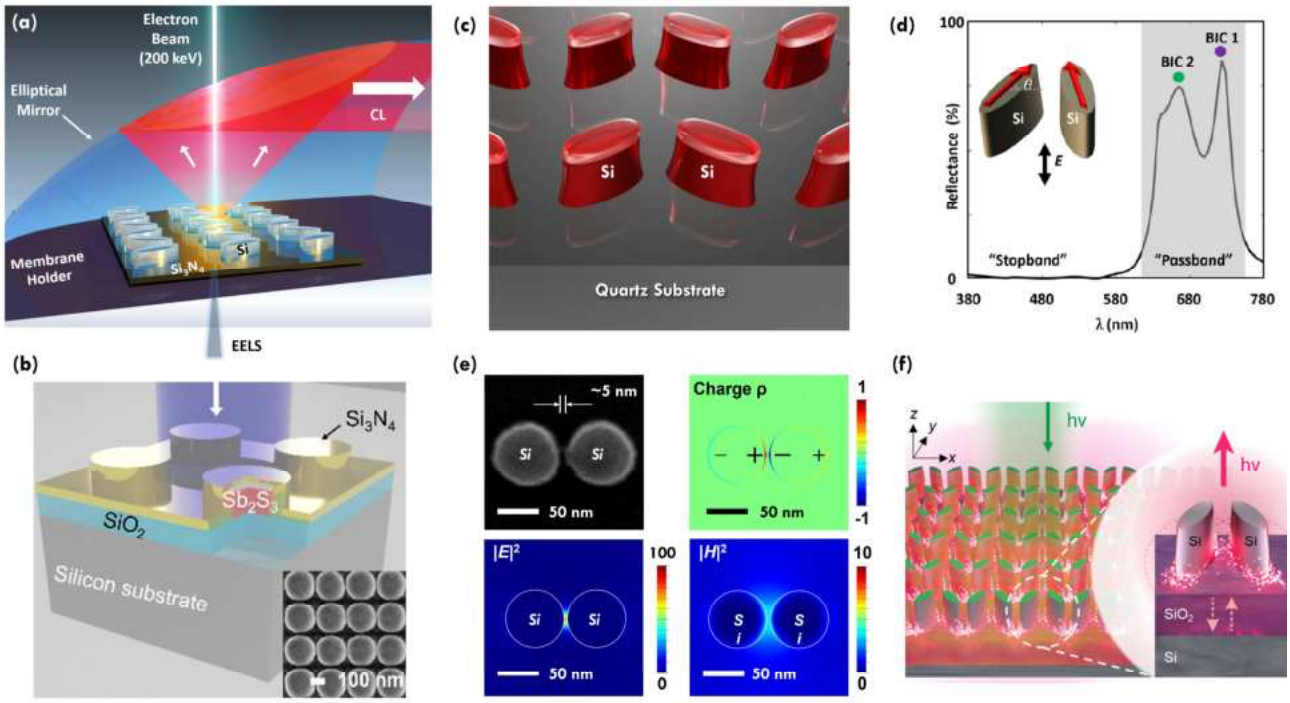


Figure 1. Nanostructural optical antennas with strong light-matter interactions. (a) Schematic illustration on probing the inaccessible BIC mode on a TEM setup via electron energy loss spectroscopy and CL emission [2]. (b) Tunable color pixels based on the phase-change material antimony trisulfide (Sb_2S_3) [6]. (c)-(d)

Schematic illustration on Si nanostructures with quasi-BIC resonance to achieve the highly saturated red color pixels [3]. (e) Schematic illustration of Si UV plasmonics and SEM image of Si dimer with ~5 nm gaps with the optical simulations [7]. (f) Schematic illustration on the tunable perovskite quantum dot emission via polarization-controlled q-BIC resonances [8].

References

1. Dong, Z., S. Gorelik, R. Paniagua-Dominguez, J. Yik, J. Ho, F. Tjiptoharsono, E. Lassalle, S. D. Rezaei, D. C.J. Neo, P. Bai, A. I. Kuznetsov, and Joel K.W. Yang, "Silicon nanoantenna mix arrays for a trifecta of quantum emitter enhancements," Nano Lett. Vol. 21, No. 11, 4853-4860, 2021.
2. Dong, Z., Z. Mahfoud, R. Paniagua-Domínguez, H. Wang, A. I. Fernández-Domínguez, S. Gorelik, S. T. Ha, F. Tjiptoharsono, A. I. Kuznetsov, M. Bosman, and Joel K.W. Yang, "Nanoscale mapping of optically inaccessible bound-states-in-the-continuum," Light: Science & Applications, Vol. 11, No. 1, 20, 2022.
3. Dong, Z., L. Jin, S. D. Rezaei, H. Wang, Y. Chen, F. Tjiptoharsono, J. Ho, S. Gorelik, R. J. H. Ng, Q. Ruan, C.-W. Qiu, and Joel K. W. Yang, "Schrödinger's red pixel by quasi-bound-states-in-the-continuum," Science Advances, Vol. 8, No. 8, eabm4512, 2022.
4. Ho, J., Z. Dong, H. S. Leong, J. Zhang, F. Tjiptoharsono, S. D. Rezaei, K. C. H. Goh, M. Wu, S. Li, J. Chee, Calvin P. Y. Wong, A. I. Kuznetsov, and Joel K.W. Yang, "Miniaturizing color-sensitive photodetectors via hybrid nanoantennas toward submicrometer dimensions," Science Advances, Vol. 8, No. 47, eadd3868, 2022.
5. Zhang, S., J. Zhang, W. P. Goh, Y. Liu, F. Tjiptoharsono, Henry Y. L. Lee, C. Jiang, J. Ding, Joel K.W. Yang, and Z. Dong, "Reversible electrical switching of nanostructural color pixels," Nanophotonics, Vol. 12, No. 8, 1387-1395, 2023.
6. Lu, L., Z. Dong, F. Tijiptoharsono, R. J. H. Ng, H. Wang, S. D. Rezaei, Y. Wang, H. S. Leong, P. C. Lim, Joel K.W. Yang, and R. E. Simpson, "Reversible tuning of Mie resonances in the visible spectrum," ACS Nano, Vol. 15, No. 12, 19722-19732, 2021.
7. Dong, Z., T. Wang, X. Chi, J. Ho, C. Tserkezis, S. L. K. Yap, A. Rusydi, F. Tjiptoharsono, D. Thian, N. Asger Mortensen, and Joel K.W. Yang, Nano Lett., Vol. 19, No. 11, 8040-8048, 2019.
8. Csányi, E., Y. Liu, S. D. Rezaei, Henry Y. L. Lee, F. Tjiptoharsono, Z. Mahfoud, S. Gorelik, X. Zhao, L. J. Lim, D. Zhu, J. Wu, K. E. Johnson Goh, W. Gao, Z.-K. Tan, G. Leggett, C.-W. Qiu, and Z. Dong, Advanced Functional Materials, Vol. 34, No. 2, 2309539, 2024.

Plasmonics and metamaterials for controlling optical properties and device applications through strong light-matter interactions

Koichi Okamoto[1*]

[1] Osaka Metropolitan University, Japan
[*]corresponding author: OkamoT@omu.ac.jp

Abstract: In this study, we examine recent advancements in plasmonics and metamaterials, spotlighting progress in light manipulation across the UV to IR spectrum and highlighting applications in high-efficiency photonic devices, sensing, imaging, and quantum technologies. Additionally, we focus on innovative fabrication techniques that expand the frontiers of nano-optical engineering.

The recent breakthroughs in plasmonics and metamaterials signify a transformative shift in nano-optics and quantum technologies, enabling unprecedented precision in nanoscale light manipulation. Our research contributes significantly to this field, enhancing light-matter interactions and unlocking novel optical properties, thereby fostering innovation across various technologies[1-9]. Groundbreaking developments such as plasmonic bandgap structures, waveguides, and enhanced light transmission through nanohole arrays underline the potential of plasmonics in future nano-optical circuits and computing, essential for a technologically advanced society.

A key application of plasmonics is the enhancement of light emission efficiency in light-emitting diodes (LEDs) through metallic films that amplify photoluminescence, utilizing InGaN/GaN quantum well (QW) materials[1-3]. This advancement is critical for reducing energy consumption in lighting, as demonstrated by the development and commercialization of InGaN-QW-based LEDs, including white-light LEDs. However, the full potential of plasmonic LEDs, such as tuning the surface plasmon (SP) resonance wavelength across the UV and infrared spectra, remains to be realized.

Metamaterials, with their ability to flexibly tune SP resonance via strong mode coupling and metallic nanoparticles, offer unique optical properties for applications in biosensing, photocatalysis, and imaging. These advancements benefit from bottom-up fabrication methods, overcoming the limitations of traditional top-down microfabrication and enabling simpler, cost-effective production of plasmonic structures. Our research highlights the promise of full-color tuning using random plasmonic metamaterials, allowing adjustments to SP resonance peak through modifications such as spacer layer thickness[4-9]. This capability not only paves the way for full-color light sources and displays but also significantly improves resonance peak quality factors, suggesting applications in nanolasers and ultra-fast LEDs. Extending localized surface plasmon resonance (LSPR) into the deep UV region, through the use of aluminum for nanohemisphere structure fabrication, demonstrates plasmonics' adaptability and its role in developing efficient deep UV LEDs for applications like water sterilization and optical lithography[5-7]. Advancements in plasmonic and metamaterial technologies have also led to significant progress in sensing, imaging, and color tuning. For instance, the creation of metal nano-hemisphere gratings and NHoM structures has yielded impressive applications in colorimetric biosensing and enhanced fluorescence imaging[8]. By manipulating LSPR wavelengths through dielectric spacer layers, we have enabled full-color tuning, marking a significant step toward full-color displays and light sources with improved efficiency and reduced energy consumption[9].

In conclusion, the evolution of plasmonics and metamaterials represents more than a scientific breakthrough; it is a paradigm shift that is redefining the capabilities of optical technologies. The progress outlined here not only demonstrates the potential for improved light emission, sensing, and imaging but also paves the way for the exploration of quantum plasmonic effects and ultrafast optical communications. As the field continues to advance, the study of plasmonics and metamaterials is poised to lead nanophotonics into a future where the manipulation of light at the nanoscale knows no bounds.

The authors wish to thank Prof. Wada and Prof. Matsuyama of Osaka Metropolitan University, Prof. K. Tamada of Kyushu University, and Prof. Y. Kawakami and Prof. M. Funato of Kyoto University for their valuable discussions and support. This work was supported by the JSPS Grants-in-Aid for Scientific Research (S) (No. JP19H05627) and Specially Promoted Research (No. JP20H05622).

References

1. K. Okamoto, M. Funato, Y. Kawakami, and K. Tamada, “High-efficiency light emission by means of exciton-surface-plasmon coupling,” Journal of Photochemistry and Photobiology C: Photochemistry Reviews, Vol. 32, 58−77, 2017.
2. K. Ikeda, K. Kawai, J. Kametani, T. Matsuyama, K. Wada, N. Okada, K. Tadatomo, K. Okamoto, “Spatial and time-resolved properties of emission enhancement in polar/semi-polar InGaN/GaN by surface plasmon resonance”, Nanophotonics, https://doi.org/10.1515/nanoph-2023-0758.
3. S. Kaito, T. Matsuyama, K. Wada, M. Funato, Y. Kawakami, and K. Okamoto, “Significant improvement of green light emission efficiency of InGaN/GaN quantum wells by depositing oxide thin films and ultraviolet light irradiations,” Research Square, DOI: 10.21203/rs.3.rs-2515057/v1; Patent Application No. 2022-014115.
4. K. Okamoto, K. Okura, P. Wang, S. Ryuzaki, and K. Tamada, “Flexibly tunable surface plasmon resonance by strong mode coupling using a random metal nanohemisphere on mirror,” Nanophotonics, Vol. 9, No. 10, 3409−3418, 2020.
5. K. Shimanoe, S. Endo, T. Matsuyama, K. Wada, and K. Okamoto, “Localized surface plasmon resonance in deep ultraviolet region below 200 nm using a nanohemisphere on mirror structure,” Scientific Reports, Vol. 11, 5169, 2021.
6. K. Shimanoe, S. Endo, T. Matsuyama, K. Wada, and K. Okamoto, “Metallic nanovoid and nano hemisphere structures fabricated via simple methods to control localized surface plasmon resonances in UV and near IR wavelength regions,” Applied Physics Express, Vol. 14, 042007, 2021.
7. S. Endo, K. Shimanoe, T. Matsuyama, K. Wada, and K. Okamoto, “Deep-ultraviolet localized surface plasmon resonance using Ga nanoparticles”, Optical Materials Express, Vol. 12, No. 7, 2444-2452, 2022.
8. N. Osaka, M. Ozawa, T. Matsuyama, K. Wada, and K. Okamoto, “Flexible tuning of the peak wavelength and intensity of localized surface plasmon resonance by heat treatment of nanodisk structures fabricated by electron beam lithography,” Optical Materials Express, Vol. 13, No. 5, 1504–1512, 2023.
9. S. Maeda, N. Osaka, R. Niguma, T. Matsuyama, K. Wada and K. Okamoto, “Plasmonic Metamaterial Ag Nanostructures on a Mirror for Colorimetric Sensing,” Nanomaterials, Vol. 13, No. 10, 1650, 2023.

Continuous wave-pumped second-harmonic generation and application from GaSe-assisted microfiber

B. Jiang[1*], Z. Hao[1], Y. Ma[1], X. Gan[1] and J. Zhao[1]

[1]Key Laboratory of Light Field Manipulation and Information Acquisition, Ministry of Industry and Information Technology, and Shaanxi Key Laboratory of Optical Information Technology, School of Physical Science and Technology, Northwestern Polytechnical University, Xi'an 710129, China.
[*]corresponding author: bqjiang@nwpu.edu.cn

Abstract: We demonstrate the realization of low-power, continuous wave-pumped second-order nonlinear optical processes with high efficiency from GaSe-assisted microfiber, and its application in the characterization of ultrashort optical pulses, with a broad measurable applicability for pico- and femto-second pulses.

Optical nonlinear frequency conversion in parametric processes includes harmonic generations, parameter oscillation and four-wave mixing has been widely applied to generate coherent light sources at new wavelengths, or with broadband spectrum, and to amplify weak signals. Unfortunately, the centrosymmetric nature of silica fiber precludes the realization of second-order nonlinear processes in optical fiber systems. Therefore, it has been a challenge to efficiently produce second-order nonlinear optical effects in a broad wavelength range under a continuous wave (CW) pump. In this work, we propose a simple strategy to efficiently realize the broadband and CW pumped second harmonics (SH), by transferring a crystalline GaSe onto a microfiber with phase-matching diameter, and characterize ultrashort pulses by incorporating the GaSe-assisted microfiber, as a frequency-doubling block, in an all-fiber interferometer. For an amorphous microfiber, by tailoring the waveguide chromatic dispersion in the fabrication process, material dispersion is compensated with mode dispersion, which makes the phase-matching approximately satisfied for SH.

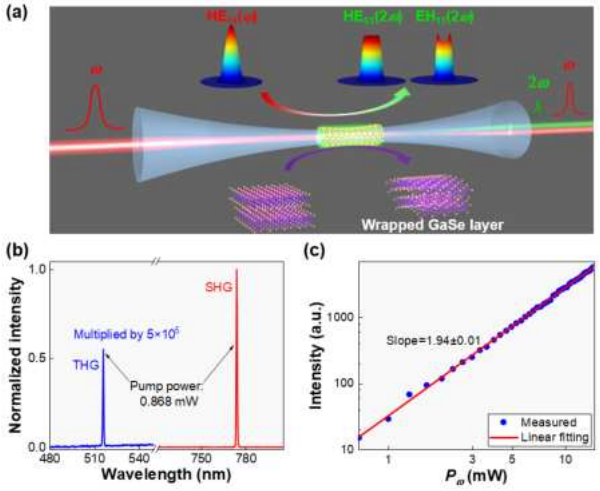


Fig.1 (a) Schematic of the microfiber for exciting SH, with the crystal structure and phase matched modes shown in the inset. (b) Spectra of SH at 775 nm and TH at 516.3 nm, pumped by a picosecond laser. (c) Power-dependence of SH when pump power of a CW laser is tuned from 0.7 to 14.5 mW.

Figure 1(a) schematically depicts the layered-GaSe coated microfiber for SH excitation and crystal structure of ε-GaSe used in experiments. To examine the device performance in the well-required C telecom band, the

1550 nm pulse light was incident into the microfiber from the picosecond laser, and the SH and third-harmonic (TH) spectra under 0.868 mW were measured and plotted in Fig. 1(b). With the assistance of crystalline GaSe layer, the SH and TH intensities have been greatly enhanced, compared with the intrinsic nonlinear signal from the microfiber. Considering the high conversion-efficiency, we replaced the pulse laser with a 1550 nm CW laser to excite the SH. According to the intensity evolution of SH signal shown in Fig. 1(c), CW-pumped SH scales quadratically with excitation power from 0.7 to 14.5 mW with a fitting slope of 1.94±0.01. The threshold of producing detectable SH in GaSe-transferred microfiber has been reduced to approximately 0.7 mW. Moreover, broadband SH spectrum is also achieved under the pump of a SLED source with a 79.3 nm bandwidth.

Further, by incorporating a GaSe-assisted microfiber into a Mach-Zehnder interferometer (MZI), we established an all-fiber autocorrelator for characterization of ultrashort optical pulses. Pulses to be retrieved were first split into the two arms of the interferometer and then overlapped, exciting the interferometric autocorrelated SH in the microfiber. By theoretical calculations, we investigated the dependence of an interferometric autocorrelation pattern on typical pulse parameters, including pulse shape, pulse duration, and unequal amplitude ratio of the two MZI arms. In the experiment, the autocorrelator shows high accuracy in measuring 7.13-ps, 1239-fs, and 683-fs pulses. In comparison with a commercial frequency-resolved optical gating, the relative errors are only 1.53%, 3.74%, and 6.86%, respectively. The proposed autocorrelator could be very compatible with current systems for future applications of in-fiber or on-chip ultrafast optical technology.

Acknowledgements

We are grateful for financial supports from National Natural Science Foundation of China (No. 62322510, 62375223, 11634010) and Key Research and Development Program (No. 2022YFA1404800). We also thank the Analytical & Testing Center of NPU for their assistance with the material and device characterizations.

References

1. Y. Zuo, W. Yu, C. Liu, X. Cheng, R. Qiao, J. Liang, X. Zhou, J. Wang, M. Wu, Y. Zhao, P. Gao, S. Wu, Z. Sun, K. Liu, X. Bai, and Z. Liu, “Optical fibres with embedded two-dimensional materials for ultrahigh nonlinearity” Nat. Nanotechnol., Vol. 15, 987-991, 2020.
2. B. Jiang, Z. Hao, Y. Ji, Y. Hou, R. Yi, D. Mao, X. Gan, and J. Zhao, "High-efficiency second-order nonlinear processes in an optical microfibre assisted by few-layer GaSe," Light Sci. Appl., Vol. 9, 63, 2020.
3. G. Q. Ngo, E. Najafidehaghani, Z. Gan, S. Khazaee, M. Per Siems, A. George, E. P. Schartner, S. Nolte, H. E.-Heidepriem, T. Pertsch, A. Tuniz, Ma. A. Schmidt, U. Peschel, A. Turchanin, and F. Eilenberger, “In-fibre second-harmonic generation with embedded two-dimensional materials” Nat. Photon., Vol. 16, 769-776, 2022.
4. Z. Hao, B. Jiang, Y. Ma, R. Yi, X. Gan, and J. Zhao, "GaSe-assisted microfiber autocorrelator for characterizing ultrashort optical pulses" Phys. Rev. Appl., Vol. 20, 044023, 2023.
5. Z. Hao, B. Jiang, Y. Ma, R. Yi, X. Gan, and J. Zhao, “Broadband and continuous wave pumped second-harmonic generation from microfiber coated with layered GaSe crystal”, Opto-Electron. Adv., Vol. 6, No. 9, 230012, 2023.
6. Z. Hao, B. Jiang, Y. Ma, R. Yi, H. Jin, L. Huang, X. Gan, and J. Zhao, “Strain-controlled phase matching of optical harmonic generation in microfibers”, Phys. Rev. Appl., Vol. 19, L031002, 2023.

Light-matter strongly coupled states in optical microcavities using highly oriented organic molecular crystals

Kenichi Yamashita[1*]

[1]Faculty of Electrical Engineering and Electronics, Kyoto Institute of Technology, Japan
[*]corresponding author: yamasita@kit.ac.jp

Abstract: Organic microcavities offer promising avenues for achieving room temperature polariton states. This study delves into the ultrafast dynamics of polariton states and optical spin-orbit coupling within an optical microcavity utilizing highly oriented molecular crystals.

Strong light-matter coupling in optical microcavities has been extensively explored for both fundamental photophysical investigations and optoelectronic device applications.[1] Organic materials are particularly promising for the active layer of the microcavities due to their large exciton binding energies and strong transition dipole moments, essential for achieving the strong coupling regime at room temperature.[2] Another area of interest in organic microcavity studies is microcavity polaritons, which are nonequilibrium quasi-particles with both light and matter characteristics.

Specifically, microcavities employing highly oriented organic crystals offer various optical functionalities. The strong macroscopic transition dipole moment of organic Frenkel excitons is achieved through highly oriented molecular alignment. Therefore, when molecular orientation aligns along the in-plane direction of the microcavity, a significantly strong light-matter interaction ensues. A crystal of 2,5-bis(4′-cyanobipheny-4-yl)thiophene (referred as BP1T-CN) is one of the appropriate materials to meet these requirements. In high-Q optical microcavities utilizing BP1T-CN single crystals, we observed the formation of polariton modes with Rabi splitting energies as large as ~200 meV.[3] Moreover, under optical pulse excitation, polariton condensation, i.e., the bosonic condensation of excited polariton particles into the energy minimum of the modes, was achieved at room temperature.[4] The excitation and relaxation dynamics of polaritons and reservoir excitons were investigated using ultrafast time-resolved photoluminescence and transient absorption spectroscopies, demonstrating the ultrafast renormalization of polariton eigenstates due to the population of polariton particles.[4]

Another intriguing aspect of BP1T-CN microcavities is the polariton states with a specific dispersion property stemming from strong optical anisotropy. The highly molecular orientation of BP1T-CN crystals results in strongly anisotropic dispersion curves for the two orthogonally polarized cavity modes. Additionally, the transition dipole moments parallel and perpendicular to the molecular axis exhibit significantly different amplitudes. These features give rise to anisotropic light-matter coupling between the two orthogonally polarized polariton modes.[5] The interaction between these modes leads to diverse polarization conversion phenomena in wavenumber space, elucidated by the optical spin-orbit coupling Hamiltonian.[6]

The author acknowledges funding from Japan Society for the Promotion of Science, JSPS KAKENHI (No. 22H00215) and from JST CREST (JPMJCR02T4).

References

1. Weisbuch, C., M. Nishioka, A. Ishikawa, and Y. Arakawa, “Observation of the coupled exciton-photon mode splitting

in a semiconductor quantum microcavity," Phys. Rev. Lett., Vol. 69, 3314–3317, 1992.
2. Sanvitto, D., and S. Kéna-Cohen, "The road towards polaritonic devices," Nat. Mater., Vol. 15, 1061–1073, 2016.
3. Goto, K., K. Yamashita, H. Yanagi, T. Yamao, and S. Hotta, "Strong exciton-photon coupling in organic single crystal microcavity with high molecular orientation," Appl. Phys. Lett., Vol. 109, 061101, 2016.
4. Yamashita, K., U. Huynh, J. Richter, L. Eyre, F. Deschler, A. Rao, K. Goto, T. Nishimura, T. Yamao, S. Hotta, H. Yanagi, M. Nakayama, and R. H. Friend, "Ultrafast dynamics of polariton cooling and renormalization in an organic single-crystal microcavity under nonresonant pumping," ACS Photon., Vol. 5, 2182–2188, 2018.
5. Tagami, T., Y. Ueda, K. Imai, S. Takahashi, H. Mizuno, H. Yanagi, T. Obuchi, M. Nakayama, and K. Yamashita, "Anisotropic light-matter coupling and below-threshold excitation dynamics in an organic crystal microcavity," Opt. Express, Vol. 29, 26433–26443, 2021.
6. Ohkura, R., T. Inukai, S. Takahashi, H. Mizuno, M. Nakayama, Y. Yamamoto, and K. Yamashita, "Rashba-Dresselhaus spin-orbit coupling and polarization-coupled luminescence in an organic single crystal microcavity," arXiv: 2310.06465, 2023.

Infrared photodetectors based on 2D heterostructures modulated by photogating

Jiong Yang[1,2*], Chao Zhang[1,2], Bining Sheng[1,2], and Xiaofeng Li[1,2]

[1]School of Optoelectronic Science and Engineering & Collaborative Innovation Center of Suzhou Nano Science and Technology, Soochow University, Suzhou 215006, China
[2]Author Affiliation, Country Key Lab of Advanced Optical Manufacturing Technologies of Jiangsu Province & Key Lab of Modern Optical Technologies of Education Ministry of China, Soochow University, Suzhou 215006, China
[*]corresponding author: jiongyang@suda.edu.cn

Abstract: Photodetectors based on 2D heterostructures can overcome bandgap limitations of individual 2D semiconductors and operate at long wavelengths. However, ultra-low interlayer absorptions result in weak photoresponsivity. Taking advantage of the photogating effect, infrared photodetectors based on 2D heterostructures are demonstrated to reach a photoresponsivity of 0.55 A/W at 1550 nm.

Infrared photodetection plays an important role in modern life and technologies, with many applications including optical communication, sensing, and night vision.[1-3] The core of photodetection lies in the efficient conversion of incident photons into electrical signals. In recent years, extensive studies on photodetectors are based on 2D materials and their heterostructures.[4-6] The working wavelengths of photodetectors are restricted by semiconductor bandgaps. Therefore, bandgap engineering of 2D semiconductors is critical for their applications in longer wavelength photodetections.

One of the frequently used methods to engineer bandgaps of 2D semiconductors is constructing their heterostructures. When forming the type-II band alignment in the heterostructure, efficient electron-hole separation into adjacent layers can occur, facilitating photodetection and photovoltaic applications.[7-9] However, interlayer absorptions are very low, typically 3 to 4 orders of magnitude smaller than intralayer absorptions,[10] resulting in low photocurrents and photoresponsivities. Photogating mechanism is a great but less investigated method in 2D heterostructures for achieving high photoresponsivity at an extended wavelength. Photogating modulation, in this case, is achieved by creating or eliminating charge carriers at or near the 2D heterostructures.

In this work, an infrared photodetector was fabricated based on a type-II heterostructure consisting of 1L MoS_2 and 1L $MoTe_2$ and operated in the photogating mode. The photodetector was in the field-effect transistor (FET) configuration. Spectral photocurrent measurements revealed broadband photodetection capabilities from 1100 to 1700 nm, beyond the energy band cut-offs of each monolayer. It was confirmed that the current was generated only between the source and drain electrodes by conducting photocurrent mapping under the 1550 nm illumination. The photoresponsivity of the 2D $MoS_2/MoTe_2$ photodetector was extracted to be 0.55 A/W under low-power 1550 nm illumination, thanks to the high gain of ~10^3 introduced by the photogating mechanism.

We acknowledge financial supports from the National Natural Science Foundation of China (62104165, 62274114, 62205227), the Natural Science Foundation of Jiangsu Province (BK20210713), and the Natural Science Research of Jiangsu Higher Education Institutions of China (22KJA510011, 22KJB140005).

References

1. Yin, J., et al., Ultrafast and highly sensitive infrared photodetectors based on two-dimensional oxyselenide crystals. Nat. Commun., 2018. 9(1): 3311.
2. Pospischil, A., et al., CMOS-compatible graphene photodetector covering all optical communication bands. Nat.

Photonics, 2013. 7(11): 892-896.
3. Hong, G., A.L. Antaris, and H. Dai, Near-infrared fluorophores for biomedical imaging. Nat. Biomed. Eng., 2017. 1(1): 0010.
4. Liu, C., et al., Silicon/2D-material photodetectors: from near-infrared to mid-infrared. Light Sci. Appl., 2021. 10(1): 123.
5. Chen, Y., et al., Unipolar barrier photodetectors based on van der Waals heterostructures. Nat. Electron., 2021. 4(5): 357-363.
6. Liu, M., et al., Photogating-assisted tunneling boosts the responsivity and speed of heterogeneous WSe_2/Ta_2NiSe_5 photodetectors. Nat. Commun., 2024. 15(1): 141.
7. Hong, X., et al., Ultrafast charge transfer in atomically thin MoS_2/WS_2 heterostructures. Nat. Nanotechnol., 2014. 9(9): 682-686.
8. Huang, D., J. Choi, C.-K. Shih, and X. Li, Excitons in semiconductor moiré superlattices. Nat. Nanotechnol., 2022. 17(3): 227-238.
9. Wu, P., et al., Van der Waals two-color infrared photodetector. Light Sci. Appl., 2022. 11(1): 6.
10. Barré, E., et al., Optical absorption of interlayer excitons in transition-metal dichalcogenide heterostructures. Science, 2022. 376(6591): 406-410.

Significant loss suppression in metasurfaces via resonances coupling

Guangyuan Li*, Xiaoqing Luo, and Xueqian Zhao

Shenzhen Institute of Advanced Technology, Chinese Academy of Sciences, China
*corresponding author: gy.li@siat.ac.cn

Abstract: We proposed and experimentally demonstrated significant loss suppression in plasmonic or all-dielectric metasurfaces via cooperative near-/far-field coupling or analogue of electromagnetically induced transparency, respectively. Both mechanisms are based on collective-collective resonances coupling, resulting to record high measured quality factors. We expect this work will advance the performance of related applications.

Metasurfaces, either plasmonic or all-dielectric, have emerged as a promising platform for a diverse range of applications, ranging from nanolasing, nonlinear optics, optoelectronic modulation, detection and biosensing to manipulation of electromagnetic field parameters, such as amplitude, phase, polarization, and wavefront. However, plasmonic metasurfaces suffer from inevitable absorption loss and scattering loss, especially in the visible regime, and all-dielectric metasurfaces suffer from considerable scattering loss although the absorption loss is zero or can be neglected. As a consequence, many of the hoped-for plasmonic devices and applications still seem a long way off or even end up unveiling fundamental limitations and dead-ends [1], and all-dielectric metasurface-based devices and applications have limited performance. How to effectively suppress the losses has been a long-standing challenge in the field of metasurfaces, especially plasmonic metasurfaces.

Recently, surface lattice resonances (SLRs), which are sometimes referred to as collective lattice resonances (CLRs), and bound states in the continuum (BICs) are two prevailing approaches for suppressing the losses of metasurfaces, and have been attracting increasing interest. Taking advantage of SLRs, the measured quality factors (Q-factors) of plasmonic metasurfaces reach up to 790 in the visible [2] and 2340 in the near-infrared regime [3]. Using BICs, measured Q-factor up to 23900 was reported [4] recently.

In this work, we propose and demonstrate a novel approach to further break the Q-factor record of plasmonic metasurfaces. It is based on cooperative near-/far-field coupling, which can be understood by the near-field strong coupling of two orthogonal SLRs supported by two silver nanorod arrays. The strong coupling further re-distributes the loss of the two SLRs, resulting in record high measured Q-factor of 3117, as shown in Figure 1.

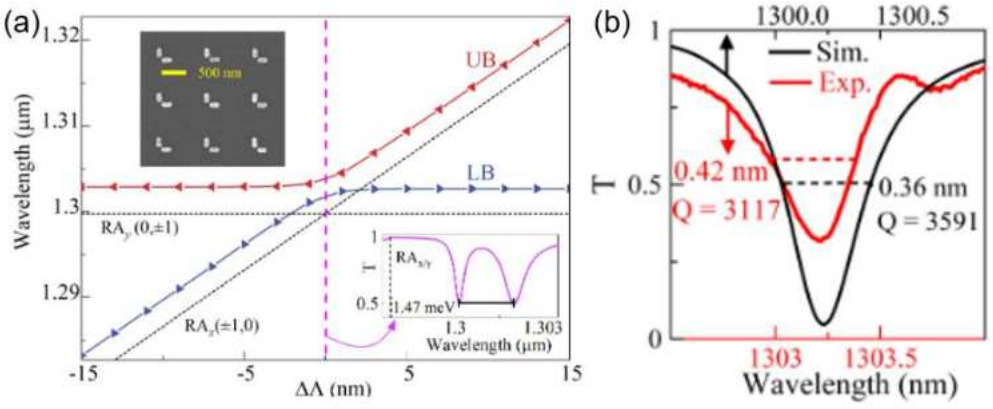


Figure 1. (a) Strong coupling of two orthogonal plasmonic SLRs in periodic L-shaped silver nanoantenna array, of which the SEM image is shown in the inset. (b) Simulated and measured transmittance spectra show that the simulated and measured Q-factors reach up to 3591 and 3117, respectively.

For all-dielectric metasurfaces, we propose and demonstrate metasurface-analogue of electromagnetically induced transparency (EIT) based on the coupling of two Mie SLRs, the electric dipole SLR (ED-SLR) and electric quadrupole SLR (EQ-SLR). We show that, compared with the high-Q EQ-SLR, the measured Q-factor is further improved by 1.2 times, from 2360 to 2750, which is more than five times of the record for metasurface-analogue of EIT [5]. This transparency window corresponds to strong slow light effect with group index reaching 12540, which indicates that the time delay through the 100 nm-thick Si metasurface is equal to that through 1.254 mm-thick vacuum [6].

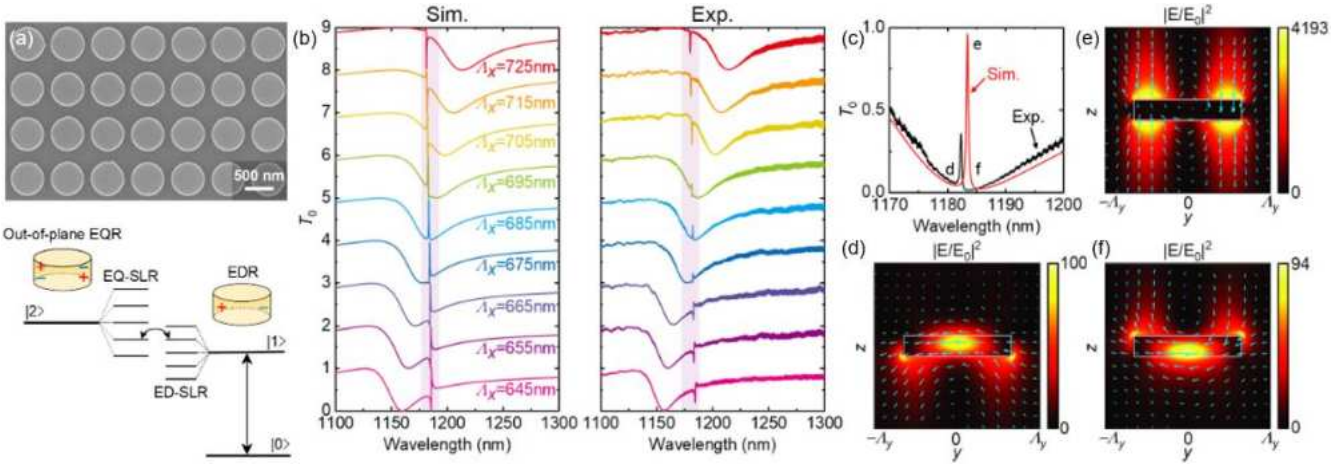


Figure 2. (a) SEM image of as-fabricated periodic Si nanodisk array and the operation principle of the EIT-analogue based on two Mie SLRs. (b) Comparison of simulation and measured transmittance spectra under normal incidence. (c) Zoom of transmittance spectra for Λ_x=685 nm. (d)-(f) Near-field electric field distributions at the wavelengths for the transmittance dips and the transparency peak in (c).

In summary, based on the strong coupling effect and the EIT effect between two SLRs, we demonstrated significant loss suppression in plasmonic and all-dielectric metasurfaces, respectively. We expect the obtained ultrahigh Q-factors will boost applications including emission enhancement, nanolasing, nonlinear optics, and biochemical sensing.

Acknowledgements: This work was supported by the National Natural Science Foundation of China (Grant No. 62275261) and the Natural Science Foundation of Guangdong Province (Grant No. 2022A1515010086).

References

1. Editorial. “Where now for plasmonics?” Nat. Nanotechnol., 11, 1, 2016.
2. Li, G., et al., “Plasmonic metasurfaces with quality factors up to 790 in the visible,” Adv. Optical Mater. 11, 2301205, 2023.
3. Bin-Alam, M.S., et al., “Ultra-high-Q resonances in plasmonic metasurfaces,” Nat. Commun. 12, 97411, 2021.
4. Huang, L., et al., “Ultrahigh-Q guided mode resonances in an all-dielectric metasurface,” Nat. Commun. 14, 3433, 2023.
5. Yang, Y., et al., “All-dielectric metasurface analogue of electromagnetically induced transparency,” Nat. Commun. 5, 5753, 2014.
6. Zhao, X., et al., “Ultrahigh-Q metasurface transparency band induced by collective-collective coupling,” Nano Lett. 24, 1238-1245, 2024.

Integrated lithium niobate photonics: from communications to metrology

Y. Li[1*]

[1] State Key Laboratory of Precision Measurement Technology and Instruments, Department of Precision Instrument, Tsinghua University, Beijing 100084, China
[*]corresponding author: yli9003@mail.tsinghua.edu.cn

Abstract: By leveraging the tunable repetition rate of integrated lithium niobate (LN) electro-optic frequency combs, we achieved ambiguity-free distance measurement system. Based on integrated LN phase modulators, we achieved 16-channel optical phased array. To achieve mass production of integrated LN devices with high fidelity and low cost, we developed wet etching-based fabrication process for integrated LN.

With the blooming of artificial intelligence technology, the distant sensing systems are highly demanded by autonomous vehicles, smart home products, virtual and augmented reality (VR and AR) systems. Ideally, these sensing systems need an agile deployment, a high refreshing rate and a high precision to map the fast-changing environment in terms of 3D point cloud under various weather and illumination conditions. At present, the mainstream distance measurement technology is evolving from amplitude modulation (time of flight, ToF) LiDAR to frequency modulation (frequency modulated continuous wave, FMCW) LiDAR. FMCW, as a coherent detection method, shows a high precision, a high selectivity against ambient light, the intrinsic capability in speed sensing and eye-safety, leading to its fast emerging in several areas such as autonomous driving.

The key components of FMCW are frequency modulated laser and coherent receiver. The laser frequency of FMCW is chirped linearly (usually with triangular waveform in frequency), enabling resolving of the distance information from the frequency difference between the transmitted and received signals over one chirping period. Such a frequency difference is usually resolved via a discrete Fourier transform (typically fast Fourier transform, FFT), imposing limitation on the integral time. Such a limitation reduces the acquisition rate, and imposes higher requirement in the frequency chirping span, speed, and linearity of the FMCW laser. This is a main challenging that prevents FMCW from being widely used in many areas such as autonomous driving despites its advantages over ToF.

Here we demonstrate an electro-optic comb-enabled absolute distance ranging technology with megahertz acquisition rate. This technology combines novel distance measurement method and light source to achieve real-time absolute distance measurement with a high acquisition rate over an arbitrary distance. Based on an on-chip lithium niobate electro-optic frequency comb, the modulation frequency scanning coherent distance measurement system can achieve an acquisition rate up to 10 kHz and a precision better than 100 mm. This on-chip integrated lithium niobate electro-optic frequency comb is designed for a deep modulation depth, an arbitrarily tunable repetition rate, and a low power consumption, resulting in more frequency comb lines based on a commercially available continuous wave laser and a frequency-sweeping microwave source. All the comb lines are transmitted to a coherent ranging system, which carries out a temporal interference with high fineness. We show that real-time distance resolving can be achieved with only two adjacent interference peaks among many peaks generated over one modulation frequency chirping period, boosting the acquisition rate of LiDAR system for ambiguity-free distance measurement.

As an excellent material platform for integrated photonics, thin film lithium niobate (TFLN) boots the

performance of various integrated photonic devices such as integrated electro-optic modulators, integrated optical frequency combs, and nonlinear wavelength converters. The performance of these devices is highly dependent on the quality of nanofabrication method. Despite the fact that conventional inductively coupled plasma–reactive ion etching (ICP-RIE) can achieve TFLN microrings with intrinsic quality factor (Q-factor) as high as 10 million, this method still shows high cost, poor reproducibility, and low throughput.

Here, we achieved z-cut TFLN micro-racetrack with an intrinsic Q factor over 11.9 million using we etching method. In this method, we first deposit a 100-nm-thick silicon dioxide film on a TFLN sample (NanoLN) using plasma-enhanced chemical vapor deposition. Then, we use electron-beam lithography to write the pattern on the electron-beam resist (ZEP 520A). We then use ICP-RIE to transfer the pattern from the electron-beam resist to the silicon dioxide film. Subsequently, we wet etch the TFLN with a solvent consisting of H2O2, NH4OH and H2O with a ratio of 2:2:1 at a temperature of 85 Celsius. Following the wet etching, we remove the silicon dioxide mask using buffered oxide etch. Eventually, we anneal the sample at 250 Celsius for 2 hours in air to recover the potential damage induced by ion slicing.

Considering that wet etching is an isotropic process and lithium niobate (LN) crystal is anisotropic, wet etched LN structures show anisotropic features. Hence, the sidewalls of wet etched ridge waveguides along distinct directions show different lateral etching properties. Our results show that the wet etching properties along three main crystal axes (x, y, z) show apparent differences. These results can help us to design TFLN devices based on wet etching.

We evaluate the fabrication quality of wet etching by characterizing Q-factors of x-cut TFLN microring and z-cut TFLN micro-racetrack. We fabricate these TFLN structures based on a 600-nm-thick TFLN and 300-nm etching depth. We design the x-cut TFLN microring with a 120-μm radius, top widths of 1.4 μm and 2.6 μm for bus waveguide and microring waveguide, respectively. And, we design the z-cut TFLN micro-racetrack with a radius of 120 μm and 3000-μm straight sections. Moreover, we design the top widths of bus waveguide and micro-racetrack as 1.6 μm and 4 μm, respectively.

Our measurement results show that the loaded Q-factor of the TE0 mode of the x-cut microring is 1.12 million with a minimum normalized transmission of 0.076, indicating an under coupling and an intrinsic Q-factor of 1.76 million. Furthermore, our measurement results show that the loaded Q-factor of the TE0 mode of z-cut TFLN micro-racetrack is 7.16 million with a minimum normalized transmission of 0.043, corresponding to an under coupling and an intrinsic Q-factor of 11.9 million. Moreover, we measured the Q-factors in a relatively broad wavelength range to see the distribution of Q-factors. These results show that the average intrinsic Q-factors of the TE0 mode of x-cut TFLN microring and z-cut TFLN micro-racetrack are 1.25 million and 7.52 million, respectively.

In summary, we presented a wet etching method for the nanofabrication of TFLN, facilitating the mass production of high-performance integrated TFLN devices with low cost, high reproducibility, and high throughput.

META 2024, TOYAMA - JAPAN, JULY 16 – 19, 2024

Multi-wavelength single-mode plasmonic nanolasing in an “H”-shape cavity

Fajun Xiao*

Shaanxi Key Laboratory of Optical Information Technology, School of Physical Science and Technology,

Northwestern Polytechnical University, Xi’an 710129, China

*corresponding author: fjxiao@nwpu.edu.cn

Abstract: A near-infrared multi-wavelength plasmonic nanolaser is demonstrated by inserting InGaAs/GaAs multi-quantum-disk (MQD) nanowires into an “H”-shape cavity. The nanolaser shows a low threshold at room temperature benefited from the enhanced energy transfer between the excitons and the standing plasmon waves in the “H”-shape cavity. Our design may open up exciting prospects for ultra-compact photonic integrated circuits and high-throughput biochemical sensing.

Multi-wavelength plasmonic nanolaser is central to the quest of ultradense and versatile photonic applications, ranging from the on-chip optical communication and optical data storage to biological detection.[1] Previous works have established two kinds of cavity architectures, namely metal-insulator-semiconductor[2] and plasmonic lattice[3], to realize the multi-wavelength plasmonic lasing. Nevertheless, the insufficient optical feedback and mode selection strategies result in high lasing threshold and multi-mode operation with limited spectral purity and stability. Here, we demonstrate the first multi-wavelength single-mode near-infrared plasmonic nanolaser by leveraging a nontrivial “H”-shape cavity. This nanolaser is constructed by inserting InGaAs/GaAs multi-quantum-disk (MQD) nanowires into a metallic F-P cavity consisting of the Ag nanowire pair positioned on ultra-smooth Au film. Our design is endowed with strong optical feedback to enhanced the energy transfer between the excitons of MQD nanowire and the standing plasmon waves in the cavity. More importantly, the design is featured with a large flexibility in tuning the resonance wavelength, where multi-wavelength lasing with virtues of single-mode and record-low threshold is realized at the room temperature by spectrally matching MQD nanowires of distinct emission energies with the wedge-shaped metallic F-P cavity. Our study makes the crucial step towards the multi-wavelength plasmonic nanolasers with the unique features of single-mode and low-threshold, opening up exciting prospects for ultra-compact multiplexed photonics circuitry and high-throughput biochemical sensing. We believe that our results should be of interest to a broad range

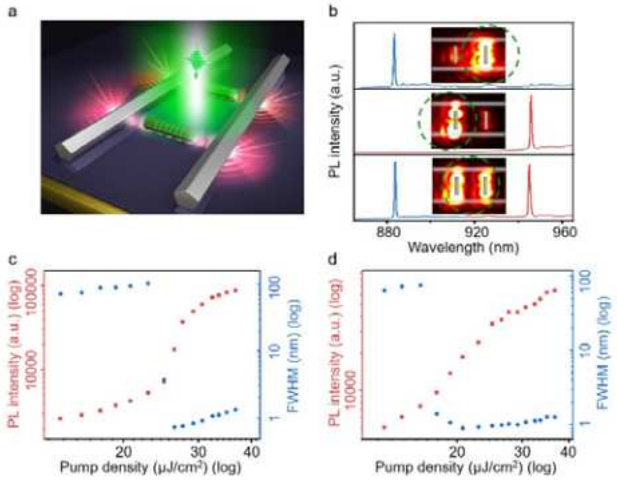


Figure 1. Realization of single-mode dual-wavelength plasmonic lasing in an "H"-shape cavity.

References

1. Zhang, G. Q., Takiguchi, M., Tateno, K., Tawara, T., Notomi, M., and Gotoh, H. , "Telecom-band lasing in single InP/InAs heterostructure nanowires at room temperature," Sci. Adv. 5, 8896 , 2019.
2. Wang, D.,Yang, A., Wang, W., Hua, Y., Schaller, R. D., Schatz, G. C., and Odom,T. W., "Band-edge engineering for controlled multi-modal nanolasing in plasmonic superlattices," Nat. Nanotechnol. 12, 889-894 2017.
3. Ma, R. M., Oulton, R. F., Sorger, V. J., Bartal, G., and Zhang, X. , "Room-temperature sub-diffraction-limited plasmon laser by total internal reflection," Nat. Mater. 10, 110-113, 2011.

Probing plasmonic light-matter interactions with Kelvin probe force microscope

S. Ishii[1,2], M-W. Yu[1,3], and K-P. Chen[3,4]
[1] National Institute for Materials Science (NIMS), Japan
[2] University of Tsukuba, Japan,
[3] National Chiao Tung University, Taiwan
[4] National Tsing Hua University, Taiwan
[*]corresponding author: sishii@nims.go.jp

Abstract: Using a Kelvin probe force microscope with external light sources, we image surface potential shifts in the nanoscale induced by the exciton–polariton coupling of MoS_2 monolayers and the plasmoelectric effect in zirconium nitride nanodisks.

A Kelvin probe force microscope (KPFM) is one of scanning probe microscopes based on an atomic force microscope which images surface potential differences or work functions differences in the nanoscale. While some KPFMs allow scanning in vacuum or in gas-controlled environment, most of KPFM measurements have been carried out in static conditions without any external excitations. In contrast, when KPFM measurements are performed with and without light irradiation, it is possible to image light-induced carrier shift or potential shift, making KPFM a powerful tool to study various effects caused by optical excitation such as plasmonic hot carriers and photocatalysts.

In the current talk, we present our recent works in which a KPFM combined with external light sources played a major role in imaging light-induced carrier shifts in the nanoscale. The first topic is the coupling between surface plasmons and MoS_2 exciton where the coupling caused the carrier shifts in the MoS_2 monolayers to the plasmonic gold grooves[1,2]. The second topic is on plasmoelectric effect which thermodynamically generates electric potential at off-resonant wavelengths. The surface potential shifts originate by the carrier shifts from the zirconium nitride nanodisks to the ITO glass substrate [3].

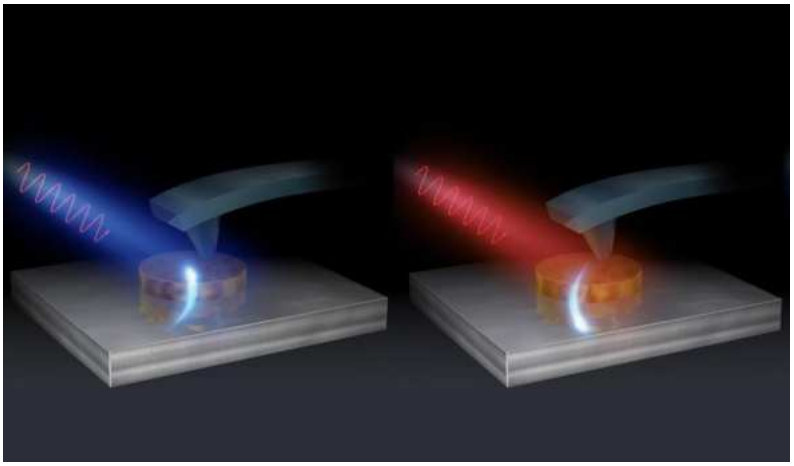


Fig. 1. Schematic of KPFM measurements with external light sources.

Acknowledgements: S.I. acknowledges the financial support from JST PRESTO (JPMJPR19I2), JST FOREST (JPMJFR2139) and Kakenhi from JSPS (22H01917), Japan.

References

1. M. Yu, et al, “Quantifying photoinduced carriers transport in exciton–polariton coupling of MoS_2 monolayers”, npj 2D Mater. Appl. 5, 47 (2021).
2. M. Yu, et al, “Enhancing Raman spectra by coupling plasmons and excitons for large area MoS_2 monolayers”, App. Surf. Sci. 605, 154767 (2022).
3. S. Ishii et al, “Observation of Plasmoelectric Effect in Plasmonic Zirconium Nitride”, Adv. Mater. Inter. 10, 2201751 (2023).

Optical Interplay between Triplet-Triplet Annihilation Upconversion Systems and Plasmons: Towards Upconverted Emission Enhancement

Kosuke Sugawa, Shota Jin, and Jotaro Honda

College of Science and Technology, Nihon University, Japan
*Kosuke Sugawa: sugawa.kosuke@nihon-u.ac.jp

Abstract: We have elucidated the effect of localized surface plasmon (LSP) resonance on a complicated triplet-triplet annihilation upconversion (TTA-UC) systems and endeavored to develop high-performance plasmonic TTA-UC systems. While the enhancement mechanism resembled conventional "metal-enhanced fluorescence," some quenching mechanisms via LSP resonance unique to the TTA-UC were demonstrated.

Among various upconversion technologies, the triplet-triplet annihilation upconversion (TTA-UC) systems, composed of sensitizer and annihilator molecules, have recently gained particular attention for integrating them into solar devices, bioimaging probes, anti-counterfeiting technologies, and more. TTA-UC has several advantages, including being driven by low-photon-density light (i.e., sunlight), being composed of low-cost organic molecules, and the ability to control excitation and emission wavelengths by manipulating the combination of sensitizer and annihilator molecules. The TTA-UC system can be driven by the following mechanisms: (i) generation of triplet-excited sensitizer molecules via photoexcitation and intersystem crossing, (ii) triplet-excited energy transfer from sensitizer to annihilator molecules, (iii) triplet-triplet annihilation between triplet-excited annihilator molecules (resulting in the generation of singlet-excited annihilator molecules), and (iv) fluorescence emission from the singlet-excited annihilator molecules. However, TTA-UC technology faces several challenges for practical applications. The processes (ii) and (iii), corresponding to Dexter-type energy transfer, are typically induced by molecular collisions. Therefore, systems embeded in solid matrices, where molecular diffusion is severely restricted, often exhibit reduced upconversion quantum yields. Moreover, the absorbance at the excitation wavelength for many sensitizer molecules is relatively low. Efforts have been dedicated to overcoming these challenges through various approaches. One strategy we have explored involves integrating metal nanoparticles that exhibit localized surface plasmon (LSP) resonance into solid-state TTA-UC systems. In this presentation, we will introduce some experimental attempts related to this research.

1. Enhancement and quenching of UC emission by LSP resonance[1]

We investigated the photophysical effect of LSP resonance of metal nanoparticles on solid-phase TTA-UC thin films. The TTA-UC system was designed with silver nanoprisms (AgPRs) with edge lengths of 27 ± 5 nm (small AgPRs: SAgPRs), 44 ± 5 nm (medium-sized AgPRs: MAgPRs), and 67 ± 10 nm (large

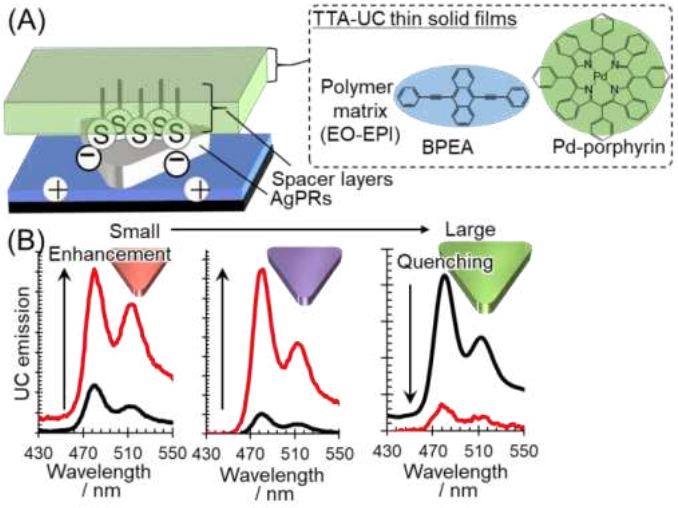


Fig. 1. (A) Schematic of plasmonic TTA-UC thin films. (B) Modification in UC emission induced by LSP resonance of AgPRs.

AgPRs: LAgPRs), inserted between a TTA-UC thin film and a quartz substrate (**Fig. 1**(A)). The TTA-UC thin film, with a thickness of 7.2 ± 0.6 nm, was composed of Pd-porphyrin as a sensitizer and BPEA as an annihilator within a polymer matrix. The UC emission (emission wavelength: 430-550 nm, excitation wavelength (λ_{ex}): 627 nm) from the TTA-UC system hybridized with SAgPRs and MAgPRs was enhanced by 3.7 times and 8.0 times, respectively, compared to the reference sample without AgPRs (**Fig. 1**(B)). This enhancement mechanism can be explained by the mechanism of "metal-enhanced fluorescence", namely, the photoexcitation enhancement of PdOEP and the Purcell effect on the singlet-excited BPEA. Conversely, the incorporation of LAgPRs significantly attenuated the UC emission. This can be attributed to the elevated radiative decay rate from the triplet-excited PdOEP caused by LAgPRs, which hinders the energy transfer from PdOEP to BPEA.

2. Optimal distance between TTA-UC thin films and AgPRs[2]

In "metal-enhanced fluorescence" by LSP resonance, the enhancement is highly sensitive to the distance between metal nanoparticles and fluorescent molecules. We investigated the optimal distance between metal nanoparticles and TTA-UC thin films for the efficient enhancement of UC emission. As shown in **Fig. 2**(A), we inserted alternating multilayer films made of polyethyleneimine and polystyrene sulfonate between AgPRs inducing the photoexcitation enhancement of sensitizer (PdOEP) and the TTA-UC thin solid films. The thickness of the multilayer films, prepared by the layer-by-layer approach, can be controlled on the nanometer scale. The maximum enhancement of UC emission was achieved when the distance between the TTA-UC thin film and AgPRs was 12.6 nm (**Fig. 2**(B)). This distance was considerably larger than the optimal distance (2.1 nm) for conventional metal-enhanced fluorescence using rhodamine 6G. This result suggests a significant quenching phenomenon induced in the TTA-UC mechanisms when AgPRs and TTA-UC thin films are in close proximity. From several experiments, we confirmed that AgPRs (or their LSP resonance) significantly quenches the triplet-excited DPA. This was verified by the fact that the triplet-excited lifetime of DPA ($\tau_{T,AgPRs}$) in the presence of AgPRs was considerably shorter than that in the absence of AgPRs (τ_T) as AgPRs and TTA-UC thin films approached each other (**Fig. 2**(C)). The shortened lifetime of triplet-excited DPA inhibited TTA (**Fig. 2**(D)), resulting in a significant attenuation of UC emission.

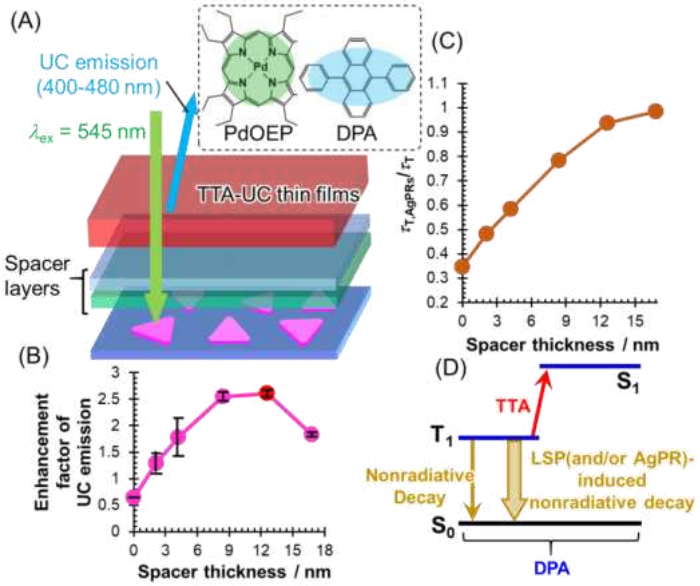


Fig. 2. (A) Schematic of plasmonic TTA-UC thin films. (B) Distance-dependent UC emission between AgPRs and TTA-UC thin films. (C) Distance dependence of $\tau_{T,AgPRs}/\tau_T$. (D) Energy diagram depicting the TTA process.

References: [1] S Jin et al., *ACS Photon.* **2018**, *5*, 5025. [2] J. Honda et al., *Langmuir* **2023**, *39*, 16138.

Acknowledgments: this work was supported by a Grant-in-Aid from JSPS KAKENHI (grant numbers 20H02850, 19H05627, and 23K17961).

Silicon BIC metasurfaces for strong interactions with molecular vibrations

K. Watanabe[1*], H. R. Devi[2], D. Hernández-Pinilla[2], M. Iwanaga[3], and T. Nagao[2,4]

[1]International Center for Young Scientists (ICYS), National Institute for Materials Science (NIMS), Japan
[2]International Center for Materials Nanoarchitectonics (MANA), National Institute for Materials Science (NIMS), Japan
[3]Research Center for Functional Materials, National Institute for Materials Science (NIMS), Japan
[4]Department of Condensed Matter Physics, Graduate School of Science, Hokkaido University, Japan
[*]corresponding author: watanabe.keisuke@nims.go.jp

Abstract: We report strong interactions between quasi-bound states in the continuum formed in silicon-on-calcium-fluoride wafers and molecular vibrations. Owing to the small losses and strong optical confinement, we demonstrate silicon-based surface-enhanced infrared absorption with a large enhancement factor and sensitivity at the monolayer level.

Material-specific molecular vibrations and phonons in the mid-infrared regime are fundamental phenomena in analytical chemistry [1] and are often used to identify structural information about molecules, including chemical bonds and configurations [2]. Although its cross section exceeds that of the Raman scattering process, the absorption cross sections of molecular vibrations in infrared spectroscopy are still small owing to the small light-molecule interactions, which pose significant difficulties when detecting small amounts of molecules or thin-film adsorbates. Surface-enhanced infrared absorption (SEIRA) spectroscopy is a technique that can enhance the sensitivity of molecular absorption based on optical resonances and their strong interactions with nearby molecules. However, the large optical ohmic loss and collisional damping of metals remain obstacles in practical sensing devices. To overcome this challenge, we focus on all-dielectric nanostructures that realize diverse tunability of optical properties based on their Mie resonances, small material absorption losses, and low-cost fabrication. In particular, a specific resonant state of light called quasi-bound state in the continuum (qBIC) in an arrayed nanostructure allows for strong light confinement with high Q factors and resonant enhancement of the electric field [3], which is experimentally obtained by breaking the symmetry of the unit structure. Thus far, we have shown tailored coupling between qBICs and molecular vibrations from weak to strong coupling regimes and demonstrated an enhanced molecular signal at a specific asymmetry parameter [4]. The coupling conditions of the qBIC-molecule system were tuned by simply changing the asymmetry parameters, whereas the upper limits of the Q factors were determined by the downward leakage losses into the high-index substrate of the silicon-on-insulator wafer, which also limited the sensitivity of the molecular absorptions.

In this work, we report interactions between qBICs formed in Si on CaF_2 wafers and molecular vibrations. Owing to the smaller losses and stronger optical confinement, we demonstrate a silicon-based SEIRA with large enhancement factors. Figure 1(a) shows the proposed silicon metasurface. By changing the lengths of the upper and lower nanorods to $L + 2\Delta L$ and $L - 2\Delta L$, respectively, the symmetry of the unit structure was broken (asymmetry parameter $\alpha = 2\Delta L/L$), controlling the amount of radiation loss of the resonance mode emitted to the far-field. For the fabrication, a 500 nm thick amorphous Si layer was first deposited by radiofrequency sputtering on a CaF_2 substrate. The pair-rod nanostructures were then patterned using electron-beam lithography and deep silicon etching. Figure 1(b) shows a representative scanning electron microscopy (SEM) image of a fabricated metasurface with asymmetry parameter α = 9%. Next, polymethyl methacrylate (PMMA) of different thicknesses was spin-coated onto a bare BIC metasurface to spatially and spectrally couple the C=O stretching modes (approximately at 5.8 μm) of the PMMA molecules and qBIC resonance modes. The enhanced molecular

signal was obtained by calculating the transmission difference with and without PMMA molecules, as shown in Figure 1(d). We found that only the 6.2 nm PMMA thin film showed a clear enhanced molecular signal. The SEIRA enhancement factor given by $(I_{SEIRA}N_{bulk})/(I_{bulk}N_{SEIRA})$ [5], where I_{SEIRA} and I_{bulk} are the vibrational signals from a metasurface with and without nanostructures, respectively, and N_{SEIRA} and N_{bulk} are the respective numbers of molecules contributing to vibrational signals, was calculated to be over 10^2. This result was roughly comparable to that obtained for typical metal nanostructures. We attribute this high enhancement factor to the low losses of the silicon nanostructures on the CaF_2 substrate and the large near-field enhancement effects derived from qBIC resonances, opening a route toward realizing highly sensitive surface-enhanced infrared spectroscopy without using metals.

This work was financially supported by JSPS KAKENHI Grant Number JP22K20496.

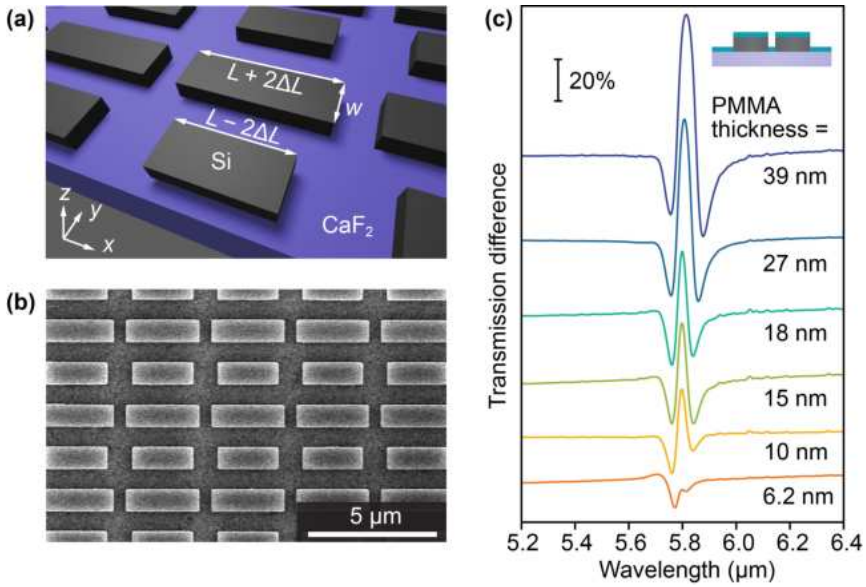


Figure. 1 Silicon metasurfaces at quasi-BICs. (a) Schematic of a silicon metasurface fabricated in Si on CaF_2 wafer composed of asymmetric pair-rod. (b) Representative SEM image of a fabricated metasurface. (c) Experimental transmission difference spectra for metasurfaces (α = 9%) coated with different thicknesses of PMMA. For clarity, the spectra are shifted vertically.

References

1. H. Altug, S. H. Oh, S. A. Maier, and J. Homola, "Advances and applications of nanophotonic biosensors," Nat Nanotechnol, vol. 17, pp. 5–16, 2022.
2. Á. I. López-Lorente and B. Mizaikoff, "Mid-infrared spectroscopy for protein analysis: Potential and challenges," Anal Bioanal Chem, vol. 408, no. 11, pp. 2875–2889, 2016.
3. T. Weber et al., "Intrinsic strong light-matter coupling with self-hybridized bound states in the continuum in van der Waals metasurfaces," Nat Mater, vol. 22, no. 8, pp. 970–976, 2023.
4. K. Watanabe, H. R. Devi, M. Iwanaga, and T. Nagao, "Vibrational coupling to quasi-bound states in the continuum under tailored coupling conditions," Adv Opt Mater, vol. 12, no.6, p. 2301912, 2024.
5. T. D. Dao, K. Chen, and T. Nagao, "Dual-band in situ molecular spectroscopy using single-sized Al-disk perfect absorbers," Nanoscale, vol. 11, no. 19, pp. 9508–9517, 2019.

NanoOptoCraft: plasmonic MEMS, nanoscale patterning, and optical low-loss film

K. Yamaguchi[1*]

[1]Institute of Post-LED Photonics, Tokushima University, Japan
[*]corresponding author: yamaguchi.kenzo@tokushima-u.ac.jp

Abstract: The NEMS drives versatile plasmomechanical devices by utilizing MEMS techniques for precise spatial control. Adiabatic plasmon wires enable manipulation of nanoscale gaps. Alternatively, narrow gaps can be realized through single-deposition techniques using stencil lithography. As a common approach, the development of low-loss single-crystalline metal films promises advancements in nanooptical devices.

Surface plasmons (SPs), which are the collective oscillations of conduction electrons, play a pivotal role in manipulating light at the nanoscale through metallic nanostructures. This study explores the potential of nano-electro mechanical systems (NEMS) technology in the development of novel multifunctional plasmomechanical devices[1-4]. Initially, we demonstrate the applicability of conventional micro-electro mechanical systems (MEMS) techniques to create plasmonic structures by utilizing metallic slits modulated by an actuator to tune the surface plasmon resonance and optical phase with voltage control[1].

Our approach extends control to single nano-order motion and space, achieved through adiabatic plasmon wires consisting of a pair of simple 50-micrometer-long nano-wires. This allows manipulation within gaps ranging from several hundred to several tens of nanometers. The proposed plasmomechanical devices exhibit versatility, serving as surface-enhanced Raman scattering (SERS) sensors, gas sensors[2], nano-lenses[3], and components in a combined fiber system.

In parallel, a fabrication method was established for metal nanopatterns with narrow gaps, utilizing a single vacuum deposition method with a hexagonal lattice period stencil. This approach simultaneously fabricates disks, rings, and holes of varying sizes and spacings, enhancing the detection patterns for unknown molecules. This method offers flexibility for wearable biosensors by applying sequential nanopatterns to the films.

To enhance the practicality of these devices, we present the development of a low-loss single-crystalline silver and gold film[5-8]. This achievement was realized through the application of epitaxial growth and film-transfer techniques, offering potential advancements in the field of nano-optical devices with improved miniaturization and power efficiency[7, 8].

This work was supported by JSPS KAKENHI Grant Numbers 16KK0150, 19K05309, 15H03546.

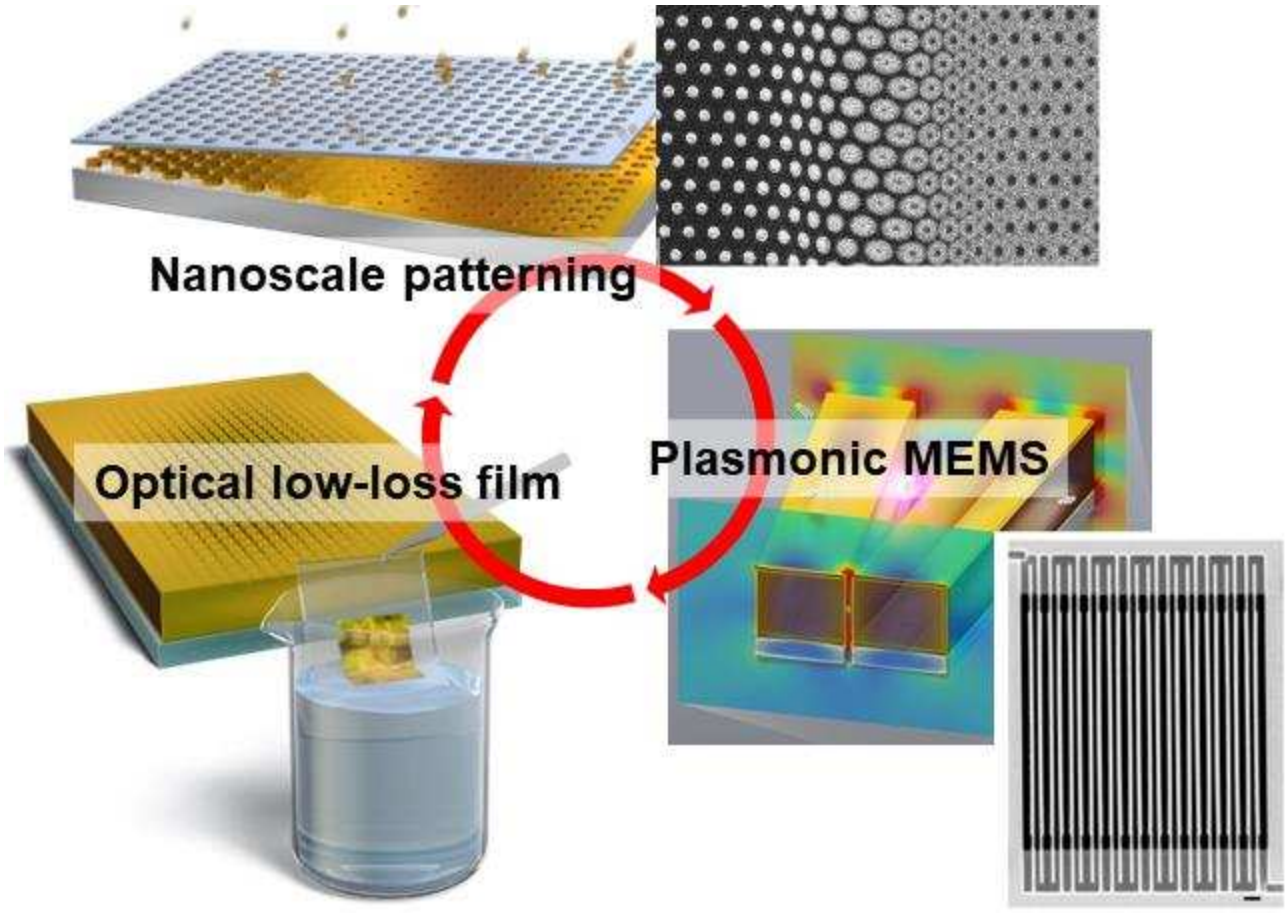


Fig 1. NanoOptoCraft.

References

1. K. Yamaguchi, M. Fujii, T. Okamoto, and M. Haraguchi, “Electrically driven plasmon chip: Active plasmon filter,” Applied Physics Express, Vol.7, No. 1, 012201, 2014.
2. K. Yamaguchi, and M. Fujii, “Electrically controlled infrared optical transmission and reflection through metallic grating using NEMS technology,” Applied Physics A, Vol.121, No. 4, pp.1353-1357, 2015.
3. K. Yamaguchi, H. Yamanaka, T. Ohtsu, and S. Ishii, “Electrically driven plasmon chip: Active plasmon lenses in visible,” Applied Physics Letters, Vol.108, No.11, 111903, 2016.
4. T. Ando, T. Kaji, K. Yamaguchi, K. Suzuki, S. Kamada, T. Okamoto, A. Mori, and M. Haraguchi, “MEMS plasmonic switch with stripe plasmonic waveguide,” Japanese Journal of Applied Physics, Vol.57, No.8S2, 08PC02, 2018.
5. T. Mori, Y. Tanaka, Y. Suzaki, and K. Yamaguchi, “Fabrication of silver thin film for single-crystalline nanopillar: effects of thickness and grain size,” Applied Physics A, Vol.121, No.4, pp.1359-1363, 2015.
6. T. Mori, Y. Tanaka, Y. Suzaki, and K. Yamaguchi, “Advanced fabrication of single-crystalline silver nanopillar on SiO_2 substrate,” Applied Physics Letters, Vol.108, No.4, 043102, 2016.
7. T. Mori, T. Mori, Y. Tanaka, Y. Suzaki, and K. Yamaguchi, “Fabrication of single-crystalline plasmonic nanostructures on transparent and flexible amorphous substrates,” Scientific Reports, Vol.7, 42859, 2017.
8. T. Mori, T. Mori, M. Fujii, Y. Tominari, A. Otomo, and K. Yamaguchi, “Optical Properties of Low-Loss Ag Films and Nanostructures on Transparent Substrates,” ACS Applied Materials & Interfaces, Vol.10, No.9, pp.8333-8340, 2018.

Robust quasi-BIC modes in a four cuboid cluster metasurface

J.F. Algorri[1,2,3], V. Dmitriev[4], H.E. Hernández-Figueroa[5], L. Rodríguez-Cobo[2], F. Dell'Olio[6], A. Cusano[7], J.M. López-Higuera[1,2,3], D.C. Zografopoulos[8]

[1]*Photonics Engineering Group, University of Cantabria, Santander, 39005, Spain*

[2]*CIBER de Bioingeniería, Biomateriales y Nanomedicina, Instituto de Salud Carlos III, Madrid, 28029, Spain*

[3]*Instituto de Investigación Sanitaria Valdecilla (IDIVAL), Santander, 39011, Spain*

[4]*Electrical Engineering Department, Federal University of Pará, PO Box 8619, Agencia UFPA, Belém, 66075-900, Brazil*

[5]*School of Electrical and Computer Engineering, University of Campinas-UNICAMP, Campinas, 13083-852, Brazil*

[6]*Department of Electrical and Information Engineering, Polytecnic University of Bari, Bari, 70125, Italy*

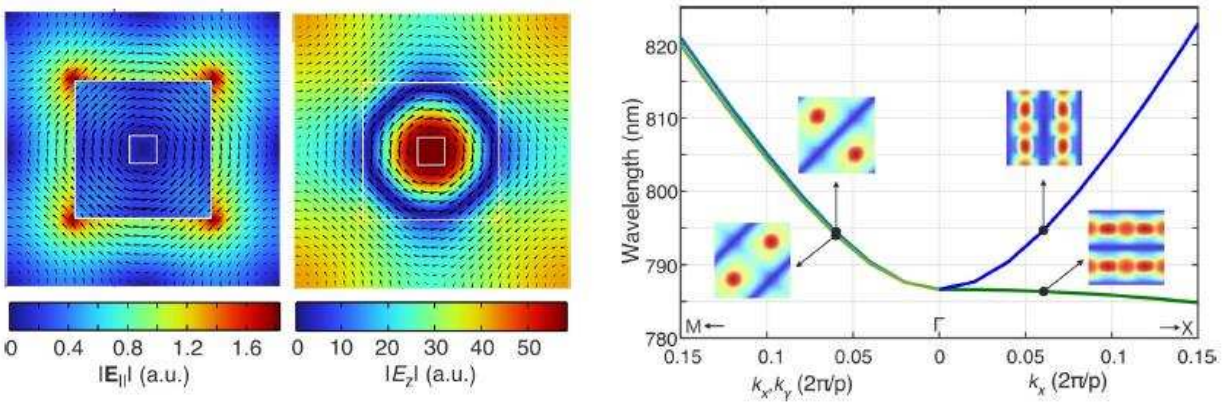
[7]*Department of Engineering, University of Sannio, Benevento, 82100, Italy*

[8]*Consiglio Nazionale delle Ricerche, Istituto per la Microelettronica e Microsistemi, Via del fosso del cavaliere 100, Rome, 00133, Italy*

Abstract: A metasurface with a unit cell composed of a cluster of four hollowed cuboids to work at the VIS spectrum is proposed. By shifting the hole asymmetrically, a qBIC resonant mode that is very robust to perturbations of the cuboid structure is produced thanks to its particular electric field profile.

Metasurfaces have emerged as a promising platform for engineering BICs. In these structures, symmetry-protected BICs are eigenmodes situated above the light cone, possessing different symmetries than the incoming wave, rendering them unexcitable within the continuum of radiation modes. By introducing some kind of perturbation, pure BICs transform into quasi-BICs with a finite lifetime, narrow linewidth and arbitrarily high radiative Q-factor. Indeed, quasi-BICs have been intensely investigated in dielectric metasurfaces with symmetry breaking, such as by introducing geometrical asymmetry or using anisotropic materials [2]. Although in most cases the resonant near fields are mainly confined to the interior of the high-index subwavelength scatterers, thus providing limited light-matter interaction with the surrounding material, it is still feasible to achieve interaction at the interface, allowing for biosensing and integration with 2D materials [3], as well as in slotted regions [4]. Furthermore, it has been recently reported that asymmetric dielectric particles arranged in clusters can be used to achieve greater flexibility in obtaining the desired near-field configuration [5] and enhancing the sensing capabilities for refractometry [6]. The operation principle in the latter case is based on plasmon-like surface waves, which are delocalised over a wide area to provide a large interaction volume with the matter but are excited in an all-dielectric structure.

In this work, we investigate a GaP metasurface supporting delocalised quasi-BIC modes. The metasurface comprises a periodic array of hollow nanocuboids patterned on a glass substrate and designed to produce ultra-high Q-factor delocalised resonances. The authors previously demonstrated this structure for toroidal responses [7,8], but the cluster arrangement has advanced features. The perturbed quadrumer arrangement retains C4v symmetry, thus allowing for polarization-independent optical response for normally incident planewaves [9]. By shifting the cuboids or a hole in the middle asymmetrically, the Brillouin zone is doubled producing a qBIC resonant mode with an antiferroelectric field configuration, which is very robust to large perturbations of the cuboid structure thanks to its particular electric field profile [9]. In addition, the resonant mode dispersion is investigated, revealing interesting features, such as low birefringence along the ΓM contour of the metasurface Brillouin zone and very low dispersion for the TM polarization along the ΓX direction [9]. Finally, this metasurface operates close to 785 nm, which is highly relevant for Raman spectroscopy.



(a) (b) (c)

Figure 1. Field structures for the investigated electric dipole mode in a metasurface with a single cuboid unit cell: magnitude of the (a) in-plane and (b) out-of-plane electric field vector. The arrow plot in both cases shows the distribution of the inplane magnetic field. (c) Band diagram of the investigated supermode along the ΓX and ΓM contour of the irreducible Brillouin zone. For oblique incidence (off-Γ point) the band splits in two branches corresponding to different polarization. The insets show the norm of the electric field calculated at $\{kx = 0.06, ky = 0\}$ and $\{kx = 0.06, ky = 0.06\}$ in units of $(2\pi/p)$ [9].

Funding

J. F.A. acknowledges the support of the projects RYC2022-035279-I and PID2019-107270RB-C21 funded by MCIN/AEI/10.13039/501100011033 and FSE+. D. C. Z. and F. D'O. acknowledge the project PRIN 2022 "ALPHA" (ALl-dielectric resonant metasurfaces enhancing PHoton emission phenomenA) 202288M84C-PE7 (CUP:D53D23001060006), Italian Ministry of University and Research (MUR), financed by the European Union, Next Generation EU.

References

1. C. Hsu et al. Bound states in the continuum. Nat Rev Mater 1, 16048,2016.
2. N. Bernhardt et al., Quasi-BIC Resonant Enhancement of Second-Harmonic Generation in WS2 Monolayers, Nano Lett. 20, 5309–5314, 2020.
3. J. Gomis-Bresco et al. Anisotropy-induced photonic bound states in the continuum. Nature Photon 11, 232–236, 2017.
4. J. F. Algorri et al., Opt. Express 29, 10374, 2021.
5. A. S. Kupriiannov et al., "Homogeneous enhancement of near-fields in all-dielectric metasurfaces with cluster-based unit cells," Opt. Lett. 45, 1527-1530, 2020.
6. D. C. Zografopoulos and V. Dmitriev, Quasi-Dark Resonances in Silicon Metasurface for Refractometric Sensing and Tunable Notch Filtering, J. Lightwave Technol. 39, 6985–6993, 2021.
7. J. F. Algorri et al. Ultrahigh-Quality Factor Resonant Dielectric Metasurfaces Based on Hollow Nanocuboids. Opt. Express 27 (5), 6320 2019.
8. J. F. Algorri et al. Anapole Modes in Hollow Nanocuboid Dielectric Metasurfaces for Refractometric Sensing. Nanomaterials, 9 (1), 1−13, 2019.
9. J.F. Algorri, et al. Polarization-independent hollow nanocuboid metasurfaces with robust quasi-bound states in the continuum, Optical Materials 147, 114631, 2023.

Optical properties of chiral plasmonic nanostructures coupled with nanocavity

T. Oshikiri[1,2*]

[1]IMRAM, Tohoku Univ., Sendai, Miyagi 980-8577, Japan
[2]RIES, Hokkaido Univ., Sapporo, Hokkaido 001-0021, Japan
[*]corresponding author: tomoya.oshikiri.c1@tohoku.ac.jp

Abstract:

We fabricated the two-dimensionally chiral Au nano-windmills (Au-NWs) by electron beam exposure and lift-off process on the Fabry-Pérot nanocavity of TiO_2 on Au-film. The chiroptical responses on Au-NWs with different geometric structures coupled with nanocavity in far and near fields are discussed.

Introduction

Many studies have investigated the interactions between circularly polarized light (CPL) and chiral molecules. Localized surface plasmon resonances (LSPRs), which are collective oscillations of conductive electrons of the metallic nanostructure, confine propagating light near the nanostructures and enhance the localized electric field (near field). Recently, it has been reported that a modal coupling between the LSPR and Fabry-Pérot (FP) nanocavity modes induces the enhancement of the near-field intensity and exhibits the homogeneous near-field distribution over LSPR particles.[1-3] Theoretical and experimental studies have shown that the interaction between plasmonic nanostructures and incident light could generate twisted near fields on the nanostructures[4-7]. In this study, we fabricated the two-dimensionally chiral Au nano-windmills (Au Au-NWs) on the FP nanocavity of TiO_2 on Au-film. We discussed the chiroptical responses on Au-NWs coupled with nanocavity.

Experimental

The Au nanostructures were fabricated by using electron beam (EB) exposure and lift-off techniques on SiO_2 substrate coated with the titanium oxide (TiO_2/SiO_2) and TiO_2 coated Au/SiO_2 ($TiO_2/Au/SiO_2$). The TiO_2 thin film with a thickness of 170 nm was deposited by an atomic layer deposition reactor at 300 °C. $TiCl_4$, and H_2O were used as precursors for the deposition. A ZEP520A (Zeon Co.) was employed as a positive resist. This study used a high-resolution EB system operating at 125 kV for sample fabrication by changing the exposure dose. After development, a 2-nm-thick titanium layer was first deposited via sputtering as an adhesive layer, followed by a 30-nm-thick Au film deposition. Lift-off was performed by successively immersing the sample in the resist remover (ZDMAC, Zeon Co.), acetone, methanol, and ultrapure water. Morphologies of nanostructures were analyzed by field-emission scanning electron microscopy (FE-SEM). Electromagnetic simulations were performed with the finite-difference time-domain (FDTD) solutions software packages (Lumerical, Inc.) to simulate the far-field reflection spectra and the electric field distribution in the near field. A plane wave light source circular polarization was irradiated to structures from the air side. Perfectly matched layer boundary conditions were imposed in the light propagation (z) direction. In the plane perpendicular to the light propagation (x and y) direction, periodic boundary conditions were applied on each boundary.

Results and Discussion

Figures 1a-c show the SEM images of three types of Au-NWs: Au-NW1, Au-NW2, and Au-NW3. Because The structural line width of Au-NW3 was broader than that of Au-NW1, the geometric two-dimensional chirality of Au-NW1 was clearer than that of Au-NW3. Figures d and e depict the near-field distribution on Au-NW1 on

TiO_2/Au/SiO_2 under left and right circularly polarized light irradiations calculated by the FDTD numerical simulation. The near-field distribution showed different responses under left and right CPL irradiations based on the two-dimensional chirality of the Au-NW1. We discuss the far-field and near-field spectra of the Au-NWs coupled with the nanocavity.

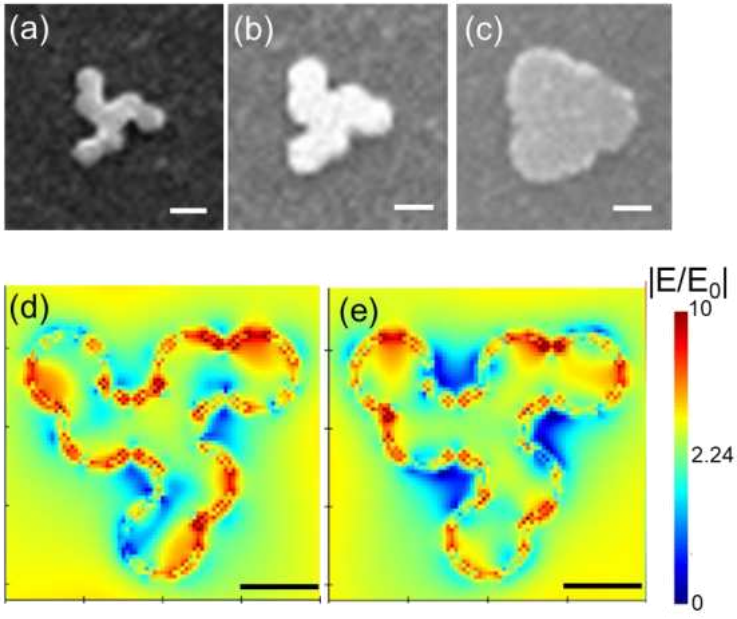


Figure 1. (a-c) FE-SEM images of Au-NW1 (a), Au-NW2 (b), and Au-NW3 (c). The scale bars indicate 200 nm. (d, e) Near-field intensity distributions on Au-NW1 on TiO_2/Au/SiO_2 under left (d) and right (e) CPL. The scale bars indicate100 nm.

Acknowledgment

We acknowledge financial support from The Japan Society for the Promotion of Science (JSPS) KAKENHI Grant Numbers JP23H01916, JP22K19003, JP22H05136, JP22H05131 (a Grant-in-Aid for Transformative Research Areas "Evolution of Chiral Materials Science using Helical Light Fields"), a project JPNP20004 (the New Energy and Industrial Technology Development Organization (NEDO)), and “Crossover Alliance to Create the Future with People, Intelligence and Materials” and Advanced Research Infrastructure for Materials and Nanotechnology (ARIM) Japan from the Ministry of Education, Culture, Sports, Science and Technology (MEXT).

References

1. Shi, X.; Ueno, K.; Oshikiri, T.; Sun, Q.; Sasaki, K.; Misawa, H., Enhanced water splitting under modal strong coupling conditions. *Nat. Nanotechnol.* **2018,** *13*, 953-958.

2. Oshikiri, T.; Jo, H.; Shi, X.; Misawa, H., Boosting Hydrogen Evolution at Visible Light Wavelengths by Using a Photocathode with Modal Strong Coupling between Plasmons and a Fabry-Perot Nanocavity. *Chem. Eur. J.* **2022,** *28*, e202200288.

3. Liu, Y.-E.; Shi, X.; Yokoyama, T.; Inoue, S.; Sunaba, Y.; Oshikiri, T.; Sun, Q.; Tamura, M.; Ishihara, H.; Sasaki, K.; Misawa, H., Quantum-Coherence-Enhanced Hot-Electron Injection under Modal Strong Coupling. *ACS Nano* **2023,** *17*, 8315-8323.

4. Hashiyada, S.; Narushima, T.; Okamoto, H., Local Optical Activity in Achiral Two-Dimensional Gold Nanostructures. *J. Phys. Chem. C* **2014,** *118*, 22229-22233.

5. Arikawa, T.; Hiraoka, T.; Morimoto, S.; Blanchard, F.; Tani, S.; Tanaka, T.; Sakai, K.; Kitajima, H.; Sasaki, K.; Tanaka, K., Transfer of orbital angular momentum of light to plasmonic excitations in metamaterials. *Sci. Adv.* **2020,** *6*, eaay1977.

6. Zu, S.; Sun, Q.; Cao, E.; Oshikiri, T.; Misawa, H., Revealing the Chiroptical Response of Plasmonic Nanostructures at the Nanofemto Scale. *Nano Lett.* **2021,** *21*, 4780-4786.

7. Oshikiri, T.; Sun, Q.; Yamada, H.; Zu, S.; Sasaki, K.; Misawa, H., Extrinsic Chirality by Interference between Two Plasmonic Modes on an Achiral Rectangular Nanostructure. *ACS Nano* **2021,** *15*, 16802-16810.

Metamaterial Technology and Its Application Prospects

High-Density Carbon Nanotube Forest Metamaterials for Advanced Photonic Applications

H. Furuta[1*], H. Kimura[1], H. Sakoda[1], R. Matsuzaki[1], S. Islam[1], and K. Kobiro[1]

[1]Kochi University of Technology, Japan
[*]Corresponding author: furuta.hiroshi@kochi-tech.ac.jp

Abstract: Carbon nanotube (CNT) forest metamaterials grown on nano-spherical substrates show flat reflectance in the visible range, showing potential for solar absorption and photonic computing applications through controlled electromagnetic resonance and isotropic optical characteristics.

Metamaterials have emerged as a frontier in manipulating electromagnetic waves, with carbon nanotubes (CNTs) representing a novel class of metamaterials that harness the unique electronic and optical properties of CNTs for advanced photonic applications. Recent progress in nano-scale lithography, such as UV and electron beam lithography, has paved the way for developing highly efficient and functional devices composed of nano-scale metamaterial circuits for energy conversion and computational applications. These advancements are underscored by the ability of metasurface to induce electromagnetic resonance at the nanoscale, which is critical for the miniaturization and enhancement of device performances. The precision offered by top-down lithographic techniques is approaching physical limits, yet the demand for finer patterning continues to grow. In this scenario, carbon nanotubes (CNTs) stand out due to their intrinsic one-dimensional structure and self-organized pattern formation, which open new avenues for metamaterial design in the optical range. As depicted in Fig. 1, our work encompasses the integration of fine patterning through Focused Ion Beam (FIB) micro-fabrication and the exploration of bottom-up processes that lead to self-aligned and self-assembled metamaterials. These processes yield CNT metamaterials with distinctive photonic properties such as enhanced infrared absorption, tunable color profiles, and VIS-IR wavelength selectivity. The figure displays the versatility of CNT forest metamaterials, highlighting the precise control of growth density and alignment critical for large-scale applications in devices such as solar heat absorbers with tailored wavelength selectivity.

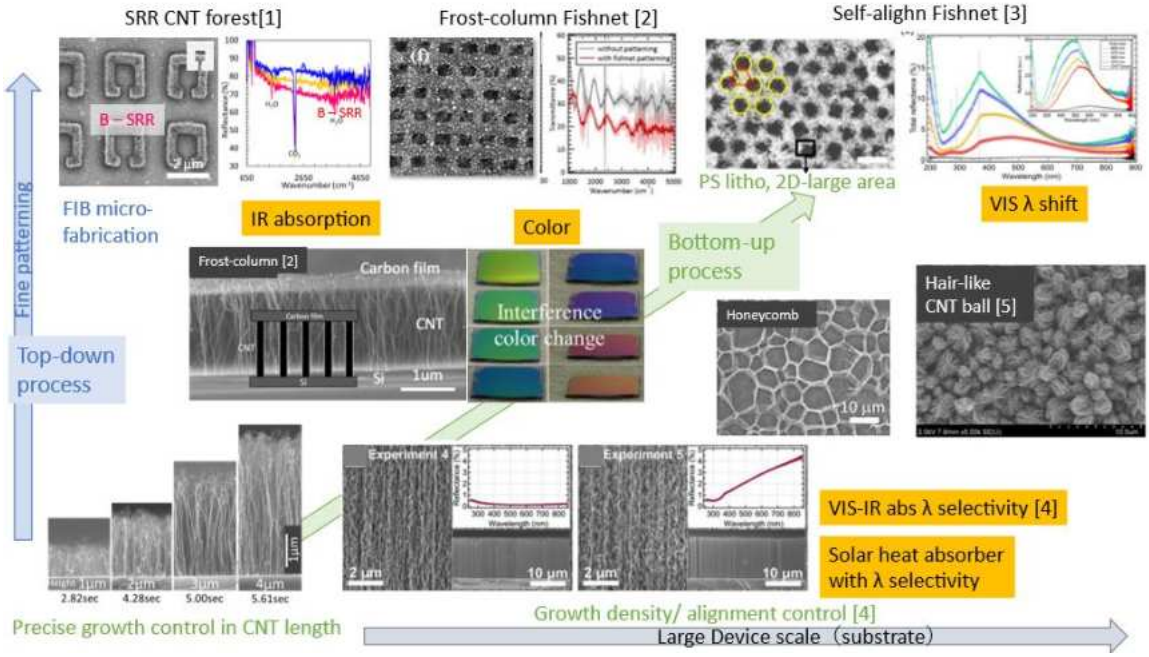


Figure 1. Fabrication of carbon nanotube forest metamaterials and their optical properties. [1-5]

CNTs were grown on FeOx-ZrO_2 MARIMO (Micro/Mesoporous Architected Roundly Integrated Metal Oxide) nano-scale spherical substrates in the thermal CVD process. Morphological characterization of the resultant metamaterials was conducted using SEM and Raman spectroscopy to evaluate the vibrational modes, indicating the quality of the CNTs. The optical properties were studied through spectrometry to measure the total and diffuse reflectance across the visible spectrum.

The SEM images (Fig.2 (a)) reveal a consistent and dense forest-like arrangement of CNTs with all-angle alignment attributable to the nano-spherical substrate geometry. This configuration contributed to flat reflectance spectra within the visible region (Fig.2(b)). The Raman spectrum in Fig.2(c) displays distinct G, D, and 2D bands, confirming high-quality multi-walled CNTs of G/D ratio ~ 2. Such a flat reflectance spectrum and the uniformity of CNT alignment indicate the material's potential for selective electromagnetic resonance control, a key factor for enhancing the efficiency of photonic devices.

The all-angle alignment of CNTs on spherical substrates exhibits the potential for isotropic optical behavior, a highly sought-after feature in photonic materials. This could lead to advancements in the design of solar wave absorbers with improved efficiency, benefiting solar power technology. Additionally, the uniform photonic response holds promise for the burgeoning field of photonic computing, where waveguides and switches require precise light control.

A part of this work was supported by Kakenhi C 23K04383 and 22K04819.

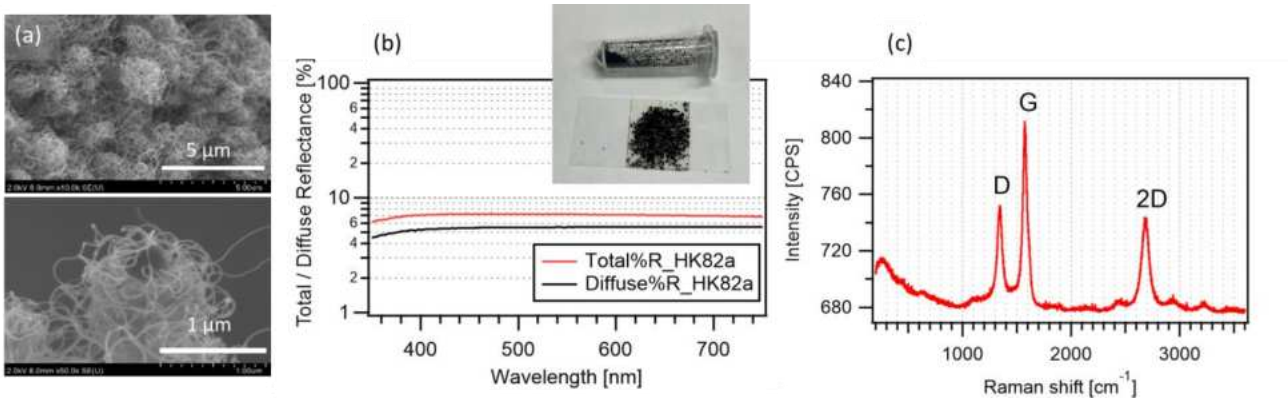


Figure 2. (a) SEM images of CNT-hair-like structures grown on nano-scale spherical oxide composite FeO_x-ZrO_2 MARIMO (CNT-MARIMO), (b) UV-VIS total and diffuse reflectance spectra, and (c) Raman spectrum.

References

1. Pander, A., K. Takano, A. Hatta, M. Nakajima, and H. Furuta, “Shape-dependent infrared reflectance properties of CNT forest metamaterial arrays,” Opt. Express, Vol. 28, No. 10, 607-625, 2020.
2. Miyaji, H., A. Pander, K. Takano, H. Kohno, A. Hatta, M. Nakajima, and H. Furuta, “Optical reflectance of patterned frost column-like CNT forest for metamaterial applications,” Dia. Rel. Mater., Vol. 83, 196–203, 2018.
3. Pander, A., T. Onishi, A. Hatta, and H. Furuta, “Fabrication of Self-Assembling Carbon Nanotube Forest Fishnet Metamaterials,” Nanomaterials, Vol. 12, 464, 2022.
4. Pander, A., K. Ishimoto, A. Hatta, and H. Furuta, “Significant decrease in the reflectance of thin CNT forest films tuned by the Taguchi method,” Vacuum, Vol. 154, 285–295, 2018.
5. Kobiro, K., H. Kimura, S. Hirose, M. Kinjo, and H. Furuta, “Solvothermal synthesis of hair-like carbon nanotubes onto sub-micron-sized spherical metal oxide catalyst cores,” RSC Advances, Vol. 13, No. 20, 13809–13818, 2023.

Effective properties of self-assembled plasmonic clusters with spatial dispersion

R. Dwivedi[1,2], A. Aradian[1*], K. Vynck[3], and A. Baron[1]

[1]Centre de Recherche Paul Pascal, University of Bordeaux & CNRS, Bordeaux, France
[2]ENSEMBLE3 Centre of Excellence, Warsaw, Poland
[3]Institut Lumière Matière, University Claude Bernard Lyon 1 & CNRS, Lyon, France
[*]corresponding author: ashod.aradian@crpp.cnrs.

Abstract: We study dense, spherical clusters made of hundreds of randomly packed plasmonic nanoparticles. We find that, using a spatial dispersion formalism, these clusters can be described as much simpler equivalent, homogeneous spheres, revealing the presence of artificial magnetism, but also of a longitudinal mode localized at the cluster borders.

Clusters made of small, plasmonic resonators, like gold or silver nanoparticles, have been an extensive source of research in nanophotonics, both before and after the emergence of the concept of metamerials. Within the field of metamerials, such clusters have been put forward as nanosize building blocks, or "meta-atoms", which could be fabricated using bottom-up, chemical techniques such as self-assembly and colloidal engineering [1]. Research efforts have for example focused on fabricating clusters able to generate a magnetic response, in order to assemble them into 3D metamaterial structures exhibiting artificial magnetism at optical frequencies [2]. Also, more recently, efforts have been devoted to fabricating clusters which could act as "Huygens scatterers," i.e., particles that scatter light with extreme asymmetry, only in the forward direction, when illuminated by a plane wave [3,4]—a feature that could lead to the obtention of metasurfaces with extraordinary capabilities to manipulate wavefronts.

In this work [5], we study the latter case of spherical clusters, made of hundreds of small plasmonic nanoparticles (here, gold nanoparticles with radius 7 nm), randomly packed together with a variable particle density or volume fraction f. Optical properties of interest, like the scattering of an incoming wave onto the cluster, and the resulting Mie coefficients, can be very accurately calculated by means of numerical simulations of like T-matrix techniques. However, such calculations become highly computationally-intensive when the number of particles in the cluster reach a few hundreds, as in realistic situations. Moreover, results from T-matrix computations do not easily lend themselves to any physical interpretation of the behavior of the internal medium composed of the plasmonic particles.

We therefore set to determine whether it is possible to describe the electromagnetic behavior of such dense plasmonic clusters with effective parameters carrying out a more intuitive picture, like electric permittivity, magnetic permeability and so on. The so-called "homogenization" of dense particulate composites is a notoriously difficult issue. No mixing law is known to efficiently describe the resulting homogenized medium except for very dilute cases (f below a few percents), and the current state of theory does not even provide clear criteria to delineate when homogenization is possible or not.

To address this issue, at least empirically, we computed the multipolar response of clusters up to 80 nm in radius and up to a particle density fraction f=44% using high-precision T-matrix calculations. Within the range of explored sizes, we find that scattering from the clusters involves an overall electric dipole Mie term, magnetic dipole, electric quadrupole, magnetic quadrupole; higher order multipoles remain insignificant. Then, we compared the obtained results with the multipolar response calculated for spheres of the same radius, but filled with a fictitious homogeneous medium. The values of the constitutive parameters (like the electric permittivity)

of the fictitious medium inside the homogeneous spheres were adjusted until an accurate agreement between the Mie coefficients of the homogeneous sphere and those of the real cluster was found, through a careful fitting procedure. When such a fit was obtained, we considered that the homogeneous spheres qualified as electromagnetic equivalents of the clusters, at least from the point of view of their scattering properties.

For clusters with small particle densities ($f < 0.15$), it was enough to use an equivalent medium with an effective dielectric permittivity only to reproduce the scattering from the clusters. But for higher densities, we found that other parameters need to be introduced. This is obviously due to the intricate, multiple interparticle couplings occurring in these systems, giving rise to "spatial dispersion" phenomena. Spatial dispersion arises frequently in complex systems, when the response of the medium becomes non-local, i.e., the polarization at one spatial point depends on the value of the electromagnetic field over a more or less spread area around it. Using a weakly spatially dispersive description for the internal medium of the homogeneous spheres, we found that it was indeed possible to successfully fit the scattering properties of clusters even in the densest cases, with f as high as 44% [5].

This weak spatial dispersion description involves three intuitive effective parameters characterizing the equivalent medium, with a transparent physical significance: -i- an electrical permittivity as in the dilute cases; -ii- a magnetic permeability, confirming that artificial magnetism emerges naturally in dense random clusters, due to particle couplings without the need of a specific ordering; -iii- a third parameter related to longitudinal waves in the system. The appearance of the latter is due to the fact that spatially dispersive systems not only support standard transverse electromagnetic waves, but also longitudinal ones; the inclusion of the longitudinal mode is required to obtain a proper fitting of the clusters. Our study shows that the longitudinal mode is strongly localized at the borders of the clusters [5].

Longitudinal modes have been largely ignored in the description of metamaterials with artificial magnetism (self-assembled or not), but this is unjustified on theoretical grounds. Our description, inclusive of the longitudinal mode, should be seen as an attempt at providing a better and more consistent approach, but still easy to understand physically.

In conclusion, our work [5] offers the opportunity to reproduce the electromagnetic properties of dense clusters with simpler equivalent, homogeneous spheres, over a wide range of particle densities. Such equivalence can be put to use when designing e.g. metasurfaces or other structures involving plasmonic clusters, for example by substituting them with the equivalent spheres in simulation steps ahead of fabrication, thereby drastically cutting down computational costs and allowing to explore a wider range of possible designs.

References

1. Baron, A., A. Aradian, V. Ponsinet and P. Barois, "Bottom-up nanocolloidal metamaterials and metasurfaces at optical frequencies," Comptes Rendus Physique, Vol. 21, 443–465, 2020.
2. Gomez-Graña, S. *et al*., "Hierarchical self-assembly of a bulk metamaterial enables isotropic magnetic permeability at optical frequencies," Mater. Horiz., Vol. 3, 596–601, 2016.
3. Elancheliyan., R. *et al*, "Tailored self-assembled nanocolloidal Huygens scatterers in the visible," Nanoscale, Vol. 12, 24177, 2020.
4. Laffite, M. *et al*, "Colloidal Self-Assembly of Silver Nanoparticle Clusters for Optical Metasurfaces," Langmuir, Vol. 40, 2601–2615, 2024.
5. Dwivedi, R., A. Aradian, V. Ponsinet, K. Vynck and A. Baron, "Effective-medium description of dense clusters of plasmonic nanoparticles with spatial dispersion," Phys. Rev. A, Vol. 109, 023507, 2024.

Optical properties and luminescence control of Ag/TiO_2 stacked metasurfaces using out-of-plane quadrupole resonance

T.Y. Lo[1], S. Murai[1*], and K. Tanaka[1]

[1]Graduate school of Engineering, Kyoto University, Japan
[*]corresponding author: murai@dipole7.kuic.kyoto-u.ac.jp

Abstract: In this study, we experimentally and numerically elucidated the optical properties of a bilayer metasurface system exhibiting out-of-plane quadrupole resonance characteristics and demonstrated the potential for bilayer metasurfaces system in directional light source application.

1. Introduction

Metasurface stickers, embedding periodic nano-structures into transparent elastomers, offer advantages such as easy attachment and detachment, even from material surfaces where direct fabrication of metasurfaces is challenging. In previous research, by utilizing the stacked metasurfaces, the fluorophore layer sandwiched between two metsurfaces can simultaneously achieve the highest efficiency in absorption enhancement and light extraction within individual metasurface[1]. In this work, we employed the out-of-plane quadrupole resonance exhibited by the first-layer Ag sticker to enhance the interaction between the first and second layers[2]. By controlling the interlayer distance, we elucidated the variations in their optical properties. Finally, we demonstrated the unique directional photoluminescence enhancement behaviour originated from the interaction of out-of-plane quadrupolar mode inside the two layers and provided the insight of their application in directional light sources.

2. Results and Discussion

Fig.1 illustrates the out-of-plane electric field distribution in the quadrupole resonance region for varying interlayer distances between two metasurfaces. As the two layers approach to each other, the quadrupole resonance of the first layer gradually extends into the underlying TiO2 metasurface. This out-of-plane oscillating electric field (Ez) forms as a new excitation source, inducing in-plane magnetic SLR within the bottom TiO2 metasurface[Fig.1(c)].

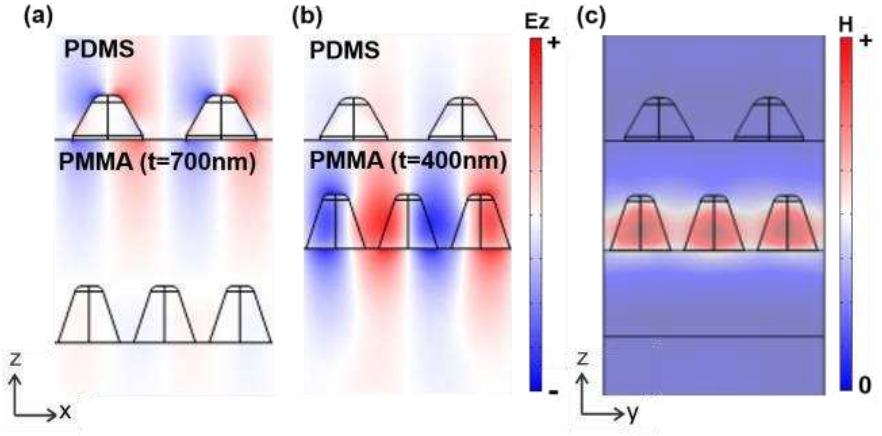


Fig 1. Numerical simulations of the out-of-plane electric field component (Ez) and magnetic field (H) distributions of Ag/TiO2 stacked metasurfaces separated by (a) 700 nm, (b and c) 400 nm.

Fig.2(a-b) shows the directional photoluminescence enhancement of the bilayer metasurfaces system with varying interlayer distances. As shown in Fig.2(b), with decreasing interlayer distance, the photoluminescence enhancement factor significantly and monotonically increases, while the directionality gradually converges towards ±5 degrees. This behavior can be attributed to the combined effect of the reduction in interlayer distance, leading to enhanced absorption in the bottom TiO2 metasurface, multiplied by the intensified field strength induced by mSLR.

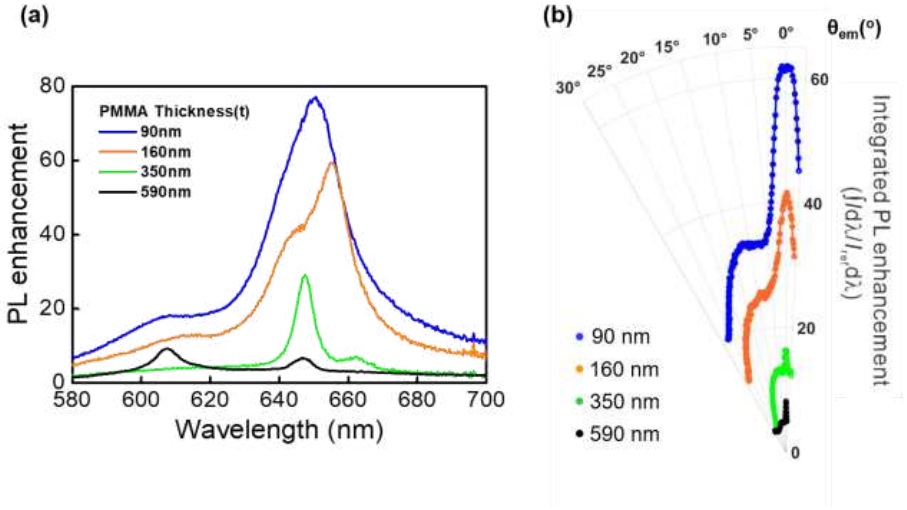


Fig 2. (a) PL enhancement spectra of Ag/TiO2 stacked collected at θem = 0 o. (b) PL enhancements calculated from the spectrally integrated PL intensity for the Ag/TiO2 stacked metasurfaces with various interlayer distances presented in a polar plot.

3. Conclusion

This study, for the first time, demonstrates both experimental and numerical simulations results showcasing the optical characteristic variations of bilayer metasurfaces at various interlayer distances. It also provides insights into their application in directional photoluminescence enhancement for the combination of the layered emitters.

References

1. Murai, S., Agata, K., & Tanaka, K, "Photoluminescence from an emitter layer sandwiched between the stack of metasurfaces," *J. Appl. Phys,* **129** (18) (2021).
2. Lo, T., Murai, S., & Tanaka, K, "Silver Nanoantenn Stickers for Photoluminescence Control," *ACS. Appl. Opt. Mater.*, **1**(4), 870-877 (2023).

Beyond Singularities: New Frontiers in Centrosymmetric Gain-Enhanced Metal Nanoparticles and Their Applications

K. Caicedo[1], M. Mora[1], N. Recalde[1], M. A Iatì[2], R. Saija[2,3], O. M. Maragó[2], A. Aradian[4], M. Infusino[1] and A. Veltri[1,*]

[1]Colegio de Ciencias e Ingenieria, Universidad San Francisco de Quito, Ecuador
[2]CNR-IPCF, Istituto per i Processi Chimico-Fisici, I-98158, Messina, Italy
[3]Dipartimento di Scienze Matematiche e Informatiche, Scienze Fisiche e Scienze della Terra, I-98166, Università degli Studi di Messina, Italy
[4]Université de Bordeaux, CNRS, CRPP,UMR5031, F-33600 Pessac, France
[*]corresponding author: aveltri@usfq.edu.ec

Abstract: In the evolving field of nanophotonics, the study of gain-enhanced metal nanoparticles presents numerous theoretical and practical possibilities. In recent years, our research group has focused on centrosymmetric gain-enhanced nanoparticles, exploring their dynamic behaviors and the intricate interplay between quantum and electromagnetic phenomena.

These systems present a largely unexplored field ripe with potential and offering a wealth of possibilities, both theoretically and in application.

In a pivotal work [1], we identified substantial behavioral changes in single metal nanoparticles within active gain mediums, particularly across the emission threshold. The interplay between local field enhancement and the corresponding depletion of population inversion, in fact typically leads to a Spatial Hole Burning (SHB) driven mode-cascade which is a phenomenon as fascinating as difficult to pinpoint in a formal theoretical framework. Notably, this cascade is absent in small nanoshells whose single-mode emission properties can be completely described with a quasi-static time-dynamic model [2].

The electromagnetic behavior of nanoshells in emissive regimes is however just one aspect of their intriguing properties. Even below the emission threshold, the ability of gain to locally amplify plasmonic fields renders these nanoparticles suitable for a wide array of applications. For instance, in this work [3], we demonstrated how the integration of externally pumped gain elements intrinsically alters the behavior of nanoshells in an optical tweezers configuration, showcasing their diverse functional capabilities. It's important to note that the conversion of electromagnetic energy into heat, a critical factor in evaluating the effect of an externally pumped nanoshell in an optical force field, was not considered in that particular study. However, we have made significant progress in this area and will be presenting some new results that delve into this aspect.

Finally, our earlier models within the quasi-static limit, while insightful, faced limitations when applied to larger particles and multi-modal phenomena such as SHB-driven mode cascades. To address this, we have developed a new time-dynamical model based on Mie Vector Spherical Harmonics [4], representing a significant advancement in the study of gain-enhanced nanoparticles. Although this new approach does not fully describe the emission regime yet, it does allow us to predict the transient states preceding emission and represents an essential step forward in the direction of a model able to adequately describe the full electromagnetic

phenomenology of these systems. Moreover, by means of this approach we have also been able to unravel a new phenomenon occurring in the sub-emissive regime: when gain is injected at the desired frequencies, higher-order and less intense modes can be selectively enhanced, allowing for a tailored spatial shaping of the electromagnetic field around the particle.

The ongoing exploration of gain-enhanced metal nanoparticles is revolutionizing the field of nanophotonics, centrosymmetric gain-enhanced nanoparticles hold promise for diverse applications. Our studies contribute to a deeper understanding of their fundamental properties and practical applications. From enhancing the operational dynamics in optical tweezers to developing advanced theoretical models. As we continue to push the boundaries of this research, we anticipate unlocking even more of their untapped potential, leading to innovative solutions in nanotechnology and beyond.

References

1. Veltri, A. et al. “Multipolar, time-dynamical model for the loss compensation and lasing of a spherical plasmonic nanoparticle spaser immersed in an active gain medium,” Scientific Reports, Vol. 6, Article No. 33018, 2016. DOI: 10.1038/srep33018.
2. Aradian, A. et al. “Gain enhanced metal nanoshells: below and above the emission threshold,” [Arxiv Preprint], 2023. arXiv:2312.13812.
3. Polimeno, P. et al. “Gain-Assisted Optomechanical Position Locking of Metal/Dielectric Nanoshells in Optical Potentials,” ACS Photonics, Vol. 7, No. 4, 1035–1042, 2020. DOI: 10.1021/acsphotonics.0c00213.
4. Recalde, N. et al. “Dynamic Multi-Mode Mie Model for Gain-Assisted Metal Nano-Spheres,” Materials, Vol. 16, No. 5, 1911, 2023. DOI: 10.3390/ma16051911.

Femtosecond pulse shaping with semiconductor Huygens' metasurfaces

K. Tanaka[1,3], D. Arslan[4], M. Weissflog[2,3], N. Geib[2], K. Gerold[4], A. Szeghalmi[4], M. Ziegler[5], F. Eilenberger[2,3,4], T. Pertsch[2,4], and I. Staude[1,3]

[1]Institute of Solid State Physics, Friedrich Schiller University Jena, Max-Wien-Platz 1, 07743 Jena, Germany
[2]Institute of Applied Physics, Abbe Center of Photonics, Friedrich Schiller University Jena, Albert-Einstein-Straße 15, 07745 Jena, Germany
[3]Max Planck School of Photonics, Hans-Knöll-Straße 1, 07745 Jena, Germany
[4]Fraunhofer Institute for Applied Optics and Precision Engineering IOF, Albert-Einstein-Straße 7, 07745 Jena, Germany
[5]Leibniz Institute of Photonic Technologies, Albert-Einstein-Straße 9, 07745 Jena, Germany

*corresponding author: katsuya.tanaka@uni-jena.de

Abstract: Manipulating ultrashort laser pulses unlocks versatile applications in laser processing, quantum state encoding, ultrafast bio-chemical reactions, and optical communication. Our study demonstrates femtosecond-scale pulse shaping with silicon Huygens' metasurfaces, enabling control over pulse dynamics. Our experimental results align closely with simulations, underscoring precise pulse manipulation capabilities.

The precise tailoring of ultrafast pulse shaping holds great promise across various domains, from laser material processing and quantum state encoding to ultrafast bio-chemical reactions and optical communication [1,2]. Optical metasurfaces, which can exert precise control over incident light fields, have emerged as a powerful tool for pulse shaping [3]. In recent years, low-loss resonant dielectric Huygens' metasurfaces gained substantial recognition for their capacity to precisely adjust the phase of incident light while maintaining nearly 100% of its original intensity [4]. In this study, we demonstrate the ability to shape pulses at femtosecond time scale using semiconductor Huygens' metasurfaces integrated into the Fourier plane of a 4-f system as shown in Figure 1. Our approach leverages spatially variant silicon metasurfaces at the Fourier plane of the setup, allowing us to selectively tune the phase and amplitude of the individual frequencies of an incident Gaussian pulse. The metasurfaces consist of locally periodic square arrays of silicon nanocylinders featuring a spatial variation of their geometric parameters (lattice constant and radius). They were designed and fabricated to induce three distinct temporal effects on the input pulse: pulse splitting, pulse stretching and pulse rectification. We utilized a Ti:Sa laser in combination with an optical parametric oscillator to generate ultrashort Gaussian input pulses at the central wavelength of 1500 nm and detected the output pulses by using the frequency-resolved optical gating method. Furthermore, the complex transmission of the fabricated metasurfaces was investigated by imaging interferometry. Figure 2 illustrates both simulated and experimental pulse profiles for both input and output signals. To demonstrate pulse stretching, we successfully fabricated a metasurface that stretches a Gaussian pulse width from 229 fs to 489 fs. In the case of pulse splitting, we fabricated a metasurface that transforms a single Gaussian pulse into two distinct Gaussian pulses with a separation of 524 fs. Finally, for pulse rectification, we have observed a nearly vertical rise and fall in temporal intensity profile in experiment although the consistency of the peak amplitude over time remains a challenge. This inconsistency can likely be attributed to fabrication errors in the diameters of the nanocylinders and surface inhomogeneities. Overall, the pulse characteristics observed in these experiments matches our numerical simulations, confirming the

metasurfaces' ability to generate desired pulse shapes. Furthermore, the resonant features of pulse shaping Huygens' metasurfaces can unlock additional opportunities for nonlinear optical effects, excitation of emissive materials, regarding pulse-shaping without the need for spectrally spreading the pulse [4] and spatiotemporal shaping [1].

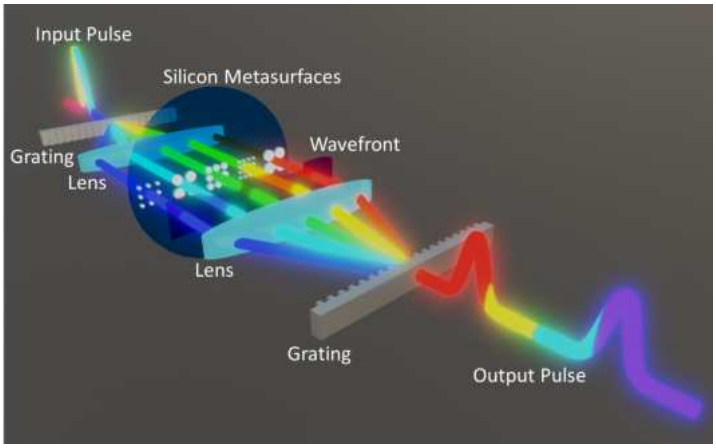


Figure 1 An artist's impression of a silicon Huygens' metasurface demonstrating pulse splitting effect using a 4-f configuration.

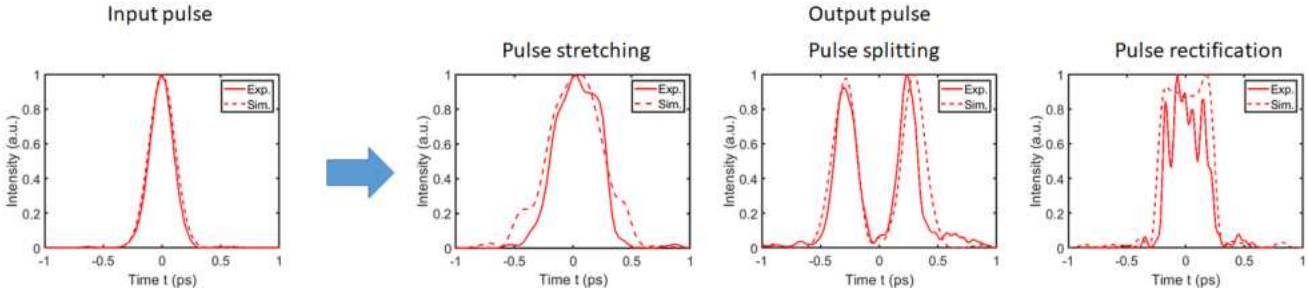


Figure 2 Input and output pulse profiles both in simulation and experiment. Numerical calculations of the pulse profiles shaped by the silicon metasurfaces were performed using COMSOL Multiphysics. Experimental data was acquired and analyzed using a standard frequency-resolved optical gating method integrated into a pulse detection system after the 4-f optical setup.

References

1. Chen, L., Zhu, W., Huo, P., Song, J., Lezec, H.J., Xu, T., Agrawal, A., "Synthesizing ultrafast optical pulses with arbitrary spatiotemporal control," Science Advances 8, 43, 2022.
2. Weiner A. M., "Ultrafast optical pulse shaping: A tutorial review," Appl. Opt. 47, A88, 2008.
3. Divitt, S., Zhu, W., Zhang, C., Lezec, H. J., and Agrawal, A., "Ultrafast optical pulse shaping using dielectric metasurfaces", Science 364, 890-894, 2019.
4. Decker, M., Staude, I., Falkner, M., Dominguez, J., Neshev, D.N., Brener, I., Pertsch, T. and Kivshar, Y.S., "High-Efficiency Dielectric Huygens' Surfaces", Advanced Optical Materials 3, 813-820, 2015.

Bottom-up fabricated metasurfaces with correlated disorder for the light management in solar cells

P. Dhawan[1], M. Gaudig[2], P. Piechulla[2], A. Sprafke[2], R. B. Wehrspohn[2], and C. Rockstuhl[1,3]

[1] Institute of Theoretical Solid State Physics, Karlsruhe Institute of Technology, Kaiserstr. 12, 76131 Karlsruhe, Germany
[2] Institute of Physics, Martin Luther University Halle-Wittenberg, Heinrich-Damerow-Str. 4, 06120 Halle (Saale), Germany
[3] Institute of Nanotechnology, Karlsruhe Institute of Technology, Kaiserstr. 12, 76131 Karlsruhe, Germany
*corresponding author: carsten.rockstuhl@kit.edu

Abstract: The bottom-up fabrication of metasurfaces with correlated disorder on large surfaces permits excellent control over light propagation characteristics and unlocks applications in the context of light management in solar cells. This contribution comprehensively describes the design, fabrication, and characterization of such devices with increasing complexity.

Metasurfaces with correlated disorder can be fabricated on large scales using a dedicated bottom-up process. Here, PMMA nanoparticles with predefined size statistics are immersed into a solution of a given ionic strength. By suitably functionalizing ordinary substrates so that their surfaces are weakly positively charged, the dip-coating of the substrate into the applied solution allows the nanospheres to be deposited onto it at a controllable density into a pattern characterized by nearly-hyperuniform disorder [1]. These hyperuniform structures are characterized by a suppressed variation of the particle density, like in a periodic structure. However, at the same time, they have the same properties in all directions at short distances, so they respond in an isotropic manner. Their scattering response is structured, their response is wavelength insensitive, and they can be designed deterministically. Metasurfaces made from high-index discs can be fabricated when using these arrays of PMMA nanospheres as an etch mask for an underlying high-index thin film. Then, additional degrees of freedom come into the game by controlling the multipolar contribution of the scattering characteristics of the individual discs.

In a sequence of contributions [2-5|, we have demonstrated the basic optical function of such disordered metasurfaces when designed to operate in the Huygens regime, i.e., when the induced electric and magnetic dipole moments are suitably balanced to suppress back-reflection. That property, combined with the vanishing structure factor of the hyperuniform interfaces, which suppresses scattering in the forward direction, and the possibility to fabricate these metasurfaces on large scales, at low costs, and in a short amount of time, makes them appealing structures for an integration into a solar cell with the purpose of light management. In essence, these metasurfaces suppress reflection and scatter light into oblique directions to maximize the absorption in the solar cell.

In our latest efforts [6], we have demonstrated that by combining these hyperuniform metasurfaces with slightly more conventional graded anti-reflection coatings, we can make the best out of the two worlds and suppress most optimal the spurious reflection from a solar cell and maximize the light absorption. Selected results are shown in Fig. 1. At the conference, we will provide all the details that concern the design, fabrication, and characterization of such devices and convincingly demonstrate that the chosen bottom-up fabrication route is a promising approach to reach structures that serve most optimal their anticipated purpose.

The authors acknowledge support from the Deutsche Forschungsgemeinde (DFG) (413644979, RO 3640/11-1 and WE 4051/26-1).

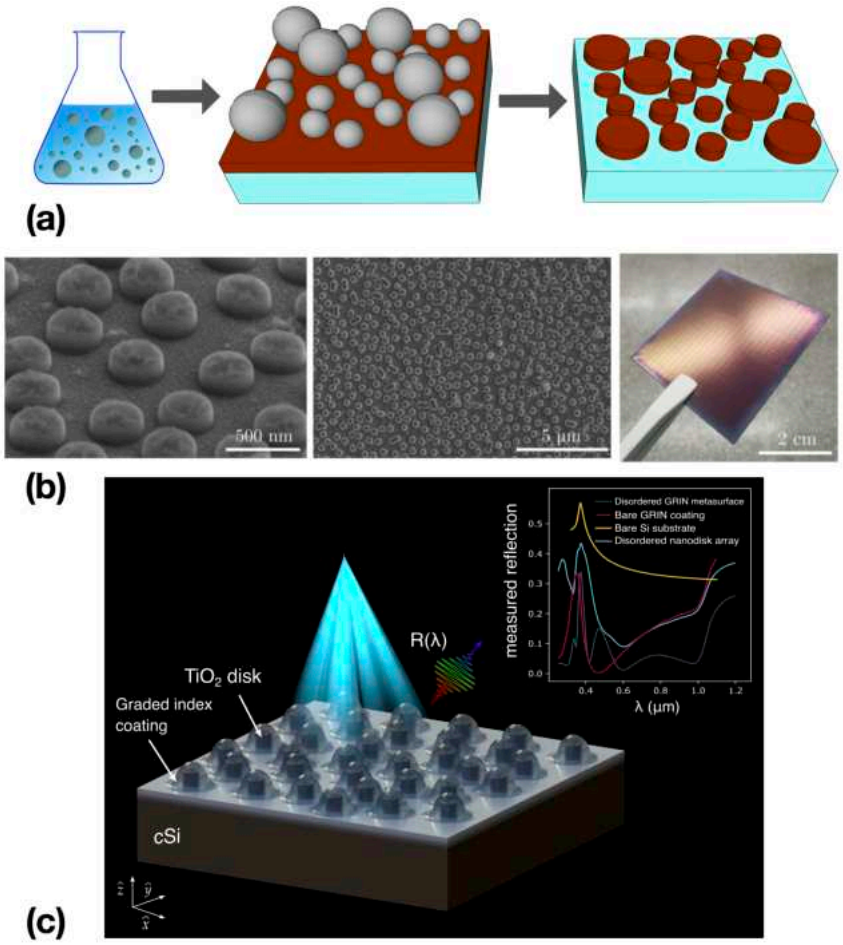


Figure 1: (a) Fabrication route of the metasurfaces with correlated disorder. (b) SEM micrographs of fabricated metasurfaces. (c) Characterization of metasurfaces upon integration as anti-reflection coating into a solar cell. Multiple devices are compared in the inset.

References

1. Piechulla P. M., A. Sprafke, L. Mühlenbein, S. Nanz, A. Abass, C. Rockstuhl, and R. B. Wehrspohn, Advanced Optical Materials, Vol. 6, 1701272, (2018)
2. Dhawan P., M. Gaudig, A. Sprafke, R. B. Wehrspohn and C. Rockstuhl, Optics Express, Vol. 29, 19903, 2021.
3. Piechulla P. M., E. Slivina, D. Bätzner, I. Fernandez-Corbaton, P. Dhawan, R. B. Wehrspohn, A. N. Sprafke, and C. Rockstuhl, ACS Photonics, Vol. 8, 3476, 2021.
4. Piechulla P. M., B. Fuhrmann, E. Slivina, C. Rockstuhl, R. B. Wehrspohn, and A. N. Sprafke, Advanced Optical Materials, Vol. 9, 2100186, 2021.
5. Dhawan P., L. Schulte, P. Piechulla, Y. Augenstein, M. Gaudig, A. Sprafke, R. B. Wehrspohn, and Carsten Rockstuhl, Journal of the Optical Society of America B, Vol. 40, B8, 2023.
6. Dhawan P., M. Gaudig, A. Sprafke, P. Piechulla, R. B. Wehrspohn, and C. Rockstuhl, „Anti-Reflective Graded-Index Metasurface with Correlated Disorder for Light Management in Planar Silicon Solar Cells,“ accepted for publication in Advanced Optical Materials

Creating Meta-Atoms Based on Gold Nanoparticle Assemblies on Polymer Microspheres

H. Yabu[1*]

[1]Advanced Institute for Materials Research (WPI-AIMR), Tohoku University, Japan
[*]corresponding author: hiroshi.yabu.d5@tohoku.ac.jp

Abstract: Fabrication of polymer microspheres densely accumulated with noble metal nanoparticles on their surface, and their applications as sensors and in metamaterials will be shown.

Particles that accumulate noble metal nanoparticles on the surface of dielectric particles can become 'meta-atoms', the building blocks of metamaterials that utilize plasmon absorption with independent of incident angle of light. Efforts have been made to realize such meta-atoms by electroless plating of silver on the surface of dielectric particles like silica or polymer microspheres, or by adsorbing noble metal nanoparticles such as gold. However, challenges existed in controlling nanoparticle size, as well as their arrangement and density.

We have reported a method for fabricating polymer microspheres with nanostructures mixing various types of polymers, using the Self-ORganized Precipitation (SORP) method, which involves adding a poor solvent to a polymer solution and removing the good solvent by evaporation to obtain a dispersion of polymer microspheres. When polystyrene (PS) and amino-terminated polybutadiene (PB-NH2) were mixed and fabricated using the SORP method, core-shell type microspheres were obtained[1], with positively charged PS as the core and PB-NH2 as the shell (Figure 1)[2]. Subsequently, by mixing a dispersion of uniformly sized gold nanoparticles, composite microspheres were obtained, where the gold nanoparticles were densely arranged on the surface due to electrostatic interactions.

The resulting composite microspheres have been demonstrated to be applicable as dispersed surface-enhanced Raman scattering (SERS) substrates[3] for analyzing adsorbed molecules, as meta-atoms in the visible to near-infrared region[4], and as probes for antigen-antibody reactions with high optical density[5].

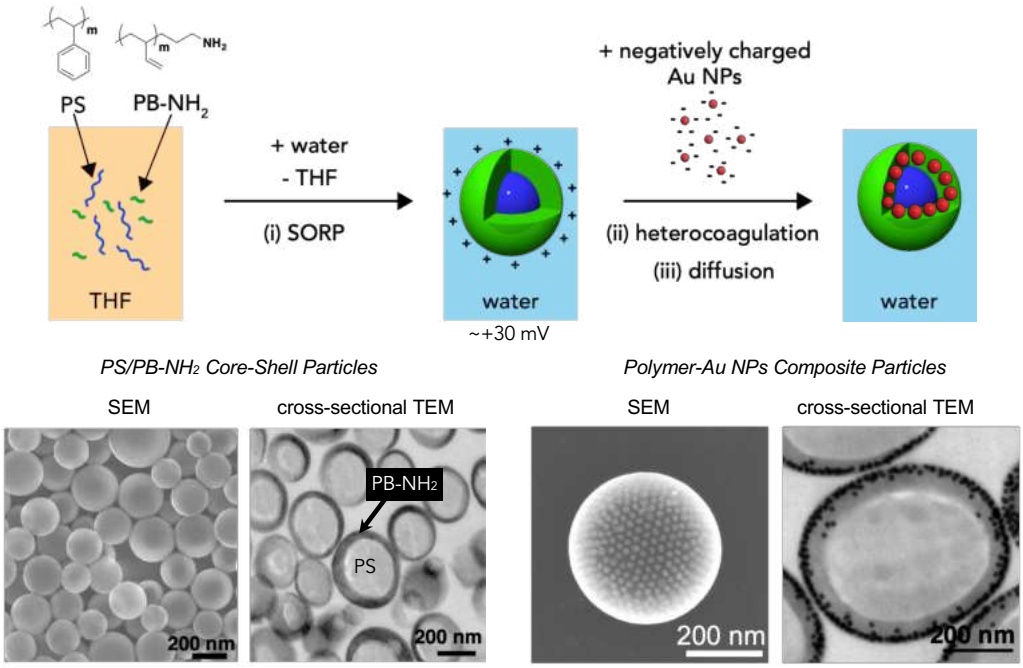


Figure 1. Schematic illustration of Au nanoparticles and polymer composite particles by SORP method (upper column), and SEM and cross-sectional TEM images of core-shell particles of PS/PB-NH2 (bottom left) and composite particles (bottom right), respectively.

References

1 Hirai, Y.; Avalos, E.; Teramoto, T.; Nishiura, Y.; Yabu, H. Ashura Particles: Experimental and Theoretical Approaches for Creating Phase-Separated Structures of Ternary Blended Polymers in Three-Dimensionally Confined Spaces. *ACS Omega* **2019**, *4* (8), 13106–13113.

2 Kanahara, M.; Satoh, H.; Higuchi, T.; Takahara, A.; Jinnai, H.; Harano, K.; Okada, S.; Nakamura, E.; Matsuo, Y.; Yabu, H. Fabrication of NIR-Excitable SERS-Active Composite Particles Composed of Densely Packed Au Nanoparticles on Polymer Microparticles. *Part. Part. Syst. Charact.* **2015**, *32* (4), 441–447.

3 Hirai, Y.; Matsuo, Y.; Yabu, H. Near-Infrared-Excitable SERS Measurement Using Magneto-Responsive Metafluids for in Situ Molecular Analysis. *ACS Appl. Nano Mater.* **2018**, *1* (9), 4980–4987.

4 Deng, T. S.; Parker, J.; Hirai, Y.; Shepherd, N.; Yabu, H.; Scherer, N. F. Designing “Metamolecules” for Photonic Function: Reduced Backscattering. *Phys. Status Solidi Basic Res.* **2020**, *257* (12), 1–11.

5 Yabu, H.; Yokokura, S.; Shimizu, S. Gold Nanoparticle-Decorated Polymer Particles for High-Optical-Density Immunoassay Probes. *Langmuir* **2024**, web released.

Aggregation of Core/Shell Quantum Rods in Composite Polymer Film for Polarization Conversion

Y. Okazaki[1*], S. Kubota[1], K. Hachiya[1], and T. Sagawa[1]

[1]Graduate School of Energy Science, Kyoto University, Japan
[*]corresponding author: okazaki.yutaka.8c@kyoto-u.ac.jp

Abstract: In this presentation, we introduce an approach for achieving both isotropy in the absorption process (low $P_{\text{LP-Abs}}$ value) and anisotropy in the emission process (high $P_{\text{LP-Lum}}$ value) by controlling aggregation formation of luminogens in uniaxially stretched luminogen/polymer composite films.

Linearly polarized luminescent (LPL) materials are attracting attention for a variety of applications including power-saving display and anti-counterfeit printing. In general, LPL materials that exhibit large polarization degree in light emission process ($P_{\text{LP-Lum}}$) also exhibit large polarization degree in light absorption process ($P_{\text{LP-Abs}}$) due to the orientation of the electronic transition dipole moment. Therefore, from the viewpoint of efficient light energy use, achieving both isotropy in the absorption process (low $P_{\text{LP-Abs}}$ value) and anisotropy in the emission process (high $P_{\text{LP-Lum}}$ value) has been considered as a challenging issue. In this presentation, we introduce an approach for overcoming this trade-off relationship by controlling aggregation formation of luminogens in uniaxially stretched luminogen/polymer composite films.

In this study, we selected CdSe/CdS core/shell quantum rod (QD) as highly emissive LPL source. QD synthesized by hot-injection method was mixed with poly(ethylene-*co*-vinyl acetate) (EVA) in toluene and was drop-casted on a glass substrate. The obtained QD/EVA composite film was peeled off from the glass substrate, stretched uniaxially, and reattached to the glass substrate. The obtained film (LPL_{QD} film) showed red-colored strong photoluminescence (PL) under UV light at 365 nm. When the PL was observed through linear polarizer placed in parallel direction to the stretching direction, it was clearly brighter than that observed through linear polarizer placed in perpendicular direction. For the quantitative evaluation, PL spectral measurements with polarization setup were performed. The large $P_{\text{LP-Lum}}$ value (0.63) at around 640 nm was confirmed under irradiation of depolarized 450 nm light. The $P_{\text{LP-Abs}}$ value was also calculated from PL intensities excited with parallel and perpendicular linearly polarized 450 nm light. Interestingly, the calculated $P_{\text{LP-Abs}}$ value (0.32) was clearly smaller than the $P_{\text{LP-Lum}}$ value (0.63). To investigate this phenomenon, we studied the effect of excitation wavelength on the PL peak position. All PL peak positions showed same wavelength even under different excitation wavelength. In addition, detection energy dependence on PL excitation (PLE) spectra was also studied and was no significant dependence was observed. These results indicate that the energy transfer between aggregated QRs in LPL_{QD} film involve in the observed polarization conversion phenomenon.

In this presentation, we will discuss about the detail mechanism of polarization conversion phenomenon observed in LPL_{QD} film.

References

1. J. Koo, S.-I. Lim, S. H. Lee, J. S. Kim, Y.-T. Yu, C.-R. Lee, D.-Y. Kim and K.-U. Jeong, “Polarized light emission from uniaxially oriented and polymer-stabilized AIE luminogen thin films,” Macromol., Vol. 52, No. 4, 1739– 1745, 2019.
2. Y. He, J. Li, J. Li, C. Zhu and J. Guo, “Photoinduced dual-mode luminescent patterns in dicyanostilbene-based liquid crystal polymer films for anticounterfeiting application,” ACS Appl. Polym. Mater., Vol. 1, No. 4, 746-754, 2019.

Development of Colloidal Silicon Nanoparticles and Composites for Photonic Applications

H. Sugimoto[1*], M. Fujii[1]

[1]Department of Electrical and Electronic Engineering, Graduate School of Engineering at Kobe University, Japan
[*]corresponding author: sugimoto@eedept.kobe-u.ac.jp

Abstract: Recently, we developed Mie resonant crystalline Si nanospheres in the size range of 100-300 nm dispersible in solution. Colloidal dispersions of Si nanospheres enable the formation of functional composites with different materials for photonic applications utilizing enhanced light matter interactions.

High index dielectric nanoparticles exhibit electric and magnetic Mie resonances and provide opportunities for manipulating and enhancing the light-matter interactions. The dielectric nanoantennas have been usually fabricated by electron beam lithographically on the solid substrate and thus the applicability of the solution-based assembly techniques have been limited compared to the plasmonic counterparts since gold and silver colloids that are commercially available.

In this talk, we present development of colloidal dispersion of perfectly spherical silicon nanoparticles dispersible in alcohol by thermal disproportionation of silicon monoxide at very high temperature (>1450°C) followed by chemical etching. We also developed monodisperse silicon nanoparticles by applying density gradient centrifugation process for the size separation.[1-4] Figure 1a shows the solution in which different sized silicon nanoparticles are dispersed. The solutions exhibit bright scattering colors depending on nanoparticles sizes. TEM image in Fig. 1b shows the monodisperse silicon nanoparticles with highly spherical shapes. In addition, Figure 1c demonstrates high crystallinity of the particle.

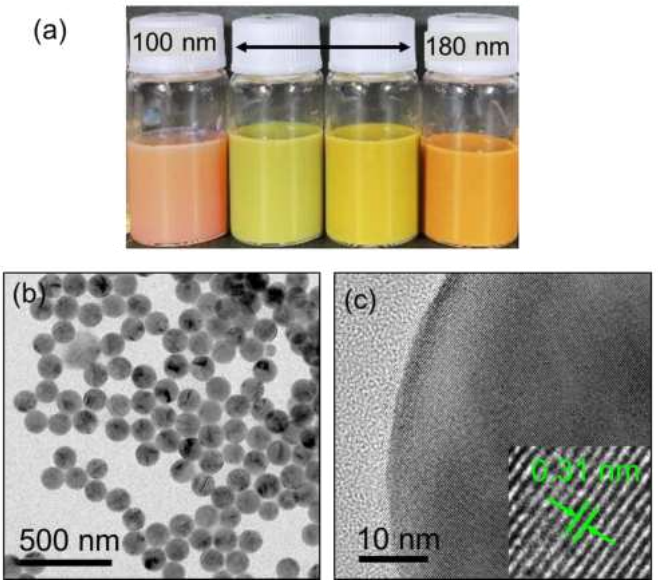


Figure 1. (a) Photo of colloidal suspension of Si nanoparticles with different average diameters. (b, c) TEM and HRTEM images of Si nanoparticles, respectively.

In this work, we also introduce the development of functional composites composed of a Si nanoparticle core and a metal and a transition metal dichalcogenide shell.[5-7] A Si-core/Au shell nanoparticles were produced by covering the surface of a Si nanosphere by Au (Si@Au). Figure 2a shows the STEM-EDS images of a Si@Au nanoparticle, demonstrating the formation of a core/shell structure.[5] We demonstrate the dark hybridized mode characteristics of the core-shell nanoparticles by the optical microscopy. Figure 2b and c demonstrate the successful formation of a Si@MoS_2 nanoparticle with ~5 MoS_2 layers. From the scattering spectroscopy on a single Si@MoS_2 nanoparticle, we show the spectral splitting of the magnetic dipole (MD) mode by the coupling with excitons in a MoS2 shell.[6]

References

1. Sugimoto, H, *et al.*, "Mie Resonator Color Inks of Monodispersed and Perfectly Spherical Crystalline Silicon Nanoparticles", Advanced Optical Materials, Vol. 8, Issue 12, 2000033, 2020.
2. Hinamoto, T *et al.*, "Colloidal Solutions of Silicon Nanospheres toward All-Dielectric Optical Metafluids", Nano Letters, Vol. 20, Issue 10, 7737-7743, 2020.
3. Sugimoto, H, Fujii, M, "Colloidal Mie Resonators for All-Dielectric Meta-Optics", Advanced Photonics Research, Vol. 2, Issue 4, 2000111, 2021.

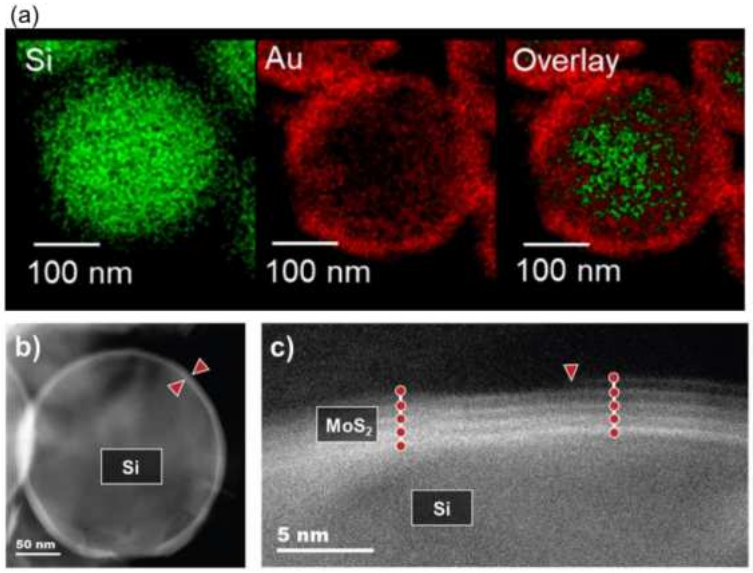


Figure 2. (a) STEM-EDS images of a Si@Au nanoparticle. (b, c) STEM images of a Si@MoS_2 nanoparticle.

4. Negoro, H, Sugimoto, H, Fujii, M, "Helicity-Preserving Optical Metafluids", Nano Letters, Vol. 23, Issue 11, pp.5101-5107, 2023.
5. Sugimoto, H, *et al.*, "Mode Hybridization in Silicon Core-Gold Shell Nanosphere", Small, Vol. 18, Issue 45, pp.2204890, 2022
6. Hinamoto, T *et al.*, "Resonance Couplings in Si@MoS2 Core-Shell Architectures", Small, Vol. 18, Issue 17, pp.2200413, 2022.
7. Adachi, M, *et al.*, "Fluorophore-Decorated Mie Resonant Silicon Nanosphere for Scattering/Fluorescence Dual-Mode Imaging", Small, Vol. 19, Issue 14, pp. 2207318, 2023.

Full-wafer fabrication of all-inorganic metalenses, waveguides and diffractive optics via direct nanoimprint lithography

Dae Eon Jung,[1] Vincent J. Einck,[1,3] Alex Dawicki,[1] Lucas D. Verrastro,[1] Amir Arbabi,[2] and James J. Watkins[1,3]*

1 Department of Polymer Science and Engineering, University of Massachusetts, Amherst, Massachusetts 01003, USA

2 Department of Electrical and Computer Engineering, Univ. of Massachusetts, Amherst, Massachusetts 01003, USA

3 Myrias Optics. Inc, Amherst, MA 01003

watkins@umass.edu, watkins@myriasoptics.com

Abstract: We fabricate all-inorganic, high refractive index optics, including metalenses, waveguides, and diffractive optical elements, via nanoimprint lithography with TiO_2 nanoparticle dispersion inks and report full-wafer fabrication of visible wavelength metalenses with absolute efficiencies greater than 80%. Atomic layer deposition is used as a post treatment to tune refractive index from 1.9 to 2.25 using less than 20 cycles.

Planar metalenses, waveguides, and diffractive optics are enabling for augmented reality, displays, compact precision imaging, 3D sensors, and other applications. Current approaches to all-inorganic metalenses involve time, materials, and cost intensive subtractive fabrication on semiconductor process platforms. For example, metalenses operating in the infrared are fabricated out of silicon, employ small device footprints, and are entering commercialization via subtractive processing. Visible wavelength devices, however, cannot be fabricated out of silicon and require high refractive index (RI) materials transparent in the visible, such as TiO_2, that are difficult to etch. Moreover, visible wavelength devices. such as waveguides for smart glasses, often require large device areas, presenting additional economic challenges for subtractive processing. Additive fabrication via nanoimprint lithography (NIL) in which devices are printed using stamps replicated from a master offers an efficient, cost-effective alternative manufacturing pathway.[1-4] We fabricate all-inorganic, high refractive index optics via NIL with TiO_2 nanoparticle dispersion inks.[2,3] The all-inorganic components offer better performance and superior mechanical and optical stability relative to devices produced via NIL using polymer/nanoparticle composites. We demonstrate full-wafer fabrication of visible wavelength metalenses lenses with absolute efficiencies greater than 80% (93% relative efficiency). We employ atomic layer deposition (ALD) as a post-imprint treatment that enables tuning of the refractive index from 1.9 to 2.25 using less than 20 cycles, which improves lens efficiency.[3] Tuning RI of the imprinted optics to match that of the substrates removes concerns about residual layer thickness, resolving an important issue for some applications. Additional cycles of ALD are used to precisely tune feature dimensions and feature spacings. Finally, we demonstrate the excellent optical and material stabilities of the all-inorganic imprinted optics.

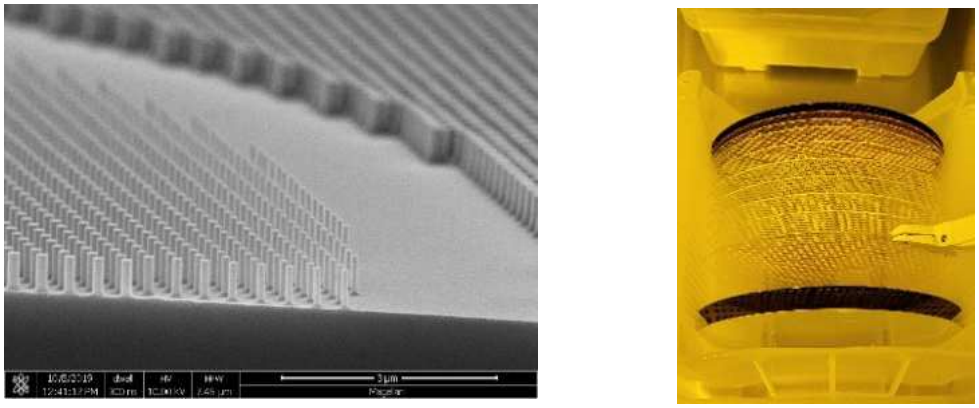


Figure 1. SEM image of a visible wavelength metalens prepared via direct NIL using nanoparticle dispersion inks (left)[1]. A cassette of wafers containing 1000 metalenses on each wafer produced via direct NIL (right).

References

1. Beaulieu, M.R.; Hendricks, N.R.; Watkins, J.J.; "Large-Area Printing of Optical Gratings and 3D Photonic Crystals Using Solution-Processable Nanoparticle/Polymer Composites." *ACS Photonics* **2014** *1*,(9) 799-805.
2. Einck, V. J.; Torfeh, M.; McClung, A.; Jung, D. E.; Mansouree, M.; Arbabi, A.; Watkins, J. J., Scalable Nanoimprint Lithography Process for Manufacturing Visible Metasurfaces Composed of High Aspect Ratio TiO2 Meta-Atoms. *ACS Photonics 2021*, 8 (8), 2400-2409.
3. Jung, D. E.; Howell, I. R.; Einck, V. J.; Arisoy, F. D.; Verrastro, L. D.; McClung, A.; Arbabi, A.; Watkins, J. J., Refractive Index Tuning of All-Inorganic TiO2 Nanocrystal-Based Films and High Aspect Ratio Nanostructures Using Atomic Layer Deposition: Implications for High-Throughput Fabrication of Metalenses. A*CS Applied Nano Materials* 2023, 6 (3), 2009-2019.
4. Yoon, G.; Kim, K.; Huh, D.; Lee, H.; Rho, J., Single-step Manufacturing of Hierarchical Dielectric Metalens in the Visible. *Nature Communications* 2020, 11 (1), 2268.

Transient dissipative structures in surface plasmon polaritons propagation

S. Derevyanko[1*] **and M. Spector**[2]
[1]School of Electrical and Computer Engineering, Ben-Gurion University of the Negev, Beer Sheva, Israel
[2]Schwartz/Reisman Science Education Center, Rehovot, Israel

[*]corresponding author: stasd@bgu.ac.il

Abstract: We suggest an easily configurable dynamical method of creating a transient periodic plasmonic lattice in a metal film by temperature induced variation of the dielectric permittivity. We demonstrate a range of effects from dissipative plasmonic crystal to induced electromagnetic transparency.

SPPs are coupled waves of electrons and light that travel along metal-dielectric interface. They can be very tightly focused, react to the surface properties, create strong electric fields near the edge, and be easily manipulated by engineering designs. These features make SPPs useful for many purposes, such as detecting molecules, making thin solar panels, producing new colors of light, enhancing light emission, connecting optical devices, switching fast signals, and computing with light, among others [1].

In the context of Drude theory of conductivity the electrons oscillate in response to the pump electric field. In this model the non-zero imaginary part of the dielectric constant is determined by electron-electron (e-e) and electron-phonon (e-ph) scattering rates. These in turn can be enhanced by various temperature effects. Therefore, by providing an external heat-dissipation source one can heat the electron and lattice subsystem and thus modulating the loss as experienced by a propagating SPP.

To model these effects, one often uses the so-called two temperature model (TTM) where the electromagnetic energy dissipated in the bulk of the metal acts as a source of heat [2]:

$$\begin{aligned} C_e\left(T_e\right)\frac{\partial T_e}{\partial t} &= \nabla\bullet\left[K_e\left(T_e,T_l\right)\nabla T_e\right]-G\left(T_e-T_l\right)+p_{abs} \\ C_l\left(T_l\right)\frac{\partial T_l}{\partial t} &= \nabla\bullet\left[K_l\left(T_l\right)\nabla T_l\right]+G\left(T_e-T_l\right) \end{aligned} \tag{1}$$

Here T_e, T_l are the temperatures of electron and lattice respectively, $C_{e,l}$ and $K_{e,l}$ are the heat capacities and thermal conductivities of the electron and lattice respectively while G is the electron-phonon coupling factor related to the rate of energy exchange between the electrons and the lattice. The energy dissipation caused by the pump field is proportional to the imaginary part of the dielectric permittivity and the intensity of the external electromagnetic field $p_{abs} \propto \varepsilon'' \left|E\right|^2$.

There are two possibilities as to how one can engineer the properties of the electron and lattice subsystems and thus control the losses experienced by the propagating SPP. In the first one [3] we can illuminate the metal-dielectric interface by two orthogonal strong pulsed beams in the near infra-red region inducing the effective periodic structure in the absorbed energy density (Figure 1a). The spatially periodic variation of the absorbed energy p_{abs} is transferred via TTM model (1) into effective transient spatially periodic variation of the electron and lattice temperatures (Figure 1b) which modulates the losses in the Drude model (the imaginary part of

dielectric permittivity) which affects the SPP propagation and creating a *dissipative plasmonic crystal* which can have different lifetimes depending on the relation between the incident pulse duration and the temperature diffusivity.

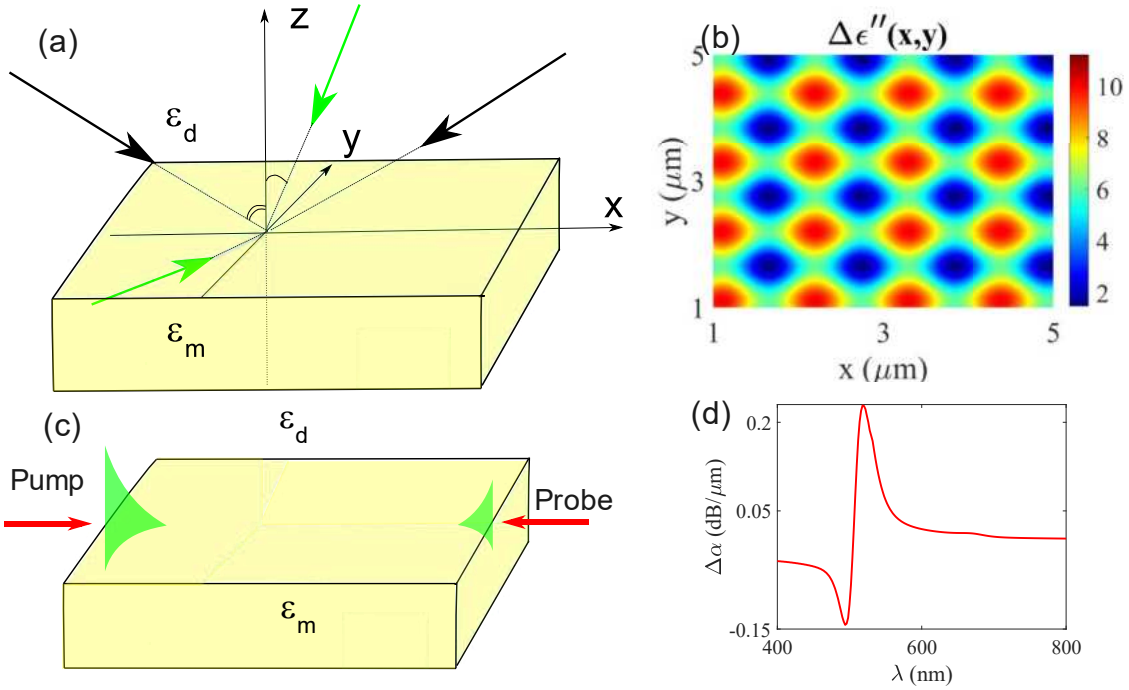


Figure 1. (a) The schematics of crossed-beam irradiation creating the transient plasmonic crystal (b) induced spatial variation of the imaginary part of the dielectric constant (c) basic pump-probe configuration (d) relative change of the absorption coefficient after pulse transit. The negative values correspond to decreased absorption.

In the second opportunity instead of using an external irradiation one can use to contra-propagating SPPs in the pump-probe configuration [4] – Figure 1c. In these settings the source of energy absorption p_{abs} is provided by a strong pump SPP and the induced change of the electron-lattice subsystems modulates the imaginary part of dielectric permittivity via interband transitions leading to increased propagation of the probe SPP in the visible-NIR region which manifests itself as an transient induced transparency of the sample.

References

1. Zayats, A, Smolyaninov, I., and Maradudin, A., "Nano-optics of surface plasmon polaritons", Phys. Rep. **408**, 131, 2005.
2. Anisimov, S, Kapeliovich, B, and Perlman, T. "Electron emission from metal surfaces exposed to ultrashort laser pulses", Sov. Phys. JETP **39**, 375, 1974.
3. Spector, M and Derevyanko. S, "Transient temperature induced plasmonic crystal", Phys. Rev. B **102**, 174308, 2020.
4. Spector, M and Derevyanko. S, "Controlling surface plasmon polariton losses in the visible spectrum by temperature-induced interband transitions", Phys. Rev. B **106**, 125111, 2022.

Optical to Terahertz Frequency Conversion using near Zero-index Nonlinear Hybrid Waveguides

C. Sheng*, X. F. Ma, N. Y. Wang, R. Z. Cao, C. Sheng, S. N. Zhu, and H. Liu

National Laboratory of Solid State Microstructures and School of Physics, Collaborative Innovation Center of Advanced Microstructures, Nanjing University, Nanjing, Jiangsu 210093, China
*corresponding author: csheng@nju.edu.cn

Abstract: Terahertz communications has emerged as an excellent candidate for the next generation of wireless communication networks. Despite of significant advances, one still looks for a high-efficiency terahertz source using nonlinear optics. Here, we propose near zero-index nonlinear hybrid waveguides to realize a high generation efficiency of terahertz waves.

Recent years have witnessed significant advancements in the fifth generation (5G) wireless communication networks. However, with the explosive growth of global wireless data traffic which increases by ~ 50% annually, 5G faces significant challenges in meeting the demands of this exponential growth. As a result, sixth generation (6G) wireless communication networks are expected to fill the gap. In this context, Terahertz (THz) wireless communications is considered a promising candidate for 6G networks. Motivated by these factors, the development of THz sources has been eagerly anticipated, as they possess distinctive characteristics including ultra-low noise, ultra-low power consumption, high integration, and ultra-fast modulation. Despite recent advancements in creating THz radiation using electronic, photonic, and hybrid approaches, THz sources that fulfill all the requirements of THz communications still face challenges. For instance, conventional electronic approaches to generate THz radiation have limitations in modulation speed, electronic-photonic hybrid approaches encounter unresolved issues related to integration and miniaturization, and photonic approaches need to improve the conversion efficiency from optical waves to THz waves for practical applications. Recently, the efficient generation THz waves [10] via on-chip difference-frequency generation (DFG) has attracted attention, since it has a unique advantage in the integration, the low-cost and the low-noise. Yet, its low conversion efficiency also urgently needs to be further optimized.

On the other hand, metamaterials[1], composite materials engineered through the structuring of subwavelength constituents, offer unparalleled flexibility in the engineering of optical materials. They enable the realization of unique and intriguing properties, including negative or zero refractive indices. Consequently, the emergence of metamaterials has led to various unprecedented applications such as perfect lenses, invisibility cloaks , and even artificial black holes. Besides of these passive linear optical elements, there have been significant advancements in metamaterials-assisted nonlinear optical processes, encompassing phase mismatch-free harmonic generation, direction-independent four-wave mixing, second-harmonic generation, and optical rectification. Notably, state-of-the-art THz sources based on nonlinear optical rectification in zero-index materials have attracted substantial attention due to their efficient generation and manipulation of broad THz waves. However, the discrete and bulky nature of these THz sources hinders their practical application in THz communications. Additionally, the broad bandwidth of these sources fails to meet the requirement of narrow-linewidth necessary for THz communications. Recently, there have been proposals and implementations of on-chip zero-index metamaterials [2,3] that manipulate nonlinear optical processes. Nonetheless, the utilization of zero-index metamaterials in integrated photonic devices to generate continuum THz waves has not

been reported thus far.

In this work, we propose a theoretical approach utilizing near zero-index nonlinear hybrid waveguides for achieving high-efficiency generation of THz waves via on-chip DFG at the telecom wavelength (Fig. 1(a)-Fig. 1(c)). Specifically, we design an optical metamaterials waveguide and a conventional hollow rectangular metallic waveguide to respectively achieve an effective refractive index of zero at telecom and THz frequency. Thanks to the simultaneous realization of near zero index both at the optical and THz waves, we have eliminated two major bottlenecks in the conversion from optical wave to THz waves: phase mismatch and weak nonlinear optical-THz waves interactions. We thus obtain the conversion efficiency as high as 3.95×10^{-3} W^{-1}at 3.21THz with a compact size on this integrated nonlinear hybrid waveguide (Fig. 1(d)).

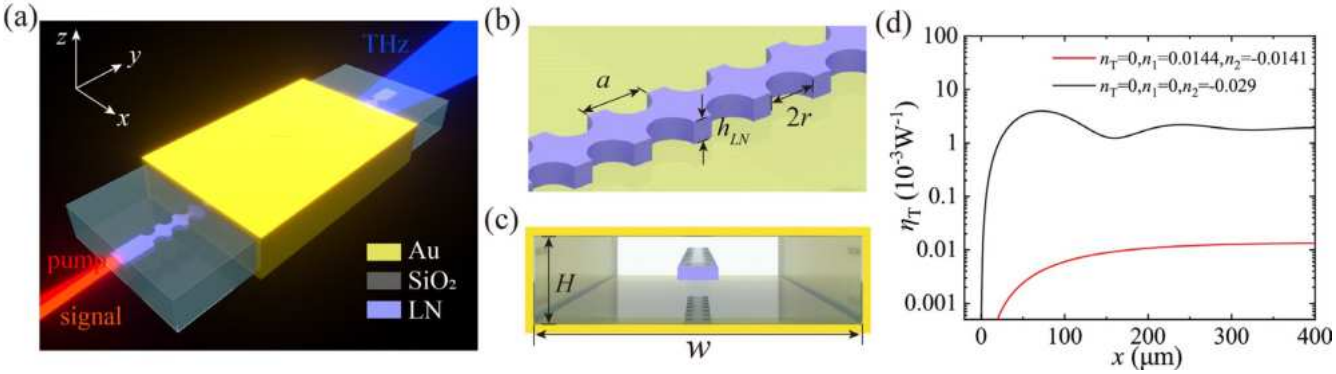


Fig.1 (a) Schematic of the designed hybrid waveguide consisting of the optical LNOI corrugated waveguide and the THz metallic rectangular Waveguide. (b) Schematic of the optical LNOI corrugated waveguide. (c) Schematic of the THz metallic rectangular waveguide. (d) Conversion efficiency versus propagation distance under the case when the refractive index is zero only for THz waves and for both THz waves and pump light.

In summary, we have presented a theoretical and numerical analysis of a highly efficient on-chip THz source based on a compact nonlinear hybrid waveguide. By leveraging the unique properties of the zero-index medium, we have successfully addressed the challenges of phase mismatch and weak nonlinear optical-THz waves interactions in the process of DFG, resulting in an impressive conversion efficiency of 3.95×10^(-3) W^(-1) over just the propagation length of several THz wavelengths. Notably, our proposed nonlinear hybrid waveguide achieves simultaneous zero refractive indices for both telecom waves and THz waves, which, to the best of our knowledge, is the first demonstration of such a feat. In future works, the conversion efficiency can be further improved by reducing the loss in such a nonlinear hybrid waveguide. Furthermore, our approach holds promise for applications in other on-chip nonlinear and quantum processes, including spontaneous parametric down-conversion and four-wave mixing.

References

1. J. B. Pendry, A. J. Holden, D. J. Robbins, and W. J. Stewart, "Magnetism from conductors and enhanced nonlinear phenomena," Ieee Transactions on Microwave Theory and Techniques 47, 2075-2084 (1999).
2. J. R. Gagnon, O. Reshef, D. H. G. Espinosa, M. Z. Alam, D. I. Vulis, E. N. Knall, J. Upham, Y. Li, K. Dolgaleva, E. Mazur, and R. W. Boyd, "Relaxed Phase-Matching Constraints in Zero-Index Waveguides," Physical Review Letters 128, 203902 (2022).
3. X. Niu, X. Hu, S. Chu, and Q. Gong, "Epsilon-Near-Zero Photonics: A New Platform for Integrated Devices," Adv. Opt. Mater. 6, 1701292 (2018).

Low-frequency sound insulation and ventilation with spiral metastructure

Shanjun LIANG[1*], and Wenjian KUANG[1]

[1]College of Professional and Continuing Education, The Hong Kong Polytechnic University, Hong Kong SAR, China
[*]corresponding author: junot.liang@cpce-polyu.edu.hk

Abstract: We report a new design of acoustic metamaterial for broadband insulation and natural ventilation. The unit cell consists of an Archimedean spiral channel and a straight pipe alongside, allowing fresh air flow and mode cancellation. It shows over 15dB transmission loss over a broad bandwidth of around 1000 Hz.

Background

Conventional noise barriers, such as walls and plates, have ideal acoustic performance. However, they also block the airflow and harm natural ventilation and cooling performance. In a low-flow state, sound insulation and ventilation of fresh air can be achieved simultaneously. A typical design is a plenum window [1]with partially opened double-glazing structures that prolong the attenuation path of noise and allow a certain degree of natural ventilation. There is still a large room to improve the insulation efficiency. The acoustic louvers [2] with a similar mechanism are widely used in heavy mechanical plant rooms, HVAC systems, and public buildings. The plenum windows and louvers require large dimensions for low-frequency performance. The emergence and development of metamaterials can help to solve the conflict between device size and wavelength. The precise control of the Fano resonance [3] introduces perfect sound insulation with structures having considerable open area. In such a kind of metamaterial, the resonant state from the meta-structure and the continuum state from the host medium in the opened area leads to the Fano-like interference, and a zero-transmission point can be observed. This phenomenon can be explained by the cancellation of resonant modes. Normally, the symmetric and anti-symmetric modes of resonance have an alternating distribution along the frequency axis. Near the resonant frequency, the dynamic behavior is dominated by the corresponding resonance state. With proper design, it is possible to have a point where the resonance state at both sides achieves an equilibrium state so that the transmission mode is canceled, referring to Fig. 1.

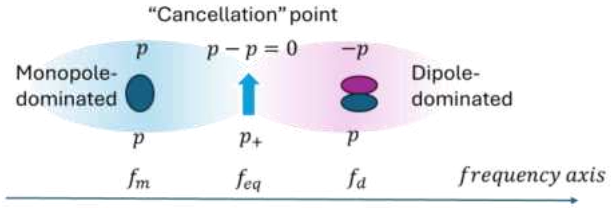


Fig. 1. Schematic of the mode cancellation. In this picture, f_m and f_d are the resonant frequencies of monopole and dipole modes, respectively; f_{eq} is the frequency where the two modes contribute equally to the state and cancel each other.

Many binary unit cells can realize the mentioned unity reflection state, such as a hollow structure surrounded by helical blades [4, 5], and a space-coiling structure with a side tube [6]. These structures inspired our design with better mechanical strength and lower working frequency.

Design and results

According to the Fano-like metamaterial, we find the binary unit cell requires a slow-wave-propagation part for resonance and an open area for ventilation; a gradient design of the resonator has better impedance matching to the host medium. Here, we adopt a gradient Archimedean spiral to slow down the wave propagation for low-frequency resonance. Two side channels are for the ventilation. The spiral shown in Fig. 2(a) is described by

$$r = a + b\theta,$$

where b, and c are constants adjust the spiral's radius and curvature distribution. The thickness of the block along wave propagation direction is about one-fourth of the shortest wavelength in the working band.

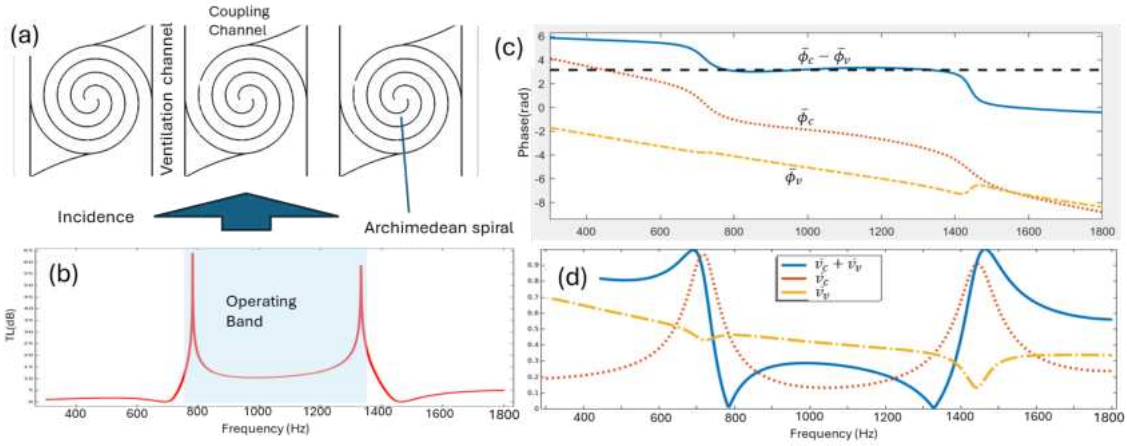


Fig. 2. The spiral metastructure's acoustic performance. (a) shows the geometry. (b) The transmission loss under normal incidence, in the operating band, $TL > 15dB$. (c) and (d) are the phase difference and amplitude summation of the transmitted ports. The subscription c represents coupling channel, while v denotes the ventilation channel.

In our design, the ventilation channel occupies 30% of the total area, offering considerable ventilation efficiency. The mode-cancelation point is located at 780 Hz and 1330 Hz, where the summation of mean velocity at the transmitted side is zero, which is illustrated in Fig. 2(d). Meanwhile, the phase difference between the coupling channel and the ventilation channel is $180°$ over a large frequency range. The out-of-phase radiation from the two channels eliminates each other and leads to a stop band.

To conclude, the reported spiral meta-structure shows broadband sound insulation with sub-wavelength thickness. The mode cancellation phenomenon has been observed through numerical results. This new type of metamaterial has great potential in green buildings.

Acknowledgments

This work was supported by the Faculty Development Scheme of the Research Grant Council (Grant No. UGC/FDS24/E04/21) in Hong Kong.

References

[1] X. Li, S. K. Tang, S. Y. C. Yim, R. Y. C. Lee, and T. Hung, "Noise reduction of plenum windows on the façade of a high-rise residential building next to heavy road traffic," *Build. Environ.*, vol. 186, p. 107353, Dec. 2020,

[2] E. B. Viveiros, B. M. Gibbs, and S. N. Y. Gerges, "Measurement of sound insulation of acoustic louvres by an impulse method," *Appl. Acoust.*, vol. 63, no. 12, pp. 1301–1313, Dec. 2002, doi: 10.1016/S0003-682X(02)00049-X.

[3] M. F. Limonov, "Fano resonance for applications," *Adv. Opt. Photonics*, vol. 13, no. 3, p. 703, Sep. 2021, doi: 10.1364/AOP.420731.

[4] M. Sun, X. Fang, D. Mao, X. Wang, and Y. Li, "Broadband Acoustic Ventilation Barriers," *Phys. Rev. Appl.*, vol. 13, no. 4, p. 044028, Apr. 2020, doi: 10.1103/PhysRevApplied.13.044028.

[5] R. Ghaffarivardavagh, J. Nikolajczyk, S. Anderson, and X. Zhang, "Ultra-open acoustic metamaterial silencer based on Fano-like interference," *Phys. Rev. B*, vol. 99, no. 2, p. 024302, Jan. 2019, doi: 10.1103/PhysRevB.99.024302.

[6] H. Zhang, Y. Zhu, B. Liang, J. Yang, J. Yang, and J. Cheng, "Omnidirectional ventilated acoustic barrier," *Appl. Phys. Lett.*, vol. 111, no. 20, p. 203502, Nov. 2017, doi: 10.1063/1.4993891.

Plasmonic Enhancement of the Performance of Integrated Phase-Change Memory and Computing Devices

J. Song[1], N. Farmakidis[2], I. Bente[3], E. Gemo[1,6], J. S. Lee[2], X. Li[2], S. Aggarwal[2], W. Zhou[2,7], N. Youngblood[5], J. Feldmann[2], W.H.P. Pernice[3,4], H. Bhaskaran[2] and C. D. Wright[1,*]

[1]Department of Engineering, University of Exeter, Exeter, EX4 4QF, UK
[2]Department of Materials, University of Oxford, Parks Road, OX1 3PH, UK
[3]Institute of Physics, University of Münster, Heisenbergstr. 11, 48149 Münster, Germany
[4]Kirchhoff-Institute for Physics, Heidelberg University, Im Neuenheimer Feld 227, 69120 Heidelberg, Germany
[5]Swanson School of Engineering, University of Pittsburgh, USA
[6]Department of Electronics and Telecommunications, Politecnico di Torino, Torino, Italy
[7]Xi'an Jiaotong University, Shaanxi 710049, P.R. China
[*]david.wright@exeter.ac.uk

Abstract: Integrated phase-change photonic memory devices are of much current interest due to their ability to provide a platform for fast, low-energy in-memory and neuromorphic computing. Here we explore the use of plasmonic enhancement of such devices to increase programming speed, reducing energy consumption and enable direct electrical access.

Integrated phase-change photonic memory devices offer a novel route to non-volatile storage and computing. Such devices generally consist of integrated waveguide structures onto which are fabricated small phase-change memory cells (e.g., $Ge_2Sb_2Te_5$, or GST), with an example being as shown in Fig. 1(a). When combined with photonic crossbar arrays and microring resonators, such photonic phase-change devices can deliver non-von Neumann forms of in-memory and neuromorphic photonic computing (see e.g. [1,2]). In the short-to-medium term, such photonic processors are probably most likely to find application as accelerators for specific processor intensive tasks, such as the matrix-vector multiplications that lie at the heart of much of today's artificial intelligence and machine learning approaches. For such applications, it is always desirable to increase computing speeds and decrease energy consumption. Moreover, since the vast majority of today's computing is carried out electronically, it is also desirable to have a seamless monolithic co-integration of electronics and photonics. One way in which these desirable features might be achieved, is via the incorporation of plasmonic antennas into the basic integrated phase-change photonic cell, and it such methods that we discuss here.

One simple approach to introduce plasmonic enhancement is to deposit plasmonic antennas on top of the phase-change cell itself, as also shown in Fig. 1(a). Here, the excitation of plasmonic resonances by the optical mode propagating in the waveguide increases the effective electric field in the GST region between the two plasmonic antennas, so increasing the optical contrast (the difference in optical transmission along the waveguide for the active GST region in its amorphous and crystalline states). This can be seen in Fig. 1(b), where the optical contrast as a function of the length of the plasmonic antennas is shown: considerable contrast is maintained (> 20%) in spite of the interaction volume with the GST being orders of magnitude smaller than in the case of a conventional cell design. More importantly, the reduced interaction volume gives rise to a very significant reduction in the time and energy required to program the GST cell (i.e. to switch it between its crystalline and amorphous states), again of around an order of magnitude or more [3]. The use of plasmonic antennas on top of the GST cell also gives access to relatively low-energy programming (switching) of the GST layer via the use of external lasers, as shown in Fig. 1(c). Here, a VCSEL laser is position above the GST cell and excites the dimer antenna from above; this leads to resonant absorption for certain antenna lengths, so improving the energy efficiency of the switching/programming of the GST layer.

The introduction of metal layers to provide plasmonic enhancement of the integrated phase-change photonic cell also brings with it the possibility for dual-mode electrical-optical operation of the device. By this we mean that the GST cell can

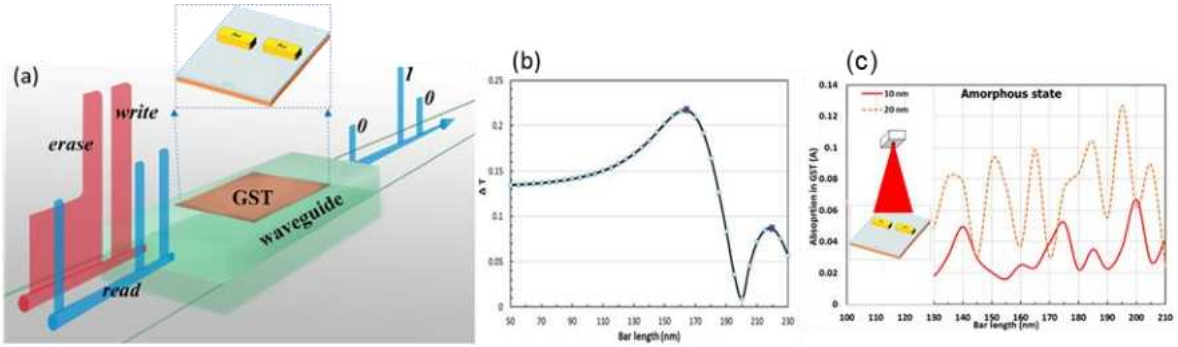


Figure. 1: (a) Schematic of a conventional integrated phase-change photonic cell showing a GST 'patch' on top of a SiN waveguide and (inset) a plasmonically-enhanced version of the GST cell. (b) The optical contrast (difference in normalized transmission for crystalline and amorphous active volumes in the GST cell) as a function of the length of the two antennas of the plasmonic cell. (c) A proposed alternative programming approach in which a VCSEL laser illuminates the plasmonic cell from above, leading to resonant absorption for certain antenna sizes.

be programmed (crystallised/amorphised) and its state read back both electrically and optically. This in turn brings closer the possibility of seamless integration of phase-change photonic processors with existing electronic hardware. An example of such a dual-mode electrical-optical device is shown in Fig. 2(a). The device consists of a shallow etched SiN waveguide which is used to efficiently route optical power to a nanoscale gap formed between two gold electrodes, into which is deposited the active GST region [4]. The functionality of the gold electrodes in this case is threefold: first, they form a metal–insulator–metal waveguide that guides and confines light into a nanoscale volume; second, they provide a means for reading the phase-state of the GST cell by measuring its conductance electrically; third, as a result of a designed-in nanoscale constriction running along the length of the nanogap, the application of a voltage pulse across said constriction produces a localized heat source to switch/program the GST cell. Successful electrical switching, with simultaneous optical readout, of such a cell is illustrated in Figs. 2(b) and 2(c) respectively.

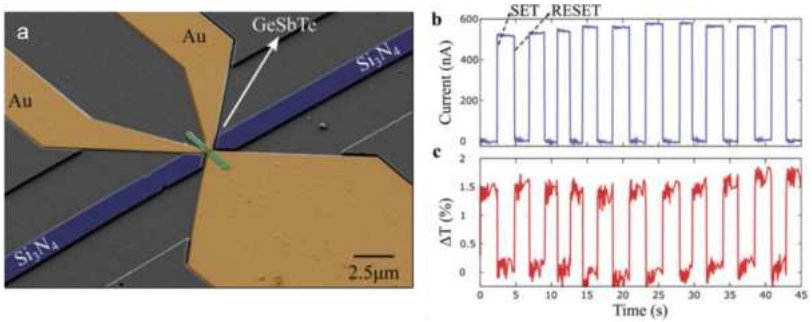


Figure. 2: (a) SEM image of a dual-mode electrical/optical integrated phase-change plasmonic photonic cell with embedded electrical heater for phase switching [4]. (b), (c) Demonstration of successful electrical switching of the GST cell along with simultaneous optical readout of the cell state.

Funding is acknowledged from the EU Horizon programme (grants 780848 & 101017237) & EPSRC (EP/W022931/1).

References

1. Feldmann J et al., *Nature*, volume 589, pages 52-58, 2021
2. Feldmann J et al., *Nature*, volume 569, pages 208-214, 2019
3. Gemo E et al., *Journal of Applied Physics*, volume 129, article no. 110902, 2021
4. Farmakidis N et al., *Advanced Science*, volume 9, article 2200383, 2022

Optical induced temperature change for ionic thermoelectric applications

D. Zhao*, M. N. Liao, and M. P. Jonsson

Linköping University, Sweden
*corresponding author: dan.zhao@liu.se

Abstract: The low energy density part of solar radiation that cannot be directly utilized by photovoltaics composes 80% of the total solar energy. Those energy was converted into heat by transparent meta-surface and black absorber to drive the operation of ionic thermoelectric devices.

In the background of energy crisis and environmental problems, more and more research are focusing on developing new technologies to generate clean and sustainable energy. As the largest available renewable energy source, the radiation from the sun would be capable of powering 100% of the worldwide demand in electricity. So far, the conversion of solar energy into electricity can be via solar thermal plants (20%) or solar cells (15-40%), such that a large amount of energy in the form of natural heat remains unused. The enormous amount of natural and waste heat is mostly stored in large volume warm fluids ($T < 250°C$). It is challenging to convert this low energy density heat into useful electricity with existing technology.

Thermoelectric material that can direct convert heat into electricity has attracted intensive research interest. As the emerging family member, ionic thermoelectric materials are mostly composed of earth abundant elements (C, N, O, H, S, etc.) and are easy to process. Moreover, the ionic thermal voltage generated in electrolytes can be 50 to 150 times larger than commercial electronic thermoelectric materials [1]. Hence, we combined the solar induced temperature change with ionic thermoelectric devices, which could generate an output voltage.

We have investigated the function of plasmonic Au-nanohole structures and black absorber in converting solar radiation into a temperature gradient across an ionic thermoelectric cells. Plasmonic metasurfaces are nanostructured metal surfaces that interact strongly with light via excitation of collective charge oscillations (i.e., plasmons). This leads to nonradiative damping and local heat generation. Meta surface with nano-holes were used to interact with light as well as the electrodes in ionic thermoelectric cells [2]. Moreover, the continues Au electrode could be used as a thermistor for temperature monitoring spontaneously. A heat of 7K was observed on the top electrode under solar radiation. A temperature difference of 2 K formed across the device and generate thermal voltage of 15 mV. We further improved the responding time of the output voltage by introducing a pyroelectric layer [3]. A sharp peak in output voltage appeared within 10 s in addition to the thermal voltage upon solar radiation, which enables radiation detection applications.

As a semi-tranparent surface, Au Nanohole based plasmonic structure could effectively convert 20% of solar light into heat to generate a thermal voltage in iTE devices. Meanwhile, black absorber typically absorbs over 95% of the solar radiation, which makes them more powerful in terms of light to heat conversion. The composite of carbon nanotube and cellulose nanofibers was investigated as the heater in iTE devices together with radiative cooling materials [4]. A temperature difference of 20K could be generated in the device exposed to the same solar radiation.

References

1. D. Zhao, A. Würger, X. Crispin, “Ionic thermoelectric materials and devices”, J. Energ. Chem., 61, 88-103, 2021,
2. D. Tordera, D. Zhao, A. V. Volkov, X. Crispin, and M. P. Jonsson, “Thermoplasmonic Semitransparent Nanohole Electrodes,” NanoLett. 17, 3145−3151, 2017.
3. M. Shiran Chaharsoughi, D. Zhao*, X. Crispin, S. Fabiano*, M. P Jonsson*, “Thermodiffusion assisted pyroelectrics—enabling rapid and stable heat and radiation sensing”, Adv. Funct. Mater. 29, 1900572, 2019
4. M N. Liao, D. Banerjee, T. Hallberg, C. Åkerlind, M. M. Alam, Q L. Zhang, H. Kariis, D. Zhao*, M. P. Jonsson*, “Cellulose-Based Radiative Cooling and Solar Heating Powers Ionic Thermoelectrics”, Adv. Sci. 10, 2206510, 2023.

Picosecond dynamics of electromagnetically-induced transparency in infrared metamaterials

The Linh Pham[1,*] , Kacper Pilarczyk[1], Nils Deßmann[2], Fei Han[1,3], Joris Van de Vondel[1] , Niels Verellen[3] , Thanh Tung Nguyen[4] and Ewald Janssens[1, **]

[1] Quantum Solid State Physics, Department of Physics and Astronomy, KU Leuven, Leuven, Belgium
[2] FELIX Laboratory, Radboud University, 6525 ED, Nijmegen, Netherlands
[3] IMEC, 3001 Leuven, Belgium
[4] Institute of Materials Science and Graduate University of Science and Technology, Vietnam Academy of Science and Technology, Hanoi, Vietnam
*corresponding author: *thelinh.pham@kuleuven.be, **ewald.janssens@kuleuven.be*

ABSTRACT: We studied the ultrafast dynamics of near-field coupling of "dark" and "bright" resonators in electromagnetic-induced transparency (EIT) metamaterials. Given the picosecond pump fluences of 8 J/m^2, we can dynamically change the optical response of the system and obtain the transient transmission change up to more than 100%. Along with this remarkable modulation depth, the knowledge of near-field coupling in complex systems will facilitate the application of ultrafast optical devices.

Electromagnetic-induced transparency (EIT) was observed for the first time in three-level atomic systems in quantum optics, when a narrow transparent state appeared in an opaque medium with a wide absorption range [1]. EIT is the result of destructive quantum interference between different pathways to the excited state. The conceptual analogue of EIT-metamaterials (EIT-MMs), proposed by Liu et. al. [2], is based on the destructive interference of two or more resonant modes that have comparable resonant frequencies, resulting in an EIT window. Due to its large dispersion, the electromagnetic wave stays longer in the medium, so-called slow light. Understanding the destructive interference and near-field coupling in EIT-MMs is crucial to optimally use this interesting phenomenon.

Our EIT-MM structure is composed of gold antennas on top, chromium as a buffer layer, and a silicon substrate underneath. As can be seen from Fig.1a, there are a vertical bar working as a dipole antenna and a pair of horizontal bars that form a quadrupole antenna under incident electromagnetic waves propagating in transverse-electric (TE) mode (inset). When they are separate, only the dipole antenna can be excited (Fig. 1b). Fig. 1c shows the static transmittance spectra of EIT-MMs obtained with FTIR spectroscopy in TE mode. When the two resonators are placed close together (g_2 = 0.1 μm), they will couple via near-field, opening an EIT transmission window. As the gap size broadens to 0.15 μm, the EIT window shrinks and it vanishes if g_2 = 0.2 μm (Fig. 1).

To study the dynamics of the EIT effect, we used a time-resolved pump-probe spectroscopy at the free electron laser facility FELIX, Radboud University, Nijmegen, The Netherlands (Fig. 2a) [3]. A train of short (2 ps) laser pulses is guided to the measurement setup and each pulse is split into a pump pulse and probe pulse. The pump takes most of the energy (95%) and was varied from 1 to 8 J/m^2 in our experiment. The given excitation sources allow us to trigger the nonlinear optical processes in the EIT structures. The arrival time of the probe relative to the pump is controlled through a delay stage, allowing us to evaluate the dynamics in the time domain of the excited state of the system after intense pump excitation. As can be seen from Fig. 2b, the system immediately responds to resonant excitation by the pump (delay of 0 ps) as the transmittance initially increases from 0.2 to 0.4 and relaxes to the original transmittance level after about 33 ps.

The mechanisms underlying the transient probe transmission change include hot electrons generation when using the pump wavelength close to the plasmonic resonance of “bright” resonators, followed by the hot carrier injection through the metal-semiconductor barrier. These processes take less than a picosecond. After that, the energetic electrons, accelerated by plasmon-induced field enhancement, will collide with bound electrons in silicon, creating additional electron-hole pairs in the so-called impact ionization (IMI) process, which leads to carrier multiplication in silicon. It changes the refractive index and conductivity of the support and thereby shifts the antenna modes, which is reflected in the probe transmission. The IMI rate and decay processes occur on time scales

from a few tens to hundreds of picoseconds [4]. This work sets the base for understanding the temporal and spatial response of EIT resonance and its coupling effect, paving the route toward optically-driven modulators and ultrafast optical devices.

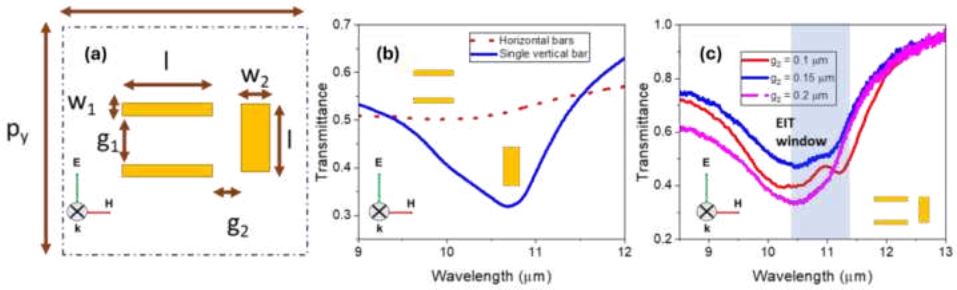


Fig. 1: *(a) Scheme of* EIT-MMs *unit cell; (b) FTIR spectra of the individual "dark" (red) and "bright" (blue) resonators and (c) FTIR transmittance spectra of EIT structures with different gap sizes* g_2.

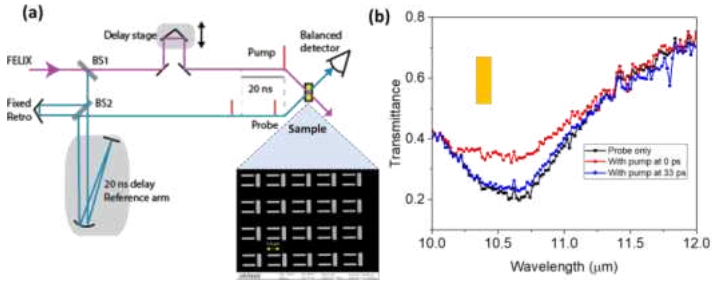


Fig. 2: *(a) Schematic layout of the pump-probe experimental setup with SEM image of EIT-MM structure (inset); (b) The transmittance spectra of a single dipole antenna at different delay times between probe and pump pulses.*

Acknowledgements

This research has been funded by a joint research project between the Research Foundation Flanders (FWO) under Grant No. G0DAX23N and the Vietnam National Foundation for Science and Technology Development (NAFOSTED) under Grant No. FWO.103-2022.01. TLP thanks the KU Leuven Research Council for an IRO Fellowship. KP acknowledges support from the Polish National Agency for Academic Exchange (project BPN/BEK/2021/1/00374) and the Polish Ministry of Science and Higher Education (scholarship 502765).

References

[1] S. E. Harris, "Electromagnetically induced transparency," *Phys Today*, vol. 50, no. 7, pp. 36–42, 1997, doi: 10.1063/1.881806.

[2] S. Liu, Z. Xu, X. Yin, and H. Zhao, "Analog of multiple electromagnetically induced transparency using double-layered metasurfaces," *Sci Rep*, vol. 10, no. 1, pp. 1–9, 2020, doi: 10.1038/s41598-020-65418-x.

[3] "User station 12: Pump-probe station - FELIX Laboratory." [Online]. Available: https://www.ru.nl/felix/facility/measurement-station/pump-probe-station/

[4] M. Bejide *et al.*, "Transient transmission of THz metamaterial antennas by impact ionization in a silicon substrate," *Opt Express*, vol. 29, pp. 170–181, 2021.

Automated Design Flow for Hybrid Metalens System with Manufacturing Awareness

Maryvonne Chalony[1], Yijun Ding[2], Larry Melvin[3], Bernd Kuechler[4], Bryan Stone[5], Evan Heller[6], Mayank Bahl[6], Rob Scarmozzino[6], and Chenglin Xu[6*]

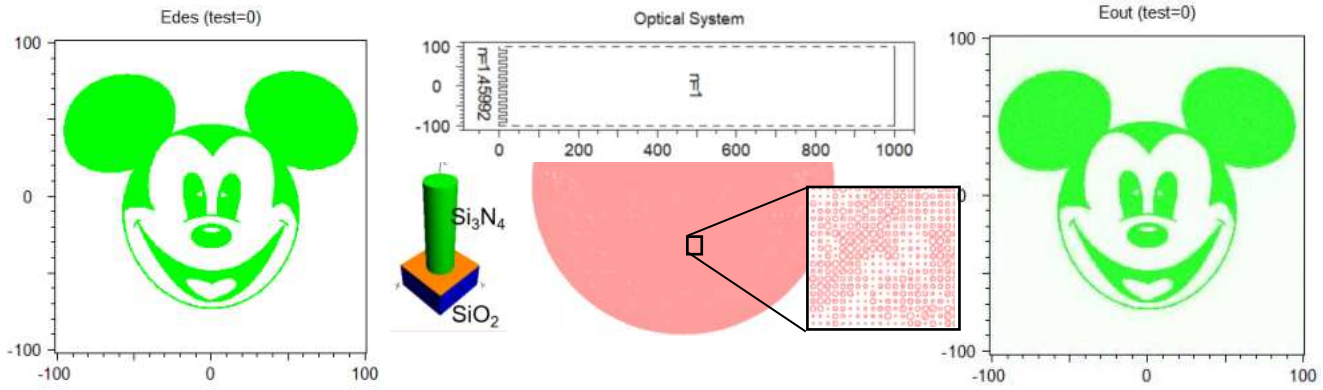
[1]Synopsys Inc., Hyeres 83400, FRANCE
[2]Synopsys Inc., Pasadena, CA 91101, USA
[3]Synopsys Inc., OR 97124, USA
[4]Synopsys Inc., Aschheim/Dornach D-85609, GERMANY
[5]Synopsys Inc., Marlborough MA 1752, USA
[6]Synopsys Inc., Ossining NY 10562, USA
[*]Corresponding author: chenglinxu@synopsys.com

Abstract

A fully automated design flow has been developed at Synopsys for hybrid metalens systems by combining macro-scale ray tracing and nano-scale electromagnetic solver. Optimum design can be automatically obtained to match desired targets. Furthermore, by taking manufacture errors into account, manufacturing aware design flow can target first print correct design.

Summary

To meet the growing demand for powerful and user-friend tools for metalens/metasurface design, Synopsys developed MetaOptic Designer (MOD), the first fully automated inverse design tool for metalens/metasurface[1]. For a given meta-atom library and incident condition, MOD can generate the best metalens layout possible to meet the specified design targets, including near-field, far-field, or modulation transfer function (MTF). Shown in Figure 1 is a design case for a desired image display.

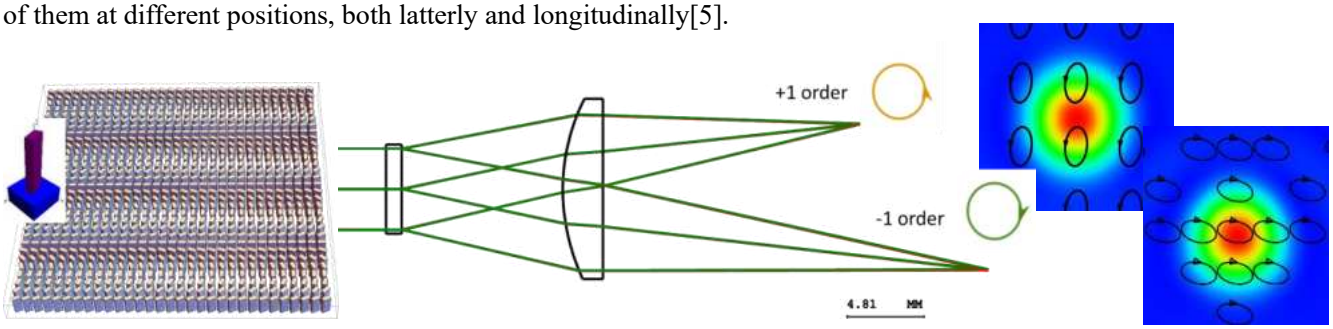


(a) (b) (c)

Figure 1. Optimization results for holographic image display (a) Desired target, (b) Meta-Atom used, optical system schematic, and optimized metasurface; (c) optimized result.

Flat and thin metalenses have great advantages over conventional curved and refractive lenses, especially with the potential of massive production with mature semiconductor fabrication technology. However, it is not feasible to completely replace refractive lenses at the current stage. In most applications, metalenses are used in hybrid optical systems to perform certain functions together with refractive lenses[2]. To design such hybrid systems, we combine both ray optics and electromagnetic optics so that refractive lenses designed in CODE V[3] can be included in the metalens design[4]. Co-design of both refractive lenses and metalenses can also be done efficiently by interfacing two products to achieve high performance from complex systems. Shown in Figure 2 is a co-designed hybrid optical system

to split left-hand circularly polarized (LCP) light and right-hand circularly polarized (RCP) light, and then focus each of them at different positions, both latterly and longitudinally[5].



(a) (b) (c)

Figure 2. Co-design a hybrid optical system for polarization beam splitter. (a) Illustration of optimized metasurface and meta-atom, (b) sketch of the optical system, (c) focused LCP and RCP beams.

Manufacturing error is inevitable during the fabrication process. As a result, the processed metalens/metasurface (Figure 3(c)) is usually different from the intended design (Figure 3(b)). To take manufacturing limitations and constrains, such as overetch, sidewall angle, roughness, etc. into account, we perform processing simulation using Sentaurus Lithography[6] to obtain manufacturing aware meta-atoms (Figure 3(d)) from which to build the meta-atom library. Metalenses/metasurfaces (Figure 3(e)) built with the manufacturing aware library naturally compensate the manufacturing errors so that their performance more closely matches the design targets.



(a) (b) (c) (d) (e) (f)

Figure 3. Manufacturing aware design flow (a) Ideal meta-atom library, (b) design based on ideal meta-atoms, (c) manufacturing predicted design, (d) manufacturing aware meta-atom library, (e) manufacturing aware design, (f), simulation results.

One of the design examples we tested is a f/5 metalens 1mm in diameter using Si_3N_4 meta-atoms. The focusing efficiency of the ideal design (Figure 3(b)) is 77.2% while the manufacturing simulated design (Figure 3(c)) gives 64.0% with 17.1% discrepancy. The manufacturing aware design (Figure 3(e)), however, has compensated the fabrication error and yields 78.4% efficiency with only 1.6% difference from the initial ideal design.

References

[1] https://www.synopsys.com/photonic-solutions/rsoft-photonic-device-tools/metaoptic-designer.html

[2] Chen, W. T., Zhu, A. Y., Sisler, J., Huang, Y. W., Yousef, K. M., Lee, E., ... & Capasso, F. (2018). Broadband achromatic metasurface-refractive optics. *Nano letters*, *18*(12), 7801-7808.

[3] https://www.synopsys.com/optical-solutions/codev.html

[4] Bos, J., Heller, E., Scarmozzino, R., Bahl, M., He, L-C., Xu, C. "Inverse Design of Metalens System Including Refractive Lenses", META, July 2023, Paris, France.

[5] Ding, Y., Stone, B. D., Bahl, M., Heller, E., & Scarmozzino, R. (2023, October). Hybrid refractive-metalens design for imaging applications. In *Current Developments in Lens Design and Optical Engineering XXIV* (Vol. 12666, pp. 13-19). SPIE.

[6] https://www.synopsys.com/manufacturing/mask-solutions/s-litho.html

The fabrication and application of 3D metamaterials

Changzhi Gu[1,2*] and Yang Guo[1,2]

[1]Beijing National Laboratory for Condensed Matter Physics, Institute of Physics, Chinese Academy of Sciences, Beijing, China
[2]School of Physical Sciences, CAS Key Laboratory of Vacuum Physics, University of Chinese Academy of Sciences, Beijing, China
[*]corresponding author: czgu@iphy.ac.cn

Abstract: We developed a nanofabrication method of 3D metamaterials based on focused-ion-beam irradiation-induced folding of low dimentional materials, which can similarly constructed 3D free-standing nanostructures and devices in the research and development of photonics. The optical characteristics of 3D plasmonic “nanograters” composed of free-standing Au films was studied, and the unusual and well-scalable Fano resonances at wavelengths ranging from 1.6 to 6.4 mm were observed, which holding great potential applications in multi-resonance differential sensing and optical communication.

The 3D metamaterials (MMs) can realize the effective constituent properties and be tuned in all propagation directions at various frequencies. Specially, nanoscaled 3D MMs responded at higher frequencies, such as in the infrared and visible regimes, remains an active focus of research. Many 3D nanofabrication technologies have been developed in decades, such as layer-by-layer stacking, multilayer electroplating, direct laser writing and ion-beam irradiation, etc. However, the fabrication technology of nanoscale 3D MMs with a hierarchical geometry remains challenging. Here, we developed a fabrication method of focused-ion-beam (FIB) folding of metallic cantilevers to construct self-supporting 3D MMs. The fabrication process employed FIB nanopatterning combined with in situ irradiation-induced folding of metallic thin-film structures. The result indicated that this method can be used to produce complex 3D metamaterials with ease and is also feasible for the production of 2D arrays of millimeter-sized 3D elements, which have practical uses in many optical applications.
In this summary, our works focused on metamaterials of U-type nanograters consisting of an array of vertical U-shape splitring resonator patterns standing along an edge of horizontal subwavelength rectangular holes. The 3D metamaterials exhibited scalable unusual Fano resonances at wavelengths ranging from 1.6 to 6.4 mm, a very strong dependence on the refractive index of the surrounding medium, with a high refractive index sensitivity, was observed. What's more, the behavior of each resonance can be modulated independently.These suggested that the local modifications to the phase and amplitude of the light wave front on a subwavelength scale induced by the nanograter structures profoundly influence the propagation of the incoming light, thereby suggesting that such nanostructures may be applied in a wide range of optical applications, including high-performance plasmonic sensing.

Acknowledgements
This work was supported by the National Natural Science Foundation of China under Grant Nos. 61888102, 11974386, 62174179, 12074420，U21A20140 and 61905274, the National Key Research and Development Program of China under Grant No. 2021YFA1400700，the Strategic Priority Research Program of Chinese Academy of Sciences (CAS) under Grant Nos. XDB33000000 and XDB28000000, the Key Research Program of Frontier Sciences of CAS under Grant Nos. QYZDJ-SSWSLH042 and XDPB22.

References:

1 C. Wu, A. B. Khanikaev, R.Adato, N.Arju, A.A.Yanik, “Fano-resonant asymmetric metamaterials for ultrasensitive spectroscopy and identification of molecular monolayers,” Nat Mater., No. 7, 69-75. 2012.

2 N. Liu, M. Hentschel, T. Weiss, A. P. Alivisatos, H. Giessen, “Three-dimensional Plasmon rulers,” Science, No. 332, 1407-1410, 2011.

3 Z. Liu, X. Xia, Y. Sun, H. Yang, R. Chen, B. Liu, B. Quan, J. Li, C. Gu, “Visible transmission response of nanoscale complementary metamaterials for sensing applications,” Nanotechnology, No. 23, 275503, 2012.

4 J. M. Hamm, S. Wuestner, K. L. Tsakmakidis and O. Hess, “Theory of Light Amplification in Active Fishnet Metamaterials,” Phys. Rev. Lett., No. 107, 167405, 2011.

5 Y. Xu, P. Bai, X. Zhou, Y. Akimov, C.E. Png, L.K. Ang, W. Knoll, L. Wu, “Optical refractive index sensors with plasmonic and photonic structures: promising and inconvenient truth”, Adv. Opt. Mater., No. 7, 1801433, 2019.

6. M.F. Limonov, M.V. Rybin, A.N. Poddubny, Y.S. Kivshar, “Fano resonances in photonics”, Nat. Photonics, No. 11, 543–554, 2017.

Low-power Laser Coloration by Oxidation and Deformation of Self-assembled AL-PS Metamaterial

M. S. Elizarov*, N. Li, F. Xiang, A. Fratalocchi

PRIMALIGHT, Faculty of Electrical Engineering, Applied Mathematics and Computational Science,
King Abdullah University of Science and Technology, Thuwal 23955-6900, Saudi Arabia
*corresponding author: maxim.elizarov@kaust.edu.sa

Abstract: We introduce a technique for wide-gamut structural coloration of a pre-processed metamaterial in 33k DPI resolution by continuous-wave laser irradiation with an average power of 10 mW. The basis of the metamaterial is self-assembled AL-PS nanosphere arrays, in which controllable material oxidation and deformation allow optical response tuning.

Conventional coloration techniques in textiles, paints, and printing often involve hazardous components, including heavy metals like lead and carcinogenic compounds [1]. Laser printing with structural colors on non-toxic materials is emerging as a promising technology to address this problem [2-4]. These structural colors originate from the interaction of nanostructures with light, causing diffraction, resonance, and interference effects that produce color without the need for pigments or dyes. Up to date, the best-performing laser coloration techniques in terms of resolution, throughput, color gamut coverage, and scalability rely on ultrafast pulsed lasers [3,4].

In this work, we present a pre-processed metamaterial based on self-assembled nanoparticles and an experimental setup for low-power laser-induced coloration of this material (Figure 1a). As depicted schematically on Figure 1a, the base unit of the metamaterial is a polystyrene nanosphere covered with a layer of aluminum polycrystalline film. Figure 1b shows results of FDTD modelling with reflectance spectra calculated for periodic arrays of a base unit with modified oxidation layer and unit shape. Our computational analysis reveals that by altering the oxidation layer of the metallic film, we can tune the resonance amplitude in the material's optical response. Additionally, deforming the spherical unit shape enables us to shift the resonance across the visible spectrum, thereby generating a spectrum of colors in the reflected light. Experimentally, we achieve such control over material by a tightly focused CW laser with variable power and exposure time. We collect experimental data for reflectivity spectra of 39 color samples and compute corresponding chromaticity values (Figure 1c)

The fabricated metamaterial is compatible with a flexible substrate, thus paving the way for the concept of 'structural paper' for laser color printing. By using a laser diode with an average power of 10 mW, we achieve laser coloration in a high-resolution of 33k DPI with the broadest gamut reported. To the authors' knowledge, the controllable gamut of color obtained with this technique also exceeds the best results currently available with inverse design [5]. With this approach, we expect that structural color laser printing can become more accessible to small-scale and end-user applications.

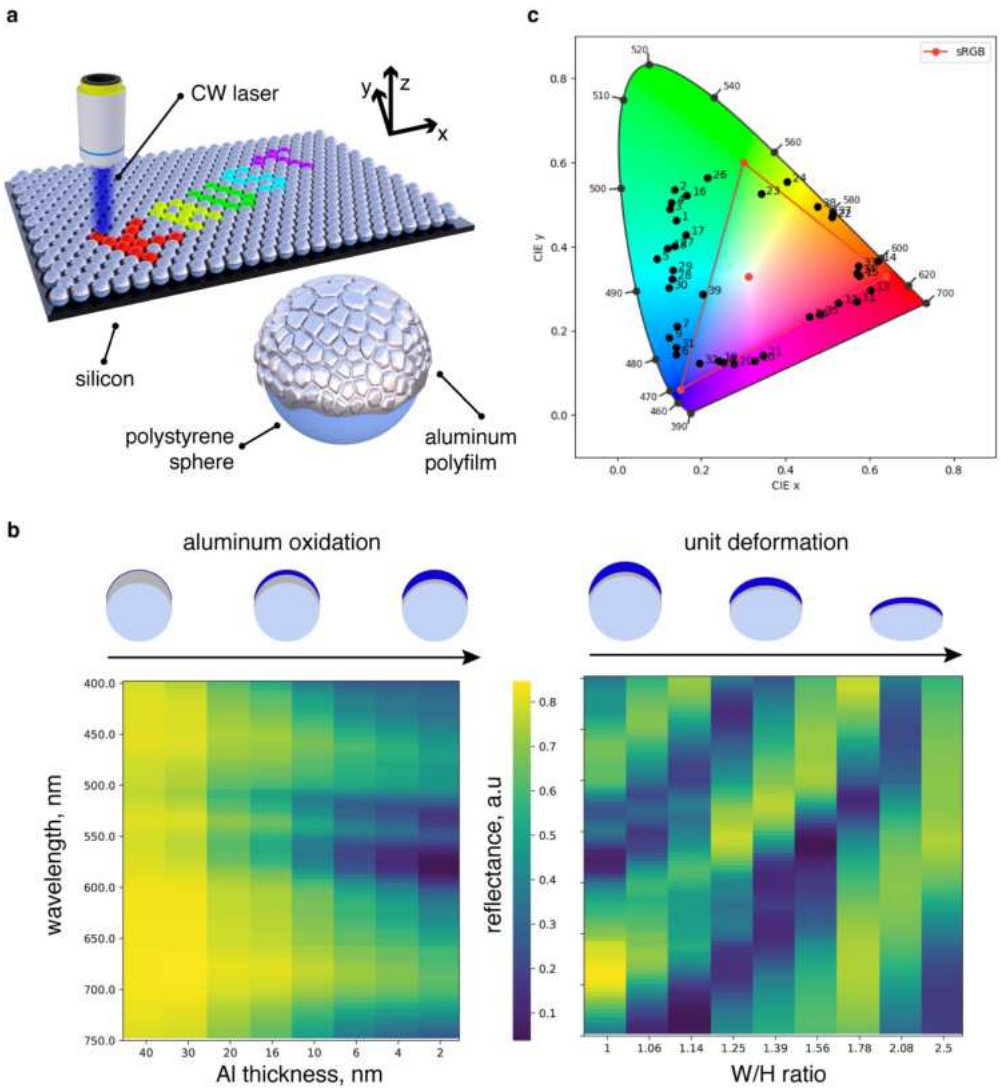


Figure 1. a - conceptual image of a described laser coloration approach and schematic image of metamaterial base unit; **b** - reflectance spectra of simulated structures; **c** - CIE 1931 chromaticity diagram with plotted chromaticities of obtained samples.

References

1. Konczol, M., *et al.*, "Oxidative stress and inflammatory response to printer toner particles in human epithelial a549 lung cells", Journal Title Abbreviation, Toxicol. Letters 216, 171–180, 2013.
2. Zhu, K., *et al.*, "Recent advances in photonic crystal with unique structural colors: A review" J. Mater. Sci. & Technol. 141, 78-99, 2022.
3. Tan, S.J., *et al.*, "Plasmonic color palettes for photorealistic printing with aluminum nanostructures", Nano letters 14, 4023–4029, 2014.
4. Geng, J., *et al.*, "High-speed laser writing of structural colors for full-color inkless printing", Nat. Comm. 14, 565, 2023.
5. Huang, Z, *et al.*, "The inverse design of structural color using machine learning", Nanoscale 11, 21748–21758, 2019

Binocular Meta-lens for Computer Vision

X. Liu[1,2*], M. K. Chen[1,2,3], T. Tanaka[4] and D. P. Tsai[1,2,3]

[1]The State Key Laboratory of Terahertz and Millimeter Waves, City University of Hong Kong, Kowloon, Hong Kong 999077, China
[2]Department of Electrical Engineering, City University of Hong Kong, Kowloon, Hong Kong 999077, China
[3]Centre for Biosystems, Neuroscience, and Nanotechnology, City University of Hong Kong, Kowloon, Hong Kong 999077, China
4Innovative Photon Manipulation Research Team, RIKEN Center for Advanced Photonics, Saitama 351-0198, Japan
5Metamaterial Laboratory, RIKEN Cluster for Pioneering Research, Saitama 351-0198, Japan
6Institute of Post-LED Photonics, Tokushima University, Tokushima 770-8506, Japan
[*]corresponding author: x.liu@cityu.edu.hk

Abstract: Meta-lenses, utilizing artificial nanoantenna arrays, offer ultra-thin, aberration-free optics, enhanced by deep learning for improved imaging and sensing. We've developed intelligent binocular meta-lens systems for computer vision applications like particle image velocimetry (PIV), underwater vision, and assisted driving, achieving compactness and high accuracy in multimodal perception.

Meta-lenses are advanced flat optical devices composed of artificial nanoantenna arrays.[1] It can manipulate the wavefront of light with the advantages of ultrathin, compact, and no spherical aberration. With the support of deep learning, meta-lens demonstrated various advanced imaging and sensing applications. We have developed a series of intelligent binocular meta-lens systems with novel applications of particle image velocimetry (PIV), underwater stereo vision, edge-enhanced depth perception for ill-posed regions, and assisted driving vision.[2,3] Traditional PIV methods require multiple cameras and conventional lens systems for image acquisition to resolve multi-dimensional velocity fields. It introduces complexity to the entire system. The 3D velocity field can be obtained by the binocular disparity and particle image displacement information of fluid flow, as shown in Figure 1(a). The measurement error of vortex-ring diameter is $\approx$1.25% experimentally validates via a Reynolds-number (Re) 2000 vortex-ring. Meta-lens PIV demonstrates a new development trend for the PIV technique for rejuvenating traditional flow diagnostic tools toward a more compact, easy-to-deploy technique. For underwater imaging, the binocular meta-lens is specifically designed and fabricated with superhydrophobicity. With deep-learning support, this stereo vision system can realize real-time depth imaging (see Figure 1(b)). Our imaging results show that depth measurement accuracy is down to 50 μm. For edge-enhanced depth perception solving the ill-posed regions, we propose a novel stereo-matching neural network, H-Net, as depicted in Figure 1(c). Our edge-enhanced system provides prompt responses in less than 0.15 seconds. This edge-enhanced depth perception meta-lens imaging system will significantly contribute to accurate 3D scene modeling and computer vision. We also developed a stereo vision meta-lens imaging system for assisted driving vision, a comprehensive perception including imaging, object detection, instance segmentation, and depth information. Our binocular meta-lens offers a comprehensive multimodal perception for scene understanding of machines, benefiting the computer vision applications of human-computer interaction, machine navigation, autonomous driving, and augmented reality.

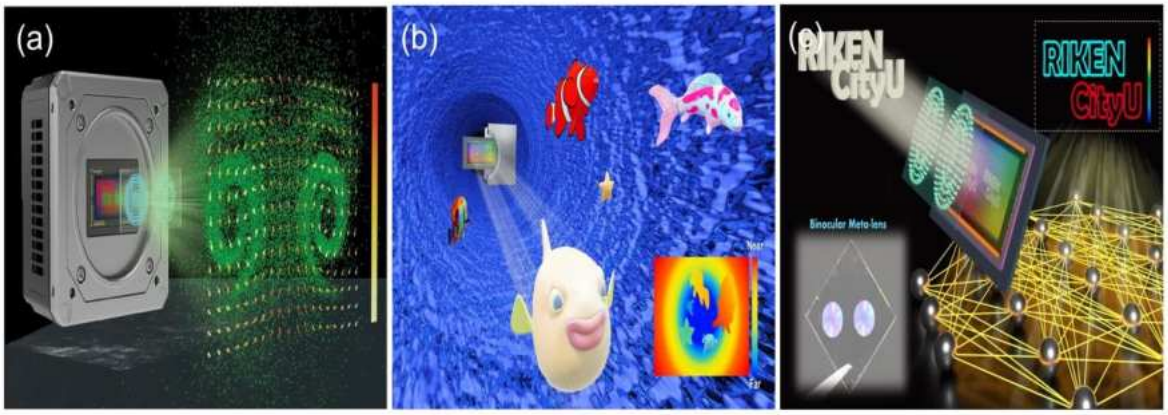


Figure 1: Binocular meta-lens for computer vision applications. (a) Particle image velocimetry. (b) Underwater stereo vision. (c) Edge-enhanced depth perception.

Acknowledgement

This work is supported by the University Grants Committee / Research Grants Council of the Hong Kong Special Administrative Region, China [Project No. AoE/P-502/20 (CityU Project No.: 9390035), CRF Project: C1015-21E (CityU Project No.: 8730064); C5031-22G (CityU Project No.: 8739072), GRF Project: CityU15303521 (CityU Project No.: 9043277); CityU11305223 (CityU Project No.: 9043572); CityU11310522 (CityU Project No.: 9043375); CityU11300123 (CityU Project No.: 9043560), and Germany/Hong Kong Joint Research Scheme: G-CityU 101/22 (CityU Project No.: 9053045)], City University of Hong Kong [Project No. 9380131, 9610628, and 7005867], National Natural Science Foundation of China [62375232] (CityU Project No.: 9680362), and JST CREST (Grant No. JPMJCR1904).

References

1. M. K. Chen, X. Liu, Y. Sun, D. P. Tsai, “Artificial Intelligence in Meta-optics,” Chem. Rev., Vol. 122, No. 19, 15356-15413, 2022.
2. X. Liu, Z. Zhao, S. Xu, J. Zhang, Y. Zhou, Y. He, T. Yamaguchi, H. Ouyang, T. Tanaka, M. K. Chen, S. Shi, F. Qi, D. P. Tsai, “Meta-lens Particle Image Velocimetry,” Adv. Mater., 2310134, 2023.
3. X. Liu, M. K. Chen, C. H. Chu, J. Zhang, B. Leng, T. Yamaguchi, T. Tanaka, D. P. Tsai, “Underwater Binocular Meta-lens,” ACS Photonics, Vol. 10, No. 7, 2382–2389, 2023.

Plasmonic Nanoplatforms – A New Generation of Efficient Heat Generators for Thermoplasmonic Detection

A. Campu [1,2*], S. Astilean[1,3], and M. Focsan [1,3]

[1] Nanobiophotonics and Laser Microspectroscopy Center, Interdisciplinary Research Institute in Bio-Nano-Sciences, Babes-Bolyai University, Treboniu Laurian No. 42, 400271 Cluj-Napoca, Romania.
[2] Environmental Science, Physics, Physical Education and Sport Department, Faculty of Sciences, Lucian Blaga University, Doctor Ion Rațiu No. 5-7, 550012 Sibiu, Romania.
[3] Biomolecular Physics Department, Faculty of Physics, Babes-Bolyai University, Mihail Kogalniceanu No. 1, 400084 Cluj-Napoca, Romania.
[*]corresponding author: andreea.campu@ubbcluj.ro

Abstract: The thermoplasmonic detection is a newly emerging application of the rapidly growing and promising field of thermoplasmonics. Despite the exploitation of the heat generated by gold nanoparticles in biomedical applications (e.g. photothermal therapy), the understanding of the influence of nanoscale photothermal processes is still subject to debate.

In this scientific context, this work aims to provide a better understanding on the thermoplasmonic mechanism leading to efficient and sensitive detection by evaluating the performances of the plasmonic nanoplatforms as thermoplasmonic generators. Specifically, various shapes of gold nanoparticles were synthesized and their intrinsic capabilities to convert light to heat were assessed by the determination of their photothermal conversion efficiencies in aqueous solution. Moreover, the photothermal performances were monitored with respect to nanoparticle's concentration, excitation wavelength and power of the excitation source at the interface with the colloidal solution. The most efficient nanoparticles were further immobilized onto different substrate types, respectively glass, paper and polymeric membrane, followed by the monitoring of their photothermal properties after immobilization. By controlling the self-assembly's formation process, it resulted that the photothermal properties of the plasmonic nanoplatforms can be modulated according to one's needs. Furthermore, by the functionalization of the plasmonic nanoplatforms with target molecules, the light-to-heat conversion performances show modifications, which can be attributed to the mass effect by the determination of the cooling constant. Thus, the obtained results contribute to the consolidation of the versatile thermoplasmonic detection technique and represent a stepping stone in the development of simple plasmonic nanoplatforms with reduced fabrication costs, facile and user-friendly implementation in thermoplasmonic-driven biomedical applications.

Acknowledgements: This work was supported by the Babes-Bolyai University, through the Starting Research Grant (SRG-UBB), contract no. 32984/ 23.06.2023.

Hyperband Multi-functional Metasurface based on Double-walled Carbon Nanotubes

Jin Zhang[1*], Peng Liu[1,2] and Zhipei Sun[1]

[1] QTF Centre of Excellence, Department of Electronics and Nanoengineering, Aalto University, Finland.
[2] Department of Applied Physics, Aalto University School of Science, Finland.
[*]Corresponding author: jin.zhang@aalto.fi

Abstract: In the past decade, metasurfaces have become a paradigm for engineering electromagnetic space due to their strong interaction with light or wave. However, mastering the cross- wavelength modulation of spatial light over the entire electromagnetic spectrum remains a challenging task. Here, we experimentally demonstrate an avenue towards hyperband multifunctionality in a single metasurface based on double-walled carbon nanotubes (DWCNTs). As a proof of concept, the proposed DWCNT-based metasurface integrates three typical functionalities including microwave selectivity, terahertz diffusion, and optical transparency.

The rapid advancement of wireless communication, digital circuits, and radar detection technologies has led to higher demands for modern electronic devices with integratable and versatile functionalities. Metasurfaces, emerging as a new class of subwavelength ultra- thin flat components, have brought disruptive innovations to the electromagnetic and nanophotonic fields. Despite the maturing developments of customized metasurfaces in specific scenarios, limited working wavelength and fixed wave manipulation remain the common defects[1]. The fixed EM properties of traditional materials enable desired responses only at specific wavelength, which limits the configuration of cross wavelength devices[2]. Recently, the electrical characteristics of DWCNT are selectable from semiconducting to conducting by controlling synthesis parameters, which promotes the development of electronic devices composed entirely of carbon materials[3]. Here, we propose a novel strategy to realize cross-wavelength multi-functionalities in an all-carbon metasurface as shown in Figure 1. Three typical functionalities including microwave frequency selectivity, Terahertz diffusion and optical transparency are realized simultaneously in a single metasurface whose resonant structures are fully made of DWCNT materials.

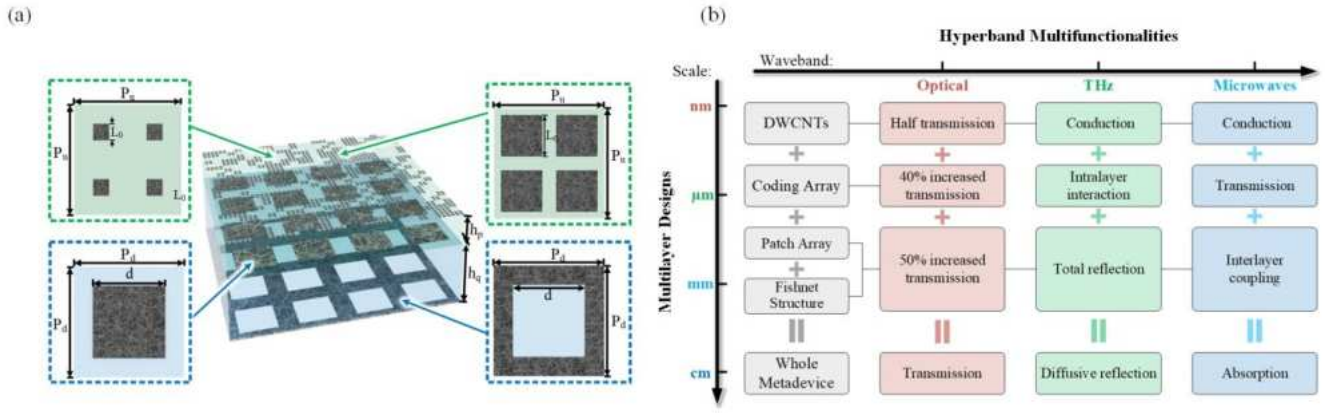


Figure 1 (a) Structural configuration of the DWCNT-based metasurface and (b) the working principle.

The proposed DWCNT-based metasurface is pictorially depicted by a three-dimensional schematic, which

consists of successively transferring thin layers of DWCNT coding array, polymer film, DWCNT patch structure, quartz glass and DWCNT fishnet structure from top to bottom. All these patterned layers are made of periodic subwavelength resonant elements and their periodic lengths are set to P_u = 150 μm and P_d = 10 mm, respectively. Therefore, the response frequency of the DWCNT coding array and the DWCNT patch/fishnet structure are correspondingly located in the THz and microwave regions to achieve different electromagnetic functions. In addition, the dielectric layers are selected as optically transparent polymer film and quartz glass materials, and they are set as h_p = 200 μm and h_q = 2 mm respectively to provide thin-film interferences for THz and microwave.

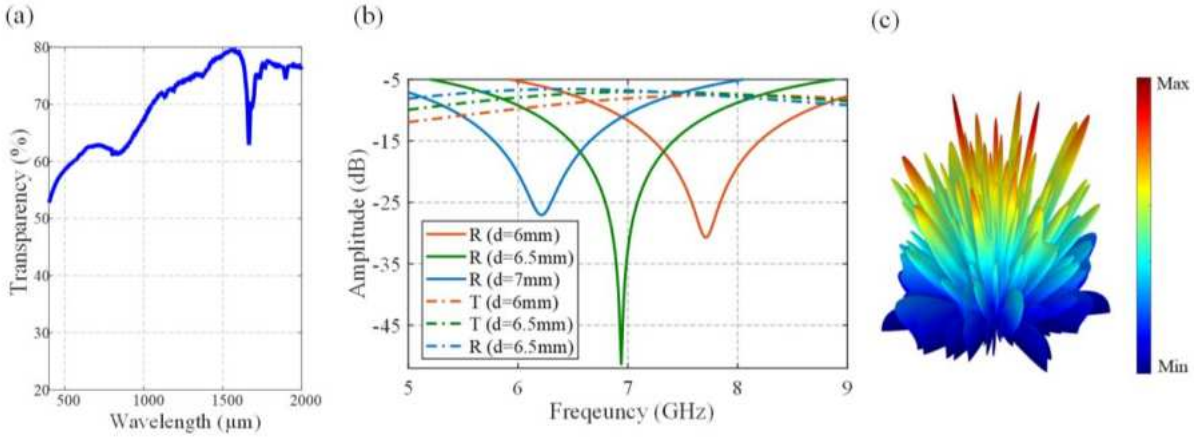


Figure 2 (a) Optical, (b) microwave and (c) terahertz responses of the proposed DWCNT-based metasurfaces.

From an optical point of view, we have quantitatively analyzed the transmittance of the proposed multilayer metasurface. Figure 2(a) illustrates that the proposed DWCNT-based metasurface enables over 60% transmittance in the wavelength range of 500 -2000 nm. To engineer the microwave responses, we simulated the reflection and transmission spectra of the proposed metasurface with different parameter d in Figure 2(b), which showing a sharp peak of reflection coefficients at resonant frequencies. For example, when d = 6.5 mm, the peak value of the reflection coefficient R is -48 dB while the transmission coefficient T is nearly -6 dB. When increasing the parameter d from 6 to 7 mm, the operating frequency of our DWCNT- based metasurface is tunable over a range from 6.2 GHz to 7.7 GHz. Furthermore, the THz scattering pattern of the proposed metasurface at 0.81 THz is demonstrated in Figure 2(c), showing diffusion-like scattering pattern randomly distributes the electromagnetic energy into numerous directions, which likes an electromagnetic wave impinging onto a rough surface, with significantly suppression of the radar cross section. In a word, we have designed a hyperband multifunctional metasurface capable of full- spectrum control of EM waves from microwaves to visible light, indicating great potentials in smart skin, electronic countermeasure, wireless communication system.

References

1. Z. Zhang, D. Wen, C. Zhang, M. Chen, W. Wang, S. Chen, and X. Chen, “Multifunctional light sword metasurface lens,” ACS Photonics, Vol. 5, 1794– 1799, 2018.
2. S. Xu, F.Y. Dong, W.R. Guo, D.D. Han, C. Qian, F. Gao, W.M. Su, H. Chen, and H.B. Sun, “Cross-wavelength invisibility integrated with various invisibility tactics,” Sci. Adv. Vol. 6, eabb3755, 2020.
3. Q. Zhang, J.S. Nam, J. Han, S. Datta et. al,“Large-diameter carbon nanotube transparent conductor overcoming performance–yield tradeoff,” Adv. Fun. Mater. Vol. 32, 2103397, 2022.

Conducting polymer-cellulose devices for tunable infrared and THz optics

C. Y. Kuang[1*], S. Z. Chen[1], and M. P. Jonsson[1,2]

[1] Laboratory of Organic Electronics (LOE), Department of Science and Technology (ITN), Linköping University, Campus Norrköping, SE 601 74, Sweden

[2] Wallenberg Wood Science Center, Linköping University, Campus Norrköping, SE 601 74, Sweden
[*]corresponding author: Chaoyang.kuang@liu.se

Abstract: Conducting polymers possess excellent reversible tunability for optical and electrical properties, enabling their various applications ranging from organic (opto)electronics to nanophotonics. In this talk, I will present our latest studies on conducting polymer devices for terahertz and infrared photonic applications.

Conducting polymers possess redox-tunable optical and electronic properties and have been explored in various areas, including electrochemical transistors, electronic skins, and thermoelectric generators. Recently, we reported their applications for plasmonic nanoantennas for near infrared applications, showing promising redox-state tunability towards spatiotemporally dynamic metasurfaces. In this study, we combined conducting polymers with sustainable cellulose nanofibrils (CNF) to form optoelectronic devices for tunable terahertz (THz) and infrared (IR) photonic applications.

The tunable electrical and optical properties of conducting polymers originate from the difference of their redox states, where at the oxidized state the polymers possess a high charge carrier density, while the charges are neutralized at the reduced state. Such redox state modulation can be realized by various ways, and in this talk, we chose both chemical and electrical switching approaches.

I will first present a conducting polymer-cellulose aerogel and demonstrate that it can provide broadband reversible tuning of THz transmission between 13% and 91% through chemical approach, while maintaining specular reflection loss below -30 dB in both states. We associate the exceptional THz modulation with the anomalous optical conductivity peak of conducting polymers, which enhances the THz absorption in its oxidized state while it decreases the reflection in its reduced state. We believe that such switchable THz materials provide a promising route towards large and broadband THz modulation for next-generation intelligent THz devices.[1]

By structural modification, we obtained a flexible conducting polymer-cellulose paper with highly suitable properties for electrically controlled IR devices. Both the specular reflection and emissivity could be modulated with large amplitudes (more than 40%) *via* the polymer redox state. This enabled various new application scenarios, where we focused on tunable radiative coolers, dynamic thermal camouflage, infrared anti-counterfeiting tags, and infrared dynamic displays. The devices are sustainable, cheap, flexible and mechanically robust, providing a versatile materials platform for active and adaptive IR optoelectronic devices.[2]

References

1. Kuang, C. Y. et al. “Switchable Broadband Terahertz Absorbers Based on Conducting Polymer-Cellulose Aerogels,” Adv. Sci., 11, 2305898, 2024.
2. Kuang, C. Y. et al. “Electrically tunable infrared optics enabled by flexible ion-permeable conducting polymer-cellulose paper”, submitted, 2024.

Boosting the tunability of Mid-infrared Metasurfaces based on graphene field-effect transistors

Fei Han[1,2*], The Linh Pham[1], Kacper Pilarczyk[1], Nguyen Thanh Tung[3], Dinh Hai Le[4], Guy A. E. Vandenbosch[5], Joris van de Vondel[1], Niels Verellen[2,1], Xuezhi Zheng[5], Ewald Janssens[1]

[1]Quantum Solid-State Physics, Department of Physics and Astronomy, KU Leuven, 3001 Leuven, Belgium
[2]IMEC, 3001 Leuven, Belgium
[3]Institute of Materials Science, Vietnam Academy of Science and Technology, 18 Hoang Quoc Viet, Hanoi, Vietnam
[4]University of New South Wales, School of Engineering and Information Technology, Campbell, 2600, ACT, Australia
[5]WaveCoRE research group, ESAT, KU Leuven, Kasteelpark Arenberg 10, 3001 Leuven, Belgium
[*]corresponding author: fei.han@kuleuven.be

Abstract: In this study, we propose a fabrication-efficient way to enhance the tuning range of mid-infrared resonances based on graphene field-effect transistors. A tuning range in the mid-infrared of 700 nm is more than two times larger than the range presented in previous studies on similar devices with multiple resonances.

Conventional metasurfaces are “passive”, i.e., their properties are determined at the design stage. It is, however, highly desirable to develop real-time controlled metasurfaces for advanced photonics applications. There have been reports on tunable metasurfaces based on thermal, electrical, mechanical, and optical stimuli.[1-3] Among the materials considered for active metasurfaces, graphene, one of the most famous two-dimensional (2D) materials, has attracted a lot of attention.

The devices shown in Figure 1a consist of a monolayer graphene sheet which was grown by chemical vapor deposition and transferred onto a SiO_2/p^{++} doped Si layer. The metasurface is designed as a stack of 30 nm Au/10 nm Pd/10 nm Al_2O_3/graphene (Metal-Dielectric-Graphene – MDG) layers. A similar metasurface without the Al_2O_3 layer (Metal-Graphene – MG) is used as a reference. Reactive ion etching was used to create a rectangular graphene sheet. A plasmonic antenna array was fabricated on the graphene sheet by electron beam lithography (EBL), followed by molecular beam epitaxy (MBE) of 10 nm Al_2O_3, 10 nm Pd and 30 nm Au, and lift-off. Metal contacts (10 nm Ti and 200 nm Au) were deposited on top of the graphene sheet by EBL and MBE. The reflectance of the hybrid metasurfaces is calculated by FDTD simulations (Lumerical Solutions, Inc.).

We used in-situ current-voltage (I-V) measurements in the FTIR setup to study the reflectivity of the device for different gate voltages, ranging from -200 V to 100 V. As shown in Figure 1b (MG-metasurface) and Figure 1c (MDG-metasurface), the tuning range of mid-infrared resonances is enhanced compared to metasurfaces without barrier layer, i.e., from 300 nm to 700 nm for the 7.3 μm resonance and from 110 nm to 140 nm for the 4.7 μm resonance.[4] To further optimize the tunability, which suffers from the required high gate voltage related to a thick SiO_2 dielectric spacer, the spacer is replaced by an ultra-thin high-k dielectric layer allowing to tune the charge carrier concentration of graphene with a low gate voltage (-3 V to 3 V). All components of this device are made of complementary metal–oxide–semiconductor (CMOS)-compatible materials, providing pathway for large-scale production.

In conclusion, we propose a fabrication-efficient approach to resolve current limitations of electrically tunable graphene-metal metasurfaces. In the mid-infrared we achieve an increase of the reflectance modulation from 26% to 36%, together with a broad tuning range of 700 nm, which is more than twice as large as that reported in previous studies on similar multiple resonance devices without insulating interlayer.[4] Our

experiments are carried out in a graphene field effect transistor configuration, which offers in-situ monitoring of graphene's electrical response while recording the reflectance spectrum from an FTIR microscope.

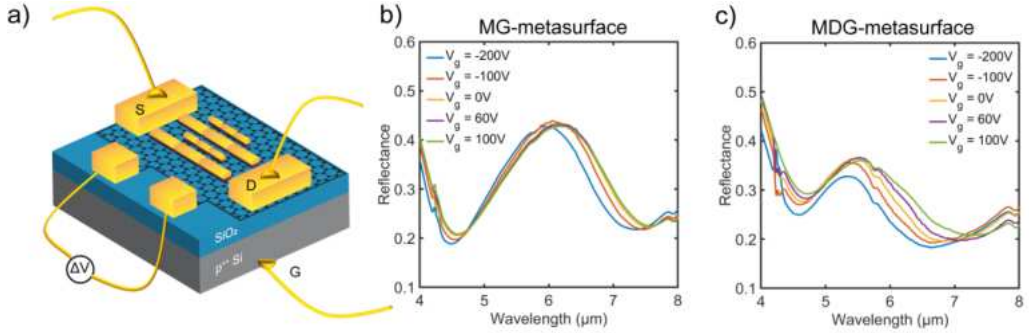


Figure 1. Device configuration and experimental results of the multi-resonant metasurfaces on top of graphene. (a) The schematic of the tunable plasmonic device based on the four-terminal measurement circuits. The device is composed of metallic antennas on a layered substrate consisting of graphene/ 300 nm SiO_2/ p^{++} doped Si substrate. Measured reflectance spectra for (b) the MG and (c) the MDG metasurfaces as a function of the gate-voltage Vg.

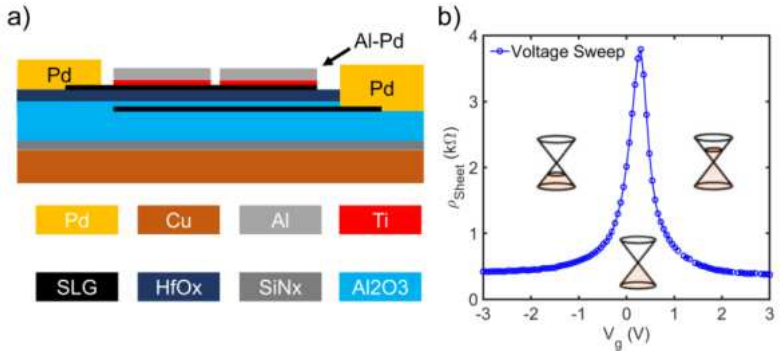


Figure 2. (a) Cross-sectional diagram of the tunable metasurfaces with a high-k dielectric layer on top of graphene, illustrating how to integrate different metals and dielectric materials into one optimized compact device. (b) Measured graphene sheet resistance as a function of gate voltage in the ambient conditions. The insets show graphene's dispersion relation, where the shaded areas represent the level filling.

Acknowledgements

This research has been funded by a joint research project between the Research Foundation Flanders (FWO) under Grant No. G0DAX23N and the Vietnam National Foundation for Science and Technology Development (NAFOSTED) under Grant No. FWO.103-2022.01. Funding by the China Scholarship Council (CSC) is acknowledged by F. Han.

References

1. Tittl, A. et al. "A switchable mid-infrared plasmonic perfect absorber with multispectral thermal imaging capability," Adv. Mater., Vol. 27, No. 31, 4597-4603, 2015.
2. Yao, Y. et al. "Electrically Tunable Metasurface Perfect Absorbers for Ultrathin Mid-Infrared Optical Modulators," Nano Lett., Vol. 14, No. 11, 6526-6532, 2014.
3. Dabidian, N. et al. "Electrical Switching of Infrared Light Using Graphene Integration with Plasmonic Fano Resonant Metasurfaces," ACS Photon., Vol. 2, No. 2, 216-227, 2015.
4. Han, F. et al. "Tunable Mid-infrared Multi-resonant Graphene-metal Hybrid Metasurfaces," Adv. Opt. Mater. (accepted 2024).

Towards Plexcitonics: Direct Plasmonic Nanostructures Lithography on 2D Transition Metal Dichalcogenides

E. Peci[1*], L. Ramò[1], M. Magnozzi[1], E. Spotorno[1], V. Venturino[1], M. Sygletou[1], M. C. Giordano[1], G. Zambito[1], F. Telesio[1], M. Canepa[1], F. Bisio[2]

[1]Dipartimento di Fisica, Università degli Studi di Genova, via Dodecaneso 33, 16146 Genova, Italy
[2]CNR-SPIN, corso Perrone 24, 16152 Genova, Italy
[*]Corresponding author: ermes.peci@edu.unige.it

Abstract: thermal scanning-probe lithography allows a direct-write fabrication route to create plasmonic nanostructures on top of exfoliated transition metal dichalcogenide (TMDC) crystals. This plasmonic-excitonic hybrid structure can be exploited to investigate heat diffusion at the nanoscale.

Semiconducting transition metal dichalcogenides (TMDCs), such as MoS_2 and WS_2, have emerged as promising candidates for next-generation optoelectronic devices, owing to their remarkable electronic and optical properties. They exhibit room-temperature excitonic effects and, when thinned down to a three-atom-thick monolayer, they are direct-gap semiconductors, endowing them with a strong photoluminescence (PL) signal. This makes TMDCs an excellent playground for exploiting light-matter interaction at the nanoscale.

By coupling a TMDC monolayer with metallic nanostructures exhibiting localized surface plasmon resonances (LSPR) it becomes possible to realize hybrid photonic systems for fundamental studies and novel applications. Within this framework, the excitons of the TMDC and the LSPR are viewed as optical resonators whose spatial coupling and spectral overlap can be freely tuned by engineering their nanoscale characteristics. Additionally, hybrid TMDC/plasmonic systems can be exploited as novel platforms to investigate the heat dynamics at the nanoscale, exploiting the thermoplasmonic effect of the plasmonic counterparts for locally generating heat, and the temperature dependence of the PL energy to act as a nano-thermometer.

Realizing these hybrid structures is by all means a complex task, that typically combines nanolithography approaches to deterministically fabricate the plasmonic counterpart with delicate growth-and-transfer methods to introduce the TMDC in the system. The issue with the realization of these systems is that the direct fabrication of plasmonic structures onto TMDCs with energetic particles (electrons, ions) is prone to damage these materials, whereas the transfer of TMDCs onto fabricated structures tends to be an aleatory process.

In this contribution, we exploit thermal scanning-probe lithography (t-SPL) as a viable alternative to electron-beam lithography or focused-ion-beam etching to directly write plasmonic nanostructures onto previously fabricated large-scale exfoliated 2D materials [1,2]. t-SPL works similarly to an atomic force microscope (AFM) with a heating tip; the desired pattern is written on a thermosensitive resist while acquiring a topological image of the sample. After gold deposition and resist lift-off, we are left with gold nanostructures over our TMDC. We demonstrated the appeal of this technique, fabricating regular, evenly spaced, 15 nm-thick plasmonic nanodisks (NDs) on square lattices onto monolayer- and bilayer-thick regions of TMDCs. Large-area MoS_2 monolayers were exfoliated from a bulk natural crystal following a procedure adapted from Ref. [3], that allowed to obtain homogeneous areas of TMDC with lateral size in excess of hundreds of μm.

The array of nanostructures consisted of a square arrangement of NDs with a nominal diameter of 200 nm and a gap of 400 nm over areas of 30×30 μm^2, realized onto monolayer and bilayer MoS_2. The NDs in object exhibit a LSPR at λ=1250 nm photon wavelength (1.0 eV), within the band gap of MoS_2. Figure 1 reports an AFM map of

the Au NDs fabricated over monolayer MoS_2. Round NDs are clearly observable on a square lattice.

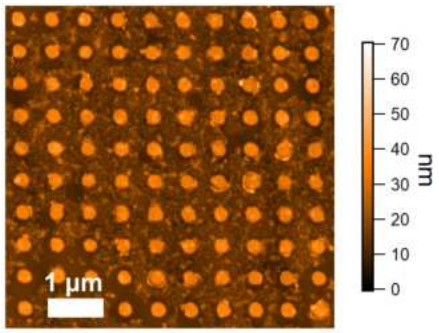


Figure 1. AFM image of Au NDs on monolayer MoS_2.

In order to verify that the fabrication procedure did not affect the structure and the optical functionality of the TMDC, Raman and PL spectra were acquired from pristine areas and from areas that had undergone fabrication. The results are reported in Figure 2. It can be clearly seen there that the fabrication has left the structural and optical functionalities intact.

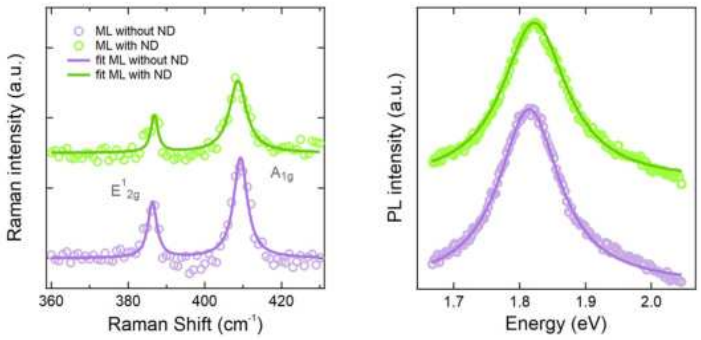


Figure 2. Left: Raman signal of monolayer MoS_2 with and without fabricated NDs. Right: PL signal of monolayer MoS_2 with and without fabricated NDs.

Summarizing, we report the application of a non-invasive nanofabrication method for realizing plasmonic nanostructures onto monolayer TMDCs while leaving their structure and functionalities intact.

References

1. Ramò L. *et al.*, "Thermal Scanning-Probe Lithography for Broad-Band On-Demand Plasmonic Nanostructures on Transparent Substrates", ACS Appl. Nano Mater., Vol. 6, No. 19, 18623–18631, 2023.
2. Ramò L., Peci E. *et al.*, "Non-Invasive Deterministic Plasmonic Nanostructures Lithography on 2D Transition-Metal Dichalcogenides", ACS Appl. Mater. Interfaces, submitted.
3. Liu F. *et al.*, "Disassembling 2D van der Waals crystals into macroscopic monolayers and reassembling into artificial lattices", Science, Vol. 367, No. 6480, 903-906, 2020.

Laser-based 3D printing of structures to control electromagnetic radiation: Bridging 2D, 2.5D, and 3D

G. Zyla[1*], Odysseas Tsilipakos[2], Dimitrios Zografopoulos[3], Savvas Papamakarios[1], Maria Farsari[1],

[1]Institute Electronic Structure Laser/Foundation for Research and Technology-Hellas, Heraklion, Greece
[2]National Hellenic Research Foundation, Athens, Greece
[3]Consiglio Nazionale delle Ricerche, Istituto per la Microelettronica e Microsistemi, Rome, Italy
[*]corresponding author: zyla@iesl.forth.gr.

Abstract: We introduce laser-based 3D printing through multi-photon lithography as an effective approach for fabricating 2D, 2.5D, and 3D structures with high resolution. Furthermore, we demonstrate these structures' capabilities to control electromagnetic radiation, offering interesting applications from the visible to the THz regimes.

Periodically arranged structures, ideally smaller than the wavelengths of interest, can effectively manipulate electromagnetic radiation through their design and material characteristics [1]. These structures often exhibit unique optical properties, making them highly suitable for a wide range of applications in optics and photonics across a broad spectral range.

A powerful technique for fabricating these structures across this extensive regime is laser-based 3D printing via multi-photon lithography (MPL). This method enables true 3D printing with ultrafast lasers without the need for masks, a vacuum atmosphere, or harsh chemicals [2]. Beyond true 3D printing, MPL also effectively supports 2D and 2.5D fabrication, making it a highly versatile tool for manufacturing structures of varying complexity designed to control electromagnetic radiation efficiently.

MPL was successfully employed to fabricate 2D, 2.5D, and 3D structures and demonstrate their application from visible wavelength to the THz regime. These structures can be inspired by nature, where, for example, certain organisms develop sophisticated surface structures for advanced light-matter interactions [3]. Another source of inspiration comes from classical metasurfaces that allow for the control of amplitude, phase, and polarization of electromagnetic radiation through precisely engineered 2D unit cells [4].

To specifically enhance MPL's efficiency for 2D and 2.5D structures, MPL was conducted in a photosensitive thin film, as illustrated in Fig. 1. These thin films were produced using spin-coating, primarily employing a hybrid photoresist synthesized via a sol-gel process. This approach significantly improves the axial resolution in MPL, positively impacting the printing speed. Notably, 2D and 2.5D structures on a 1 cm² area could be printed in just 1.5 hours using this technique.

To demonstrate the versatility of MPL, structures were fabricated on various reflective substrates, including glass, silicon (Si), and silicon-on-insulator (SOI). Specifically, we showcase the application of these structures to generate angle-insensitive coloration, inspired by the blue Morpho butterflies, as anti-counterfeit features. Furthermore, large-area metasurfaces were fabricated to modulate the dielectric permittivity atop an SOI wafer. This facilitates the coupling of an incident wave to leaky photonic modes guided in the Si device layer at discrete wavelengths—a phenomenon known as guided-mode resonances (GMRs), highly benefical for mid-IR spectroscopy. Additionally, 3D low THz-metasurfaces were explored, focusing on electromagnetically induced

transparency (EIT). In this context, we investigated that two metallic split-ring resonators (SRRs)—one exhibiting asymmetry—can generate such an extraordinary effect, proving highly effective for sensing applications. The EIT effect arises from asymmetric features, which induce a shift in the magnetic dipole moment. As a proof of concept, such 3D structures were fabricated via MPL and subsequently post-processed using selective electroless plating with silver. The structures were characterized using time-domain spectroscopy (TDS). The resulting optical properties compared to the simulations.

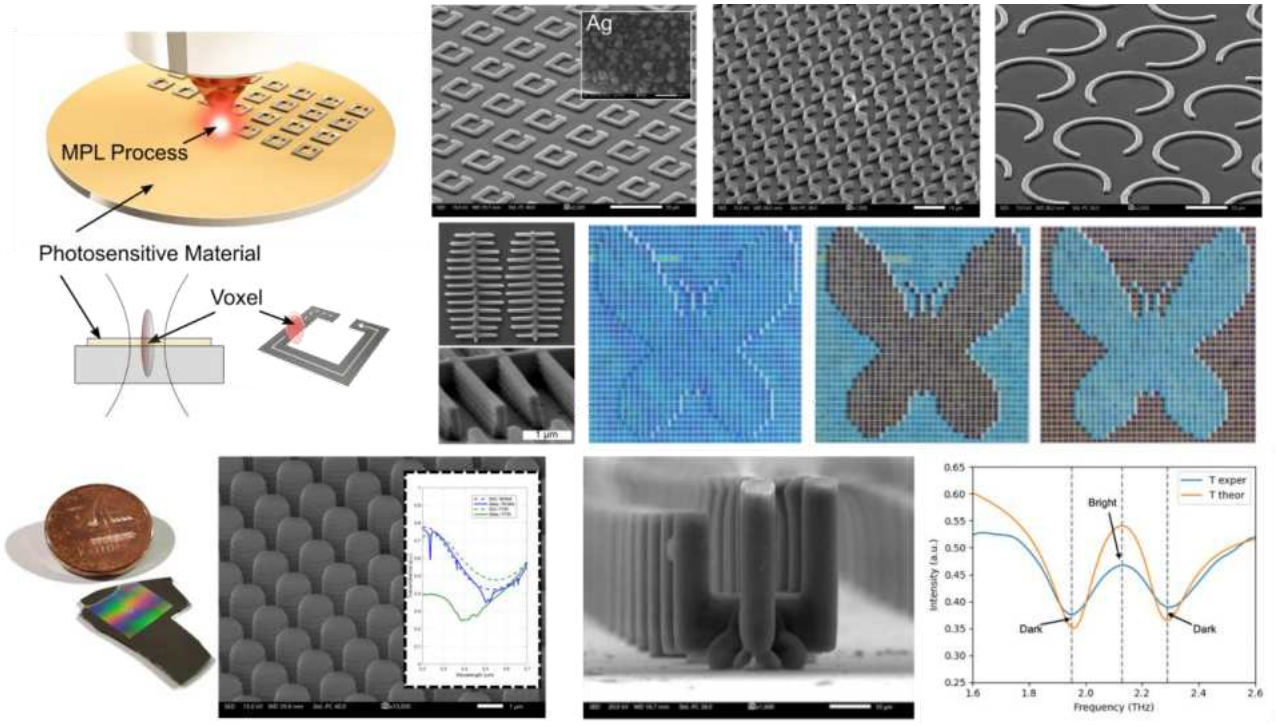


Fig.1: Laser-based 3D printing through MPL of structures capable to control electromagnetic radiation.

Acknowledgements:

This work was supported by the Marie Sk lodowska-Curie Actions, under grant agreement No. 101059253, as part of the European Union's Horizon Europe research and innovation programme.

References

1. Soukoulis, C. M., and Wegener, M., "Past achievements and future challenges in the development of three-dimensional photonic metamaterials," Nat. Photonics 5, 523–530, 2011.
2. Faraari, M., and Chichkov, B.N., "Two-photon fabrication," Nature Photon. 3, 450–452 2009.
3. Vukusic, P, and Sambles, J.R., "Photonic structures in biology," Nature 424, 852–855, 2003.
4. Zhao, X., Sun, Z., Zhangm L., Wang, Z., Xie, R:, Zhao, J., You, R., and You, Z, "Review on Metasurfaces: An Alternative Approach to Advanced Devices and Instruments," Adv Devices Instrum., 2022, 9765089, 2022.

Slime mold algorithm for topology optimization of photonics structure

K.S. Edee[1*] and P. Bonnet[1]

[1]Université Clermont Auvergne, Clermont Auvergne INP, CNRS, Institut Pascal, Clermont-Ferrand F-63000, France.

Abstract: We introduce an innovative approach to photonics structure design, incorporating the slime mold algorithm (SMA) [1], a gradient-free metaheuristic optimization method, in tandem with the topology optimization (TO) method, and utilizing a spectral modal method. Through the integration of TO with SMA, (TO-SMA) we achieve successfully metagrating designs [2].

In this paper, we present the application of the Slime Mold Algorithm (SMA) to topology optimization for a 1D dielectric metagrating (see Fig. 1), within the framework of a spectral method. The primary objective of this design is to formulate a 1D metagrating composed of a sequence of nanorods and air gaps with varying widths, strategically optimized to efficiently redirect incident plane wave power into a specified transmission order. The proposed SMA initiates by generating a random set of widths for the nanorods and air gaps. A corresponding set of binary permittivity functions is defined for this sequence of nanorods/air gap widths. However, since our focus is on a Topology Optimization (TO) method, we apply a blurring process to this initial population. This process transforms the discrete set of widths into a continuous sequence of permittivity functions. A noteworthy aspect and a key feature of our proposed method lie in the choice of the filter employed during this blurring process. Instead of opting for classical Gaussian or binary functions as filters, we introduce the Schwartz function. The shape of the function can be significantly altered by adjusting some of its key parameters, providing enhanced flexibility and control over the continuous permittivity function at each iteration during the optimization process.

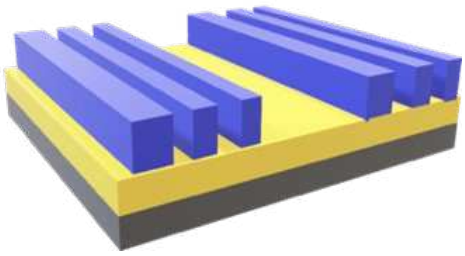


Figure 1 : A 1D deflector to be designed

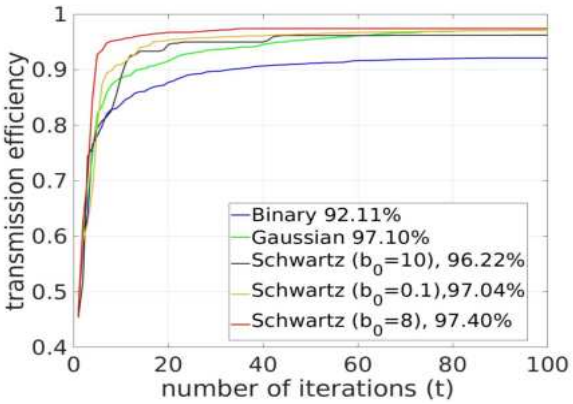


Figure 2: Performances of the TO-SMA using different filter functions: the Schwartz, Gaussian and binary functions

In Fig. 2 we emphasize the impact of the Schwartz function on numerical results, we compare the

performance of TO-SMA using the Schwartz filter with different shapes. This assessment involves a comparison with Gaussian and binary functions. The Schwartz filter demonstrates a remarkable ability to converge rapidly towards high-performance solutions. A flow chart of the proposed algorithm is shown in Fig.3

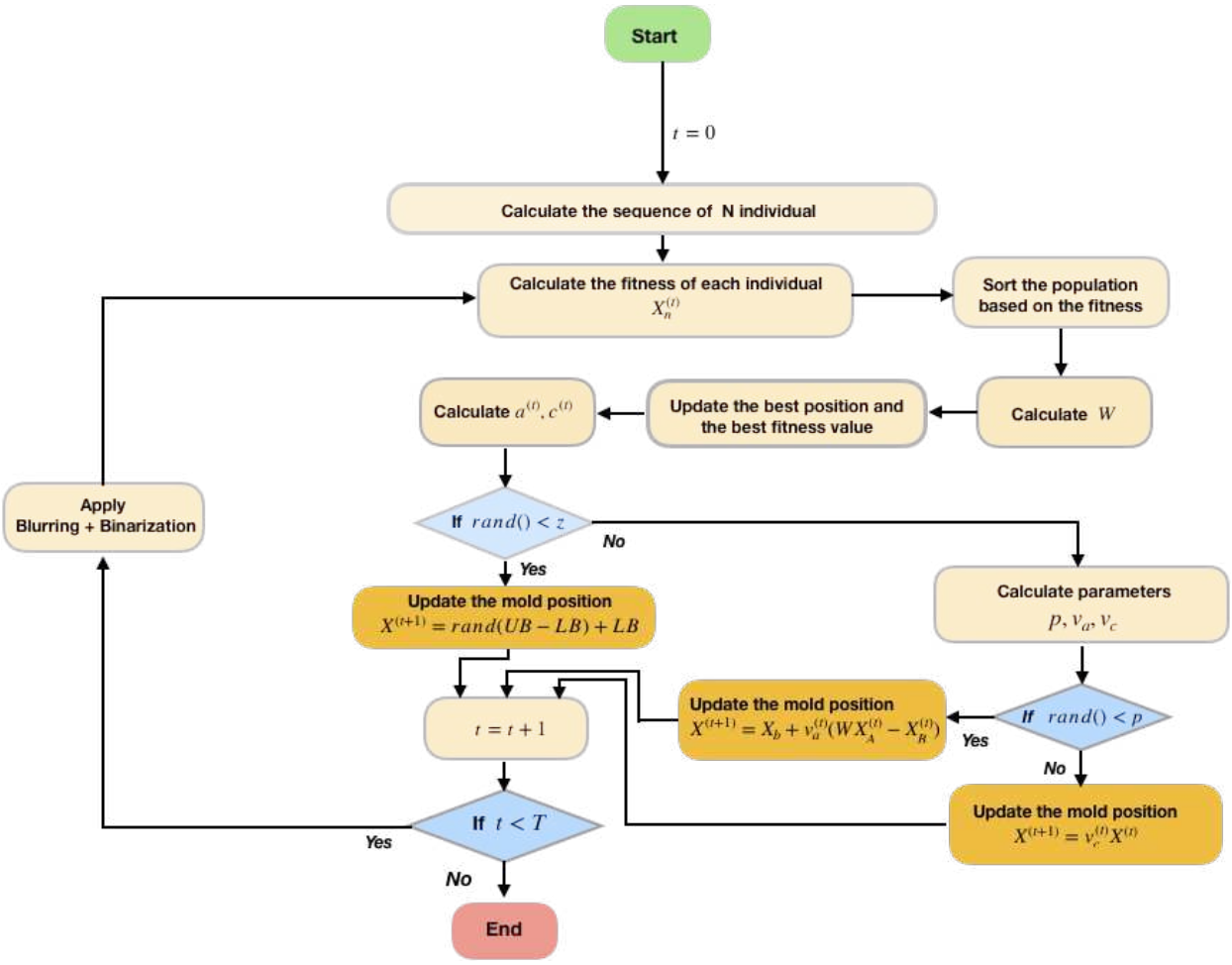


Figure: 3 A flow chart of the algorithm

References

1. Li S, Chen H, Wang M, Heidari AA, Mirjalili S. Slime mould algorithm: a new method for stochastic optimization. Fut Gener Comput Syst. 2020;111:300–23.
2. Edee, K., Granet, G. & Bonnet, P. "Slime mold algorithm for topology optimization: metagratings inverse design," Discov Appl Sci **6**, 68 (2024).

Tailoring gold plasmonic metasurfaces for efficient harmonic generation

S. Mukhopadhyay[1*], **C. Cojocaru**[1], **M. A. Vincenti**[2], **K. Hallman**[3], **A. Mihi**[4], **M. Scalora**[5], and **J. Trull**[1]

[1] Department of Physics, Universitat Politècnica de Catalunya, Rambla Sant Nebridi 22, 08222 Terrassa (Barcelona), Spain
[2] Department of Information Engineering – University of Brescia, Via Branze 38, 25123 Brescia, Italy
[3] PeopleTec, Inc. 4901-I Corporate Dr., Huntsville, AL 35805, USA
[4] Institute of Materials Science of Barcelona ICMAB – CSIC, 08193 Bellaterra (Barcelona), Spain
[5] Aviation and Missile Center, US Army CCDC, Redstone Arsenal, AL 35898-5000, USA
[*]corresponding author: shroddha.mukhopadhyay@upc.edu

Abstract: We report a combined experimental-theoretical investigation on more than three orders of magnitude enhancement in the second and third harmonic generation from plasmonic metasurfaces in the visible and UV ranges. Our experimental results are validated by our unique microscopic, hydrodynamic model for linear and nonlinear interactions in metal surfaces.

In the last few decades, both experimental and theoretical nonlinear optics (NLO), have focused on illuminating thick materials under phase matching conditions in the low absorption spectral range, to maximize the bulk nonlinear (NL) interaction and achieve very high NL efficiencies. The NL polarization term plugged into the Maxwell's equations, primarily consists of the electric-dipole/bulk contribution ($\chi^{(2)}$) while other contributions coming from the surface or magnetic effects, are usually many order of magnitude smaller and thus neglected. However, as the material thickness is reduced down to nanometer size, the bulk nonlinearity reduces drastically producing second (SH) and third harmonic (TH) signals with efficiencies of the order of 10^{-7}-10^{-13}, thus becoming comparable to surface nonlinearity, electric quadrupole and magnetic sources [1]. In this scenario, optical nanomaterials have emerged as a very promising platform to capture new and unique aspects of light localization and light-matter interaction at the nanoscale. The rapid development in nano-fabrication techniques lead to precision designs of subwavelength optical metamaterials (nanospheres, gratings, pillars etc.). But soon it became clear that classical NLO theories rely on approximations that cannot fully explain metals/metallic nanostructures, the observed effects and an effort is needed to fully describe the behavior of light propagation and interaction at the nanoscale and in particular in metasurfaces.

Here we porpose a novel approach to face this problem that considers in first place the nontrivial problem of how the strategic materials used in the photonics nanostructure fabrication (i.e. metals, semiconductors, or conductive oxides) respond to linear and NL excitation by ultrashort laser pulses in different spectral range. These studies, performed on layers a few nanometers thick, remove the usual approximations and identify new mechanisms that may trigger the interaction, and must be consistently accounted for in the theoretical models in order to understand the physics involved. Recently we have studied, both experimentally and theoretically, the behavior of different materials and gained new understanding about the basic physical mechanisms responsible for their optical response. Our theoretical approach is based on a Maxwell Hydrodynamic model that accounts for competing surface, magnetic, and bulk nonlinearities arising from both free (conduction) and bound (valence) electrons and preserves linear and NL material dispersions, nonlocal effects, and the influence of hot electrons [2]. Our previous studies on SH and TH generation from 20 nm and 70 nm-thick gold nano layers allowed us to extract its basic physical intrinsic properties [4].

However, the NL efficiency from nanolayers are extremely low. An important enhancement can be envisaged by tailoring and enhancing the NL optical properties of metals in specifically designed metasurfaces by taking profit of plasmonic resonances responsible for the strong spatial confinement of electromagnetic field near the surface of the metal. The properties of the nanostructures are determined by the geometrical (shape, size, and sharpness) and physical parameters (dielectric functions at a given wavelength) of both the metal and the surrounding dielectric materials. A strong plasmonic

interaction can significantly enhance light-matter interaction, and generate very large surface nonlinearities [3,5], giving rise to HHG conditions under relatively low input laser intensities. This enables the manipulation of optical fields with unprecedented spatial (far beyond the diffraction limit) and time resolutions.

Fig.1 shows several of the considered configurations and demonstrates the E-field localization within two kinds of SP surface plasmonic localization (E-field is confined around the corner of a 2-D grating [5], E-field is confined inside a nanohole). Our very recent results from the 2D nanograting show that under the right excitation conditions we can achieve between three and five orders of magnitude enhancement factor in the SH and TH harmonic generation (Fig 1(a)). Although a more sophisticated quasi-3D structure consisting of nanoholes in gold, provides more tunability and shaping of the plasmonic resonance, however the NL enhancement is much lower. Fig-1(b) shows the narrow plasmonic resonance centered around 790 nm, both measured and simulated using Finite Difference Time Domain, the depth and position of which depends on the period of the hole pattern, the diameter and depth of the hole and thickness of the gold layer deposited on top. Under the resonant illumination conditions as in ref 5, the nanoholes show a TH enhancement factor of ~100 (Fig-1(c)).

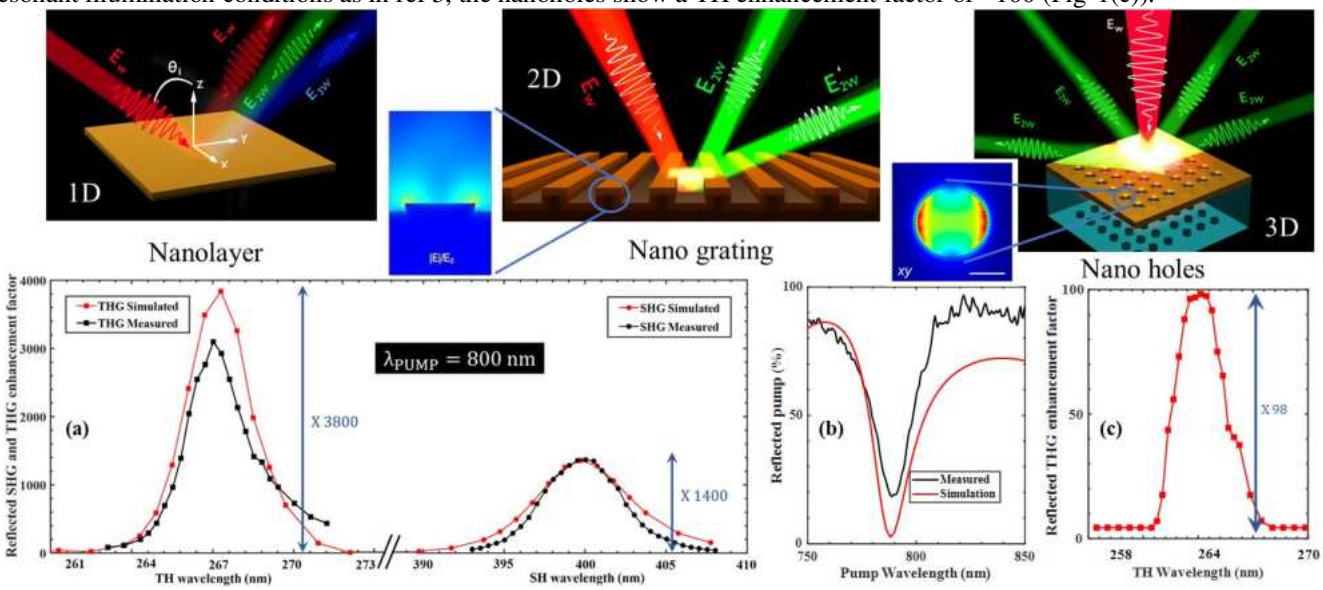


Fig 1. Examples of 1D, 2D and 3D nanostructures, light confinement and enhancement in nonlinear interaction [4-5]

Plasmon induced NL generation can be directional or diffused, the periodicity of the structures may enable constructive interference of the generated SH/TH in certain directions, producing diffraction orders, proving experimental retrieval of the total generated SH/TH to be challenging. A 2D grating will diffract in the plane of incidence while the diffraction from a 3D structure is more complicated (Fig-1). Our sophisticated detection system and precision calibration enables us to detect and quantify SH/TH efficiencies, and corroborate our theoretical and experimental observations of shape, spectral width, and maximum amplitude of the spectral response.

Apart from Au, successful detection of SH from few nm thick aluminium also unraveled remarkable consequences of resonant absorption, a critical role that bound electrons play in light-matter interactions across the optical spectrum. Precise engineering of metasurface geometry and modern fabrication methods promise very well-tailored plasmonic structures and is the way to produce compact higher frequency light sources embedded with nonlinear components beam-deflecting, metalenses, meta-holograms, orbital-angular-momentum (OAM) beams etc [3].

References

1. J. A. Armstrong, N. Bloembergen, J. Ducuing et al, Phys. Rev. 127, 1918 (1962)
2. M. Scalora, M. A. Vincenti, D. de Ceglia, et al, Phys. Rev. A 82, 043828 (2010)
3. San Kim, Tae-In Jeong, Jongkyoon Park, et al, Nanophotonics, 11 (11), 2393-2431 (2022).
4. L. Rodriguez-Suñé, J. Trull, C. Cojocaru, et al, Optics Express 29, 8581 (2021).
5. S. Mukhopadhyay, L. Rodriguez-Suné, C. Cojocaru, et al, APL Photonics 8, 046108 (2023).

Synthesis and plasmonic properties of Fe_3O_4-Au-Pd hybrid nanoparticles

Y. Yokota[1*] and Mao. Takeda[1]

[1] Department of Materials and Life Sciences, Faculty of Science and Technology, Sophia University, 7-1Kioicho, Chioyoda, Tokyo 102-8554, Japan
[*]corresponding author: y_yokota@sophia.ac.jp

Abstract: In this study, we focused on iron oxide to magnetically resolve noble metal nanoparticle arrays or to construct noble metal nanoparticle three-dimensional structures. By adding gold and palladium to iron oxide nanoparticles synthesized in the liquid phase, we developed a method for synthesizing iron oxide-gold-palladium nanoparticles (Fe_3O_4-Au-Pd nanoparticles) that can be recovered with a magnet.

The fabrication of metasurfaces and metamaterials requires the precise 2-D or 3-D alignment of noble metal nanoparticles. In the past, for example, controlled orientation of Pd nanosheets [1] was achieved by liquid-phase synthesis. In this study, we focus on iron oxide with magnetic force as a means to resolve the alignment of noble metal nanoparticles by magnetic force or to construct a three-dimensional structure of noble metal nanoparticles. In addition, when used as individual nanoparticles, the nanoparticles are light in weight and need to be collected by centrifugation after the reaction is completed in order to be reused. As noble metals to be combined as nanoparticles, we used not only gold, which can induce high electric field enhancement by localized surface plasmon resonance, but also Pd, which has high catalytic activity. By adding Au and Pd to iron oxide nanoparticles synthesized in the liquid phase, we developed a method for synthesizing iron oxide-gold-palladium nanoparticles (Fe_3O_4-Au-Pd nanoparticles) that can be recovered using a magnet.

The Fe_3O_4 nanoparticles were prepared by coprecipitation of iron (II) chloride tetrahydrate and iron (III) chloride hexahydrate with ammonia water dropwise in the liquid phase [2]. After collection and purification with a magnet, the Fe_3O_4 nanoparticles were protected with a surfactant, CTAB, and $HAuCl_4$ was added to synthesize Fe_3O_4-Au nanoparticles. Fe_3O_4-Au-Pd nanoparticles were then synthesized by adding H_2PdCl_4. The synthesized nanoparticles were collected with a magnet, measured for absorbance, and observed for shape by scanning electron microscopy (SEM) and transmission electron microscopy (TEM).

Fig. 1(a) shows the absorption spectra of the synthesized Fe_3O_4 nanoparticles (blue line) and Fe_3O_4-Au nanoparticles (red line), respectively. The absorbance spectra of Fe_3O_4-Au nanoparticles show a clear peak at a wavelength of 525 nm, which are attributed to the plasmon resonance of the Au nanoparticles. From the absorption spectrum in Fig. 1(b), the Fe_3O_4-Au-Pd nanoparticles have a larger absorbance toward longer wavelengths and may show

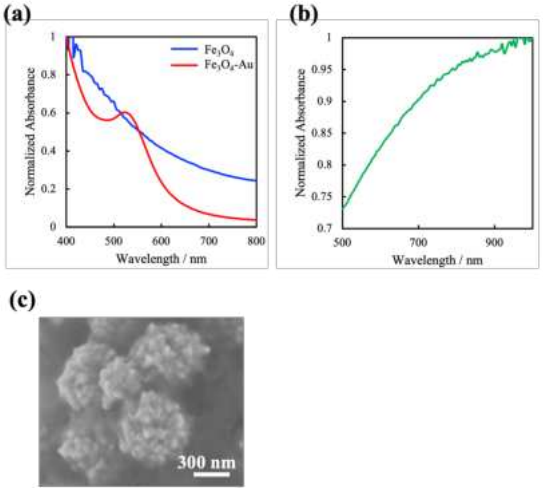


Fig. 1 UV-Visible absorption spectra of (a) Fe_3O_4 and Fe_3O_4-Au nanoparticles and (b) Fe_3O_4-Au-Pd hybrid-nanoparticles. (c) SEM images of Fe_3O_4-Au-Pd hybrid-nanoparticles.

a peak after 1000 nm. When Pd is grown on the surface of Au nanoparticles, the localized surface plasmon resonance-derived peak is also reported to become broadened [3], so this change can be considered to be due to Pd growth. Fig. 1(c) shows SEM images of Fe_3O_4-Au-Pd nanoparticles. For the Fe_3O_4-Au-Pd nanoparticles, a needle-like growth shape was observed on the surface. Although not shown in the figure, TEM and EDS mapping confirmed the presence of Fe, Au, and Pd in the nanoparticles. From these results, the amount of Pd deposited on the surface relative to the Fe_3O_4-Au nanoparticles was large, which may have shifted the absorption peak derived from plasmon resonance to the long wavelength side.

In conclusion, we were able to synthesize hybrid nanoparticles with a diameter of about 200 nm that can be recovered by a magnet that exhibits a plasmon resonance peak in the near infrared by adding Au and Pd to the liquid phase synthesized iron oxide nanoparticles.

Acknowledgements: This work was supported by "Advanced Research Infrastructure for Materials and Nanotechnology in Japan (ARIM)" of the Ministry of Education, Culture, Sports, Science and Technology (MEXT), Grant Number JPMXP1223UT0315 and JSPS KAKENHI "Grant-in-Aid for Scientific Research (C)", Grant Numbers 23K04823.

References

1. Yokota, Y., Takatsuki, T., Tsuyoshi, T., Yabuki, Y., and Watanabe, K. "Synthesis and Plasmonic Properties of Au Double Nanorings Supported by Pd Cyclic Nanosheets," META2019, 2019.
2. Zhou, T., Wu, B. and Xing, D. "Bio-modified Fe_3O_4 core/Au shell nanoparticles for targeting and multimodal imaging of cancer cells,"J. Mater. Chem., Vol. 22, 470, 2012.
3. Yin, Y. *et al.*, "Facile synthesis of Au/Pd nano-dogbones and their plasmon-enhanced visible-to-NIR light photocatalytic performance," *RSC Adv.*, Vol. 7, 36923, 2017.

From synthesis to assembly: a Silicon based metasurface fabrication

Juan Xin[1], Julien Proust[1] and Jérôme Plain[1*]

[1] Lumière, nanomatériaux et nanotechnologie (L2n), CNRS UMR 7076 & Université de Technologie de Troyes, 12 rue Marie Curie, 10004 Troyes Cedex, France

[*]Corresponding author: jerome.plain@utt.fr

Abstract: In this study, we present an assembly technique based on the use of the capillarity force and allowing the obtaining of metasurfaces from silicon nanoparticles. Particularly, we will present the use of such technique to obtained complicated pattern thus paving the way to the fabrication of engineering metasurfaces.

In our synthesis technique, we simply grind bulk silicon to obtain nanoparticles[1]. This technique allows us to obtain in solution Si nanoparticles with a diameter ranging from 80 nm to about 250 nm. By centrifugation steps, it is possible to obtain a final mean size of about 120 nm ± 20 nm.

In the second step, nanoparticles are deposited in a pattern obtained by electron lithography. This technique, based on the assistance of capillary forces, makes it possible to obtain large surfaces from a colloidal solution of nanoparticles, as shown schematically in figure 1a. In this step, nanoparticles in solution are deposited in patterns formed in a PMMA layer. Figure 1b shows nanoparticles of two different sizes distributed in a complex pattern with a fill rate close to 100%. During the lift-off step, the Si NP arrays remain well organized on the substrate. We carried out a systematic study of nanoparticles sorted by four sizes of size patterns. This enabled us to obtain a regular square pattern of 4 nanoparticles separated by 600 nm and formed by nanoparticles of diameter D1≈300 nm, D2≈250 nm, D3≈200 nm and D4≈150 nm. To take our analysis a step further, we measured the average size of nanoparticles on the drawing containing 4 types of holes (add sizes) and the corresponding RGB colors.

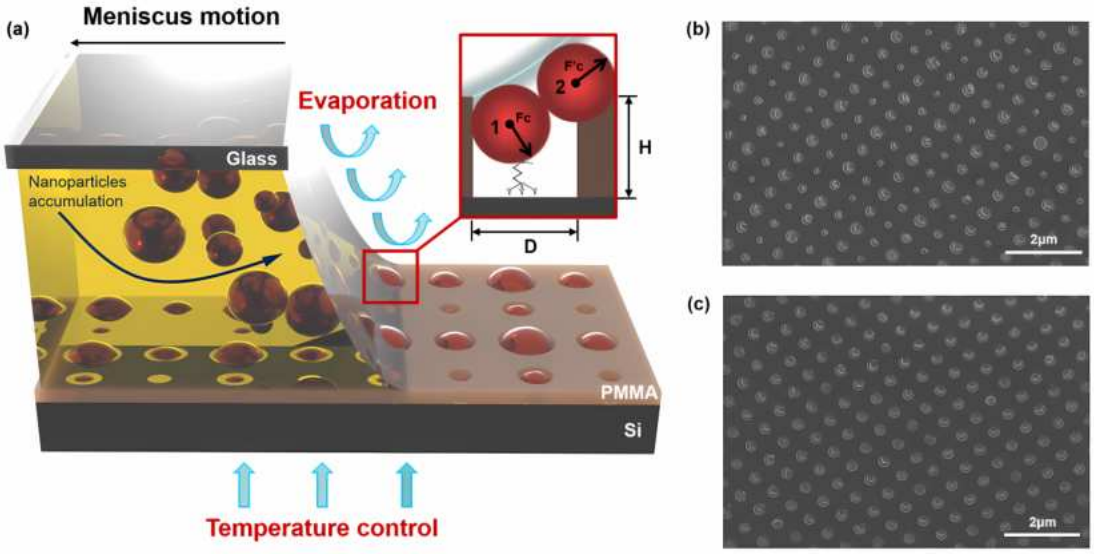


Figure 1. NP assembly. (a) Schematic diagram of capillary force assisted Si NP assembly process. SEM

micrograph of a randomly selected assembly (b) area 1 and (c) area 2 showing the deposition of single NPs.

We have demonstrated that it is possible to organize naonaoparticles obtained in solution on a surface using a technique that is relatively simple to implement and compatible with all nano-lithography techniques.

References

(1) Chaabani W., Proust J., Movsesyan A., Beal J., Baudrion A-L., Adam P-M., Chehaidar A., and Plain J., Large-Scale and Low-Cost Fabrication of Silicon Mie Resonators ACSnano 2019,13 4199-4208

Acknowledgment: Samples were fabricated in the Nanomat platform (www.nanomat.eu). The authors acknowledge support from the French Agence Nationale de la Recherche (ANR) under grant NOSE (ANR-21-CE39-0014). This work was done within the framework of the Graduate School NANO-PHOT (École Universitaire de Recherche, grant ANR-18-EURE-0013). JX thanks the China Scholarship Council (CSC), (contract 202208070142) for the financial support.

All-Garnet Magnetooptical Microcavity

Taichi Goto[1,*]

[1]Research Institute of Electrical Communication, Tohoku University, Japan
[*]corresponding author: taichi.goto.a6@tohoku.ac.jp

Abstract: Magnetooptical device using magnetic domains have attract many interests because of its quick response and large diffraction angle. To develop these devices, we grew all-garnet magnetooptical microcavity using rf ion-beam sputtering, showing nano-scale magnetic domain and a large Faraday rotation angle.

Magnetooptical devices, including magnetooptical Q-switched lasers [1], spatial light modulators, optical isolators [2], and magnetic holographic memory, have attracted significant interest due to their unique properties. In these applications, a large magnetooptical response and small magnetic domains are crucial parameters. However, achieving a large magnetooptical response with magnetic films that exhibit tiny magnetic domains is challenging due to the relationships among film thickness, magnetooptical response, perpendicular magnetic anisotropy, and magnetic domain width. As thickness increases, so does the magnetooptical response. Conversely, perpendicular magnetic anisotropy decreases due to the relaxation of strain between the film and the substrate, leading the easy axis of magnetization to orient in-plane and resulting in the disappearance of magnetic domains from the magnetic film. Hence, in this study, we employed a microcavity structure to achieve a large magnetooptical response and tiny magnetic domains generated by perpendicular magnetic anisotropy.

Magnetic garnet films were epitaxially grown on a gadolinium gallium garnet (GGG) substrate using RF ion beam sputtering [3]. During growth, the sample temperature was maintained at 900°C. Two types of magnetic garnets, cerium-substituted yttrium iron garnet (Ce:YIG) and GGG, were alternately grown to create Bragg mirrors. Within the Bragg mirror, a defect layer, twice as thick, was introduced to provide a localized mode within a photonic band gap and enhance the Faraday rotation angle. This structure is referred to as a microcavity or magnetophotonic crystal. The Ce:YIG and GGG have slightly different lattice constants, generating lattice strain, perpendicular magnetic anisotropy, and magnetic domains.

The magnetic domains of the fabricated Bragg mirror and microcavity were observed using a magnetooptical microscope, as shown in Figure 1. The width of the magnetic domain was less than 500 nm, and the domain wall width was less than 100 nm. The detail will be shown in the symposium.

The Faraday rotation angle was enhanced by the microcavity resonance at a near-infrared wavelength. Therefore, large magnetooptical responses and tiny magnetic domain structures were simultaneously obtained using the all-garnet magnetooptical microcavity sample.

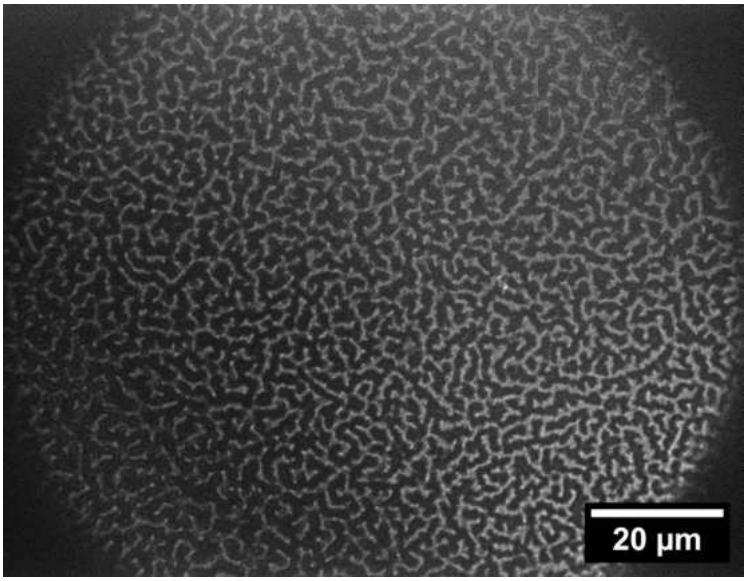


Figure 1. Magnetooptical microscope image of the sample. The observed wavelength was 470 nm. The magnetic field was not applied to the sample.

This work was partly supported by the Japan Society for the Promotion of Science (JSPS) KAKENHI Nos. 20H02593, 20K20535, 23H01439, and 23K17758; the New Energy and Industrial Technology Development Organization (NEDO) No. 23200047-0, and the Inamori Foundation. We also acknowledge the Center for Integrated Nanotechnology Support (CINTS), the Laboratory for Nanoelectronics and Spintronics (LNS), and the Fundamental Technology Center of Tohoku University (FTCTU).

References

1. T. Goto, R. Morimoto, J. W. Pritchard, M. Mina, H. Takagi, Y. Nakamura, P. B. Lim, T. Taira, and M. Inoue, "Magneto-optical Q-switching using magnetic garnet film with micromagnetic domains," Opt. Express 24, 17635-17643 (2016).
2. T. Goto, M. C. Onbasli, D. H. Kim, V. Singh, M. Inoue, L. C. Kimerling, and C. A. Ross, "A nonreciprocal racetrack resonator based on vacuum-annealed magnetooptical cerium-substituted yttrium iron garnet," Opt. Express 22, 19047-19054 (2014).
3. Y. Yoshihara, K. Ishiyama, T. Watanabe, P. B. Lim, M. Inoue, C. A. Ross, and T. Goto, "Growth of magnetooptical cerium-substituted yttrium iron garnet on yttrium aluminum garnet using ion beam sputtering," Appl. Phys. Lett. 123, 112404 (2023).

Microscale concave interfaces: a new reflective colorimetric platform

Jacob Rada[1,2], **Chi Zhou**[2] and **Qiaoqiang Gan**[1,*]

[1]King Abdullah University of Science and Technology, Saudi Arabia

[2]University at Buffalo, The State University of New York, Buffalo, NY, US
[*]corresponding author: qiaoqiang.gan@kaust.edu.sa

Abstract: This talk will discuss the novel use of microscale concave interfaces (MCI) for generating structural colors through total internal reflection interference. Highlighting both theoretical understanding and experimental research, it promises significant applications in information display, traffic safety, and photonics.

In our daily lives, both humans and machines utilize various colors to decipher and process critical information. As the field of modern physics has advanced, our understanding of color generation has significantly expanded, enabling the characterization of diverse coloration phenomena. These phenomena range from optical dispersion, exemplified by prism-induced rainbows; spectrally selective absorption, observed in chemical pigments and resonant photonic structures; to thin-film interference, visible in the iridescence of bubbles and oil slicks. Among these, structural colors are particularly noteworthy for their reliance on geometric optimization to produce color, eschewing traditional pigments or dyes. This method of coloration has piqued the interest of the scientific and industrial sectors due to its innovative ability to manipulate light flow.

A notable advancement in this realm is the exploration of total internal reflection (TIR) interference through microscale concave interfaces (MCI), as recently proposed [1,2]. This mechanism stands apart from conventional coloration processes, presenting both exciting possibilities and significant challenges for incorporation into large-scale displays and sensors. This presentation aims to delve into a combined approach of fundamental and experimental research to demystify the physical underpinnings of MCI. Emphasizing the exploration of an unambiguous physical mechanism for this new MCI structure, our discourse is grounded in systematic experimental characterization [3]. As a result of this characterization, we realized a previously unseen multiple concentric ring phenomena, as shown in **Fig**. **1**.

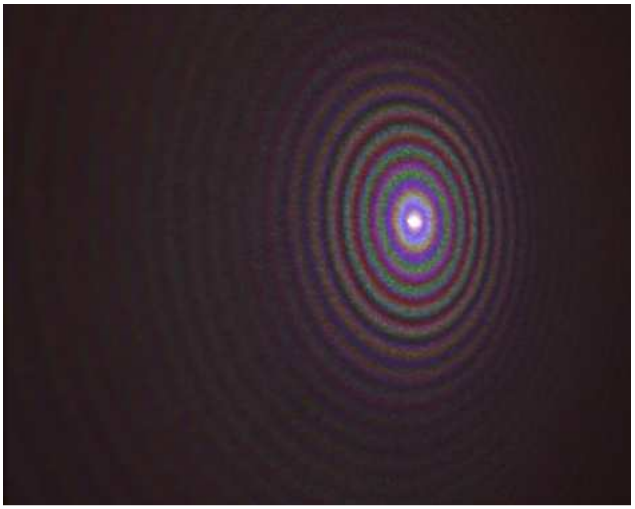


Fig. 1| Multiple concentric rainbow rings generated by an MCI sample containing polystyrene microspheres with a mean diameter of 42μm.

Building on these insights into novel optical interface structures, we will highlight advancements in selected hybrid technologies spanning both visible and infrared display and spectroscopy [4]. The realization of these cutting-edge reflective coloration strategies is anticipated to drive pivotal technological breakthroughs, particularly in information display applications. Furthermore, the development of micro-optics structures is set to propel research and development efforts, with wide-ranging impacts from enhancing traffic safety [5] to anti-counterfeiting and optical encryption [6-10].

Acknowledgements: This work is partially supported by NSF (ECCS-2111056) and the baseline from KAUST ((BAS/1/1415-01)).

References

1. Goodling, A.E., et al. Colouration by total internal reflection and interference at microscale concave interfaces. *Nature* **566**, 523–527 (2019)
2. Fan, W., et al. Iridescence-controlled and flexibly tunable retroreflective structural color film for smart displays. *Sci. Adv.* **5**, eaaw8755 (2019)
3. Rada, J., et al. Multiple concentric rainbows induced by microscale concave interfaces for reflective displays. *Appl. Mater. Today* **24**, 101145 (2021)
4. Yang, Z., et al. Miniaturization of optical spectrometers. *Science* **371**, 480 eabe0722 (2021)
5. Qi, Y., et al. Retroreflection and wettability controlled smart indicator based on a responsive bilayer photonic crystals for traffic warning. *Adv. Opt. Mat.* **8**, 2001367 (2020)
6. Ji, C., Chen, M., Wu, L., Quadruple anti-counterfeiting retroreflective structural color films. *Adv. Opt. Mater.* **10**, 2102383 (2022)
7. Ji, C., Chen, M., Wu, L., Patternable and rewritable retroreflective structural color shape memory polymers. *Adv. Opt. Mat.* **9**, 2100739 (2021)
8. Kaixuan, L., et al. Facile full-color printing with a single transparent ink. *Sci. Adv.* **7**, eabh1992 (2021)
9. Yang, Y., et al. Nanostructure-free crescent-shaped microparticles as full-color reflective pigments. *Nat. Comm.*, **14**, 793 (2023)
10. Li, D. Y., et al. Tunable structural coloration in eccentric water-in-oil-in-water droplets. *Nano Lett.*, **23**, 20, 9657–9663 (2023)

Periodically nanostructured anisotropic coatings for spatial filtering and polarization control

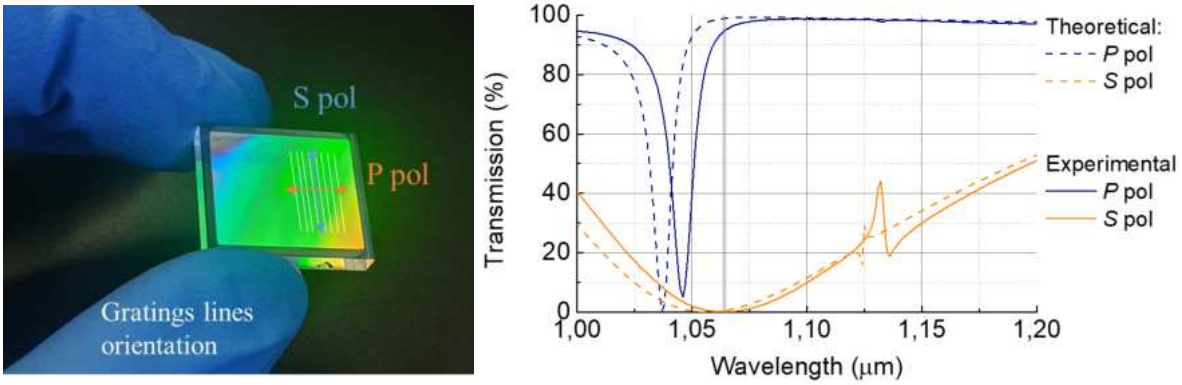
J. Nikitina[1], M. Plukys[2], D. Gailevičius[2], K. Staliunas[3,4], L. Grineviciute[1,2*]

[1] Center for Physical Sciences and Technology, Savanoriu Ave. 231, LT-02300 Vilnius, Lithuania
[2]Vilnius University, Faculty of Physics, Laser Research Center, Sauletekio Ave. 10, Vilnius, Lithuania
[3]ICREA, Passeig Lluís Companys 23, 08010, Barcelona, Spain
[4]UPC, Dep. de Fisica, Rambla Sant Nebridi 22, 08222, Terrassa (Barcelona) Spain
[*]corresponding author: lina.grineviciute@ftmc.lt

Abstract: This study aimed to investigate the growth process of thin films on a nanostructured surface and to analyze the perspective to use such elements in micro lasers. Optical characterization revealed the presence of Fano-like resonance phenomenon in such single-layer structure, surrounded by a lower refractive index media. Moreover, we demonstrate a 5 μm thick photonic multilayer structure composed of alternating high- and low-index materials, providing angular selectivity of light. The proposed 2D photonic structure can be considered as a promising component for intracavity spatial filtering and polarization control, even in high-power microlasers.

In micro-lasers, especially in high-power emission regimes, the spatial quality of the laser light beam deteriorates. Typically, a confocal arrangement of lenses with a diaphragm in the focal plane is used for intracavity spatial filtering; however, such conventional filtering requires access to the far-field domain. Conventional filtering is impossible in microlasers due to the lack of space in micro-resonators to access the far-field. Therefore, a novel concept for compact and efficient spatial filtering is necessary.

This work presents the investigation of 2D periodic structures made by conformal deposition of dielectric thin films on the modulated surface, where the deposited layers repeat the primary surface [1,2]. The investigation revealed that Fano-like resonance can be exited even in a periodically modulated single layer with a higher refractive index than the surrounding media. The proposed structure shows high angle-wavelength sensitivity of light transmission/reflection, which can be used to manipulate the properties of the beam radiation perpendicular to the surface. Moreover, we experimentally demonstrate a 5 μm thick photonic multilayer structure composed of alternating high- and low-index materials providing spatial filtering in the near-infrared frequencies with a 2° low-angle passband. Depending on the architecture, such spatial filtering may be performed in transmission or reflection with the incidence of radiation perpendicular to the surface. Furthermore, due to the linear structure, such elements can work as 0° AOI polarizers.



Fg.1. The image of fabricated sample (left) and transmission spectra of nanostructured coating polarizer for both S and P polarizations (right).

In the presentation, the overview of different technologies to form conformal coatings on periodically modulated surfaces will be presented. As the proposed 2D photonic structure can be considered a promising component for intracavity spatial filtering, the integration into microchip laser will be presented. A significant reduction of M^2 and brightness increase of two times was recorded for the microchip laser when the fabricated spatial filter was used as one of the resonator mirrors. Moreover, the investigation on resistivity to laser radiation and further improvements will be presented.

References

1. Grineviciute L., Nikitina J., Babayigit C., Staliunas K., “Fano-like Resonances in Nanostructured Thin Films”, Applied Physics Letters, 118, 2021.
2. Grineviciute L., Babayigit C., Gailevičius D., et al., “Nanostructured Multilayer Coatings for Spatial Filtering”, Adv. Optical Mater. 9, 2001730 2021.

Engineering spin-orbit coupling of light in weak and strong light-matter coupling regimes for topological photonics

Jacek Szczytko[1*], M. Muszyński[1], P. Oliwa[1], P. Kapuściński[1], P. Kokhanchik[2], M. Kędziora[1], K. Łempicka-Mirek[1], E. Oton[3], R. Mazur[3], P. Morawiak[3], W. Piecek[3], P. Kula[4], D. Bobylev[2], D. Solnyshkov[2,5], G. Malpuech[2], W. Bardyszewski[6], B. Piętka[1]

[1]Institute of Experimental Physics, Faculty of Physics, University of Warsaw, Poland
[2]Université Clermont Auvergne, Clermont Auvergne INP, CNRS, Institut Pascal, F-63000 Clermont-Ferrand, France
[3]Institute of Applied Physics, Military University of Technology, Warsaw, Poland
[4]Institute of Chemistry, Military University of Technology, Warsaw, Poland
[5]Institut Universitaire de France (IUF), 75231 Paris, France
[6]Institute of Theoretical Physics, Faculty of Physics, University of Warsaw, Poland
[*]corresponding author: Jacek.Szczytko@fuw.edu.pl

Abstract: We have developed a method to control the spin-orbit coupling of light by embedding emitters within liquid-crystal microcavities. We explore light-matter interactions in both weak and strong coupling regimes, which extend beyond traditional optical properties. This approach has enabled us to achieve tunable lasing, including dual and circularly polarized lasing.

Metamaterials are artificial materials engineered to achieve properties not found naturally, using specialized functional units. Especially, these structures are designed to manipulate electromagnetic waves in unique ways. The physics of microcavities has become rich over recent decades, enhanced by the diversity of materials that can be embedded within them. These materials can significantly alter cavity mode properties, and conversely, the response of the materials can be influenced by the cavity, extending beyond optical properties.

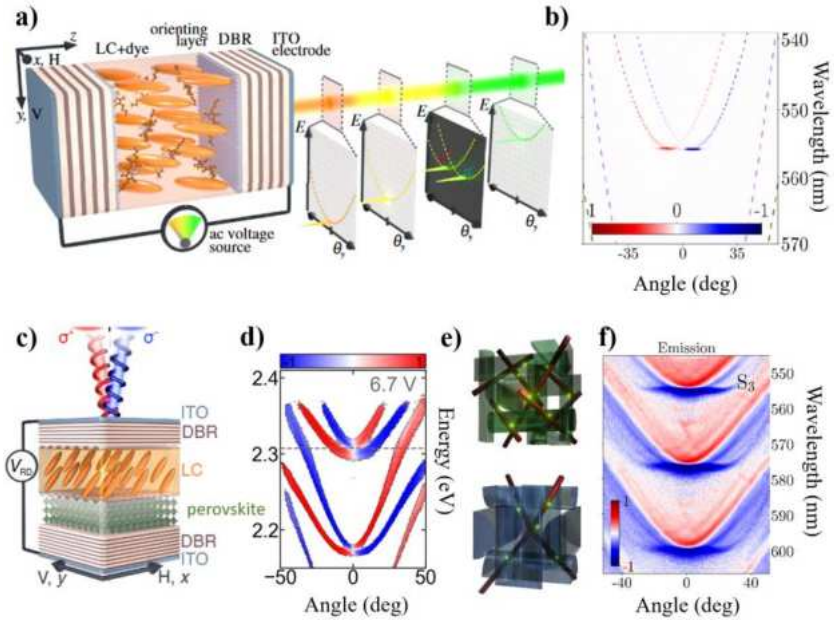


Figure a) scheme of the tunable dye-doped LC microcavity [5]; **b)** lasing in RD spin-orbit regime [5] (experiment); **c)** schematic representation of the LC microcavity with the two-dimensional (2D) hybrid organic-inorganic perovskite layer [7,8]; **d)** circularly polarized emission in strong light-matter coupling [7] (experiment, Stokes S_3 parameter); **e)** Blue phase LCs in phases BPI and BPII (top and bottom respectively): 3D self-organizing photonic crystal [10]; **f)** circularly polarized emission from a laser dye-doped blue phase integrated within a microcavity (Stokes S_3).

We have developed a method to electrically control the spin-orbit coupling (SOC) of light using specially designed photonic structures – birefringent microcavities (**Fig. a**). These consist of a 2-3 μm thin liquid crystal layer enclosed between two parallel distributed Bragg reflectors deposited on transparent electrodes. In solid-state systems with broken inversion symmetry, SOC gives rise to the Dresselhaus and Bychkov-Rashba

SOC Hamiltonians, key to spintronics, topological insulators, and superconductors. Unlike SOC in solid-state matter, which is challenging to manipulate, birefringent optical cavities offer substantial tunability of photonic modes. This has led to observing an optical analog of the spin Hall effect and creating artificial gauge fields for parameters extending far beyond those previously considered experimentally and theoretically [1]. We discovered Rashba-Dresselhaus spin-orbit coupling in a photonic system and showed control of an artificial Zeeman splitting [2]. Additionally, we've shown how to structure light so its polarization mimics spins in a ferromagnet, forming half-skyrmions (merons) [3]. Recently we observed an optical analog of persistent spin helix, reciprocal Young's and Stern-Gerlach experiments [4], and a new type of chiral Rashba-Dresselhaus lasing [5] (**Fig. b**). Our results illustrate an effective approach to engineering artificial gauge fields and synthetic Hamiltonians with photons for the simulation of nontrivial condensed matter and quantum phenomena, promising new directions in topological photonics [6-8], non-Hermitian systems [6,9] and condensates of light. By embedding emitters within birefringent microcavities, we explore light-matter interactions in both weak [5] (**Fig. a,b**) and strong coupling regimes [7-8] (**Fig. c,d**).

The platform we proposed opens new possibilities in topological photonics [7-9]. Beyond the standard lithographic methods, our approach with liquid crystal cavities enables the creation of self-organizing macro-molecular structures, whose sizes and shapes can be controlled by temperature or electric fields. Our team has successfully integrated a self-organizing liquid crystal structure – specifically, a blue phase, whose structure can be regarded as a 3D photonic crystal (**Fig. e,f**) – within a microcavity [10]. Additionally, these periodic photonic structures allow for precise control over optical modes, enhancing their functionality and application potential.

Acknowledgements: This work was supported by the National Science Centre grants 2019/35/B/ST3/04147, 2019/33/B/ST5/02658 and 2021/43/I/ST5/02632, 2022/47/B/ST3/02411, and the European Union's Horizon 2020 program, through a FET Open research and innovation action under the grant agreements No. 964770 (TopoLight). Additional support was provided by the ANR Labex GaNext (ANR-11-LABX-0014), the ANR program "Investissements d'Avenir" through the IDEX-ISITE initiative 16-IDEX-0001 (CAP 20-25), and the ANR project "NEWAVE" (ANR-21-CE24-0019).

References

[1] K.Lekenta, et al., *Tunable optical spin Hall effect...* Light Sci. & Appl. **7**, 74 (2018).

[2] K.Rechcińska, et al. *Engineering spin-orbit synthetic Hamiltonians…,* Science **366**, 727 (2019)

[3] M. Król et al. *Observation of second-order meron polarization textures …,* Optica **8**, 255 (2021)

[4] M.Krol et al. *Realizing Optical Persistent Spin Helix*…, Phys. Rev. Lett., **127**, 190401 (2021)

[5] M.Muszynski, et al. *Persistent-Spin-Helix Lasing*…, Phys. Rev. Appl. **17**, 014041 (2022);

[6] M. Król, I. Septembre et al. *Annihilation of exceptional points…* Nature Commun.**13**, 5340 (2022)

[7] K. Łempicka-Mirek et al., *Electrically tunable Berry curvature* … Sci. Adv. **8**, eabq7533 (2022)

[8] K. Łempicka-Mirek et al., *Electrical switching…* doi.org/10.1515/nanoph-2023-0829 Nanophotonics (2024)

[9] P. Oliwa et al. *Quantum mechanical-like approach*… Phys. Rev. Research **6**, 013324 (2024)

[10] E. Otón, et al. *Orientation control of ideal blue phase photonic crystals*. Sci Rep **10**, 10148 (2020)

Energy- and Time-resolved NIR to Visible Upconversion Luminescence from Single $NaYF_4:Yb^{3+},Tm^{3+}$ Nanoparticles on Self-assembled Chiral Metasurfaces

A. Ahmed[1], K.Y. Chiok[1], S. May[2], A. Baride[2], R.B. Anderson[1], S. Zhou[1], S. Smith[1]

[1]South Dakota School of Mines and Technology, Rapid City, South Dakota, USA
[2]University of South Dakota,Vermillion, South Dakota, USA

Corresponding author email: Steve_Smith@mailaps.org

Abstract: We use time- and energy-resolved single particle spectroscopic imaging to assess the plasmonic enhancement of NIR-to-visible upconversion luminescence (UCL) from single β-$NaYF_4:Yb^{3+}:Tm^{3+}$ upconverting nanoparticles (UCNPs) supported on self-assembled chiral metasurfaces[1]. By examining the effects at the single particle level, we assess the plasmon-enhanced radiative decay and polarization of upconversion luminescence on metasurfaces self-assembled from tetrahedral Au nanoparticles. We obtain a statistical description of UCL emission enhancement in the Tm-doped UCNPs and map out the statistical distribution of excitation and luminescence enhancement on plasmonic substrates[2–4]. We use both wide field and confocal scanning spectroscopic imaging of single UCNPs on and off the plasmonic substrates in combination with energy and time resolved spectroscopy, and compare these results to a coupled rate equation analysis to elucidate the energy transfer upconversion enhancement mechanisms. The results obtained are compared to Finite Difference Time Domain (FDTD) calculations of the fields near the plasmonic substrate.

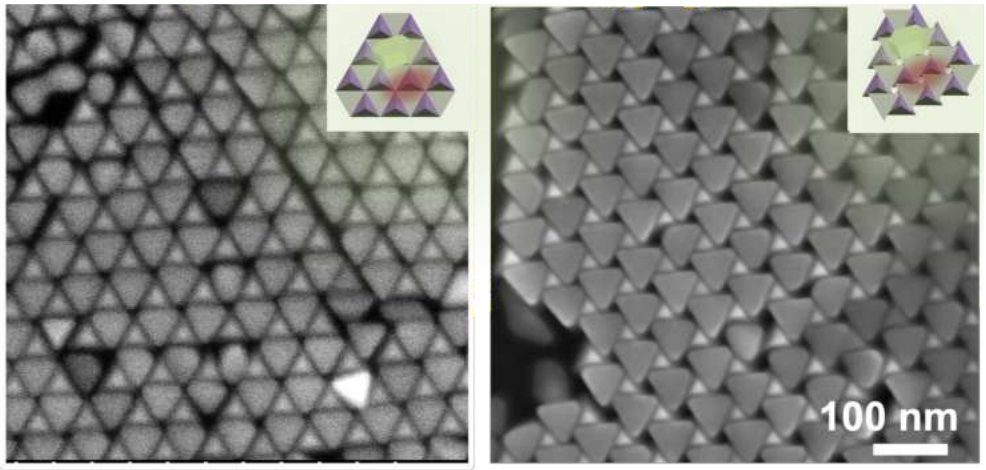


Figure: SEM images of self-assembled symmetric (left) and chiral (right) metasurfaces obtained by self-assembly of Au tetrahedra. Inset: Schematic of self-assembled metasurfaces supporting single UCNPs.

References:

(1) Zhou, S.; Li, J.; Lu, J.; Liu, H.; Kim, J. Y.; Kim, A.; Yao, L.; Liu, C.; Qian, C.; Hood, Z. D.; Lin, X.; Chen, W.; Gage, T. E.; Arslan, I.; Travesset, A.; Sun, K.; Kotov, N. A.; Chen, Q. Chiral Assemblies of Pinwheel Superlattices on Substrates. *Nature* **2022**, *612* (7939), 259–265.

(2) Fisher, J.; Zhao, B.; Lin, C.; Berry, M. T.; May, P. S.; Smith, S. Spectroscopic Imaging and Power Dependence of NIR to Visible Upconversion Luminescence from NaYF4:Yb3+,Er3+ Nanoparticles on Nano-Cavity Arrays. *Journal of Physical Chemistry C* **2015**, *119* (44), 24976–24982.

(3) Hor, A.; Luu, Q.; May, P.; Berry, M.; Smith, S. Non-Linear Density Dependent Upconversion Luminescence Enhancement of β-NaYF4: Yb3 : Er3 Nanoparticles on Random Ag Nanowire Aggregates. *MRS Adv* **2016**, *1* (38), 2677–2682.

(4) Hossan, M. Y.; Hor, A.; Luu, Q.; Smith, S. J.; May, P. S.; Berry, M. T. Explaining the Nanoscale Effect in the Upconversion Dynamics of β-NaYF 4 :Yb 3+ , Er 3+ Core and Core–Shell Nanocrystals. *The Journal of Physical Chemistry C* **2017**, *121*, 16592–16606.

Advanced Computational Electromagnetics for the Analysis and Design of Nanophotonic Devices

Refined Quantum Hydrodynamic Model for Deep Nanoscale Plasmonics with Noble Metal and Dielectrics

Xue-Wen Chen[1,2*]

[1]School of Physics and Wuhan National Laboratory for Optoelectronics, Huazhong University of Science and Technology, Wuhan, China.
[2]Wuhan Institute of Quantum Technology, Wuhan, China.
[*]Corresponding author: xuewen_chen@hust.edu.cn

Abstract: Quantum hydrodynamic model has become a versatile and efficient tool for plasmonics at the deep nanoscale, but the current model is in principle only applicable to simple metals, not for noble-metal structures. We present a refined quantum hydrodynamic model to effectively account for various effects from noble metals.

Plasmonic resonances of metallic nanostructures, especially those made from noble metals, have the capability of confining light down to the deep nanometer scale. As optical fields are concentrated below ~10 nm and towards the Thomas-Fermi screening length scale, the nonlocal and quantum effects of conduction electrons become significant. The quantum hydrodynamic model (QHDM) directly computes the conduction electron density and current by solving a hydrodynamic equation. The equation retains the quantum and many-body effects with internal energy functionals and viscoelastic tensors of conduction electrons. Consequently, the QHDM could account for various quantum effects with affordable computational cost, and thus outstands as a promising method for studying nanoplasmonics.

However, the existing QHDMs are designed for simple metals. The application to noble metals hasn't been duly justified. For noble metal, while the direct effect from the d-band (or bound electrons) could be depicted with a background optical permittivity in Ampere's law, the indirect effect from these d-band electrons on the conduction electrons has not been taken into account. In addition, when the noble-metal structures interface with dielectrics, the electron affinity of the dielectrics near the interface should be properly described. Here we report a refined QHDM, where the missing effects of the d-band electrons are identified and included [1]. The near-field effects of the d-band electrons and electron affinity of the dielectric are encompassed with an extra potential U_{aff} in the refined QHDM [2]. Material-independent model parameters are fitted with density functional theory (DFT) calculations for simple metal. Our calibrated QHDM is lastly benchmarked against DFT and time-dependent DFT for Ag, Au and Al nanostructures interfacing with dielectrics. We expect our QHDM would be a valuable asset for the rapidly developing field of extreme nanophotonics.

We acknowledge partial financial support from the National Natural Science Foundation of China (Grants No. 92150111 and No. 62235006).

References

1. Q. Zhou, P. Zhang, X.-W. Chen, "General framework of canonical quasinormal mode analysis for extreme nano-optics", *Phys. Rev. Lett.* 127, 267401 (2021).
2. Q. Zhou, W. Li, Z. He, P. Zhang, X.-W. Chen, "Quantum hydrodynamic model for noble metal

nanoplasmonics," Phys. Rev. B 107, 205413 (2023).

Slime mold algorithm for topology optimization of photonics structure

K.S. Edee[1*] and P. Bonnet[1]

[1]Université Clermont Auvergne, Clermont Auvergne INP, CNRS, Institut Pascal, Clermont-Ferrand F-63000, France.

Abstract: We introduce an innovative approach to photonics structure design, incorporating the slime mold algorithm (SMA) [1], a gradient-free metaheuristic optimization method, in tandem with the topology optimization (TO) method, and utilizing a spectral modal method. Through the integration of TO with SMA, (TO-SMA) we achieve successfully metagrating designs [2].

In this paper, we present the application of the Slime Mold Algorithm (SMA) to topology optimization for a 1D dielectric metagrating (see Fig. 1), within the framework of a spectral method. The primary objective of this design is to formulate a 1D metagrating composed of a sequence of nanorods and air gaps with varying widths, strategically optimized to efficiently redirect incident plane wave power into a specified transmission order. The proposed SMA initiates by generating a random set of widths for the nanorods and air gaps. A corresponding set of binary permittivity functions is defined for this sequence of nanorods/air gap widths. However, since our focus is on a Topology Optimization (TO) method, we apply a blurring process to this initial population. This process transforms the discrete set of widths into a continuous sequence of permittivity functions. A noteworthy aspect and a key feature of our proposed method lie in the choice of the filter employed during this blurring process. Instead of opting for classical Gaussian or binary functions as filters, we introduce the Schwartz function. The shape of the function can be significantly altered by adjusting some of its key parameters, providing enhanced flexibility and control over the continuous permittivity function at each iteration during the optimization process.

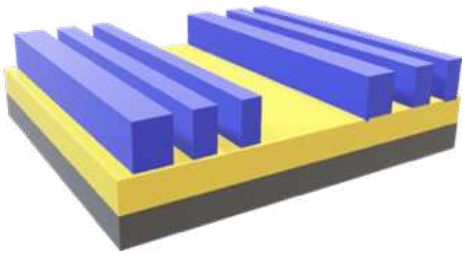


Figure 1 : A 1D deflector to be designed

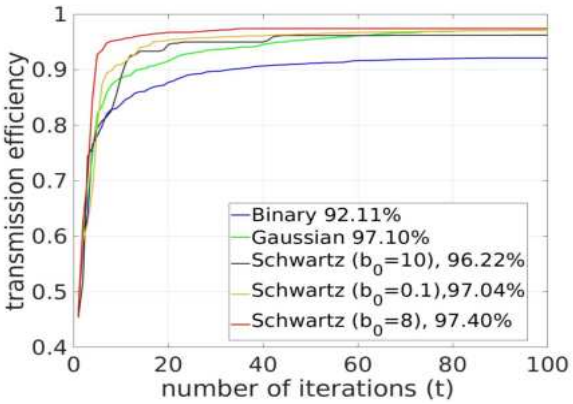


Figure 2: Performances of the TO-SMA using different filter functions: the Schwartz, Gaussian and binary functions

In Fig. 2 we emphasize the impact of the Schwartz function on numerical results, we compare the

performance of TO-SMA using the Schwartz filter with different shapes. This assessment involves a comparison with Gaussian and binary functions. The Schwartz filter demonstrates a remarkable ability to converge rapidly towards high-performance solutions. A flow chart of the proposed algorithm is shown in Fig.3

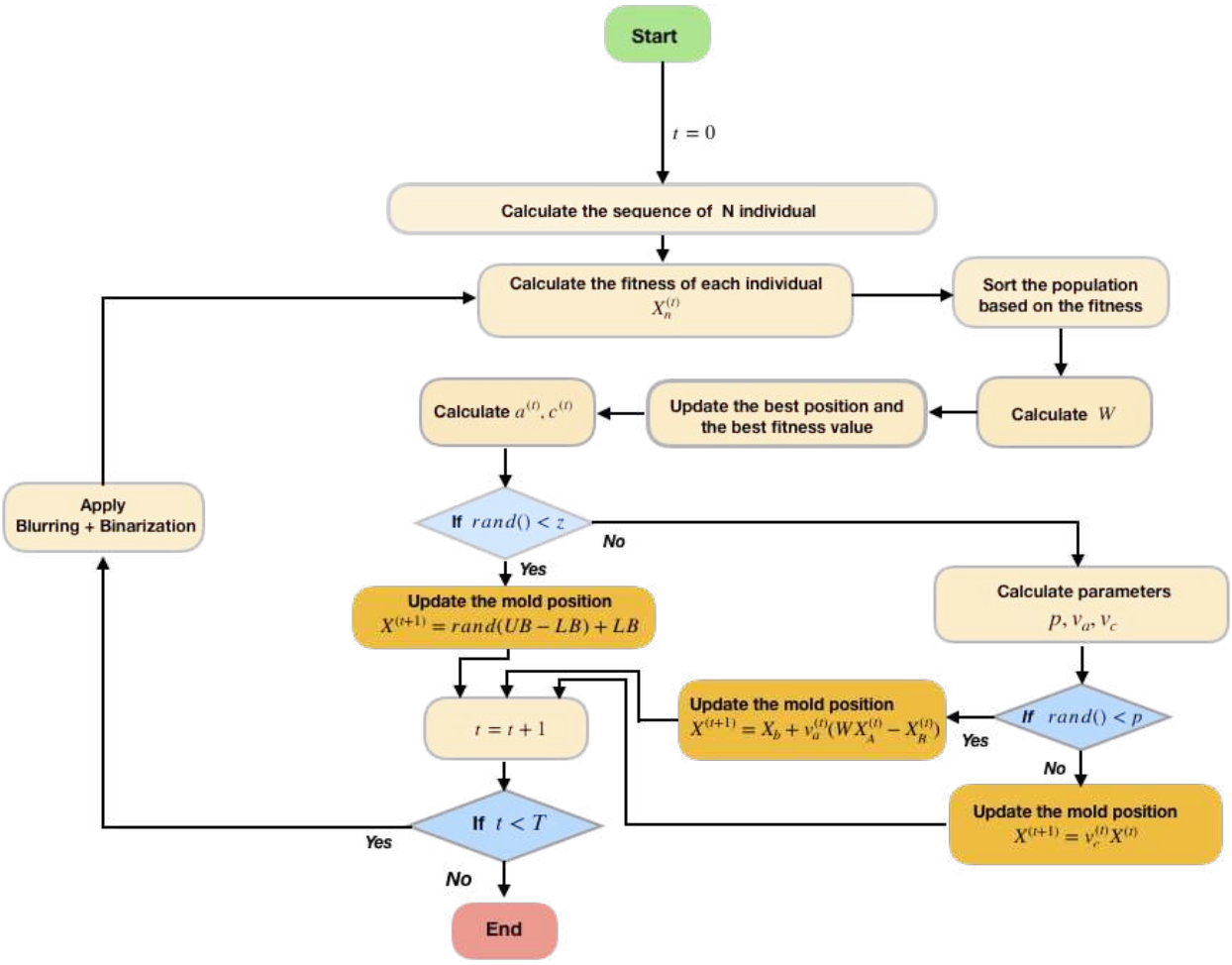


Figure: 3 A flow chart of the algorithm

References

1. Li S, Chen H, Wang M, Heidari AA, Mirjalili S. Slime mould algorithm: a new method for stochastic optimization. Fut Gener Comput Syst. 2020;111:300–23.
2. Edee, K., Granet, G. & Bonnet, P. "Slime mold algorithm for topology optimization: metagratings inverse design," Discov Appl Sci **6**, 68 (2024).

Nanophotonic chirality transfer to dielectric Mie resonators

E. Mohammadi[1], T. V. Raziman[1], Alberto G. Curto[1,2,3*]

[1] Department of Applied Physics and Eindhoven Hendrik Casimir Institute,
Eindhoven University of Technology, Eindhoven, The Netherlands
[2] Photonics Research Group, Ghent University-imec, Ghent, Belgium
[3] Center for Nano- and Biophotonics, Ghent University, Ghent, Belgium

[*]Corresponding author: Alberto.Curto@UGent.be

Abstract: Nanophotonics can boost the weak circular dichroism of chiral molecules. One mechanism relies on creating fields with high optical chirality at the molecular position using resonators. Here, we elucidate how the reverse interaction between molecules and the resonator, called chirality transfer, can produce stronger circular dichroism in dielectric Mie resonators.

Chiral molecules exist in right- and left-handed forms known as enantiomers. Their biological functionality depends on handedness, which makes chiral sensing crucial to biochemistry and medicine. Circular dichroism (CD) can detect the handedness of enantiomers through the differential absorption of circularly polarized light. However, it is typically very weak, particularly at low molecular concentrations. To overcome this, nanophotonics offers enhanced optical chirality to increase the interaction of light with chiral molecules. Nanophotonic structures such as metal and dielectric nanoparticles can generate chiral fields at the location of the chiral molecules.[1,2] The resulting CD enhancement is proportional to the average value of the optical chirality over the chiral sample volume. It is challenging to obtain high average values because high optical chirality usually occurs in hotspots with limited volumes.

Here, we show that the reverse interaction between chiral molecules and nanoresonators is also relevant and can dominate chiral sensing with dielectric nanostructures. A chiral molecule can transfer its chirality to an achiral dielectric resonator, resulting in chiroptical signals orders of magnitude higher than those from optical chirality alone. The underlying physics is the back action of the chiral molecules onto the nanostructures through dipole-dipole interactions. For right- and left-handed circularly-polarized excitations, the presence of the chiral molecules changes the otherwise equal electric fields (and thus the dipole moments) in an achiral nanoparticle. Consequently, the circular dichroism of the system consisting of a nanoresonator and chiral molecules arises from both chirality transfer and optical chirality. Most studies thus far focused *ad hoc* on only one of these two mechanisms, which has been a source of mismatch between experimental results and theoretical predictions and prevented a rational design of nanostructures.

We demonstrate that chirality transfer to dielectric resonators offers higher CD enhancement compared to metallic ones thanks to the tunable co-existence of electric and magnetic resonances.[3] We derive closed-form equations revealing its dependence on the molecular chirality (Pasteur parameter), molecule-resonator distance, and the resonator Mie coefficients. Our complete theoretical framework allows us to find the fundamental upper limits for chirality transfer for electric and magnetic Mie resonances. Importantly, we clarify the different requirements for CD enhancement based on the chirality transfer and optical chirality mechanisms. We decompose the contribution of chirality transfer to CD into electric and magnetic terms and recognize the

magnetic contribution as responsible for the unique performance of dielectric resonators. Finally, for practical purposes, we introduce a dielectric metasurface composed of silicon disks showing a 900-fold CD enhancement. Our insights into chirality transfer and its opportunities pave the way towards more efficient nanophotonic platforms for ultrasensitive chiral detection.

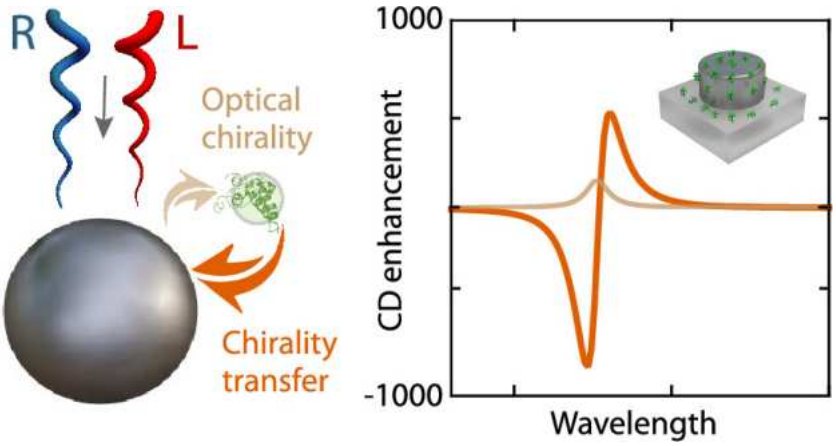


Figure 1. Imprinting of circular dichroism into the resonance of an achiral Mie resonator through its interaction with a chiral material.

References

1. E. Mohammadi, A. Tittl, K. L. Tsakmakidis, T. V. Raziman, and A. G. Curto, Dual Nanoresonators for Ultrasensitive Chiral Detection, *ACS Photonics*, vol. 8, no. 6, 2021.
2. T. V. Raziman, R. H. Godiksen, M. A. Müller, and A. G. Curto, Conditions for Enhancing Chiral Nanophotonics near Achiral Nanoparticles, *ACS Photonics*, vol. 6, no. 10, 2019.
3. E. Mohammadi, T. V. Raziman, and A. G. Curto, Nanophotonic Chirality Transfer to Dielectric Mie Resonators, *Nano Letters*, vol. 23, no. 9, 2023.

Consensus ADMM for Photonic Design

Hyeonhee Kim[1], Myungjoon Kim[1], Zeyu Kuang[2], Owen D. Miller[2,*], and Jonghwa Shin[1,*]

[1]Department of Materials Science and Engineering, KAIST, Daejeon, 34141, Republic of Korea
[2]Department of Applied Physics and Energy Sciences Institute, Yale University, New Haven, CT 06520, USA
[*]corresponding authors: owen.miller@yale.edu, qubit@kaist.ac.kr

Abstract: We propose a novel photonic design approach by formulating the problem as quadratically constrained quadratic programming and applying a consensus-based alternating direction method of multipliers. We demonstrate that for a metalens design, our algorithm outperforms conventional inverse design methods, achieving superior outcomes in terms of solution quality and optimization speed.

Photonic design plays a pivotal role in modern optics to create devices with enhanced functionalities. Inverse design processes, often leveraging gradient-based optimization, have been used to design numerous optical devices. However, the inherent highly nonconvex nature of the objective functions often leads to convergence at local optima of poor quality. In contrast, a fundamentally different strategy has been proposed, leveraging the well-established convex optimization theories and algorithms. The photonic design problem is formulated as a quadratically constrained quadratic programming (QCQP) and subsequently the QCQP is translated into semidefinite programming by relaxation [1]. This translation makes possible to obtain computational bounds of defined objective values. More recently, this QCQP formulation has been applied to photonic design problems, enabling the derivation of physical structures through convex optimization techniques under sparse conditions [2].

Here, we introduce a novel algorithm for photonic design that directly tackles general QCQP by employing the alternating direction method of multipliers (ADMM). The ADMM is well-established convex optimization algorithm, well-suited for distributed and parallel computation [3]. This algorithm has been demonstrated to be effective in addressing general nonconvex QCQP using the consensus method [4]. We reformulate the photonic design problem into a consensus optimization framework as follows:

$$minimize \quad \boldsymbol{p}^{\dagger}\boldsymbol{A}_0\boldsymbol{p} + 2\Re\{\boldsymbol{b}_0^{\dagger}\boldsymbol{p}\} + \boldsymbol{c}_0$$

$$subject\ to \quad \boldsymbol{z}_i^{\dagger}\mathbb{D}_i\{(\boldsymbol{G_0} - \boldsymbol{\chi}^{-1})\boldsymbol{z}_i + \boldsymbol{e_{inc}}\} = 0,$$

$$\boldsymbol{z}_i = \boldsymbol{p}, \forall i = 1,2,\dots,m,$$

where the global variable $\boldsymbol{p}$ represents the polarization field and objective functions are defined with the Hermitian matrix $\boldsymbol{A}_0$, vector $\boldsymbol{b}_0$, constant $\boldsymbol{c}_0$. Additionally, each local variable $\boldsymbol{z}_i$ is constrained to satisfy a weighted quadratic form of the Green's function integral equation. The key step of the algorithm is to separate QCQP, each characterized by a single constraint. At each iteration, the separated problems are solved independently and update global variable to reflect a consensus among the local variables. Through a series of iterations, the local variables gradually align with the global variable, thereby achieving a consensus while minimizing the objective functions (Figure 1.a).

As a proof of concept, we demonstrate metalens design with the objective of maximizing light intensity at a specific point within a two-dimensional space. Consensus-ADMM shows faster convergence (T^{ADMM}=430s) and better objective value (f_{obj}^{ADMM}=1.4) than conventional adjoint-based optimization ($f_{obj}^{adj} = 1.2, T^{adj} = 5500s$).

The solution achieved is feasible, indicating that the optimized polarization fields are physically realizable (Figure 1.b). We convert the field into corresponding metasurface structure and the device shows focusing incoming light toward the designated target point (Figure 1.c).

In summary, we have proposed an innovative optimization framework for photonic design problems, utilizing a convex optimization algorithm. This approach demonstrates enhanced performance over traditional optimization methods, presenting its potential for further advancements and integration with additional optimization strategies. This framework can be widely applicable to a broad spectrum of problems in linear optics and photonics.

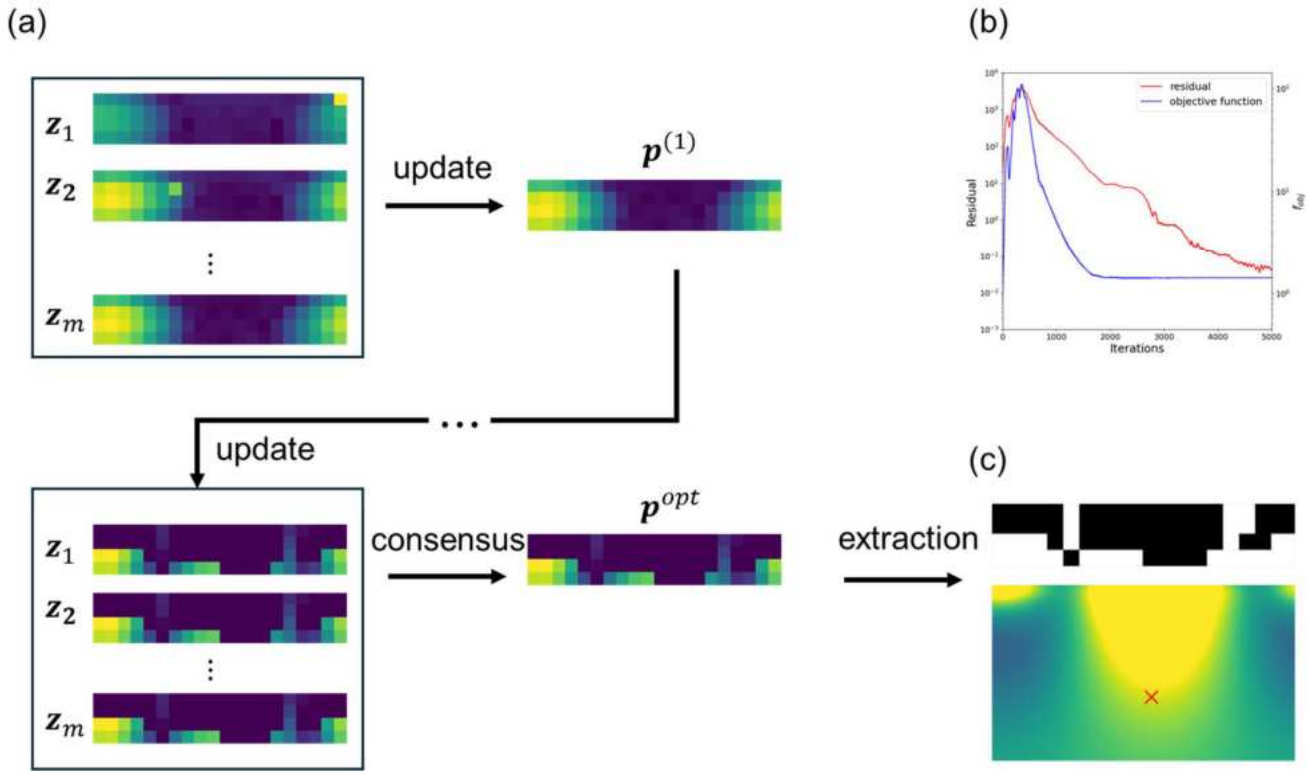


Figure 1. Design of a cylindrical metalens using consensus-ADMM (a) Schematic of consensus-ADMM for photonic design. (b) Residual and objective function versus Iterations. (c) Extracted Structure from p^{opt} and numerically obtained electric field profile.

References

1. Zeyu Kuang and Owen D. Miller, “Computational Bounds to Light–Matter Interactions via Local Conservation Laws,” Phys. Rev. Lett., Vol. 125, No. 26, 263607(7), 2020.
2. Shai Gertler, Zeyu Kuang, Colin Christie and Owen D. Miller, “Many Physical Design Problems are Sparse QCQPs,” arXiv:2303.17691, 2023.
3. Stephen Boyd, Neal Parikh, Eric Chu, Borja Peleato and Jonathan Eckstein, “Distributed Optimization and Statistical Learning via the Alternating Direction Method of Multipliers,” Found. Trends Mach. Learn., Vol. 3, No. 1, 1–122, 2010.
4. Kejun Huang and Nicholas D. Sidiropoulos, “Consensus-ADMM for General Quadratically Constrained Quadratic Programming, IEEE, Vol. 64, No. 20, 5297–5310, 2016.

Optimizing Metasurface Design for Interference Lithography: Achieving Two-Dimensional Bravais Lattices with Arbitrary Motifs

Myungjoon Kim[1], Nayoung Kim[1], and Jonghwa Shin[1,*]

[1]Department of Materials Science and Engineering, KAIST, Daejeon, 34141, Republic of Korea
[*]corresponding author: qubit@kaist.ac.kr

Abstract: Periodic metasurface masks are utilized in interference lithography. In this study, we demonstrate that through the inverse design of metasurfaces, it is possible to achieve all two-dimensional Bravais lattices with any desired motifs by manipulating the amplitude, phase, and polarization of individual diffraction beams.

Proximity-field nanopatterning (PnP) is considered a promising technology for creating 3D nanostructures through the interference and diffraction of light sources. The PnP method uses binary gratings to produce multiple diffraction orders from a single incident beam. The pattern created by the process is determined by the design of the grating masks. Recently, the inverse design of metasurface masks in the PnP process has been proposed, presenting the potential for patterning that was previously unachievable. [1, 2, 3].

We can model the PnP system mathematically to analyze how an incident beam, after passing through a periodic metasurface mask, is diffracted into multiple coherent beams described by $\boldsymbol{E}_i(\boldsymbol{r}) = E_i \boldsymbol{p}_i \exp(\boldsymbol{k}_i \cdot \boldsymbol{r} + \varphi_i)$, where $\boldsymbol{r}$ corresponds to the position vector, and $\boldsymbol{p}_i, \boldsymbol{k}_i,$ and φ_i are the polarization vector, wavevector, and phase offset i^{th} diffraction beam, respectively. The resultant interference pattern is defined by $I(\boldsymbol{r}) = |\sum_i \boldsymbol{E}_i(\boldsymbol{r})|^2$. Ultimately, the nanopattern generated by the PnP process is determined by applying a simple threshold to this intensity pattern.

The five types of two-dimensional Bravais lattices, including rectangular, square, centered rectangular, hexagonal, and oblique, are determined by their primitive vectors. These primitive vectors for every Bravais lattice are obtained from the diffracted beam by selecting specific orders, in conjunction with the period of the metasurface and the wavelength of the source [3]. Moreover, the motifs within these lattices can be customized at will through adjustments in amplitude, phase, and polarization of diffraction beams. For example, to achieve a rectangular lattice, orders {-3, -1, +1, +3} are selected, with all other orders being suppressed. In such four-beam configuration, diverse motifs, from circular to V-shaped, can be implemented by modifying the relative amplitude and phase for each polarization.

We present the inverse design of bilayer metasurface mask for PnP that manipulate each diffraction beam. Using adjoint-based topology optimization, the PnP system, featuring a period of 1 μm and a wavelength of 355 nm, is optimized under conditions suitable for fabrication. We illustrate that the optimized metasurface effectively induces the desired diffraction amplitude, phase, and polarization. We further demonstrate that adjusting the geometric configuration of metasurfaces enables the creation of a variety of lattice distances and motifs within rectangular lattices.

References

1. S.-H. Nam, M. Kim, N. Kim, D. Cho, M. Choi, J. H. Park, J. Shin, and S. Jeon, “Photolithographic realization of target nanostructures in 3D space by inverse design of phase modulation,” *Science. adv.*, Vol. 8, No. 21, eabm6310, 2022.
2. C. Lee, G. Chang, J. Kim, G. Hyun, G. Bae, S. So, J. Yun, J. Seong, Y. Yang, D. Y. Park, S. Jeon, and J. Rho, “Concurrent Optimization of Diffraction Fields from Binary Phase Mask for Three-Dimensional Nanopatterning,” *ACS Photon.*, Vol.

10, No. 4, 919–927, 2022.

3. M. Kim, N. Kim, and J. Shin, “Realization of all two-dimensional Bravais lattices with metasurface-based interference lithography,” *Nanophotonics*, 2024. https://doi.org/10.1515/nanoph-2023-0786

Plasmonic semiconductor waveguides with tunable nonlinear optical response

G. Álvarez-Pérez[1,*], H. Hu[1], and C. Ciracì[1]

[1]Center for Biomolecular Nanotechnologies, Istituto Italiano di Tecnologia, via Barsanti 14, Arnesano, 73010, Italy
[*]corresponding author: gonzalo.alvarezperez@iit.it

Abstract: We design tunable nonlinear plasmonic waveguides made of heavily doped semiconductors to boost third harmonic generation. Employing a hydrodynamic nonlocal description, we calculate the power transfer and nonlinear efficiency. Our work has applications in advancing the realization of all-semiconductor photonic integrated circuits and all-optical neural networks.

Heavily doped semiconductors offer a promising platform for realizing nanoscale nonlinear optics due to their distinctive characteristics. Compared to noble metals, semiconductors exhibit much lower free carrier densities and smaller effective carrier masses. These differences lead to stronger nonlocal effects and larger nonlinear active volumes, surpassing those achievable with noble metals by up to 1000 times. Moreover, the limitations imposed by anharmonic potentials on the nonlinear susceptibilities—$\chi^{(2)}$ and $\chi^{(3)}$— that limit the nonlinear response of dielectrics do not apply to free-electron nonlinearities, thus making heavily doped semiconductors a unique platform for developing nanoscale nonlinear elements in photonic integrated circuits.

Nonlinearities in heavily doped semiconductors are fundamentally nonlocal and are linked to the kinetic energy of the free-electron gas. This behavior can be accurately modeled using a set of hydrodynamic equations of motion, akin to classical fluid dynamics [1-3]. Building on this, here we design nonlinear plasmonic waveguides using heavily doped semiconductors to boost third harmonic generation. Our chosen material platform is InGaAs/InP due to its broad appeal for the future exploitation of plasmonic nonlinearities in all-semiconductor photonic integrated circuits. To model the nonlinear response of the structure, we develop a generalized framework that employs a hydrodynamic nonlocal description and allows for the computation of second harmonic (SH) and third harmonic (TH) free-electron nonlinearities in hybrid plasmonic waveguides made of both heavily doped and undoped semiconductors (Fig. 1a). Our method allows studying the structure on a two-dimensional cross-section, thereby circumventing the challenges posed by the scale mismatch between surface effects and overall mode propagation in three-dimensional simulations.

The general solution is shown to be the sum of the solutions with and without free electron nonlinearities. Both can be expressed as linear combinations of the eigenmodes of the system, which in turn can be determined using an eigenmode solver that we implement in Comsol Multiphysics with a customized weak form (Fig. 1b,c). This approach is valid under the undepleted pump approximation, assuming minimal modulation of the refractive index by the pump's strength.

This framework allows for the calculation of the power transfer from the fundamental frequency mode to the second and third harmonic and predicts the efficiency of the nonlinear waveguide (Fig. 1d). This includes direct and cascaded processes, along with third-order lattice nonlinearities, allowing to optimize the structure of the

waveguide to maximize the nonlinear efficiency. Additionally, given the tunability of the plasma frequency in heavily doped semiconductors, gating effects can be implemented to actively tune and control the plasmonic nonlinearities through external stimuli, a critical step towards the practical implementation of these advancements. Our nonlinear plasmonic waveguides could be integrated in all-semiconductor photonic circuits and could, for instance, play a key role in emulating, through optical means, the nonlinear activation function—a critical part of the computational capability of neural networks.

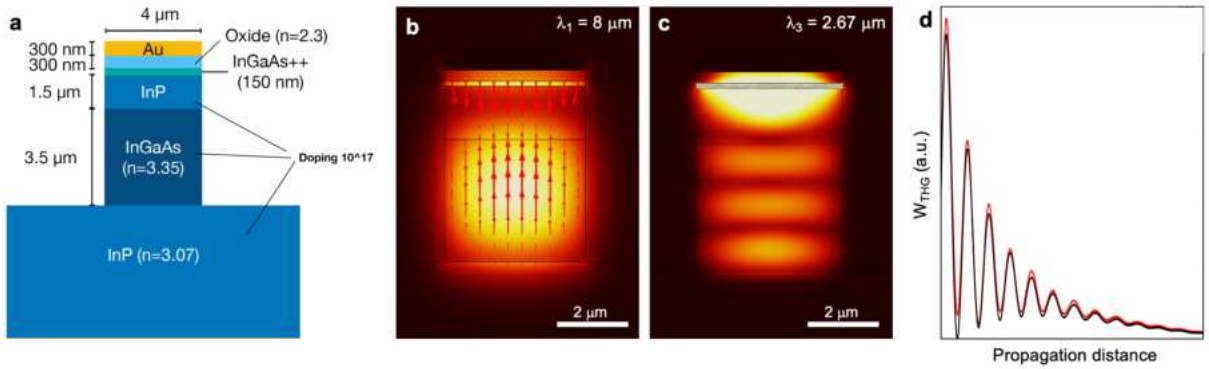


Fig. 1. Hybrid plasmonic waveguides based on free-electron nonlinearities in heavily doped semiconductors. (a) Schematics of the hybrid plasmonic waveguide. **(b)** Norm of the electric field of one of the eigenmodes at the fundamental frequency. The red arrows represent the free-electron polarization. **(c)** Norm of the electric field of the particular solution at the third harmonic. **(d)** Power of the third harmonic as a function of the propagation distance along the waveguide.

Acknowledgements: We acknowledge funding by the European Innovation Council (NEHO, 101046329). Views and opinions expressed are however those of the authors only and do not necessarily reflect those of the European Union. Neither the European Union nor the granting authority can be held responsible for them.

References

1. De Luca, F. and Ciracì, C. “Impact of Surface Charge Depletion on the Free Electron Nonlinear Response of Heavily Doped Semiconductors,” Phys. Rev. Lett., Vol. 129, No. 123902, 2022.
2. Noor, A., Khalid, M., De Luca, F., Baghramyan, H. M., Castriotta, C., D'Orazio, A. and Ciracì, C. “Second-harmonic generation in plasmonic waveguides with nonlocal response and electron spill-out,” Phys. Rev. B, Vol. 106, No 045415, 2022.
3. Rossetti, A., Hu H., Venanzi, T., Bousseksou, A., De Luca, F., Deckert, T., Giliberti, V., Pea, M., Sagnes, I., Beaudoin, G., Biagioni, P., Baù, E., Maier, S. A., Tittl, A., Brida, D., Colombelli, R., Ortolani, M. and Ciracì, C. “Origin of optical nonlinearity in plasmonic semiconductor nanostructures”, arXiv:2402.15443v1, 2024.

META 2024, TOYAMA - JAPAN, JULY 16 – 19, 2024

Adaptive Meshing Using A Posteriori Error Estimation

Albin J. Svärdsby and Philippe Tassin

Department of Physics, Chalmers University of Technology, 41296 Göteborg, Sweden

Abstract: We present our work on adaptive meshing of electromagnetic simulations based on a posteriori error estimation. We present our implementation and demonstrate that our adaptive meshing technique can lead to faster convergence with lower memory footprint, especially for simulations of complex three-dimensional nanophotonic structures.

It is becoming increasingly important to solve large computational models of nanophotonic devices efficiently, with low memory footprint and short wall-clock times. This is important for, e.g., inverse design—the computer-aided selection of a device geometry with a desired optical response—which requires a large number of successive simulations in gradient-descent optimization techniques or an even larger number of independent simulations in data-driven inverse design using machine learning [1]. One way to achieve more efficient computational models is to make use of adaptive meshing [2]. Adaptive meshing is today often based on geometric considerations, i.e., small geometric features are meshed more densely. However, it would be much more effective to base adaptive meshing on a calculation of the relative error of mesh elements.

In this contribution, we will present our work on adaptive meshing based on a posteriori error estimation [3]. We implement a technique that involves a computationally cheap, secondary finite-element model and is able to calculate the relative contribution to the simulation error of each individual mesh element [4]. This we can in turn use to strategically refine and coarsen the mesh of an electromagnetic simulation.

We show how the method works and we present a number of example, allowing us to study the time complexity compared to traditional meshing. This suggest that our adaptive meshing method is able to speed up simulations for large electromagnetic models. We discuss a number of pitfalls and provide guidance for best practice when using adaptive meshing.

We acknowledge support from Chalmers' Excellence Initiative Nano and from the Swedish Research Council under Grant No. 2020-05284. The training data generation and ANN training were performed on resources provided by the Swedish National Infrastructure for Computing (NAISS), at the Chalmers/C3SE and KTH/PDC sites, partially funded by the Swedish Research Council under Grant No. 2022-06725.

References

1. Gahlmann, T. and P. Tassin, "Deep neural networks for the prediction of the optical properties and the free-form inverse design of metamaterials," Phys. Rev. B, Vol. 106, 085408, 2022.
2. Li J. and Y. Huang, Time-Domain Finite Element Methods for Maxwell's Equations in Metamaterials (Springer, 2013).
3. Izsak F., D. Harutyunyan, and J. J. W. Van Der Vegt, "Implicit a posteriori error estimates for the Maxwell equations," Math. Comput., Vol. 77, 1355, 2008.
4. Svärdsby, Albin J. and P. Tassin, "Adaptive meshing strategies for nanophotonics using a posteriori error estimation," in press, 2024.

Hardware-Accelerated FDTD Simulation

Zongfu Yu, Tyler Hughes, Shanhui Fan
Flexcompute, Inc

In this talk, we will demonstrate the application of novel computing hardware to electromagnetic simulation. We will discuss how electromagnetic simulation compute requirements motivate new approaches to hardware architecture. Then, we will demonstrate how our technology leverages these understandings to enable the simulation and design of novel photonic devices at speeds and scales not possible with conventional approaches.

First, we will discuss the specific computing requirements of electromagnetic simulations, specifically the FDTD method. A simplified model of simulation performance based on computing speed and memory bandwidth will be presented. This understanding intuitively demonstrates a fundamental problem with the CPU-based simulation technology that is most commonly employed in both industry and academia. We show how to overcome this limitation through the application of novel computing hardware platforms with a high memory bandwidth, such as GPUs, to electromagnetic simulations, and discuss performance bounds achievable through this framework.

Next, we will introduce our FDTD solver (Tidy3D), which leverages these understandings to perform cloud-based electromagnetic simulations. We will give several examples of Tidy3D outperforming conventional CPU-based FDTD solvers by orders of magnitude in both speed and maximum problem size. We will also provide a basic overview of the features and capabilities provided by this solver and its interface. Specifically, we will give an explanation of how to perform "inverse design" using this framework, which is a method that enables automated design of devices based on a user-defined objective function. We demonstrate how machine learning libraries are integrated with our solver to perform the automatic differentiation needed.

Finally, we will show examples of how we and our collaborators have leveraged this technology to enable novel findings in various applications. Topics will include (a) three-dimensional modeling of large scale photonic integrated circuits (b) full-wave simulation of large area metasurfaces (c) using electromagnetic simulation to answer long standing questions in fundamental physics.

Quasinormal mode expansion theory for mesoscale plasmonic nanoresonators with an analytical treatment of nonclassical electromagnetic boundary condition

Haitao Liu[1,2*], Can Tao[1,2], and Ying Zhong[3]

[1]Institute of Modern Optics, College of Electronic Information and Optical Engineering, Nankai University, Tianjin, 300350, China
[2]Tianjin Key Laboratory of Micro-scale Optical Information Science and Technology, Tianjin, 300350, China
[3]State Key Laboratory of Precision Measurement Technology and Instruments, Tianjin University, Tianjin 300072, China
[*]corresponding author: liuht@nankai.edu.cn

Abstract: We propose a quasinormal mode (QNM) expansion theory for mesoscale plasmonic nanoresonators with nanometric feature sizes. Our theory can analytically unveil the impact of nonclassical quantum effects described by the nonclassical electromagnetic boundary condition (NEBC) on the optical response and thus provides an efficient tool for various design tasks.

For plasmonic nanoresonators, the QNM expansion theory, in which the source-excited electromagnetic field is expanded upon the basis of source-free eigen/resonance modes of QNMs, can provide an analytical dependence of electromagnetic field on the excitation source and frequency, and therefore is physically intuitive and computationally efficient [1]. However, for mesoscale plasmonic nanoresonators with highlighted nonclassical quantum effects, which can be fully described by the NEBC using the surface-response Feibelman *d* parameters $d_\perp$ and $d_\parallel$, the QNM expansion theory is still in its infancy [2-5]. For the case of non-perturbative NEBC and with the presence of excitation source, a QNM expansion theory with an analytical dependence on the NEBC, which is crucial for a transparent and fast analysis of the impact of NEBC on the mesoscale plasmonic response, is still absent.

In this talk, we report a rigorous nonclassical QNM expansion theory with an analytical dependence on the non-perturbative NEBC (incorporating both $d_\perp$ and $d_\parallel$) for mesoscale plasmonic nanoresonators [6]. By taking the easy-to-solve classical QNMs under classical electromagnetic boundary condition (CEBC) as a complete set of basis functions, the source-excited nonclassical electromagnetic field $\mathbf{\Psi}$ under NEBC can be rigorously expanded as,

$$\mathbf{\Psi}(\mathbf{r},\omega)=\mathbf{\Phi}(\mathbf{r})^{\mathrm{T}}[i(\omega\mathbf{I}-\mathbf{W})-\mathbf{K}(\omega)]^{-1}\mathbf{b}(\omega)\,, \tag{1}$$

where $\mathbf{r}=(x, y, z)$ are Cartesian coordinates, ω is the real-valued excitation angular frequency, $\mathbf{I}$ represents the identity matrix, and $\mathbf{W}$ is a diagonal matrix with the complex eigenfrequency ω_p of the pth classical QNM $\mathbf{\Psi}_p$ as its pth diagonal element. $\mathbf{\Phi}^{\mathrm{T}}$ is a row vector with its pth element being $\mathbf{\Psi}_p$. $\mathbf{b}(\omega)$ is a frequency-dependent column vector with its pth element β_p describing the excitation of $\mathbf{\Psi}_p$ by the external source. The matrix $\mathbf{K}(\omega)$ depends on both $d_\perp$ and $d_\parallel$ *in an analytical way*, with its pth-row and qth-column element $\kappa_{p,q}$ describing the coupling between $\mathbf{\Psi}_p$ and $\mathbf{\Psi}_q$ caused by the NEBC. Starting from Eq. (1) (called Model 1), we can further solve the source-free ($\mathbf{b}=\mathbf{0}$) nonclassical QNMs under NEBC, and then expand the source-excited ($\mathbf{b}\neq\mathbf{0}$) electromagnetic field (called Model 2A) and Green's function tensor (called Model 2B) upon the basis of nonclassical QNMs. Our theory exhibits high physical intuitiveness and computational efficiency if the optical response of resonator is dominated by a small set of classical QNMs. For example, by considering the two dominant classical QNMs in the numerical example in Fig. 1, the eigenfrequencies $\omega=\tilde{\omega}_p$ (p=1, 2) of

nonclassical QNMs is given by

$$\omega=\frac{1}{2}\left[(\sigma_1+\sigma_2)\pm(\sigma_1-\sigma_2)\sqrt{1-4\kappa_{1,2}\kappa_{2,1}/(\sigma_1-\sigma_2)^2}\right], \tag{2}$$

where $\sigma_q=\omega_q-i\kappa_{q,q}(\omega)$ (q=1, 2). Equation (2) explicitly unveils the impact of NEBC-induced cross coupling between different classical QNMs (represented by $\kappa_{p,q}$ with $p\neq q$) on the nonclassical QNMs which is not considered in previous theories [3-5].

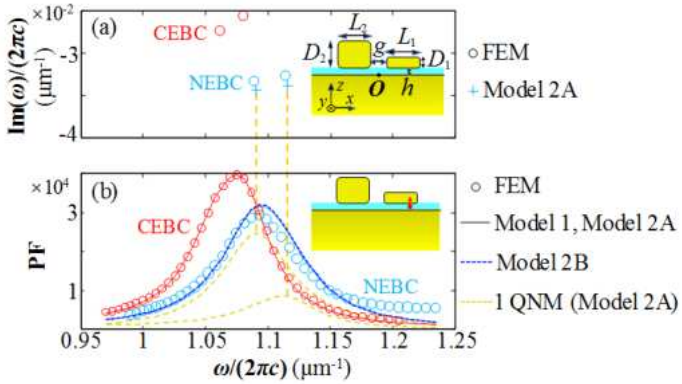


Fig. 1. (a) Complex eigenfrequencies of the two dominant QNMs with the highest quality factors for an asymmetrical dimer of gold nanowires (lengths L_1=60 nm, L_2=72 nm) with square cross-sections (side lengths D_1=20 nm, D_2=110 nm) on gold substrate (g=15 nm, h=6 nm). c is the light speed in the vacuum. (b) Frequency spectrum of Purcell factor (PF) for the excitation by a z-polarized point source (red dot) at (x, y, z)=(g/2+L_1−d, 0, h/2) (origin denoted by O) in the AlO_x nanogap (blue layer). The circles and other curves show the full-wave finite element method (FEM) results and theoretical predictions, respectively. The yellow-dashed curves show the respective contributions from the two dominant nonclassical QNMs.

Acknowledgements: Financial support from the National Natural Science Foundation of China (62075104, 61775105) is acknowledged.

References

1. Lalanne, P., W. Yan, K. Vynck, C. Sauvan and J.-P. Hugonin, "Light interaction with photonic and plasmonic resonances," Laser Photon. Rev., Vol. 12, No. 5, 1700113, 2018.
2. Zhou, Q., P. Zhang and X.-W. Chen, "Quasinormal mode theory for nanoscale electromagnetism informed by quantum surface response," Phys. Rev. B, Vol. 105, No. 12, 125419, 2022.
3. Yang, Y., D. Zhu, W. Yan, A.Agarwal, M. Zheng, J. D. Joannopoulos, P. Lalanne, T. Christensen, K. K. Berggren and M. Soljačić, "A general theoretical and experimental framework for nanoscale electromagnetism," Nature, Vol. 576, No. 7786, 248–252, 2019.
4. Christensen, T., W. Yan, A. P. Jauho, M. Soljacic and N. A. Mortensen, "Quantum corrections in nanoplasmonics: shape, scale, and material," Phys. Rev. Lett., Vol. 118, No. 15, 157402, 2017.
5. Goncalves, P. A. D., T. Christensen, N. Rivera, A. P. Jauho, N. A. Mortensen and M. Soljacic, "Plasmon–emitter interactions at the nanoscale," Nat. Commun., Vol. 11, No. 1, 366, 2020.
6. Tao, C., Y. Zhong and H. Liu, "Quasinormal mode expansion theory for mesoscale plasmonic nanoresonators: an analytical treatment of nonclassical electromagnetic boundary condition," Phys. Rev. Lett., Vol. 129, No. 19, 197401, 2022.

Effective Medium Theory for Photonic Parallel Universes

Yun Lai[1*]

[1] National Laboratory of Solid State Microstructures, School of Physics, and Collaborative Innovation Center of Advanced Microstructures, Nanjing University, Nanjing 210093, China
[*]corresponding author: laiyun@nju.edu.cn

Abstract: Conventional wisdom tells us that a physical space corresponds to only one optical medium, e.g. an optical space cannot behave like vacuum and glass simultaneously. Surprisingly, this fundamental limitation can be broken in photonics. Here, I demonstrate multiple effective media associated with one physical space, effectively creating photonic parallel universes.

The development of metamaterials in the past decades have significantly expanded the realm of effective medium theories. Extraordinary effective parameters such as negative, near-zero, and indefinite values have been realized, which can be numerically retrieved via effective medium theories. Nevertheless, a fundamental law is obeyed all the time, i.e. one physical space can only correspond to one optical effective medium. This law is intuitive, as it is obvious that a space cannot be occupied by two media or two objects simultaneously.

Now, imagine that a physical space occupied by a metamaterial can behave like two distinct optical media, e.g. vacuum and glass, with different refractive indices and impedances. In other words, such a metamaterial has two independent effective media, one is vacuum and the other is glass. This amazing phenomenon turns out to be surprisingly feasible, around a certain working frequency. The choice of the effective media depends on which surface of the metamaterial the external photons choose to enter. In this sense, photonic parallel universes, corresponding to different optical media, have been realized at the same physical space.

We have established an effective medium theory to explain this unprecedented phenomenon of photonic parallel universes. Our theory is validated by simulations and microwave experiments. Deep learning can be applied to design parallel universes efficiently. This concept creates a plethora of exciting new phenomena, such as cladding-free waveguide systems [1, 2] and photonic wormholes [3].

References

1. T. T. Song et al., “Ultracompact Photonic Circuits without Cladding Layers,” Physical Review X, Vol. 12, 011053, 2022.
2. T. T. Song, J. Luo and Y. Lai, “A road toward zero-spacing photonic waveguides and circuits,” EPL, Vol. 141, 15001, 2023.
3. T.T. Song et al., submitted.

Space-time metasurfaces for photonics

S. Vezzoli[1*], A. Hartwood[1], and R. Sapienza[1]

[1]Imperial College London, United Kingdom
[*]corresponding author: svezzoli@imperial.ac.uk

Abstract: Metamaterials control light by acting on its momentum, yet they are static devices and bounded by energy conservation. Here we discuss spatial and temporal diffraction in a film of Indium Tin Oxide, as a first step towards a space-time metasurface for photonic applications.

Metamaterials have revolutionised the way we control light waves. By engineering light scattering on sub-wavelength scales, one can design exotic new materials and applications, like invisibility cloaks and negative refraction. Yet, static metamaterials only act on the momentum of light and thus are still bounded by Lorentz reciprocity and energy conservation. A dynamical metasurface, whose optical response can be arbitrarily modulated at the speed of light through a time-varying complex refractive index n(t), would offer access to the manipulation of the frequency spectrum and a whole new range of functionalities. Yet, despite the abundance of theoretical proposals [1], experimental realisations remain elusive, due to the challenge of finding a material platform that can support large and ultrafast modulations without incurring damage.

Here I will discuss our first steps towards optically driven metasurfaces for photonics, based on Indium Tin Oxide, an epsilon-near-zero material with strong nonlinearities and ultrafast time response [2]. I will report on our recent demonstration of double-slit time diffraction from a deeply subwavelength and resonant film of Indium Tin Oxide in the near-infrared [3], the first step towards the creation of more complex time modulations. I will then discuss one possible extension of this experiment to the visible range, which employs the non-perturbative modulation of second harmonic generation at the time-varying interface. Finally, I will present our most recent results, aimed at coupling space and time modulations in a time-varying medium: the observation of slits that diffract light both in time and space. These results represent the basic building blocks for the generation of complex spatiotemporal modulations and one of the first evidence of synthetic motion at optical frequencies.

References

1. Galiffi, E. et al, Advanced Photonics, Vol. 4, Issue 1, 014002 (2022)
2. Alam, M.Z. et al., Science 10.1126/science.aae0330 (2016)
3. Tirole, R. et al, Nat Phys Vol. 19, 999 (2023)

Topological transition from bound states in the continuum of plasmonic lattices

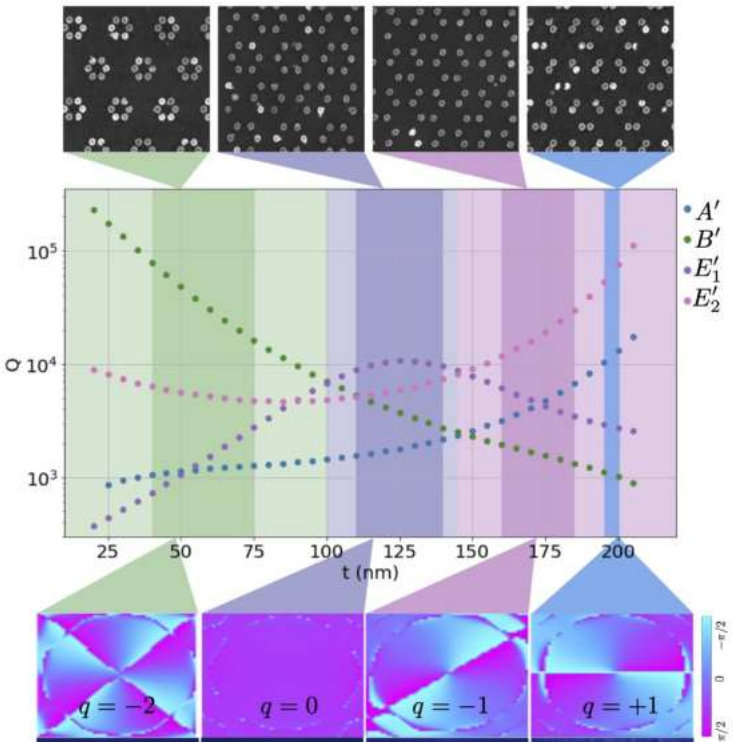
G. Salerno[1#], R. Heilmann[1], K. Arjas[1], K. Aronen[1], J.P. Martikainen[1] and P. Törmä[1*]

[1] Department of Applied Physics, Aalto University School of Science, Aalto FI-00076, Finland

[*]corresponding author: paivi.torma@aalto.fi

[#]corresponding and presenting author: grazia.salerno@aalto.fi

Abstract: We study lasing of plasmonic BIC modes with topological charge 0, ±1 and -2. We evidence a loss-driven topological phase transition in the lasing mode, as the scale of the unit cell is varied. Our work shed light on the interplay between non-Hermitian systems and the topology of polarization singularities.



Bound states in the continuum (BICs) are general solutions of wave equations that arise as topological defects protected by system symmetries. In photonics, BICs show a winding of the light polarization around a specific momentum, akin to a vortex with a non-trivial topological charge [1-2]. These modes are also known as polarization singularities, and have extremely-high quality factors, which, in combination with their topological origin, may open opportunities for designing novel topological photonic devices [3].

We study BICs in plasmonic lattices composed of complex unit cells containing multiple gold nanoparticles [4-5]. The system is brought to the lasing regime by combining it with a dye molecule liquid acting as a gain medium. These structures exhibit lasing emission with non-trivial polarization properties attributed to BICs. Combining group theory with a careful lattice design demonstrates that different BICs with distinct topological charges can lase in various regimes, as the internal structure of

the unit cell is varied. Using T-matrix simulations, we confirm that the modes' quality factors undergo a loss-induced topological transition. Our findings are further supported by finite element method simulations, where we see that the modes' electric field intensity distribution in the unit cell changes significantly due to losses, despite the symmetry of the modes being the same. As our results introduce a versatile new platform for studies of non-Hermitian topological polarization singularities, we will also discuss our recent unpublished results on topological photonics.

References

1. Hsu, Zhen, Stone, Joannopoulos, and Soljačić, *Nat. Rev. Mater.* **1**, 1 (2016)
2. Zhen; Hsu, Lu, Stone, and Soljačić, *Phys. Rev. Lett.* **113**, 257401 (2014)
3. Xu, Xing, Xue, Lu, Fan, Fan, Shum, and Cong, *Ultrafast Science* **3**, 0033 (2023)
4. Heilmann, Salerno, Cuerda, Hakala, and Törmä, *ACS Photonics* **9**, 224 (2022)
5. Salerno, Heilmann, Arjas, Aronen, Martikainen, and Törmä, *Phys. Rev. Lett.* **129**, 173901 (2022)

Singularity and topology in structured near fields

Shubo Wang[1,2*], Tong Fu[1], Shiqi Jia[1], Jie Peng[1], and Ruo-Yang Zhang[3]

[1]Department of Physics, City University of Hong Kong, Hong Kong, China
[2]City University of Hong Kong Shenzhen Research Institute, Guangdong, China
[3]Department of Physics, The Hong Kong University of Science and Technology, Hong Kong, China
[*]corresponding author: shubwang@cityu.edu.hk

Abstract: Under external excitations, simple metal structures can generate strong near fields with rich subwavelength vector properties. These near fields can exhibit complex structures of polarization with interesting topological and singularity properties fundamentally connected to the real-space topology of the metal structures.

Simple metal structures can generate strong near fields under external excitations due to their plasmonic response. The near fields are characterized by full vector properties in the subwavelength scale, offering rich degrees of freedom for manipulating the various properties of light, including intensity, polarization, phase, etc. Besides, the near fields can induce strong light-matter interactions with broad applications in optical sensing, optical metrology, and optical micromanipulations. Therefore, it is essential to understand various properties of optical near fields and uncover their relationships with the geometric and material properties of optical structures.

For a single metal scatterer under the illumination of external light, the interference of the electromagnetic multipoles induced in the scatterer can give rise to polarization singularities in the near fields, including C points and V points [1, 2]. The C points are particularly interesting because they carry intrinsic optical chirality that can be applied for chiral sensing and discrimination [3, 4]. In addition, the C points carry nontrivial topological properties that can be characterized by both a polarization index and a phase index. We find that the total index of the C points on the smooth surfaces of metal structures is fundamentally decided by the Euler characteristic of the structures and is irrelevant to the geometric details or external excitations [2]. The C points grow from the structures' surfaces and extend to free space to form C lines. Their merging and bifurcation are determined by the conservation of the phase index.

Since the near fields are nonuniform and exhibit complex structures, their spatial variation can give rise to a geometric phase, which generally comprises two parts: the spin-redirection geometric phase and the Pancharatnam-Berry geometric phase. We find that the geometric phase of the near fields in finite-sized metal structures can be applied to define a spin Chern number $\mathbb{C}_{\mathrm{spin}}$. Unlike the Chern number in the momentum space of periodic systems, this real-space spin Chern number has an intrinsic relationship with the topology of the metal structures [5]:

$$\mathbb{C}_{\mathrm{spin}}(M) = \frac{1}{2\pi}\oint_M \mathbf{\Omega}_{\mathrm{spin}} \cdot d\mathbf{S} = \sum_i I_{\mathrm{pl}}(\mathbf{r}_i) = \chi(M)$$

Here, $\mathbf{\Omega}_{\mathrm{spin}}$ denotes the spin Berry curvature of the near fields, $I_{\mathrm{pl}}(\mathbf{r}_i)$ denotes the polarization index of the singularity at $\mathbf{r}_i$, and $\chi(M)$ is the Euler characteristic of the manifold M (i.e., the surface of the optical structure). The above equation indicates that the spin Chern number of optical near fields is quantized and equal to the Euler characteristic of the optical structures and thus decided solely by the number of "holes" in the structure's surface. We verified the above equation by conducting full-wave simulations for metal structures with different Euler characteristics and under different excitations.

The work was supported by the Research Grants Council of the Hong Kong Special Administrative Region, China (CityU 11306019, AoE/P-502/20) and the National Natural Science Foundation of China (12322416, 11904306).

References

1. J. Peng, W. Liu, and S. Wang, “Polarization singularities in light scattering by small particles”, Physical Review A 103, 023520 (2021).
2. J. Peng, R.-Y. Zhang, S. Jia, W. Liu and S. Wang. “Topological near fields generated by topological structures,” Science Advances 8, eabq0910 (2022).
3. S. Jia, J. Peng, Y. Cheng and S. Wang, “Chiral discrimination by polarization singularities of a metal sphere”, Physical Review A 105, 033513 (2022).
4. S. Jia, T. Fu, J. Peng, and S. Wang, “Broadband and large-area optical chirality generated by an achiral metasurface under achiral excitation”, Physical Review A 108, 053504 (2023).
5. T. Fu, R.-Y. Zhang, S. Jia, C. T. Chan, and S. Wang, “Near-field spin Chern number quantized by real-space topology of optical structures”, Physical Review Letters 132, 233801 (2024).

Electron-tunneling-induced thermoelectric effects

M. Gómez Viloria[1], R. Messina[1*], and P. Ben-Abdallah[1]

[1]Laboratoire Charles Fabry, UMR 8501, Institut d'Optique, CNRS, Université Paris-Saclay, 2 Avenue Augustin Fresnel, 91127 Palaiseau Cedex, France
[*]corresponding author: riccardo.messina@institutoptique.fr

Abstract: We introduce direct (Seebeck) and inverse (Peltier) thermolectric effect induced by electron tunneling between closely separated conducting films: a transverse temperature gradient applied along one film induces a bias voltage in the second, whereas an electric current passing through one film can allow to extract or deliver a thermal power.

Thermoelectric effects are the direct conversion of the temperature difference inside a material into a bias voltage (Seebeck effect) and the conversion of an electric current flowing through this material into a negative or positive thermal power (Peltier effect). The efficiency of a thermoelectric system can be evaluated with the figure of merit ZT, depending on the Seebeck coefficient of the material, as well as on its electrical and thermal conductivities. Recent efforts have been performed to manipulate these quantities in order to increase the ZT [1,2].

We have recently shown [3] that when two planar substrates are placed in the extreme near field (distances in the nanometer range and below), in addition to evanescent photons tunneling across the vacuum gap and inducing an amplification of heat transfer [4], also phonons and electrons can tunnel through the vacuum gap and contribute as additional channels to energy transfer. By introducing a general formalism to describe this multi-channel energy transfer, we have shown that for metallic bodies electron tunneling becomes the dominant effect close to contact [3].

Here we introduce thermoelectric effects induced by the tunneling of electrons between two coupled conductors separated by a small gap [5]. When the size of this gap is sufficiently small and a temperature difference is applied along one of two conductors, a spatially varying density of free charges can be induced across the gap by tunneling effect giving rise to a drift and a diffusion current into the second conductor. Conversely, when a bias voltage is applied along one of the conductors, a heat flux can be extracted from or inserted into the second conductor. We develop a general theory to describe these thermoelectric effects between two metallic films and analyze its main characteristics with respect to the separation gap and films thicknesses, showing that in some scenarios their performance can exceed the classical thermoelectric properties of bulk material. These thermoelectric effects could be exploited for nanoscale energy conversion and to develop solid-state refrigeration devices.

References

1. Majumdar, A., "Thermoelectricity in Semiconductor Nanostructures", Science **303**, 777 (2004).
2. Rodgers, P., "Silicon goes thermoelectric", Nature Nanotech. **3**, 76 (2008).
3. Gómez Viloria, M., Guo, Y., Merabia, S., Ben-Abdallah, P. and Messina, R., "Role of the Nottingham effect in heat transfer in the extreme near-field regime", Phys. Rev. B **107**, 125414 (2023).
4. Joulain, K., Mulet, J.-P., Marquier, F., Carminati, R. and Greffet, J.-J., "Surface electromagnetic waves thermally excited: Radiative heat transfer, coherence properties and Casimir forces revisited in the near field", Surf. Sci. Rep. **57**, 59 (2005).
5. Gómez Viloria, M., Messina, R. and Ben-Abdallah, P., "Electron-tunneling-induced thermoelectric effects", preprint arXiv: 2312.13017 (2023).

High-Accuracy DDA

O. D. Miller[1*]

[1]Dept of Applied Physics and Energy Sciences Institute, Yale University, New Haven, CT, USA
[*]corresponding author: owen.miller@yale.edu

Abstract: The discrete dipole approximation (DDA) is a simple but typically low-accuracy simulation technique. We describe two straightforward modifications that reduce the error from first order to fourth order in resolution. We demonstrate fast, accurate simulation in the regime DDA typically struggles: high-complexity, three-dimensional structures with large refractive indices.

Thermal radiation at the nanoscale, electroluminescence, single and dual radiative heat engines

J. Legendre[1], T. Châtelet[1], M. Thomas[1], O. Merchiers[1], and P.-O. Chapuis[1*]

[1]Centre for Energy and Thermal Sciences of Lyon (CETHIL), CNRS – INSA Lyon, Villeurbanne, France
[*]corresponding author: olivier.chapuis@insa-lyon.fr

Abstract: At the crossroad of nanophotonics and energy harvesting, a novel class of heat engines in the near field is being developed. Building on the experimental confirmation of near-field thermophotovoltaics and on the physics of light-emitting diodes, dual radiative heat engines, e.g. thermophotonic ones, are attractive for heat-to-electricity conversion and refrigeration.

Thermal emission can be described with the Poynting vector associated to the electromagnetic field generated by the random fluctuations of electrical charges in matter. Such approach known as fluctuational electrodynamics has proved to be extremely powerful in the last two decades, being able to address radiative heat transfer involving objects of sub-wavelength size or short distances [1]. In these two regimes, Planck's blackbody law, known to be an upper bound for the radiative exchange of large opaque surfaces, does not apply anymore. In particular, it was shown that near-field radiative heat transfer induces fluxes that exceed the prediction limited to propagative waves (blackbody limit) [2] and that the exponent and constant involved in the Stefan-Boltzmann law are distance dependent when the bodies are close [3]. The strong radiative power increase observed in the near field is attractive for energy-harvesting applications where radiation is converted into electricity. An increased electrical power output could indeed be obtained in near-field thermophotovoltaics (TPV) [4].

(a) (b)

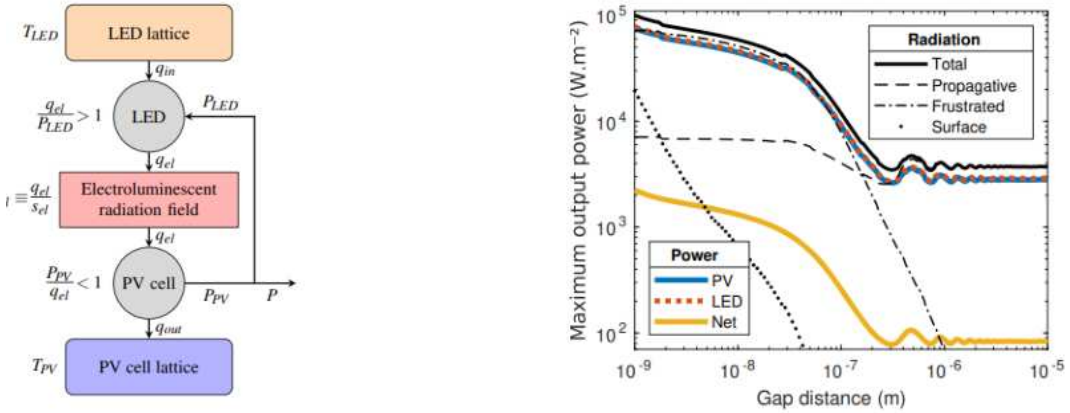


Figure 1. (a) Schematic of a thermophotonic energy harvester, highlighting the LED heat pump and the PV cell heat engine as elements of the dual radiative heat engine. (b) Radiative power exchanged (black) and power output of an ideal GaAs near-field thermophotonic device as a function of gap distance. Internal quantum efficiency, describing non-radiative losses, is spectrally flat with a value of 0.9.

Another way to surpass Planck's blackbody limit at a given wavelength is to generate electroluminescence, as exemplified by the bright emission of light-emitting diode (LED), which is another optoelectronic device based on pn or pin junctions. Interestingly, LEDs and TPV cells can be seen respectively as heat pumps and heat engines, i.e. radiative heat engines. The combination of a hot illuminating LED and a wavelength-matched illuminated room-temperature PV cell is known as a thermophotonic energy harvester [5], since the net electrical power produced can be positive in spite of the LED consumption. As it is made of two optoelectronic components, such a device is a dual radiative heat engine. We have studied the conditions for operation of such engine both in the far field and in the near field, where the harvested power is expected to be larger. This is done either in a detailed-balance approach [6] or by fully considering temperature and spatially-dependent losses associated with non-radiative recombinations [7]. In the second case, fluctuational electrodynamics is coupled to a numerical code solving the drift-diffusion equations able to account for high carrier injection and discontinuity of the valence/conduction bands in heterostructures. One advantage of such devices over TPV ones is their working temperature, expected to be significantly lower (few hundreds of degrees Celsius).

The versatility of these devices allows also designing a thermophotonic refrigerator if the LED, initially at room temperature or below, is cooling by extracting heat from its surroundings [8]. In general, exploiting the phase space opened by the combination of these optoelectronic devices seen as heat engines allows selecting thermodynamic performances such as high efficiency (Carnot-like) or large power output, depending on the targeted application.

We acknowledge funding from EU projects FETProactive TPX-Power (GA951976) and FETOpen OPTAGON (GA 964698). We thank J. Oksanen and R. Vaillon for useful discussions.

References

1. Chapuis, P.-O., B.-J. Lee and A. Rodriguez, "Thermal radiation at the nanoscale and applications", Appl. Phys. Lett., Vol. 123, 220401, 2023.
2. Lucchesi, C., R. Vaillon and P.-O. Chapuis, "Radiative heat transfer at nanoscale: experimental trends and challenges", Nanoscale Horiz., Vol. 6, 201, 2021.
3. Lucchesi, C., R. Vaillon and P.-O. Chapuis, "Temperature dependence of near-field radiative heat transfer above room temperature", Materials Today Phys., Vol. 21, 100562, 2021.
4. Lucchesi, C., *et al*., "Near-field thermophotovoltaic conversion with high energy density and efficiency above 14%", Nano Lett., Vol. 21, 4524, 2021.
5. Harder, N.-P. and M. A. Green, "Thermophotonics", Semicond. Sci. Tech.., Vol. 18, S270–S278, 2003.
6. Legendre, J. and P.-O. Chapuis, "GaAs-based near-field thermophotonic devices: approaching the idealized case with one-dimensional pn junctions", Sol. Energy Mater Sol. Cells, Vol. 238, 111594, 2022.
7. Legendre, J. and P.-O. Chapuis, "Overcoming non-radiative losses in near-field thermophotonics with AlGaAs PIN junctions", Appl. Phys. Lett., Vol. 121, 193902, 2022.
8. Santhanam, P., D.J. Gray, Jr. and R. J. Ram, "Thermoelectrically pumped light-emitting diodes operating above unity efficiency", Phys. Rev. Lett., Vol. 108, 097403, 2012.

Quantum Effects in Plasmonic/Nonlinear Meta-Surfaces: Development and Applications of Maxwell-TDDFT Method

T. Takeuchi[1], M. Uemoto[2], and K. Yabana[3,*]

[1]Metamaterials Laboratory, RIKEN Cluster for Pioneering Research, Japan
[2]Department of Electrical and Electric Engineering, Kobe University, Japan
[3]Center for Computational Sciences, University of Tsukuba, Japan
[*]corresponding author: yabana@nucl.ph.tsukuba.ac.jp

Abstract: We develop a computational method coupling time-dependent density functional theory for electron dynamics and Maxwell equations for light propagation. We apply the method for various nonlinear and/or nonlocal optical phenomena where quantum electronic motion is significant, including plasmonic and semiconductor meta-surfaces.

As the size of nanoparticles decreases in meta-surfaces, quantum effects become more pronounced in their optical response. Most commonly seen is the effect of surface spill-out of electrons, and as the distance between nanoparticles decreases, the effect of tunneling currents flowing between nanoparticles appears. As the intensity of the pulsed light increases, nonlinear light-matter interaction becomes significant. High order harmonic generations from dielectric meta-surfaces have been attracting interest. To describe the optical response of meta-surfaces with such quantum and/or nonlinear effects, it is important to develop a method that simultaneously describes the quantum dynamics of electrons and the propagation of light. We have been developing a theoretical and computational method for the interaction of optical pulses with various materials based on the time-dependent density functional theory (TDDFT), either within the jellium approximation, which replaces the detailed atomic structure with smooth positive background charge, or by an ab initio calculation. Coupling Maxwell equations with electronic motion described by TDDFT, nonlinear and/or nonlocal light propagation of pulsed light can be described. The method has been implemented in an open-source software SALMON, developed by the authors' group [1]

To connect electron dynamics described by TDDFT and light propagation by Maxwell equations, we make

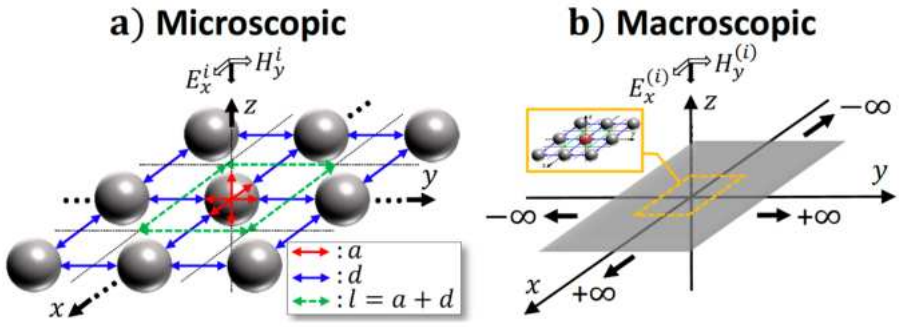


Fig. 1: Schematic description of computational method for small nanoparticles. (a) In microscopic scale, we solve time-dependent Kohn-Sham equation with periodic boundary condition. (b) In macroscopic scale, meta-surface is treated as uniform thin layer with two-dimensional current density.

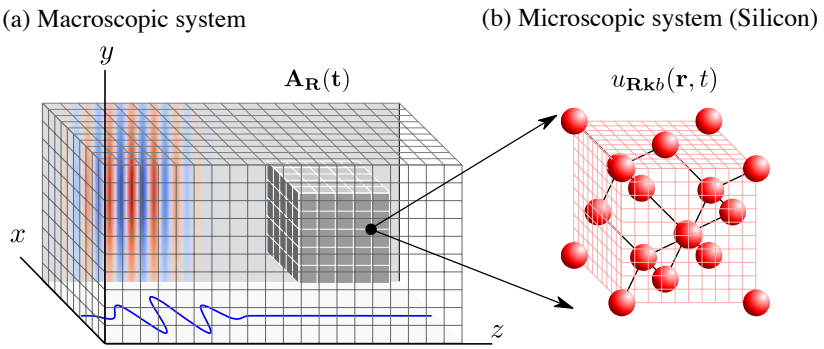


Fig. 2: Schematic description of computational method for large nanoparticles. (a) In macroscopic scale, Maxwell equation is solved in course-grid. (b) In microscopic scale, electronic motion is described assuming electronic motion in an infinite system under a spatially-uniform, time-dependent electric field.

use of a course-graining approximation. We explain it for two distinct cases: For nanoparticles whose size is less than a few nano-meters, we can describe electronic motion by solving time-dependent Kohn-Sham (TDKS) equation, the basic equation of TDDFT, for the nanoparticle in real time and real space. To connect with macroscopic Maxwell equation, we make a course-graining approximation that produces 2D current. (See Fig. 1)

For nanoparticles whose size is comparable to the wavelength of light (a few hundred nano-meters), it is impossible to solve the TDKS equation for electrons in the nanoparticle. Instead, we make use of a course-graining approximation for the nanoparticle: The nanoparticle is considered to be composed of a number of small cubes and electronic motion in the cubes is described by the TDKS equation for an infinitely periodic system under a spatially-uniform electric field (See Fig. 2). In this method, although we cannot take into account the surface effects, nonlinear light-matter interaction can be fully taken into account.

We have been applying both methods for various phenomena. The former method has been applied to investigate quantum effects in plasmonic meta-surfaces. Effects of quantum tunneling and electron spill-out have been reported in the linear [2] and nonlinear [3] responses. The latter method has been applied to investigate light propagation under extremely nonlinear conditions such as high harmonic generations in thin films [4,5] and nonlinear light propagation in semiconductor meta-surface [6].

References

1. L M. Noda et.al, “SALMON: Scalable Ab-initio Light-Matter simulator for Optics and Nanoscience”, Comp. Phys. Comm. **235**, 356 (2019); https://salmon-tddft.jp.
2. T. Takeuchi and K. Yabana, “Operation of Quantum Plasmonic Metasurfaces Using Electron Transport through Subnanometer Gaps”, ACS Photonics 6, 2517 (2019).
3. T. Takeuchi and K. Yabana, “Extremely large third-order optical effects caused by electron transport in quantum plasmonic metasurfaces with subnanometer gaps”, Sci. Reports 10, 21270 (2020).
4. T. Takeuchi and K. Yabana, “Electron spill-out effect on third-order optical nonlinearity of metallic nanostructure”, Phys. Rev. A106, 063517 (2022).
5. S. Yamada, T. Otobe, D. Freeman, A. Kheifets, and K. Yabana, “Propagation effects in high-harmonic generation from dielectric thin films”, Phys. Rev. B107, 035132 (2023).
6. K. Kihara, G. Matsuura, S. Yamada, and M. Uemoto, “First-principles simulation of nonlinear optical properties of nanostructured semiconductors”, Proc. 34th Symp. Of Association for Condensed Matter Photophysics.

Computing free-electrons Kerr nonlinearities in semiconductor plasmonic systems

C. Ciracì[1*] and H. Hu[1]

[1]Center for Biomolecular Nanotechnologies, Istituto Italiano di Tecnologia, Italy
[*]corresponding author: cristian.ciraci@iit.it

Abstract: We present a time-domain numerical approach based on finite-elements to solve hydrodynamic equations for free-electrons and demonstrate giant free-electron Kerr nonlinearities supported by the longitudinal bulk plasmon mode in heavily doped semiconductors.

Ultra-fast nonlinear optical response in integrated systems is a long-standing sought-after technological achievement that could enable manipulation of light on extremely short timescales and small volumes, allowing for efficient and high-performance photonic integrated circuits. This rapid response is fundamental for applications in telecommunications and data processing, including artificial intelligence training algorithms [1].

Nonlinear optics traditionally hinges on the interaction between light and dielectric materials, often requiring propagation for distances much longer than the involved wavelengths. On the other hand, the use of the metals in plasmonics as a way to confine radiation below diffraction limit has open a path toward miniaturization of nonlinear optical systems. The nonlinear response in a plasmonic structure is due to the collective motion of free electrons under an external radiation field. These oscillations are ultimately related to the kinetic energy of the free-electron gas and can be modelled by a set of hydrodynamic equations of motion in analogy with a classical fluid [2], i.e.:

$$\ddot{\mathbf{P}} + \gamma\dot{\mathbf{P}} = \frac{n_0 e^2}{m}\mathbf{E} + \beta^2\nabla(\nabla\cdot\mathbf{P}) + \mathbf{S}_{\mathrm{NL}}^{(2)} + \mathbf{S}_{\mathrm{NL}}^{(3)} \tag{1}$$

$$\mathbf{S}_{\mathrm{NL}}^{(3)} = -\frac{1}{e^2 n_0^2}\left(\nabla\cdot\mathbf{P}(\dot{\mathbf{P}}\nabla\cdot\dot{\mathbf{P}} + \dot{\mathbf{P}}\cdot\nabla\dot{\mathbf{P}}) + \dot{\mathbf{P}}\cdot\dot{\mathbf{P}}\nabla\nabla\cdot\mathbf{P}\right) - \frac{1}{27}\frac{\beta^2}{e^2 n_0^2}\nabla(\nabla\cdot\mathbf{P})^3 \tag{2}$$

Compared to traditional dielectric nonlinearities that can be described by a local susceptibility tensor, free-electrons nonlinearities are intrinsically nonlocal and depend on the product of field gradients and the electron density, which might vary at deep subwavelength scales.

We employ a time-domain numerical method based on finite-elements to solve Eqs. (1)-(2) coupled with Maxwell's equations. We apply the hydrodynamic model to a system based on heavily doped semiconductors and we demonstrate giant free-electron Kerr nonlinearities supported by the longitudinal bulk plasmon mode.

The authors acknowledge funding from the European Union's Horizon Europe Research and Innovation Program (NEHO, 101046329).

References

1. J. Niu, H. Shao, Y. Feng, B. Gao, Y. Zhang, Y. Li, H. Chen, and H. Qian, *Advanced Optical Materials*, 11, 2300223 (2023).
2. F. De Luca, M. Ortolani and C. Ciracì, *Phys. Rev. B,* 103, 115305 (2021).

Is photonic band topology rare or common?

T. Christensen[1]

[1] Department of Electrical and Photonics Engineering, Technical University of Denmark, 2800 Kgs. Lyngby, Denmark
[*] thomas@dtu.dk

Abstract: Overall, rather common. Although intensely researched for more than a decade, it remains unclear whether photonic crystal band topology is a rare or common feature. I will present our answers, obtained from statistical analysis of high-throughput symmetry-based calculations in two-dimensional photonic crystals, and spanning stable, fragile, and high-order band topology.

Put differently, what are the odds of finding band topology in "generic" photonic band structures and what do these odds depend on? To address this, we have analyzed roughly half a million two-dimensional, randomly generated photonic crystals across the eleven symmetry settings that admit a symmetry-based diagnosis of photonic band topology [1]. Our answers span stable topology, both in time-reversal symmetric and broken settings, fragile topology, and higher-order topology associated with corner filling anomalies. By analyzing the statistics of these calculations, we determine that most varieties of photonic band topology are rather common – and certainly more common than earlier associations might suggest; conclusions that are broadly consistent with recent findings from the condensed-matter context. Some topological features remain scarce, however, including "cumulatively" fragile topology (i.e., sets of fragile bands connected to zero frequency) which is virtually absent in our dataset. Similarly, certain symmetry settings, such as C_3, are far less amenable to hosting topological bands. We find that the prevalence of photonic topology is mostly affected by crystal symmetry, modal polarization, and geometric features – and only to a lesser extent by dielectric contrast and the amplitude of time-reversal breaking effects.

While our findings demonstrate that topology is mostly a rather common attribute in photonic band structures, our results also demonstrate that it is rare to find photonic band topology simultaneously with good spectral features (e.g., well-separated topological nodal features or gaps). This underscores the central and enduring design challenge in photonic topology. More broadly, the underlying dataset, individual data samples, and identified parameter trends may serve as guidelines to realizing new photonic topological phases in experiments.

Time allowing, I will also discuss the outlook for whether frequency-isolated photonic Weyl points can exist at the maximal high-symmetry points of the Brillouin zone, which can be addressed using $\mathbf{k}\cdot\mathbf{p}$ and graph theory.

References

1. A. Ghorashi, S. Vaidya, M. Rechtsman, W. Benalcazar, M. Soljačić, and T. Christensen, "Prevalence of two-dimensional photonic topology," arXiv:2307.15701 (2023).

THz Plasmonic Detectors Based on Field-Effect Transistors with Metallic Diffraction Grating Metasurfaces

A. Satou[1*] and T. Otsuji[1]

[1]Research Institute of Electrical Communication, Tohoku University, Japan
[*]Corresponding author: akira.satou.d2@tohoku.ac.jp

Abstract: We review our recent experimental and numerical studies on terahertz (THz) plasmonic detectors based on field-effect transistors with metallic diffraction grating metasurface structures for fast, ultra-sensitive, and room-temperature-operating THz detection.

To realize beyond-5G (6G/7G) wireless communication networks, where the use of the THz bands for the wireless carrier frequencies is assumed, fast, highly sensitive, and room-temperature-operating THz detectors are required. For this purpose, we have developed THz plasmonic detectors based on field-effect transistors (FETs) with metallic diffraction grating metasurface structures [1]. The plasmonic detectors utilize an efficient coupling of incident THz waves with two-dimensional (2D) plasmons in transistor channels via diffraction grating metasurfaces, which also serves as gate fingers, and their hydrodynamic nonlinearities to generate rectified photocurrent. In this talk, we review our recent experimental and numerical studies on the THz plasmonic detectors towards their applications to wireless communications.

With a conventional 1D grating THz plasmonic detector (Fig. 1(a)), the polarization component of the incident THz wave in the channel-width direction cannot be coupled with the 2D plasmons in the channel-length direction, so that the responsivity for that polarization direction is weak. To overcome this, we proposed a new 2D diffraction grating metasurface structure (Fig. 1(b)) which comprises the one-dimensional (1D) grating gate fingers and floating metallic rectangular patches (i.e., 2D nano-antennas). The nano-antennas act as a grating coupler in both channel-length and channel-width directions and also enable an efficient conversion of the THz wave polarized in the channel-width direction into a plasmon mode oscillating in the channel-length direction, as demonstrated by electromagnetic simulation in Fig. 1(c) [2]. A THz pulse detection measurement on fabricated plasmonic detectors based on InGaAs-channel high-electron-mobility transistors (HEMTs) with the 1D and 2D grating structures verified that the strong alteration of the polarization characteristics of the output photovoltage due to the introduction of the nano-antennas, as shown in Figs. 1(d) and (e) [3]. More flexible control of polarization characteristic of the responsivity is expected by designing the nano-antenna metasurfaces [3].

Moreover, we have succeeded in a significant enhancement of the detector responsivity by a newly discovered three-dimensional (3D) rectification effect in InGaAs-HEMT-based detectors with the gate-readout configuration at a forward (positive) gate bias voltage application [4]. The 3D rectification effect is a multiplication of horizontal hydrodynamic nonlinearities of 2D plasmons with a vertical diode-like current nonlinearity at the heterobarrier between the InGaAs channel and the InAlAs barrier layer (Fig. 2(a)). As shown in an electromagnetic simulation of the electric field distribution in a detector with a 1D grating structure upon the THz radiation incidence (Fig. 2(b)), the excited 2D plasmon generates a strong vertical field between the gate and channel that drives the diode-like current at the heterobarrier. We experimentally demonstrated that the internal current responsivity of a fabricated 1D grating-gate detector exponentially enhances as the gate bias voltage increases and that its characteristic agrees excellently with the I-V characteristic (Fig. 2(c)) [4]. Device simulation to reveal deeper physics inside the 3D rectification effect will be the subject of future work.

The authors thank Dr. Y. Takida and Dr. H. Minamide at RIKEN Center for Advanced Photonics, RIKEN, Japan, Dr. T.-T. Lin, C. Tang, Mr. K. Tamura, Mr. K. Narita, Mr. M. Nagatsu, and Mr. P.-E. Retaux at RIEC, Tohoku University, Japan, and Dr. T. Suemitsu at NICHe, Tohoku University, Japan, for their contributions throughout the work. The devices presented here were fabricated using the facility and equipment in the Nano-Electronics & Spintronics Lab., RIEC, Tohoku Univ., Japan. This work was financially supported by JSPS KAKENHI #21H01380. This work was conducted in the frameworks of NICT Beyond 5G R&D Promotion Project #JPJ012368C01301, Japan.

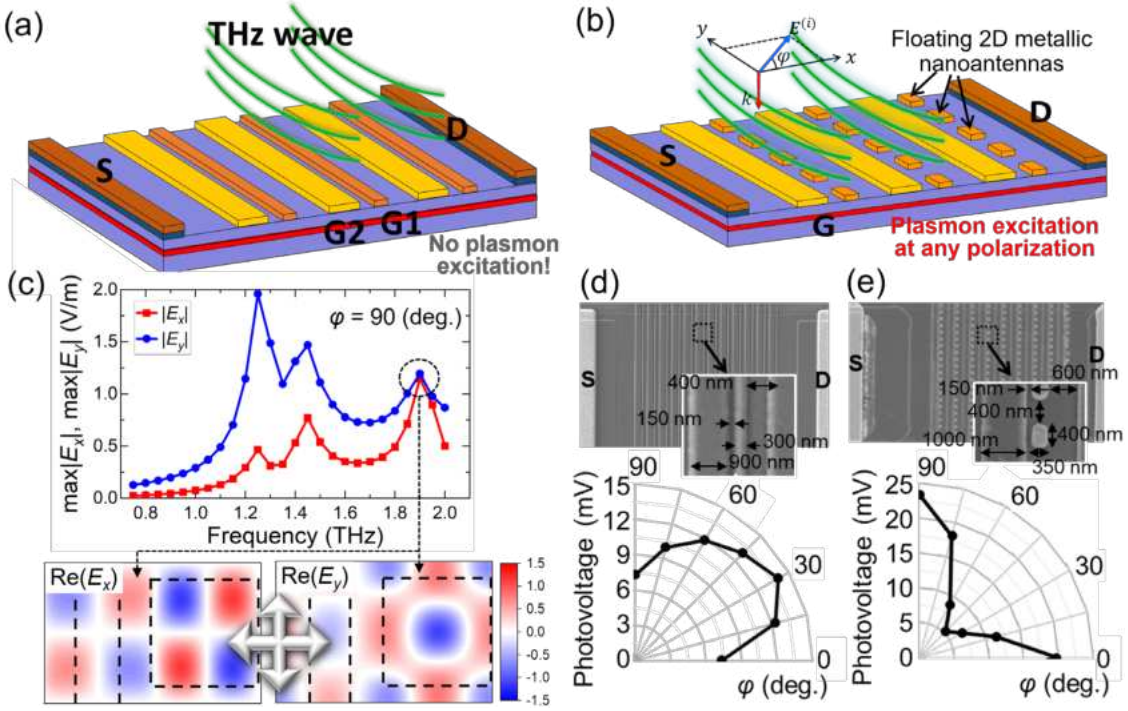


Fig. 1. Schematic views of THz plasmonic detectors with (a) a conventional 1D grating and (b) a new 2D grating structure, (c) simulated electric field distribution and frequency-dependent maximum field in the channel of the detector with the 2D grating structure [2], scanning-electron-microscope images and polarization characteristics of output photovoltage of fabricated THz plasmonic detectors with (d) a conventional 1D grating and (e) a new 2D grating structure [3].

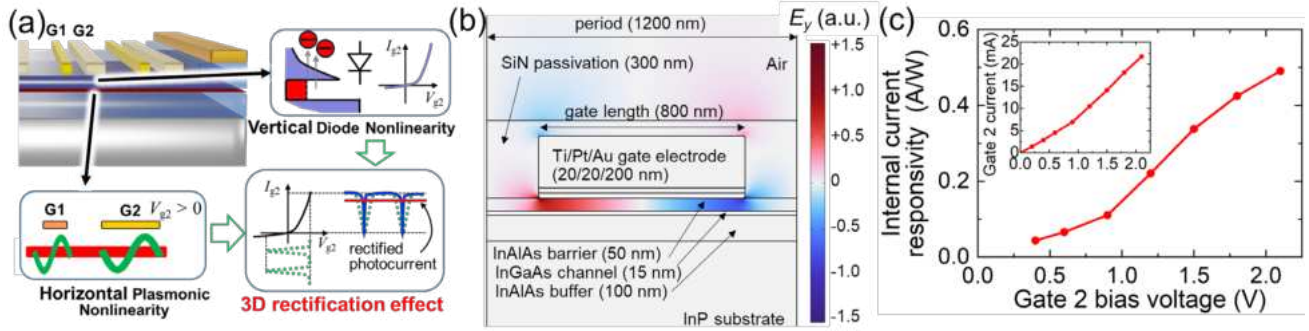


Fig. 2. (a) A schematic view of the 3D rectification effect in a 1D grating-gate THz plasmonic detector in the gate-readout configuration, (b) simulated electric-field component in the vertical direction in the detector (one period of the 1D grating structure) upon THz radiation incidence, (c) internal current responsivity of a fabricated detector vs gate bias voltage (the inset shows its I-V characteristic) [4].

References

1. Otsuji, T., IEEE Trans. Terahertz Sci. Tech., Vol. 5, Iss. 6, 1110–1120, 2015.
2. Sasaki, Y., Otsuji, T., and Satou, A., IRMMW-THz 2021, Chengdu, China, WE-PO-76, Aug. 29-Sep. 3, 2021.
3. Suzuki, M., *et al*., IRMMW-THz 2018, Nagoya, Japan, Tu-A2-1a-2, Sep. 10-14, 2018.
4. Satou, A., *et al*., Nanophotonics, Vol. 12, Iss. 23, 4283–4295, 2023.

Advancing Nano- and Quantum Photonics with Machine Learning

B. Wilson[1,2], Y. Chen[1,2], V. Shalaev[1,2], A. Kildishev[1], A. Boltasseva[1,2]

[1]Elmore Family School of Electrical and Computer Engineering, Birck Nanotechnology Center and Purdue Quantum Science and Engineering Institute, Purdue University, West Lafayette, IN 47907, USA,

[2]The Quantum Science Center (QSC), a National Quantum Information Science Research Center of the U.S. Department of Energy (DOE), Oak Ridge, TN 37931

*Corresponding author e-mail address: aeb@purdue.edu

Abstract: We report on advancing machine-learning techniques for improving nanophotonics experiments and device designs with applications in thermophotovoltaics, reflective optics, and lightsail technology as well as for on-chip quantum photonic components and super-resolution imaging.

Applying machine learning techniques to nanophotonics promises to advance on-chip circuitry, imaging, sensing, energy, and quantum information technology. In this talk, we discuss machine-learning assisted techniques in photonic inverse design optimization, measurements, and simulations. Our approaches showcase the use of new techniques for platform applications in thermophotovoltaics, reflective optics, quantum photonic circuitry and lightsail technology. We demonstrate the effectiveness of autoencoders and diffusion models for compressing the vast design space of metasurfaces into a smaller search space. By employing global optimization via adjoint methods or quantum annealing, one can find the optimal metasurface designs within the smaller space constructed by the autoencoder. We also apply machine learning approaches to advance measurements through super-resolution imaging, clustering algorithms for fabrication techniques, and attention networks for semiconductor authentication.

Acknowledgements

This work is supported by the U.S. Department of Energy (DOE), Office of Science through the Quantum Science Center (QSC), a National Quantum Information Science Research Center, and Purdue's Elmore ECE Emerging Frontiers Center 'The Crossroads of Quantum and AI'. The authors also acknowledge support from the National Science Foundation award 2029553-ECCS.

Fast Multi-channel Full-wave Solver and Inverse Design with Augmented Partial Factorization

Chia Wei Hsu[1*]

[1]Ming Hsieh Department of Electrical and Computer Engineering, University of Southern California, Los Angeles, California 90089, United States
[*]corresponding author: cwhsu@usc.edu

Abstract: I will describe a numerical approach called "augmented partial factorization" (APF) that bypasses the computation of unnecessary quantities to enable single-shot full-wave computation of the complete response of multi-channel optical systems and efficient inverse design. APF can reduce the computing time by orders of magnitude compared to existing frequency-domain methods.

We need full-wave solutions of Maxwell's equations to make quantitative predictions about wave propagation and scattering in multi-channel systems such as aperiodic metasurfaces, disordered media, and channel [de]multiplexers. However, these simulations are often prohibitively slow given the multiple length scales and large number of input channels involved. Conventional methods have two deficiencies: (1) After discretizing Maxwell's equations on a basis, they solve for all unknowns in this large basis, which may contain millions to billions of elements even though we only extract much fewer data points from it (e.g., the amplitude of light scattered to the directions of interest). (2) A loop over the many inputs is repetitive.

In this talk, I will describe a more efficient strategy that computes only the quantities of interest. Any set of linear responses in the frequency domain can be written as a generalized scattering matrix $CA^{-1}B$ where A discretizes the Maxwell differential operator, the columns of matrix B contain different input source profiles of interest, and the rows of matrix C contain different output projection profiles of interest. Instead of evaluating the full-basis solution $X = A^{-1}B$, we directly compute the orders-of-magnitude-smaller projected matrix $CA^{-1}B$ through a partial LU factorization of an augmented matrix $K = [[A, B]; [C, 0]]$ as shown in the figure below. Doing so is equivalent to a partial Gaussian elimination that projects the Green's function A^{-1} onto the inputs B and outputs C, bypassing the forward and backward substitutions that solve for the many unknown variables in $A^{-1}B$. This approach, which we call "augmented partial factorization" (APF) [1], is ideal for multi-channel problems since it jointly handles all inputs without a loop over them. It is exact and applicable to any discretization scheme in any dimension.

APF can reduce the computing time by three to seven orders of magnitude while lowering memory usage without compromising accuracy [1]. This drastic speed-up enabled us to perform full-wave simulations of scattering matrix tomography and other imaging methods [2] and demonstrate the enhanced correlations in the backscattering direction for entangled photon pairs scattered from disorder [3]. We also developed multi-channel gradient computation using APF and used it for the inverse design of aperiodic metasurfaces [4].

We developed an open-source APF solver called MESTI (Maxwell's Equations Solver with Thousands of Inputs) in Julia [5] and MATLAB [6]. It uses finite-difference discretization on the Yee grid. MESTI supports any relative permittivity profile, any set of input source profiles, any set of output projection profiles, and comes with PML and the common boundary conditions. Multithreading and MPI are supported via the MUMPS linear-solver package.

If time permits, I will mention fundamental thickness bound [7] and efficiency bound [8] for multi-channel optical systems, and inverse designs that reach these bounds and break performance records [9].

References

1. Lin, H.-C., Z. Wang and C. W. Hsu, "Fast multi-source nanophotonic simulations using augmented partial factorization," Nat. Comput. Sci., Vol. 2, 815–822, 2022.
2. Wang, Z., Y. Zhang and C. W. Hsu, "Full-wave simulations of tomographic optical imaging inside scattering media," arXiv:2308.07244.
3. Safadi, M., O. Lib, H.-C. Lin, C. W. Hsu, A. Goetschy and Y. Bromberg, "Coherent backscattering of entangled photon pairs," Nat. Phys., Vol. 19, 562–568, 2023.
4. Li, S., H.-C. Lin and C. W. Hsu, "Fast multichannel inverse design through augmented partial factorization," ACS Photonics, Vol. 11, 378–384, 2024.
5. https://github.com/complexphoton/MESTI.jl
6. https://github.com/complexphoton/MESTI.m
7. Li, S. and C. W. Hsu, "Thickness bound for nonlocal wide-field-of-view metalenses," Light: Science & Applications, Vol. 11, 338, 2022.
8. Li, S. and C. W. Hsu, "Transmission efficiency limit for nonlocal metalenses," Laser Photonics Rev., Vol. 17, 2300201, 2023.
9. Li, S., H.-C. Lin and C. W. Hsu, "High-efficiency high-NA metalens designed by maximizing the efficiency limit," arXiv:2311.13592.

Physics-based design of dielectric particle accelerators

A. Locatelli[1*], R. Palmeri[2,3], N. Salerno[4], G. S. Mauro[5], G. Torrisi[5], G. Sorbello[4,5], D. Rocco[1]

[1]Department of Information Engineering, University of Brescia, Italy
[2]DIIES, University Mediterranea of Reggio Calabria, Italy
[3]Institute for the Electromagnetic Sensing of the Environment, National Council of Research (IREA-CNR), Italy
[4]Department of Electric, Electronics, and Computer Engineering, University of Catania, Italy
[5]Southern National Laboratories – National Institute for Nuclear Physics, Italy
[*]corresponding author: andrea.locatelli@unibs.it

Abstract: We illustrate a methodology for designing sub-relativistic dielectric laser accelerators. We focus on slot waveguides where an optimal taper can ensure particle-wave synchronicity and maximum energy gain. The optimization is carried out through a physics-based approach, which is validated by comparison with a downhill simplex method searching algorithm.

Several scientific and industrial applications would benefit from miniaturized particle accelerators with a reduced cost compared to the state-of-the-art equipment. However, it is well known that the performance of conventional accelerators is limited by metal breakdown and by the power required to guarantee large accelerating gradients. In this framework, laser-driven accelerating structures made of dielectric materials have been conceived, by exploiting commonly used nano-fabrication technologies [1]. This approach can be effective for miniaturization of particle accelerators, since dielectrics exhibit a larger breakdown threshold with respect to metals and powerful laser sources are available for telecommunications. As a matter of fact, dielectric waveguides are a promising platform which overcomes the limitations of side-pumped geometries, because the accelerating field is a guided mode co-linear with the particles. In this context, it was reported that slot waveguides composed of high-index dielectric strips placed over a substrate (see Fig. 1) can be employed for acceleration of sub-relativistic electrons if synchronization between particles and field is guaranteed by tapering the waveguide cross-section [2].

In this work we have investigated optimization methodologies for design of a tapered waveguide tailored for particle acceleration. In details, we adopt a physics-based approach aimed at maximizing the output energy gain by imposing that the phase velocity is equal to the particle velocity at each cross section. This procedure is rather efficient from a computational point of view since it requires a simple parametric study of the modal properties of the slot waveguide in combination with solution of single-particle relativistic dynamics. Moreover, numerical optimization has been carried out by using the Nelder-Mead method (also called downhill simplex method), which allows to determine the optimum value of a figure of merit in a multidimensional space [3]. Comparison between the optimal width *a* of the high-index strips determined through the previously mentioned techniques is reported in Fig. 2 for two different lengths of the accelerating waveguide. Notice that for shorter structures agreement between different methods is excellent, whereas results tend to diverge for longer waveguides (see Fig. 3). This is an expected result due to the field approximation used in [3], where a proper model correction was also envisaged.

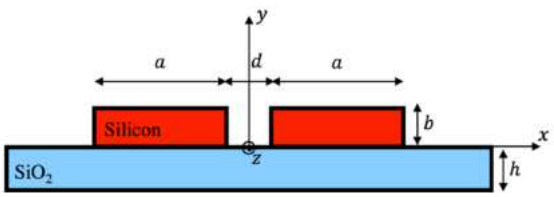


Figure 1. Schematic view of the cross-section of a slot waveguide composed of silicon strips over a silica substrate [2].

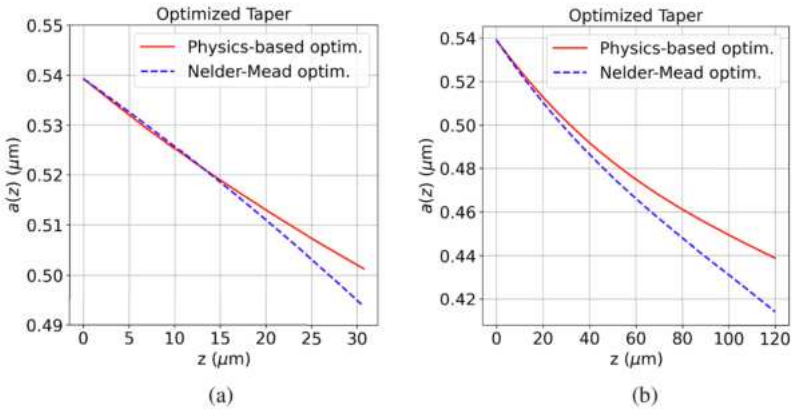


Figure 2. Optimal taper profiles obtained with the physics-based approach (red lines) and the Nelder-Mead algorithm (blue lines), respectively. (a) $L = 30\ \mu m$. (b) $L = 120\ \mu m$.

Temporal effects due to the pulsed nature of the accelerating field have also been investigated. It is indeed well-known that conventional metallic structures typically work at room temperature with low repetition rate (tens of Hz). Instead, dielectric particle accelerators can achieve MHz repetition rates, and even CW operation can be envisaged. In this scenario, short pulses are characterized by larger peak power, but the interaction length can be limited by low group delay and by waveguide dispersion. Notice that in general longer pulses exhibit an opposite behavior. In this study the effect of pulse duration has been analyzed, with the goal of identifying a recipe for choosing the pulse duration that maximizes the energy gain.

The authors acknowledge financial support from INFN V National Committee through the MICRON grant, and from the National Ministry of University and Research as part of the PRIN 2022 projects DOSE (2022MANFK5), GRACE6G (2022H7RR4) and IDEAS (202293B5X).

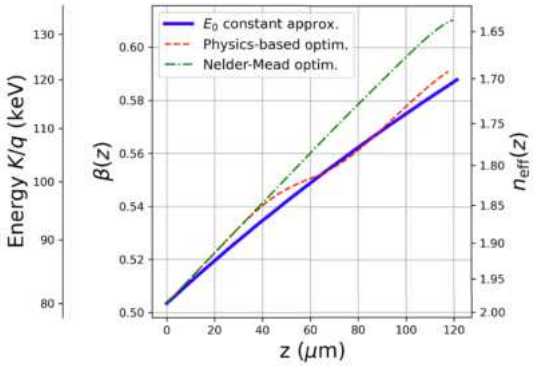


Figure 3. Comparison between acceleration profile and output energy achievable with different optimization strategies.

References

1. England, R. J., D. Filippetto, G. Torrisi, et al., "Laser-driven structure-based accelerators," arXiv, 2203.08981, 2022
2. Zhao, Z., T. W. Hughes, S. Tan, H. Deng, N. Sapra, R. J. England, J. Vuckovic, J. S. Harris, R. L. Byer, and S. Fan, "Design of a tapered slot waveguide dielectric laser accelerator for sub-relativistic electrons," Opt. Express Vol. 26, 22801–22815, 2018.
3. Palmeri, R., N. Salerno, G. S. Mauro, D. Rocco, A. Locatelli, G. Torrisi, and G. Sorbello, "Optimization of sub-relativistic co-propagating accelerating structures," Optics Express, Vol. 31, 38891-38909, 2023.

Quantifying Symmetry of Metasurfaces and Eigenmodes for Optimisation Design

Matthew Parry[1,*], Andrey A. Sukhorukov[1], and Dragomir N. Neshev[1]

[1]ARC Centre of Excellence for Transformative Meta-Optical Systems (TMOS), Department of Electronic Materials Engineering, Research School of Physics, Australian National University, Canberra, ACT 2600, Australia
[*]corresponding author: Matthew.Parry@anu.edu.au

Abstract: We demonstrate a novel technique to numerically quantify the symmetry of metasurface eigenmodes. We show its application to the optimization of a metasurface laser for multiple objectives such as enhancing pump absorption by four times relative to a Fabry-Perot cavity as well as controlling the mode dispersion.

Symmetry has recently become an important element of metasurface (MS) design, finding uses in the engineering of quasi-bound states in the continuum, chirality, geometric phase and the effective permittivity and permeability of MSs. The properties of the individual modes themselves can also be determined by symmetry, such as in the engineering of Dirac cones from the overlap of modes of certain symmetries. At the same time, inverse design methods are becoming increasingly important for the engineering of specific linear and nonlinear responses [1]. It is clear that an important advance can be made in metasurface applications if one is able to introduce symmetry constraints on both the MS design and the selection of modes in inverse design algorithms.

We demonstrate a novel technique to numerically quantify the symmetry of both MSs and their eigenmodes [2] through the example of an Up-Converting Nano-Particle (UCNP) based MS laser [3]. In contrast to conventional active media, the absorption band of the UCNPs is at longer wavelengths than the lasing spectral band (Fig. 1(a)). In [3], UCNP MS laser was demonstrated, however, the MS was only resonant at the lasing wavelength, having no enhancement for the absorption. Therefore, new dielectric MS designs are required to increase the infrared absorption with low dispersion to increase the acceptance angle. These goals can be achieved by selecting modes of a particular symmetry and here we demonstrate a novel technique to numerically quantify the mode symmetry so that it can be included as an optimization objective [2].

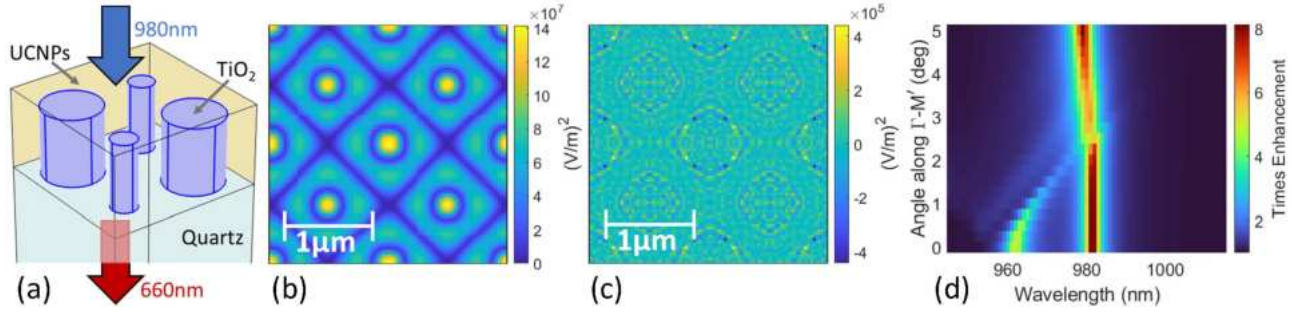


Figure 1. (a) Conceptual diagram of lasing up-conversion. (b) A scalar field with C_{4v} A_1 symmetry, over four unit cells. (c) The effect of applying the C_{4v} B1 projector to the field in (b). (d) The absorption enhancement, relative to a thin film, of the optimized metasurface.

The MS design is of C4v symmetry (Fig. 1(a)), which means that some of the modes will have the symmetry of the C4v E irreducible representation. These are degenerate, polarization independent modes with relatively

low dispersion (as required for the absorption band) for P-polarised incident light. They are also bright modes since the E irreducible representation has the same symmetry as a vector and they will therefore couple to the radiation channels. We accordingly wish to select only these modes for the absorption band and therefore require a method to recognize the symmetry of a mode from an eigenfrequency study.

Since the lattice modes in a MS have either transverse electric or transverse magnetic fields, we can characterize the vector field by taking a slice through the center of the MS. We express the fields (such as that shown in Fig. 1(b)) as a vector and then subdivide this vector space by symmetry [2]. We can therefore test for the presence of a particular symmetry by projecting the vector representing the field onto the subspace for the symmetry to be tested for. For example, the mode in Fig. 1(b), chosen for illustrative purposes, has C4v A1 symmetry. That is, it is symmetric across the horizontal and vertical as well as both diagonal mirror symmetries. If we project this vector onto the C4v B1 subspace then we get the result shown in Fig. 1(c), which is two orders of magnitude weaker. We can then use the ratio of the magnitude of this projected vector to that of the original vector to quantify the degree to which it has the given symmetry. We have thus formulated a numerical method that distinguishes between the MS eigenmodes by their symmetry.

For the optimisation of the absorption band, we used this symmetry analysis technique to eliminate all modes that are not of C4v E symmetry and then optimized for absorption within the UCNP layer. In Fig. 1(d) we can see an up to 8-fold enhancement of absorption for the optimized design relative to a UNCP thin film without the MS. This can be compared to a Si-UCNP-Si Fabry-Perot cavity, which would only provide and enhancement of 2.23 times. Note that the emission enhancement would be approximately the square of this figure since the up-conversion process is sequential two-photon absorption.

To demonstrate the general utility of projection operators we also formulate a universal definition of MS asymmetry and use it to numerically quantify the polarization of quasi-bound states in the continuum. We use these developments to provide a deeper understanding of MS asymmetry and its relationship to the mode quality factor. We also provide an analysis of the interaction of MS asymmetry and eigenmode symmetry in the context of third harmonic generation (THG). The method presented is algorithmic in nature and thus also amenable to use in optimisation routines.

In summary, we have developed a powerful technique based on projection operators that allows one to numerically quantify the symmetry of both MSs and their eigenmodes. With this new technique we designed a MS with resonances at both the absorption and lasing bands of a UCNP based MS laser and used our technique to ensure that these two modes have the properties required. We have also used projection operators to optimize a MS for THG. We believe that these projection operator techniques will be of general use wherever symmetry considerations must be taken into account in MS design.

This work was supported by Australian Research Council (CE200100010) and DARPA (HR001121S0013).

References

1. S. D. Campbell, D. Sell, R. P. Jenkins, E. B. Whiting, J. A. Fan, and D. H. Werner, “Review of numerical optimization techniques for meta-device design”, Optical Materials Express **9**, 1842 (2019).
2. M. Parry, K. B. Crozier, A. A. Sukhorukov, and D. N. Neshev, “Optimization of metasurfaces for lasing with symmetry constraints on the modes,” Phys. Rev. B **109**, 075406 (2024).
3. A. Fernandez-Bravo, D. Q. Wang, E. S. Barnard, A. Teitelboim, C. Tajon, J. Guan, G. C. Schatz, B. E. Cohen, E. M. Chan, P. J. Schuck, and T. W. Odom, “Ultralow-threshold, continuous-wave upconverting lasing from subwavelength plasmons,” Nat. Mater. **18**, 1172 (2019).

Efficient modelling and tailoring of nonlinear wavefront and enhanced third harmonic generation in dielectric metasurfaces

V. Myroshnychenko[1]

[1]Theoretical Electrical Engineering and CeOPP, Paderborn University, Paderborn, Germany
viktor.myroshnychenko@gmail.com

Abstract: We present an effective geometry optimization approach for tailoring phase and amplitude of the third-harmonic wavefront with a high emission efficiency using dielectric metasurfaces. We demonstrate optimal metasurface designs operating as a third harmonic beam deflector and possessing a strong third harmonic generation originating from a multi-mode Fano mechanism.

Dielectric metasurfaces provide a unique platform for efficient harmonic generation and optical wavefront manipulation at the nanoscale [1]. Tailoring phase and amplitude of a nonlinearly generated wave with a high emission efficiency using resonance-based metasurfaces is a challenging task that often requires state-of-the-art numerical methods. Here, we propose a simple yet effective approach combining a sampling method with a Monte Carlo method to design the third-harmonic wavefront generated by all-dielectric metasurfaces composed of elliptical silicon nanodisks [2,3]. Using this approach, we theoretically demonstrate the full nonlinear 2π phase control with a uniform and highest possible amplitude in the considered parameter space. This allows us to design metasurfaces operating as third harmonic (TH) beam deflectors capable of steering light into a desired direction with high emission efficiency (Figure 1). The TH beam deflection with a record calculated average conversion efficiency of 1.2×10^{-1} W^{-2} is achieved [2].

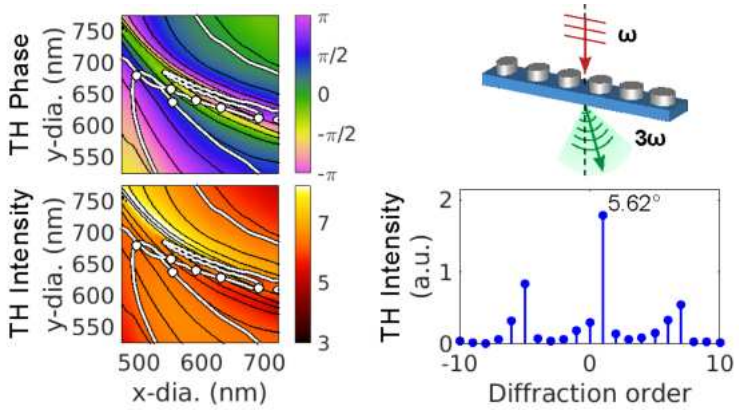


Figure 1. An artistic view of a designed supercell of a dielectric metasurface with tailored phase and amplitude used for nonlinear beam deflection. The TH phase and intensity maps are used to select the nanodisks generating the required phase and amplitude.

By employing the Monte Carlo protocol to sample over a large ensemble of geometrical parameters, one can also find the optimal metasurface designs possessing strong enhancement of third harmonic generation (THG). We demonstrate one example where extremely enhanced TH is generated by the interaction of an ultra-narrow high-Q quadrupolar magnetic mode with the two broad electric dipole and electric quadrupole

modes, which are spectrally brought so close together that they form what we call a 'Super-Fano' resonance (see Figure 2). The theoretically predicted behaviour of the metasurface is experimentally verified by linear and nonlinear transmission spectroscopy. We achieve a THG enhancement up to ~900 compared to an unpatterned amorphous silicon film of the same thickness and an absolute conversion efficiency of $\eta_{max} \approx 2.8 \times 10^{-7}$ at a peak power intensity of 1.2 GWcm^{-2} and a pulse duration of 80 fs [4].

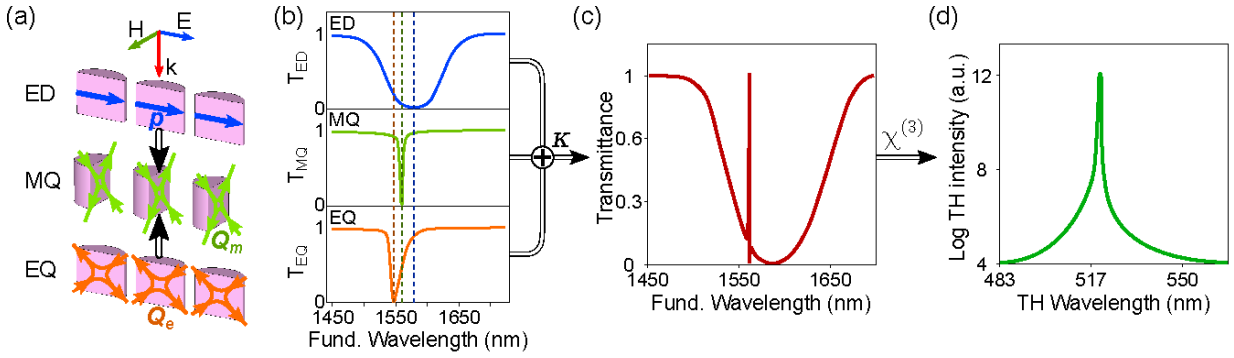


Figure 2. (a) Illustration of the enhanced third harmonic generation scheme by the multi-mode Fano resonance mechanism involving electric dipole, magnetic quadrupole, and electric quadrupole modes. (b) Transmittance spectra associated with the corresponding modes forming single resonances. (c) The resultant transmittance spectrum originated from coupling of these three modes with the coupling strength κ, forming the Fano-like sharp asymmetric resonance profile. (d) The corresponding TH spectrum of high intensity.

The authors gratefully acknowledge financial support from the Deutsche Forschungsgemeinschaft (DFG) via TRR142/3, project number 231447078, subprojects C05 and B06, and computing time support provided by the Paderborn Center for Parallel Computing (PC^2).

References

1. Wang, L., S. Kruk, K. Koshelev, I. Kravchenko, B. Luther-Davies and Y. Kivshar, "Nonlinear wavefront control with all-dielectric metasurfaces, " Nano Letters Vol. 18, No. 6, 3978–3984, 2018.
2. Hähnel, D., J. Förstner and V. Myroshnychenko, "Efficient modeling and tailoring of nonlinear wavefronts in dielectric metasurfaces," ACS Photonics, Vol. 10, No. 8, 2502–2510, 2023.
3. Almeida, E., O. Bitton and Y. Prior, "Nonlinear metamaterials for holography," Nature Communications, Vol. 7, No. 1, 12533, 2016.
4. Hähnel, D., C. Golla, M. Albert, T. Zentgraf, V. Myroshnychenko, J. Förstner and C. Meier, "A multi-mode super-fano mechanism for enhanced third harmonic generation in silicon metasurfaces," Light: Science & Applications, Vol. 12, No. 1, 97, 2023.

Modeling and Implementation of Asymmetric Angular Transmittance

M. A. A. Abouelatta[1*] and K. Achouri[1]

[1]Swiss Federal Institute of Technology in Lausanne (EPFL), Switzerland
[*]corresponding author: mahmoud.abouelatta@epfl.ch

Abstract: We demonstrate theoretically and experimentally how asymmetric angular transmittance may be achieved using a meta-grating. We develop two approaches for predicting the response of this system based on generalized sheet transitions conditions and effective polarizabilities. This concept may find applications in the design of compact spatial analog processing systems.

Metasurfaces have enabled precise manipulation of the amplitude, phase, polarization and even frequency of electromagnetic waves. Yet, controlling how light responds at different angles of propagation, an ability that is a critical aspect for enabling analog computing or spatial processing in very compact optical systems, remains one of the main ongoing challenges in metasurface design. In this work, we develop a meta-grating system that exhibits angular asymmetry in transmittance. As depicted in Figure 1, the meta-grating reflects TM light which is incident from the left side, while it efficiently transmits TM light which is incident from the right side. This is evident in the magnetic field distributions shown in the far left and right sides of Figure 1 for incidence angles equal to 55° and -55°, respectively.

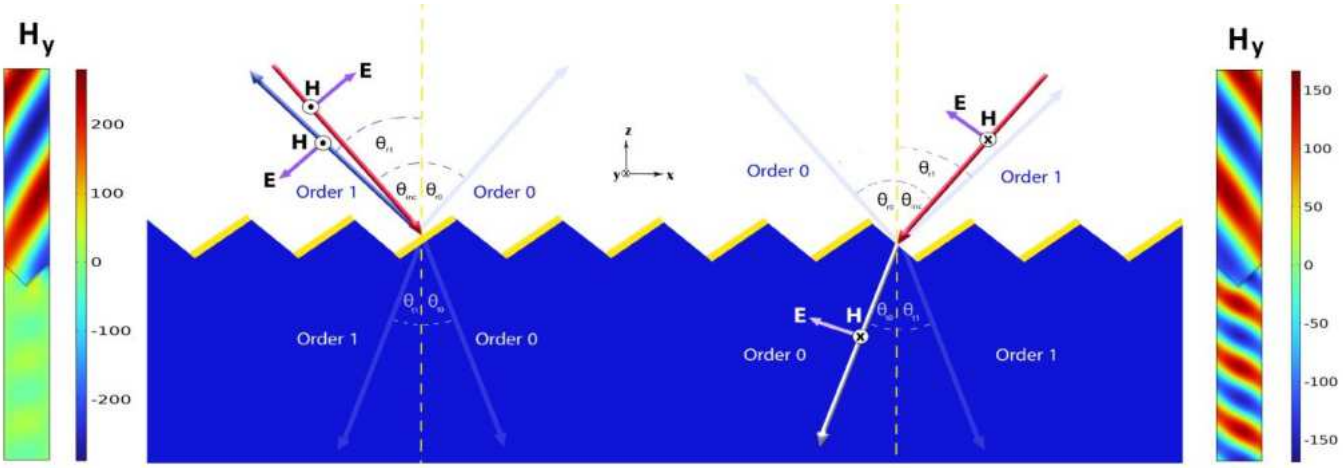


Figure 1. Schematic of the suggested meta-grating exhibiting asymmetric angular scattering.

Figure 2 (a), (b), and (c) show the 0th order, 1st order, and total transmittance, respectively, for incidence angles equal to 55° and -55°. The 0th order, 1st order, and total reflectance are also depicted in Figure 2 (d), (e), and (f), respectively. It can be noted that there is remarkable asymmetry in the total transmittance for a wavelength range starting from 0.8 to 0.95 µm. For the incidence angle (55°) where there is no transmission, the energy is rerouted to the first diffraction order in reflection as depicted in Figure 1 (e).

At the conference, we will show the response of the meta-grating in Fourier space for all three-dimensional incidence orientations. Physical insights about the inner workings of the meta-grating will be provided based

on the propagation conditions in Fourier space for each diffraction order. Moreover, two approaches for modeling and predicting the angular response of the meta-grating will be discussed. The first approach relies on the generalized sheet transition conditions [1, 2], which works only in the non-diffractive regime. The second approach is based on effective polarizabilities and Floquet expansion, which could work both in the non-diffractive and diffractive regimes. We will additionally show the fabrication process and the experimental results, which prove the asymmetric response of the transmittance. The process flow for fabrication starts with a nitride mask created on top of a silicon wafer by E-beam lithography and plasma etching. KOH is then used to create the triangular pattern since it etches the 111 plane of crystalline silicon 200 faster than the 100 plane. After that, wet thermal oxidation is applied to convert the silicon ridges to silica without deformation. Finally, oblique evaporation of gold on only one side of the ridges completes the process flow. Experimental measurements for the 0^{th} order transmittance as a function of the incidence angle and wavelength are obtained by an optical setup made of a supercontinuum light source, a polarizer, a holder, and an optical spectrum analyzer to show the angularly asymmetric response of the transmittance.

Such a meta-grating could be used for Schlieren imaging, which is typically realized by a free-space setup in which half of Fourier space is filtered. It may also be used in other applications such as angular selective thermal emission [3].

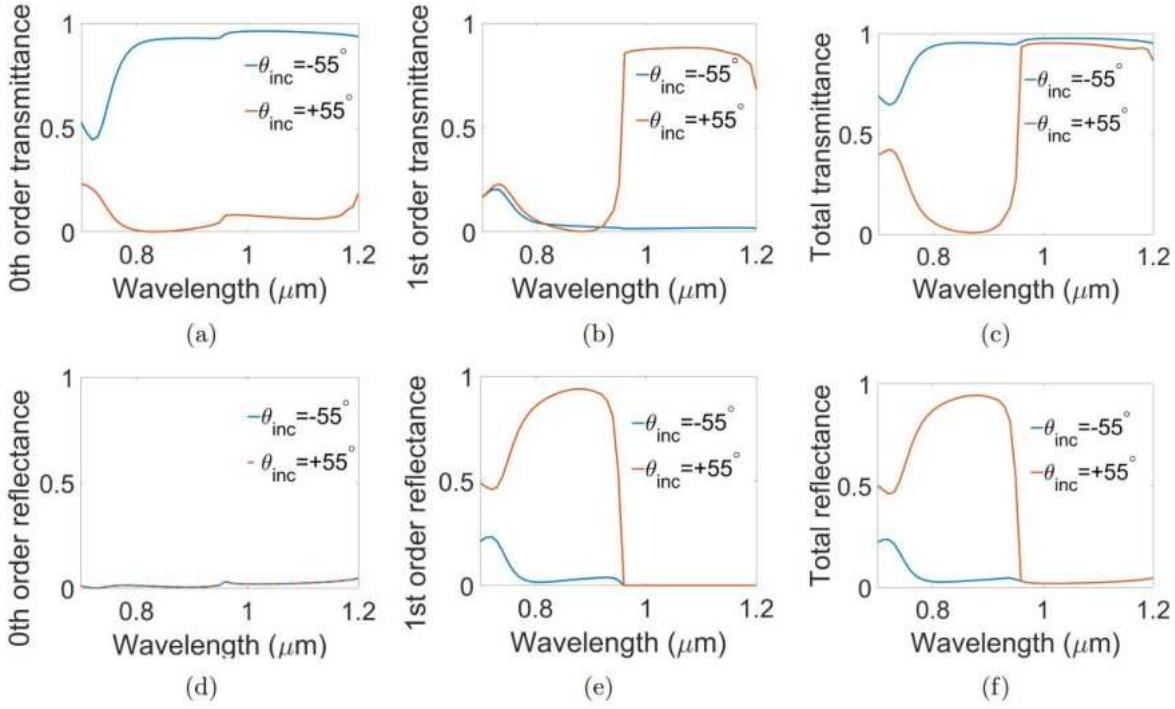


Figure 2. Full-wave simulations of the 0^{th} and 1^{st} order transmittance and reflectance as well as total transmittance and reflectance for the meta-grating in Fig. 1.

References

1. K. Achouri and C. Caloz, Electromagnetic metasurfaces: theory and applications. Hoboken, NJ: Wiley-IEEE Press, 2021.
2. K. Achouri and O. J. F. Martin, "Angular Scattering Properties of Metasurfaces," IEEE Trans. Antennas Propagat., vol. 68, no. 1, pp. 432–442, Jan. 2020
3. E. Sakr, S. Dhaka, and P. Bermel, "Asymmetric angular-selective thermal emission," presented at the SPIE OPTO, A. Freundlich, L. Lombez, and M. Sugiyama, Eds., San Francisco, California, United States, Mar. 2016, p. 97431D.

Anamorphic meta-lenslet array for laser guide star wavefront sensing

Josephine Munro[1*], Sarah Dean[1], Neuton Li[1], Israel Vaughn[2], Andrew W. Kruse[2], Tony Travouillon[2], Dragomir N. Neshev[1], Robert Sharp[2], and Andrey A. Sukhorukov[1]

[1]ARC Centre of Excellence for Transformative Meta-Optical Systems (TMOS), Department of Electronic Materials Engineering, Research School of Physics, Australian National University, Canberra, ACT 2600, Australia
[2]Research School of Astronomy and Astrophysics, Australian National University, Weston Creek, ACT 2611, Australia
[*]corresponding author: Josephine.Munro@anu.edu.au

Abstract: Laser guide star wavefront sensing will be a major challenge for next generation extremely large telescopes, as Shack-Hartmann wavefront sensors will suffer from laser guide star elongation. We present the design of a meta-lenslet array which efficiently uses detector space by anamorphically rescaling the image space uniquely for each subaperture.

Laser guide star facilities for Extremely Large Telescopes (ELTs) will be crucial to correct atmospheric aberrations over a large fraction of the sky, for example the Laser Tomography Adaptive Optics (LTAO) facility for the Giant Magellan Telescope [1]. LTAO will be equipped with six laser launchers, located around the periphery of the primary mirror, to excite an asterism of artificial guide stars in the sodium layer of Earth's upper atmosphere (altitude ~95km). But the sodium layer is not infinitely thin, the 10-20km thickness of the sodium layer means a laser guide star is a vertical column of illumination rather than a point source [2]. This is particularly challenging for a Shack-Hartmann wavefront sensor (SHWFS), where each subaperture images a unique perspective elongation that is radially dependent on its off-axis position compared to the laser launcher, as depicted in Fig. 1(a). The elongation ratio for the SHWFS subapertures for ELTs varies between 1:1 and 1:10 across the aperture, see Fig. 1(b). The conventional solution is to use detectors with many pixels to adequately sample the non-elongated spots while avoiding excessive truncation of the elongated spots. But the disadvantages of using very large detectors include increased readout noise, longer readout time, decreased iteration speed, and the engineering challenges of mounting the large, heavy system on the telescope.

We present an innovative solution; a meta-lenslet array, where each meta-lenslet subaperture delivers a custom anamorphic image scale compression, allowing efficient detector packing. A SHWFS using a single layer of dielectric metalenses as the lenslet array was previously demonstrated for polarimetric beam profiling [3]. However, for our meta-lenslet array to achieve both parfocal operation and correct a broad range of elongation ratios, we developed an original design based on a metasurface bilayer configuration [4], as sketched in Fig. 1(c).

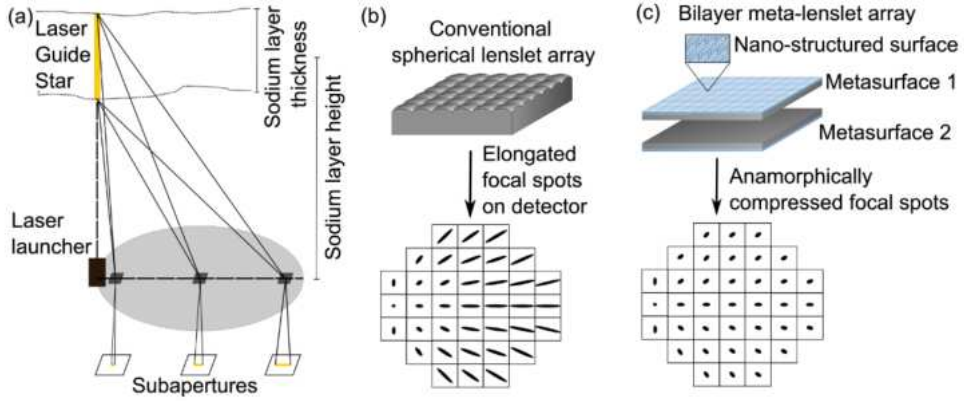


Figure 1: (a) Depiction of spot elongation due to the finite thickness of the sodium layer in the atmosphere. (b) SHWFS conventional lenslet array with variable laser guide star perspective elongation across the aperture. (c) Bilayer arrangement of the meta-lenslet, with a 6.6mm air gap between the metasurfaces.

We have designed multiple bilayer meta-lenslets with the varying the anamorphic compression ratios from 1:1 to 1:10. We matched the effective focal length of 2 mm from the LTAO design, and also investigated longer effective focal lengths up to 10mm. The Optics Studio (Zemax) simulation of our bilayer meta-lenslet and equivalent spherical lenslet showed that for f=2 mm, a 50% reduction in spot size was achieved for the most elongated spots, as seen in Fig. 2(a)-(c). For an effective focal length of f=10 mm, the spot size was completely anamorphically corrected, reducing the 104 μm spot size for the spherical lenslet to a 12 μm spot size, see Fig. 2(d)-(f). The metasurfaces can be fabricated from silicon using established research or industry facilities, or potentially titanium dioxide for increased efficiency due to a lower material absorption at the 589nm target wavelength.

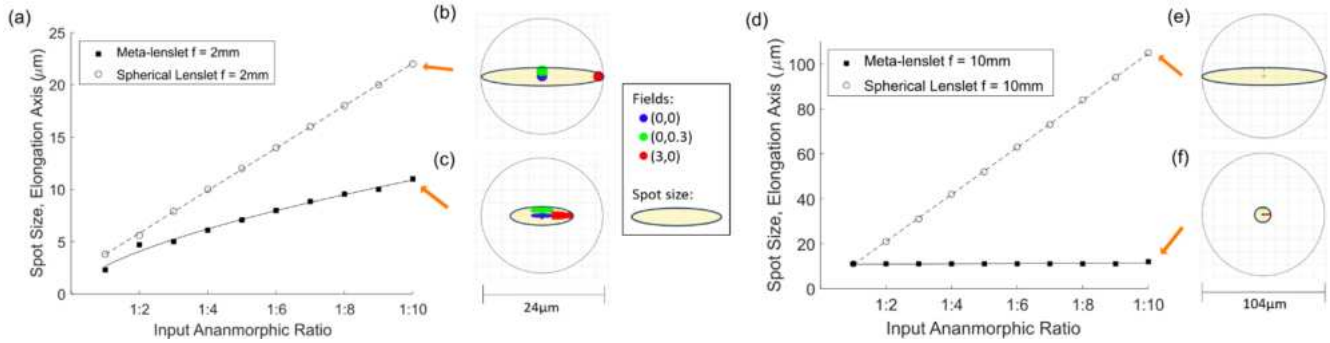


Figure 2: (a,d) Spot size versus input anamorphic ratio for a meta-lenslet and a spherical lenslet. (b,c,e,f) Focal plane field angle positions and spot size at 1:10 anamorphism for (b,e) spherical lenslet and (c,f) meta-lenslet. The effective focal lengths are (a-c) f =2 mm and (d-f) f=10 mm.

In summary, our study reveals new opportunities for anamorphic optics with meta-lenslet arrays that can find applications in telescopes and other systems requiring tailored image rescaling.

We acknowledge the support of the Australian Research Council (NI210100072, CE200100010).

References

1. R. Conan, F. Bennet, A. H. Bouchez, M. A. van Dam, B. Espeland, W. Gardhouse, C. d'Orgeville, S. Parcell, P. Piatrou, I. Price, F. Rigaut, G. Trancho, and K. Uhlendorf. "The Giant Magellan Telescope laser tomography adaptive optics system," Brent L. Ellerbroek, Enrico Marchetti, and Jean-Pierre Véran, editors, In Adaptive Optics Systems III, volume 8447, page 84473P. International Society for Optics and Photonics, SPIE, 2012.
2. S. J. Thomas, S. Adkins, D. Gavel, T. Fusco, and V. Michau. "Study of optimal wavefront sensing with elongated laser guide stars," Mon. Not. R. Astron. Soc., 387(1):173–187, 05 2008.
3. Z. Y. Yang, Z. K. Wang, Y. X. Wang, X. Feng, M. Zhao, Z. J. Wan, L. Q. Zhu, J. Liu, Y. Huang, J. S. Xia, and M. Wegener. "Generalized hartmann-shack array of dielectric metalens sub-arrays for polarimetric beam profiling," Nat. Commun., 9:4607, Nov 2 2018.
4. F. Yang, H. I. Lin, M. Y. Shalaginov, K. Stoll, S. An, C. Rivero-Baleine, M. Kang, A. Agarwal, K. Richardson, H. L. Zhang, J. J. Hu, and T. Gu. "Reconfigurable parfocal zoom metalens," Adv. Opt. Mater., 10(17):2200721, Sep 2022.

One-way excitation of normal incident light for a plasmonic grating coupler with trapezoidal dielectric gratings

J. Shibayama[1*], H. Nakasaka[1] and K. Takeya[1]

[1]Faculty of Science and Engineering, Hosei University, Japan
[*]corresponding author: shiba@hosei.ac.jp

Abstract: We investigate the coupling problem of a plasmonic grating coupler with trapezoidal dielectric gratings. The coupler is analyzed using the frequency-dependent finite-difference time-domain method. It is shown that the normal incident light is coupled to the grating and the coupled light propagates in one direction.

When a light field is incident to gratings, the field is coupled to them provided that the phase matching condition is satisfied [1]. When gratings are used for an optical link, it is highly expected that the coupled light propagates in one direction in order to maximize the use of the incident light. Unfortunately, at normal incidence, the coupled light propagates in both directions in a plasmonic grating coupler with rectangular dielectric gratings. On the other hand, at oblique incidence, the coupled light propagates in one direction. However, it is cumbersome to precisely control the angle of incidence in a practical device.

In this article, we investigate a plasmonic grating coupler with trapezoidal dielectric gratings for one-way excitation of normal incident light. Fig. 1 shows the configuration of the plasmonic coupler, in which trapezoidal dielectric gratings made of SiO_2 are placed on an Ag substrate. The grating period Λ is set to be 1.2 μm and the lengths of the top and bottom sides of the trapezoid are determined by the conditions under which normal incident light enters the Ag substrate at the appropriate angle.

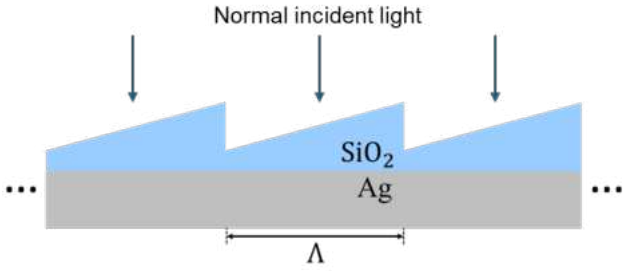
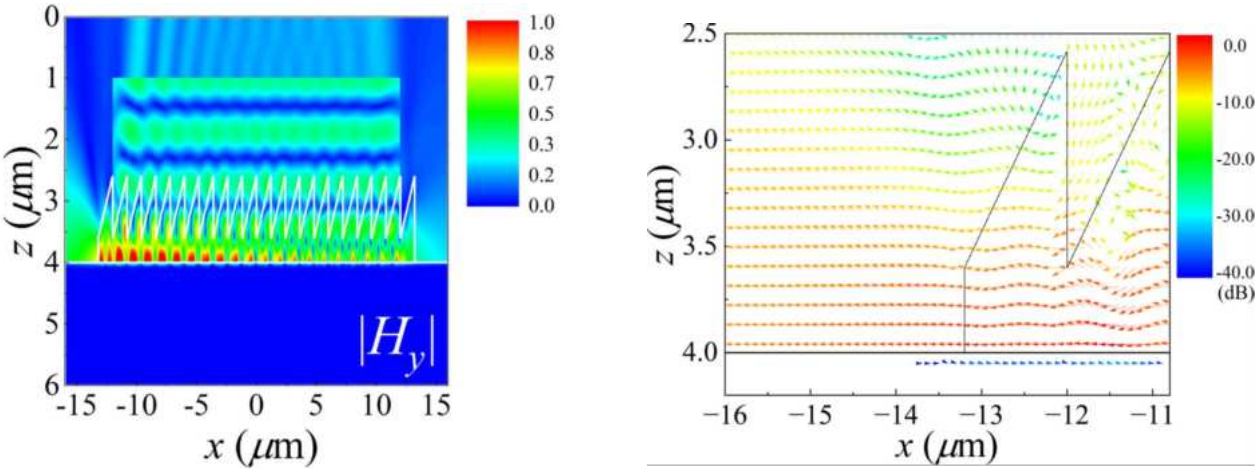


Fig. 1 Configuration of a plasmonic grating coupler with trapezoidal dielectric gratings.

To analyze a metal material using the finite-difference time-domain (FDTD) method at optical frequencies, we need to perform the frequency-dependent formulation [2]. Here, we employ the trapezoidal recursive convolution (TRC) technique [3],[4], in which only one convolution calculation is required for second-order accuracy in time. Note that the frequently used piecewise liner recursive convolution (PLRC) technique requires two convolution calculations. In the practical simulation, we apply the total-field/scattered field formulation to the FDTD method.

Figs. 2(a) and (b) show the field distribution of the H_y component at λ=1.69 μm, and the Poynting vector at

the end of the grating, respectively. In Fig. 2(a), it is found that the normal incident light is coupled to the grating, in which the field intensity is stronger on the left side of the grating. In Fig. 2(b), calculation of the Poynting vector shows that the field propagates only in the left direction, even though the field is vertically incident. It is interesting to note that the Poynting vector in the metal (blue arrows) is pointing to the right. This is because the real part of the permittivity of the metal is negative.



(a) Field distribution (b) Poynting vector

Fig. 2 Result of the plasmonic grating coupler with a 22-period grating.

In summary, we have analyzed a plasmonic grating coupler with trapezoidal dielectric gratings using the FDTD method based on the TRC technique. It is found that the coupled field propagates only in one direction, even though the field is vertically incident. Our future work is to reduce the reflected field from the gratings.

References

1. Shibayama, J., S. Takahashi, J. Yamauchi, and H. Nakano, "Fundamental investigation of a grating consisting of InSb-coated dielectric cylinders on a substrate in the THz regime," IEICE Trans. Electron., Vol. E103-C, No. 11, 567-574, 2020.
2. Takeya, K., J. Chakarothai, J. Shibayama, Y. Suzuki, and K. Fujii, "Novel surface impedance formulation via FILT and Prony method for FDTD analyses of lossy media," IEEE Antennas Wirel. Propag. Lett., Vol. 23, 2024. (to be published)
3. Shibayama, J., H. Kawai, J. Yamauchi, and H. Nakano, "Analysis of a 3D MIM waveguide-based plasmonic demultiplexer using the TRC-FDTD method," Opt. Commun., Vol. 452, 360-365, 2019.
4. Shibayama, J., K. Suzuki, J. Yamauchi, and H. Nakano, "Simple trapezoidal recursive convolution technique for the frequency-dependent FDTD analysis of a Drude-Lorentz model," IEEE Photon. Technol. Lett., Vol. 21, No. 2, 100-102, 2009.

Machine-Learning Assisted Multi-User Frequency Selective Beam Steering with a Reconfigurable Intelligent Surface

Alexander Wolff[1], Lukas Mueller[1], Steffen Klingel[1], Janis Krieger[1], Lars Franke[1], Ralf Stemler[1], and Marco Rahm[1]

[1]Department of Electrical and Computer Engineering and Research Center OPTIMAS, Erwin-Schroedinger-Strasse, RPTU Kaiserslautern-Landau, 67663 Kaiserslautern, Germany

[*]corresponding author: marco.rahm@rptu.de

Abstract: We used a Machine Learning approach to design, optimize and experimentally implement a Reconfigurable Intelligent Surface (RIS) that allows simultaneous, dynamic beam steering of microwave signals at 27 GHz and 31 GHz to two users that locally move at two different locations.

In the realm of 5G and 6G mobile communication, beam obstruction caused by structures or obstacles is a significant challenge due to the utilization of higher frequency bands [1]. In this context, Reconfigurable Intelligent Surfaces (RIS) provide a remedy by redirecting radiation emitted by base stations towards obstructed regions. As shown in [2,3], continuous beam steering can be achieved within a dedicated frequency range by use of varactor diodes as tuning elements. By exploiting the frequency dependence of the S11-Parameter in such RIS, we can find tuning patterns on the unit cell level that allow us to deliberately deflect incident waves of different frequencies towards distinct directions. The determination of the required unit cell bias voltages for this task is accomplished by a semi-analytical technique that merges Kirchhoff diffraction theory with neural network algorithms. In experimental trials, we successfully demonstrate beam steering in a single plane concurrently at 27 GHz and 31 GHz, spanning deflection angles from 10° to 45°.

This research aims to enhance signal strength for two distinct users positioned at different angles relative to the normal vector of the RIS. One user operates at 27 GHz carrier frequency, while the other uses 31 GHz. Both users must receive signals simultaneously. Achieving this necessitates selecting bias voltages for the RIS varactor diodes to generate a beam lobe at the target deflection angle and frequency for each user. Yet, the voltage pattern selection is non-trivial.

For this reason, we employed a machine learning architecture, where we use the Kirchhoff diffraction formula to first analytically calculate the spatial phase distribution that is required in an ideal RIS to generate the desired spatial electromagnetic diffraction pattern at the target frequencies of 27 GHz and 31 GHz. At this point, it is important to note that the Kirchhoff formula assumes a RIS with constant, ideal reflection amplitude, which cannot be achieved in our fabricated RIS. For this reason, we pass the calculated phase pattern to a neural network that translates the phase distribution into a unit cell bias voltage distribution of the RIS with the goal to generate an identical electromagnetic diffraction pattern as previously calculated in the ideal case. As an additional constraint, the neural network is only allowed to generate bias voltages within a maximum range that is determined by the used varactor diodes in the RIS. By means of a calibration measurement that relates the applied bias voltage to the corresponding diffraction amplitude and phase from our fabricated RIS at the target

frequencies of 27 GHz and 31 GHz, we can calculate the diffractive amplitude and phase pattern of the RIS from the bias voltage matrix output of the neural network and can again use the Kirchhoff diffraction integral to calculate the resulting electromagnetic field diffraction pattern. In the training, we used a categorical cross-entropy function for the comparison between the ideal field diffraction pattern and the generated field diffraction pattern from the neural network.

With the used method, we were capable of creating bias voltage matrices for the RIS that simultaneously steered the two main lobes of the 27 GHz field pattern and the 31 GHz field pattern continuously between 10° and 45° at will.

The authors acknowledge the financial support by the Federal Ministry of Education and Research of Germany in the project “Open6GHub” (grant number: 16KISK004).

References

1. C. Pan, H. Ren, K. Wang, J. F. Kolb, M. Elkashlan, M. Chen, M. Di Renzo,Y. Hao, J. Wang, A. L. Swindlehurst, X. You and L. Hanzo, “Reconfigurable Intelligent Surfaces for 6G Systems: Principles, Applications, and Research Directions,” IEEE Communications Magazine, vol. 59, No. 6, pp. 14-20, June, 2021.Lastname, F. M. and F. M. Lastname, “Title of the journal paper,” Journal Title Abbreviation, Vol. 34, No. 10, 1064–1076, 1986.
2. A. Wolff, L. Franke, S. Klingel, J. Krieger, L. Mueller, R. Stemler, M. Rahm, “Continuous beam steering with a varactor-based reconfigurable intelligent surface in the Ka-band at 31 GHz,” J. Appl. Phys. vol. 134, pp. 114502-1 – 7, September 2023.
3. A. Wolff et al., "Continuous asymmetric beam steering with a reconfigurable intelligent surface in the Ka-Band at 31 GHz," 2023 48th International Conference on Infrared, Millimeter, and Terahertz Waves (IRMMW-THz), Montreal, QC, Canada, 2023, pp. 1-2, October 2023.

Modelling and design of complex light matter interactions on the nanoscale

L. Ramunno[1*]

[1]Department of Physics and Nexus for Quantum Technologies Institute, University of Ottawa, Canada
[*]corresponding author: lramunno@uottawa.ca

Abstract: Computational electrodynamics is ubiquitous in nanophtonics modelling. I will describe our in-house electrodynamics software that goes beyond usual FDTD, in order to model complex light matter interactions on the nanoscale (including nonlinear and time-dependent materials) as well as our approach to the inverse design of complex light-matter interactions.

End-to-end Nanophotonic Inverse Design for Computational Imaging

Zin Lin[1*]

[1]Bradley Department of Electrical and Computer Engineering, Virginia Polytechnic Institute and State University, Arlington Research Center, 900 N Glebe Road, Arlington VA, 22203, USA
[*]Corresponding author: zinlin@vt.edu

Abstract: We introduce end-to-end inverse design in which a nanophotonics frontend is optimized in conjunction with a computational-imaging backend to minimize reconstruction errors. We present several nanophotonics designs for snapshot multi-dimensional imaging.

Nanophotonics inverse design [1] enhances spatial, spectral and polarization sensitivities by leveraging full-wave Maxwell physics—electromagnetic interactions largely ignored by refractive or diffractive optics. Computational imaging transcends conventional optics by algorithmic reconstruction of high-fidelity information from limited optical measurements. We integrate nanophotonics inverse design and computational imaging into a holistic end-to-end framework: a single-piece nanophotonics frontend is optimized in conjunction with an image-processing backend to minimize reconstruction errors. The optics and computation are tightly coupled because the gradient of the backend error is propagated through the entire pipeline to the physical parameters of the frontend nanophotonics. In contrast to optics-only or computation-only designs, the functionality or the operating principles of the frontend optics is not prescribed *a priori* but *spontaneously* emerges during the end-to-end optimization. Unfettered by human intervention, end-to-end discovery reveals nano-structures with enhanced data-acquisition capabilities and ultra-compact form factors.

A general formulation of our end-to-end framework is described below [2,3,4]:

$$\min_{\varepsilon,\alpha} L(\tilde{u},u) \;\equiv\; \langle ||\boldsymbol{u}-\tilde{\boldsymbol{u}}||^2\rangle_{u,\eta} \tag{1a}$$

$$\tilde{u} = \mathrm{argmin}_{\mu}||\boldsymbol{G}\mu-\boldsymbol{v}||^2 + R(\mu;\alpha) \tag{1b}$$

$$v = Gu+\eta,\; G\sim|E(r_{CCD},\lambda)|^2 \tag{1c}$$

$$\nabla\times\nabla\times E(r)-\omega^2\epsilon(r)\,E(r) = i\omega\,\delta(r-r_{\mathrm{OS}})\hat{p}, \tag{1d}$$

$$\omega=\frac{2\pi}{\lambda},\; \hat{p}\in\{\hat{x},\hat{y},\hat{z}\} \tag{1e}$$

Here, the loss function L is given by the averaged reconstruction error over several training objects u and noise realizations η. For each u, the estimate $\tilde{u}$ is obtained by solving a *nested* minimization problem (commonly known as the inverse scattering problem in computational imaging); the latter seeks to recover u from a raw image v (for example, noise-corrupted readings from a CCD sensor) by minimizing the data-fitting term $\left||G\mu-v|\right|^2$ and an additional regularization function R. The measurement matrix G embodies the imaging optics and can be computed from the electric field intensities $|E|^2$ on the CCD sensor in response to a point dipole $\delta(r-r_{\mathrm{O}})\hat{p}$ at each position within the object space (OS). In our image-formation models, G can vary from convolutional kernels to full dense

matrices. In fact, the richness and complexities of G that arise from the underlying Maxwell equation differentiate our framework from traditional refractive or diffractive optics. In particular, accurate computations of G require detailed simulations of the nanophotonic permittivity $\varepsilon(r)$ as well as the gradient $\nabla_\varepsilon G$ using the full Maxwell equation and its adjoint, taking into account strong spatio-spectral and polarization dispersions. We present several examples to illustrate the capabilities of our framework [2,3,4].

References

1. Sean Molesky, Zin Lin, Alexander Y Piggott, Weiliang Jin, Jelena Vučković, and Alejandro W Rodriguez. Inverse design in nanophotonics. Nature Photonics, 12(11):659, 2018.
2. Zin Lin, Raphael Pestourie, Charles Roques-Carmes, Zhaoyi Li, Federico Capasso, Marin Soljačić, Steven G Johnson. End-to-end metasurface inverse design for single-shot multi-channel imaging. Optics Express, 30(16):28358, 2022.
3. Zin Lin, Charles Roques-Carmes, Raphael Pestourie, Marin Soljačić, Arka Majumdar, and Steven G Johnson. End-to-end nanophotonic inverse design for imaging and polarimetry. Nanophotonics, 10(3):1177–1187, 2021.
4. Gaurav Arya, William F. Li, Charles Roques-Carmes, Marin Soljačić, Steven G. Johnson, and Zin Lin. End-to-End Optimization of Metasurfaces for Imaging with Compressed Sensing. arXiv:2201.12348, 2022.

On the different models of Graphene conductivity and its effects on Casimir forces and on radiative heat transfer in nanostructured systems

Mauro Antezza[1,2]

[1]Laboratoire Charles Coulomb (L2C), UMR 5221 CNRS-University of Montpellier, F-34095 Montpellier, France
[2]Institut Universitaire de France, Ministère de l'Enseignement Supérieur et de la Recherche, 1 rue Descartes, F-75231, Paris, France
[*]corresponding author: mauro.antezza@umontpellier.fr

Abstract: We discuss different available models of graphene conductivity, and graphene effects two main fluctuational electrodynamics effects in nanostructured systems.

We will start discussing three available models of graphene conductivity: a non-local Kubo model, a local model, and finally a non-local Quantum Field Theory based (QFT-b) model [1]. While we confirm that the local model is a proper limit of the non-local Kubo model, we find some inconsistencies in the QFT-b model as derived and used in literature. We show that the inconsistencies of QFT-b model predictions are due to a non-correct regularization-scheme which allows for the gauge invariance violation. We show how to correctly regularize the QFT-b model in order to satisfy the gauge invariance and, once also losses are correctly included, we show that the Kubo and QFT-b model exactly coincide. In the second part we will discuss the effect of graphene through its conductivity and shape on two paradigmatic fluctuation induced phenomena in periodic nanostructured graphene-based nano-systems: the Casimir forces [2] and the radiative heat transfer [3].

References

1. Pablo Rodriguez-Lopez, and Mauro Antezza "Graphene conductivity: Kubo model versus QFT-based model", arXiv:2403.02279 (2024)

2. Youssef Jeyar, Minggang Luo, Kevin Austry, Brahim Guizal, Yi Zheng, H. B. Chan, and Mauro Antezza, "Tunable nonadditivity in the Casimir-Lifshitz force between graphene gratings", Phys. Rev. A 108, 062811 (2023)

3. Minggang Luo, Youssef Jeyar, Brahim Guizal, Junming Zhao, and Mauro Antezza "Effect of the graphene grating coating on near-field radiative heat transfer" Appl. Phys. Lett. 123, 253902 (2023)

Low Dimensional Thermal Radiation

S. Volz[1]

[1]LIMMS/CNRS-IIS(IRL2820)
Institute of Industrial Science, The University of Tokyo
4-6-1 Komaba, Meguro-ku, Tokyo 153-8505 JAPAN

Abstract: Heat carried by Surface Phonon-Polaritons is investigated in thin films with contributions in the range of the one of heat conduction and of the Planck emission.

The Phonons are the quasiparticles of lattice vibrations and represent the primary heat carriers in bulk dielectric materials. The thermal conductivity of dielectric membranes is thus typically driven by acoustic phonons that is usually assimilated to a gas of particles, and generally reduces with the membrane thickness due to the increasing frequency of surface scattering events [1]. In the light of the ever-increasing miniaturization of devices with enhanced rates of operation, this reduction in the thermal conductivity causes overheating, low reliability, and reduced lifetime of electronic components [2–4]. Yet, while the thermal transport via acoustic phonons might be at the limit, the heat dissipation might be enhanced via optical phonons coupled with surface electromagnetic waves.

Over the past decade, substantial research efforts have been devoted to the study of these surface waves, because the surface effects predominate over the volumetric ones in nanostructures with high surface-to-volume ratio. Some types of surface electromagnetic waves may even carry heat [5] and thus improve the thermal performance and stability of nanoscale devices.

One type of such surface waves is the surface phonon-polaritons (SPhPs), which occurs as a hybrid of optical phonons and surface electromagnetic waves. The SPhPs are essentially evanescent waves that propagate along the surface of polar dielectric membranes [6,7].

We will first demonstrate the existence and the properties of those SPhPs in thin SiO2 films and especially uncover that the propagation lengths of those waves reach the range of hundreds of micrometers [8], which is orders of magnitude longer than the typical mean free path of acoustic phonons. Theoretical models predict that such a long propagation length enables SPhPs to conduct more thermal energy than phonons when the membrane thickness is reduced below 100 nm.

We will then corroborate the significant contribution of SPhPs to heat flux in silica membranes [9], in a restricted temperature range and also, in a wide temperature range, in silicon nitride membranes where SPhP thermal conductivity becomes predominant at 800K [10]. An additional confirmation was finally provided by showing the size dependence of thermal conductivity due to the ballistic contribution of SPhP.

This work was supported by the CREST Japan Science and Technology Agency (Grant No. JPMJCR19I1), the JSPS Kakenhi (Grant No. 21H04635).

References

1. P. Nath, K. L. Chopra, “Thermal conductivity of amorphous vs crystalline Ge and GeTe films”. Jpn. J. Appl. Phys. 13,

781, 1974.

2. S. Volz, J. Shiomi, M. Nomura, K. Miyazaki, “Heat conduction in nanostructured materials”. J. Therm. Sci. Technol. 11, JTST0001, 2016.
3. S. Volz, J. Ordonez-Miranda, A. Shchepetov, M. Prunnila, J. Ahopelto, T. Pezeril, G. Vaudel, V. Gusev, P. Ruello, E. M. Weig, M. Schubert, M. Hettich, M. Grossman, T. Dekorsy, F. Alzina, B. Graczykowski, E. Chavez-Angel, J. S. Reparaz, M. R. Wagner, C. M. Sotomayor-Torres, S. Xiong, S. Neogi, D. Donadio, “Nanophononics: State of the art and perspectives”. Eur. Phys. J. B 89, 15, 2016.
4. M. Nomura, J. Shiomi, T. Shiga, R. Anufriev, “Thermal phonon engineering by tailored nanostructures”. Jpn. J. Appl. Phys. 57, 080101, 2018.
5. K. Joulain, J.-P. Mulet, F. Marquier, R. Carminati, J.-J. Greffet, “Surface electromagnetic waves thermally excited: Radiative heat transfer, coherence properties and Casimir forces revisited in the near field”. Surf. Sci. Rep. 57, 59–112, 2005.
6. D.-Z. A. Chen, A. Narayanaswamy, G. Chen, “Surface phonon-polariton mediated thermal conductivity enhancement of amorphous thin films”. Phys. Rev. B 72, 155435, 2005.
7. J. Ordonez-Miranda, L. Tranchant, T. Tokunaga, B. Kim, B. Palpant, Y. Chalopin, T. Antoni, S. Volz, “Anomalous thermal conductivity by surface phonon-polaritons of polar nano thin films due to their asymmetric surrounding media”. J. Appl. Phys. 113, 084311, 2013.
8. S. Gluchko, B. Palpant, S. Volz, R. Braive, T. Antoni, “Thermal excitation of broadband and long-range surface waves on SiO2 submicron films”. Appl. Phys. Lett. 110, 263108, 2017.
9. L. Tranchant, S. Hamamura, J. Ordonez-Miranda, T. Yabuki, A. Vega-Flick, F. Cervantes-Alvarez, J. J. Alvarado-Gil, S. Volz, K. Miyazaki, “Two-dimensional phonon polariton heat transport”. Nano Lett. 19, 6924–6930, 2019.
10. Y. Wu, J. Ordonez-Miranda, S. Gluchko, R. Anufriev, D. De Sousa Meneses, L. Del Campo, S. Volz, and M. Nomura, “Enhanced thermal conduction by surface phonon-polaritons”, Science Advances 6(40):eabb4461, 2020.
11. Y Wu, J Ordonez-Miranda, L Jalabert, S Tachikawa, R Anufriev, H Fujita, S Volz, M Nomura, “Observation of heat transport mediated by the propagation distance of surface phonon-polaritons over hundreds of micrometers”, Applied Physics Letters 121 (11), 112203, 2022.

Duality Gaps in Photonic Inverse Design

S. Molesky

Polytechnique Montréal, Canada
*sean.molesky@polymtl.ca

Abstract: Lagrange duality and semi-definite programming relaxations have been recently employed to bound a variety of photonic design objectives. Here, I will describe why these techniques work so well, and provide limits on how much the associated bounds may differ from an optimal device.

Existence of Friedrich-Wintgen bound states in the continuum in periodically perturbed slabs

Amgad Abdrabou[1], **Wangtao Lu**[2], **and Ya Yan Lu**[3,*]

[1]Elmore Family School of Electrical and Computer Engineering, Purdue University, West Lafayette, USA
[2]School of Mathematical Sciences, Zhejiang University, Hangzhou, China
[3]Department of Mathematics, City University of Hong Kong, Hong Kong, China
*corresponding author: mayylu@cityu.edu.hk

Abstract: Bound states in the continuum (BICs) have been used to improve and enhance many photonic devices, but their existence has only been justified in some special or simple cases. In this paper, we present a general existence theory for Friedrich-Wintgen BICs in a wide class of periodically perturbed slabs.

A bound state in the continuum (BIC) is guided or trapped mode with a frequency in the radiation continuum [1]. Although numerous applications of BICs have been realized, their existence is only proved for a few simple cases or special examples. The appearance of BICs in wave systems are due to a number of different physical mechanisms [1]. The so-called Friedrich-Wintgen (FW) BICs are related to the destructive interference of two resonant modes, but the original work by Friedrich and Wintgen is for a system of three 1D Schrödinger equations [2]. In a photonic system, decomposing a resonant mode as a linear combination of two independent resonant modes is not exact, and the existence of FW-BICs has not been justified rigorously in a general setting.

In this paper, we present a general existence theory for FW-BICs in periodically perturbed slabs. For simplicity, we consider the E polarization for 2D structures with a 1D periodicity. The dielectric function is given by $\epsilon(y,z) = \epsilon_*(z) + \delta F(y,z)$, where ϵ_* describes a slab of thickness $2D$ surrounded by air, F is the perturbation profile (real, periodic in y with minimum period L, even in both y and z, and $F = 0$ if $|z| > D$), and δ is the amplitude of the perturbation. A BIC of frequency ω is a Bloch mode with the x component of the electric field given by $u_{\text{bic}} = \varphi(y,z)e^{i\beta z}$, where φ is periodic in y with period L, $\varphi \to 0$ as $z \to \pm\infty$, $\beta \in [-\pi/L, \pi/L]$, $\omega > c|\beta|$, and c is the speed of light in vacuum. A guided mode of the uniform slab (i.e., $\delta = 0$) with frequency ω_0 can be written as $u_{\text{slab}} = \phi(z)e^{i\beta y} = [\phi(z)e^{i2p\pi y/L}]e^{i\beta_0 y}$, where ϕ is the mode profile (a real function of z), β is the propagation constant, p is an integer such that $\beta_0 = \beta - 2p\pi/L \in [-\pi/L, \pi/L]$. The guided modes form bands, and each band is given by a dispersion relation $\omega_0 = \hat{\omega}_{\text{slab}}(\beta) = \omega_{\text{slab}}(\beta_0; p)$. The dispersion relation for $p \neq 0$ corresponds to a folded band of the slab mode. Two folded bands may cross at a particular point (β_*, ω_*) in the β-ω plane. That is,

$$\omega_* = \omega^{(1)}_{\text{slab}}(\beta_*; p_1) = \omega^{(2)}_{\text{slab}}(\beta_*; p_2), \quad \frac{d}{d\beta_0}\omega^{(1)}_{\text{slab}}(\beta_*; p_1) \neq \frac{d}{d\beta_0}\omega^{(2)}_{\text{slab}}(\beta_*; p_2), \tag{1}$$

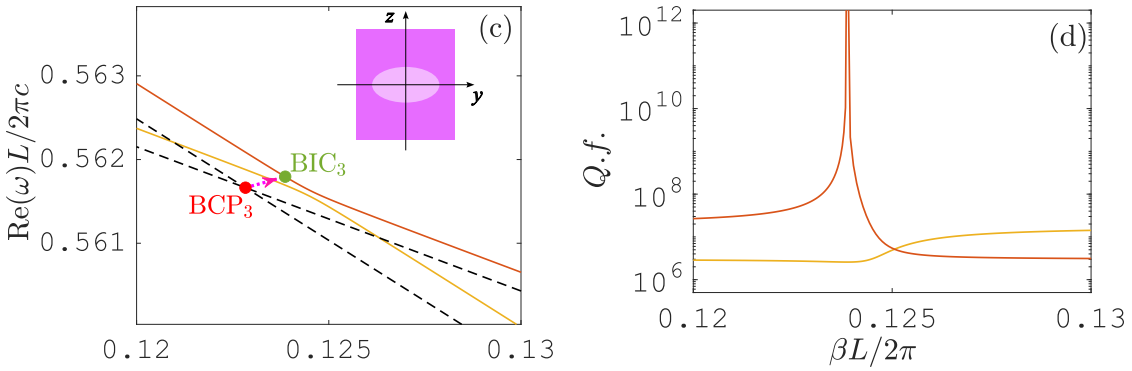
where the superscript (j) for $j = 1, 2$, corresponds to a slab mode with mode profile $\phi^{(j)}(z)$ and propagation constant $\beta^{(j)}$, and p_j is the related folding index. We have the following proposition: *If* (β_*, ω_*) *satisfies*

$$|\beta_*| < \pi/L, \quad |\beta_*| < \omega_*/c < 2\pi/L - |\beta_*|, \tag{2}$$

and is a crossing point of folded bands of two slab modes with the same parity in z, then for any sufficiently small δ near 0 and any perturbation profile F, the perturbed slab has a BIC $\{\varphi, \omega, \beta\}$ with frequency ω near ω_* and Bloch wavenumber β near β_*.

In the above, condition (2) ensures that there is exactly one radiation channel in the positive or negative z direction. The profile F must satisfy the conditions stated in the second paragraph above. Our result guarantees the existence of a BIC for all sufficiently small δ. The BIC depends on δ continuously and tends to a linear combination of the two slab modes at the crossing point as $\delta \to 0$. This is related to the assumptions on F and the robustness of BICs in 2D periodic structures with reflection symmetries in both y and z [3]. The robustness theory also implies that the BIC will continue its existence when $|\delta|$ is increased until (β, ω) fails to satisfy condition (2). Notice that the crossing point is only related to the slab modes and it unrelated to the perturbation profile F. For a small nonzero δ, the perturbed slab has two bands of resonant modes (near the crossing point) given by dispersion relations $\omega = \omega_{\text{res}}^{(j)}(\beta)$, $j = 1, 2$, where β is real and ω is complex. Due to the avoided crossing, $\text{Re}[\omega_{\text{res}}^{(j)}(\beta)]$ (for $j = 1$ or 2) is partially close to $\omega_{\text{slab}}^{(1)}(\beta; p_1)$ and partially close to $\omega_{\text{slab}}^{(2)}(\beta; p_2)$. Our theory implies that there is always a β near β_*, such that the imaginary part of $\omega_{\text{res}}^{(1)}(\beta)$ or $\omega_{\text{res}}^{(2)}(\beta)$ is exactly zero.

As an example, we consider a slab with $\epsilon_*(z) = 11.56$ for $|z| < D = 0.625L$ and a perturbation corresponding to a periodic array of elliptic cylinders. In the yz plane, the cross sections of the cylinders are elliptic disks with a semi-major axis $a = 0.3L$ (along the y axis) and semi-minor axis $b = 0.28618L$. The profile $F(y, z)$ equals -1 or 0, for (y, z) inside or outside the elliptic disks, respectively. In Fig. 1(c), we show two folded bands of the



uniform slab as the dashed lines and a crossing point denoted as BCP_3. For the perturbed slab with $\delta = 0.05$ (the dielectric constant of the elliptic cylinders is $\epsilon = 11.51$), We have two bands of resonant modes near the crossing point, and show $\text{Re}[\omega_{\text{res}}^{(j)}(\beta)]$ (for $j = 1, 2$) as the solid lines and a BIC denoted as BIC_3 in Fig. 1(c). The quality factors, $Q = -0.5\text{Re}[\omega_{\text{res}}^{(j)}(\beta)]/\text{Im}[\omega_{\text{res}}^{(j)}(\beta)]$, of the two bands are shown in Fig. 1(d).

References

1. C. W. Hsu, B. Zhen, A. D. Stone, J. D. Joannopoulos, and M. Soljačić, Bound states in the continuum, *Nat. Rev. Mater.* Vol. 1, 16048, 2016.
2. H. Friedrich and D. Wintgen, Interfering resonances and bound states in the continuum, *Phys. Rev. A*, Vol. 32, 3231–3242, 1985.
3. L. Yuan and Y. Y. Lu, Bound states in the continuum on periodic structures: perturbation theory and robustness, *Optics Letters*, Vol. 42, 4490–4493, 2017.

Design for quality: multifunctional flat optics using metasurfaces

Hanyu Zheng[1], Fan Yang[1], Hung-I Lin[1], Yunxi Dong[2], Hualiang Zhang[2], Juejun Hu[1], Tian Gu[1]

[1]Materials Science and Engineering Dept., Massachusetts Institute of Technology, Cambridge, Massachusetts, USA

[2]ECE Dept., University of Massachusetts Lowell, Lowell, Massachusetts, USA

*corresponding author, E-mail: gutian@mit.edu

***Abstract*—** In this talk, I will discuss the prospects and hurdles of utilizing multifunctional metasurfaces across multiple applications. Leveraging advanced materials and designs, we develop ultra-compact meta-optics with unprecedented performance and new imaging and sensing architectures. The judiciously engineered metasurfaces show significantly lower the size, weight, power and cost (SWaP-C).

META 2024, TOYAMA - JAPAN, JULY 16 – 19, 2024

Second harmonic generation of optical beams with orbital angular momentum on dielectric films and metasurfaces

L. Coudrat[1], D. De Ceglia[2,3], R. Tanos[4], J.-M. Gérard[4], C. De Angelis[2,3], A. Degiron[1], and G. Leo[1,4*]

[1] MPQ, Université Paris Cité and CNRS, France
[2] CNIT and DIE, University of Brescia, Italy
[3] INO, CNR, Italy
[4] Université Grenoble Alpes, CEA, INP, IRIG, PHELIQS, France
[5] Institut Universitaire de France (IUF)

[*]corresponding author: giuseppe.leo@u-paris.fr

Abstract: We report on the generation of second-harmonic vortices with either a uniform film or an optical metasurface, fabricated in a hybrid AlGaAs-on-sapphire platform. In the former case we demonstrate spin-to-orbital angular momentum transfer, while in the latter we generate orbital angular momentum with arbitrary topological charge via a nonlinear meta-hologram.

Calculation of surface state spectra for topological photonic and acoustic crystals

Y. X. Sha[1*], and Y. Yang[1*]

[1] Department of Physics, The University of Hong Kong, Pokfulam, Hong Kong, China
[*]corresponding author: yxsha@hku.hk; yiyg@hku.hk

Abstract: We present efficient algorithms for calculating the surface state spectra of photonic and acoustic crystals, which are highly beneficial in studying topological materials in classical systems.

In recent years, various novel topological surface effects have been experimentally observed in optical and acoustic systems. However, there is currently no ideal method available for calculating the surface state spectrum of such systems, so as to directly compare it with the results of near-field scanning experiments.

The existing method for obtaining surface states in these classical systems involves calculating the eigenvalues of a finite size supercell, which has drawbacks such as large memory consumption and high requirements for absorption boundary. In contrast, the relatively mature method of doing so in electronic systems involves calculating the surface Green's functions (i.e., surface density of states) for a semi-infinite structure, which directly highlights the surface states on a single surface in the spectrum. Moreover, various fast algorithms have been proposed for solving the surface Green's function of electronic materials, effectively reducing the consumption of computational memory. Inspired by this, here we develop various numerical algorithms for calculating the surface density of states in topological photonic and phononic crystals.

Firstly, we will introduce the relationship between the Green's functions and the local density of states (LDOS). The Green's function $\boldsymbol{G}$ for electromagnetic and acoustic waves can be defined as

$$\underbrace{\left[\boldsymbol{X}(\boldsymbol{r})-\omega^2\boldsymbol{Y}(\boldsymbol{r})\right]}_{\boldsymbol{Z}(\boldsymbol{r};\omega)}\boldsymbol{G}(\boldsymbol{r},\boldsymbol{r}';\omega)=\boldsymbol{I}\delta(\boldsymbol{r}-\boldsymbol{r}') \tag{1}$$

where $\boldsymbol{X}$ is the differential operator, $\boldsymbol{Y}$ is the material parameter and $\boldsymbol{I}$ is the unit dyad. The LDOS can be directly derived from the imaginary part of $\boldsymbol{G}$:

$$\mathrm{LDOS}\,(\boldsymbol{r};\omega)=\frac{2\omega}{\pi}\,\mathrm{Im}\left\{\mathrm{Tr}\left[\boldsymbol{Y}\,(\boldsymbol{r})\lim_{\eta\to 0^+}\boldsymbol{G}\,(\boldsymbol{r},\boldsymbol{r};\omega+j\eta)\right]\right\} \tag{2}$$

Next, we will calculate the surface Green's function for a semi-infinite photonic system. If each layer of the photonic crystal is discretized with the same finite element mesh, then the operator $\boldsymbol{Z}$ in Eq. (1) will become a semi-infinite block cyclic tridiagonal matrix, i.e., $\boldsymbol{Z}_{m,m}=\boldsymbol{Z}_{0,0}$, $\boldsymbol{Z}_{m,m+1}=\boldsymbol{Z}_{0,1}$, $\boldsymbol{Z}_{m+1,m}=\boldsymbol{Z}_{1,0}$ (the subscripts represent the layer numbers from the surface). Many efficient algorithms such as cyclic reduction method[1] and transfer matrix method[2] have been proposed to invert such a matrix. These methods deal only with one or two cells of a crystal rather than a large supercell structure, which saves lots of computational memory. They are summarized in Tab. 1 and Tab. 2 in the form of pseudocodes.

Finally, we will verify the effectiveness of our algorithms through a simple example. Fig. 1(a) is a semi-infinite acoustic crystal having two Dirac points and four helicoid surface states protected by the glide symmetries. Fig. 1(c) is the calculated surface density of states, which agrees well with those bands on a single surface in Fig. 1(b). Fig. 1(d)-1(f) are the iso-frequency cuts of the band diagram, which clearly shows the evolution of the surface states near the Dirac point.

Table 1: Pseudocode of cyclic reduction method.

Initialization:
maximum iterations > 0, accuracy > 0
$\alpha_0 = \mathbf{Z}_{0,1}$, $\beta_0 = \mathbf{Z}_{1,0}$, $\zeta_0 = \mathbf{Z}_{0,0}$
$\zeta_0^s = \mathbf{Z}_{0,0}$
for $i = 1$ **to** maximum iterations **do**
  $\alpha_i = \alpha_{i-1}(\zeta_{i-1})^{-1}\alpha_{i-1}$
  $\beta_i = \beta_{i-1}(\zeta_{i-1})^{-1}\beta_{i-1}$
  $\zeta_i = \zeta_{i-1} - \alpha_{i-1}(\zeta_{i-1})^{-1}\beta_{i-1} - \beta_{i-1}(\zeta_{i-1})^{-1}\alpha_{i-1}$
  $\zeta_i^s = \zeta_{i-1}^s - \alpha_{i-1}(\zeta_{i-1})^{-1}\beta_{i-1}$
  if $(\zeta_i^s - \zeta_{i-1}^s)/(\zeta_{i-1}^s) <$ accuracy **then**
    Break
  end
end
$G_{0,0} = (\zeta_i^s)^{-1}$

Table 2: Pseudocode of the transfer matrix method

Initialization:
$T_1 = \begin{pmatrix} \mathbf{0} & I \\ -\mathbf{Z}_{0,1} & \mathbf{0} \end{pmatrix}$, $T_2 = \begin{pmatrix} I & \mathbf{0} \\ \mathbf{Z}_{0,0} & \mathbf{Z}_{1,0} \end{pmatrix}$
Eigenanalysis $T_2 S = T_1 S \Lambda$
\\ sort all the eigenvalues λ and the corresponding eigenvectors s in Λ and S
for $i = 1$ **to** length (T_1) **do**
  for $j =$ length (T_1) **to** $i + 1$ **do**
    if $|\lambda(j)| < |\lambda(j-1)|$ **then**
      swap $\lambda(j)$ with $\lambda(j-1)$
      swap $s(j)$ with $s(j-1)$
    end
  end
end
\\ obtain partitioned $S = \begin{pmatrix} S_1 & S_3 \\ S_2 & S_4 \end{pmatrix}$
$G_{0,0} = \left(\mathbf{Z}_{0,0} + \mathbf{Z}_{0,1} S_2 S_1^{-1}\right)^{-1}$

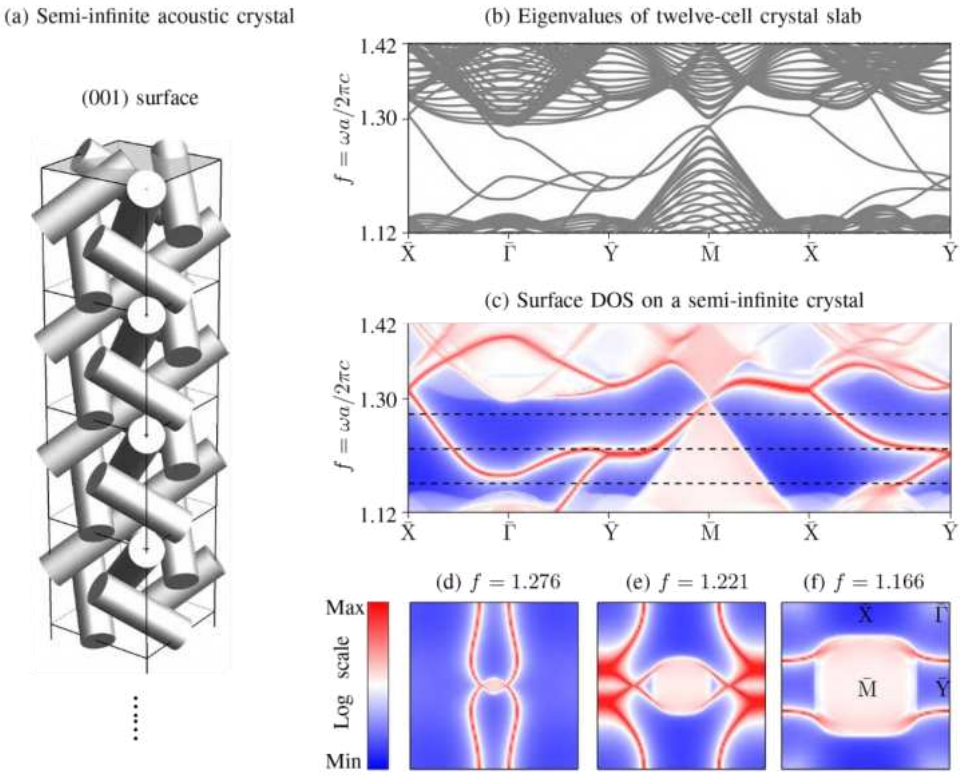


Figure 1: Surface DOS of a semi-infinite Dirac acoustic crystal.

We acknowledge support from the NSFC Excellent Young Scientists Fund (HKU 12222417); the start-up fund of The University of Hong Kong; and an Asian Young Scientist Fellowship.

References

1. M. L. Sancho, J. L. Sancho, J. L. Sancho, and J. Rubio, Highly convergent schemes for the calculation of bulk and surface Green functions, J. Phys. F: Met. Phys. 15, 851 (1985).
2. D. H. Lee and J. D. Joannopoulos, Simple scheme for surface band calculations. II. The Green's function, Phys. Rev. B 23, 4997 (1981).

Modeling the Acousto-Plasmonic Coupling: Raman Energy Density Framework

N. Large[1*], Montaño-Priede[1], and A. Mlayah[2]

[1]Department of Physics and Astronomy, University of Texas at San Antonio, United States
[2]Laboratoire d'Analyse et d'Architecture des Systèmes, CNRS – Université de Toulouse, France
[*]corresponding author: Nicolas.Large@utsa.edu

Abstract: We present a theoretical study of the interactions between confined acoustic phonons and localized surface plasmons in metallic nanoparticles. We introduce a new physical quantity, the Raman energy density, which is a local quantity that serves as a tool for the study of Raman scattering mediated by plasmons in nanoparticles.

Most of the studies focusing on metallic nanoparticles consider them as static bodies at rest. However, localized surface plasmons (LSPs) can be temporally modulated by acoustic vibrations, also known as acoustic phonons, naturally present in the nanomaterial and surrounding environment. Very recently, there has been a renewed interest on the modulation effect of the LSPs by (opto)mechanical modes and elastic waves [1-6]. Such high-frequency (GHz-THz) modulation can be used to increase detection and sensing accuracy of nano-objects and molecules. For instance, these vibrating nanoparticles, acting as simple optomechanical nanoresonators, can be seen as nanoscale analogs to quartz crystal microbalances. Acoustic-phonons Raman scattering is a very effective, high-precision, and non-invasive technique for nanometrology. It uses the acoustic vibrations as local probes to determine sizes and distances at the nanoscale with very high accuracy. However, the effectiveness of this technique is directly related to the knowledge of the interaction mechanisms between electrons (plasmons) and phonons (acoustic vibrations). Therefore, it is necessary to know what are the vibrational modes sustained by a given nanostructure (amplitude, frequency, symmetry) and know how they interact with the LSPs to completely determine the Raman efficiencies and selection rules.

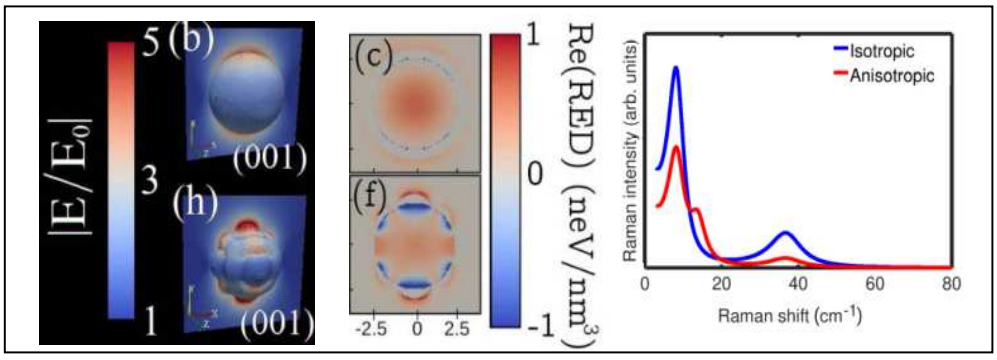


Fig. 1 Left: Isotropic (l=0) and Anisotropic (A_{1g}) breathing acoustic mode of a AuNP modulating the near electric field induced par the dipolar localized surface plasmon (LSP). **Center**: Raman energy density (RED) resulting from the interaction of the l=0 and A_{1g} vibration mode with the dipole LSP. **Right**: Calculated acoustic Raman spectra for the isotropic and anisotropic nanoparticles.

Here, we investigate the dynamic properties of metallic nanoparticles by focusing on the interaction between confined acoustic vibrations and LSPs (**Fig. 1, left**) [5, 7]. The dynamic properties of LSPs are responsible for the transient optical absorption modulation, that can be observed in time-resolved transient absorption experiments [6], and for the acoustic SERS effect [4], We describe the resonant Raman scattering process using a new approach based on a single direct acousto-plasmonic interaction process described by Fermi golden rule [7]. Within this framework, we introduce a new physical quantity, namely, the Raman energy density (RED; **Fig. 1, center**). Similarly to the Raman-Brillouin electronic density (RBED) introduced in semiconducting nanostructures [8, 9], the RED allows for studying and monitoring the acousto-plasmonic Raman scattering in the near-field. We modeled the acousto-plasmonic interaction by implementing vibrational dynamics (resonant ultrasound method, RUS), into electrodynamic calculations (discrete dipole approximation, DDA). We used this methodology to compute the acoustic Raman spectra (**Fig. 1, right**) and investigate the interaction between LSPs and (an)isotropic acoustic vibrations, thus leading to the full determination of Raman efficiencies and selection rules. We show that the RED (**Fig. 1, center**), which can be mapped in the near-field for each vibration mode, correlates the far-field Raman scattering (**Fig. 1, right**) to the local acousto-plasmonic hot spots (**Fig. 1, left**), provides a deeper understanding of the Raman scattering process (*e.g.*, Raman selection rules), and serves to study the acousto-plasmonic coupling of complex nanostructures.

This work received financial support from the U.S. Office of Naval Research (ONR) under Grant No. N00014-21-1-2729.

References

1. A. Ahmed, M. Pelton, and J. R. Guest, "Understanding How Acoustic Vibrations Modulate the Optical Response of Plasmonic Metal Nanoparticles," ACS Nano **11**, 9360-9369 (2017).
2. O. Saison-Francioso, G. Lévêque, and A. Akjouj, "Numerical Modeling of Acousto–Plasmonic Coupling in Metallic Nanoparticles," J. Phys. Chem. C **124**, 12120-12133 (2020).
3. K. O'Brien, N. D. Lanzillotti-Kimura, J. Rho, H. Suchowski, X. Yin, and X. Zhang, "Ultrafast acousto-plasmonic control and sensing in complex nanostructures," Nat. Comm. **5**, 4042-4042 (2014).
4. S. Tripathy, R. Marty, V. K. Lin, S. L. Teo, E. Ye, A. Arbouet, L. Saviot, C. Girard, M. Y. Han, and A. Mlayah, "Acousto-Plasmonic and Surface-Enhanced Raman Scattering Properties of Coupled Gold Nanospheres/Nanodisk Trimers," Nano Lett. **11**, 431-437 (2011).
5. N. Large, L. Saviot, J. Margueritat, J. Gonzalo, C. N. Afonso, A. Arbouet, P. Langot, A. Mlayah, and J. Aizpurua, "Acousto-plasmonic hot spots in metallic nano-objects," Nano Lett. **9**, 3732 (2009).
6. W. M. Deacon, A. Lombardi, F. Benz, Y. del Valle-Inclan Redondo, R. Chikkaraddy, B. de Nijs, M.-E. Kleemann, J. Mertens, and J. J. Baumberg, "Interrogating Nanojunctions Using Ultraconfined Acoustoplasmonic Coupling," Phys. Rev. Lett. **119**, 023901 (2017).
7. J. L. Montaño-Priede, A. Mlayah, and N. Large, "Raman energy density in the context of acoustoplasmonics," Phys. Rev. B **106**, 165425 (2022).
8. N. Large, J. R. Huntzinger, J. Aizpurua, B. Jusserand, and A. Mlayah, "Raman-Brillouin electronic density in short period superlattices," Phys. Rev. B **82**, 075310-075318 (2010).
9. A. Mlayah, J.-R. Huntzinger, and N. Large, "Raman-Brillouin light scattering in low-dimensional systems: Photoelastic model versus quantum model," Phys. Rev. B **75**, 245303-245303 (2007).

Limits and opportunities for nonlinear nanophotonics

Alejandro Rodriguez*

Princeton University, USA
*arod@princeton.edu

Abstract: The ability to tailor light--matter interactions by structuring materials is crucial to a wide range of disciplines, e.g., spectroscopy and quantum communication. Advances in nanofabrication make it possible to investigate optical devices at the fundamental limits of achievable performance --- limited only by available material response and attainable feature sizes. In this talk, we review recent advances and applications of large-scale optimization techniques to nonlinear processes, including limitations on the ability of structuring to control spontaneous emission, second harmonic generation, and Raman scattering in resonant media.

Design and simulation of a metalens-based eye-tracking system

Han-Hsiang (Michael) Cheng[1*], Dan-Nha Huynh[2], Thibault Leportier[3], Jens Niegemann[3], Vlad Smagley[4], Erin Elliot[4] and Allen Cheng[5]

[1]Ansys Japan K.K., Japan
[2]Ansys Germany GmbH, Germany
[3]Ansys Canada Ltd., Canada
[4]Ansys Inc., United States
[5]Ansys Taiwan, Taiwan
[*]Corresponding author: Michael.Cheng@Ansys.com

Abstract

We present a computational workflow that integrates metalens design principles into the classical optical design process. Our approach encompasses the design of phase profiles, meta-atoms, and introduces an innovative method for system-level simulation within a ray-tracing environment. As a practical application, we employ this workflow to develop a metalens-based eye-tracking system, seamlessly embedded within a VR device.

1. Introduction

Recently, an increasing interest in utilizing metalens for various optical systems has been observed due to their lightweight and compact size compared to their traditional equivalents. Some applications require integration of large-scale metalens, usually exceeding hundreds of times the wavelength, into a macro system that often includes refractive optical components. These systems are typically designed and simulated with ray-tracing methods. However, it becomes challenging to simulate metalens in this type of system. Ray-tracing is generally not suitable for simulating sub-wavelength structure, while FDTD or RCWA struggle with the large-scale system. In this paper, we will introduce a new method to simulate metalens with the ray-tracing approach to effectively simulate a metalens within a macro system. To demonstrate this new approach, we will design and demonstrate an eye-tracking system used within a VR pancake system.

2. Ray-tracing method for metalens

In this paper, we propose an innovative method for metalens design workflow where RCWA and ray-tracing are combined for an efficient way to transport nano-scale information into the mm-scale system.

This method requires a pre-calculated database of meta-atom's far field response data, amplitude and phase, for plane wave inputs in different incident angles. The pre-calculation is performed for different types of meta-atom with different geometry. For example, if the meta-atom is a cylinder, we may pre-calculate for different radius and save in the database. The response of each individual meta-atom is computed via the RCWA method with locally periodicity approximation (LPA). Another required data is a meta-atom map, which describes how meta-atom with different geometries are distributed on the metalens substrate. This meta-atom map can be derived from the meta-atom database along with an ideal phase profile that is designed in a ray-tracing process.

With the meta-atom database and a given meta-atom map, we can fully simulate a metalens in a macro system in ray-tracing process. During the ray-tracing, when a ray hits the metalens surface, we consider the ray locally as a plane wave and look up the database for the corresponding response based on the plane wave's incident angle and the corresponding meta-atom type where the ray hits. From the response data, the phase gradient of the output field at the ray position can be derived and the output ray's direction and amplitude is further calculated, as shown in Fig 1.

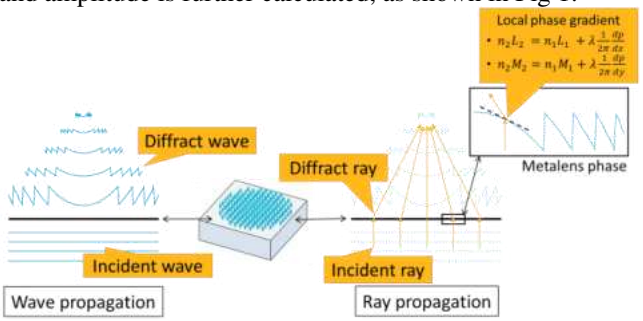


Figure 1: The left side shows how a beam passes through the metalens in viewpoint of wave propagation. The right side shows how the phase gradient data is used to decide the diffract rays. In the picture, (n1, n2) are the refractive index at two sides of the metalens. (L1,M1) and (L2,M2) are direction cosines x and y for incident and diffract rays. λ is wavelength. dp/dx and dp/dy are the phase gradient in x and y directions.

3. System design

The workflow is demonstrated with a metalens-based eye-tracking system, integrated into a compact pancake-style virtual reality (VR) device (as depicted in Fig. 2). The eye-tracking system is constructed using a glass plate with meta-surfaces on both sides (ML1 and ML2 in Fig. 2). Our specific focus lies on pancake-type VR devices, which have gained significant popularity recently. By strategically

positioning the eye-tracking system behind the VR lenses, we achieve an extended optical path, thereby able to capture image of same area around eye with smaller field of view (FOV) requirement. The tradeoff is we them have more aberration to correct because there are two traditional lenses in between the eye-tracking system and the human eye to be imaged.

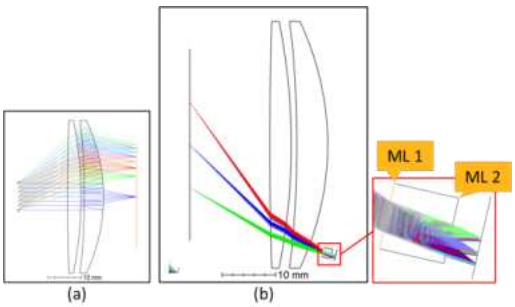


Figure 2: (a) The layout of pancake VR design. (b) The metalens based eye-tracking design embedded in pancake VR system.

The basic specifications and constraints of the system used during the design process are shown as in Table 1.

Table 1: specifications and constraints

Eye box	16 mm x 32 mm
Diameter	< 2 mm
Length	< 4 mm
Wavelength	0.85 µm
Meta-atom size	0.4 µm

3.1. Phase profile

The first step to build the system is to design the ideal phase profile in pure ray-tracing process. The phase profile on the metalens is described in the equation (1). Ai and Bi are the coefficients to be optimized for best image performance.

$$\phi = \frac{2\pi}{\lambda}\left(\sum_{i=1}^{P} A_i r^i + \sum_{i,j=1}^{N,M} B_{i,j} x^i y^j\right) \quad (1)$$

In the equation, the first part in the parentheses is rotationally symmetric phase which focuses light on the image plane and compensates most of on-axis aberrations. The second part, on the other hand, is a freeform phase, which is responsible for compensating for those aberrations caused by the off-axis nature of the system. We use the same equation for both metalenses at the two sides.

At this stage, the main goal is to optimize the coefficients Ai and Bi for the best image quality, which means the smallest spot size for sampling field of view. Note the distortion is not considered during the optimization as they can often be compensated later in the digital post-processing.

During the optimization, it is needed to constraints the phase slope not to be too large. In this design, the meta-atom size is 0.4 µm. Following the Nyquist frequency, it means there should be at least two meta-atoms in every 2π phase change, which corresponds to maximum allowed phase slope of 1/(0.4*2)=1250 mm^-1. However, in this case, the error between ideal phase and phase reproduced by meta-atom can be large. For a better quality, here we choose to constraint the maximum allowed phase slope to be <250 mm^-1, which means there are at least 10 meta-atoms in every 2π phase change on the metalens.

The optimized phase profile and its phase slope are shown in Fig 3. For first metalens, phase slope is stronger in tangential direction and works like a rotationally symmetric lens. The second metalens, on the other hand, has more phase slope in sagittal direction and works more like a freeform lens which compensates off-axis aberrations.

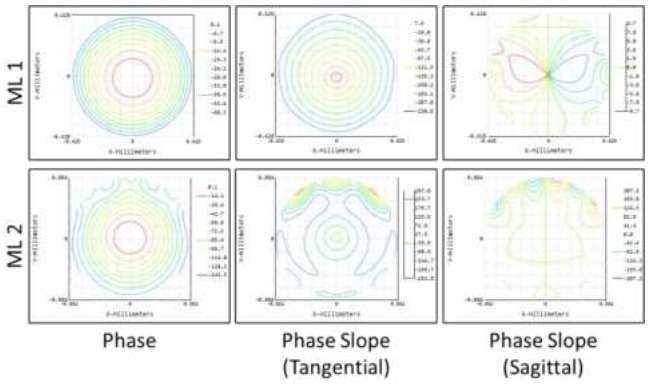


Figure 3: The optimized ideal phase and phase slope for first and second metalens in the system.

3.2. Meta-atom

The next step is to get meta-atom database by scanning the field response of the meta-atom with different incident wave and different geometry. In this design, meta-atom geometry is a simple cylinder pillar. We scan to find how phase varies with different radius and height of the cylinder as shown in Fig 4. The purpose is to find a range of radius, where the corresponding phase delay covers 0 ~ 2π range. In addition, the range of the radius is the larger the better and the minimum radius is 0.05 µm, which we assume is the minimum manufacturable size. Based on the result, we decide to fix the heigh of cylinder to 1.7357 µm and vary radius from 0.072 to 0.165 µm to include a 2π range of phase variation.

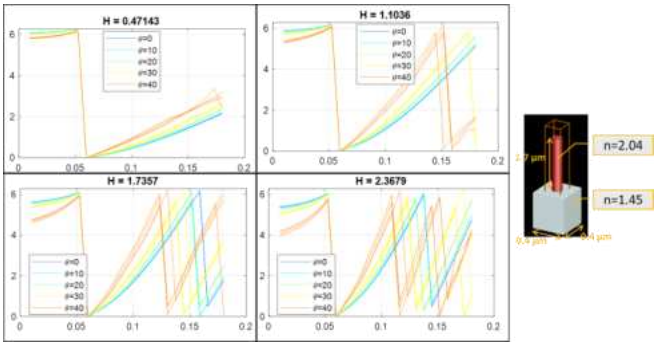


Figure 4: Phase delay introduced by the meta-atom with different cylinder radius. Different color of line corresponds to different incident polar angle, where azimuthal angle is fixed to 0 degree, as shown in the legend. Different sub plots show results with different cylinder height.

A more detailed analysis of the selected meta-atom is shown in Fig 5. where the results are shown for both phase and amplitude. The results for first and second metalens are also shown. The response of the two metalenses are different because the light is incident from different side.

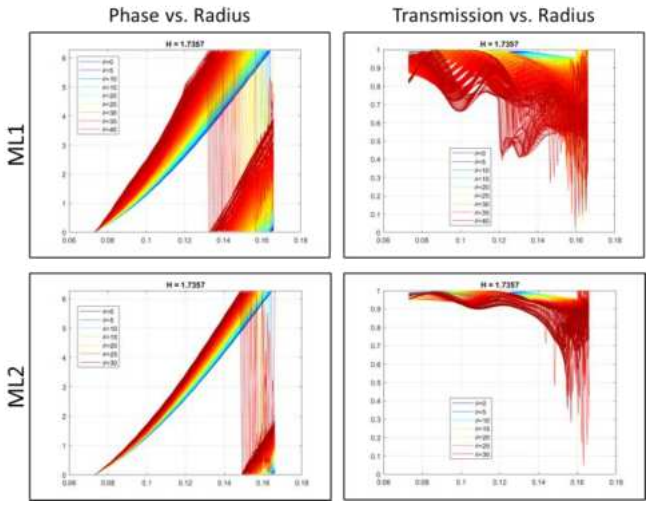


Figure 5: Phase delay and amplitude transmission introduced by the meta-atom with different cylinder radius for first and second metalens. Different color of line means different incident polar angle. For same color, there can be several lines, which correspond to different incident azimuthal angles.

It is worth mentioning that the manufacturable cylinder radius can be discrete depending on fabrication method. Thus, the generatable phase delay is also discrete. In this paper, it's assumed that the minimum phase difference between two different meta-atoms is 1 degree. This will be the source of imperfections of the metalens, as will be shown in the next section.

3.3. Macro-scale system simulation with ray-tracing method

As explained in section 2, the ideal phase created in section 3.1 and the meta-atom database generated in section 3.2 are then loaded into a ray-tracing engine by a plugin for a system-level simulation.

4. Simulation result

4.1. System performance

After applying the phase profile and the meta-atom database, the ray-tracing result shows a similar result to ideal phase but with worse performance, as shown in Fig. 6. It can also be seen that the spot size is larger with our metalens model than the result with ideal phase in Fig. 7. This is expected as the metalens cannot perfectly reproduce the designed phase, which introduces error to the diffract rays.

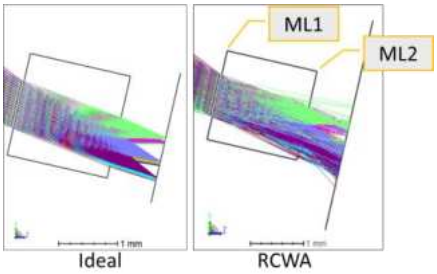


Figure 6: Layout of ray-tracing result between ideal phase and exact phase from RCWA.

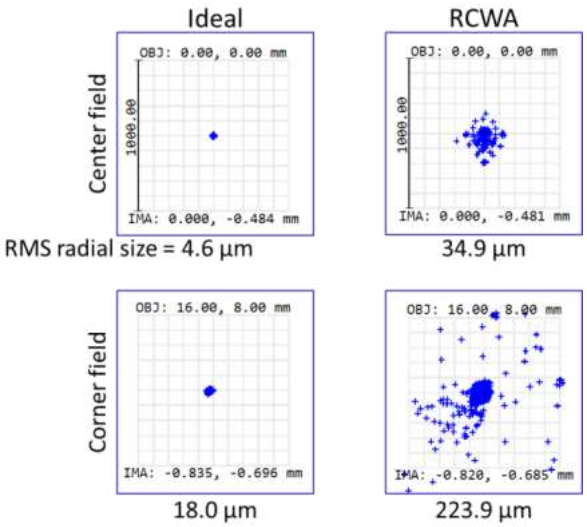


Figure 7: Spot diagram for center field and corner field with ideal and RCWA phase profile.

4.2. Image simulation

In addition to efficiency in large scale system, another benefit of ray-tracing method is the ability of doing image simulation. The result of image simulation for ideal phase and the metalens model are shown in Fig. 8. As expected, the distortion is significant because they are not considered during optimization. The image with metalens model is more blurred than image with ideal phase as the metalens doesn't perfectly reproduce the phase. It can also be seen the relative illumination is lower and the image is less sharp at the corner of the image. This is as expected because, at larger incident angle, the amplitude transmission of the meta-atom is lower and the phase error is larger.

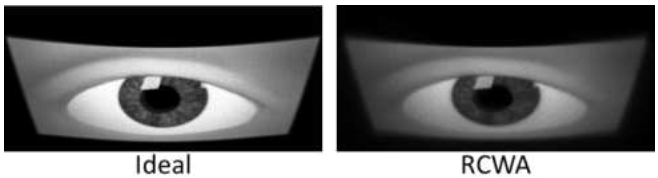


Figure 8: Image simulation result with ideal and RCWA phase profile.

5. Conclusions

We introduced a new method to simulate metalens with ray-tracing. This method requires a meta-atom database, pre-

calculated in RCWA, and a meta-atom map describing how meta-atoms are distributed on the metalens substrate. The database and the meta-atom map are loaded in ray-tracing engine to handle the metalens response. To demonstrate the method, a metalens-based eye-tracking system built in a pancake VR lens system are designed and simulated with this new method. We have compared the spot diagram and image simulation results between using ideal phase and our metalens model. It can be observed that the result with the metalens model shows similar but worse performance compared to ideal phase model, as expected.

References

[1] J. Niegemann, D. Huynh, A. Reid, H. (M.) Cheng, E. Elliot, F. Gomez, and J. Pond, "Design and Simulation of Large-Scale Metalenses," in Frontiers in Optics + Laser Science 2023 (FiO, LS), Technical Digest Series (Optica Publishing Group, 2023), paper FTu6D.5.

[2] Z. Zhu, Z. Liu, and C. Zheng, "Metalens enhanced ray optics: an end-to-end wave-ray co-optimization framework," Opt. Express 31, 26054-26068 (2023)

Chiro-optical and chiral-acoustic phenomena

TiO_2 Nanoantenna Stickers for Fabricating Large-Area Twisted Metamaterials with Tunable Chiroptical Effects

Jiayang He [1], Shunsuke Murai[1*], Tienyang Lo[1], Katsuhisa Tanaka[1 *]

[1]Kyoto university, Japan
[*] murai@dipole7.kuic.kyoto-u.ac.jp

Abstract: Twisted metamaterials, created by stacking and twisting two achiral nanostructured layers exhibit chirality. We propose a simple method employing nanoantenna stickers to fabricate such metamaterials, achieving precise control of giant circular dichroism via twist angle adjustment with the largest effect at 22.5°, holding promise for chiral optics and sensing development.

1. Introduction

Chiral metamaterials, known for their chiroptical effects, exhibit asymmetric responses to left- and right-circularly polarized light, resulting in higher circular dichroism (CD) compared to natural materials[1,2]. Currently, some chiral metamaterials, exemplified by helices[3], offers inherent handedness, but their 3D nanostructure fabrication can be complex [2].

In this study, we present a novel chiral metamaterial composed of two identical achiral TiO_2 nanoantenna stickers stacked together. Its chiroptical response is precisely tunable by varying the in-plane rotation angle or twist angle between the sticker layers, yielding some CD spectra varied with the twist angle.

2. Results and discussion

The TiO_2 nanoparticles array is embedded into a transparent, flexible PDMS substrate to create stickers that are reusable and handled with ease (Fig. 1). Then we stick a pair of identical TiO_2 nanoantenna stickers with a twist angle in between (Fig. 2a-c). The transmission intensities for the right- (I_R) and left- (I_L) circularly polarized light were measured, and the CD value, defined as CD = $(I_R - I_L) / (I_R + I_L)$ was plotted as a function of incident angle (Fig. 2d, e). The flip of the sign of the CD signal is notable between the twist angles in opposite directions. The flip was further compared at normal incidence (Fig. 2f).

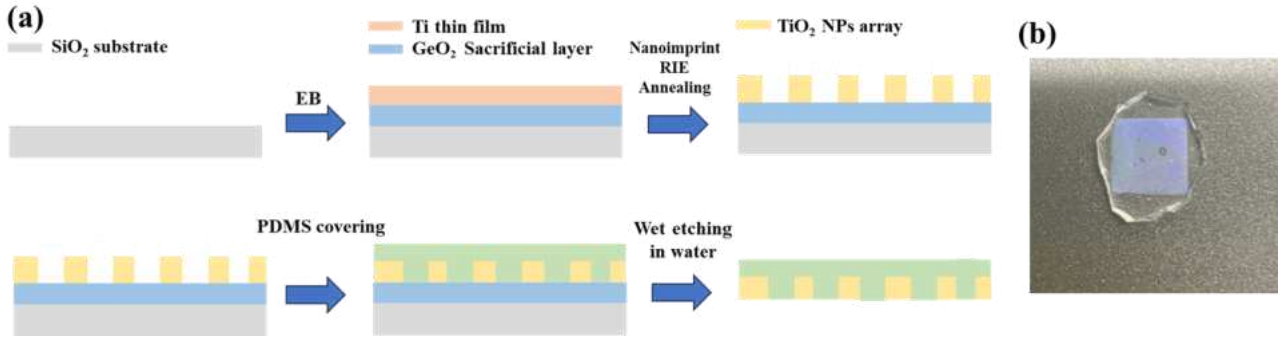


Fig. 1. (a) TiO_2 nanoantenna sticker is fabricated by nanoimprint on a sacrifice GeO_2 layer and reactive ion etching of Ti thin film followed by thermal oxidation, next, the TiO_2 array is covered with a PDMS film and transferred onto the PDMS layer by dissolving the underlying GeO_2 film in water. (b) Photograph of TiO_2

nanoantenna sticker.

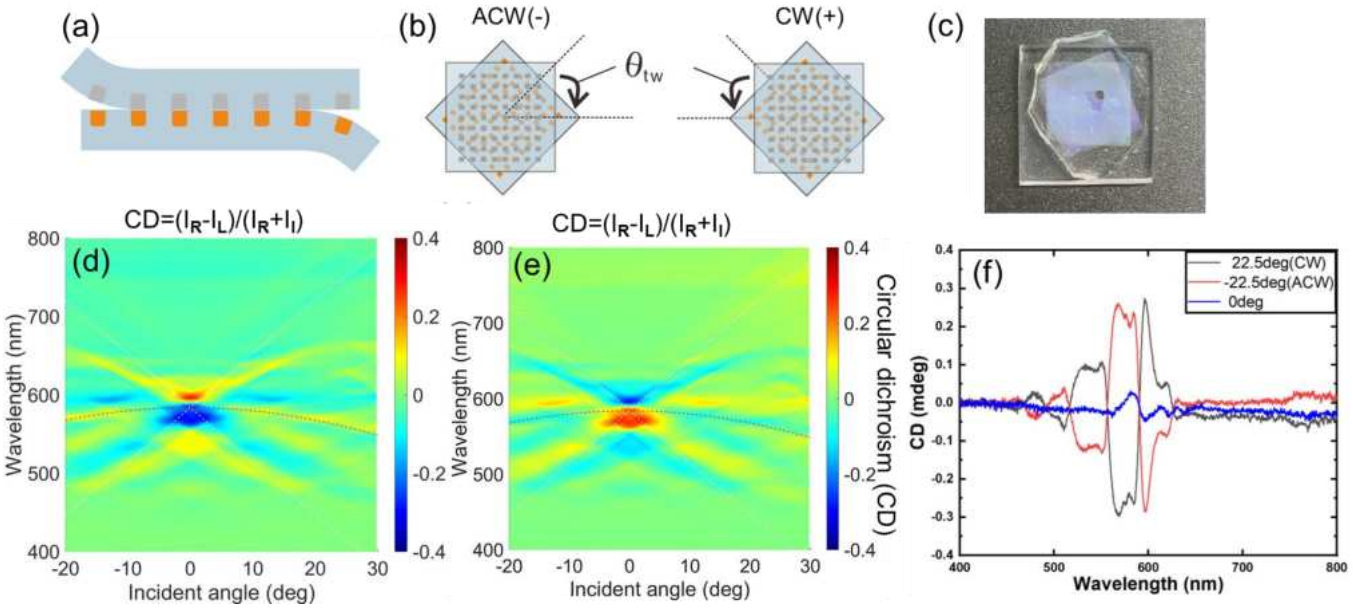


Fig. 2. (a-c) The sketch(a) and photograph (c) of the twisted metamaterial configuration composed of two identical nanoantenna stickers adhered to each other. (b) illustrates the definition of the twist angle. The incident angle dependence of the CD values at twist angles of 22.5° (d) and -22.5° (e) is depicted. CD spectra of (f) the stacked stickers with twist angles of 0 and ±22.5° at normal incidence.

3. Conclusion

The TiO_2 nanoantenna stickers embedded in PDMS were successfully fabricated through a series of treatments such as heat treatment and transfer technology and can be utilized as chiral metamaterial.

The CD results for the stacked identical stickers exhibit dependence on incident angles, revealing symmetry in CD response intensity for equal clockwise (CW) and anticlockwise (ACW) rotations.

References

1. Wu, Zilong, and Yuebing Zheng. "Moiré chiral metamaterials." Adv. Opt. Mater., Vol. 5, No. 16, 1700034, 2017.
2. Hentschel, M., Schäferling, M., Duan, X., et al. "Chiral plasmonics." Sci. Adv., Vol. 3, No. 5, e1602735, 2017.
3. Gansel, J. K., Latzel, M., Frölich, A., et al. "Tapered gold-helix metamaterials as improved circular polarizers." Appl. Phys. Lett., Vol. 100, No. 10, 2012.

Directional sources realized by toroidal dipoles

Junho Jung[1], Yuqiong Cheng[1], and Shubo Wang[1,2*]

[1]Depaartment of Physics, City University of Hong Kong, Tat Chee Avenue, Kowloon, Hong Kong, China
[2]City University of Hong Kong Shenzhen Research Institute, Shenzhen, Guangdong, China
[*]corresponding author: shubwang@cityu.edu.hk

Abstract: We demonstrate that toroidal dipole can be applied to realize three new types of directional sources: pseudo-circular dipole, pseudo-Huygens dipole, and pseudo-Janus dipole. These directional sources exhibit near-field directional behavior analogous to conventional directional sources, while they provide more degrees of freedom to tune the directionality.

It is well known that circularly polarized dipole, Huygens dipole, and Janus dipole can give rise to near-field directional coupling along a waveguide due to its intriguing properties associated with spin, power flow, and reactive power. [1] These directional dipole sources are composed of electric and/or magnetic dipoles. There is another type of dipole source called a toroidal dipole, which has analogous properties and the same far-field radiation pattern as an electric dipole.[2] Here, we demonstrate numerically and analytically that the toroidal dipole can replace an electric dipole component of the conventional directional dipole sources to achieve the same near-field directional coupling along a silicon waveguide. Moreover, we find that the directionality can be controlled by changing the geometric parameters of the toroidal dipole, leading to tunable asymmetric coupling between the dipole sources and the waveguide. These new types of directional sources provide more degrees of freedom to tailor the directionality compared to conventional sources. Furthermore, we demonstrate that we can optimize a toroidal dipole component of the pseudo sources to obtain the unidirectional coupling. This novel approach suggests a new way to design directional light sources and directional optical devices, which can be applied to on-chip optical routing, waveguiding, and nanophotonic communications.

References

1. Picardi, M. F., Zayats, A. V., & Rodríguez-Fortuño, F. J. (2018). Janus and Huygens Dipoles: Near-field directionality beyond spin-momentum locking. *Physical Review Letters*, *120*(11).
2. Miroshnichenko, A. E., Evlyukhin, A. B., Yu, Y. F., Bakker, R. M., Chipouline, A., Kuznetsov, A. I., Luk'yanchuk, B., Chichkov, B. N., & Kivshar, Y. S. (2015). Nonradiating anapole modes in dielectric nanoparticles. *Nature Communications*, *6*(1).

Robust chiral optical force for small chiral molecules

Robert P. Cameron[1*], Duncan McArthur[1], and Alison M. Yao[1]

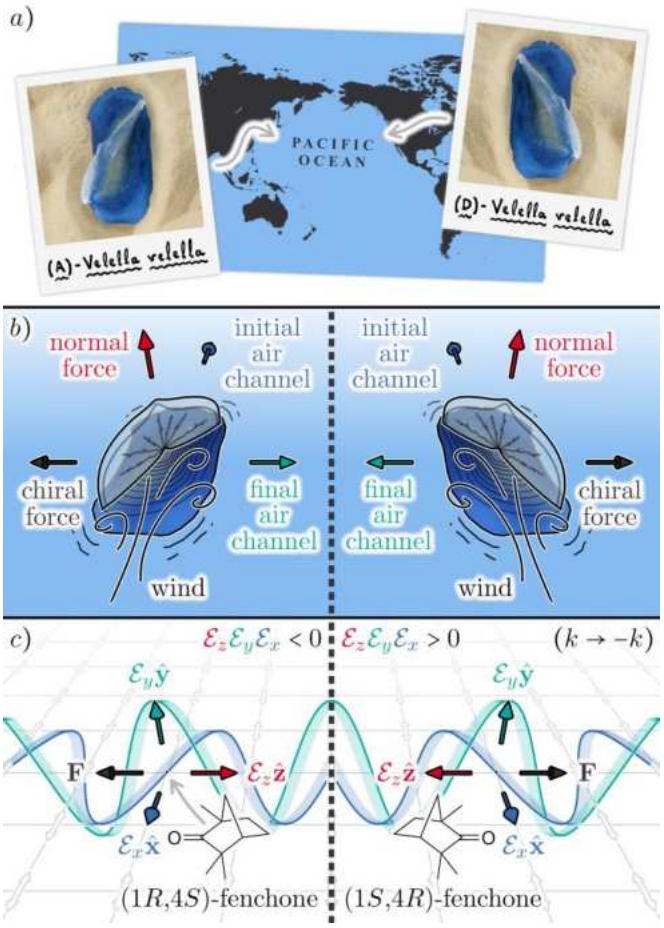
[1] SUPA and Department of Physics, University of Strathclyde, Glasgow G4 0NG, United Kingdom

[*]corresponding author: robert.p.cameron@strath.ac.uk

Abstract: We draw inspiration from nature to identify a robust chiral optical force for small chiral molecules that can be several orders of magnitude stronger than other chiral optical forces proposed to date. Potential applications range from chiral molecular matter-wave interferometry to the resolution of enantiomers.

Interest is growing in the possibility of an optical force that discriminates between the enantiomers of a small chiral molecule. Such a force could find use in a wealth of potential applications, however the chiral optical forces proposed to date are extremely weak, as they rely on magnetic-dipole and electric-quadrupole interactions.

Drawing inspiration from a remarkable chiral force found in nature for the "by-the-wind sailor" *Velella velella*, we show that a static electric field combined with a linearly polarized travelling wave and a lin⊥lin standing wave can exert a chiral optical force on small chiral molecules that is several orders of magnitude stronger than other chiral optical forces proposed to date, being based on leading electric-dipole interactions rather than relying on weak magnetic-dipole and electric-quadrupole interactions.



The two distinct mirror-image forms of *Velella velella* are found on opposite sides of the Pacific a), having been separated by the wind b). Our chiral optical force is constructed by analogy c).

Our chiral optical force applies to most small chiral molecules, including isotopically chiral molecules, and does not require a specific energy-level structure. Potential applications range from chiral molecular matter-wave interferometry for precision metrology and tests of fundamental physics to the resolution of enantiomers for use in chemistry and biology.

This work was supported by RPC's Royal Society University Research Fellowship (URF/R1/191243).

References

1. Cameron, R. P., D. M. McArthur and A. M. Yao, "Strong chiral optical force for small chiral molecules based on electric-dipole interactions, inspired by the asymmetrical hydrozoan *Velella velella*," New J. Phys., Vol. 25, 083006, 2023.

Acoustic Fullerene Metamaterials

Danwei Liao[1], Jingyi Zhang[2], Shuochen Wang[1], Zhiwang Zhang[1], Alberto Cortijo[3], Maria A. H. Vozmediano[3], Francisco Guinea[4], Ying Cheng[1], Xiaojun Liu[1] and Johan Christensen[2*]

[1]Department of Physics, MOE Key Laboratory of Modern Acoustics,

Collaborative Innovation Center of Advanced Microstructures,

Nanjing University, Nanjing 210093, China

[2]IMDEA Materials Institute, Calle Eric Kandel, 2, 28906 Getafe, Madrid, Spain

[3]Instituto de Ciencia de Materiales de Madrid,

CSIC, Cantoblanco, E-28049 Madrid, Spain

[4]IMDEA Nanociencia, C/Faraday 9, 28049 Madrid, Spain

Abstract: In this contribution we focus on various acoustic analogies of carbon allotropes and discuss their topological origins and characteristics. Through theoretical insight, numerical studies, and experimental verifications we demonstrate acoustic examples with their various nontrivial confinements.

Ultrafast topological phase switching of non-Hermitian photonic metasurfaces

Sangha Lee[1], Donghak Oh[2], Junho Park[2], Soojeong Baek[1], Fabian Rotermund[2], Bumki Min[1,2*]
[1]Department of Mechanical Engineering, Korea Advanced Institute of Science and Technology, Republic of Korea
[2]Department of Physics, Korea Advanced Institute of Science and Technology, Republic of Korea
[*]corresponding author: bmin@kaist.ac.kr

Abstract: In this work, we report ultrafast switching of topological phases in a time-varying system both numerically and experimentally, using FDTD simulations and optical-pump terahertz-probe (OPTP) spectroscopy.

Topological phase transitions are typically observed at Dirac or Weyl points in Hermitian systems but often manifest at exceptional points (EPs) in non-Hermitian systems, where eigenvalues and eigenstates coalesce concurrently [1]. While EPs in time-invariant systems have been extensively elucidated, the characteristics of Eps in time-varying contexts remain comparatively underexplored [2-3]. In this work, we prepare a non-Hermitian metasurface on a gallium arsenide (GaAs) substrate for the observation of ultrafast topological phase switching. Through the utilization of optical pumping, we achieve instantaneous modulation of material loss, a phenomenon attributed to the photoexcited carriers in the GaAs substrate. In a time-invariant situation, where input frequency and pump power were controlled, we identify an EP where the transmission coefficient for right- to left-circularly polarized light approaches zero. By pumping the metasurface with varying input frequencies and pump-probe delay, we demonstrate ultrafast traversal past the EP on a subpicosecond scale. Our findings are corroborated through finite-difference time-domain (FDTD) simulations and optical-pump terahertz-probe (OPTP) measurements. This work not only confirms the presence of EPs but also introduces an innovative approach for ultrafast topological phase switching.

References

1. Baek, S. et al. Non-Hermitian chiral degeneracy of gated graphene metasurfaces. Light Sci Appl 12, (2023).
2. Li, S. et al. Exceptional point in a metal-graphene hybrid metasurface with tunable asymmetric loss. Opt Express 28, 20083 (2020).
3. Chen, W., Özdemir, Ş. K., Zhao, G., Wiersig, J. & Yang, L. Exceptional points enhance sensing in an optical microcavity. Nature 548, 192–195 (2017).

Directional manipulation of guided light by anisotropic chirality

Yuqiong Cheng [1], Kayode Adedotun Oyesina [2], Bo Xue [2], Dangyuan Lei [3], Alex M. H. Wong[2,4*], and Shubo Wang [1,5*]

[1]Department of Physics, City University of Hong Kong, Hong Kong, China
[2]Department of Electrical Engineering, City University of Hong Kong, Hong Kong, China
[3]Department of Materials Science and Engineering, City University of Hong Kong, Hong Kong, China
[4]State Key Laboratory of Terahertz and Millimeter Waves, City University of Hong Kong, Hong Kong, China
[5]City University of Hong Kong Shenzhen Research Institute, Guangdong, China
[*]corresponding author: alex.mh.wong@cityu.edu.hk; shubwang@cityu.edu.hk.

Abstract: We theoretically and experimentally construct a complete near-field directionality space by the synergy of chirality and anisotropy. An anisotropic chiral particle can serve as a directional dipole dice, achieving all types of directional dipoles via different "faces" of the particle and realizing face-multiplexed and high-dimensional routing of guided light.

Near-field optical directionality plays an essential role in almost every aspect of photonics and plasmonics. The most elemental system with this property is the class of directional dipoles, including circular dipole, Huygens dipole, and Janus dipole. Their unified realization are highly desirable for developing compact and multifunctional directional sources and switches. Here, we propose a general physical mechanism, the synergy of chirality and anisotropy, for unifying all three dipole types in one structure at the same frequency under the linearly polarized plane wave excitations. This mechanism enables a simple helix particle to generate different directional dipoles on different "faces", corresponding to a directional dipole dice (DDD). To understand the underlying physics, we apply the mode expansion analysis to reveal the origin of the DDD. The emergence of directional dipoles is attributed to the selective excitation of orthogonal chiral and achiral eigenmodes by tuning the incidence. To demonstrate the light-manipulation ability of the DDD, we employ three "faces" of the helix to realize the face-multiplexed and high-dimensional control of directional coupling to a dielectric waveguide in the infrared regime. Different dipole faces generate different types of optical directionalities in different orthogonal directions based on three degrees of freedom: spin, power flow, and reactive power. The phenomena are experimentally verified in the microwave regime using a copper helix placed near waveguides. The results can find promising applications in photonic integrated circuits, quantum information processing, and subwavelength-resolution imaging.

Acknowledgements: The work described in this paper was supported by the National Natural Science Foundation of China (No. 11904306) and grants from the Research Grants Council of the Hong Kong Special Administrative Region, China (Project Nos. C6013-18G, CityU 11301820, and AoE/P-502/20).

References

1. Y. Cheng, K. A. Oyesina, B. Xue, D. Lei, A. M. H. Wong, and S. Wang, "Directional dipole dice enabled by anisotropic chirality," Proc. Natl. Acad. Sci. U.S.A., Vol. 120, No. 25, e2301620120, 2023.

Peculiar wave transports in elastic valley-chiral phononic crystal plates

Weitao Yuan[1*], Jinfeng Zhao[2]

[1]Applied Mechanics and Structure Safety Key Laboratory of Sichuan Province, School of Mechanics and Aerospace Engineering, Southwest Jiaotong University, Chengdu, Sichuan 610031, People's Republic of China

[2]School of Aerospace Engineering and Applied Mechanics, Tongji University, 100 Zhangwu Road, Shanghai 200092, People's Republic of China

[*]corresponding author: weitao_yuan@swjtu.edu.cn

Abstract: We report on the peculiar behavior of waves in elastic valley-chiral phononic crystal plates, including the multi-branch topological edge states (TES) in one single devices, the transversely symmetric and antisymmetric feature of TES, the abnormal refractions, and etc. These wave behaviors provide efficient path to precisely control the wave transports.

The topological edge states (TES) have attracted great interest in optical[1], acoustic[2] and elastic[3] wave fields in recent years, due to the robustness against defects and the spin dependent wave transports. The TES with excellent features have arisen novel path to design phononic devices which possess good functionalities. Usually, the TES can be realized by mimicking the quantum Hall effect, quantum spin Hall effect, and etc. Particularly, the valley degree of freedom[1, 3] provides a convenient way to design topological devices, i.e., valley-chiral devices, however without either the complicated design of structures or the precise control of systems.

The TES in valley-chiral PC plates feature rich behaviors. For example, the valley PC plate can support multi-branch TES in one single device[4, 5], which provides multiple operating frequency bands to increase the information capacity or bandwidth of the device, and also the topological protection to enhance device stability. The valley TES also feature the transversely symmetric and antisymmetric property attributing to the valley chirality, which can tune the wave couplings and refractions[4, 6]. The transversely symmetric and antisymmetric property is efficient to control the connection between the topological PC waveguide and the external field, e.g., control the intensity of the waves coupled into the waveguide or the refraction of the outgoing waves. Besides, the valley-chiral TES can be combined with the rainbow effect, i.e., topological rainbow effect, which will benefit from both the backscattering immunity of TES and the special-spectral control of rainbow effect. The peculiar wave behaviors in valley-chiral PC plates are of great benefit to the control of wave transports, and are prospective to enrich the potential applications in wave and communication communities.

References

1.Zeng, Y.Q., et al., *Electrically pumped topological laser with valley edge modes.* Nature. Vol.**578**: 246-250. 2020

2.He, C., et al., *Acoustic topological insulator and robust one-way sound transport.* Nature Physics. Vol.**12**: 1124-1128. 2016

3.Zhang, Q.C., et al., *Gigahertz topological valley Hall effect in nanoelectromechanical phononic crystals.* Nature Electronics. Vol.**5**: 157-163. 2022

4.Yuan, W., et al., *Multi-branch valley-chiral edge states of antisymmetric plate wave in phononic crystal plates with double-sided symmetric pillars.* International Journal of Mechanical Sciences. Vol.**197**: 106347. 2021

5.Yuan, W., et al., *Observation of triple-branch valley topological edge states and abnormal refraction in elastic phononic crystal plates.* International Journal of Mechanical Sciences. Vol.**264**: 108825. 2024

6.Yuan, W., et al., *Theoretical and experimental demonstrations of the transversely symmetric and antisymmetric properties of topological edge states.* Journal of Physics D: Applied Physics. Vol.**56** No.44: **445305**. 2023

Chiral Plasmonic Structures as Acoustoplasmonic Transducers

B. Castillo López de Larrinzar[1], C. Xiang[2], E. R. Cardozo de Oliveira[2], N.D. Lanzillotti-Kimura[2] and A. García-Martín[1]*

[1]Instituto de Micro y Nanotecnología IMN-CNM, CSIC (CEI UAM+CSIC), Tres Cantos, Madrid, Spain
[2]Centre de Nanosciences et de Nanotechnologies, Université Paris-Saclay, Palaiseau, France
*corresponding author: a.garcia.martin@csic.es

Abstract: The study demonstrates that absorption and scattering cross sections can be qualitatively different for two circular polarizations. Thus, the dominating cross section, absorption/scattering, changes with the polarization of the beam. This allows coherent phonon generation and detection by separating absorption and scattering *for the same wavelength* using the appropriate helicity.

Summary

The possibility of creating and manipulating nanostructured materials encouraged the exploration of new strategies to control electromagnetic properties. Among the most intriguing nanostructures are those that respond differently to helical polarization, i.e., exhibit chirality.[1] Circularly polarized light can be used to probe and determine the chiral nature of a plasmonic structure, which is usually reflected as quantitative differences in the values of the absorption or scattering cross-sections. However, reaching maximum absorption and minimum scattering for one helicity, and the opposite for the other is not usually found to occur at the same wavelength.[2] In the present work, we propose a simple chiral plasmonic structure based on crossed elongated bars where light-handedness defines the dominating cross-section absorption or scattering, as it identifies the two different enantiomers in a chiral structure which determine how the system interacts with its environment. The system is yet maintained simple enough to understand the actual nature of the response observed, be open to future developments, and warrant fabrication for future experimental verification [3,4]. Based on this structure, our work demonstrate that, not only through the interactions between different elements it is possible to make the absorption and scattering cross-sections radically and qualitatively different for the two circular polarizations, but also that the dominating cross-section can be switched from absorption to scattering by simply changing the polarization of the impinging beam. Also, we theoretically propose a simple pump-probe experiment using circularly polarized light. [5] In the reported structures, the generation of acoustic phonons is optimized by maximizing the absorption, while the detection is enhanced at the same wavelength -and different helicity- by engineering the scattering properties [6]. Thus, the presented results constitute one of the first steps towards harvesting chirality effects in the design and optimization of efficient and versatile acoustoplasmonic transducers.

References

1. Barron, L. D., Molecular Light Scattering and Optical Activity, Cambridge, Cambridge Univeristy Press, (2004)
2. Hopkins, B., et al., Laser Phot. Rev. 10, 137 (2016)
3. Auguié, B., et al., J. Phys. Chem. Lett. 2, 846 (2011)
4. de Dios, C., et al., Opt. Express 27, 21142 (2019)
5. Castillo López de Larrinzar, B., et al., Nanophotonics 12, 1957 (2023)
6. Lanzillotti-Kimura, N. D., et al., Phys. Rev. B 83, 201103 (2011)

Chiral phonon-originated nonreciprocal phenomena in magnets

Y. Nii

Institute of Materials Research, Tohoku University, Japan
*corresponding author: yoichi.nii.c1@tohoku.ac.jp

Abstract: Surface acoustic wave (SAW) devices serve a versatile platform in both classical and quantum technologies, gaining increasing prominence in modern research. This work unveils a novel facet of SAW phenomena – the manifestation of nonreciprocal responses arising from the coupling between phonon and spin angular momentum.

In media without spatial inversion symmetry, acoustic modes may adopt chirality, involving a circulating motion of the lattice [1]. Surface acoustic wave (SAW), where spatial inversion symmetry is inherently broken at the surface, stands out as the archetypal platform that provides a circular eigenmode known as the Rayleigh-wave. Owing to the superposition of the longitudinal and transverse modes, Rayleigh-SAW inherently possesses nonzero phonon angular momentum [1]. Analogous to electronic states with broken spatial inversion symmetry, the direction of phonon angular momentum varies with the SAW momentum $\boldsymbol{k}$. Consequently, various $\boldsymbol{k}$-dependent responses may emerge in SAW when coupled with magnetism.

This study presents experimental demonstrations of the $\boldsymbol{k}$-dependent, nonreciprocal phenomena of SAW using magnetoelastic devices implemented on a $LiNbO_3$ piezoelectric substrate. Initially, we show nonreciprocal propagation of SAW [2], where the transmission amplitude varies upon reversing the propagation direction. Subsequently, we elucidate the inverse effect of nonreciprocity [3], where magnetization of ferromagnetic Ni was deterministically controlled by SAW. Finally, we show nonreciprocal SAW diffraction, characterized by the asymmetric intensity of upward and downward scattered SAWs, achieved by a periodic array of magnetoelastic nanowires on a SAW device [4]. We discuss that transfer of angular momentum between phonon and spin systems is pivotal in all these phenomena. Our experimental demonstrations highlight the importance of chiral phonon states, opening avenues for further advancement of SAW-based technologies across diverse applications, including microwave communications and quantum engineering applications.

This work was supported by JSPS KAKENHI (JP20K03828, JP 21H01036, JP 22H04461), PRESTO (JPMJPR19L6), and FOREST (JPMJFR2133).

References

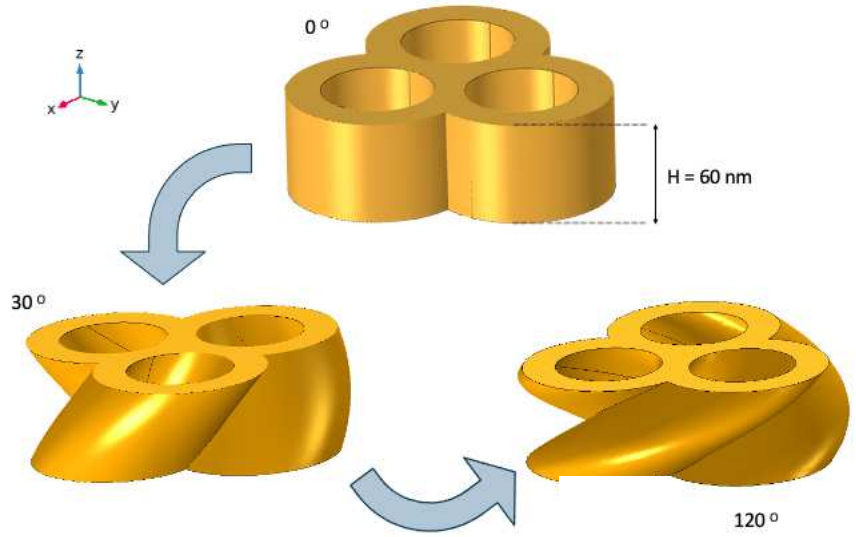
1. L. Zhang and Q. Niu, Phys. Rev. Lett. **112**, 085503 (2014)
2. R. Sasaki, Y. Nii, Y. Iguchi, and Y. Onose, Phys. Rev. B, **95**, 020407(R) (2017)
3. R. Sasaki, Y. Nii, and Y. Onose, Nat. Commun., 12 2599 (2021)
4. Y. Nii, K. Yamamoto, M. Kanno, S. Maekawa, and Y. Onose, *submitted*.

Photonic and phononic characterization of twisted acoustoplasmonic nanostructures

B. Castillo López de Larrinzar[1,*], Jorge García Martínez[1], C. Xiang[2], E. R. Cardozo de Oliveira[2], N.D. Lanzillotti-Kimura[2] and A. García-Martín[1]

[1]Instituto de Micro y Nanotecnología IMN-CNM, CSIC (CEI UAM+CSIC), Tres Cantos, Madrid, Spain
[2]Centre de Nanosciences et de Nanotechnologies, Université Paris-Saclay, Palaiseau, France
[*]corresponding author: beatriz.castillo@csic.es

Abstract: The excitation of modes in structures depends on the spatial profile of the acoustic eigenmodes and the optics of the system. In this work we present a system that is composed of a twisted metallic propeller-like structure, that give rise to the excitation of new optical and acoustic modes.



Summary

Simple acoustoplasmonic resonators, such as nanobars and crosses, are efficient light-hypersound transducers.[1] The excitation of hypersonic modes in these structures strongly depends on the spatial profile of the acoustic and plasmonic eigenmodes and the optical properties of the system's resonances.[2] Lately, it has been made possible to selectively excite and detect phonon modes via plasmon resonances at the same frequency using chiral nanostructures and circularly polarized light.[3] In this work the structure to be analyzed is a metallic propeller-like structure, based in a three lobed perforated clover whose top face is twisted with respect to the bottom one. Only for the twisted cases the structure becomes chiral, leading to an optical response that depends on the helicity of the impinging beam. Having handedness-dependent absorption and scattering cross-sections unlocks an invaluable tool to decouple the generation and detection of coherent acoustic phonons in nanostructures. Furthermore, the plasmon-phonon transduction is an extremely useful tool for launching phonons. If the symmetry characteristics of the plasmon is transferred to the phonon launching, then the phonons to be excited in the

substrate are expected to present a chiral profile. Moreover, the presence of the twisting angle gives rise to the excitation of non-conventional phononic modes. Herewith, we will present a comprehensive theoretical analysis of the phononic and plasmonic modes alongside their surface deformation field and electromagnetic field profiles.[4]

References

1. Ultrafast acousto-plasmonic control and sensing in complex nanostructures, K O'Brien, ND Lanzillotti-Kimura, J Rho, H Suchowski, X Yin, X Zhang Nature communications 5, 4042, (2014)
2. Polarization-controlled coherent phonon generation in acoustoplasmonic metasurfaces, ND Lanzillotti-Kimura, KP O'Brien, J Rho, H Suchowski, X Yin, X Zhang Physical Review B 97, 235403, (2018)
3. Towards chiral acoustoplasmonics, B. Castillo López de Larrinzar, C. Xiang, E.R. Cardozo de Oliveira, N.D. Lanzillotti-Kimura, and A. García-Martín. Nanophotonics, 12, 1957-1964 (2023).
4. B. Castillo López de Larrinzar, C. Xiang, J. M. García, N.D. Lanzillotti-Kimura, and A. García-Martín, (to be submitted 2024)

How can planar become chiral? Maximum-chiral optics with flat metasurfaces

M.V. Gorkunov[1*], A.A. Antonov[1,2], and Y.S. Kivshar[3]

[1] Shubnikov Institute of Crystallography, NRC "Kurchatov Institute", Moscow 119333, Russia
[2] Chair in Hybrid Nanosystems, Ludwig-Maximilians-University of Munich, Munich 80539, Germany
[3] Nonlinear Physics Centre, Research School of Physics, Australian National University, Canberra ACT 2601, Australia
[*]corresponding author: gorkunov@crys.ras.ru

Abstract: Dielectric metasurfaces are game-changing platform for chiral optics. Designs relying on mirror symmetry breaking by variable height or elevation of meta-atoms are technologically inconvenient. We consider optical chirality of flat metasurfaces including extrinsic-chiral single-layered and intrinsic-chiral multilayered ones, and especially focus on the effects of mirror symmetry breaking by substrates.

Metasurfaces built as subwavelength arrays of meta-atoms made of highly refracting materials manifest versatile high-quality photonic resonances. Recently, it was understood that they offer a game-changing platform for chiral optics: unprecedented strong optical chirality can be realized if the resonant eigenstates are adjusted for selective interaction with circularly polarized waves. To date, the known examples of chiral eigenstate engineering rely on combinations of perturbations breaking the in-plane and out-of-plane mirror symmetries in order to isolate a particular state from waves of one circular polarization incident on one or both metasurface sides. Inconveniently for practice, most designs require variable meta-atom elevation [1] or height [2,3]. From the practical viewpoint, structures feasible for conventional lithographic processing of flat layers are much more attractive. Lithography is capable of producing precisely shaped holes and slits with vertical walls in layers of constant thickness. The resulting structures on their own, however, inevitably retain a mirror symmetry plane, and the lack of geometric chirality substantially limits the optical chirality.

There are different ways of achieving strong optical chirality using dielectric metasurfaces made of flat layers. One is to employ the phenomenon of extrinsic chirality, when the mirror symmetry plane is broken not at the structural level but by the optical setup. In such case, maximum-chiral transmission and reflection of light waves occurs if the corresponding eigenstates selectively interact with obliquely incident waves of a particular circular polarization. Remarkably, this can be achieved in meta-atoms of such simple shapes as triangular silicon particles [4].

Alternatively, the planar mirror symmetry can be lifted if flat meta-atoms are made of stacks of layers of transparent materials having different refractive indexes. Then the displacement current density of photonic quasi-bound states in the continuum becomes asymmetrically distributed within the multilayered structure. By carefully adjusting the parameters of meta-atom shape and the thickness of different layers, one can isolate a state from waves of a particular circular polarization to achieve the maximum intrinsic chirality

Finally, the planar mirror symmetry is formally broken in all lithographically cut metasurfaces supported by a substrate as long as its refractive index is different from the rest of the environment. This is rarely recognized as an important factor, as the substrate effects on metasurface optics typically remain subtle. We demonstrate, however, that it is possible to maximize the intrinsic optical chirality of a flat metasurface on substrate relying on peculiar hybridization of photonic eigenstates. In the absence of substrate, such states possess spatial parity and equally strongly contribute to the transmission and reflection of left and right circularly polarized waves. When

placed upon a substrate, the states merge into peculiar hybrids with chiral distributions of the displacement current, and, therefore, underpin sharp peaks of circular dichroism with close-to-maximum optical chirality. The metasurface remains transparent to waves of one circular polarization and resonantly blocks those of the opposite polarization.

As all discussed realizations of maximum chirality rely on selective excitation of high-quality photonic eigenstates, they can be straightforwardly employed for various chiral light transformations desired for emerging applications. For example, the extrinsic chiral metasurface stacked with an ordinary metal mirror forms an optical cavity selectively coupled to obliquely incident circularly polarized waves, which can serve as an ultracompact source of chiral light [4]. Reciprocally, maximum chiral structures made of emerging optoelectronic materials can be used in sensitive detectors of chiral light. As the excitation of high-quality chiral eigenstates is accompanied by enhancement of near-fields by orders of magnitude, they pave the way for numerous nonlinear-optical chiral light transformations including the harmonic generation [5].

Support from the Russian Science Foundation (project 23-42-00091) is gratefully acknowledged.

References

1. Gorkunov, M. V., A. A. Antonov, and Y. S. Kivshar, “Metasurfaces with maximum chirality empowered by bound states in the continuum,” Phys. Rev. Lett., Vol. 125, No. 9, p. 093903, 2020.
2. Gorkunov, M. V., A. A. Antonov, V. R. Tuz, A. S. Kupriianov, and Y. S. Kivshar, “Bound states in the continuum underpin near-lossless maximum chirality in dielectric metasurfaces,” Adv. Optical Mater., Vol. 9, No. 19, p. 2100797, 2021.
3. Kühner, L., F. J. Wendisch, A. A. Antonov, J. Bürger, L. Hüttenhofer, L. de S. Menezes, S. A. Maier, M. V. Gorkunov, Y.S. Kivshar, and A. Tittl, “Unlocking the out-of-plane dimension for photonic bound states in the continuum to achieve maximum optical chirality,” Light Sci. Appl. Vol. 12, No. 1, p. 250, 2023.
4. Kim, S., S.-C. An, Y. Kim, Y.S. Shin, A.A. Antonov, I.C. Seo, B.H. Woo, Y. Lim, M.V. Gorkunov, Y.S. Kivshar, J.Y. Kim, Y.C. Jun, “Chiral electroluminescence from thin-film perovskite metacavities”, Sci. Adv., Vol. 9, p. eadh0414, 2023.
5. Antonov, A., M. Gorkunov, and Y. Kivshar, “Chiral Harmonic Generation by Quasi-Bound States in the Continuum”, in: 2023 Seventeenth International Congress on Artificial Materials for Novel Wave Phenomena (Metamaterials)., IEEE, Chania, Greece, p. X-013-X–015, 2023.

Circularly-Polarized Light for Probing and Controlling Spins and Magnetization in Atomically-Thin Materials

M. H. D. Guimaraes[1*]

[1]Zernike Institute for Advanced Materials, University of Groningen, The Netherlands
[*]corresponding author: m.h.guimaraes@rug.nl

Abstract:
Two-dimensional materials provide an exciting platform for studying spin-dependent (chiral) light-matter interaction. In this talk I will show how (chiral) light can be used to control the spin accumulation and magnetization in two-dimensional magnets and semiconductors.

Summary:
Van der Waals (vdW) materials are ideal systems to probe how spins and magnetism behave in low dimensions since they maintain their excellent optical, magnetic and electronic properties down to the atomically-thin limit. Because of their low dimensionality, these materials possess another exciting property, they are extremely sensitive to external stimuli, such as light and electric fields.

In this talk, I will give a brief introduction to vdW two-dimensional semiconductors and magnets, particularly focusing on their (chiral) light-matter interaction. I will also show how we can use time-resolved magneto-optical Kerr effect (TR-MOKE), a technique able to detect the differences in the index of refraction for the two helicities of light, to probe the spin and magnetization dynamics in these materials.

I will then present our recent results which show how (ultrashort) circularly-polarized light pulses can be used to excite a spin accumulation in two-dimensional semiconductors [1,2], and how we can use magnetic fields to control the dynamics of this spin accumulation [3]. I will also show examples on how the magnetization of vdW magnets can be similarly controlled and probed using ultrashort laser pulses [4]. Particularly, I will focus on the material $Cr_2Ge_2Te_6$, for which we demonstrated that linearly-polarized light pulses can be used to apply a magnetic torque on the magnetization [5]. These light-induced magnetic torques can be effectively controlled using electric fields and be turned on and off at will through electrostatic gates.

Our studies illustrate the potential of vdW materials for combining optics, spintronics and magnetism, making them appealing for new opto-spintronic and opto-magnetic device architectures for future integrated photonic systems.

Acknowledgements
This research has been funded by the Dutch Research Council (NWO) through grants STU.019.14 and OCENW.XL21.XL21.05, the Gravitation program financed by the Dutch Ministry of Education, Culture and Science (OCW) QuMat (024.005.00), the European Union through the ERC grant 2D-OPTOSPIN (101076932), and the Zernike Institute for Advanced materials of the University of Groningen. The device fabrication and nanocharacterization were performed using Zernike NanoLabNL facilities.

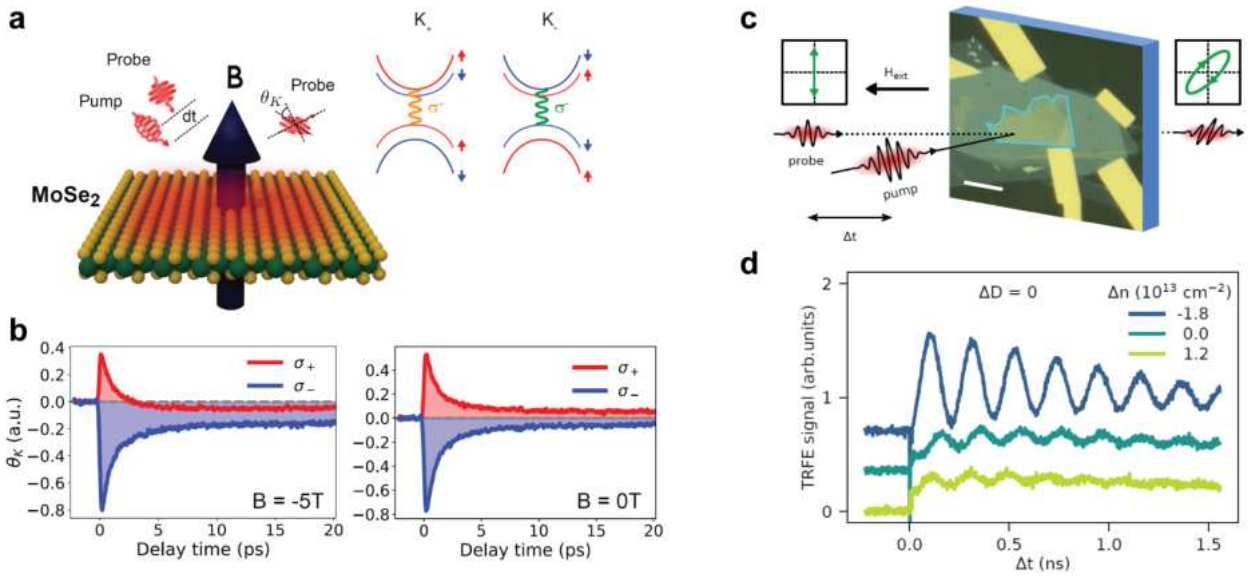


Figure 1: (a) Time-resolved magneto-optical Kerr effect for probing spins in a two-dimensional semiconductor. The spin accumulation is generated with circularly-polarized light. **(b)** The dynamics of the spin accumulation – probed using the Kerr rotation of a linearly-polarized probe pulse – can be manipulated using an out-of-plane magnetic field. **(c)** A similar optical pump-probe technique can be used to study the dynamics of a two-dimensional ferromagnet, where a linearly polarized pump-pulse applied a torque on the magnetization, which then precesses around an applied magnetic field. **(d)** The initial torque and subsequent magnetization dynamics can be tuned using electrostatic gating. Panels (a) and (b) are adapted from reference 3 and panels (c) and (d) are adapted from reference 5.

References

1. M.H.D. Guimarães, and B. Koopmans, "Spin accumulation and dynamics in inversion-symmetric van der Waals crystals", Phys. Rev. Lett. 120, 266801 (2018).
2. C.M. Gilardoni, F. Hendriks, C.H. van der Wal, and M. H. D. Guimarães, "Symmetry and Control of Spin-Scattering Processes in Two-Dimensional Transition Metal Dichalcogenides", Phys. Rev. B 103, 115410 (2021).
3. R.R. Rojas-Lopez, F. Hendriks, C. H. van der Wal, P. S. S. Guimarães, and M. H. D. Guimarães, "Magnetic Field Control of Light-Induced Spin Accumulation in Monolayer $MoSe_2$", 2D Materials 10, 035013 (2023).
4. T. Lichtenberg, C. F. Schippers, S. C. P. van Kooten, S. G. F. Evers, B. Barcones, M. H. D. Guimarães, and B. Koopmans, "Anisotropic Laser-Pulse-Induced Magnetization Dynamics in van der Waals Magnet Fe_3GeTe_2", 2D Materials 10, 015008 (2022).
5. F. Hendriks, R. R. Rojas-Lopez, Bert Koopmans, and M. H. D. Guimarães, "Electric control of optically-induced magnetization dynamics in a van der Waals ferromagnet", Nature Communications, in press.

Far-field and near-field chirality in plasmonic metamolecules

T. Aoudjit[1], F. Lamaze[1], J. Béal[1], A. Hmima[1], W. d'Orsonnens[1], T. Maurer[1], J. Plain[1], J. Proust[1], D. Gérard[1*]

[1]Light, nanomaterials, nanotechnologies (L2n), Université de Technologie de Troyes & CNRS UMR 7076, Troyes, France
[*]corresponding author: davy.gerard@utt.fr

Abstract: We study metamolecules consisting of coupled metallic nanoparticles. We show that the local field dissymmetry under left- and right-handed circular polarization can be directly imaged using a photopolymer. Then, we show experimentally that both the far- and near-field chirality can be controlled by fabricating the metamolecules onto a stretchable substrate.

Although optical chirality is generally studied in the far field, many interesting chiral effects occur in the near field. For example, in plasmonic metamolecules (i.e., complex nanostructures using metal nanoparticles as elementary building blocks), chirality can appear due to the complex interplay between the coupled nanoparticles. This leads to the existence of "hidden chirality" in otherwise achiral nanostructures [1] and to the appearance of "chiral hot spots", which can be switched on and off depending on the handedness of the exciting light [2]. Near-field characterization of chiral plasmonic nanostructures is however more difficult, and relies on advanced tools such as near-field microscopy or cathodoluminescence. Here, we take advantage of a photochemical imaging technique allowing us to directly probe the dissymmetry of the electromagnetic near-field around chiral nanostructures. Our approach is demonstrated using coupled gold nanorods as a simple chiral metamolecule [2].

Then, using a more complex chiral geometry, we show that chirality can be engineered by fabricating the metamolecule onto a stretchable substrate. Under the application of strain, the metamolecule undergoes deformation, leading to a significant change in its chiroptical response. This mechanically-induced changes are experimentally tracked both in the far-field (using circular dichroism measurements) and in the near-field (using photochemical imaging)

References

1. Horrer, A., Zhang, Y., Gérard, D., Béal, J., Kociak, M., Plain, J. and Bachelot, R. "Local optical chirality induced by near-field mode interference in achiral plasmonic nanostructures," Nano Lett., Vol. 20, 509–516, 2020.
2. Aoudjit, T., Horrer, A., Kostcheev, S, Bachelot, R., Plain, J. and Gérard, D. "Photochemical Imaging of Near-Field and Dissymmetry Factor in Chiral Nanostructures," Adv. Opt. Mater., Vol. 11, 2203015, 2023.

1D and 2D topological solitons in nanoelectromechanical resonator arrays

Hiroshi Yamaguchi[1*], Daiki Hatanaka[1], Motoki Asano[1], and Samer Houri[1#]

[1]NTT Basic Research Laboratories, NTT Corporation, Kanagawa 243-0198, Japan
[*]corresponding author: hrsh.yamaguchi@ntt.com

Abstract: We theoretically and numerically demonstrate 1D and 2D coupled parametric resonator arrays generating a topological soliton in its rotating-frame phase space. The topological soliton can be implemented by using electromechanical resonators in both 1D and 2D systems providing a fully controlled on-chip test bed for the study of a topological soliton.

Topological soliton is a commonly observed stable excitation in various nonlinear dynamical systems. In a one-dimensional (1D) system, for example that described by Sine-Gordon equation [1], the topological soliton is the boundary between two identical, but topologically distinguished phase domains, generated as a zero-mass Goldstone mode by the spontaneous breaking of translational symmetry. Its annihilation requires an energy to overcome the phase rotation and the existence is energetically protected by the topological properties. As has been widely demonstrated in the system of topological insulators, importing the concept of topology into artificial 2D lattice systems, such as photonics, microwave, and acoustics structures, is promising to open up new directions in device and material technologies based on the topologically robust properties. In this invited talk, we present our theoretical and numerical works that demonstrate 1D and 2D topological solitons using the arrays of parametric resonators. The key idea is to use quadrature variables, i.e. the sine and cosine oscillation amplitudes, in parametric oscillation to define the phase of dynamical variables. In 1D system, the boundary between 0-phase and π-phase parametric oscillation shows the feature of topological solitons and the motion can be driven by the electromechanical harmonic actuation of resonators [2]. In 2D system, four quadrature components in the square array of doubly degenerate circular membrane resonators play as the similar role as magnetic moments in ferromagnetic systems and the numerical simulation shows that the texture of skyrmion, which is one of the most important 2D topological solitons, can be generated by the parametric excitation. We performed a FEM calculation to prove the feasibility using realistic device designs [3]. In both 1D and 2D cases, we also discuss the robustness against the frequency fluctuation of resonator arrays.

This work was partially supported by JSPS KAKENHI Grant-in-Aid for Scientific Research (JP21H05020 and JP23H05463).

References

1. J. Rubinstein, “Sine‐Gordon Equation”, J. Math. Phys. Vol. 11, 258-266, 1970.
2. H. Yamaguchi and S. Houri, “Generation and propagation of topological solitons in a chain of coupled parametric-micromechanical-resonator arrays”, Phys. Rev. Applied Vol. 15, 034091-1-12, 2021
3. H. Yamaguchi, D. Hatanaka, and M. Asano, “Quadrature skyrmions in two-dimensionally arrayed parametric resonators”, Phys. Rev. Research Vol 5, 043076-1-11, 2023.

[#] Present address: imec, Leuven, Belgium

Valley pseudospin polarized transports of ultrahigh frequency phonons in topological ring-waveguide coupled systems

D. Hatanaka[1]*, H. Takeshita[2], M. Kataoka[2], H. Okamoto[1], K. Tsuruta[2], and H. Yamaguchi[1]

[1]NTT Basic Research Laboratories, NTT Corporation, Japan
[2]Department of Electrical and Electronic Engineering, Okayama University, Japan
*corresponding author: daiki.hatanaka@ntt.com

Abstract: We investigate propagation characteristics of microwave phonon waves in valley topological ring and waveguide coupled systems. The coupled system sustains valley polarization of phonons so that we successfully excite resonant vibrations in wavelength-scale micro-rings without significant backscattering. The results indicate capability of the topological technology to finely manipulate phonons.

Phonons are elementary excitations of lattice vibrations in solids and are being recognized for their capability as one of the next generation information carriers. In particular, acoustic phonons at microwave frequencies (> 0.3 GHz) possess short wavelength and radiation-free structures compared with electromagnetic waves at similar frequencies [1]. Therefore, establishing their control technology and understanding their propagation dynamics can lead to development of miniaturized and high-performance microwave devices for application of wireless communications and quantum technologies [2]. However, they are susceptible to micro and nanoscale structural disturbance and defects which induce backscattering, thus generating undesired spatial and spectral wave localization and hampering their stable operations.

We utilize topological technology to operate wavelength-scale fundamental circuits composed of phononic ring and waveguide [3]. Ultrahigh frequency phonon waves propagate in a boundary between two phononic crystals with different valley Hall phases and the valley pseudospin polarized waves are immune to backscattering due to time-reversal symmetry. As results, we successfully observe resonant oscillations in tiny phononic rings by their spectral response and spatial mapping measurements. Furthermore, the valley preserved ring circulations interfere to phonons with the same valley propagating in the evanescently coupled waveguide, which enables the phonon transmission efficiency to be regulated by the ring resonator. Our findings provide a proof of the capability of topological technology for dealing with microwave phonons and constructing their integrated systems, which are useful for microwave information processing applications.

This work was partially supported by JSPS KAKENHI(S) Grant Number JP21H05020 and JP23H05463.

References

1. Shah, T., Brendel. C., Peano. V., and Marquardt. F. “Topologically Protected Transport in Engineered Mechanical Systems,”arXiv:2206:12337.
2. Qiao. H. *et al*., “Splitting phonons: Building a platform for linear mechanical quantum computing,”Science, Vol. 380, 1030–1033, 2023.
3. Hatanaka., D. Takeshita. H., Kataoka. M. Okamoto. H. Tsuruta. K., and Yamaguchi. H., “Evanescently coupled topological ring-waveguide systems for chip-scale ultrahigh frequency phononic circuits,” arXiv:2310:04008

Non-reciprocal coupling between chiral phonons and magnons in ferromagnetic-semiconductor hybrid structures

A. Hernández-Mínguez[1*], F. Macià[2], J. M. Hernàndez[2], J. Herfort[1] and P. V. Santos[1]

[1]Paul-Drude-Institut für Festkörperelektronik, Leibniz-Institut im Forschungsverbund Berlin e.V., Hausvogteiplatz 5-7, 10117 Berlin, Germany

[2]Dept. of Condensed Matter Physics, University of Barcelona, Martí i Franquès 1, 08028 Barcelona, Spain

[*]corresponding author: hernandez-minguez@pdi-berlin.de

Abstract: We demonstrate a high degree of non-reciprocity for surface acoustic waves (SAWs) at GHz frequencies propagating in an epitaxial ferromagnetic layer. The non-reciprocal behavior depends on the relative chirality between the SAW strain field (phonons) and spin waves (magnons) in the ferromagnetic film.

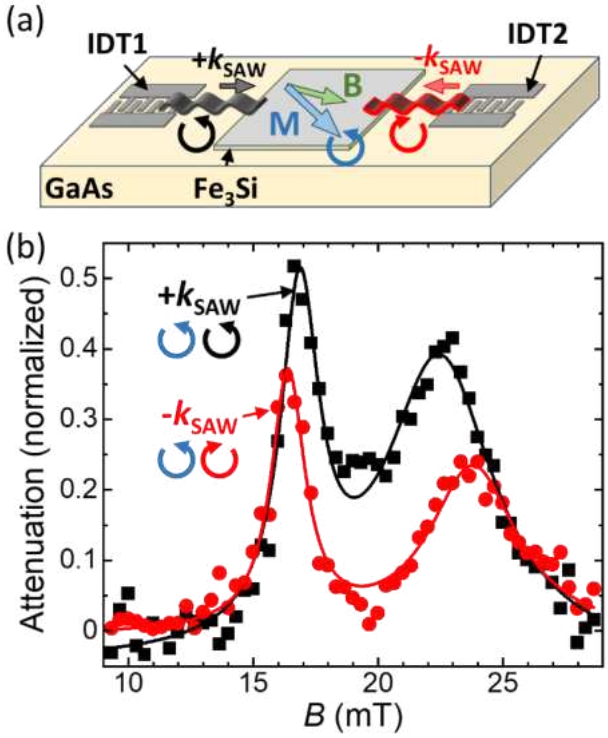


Figure 1. (a) Schematics of the magneto-acoustic system. Interdigital transducers (IDTs) at opposite ends of a ferromagnetic Fe_3Si film launch and detect SAWs with opposite wave vectors, $\pm k_{SAW}$, and chiralities. (b) SAW attenuation as a function of an external in-plane magnetic field, B. The magneto-acoustic resonances cause stronger SAW attenuation for $+k_{SAW}$ than for $-k_{SAW}$.

In the last years, there has been an increasing interest in non-reciprocal systems for the efficient manipulation of sound. Especially appealing for applications are surface acoustic waves (SAWs) [1]. Due to their efficient piezoelectric generation and detection, and their low propagation velocities, SAWs are ideally suited for controlling and interfacing elementary excitations in the solid state [2].

One way to achieve non-reciprocal SAW propagation is to break time-inversion symmetry by coupling the strain field of the SAW (phonons) to spin waves (magnons) [3]. The non-reciprocity arises from the chiral nature of both the SAW and the spin wave. In this contribution, we demonstrate non-reciprocal transmission of high-frequency SAWs (3.4 GHz) traveling along a hybrid structure consisting of a ferromagnetic Fe_3Si thin film epitaxially grown on a GaAs substrate [4]. When the SAW and the spin wave have the same frequency and wave vector, then the magneto-elastic and magneto-rotational coupling transfer energy from the acoustic to the magnetic system, resulting in SAW attenuation, see Fig. 1. The efficiency of this coupling depends on the relative chirality of the SAW and spin wave, which is determined by the orientation of the magnetization with respect to the SAW wave vector and can be controlled with an external magnetic field. The resulting transmission non-reciprocity, defined as the difference between the transmitted acoustic power for forward and backward SAW propagation, reaches values up to 20% under magneto-acoustic resonance.

References

1. Delsing, P. *et al.*, “The 2019 surface acoustic waves roadmap”, J. Phys. D: Appl. Phys., Vol. 52, 353001, 2019.
2. Schuetz, M. J. A. *et al.*, “Universal Quantum Transducers Based on Surface Acoustic Waves”, Phys. Rev. X, Vol. 5, 031031, 2015.
3. Sasaki, R. *et al.*, “Nonreciprocal propagation of surface acoustic wave in $Ni/LiNbO_3$”, Phys. Rev. B, Vol. 95, 020407(R), 2017.
4. Hernández-Mínguez, A. *et al.*, “Large Nonreciprocal Propagation of Surface Acoustic Waves in Epitaxial Ferromagnetic/Semiconductor Hybrid Structures”, Phys. Rev. Appl., Vol. 13, 044018, 2020.

Diffraction of OAM beams assisted by Bloch Surface Waves

N. Marcucci[1], Z. Tang[2,3], T. Guo[4], M. Roussey[4], Y. Liu[3] and E. Descrovi[2*]

[1]CNR-IFAC, Italy
[2]Politecnico di Torino, Italy
[3]SusTech, China
[4]University of Eastern Finland, Finland
[*]corresponding author: emiliano.descrovi@polito.it

Abstract: Beams carrying Orbital Angular Momentum are produced from multilayered structures upon excitation of surface modes. Such structures are axially-symmetric and exhibit a high Local Density of States to facilitate radiation coupling from localized, possibly individual emitters located on the surface, such as q-dots or defected 2D materials.

In the perspective of mitigating the forthcoming issue of the “capacity crunch” in optical communications, the use of spatial degrees of freedom of light has been proposed, in addition to wavelength and polarization, for information coding. Vortex beams (VBs) are structured electromagnetic paraxial modes characterized by a phase singularity along the optical axis, surrounded by a helical wavefront. A convenient way to describe such axis-symmetric VBs is by means of Laguerre-Gauss functions. In 1992, Allen and co-workers demonstrated that the topological charge m appearing in the L-G representation of a VB unveils the existence of an Orbital Angular Momentum (OAM) associated thereto [1]. Most of the previous-art approach for generating OAM beams rely on the conversion of an incoming radiation into specifically controlled vortex beams. This is done with planar devices based on Liquid Crystals (LC) technology and anisotropic media, holographic or diffractive optical elements (DOEs) and more recently, meta-surfaces (MSs). The large majority of these solutions lead to very energy-efficient mode-converters. The coherence properties required to a VB are inherited from the input beam, which is usually extracted out of a laser source. In an attempt to increase the level of integration, sometimes, MSs or DOEs have been directly inserted within laser cavities, on a more macroscopic scale. However, according to this previous art, the source device is functionally separated from the LC/DOE/hologram/MS element producing VBs. Hence, the resulting VB is obtained upon manipulation of a far-field radiation. When single emitters are concerned, approaches based on MS or holographic/DOE are hardly suitable for a single, localized source integrated therein. In fact, since the beam conversion through DOE/MS relies on a spatial-dependent phase transformation, an emitter located in a specific position on a MS would be insensitive to the overall geometry of the MS itself. Instead, the emission will be only affected by the local MS optical properties, unless some collective modes are intervening.

In this work we propose all-dielectric structures based on planar multilayers that are suitable for integration with single emitters. More specifically, a stack of dielectric materials, such as TiO_2 and SiO_2 or Al_2O_3 carrying Bloch Surface Waves (BSW) in a specific wavelength range, is decorated with axially-symmetric resonant and diffractive structures on the top surface, such that the outcoupled radiation can carry OAM.

In a first implementation, a multilayer supporting TE-polarized BSW is considered, wherein the top surface is patterned with spiral gratings with different topological charge. In order to couple BSW, a rotating dipole laying on the stack top plane is emulated by focusing a circularly polarized optical beam at high Numerical Aperture (NA=1.49) through oil-immersion optics. Different OAM for right- and left- circularly polarized light (RHC and LHC respectively) are observed, according to the conservation of total momentum [2].

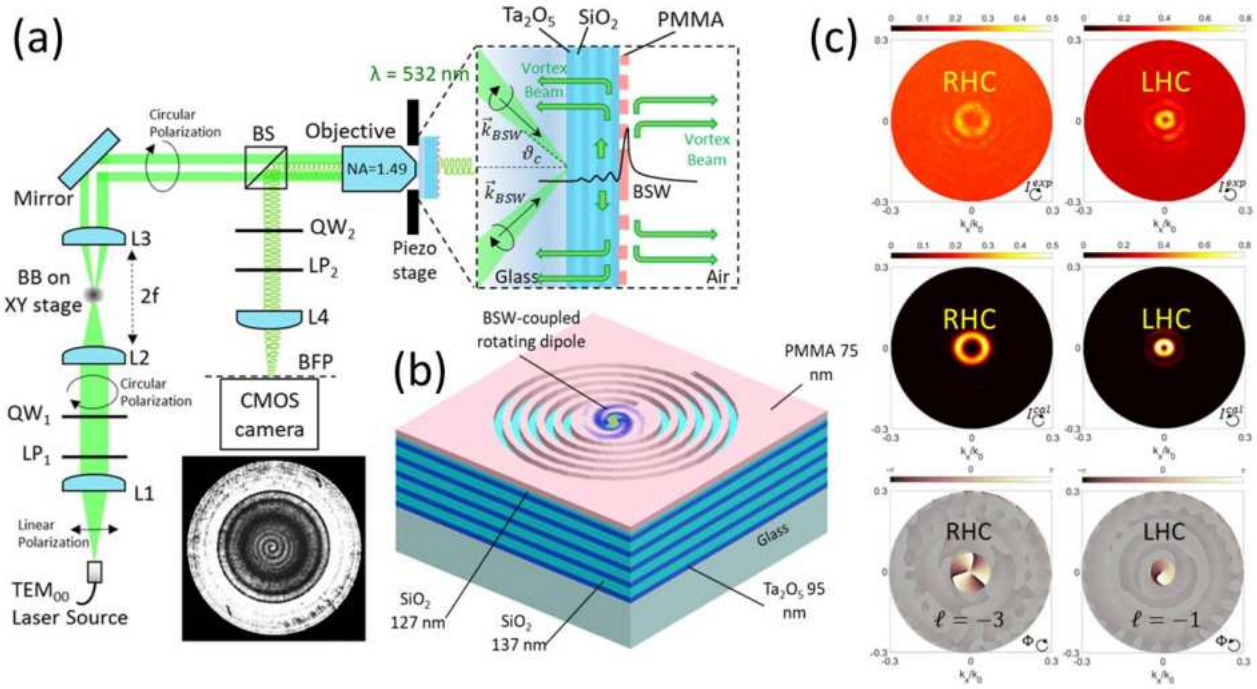


Figure 1. (a) Experimental setup for BSW coupling and diffraction with OAM imparted by spiral gratings; (b) sketch of the sample, with the source being a rotating in-plane electric dipole emulated by a focused circularly polarized light; (c) illustrative examples of diffracted beams carrying OAM for RHC and LHC light.

In a second implementation, a multilayer sustaining TM-polarized BSW is used. Here, the wavefront of the coupled BSW is circular. In addition, space-variant patterns are used to provide different diffraction efficiencies for RHC and LHC radiation, so that separation of two perpendicular polarization states is facilitated thanks to anomalous diffraction effects.

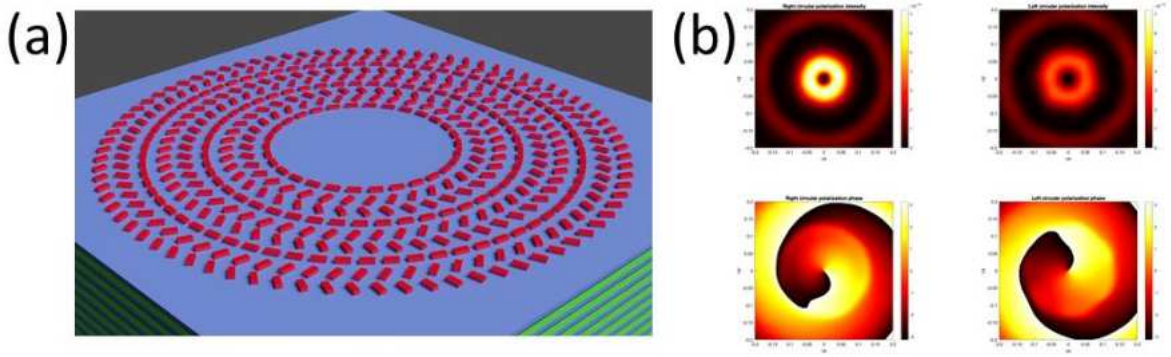


Figure 2. (a) Sketch of the multilayer, carrying a null topological charge metasurface; (b) calculated intensity and phase of RHC and LHC components of the diffracted radiation upon BSW coupling.

References

1. Molina-Terriza, G., Torres, J. & Torner, L., "Twisted photon", Nature Phys. 3, 305–310, 2007.
2. Stella, U., et al. ,"Vortex Beam Generation by Spin-Orbit Interaction with Bloch Surface Waves," ACS Photonics, Vol. 7, 774–783, 2020.

Angular momentum addition for flexural waves using transformation approach

Pengfei Zhao[1+], **Xiaofan Wang**[2+], **Liyou Luo**[1+], **Jensen Li** [1*] **and Huanyang Chen** [2*]
[1] Department of Physics, The Hong Kong University of Science and Technology, Clear Water Bay, Hong Kong, China
[2] Department of Physics, Xiamen University, Fujian, Xiamen, China
[*]corresponding author: kenyon@xmu.edu.cn, jensenli@ust.hk

Abstract: We propose to add flexural wave angular momentum on the plate with tailor-made thickness profile using transformation approach. The experimental result illustrates that two vortexes with same topological charge l located at different positions in space appear like a new single vortex with topological charge $2l$ in the near field.

In the past three decades, orbital angular momentum (OAM) has become a rapidly emerging field of research, in both classical and quantum systems, which deepened the understating of the wave-matter interaction [1]. It also has facilitated distinctive applications across various domains including communications, metrology, tweezers, and nanophotonics. Recently, the OAM in elastics has been theoretically studied [2] and experimentally realized [3]. The transverse OAM [4], described by a transverse spirally azimuthal phase $\exp(-il\phi)$ with l as the topologic charge (TC) and ϕ the azimuthal angle, draws much attention and has been experimentally verified in elastic waves by metamaterials [5]. When considering the flexural wave on the thin plate, we can utilize thickness profile to manipulate flexural wave by transformation approach [6]. Therefore, we can simply use the thickness profile of the plate to investigate the OAM in elastics instead of complex metamaterials. By designing a proper thickness profile through transformation approach, two OAM with the same TC can appear like a single vortex source with added TC in the near field. The experimental result confirms the TC addition and shows the evolution of wavefronts over distance.

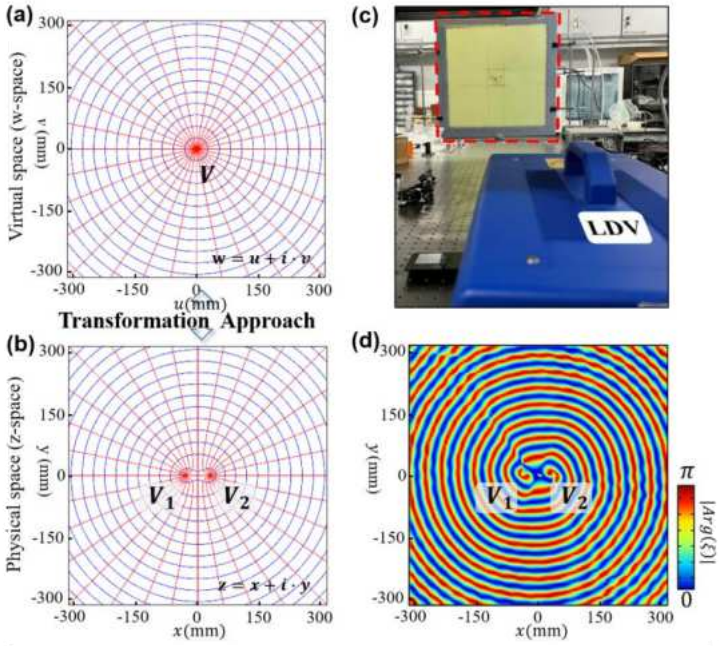


Figure 1. Transformation approach between (a) virtual space (w-space) and (b) physical space (z-space). (c) The experimental setup including Laser Doppler Vibrometer (marked as LDV) and curved plate with tailor-made thickness profile with Blu tack on the boundaries (red dashed box). (d) Experimental measurement (phase of out-of-plane velocity field) obtained for the two vortexes , with the vortex realizing $1 + 1 = 2$ at 6kHz.

We introduce one kind of conformal mapping $w = f(z)$ between physical space defined by coordinates (x, y) and virtual space defined by coordinates (u, v). Fig. 1(a) shows the virtual space with polar coordinates, where the blue and red lines indicate contours of the magnitude $|w|$ and argument $\mathrm{Arg}(w)$. Here, we choose two centers (V_1, V_2) in the physical space from the mapping. Then, contours of magnitude $|f(z)|$ in blue and argument $\mathrm{Arg}(f(z))$ in red in Fig. 1(b) will share the similar distributions away from the origins in physical space. Now we consider flexural wave propagation on a thin plate. Once a flat plate in virtual space is set as h_0, the corresponding inhomogeneous thickness profile h in physical space is obtained. In this case, our target is that the customized thickness profile h enables flexural vortex waves from V_1 and V_2 to act as a single vortex at V in a plate with constant thickness h_0. In order to produce a vortex source for various topological charges in elastics, we typically use an array of transducers with different phases. Here, we excite two vortex sources with the same topological charge $l_{1,2} = 1$ at V_1 and V_2 in physical space with the same amplitude. Certain significant optimizations are required for the real sample for available thickness range. Fig. 1(c) shows the experimental setup including a Laser Doppler Vibrometer (LDV) as a sensor and our experimental sample bounded by Blu tack strips. As we can see, in Fig. 1(d), the measured $|\mathrm{Arg}(\xi)|$ on the tailor-made thickness profile remains original TC as 1 around V_1 and V_2 which we also plot in the Fig. 1(c). The flexural waves gradually superpose when the flexural wave travels several wavelengths away from the V_1 and V_2, showing that the total TC becomes 2 from a virtual vortex located at V. We will also discuss other possible additions of TC for the OAM in the talk.

In conclusion, we demonstrate adding angular momentum with tailor-made thickness profile which is calculated by the transformation approach. Generally speaking, the two vortexes share the same TCs will interfere to each other and observer can easily distinguish them by scattering fields. In our design, by simply adding the tailor made thickness profile near the sources, the observer will see only one vortex source at the origin. Furthermore, the total TC of the field will appear as 2. Our experimental result verifies this vortex illusion effect by employing two vortex sources ($\mathrm{TC} = 1$) at two different positions and then achieving desired vortex image ($\mathrm{TC} = 2$) at the origin. The developed transformation approach for manipulating the vortex waves will be useful for studying vibration control and wavefront shaping in theory. Understanding how angular momentums are added or combined can provide insights into the manipulation of the TCs in other classical waves and has potential to achieve applications such as signal isolation and signal detector.

Acknowledgments

The work is supported by Research Grants Council (RGC) of Hong Kong through projects no. 16307522, STG3/E-704/23N and AoE/P-502/20, and the Croucher Foundation (CAS20SC01).

References

1. Y. Shen, X. Wang, Z. Xie, C. Min, X. Fu, Q. Liu, M. Gong, and X. Yuan, Optical Vortices 30 Years on: OAM Manipulation from Topological Charge to Multiple Singularities, Light Sci Appl 8, 90 (2019).
2. K. Y. Bliokh, Elastic Spin and Orbital Angular Momenta, Phys. Rev. Lett. 129, 204303 (2022).
3. G. J. Chaplain and J. M. De Ponti, The Elastic Spiral Phase Pipe, Journal of Sound and Vibration 523, 116718 (2022).
4. K. Y. Bliokh and F. Nori, Transverse and Longitudinal Angular Momenta of Light, Physics Reports 592, 1 (2015).
5. Y. Liu, Z. Liang, F. Liu, O. Diba, A. Lamb, and J. Li, Source Illusion Devices for Flexural Lamb Waves Using Elastic Metasurfaces, Phys. Rev. Lett. 119, 034301 (2017).
6. D. W. Lee, Y. R. Hao, J. H. Park, I. S. Kang, S. H. Kim, J. Li, and J. Rho, Singular Lenses for Flexural Waves on Elastic Thin Curved Plates, Physical Review Applied 15, 034039 (2021).

Topological boundary modes in a hexagonal flexural wave machine

M. Tomoda[1*], H. Takeda[1], R. Minami[1], O. Matsuda[1], and O. B. Wright[1,2]

[1]Graduate School of Engineering, Hokkaido University, Sapporo 060-8628, Japan
[2]Graduate School of Engineering, Osaka University, Osaka 565-0871, Japan
[*]corresponding author: mtomoda@eng.hokudai.ac.jp

Abstract: We construct a two-dimensional mechanical wave machine based on a hexagonal lattice to investigate low-frequency flexural plate waves whose propagation mimics a topological quantum valley Hall system. Imaging experiments, backed up by simulations, reveal the presence of boundary modes along a topological interface.

Concepts in topological physics, which have been utilized in condensed matter physics, have recently been extended to classical physical systems. Topological boundary modes arising at interfaces of different topological phases have garnered attention in the control of classical wave fields due to their robustness and low energy loss, representing a localized phenomenon in both photonics [1] and phononics [2]. Quantum Valley Hall (QVH) systems, known for their compatibility with photonic/phononic crystals, can be realized by breaking the spatial inversion (*P*) symmetry of the unit cell. While QVH phononic crystals have been extensively studied from kilohertz to gigahertz frequencies, they face challenges in the observation of the motion of mechanical vibrational modes with small displacements, which are beyond the capability of conventional cameras. Although a low-frequency experimental study on a mechanical QVH system at ~10 Hz based on magnetically coupled spinners has been reported, observing the motion of modes with a high degree of freedom, such as those involving chiral phonons, is not feasible with such a system that exhibits a single degree of freedom for each lattice point [3].

In this study, we construct a two-phase mechanical hexagonal-lattice model to elucidate the behavior of a phononic QVH-like system for low-frequency flexural plate waves [4]. Figure 1 shows photographs of the constructed two-dimensional structure consisting of stainless-steel thin plates, plastic hollow rods, and brass weights, measuring overall 1300 mm on each side, and oriented in a vertical plane. The rods and weights enhance the moment of inertia, lowering the eigenfrequencies of the lowest modes to ~1 Hz. To break *P*-symmetry and

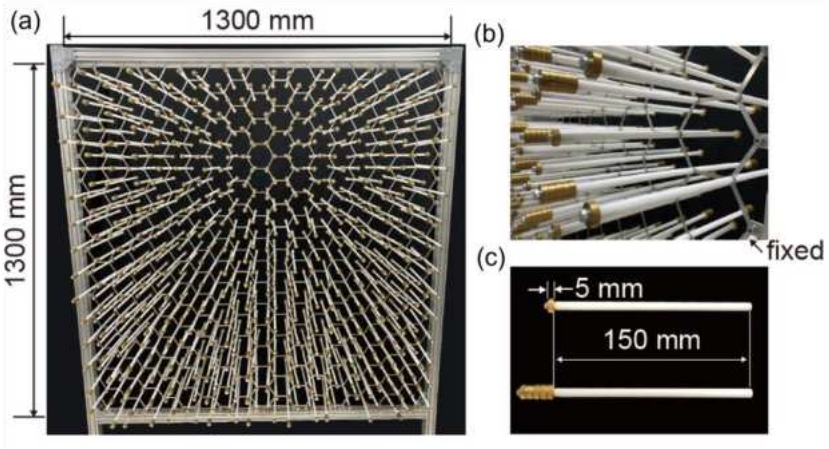


Fig. 1 (a) Photograph of the constructed model. (b) Close-up view of some unit cells. One site rods are loaded with 5 weight, and the other site rods are loaded with a single weight. (c) Close-up view of the polyoxymethylene plastic rods.

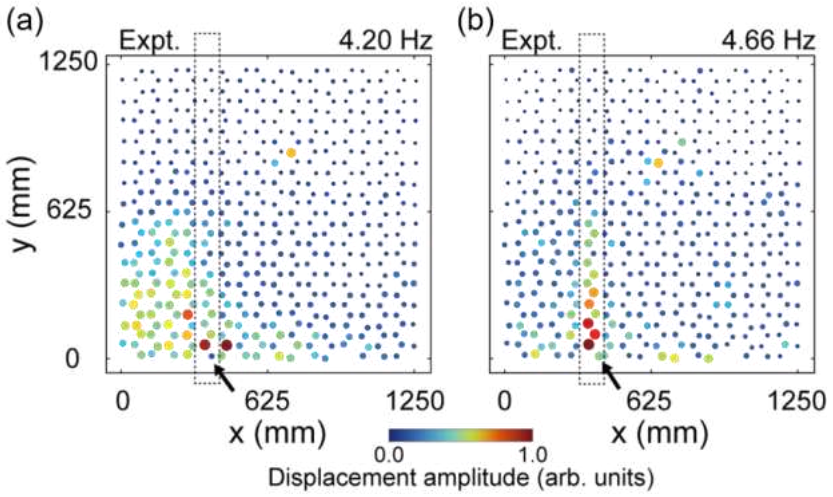


Fig. 2 Displacement fields in the experiment: (a) Bulk mode at 4.20 Hz. (b) Topological boundary mode at 4.66 Hz. The dotted box and arrow indicate the topological interface and excitation point. The point size reflects the normalized displacement amplitude.

induce valley polarization, we adjust the brass weights within each unit cell. In the lefthand 1/3 of the structure, A-site rods are loaded with 5 weights and B-site rods with a single weight. In order to produce a region with a second topological phase, in the center 1/3 of the structure A-site rods are loaded with a single weight and B-site rods with 5 weights. The vertical boundary of the left-hand and central regions consists of a bearded boundary composing single-weight rods forming a zigzag ribbon.

We measured the dynamics of this system. Single-frequency in-plane mechanical vibration was applied to a rod at the lowest position of the interface using an electrodynamic shaker. The motion of each cell was monitored with a motion capture system. The experimental vibration maps based on displacement amplitude are shown in Figs. 2(a) and 2(b), which correspond to bulk and topological boundary modes at 4.20 and 4.66 Hz, respectively.

In future, it would be interesting to vary the structure, for example by changing the dimensions, material or lattice of the cellular plate, in order to investigate the effect on the topological phononics and waveguiding. In addition, our approach should be applicable to metamaterials, including reconfigurable and active systems.

References

1. L. Lu, J.D. Joannopoulos, and M. Soljačić, “Topological photonics,” Nat. Photon. Vol. 8, 821 (2014).
2. G. Ma, M. Xiao and C.T. Chan, “Topological phases in acoustic and mechanical systems,” Nat. Rev. Phys. Vol. 1, 281, 2019.
3. K. Qian, D.J. Apigo, C. Prodan, Y. Barlas. And E. Prodan, “Topology of the valley-Chern effect,” Phys. Rev. B, Vol. 98, 144138 (2018).
4. H. Takeda, R. Minami, O. Matsuda, O. B. Wright, and M. Tomoda “Phononic band calculations and experimental imaging of topological boundary modes in a hexagonal flexurual wave machine, ” Appl. Phys. Express, Vol. 17, 017004, 2024.

Some three-dimensional acoustic flat bands

Baile Zhang[1,2]

[1]Division of Physics and Applied Physics, School of Physical and Mathematical Sciences,
Nanyang Technological University, Singapore 637371, Singapore
[2]Centre for Disruptive Photonic Technologies, Nanyang Technological University, Singapore 637371, Singapore
corresponding authors: ‡blzhang@ntu.edu.sg

Abstract: Flat bands are momentum-independent energy levels, whose history can be traced back to the Landau levels introduced in 1930. Here we discuss the construction of 3D flat Landau levels in an acoustic crystal. We also discuss the construction of highly degenerate 3D flat bands with acoustic waves.

Flat bands are of broad interest in multiple fields of physics since their high density of states provides access to strong-interaction regimes. The first concept of flat bands might be Landau levels introduced by Landau in 1930, which refer to the quantized energy levels of 2D electrons exposed to perpendicular strong magnetic fields. Related to 3D flatbands, we will discuss two works. One is that the construction of 3D flat Landau levels. The other is the construction of highly degenerate flatbands.

In the first part, we design and demonstrate a 3D lattice exhibiting Landau levels that are flat in all three directions. This is accomplished with an acoustic crystal (Fig. 1a) that incorporates an inhomogeneous structural distortion. In the absence of the distortion, the band structure contains a circular nodal ring (i.e., a ring in momentum space along which two bands touch). The introduction of the distortion generates a pseudo magnetic vector potential pointing radially from the nodal ring's center in momentum space, as well as varying in real space. The nodal ring spectrum hence splits into 3D flat bands, in a manner analogous to the formation of 2D Landau levels from Dirac points. In presence of a speaker at the center of the crystal, we can measure the acoustic response, and observe multiple peaks that correspond to different orders of Landau levels in the 3D crystal (Fig. 1b).

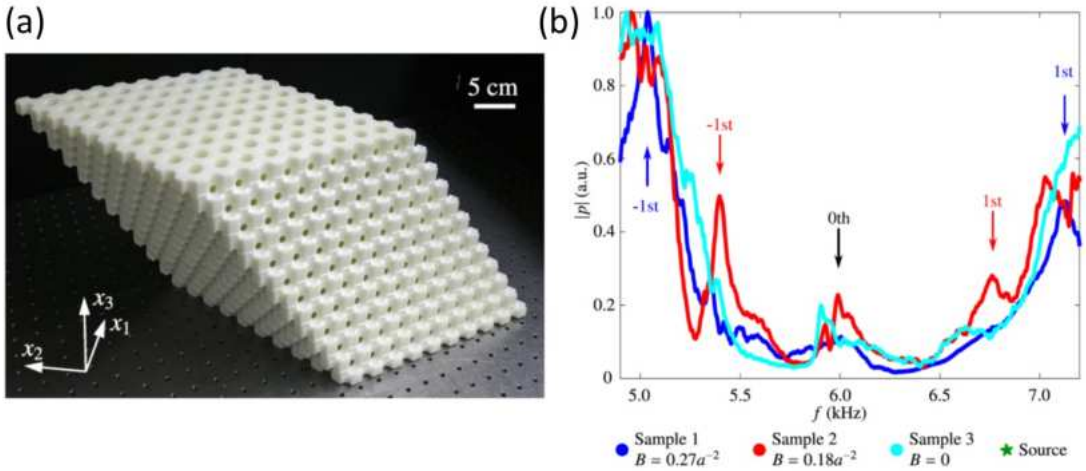


Figure 1 Construction of acoustic Landau levels. (a) The inhomogeneous acoustic crystal. (b) Measured acoustic response when a speaker is placed at the center of the crystal

In the second part, we design and construct an acoustic crystal that exhibits 3D flat bands that are highly degenerate. We start with 1D structures that exhibit bound states in the continuum (BIC), and then stack them up to form 2D and 3D structures. The resultant 3D structure can exhibit 12-fold degeneracy, and thus allow the localization of vortices in 3D spaces.

Jet formation induced by sub-nanosecond optical vortex optical pulses

K. Yamane[1*], R. Tamemoto[1], K. Sato[1], Y. Toda[1], T. Omatsu[2,3], and R. Morita[1]**

[1]Department of Applied Physics, Hokkaido University, Kita 13, Nishi 8, Kita-ku, Sapporo, 060-8628, Japan
[2]Graduate School of Engineering, Chiba University, 1-33 Yayoi-cho, Inage-ku, Chiba, 263-8522, Japan
[3]Molecular Chirality Research Center, Chiba University, 1-33 Yayoi-cho, Inage-ku, Chiba, 263-8522, Japan
*corresponding author: k-yamane@eng.hokudai.ac.jp
**corresponding author: morita@eng.hokudai.ac.jp

Abstract: The jet formation was induced by a 120-ps optical vortex pulse irradiation with a topological charge of 1. The generated jet was monitored by a snapshot imaging system and its speed was evaluated to be about 40 m/s.

Laser-induced forward transfer (LIFT) is one of the direct writing techniques and offers us flexible maskless fine prototyping for printed electronics/photonics structure, bioprinting as well as screen-printing. Since LIFT does not require any nozzles for droplet ejection unlike inkjet technology, it is free from clogging problems [1]. Therefore, it is applicable to a wide variety of donor materials such as high-viscosity fluids, solid, dielectric particles.

When optical vortex pulses are utilized as laser sources, their orbital angular momentum (OAM) causes the generated “jets” or the ejected droplets to rotate. This is called ‘spin jet’ phenomena, which makes patterning possible with high resolution and long working distance [2]. Although such “spin” jet formation occurs basically in the microsecond regime, the light-matter interaction takes place only within pulse duration (typically, few nanoseconds) of irradiated pulses. The questions of why the OAM influences trajectory of donor materials despite the significant different time scales has not been investigated in detail. In previous works, only nanosecond optical vortex pulses have been utilized so far for driving laser source in all the cases. To clarify the mechanism of “spin jet” formation, we focus on the interaction time between light waves and (donor) materials, namely, pulse duration. In this paper, we present jet formation induced by 120-ps optical vortex pulses.

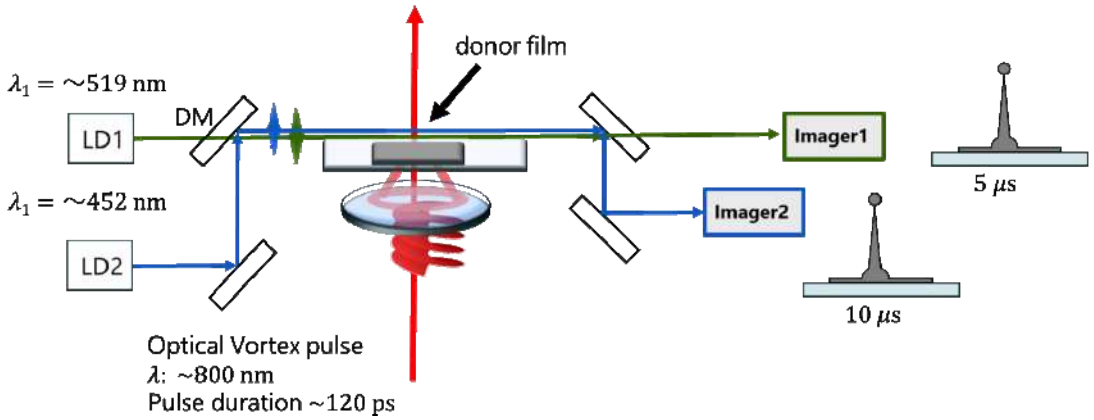


Fig. 1 Schematic of experimental setup. DM: dichroic mirror. Imager1,2: CMOS cameras with imaging lenses.

The schematic of experimental setup is shown in Fig.1. A 120-ps optical pulse from a Ti:Sa multipass amplifier (repetition rate of 1 kHz, center wavelength of ~800 nm) was converted into a linearly-polarized optical

vortex pulse with topological charge of 1 by using a *q*-plate, and focused onto a 40-μm-thick donor film by using a lens with a focal length of 40 mm. The donor film was made of a black ink (SAILOR, Kiwaguro) diluted 100 times with glycerol, and formed on a borosilicate glass substrate. The jet formation was monitored by a snapshot imaging system consisting of two directly modulated laser diodes with pulses durations of 60 ns and two CMOS cameras. Figure 2 shows the snapshot images at 5 μs and 10 μs after sub-nanosecond optical vortex pulse irradiation. The input pulse energy was 14 μJ, and the beam diameter on the donor film was about 40 μm. As clearly seen in Fig. 2, the long stable jet was successfully generated by even sub-nanosecond pulse irradiation, and its speed was evaluated to be about 40 m/s. In addition, we have verified that 23-ps optical vortex pulse irradiation also induced "jet formation".

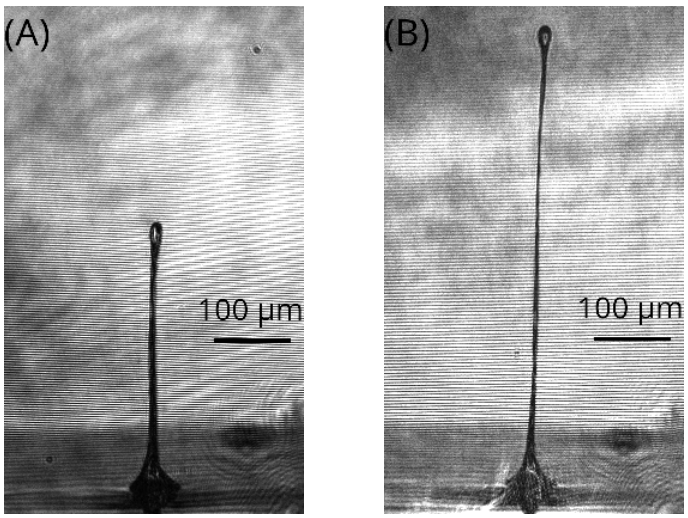


Fig. 2 Snapshot images of jet formation (A) 5 μs and (B) 100 μs after optical vortex irradiation.

References

1. J. Bohandy, et al., "Metal deposition from a supported metal film using an excimer laser," J. Appl. Phys. Vol. 60, 1538-1539 (1986).
2. R. Nakamura et al., "Optical vortex-induced forward mass transfer: manifestation of helical trajectory of optical vortex," Opt. Express, Vol. 27, 38019-38027 (2019).

Control of Circular Polarization Using Nonlinear Optical Effect in Dielectric Membrane Nanostructures

K. Konishi

Institute for Photon Science and Technology, The University of Tokyo, Japan
*corresponding author: kkonishi@ipst.s.u-tokyo.ac.jp

Abstract: Circular polarization is crucial for exploring chiro-optical effects. However, in the vacuum ultraviolet region, generating and controlling circular polarization proves difficult. We discovered that the nonlinear optical effect of nanostructures fabricated on free-standing films with a sub-micron thickness enables the generation and control of circular polarization in such short-wavelength region**s.**

Circular polarization is essential in exploring the chiro-optical effect. However, absorption is high for many materials in the short wavelength region below the ultraviolet. Therefore, the materials needed for circular polarization control elements are limited, and unlike in the visible light region, it is difficult to obtain high-performance circular polarization control optics. Recently, polarization control technology using plasmonic metasurfaces has also been developed. Still, polarization control utilizing plasmonics is also difficult because metal plasmon resonance does not occur in the vacuum ultraviolet region. As a result, it is also challenging to generate and control circular polarization even with nanostructures. We have recently discovered that the nonlinear optical response of nano-periodic structures fabricated on freestanding thin films (nanomembrane) several hundred nanometers thick enables generating and controlling circular polarization in such an ultra-short wavelength region [1,2]. We have succeeded for the first time in generating circularly polarized light in the vacuum ultraviolet region directly from nanostructured materials by the third harmonic generation of a circularly polarized visible femtosecond laser. Recently, we have also succeeded in fabricating such dielectric membrane nanostructures using a more versatile material, SiO2. In this presentation, I will introduce our new approach.

References

1. Kuniaki, K. et al., “Tunable third harmonic generation in the vacuum ultraviolet region using dielectric nanomembranes,” APL Photonics Vol. 5, 066103, 2020.
2. Kuniaki, K. et al., “Circularly polarized vacuum ultraviolet coherent light generation using a square lattice photonic crystal nanomembrane,” Optica Vol. 7, No. 8, 855-863, 2020.

Three-dimensional Design of Acoustic/Elastic Waveguides based on Higher Order Topological Modes

K. Tsuruta,[1] Y. Hata,[1] and M. Anzan-Uz-Zaman[1,2]

[1] Department of Electrical and Electronic Engineering, Okayama University, 3-1-1 Tsushima-naka, Kita-ku, Okayama 700-8530, Japan

[2] Institute of Electronics, Atomic Energy Research Establishment, Gonokbari, Savar, Dhaka-1349, Bangladesh

tsuruta@okayama-u.ac.jp

Abstract: We designed three-dimensional acoustic/elastic waveguides based on higher-order topological modes in stacked layer phononic crystals. A hierarchical property of phononic bandgaps was utilized for designing two-dimensional edge modes and one-dimensional hinge modes. The elastic-wave propagation normal to the layers is demonstrated numerically and experimentally in a layered Kagome lattice.

As the demand for higher integration of information processing increases, elastic and/or acoustic devices are also required to have a higher degree of freedom in their propagation paths. Conventional elastic devices are implemented in 2-dimensional substrates, which prevent additional devices mounted on top of the device. Thus 3-dimensional elastic devices have advantages in developing multichannel and multifunctionality, however, there is an obstacle in making a waveguide perpendicular to a substrate without energy loss.

Topological phononic crystals (PnCs) are artificial acoustic/elastic structures to realize efficient acoustic-/elastic-wave propagations. Topological insulators have robust boundary states against bend, disorder, and defects [1]. Recently, new topological material, named higher order (HO) topological insulator, has been proposed [2]. This material has topological state at boundary of a lower dimension. Especially, a second order topological insulator has a localized hinge state, leading to wave transport perpendicular to substrates.

In this study, we investigate topological boundary modes in stacked layer lattices, aiming to develop an efficient multichannel waveguide through the topological band design. Starting from highly degenerate Dirac band in stacked layer PnCs, it is shown theoretically and numerically that the degeneracies can be split into several distinct modes that exhibit 1st and 2nd order topological states by changing intra- and inter-layer bonds.

To engineer this controllability of the HO modes, we design a topological elastic waveguide based on a 3-dimensional phononic crystal with stacked Kagome lattices. Topological corner modes are shown to be elaborated by changing the intracell- and intercell-bonds. We demonstrate numerically and experimentally that such topological corner modes can be extended to one-dimensional hinge mode [3].

This work was supported by JSPS KAKENHI(S) Grant Number JP21H05020.

References

1. Kataoka, M., Misawa, M., and Tsuruta, K., “Design and Robustness Evaluation of Valley Topological Elastic Wave Propagation in a Thin Plate with Phononic Structure,” Symmetry Vol.14, 2133, 2022.
2. Ezawa, M.,“Higher-order topological insulators and semimetals on the breathing Kagome and pyrochlore lattices,” Physical Review Letters, Vol.120, 026801, 2018.
3. Hata, Y., Misawa, M., and Tsuruta, K., “Second-order topological hinge modes in a 3-dimensional phononic crystal,” 2023 IEEE International Ultrasonics Symposium, 10307189, 2023.

Fourier-based band structure computation for quasicrystalline media

Marc Martí-Sabaté[1], Matheus I.N. Rosa[2], Sebastien Guenneau[3] and Daniel Torrent[4*]

[1]The Blackett Laboratory, Department of Physics, Imperial College London, London SW7 2AZ, UK

[2]Department of Mechanical and Process Engineering, ETH Zurich, Zurich, Switzerland

[3] The Blackett Laboratory, Department of Physics, Imperial College London, London SW7 2AZ, UK

[4]GROC-UJI, Institut de Noves Tecnologies de la Imatge, Universitat Jaume I, 12080 Castello, Spain
[*]corresponding author: dtorrent@uji.es

Abstract: This presentation introduces a novel method for computing the band structure of nonperiodic crystals using Fourier-based techniques and plane wave expansion. It discusses applications to Moiré lattices, cut-and-project quasicrystals, and incommensurable modulated crystals. The method is broadly applicable to wave systems like photonic, acoustic, and phononic quasicrystals.

In this presentation, we introduce an analytical approach for computing the band structure of quasicrystalline materials using Fourier-based methods. Departing from traditional periodic crystal analyses, our method offers a novel perspective on understanding the properties of nonperiodic structures.

Through an examination of plane wave expansion and Fourier space characteristics, we unveil a set of mathematical expressions capable of accurately determining the band structure and phase space diagrams of modulated potentials within Schrödinger's equation. Notably, our method transcends the limitations of conventional analyses by accommodating various incommensurable structures.

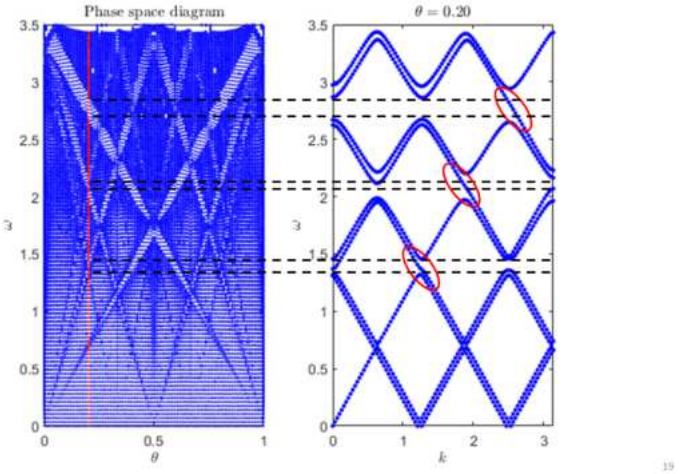


Figure 1 Example of dispersion relation calculation for modulated 1-D quasi crystals as a function of the modulation parameter (left panel) and the wave vector (right panel)

Throughout the discourse, we illustrate the versatility of our approach by exploring three distinct examples: the incommensurate superposition of periodic lattices, exemplified by Moiré lattices; cut-and-project

quasicrystals; and incommensurable modulated crystals. Importantly, while our investigation primarily revolves around the Schrödinger's equation framework, the applicability of our findings extends to diverse wave systems, encompassing photonic, acoustic, and phononic quasicrystals.

Our numerical simulations yield profound insights into the behavior of quasicrystalline materials, revealing the emergence of stop bands with chiral states in accordance with the Cantor spectrum properties inherent to quasicrystals. Furthermore, we elucidate that essential band structure information can be gleaned from the projection of modes aligned with the anticipated diffraction directions dictated by the structure's geometry.

To validate the robustness of our computational predictions, we complement our numerical analyses with rigorous time-domain simulations, thus reinforcing the reliability and accuracy of our methodology. Through this comprehensive investigation, we not only advance the understanding of quasicrystalline band structures but also pave the way for future applications in several wave-based systems.

References

1. Martí-Sabaté, M., & Torrent, D. (2021). Dipolar localization of waves in twisted phononic crystal plates. Physical Review Applied, 15(1), L011001.
2. Martí-Sabaté, M., & Torrent, D. (2021). Edge modes for flexural waves in quasi-periodic linear arrays of scatterers. *APL Materials*, *9*(8).
3. Massimo, R., & Emil, P. (2021). Topological gaps by twisting. Communications Physics, 4(1).

Acoustic Spin and Phonon Spin

Jie Ren[1]

[1] Center for Phononics and Thermal Energy Science, China-EU Joint Lab on Nanophononics, Shanghai Key Laboratory of Special Artificial Microstructure Materials and Technology, School of Physics Science and Engineering, Tongji University, Shanghai 200092, China

*corresponding author: xonics@tongji.edu.cn

Abstract: Spin angular momentum is an inherent property of classical waves. It was believed that only circularly polarized transverse waves carry spin, while longitudinal waves lack spin structures. However, recent progress has challenged this understanding. Here, I'll share recent progress on acoustic and phonon spin, along with spin related chiral phenomena.

1) SAM of elastic wave and acoustic wave

Elastic waves, which refer to vibrations in elastic media, can be described by the displacement field $\boldsymbol{u}(\boldsymbol{r},t) = \boldsymbol{u}_0(\boldsymbol{r})e^{i(\boldsymbol{k}\cdot\boldsymbol{r}-\omega t)}$. The SAM density carried by elastic waves can be expressed as [1,2]: $\boldsymbol{S} = \frac{\rho\omega}{2}\mathrm{Im}[\boldsymbol{u}^* \times \boldsymbol{u}]$

Taking into account that air acoustic waves are a special case where the $\nabla \times \boldsymbol{u}$ is zero, Eq. (1) is also applicable to acoustics waves. Experimentally, we can utilize absorbers that absorb acoustic waves to actually measure the torque induced by SAM of acoustics and verify its existence [3].

2) Spin related chirality in acoustic meta waveguides

The chiral phenomena associated with the spin of air acoustics can be harnessed as a tool for manipulating acoustic waves. For example, by disrupting the symmetry of an acoustic waveguide, we can establish a fixed chiral relationship among SAM, wave vector, and the waveguide's structure [4]. Leveraging this relationship, we can tailor specific propagation paths for acoustic waves, as demonstrated in Figure 1a. Furthermore, by exploiting the chiral relation between spin, energy flow, and reactive power in surface waves [5], we can achieve selective excitation of acoustic waves [6], as exemplified in Figures 1b and 1c.

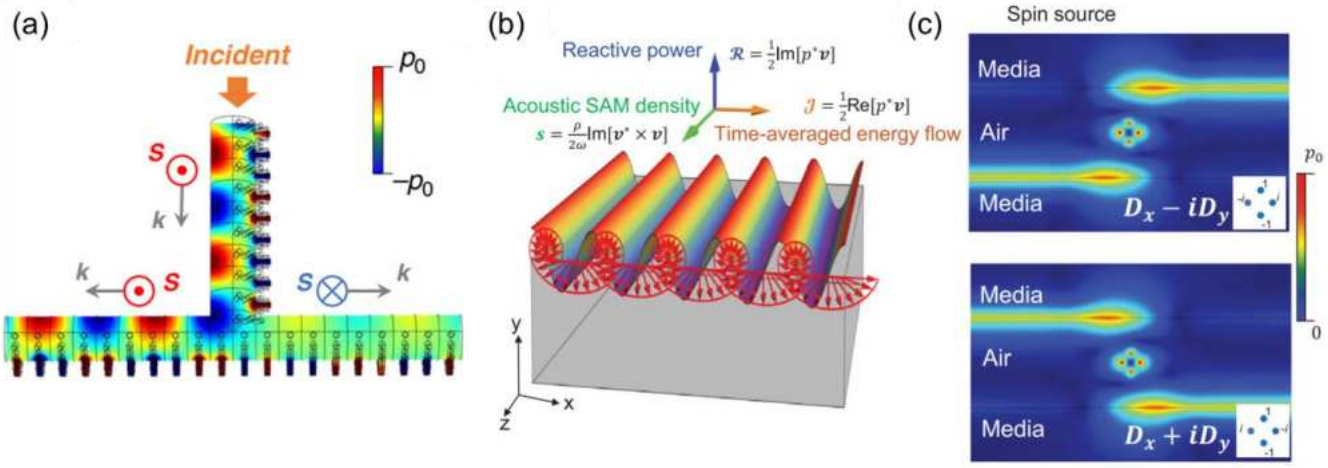


Figure 1. (a) A metasurface waveguide for sound carrying non-zero acoustic spin with tight spin-momentum coupling can be achieved by imposing an effective soft boundary. Assuming that the direction vector from the soft boundary to the hard boundary is denoted as $\boldsymbol{n}$, we can obtain the right-handed chirality as $\boldsymbol{s}\cdot(\boldsymbol{n}\times\boldsymbol{k}) > 0$. The acoustic wave will selectively propagate along one side due to the SAM match when facing multiple channels. (b) The evanescent wave can be supported on the interface between conducting (air in the acoustic case) and insulating media (gray block). We can obtain the right-handed chirality as $\boldsymbol{s}\cdot(\boldsymbol{\mathcal{J}}\times\boldsymbol{\mathcal{R}}) > 0$. (c) Selective excitation according to the spin-related symmetry.

3) Hybrid Spin in elastic waves

Electromagnetic waves belong to the category of transverse waves. In a vacuum devoid of free charges, the electric field's divergence vanishes, mathematically expressed as $\nabla \cdot \boldsymbol{E}$. Longitudinal waves, such as those found in air acoustics, exhibit a velocity field with zero vorticity due to the inability of ideal fluids to transmit shear forces, resulting in $\nabla \times \boldsymbol{v}$. Elastic waves, however, stand apart from both of these types, display both divergence-free and cure-free parts. Their displacement field can be represented by $\boldsymbol{u} = \boldsymbol{u_l} + \boldsymbol{u_t}$, satisfying $\nabla \times \boldsymbol{u}_l = 0$ and $\nabla \cdot \boldsymbol{u}_t = 0$. The spin of elastic waves is expressed as $\boldsymbol{S} = \frac{\rho\omega}{2}\mathrm{Im}[\boldsymbol{u}^* \times \boldsymbol{u}] = \frac{\rho\omega}{2}(\mathrm{Im}[\boldsymbol{u}_l^* \times \boldsymbol{u}_l] + \mathrm{Im}[\boldsymbol{u}_t^* \times \boldsymbol{u}_t] + \mathrm{Im}[\boldsymbol{u}_l^* \times \boldsymbol{u}_t] + \mathrm{Im}[\boldsymbol{u}_t^* \times \boldsymbol{u}_l])$, which possess the hybrid parts $\boldsymbol{u}_l^* \times \boldsymbol{u}_t$ and $\boldsymbol{u}_l^* \times \boldsymbol{u}_t$ [1,2,7]. Therefore, even within similar systems, the spin distribution of elastic waves may vary significantly, as illustrated in Figure 2. This uniqueness endows elastic waves with manipulation techniques that are unparalleled in other systems.

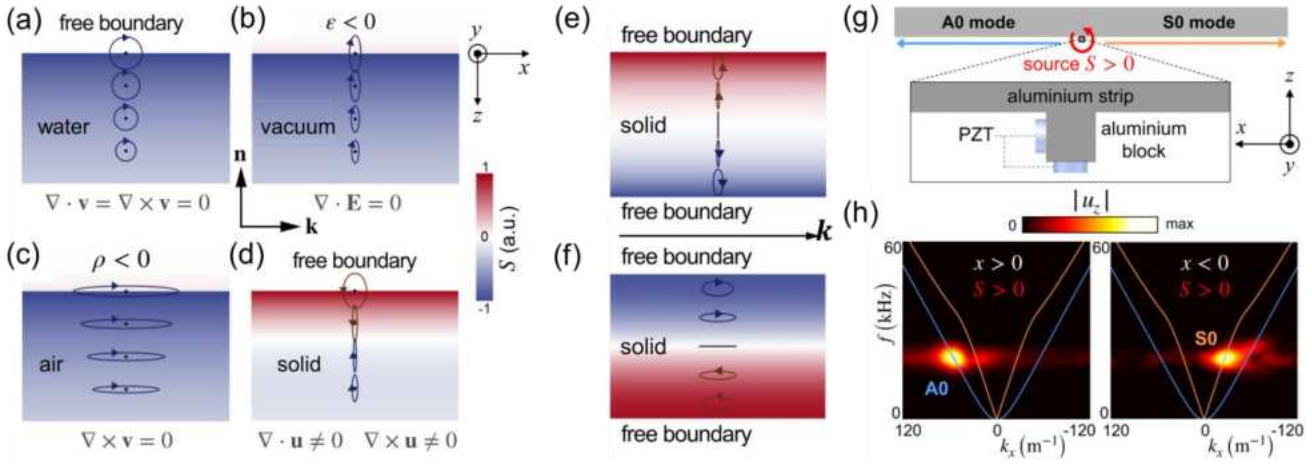


Figure 2. Anomalous spin-momentum locking in elastic waves. Transverse spin density in surface water (a), electromagnetic (plasmon-polariton) (b), acoustic (c), and elastic Rayleigh (d) waves. The spin-normal-momentum triad is right-handed in (a), (b) and (c) as $\boldsymbol{s} \cdot (\boldsymbol{n} \times \boldsymbol{k}) > 0$ and left-handed near the surface for Rayleigh waves as $\boldsymbol{s} \cdot (\boldsymbol{n} \times \boldsymbol{k}) < 0$. In Lamb wave, the A0 mode (e) has a reversed spin sign with S0 mode (f). As such, a spin source will induce the spin-induced directional excitation of the Lamb modes, as shown in (g) and (h).

References

1. Y. Long, J. Ren and H. Chen, "Intrinsic spin of elastic waves," PNAS, Vol. 115, No.40, 9951-9955, 2018.
2. J. Ren, "From Elastic Spin to Phonon Spin: Symmetry and Fundamental Relations," Chin. Phys. Lett., Vol. 39, No.12, 126301, 2022.
3. C. Shi, R. Zhao, L. Yang, S. Yang, Y. Wang, H. Chen, J. Ren and X. Zhang, "Observation of acoustic spin," Nati. Sci. Rev., Vol. 6, No.4, 707-712, 2019.
4. Y. Long, D. Zhang, C. Yang, J. Ge, H. Chen and J. Ren, "Realization of acoustic spin transport in metasurface waveguides," Nat. Commun., Vol. 11, No. 1, 4716, 2020.
5. Y. Long, C. Yang, H. Chen and J. Ren, "Universal Geometric Relations of Acoustic Spin, Energy Flux, and Reactive Power," Phys. Rev. Applied, Vol. 19, No. 6, 064053, 2023.
6. Y. Long, H. Ge, D. Zhang, X. Xu, J. Ren, M.-H. Lu, M. Bao, H. Chen and Y.-F. Chen, "Symmetry selective directionality in near-field acoustics," Nati. Sci. Rev., Vol.7, No.6, 1024-1035, 2020.
7. C. Yang, D. Zhang, J. Zhao, W. Gao, W. Yuan, Y. Long, Y. Pan, H. Chen, F. Nori, K. Y. Bliokh, Z. Zhong and J. Ren, "Hybrid Spin and Anomalous Spin-Momentum Locking in Surface Elastic Waves," Phys. Rev. Lett., Vol.131, No.13, 136102, 2023

Towards chiral phononic modes in silicon

C. M. Sotomayor Torres[1,2*] and O. Florez[2]

[1]International Iberian Nanotechnology Laboratory, Portugal
[2]Catalan Institute of Nanoscience and Nanotechnology, Spain
[*]corresponding author: clivia.sotomayor@inl.int

Abstract: We present simulations of phononic crystals supporting interface modes in the GHz range, which are treated as waveguides. Under certain conditions chiral phononic modes are predicted. The sensitivity to critical dimensions variability is discussed.

Phononic waveguides could eventually become an alternative to in-chip interconnects if their losses are minimal. This leads to consider the concept of topological protection of phonons in a waveguide as a legitimate aim to explore phononic waveguides formed at the interface between two phononic crystals with different phases.

We have already demonstrated the presence of waveguide modes in a mechanical phononic structure realized in silicon-on-insulator, exhibiting a gap of 5.3 GHz centered at 8.4 GHz where the frequencies of the waveguide modes were found to be 5.7 and 7.1 GHz at room temperature [1]. The simulations were successfully compared to data from Brillouin scattering to obtain the dispersion relations of phonons in the phononic waveguide by solving the full 3-dimensional elastic wave equation by FEM simulation in COMSOL Multiphysics.

Here we will present simulations of selected phononic crystal structures with an interface waveguide between phononic crystals with similar but not identical geometry and a distinct variation of mass density in the unit cell. We will discuss the dramatic impact of a few nm variability in critical dimensions on dispersion relation, on a topological invariance and on the topological waveguide modes. The cases where chiral modes are expected will be illustrated [2].

References

1. Flores, O. et al., “Engineering nanoscale hypersonic phonon transport,” Nature Nanotechnology, Vol. 17, 947-951, 2022.
2. Florez, O. et al, in preparation.

Funding

This work was supported by the European Research Council H2020 GA No. 885689LEIT and the Marie Sklodowska Curie COFUND PreBIST GA No. 754558.

Tunable spiraling metamaterial as a platform for controlling sound waves, electromagnetic waves, and enhancing optomechanical coupling

Osama R. Bilal[1*]

[1]Department of Mechanical, Aerospace, and Manufacturing engineering, University of Connecticut, Storrs, Connecticut 06269, USA Affiliation, Country
[*]corresponding author: Osama.bilal@uconn.edu

Abstract: In this work we present a platform for designing phononic and photonic materials utilizing a periodic tessellation of Archimedean spirals. Such tessellations are capable of opening band gaps for both sound and electromagnetic waves and enhancing opto-mechanical coupling in a programmable manner.

Metamaterials are repeating geometric patterns in space that construct artificial lattices. Such lattices can be utilized as platforms to realize peculiar behavior for both electromagnetic and sound waves. The design approaches for engineering such lattices are vastly different (from material layering and holes, pillar coatings and heavy inclusions to hinged mechanisms [1-6]). In this work, we present a generic platform, based on Archimedean spirals, to engineer a wide spectrum of wave manipulation capabilities by varying the spirals' geometry [7-10]. These spiraling materials can be easily manufactured using either additive or subtractive manufacturing technologies and can be easily programmed in a reversible manner. In addition to the realization of the different band gap physics through the proposed platform, we capitalize on the internal unit cell symmetry creating partial propagating bands within full band gaps. Such symmetry breaking allows for the demonstration of two cases of wave beaming. Moreover, we modify the packing symmetry of the spiraling unit cells to create topologically protected wave behavior. Our demonstrations show the potential of coupling various wave phenomena within unified and easy-to-design and fabricate building blocks, enabling the design of novel phononic and photonic materials for different applications. The presented advances highlight the versatility of spirals-based metamaterials.

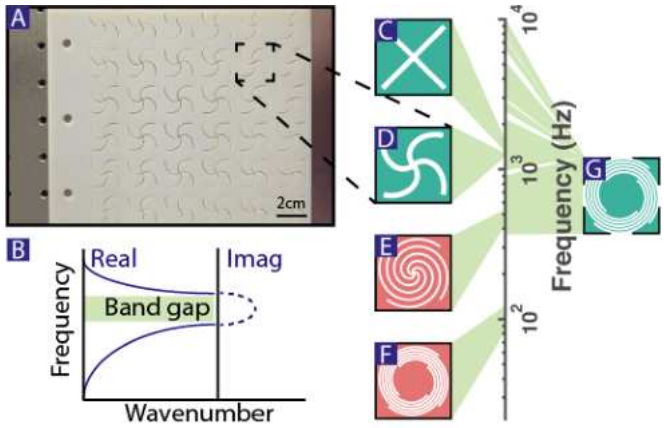


Figure 1: Spiraling metasurfaces: (a) A 3D printed metasurface with arrays of spiraling unit cells, (b) a dispersion curve with both real and imaginary solutions highlighting a band gap, and (c-g) variations of the spiral pattern along with the frequency ranges of their band gaps.

References

1- Kushwaha, Manvir S., et al. "Acoustic band structure of periodic elastic composites." *Physical review letters* 71.13 (1993): 2022.
2- Sigalas, Michael, and Eleftherios N. Economou. "Band structure of elastic waves in two dimensional systems." *Solid state communications* 86.3 (1993): 141-143.
3- Liu, Zhengyou, et al. "Locally resonant sonic materials." *science* 289.5485 (2000): 1734-1736.

4- Pennec, Yan, et al. "Low-frequency gaps in a phononic crystal constituted of cylindrical dots deposited on a thin homogeneous plate." *Physical Review B* 78.10 (2008): 104105.
5- Wu, Tsung-Tsong, et al. "Evidence of complete band gap and resonances in a plate with periodic stubbed surface." *Applied Physics Letters* 93.11 (2008).
6- Yilmaz, Cetin, Gregory M. Hulbert, and Noboru Kikuchi. "Phononic band gaps induced by inertial amplification in periodic media." *Physical Review B* 76.5 (2007): 054309.
7- Foehr, André, et al. "Spiral-based phononic plates: From wave beaming to topological insulators." *Physical review letters* 120.20 (2018): 205501.
8- Bilal, Osama R., Foehr, André and Daraio, Chiara. "Reprogrammable phononic metasurfaces." *Advanced materials* 29.39 (2017): 1700628.
9- Bilal, Osama R., Foehr, André and Daraio, Chiara. "Bistable metamaterial for switching and cascading elastic vibrations." *Proceedings of the National Academy of Sciences* 114.18 (2017): 4603-4606.
10- Kheybari, Majid, and Bilal, Osama R. "Harnessing asymmetry to reprogram nonlinear metamaterials on-the-fly with no moving parts." *Materials & Design* 233 (2023): 112168.

Acoustic Metasurface in a Nano-Opto-Electro-Mechanical Device for High Optomechanical Coupling Rate

A. Guedidda, Y. Pennec[1*], L. Carpentier[1], G. Lévêque and B. Djafari-Rouhani[2]
[1]IEMN University of Lille, Cité Scientifique, 59650, Villeneuve d'Ascq, France

[*]corresponding author: yan.pennec@univ-lille.fr

Abstract: We theoretically investigate a phoXonic nanobeam for optomechanical coupling. Our focus lies to explore high-frequency (10 GHz) phonons trapped inside tapered or topologic high-Q cavities. To reach this objective, we propose the design of a metasurface to focus the acoustic wave into the nanobeam.

The Nano-Opto-Electro-Mechanical device comprises an optomechanical (OM) cavity housed within a phoXonic nanobeam. It is connected with two sets of inter-digitated transducers (IDT) at its input and output, facilitating the excitation and detection of acoustic waves. The optical modes within the OM cavity are stimulated by an external optical waveguide, which terminates with a Bragg mirror constructed from tapered holes. A scheme of the device is presented in Figure 1(a).

The phoXonic cavity is constructed with a periodic arrangement of holes and stubs, which concurrently generate an acoustic bandgap within the GHz range and an optical bandgap around 1550 nm for telecommunications. Our research has showcased[1,2] different cavity designs that sustain both acoustic modes spanning from 2 to 4 GHz and optical modes characterized by high-quality factors. Moreover, these cavities exhibit a substantial optomechanical coupling rate, denoted as g, on the order of MHz. Additionally, we explored the feasibility of exciting the phononic cavity modes using a set of inter-digitated transducers positioned in front of the nanobeam[3].

An acoustic metasurface, made of an array of sub-wavelength resonant pillars is tailored to concentrate the elastic wave emanating from the IDTs towards the nanobeam entrance. We proposed to obtain the focalization functionality by using elliptical pillars[4,5] with a constant height but a gradient in their ellipticity, which is suitable for the microfabrication technologies. We demonstrated that the proposed metasurface allows to focus the incident flexural waves into a focal spot with an intensity six times that of the incident wave with a full width at half maximum (FWHM) of the focal spot equal to $0.39\times\lambda$ (Figure 1(b)).

We then explored high-frequency acoustic cavities operating within the 6-10 GHz range. The design of OM cavities that support phonon localized modes in the range of 10 GHz while the optical cavity modes need to have both a high-quality factor and a strong OM coupling rate. In some of our previous works[1,2], we proposed tapered cavities where the sizes of the holes and stubs in the center of the cavity were increased (resp. decreased) with respect to the phoxonic crystal parameters in order to decrease (resp. increase) the cavity phonon frequency in the range of 2-4 GHz. In contrast, to go to 10 GHz frequencies, we adopted here an opposite solution, namely putting a long length stub at the center and relying on its high frequency second order breathing mode to compresse the holes and create the conditions for strong OM coupling. Different tapered cavities are under

investigation and some promising solutions are expected. One example is presented in Figure 1(c) where we show the acoustic and optical fields of the cavity with a coupling rate of g = 5 MHz.

In parallel, we are exploring the possibility of using simultaneous localized acoustic and optical modes at the interface between two topologically different phoXonic crystals. The principle is based on the analogy with the Su-Schrieffer-Heeger (SSH) model by making a pairing of the pillars and constructing a unit cell with two sub-units. Both photonic and phononic topological interface modes have been obtained by this approach.

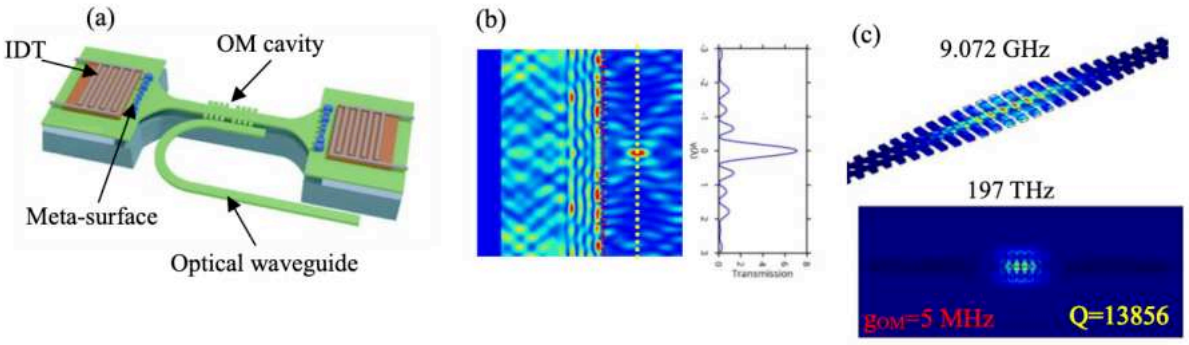


Figure 1: Schematic view of the opto-electromechanical device. (b) Elastic wave focusing effect of the metasurface. The blue curve represents the transverse intensity evaluated along the yellow line crossing the focal spot. (c) An example of phononic and photonic cavity modes providing high OM coupling rate g_{OM}.

Acknowledgements. This work is part of the project MAGNIFIC of the European Union's Horizon Europe research and innovation program under grant agreement No 101091968 and the CHIST-ERA Call 2021 under the grant agreement No CHIST-ERA-20-NOEMS-003.

References

1. Djafari Rouhani, B. et al, "Phoxonic crystals and cavity optomechanics", Comptes Rendus Physique 17, 555, 2016.
2. Gueddida, A. et al, "Coupling of integrated waveguide and optomechanic cavity for microwave phonon excitation in Si nanobeams", Photonics. 7, 67, 2020.
3. Korovin, A. et al, "Conversion between surface acoustic waves and guided modes of a quasi-periodic structured nanobeam", J. Phys. D : Applied Physics. 52, 32LT01, 2019.
4. Djafari Rouhani, B. et al, "Elastic metasurface made of elliptic shape pillars for acoustic wave focusing", Proceedings of 2022 IEEE International Ultrasonics Symposium.
5. Carpentier, L. et al, "Elliptic pillars based metasurface for elastic waves focusing in a plate", Submitted to APL Materials

Intrinsic Three-dimensional Spin Angular Momentum of Gigahertz Evanescent Acoustic Phonons

Yi He[1], Hoon Sohn[2], Osamu Matsuda[3], and Zhongqing Su[1*]

[1]Department of Mechanical Engineering, The Hong Kong Polytechnic University, Kowloon, Hong Kong SAR

[2]Department of Civil and Environmental Engineering, Korea Advanced Institute of Science and Technology, Daejeon 34141, Republic of Korea

[3]Division of Applied Physics, Faculty of Engineering, Hokkaido University, Sapporo 060-8628, Japan

[*]corresponding author: Zhongqing.su@polyu.edu.hk

Abstract: Burgeoning study on the spin angular momentum (SAM) of phonons has advanced profound understanding of fundamentals of SAM, from its classical to quantum aspects, and also envisioned intriguing applications of SAM in controlling elementary particles (e.g., photons, magnons, and electrons) via the spin–orbit interaction. Notwithstanding, prevailing studies on SAM of phonons are restricted to isotropic media in a frequency domain up to megahertz, in part due to the challenges in acquiring the full-field information of phonons using interferometry at a gigahertz (GHz) frequency. The present work is dedicated to gaining insight into the SAM of GHz evanescent acoustic phonons (EAP) in the lattice of monocrystalline materials, in which the temporally averaged Poynting vector of EAP is zero along specific directions. Theoretical modelling on lattice dynamics reveals that the EAP carries intrinsic three-dimensional (3-D) SAM – a trait that the bulk acoustic phonons do not manifest. A femtosecond-laser pump-probe set-up with the assembly of a knife-cutting-interferometer is configurated, to optoacoustically generate GHz surface acoustic phonons (SAP) -- a typical type of EAP, and measure the corresponding 3-D SAM. Experiment results evidence the detectability of the knife-cutting-interferometry to the in-plane components of atomic velocity of EAP, on which basis the 3-D SAM is imaged for intuitive observation. Experimental observation corroborates the 3-D intrinsic nature of the SAM carried by EAP as predicted using the theoretical modelling. The 3-D intrinsic SAM of EAP displays spin-momentum locking and omnidirectional conservation. We also reveal that the propagation of EAP along specific orientations can lead to the orthogonalization of SAM. Results of this study accentuate an application prospect of navigating elementary particles based on the conservation and transfer of angular momentum.

Keywords: Ultrafast optoacoustics; Spin angular momentum; Femtosecond-laser pump-probe measurement; Evanescent acoustic phonons; Lattice dynamics

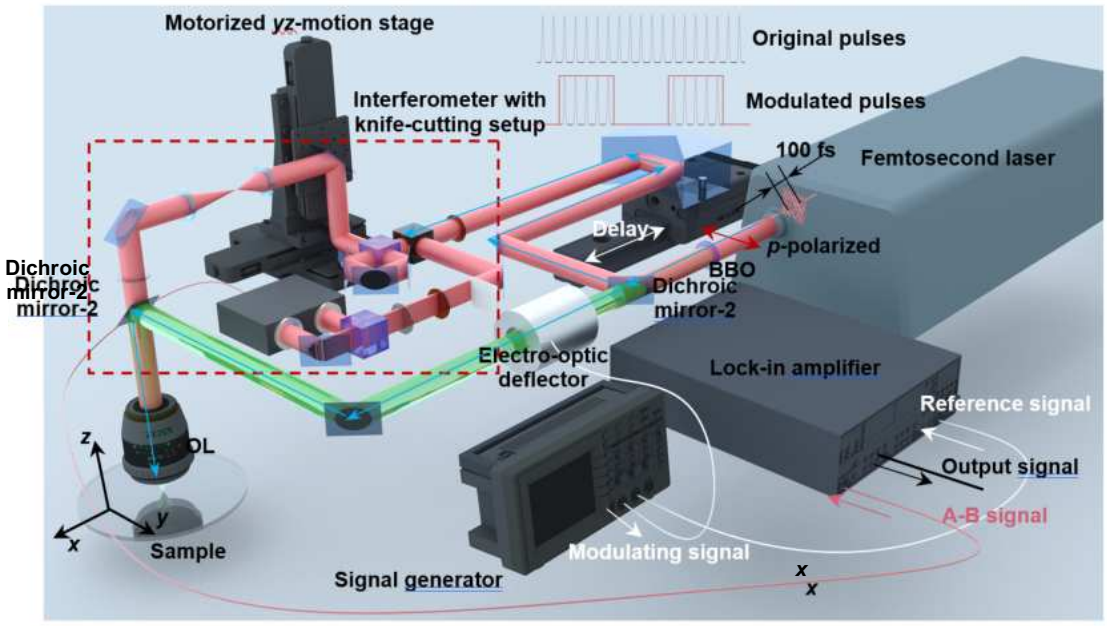


Figure 1 Schematic of the femtosecond-laser pump-probe system with a knife-cutting setup, the blue vectors signify the propagating direction of laser beams.

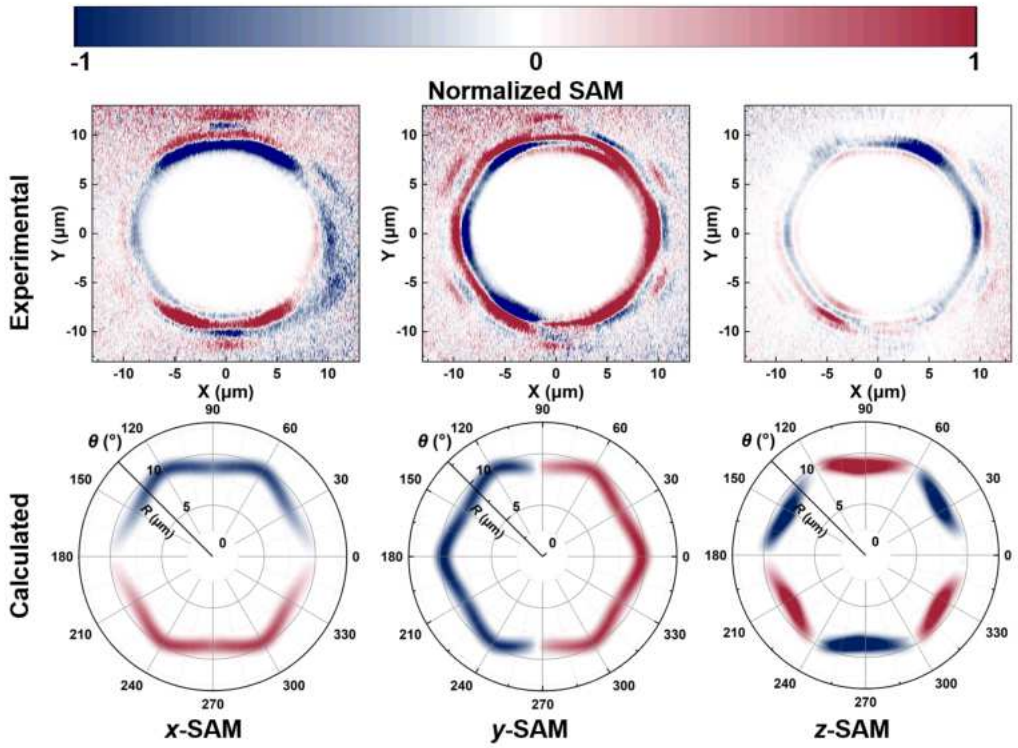


Figure 2 The calculated and experimental SAM images sampled using the femtosecond-laser pump-probe system with a knife-cutting setup.

Quantum Metasurfaces

Quasi-BIC Mode Lasing in a Quadrumer Plasmonic Lattice

R. Heilmann[1], G. Salerno[1#], J. Cuerda[1], T.K. Hakala[2], and P. Törmä[1*]

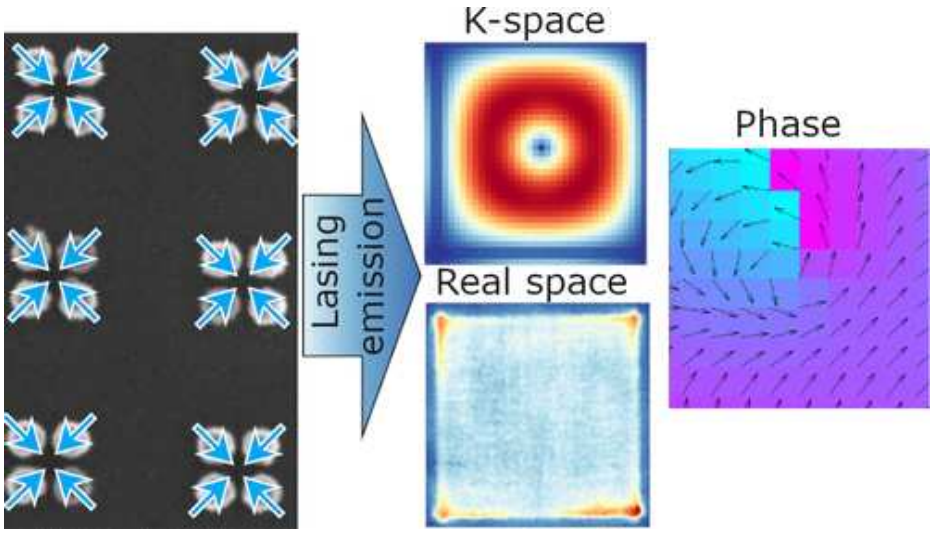
[1] Department of Applied Physics, Aalto University School of Science, Aalto FI-00076, Finland

[2]Institute of Photonics, University of Eastern Finland, Joensuu FI-80101, Finland

[*]corresponding author: paivi.torma@aalto.fi

[#]presenting author: grazia.salerno@aalto.fi

Abstract: Multiparticle unit cells of nanoparticle arrays are a promising concept for realizing quasi-BIC modes whose darkness in the far-field is topologically protected against imperfections. By combining theory with polarization-resolved measurements of the emission, we show that the lasing emission from a plasmonic quadrumer array has a topological charge.



Metal nanoparticle arrays exhibit surface lattice resonances (SLRs), creating plasmonic-photonic modes with controllable dispersion. When combined with a gain medium, SLRs provide light-matter interaction, resulting in various phenomena such as lasing and Bose-Einstein condensation [1,2]. Thus far, simple unit cells of only one or two particles have been studied extensively, while the potential of complex unit cells with many particles is only starting to be explored. Our work focuses on a quadrumer nanoparticle arrays, and we show the unique characteristics of the multiparticle unit cell enables unique lasing characteristics [3].

We study lasing from a bound-state-in-continuum (BIC) mode, arising from the quadrupolar nature enforced by the quadrumer unit cell. BICs are localized states decoupled from the extended modes of the continuum, and are appealing for applications in lasing, filtering, or sensing [4-5]. They possess a quantized topological charge and are dark in outgoing radiation [6]. Our work combines a two-dimensional SLR lattice with a gain medium, observing emission primarily at sample edges and

corners. Under optical pumping, we experimentally observe the strongest emission at the corners and edges of the sample. By theoretical analysis of the isolated quadrumer, combined with numerical analysis of the electromagnetic fields both in finite and infinite systems, we identify BIC modes in an infinite lattice, and quasi-BIC in a finite one. Comparison of polarization-resolved lasing images to the numerical calculations reveals the lasing occurs in a quasi-BIC mode. The mechanism of coupling the BIC light to far field is in our system provided by the edges of the sample. We observe a nontrivial winding of the polarization field both in the experiments and simulations, indicating a nonzero topological charge.

The lasing BIC mode exhibits a high Q-factor (Q ~ 1400), surpassing typical SLR modes (Q ~ 300) [7]. The potential of nanoparticle complexes in designing topologically protected high-Q modes for lasing is demonstrated, with implications for understanding loss-dependent momentum dependence of the Q-factor. This study showcases lasing in a system with complex unit cells, highlighting the role of structure in determining mode characteristics and the potential of sample edges as leakage mechanisms for quasi-BICs, where losses significantly impact the quasi-BIC mode [8].

References

1. Moerland, Rekola, Eskelinen, Martikainen, Kim, and Törmä, *Nano Letters* **14**, 1721 (2014)
2. Hakala, Moilanen, Vakevainen, Guo, Martikainen, Daskalakis, Rekola, Julku, and Törmä, *Phys.14*, 739 (2018)
3. Heilmann, Salerno, Cuerda, Hakala, and Törmä, *ACS Photonics* **9**, 224 (2022).
4. Hsu,Zhen,Stone,Joannopoulos, andSoljačić, *Rev. Mater.* **1**, 1 (2016)
5. Kodigala,Lepetit,Gu,Bahari, Fainman, and Kante,*Nature* **541**, 196 (2017)
6. Zhen; Hsu,Lu, Stone, and Soljačić, *Rev. Lett.* **113**, 257401 (2014)
7. Kravets,Kabashin, Barnes, and Grigorenko, *Rev.* 118, 5912 (2018)
8. Salerno, Heilmann, Arjas, Aronen, Martikainen, and Törmä, *Rev. Lett.* **129**, 173901 (2022)

Stable-to-unstable transition in quantum friction

D. Oue[1,2*], J. B. Pendry[2], and M. G. Silveirinha[1]

[1]Instituto de Telecomunicações, Instituto Superior Técnico, University of Lisbon, Portugal
[2]The Blackett Laboratory, Department of Physics, Imperial College London, the United Kingdom
[*]corresponding author: daigo.oue@gmail.com

Abstract: We utilise a fully quantum-mechanical theory without perturbative approximations to investigate non-contact friction between two metallic bodies in relative motion, employing modified fluctuation-dissipation relations.

We demonstrate that when the metallic slabs are engaged in relative motion (Figure 1), low-frequency waves can undergo amplification, fundamentally altering the fluctuation-dissipation relation. Thereby, the metallic slabs can behave as gain media. This amplification, tailored by the Doppler effect, occurs in a directionally selective manner. By incorporating the modified fluctuation-dissipation relations for gain media, we rediscover the formula for frictional force previously postulated by Pendry et al. [1-3]. The directionally selective wave amplification results in the frictional force.

Moreover, the strength of interaction between the two slabs, their relative velocity, and the degree of dissipation jointly determine the stability of the system. In an unstable scenario, the modes of the system may experience exponential growth, culminating in the divergence of the frictional force. This shift from stability to instability is governed by the poles of Green's function. When one of the poles traverses the real frequency axis and enters the upper half of the complex frequency plane, the associated mode undergoes time growth rather than damping. Consequently, above the instability threshold, the quantum friction process is not stationary in time.

Furthermore, our study establishes a link between the quantum friction between two metal sheets and the classical Kelvin-Helmholtz instability (KHI). In the quasistatic limit, the equations of motion of the electromagnetic problem coincide with those governing KHI. Consequently, the instability in our quantum system emerges as a quantum electromagnetic analogue of the well-known Kelvin-Helmholtz instability, providing new insights into non-contact friction physics.

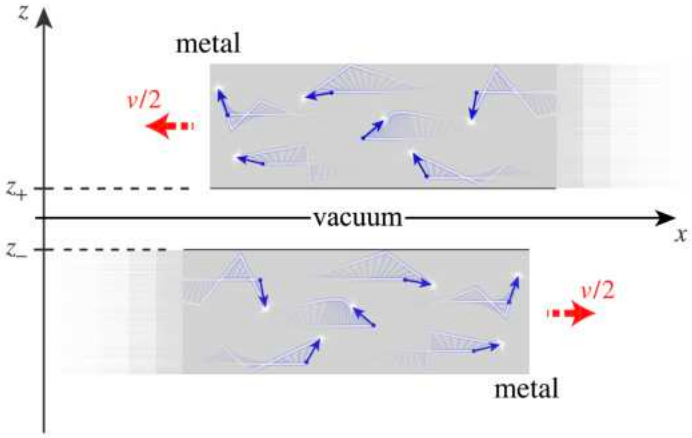


Figure 1. Schematic of the system analysed in this work: two metal sheets in a shear motion separated by a vacuum gap. The metallic medium is subject to finite damping, which implies the existence of noise currents in the medium (indicated by blue arrows).

Acknowledgements. D.O. is supported by JSPS Overseas Research Fellowship, by the Institution of Engineering and Technology (IET), and by Fundação para a Ciência e a Tecnologia and Instituto de Telecomunicações under project UIDB/50008/2020. J.B.P. acknowledges support from the Gordon and Betty Moore Foundation.

References

1. Pendry, J. B. “Shearing the vacuum—quantum friction,” J. Phys.: Condens. Matter Vol. 9, 10301–10320, 1997.
2. Volokitin, A. and Persson, B. “Theory of friction: the contribution from a fluctuating electromagnetic field,” J. Phys.: Condens. Matter 11, 345–359, 1999.
3. Brevik, I., Shapiro, B. and Silveirinha, M. G. “Fluctuational electrodynamics in and out of equilibrium,” Int. J. Mod. Phys. A 37, 2241012, 2022.

On-Chip Metaphotonics Empowered Single-Photon Emission

Yinhui Kan[1*], Xujing Liu[1], and Sergey I. Bozhevolnyi[1*]

[1] Center for Nano Optics, University of Southern Denmark, DK-5230 Odense M, Denmark
[*]corresponding author: yk@mci.sdu.dk; seib@mci.sdu.dk

Abstract: We present a new avenue by introducing array of subwavelength nanostructures to on-chip couple with quantum emitters (QEs), which can efficiently outcouple the QEs-excited nonradiative surface plasmon polaritons to photon emission encoded with desired properties, i.e., directionality, specific spin and orbital angular momenta.

Generation of single photon beams with desired directionality, polarizations, and phase fronts is at the cornerstone of both classical and quantum optics.[1] However, conventional approaches for molding single-photon emission, relying on external bulky devices, such as polarization filters and spiral phase plates, decrease not only the compactness of single-photon configurations but also their efficiency and brightness. Efficient integration of quantum emitters (QEs) with beam shaping and polarization encoding functionalities has always been on the agenda but heretofore remained elusive.

Here, we present a new avenue by introducing metasurfaces to on-chip couple with QEs, which can efficiently outcouple the QEs-excited nonradiative surface plasmon polaritons to photon emission encoded with specific spin and orbital angular momenta (SAM and OAM), respectively.[2-4] We have also realized independent manipulation of the single-photon SAM and OAM states by using metasurface dimers of orthogonal nanobricks that generate (by scattering) high purity SAM (98% for S3 > 0.9).[5] By arranging the nanobrick dimers along different metasurface trajectories controlling OAM, high-purity SAM states are superimposed with OAM states corresponding to different phase-front helicities, for example, l = 0, 1, and 2. Furthermore, we have demonstrated the generation of high-purity linearly polarized (LP) single-photon vortex beams. Remarkably, the design strategy enables simultaneous generation of high-purity orthogonal LP single-photon beams with arbitrary different OAMs, meeting thereby growing demands for increasing the quantum information channel capacity.[6] Thus, by selectively covering azimuthally different metasurface areas with differently arranged nanobricks, we realize multiplexing of single-photon emission channels with orthogonal LPs carrying different topological charges (OAMs) and confirm their entanglement.

Moreover, we develop the vectorial scattering holography approach, as an inverse design method, with both single-channel and multiple-channel regimes for flexibly designing versatile on-chip QE-coupled metasurfaces.[7-9] Based on the proposed approach, we design, fabricate, and characterize on-chip quantum light sources of two well-collimated single-photon beams propagating along different off-normal directions with orthogonal linear polarizations.[8] Furthermore, we experimentally demonstrate on-chip generation of multichannel quantum emission encoded with different SAMs and OAMs in each channel.[9] The multichannel holography approach is further extended for tempering the strength of QE emission into a particular channel. The holography-based inverse design approach developed and demonstrated on-chip quantum light sources with multiple degrees of freedoms enable thereby a powerful platform for quantum nanophotonics, especially relevant for advanced quantum photonic applications, e.g., high-dimensional quantum information processing.

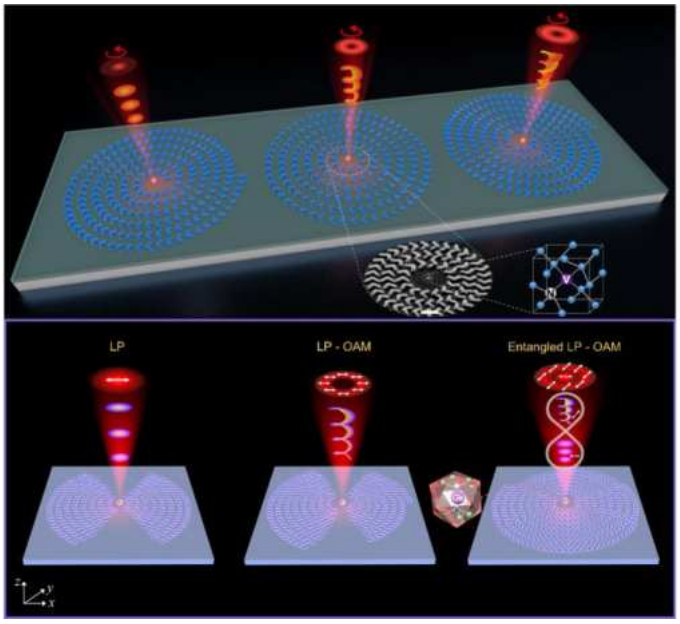


Figure 1. On-chip metaphotonics empowered single-photon emission.

Acknowledgements References

The authors acknowledge the support from National Natural Science Foundation of China (Grant No. 62105150), Natural Science Foundation of Jiangsu Province (BK20210289), European Union's Horizon Europe research and innovation programme under the Marie Skłodowska-Curie Action (Grant agreement No. 101064471), and Villum Kann Rasmussen Foundation (Award in Technical and Natural Sciences 2019).

References

1. Forbes, A., Oliveira, M. de and Dennis, M. R. "Structured light," Nat. Photonics, 15, 253–262, 2021.
2. Kan, Y. H., Andersen, S. K. H., Ding, F., Zhao, C. Y., Bozhevolnyi, S. I., "Metasurface-enabled generation of circularly polarized single photons," Adv. Mater., 32 (16), 1907832, 2020.
3. Kan, Y. H., Ding, F., Zhao, C. Y., Bozhevolnyi, S. I., "Directional off-normal photon streaming from hybrid plasmon-emitter coupled metasurfaces." ACS Photonics, 7(5), 1111-1116, 2020.
4. Wu, C., Kumar, S., Kan, Y. H., Komisar, D., Wang Z., Bozhevolnyi, S. I., Ding, F., "Room-temperature on-chip orbital angular momentum single-photon sources," Sci. Adv., 8 (2), eabk3075, 2022.
5. Liu, X., Kan, Y. H., Kumar, S., Komisar, D., Zhao, C. Y., Bozhevolnyi, S. I., "On-chip generation of single-photon circularly polarized single-mode vortex beams," Sci. Adv. 9 (32), eadh0725, 2023.
6. Liu, X., Kan, Y. H., Kumar, S., Kulikova, L. F., Davydov, V. A., Agafonov, V. N., Zhao, C. Y., Bozhevolnyi, S. I., "Ultracompact single-photon sources of linearly polarized vortex beams," Adv. Mater., 36, 202304495, 2024.
7. Kan, Y. H., Bozhevolnyi, S. I., "Molding photon emission with hybrid plasmon-emitter coupled metasurfaces," Adv. Opt. Mater., 10 (12), 2102697, 2022.
8. Komisar, D., Kumar, S., Kan, Y. H., Meng, C., Kulikova, L. F., Davydov, V. A., Agafonov, V. N., Bozhevolnyi, S. I., "Multiple channelling single-photon emission with scattering holography designed metasurfaces," Nat. Commun., 14 (1), 6253, 2023.
9. Kan, Y. H., Liu, X., Kumar, S., Bozhevolnyi, S. I., "Multichannel quantum emission with on-chip emitter-coupled holographic metasurfaces," ACS Nano, 17, 20, 20308–20314, 2023.

Dual-Band Control of Bound States in the Continuum with Pairwise Positioning of Singularities in Metasurfaces

Chloe F. Doiron[1]

[1]Sandia National Laboratories, USA
*corresponding author: cfdoiro@sandia.gov

Abstract: Applications of metasurfaces in classical and quantum optics are driving the need for polarization control of nearly-degenerate, high quality-factor (Q) modes. To address this need, we developed and experimentally demonstrated a design paradigm for controlling the Q-factors, mode splittings, and polarization responses of pairs of high-Q modes in dielectric metasurfaces.

Controlling the quality (Q) factor and far-field polarization response of a metasurface is critical for many applications in classical and quantum optics with new applications driving the creation of increasingly sophisticated devices that require multi-dimensional control. In particular, one emerging need is the ability to robustly create and control nearly-degenerate pairs of high-Q modes while shaping the frequency splitting, Q-factors, and polarization responses across two bands simultaneously. Achieving such comprehensive control would create pathways for enhancing metasurfaces in applications ranging from sensing to generating entangled photon-pairs, as well as enhancing non-linear mixing.

Here, we present and experimentally demonstrate a paradigm rooted in group theory for creating and choreographing guaranteed pairs of bound states in the continuum (BICs) — modes that are completely decoupled from the radiation continuum and therefore have infinite Q-factors [1]. By starting with guaranteed pairs of symmetry-protected BICs found in triangular lattices with six-fold rotational symmetry, symmetry breaking operations can independently control the frequency splitting and Q-factor with two-fold rotational symmetry breaking controlling Q-factors and three-fold rotational symmetry breaking controlling mode splitting (Figure 1) [2].

Moreover, the presence of BICs results in the formations of polarization singularities (points where the major axis of the polarization ellipse orientation is ill-defined). Because the variation of polarization away from these singularities is smooth and predictable, the positioning of these singularities can control the polarization response of the entire band. We will show pairwise generation, annihilation, and positioning of polarization singularities,

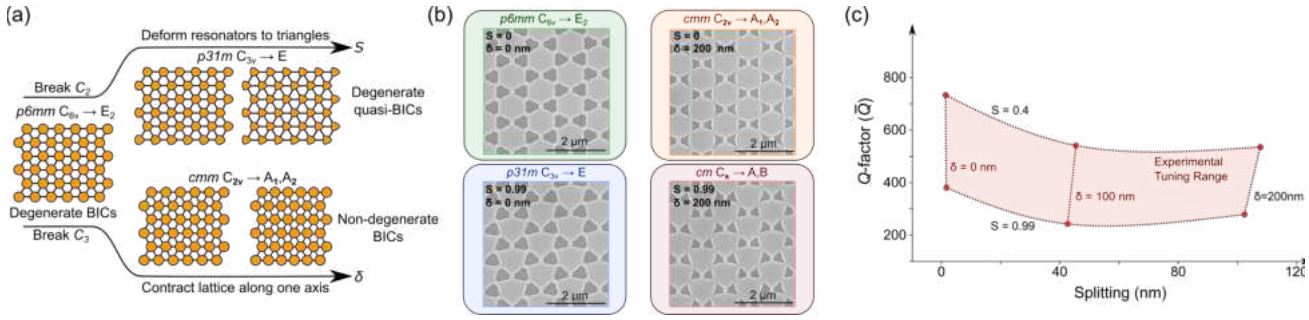


Figure 1: (a) By deforming the circular resonators into triangles, two-fold rotational symmetry (C_2) can be broken. Correspondingly, three-fold rotational symmetry (C_3) can be broken by contracting the lattice along one axis. (b) Scanning electron micrographs of silicon metasurfaces in all four symmetry phases. (c) Experimentally measured Q-factors and mode splitting for silicon metasurfaces with three-fold symmetry breaking (δ) controlling splitting and two-fold rotational symmetry breaking (S) controlling Q-factors.

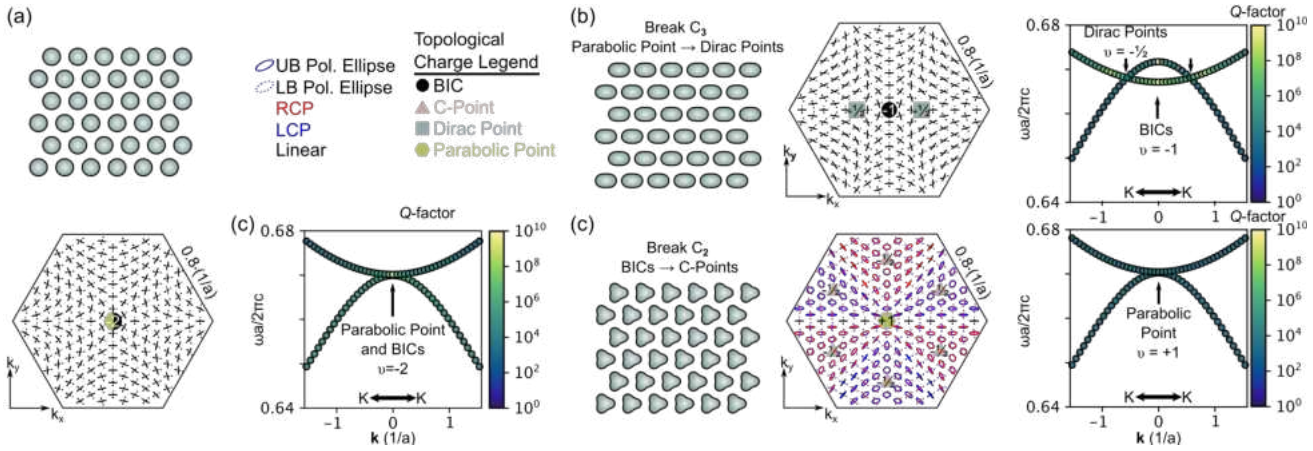


Figure 2: (a) When all symmetries of the triangular lattice are preserved, symmetry-guaranteed pairs of symmetry-protected BICs can form. Looking at the eigenpolarization near the **Γ**-point, a topological singularity exists at the **Γ**-point with topological charge (-2) arising from the presence of BICs and a parabolic degeneracy. (b) When a C_3 symmetry breaking deformation is applied to the resonators in the triangular lattice, the degeneracy is lifted resulting in the creation of two Dirac-points, but two symmetry-protected BICs remain. (c) Correspondingly, when a C_2 symmetry breaking deformation is applied, the parabolic degeneracy is preserved but the symmetry-protected BICs are converted to quasi-BICs resulting in the creation of 6 C-points per band.

derived from symmetry-guaranteed pairs of symmetry-protected bound states in the continuum in silicon metasurfaces (Figure 2) [3]. Building upon these demonstrations, we will conclude by presenting a design methodology for narrowband wavefront shaping without deeply sub-wavelength features.

Work supported by the US Department of Energy, Office of Basic Energy Sciences, Division of Materials Sciences and Engineering (grant BES 20-017574). The work was performed, in part, at the Center for Integrated Nanotechnologies, an Office of Science User Facility operated for the US Department of Energy, Office of Science. Sandia National Laboratories is a multi-mission laboratory managed and operated by National Technology and Engineering Solutions of Sandia LLC, a wholly owned subsidiary of Honeywell International Inc., for the US Department of Energy's National Nuclear Security Administration under contract DE-NA0003525. This paper describes objective technical results and analysis. Any subjective views or opinions that might be expressed in the paper do not necessarily represent the views of the US Department of Energy or the United States government.

References

1. Hsu, C., Zhen, B., Stone, A. *et al.* Bound states in the continuum. *Nat Rev Mater* 1, 16048, 2016.
2. Doiron, C. F., Brener, I., & Cerjan, A., Realizing symmetry-guaranteed pairs of bound states in the continuum in metasurfaces. *Nature Communications*, *13*(1), 7534, 2022.
3. Doiron, C. F., Brener, I., & Cerjan, A., Topological Polarization Singularities for Full Polarization Control of High-Q Modes. In *CLEO: Fundamental Science* (pp. FF1D-1), 2023.

Tailored generation of biphoton polarization Bell state from an InGaP metasurface

Jinyong Ma[†,1], Tongmiao Fan[†,1], Tuomas Haggren[†,1], Jihua Zhang[1], Saniya Shinde[1,2], Frank Setzpfandt[2,3], Hark Hoe Tan[1], Chennupati Jagadish[1], Dragomir N. Neshev[1], Andrey A. Sukhorukov[1]

†Co-first authors with equal contribution

[1]ARC Centre of Excellence for Transformative Meta-Optical Systems (TMOS), Department of Electronic Materials Engineering, Australian National University, Canberra, ACT 2600, Australia

[2]Abbe Center of Photonics, Friedrich Schiller University Jena, Jena, Germany

[3]Fraunhofer Institute for Applied Optics and Precision Engineering, Jena, Germany

Abstract: We develop, for the first time, an ultrathin source of two-photon polarization Bell states based on an InGaP nonlinear metasurface. The metasurface facilitates a local optical resonance with a tailored angular dispersion, enabling the all-optical tuning of polarization entanglement.

Nonlinear dielectric metasurfaces incorporating subwavelength nanostructures are emerging as promising platforms for generating versatile and highly flexible miniaturized photon pair sources via spontaneous parametric down-conversion (SPDC) [1]. Unlike conventional nonlinear crystals, metasurfaces can enhance and customize SPDC by leveraging optical resonances in the nanostructures. Recent experiments demonstrated strongly enhanced generation of spatially [2] and spectrally [3] entangled photon pairs, as well as counterpropagating emission [4]. While polarization entanglement was proposed in a multiplexed metasurface [5] and was demonstrated in Transition Metal Dichalcogenide thin film [6], the generation in metasurfaces remained an open challenge.

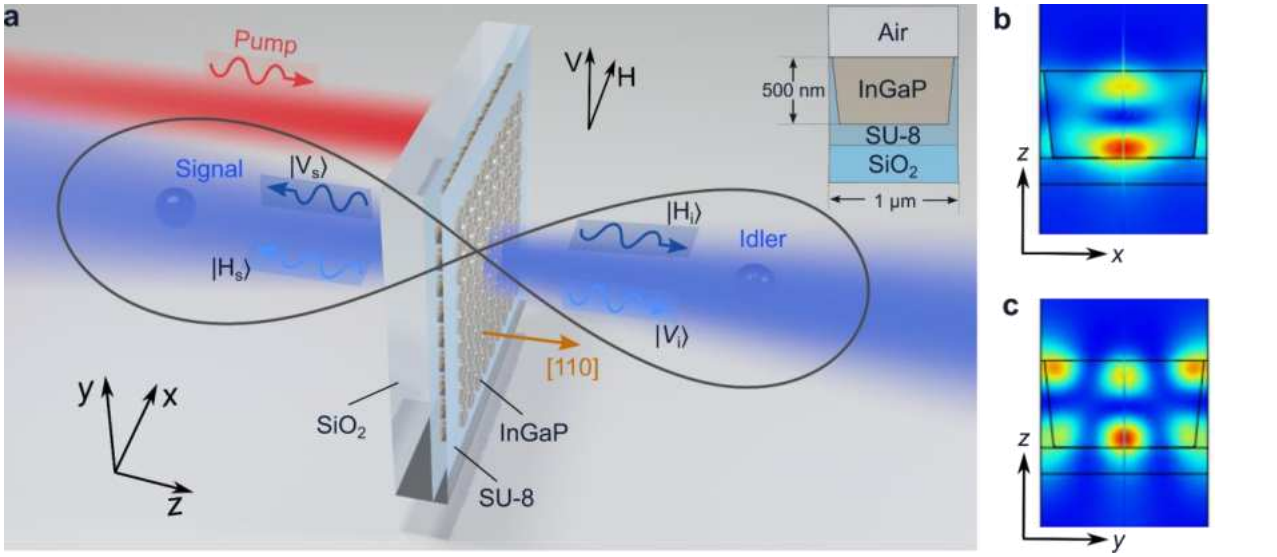


Figure 1 Concept. a. Polarization entanglement from an InGaP nonlinear metasurface. The metasurface incorporating nanostructured <110> InGaP film emit a pair of counter-propagating photons with crossed polarization. The polarization of each photon is uncertain before performing measurements, producing biphoton polarization entanglement. The inset presents the cross-section of a unit cell of the metasurface. **b-c.** Optical mode profile of the metasurface. The metasurface manifests an optical resonance at ~1571 nm, where the optical field inside the InGaP nanostructures is enhanced. The resonance enables enhanced and tailored generation of polarization entanglement.

Here we reveal, for the first time to our knowledge, that enhanced and tailored generation of polarization Bell state can be realized with an InGaP nonlinear metasurface through the SPDC process. The metasurface incorporates nanostructured InGaP film of 500 nm thickness and supports a local optical resonance at 1571 nm, as shown in Fig. 1. The resonance reveals strong field enhancement within the nanostructure (Fig. 1**b-c**), allowing enhanced generation of counterpropagating photon pairs. The InGaP material exhibits low fluorescence and a notably high

second-order susceptibility of 110 pm/V and the selected crystal orientation [110] offers a specific nonlinear tensor for generating cross-polarized photon pairs. Our experiments, displayed in Fig. 2, show that photon-pair rate is enhanced by 25 times in comparison to unstructured film (Fig. 2**a**). The density matrix reconstructed using maximum likelihood estimation confirms the generation of the polarization-entangled state, manifesting a concurrence of 0.92 and fidelity of 95% with the Bell state $|\psi^-\rangle = \frac{1}{\sqrt{2}}(|H_s V_i\rangle - |V_s H_i\rangle)$ (Fig. 2**c-d**). More importantly, we observe that the amplitude α of polarization entanglement $|\psi\rangle = \frac{1}{\sqrt{\alpha^2+1}}(|H_s V_i\rangle - \alpha|V_s H_i\rangle)$ is optically tunable via pump wavelength (Fig. 2**b**) due to nanostructure asymmetry along the light propagation, which is a unique feature unattainable with unstructured nonlinear films. The results will establish the first metasurface-based source of tunable polarization entanglement and manifest an important step closer to quantum communications with quantum light sources from metasurfaces.

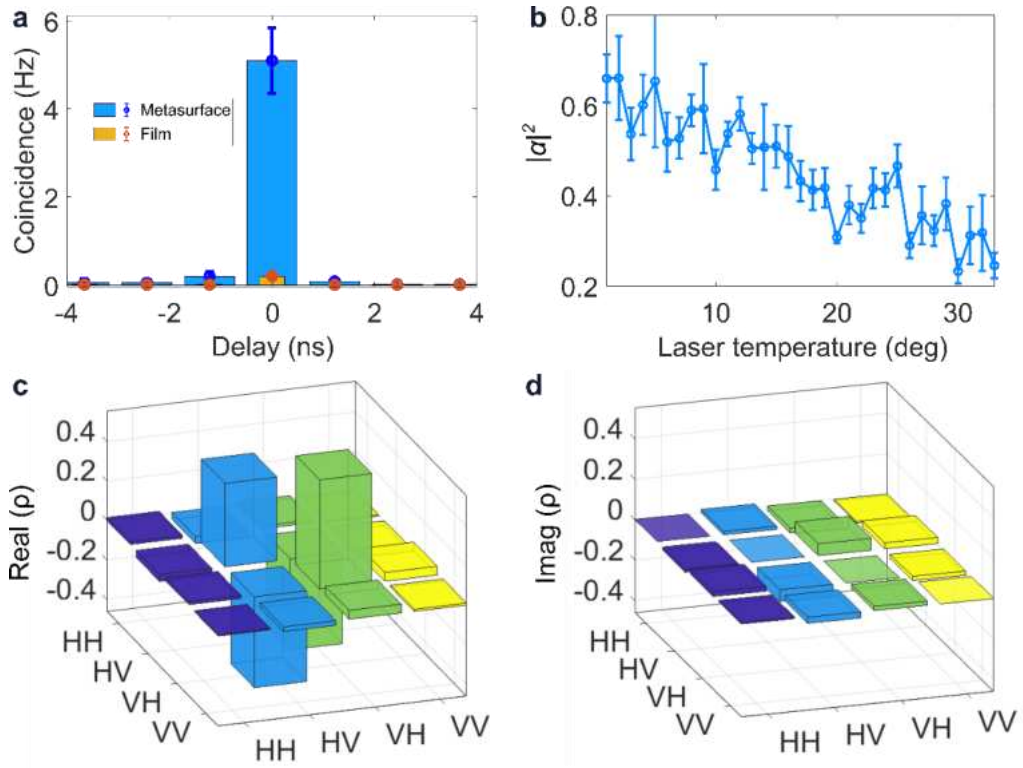


Figure 2 Experimental characterization of tunable polarization entanglement. a. Enhanced SPDC rate with metasurface. The generation rate and coincidence-to-accidental ratio of photon pairs from metasurfaces are both enhanced by ~25 times, as compared to unstructured thin film. **b. All-optical tuning of polarization entanglement.** The amplitude $|\alpha|^2$ of the polarization entanglement is tunable via pump wavelength, which is controlled by the laser temperature in our experiment. **c-d. Quantum tomography of polarization entanglement.** The reconstructed density matrix reveals the generation of a polarization-entangled state, having a concurrence of 0.92 and fidelity of 95% with Bell state. The pump wavelength considered here is ~782 nm.

References

1. Y. Kan and S. I. Bozhevolnyi, Advanced Optical Materials 11, 2202759 (2023).
2. J. Zhang, J. Ma, M. Parry, M. Cai, R. Camacho-Morales, L. Xu, D. N. Neshev, and A. A. Sukhorukov, Sci. Adv. 8, eabq4240 (2022).
3. T. Santiago-Cruz, S. D. Gennaro, O. Mitrofanov, S. Addamane, J. Reno, I. Brener, and M. V. Chekhova, Science 377, 991 (2022).
4. C. Son, V. Sultanov, T. Santiago-Cruz, A. P. Anthur, H. Zhang, R. Paniagua-Dominguez, L. Krivitsky, A. I. Kuznetsov, and M. V. Chekhova, Nanoscale 15, 2567 (2023).
5. J. Ma, J. Zhang, Y. Jiang, T. Fan, M. Parry, D. N. Neshev, and A. A. Sukhorukov, Nano Lett. 23, 8091 (2023).
6. M. A. Weissflog et al., A Tunable Transition Metal Dichalcogenide Entangled Photon-Pair Source, arXiv:2311.16036.

Spontaneous Parametric Downconversion Facilitated by Intrinsic Nonlinear Response of Plasmonic Metal Nanoparticles

A. Piryatinski[1*], S. A. Shah[1], M. R. Clark[2], J. Zyss[3], and M. Sukharev[2,4]

[1]Theoretial Division, Los Alamos National Laboratory, Los Alamos, NM 87545, USA.
[2]Department of Physics, Arizona State University, Tempe, AZ 85287, USA
[3] LUMIN Laboratory and Institut d'Alembert, Ecole Normale Supérieure Paris Saclay, CNRS, Université Paris-Saclay, 4, Avenue des Sciences, Gif-sur- Yvette, France
[4] College of Integrative Science and Arts, Arizona State University, Mesa, Arizona, 85212, USA
[*]corresponding author: apiryat@lanl.gov

Abstract: Our theoretical study explores using L-shaped gold metal nanoparticles with intrinsic plasmonic second-order nonlinearity for spontaneous parametric downconversion. Through quantum optical modeling parameterized by FDTD simulations, it demonstrates the MNPs' potential as probabilistic quantum photon sources suitable for applications as building units of quantum metasurface.

Metal nanoparticles (MNPs) exhibiting plasmonic resonances can serve as essential building blocks of quantum metasurfaces[1]. When paired with semiconductor quantum emitters, they can be used to control quantum light properties, particularly in quantum photon sources. Here, we present a theoretical study of the effect of spontaneous parametric downconversion (SPDC) carried out by the plasmonic MNPs. Leveraging our prior investigation[2], which involved the classical effect of difference-frequency generation within an array of L-shaped Au-MNPs, along with a semiclassical analysis of the SPDC, we now focus on quantum calculations of the SPDC energy conversion rate. The novelty of this research lies in harnessing the intrinsic plasmonic second-order nonlinearity exhibited by the L-shaped MNPs. This property of the MNPs eliminates using quantum emitters or additional nonlinear media as the source of nonlinearity.

As depicted in Fig. 1(a), we examine a 1D array of noninteracting L-shaped MNPs with arms l= 130 nm in length and w=40 nm in width. The thickness, d, of the MNPs is a variable parameter. The array is subject to incident pump pulse of frequency ω_p and intensity I_p polarized in the plane of the MNP array and tuned to the second harmonic frequency of the MNP plasmonic resonance, i.e., $\omega_p = 2\omega_{sp}$. The second-order susceptibility, $\chi^2(\omega_p;\omega,\omega_p-\omega)$, attributed to the MNP plasmonic nonlinearity, facilitates the SPDC of the pump pulse into the signal and idler photon pair of frequencies ω and $\omega_p-\omega$, respectivly. Our quantum optical model provides the following expression for the energy conversion yield, i.e., the ratio of the total plasmon energy of the signal and idler normalized per energy due to the pump photons

$$\eta = \frac{2\hbar}{A\pi\varepsilon_o c^5\left|1+n(\omega_p)\right|^2}\int d\omega\,\omega^3\left[\omega_p-\omega\right]^2\left\{\left|\chi^{(2)}(\omega_p;\omega,\omega_p-\omega)\right|^2+\left|\chi^{(2)}(\omega_p;\omega_p-\omega,\omega)\right|^2\right. \quad (1)$$

$$\left.+2\,\mathrm{Re}\left[\chi^{(2)*}(\omega_p;\omega,\omega_p-\omega)\chi^{(2)}(\omega_p;\omega_p-\omega,\omega)\right]\right\}\iint d^3r d^3r'\,\mathrm{Im}[G(r,r';\omega)]\,\mathrm{Im}\left[G(r,r';\omega_p-\omega)\right].$$

Here, A is the MNP area exposed to the pump, ε_o is the vacuum permittivity, c the speed of light in vacuum, and $n(\omega)$ is the refractive index accounting for the plasmon resonance. $G(r,r';\omega)$ is the MNP Green function defining the signal and idler joint density of states in Eq. (1), represented using the plasmon pole approximation

$$G(r,r';\omega) = \frac{e^{ik(\omega_{sp})(z-z')}}{V(\omega_{sp})\left[\partial(\omega n(\omega))^2/\partial\omega\right]_{\omega=\omega_{sp}}(\omega-\omega_{sp}-i\gamma_{sp})}. \quad (2)$$

In Eq. (2), $k(\omega_{sp}) = n(\omega_{sp})\omega_{sp}/c$ and $V(\omega_{sp}) = \int d^3r\, n(\omega_{sp}, r) e^{2Im[k(\omega_{sp})]z}$ is the surface plasmon mode volume. For comparison, we also consider the semiclassical expression for the idler photon energy yield[2]

$$\kappa = \frac{\hbar d^2}{2\varepsilon_o c^4}\left|\frac{[1+n(\omega_p)]}{1+n(\omega_p-\omega)}\right|^2 \int d\omega\omega^2\left[\omega_p-\omega\right]^2 \left|\chi^{(2)}(\omega_p;\omega,\omega_p-\omega)\right|^2 \mathrm{Im}\left[G(0,0;\omega_p-\omega)\right] \quad (3)$$

$$\times \left|\frac{\sin([k(\omega_p-(\omega_p-\omega)+k(\omega)]d/2)}{[k(\omega_p-(\omega_p-\omega)+k(\omega)]d/2}\right|^2 e^{-\mathrm{Im}[k(\omega_p-\omega)+k(\omega)]d}.$$

To parameterize Eqs. (1)-(3), we consider the Au MNPs. We performed FDTD simulations of the linear and nonlinear plasmonic response using the hydrodynamic model for the conduction electrons coupled with the Maxwell equations for the electromagnetic field. Using the approach developed in Refs.[2,3], we have extracted the linear response, *n(ω)*, characterized by the plasmon energy $\hbar\omega_{sp}$= 1.23eV, linewidth $\hbar\gamma_{sp}$= 0.077eV, and transition dipole p_{sp}= 4.75 10^3D. The nonlinear susceptibility was fit to the anharmonic response model with $|\chi^{(2)}| = 4$ pm/V at the second harmonic energy of the plasmon resonance.[2]

The calculated quantum and semiclassical energy conversion yields are shown in Fig. 1(b) as a function of the MNP thickness *d*. According to the plot, the total energy conversion rate of the signal photons to the signal and idler plasmon quanta is $\eta \sim 10^{-10}$. The energy yield for converting the pump photons to the outgoing idler photons saturates at $\kappa \sim 10^{-11}$. For comparison $\kappa \sim 10^{-12}$ is typical for SPDC process in 1mm thick BBO crystal, suggesting superior performants of the considered MNP of the sizes allowing their incorporation into metasurfaces. It is noteworthy that the difference between η and κ yields can be associated with the nonradiative plasmonic losses. The inset to Fig. 1(b) presents the yield energy distributions peaked at the surface plasmon energy resulting from the plasmon-enhanced SPDC processes.

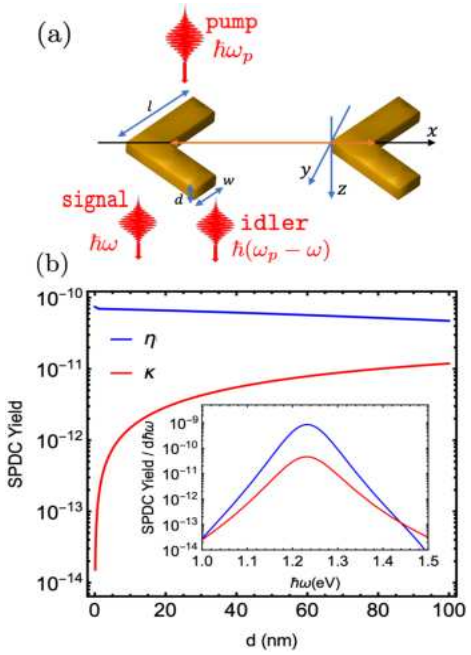


Figure 1 (a) Geometry of MNP subject to incident pump pulse and outgoing signal and idler photon pair. (b) Calculated energy yields vs. MNP thickness *d*. The inset shows yield energy distributions $d\eta/d\hbar\omega$ & $d\kappa/d\hbar\omega$ at *d* = 30 nm.

Acknowledgments: Research at LANL is supported by the LDRD projects No.20230363ER and No.3W400A-XXJ4. Research at ASU is supported by the Air Force Office of Scientific Research under Grant No. FA9550-22-1-0175. This work is performed, in part, at the CINT, an Office of Science User Facility operated for the U.S. Department of Energy (DOE) Office of Science by Los Alamos National Laboratory (Contract 89 233 218CNA000001) and Sandia National Laboratories (Contract DE-NA-0003525) (user project No. 2021BC0087).

References:

1. Solntsev, A. S., Agarwal, G. S., and Y. S. Kivshar, "Metasurfaces for quantum photonics," Nat. Photonics, Vol. 15, 327–336, 2021.
2. Shah, S. A., Clark, M. R., Sukharev, M., and A. Piryatinski, "Interplay of gain and loss in arrays of nonlinear plasmonic nanoparticles: toward parametric downconversion and amplification", Opt. Lett. (in press), arXiv:2312.06897.
3. Minh Ngo, H., Drobnyh, E., Sukharev, M. KhuongVo, Q., Zyss, J., and I. Ledoux-Rak "High yield synthesis and quadratic non-linearities of gold nanoprisms in solution: The role of corner sharpness," Isr. J. Chem. Vol. 63, e202200009, 2023.

Quantum light-matter interfaces with arrays of trapped atoms

E. Shahmoon[1,*]

[1]Department of Chemical & Biological Physics, Weizmann Institute of Science, Rehovot 7610001, Israel
[*]corresponding author: ephraim.shahmoon@weizmann.ac.il

Abstract: We develop a general framework for the design of efficient atom-array quantum interfaces. Our approach relies on the mapping of realistic, collective atomic systems to a generic 1D model of a quantum interface, characterized by a reflectivity parameter. This gives a universal relation between a simple measurable quantity – the reflectivity – and various desired quantum tasks, from quantum memories to entanglement generation.

Arrays of laser-trapped atoms, such as optical lattices or tweezer arrays, form some of the most prominent quantum platforms, with applications in quantum simulations, metrology and computation. Recent studies highlighted that they may also couple strongly to light, as evident by their strong reflectivity [1-3]. For spatially ordered arrays, this strong coupling results from the combination between spatial order and the collective response to light, established by photon-mediated dipole-dipole interactions between the atoms. Subsequent studies found that this strong coupling is also useful in various quantum tasks such as quantum memories [4] and entanglement generation between photons [5-7]. This motivates a systematic study of atomic arrays as a new type of quantum interfaces which rely on collective effects to enable the efficient transfer of quantum information from propagating photons to atoms, crucial for a variety of quantum tasks.

To this end, we develop a universal approach for the analysis of two-sided quantum interfaces in collective atomic systems, relying on the mapping to a generic 1D scattering model characterized by a reflectivity [8]. This entails two important consequences: (i) the efficiency of the quantum interface in performing various quantum tasks is characterized by a measurement or a simple classical calculation of a reflectivity; (ii) we show how the reflectivity, and hence the efficiency, can be greatly enhanced by a properly designed photon mode which spatially matches the collective eigenmodes of the array structure.

Our methodology consists of two parts: (i) 1D model of a quantum interface and its characterization by a reflectivity; (ii) procedure for the mapping of a collective atom-photon system to the 1D model. Beginning with the former, we consider a minimal 1D model for a two-sided atom-photon interface: a collective mode of atomic dipoles P is coupled to a 1D-propagating ``target" photon mode E, while also scattering to other modes considered as loss. Denoting the ratio of these couplings by the cooperativity $C=\Gamma/\gamma_{\rm loss}$, we find that the on-resonance reflectivity of the target mode, given by $r_0=C/(C+1)$, fully characterizes atom-photon coupling. In particular, r_0 is equal to the efficiency of energy conversion between the dipole P and the target mode E and hence emerges as a universal figure of merit of quantum tasks. This can be demonstrated for efficiencies of quantum memory and entanglement generation [8].

The second part is to identify the mapping of given atom-photon systems to the two-sided 1D model. We consider a general collection of atoms interacting with a paraxial target photon mode in free space, accounting for collective dipole-dipole interactions between the atoms. For atoms on a single plane, we find that the mapping is possible if the transverse profile of the target mode E spatially matches an eigenmode P of the dipole-dipole interaction kernel whose eigenvalue is denoted by D_0. While P can decay to both the target mode E and to other photon modes at a total rate $\Gamma_0 = 2\mathrm{Im}[D_0]$, we find a general formula for its coupling rate to the target mode $\Gamma<\Gamma_0$, yielding the mapping parameters Γ and $\gamma_{\rm loss} = \Gamma_0 - \Gamma$ [9]. For multiple planar atomic layers, the mapping is possible when the inter-layer distance is an

integer multiple of half of the wavelength, yielding Γ that increases linearly with the number of layers.

We apply our approach for the description and design of realistic atom-array interfaces [8]:

2D and 3D lattice arrays: We derive analytical expressions for typical cases of ordered arrays considering their finite size and position disorder. The mapping to the 1D model is established, showing that a target photon mode in a typical Gaussian-beam shape matches an approximate eigenmode of the dipole-dipole interaction, whereas deviations due to imperfections are accounted for by the loss parameter γ_{loss}. Analytical results for r_0 derived from the mapping theory agree with numerical results of both the reflectivity and the efficiency of a quantum memory protocol.

Beyond lattice symmetry: Considering a 2D ordered array with a finite filling fraction, we show how the reflectivity can be greatly enhanced if we go beyond the typical case of a Gaussian-beam target mode. Choosing a target mode that matches a dipole eigenmode, we obtain efficiencies of r_0=0.99 and r_0=0.94 for filling fractions as low as 85% and 70%, instead of much lower efficiencies with a typical Gaussian-beam target mode. Analytical results agree with numerical ones, showing that the mapping is valid so that enhancement of r_0 implies enhanced efficiencies of quantum tasks. We also consider a circular array, again demonstrating efficient coupling of corresponding paraxial dipole eigenmodes.

Going forward, this approach opens the prospect for a unified treatment of more applications and platforms, as demonstrated by our subsequent works. First, considering quantum tasks beyond those discussed here, e.g. the dissipative transfer of squeezing correlations [9]; Second, considering atom-array interfaces beyond the geometries discussed above, e.g. using tweezer atom arrays [10,11].

We acknowledge financial support from the Israel Science Foundation (ISF) the Directorate for Defense Research and Development (DDR&D), the Center for New Scientists at the Weizmann Institute of Science, the Council for Higher Education (Israel), and QUANTERA (PACE-IN). This research is made possible in part by the historic generosity of the Harold Perlman Family.

References

1. R. J. Bettles, S. A. Gardiner and C. S. Adams, Phys. Rev. Lett. 116, 103602 (2016).
2. E. Shahmoon, D. S. Wild, M. D. Lukin and S. F. Yelin, Phys. Rev. Lett. 118, 113601 (2017).
3. J. Rui et al., Nature, 583, 369 (2020).
4. M. T. Manzoni, M. Moreno-Cardoner and A. Asenjo-Garcia, J. V. Porto, A. V. Gorshkov, and D. E. Chang, N. J. Phys. 20, 083048 (2018).
5. M. Moreno-Cardoner, D. Goncalves, and D. E. Chang, Phys. Rev. Lett., 127 (26), 263602 (2021).
6. L. Zhang, V. Walther, K. Molmer, and T. Pohl, Quantum, 6, 674, (2022).
7. Y. Solomons, and E. Shahmoon, Phys. Rev. A 107, 033709 (2023).
8. Solomons Y., Ben-Maimon R., and Shahmoon E., PRX Quantum (accepted 2024), preprint: arXiv:2302.04913
9. R. Ben-Maimon, Y. Solomons and E. Shahmoon, preprint: arXiv:2311.03898
10. Y. Solomons, I. Shani, O. Firstenberg, N. Davidson, and E. Shahmoon, preprint: arXiv:2312.11104
11. R. Ben-Maimon, Y. Solomons, N. Davidson, O. Firstenberg, and E. Shahmoon, preprint: arXiv: 2402.06839

Lattice Resonances in Periodic Arrays with Multiparticle Unit Cells

A. Manjavacas[1*]

[1]Instituto de Óptica (IO-CSIC) Consejo Superior de Investigaciones Científicas, Spain
[*]corresponding author: a.manjavacas@csic.es

Abstract: We explore novel functionalities provided by the lattice resonances supported by periodic arrays of nanostructures with multiparticle unit cells.

Two-dimensional periodic arrays of metallic nanostructures can support collective optical modes known as lattice resonances. These excitations occur at wavelengths commensurate with the periodicity of the array and give rise to very strong and spectrally narrow optical responses. Thanks to these exceptional properties, periodic arrays are being exploited in a wide variety of applications [1]. In this contribution, we will discuss some recent theoretical advances on the topic of lattice resonances. In particular, we will analyze the response of arrays with multi-particle unit cells using an analytical approach based on hybridization theory [2], which provides a simple and efficient way to design periodic arrays with engineered properties [3,4]. Furthermore, we will explore how the response of a periodic array is affected by the characteristics of the source used to excite it [5-7]. Finally, we will analyze different array geometries that support lattice resonances with extraordinary properties such as perfect circular dichroism [8] and perfect absorption [9].

References

1. Kravets, V. G.; Kabashin, A. V.; Barnes, W. L.; and Grigorenko, A. N., “Plasmonic Surface Lattice Resonances: A Review of Properties and Applications,” Chem. Rev., 118, 5912, 2018.
2. Baur, S.; Sanders, S.; and Manjavacas, A., “Hybridization of Lattice Resonances,” ACS Nano, 12, 1618, 2018.
3. Cuartero-González, A.; Sanders, S.; Zundel, L., Fernández-Domínguez, A. I.; and A. Manjavacas, “Super- and Subradiant Lattice Resonances in Bipartite Nanoparticle Arrays,” ACS Nano, 14, 11876, 2020.
4. Alvarez-Serrano, J. J.; Deop-Ruano, J. R.; Aglieri, V.; Toma, A.; and Manjavacas, A., “Normal Incidence Excitation of Out-of-Plane Lattice Resonances in Bipartite Arrays of Metallic Nanostructures,” ACS Photonics, 11, 301, 2024.
5. Zundel, L.; Cuartero-González, A.; Sanders, S.; Fernández-Domínguez, A. I.; and Manjavacas, A., “Green Tensor Analysis of Lattice Resonances in Periodic Arrays of Nanoparticles,” ACS Photonics, 9, 540, 2022.
6. Zundel, L.; Deop-Ruano, J. R.; Martínez-Herrero, R.; and Manjavacas, A., “Lattice Resonances Excited by Finite-Width Light Beams.,” ACS Omega, 7, 31431, 2022.
7. Zundel, L.; Malone, K.; Cerdán, L.; Martínez-Herrero, R.; and Manjavacas, A., “Lattice Resonances for Thermoplasmonics,” ACS Photonics, 10, 274, 2023.
8. Cerdán, L.; Zundel, L.; and Manjavacas, A., “Chiral Lattice Resonances in 2.5-Dimensional Periodic Arrays with Achiral Unit Cells.,” ACS Photonics, 10, 1925, 2023.
9. Cerdán, L.; Deop-Ruano, J. R.; Alvarez-Serrano, J. J.; and Manjavacas, A., “Perfect Absorption with Independent Electric and Magnetic Lattice Resonances in Metallo-Dielectric Arrays,” Adv. Optical Mater., 2302737, 2024.

Controlling quantum states and quantum noise with nonlinear photonics

Nicholas Rivera[1]

[1]Department of Physics, Harvard University, Cambridge MA 02138
[*]corresponding author: nrivera@fas.harvard.edu

Abstract: We present recent theoretical and experimental results on using engineered nonlinear interactions to generate elusive quantum states of light and control quantum noise of electromagnetic fields.

The quantum mechanical nature of electromagnetic fields has a variety of important consequences for fields such as sensing, microscopy, laser physics, communications, and quantum information processing. There are several bottlenecks in realizing broad application of quantum states of light. One is that it is currently challenging to deterministically produce an important class of quantum light states called non-Gaussian quantum states, even given powerful resources like single and few-photon nonlinearities realizable in cavity quantum electrodynamics and excitonic systems. The other bottleneck is that many applications, even those that rely on Gaussian states (e.g., squeezed states), require control over highly multimode systems, where quantum noise dynamics are not well-understood. With respect to the first bottleneck, we present a new approach which enables deterministic generation of important non-Gaussian states. The approach is based on combining few-photon nonlinearities with engineered loss and/or gain to create nonlinear loss and gain that promotes the creation of these states. As an example, we will show how certain types of nonlinear cavities and beamsplitters can enable creation of Fock and Schrodinger cat states from simple coherent-state inputs [1-4]. Along the lines of controlling highly multimode quantum systems, we present a new theoretical approach called quantum sensitivity analysis that enables prediction of quantum noise dynamics in highly multimode nonlinear systems [5]. Guided by this theoretical framework, we experimentally demonstrated new low-noise correlated states in the phenomenon of supercontinuum generation [5], as well as quantum correlated states in highly multimode nonlinear fibers [6].

N. R. acknowledges support of a Junior Fellowship from the Harvard Society of Fellows.

[1] **Rivera, Nicholas***, Jamison Sloan*, Yannick Salamin, John D. Joannopoulos, and Marin Soljačić. "Creating large Fock states and massively squeezed states in optics using systems with nonlinear bound states in the continuum." *Proceedings of the National Academy of Sciences* 120.9 (2023): e2219208120.

[2**]** Sean Chen, **Nicholas Rivera**, Jamison Sloan, and Marin Soljačić. "Deterministic quantum state generators and stabilizers from nonlinear photonic filter cavities." *arXiv preprint arXiv:2312.07386* (2023).

[3] Jamison Sloan, **Nicholas Rivera***, and Marin Soljačić. "Driven-dissipative phases and dynamics in non-Markovian nonlinear photonics." *arXiv preprint arXiv:2309.09863* (2023).

[4] Nguyen, Linh, Jamison Sloan, **Nicholas Rivera**, and Marin Soljačić. "Intense squeezed light from lasers with sharply nonlinear gain at optical frequencies." *Physical Review Letters* 131.17 (2023): 173801.

[5] Shiekh Zia Uddin* and **Nicholas Rivera*** et al. "An ab initio framework for understanding and controlling quantum fluctuations in highly multimoded light-matter systems." *arXiv preprint arXiv:2311.05535* (2023).

[6] Shiekh Zia Uddin *, Jamison Sloan*, **Nicholas Rivera**, Sahil Pontula, Yannick Salamin, Michael Birk, Pavel Sidorenko, Ido Kaminer, and Marin Soljačić. "Quantum correlations in multimode nonlinear optics." Conference on Lasers and Electro-Optics (2024).

Recent progress on photon pair generation in semiconductor metasurfaces

T. Santiago-Cruz[1,2*], J. Noh[1,2], V. Sultanov[3,4], S. D. Gennaro[1,2], C. F. Doiron[1,2], H. Jung[1,2], M. V. Chekhova[3,4], and I. Brener[1,2]

[1]Sandia National Laboratories, Albuquerque, New Mexico 87185, USA.
[2]Center for Integrated Nanotechnologies, Sandia National Laboratories, Albuquerque, New Mexico 87185, USA.
[3]Max Planck Institute for the Science of Light, 91058 Erlangen, Germany.
[4]Friedrich-Alexander-Universität Erlangen-Nürnberg, 91058 Erlangen, Germany.
[*]corresponding author: tomasstgox@gmail.com

Abstract: In this talk, I will discuss the generation of photon pairs driven by quasi bound states in the continuum resonances in metasurfaces made of gallium arsenide of two different crystallographic orientations, and how these resonances can shape the polarisation state of the emitted photons.

Metasurfaces hold a big potential for the engineering of the quantum state of photon pairs. Indeed, since the first demonstration of photon pair generation from metasurfaces via Mie-type resonances [1] in 2021, it was clear that metasurfaces could shape the emission of photon pairs in different degrees of freedom such as frequency, direction of emission, and polarisation.

We generate photon pairs via spontaneous parametric down-conversion (SPDC) in metasurfaces made of GaAs wafers. SPDC is a quantum process where a higher-energy pump photon is split into two lower-energy photons after interacting with a second-order nonlinear material (e.g. a GaAs metasurface). The metasurfaces studied here feature quasi bound states in the continuum (qBIC) resonances of relatively high quality factors ($300 < Q < 1600$) at multiple wavelengths in the telecom range. The mechanism of photon pair generation is the following. The qBIC resonance enhances the zero-point vacuum fluctuations at a particular wavelength. Then, when a pump photon interacts with the metasurface, its energy is split into two photons, one of them being emitted by the qBIC mode which is driving the nonlinear interaction, forcing the emission of the other (conjugate) photon at the wavelength that conserves the energy. The resonance not only fixes the wavelengths of emission but also enhances the conversion efficiency. Using qBIC resonances, it was possible to demonstrate the spatially-entangled emission of photon pairs [2], and the frequency-multiplexed emission of photon pairs [3] using multiple qBIC resonances. More complex scenarios have been demonstrated too, such as bidirectional and collinear emission of frequency non-degenerate photon pairs [4], and the more general case of photon pairs being emitted in opposite directions at complementary angles, where the angle of emission can be tuned via the pump wavelength [5].

Most studies have focused on the spectral and emission direction degrees of freedom, but polarisation, which is essential in quantum information applications, remains practically unexplored. A recent work [6] characterized the polarisation state of photon pairs emitted in nonlocal metasurfaces and suggested a configuration for the generation of Bell states.

In this work, we performed a complete polarisation tomography of photon pairs emitted by qBIC resonances in metasurfaces made of (001)-oriented GaAs [3]. By carrying out two-photon polarisation tomography measurements of frequency-nondegenerate photon pairs, we reconstructed the density matrix and calculated the

purity of the photons. Here, the nondegenerate emission was driven by a single resonance, that is, one photon is emitted at the resonance wavelength, and the conjugate photon is emitted at the wavelength that conserves energy according to the pump laser wavelength. The two-photon tomography results show that the polarisation state is mixed with no sign of polarisation entanglement. To understand the origin of the mixedness, we carried out further polarisation tomography measurements on each photon of the pair. The results show that photons within the same pair are in different polarisation states. Moreover, photons emitted by the resonance have higher purity (> 0.9) than their conjugates, indicating that the mixedness of the two-photon quantum state might be a consequence of the conjugate photon populating more than one eigenmode of the metasurface.

A drawback of metasurfaces for SPDC is the low conversion efficiency, which is a consequence of their ultrathin profile. Despite featuring relatively large quality factors ($300< Q \leq 1600$) and one of the largest second-order susceptibilities ($\chi^{(2)} \sim 240$ pm/V), the emission rate of SPDC in (001)-oriented GaAs metasurfaces does not surpass 8 Hz/W, which is low for practical quantum applications. In an effort to improve the generation rate, we fabricated metasurfaces using (110)-oriented GaAs wafers using the same design and target wavelengths as in our (001)-oriented GaAs metasurfaces [3]. The advantage of this crystallographic orientation is a direct access to the components of the second-order susceptibility tensor. Our preliminary results show that the rate is improved by a factor of 20x when compared to its (100) counterpart [3], and the enhancement (10^3) with respect to an unpatterned film of the same thickness is maintained. We believe that the rate can be further improved by adjusting the in-plane orientation of the nanoresonators, which is subject of current investigation.

Acknowledgments

This work was supported by the US Department of Energy, Office of Basic Energy Sciences, Division of Materials Sciences and Engineering. Sandia National Laboratories is managed and operated by NTESS under DOE NNSA contract DE-NA0003525. This work was supported by the US Department of Energy (DOE), Office of Basic Energy Sciences, Division of Materials Sciences and Engineering and performed, in part, at the Center for Integrated Nanotechnologies, an Office of Science User Facility operated for the US DOE Office of Science.

References

1. Santiago-Cruz, T. et al., “Photon pairs from resonant metasurfaces,” Nano Lett. 21, 4423–4429, 2021.
2. Zhang J. et al., “Spatially entangled photon pairs from lithium niobate nonlocal metasurfaces,” Sci. Adv. 8, eabq4240, 2022.
3. Santiago-Cruz, T. et al., “Resonant metasurfaces for generating complex quantum states,” Science, 377 991-995, 2022.
4. Son, C. et al., “Photon pairs bidirectionally emitted from a resonant metasurface,” Nanoscale, 15, 2567–2572, 2023.
5. Weissflog, M. A., et al. "Directionally tunable co-and counter-propagating photon pairs from a nonlinear metasurface," arXiv preprint arXiv:2403.07651, 2024.
6. Ma J. et al., “Polarization engineering of entangled photons from a lithium niobate nonlinear metasurface,” Nano Lett. 23, 8091–8098, 2023.

Applications of Spacetime Quantum Metasurfaces to Simulating Hawking Radiation

Patrick Brown[1,2], Wilton J. M. Kort-Kamp[3], Gerald Cleaver[1,2], and Diego Dalvit[3]

1. *Early Universe, Cosmology and Strings (EUCOS) Group, Center for Astrophysics, Space Physics and Engineering Research (CASPER).*
2. *Department of Physics, Baylor University, Waco, TX 76798, USA.*
3. *Los Alamos National Laboratory, Los Alamos, New Mexico 87545, USA.*

The Dynamical Casimir Effect (DCE) was first theorized by Gerald T. Morre in 1970 where he demonstrated that a moving mirror would create excitations in the quantum vacuum resulting in the production of real photons. This photon production effect arose from the fluctuations in the quantum vacuum caused by the time dependent boundary conditions created by the moving mirror. It was later shown that this effect could be enhanced if the mirror was instead made to oscillate at one end of a closed cavity at roughly twice the cavity's resonant frequency. Many detailed analyses of closed and open cavity systems have been conducted as well as detailed studies of single oscillating mirror systems. These studies have included the use of $\delta - \delta'$ b mirrors to analyze not only the time dependent boundary conditions, but also the presence and consequences of asymmetry (Silva et. al. and Gorban et. al.). However, it has been shown that in all scenarios involving mechanical oscillation of the mirror, it would need to be oscillating at a sizable percentage of the speed of light posing an obvious problem for experimental application. Yablonovich, however, showed that the DCE could be modeled by modulating the optical properties of a material. This was first theorized to be possible in a nonlinear optical medium whose index of refraction was rapidly oscillating in time, which Yablonovich chose to be a rapidly growing plasma. It was quickly shown that this effect was not limited to plasmas, but was in fact possible with nonlinear materials through the rapid oscillations of their optical properties. Since then much research has been devoted to designing new materials and systems to produce the DCE through optical modulation. The first successful observation of DCE photons was performed through the use of a wave guide terminated by a SQUID (Wilson et. al). There are, however, limitations to the use of SQUID systems including the very low temperatures at which SQUIDs must be operated and the low DCE photon generation rate that this system produces. It is then necessary to look for new systems capable of much higher DCE photon generation rates.

In recent years, Spacetime Quantum Metasurfaces (STQMs) have garnered a lot of interest due to their unique quantum and optical properties through the use of both spatial and temporal modulation (Wilton et. al.). These include the application of electrical bias for the creation of metalenses by modulating their index of refraction, magnetic field modulation taking advantage of the near instantaneous response of metasurfaces and metamaterials to magnetic fields, temperature modulation through the use the thermo-optic effect, optical modulation through their ultra-fast responses to photon interactions, and of course mechanical modulations. The most attractive feature of STQMs is the enhancement of their response to these modulations by combining two or more of these modulation schemes in conjunction with each other. This allows for the generation of unique physical phenomena including on demand control of entanglement among all degrees of freedom of a single photon, encoding quantum information into high-dimensional color qudits, higher degrees of control of multispectral and multispatial modes in spontaneous emission, and the generation of steered and vortex photon pairs out of the

vacuum. For this talk we will be solely interested in STQMs ability to create real photons from vacuum fluctuations (DCE) and the applications therein. One such application is the analysis of the quantum aspects of curved spacetime, specifically Hawking Radiation.

In 1975, Hawking first theorized that black holes could indeed evaporate, or decrease in size, through the emission of real photons. He demonstrated that this emission of photons came from the excitation of the quantum vacuum near the event horizon of a black hole. Specifically, he demonstrated that the difference in the creation and annihilation operators of both the quantized scalar and electromagnetic fields near the event horizon and past null infinity are realized as the creation of real photons from vacuum excitations. It was then shown by Davies and Fulling that this process could be simulated by a moving mirror. They demonstrated that if the mirror was made to move on an asymptotically null trajectory that the emission of particles from the vacuum would model the same mechanism of particle production predicted by Hawking for black holes. Since the Dynamical Casimir Effect is characterized by the emission of real photons from the vacuum, it was proposed that Hawking radiation could be simulated by modulating the optical properties of a material. Since then much work has been done to analyze these so-called “optical event horizons.” Nation et. al. proposed the use of a superconducting transmission line though the use of SQUIDs. The biasing of such a circuit with a space-time varying flux creates the necessary effective metric and “analogue” horizon. Horsley and Pendry, however, proposed the use of diffraction gratings synthetically moving at trans-luminal velocities. Here it is the creation of vacuum excitations when the grating and wave velocities are equal which create the “optical” event horizons.

STQMs allow for the engineering of not only spatial and temporal modulations of the material, but also allow for the steering and control over the quantum properties of the output photons. These features could provide methods for not only the emission of Hawking photons but also the use of such emissions to probe much deeper into the quantum aspects of curved spacetime. In this talk I discuss how these unique quantum properties of STQMs could provide a novel and unique platform for the simulation of Hawking radiation and other quantum effects predicted in curved spacetimes.

Space-Time Quantum Metasurfaces

Diego Alejandro Roberto Dalvit

Los Alamos National Lab., USA
*corresponding author: dalvit@lanl.gov

Abstract: Metasurfaces have recently entered the realm of quantum photonics, enabling manipulation of quantum light using a compact nanophotonic platform. Realizing the full potentential of metasurfaces at the deepest quantum level requires the ability to tune coherent light-matter interactions continuously in space and time. Here, we introduce the concept of space-time quantum metasurfaces for arbitrary control of the spectral, spatial, and spin properties of nonclassical light using a compact photonic platform. We show that space-time quantum metasurfaces allow on-demand tailoring of entanglement among all degrees of freedom of a single photon. We also show that spatiotemporal modulation induces asymmetry at the fundamental level of quantum fluctuations, resulting in the generation of steered and vortex photon pairs out of vacuum. Space-time quantum metasurfaces have the potential to enable novel photonic functionalities, such as encoding quantum information into high-dimensional color qudits using designer modulation protocols, sculpting multispectral and multispatial modes in spontaneous emission, and generating reconfigurable hyperentanglement for high-capacity quantum communications.

Analog of Quantum Bit Empowered by A Novel Electromagnetic Metasurface

Long Chen[1], Jian Wei You[1,*], Xin Yu Li[1], Ze Gu[1], Qian Ma[1], and Tie Jun Cui[1,*]

[1]State Key Laboratory of Millimeter Waves, School of Information Science and Engineering, Southeast University, Nanjing, China
*corresponding author, E-mail: jvyou@seu.edu.cn, tjcui@seu.edu.cn

Abstract

Current metamaterial research mainly focuses on the classical bit as the fundamental unit of information. To overcome the limitations of classical information capacity, we recently have proposed a new electromagnetic metasurface to implement analog quantum bit. This presentation would summarize our recent works in the field of analog quantum metasurfaces.

1. Introduction

Information transmission has ancient roots, dating back 5,000 years with fire signals and drumming for distance communication. In 2014, Cui et al. pioneered the digital coding metamaterials concept [1], marking a significant leap in the integration of information technology with material science. These metamaterials serve as intermediaries between the physical and digital worlds [2][3], acting as a bridge that enables the seamless exchange of data across domains. Presently, the focus in metamaterials research is on leveraging the classical bits for information processing [5][6]. For instance, electromagnetic (EM) metamaterials can be designed to enhance wireless communication signals and develop stealth technologies for cloaking objects [7][8]. Our research has shown that quantum-inspired information metamaterials have the potential to go beyond the limitations of classical information capacity, and this has been reported [9]. By drawing inspiration from quantum mechanics, these metamaterials can exhibit properties such as superposition, which are not found in classical systems.

In this paper, we summarize and report the latest research results achieved by our team in the field of quantum-inspired metasurfaces [9][12]. Specifically, we have successfully created an analog quantum information metasurface, which is different from another representative of analog quantum metasurfaces (topological metasurfaces) and from real quantum metasurfaces, please refer to Ref. [9]. Our work is progressively bridging the gap between classical and quantum systems, paving new paths for the realization of quantum-inspired information metamaterials.

2. Results and discussion

2.1. Principle

This section introduces a novel concept, the analog quantum bit (qubit), inspired by the qubit.

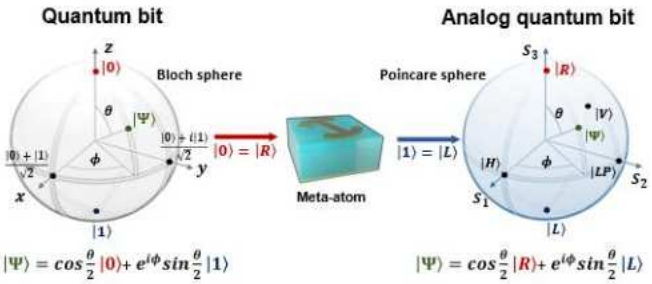


Figure 1: The concept of quantum bit and analog quantum bit.

As is well-known, the state of a qubit $|\Psi\rangle$ can be mathematically represented as a linear superposition of two orthogonal states, that is $|\Psi\rangle = cos\frac{\theta}{2}|0\rangle + e^{i\phi}sin\frac{\theta}{2}|1\rangle$, with the sum of their squared amplitudes equaling one, in accordance with probabilistic constraints. Furthermore, the state of a qubit can be visualized geometrically using the Bloch sphere. This superposition property significantly surpasses the binary nature of classical bits. Based on these principles, we propose the concept of an analog qubit and demonstrate its physical realization using a Pancharatnam-Berry (PB) phase metasurface, as illustrated in Fig. 1. In the design and analysis of the metasurface, we focus on the transformation of the Jones matrix, successfully achieving the analysis of conversion between linear and circular polarizations and deriving the corresponding mathematical representations.

$$\begin{cases} |r_{RR}| = \sqrt{\frac{|r_{uu}|^2[1+\cos(\theta_{vv}-\theta_{uu})]}{2+|r_{uu}||r_{uv}|[sin(\theta_{vv}-\theta_{uv})+sin(\theta_{uv}-\theta_{uu})]}} \\ |r_{LR}| = \sqrt{\frac{2+|r_{uu}||r_{uv}|[sin(\theta_{vv}-\theta_{uv})+sin(\theta_{uv}-\theta_{uu})]-|r_{uu}|^2[1+\cos(\theta_{vv}-\theta_{uu})]}{2+|r_{uu}||r_{uv}|[sin(\theta_{vv}-\theta_{uv})+sin(\theta_{uv}-\theta_{uu})]}} \end{cases} \quad (1)$$

$$\begin{cases} \phi_{RR} = arg(r_{uu}+r_{vv}) \\ \phi_{LR} = 2\alpha + arg([(r_{uu}-r_{vv})-i(r_{uv}+r_{vu})]) \end{cases} \quad (2)$$

where r_{ij} denotes the reflection coefficient from the j-th incident wave to the i-th reflected wave, with i, j belonging to the sets $\{u, v\}$ for linear polarization and $\{R, L\}$ for circular polarization. It should be noted that the aforementioned expressions are valid under the excitation of a right-hand circularly polarized (RCP) incident wave. In this case, we can further derive the mathematical representation of the analog qubit.

$$|\Psi\rangle = cos\frac{\theta}{2}|R\rangle + e^{i\phi}sin\frac{\theta}{2}|L\rangle \quad (3)$$

$$\begin{cases} \theta = 2arccos\left(\sqrt{\frac{|r_{uu}|^2[1+\cos(\theta_{vv}-\theta_{uu})]}{2+|r_{uu}||r_{uv}|[sin(\theta_{vv}-\theta_{uv})+sin(\theta_{uv}-\theta_{uu})]}}\right) \\ \phi = 2\alpha + arg([(r_{uu}-r_{vv})-i(r_{uv}+r_{vu})]) - arg(r_{uu}+r_{vv}) - \pi \end{cases} \quad (4)$$

Based on this mathematical representation, we can geometrically visualize the qubit-like states using the Poincaré sphere, where RCP and LCP are represented as two orthogonal vector states (i.e., $|R\rangle$ and $|L\rangle$). For more details on the principle, please refer to Ref. [9].

2.2. Verification of the mathematical representation

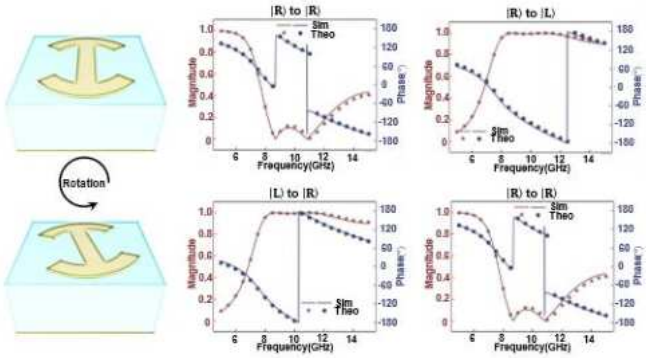


Figure 2: Mathematical representation verification of the analog qubit.

We have developed a PB phase metasurface to physically validate the mathematical representation of the proposed analog qubit. Specific details on the dimensions of the meta-atoms can be found in Ref. [9]. By rotating any structured meta-atom to arbitrary angles, the theoretical predictions of circularly polarized reflection coefficients can be derived from the linearly polarized reflection coefficients using equations (1) and (2). As depicted in Fig. 2, one set of examples (i.e., $\gamma = 105°$, $\kappa = 105°$, and $\alpha = 15°$) illustrates that the theoretical predictions of the magnitudes and phases of the four circularly polarized reflection coefficients are in high agreement with the numerical simulations. This agreement confirms the correctness of our theory and, by extension, the mathematical representation of the analog qubit. It is also noteworthy that this theory is not only applicable to the symmetrical structures (as shown in Fig. 2) but also to anisotropic structures.

2.3. Verification of the geometrical representation

We further validated the geometric representation of the analog qubit within PB phase metasurfaces. To study the polarization evolution paths on the Poincaré sphere, we employed Stokes parameters $\{S_0, S_1, S_2, S_3\}$to evaluate the positions of the electric field polarization states at different locations in the incident and reflection regions. Figure 3 illustrates the polarization evolution path when excited by an RCP wave for a specific metasurface structure. In the incident region, the polarization state remains unchanged due to the absence of interaction; conversely, in the reflected region, the RCP state gradually transitions into various other polarization states, eventually stabilizing as the far-field polarization state. We marked the numerically simulated state on the Poincaré sphere with green dots and calculated the theoretical predictions using equations (3) and (4), represented by red dots. The high overlap between these points confirms the accuracy of the geometric representation of the analog qubit. Additionally, we conducted broadband validation, further enhancing the reliability and robustness of our findings (refer to [9]).

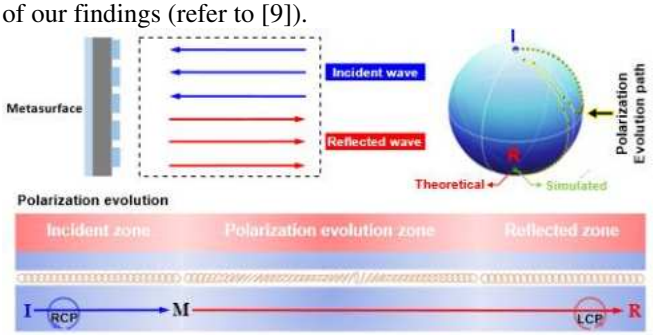


Figure 3: Geometrical representation verification of the analog qubit.

2.4. Demonstration of the analog quantum bits

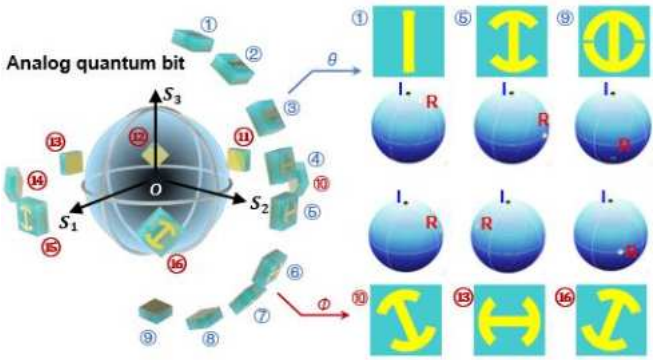


Figure 4: Modulation of the realization of the analog quantum bit.

To achieve the superposition state characterization property of the analog qubit, and considering that these superposition states are governed by two degrees of freedom on the (θ and ϕ) Poincaré sphere, we have proposed a feasible scheme.

As shown in Fig. 4, the latitude angle is primarily influenced by the magnitude of the reflection coefficient. By maintaining a constant rotation angle for the meta-atom and varying the lengths of two equal arcs, we can achieve a full coverage of magnitudes from 0 to 1, thereby enabling precise control of the latitude angle across any meridian. Since the meta-atom adheres to the PB phase, by keeping the arc length constant and rotating around the central z-axis, we can induce a twofold change in the longitude angle, thus enabling precise control over the longitude angle along any latitude.

To quantitatively demonstrate our control strategy, theoretical predictions and numerical simulations are presented in Tables 1 and 2, further validating the correctness of our approach. More detailed results are available in Ref. [9]. The high degree of overlap between the numerical simulations and theoretical predictions

verifies our comprehensive coverage of polarization states across the Poincaré sphere.

Table 1: Quantitative analysis of the modulation of the latitude angle θ.

No.	$\gamma = \kappa[^\circ]$	Theoretical	Simulated
1	20	90.01	89.80
5	105	89.99	89.75
9	175	90.05	88.96

Table 2: Quantitative analysis of the modulation of the longitude angle ϕ.

No.	$\alpha[^\circ]$	Theoretical	Simulated
10	22.5	134.99	127.91
13	90	269.99	269.89
16	157.5	44.99	51.59

2.5. Experimental Verification

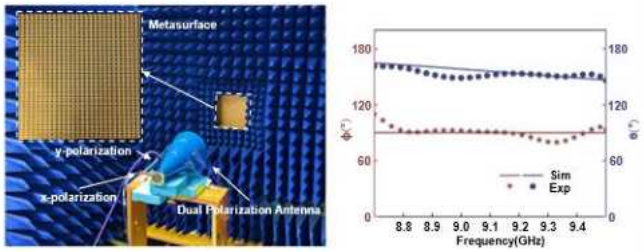


Figure 5: Experimental setup and results.

We constructed a small anechoic chamber experimental platform to verify the accuracy of our theoretical predictions, as illustrated in Fig. 5. By interfacing a dual-polarized horn antenna with a vector network analyzer (VNA), we measured the four linear polarization complex reflection coefficients ($\{r_{uu}, r_{vu}, r_{uv}, r_{vv}\}$). This enabled us to obtain experimental results for the two components of the analog qubit at corresponding positions on the Poincaré sphere. The high degree of consistency between the experimental results and numerical simulations further validates the feasibility of using the proposed analog qubit to emulate quantum bits.

3. Conclusions

In summary, this paper presents our recent advancements in the field of quantum-inspired metasurfaces, with a particular focus on introducing the concept of the analog qubit. We developed a feasible metasurface-based physical platform, which has been validated through mathematical and geometrical representations. Additionally, we conducted relevant experiments to verify the effectiveness of this concept. It should be noted that this study is still limited to passive metasurfaces. Our team is currently working on extending this research to tunable and even active metasurfaces, aiming to advance the development of analog qubit and create new opportunities for the fields of information science and quantum science.

Acknowledgements

This work was supported by the National Natural Science Foundation of China (Grant Nos. 62101124, and 62288101), the National Key Research and Development Program of China (Grant Nos. 2017YFA0700201, 2017YFA0700202, 2017YFA0700203, and 2022YFA1404903), the Natural Science Foundation of Jiangsu Province (Grant Nos. BK20210209, and BK20212002), the Fundamental Research Funds for the Central Universities (Grant No. 2242023K5002), and 111 Project (Grant No. 111-2-05).

References

[1] T. J. Cui, M. Q. Qi, X. Wan, J. Zhao, Q. Cheng, Coding metamaterials, digital metamaterials and programmable metamaterials, *Light: Sci. Appl* 3: e218, 2014.

[2] J. W. You, Q. Ma, Z. Lan, Q. Xiao, N. C. Panoiu, T. J. Cui, Reprogrammable plasmonic topological insulators with ultrafast control, *Nat. Commun* 12: 1−7, 2021.

[3] Q. Ma, W. Gao, Q. Xiao, L. Ding, T. Gao, Y. Zhou, X. Gao, T. Yan, C. Liu, Z. Gu, X. Kong, Q. H. Abbasi, L. Li, C.-W. Qiu, Y. Li, T. J. Cui, Directly wireless communication of human minds via non-invasive brain-computer-metasurface platform, *eLight* 2: 132–142, 2022.

[4] X. Li, J. W. You, Z. Gu, Q. Ma, J. Zhang, L. Chen, T. J. Cui, Multiperson detection and vital-sign sensing empowered by space-time-coding reconfigurable intelligent surfaces, *IEEE Internet Things* (early access) 2024, doi: 10.1109/JIOT.2024.3400960.

[5] J. W. You, Z. Lan, Q. Ma, Z. Gao, Y. Yang, F. Gao, M. Xiao, T. J. Cui, Topological metasurface: from passive toward active and beyond, *Photonics. Res* 11: B65–102, 2023.

[6] J. W. You, Q. Ma, L. Zhang, C. Liu, J. N. Zhang, S. Liu, T. J. Cui, Electromagnetic metamaterials: from classical to quantum, *Em. Sci* 1: 1–33, 2023.

[7] J. N. Zhang, L. Chen, X. M. Lin, X. Y. Yu, Q. Ma, W.-B. Lu, J. W. You, T. J. Cui, Feature-assisted neuro-CMT approach to fast design optimization of metasurfaces, *IEEE Microw. Wireless. Tech. Lett* 34: 467–470, 2024.

[8] J. L. Su, J. W. You, L. Chen, X. Y. Yu, Q. C. Yin, G. H. Yuan, S. Q. Huang, Q. Ma, J. N. Zhang, T. J. Cui, MetaPhyNet: intelligent design of large-scale metasurfaces based on physics-driven neural network, *J. Phys. Photonics* 6: 035010, 2024.

[9] L. Chen, J. W. You, Z. Gu, Q. Ma, T. J. Cui, Analog quantum bit based on Pancharatnam-Berry phase metasurfaces, *Adv. Quantum. Technol* 6: 2300135, 2023.

[10] L. Chen, Z. Lan, X. W. Wu, Q. Ma, J. W. You, T. J. Cui, Analog quantum valley–Hall and quantum spin Hall plasmons in graphene metasurfaces with low point group symmetry, *Adv. Phys. Res* 2: 2200076, 2023.

[11] J. W. You, Z. H. Lan, N. C. Panoiu, Four-wave mixing of topological edge plasmons in graphene metasurfaces, *Sci. Adv* 6: eaaz3910, 2020.

[12] L. Chen, Z. Lan, X. W. Wu, Q. Ma, J. W. You, T. J. Cui, Low-symmetrical topological graphene metasurfaces with quantum valley and spin Hall effects, *Proc. Progress in Electromagnetics Research Symposium (PIERS 2023),* Prague, Czech Republic, pp. 1622−1627, 2023.

Integrated metasurfaces/metamaterials on photonic platform

Observation of momentum-gap topology of light

Y. Yang[1*]

[1]Zhejiang University, Hangzhou 310027, China
[*]corresponding author: yangyihao@zju.edu.cn

Abstract: Topological phases have prevailed across diverse disciplines. Hitherto, the understanding of these phases has centered on frequency bandstructures, showcasing topological boundary states at spatial interfaces. Here, we report the experimental observation of momentum-gap topology of light, manifesting as topological boundary states at temporal interfaces between systems with distinct momentum-gap topology.

Topological phases, which are pivotal in the fields of electronics, photonics, and acoustics, have traditionally been centered on the study of energy bandstructures and the exploration of spatial topological boundary states. Yet, recent advancements have led to the discovery of a novel class of bandstructures characterized by momentum bandgaps, or 'k gaps', particularly prominent in photonic time crystals. This seminal development heralds a diverse array of topological phases within momentum bands, alongside numerous topological boundary states in the temporal domain. In this talk, we will present the experimental observation of k-gap topology within an optical temporal synthetic lattice, demonstrating temporal topological boundary states. These states manifest at the temporal interfaces between two subsystems, each characterized by distinct k-gap topologies. Our findings present a novel perspective in the study of k gaps, temporal topological states, and the dynamics of time-varying physical systems, thus catalyzing further research and exploration in this burgeoning field.

Approaching unity quantum coupling of free electrons and photons using nanophotonic structures

Yuval Adiv[1]

[1] Department of Electrical and Computer Engineering, Technion-Israel Institute of Technology, 32000 Haifa, Israel
*corresponding author: yuvalad@campus.technion.ac.il

Abstract: Using a dispersion-engineered nanophotonic structure we achieve a unity quantum coupling strength between free electrons and 2D photons. This record coupling strength enables the first observation of 2D Cherenkov radiation and provides insights into the quantum nature of free-electron radiation.

The quantum coupling strength between free electrons and photons is a unitless measure reflecting the average number of photons emitted by a single electron when interacting with an optical medium. Typically, free-electron radiation phenomena, like Cherenkov and Smith-Purcell radiation, exhibit relatively weak coupling, on the order of 10^{-4} to 10^{-2}. Intriguingly, the dimensionality of the medium into which the radiation is emitted can fundamentally change the radiation properties such as its spectrum, intensity, directionality, and polarization. The manipulation of these properties can potentially lead to an enhancement of the quantum coupling strength by orders of magnitude.

This is particularly true for Cherenkov radiation (CR). The CR first observed and explained over 80 years ago as an electromagnetic shockwave emitted by a charged particle when it exceeds the phase velocity of light in a medium [1]. Since then, CR has been mostly conceived as a 3D phenomenon where the radiation creates a cone around the emitting particle. Theory papers predicted two-dimensional CR (2D-CR) to have a sharper bandwidth emitted into longitudinal modes [2], but, until this work, only phenomena analogous to it were demonstrated experimentally [3,4], and such radiation has yet to be observed.

In this work, we present the first observation of 2D-CR, which we generate in a transmission electron microscope (TEM) by aligning an electron beam to propagate close and parallel to a dispersion-engineered multi-layered structure. We tune the electron velocity and observe a corresponding shift in the electron energy loss spectrum (EELS) that follows the Cherenkov (phase-matching) condition and matches the dispersion of the surface photonic mode. The reduced dimensionality leads to sharp EELS characteristics, allowing us to unveil the quantum-optical nature of CR emission. The EELS data shows up to three quantized emission events by each electron – the first such observation in any process of coherent free-electron radiation (i.e., coherent cathodoluminescence). Most importantly, a thorough analysis of our measurements reveals a quantum coupling strength of unity between the free electron and the photon it emits, indicating, for the first time, on the single-electron–single-photon interaction regime.

This experiment arises from theory papers and a scientific debate on the quantum state of radiation emitted by free electrons, which recently led to a paradigm shift: For many years, radiation emitted by a free electron was considered as classical light (i.e. a Glauber coherent state). However, recent theoretical works showed this to be generally incorrect [5-7]. Instead, the electrons can become entangled with the photons they emit – changing the quantum state of the emitted photons. Our work provides experimental support to this paradigm shift.

References

1. P.A. Cherenkov, Dokl. Akad. Nauk SSSR 2, 451 (1934).
2. O. Keller, Phys. Lett. A 188, 272 (1994).
3. P. Genevet, et al., Nature Nano. 10, 804 (2015).

4. Y. Zhang, et al., Nano Lett. 20, 2770–2777 (2020).
5. A. Karnieli, et al., Sci. Adv. 7, eabf8096 (2021).
6. O. Kfir, et al., Sci. Adv. 7, eabf6380 (2021).
7. V. Di Giulio, et al., ACS Nano 15, 7290–7304 (2021).

Time Edge States Protected by Chiral Symmetry

Hao Hu[1*]

[1]National Key Laboratory of Microwave Photonics, Nanjing University of Aeronautics and Astronautics, Nanjing, China
[*]corresponding author: hao.hu@nuaa.edu.cn

Abstract: This talk will introduce a novel type of edge states that are localized in the time domain. As protected by the chiral symmetry, the time edge states are proven to be robust against the external perturbations.

Time photonic crystals whose electromagnetic parameters are modulated periodically in time, are of paramount significance, owing to their promising applications in non-resonant laser, reconfigurable intelligence surfaces, and particle accelerators. Inspired from recent advances in space photonic crystals, the topological band theory has been transferred to the time photonic crystals whose unit cells preserve time-reversal symmetry, enabling the temporal version of topological edge states. However, disorders will readily break the time-reversal symmetry, hence heavily impacting the behaviors of corresponding edge states. To this end, we propose a novel type of time photonic crystals that respect the chiral symmetry, only if the temporal duration over the refractive index for each layer is a constant. The chiral symmetry of time photonic crystals gives rise to the quantized winding number (i.e., 0 or 1) that is defined in the Bloch frequency. Contacting time photonic crystals with different winding number results in the emergence of chiral-symmetry protected edge states localized at the temporal domain wall and spectrally manifested as sharp dips in the momentum gap. Importantly, the chiral symmetry remains unbroken even if the applied disorders are sufficiently strong. This remarkable property favorably enhances the robustness of behaviors (e.g., the resonant frequencies and field patterns) of topological edge states in time photonic crystals.

Thin film lithium niobate double notch filter

Songyan Hou[1*]

[1]Xidian University, China
[*]corresponding author: housongyan@xidian.edu.cn

Abstract: We propose a tunable double notch filter on thin-film lithium niobate using dual micro-ring architecture. This unique integrated filter is essential for complex photonic integrated circuits, along with multiple channels and various frequency spacing.

Integrated optical filter is one of fundamental building blocks in many optical applications, notably in the context of wavelength division multiplexing (WDM) networks[1, 2]. To meet the flexibility requirements of the wavelength selection in the forthcoming highly functional optical circuits, the optical filter featuring continuous tunability has attracted increasing attention. To realize the tunable optical filter, widely adopted approaches are implemented based on silicon photonics. For example, arrayed waveguide grating[3] and cascaded micro-ring filter[4] on silicon platform have been demonstrated a wide tunability. However, the lack of intrinsic electro-optic effect in silicon photonics makes the optical filter suffer from extra optical transmission losses and high power consumption when the functionality is achieved by the means of carriers doping and thermal tunning, prompting the exploration of alternative materials with robust Pockels electro-optic coefficient, such as lithium niobate (LN)[5-10].

Here, a tunable double notch filter is proposed and experimentally demonstrated on thin-film LN. The design consists of two cascaded microring resonators, whose electric filed are revised by one external voltage. The frequency spacing of the filter is tunable by reversely tuning the resonances of the two microrings. A wide separation tunability range from 16.1 GHz to 89.9 GHz is demonstrated, and the separation can be increased to free spectral range (FSR) of 423 GHz when further increase the voltage. With an ultracompact footprint of 0.0248 mm2, the device provides a frequency separation tunability of 0.82 GHz/V with a contrast of 10~16 dB.

References

[1]. R. Magnusson, S. Wang. New principle for optical filters [J]. Applied physics letters, 1992, 61(9): 1022-1024.

[2]. M. Uenuma, T. Motooka. Temperature-independent silicon waveguide optical filter [J]. Optics letters, 2009, 34(5): 599-601.

[3]. D. Liu, H. Wu, D. Dai. Silicon multimode waveguide grating filter at 2 μm [J]. Journal of Lightwave Technology, 2019, 37(10): 2217-2222.

[4]. T. Dai, A. Shen, G. Wang, Y. Wang, Y. Li, X. Jiang, J. Yang. Bandwidth and wavelength tunable optical passband filter based on silicon multiple microring resonators [J]. Opt Lett, 2016, 41(20): 4807-4810.

[5]. Z. He, H. Guan, X. Liang, J. Chen, M. Xie, K. Luo, R. An, L. Ma, F. Ma, T. Yang, H. Lu. Broadband, Polarization-Sensitive, and Self-Powered High-Performance Photodetection of Hetero-Integrated MoS₂ on Lithium Niobate [J]. Research, 2023, 6: 0199.

[6]. C. Wang, M. Zhang, X. Chen, M. Bertrand, A. Shams-Ansari, S. Chandrasekhar, P. Winzer, M. Loncar. Integrated lithium niobate electro-optic modulators operating at CMOS-compatible voltages [J]. Nature, 2018, 562(7725): 101-104.

[7]. M. He, M. Xu, Y. Ren, J. Jian, Z. Ruan, Y. Xu, S. Gao, S. Sun, X. Wen, L. Zhou, L. Liu, C. Guo, H. Chen, S. Yu, L. Liu, X. Cai. High-performance hybrid silicon and lithium niobate Mach–Zehnder modulators for 100 Gbit/s and beyond [J].

Nature Photonics, 2019, 13(5): 359-364.
[8]. Q. Luo, C. Yang, Z. Hao, R. Zhang, R. Ma, D. Zheng, H. Liu, X. Yu, F. Gao, F. Bo, Y. Kong, G. Zhang, J. Xu. On-chip erbium–ytterbium-co-doped lithium niobate microdisk laser with an ultralow threshold [J]. Optics Letters, 2023, 48(13): 3447-3450.
[9]. D. Zhu, L. Shao, M. Yu, R. Cheng, B. Desiatov, C. Xin, Y. Hu, J. Holzgrafe, S. Ghosh, A. Shams-Ansari. Integrated photonics on thin-film lithium niobate [J]. Advances in Optics and Photonics, 2021, 13(2): 242-352.
[10]. M. Xu, M. He, H. Zhang, J. Jian, Y. Pan, X. Liu, L. Chen, X. Meng, H. Chen, Z. Li, X. Xiao, S. Yu, S. Yu, X. Cai. High-performance coherent optical modulators based on thin-film lithium niobate platform [J]. Nature Communications, 2020, 11(1): 3911.

The Proposal of the Substrate-inverted Multi-Material Technology (SuMMIT) for Scalable Heterogeneously-Integrated Photonics

Jia Xu Brian Sia[1,2]

[1]School of Electrical and Electronic Engineering, Nanyang Technological University, 50 Nanyang Avenue, 639798, Singapore
[2]Department of Material Science & Engineering, Massachusetts Institute of Technology, Cambridge, M.A., USA
[*]corresponding author: jiaxubrian.sia@ntu.edu.sg

Abstract: Current silicon photonic heterogeneous integration has displayed challenges with contemporary foundry-compatible, wafer-scale silicon photonics. Through the integration of industrial foundry-level silicon photonics and hybrid Cu bonding technologies, the SuMMIT platform is proposed, where heterogeneous photonic integration can be realized in a scalable fashion.

The silicon photonic platform possesses significant limitations, arising from the material limitations of Group IV materials. The abovementioned has led to a distinct split in the development of the silicon photonics between industry and academia. Firstly, there is the development of foundry-driven, wafer-level silicon photonics consisting of complex back-end-of-line (BEOL) layers which facilitates the realization of high-speed silicon modulators and germanium-based photodetectors, widely adopted by industry [1]. Heterogeneous silicon photonics, on the other hand, has attracted considerable interest from the academic front, where functional materials (i.e., III-V gain medium [2], Ce:YIG [3]) have been integrated close to the silicon waveguide core to extend the suite of functionalities possible within the platform. However, heterogeneous material integration in silicon photonics could lead to a reduction in scalability.

To that effect, the SuMMIT platform is proposed, illustrated in Fig. 1(a); the detailed fabrication process flow is elucidated in [4]. A 200 mm silicon foundry-manufactured silicon photonic wafer is shown at the inset of Fig. 1(a). The SuMMIT platform can be categorized into 4 technology layers: 1.) CMOS electronics, 2.) Through-glass/silicon via (TGV/TSV), silicon photonics, and multi-material integration layer. The substrate removal of the silicon photonic wafer (silicon substrate and buried oxide) results in the formation of a surface at the backside of the silicon waveguides with low rms values (< 0.5 nm). This results in compatibility with multi-material integration via techniques such as hydrophilic bonding, and material deposition.

An example of material integration on SuMMIT is shown in Fig. 1(b), where the back-end-of-line (BEOL) layers, preserved by the SuMMIT vertical architectures enables the electrothermal control of the Sb_2Se_3, a phase change material used for non-volatile photonic memory [4]. A 30 nm thick, and 5 μm long Sb_2Se_3 strip is integrated on a straight PIN junction, embedded within a silicon racetrack resonator. The silicon waveguide has a width of 500 nm. The PIN junction, which makes use of a rib waveguide has a rib height of 130 nm, where the rest of the racetrack resonator comprises of strip waveguides, with height of 220 nm. The N++ and P++ regions of the PIN junction are spaced 250 nm from the edge of the rib waveguide (intrinsic) to prevent optical loss due to carrier absorption. The electrothermal characteristics of the PIN junction, simulated via the IV curve of the PIN junction shows a thermal time constant of 248 ns (1/e from peak temperature). This is commensurate for

Sb_2Se_3 to bypass crystallization. The non-volatile photonic memory of the Sb_2Se_3-integrated racetrack resonator is shown in Fig. 1(c) and (d), via the through and drop port, where a large contrast can be seen between the crystalline and amorphous states. By fixing a laser wavelength a $\lambda_{res.}$, a non-volatile photonic transmission states can be addressed via electrothermal switching.

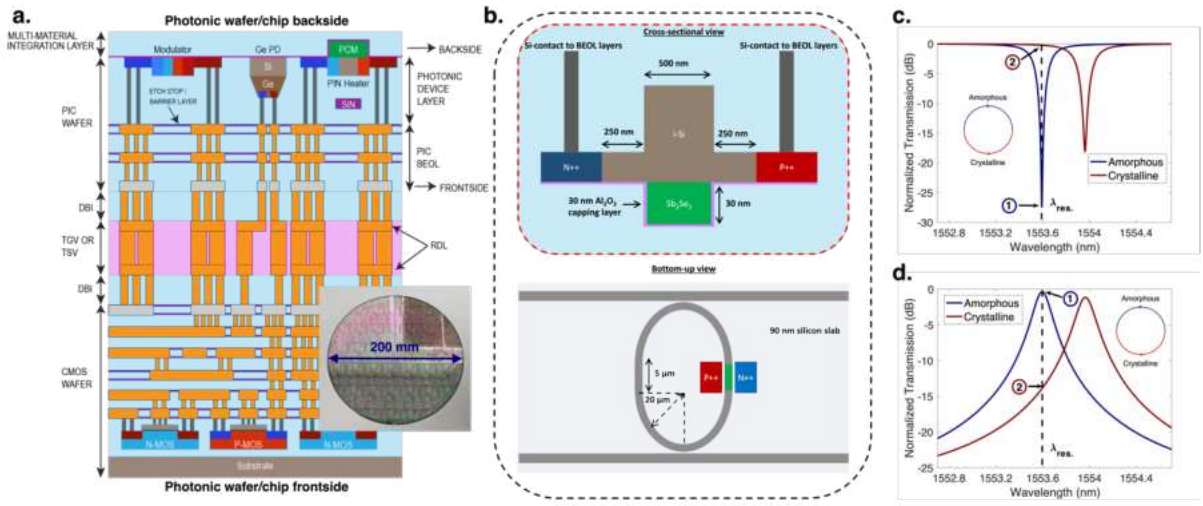


Fig. 1. (a) Illustration of the SuMMIT technology platform. The photograph of the 200 mm silicon photonic wafer is shown at the inset. (b) Sb_2Se_3-integated racetrack resonator via the SuMMIT platform, facilitating the on-chip non-volatile photonic memory. The (c) through, and (d) drop port of the Sb_2Se_3-integated racetrack resonator when the Sb_2Se_3 is switched to a crystalline and amorphous state via electrothermal switching of the PIN junction.

SuMMIT will provide a high-scalable approach for heterogeneous integration of various optical materials. Via the innovative architecture, the preservation of the BEOL layers within the silicon photonic wafer can facilitate light-matter control.

Jia Xu Brian Sia would like to acknowledge the Ministry of Education/NTU College of Engineering International Postdoctoral Fellowship.

References

1. Sia, J. X. B. *et al.* "Wafer-Scale Demonstration of Low-Loss (~0.43 dB/cm), High-Bandwidth (>38 GHz), Silicon Photonics Platform Operating at the C-Band," IEEE Photonics J., Vol. 14, 1-9, 2022.
2. Tran. M. A. *et al.* "Tutorial on narrow linewidth tunable semiconductor lasers using Si/III-V heterogeneous integration," APL Photonics, Vol. 4, 111101, 2019.
3. Huang *et al.*, "Dynamically reconfigurable integrated optical circulators," Optica, Vol. 4, 23-30, 2017.
4. Ranno *et al.*, "Multi-Material heterogeneous integration on a photonic-CMOS platform" Opt. Mater. Express, Vol. 13, No. 10, 2711-2725, 2023.

Extending the bandwidth of nonlinear optics

Yu Luo[1*], Chunyu Huang[2], and Hui Liu[2]

[1] National Key Laboratory of Microwave Photonics, Nanjing University of Aeronautics and Astronautics, Nanjing 211106, China

[2] Collaborative Innovation Center of Advanced Microstructures National Laboratory of Solid State Microstructures，School of Physics Nanjing University Nanjing Jiangsu 210093 China

[*]corresponding author: yu.luo@nuaa.edu.cn

Abstract: Integrated nonlinear optical devices play an important role in modern optical communications. However, the realization of efficient nonlinear optical conversion on chip over a broadband frequency range is widely acknowledged as a challenging task. In the first part of my talk, I will present a universal strategy based on the theory of transformation optics to design broadband nonlinear optical devices on chip [1]. In the second part of this talk, I will show how stacked perfect-electric-conductor (PEC) and epsilon-near-zero (ENZ) metamaterial consisting of nonlinear varactors can be used for strong second harmonic generation over a wide range of illumination angles.

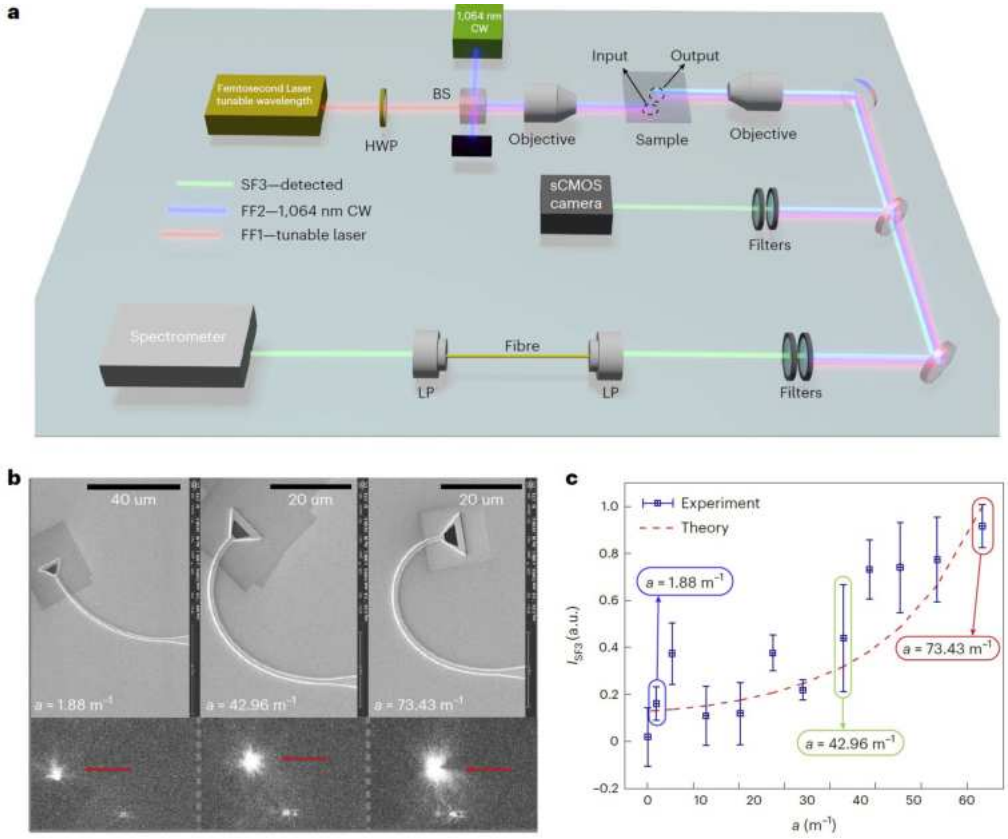


Figure 1: **Experimental demonstration of enhanced SFG.** (a) Schematic of the experimental setup. The wavelength-tunable femtosecond laser and the steady-state light source are used at the fundamental frequency. (b) The electron microscope images of the accelerated waveguides with different gradient curvatures and the corresponding CMOS images. The three sub-figures clearly demonstrate that the larger the acceleration, the

higher the light intensity. (c) The intensity of the sum-frequency light as a function of the acceleration. The red line represents the theoretical calculation, the blue points correspond to the experimental mean values, and the vertical error bars denote the range of standard deviation, respectively.

We will first demonstrate from the theoretical point of view that accelerating waveguides with gradient curvatures provide a powerful platform to extend the bandwidth of various nonlinear optical processes on chip. As an experimental proof, we will show how this method can be applied to boost the efficiency of sum-frequency generations for infrared signal upconversion (SFG-ISU) in curved accelerating waveguides (CAWs) made of LiNbO3, as shown in Fig. 1. Especially, we will discuss the relationship of the gradient of the waveguide curvature (i.e. the acceleration) and the bandwidth of the SFG process. Such a broadband SFG process offers a promising method in the long wavelength detection and imaging in the mid/far-infrared [1].

The conformal transformation approach presented in this talk is general and can be extended to other nonlinear optical processes at any wavelength range. It can also be realized with various nonlinear optical materials. Besides, our scheme does not require complicated fabrications or accurate designs. It is mass producible and compatible with the CMOS process.

References

1. C. Huang, Y. Luo, Y. Zhao, X. Ma1, Z. Yan1, Z. Liu, C. Sheng, S. Zhu, Hui Liu, “A conformal mapping approach to broadband nonlinear optics on chip”, Nat. Photon., https://doi.org/10.1038/s41566-024-01386-2

Spoof Plasmonic Skyrmions and Sensing Application

Liangliang Liu
National Key Laboratory of Microwave Photonics, Nanjing University of Aeronautics and Astronautics, Nanjing, 211106, China
corresponding author: llliu@nuaa.edu.cn

Abstract: Recent concept of spoof plasmonic skyrmions (SPSs) has attracted much attention for their topologically robust and multiple equidistance sharp resonances. However, highly-efficient excitation and its application for broadband sensing still remain elusive. Here, we developed an ultracompact and topologically robust sensor based on SPSs for characterizing dielectric materials in a wideband with ultrahigh sensitivity. Moreover, a shape-immuned hybridization model with SPSs is proposed to offer remarkable field enhancement. Simulation and experimental results show that SPSs sensor features highly sensitive (>4.82%) and extremely accurate (≈99.99%) sensing performance against continuous shape deformations. These results open up an avenue for multiple resonant measurements of dielectric materials in broadband and provide a very versatile platform for the design and fabrication of ultracompact, highly sensitive and topologically robust plasmonic sensors.

References

1. Z. L. Deng, T. Shi, A. Krasnok, X. P. Li, A. Alù, “Observation of localized magnetic plasmon Skyrmions,” Nature Communications, 13:8, 2022.
2. X. H. Li, L. L. Liu, Z. X. Zhou, J. R. Shen, Y. R. Zhang, G. D. Han and Z. Li, “Highly Sensitive and Topologically Robust Multimode Sensing on Spoof Plasmonic Skyrmions,” Adv. Optical Mater., 2200331, 2022.
3. S.-Q. Li, C.-H. Du, D.-L. Yin, X.-W. Cai, T.-Q. Xu, Y. Wang, F.-H. Li, Y. Zhu, and F. Zhang, “Localized Spoof Surface Plasmon Skyrmions Excited by Guided Waves,” Adv. Funct. Mater. , 33, 2305789, 2023.
4. X. H. Li, L. L. Liu, Y. R. Zhang, Y. Feng, G. D. Han, H. L. Yang, H. Hu, Y. Luo, and Z. Li, Hybridization of Localized Spoof Plasmonic Skyrmions and its Application in Micro-Displacement Sensing, Adv. Optical Mater. , 2302744, 2023.

Self-focusing beam in hyperbolic media

Yueqian Zhang[1,2], Chongwu Wang[1], Qian Wang[2*], Qi Jie Wang[1*], and Yu Luo[3*]

[1] School of Electrical and Electronic Engineering, Nanyang Technological University, Singapore 639798, Singapore
[2] Institute of Materials Research and Engineering, Agency for Science, Technology and Research (A*STAR), 2 Fusionopolis Way, Innovis, Singapore, 138634, Singapore
[3] Key Laboratory of Radar Imaging and Microwave Photonics, Ministry of Education, College of Electronic and Information Engineering, Nanjing University of Aeronautics and Astronautics, Nanjing 211106, China
[*]Qian Wang: wangqian@imre.a-star.edu.sg
[*]Qi Jie Wang: qjwang@ntu.edu.sg
[*]Yu Luo: yu.luo@nuaa.edu.cn

Abstract: Special beams, exemplified by the Airy beam since 2007, exhibit intriguing properties. However, their behavior in hyperbolic media remains poorly explored. We propose a method to convert half Bessel beams in isotropic media into self-focusing special beams in hyperbolic media, expanding avenues for advanced beam manipulation.

Special beam is a beam family typical of non-diffracting main lope. The first found special beam is Airy beam which originates from the special solution to Schrodinger equation and was introduced to optical system in 2007 [1]. The most striking property is that the main lope always remains its energy without diverging into other directions. It can remain the beam shape when propagating and the main lope trajectory follows a parabola in the paraxial range. After that, people have been trying to push the special beam into non-paraxial regime with different main lope trajectories and a series of special beams are proposed. The main lope of Half Bessel beam [2] follows a circle and Weber beam [3] follows an parabola while Mathieu beam [3] follows an ellipse. They can overcome the paraxial limit and the beam can bend to nearly 90°.

However, all these special beams are derived in the isotropic media such as in free space and it also requires complicated derivation. How to build up a special beam with one simple design principle that can be applied to all kinds of media, including isotropic, ellipse and even hyperbolic media, remains unexplored. Regarding this blankness, this work reports a general design principle which can be applied to all kinds of media.

Based on this design method, we can realize special beams in elliptical media and even hyperbolic media. Especially, in the hyperbolic media we realize non-diffracting special beams with unique properties, which are transformed from the half Bessel beams in isotropic media. Compared with the original half Bessel beam, the transformed beams have the following new properties:

1. Finite aperture
2. Self-focusing
3. Longer propagation length

Moreover, two different self-focusing mechanisms are realized. The beam in Figure1(a) shows only one focal point when the main lope meets the asymptote. While the beam in Figure1(b) illustrates multi-focusing effect each time when side lopes meet the asymptote.

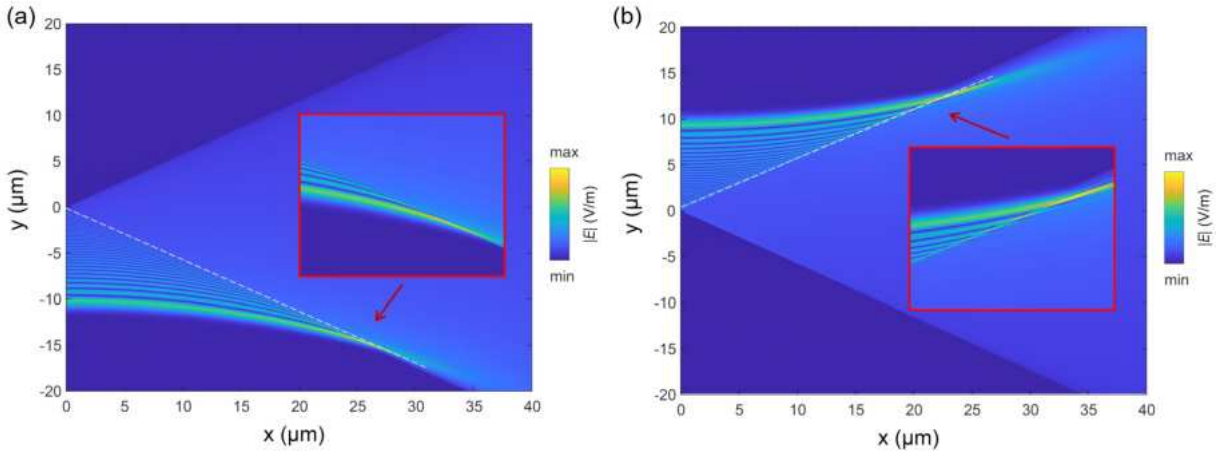


Figure1 The field distribution of two different self-focusing beams in hyperbolic media. (a) Focusing will only happen when the main lope meets the asymptote. (b) Focusing will happen multi-times when each side lopes meet the asymptote. The insets show the detailed light behavior along the asymptote.

Acknowledgement:
This research was supported by National Research Foundation Singapore programme (NRF-CRP22-2019-0007, NRF-CRP23-2019-0007, and NRF-CRP23-2019-0007), A*STAR grant numbers (M22K2c0080 and M23M2b0056), National Medical Research Council (NMRC) MOH-000927 and the Distinguished Professor Fund of Jiangsu Province (Grant No. 1004-YQR24010).

References

1. G. A. Siviloglou, J. Broky, A. Dogariu, and D. N. Christodoulides, Observation of Accelerating Airy Beams, Phys. Rev. Lett. 99, 213901 (2007).
2. I. Kaminer, R. Bekenstein, J. Nemirovsky, and M. Segev, Nondiffracting Accelerating Wave Packets of Maxwell's Equations, Phys. Rev. Lett. 108, 163901 (2012).
3. P. Zhang, Y. Hu, T. Li, D. Cannan, X. Yin, R. Morandotti, Z. Chen, and X. Zhang, Nonparaxial Mathieu and Weber Accelerating Beams, Phys. Rev. Lett. 109, 193901 (2012).

Meta-optics for imaging, microscopy and information processing

The Multi-angle Beam Bender with Transformation Materials

Wen-xiu Dong[1,2], **Yun-yun Lai** [1,2], **and Jin Hu**[1,2 *]

[1] Beijing Institute of Technology, China
[2] China Beijing Key Laboratory of Fractional Signals and Systems, China
[*]corresponding author: bithj@bit.edu.cn

Abstract: In contrast to the usual bender that can only bending fixed angle of the beam path no matter what the incidence angle is, a new bender that can guiding the beam path to wide range bending angles is proposed, which can adjust the path directions according to the incidence angles.

The beam bender is a useful device that can control the wave propagation path along the predefined direction with no limitation such as cut-off frequency as the waveguide tube has [1]. The usual bender is fixed by its bending angle no matter what the incidence angle is, as shown in Fig.1. This means if one wants to adjust the wave path bending angle then the corresponding bender must be replaced to fit the new angle, such situation limits the flexibility of the bender applications.

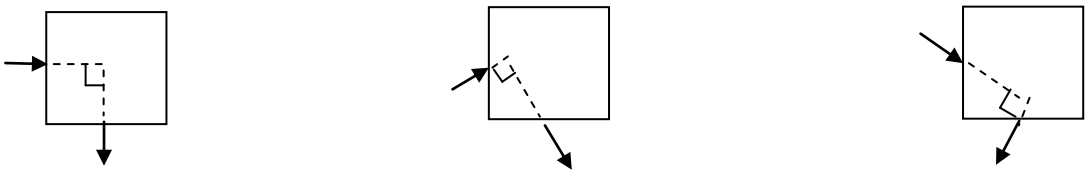


Figure 1. The conventional bender can only turn the beam path at fixed angle no matter what the incidence angle is; here is 90 degree as an example.

In this study, we propose a new kind of beam bender that can tailor the input wave path to different bending angle using the same device, provided the incidence angle is set to an appropriate one. The proposed bender is transformed from the circular Eaton lens based on transformation optics (TO) [2], with planar input and output surfaces. As a characteristic of the Eaton lens, the incident angle of the ray equals to its emergence angle on the boundaries; therefore, when transformed to rectangle, this feature turns to be an arbitrary angle bender that the turning angle of the ray path is controlled by the incident-angle. The space mapping and this bending-control principle are shown in Fig.2.

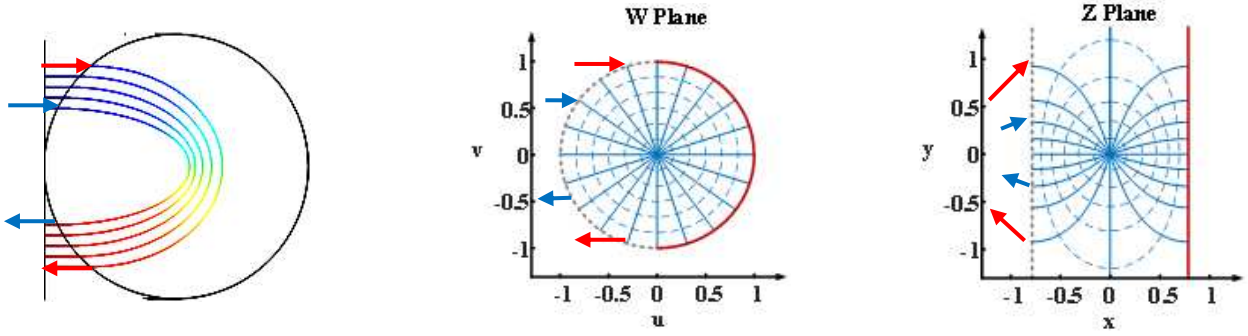


Figure 2. The multi-angle bending control principle. Left: the ray path in the circular Eaton lens; mid: the original space before the mapping; right: the transformation space after the mapping, where, as a result, different incident angle will have different emergence angle on the boundaries.

The effectiveness of the bender is verified by numerical simulations, as shown in Fig.3, which clearly shows that the same device can provide quite wide range of beam bending angles, even can greater than 180 degree. Such a multi-angle angle beam bender may greatly improve the flexibility and conveniences of wave path manipulation.

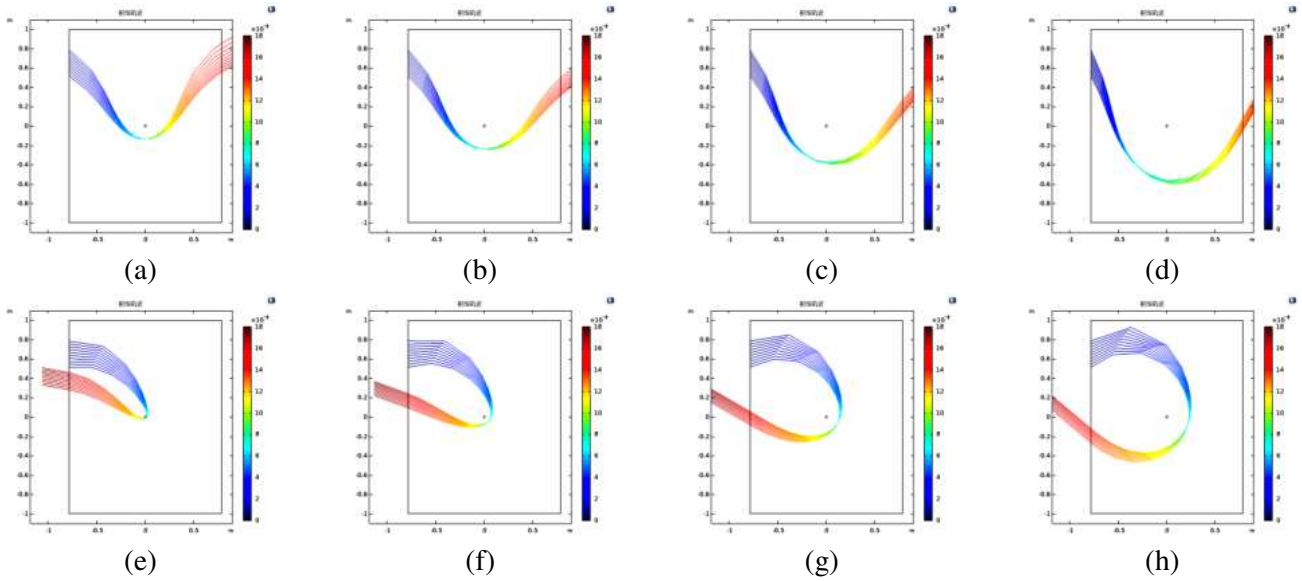


Figure 3. The simulation results of the wide range angle beam bender. (a) 60 degree bending with incident and emergence angles are 30 degree; (b) 80 degree bending with incident and emergence angles are 40 degree; (c) 100 degree bending with incident and emergence angles are 50 degree; (c) 120 degree bending with incident and emergence angles are 60 degree;(e) 200 degree bending with incident and emergence angles are 100 degree; (f) 220 degree bending with incident and emergence angles are 110 degree; (g)240 degree bending with incident and emergence angles are 120 degree; (h) 260 degree bending with incident and emergence angles are 130 degree.

Acknowledgements: This work was supported by National Natural Science Foundation of China (62375017)

References

1. Jiang, W. X., Cui, T. J., Zhou, X. Y., et.al, “Arbitrary bending of electromagnetic waves using realizable inhomogeneous and anisotropic materials,” Phys. Rev. E, Vol.78, 066607, 2008.
2. Pendry, J. B., Schurig, D. and Smith, D. R., “Controlling Electromagnetic Fields,” Science Smith Vol. 312, 1780-1782, 2006.

Computer-generated holography and its applications to metasurfaces

Kexuan Liu[1], Yunhui Gao[1], Jiachen Wu[1], Zehao He[1], and Liangcai Cao[1*]

[1] Department of Precision Instruments, Tsinghua University, Beijing 100084, China
[*]corresponding author: clc@tsinghua.edu.cn

Abstract: Optical metasurfaces offer unprecedented light manipulation capabilities for various applications including holography. In this talk, we introduce the general inverse problem approach for computer-generated holography and discuss its potential applications with the emerging field of optical metasurfaces.

Computer-generated holography (CGH), as a powerful means of light field control, has important applications in computational display and imaging with the help of diffractive optical elements and metasurfaces. Typically, the hologram for optical reconstruction is obtained by solving an ill-posed inverse problem. The reconstruction quality of CGH is greatly limited by the accuracy of the forward model and the reliability of the inverse solver. Currently, realizing high-speed and high-quality hologram generation remains a key challenge, and iterative optimization algorithms and deep learning algorithms provide promising solutions.

In this talk, we present a general inverse problem approach for CGH. CGH algorithms based on numerical optimization and deep learning will be briefly introduced and analyzed. Specifically, model-based deep learning methods, which combine the unique advantages of both model-based methods and deep learning methods, will be highlighted and discussed in detail. [1] We demonstrate the realization of high-speed, high-quality 4K hologram generation with the recently proposed 4K-DMDNet.[2]

While conventional CGH has primarily been realized using liquid-crystal spatial light modulators (SLMs), optical metasurfaces offer unique light manipulation capabilities that are favorable in holographic applications. This talk will conclude with a discussion on the potential application of metasurfaces in the field of holography, particularly towards higher dimensions and higher information capacity.[3]

This work is partially supported by the National Natural Science Foundation of China (62035003, 61775117), China Postdoctoral Science Foundation (BX2021140), and Tsinghua University Initiative Scientific Research Program (20193080075).

References

1. Wu, J., K. Liu, X. Sui and L. Cao, “High-speed computer-generated holography using an autoencoder-based deep neural network,” Opt. Lett., Vol. 46, 2908-2911, 2021.
2. Liu, K., J. Wu, Z. He and L. Cao, “4K-DMDNet: diffraction model-driven network for 4K computer-generated holography,” Opto-Electron. Adv., Vol. 6, 220135, 2023.
3. Jiang, Q., G. Jin and L. Cao, “When metasurface meets hologram: principle and advances,” Adv. Opt. Photonics, Vol. 11, 518-576, 2019.

Super-Resolution Exciton Imaging of Nanodefects in 2D Semiconductors

Jia-Tai Huang[1], **Benfeng Bai**[1*]

[1]State Key Laboratory of Precision Measurement Technology and Instruments, Department of Precision Instrument, Tsinghua University, Beijing 100084, China
[*]corresponding author: baibenfeng@tsinghua.edu.cn

Abstract: The nanodefects in Two-dimensional (2D) semiconductors rise during growth and transfer inevitably and may significantly alter the optoelectronic properties of composed devices. We provide a near-field nanophotoluminescence method that can investigate their impact on local excitonic properties of 2D semiconductors with a very high spatial resolution of 10 nm.

2D semiconductors, such as transition metal dichalcogenides, have emerged as important candidate materials for next-generation chip-scale optoelectronic devices with the development of large-scale production techniques, such as chemical vapor deposition (CVD). However, 2D materials need to be transferred to other target substrates after growth, during which various micro- and nanoscale defects, such as nanobubbles, are inevitably generated. These nanodefects not only influence the uniformity of 2D semiconductors but also may significantly alter the local optoelectronic properties of the composed devices. Hence, super-resolution discrimination and characterization of nanodefects are highly demanded. Here, we report a near-field nanophotoluminescence (nano-PL) microscope that can quickly screen nanobubbles and investigate their impact on local excitonic properties of 2D semiconductors by directly visualize the PL emission distribution with a very high spatial resolution of ~10 nm, far below the optical diffraction limit, and a high speed of 10 ms/point under ambient conditions.

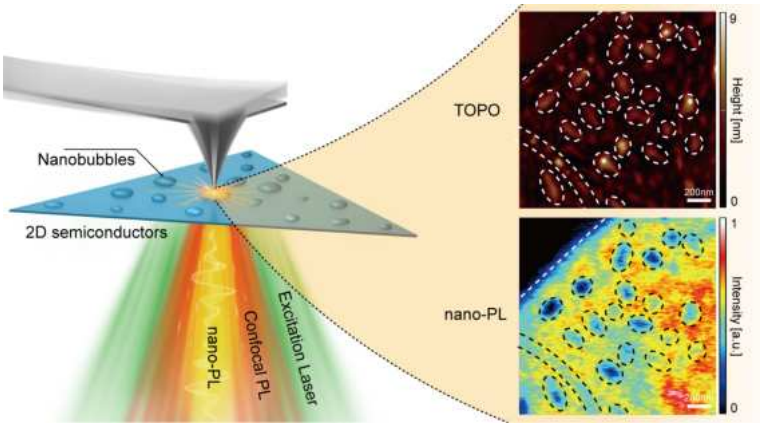


Figure 1. Left: Schematic illustration of the working principle of the nano-PL method. Right: Topography and nano-PL mapping images of the 1L-WS2 sample obtained with the nano-PL system simultaneously.

By using nano-PL microscopy to map the exciton and trion emission intensity distributions in transferred CVD-grown monolayer tungsten disulfide (1L-WS2) flakes, it is found that the PL intensity decreases by 13.4% as the height of the nanobubble increases by every nanometer, which is mainly caused by the suppression of trion emission due to the strong doping effect from the substrate. In addition to the nanobubbles, other types of nanodefects, such as cracks, stacks, and grain boundaries, can also be characterized. The nano-PL method is

proven to be a powerful tool for the nondestructive quality inspection of nanodefects as well as the super-resolution exploration of local optoelectronic properties of 2D materials.

The authors acknowledge the financial support of the National Natural Science Foundation of China (62175121, 61960206003) and Tsinghua-Foshan Innovation Special Fund grant (2021THFS0102).

References

1. Jia-Tai Huang, Benfeng Bai, Yu-Xiao Han, Peng-Yi Feng, Xiao-Jie Wang, Xiao-Ze Li, Guan-Yao Huang, and Hong-Bo Sun, “Super-Resolution Exciton Imaging of Nanobubbles in 2D Semiconductors with Near-Field Nanophotoluminescence Microscopy,” ACS Nano, Vol. 18, No. 1, 272-280, 2024.

Manipulation of Electromagnetic field based on Plasmonic-ENZ Nonlinear Metasurface

Junhong Deng[1]*, Guixin Li[2,3]*

[1]Shenzhen Institute for Quantum Science and Engineering, Southern University of Science and Technology, Shenzhen 518055, China.
[2]Department of Materials Science and Engineering, Southern University of Science and Technology, Shenzhen, 518055, China.
[3]Institute for Applied Optics and Precision Engineering, Southern University of Science and Technology, Shenzhen 518055, China.
*E-mail: dengjh@sustech.edu.cn, ligx@sustech.edu.cn

Abstract: An abstract section (limited to 50 words max) should appear on the top of the page, after the names of the authors and the contact information of the corresponding author.

In epsilon-near-zero (ENZ) materials, second-harmonic generation (SHG) is significantly enhanced but the oblique incidence is required to address nonlinearity. We show that Au meta-atoms on an indium-tin-oxide (ITO) layer provide an approximately 10^4-fold experimentally measured SHG enhancement at normal incidence at the fundamental wavelength near the ENZ condition of ITO.

References

1. Deng, J., Tang Y., Chen S., Li K., Zayats, A. V. & Li, G. “Giant enhancement of second-order nonlinearity of epsilon-near-zero-medium by a plasmonic metasurface,” Nano Letters, Vol. 20, No. 7, 5421-5427, 2020.

Metasurface array for single-shot spectroscopic ellipsometry

Shun Wen[1#], Xinyuan Xue[1#], and Yuanmu Yang[1*]

[1] State Key Laboratory of Precision Measurement Technology and Instruments, Department of Precision Instrument, Tsinghua University, Beijing 100084, China
#These authors contributed equally.
[*]corresponding author: ymyang@tsinghua.edu.cn

Abstract: We demonstrated a compact metasurface array-based spectroscopic ellipsometry system that allows single-shot spectropolarimetric detection and accurate determination of thin film properties without any mechanical movement.

Spectroscopic ellipsometry is widely adopted in semiconductor processing, such as in the manufacturing of integrated circuits, flat display panels, and solar cells. However, a conventional spectroscopic ellipsometer, as shown in Fig.1a, typically modulates the polarization state via mechanical rotation of the compensator or analyzer[1-2]. For spectral detection, it either requires wavelength scanning or the use of a multi-channel spectrometer[3-4]. The resulting system is often bulky, complex, and require multiple measurements.

Here, we proposed and experimentally demonstrated a compact metasurface array-based system for single-shot spectroscopic ellipsometry measurement, as shown in Fig.1b. The proposed system utilizes a silicon-based metasurface array to encode the full Stokes polarization spectrum of light reflected from the thin film. Subsequently, the polarization and spectral information is decoded based on the intensity signals collected by a CMOS sensor using convex optimization algorithms. It can reconstruct the full Stokes polarization spectrum of the thin film, which then further allow the determination of film thickness and refractive index. This approach significantly simplifies conventional spectroscopic ellipsometry systems and enables single-shot thin film parameter measurements.

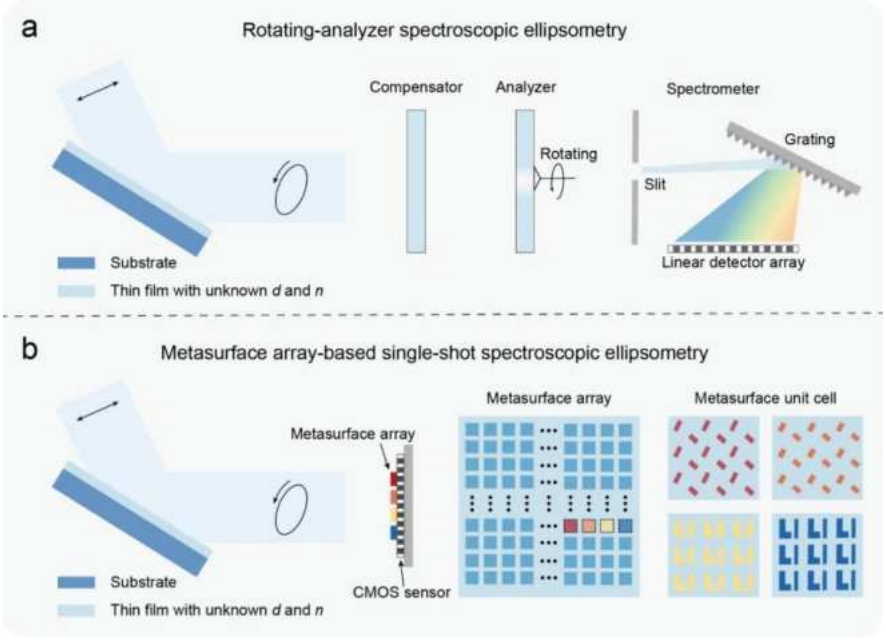


Figure 1. Comparison between conventional (a) and metasurface array-based (b) spectroscopic ellipsometry. a,

Schematics of a conventional spectroscopic ellipsometry system. b, Schematics of a metasurface array-based single-shot spectroscopic ellipsometry system.

The spectropolarimetric detection section of the ellipsometer is composed of a metasurface array integrated onto a commercial CMOS sensor, resulting in an extremely compact system. The metasurface array consists of 20 × 20 optimized elements designed to support anisotropic and spectrally-diverse response, ensuring accurate reconstruction of the full Stokes polarization spectrum. In this work, five SiO_2 thin films with thicknesses ranging from 100 nm to 1000 nm deposited on a silicon substrate were selected as samples for testing. The fitted thicknesses and refractive index dispersions of the tested thin films closely matched the ground truth obtained from a commercial spectroscopic ellipsometer, with errors of only 2.16% and 0.84% for thickness and refractive index measurements, respectively.

The metasurface array also holds promise for spectropolarimetric imaging[5-7], which may further allow the non-destructive characterization of spatially-inhomogeneous thin films. Our approach opens up a new pathway towards a compact and robust spectroscopic ellipsometry system for the high throughput measurement of thin film properties.

This work was supported by the National Natural Science Foundation of China (62135008, 61975251) and by the Guoqiang Institute, Tsinghua University.

References

1. Collins, R. W. & Koh, J. Dual rotating-compensator multichannel ellipsometer: instrument design for real-time Mueller matrix spectroscopy of surfaces and films. Journal of the Optical Society of America A 16, 1997-2006, 1999.
2. Shan, A. et al. High-speed imaging/mapping spectroscopic ellipsometry for in-line analysis of roll-to-roll thin-film photovoltaics. IEEE Journal of Photovoltaics 4, 355-361, 2014.
3. Lee, J. et al. Rotating-compensator multichannel ellipsometry: applications for real time stokes vector spectroscopy of thin film growth. Review of Scientific Instruments 69, 1800-1810 (1998).
4. Fujiwara, H. Spectroscopic Ellipsometry: Principles and Applications. (Hoboken: Wiley, 2007).
5. Zhang, W. Y. et al. Deeply learned broadband encoding stochastic hyperspectral imaging. Light: Science & Applications 10, 108 (2021).
6. Xiong, J. et al. Dynamic brain spectrum acquired by a real-time ultraspectral imaging chip with reconfigurable metasurfaces. Optica 9, 461-468 (2022).
7. Yako, M. et al. Video-rate hyperspectral camera based on a CMOS-compatible random array of Fabry-Pérot filters. Nature Photonics 17, 218-223 (2023).

Metasurface-enabled Wavefront Engineering for Advanced Imaging Technologies: 3D Sensing and Biomedical Imaging

Inki Kim[1,2]

[1] Dept. of Biophysics, Institute of Quantum Biophysics, Sungkyunkwan University, Suwon 16419, Korea
[2] Dept. of Intelligent Precision Healthcare Convergence, Sungkyunkwan University, Suwon 16419, Korea
*corresponding author: inki.kim@skku.edu

Abstract: In this talk, I will introduce metasurface-enabled advanced imaging techniques: (1) Electrically tunable varifocal metalens and point cloud generating metasurface for 3D depth imaging, (2) Dual-mode metalens for switchable bright-field and edge-enhanced imaging (3) Multifunctional metalens for photoacoustic microscopy

Metamaterials or metasurfaces – materials that are engineered to have properties that are not found in natural materials – allow us to overcome physical limitations. Metasurface science is further not only expanding field of optics and photonics by providing ultra-compact and multifunctional flat optical devices, also resolves challenging problems in diverse sectors like healthcare, optical display, imaging, and military affairs.

In this talk, I will introduce metasurface-enabled wavefront engineering applications, especially advanced imaging technologies. First, I will explain an electrically tunable varifocal metalens that operates at visible wavelengths and a point cloud generating metasurface for advanced 3D depth imaging or LiDAR applications [1,2]. The electrically tunable varifocal metalens will enable solid-state zoom tuning camera. The point cloud generating metasurface is able to spread 10K dots over 2π full space with over 80% diffraction efficiency, which is promising for scanning-free LiDAR technology. Second, I will show a dual-mode metalens integrated with a liquid crystal cell that can be electrically switched between bright-field and edge-enhanced imaging on the millisecond scale [3]. We demonstrate the focusing and vortex generation ability of the metalens under different states of circular polarization and prove its use for biological imaging. Third, we will introduce metasurface-enhanced photoacoustic microscopy for label-free biomedical imaging. We design an achromatic transmissive lens for 266 and 532 nm wavelength with NA of 0.8 for multispectral photoacoustic microscopy [4]. Also, we demonstrate a diffraction-limited needle beam generating metasurface with an aspect ratio of 260 (along the beam propagation direction) for deep tissue photoacoustic imaging.

References

1. Badloe, T. et al., “Electrically tunable bifocal metalens with diffraction-limited focusing and imaging at visible wavelengths,” Adv. Sci., Vol. 8, No. 21, 2102646, 2021.
2. Kim, G. et al., “Metasurface-driven full-space structured light for three-dimensional imaging,” Nat. Commun., Vol. 13, 5920, 2022.
3. Badloe, T. et al., “Bright-field and edge-enhanced imaging using an electrically tunable dual-mode metalens,” ACS Nano, Vol. 17, No. 15, 14978-14685, 2023.
4. Barulin, A. et al., “Dual-wavelength UV-visible metalens for multispectral photoacoustic microscopy: A simulation study,” Photoacoustics, Vol. 32, 100545, 2023.

Monocular polarimetric metalens for ultracompact snapshot stereo-imaging

Shuming Wang[1]

[1] National Laboratory of Solid State Microstructures, School of Physics, Nanjing University, Nanjing 210093, China

[*]corresponding author: wangshuming@nju.edu.cn

Abstract: We propose a non-interfering, all-Stokes imaging polarimeter based on a single-layer metasurface to demonstrate the stereo-imaging in an ultracompact size.

Polarization, as an optical degree of freedom, provides spatially varying information that can be detected through polarization imaging. Analyzing the polarized reflection information of objects represents a rapid, passive, and interference-resistant monocular three-dimensional (3D) depth recovery method. Metasurfaces, as subwavelength-scale 2D arrays, offer versatile control over the wavefront and polarization of light. In this paper, we propose a non-interfering, all-Stokes imaging polarimeter based on a single-layer metasurface. This polarimeter achieves compact snapshot coverage of the entire Poincaré sphere for full polarization information acquisition, overcoming the inherent limitations of 50% efficiency in conventional polarizers. We explore a matching algorithm for 3D reconstruction, providing a comprehensive technical roadmap for monocular detection. The achievable minimum pixel accuracy of our system is 5 μm, paving the way for high-resolution polarization cameras. Innovatively introducing circular polarization information into the 3D reconstruction system enhances surface detail and texture information, especially for miniature and circular objects. This breakthrough provides an ultra-compact depth perception platform for applications such as face recognition and visual systems for automotive robots.

Towards thinner imaging systems with Huygens' spaceplates

F. J. Díaz-Fernández[1,2], L. M. Máñez-Espina[1], A. Díaz-Rubio[1], and V. Asadchy[2,*]

[1]Universitat Politècnica de València, Camí de Vera s/n, Valencia 46022, Spain
[2]Aalto University, Maarintie 8,Espoo 02150, Finland
[*]viktar.asadchy@aalto.fi

Abstract: Spaceplates are designed to replace free-space gaps in optical systems. We show that by leveraging Huygens'-type condition in a photonic crystal slab supporting two resonance modes it is possible to strongly enhance spaceplates characteristics and make it transparent across a wide frequency range, laying the foundation for multicolor spaceplate systems.

The advent of spaceplates marks a significant development in non-local metasurfaces, enabling the compression of the optical path in systems between the detector and the lens. Unlike traditional optics advancements that focused on miniaturizing lenses and sensors, spaceplates manipulate the intervening space [1,2]. They reduce the optical system's free space, effectively decreasing its size by the factor called reduction ratio $h_{\text{eff}}/h_{\text{s}}$, where h_{s} and h_{eff} are the actual spaceplate thickness and the thickness of an air slab it can emulate, respectively (see illustration in Figure 1). Primarily, spaceplates aim to compact optical systems, benefiting devices from smartphone cameras to medical instruments, potentially fostering new human body study techniques. Recently, the spaceplates have been achieved based on the Fano resonances in photonic crystal slabs [2] and Fabry-Perot resonances in multilayer films [3,4]. In both cases, the required properties have been produced with a single resonance or by cascading structures with the same-type (with even or odd symmetry) resonances.

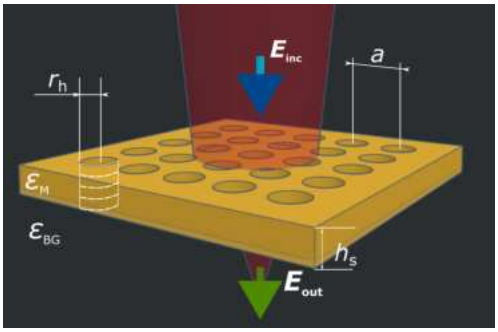


Figure 1. Spaceplate concept. The spaceplate slab with thickness h_{s} emulates an air slab of thickness h_{eff}. The spaceplate allows for a decrease in the air distance between any optical component. For example, in the figure, the convergence of an optical beam is enhanced through interaction with the spaceplate.

In this study, we study the performance limits of spaceplates with two spectrally overlapped even and odd (orthogonal) resonances and demonstrate strong enhancement of the reduction ratio. The spectral overlap of resonances with opposite mode symmetries, fulfilling the so-called Huygens' condition, has been utilized over the past decade through Huygens' metasurfaces [5]. Very recently, a similar idea of combining two resonances in spaceplates was suggested in [6] based on the susceptibility model, however, the model is recognized for its complexity in application to optical designs, and no feasible geometry has been presented. Our results

demonstrate that the overlap of two orthogonal resonances in a spaceplate not only doubles its reduction ratio $h_{\text{eff}}/h_{\text{s}}$, but also drastically expands its operational bandwidth and transparency window. Additionally, we explore the use of nearly overlapping resonances, examining their performance beyond the Huygens' configuration.

Figure 2 compares the conventional (single-resonance) and proposed Huygens' (double-resonance) spaceplates. The notations used in the figure are explained in its caption. From the second raw of plots, one can observe the double enhancement of the reduction ratio $\Phi \sim h_{\text{eff}}/h_{\text{s}}$ and full-transparency regime for large range of frequencies and incident angles available only in Huygens'-type spaceplates.

In the presentation, we will show the developed temporal coupled-mode theory for such Huygens'-type spaceplates and several realistic designs of them implemented based on a photonic-crystal-slab geometry [7].

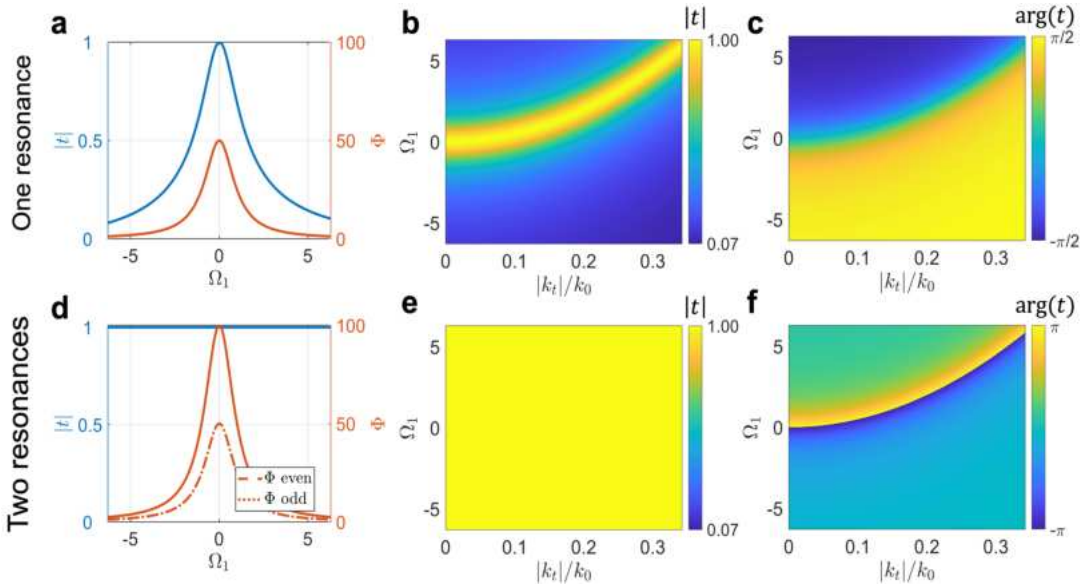


Figure 2. Comparison of conventional (a-c) and Huygens'-type (d-f) spaceplates. For the latter, the electric and magnetic resonances share the same frequency. (a,d) Transmission coefficient for normally incident light (blue) and compression parameter Φ proportional to $h_{\text{eff}}/h_{\text{s}}$ for the conventional (top) and Huygens'-type (bottom) spaceplate. Ω_1 is the frequency shift with respect to the resonance frequency of the spaceplate and normalized by the resonance width. (b,e) Transmission coefficient amplitude and (c,f) phase of the spaceplate versus frequency and the incident angle defined as asin($|k_t|/k_0$).

References

1. Reshef, O., DelMastro, M. P., Bearne, K. K. M., Alhulaymi, A. H., Giner, L., Boyd, R. W., and Lundeen, J. S., "Towards ultra-thin imaging systems: an optic that replaces space," Nat. Comm., Vol. 12, 3512, 2021.
2. Guo, C., Wang, H., and Fan, S., "Squeeze free space with nonlocal flat optics," Optica, Vol. 7, No. 9, 1133, 2020.
3. Chen, A. and Monticone, F., "Dielectric nonlocal metasurfaces for fully solid-state ultra-thin optical systems", ACS Photonics, Vol. 8, No. 5, 1439–1447, 2021.
4. Pahlevaninezhad M. and Monticone, F., "Multi-color spaceplates in the visible", arXiv:2312.02378, 2023.
5. Epstein A. and Eleftheriades, G.V., "Huygens' metasurfaces via the equivalence principle: Design and applications", JOSA B, Vol. 33, No. 2, A31, 2016.
6. Dugan, J., Smy, T. J., Monticone, F., and Gupta, S., "Surface susceptibility synthesis of spatially dispersive metasurfaces for space compression and spatial signal processing", techrxiv.24174513, 2023.
7. Yang, Q., Kruk, S., Xu, Y., Wang, Q., Srivastava, Y. K., Koshelev, K., Kravchenko, I., Singh, R., Han, J., Kivshar, Yu., and Shadrivov, I., "Mie-resonant membrane huygens' metasurfaces", Adv. Fun. Mat., Vol. 30, No. 4, 1906851, 2019.

Varifocal Meta-lenses for Bio-imaging and 6G Communication

Mu Ku Chen[1,2,*], Jing Cheng Zhang[1], Xiaoyuan Liu[2], Yin Zhou[1], Jialuo Cheng[1], Takuo Tanaka[3], and Din Ping Tsai[1,2]

[1]Department of Electrical Engineering, City University of Hong Kong, Kowloon, Hong Kong.

[2]The State Key Laboratory of Terahertz and Millimeter Waves, City University of Hong Kong, Kowloon, Hong Kong.

[3]Innovative Photon Manipulation Research Team, RIKEN Center for Advanced Photonics, Saitama, Japan.

[*]corresponding author: mkchen@cityu.edu.hk

Abstract: Meta-device is a new type of flat optical device composed of artificial nanostructures that can manipulate the incident electromagnetic wave. We developed varifocal meta-lenses to manipulate the focusing spot for bioimaging and 6G communication from 1D to 3D.

Introduction

The manipulation of focused light beams is widely used in our lives, such as camera lenses and signal transmission. Although there are traditional lenses that realize off-axis focusing, the requirements of tilting need extra space, and the tilting stage hinders its compact integration. These disadvantages hinder the development of device miniaturization or increased construction complexity. Meta-devices composed of artificial nanostructures can manipulate the incident electromagnetic wave's phase, polarization, and amplitude. Here, we demonstrate Moire meta-devices for focal length tuning in the z-axis (1 dimensional, 1D), focal spots manipulation in the x-y plane (2 dimensional, 2D), and x-y-z axis (3 dimensional, 3D).

Results and Discussion

Following the Moiré technique, a variable focus dielectric meta-device in 1D is designed and implemented for high-contrast optical sectioning fluorescence microscopy at the visible spectral region in Fig 1(A). Fig.1(B) shows the designed phase, and the SEM images. Measured focus beam profiles of the varifocal meta-devices along the propagation direction under different rotation angles (θ = 180-350°) in a step of 30° are shown in Fig.1(C). The focal length can be tuned from 20 mm to 10 mm, which is a function of rotation angle (θ) and decreases with the increasing relative rotation angles of the metasurfaces. We demonstrated telecentric imaging equipped with variable focus meta-lens, which performs high-contrast multi-plane fluorescence imaging for mouse intestine tissue samples, as shown in Fig.1(D).

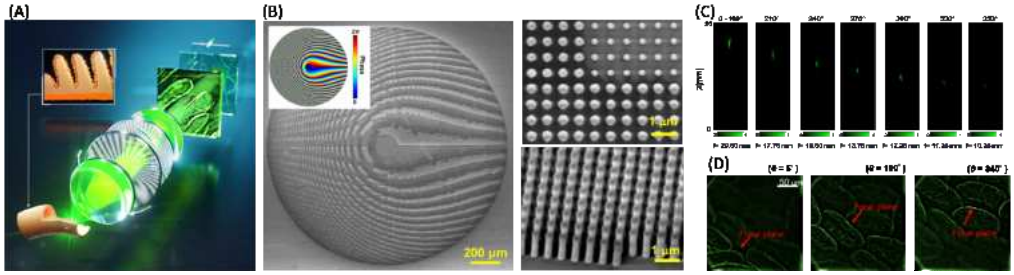


Fig. 1. Varifocal meta-devices for 1D. (A) 1D varifocal for bio-imaging. (B) SEM images of meta-devices. Insert image is the designed phase. (C) focusing profile of varifocal in the z-axis with various rotation angles. (D) Bio-imaging of mouse intestine tissue with different focus depths by this meta-device.

The synthetic phase design of rotary doublet Airy beam and triplet Gaussian beam varifocal meta-devices to fully control the 300GHz beam's propagation direction and coverage area are shown in Fig.2(A-B) and (D-E), respectively. The focusing spot can be delivered to arbitrary positions in a two-dimensional plane or a three-dimensional space, as shown in Fig.2(C) and (F), respectively. The highly concentrated signal can be delivered to a specific position, and the transmission direction can be adjusted freely to enable secure, flexible, and high-directivity 6G communication systems. This metasurface technology avoids the high costs associated with extensive use of active components (e.g., pin diodes and varactor diodes). 6G communication systems, wireless power transfer, zoom imaging, and remote sensing will benefit from the large-scale adoption of such a technology.

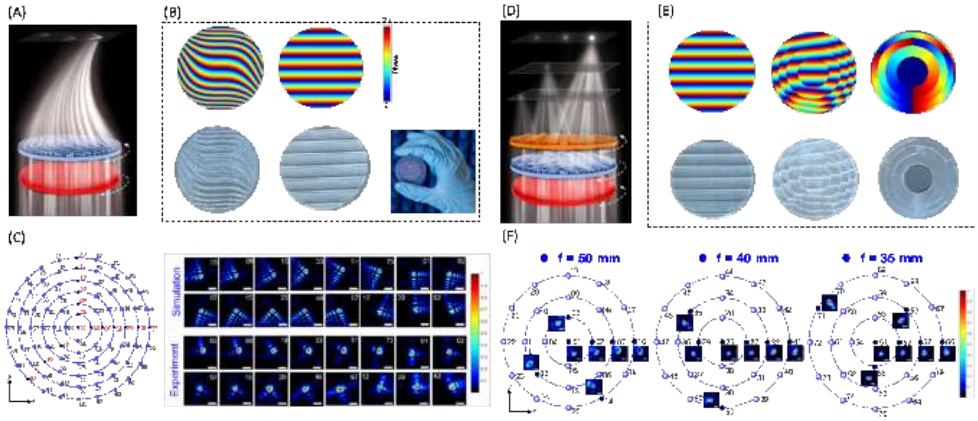


Fig. 2. (A) Varifocal meta-devices for 2D manipulation. (B&E) Designed phase and fabrication sample by 3D printing. (C) Varifocal focusing map in 2D. (D) Varifocal meta-devices for 3D manipulation. (F) Varifocal focusing map in 3D.

Summary

We demonstrate Moire meta-devices for the focal spot tuning in 1D, focal spots manipulation in 2D and 3D. The varifocal meta-devices are used for bio-imaging and 6G signal transmission. We show the telecentric imaging equipped with variable focus meta-lens, which performs high-contrast multi-plane fluorescence imaging for mouse intestine tissue samples. The sixth-generation (6G) communication technology is being developed in full swing and is expected to be faster and better than the fifth generation.

Acknowledgements

This work is supported by the University Grants Committee / Research Grants Council of the Hong Kong Special Administrative Region, China [Project No. AoE/P-502/20, CRF Project: C5031-22G, GRF Project: CityU15303521; CityU11305223; CityU11310522; CityU11300123, City University of Hong Kong [Project No. 9380131, 9610628, and 7005867], and National Natural Science Foundation of China [62375232].

References

1. J. Zhang, G. -B. Wu, M. K. Chen, X. Liu, K. F. Chan, D. P. Tsai, and C. H. C, “A 6G Meta-device for 3D Varifocal”, Science Advances, 9(4), eadf8478 (2023).
2. Y. Luo, C. H. Chu, S. Vyas, H. Y. Kuo, Y. H. Chia, M. K. Chen, X. Shi, T. Tanaka, H. Misawa, Y.-Y. Huang, and D. P. Tsai, "Varifocal Metalens for Optical Sectioning Fluorescence Microscopy", Nano Letters, 21, 5133-42 (2021).

Subnanometer-matter's Farfield Optical Fingerprints and Metrology Applications

Xue-Wen Chen[1,2*]

[1]School of Physics and Wuhan National Laboratory for Optoelectronics, Huazhong University of Science and Technology, Wuhan, China.
[2]Wuhan Institute of Quantum Technology, Wuhan, China.
[*]Corresponding author: xuewen_chen@hust.edu.cn

Abstract: We report that subnanometer-dielectric surface undulations feature deterministic and pronounced speckles in the farfield via interference scattering microscopy. We show they could serve as the optical fingerprints of the dielectric substrate surface. Consequently, we demonstrate their applications for marker-free position identification and displacement sensing with sub-nanometer precisions.

Interferometric scattering microscopy, as an ultrasensitive fluorescence-free imaging modality, has recently gained enormous attention and has been rapidly developing from demonstration of principle to quantitative sensing and bioanalytics. A substrate, such as a coverslip or wafer, is an indispensable component of any modern optical microscope. The interaction between the substrate and sample naturally imprints the substrate's signatures into the observations, in particular, for interferometric scattering microscopy, where the image directly relies on the interference between the reflected/transmitted field from the substrate surface and scattering of the sample. Thus, typical microscope substrates used in the laboratory, such as glass coverslips, have been made extremely at, often with surface roughness well below 0.5 nm. However, even employing such flat substrates, images obtained in interferometric scattering microscopy still exhibit seemingly mysterious “random" speckle patterns, which have been speculated to originate from combined effects of uncontrollable imperfections including uneven illumination, glass inhomogeneity, surface roughness, dust, or stray light in the setup. The speckles set a lower limit for the size of detectable scatterers.

In this talk, we report that substrates commonly used in the laboratory feature deterministic speckle patterns in interference microscopy, which originate, counterintuitively, from the sub-nanometer surface roughness [1]. We show they serve as the optical fingerprints of the substrate surface. We demonstrate their applications for marker-free position identification and displacement detection with sub-nanometer precisions, which are essential for many modern technologies, including positioning of wafers in the semiconductor industry and accurate localizations of single-molecule labels in super-resolution microscopies. We also discuss approaches to remove the speckle pattern [2].

We acknowledge partial financial support from the National Natural Science Foundation of China (Grants No. 92150111 and No. 62235006).

References

1. S. Lin, Y. He, D. Feng, M. Piliarik, X.-W. Chen, “Optical fingerprint of flat substrate surface and marker-free

lateral displacement detection with Angstrom-level precision", *Physical Review Letters* 129, 213201 (2022).
2. N. Jiao, S. Lin, D. Feng, Y. He, X.-W. Chen, "Defocus-integration interferometric scattering microscopy for speckle suppression and enhancing nanoparticle detection on substrate", Submitted (2024).

Photothermal inspection of optoelectronic chips

Xiangping Li

Institute of Photonics Technology, Jinan University, P.R.China
*corresponding author: xiangpingli@jnu.edu.cn

Abstract: In this paper, we report the microscopic excitation and imaging of dielectric Mie resonators. The interaction of tightly focused vector beams with dielectric nanoparticles leads to exotic phenomena including multipolar excitation by displacement resonances, directional scattering, as well as superresolution imaging.

The studies of Mie scattering in dielectric nanostructures reveal strong electro-magnetic multipolar resonances, laying foundation for emerging nanophotonic applications [1]. Canonically, the morphology-sensitive resonances hinge on excitations under plane wave illuminations. The tight focusing condition under microscope, a typical scenario of nanophotonics, leads to a plethora of freedom in manipulation of light-matter interactions. In this talk, we show that the confocal microscopic imaging of silicon nanostructures exhibits distinctive patterns of the scattering point spread functions, which manifests the excitation of higher-order multipolar modes associated to displacement resonance by tight focusing. In addition, the manipulation of focal field component of vector beams can lead to directional scattering of dielectric dimer structures by judicious configuring the multipolar excitations. Moreover, the strong multipolar electro-magnetic resonance by microscopic excitations empowers pronounced photothermal heating effect. At a mild light irradiance on the order of MW/cm2, it enables a giant nonlinear modulation of the confocal reflection intensity from dielectric nanostructures and their imaging patterns [2]. Thereby, it opens up an entirely new paradigm for label-free sub-diffraction imaging with a demonstrated ~λ/7 feature size [3].

References

1. Yuri, Kivshar, “The rise of Mie-tronics,” Nano Letters, 22, 3513, 2022.
2. Yu-Lung Tang, Te-Hsin Yen, Kentaro Nishida, Chien-Hsuan Li, Yu-Chieh Chen, Tianyue Zhang, Chi-Kang Pai, Kuo-Ping Chen, Xiangping Li, Junichi Takahara & Shi-Wei Chu, Multipole engineering by displacement resonance: a new degree of freedom of Mie resonance, Nature Communications. 14, 7213, 2023.
3. Ying Che, Tianyue Zhang, Xiaowei Liu, Dejiao Hu, Shichao Song, Yan Cai, Yaoyu Cao, Jie Zhang, Shi-Wei Chu, Xiangping Li, “Nanophotonic inspection of deep-subwavelength integrated optoelectronic chips,” arXiv:2404.02528, 2024.

Optical Information Processing on Thin Film Lithium Niobate

Mengjie Yu

Department of Electrical and Computer Engineering, University of Southern California, Los Angeles, CA 90089, United States
E-mail: mengjiey@usc.edu

Abstract:

Lithium niobate (LN) is an excellent nonlinear photonic material due to its large electro-optic (EO) coefficient, second order ($\chi^{(2)}$) and Kerr ($\chi^{(3)}$) nonlinearity, along with a wide optical transparency window. Thanks to the recent advances in nanofabrication technology, monolithic LN waveguides with high optical confinement and ultralow linear loss has been achieved, which was critical to the success of the silicon-based platform in the past decade. Highly efficient and controllable light-matter interactions can be achieved using optical, electrical, or mechanical waves at extremely compact footprints. In this talk, I will review our recent developments of generation and measurement of ultrafast optical waveforms, optical modulation for free space communication and optical neutral network on thin-film LN nonlinear platform.

Quantum metamaterials for artificial intelligence

Analyzing qubit arrays via a multiresolution approach

M. Bidarvand[1*], A. Sowa[1]

[1]University of Saskatchewan, Canada
[*]corresponding author: mab867@usask.ca

Abstract: Utilizing a multiresolution approach, we analyze the properties of infinite qubit arrays. Our method merges the classical Borel isomorphism and the Haar basis, connecting the qubit system's Hilbert space to $L_2(0,1]$. This furnishes a geometric representation of fundamental operators and reveals an unexpected integration of classical calculus in this structure.

Introduction: Qubit arrays are a type of quantum metamaterial that interact with a mode of the electromagnetic field in a manner that depends on its quantum state. The fundamental problem is the solvability of mathematical models describing such systems. A systematic investigation originated in the physics literature [2, 5, 6]. Solvability of the model, with a certain choice of constituent parameters, was demonstrated in [3]. We further refine the mathematical methods introduced therein. Specifically, we use the multiresolution methods to rigorously establish a correspondence between $L_2(0,1]$ and the Hilbert space of an array of qubits, which may be finite or infinite.

The Model: We adopt the generalized Jaynes-Cummings model, which describes a system consisting of n qubits and a quantum harmonic oscillator, which represents a single mode of the electromagnetic field. In this model the Hamiltonian consists of three components, which capture the qubits, the field, and the interaction between them. The interaction part is the most important, [3]. It assumes the form

$$\mathcal{H}_I = C_x^{(n)} \otimes (\hat{a} + \hat{a}^\dagger), \tag{1}$$

with $\hat{a}$ and $\hat{a}^\dagger$ being the harmonic oscillator's annihilation and creation operators, respectively, while

$$C_x^{(n)} = \sum_{k=1}^{n} \lambda_k \, \sigma_x^k, \qquad \sigma_x^k = I \otimes \ldots I \otimes \sigma_x \otimes I \ldots \ (\sigma_x \text{ in k-th place}) \tag{2}$$

where σ_x is the Pauli matrix. Here, we provide rigorous interpretation for the limit $n \to \infty$, for a specific choice of the weights λ_k. We also discuss what happens when σ_x is replaced by, say, σ_y, which in the case of an infinite array is deeply nontrivial.

Let $\mathbb{H}_Q = \text{span}\{|0\rangle, |1\rangle\}$, so that the Hilbert space of an n-tuple of qubits is $\bigotimes_{j=1}^{n} \mathbb{H}_Q$. Naturally, one envisions the state space of an infinite array to be $\bigotimes_{j=1}^{\infty} \mathbb{H}_Q$. Viewing $\mathbb{H}_Q$ as the space of functions on $\mathbb{Z}_2$, the infinite tensor product of such spaces should embody functions on the infinite Cartesian product $\mathbb{Z}_2 \times \mathbb{Z}_2 \times \mathbb{Z}_2 \times \ldots$. The latter can be correlated with the interval $(0,1]$ through binary expansion. Moreover, the Haar basis and its associated multiresolution enable the representation of quantum states via square-integrable functions on the interval $(0,1]$. Furthermore, operations on states can be represented through integral operators, typically with distributional kernels. This structural setup simplifies the characterization of the spectral properties of the central operators. A key example is C_x (i.e., the $n \to \infty$ limit of $C_x^{(n)}$), which takes on the form

$$C_x[\Phi](x) = \sum_k \frac{1}{2^k} \Phi\left(x + \frac{(1)^{\epsilon_k(x)}}{2^k}\right) \quad x \in (0,1], \tag{3}$$

for a continuous function Φ. Note that $\epsilon_k(x) \in \{0,1\}$ denotes, the k-th digit in the dyadic expansion of $x \in (0,1]$, i.e.

$$x = \sum_{k=1}^{\infty} \frac{\epsilon_k(x)}{2^k}.$$

As it turns out, the Haar transform reduces the operator (4) to a block matrix with consecutive diagonal blocks increasing in size, see Fig. (1) . This is sufficient to characterize the spectrum of C_x. Perturbing the entire array along the Bloch sphere, we are led to consider

$$C_y[\Phi](x) = \sum_k \frac{(-1)^{\epsilon_k(x)} i}{2^k} \Phi\left(x + \frac{(-1)^{\epsilon_k(x)}}{2^k}\right) \quad x \in (0,1]. \tag{4}$$

At first glance, one might expect a similar scenario for C_y as for C_x, given the unitary equivalence between σ_x and σ_y. However, the situation is more intricate: the Haar transform fails to convert C_y into a block matrix. Instead, C_y emerges as the combination of such an operator and a compact operator.

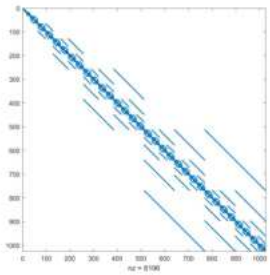


Figure 1: The block matrix representing C_x in the Haar basis.

The block structure remains the same for C_x and C_y (with different numerical entries). The aforementioned necessary compact correction, denoted K, is defined as follows:

$$K = i(L' - L), \qquad L[u](x) = \int_0^x u(y)dy, \tag{5}$$

where L'represents the adjoint of L. Defining operators

$$C_- = \sum_{k=1}^{\infty} \frac{1}{2^k}\, \sigma_-^k, \quad C_+ = \sum_{k=1}^{\infty} \frac{1}{2^k}\, \sigma_+^k, \tag{6}$$

where $\sigma_\pm$ are the raising/lowering operators, we obtain

$$C_y = i((C_+ + L') - (C_- + L)) - K. \tag{7}$$

The first two terms turn into block matrices when represented by the Haar transform.

Conclusion: As is well known, due to the exponential dependence of the underlying Hilbert space dimension on the number of qubits, generic classical simulations of quantum systems have scaling limitations. Furthermore, the standard approaches to quantum many-body theory often ignore real quantum effects in favor of roughly factorized quantum states. Quantum engineering has great potential due to the fact that it can harness the quantum correlations seen in non-factorized states, [4]. The explicitly solvable quantum models, like the ones discussed here, provide unique insight that could not be obtained via simulation. The conceptual framework presented here amounts to an alternative, scale-based, model of quantum information. While it is equivalent to the canonical one, it provides advantage in certain types of analysis. In particular, it enables rigorous analysis of systems that comprise an infinite number of qubits.

References

[1] Haar, A. "Zur theorie der orthogonalen Funktionensysteme," Math. Annalen. 69, PP. 331–371, 1910.

[2] Rakhmanov, A.L., A.M. Zagoskin, S. Savel'ev and F. Nori, "Quantum metamaterials: Electromagnetic waves in a Josephson qubit line," Phys. Rev. B, 77, 144507, 2008.

[3] Sowa, A.P. and A.M. Zagoskin, "An exactly solvable quantum-metamaterial type model," Journal of Physics A: Mathematical and Theoretical, 52, 395304 (12pp), 2019.

[4] Zagoskin. A. M. "Quantum Engineering, Theory and Design of Quantum Coherent Structures," Cambridge University Press: Cambridge, 2011.

[5] Zagoskin. A. M., D. Felbacq and E. Rousseau, "Quantum metamaterials in the microwave and optical ranges," EPJ Quantum Technology, 3 (1): 2, 2016.

[6] Zagoskin. A. M. "Superconducting quantum metamaterials in: Nonlinear, Tunable and Active Metamaterials," Springer, 255–279, 2015.

Effects of Strong Capacitive Coupling Between Meta-Atoms in Three-Dimensional rf SQUID Superconducting Metamaterials

Jingnan Cai[1], Yilin Li[1], and Steven M. Anlage[1*]

[1] Quantum Materials Center, Physics Department, University of Maryland, College Park, MD 20742-4111 USA
[*]corresponding author: anlage@umd.edu

Abstract: We model and measure a nonlinear three-dimensional superconducting metamaterial with qualitatively new properties enabled by strong capacitive coupling between the meta-atoms. The new form of coupling creates a multitude of resonant modes. The model is verified with rf current images produced by laser scanning microscopy of the operating metamaterial.

Superconducting macroscopic quantum metamaterials have been of interest since the first experimental demonstration in 2005 [1-4]. We consider, for the first time, the effects of strong capacitive and inductive coupling between radio frequency Superconducting Quantum Interference Devices (rf SQUIDs) in a three-dimensional overlapping metamaterial geometry when driven by rf flux at and near their self-resonant frequencies [5]. The equations of motion containing the gauge-invariant phases on the Josephson junctions in each SQUID are set up and solved which include the high-frequency displacement currents through capacitive overlap between the wiring of SQUID loops. We begin by modeling two overlapping SQUIDs and studying the response in both the linear and nonlinear high-frequency driving limits. By exploring a sequence of more and more complicated arrays, the formalism is eventually extended to the $N \times N \times 2$ overlapping metamaterial array, where we develop an understanding of the many $(8N^2 - 8N + 3)$ resulting resonant modes in terms of three classes of resonances. The capacitive coupling gives rise to qualitatively new self-resonant response of rf SQUID metamaterials, and is demonstrated through analytical theory, numerical modeling, and experiment in the 10-30 GHz range on capacitively and inductively coupled rf SQUID metamaterials [5]. To further investigate the predictions of the theory, we image the rf current distributions in the SQUID metamaterial while it is under rf magnetic flux illumination in the superconducting state, by means of laser scanning microscopy [6]. We also discuss the use of machine learning to design structured light perturbations to bring the rf SQUID metamaterial into coherent oscillation.

This work was supported by ONR under grant N000142312507, and NSF/DMR under grant 2004386.

References

1. S. M. Anlage, “The physics and applications of superconducting metamaterials,” Journal of Optics, Vol. 13, 024001 (2011).
2. P. Jung, A. V. Ustinov, and S. M. Anlage, “Progress in superconducting metamaterials,” Superconductor Science and Technology, Vol. 27, 073001 (2014).
3. N. Lazarides and G. P. Tsironis, “Superconducting metamaterials,” Physics Reports, Vol. 752, 1-67 (2018).
4. M. Ricci, N. Orloff, and S. M. Anlage, "Superconducting Metamaterials," Appl. Phys. Lett., Vol. 87, 034102 (2005).
5. J. Cai, *et al.*, “Effects of Strong Capacitive Coupling Between Meta-Atoms in rf SQUID Metamaterials,” arXiv:2402.07044.
6. A. P. Zhuravel, *et al.*, “Imaging the paramagnetic nonlinear Meissner effect in nodal gap superconductors,” Phys. Rev. B, Vol. 97, 054504 (2018).

Point defect-based material solutions for quantum sensing and quantum reservoir computing

V. Ivády[1,2,3,*]

[1]Department of Physics of Complex Systems, Eötvös Loránd University, Egyetem tér 1-3, H-1053 Budapest, Hungary
[2]MTA–ELTE Lendület "Momentum" NewQubit Research Group, Pázmány Péter, Sétány 1/A, 1117 Budapest, Hungary
[3]Department of Physics, Chemistry and Biology, Linköping University, SE-581 83 Linköping, Sweden
[*]corresponding author: ivady.viktor@ttk.elte.hu

Abstract: Point defects with controllable electron and nuclear spin states provide a versatile toolbox for developing quantum applications in the fields of sensing, information processing, and computation. My talk outlines the physics of point defect quantum bits and discusses recent advances in light of sensing and quantum reservoir computing.

Quantum applications are about to revolutionize several key areas of science and technology, including but not limited to computation, communication, and sensing. Quantum bits (qubits) realized by point defects in semiconductors are the building blocks for several of these developing applications. For example, the unprecedented properties of point defect qubits have opened new horizons for nano-scale sensing in material science and biology. Point defect qubits are complex atomic-scale structural imperfections in wide-bandgap semiconductors that can be comprehensively characterized by measurements and first-principles calculations.

Point defect qubits that utilize both the optical and the spin degree of freedoms exhibit extraordinary controllability and long coherence time. Their most prominent representative is the NV center in diamond1, which can be read out by electrical and optical means, remain coherent as long as 1.8 ms at room temperature, and operate at high temperatures up to 1000 K. Besides the NV center, the divacancy in silicon carbide [1] (SiC) and the silicon vacancy in SiC [2] have recently gained considerable interest in the field of quantum sensing and quantum computation, respectively. In particular, 64 ms coherence time, 30% room temperature read-out contrast, emission at the edge of the O-band (~1100 nm) with lifetime limited linewidth, and spin-to-photon conversion are only the most recent demonstrations in SiC that underline the potential of this material for advanced quantum technologies.

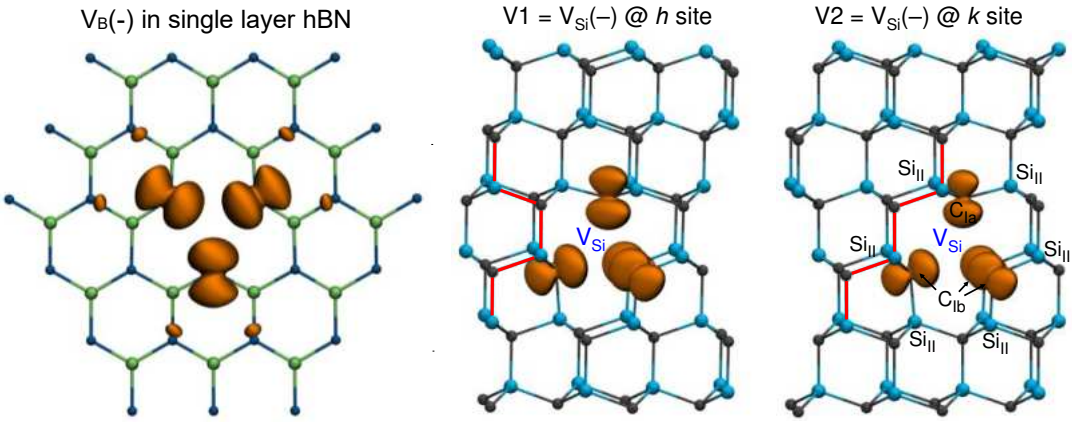


Fig. 1. The spin density of a) the boron vacancy in single-layer hexagonal boron nitride and b), c) the silicon vacancy in the 4H polytype of silicon carbide. b) and c) the so-called *h* and *k* site of the defect in 4H-SiC.

It is worth noting, however, that there are countless qubit candidates in diamond, SiC, and other wide-bandgap semiconducting materials. Very recently, two-dimensional semiconductor hosts have gained considerable attention due to their rich physics with potential technological advantages over their bulk counterparts. The negatively charged boron vacancy ($V_B(-)$) [3] is among the first color centers in hexagonal boron nitride (hBN), whose spin could be initialized, coherently manipulated, and read out.[4] The possibility of exfoliation of hBN and the creation of vacancy centers close to the surface open new horizons for quantum sensing.[5]

In my talk, I briefly introduce the most relevant features of point defect quantum bits in wide band-gap semiconductors. In particular, I will discuss the boron vacancy in hBN and the silicon vacancy in 4H-SiC, see Fig. 1. I will discuss the properties and use of the high spin ground state of the defect in light low dimensional sensing applications and quantum reservoir computing.

Acknowledgments

This research was supported by the National Research, Development, and Innovation Office of Hungary within the Quantum Information National Laboratory of Hungary (Grant No. 2022-2.1.1-NL-2022-00004) and within the grant FK 145395. Support from the Knut and Alice Wallenberg Foundation through WBSQD2 project (Grant No. 2018.0071) is also acknowledged.

References

1. Koehl, W. F. and Buckley, B. B. and Heremans, F. J. and Calusine, G. and Awschalom, D. D. “Room temperature coherent control of defect spin qubits in silicon carbide”, Nature, Vol. 479, No. 84, 2011.
2. Ivády, V. and Davidsson, J. and Son, N.T. and Ohshima, T. and Abrikosov, I. A. and Gali, A. “Identification of Si-vacancy related room-temperature qubits in silicon carbide”, Physical Review B, Vol. 96, No. 161114, 2017.
3. Ivády, V. and Barcza, G. and Thiering, G. and Li, S. and Hamdi, H. and Chou, J. P. and Legeza, Ö. and Gali. A. “Ab initio theory of the negatively charged boron vacancy qubit in hexagonal boron nitride”, npj Computational Materials, Vol 6, No. 41, 2020.
4. Gottscholl, A. and Kianinia, M. and Soltamov, V. and Orlinskii, S. and Mamin, G. and Bradac, and C. and Kasper, C. and Krambrock, K. and Sperlich, A. and Toth, M. and Aharonovich, I. and Dyakonov, V. “Initialization and read-out of intrinsic spin defects in a van der Waals crystal at room temperature”, Nature Materials, Vol. 19, No. 540, 2020.
5. Healey, A. J. and Scholten, S. C. and Yang, T. and Scott, J. A. and Abrahams, G. J. and Robertson, I. O. and Hou, X. F. and Guo, Y. F. and Rahman, S. and Lu, Y. and Kianinia, M. and Aharonovich, I. and Tetienne, J-P. “Quantum microscopy with van der Waals heterostructures”, Nature Physics, Vol. 19, No. 87, 2023.

An infinite array of boson sites—a rigorous approach

Artur Sowa[1]∗**, Jonas Fransson**[2]**,**

[1]Department of Mathematics and Statistics, University of Saskatchewan, Saskatoon, Canada
[2]Department of Physics and Astronomy, Uppsala University, Uppsala, Sweden
*corresponding author, E-mail: sowa@math.usask.ca

Abstract: We demonstrate how to analyze an infinite array of boson sites with the use of the Dirichlet series. The results apply to the Bose-Hubbard model, which is of relevance to various types of physics, including anisotropic magnetism. Our approach leads to the construction of coherent states in the Fock space.

Our strategy to tackle the case of an infinite array of boson sites relies on a known device, perhaps first explored in [1] and [2]. Namely, we label the sites by primes rather than by consecutive integers. This has the effect of revealing the structure of the Fock space as that of $\ell_2(\mathbb{N})$ with a major role to play by the multiplicative number theory. In particular, some techniques of the analytic number theory become indispensable and, indeed, enable a rigorous theoretical approach to a system with infinitely many degrees of freedom. This framework emphasizes the role of the multiplicative group of positive rationals $\mathbb{Q}_+$, which was investigated in depth in [3]. While the generalized Fourier transform on $\mathbb{Q}_+$ has been part of the abstract harmonic analysis expositions, e.g., [4], it has not been applied in quantum theory before.

One of the main developments is the construction of a new type of coherent states. We refer to them as nonlocal coherent states (NCS), as indeed they are distributed over the entirety of the infinite array of sites. The NCS are structurally akin to the Dirichlet series. In particular, we discover yet another representation of the Fock space that is imprinted on a set of the Dirichlet series. This representation may be viewed as a many-body analogue of the Bargmann-Segal representation of the single-particle Hilbert space. The main technical result consists of a demonstration that NCS arise from the vacuum state via an application of a suitably defined displacement operator, an effect analogous to that known in the context of the canonical coherent states. We also obtain a suitable resolution-of-the-identity formula, based on the NCS. Furthermore, we demonstrate how the NCS lead to explicit formulas for the expectation of certain types of Hamiltonians. We also discuss additional physical insights that can be derived from the proposed mathematical approach.

The 1985 compendium, [5], features a historical introduction which states that already at that point there were over 1000 publications on the subject. Contemporarily, the 'mathscinet' displays a steady stream of mathematics publications involving CS in over half a century, with the total of over 1500 papers. A search on the 'arxiv' reveals over 5600 papers that involve the CS or the related squeezed states. However, to our best knowledge, none of the preexisting work refers in any way to the Dirichlet series which, in a way, are the centerpiece of this work.

Acknowledgement: The authors acknowledge partial support via the Global Ambassador Program, University of Saskatchewan 2022-23 and 2023-24.

References

[1] D. Spector, *Supersymmetry and the Möbius Inversion Function*, COMM. MATH. PHYS. **127** (1990), 239–252

[2] J.-B. Bost and A. Connes, Hecke Algebras, Type III Factors and Phase Transitions with Spontaneous Symmetry Breaking in Number Theory, SELECTA MATHEMATICA New Series 1 (1995) 411-457.

[3] A. Sowa, J. Fransson, *Solving the Bose-Hubbard model in new ways*, QUANTUM **6** (2022) 728.

[4] G.B. Folland, A Course in Abstract Harmonic Analysis, CRC Press: Boca Raton, Ann Arbor, London, Tokyo 1995

[5] J. R. Klauder, B.-S. Skagerstam, Coherent States, Applications in Physics and Mathematical Physics, World Scientific 1985

Bloch transistor for quantum electronics

I. Antonov[1] R. Shaikhaidarov[1, 2] K.H. Kim[1], D. Golubev[3, 4], V.N. Antonov[1] and O.V. Astafiev[1]

[1]Physics Department, Royal Holloway, University of London, United Kingdom
[2]National Physical Laboratory, United Kingdom
[3]QS Quantum Simulations GmbH, 76131, Germany
[4]Department of Applied Physics, QTF Centre of Excellence, Finland
*corresponding author: v.antonov@rhul.ac.uk

Abstract: We report a Bloch transistor for the emerging platform of quantum electronics. The fully quantum device facilitates precise control of electronic current in quantum circuits. The transistor maintains the source-drain current at quantized values, $I=2efn$, through four controls: the gate or bias voltage and the frequency or amplitude of the microwave.

The emerging new quantum paradigm necessitates devices with functionalities that differ from their classical counterparts. The envisaged applications of these devices are quantum calculations, sensing, and imaging. We report one of these devices, the Bloch transistor (BT). It can deliver the precisely controlled quantized current $I=2efn$ (e is the charge of an electron, f is the microwave driving frequency, and n is the integer). The transistor operation is based on the manipulation of two quantum conjugates, the charge and phase in a superconducting circuit [1]. The BT operates at a bias voltage of a few microvolts and can deliver quantized current up to 10 nA. The amplitude of the quantized current is adjustable through four controls: the gate or bias voltage and the frequency or amplitude of the microwave. The design of the BT is shown in the left panel of Fig. 1. Inductances, L1 and L2 are made of TiN thin film with L_{sq}~2 nH [2]. They turn to a superconducting state at ~1.5 K. The Pd resistors R have a value ~10 kΩ. When the JJ are biased with V_b and the microwave drive is applied the quantized current steps are developed, see right panel of Fig. 1. They correspond to n =1, 2, 3. The width of the step can

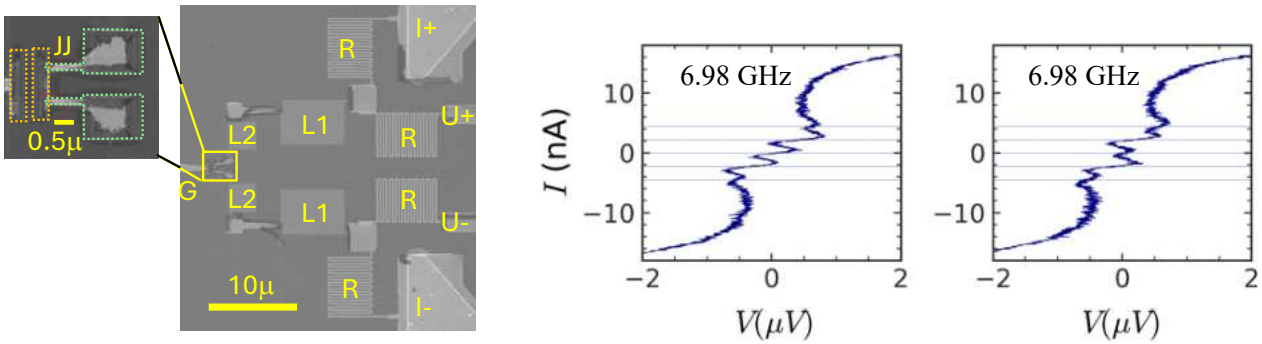


Fig. 1 Left: SEM photo of the Bloch transistor (BT). There are two JJs (blow-up) embedded in a circuit with inductances (L1, L2) and resistances (R). A gate electrode (G) serves also as the feeding line for the MW. BT needs five electrodes for operation (V+, V-, I+, I-, G). Right: Current quantization with f = 6.91GHz and two MW amplitudes, $I_{ac}/2ef$=1.44, 1.76. BT is kept at T=15 mK.

be as large as ~1 μV. One can change the width of the step and even dissolve the current steps by changing the amplitude of the drive MW. Similarly, one can change the quantized current from one to another value by changing the bias voltage. The gate control of the quantized current is shown in Fig. 2. The peaks in the intensity

plot of dV/dI correspond to the quantized current. By changing the gate voltage V_g one can change the current from the quantized value to zero and back. The last control of the BT is the frequency of the MW. By varying the MW frequency, the amplitude and position of the current can be continuously varied. In this work, we discuss the operation of the BT and explain its limits and applications.

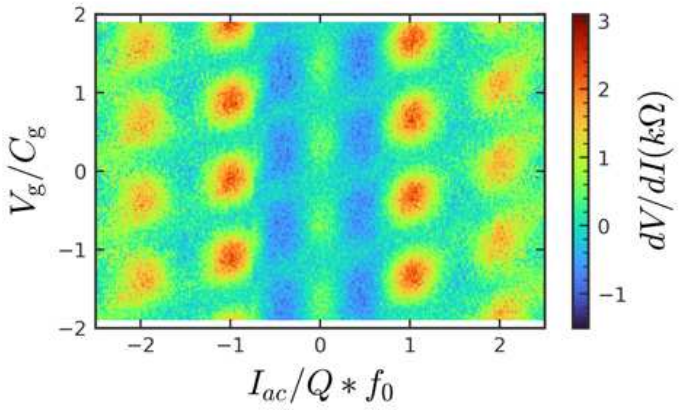


Fig. 2 Intensity plot of dV/dI in coordinates of MW amplitude and induced charge V_g/C_g. The peaks correspond to the quantized current.

References

1. S. E. de Graaf et al, “Charge quantum interference device”, Nature Physics, Vol. 14, 590–594, 2018.
2. R Shaikhaidarov et al , “Quantized current steps due to the a.c. coherent quantum phase-slip effect”, Nature, Vol. 109, 45–49, 2022.

Simultaneous AC bias and gate drive to control a SINIS turnstile

M. Marín-Suárez[1], Yu. A. Pashkin[2*], J. T. Peltonen[1] and J. P. Pekola[1]

[1]Department of Applied Physics, Aalto University, Aalto FI-000 76, Finland
[2]Department of Physics, Lancaster University, Lancaster LA1 4YB, United Kingdom
[*]corresponding author: y.pashkin@lancaster.ac.uk

Abstract: We experimentally demonstrate a driving protocol in which, in addition to the conventional AC gate drive, we also apply an AC bias drive. This improves the single-electron current accuracy by one order of magnitude and allows accurate single-electron current generation even at zero DC bias.

Hybrid turnstiles have proven to generate accurate single-electron currents that underpin electric current metrology.[1] A hybrid turnstile, nicknamed SINIS, consists of a normal-metal island tunnel coupled to two superconducting electrodes, and the island potential is controlled by the nearby gate, as shown schematically in Fig.1(a). The usual turnstile operation involves setting the working point of the device by adjusting the DC bias, V_{0b}, and gate, V_{0g}, voltages, and application of an AC harmonic signal to the gate, $V_g \sin \omega t$.[2] This corresponds to the straight pumping trajectory on the SINIS stability diagram, that links two charge states differing by one electron, as shown by the horizontal magenta line in Fig.1(b). Ideally, one electron is transferred through the device per pumping cycle resulting in the well-defined current plateaus in the transport characteristics. However, the accuracy of charge pumping at high operation frequencies is limited by the so-called back-tunnelling events when electrons tunnel in the direction against the applied bias.[3] The increase of the barrier transparency between the island and the superconducting electrodes as well as the source-drain bias suppresses these events but leads

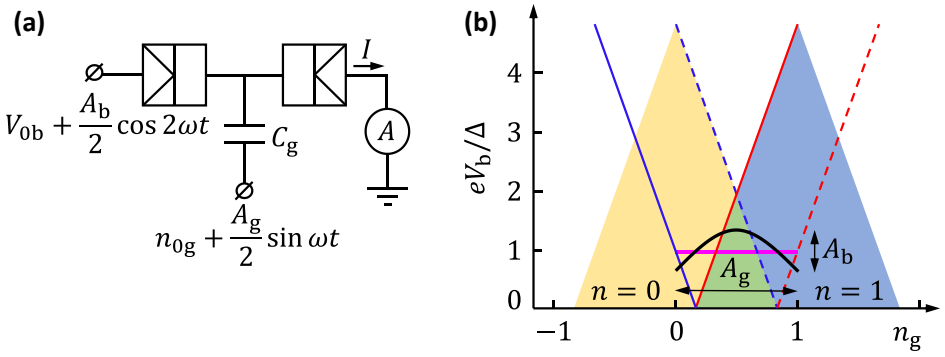


Figure 1. (a) Schematic diagram of the SINIS turnstile and measurement circuitry. (b) Stability diagram of a SINIS turnstile with two identical tunnel junctions for positive bias and gate voltages, showing two charge states (Coulomb diamonds) $n = 0$ and $n = 1$. Ideally, no current flows in the DC regime inside the Coulomb diamonds. The blue and red lines are tunneling thresholds: blue (red) corresponds to the right (left) junction, continuous (dashed) lines correspond to tunneling into (out of) the island. Crossing the line adds or removes one electron to or from the island. The horizontal magenta line is a pumping trajectory when AC signal is applied to the gate only. The black parabola is a pumping trajectory when AC signals are applied to both the gate and the bias.

to some additional errors.

We experimentally demonstrate a novel driving protocol that suppresses back-tunnelling, thus extending the range of frequencies for generating accurate single-electron currents. The main feature of this approach is an additional AC harmonic signal applied to the bias with frequency twice that applied to the gate electrode.[4] This allows additional modulation of the island chemical potential and improves the single-electron current accuracy by one order of magnitude. This can be seen in Fig.2 in which the current plateau at zero AC bias deviates strongly from the expected magnitude indicated by the dashed red line. However, the agreement becomes better when AC drive is applied to the bias. We also show that accurate single-electron currents can be generated at zero average bias voltage by applying only AC drive to the bias.[5] Furthermore, we show that within this protocol, the current direction can be reversed by shifting the phase of the source signal. Besides metrology, this novel drive method can find applications in quantum sensing and quantum computing.

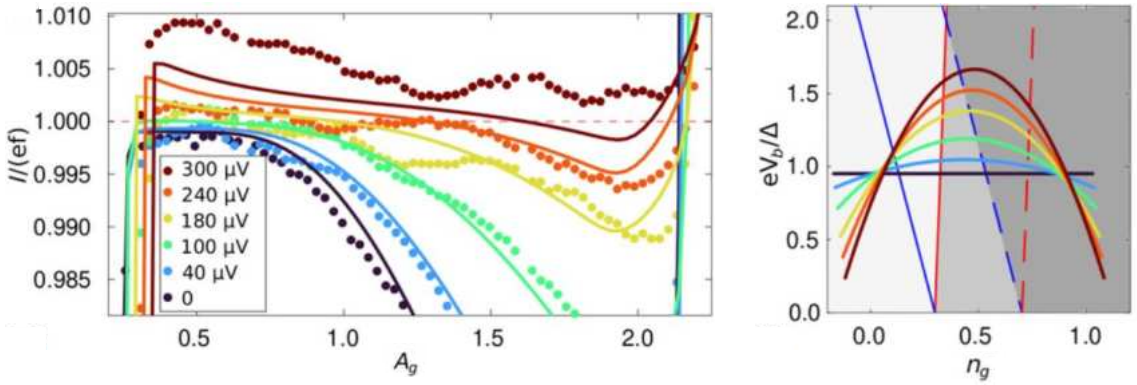


Figure 2. (a) Current plateaus using parabolic driving at $f = 5$ MHz and $V_{0b} = 200$ μV; the legend designates the peak-to-peak bias amplitude used. Dots represent measurements, solid lines simulations based on the semiclassical theory of charge tunnelling. The right panel shows the corresponding pumping trajectories.

M.M.-S., J.T.P., and J.P.P. acknowledge support from the Academy of Finland under Grant No. 312057. Yu.A.P. acknowledges support from the QSHS project ST/T006102/1 funded by STFC.

References

1. Pekola, J. P., Saira, O.-P., Maisi, V. F., Kemppinen, A., Möttönen, M., Pashkin, Yu. A. and D. V. Averin, "Single-electron current sources: Toward a refined definition of the ampere," Rev. Mod. Phys. Vol. 85, 1421–1472 (2013).
2. Pekola, J. P., Vartiainen, J.J., Mötönen, M., Saira, O.-P., Meschke, M. and D.V. Averin, "Hybrid single-electron transistor as a source of quantized electric current," Nat. Phys. Vol. 4, 120–124 (2008).
3. Kemppinen, A., Kafanov, S., Pashkin, Yu. A., Tsai, J. S., Averin, D. V. and J. P. Pekola, "Experimental investigation of hybrid single-electron turnstiles with high charging energy," Appl. Phys. Lett. Vol. 94, 172108 (2009).
4. Marín-Suárez, M., Pashkin, Yu. A., Peltonen, J. T. and J. P. Pekola, "Suppression of back-tunneling events in hybrid single-electron turnstiles by source-drain bias modulation," Phys. Rev. Applied Vol. 19, 044088 (2023).
5. Marín-Suárez, M., Pashkin, Yu. A., Peltonen, J. T. and J. P. Pekola, "Zero-average bias bidirectional single-electron current generation in a hybrid turnstile," J. Low Temp. Phys. Vol. 210, 232–240 (2023).

Recent Advances in Metamaterials and their Applications

Optoelectronic metasurface based on photodiodes

Y. L. Sun[1*]

[1] State Key Laboratory of Millimeter Waves, Southeast University, Nanjing, China
[*]corresponding author: huolunyou@163.com

Abstract: We present an optoelectronic metasurface that can realize direct and efficient optical-microwave interactions in free space. This metasurface is realized by integrating microwave resonant meta-structure with photoresponsive materials. We construct an optoelectronic metasurface based on photodiodes, in which the phase of output microwave can be tuned by input laser intensity.

Interactions between light and matter are fundamental to both contemporary classical and quantum physics [1]. An enormous amount of work has been focused on how to improve and manage the interactions between matter and electromagnetic (EM) waves in various spectrum [2]. Traditionally, these kinds of interactions in the optical and microwave bands have included distinct mechanisms and approaches that are developed in parallel. However, a significant convergence is occurring at the interface between material science and information technology, due to the fast expansion of both sciences, giving rise to other emergent fields, such as lightwave electronics [3] and microwave photonics [4]. Among them, the convergence of the optical and microwave domains forms the basis for several appealing applications, including coherent quantum transduction, electro-optic modulation, microwave-to-optical conversion [5], and optically-controlled microwave transmission [6]. Many physical platforms have been built recently in order to carry out the multi-physics field coupling. Nevertheless, it is challenging for the already proven metasurfaces to react to optical and microwave simultaneously.

Here, we present and realize an optoelectronic metasurface that is able to interact with the incident optical and microwave fields simultaneously, thus generating optical-microwave coupling effects. This metasurface is achieved by integrating photosensitive materials into microwave metasurface. The hybrid integration involves a relationship between the input optical intensity and the output microwave phase. This optoelectronic metasurface is theoretically simulated and experimentally verified by a manufactured photodiode-based metasurface sample. In Figure. 1, we show the specific design of optoelectronic metasurface by employing photodiodes as the photosensitive materials integrated into metasurface units. When light and microwave irradiated on this optoelectronic metasurface concurrently, the impedance of photodiode varies by light absorption, thus leading to different microwave reflected phases. The output microwave reflected phases depend on the input light intensity. Therefore, we realize the efficient free-space interaction between the optical intensity and microwave phase. This spatial optical-microwave interaction offers a compelling foundation for a variety of applications in signal processing, energy conversion, wave manipulation, photoelectric sensing, and nonlinear microwaves.

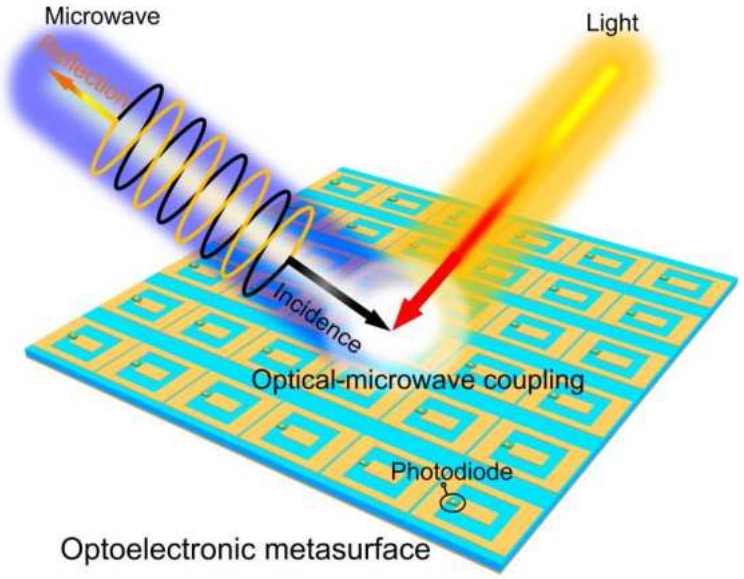


Figure. 1 Illustration of photodiode-based optoelectronic metasurface

References

1. P. Forn-Díaz, L. Lamata, E. Rico, J. Kono, and E. Solano, "Ultrastrong Coupling Regimes of Light-Matter Interaction," Rev. Mod. Phys., vol. 91, no. 2, p. 025005, 2019.
2. X. G. Zhang, et al., "A metasurface-based light-to-microwave transmitter for hybrid wireless communications," Light: Sci. Appl., vol. 11, p. 126, 2022.
3. J. Bloch, A. Cavalleri, V. Galitski, M. Hafezi, and A. Rubio, "Strongly Correlated Electron-Photon Systems," Nature, vol. 606, pp. 41-48, 2022.
4. D. Marpaung, J. Yao, and J. Capmany, "Integrated Microwave Photonics," Nat. Photon., vol. 13, pp. 80-90, 2019.
5. X. G. Zhang, et al., "An optically driven digital metasurface for programming electromagnetic functions," Nat. Electron., vol. 3, no. 3, pp. 165-171, 2020.
6. X. G. Zhang, et al., "Light-controllable time-domain digital coding metasurfaces," Adv. Photon., vol. 4, no. 2, p. 025001, 2022.

Smart Electromagnetic Manipulation Based on Programmable Metasurfaces with Space Sensing

Yuanke Liu[1*]

[1*]Southeast University, China

Abstract: We introduce a programmable metasurface with smart control system that can detect multiple parameters of environment such as the orientation, distance and shape of an external target. Based on the detected information, electromagnetic manipulation is realized in a non-contact and self-adaptive way.

Digital coding and programmable metasurfaces develop a new way of realizing more different functions in real time. However, most programmable metasurfaces could only be triggered artificially to perform the predefined functions[1-3]. How to realize the intelligent or cognitive metasurfaces that can work without hunman intervetion are the directions of future development. Compare to the conventional control method with field-programmable gate array (FPGA), intelligent control provides an automatic way to manipulate the electromagnetic (EM) waves without human intervention[4]. In this study, we introduce a programmable metasurface with smart control system, through which non-contact electromagnetic manipulation is realized.

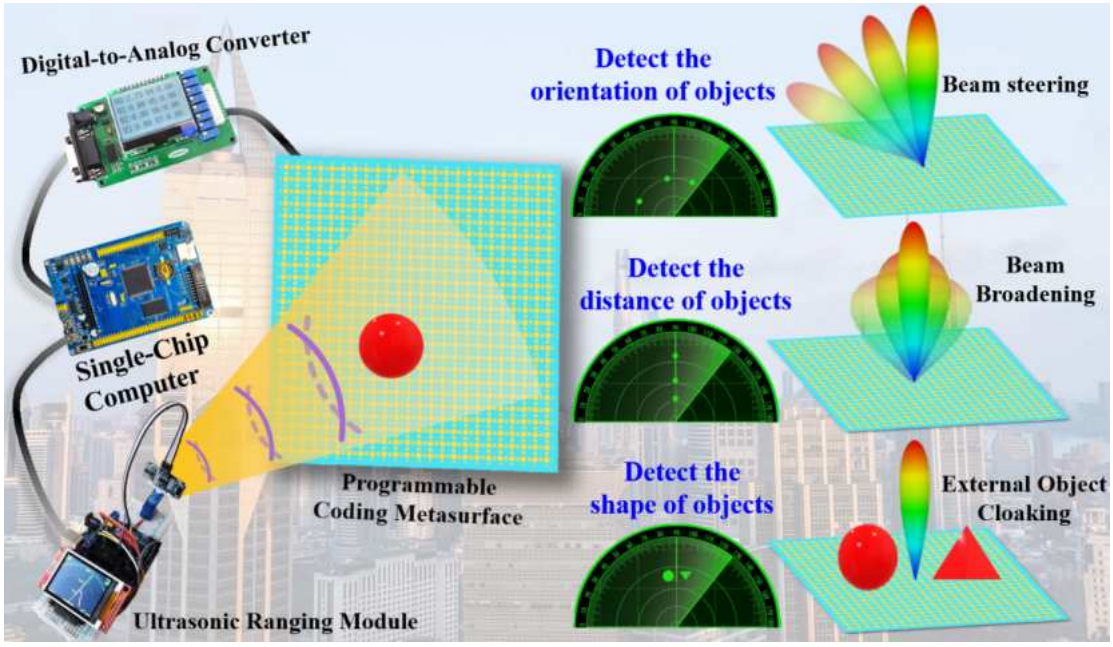


Figure 1. Schematic of the proposed self-adaptively metasurface based on ultrasonic ranging.

As shown in Figure 1, the high intelligent metasurface platform based on ultrasonic ranging that can detect multiple parameters such as the orientation, distance and shape of an external object. We integrate a broadband and full polarizations programmable metasurface a with ultrasonic ranging module, a single-chip computer and several digital-to-analog converters (DACs). By alternating the bias voltage supplied to varactor diodes

embedded on metasurface, 3-bit reflection states are achieved and each super unit cell can be controlled independently. The bias voltage sequences generated by DACs are changed according to the positional data of object captured by ultrasonic ranging module. Therefore, a non-connect and remote control of metasurface is accomplished without the intervention of human beings.

This study sets up a new paradigm for intelligent and cognitive metasurface, which is expected to find extensive applications in advanced EM device and communication system.

References

1. Zhang, X. G., W. X. Tang, W. X. Jiang, et al, "Light-controllable digital coding metasurfaces," Advanced Science, 1801028, 2018.
2. Sun, S. Y., W. Jiang, S. X. Gong, and T. Hong, "Reconfigurable linear-to-linear polarization conversion metasurface based on PIN diodes," IEEE Antenna and Wireless Propagation Letters, vol. 17, no. 9, 1722-1726, 2018.
3. Li, W. H., T. S. Qiu, J. F. Wang, et al. "Programmable coding metasurface reflector for reconfigurable multibeam antenna application," IEEE Transaction on Antennas and Propagation, vol. 69, no. 1, 296-301, 2021.
4. Cui, T. J., S. Liu, and L. Zhang, "Information metamaterials and metasurfaces," Journal of Materials Chemistry C, 5, 3644-3668, 2017.

Photonic topological states with auxiliary orbital degree of freedom in Kekulé modulation surface-wave metamaterials

Liyun Tao[1], Yahong Liu[1*], Xin Zhou[2], Lianlian Du[1], Meize Li[1], Kun Song[1], Zhenfei Li[1], Xiaopeng Zhao[1]

[1]School of Physical Science and Technology, Northwestern Polytechnical University, Xi'an 710129, China.
[2]The National Research Institute of Radio Spectrum Management, Xi'an 710061, China. School of Information Engineering, Xi'an Mingde Institute of Technology, Xi'an 710124, China.
* E-mail: yhliu@nwpu.edu.cn

Abstract: We design and demonstrate topological metamaterials with an arbitrary auxiliary orbital DOF by applying continuous generalized Kekulé modulations in honeycomb surface-wave metamaterials. Three kinds of photonic platforms are constructed . The perfect electrical conductor boundaries in finite structures, the interface of the two topological metamaterials and a band-notch line-defect waveguide.

Photonic topological insulators have unique advantages as regards ensuring lossless transmission and realizing stable energy locality of electromagnetic waves. More complex requirements to manipulate discrete degrees of freedom of photons, such as orbital degree of freedom (DOF), show a great foresight. With the development of topological band theory for electromagnetics, photonics and acoustics, topological insulators can be realized by resorting to spin,[1] polarizations,[2] or valley-pseudospin DOF.[3,4] Recently, an emerging type of Nano mechanical topological systems with auxiliary orbital DOF has been introduced in integrated circuits accommodating distinct topological edge channels.[5] Similar to spin DOF, orbital DOF constitutes another fundamental attribute of Bloch waves that describes the spatial distribution of wave functions inside the unit cell of crystals. Exploration of additional DOF, particularly orbital DOF provides a powerful approach to investigate novel topological insulators. However, nanoscale platform requires a higher vacuum environment with considerable Nano membrane air damping, limiting its practical value. By adopting additional spatial [6] or temporal [7] DOF, adiabatic topological transition has been realized. However, it is difficult to apply to on-chip two-dimensional (2D) topological circuits. It will be undoubtedly promising that optimizing topological photonic circuits with the control of orbital states is achieved by using a simple solid metamaterial structure. Moreover, it is rare to report topological photonic insulators with an arbitrary auxiliary orbital DOF. Based on surface wave metamaterial microstructure, the physical mechanism to achieve additional DOF also needs to be demonstrated clearly in the domain of synthetic dimensions. [8]

To this end, we explore a more generic type of topological photonic insulator with arbitrary orbital DOF, and demonstrate the mechanism of multiple platforms carrying photonic topological states. It is expected that the present results can become an alternative means to manipulate topological phase transition, and provide a underlying platform for exploration of additional DOF. The novelty of the work is shown as follows:

1. By applying continuous generalized Kekulé modulations in honeycomb surface-wave metamaterial

lattice, translational symmetry and mirror symmetry are broken, we explore a more generic type of topological photonic insulator with arbitrary orbital DOF.

2. By setting different boundary conditions in finite structure, we construct three kinds of photonic platforms carrying abundant topological phenomena, including the perfect electrical conductor boundaries of finite topological phase structure, the domain wall interface consisting of two topological phase structures, and the line-defect channels.
3. We investigate 1D edge states and 0D corner states with auxiliary orbital DOF at perfect electrical conductor boundaries of finite topological metamaterial. At the interface of two topological metamaterials, we obtained helical edge states with arbitrary auxiliary orbital DOF and demonstrated adiabatic waveguide states transition. By adjusting structure defect, we design a curved waveguide path of 90°.

Acknowledgments: Y. L. acknowledges support from the National Natural Science Foundation of China (Grant No. 12374296), the Key Research and Development Program of Shaanxi Province of China (Grant No. 2023-YBGY-247), and the Natural Science Foundation of Guangdong Province of China. X. Z. acknowledges support from the Innovation Foundation of Xi'an Mingde Institute (Grant No. 2023MDE01). K. S. acknowledges support from the Fundamental Research Funds for the Central Universities (Grant No. D5000230165).

References

1. J. Cha, K. W. Kim, C. Daraio, Nature 2018, 564, 229.
2. B. Z. Xia, T. T. Liu, G. L. Huang, Phys. Rev. B 2017, 96, 094106.
3. L. Ju, Z. Shi, N. Nair, Y. Lv, C. Jin, J. Velasco, C. Ojeda-Aristizabal, H. A. Bechtel, M. C. Martin, A. Zettl, J. Analytis, F. Wang, Nature 2015, 520, 650.
4. J. Lu, C. Qiu, W. Deng, X. Huang, F. Li, F. Zhang, S. Chen, Z. Liu, Phys. Rev. Lett. 2018, 120, 116802.
5. J. Ma, X. Xi, Y. Li, X. Sun, Nat. Nanotechnol. 2021, 16, 576.
6. M. Lohse, C. Schweizer, H. M. Price, O. Zilberberg, I. Bloch, Nature 2018, 553, 55.
7. Y. Xia, E. Riva, M. I. N. Rosa, G. Cazzulani, A. Erturk, F. Braghin, M. Ruzzene, Phys. Rev. Lett. 2021, 126, 095501.
8. T. Ozawa, H. Price, Nat. Rev Phys 2019, 1, 349.

Particle Image Velocimetry Utilizing Binocular Polarization-independent Meta-lens

Y. He[1], Z. Zhao[1], X. Liu[2], Y. Ji[1], T. Tanaka[3], M. K. Chen[2*], S. Shi[1*] and D. P. Tsai[2]

[1] School of Mechanical Engineering, Shanghai Jiao Tong University, China
[2] Department of Electrical Engineering, City University of Hong Kong, China
[3] Institute of Post-LED Photonics, Tokushima University, Japan
[*]corresponding author: mkchen@cityu.edu.hk; kirinshi@sjtu.edu.cn.

Abstract: Experimental fluid dynamics is mainly studied using PIV, but traditional methods need complex optical system. Binocular meta-lens PIV, utilizing polarization-independent GaN meta-lenses and CMOS sensors, offers a compact solution for obtaining three-dimensional velocity fields. Measurement error of 1.3% on vortex ring shows promise for space-constrained applications.

Our speech will present a particle image velocimetry (PIV) system employing a binocular meta-lens based on GaN[1]. The performance of the binocular meta-lens PIV system was verified and evaluated through a typical vortex ring experiment [2]. Experimental setup of binocular meta-lens PIV is performed in Figure 1(a), (b), and (c). The system demonstrated the capability to capture high-quality particle images (as shown in Figure 1(d)) and provide two-dimensional three-component (2D-3C) velocity fields.

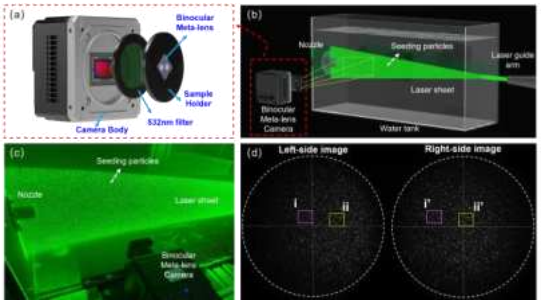


Figure 1. Binocular meta-lens camera and experimental setup of binocular meta-lens PIV.

We assembled the compact custom-built binocular meta-lens camera utilizing a single high-speed CMOS sensor, a 532nm filter, and two thin, light-weight, high-quality meta-lenses with a diameter of 2.6mm and 4mm distance apart. The binocular meta-lens is fabricated with GaN cylindrical nanopillars on a sapphire substrate. Scanning electron microscope (SEM) image of fabricated meta-lens are shown in Figure 2(b), (c). Efficiency and phase response of nanopillars with different radius has been simulated and presented in Figure 2(d). Characterizations show successful fabrication with varying diameter nanopillars and high aspect ratio. Experimental results demonstrate close-to-diffraction-limited focusing performance with a full-width at half-maximum (FWHM) of 2.2 μm in Figure 2(e), (f). Additionally, the system's binocular vision allows for depth perception in a range of 6 to 45 cm in accordance with Figure 2(g).

For the calibration and data processing of the binocular meta-lens PIV system, calibration images were captured with a calibration board placed inside the water tank. The acquired calibration images and particle images underwent data processing. The direct linear transformation (DLT) method based on the pinhole model was utilized to compute mapping matrices between pixels and world coordinates for each sub-lens. A self-calibration process based on particle images iteratively updated these mapping matrices. Standard

two-dimensional two-component (2D-2C) velocity fields (as illustrated in Figure 3(a)) were obtained through cross-correlation analysis of segmented left and right images, followed by the reconstruction of 2D-3C velocity fields using Soloff 's method (as shown in Figure 3(b)). The 2D cross correlation is performed upon an interrogation window and an interrogation grid. Mark the 1st and 2nd images as f_1 and f_2, then the cross-correlation can be expressed as [3]:

$$\Phi(m,n)|_{(i,j)} = \sum_{i}^{i+M-1} \sum_{j}^{j+N-1} f_1(i,j) \cdot f_2(i+m, j+n), \left(|m| \leq \frac{M_g - M}{2}, |n| \leq \frac{N_g - N}{2} \right) \quad (1)$$

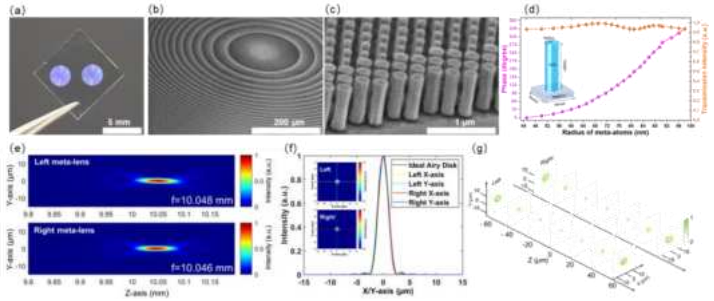


Figure 2. The optical characterization of the binocular meta-lens.

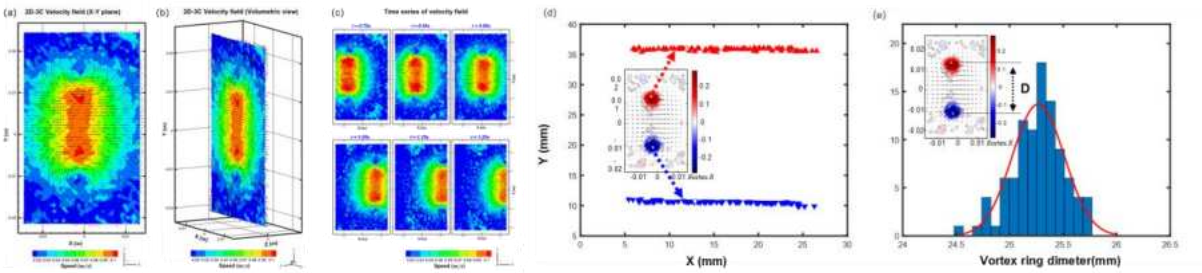


Figure 3. Results of the phase-averaged 2D-3C velocity field at the central plane of the vortex ring (Reynolds number = 2000) obtained using our binocular meta-lens PIV system.

The diameter of the vortex ring (core-to-core diameter) can be determined directly by measuring the distance between the two vortex cores. Figures 3(d) and (e) illustrate the diameter distribution between t = 0.75s and t = 1.25s in Figure 3(c), with the red line representing the normal distribution curve fit. The peak value of the fitted line is D' = 25.27 mm, with a standard deviation (STD) of σ = 0.24 mm. Additionally, the theoretical diameter value can be calculated as D_{ideal} = $1.18D(L/D)^{1/5}$~ 25.59 mm, indicating that the measured uncertainty in the vortex ring diameter is 1.25%.

In conclusion, the binocular meta-lens PIV system provides a reliable and accurate method for capturing and analyzing flow fields, with potential for improved depth direction performance through modifications in the setup configuration.

References

1. Liu, X., Chen, M. K., et al. “Underwater Binocular Meta-lens,” ACS Photonics, Vol. 10, No. 7, 2382–2839, 2023.
2. New, T.H., Shi, S. and Liu, Y. “On the flow behaviour of confined finite-length wavy cylinders,” J. Fluids Struct, Vol. 54, 281–296, 2015.
3. Raffel, M., Willert, C. E., et al. “Particle Image Velocimetry: A Practical Guide”, Springer Cham, 2018.

META 2024, TOYAMA - JAPAN, JULY 16 – 19, 2024

Reflective Moiré Metasurfaces: A Paradigm of Innovation and Challenge

Shuo Liu[1*], Lei Zhang[1], and Xiaoqing Chen[1]

[1]State Key Laboratory of Millimeter Waves, Southeast University, Nanjing 210096, China
[*]corresponding author: liushuo.china@seu.edu.cn

Abstract: Reflective moiré metasurface offers a cost-effective solution for dynamic beamforming in RIS applications and importantly, paves new ways for synthesizing far-field scattering using tightly stacked ultrathin metallic patterns of varying plane symmetries. This innovation is expected to have widespread impact across the fields of electromagnetics, antenna development, and wireless communication.

Dynamic beamforming plays a pivotal role in various technological applications, including radar systems, holographic imaging, and the development of reconfigurable intelligent surfaces (RIS).[1-3] Traditional methods for achieving this dynamic control rely heavily on active electronic components, such as pin-diodes and varactor diodes. This reliance significantly escalates costs for large-scale implementations, a challenge that becomes even more pronounced at millimeter-wave and sub-terahertz frequencies where these components are notably costly or may not be readily available.

Recently, the fascinating physical properties of moiré patterns created by overlaying two differently twisted two-dimensional (2D) materials have drawn renewed attention. In this context, we introduce a novel approach for dynamic beam steering using two closely attached metasurfaces. By adjusting the in-plane rotation of these two metasurfaces relative to each other, we can continuously manipulate the direction of reflected beams [4], as demonstrated in **Figure 1**. This method allows for a variety of beam configurations, directions, and paths by varying the twist angle and designing different patterns for each metasurface layer. In this work, we design and experimentally demonstrate two different moiré metasurfaces, the chessboard-type and triangular-type, which produce four-beam and six-beam radiations, respectively. Remarkably, the beam efficiency achieved by our moiré metasurfaces is even greater than the conventional metasurface designed with super unit cell configuration. Note that the design of moiré metasurfaces is fundamentally different from all previously reported moiré metasurfaces, in which the separation between the two metasurfaces is designed large enough to ensure linear combination of the functionality of each individual layer.

Our design offers a cost-effective solution for dynamic beamforming in RIS applications and unveils a novel approach to exploring new physics in programmable metasurfaces. Their compact profile makes them highly adaptable for use in a variety of applications, effortlessly blending into indoor environments as part of walls, ceilings, and decorative art, as well as enhancing outdoor infrastructures like building facades, streetlights, and advertising boards to extend signal reach. Beyond the cost-saving advantage, our fully passive reflective moiré metasurface architecture boasts several remarkable features, including zero static power consumption, no receiver noise, and a high capacity for handling power, showcasing its vast potential for applications in RIS and electronic warfare.

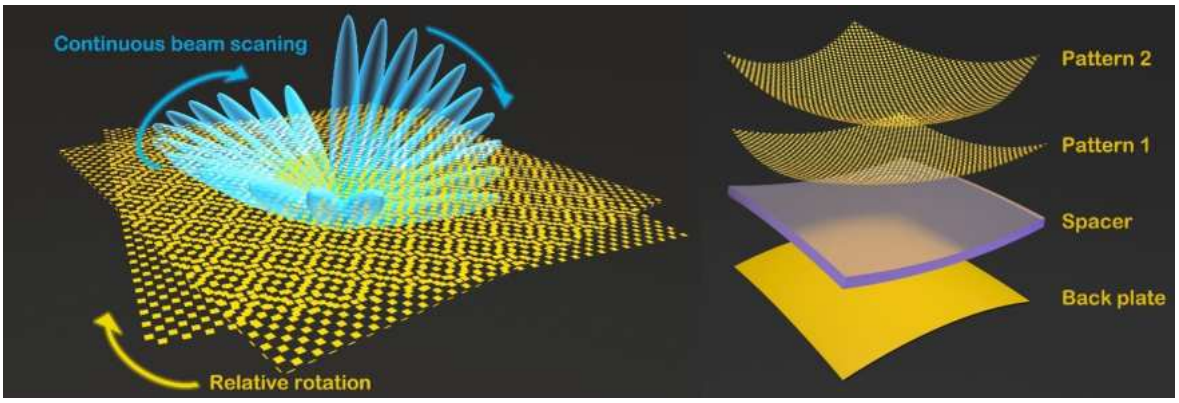


Figure 1 Schematic illustration and composition of a moiré metasurface.

However, the exploration of reflective moiré metasurfaces presents unique challenges and issues across various aspects, diverging significantly from the traditional design paradigms of conventional metasurfaces. Unlike their conventional counterparts, which rely on the repetitive nature of unit cells with locally periodic boundary conditions, reflective moiré metasurfaces cannot be described using a similar approach. This is because the moiré patterns, although periodically perceivable by the human eye under most conditions, do not exhibit true two-dimensional crystallinity except at certain discrete twist angles where the overlaid grid lattices of the two patterns align exactly.

Further complicating the design and understanding of moiré metasurfaces is their inherent high anisotropy. Traditional metasurface designs often leverage straightforward geometric shapes arranged in square or hexagonal lattices, resulting in predictable electromagnetic (EM) responses. Reflective moiré metasurfaces, however, introduce an additional layer of complexity due to the complex moiré pattern that changes with the twist angle. The moiré pattern not only complicates the polarization state of reflected waves, which may contain both co-polarized and cross-polarized components, but also leads to a shift in moiré periodicity across various lattice types as the twist angle changes. Such changes significantly affect the radiation pattern, making the design process more intricate.

Our research paves the way for novel methods of engineering far-field scattering by closely aligning ultra-thin metal patterns from different symmetry groups, a breakthrough with significant theoretical and practical implications. This innovation is expected to have widespread impact across the fields of electromagnetics, antenna development, and wireless communication, marking a significant step forward in these disciplines.

References

[1] T. J. Cui, S. Liu, and L. Zhang, Information metamaterials and metasurfaces, J. Mater. Chem. C 5, 3644-3668 (2017).

[2] T. J. Cui, L. Li, S. Liu, Q. Ma, L. Zhang, X. Wan, W. X. Jiang, and Q. Cheng, Information Metamaterial Systems, iScience 23, 101403 (2020).

[3] W. Tang, M. Z. Chen, X. Chen, J. Y. Dai, Y. Han, M. D. Renzo, Y. Zeng, S. Jin, Q. Cheng, and T. J. Cui, Wireless communications with reconfigurable intelligent surface: path loss modeling and experimental measurement, IEEE Trans. Wirel. Commun. 20, 421-439 (2021).

[4] S. Liu, S. Ma, R. Shao, L. Zhang, T. Yan, Q. Ma, S. Zhang, and T. J. Cui, Moiré metasurfaces for dynamic beamforming, Sci. Adv. 8, abo1511 (2022).

Metasurface-enabled light-to-microwave hybrid wireless communications

Xin Ge Zhang, Ya Lun Sun, and Wei Xiang Jiang*

State Key Laboratory of Millimeter Waves, Southeast University, Nanjing 210096, China
*corresponding author: wxjiang81@seu.edu.cn

Abstract: We will introduce an optically-controlled programmable metasurface for remote microwave control and hybrid light/microwave signal processing. A hybrid wireless communication system that allows dual-channel data transmissions in a light-to-microwave link is demonstrated, and the experimental results show that two different videos can be transmitted and received simultaneously and independently.

Metasurfaces are ultrathin array structures consisting of artificial subwavelength elements arranged on a specific two-dimensional surface, and have shown great capabilities to manipulate phase, amplitude, frequency, and polarization features of electromagnetic (EM) waves flexibly. Recently, programmable metasurface with real-time EM control and digital information processing capabilities has been a hot topic in the EM and communication communities[1,2].

In this talk, we will introduce an optically-controlled programmable metasurface for remote microwave control and hybrid light/microwave signal processing. First, we present the design and realization of the spatial-domain optically-controlled programmable metasurface that can manipulate microwave scatterings by light, achieving different EM functions including beam tuning, external cloaking, and vortex beam generation. The unique advantage of optically-controlled programmable metasurface is that it can avoid effectively complex bias network design and adverse DC-EM signal crosstalk. Then, we present the design and implementation of a time-domain optically-controlled programmable metasurface that can tailor microwave spectra by time-varying light signals. Next, we will show how the time-domain optically-controlled programmable metasurface is used to construct a light-to-microwave hybrid wireless communication system that can convert light signal to microwave signal directly, without using down-conversion process to baseband. More importantly, one designed light signal channel can carry two independent original information that can be encoded onto two microwave carriers with different incidence frequencies by using the dispersion characteristic of the metasurface. As an attractive example, we realize a dual-channel light-to-microwave hybrid wireless communication system that can transmit simultaneously two different videos with the aid of frequency division multiplexing scheme. Different from the microwave photonics technologies typically target fiber and on-chip methods, the optically-controlled programmable metasurface can realize hybrid signal processing based on wave modulations, which could stimulate attractive information-oriented applications.

References

1. Zhang, X. G. et al., “A metasurface-based light-to-microwave transmitter for hybrid wireless communications,” Light: Sci. Appl., Vol. 11, 126, 2022.
2. Zhang, X. G. et al., “Light-controllable time-domain digital coding metasurfaces,” Adv. Photon., Vol. 4, 025001, 2022.

Meta-lens Digital Image Correlation

Y. Ji[1], Z. Zhao[1], M. K. Chen[2*], S. X. Shi[1*] and D. P. Tsai[2]

[1] School of Mechanical Engineering, Shanghai Jiao Tong University, China

[2] Department of Electrical Engineering, City University of Hong Kong, China

[*]corresponding author: mkchen@cityu.edu.hk; kirinshi@sjtu.edu.cn

Abstract: An approach for digital image correlation (DIC) measurement using a single camera is reported in this work, utilizing the polarization-independent GaN binocular meta-lens to measure the displacement of the flat-plate. Finally, the depth and displacement of the cylinder are measured through binocular imaging, validating the feasibility of the proposed approach.

Digital Image Correlation (DIC) is a non-interferometric optical technique used to measure full-field displacements and strains on the surface of an object [1]. This study introduces a digital image correlation (DIC) system utilizing a binocular meta-lens based on GaN. The basic principle of DIC is shown in Figure 1. In this system, binocular meta-lens is employed to image the specimen, replacing traditional lens. The binocular meta-lens is shown in Figure 1(a). We demonstrate the setup image for the flat plate displacement experiment of meta-lens DIC in Figure 1(b). Generally, the implementation of DIC involves the following steps [2]: (1) specimen preparation;(2) image capture before and after deformation;(3) calculation of the displacement field and strain field. We illustrate a high-quality speckle pattern on a flat plate specimen in Figure 1(c) [3]. Subsequently, speckle patterns before and after deformation, as shown in Figure 1(d) and Figure 1(e), can be captured using the camera.

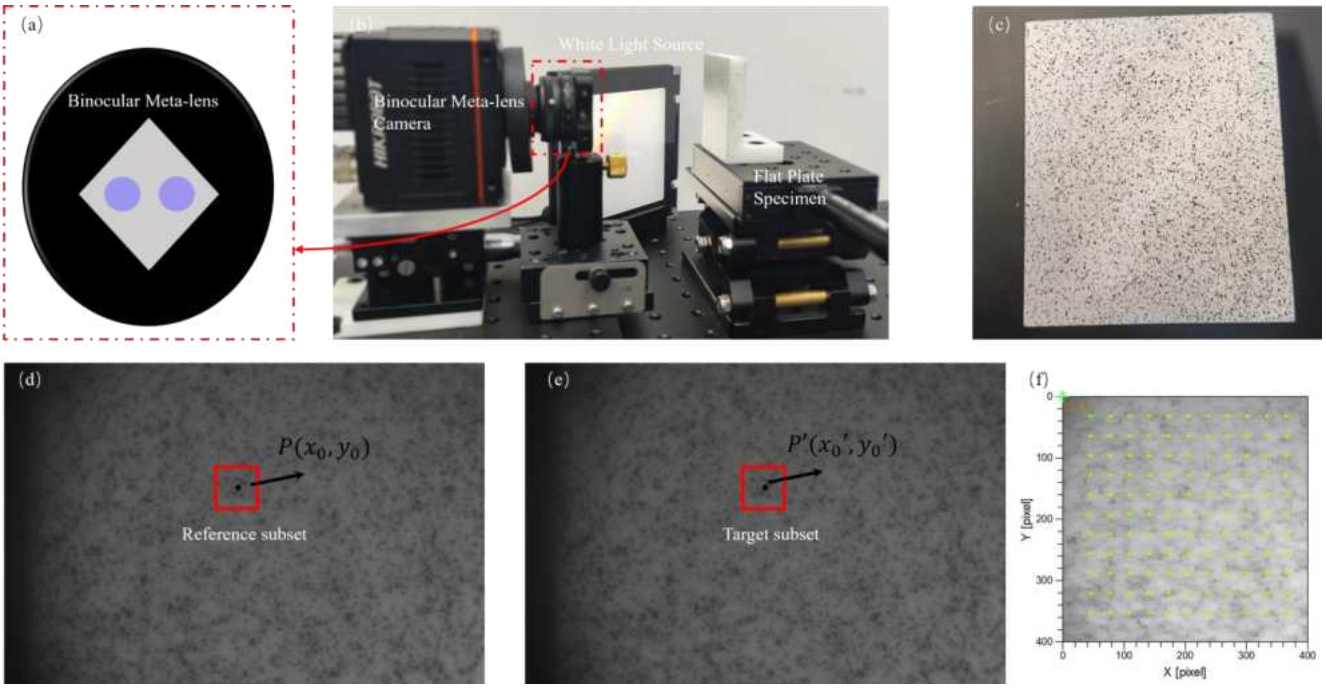


Figure 1 Schematic image of Meta-lens DIC. (a)binocular meta-lens; (b) experimental setup image of meta-lens DIC; (c)specimen preparation; (d)schematic illustration of a reference square subset before deformation; (e)schematic illustration of a target subset after deformation; (f)calculated displacement field.

In implementation of the DIC method, the region of interest (ROI) should be defined at first similar to the region outlined by the red lines in Figure 1(d). The ROI region is generally a (2M+1) * (2M+1) area centered at the point $P(x_0, y_0)$. Then, we calculate the correlation criterion to find where reference subset has moved to after deformation. As shown in Figure 1(f), the reference subset has moved to the target subset, and the point $P(x_0, y_0)$ has moved to the point $P'(x_0', y_0')$.Finally, we can calculate the displacement corresponding to each subset, thereby obtaining the displacement field.

We initially validated the feasibility of this system through the in-plane displacement experimental, the experimental setup is shown in the Figure 1(b). The pixel size of this image is 0.08 mm/pixel. We conducted 30 sets of displacement experiments with a step size of 0.1 pixels [4]. We conducted 2D-DIC in-plane experiments using the right eye of the binocular meta-lens. The images we obtained before and after deformation are shown in the Figure 1(d) and Figure 1(e). We use the cross-correlation (CC) to evaluate the similarity degree between the reference subset and the deformed subset. Then, we use the inverse compositional Gauss-Newton (IC-GN) algorithm as a sub-pixel displacement registration algorithm to calculate the precise sub-pixel displacement of each subset [5]. Ultimately, we obtain the displacement field as shown in Figure 1(f).

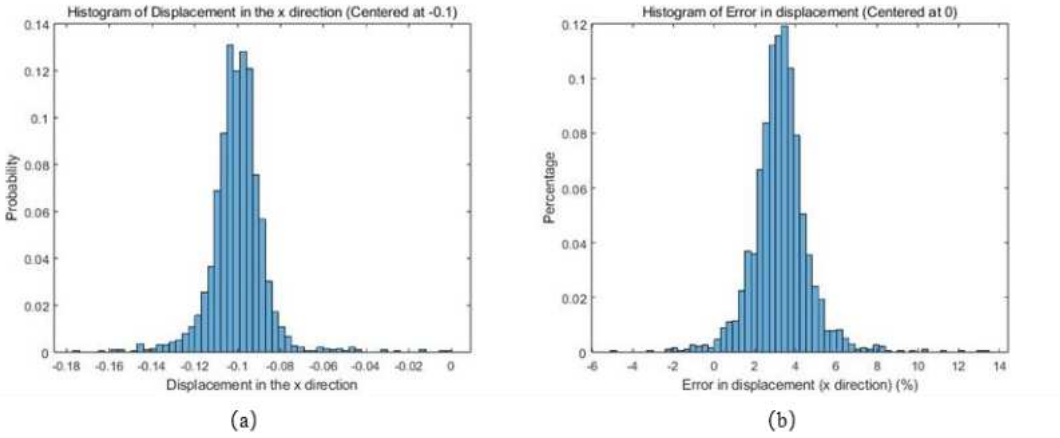


Figure 2. Histogram of in-plane displacement and error. (a) Histogram of in-plane displacement. (b) Histogram of in-plane displacement error.

We conducted a statistical analysis of the calculated sub-pixel displacements, as shown in Figure 2(a). Figure 2(b) illustrates the errors between these displacement values and the ground truth. The majority of displacement errors fall between 1.8% and 5%. However, due to edge distortion of the meta-lens, approximately around 10% of the displacement errors increase.

References

1. TC, Chu., Ranson, WF and Sutton, Michael A. “Applications of digital-image-correlation techniques to experimental mechanics,” Experimental Mechanics, Vol. 25, 232-244, 1985.
2. B, Pan. Qian, Kemao and Xie, Huimin., et al. “Two-dimensional digital image correlation for in-plane displacement and strain measurement: a review,” Measurement science and technology, Vol. 20, 062001, 2009.
3. Giacomo, Lionello and Cristofolini, Luca. “A practical approach to optimizing the preparation of speckle patterns for digital-image correlation,” Experimental Mechanics, Vol. 25, 107001, 2014.
4. L, Reu. Phillip., Toussaint, Evelyne and Jones, Elizabeth., et al. “DIC challenge: developing images and guidelines for evaluating accuracy and resolution of 2D analyses,” Experimental Mechanics, Vol. 58, 1067-1099, 2018.
5. B, Pan. and Wang, B, “Digital image correlation with enhanced accuracy and efficiency: a comparison of two subpixel registration algorithms,” Experimental Mechanics, Vol. 56, 1395-1409, 2016.

Combinatorial Optimization of Electromagnetic Devices using metamaterial Function Units

Guoyan Dong*

Center of Materials Science and Optoelectronics Engineering, School of Optoelectronics, University of Chinese Academy of Sciences, Beijing 100049, China
*corresponding author: gydong@ucas.ac.cn

Abstract: Periodic or aperiodic spatial arrangements of metamaterial resonant elements can not only enhance and extend the resonant characteristics through mutual coupling resonance effects but also design and optimize the performance of devices according to specific application requirements. These designs have significant applications in light modulation and performance enhancement.

Keywords: Metamaterials, Functional element, Photonic crystal, Device Engineering, Mie resonance.

The scattering properties of periodic or aperiodic structural materials empower them to efficiently manipulate electromagnetic wave (EMW) propagation by adjusting their characteristics. For instance, by altering the alignment and percentage of different materials inside the periodic structure, the location and breadth of the band gap can be changed to achieve the limiting or transmission of electromagnetic waves in a given frequency range [1]. Changes in structural parameters can regulate the effective permittivity and permeability. These synthetic functional units are arranged and integrated in a way that allows them to display unusual electromagnetic properties lacking in natural materials. The versatile design of electromagnetic metamaterials provides more potential for the development of resonant devices.

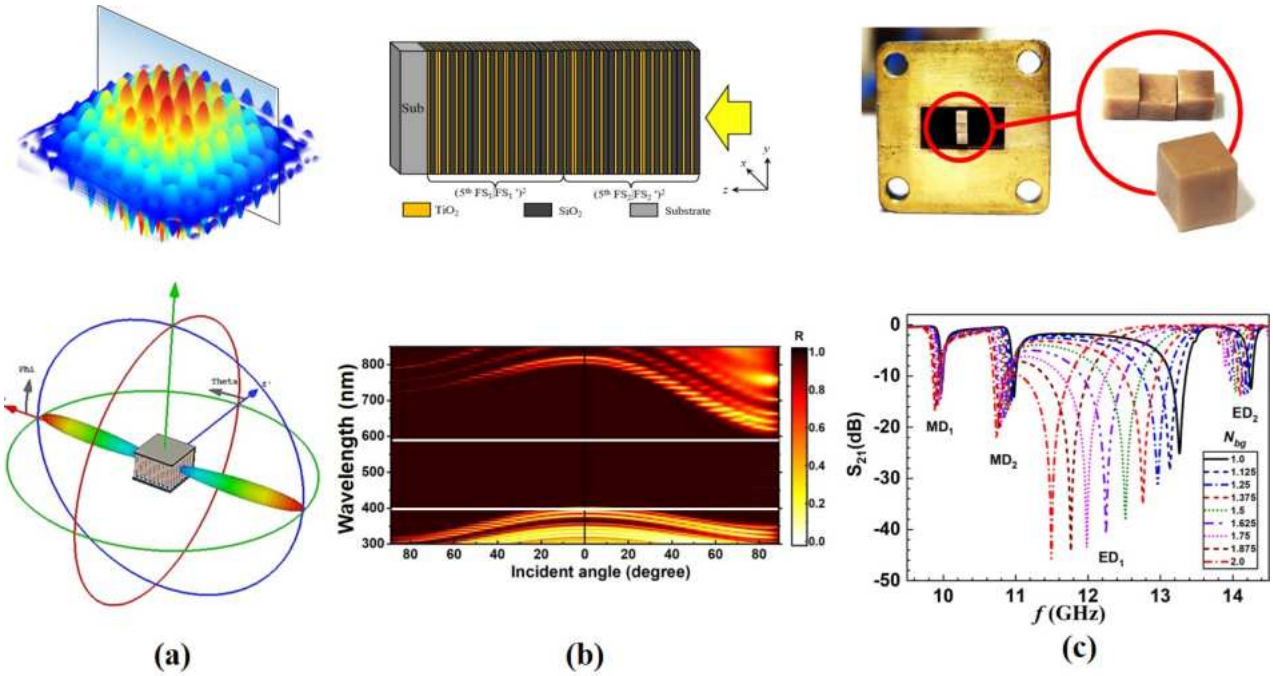


Figure 1. (a) Resonance and radiation pattern of PhC-antenna, (b) Structure and reflectivity spectra of dielectric-reversal quasicrystal sequence, (c) Dielectric-particle trimer and measured spectra detecting on ambinent refractive index changes.

First, metamaterials are used to create functional elements that have characteristics not found in nature. These elements then work as platforms for creating useful devices. Employing the near-zero effective refractive index of photonic crystal (PhC) at the center of the first Brillouin zone (FBZ), as shown in Fig. 1(a), we develop a PhC antenna composed of dielectric cylinders for splitting and directional radiation [2]. Microwave simulation and tests have confirmed that the space incident light may be redirected orthogonally and radiated symmetrically with high directional gain by inducing the PhC array resonance near the band edge scope [3]. Compared with traditional directional antennas, this PhC array antenna has the advantages of compact size, simple structure, economical cost, high coupling efficiency, and directivity.

Second, metamaterial components of diverse properties are devised and ingeniously integrated to create unique functional devices. In Fig. 1(b), we proposed a dielectric-reversal quasicrystal sequence to expand the bandgap while eliminating its inherent defects for impeccable omnidirectional reflection with fewer dielectric layers [4]. Although defects can be mitigated, it is challenging to entirely eliminate transmission flaws in quasicrystal sequences. Consequently, through the ingenious design of the central wavelength, we integrate it with periodic sequences or other quasi-periodic sequences, resulting in an omnidirectional high reflectance function surpassing 98% in the visible light band spanning approximately 150nm.

Thirdly, resonance coupling between structural units is exploited to amplify and optimize the functional features of metamaterials. The Mie resonant interactions of rectangular particles can serve as the foundation to enhance anisotropic light-matter interactions and enable increased sensitivity towards particular spectral regions. The coupled Mie resonances in a symmetrical linear rectangular-particle trimer (Fig. 1c) ensure the enhancement of electric dipole and magnetic dipole resonances. The symmetrical nature of the trimer overcomes the split dipolar resonance challenge presented in earlier designs and shows the potential for advanced sensing devices.

In summary, modifying the structure of electromagnetic metamaterials has expanded their functionality by inducing specific resonance, integrating different sequences, and coupling Mie resonances. This research introduces a promising method for broadening metamaterial functions and may pave the way for next generation metamaterial devices.

Acknowledgements

This work is supported by National Key Research and Development Program of China (2022YFB3806003); Natural Science Foundation of Beijing Municipality (4222081); National Natural Science Foundation of China (12374398); Fundamental Research Funds for the Central Universities.

References

1. G. Dong, P. Qiao, S. Zheng, X. Yang, X. Meng, and J. Zhou, "Efficient light redirection via stretched field resonance in dielectric meta-resonator," Opt. Express **27**, 32846-32854 (2019).
2. S. Zheng, G. Dong, Q. Yang, H. Wang, and J. Zhou, "Ultra-compact photonic crystal couplers for optical switches based on band-edge resonance," Advanced Composites and Hybrid Materials **4**, 1302-1308 (2021).
3. G. Dong, X. Guo, and Q. Yang, "Spatial observation of highly directional radiation from a compact 3D photonic-crystal antenna in Ku band," Applied Physics Letters **121**, 252901 (2022).
4. H. Wang, X. Guo, X. Zhao, and G. Dong, "Ultra-broadband polarization-independent omnidirectional reflectors via dielectric-reversal quasicrystal heterostructure multilayer films," Advanced Composites and Hybrid Materials **6**, 17 (2023).

Phase Change Materials-based Metasurface Discs

S. Du[1,2*], P. X. Liang[1], S. Hu[3], C. S. Li[2], C. Z. Gu[2], and X. C. Chen[1]

[1] BOE Technology Group Co., Ltd., Beijing 100176, China

[2] Beijing National Laboratory for Condensed Matter Physics, Institute of Physics, Chinese Academy of Sciences, Beijing 100190, China

[3] School of Sciences, Henan University of Technology, Zhengzhou, Henan 450001, China

[*]corresponding author: dosure@126.com

Abstract: Based on the phase-change materials, we propose a storage technology capable of writing and erasing the functions of metasurfaces. By constructing phase storage units using phase-change materials, the phase of pixels can be written and erased with a laser.

Metasurfaces have contributed to many hotspots in the optical field over the past decade, with their powerful capability to modulate light fields, becoming the darling of researchers and technologists in various optical scenarios and interdisciplinary fields. However, most existing metasurfaces are static, which means that their functionalities cannot be changed once the sample fabrication is completed. This limitation significantly constrains the practicality of metasurfaces in scenarios oriented towards storage, display, encryption, and the like.

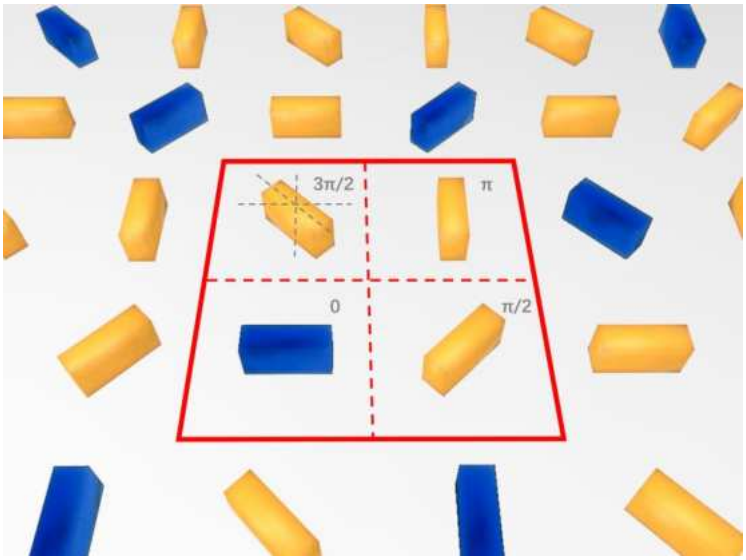


Fig.1 Schematic diagrams of designed the rewritable metasurface

The emergence of phase-change materials has provided a new approach to addressing this issue. Here, we utilize the phase-change material GST ($Ge_2Se_2Te_5$) [1] to construct rewritable metasurface phase storage units. The basic configuration is illustrated in Fig. 1, where four units form a storage pixel according to the geometric phase. The specific units within each pixel are irradiated with a focused laser to induce a phase change in the material, resulting in a reduced polarization conversion efficiency [2]. Meanwhile, the efficiency of the non-irradiated units remains high, determining the phase state of that pixel. As a result, the functionality of the metasurface can be defined.Owing to the non-volatile nature of the phase transition of GST, its functionality can

be preserved for an extended period. To erase the functionality, it is only necessary to anneal the metasurface at high temperature, which resets the phase state of each unit, thus allowing new functions to be written.

References

1. Wang, Y., Landreman, P., Schoen, D., Okabe, K., Marshall, A., Celano, U., Wong, H.P., Park, J., Brongersma,.M.L., “Electrical tuning of phase-change antennas and metasurfaces” Nat. Nanotechnol., Vol. 16, No. 6, 667-672, 2021.
2. Li, C., Du, S., Pan, R., Xiong, X., Tang, Z., Zheng, R., Liu, Y., Geng, G., Sun, J., Gu, C., Guo, H., Li, J., “Phase Change Materials Based Bilayer Metasurfaces for Near Infrared Photonic Routing”. Adv. Funct. Mater., 2310626, 2023.

Chiral meta-coder for target camouflage and identification

Zhenfei Li[1*] and Weiren Zhu[2]

[1]School of Physical Science and Technology, Northwestern Polytechnical University,
Xi'an 710129, China
[2]Department of Electronic Engineering, Shanghai Jiao Tong University,
Shanghai 200240, China
[*]corresponding author: zhenfei_li@nwpu.edu.cn

Abstract: We present an innovative method for achieving spin switchable electromagnetic camouflage and target identification functionalities using an irregular chiral meta-coder. This meta-coder is designed by combining chiral meta-atoms with an irregular phase encoding method. It could potentially open up new avenues for applications in the field of information security.

Electromagnetic camouflage, which is crucial for concealing an object's physical identity from external electromagnetic detection, has been extensively researched in recent years. While metamaterial advances have introduced transformative solutions, such as cloaking devices enabled by transformation optics, they often suffer from limitations due to bulky or static materials [1]. The emergence of metasurfaces has revolutionized our control over the propagation of electromagnetic waves [2]. By precisely arranging meta-atoms over curved surfaces, metasurfaces can mimic flat mirrors, effectively rendering objects invisible [3]. Advances in metasurfaces have led to significant advances in skin cloaking technology, with spin decoupled metasurfaces enabling cloaking under arbitrary polarization states, and tunable metasurfaces facilitating dynamic switching for reconfigurable camouflage [4,5]. The reported metasurface cloaking strategy relies on a conformal approach, requiring a metasurface equivalent to the volume of the cloaked object. However, this approach has limitations for larger objects and introduces manufacturing complexities due to conformal design requirements. A seamless transition between camouflage and visualization functions is critical. Addressing these challenges, including concealing objects while ensuring secure communication, has been the focus of extensive research and development efforts.

In this paper, we present an innovative chiral meta-coder to achieve spin switchable electromagnetic camouflage and target identification. By integrating chiral meta-atoms with an irregular phase encoding method, our approach eliminates the need for complex conformal designs and experimental operations on metasurfaces, providing a more efficient strategy. The core concept involves the dense arrangement of meta-atoms around a target object, coupled with the encoding of appropriate phase sequences for wavefront shaping and camouflage. At the same time, the target object can be identified by modulating the helical state of the incident wave based on the chiral resonance property of the meta-atoms. To validate our approach, we have provided a proof of concept through the design and experimental demonstration of a chiral meta-coder applied to a camouflaging "A" shaped target object. For contrast, Figure 1(a) shows a single "A" target without meta-atoms. When an electromagnetic wave hits an "A" shaped object, reconnaissance systems can easily decipher the target from the far-field scattering pattern. For the target object surrounded by meta-atoms, as shown in Figure 1(b), our results indicate that by encoding an appropriate sequence of meta-atoms, these meta-atoms can adapt the wavefront to effectively conceal target information when exposed to right circularly polarized (RCP) waves. The resulting camouflage pattern exhibits diffuse scattering in the far field and three focal patterns in the near field. Conversely, under the excitation of left-circularly polarized (LCP) waves, these meta-atoms transform into a

wave-absorbing configuration, facilitating the precise identification of target information, as shown in Fig. 1(c). We believe that this innovative strategy may have promising applications in the fields of data security, privacy, and communication.

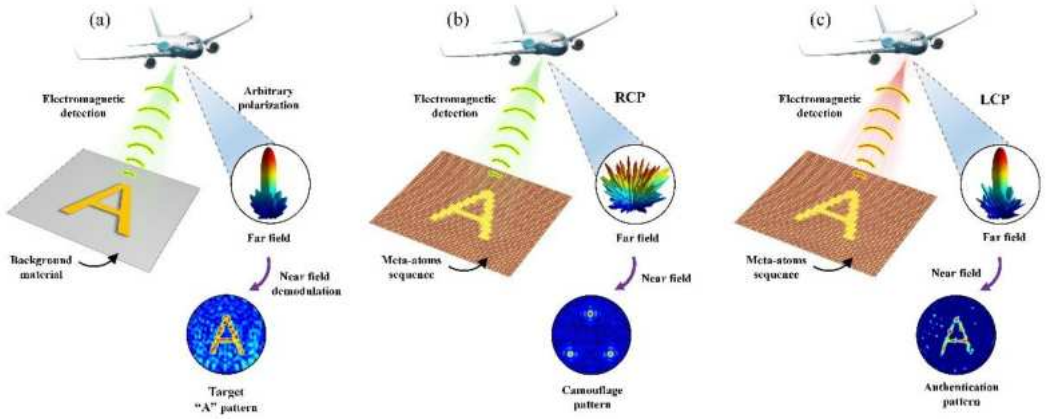


Figure 1 Schematic diagram of a chiral meta-coder for information camouflage and authentication. (a) a single target object without meta-atoms, (b) a target object surrounded by meta-atoms excited with RCP waves, (c) a target object surrounded by meta-atoms excited with LCP waves.

Acknowledgements

This work was supported by National Natural Science Foundation of China (NSFC) (61601375, 62071291, 12374296, 12304354); and Fundamental Research Funds for the Central Universities (D5000230353, D5000230165); and Natural Science Basic Research Plan in Shaanxi Province of China (2024JC-YBMS-554).

References

1. Pendry, J. B., Schurig, D., and Smith, D. R., "Controlling Electromagnetic Fields," Science, Vol. 312, No. 5781, 1780-1782, 2006.
2. Yu, N., Genevet, P., Kats, M. A., Aieta, F., Tetienne, J., Capasso, F., and Gaburro, Z., "Light Propagation with Phase Discontinuities: Generalized Laws of Reflection and Refraction," Science, Vol. 334, No. 6054, 333-337, 2011.
3. Ni, X., Wong, Z. J., Mrejen, M., Wang, Y., and Zhang, X., "An ultrathin invisibility skin cloak for visible light," Science, Vol. 349, No. 6254, 1310-1314, 2015.
4. Xu, H.-X., Hu, G., Wang, Y., Wang, C., Wang, M., Wang, S., Huang, Y., Genevet, P., Huang, W., Qiu, and C.-W., "Polarization-insensitive 3D conformal-skin metasurface cloak," Light: Sci. Appl., Vol. 10, No. 1, 75, 2021.
5. Qian, C., Zheng, B., Shen, Y., Jing, L., Li, E., Shen, L., and Chen, H., "Deep-learning-enabled self-adaptive microwave cloak without human intervention," Nat. Photonics, Vol. 14, No. 6, 383-390, 2020.

Versatile and Flexible Membrane Metasurfaces for Optimal Optoelectronic Device Efficiency

Shaojun Wang[1,2*]

[1]School of Optoelectronic Science and Engineering & Collaborative Innovation Center of Suzhou Nano Science and Technology, Soochow University, Suzhou 215006, China

[2]Key Lab of Advanced Optical Manufacturing Technologies of Jiangsu Province & Key Lab of Modern Optical Technologies of Education Ministry of China, Suzhou 215006, China

[*]corresponding author: swang.opto@suda.edu.cn

Abstract: We present a novel technique for transferring a polymer membrane incorporating monocrystalline silicon (c-Si) nanoparticle arrays (NPAs) onto diverse support substrates. Leveraging the collective resonances of the c-Si NPAs, this device exhibits efficient capabilities for beaming the fluorescence of μ-LED color-converters, serving as an étendue reducer for wireless optical detection, and enhancing light outcoupling in scintillators for low-dose X-ray imaging.

Luminescent films, demonstrating fundamental absorption and re-emission phenomena, are versatile in applications, spanning traditional white light emitting diodes and displays. They also play a crucial role in down-converting optoelectronics for detecting propagating light and high-energy particles from free space. This innovative technique broadens the detection range beyond commercially available silicon-based detectors, finding utility in luminescent solar concentrators, information storage, fluorescence anti-counterfeiting, scintillators for ionizing radiation detection, and wireless optical communications. The effectiveness of these down-converters hinges on factors like absorption, internal quantum yield, and external out-coupling efficiency. Despite design strategies, the high refractive index of the emitter matrix limits the external efficiency of luminescent slabs due to total internal reflection. This results in the majority of luminescent photons leaking into the substrate and being guided to the side where detectors are positioned, significantly constraining the integration of the optoelectronic system.

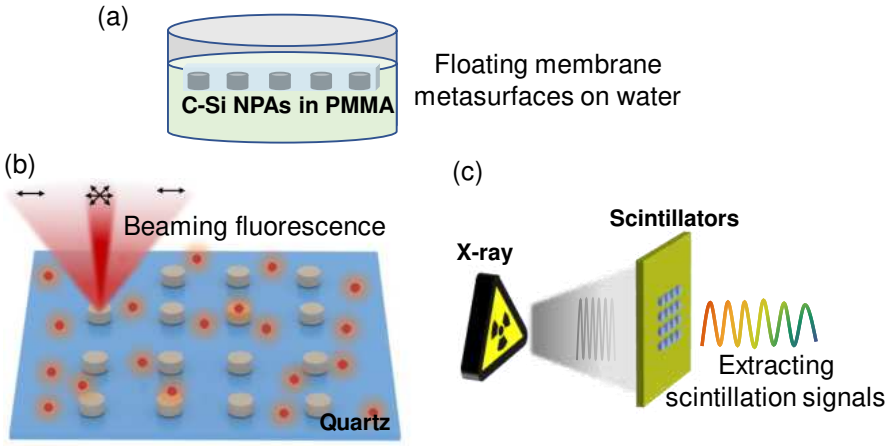


Figure 1. Floating membrane metasurfaces on water (a) can be transferred onto target substrates for beaming the fluorescent emission and act as an étendue reducer (b) or extracting the scintillation light from the crystals.

To overcome inherent limitations, optical metasurfaces emerge as a promising solution. These ultra-thin, lightweight two-dimensional elements integrate seamlessly onto down-converters due to their flat structure and natural alignment with detectors. Leveraging metallic or dielectric nanoparticle arrays (NPAs), these metasurfaces position luminescent materials within the strong near-field range of nanoantenna resonances, forming light-emitting metasurfaces. Various configurations include coating emitters on top of NPAs, depositing NPAs on luminescent slabs, or embedding emitters inside NPAs.

In Figure 1, we successfully crafted a metasurface using c-Si, known for its low loss and high refractive indices in the visible light range.[1-3] This metasurface, designed to enhance the directional emission of fluorescence layers, was transferred onto a quartz or scintillator substrate using the 'floating off' technique. It was securely affixed to quartz through dangling bonding at the interface between c-Si and substrates. We present an adaptive approach to enhance quasi-BIC emission from a resonant monocrystalline silicon (c-Si) metasurface through lattice and multipolar engineering. Dual-BICs, originating from electric quadrupoles (EQ) and out-of-plane magnetic dipoles, are identified. EQ quasi-BICs concentrate near-fields near c-Si nanodisks, enhancing fractional radiative local density of states and promoting efficient out-coupling. Coupling EQ quasi-BICs with Rayleigh anomalies enhances directional emission intensity, revealing inherent opposite topological charges in multipolar-controlled dual-BICs. Our work paves the way for fundamental research in strong light-matter interactions, the design of highly efficient light-emitting metasurfaces, and other relevant optoelectronic devices.

Acknowledgements

This work was financially supported by the National Natural Science Foundation of China (62275184, 6231101594, 62274114, and 62120106001), Natural Science Foundation of Jiangsu Province (BK20200859 and BK20210713), and the Priority Academic Program Development (PAPD) of Jiangsu Higher Education Institutions.

References

1. F. Shen, Z. Zhang, Y. Zhou, J. Ma, K. Chen, H. Chen, S. Wang, J. Xu, Z. Chen, “Transition metal dichalcogenide metaphotonic and self-coupled polaritonic platform grown by chemical vapor deposition”, Nat. Commun. 13, 5597 (2022).
2. Z. Zhang, P. Liu, W. Lu, P. Bai, B. Zhang, Z. Chen, S. A. Maier, J. Gómez Rivas, S. Wang, X. Li, High-Q Collective Mie Resonances in Monocrystalline Silicon Nanoantenna Arrays for the Visible Light, Fundam. Res. 3, 822 (2023).
3. Z. Zhang, C. Xu, C. Liu, M. Lang, Y. Zhang, M. Li, W. Lu, Z. Chen, C. Wang, S. Wang, X. Li, Dual Control of Enhanced Quasi-Bound States in the Continuum Emission from Resonant c-Si Metasurfaces, Nano Lett. 16, 7584 (2023).

Plasmonic nanoparticle clusters with tiny gaps fabricated with self-assembly superlattices

Shao-Ding Liu[1,2*], Lan-Qi Lian[1], and Qiang Zhang[1,2]

[1] Key Lab of Advanced Transducers and Intelligent Control System of Ministry of Education, Taiyuan University of Technology, Taiyuan 030024, P. R. China
[2] Department of Physics and Optoelectronics, Taiyuan University of Technology, Taiyuan 030024, P. R. China
[*]corresponding author: liushaoding@tyut.edu.cn

Abstract: Plasmonic nanoparticle clusters are reliably fabricated with a modified electron-beam lithography method using self-assembly superlattices, where the interparticle separations is less than 5 nm, the non-radiative losses can be suppressed, and the fabrication processes are simplified compared with conventional top-down approaches.

Plasmonic nanoparticle clusters have gained considerable attentions due to their versatile collective optical responses, and the interparticle separations have to be reduced as far as possible to enhance the plasmon coupling, which is hard to achieve with conventional top-down approaches (e.g., electron-beam lithography).[1, 2] This study proposes and demonstrates that using self-assembly nanoparticle superlattices, plasmonic nanoparticle clusters are reliably fabricated with a two-step lithography method (electron-beam exposure and washing process). Since the nanoparticles are separated with the coated polymer molecules. the interparticle separations are less than 5 nm (Figure 1). Besides that, the non-radiative losses of the metallic material can also be effectively suppressed due to the good crystallization for the nanoparticles fabricated with the wet-chemistry method.

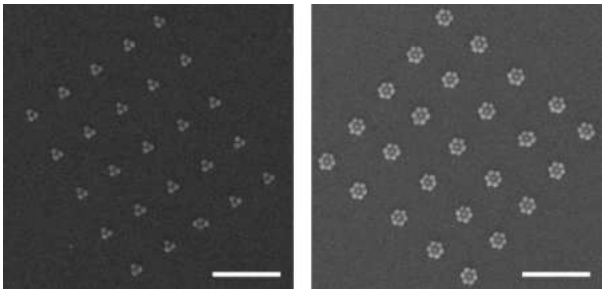


Figure 1. Gold nanoparticle clusters fabricated with the modified electron-beam lithography (Scale bars: 1 μm).

Acknowledgements: The National Natural Science Foundation of China (12004273), and the Key Research and Development Program of Shanxi Province (201903D121131).

References

1. Cai, Y. Y., Fallah, A., Yang, S., Choi, Y. C., Xu, J., Stein, A., Kikkawa, J. M., Murray, C. B., Engheta, N. and Kagan, C. R., “Open and Close-Packed, Shape-Engineered Polygonal Nanoparticle Metamolecules with Tailorable Fano Resonances,” Adv. Mater., Vol. 35, No. 33, 2301323, 2023.
2. Zhang, S., Li, G. C., Chen, Y., Zhu, X., Liu, S. D., Lei, D. Y. and Duan, H. G., “Pronounced Fano Resonance in Single Gold Split Nanodisks with 15 nm Split Gaps for Intensive Second Harmonic Generation,” ACS Nano, Vol. 10, 11105, 2016.

Optomechanical metasurfaces based on kirigami technology

Nanzhong Deng[1,2], Ashish Pandey[1,3], Gregory Roberts[1,3], Haogang Cai[1,2,3*]

[1]Tech4Health Institute, NYU Langone Health, New York, USA
[2]Department of Biomedical Engineering, New York University, Brooklyn, USA
[3]Department of Radiology, NYU Langone Health, New York, USA
[*]corresponding author: haogang.cai@nyu.edu

Abstract: As inspired by the Japanese art of paper cutting, kirigami technology has been used to create mechanical and optical metamaterials. Based on our recent nano-kirigami actuators whose tilting angle can be predefined by the geometry, we demonstrated deformable mirrors, dynamic tunable optical metasurfaces and photonics crystals with broad applications.

As inspired by the Japanese art of paper folding and cutting, “origami” and “kirigami” technologies provide a unique solution to create three-dimensional (3D) complex architectures and metamaterials with predefined two-dimensional (2D) geometry of creases and hinges (Fig. 1a) [1]. Through various processes of cutting, folding, bending, twisting, 2D thin films could pop up with a “nonlinear” expansion in 3D space by several orders of magnitude, adding an extra degree of freedom in 3D nanofabrication and actuation beyond the design possibilities through conventional approaches [2]. In particular, kirigami leverage existing 2D lithographic techniques, enabling a high compatibility with standard semiconductor manufacturing processes. The buckling-induced deformation mechanism is universal across many size scales (Fig. 1b, c) and can be applied to a broad range of materials, from conventional silicon-based materials, 2D materials, to soft and biomaterials. Therefore, kirigami is not only widely utilized in micro-electromechanical systems (MEMS) [3], but also suitable for biomimetic design of robotic, biomedical, and consumer devices [4].

Recently, kirigami technology has been used to create chiral and reconfigurable metasurfaces [5, 6]. Here, we adopted a simple kirigami design using only perpendicular cuts in a thin membrane. Two suspended panels are connected through hinged regions in the middle (Fig. 1a). When a tensile stress is applied to the membrane, kirigami panels are tilted by buckling-induced out-of-plane deformation. By changing the geometric parameters of hinge size h and cut width c, we obtained distinct deformation configurations, which are referred to as “symmetric” and “asymmetric” tilting modes [1]. The actuation of a kirigami results in a panel tilting angle θ (Fig. 1c) under a tensile stress $\sigma_{xx} = N_{xx}/t$, where N_{xx} is the load per unit length, t is the membrane thickness. We investigated the relationship of θ vs. σ_{xx} or strain ε (Fig. 1d), which is determined by the geometric parameters. Each kirigami actuator could work as a meta-atom to build novel optomechanical metasurfaces. Since the kirigami tilting angle can be predefined by its geometry, kirigami with different angles can be arranged in an array to form deformable mirrors with desired topographic profiles. Moreover, kirigami provides an ultra-compact thin-film mechanical actuation platform for dynamic tunable optical metasurfaces and photonics crystals. As an example, a photonic crystal film was integrated on top of a kirigami array, by self-assembly of a monolayer of polystyrene spheres, displaying structural colors at a given view angle [7]. The kirigami pixels can be engineered to encode different colors for optical information display, encryption and anti-counterfeiting.

Acknowledgements: The authors acknowledge support from the National Institute of General Medical Sciences of the National Institutes of Health under Award Number R35GM147406.

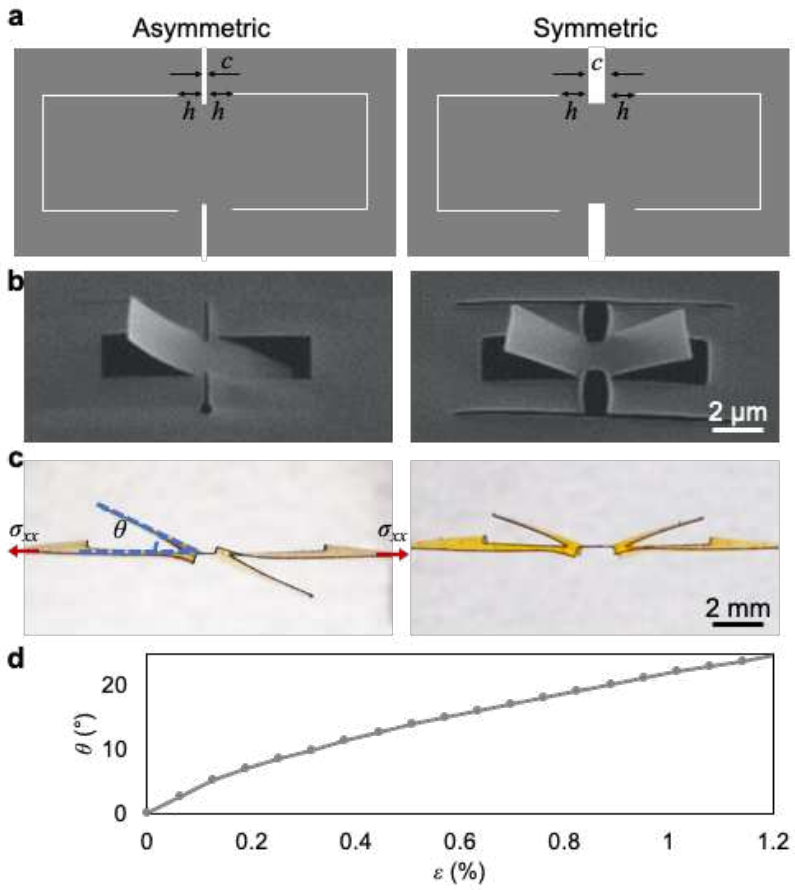


Figure 1. (a) Kirigami meta-atom layout. (b) Nano-kirigami patterned by focused ion beam in silicon nitride membrane. (c) Kirigami actuators made in Kapton film. (d) Tilting angle θ vs. membrane strain ε for the asymmetric actuation mode.

References

1. Zhang, X., Medina, L., Cai, H., Aksyuk, V., Espinosa, H.D., and Lopez, D., Kirigami Engineering-Nanoscale Structures Exhibiting a Range of Controllable 3D Configurations. *Adv Mater.* 2021, 33, e2005275.
2. Chen, S., Chen, J., Zhang, X., Li, Z.-Y., and Li, J., Kirigami/origami: unfolding the new regime of advanced 3D microfabrication/nanofabrication with "folding". *Light: Science & Applications.* 2020, 9.
3. Rogers, J., Huang, Y., Schmidt, O.G., and Gracias, D.H., Origami MEMS and NEMS. *MRS Bulletin.* 2016, 41, 123-129.
4. Rossiter, J. and Sareh, S., *Kirigami design and fabrication for biomimetic robotics*. SPIE Smart Structures and Materials + Nondestructive Evaluation and Health Monitoring. Vol. 9055. 2014: SPIE.
5. Liu, Z., Du, H., Li, J., Lu, L., Li, Z.Y., and Fang, N.X., Nano-kirigami with giant optical chirality. *Sci Adv.* 2018, 4, eaat4436.
6. Zheng, Y., Chen, K., Yang, W., Wu, L., Qu, K., Zhao, J., et al., Kirigami Reconfigurable Gradient Metasurface. *Advanced Functional Materials.* 2022, 32, 2107699.
7. Lai, X., Peng, J., Cheng, Q., Tomsia, A.P., Zhao, G., Liu, L., et al., Bioinspired Color Switchable Photonic Crystal Silicone Elastomer Kirigami. *Angewandte Chemie International Edition.* 2021, 60, 14307-14312.

Multiband and broadband acoustic topological metamaterial

C. L. Ding[1*], Y. Sun[1], and X. P. Zhao[1]

[1]Smart Materials Laboratory, School of Physical Science and Technology, Northwestern Polytechnical University, Xi'an 710129, People's Republic of China
[*]corresponding author: dingchanglin@nwpu.edu.cn

Abstract: We firstly present a dual-band acoustic high-ordered topological metamaterial (AHOTM) composed of meta-atoms and meta-molecules with edge states and corner states in two frequency regions. And then the dual-band negative refraction, valley-locked topological transport and local enhancement are investigated. At last, we realize broadband AHOTM with topological edge states.

Acoustic topology is a hot spot in recent year, because Acoustic topological insulator presents topological transport with defect immunity, backscattering immunity, and robust edge states.[1-4] Although some ATIs have been achieved by phononic crystals based on Bragg scattering, the narrow work frequency band related to the lattice constant limits their applications.[5-8] Acoustic metamaterials (AMs)[7-10] based on local resonance are another kind of candidate for the design of ATIs.[11]

In this paper, we propose a dual-band and broadband composite acoustic higher-order topological metamaterial (AHOTM)[12] based on the concepts of local resonance and weak interaction. The dual-band AHOTM is composed of meta-atoms of hollow tubes (HTs) and meta-molecules of opened-hole hollow tubes (OHTs) arrayed as a regular triangle in a hexagonal lattice with C3v symmetry. The two edge states and corner states can be separately tuned by the geometry sizes of HTs and OHTs because of their local resonances and weak interactions. The dual-band AHOTM also presents frequency-selective topological transport of edge states and higher-order corner states by rotating one structure and can sustain the topologically robust edge states against some defects. By designing three kinds of arrays A, B and C with different rotated angles of -30 ˚, 0 ˚, 30 ˚, respectively, the topological transport of edge states occurs in the wide region of array B in two bands. The AHOTM also present other dual-band acoustic effects, such as negative refraction, valley-locked topological transport and local enhancement. The concept of the dual-band AHOTM can be extended to design multiband and broadband acoustic topological insulators for their flexible manipulation of sound waves with broadband topological edge states.

References

1. K. v. Klitzing, G. Dorda, and M. Pepper, “New Method for High-Accuracy Determination of the Fine-Structure Constant Based on Quantized Hall Resistance,” Phys. Rev. Lett. 45, 494, 1980.
2. R. B. Laughlin, “Anomalous Quantum Hall Effect: An Incompressible Quantum Fluid with Fractionally Charged Excitations,” Phys. Rev. Lett. 50, 1395, 1983.
3. M. Z. Hasan and C. L. Kane, “Colloquium: Topological insulators,” Rev. Mod. Phys. 82, 3045, 2010.
4. X. L. Qi and S. C. Zhang, “Topological insulators and superconductors,” Rev. Mod. Phys. 83, 1057, 2011.
5. R. Fleury, D. L. Sounas, C. F. Sieck, M. R. Haberman, and A. Alù, “Sound isolation and giant linear nonreciprocity in a compact acoustic circulator,” Science 343, 516, 2014.
6. C. He, X. Ni, H. Ge, X. C. Sun, Y. B. Chen, M. H. Lu, X. P. Liu, and Y. F. Chen, “Acoustic topological insulator and robust one-way sound transport,” Nat. Phys. 12, 1124, 2016.
7. C. L. Ding, Y. B. Dong, Y. B. Wang, J. B. Shi, S. L. Zhai, and X. P. Zhao, “Acoustic metamaterials and metasurfaces composed of meta-atoms and meta-molecules,” J. Phys. D: Appl. Phys. 55, 253002, 2022.
8. C. L. Ding, Y. B. Dong, and X. P. Zhao, Research advances in acoustic metamaterials and metasurface, Acta Phys. Sin. (Beijing, China) 67, 194301, 2018.
9. H. J. Chen, H. Li, S. L. Zhai, C. L. Ding, L. M. Hao, C. R. Luo, and X. P. Zhao, “Ultrasound acoustic metamaterials with double-negative parameters,” J. Appl. Phys. 119, 204902, 2016.
10. C. L. Ding, H. J. Chen, S. L. Zhai, and X. P. Zhao, “Acoustic metamaterial based on multi-split hollow spheres,” Appl. Phys. A 112, 533, 2013.
11. Y. B. Wang, Y. B. Dong, S. L. Zhai, C. L. Ding, C. R. Luo, and X. P. Zhao, “Reconfifigurable topological transition in acoustic metamaterials,” Phys. Rev. B 102, 174107, 2020.
12. C. L. Ding, J. B. Shi, Y. B. Dong , Y. Bai , S. L. Zhai, and X. P. Zhao, “Dual-band acoustic higher-order topological metamaterial composed of meta-atoms and meta-molecules,” Phys. Rev. B 108, 094103 (2023)

The Design, Control and Optimization of Cavity-based Metamaterials for Miniature Spectrometer Application

Ruonan Ji[1*], Qingquan Liu[1], and Shaowei Wang[1]

[1] State Key Laboratory of Infrared Physics, Shanghai Institute of Technical Physics, Chinese Academy of Sciences, China
[*]corresponding author: jiruonan@mail.sitp.ac.cn

Abstract: Spectrometers are vital for diverse applications but face limitations like size and cost. This paper focuses on developing compact, integrated miniature spectrometers using dielectric cavity-based metamaterials, enhancing portability and performance through innovative spectrometric metamaterials and advanced reconstruction algorithm. This research contributes to the ongoing progress in miniaturized optical sensing systems.

Spectrometers are indispensable tools in a wide range of applications, including environmental monitoring, biomedical diagnostics, food quality analysis, agriculture, and industrial process control. However, traditional spectrometers often suffer from limitations such as large size, high cost, and limited mobility, restricting their usability in many real-world scenarios, including real-time analysis, in situ measurements, space and field-deployable capabilities. To overcome these limitations and meet the demands of diverse applications, the development of miniature spectrometers has gained significant attention[1]. The all-dielectric optical microcavity, featuring exceedingly low losses, can confine light within a very small volume, significantly enhancing the interaction between light and matter. This enhancement leads to improved performance of photonic devices. Moreover, its simple fabrication process and ease of integration provide an excellent platform for developing photonic spectroscopic devices suitable for miniaturized spectrometers. This paper presents various applications of all-dielectric microcavity-based metamaterials in miniaturized spectrometers and how spectral super-resolution reconstruction techniques can be used to enhance spectral resolution, addressing the challenges of size, cost, and spectral resolution faced by miniaturized spectrometers.

A short-wave infrared broad-spectrum detection chip based on an F-P (Fabry-Perot) microcavity array is proposed. Using ultraviolet laser direct writing grayscale lithography, the F-P microcavity array is rapidly fabricated directly on the InGaAs focal plane detector. Combined with spectral reconstruction methods, this allows for a very wide spectral detection range with few spectral channels, covering 900 to 1700 nm in the short-wave infrared range, and achieving a spectral resolution of 2 nm[2]. Furthermore, by integrating a two-dimensional metasurface with an all-dielectric optical microcavity, a novel optical metainterface device capable of simultaneous polarization and spectral splitting is proposed[3]. This device achieves simultaneously polarization extinction ratio(PER) of 800 and a spectral resolution power (SRP, $\lambda/\Delta\lambda$) of 113 with a very thin metal grating, and its fabrication process is simple and easy to manufacture. Moreover, it can break the limitation of diffraction and achieve much higher polarization extinction ratio with limited size gratings. This research contributes to the ongoing progress in miniaturized optical sensing systems, opening up possibilities for advancements in diverse application domains.

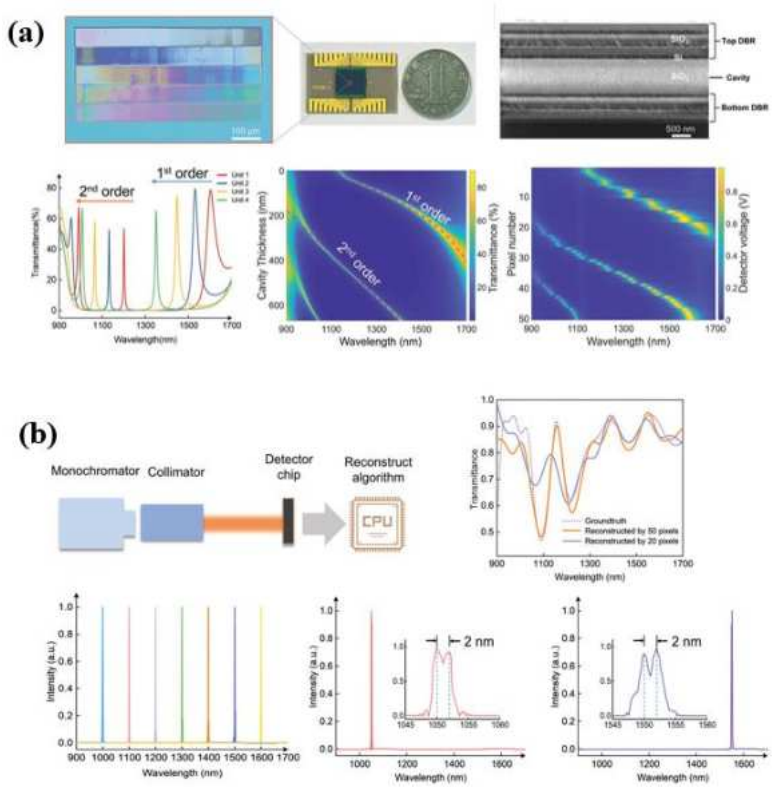


Fig 1. Snapshot Spectral Chip Based on Optical Microcavity

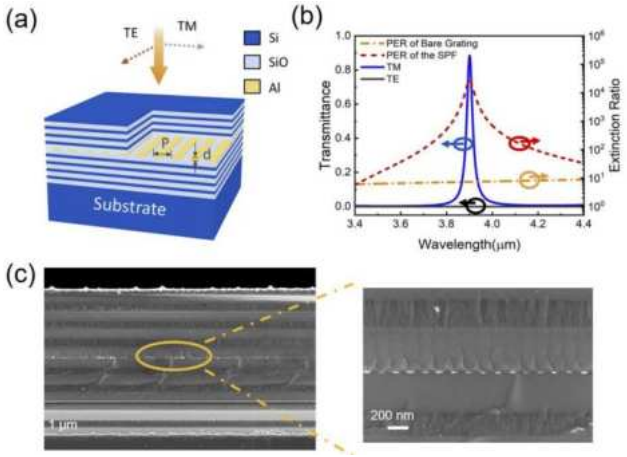


Fig 2. Multidimensional spectroscopic device based on optical metainterface

References

1. Yang, Z., Albrow-Owen, T., Cai, W. & Hasan, T. Miniaturization of optical spectrometers. *Science* **371**, eabe0722 (2021).
2. Xuan, Z. *et al.* Short-Wave Infrared Chip-Spectrometer by Using Laser Direct-Writing Grayscale Lithography. *Advanced Optical Materials* **10**, 2200284 (2022).
3. Liu, Q. *et al.* Metainterface and Application for High-Performance Spectro-Polarimetric Filter. *ACS Photonics* **10**, 125–133 (2023).

Overlapped Bandgap and Ultrabroadband Transmission in a Valley Photonic Insulator Based on Dendritic Structure

Yahong Liu[1,2*], Meize Li[1,2], Peng Li[1], Liyun Tao[1,2], Lianlian Du[1]

[1] School of Physical Science and Technology, Northwestern Polytechnical University, Xi'an 710129, China
[2] Research & Development Institute of Northwestern Polytechnical University in Shenzhen, Shenzhen, 518063, China
*corresponding author: yhliu@nwpu.edu.cn

Abstract: Exploring multi-dimensional manipulation waves will greatly promote the development of physical systems. In topological insulators[1-2], overlapped bandgap with nontrivial topology has never been reported. Besides, it is urgent to improve the bandwidth of topological transmission[3-4]. In this work, overlapped bandgap and ultrabroadband transmission are realized in dendritic valley photonic insulator.

Keywords: overlapped bandgap, edge states, corner states, valley photonic insulator, ultrabroadband, dendritic Structure.

Topological insulators have attracted considerable attention due to their strong backscatter immune transmission. A higher-order valley photonic insulator composed of arrays of dendritic structure is designed. As in any uniaxial structure, eigenmodes propagating can be classified as TE mode and TM mode. As shown in Fig.1, based on the two modes of dendritic structure, overlapped bandgap and ultrabroadband valley transmission are realized, respectively.

Firstly, we discuss TM mode. The band structure shows an overlapped bandgap is observed, and the overlapped bandgap divides the band structure to three bandgaps. The evolution of the overlapped bandgap is investigated by changing the geometric parameters and increasing fractal to break the C_{3v} symmetry drastically. Besides, it is notable that the band structure of the proposed valley photonic insulator is flat bands. It is demonstrated that undistorted transmission can be observed as a plane electromagnetic wave transmits through the proposed valley photonic insulator. The interface consisting of two valley photonic structures with distinct topological nontrivial phases is constructed. Edge states and corner states with strong energy localization are obtained in multi-band frequencies. Remarkably, two triangular structures with different Wannier center configurations both have corner states in the same bandgap, which does not obey the valley selectivity. The phenomenon is caused by the weak valley locking property due to the overlapped bandgap.

Secondly, we discuss TE mode. The valley photonic crystal composed of dendritic structure can realize valley transmission with a relative bandwidth up to 59.65%. Theoretical analysis, numerical simulation and experimental measurement all confirm flexible manipulation of electromagnetic

wave propagation paths. Ultrabroadband topological waveguides with the zigzag and armchair interface are demonstrated, which can achieve experimentally 58.71% and 36.78% relative bandwidth, respectively. Several topological channel intersections are designed, and two types of corner states with topological switchability and valley selectivity are demonstrated.

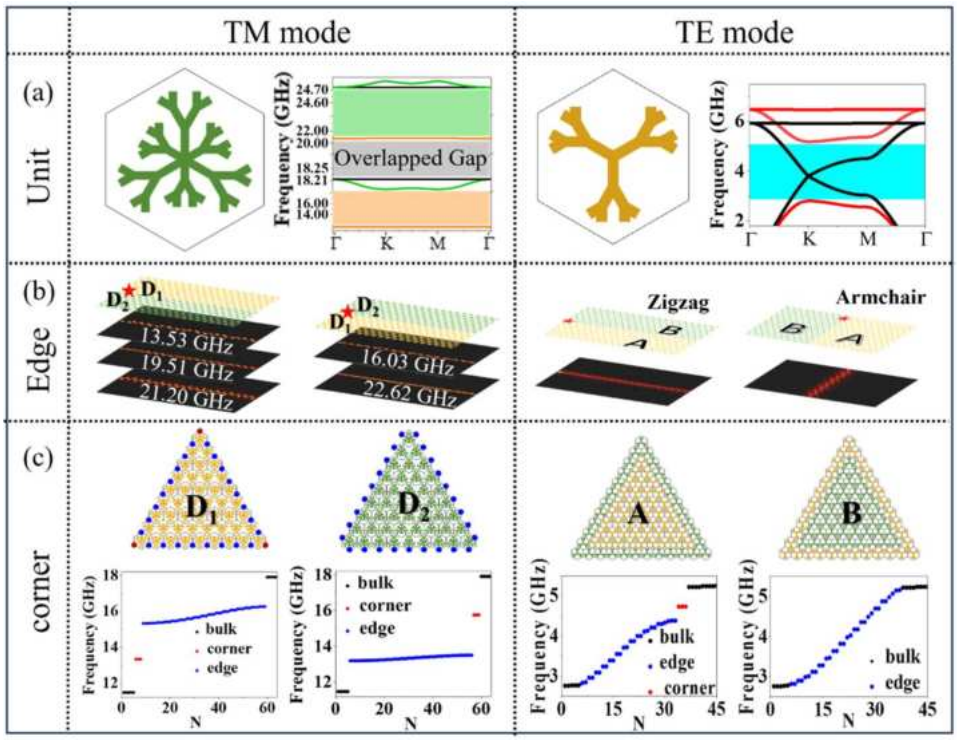


Figure 1. (a) Schematics and the band structures. (b) Schematic and electric field distributions for waveguides. (c) Schematic and eigenspectral for corner structures.

Acknowledgements

The work is supported from the National Natural Science Foundation of China (Grant No. 12374296), the Key Research and Development Program of Shaanxi Province of China (Grant No. 2023-YBGY-247), and the Guangdong Basic and Applied Basic Research Foundation (Grant No. 2024A1515011725).

References

1. X. Zhang, L. Liu, M. H. Lu, Y. F. Chen, *Phys. Rev. Lett.* 126, 156401, (2021).
2. H. X. Wang, L. Liang, B. Jiang, J. Hu, X. Lu, J. H. Jiang, *Photonics Res.* 9, 1854, (2021).
3. Kumar, A., Tan, Y. J., Navaratna, N., Gupta, M., Pitchappa P. Singh R, *Nat. Commun.* 15, 926 (2024).
4. Zhang, Z., Li, F., Lu, J., Liu, T., Heng, X., He, Y., Liang, H., Gan, J. Yang, Z, *Nanophotonics* 9(9), 2839-2846 (2020).

Perovskite Photovoltaics: Light-Matter Interaction

Subcell Characterization Platforms for Emerging Tandems

J. Y. Kim[1*]

[1]Department of Materials Science and Engineering, Seoul National University, Seoul 08826, Republic of Korea
[*]corresponding author: jykim.mse@snu.ac.kr

Abstract: We report comprehensive electrical characterization methods based on either 2-terminal or 3-terminal platform that can accurately and easily analyze the subcells of monolithic emerging tandems. In addition to the current-voltage and external quantum efficiency measurements, advanced characterization for subcells such as impedance spectroscopy and thermal admittance spectroscopy will be demonstrated.

Introduction

The efficiencies of emerging tandems are rapidly increasing in recent years. Among them, the perovskite/Si tandem solar cells (PVSK/Si TSCs) are particularly attracting interest from both of academia and industry, because its highest certified efficiency (33.9%) has already surpassed the efficiency limit of the single junction solar cells.[1] Despite this extensive improvement in device performance, subcells are relatively poorly understood because of the limited availability of their characterization methods. Optical methods such as photoluminescence and electroluminescence have been reported as possible tools for characterizing subcells; however, they can only provide indirect information regarding the device performance. Moreover, a few facile electrical characterization methodologies have been reported, but their applications for PVSK/Si TSCs have not been fully investigated. Indeed, most of the electrical characterization methods that have been developed for single-junction solar cells are inadequate for probing the subcells of monolithic TSCs. Given that the performance optimization of PVSK/Si TSCs is currently mostly realized through the independent characterization of single-junction cells, this lack of tools for characterizing subcells represents a severe obstacle to further enhance the device performance. In this study, we report a comprehensive methodoloty based on either 2-terminal or 3-terminal characterization platform. Examples of subcell characterizations such as the current density-voltage (J-V) curves, external quantum efficiency (EQE) curves, impedance spectroscopy (IS), transient photovoltage decay (TPVD), and thermal admittance spectroscopy (TAS) will be presented based on highly efficient PVSK/Si TSCs.

Contents

A. Subcell Characterization Methods using the 3-Terminal Platform[2]

The 3-terminal platform utilizes the internal recombination layer as an auxiliary contact for the subcell characterization. We will present the examples of subcell characterization using 3-terminal platform, where accurate current density-voltage (J-V) and external quantum efficiency (EQE) curves of each subcell can be obtained without any additional light bias. Further studies such as the electron dynamics study of subcells and the current-mismatch effect on the fill factor will also be presented.

B. 2-Terminal Characterization Protocols based on Subcell-selective Illumination[3]

Unlike the 3-terminal platform, the 2-terminal platform is based on subcell-selective illumination, and can be applied to general 2-terminal monolithic TSCs without the auxiliary contact. The way how we can obtain subcell characteristics and examples of the accurate characterization of the subcells will also be presented for highly

efficient PVSK/Si TSCs.

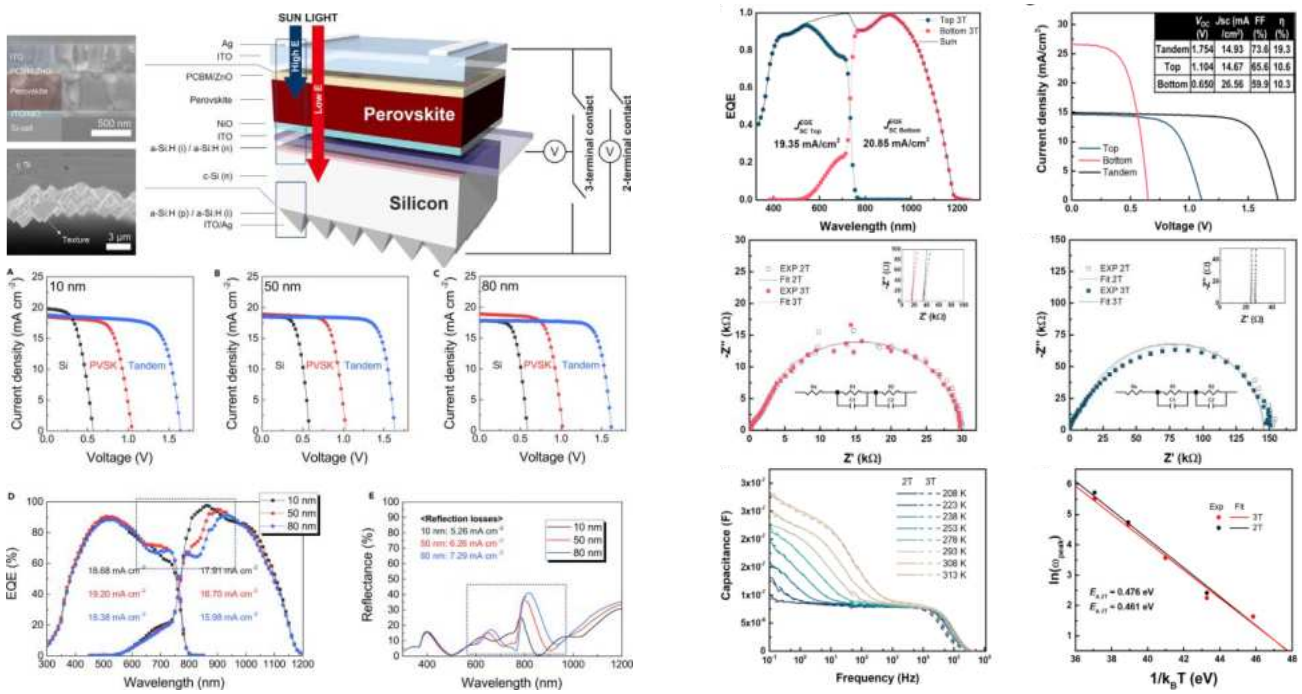


Fig. 1. (Left) Structure of 3-terminal characterization platform and example of subcell characteristics.
Fig. 2. (Right) Example of subcell characterization using the 2-terminal protocol.

Summary

We present 2-terminal and 3-terminal characterization platforms for accurate subcell characterization of emerging tandem solar cells using a model system of highly efficient perovskite/Si tandem solar cells. The 3-terminal platform utilizes the internal recombination layer as an auxiliary contact for the subcell characterization, whereas the 2-terminal platform is based on subcell-selective illumination, which can be applied to general 2-terminal monolithic TSCs without the auxiliary contact. The presented protocols for the accurate subcell characterization of monolithic tandem cells will be beneficial to the further development of high efficiency tandem cells and their successful commercialization.[4-6]

References

1. NREL, Best Research-Cell Efficiencies Chart (https://www.nrel.gov/pv/cell-efficiency.html.)
2. I. J. Park et al., *Joule*, 3, 807-818 (2019)
3. J. H. Park, et al., *Cell Reports Physical Science*, 3, 101076 (2022)
4. D. Kim et al., *Science*, 368, 155-160 (2020)
5. Y. J. Choi et al., *ACS Energy Lett.*, 8, 3141-3146 (2023)
6. S. K. Hwang et al., *Energy Environ. Mater.*, DOI: 0.1002/eem2.12489 (2024)

Nano-photonics as a route to enhance the open circuit voltage from perovskite and organic photovoltaic cells

Jordi Martorell

ICFO-The Institute of Photonic Sciences, The Barcelona Institute of Science and Technology, 08860 Castelldefels, Barcelona Spain.
Departament de Física Universitat Politécnica de Catalunya, Terrassa 08222, Spain.

Abstract
A nanophotonic structuration of perovskite and organic solar cell architectures is considered for enhancing the open-circuit voltage (Voc). Numerical and experimental results to limit Boltzmann losses and set the path to push the efficiency from planar geometry single junction cells from 33% to levels exceeding 41% will be presented.

Summary
While existing light management strategies predominantly target an effective sunlight absorption and short-circuit current density enhancement, optical approaches to reduce Voc losses in solar cells are seldom explored. In the current work we take a radical shift for enhancing the efficiency of perovskite and organic solar cells, with a specific focus on improving the open-circuit voltage (Voc) by considering the incorporation of a nanophotonic structuration designed to serve as angular restrictor for the emission photons in thin film solar cells.

We will present different nanophotonic structures which primary objective is to mitigate losses associated with bimolecular radiative recombination, specifically Boltzmann losses, without the reliance on sunlight concentration. This approach aims to preserve the advantages inherent from a planar configuration in solar cells. We will discuss numerical and experimental results where light emission and quasi-Fermi level splitting in perovskite and organic solar cells is modified by the incorporation of different nanophotonic structures. We will also discuss how the nanophotonic structuration can control the Voc to open paths for surpassing the planar geometry single junction solar cell power conversion efficiency limit and push it from 33% to reaching levels exceeding 41%. Through such unconventional approach we aim at taking planar geometry single junction solar cells to reach the high efficiencies obtained by sunlight concentration in simple and commercially viable photovoltaic configurations.

Interface study for Sn-Pb mixed perovskite solar cells

D. H. Kim[1*]

[1] Department of Materials Science and Engineering, Korea University, Republic of Korea
[*]corresponding author: donghoekim@korea.ac.kr

Abstract: Most studies of Sn-Pb perovskite have focused mainly on itself. In this presentation, I introduce our diverse works on the interfaces between Sn-Pb perovskite and charge transport layers to improve the electrical and physical properties on the device.

The perovskites are an attractive choice as ideal light absorbing materials for next generation solar cells due to their unique bandgap tunability and excellent optoelectrical properties. As a result, various perovskite-based solar cells have shown many outstanding performances, such as the highest certified efficiency in thin-film criteria (26.1%) and in silicon-based dual-junction tandem device (33.9%).[1]

Among the various types of perovskites, those with a mix of tin (Sn) and lead (Pb) in the B-site have a narrow bandgap. This allows them to absorb light up to the near-infrared region. Theoretically, this means they could be used to create higher-efficiency single-junction solar cells than that of Pb-based perovskite solar cells. Moreover, they could be part of tandem solar cells that surpass 30% efficiency. As a result, narrow bandgap perovskites have gained importance in perovskite solar cell research. To tap into the potential of Sn-Pb perovskites, researchers have explored various aspects such as composition, morphology, and how to prevent Sn^{2+} from oxidizing.[2] So far, the efficiency of Sn-Pb perovskite solar cells has reached up to 23.8%.[3] However, most studies have focused mainly on the Sn-Pb perovskite itself. For further breakthroughs, it's crucial to look at the interface between materials.

For example, from the beginning, poly[3,4-ethylene dioxythiophene]-poly[styrene sulfonate] (PEDOT:PSS) has been commonly used as the hole transport layer because it matches the energy levels well. But, the PEDOT:PSS layer has several downsides. First, its acidic nature; second, its sensitivity to moisture; and third, its lower electrical conductivity for moving charges because the PEDOT is encased in PSS. These issues mainly cause defects at the interface between PEDOT:PSS and the perovskite, making it less stable compared to Pb-based perovskites. Despite these disadvantages, it is still in use because the interface with PEDOT:PSS has not been changed or replaced by a new HTL material.

In this talk, I will introduce how we enhanced the electrical properties of the interface between the electron transport layer and Sn-Pb mixed perovskite through additives and introduced molecular engineering on the PEDOT:PSS surface to improve the electrical and physical junction properties of the PEDOT:PSS/perovskite interface. I believe that the results of these surface studies will provide some insights to open the next chapter of Sn-Pb perovskite research.

References

1. https://www.nrel.gov/pv/cell-efficiency.html
2. Lee, H., Kang, S. B., Lee, S. Zhu, K. and Kim, D. H., “Progress and outlook of Sn–Pb mixed perovskite solar cells,” Nano Converg., Vol. 10, 27, 2023.
3. Green, M. A., Dunlop, E. D., Yoshita, M., Kopidakis, N., Bothe, K., Siefer, G., Hao, X., “Solar cell efficiency tables (version 62),” Prog. Photovolt. Res. Appl. Vol. 31, 651-663, 2023.

Crystal Growth and Composition Engineering for Reproducible Fabrication of High-Performance Perovskite Solar Cells

Jin-Wook Lee *

Department of Nano Science and Technology and Department of Nanoengineering, SKKU Advanced Institute of Nanotechnology (SAINT), Sungkyunkwan University, Suwon 16419, Republic of Korea.
SKKU Institute of Energy Science & Technology (SIEST), Sungkyunkwan University, Suwon, 16419, Republic of Korea

Metal halide perovskite solar cells (PSCs) have been spotlighted as a promising next-generation photovoltaic technology. Recently, there has been a surge of efforts in the commercialization of PSCs in academia and industries worldwide with record power conversion efficiencies over 26% for both n-i-p and p-i-n structured devices. Nevertheless, their subpar operational durability, module scalability, and material toxicity are challenges often brought up as the major barriers hindering practical commercialization. The poor reproducibility of PSCs has been relatively overlooked, but negatively impacts institutional research laboratories, start-up companies, and large established corporations all alike. Reproducible fabrication of PSCs is a critical consideration for market viability and practical commercialization. In this work, I will discuss the critical functions of atmospheric humidity to regulate the crystallization and stabilization of formamidinium lead triiodide ($FAPbI_3$) perovskites. We demonstrate that the humidity content during processing underlies profound variations in perovskite stoichiometry, thermodynamic stability, optoelectronic quality and thus reproducibility of PSCs. In second part of the presentation, I will discuss the interplay between composition of perovskite, and performance and stability of inverted PSCs. We rationalize the difference in widely used perovskite compositions in n-i-p and p-i-n PSCs.

Vacuum-Processed Additive: A Novel Approach for Controlling Growth of Perovskite Crystals in All Vacuum Processed Perovskite Solar Cell

K. Lee[1], and K. Kim[1]

[1] Department of Chemistry and Nano Science, Ewha Womans University, Seoul 03760, Republic of Korea
*corresponding author: kimkk@ewha.ac.kr

Abstract: We present a novel method for controlling the growth of perovskite crystals in a vacuum thermal evaporation process by utilizing a vacuum-processable additive, propylene urea (PU). Co-evaporating of perovskite precursors and PU retards the direct reaction between the perovskite precursors. This facilitates larger domain size and reduced defect density.

In this study, we present a novel method for controlling the growth of perovskite crystals in a vacuum thermal evaporation process by utilizing a vacuum-processable additive, propylene urea (PU). By co-evaporating perovskite precursors with PU to form the perovskite layer (Figure1), PU, acting as a Lewis base additive, retards the direct reaction between the perovskite precursors. This facilitates larger domain size and reduced defect density (Figure 2). Following the removal of the residual additive, the perovskite layer, exhibiting improved crystallinity, demonstrates reduced charge recombination, as confirmed by time-resolved microwave conductivity analysis. Consequently, there is a notable enhancement in open-circuit voltage and power conversion efficiency, increasing from 1.05 V to 1.15 V and from 17.17% to 18.31%, respectively. The incorporation of a vacuum-processable and removable Lewis's base additive into the fabrication of vacuum-processed perovskite solar cells offers new avenues for optimizing these devices.

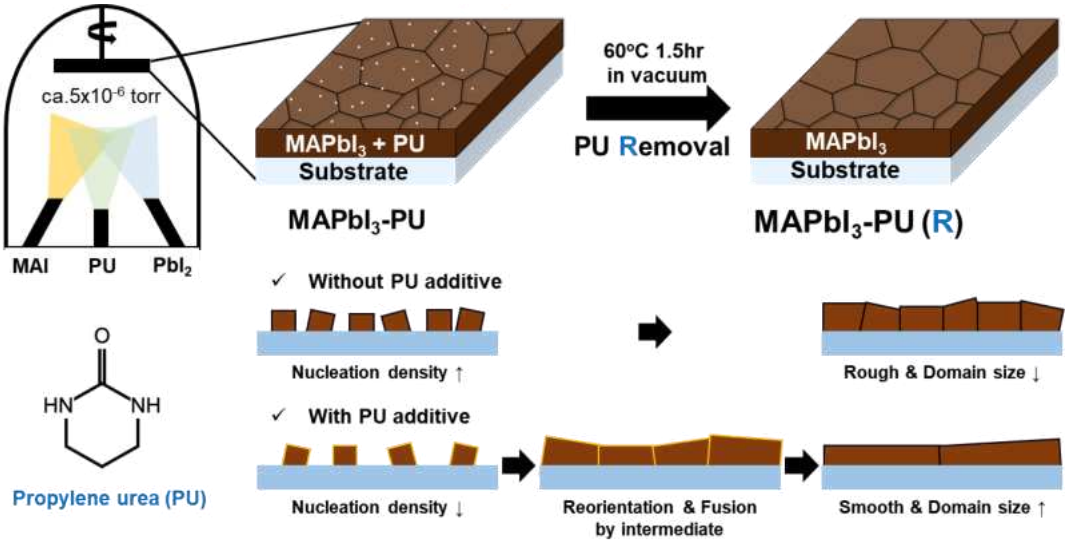


Figure 1. Schematic diagram of the vacuum-processed perovskite fabrication process with a vacuum-processable propylene urea (PU) additive and subsequent removal step for residual PU additive. Schematic representation of perovskite crystal formation without and with PU additive and corresponding chemical structure of PU are also shown.

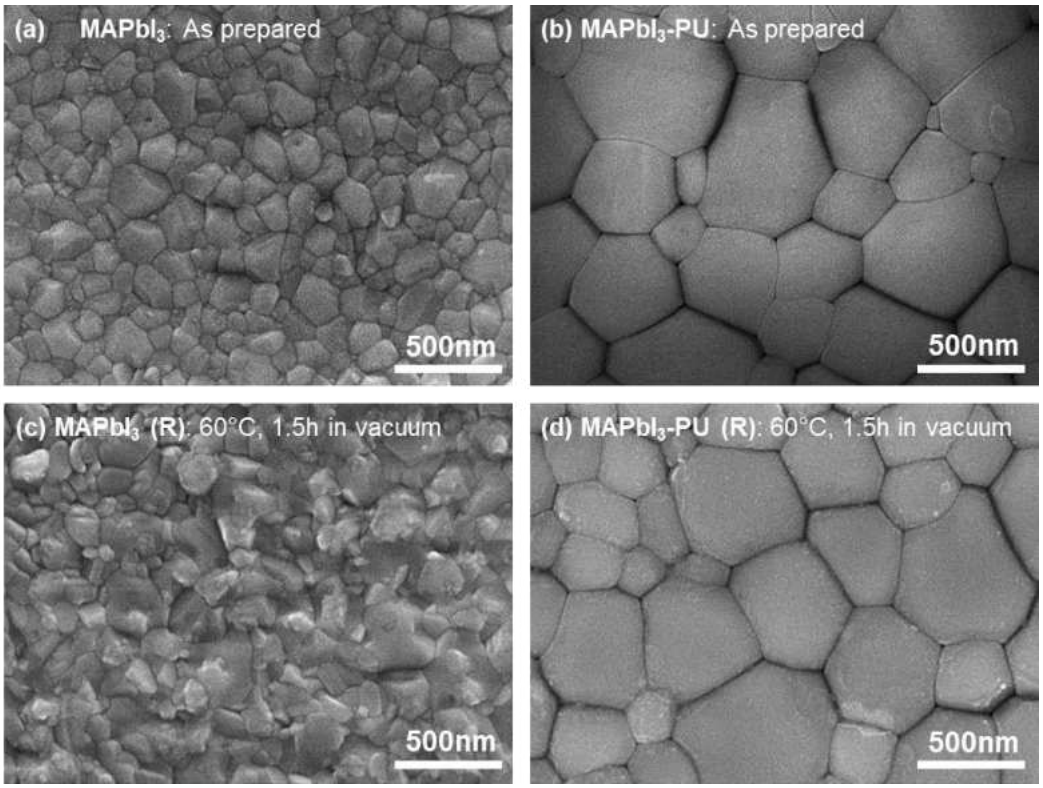


Figure 2. Top view scanning electron microscopy (SEM) images of vacuum-processed $MAPbI_3$ film with different fabrication condition. (a) $MAPbI_3$ film without PU additive and (b) with PU additive before the subsequent annealing step and (c) $MAPbI_3$ film without PU additive and (d) with PU additive after the subsequent annealing step.

Performance-limiting processes in $Cs_2AgBiBr_6$ double perovskite solar cells

Wolfgang Tress*

Institute of Computational Physics, Zurich University of Applied Sciences, 8400 Winterthur, Switzerland

*corresponding author: wolfgang.tress@zhaw.ch

Abstract: $Cs_2AgBiBr_6$ double perovskite solar cells are one of the sister devices of the lead-based perovskites. However, their photophysics is highly distinct posing various open questions. Some of those are addressed by photo and electro-luminescence spectroscopy and sensitive spectral response measurements, all performed on working devices and temperature-dependent.

Highly-efficient perovskite solar cells contain the heavy metal lead. One way to avoid lead consists of employing double perovskite materials. One of the most common representatives in photovoltaics research is $Cs_2AgBiBr_6$, so far commonly yielding power-conversion efficiencies below 5%. Although the potential of this material as an absorber in solar cells is limited due to an absorption onset above 2 eV, it is a highly interesting optoelectronic material. Understanding its properties might contribute to pave the way for the development of further lead-free perovskite(-similar) materials.

In this contribution, the performance-limiting factors in $Cs_2AgBiBr_6$ solar cells are discussed based on a temperature-dependent study of the optoelectronic properties. The findings are very distinct from the lead-halide perovskites, which can be described as a semiconductor, where e.g. the common reciprocity relations are applicable.

The large Stokes shift between absorption (peak at 2.8 eV) and emission (peak at 2.0 eV) of $Cs_2AgBiBr_6$ and the broad emission were early observations that gave rise to still ongoing debates. We find that it is indeed not straight-forward to employ reciprocity relations to deduce radiative open-circuit voltage (Voc) limits from sensitive measurements of the photocurrent onset. Fitting a Gaussian allows to calculate a radiative Voc limit of 1.95 V and roughly reproducing the photoluminescence (PL) spectra.[1] However, using an exponential fit, a strongly temperature dependent Urbach energy with a value of ca. 50 meV at room temperature can be found. Furthermore, the PL, which increases by two to three orders of magnitude when decreasing the temperature to 100 K, can be separated into two peaks: One (630 nm), whose shape is hardly affected by temperature similarly to the absorption peak and a second one further in the red (670 nm) that shows a stronger temperature dependence. The first confirms earlier suggestions of a rather localized excitonic transition in contrast to a transition between a valence and conduction band of the crystal. Since the absorption peak remains mainly unaffected by temperature as well, this indicates the same origin of absorption and PL despite the large shift. From impedance spectroscopy, we deduce a dielectric constant of 21, which indicates efficient charge screening. Analyzing light- and temperature dependent open circuit voltage data in the range above 250 K allows for a linear extrapolation to values at 0 K, yielding a value of around 2 V. The open-circuit voltage is limited by non-radiative recombination as electroluminescence yields of 1e-8 show, where interestingly the EL spectrum is further redshifted compared to the PL. One part of the rather low Voc of 1.1 V can be explained by poor contact selectivity as voltage-dependent external quantum efficiency measurements indicate. Also scan-rate dependent current-voltage curves unravel slow processes that counteract efficient charge collection. Adding a 2D perovskite layer on top of the 3D one could slightly attenuate these losses.[2]

References

1. Sirtl, M. T. *et al.* The Bottlenecks of Cs2AgBiBr6 Solar Cells: How Contacts and Slow Transients Limit the Performance. *Advanced Optical Materials* **9**, 2100202 (2021).
2. Sirtl, M. T. *et al.* 2D/3D Hybrid Cs2AgBiBr6 Double Perovskite Solar Cells: Improved Energy Level Alignment for Higher Contact-Selectivity and Large Open Circuit Voltage. *Advanced Energy Materials* **12**, 2103215 (2022).

Functions of Porous Carbon in Multi-Porous-Layered-Electrode Perovskite Solar Cells (MPLE-PSCs)

S. Ito[1]

[1]University of Hyogo, Japan
corresponding author: userid@institution.edu

Abstract: Information of carbon materials (carbon black and graphite) for fully-printed carbon-based perovskite solar cells has been disclosed. TEM images and conductivity variation with the mixing ratio are shown. And, the hole extraction ability has been discussed with the results of J-V curves by inversed-structured multi-porous- layered-electrode perovskite solar cells (MPLE-PSCs).

For commercialization of perovskite solar cells, utilization of carbon back contact is quite important, because of the reasons below:

[1] Printability (without vacuum deposition)
[2] Low sheet resistance (small resistibility as TCO in solar cells)
[3] Chemical stability (stable against iodide)
[4] Hole extraction
[5] Moisture blocking with perovskite crystal
[6] Water adsorption (as activated charcoal)

If solar cells will be fabricated via vacuum deposition, the system cost must be larger than printing one. Moreover, printing procedure is faster than vacuum deposition, which is important to fabricate cost-effective solar cells. And, the printed carbon layer can be a good conducting film. The sheet resistance of printed-carbon layer is as low as transparent conducting oxide (TCO) [8 - 10 Ω/sq.]. We have used conducting carbon black (about 30 nm diameter) (Figure 1) and graphite (about 1 - 30 μm) (Figure 2). Specially, combination of carbon black and graphite is quite important (Figure 3). The standard materials in perovskite solar cells for used back contact electrodes are gold and/or silver, which can react with iodin in perovskite solar cells. For the long-time stability, elimination of Au and Ag is quite important about perovskite solar cells.

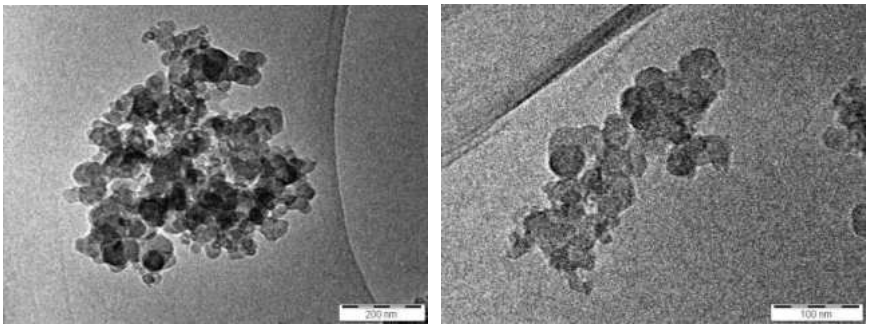


Figure 1. TEM images of carbon black for MPLE-PSCs; left: large view; light magnified view.

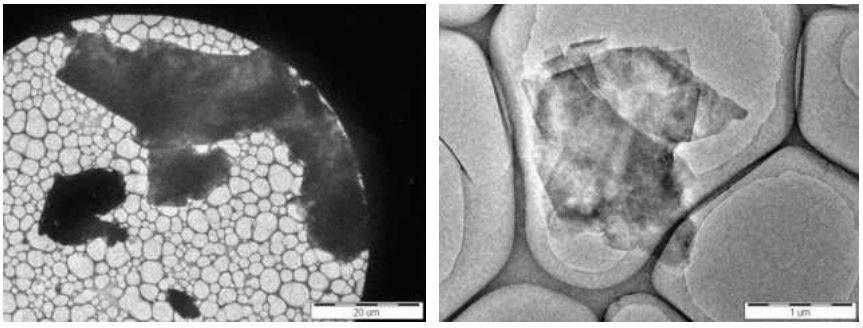


Figure 2. TEM images of graphite for MPLE-PSCs; left: large view; light magnified view.

The conducting carbon layer has the function of hole extraction. In order to confirm it, we have compared J-V curves of inversed-structured multi-porous-layered-electrode perovskite solar cells (MPLE-PSCs) of <porous carbon/porous In-Zn-O(IZO)/porous ZrO_2/compact NiO/FTO/glass> and <Ag/BCP/porous In-Zn-O(IZO)/porous ZrO_2/compact NiO/FTO/glass> (Figure 4). The porous layers were filled with organo-lead-iodide perovskite crystal ($(5\text{-AVA})_{0.05}MA_{0.95}PbI_3$). Since Nickel oxide and carbon compete for holes, the Voc of "carbon electrode" became quite smaller than that of "Ag electrode". Hence, we have confirmed that caron has strong ability to extract holes in perovskite crystal.

Moreover, the porous carbon layer has the ability of moisture blocking with filled perovskite crystal in the pore. And, water can be adsorbed like activated charcoal, which can work as getter material in solar cells. The details would ne In the conference, the details will be discussed.

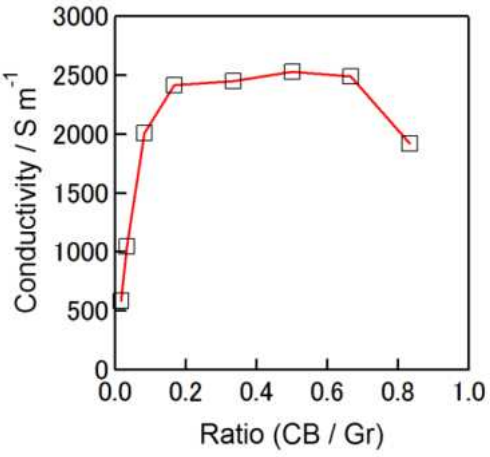


Figure 3. Variation of conductivity with the mixing ratio of carbon black (CB) and graphite (Gr.)

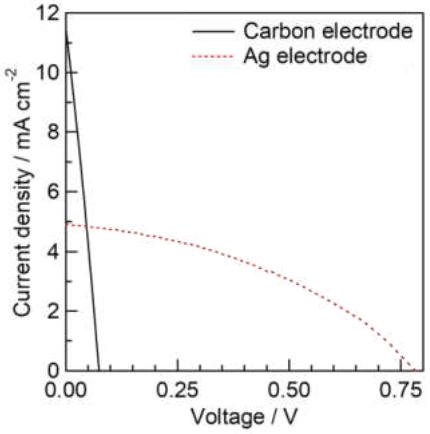


Figure 4. J-V curves of inversed-structured multi-porous-layered-electrode perovskite solar cells (MPLE-PSCs) of <porous carbon/porous In-Zn-O(IZO)/porous ZrO_2/compact NiO/FTO/glass> (as "Carbon electrode" in figure) and <Ag /BCP /porous In-Zn-O(IZO) /porous ZrO_2/compact NiO /FTO /glass> (as "Ag electrode" in figure).

Halide Interfacial Layers for Perovskite Solar Cells

Jun Hong Noh[1*]

[1]School of Civil, Environmental & Architectural Engineering, KoreaUniversity,

Seoul, South Korea

[*]corresponding author: junhnoh@korea.ac.kr

Abstract: Halide perovskite solar cells have a thin-film device architecture including interfaces between hetero-materials such as oxides, halides, and organic materials. Here, the wide-band gap halide interfacial layers will be discussed to ensure compatibility with the light absorbing halide perovskite layer for achieving high photovoltaic performance.

The light absorbing halide perovskite layer with narrow band gap of ~ 1.5 eV is used in perovskite solar cells. The interface between the light absorbing layer and charge transporting layers such as Spiro-OMeTAD, P3HT, and SnO_2 is a crucial location where non-radiative recombination sites are predominantly formed, and it serves as a key site where charge transfer must take place. The articles show wide band gap halide perovskite layers that do not only successfully passivate the interfacial trap sites but also design the interfacial electric field.

References

1. EH Jung, NJ Jeon, EY Park, CS Moon, TJ Shin, TY Yang, JH Noh, J Seo. “Intact 2D/3D halide junction perovskite solar cells via solid-phase in-plane growth,” Nature Energy, Vol. 6, 63–71, 2021.
2. YW Jang, S Lee, KM Yeom, K Jeong, K Choi, M Choi, JH Noh., “Efficient, stable and scalable perovskite solar cells using poly (3-hexylthiophene),” Nature, Vol. 567, 511–515, 2019.
3. MJ Jeong, CS Moon, S Lee, JM Im, MY Woo, JH Lee, H Cho, SW Jeon, JH Noh., “Boosting radiation of stacked halide layer for perovskite solar cells with efficiency over 25%,” Joule, Vol. 7, 112-127, 2023

Surface Chemistry for Efficient Sn- and Pb-based Perovskite Photovoltaics

A. Wakamiya[1*], M. A. Truong[1], N. Ohashi[1], T. Nakamura[1], C.-Y. Chen,[1] R. Murdey[1]

[1]Institute for Chemical Research, Kyoto University, Gokasho, Uji, Kyoto 611-0011, Japan
[*]corresponding author: wakamiya@scl.kyoto-u.ac.jp

Abstract: Perovskite solar cells are emerging as a game-changer in photovoltaics, offering a path to highly efficient solar energy conversion.[1–3] Surface modification of perovskite layer is crucial to improve device performance and durability. In this talk, we will present recent progress on the development of charge collecting materials and surface modification with dipole strategy.

Tripodal Triazatruxene Derivative as a Face-On Oriented Hole-Collecting Monolayer for Efficient and Stable Inverted Perovskite Solar Cells[1]

Hole-collecting monolayers have drawn attention in perovskite solar cell research due to their ease of processing, high performance, and good durability. Since molecules in the hole-collecting monolayer are typically composed of functionalized π-conjugated structures, hole extraction is expected to be more efficient when the π-cores are oriented face-on with respect to the adjacent surfaces. However, strategies for reliably controlling the molecular orientation in monolayers remain elusive. In this work, multiple phosphonic acid anchoring groups were used to control the molecular orientation of a series of triazatruxene derivatives chemisorbed on a transparent conducting oxide electrode surface. Using infrared reflection absorption spectroscopy and metastable atom electron spectroscopy, we found that multipodal derivatives align face-on to the electrode surface, while the monopodal counterpart adopts a more tilted configuration. The face-on orientation was found to facilitate hole extraction, leading to inverted perovskite solar cells with enhanced stability and high-power conversion efficiencies up to 23.0%.[4]

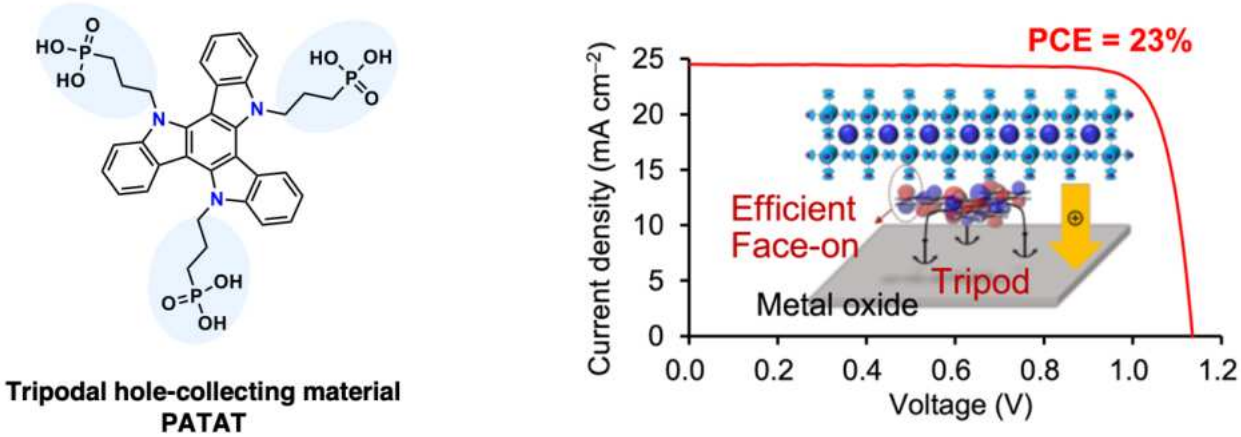


Fig. 1. Triazatruxene-based tripodal hole collecting monolayer for inverted perovskite solar cells.

Optimized Carrier Extraction at Interfaces for Efficient Perovskite Solar Cells[5–7]

Carrier extraction in mixed tin–lead perovskite solar cells is improved by modifying the top and bottom perovskite surfaces with ethylenediammonium diiodide and glycine hydrochloride, respectively. Trap densities in the perovskite layers are reduced as a result of surface passivation effects and an increase in film crystallinity.

In addition, the orientated aggregation of the ethylenediammonium and glycinium cations at the charge collection interfaces result in the formation of surface dipoles, which facilitate charge extraction. As a result, the treated mixed tin–lead perovskite solar cells showed improved performance, with a fill factor of 0.82 and a power conversion efficiency up to 23.6%. The unencapsulated device also shows improved stability under AM1.5G, retaining over 80% of the initial efficiency after 200 h continuous operation in inert atmosphere. Our strategy is also successfully applied to centimeter-scale devices, with efficiencies up to 21.0%.[5]

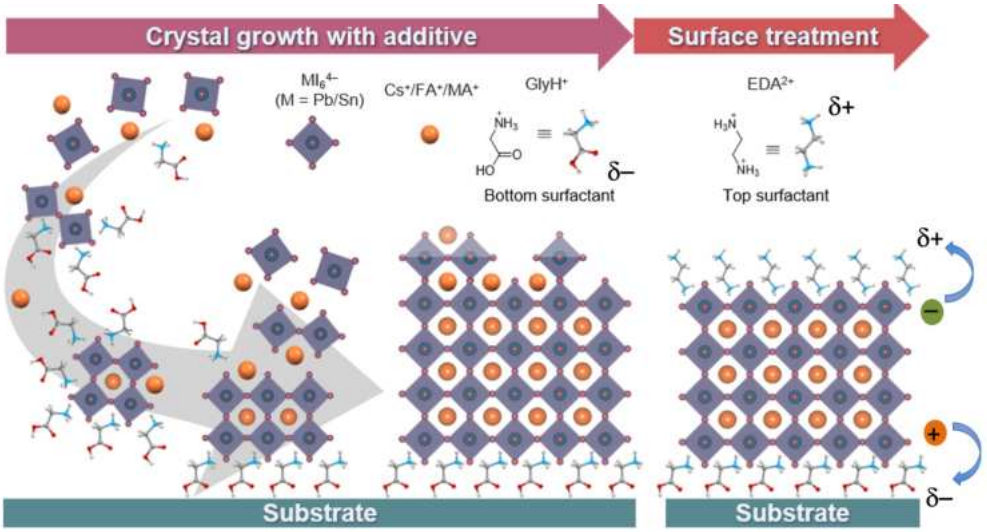


Fig. 2. Surface modification with dipole strategy: Perovskite films with top and bottom interface modification.

Acknowledgement

This work was partially supported by JST–MIRAI (JPMJMI22E2), JSPS KAKENHI Grant-in-Aid for Scientific Research (A) (JP21H04699), NEDO, International Collaborative Research Program of ICR, Kyoto University, and Grants for Integrated Research Consortium on Chemical Sciences, etc. We thank to all collaborators.

References

1. T. Nakamura, A. Wakamiya, et al. "Sn(IV)-free Tin Perovskite Films Realized by In Situ Sn(0) Nanoparticle Treatment of The Precuarsor Solution", *Nat. Commun.* **2020**, *11*, 3008.
2. S. Hu, J. A. Smikth, H. J. Snaith, A. Wakamiya, "Prospects for Tin-Containing Halide Perovskite Photovoltaics", *Precis. Chem.* **2023**, *1*, 69.
3. T. Nakamura, Y. Kondo, N. Ohashi, M. A. Truong, R. Murdey, A. Wakamiya, et al. "Materials Chemistry for Metal Halide Perovskite Photovoltaics", *Bull. Chem. Soc, Jpn.* **2024**, in press. (DOI: 10.1093/bulcsj/uoad025).
4. M. A. Truong, A. Wakamiya, et al. "Tripodal Triazatruxene Derivative as a Face-On Oriented Hole-Collecting Monolayer for Efficient and Stable Inverted Perovskite Solar Cells", *J. Am. Chem. Soc.* **2023**, *145*, 7528.
5. S. Hu, A. Wakamiya, et al. "Optimized Carrier Extraction at Interfaces for 23.6% Efficient Tin-Lead Perovskite Solar Cells", *Energy Environ. Sci.,* **2022**, *15*, 2096.
6. S. Hu, J. Pascual, A. Wakamiya, et al. "A Universal Surface Treatment for p-i-n Perovskite Solar Cells", *ACS Appl. Mater. Interfaces*, **2022**, *14*, 56290.
7. S. Hu, H. J. Snaith, A. Wakamiya, et al. "Synergistic Surface Modification of Tin-Lead Perovskite Solar Cells", *Adv. Mater.* **2023**, *35*, 2208320.

New Class of Semiconducting Organic-Inorganic Metal Halides for Photovoltaic Devices

Hyunjung Shin*

Department of Energy Science, Department of Future Energy Engineering, SKKU Institute of Energy Science and Engineering, Sungkyunkwan University, Suwon, Korea

*corresponding author: hshin@skku.edu

Abstract: Organic-inorganic hybrid metal halides are now emerging as new class of semiconductors. It shows "Perovskite" crystal structure and is used as a main light absorber in photovoltaic cells, known as 'Perovskite Solar Cell (PSC)'. The notable examples are $MAPbI_3$ (methyl ammonium lead triiodides) and $FAPbI_3$ (formamidinium lead triiodides). The PSC now shows a remarkable power conversion efficiency (PCE) of 26.1%. These halides are truly unique semiconducting materials showing excellent optoelectronic properties, even their preparation methods are simple like spin coatings of precursor solution with a low temperature annealing. Unlike monocrystalline Si, and GaAs, these halides contain lot of defects, which are potentially non-radiative recombination centers. Defect tolerating in these halides is now under debating and thus defect engineering is the key to increase further the PCE. In this talk, the unique semiconducting properties studied are summarized and understanding of the materials' structure-properties relationship will be discussed. Further, we examined the crystallization process of MACl, as higher concentration of MACl induces slower crystallization kinetics. Microscopic observations, such as electron back-scattered diffraction (EBSD), confocal photoluminescence (PL), time-resolved photoluminescence (TRPL) mapping, and conductive atomic force microscopy (C-AFM), were conducted to examine the optoelectronic properties of [001] preferentially oriented grains. Reduction in the non-radiative recombination, a longer lifetime of charge carriers and less photocurrent deviation between each grain induce higher short-circuit current density (J_{sc}) and fill factor (FF) in α-$FAPbI_3$ based PSCs with MACl40%.
It highlights the importance of crystallization kinetics resulting in desirable microstructures for device engineerin g.

References

1. Shin, H., et al., "Superhalogen Modulation: An Effective Approach for Minimizinng Light-Induced Halide Segregation in $MAPb(I_{0.7}Br_{0.3})_3$," J. Mater. Chem. A., Vol. 11, 19004–19016, 2023.
2. Shin, H., et al., "Aging of Perovskite Solar Cells: A Mini Review," Mater. Today Energy, Vol. 37, 101381, 2023.
3. Shin, H., et al., "Enhancing the Stability of Efficient Perovskite Solar Cells (PCE ~ 24.5%) by Suppression PbI_2 Inclusion Formation," Adv. Funct. Mater., Vol. 33, 2301213, 2023.
4. Shin, H., et al., "Kinetic-Controlled Crystallization of a-$FAPbI_3$ Inducing Preferred Crystallographic Orientation Enhances Photovoltaic Performance," Adv. Mater, 10, 2300798, 2023.

Orientation control of perovskites using asymmetric amines

Y. Takeoka[1*], H. Kobayashi[1], D. Hishida[1], Masahiro Yoshizawa-Fujita[1], and M. Rikukawa[1]

[1]Sophia University, Japan
[*]corresponding author: y-tabuch@sophia.ac.jp

Abstract: q-2D organic-inorganic perovskites are expected as solar cell materials due to their high stability. Because the orientation q-2D perovskites affets carrier transport properties, the orientation is important. In this study, we focused on the orientation control of q-2D perovskites prepared from asymmetric diamines and evaluated their solar cell performance.

Lead halide-based perovskite compounds have attracted significant attention since their initial application to photovoltaic devices by Miyasaka *et al*. in 2009.[1] As research into perovskite solar cells (PSCs) has progressed over the last several years, the power conversion efficiency (PCE) values of PSCs have increased from 3.8% to more than 25%, that reaches the level of practical application. Among the lead halide-based PSCs, three-dimensional (3D) perovskites have been mainly used. However, they are easily affected by moisture, oxygen, and heat, and are susceptible to degradation by water. To address this issue, two-dimensional (2D) perovskites have attracted much attention because of their excellent stability against moisture. Because 2D perovskites possess an organic ammonium layer that acts as an insulator and the $[PbX_6]^{4-}$ (X: halogen) layers are connected two-dimensionally, the diffusion of photo-generated carriers is limited. Therefore, quasi two-dimensional (q-2D) organic-inorganic perovskite compounds which are intermediate compounds of 2D and 3D perovskites show potential to solve the stability issue of PSCs. In solar cells, the direction of carrier transport is perpendicular to a substrate. However, q-2D perovskites have a strong tendency to orient parallel to a substrate and this trend renders the migration of transport carriers in the vertical direction difficult. As a result, the power generation performance of PSCs based on q-2D perovskites is significantly reduced. Our group has reported the orientation control of 2D and q-2D perovskites which has one or more inorganic sheets by changing organic ammoniums with various film preparation methods.[2-4] As a result of these considerations, although the verticality of the inorganic layer improved, it was not possible to achieve a completely single crystal orientation.

In this study, we focused on the structural orientation and improvement of crystallinity brought about by the asymmetry of diamine and aromatic ring-containing organic ammonium. We investigated the structure, optical properties, and crystal morphology of q-2D perovskites using asymmetric phenyleneammonium and its counterpart of asymmetric alkylammonium.

By introducing a rigid aromatic ring to the asymmetric diammonium, a q-2D perovskite compound with a controlled orientation of certain angle was obtained. It was suggested that carrier transport is possible because the inorganic layer forms a structure that is oriented out of plane with respect to the substrate. In addition, by changing the self-organization, a thin film containing many large-n phases was obtained, the band edge was red-shifted, and the crystallinity was improved. A q-2D perovskite compound using asymmetric phenylene diammonium was suggested to be a promising material for solar cells.

Acknowledgements

This work was supported by JST-ALCA-Next Program Grant Number JPMJAN23B2, Japan.

References

1. Kojima, A. Teshima, K. Shirai, Y. Miyasaka, T. Organometal Halide Perovskites as Visible-Light Sensitizers for Photovoltaic Cells", *J. Am. Chem. Soc*., Vol. 131, 6050, (2009).
2. Hamaguchi, R. Yoshizawa-Fujita, M. Miyasaka, T. Kunugita, H. Ema, K. Takeoka, Y. Rikukawa, M. "Formamidine and cesium-based quasi-two-dimensional perovskites as photovoltaic absorbers", *Chem.Commun*., Vol. 53, 4366, (2009).
3. Arai, E. Yoshizawa-Fujita, M. Takeoka, Y. Rikukawa, M. "Factors determining the vertical orientation of two-dimensional perovskites", *CrystEngComm*, Vol. 21, 2334 (2019).
4. Akiyoshi, M. Yoshizawa-Fujita, M. Takeoka, Y. Rikukawa, M. "Perpendicularly oriented 2D perovskite thin films prepared using the bar-coating method and DMSO additive", *Chem.Comm.*, Vol. 57, 3395 (2021).

Improving efficiency and stability of hybrid perovskite devices

Yeng Ming Lam[1*], Haixia Rao[1], Tze Chian Sum[2], Senyun Ye[2]

[1]School of Materials Science and Engineering, Nanyang Technological University, 50 Nanyang Avenue, Singapore 639798.

[2]Division of Physics and Applied Physics, School of Physical and Mathematical Sciences, Nanyang Technological University, 21 Nanyang Link, Singapore 637371

[*]corresponding author: ymlam@ntu.edu.sg

Abstract: Organic-inorganic hybrid perovskites have emerged in recent years as one of the most promising materials for solution-processed electronics and optoelectronics. We showed that through a full precursor technology option, it is possible to access a wider cation library for these capping layers.

Organic-inorganic hybrid perovskites have emerged in recent years as one of the most promising materials for solution-processed electronics and optoelectronics including solar cells, light-emitting diodes (LED) and field-effect transistors (FET). There is an active exploration of different organic molecules contribution to the materials behaviour and also the use of novel interfacial layer and their functions to improve the performance of the devices. The key to the successful implementation of any materials systems depends very much on the how facile is the methodology. In this presentation, two examples will be shown on how the understanding of the materials can lead to simple solution with good outcome. In solar cells application, there are two critical performance indicators – efficiency and stability. Two layers combination making up of three-dimensional (3D) perovskite capped with low-dimensional (LD) perovskites materials have shown be an effective strategy in resolving the compromise that we have to live with for hybrid perovskites – compromise between photovoltaic efficiency and operational stability. In the study, instead of the conventional LD capping layers containing Pb2+ or Sn2+, we showed that through a full precursor technology option, it is possible to access a wider cation library for these capping layers.[1] Through this method, high efficiency cells can be achieved. Hybrid perovskites also have shown to have great potential to be used as emitters with tunable emission, high color purity and good ease of fabrication. A lot of studies have so far been focused on three-dimensional (3D) perovskites, such as CH3NH3PbBr3 and CH3NH3PbI3 for green and infrared emission. The organic molecules used in these systems can be varied and it can give rise to different optical behaviour. I will also share some work that we have done with active cations which of energy levels that can be made use of to encourage the harvesting of triplets and this opens up a very interesting optoelectronic behavior[2,3].

References

1. Ye S., Rao H., Feng M., Xi L., Yen Z., Seng D.H.L., Xu Q., Boothroyd C., Chen B., Guo Y., Wang B., Salim T., Zhang Q., He H., Wang Y., Xiao X., Lam Y.M., and Sum T.C. Expanding the low-dimensional interface engineering toolbox for efficient perovskite solar cells. Nature Energy, 8, 3, 284-293, 2023.
2. Hu H., Zhao D., Gao Y., Qiao X., Salim T., Chen B., Chia E.E.M., Grimsdale A.C., and Lam Y.M. Harvesting Triplet Excitons in Lead-Halide Perovskites for Room Temperature Phosphorescence. Chemistry of Materials, 31, 7, 2597-2602, 2019.
3. Hu H., Meier F., Zhao D., Abe Y., Gao Y., Chen B., Salim T., Chia E.E.M., Qiao X., Deibel C., and Lam Y.M., Efficient Room-Temperature Phosphorescence from Organic-Inorganic Hybrid Perovskites by Molecular Engineering. Advanced Materials, 30, 36, 1707621, 2018.

Tailoring Charge Transport in Mixed-Valence Coordination Polymers for Emerging Molecular Devices

M. Freitag
Newcastle University, UK
*corresponding author: Marina.Freitag@newcastle.ac.uk

Abstract: Coordination polymers offer exceptional tunability and sustainability as charge transport materials for emerging technologies, including photovoltaics, batteries, and sensors. This comprehensive study elucidates their structure-function relationships, charge transport mechanisms, and applications, showcasing their potential to outperform conventional charge extracting materials. Tailoring mixed-valence copper polymers yielded high efficiencies and stability in hybrid solar cells.

The relentless pursuit of sustainable energy solutions has spurred the development of emerging technologies, including photovoltaics, batteries, and sensors. However, their widespread adoption has been hindered by the lack of efficient, stable, and tuneable charge transport materials. Coordination polymers (CPs), comprising metal centres bridged by organic or inorganic ligands, present an unprecedented opportunity to address this challenge. This comprehensive study delves into the intricate structure-function relationships governing charge transport in CPs and their applications in cutting-edge molecular devices.

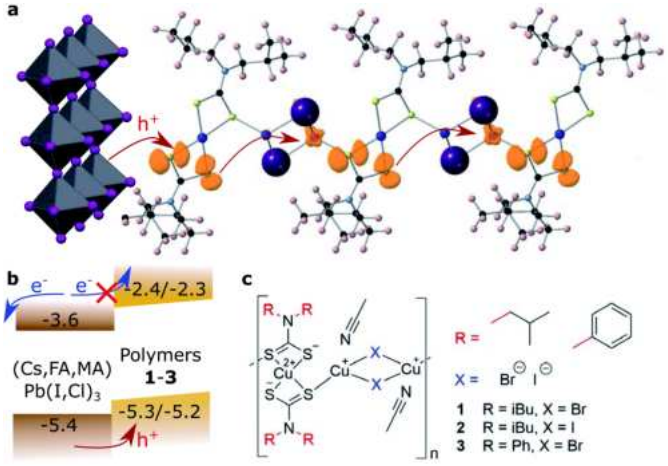


Figure 1 Copper coordination polymers as hole conducting materials. (a) Polarons hop along a computational model of a coordination polymer chain. (b) Energetic position of the frontier orbitals in relation to the halide perovskite valence and conduction band edges. (c) General structure of the coordination polymers presented in this work

Through a synergistic approach combining experimental and theoretical methods, the charge transport mechanism in a series of mixed-valence $Cu^{(II/I)}$ coordination polymers is elucidated. Electrochemical analysis, Raman spectroscopy, and X-ray diffraction techniques are employed to unravel the electronic and structural properties of these materials. Density functional theory calculations reveal that the bridging halide ligands play a pivotal role in modulating the electronic conductivity. The iodide-bridged polymer exhibits superior transport characteristics, with a conductivity of 1 mS cm^-1 and a hole mobility of 5.8×10^{-4} cm^2 $(V\ s)^{-1}$ at room

temperature, attributed to the enhanced orbital conjugation between copper ions facilitated by the more polarizable iodide anions.

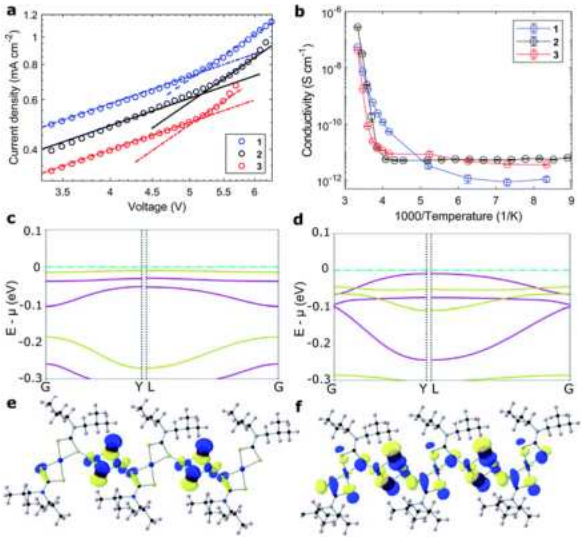


Figure 2 Charge transport in the coordination polymers. (a) Space-charge limited current hole mobility and (b) temperature-dependent conductivity of coordination polymers 1–3. (c and d) Band structure around the valence band of polymers 1 and 2 along high symmetry paths. (e and f) Orbital projections of the top of the valence band for 1 and 2.

The exceptional charge transport properties of CPs are harnessed in the development of perovskite solar cells. Picosecond photoluminescence spectroscopy confirms the rapid charge extraction from halide perovskite films by the CP hole-conducting layers. Remarkably, carbon-based perovskite solar cells incorporating the iodide-bridged CP achieve high power conversion efficiency with carbon electrodes outperforming state-of-the-art organic hole conductors and exhibiting improved long-term stability, retaining stability over months.

This comprehensive study underscores the pivotal role of coordination polymers as sustainable, high-performing charge transport materials for emerging molecular devices. By elucidating the structure-function relationships and charge transport mechanisms, researchers can harness the unique advantages of CPs, such as their exceptional tunability through molecular design. The ability to fine-tune the electrical and structural properties paves the way for the development of environmentally friendly and efficient technologies, addressing the pressing need for sustainable energy solutions.

References

1. (Chen, C.-T.; Suslick, K. S. One-Dimensional Coordination Polymers: Applications to Material Science. *Coord Chem Rev* **1993**, *128* (1), 293–322.
2. Michaels, H.; Golomb, M. J.; Kim, B.; Edvinsson, T.; Cucinotta, F.; Waddell, P. G.; Probert, M.; Konezny, S. J.; Boschloo, G.; Walsh, A.; Freitag, M. Copper Coordination Polymers with Selective Hole Conductivity. *J Mater Chem A Mater* **2022**.
3. Morritt, G. H.; Michaels, H.; Freitag, M. Coordination Polymers for Emerging Molecular Devices. *Chemical Physics*

Reviews **2022**, *3* (1), 011306.

Plasmonics: Fundamentals and Applications

Plasmon-based chiroptical sensing

S. Liu, R.-Y. Wang *

School of Physics, Beijing Institute of Technology, Beijing 100081, China.
*corresponding author: wangry@bit.edu.cn

Abstract: In this talk, we report a chiral plasmonic nanosensor capable of transforming molecularly enantioselective recognition into asymmetrically amplified plasmonic circular dichroism (CD) readouts. This chiral nanosensor enables the enantiospecific recognition and determination of enantiomeric excess of amino acid molecules.

Plasmonic nanosensors with strong chiroptical activities can provide a novel approach for analyzing molecular chirality. In particular, plasmonic CD spectral readouts can greatly enhance the detection sensitivity for trace amounts of biomolecules that cannot be detected using ordinary electronic CD techniques [1,2]. In this presentation, we introduce a new scheme for plasmon-based chiroptical sensing in the solution phase to detect and characterize molecular chirality at nanoscale interfaces. Unlike previous studies [2,3] that focused on plasmonic chirality induced by a single molecularly chiral source, our approach involves a molecules-to-nanoparticles chirality transfer system with two molecularly chiral inputs. In this chiral sensing scheme (Figure 1), gold nanorods arranged in a chiral manner serve as plasmonic nanotransducers to convert enantioselective recognition between two molecular inputs into asymmetrically amplified plasmonic CD readouts. The utilization of plasmonic CD-based chiral probes enables enantiospecific recognition and quantitative determination of the enantiomeric excess of amino acid molecules [4]. This chiroptical method exhibits advantages such as easy processing and cost-effectiveness, which hold great promise for high-throughput chiral analyses in fields such as biology, stereochemistry, and pharmaceutics.

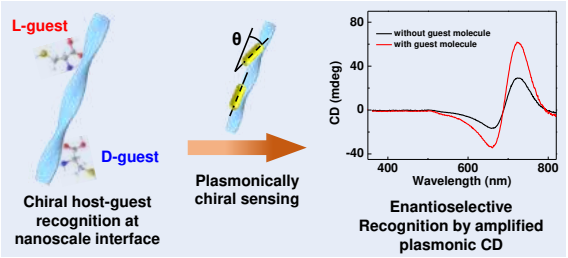


Figure 1. plasmon-based chiroptical sensing scheme.

References

1. Ma, W.; Kuang, H.; Xu, L.; Ding, L.; Xu, C.; Wang, L.; Kotov, N. A. Attomolar DNA Detection with Chiral Nanorod Assemblies. Nat. Commun. 2013, 4, 2689.
2. Kumar, J.; Eraña, H.; López-Martínez, E.; Claes, N.; Martín, V. F.; Solís, D. M.; Bals, S.; Cortajarena, A. L.; Castilla, J.; Liz-Marzán, L. M. Detection of Amyloid Fibrils in Parkinson's Disease Using Plasmonic Chirality. Proc. Natl. Acad. Sci. U. S. A. 2018, 115, 3225-3230.
3. Hao, C.; Xu, L.; Kuang, H.; Xu, C. Artificial Chiral Probes and Bioapplications. Adv. Mater. 2020, 32, 1802075.
4. Liu, S. L.; Ma, X. Y.; Song, M.; Ji, C. Y.; Song, J.; Ji, Y. L.; Ma, S. J.; Jiang, J.; Wu, X. C.; Li, J. F.; Liu, M. H.; Wang,

R. Y. Plasmonic Nanosensors with Extraordinary Sensitivity to Molecularly Enantioselective Recognition at Nanoscale Interfaces, ACS Nano 2021, 15, 19535−19545.

Multifunctional Dynamic MEMS-based Optical Metasurfaces

C. Meng[1*], P. C. V. Thrane[1, 2], Y. D. Deng, F. Ding[1], and S. I. Bozhevonyi[1]

[1]Centre for Nano Optics, University of Southern Denmark, Campusvej 55, Odense DK-5230, Denmark
[2]SINTEF Microsystems and Nanotechnology, Gaustadalleen 23C, 0737 Oslo, Norway

[*]corresponding author: chao@mci.sdu.dk

Abstract: Recent advances in piezoelectric MEMS enabled multifunctional optical metasurfaces (OMSs) for dynamic phase and polarization control are presented. Moreover, theoretical investigations on the MEMS-OMS configuration show that control over scattering phase singularities in the parameter space determined by the MEMS-OMS separations and meta-atom sizes with the OMS, underpins these developments.

Main:

Dynamic optical metasurfaces (OMS) stand at the forefront of advancing intelligent and adaptable optical systems and networks due to their ultra-compact design and reconfigurable responses[1]. The evolution of dynamic OMS has significantly benefited from the incorporation of active materials such as 2D materials, phase-change materials (PCMs), liquid crystals (LCs) and others[2]. However, challenges persist in achieving an optimal balance between speed and efficiency. For instance, while dynamic OMS using 2D materials offer rapid response times, they tend to have limited modulation strength. Conversely, dynamic OMS that integrate PCMs and LCs can attain high modulation strength but typically suffer from slower response times. Additionally, LC-based dynamic OMS encounter issues related to polarization dependence, presenting a critical area for further improvement.

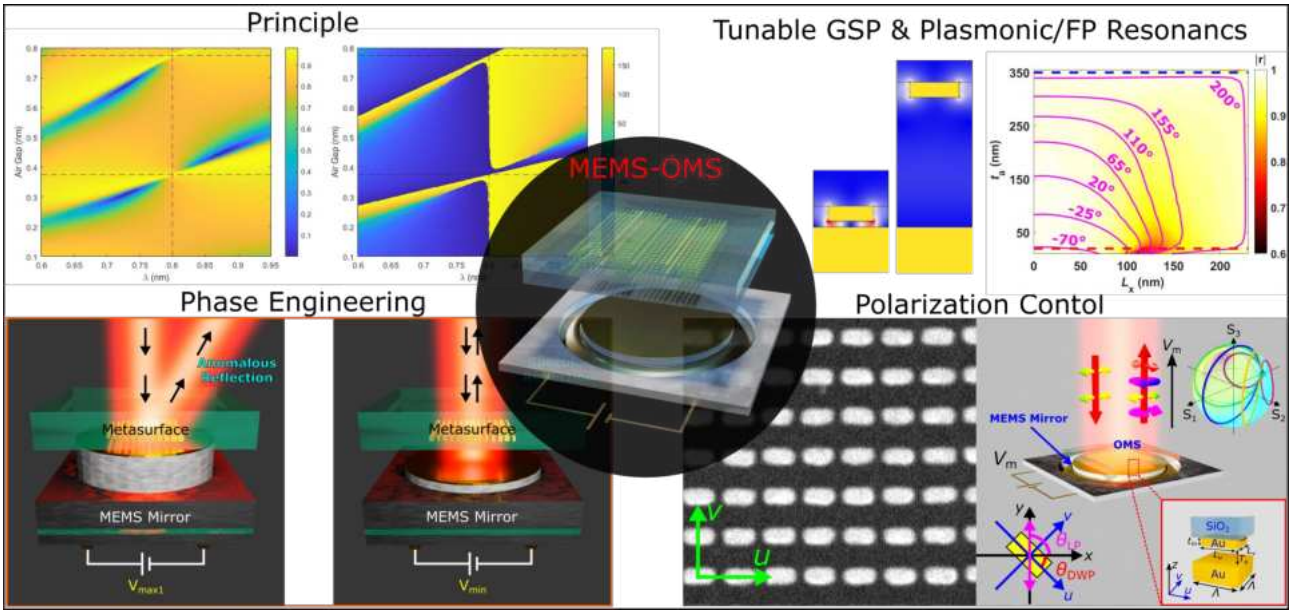


Fig. 1 MEMS-OMS platform: principles and implementations.

In a recent breakthrough, we have developed a MEMS-OMS platform that synergizes a piezoelectric MEMS mirror with a plasmonic OMS. This innovative combination has led to a ultracompact system capable of dynamically manipulating reflection phase and polarization with high efficiency, substantial modulation strength, and rapid response, as showcased in our demonstrations (Fig.1). We have successfully demonstrated a variety of

dynamic optical functionalities, such as blazed gratings[3,4], focusing lenses[3], waveplates[5] as well as both linear and chiral polarizer[6,7].

Our investigation into the mechanism behind this dynamic response has unveiled that it stems from the controllable and tunable scattering phase singularities within a specific parameter space. This parameter space is defined by the MEMS-OMS separation and the dimensions of the meta-atoms. We have explored both tunable gap-surface-plasmon (GSP) resonances and hybrid plasmonic/Fabry-Pérot resonances to design the phase singularities within this parameter space.

To summarize, we will discuss the future outlooks for this platform, highlighting its potential to revolutionize the field of dynamic meta-optics with its innovative approach to achieving rapid, efficient, and strong modulation capabilities.

Acknowledgements.
The authors acknowledge Villum Fonden (37372, 50343, award in Technical and Natural Sciences 2019); Danmarks Frie Forskningsfond (1134-00010B), Research Council of Norway (Project number 323322), China Scholarship Council (202108330079).

References

(1) Gu, T.; Kim, H. J.; Rivero-Baleine, C.; Hu, J. Reconfigurable Metasurfaces towards Commercial Success. *Nat. Photon.* **2023**, *17* (1), 48–58.

(2) Abdelraouf, O. A. M.; Wang, Z.; Liu, H.; Dong, Z.; Wang, Q.; Ye, M.; Wang, X. R.; Wang, Q. J.; Liu, H. Recent Advances in Tunable Metasurfaces: Materials, Design, and Applications. *ACS Nano* **2022**, *16* (9), 13339–13369.

(3) Meng, C.; Thrane, P. C. V.; Ding, F.; Gjessing, J.; Thomaschewski, M.; Wu, C.; Dirdal, C.; Bozhevolnyi, S. I. Dynamic Piezoelectric MEMS-Based Optical Metasurfaces. *Sci. Adv.* **2021**, *7* (26), eabg5639.

(4) Thrane, P. C. V.; Meng, C.; Ding, F.; Bozhevolnyi, S. I. MEMS Tunable Metasurfaces Based on Gap Plasmon or Fabry-Pérot Resonances. *Nano Lett.* **2022**, *22*, 6951–6957.

(5) Meng, C.; Thrane, P. C. V.; Ding, F.; Bozhevolnyi, S. I. Full-Range Birefringence Control with Piezoelectric MEMS-Based Metasurfaces. *Nat. Commun.* **2022**, *13* (1), 2071.

(6) Ding, F.; Deng, Y.; Meng, C.; Thrane, P. C. V.; Bozhevolnyi, S. I. Electrically Tunable Topological Phase Transition in Non-Hermitian Optical MEMS Metasurfaces. *Sci. Adv.* **2024**, *10* (5), eadl4661.

(7) Deng, Y.; Meng, C.; Thrane, P. C. V.; Sande, S. im; Bozhevolnyi, S. I.; Ding, F. MEMS-Integrated Metasurfaces for Dynamic Linear Polarizers. *Opitca* **2024**, *11* (3), 3–9.

Chiroptics of hybrid nanostructures: Strong coupling effect and interference effect

Wei Zhang[1*]

[1] Institute of Applied Physics and Computational Mathematics, Beijing 100088, China
[*]corresponding author: zhang_wei@iapcm.ac.cn

Abstract: We study chiroptical properties of hybrid nanostructures, paying attention to the strong coupling effect and interference effect. Strong plasmon-exciton coupling leads to double Rabi splitting in the circular dichroism spectroscopy. Mode hybridization leads to chirality transfer between bright modes and dark modes and chirality selective Rabi splitting/Fano effect.

Chiroptics plays an important role in understanding light-matter interaction and has various applications [1-6]. In this talk, I will present our recent studies on the chiroptical properties of hybrid nanostructures made of (chiral) molecules and metallic/dielectric nanoparticles, paying attention to the strong coupling dynamics and interference effect.

We explore the chiroptical response of the hybrid systems with the chirality from exciton (of molecules) or from the plasmon (of nanoparticles). The strong coupling between and plasmon and exciton leads to avoided crossing and Rabi splitting in the circular dichroism (CD) spectroscopy. We propose and justify a new criterion of strong plasmon−exciton interaction: the mode splitting in the CD spectra (at zero detuning) is larger than half of that in the extinction spectra.

We develop a plexcitonic Born−Kuhn model to take into account both effects from chirality and strong coupling dynamics of the chiral hybrid nanostructures made of nanorods and molecules. As a consequence of strong interaction between plasmons and excitons, double Rabi splittings and an anti-crossing phenomenon appear in the CD spectroscopy. The character of dual plexciton (symmetric and anti-symmetric plexciton, the hybridized states resulting from the strong coupling between plasmons and excitons) and associated chiroptical properties have been demonstrated. The interplay between mirror symmetry breaking and plasmon−plasmon/plasmon−exciton interaction leads to an optimal configuration with the maximal chiroptical response. Moreover, chirality (of incident light) selective excitation of plexcitonic modes has been achieved by structural design.

We investigate the modulation of chiroptics of metasurface with unit cell of corner-stacked nanorods and stacked nanorings, paying attention to the bright-dark-mode coupling effects and interference effect. With the help of phase modulation and mode hybridization, we can realize chirality transfer from bright modes to dark modes, which results in chirality-selective transparency due to chirality-selective excitation of binding/antibonding dark modes. Moreover, one can switch between different coupling regimes with a distinct physical effect (Fano effect vs Rabi splitting) by changing only the chirality of the incident field without varying the structure of the metasurface. Based on the mechanisms of chirality transfer and mode hybridization, our designed metasurface has achieved chirality-selective transparent window with tunable central frequency and bandwidth, which provides insight and guidance for the optoelectronic device design.

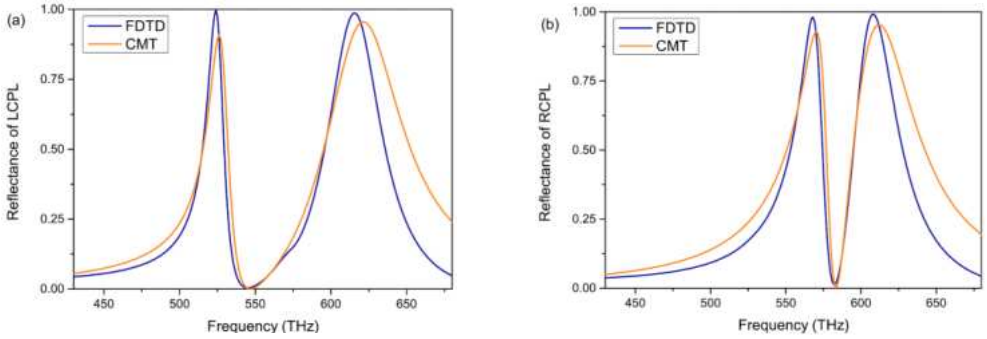


Figure 1. Chirality selective Rabi splitting (a, for left circularly polarized incident light) and Fano effect (b, for right circularly polarized incident light).

References

1. Cai, J. M.[#], Zhang, W.[#], et al., "Polarization-sensitive optoionic membranes from chiral plasmonic nanoparticles," Nature Nanotechnology, Vol. 17, 408–416, 2022.
2. Chen, Y., Zheng, J., Zhang, L., Li, S., Chen, Y., Ka Kit Chui, K. K., Zhang, W.*, Shao, L., and Wang, J.*, "Inversion of the Chiroptical Responses of Chiral Gold Nanoparticles with a Gold Film," ACS Nano, Vol. 18, No. 1, 383–394, 2024.
3. Zhang, L., Chen, Y., Zheng, J., Lewis, G. R., Xia, X., Ringe, E., Zhang, W.*, and Wang, J.*, "Chiral Gold Nanorods with Five-Fold Rotational Symmetry and Orientation-Dependent Chiroptical Properties of Their Monomers and Dimers," Angew. Chem. Int. Ed., Vol. 62, No. 52, e202312615, 2024.
4. Zhao, S., Gao, L.*, and Zhang, W.*, "Chirality-selective electromagnetically induced transparency in a dielectric metasurface based on chirality transfer between bright and dark modes," Appl. Phys. Lett., Vol. 123, No. 15, 151701, 2023.
5. Wu, F., Li, N., Ding B.*, and Zhang, W.*, "Plasmon–Exciton Strong Coupling Effects of the Chiral Hybrid Nanostructures Based on the Plexcitonic Born–Kuhn Model," ACS Photonics, Vol. 10, No. 5, 1256–1366, 2023.
6. Wu, F., Guo, J., Huang, Y., Liang, K., Jin, L., Li, J., Deng, X., Jiao, R., Liu, Y., Zhang, J.*, Zhang, W.*, and Yu, L.*, "Plexcitonic Optical Chirality: Strong Exciton-Plasmon Coupling in a Chiral J-Aggregate-Metal Nanoparticle Complex," ACS Nano, Vol. 15, No. 2, 2292–2300, 2021.

On-chip electrical detection of plasmon in the top-down fabricated plasmonic waveguides on SOI substrate

Xiangqian Li[1], Weikang Liu[1], Huijie Wang[1], Li Chen[5], Zhiqiang Guan[1,2,3,4,*], Hongxing Xu[1,3,4,*]

[1] School of Physics and Technology, Center for Nanoscience and Nanotechnology, and Key Laboratory of Artificial Micro- and Nano-structures of Ministry of Education, Wuhan University, Wuhan 430072, China

[2] Hubei Luojia Laboratories, Wuhan 430079, China

[3] School of Microelectronics, Wuhan University, Wuhan 430072, China

[4] Wuhan Institute of Quantum Technology, Wuhan 430206, China

[5] Material Science and Engineering, University of California, San Diego, 9500 Gilman Drive, La Jolla, California 92093-0407, USA

[*]corresponding author: Zhiqiang Guan: zhiqiang.guan@whu.edu.cn; Hongxing Xu: hxxu@whu.edu.cn

Abstract: On-chip plasmon detection is highly demanding in the plasmonic-integrated circuits. We demonstrated an on-chip plasmonic detector by placing an externally biased silicon strip at the end of the top-down fabricated gold plasmonic waveguides. The polarization and wavelength-dependent photocurrent confirm plasmonic detection under optimized near-field coupling geometry.

Owing to the advantage of small size and fast speed, plasmonic devices are promising to integrate with microelectronic chips for high-performance hybrid optoelectronic circuits. Despite the on-chip plasmon detector demonstration on chemically synthesized metallic nanowires [1] and metallic film [2], the on-chip plasmon detector remains to be explored for the top-down fabricated metallic plasmonic waveguides. Here, we demonstrated an on-chip plasmon detector solution for this purpose. The gold strip and silicon strip are top-down fabricated on the silicon-on-insulator substrate. The direct energy transfer from plasmons to electrons is achieved by optimized near-field coupling between the plasmon waveguide and silicon nanostrip. The detection is accomplished by converting the plasmons into a photocurrent signal. We confirmed the detection of plasmons through polarization and wavelength dependence of the photocurrent. Periodic oscillations in the wavelength-dependent photocurrent are attributed to the characteristic Fabry-Perot resonance in the plasmonic waveguide. According to the simulation results, up to 70% of the plasmonic energy could be absorbed in the silicon nanostrips by optimizing the thickness, width, and gap between the gold strip end and the silicon strip. Our design provides a promising on-chip plasmonic detector solution for plasmonic photocircuits.

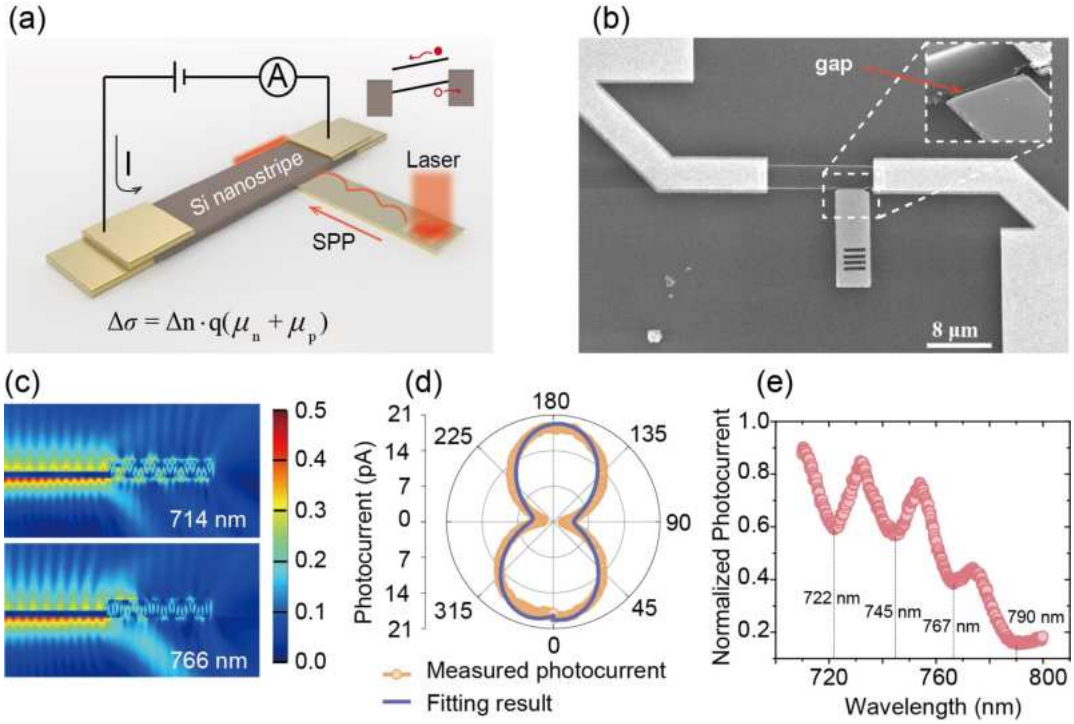


Figure 1. (a) Schematic diagram of the on-chip plasmon detector. The carriers are photo-generated through plasmon coupling into a Si strip and detected as photocurrents under external bias. (b) The SEM image of the prepared sample. It is composed of a Si strip and an Au strip. The inset showed the gap size in the coupling structure. (c) The electric field distribution in the coupling structure was calculated using the FDTD simulation for 714 nm (matching condition) and 766 nm wavelength laser(non-matching condition) excitation. (d) Measured polarization-dependent photocurrent. The angle θ was the included angle between incident laser polarization and the Au strip direction. (e) Measured wavelength-dependent photocurrent. A Fabry-Perot resonance is observed with a 23 nm oscillation period.

Acknowledgments: The work is supported by the National Key R&D Program of China (Grant No. 2021YFA1401100), the National Natural Science Foundation of China (No. 12174293), the Fundamental Research Funds for the Central Universities (No. 2042022kf0047), and the Special Fund of Hubei Luojia Laboratory. We acknowledge the nanofabrication assistance from the Center for Nanoscience and Nanotechnology at Wuhan University.

References

1. Abram L. Falk, Frank H. L. Koppens and Chun L. Yu, et al. “Near-field electrical detection of optical plasmons and single-plasmon sources.” Nat. Phys. Vol. 5, No. 7, 475-479, 2009.
2. Xiaobo He, Huatian Hu and Zhenyu Yang, et al., “On-Chip Detection of Multiwavelength Surface Plasmon Polaritons Based on Plasmonic Demultiplexers.” ACS Photonics, Vol. 9, No. 2, 391-397, 2022.

Dynamic plasmonics with structured alkali metals

Jie Liang[1], Yan Jin[1], Jia Zhu[1] and Lin Zhou[1*]

[1]College of Engineering and Applied Sciences, Nanjing University, China
[*]corresponding author: linzhou@nju.edu.cn

Abstract: Dynamic plasmonics has long been regarded as one of the most crucial branches for nanophotonics and integrated optics, which is urgent for active subwavelength optical devices. This report will present the recent advancements on alkali metals based dynamic plasmonics, from the fundamental optical properties to the potential applications.

Alkali metals, with their simple electronic structure, low free carrier density, and weak interband optical transition, are promising plasmonic materials expected to exhibit lower optical damping rates than conventional noble metals. Additionally, their potential as negative electrode materials in high-capacity, high-energy-density batteries offers a natural platform for dynamic plasmonics control.

I will first briefly present the basis of the electric-field driven microstructure transformation of lithium metals by employing a lithium metal battery platform. Then two kinds of application devices are explored. On the one hand, we try to utilize the real-time plasmonic signals to identify the morphology of lithium metals on the electrodes, which can serve as an in-operando monitoring technique for the lithium metal battery. On the other hand, we have developed the electric-field driven dynamic display through the reconfigurable plasmonic color of lithium particles.

A notable study involves in situ monitoring of lithium metal batteries. There's a pressing need for in situ, nondestructive techniques to monitor and control lithium metal morphology, crucial for rejuvenating lithium metal batteries. Leveraging lithium plasmonics, we devised an in situ monitoring platform (Figure 1) to study lithium deposition across various conditions and electrolytes. This technology, correlating evolving lithium morphologies with in situ optical spectra, offers an efficient means to investigate lithium morphology during electrochemical processes, accelerating electrolyte design and alkali metal-based energy storage system development.

Another most representative example, the electric-driven dynamic plasmonics for self-powered display, is shown in Figure 2. It is well known that, display and power supply have been two essential and independent cornerstones of modern electronics. A low power or even self-powered display devices are highly desired but rather challenging thus far. Our recent work reported a lithium plasmon based low-powered dynamic color display with inherited dual functionalities, the plasmonic display and energy recycling unit (see Figure 2a), through electric-driven transformation of nanostructured lithium metals. In such an intriguing operation configuration, each display pixel can work as a micro-battery cell and most excitingly, each micro-pixel (micro-battery) can be powered by its adjacent counterpart, making the manipulation of dual functionalities (information and energy) more flexible (Figure 2b).

We acknowledge the micro-fabrication center of National Laboratory of Solid State Microstructures (NLSSM) for technique supports, and these research works are supported by the National Key Research and Development Program of China (Nos. 2022YFA1404300, 2021YFA1400700); the National Natural Science Foundation of China (Nos. 12022403, 62375123) and the Excellent Research Program of Nanjing University (ZYJH005).

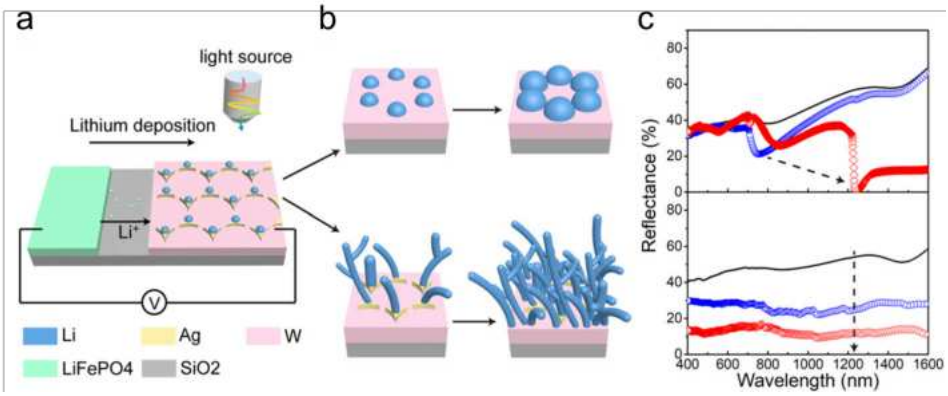


Figure 1. In operando plasmonic monitoring of lithium morphological evolution in a battery. (a) Schematic of in operando monitoring device. (b) Two pathways of lithium morphological evolution: growth of periodic lithium particle arrays (Upper) and formation of random lithium dendrites (Lower). (c) corresponding simulated reflectance spectra.

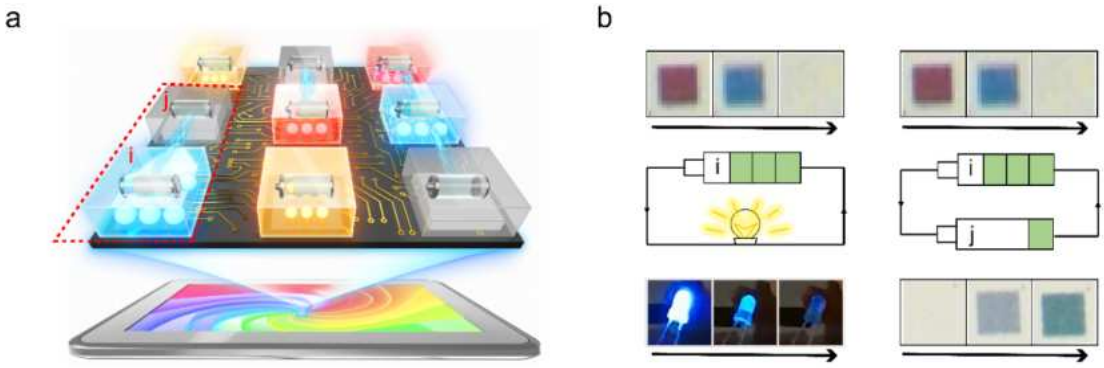


Figure 2. Low-powered dynamic plasmonic color display. (a) The operation schematic of the low-powered dynamic plasmonic color display. (b) The dual functionalities of the power supplier and information display of the device.

References

1. Jie Liang, Yan Jin, Huiling Yu, Xinjie Chen, Lin Zhou*, Pengcheng Huo, Ye Zhang, Haiyang Ma, Yi Jiang, Bin Zhu, Ting Xu, Hui Liu, Shining Zhu, Jia Zhu*. Lithium-plasmon-based low-powered dynamic color display, ***National Science Review*** nwac120, (2022)
2. Yan Jin, Jie Liang, Shan Wu, Ye Zhang, Lin Zhou*, Qianjin Wang, Hui Liu, and Jia Zhu*, Electrical Dynamic Switching of Magnetic Plasmon Resonance Based on Selective Lithium Deposition, ***Advanced Materials*** 32, 2000058 (2020)
3. Yan Jin, Lin Zhou*, Jianyu Yu, Jie Liang, Huigang Zhang, Wenshan Cai, Shining Zhu, Jia Zhu*, "In operando plasmonic monitoring of electrochemical evolution of lithium metal", ***PNAS*** 115, 11168-11173 (2018)
4. Yan Jin, Lin Zhou*, Jie Liang, Jia Zhu*, Electrochemical driven dynamic plasmonics, ***Advanced Photonics*** 3, 044002 (2021)

Nanometer-Scale Spatial and Spectral Mapping of Exciton Polaritons in Structured Plasmonic Cavities

David J. Masiello[1]

[1]University of Washington, Seattle, WA, USA
*corresponding author: masiello@uw.edu

Abstract: Exciton polaritons (EPs) are ubiquitous light-matter excitations under intense investigation as test beds of fundamental physics and as components for all-optical computing. Owing to their unique attributes and facile experimental tunability, EPs potentially enable strong nonlinearities, condensation, and superfluidity at room temperature. However, the diffraction limit of light and broad momentum content of fast electron probes preclude the characterization of EPs in nanoscale structured cavities exhibiting energy-momentum dispersion. Through an innovative combination of electron beam and optical probes, I will show theoretically that these limitations can be overcome to measure EPs in periodic nanophotonic cavities at their natural energy, momentum, and length scales via lattice electron energy gain spectroscopy. With the combined high momentum resolution of light and nanoscale spatial resolution of free-space focused electron beams, lattice electron energy gain spectroscopy can expose deeply subwavelength EP features using currently available monochromated, aberration-corrected scanning transmission electron microscopes (STEMs). Time permitting, I will also discuss the addition of polarization structure to the STEM electron probe and demonstrate theoretically how this degree of freedom can be harnessed to characterize the 3D polarization-resolved response field and local chirality of an optically excited target with nanoscale spatial resolution.

Alongside the recent proliferation of quantum materials comes the companion need to develop new measurement techniques to characterize these materials on their natural energy, length, momentum, and polarization scales. While optical methods offer unparalleled momentum and energy resolution, diffraction limits the achievable spatial resolution to hundreds of nanometers in the visible spectrum. Modern monochromated and aberration-corrected scanning transmission electron microscopes (STEMs), on the other hand, offer nanometer spatial resolution and $5-10$ meV energy resolution with a broadband spectrum spanning from vibrational to core excitations. This talk will discuss new STEM/TEM observables designed to map nanophotonic structures as well as 2D materials with simultaneously high energy, momentum, space, and polarization resolution.

All work was supported by the U.S. Department of Energy (DOE), Office of Science, Office of Basic Energy Sciences (BES), Materials Sciences and Engineering Division under award no. DOE BES DE-SC0022921.

References

1. Marc R. Bourgeois, Elliot K. Beutler, Siamak Khorasani, Nicole Panek, and David J. Masiello, Nanometer-Scale Spatial and Spectral Mapping of Exciton Polaritons in Structured Plasmonic Cavities, Physical Review Letters 128, 197401 (2022)
2. Marc R. Bourgeois, Austin G. Nixon, Matthieu Chalifour, Elliot K. Beutler, and David J. Masiello, Polarization-Resolved Electron Energy Gain Nanospectroscopy With Phase-Structured Electron Beams, Nano Letters 22, 7158–7165 (2022)
3. Marc R. Bourgeois, Austin G. Nixon, Matthieu Chalifour, and David J. Masiello, Optical Polarization Analogs in Inelastic Free Electron Scattering, Science Advances 9, eadj6038 (2023)
4. Andrew W. Rossi, Marc R. Bourgeois, Caleb Walton, and David J. Masiello, Probing the Polarization of Low-Energy Excitations in 2D Materials from Atomic Crystals to Nanophotonic Arrays using Momentum-Resolved Electron Energy Loss Spectroscopy, arXiv:2402.04481
5. Austin G. Nixon, Matthieu Chalifour, Marc R. Bourgeois, Michael Sanchez, and David J. Masiello, Inelastic scattering of transversely structured free electrons from nanophotonic targets: Theory and computation, arXiv:2312.08513

Photoluminescence modulation of 2D semiconductors by individual plasmonic metal nanocrystals

Lei Shao[1*]

[1]State Key Laboratory of Optoelectronic Materials and Technologies, Guangdong Province Key Laboratory of Display Materials and Technologies, School of Electronics and Information Technology, Sun Yat-sen University, Guangzhou 510275, China

[*]corresponding author: shaolei5@mail.sysu.edu.cn

Abstract: Integrating plasmonic nanostructure with 2D semiconductor materials has great potential in developing compact, high-performance photonic devices and nanoscale optoelectronic devices. In this presentation, we will introduce our recent work of employing individual plasmonic noble metal nanocrystals to integrated with 2D WS_2 and modulate the photoluminescence properties of the latter.

Two-dimensional transition-metal dichalcogenides exhibit rich excitonic properties. It is of great interest to achieve the modulation of the 2D semiconductor emission properties with spatial, spectral, polarization, and direction control. Plasmonic nanostructures can confine light to the nanoscale or even atomic scale and at the same time work as optical antennas to control light. Integrating plasmonic nanostructure with 2D semiconductor materials therefore has great potential in developing compact, high-performance photonic devices and nanoscale optoelectronic devices. In this presentation, we will introduce our recent work of employing individual plasmonic noble metal nanocrystals to integrated with 2D WS_2 and modulate the photoluminescence properties of the latter. We will first demonstrate the use of Au nanodisks and nanorods in generating and room-temperature detecting localized excitons of monolayer WS_2 with defined spatial confinement and an energy shift up to 200 meV[1]. We will then present the emission polarization and direction control of WS_2 monolayer excitons by individual plasmonic nanocrystals[1–3]. Besides the photoluminescence modulation of monolayer excitons, the plasmonic nanocrystals can form high-quality Fabry–Pérot resonators with integrating with WS_2 flakes and a Au mirror[4], providing a platform for controlling the WS_2 indirect band gap emissions.

Acknowledgements: L.S. acknowledges support from the National Natural Science Foundation of China (62375290), the Pearl River Talent Recruitment Program (2019QN01C216), the Shenzhen Science and Technology Program (JCYJ20210324140805014), the Sun Yat-Sen University research fund (Grant No. 23PTPY03), and the Science and Technology Planning Project of Guangdong Province (2023B1212060025).[1234]

References

1. Li, S., Chui, K. K., Shen, F., Huang, H., Wen, S., Yam, C., Shao, L., Xu, J. and Wang, J. Generation and Detection of Strain-Localized Excitons in WS_2 Monolayer by Plasmonic Metal Nanocrystals. *ACS Nano* **2022**, *16*, 10647–10656.
2. Wang, J., Zheng, J., Li, K. H., Wang, J., Lin, H.-Q. and Shao, L. Excitation of Chiral Cavity Plasmon Resonances in Film-coupled Chiral Au Nanoparticles. *Adv. Opt. Mater.* **2023**, *11*, 2202865.
3. Li, S., Ai, R., Chui, K. K., Fang, Y., Lai, Y., Zhuo, X., Shao, L., Wang, J. and Lin, H.-Q. Routing the Exciton Emissions of WS_2 Monolayer with the High-Order Plasmon Modes of Ag Nanorods. *Nano Lett.* **2023**, *23*, 4183–4190.
4. Huang, H., Wang, H., Li, S., Jiang, J., Liu, Y., Cai, M., Shao, L., Chen, H. and Wang, J. WS_2–Flake-Sandwiched,

Au-Nanodisk-Enabled High-Quality Fabry–Pérot Nanoresonators for Photoluminescence Modulation. *ACS Nano* **2022**, *16*, 14874–14884.

Plasmonic-assisted 2D hybrid broadband photodetectors

I. Goykhman

[1]Institute of Applied Physics, The Faculty of Science and The Center for Nanoscience and Nanotechnology, The Hebrew University of Jerusalem, Jerusalem 91904, Israel.

[*]corresponding author: ilya.goykhman@mail.huji.ac.il

Abstract: The rich portfolio of 2D materials and favorable heterogeneous integration with silicon technology set up new horizons for integrated photonics and optoelectronics. In this talk, I will discuss the advanced plasmonic-assisted 2D hybrid broadband photodetectors for free-space and guided mode configurations. I will present key aspects of material properties, device physics, nanofabrication, and system performances.

Tip-enhanced cavity-spectroscopy for quantum light-matter interactions at the nanoscale

Kyoung-Duck Park[1]

[1]Department of Physics, University of Science and Technology (POSTECH), Pohang 37673, Republic of Korea
*corresponding author: parklab@postech.ac.kr

Abstract: In this talk, we provide a novel concept of tip-enhanced cavity-spectroscopy (TECS) overcoming the limitations of previous approaches to induce, probe, and dynamically control ultrastrong light-matter interactions. We will then talk about exciton funneling and exciton-to-trion conversion properties in 2D semiconductors at the nanoscale.

Structure, functions, dynamics, and interactions are the basic properties to systematically understand physical systems existing in nature. In particular, there have been many scientific adventures to understand light-matter interactions, yet in the classical regime at the microscale due to the diffraction-limited optical resolution. Recently, plasmonic nano-cavity enables to induce light-matter interactions and tip-enhanced nano-spectroscopy enables to probe them at the nanoscale. However, these two approaches have developed independently with their own weaknesses so far. In this presentation, we provide a novel concept of tip-enhanced cavity-spectroscopy (TECS) overcoming the limitations of previous approaches to induce, probe, and dynamically control ultrastrong light-matter interactions in the quantum tunneling regime. Furthermore, we provide several new directions of nano-spectroscopy and -imaging. First, we exploit extremely high tip-pressure (~GPa scale) to directly modify the lattice structure and electronic properties of materials. Second, we dynamically control the near-field polarization by adopting adaptive optics technique to near-field optics. Third, we develop conductive TECS to modify electrical properties of materials by directly flowing an electric current through the cavity junction.

We will then talk about the exciton funneling behaviors of 2D semiconductors at the nanoscale. Understanding and controlling the nanoscale transport of excitonic quasiparticles in atomically thin semiconductors are crucial to produce highly efficient nano-excitonic devices. Here, we present a nanogap device to selectively confine excitons or trions of 2D transition metal dichalcogenides at the nanoscale, facilitated by the drift-dominant exciton funneling into the strain-induced local spot. We investigate the spatiospectral characteristics of the funneled excitons in a WSe_2 monolayer (ML) and converted trions in a MoS_2 ML using hyperspectral tip-enhanced photoluminescence imaging with <15-nm spatial resolution. In addition, we dynamically control the exciton funneling and trion conversion rate by the gigapascal-scale tip pressure engineering. Through a drift-diffusion model, we confirm an exciton funneling efficiency of ~25% with a significantly low strain threshold (~0.1%), which sufficiently exceeds the efficiency of ~3% in previous studies. This work provides a previously unexplored strategy to facilitate efficient exciton transport and trion conversion of 2D semiconductor devices [1].

We will then talk about high purity exciton-to-trion conversion in ambient conditions. The generation of high-purity localized trions, dynamic exciton-trion interconversion, and their spatial modulation in 2D semiconductors are building blocks for the realization of trion-based optoelectronic devices. Here, we present a method for the all-optical control of the exciton-to-trion conversion process and its spatial distributions in a

MoS_2 ML. We induce a nanoscale strain gradient in a 2D crystal transferred on a lateral metal–insulator–metal (MIM) waveguide and exploit propagating surface plasmon polaritons (SPPs) to localize hot electrons. These significantly increase the electrons and efficiently funnel excitons in the lateral MIM waveguide, facilitating complete exciton-to-trion conversion even at ambient conditions. Additionally, we modulate the SPP mode using adaptive wavefront shaping, enabling all-optical control of the exciton-to-trion conversion rate and trion distribution in a reversible manner. Our work provides a platform for harnessing excitonic quasiparticles efficiently in the form of trions at ambient conditions, enabling high-efficiency photoconversion [2].

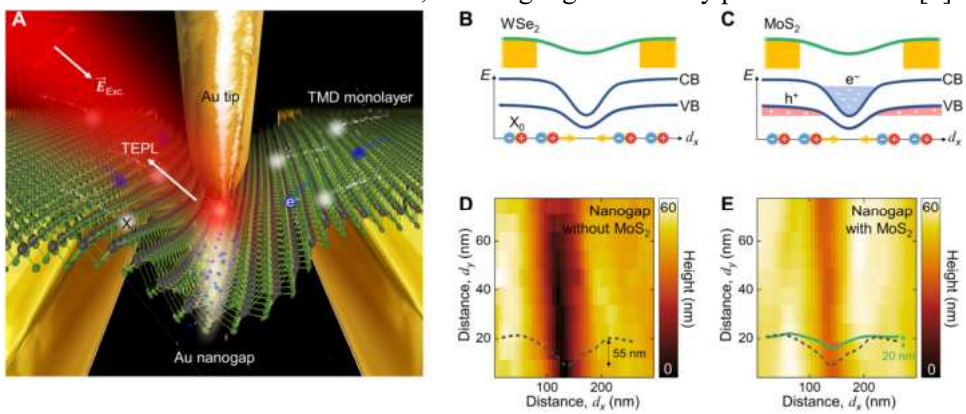


Fig. 1. a The Au nanogap device and transferred TMD MLs combined with TEPL spectroscopy to probe and control the electric charges (e-) and exciton (X_0) dynamics at the nanoscale. Illustrations of the energy band diagram for WSe_2 (**b**) and MoS_2. (**c**) MLs on the nanogap and spatial distributions of electric charges (e- and h+) and photoexcited excitons (X_0). AFM topography images and height profiles of the nanogap without (**d**) and with (**e**) MoS_2 ML exhibiting a wrinkled crystal structure, which leads to a nanoscale strain gradient.

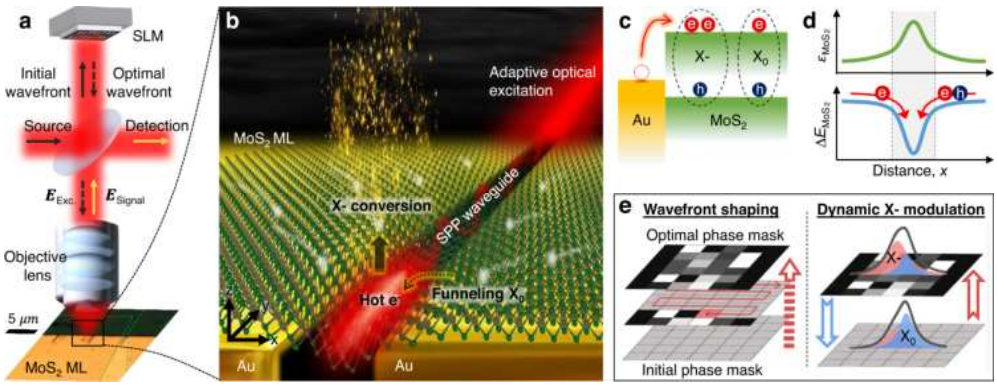


Fig. 2. a Schematic diagram of all-optical trion control platform operating with adaptive optical excitation. Green dashed line indicates transferred MoS_2 ML. **b** Illustration of all-optical trion control platform facilitated by nanoscale strain gradient, plasmon-induced hot electrons, and resultant exciton-to-trion conversion. **c** Illustration of hot electron injection process from Au to MoS_2 ML in SPP mode. **d** Strain (ϵ) and corresponding bandgap energy change (ΔE) diagram of MoS_2 ML as function of distance x, where gray region indicates nanogap area. **e** Adaptive wavefront shaping using stepwise sequence feedback algorithm to find optimal phase mask (left) and dynamic excitonic emission modulation through phase mask control (right).

References

1. Lee, H. et al., "Drift-dominant exciton funneling and trion conversion in 2D semiconductors on the nanogap," Sci. Adv., Vol. 8, eabm5236, 2022.
2. Lee, H. et al., "All-optical control of high-purity trions in nanoscale waveguide," Nat. Commun., Vol. 14, 1891, 2023.

White-nanolight-source through plasmon nanofocusing for nanoimaging, nanosensing, and nano-optical switching

Takayuki Umakoshi and Prabhat Verma*

Department of Applied Physics, Osaka University, Yakadaoka 2-1, SuitaOsaka, Japan
*corresponding author: verma@ap.eng.osaka-u.ac.jp

Abstract: Plasmon nanofocusing is an alternate technique that confines the light field at the apex of a metalized nanotip, enabling background-free detection. This non-resonant method confines all wavelengths simultaneously, producing a white nanolight at the apex for multi-color optical investigations and applications such as nanoimaging, nanosensing, and nano-optical switching.

Spectroscopic methods that benefit from plasmonic enhancement, such as surface-enhanced Raman spectroscopy (SERS) and tip-enhanced Raman spectroscopy (TERS), have been extensively applied for nanospectroscopy, nanoimaging, and the detection of minuscule quantities of molecules for nanosensing [1–5]. The crux of these techniques lies in the selective amplification of the Raman signal from a sample's nanometric volume, enabling investigations at extremely high spatial resolutions and low concentrations. This necessitates precise tuning of the plasmon resonance wavelength, which is accomplished by directing a diffraction-limited focused laser beam upon a plasmonic nanoantenna, be it the apex of a metallic nanotip in TERS or metallic nanoparticles in SERS, thereby generating an enhanced and confined nanolight-source in the close vicinity of the antenna through the resonant oscillation of surface plasmons. Since the resonance condition is achieved only for a very narrow wavelength range that matches the plasmon resonance for a chosen antenna, the nanolight-source also has a narrow wavelength range. In addition, alongside the desired nanolight-source obtained in this process, one also encounters undesirable background scattering, a consequence of the sample being illuminated by the diffraction-limited laser beam at a micrometer scale. One would like to avoid this unwanted background scattering for nanoimaging with higher contrast, and in some cases, one would also like to have fast wavelength switching or even multiple wavelengths at the nanolight-source without changing or replacing the antenna for experiments involving nanosensing or nano-optical switching.

As a viable alternative, plasmon nanofocusing, which is not reliant on plasmon resonance, offers a method to produce a nanolight-source at the apex of the tip [6–9]. This phenomenon involves the excitation of plasmons at the broader end far from the apex of a metallic taper or a conical metallic tip, which then propagate towards the apex of the structure, slowing down by adiabatically compressing their energies, ultimately culminating near the apex where the energy is transmuted into light, creating a strong, localized light field at the nanometrically tapered apex. Here, plasmons are excited by transferring energy from propagating photons to plasmons using a grating that serves as the plasmon coupler. Owing to the grating and the tip apex being separated by a substantial distance, typically around 5 to 8 micrometers, the illuminating beam does not directly impinge upon the sample, thus precluding the unwanted background scattering. Moreover, as the generation of the nanolight-source arises through plasmon propagation rather than localized resonance, the technique works across a broad wavelength spectrum from ultraviolet to near-infrared. Nonetheless, the efficiency of the grating coupler is generally limited to a narrow wavelength range, which inherently constrains the spectral range of the nanolight-source at the apex.

This limitation can be overcome by designing a coupler that can couple a wide spectral range, or in other words, the white light. We have discovered that a suitably designed single slit, which mimics the superimposition of multiple gratings, can function as an effective plasmon coupler for white light, hence generating a white-nanolight-source. We have recently proposed the generation of a white-nanolight-source via broadband plasmon nanofocusing, which has been successfully employed for high-resolution spectroscopy and optical imaging.

Furthermore, sensing and controlling the physical and electronic properties of materials via optics is highly desired for both foundational scientific exploration and the advancement of optoelectronic technologies. The transition towards nanoscale devices demands that the optical interaction volume be similarly scaled down. Although optical antennas can localize light, they fall short due to the requirement of illuminating them with a diffraction-limited focal spot, resulting in unintentional illumination of the sample over a larger volume, as well as due to the significantly narrow spectral range of the enhanced light field. Since plasmon nanofocusing physically separates the illumination and the nanolight generation sites and, at the same time, also offers the generation of nanolight across a broad spectrum of wavelengths or the creation of a white nanolight-source, it is suitable for nanoscale multi-sensing and optical switching applications. The implications of broadband plasmon nanofocusing are profound, not only in optical imaging, sensing, and optical switching but across various scientific domains, serving as a versatile nanoscale broadband light source. This talk will elucidate the generation of background-free, wavelength-independent nanolight and its various interesting potential applications.

References

1. Verma, P. “Tip-Enhanced Raman Spectroscopy: Technique and Recent Advances” Chem. Rev., Vol. **117**, 6447–6466, 2017.
2. Verma, P., Ichimura, T., Yano, T., Saito, Y. and Kawata, S. “Nano-imaging through tip-enhanced Raman spectroscopy: Stepping beyond the classical limits” Laser Photon. Rev., Vol. **4**, 548–561, 2010.
3. Yano, T., Verma, P., Saito, Y., Ichimura, T. and Kawata, S. “Pressure-assisted tip-enhanced Raman imaging at a resolution of a few nanometres” Nature Photon., Vol. **3**, 473–477, 2009.
4. Yano, T., Ichimura, T., Kuwahara, S., H’Dhili, F., Uetsuki, K., Okuno, Y., Verma, P. and Kawata, S. “Tip-enhanced nano-Raman analytical imaging of locally induced strain distribution in carbon nanotubes” Nature Commun. Vol. **4**, 2592, 2013.
5. Kato, R., Moriyama, T., Umakoshi, T., Yano, T. and Verma, P. “Ultrastable tip-enhanced hyperspectral optical nanoimaging for defect analysis of large-sized WS2 layers” Science Adv., Vol. **8**, eabo4021, 2022.
6. Umakoshi, T., Saito, Y. and Verma, P. “Highly efficient plasmonic tip design for plasmon nanofocusing in near-field optical microscopy” Nanoscale, Vol. **8**, 5634–5640, 2016.
7. Yadav, R., Arata, H., Umakoshi, T. and Verma, P. “Plasmon nanofocusing for the suppression of photodegradation in fluorescence imaging using near-field scanning optical microscopy” Opt. Commun., Vol. 497, 127206, 2021.
8. Umakoshi, T., Tanaka, M., Saito, Y. and Verma, P. “White nanolight source for optical nanoimaging” Science Adv., Vol. **6**, eaba4179, 2020.
9. Taguchi, K., Umakoshi, T., Inoue, S. and Verma, P. “Broadband Plasmon Nanofocusing: Comprehensive Study of Broadband Nanoscale Light Source” J. Phys. Chem. *C*, Vol. **125**, 6378–6386, 2021.

Nanocavity-dependent photon output from WSe_2 single quantum emitter with broken valley symmetry

Xulai Xu[1*]

[1]School of Physics, Peking University, China
[*]email: xlxu@pku.edu.cn

Abstract: We show experimental evidence of valley symmetry breaking for quantum emitters in WSe_2 monolayer by interacting with chiral plasmonic nanocavities. And a cavity-dependent circularly polarized single-photon output is also demonstrated.

We investigated the coupling of single localized defect excitons in a two-dimensional layer with chiral plasmonic nanocavity, as shown in Fig. 1. By designing a chiral plasmon mode with high quality factor and coupling it with a WSe_2 monolayer, we demonstrated cavity-dependent photon output from single quantum emitters. The dynamics of this coupled system shows that the chiral photon output mainly comes from the spontaneous emission of the quantum emitter which is strongly modified by the chiral plasmonic nanocavity, which proves that the valley-dependent optical selection rules are absent in such quantum emitters [1]. The coupling interactions of plasmonic nanocavity with two-dimensional excitons at the level of single quanta by using the single quantum emitter in monolayer, instead of small number of two-dimensional excitons [2], will provide platform for future research of quantum plasmonic photonics and integrated photonics.

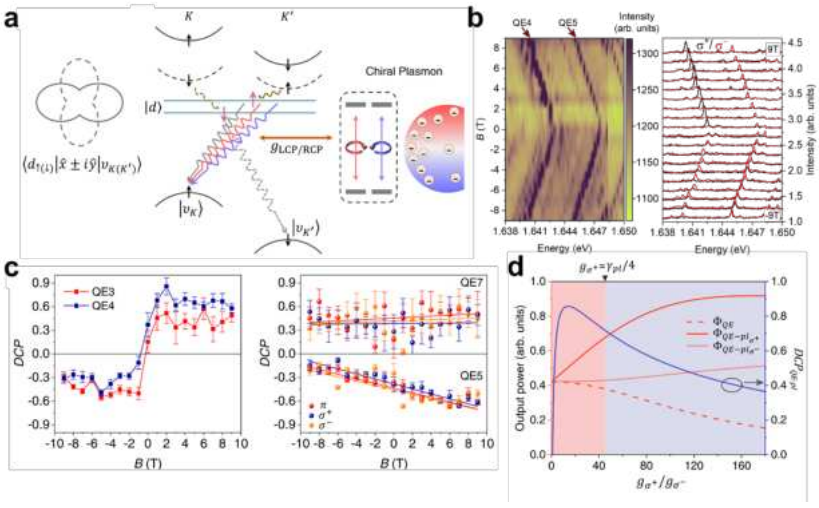


Figure 1 (a) Schematic diagram of the manipulation of circular polarization output of quantum emitter in WSe_2 by chiral plasmon field. (b) Polarization-resolved magneto-PL spectroscopy of QEs on the chiral plasmonic lattices. (c) Degree of circular polarization of QEs uncoupled and coupled with the chiral plasmon field. (d) The study of cavity quantum electrodynamics of the coupled system.

References

1. Yang L., Yuan Y., Fu B. et al. "Revealing broken valley symmetry of quantum emitters in WSe2 with chiral nanocavities," Nat. Commun., 14, 4265, 2023.
2. Yang L., Xin X., Yang J. et al. "Strong light-matter interactions between gap plasmons and two-dimensional excitons under ambient conditions in a deterministic way," Nano Lett., 22, 2177-2186, 2022.

Subnanometer Resolved Single-Molecule Optical Spectroscopy

Z. C. Dong*

University of Science and Technology of China, Hefei, China
*corresponding author: zcdong@ustc.edu.cn

Abstract: Recent progresses on two STM-based optical phenomena will be presented. One is single-molecule Raman spectromicroscopy down to single-bond resolution, allowing to track bond breaking and forming of surface reactions; the other is single-molecule electro-phosphorescence with the discovery of a new optomagnetic channel to activate the emission from triplet-to-singlet transition.

Aspirations for reaching atomic resolution with light have been a major force in shaping nano-optics, whereby a central challenge is to achieve highly localized optical fields. The plasmonic picocavity defined by the coinage-metal tip and substrate in a scanning tunneling microscope (STM) can provide highly confined and dramatically enhanced electromagnetic fields, which can modify both the excitation and emission of a single molecule inside the picocavity and improve the spatial resolution down to the subnanometer scale [1]. In this talk, I shall demonstrate two recent STM-based phenomena related to single-molecule optical spectroscopy.

The first is single-molecule Raman scattering [2]. The spatial resolution of tip enhanced Raman spectroscopy (TERS) has been further driven down to the angstrom scale at the single-bond limit [3,4]. Such a capability not only allows to track bond breaking and forming of surface reactions [5,6] as well as the local heating effect of a non-equilibrium single molecule [7], but also enables to clarify the chemical enhancement mechanism in TERS through well-controlled local contact environments [8].

The second phenomenon is single-molecule electroluminescence. Through managements over molecular quenching and energy level alignment, clear single-molecule electroluminescence and even single-photon emission can be realized [9]. By precisely controlling intermolecular distances, we can not only demonstrate coherent dipole–dipole coupling in homodimers [10], but also reveal intriguing transitions from incoherent hopping-like Forster energy transfer to coherent wavelike electronic energy transfer in donor–acceptor heterodimers [11]. Furthermore, in addition to the emission via the electric channel, the optomagnetic field is also found to be significantly enhanced in a confined plasmonic picocavity, leading to a new observation of optomagnetism induced molecular phosphorescence via the magnetic channel that goes beyond the conventional spin-orbit coupling mechanism. The microscopic mechanism for the single-molecule electroluminescence including upconversion electroluminescence will also be addressed in this talk [12,13]. Our results provide new routes to optical imaging, spectroscopy and engineering of light–matter interactions and intermolecular coupling at the sub-nanometer scale.

Acknowledgements: This work was supported by National Key R&D Program of China, the National Natural Science Foundation of China, Anhui Initiative in Quantum Information Technologies, and Innovation Program for Quantum Science and Technology.

References

1. B. Yang, et al., "Sub-nanometre resolution in single-molecule photoluminescence imaging", *Nat. Photonics* **14**, 693–699 (2020)

2. R. Zhang, et al., "Chemical mapping of a single molecule by plasmon-enhanced Raman scattering", *Nature* **498**, 82–85 (2013).
3. J. Lee, K. T. Crampton, N. Tallarida and V. A. Apkarian, "Visualizing vibrational normal modes of a single molecule with atomically confined light", *Nature* **568**, 78–82 (2019).
4. Y. Zhang, et al., "Visually constructing the chemical structure of a single molecule by scanning Raman picoscopy", *Natl. Sci. Rev.* **6**, 1169–1175 (2019).
5. J. Y. Xu, et al., "Determining structural and chemical heterogeneities of surface species at the single-bond limit", *Science* **371**, 818 (2021).
6. R. P. Wang, et al., "Raman detection of bond breaking and making of a chemisorbed up-standing single molecule at single-bond level", *J. Phys. Chem. Lett.* **12**, 1961-1968 (2021).
7. Q. S. Meng, et al., "Local heating and Raman thermometry in a single molecule", *Sci. Adv.* **10**, eadl1015 (2024).
8. B. Yang, et al., "Chemical enhancement and quenching in single-molecule tip-enhanced Raman spectroscopy", *Angew . Chem. Int. Ed.* **62**, e202218799 (2023).
9. L. Zhang, et al., "Electrically driven single-photon emission from an isolated single molecule", *Nat. Commun.* **8**, 580 (2017).
10. Y. Zhang, et al., "Visualizing coherent intermolecular dipole–dipole coupling in real space", *Nature* **531**, 623–627 (2016).
11. F. F. Kong, et al., "Wavelike electronic energy transfer in donor--acceptor molecular systems through quantum coherence", *Nat. Nanotechnol.* **35**, 713-719 (2022).
12. G. Chen, et al., "Spin-triplet-mediated up-conversion and crossover behavior in single-molecule electroluminescence", *Phys. Rev. Let.* **122**, 177401 (1019).
13. Y. Luo, et al., "Anomalously bright single-molecule upconversion electroluminescence", *Nat. Commun.* **15**, 1677 (2024).

Strong Coupling between Surface Plasmons and Excitons

Hong Wei*

Institute of Physics, Chinese Academy of Sciences, Beijing 100190, China
*corresponding author: weihong@iphy.ac.cn

Abstract: The strong coupling between surface plasmons and excitons leads to the formation of plasmon-exciton polariton states in nanoscale systems at room temperature. In this presentation, I will talk about our research on the strong coupling of single plasmonic nanogap structures and nanowires with monolayer transition metal dichalcogenides.

When the interaction between an optical cavity and quantum emitters is strong enough to reach the strong coupling regime, exciton polaritons are produced. The exciton polaritons inherit the properties of both light and matter, and show great potentials for applications in physical and chemical sciences and related technologies. Metal nanostructures can confine electromagnetic field into tiny spaces of deep subwavelength scale due to the excitation of surface plasmons and result in a very small mode volume, which leads to a large plasmon–exciton coupling strength. Therefore, plasmonic nanocavities are favorable for realizing strong coupling at room temperature. In recent years, the strong coupling of plasmonic nanostructures and excitons has attracted intense interest [1].

In this presentation, I will talk about our research on the strong coupling of single plasmonic nanogap structures [2, 3] and nanowires [4, 5] with monolayer transition metal dichalcogenides. We achieved the strong coupling of monolayer WSe_2 and lithographically defined single gold nanobowties, and the intermediate coupling of two exciton states in monolayer MoS_2 and the nanogap structure of silver nanowire on gold film. In the coupling system of single silver nanowires and monolayer WSe_2, we found that the photoluminescence and scattering light share the same spectral profiles resulting from strong coupling, which unifies the photoluminescence and scattering spectra in the plasmon–exciton strong coupling systems and sheds new light on understanding the rich spectral phenomena in the strong coupling regime.

References

1. Wei, H.; Yan, X. H.; Niu, Y. J.; Li, Q.; Jia, Z. L.; Xu, H. X., “Plasmon–exciton interactions: spontaneous emission and strong coupling”, Adv. Funct. Mater. 31, 2100889, 2021.
2. Yan, X. H.; Wei, H., “Strong plasmon-exciton coupling between lithographically defined single metal nanoparticles and monolayer WSe2”, Nanoscale 12, 9708–9716, 2020.
3. Zhang, W. J.; Gao, L.; Yan, X. H.; Xu, H. X.; Wei, H., “Excitation and emission distinguished photoluminescence enhancement in a plasmon–exciton intermediate coupling system”, Nanoscale 15, 7812–7819, 2023.
4. Niu, Y. J.; Xu, H. X.; Wei, H., “Unified scattering and photoluminescence spectra for strong plasmon-exciton coupling”, Phys. Rev. Lett. 128, 167402, 2022.
5. Niu, Y. J.; Gao, L.; Xu, H. X.; Wei, H., “Strong coupling of multiple plasmon modes and excitons with excitation light controlled active tuning”, Nanophotonics 12, 735–742, 2023.

Chiral Response of plasmonic metasurface

Jinwei Shi[1]

[1] Department of Physics, Beijing Normal University, Beijing, 100875
[*]corresponding author: shijinwei@bnu.edu.cn

Abstract: By breaking the interlayer symmetry, we demonstrated a bilayer metasurface that can achieve circular dichroism close to 1. A triple-layer metasurface is then designed to obtain multiple chiral bands with near unity circular dichroism. Finally, we experimentally achieved an chiral exceptional point in the optical communication band.

The chiral metasurface has broad prospects in various fields such as chiral drugs and polarized optics. Conventional bilayer chiral metasurfaces are constrained by interlayer alignment, and the resulting circular dichroism is limited. Moiré metasurfaces are not restricted by interlayer alignment, reducing the requirements for fabrication technology. However, the chirality of existing Moiré metasurfaces is still not good enough. On the other hand, non-Hermitian chiral metasurfaces based on PT symmetry have also attracted interest, but the fabrication of metamsurface within the visible to near-infrared wavelength range is hindered by multi-step processing requirement.

In this report, I will present three recent works of our group on chiral metasurfaces. Firstly, we analyzed the chirality of Moiré metasurfaces composed of anisotropic materials. Based on the analysis, by breaking the symmetry of the bilayer metasurface, we constructed a chiral device that can achieve circular dichroism close to 1 in a single direction and conducted experimental verification. Furthermore, to obtain multiple chiral bands with circular dichroism close to 1, we designed a triple-layer metasurface. In the forward direction, we used two sets of nearly independent bilayer structures to achieve two nearly ideal chiral bands, while in the backward direction, we used the overall chirality of the three layers to achieve a third nearly ideal chiral band. Finally, using the coupling of local modes and propagating modes, we experimentally achieved an exceptional point (EP) in the optical communication band in a structure made by a single material through one-step fabrication, obtaining a high chiral conversion contrast.

Statistical quantitative SERS beyond the single-molecule level and its physical foundations

Zhipeng Li [1*], Longkun Yang[1], Hao Zhang[1], and Hongxing Xu[2]

[1]Beijing Key Laboratory of Nano-Photonics and Nano-Structure (NPNS), Department of Physics, Capital Normal University, Beijing, 100048, China

[2]School of Physics and Technology, Center for Nanoscience and Nanotechnology, and Key Laboratory of Artificial Micro- and Nano-structures of Ministry of Education, Wuhan University, Wuhan 430072, China
[*]corresponding author: zpli@cnu.edu.cn

Abstract: We proposed a new physical principle for ultra-sensitive quantitative SERS detection. Based on Poisson statistical distribution, the relationship between probability and average molecular number is established. Quantitative SERS of 1 fM beyond the single-molecule level is realized.

Since the discovery of single-molecule SERS nearly 30 years ago, ultrasensitive quantitative sensing is always the ultimate goal of SERS spectroscopy[1]. However, due to the intrinsic quantum fluctuation and molecule diffusion, quantitative SERS down to single-molecule level following the traditional intensity gauging is unachievable. Our work opens up a new field of statistical quantitative SERS[2,3]. By introducing a statistical physical quantity "SERS probability" (Figure 1), we accomplished quantitative SERS even beyond single-molecule level. Moreover, we reported ultra-broad quantitative concentration range from 10^{-4} to 10^{-15} M. We also established a sound physical foundation for the field of statistical quantitative SERS. For the first time, we revealed SERS probability P based on Poisson distribution which indicates the microscopic essence of SERS probability. We corroborated this discovery by correlating the measured SERS probability P and the alpha determined from bi-analytes analysis.

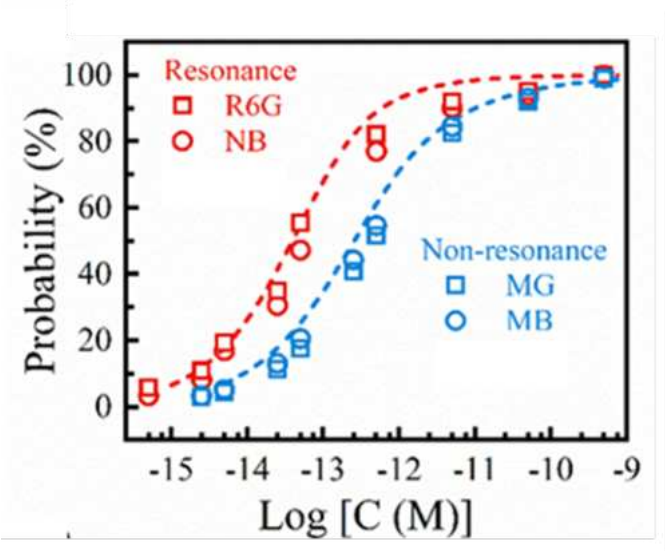


Figure 1. SERS probability as a function of concentration.

Acknowledgements. This work was supported by the National Key Research and Development Program of China (2021YFA1400800); National Natural Science Foundation of China (12374028); Beijing Natural Science

Foundation (Z190006); Scientific Research Base Development Program of Beijing Municipal Commission of Education.

References

1. Xu, H. X.; Bjerneld, J.; Käll, M.; Börjesson L., “Spectroscopy of Single Hemoglobin Molecules by Surface Enhanced Raman Scattering”, Phys. Rev. Lett. Vol. 83, 4357, 1999.
2. Yan, W. J.; Yang, Y.; Chen, J.; Wu, Y.; Wang, P.; Li, Z. P., “In Situ Two-Step Photoreduced SERS Materials for On-Chip Single-Molecule Spectroscopy with High Reproducibility”, Adv. Mater. Vol. 29, 1702893, 2017.
3. Zhang, H.; Yang, L.; Zhang, M.; Tong, L.; Xu, H. X.; Li, Z. P., “A Statistical Route to Robust Quantitative SERS Beyond the Single-Molecule Level”, submitted on 2023-08.

Recent Developments in Optical Nanoantennas for Enhanced Light Matter Interaction

Dynamics of Thermal Asymmetry: Interfacial Thermal Conductance in Plasmonic Janus Nanostructures

Javier González-Colsa[1], Fernando Bresme[2*], and Pablo Albella[1#]

[1]Group of Optics, Department of Applied Physics, University of Cantabria, 39005, Santander, Spain.
[2]Department of Chemistry, Molecular Sciences Research Hub, Imperial College London, W12 0BZ UK.

Corresponding authors: [*]f.bresme@imperial.ac.uk and [#]pablo.albella@unican.es

Abstract: Plasmonic Janus nanoparticles have shown as promising agents in biomedicine due to their controllable photothermal response. Here, we study how interfacial thermal conductance affects their thermal relaxation. The main result is a directional heat dissipation under nanosecond pulsed light, something that supports their potential in photothermal therapies and temperature-controlled devices.

Plasmonic structures and in particular Plasmonic Janus Nanoparticles have attracted great attention due to their capability to generate and control heat at the nanoscale by means of the excitation of Localized Surface Plasmons Resonances (LSPRs) [1-5]. Therefore, these nanoparticles can induce substantial temperature increases, making them valuable in hyperthermia cancer treatments. Recent studies [6] have shown that Plasmonic JNPs with contrasting thermal conductivities can asymmetrically generate heat, particularly under continuous wave excitation, holding promise for this area. However, pulsed illumination is often used in photothermal therapies as different tissues can be targeted by simply modifying the pulse features. Under these conditions, Interfacial Thermal Conductance (ITC) plays a pivotal role in accurately describing the thermoplasmonic response of JNPs.

Our work [7] investigates the impact of ITC on the transient heating and cooling of Plasmonic JNPs under nanosecond-pulsed illumination, using as an example a core-semishell structure made of a polymeric nanosphere coated with a gold spherical cap. To do so, we build a Comsol Multiphysics model able to calculate the thermoplasmonic response of arbitrary JNP geometries, implementing the ITC together with temperature dependent physical properties.

As it can be seen in Figure 1a, the gold nanocap heats first upon pulsed illumination, transferring afterwards heat internally to the polymer core and later externally to the solvent. Interestingly, during the cooling process there is a time where the temperature inside PMMA becomes higher than that of the gold side. Consequently, the conductive thermal flux is inverted towards gold, acting this as a heat sink. This suggests that the structure is inherently more efficient than homogeneous particles since part of the thermal energy is blocked backwards and redirected forwards. Furthermore, as can be observed in Figure 1b, our analysis reveals significant temperature contrasts induced by these interfaces (ITCs), with distinct temperature profiles at interfacial regions. The maximum temperature is observed inside the gold semishell. Temperature gaps at the gold/polymer and gold/water interfaces are associated with their respective ITCs, with larger jumps attributed to higher heat fluxes.

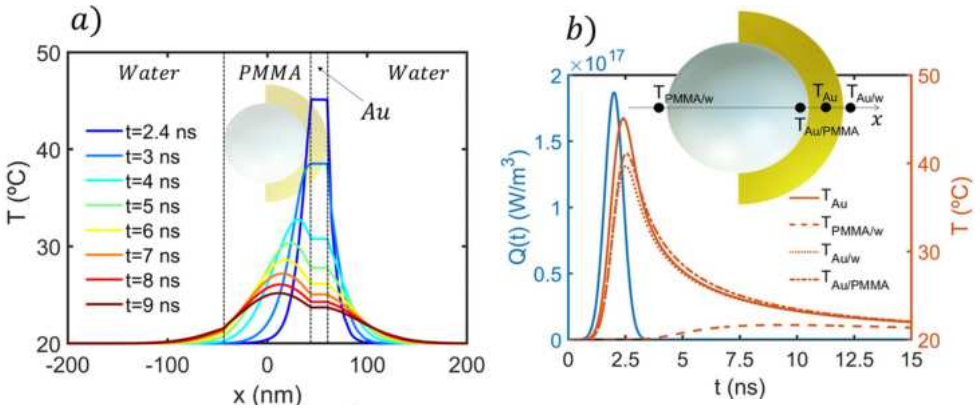


Figure 1. (a) Transient temperature profiles taken along the x-axis. The initial profile is taken at the maximum temperature increase (t = 2.4 ns), so that the cooling process is shown. The vertical lines and the inset display the the interfaces. (b) Input heat power density pulse (left plot) and temporal evolution of the temperature (right plot) taken at points T_{Au}, $T_{Au/PMMA}$, $T_{Au/w}$, and $T_{PMMA/w}$ as seen in the upper inset. Image taken from [7].

Interestingly, the PMMA/water interface exhibits a much slower temperature rising. This is associated to the low thermal conductivity of PMMA and to the ITC of PMMA/water interface. Therefore, this Plasmonic JNP shows a significant temperature contrast across opposite nanoparticle regions at nanosecond timescales. This aspect can become critical in biomedicine since photothermal therapies can benefit from the asymmetric heating. Target cells can be affected by sudden temperature rises preventing the healthy tissue from being overheated and ultimately damaged.

Acknowledgements

This work was funded by the MOPHOSYS Project (PID2022-139560NB-I00) from Proyectos de Generación de Conocimiento provided by the Spanish Agencia Estatal de Investigación. J.G.-C. thanks the Spanish Ministerio de Ciencia e Innovación for his FPI grant.

References

1. Govorov, A. O.; Richardson, H. H. “Generating Heat with Metal Nanoparticles”. Nano Today 2007, 2 (1), 30–38.
2. Baffou, G.; Quidant, R.; García De Abajo, F. J. “Nanoscale Control of Optical Heating in Complex Plasmonic Systems”. ACS Nano 2010, 4 (2), 709–716.
3. González-Colsa, J.; Serrera, G.; Saiz, J. M.; Ortiz, D.; González, F.; Bresme, F.; Moreno, F.; Albella, P. “Gold Nanodoughnut as an Outstanding Nanoheater for Photothermal Applications”. Opt Express 2022, 30 (1), 125.
4. González-Colsa, J.; Olarte-Plata, J. D.; Bresme, F.; Albella, P. “Enhanced Thermo-Optical Response by Means of Anapole Excitation”. Journal of Physical Chemistry Letters 2022, 13 (26), 6230–6235.
5. Olarte-Plata, J. D.; Gabriel, J.; Albella, P.; Bresme, F. “Spatial Control of Heat Flow at the Nanoscale Using Janus Particles”. ACS Nano 2022, 16 (1), 694–709.
6. González-Colsa, J.; Franco, A.; Bresme, F.; Moreno, F.; Albella, P. “Janus-Nanojet as an Efficient Asymmetric Photothermal Source”. Sci Rep 2022, 12 (1), 14222.
7. González-Colsa, J. Bresme F., and Albella P. “Impact of the Interfacial Thermal Conductance on the Thermoplasmonic Response of Metal/Polymer Hybrid Nanoparticles under Nanosecond Pulsed Illumination”. J. Phys. Chem. C 2023, 127, 38, 19152–19158.

Enhancement and Directional Control of Light Emission from Monolayer MoS_2 by Silicon Nanosphere Antennas

K. Ozawa,[1] D. Shima,[1] S. Raza,[2] K. Imaeda,[3] K. Ueno,[3] H. Sugimoto,[1*] and M. Fujii[1]

[1]Graduate School of Engineering, Kobe University, Japan
[2]Department of Physics, Technical University of Denmark, Denmark
[3]Faculty of Science, Hokkaido University, Japan
[*]corresponding author: sugimoto@eedept.kobe-u.ac.jp

Abstract: High-index dielectric nanostructures work as optical antennas to control the light emission from quantum emitters, including the intensity enhancement and the directional control by Mie resonances. In this work, we demonstrate the enhancement and modification of the light emission from monolayer molybdenum disulfide by a crystalline silicon nanosphere.

Controlling the light emission from quantum emitters by nanoantennas is of great importance for the photonic application. Recently, nanostructures of high-index dielectrics such as silicon (Si) have been suggested as the highly efficient nanoantennas for the light emission control by Mie resonances. The high-index nanoantennas are capable of not only localizing the incident light in the volume much smaller than the light wavelength but also enhancing the radiative rate of the emitter that is so-called Purcell effect. Moreover, because they exhibit both the electric- and magnetic-type Mie resonances, they modify the directional properties of the emitter, including the generation of the magnetic dipole (MD) and magnetic quadrupole (MQ) radiation patterns and the unidirectionality through the interference among the multiple Mie resonances. In this work, we demonstrate the light emission control from monolayer transition-metal dichalcogenides (TMDCs) by a crystalline Si nanosphere (Si NS). As a quantum emitter, monolayer molybdenum disulfide (MoS_2) has been employed since the dipole moments of the exciton emission are oriented in-plane and benefit the efficient coupling with Mie resonances. There have been several reports on the modification of the exciton emission of TMDCs by a Si nanowire [1] and an amorphous Si NS [2]. On the other hand, the system composed of a crystalline Si NS have advantage of the higher-order Mie resonances with high-Q factors and compact size much smaller than the wavelength.

Figure 1a shows the calculated scattering efficiency (Q_{sca}) of a crystalline Si NS as a function of the diameter. The wavelength is 675 nm, corresponding to the photoluminescence (PL) wavelength of MoS_2. The contributions of magnetic dipole (MD), electric dipole (ED), and magnetic quadrupole (MQ) Mie resonances are also shown. Figure 1b shows the calculated radiative rate enhancement factor for the dipole placed 3 nm from the Si NS surface with its orientation parallel to the surface. While the

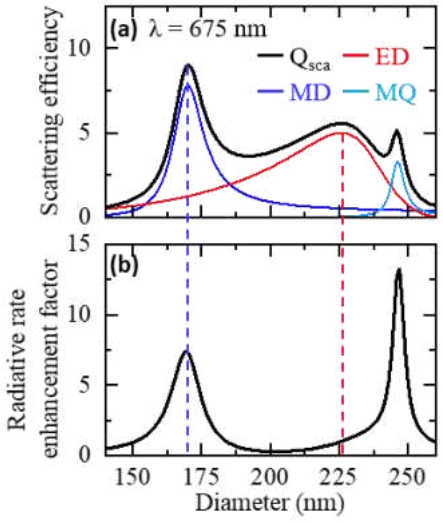


Figure 1. (a) Calculated scattering efficiency (Q_{sca}) and (b) radiative rate enhancement factor at 675 nm for the dipole placed 3 nm from the Si NS surface as a function of the diameter. The wavelength (λ) is 675 nm, corresponding to the PL wavelength of MoS_2. The contributions of ED (red curve), MD (blue curve) and MQ (light-blue curve) Mie resonances are also shown in (a).

radiative rate is not enhanced at ED resonance, it is strongly enhanced at MD and MQ resonances, leading to the intensity enhancement and the spectral modification of the PL.

Figure 2a shows transmission electron microscope (TEM) image of Si NSs developed in our group.[3] They have high sphericity and crystallinity, thus exhibiting the high-Q Mie resonances. Figure 2b shows the schematic of the preparation procedure of Si NSs placed on MoS_2 (Si/MoS_2). MoS_2 is prepared by the chemical vapor deposition (CVD) method and transferred onto a silica substrate. Colloidal solution of Si NSs is deposited on a MoS_2 and the sample is subjected to Ar^+ etching to remove MoS_2 except for the regions underneath the Si NSs. Figure 2c shows the scattering spectrum of the single Si/MoS_2 (diameter of Si NS: 248 nm). The Si NS exhibits MQ resonance around 675 nm. The peak around 575 nm shows the electric quadrupole (EQ) resonance. Figure 2d shows normalized PL spectra of Si/MoS_2 (red curve) and MoS_2 (black curve). The excitation wavelength is 532 nm. The spectral shape of Si/MoS_2 shows narrow linewidth; the full width at half maximum (FWHM) of the PL changes from 106 meV (MoS_2) to 55 meV (Si/MoS_2). From the calculation in Figure 1b, we can conclude that the PL modification is due to the radiative rate enhancement by the coupling with MQ resonance (FWHM: 30 meV).

In the presentation, we discuss the PL enhancement factors and theoretically and experimentally demonstrate the directional control of the exciton emission by a Si NS.

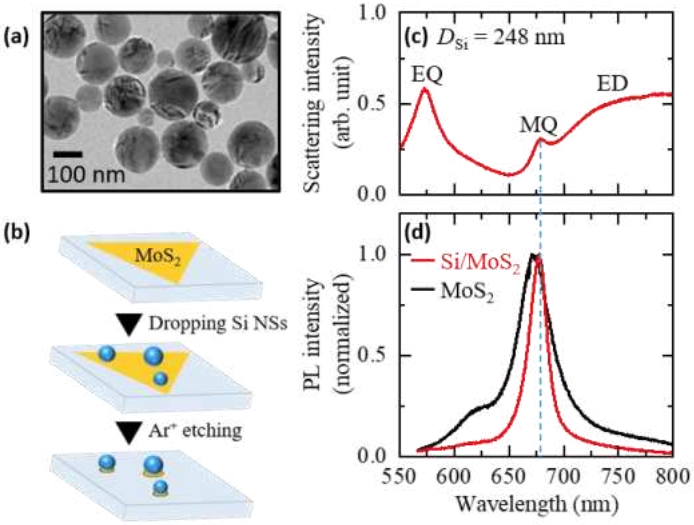


Figure 2. (a) Schematic of the preparation procedure of Si/MoS_2. (b) Scattering spectrum of Si/MoS_2. The diameter of a Si NS (D_{Si}) is 248 nm. (c) Normalized PL spectra of Si/MoS_2 (red curve) and MoS_2 (black curve). The excitation wavelength is 532 nm.

References

1. A.F. Cihan, A. G. Curto, S. Raza, P. G. Kik and M. L. Brongersma. “Silicon Mie resonators for highly directional light emission from monolayer MoS_2,” Nat. Photonics, Vol. 12, No. 5, 284-290, 2018.
2. J. Fang, M. Wang, K. Yao, T. Zhang, A. Krasnok, T. Jiang, J. Choi, E. Kahn, B. A. Korgel, M. Terrones, X. Li, A. Alù and Y. Zheng, “Directional Modulation of Exciton Emission Using Single Dielectric Nanospheres,” Adv. Mater., Vol. 33, No. 20, 2007236, 2021.
3. H. Sugimoto, T. Okazaki and M. Fujii, “Mie Resonator Color Inks of Monodispersed and Perfectly Spherical Crystalline Silicon Nanoparticles,” Adv. Opt. Mater., Vol. 8, No. 12, 2000033, 2020.
4. H. Shinomiya, H. Sugimoto, T. Hinamoto, Y. Lee, M. L. Brongersma, M. Fujii, "Enhanced Light Emission from Monolayer MoS2 by Doubly Resonant Spherical Si Nanoantennas", ACS Photon., Vol. 9, Issue 5, pp. 1741-1747 (2022). (First published: 19 April 2022)

Optical Heating Triggered by Multipolar Mie Resonance of Silicon Nanoparticles

M. Karimi Habil[1], K. Kondo[1], H. Sugimuto[1*], M. Fujii[1]

[1]Department of Electrical and Electronic Engineering, Graduate School of Engineering, Kobe University, 657-8501 Kobe, Japan

[*]corresponding author: sugimoto@eedept.kobe-u.ac.jp

Abstract: We experimentally demonstrate temperature raising over 300 K of crystalline spherical silicon nanoparticles (Si NPs) when the low-power laser light is coupled to the multipole Mie resonances. The experimental results are supported by numerical simulations. These hot Si NPs may have potential applications in biosensing and photothermal therapy.

Keywords: Mie resonances, spherical silicon nanoparticles, temperature raising.

Introduction

High-refractive-index dielectrics supporting magnetic and electric multipole Mie-type resonances in the visible and infrared spectrum have attracted attention in different fields of optics and photonics [1]. Crystalline silicon nanoparticles, unlike their metallic counterpart suffering from high dissipative losses, owing to the low dissipation can strongly confine the electric and magnetic fields in a subwavelength scale. This light-mater interaction can be utilized in light-to-heat conversion through the absorption by Si NPs. For instance, colloidal spherical Si NPs thermally tuning the near- and far-filed of Mie resonances [2], and Si NPs fabricated by femtosecond laser ablation [3] have been proposed for applications in nonlinear optics, Raman scattering, and light-to-heat conversion. Here, we experimentally demonstrate temperature increase in well-defined spherical Si NPs supported by a glass substrate through relatively low-power laser. Due to the high-Q Mie resonances the particles and the ambient temperature can be dynamically controlled through the size of the particles and the laser wavelength.

Theory and Numerical Calculations

When a particle is illuminated by an electromagnetic (EM) wave, the EM energy can be absorbed by the particle. This absorption is quite pronounced at the resonances which leads to the elevation of the particle temperature and its surrounding matrix. In the simplest case, for spherical particles with the thermal conductivity much higher than their homogenous surrounding medium, the temperature increase can be easily calculated using Mie theory [3,4]. When the surrounding medium of the particle is inhomogeneous, for instance, the particle supported by a substrate, one can numerically solve the thermal diffusion equation [3,4]. For this purpose, we perform numerical simulations using finite element method with the implement of COMSOL Multiphysics by coupling electromagnetic wave and heat transfer modules.

Experimental Method

Colloidal spherical Si NPs were prepared by thermal disproportionation of silicon monoxide followed by hydrofluoric acid etching to liberate NPs in solution [1]. The temperature of the single NPs of different diameters on a silica glass were measured by micro Raman spectroscopy under different excitation wavelengths of 488, 532 and 633 nm. The shift of Raman frequency of crystalline Si peak from 520 cm^{-1} was converted to the temperature according to literature [5].

Results and discussion

Figure 1 shows the TEM image and scattering spectra of Si NPs. The TEM images demonstrate the sphericity and crystallinity of Si NPs. As seen in the scattering spectra for NPs with different sizes, the magnetic dipole

(MD) and electric dipole (ED) modes are quite pronounced in the visible spectrum for a smaller NP, whereas the magnetic quadrupole (MQ) and electric quadrupole (EQ) are highly excited in the larger NP.

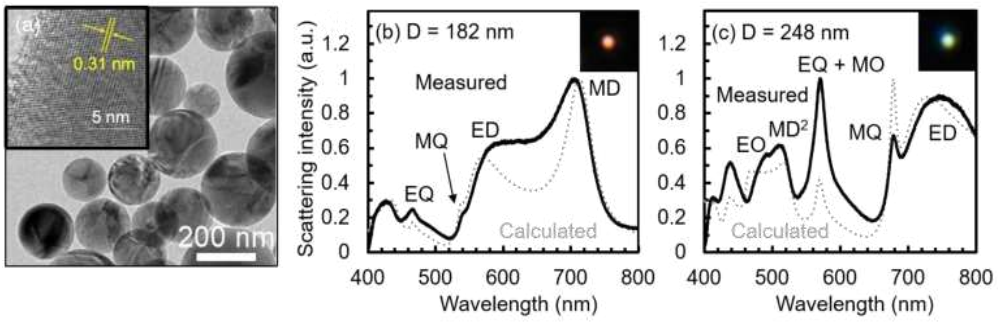


Figure 1: (a) TEM images of a Si NPs. The inset shows high-resolution of Si NP. (b) and (c) Measured (solid curve) and calculated (dashed curve) scattering spectra of a single Si NP of diameter D. The inset, located in the upper right corner, shows the dark-field image of each NP.

Figure 2 shows the experimental temperature increase of Si NPs of different sizes under a laser illumination obtained from Raman measurements together with COMSOL simulation results when the particle is supported by a glass substrate. As it is shown, the multipoles Mie resonances are excited in different particles of different sizes. However, the particles supporting MQ can be strongly coupled to the incoming EM wave and heated up over 300 K with relatively low intensity laser. In the presentation, we will discuss the experimental and the numerical calculation in more detail.

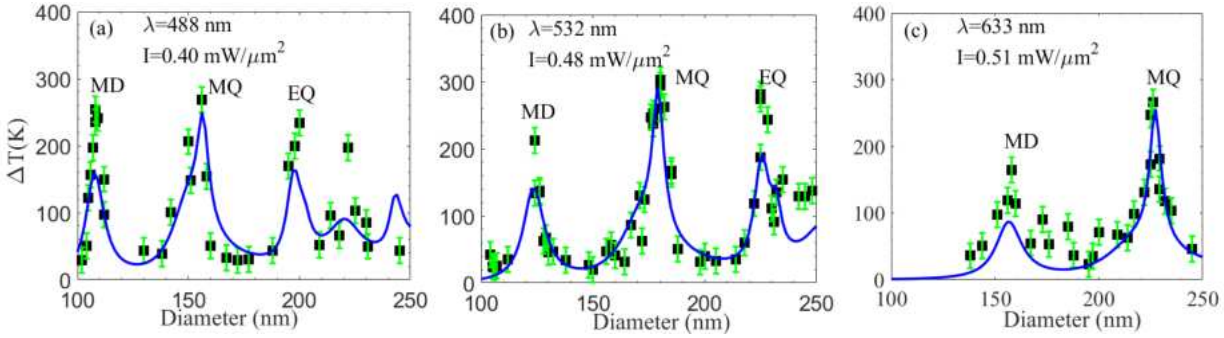


Figure 2: Measured (black dots) and calculated simulations (blue curve) temperature increase of Si NPs. The laser intensity and its corresponding wavelength, and the dominant multipoles are indicated in the inset.

Acknowledgments

This work was supported by Kobe University Strategic International Collaborative Research Grant (Type C Creating Joint Researcher).

References

1. Sugimoto, H., Okazaki, T., Fujii, M. "Mie resonator color inks of monodispersed and perfectly spherical crystalline silicon nanoparticles". Adv. Opt. Mater., Vol. 8, No. 12, 2000033, 2020.
2. Assadillayev, A., et al. "Thermal near-field tuning of silicon Mie nanoparticles". Nanophotonics, Vol. 10. No. 16, 4161-4169, 2021.
3. Zograf, G. P., et al. "Resonant nonplasmonic nanoparticles for efficient temperature-feedback optical heating". Nano let., Vol. 17, No. 5, 2945-2952, 2017.
4. Govorov, A. O., Richardson H. H. "Generating heat with metal nanoparticles". Nano Today, Vol. 2, No. 1, 30-38, 2007.
5. Balkanski, M., Wallis, R. F., Haro, E. "Anharmonic effects in light scattering due to optical phonons in silicon". Phys. Rev. B, 1983, Vol. 28, No. 4, 1928, 1983.

Plasmonic lightning-rod effect

V. Křápek[1*], R. Řepa[1], M. Foltýn[1], T. Šikola[1], and M. Horák[1]

[1]Brno University of Technology, Technická 2, 616 69 Brno, Czechia
[*]corresponding author: krapek@vutbr.cz

Abstract: We study the role of the local curvature of plasmonic antennas on the local electromagnetic field enhancement and disentangle it from other effects contributing to the field enhancement. Our findings are supported by electromagnetic simulations and electron energy loss spectroscopy. We provide a phenomenological model for the field enhancement.

The lightning-rod effect is a well-known phenomenon in electrostatics characterized by the formation of a strong electric field near the sharp features of a charged conductor. Field enhancement is one of the key targets in plasmonics and one of the main characteristic features of localized surface plasmon resonances (LSPR) supported by metallic nanostructures known as plasmonic antennas (PAs). Intuitively, it is expected that PAs will produce a particularly strong electromagnetic field around their features with high curvature and this consideration translates to meticulous design of plasmonic structures with applications e.g. in enhanced photoluminescence [1] or strong light-matter coupling [2]. However, this so-called plasmonic lightning-rod effect (PLRE) is not rigorously understood despite studies addressing its particular aspects [3,4]. Importantly, the field enhancement in plasmonics stems from additional contributions besides local curvature, including the evanescent nature of LSPR or the magnitude of the induced charge for a specific excitation. In our communication, we isolate the contribution of the local curvature of a plasmonic antenna to the magnitude of the electric field of its dipole LSPR.

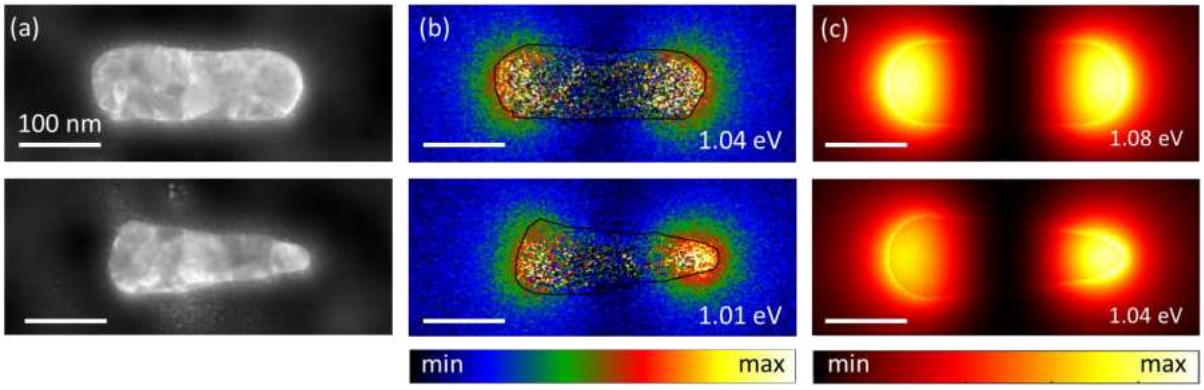


Figure 1: Two PAs with a fixed radius r_{fix} (50 nm) at the left side and a variable radius r_{var} (50 nm and 20 nm) at the right side imaged by transmission electron microscope (a) together with EELS of their dipole localized surface plasmon resonance: (b) measured, (c) calculated. The plasmonic lightning-rod effect is manifested as the intense loss signal at the sharp side of the PAs at the bottom panel ($r_{\mathrm{var}} = 20$ nm).

We design a set of rod-like PAs of identical length with two cylindrical terminations, one with a fixed radius r_{fix} and one with a variable radius r_{var}. Gold PAs are fabricated by focused ion beam lithography [Fig. 1(a)] and characterized by electron energy loss spectroscopy (EELS) and electromagnetic simulations [Fig. 1(b,c)]. A

comparison of responses at both terminations allows for assessing the role of the local curvature in the field enhancement. At the fixed-radius end, we observe the identical loss intensity [Fig. 2(b)] and field enhancement for all the PAs independent of their variable radius. This ensures that the variations in the response at the variable-radius end can be attributed purely to the local curvature. A good quantitative agreement between the experiment and simulations in both spatial [Fig. 1(b,c)] and spectral [Fig. 2(a)] domains verifies the validity of the simulations and allows to employ them for retrieval of the electric field, whose magnitude at the axis of the PA 20 nm away from the variable-radius end is shown as a function of the PA local radius r_{var} in Fig. 1(c). Finally, we present an intuitive phenomenological model for the induced electric field based on an effective induced point charge.

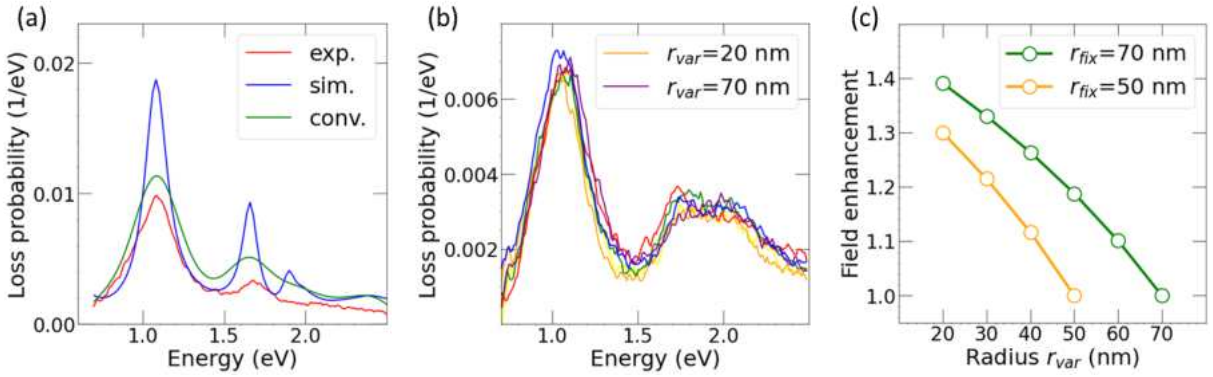


Figure 2: (a) The loss probability spectrum obtained from the experiment (red line), calculated (blue line), and calculated followed by the convolution with the instrumental broadening profile (green line). (b) The loss probability measured at the fixed-radius side of PAs demonstrates that the effects beyond the local curvature do not alter the induced field for our set of PAs. (c) The magnitude of the electric field calculated at the distance of 20 nm from a variable-radius side of the PA divided by the same quantity for $r_{\mathrm{var}} = r_{\mathrm{fix}}$ is displayed as a function of the local radius. Stronger fields obtained from sharper features of PAs represent the quantified manifestation of PLRE.

We acknowledge the support of the Czech Science Foundation (project No. 22-04859S), and the Ministry of Education of the Czech Republic (project CzechNanoLab Research Infrastructure, No. LM2018110, and QM4ST, No. CZ.02.01.01/00/22_008/0004572).

References

1. Kinkhabwala, A., Yu, Z., Fan, S., Avlasevich, Y., Müllen, K, and Moerner, W. E, "Large single-molecule fluorescence enhancements produced by a bowtie nanoantenna," Nature Photon., Vol. 3, 654–657, 2009.
2. Bitton, O., Gupta, S.N., Houben, L, Kvapil, M., Křápek, V. Šikola, T, and Haran, G., "Vacuum Rabi splitting of a dark plasmonic cavity mode revealed by fast electrons," Nat. Commun., Vol. 11, 487, 2020.
3. García-Etxarri, A., Apell, P, Käll, M., and Aizpurua, J., "A combination of concave/convex surfaces for field-enhancement optimization: the indented nanocone," Opt. Express, Vol. 20, 25201–25212, 2020.
4. Hrtoň, M., Konečná, A., Horák, M., Šikola, T. and Křápek, V., "Plasmonic Antennas with Electric, Magnetic, and Electromagnetic Hot Spots Based on Babinet's Principle," Phys. Rev. Appl., Vol. 13, 054045, 2020.

Controlled radiation modes of second harmonic generation from plasmonic nanoantennas

Yoshito Y. Tanaka[1]

[1] Research Institute for Electronic Science, Hokkaido University, Japan
*corresponding author: ytanaka@es.hokudai.ac.jp

Abstract: We have theoretically and experimentally investigated the control of the radiation mode of second harmonic (SH) generation from plasmonic nanonantennas by near-field coupling of surface SH polarization induced by the fundamental field into the plasmonic eigenmodes at the SH wavelength.

Controlling the process of second-harmonic (SH) generation in plasmonic nanostructures is important for practical applications in imaging, label-free sensing, and the selective identification of biomaterials, but remains challenging in nanophotonics. Although second-order nonlinear-optical effects are forbidden in metals within the electric-dipole approximation, a SH polarization that radiates the electromagnetic field with doubled frequency of the incident light is generated at the surface of the metal nanostructures and can be strongly enhanced by plasmonic near-field concentration, resulting in SH signals that are observable even at the nanoscale. Generally, SH radiation patterns from metal nanostructures are based on quadrupole and are strongly influenced by uncontrollable defects in the realistic metal nanostructures, such as surface roughness. Therefore, direct shaping of the SH radiation patterns is difficult. To address this issue, we control SH radiation mode through near-field coupling of surface SH polarization into plasmonic eigenmodes of nanoantennas.

To reveal plasmonic modes that can be coupled by the SH polarization, we have focused on a cross-shaped single-element plasmonic nanoantenna (Fig. 1). Owing to the symmetry of the structure, the excited plasmon modes can be expanded into many orthogonal basis modes, making it easy to determine the plasmon modes that affect the SH process. Based on theoretical and experimental studies, we found that the nanonatenna resonating with bright and dark modes at the fundamental and SH wavelengths, respectively, generates radially polarized ring-shaped SH radiations with axial symmetry by exciting the bright dipole mode with linearly polarized light [1]. Mode expansion analysis of the generated SH radiation revealed that the radial polarization arises from a dark breathing mode in which coherent dipoles are radially distributed along the arms of the cross-shaped antenna. Our results reveal that surface SH polarization generated by the electric near-field of the bright mode at the fundamental wavelength is efficiently coupled to the dark modes rather than the bright mode because its spatial distribution has the same symmetry as the dark modes. By engineering bright and dark modes at the fundamental and SH wavelengths, respectively, novel plasmonic nanodevices that simultaneously perform polarization control and efficient wavelength conversion are expected.

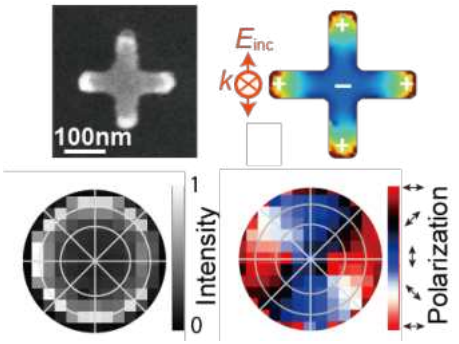


Fig. 1 SEM image of a cross-shaped nanoantenna and its measured intensity and polarization patterns of SH radiation from dark breathing mode induced by SH polarization.

However, the dark modes can not be efficiently coupled to the radiation fields. Furthermore, established approaches in linear optical processes for controlling the radiation field of bright modes are not available. To

couple the surface SH polarization into the bright modes, we studied SH radiations from symmetry-breaking V- and Y-shaped plasmonic nanoantennas [2]. Owing to spatial overlap of two orthogonal plasmonic bright (dipole) modes at the fundamental and SH wavelengths of the nanoantennas, surface SH polarizations induced by the fundamental field is efficiently near-field coupled to the SH plasmon mode, resulting in dipolar SH radiation from the antennas. Moreover, the phase of this radiation can be tuned simply by altering the part of the Y-antenna shape, which changes the SH plasmon resonance while keeping the fundamental resonance. Based on the same design approach as Yagi-Uda nanoantenna, unidirectional SH radiation perpendicularly to an incident light direction has been theoretically and experimentally demonstrated using a pair of the V-and Y-shaped antennas (Fig. 2). Our approach is a promising platform for engineering not only directional nonlinear nanoantennas but also nonlinear metamaterials.

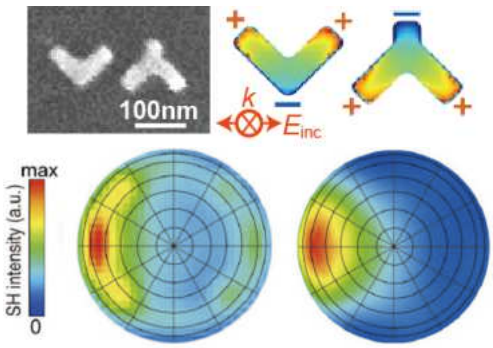


Fig. 2 SEM image of a pair of V- and Y-shaped nanoantennas and its measured and calculated intensity patterns of SH radiation from bright modes induced by SH polarization.

This work was supported by JST FOREST Program, Grant Number JPMJFR213O, Japan, and JSPS KAKENHI grant no. 22H05132 in Grant-in-Aid for Transformative Research Areas “Revolution of chiral materials science using helical light fields”.

References

1. Tanaka, Y. Y., Kimura, T. and Shimura, T., “Radially Polarized Second-Harmonic Generation from a Single-Element Nanoantenna via Dark Plasmon Coupling of Nonlinear Polarization,” ACS Photon., Vol. 9, 3649–3655, 2022.
2. Tanaka, Y. Y., Kimura, T. and Shimura, T., “Unidirectional emission of phase-controlled second harmonic generation from a plasmonic nanoantenna,” Nanophotonics, Vol. 10, No. 18, 4601–4609, 2021.

Beam Engineering for Enhanced Light-Matter Interactions in Optical Nanostructures

Uttam Manna*, and Mahua Biswas

Department of Physics, Illinois State University
*corresponding author: umanna@ilstu.edu

Abstract: The state of polarization of scalar beams (e.g., linearly, circularly polarized beams) does not depend on the spatial location of the beam. Alternately, the cylindrical vector beams (CVBs) possess spatially variant polarization states with axial symmetry in both amplitude and phase.[1] Such beams can have their electric fields aligned in azimuthal (radial) orientations, while the magnetic fields are aligned in radial (azimuthal) directions with respect to the optical axis, known as *azimuthally (radially) polarized* beam.[1-3] For focused azimuthally polarized beam (APB) with a high numerical aperture (NA), the longitudinal (*z*)-component of the magnetic field can exceed the transverse component of the magnetic field in the focal region; whereas the electric field component is purely transverse.[3] In this talk, I will review our recent works on enhanced light-matter interactions in various optical nanostructures under illumination with cylindrical vector beams that demonstrate selective excitation of multipolar resonances and excitation of optical anapoles in high-index dielectric nanoparticles,[6] selective induction of optical magnetism in dielectric core−metal nanoparticle nanostructures,[7] etc.

This material is based upon work supported by the National Science Foundation (NSF), Division of Material Research under Grant No. DMR-2208240. We also thank John A. Parker, Norbert Scherer, Stephen Gray, Hiroshi Sugimoto, and Minoru Fujii for their valuable contributions.

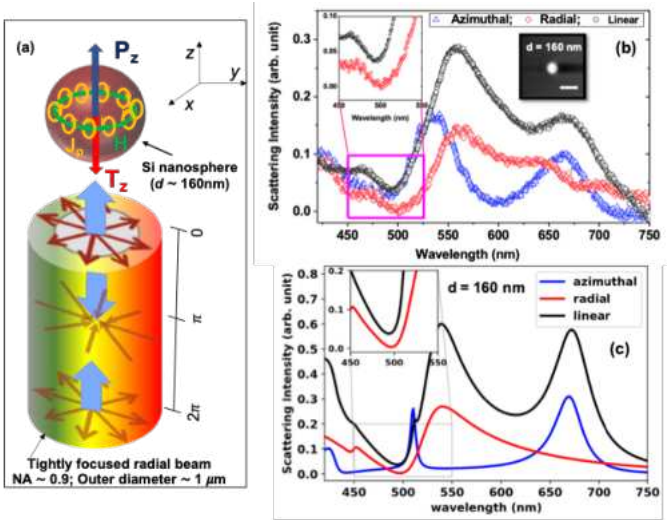


Figure 1: (a) Schematic diagram showing excitation of a Si nanosphere (d ~ 160 nm) for radially polarized beam excitation leads to the excitation of optical anapoles. The experimental (b) and simulated (c) scattering spectra of single Si nanospheres (d ~ 160 nm) for linearly, radially, and azimuthally polarized beam illuminations.

References

1. Hall, D. G. "Vector-beam solutions of Maxwell's wave equation," Opt. Lett., 21, 9-11, 1996.
2. Novotny, L. and Hecht. B. Principles of Nano-Optics, Cambridge University Press, 2006.
3. Youngworth, K. S. and Brown, T. G. "Focusing of high numerical aperture cylindrical-vector beams", Opt. Express, 7, 77-87, 2000.
4. Kasperczyk, M. Person, S. Ananias, D. Carlos, L. D. and Novotny, L. "Excitation of Magnetic Dipole Transitions at Optical Frequencies," Phys. Rev. Lett., 114, 5, 2015.
5. Wozniak, P. Banzer, P. and Leuchs, G. "Selective switching of individual multipole resonances in single dielectric nanoparticles," Laser Photonics Rev., 9, 231-240, 2015.
6. Parker, J. A. Sugimoto, H. Coe, B. Eggena, D. Fujii, M. Scherer, N. F. Gray, S. K. and Manna, U. "Excitation of Nonradiating Anapoles in Dielectric Nanospheres," Phys. Rev. Lett., 124, 097402, 2020.
7. Manna, M. Lee, J. H. Deng, T. S. Parker, J. Shepherd, N. Weizmann, Y. and Scherer, N. F. "Selective Induction of Optical Magnetism," Nano Lett., 17, 7196-7206, 2017.

Spin-valley nanophotonics with atomically thin semiconductors

Alberto G. Curto[1,2,3*]

[1] Department of Applied Physics and Eindhoven Hendrik Casimir Institute,
Eindhoven University of Technology, Eindhoven, The Netherlands
[2] Photonics Research Group, Ghent University-imec, Ghent, Belgium
[3] Center for Nano- and Biophotonics, Ghent University, Ghent, Belgium

[*]Corresponding author: Alberto.Curto@UGent.be

Abstract: Atomically thin semiconductors such as WS_2 can sustain spin-valley polarization and emit circularly polarized light. Using few-layer WS_2, we investigate the electrodynamic nature of valley-polarized emission using back focal plane imaging. We also demonstrate a Drexhage experiment to enhance and control valley-polarized emission.

Two-dimensional semiconductors hold great promise for nanoscale photonics and optoelectronics. Based on robust excitons at room temperature, they exhibit strong light absorption and emission, and they are easy to integrate into nanophotonic structures. One of their most promising properties is spin-valley polarization. In atomically thin semiconductors such as monolayer MoS_2 or WS_2, the spin and momentum direction of carriers can be locked. As a result, using circularly polarized light, we can populate carriers with a momentum direction that depends on the handedness of the optical excitation.[1] This degree of freedom, known as valley polarization, could be exploited to add a new dimension to information processing and optoelectronics. To fully take advantage of valley polarization for nanophotonics, it is necessary to better understand the conditions for it to occur, its electrodynamic nature, and the possibilities for enhancing it through optical means.

In this presentation, we characterize the microscopic electrodynamic character of valley polarization and valley coherence in few-layer WS_2 at room temperature. We employ back focal plane (BFP) imaging to record polarization-resolved angular radiation patterns. By analyzing the spin of the evanescent part of the angular spectrum, we identify circular and linear electric dipole characteristics in WS_2 excitons under circularly and linearly polarized excitations, respectively. Such evanescent optical spin is transferable to the far field using a glass substrate and has peculiar characteristics. Our investigation compares theory and experimental results for a dipolar source of photoluminescence in few-layer WS_2 semiconductors on a glass substrate. Utilizing polarization-resolved BFP imaging, we attribute valley-polarized emission to circularly polarized electric dipoles and valley-coherent emission to linearly polarized dipoles. Interestingly, it is possible to observe emission with linear polarization under certain angles for valley-polarized emission, and radiation with circular polarization for valley-coherent emission.

The ideal valley-polarized material should exhibit high emission quantum efficiency together with high polarization. However, currently available transition metal dichalcogenides suffer from either low efficiency or low polarization. In the second part of this presentation, we follow a nanophotonic route to enhance circularly polarized emission capable of enhancing both the emission intensity and the degree of polarization. We introduce a Drexhage experiment for valley polarization, where we control the distance between a WS_2 bilayer and a mirror using dielectric spacers. Our experiment achieves nearly complete control over valley-polarized

emission at room temperature, with a degree of circular polarization varying from 0.1 to 0.75 at different distances. We characterize the lifetime of the polarized emitted photons and the angular radiation patterns. We interpret the results using a rate equation model and highlight the impact of distance and power-dependent polarization on valley dynamics, providing a new path to control valley polarization. Unlike complex arrays of nanostructures,[2] our Drexhage experiment is a simple yet effective method to exert robust control over valley polarization by exploiting exciton dynamics. Our findings elucidate the spin-valley dynamics influenced by exciton-exciton annihilation.

Our results offer valuable insights into the dipolar nature of exciton emitters with valley polarization and their intrinsic evanescent fields. By understanding, controlling, and enhancing the circular polarization of light emitted by WS_2, our results open up new possibilities for spin-based nanophotonic and optoelectronic devices. Our findings have implications for applications such as polarization-controlled light on-chip and the development of valley-based technologies and integrated photonic devices.

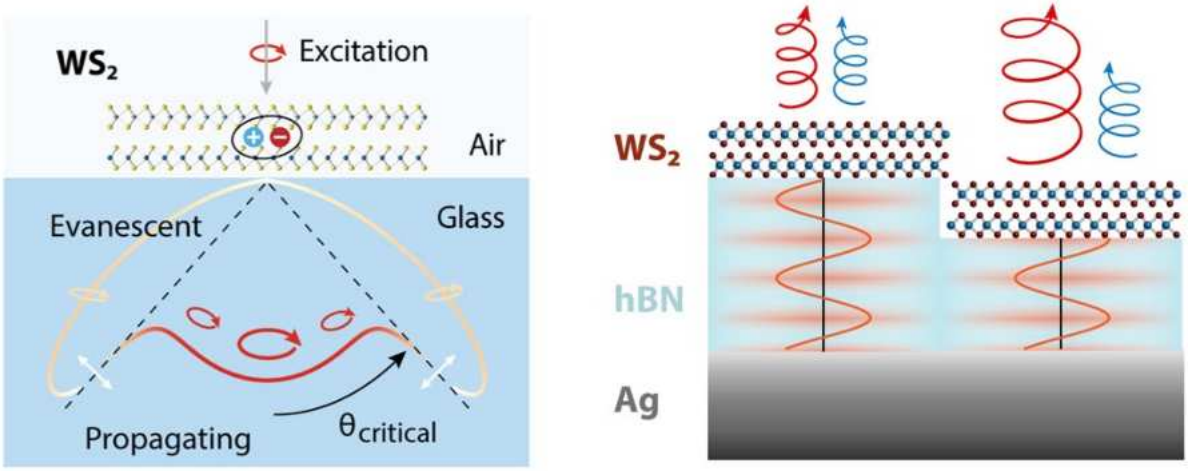


Figure 1. Polarization-resolved angular radiation patterns of few-layer WS_2 and enhanced valley-polarized emission near a mirror.

References

1. Godiksen, R. H., Wang, S. Raziman, T. V., Gómez Rivas, J., Curto, A. G. Impact of indirect transitions on valley polarization in WS_2 and WSe_2, *Nanoscale* 14, 17761, 2022.
2. Raziman, T. V., Godiksen, R. H. , Müller, M. , Curto, A. G.. Conditions for enhancing chiral nanophotonics near achiral nanoparticles, *ACS Photonics* 6, 2583 (2019).

Multiplexed single-molecule plasmon sensing by spectral decomposition

V. Lamberti, S. Nooteboom, T. Schellekens, and P. Zijlstra[1]

[1]Eindhoven University of Technology, Department of Applied Physics and Science Education, The Netherlands
*corresponding author: p.zijlstra@tue.nl

Abstract: Narrowband light-matter interactions mediated by plasmonic nanoantennae strongly modify a nearby emitter's emission spectrum. Such reshaping shrouds the original emission spectrum of the dye and hampers multicolor applications. Here, I will describe our recent efforts to elucidate single-molecule spectral reshaping and use it for continuous and multicolor single-molecule plasmon sensing.

Light-matter interactions between a plasmonic nanoantenna and a molecule have proven their value in applications like biosensing and spectroscopy. Herein coupling between the molecule and plasmonic modes in the antenna result in strongly enhanced excitation rates, modification of decay rates by the local density of states, and modulation of the radiation pattern of the emitter. In recent years this has enabled highly directional nanoantennas, fast probing of single-molecule SERS, and single-molecule biosensing mediated by plasmon-enhanced fluorescence.

These applications employ nanoantennas that are functionalized with e.g. protein or DNA using thiol-mediated surface chemistry. I will describe the use of these DNA-coated nanoparticles [1] for multiplexed single-molecule biosensing [2]. We use a sandwich assay whereby the presence of analyte is revealed by reversible binding of a fluorescently labeled detection probe. We perform spectroscopy of each single-molecule binding event, and study the spectral reshaping induced by plasmon-fluorophore coupling. Spectral decomposition enables us to extract the underlying dye spectrum from the strongly reshaped overall emission spectrum. Despite the strong spectral reshaping by the antenna we achieve 3-color multiplexed single-molecule sensing. This will pave the way toward single-molecule and multiplexed digital diagnostics

References

1. Dey et al. “Biomolecular interactions on densely coated nanoparticles: a single-molecule perspective,” Nanoscale 16, 4872-4879 (2024).
2. Lamberti, V. et al. “Continuous Monitoring Biosensing Mediated by Single-Molecule Plasmon-Enhanced Fluorescence in Complex Matrices,” ACS Nano 18, 5805–5813 (2024).

Mie resonances in silicon nanospheres probed by pump-probe cathodoluminescence spectroscopy

S. Fiedler[1*], Evelijn Akerboom[1], Patrick Spaeth[1], Hiroshi Sugimoto[2], Minoru Fujii[2], and A. Polman[1]

[1]Photonic Materials, NOW-Institute AMOLF, Science Park 104, 1098 XG Amsterdam, The Netherlands
[2]Department of Electrical and Electronic Engineering, Kobe University, Rokkodai, Nada, Kobe 657-8501, Japan
[*]corresponding author: s.fiedler@amolf.nl

Abstract: We study optical Mie resonances in individual Si nanospheres (NPs) using cathodoluminescence (CL) spectroscopy, complemented with theoretical CL calculations. We couple light into the SEM-CL system to locally heat NPs and observe spectral shifts of Mie modes. Delaying the synchronized laser and electron pulses enables *in-situ* pump-probe CL for nanothermometry.

The fabrication of nanostructures with ever-decreasing sizes has increased the demand of suitable characterization methods allowing to determine their shape and size at the nanoscale and enable the investigation of their optical properties beyond the diffraction limit. Due to the high spectral and spatial resolution, cathodoluminescence spectroscopy (CL), has become a powerful characterization tool to study plasmonic and dielectric nanostructures. Of particular interest is the control over the nanoscale distribution of light fields in the optical spectral range which can be readily investigated using CL nanoscopy.

In this work, we systematically study the electric near-fields induced by free electrons coupling to optical Mie modes in individual Si nanospheres[1] (NPs) using both hyperspectral CL mapping[2] and angle-resolved CL. Furthermore, we present the first exploration of using a pulsed laser in our scanning electron microscope (SEM) to perform ultra-fast pump-probe CL spectroscopy of such single Si NPs.

First, we collect hyperspectral CL maps to identify the spectral and spatial signature of the different (magnetic and electric) Mie modes within an individual Si NP (d ~ 240 nm) suspended on a 15 nm-thin SiN membrane, as shown in figure 1. We find that the intensity of the NP's eigenmodes (electric (EQ) and magnetic (MQ) quadrupole Mie mode) changes depending on the electron beam position within the NP.

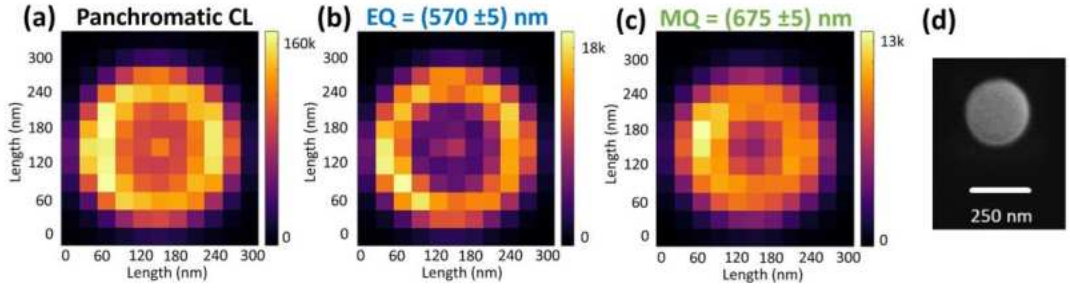


Figure 1 30 keV-CL maps integrated (a) over the entire spectral range from 350 nm to 850 nm, (b) over the electric quadrupole (EQ) and (c) magnetic quadrupole (MQ) Mie mode of the 240 nm-sized Si nanosphere suspended on a 15 nm-thin SiN membrane. (d) Corresponding SEM image.

To gain a more fundamental insight into these excited near-fields, we perform theoretical calculations of the coupling strength[3] between the incoming electron and individual Mie modes which has shown to be strongly dependent on the electron's velocity, electron beam position within the NP and the selected Mie mode. The

exemplary decomposition of the electric (ED) and the magnetic dipole (MD) Mie mode of a 180 nm-sized Si NP using a 25 keV-electron beam excitation is displayed in figure 2. We note that a swift electron moving along the z-axis only allows for coupling to the z-component of an electric near-field. To complement the near-field imaging, we also perform angle-resolved CL maps, allowing us to explore the radiation into the far-field both experimentally and theoretically.

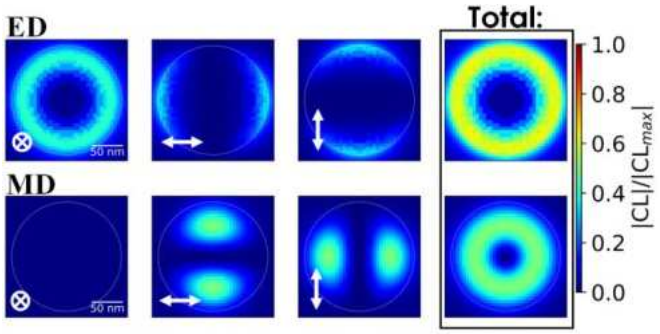


Figure 2 Calculated coupling strength between 25 keV-electron and electric (ED) and magnetic dipole (MD) mode in a 180 nm-sized Si nanosphere (top view).

Second, we couple a pulsed laser into the SEM to locally heat a single Si NP. Due to the thermo-optical effect in Si, a spectral shift of Mie modes can be observed (cf. figure 3) and ultimately, used for nanothermometry. Using an ultra-fast electrostatic beam blanker, we generate ns-electron pulses to probe those spectral shifts in Mie modes upon laser heating. We then systematically delay the synchronized laser and electron pulses to study the time evolution of temperature changes using these Mie modes.

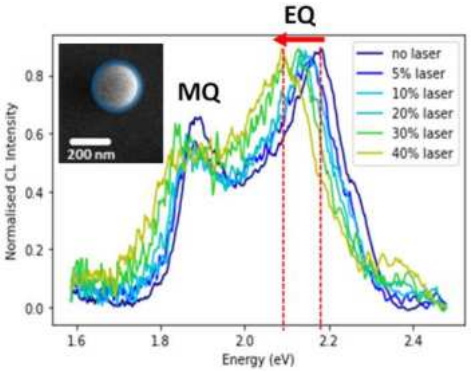


Figure 3 cw-laser (λ = 440 nm) heated Si NP (d ~240 nm) showing 100 meV-spectral shift of EQ Mie mode.

Introducing a pulsed laser in the SEM-CL chamber ultimately opens up a new world of *in-situ* studies of electron-light-matter interactions with applications in photovoltaics, photocatalysis and more.

Acknowledgements: FET-Proactive EBEAM (Grant No. 101017720).

References

1. Sugimoto, H., Okazaki, T., and Fujii, M., "Mie Resonator Color Inks of Monodispersed and Perfectly Spherical Crystalline Silicon Nanoparticles," Adv. Optical Mater., 8, 2000033, 2020.
2. Fiedler, S., Stamatopoulou, P. E., Assadillayev, A., Wolff, C., Sugimoto, H., Fujii, M., Mortensen, N. A., Raza, S., and Tserkezis, C., "Disentangling Cathodoluminescence Spectra in Nanophotonics: Particle Eigenmodes vs Transition Radiation," Nano Lett., 22, 6, 2320-2327, 2022.
3. De Abajo, F. G., "Optical excitations in electron microscopy," Rev. Mod. Phys., 82, 209, 2010.

Optical Metafluid Made from Silicon Nano-spheres

Minoru Fujii[1], **and Hiroshi Sugimoto**[1]

[1]Department of Electrical and Electronic Engineering, Graduate School of Engineering, Kobe University, Japan

Abstract: A silicon nanoparticle exhibits optical magnetism, and can satisfy the electromagnetic duality symmetry condition at the 1st Kerker condition. We demonstrate that the colloidal suspension also has the optical magnetism and acts as a metafluid that preserves the handedness of circularly polarized light.

A colloidal suspension of photonic nanostructures exhibiting optical magnetism is dubbed an optical metafluid. A promising constituent of a metafluid is a nanoparticle of high-refractive index dielectrics having the magnetic-type Mie resonances in the optical frequency. A nanosphere of crystalline silicon 100 to 300 nm in diameters is an almost ideal constituent of an optical metafluid because of the high refractive index and the low extinction coefficient in the visible to near infrared spectral range. Recently, a process to produce high-quality silicon nanospheres in large quantities has been developed [1]. This makes experimental researches on optical metafulids possible. In this work, we will show our recent work on silicon nanosphere-based optical metafluids.

Figure 1a shows water solutions of different diameter silicon nanospheres. Because of the small size distributions, distinctive size-dependent scattering color can be seen. Figure 1b and c shows the TEM images. The silicon nanospheres are almost perfectly spherical and have high crystallinity. In these solutions, the magnetic dipole (MD) resonance is as large as that of the electric dipole (ED) resonance [2]. This almost unity magnetic-to-electric response ratio is very difficult to achieve in plasmonic nanoparticle-based metafluids, and is an advantage of dielectric nanoparticles having the magnetic-type Mie resonances.

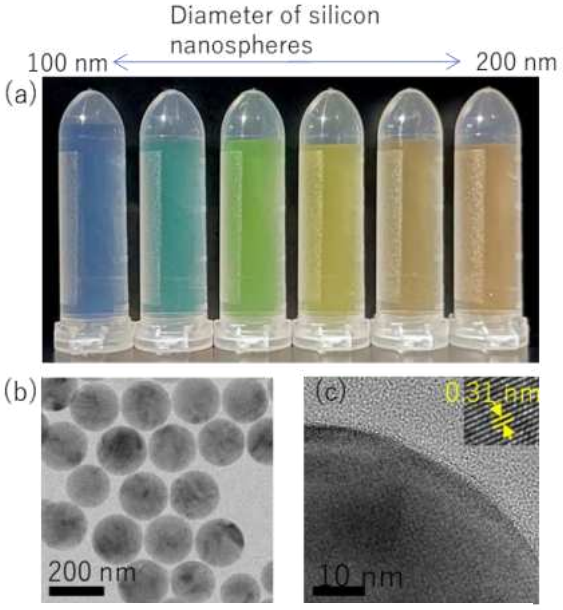


Figure 1. (a) Photos of water solutions of size-purified silicon nanospheres. (b, c) TEM images of silicon nanospheres.

Because of the strong optical magnetism, an individual silicon nanosphere can satisfy the electromagnetic duality symmetry condition at a specific wavelength, and thus can preserve the handedness of circular polarization of incident light in the scattering event to all directions. This suggests that a metafluid of silicon nanospheres also preserves the helicity of incident light. In order to experimentally demonstrate the helicity preservation in silicon nanosphere-based metafluids, we perform polarization- and angle-resolved scattering measurements.

Under illumination by circularly polarized plane wave, the expected value of the electromagnetic helicity density of a silicon nanosphere for the whole solid angle is given by,

$$\langle \Lambda \rangle = \frac{2|a_1||b_1|\cos(\varphi_{MD}-\varphi_{ED})}{|a_1|^2+|b_1|^2}, \qquad (1)$$

where a_1 and b_1 are the Mie coefficients corresponding to the ED and MD modes, respectively, and $\varphi_{MD} -$

φ_{ED} is the phase difference. This equation is equivalent to that of the degree of circular polarization of scattered light to a right angle ($\theta = \pi/2$) under RHC polarized light illumination,

$$\eta\left(\frac{\pi}{2}\right) = \frac{I_{RHC}(\pi/2) - I_{LHC}(\pi/2)}{I_{RHC}(\pi/2) + I_{LHC}(\pi/2)}, \qquad (2)$$

where $I_{RHC}(\pi/2)$ and $I_{LHC}(\pi/2)$ are the intensities of RHC and LHC-polarized componetns of scattered light, respectively [3]. Therefore, by simple scattering measurements to $\theta = \pi/2$ direction (Figure 2a), averaged helicity density for the whole solid angle is obtained. Figure 2b shows the spectra of $I_{RHC}(\pi/2)$ and $I_{LHC}(\pi/2)$, and Figure 2c shows that of the degree of circular polarization $\eta(\pi/2)$ obtained from Figure 2b. The calculated helicity density spectrum is also shown in Figure 2c. The measured spectrum agrees well with the calculated one. The measured helicity density is around 0.70 at the maximum (685 nm), i.e., at the 1st Kerker condition, where the ED and MD Mie resonances have the same amplitude and are in-phase. The slight degradation of the helicity density value compared to the calculated one is mainly due to the imperfection of the broadband λ/4 plates and other optical components. The observed large helicity density value in combination with calculations indicates that the local chiral fields around the silicon nanospheres are strongly enhanced. This enhances the chiral light-matter interaction, and may be used to improve the sensitivity of enantiomer-selective chiral molecular sensing [4].

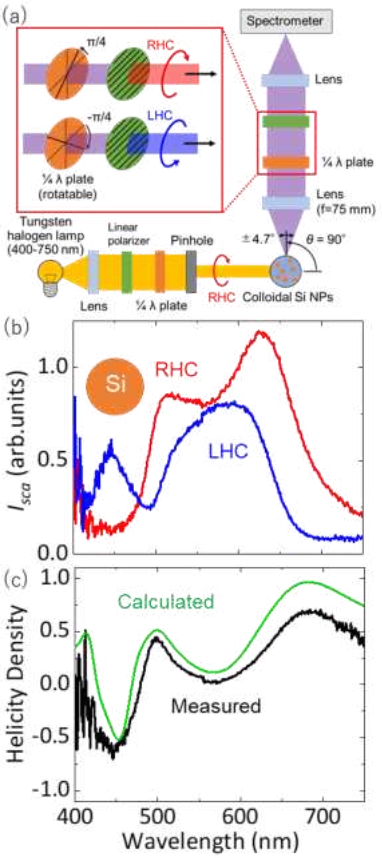


Figure 2. (a) Setup for polarization-resolved scattering measurement. (b) RHC- and LHC-polarized components of scattering spectra of a metafluid under RHC polarized light illumination. (c) Measured degree of circular polarization spectrum ($\eta(\pi/2)$) and calculated expected value of helicity density $\langle\Lambda\rangle$ spectrum.

Acknowledgements: This work was supported by JSPS KAKENHI, Grant Number 22K18949, and JST FOREST Program, Grant Number JPMJFR213L, and partially supported by JSPS KAKENHI, Grant Numbers 18KK0141, 21H01748, and 21H01782.

References

1. Hiroshi Sugimoto, Takuma Okazaki, and Minoru Fujii, "Mie Resonator Color Inks of Monodispersed and Perfectly Spherical Crystalline Silicon Nanoparticles", Advanced Optical Materials, Vol. 8, No. 2000033 (2020).
2. Tatsuki Hinamoto, Shinnosuke Hotta, Hiroshi Sugimoto, and Minoru Fujii, "Colloidal Solutions of Silicon Nanospheres toward All-Dielectric Optical Metafluids", Nano Letters, Vol. 20, P.7737 (2020).
3. Hidemasa Negoro, Hiroshi Sugimoto, Minoru Fujii, "Helicity-Preserving Optical Metafluids", Nano Letters, Vol. 23, P.5101 (2023).
4. Jorge Olmos-Trigo, Hiroshi Sugimoto, Minoru Fujii, "Far-Field Detection of Near-Field Circular Dichroism Enhancements Induced by a Nanoantenna", Laser & Photonics Reviews, (2024) (DOI: 10.1002/lpor.202300948).

Solving Maxwell Equations from a Single Polarimetry Measurement

Jorge Olmos-Trigo[1*]

[1]Departamento de Física, Universidad de La Laguna, Apdo. 456. E-38200, San Cristóbal de La Laguna, Santa Cruz de Tenerife, Spain.
[*]corresponding author: jolmostrigo@gmail.com

Abstract: Maxwell's equations are solved when the amplitude and phase of the electromagnetic field are determined at all points in space [1]. The Stokes parameters can only capture the amplitude and polarization state of the electromagnetic field in the radiation (far) zone [2]. Therefore, the measurement of the Stokes parameters is, in general, insufficient to solve Maxwell's equations. In this Letter, we demonstrate that measuring the Stokes parameters at a single scattering angle is sufficient to solve Maxwell's equations for a set of objects widely used in Nanophotonics. Our method for solving Maxwell's equations endows the Stokes parameters, commonly used to capture only the polarization of light, an even more fundamental role in the electromagnetic scattering theory.

The determination of the amplitude and phase of the electromagnetic field at all points in space solves Maxwell's equations. Currently, electromagnetic software packages can provide the numerical solution to Maxwell's equations. However, solving Maxwell's equations in the optical laboratory is exceptionally challenging due to the need to measure the scattered field produced by the object at all points of the radiation zone. On top of that, the internal field induced in the excited object is experimentally inaccessible.

In stark contrast, the Stokes parameters can be readily measured using a photodiode and waveplates. The Stokes parameters can capture the amplitude and polarization state of the electromagnetic field in the radiation (far) zone. As we mentioned earlier, the determination of the electromagnetic phase is necessary to solve Maxwell's equations. Therefore, the measurement of the Stokes parameters is, in general, insufficient to solve Maxwell's equations (even if restricted to the far-field).

In this tak, we demonstrate that a measurement of the Stokes parameters at a single scattering angle is sufficient to solve Maxwell's equations for a widely used set of objects [3]. This set of objects shares the following features: they are lossless, axially symmetric, and their optical response is well- described by a single multipolar order. The key to our procedure lies in linking the measurement of the Stokes parameters in the radiation (far) zone with the electric and magnetic scattering coefficients of the multipolar expansion of the scattered electromagnetic field. As we show, the determination of these scattering coefficients solves Maxwell's equations at all points of the radiation zone, ranging from far-to-near field. Additionally, in the case of spherical objects, we solve Maxwell equations at all points in space (also inside the object).

Let us highlight the main features of our procedure for solving Maxwell's equations in the radiation zone:

- Simplicity in the measurement: Our method only relies on a measurement of the Stokes parameters at a single scattering angle in the far-field.

- Generality of the material and shape of the object: Our method works for axially symmetrical objects such as disks, pillars, spheres, and spheroids. Note that these objects can be composed of a single material or not (coated objects). The only requirement is that the absorption cross-section of these objects must be zero.

- Wide range of illumination conditions: Our method can accommodate plane waves, Gaussian beams, or even vortex wavefields. The only requirement is that the angular momentum m of the light-scattering system must be well-defined.

To the best of our knowledge, this study represents the first proposal of a method capable of solving Maxwell's equations from a single polarimetry measurement. This feature endows the Stokes parameters an even more fundamental role in the electromagnetic scattering theory. Consequently, our findings, supported by analytical theory and exact numerical simulations, can find applications in all branches of Nanophotonics and Optics.

References

1. J. C. Maxwell, Philosophical transactions of the Royal Society of London , 459 (1865).
2. G. G. Stokes, Transactions of the Cambridge Philosophical Society 9, 399 (1851).
3. J. Olmos-Trigo, arXiv preprint arXiv:2310.17946 (2023).

Probing the quantum tunneling in plasmonic gaps with magnetic plasmon resonances

Haisheng Luo[1], Ruizhao Yao[1], Helene Giesler[2], Sebastian Schlücker[2], Sheng Lan[1] and Guang-Can Li*

[1]School of Information and optoelectronic Science and Engineering, South China Normal University, China
[2]Faculty of Chemistry, University Duisburg-Essen, Germany
*corresponding author: Guangcan.li@m.scnu.edu.cn

Abstract: The quantum tunneling (QT) effects in metal plasmonic gaps were revisited in a nanoparticle-dimer-on-mirror (NDoM) structure exhibiting concurrent electric and magnetic plasmon resonances. The distinct response of the magnetic resonance to the gap conductivity enable a reliable and robust strategy to deterministically probe QT events in thin metal gaps.

The electron tunneling in between two closely separated plasmonic nanoparticles constituents one of the most fundamental quantum effects in plasmonic optics. The probing of this quantum event in the particle gaps conventionally relies on inspecting the shifting trend of the bonding dipole plasmon (BDP) resonances when shrinking the gap distances, i.e., the resonance initially red shift with narrowing gaps at larger gap distance and then blue shift when the quantum tunneling effect sets on at smaller gap distances. This criterion is problematic in experimental implementation as it is difficult to precisely tune the gap distances while keeping the other geometry parameters (particle sizes, morphologies, etc.) constant. On the other hand, there is no way to deterministically confirm the occurrence of QT events in a specific plasmonic gap without reference to control experiments.

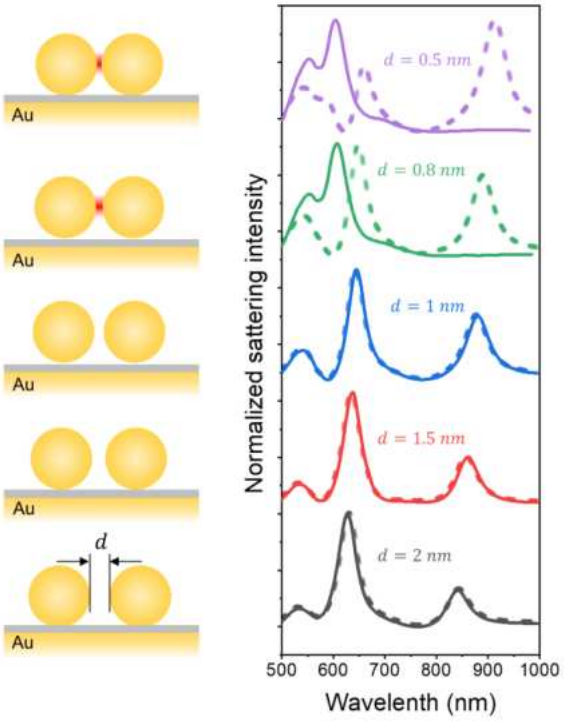


Figure 1 Schematic of nanosphere-dimer-on mirror (NDoM) structures with varying dimer gaps (left panel) and their scattering responses (right panel) simulated with the classical electromagnetic model (CEM, dashed lines) and the quantum-corrected model (QCM, solid lines).

In this work, established a new paradigm of inspecting quantum tunneling events in single plasmonic gaps with magnetic resonances, which does not rely on any control experiment. The testing nanoconstruct consists of a gold nanoparticle dimer on mirror (NDoM) structure, which exhibits concurrent electric (see Fig.1, the BDP at 625 nm for d = 2 nm) and magnetic dipole (The MD at 850 nm for d = 2 nm) resonances. We separate the dimer from the gold film with a dielectric spacer of a constant thickness of 3 nm, to avoid electron tunneling at the nanoparticle-mirror junctions. The quantum-corrected model (QCM), in contrast to the classical electromagnetic model (CEM) without counting in the quantum effects, was employed to calculate and predict the plasmonic responses of the NDoM with decreasing dimer gap distances. We saw the BDP resonances red shift first and then blue shift, indicating the occurrence of quantum tunneling at small gap distances (d = 0.8 and 0.5 nm). The magnetic resonances first slowly red shift with narrowing gaps at larger separation distances, but fully vanished when entering the quantum tunneling regime. These characters are in line with our experimental observations and suggest we can determine the occurrence of quantum tunneling events in single plasmonic gaps by inspecting only the magnetic resonances.

Funding: National Natural Science Foundation of China (Grant No 12274147); Natural Science Foundation of Guangdong Province (Grant No. 2023A1515012368); Natural Science Foundation of Guangzhou (Grant No. 202201010445); International Academic Exchange Program of Guangdong Province (Grant No. 2022A0505030012).

References

1. H-S Luo, R-Z Yao, H Giesler, S Schlücker, S Lan and G. -C. Li. 2024, In submission.
2. M Wersall, B Munkhbat, DG Baranov *et al*. ACS Photon. 2019, 60, 2570
3. J Jose, L Schumacher, M Jalali *et al*. ACS Nano 2022, 16, 21377
4. WQ Zhu, R Esteban, AG Borisov *et al*. Nat. Comm. 2016, 7, 11495
5. KJ Savage, MM Hawkeye, R Esteban *et al*. Nature 2012, 491, 574

Topology, Geometry, and Quantumness of Textured Light

Nonclassical states of light after high-harmonic generation in semiconductors: A Bloch-based perspective

J. Rivera-Dean[1], P. Stammer[1], A. S. Maxwell[2], Th. Lamprou[3,4], A. F. Ordóñez[1], E. Pisanty[5], P. Tzallas[3,6], M. Lewenstein[1,7], and M. F. Ciappina[8,9,10,*]

[1] ICFO–Institut de Ciencies Fotoniques, The Barcelona Institute of Science and Technology, 08860 Castelldefels (Barcelona)
[2] Department of Physics and Astronomy, Aarhus University, DK-8000 Aarhus C, Denmark
[3] Foundation for Research and Technology-Hellas-IESL, GR-70013 Heraklion (Crete), Greece
[4]Department of Physics, University of Crete, P.O. Box 2208, GR-70013 Heraklion (Crete), Greece
[5]Department of Physics, King's College London, WC2R 2LS London, United Kingdom
[6]ELI-ALPS, ELI-Hu Non-Profit Ltd., Dugonics tér 13, H-6720 Szeged, Hungary
[7]ICREA, Pg. Lluís Companys 23, 08010 Barcelona, Spain
[8]Physics Program, Guangdong Technion–Israel Institute of Technology, Shantou, Guangdong 515063, China
[9]Technion – Israel Institute of Technology, Haifa, 32000, Israel
[10]Guangdong Provincial Key Laboratory of Materials and Technologies for Energy Conversion, Guangdong Technion – Israel Institute of Technology, Shantou, Guangdong 515063, China
[*]corresponding author: marcelo.ciappina@gtiit.edu.cn

Abstract: We investigate high-harmonic generation in semiconductors from a quantum optical perspective and demonstrate the generation of non-classical light states. We analyze the dependence of their features on the solid characteristics and the driving field strength. Our study provides insights for generating non-classical light sources using bulk matter.

Since the first observations of the high-harmonic generation process (HHG) in gases, in the last quarter of the 20th century, strong-field physics has undergone tremendous and steady progress. Nowadays, HHG stands as one of the primary mechanisms behind extreme ultraviolet (XUV) radiation sources and attosecond pulse generation. It has found diverse applications in nonlinear XUV optics, attosecond science, molecular tomography, and high-resolution spectroscopy [1]. HHG in solid-state systems has also demonstrated significant potential for quantum technology applications. For instance, it was revealed that driving HHG in strongly correlated materials can serve as a tool for detecting topological order and for scrutinizing phase transitions [2].

Concerning the actual applications of semiconductors in the context of quantum information science, one of its main prospects is to use them as nonclassical compact light sources [3]. In this direction, the emergent connection between quantum optics and strong-laser field physics [4] has shown that, by means of HHG processes in atomic systems, one can generate nonclassical states of light with intensities strong enough to drive nonlinear processes in matter, as well as massive frequency-entangled states. Notably, these findings extend beyond HHG processes [5] in atomic systems. Specifically, for the case of solids, recent studies have demonstrated that the effect of electronic acceleration within the valence band could potentially yield analogous outcomes. While Wannier-based studies in solid-state systems have provided essential insights about the generation of nonclassical states of light after HHG in this kind of media, they are either limited to specific electron dynamics within the solid, or involve simplifications on the interaction with the material, restricting the analysis to a limited number of Wannier sites and neglecting dephasing effects. These limitations can be addressed by employing a Bloch-based description of the solid system, where the semiconductor Bloch equations (SBEs) offer a straightforward framework for describing dephasing times and the incorporation of many-body effects.

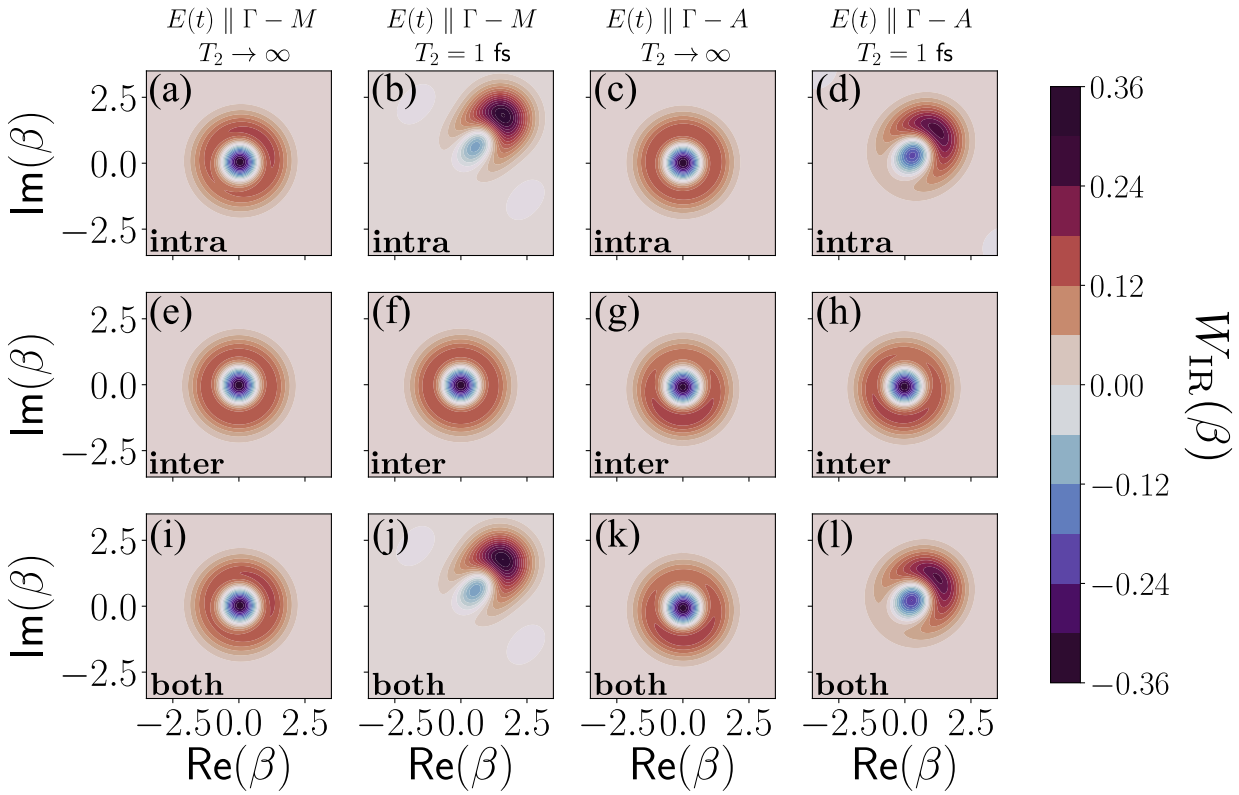


Figure 1. Wigner function representations of the generated entangled coherent state superposition under various conditions. Each column corresponds to distinct values of the dephasing time, T_2, along with different orientations of the applied linearly polarized laser field, specifically aligned with the Γ-M and Γ-A directions. The first two rows focus individually on the intraband and interband contributions, while the last row displays their combined effect. The laser parameters used in this case correspond to λ_L = 3.25 μm, field strength of 0.5 V/Å, and a duration of $\approx$ 96 fs (equivalent to nine optical cycles).

We present investigations of HHG in semiconductor materials under a quantum optical perspective. Our study focuses on the interaction of a strong infrared laser field, linearly polarized along different crystal orientations of a ZnO material, which has been extensively examined both experimental and theoretically. Similar to atomic systems, our findings show that conditioning measurements on the high-harmonic generation process, enable the creation of entangled coherent state superpositions. Thus, these results suggest that the experiments already conducted in atomic gases could potentially be conducted in typical semiconductor samples, utilized in much of the current technology.

We acknowledge financial support from the Guangdong Province Science and Technology Major Project (Future functional materials under extreme conditions - 2021B0301030005) and the Guangdong Natural Science Foundation (General Program project No. 2023A1515010871).

References

1. F. Krausz and M. Ivanov, Rev. Mod. Phys. **81**, 163 (2009)
2. J. Alcalà, et al., Proc. Natl. Acad. Sci. USA **119**, e2207766119 (2022)
3. J. Rivera-Dean, et al., Phys. Rev. B (in press) (2024)
4. M. Lewenstein, et al., Nat. Phys. **17**, 1104 (2021)
5. J. Rivera-Dean, et al., Phys. Rev. A **106**, 063705 (2022)

Lie Group Theory and Topology of Structured Light

S. Saito

Center for Exploratory Research Laboratory, Research & Development Group, Hitachi, Ltd. Tokyo 185-8601, Japan.
*corresponding author: shinichi.saito.qt@hitachi.com

Abstract: We have developed a Lie Group theory for the SU(*N*) symmetry of structured light, and experimentally demonstrated their controls over a full Poincaré sphere. We show trajectories of Stokes parameters exhibit non-trivial topological features like a torus, a Möbius strip, and a bosonic Dirac cone.

Structured light attracted significant attentions in the last three decades and it is still an active area for quantum optics and potential applications in communications, computing, and sensing [1-10]. It is typically characterised as an optical vortex with the unique mode profile, described by a Laguerre-Gauss mode [1-10]. Here, we show that the structure of coherent photons is mathematically characterised by a Lie group theory, which predicts various topological features in the expectation values of SU(*N*) generators of rotations [11].

The ray of coherent photons with the SU(*N*) symmetry [11] is described by

$$|\alpha_1, \cdots, \alpha_N\rangle = \prod_{\sigma=1}^{N} \mathrm{e}^{-\frac{|\alpha_\sigma|^2}{2}} \mathrm{e}^{\hat{a}_\sigma^\dagger \alpha_\sigma} |0\rangle \quad , \tag{1}$$

where we have defined creation and annihilation operators to satisfy the Bose commutation relationship, $[\hat{a}_\sigma, \hat{a}_{\sigma'}^\dagger] = \delta_{\sigma,\sigma'}$, and σ (σ') stands for the internal structure. The state is characterised by *N* values of complex numbers, $(\alpha_1, \ldots, \alpha_N) \in \mathbb{C}^N$. The generators of rotations (X_i, i=1, …, N^2-1) satisfy the commutation relationship as $[X_i, X_j] = i\sum_k f_{ijk} X_k$, where $f_{ijk} \in \mathbb{R}$ is a real number, named as the structure constant [11]. It is important to recognise that the coherent state of (1) is a many-body state, such that the macroscopic number of photons are occupying a few states of *N*, while allowing the superposition states among them. The corresponding many-body field-operator for spin and orbital angular momentum becomes

$$\hat{X}_i = \hbar \sum_{\sigma,\sigma'} \hat{a}_\sigma^\dagger (X_i)_{\sigma\sigma'} \hat{a}_{\sigma'} \ . \tag{2}$$

It is straightforward to calculate the expectation values of generators of rotations, since the coherent state of (1) is the eigenstate of annihilation operators, such that the operators are simply converted to complex numbers. In general, we have N^2-1 generators of rotations, such that the expectation values are describe by SO(N^2-1).

The simplest example of SU(2) states of coherent photons is found in polarisation states, for which we have N=2 orthogonal states controlled by N^2-1=3 generators of rotations. Then, we can recognise that the Stokes parameters, $\mathbf{S}=(S_1,S_2,S_3)$, are quantum-mechanical expectation values of Spin operator, $\langle\hat{\mathbf{S}}\rangle$. Moreover, the radius of the Poincaré sphere (S_0) corresponds to the average number of photons per second (n_0), passing through the cross section of the beam, $S_0=\hbar n_0$. In order to confirm this picture, we have developed the arbitrary SU(2) operator, name as a Poincaré rotator [11], and demonstrated to realise the photonic C_{60} and the coastline of the earth on the Poincaré sphere (Fig. 1).

The surface of the Poincaré sphere is mathematically described as the two-dimensional sphere, S^2. We can also realise a polarisation torus, $T=S^1 x S^1$, simply preparing a polarisation dependent interferometer [11]. It is

also possible to realise a polarisation Mobius strip and a bosonic Dirac cone (Fig. 2). By extending the analysis of photonic angular momentum to include orbital angular momentum, we can realise various SU(*N*) states, which exhibit classical entanglement and associated Bell projections of coherent photons [11].

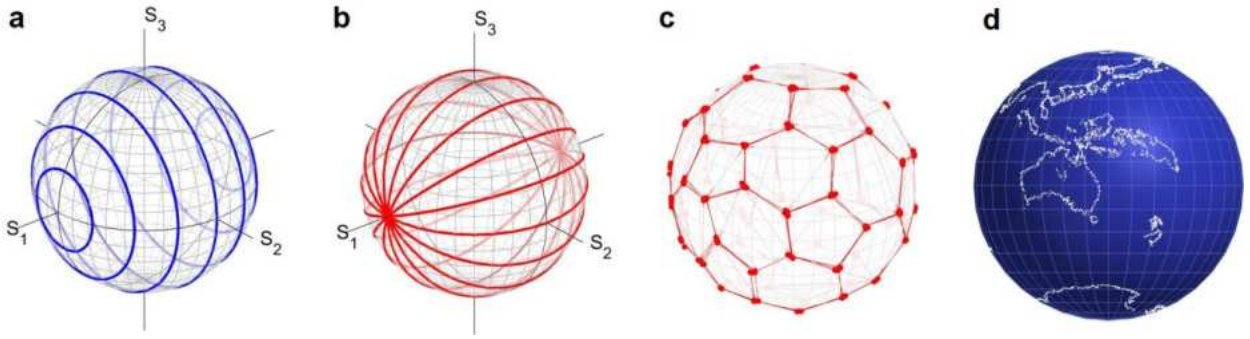


Fig. 1 Poincaré rotator to realise an arbitrary SU(2) operation for spin states of coherent photons, using a laser with the wavelength of 1533nm. (a) and (d) simulated trajectories for phase-shifter and rotator operations, respectively. Experimental data to draw (c) fullerene C_{60} and (d) the earth by Stokes parameters.

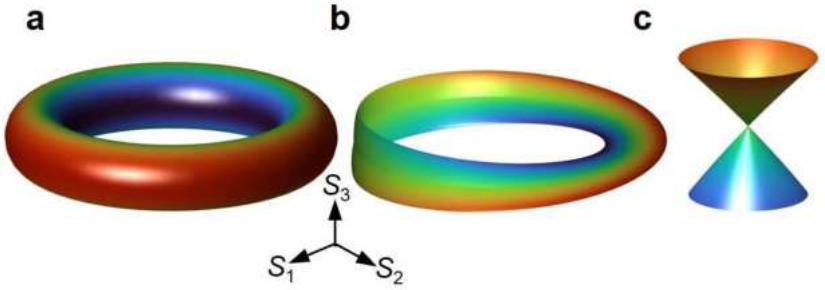


FIG. 2. Topological polarisation states. Stokes parameters were theoretically calculated for (a) a torus, (b) a Möbius strip, and (c) a bosonic Dirac cone.

Acknowledgements: This work is supported by JSPS KAKENHI Grant Number JP 18K19958. The author would like to express sincere thanks to Prof I. Tomita for continuous discussions and encouragements.

References

1. E. Abramochkin and V. Volostnikov, Opt. Comm. **83**, 123 (1991).
2. L. Allen, M. W. Beijersbergen, R.J. C. Spreeuw, and J. P. Woerdman, Phys. Rev. A **45**, 8185 (1992).
3. B. J. C. Spreeuw, Found. Phys. **28**, 361 (1998).
4. S. M. Barnett, L. Allen, R. P. Cameron, C. R. Gilson, M. J. Padgett, F. C. Speirits, and A. M. Yao, J. Opt. **18**, 064004 (2016).
5. G. Milione, H. I. Sztul, D. A. Nolan, and R. R. Alfano, Phys. Rev. Lett. **107**, 053601 (2011).
6. S. Naidoo, F. S. Roux, and A. Dudley, I. Litvin, B. Piccirillo, L. Marrucci, and A. Forbes, Nat. Photon. **10**, 327 (2016).
7. Y. Shen, X. Wang, Z. Xie, C. Min, X. Fu, Q. Liu, M. Gong, and X. Yuan, Light: Sci. Appl. **8**, 90 (2019).
8. A. Forbes, M. d. Oliveira, and M. R. Dennis, Nat. Photon. **15**, 253 (2021).
9. J. Wang and Y. Liang, Front. Phys. **9**, 688284 (2021).
10. O. V. Anelsky, A. Y. Bekshaev, S. G. Hanson, C. Y. Zenkova, I. I. Mokhun, and J. Zheng, Front. Phys. **8**, 114 (2020).
11. S. Saito, Front. Phys. **11**, 1225419; 1225346; 1225360; 1225387; 1225462; 1225488; 1289062; 1225334 (2023).

Selective Photoexcitation of Finite Momentum Excitons in 2D Materials by Using Structured Lights

Shun-Jen Cheng[1*], Guan-Hao Peng[1], Ping-Yuan Lo[1], Wei-Hua Li[1], Oscar J. G. Sanchez[1], Jhen-Dong Lin[1], Kristan Bryan Simbulan[2], Ting-Hua Lu[2], and Yann-Wen Lan[2]

[1] Department of Electrophysics, National Yang Ming Chiao Tung University, Hsinchu 300, Taiwan
[2]Department of Physics, National Taiwan Normal University, Taipei 11677, Taiwan
[*]corresponding author: sjcheng@nycu.edu.tw

Abstract: In this work, we will review our recent experiment-theory-joint studies and the developed theory of the light-exciton interactions between excitons in 2D materials and structured lights, including scalar twisted lights carrying orbital angular momenta and vector vortex beams.

A twisted light (TL) is a spatially structured light where the wavefront of the amplitude is engineered to be in a twisted form to acquire the orbital angular momentum (OAM), being a new degree of freedom of light in addition to that of spin angular momentum (SAM), i.e. polarization. To date, spatially structured light sources, including scalar TL and vector vortex beams, have given rise to broad interest and rapidly ongoing progress in the exploration of the fascinating optical physics and OAM-based photonic technology, [1] ranging from optical control of microscopic systems, high-resolution imaging techniques to high dimensional quantum information technology. Following the rapid advancement in the optical technology of TL, it is timely crucial and desired to explore the intriguing optical interaction of structured light with emergent optoelectronic nano-materials, e. g. transition metal dichalcogenide monolayers (TMD-ML). However, the research on the intriguing interplay between twisted lights and the emergent 2D TMD-MLs (MoS_2, WSe_2, etc) still remains rarely explored.

Only a few years ago, the first photoluminescence (PL) spectrum of a 2D MoS_2 monolayer under the photo-excitation of twisted light with controlled OAM was measured by Ref.[2]. With the increment of OAM of the incident TL, the measured PLs from a hBN-encapsulated MoS2-ML under the excitation of the TL are shown blue-shifted, as consequence of OAM transfer from a light to excitons and selective photo-excitation of finite momentum exciton states well explained by our theoretical analysis and numerical simulation. Theoretically, we have established the theory of the light-matter interaction between a 2D exciton and structured light by using the time-dependent perturbation theory within the electric dipole approximation. We calculate the dispersive fine structures and microscopic wave functions of exciton complexes, including bright exciton and various dark excitons, in 2D materials by numerically solving the Bethe Salpeter equation (BSE) established on the base of first principles.[3] In classical electrodynamical theory, the vector potential of twisted light in the Coulomb gauge is explicitly derived from the Helmholtz equation in the paraxial approximation.

By using the developed theory, it is established that the photo-excitation of finite momentum exciton states by a TL forms a localized exciton wave packet, whose spatially structured pattern is encoded by the OAM carried by the incident TL and suggested to read-out by using the angle-resolved optical spectroscopy.[4] Further, the developed theory of twisted-light-exciton interaction is applied to the investigation of focal TL beam and its interaction with exciton complexes, including bright and various dark exciton. Notably, the SAM and OAM in

a focal TL beam are actually coupled to each other and the resulting polarization is no longer purely transverse. The existence of the longitudinal field in a focal TL manifests the effect of optical spin orbit interaction, which makes it possible to optically access one of the dark exciton doublet of TMD-MLs, i.e. gray exciton, that is a long-lived exciton state and advantageous for the preservation of the transferred OAM from a TL. Regarding the recent study of vector vortex beam (VVB) that is formed by the superposition of two TLs with opposite angular momenta, we show that the spin-orbit non-separability of VVB enables the OAM-imprinting of gray excitons in 2D materials.

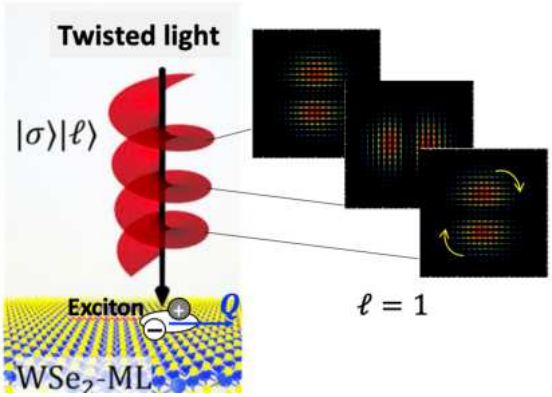


Fig.1 Schematics of a twisted light that carries an orbital angular momentum, $\hbar\ell$, normally incident to a 2D WSe_2 monolayer and photo-generates an exciton with the center-of-mass momentum, $\boldsymbol{Q}$. The square insets show the spatially structured patterns of the vector potential of the incident TL in the different cross-section planes.

References

1. Shen, Y., Wang, X., Xie, Z., Min, C., Fu, X., Liu, Q., Gong, M., Yuan, X. 'Optical Vortices 30 Years On: OAM Manipulation from Topological Charge to Multiple Singularities", Light: Sci. Vol. 8 No.1, 90, 2019.
2. Simbulan, K.B., Huang, T.D., Peng, G.H., Li, F., Gomez Sanchez, O.J., Lin, J.D., Lu, C.I., Yang, C.S., Qi, J., Cheng, S.J. and Lu, T.H., "Selective Photoexcitation of Finite- Momentum Excitons in Monolayer MoS2 by Twisted Light", ACS Nano Vol. 15 No.2, 3481-3489, 2021.
3. Peng, G.H., Lo, P.Y., Li, W.H., Huang, Y.C., Chen, Y.H., Lee, C.H., Yang, C.K. and Cheng, S.J., "Distinctive Signatures of the Spin- and Momentum-Forbidden Dark Exciton States in the Photoluminescence of Strained WSe2 Monolayers under Thermalization", Nano Lett. Vol. 19, 2299, 2019.
4. Peng, G.-H., Sanchez, O. J. G., Li, W.-H., Lo, P.-Y., and Cheng, S.J. "Tailoring the superposition of finite-momentum valley exciton states in transition-metal dichalcogenide monolayers by using polarized twisted light", Phys. Rev. B Vol. 106 No. 15, 155304 (2022).

Propagation-Independent Polarization Features Near Phase Singularities of Electromagnetic Fields

Andrei Afanasev*

The George Washington University, Washington, DC 20052, USA

**corresponding author: afanas@gwu.edu*

Abstract: We considered polarization properties of optical vortex beams beyond the paraxial approximation, which requires inclusion of the longitudinal component of the electric field. It is shown that even though the vortex beams expand under propagation due to diffraction, the polarization features near phase singularities remain constant. Polarization behaviors near the phase singularity is illustrated with Young's double-slit interference example. We also demonstrate propagation independence of spatial separation of magnetic end electric polarization singularities.

OCIS codes: (270.0270) Quantum Optics; (260.6042) Singular Optics; (050.4865) Optical Vortices

We have studied [1] the polarization of vector beams carrying optical angular momentum. We show the existence of polarization features within optical vortex beams that maintain constant transverse spatial dimensions independently of the beam divergence due to diffraction. The exact size of these vortex polarization structures is dictated by the presence of the longitudinal electric field in the beam, and such structures are expected for vortex beams of all topological charges. An analytical paraxial model predicts their presence in weakly focused beams and a numerical angular spectrum approach further extended this prediction to tightly focused beams, thereby proving applicability to all vortex beams. These polarization features are not affected by finite NAs and so should be experimentally measurable. It should be noted that the predicted nondiffractive polarization features have relatively small transverse dimensions of the order $\Delta\rho \approx l\lambda/\pi$, centered on a low-intensity region of the optical vortex wavefront. Therefore, future measurements will require subwavelength resolution at low l and increased sensitivity of the probe for larger values of l. The demonstrated effect allows one to pinpoint the position of a phase singularity with subwavelength accuracy independently of the size of a beam spot. This property may have useful applications in metrology, optical communications, optical networking, laser sensing, and radar operations.

These results were extended [2] to a general case of field zeros in the wavefronts of electromagnetic fields: while the transverse field might turn to zero due to interference effects, the longitudinal field becomes essential, leading to novel polarization features. Remarkably, these polarization features remain unchanged under propagation, providing a new tool for application. The effect is illustrated in Fig.1 using an example of Young's double-slit interference.

Next, we show that Michael Berry's observations [3] of magnetic vs electric singularity separation are in fact also propagation-independent. Separation of magnetic and electric singularities is considered for phased arrays of atoms [4].

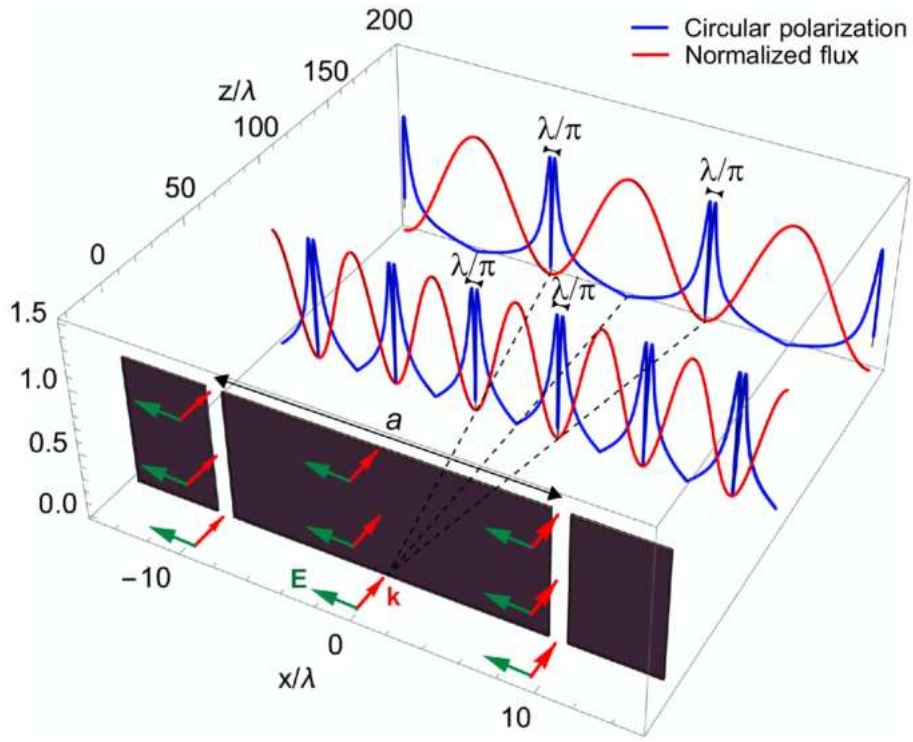


Figure 1. Non-diffractive behavior of polarization Young's double-slit interference. Shown are intensity (red curves) and circular polarization |**s**|. The incident light is linearly polarized perpendicular to the slits. Pairs of C-lines are developed due to interplay between small but nonzero z components of the electric field normal to the screen and (otherwise dominant) in-plane x-components that turn to zero due to destructive interference between two slits. For each C-line pair, photon polarization vectors point along the y-axis, reaching unit length, and are opposite in sign: s_y=±1.

Acknowledgements. This work was supported by US ARO Award W911NF-23-1-0085.

References

[1] A. Afanasev, J. Kingsley-Smith, F.J. Rodríguez-Fortuño, A.V. Zayats, Advanced Photonics Nexus **2**, 026001 (2023).

[2] A.J. Vernon, A. Kille, F.J. Rodríguez-Fortuño, A. Afanasev, Optica **11**, 120 (2024).

[3] M.V. Berry, J. Opt. A: Pure Appl. Opt. **6**, 475 (2004).

[4] A. Afanasev, H. Wang, Appl. Sci. **13**, 5672 (2023).

Optical skyrmions

J. B. Götte[1,2*], **Z. Ye**[1], **A. McWilliam**[1], **F. C. Speirits**[1], **C. M. Cisowski**[1], **S. Franke-Arnold**[1], **and S. M. Barnett**[1]

[1]School of Physics and Astronomy, University of Glasgow, Glasgow, G12 8QQ, UK
[2]College of Engineering and Applied Sciences, Nanjing University, Nanjing, China
[*]corresponding author: Joerg.Goette@glasgow.ac.uk

Abstract: We show how optical skyrmions and their associated skyrmion field provide the natural framework to analyse the topology and geometry of fully structured light.

Structured light beams display a spatial variation in their amplitude, phase and polarization. They can exhibit topological features such as phase and polarization singularities, which in turn can trace out links and knots. Structured light beams which contain the whole Poincaré sphere of possible polarizations in every cross section are aptly called Poincaré beams. If this complete covering of the Poincaré sphere supports a mapping of the polarisation structure reminiscent of the arrangement of the magnetization in magnetic skyrmions at the surface of magnetic media, the light beam forms an optical skyrmion.

The polarization pattern of optical skyrmions can readily be formed by superimposing two vortex beams of different topological charge with orthogonal polarization. Adopting a notation from quantum mechanics and denoting the two orthogonal polarisations as $|0\rangle$ and $|1\rangle$, the local polarization of a skyrmion beam can be constructed as

$$|\psi(\boldsymbol{r})\rangle = \frac{|0\rangle + v(\boldsymbol{r})|1\rangle}{\sqrt{1+|v(\boldsymbol{r})|^2}}, \qquad (1)$$

where $v(\boldsymbol{r}) = \beta u_1(\boldsymbol{r})/\alpha u_0(\boldsymbol{r})$ contains the amplitude of the superposition $\alpha u_0(\boldsymbol{r})\,|0\rangle + \beta u_1(\boldsymbol{r})|1\rangle$, and u_1 and u_2 are spatial modes with different topological charges. The local direction on the Poincaré sphere is then simply given by $\boldsymbol{S} = \langle \psi(\boldsymbol{r}) \,|\, \boldsymbol{\sigma} |\, \psi(\boldsymbol{r}) \rangle$, where $\boldsymbol{\sigma}$ is a vector of Pauli matrices. Skyrmions are characterized by an integer winding number, or skyrmion number, which encapsulates how often the Poincaré sphere is covered, and is given by

$$n(z) = \frac{1}{4\pi}\int \boldsymbol{S} \cdot \left(\frac{\partial \boldsymbol{S}}{\partial x} \times \frac{\partial \boldsymbol{S}}{\partial y}\right) dx\, dy. \qquad (2)$$

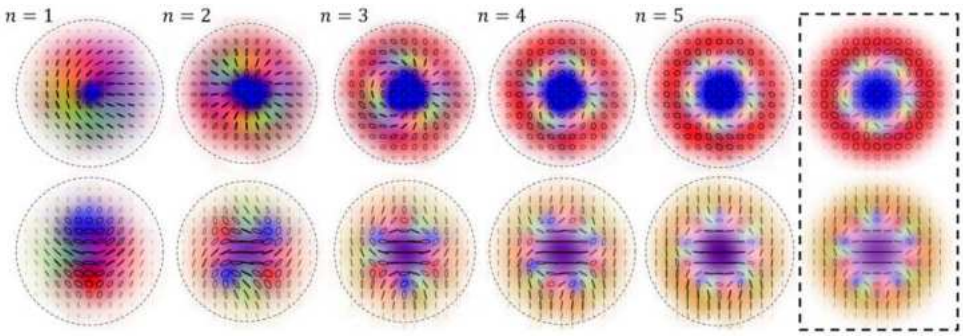


Figure 1: Experimentally measured polarization textures for beams with skyrmion numbers n = 1 to 5. The top row shows N´eel-type skyrmions defined in the circular basis (|0⟩ = |l⟩ , |1⟩ = |r⟩), and the bottom row Neel-type bimerons in the linear basis (|0⟩ = |h⟩ and |1⟩ = |v⟩). The inset at the right shows the theoretical polarization textures for n = 5.[3]

The polarization structure of skyrmion and more generally any fully structured light beam is given by the transverse, that is divergence-less, skyrmion field, $\boldsymbol{\Sigma}$, defined as

$$\Sigma_i = \frac{1}{2}\varepsilon_{ijk}\boldsymbol{S}\cdot\left(\frac{\partial \boldsymbol{S}}{\partial x_j}\times\frac{\partial \boldsymbol{S}}{\partial x_k}\right), \qquad (3)$$

which makes it possible to write the skyrmion number as

$$n(z) = \frac{1}{4\pi}\int \Sigma_z \, \mathrm{d}x \, \mathrm{d}y \, .$$

The streamlines of the skyrmion field have a significance beyond their connection with skyrmion beams, they form the skeleton of all smoothly varying, fully structured light beams. Interestingly the family of streams lines is invariant under a basis transformation of the underlying polarisation structure.[2]

The transverse nature of $\boldsymbol{\Sigma}$ allows us to write it as the rotation of a skyrmion potential $\boldsymbol{\Sigma} = \boldsymbol{\nabla}\times\boldsymbol{V}$. This potential, although not unique, provides a simple expression for the skyrmion number in paraxial optical skyrmion fields based solely on topological considerations. This has the advantage that the surface integral in Eqs. (2) and (3) can be replaced by a line integral utilizing Stokes's theorem. We have shown that this technique allows an experimental determination of skyrmion numbers with exceptional precision.[3]

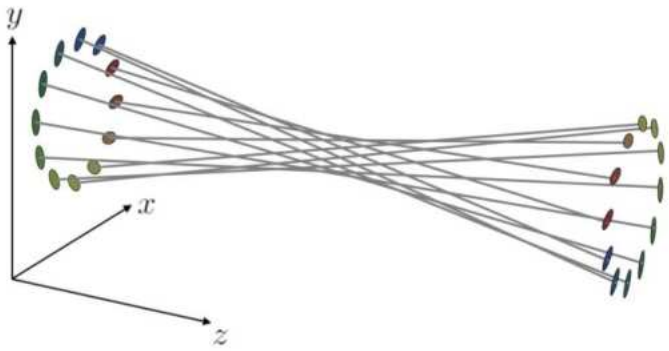


Figure 2: Field lines of the skyrmion field map out lines of constant polarization and show the rotation of the skyrmion pattern on propagation.

While optical skyrmions fall into a specific category of structured light beams, studying their fundamental properties uncovers powerful tools for examining the topological properties of paraxial light beams.

We acknowledge support from the Royal Society, the UK Research and Innovation Council and the Leverhulme Trust.

References

1. Gao, S., Speirits, F. C., Castellucci, F., Franke-Arnold, S., Barnett, S. M. and Götte, J. B. "Paraxial skyrmionics beams," Physical Review A, Vol. 105, No. 5, 053513, 2020.
2. Barnett, S. M., Speirits F. C and Götte, J. B., "On the lines of constant polarizartion in structured light beams," Europhysics Letters, Vol. 143, No. 3, 35002, 2023.
3. McWilliam, A., Cisowski, C. M., Ye Z., Speirits F. C., Götte, J. B., Barnett, S. M. and Franke-Arnold, S. "Topological Approach of Characterizing Optical Skyrmions and Multi-Skyrmions," Laser and Photonics Reviews, Vol. 17, No. 9, 2300155, 2023.

Generation and application of structured attosecond light pulses with controlled topology

C. Hernández-García[1, 2, *]

[1] Grupo de Investigación en Aplicaciones del Láser y Fotónica, Departamento de Física Aplicada, Universidad de Salamanca, Salamanca E-37008, Spain
[2]Unidad de Excelencia en Luz y Materia Estructuradas (LUMES), Universidad de Salamanca, Salamanca, Spain
[*]corresponding author: carloshergar@usal.es

Abstract: Structured attosecond light pulses with designed light properties can be currently generated in the extreme ultraviolet thanks to high harmonic generation. We demonstrate how the topological properties of the structured harmonic beams can be properly controlled, and how they can be used to reveal ultrafast electronic dynamics within matter.

The development of structured ultrafast laser sources is a key ingredient to advance our knowledge about the fundamental dynamics of electronic and spin processes in matter. It is widely recognized the relevance of ultrafast sources structured in their spin angular momentum (SAM)—associated to the polarization of light—and orbital angular momentum (OAM)—associated with the transverse phase profile, or vorticity of a light beam—to study chiral systems and magnetic materials in their fundamental temporal and spatial scales. In the last decade, the possibility to generate high frequency structured ultrafast laser pulses–in the extreme-ultraviolet (EUV) or even soft x-rays—has triggered substantial developments in nonlinear optics. Among other x-ray sources such as free electron lasers or plasma-based soft x-ray lasers, high-harmonic generation (HHG) stands as a robust mechanism to generate highly spatially and temporally coherent radiation from the EUV to the soft x-ray regimes [1], with exquisite temporal accuracy in the attosecond regime [2]. During the last decade several works have explored the possibility of up-convert light's angular momentum from the infrared into the high frequency regime thanks to HHG [3].

In this contribution we will review our recent advances in the generation of structured coherent EUV/soft x-ray pulses through HHG, and their applications to reveal ultrafast electronic dynamics within matter. Since the first works of HHG driven by vortex beams [4], the use of driving field configurations with custom OAM is opening novel control opportunities over the properties of the high-order harmonics. The generation of attosecond vortices with controlled polarization [5], high harmonic pulses with time-dependent OAM or self-torque [6], or low-divergence harmonic combs with controlled frequency line spacing extending into the soft x-rays [7], represent some of the most exciting advances. More recently, the generation of attosecond vortex pulse trains (Fig. 1) has been realized [8] thanks to the generation of high-order harmonic vortex beams with the same topological charge. In addition, the application of structured light to HHG driven in solids, is opening interesting avenues for the study of ultrafast electronic dynamics. For instance, the anisotropic nonlinear response of thin materials such as graphene [9] allowed us to propose topological harmonic spectroscopy to reveal ultrafast nonlinear dynamics through light's topology [10]. Finally, ultrafast vector beams offer the opportunity to obtain magnetic pulses that are spatially isolated from the electric field [11]. Such unique magnetic pulses can be used to drive nonlinear magnetization dynamics [12] or to assist HHG in order to achieve Fourier limited attosecond pulses [13].

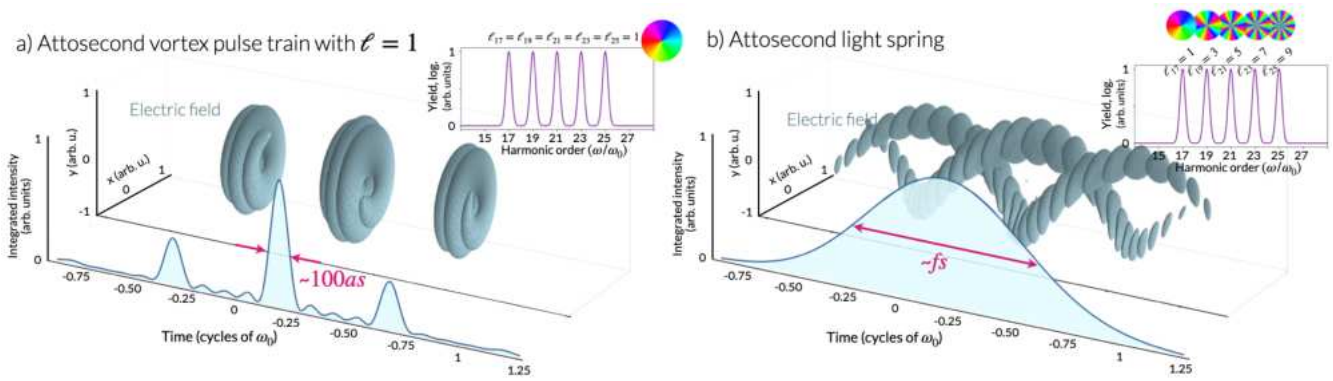


Figure 1. a) Attosecond vortex pulse train obtained after synthesizing several harmonic orders with the same topological charge [8]. If the topological charge scales with the harmonic order, an attosecond light spring is obtained [4].

We acknowledge funding support from the Spanish Ministerio de Ciencia, Innovación y Universidades (PID2022-142340NB-I00). This project has also received funding from the European Research Council (ERC) under the European Union's Horizon 2020 research and innovation program (Grant Agreement No. 851201).

References

1. T. Popmintchev, et al. "Bright coherent ultrahigh harmonics in the keV x-ray regime from mid-infrared femtosecond lasers". Science **336,** 1287 (2012).
2. X. Shi, et al., "Attosecond light science and its application for probing quantum materials", J. Phys. B 53, 184008 (2020).
3. C. Hernández-García, "A twist in coherent X-rays", Nature Physics 13, 327-329 (2017).
4. C. Hernández-García et al. "Attosecond Extreme Ultraviolet vortices from high-order harmonic generation", Physical Review Letters 111, 083602 (2013).
5. K. M. Dorney, et al. "Controlling the polarization and vortex charge of attosecond high-harmonic beams via simultaneous spin-orbit momentum conservation". Nat. Photon. 13, 123-130 (2019).
6. L. Rego, et al., "Generation of extreme-ultraviolet beams with time-varying orbital angular momentum". Science 364, eaaw9486 (2019).
7. L. Rego et al. "Necklace-structured high harmonic generation for low-divergence, soft X-ray harmonic combs with tunable line spacing", Science Advances 8, eabj7380 (2022).
8. A. de las Heras et al. "Attosecond vortex pulse trains", arXiv:2402.15225
9. O. Zurrón-Cifuentes, et al., "Optical anisotropy of non-perturbative high-order harmonic generation in gapless graphene", Opt. Exp. 27, 7776–7786 (2019).
10. A. García-Cabrera, et al. "Topological harmonic spectroscopy", Communications Physics 7, 28 (2024).
11. M. Blanco et al. "Ultraintense femtosecond magnetic nanoprobes induced by azimuthally polarized laser beams", ACS Photonics 6, 38–42 (2019),
12. L. Sánchez-Tejerina et al. "All-optical non-linear chiral ultrafast magnetization dynamics driven by circularly polarized magnetic fields", High Power Laser Science and Engineering 11, e82 (2023)
13. R. Martín-Hernández et al. "Fourier-limited Attosecond Pulse from High Harmonic Generation Assisted by Ultrafast Magnetic Fields", Ultrafast Science 3, 0036 (2023).

Interaction of structured light with a trapped ion

A. A. Peshkov[1,2*], R. Lange[1], Y. M. Bidasyuk[1], R. P. Schmidt[1], E. Jordan[1], M. Kromrey[1], K. K. Mehta[3], T. E. Mehlstäubler[1,4], N. Huntemann[1], E. Peik[1], and A. Surzhykov[1,2]

[1]Physikalisch-Technische Bundesanstalt, Braunschweig, Germany
[2]Technische Universität Braunschweig, Germany
[3]Cornell University, Ithaca, USA
[4] Leibniz Universität Hannover, Germany
[*]corresponding author: anton.peshkov.ext@ptb.de

Abstract: We study the nondipole excitation of trapped ions by structured light. Particular attention is paid to finding the optimal light polarization and external magnetic field orientation to obtain simultaneously the maximum Rabi frequency and the minimum light shift. The theoretical predictions are compared with experimental data.

The production and use of structured (or twisted) light beams has been intensively discussed over the past decades in many areas of modern physics [1]. In contrast to “usual” plane-wave radiation, these beams possess phase singularities, complex polarization patterns and highly inhomogeneous intensity profiles. The latter feature is of particular interest to metrology because it can allow the excitation of narrow-line clock transitions with simultaneous suppression of the undesirable light (or a.c. Stark) shift. This is achieved as follows. An atom or ion, placed in the dark (low-intensity) center of a structured light beam, is exposed to an electric field of low strength but high gradient, which favors the excitation of non-dipole transitions and at the same time weakly perturbs atomic levels. Such “excitation in the darkness” has been successfully demonstrated on the example of an electric quadrupole transition in a single trapped $^{40}Ca^{+}$ ion in the experiment performed by the group of F. Schmidt-Kaler [2].

In the present study we evaluate the effectiveness of the “excitation in the darkness” scheme for the case of higher-multipole transitions which are of interest for use in optical atomic clocks. In particular, we have developed a theory to describe the excitation of electronic transitions in atoms by structured Bessel and Laguerre-Gaussian modes for arbitrary orientation of the atomic quantization axis [3]. Based on our theoretical results, the group of E. Peik and N. Huntemann conducted an experimental study of the excitation of the $^{2}S_{1/2} \rightarrow {}^{2}F_{7/2}$ electric octupole transition in a single trapped $^{171}Yb^{+}$ ion [4]. In the dark center of the Laguerre-Gaussian beam, excitation was observed with a fivefold reduction of the light shift compared to excitation by plane-wave radiation at the same Rabi frequency. The dependence of the transition probability on the direction of the applied magnetic field was also measured. We compared the experimental data with theoretical predictions and found good qualitative agreement.

The experiment with $^{171}Yb^{+}$ represents an important step towards precision spectroscopy with structured light. In this experiment, however, suppression of the light shift was limited by imperfect ion positioning relative to the low-intensity center of the laser beam. Such uncertainty in the localization of the target arises not only due to the thermal motion of an ion in a trap, but also due to the lack of laser beam pointing stability. The group of T. Mehlstäubler proposed to partially solve the latter problem using the integrated schemes in which the light

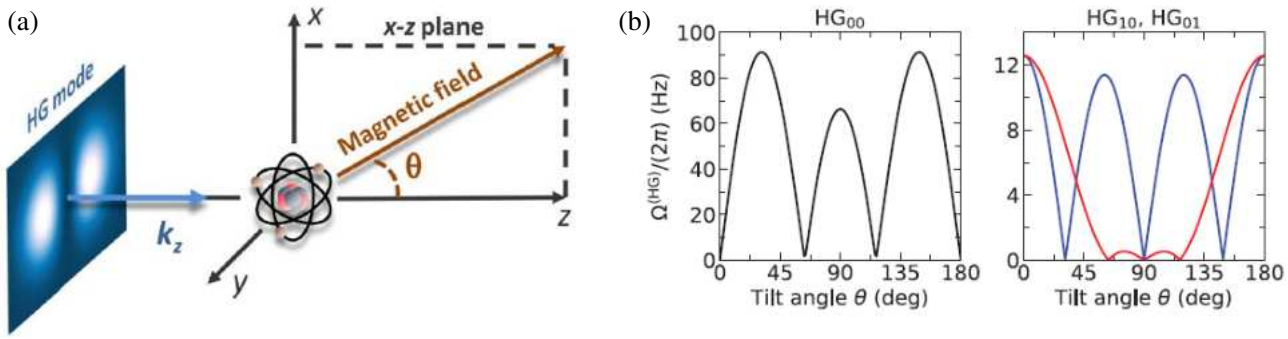


Figure 1: (a) Geometry of the excitation of a single trapped atom by Hermite–Gaussian (HG) modes. (b) Rabi frequencies as a function of the magnetic field tilt angle for HG_{00} (black line) and HG_{10} (blue line) modes linearly polarized in the x-direction and for HG_{01} (red line) mode linearly polarized in the y-direction. The atom is placed in the beam center.

delivery optics is fabricated directly into the ion trap. The geometry of such structures allows fairly straightforward excitation of Hermite-Gaussian modes, which, unlike Laguerre-Gaussian modes, do not have rotational symmetry. To assess the feasibility of this approach, we have conducted a theoretical study of the interaction between a single trapped $^{171}Yb^{+}$ ion and structured Hermite-Gaussian beams [5]. For example, we found that the Rabi frequency of the $|F=0, M=0\rangle + \gamma \rightarrow |F=3, M=0\rangle$ transition can be enhanced by choosing the polarization of the HG_{10} mode along the *x* axis and the direction of the external magnetic field along the *z* axis.

References

1. H. Rubinsztein-Dunlop *et al*, "Roadmap on structured light", J. Opt. , Vol. 19, 013001, 2017.
2. C. T. Schmiegelow, J. Schulz, H. Kaufmann, T. Ruster, U. G. Poschinger, and F. Schmidt-Kaler, "Transfer of optical orbital angular momentum to a bound electron", Nat Commun, Vol. 7, 12998, 2016.
3. S. A.-L. Schulz, A. A. Peshkov, R. A. Müller, R. Lange, N. Huntemann, Chr. Tamm, E. Peik, and A. Surzhykov, "Generalized excitation of atomic multipole transitions by twisted light modes", Phys. Rev. A, Vol. 102, 012812, 2020.
4. R. Lange, N. Huntemann, A. A. Peshkov, A. Surzhykov, and E. Peik, "Excitation of an electric octupole transition by twisted light", Phys. Rev. Lett., Vol. 129, 253901, 2022.
5. A. A. Peshkov, E. Jordan, M. Kromrey, K. K. Mehta, T. E. Mehlstäubler, and A. Surzhykov, "Excitation of forbidden electronic transitions in atoms by Hermite-Gaussian modes", Ann. Phys., Vol. 535, 2300204, 2023.

Non-Hermitian Photonics: Topological, Disordered and Quantum systems

Electrical tuning of exceptional points in microwave plasmonic structures

H. Y. Jeong[1*]

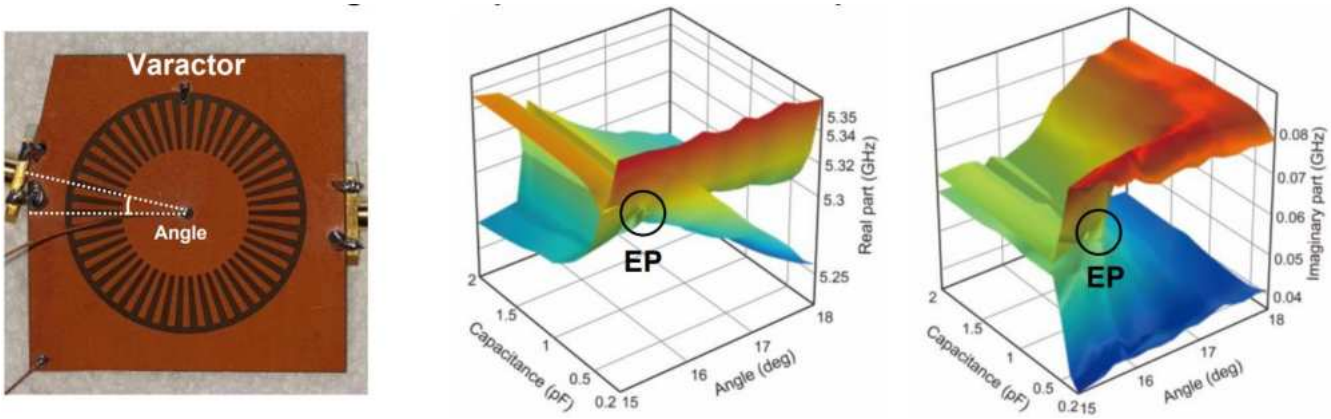
[1]Korea University, Republic of Korea
[*]corresponding author: hoonyeub@gmail.com

Abstract: We propose and experimentally demonstrate electrically addressable EP in a plasmonic structure. We employ a localized spoof plasmon structure that supports circulating plasmonic modes in compact single-resonator geometry. Plasmonic modes are perturbed by an angled metal line, and the interaction between the plasmonic modes is electrically controlled using a varactor.

Exceptional points (EPs) are intriguing phenomena arising within non-Hermitian systems, where eigenvalues and eigenvectors converge simultaneously. These singularities are pivotal in energy exchange dynamics with their environment and have emerged as pivotal elements across diverse domains, spanning novel laser, nonlinear optics, and high-precision measurements. EPs and non-Hermitian photonic systems have attracted considerable attention and may provide new platforms for photonic device design.

Optical microdisks and microtoroidal cavities have notably served as versatile platforms for probing EPs, particularly by manipulating the circulating optical modes influenced by particles strategically positioned along their circumference [1, 2]. This control affords manipulation of the real and imaginary components of the complex eigenfrequency, enabling the observation of EP-related phenomena such as mode crossing or anti-crossing. Despite these strides, much of the research surrounding EPs has been confined to static configurations, posing inherent challenges in precisely targeting and manipulating these points.

In recognition of the potential of dynamically tunable systems, recent endeavors have ventured into the realm of electrically controlled EPs, particularly within the terahertz range such as ionic electrolyte gating of graphene and the manipulation of reflection properties using phase-change materials have been explored [3]. However, the quest for compact, integrated device platforms capable of dynamically tuning EPs remains an active pursuit.



In this context, we propose a novel paradigm centered around a single-resonator structure inspired by insights gleaned from optical microcavity structures. Leveraging a spoof plasmon configuration, we introduce an angled metal line to perturb circulating plasmonic modes, thereby realizing EPs within a compact resonator geometry.

Our innovative approach integrates a voltage-controlled capacitor (varactor), offering precise electrical control over EPs' characteristics. Through a comprehensive exploration comprising numerical simulations and experimental validations, we delve into the intricate coupling dynamics of plasmonic resonances, demonstrating the feasibility of dynamically and continuously tuning EPs.

Acknowledgements

This research was supported by Basic Science Research Program through the National Research Foundation of Korea (NRF) funded by the Ministry of Education (RS-2023-00274366)

References

1. J. Zhu, Ş. K. Özdemir, L. He, and L. Yang, "Controlled manipulation of mode splitting in an optical microcavity by two Rayleigh scatterers," Opt. Express, vol. 18, pp. 23535–23543, 2010.

2. J. Wiersig, "Structure of whispering-gallery modes in optical microdisks perturbed by nanoparticles," Phys. Rev. A, vol. 84, p. 063828, 2011.

3. Y. Huang, Y. Shen, C. Min, and G. Veronis, "Switching of the direction of reflectionless light propagation at exceptional points in non-PT-symmetric structures using phase-change materials," Opt. Express, vol. 25, pp. 27283–27297, 2017.

Spontaneous disentanglement and thermalisation

Eyal Buks[1]

[1]Technion, Israel
[*]corresponding author: eyal@ee.technion.ac.il

Abstract: The problem of quantum measurement can be partially resolved by incorporating a process of spontaneous disentanglement into quantum dynamics. We propose a modified master equation, which contains a nonlinear term giving rise to both spontaneous disentanglement and thermalisation. We find that the added nonlinear term enables limit cycle steady states, which are prohibited in standard quantum mechanics.

The problem of quantum measurement is considered as one of the most important open questions in physics. This problem arguably originates from a self-inconsistency in quantum theory. This long-standing problem has motivated some proposals for nonlinear extensions to quantum theory. Moreover, processes giving rise to spontaneous collapse have been explored. For some cases, however, nonlinear quantum dynamics may give rise to conflicts with well-established physical principles, such as causality and separability. In addition, some predictions of standard quantum mechanics (QM), which have been experimentally confirmed to very high accuracy, are inconsistent with some of the proposed extensions.

A modified Schrödinger equation having a nonlinear term that gives rise to suppression of entanglement (i.e. disentanglement) has been recently proposed [1]. This nonlinear extension partially resolves the self-inconsistency associated with the measurement problem by making the collapse postulate of QM redundant. The proposed modified Schrödinger equation can be constructed for any physical system whose Hilbert space has finite dimensionality, and it does not violate norm conservation of the time evolution. The nonlinear term added to the Schrödinger equation has no effect on product (i.e. disentangled) states. The spontaneous disentanglement generated by the modified Schrödinger equation gives rise to a process similar to state vector collapse.

The nonlinear extension that was proposed in Ref. [1] is applicable only for bipartite systems, and only for pure states. To allow incorporating spontaneous disentanglement for more general cases, we propose a modified master equation for the time evolution of the density operator ρ. The modified master equation contains a nonlinear term that gives rise to spontaneous disentanglement. For a multipartite system, disentanglement between any pair of subsystems can be introduced by the added nonlinear term. Moreover, thermalisation can be incorporated by an additional nonlinear term added to the master equation.

In contrast to the above-discussed modified master equation, which is nonlinear in ρ, in standard QM the time evolution of ρ is governed by the Gorini-Kossakowski-Sudarshan-Lindblad (GKSL) master equation, which is linear in ρ. This linear dependency excludes any nonlinear dynamics in the time evolution of ρ, and, in particular, it excludes a limit cycle steady state for any quantum system having a Hilbert space of finite dimensionality and time independent Hamiltonian. On the other hand, the modified master equation yields rich nonlinear dynamics. In particular, both a Hopf bifurcation and a limit cycle steady state may occur.

References

1. EB, Advanced Quantum Technologies, 2300103 (2023).

Generation of orbital angular momentum by optical non-Hermitian skin effect in mirror-time symmetric media

Issei Takeda[1*], Taiki Yoda[1], Yuto Moritake[1], Kenta Takata[2,3], and Masaya Notomi[1,2,3]

[1]Department of Physics, Tokyo Institute of Technology, Tokyo, Japan
[2]NTT Basic Research Laboratories, NTT Corporation, Kanagawa, Japan
[3]Nanophotonics Center, NTT Corporation, Kanagawa, Japan
[*]corresponding author: takeda.i.ab@m.titech.ac.jp

Abstract: In this study, we investigate propagation states of two-dimensional optical non-Hermitian skin effect in closed mirror-time (MT)-symmetric media and have found that skin modes rotating around the edges of the system can be realized and orbital angular momentum is generated, especially in rectangular cavities with MT-symmetric medium.

The phenomenon called the Non-Hermitian Skin Effect (NHSE), in which all bulk eigenstates are localized at the edge of a non-Hermitian system, is a unique phenomenon that occurs only in non-Hermitian systems and has been actively studied recently as a new method of localized state formation [1,2]. Although conventional NHSE systems are based on periodic lattices, we have recently shown that optical NHSE can be realized in anisotropic uniform media [3].

In this study, we numerically investigate the propagation state using optical NHSE in two-dimensional MT-symmetric anisotropic uniform media. The basic model of MT-symmetric NHSE media in the present study is shown in Fig. 1(a). The mirror plane of the inversion is shown in Fig. 1(a), and the time reversal is complex conjugation of the dielectric constant. In infinitely long MT-symmetric media with reflective boundaries (perfect electric conductor (PEC)) on the left and right (Fig. 1(b)), a skin mode without amplification or attenuation propagates in one direction. The location of the skin mode depends on the sign of k_y.

First, we examine the nature of this one-way propagating mode by adding a defect at the edge. We numerically simulate the structure shown in Fig. 1(c) assuming MT-symmetric anisotropic permittivity $\varepsilon_{\parallel} = \varepsilon_{\perp}^{*} \sim 1.67 + 0.97i$ and place a defect at the left edge. When we excite a left-side skin mode propagating in the +y direction at the excitation port, light travels in the +y direction at the left edge without reflection but a right-side edge mode propagating in the -y direction is also generated. As a total, a rotating-like mode is formed. We regard that this is due to the inter-edge coupling resulting from the scattering by a defect.

Inspired from this unique phenomenon, we then investigate a closed structure which has PEC boundaries on the top, bottom, left, and right sides. We found that in the symmetric square structure, clockwise rotating modes localized at the left-right boundary and counterclockwise rotating modes localized at the top-bottom boundaries appear at the same time (Fig. 1(d)). In this case, the counterclockwise rotation and the clockwise rotation are balanced, resulting zero orbital angular momentum (OAM). However, when the structure become rectangular, one can select either of clockwise or counterclockwise rotation. In Fig. 1(e), the clockwise rotating modes localized on the left and right sides selectively emerge and generate substantially large OAM (Fig. 1(f)). Here we define the degree of asymmetry by $r = L_y/L_x$ and examine the dependence of OAM on the asymmetry r in Fig. 1(f). First, OAM grows with r. Then it saturates around $r = 5$ and reaches its maximum value.

In summary, we have found an interesting way to generate OAM by employing NHSE in a closed MT-symmetric anisotropic media. We will discuss other methods to generate OAM by breaking the symmetry in NHSE

systems. Since OAM of light is important due to its applicability for high-capacity and high-efficiency optical communications, and this study is expected to be applied as one of the new methods for generating optical OAM.

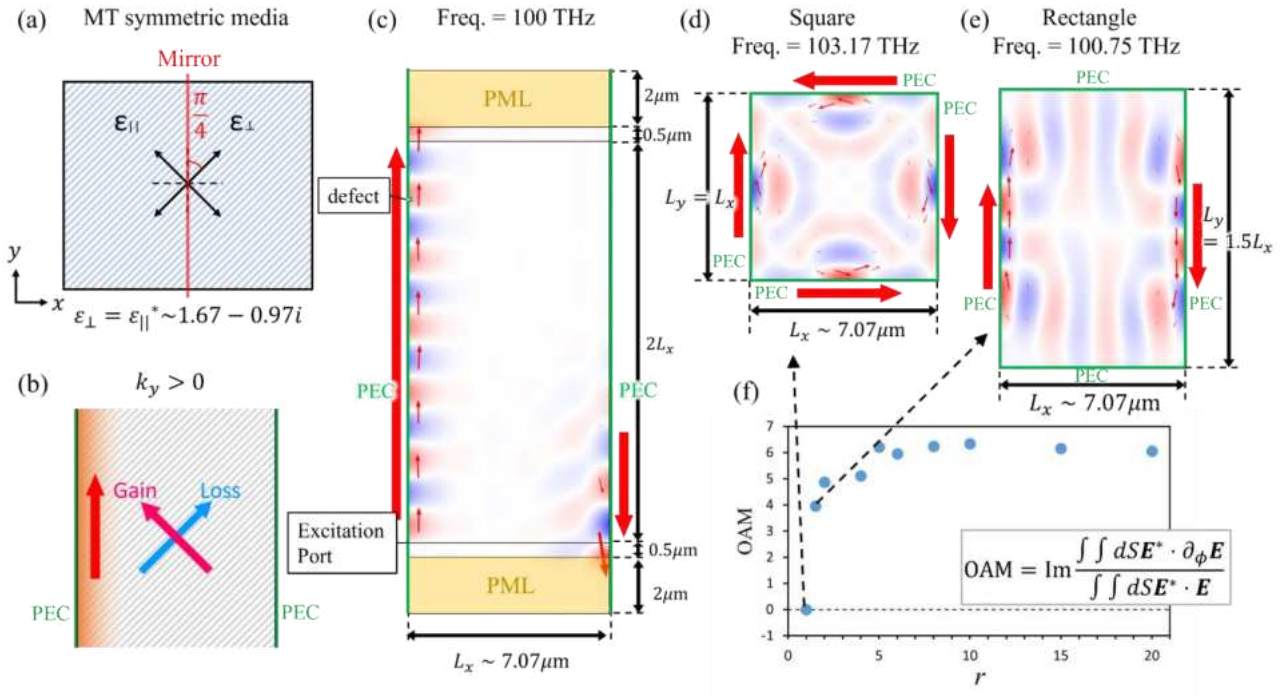


Fig. 1 (a) Anisotropic dielectric medium with MT symmetry. (b) Skin mode with $k_y > 0$ and real eigenfrequency. (c) Scattering of skin modes in structures with defects. (d) Eigenmodes in MT-symmetric square system bounded by PEC. (e) Eigenmodes in MT-symmetric rectangular system bounded by PEC. (f) Dependence of OAM on rectangle length, where r is the ratio of the length of the rectangle to the length of the sides of the original square.

Acknowledgements

This work was supported by Grant-in-Aid for Scientific Research (20H05641, 21K14551).

References

1. Shunyu Yao and Zhong Wang, “Edge States and Topological Invariants of Non-Hermitian Systems,” Phys. Rev. Lett. 121, 086803, 2018.
2. Shunyu Yao, Fei Song, and Zhong Wang, “Non-Hermitian Chern Bands,” Phys. Rev. Lett. 121, 136802, 2018.
3. Taiki Yoda, Yuto Moritake, Kenta Takata, Kazuki Yokomizo, Shuichi Murakami, and Masaya Notomi, “Optical non-Hermitian skin effect in two-dimensional uniform media,” arXiv:2303.05185, 2023.

Non-Hermitian quasicrystals

A. Ghatak[1], I. Komis[1], Z. H. Musslimani[3], and K. G. Makris[1,2]

1Institute of Electronic Structure and Laser (IESL), FORTH, 71110 Heraklion, Greece

2ITCP-Department of Physics, University of Crete, Heraklion, 70013, Greece

3Department of Mathematics, Florida State University, Tallahassee, Florida, 32306-4510, USA

*Corresponding author: gananya04@gmail.com

Abstract: In the framework of non-Hermitian photonics, we investigate the wavepacket diffraction dynamics in non-Hermitian one-dimensional quasiperiodic and two-dimensional quasicrystal waveguide lattices. In particular, the effect of spatial symmetries and localization on the spectral sensitivity is examined in terms of pseudospectra.

Recently it was understood that the non-Hermitian analogue of the Anderson original problem can be experimentally realized [1]. Since then, in the context of non-Hermitian photonics [2], there has been a renewed interest in non-Hermitian Anderson localization problems [3–8].

In this work, we provide a systematic study of wavepacket diffraction on two different non-Hermitian potentials: a one –dimensional quasiperiodic Aubry-André-Harper [9,10] lattice and a two-dimensional generalization of Penrose lattices [11–13]. We investigate the possible ways that one can realize these types of quasicrystal optical waveguide arrays, by appropriate spatial combinations of gain-loss materials. We consider parity-time (PT)-symmetric potentials, as well as, purely dissipative ones. The spectral sensitivity is studied in terms of pseudospectra. On the other hand, the dynamics is based on the global quantity of optical power and its logarithmic derivative. In fact, the wave diffraction in a disordered non-Hermitian lattice is highly non-trivial [4, 6–8]. Even though all the eigenstates are localized, the wave exhibits “non-Hermitian jumps” between distant sites, and thus we obtain short-range transport. In our case, of a non-Hermitian quasicrystal, the situation is far more complex, since not all the eigenmodes are localized. Thus, we investigate the conditions under which such jumps occur or not. Our results, are highly relevant to disordered photonics and complex media, where wave transport through highly scattering media is the ultimate goal.

Acknowledgements: This project was funded by the European Research Council (ERC-Consolidator) under the grant agreement No. 101045135 (Beyond Anderson).

References

1. S. Weidemann, M. Kremer, S. Longhi and A. Szameit, ”Coexistence of dynamical delocalization and spectral localization through stochastic dissipation”, Nat. Phot. 15, 576 (2021).
2. R. El-Ganainy, et. al., ”Non-Hermitian physics and PT symmetry,” Nat. Phys., 14, 11 (2018).
3. N. Hatano and D. R. Nelson, ”Non-Hermitian delocalization and eigenfunctions” Phys. Rev. B 58, 8384 (1998).
4. J. Feinberg and A. Zee, ”Non-Hermitian localization and delocalization” Phys. Rev. E 59, 6433 (1999).
5. A. F. Tzortzakakis, K.G. Makris, and E. N. Economou ”Non-Hermitian disorder in two-dimensional optical lattices,” Phys. Rev. B 101, 014202 (2020).
6. Y. Huang and B. I. Shklovskii, ”Anderson transition in three-dimensional systems with non-Hermitian disorder,” Phys.Rev. B, 101, 014204 (2020).

7. A.F. Tzortzakakis, K.G. Makris, A. Szameit, and E.N. Economou ”Transport and spectral features in non-Hermitian open systems”, Phys. Rev. Res. 3, 013208 (2021).
8. A. Leventis, K.G. Makris, and E.N. Economou, ”Non-Hermitian jumps in disordered lattices”, Phys. Rev. B 106, 064205 (2022).
9. P. G. Harper, Single band motion of conduction electrons in a uniform magnetic field, Proc. Phys. Soc. London A 68, 874 (1955).
10. S. Aubry and G. André, Analyticity breaking and Anderson localization in incommensurate lattices, Ann. Israel Phys. Soc.3, 133 (1980).
11. B. Freedman, G. Bartal, M. Segev, R. Lifshitz, D.N. Christodoulides, and J. W. Fleischer, ”Wave and defect dynamics in nonlinear photonic quasicrystals”, Nature 440, 1166 (2006).
12. B. Freedman, R. Lifshitz, J.W. Fleischer, and M. Segev, ”Phason dynamics in nonlinear photonic quasicrystals”, Nat. Mater. 6, 776 (2007).
13. L. Levi, M. Rechtsman, B. Freedman, T. Schwartz, O. Manela, M. Segev, ”Disorder-enhanced transport in photonic quasicrystals”, Science 332, 1541 (2011).

Extremely Narrow, Sharp-Peaked Resonances at the Edge of the Continuum

I. Lukosiunas[1], L. Grineviciute[2], J. Nikitina[2], D. Gailevicius[1], and K. Staliunas[3,4,*]

[1]Vilnius University, Laser Research Center, Sauletekio Ave. 10, Vilnius, Lithuania
[2]Center for Physical Sciences and Technology, Savanoriu Ave. 231, LT-02300 Vilnius, Lithuania
[3]UPC, Dep. de Fisica, Rambla Sant Nebridi 22, 08222, Terrassa, Spain
[4]ICREA, Passeig Lluís Companys 23, 08010, Barcelona, Spain

[*]corresponding author: kestutis.staliunas@icrea.cat

Abstract: We report a critical narrowing and sharpening of resonances of a potential well when their eigenfrequencies approach the edge of the continuum. The situation was realized for the electromagnetic wave propagating across the dielectric thin films with a periodically modulated interfaces.

It is well known that the wavefunctions in a potential well can form bound states for their energies below the background of the potential well, and the continuum states for their energies above the background. Although the basic wave behavior in the potential wells has been established since the beginning of quantum mechanics, new findings are constantly being reported. One such example is the phenomenon of Bound States in the Continuum,. Here we report another effect never considered before –extreme sharpening of the peaks of the resonances when their energies approach the background energy of the potential well, just before crossing the boundary of the continuum.

The physical situation is depicted in Fig.1. The situation can be realized in thin, nano-modulated dielectric films, where the periodic modulation of the interface serves as a drive of the potential well. The situation mathematically can be described by an externally driven Schrödinger equation:

$$\frac{\partial^2 A_1(z)}{\partial z^2} + \big(E - V(z)\big)A_1(z) - i\gamma(z)e^{ik_{0,z}z}A_0(z) = 0 \qquad (1)$$

The γ(z) is the normalized coupling profile, see Fig.1, V(z) is the profile of the potential (corresponding to the refraction index profile in optics), and E is the position of the driving ion the energy (frequency) domain (corresponds to frequency of excitation in optics).

When the energy of the driving force is below the edge of the continuum, the usual discrete resonances are excited. These are Fano resonances with their typical (asymptotically Lorenz-like) form [2]. However when the potential is deformed so, that one of the resonances approaches the edge of a continuum, a critical sharpening of the resonance is observed. The usual Lorentzian-like shapes, which asymptotically at around their peaks follow the parabolic law 1-dw^2, deforms into sharp-peaked ones with the asymptotical shapes of 1-|dw|. Also the scalings of the width of the resonance with the coupling parameter at the continuum boundary is different from the usual scalings of Fano resonances.

We demonstrated such sharpening of the resonances also experimentally, in thin, nano-modulated dielectric films,

We will discuss the possible realisation of the effect in passive systems (the thin film on the dielectric substrate) as well as in active (the film on amplifying material).

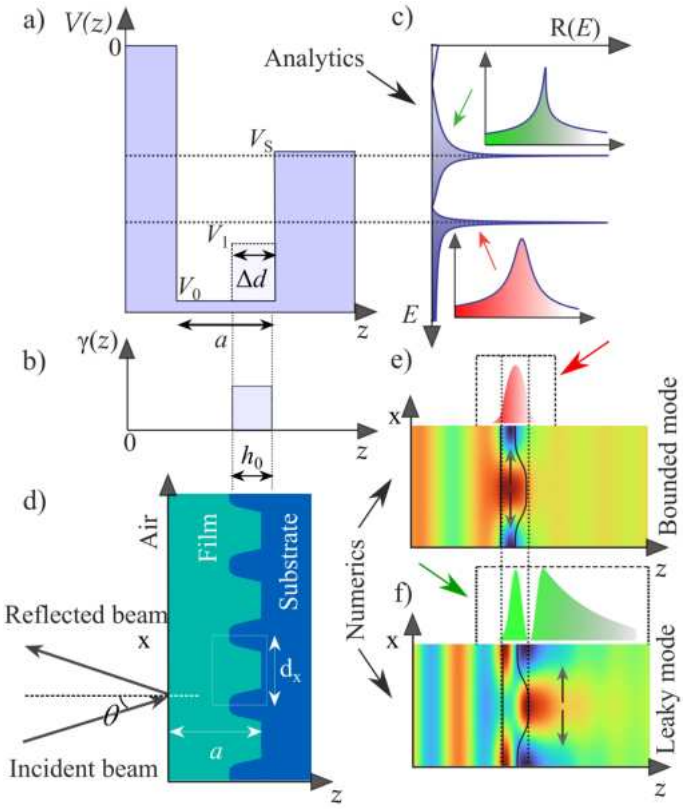


Fig.1. (a) A driven potential well (a,b) is equivalent to the thin film of high refraction index with periodically modulated interface (d). Mathematically driving is equivalent to imaginary part of the potential (b). The interface modulation couples the nearly-normal FP mode into the bounded waveguided modes (e) or leaky surface modes (f), resulting in the usual Lorenz-shaped resonance, or sharp-peaked resonances, respectively (c).

References

1. Ignas Lukosiunas, Lina Grineviciute, Julianija Nikitina, Darius Gailevicius, and Kestutis Staliunas, Extremely Narrow, Sharp-Peaked Resonances at the Edge of the Continuum, Phys. Rev. A **107**, L061501 (2023).
2. Lina Grineviciute, Julijana Nikitina, Ceren Babayigit, and Kestutis Staliunas, Fano-like resonances in nanostructured thin films for spatial filtering, Appl. Phys. Lett. **118**, 131114 (2021).

Topological enhancement of non-normality in non-Hermitian systems

Masatoshi Sato[1]

[1]Yukawa Institute for Theoretical Physics, Kyoto University
msato@yukawa.kyoto-u.ac.jp

Abstract: The non-Hermitian skin effects are representative phenomena intrinsic to non-Hermitian systems. Whereas a non-trivial topology under the PBC characterizes the non-Hermitian skin effects, their proper measure under the OBC has not been clarified yet. In this talk, I argue that topological enhancement of non-normality under the OBC accurately quantifies the non-Hermitian skin effects. The topological enhancement of non-normality governs the perturbation sensitivity of the non-Hermitian systems and the anomalous time-evolution dynamics. I also discuss related subjects intrinsic to non-Hermitian systems.

References

1. Y. O. Nakai, N. Okuma, D. Nakamura, K. Shimomura, M. Sato, arXiv:2304.06689.

Bunching states and memory loss in noisy non-unitary dynamics of bosons

K. Mochizuki[1,2], **R. Hamazaki**[2,3]

[1] Department of Applied Physics, University of Tokyo, Japan.
[2] Nonequilibrium Quantum Statistical Mechanics RIKEN Hakubi Research Team, Japan.
[3] RIKEN Interdisciplinary Theoretical and Mathematical Sciences Program (iTHEMS),Japan.
[*]corresponding author: ken-mochizuki@ap.t.u-tokyo.ac.jp

Abstract: We explore noisy non-unitary dynamics of bosons exposed to random measurements and postselections. We find that noisy dynamics typically exhibit bunching states with no memory of initial states, where all bosons occupy one time-dependent mode. We also show a universal power law of relaxation times to the fluctuating bunching state.

Spectral analysis has played a key role for understanding noiseless linear dynamics described by time-independent generators. Indeed, various intriguing phenomena have been uncovered through the eigenvalues and eigenmodes of the generator. Examples include Parity-Time symmetry breaking related to the complexity of bosons [1] and steady state phase transitions accompanied by gap closing [2]. Meanwhile, temporally noisy dynamics has also gathered huge attention as versatile platforms for exploring intriguing phenomena and universal features of non-equilibrium dynamics. Examples include information scrambling in unitary dynamics [3] and measurement-induced transitions in non-unitary dynamics of monitored systems [4]. However, the direct spectral analysis for noisy dynamics has not been fully developed, which is contrasted to noiseless dynamics with time-independent generators.

In this work, we propose an analysis based on a noisy spectral gap, which is a generalization of the spectral gap in noiseless systems. We apply the analysis to noisy non-unitary dynamics of bosons where the system is coupled to the environment. As a result, we reveal that bosons typically exhibit the fluctuating bunching state in the long run; all bosons asymptotically occupy one time-dependent mode [5]. The fluctuating bunching state has several unique features. First, the bunching state is distinct from stationary states in noiseless dynamics since the former is largely fluctuating in time while the latter is independent of time. Second, the occupation of one mode leads to the memory loss where there is no information about the initial state, which is contrasted to unitary dynamics. Third, the probability distribution of bosons corresponds to that of distinguishable particles that classical computers can easily sample, which is contrasted to unitary dynamics where the boson sampling problem can exhibit quantum supremacy [6]. We also find a universal power law of relaxation times, which bosons take to reach the bunching state, with respect to the strength of noise [5].

References

1. K. Mochizuki and R. Hamazaki, Physical Review Research **5**, 013177 (2023).
2. E. M. Kessler *et. al*, Physical Review A **86**, 012116 (2016).
3. A. Nahum *et. al*, Physical Review X **7**, 031016 (2017).
4. B. Skinner, J. Ruhman and A. Nahum, Physical Review X **9**, 031009 (2019).
5. K. Mochizuki and R. Hamazaki, Physical Review Research **6**, 013004 (2024).
6. S. Aaronson and A. Arkhipov, Theory of Computing **9**, 143 (2013).

Resonance energy transfer near PT-symmetric and non-Hermitian multilayer systems

F. Marozka[1], A. Arlouski[2], A. Karabchevsky[1], and A. Novitsky[2*]

[1]School of Electrical and Computer Engineering, Ben-Gurion University of the Negev, Beer-Sheva, Israel
[2]Belarusian State University, Minsk, Belarus
[*]corresponding author: andreyvnovitsky@gmail.com

Abstract: Non-Hermiticity provides a fascinating route for the control over nanophotonic phenomena. Here we study the resonant energy transfer (RET) between acceptor and donor molecules for optically thick PT-symmetric layers. We relate spectral and RET features, show stochastic-like behavior of exceptional point positions, and give insights into machine-learning optimization of RET.

Non-Hermitian photonics is an important part of modern physics that allows realizing fundamental ideas in practice [1,2]. PT-symmetric systems exhibit prominent topological and scattering phenomena in pure form. The PT symmetry can be obtained in different designs, the simplest of which is a multilayer one, which supports a plethora of famous properties known for non-Hermitian systems. Many properties are related to the exceptional points bordering PT-symmetric and broken-PT-symmetric phases. Exceptional points facilitate enhancing of physical effects; they can be used for realization of lasing and improvement of the sensor's sensitivity [3].

Here we study the resonance energy transfer (RET) as a non-radiative energy transfer between quantum dipole emitter and receiver. The rate of RET is expressed by means of the emission and absorption spectra of the respectively donor and acceptor chromophores and spectral function presented below

$$T(\omega) = \frac{2\pi\omega^4}{\hbar^2 c^2 \varepsilon_0^2} \left| \overline{d}_d G(\omega, \overline{r}_d, \overline{r}_a) \overline{d}_a \right|^2 \quad . \tag{1}$$

The spectral function depends on non-Hermitian environment through Green's function and, hence, is of our interest. Here $\overline{d}_d$ and $\overline{d}_a$ are the electric dipole moments at the points $\overline{r}_d$ and $\overline{r}_a$, respectively.

We consider a couple of dipoles in vicinity of the gain layer boundary as shown in Fig. 1(a). The gain (dielectric permittivity $\varepsilon_g = \varepsilon' - i\varepsilon''$) and loss (permittivity $\varepsilon_l = \varepsilon' + i\varepsilon''$) slabs form a bilayer PT-symmetric system, which exceptional points can be found using the scattering matrix technique. In Fig. 1(b), the exceptional points for various layer thicknesses *L* and non-Hermiticity parameters ε'' are demonstrated [4]. The exceptional points in Fig. 1(b) look random due to dense oscillations of the spectral reflection and transmission functions for optically thick layers. The total intensity as a sum of reflection and transmission is illustrated in Fig. 2(a). Positions of the exceptional points well correspond to the maximum of the total intensity, because this exceptional point is a predecessor of the lasing-like phenomenon.

In Fig. 2(b), the spectral function *T* normalized by the spectral function in vacuum T_0 is depicted. At small values of the slab thickness *L* the PT symmetry feebly alters. The peak value at greater *L* is related to the spectral peak in Fig. 2(a). Besides the high peak of the spectral function, we observe also the suppression of *T*. The spectral function has an asymptote at extremely large slab thicknesses, which might be useful for the stable achieving of the resonance energy transfer enhancement.

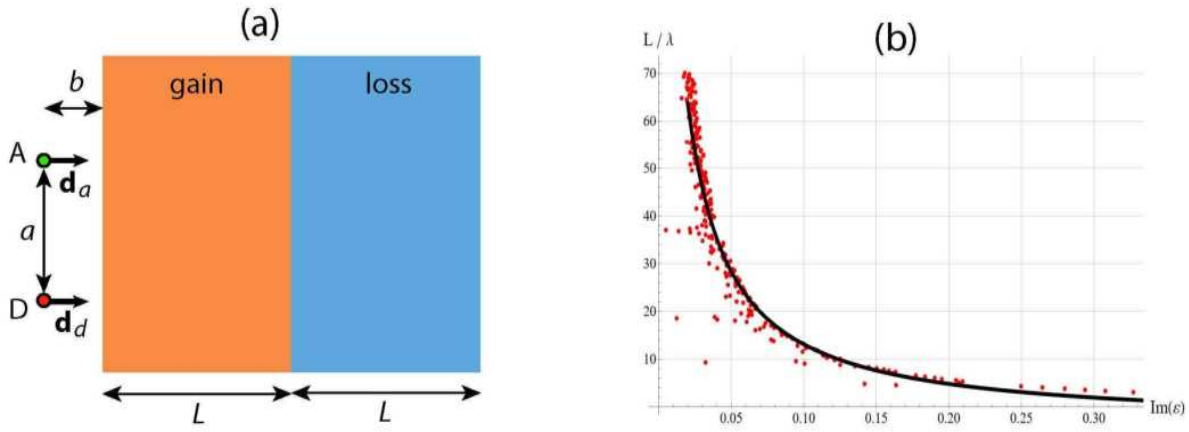


Fig. 1. (a) Sketch of the system in question. (b) Exceptional points depending on layer's thickness L and imaginary part of dielectric permittivity.

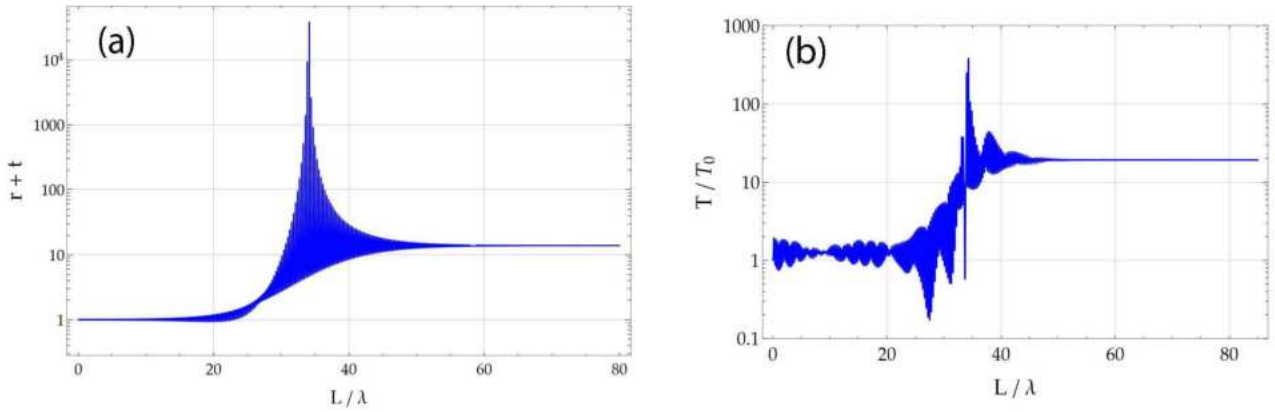


Fig. 2. (a) Total intensity and (b) normalized spectral function of the resonance energy transfer rate. Parameters: $\lambda = 500$ nm, a=10 nm, b=50 nm, and $\varepsilon'' = 0.05$. Dipoles are oriented as in Fig. 1(a).

To sum up, we have revealed that the resonant energy transfer rate might be enhanced owing to strong enlargement of the spectral function near exceptional points. Deeper analysis into this problem can be carried out using the machine learning algorithms.

References

1. L. Feng, R. El-Ganainy and L. Ge, "Non-Hermitian photonics based on parity-time symmetry," Nat. Photonics, Vol. 11, 752, 2017.
2. R. El-Ganainy, K. G. Makris, M. Khajavikhan, Z. H. Musslimani, S. Rotter and D. N. Christodoulides, "Non-Hermitian physics and PT symmetry," Nat. Phys., Vol. 14, 11, 2018.
3. S. K. Özdemir, S. Rotter, F. Nori and L. Yang, "Parity-time symmetry and exceptional points in photonics," Nat. Mater., Vol. 18, 783, 2019.
4. A. Arlouski and A. Novitsky, "Planar Bilayer PT-Symmetric Systems and Resonance Energy Transfer," Photonics, Vol. 11, 169, 2024.

Non-Bloch band theory of photonic crystals

K. Yokomizo[1*], T. Yoda[2], Y. Ashida[1,3], and S. Murakami[2]

[1]Depertment of physics, The University of Tokyo, 7-3-1 Hongo, Bunkyo-ku, Tokyo, 113-0033, Japan
[2]Depertment of Physics, Tokyo Institute of Technology, 2-12-1 Ookayama, Meguro-ku, Tokyo, 152-8551, Japan
[3]Institute for Physics of Intelligence, The University of Tokyo, 7-3-1 Hongo, Bunkyo-ku, Tokyo, 113-0033, Japan
[*]corresponding author: yokomizo@phys.s.u-tokyo.ac.jp

Abstract: We study the non-Hermitian skin effect of photonic crystals by establishing the non-Bloch band theory, which allows us to calculate the continuum band of the localized eigenmode. We reveal the qualitative and quantitative properties of the skin modes in photonic crystals.

Optics is an ideal platform for studying non-Hermitian physics due to the ease of incorporating optical gain and loss. Recent years have witnessed remarkable developments to emulate a variety of non-Hermitian phenomena. One of the most important progresses in non-Hermitian optics is to observe a parity-time symmetry breaking and associated exceptional points [1]. On another front, the non-Hermitian skin effect, a phenomenon localizing numerous eigenmodes at boundaries, has played a vital role in non-Hermitian physics. While the non-Hermitian skin effect gives rise to rich, intriguing phenomena, it has not been a research subject in optics. So far, the non-Hermitian skin effect has been mainly investigated by using tight-binding models.

To study the non-Hermitian skin effect in optics, we establish the non-Bloch band theory in continuous models and apply the theory to several photonic crystals. The non-Bloch band theory allows us to calculate the continuum band under the non-Hermitian skin effect, reproducing the eigenvalue of the finite-size system with open boundary conditions. The key idea is that one can determine the generalized Brillouin zone for the complex-valued Bloch wave number. We remark that the inverse of the imaginary part of the complex-valued Bloch wave number means the localization length of the skin mode.

We first consider the eigenmode of the photonic crystal composed of the layered dielectric media [2]. Let us suppose that the dielectric tensors of the layers are given by

$$\hat{\varepsilon}_j = \begin{pmatrix} \varepsilon_{xx,j} & \varepsilon_{xy,j} & 0 \\ \varepsilon_{yx,j} & \varepsilon_{yy,j} & 0 \\ 0 & 0 & \varepsilon_{zz} \end{pmatrix}, (j = 1,2). \tag{1}$$

The magnetic field of the transverse-electric mode then obeys the Strum-Liouville type equation written as

$$\left\{ -\frac{d}{dx}\eta_{yy}(x)\frac{d}{dx} - \frac{i}{2}\left[-2k_y\eta_{xy}(x)\frac{d}{dx} + \frac{d}{dx}\left[-2k_y\eta_{yx}(x) \right] \right] + k_y^2\eta_{xx}(x) \right\} H(x) = \left(\frac{\omega}{c}\right)^2 H(x), \tag{2}$$

where c is the speed of light in vacuum, and $\hat{\eta}(x)$ is the inverse of $\hat{\varepsilon}(x)$. Based on the original non-Bloch band theory [3], we analytically derive the localization length of the skin mode as follows:

$$\lambda = \left| \frac{2a}{k_y \mathrm{Im}\left(\sum_{j=1}^{2} \frac{\varepsilon_{xy,j} + \varepsilon_{yx,j}}{\varepsilon_{xx,j}} a_j \right)} \right|, \tag{3}$$

where $a(= a_1 + a_2)$ is the lattice constant. Thus, Eq. (3) indicates that the anisotropy of the permittivity and the

optical gain and loss give rise to the non-Hermitian skin effect in the photonic crystal. Furthermore, based on Eq. (3), one can define the Zak phase from the generalized Brillouin zone to discuss the topology of the photonic crystal. Indeed, we demonstrate the bulk-edge correspondence of the nonzero Zak phase and the existence of the topological edge mode.

We next consider the eigenmode of the photonic crystal composed of the layered chiral metamaterials [4]. Let $\hat{\xi}_j$ and $\hat{\zeta}_j$ denote the chirality tensors of the layers. We remark that the form of the chirality tensors determines the polarization of the eigenmode of the photonic crystal. For example, when the chirality tensors are given by

$$\hat{\xi}_j = \begin{pmatrix} 0 & \xi_{xy,j} \\ \xi_{yx,j} & 0 \end{pmatrix}, \hat{\zeta}_j = \begin{pmatrix} 0 & \zeta_{xy,j} \\ \zeta_{yx,j} & 0 \end{pmatrix}, (j = 1,2), \tag{4}$$

the photonic crystal has the linearly polarized eigenmode. The non-Bloch band theory based on the transfer-matrix method allows us to derive the analytical form of the localization length of the skin mode as follows:

$$\lambda = \left| \frac{2ca}{\mathrm{Im}\left(\sum_{j=1}^{2} \omega\left(\xi_{xy,j} + \zeta_{yx,j}\right) a_j\right)} \right|. \tag{5}$$

Meanwhile, when the chirality tensors are given by

$$\hat{\xi}_j = \begin{pmatrix} \xi_j & 0 \\ 0 & \xi_j \end{pmatrix}, \hat{\zeta}_j = \begin{pmatrix} \zeta_j & 0 \\ 0 & \zeta_j \end{pmatrix}, (j = 1,2), \tag{6}$$

the photonic crystal has the circularly polarized eigenmode. Notably, under the non-Hermitian skin effect, the left- and right-circularly polarized eigenmodes are localized at the opposite boundaries with the localization lengths represented by

$$\lambda = \left| \frac{2ca}{\mathrm{Re}\left(\sum_{j=1}^{2} \omega\left(\xi_j - \zeta_j\right) a_j\right)} \right|. \tag{7}$$

Equations (5) and (7) indicate that the chirality parameters contribute to the non-Hermitian skin effect in the photonic crystal. In the former, the non-Hermitian skin effect vanishes when the system becomes reciprocal, i.e., $\hat{\xi}^{\mathrm{T}} = -\hat{\zeta}$. Meanwhile, in the latter, the non-Hermitian skin effect persists even if $\hat{\xi}^{\mathrm{T}} = -\hat{\zeta}$. Furthermore, while all the eigenmodes have the typical localization length in the photonic crystal composed of the dielectric media, the localization lengths of the eigenmodes depend on the corresponding eigenvalue in the present case.

References

1. C. E. Rüter, K. G. Makris, R. El-Ganainy, D. N. Christodoulides, M. Segev, and D. Kip, "Observation of parity-time symmetry in optics," Nat. Phys. **6**, 192 (2010).
2. K. Yokomizo, T. Yoda, and S. Murakami, "Non-Hermitian waves in a continuous periodic model and application to photonic crystals," Phys. Rev. Research, **4**, 023089 (2022).
3. K. Yokomizo and S. Murakami, "Non-Bloch band theory of non-Hermitian systems", Phys. Rev. Lett., **123**, 066404 (2019).
4. K. Yokomizo, T. Yoda, and Y. Ashida, "Non-Bloch band theory of generalized eigenvalue problems," appear in Phys. Rev. B.

Classifying topology in photonic crystal slabs despite their radiative environment

S. Wong[1*], T. A. Loring[2], and A. Cerjan[1]

[1]Center for Integrated Nanotechnologies, Sandia National Laboratories, Albuquerque, New Mexico 87185, USA
[2]Department of Mathematics and Statistics, University of New Mexico, Albuquerque, New Mexico 87131, USA
[*]corresponding author: stewong@sandia.gov

Abstract: The spectral localizer is used to probe the topology in a full-wave simulated photonic systems. Using a topological photonic crystal slab, we show the genuine topological protection where the radiative loss is taken into account.

Over the past few years, there has been significant work on photonic topological insulators (PTIs) because of their potential to improve photonic devices through their topological protected edge states [1]. The study of PTIs has first focused on two-dimensional (2D) photonic crystals using topological band theory, and soon after was realized in photonic crystal slabs where a 2D, and Hermitian, approximations are assumed for the characterization of the topology. However, the out-of-plane radiative loss, an important aspect of photonic crystal slabs, has been neglected in previous theoretical treatments and cannot be accounted for using a band theoretic approach. In particular, above the light-line, photonic crystal slabs do not possess a true band structure of bound states – instead, while a resonance band structure can be defined, resonances are not true eigenstates of a Hermitian Hamiltonian. Moreover, it is not known whether topological invariants can be meaningfully calculated, especially given that the surrounding environment is gapless [2]. Here, we present a general framework for studying topology in realistic three-dimensional (3D) photonic systems that directly accounts for out-of-plane losses. The framework relies on the spectral localizer, a real-space approach that uses the position matrices and the Hamiltonian matrix of the system to draw a local picture of the topology of the system, along with finite element method (FEM) to discretize the system describe by the full-wave Maxwell equations. Finally, we illustrate this general framework using a non-trivial topological photonic crystal slab, specifically a Chern slab.

The spectral localizer takes an operator-based approach to classify the topology of a system. This approach directly uses the positions matrices and Hamiltonian matrix of the system to assess any obstructions to continuously deforming the system to an atomic limit. To some extent, this local approach can be seen as a real-space analogue to topological quantum chemistry. For a d-dimensional Hermitian system, the localizer can be defined as [3]

$$L_{\lambda=(x_1,\dots,x_d,E)}(X_1,\dots,X_d,H) = \sum_{j=1}^{d} \kappa\left(X_j - x_j I\right) \otimes \Gamma_j + (H - EI) \otimes \Gamma_{d+1}, \quad (1)$$

where $X_1,\dots,X_d$ are the positions matrices and H is the Hamiltonian matrix of the system, I is the identity matrix, and $\lambda = (x_1,\dots,x_d,E)$ is to be seen as an input for the local probing of the topology in space $(x_1,\dots,x_d)$ and energy (E). κ is a hyperparameter that makes the units consistent between the position and Hamiltonian matrices. The eigenvalues of the spectral localizer $\sigma(L_\lambda)$ can heuristically be understood as a real-space, local analogue of the bulk bands. Similarly, the topology of the system can only change through a gap closing of the localizer spectrum, namely when $\min(|\sigma(L_\lambda)|) = 0$. The topological robustness can then be represented by its localizer gap $\mu_\lambda^{\mathrm{C}} := \min\left(\sigma(L_\lambda)\right)$. The spectral localizer is applied to the study of topology in photonic systems as follows. A photonic system is typically described by the full-wave Helmholtz equation which we discretize using FEM via COMSOL Multiphysics [4]. The position matrices are then diagonal matrices with entries corresponding to the positions of the FEM degree of freedom. The effective Hamiltonian matrix H_{eff} is the FEM matrix from the Helmholtz equation after FEM discretization where the eigen-solution of $H_{\mathrm{eff}}(\omega)\Psi = 0$ gives the physical states at frequency ω. As only the zero eigenvalue of H_{eff} is physically meaningful, the topology in photonic system via FEM is probed using the following version of the spectral localizer $L_{\lambda=(x_1,\dots,x_d,0)}\left(X_1,\dots,X_d,H_{\mathrm{eff}}(\omega)\right)$. This approach directly incorporates radiative boundary conditions by using the non-Hermitian line-gap extension of the localizer [5].

As an example of a photonic system which is not fully describe by topological band theory, we consider here a free-standing Chern slab in air as shown in Fig. 1(a)-(b). The slab of thickness $t_{\text{slab}} = 0..5a$ is made of gyro-electric material that breaks time-reversal symmetry with $\epsilon_{jj} = 1, \epsilon_{xy} = 0.4i$ and dielectric rods with $\epsilon_{jj} = 14$ of radius $r = 0.37a$ patterned as a triangular lattice with lattice constant $a = 1\mu m$. Although the system is genuinely 3D, the z-dimension is projected into a single z value and the effective 2D version is used for the spectral localizer in Eq. (1). This projection allows us to restrict the study of the topology via the point-of-view of a path from one topological insulator to another into the xy-plane while keeping all the 3D information, such as the radiative loss, in the effective Hamiltonian H_{eff} derived from the full 3D system. Physically, this dimensional reduction is necessary for a Chern number to have meaning; complex 3D systems do not generally possess an integer topological invariant. The non-Hermitian spectral localizer used for classifying 2D systems is then written as [5]

$$L_{\lambda=(x,y,0)}(X, Y, H_{\text{eff}}(\omega)) = \begin{pmatrix} H_{\text{eff}}(\omega) & \kappa(X - xI) - i\kappa(Y - yI) \\ \kappa(X - xI) + i\kappa(Y - yI) & -H_{\text{eff}}(\omega)^{\dagger} \end{pmatrix}. \quad (2)$$

Given a position in y, the topology is probed from outside the topological photonic crystal in the slab to the middle in Fig. 1(c). The figure demonstrates a crossing in the spectrum of L_λ which is representative of a change of topology (red arrow) in accordance with topological band theory. However, the topological protection given by the localizer gap now takes into account the radiative loss of the topological edge slab state and is not just a single value corresponding to the bulk band gap in the bandstructure.

To conclude, using the operator-based approach of the spectral localizer, we study the topology in photonic system derived directly from the full-wave Maxwell equations. Besides, the spectral localizer allows us to give the genuine topological protection of the topological edge slab state when taking into account possible radiative loss of the slab state. Moving forward, this framework is suitable to accurately probe the topological information of a photonic system for future practical application but is also general for tackling problem in other platforms such as in acoustic materials.

SNL is managed and operated by NTESS under DOE NNSA contract DE-NA0003525.

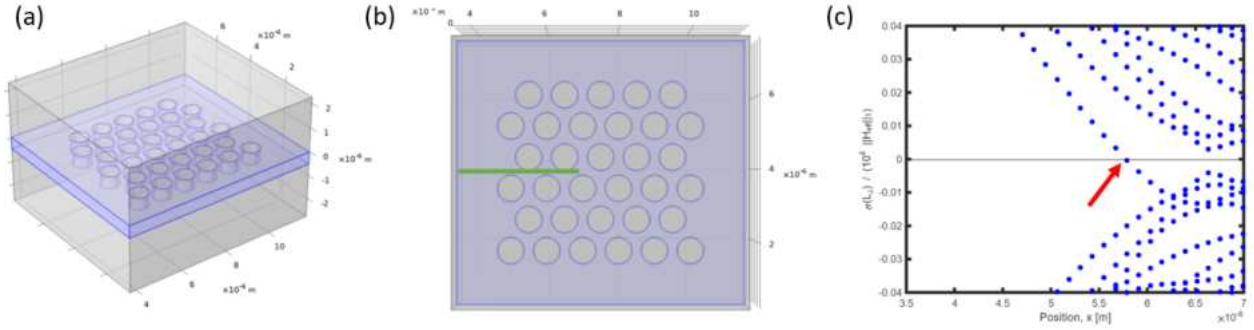


Figure 1: (a) Design of the free-standing Chern slab with the slab highlighted in blue. (b) xy-view of the Chern slab. (c) Spectrum of the localizer $\sigma(L_\lambda)$ normalized by $10^4\|H_{\text{eff}}\|_1$ with $\kappa = 0.5$ $\|X\|_1/(10^4\|H_{\text{eff}}\|_1)$ along the green line in (b). The red arrow indicates the change in topology at the given position.

References

1. T. Ozawa, H. M. Price, A. Amo, et al, "Topological photonics", Rev. Mod. Phys. 91, 015006 (2019).
2. C.-K. Chiu, J. C. Y. Teo, A. P. Schnyder, and S. Ryu, "Classification of Topological Quantum Matter with Symmetries", Rev. Mod. Phys. 88, 035005 (2016).
3. T. A. Loring, "K-theory and pseudospectra for topological insulators", Ann. Phys. 356, 383-416, (2015).
4. COMSOL Multiphysics® v. 6.2. www.comsol.com. COMSOL AB, Stockholm, Sweden.
5. A. Cerjan, L. Koekenbier, and H. Schulz-Baldes, "Spectral localizer for line-gapped non-Hermitian systems", Journal of Mathematical Physics 64, 082102 (2023).

META 2024, TOYAMA - JAPAN, JULY 16 – 19, 2024

Non-hermitian coupled modes controlled by the slot chirality in a parity-time symmetric waveguide pair.

A. De Corte[1], B. Maes[1], H. Benisty[2] and M. Besbes[2]

[1]Micro- and Nanophotonic Materials Group, Research Institute for Materials Science and Engineering, University of Mons, Belgium

[2]Laboratoire Charles Fabry, Institut d'Optique Graduate School, CNRS, Université Paris Saclay, France

Henri.benisty@institutoptique.fr

Abstract: Chiral materials inserted in the gap of PT-symmetric coupled dielectric waveguides induce a coupling of their non-Hermitian modes. The interplay of chirality-induced polarization-related anticrossing and exceptional points unveils a rich physics, featuring enhancement mechanisms such as slot geometries and providing unusual dispersion around exceptional points.

Coupling of two polarizations is at the core of chirality. Another coupling, the coupling of two waveguides, has been widely revisited in the presence of parity-time symmetric setting, i.e. a gain waveguide and a lossy waveguide, leading to the occurrence of an exceptional point (EP) where eigenvalues and eigenmodes coalesce. The aim of this exploration is to investigate the interplay of polarization coupling and mode coupling in terms of dispersion and fate of exceptional point, but in the waveguide geometry[1], unlike studies of layered systems such as [2]. To this aim we chose to study the case of two waveguides of identical elongated shape with a thin spacer between them, filled of chiral or achiral material (see black contours on Fig.1, the single guide cross section is 100x400 nm and the real part of its refractive index has a real part Re(n)= 2, the gap has index n=1.479 (achiral basis), the rest around is vacuum n=1). Among the scopes of keeping the chiral material thin is the issue of performing sensing of very small, comparable to those of the most sensitive biomolecular label-free techniques.

We thus study the dispersion and eigenmodes of coupled waveguides with a "chiral gap" as compared to an achiral gap, and attempt to get interactions that involve on a similar footing the PT symmetry features and the chiral features. Specifically, the chosen geometry, basically establishing non-interacting TE and TM polarization in the achiral case, is such that the achiral EP due to gain+loss in one polarization is also met by one of the branches of the other dispersion, so that the study can be seen as the quest of the nontrivial features arising from the anticrossing induced by chirality combined with a standard EP. Prior studies of 4-mode coupling [3] unveiled "symmetry recovery" effects, for instance, that we find as well here.

We model waveguide structures with using the SimPhotonics software implementing the finite element method. SimPhotonics is a Matlab toolbox developed at the Laboratoire Charles Fabry, it was modified to include the core coupling of chirality, the direct local coupling of E-field to H-field with a linear coefficient.

Besides the results of exact modal calculations, we have also exploited various basis to provide a quasi-analytical form to the dispersion. Specifically, we use either the individual mode basis (TE,TM in each waveguide) or the supermode basis (coupled waveguide) to interpret the various phenomena and check the underlying physical mechanisms.

Beside the specific interplay of the two effects (the EP behavior and the chirality), we explore the amount of "effective chirality" as observed from the coupling of modes and compare it to the bulk coupling. With a specific

gap of 32 nm, we find the E-field patterns of Fig.1 (*x* is horizontal, *y* is vertical, *z* is along the waveguide), whereby a large field enhancement exists for the E_x component in the slot in the achiral case (top). We hypothesize that this slot effect is of foremost importance to get to the same degree of "effective chirality" as a bulk medium with the same chiral constant (κ=0.012 here, a value to make coupling appear neatly enough) as the one present only in the 32 nm gap.

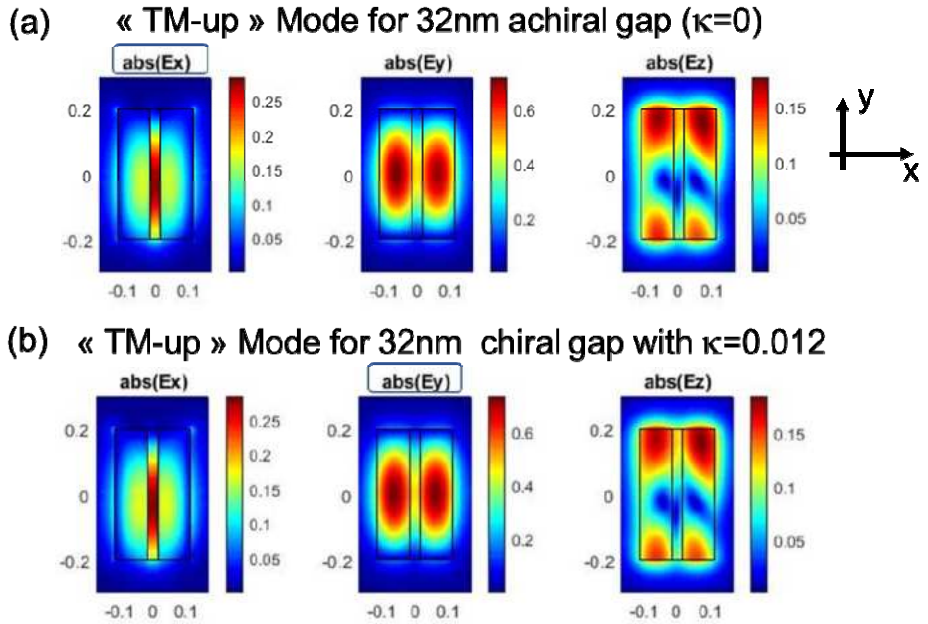


Figure 1 : Modes and coupled PT-symmetric waveguide geometry (black lines), operated at λ=350 nm, with a 32 nm gap. The right-side guide has gain and the left-side guide has loss. The gap is either achiral for the mode pictured in (a) or chiral for the mode pictured in (b). The mode is the « TM up » mode [1].

To conclude, we have unveiled a novel potential of PT-symmetric waveguides to get sensitive responses to chiral materials in small volume, thanks to the interplay of the various coupling operating in this situation.

Acknowledgements: A.D.C. acknowledges support from the Fund for Scientific Research F.R.S.-FNRS through a FRIA grant.

References

1. A. De Corte, M. Besbes, H. Benisty, B. Maes, "Chiral materials to control exceptional points in parity-time-symmetric waveguides," Phys. Rev. A Vol.109, 023521, 2024.
2. I. Katsantonis, S. Droulias, C. M. Soukoulis, E. N. Economou,T. P. Rakitzis, and M. Kafesaki, "Chirality sensing employing parity-time-symmetric and other resonant gain-loss optical systems," Phys. Rev. B, Vol.105, 174112, 2022.
3. N. X. A. Rivolta and B. Maes, "Symmetry recovery for coupled photonic modes with transversal PT symmetry," Opt. Lett., Vol.40, 3922 (2015).

Dual symmetry classification of non-Hermitian systems and point-gap topology

Zhiyu Jiang[1], Geonhwi Hwang[1], and Hideaki Obuse[1,2*]

[1]Department of Applied Physics, Hokkaido University, Sapporo 060-8628, Japan

[2]Institute of Industrial Science, The University of Tokyo, 5-1-5 Kashiwanoha, Kashiwa, Chiba 277-8574, Japan
[*]corresponding author: hideaki.obuse@eng.hokudai.ac.jp

Abstract: Since there is no distinct difference in mathematical definitions for Hamiltonians and time-evolution operators in non-Hermitian systems, we show that the systems can be always classified by two ways. We demonstrate this for point-gap topology of quantum walks. We also explain the bulk-edge correspondence for point-gap topology in junction systems.

It is widely known that non-Hermitian Hamiltonians exhibit richer topological properties compared to their Hermitian counterparts. This distinction arises due to the presence of two types of energy gaps—line gaps and point gaps—as well as an increased number of symmetries[1]. Additionally, the symmetry of time-evolution operators plays a crucial role in Floquet topological phases. However, the symmetry relation for time-evolution operators is described differently from that of Hamiltonians. These concepts extend to non-Hermitian systems, where the time-evolution operator becomes non-unitary. Until now, non-Hermitian systems have been classified based on the symmetry descriptions for non-Hermitian Hamiltonians[1] or the symmetry descriptions for non-unitary time-evolution operators[2].

In this talk, we show that since there is no distinct mathematical difference between the definitions of non-Hermitian Hamiltonians and non-unitary time-evolution operators, non-Hermitian systems can always be classified in two ways: the non-unitary time-evolution operator can be categorized using the symmetry relations for non-Hermitian Hamiltonians, and vice versa. We refer to this dual classification as dual symmetry classifications[3]. Furthermore, we delve into the bulk-edge correspondence for point-gap topology in junction systems[4].

To illustrate the dual symmetry classifications with a specific example, we introduce a non-unitary quantum walk classified in class AII† using the symmetry relations for non-Hermitian Hamiltonians. Notably, this non-unitary quantum walk exhibits point gaps with a Z2 topological phase and satisfies the bulk-edge correspondence for Z_2 point-gap topology, demonstrating Z_2 skin effects.

We also discuss the bulk-edge correspondence for point-gap topology in junction systems. In Hermitian systems, it is well known that the bulk-edge correspondence can predict the number of edge states appearing at an interface where two subsystems with their own topological numbers are attached. This prediction is based on considering the difference in the topological numbers. Now, we extend the concept of the bulk-edge correspondence to non-Hermitian junction systems, specifically focusing on point-gap topology[4] and clarify that the difference in the topological numbers in point gap for subsystems.

Zhiyu Jiang was supported by JST SPRING (Grant No. JPMJSP2119). This work was supported by JSPS

KAKENHI (Grants No. JP19H00658, No. JP20H01828, No. JP21H01005, No. JP22K03463 and No. JP22H01140).

References

1. Kawabata, K., K. Shiozaki, M. Ueda and M. Sato, “Symmetry and Topology in Non-Hermitian Physics,” Phys. Rev. X **9**, 041015 (2019).
2. Kawasaki, M., K. Mochizuki, N. Kawakami, and H. Obuse, “Bulk–edge correspondence and stability of multiple edge states of a PT –symmetric non-Hermitian system by using non-unitary quantum walks,” Prog. Theor. Exp.Phys. **2020**, 12A105 (2020)
3. Jiang, Z., R. Okamoto and H. Obuse, “Dual Symmetry Classification of Non-Hermitian Systems and Z2 point-gap toplogy of a Non-Unitary Quantum Walk,” (in preparation)
4. Hwang, G. and H. Obuse, “Bulk-edge correspondence for point-gap topological phases in junction systems” Phys. Rev. B **108**, L121302 (2023).

Topological control of OAM in photonic lattices

Zhigang Chen
The MOE Key Laboratory of Weak-Light Nonlinear Photonics, TEDA Applied Physics Institute and School of Physics, Nankai University, Tianjin, China
zgchen@nankai.edu.cn

Graphene has attracted immense attention due to its fundamental interest and highly exploited applications. Apart from carbon-based monolayer graphene materials, various synthetic honeycomb lattices (HCLs) have been employed as artificial graphene for electrons, atoms and photons. In particular, photonic graphene - an HCL of evanescently coupled waveguide arrays, has been proposed and demonstrated as an ideal platform for investigation of unconventional edge states and pseudospin angular momentum, among other intriguing phenomena. In this talk, I will present a few examples of our recent demonstrations on topological control and manipulation of OAM modes in photonic graphene-like structures, including topological singularity mapping that leads to stair-wise generation of OAM beams and topological protection of OAM transport.

Sub-symmetry protected topological states

Ziteng Wang[1†], Xiangdong Wang[1†], Zhichan Hu[1†], Domenico Bongiovanni[1,2†], Dario Jukić[3], Liqin Tang[1], Daohong Song[1], Roberto Morandotti[2], Zhigang Chen[1*], and Hrvoje Buljan[1,4*]

[1]TEDA Applied Physics Institute and School of Physics, Nankai University, Tianjin 300457, China
[2]INRS-EMT, 1650 Blvd. Lionel-Boulet, Varennes, Quebec J3X 1S2, Canada
[3]Faculty of Civil Engineering, University of Zagreb, A. Kačića Miošića 26, 10000 Zagreb, Croatia
[4]Department of Physics, Faculty of Science, University of Zagreb, Bijenička c. 32, 10000 Zagreb, Croatia
[*]corresponding author: zgchen@nankai.edu.cn, hbuljan@phy.hr

Abstract: A hallmark of symmetry-protected topological phases are topological boundary states, which are immune to perturbations that respect the protecting symmetry. It is commonly believed that any perturbation that destroys such topological phase simultaneously destroys the boundary states. However, we find that the boundary states are protected by a weaker sub-symmetry condition when the symmetry equation holds only in part of the Hilbert space. By precisely controlling symmetry-breaking in photonic lattices, we experimentally demonstrate such sub-symmetry protection of topological states.

Symmetry protected topological (SPT) phases of matter are ubiquitous in nature and exist on versatile platforms including condensed matter physics, ultracold atomic gases, and photonics [1,2]. Topological insulators (TIs) induced by spin-orbit coupling protected by time-reversal symmetry (TRS) are a paradigm for SPT phases [1-3]. In topological crystalline insulators, a crystalline point group symmetry protects topological metallic boundary states [1,4]. Imagine an SPT phase with a topological invariant characterizing the bulk states and the associated symmetry protected boundary states. Any perturbation that respects the protecting symmetries will not destroy these boundary states or change the topological invariant without closing the gap between bands [1,2]. However, as pictured in Fig. 1, the situation can be more complex: there are perturbations that preserve the topological invariant but oppose the existence of boundary states [5,6], and vice versa, there are perturbations that leave the boundary states unhurt while destroying the topological invariant [7]. We explore these questions by using the concept of sub-symmetry (SubSy), where the symmetry equation does not hold in the whole Hilbert space, but only in its subspace. For a one-dimensional (1D) Su-Schrieffer–Heeger (SSH) and breathing Kagome lattice (BKL) models, the SubSys arise from their chiral symmetries.

We demonstrate, theoretically and experimentally, that the boundary states in the SSH and BKL models are protected by their pertinent SubSy. Any SubSy-preserving perturbation will leave its corresponding boundary state eigenvalue at zero, even though the bulk topological invariant is lost. We utilize zigzag and twisted lattices, and “bridge” waveguides to experimentally introduce SubSy-breaking and -preserving perturbations in a controlled manner, and thereby demonstrate SubSy protected topological states. In the case of non-negligible long-range hopping (i.e., non-negligible coupling between distant lattice sites) in BKLs, we find that SubSy and an additional long-range hopping symmetry are sufficient to protect the corner states. Our experiments are performed in photonic structures, which have been established as a fertile platform for exploring novel topological phenomena [8-10]. The main message from our findings is summarized in Fig. 1, and more details can be found in Ref. [11].

Based on the concept of sub-symmetry, we propose a method that transforms an in-gap topological boundary state into a bound-state in continuum (BIC) [12]. More specifically, we design coupling between a

system possessing an in-gap topological modes and a system possessing a continuum of states that results in topological BICs. We define the criteria for the coupling that yields the desired results. Finally, we will present our recent results related to the non-Hermitian Skin effect induced by the synthetic gauge fields [13].

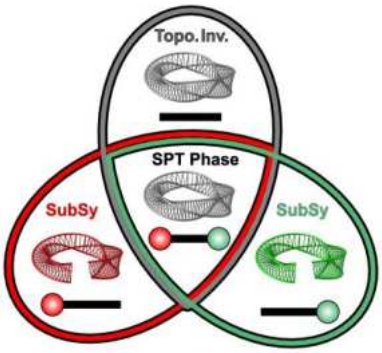


Fig. 1. Classification of perturbations with respect to symmetries in SPT phases. A set of perturbations, that preserves the topological invariant (or invariants) and respects a particular symmetry (or symmetries), is encircled with a grey line. Every boundary state is protected with its pertinent sub-symmetry (SubSy). In the illustration, two sets of SubSy-preserving perturbations (encircled with red and green lines) are sketched, but their number depends on the actual system. At the overlap region, one has an SPT phase with a topological invariant characterizing the bulk, and all associated boundary states. See Ref. [11] for details.

References

1. Chiu, C.-K. et al. Classification of topological quantum matter with symmetries. Rev. Mod. Phys. 88, 035005 (2016).
2. Ozawa, T. et al. Topological photonics. Rev. Mod. Phys. 91, 015006 (2019).
3. Kane, C. L. & Mele, E. J. Z2 topological order and the quantum spin Hall effect. Phys. Rev. Lett. 95, 146802 (2005).
4. Fu, L. Topological crystalline insulators. Phys. Rev. Lett. 106, 106802 (2011).
5. Longhi, S. Probing one-dimensional topological phases in waveguide lattices with broken chiral symmetry. Opt Lett 43, 4639-4642 (2018).
6. Jiao, Z. Q. et al. Experimentally detecting quantized Zak phases without chiral symmetry in photonic lattices. Phys. Rev. Lett. 127, 147401 (2021).
7. Poli, C. et al. Partial chiral symmetry-breaking as a route to spectrally isolated topological defect states in two-dimensional artificial materials. 2D Mater. 4, 025008 (2017).
8. Wang, Z. et al. Nature 461, 772 (2009).
9. Rechtsman, M. C. et al. Photonic Floquet topological insulators. Nature 496, 196-200 (2013).
10. Hafezi, M. et al. Imaging topological edge states in silicon photonics. Nat. Photon. 7, 1001-1005 (2013).
11. Z. Wang, X. Wang, Z. Hu, D. Bongiovanni, D. Jukić, L. Tang, D. Song, R. Morandotti, Z. Chen, H. Buljan, Sub-symmetry protected topological states, Nature Physics (2023), https://doi.org/10.1038/s41567-023-02011-9
12. X. Wang, D. Bongiovanni, Z. Wang, A. Abdrabou, Z. Hu, D. Jukić, D. Song, R. Morandotti, R. El-Ganainy, Z. Chen, and H. Buljan, Construction of topological bound states in the continuum via sub-symmetry, submitted.
13. H. Tang, Z. Wang, L. Tang, D. Song, Z. Chen and H. Buljan, Control of non-Hermitian skin effect by staggered synthetic gauge fields, submitted.

Non-Hermitian Many-body Landau-Zener Systems: Quantum Dynamics & Correlations

Avadh Saxena[1], Rajesh K. Malla[2], Julia Cen[1] and Wilton J. M. Kort-Kamp[1]

[1] Los Alamos National Lab. [2] Brookhaven National Lab.

We provide a general framework to solve a diverse class of linearly driven non-Hermitian quantum systems. In the context of Hermitian systems such models are commonly known as multistate Landau-Zener models. The anti-Hermitian couplings between the diabatic levels introduce non-Hermiticity. We find a conservation law which is unique to this class of models that describes the simultaneous growth of the unnormalized wave functions. For practical applications these models are pertinent to Bose-Einstein condensates, and can describe the dynamics of multispecies bosonic systems. The conservation law is related to a pair-production mechanism that is relevant to the dissociation of diatomic molecules into atoms. We address both solvable and semiclassically solvable non-Hermitian Landau-Zener models. These results are also useful in studying emergent phenomena in time-dependent non-Hermitian quantum systems. Finally, we make some general remarks about out-of-time ordered correlations in non-Hermitian systems.

2D Materials and Nanophotonics

Deep-Ultraviolet High-Quality-Factor Metasurfaces

Bo Ray Lee[1], Shang Jie Shen[1], Ting An Hsu[1], Mao Feng Jiang[1], Pei Ying Ho[1], Kuan-Heng Chen[1], Jia Hua Lee[1], Tzu-En Lin[2], Yao-Wei Huang[3], Ray-Hua Horng[1], Ming Lun Tseng[1]*

[1]Institute of Electronics, National Yang Ming Chiao Tung University, Hsinchu 300, Taiwan
[2]Institute of Biomedical Engineering, National Yang Ming Chiao Tung University, Hsinchu 300, Taiwan
[3]Department of Photonics, College of Electrical and Computer Engineering, National Yang Ming Chiao Tung University, Hsinchu 30010, Taiwan

Corresponding author: mltseng@nycu.edu.tw

Abstract: We demonstrate high-quality-factor dielectric metasurfaces working in the deep-ultraviolet (DUV) range. The metasurfaces were designed by incorporating several device schemes to enable the strong light confinement for high Q resonances. The applications of the reported metasurfaces will be discussed.

DUV light plays a critical role in many key technologies ranging from nanolithography, clinical imaging, to biomolecular spectroscopy(1). It has been shown that metasurfaces can improve those applications by their capability to enhance electromagnetic fields (2). Previously, metasurfaces and plasmonic devices in the DUV range are majorly made of aluminum(3-5). It is because that aluminum has a larger plasma frequency compared with other metals and thus still shows proper plasmonic properties below 300 nm. Despite many novel advancements with plasmonic metasurfaces in the DUV, the intention to further boost the light-matter interactions using metasurfaces usually suffers from their relatively moderate resonance quality due to the resistive loss of aluminum. This issue can be circumvented by replacing aluminum with low-loss dielectric materials. Dielectric metasurfaces made of high-index materials such as Ge, TiO2, and GaN have been used for many applications in the visible and IR range including light focusing, biosensing, and nonlinear optics. However, as commonly available low-loss DUV dielectric materials show moderate refractive index, it is challenging to realize high-Q metasurfaces due to the insufficient dielectric contrast between the resonance unit cells and the substrate. Here, we demonstrate feasible approaches to realize high-Q metasurfaces by introducing various device schemes in the designs. One of the reported methods is shown in Figure 1a, which is to place the metasurface on a freestanding membrane with a refractive index of 1.8. The thickness of the membrane is 15 nm. In our work, we tested aluminum nitride and hafnium oxide as the constituent materials for our DUV high-Q metasurfaces due to their neglectable optical absorption beyond ~230 nm. We use commercial simulation software Lumerical to design and characterize the optical properties of the metasurfaces. The resulting metasurface shows a high Q factor beyond 1000 with field enhancement of more than 30-fold compared with the incident light. As shown in Figure 1c, by gradually scaling the size of the resonance unit cells, we can move the resonance of the metasurface across the DUV range. In addition, we performed tests to verify the capability of the reported metasurfaces for biomolecular sensing. The results show that the reported high-Q metasurfaces can provide a striking platform for biomolecular sensing in the DUV range. The other design schemes and the applications of the reported metasurfaces for various surface-enhanced spectroscopy techniques and DUV chiral optics will be reported.

In conclusion, we demonstrate high-Q metasurfaces made of low-loss dielectric materials for DUV applications. The reported design schemes enable many novel applications in this critical wavelength range. This work will pave a novel route toward novel nanophotonic devices for sensing, quantum optics, and nonlinear

optics in this critical wavelength range.

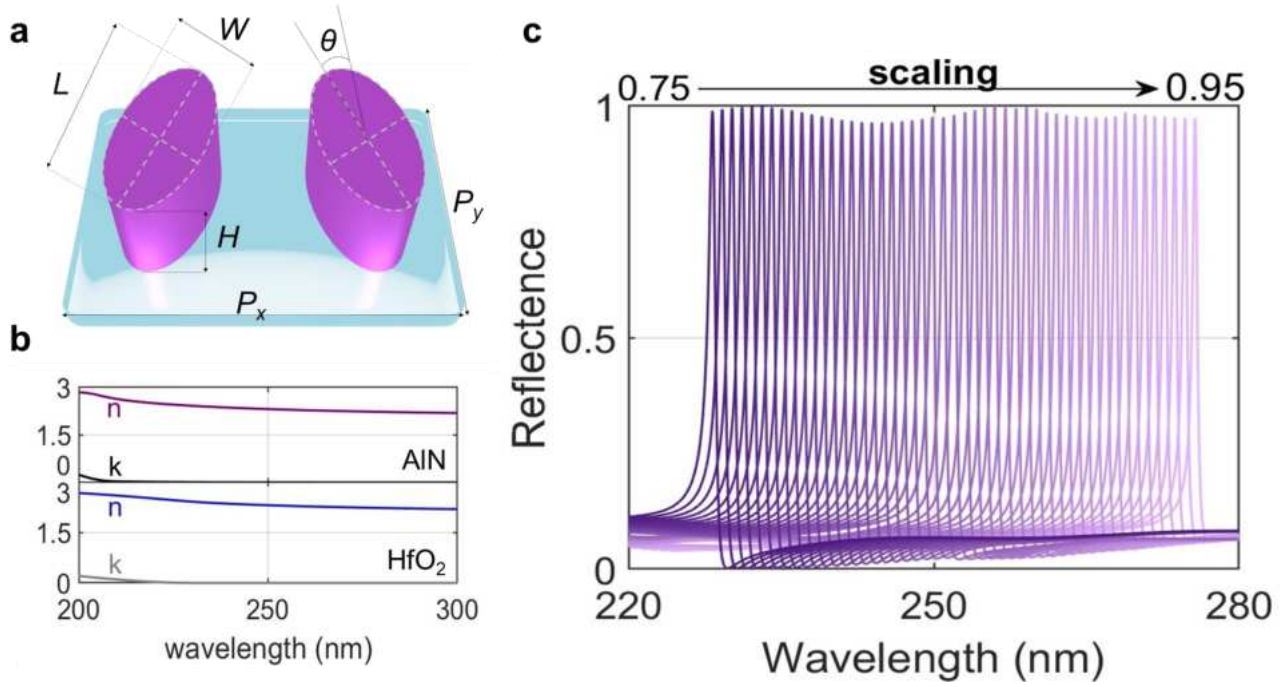


Figure 1. High-Q metasurface working in the DUV range. (a) The design of the high-Q metasurface. L: 114, W: 57, H:50, Py:168, Px: 236 nm, θ: 15 degrees. (b) The optical constants of AlN and HfO2 used for the DUV metasurface designs. (c) Simulation spectra of the metasurfaces with different scaling factors.

Acknowledgements. The authors acknowledge support from the National Science and Technology Council ((NSTC 112-2636-M-A49-001)) in Taiwan, the Ministry of Education in Taiwan under the Yushan Fellow Program, and the Center for Integrated Electronics-Optics Technologies and Systems, National Yang Ming Chiao Tung University. This work was also supported by the Higher Education Sprout Project of National Yang Ming Chiao Tung University and the Ministry of Education (MOE), Taiwan.

References

1. Y. Kumamoto, A. Taguchi, S. Kawata, "Deep‐Ultraviolet Biomolecular Imaging and Analysis." *Advanced Optical Materials* **7**, 1801099 (2018).
2. M. L. Tseng, Y. Jahani, A. Leitis, H. Altug, "Dielectric Metasurfaces Enabling Advanced Optical Biosensors. " *ACS Photonics* **8**, 47-60 (2020).
3. S. K. Jha, Z. Ahmed, M. Agio, Y. Ekinci, J. F. Löffler, "Deep-UV Surface-Enhanced Resonance Raman Scattering of Adenine on Aluminum Nanoparticle Arrays. " *J. Am. Chem. Soc.* **134**, 1966-1969 (2012).
4. A. Barulin *et al.*, "Preventing Aluminum Photocorrosion for Ultraviolet Plasmonics. " *J Phys Chem Lett* **10**, 5700-5707 (2019).
5. R. G. Hobbs *et al.*, "High-Energy Surface and Volume Plasmons in Nanopatterned Sub-10 nm Aluminum Nanostructures. " *Nano Lett.*, **16**, 4149 (2016).

Electric Field Driven Trion Drift in suspended 2D Transition Metal Dichalcogenides

Woo Hun Choi[1,2], Seong Won Lee[1,2] and Su-Hyun Gong[1,2*]

[1]Department of physics, Korea University, Seoul, Korea
[2]KU Photonics center, Korea University, Seoul, Korea
[*]Su-Hyun Gong: shgong@korea.ac.kr

Abstract: Trions, quasiparticles composed of an exciton bound to an excessive charge, in transition metal dichalcogenide (TMD) are potential candidate of information carriers that can be controlled using external electric fields. In this work, we demonstrate drift of trions in a suspended TMD monolayer by using a simple electromechanical device.

Transition-metal dichalcogenide (TMD) materials emerged as an indispensable platform for studying exciton-related physics because of their rich exciton landscape[1]. Among the diverse research field, controlling the exciton transport in a TMD monolayer are considered as a crucial step for developing TMD-based excitonic devices[2]. However, an external electric field cannot be utilized since excitons are charge-neutral quasiparticles. In contrast to neutral excitons, trions (charged excitons) carry a nonzero net charge, which provides great potential for their manipulation using externally applied electric fields as in conventional electronic devices[3,4]. In this study, we achieved free-trion drift in a suspended TMD monolayer by exerting a gate-tunable electric field using a simple bottom-gate device. Our device consists of TMD monolayer suspended on a patterned SiO2/Si substrate, Si bottom gate, and top Au contact (Fig. 1a). When a voltage was applied at the bottom gate, electric fields were induced in the vicinity of the monolayer (Fig. 1b). Induced electric field plays two roles in our device. First, because the monolayer is connected to the ground through the top contact, the electric field leads to electrostatic doping in the monolayer result in increasing the density of trions. The second role of the electric field in our device is to apply an electric force to the suspended monolayer which pulls down the suspended layer and induces in-plane trion motion.

Figure 1

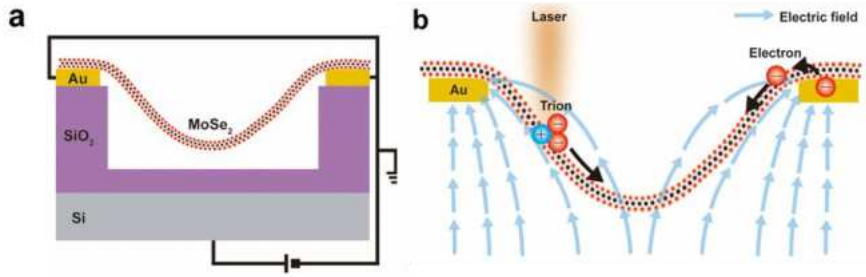


Figure 1. Gate-tunable suspended MoSe2 monolayer device. **a**. Schematic diagram of the suspended MoSe2 monolayer on a patterned SiO2/Si substrate. **b**. Schematic diagram of the suspended MoSe2 monolayer under the electric fields.

To confirm the trion drift motion, we locally excited trions and compare the PL distribution at various position in the suspended region. Figure 2a–d shows the spatial distribution of the trion PL intensity for different excitation positions at a bottom-gate voltage of 170 V at a cryogenic temperature (3 K). At the hole center, trion PL distribution followed the symmetry of the Gaussian profile. However, PL distribution at about 350 nm away from the hole center exhibited

an asymmetric behavior along the radial direction. The asymmetric intensity with a stretched tail toward the hole center suggests that the trions tend to drift toward the center at a finite positive gate voltage. Furthermore, in order to utilize trions as information carrier at practical usage, they must be able to exhibit same phenomena even at room temperature. Therefore, we also conducted a similar study in WS_2 monolayer at room temperature and successfully observed trion drift.

Figure 2

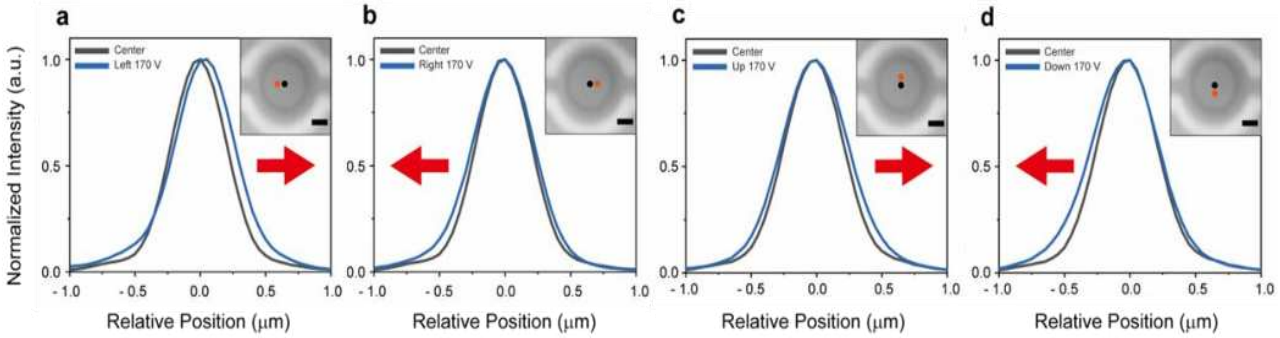


Figure 3. Drift of trions toward the center of the hole. (a–d) Cross-sectional PL intensity distribution of trions for different excitation positions at a gate voltage of 170 V.

In conclusion, we successfully demonstrated the drift motion of a trions in a suspended TMD monolayer at both cryogenic and room temperature. We emphasize that previous studies on the transport of excitons or excitonic complexes in TMD monolayers conducted on time-resolved techniques under pulse-excitation[4,5]. In this study, we observed the drift of trions under continuous-wave (CW) excitation without time-resolved spectroscopy which provides more direct result that are easy to interpret. It is recently reported that the suspended geometry of the device and electrostatic doping increase the trion lifetime hence enabling us to observe enhanced transport phenomena of trions[6]. Our findings clearly demonstrate the untapped potential of trion-based optoelectronic devices.

References

1. Malic, E., Perea-Causin, R., Rosati, R. et al., "Exciton transport in atomically thin semiconductors" *Nat Commun*, 14, 3430, 2023.
2. Lee, H., Kim, Y.B., Ryu, J.W. et al., "Recent progress of exciton transport in two-dimensional semiconductors" *Nano Converg*, 10, 57, 2023.
3. Sanvitto, D., et al., "Observation of Charge Transport by Negatively Charged Excitons" *Science*, 294, 837-839, 2001.
4. Cheng, G., Li, B., Jin, Z., Zhang, M., Wang, J., "Observation of Diffusion and Drift of the Negative Trions in Monolayer WS2" *Nano Lett*, 21, 6314-6320, 2021.
5. Harats, M. G., Kirchhof, J. N., Qiao, M., Greben, K., Bolotin, K. I., "Dynamics and Efficient Conversion of Excitons to Trions In Non-Uniformly Strained Monolayer WS2" *Nat. Photon*, 14, 324-329, 2020.
6. Sharma, A., Zhu, Y., Halbich, R., Sun, X., Zhang, L., Wang, B., Lu, Y., "Engineering the Dynamics and Transport of Excitons, Trions, and Biexcitons in Monolayer WS2" *ACS Appl. Mater. Interfaces*, 14, 36, 41165-41177, 2022.

Tunable Transition Metal Dichalcogenide Based Metasurfaces in Liquid Crystal Medium

K. M. Anu[1], and Jayasri Dontabhaktuni[1*]

[1] Department of Physics, Mahindra University, Hyderabad, India

*corresponding author: jayasri.d@mahindrauniversity.edu.in

Abstract: In this work, we demonstrate versatility and tunability of transition metal dichalcogenide based metasurfaces in air and liquid-crystal medium. We explore the tunability in electromagnetic response, near-field, far-field radiation profiles, sensitivity, strong coupling between excitons and polaritons in WS_2 based metasurfaces as a function of liquid-crystal orientations in visible region.

Summary:

Transition metal dichalcogenides (TMDCs) is a rapid growing field in the nanophotonics due to their extraordinary excitonic, optical, mechanical, thermal and electronic properties [1-3]. The creation of innovative dielectric metasurfaces with a high refractive index has garnered significant attention and research interest due to TMDCs. Compared to commonly utilized dielectric materials with high refractive indices, bulk TMDC materials have naturally very high refractive indices in the visible and near-infrared spectral region. TMDCs, specifically MoS_2 and WS_2 have direct bandgap and strong excitonic characteristics. Bulk WS_2 exhibits self-coupled exciton-polaritons and distinct Mie modes [4, 5]. WS_2 metasurface has been useful for sensing applications [6], light harvesting [4, 6] and exciton-polariton devices [4, 6, 7]. Liquid crystals (LC's) are a flexible medium that can support programmable, multifunctional, and tunable electromagnetic response through optical, thermal, electrical, and magnetic tuning [8, 9]. WS_2 has variety of uses in electronics and optoelectronics and we investigate the tunability liquid crystal (LC) can bring in the light matter interaction in bulk WS_2 metasurface.

We designed the model using finite element method (FEM) simulations in commercially available CST software. A nanocuboid metasurface made out of bulk WS_2 is deposited onto a SiO_2 substrate of thickness t = 100 nm, illuminated by a normally incident y-polarized plane wave. The periodicity of each unit cell is p = 300 nm and every nanocuboids has sides a = 240 nm and a height h = 30 nm, respectively. Each nanocuboids consists of a rectangular hole (100 × 50 nm) at a fixed distance d = 25 nm between center of WS_2 to center of rectangular hole. The simulated design has been studied in the air medium and liquid crystal (LC) medium of thickness 200 nm. Results are obtained by simulating unit cell with periodic boundary condition (PBC) along X and Y directions in the visible frequency range.

Conclusions:

The tunability that LC gives to the bulk WS_2 metasurfaces light matter interaction has been investigated in this paper. As per the literature, for the first time, we are showing LC's can tune quasiparticle interactions. We numerically examine the effect of electrically driven anisotropic LC medium on bulk WS_2 metasurface and their orientation in Quality factor, sensitivity, strong coupling between excitons and non-radiating states, near and far-fields, and thus expanding the possibilities of applications for phase modulators, multifunctional metasurfaces, tunable exciton-polariton devices and sensing.

Acknowledgements:

We are thankful to Mahindra University, Hyderabad, for supporting and providing necessary funds for our research.

References:

1. Zhou, J. et.al. "A library of atomically thin metal chalcogenides," Nature, 556,770,355-359, 2018.
2. Bhimanapati, G. R. et.al. "Recent advances in two-dimensional materials beyond graphene," ACS nano, 9, 12, 11509 - 11539, 2015.
3. Butler, S. Z. et al. "Progress, challenges, and opportunities in two-dimensional materials beyond graphene,"ACS nano, 7, 4, 2898-2926, 2013.
4. Verre, R. et al. "Transition metal dichalcogenide nanodisks as high-index dielectric Mie nanoresonators," Nature nanotechnology, 14, 7, 679-683, 2019.
5. Shen, F. et al. "Transition metal dichalcogenide metaphotonic and self-coupled polaritonic platform grown by chemical vapor deposition," Nature Communications, 13, 1, 5597, 2022.
6. Zong, X. et al. "Enhanced light--matter interactions in ultrathin transition-metal-dichalcogenide metasurfaces by magnetic and toroidal dipole bound states in the continuum," Optics Express, 30, 24, 43104-43117, 2022.
7. Qin, M. et al. "Strong coupling between excitons and quasibound states in the continuum in bulk transition metal dichalcogenides," Physical Review B, 107, 4, 045417, 2023.
8. Sakhare, P. A. and Jayasri Dontabhaktuni, "Ultra fast switching of dflc based dynamic metasurfaces," Frontiers in Physics, 10, 207, 2022.
9. Santonocito A., B. Patrizi, and G. Toci, "Recent Advances in Tunable Metasurfaces and Their Application in Optics", Nanomaterials, 13, 10, 1633, 2023.

Photoluminescence and electroluminescence control of 2D semiconductors coupled to nanophotonic structures

A. J. Moilanen[1*], T. Taniguchi[2], K. Watanabe[2], and L. Novotny[1]

[1]ETH Zürich, Switzerland
[2]National Institute for Materials Science, Japan
[*]corresponding author: amoilanen@ethz.ch

Abstract: We present control of photoluminescence and electroluminescence properties of two-dimensional (2D) semiconducting materials, monolayers of transition metal dichalcogenides (TMDs), by incorporating them into plasmonic and photonic cavities as well as waveguides. As another way to control the emission properties, we exploit electrostatic doping of the TMDs by using gate electrodes.

Nanophotonic cavities, such as plasmonic lattices (periodic arrays of metal nanoparticles) have been used to modify the photoluminescence (PL) properties of emitters such as fluorescent molecules and quantum dots, leading ultimately to the generation of coherent light in the nanoscale by lasing or Bose–Einstein condensation (BEC) [1-4]. While most of the previous works have relied on optical excitation of the gain material, electrically excited and controlled active materials would be desirable for on-chip integration. Two-dimensional (2D) semiconducting materials, monolayers of transition metal dichalcogenides (TMDs), have a direct optical bandgap and excitons with high binding energies, making TMDs a promising class of materials for light-emitting optoelectronic devices. We present ways to control the PL of these materials by coupling them into nanophotonic cavities and by applying gate electrodes to our devices. In addition, we demonstrate the integration of a 2D light-emitting device into a photonic waveguide made of hexagonal boron nitride (h-BN) [5]. Our results pave the way for novel on-chip optoelectronic devices such as integrated nanoscale light sources and optical interconnects.

This work has been supported by the Swiss National Science Foundation (Grant 200020_192362/1). A.J.M. acknowledges financial support by the ETH Zürich Postdoctoral Fellowship programme. The use of the facilities of the FIRST center for micro- and nanoscience at ETH Zürich is gratefully acknowledged. K.W. and T.T. acknowledge support from JSPS KAKENHI (Grants 19H05790, 20H00354, and 21H05233).

References

1. T. K. Hakala*, H. T. Rekola*, A. I. Väkeväinen, J.-P. Martikainen, M. Nečada, A. J. Moilanen, and P. Törmä., "Lasing in dark and bright modes of a finite-sized plasmonic lattice", Nat. Comm. 8: 13687, 2017.
2. T. K. Hakala*, A. J. Moilanen*, A. I. Väkeväinen, R. Guo, J-P. Martikainen, K. S. Daskalakis, H. T. Rekola, A. Julku, and P. Törmä, "Bose–Einstein condensation in a plasmonic lattice", Nat. Phys. 14, 739–744 (2018).
3. A. I. Väkeväinen, A. J. Moilanen, M. Nečada, T. K. Hakala, K. S. Daskalakis, and P. Törmä, "Sub-picosecond thermalization dynamics in condensation of strongly coupled lattice plasmons", Nat. Comm. 11, 3139, 2020.
4. A. J. Moilanen, K. S. Daskalakis, J. M. Taskinen, and P. Törmä, "Spatial and temporal coherence in strongly coupled plasmonic Bose–Einstein condensates", Phys. Rev. Lett. 127, 255301 (2021)
5. R. Khelifa*, S. Shan*, A. J. Moilanen, T. Taniguchi, K. Watanabe, and L. Novotny, "WSe_2 light-emitting device coupled to an h-BN waveguide", ACS Photonics 10, 5, 1328–1333, 2023

*these authors contributed equally

Strong nonlinear optical activities in the asymmetric 2D material with inversion-symmetry breaking

Song Zhu[1], Ruihuan Duan[2], Zheng Liu[2], and Qi Jie Wang[1]

[1]School of Electrical and Electronic Engineering, Nanyang Technological University, 639798, Singapore
[2]School of Material Science and Engineering, Nanyang Technological University, 639798, Singapore
150001, China
*corresponding author: qjwang@ntu.edu.sg

Abstract: Here, we demonstrate strong second-order and third-order susceptibilities of 64 pm/V and 6.2×10^{-19} m^2/V^2, respectively, in the even-layer PdPSe. It also simultaneously exhibited strong SHG anisotropy with an anisotropic ratio of ~45, which is the largest reported among all 2D materials to date, to the best of our knowledge.

Nonlinear optics has been a fundamental building block of modern optics and lies at the core of laser technology, optical spectroscopy, and quantum networks. Second-harmonic generation (SHG) and third-harmonic generation (THG) processes in 2D materials are emerging branches of nonlinear optics and have been widely exploited for various applications, such as nonlinear optical modulators[1], nonreciprocal optical devices[2], and quantum sources[3]. Several methods have been proposed to generate SHG in 2D materials by breaking the inversion symmetry.

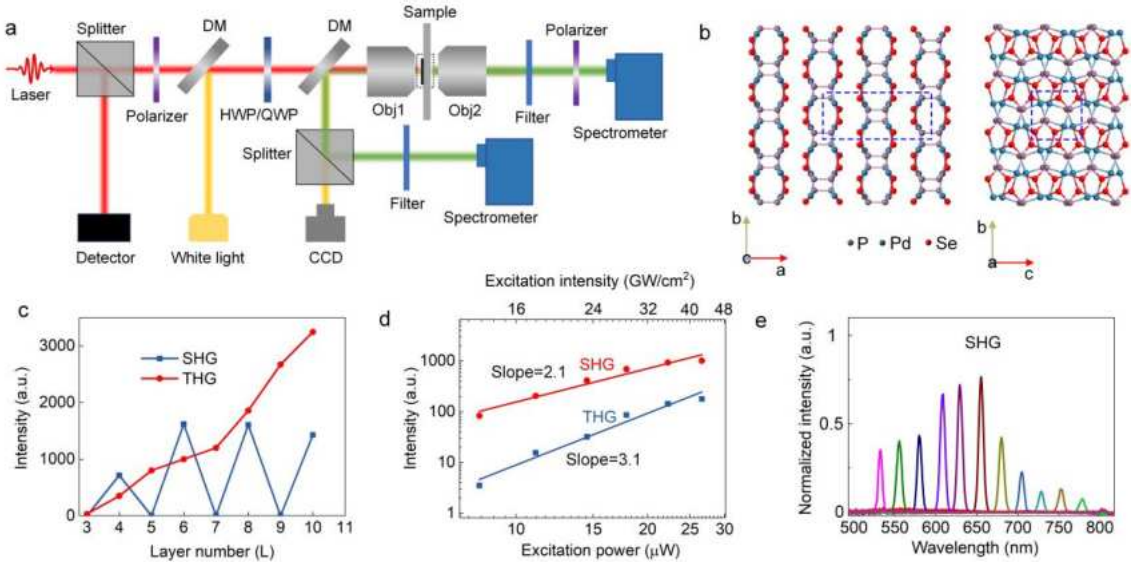


Figure 1. (a) Experimental setup. (b) The crystal structure of PdPSe. (c) SHG and THG intensities as functions of the layer number (L). (d) Excitation power (intensity) dependent SHG and THG intensities in 6 L PdPSe. (e) The SHG spectra with the excitation wavelength from 1064 to 1600 nm in 4 L PdPSe.

Anisotropic nonlinear optical responses generated from the difference of polarization P(t) in two crystal orientations have become a recent research focus, such as anisotropic nonlinear absorption, anisotropic SHG, and anisotropic THG in asymmetric 2D materials. Exploring new inversion-symmetry-broken 2D materials with the coexistence of strong nonlinear optical anisotropy and strong optical nonlinearity (including SHG and THG) is highly desirable for fundamental research as well as novel optoelectronic applications. Here, we describe our finding that even-layer PdPSe has strong inversion-symmetry-broken behaviors, which are distinct from other

common TMDCs[4], with a strong second-order susceptibility of 64 pm/V and a third-order susceptibility of 6.2×10^{-19} m^2/V^2. Importantly, in contrast to MoS_2 and GaSe without in-plane anisotropy, we showed that 2D PdPSe possesses strong nonlinear optical anisotropy with a maximum anisotropic ratio (ρ_{SHG}) of ~45, which is the largest in all atomically layered 2D materials, to the best of our knowledge. The maximum ρ_{THG} value of PdPSe crystal is ~7, which is also larger than that in all the 2D layered materials. The simultaneous realization of strong nonlinear optical anisotropy and strong nonlinear optical coefficients in 2D PdPSe opens up opportunities for the next-generation miniaturized photonic devices with polarization functions.

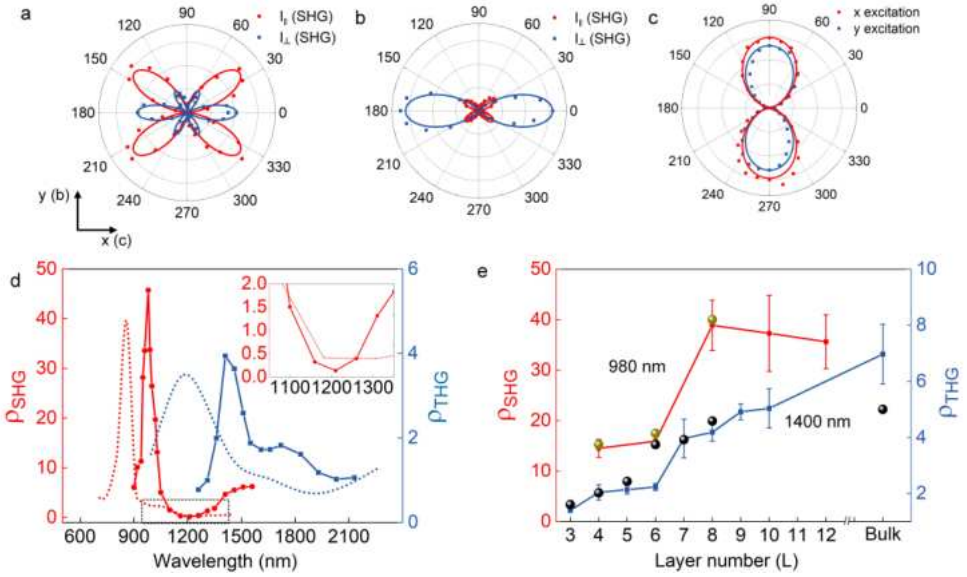


Figure 2. (a-b) Polar plots of the SHG intensity versus the polarization angle (θ) with parallel (red) and perpendicular (blue) configurations under 1550-nm and 980-nm excitations. (c) SHG polarization orientation with excitation polarization along x-(red) and y-(blue) axes of PdPSe under 1300-nm excitation. (d) ρ_{SHG} (red) and ρ_{THG} (blue) versus the excitation wavelength for 8 L PdPSe. (e) ρ_{SHG} (red) and ρ_{THG} (blue) as functions of the layer number under 980-nm and 1400-nm excitations, respectively.

This work is partially supported by A*STAR funding in Singapore (R23I0IR041, M22K2c0080, and M23M2b0056), and National Research Foundation Competitive Research Program (NRF-CRP29-2022-0003).

References

1. Seyler, K. L. *et al.* Electrical control of second-harmonic generation in a WSe_2 monolayer transistor. *Nat. Nanotechnol.* 10, 5, 407-411, 2015.
2. Sun, Z. *et al.* Giant nonreciprocal second-harmonic generation from antiferromagnetic bilayer CrI_3. *Nature* 572, 7770, 497-501, 2019.
3. Guo, Q. *et al.* Ultrathin quantum light source with van der Waals $NbOCl_2$ crystal. *Nature* 613, 7942, 53-59, 2023.
4. Saynatjoki, A. *et al.* Ultra-strong nonlinear optical processes and trigonal warping in MoS_2 layers. *Nat. Commun.* 8, 1, 893, 2017.

Revealing the Local Band Structures of Sharp WS_2/MoS_2 Heterojunction and Graded $W_xMo_{1-x}S_2$ Alloy by Near-Field Optical Imaging

Po-Wen Tang[1], He-Chun Chou[1], Shiue-Yuan Shiau[2], Xin-Quan Zhang[3], Yi-Hsien Lee[3], and Chi Chen[1*]

[1] Research Center for Applied Sciences, Academia Sinica, Taipei,115, Taiwan

[2] Physics Division, National Center for Theoretical Sciences, Taipei, 106, Taiwan

[3] Department of Materials Science and Engineering, National Tsing-Hua University, Hsinchu, 300, Taiwan

[*]corresponding author: chenchi@sinica.edu.tw

Abstract: We demonstrate the state-of-the-art scanning near-field optical microscopy (SNOM) imaging of 2D materials. We identified the exciton quenching behavior at sharp WS_2 and MoS_2 lateral heterojunctions with a 68 nm NF-photoluminescence resolution. Furthermore, the bandgap evolution and interlayer coupling in the $W_xMo_{1-x}S_2$ alloy were visualized using the NF-transmission method.

With the development of advanced chemical vapor deposition (CVD) methods [1], many artificial 2D semiconductors have been synthesized, which increases the chances of forming disrupted interfaces and nonperiodic or small-sized systems (defects and grain boundaries). All such systems create local electronic band structures within a finite scale, which cannot be readily explained by solid-state band theory or probed easily by confocal microscopy and macroscopic transport.

In this study, we investigated abrupt heterojunctions and graded alloys between two transition metal dichalcogenides (TMD), which involve nonperiodic band structures and require high spatial resolution. We employed near-field photoluminescence (NF-PL) imaging to study the atomically sharp 1D interfaces between WS2 and MoS2 (Fig. 1b). With an optical resolution of 68 nm, a 105 nm-wide region for quenched PL was confirmed using NF-PL imaging [2]. Our NF-PL imaging resolved the narrowest quenching width and sharpest strain mapping because of the superior spatial resolution and stability of our home-built SNOM [3].

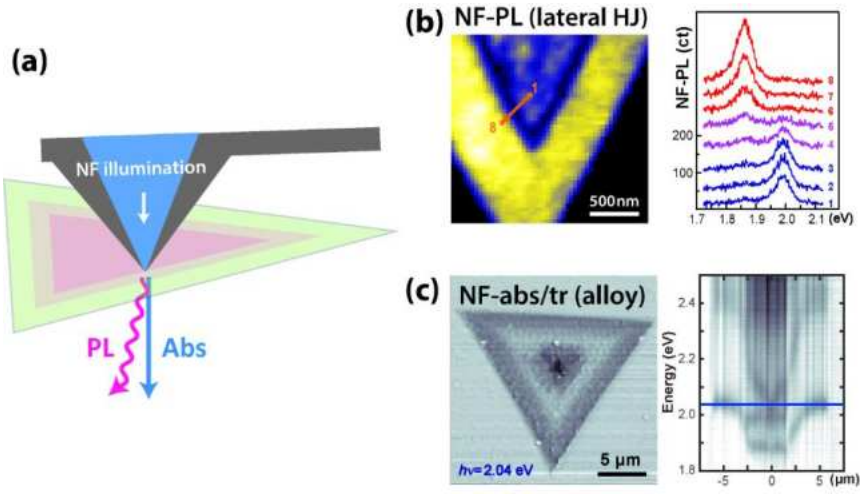


Fig. 1 (a) Schematic of the near-field absorption/transmittance (NF-abs/tr) and near-field photoluminescence (NF-PL) measurements. **(b)** NF-PL imaging and spectra of the lateral heterojunction. **(c)** NF-tr spectroscopic imaging and band structure of graded alloy.

We further developed a near-field broadband absorption (or transmittance, NF-tr) imaging method to overcome the limitations of NF-PL in low-quantum-yield materials. The NF-tr technique provides abbreviation-free and nanoscale-resolution imaging capabilities of the entire conduction band over a highly lateral inhomogeneity. We utilized NF-tr microscopy to investigate the varying bandgap and bowing factor of a single-layer WxMo1-xS2 alloy [4]. For the bilayer WxMo1-xS2 alloy, the energy contour maps present the bandgap evolution in the alloy and reveal bilayer coupling between the top and bottom layers (Fig. 1c). We can conclude that the bottom layer is alloy in nature, whereas the top layer is composed of pure WS2. High-spatial-resolution spectral capability is essential for analyzing compositional and location-dependent bandgap evolutions.

References

1. K.-C. Chiu and Y.-H. Lee *et al.,* Synthesis of In-Plane Artificial Lattices of Monolayer Multijunctions. *Adv. Mater.* 30, 1704796 (2018)
2. H.-C. Chou and C. Chen *et al.,* Near-field spectroscopic imaging of exciton quenching at the atomically sharp MoS2/WS2 lateral heterojunction. *Nanoscale* 14, 6323 (2022)
3. J.-R. Yu and C. Chen *et al.,* A horizontal-type scanning near-field optical microscope with torsional mode operation toward high-resolution and non-destructive imaging of soft materials. *Rev. Sci. Instrum.* 91, 073703 (2020)
4. P.-W. Tang and C. Chen *et al.,* Visualization of bandgap evolution and bilayer coupling in WxMo1-xS2 alloy by near-field broadband absorption microscopy.. *ACS Nano*, 16, 5, 7503 (2022)

Absorption Enhancement of Exciton of WS_2 by Silicon Metasurface Based on Degenerate Critical Coupling

Dingwei Chen[1], **Junichi Takahara**[1, 2*]

[1]Graduate School of Engineering, Osaka University, Japan
[2]Photonics Center, Graduate School of Engineering, Osaka University, Japan
[*]Corresponding author: takahara@ap.eng.osaka-u.ac.jp

Abstract: We study an absorption enhancement of two-dimensional transition-metal dichalcogenides coupled to a Silicon metasurface by degenerate critical coupling. Here, we demonstrate in numerical simulations that the absorption of A mode of exciton in WS_2 can be increased 15.5 times by degenerated Mie modes.

Atomically thin two-dimensional (2D) transition-metal dichalcogenides (TMDCs), such as WS_2, have gained prominence in recent years due to their unique optical and transport characteristics, particularly in the field of optoelectronics and photonics applications[1, 2]. Nevertheless, their ultrathin thickness results in weak optical absorption. To accomplish light absorption enhancement, an all-dielectric metasurface utilizing Mie resonance along with degenerate critical coupling (DCC)[3] has been developed, achieving synergistic enhancement effects on WS_2. With increasing light-matter interactions, the emergence of exciton-polaritons in strong coupling is poised to engender more interesting phenomena, thereby expanding the potential applications significantly.

In this study, we achieve a huge absorption increase of WS_2 with an all-dielectric metasurface, when peaks of electric and magnetic dipole (ED and MD) modes of metasurface overlaps in the wavelength near the peak related to A excitonic transitions in monolayer WS_2.

First, we design the Mie resonator metasurface substrate to increase absorption of WS_2 and study its optical spectrum. Figure 1 shows the structure of WS_2 on the Silicon (Si) metasurface. Among them, the metasurface is comprised by cylindrical resonator arrays with period *d*, radius *r*, and thickness *h*.

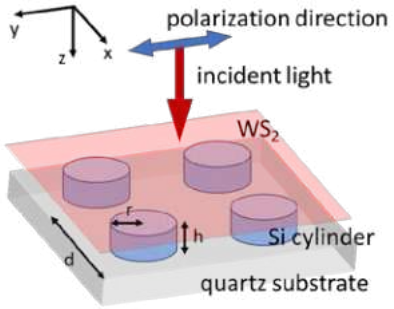


Fig. 1: Schematic view of WS_2 on Si metasurface composed of Mie resonator arrays.

Figure 2(a) shows the calculated absorption spectral map of Si Mie resonators with h = 55-115 nm. The resonant wavelengths of ED and MD modes increase as h increases, while the MD mode experience a larger red shift compared to the ED mode. We observe an overlap of two modes at h = 89 nm. When ED and MD modes overlap, DDC is realized and simulated absorption of metasurface is shown as the red dotted line in Fig. 2(b). Furthermore, in Fig. 2(b), we fabricated the designed sample shown in the inset and measured its spectrum shown in the blue dotted line. Because the height and radius of prepared sample was different from designed, overlap was not completely achieved. However, we partially realized DDC with ED and MD modes shown as the fitting curve 1 and 2.

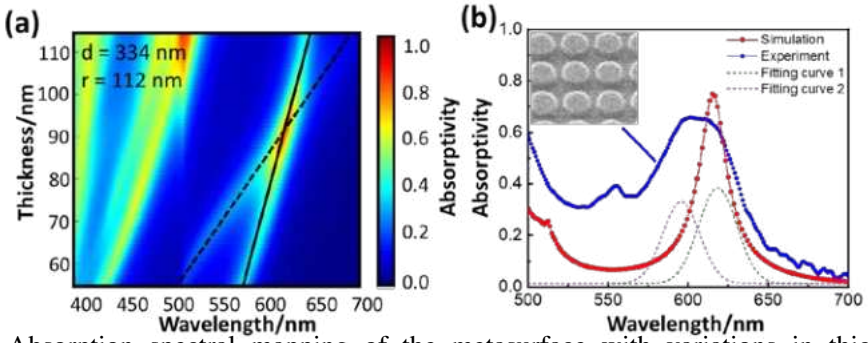


Fig. 2:(a) Absorption spectral mapping of the metasurface with variations in thickness *h*, (b) experimental and simulated[4] absorptivity for the metasurface, and modes fitting curve of experimental spectrum. Inset: Scanning Ion Microscope image of the sample.

We simulate the absorption spectrum of WS_2 on metasurface, and obtain the A exciton absorption peak of WS_2 by fitting as shown in Fig. 3(a). By subtracting background from Fig. 3(a), we obtain the absorptivity of WS_2, which is increased by about 0.52 (15.5 times) under DCC condition compared with WS_2 on Si substrate as shown in Fig. 3(b). At the same time, we observe that the peak position shows a 9 nm red shift. Note that such red shift is attributed to the coupling effect of exciton and dipole modes.

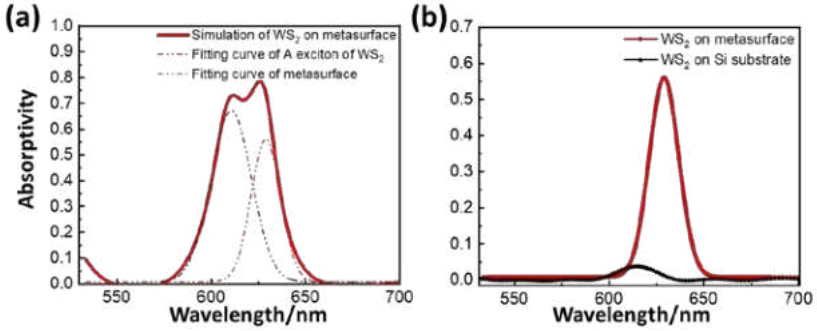


Fig. 3:(a) Simulated absorptivity of WS_2 on the metasurface and corresponding fitting curves. (b) Simulated absorptivity subtracting background for WS_2 on Si substrate and the metasurface in 2(b).

In summary, we designed an all-dielectric Si Metasurface based on DCC, and found that the absorption of WS_2 monolayer as high as 0.56 (before 0.036) was achieved. This architecture could be used in the future as a highly efficient tunable single-color photodetector. Moreover, the suggested dielectric metasurface holds promise for improving application possibilities of semiconductor 2D materials in visible wavelength range.

Acknowledgements

This work was supported by the Japan Society for the Promotion of Science (JSPS) KAKENHI 23H00274. Dingwei Chen was supported by the China Scholarship Council (No. 202204910108.).

References

1. Q. Wang, K. Kalantar-Zadeh and et al., “Electronics and optoelectronics of two-dimensional transition metal dichalcogenides,” Nat. Nanotechnol., Vol. 7, 699–712, 2012.
2. W. Xu, W. Liu and et al., “Correlated fluorescence blinking in two-dimensional semiconductor heterostructures,” Nature, Vol. 541, 62–67, 2017.
3. R. Xu and J. Takahara, “Radiative loss control of an embedded silicon perfect absorber in the visible region,” Opt. Lett., Vol. 46, No. 4, 805–808, 2021.
4. J. Gwang-Hun, Y. SeokJae and P. Q-Han, "Measuring the optical permittivity of two-dimensional materials without a priori knowledge of electronic transitions," Nanophotonics, Vol. 8, No. 2, 263–270, 2019.

Hundred- to thousand-fold enhanced luminescence and the quantum nature manifested in continuous 2D materials coupled with metasurfaces

Masanobu Iwanaga*, Xu Yang, Vasilios Karanikolas, Takashi Kuroda, and Yoshiki Sakuma

National Institute for Materials Science (NIMS), Japan
*corresponding author: iwanaga.masanobu@nims.go.jp

Abstract: Atomic-layer 2D materials are attracting huge research interest. Transition metal dichalcogenide (TMDC) monolayers exhibit efficient luminescence. By coupling a continuous TMDC monolayer with all-dielectric metasurfaces or plasmo–photonic metasurfaces, significant luminescence enhancement was achieved. Furthermore, the quantum nature of the enhanced luminescence was visualized in confocal microscopy.

TMDC monolayers, specifically MoS_2 monolayers, were found to have direct-transition exciton luminescence at room temperature in 2010 [1,2]. They were microscale triangles at the early stage. Now, wafer-scale continuous TMDC monolayers can be grown by some groups [3,4]. Here, we address our recent experimental findings regarding coupled systems of the continuous cm-scale TMDC monolayer and metasurfaces that were shown to have prominent fluorescence-enhancing ability [5–7].

Figure 1A illustrates a TMDC monolayer located on an all-dielectric metasurface that is periodic array of Si nanocolumns on an SiO_2 layer. Actual sample [8] is shown in Figure 1B. The metasurfaces were fabricated on a silicon-on-insulator substrate of 2 cm square, being aligned vertically at the center (orange in Figure 1B). The continuous TMDC monolayer of almost 1 cm square, which was nearly WS_2 monolayer, was transferred onto the metasurface substrate, indicated by four arrows. Photoluminescence (PL) of the TMDC monolayer was greatly enhanced on the metasurface, exhibiting 300-fold PL intensity in comparison with the PL intensity off the metasurface [8].

Figure 1C shows a confocal PL image recorded in a photon-counting manner; the white rectangular part corresponds to a metasurface area. It is evident that the image is dark outside the metasurface, meaning that PL is at zero photon level. We analyzed the photon number distribution at the pixels in the image and determined that the distribution is reproduced using the Poisson distribution. This result indicates that the PL emission comes from a coherent single-mode emission [9].

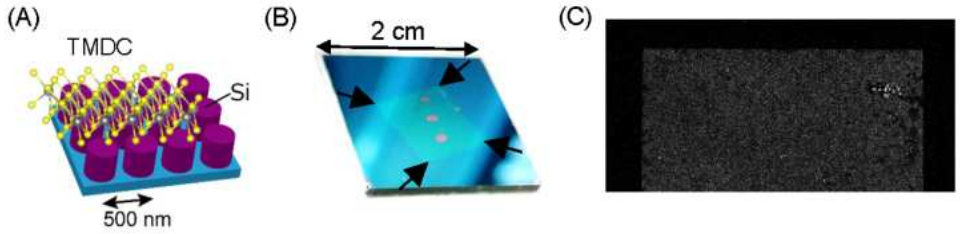


Figure 1. (A) Illustrations of TMDC monolayer transferred onto an all-dielectric metasurface of Si nanocolumn array. (B) Photograph of a sample, cited from [8]. The TMDC monolayer is almost 1 cm square, whose corners are indicated by four arrows. Three metasurfaces (orange) are aligned vertically at the center of substrate. (C) A confocal PL image of the TMDC monolayer shown in gray scale. The PL was observed only on the metasurface area of rectangular shape in the image.

Plasmo–photonic metasurfaces were also found to exhibit strong PL-intensity enhancement, exceeding 1000-fold in comparison with the PL intensity off the metasurface, where flat Au film existed. The PL was also found to have quantum nature, similarly to the case of the all-dielectric metasurface in Figure 1.

Thus, the metasurfaces are good platform to efficiently extract PL from the TMDC monolayer without losing the quantum nature. The details of the experimental results and analysis, as well as the designs and optical properties of the metasurfaces, will be shown in the presentation.

This study was partially supported by the midterm project in NIMS. M.I. thanks a financial support by JSPS KAKENHI (Grant number JP20K21134), Japan. T.K thanks a financial support of Innovative Science and Technology Initiative for Security, Grant Number JPJ004596, ATLA, Japan. Nanofabrication and confocal PL measurement were conducted at "Advanced Research Infrastructure for Materials and Nanotechnology in Japan (ARIM)" of the MEXT, Japan (Proposal Number JPMXP1223NM5310). Numerical implementations for the optical spectra and EM fields were conducted using supercomputing resources at Cybersceience Center, Tohoku University.

References

1. Splendiani, A., L. Sun, Y. Zhang, T. Li, J. Kim, C.-Y. Chim, G. Galli and F. Wang, “Emerging Photoluminescence in Monolayer MoS_2,” Nano Lett., Vol. 10, No. 4, 1271–1275, 2010.
2. Mak, K. F., C. Lee, J. Hone, J. Shan and T. F. Heinz, “Atomically Thin MoS_2: A New Direct-Gap Semiconductor,” Phys. Rev. Lett., Vol. 105, No. 13, 136805, 2010.
3. Yang, X., S. Li and Y. Sakuma, “Highly Efficient Deposition of Centimeter-Scale MoS_2 Monolayer Film on Dragontrail Glass with Large Single-Crystalline Domains,” Small Methods, Vol. 6, No. 12, 2022017079, 2022.
4. Yang, X., S. Li, N. Ikeda, A. Ohtake and Y. Sakuma, “Scalable growth of atomically thin MoS_2 layers in a conventional MOCVD system using molybdenum dichloride dioxide as the molybdenum source,” Appl. Surf. Sci., Vol. 636, No. 1, 157756, 2023.
5. Iwanaga, M. and B. Choi, “Heteroplasmon Hybridization in Stacked Complementary Plasmo–Photonic Crystals,” Nano Lett., Vol. 15, No. 3, 1904–1910, 2015.
6. Choi, B., M. Iwanaga, H.T. Miyazaki, Y. Sugimoto, A. Ohtake and K. Sakoda, “Overcoming metal-induced fluorescence quenching on plasmo-photonic metasurfaces coated by a self-assembled monolayer,” Chem. Commun., Vol. 51, No. 57, 11470–11473, 2015.
7. Iwanaga, M., “All-Dielectric Metasurfaces with High-Fluorescence-Enhancing Capability,” Appl. Sci., Vol. 8, No. 8, 1328, 2018.
8. Iwanaga, M., X. Yang, V. Karanikolas, T. Kuroda and Y. Sakuma, “Prominently enhanced luminescence from a continuous monolayer of transition metal dichalcogenide on all-dielectric metasurfaces,” Nanophotonics, Vol. 13, No. 1, 95–105, 2024.
9. Loudon, R., *The Quantum Theory of Light*, Oxford Univ. Press, 3rd ed., 2000. Chap. 5.

Membrane Nanophotonic Platform for Enhanced Light-Matter Interaction of Transition Metal Dichalcogenide Monolayer

Y.-L. Ho[1*], C. F. Fong[2], Y.-J. Wu[3], K. Konishi[4], J.-H. Fu[5], Y. K. Kato[2,6], V. Tung[5], and C.-W. Chen[7]

[1]Research Center for Electronic and Optical Materials, National Institute for Materials Science (NIMS), Japan
[2]Nanoscale Quantum Photonics Laboratory, RIKEN Cluster for Pioneering Research, Japan
[3]Center for Basic Research on Materials, National Institute for Materials Science (NIMS), Japan
[4]Institute for Photon Science and Technology, The University of Tokyo, Japan
[5]Department of Chemical System Engineering, School of Engineering, The University of Tokyo, Japan
[6]Quantum Optoelectronics Research Team, RIKEN Center for Advanced Photonics, Japan
[7]Department of Materials Science and Engineering, National Taiwan University, Taiwan
[*]corresponding author: HO.Ya-Lun@nims.go.jp

Abstract: Strong coupling between the membrane metasurface and TMDC monolayer via the quasi-BIC mode is demonstrated, presenting enhanced photoluminescence emission. The significance of membrane metasurface design for achieving highly confined quasi-BIC modes, distinct from conventional photonic guided modes, is clarified, offering new possibilities for 2D material-based nanophotonic and quantum devices.

In recent years, there has been significant interest in the strong light-matter coupling observed in monolayers of transition metal dichalcogenides (TMDCs) within the fields of optoelectronics and nanophotonics. A crucial aspect of improving the coupling between photonic structures and TMDC materials, facilitating interactions between photons and excitons, is optimizing the design of photonic structures specifically tailored for materials in the atomic-scale thickness. In the photonic structures, the dielectric metasurface supports the photonic bound state in the continuum (BIC), representing an optical mode confined within a structure without radiative losses. This unique characteristic results in exceptional light-matter interactions, making it an ideal choice for designing TMDC monolayer-based nanophotonic devices [1-3]. In the field of two-dimensional (2D) materials nanophotonics, there has been growing attention towards nanophotonic applications involving BIC modes.

To achieve BIC with a strong field enhancement and a quality factor at resonance approaching infinity in practicality, membrane structures, with their inherent two-dimensional nature, provide an ideal platform. The confinement and manipulation of light within the membrane structures introduce novel possibilities for enhancing light-matter coupling. Additionally, they enable control over optical properties when compared to conventional waveguide modes. Here, we demonstrate the strong coupling between the membrane metasurface and the TMDC monolayer via a quasi-BIC mode. Utilizing the membrane metasurface, the enhanced photoluminescence (PL) emission from the quasi-BIC mode is observed, presenting distinct differences from the emission behaviors of the conventional photonic waveguided mode.

Figure 1(a) illustrates the electric field enhancement distribution of the quasi-BIC mode in the membrane metasurface, demonstrating a significantly larger enhancement than that of the quasi-BIC mode in the substrate-based metasurface. This suggests the significance of the membrane metasurface design for achieving a highly confined quasi-BIC mode. Following the investigation of the membrane metasurface, the emission enhancement

of the WSe_2 monolayer through the strong coupling of the TMDC monolayer to the membrane metasurface via the quasi-BIC mode, deviating from the conventional photonic guided mode, is demonstrated as shown in Figure 1(b). This study underscores the importance of membrane design for nanophotonic metasurfaces supporting BIC, opening a new window for 2D material-based nanophotonic and quantum devices.

This work was supported by JSPS KAKENHI (JP23H01461, JP22K14623). C.F.F. is supported by the RIKEN SPDR fellowship.

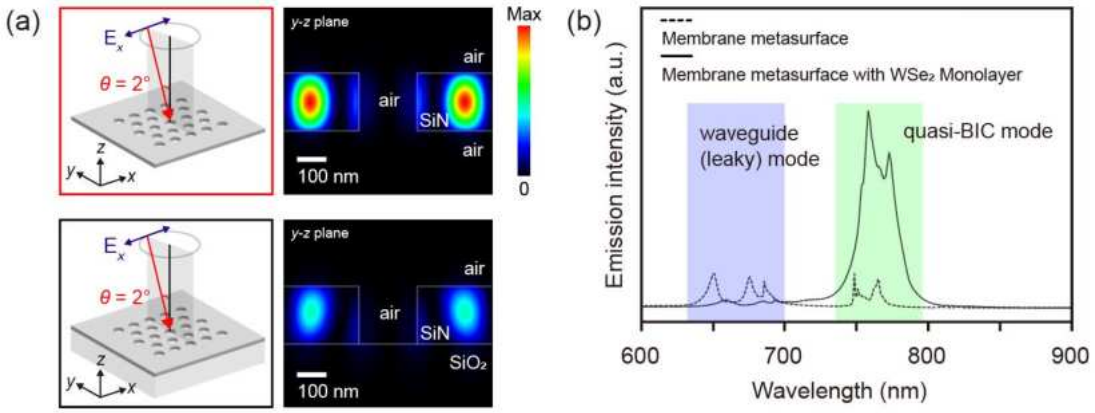


Figure 1. (a) Simulated electric energy density distribution at the quasi-BIC mode of the membrane metasurface (top) and the metasurface on the top of the SiO_2 substrate (bottom), with the incident angle and polarization indicated. (b) The PL emission spectra from the SiN membrane metasurface and the WSe_2 monolayer-membrane metasurface.

References

1. Maggiolini, E., Polimeno, L., Todisco, F. et al. "Strongly enhanced light–matter coupling of monolayer WS_2 from a bound state in the continuum," Nat. Mater. Vol. 22, 964–969, 2023.
2. Kravtsov, V., Khestanova, E., Benimetskiy, F.A. et al. "Nonlinear polaritons in a monolayer semiconductor coupled to optical bound states in the continuum," Light Sci. Appl. Vol. 9, 56, 2020.
3. Bernhardt, N., Koshelev, K., White, S.J.U., et al. "Quasi-BIC Resonant Enhancement of Second-Harmonic Generation in WS2 Monolayers," Nano Lett. Vol. 20, 5309–5314, 2020.

Nanoengineered Transition Metal Dichalcogenides Platform for Quantum Photonics: Generation and interference of single photons

A. Paralikis[1], C. Piccinini[1], P. Metuh[1], J. F. Neto[1], P. Wyborski[1], A. A. Madigawa[1], L. Vannucci[1], N. Gregersen[1], and B. Munkhbat[1*]

[1]Department of Electrical and Photonics Engineering Technical University of Denmark, Kongens Lyngby, Denmark
[*]corresponding author: bamunk@dtu.dk

Abstract: Our recent progress in nanoengineered transition metal dichalcogenides (TMDs) enables high-quality single-photon sources (SPSs). I will present a method for fabricating highly polarized, pure single-photon emitters. Additionally, I discuss the importance of employing advanced optical excitation in improving single photon characteristics and discuss on-chip SPS developments with the TMD platform.

Transition metal dichalcogenides (TMDs) have attracted significant attention as a unique excitonic and photonic platform for nano- and quantum photonics. One remarkable feature of TMDs is their easy exfoliation via the scotch tape, thanks to their van der Waals stacking nature. This feature opens the door to assembling and stacking various TMD materials to possess new properties and integrating them into other photonic platforms. Additionally, TMD mono- and bilayers can yield single photons through strain- and defect-engineering, ranging in visible [1] and telecom [2] wavelengths.

Integrating these TMD quantum emitters with photonic nanostructures and cavities promises efficient single-photon generation [3-5]. In addition to monolayers, multilayer TMDs possess exceptional optical properties, e.g., high index **($n \geq 4$) and low loss ($k \leq 10^{-4}$)** [6]**,** despite their indirect bandgap. These exceptional optical properties combined with optimized nanostructuring offer new possibilities to exploit multilayer TMDs in developing novel photonic components [7-8] for fully integrated quantum photonic circuits.

In the first part of my talk, I will present our recent advancements in fabricating highly polarized mono- and bilayer TMD single photon emitters through strain engineering [9]. This technique allows precise control over the polarization of these quantum emitters, a crucial step in their integration into desired photonic cavities for developing efficient single-photon sources. Our fabricated quantum emitters not only feature a high degree of single photon purity but also exhibit narrow zero-phonon lines with visible phonon sidebands [10]. This provides crucial details on the exciton-phonon coupling of the system and allows us to predict exciton preparation under different excitation schemes [11]. Moreover, we have explored experimentally various optical excitation schemes [10], including quasi- and resonant excitations, to understand their impact on single photon characteristics and the stability of emission lines, especially when compared to above-band excitation.

In the last part of my talk, I will discuss our ongoing research activities in developing on-chip TMD photonic components such as nanobeam cavities, on-chip beam splitters, and waveguides, harnessing the unique properties of nanoengineered multilayer TMD materials. These novel photonic components combined with our TMD quantum emitters could be a promising platform for realizing fully integrated quantum photonic circuits in future scalable quantum information technology.

Acknowledgments

The authors acknowledge support from the European Research Council (ERC-StG ``TuneTMD", grant no. 101076437) and the Villum Foundation (grant no. VIL53033). The authors also acknowledge the European

Research Council (ERC-CoG``Unity", grant no.865230). NG acknowledges support from the European Union's Horizon 2020 Research and Innovation Program under the Marie Skolodowska-Curie Grant Agreement no. 861097.

References

1. Srivastava, A., Sidler, M., Allain, A. V., Lembke, D. S., Kis, A., & Imamoğlu, A., Optically active quantum dots in monolayer WSe_2. Nature Nanotechnology, 10(6), 491-496, 2015.
2. Zhao, H., Pettes, M. T., Zheng, Y., & Htoon, H., Site-controlled telecom-wavelength single-photon emitters in atomically-thin $MoTe_2$. Nature Communications, *12*(1), 6753, 2021.
3. Iff, O., Buchinger, Q., Moczała-Dusanowska, M., Kamp, M., Betzold, S., Davanco, M., ... & Schneider, C., Purcell-enhanced single photon source based on a deterministically placed WSe_2 monolayer quantum dot in a circular Bragg grating cavity. *Nano letters*, *21*(11), 4715-4720, 2021.
4. Errando-Herranz, C., Schöll, E., Picard, R., Laini, M., Gyger, S., Elshaari, A. W., ... & Jöns, K. D., Resonance fluorescence from waveguide-coupled, strain-localized, two-dimensional quantum emitters. *ACS Photonics*, *8*(4), 1069-1076, 2021.
5. von Helversen, M., Greten, L., Limame, I., Shih, C. W., Schlaugat, P., Antón-Solanas, C., ... & Reitzenstein, S., Temperature dependent temporal coherence of metallic-nanoparticle-induced single-photon emitters in a WSe_2 monolayer. *2D Materials*, *10*(4), 045034, 2023.
6. Munkhbat, B., Wróbel, P., Antosiewicz, T. J., & Shegai, T. O., Optical constants of several multilayer transition metal dichalcogenides measured by spectroscopic ellipsometry in the 300–1700 nm range: high index, anisotropy, and hyperbolicity. *ACS photonics*, *9*(7), 2398-2407, 2022.
7. Munkhbat, B., Yankovich, A. B., Baranov, D. G., Verre, R., Olsson, E., & Shegai, T. O., Transition metal dichalcogenide metamaterials with atomic precision. *Nature Communications*, *11*(1), 4604, 2020.
8. Munkhbat, B., Küçüköz, B., Baranov, D. G., Antosiewicz, T. J., & Shegai, T. O., Nanostructured transition metal dichalcogenide multilayers for advanced nanophotonics. *Laser & Photonics Reviews*, *17*(1), 2200057, 2023.
9. Paralikis, A., Piccinini, C., Madigawa, A. A., Metuh, P., Vannucci, L., Gregersen, N., & Munkhbat, B., Tailoring Polarization in WSe_2 Quantum Emitters through Deterministic Strain Engineering. *arXiv preprint arXiv:2402.11075*, 2024.
10. Piccinini, C., Paralikis, A., Madigawa, A. A., Neto, J. F., Vannucci, L., Gregersen, N., & Munkhbat, B., Advanced optical excitation schemes in WSe_2 Quantum Emitters, *In preparation,* 2024.
11. Vannucci, L., Neto, J. F., Piccinini, C., Paralikis, A., Gregersen, N., & Munkhbat, B., Single-photon emitters in WSe_2: The critical role of phonons on excitation schemes and indistinguishability. *arXiv preprint arXiv:2402.10897*, 2024.

Excitons in 2D TMDCs for metaoptics and photodetector applications

Zeng Wang[1*], and Jinghua Teng[1]

[1] Institute of Materials Research and Engineering (IMRE), Agency for Science, Technology and Research (A*STAR), Singapore

[*]Corresponding author: wang_zeng@imre.a-star.edu.sg

Abstract: Our research explores excitons in two-dimensional TMDCs for metaoptics and photodetectors, highlighting advancements in exciton-enabled metaoptics, tunable exciton-trion conversion, and ambipolar photoconductivity control. This demonstrates the promise of TMDCs in optoelectronics, offering enhanced performance for next-generation imaging and sensing technologies.

Excitons in 2D transition metal dichalcogenides (TMDCs) are quasiparticles formed by the pairing of electrons and holes, exhibiting strong binding energies due to reduced dielectric screening and enhanced Coulomb interactions in the atomically thin layers[1]. This results in pronounced optical properties, making 2D TMDCs promising materials for novel optoelectronic devices.

Based on the unique excitonic features, firstly, we demonstrate atomic thin metaoptics utilizing the strong excitonic resonances in MoS_2 multilayers[2]. These devices, including a photon-sieve hologram and a supercritical 2D lens, offer enhanced efficiency and resolution beyond the diffraction limit, leveraging the atomically thin MoS_2 for advanced optical wavefront engineering and imaging applications. Secondly, we show a significant enhancement in exciton-trion conversion in atomically thin WS_2[3]. This achievement, facilitated by an optical cavity and electrical modulation, leads to a 40% modulation in reflectivity for excitons and 7% for trions at room temperature, suggesting potential for tunable and ultra-compact optical devices using two-dimensional materials. Last, we present a significant advancement in photodetection technology using n+-SnSe2/n-MoS2 heterojunctions[4]. It showcases a broad wavelength operation from deep ultraviolet to near-infrared, featuring high responsivity, self-powered operation, and unique ambipolar photoresponse with both positive and negative photoconductance under various control parameters. This work highlights the potential for multifunctional optoelectronic devices leveraging the ambipolar photoresponse capabilities of transition metal dichalcogenides heterostructures.

References

1. Mak, K. F., & Shan, J. (2016). Photonics and optoelectronics of 2D semiconductor transition metal dichalcogenides. Nature Photonics, 10(4), 216-226.
2. Wang, Z., Yuan, G., Yang, M., Chai, J., Steve Wu, Q. Y., Wang, T., ... & Teng, J. (2020). Exciton-enabled meta-optics in two-dimensional transition metal dichalcogenides. Nano Letters, 20(11), 7964-7972.
3. Wang, Z., Sebek, M., Liang, X., Elbanna, A., Nemati, A., Zhang, N., ... & Teng, J. (2023). Greatly Enhanced Resonant Exciton‐trion Conversion in Electrically Modulated Atomically Thin WS2 at Room Temperature. Advanced Materials, 2302248.
4. Elbanna, A., Wang, Z., Liu, Y., Wu, Q. Y. S., Liang, X., Liu, H., ... & Teng, J. (2023). Multi‐Controllability of Ambipolar Photoconductivity in Transition Metal Dichalcogenides Van der Waals Heterostructures. Advanced Materials Technologies, 8(23), 2301079.

Plasmonic photodetectors with superior optoelectronic performance demonstrated in MIR, NIR, visible and UV regions

Yu-Te Chu[1], Shyam Narayan Singh Yadav[1], Ching-Han Mao[1], Yu-Ping Kuang[1], Chang Hua Liu[2], Shangjr Gwo[3], Yu-Jung Lu[4], Pin-Chieh Wu[5], Ta-Jen Yen[*1]

[1]Department of Material Sciences and Engineering, National Tsing Hua University, Hsinchu Taiwan.
[2]Institute of Photonics Technology, National Tsing Hua University, Hsinchu Taiwan.
[3]Department of Physics, National Tsing Hua University, Taiwan.
[4]Research Centre for Applied Science, Academia Sinica, Taipei, Taiwan.
[5]Department of Photonics, National Cheng Kung University, Taiwan.
[*] Ta-Jen Yen: tjyen@mx.nthu.edu.tw; +886-922249996

Abstract: Incorporating plasmonic nanostructures with semiconductor compounds offers a new route to significantly improving the performance of photodetectors. Herein, we developed six hybrid structures comprised of 2D semiconductors, perovskite QDs and GaN with different design of plasmonic nanostructures to demonstrate ultrasensitive photodetection in MIR, NIR, visible and UV regions, respectively.

These six demonstrations are, 1. Plasmonic Metasurface Integrated Black Phosphorus-Based Mid-Infrared Photodetector with High Responsivity and Speed **(Figure 1**a), 2. MoS_2 Plasmonic Grating Integrated Indium Selenide for Polarization-Sensitive Multi-Band Photodetection in Near-Infrared **(Figure 1**b),

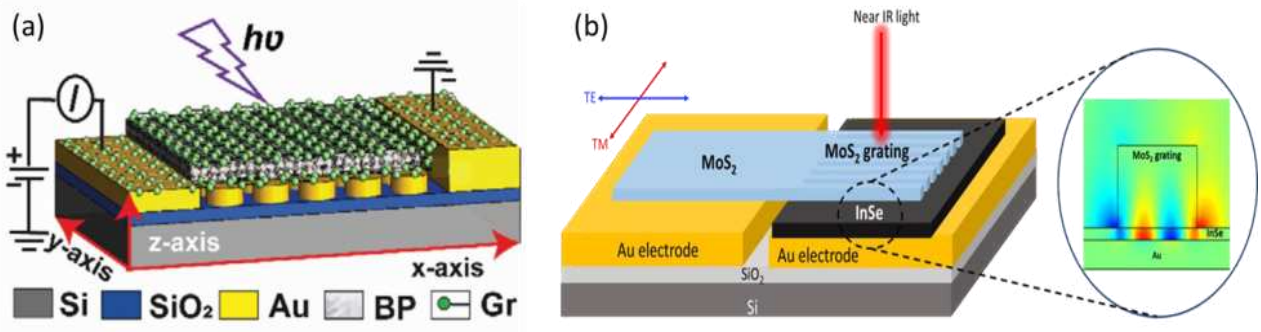


Figure 1. Schematic illustration of the (a) Plasmonic metasurface/BP MIR photodetector and (b) MoS_2 grating/InSe NIR photodetector.

3. Ultrasensitive Gateless Photodetector based on 2D Bilayer MoS_2-1D Si Nanowire-0D Ag Nanoparticle Hybrid Structure **(Figure 2**a), 4.Enhanced Photoresponsivity of Perovskite QDs/Graphene Hybrid Gate-free Photodetector by Morphologically Controlled Plasmonic Au Nanocrystals **(Figure 2**b),

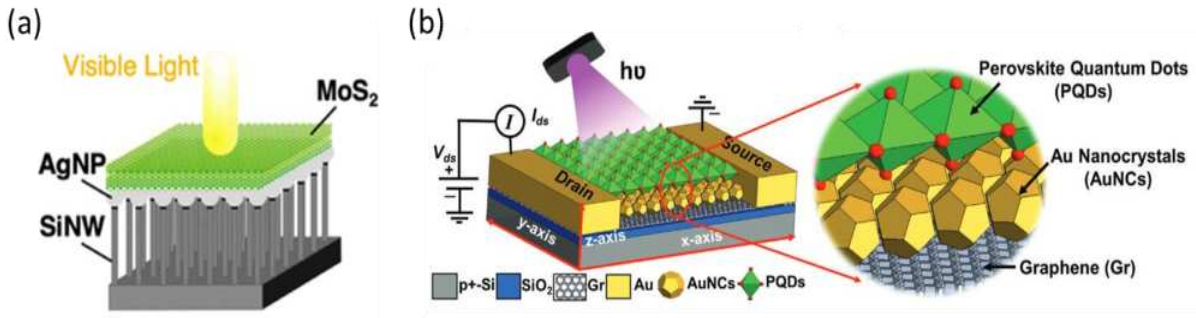


Figure 2. Schematic illustration of the (a) 2D bilayer MoS_2-1D Si nanowire-0D Ag nanoparticle hybrid visible photodetector and (b) PQDs/AuNCs/Gr hybrid electrostatic gate-free visible photodetector.

5.Ultrasensitive Photodetection of Monolayer MoS_2 using Semimetal Plasmonic Structure and Ohmic Contact (**Figure 3**a), and 6. A Multifunctional Plasmonic Sensor for Excellent UV Photodetection and NO_2 Gas Sensing by an Array of Al Nanocaps on GaN Truncated Nanocones (**Figure 3**b). These studies provide novel approaches for designing high-performance plasmonic photodetectors in different frequency regions.

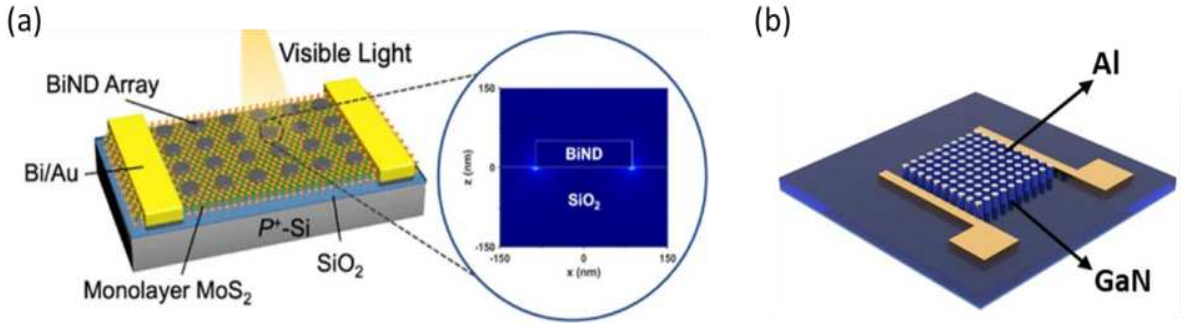


Figure 3. Schematic illustration of the (a) BiND-MoS_2 visible photodetector and (b) GaN-TNC array with Al nanocaps UV photodetector.

References

1. Yadav, Shyam Narayan Singh, et al. "Plasmonic Metasurface Integrated Black Phosphorus‐Based Mid‐Infrared Photodetector with High Responsivity and Speed." Advanced Materials Interfaces 10.10 (2023): 2202403.
2. Chu, Yu-Te, and Ta-Jen Yen. "MoS2 plasmonic grating integrated indium selenide for polarization-sensitive multi-band photodetection in near-infrared." Plasmonics: Design, Materials, Fabrication, Characterization, and Applications XXI. Vol. 12648. SPIE, 2023.
3. Mao, Ching-Han, et al. "An ultrasensitive gateless photodetector based on the 2D bilayer MoS2–1D Si Nanowire–0D Ag nanoparticle hybrid structure." ACS Applied Materials & Interfaces 13.3 (2021): 4126-4132.
4. Yadav, Shyam Narayan Singh, et al. "Enhanced Photoresponsivity of Perovskite QDs/Graphene Hybrid Gate‐Free Photodetector by Morphologically Controlled Plasmonic Au Nanocrystals." Advanced Optical Materials (2023): 2300131.
5. Mao, Ching-Han, et al. "Bifunctional Semimetal as a Plasmonic Resonator and Ohmic Contact for an Ultrasensitive MoS2 Photodetector." ACS Photonics 10.5 (2023): 1495-1503.
6. Kuang, Yu‐Ping, et al. "Multifunctional Plasmonic Sensor for Excellent UV Photodetection and NO2 Gas Sensing by an Array of Al Nanocaps on GaN Truncated Nanocones." Advanced Optical Materials 11.17 (2023): 2300252.

Resonant exciton transfer in mixed-dimensional heterostructures for overcoming dimensional restrictions in optical processes

N. Fang[1], Y. R. Chang[1], D. Yamashita[2,3], S. Fujii[2,4], M. Maruyama[5], Y. Gao[5], C. F. Fong[1], K. Otsuka[1,6], K. Nagashio[7], S. Okada[5], Y. K. Kato[1,2*]

[1]Nanoscale Quantum Photonics Laboratory, RIKEN Cluster for Pioneering Research, Saitama 351-0198, Japan
[2]Quantum Optoelectronics Research Team, RIKEN Center for Advanced Photonics, Saitama 351-0198, Japan
[3]Platform Photonics Research Center, National Institute of Advanced Industrial Science and Technology (AIST), Ibaraki 305-8568, Japan
[4]Department of Physics, Keio University, Yokohama 223-8522, Japan
[5]Department of Physics, University of Tsukuba, Ibaraki 305-8571, Japan
[6]Department of Mechanical Engineering, The University of Tokyo, Tokyo 113-8656, Japan
[7]Department of Materials Engineering, The University of Tokyo, Tokyo 113-8656, Japan
[*]corresponding author: yuichiro.kato@riken.jp

Abstract: We report on exciton transfer in carbon-nanotube/tungsten-diselenide heterostructures, where the excitons within the two-dimensional semiconductor are funneled into carbon nanotubes through diffusion. When band alignment is resonant, we observe substantially more efficient excitation via tungsten diselenide compared to direct excitation of the nanotube.

Nanomaterials exhibit unique optical phenomena, in particular excitonic quantum processes occurring at room temperature. For example, excitons in one-dimensional carbon nanotubes exhibit extended diffusion lengths [1], efficient exciton-exciton annihilation [2], near-unity quantum efficiency [3], and single-photon emission at room temperature [4]. The low dimensionality, however, imposes strict requirements for conventional optical excitation, and an approach for bypassing such restrictions is desirable. Here we report on exciton transfer in carbon-nanotube/tungsten-diselenide heterostructures [5], where several advantages are offered including larger absorption areas, broadband spectral response, and polarization-independent efficiency.

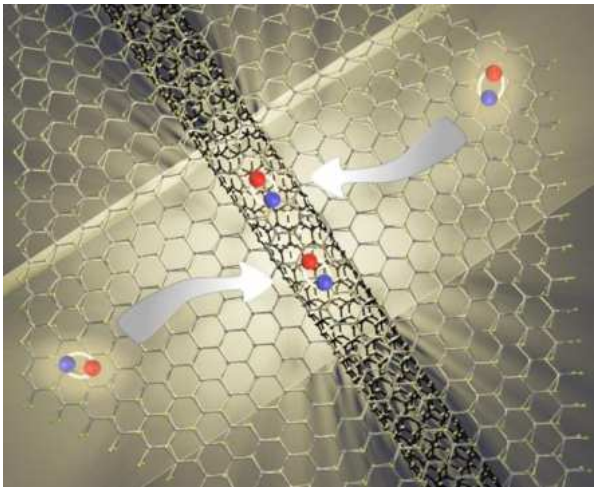


Figure 1: Schematic of the exciton transfer process in a mixed-dimensional heterostructure.

The mixed-dimensional heterostructures are fabricated by transferring a tungsten diselenide flake on top of an individual air-suspended carbon nanotube. The nanotubes are grown over trenches by chemical vapor deposition [2], and a tungsten diselenide flake is placed on top of the tubes by utilizing the anthracene-assisted transfer technique [6, 7]. The nanotube/tungsten-diselenide heterostructures are therefore entirely free-standing, which eliminates substrate-induced inhomogeneity and dielectric screening effects.

Photoluminescence excitation spectroscopy [2] and time-resolved photoluminescence measurements [1, 3] are performed to elucidate the absorption and emission characteristics. We observe a peak in the excitation spectrum corresponding to the A exciton resonance in tungsten diselenide and an emission peak corresponding to the E_{11} exciton in carbon nanotubes. Time-resolved luminescence data reveal an exciton reservoir effect where the longer-lifetime excitons within the two-dimensional semiconductor are funneled into carbon nanotubes through diffusion. Taking advantage of the chirality-dependent band gap in carbon nanotubes, band alignment in the heterostructure can be systematically varied. When band alignment is resonant, we observe substantially more efficient excitation via tungsten diselenide compared to direct excitation of the nanotube. We further demonstrate simultaneous bright emission from an array of carbon nanotubes with varied chiralities and orientations.

These observations propose that the exciton transfer process in mixed-dimensional heterostructures could be harnessed for generation of excitons in carbon nanotubes, thus providing an avenue to surpass the excitation constraints in low-dimensional materials. The high tunability of the band alignment indicates the potential for more intriguing excitons to emerge in this system, for example, indirect excitonic states at the mixed-dimensional interface under type-II band alignment. Our findings show the potential of mixed-dimensional heterostructures and band alignment engineering for energy harvesting and quantum applications through exciton manipulation.

Parts of this study are supported by JSPS (KAKENHI JP22K14624 to D.Y., JP22K14625 to S.F., JP21K14484 to M.M., JP22K14623 to C.F.F., JP21H05233 to S.O., JP22F22350 to Y.R.C., JP23H00262, JP20H02558 to Y.K.K.) and MEXT (ARIM JPMXP1222UT1135). Y.R.C. is supported by JSPS (International Research Fellow). N.F. and C.F.F. are supported by the RIKEN Special Postdoctoral Researcher Program. We thank the Advanced Manufacturing Support Team at RIKEN for technical assistance.

References

1. A. Ishii, H. Machiya, Y. K. Kato, "High efficiency dark-to-bright exciton conversion in carbon nanotubes," Phys. Rev. X **9**, 041048 (2019).
2. A. Ishii, M. Yoshida, Y. K. Kato, "Exciton diffusion, end quenching, and exciton-exciton annihilation in individual air-suspended carbon nanotubes," Phys. Rev. B **91**, 125427 (2015).
3. H. Machiya, D. Yamashita, A. Ishii, Y. K. Kato, "Evidence for near-unity radiative quantum efficiency of bright excitons in carbon nanotubes from the Purcell effect," Phys. Rev. Research **4**, L022011 (2022).
4. A. Ishii, T. Uda, Y. K. Kato, "Room-temperature single-photon emission from micrometer-long air-suspended carbon nanotubes," Phys. Rev. Applied **8**, 054039 (2017).
5. N. Fang, Y. R. Chang, D. Yamashita, S. Fujii, M. Maruyama, Y. Gao, C. F. Fong, K. Otsuka, K. Nagashio, S. Okada, Y. K. Kato, "Resonant exciton transfer in mixed-dimensional heterostructures for overcoming dimensional restrictions in optical processes," Nature Commun. **14**, 8152 (2023).
6. K. Otsuka, N. Fang, D. Yamashita, T. Taniguchi, K. Watanabe, Y. K. Kato, "Deterministic transfer of optical-quality carbon nanotubes for atomically defined technology," Nature Commun. **12**, 3138 (2021).
7. N. Fang, D. Yamashita, S. Fujii, K. Otsuka, T. Taniguchi, K. Watanabe, K. Nagashio, Y. K. Kato, "Quantization of mode shifts in nanocavities integrated with atomically thin sheets," Adv. Opt. Mater. **10**, 2200538 (2022).

Abundant optical properties of hexagonal boron nitride

Kenji Watanabe[1*], and Takashi Taniguchi[2]

[1] Research Center for Electronic and Optical Materials, National Institute for Materials Science
[2] Research Center for Materials Nanoarchitectonics, National Institute for Materials Science
[*]corresponding author: WATANABE.Kenji.AML@nims.go.jp

Abstract: We will review the new aspects of hexagonal boron nitride (h-BN), especially the peculiar and outstanding optical characteristics originating from the anisotropic two-dimentional crystal structure.

Hexagonal boron nitride (h-BN) single crystal is a layered material consisting of atomically flat atomic layers with boron and nitrogen atoms bonded with sp^2 hybridized orbital. Each layer is weakly stacked by van der Waals interactions[1]. Since the early stages of graphene research, high crystalline h-BN single crystals grown by high-pressure, high-temperature (HPHT) synthesis method have been used as the best substrate dielectrics for studying two-dimensional physics[2]. It supplies "a stage" for the emergence of new two-dimensional physical phenomena[3] by the use of the clean surface of the cleaved h-BN layer, which has almost no dangling bonds or charged traps[4].

Derived from this anisotropic two-dimensional crystal structure, this material is also known for its very interesting optical properties, such as the high luminous efficiency of excitons in the far-ultraviolet region[5], three-dimensionally confined hyperbolic polaritons[6], symmetrically controlled polarization properties[7], and single-photon emission from intentionally created point defect centers[8]. Although h-BN is an indirect bandgap material, its luminous efficiency is comparable to typical direct transition materials such as ZnO[9]. The feature of a confined hyperbolic polariton is known as a "natural metamaterial". Polar switching with a twisted layer is promising for the application of atomic-thin non-volatile memory, and single-photon sources due to intentionally introduced point defects are attracting attention as future quantum devices. We review these new aspects of h-BN, especially their abundant optical properties.

Acknowledgements: K.W. and T.T. acknowledge support from the JSPS KAKENHI (Grant Numbers 20H00354, 21H05233, 22H01975 and 23H02052) and World Premier International Research Center Initiative (WPI), MEXT, Japan.

References

1. Mishima, O. and Era, K. in: Electric Refractory Materials, edited by Kumashiro, Y (Marcel Dekker, Inc., New York, 2000), p. 495.
2. Dean.C. R., A. F. Young, I. Meric, C.-H. Lee, L. Wang, S. Sorgenfrei, K. Watanabe, T. Taniguchi, P. Kim, K. L. Shepard, and J. Hone, “Boron nitride substrates for high-quality graphene electronics,” Nat. Nanotech., Vol. 5, No. 722-726, 2010.
3. Hunt.B., J. D. Sanchez-Yamagishi, A. F. Young, M. Yankowitz, B. J. Leroy, K. Watanabe, T. Taniguchi, P. Moon, M. Koshino, P. Jarillo-Herrero, and R. C. Ashoori, “Massive Dirac Fermions and Hofstadter Butterfly in a van der Waals Heterostructure,” Science, Vol. 340, No. 6139, 1427-1430, 2013; Dean.C. R., L. Wang, P. Maher, C. Forsythe, F.

Ghahari, Y. Gao, J. Katoch, M. Ishigami, P. Moon, M. Koshino, T. Taniguchi, K. Watanabe, K. L. Shepard, J. Hone, and P. Kim, “Hofstadter’s butterfly and the fractal quantum Hall effect in moire superlattices,” Nature, Vol. 497, No. 7451, 598-602, 2013; Cao.Y., V. Fatemi, S. Fang, K. Watanabe, T. Taniguchi, E. Kaxiras, and P. Jarillo-Herrero, “Unconventional superconductivity in magic-angle graphene superlattices,” Nature, Vol. 556, No. 43-50, 2018.

4. Xue.J., J. Sanchez-Yamagishi, D. Bulmash, P. Jacquod, A. Deshpande, K. Watanabe, T. Taniguchi, P. Jarillo-Herrero, and B. J. Leroy, “Scanning tunnelling microscopy and spectroscopy of ultra-flat graphene on hexagonal boron nitride,” Nat. Mater., Vol. 10, No. 4, 282-285, 2011.
5. Watanabe.K., T. Taniguchi, and H. Kanda, “Direct-Bandgap Properties and Evidence for Ultraviolet Lasing of Hexagonal Boron Nitride Single Crystal,” Nat. Mater., Vol. 3, No. 6, 404-409, 2004.
6. Caldwell.J. D., A. V. Kretinin, Y. Chen, V. Giannini, M. M. Fogler, Y. Francescato, C. T. Ellis, J. G. Tischler, C. R. Woods, A. J. Giles, M. Hong, K. Watanabe, T. Taniguchi, S. A. Maier, and K. S. Novoselov, “Sub-diffractional volume-confined polaritons in the natural hyperbolic material hexagonal boron nitride,” Nat. Commun., Vol. 5, No. 5221, 2014; Dai.S., Z. Fei, Q. Ma, A. S. Rodin, M. Wagner, A. S. Mcleod, M. K. Liu, W. Gannett, W. Regan, K. Watanabe, T. Taniguchi, M. Thiemens, G. Dominguez, A. H. Castro Neto, A. Zettl, F. Keilmann, P. Jarillo-Herrero, M. M. Fogler, and D. N. Basov, “Tunable Phonon Polaritons in Atomically Thin van der Waals Crystals of Boron Nitride,” Science, Vol. 343, No. 6175, 1125-1129, 2014.
7. Woods.C. R., P. Ares, H. Nevison-Andrews, M. J. Holwill, R. Fabregas, F. Guinea, A. K. Geim, K. S. Novoselov, N. R. Walet, and L. Fumagalli, “Charge-polarized interfacial superlattices in marginally twisted hexagonal boron nitride,” Nat. Commun., Vol. 12, No. 1, 347, 2021; Vizner.S. M., Y. Waschitz, W. Cao, I. Nevo, K. Watanabe, T. Taniguchi, E. Sela, M. Urbakh, O. Hod, and S. M. Ben, “Interfacial ferroelectricity by van der Waals sliding,” Science, Vol. 372, No. 6549, 1462-1466, 2021; Yasuda.K., X. Wang, K. Watanabe, T. Taniguchi, and P. Jarillo-Herrero, “Stacking-engineered ferroelectricity in bilayer boron nitride,” Science, Vol. 372, No. 6549, 1458-1462, 2021..
8. Tran.T. T., C. Zachreson, A. M. Berhane, K. Bray, R. G. Sandstrom, L. H. Li, T. Taniguchi, K. Watanabe, I. Aharonovich, and M. Toth, “Quantum Emission from Defects in Single-Crystalline Hexagonal Boron Nitride,” Phys. Rev. Applied, Vol. 5, No. 034005, 2016; Tran.T. T., K. Bray, M. J. Ford, M. Toth, and I. Aharonovich, “Quantum emission from hexagonal boron nitride monolayers,” Nat. Nanotech., Vol. 11, No. 1, 37-41, 2016; Tran.T. T., C. Elbadawi, D. Totonjian, C. J. Lobo, G. Grosso, H. Moon, D. R. Englund, M. J. Ford, I. Aharonovich, and M. Toth, “Robust Multicolor Single Photon Emission from Point Defects in Hexagonal Boron Nitride,” ACS Nano, Vol. 10, No. 8, 7331-7338, 2016; Gottscholl.A., M. Kianinia, V. Soltamov, S. Orlinskii, G. Mamin, C. Bradac, C. Kasper, K. Krambrock, A. Sperlich, M. Toth, I. Aharonovich, and V. Dyakonov, “Initialization and read-out of intrinsic spin defects in a van der Waals crystal at room temperature,” Nat. Mater., Vol. 19, No. 5, 540-545, 2020.
9. Schué.L., L. Sponza, A. Plaud, H. Bensalah, K. Watanabe, T. Taniguchi, F. Ducastelle, A. Loiseau, and J. Barjon, “Bright Luminescence from Indirect and Strongly Bound Excitons in h-BN,” Phys. Rev. Lett., Vol. 122, No. 6, 067401, 2019.

Plasmonic Strong Coupling and Tamm Plasmon Polaritons Photodetectors Enabled by 2D materials Hot Electrons

Kuo-Ping Chen*
Institute of Photonics Technology, National Tsing Hua University, Taiwan
**kpchen@ee.nthu.edu.tw*

Abstract: Two-dimensional materials are being studied for their unique optical characteristics and miniaturization capabilities. We proposed that by combining Tamm plasmon polariton (TPP) resonance and a graphene layer at the point of strong field confinement, a wavelength- and angle-selective photodetector that significantly enhances photocurrent response. This graphene-TPP photodetector could have applications in LiDAR detection, sun sensors, laser beacon tracking, and navigational instruments.

***Key Word**-- Tamm plasmon polariton; graphene; photodetectors; wavelength and angle selectivity;*

1. Introduction

In this study, an idea was developed for a graphene photodetecting device employing the Tamm plasmon polariton (TPP) structure [1]. As graphene was transferred onto the DBR, a metal film was fabricated on the graphene layer. The proposed graphene-TPP photodetector was devised and fashioned using gold electrodes to collect electrical signals. The graphene layer does not affect the TPP resonance thanks to the atomic layer thickness of graphene; however, the graphene locates the localized electric field formed by the TP structure. The structure converts incident light into TPPs that are collected and transferred into photocurrents by the graphene layer. The photocurrent generation mechanism of our device is related to the PV effect. In our proposed graphene–TPP photodetector, the photoresponse of graphene can be enhanced by the localized electric field, and the device facilitates angle and wavelength selectivity by means of the TP structure. Our device can be utilized as a miniaturized Li-DAR detector for suitable applications, lowering the processing cost, and optimizing the processing yield.

In addition, the coupling between excitons in transition metal dichalcogenide (TMD) monolayers and plasmons in nanostructures will be discussed [2]. The study focuses on enhancing exciton-polariton coupling by utilizing one-dimensional plasmonic nanogrooves (NGs) to align excitons in MoS2 monolayers with plasmon polaritons. Our approach addresses the inefficiency in coupling due to the misalignment of exciton orientations in conventional systems. We demonstrate significant Rabi splitting at room temperature and attribute the enhanced photoluminescence to parallel exciton-polariton interactions, paving the way for improved photonic device performance.

2. Results and discussion

Figure 1(a) shows the schematic of the proposed graphene–TPP photodetector. The device was constructed by stacking a glass substrate, alternating dielectric layers of the DBR, transferred graphene, and deposited TPP metal film (35 nm gold) and gold electrodes on top of each other using an E-beam evaporation machine. The graphene channel is where the strong electric field confinement caused by the TP structure is located. The SEM image of the cross-section of the dielectric layers in our DBR is shown in Figure 1(b); the thickness of all the silicon dioxide (SiO_2, refractive index n = 1.475) layers is approximately 144 nm, and that of all the titanium dioxide (TiO_2, refractive index n = 2.237) layers is about 95 nm, giving rise to the central wavelength of the DBR at 850 nm, which could be considered as an NIR-region sample.

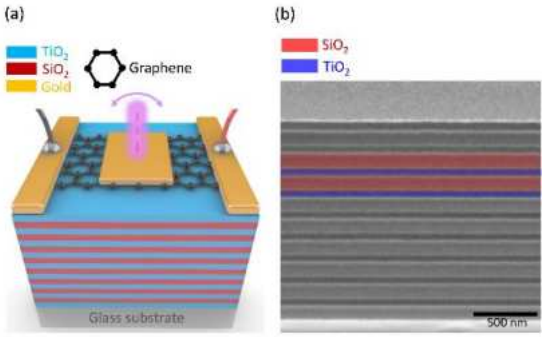


Fig. 1 (a) A schematic of the graphene Tamm plasmon polariton photodetector. (b) Scanning electron micrograph of the dielectric layers of the DBR

3. Conclusion

In summary, the contribution of this work is the simplification of the structure of the photodetector device by stacking layers to form the plasmonic structure. The results confirm that our Graphene-TPP photodetector can be universally applied to various optoelectronic materials. With the field confinement located at the metal-DBR interface, the TPP signal can be detected and converted into electrical signals.

4. References

[1] Huang, Cheng-Han, Chia-Hung Wu, Rashid G. Bikbaev, Ming-Jyun Ye, Chi-Wen Chen, Tung-Jung Wang, Ivan V. Timofeev, Wei Lee, and Kuo-Ping Chen. "Wavelength-and Angle-Selective Photodetectors Enabled by Graphene Hot Electrons with Tamm Plasmon Polaritons." *Nanomaterials* **2023**, 13, no. 4: 693.

[2] Yu, Min-Wen, Satoshi Ishii, Shisheng Li, Ji-Ren Ku, Jhen-Hong Yang, Kuan-Lin Su, Takaaki Taniguchi, Tadaaki Nagao, and Kuo-Ping Chen. "Quantifying photoinduced carriers transport in exciton–polariton coupling of MoS2 monolayers." npj 2D Materials and Applications 5, no. 1 (2021): 1-7.

Unlocking the technology of wafer-scale layered atomic crystal growth on dielectric substrates for electronic and photonic applications

X. Yang[1*], Y. Sakuma[2], M. Pristovsek[1], and H. Amano[1]

[1]Nagoya University, Japan
[2]National Institute for Materials Science, Japan
[*]Corresponding author: yang.xu.y2@f.mail.nagoya-u.ac.jp

Abstract: **This study reports on wafer-scale high-quality two-dimensional atomic crystals of hBN and MoS_2 on technologically relevant dielectric substrates. Chemical vapor deposition and annealing resulted in highly ordered hBN and MoS_2 crystal layers with a quality that is comparable to or even better than the state-of-the-art.**

To bring two-dimensional (2D) atomically thin crystals such as transition metal dichalcogenides (TMDs) and hexagonal boron nitride (hBN) to practical applications, they must be produced in a highly controllable process on a large scale and with excellent homogeneity. Metalorganic chemical vapor deposition (MOCVD) has demonstrated this for conventional semiconductors (e.g., GaAs and GaN). In contrast, the scalable growth of 2D materials, including MoS_2 and hBN, using MOCVD is still in its infancy,[1,2] where the level of impurity, defect, and crystallographic misalignment in the resulting 2D crystal films is high and thus challenges practical applications.

To overcome the above issues, highly controllable routes for scalable production of high-quality 2D crystal layers of MoS_2 and hBN over larges-sized dielectric substrates were developed based on our efforts. We pioneeringly chose molybdenum oxychloride (MoO_2Cl_2) as the Mo source together with H_2S and could thus use a standard MOCVD system for MoS_2 growth. By using this carbon-free route, the scalable growth of low-defect monolayer MoS_2 free of carbon contamination was realized. Using catalytic Dragontrail glass as the substrate, we investigated the effect of MoO_2Cl_2 flux, temperature, and deposition time on the growth. The vapor pressures MoO_2Cl_2 is well compatible with the MOCVD system, enabling precise control for uniform nucleation and reasonable growth time of large-area MoS_2 monolayers. Based on the above-mentioned findings, we demonstrated the growth of carbon-free MoS_2 monolayers on glass and other technologically important substrates (e.g., SiO_2/Si). The MoS_2 monolayers were uniform over the 2” wafer with narrow intensity photoluminescence that is on par with the best data reported so far.[3,4] Based on this, working transistors with good and uniform properties over the wafer.

Another material is hBN. The challenging epitaxial growth of high-quality hBN multilayers was enabled by pulsed-mode MOCVD[5] and the quality was further enhanced by subsequent high-temperature annealing. Besides the typically used substrates like sapphire or silicon, we explored aluminum nitride (AlN), which has a very high thermal robustness. Since highly ordered hBN epitaxy on dielectric substrates requires high temperatures (1400°C and higher), AlN is a very promising substrate. Annealing over 1600°C of epitaxially-grown hBN/AlN heterostructures resulted in higher crystallinity and optical quality in hBN multilayer. Furthermore, carbon and oxygen impurities were strongly reduced by the annealing. Especially, the low residual carbon concentration allowed the observation of single-photon emission centers in hBN at room temperature. More than 82% of them emitted with their zero-phonon line at (578.5 ± 5) nm, a narrower distribution than previously reported for CVD-grown BN. These results bring high-quality homogenous hBN multilayers close to a fully

industry-compatible and scalable synthesis with the control of the separation of carbon-related single photon emission centers for next-generation quantum devices.

In summary, our work has yielded novel insights into the wafer-scale manufacturing of high-quality 2D layers, especially hBN and MoS_2, for their development for practical electronic and photonic applications.

References

1. Eichfeld, S.M., Hossain, L., Lin, Y.-C., Piasecki, A.F., Kupp, B., Birdwell, A.G., Burke, R.A., Lu, N., Peng, X., Li, J., Azcatl, A., McDonnell, S., Wallace, R.M., Kim, M.J., Mayer, T.S., Redwing, J.M., Robinson, J.A., Highly Sscalable, atomically thin WSe_2 grown via metal–organic chemical vapor deposition, ACS Nano. 9, 2080–2087, 2015.
2. Choudhury, T. H., Simchi, H, Boichot, R, Chubarov, M., Mohney, S. E., Redwing, J. M., Chalcogen precursor effect on cold-wall gas-source chemical vapor deposition growth of WS_2, Cryst. Growth Des. 18, 4357–4364, 2018.
3. Yang, X., Li, S., Sakuma, Y., Highly efficient deposition of centimeter-scale MoS_2 monolayer film on Dragontrail glass with large single-crystalline domains, Small Methods. 6, 2201079, 2022.
4. Yang, X., Li, S., Ikeda, N., Ohtake A., Sakuma, Y., “Scalable growth of atomically thin MoS_2 layers in a conventional MOCVD system using molybdenum dichloride dioxide as the molybdenum source”, Appl. Surf. Sci. 636, 157756, 2023.
5. Yang, X., Nitta, S., Pristovsek, M., Liu, Y. H., Liao, Y. L., Kushimoto, M., Honda, Y., and Amano, H., “Scalable synthesis of multilayer h-BN on AlN by metalorganic vapor phase epitaxy: nucleation and growth mechanism”, 2D Mater. 7, 2020.

Nano-optical imaging and spectroscopy

Dynamics and delocalized emissions of surface plasmon polaritons in one-dimensional plasmonic crystals

Izzah Machfuudzoh[1*], Sotatsu Yanagimoto[1], Naoki Yamamoto[1], Takumi Sannomiya[1]

[1]Department of Materials Science and Engineering, Tokyo Institute of Technology, Yokohama, Japan
[*]corresponding author: machfuudzoh.i.aa@m.titech.ac.jp

Abstract: Surface plasmon polaritons (SPPs) are vital in nanophotonics, yet local optical properties of SPP-based nanostructures remain underexplored due to their sub-wavelength field localization and propagating nature. Employing cathodoluminescence techniques, we investigate their interaction with plasmonic crystals, revealing distinctive dispersion patterns, further elucidated by SPP scattering dynamics through optical spot analysis.

Surface plasmon polaritons (SPPs) are electromagnetic surface modes existing at the dielectric/metal interface, playing a key role in nanophotonic fields. However, the underexplored optical properties of plasmonic nanostructures based on SPPs, particularly in the context of spatially-resolved dispersion curves and the simultaneous revelation of nanoscale excitation and emission, have resulted in an insufficient understanding of SPP propagation and conversion to photons upon excitation. In this work, we employ combined cathodoluminescence (CL) techniques of momentum-resolved CL and emission-position-resolved CL, by means of electron-beam approach, to investigate the interaction of excited SPPs with plasmonic crystals (PlCs).

One-dimensional (1D) PlCs with a periodicity of 600 nm, patterned on an otherwise a flat 200 nm-thick silver surface, served as the sample, with a terrace width of 420 nm and height of 100 nm. Mode excitation and data acquisition were performed using CL-based scanning transmission electron microscopy (STEM-CL), operated at an accelerating voltage of 80 kV with *p*-polarization, by scanning the electron beam across the samples. Two different sample setups, namely the “flat at top” and the “flat at bottom” setups, were analyzed, with the planar surface oriented respectively closer to and farther from the light-collecting parabolic mirror as shown in Figure 1.

The distinctive optical properties of SPP were observed when the sample orientation was flipped relative to the parabolic mirror, attributed to the phase difference between the at-impact emission of transition radiation (TR) and the grating-scattered emission of SPP [1]. In the “flat at top” setup, the backward-propagating SPP dominates with a decreasing group velocity as the spatial frequency increases (Figure 1(a)). Conversely, in the “flat at bottom” setup, it is the forward-propagating SPP that travels faster as the wavenumber increases (Figure 1(b)), as depicted by the opposing slopes in the respective area-resolved dispersion curves.

Studies on the photon emission position were also performed to evaluate where in space the light is being emitted by the samples. Through the synchronization of emission imaging with electron beam scanning, different numbers of optical emission spots (i.e., either three, two, or one spot) were observed, depending on both the sample orientation and the beam excitation position, which is understood as a result of constructive or destructive interference between the outcoupled SPP and the simultaneously excited TR. Moreover, with the aid

of emission-spot-decomposed CL maps capable of extracting the emission position, it was uncovered that photons mainly emerge not where the electron beam is being irradiated but rather at more delocalized locations on the sample, indicating the occurrence of the propagating SPP mode being scattered [2]. Additionally, the shift of the emission spots with respect to the beam excitation position shows a non-linear trend, in which the spot positions tend to be held stronger at the antinode positions of the surface charge distribution on the sample.

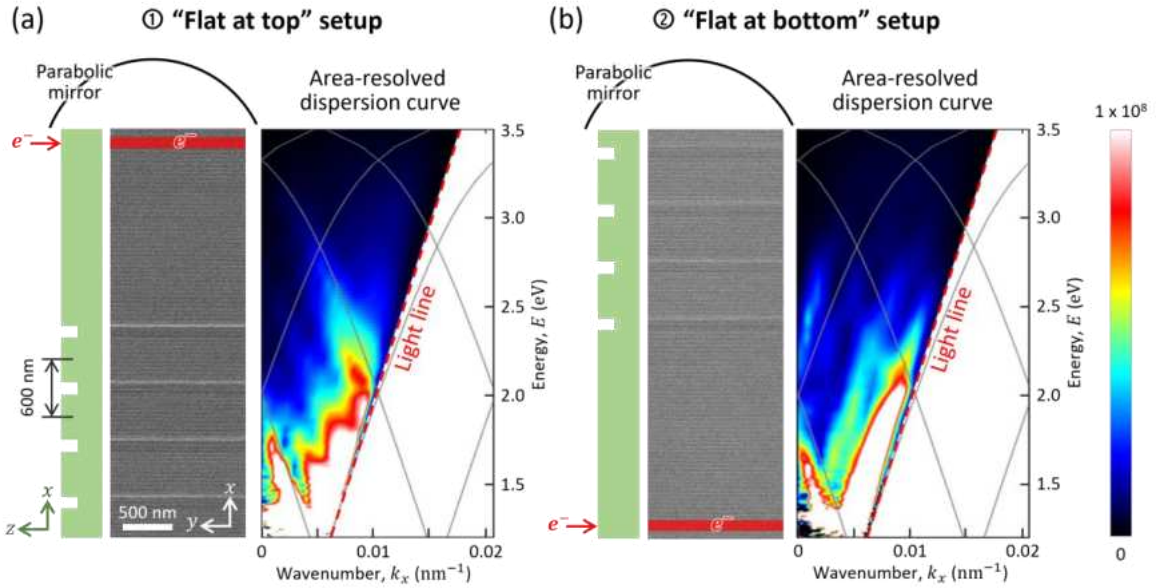


Figure 1. Illustrated *x*-*z* side view and STEM image *x*-*y* top view of a 1D silver plasmonic crystals with a 600 nm periodicity (left panel) for (a) "flat at top" setup and (b) "flat at bottom" setup, with the measured area-resolved dispersion curves integrated over an area indicated by a red arrow or rectangle shown on the sample (right panel). The solid gray curves represent the calculated SPP dispersion curves, and the dashed red line depicts the light line. The *x*-*y*-*z* coordinates, scale bar, and color bar apply to both sample setups.

In conclusion, our studies unravel how the SPPs interact with the 1D-PlCs through their propagation behavior and interference with the transition radiation, using nanoscale resolution of field mapping and optical spot analyses. These findings provide valuable insights into comprehensive details on the SPP modes, with implications for optical devices such as plasmonic sensing and antennas, and photonic integrated circuits. This work was financially supported by JSPS Kakenhi (21H01782, 22H05033) and JST FOREST (JPMJFR213J).

References

1. Sannomiya, T., T. Matsukata, and N. Yamamoto, "Controllable chiral light generation and vortex field investigation using plasmonic holes revealed by cathodoluminescence", Nano Letters, Vol. 24, No. 3, 929-934, 2024.
2. Matsukata, T., S. Ogura, F. J. Garcia de Abajo, and T. Sannomiya, "Simultaneous nanoscale excitation and emission mapping by cathodoluminescence", ACS Nano, Vol. 16, No. 12., 21462-21470, 2022.

Optical spin sorting in a plasmonic crystal waveguide

K. Kihara[1], M. Ikeuchi[2], I. Machfuudzoh[3], T. Sannomiya[3] and H. Saito[2,3,*]

[1] Department of Energy Science and Engineering, Kyushu University, Japan
[2] Institute for Materials Chemistry and Engineering, Kyushu University, Japan
[3] Department of Materials Science and Engineering, Tokyo Institute of Technology, Japan
[*]corresponding author: saito.hikaru.961@m.kyushu-u.ac.jp

Abstract: We designed a unique plasmonic crystal waveguide composed of metallic nanodisk arrays on a metal film (MIM structure) that can convert circularly polarized light into a unidirectionally guided plasmon mode. The plasmon propagation direction can be switched depending on the orientation of circular polarization.

Spin-momentum locking is an indispensable technique for quantum information communication, where photons with opposite spins emitted from a quantum emitter must be guided to different destinations [1]. Plasmonic waveguides can compress electromagnetic fields to a small size far beyond the diffraction limit of light, drastically enhancing light-matter interactions and realizing high-speed and energy-saving active devices [2]. However, spin-momentum locking has rarely been achieved in plasmonic waveguides. To accomplish this task, we have proposed a use of plasmonic crystals (PlCs) [3], i.e., waveguiding based on band engineering. We demonstrated a valley PlC waveguide that can support topologically protected edge states [4], offering a feasible strategy for spin-momentum-locked plasmonic waveguides. The next step is to achieve optical spin sorting by attaching optical antennas to such a PlC-based waveguide, where external circularly polarized light is guided to different destinations depending on the orientation of circular polarization.

We designed a PlC with a MIM structure [5] as shown in Fig. 1(a) by using finite-difference time-domain (FDTD) simulation. In this PlC, aluminum (Al) nanodisks with a diameter of 160 nm and a height of 70 nm are arranged in a triangular lattice with a period of 380 nm. This nanodisk array is placed on 30-nm-thick SiO_2/silver (Ag) substrate. The Al nanodisks not only works as scatterers for surface plasmon polaritons (SPPs) propagating on the Ag substrate, but also supports localized surface plasmon (LSP) modes since they are isolated by the SiO_2 spacer. By utilizing the LSP modes as optical antenna effects, external light can be coupled to lattice modes or waveguide modes formed in the PlC. Figure 1(b) shows the calculated band dispersions of the designed PlC, indicating the full band gap formation from 1.5 eV to 1.9 eV. Waveguide modes are expected to appear in this energy range by introducing modified structures such as defects.

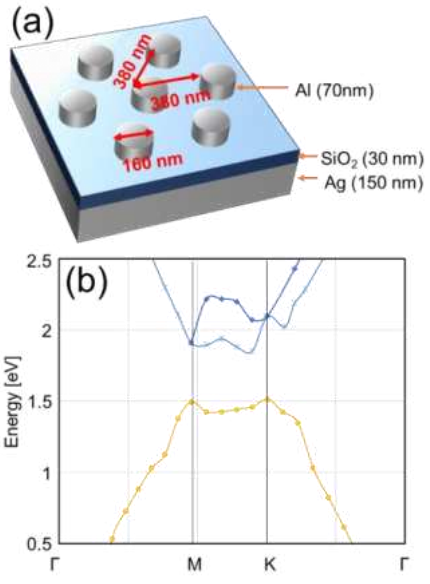


Figure 1 (a) Schematic of the designed PlC. (b) Calculated band dispersions of the PlC.

Based on the above PlC structure, we further designed a waveguide structure by introducing a flat region with a width of 780 nm, which is sandwiched by two PlCs (Fig. 2(a)). Nanodisks facing the waveguide are arranged in a zigzag manner [1] to prevent Bragg reflections in the

propagation direction (horizontal direction in Fig. 2). Figure 2(b) shows a simulation of the guided SPPs. A rotating in-plane electric dipole with the left-handed (down) spin was used to excite SPPs, which was placed at the center of one of the Al nanodisks facing the waveguide and at mid-height of the SiO_2 layer (labeled "excitation source" in Fig. 2(b)). The result shows that the excited SPPs are guided to the right side with greater intensity. Due to the symmetry of the structure, when the spin orientation of the excitation source is flipped, the propagation direction of SPPs is reversed. Figure 2(c) shows a phase map near the Al nanodisks. The black circles indicate the locations of the Al nanodisks. The result indicates that this guided SPPs generate orbital angular momentum around the Al nanodisks. This is consistent with the fact that unidirectional guided SPPs were excited by the rotating in-plane electric dipole placed at the center of the Al nanodisk. Accordingly, the designed structure can function as an optical spin sorter by modifying the structure so that the resonance energy of the in-plane dipole LSP mode of Al nanodisks facing the waveguide is matched with the waveguide mode.

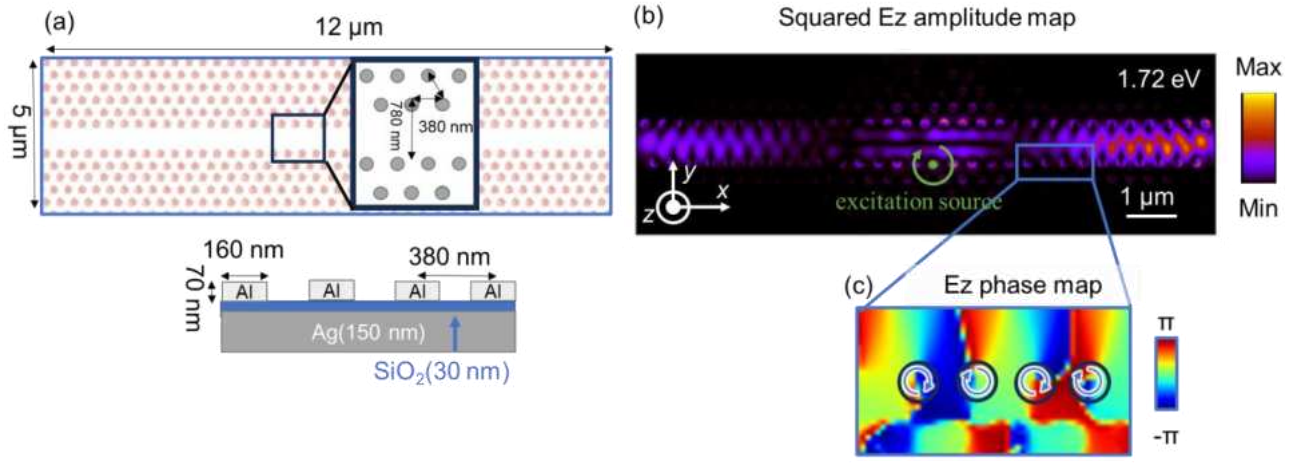


Figure 2 (a) Schematic of the designed waveguide. (b) Squared electric field amplitude in the *z* direction (*Ez*). The excitation energy was 1.72 eV. (c) Phase map of the *Ez* component in the part of calculation space indicated.

References

1. I. Söllner, S. Mahmoodian, S. L. Hansen, L. Midolo, A. Javadi, G. Kiršanskė, T. Pregnolato, H. El-Ella, E. H. Lee, J. D. Song, S. Stobbe and P. Lodahl, "Deterministic photon–emitter coupling in chiral photonic circuits," Nat. Nanotech, Vol. 10, 775–778, 2015.
2. M. Ono, M. Hata, M. Tsunekawa, K. Nozaki, H. Sumikura, H. Chiba and M. Notomi, "Ultrafast and energy-efficient all-optical switching with graphene-loaded deep-subwavelength plasmonic waveguides," Nat. Photonics, Vol. 14, 37–43, 2020.
3. J. Erland, K. Leosson, P.M. W. Skovgaard, and J.M. Hvam, "Waveguiding in Surface Plasmon Plariton Band Gap Structures," Phys. Rev., Vol. 86, No. 14, 3008–3011, 2001.
4. H. Saito, D. Yoshimoto, Y. Moritake, T. Matsukata, N. Yamamoto and T. Sannomiya, "Valley-Polarized Plasmonic Edge Mode Visualized in the Near-Infrared Spectral Range," Nano Lett., Vol. 21, 6556–6562, 2021.
5. H. Saito, D. Yoshimoto, H. Lourenco-Martins, N. Yamamoto, T. Sannomiya "Hybridization of Gap Modes and Lattice Modes in a Plasmonic Resonator Array with a Metal–Insulator–Metal Structure," ACS Photon., Vol. 6, No. 11, 2618–2625, 2019.

Lifetime analysis of nitrogen-vacancy centers in nanodiamond particles using cathodoluminescence microscopy

S. Yanagimoto[1*], N. Yamamoto[1], K. Akiba[1,2], and T. Sannomiya[1]

[1]Tokyo Institute of Technology, Japan
[2] National Institutes for Quantum Science and Technology (QST), Japan
[*]Corresponding author: yanagimoto.s.aa@m.titech.ac.jp

Abstract: We measured the lifetimes of nanodiamond particles with nitrogen-vacancy centers using cathodoluminescence microscopy combined with Hanbury Brown-Twiss interferometry. The experimental results showed the lifetime distribution due to the size effect of the particles. The lifetime can be further modified by coupling with surface plasmons.

Nitrogen-vacancy (NV) emission centers in nanodiamond (ND) particles exhibit highly stable optical properties even at room temperature, making them promising candidates as quantum emitters (QEs) for quantum communications and optical computing [1]. The transition probability from the excited state is one of the speed-limiting factors for the information processing using QEs. When the electromagnetic local density of states (EMLDOS) surrounding the QE is enhanced, the transition probability increases, known as the Purcell effect [2]. However, since the lifetime of the NV center may be sensitively influenced by the dielectric environment of the ND particle itself, it is essential to investigate the lifetime distribution of bare ND particles before evaluating the Purcell effect by coupling with other enhancing structures. To measure the lifetime of individual ND particle to obtain the distribution, an optical lifetime measurement technique with spatial resolution beyond the diffraction limit of light is required. Cathodoluminescence (CL) microscopy, utilizing an electron beam of a scanning transmission electron microscope (STEM), is a powerful approach for accessing nanoscale optical information, which also allows lifetime measurements by combining with Hanbury Brown–Twiss (HBT) interferometry [3]. The HBT measurement of light provides a second-order time correlation function defined by

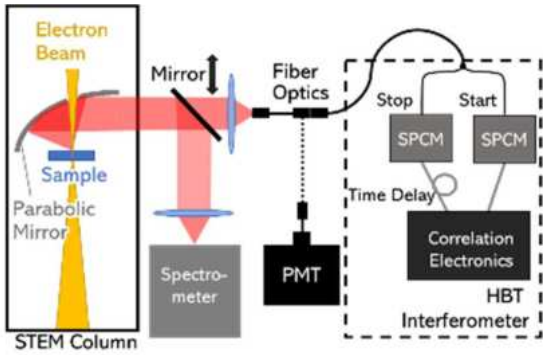


Fig 1. Schematic illustration of the CL-STEM and optical setup for the HBT measurement. A parabolic mirror collimates the emitted light to optical system.

$$g^{(2)}(\tau) = \frac{\langle I(t)I(t+\tau)\rangle}{\langle I(t)\rangle\langle I(t+\tau)\rangle}, \quad (1)$$

where $I(t)$ is the light intensity as a function of time t and τ denotes the time delay. In the case of CL, it is known that the value of $g^{(2)}(0)$ typically exceeds one [4], which is called photon bunching. The lifetime of photon emitters can be obtained by fitting the bunching curve.

In this work, we measured the lifetime of NV centers in ND particles on a SiO_2 self-standing membrane using STEM-based CL-HBT. The experimental setup is illustrated in Fig 1. The light emitted from the sample was guided out of the STEM column by a parabolic mirror and transferred either to a spectrometer for CL spectrum measurement, to a photomultiplier tube (PMT) for panchromatic CL mapping, or to the HBT measurement system. We performed the measurement at room temperature at an accelerating voltage of 80 kV and a beam current of

between 17 and 60 pA. The ND particles used in the experiment have an average diameter of 100 nm and a distribution of 70 to 125 nm . Figure 2(a) illustrates the $g^{(2)}(\tau)$ curves obtained from HBT measurements for three different ND particles. Each particle shows a $g^{(2)}(\tau)$ curve with bunching features with ~ 15 ns lifetime. We statistically evaluated the lifetime of ND particles by performing the HBT measurement of 53 ND particles, as shown by the histogram in Fig 2(b). To evaluate the particle size effect on such lifetime distributions, we performed electromagnetic field simulations with the finite element method (FEM). Figure 2(c) shows plots of the ratio of lifetimes normalized by a diameter of 100 nm, calculated from the simulations with the particle diameter varied from 70 to 130 nm. The simulation demonstrates that the Purcell factor can vary with the particle size. In the experiment, additional effects related to the shape of the particle and the location of the dipole would be included. Due to these combined effects, even bare NDs have a wide lifetime distribution [5]. We also demonstrate that this lifetime distribution shifts to smaller values by coupling with surface plasmons.

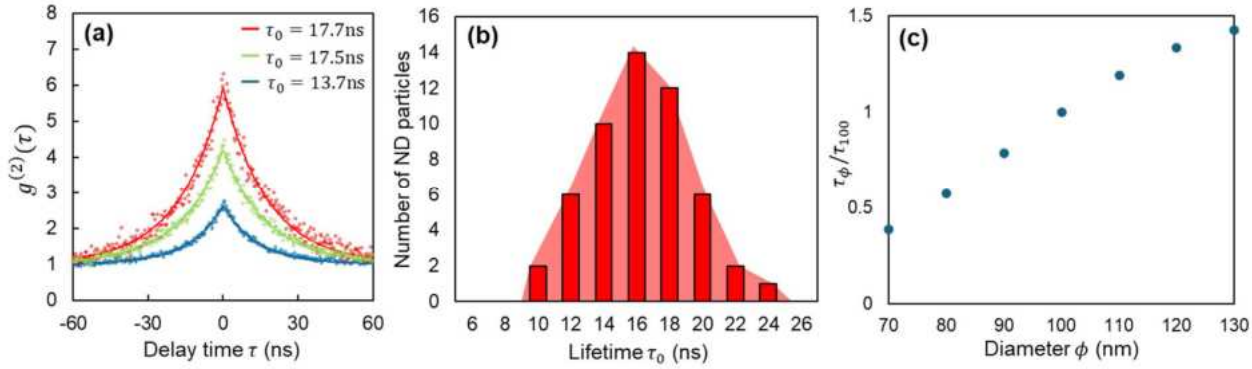


Fig.2. (a) $g^{(2)}(\tau)$ curves obtained from three different ND particles. Scattered plots are experimental data, and solid line are fitted line with exponential function. (b) Histograms of the lifetime obtained from 53 ND particles. (c) Size dependence of the lifetime with the ND particle diameter.

Acknowledgments

This work was financially supported by JST PRESTO (Grant No. JPMJPR17P8), Murata Science Foundation, JSPS KAKENHI Grant No. 17K14321, and Research Foundation for Opto-Science and Technology.

References

[1] C. Kurtsiefer, S. Mayer, P. Zarda, and H. Weinfurter, *Stable Solid-State Source of Single Photons*, Phys Rev Lett **85**, 290 (2000).

[2] H. Lourenço-Martins, M. Kociak, S. Meuret, F. Treussart, Y. H. Lee, X. Y. Ling, H. C. Chang, and L. H. Galvão Tizei, *Probing Plasmon-NV0 Coupling at the Nanometer Scale with Photons and Fast Electrons*, ACS Photonics **5**, 324 (2018).

[3] L. H. G. Tizei and M. Kociak, *Spatially Resolved Quantum Nano-Optics of Single Photons Using an Electron Microscope*, Phys Rev Lett **110**, 1 (2013).

[4] S. Meuret, L. H. G. Tizei, T. Cazimajou, R. Bourrellier, H. C. Chang, F. Treussart, and M. Kociak, *Photon Bunching in Cathodoluminescence*, Phys Rev Lett **114**, (2015).

[5] S. Yanagimoto, N. Yamamoto, T. Sannomiya, and K. Akiba, *Purcell Effect of Nitrogen-Vacancy Centers in Nanodiamond Coupled to Propagating and Localized Surface Plasmons Revealed by Photon-Correlation Cathodoluminescence*, Phys Rev B **103**, 205418 (2021).

Theory for single molecule imaging with photo-induced force microscopy: A comparative study of phthalocyanine molecules

M. Tamura[1,2*], H. Yamane[3], and H. Ishihara[1]

[1]Graduate School of Engineering and Science, Osaka University, 1-3 Machikaneyama-cho, Toyonaka-shi, Osaka 560-8531, Japan
[2]RILACS, Osaka Metropolitan University, 1-1 Gakuen-cho, Naka-ku, Sakai-shi, Osaka 599-8231, Japan
[3]Osaka Research Institute of Industrial Science and Technology, 7-1 Ayumino-2, Izumi-city, Osaka 594-1157, Japan
[*]m.tamura.es@osaka-u.ac.jp

Abstract: Using our developed theoretical framework for photo-induced force microscopy (PiFM), we successfully visualized single molecule images of phthalocyanine molecules. The obtained PiFM images reflected the characteristics of Zinc and H_2 phthalocyanines. This not only affirms the capability of our theoretical framework but also contributes to the advancement of material science.

Photo-induced force microscopy (PiFM), a technique that detects the optical force between the probe tip and the sample in scanning probe microscopy environments like atomic force microscopy, enables the spectroscopic imaging of samples with high resolution. Typically, the performance of optical microscopy is restricted by the diffraction limit of light. However, in systems employing a probe tip, the enhanced and localized electric field at the probe tip contributes to achieving the high resolution. For example, in an experiment using dumbbell-shaped quantum dots, the surface roughness was visualized with a resolution of 0.7 nm [1]. Moreover, our group has developed a theoretical framework to evaluate the PiFM of single molecules based on the nonlocal response theory. We have successfully visualized PiFM images that depend on the molecular orbitals and the transition dipole moment of target molecules [2]. Nevertheless, despite its potential, theoretical research on PiFM under various conditions has not been sufficiently explored. Therefore, in this study, selecting the phthalocyanine as our subject, we aim to discuss the variation of PiFM image based on the differences among molecular types, and seek to contribute to the theoretical understanding of PiFM.

Figure 1 shows the simulation model, where the phthalocyanine molecule is located between the metal substrate and probe. The probe consists of two hemispheres: a smaller one (diameter approx. 0.8 nm) was attached to the bottom of a larger one (diameter 10 nm), assuming the presence of small apex. As shown in Figure 2(a) and 2(b), we employed Zinc phthalocyanine (ZnPc) and H_2-phthalocyanine (H_2Pc) as target molecules. In the energy level diagrams, S_0 represents their highest occupied molecular orbital (HOMO) and S_1 represents lowest unoccupied molecular orbital (LUMO), with LUMO+1 also indicated by S_2. The molecular orbitals and eigen energies were calculated using GAMESS, a quantum chemical calculation software [3]. To evaluate the optical force exerted on the probe under plane wave illumination, we employed the discrete dipole approximation method. In this approach, both metal structure and the molecule were discretized into cubic cell. The response electric field and induced polarization in each cell were self-consistently determined. Figure 1(b) shows the response field in the case without the molecule. The

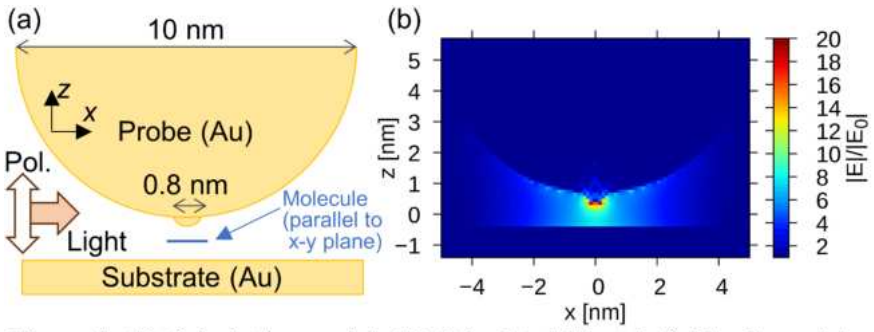


Figure 1. (b) Calculation model. (b) Calculated Electric field enhanced by the metal probe and substrate (incident light energy $\hbar\omega$ = 2.18508 eV).

molecule susceptibility was modeled as nonlocal. We assumed an incident light intensity of 10 kW/cm^2. Further detail of the method was discussed in the referenced literature [2].

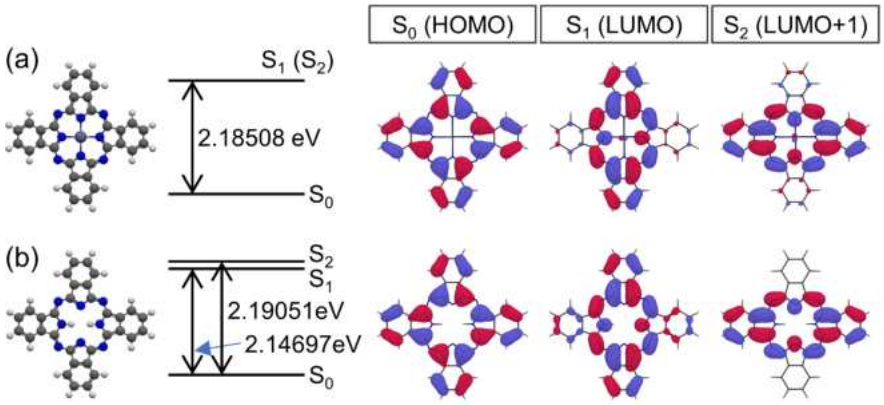


Figure 2. Molecular structure, energy level diagram, and molecular orbitals for (a) ZnPc and (b) H_2Pc. S_1 and S_2 of ZnPc is degenerate. The contour of molecular orbitals indicates the value of ± 0.05.

Figure 3 shows the calculation results of PiFM image. To simulate the scanning of probe, the molecule was displaced in x-y plane relatively. The incident light energy was varied to be resonant for each transition. In the case of H_2Pc, the PiFM image corresponding to transitions from S_0 to S_1 and from S_0 to S_2 were visualized in Figure 3(b) and 3(c), respectively. This agrees with the results we reported previously [2]. Conversely, Figure 3(a) shows that, due to degeneracy, the distribution in PiFM image reflects both transitions. A similar distribution was reported in other scanning probe microscopy technique using light, such as tip-enhanced photoluminescence [4,5].

The obtained result indicates the validity of our theoretical framework in visualizing single molecules with optical forces that are dependent on the unique characteristics of each molecule. It paves the way for future research that bridges theoretical insights with practical applications and contributes to the development of material science.

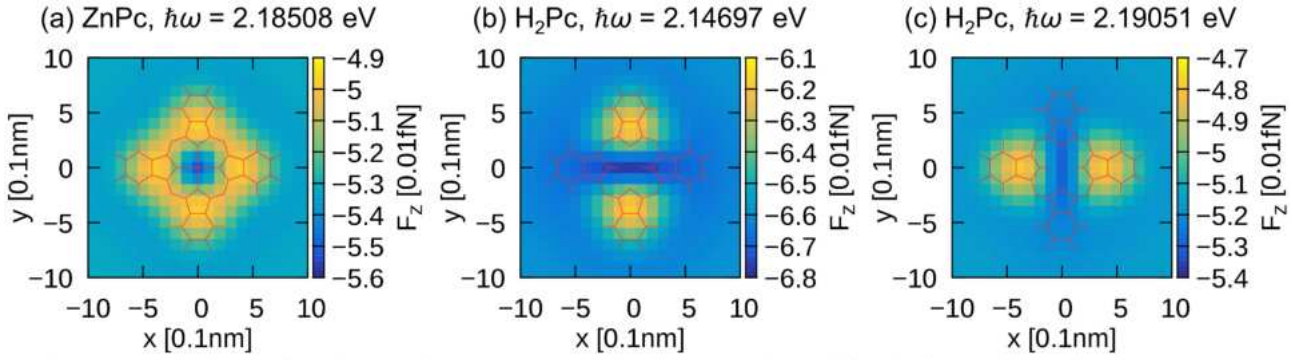


Figure 3. Calculated PiFM image for (a) ZnPc and (b)(c) H_2Pc. The red line indicates the molecular structure.

Acknowledgments

This work was supported by JSPS KAKENHI (Grant Numbers JP16H06504, JP20K15196, JP21H05019, JP21K14554 and JP23H04594), JST-Mirai Program (Grant Numbers JPMJMI18GA and JPMJMI21G1) and JST CREST (Grant Number JPMJCR1903).

References

1. J. Yamanishi, et al., "Optical force mapping at the single-nanometre scale," Nat. Commun., Vol. 12, 3865, 2021.
2. H. Yamane, et al., "Near-field circular dichroism of single molecules," Opt. Express, Vol. 31, No. 3, 3415–3426, 2023.
3. M. W. Schmidt, et al., "General atomic and molecular electronic structure system," J. Comput. Chem., Vol. 14, No. 11, 1347–1363, 1993.
4. B. Yang, et al., "Sub-nanometre resolution in single-molecule photoluminescence imaging," Nat. Photonics, Vol. 14, 693–699, 2020.
5. S. Lyu, et al., "Picocavity-Controlled Subnanometer-Resolved Single-Molecule Fluorescence Imaging and Mollow Triplets," J. Phys. Chem. C, Vol. 126, No. 27, 11129–11137, 2022.

Light-matter interaction probed by cathodoluminescence spectroscopy

Fatemeh Chahshouri[1*], Masoud Taleb[1], Maximilian Black[1], Nahid Talebi[1,2]

[1]Institute of Experimental and Applied Physics, Kiel University, 24098 Kiel, Germany

[2]Kiel, Nano, Surface, and Interface Science − KiNSIS, Kiel University, 24098 Kiel, Germany

[*]corresponding author: Chahshouri@physik.uni-kiel.de, Talebi@physik.uni-kiel.de,

Abstract: We show how electron beams can be used to study nanooptical excitations of van der Waals materials and group III nitride heterostructures. In addition, we present methods for coherently controlling the shape of free-electron wavepackets using nanooptical excitations.

Recently, electron-beam spectroscopy techniques have become powerful probes in nanoscience, revealing detailed views of biological, chemical, and semiconductor structures with atomic-scale resolution. Moreover, this method enables the study of quantum phenomena at the nanoscale for inspecting quantum-optical excitation with spatially-resolved cathodoluminescence (CL) spectroscopy [1]. CL holds great potential for probing optoelectronic properties of nanoscale materials by collecting and analyzing the electron-beam-induced radiation inside an electron microscope. Here, we focus on the functionality of CL spectroscopy in investigating the strong interaction between excitons and photons in transition metal dichalcogenides, which gives rise to propagating exciton polaritons through the self-hybridization effect in WSe_2 thin films [2,3]. Moreover, we utilize CL spectroscopy to investigate the optical properties of undoped AlGaN/GaN heterostructures [4]. By tuning the energy and current of the incident electron beam (Fig. 1), we explore the emission from defects in GaN, as well as quantized energy levels trapped at the AlGaN/GaN interface. Indeed, the correlation between the initial electron energy and electron diffusion length in the channel formed at the interface, along with the percentage of the secondary electrons captured at the heterojunction (Fig. 1), allows for controlling the spectral luminescent peaks.

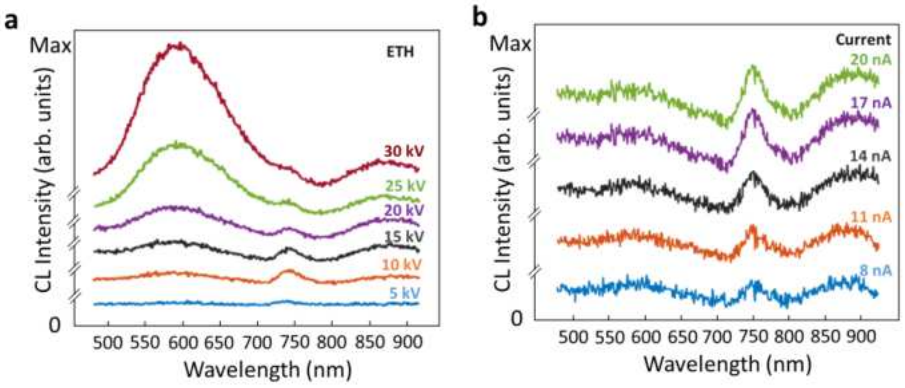


Fig. 1. Room temperature CL spectra of a heterostructure. (a) CL spectrum obtained at depicted electron beam acceleration voltages with a beam current of 12 nA. (b) Acquired CL spectrum corresponding to the 10 kV acceleration voltage at different depicted beam currents.

Recently, merging laser and electron beam spectroscopies into a single setup [5] ushered in a new era for

nanooptics within the realm of electron-beam science. This new domain revolutionized quantum-mechanical electron-light interactions to enter femtosecond and picosecond time resolutions, enabling shaping the electron wavepackets with near-field oscillations. Here, we developed a self-consistent Maxwell-Schrödinger numerical toolbox to evaluate the interaction between slow electron wavepackets and laser-induced gold nanorods [6]. Our numerical studies show that the direction and the spatial profile [7] of the dipolar near-field (Fig. 2), as well as the phase offset in a sequential-interaction system [8], can be used to control the phase and amplitude of the slow electron wavepackets. When the free electron experiences both inelastic longitudinal energy transfer as well as elastic transverse recoil (momentum exchange). These findings demonstrate that one can chart a roadmap for realizing the next generation of ultrafast electron microscopes, enriching the interaction of shaped electron wavepackets with light and matter.

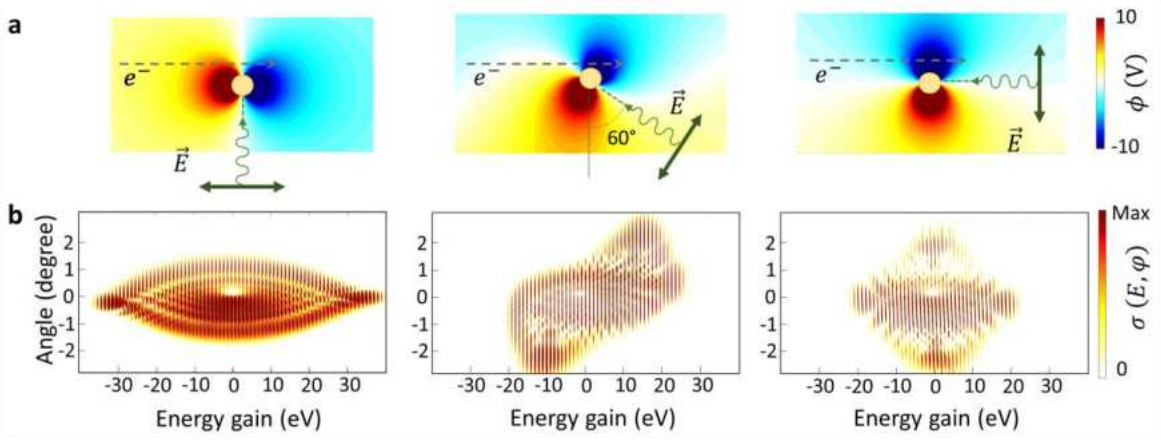


Fig 2**.** Electron wavepacket modulation after interaction with laser-induced near-field localized plasmons of a gold nanorod. (a) Schematics of laser inclination angles and spatial profile of the near-field, and (b) Inelastic scattering cross section.

References

1. Coenen, T. and N. M. Haegel, "Cathodoluminescence for the 21st century: Learning more from light," Appl. Phys. Rev, Vol. 4, No. 3, 2017.
2. Chahshouri, F. et al. "Interaction of excitons with Cherenkov radiation in WSe_2 beyond the non-recoil approximation," J. Phys. D, Vol, 55, No. 14, 145101, 2022.
3. Taleb, M, et al. "Charting the exciton–polariton landscape of WSe_2 thin flakes by cathodoluminescence spectroscopy." Adv. Photonics, Vol. 3, No. 1, 2100124, 2022.
4. Chahshouri, F, et al. "Cathodoluminescence of quantized energy states at AlGaN/GaN interface," arXiv preprint arXiv:2401.05748, 2024.
5. Park, S. T., M. Lin and A. H. Zewail, "Photon-induced near-field electron microscopy (PINEM): theoretical and experimental," New J. Phys, Vol. 12, No. 12 (2010): 123028.
6. Talebi, N. "Near-field-mediated photon-electron interactions," Cham: Springer, 2019.
7. Chahshouri, F., and N. Talebi, "Tailoring near-field-mediated photon electron interactions with light polarization," New J. Phys, Vol. 25, No. 1, 013033, 2023.
8. Chahshouri, F., and N. Talebi, "Numerical investigation of sequential phase-locked optical gating of free electrons," Sci. Rep, Vol. 13, No. 1, 18949, 2023.

This project has received funding from the European Research Council (ERC) under the European Union's Horizon 2020 research and innovation program, Grant Agreement No. 802130 (Kiel, NanoBeam) and Grant Agreement No. 101017720 (EBEAM).

A plasmonic resonator array enhancing luminescence from a phosphor thin film studied by cathodoluminescence

H. Saito[1,2*], Y. Kimura[3], K. Matsuzaki[3], K. Watanabe[4], M. Inada[5], T. Sannomiya[2]

[1] Institute for Materials Chemistry and Engineering, Kyushu University, Japan
[2] Department of Materials Science and Engineering, Tokyo Institute of Technology, Japan
[3] Department of Applied Science for Electronics and Materials, Kyushu University, Japan
[4] Department of Mechanical Engineering, Faculty of Engineering, Kyushu University, Japan
[5] Department of Applied Chemistry, Faculty of Engineering, Kyushu University, Japan
[*]corresponding author: saito.hikaru.961@m.kyushu-u.ac.jp

Abstract: Cathodoluminescence saturation imaging is proposed as a new approach to discriminate coherent and incoherent emissions in phosphor-resonator systems. This method was applied to an integrated system of a Zn_2SiO_4 phosphor film and a plasmonic resonator array, successfully visualized plasmon-enhanced luminescence at the nanoscale.

Plasmonic resonators have realized remarkable Purcell effect for extremely small emitters as well as quantum emitters due to the small mode volume. Cathodoluminescence (CL) is a powerful imaging technique to visualize emitters with a high spatial resolution far beyond the diffraction limit. However, electron beam excitation lacks wavelength selectivity, and thus, an electron beam inevitably excites not only the emitter but also the coherent electromagnetic modes. This problem has made it difficult for CL analysis to quantify luminescence enhancement in the integrated emitter-resonator systems. Recent time-resolved or time correlation CL measurements can be reliable approaches to evaluate Purcell effect at the nanoscale [1,2]. However, especially for long-lifetime emitters such as rare-earth or transition metal dopants, time domain measurements can not be practical due to huge amount of accumulation time for real space mapping of lifetimes. There is an example in which plasmon-enhanced luminescence from an atomically thin semiconductor has been visualized by time-integrated CL [3], where the enhancement can be evaluated based on the reference CL obtained from each of the used resonator array and the luminescent material. However, general phosphor materials having an unignorable volume modifies the dielectric environment and the electromagnetic modes. Here, to directly discriminate incoherent emissions from coherent emissions in integrated phosphor-resonator systems, a simple new method utilizing CL saturation is proposed.

A phosphor-resonator structure including a 20-nm-thick Zn_2SiO_4 film was fabricated (Fig. 1a). A SiO_2 (20 nm thick) / ZnO (9.4 nm thick) bilayer film was first deposited on a commercially available Si_3N_4 film (20 nm thick) by RF magnetron sputtering. Then, by annealing this multilayer film for 1 hour at 1273 K, a Zn_2SiO_4 phosphor layer was produced at the SiO_2/ZnO interface. After covering the Zn_2SiO_4 phosphor film with a 6-nm-thick SiO_2 film, an Al nanodisk array with a triangular lattice of a 520 nm period was fabricated on top of the $SiO_2/Zn_2SiO_4/Si_3N_4$ multilayer film by electron beam lithography and thermal evaporation. The nanodisk diameter and height are 190 nm and 40 nm, respectively. From the backside of the multilayer film, a 50-nm-thick Al film was finally deposited by thermal evaporation. To study luminescence enhancement in this sample at the nanoscale, four-dimensional (4D) scanning transmission electron microscopy (STEM)-CL mapping [4] was conducted. A CL peak was observed at the wavelength of 525 nm, and its intensity depended on sweep speed of the electron probe. This 525 nm peak is due to incoherent emissions from the Zn_2SiO_4 layer

because the intensity decreases as the probe sweep becomes slower, i.e., the number of electrons per pulse increases. This CL saturation is peculiar to incoherent emissions, and thus, can be utilized to discriminate them from coherent emissions linearly depending on the sweep speed or probe current.

In the phosphor-resonator structure in which plasmonic modes have the resonance wavelength of 525 nm, three paths can be considered as the CL mechanism (Fig. 1b). Zn_2SiO_4 has a wide bandgap of ~5 eV [5], and the observed green emission suggests existence of impurity or defect levels in the bandgap of the fabricated Zn_2SiO_4 film. This radiative electron transition is path 1. The electron transition inside the Zn_2SiO_4 can partially be coupled with the plasmon modes. This resonator-mediated emission is path 2. However, lack of the wavelength selectivity in the electron beam excitation brings about the third path in CL, i.e., direct excitation of the plasmon modes (path 3). To solve the above difficulty, 4D STEM-CL mappings were performed with two different probe current 1.5 nA and 16 pA on the identical field of view. Under both the two conditions, incoherent emissions (path 1 and path 2) and coherent emissions (path 3) were contained in the data. However, at the wavelength of 525 nm, incoherent emissions from Zn_2SiO_4 (path 1 or path 2) became relatively dominant under the low current condition (16 pA) due to less CL saturation. Incoherent emission maps without the path 3 contributions were extracted by taking differences between the two current conditions. The observed luminescence enhancement distributions were similar to the field distributions of the plasmon modes, indicating the existence of near-field coupling between the luminescence centers and the plasmon modes in the used phosphor-resonator system.

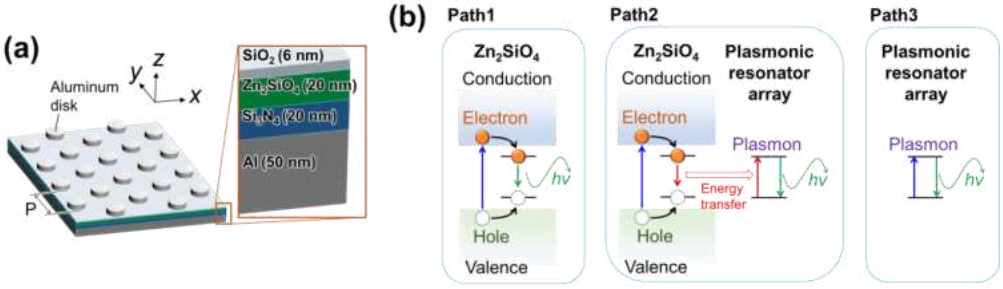


Figure 1 (a) Schematic drawing of the fabricated phosphor-resonator structure. (b) Schematic drawings of the three possible CL paths at the emission wavelength of 525 nm in the phosphor-resonator structure.

References

1. Lourenço-Martins, H., Kociak, M., Meuret, S., Treussart, F., Lee, Y. H., Ling, X. Y., Chang H. C., Tizei, L. H. G. "Probing Plasmon-NV^0 Coupling at the Nanometer Scale with Photons and Fast Electrons," ACS Photon., Vol. 5, No. 2, 324–328, 2018.
2. Yanagimoto, S., Yamamoto, N., Sannomiya, T., Akiba, K. "Purcell effect of nitrogen-vacancy centers in nanodiamond coupled to propagating and localized surface plasmons revealed by photon-correlation cathodoluminescence," Phys. Rev. B, Vol. 103, 205418, 2021.
3. Vu, D. T., Matthaiakakis, N., Sannomiya, T. "Plasmonic Nanopyramid Array Enhancing Luminescence of MoS_2 Investigated by Cathodoluminescence," Adv. Optical Mater., Vol. 11, 2300598, 2023.
4. Matsukata, T., García de Abajo, F. J., Sannomiya, T. "Chiral Light Emission from a Sphere Revealed by Nanoscale Relative-Phase Mapping," ACS Nano, Vol. 15, No. 2, 2219–2228, 2021.
5. Diana, P., Sivaganesh D., Sivakumar, V., Gopal, J. N., Sebastian, S., Saravanakumar, S. "UV-induced photoluminescence and X-ray-induced thermoluminescence of Zn_2SiO_4: Mn phosphor," J. Mater. Sci.-Mater. Electron, Vol. 34, 1992, 2023.

Optical chiral fields and plasmon modes in gold nanostructures studied by apertured near-field spectroscopic imaging

K. Imura[1*]

[1]Department of Chemistry and Biochemistry, School of Advanced Science and Engineering, Waseda University, Japan
[*]corresponding author: imura@waseda.jp

Abstract: We have developed various types of near-field imaging methods to elucidate optical properties of nanomaterials. Plasmonic materials have gained much attention due to the enhancement of plasmonic and chiral fields. To gain deep insights into the localized fields, various near-field imaging methods are applied to plasmonic nanostructures.

Near-field imaging methods overcome the diffraction limit of light and achieve a nanometer spatial resolution. Scattering and apertured near-field methods developed have been utilized to examine optical properties of nanomaterials. We are developing various types of apertured near-field imaging methods to elucidate optical properties of nanomaterials from various spectroscopic points of views.[1-4] For instance, near-field nonlinear imaging is of great use for visualization of enhanced optical fields, and time-resolved imaging is for revealing spatio-temporal dynamics of elementary excitations.[2] Plasmonic materials with subwavelength dimensions have gained much attention due to the enhancement of optical and chiral fields. To reveal physical origins of the chiral fields based on the plasmon mode, near-field spectroscopic imaging is essential. In this study, various near-field imaging methods are utilized to gain deep insights into the chiral near-fields induced in the plasmonic structures.

We have performed near-field transmission and reflection imaging of single gold nanoplates.[1,2] We reveal from the near-field imaging that periodic spatial features are visualized depending on the observed wavelengths and are assignable to plasmon mode excited. The spatial features are well reproduced by eigen functions calculated for a particle confined in a two-dimensional potential well. The eigen modes are classified using the point group analysis, and by using a Lippmann-Schwinger equation, the optical selection rule can be understood.[1,3] For instance, gold nanoplate on a substrate is illuminated from a normal incidence (along z direction), plasmon mode assigned to E and A_1 modes are interpreted as the allowed (bright) and forbidden (dark) modes, respectively, as shown in Figure 1. Near-field transmission imaging indicates that the near-field local illumination enables to excite the optically dark mode.

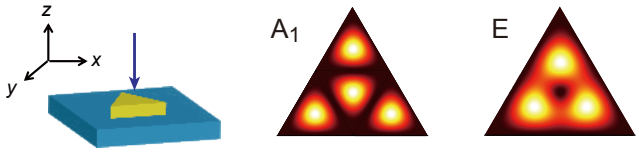


Figure 1. Schematic image of the illumination configuration and calculated eigen modes for a gold nanoplate.

Spectral bandwidth of the plasmon resonance provides the dephasing time of the plasmon. However, as two bands are spectrally overlapped, determination of the dephasing time becomes challenging. To reveal dephasing time of the plasmon mode, we performed near-field time resolved imaging of the gold nanoplate.[1] The near-field excitation image of the plate shows unique spatial features assignable to superposition of the dark and bright plasmon modes. Time-resolved autocorrelation trace taken at the apex of the plate shows indicates that the

plasmon dephasing time is an order of fs time scale. We visualized spatial distribution of the dephasing time on the plate and reveal that the dark mode exhibits longer dephasing time than the bright mode.

Three dimensional near-field imaging is also capable to reveal light confinement capability of the plasmons.[4,5] By regulating a distance between the near-field aperture-tip and sample surface, physical properties of plasmon are examined. Near-field images taken at normal operation indicates that two modes are overlapped in both spatial and spectral manners, while by regulating the distance, two-modes are spatially discriminated. Spatial extensions of the modes are examined and found that the dark mode exhibits tight light confinement compared to that of the bright mode, consistent with the result obtained in the time-resolved near-field imaging.

The dark mode discussed so far is radially polarized mode and/or out-of-plane mode. To examine the excitation probability of these two-modes, we carried out nonlinear confocal microscopy of the plate using the focused cylindrical vector beams.[6] Observed excitation image show unique spatial distributions depending on the excitation fields. Electromagnetic field simulation well reproduces the observed images and indicates that the observations are consistent with the excitation of the dark mode. From a detailed analysis of the electromagnetic simulations, we found that the out-of-plane mode is dominantly excited.

We have examined optical chiral fields in the vicinity of gold nanoplate by using three-dimensional near-field polarization imaging. Near-field transmission images taken by detecting right and left circular polarization components show very similar spatial features with the one observed by conventional transmission imaging. By subtracting the left circular polarization component from the right one in the transmission images, S_3 Stokes parameter is obtained. Optical chiral density is closely related to the S_3 parameter, and thus in this way, chiral near-field can be visualized. Spatial feature of the observed image (Figure 2) is not identical with that of the one visualized by conventional method. Electromagnetic field simulations reproduce the spatial distributions under various incident polarizations, indicating that the visualized spatial distribution is assignable to the chiral near-field. We examine spatial extension of the optical chiral field and reveal that the chiral field is more strongly localized than that of the optical field. We will discuss the plasmon mode dependency of the chiral fields and physical origins of the spatial and steric properties of the optical chiral field in the conference.

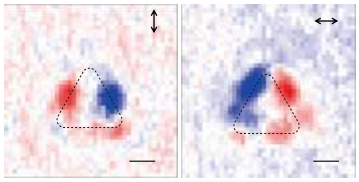


Figure 2. Optical chiral fields visualized for a gold nanoplate. Arrow: incident polarization. Scale bar: 200 nm.

The author is grateful to the collaborators who contributed to this study, in particular, Drs. S. Hasegawa, K. Imaeda, and H. Mizobata. This work was supported in part by JSPS KAKENHI (grant nos. 20H02700, 20K21179, 22K19013, 23H04604, 23H01927) from the Japan Society for the Promotion of Science.

References

1. Imaeda, K., S. Hasegawa, S., K. Imura, K. *J. Phys. Chem. Lett.* 9, 4075 (2018).
2. Mizobata, H., Hasegawa, S., Tamura, M., Iida, T., Imura, K. *J. Chem. Phys.* 153, 144703 (2020).
3. Imaeda, K., Hasegawa, S., Imura, K. *J. Chem. Phys.* 156, 044702 (2022).
4. Matsuura, T., Imaeda, K., Hasegawa, S., Suzuki, H., Imura, K. *J. Phys. Chem. Lett.* 10, 819 (2019).
5. Suzuki, H., Imaeda, K., Mizobata, H., Imura, K. *J. Chem. Phys*. 152, 014708 (2020).
6. Hasegawa, S., Ichikawa, H., Imura, K. *J. Phys. Chem. C*. 128, 2536 (2024).

New insights into optical property characterization of 2D semiconductor materials through time-correlated photon/electron spectroscopies

F. Castioni[1*], Y. Auad[1], N. Varkentina[1], A. Freilinger[1], S. Y. Woo[1], N. Bonnet[1], J.-D. Blazit[1], X. Li[1], M. Tencé[1], K. Watanabe[2], T. Taniguchi[3], O. Stéphan[1], M. Kociak[1] and L. H. G. Tizei[1*]

[1] Université Paris-Saclay, CNRS, Laboratoire de Physique des Solides, Orsay, France
[2]Research Center for Electronic and Optical Materials, National Institute for Materials Science, 1-1 Namiki, Tsukuba, Japan
[3]Research Center for Materials Nanoarchitectonics, National Institute for Materials Science, 1-1 Namiki, Tsukuba, Japan
[*]corresponding authors: florian.castioni@universite-paris-saclay.fr, luiz.galvao-tizei@universite-paris-saclay.fr

Abstract:

This contribution investigates the possibilities presented by the latest advancements in STEM techniques, specifically focusing on electron-photon time-correlations. Utilizing techniques such as CLE and EEGS, the objective is to gain deeper insights into the optical characteristics of model systems like TMD 2D semiconductors at the nanometer scale.

The optical properties of luminescent materials are intricately tied to their structural and chemical characteristics at the nanometric, or even atomic scale. Understanding this relationship has long relied on the combination of scanning transmission electron microscopy (STEM) with external optical techniques such as absorption or photoluminescence spectroscopies, probing the excitation and emission mechanisms at the micrometric scale. However, the significant gap in spatial resolution between these methods and phenomena of interest often leads to ambiguous or even impossible interpretations of the measurements.

Recent advancements in nano-optics seek to address this resolution disparity by enabling observation of luminescent material properties at nanometric scales. In that sense, STEM has undergone substantial instrumental and theoretical progress, providing valuable insights into optical properties through conventional inelastic electron scattering (electron energy loss spectroscopy, EELS) and photon emission (cathodoluminescence, CL) spectroscopies [1]. However, both techniques are hindered by spectral resolution limitations and the broadband excitation process of the electron beam. To overcome these challenges, two techniques currently in development will be highlighted in this contribution:

- **Cathodoluminescence Excitation Spectroscopy (CLE, Figure 1b)**, based on coincidence measurements between EELS and CL events. CLE offers insights into energy transfer pathways and excitation lifetimes at the nanometer scale, as previously reported [2,3].
- **Electron Energy Gain Spectroscopy (EEGS, Figure 1c)**, an extension of the photon-induced near-field electron microscopy (PINEM) technique, investigates primary electron acceleration when the beam interacts with a strong optical field generated by a laser. By changing the energy of the photons, this technique can resolve ultra-fine optical resonances in the sub-meV range, revealing novel physical properties below the energy resolution achievable with state-of-the-art monochromated electron beams. So far, it has only been applied to photonic excitations, such as plasmons or surface polaritons [4].

These techniques, with their distinct excitation and deexcitation processes (**Figure 1a**), are expected to be highly complementary, offering deeper insights into optical mechanisms at the nanometer scale. The present contribution focuses on using transition metal dichalcogenides (TMDs) as a model system of functional luminescent material to explore the insights provided by these correlated techniques.

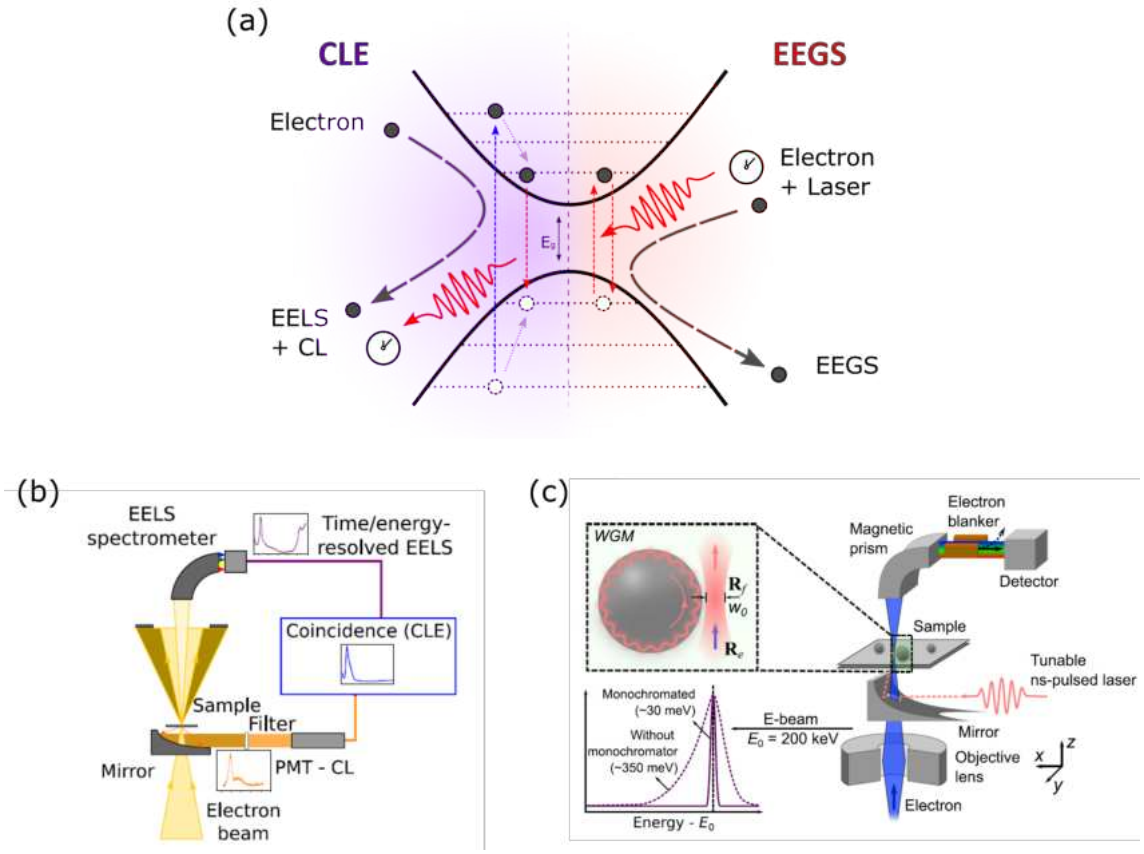


Figure 1. Illustration of correlated photon/electron spectroscopies principles. (a) Band diagram schematic of excitation processes comparing cathodoluminescence excitation spectroscopy (CLE) and energy electron grain spectroscopy (EEGS). (b-c) Experimental set-ups developed at the Orsay laboratory for CLE **[2]** and EEGS [5] spectroscopies, respectively.

References

[1] N. Bonnet, H.Y. Lee, F. Shao, S.Y. Woo, J.-D. Blazit, K. Watanabe, T. Taniguchi, A. Zobelli, O. Stéphan, M. Kociak, S. Gradečak, L.H.G. Tizei, "Nanoscale Modification of WS $_2$ Trion Emission by Its Local Electromagnetic Environment", Nano Lett. 21 (2021) 10178–10185.

[2] N. Varkentina, Y. Auad, S.Y. Woo, A. Zobelli, L. Bocher, J.-D. Blazit, X. Li, M. Tencé, K. Watanabe, T. Taniguchi, O. Stéphan, M. Kociak, L.H.G. Tizei, "Cathodoluminescence excitation spectroscopy: Nanoscale imaging of excitation pathways", Sci. Adv. 8 (2022) eabq4947.

[3] N. Varkentina, Y. Auad, S.Y. Woo, F. Castioni, J.-D. Blazit, M. Tencé, H.-C. Chang, J. Chen, K. Watanabe, T. Taniguchi, M. Kociak, L.H.G. Tizei, "Excitation lifetime extracted from electron–photon (EELS-CL) nanosecond-scale temporal coincidences", Applied Physics Letters 123 (2023) 223502.

[4] J.-W. Henke, A.S. Raja, A. Feist, G. Huang, G. Arend, Y. Yang, F.J. Kappert, R.N. Wang, M. Möller, J. Pan, J. Liu, O. Kfir, C. Ropers, T.J. Kippenberg, "Integrated photonics enables continuous-beam electron phase modulation", Nature 600 (2021) 653–658.

[5] Y. Auad, E.J.C. Dias, M. Tencé, J.-D. Blazit, X. Li, L.F. Zagonel, O. Stéphan, L.H.G. Tizei, F.J. García De Abajo, M. Kociak, "μeV electron spectromicroscopy using free-space light", Nat Commun 14 (2023) 4442.

Femtosecond time-resolved microscopy for spatio-temporal characterization of structured surface plasmon polariton wave packets

Atsushi Kubo[1*]

[1]Faculty of Pure and Applied Sciences, University of Tsukuba,1-1-1 Tennodai, Tsukuba-shi, Ibaraki 305-8571, Japan
[*] kubo.atsushi.ka@u.tsukuba.acjp

Abstract: Recent studies of structured light (SL) have generated various optical fields with internal structures of energy flow density and angular momentum. The surface-wave correspondence of SL, structured surface plasmon polaritons (SPPs), can also be formed. We investigate the generation and visualization of structured SPPs using femtosecond time-resolved microscopy methods.

Recent progress in the study of structured light has advanced the generation and evaluation techniques for various types of light beams with complex structures of energy flow density and angular momentum (AM) states in the beam cross-section, such as optical vortices, non-diffraction beams, and skyrmion beams [1]. When pulsed light is used as a source, a so-called "light bullet" is realized in which the optical field is confined in three dimensions. Recent studies have shown that the group velocity of an optical wave packet (WP) is not simply determined by the space or material dispersion relation, but rather is a quantity that can be manipulated by applying a designed wavenumber vector to each frequency component of the wave packet [2,3]. Control of both the temporal and spatial frequencies of the optical field is the key to uncovering novel phenomena in the space-temporal regime of the WP. Surface plasmon polaritons (SPPs) are another type of structured light with strong confinement of the field perpendicular to the interface. Recent studies have realized the generation of various "structured plasmons", such as SPP vortices [4], plasmonic spin skyrmions/ melons [5,6], and non-diffractive SPP beams [7]. In these studies, time-resolved microscopy has played a critical role in observing the dynamical behavior of the SPP field in space and time. When pulsed light is used as an excitation source, three-dimensional confinement of the SPP field is realized. Such SPP WPs propagate with a three- dimensional spin angular momentum (SAM) texture associated with the localized field energy density [8,9]. Therefore, they are expected to serve as carriers of electron spin information in novel devices.

In this paper, we describe the imaging of SPP wave packets using femtosecond time-resolved two-photon fluorescence microscopy (TR-2PFM) [10].

The first is the imaging of the deformation of a femtosecond SPP WP during transmission through a metal-insulator-metal nanocavity (MIM-NC) (Fig. 1) [11]. The SPP WP is launched by irradiating a laser pulse with a center wavelength of 810 nm and a time duration of 10 fs onto the surface of deposited Au film with a linear coupler. After propagating on the Au surface, the SPP WP passes through

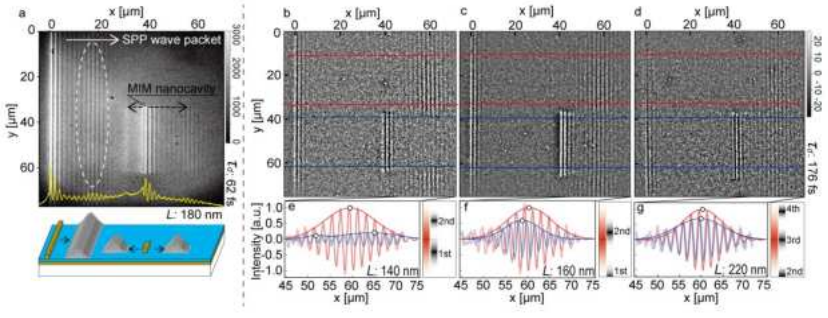


Fig.1: (a) Schematic of the TR-2PFM of a SPP WP interacting with a MIM -NC on Au surface. (b-c) Micrographs of SPP WPs after transmission through a MIM-NC with the width *L* of (b) 140 nm, (c) 160 nm and (d) 220 nm. (e-f) Profiles of (b-c). [11]

the MIM-NC with a structure width of L (50 ~ 220 nm). During this process, the SPP field is visualized by detecting two-photon fluorescence emission from a very thin fluorescent film coated on the Au surface using an optical microscope and a CCD camera. The micrographs revealed that the transmittance, shape, and peak position of the SPP WP are significantly modulated in dependence on L. The results are interpreted in terms of up-chirping in the propagation path of the SPP WP and resonant transmission in the eigenmode band of the MIM-NC. In the case of L=160 nm, a backward shift of ~2 μm in the peak position of the SPP WP transmitted through the MIM-NC was observed compared to a WP without interaction with the NC. For this MIM-NC, the second-order eigenmode overlaps with the high-energy side of the SPP spectrum. The backward shift is caused by the selective transmission of the tail part of the up-chirped WP through the MIM-NC. This result constitutes a visualization of a spatio-temporal correlation of the SPP WP.

The second is a generation and observation of a space-time SPP (ST-SPP) WP [12]. Femtosecond laser pulses are formed into optical ST-WPs using a 4f system and irradiated onto an Au surface with a linear coupler to generate non-diffractive ST-SPP WPs (Fig.2). To form striped ST-SPP, fs pulses are spectrally resolved by a grating, then all frequency components are given constant transverse momentum using a two-dimensional spatial light modulator. The spatial distribution of the SPP field was again visualized by the two-photon fluorescence from the fluorescent film applied on the sample surface. In Fig. 2, many SPP stripes with a period of about 5 μm are generated. The intensity contrast between adjacent stripes remains high after the propagation of the SPP wave, indicating that non-diffractive properties are realized.

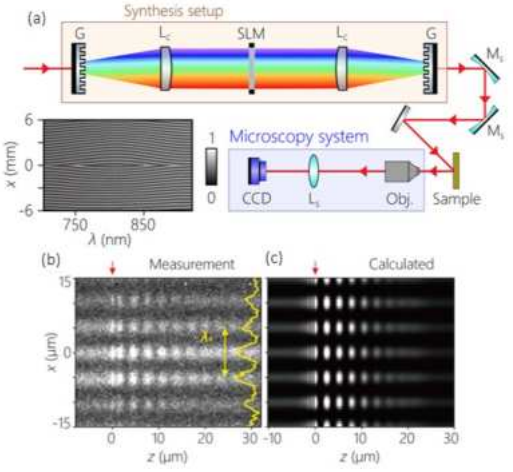


Fig.2: (a) Schematic of an experimental setup for synthesis of ST-WPs and 2PFM imaging of ST-SPP WPs. (b) Micrograph of the striped ST-SPP. (c) Simulated image of (b). [12]

References

1. A. Forbes, M. de Oliveria, M. R. Dennis, "Structured light," Nat. Photonics, 15, 253-262 (2021).
2. D. H. Froula, et al., "Spatiotemporal control of laser intensity," Nat. Photonics, 12, 262-265 (2018)
3. M. Yessenov, L. A. Hall, K. L. Schepler, A. F. Abouraddy, "Space-time wave packets," Adv. Opt. Photonics, 14, 455 (2022).
4. G. Spektor, et al., "Mixing the Light Spin with Plasmon Orbit by Nonlinear Light-Matter Interaction in Gold, " Phys. Rev. X 9, 021031 (2019)
5. Y. Dai, Z. Zhou, A. Ghosh, R. S. K. Mong, A. Kubo, C. B. Huang, H. Petek, "Plasmonic topological quasiparticle on the nanometre and femtosecond scales," Nature, 588, 616 (2020).
6. Y. Dai, Z. Zhou, A. Ghosh, K. Kapoor, M. Dabrowski, A. Kubo, C. B. Huang, H. Petek, "Ultrafast microscopy of a twisted plasmonic spin skyrmion," Appl. Phys. Rev., 9, 011420 (2022)
7. K. L. Schepler, M. Yessenov, Y. Zhiyenbayev, A. F. Abouraddy, "Space–Time Surface Plasmon Polaritons: A New Propagation-Invariant Surface Wave Packet," ACS Photonics, 7, 2966-2977 (2020).
8. N. Ichiji, D. Oue, M. Yessenov, K. L. Schepler, A. F. Abouraddy, A. Kubo, "Transverse spin angular momentum of a space-time surface plasmon polariton wave packet," Phys. Rev. A 107, 063517 (2023).
9. N. Ichiji, M. Yessenov, K. L. Schepler, A. F. Abouraddy, A. Kubo, "Exciting space-time surface plasmon polaritons by irradiating a nanoslit structure," J. Opt. Soc. Am. A 41, 396-405 (2024)
10. T. Hattori, A. Kubo, K. Oguri, H. Nakano, H. T. Miyazaki, "Femtosecond Laser-Excited Two-Photon Fluorescence Microscopy of Surface Plasmon Polariton", Jpn. J. Appl. Phys., 51, 04DG03 (2012)
11. N. Ichiji, Y. Otake, A. Kubo, “Femtosecond imaging of spatial deformation of surface plasmon polariton wave packet during resonant interaction with nanocavity”, Nanophotonics, 11, 1321-1333 (2022)
12. N. Ichiji, H. Kikuchi, M. Yessenov, K. L. Schepler, A. F. Abouraddy, A. Kubo, "Observation of ultrabroadband striped space-time surface plasmon polaritons", ACS Photonics, 10, 374-382 (2023)

Photon-STM study of exciton creation and annihilation processes in a single molecule

M. Imai-Imada[1,2*]

[1]SISL RIKEN, Japan
[2]JST PRESTO, Japan
[*]corresponding author: miyabi@riken.jp

Abstract: we report atomic-scale investigation of the electron dynamic processes that drive exciton creation and annihilation, including luminescence and photocurrent generation, in a single molecule.

The creation and annihilation of an exciton induced by electron dynamics, such as transition in a molecule or transfer between a molecule and an electrode, play crucial roles in optoelectronic energy conversion. However, the correlation between the exciton and electron dynamics in a molecule is yet to be thoroughly described, mainly because the spatial resolution of conventional techniques is not enough to resolve individual molecules. Recently, we have developed Photon-STM (Fig. 1**a**) by combining low-temperature scanning tunneling microscope with laser irradiation and photo-detection systems, and realized to investigate the exciton dynamics, such as luminescence and photocurrent generation in a single molecule [1-3].

In this study, we report Photon-STM study of photocurrent generation in a single-molecule free-base phthalocyanine (FBPc) molecule at atomic resolution. The experimental setup was carefully designed to optimize the efficiency of molecular excitation; as a result, the excitation laser energy can be tuned to the single-molecule absorption resonance with μeV precision. Moreover, the laser light field is strongly enhanced in the plasmonic nanogap between a gold tip and a silver substrate[5,6]. Figure 1**b** shows an STM image of our sample, in which an FBPc molecule is adsorbed on a 4-monolayer (ML) NaCl(100) film grown on the Ag(111) substrate. The NaCl film was used to decouple the molecule from the metal substrate[7] in order to preserve its intrinsic optical properties.

To measure the photocurrent, the STM tip was placed on a molecule while the STM feedback loop was opened, and the STM junction was then irradiated with a wavelength of 683 nm, corresponding to the molecular resonance. After adjusting the sample voltage V_s to −2.0 V, which made the dark current flowing through the molecule negligible, the tunnelling current I_t trace was measured on the molecule

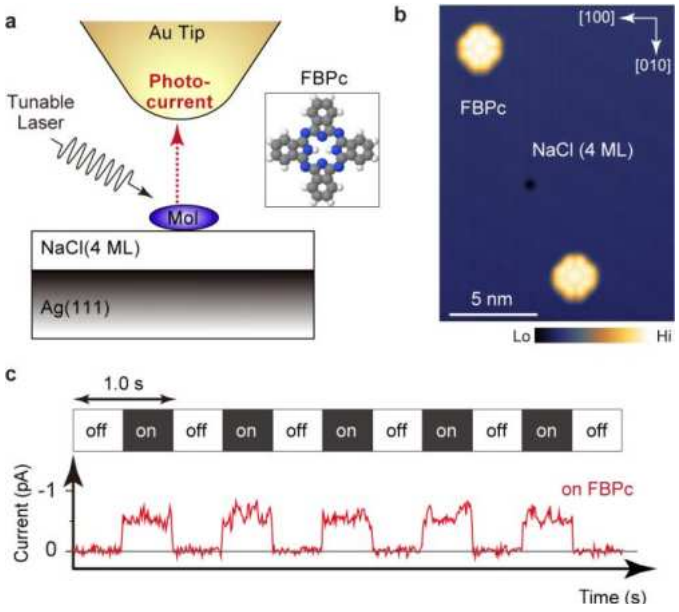


Figure 1 a, A schematic illustration of the experiment and the structure of free-base phthalocyanine (FBPc, grey, C; blue, N; white, H, D).
b, An STM image of the sample (sample bias voltage V_s = 1.0 V, tunnel current I_t = 5 pA).

while turning the laser irradiation on and off at 1 Hz using a shutter (Fig. 1**c**). The I_t flows in the laser-on state and is zero in the laser-off state. This irradiation-induced I_t switching was not detectable at the initial tip-molecule separation (where I_t = 3 pA flows at V_s = −2.5 V on the molecule with closed STM feedback loop under laser-off condition) but became so as the tip is approached the molecule by ~0.2 nm. The laser energy (hν) dependence revealed that the irradiation-induced I_t can be detected only when the laser energy is at 1816 meV corresponding to the molecular excitation energy from the ground state (S_0) to the first singlet excited state (S_1). We, therefore, conclude that the detected photocurrent is triggered by the S_0-S_1 electronic excitation.

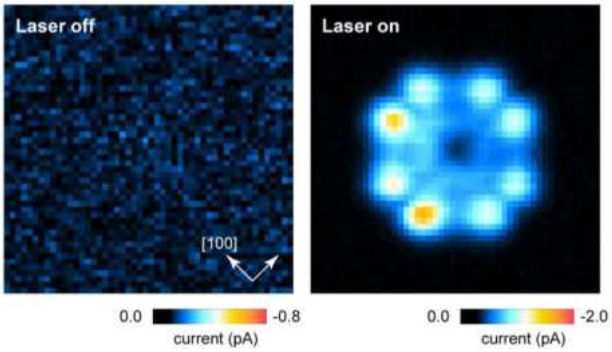


Figure 2 the current images of a molecule measured at V_s = -2.0 V under the laser-off (left) and laser-on (right) conditions.

Figure 2 shows I_t images under the laser-off and laser-on conditions. While the observed signals under the laser-off condition were within the margin of error for current measurement, signals far exceeding the noise level were obtained under illumination. The photocurrent image clearly reveals a four-fold symmetric pattern with nodes and lobes having similar characteristics to the molecular orbitals (MOs) of phthalocyanines that have been visualized by STM. Photocurrent flowing through MOs was thus successfully visualized at an atomic resolution.

Depending on the applied bias voltage, not only the direction but also the spatial distribution of the photocurrent changes markedly. Comparing the spatial distribution of photocurrent and the frontier MOs of an FBPc molecule allowed us to identify the frontier MOs which play essential roles in the photocurrent generation. Moreover, the photocurrent images, measured in the voltage region where the direction of the current is inverted, allowed us to discovered multiple counterflowing photocurrent channels even at a voltage where the averaged photocurrent is almost zero. The detailed mechanism of photocurrent generation will be discussed in the presentation.

References

1. M. Imai-Imada et al., “Energy-level alignment of a single molecule on ultrathin insulating film”, *Phys. Rev. B* **98**, 201403(R) (2018).
2. M. Imai-Imada *et al*., “Orbital-resolved visualization of single-molecule photocurrent channels”, *Nature* **603**, 829 (2022).
3. H. Imada, M. Imai-Imada *et al*., “Single-molecule laser nanospectroscopy with micro–electron volt energy resolution”, *Science* **373**, 95 (2021).

Single-molecule photonics with scanning tunneling microscopy: nanospectroscopy and beyond

H. Imada[1]

[1]Surface and Interface Science Laboratory, RIKEN, Japan
himada@riken.jp

Abstract: The study introduces a novel single-molecule nanospectroscopy technique combining scanning tunneling microscopy and near-field optics, enabling precise investigation of molecular excited states and energy conversions at the submolecular level. This approach overcomes previous limitations in optical spectroscopy, offering new insights into organic material functions.

The electronic excitation of molecules triggers diverse energy conversion phenomena, including luminescence, photovoltaic effects, and various chemical reactions. Understanding and controlling dynamic processes of molecules in excited states are of primary importance for creating novel functions with organic materials. Optical spectroscopy has been widely used to investigate such electronic excited states, determine emission and absorption energies, elucidate dynamic phenomena occurring in materials, and so on. However, because of its limited spatial resolution, it cannot provide direct information about the local spatial distribution of molecular orbitals, which governs excitation. Conversely, atomic-resolution microscopy techniques such as electron microscopy and scanning probe microscopy can visualize local structure, but spectroscopic techniques using such microscopes are very underdeveloped. Consequently, there have been few studies on electronic excitations and succeeding processes at the atomic or molecular level and much remains to be learned about the associated energy conversions.

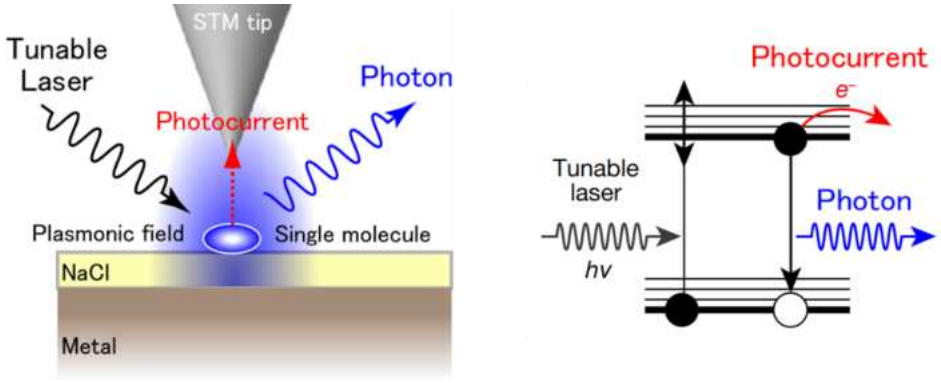


Figure: Illustration of the experimental setup of near-field optical spectroscopy in STM. Single molecule is photo excited by the laser-driven localized plasmonic field, and photon (luminescence, Raman) or electric current is measured.

Recently we have developed single-molecule nanospectroscopy techniques that combined scanning tunneling microscopy (STM) and near-field optics [1-3], which are based on plasmon-enhanced light-matter interaction at the molecular scale (Figure). STM allows us to observe molecular orbitals at the atomic scale, and various kinds of near-field spectroscopy (Raman, photoluminescence, photocurrent) now allows us to directly investigate the electronic, optical, and vibrational properties of the materials with submolecular spatial resolution.

In this talk, I will introduce recent progress of the single-molecule nanospectroscopy techniques, and discuss perspectives of the technique.

References

1. H. Imada et al., Science 373 (2021) 95-98.
2. R. B. Jaculbia, H. Imada et al., Nat. Nanotechnol. 15 (2020) 105-110.
3. M. Imai-Imada, H. Imada et al., Nature 603 (2022) 829-834.

Meta and plasmonic materials for advanced biosensing and bioimaging

Deep subwavelength titanium nitride grating structures for mid-infrared vibrational absorption sensing

L. Yu. Beliaev[1], E. Shkondin[2], A. V. Lavrinenko[1], and O. Takayama[*1]

[1]DTU Electro – Department of Electrical and Photonics Engineering, Technical University of Denmark, Ørsteds Plads 343, DK-2800 Kgs. Lyngby, Denmark

[2]DTU Nanolab - National Center for Micro- and Nanofabrication, Technical University of Denmark, Ørsteds Plads 347, DK-2800 Kgs. Lyngby, Denmark

[*]corresponding author: otak@dtu.dk

Abstract: The mid-infrared vibrational spectroscopy has been used for the detection of various molecules due to the characteristic infrared absorption features of chemical bondings. We realize high-aspect ratio plasmonic titanium nitride gratings where infrared absorption by vanillin molecules is significantly enhanced due to stronger electric fields within the deep subwavelength structures.

Vibrational spectroscopy in the mid-infrared (IR) wavelength region spanning from 2.5 to 20 μm has been extensively used for the detection and identification of molecules since molecular bondings exhibit characteristic absorption peaks in the wavelength region, allowing various sensing applications, such as production process, gas sensing for environmental monitoring, and label-free detection of proteins. In order to improve the mid-IR absorption signals of analyte molecules, surface-enhanced infrared absorption (SEIRA) spectroscopy has been developed by incorporating both plasmonic and dielectric nanostructures to confine mid-IR light at the nanoscale [1]. SEIRA employs various nanostructures supporting highly localized plasmon modes, which are made of gold and transparent conductive oxides, like Al-doped zinc oxide (AZO) [2].

Here, we report that high-aspect ratio titanium nitride (TiN) grating structures can enhance mid-IR light absorption of molecules [3]. Titanium nitride is a plasmonic material whose permittivity becomes negative from the visible to mid-IR wavelengths [4]. Up to present, a TiN-based nanostructure has not been used for SEIRA applications. The TiN nanostructures have been fabricated by the combination of deep ultraviolet (DUV) lithography, dry etching, and atomic layer deposition (ALD) techniques [5]. As shown in Figure 1(a), the fabricated TiN grating structures have the periodicity of 0.4 μm, TiN wall thickness of 0.2 μm, and height of 2.4 μm with high aspect ratio on a Si substrate. The TiN nanostructures become hyperbolic metamaterials (HMMs) for mid-IR wavelengths where permittivity tensor components parallel to trench walls are negative (plasmonic behavior) while the perpendicular component is positive (dielectric behavior) [6].

The TiN grating structures support Fabry-Pérot modes propagating within the deep subwavelength plasmonic trenches and possess strong electric field, which enhances infrared absorption by analyte molecules. We use vanillin as a model analyte that exhibits several characteristic absorption peaks for mid-infrared wavelengths of λ = 6 – 7 μm (1666 – 1427 cm−1), as shown in Figure 1(b). We observe enhancement of vibrational signal in TiN gratings, compared with unstructured Si substrate. Apart from intense electric field within gratings, the high aspect ratio geometry increases the working surface of the sensor, resulting in improved vibrational signals. Titanium nitride grating structures may serve as a highly sensitive chemical sensing platform for mid-infrared absorption spectroscopy. Additionally, such TiN grating structure can also be used for

refractometric sensing where analyte is detected as the change of local refractive index [5] and photothermal applications [7].

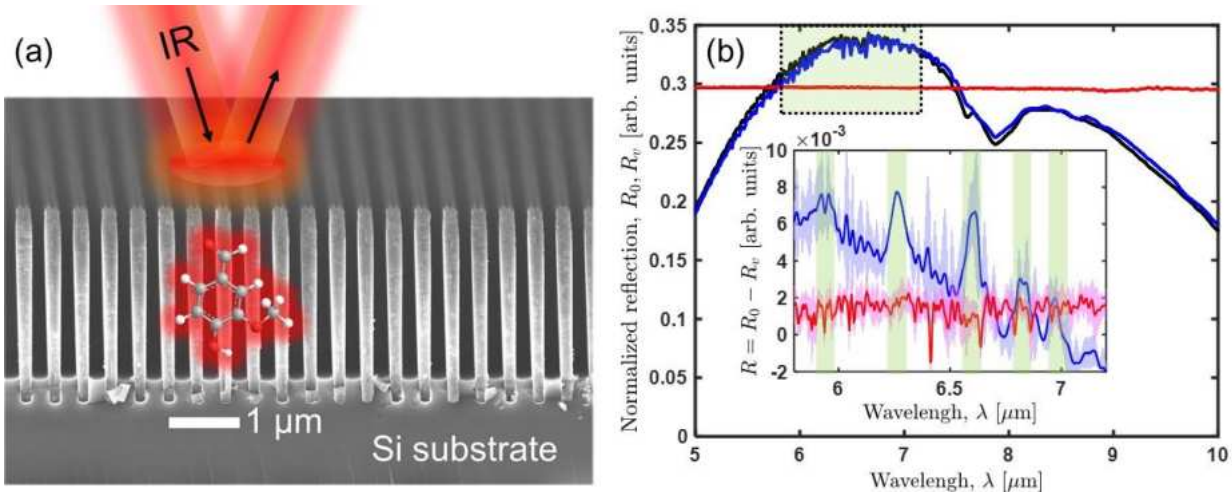


Figure 1: (a) Scanning electron microscope (SEM) image of the fabricated TiN gratings. (b) Measured free-space reflection spectra from TiN gratings (blue) and Si substrate (red) with and without vanillin sample, Rv, R_0, respectively. The inset is the reflection difference between samples with and without vanillin $R = R_0 - Rv$. Green shades show five absorption peaks of vanillin.

This research was funded by Independent Research Fund Denmark, DFF Research Project 2 ”PhotoHub” (8022-00387B). The authors would like to acknowledge the support from the Danish National Center for Micro- and Nanofabrication (DTU Nanolab).

References

1. Takayama, O., “Mid-infrared nanophotonics for biochemical sensing: a review,” Rom. Rep. Phys. Vol. 72 No. 3, 408 2020.
2. Shkondin, E., T. Repän, M. E. Aryaee Panah, A. V. Lavrinenko and O Takayama, “High aspect ratio plasmonic nanotrench structures with large active surface area for label-free mid-infrared molecular absorption sensing,” ACS Appl. Nano Mater. Vol. 1, No. 3, 1212–1218, 2018.
3. Beliaev, Yu. L., E. Shkondin, A. V. Lavrinenko and O. Takayama, “Titanium Nitride Nanotrench Metasurfaces for Mid-infrared Chemical Sensing,” ACS Appl. Opt. Mater. DOI: 10.1021/acsaom.3c00355. 2023.
4. Beliaev, L. Y., E. Shkondin, A. Lavrinenko and O. Takayama, “Optical Properties of Plasmonic Titanium Nitride Thin Films from Ultraviolet to Mid-Infrared Wavelengths Deposited by Pulsed-Dc Sputtering, Thermal and Plasma-Enhanced Atomic layer deposition,” Optical Materials Vol. 143, 114237, 2023.
5. Shkondin, E., T. Repän, O. Takayama and A. V. Lavrinenko, “High aspect ratio titanium nitride trench structures as plasmonic biosensor,” Opt. Mater. Express Vol. 7, No. 11, 4171–4182, 2017.
6. Beliaev, L., O. Takayama, P. N. Melentiev and A. V. Lavrinenko, “Photoluminescence control by hyperbolic metamaterials and metasurfaces: a review,” Opto-Electro. Adv. Vol. 4, No. 8, 210031, 2021.
7. Ishii, S., M Higashino, S Goya, E Shkondin, K Tanaka, T Nagao, O. Takayama and S. Murai, “Extreme thermal anisotropy in high-aspect-ratio titanium nitride nanostructures for efficient photothermal heating,” Nanophotonics Vol. 10, No. 5, 1487–1494 2021.

Embryonic stem cell sensing with terahertz plasmonic exceptional points

Y. Guo[1,2*], L. Y. Hu[1,2], C. Luo[1,3], W. Y. Chang[1,3] and C. Z. Gu[1,2*]

[1] Beijing National Laboratory for Condensed Matter Physics, Institute of Physics, Chinese Academy of Sciences, Beijing, China

[2] School of Physical Sciences, CAS Key Laboratory of Vacuum Physics, University of Chinese Academy of Sciences, Beijing, China

[3] Key Laboratory for Microstructural Material Physics of Hebei Province, School of Science, Yanshan University, Qinhuangdao 066004, China

[*]Corresponding authors: yangguo@iphy.ac.cn, czgu@iphy.ac.cn

Abstract: Singularities of non-Hermitian systems, also known as exceptional points (EPs), have been shown to be highly sensitive to external disturbances[1,2]. By inducing a phase transition of parity-time symmetry, we have theoretically proposed and practically demonstrated a terahertz metasurface capable of supporting a plasmonic EP. This terahertz EP-based metasurface serves as a sensor for detecting residual embryonic stem cells (ESCs) among differentiated cells, offering significant value in medical diagnosis.

Summary

In this study, we introduce a planar microstructure with plasmonic EPs controlled by the breaking of parity-time (PT) symmetry. By utilizing temporal coupled mode theory (TCMT), we analyze two-mode and two-port photonic systems, identify the simple conditions for EP occurrence, and design a planar metasurface that numerically and experimentally supports EP. We successfully demonstrate the ability of a plasmonic EP-based metasurface to detect the concentration of embryonic stem cells (ESCs). Our research presents a straightforward approach to achieve second-order EP in the terahertz spectrum, showcasing that EP-based terahertz biosensors do not demand high-Q resonators, which is advantageous for conventional THz-TDS measurements. Both practical applications and theoretical investigations involving plasmonic EP hold paramount importance.

To elucidate the realization of EPs, we initially examine a dual-port photonic system comprising of a dark mode M_d, a bright mode M_b and their interactions. Assuming M_d and M_b share the same resonant frequency ω_0, with M_b having a decay rate of γ while Md possesses a vanished decay rate, and they are coupled to each other with a coupling strength of κ. By neglecting the non-radiative decay as a reasonable assumption, we describe the dynamics of the resonant modes using TCMT[3]. We discuss three scenarios based on the coupling strength κ, leading to the emergence of an EP, a passive PT-symmetric phase, or a broken PT-symmetric phase. By tuning the coupling strength κ, one can manipulate PT-symmetry to realize a second-order EP. To construct a practical planar metasurface guided by the effective Hamiltonian, we design a structure containing parallel plasmonic antennas along the x-axis and a vertical plasmonic antenna adjacent to them at a distance of g.

To experimentally validation of the EP in our designed structure, we first fabricated the metasurfaces by using regular electron beam lithography (EBL) technique on silicon substrates. The EBL provides enough accuracy to tune the structure dimension to an EP. The sample is composed of a single layer of 150-nm-thick aluminum microstructures with a lattice constant of 110 μm along the x-axis and 70 μm along the y-axis on a 1-mm-thick silicon substrate. Following that, we investigated at the possibility of using our EP-based sensor to detect residual stem cells in differentiated functional cells in vitro. We used neural cells mixed with a portion of ESCs as

analytes; these neural cells were produced from ESCs in vitro at a cell density of 400 cells/mm^2, and the proportion of ESCs was set to 0%, 1%, 10%, 20%, 30%, and 40%.

It is found that the Δω produced by the neuronal cell layer is approximately 0.05 THz, which is less than that produced by the ESCs layer with the same density (Δω~ 0.09), by varying types and quantities of chemicals contained in the cells. This result indicates that our sensor is capable of discriminating between different cell types, and that the Δω produced by mixed cells steadily increases as the number of ESCs increases. In particular, our EP-base terahertz sensor can detect the ESCs with proportion as low as 1%, which can be extremely useful in medical diagnosis. We emphasize that our method for detecting ESCs is label-free, and the detection process as a whole does not induce cell harm. It takes only about half an hour in our THz-TDS to measure terahertz pulses and extract the Δω, which is significantly faster than existing approaches for detecting remaining stem cells. Additionally, because the metasurface is chemically stable, washing with acetone and boiling water can be used to remove cells adhered to the metasurface without affecting the performance of metasurface. The reusability of EP-based biosensors proves that the device has great application potential.

In conclusion, through a combination of TCMT analysis, FDTD simulation, and THz-TDS measurements, we have developed a planar metasurface supporting a plasmonic EP in the terahertz frequency range. Our work demonstrates that the resonant frequency of the terahertz metasurface at the EP is highly sensitive to minute external perturbations, enabling the detection of ESCs at low proportions efficiently. This EP-based biosensor showcases faster detection of stem cells compared to existing methods and exhibits great potential for various applications in the field of terahertz biosensing.

Acknowledgements

This work was supported by the National Natural Science Foundation of China (Grant Nos. 92265110, 62174179, 61888102 and 62204259), the Strategic Priority Research Program of Chinese Academy of Sciences (Grant Nos. XDB33000000 and XDB28000000) and the Key Research Program of Frontier Sciences of CAS (Grant Nos. QYZDJ-SSWSLH042 and XDPB22).

References

1. J. H. Park, A. Ndao, W. Cai, L. Hsu, A. Kodigala, et al. “Symmetry-breaking-induced plasmonic exceptional points and nanoscale sensing,” Nature Physics 16, 462, 2020.
2. J. Wiersig, “Review of exceptional point-based sensors,” Photonics Research **8**, 1457, 2020.
3. F. Alpeggiani, N. Parappurath, E. Verhagen, and L. Kuipers, “Quasinormal-mode expansion of the scattering matrix,” Physical Review X **7**, 021035, 2017.

Exceptional point sensing in planar terahertz metasurface

Bo Wang*, Leyong Hu, and Junjie Li*

Beijing National Laboratory for Condensed Matter Physics,

Institute of Physics, Chinese Academy of Sciences, Beijing 100190, China

*Corresponding authors: wangbo2014@iphy.ac.cn, jjli@iphy.ac.cn

Abstract: We experimentally demonstrate a plasmonic metasurface supporting exceptional points at terahertz frequencies, based on wisely tailored coupling between bright and dark modes. As an application, we use the metasurface EP sensor to trace residual embryonic stem cells in differentiated cells with a detection limit of less than 1%.

Exceptional points (EPs) [1], singularities of non-Hermitian systems, exhibit remarkable sensitivity to small external perturbations and have found applications in biosensors to enhance performance. However, these EPs have typically been realized on large and bulky platforms, such as coupled ring resonators, coupled silicon waveguides, and stacked metamaterials [2]. The advent of metasurfaces, a flat optics infrastructure, offers a revolutionary platform for compact and planarized optical devices. Plasmonic metasurfaces have been extensively utilized for optical biosensing, particularly in the terahertz frequency range. However, the sharp resonances and their shifts are challenging to measure due to the frequency resolution limitations of conventional terahertz time-domain spectrometers (THz-TDS) [3]. To address this issue, leveraging the concept of EPs in combination with terahertz metasurfaces holds promise for enhancing the sensitivity of biosensors.

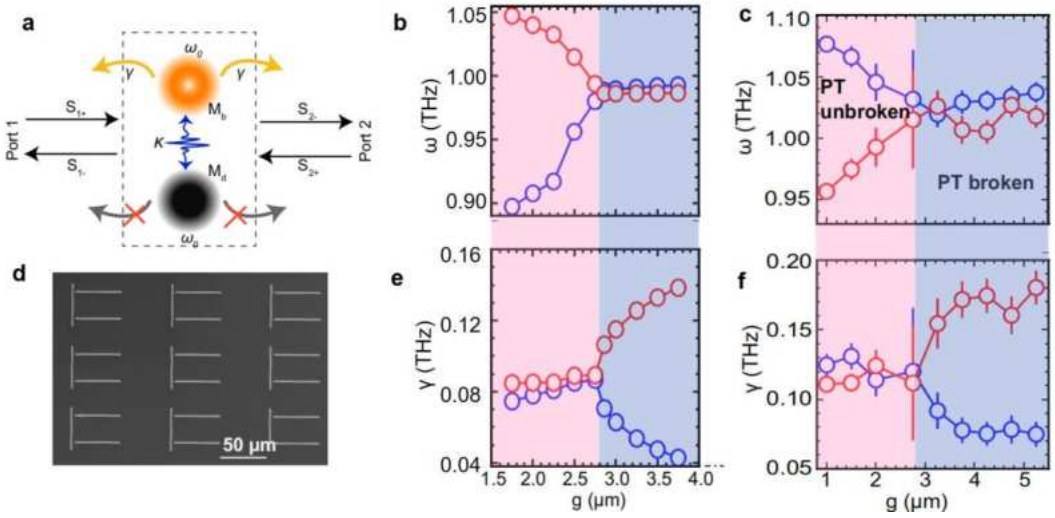


Figure 1: (a) A dual-port system consisting of adark resonant mode and a bright resonant mode. (b,e) Simulted resonant frequencies (b) and damping rates (e) changing with the parameter *g*. (c,f) Measured resonance frequencys (c) and damping rates (f).

Utilizing the temporal-coupled-mode-theory, we conducted an analysis of a two-mode and two-port photonic system illustrated in Figure 1a. Our study led us to propose a single-layered terahertz extraordinary optical transmission (EP) metasurfaces, depicted in Figure 2d. The resonant modes of the metasurfaces designed exhibit a plasmonic EP that is influenced by the breaking of parity-time (PT) symmetry [4]. Simulation results displayed in Figure 1b and 1e reveal the resonant frequencies and damping rates of our structures obtained through full-wave simulations. The EP phenomenon is observed at a specific parameter value of g = 2.75 μm, and these findings were experimentally validated using terahertz time-domain spectroscopy (THz-TDS) measurements, as depicted in Figure 1c and 1f.

Resonant-frequency splitting around the plasmonic EP sensitively characterize tiny external perturbation. We seed neural cells mixed with a portion of embryonic stem cells as analytes on the terahertz-exceptional-point metasurfaces, as shown in Figure 2a. We found that the resonance frequency split is not only sensitive to cell concentration (see Figure 2b) but also to cell proportion when mixed with neural cells (see Figure 2c). our EP-base terahertz sensor can detect the ESCs with proportion as low as 1%, which can be extremely useful in medical diagnosis.

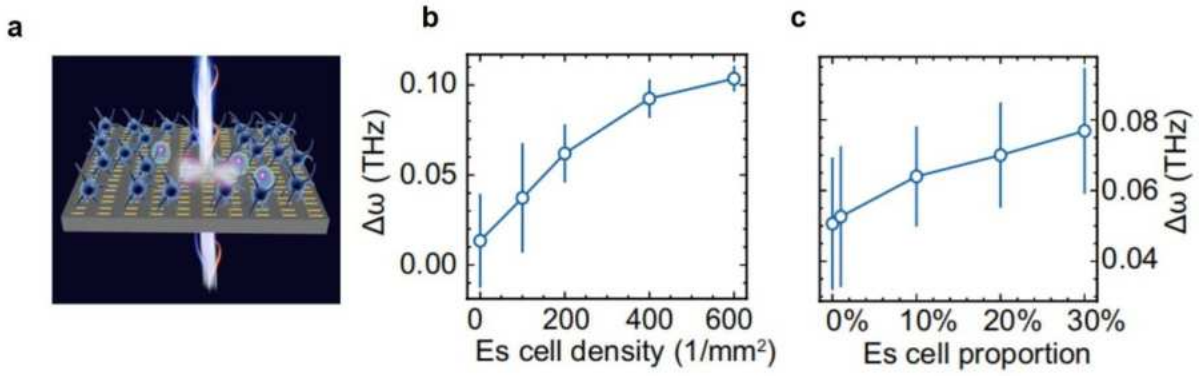


Figure 2: (a) Schematics for sensing ESC trace with the EPMS. (b) Resonant-frequency split induced by ESCs with different concentrations. (c) Resonant-frequency split at different proportions of ESCs.

This work was supported by the National Natural Science Foundation of China (1230446, 12074420 and U21A20140,)

References

1. W. Chen, S¸. Kaya Ozdemir, G. Zhao, J. Wiersig, and L. Yang, “Exceptional points enhance sensing in an optical micro-¨ cavity,” *Nature*, vol. 548, no. 7666, pp. 192–196, 2017.
2. J.-H. Park, A. Ndao, W. Cai, L. Hsu, A. Kodigala, T. Lepetit, Y.-H. Lo, and B. Kante, “Symmetry-breaking-induced´ plasmonic exceptional points and nanoscale sensing,” *Nature Physics*, vol. 16, no. 4, pp. 462–468, 2020.
3. M. Koch, D. M. Mittleman, J. Ornik, and E. Castro-Camus, “Terahertz time-domain spectroscopy,” Nature Reviews Methods Primers, vol. 3, no. 1, p. 48, 2023
4. R. El-Ganainy, K. G. Makris, M. Khajavikhan, Z. H. Musslimani, S. Rotter, and D. N. Christodoulides, “Non-hermitian physics and pt symmetry,” Nature Physics, vol. 14, no. 1, pp. 11–19, 2018

Topologically dark metamaterials for optical biosensing

G. I. Tselikov[1*], G. A. Ermolaev[1], A.V. Arsenin[1], A.V. Kabashin[2] and V. S. Volkov[1]

[1] Emerging Technologies Research Center, XPANCEO, Internet City, Emmay Tower, Dubai 00000, United Arab Emirates
[2] Aix Marseille University, CNRS, UMR 7341 CNRS, LP3, 13288 Marseille Cedex 9, France
[*]corresponding author: celikov@xpanceo.com

Abstract: Our research focuses on utilizing topologically dark metamaterials to achieve exceptionally high spectral and phase sensitivity in detecting biological binding events. The proposed approach can provide a plenty of sensing modalities in wearable electronic devices like multifunctional smart contact lenses. Moreover, it was used to probe two dimensional materials.

The analysis of affinity binding interactions between a target analyte (e.g., antigen, protein, peptide, DNA, RNA segments) from a biological sample solution and its selective receptor (e.g., antibody, protein, peptide, etc.) immobilized on the surface presents one of key tasks in biomedical diagnostics [1]. Traditional label-based biosensing currently used in hospitals and laboratories uses fluorescent or radiolabels to mark analytes and thus reports biomolecular binding, but this approach is inaccurate due to the presence of a reaction that interferes with labeling, expensive in terms of required laboratory facilities, and too time-consuming. An alternative is optical transduction biosensing, which allows the recording of biomolecular interactions by monitoring the optical refractive index (RI) change associated with increasing biolayer thickness, providing immediate report of binding results and obtaining kinetic constants within minutes [2]. The most used transduction biosensing architectures are based on spectral (or angular) interrogation under surface plasmon resonance (SPR) or localized plasmon resonance (LPR) [2]. However, these schemes provide order of magnitude lower limit of detection (LOD) levels compared to label-based sensors. The solution of this problem can be found in utilizing ultrasensitive phase interrogation scheme for studying the reflection of light by properly designed plasmonic structures under the conditions of topological darkness (TD).

Recently the phenomenon of TD was proposed as a possible solution for label-free single-molecule detection [3]. It implies the exact zero linear polarized light reflection from a dedicated optical system and manifest itself as a resonant feature in reflection spectra with a point of zero light intensity. At the same time the phase of light under conditions of TD demonstrates an exact Heaviside π-jump which allows one to use it as a sensing parameter that can radically improve the sensitivity of label-free biosensors. Moreover, thanks to Jordan-Brouwer theorem the TD point is topologically protected, it means that it will be achieved regardless of any imperfection in the fabrication of topologically dark structures [4]. Recently it was demonstrated that the light phase singularities under TD can be provided by a variety of structures including the plasmonic metasurfaces and thin layers of 2D materials on the Fabry-Perot substrates [5]. However, despite the high phase sensitivity of the proposed sensing substrates its spectral sensitivity was lower than one of SPR sensors.

Here we introduce the concept of topologically dark metamaterials that assure extremely high values of both spectral and phase sensitivities due to so-called “scissor effect”. This effect can be realized by the proper design of metamaterials and implies the intersection of zero reflection surface with a spectral curve of optical constants at a small angle. The smaller the angle of incidence the higher the spectral sensitivity of TD structures (the

scissor analogy). As an example, we demonstrate the applicability of this approach for the arrays of gold nanodimers on a glass substrate fabricated by electron-beam lithography (Fig. 1).

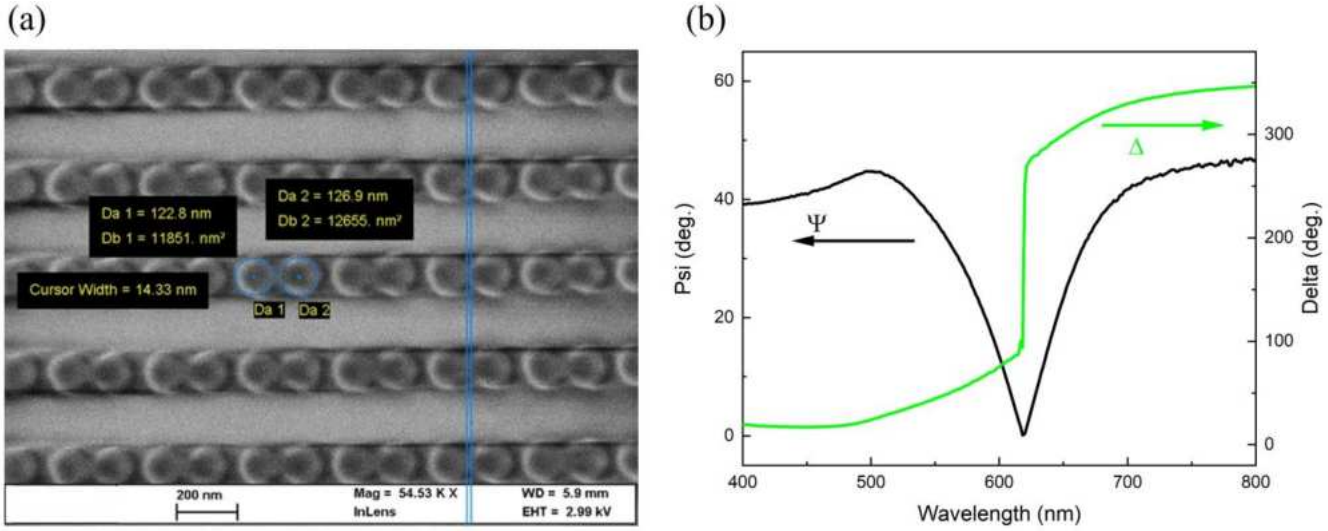


Fig.1 SEM image of topologically dark metamaterial based on 320-nm period arrays of glass-supported Au nanodimers (a) and spectral ellipsometry observation of TD phenomenon (b).

We show that for nanodimer-based TD plasmonic metamaterial the spectral sensitivity of resonances can reach values of 10^4 nm/RIU while phase sensitivity can be as high as 10^5 nm/RIU when the refractive index of local environment is changed for the model system – water-glycerol mixture. Moreover, we performed label-free biosensing tests using protocol for quantitative detection of folic acid. We show that TD metamaterials are capable of monitoring folic acid in a 3-log wide range of concentrations (5−5000 nM), while the observed LOD of 0.22 nM was orders of magnitude better than those of previously used label-free and label-based methods [4].

Finally, we have also demonstrated that high localization and concentration of electromagnetic fields that is achieved at the conditions of TD over the array of plasmonic metamaterials can be used to probe the atomically thin two-dimensional materials like graphene and molybdenum disulfide and to resonantly increase the Raman scattering of light in these layers.

References

1. Banica, F.-G., Chemical Sensors and Biosensors: Fundamentals and Applications; Wiley: 2012.
2. Kravets, V. G., A.V. Kabashin, W.L. Barnes and A.N. Grigorenko, “Plasmonic Surface Lattice Resonances: A Review of Properties and Applications,” Chem. Rev., Vol. 118, No. 12, 5912−5951, 2018.
3. Danilov, A., G. Tselikov, F. Wu, V.G. Kravets, I. Ozerov, F. Bedu, A.N. Grigorenko and A.V. Kabashin, “Ultra-narrow surface lattice resonances in plasmonic metamaterial arrays for biosensing applications,” Biosens. Bioelectron., Vol. 104, 102−112, 2018.
4. Tselikov, G.I., A. Danilov, V.O. Shipunova, S.M. Deyev, A.V. Kabashin and A.N. Grigorenko, “Topological Darkness: How to Design a Metamaterial for Optical Biosensing with Ultrahigh Sensitivity,” ACS Nano., Vol. 17; No. 19, 19338-19348, 2023.
5. Ermolaev, G. A., K.V. Voronin, D. G. Baranov, V. G. Kravets, G. Tselikov, Y. V. Stebunov, D. I. Yakubovsky, S. M. Novikov, A. A. Vyshnevyy, A. B. Mazitov, I. A. Kruglov, S. Zhukov, R. I. Romanov, A. M. Markeev, A. V. Arsenin, K. S. Novoselov, A. N. Grigorenko and V. S. Volkov, “Topological Phase Singularities in Atomically Thin High-Refractive-Index Materials,” Nat. Comm., Vol. 13, 2049, 2022.

Plasmon-enhanced fluorescence immunosensor using polymer-coated silver nanoparticles

Nahoko Okimi[1], Setsuko Yano[2], Yoshie Komatsu[2], Toshifumi Nanjyo[2], Mitsuhiro Uesugi[2], Ryo Kato[1], Takuo Tanaka[1], Fumihisa Kitawaki[2], and Taka-aki Yano[1*]

[1]Institute of Post-LED Photonics, Tokushima University, Japan
[2]PHC Corporation, Japan
[*]corresponding author: yano.takaaki@tokushima-u.ac.jp

Abstract: We developed a one-pot method for synthesizing polymer-coated silver nanoparticles, which are suitable for plasmon-enhanced fluorescence immunosensing. The coating with the polymer layer is sufficiently thin to plasmonically enhance fluorescence, yet thick enough to effectively suppress fluorescence quenching. This enables the highly sensitive detection of blood biomarkers at picomolar(pM) concentrations.

Plasmon-enhanced fluorescence spectroscopy has attracted attention as a highly sensitive biosensing technique because the fluorescence intensity of labeled molecules can be enhanced by the electric field enhancement effect near the metal surface [1]. When fluorescent molecules are in close proximity to a metal surface, the electric field enhancement effect increases, while the quenching effect is dominant due to energy transfer on the metal surface.

In this study, we developed polymer-coated plasmonic nanoparticles by forming a functional polymer film of a few nm on the surface of silver nanoparticles to suppress the quenching effect [2]. The polymer-coated metal nanoparticles were prepared in a one-pot process using a functional polymer (PLL: Poly-L-Lysine) conjugated with disulfide-containing crosslinkers. As shown in Fig. 1(a), the disulfides played a crucial role in covalently bonding PLL polymers to the surface of the Ag nanoparticles. The covalent bond enabled the PLL layer to form a long-term stable coating on the Ag nanoparticles. The shell of the PLL layer was thick enough to effectively suppress the quenching of fluorescence and was also thin enough to efficiently produce plasmonic enhancement of fluorescence, thereby maximizing the net enhancement of fluorescence in the vicinity of the PLL-coated Ag nanoparticles.

Highly sensitive fluorescence detection of CRP (C-reactive protein), an inflammatory marker in blood, was demostrated using the polymer-coated silver nanoparticles. As shown in Figure 2(a), antibody molecules and fluorescent dye (Alexa 594) were chemically modified on the surface of polymer-coated silver nanoparticles, and CRP antigen was added to the particle solution. Figure 2(b) shows the dark-field scattering spectra of silver nanoparticles before and after antigen addition. Before the antigen-antibody reaction, the silver nanoparticles are isolated and dispersed, and have a plasmon resonance wavelength near 440 nm. When the silver nanoparticles are aggregated by the antigen-antibody reaction, a new plasmon resonance mode appears around

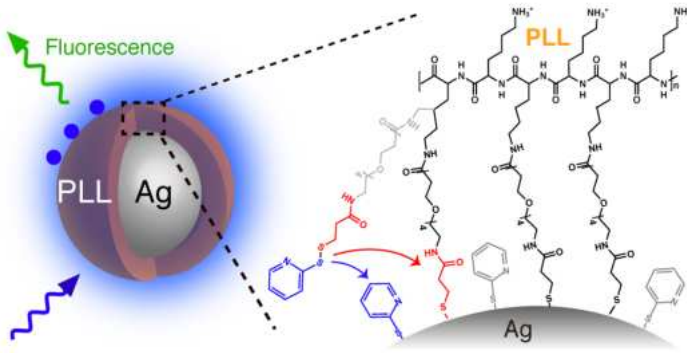


Fig. 1 Schematic of a polymer-coated silver nanoparticle for plasmon-enhanced fluorescence spectroscopy.

590 nm. This mode is derived from the gap-mode plasmon induced between nanoparticles when polymer-coated metal nanoparticles aggregate, and a high fluorescence enhancement effect can be expected between the gaps when this mode is used. Figure 2(c) shows the fluorescence spectrum measured at different concentrations of antigen (CRP). The fluorescence excitation wavelength (594 nm) coincides with the resonance wavelength of gap-mode plasmons between nanoparticles, and the fluorescence is specifically enhanced only during aggregation, resulting in a fluorescence enhancement of about two orders of magnitude. The fluorescence intensity increased in proportion to the antigen concentration, and a detection limit on the order of pM was obtained.

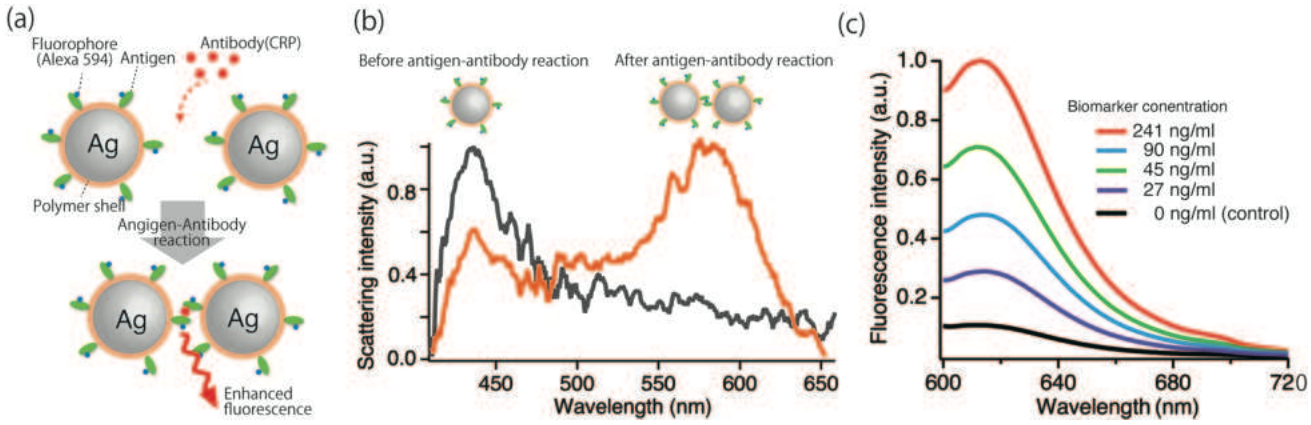


Fig. 2 (a) Principle of antigen detection using polymer-coated silver nanoparticles, (b) dark-field scattering spectra of silver nanoparticles before and after antigen-antibody reaction, (c) antigen concentration dependence of plasmon-enhanced fluorescence spectra.

References

[1] Semeniak, D., et al., "Plasmonic Fluorescence Enhancement in Diagnostics for Clinical Tests at Point-of-Care: A Review of Recent Technologies," Adv. Mater., Vol. 35, 2107986, 2023.

[2] Kato, R., et al., "Highly Stable Polymer Coating on Silver Nanoparticles for Efficient Plasmonic Enhancement of Fluorescence," ACS Omega, Vol. 7, 4286, 2022.

Orthogonal chemical toolbox for antifouling biointerface on gold nanoparticle arrays serving in plasmonic biosensing applications

D. Cattozzo Mor[1], A. B. Plšek[1], V.T. Vu[2], G. Aktug[1], Z. Hubička[1], Chun-Jen Huang[2] and J. Dostalek[1,3*]

[1] FZU-Institute of Physics, Czech Academy of Sciences, Czech Republic
[2] Department of Chemical and Materials Engineering, National Central University, Taiwan
[3] Laboratory for Life Sciences and Technology, Danube Private University, Austria

[*]corresponding author: dostalek@fzu.cz

Abstract: In plasmonic biosensing applications, gold nanostructures are typically attached to oxide surfaces. Here, we present an orthogonal chemical toolbox to promote adhesion of gold to glass and to selectively modify arrays of gold nanoparticles by antifouling and biofunctional moieties, based on a set of dedicated silatrane and thiol molecules bearing carboxy- and sulfo-betaine headgroups.

Surface plasmons are optical resonances originating from collective oscillations of charge density at metal/dielectric interfaces (e.g., thin metallic films or metallic nanostructures on glass substrates). They are associated with increased intensity of tightly confined electromagnetic field and become frequently employed for optical probing of chemical and biological species in numerous bioanalytical methods, including surface plasmon resonance (SPR) biosensors, surface enhanced Raman spectroscopy (SERS) or plasmon-enhanced fluorescence (PEF). The electromagnetic field intensity enhancement and quality factor of plasmonic resonances depend strongly on the employed materials and typically for gold nanostructures attached to glass an intermediate adhesion layer is required. Most commonly, thin chromium or titanium layers are used as adhesion promoting coating [1], which, however, introduce damping to the surface plasmon field. In addition, the surface of plasmonic nanostructures needs to be modified in order to preferably dock the target molecules at the metal surface and not at the oxide substrate, which is not probed by the plasmonically enhanced electromagnetic field.

In our work, we exploited a chemical toolbox containing thiol and silatrane molecules to serve as adhesion-promoting layers, antifouling coatings, and to introduce biofunctional moieties on arrays of gold nanoparticles. Silatranes are tricyclic caged structures that take advantage of silane chemistries and allow for high homogeneity and ordered assembly, to densely coat glass substrates over large surfaces [2]. The toolbox consists of mercatopropyl silatranes (MPS) for gold/glass adhesion promotion, sulfobetaine silatranes (SBSiT) for glass surface antifouling properties, carboxybetaine-thiols (CB-thiols) for functionalization with bio-recognition elements, and Sulfobetaine-thiols (SB-thiols) for antifouling properties of the sensing area. Each component of the toolbox serves a different function, and it is engineered to bind only to a specific material, making the process orthogonal (see Figure 1). Here, we carried out a comprehensive comparison between metallic (chromium) and chemical (MPS) adhesion layers and we present the benefits obtained using chemical layers. In addition, we monitored the influence of antifouling layers in biosensing sensitivity in SPR and PEF – based biosensor applications.

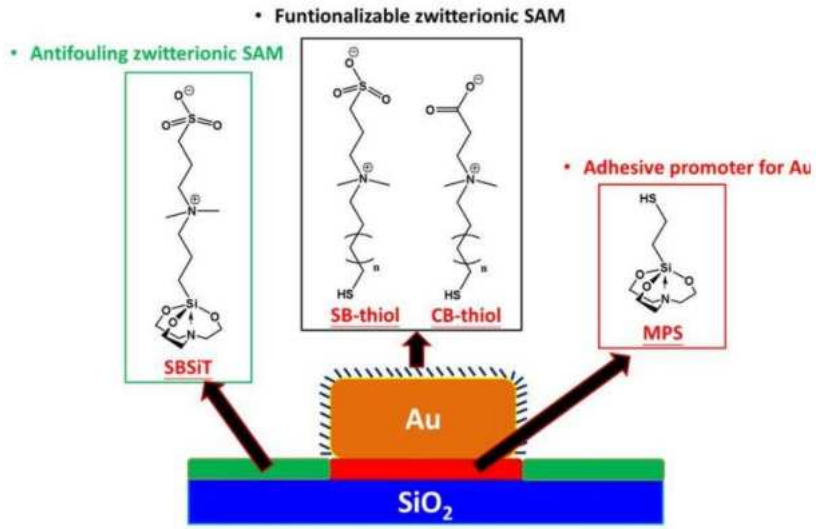


Figure 1 Components of the orthogonal chemical toolbox, in the context of gold nanostructures on a glass substrate.

This work was supported by the Czech Science Fund, project APLOMA (22-30456J) and by the European Union's European Innovation Council (EIC) under Horizon Europe program project VerSiLiB (grant agreement No 101046217), and by the Czech Academy of Sciences Mobility Plus project (JSPS-24-16).

References

1. F. Colas et al., Comparison of adhesion layers of gold on silicate glasses for SERS detection. Journal of Optics 2015, 17, 114010;
2. T.-J. Lee et al., Controlled Silanization: High Molecular Regularity of Functional Thiol Groups on Siloxane Coatings. Langmuir 2020, 36 (21), 5935-5943.

Utilizing Flexible Polymer Linkers in a Continuous Monitoring Plasmonic Biosensor for Detecting Low Molecular Weight Analytes

Aktug G.[1], Asai N.[2], Van-Truc, V.[3], Huang C-J[3], Monteiro da Santa, C. [4], Park, S.[4], Sergelen, K.[4], Dostalek J.[1,2]

[1]FZU-Institute of Physics, Czech Academy of Sciences, Na Slovance 2, Prague, 182 21, Czech Republic

[2]LiST – Laboratory for Life Sciences and Technology, Danube Private University (DPU), Tulln 3430, Austria

[3]Department of Chemical and Materials Engineering, National Central, University, Jhong-Li, Taoyuan 320, Taiwan
[4]BioMed X Institute, Heidelberg 69120, Germany

aktug@fzu.cz

https://www.fzu.cz/en/research/divisions-and-departments/division-4/department-21/laboratory-2107

This research aims to develop a plasmonic sensor capable of continuously monitoring low molecular weight analytes by exploiting reversible interactions with ligands, coupled with a plasmonically enhanced fluorescence (PEF) energy transfer readout[1]. A specific aptamer-based ligand, attached to a metallic sensor surface via a fluorophore-labeled flexible polymeric linker (FPL), regulates the distance between the fluorophore label and the surface through its affinity interaction with the target analyte. The study investigates the use of FPL based on both single-stranded and double-stranded DNA chains to switch between enhancing (>15 nm) and quenching (<10 nm) the fluorescence signal via plasmonic effects. The potential application for continuous monitoring of the antibiotic Vancomycin[2] is investigated, and the conformational changes of FPL are examined using Quartz Crystal Microbalance with Dissipation (QCM-D). Additionally, a novel toolkit for constructing a thin biointerface with antifouling zwitterionic moieties is employed[3]. This comprehensive approach aims to enhance therapeutic drug monitoring in clinical applications.

Acknowledgments

GA and JD are Czech Grant Agency through the project APLOMA (#22-30456J). NA and JD were supported by the Austrian Science Fund (FWF) through the project DIPLAB (I 5119-B).

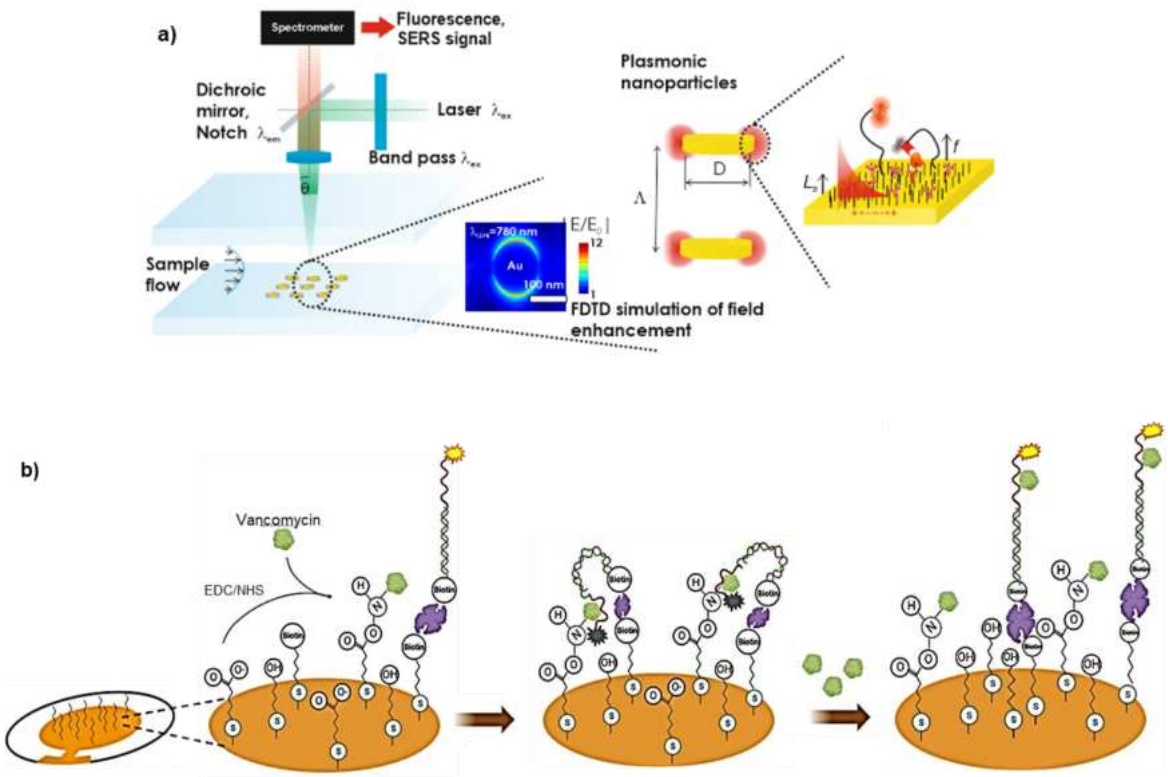


Figure (a) Schematic of the optical readout with plasmon-enhanced fluorescence (PEF) by the use of metallic nanostructures and biointerface with ligands immobilized by flexible polymer linkers and (b) the utilization of double-stranded DNA brush architecture for flexible polymer linker – based reversible assay.

References

1. K. Sergelen et al., *ACS Sens*., 2017, 2, 916-923
2. Shaver et al., *ACS Sens.,* 2022, 7, 3895-3905.
3. Y.S. Wang et al., *Langmuir* 2019, 35, 5, 1652–1661

Understanding on Light-matter Interaction in Chiral Plasmonics

Jeong Hyun Han[1], Ryeong Myeong Kim[1], and Ki Tae Nam[1*]

[1]Department of Materials Science and Engineering, Seoul National University, Seoul 08826, Republic of Korea
[*]corresponding author: nkitae@snu.ac.kr

Abstract: Plasmonic materials enhance chiral sensing in a noninvasive, ultra-sensitive manner. We take note of principles of chiral light-matter interactions in chiral plasmonics driven by optical chirality and chiral perturbation. We demonstrate two strategies based on them: collective resonances in periodic chiral plasmonic nanoparticles and nanostructure optimization via machine learning.

Identifying the molecular chirality is important for many biochemical applications. Plasmonic metamaterials are of particular interest because they can enhance local chiral light-matter interaction in deep-subwavelength scale, significantly improving spectroscopic detection limits using circular dichroism. When discussing chiral molecule detection via plasmonic resonances, the focus often lies on the intensified electromagnetic fields strongly confined by plasmonic materials that enhance the molecule's intrinsic optical excitation rate and corresponding signal amplification. However, a theoretical gap has persisted due to the disparity between the wavelength of molecular electronic absorption, typically in the UV region, and the optical response of plasmonic materials in the visible and near-infrared ranges. Recent noteworthy research shifts attention to interpreting plasmonic sensing based on perturbation theory, considering the backaction of molecular energy absorption from the electromagnetic energy stored in plasmonic structures. In this case, the shift in plasmonic resonance modes can be understood as a collective effect between 1) dielectric perturbation in electric energy capacitively stored in nanostructures caused by the refractive index change and 2) chiral perturbation arising from the effect of near-field optical chirality and media's chirality parameter. Thus, this interpretation enables broad detection capabilities concerning sample type, concentration, and chirality. We introduce the physical significance of this theoretical background and present two innovative enantioselective chiral plasmonic sensing strategies derived from the chiral perturbation theory. Firstly, the fabrication and incorporation of chiral plasmonic nanoparticles into 2D photonic crystals to form spinning dipoles responsive to circularly polarized light, resulting in the strong and uniform optical chirality in three dimensions, showcases extraordinary sensing feasibility in various regimes (transmission, reflection, and sample immobilization methods). Secondly, a machine learning-based simultaneous optimization of dielectric and chiral perturbations efficiently optimizes the effect of medium backaction on electric fields, optical chirality, and spectroscopic responses, achieving tailored sensing.

References

1. Kim, R. M., Han, J. H., ..., Nam, K. T. "Chiral plasmonic sensing: From the perspective of light–matter interaction," The Journal of Chemical Physics, Vol. 160, No. 6, 2024.
2. Kim, R. M., ..., Nam, K. T, "Enantioselective sensing by collective circular dichroism," Nature, Vol. 612, No. 7940, 470-476, 2022.
3. Han, J. H., ..., Nam, K. T, "Neural-Network-Enabled Design of a Chiral Plasmonic Nanodimer for Target-Specific Chirality Sensing," *ACS nano*, Vol. 17, No. 3, 2306-2317, 2023.

Spectrometer-free colorimetric plasmonic biosensor for detection of food allergens

D. Hirabayashi[1], K. Kajikawa[1], and M. Toma[1*]

[1] Tokyo Institute of Technology, Nagatsuta-cho 4259, 226-8503 Yokohama, Japan
[*]corresponding author: toma@ee.e.titech.ac.jp

Abstract: The direct detection of a food allergen, ovomucoid from egg white, is demonstrated by a colorimetric plasmonic biosensor. Plasmonic colors of our metal nanodome arrays allow us to realize biosensing with portable equipment such as smartphones.

The development of portable plasmonic biosensors suitable for on-site detection of biomolecules is one of the important research topics for practical applications. Metal nanostructure arrays working as plasmonic metasurfaces offer a means to engineer key characteristics in plasmonic biosensors. The plasmonic coloration exhibited by metal nanodome arrays illustrated in Figure 1(a) presents an appealing property for biosensor applications. Because their color changes induced by the binding of biomolecules at the sensor surface can be detected by a normal camera including a smartphone [1-2]. This paper introduces a plasmonic biosensor capable of sensitively detecting food allergen, ovomucoid (OVM) from egg white, through the observation of color changes in metal nanodome arrays.

The metal nanodome arrays used as a sensor substrate consist of polystyrene beads (diameter: 250 nm) monolayer covered with a 50 nm-thick Ag layer and a 5 nm-thick Au layer on the top. The surface of the sensor substrate was chemically modified with a polydopamine thin film and blocked with a blocking agent after the immobilization of the anti-OVM antibody. Then, sample solutions spiked with OVM at a concentration of 0.1~3 ug/mL were flowed over the sensor surface for 20 minutes and rinsed. Measurements were made using an optical system capable of measuring reflectance spectra and acquiring reflectance images at the same spot. The color change of the sensor substrate was evaluated as the change in hue angle ΔH by converting RGB values to hue angle H in the HSV color space coordinate.

The sensor surface exhibited bluish-purple when it was in contact with an aqueous solution as shown in Figure 1 (b). When the sample solution containing 1 ug/mL OVM was introduced, the color changed by -0.39 deg in hue angle due to the binding of OVM. These results indicate that the colorimetric plasmonic biosensor can detect concentrations below the 10 ug/mL labeling threshold for food allergens.

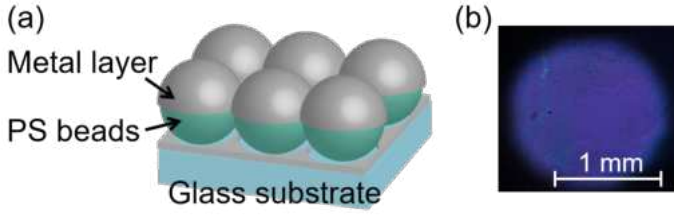


Figure 1 (a) A schematic illustration of metal nanodome arrays used as a sensor substrate. (b) A reflection image of the sensor substrate in contact with a buffer solution.

References

1. Toma, M., Tawa, K., Nanoscale advances 1, 3699-3708 (2019).
2. Toma, M., Itakura, Y., Namihara, S., Kajikawa, K. Advanced Engineering Materials 25, 2200912 (2023).

Acknowledgments: This work was supported by JST A-STEP Grant Number JPMJTM22C7, Japan.

High-speed near-field optical microscopy: super-resolution plasmonic imaging for biological studies

T. Umakoshi[1,2*]

[1]Institute for Advanced Co-Creation Studies, Osaka University, Japan
[2]Department of Applied Physics, Osaka University, Japan
[*]corresponding author: umakoshi@ap.eng.osaka-u.ac.jp

Abstract: We developed high-speed near-field optical microscopy by combining near-field optical microscopy and high-speed atomic force microscopy, holding a great promise for biological studies owing to the real-time label-free imaging capability. In this talk, details of the constructed setup and its applications are discussed.

Near-field optical microscopy has been well recognized as a type of super-resolution optical microscope, which utilizes near-field light localized within a nanometric volume at a plasmonic tip. Super-resolution optical images are obtained by raster-scanning the tip or samples,. Compared to the super-resolution fluorescence microscope, which is another well-known super-resolution microscope, one of its advantages is that it is label-free because near-field optical microscopy achieves super-resolution owing to the physically small near-field light without any fluorescent molecules. Therefore, it can be combined with Raman spectroscopy and infrared absorption spectroscopy, which enables the analysis of the nanoscale label-free nature of biological samples through molecular vibrations or chemical properties. However, the imaging rate is slow because the plasmonic tip needs to be raster-scanned, typically taking several minutes or more to acquire one image. It has been possible to observe fixed samples in air, but observation of living, moving biological samples remains highly challenging. Near-field optical microscopy capable of high-speed imaging would be a powerful tool to visualize natural biological phenomena at the nanoscale in a label-free manner, greatly contributing to life science.

In this study, we developed high-speed near-field optical microscopy with an imaging rate of a few seconds per image [1]. To increase the imaging rate, we employed a high-speed atomic force microscope (HS-AFM) for rapid tip scanning [2,3]. HS-AFM enables high-speed AFM imaging, typically up to 10 frames/s. In addition, in spite of such rapid tip-scanning, it is gentle enough not to disturb biological behavior owing to sophisticated quick feedback and a soft cantilever tip. By combining it with near-field optical microscope setup, we constructed a high-speed near-field optical microscope. We successfully obtained the near-field optical image of a fluorescent polystyrene bead within 3.5 s (Fig. 1(a)). The near-field optical image of DNA was also obtained in 10 s (Fig. 1(b)). Importantly, our technique is highly biocompatible as these were demonstrated in physiological conditions (in buffer solution). We further demonstrated high-speed successive imaging, showing the dynamic behavior of a DNA fraction through frame-by-frame observation (Fig. 1(c)).

In this talk, we will describe the details of the construction of the experimental setup, including tip fabrication. Moreover, further developments recently made in high-speed near-field optical microscopy will be discussed, which further increased the imaging rate up to the sub-second order. In addition to high-speed near-field optical microscopy, we will introduce various developments made in near-field optical microscopy, which would be highly beneficial for biological studies [3].

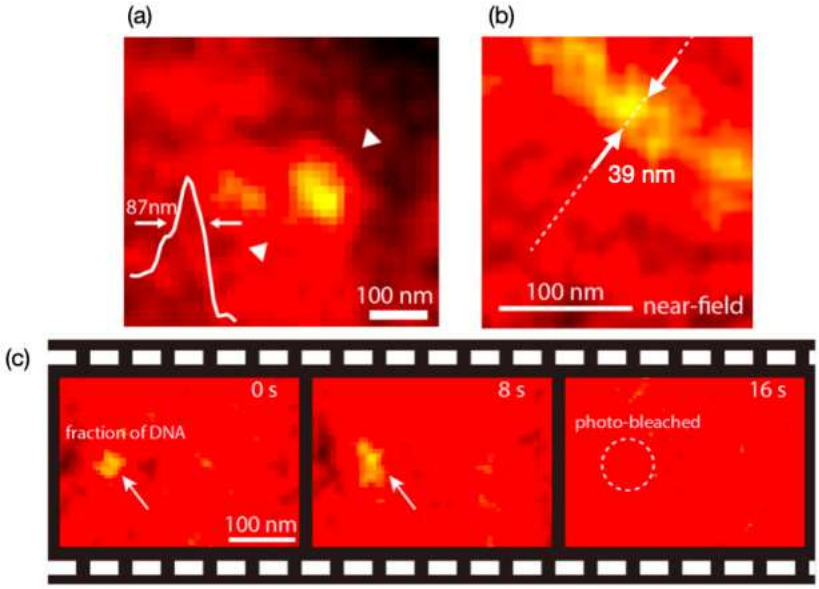


Figure 1. High-speed near-field optical images. (a) Fluorescent polystyrene bead (imaging rate: 3.5 s/frame), (b) DNA (imaging rate: 10 s/frame), (b) Successive images of a DNA fraction (imaging rate: 8 s/frame). [1]

References

1. T. Umakoshi, S. Fukuda, R. Iino, T. Uchihashi, and T. Ando*, "High-speed near-field fluorescence microscopy combined with high-speed atomic force microscopy for biological studies," BBA Gen. Sub., **1864**, 129325, 2020.
2. T. Ando*, N. Kodera, E. Takai, D. Maruyama, K. Saito, and A. Toda, "A high-speed atomic force microscope for studying biological macromolecules", PNAS, **98**, 12468, 2001.
3. T. Umakoshi, H. Udaka, T. Uchihashi, T. Ando, M. Suzuki, and T. Fukuda*, "Quantum-dot antibody conjugation visualized at the single-molecule scale with high-speed atomic force microscopy", Colloids Surf. B, **167**, 267-274, 2018.
4. T. Umakoshi*, M. Tanaka, Y. Saito, and P. Verma*, "White nanolight source for optical nanoimaging", Sci. Adv., **6(23)**, eaba4179, 2020.

Recent advances in metasurface fluorescence biosensors for diverse targets

Masanobu Iwanaga[1*]

[1]Research Center for Electronic and Optical Materials, National Institute for Materials Science (NIMS), Japan
[*]corresponding author: iwanaga.masanobu@nims.go.jp

Abstract: Metasurfaces have been activated as resonant-wavelength shift and fluorescence biosensors. Here, we address recent advances in metasurface fluorescence (FL) biosensors that can detect diverse targets from antigen/antibody to DNA even at one molecule per test. The metasurface FL biosensors have been realized in both all-dielectric and plasmonic types.

Among the numerous metasurface reported so far, a small number of them was found to work as extremely efficient fluorescence (FL)-enhancing platforms, which exhibited more than 1000-fold FL-intensity enhancement compared to flat non-enhancing substrates such as silicon wafers and, simultaneously, high reproducibility of the FL enhancement effect [1–3]. We found two types of the FL-enhancing metasurfaces: plasmo–photonic and all-dielectric. Figure 1A,B illustrates the plasmo–photonic and all-dielectric metasurfaces, respectively. The former comprises complementary stacked structure of Au and periodically perforated Si slab: the latter is a periodic array of Si nanocolumns. Both have the periodicity less than 400 nm and are subwavelength structures for the working wavelengths of 530 nm and longer.

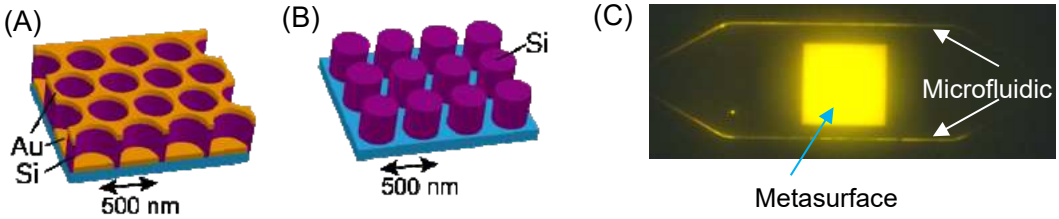


Figure 1. (A) and (B) Illustrations of plasmo–photonic and all-dielectric metasurfaces, respectively. (C) A representative FL image of the metasurface FL biosensor. Metasurface area is the central bright square of 0.72 mm × 0.72 mm, indicated by a light blue arrow. Microfluidic boundary is indicated by white arrows.

Thanks to the significant FL-enhancing ability, FL detections of biomolecules became far more feasible and simpler than before. Metasurface FL biosensors were constructed by combining the FL-enhancing metasurface substrate with a microfluidic chip. Figure 1C shows a typical FL image of captured proteins on the plasmo–photonic metasurface. The secondary FL-labeled antibody emitted the yellow FL. Evidently, the metasurface area indicated by a light blue arrow is far brighter than the area around. Microfluidic boundary is indicated by white arrows. To date, various targets such as immunoglobulin G antibody [4,5], cancer marker proteins (anti-p53 antibody [4,5], carcinoembryonic antigen, CEA [4,6], and prostate specific antigen, PSA [6]), spike proteins of the COVID-19 [7], nucleic acids of the COVID-19 [8,9], and cell-free DNA (cfDNA) [10] were detected in the metasurface FL biosensors very precisely. Especially, we achieved an ultimate limit of detection for the cfDNA to discriminate one cfDNA from zero. We realize the ultimate detection by combining short-cycle polymerase chain reaction (PCR) with the all-dielectric metasurfaces. To the best of our knowledge,

this ultimate detection has not been attained in any other techniques such as a current gold-standard technique of digital PCR.

This study was partially supported by NIMS project “Biomaterials” and a cross-ministerial Strategic Innovation Promotion (SIP) Program, Japan.

References

1. Choi, B., M. Iwanaga, H.T. Miyazaki, Y. Sugimoto, A. Ohtake and K. Sakoda, “Overcoming metal-induced fluorescence quenching on plasmo-photonic metasurfaces coated by a self-assembled monolayer,” Chem. Commun., Vol. 51, No. 57, 11470–11473, 2015.
2. Iwanaga, M., B. Choi, H.T. Miyazaki and Y. Sugimoto, “The artificial control of enhanced optical processes in fluorescent molecules on high-emittance metasurfaces,” Nanoscale, Vol. 8, No. 21, 11099–11107, 2016.
3. Iwanaga, M., “All-Dielectric Metasurfaces with High-Fluorescence-Enhancing Capability,” Appl. Sci., Vol. 8, No. 8, 1328, 2018.
4. Iwanaga, M., “All-Dielectric Metasurface Fluorescence Biosensors for High-Sensitivity Antibody/Antigen Detection,” ACS Nano, Vol. 14, No. 12, 17458–17467, 2020.
5. Iwanaga, M., “Highly sensitive wide-range target fluorescence biosensors of high-emittance metasurfaces,” Biosens. Bioelectron., Vol. 190, No. 1, 113423, 2021.
6. Iwanaga, M., “Robust Detection of Cancer Markers in Human Serums Using All-Dielectric Metasurface Biosensors,” Biosensors, Vol. 13, No. 3, 377, 2023.
7. Iwanaga, M. and W. Tangkawsakul, “Two-Way Detection of COVID-19 Spike Protein and Antibody Using All-Dielectric Metasurface Fluorescence Sensors,” Biosensors, Vol. 12, No. 11, 981, 2022.
8. Iwanaga, M., “High-Sensitivity High-Throughput Detection of Nucleic-Acid Targets on Metasurface Fluorescence Biosensors,” Biosensors, Vol. 11, No. 2, 33, 2021.
9. Iwanaga, M., “Rapid Detection of Attomolar SARS-CoV-2 Nucleic Acids in All-Dielectric Metasurface Biosensors,” Biosensors, Vol. 12, No. 11, 987, 2022.
10. Iwanaga, M., T. Hironaka, N. Ikeda, T. Sugasawa and K. Takekoshi, “Metasurface Biosensors Enabling Single-Molecule Sensing of Cell-Free DNA,” Nano Lett., Vol. 23, No. 12, 5755–5761, 2023.

Polymeric Grating Prism-based Dual-mode Miniature Surface Plasmon Resonance Sensor

A. Baba[1*], W. Jaikeandee[1], C. Lertvachirapaiboon[2], K. Shinbo[1], K. Kato[1] and S. Ekgasit[3]

[1]Graduate School of Science and Technology, Niigata University, Japan
[2]National Nanotechnology Center (NANOTEC), National Science and Technology Development Agency, Thailand
[3]Department of Chemistry, Faculty of Science, Chulalongkorn University, Thailand
[*]corresponding author: ababa@eng.niigata-u.ac.jp

Abstract: In this study, we demonstrate the fabrication of a dual-mode miniature surface plasmon resonance (SPR) sensor using a polymeric grating prism made from a UV-curable adhesive, specifically Norland Optical Adhesive 61 (NOA 61), employing a confined sessile drop technique.

The uniform grating pattern was replicated on a polydimethylsiloxane (PDMS) circular disk with a 6-mm diameter. A hemispherical prism with a grating structure was created by directly dropping liquid NOA 61 onto the grating–PDMS circular disk. The resulting NOA61 polymeric grating prism was obtained after curing under UV irradiation. Subsequently, a 3-nm chromium layer and a 47-nm gold layer were deposited on the grating side of the fabricated prism, followed by the integration of a microfluidic cell, resulting in the complete dual-mode miniature SPR sensor chip. The SPR excitation of the dual-mode SPR sensor chip was observed through wavelength modulation at fix incident angles. As shown in Fig. 1, the results demonstrated SPR reflectivity curves spanning the vis–NIR region. The mode of each SPR reflectivity curve was elucidated by comparing the SPR dip of the experimental results with the calculated surface plasmon (SP) dispersions. Two types of SPR modes were identified: prism-coupling SPR mode (PC-SPR mode, corresponding to $+SP^{0}$ of the gold–NOA 61 interface) and grating-coupling SPR mode (GC-SPR mode, corresponding to $-SP^{+1}$ of the gold–air and gold–NOA 61 interfaces). The dual-mode SPR sensor demonstrated selective sensitivity by incorporating materials onto a gold-coated grating prism that matched the refractive index of the target analyte and exhibited overlapping absorption at the specific SPR excitation wavelength. Its enhanced response and significant wavelength amplification allow accurate performance in selective sensing situations.

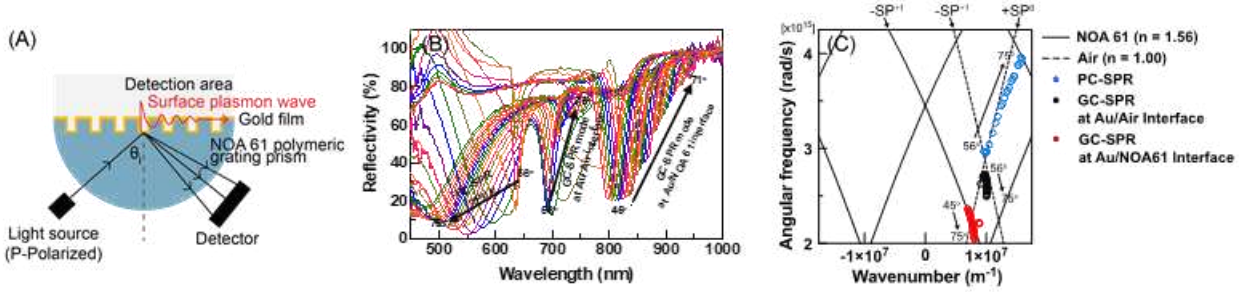


Fig. 1. (A) Schematic drawing of the dual-mode miniature SPR sensor chip. (B) SPR reflectivity curves in the air. (C) Experimental results of dual-mode SPR and calculated results of the dispersion of SPs at the gold-NOA 61 (full lines) and gold-air (dash line) interfaces.

References

1. S. Nootchanat, W. Jaikeandee, P. Yaiwong, C. Lertvachirapaiboon, K. Shinbo, K. Kato, S. Ekgasit, A. Baba, "Fabrication of Miniature Surface Plasmon Resonance Sensor Chips by Using Confined Sessile Drop Technique", ACS Appl. Mater. Interfaces. 11, 11954–11960, 2019.

Plasmonic biosensor platforms for digital single molecule assay readout

K. Schmidt[1], N. Asai[1], G. Aktug[2], D. Cattozzo Mor[2], P. Asokan[2], S. Fossati[2], Y. Morozov[3], A. Weinhaeusel[3], T. Riedel[4], A. de los Santos Pereira[4], and J. Dostalek[1,2*]

[1]Laboratory for Life Sciences and Technology, Danube Private University, Austria
[2]Institute of Physics, Czech Academy of Sciences, Czech Republic
[3]AIT-Austrian Institute of Technology, Austria
[4]Institute of Macromolecular Chemistry, Czech Academy of Sciences, Czech Republic

[*]corresponding author: dostalek@fzu.cz

Abstract: Optical biosensors with digital readout format for ultrasensitive biomarker analysis will be presented. It is based on counting of individual affinity-captured biomolecules by using the combination of optical plasmonic enhancement and enzymatic as well as non-enzymatic amplification without the need of compartmenting the analyzed sample.

In order to reach the ultimate single molecule sensitivity of affinity biosensors, a combination of optical and molecular interaction - based amplification means is pursued. Firstly, tailored metallic nanostructures are employed for the plasmonically-enhanced fluorescence detection that is suitable for readout on sufficiently large sensor surface areas.[1,2] These metallic nanostructures carry biorecognition elements that allow to specifically capture target analyte molecules from the analyzed liquid sample. In order to maximize the optical sensor response associated with probing the captured target analyte by the enhanced electromagnetic field of resonantly excited surface plasmons, approaches for nanoscale control of the attachment to the so called 'plasmonic hotspots' are explored through plasmon-enhanced photochemistry[3]. The response to specific affinity binding events is further enhanced by rolling circle amplification or through enzyme-free catalytic hairpin assembly method in order to associate the individual affinity capture target molecules with bright fluorescence spots.[4] Lastly, the important issue on the mitigation of false positive response events due to the unspecific sorption of bioassay constituents to the surface is addressed by antifouling polymer biointerfaces.[5] The presented methods will be put to context with liquid biopsy – based lung and melanoma cancer diagnostics through ultrasensitive detection of trace amounts of specific biomarkers circulating in blood.

Support from Gesellschaft für Forschungsförderung Niederösterreich m.b.H. project LS20-014 ASPIS, Austrian Science Fund and Czech Science Foundation via the project DIPLAB (I 5119-B and 21-16729K) and Lise Meitner project PLAHOSA (M 2925), European Union's European Innovation Council (EIC) under Horizon Europe program project VerSiLiB (grant agreement No 101046217), Czech Academy of Sciences Mobility Plus project (JSPS-24-16) is acknowledged.

References

1. M. Bauch et al., Surface plasmon-enhanced fluorescence biosensors: a review, Plasmonics, 2014, 9 (4), 781-799.
2. S. Fossati et al., Multi-resonant plasmonic nanostructure for ultrasensitive fluorescence biosensing,

Nanophotonics, 2020, 9, 11, 3673–3685.

3. Yevhenii M. Morozov, Fiona Wiesner (née Diehl), Jonas J. Grün, Matthias Pertiller, Stefan Fossati, Katharina Schmidt, Nestor Gisbert Quilis, Claudia Gusenbauer, Barbara Zbiral, Jose Luis Toca-Herrera, Sven Klees, Clinton Richard Victor Thiagarajan, Ulrich Jonas, Jakub Dostalek, Microstructuring of Thermoresponsive Biofunctional Hydrogels by Multiphoton Photocrosslinking, Advanced Functional. Materials, 2024, 2315578
4. Schmidt et al., Affinity interaction-based manipulation of oligonucleotide chains generated by rolling circle amplification for surface plasmon-enhanced fluorescence, 2022, ACS Applied Materials & Interfaces, 2022, 14, 49, 55017–55027.
5. Hageneder et al., Responsive hydrogel binding matrix for dual signal amplification in fluorescence affinity biosensors and peptide microarrays, ACS Applied Materials & Interfaces, 2021, 13, 27645-27655.

Plasmonic Immunosensor Platform Composed of a Capture Interface Formed by Photochemical Reaction

K. Tawa[1*]

[1]Kwansei Gakuin University, Japan
[*]corresponding author: ktawa@kwansei.ac.jp

Abstract: Plasmonic chips were prepared by coating periodic patterns with metal films. By exposing the surface modified with photoreactive P-*O*-MBA to the light, the intermediate was photochemically reacted with maleimide-labeled molecules on the pattern within the exposure spots. Multi-arrayed spots can induce high-throughput detection with reaction promotion and enhanced fluorescence.

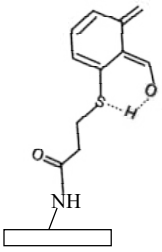


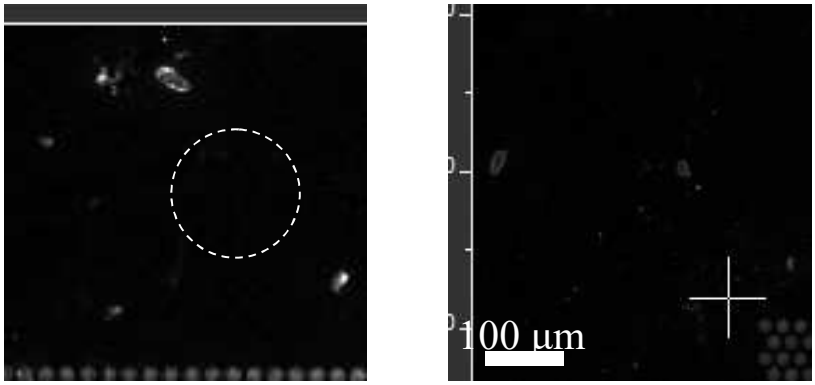
Figure 1. Intermediate of P-O-MBA formed on a plasmonic chip exposed to the light.

Plasmonic sensor platform is available to the photochemical reaction promotion and emission enhancement. Plasmonic chip surface was modified with a photoreactive molecule 3-((2-formyl-3-methylphenyl) thio)propanoic acid (*O*-MBA) (Figure 1) [1] and it has photochemically reacted with Cy5-maleimide (Cy5-M) after exposure to UV light. The plasmonic chip enhancement factor for fluorescence E_p and photochemical reaction promotion rate R_p were evaluated using fluorescence intensities inside the plasmonic pattern and outside. As the result, the mean values of E_p and R_p were 12.8 and more than two, respectively [2]. In this study, to prepare the interface capturing a protein, biotin-maleimide (Biotin-M) was added to the *O*-MBA surface of a plasmonic chip after UV or visible light irradiation. A fluorescence intensity was evaluated for the target concentration of Cy5-Streptavidin (Cy5-SA).

The replica of concentric circle called “Bull’s eye” pattern array was fabricated by UV-nanoimprint method. It was coated with silver and silica layers by rf-sputtering method, in which the silver and silica film thickness was prepared at 50 $\pm$ 5 nm and 20 nm, respectively. The pitch of a periodic structure was 480 nm and 2000 of Bull's-eye patterns with 20 μm in diameter were arrayed. *O*-MBA was modified to the aminated chip. The UV (365nm) or visible (417 nm) light was illuminated from back side of plasmonic chip using 100x objective with the upright-inverted microscope (special made, Olympus). After light exposure, *O*-MBA reacted with Biotin-M. Then, fluorescently labeled protein Cy5-SA solution was injected and fluorescence image was observed with upright-inverted fluorescence microscope under the transmitted-light. In the single plasmonic chip, multi-spots were prepared with UV exposure and Cy5-SA solution was individually injected for each spot. Fluorescence image was taken using Cy5 filter unit and 20x objective for excitation (inverted side) and Cy5 filter unit and 10x objective for emission (upright side).

Figures 2(a) and 2(b) show the fluorescence images of Cy5-SA prepared at 10 nM after the UV light exposure and without exposure, respectively. The broken lines depicted in Figure 2(a) corresponds to the UV exposure spot. The fluorescence intensity was evaluated inside the Bull’s eye patterns within the UV exposure spot and it was plotted against Cy5-SA concentration. The linear relationship was found in the calibration curve and it shows that a highly sensitive detection platform for protein detection was constructed by promoting

photochemical reactions and enhancing fluorescence on the plasmonic chip



(a) (b)

Figure 2. Fluorescence images of Cy5-SA prepared at 10 nM: (a) fluorescence image after exposure to UV light and (b) fluorescence image without exposure to UV light. The broken circle corresponds to UV exposure spot.

Acknowledgements, KT thank Toyo Gosei for providing UV-curable resin.

References

1. Menzel, P. J., B. B. Noble, A.Lauer, L.M. Coot, P. J. Blinco, and C. Barner-Kowollik, "Wavelength dependence of light-induced cycloadditions," J. Am. Chem. Soc. Vol.139, 15812−15820, 2017.
2. Koji M., M. Kanda, H. Sunayama, T, Takeuchi, and K. Tawa, "New plasmonic sensor platform using a spatially controlled photochemical reaction and enhanced fluorescence", J. Photochem. Photobiolo., A, Vol.433, 114177 (2022).

Recent Trends in Metaoptical and Plasmonic Systems

High Diffraction Efficiency Top-hat Beam Shaper Metasurface for Fluorescence Observation

T. Shimatani[1], L. Jie[2], R. Yamada[1], S. Ikezawa[3], and K. Iwami[1*]

[1] Tokyo University of Agriculture and Technology,
[2] R&D Technology Center, Tamron Co., Ltd.,
[3] Waseda University
[*] K. Iwami: k_iwami@cc.tuat.ac.jp

Abstract: We developed a Gaussian-to-top-hat metasurface beam shaper for spherical incident waves. Using dielectric pillar meta-atoms made of a-Si, a uniform intensity distribution of ±9.31%RMS and absolute diffraction efficiency of 72.1% were obtained. Fluorescent imaging was demonstrated using the fabricated metasurface.

1. Introduction

Highly uniform illumination is a crucial requirement for observation in the medical field. For this purpose, top-hat beam shapers based on refractive optical elements (ROE) or diffractive optical elements (DOE) are widely used. However, their bulky size, fabrication difficulty, and deterioration of uniformity due to zero-order light have been problems. In this study, we aim to develop a top-hat beam shaper based on dielectric metasurface for the near-infrared region using waveguide-type meta-atoms. As a result, we realized an ultra-thin optical element that converts the incident-diverging Gaussian beam from an optical fiber into a wide top-hat beam.

2. Methods

From the geometric transformation technique[1], the phase profile of a top-hat beam shaper $\varphi_{\mathrm{gt}}(r)$ is given by:

$$\varphi_{\mathrm{gt}}(r) = \frac{2\pi}{\lambda l}\int_0^r \left[\frac{w_2}{2}\left[\frac{1-\exp(-8\xi^2/w_1^2)}{1-\exp(-2D^2/w_1^2)}\right]^{1/2} - \xi\right] d\xi, \tag{1}$$

where r is the radius from the optical axis, λ is the wavelength, D is the diameter of the beam shaper, w_1 is the waist diameter of the incoming collimated Gaussian beam, w_2 is the diameter of the outgoing top-hat beam, and l is the propagation distance. As equation (1) assumes collimated input, we have to take the phase profile of a spherical lens into account to consider the diverging Gaussian beam:

$$\varphi_{\mathrm{sph}}(r) = -\frac{2\pi}{\lambda}\left(\sqrt{r^2+f^2} - f\right), \tag{2}$$

where f is the focal length. Thus, in this study, the total phase profile of $\varphi(r) = \varphi_{\mathrm{gt}}(r) + \varphi_{\mathrm{sph}}(r)$ is used to design the metasurface beam shaper.

3. Fabrication

The phase profile $\varphi(r)$ designed at the wavelength of 805 nm is expressed as a dielectric metasurface that consists of amorphous silicon (a-Si) pillar waveguide meta-atoms. Pillars are arranged in a square lattice and have square cross-sections with widths w = 110–220 nm. The phase delay and transmittance were obtained by electromagnetic field analysis.

The fabrication procedure of the metasurface is shown in Fig. 2. An a-Si layer is deposited on a 2 cm square glass substrate; a resist pattern was drawn on the substrate using an electron-beam (EB) lithography. Chromium was vacuum-deposited, and the resist was removed by lift-off. Finally, silicon was etched by deep-reactive ion etching (DRIE), and the chromium was removed to complete the process.

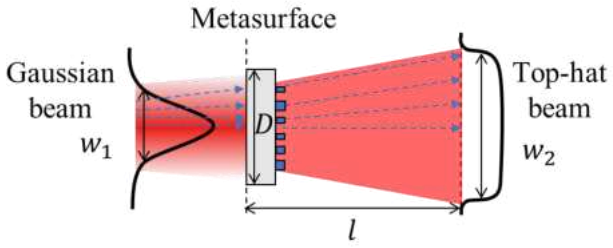


Fig. 1 Schematic of top-hat metasurface

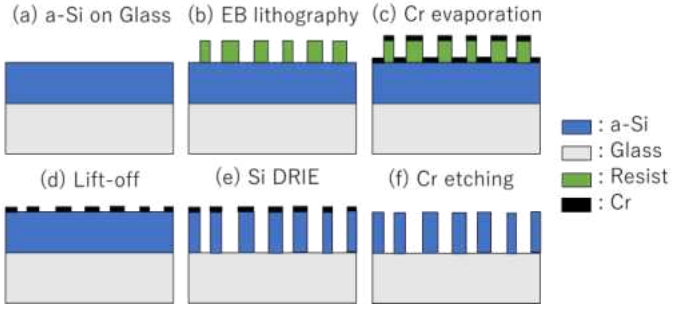


Fig. 2 Schematic diagram of metasurface fabrication procedure.

4. Results

Fig. 3 shows the observed beam intensity profile of the fabricated metasurface at a propagation distance of 100 mm. A fiber-coupled laser source with a wavelength of 808 nm and a numerical aperture of 0.37 was used. As a result, a highly uniform top-hat profile with an intensity variation of ±9.31%RMS and a high diffraction efficiency of 72.1% were obtained. Fluorescence observation was performed using the shaped top-hat beam. Fig. 4 shows the setup of the optical system, and Fig. 5 shows the observed fluorescence image. As a result, we confirmed the fluorescence was stable enough to recognize a letter.

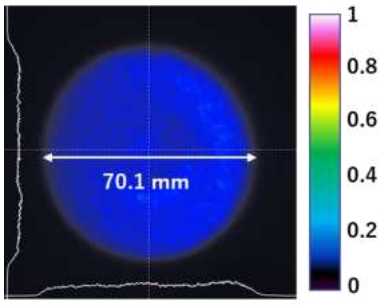


Fig. 3 Observed beam profile.

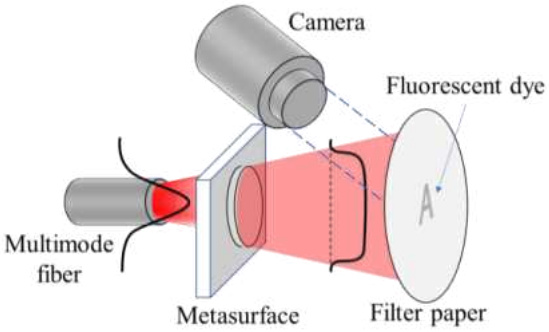


Fig. 4 Schematic image of the optical system of fluorescence observation.

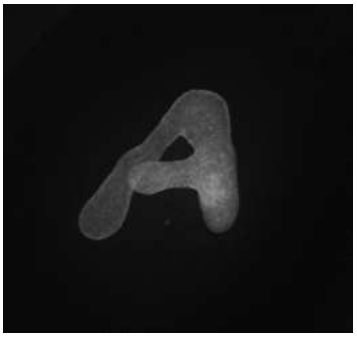


Fig. 5 Fluorescence image.

5. Conclusion

In summary, we developed a Gaussian-to-top-hat metasurface beam shaper for spherical incident waves. As a result, a highly uniform top-hat profile with an intensity variation of ±9.31%RMS and a high diffraction efficiency of 72.1% were obtained. Furthermore, observation using the shaped top-hat beam confirmed that the fluorescence was stable enough to recognize a letter.

Acknowledgements

This work was supported by the "Advanced Research Infrastructure for Materials and Nanotechnology (ARIM)" under Grant No. of JPMXP1223UT1010.

References

1. G. Z. Yang, B. Y. Gu, and B. Z. Dong, ‘‘Theory of the amplitude-phase retrieval in any linear transform system and its applications,’’ Intl. J. Mod. Phys. B 7, 3152–3224, 1993.

High Transmittance 3D Metasurface Holograms Made of SiN for Multicolor Projection with Time-division-multiplexing Method

T. Onozawa[1], J. Beppu[1], M. Yamaguchi[1], and K. Iwami[1*]

[1]Tokyo University of Agriculture and Technology, Japan
[*]corresponding author: k_iwami@cc.tuat.ac.jp

Abstract: We developed large-area 3D metasurface holograms observed with the naked eyes for multicolor projection in the time-division-multiplexing method. Using dielectric SiN pillar meta-atoms, a high transmittance of 81 % was achieved. We also demonstrated an automatic optical system for the multicolor projection.

Holography is a technology that records and reconstructs light waves. Three-dimensional (3D) holography provides natural stereopsis without eye fatigue, and they are expected to be applied to displays, AR/VR devices, and high-security systems. Especially, as metasurface holograms have a wide viewing angle Θ, which is given by $2\arcsin(\lambda/2p)$, due to an array period p of meta-atoms that is smaller than a wavelength λ, it is assumed to be a key technology for these applications. In this context, it is necessary to be reproduced as a multicolor animation with naked eyes observation without using bulky objective lens[1]. In this study, we aim to large-area dielectric 3D metasurface holograms for multicolor projection. As shown in Fig. 1, we made an array of metasurface holograms for the three primary colors respectively, and we projected it by a time-division-multiplexing method.

Metasurface holograms consist of a square lattice of silicon nitride (SiN) meta-atom with a regular octagonal cross section. SiN is chosen due to its high transmittance in the visible light range[2]. We calculated the phase distribution φ of holograms by angular spectrum method. We also overlayed the prism phase given by:

$$\psi = \left(2\pi x/\lambda\right)\sin\theta\,, \tag{1}$$

where λ is the wavelength, x is the position in the direction of each pixel, and θ is the bending angle ($\theta = 20$ deg), on the calculated phase distribution to avoid overlap between the $+1^{st}$ image and the -1^{st} image. Thus, the reproduced the total phase distribution Φ given by:

$$\Phi = \varphi + \psi. \tag{2}$$

To reproduce this phase distribution, we calculated meta-atoms' phase delays and transmittance by the finite element method. They are the height of 1625 nm, and an array period of 404 nm, 340 nm, and 284 nm for λ_1, λ_2, λ_3= 638 nm, 532 nm, and 450 nm. Based on the results, as shown Table 1, we adopted the meta-atoms whose width ranges is 100-280 nm for λ_1, 90-210 nm for λ_2, and 90-180 nm for λ_3 to cover the 2π phase range with an average transmittance over 96 %. By these meta-atoms, the hologram phase distributions were finely discretized in 16384 $\times$ 16384 pixels to realize the large-area metasurface holograms. We adopt the time-division-multiplexing method for multicolor holographic projection. Each hologram is designed to reconstruct each color part of a 3D multicolor model so that they can be seen as overlayed by high-speed frame switching as Fig. 1.

The fabrication procedure of metasurface holograms is shown in Fig. 2. We used a glass substrate on which SiN was sputter-deposited. The substrate was coated with a resist, the pattern was drawn by electron beam lithography, and chromium was deposited by vacuum evaporation. The resist was removed by lift-off, the SiN was

scraped by reactive ion etching (RIE), and finally, the chromium was removed by wet etching to complete the

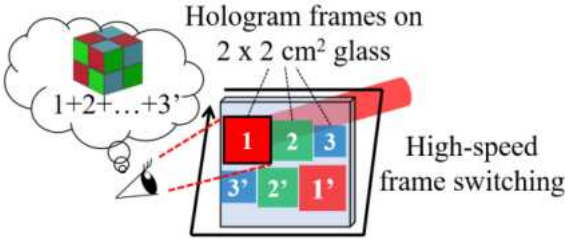


Fig. 1 Schematic of metasurface hologram for multicolor projection hologram. Their structures captured by SEM are shown in Fig. 2.

Table 1 Meta-atoms at each wavelength

Wavelength [nm]	638	532	450
Array period [nm]	404	340	284
Width range [nm]	100-280	90-210	90-180
Ave. transmittance	0.973	0.970	0.962

Fig. 3 shows the reproduced holographic images for each wavelength by the fabricated metasurface holograms. For red and green wavelengths, reconstruction was successful without overlapping with the 0^{th} and -1^{st} images due to the prism phase of 20 deg, as shown in Fig. 3. The blue reconstructed image was blurred because wide meta-atoms were not scraped by RIE in such a narrow array period of 284 nm. Hologram sizes were 6.6 mm, 5.6 nm, and 4.7 nm square for λ_1, λ_2, λ_3, respectively, so that they are large enough to be observed with the naked eyes. Their transmittance was 83 %, 81 %, and 78 % for each wavelength. We demonstrated the time-division-multiplexing method, in which the hologram array is mounted on a biaxial automatic stage and all frames are projected alternately with laser blinking repeatedly. When fast-forwarded in 42 fps (frame per second), images were multiplexed. However, it occurred deviations between each image. Simulating of the correction for them, less than 10 % deviation is required for multiplexing holographic images.

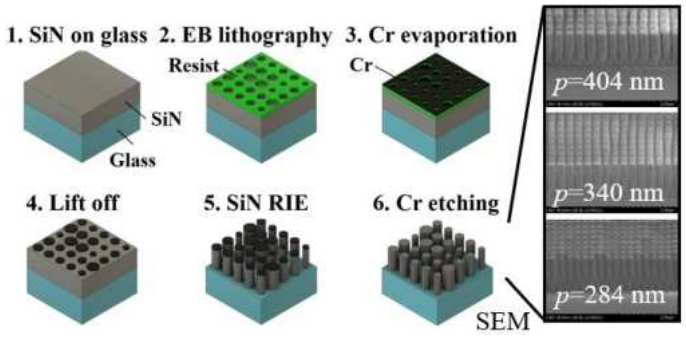


Fig. 2 Fabrication procedure and SEM

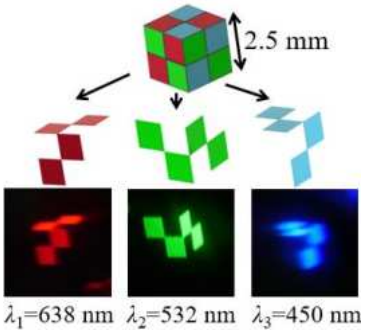


Fig. 3 Reconstructed images

We achieved 3D metasurface hologram for the three primary colors and evaluated 3D holographic multicolor projection by time-division-multiplexing method. The future plans are correction for the deviations between the images and developing holograms of simultaneous multicolor projection.

Acknowledgment

JSPS KAKENHI 22K04894, ARIM grant number JPMXP1223UT1007. We would also like to thank Prof. K. Matsushima, the developer of the "WaveField Library" used to calculate the phase distribution.

References

1. Yamaguchi, M., et al., "Naked-eye Observable Animation with 3D Metasurface Holograms," Metamaterials, 2023., pp. X-442-X-444
2. Yamaguchi, M., et al., "Highly-efficient full color holographic movie based on silicon nitride metasurface," Nanophotonics, *Accepted* 2024.

Hyperspectral Imaging for Flat Optics enabled by Dielectric Metasurfaces

M. Braasch[1,*], **T. Pertsch**[1], **P. Manley**[2], **S. Burger**[2], **B. Wegner**[3], **P. Heimel**[3], and **T. Miteva**[3]

[1]Institute of Applied Physics, Friedrich Schiller University, Jena, Germany
[2]JCMwave GmbH, Berlin, Germany
[3]Stuttgart Laboratory 2, Sony Semiconductor Solutions Europe, Sony Europe BV, Germany Branch, Stuttgart, Germany
[*]corresponding author: marie.braasch@uni.jena.de

Abstract

Optical spectroscopy has become a widely used tool for various areas in science and technology. Most commercial spectrometers are bulky and exploit diffractive optics. Here we present a miniaturized design that can be utilized for hyperspectral imaging. Based on dielectric metasurfaces and Fabry-Perot resonances it facilitates optics which are directly compatible with photodetectors.

Development of Vapor Cells Based on Tri-functional Metasurface for Microfabricated Atomic Clock

R. Ito[1], P. Prutphongs[1], K. Aoki[1], S. Ikezawa[2], M. Hara[3], and K. Iwami[1*]

[1]Tokyo University of Agriculture and Technology, Japan
[2]Waseda University, Japan
[3]National Institute of Information and Communication Technology, Japan
[*]K. Iwami: k_iwami@cc.tuat.ac.jp

Abstract: We report on a microfabricated vapor cell based on tri-functional metasurfaces that combine lens, prism, and quarter-wave plate. The fabricated metasurface showed a high deflection efficiency of 65.4%, a degree of circular polarization (DoCP) of -0.78, and a focal length of 511 μm.

Atomic clocks are the most precise timing device, and the importance of time synchronization in the realization of ultra-high-speed communication between IoT devices and smartphones requires the development of microfabricated atomic clocks that can be installed in these devices. Based on the reflective vapor cells in the previous studies[1,2], this research aims to develop a highly efficient and compact reflective optical cell combining a metasurface and Si cavity with integrated deflection, quarter-wave plate (QWP), and collimating functions.

In this study, we fabricate a tri-functional metasurface consisting of a square lattice of subwavelength pillars made of hydrogenated amorphous silicon (a-Si:H) meta-atoms. The QWP function can be achieved by satisfying equation, and the library was created with meta-atoms that satisfy this equation.

$$\varphi_y(w_x, w_y) = \varphi_x(w_x, w_y) + \frac{\pi}{2}, \tag{1}$$

where φ_x, φ_y are phase delay, and w_x, w_y are pillar widths. Phase profiles φ_{prism} and φ_{lens} for the prism and collimator lens are expressed as follows;

$$\varphi_{\text{prism}} = \frac{2\pi}{\lambda} x \sin\theta, \tag{2}$$

$$\varphi_{\text{coll}} = -\frac{2\pi}{\lambda}\left(\sqrt{x^2 + y^2 + f^2} - f\right), \tag{3}$$

where λ is operating wavelength, and f is the focal length of lens, θ is the beam deflection angle, and (x, y) are the coordinate on the metasurface. The prism and collimator functions can be integrated by superposition of the phase profiles of equations. (2) and (3), and the three functions are integrated by placing meta-atoms from the meta-atom library that satisfy equation. 1.

Electromagnetic field analysis was performed for a-Si:H pillars to determine meta-atom parameters. The shape of the pillar is rectangular. As a result of the analysis, it was decided to use a 750-nm-high column that exhibits high transmittance and a phase delay of 0-2π at 795 nm, the operating wavelength.

The fabrication process of the metasurface is shown in Fig. 2. Initially, resist patterns were drawn by electron beam (EB) lithography on a glass substrate on which a-Si:H layers were deposited. Next, chromium was vacuum deposited and the resist was removed by lift-off. Finally, the process was completed by etching the silicon by deep reactive ion etching (DRIE) to remove the chromium.

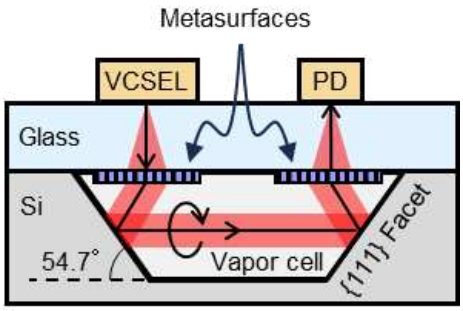


Fig. 1 Schematic of vapor cell

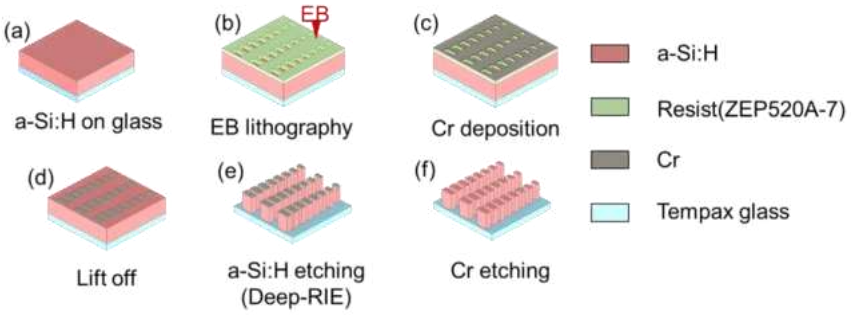


Fig. 2 Fabrication process

First, as a prototype, we fabricated metasurface with only two functions, deflection and QWP functions. The metasurface showed a high deflection efficiency of 84.1% and a DoCP of -0.90. Subsequent, the prototype metasurfaces and Si cavity were combined to simulate a vapor cell as shown in Fig. 3. The optical system shown in Figure 4 was used to measure the light yield of the vapor cell. The measurement showed a light yield of 2.2%. While there is room for improvement in light yield, as the theoretical value is 7.05%, we confirmed that the vapor cell function. Moreover, a 56.8% of light yield can be expected by depositing HR coating on the cavity surface.

Next, we fabricated tri-functional metasurface with deflection, QWP and collimating functions. The fabricated metasurface showed a high deflection efficiency of 65.4%, a DoCP of -0.78, and a focal length of 511 μm. From the above, it was confirmed that the three functions are performed simultaneously.

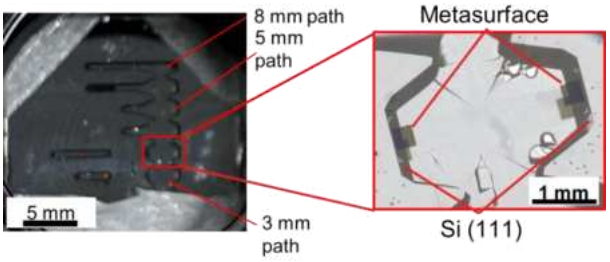


Fig. 3 Fabricated vapor cell

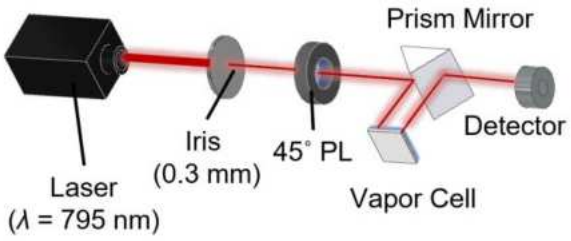


Fig. 4 Optical system used for light yield measurement

The objective of this study was to develop a reflective vapor cell with metasurfaces that integrate three functions. The two-function metasurfaces successfully measure light yield when combined with Si cavity. On the other hand, there is room for efficiency improvement in the tri-functional metasurface, so the light yield has not yet been measured. In the future, we would like to improve the efficiency of tri-functional metasurface and combine them with HR coated Si cavities for evaluation.

Acknowledgements, this work was supported by JSPS Grant-in-Aid for Challenging Research Exploratory 23K17858, “Advanced Research Infrastructure for Materials and Nanotechnology(ARIM)” JPMXP1223UT1006 .

References

1. R. Chutani, *et al*., “Laser light routing in an elongated micromachined vapor cell with diffraction gratings for atomic clock applications,” *Sci. Rep*, Vol.5, No. 14001, 1-12, 2015
2. H. Nishino, *et al*., “Reflection-type vapor cell for micro atomic clocks using local anodic bonding of 45◦ mirrors,” *Opt. Lett*, Vol. 46, No. 10, 2272-2275, 2021

All-optical spectral control by perfect absorber based on quadrupole resonance and photothermal effect

Seiya Shinkai[1], **and Junichi Takahara**[1*,2]

[1]Graduation School of Engineering, Osaka University, Japan
[2]Photonics Center, Osaka University, Japan
[*]corresponding author: takahara@ap.eng.osaka-u.ac.jp

Abstract: We study all-optical spectral control of silicon metasurface by photothermal effect. We fabricated a perfect absorber based on metasurface which supports two degenerated quadrupole modes. In this study, we demonstrate 8nm red-shift and the modulation of transmission spectra induced 3% increase by 90K temperature rise.

1. Introduction and purpose

The importance of all-dielectric metasurfaces made of high refractive index materials for nanophotonics have been increasing year and year because of the development of large scale optical integrated circuit. The metasurfaces can support some kinds of Mie-resonances, such as dipole and quadrupole modes. It's known that they can achieve perfect absorption (PA) based on degenerate critical coupling (DCC) theory. The absorption equation is as follows,

$$A(\omega) = \frac{2\gamma_1\delta_1}{(\omega-\omega_1)^2+(\gamma_1+\delta_1)^2} + \frac{2\gamma_2\delta_2}{(\omega-\omega_2)^2+(\gamma_2+\delta_2)^2}, \quad (1)$$

where ω, ω_1 and ω_2 are the resonance frequencies of the incoming wave, one resonance mode, and the other mode, respectively, and γ_1, δ_1, γ_2, and δ_2 are the radiative and intrinsic losses of each mode, respectively [1]. According to Eq. (1), the absorption becomes unity at the resonance ($\omega = \omega_1 = \omega_2$) when the radiative and intrinsic losses for two modes ($\gamma_1 = \delta_1$, $\gamma_2 = \delta_2$) are matched. Hence, we can achieve PA of the dipole as well as quadrupole modes. The advantage of PA based on quadrupole modes is that they show strong confinement inside the Mie-resonator, hence the dependence on period is small.

Photothermal effect, which changes refractive index of materials, is studied as one of the methods of controlling optical properties [2]. The superior of thermal tuning is that it can realize active control without adding another structure and refractive index changes continuously. The merit keeps metasurface flat and leads to realize various modulations. Recent studies combinate nanostructure and thermo-optical (TO) effect and realized the high modulation of near-field optical properties from Mie-scattering in nanoseconds scale [3]. In this study, we design the metasurface to control transmission of signal light by controlled light, which induces TO effect at the far-field. We experimentally demonstrated the spectral shift of transmission by TO effect.

2. Result and discussion

Figure 1(a) shows the all-optical switching of periodic crystalline-silicon (c-Si) nanostructure on quartz is shown in Fig. 1(a). The mechanism is such temperature rising by photothermal effect due to absorption of light energy excites TO effect and modulates the optical responses of c-Si. We design the metasurface such that PA is achieved at light wavelength $\lambda = 450$nm by DCC of electric quadrupole (EQ) and magnetic quadrupole (MQ) and 0% transmission at $\lambda = 543$nm caused by electric dipole (ED) at the condition of radius r =89nm, height h = 100nm and period P = 265nm (see Fig. 1(b)). Since ED mode is sensitive to temperature, it is suitable to control the transmission of light. The transmission increases ~30% at maximum. The excitation intensity is only $1.1\text{mW}/\mu m^2$.

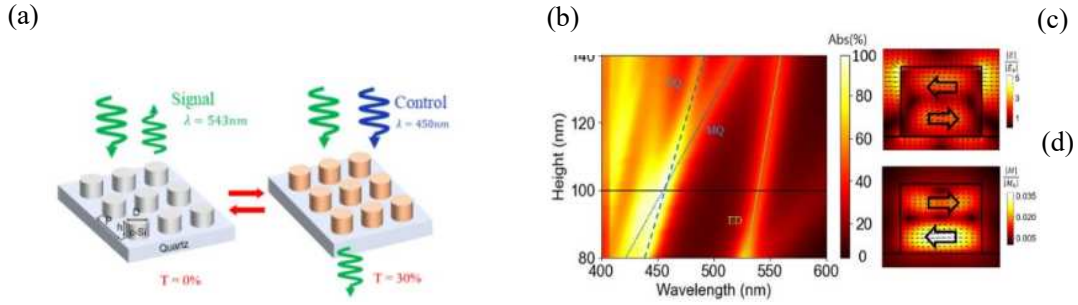


Fig. 1 (a) Concept of all-optical control based on Si metasurface, (b) absoption spectral map for different heights and the spatial distributions of (c) EQ and (d) MQ modes, which are normalized to the amplitude of the incident E_0 and M_0, respectively.

We fabricated the sample by using a silicon-on-quartz substrate (SOQ). Figure 2(a) shows the image of the sample taken by the focused ion beam (FIB) system. It is observed that the top shape of Mie resonator is not circle perfectly but ellipsoidal. Figure 2(b) shows the experiment results of transmission and absorption spectra. Regarding to the measurement, we heated the sample placed on a ceramic heater and measured temperature dependence of transmission. The result is shown in Fig. 2(c), where the red-shift of transmission spectra by TO effect is observed. Due to temperature rise, both of real and imaginary parts of refractive index increase, which leads spectral red-shift and the decrease of Transmission. We observed that higher Transmission at 300K becomes lower one at 393K. In the future, we will use CW laser to heat up samples and expand spectral range from visible to telecommunication wavelength. Our research suggests that the proposed structure can be applied for photodetectors, wave front control and all-optical switches.

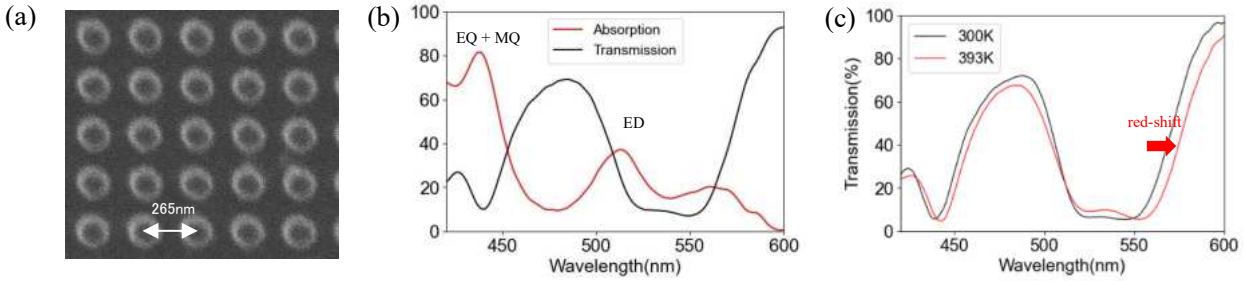


Fig. 2 (a) FIB image of the fabricated sample, (b) measured results transmission (black line) and absorption (red line) spectra and (c) transmission spectra measured at 300K (black line) and 393K (red line).

References

1. X, Ming *et al.*, “Degenerate critical coupling in all-dielectric metasurface absorbers”, Opt. Express, 25, 20, 24658-24669, 2017.
2. K, Nishida *et al.*, “All-optical scattering control in an all-dielectric quasi-perfect absorbing Huygens’ metasurface”, Nanophotonics, 12, 1, 139-146, 2023.
3. YS, Duh *et al.*, “Giant photothermal nonlinearity in a single silicon nanostructure”, Nature. Commun, 11, 4101, 2020.

Development of wide-angle metalenses capable of simultaneously capturing near and far-view images

A. Hasegawa[1], R. Yamada[1], K. Ozawa[2], Y. Abe[2], M. Taoka[2], T Yamagishi[2], and K. Iwami[1*]

[1]Tokyo University of Agriculture and Technology, Japan
[2]Samsung R&D Institute Japan, Japan
[*]K. Iwami: k_iwami@cc.tuat.ac.jp

Abstract: We developed wide-angle metalenses capable of simultaneously capturing near and far view images. From the imaging evaluation at object distances of 5.3 mm and 15.7 mm, near and far view metalenses had angular field of views of 86.7° and 103.7°, respectively. We successfully captured simultaneous images using the fabricated metasurface.

Miniaturization of imaging lenses is strongly demanded from the viewpoint of applications in the automotive and medical industries. However, this is difficult to achieve with conventional lenses. In this study, our objective is to develop wide-angle metalenses that can simultaneously capture objects at the near and far regions with a single image sensor, as shown in Fig. 1. Our metalenses are to operate in visible light while utilizing the principle of an aperture integrated ultra-wide-angle metalens proposed in a previous study[1].

In this study, we fabricate a metalens consisting of a square lattice of tiny SiN pillars (meta-atoms). The phase distribution of the metalens fabricated in this research follows the following equation;

$$\varphi(r) = \sum_{j=1}^{9} C_j \cdot r^{2j}, \tag{1}$$

where r is the radial coordinate of the lens, C_j are coefficients to optimize the phase distribution so that the metalens has a wide field of view and high resolution. C_j for far and near metalenses are optimized using commercial ray optics software.

Electromagnetic field analysis was performed to determine the relationship between the width of the SiN pillars and the transmittance and phase delay of the transmitted light. The pillars are arranged in a square lattice and have a regular octagonal cross section. The design wavelength is 633 nm, the pillar height is 1625 nm, and the meta-atom pitch is 404 nm. Based on the analysis results, a design value of 114 nm to 312 nm was determined for the design width, which satisfies high transmittance and a phase delay of 0–2π.

The fabrication process of the metalens is shown in Fig. 2. First, (a) resist is coated glass substrate on SiN, and the structure is transferred using an electron beam lithography system. (b) Next, Cr is deposited, and (c) the resist is removed by lift off. (d) The substrate is then inverted, resist is applied, and the structural pattern on the aperture surface is exposed using a photolithography system. (e) After depositing Al, (f) the resist is removed by lift off to complete the aperture surface. (g) After the aperture surface is completed, the substrate is reversed and SiN is removed by reactive ion etching, and (h) unnecessary Cr is removed by Cr etching to complete the metalens.

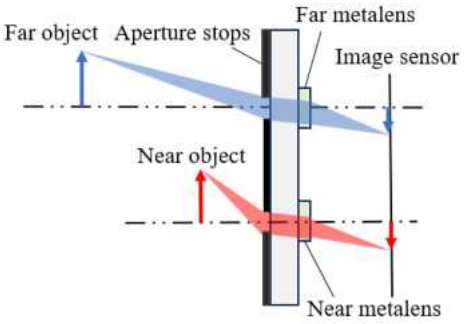


Fig. 1 Schematic of simultaneous capturing metalenses

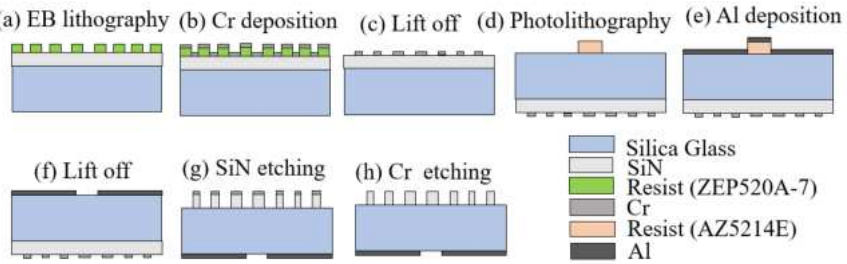


Fig. 2 Fabrication process

Fig. 3 shows photographs of a plastic ruler taken under ring illumination at a wavelength of 633 nm with (a) near and (b) far metalenses at object distances of (a) 5.3 mm and (b) 15.7 mm, respectively. A transparent plate was inserted between the object and the lens. The angular fields of view of the near and far-view metalenses read from the captured images were 86.7° and 103.7°, respectively, which decreased compared to the designed values. The reasons for the decrease in the angular field of views are the meta-atom design that limits the maximum oblique incident angle and the meta-atom fabrication error. Fig. 4 shows a photograph that consists of near and far-views captured simultaneously by a single image sensor. Two objects of a barcode placed at 16 mm and the logo mark of the Tokyo University of Agriculture and Technology at 5.3 mm are used, and the right and left halves of Fig. 4 show the near and far-views, respectively. The barcode and the logo mark were clearly imaged in the far and near view images, respectively, and simultaneous imaging was achieved.

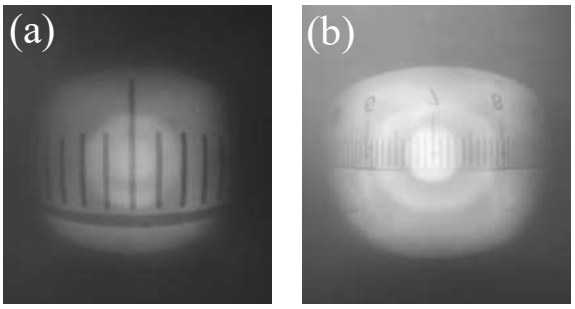


Fig. 3 Images of a plastic ruler taken with fabricated metalenses for (a) near, and (b) far views

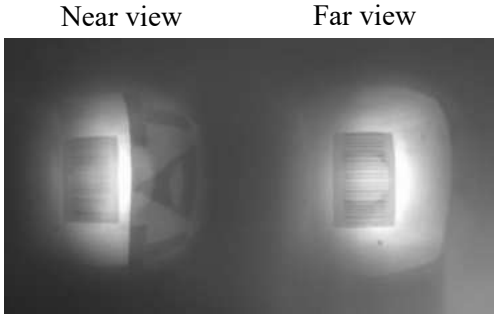


Fig. 4 Simultaneously captured near and far views

The purpose of this study was to design, develop, and demonstrate wide-angle metalenses capable of simultaneously capturing near and far views. From the imaging evaluation, near and far view metalenses had angular field of views of view of 86.7° and 103.7°. And the near and far view images were clearly formed together. In the future, we aim to bring the angles of view of metalenses closer to the designed value.

Acknowledgements, this research was supported by the “Advanced Research Infrastructure for Materials and Nanotechnology(ARIM)”

References

1. Shalaginov, M. Y., et al., “Single-Element Diffraction-Limited Fisheye Metalens” *Nano Letters*, Vol. 20, No. 10, 7429–7437, 2020.

Enhancing the photo sensitivity of photo detector using nanophotonics approach

Soh Uenoyama[1*]

[1]Central Research Laboratory, Hamamatsu Photonics K.K.,

5000, Hirakuchi, Hamana-ku, Hamamatsu City, 434-8601, Japan
[*]Corresponding author: so.uenoyama@crl.hpk.co.jp

Abstract: Silicon photomultiplier has been used in various applications due to its excellent photon counting ability. We demonstrated the enhancement of the sensitivity by focusing incident photon on the photo-sensitive area of pixel using metalens array. Additionally, we report on various nanophotonic approaches for enhancing the performance of the photodetector.

Silicon photomultiplier (SiPM) has been applied in many kinds of applications such as flow-cytometry, light detection and ranging (LiDAR) due to its excellent photon counting ability. SiPM contains many single avalanche photo diode (SPAD), which operates at a Geiger mode. SPADs usually have a trench area at the boarder of each SPAD. However, it not only enables to shield crosstalk but also has known to be low-photo sensitive area. Thus, improve the performance of SiPM, such as photon detection efficiency (PDE) and timing performance requires the focusing incident photon on the photo sensitive area of SPAD while avoiding illumination to the trench areas. Our previous work demonstrated the improvement of the performance of SiPM for focusing incident photon on the photosensitive area of each SPAD using metalens array [1]. However, separated configuration between metalens and SiPM can cause the miss alignment even at a small vibration.

We thus monolithically integrated metalens with SPAD using whole CMOS process at a chip-scale for providing stable enhancement of using metalens [2]. As a result, we experimentally demonstrated the improvement of PDE >70% at a wavelength of 404 nm. Additionally, we investigated wavelength-dependent and incident angle dependent characterization for considering scintillation applications. For angle-dependent characterization, the metalens-integrated SiPM exhibits the robust performance toward the oblique incidence even at 45 degrees. In addition, for wavelength-dependent characterization, it exhibits the robust performance toward the broad wavelengths >50%, in the wavelength of 375- 450 nm. Furthermore, we are going to introduce the nanophotonis approach which effectively affects the improvement of photo sensitivity at a near infrared wavelength band.

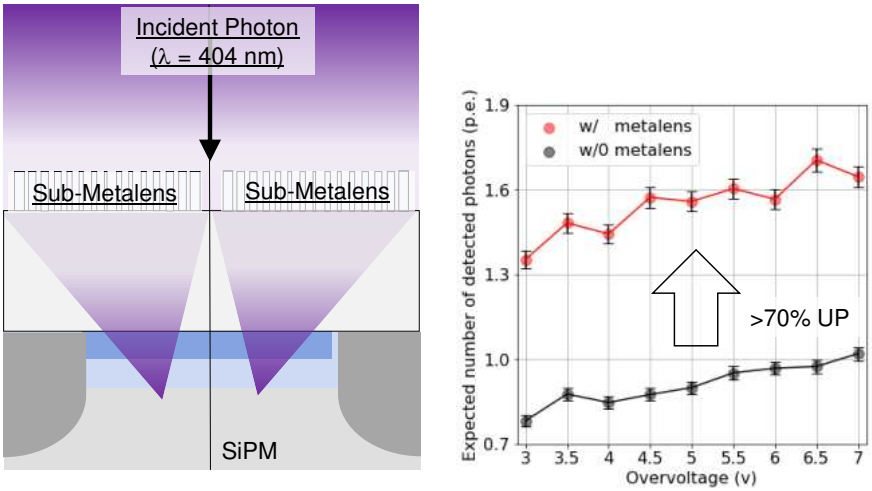


Figure.1. Schematic illustration of the metalens integrated Silicon photomultipliers and photo detection efficiency plot as a function of applied overvoltage.

References

1. Uenoyama, S. and R. Ota, "40 × 40 Metalens Array for Improved Silicon Photomultiplier Performance" ACS Photonics, Vol. 8, No. 6, 1548–1555, 2021.
2. Uenoyama, S. and R. Ota, "Monolithic integration of Metalens in Silicon Photomultiplier for Improved Photodetection efficiency" Advanced Optical Materials, Vol. 10, No. 9, 202102707, 2022.

Enhancement of photothermal nonlinear scattering from Mie-resonant silicon nanostructures

K. Nishida[1] and S.-W. Chu[1,2,3*]

[1]Department of Physics, National Taiwan University, No. 1, Sec. 4, Roosevelt Rd., Taipei 10617, Taiwan
[2]Molecular Imaging Center, National Taiwan University, No. 1, Sec 4, Roosevelt Rd., Taipei 10617, Taiwan
[3]Brain Research Center, National Tsing Hua University, 101, Sec 2, Guangfu Road, Hsinchu 30013, Taiwan
[*]corresponding author: swchu@phys.ntu.edu.tw

Abstract:
Signal nonlinearity is an essential factor in all-optical switching and super-resolution imaging applications. In our research, we demonstrated strong photothermal nonlinear scattering from silicon Mie nanoresonator via utilizing several different approaches: quasi-perfect absorbing metasurface, displacement excitation by focused laser beam and optical bistability.

Silicon nanostructures efficiently support multiple modes of Mie resonances in visible wavelength region due to silicon's high refractive index and low loss optical properties, forming an important basis of the future Mie-tronics devices including optical nanoantenna, structural color pixels and metasurface[1]. While these linear scatterings in the silicon Mie resonators are widely utilized, the nonlinear property of scattering intensity is critical to extending the applications of Mie-tronics toward all-optical switching and super-resolution imaging[2,3]. In particular, our group previously discovered that the iterative photothermal and thermo-optic effect in Mie-resonant silicon nanostructure triggers the giant nonlinear relationship between scattering and excitation intensities, which is a few orders larger than that induced by Kerr nonlinearity[4], leading to significantly improved modulation depth in all-optical switching and spatial resolution in optical imaging.

In this talk, we would like to present our recent studies to further enhance the photothermal nonlinear scattering from Mie resonant silicon nanostructures. The first approach is based on critical coupling in silicon metasurface to enhance optical absorption as well as photothermal effect[5]. We designed a silicon Huygens' metasurface that exhibits quasi-perfect absorption and unidirectionality of scattering signal through matching the material loss with its radiative loss, i.e. critical coupling. By illuminating the metasurface with the single wavelength laser light at the resonance, the forward scattering signal shows sub-linear increases versus excitation intensity, while the backward scattering signal presents a super-linear trend, featuring all-optical dynamic scattering controls. Due to the high absorption of the metasurface, the required excitation intensity to induce nonlinear scattering is one-order reduced compared with that of the single silicon nanoparticle, representing low-energy consumption switching.

Another approach is the introduction of "displacement resonance", which we discovered by applying confocal laser scanning microscopy to observe silicon nanostructures[6]. The surprising finding is that when a focused light spot diameter and a silicon nanostructure are of similar sizes, not much smaller nor much larger, changing their relative positions triggers new high-order resonances that are not allowed with conventional paraxial excitation. The displacement resonance leads to a counterintuitive situation that the light-matter interactions, including scattering and absorption-induced nonlinear optical effects, are not maximal when laser focus is aligned with the particle, but become maximized when the focus spot is about 100 nanometers off-center. Combining displacement

resonance with photothermal nonlinearity, we are going to show application examples including reduction of nonlinearity threshold, sign flip of all-optical switching, and resolution enhancement, etc.

Furthermore, we recently proposed to use optical bistability to generate a steep super-linear scattering response in silicon Mie resonator[7]. It is well known that optical bistability requires the combination of nonlinear refractive index and a resonant cavity. Conventionally, because of the small nonlinear refractive index of silicon, the optical bistability of silicon optical devices was mainly limited to high-Q microcavities, for example, ring resonators or photonics crystal, whose footprints are in the order of 1-10 micrometers. As mentioned earlier, we efficiently utilized the photothermal and thermo-optic effects responses to enhance the nonlinear refractive index magnitude in nano-silicon, thus relaxing the requirement of the high-Q cavity. We experimentally and theoretically discovered optical bistable states in a single silicon nanoparticle with a Q-factor < 10 and cavity volume size of 10^{-3} μm^3, both are record low. The bistability leads to an abrupt super-linear jump of scattering intensity, reaching over ~100th order of excitation intensity. We expect it would dynamically improve both performances of all-optical switching and super-resolution microscopy.

References

1. Kivshar, Y. The rise of Mie-tronics. *Nano Lett.,* Vol. 22, No. 9, 3513–3515, 2022.
2. Tang, Y.-L. *et al.* Mie-enhanced photothermal/thermo-optical nonlinearity and applications on all-optical switch and super-resolution imaging [Invited]. *Opt. Mater. Express,* Vol. 11, No.11, 3608-3626, 2021.
3. Astratov, V. N. et al. Roadmap on label-free super-resolution imaging. *Laser Photon. Rev.* Vol. 17, 2200029, 2023
4. Duh, Y.-S. *et al.* Giant photothermal nonlinearity in a single silicon nanostructure. *Nat. Commun.* Vol. 11, 4101, 2020.
5. Nishida, K. *et al.* All-optical scattering control in an all-dielectric quasi-perfect absorbing Huygens' metasurface. *Nanophotonics* Vol. 12, No.1, 139–146, 2023.
6. Tang, Y.-L. *et al.* Multipole engineering by displacement resonance: a new degree of freedom of Mie resonance. *Nat. Commun.* Vol. 14, 7213, 2023.
7. Nishida, K. *et al.* Optical bistability in nanosilicon with record low Q-factor. *Nano Lett.* Vol. 23, No. 24 11727–11733, 2023.

High-sensitivity image sensors based on dispersion-engineered metalenses

Masashi Miyata*

NTT Device Technology Laboratories, NTT Corporation, 3-1, Morinosato Wakamiya, Atsugi, Kanagawa 243-0198, Japan
*corresponding author: masashi.miyata@ntt.com

Abstract: This talk will review our recent work on dispersion-engineered metalenses for color splitting on sensor pixels, which provide a path toward the development of high-sensitivity color image sensors while maintaining consistency with CMOS sensor technology.

Boosting the sensitivity of image sensors, e.g., to enable optical imaging even in low-light environments, is a never-ending issue in sensor technology [1, 2]. In particular, the development of smartphones with numerous image sensors has increased the importance of this issue. Unfortunately, in most image sensors in use today, the bulk of the incident light does not reach the sensor's photodetectors because all of the photodetectors are covered with light-absorptive color filters. Therefore, the light power detected by the image sensors is essentially capped at around 30% of the incident light power.

Recent advances in optical metasurfaces have enabled the creation of miniature color splitters, which present an opportunity to enhance sensor sensitivity [3–6]. These metasurface-based color splitters can be used as an alternative to color filters for extracting red (R), green (G), and blue (B) color information from photodetectors. Importantly, in contrast to color filters, they can guide the incident light to the photodetectors without significant optical losses, thus maximizing the detectable light power.

Our recent work has enhanced their design by making extensive use of the dispersion-engineered metasurface concept and has resulted in color-sorting metasurface-lenses (metalenses) that simultaneously act as efficient color splitters and micro-lenses [7–9]. The metalenses are consist of a single-layer pattern made of a dielectric material commonly used in the CMOS process, making them compatible with CMOS sensor technology. We demonstrated through both experiments and simulations that image sensors using such metalenses in place of filters dramatically increase the detected light power while maintaining image quality and compatibility with a variety of imaging optics. In addition, a prototype of a metalens-integrated image sensor was built and tested, which revealed its superior sensitivity [10]. Furthermore, the same concept can potentially be applied to a metalens design for splitting RGB and near-infrared (NIR) light, which would improve the sensitivity of RGB-NIR image sensors [11, 12]. This talk introduces these color-sorting metalenses and shows their potential for making filter-free, high-sensitivity color image sensors.

References

1. Iwabuchi, S. *et al*., "A back-illuminated high sensitivity small-pixel color CMOS image sensor with flexible layout of metal wiring," in *2006 IEEE International Solid State Circuits Conference (ISSCC)* (February 2006), 1171–1178.
2. Okawa, T. *et al*., "A 1/2inch 48M all PDAF CMOS image sensor using 0.8 µm Quad Bayer coding 2× 2OCL with 1.0 lux minimum AF illuminance level," in *2019 IEEE International Electron Devices Meeting (IEDM)* (December 2019), 16.3.1–16.3.4.
3. Chen, B. H. *et al*., "GaN metalens for pixel-level full-color routing at visible light," Nano Lett. **17**, 6345–6352 (2017).

4. Miyata, M. *et al*., "High-sensitivity color imaging using pixel-scale color splitters based on dielectric metasurfaces," ACS Photon. **6**, 1442–1450 (2019).
5. Camayd-Muñoz, P. *et al*., "Multifunctional volumetric meta-optics for color and polarization image sensors," Optica **7**, 280–283 (2020).
6. Yun, S. *et al.*, "Highly efficient color separation and focusing in the sub-micron CMOS image sensor," in *2021 IEEE International Electron Devices Meeting (IEDM)* (December 2021), 30.1.1-30.1.4.
7. Miyata, M. *et al*., "Color splitting micro-metalenses for high-sensitivity color image sensors," in *2021 Conference on Lasers and Electro-Optics (CLEO)* (May 2021), FTu2M.5.
8. Miyata, M. *et al*., "Full-color-sorting metalenses for high-sensitivity image sensors," Optica **8**, 1596–1604 (2021).
9. Miyata, M. *et al*., "Metasurfaces Boost Color-Imaging Sensitivity," Optics & Photonics News **33**, 42 (Optica, December 2022).
10. Miyata, M. *et al*., "Filter-free color image sensors with a full-color-sorting metalens array," in *2022 Conference on Lasers and Electro-Optics (CLEO)* (May 2022), FM1B.8.
11. Miyata, M. *et al*., "Optical element, image sensor and imaging device," WO2022113363, 2022-06-02.
12. Miyata, M. and Hashimoto, T., "Four-color-sorting metalenses for high-sensitivity RGB-NIR image sensors," in *2023 The 84th JSAP Autumn Meeting* (September 2023), 21p-A309-4.

Reconstructive Spectrometer Using Plasmonic Photodetector

Y. Kaneda[1], E. Abubakr[1, 2], A. Abadi[1], S. Yasunaga[3], M. Oshita[1], and T. Kan[1 *]

[1]The University of Electro-Communications, Japan
[2]Aswan University, Egypt
[3]The University of Tokyo, Japan
[*]corresponding author: tetsuokan@uec.ac.jp

Abstract: When a metallic structure is formed on a semiconductor surface, the hot electrons in the metal excited by surface plasmon resonance (SPR) are extracted as an electric current. By configuring the structure that generates SPR as a continuous one-dimensional metallic diffraction grating structure, it is possible to sharply define the resonance of SPR and perform reconstructive spectroscopy.

Surface plasmon resonance (SPR) is a collective resonance of free electrons on a metal surface in contact with a dielectric. When the light incident on a metal structure satisfies the SPR matching condition, the incident light couples to the free electron resonant vibration on the metal surface. Since the resonance mode changes depending on the metal geometry, a device can operate for specific wavelengths and polarizations. Furthermore, suppose the metallic structure is formed on a semiconductor. In that case, a Schottky barrier is formed at the metal-semiconductor interface, allowing hot electrons to be injected into the semiconductor and extracted as a current, enabling electrical readout of SPR. Furthermore, since the Schottky barrier height can be tuned lower than the silicon band gap, infrared detection becomes possible on a silicon device[1].

By configuring the structure that generates SPR as a continuous one-dimensional metallic diffraction grating structure, it is possible to sharply define the resonance of SPR. Diffraction grating structures have been traditionally used as SPR coupling elements, but combining this surface plasmon coupling function with a current measurement function has revealed the potential for a new type of compact spectrometric device called a reconstruction method. When a device is irradiated with Transverse Magnetic (TM) polarized light of a single wavelength, SPR occurs at an angle satisfying the following dispersion relation (1)[2]:

$$\frac{\omega}{c}\sqrt{\varepsilon_{\mathrm{air}}}\sin\theta + \frac{2m\pi}{a} = \frac{\omega}{c}\sqrt{\frac{\varepsilon_{\mathrm{air}}\varepsilon_{\mathrm{metal}}}{\varepsilon_{\mathrm{air}} + \varepsilon_{\mathrm{metal}}}} \qquad (1)$$

By determining the frequency of the incident light and the permittivity, and solving the dispersion relation (1), the angle at which SPR occurs for a specific wavelength is essentially uniquely determined. Therefore, when TM light of different single wavelengths λ_1, λ_2, and λ_3 is irradiated and the device is angle-scanned relative to the incident light, the angular SPR photocurrent presents peaks at different SPR generation angles θ_1, θ_2, and θ_3 corresponding to λ_1, λ_2, and λ_3, respectively. If these three wavelengths are irradiated simultaneously and angle scanning measurement is performed, the photocurrent measurement value at each angle is expressed as a linear sum of the current amounts for each wavelength, for example, the current measurement value $I_{\theta 1}$ at angle θ_1 becomes

$$I_{\theta_1} = R_{\lambda_1\theta_1}P_{\lambda_1} + R_{\lambda_2\theta_1}P_{\lambda_2} + R_{\lambda_3\theta_1}P_{\lambda_3} \qquad (2)$$

and can be expressed as the sum of the product of the incident intensity and the sensitivity value at that angle. If

the number of irradiation wavelengths is extended to n and current measurement is performed at m angular positions, the current measurement value at each angular position will be a linear sum of the current amounts for each wavelength, so

$$\begin{bmatrix} I_{\theta_1} \\ \vdots \\ I_{\theta_m} \end{bmatrix} = \begin{bmatrix} R_{\lambda_1\theta_1} & \cdots & R_{\lambda_n\theta_1} \\ \vdots & \ddots & \vdots \\ R_{\lambda_1\theta_m} & \cdots & R_{\lambda_n\theta_m} \end{bmatrix} \begin{bmatrix} P_{\lambda_1} \\ \vdots \\ P_{\lambda_n} \end{bmatrix} \quad (3)$$

and it can be written in matrix form as $\boldsymbol{I} = \boldsymbol{RP}$. If the $\boldsymbol{R}$ matrix is derived in advance using a light source with known wavelengths and intensities, the spectral $\boldsymbol{P}$ can be obtained from the vector of current measurement values $\boldsymbol{I}$ at each measurement angle through the simple calculation of the inverse matrix $\boldsymbol{P} = (\boldsymbol{R}^{\mathrm{T}}\,\boldsymbol{R})^{-1}\boldsymbol{R}^{\mathrm{T}}\boldsymbol{I}$. Currently, we have confirmed spectroscopy performance using this method[3], application to gas sensing[4], integration with MEMS[5,] and extension of the measurement wavelength[6].

References

1. Berini, P. “Surface Plasmon Photodetectors and Their Applications,” Laser and Photonics Reviews, Vol. 8, No. 2, 197-220, 2014.
2. Raether, H. “Surface Plasmons on Smooth and Rough Surfaces and on Gratings,” Springer: Berlin, Heidelberg, 1988.
3. Chen W., Kan T., Ajiki Y., Matsumoto K., Shimoyama I. “NIR spectrometer using a Schottky photodetector enhanced by grating-based SPR,” Opt Express, Vol. 24, No. 22, 25797-25804, 2016.
4. Yamamoto Y., Oshita M., Saito S., Kan T. “Near-infrared spectroscopic gas detection using a surface plasmon resonance photodetector with 20 nm resolution,” ACS Applied Nano Materials, Vol. 4, No. 12, 13405-13412, 2021.
5. Oshita, M., Saito, S. and Kan, T. “Electromechanically reconfigurable plasmonic photodetector with a distinct shift in resonant wavelength,” Microsyst Nanoeng, Vol. 9, 26, 2023.
6. Abubakr E., Abadi A., Oshita M., Saito S., Kan T. “Optimizing geometry and metal-dependent performance of Si-based Schottky plasmonic photodetectors,” Optical Materials, Vol. 150, 115175, 2024.

Spatiotemporal Metamaterials and Metasurfaces

Physics-Driven Vector-Quantized Autoencoder for Space-Time-Coding Matrix

Xiao Qing Chen[1], and Lei Zhang[1] *

[1]State Key Laboratory of Millimeter Waves, Southeast University, Nanjing 210096, China
*Corresponding author: njzhanglei@seu.edu.cn

Abstract: We have designed and trained a physics-driven vector-quantized (PD-VQ) autoencoder model that takes the target harmonic scattering pattern as an input, and this PD-VQ autoencoder model quickly outputs the optimal discrete space-time coding (STC) matrix, which can help the STC digital metasurface to perform agile multi-frequency harmonic beamforming in real-time.

The space-time coding (STC) digital metasurface was proposed by Zhang et al. in 2018[1], whose coding elements can respond dynamically in space and time so that electromagnetic waves can be accurately modulated in both the spatial and frequency domains. The STC matrix is used to characterize the dynamic coding state of each element in space and time, and its design is both critical and complex for STC digital metasurfaces. The computational complexity of traditional optimization algorithms for obtaining STC matrices is very high, which makes the efficiency of obtaining STC matrices very low (especially when the matrix dimensions become large), thus hindering the practical application of STC digital metasurfaces to a certain extent.

Therefore, we propose an encoding strategy based on a physics-driven vector-quantized (PD-VQ) autoencoder [2, 3], which consists of an encoder, a vector-quantizer layer, and a physics-driven decoder. The target scattering pattern is used as the input to the encoder and the corresponding optimized STC matrix is output. Considering that the operating states of the elements are discrete, the discrete STC matrix is obtained with the help of the vector quantization layer. Finally, the physical operation mechanism between the STC matrices and the harmonic scattering patterns is introduced so that the decoder outputs the reconstructed harmonic scattering pattern and therefore the autoencoder can be trained in an unsupervised manner. Based on the target harmonic scattering pattern, the PD-VQ autoencoder model can quickly generate the optimized discrete STC matrix with high reliability, accuracy, and generalization.

The conceptual illustration is shown in Figure 1, the target harmonic scattering pattern is fed into the autoencoder, which immediately generates the corresponding optimized discrete STC matrix. Based on the generated STC matrix, the control module periodically changes the control voltage of the elements to modulate the incident wave into the desired harmonic scattering pattern.

The proposed PD-VQ autoencoder shows high reliability and accuracy on both the training and test datasets, indicating that the autoencoder has good generalization ability. Moreover, for the target harmonic scattering patterns that are not included in the training and test sets, the autoencoder still outputs the corresponding optimized STC matrices, and the reconstructed harmonic scattering pattern matches the target very well.

In summary, we propose the encoding strategy based on the PD-VQ autoencoder to realize the inverse design of the STC matrix with high accuracy and reliability. This autoencoder is trained in an unsupervised way, which does not require a large amount of manually labeled data and greatly reduces the workload of obtaining the training set. According to the application scenario and the desired harmonic scattering pattern, we can easily construct the data set for training. Based on this encoding strategy, STC digital metasurfaces can be more easily and quickly modulated harmonics on demand, thus finding more potential applications in imaging, sensing, radar,

communication, and other intelligent information systems.

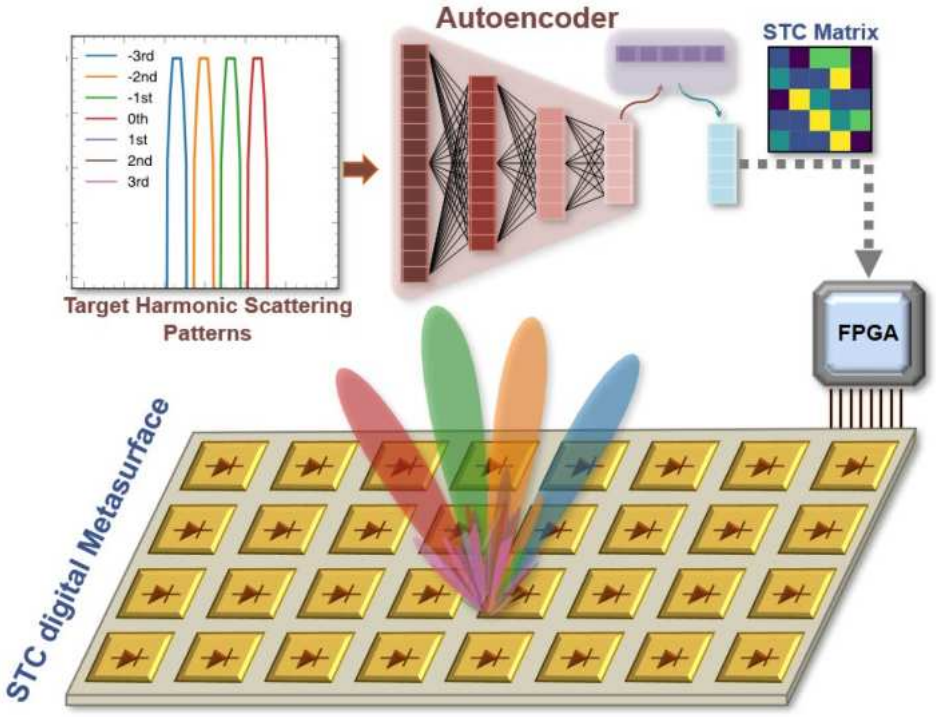


Figure 1. The autoencoder takes the target harmonic scattering patterns as input and generates the corresponding optimized discrete STC matrix with high reliability and accuracy. Thus, the STC digital metasurface can modulate the incident wave into desired harmonics scattering patterns in real time under the control of the generated STC matrix.

References

1 Zhang, L., Chen, X.Q., Liu, S., Zhang, Q., Zhao, J., Dai, J.Y., Bai, G.D., Wan, X., Cheng, Q., Castaldi, G., Galdi, V., and Cui, T.J.: 'Space-time-coding digital metasurfaces', Nature communications, 2018, 9, (1), pp. 4334

2 Oord, A.v.d., Vinyals, O., and Kavukcuoglu, K.: 'Neural Discrete Representation Learning', 2017

3 Liu, C., Yu, W.M., Ma, Q., Li, L., and Cui, T.J.: 'Intelligent coding metasurface holograms by physics-assisted unsupervised generative adversarial network', Photonics Research, 2021, 9, (4)

Enhanced optical effects based on the bound states in the continuum

Haitao Jiang*, Zhiwei Guo, and Yong Sun

MOE Key Laboratory of Advanced Micro-Structured Materials, School of Physics Science and Engineering, Tongji University, Shanghai, 200092, China

*corresponding author: jiang-haitao@tongji.edu.cn

Abstract: We reveal that the bound states in the continuum in meta-grating or metasurface structures can strongly enhance the optical effects including giant Goos-Hänchen shift, optical chirality and nonlinear optical effects. Our work provides a direct avenue towards the realization of ultra-sensitive sensors, high-efficiency chiral optical and nonlinear optical devices.

The conventional bound state can have an ultra-high quality factor, but it would be localized within a small part of the structure. However, the bound states in the continuum (BICs) can not only have ultra-high quality factors, but also have very large mode profile within the structure. As a result, the bound states in the continuum would strongly enhance the optical effects as well as the interaction between the light and matter. In this presentation, we mainly discuss how to realize the BICs in various meta-grating structures including compound single-grating structure and double-grating structures. We also discuss how to realize chiral BICs in metasurfaces by breaking the symmetry of the structures. Based on the BICs, one can greatly boost the optical effects including giant Goos-Hänchen shift [1], optical chirality [2, 3] and high-efficiency second-harmonic generation [4, 5]. The enhanced optical effects assisted by the BICs can be utilized for the design of ultra-sensitive sensors, high-efficiency chiral optical and nonlinear optical devices.

Acknowledgements: This work is supported by the National Key Research and Development Program of China (No. 2021YFA1400602), the NSFC (No. 12274325, No. 11974261).

References

1. F. Wu, J. J. Wu, Z. W. Guo, H. T. Jiang, Y. Sun, Y. H. Li, J. Ren, and H. Chen, "Giant enhancement of the Goos-Hänchen shift assisted by quasibound states in the continuum," Phys. Rev. Applied, **12,** 014028 (2019).
2. J. J. Wu, X. T. Xu, X. Q. Su, S. Zhao, C. Wu, Y. Sun, Y. H. Li, F. Wu, Z. W. Guo, H. T. Jiang, and H. Chen, "Observation of giant extrinsic chirality empowered by quasi-bound states in the continuum," Phys. Rev. Applied, **16**, 064018 (2021).
3. X. Qi, J. J. Wu, F. Wu, S. Zhao, C. Wu, Y. Y. Min, M. N. Ren, Y. F. Wang, H. T. Jiang, Y. H. Li, Z. W. Guo, Y. P. Yang, W. H. Zheng, H. Chen, and Y. Sun, "Observation of maximal intrinsic chirality empowered by dual quasi-bound states in the continuum in a planar metasurface," Photonics Research, **12** (2), 244–252 (2024).
4. X. Qi, J. J. Wu, F. Wu, M. N. Ren, Q. Wei, Y. F. Wang, H. T. Jiang, Y. H. Li, Z. W. Guo, Y. P. Yang, W. H. Zheng, Y. Sun, and H. Chen, "Steerable merging bound states in the continuum on a quasi-flatband of photonic crystal slabs without breaking symmetry", Photonics Research, **11** (7), 1262–1274 (2023).
5. J. J. Wu, J. G. Chen, X. Qi, Z. W. Guo, J. J. Wang, F. Wu, Y. Sun, H. T. Jiang, L. Shi, J. Zi, and H. Chen, "Observation of accurately designed bound states in the continuum in momentum space", Photonics Research, in press, to be published.

Down-conversion of terahertz wave frequencies by mode coupling at temporal boundaries in semiconductor waveguides

Keisuke Takano[1,*], Satoko Uchiyama[1], Shintaro Nagase[1], Yuka Tsuchimoto[1], Toshihiro Nakanishi[2], Yosuke Nakata[3,4], Joel Pérez-Urquizo[5,6], Julien Madéo[5], Keshav M. Dani[5], and Fumiaki Miyamaru[1]

[1]Department of Physics, Faculty of Science, Shinshu University, Japan
[2]Department of Electronic Science and Engineering, Kyoto University, Japan
[3]Graduate School of Engineering Science, Osaka University, Japan
[4]Center for Quantum Information and Quantum Biology, Osaka University, Japan
[5]Femtosecond Spectroscopy Unit, Okinawa Institute of Science and Technology Graduate University, Japan
[6]Laboratoire de Physique de l'École Normale Supérieire ENS, Université PSL, CNRS, Sorbonne Université, Université de Paris, France
[*]Corresponding author: ksk_takano@shinshu-u.ac.jp

Abstract: Photoexcitation can induce a temporal boundary that alters dispersion relations of electromagnetic waves in semiconductor waveguides, leading to frequency conversion. In this study, we demonstrate frequency down-conversion of terahertz waves via coupling between transverse-magnetic and transverse-electromagnetic modes at a photoexcited temporal boundary in a waveguide made of semi-insulating GaAs.

A highly efficient device that converts frequencies of terahertz waves to desired frequencies is essential for developing high-capacity communication. To realize such a device, we can exploit time-varying systems. When a dispersion relation varies temporally during wave propagation, the frequency can be shifted. As this process involves linear wave scattering by the temporal variation, its conversion efficiency is independent of the intensity of the input electromagnetic waves. In particular, time-varying waveguides have the potential to realize highly efficient frequency conversion devices due to their strong energy confinement. So far, frequency up-conversion of terahertz waves has been reported for the transverse-electric (TE) mode terahertz waves in semiconductor GaAs waveguides[1]. In Ref. 1, an ultrashort laser pulse excited conduction electrons on the surface of the semiconductor waveguide, inducing a temporal boundary where the propagation mode switches instantaneously. The frequency up-conversion occurs due to the coupling of the incident TE mode with higher-frequency TE modes at the temporal boundary. On the other hand, photoexcitation of the semiconductor waveguide surface shrinks the electromagnetic field distribution of the propagating modes, so that frequency down-conversion usually does not occur. The waveguide structures and mode conditions for the down-conversion have not been clarified yet. In this study, we demonstrate the frequency down-conversion of terahertz waves in a GaAs waveguide by coupling an incident transverse-magnetic (TM) mode with a transverse-electromagnetic (TEM) mode at the optically excited temporal boundary.

Figure 1(a) depicts a schematic of the GaAs waveguide structure designed for the frequency down-conversion of the terahertz waves and the experimental setup. An Au film was deposited on the entire bottom surface of a GaAs substrate, which was 100 μm thick, 1 mm wide, and 10 mm long. The top surface of the waveguide was also coated with Au, leaving a 4 mm long area for photoexcitation. For TM-mode excitation, *y*-polarized terahertz wave packets were injected into the waveguide. While the terahertz wave packet was propagating through the photoexcitation region in Fig. 1(a), the top surface of the waveguide was optically excited with a time delay of $\Delta\tau$ by the pump laser pulse (center wavelength ~800 nm and pulse width ~100 fs).

The spectra of the terahertz wave packets transmitted through the waveguide are shown in Fig. 1(b).

Without the pump pulse, a peak at 0.42 THz was observed, whereas a peak at 0.36 THz was observed in a certain $\Delta\tau$ range. Thus, the pump pulse irradiation causes the frequency down-conversion. The range of $\Delta\tau$ where the frequency conversion occurs corresponds to the time range where the wave packet exists in the 4 mm long photoexcitation area at the photoexcitation timing. As the electric fields in the photoexcited surface are shielded by the conduction electrons, the semiconductor waveguide is regarded as a parallel-plate waveguide after the temporal boundary. The parallel-plate waveguide has a TEM mode with a uniform electric field distribution in the *y*-direction. The dispersion curve of the TEM mode is positioned below that of the lowest-order TM mode before the photoexcitation. The frequency down-conversion is attributed to the coupling of the incident TM and TEM modes at the temporal boundary. The power of the observed down-converted terahertz wave was more than 20% of that of the incident TM mode.

By combining the frequency up-conversion for the TE mode[1] with the frequency down-conversion for the TM mode excited by the *y*-polarized incident terahertz waves in this study, the frequency up- or down-conversion can be selected by switching the polarization of the incident terahertz waves. The frequency-conversion waveguide capable of up- and down-conversion with high efficiency can contribute to developing terahertz wave integrated circuit systems for forthcoming high-capacity communication.

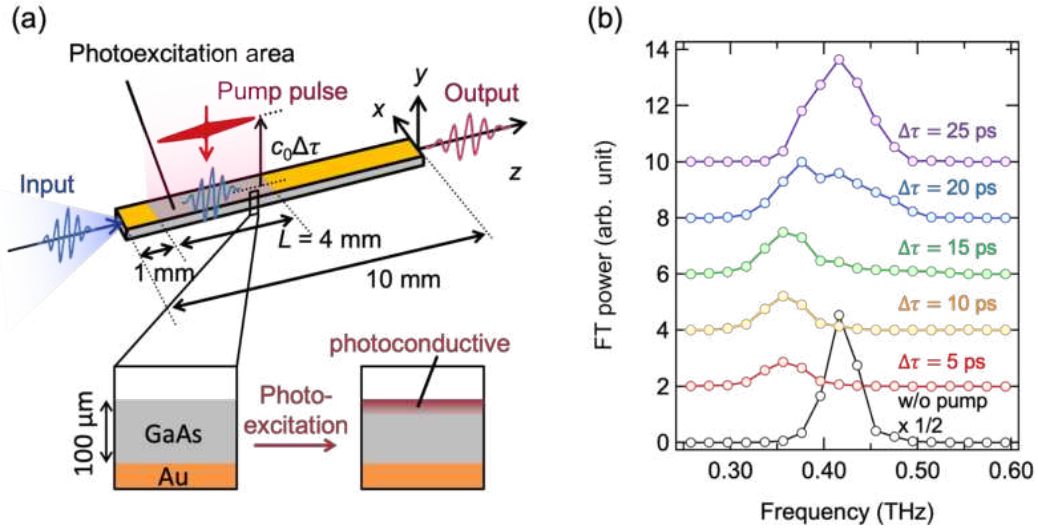


Figure 1: (a) Schematics of the GaAs waveguide and experimental setup of the frequency conversion for the TM modes. (b) Spectra of the terahertz waves transmitted through the waveguide with and without the pump pulses having several relative time delays $\Delta\tau$. The fluence of the pump pulses was 0.186 mJ/cm^2.

This work was supported by JSPS KAKENHI under grant numbers 22K20493 and 22K04964. Y.N. is supported by JST PRESTO (Grant Number JPMJPR20L6). K.T. is partly supported by a research grant from the Takano Gakujutsu-Shinko-Zaidan Foundation. J.P.-U., J.M. and K.M.D. are supported by the Femtosecond Spectroscopy Unit at the Okinawa Institute of Science and Technology Graduate University.

References

1. Miyamaru, F., C. Mizuo, T. Nakanishi, Y. Nakata, K. Hasebe, S. Nagase, Y. Matsubara, Y. Goto, J. Pérez-Urquizo, J. Madéo, and K. M. Dani, "Ultrafast Frequency-Shift Dynamics at Temporal Boundary Induced by Structural-Dispersion Switching of Waveguides," Phys. Rev. Lett., vol. 127, no. 5, pp. 053902-1-6, 2021.

Waveform-Selective Metasurfaces Varying in Time and Space at the Same Frequencies in Accordance with Pulse Width

H. Wakatsuchi* and A. A. Fathnan

Department of Engineering, Nagoya Institute of Technology, Japan
*corresponding author: wakatsuchi.hiroki@nitech.ac.jp

Abstract: In this invited talk, we report recently developed circuit-based metasurfaces that show distinct behavior while operating at the same frequencies in accordance with the pulse width of incoming waves. We also demonstrate how such waveform-selective metasurfaces can be exploited for specific applications in antenna design, wireless communications, and electromagnetic compatibility.

In recent years, time-varying metasurfaces have been broadly and intensively explored to enhance control over electromagnetic waves and related phenomena [1]. These metasurfaces may adjust to their surrounding environments to establish the connection of wireless communications and enhance their quality as intelligent reflecting surfaces (IRSs) or reconfigurable intelligent surfaces (RISs) [2, 3]. However, most time-varying metasurfaces were so far developed with external power supply as active metasurfaces, which restricts the practical usage and application of these smart metasurfaces. In contrast, circuit-based metasurfaces were recently developed by introducing lumped circuit elements including diodes. These metasurfaces allow for electromagnetic response control in the time domain dependent on the pulse width of the incoming wave, without the need for extra power supply [4-10]. In this invited talk, we report such waveform-selective metasurfaces that show distinct behavior while operating at the same frequency. In particular, we present the most recent results on the design of these time-varying metasurfaces for advanced electromagnetic control, including frequency-sequence-based selectivity and ultra-fast impedance switching, which overcome long-standing physical limitations. We also demonstrate that these properties can be utilized in a range of applications such as antennas, absorbers, RISs, and cloaks. These novel time-varying metasurfaces provide a valuable contribution to addressing electromagnetic challenges with a higher degree of freedom in accordance with pulse width.

This work was supported in part by the Japan Science and Technology Agency (JST) under Fusion Oriented Research for Disruptive Science and Technology, KAKENHI grants from the Japan Society for the Promotion of Science (JSPS) (No. 22F22359, and 23H00470), and National Institute of Information and Communications Technology (NICT), Japan under the commissioned research (No. 06201).

References

1. Won, R., “A new knob for metamaterials,” *Nat. Photonics*, Vol. 15, 718–719, 2021.
2. Zhang, L. et al., “Space-time-coding digital metasurfaces,” *Nat. Commun.*, Vol. 9, 4334, 2018.
3. Wu., Q. and Zhang, R., “Towards smart and reconfigurable environment: intelligent reflecting surface aided wireless network,” *IEEE Commun. Mag.*, Vol. 58, No. 1, 106–112, 2020.
4. Wakatsuchi, H., et al., “Waveform-dependent absorbing metasurfaces,” *Phys. Rev. Lett.*, Vol. 111, No. 24, 245501, 2013.
5. Wakatsuchi, H, Long, J., and Sievenpiper, D., “Waveform selective surfaces,” *Adv. Funct. Mater.*, Vol. 29, No. 11,

1806386, 2019.
6. Vellucci, S. et al., “Waveform-selective mantle cloaks for intelligent antennas,” *IEEE Trans. Antennas Propag.*, Vol. 68, No. 3, 1712-1725, 2019.
7. Imani, M. F. and Smith, D. R., “Temporal microwave ghost imaging using a reconfigurable disordered cavity,” Appl. Phys. Lett., Vol. 116, 054102, 2020.
8. Ushikoshi, D. et al., “Pulse-driven self-reconfigurable meta-antennas,” *Nat. Commun.*, Vol. 14, 633, 2023.
9. Takimoto, K., et al., “Perfect pulse filtering under simultaneous incidence at the same frequencies with waveform-selective metasurfaces,” *APL Mater.*, Vol. 11, No. 8, 08116, 2023.
10. Takeshita, T. et al., “Frequency-hopping wave engineering with metasurfaces,” *Nat. Commun.*, Vol. 15, 196, 2024.

Direction-of-arrival (DOA) estimation with a programmable space-time-modulated metamaterial receiver

Shaghayegh Vosoughitabar[1], **Chung-Tse Michael Wu**[1,2*]

[1]Department of Electrical and Computer Engineering, Rutgers, the State University of New Jersey, USA
[2]Department of Electrical Engineering, National Taiwan University, Taiwan
[*]corresponding author: ctm.wu@rutgers.edu

Abstract: A space-time-modulated metamaterial antenna is leveraged as a receiver to estimate the direction-of-arrival (DOA) of an incoming signal. This approach uses the power levels of first-order harmonics, generated due to the periodic time-modulation of the metamaterial unit-cells' phase constants, allowing for precise DOA estimation of waves impinging on the antenna.

DOA finding holds importance in wireless communication, radar tracking, and remote sensing. In this context, multiple methods and signal processing algorithms have been developed to estimate the direction of an incoming signal [1]. Furthermore, DOA estimation by employing a reflective metasurface has been recently proposed to reduce computational complexity and hardware costs [2], [3]. For example, in [2] a reflective space-time modulated metasurface is employed for DOA estimation of an incident plane wave through creating a pattern asymmetry for the scattered fields at the two first-order harmonics. In this method, a detecting antenna is required to collect the scattered waves from the metasurface for DOA finding. Here, we propose a method utilizing only one space-time modulated metamaterial antenna to estimate the DOA of a signal impinging on the antenna.

Very recently, a space-time-modulated composite right/left-handed (CRLH) antenna has been proposed in [4], exhibiting interesting properties such as non-reciprocity and harmonic beam-scanning, which can be used for simultaneous transmission and reception of signals. In this antenna, the phase constant (β) of each CRLH unit cell can be either positive or negative, depending on the bias voltages of the integrated varactors into the unit cell. By toggling β between these two states (i.e. β_0 and β_1 shown in Figure 1) in a periodic fashion, harmonics are produced within the receiving antenna upon receiving a signal at frequency f_0 arriving from angle θ. Figure 1 displays the received fundamental and first harmonic patterns for the illustrated space-time-modulated sequence, obtained by mathematically formulating the received patterns based on the array factor approach. By looking at the 1st harmonic and -1st harmonics' patterns ($f_0 \pm \Delta f$), it is noted that if the received powers at these harmonics are deducted from each other (Δ), in each θ angle within a particular range, a distinct value is achieved, as can be seen in (1) and Figure 1. Therefore, when a wave with a frequency of f_0, coming from an angle of θ within the detection range, is captured by the antenna, by calculating Δ and referring to the plotted curve in Figure 1, the DOA of the signal can be estimated. It is noted that there is a trade-off between the detection resolution and detection range. As such, it is worth mentioning that while increasing the amount of $|\beta_0 p|$ and $|\beta_1 p|$ leads to a higher slope of the Δ curve (better detection resolution), this will also result in a decrease in the detection range.

$$\Delta = Power\ of\ (f_0 - \Delta f)(dB) - Power\ of\ (f_0 + \Delta f)(dB) \quad (1)$$

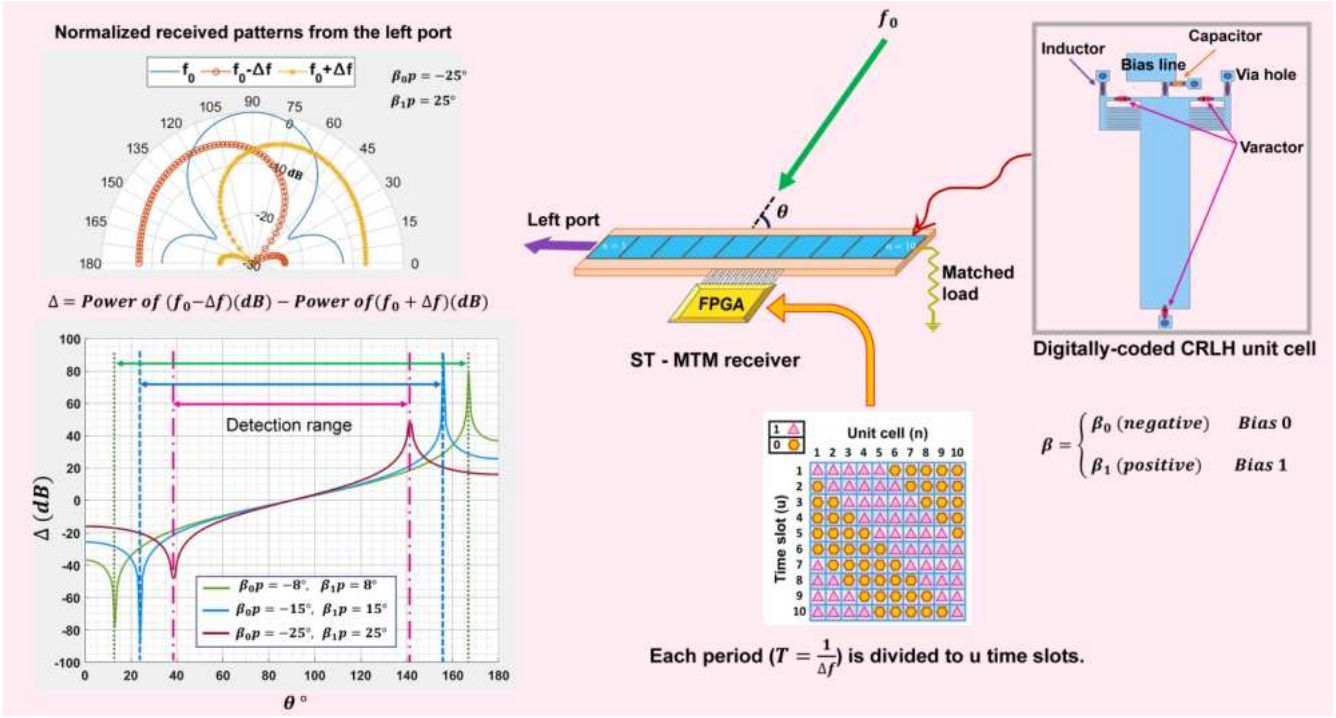


Figure 1. Space-time modulated metamaterial (ST-MTM) receiving antenna with 10 CRLH unit-cells for DOA estimation where *p* denotes the unit-cell length.

Acknowledgements

This work is supported by the National Science Foundation (NSF) under Grant ECCS-2229384 and ECCS-2028823.

References

1. He, Chong, et al. "Direction finding by time-modulated array with harmonic characteristic analysis," IEEE Antennas and Wireless Propagation Letters, Vol. 14, 642-645, 2015.
2. Fang, Xinyu, et al. "Accurate Direction-of-Arrival Estimation Method based on Space-Time Modulated Metasurface," IEEE Transactions on Antennas and Propagation, Vol. 70, No. 11, 10951-10964, 2022.
3. Bai, Lin, et al. "1-Bit Programmable Metasurface-Based 2-D Direction Finding," IEEE Antennas and Wireless Propagation Letters, Vol. 22, No. 9, 2160-2164, 2023.
4. S. Vosoughitabar and C.-T. M. Wu "Programming nonreciprocity and harmonic beam steering via a digitally space-time-coded metamaterial antenna," Scientific Reports, Vol. 13, No. 1, 7338, 2023.

Acoustic Fiber via Rotational Motion

M. Farhat[1] and Y. Wu [1,2*]

[1]Computer, Electrical and Mathematical Sciences and Engineering Division, King Abdullah University of Science and Technology, Thuwal, Saudi Arabia

[2] Physical Sciences and Engineering Division, King Abdullah University of Science and Technology, Thuwal, Saudi Arabia

[*]corresponding author: ying.wu@kaust.edu.sa

Abstract. We will discuss our recent work on acoustic wave propagation in spinning fluid (air or water) that may lead to fiber applications. We reveal that spin can alter the refractive index and therefore can support waveguide modes. The propagation is asymmetric: allowing right-hand propagation and prohibiting left-hand propagation.

Propagation of acoustic waves in time-varying and/or moving media has attracted a lot of attentions and is expected to lead to many intriguing applications. In this summary, we discuss our recent work on realizing acoustic fiber via spinning motion. Most solid and liquid materials support acoustic speed that are much higher than that in air, making the confinement of the guided mode difficult. Recently, we found that by introducing rotational motion, the effective refractive index of the medium is altered and therefore, it can support guided modes. The angular velocity of the spinning determines the properties of the guided mode, and interestingly can be viewed as the strength of the acoustic analogue of Zeeman effect.

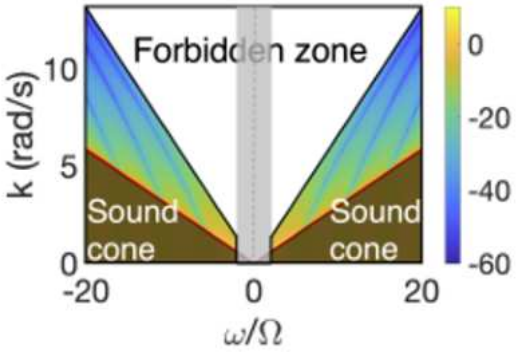


Fig. 1 Counterplot of the dispersion relation for the zero-th order mode.

Acknowledgements: This work is supported by King Abdullah University of Science and Technology via baseline research fund BAS/01/1626-01-01 and OSR-2020-CRG9-4374.

References

1. Farhat M, Chen P. Y, and Wu Y. Phys. Rev. Appl. Vol.19, L041002 (2023)

A Physical Unclonable Function Based on Time-Modulated Systems with Exceptional Points of Degeneracy

Pai-Yen Chen[1,*]

[1]Department of Electrical and Computer Engineering, University of Illinois, Chicago, IL 60607, U.S.A.
[*]corresponding author: pychen@uic.edu

Abstract: I will outline my recent findings on hardware security primitives built based upon time-variant electronic system with exceptional points at which high entropy occurs. I will show that the proposed encryption notion can provide excellent performance metrics in terms of randomness, uniqueness, and robustness against modeling attacks.

Over the past decade, non-Hermitian physical systems and their unusual singularities, known as exceptional points (EPs), have deepen understanding of engineering spectral, spatial, and temporal properties of waves, enabling new applications in signal generation, routing, and sensing across the spectrum. Particularly, the effect of eigenvalue bifurcation in the proximity of EPs has been extensively studied, as it may drastically improve the sensitivity of optical, optomechanical, acoustic, elastic, and electronic sensors[1],[2]. Furthermore, high entropy at EP degeneracy has been recently proposed to implement physical unclonable functions (PUFs) and cryptographic random number generators (CRNG)[3],[4], opening up a new pathway for development of hardware security primitives. In general, these non-Hermitian physical systems with EPs are built based on the parity-time reversal (PT)-symmetric structures with spatially-distributed, balanced gain and loss. Nevertheless, recent studies reported that contrary to PT-symmetric structures that require a delicate balance between gain and loss, EPs can occur in linear periodically time-varying systems without gain and loss. In this talk, I will present new types of PUFs and CRNGs based on simple, lightweight, and low-cost time-modulated electronic systems with EPs, along with some experimental evidence. I will show that proposed PUFs and CRNGs can exhibit excellent randomness (i.e., Shannon entropies) and uniqueness (i.e., inter-device Hamming distance), and, most importantly, robustness against machine learning-based modeling attacks. The proposed notion of PUFs based on EPs in time-modulated electronic systems may shed light on unforeseen cryptographic applications, such as RF and optical fingerprinting, anticounterfeiting labels, true random number generators, and secure wireless communications, to name a few.

References

1. Chen, P. Y., Sakhdari, M., Hajizadegan, M., Cui, Q., Cheng, M. M. C., El-Ganainy, R., & Alù, A. (2018). Correction: Generalized parity-time symmetry condition for enhanced sensor telemetry (Nature Electronics (2018. Nature Electronics, 1(6), 371.
2. Sakhdari, M., Hajizadegan, M., Zhong, Q., Christodoulides, D. N., El-Ganainy, R., & Chen, P. Y. (2019). Experimental Observation of P T Symmetry Breaking near Divergent Exceptional Points. Physical review letters, 123(19), 193901.
3. Yang, M., Ye, Z., Pan, H., Farhat, M., Cetin, A. E., and Chen, P. Y. (2023). Electromagnetically unclonable functions generated by non-Hermitian absorber-emitter. Science Advances, 9(36), eadg7481.
4. Yang, M., Zhu, L., Zhong, Q., El-Ganainy, R., and Chen, P. Y. (2023). Spectral sensitivity near exceptional points as a resource for hardware encryption. Nature Communications, 14(1), 1145.

Near-infrared metasurface with simultaneous control of dielectric and magnetic properties in the 100-THz band

Harumi Asada[1,2], Kumiko Ryu[3], and Takehito Suzuki[4*]

[1] Department of Electronic and Information Engineering, Graduate School of Engineering, Tokyo University of Agriculture and Technology, Japan
[2] Research Fellow of Japan Society for the Promotion of Science, JSPS, Japan
[2] Department of Electrical and Electronic Engineering, Graduate School of Engineering, Tokyo University of Agriculture and Technology, Japan
[4] Division of Advanced Electrical and Electronics Engineering, Institute of Engineering, Tokyo University of Agriculture and Technology, Japan
[*]corresponding author: takehito@go.tuat.ac.jp

Abstract: This report presents a metasurface that controls the dielectric and magnetic properties for the directivity control of near-infrared thermal radiation. We fabricate the metasurface with three-layered square Au, SiO_2, and Au patches on a supporting Si substrate. Measurements verify that the metasurface has a resonance at approximately 120 THz.

Thermal radiation is electromagnetic waves emitted from objects. The control of thermal radiation emitted from hot objects around us by artificial materials would be a welcome contribution to develop trailblazing applications such as for thermal management and energy harvesting [1,2]. A metasurface is an artificial material composed of periodically arranged subwavelength meta-atoms. Metasurfaces that control the dielectric and magnetic properties in the terahertz waveband have been applied to directivity control of terahertz waves radiated from terahertz continuous wave sources [3,4]. A metasurface that controls the dielectric and magnetic properties in the near-infrared region could be applied to directivity control of thermal radiation from hot objects. In this report, we fabricate and demonstrate a near-infrared metasurface that controls the dielectric and magnetic properties in the 100-THz band [5].

Figures 1(a) and (b) show an overall and an enlarged view, respectively, of a near-infrared metasurface. The near-infrared metasurface is composed of periodically arranged three-layered square metal, dielectric, and metal patches. The side length l and spacing s of a square patch, the thickness of the metal layer t, and the thickness of the dielectric layer d are 320 nm, 170 nm, 20 nm, and 50 nm, respectively. An adhesive layer is sandwiched between the metal and dielectric layers to improve adhesion between the metal and the dielectric. Figures 2(a)–(f) show the fabrication process of the near-infrared metasurface on a supporting Si substrate. Figures 3(a) and (b) are a photograph of the near-infrared metasurface by (a) a digital camera and (b) an image by field emission scanning electron microscopy (FE-SEM). The FE-SEM image shows the three-layered square Au, SiO_2, and Au patches periodically arranged in an area of 2.5×2.5 mm^2 of the supporting Si substrate.

Figures 4(a) and (b) show the reflectance and transmittance measurements by microscopic Fourier transform infrared spectroscopy (FT-IR) of the near-infrared metasurface and an one layer of silicon substrate, respectively. Figures 4(a) and (b) show that the near-infrared metasurface has a resonance at approximately 120 THz. Figures 4(a) and (b) show that the one layer of silicon substrate has almost constant values from approximately 40 to 210 THz and no resonance at approximately 120 THz. The resonances in the measurements of the near-infrared metasurface at approximately 120 THz could be the cause of the simultaneous control of the dielectric and

magnetic properties due to the three-layered square Au, SiO2, and Au patches on the supporting Si substrate.

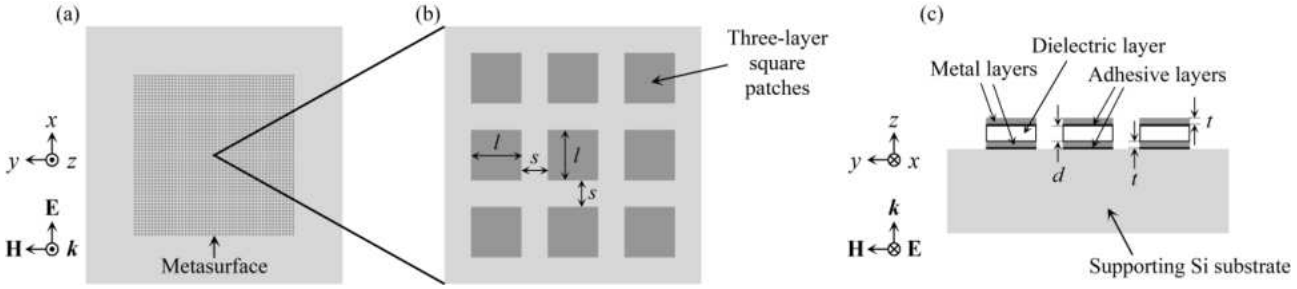


Fig. 1 (a) Overall and (b) enlarged views of a near-infrared metasurface with three-layered square metal, dielectric, and metal patches.

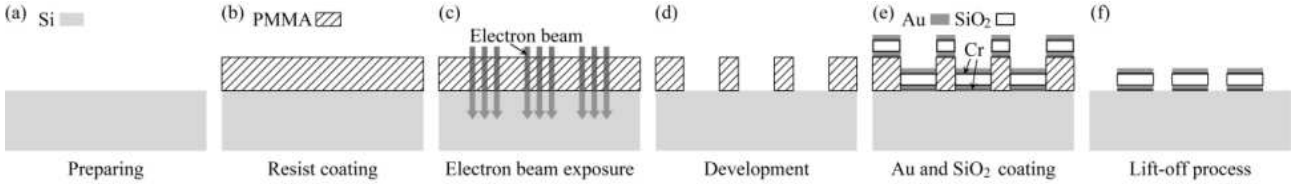


Fig. 2 Fabrication processes for the near-infrared metasurface with three-layered square metal, dielectric, and metal patches.

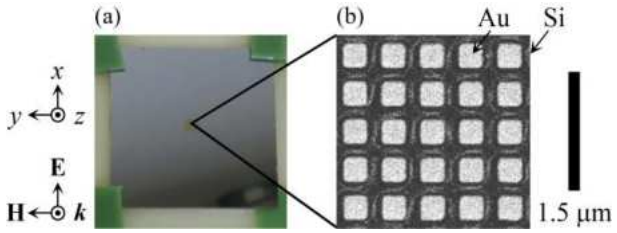


Fig. 3 (a) Photograph and (b) FE-SEM image of the near-infrared metasurface fabricated on a supporting Si substrate.

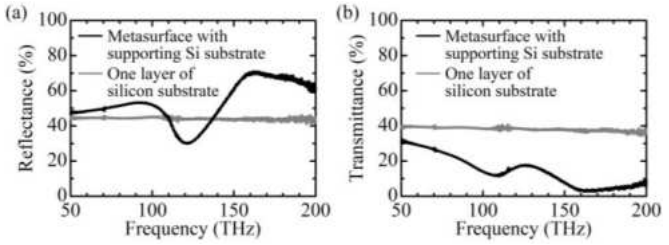


Fig. 4 (a) Reflectance and (b) transmittance measurements of the near-infrared metasurface and one layer of silicon substrate.

Acknowledgements

This research was supported by Grant-in-Aid for JSPS Fellows (No. 21J22822), FOREST from the Japan Science and Technology Agency (JST) (JPMJFR222I), Grants-in-Aid for Scientific Research (B) from the Japan Society for the Promotion of Science (JSPS) (No. 21H01839), and Research Foundation for the Electrotechnology of Chubu. The part of the fabrication of the sample was conducted at Nanofabrication Platform, Tokyo Institute of Technology, supported by Nanotechnology Platform Japan (No. F-21-IT-029) and Advanced Research Infrastructure for Materials and Nanotechnology in Japan (No. 22IT0005).

References

1. J.-J. Greffet, R. Carminati, K. Joulain, J.-P. Mulet, S. Mainguy, and Y. Chen, “Coherent emission of light by thermal sources,” Nature, Vol. 416, No. 6876, 61–64, 2002.
2. W. Li and S. Fan, “Nanophotonic control of thermal radiation for energy applications,” Opt. Express, Vol. 26, No. 12, 15995–16021, 2018.
3. K. Endo, M. Sekiya, J. Kim, K. Sato, and T. Suzuki, “Resonant tunneling diode integrated with metalens for high-directivity terahertz waves,” Appl. Phys. Express, Vol. 14, No. 8, 082001, 2021.
4. T. Suzuki, K. Endo, J. Kim, K. Tsuruda, and M. Sekiya, “Metalens mounted on a resonant tunneling diode for collimated and directed terahertz waves,” Opt. Express, Vol. 29, No. 12, 18988–19000, 2021.
5. K. Ryu, H. Asada, and T. Suzuki, Symposium on Frontier of Terahertz Science IX, P-16, Fukui, Nov. 2022 (in Japanese).

Application of Deutsch-Jozsa Algorithm via an Inverse-Designed Polyimide Metamaterial

A. Blackwell[1], R. Yahiaoui[1], Y-H. Chen[1], P-Y. Chen[1], T.A. Searles[1], Z.A. Chase[1*]

[1]Department of Electrical and Computer Engineering, University of Illinois at Chicago, Illinois, USA

[*]corresponding author: chase8@uic.edu

Abstract: Using inverse design, a quantum algorithm emulator, made of a polyimide gradient-index and silicon, is optimized to enhance the interaction of incident light with the metamaterial showing improvements in the amplitude and FWHM of the outgoing wave in the terahertz region for the implementation of the Deutsch-Josza algorithm.

Metamaterials can be used to exploit the least used terahertz (THz) region for devices that have applications in analog computing. Gradient index (GRIN) lenses have not only been proven to operate at THz frequencies but can be integrated into photonic devices that consist of multiple subblocks for quantum algorithm emulators (QAEs). They have been used to simulate quantum search algorithms with classical light but only in the microwave region.[1] We report a new design for a QAE that operates at THz frequencies and is optimized by machine learning using an inverse design approach.

In the QAE, as shown in Figure 1, the oracle and Fourier transform (FT) subblocks are in optical contact. The oracle subblock modulates the electric field profile of the incident THz light by assigning a phase shift of 0 or π on each spatial position along y-axis via physically varying the radii of the hole array drilled in the silicon substrate which varies the effective electric permittivity along the y-axis. The FT block has various hole sizes acting as an all-dielectric GRIN lens that determines the output wave. Numerical analysis, done by finite-difference time-domain (FDTD), computed the initial optimized radii for the GRIN lens, $r_1 < r_2 < r_3 = r_4 < r_5 = r_6$, with a thickness of 127 μm and a period of 70 μm for the array. Defining the phase shift of 0 or π along the transversal axis of the QAE, two different solutions of the DJ algorithm can be realized. Either a constant or balanced function results. The constant function shows a maximum electric field intensity at y=0 and the balanced function shows a minimum intensity at y=0 with two separate peaks with an input frequency of 0.8 THz. Table 1 shows the optimized parameters for the radii and thickness of the GRIN lens after inverse design via machine learning was used. The improvement in the design shows increases in the amplitude and decreases of the FWHM as shown in Table 2 while only the third radius changes most significantly (15%). There is a two-fold increase in the thickness of the GRIN lens. Use of inverse design ML has helped construct a QAE that has an optimal distribution of the output wave intensity that creates a device that can be better equipped to handle a greater number of database inputs.[2]

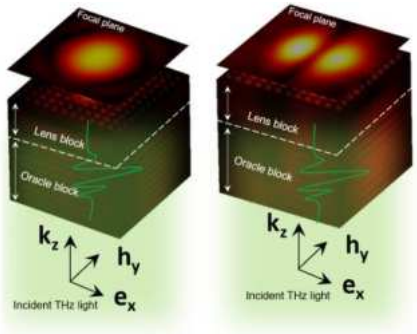


Figure 1: Schematic of the QAE showing outputs for both constant (left) and balanced (right) functions.

Table 1. Machine learning optimized structural parameters for the GRIN lens.

Parameter	r_1	r_2	r_3	r_4	r_5	r_6	h
Initial	10	15	25	25	30	30	127
Optimal	11.97	16.09	21.24	27.88	31.59	34.91	289.86

Table 2. Machine learning optimized output wave characteristics for both the constant and balance functions for the GRIN lens.

Case	All zero / All one		Half-zero half-one			
Parameter	Ap	FWHM	Ap_1	$FWHM_1$	Ap_2	$FWHM_2$
Initial	41.872	449.96	26.795	264.50	46.813	208.50
Optimal	53.455	218.15	40.976	195.16	42.792	217.25

This work is supported by the U.S. Department of Energy, Office of Science, National Quantum Information Science Research Centers, Co-design Center for Quantum Advantage (C2QA).

References

1. Wei, Z., et al., Micromachines 13 1204 (2022)
2. Cheng, K., et al., Opt. Express 28 16230–16243 (2020)

Recent advances in non-Hermitian metamaterials

Realization of Geometry-Dependent Skin Effect in a Reciprocal Two-Dimensional

M. Hu[1*], and K. Ding[1]

[1]Department of Physics, State Key Laboratory of Surface Physics, and Key Laboratory of Micro and Nano Photonic Structures (Ministry of Education), Fudan University, Shanghai 200438, China
[*]corresponding author: myhu@fudan.edu.cn

Abstract: We theoretically and experimentally demonstrate the non-Hermitian skin effect in a 2D spectral and Lorentz reciprocal mechanical system in which the only non-Hermiticity is the gain and loss.

Non-Hermitian skin effect (NHSE) is characterized by the confinement of bulk modes to the boundary under open boundary conditions (OBCs), contrasting with their distribution under periodic boundary conditions (PBCs). This phenomenon is governed by the distinctive topological characteristics of complex eigenvalues specific to non-Hermitian systems. The NHSE, rooted in the non-trivial spectral winding, naturally manifests in non-reciprocal systems. Consequently, established methodologies rely on non-reciprocity to induce the NHSE. Here, we theoretically and experimentally demonstrate the NHSE in a 2D spectral and Lorentz reciprocal mechanical system in which the only non-Hermiticity is the gain and loss [Figure 1(a)]. Such NHSE exclusively occurs at boundaries where the macroscopic symmetry deviates from lattice symmetry, termed the geometry-dependent skin effect (GDSE), as shown in Figure 1(b). Experimentally, we confirm that the GDSE occurs only at the boundary where there is a mismatch between macroscopic symmetry and lattice symmetry by applying different pulse signals, as shown in Figure 1(c, d). Conversely, at the boundaries where macroscopic symmetry matches lattice symmetry, no GDSE is observed, as depicted in Figure 2.

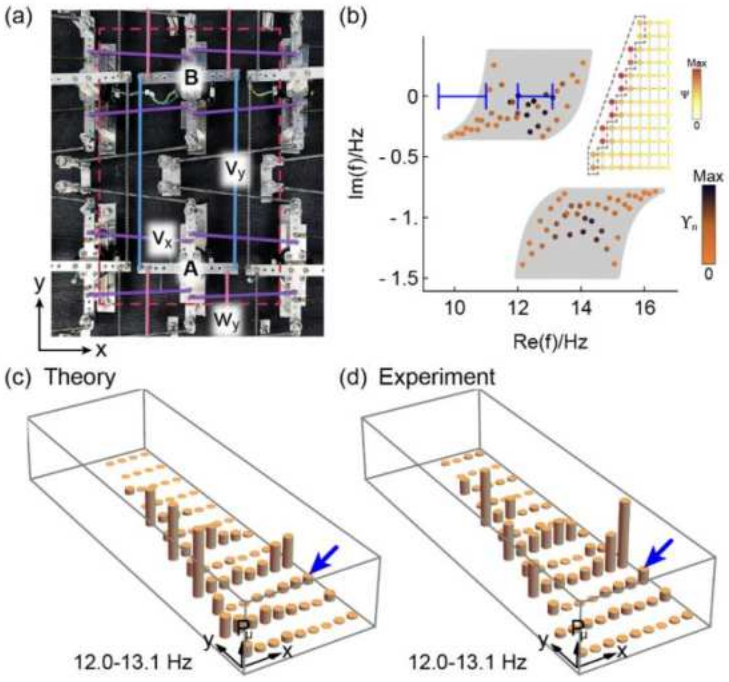


Figure 1 (a) The photo of the coupled rotational oscillators. (b) The OBC complex spectrum (colorful dots) of the trapezoidal structure with 78 sites. The gray background displays the corresponding PBC complex spectrum.

The plots of the (c) theoretical and (d) experimental spectral sum with different input chirp signals.

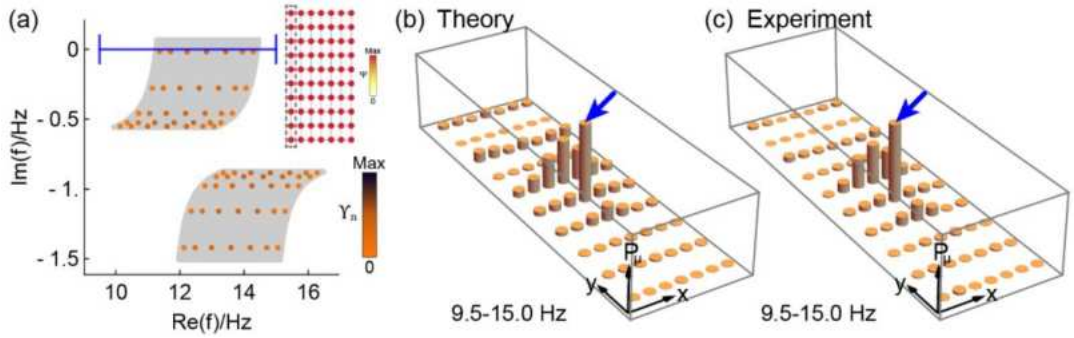


Figure. 2 (a) The OBC complex spectrum (colorful dots) of the rectangular structure with 70 sites. The plots of the (b) theoretical and (c) experimental spectral sum with different input chirp signals.

Our work not only reveals the universality of NHSEs in high-dimensional systems, but also underscores the critical influence of reciprocity and macroscopic geometry on the NHSE in two-dimensional systems and above, paving the way for novel approaches to wave structuring through non-Hermitian effects.

Acknowledgements: This work is supported by the National Natural Science Foundation of China (12174072, 11922416, 2021hwyq05), the Hong Kong Research Grants Council (RFS2223-2S01, 12302420, 12300419, 12301822), and the Natural Science Foundation of Shanghai (No. 21ZR1403700).

References

1. F. M., W. Wang, M. Hu, X. Wang, G. Ma and K. Ding, “Experimental Realization of Geometry-Dependent Skin Effect in a Reciprocal Two-Dimensional,” Phys. Rev. Lett., 131, 207201, 2023.

Arbitrary Chern Vectors in Non-Reciprocal 3D Acoustic Crystals

Yan Meng[1,2,*], Linyun Yang[2], Xiang Xi[1,2], Zhenxiao Zhu[2], Bei Yan[2], Yihao Yang[3], Gui-Geng Liu[4], Baile Zhang[4,5], and Zhen Gao[2,†]

[1] *School of Electrical Engineering and Intelligentization, Dongguan University of Technology, Dongguan, 523808, China*

[2] *Department of Electronic and Electrical Engineering, Southern University of Science and Technology, Shenzhen, 518055, China*

[3]*Interdisciplinary Center for Quantum Information, State Key Laboratory of Modern Optical Instrumentation, ZJU-Hangzhou Global Science and Technology Innovation Center, College of Information Science and Electronic Engineering, ZJU-UIUC Institute, Zhejiang University, 310027 Hangzhou, China*

[4]*Division of Physics and Applied Physics, School of Physical and Mathematical Sciences, Nanyang Technological University, 21 Nanyang Link, Singapore 637371, Singapore*

[5]*Centre for Disruptive Photonic Technologies, The Photonics Institute,Nanyang Technological University, Singapore, Singapore*

[*]presenting author: mengy@sustech.edu.cn
[†]corresponding author: gaoz@sustech.edu.cn

Abstract:
In this talk, we extend the 3D Chern insulator phase into acoustic crystals, introducing a strategy for constructing arbitrary Chern vectors. This approach facilitates surface-state torus knots or links on the surface of a single crystal with non-reciprocal coupling, offering a comprehensive understanding of bulk-boundary correspondence in topological Chern vectors.

Summary:
The topological invariant that characterizes Chern insulators (the celebrated Haldane model [1]) has recently evolved from a scalar Chern number to a topological Chern vector, extending the Chern-type bulk-boundary correspondence from one-dimensional (1D) edge states to two-dimensional (2D) surface states and forming nontrivial torus knots or links in the surface Brillouin zone [2]. However, so far, the exploration of topological Chern vector has been limited to its simplest form, $\boldsymbol{C} = (0,0,C_3)$, with only a single nonzero Chern number, resulting in the surface-state torus knots or links emerging only along an internal domain wall between two three-dimensional (3D) Chern insulators with perpendicular Chern vectors[2]. The arbitrary Chern vector $\boldsymbol{C} = (C_1, C_2, C_3)$ with multiple nonzero Chern numbers is still unexplored. On the other hand, since the first theoretical proposal[3] and experimental realization [4] of acoustic Chern insulators, it is still limited to 2D, and the acoustic 3D Chern insulators are still excluded.

As shown in Fig. 1, we extend the concept of the Chern vectors to the acoustic 3D Chern insulators that exhibit arbitrary Chern vectors, which allow the emergence of torus knots or links on the surface of a single crystal[5]. Additionally, we unveil the phenomenon of successive topological negative refraction at three adjacent faces of a single crystal, enabling acoustic chiral surface states pass through sharp edges continuously in 3D space via negative refraction without backscattering. Lastly, we illustrate that nontrivial torus knot or link surface states can manifest on the surface of a single 3D Chern insulator with arbitrary Chern vectors. This represents a stark contrast to previous findings and may find potential applications in topological acoustics.

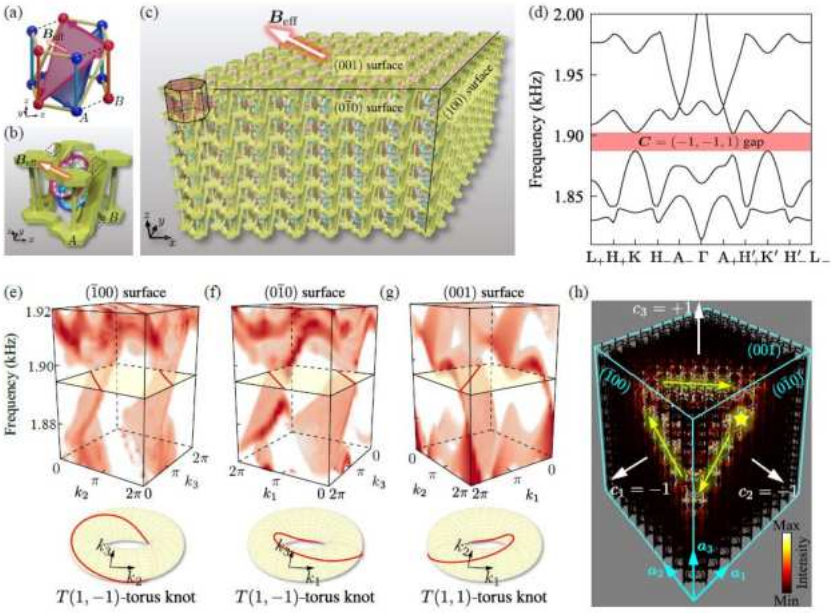


FIG. 1. Acoustic 3D Chern insulator with a Chern vector $\boldsymbol{C} = (-1, -1, 1)$. (a) The tilted 3D Haldane model and (b) its acoustic realization, in which the circulating airflows (blue and red arrows) are tilted to induce nonreciprocal hoppings between adjacent layers. (c) Schematic view of the acoustic 3D Chern insulator with a Chern vector $\boldsymbol{C} = (-1, -1, 1)$. (d) The simulated bulk band structure of the acoustic 3D Chern insulator with a 3D topological $\boldsymbol{C} = (-1, -1, 1)$ bandgap. (e)-(g) The chiral surface states dispersions (surface DOS) of the left ($\bar{1}$00), front (0$\bar{1}$0) and top (001) surfaces, respectively. The lower panels show the torus knots formed by winding the Fermi loops on three different surface BZs. (h) Full-wave simulated acoustic intensity distributions of the chiral surface states excited by a point source (yellow star) at 1.897 kHz on the surfaces of an acoustic 3D Chern insulator with a Chern vector $\boldsymbol{C} = (-1, -1, 1)$.

Acknowledgements: Y.M. acknowledges the support from the National Natural Science Foundation of China under Grant No. 12304484. Z.G, Basic and Applied Basic Research Foundation of Guangdong Province under Grant No. 2414050002552, and Shenzhen Science and Technology Innovation Commission under Grant No. 202308073000209. Z. G. acknowledges the support from the National Natural Science Foundation of China under Grant No. 62375118 and 12104211, Shenzhen Science and Technology Innovation Commission under Grant No. 20220815111105001, and SUSTech under Grant No. Y01236148 and No. Y01236248. L.Y. acknowledges the support from China Postdoctoral Science Foundation under Grant No. 2023M731533, Shenzhen Science and Technology Program under Grant No. RCBS20221008093326054 and SUSTech Presidential Postdoctoral Fellowship. B.Z. acknowledges the support from National Research Foundation Singapore Competitive Research Program No. NRF-CRP23-2019-0007, and Singapore Ministry of Education Academic Research Fund Tier 2 under grant No. MOE2019-T2-2-085.

References

1. Haldane, F. D. M. Model for a quantum Hall effect without Landau levels: Condensed-matter realization of the" parity anomaly". *Physical Review Letters* **61**, 2015 (1988).
2. Liu, G.-G. *et al.* Topological Chern vectors in three-dimensional photonic crystals. *Nature* **609**, 925–930 (2022).
3. Yang, Z. *et al.* Topological acoustics. *Phys Rev Lett* **114**, 114301 (2015).
4. Ding, Y. *et al.* Experimental Demonstration of Acoustic Chern Insulators. *Phys. Rev. Lett.* **122**, 014302 (2019).
5. Linyun, Y. *et al.* Acoustic Three-dimensional Chern Insulators with Arbitrary Chern Vectors. Preprint at http://arxiv.org/abs/2401.07040 (2024).

Observation of Discrete-Light Temporal Refraction by a Quantized Moving Gauge Potential Barrier

Chengzhi Qin[1*], Bing Wang[1], Stefano Longhi[2] and Peixiang Lu[1]

[1]School of Physics and Wuhan National Laboratory for Optoelectronics and, Huazhong University of Science and Technology, Wuhan 430074, China.
[2]Dipartimento di Fisica, Politecnico di Milano, Piazza Leonardo da Vinci 32, I-20133 Milano, Italy.
[*]corresponding author: qinchengzhi@hust.edu.cn

Abstract: We observe discrete-light temporal refraction by a moving gauge-potential barrier, which obeys a different Snell's law compared to traditional refraction at a static boundary. To eliminate beam splitting we find the barrier can only move at a quantized speed of integer and fractional values, which exhibit reflectionless and reflective refractions.

Main results:

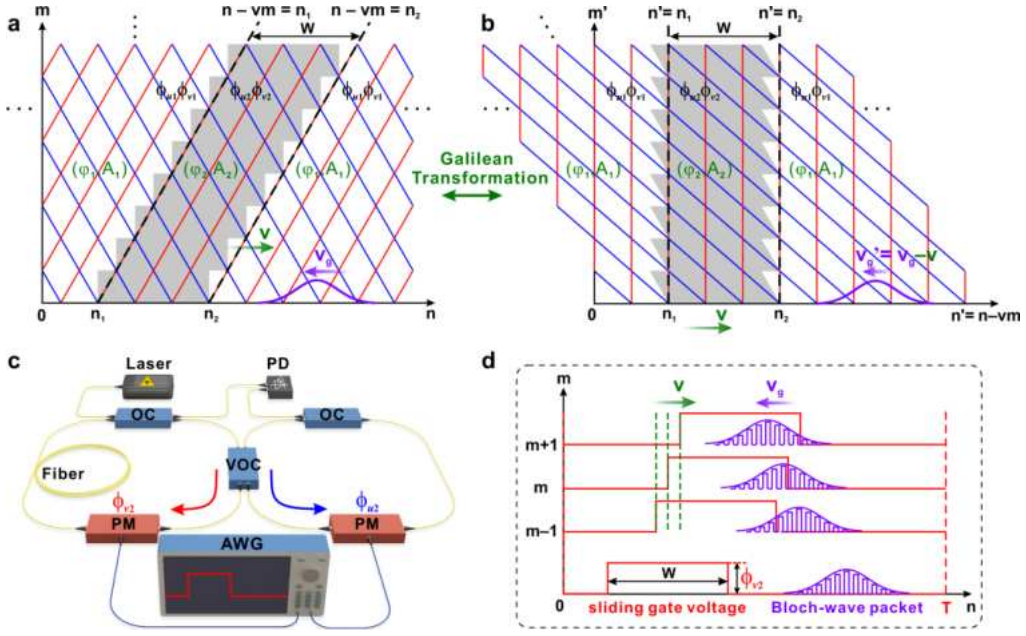


Fig. 1. a, b. Schematic of a moving gauge potential barrier in a synthetic temporal lattice described in laboratory and moving reference frames. **c.** Schematic of coupled fiber circuit to create the temporal lattice. **d.** The required sliding gate voltage to create the moving gauge potential barrier.

Figure. 1a shows a moving gauge potential barrier in a synthetic discrete-time quantum walk lattice made of leftward (blue) and rightward (red) links towards scattering nodes labeled by position n and step m. The phase modulations are (ϕ_{u2}, ϕ_{v2}) and (ϕ_{u1}, ϕ_{v1}) inside and outside the moving barrier, corresponding to a gauge potential distribution of (φ_2, A_2) and (φ_1, A_1). The two moving boundaries are $n - vm = n_{1,2}$, where v is the moving speed, n_1 and n_2 are initial positions of the two boundaries and $W = n_2 - n_1$ is barrier's width. The Bloch-wave packet (purple) is incident from the barrier's right side. Figure 1b shows the lattice and gauge potential distribution in the moving reference frame (n', m') obtained through Galilean transformation $m' = m$, $n' = n - vm$ from laboratory frame (n, m). The reason why we need to apply Galilean transformation is that in the laboratory frame, the boundaries are tilted, such that Snell's law, conservation of tangential propagation constants is not applicable.

By contrast, if we choose the moving frame (n', m') where the two boundaries become vertical that are parallel to the m' axis, the Snell's law is applicable. The Snell's law in moving frame is $\theta_{\pm}'(k_{t,\pm}) = \theta_{\pm}'(k_{r,\pm}) = \theta_{+}'(k_i)$, where

$$\begin{cases} \theta'_{\pm}(k_{t,\pm}) = \pm\cos^{-1}[\cos(\beta)\cos(k_{t,\pm} - \Delta A)] - \Delta\varphi - vk_{t,\pm} \\ \theta'_{\pm}(k_{r,\pm}) = \pm\cos^{-1}[\cos(\beta)\cos(k_{r,\pm})] - vk_{r,\pm} \\ \theta'_{+}(k_i) = \pm\cos^{-1}[\cos(\beta)\cos(k_i)] - vk_i \end{cases} \quad (1)$$

from which we can solve the refracted and reflected Bloch momenta k_r and k_t for a given incident k_i. To eliminate beam splitting during refraction, one requires $v'_g(k_{t,+}) = v'_g(k_{t,-}) = \partial\theta_{\pm}'(k)/\partial k = \pm\cos(\beta)\sin(k_{t,\pm} - \Delta A) - v$, which gives rise to the quantized condition of moving speed $v = 1/q = 1$ for integer value or 1/3, 1/5, … for fractional values.

The band structures for $v = 1$ are shown in Fig. 2a, where incident/refracted packets are denoted by blue and red circles. Figure 2b shows the field evolution for integer speed $v = 1$, $k_i = -0.5\pi$, showing the beam-splitting-free refraction. Figure 2c shows field evolution for $k_i = -0.148\pi$, which exhibit the refractionless effect, thus realizing transparent moving potential. Figures 2d-2f show the case of fractional speed $v = 1/3$, showing beam reflection compared to $v = 1$, as evidenced by Fig. 2e. Figure 2f proves the existence of transparent potential for $v = 1/3$.

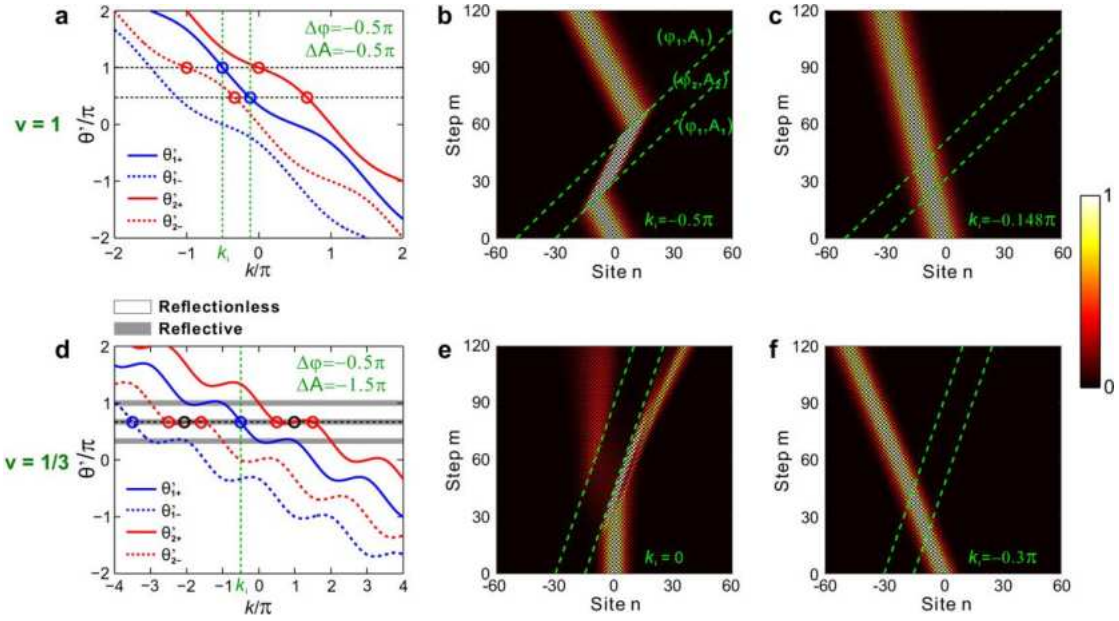


Fig. 2. a. Band structures for the $v = 1$ case. **b. c.** Field evolutions for $k_i = -0.5\pi$ and $k_i = -0.148\pi$ under $v = 1$. **d.** Band structures for the $v = 1/3$ case. **e. f.** Field evolutions for $k_i = 0$ d $k_i = -0.3\pi$ under $v = 1/3$.

Acknowledgements: The work was supported by National Natural Science Foundation of China (No. 12204185, 12374305, 62305122 and 12021004), and Natural Science Foundation of Hubei Province (No. 2022CFB036).

References

1. C. Qin *et al.*, "Observation of discrete-light temporal refraction by moving potentials with broken Galilean invariance," Nature Communications, under review.
2. S. Longhi, "Reflectionless and invisible potentials in photonic lattice," Optics Letters, Vol. 42, No. 16, 3229-3232, 2017.
3. S. Longhi, "Refractionless propagation of discretized light," Optics Letters, Vol. 42, No. 24, 5086–5089, 2017.

Heat circulation metadevices

Ran Ju[1,2,3,4], Pei-Chao Cao[1,2,3,4], Dong Wang[1,2,3,4], Minghong Qi[1,2,3,4], Liujun Xu[6], Shuihua Yang[5], Cheng-Wei Qiu[5]*, Hongsheng Chen[1,2,3,4]* Ying Li[1,2,3,4]*

[1] Interdisciplinary Center for Quantum Information, State Key Laboratory of Extreme Photonics and Instrumentation, ZJU-Hangzhou Global Scientific and Technological Innovation Center, Zhejiang University, Hangzhou 310027, China
[2] International Joint Innovation Center, The Electromagnetics Academy at Zhejiang University, Zhejiang University, Haining 314400, China
[3] Key Lab. of Advanced Micro/Nano Electronic Devices & Smart Systems of Zhejiang Jinhua Institute of Zhejiang University, Zhejiang University, Jinhua 321099, China
[4] Shaoxing Institute of Zhejiang University, Zhejiang University, Shaoxing 312000, China
[5] Department of Electrical and Computer Engineering, National University of Singapore, Singapore 117583, Singapore
[6] Graduate School of China Academy of Engineering Physics, Beijing 100193, China
*corresponding author: chengwei.qiu@nus.edu.sg; hansomchen@zju.edu.cn; eleying@zju.edu.cn

Abstract: Having developed a comprehensive thermal scattering theory that describes the nonreciprocal transmission properties of temperature field effectively, this work creates a metadevice that supports both dynamic and steady-state nonreciprocal heat transfer. It uncovers the unique multiple-scattering effect at steady state, as well as the resonance enhanced nonreciprocity of thermal fields.

Nonreciprocal heat transfer is of great significance for efficient thermal energy utilization, thermal management, and performance improvement of thermal logic processing[1]. However, most existing approaches to macroscopic thermal nonreciprocity rely on nonlinear or spatiotemporal-modulation effects[2], which come with apparent drawbacks, such as limited operating temperature ranges and complex experimental setups[3]. Meanwhile, constrained by their inherent mechanisms, these methods can hardly be effective under both dynamic and static excitations[4,5].

Confronted with these challenges, here we develop a convection-based thermal metadevice where nonreciprocity can be realized under both the dynamic and steady-state temperature excitations, shown in Figure 1a. Starting from the convection-diffusion equation and the plane wave solution of the propagating thermal field[6], the scattering matrix $\boldsymbol{S}$ which relates the outgoing and ingoing signals ($(B_1, B_2, B_3)^{\mathrm{T}} = \boldsymbol{S}(A_1, A_2, A_3)^{\mathrm{T}}$) can be derived by thermally intercoupling all parts of the thermal metadevice, and the strength of nonreciprocity can be defined as $\Gamma = |S_{21}/S_{31}|$. Consequently, the dynamic thermal nonreciprocity is attributed to an asymmetric scattering matrix [7], where the nontrivial dependencies between nonreciprocity and dynamic parameters are shown in Figure 1b. However, this matrix approaches a symmetric limit at the steady state but still conveys significant steady-state nonreciprocity counterintuitively. By delving into the physical implication of the thermal scattering process, we reveal a unique nonreciprocal mechanism where the boundary-induced multiple scattering counterbalances the diminishing asymmetry[8] (Figure 1c). Then we observe a strong resonance phenomenon in this metadevice (Figure 1d and 1e). The multiple-scattering nonreciprocity Γ' can be expressed as a function of the single scattering coefficients when the number of scattering iterations n tends to infinity, where

$$\Gamma' = \left| \frac{\tilde{r} S_{31}^2 + S_{21} - \tilde{r} S_{11} S_{21}}{\tilde{r} S_{21}^2 + S_{31} - \tilde{r} S_{11} S_{31}} \right| \tag{1}$$

This theory serves as a bridge between thermal scattering analysis and traditional heat-flux analysis. Based on it, we have finally verified the nonreciprocal heat transfer effect in this metadevice experimentally (Figure 1e).

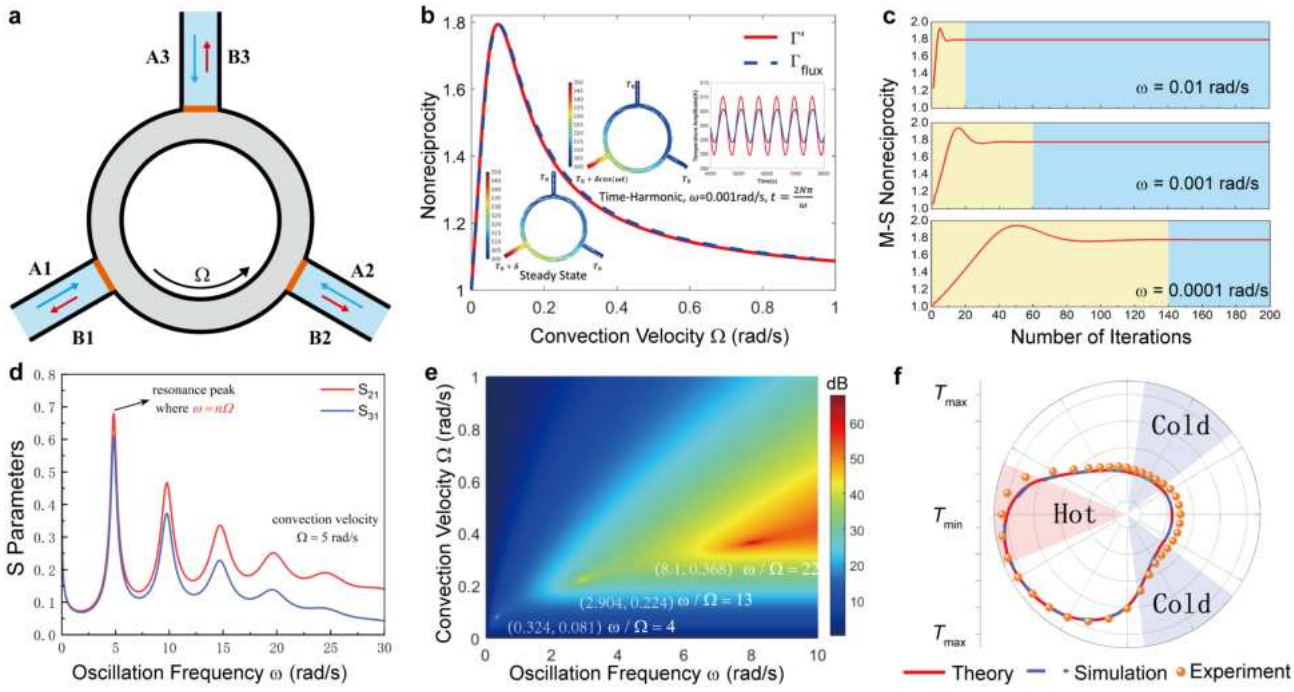


Figure 1. Heat circulation metadevices. a) The sketch of the thermal circulator. b) Nontrivial nonreciprocity dependencies. c) Boundary-induced multiple scattering effect. d) & e) Resonance phenomena. f) Nonreciprocal temperature distribution.

The work was sponsored by Key Research and Development Program of the Ministry of Science and Technology under Grants Nos. 2023YFB4604100 and 2022YFA1405200, and the National Natural Science Foundation of China (NNSFC) under Grants Nos. 92163123 and 52250191. C.-W.Q. acknowledges financial support from the Ministry of Education, Singapore (Grant No. A-8000107-01-00).

References

1. F. Yang, Z. Zhang, L. Xu, Z. Liu, P. Jin, P. Zhuang, M. Lei, J. Liu, J.-H. Jiang, X. Ouyang, F. Marchesoni, J. Huang, "Controlling mass and energy diffusion with metamaterials." Rev. Mod. Phys. Vol. 96, No. 015002, 2024.
2. Y. Li, X. Shen, Z. Wu, J. Huang, Y. Chen, Y. Ni, J. Huang, "Temperature-Dependent Transformation Thermotics: From Switchable Thermal Cloaks to Macroscopic Thermal Diodes." Phys. Rev. Lett. Vol. 115, No. 195503, 2015.
3. D. Torrent, O. Poncelet, J.-C. Batsale, "Nonreciprocal Thermal Material by Spatiotemporal Modulation." Phys. Rev. Lett. Vol. 120, No. 125501, 2018.
4. A. A. Maznev, A. G. Every, O. B. Wright, "Reciprocity in reflection and transmission: What is a 'phonon diode'?" Wave Motion, Vol. 50, No. 776–784, 2013.
5. J. Li, Y. Li, P.-C. Cao, M. Qi, X. Zheng, Y.-G. Peng, B. Li, X.-F. Zhu, A. Alù, H. Chen, C.-W. Qiu, "Reciprocity of thermal diffusion in time-modulated systems." Nat. Commun. Vol. 13, No. 167, 2022.
6. Y. Li, Y.-G. Peng, L. Han, M.-A. Miri, W. Li, M. Xiao, X.-F. Zhu, J. Zhao, A. Alù, S. Fan, C.-W. Qiu, "Anti–parity-time symmetry in diffusive systems." Science, Vol. 364, No. 170–173, 2019.
7. Y. Li, J. Li, M. Qi, C.-W. Qiu, H. Chen, "Diffusive nonreciprocity and thermal diode." Phys. Rev. B, Vol. 103, No. 014307, 2021.
8. Y. Li, M. Qi, J. Li, P.-C. Cao, D. Wang, X.-F. Zhu, C.-W. Qiu, H. Chen, "Heat transfer control using a thermal analogue of coherent perfect absorption." Nat. Commun. Vol. 13, No. 2683, 2022.

The Manipulation of Topological Modes and Anderson Localized Modes via non-Hermicity

Xulong Wang[1, 2*], Wei Wang[1, 2], Guancong Ma[1, 2]
[1]Department of Physics, Hong Kong Baptist University, Kowloon Tong, Hong Kong, China
[2]Shenzhen Institute for Research and Continuing Education, Hong Kong Baptist University, China
[*]corresponding author: 20482698@life.hkbu.edu.hk

Abstract: In this work, we utilize active resonant platforms to demonstrate the manipulation of topological modes (TMs), and Anderson localized modes (ALMs) through non-Hermicity. Localized topological modes can be reconfigured into diverse shapes via non-Hermitian interactions. Complex Anderson modes can be formed in a one-dimensional non-Hermitian disordered ring.

Non-Hermitian systems, characterized by their complex spectra, are intrinsically well-suited for simulating open systems engaged in environmental interactions. These interactions facilitate the emergence of unique effects such as energy modulation through gain and loss and nonreciprocal interaction, catalyzing a spectrum of novel phenomena. One of the most fascinating phenomena is the non-Hermitian skin effect (NHSE), where the bulk states become skin modes localized at the open boundaries. The incorporation of non-Hermiticity introduces intricate challenges in the analysis of topological modes (TMs) and Anderson localized modes (ALMs), which may yield fresh perspectives on the underlying behaviors of these systems.

In the first part, we harness the NHSE to manipulate the wavefunctions of TMs. By laying out an active mechanical lattice as a one-dimensional (1D) non-Hermitian Su-Schrieffer-Heeger (NH-SSH) model, we witness the complete delocalization of a topological zero mode (TZM) [1-3]. Advancing to two-dimensional (2D) topological lattices, our work showcases the transformation of 1D topological edge modes (TEMs) and 0D second-order topological corner modes (TCMs) into various configurations by tailoring the non-Hermiticity distribution. Despite the TMs spreading out due to the NHSE, they maintain spectral isolation within the bandgap and preserve their topological robustness. Our discoveries release TMs from their usual confinement to boundaries, opening new avenues for their application in the realm of topological phenomena.

In a chain with a topological interface, the left side is a trivial NH-SSH chain containing non-reciprocal coupling (δ), and the right side is a non-trivial Hermitian SSH chain with reciprocal coupling. With the increase of $|\delta|$, the TZM spread out more in the NH-SSH chain. The TZM re-localizes at the left end of the system for larger $|\delta|$. As for 2D non-Hermitian topological quadrupole insulator (NH-TQI):

$$H_Q(k_x, k_y) = \begin{bmatrix} 0 & R_x(k_x) & R_y(k_y) & 0 \\ M_x(k_x) & 0 & 0 & -R_y(k_y) \\ M_y(k_y) & 0 & 0 & R_x(k_x) \\ 0 & -M_y(k_y) & M_x(k_x) & 0 \end{bmatrix} \quad (1)$$

where $R_\mu(k_\mu) = v_\mu + w_\mu e^{-ik_\mu}$ and $M_\mu(k_\mu) = (v_\mu + \delta_\mu) + w_\mu e^{ik_\mu}$ with $\mu = x, y$.
v_μ and w_μ denoting the magnitude of intra/intercell hopping, respectively. δ_μ are the additional non-Hermitian terms introduced in the lattice, as shown in Fig. 1(d).

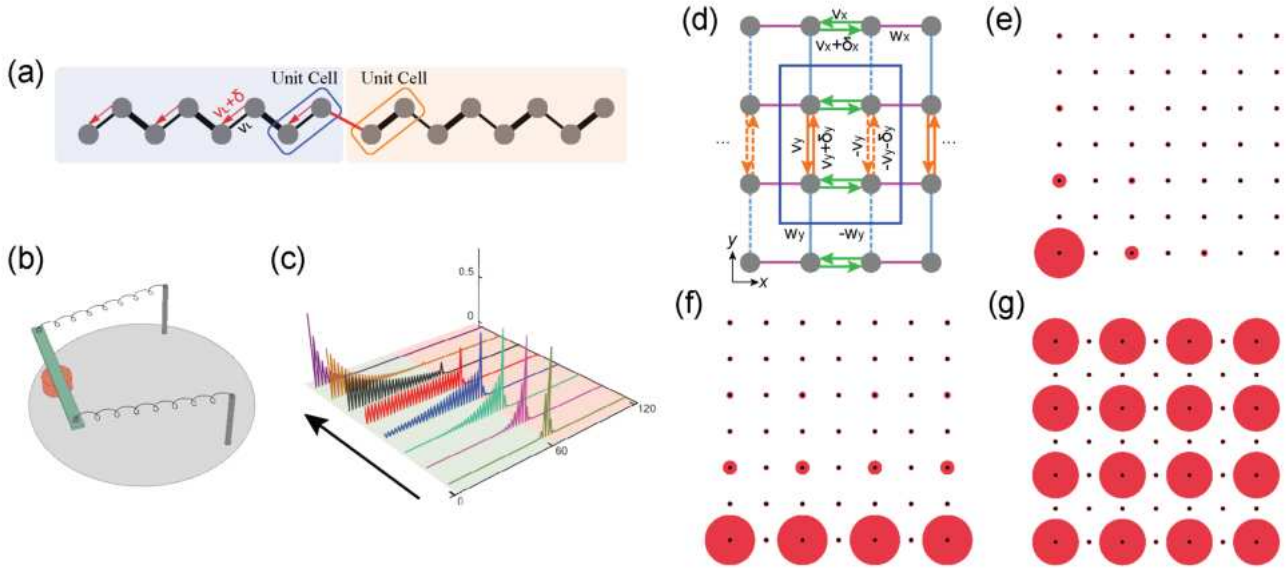


Figure. 1 (a) 1D NH-SSH chain with TZM localized at the interface. (b) The schematic of a rotational oscillator that functions as the on-site orbital within our experimental lattice. (c) The real space wavefunctions of TZMs for different δ. (d) The model of NH-TQI. The wavefunction of TCM in the NH-TQI is localized at the lower-left corner for the Hermitian case (e). The extension of the TCM along the lower edge (f), and into the 2D surface (g) under different non-Hermicity distributions.

In addition, we will also discuss the effect of non-Hermiticity on Anderson localization. The seminal contributions to this area belong to Hatano and Nelson stand out [4]. They uncovered a localization transition triggered by the introduction of a sufficiently large constant imaginary vector potential into the Schrödinger equation. Inspired by the groundbreaking work of Hatano and Nelson and recent insights into non-Hermitian systems, we explore new configurations of random potential effects in a 1D non-Hermicity ring and identify new types of localization-delocalization behaviors that relate to the complex spectrum of the system.

Acknowledgement: The National Key R&D Program of China No. 2022YFA1404400

References

1. Wang, W., Wang, X. and Ma, G., "Non-Hermitian morphing of topological modes." Nature 608.7921, 2022
2. Wang, W., Wang, X. and Ma, G., Extended State in a Localized Continuum. Phys. Rev. Lett., 129(26), 264301, 2022
3. Wang, X., Wang, W. and Ma, G., Extended topological mode in a one-dimensional non-Hermitian acoustic crystal. AAPPS Bulletin, 33(1), 23, 2023
4. Hatano, N., and Nelson, D.R., Localization transitions in non-Hermitian quantum mechanics. Phys. Rev. Lett., 77(3), 570, 1996

Acoustic orbital-related topological states and phase transitions

Feng Gao, Yu-Gui Peng*, Xue-Feng Zhu*

School of Physics and Innovation Institute, Huazhong University of Science and Technology, Wuhan 430074, China
*corresponding author: ygpeng@hust.edu.cn, xfzhu@hust.edu.cn, aalu@gc.cuny.edu

Abstract: In this talk, we concentrate on the topological states and phase transitions induced by orbital-interactions. The introduction of acoustic orbitals enables counterintuitive orbital-dependent topological edge states and versatile corner states, opening avenues for exploring orbital-related topological physics and sound-wave interaction.

Summery: Topological insulators are enabled by broken crystal symmetries and associated degrees of freedom (DoFs), such as spin or valley DoFs in a periodic lattice, significant to unveil different topological phases[1]. Beyond the degree of spin, the intrinsic orbital DoF also plays a significant role in correlated electrons and solid state materials, which induce many unique topological phases such as orbital superfluidity[2] and topological semimetals[3]. Recently, employing ODoFs on the investigation of topological matter has been frequently extended to photonics[4] and electronics[5], which has not yet been extensively explored in acoustics.

Exploiting paired degenerate *p* orbitals and the correlated orbital-interactions in the acoustic resonators, we first demonstrate counterintuitive topological edge modes and topological phase transitions in 1D orbital SSH lattices[6]. As shown in Fig. 1(a), for the leftmost and rightmost resonators, they are strongly and weakly coupled to the topological chain with different coupling tubes d_1 and d_2 ($d_2<d_1$=0.6cm), respectively. Unlike the conventional SSH model, with edge modes residing on the rightmost resonator, topological phase transitions emerge in our orbital SSH chains. Keeping the bonding angle at 90°, the p_x-like edge mode displays tunneling through the bulk chain from the right to the left termination by varying d_2 from 0.1cm to 0.4cm, and the transition appears at d_2=0.25cm in the simulations, which can be not found in the conventional counterpart obtained by setting the bonding angle as 180°. In experiments, the counterintuitive edge mode on leftmost resonator is evidenced with a p_x-like source, as shown in Fig 1(c), agreeing well with the simulations. Meanwhile, a p_y-like source cannot excite the leftmost resonator, featuring strong orbital-selectivity.

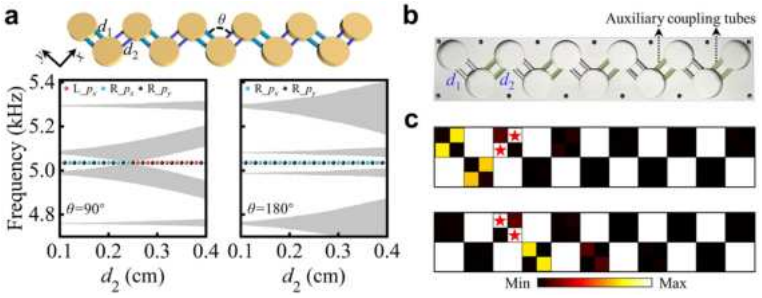


Fig. 1. Topological transitions and edge modes in dimerized orbital SSH model. (a) Top: Sketch of the orbital SSH model with dimerized coupling tubes. Bottom: Energy spectra for orbital SSH models and conventional SSH models. (b) Experimental sample. (c) Measured pressure amplitude fields.

Then, we extended exploration of orbitals of topological matter to acoustic higher-order insulators[7]. Here, we exploit degenerate orbitals in acoustic resonant cavities to demonstrate versatile, orbital-selective, higher-order topological corner states. Type-II corner states are theoretically investigated and experimentally demonstrated based on tailored orbital interactions, without the need for long-range hoppings that has so far served as a key ingredient for Type-II corner states in single-orbital systems. Moreover, we employed a judicious excitation mechanism combining both frequency and source polarization to excite and visualize these orbital corner states, and four types of orbital states can be well excited at the corners as displayed in Fig. 2.

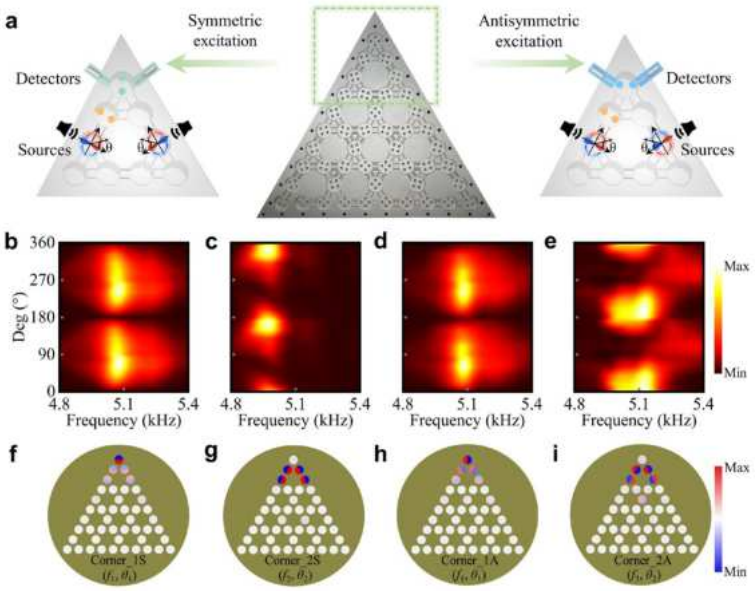


Fig. 2. Experimental characterization of orbital corner states. (a) Middle panel: The fabricated sample. Left and right panels display the schematics of symmetric and antisymmetric excitation and detection. (b-e) The measured spectra for versatile corner states. (f-i) The measured pressure field distributions under symmetric excitations and antisymmetric excitations.

References

1. Hasan, M. Z. *et al*. "Colloquium: Topological insulators," Rev. Mod. Phys. 82, 3045-3067, 2010.
2. Wirth, G. *et al*. "Evidence for orbital superfluidity in the *P*-band of a bipartite optical square lattice," Nat. Phys. 7, 147-153, 2011.
3. Sun, K. *et al*. "Topological semimetal in a fermionic optical lattice," Nat. Phys. 8, 67-70, 2012.
4. Milićević, M. *et al*. "Type-III and Tilted Dirac Cones Emerging from Flat Bands in Photonic Orbital Graphene," Phys. Rev. X 9, 031010, 2019.
5. Slot, M. R. *et al*. "p-Band Engineering in Artificial Electronic Lattices," Phys. Rev. X 9, 011009, 2019.
6. Gao, F. *et al*. "Orbital topological edge states and phase transitions in one-dimensional acoustic resonator chains," Nat. Commun. 14, 8162, 2023.
7. Gao, F. *et al*. "Acoustic Higher-Order Topological Insulators Induced by Orbital-Interactions," Adv. Mater. 2312421, 2024

Non-Hermitian skin effects in anisotropic metamaterials

Y. Tian[1], and X. Zhang[1*]

[1] National Laboratory of Solid State Microstructures and Department of Materials Science and Engineering, Nanjing University, Nanjing 210093, China

[*]corresponding author: xiujuanzhang@nju.edu.cn

Abstract: We demonstrate the occurrence of non-Hermitian skin effect (NHSE) in anisotropic metamaterials. Our experiments reveal selective excitation of skin modes based on the wave vector, where the localization of these modes is precisely controlled by an effective gauge potential stemming from the anisotropy of the non-Hermitian density tensor.

Beyond the scope of Hermitian physics, non-Hermiticity has significantly advanced our understanding of non-equilibrium phenomena, revealing novel effects such as the non-Hermitian skin effect (NHSE). While NHSE is commonly predicted in periodic lattice systems, its exploration in more general continuum and homogeneous media remains limited. Here, we demonstrate the occurrence of NHSE in anisotropic homogeneous media using subwavelength acoustic multilayer metamaterials. Our experiments reveal selective excitation of skin modes based on the wave vector, where the localization of these modes is precisely controlled by an effective gauge potential stemming from the anisotropy of the non-Hermitian density tensor. Additionally, we identify the emergence of corner skin modes, showcasing the potential of higher-order NHSE. Our research opens a new pathway for exploring NHSE in homogeneous systems, rooted in the interplay between non-Hermitian physics and anisotropy, and offers a novel method for guiding sound, light, and other types of waves.

Nanophotonics in Biomedical Applications

Ultrafast Photonic PCR with All-Solution Processed Perfect Absorber

Seho Lee[1,2], Abdulrahman Alsaadi[1,2], and Inki Kim[1,2*]

[1]Department of Biophysics, Institute of Quantum Biophysics, Sungkyunkwan University, Suwon 16419, Republic of Korea
[2]Department of Intelligent Precision Healthcare Convergence, Sungkyunkwan University, Suwon 16419, Republic of Korea
[*]corresponding author: inki.kim@skku.edu

Abstract: We developed a low-cost all-solution processed metaplasmonic PCR chip using a metal-insulator-meal configuration with gold nanoparticles and MXene $Ti_3C_2T_x$. This chip featuring ultra-high absorption and low-power consumption, overcomes cost challenges associated with traditional methods. Utilizing a solution processing approach, we achieved 30 cycles of the PCR process within 8 minutes.

Research on polymerase chain reaction (PCR) technology for rapid and accurate detection of pathogens is still actively being conducted. However, PCR amplification requires more than 30 cycles of thermal cycling and high power consumption, making it generally restricted to laboratory environments. Therefore, there is a need for portable and rapid nucleic acid-based diagnostic technologies that can be used outside of the laboratory. Recently, photonic PCR technology using low-power LEDs has garnered attention [1]. However, the fabrication of metamaterial surfaces still relies heavily on equipment such as E-beam lithography and E-beam evaporators, which pose significant drawbacks in terms of cost and time [1,2].

We conducted PCR using an efficient and low-cost all-solution processed perfect absorber based on MXene. We utilized a MXene-SiO_2-Gold-nanoparticles structure to enhance absorption efficiency, achieving over 98% absorption at the targeted wavelength of 940nm for infrared LED. The high absorption efficiency of the MXene-SiO_2-Gold-nanoparticles is attributed to the plasmonic effect. In this structure, the gold-nanoparticles induce surface plasmon resonance, concentrating incident light at specific wavelengths to enhance absorption efficiency. Additionally, the MXene and SiO_2 coatings improve the efficient generation and interaction of surface plasmons, contributing to the enhancement of absorption efficiency. These plasmonic effects enable wavelength-selective absorption and overall improvement of the structure's optical performance. In the fabrication process, we circumvented the significant drawbacks in terms of cost and time by completing the fabrication using a spin-coater apparatus, without the need for equipment such as E-beam lithography or E-beam evaporators, often associated with high expenses and time consumption. Gold-nanoparticles were deposited using the drop-casting method, covering approximately 75% of the overall surface area.

We performed 30 thermal cycles from the denaturation temperature of 95°C to the annealing temperature of 65°C, achieving a heating rate of 14.7°C/s and a cooling rate of 6.3°C/s in an ultrafast photonic quantitative PCR. Overall, the low power consumption and highly efficient photo-thermal effect of our meta-absorber demonstrate the potential use of metasurfaces for ultrafast qPCR for point-of-care (POC) molecular diagnostics. This highlights MXene-based metamaterial absorbers as promising for high-speed on-site molecular diagnostics.

References

1. Kang, B.-H. et al. "Ultrafast and Real-Time Nanoplasmonic On-Chip Polymerase Chain Reaction for Rapid and Quantitative Molecular Diagnostics." ACS Nano 15, 10194-10202, 2021.
2. Son, Jun Ho, et al. "Ultrafast photonic PCR." Light: Science & Applications 4.7, e280-e280, 2015.

Au film-porous anodic aluminum oxide-Al hybrid nanomaterial-based optical biosensor for detection of the VEGFA protein.

U. Malinovskis[1*], A. Reke[1], R. Poplausks[1], A. Dutovs[1], O. Putans[1], I. Oliseveca[1], D. Erts[1,2], I. Muiznieks[3], J. Prikulis[1,4]

[1]Institute of Chemical Physics, University of Latvia, 19 Raina Blvd., Riga LV-1586, Latvia,
[2]Faculty of Chemistry, University of Latvia, 1 Jelgavas Str., Riga LV-1004, Latvia,
[3]Faculty of Biology, University of Latvia, 1 Jelgavas Str., Riga LV-1004, Latvia,
[4]Faculty of Physics, Mathematics and Optometry, University of Latvia, 3 Jelgavas Str., Riga LV-1004, Latvia
[*]corresponding author: uldis.malinovskis@lu.lv

Abstract: We tested the suitability of Au film-porous anodic aluminum oxide (PAAO)-Al plasmonic nanomaterials as sensor substrate for optical detection of vascular endothelial growth factor A (VEGFA). These substrates are suitable for refractometric detection of elevated concentrations of VEGFA protein using simple optical microscopy setup.

The PAAO acts as a cost-effective template for the lithography-free manufacturing of nanostructured sensor substrates. This approach has the potential to overcome challenges in producing localized surface plasmon resonance (LSPR) sensor substrates, given its simplicity and applicability in standard chemistry labs. In our study, we tested the usability of Au film-PAAO-Al to detect the molecular biomarker VEGFA in water-based solutions. Vascular endothelial growth factor A plays a key role in normal and pathological angiogenesis. Increased levels of VEGFA protein in human body fluids are associated with malignant tumor development and degenerative eye diseases [1]

The two-step anodization method was used to fabricate thin PAAO layers on an aluminum surface in 0.3 M oxalic acid electrolyte at 40 V potential [2,3]. These layers feature a pore diameter of 40 nm and an interpore distance of approximately 110 nm. The obtained PAAO templates were coated with an optically thin (20-30 nm) layer of gold [4]. The gold surface of Au film-PAAO-Al substrates was functionalized with modified anti-VEGF 3'-thiolated DNA aptamer [5]. After functionalization, substrates were treated with bovine serum albumin to prevent non-specific protein absorption on sensor surfaces. The prepared substrates were used for the detection of the human $VEGF_{165}$ isoform in phosphate-buffered saline solution. Two methods of signal detection were investigated: the LSPR scattering setup and reflectance spectroscopy.

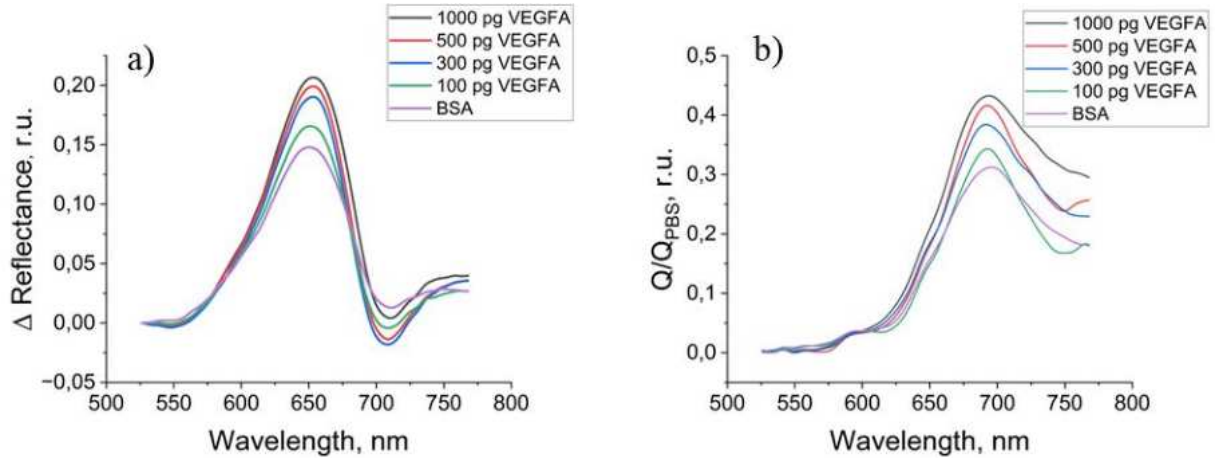


Figure 1. VEGFA protein detection sensitivity a) in reflectance mode spectroscopy (difference between VEGFA signals and reference) and b) in scattering mode spectroscopy (s-polarized illumination).

Reflection mode spectroscopy (Fig.1 a) showed good signal to background ratio and change of signal intensity was detected at presence of 100 – 1000 pg/mL VEGF protein. Scattering mode illumination with s-polarized light source (Fig.1 b) produced wider and asymmetrical spectral peaks in comparison with reflection mode spectroscopy.

Acknowledgements: the work was performed within the Latvian Council of Science fundamental and applied research project LZP-2020/1-0200 "Nanostructured multilayer hybrid coatings for interferometric and optoelectronic sensors".

References

1. Ferrara, N., "Vascular endothelial growth factor: Basic science and clinical progress," Endocr. Rev., Vol. 25, No. 4, 581–611, 2004.
2. Masuda, H. and K. Fukuda, "Ordered Metal Nanohole Arrays Made by a Two-Step Replication of Honeycomb Structures of Anodic Alumina," Science, Vol. 268, No. 5216, 1466–1468, 1995.
3. Malinovskis, U., R. Popļausks, A. Jurkevičiūtė, A. Dutovs, K. Berzins, V. Perkanuks, W. Simka, I. Muiznieks, D. Erts, and J. Prikulis, "Optimization of Colloidal Gold Nanoparticles on Porous Anodic Aluminum Oxide Substrates for Refractometric Sensing," ACS Omega, Vol. 7, No. 44, 40324–40332, 2022.
4. Prikulis, J., T. Tamulevičius, R. Popļausks, G. Bergs, I. Apsite, U. Malinovskis, A. Actins, and D. Erts, "Optical properties of thin metal films with nanohole arrays on porous alumina-aluminum structures," RSC Adv., Vol. 5, No. 83, 68143-68150, 2015.
5. Kaur, H. and L.Y.LYung, "Probin. g high affinity sequences of DNA aptamer against VEGF165". PLoS ONE, Vol. 7, No. 2, 19–26, 2012.

Biomedical applications of laser reirradiated metallic nanoparticles

AM Vilas[1], M. Boutinguiza[1,2], M. Fernández-Arias[1], D. Rodríguez[3], O. Barro[1], F. Arias-González[1], P. Pou-Álvarez[1], R.F. Soto[1], J. Pou[1,2*]

[1]LaserON Research Group, CINTECX, School of Engineering, University of Vigo, Vigo, Spain
2Galicia Sur Health Research Institute (IIS Galicia Sur), SERGAS-UVIGO, 36213 Vigo, Spain
3Biomaterials, Biomechanics and Tissue Engineering Group, Mat.Sci. Dept., UPC-Barcelona TECH, 08930 Barcelona, Spain
[*]corresponding author: jpou@uvigo.es

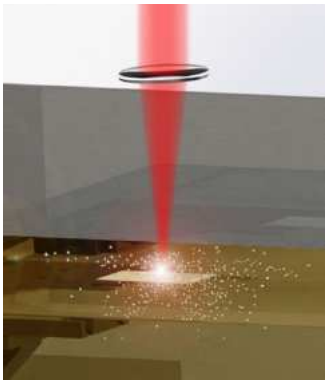
Abstract: Laser ablation allows controlling the main features of metallic nanoparticles by tuning the processing parameters. In addition, reirradiation of nanoparticles reduces its size and allows obtaining bimetallic nanoparticles without any additional reagent or contaminant that can be harmful to the healthy tissues. Applications such as antibacterial agent will be presented.

Introduction & main results

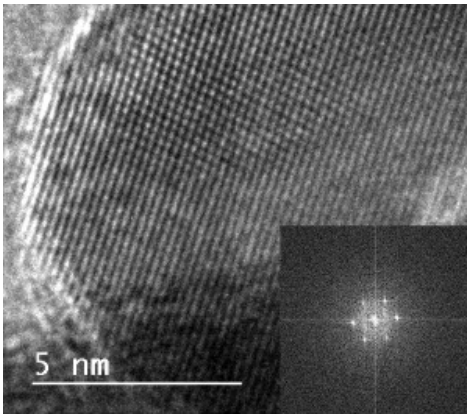
Metallic nanoparticles have attracted much attention as a subject of investigation due to their well-known properties, such as high electrical and thermal conductivity, catalytic activity, localized surface plasmon resonances, antibacterial and antifungal effects, etc. They are used in many different areas, medicine, photovoltaic solar cells, industrial applications, and scientific investigation, etc. The size as well as the shape is very important for certain applications.

There are different techniques for producing metallic nanoparticles using chemical, physical and biological routes. Each method presents its own disadvantages and restrictions, being the most used the chemical ones. But nanoparticles obtained via the chemical route could have byproducts of the reactions that could be harmful when nanoparticles are used for biomedical applications.

In the present work, laser-assisted methods such as ablation of solids in liquid phase (LASL) and laser reirradiation have been utilized to prevent the presence of contamination and impurities in obtained products. These methods are good alternatives to chemical reduction, especially when biological applications are taken into account. Different types of metallic nanoparticles, such as silver, copper or palladium, were successfully obtained as shown in figure 1.



a)



b)

Figure 1. *a) Schematic illustration of the Laser Ablation technique. b) Example of the silver nanoparticles produced by this technique. [1].*

Laser reirradiation consists on submitting the obtained solutions from the LASL to pressure to give a horizontal homogeneous and constant stream flowing from a capillary to be re-irradiated once and three times using the same laser sources with the same parameters used for the initial colloidal solution (see figure 2). As can be observed, the laser reirradiation treatment allows reducing the size (compare size of nanoparticles in figure 2b with that of figure 1b).

Also, laser reirradiation allows obtaining bimetallic nanoparticles that have synergistic effect as bactericidal agent.

Physico-chemical characterization included field-emission scanning electron microscopy (FSEM), transmission electron microscopy (TEM), selected area electron diffraction (SAED), energy dispersive spectroscopy (EDS), Ultraviolet-visible spectroscopy, High-resolution transmission electron microscopy (HRTEM)

Antibacterial activity against different bacteria such as Staphylococcus aureus, Escherichia coli, and Lactobacillus Salivarius was assessed by minimal inhibitory concentration assays. Results show that silver, copper and palladium nanoparticles are effective agents against bacteria proliferation.



a) b)

Figure 2. *a) Schematic illustration of the Laser reirradiation technique. b) Example of the nanoparticles obtained by Laser reirradiation. [1].*

Acknowledgements

This work was partially supported by the Government of Spain [PID2020-117900RB-I00 (MCI/AEI/FEDER, UE)], and by Xunta de Galicia (ED431C 2023/25).

References

1. Fernández-Arias, M.; Boutinguiza, M.; del Val, J.; Medina, E.; Rodríguez, D.; Riveiro, A.; Comesaña, R.; Lusquiños, F.; Gil, F.; Pou, J. RE-irradiation of silver nanoparticles obtained by laser ablation in water and assessment of their antibacterial effect. Appl. Surf. Sci. 2018, 473, 548–554.

New materials for photonics

Demonstration of hybrid photonic crystal nanocavity using atomically thin van der Waals flakes

C. F. Fong[1*], D. Yamashita[2,3], N. Fang[1], S. Fujii[2,4], Y.-R. Chang[1], T. Taniguchi[5], K. Watanabe[6], and Y. K. Kato[1,2]

[1]Nanoscale Quantum Photonics Laboratory, RIKEN Cluster for Pioneering Research, Japan
[2]Quantum Optoelectronics Research Team, RIKEN Center for Advanced Photonics, Japan
[3]Platform Photonics Research Center, National Institute of Advanced Industrial Science and Technology (AIST), Japan
[4]Department of Physics, Faculty of Science and Technology, Keio University, Japan
[5]Research Center for Materials Nanoarchitectonics, National Institute for Materials Science, Japan
[6]Research Center for Electronic and Optical Materials, National Institute for Materials Science, Japan
[*]corresponding author: cheefai.fong@riken.jp

Abstract: We demonstrate the formation of hybrid nanocavities by partially covering silicon photonic crystal (PhC) waveguides with suitably-sized 2D material flakes, obtaining cavity quality (Q) factors as high as 4.0×10^5.

The field of hybrid photonics has seen exciting progress with the advent of 2D van der Waals materials such as graphene, hexagonal boron nitride (hBN) and transition metal dichalcogenides (TMD) [1]. In particular, semiconducting TMDs have a direct bandgap at monolayer [2], making them optically active. For practical applications, 2D materials are often coupled to photonic structures such as cavities to manipulate light-matter coupling [3]. However, the transfer of 2D materials changes the dielectric environment of the cavities and also induce other losses which degrade the cavity quality (Q) factor. The situation becomes complicated with stacks of 2D materials with irregular shapes and thicknesses. Instead of being a detriment, the change in the dielectric environment caused by the 2D materials can be utilized to enable alternative methods for 2D material and cavity light-matter coupling.

In our work, we demonstrate a novel method to the form high Q factor nanocavities by partially covering a photonic crystal (PhC) waveguide post-fabrication with a suitably-sized 2D material flake (Fig. 1a) [4]. The presence of the flake increases the local refractive index causing a frequency mismatch of the optical fields in the regions with and without the flake which results in the formation of a nanocavity. We first performed numerical finite-difference time-domain (FDTD) and finite element method (FEM) simulations, considering specifically the air-suspended W1 line defect PhC waveguide made of silicon with a triangular array of air holes with lattice period a, with a 2D material flake covering a section of the waveguide. Fig. 1b shows a typical distribution of the E_y field amplitude of the cavity mode, indicating that the fields are largely confined to the regions with the 2D material flake. From our simulation results, the Q factor increases with decreasing flake thickness, approaching ultrahigh Q factors of the order of 10^7 at monolayer thickness (Fig. 1c). The atomically thin nature of the flake causes a less abrupt change of the refractive index in space, minimizing loss and thus resulting in ultrahigh Q factors.

WSe_2 flakes are transferred onto the PhC waveguide using the anthracene-assisted dry transfer method [5]. Figure 1d shows a fabricated hybrid nanocavity device with a trilayer tungsten diselenide (WSe_2) flake. The flake width is about $10a$. To obverse the cavity mode, we performed laser transmission measurement by exciting the laser at the grating coupler at one end of the waveguide and detecting the signal from the opposite end. The cavity peak is clearly observed in the transmission spectrum, giving a loaded cavity Q factor as high as 4.0×10^5. We have also successfully fabricated hybrid nanocavities using hBN and molybdenum ditelluride ($MoTe_2$). In particular, $MoTe_2$ is optically active in the near infrared. Since the nanocavity and the flake are spatially self-aligned, they

could couple to each other readily. We managed to observe such self-aligned optical coupling in a $MoTe_2$-hybrid nanocavity device exhibiting enhanced photoluminescence emission, as well as a reduced emission decay time due to the cavity Purcell effect.

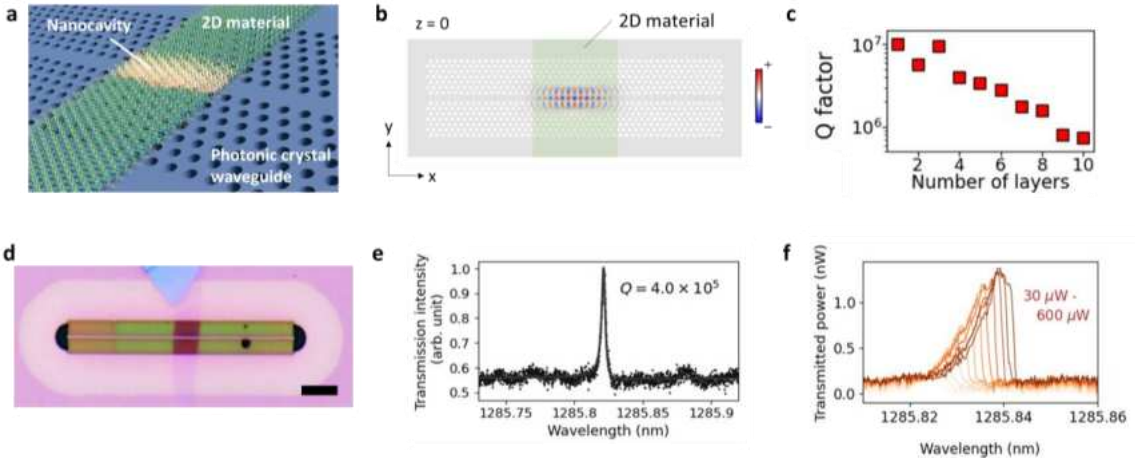


Fig. 1 (a) Schematic of the PhC hybrid nanocavity. (b) Simulated cavity mode profile for a WSe_2 flake with lateral width of 14*a*, showing that the fields are confined to the regions with the 2D material flake. (c) Theoretical Q factor against the WSe_2 flake layer number obtained from FEM simulations. The width of the flake is fixed to 14*a*. (d) Optical micrograph of a fabricated hybrid nanocavity with a trilayer WSe_2 flake. The color and contrast have been adjusted to improve clarity. (e) Transmission spectrum showing the cavity peak with a Q factor of 4.0×10^5. (f) Asymmetric cavity peak indicating optical bistability.

Our work unambiguously show hybrid nanocavity formation and self-aligned optical coupling using atomically thin materials. This versatile approach can be extended to a wide variety of materials, with further room for more complex material and photonic engineering to manipulate light-matter interaction. Therefore, our results will have a significant impact on numerous fields including layer materials nanoscience, hybrid device applications and integrated photonics.

Acknowledgement: This work is supported in part by JSPS KAKENHI (JP22K14623, JP20H02558, JP20J00817, JP22K14624, JP22K14625, JP22F22350 and JP23H00262) and MEXT ARIM (JPMXP1222UT1138), as well as the RIKEN Incentive Research Projects. The growth of hBN crystals is supported by the JSPS KAKENHI (Grant Numbers 20H00354, 21H05233 and 23H02052) and World Premier International Research Center Initiative (WPI), MEXT, Japan. C.F.F. is supported by the RIKEN SPDR fellowship. Y.-R.C. is supported by the JSPS Postdoctoral Fellowship. We acknowledge support by the RIKEN Information Systems Division for the use of the Supercomputer HOKUSAI BigWaterfall and SailingShip, as well as the use of the COMSOL license.

References

1. A. Krasnok, S. Lepeshov, and A. Alú, "Nanophotonics with 2D transition metal dichalcogenides," Opt. Express **26**, 15972 (2018).
2. K. F. Mak, C. Lee, J. Hone, J. Shan, and T. F. Heinz, "Atomically Thin MoS_2: A New Direct-Gap Semiconductor," Phys. Rev. Lett. **105**, 136805 (2010).
3. N. Fang, D. Yamashita, S. Fujii, K. Otsuka, T. Taniguchi, K. Watanabe, K. Nagashio, and Y. K. Kato, "Quantization of Mode Shifts in Nanocavities Integrated with Atomically Thin Sheets," Adv. Opt. Mater. **10**, 2200538 (2022).
4. C. F. Fong, D. Yamashita, N. Fang, S. Fujii, Y.-R. Chang, T. Taniguchi, K. Watanabe, and Y. K. Kato, "Self-aligned hybrid nanocavities using atomically thin materials," arXiv:2308.10566 (2023).
5. K. Otsuka, N. Fang, D. Yamashita, T. Taniguchi, K. Watanabe, and Y. K. Kato, "Deterministic transfer of optical-quality carbon nanotubes for atomically defined technology," Nat. Commun. **12**, 3138 (2021).

The reduced loss of guided exciton–polariton modes in WS_2 multilayers by hBN-encapsulation

Ho Seung Lee[1], Junghyun Sung[1], Dong-Jin Shin[1], and Su-Hyun Gong[1]

[1]Department of Physics, Korea University, Republic ofKorea

Abstract: Guided exciton–polariton modes, innately form in bare TMDC layers due to self-hybridization between excitons and photons, exhibit a limited propagation distance owing to the substantial exciton absorption within the material. We overcome this limitation and increased propagation distance by utilizing hBN layers to provide flat substrates and protect surface.

Atomically thin two-dimensional (2D) transition metal dichalcogenides (TMDCs) are remarked for their outstanding potential in photonic and optoelectronic devices. 2D TMDCs experience strong light-matter interactions and valley degrees of freedom by increased excitonic effect in 2D limits and broken inversion symmetry. The unique properties of TMDCs led to studies in various fields such as exciton-polaritons demonstrated by cavity engineering [1]. Further studies have shown guided exciton–polariton modes naturally exist in bare TMDCs layers due to self-hybridization between excitons and photons [3]. However, these guided polariton modes exhibit a limited propagation distance owing to the substantial exciton absorption within the material.

Here, we demonstrated improvement of guided exciton-polariton modes in TMDCs multilayers by integrating protection layers. Tungsten Disulfide (WS_2) is selected from the TMDCs due to its outstanding excitonic properties in room-temperature regime. For protection layers, hexagonal Boron Nitride (hBN) is chosen due to its outstanding properties as protection layers and flat substrates: wide band gap, high permittivity, little dangling bonds, and continuous hexagonal lattice structure with flat plain similar to graphene. By encapsulating WS_2 layers with atomically thin layers of hBN, WS_2 layers were isolated from charge disorder at the surface of substrates and protected physical flatness [3, 4]. We observed that the hBN encapsulation reduced the inhomogeneous linewidth of exciton in the photoluminescence spectrum. The reduced linewidth of the exciton emission indicates a stronger excitonic resonance, which leads exciton-polaritons to have improved properties. To directly compare the optical properties of exciton-polaritons with and without hBN encapsulation, their spectra scattered at the sample edge were systematically investigated. We experimentally observed that the propagation distance of polariton modes substantially increased with hBN layers. Additionally, the polariton spectrum broadened due to efficient exciton relaxation to the polariton states at lower energies. The promising outcomes with hBN encapsulation suggest its potential to overcome strong excitonic losses of the guided exciton polariton in implementing nanophotonic devices.

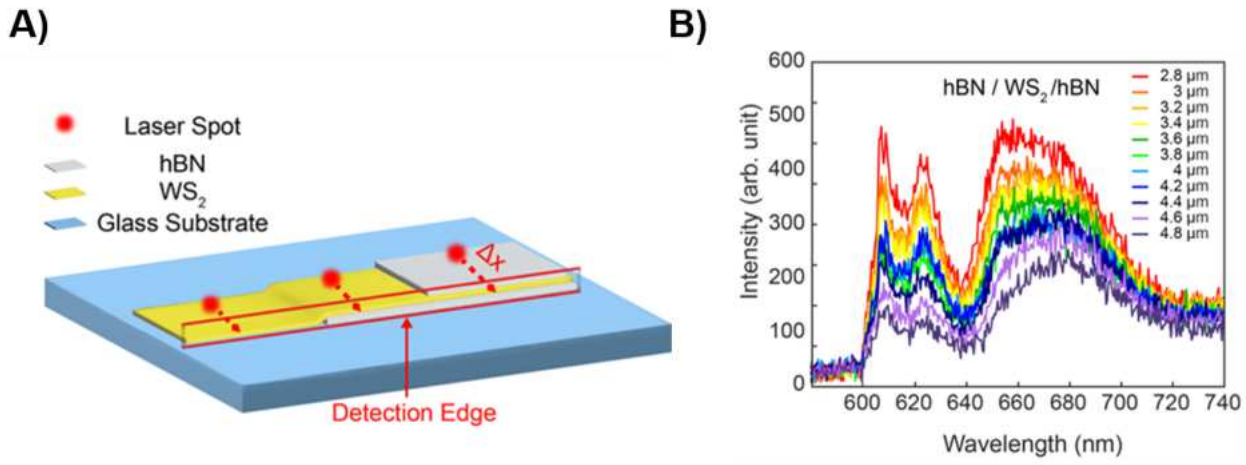


Figure A and B: (A) Schematic representation of the hBN-encapsulated WS_2 sample designed for three different measurement positions: bare WS_2, WS_2 on top of hBN, and WS_2 sandwiched with hBN. (B) PL spectra of scattered emissions of exciton–polaritons at the edge of the sample with increasing distances between the pumping spot and the edge for three different sample positions.

References

1. Dufferwiel, S., Schwarz, S., Withers, F. et al. "Exciton–polaritons in van der Waals heterostructures embedded in tunable microcavities," Nat Commun, 6, 8579, 2015.
2. Hu, F., Luan, Y., Scott, M. et al, "Imaging exciton-polariton transport in MoSe2 waveguides," Nature Photon, 11, 356–360, 2017.
3. Man, M., Deckoff-Jones, S., Winchester, A. et al, "Protecting the properties of monolayer MoS2 on silicon based substrates with an atomically thin buffer," Sci Rep, 6, 20890, 2016.
4. H. S. Lee, J. Sung, D.-J. Shin, and S.-H. Gong. "The impact of hBN layers on guided exciton–polariton modes in WS2 multilayers," Nanophotonics, no. 0, 2024.

Titanium nitride as an alternative metamaterial fabricated via gas nitridation

Liya Tony, I Packia Selvam, S.N. Potty*
Centre for Materials for Electronics Technology (C-MET)
Scientific Society, Ministry of Electronics & Information Technology, Government of India
Shoranur Road, Athani P.O, Thrissur 680 581, India
* Corresponding author – snpotty@cmet.gov.in

Abstract

Distinctive structural, electrical and optical characteristics of titanium nitride films made them highly sought-after for a variety of technological applications. Investigations in their material property perspective proved it as an alternative metamaterial. Typically, these materials are produced via physical vapor deposition (PVD) and chemical vapor deposition (CVD) techniques [1]. This study focuses on the development of titanium nitride thin films by gas nitridation process of RF sputtered titanium metal films at a temperature of 600°C, utilizing ammonia gas. The fabricated films possess enhanced opto-electrical properties compared to other fabrication routes. We investigated here the titanium nitride film as new platform for further metamaterial applications with an evaluation of the dielectric function. The films that are being studied range from 50 to 150 nm in thickness. Structural analysis is carried out with the aid of Raman and GI-XRD spectroscopic methods. The reflection and transmission spectra analysis in the visible region (400–900 nm) was used to investigate the optical characteristics. The bandgap variation has been studied by processing optical transmission spectra using Tauc plot. Hall measurement in the van der Pauw arrangement was used to examine the electrical properties of the films. Study was concentrated on their electrical and optical properties to establish a correlation and also to illustrate the metamaterial characteristics of the coated titanium nitride films.

1. Introduction

The advancement in the field of hyperbolic metamaterial (HMM) requires a material, which offers low loss and negative permittivity compared to the conventional metals used for the purpose[1]. In 2017, Naik et al investigated the optical performance of layered titanium nitride and a dielectric material for HMM device application [2] and confirmed the improved performance of the same. The fabrication of each layer was done with magnetron sputtering technique.

In general, titanium nitride films were fabricated by physical vapour deposition, plasma laser deposition, and chemical vapour deposition techniques. In this work, we used gas nitridation route to incorporate nitrogen into the titanium metal films fabricated via sputtering. Purged ammonia gas will split up to nascent nitrogen and hydrogen at high temperature, the produced hydrogen creates a reduced atmosphere and prevents the traces of residual oxygen in the samples.

2. Methodology

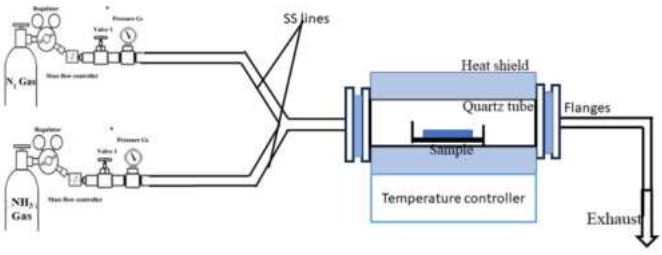


Fig 1 Ammonia gas nitridation apparatus

The Titanium metal films were fabricated via magnetron sputtering on soda lime glass substrate using metal target (99.99%) of 2 inch diameter with a sputtering power of 120W and working pressure 3×10^{-3}mbar. The films were coated with variable thickness ranging from 50 to 150nm, confirmed by Field emission scanning electron microscopic images. The sputtered metal films were immediately transferred to the nitridation chamber to avoid possible oxidation. Fig 1 shows the experimental setup for nitridation. Gas nitridation is carried out by initially purging nitrogen (99.99%) gas and then shifting to ammonia (99.99%). The nitridation is carried out at a ramp rate of 5°C/min up to temperature of 600°C for duration of 30 minutes. The samples were named according to the average thickness of the precursor metal films, as T1(50nm), T2 (100nm), and T3(150nm), respectively

Nitridated samples were subjected to structural, electrical and optical characterizations by using grazing

incident x-ray diffraction, hall measurements and UV-visible transmittance spectra, respectively. The phase formation was confirmed with x-ray diffraction (Rigaku Ultima IV) with Cu K_α radiation, at a glancing angle of 0.5°. Hall effect measurements of the films were carried out using the four-probe van der Pauw method (ECOPIA HMS3000). UV-vis-NIR reflectance spectra were recorded using a spectrophotometer (JASCO V-570)

3. Results and discussion

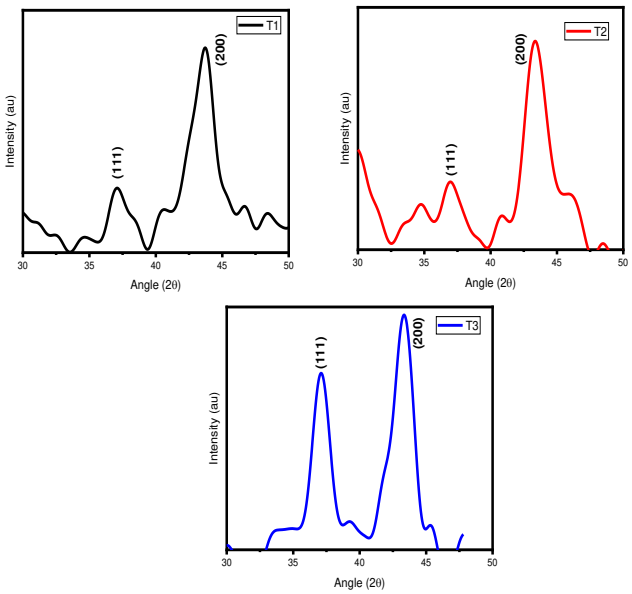


Fig 1 Grazing incident XRD patterns of the nitridated metal films, T1, T2 and T3

As shown in figure, the films prepared are having a cubic symmetry with peak orientation corresponding to (111) and (200) planes in 2θ angles at 36.5° and 42.6°, respectively (ICDD pattern, 00-038-1420). The samples were subjected to same nitridation conditions. However, being a non-stoichiometric compound, the samples after nitridation differs with respect to the film thickness. Hence, one can expect variations in the overall properties of the samples with stoichiometry. May be the increased titanium content in the film T3 contributed to an increased peak orientation in (111) direction exhibiting better crystallinity for the film [3].

Table 1 Hall measurement data of the nitridated metal films

Sample name	Carrier concentration (/cc)	Mobility (cm^2/Vs)
T1	4.19×10^{21}	0.0125
T2	8.05×10^{20}	0.493
T3	4.68×10^{20}	0.695

Table 1 shows the hall measurement data obtained for the nitridated metal films. Electrical conductivity and other properties of transition metal nitride largely depend on the stoichiometric nature of the material. Both metal rich condition and stoichiometric condition generally provide high carrier concentration in TiN films. Here, high carrier concentration exhibited by the sample T1 may be due to the stoichiometric condition. The sample T3 showed higher hall mobility among the three films, which may be due to the improved crystallinity in the film.

The measured transmittance spectra of nitridated films T1, T2, and T3 are shown in figure 2. The bandgap determinations are carried out with Tauc plot analysis. According to tauc plot the strength of optical absorption depends on the [4-5] difference between the photon energy and bandgap as

$$\alpha h\upsilon = A\,(h\upsilon - E_g)^n \ldots\ldots\ldots (1)$$

where h is Planck's constant, ν is the photon's frequency, α is the absorption coefficient, Eg is the band gap and A is the constant.

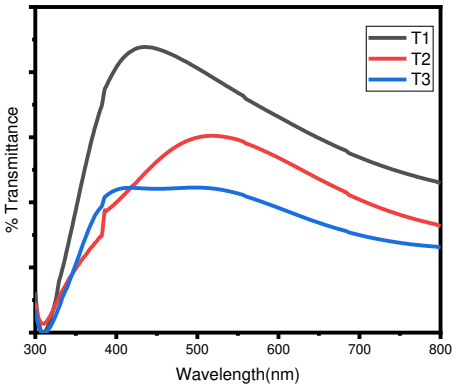


Fig 2 Transmittance spectra of nitridated metal films

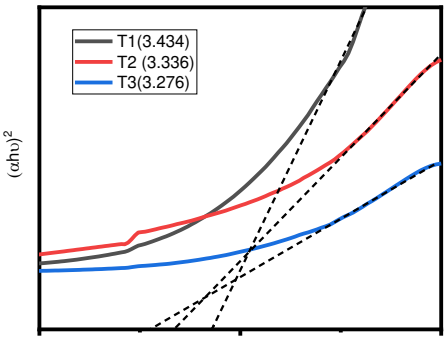
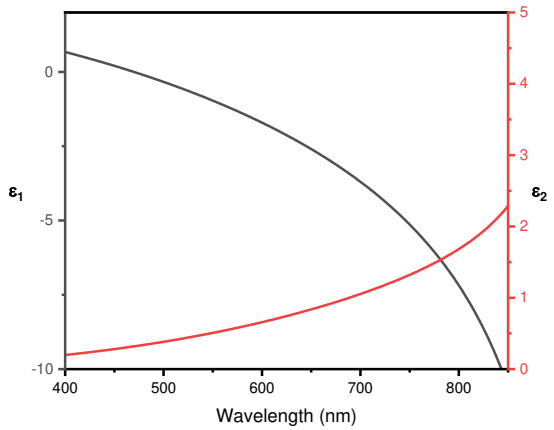


Fig 3 bandgap of metal films after nitridation

The plot $(\alpha h\upsilon)^2$ vs energy provides information about the bandgap. Bandgap values show a decreasing trend as the sample film thickness is increased. The wide band gap exhibited by the sample T1 may be due to the stoichiometric dependent nature of the film. Bandgap values showed a variation from 3.27 to 3.43eV with respect to the thickness.

Patasalas et al extracted the dielectric function from the reflectance pattern of the titanium nitride films using Drude -Lorentz approximation, by considering both free carriers and bound electrons in the sample. [6]. In a similar manner, extracted the dielectric function of the sample, and obtained the permittivity values in the visible range, are as shown in Fig. 4. The existence of negative permittivity and low loss nature is confirmed, and this indicates that the titanium nitride films prepared in this work can behave as a suitable metamaterial in visible region.



Employing wide band gap materials with negative permittivity in the desired wavelength will reduce the dielectric loss and enhance the performance of HMM devices applications [7].

4. Conclusions

Titanium nitride thin films with variable thickness were successfully fabricated from RF sputtered metal films by subjecting to ammonia gas nitridation. Structural confirmations were obtained through grazing incident x-ray diffraction. The films with stoichiometric nature exhibited higher carrier concentration with wide bandgap nature. Negative permittivity and low loss nature of the nitridated thin films were confirmed in the visible region, and this make titanium nitride a suitable hyperbolic metamaterial. Further investigations are required by combining them with dielectric material for complete understanding of metamaterial characteristics.

Acknowledgements

This work was supported by Department of Science and Technology, Government of India, INSPIRE division. We acknowledge the support of International Travel Support (ITS) Scheme of Science and Engineering Research Board (SERB), India for the travel grant.

References

1. Dip Sarker, Ahmed Zubair, Titanium nitride-based hyperbolic metamaterial for near-infrared ultrasensitive sensing of microbes, Phys. Chem. Chem. Phys.,26, 10273-10283, 2024
2. G. V. Naik, A titanium nitride based metamaterial for applications in the visible, CLEO: 2013, San Jose, CA, USA. 1-2, 2013.
3. P. Patsalas, S. Logothetidis; Optical, electronic, and transport properties of nanocrystalline titanium nitride thin films. J. Appl. Phys.; 90 (9): 4725–4734,2001.
4. Tauc J., Grigorovici, R. and Vancu, A., Optical Properties and Electronic Structure of Amorphous Germanium. phys. stat. sol. (b), 15: 627-637, 1966.
5. J. Tauc, Optical properties and electronic structure of amorphous Ge and Si, Mat. Resea, Bull.,37-46, 1968.
6. Patsalas, P.; Kalfagiannis, N.; Kassavetis, S. Optical Properties and Plasmonic Performance of Titanium Nitride. Materials, 8, 3128-3154,2015.
7. Naik, G.V., Shalaev, V.M. and Boltasseva, A, Alternative Plasmonic Materials: Beyond Gold and Silver. Adv. Mater., 25: 3264-3294, 2013.

Super-resolution imaging of sulfur vacancies in 2D molybdenum disulfide using expansion microscopy and dSTORM

Pin-Jen Wang[1*], Ting-Jui Ben Chang[1,2], Hui-Jen Lin[3], Shun-Min Yang[4], Mor-Pal Vikram[1], Kai-Chun Huang[5], Tsung-Hsin Liu[6], Chih-Yang Huang[7], T. Tony Yang[2,8], Ann-Shyn Chiang[3], Yeu-Kuang Hwu[3,4], Chun-Wei Chen[5], Li-Chyong Chen[7], Han-Chun Wu[9], and Shi-Wei Chu[1,3]

[1]Department of Physics, National Taiwan University, Taiwan
[2]Department of Electrical Engineering, National Taiwan University, Taiwan
[3]Brain Research Center, National Tsing Hua University, Taiwan
[4]Institute of Physics, Academia Sinica, Taiwan
[5]Department of Material Science and Engineering, National Taiwan University, Taiwan
[6]International Graduate Program of Molecular Science and Technology, National Taiwan University, Taiwan
[7]Center for Condensed Matter Sciences, National Taiwan University, Taiwan
[8]Graduate Institute of Biomedical Electronics and Bioinformatics, National Taiwan University, Taiwan
[9]School of Physics, Beijing Institute of Technology, China
[*]corresponding author: r11222041@ntu.edu.tw

Abstract: Defect inspection in 2D transition metal dichalcogenides has been limited to electron microscopy which has low field-of-view and low imaging speeds. Here we propose to use expansion microscopy (ExM) to embed the defect distribution onto a swellable hydrogel and combine with localization microscopy to achieve sub-10-nm resolution with optical microscopy.

Atomic defects in 2D materials are of great interest due to their role in modifying the optical and electrical properties of their host material. The observation of such defects is of high importance when considering fabrication of 2D semiconductor devices. Currently, defect mapping in MoS_2 is carried out at both small and large scales, the former by transmission electron microscopy (TEM) and scanning tunneling microscopy (STM) and the latter by photoluminescence mapping and Raman spectroscopy. TEM and STM offer atomic resolution, but are limited by the small field of view and slow imaging speed, thus impeding large-scale defect identifications. On the other hand, optical methods are much more efficient in characterizing millimeter to centimeter scale defect distributions, but the resolution is limited by diffraction, i.e. ~300 nm with visible light.

Over the past three decades, the diffraction limit has been repeatedly broken by significant improvements in optical microscopy. For example, single-molecule localization microscopy (SMLM) has the capability to localize blinking fluorescent molecules with precision near ~20 nm, but due to their biomolecular nature, such applications have been limited to bioimaging and cannot be utilized on semiconductor samples. Recently, two works have demonstrated the capability of using thiol-containing fluorescent probes such as DNA molecules[1] or antibody fragments[2] to attach a fluorescent signal to sulfur vacancies in MoS_2. Such approaches have already pushed the resolution of defect imaging down to ~20 nm.

We extend these works further by using antibody fragments to anchor to a swellable hydrogel matrix and physically expand the hydrogel, allowing for ~4X effective resolution improvements using a conventional fluorescence microscope. This process is known as expansion microscopy[3,4] (ExM). In Figure 1, we detail the process of embedding the defect distribution onto the hydrogel and demonstrate sub-10 nm resolution imaging by also using dSTORM[5] to localize the fluorescent probes.

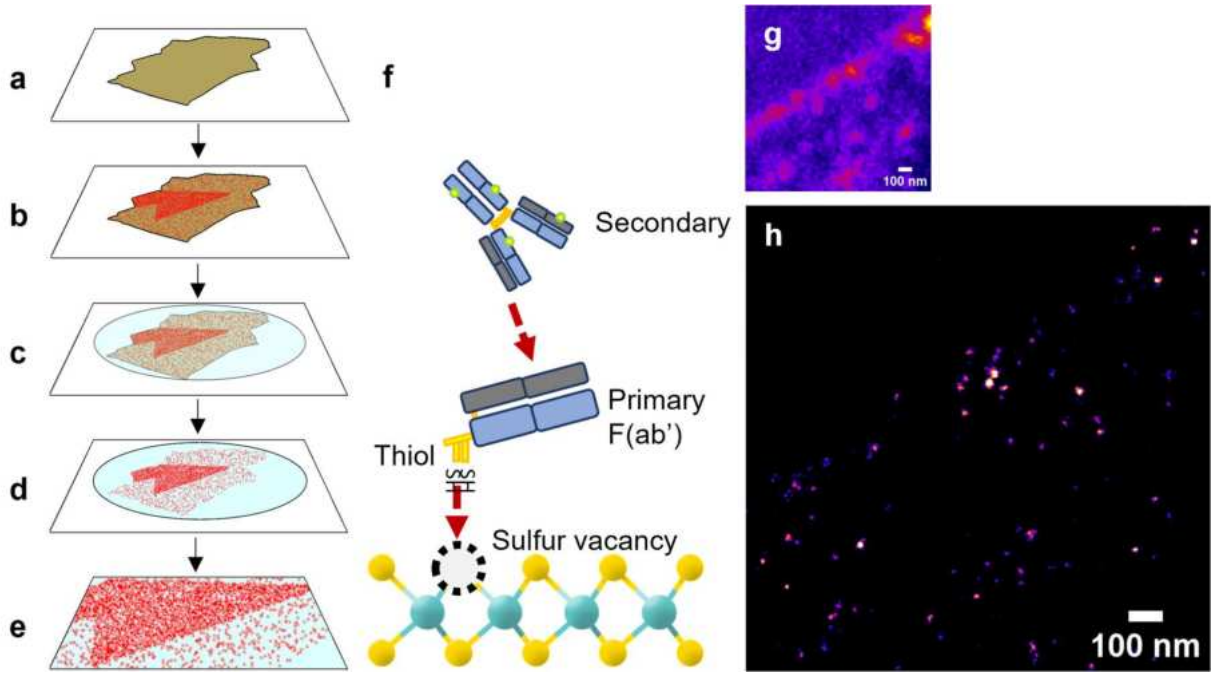


Figure 1. (a-e) Schematic of expansion microscopy on MoS_2. (b) Labelling with fluorescent probes. (c) Probes are embedded in gel. (d) Gel is digested to allow for free expansion. (e) Gel is physically expanded up to ~4X linearly. (f) Molecular view of labeling step shown in (b). (g) Fluorescence image of 4.0X expanded gel. (h) dSTORM image of the same region in (g).

While ExM alone can provide a fourfold improvement in resolution, as seen in Figure 1g, dSTORM (Figure 1h) pushes the resolution limit even further, allowing us to resolve individual defects with a distance of sub-10 nm, with a massive field of view of 50 by 50 micrometers (full image not shown). In conclusion, we successfully demonstrate using ExM to achieve super-resolution defect imaging in MoS_2. This opens exciting avenues for utilizing ExM for large-scale, high-resolution defect mapping in 2D materials.

References

1. Zhang, Miao, Martina Lihter, Tzu-Heng Chen, Michal Macha, Archith Rayabharam, Karla Banjac, Yanfei Zhao, et al. "Super-Resolved Optical Mapping of Reactive Sulfur-Vacancies in Two-Dimensional Transition Metal Dichalcogenides." ACS Nano, Vol. 15, No. 4, 7168-7178, 2021.
2. Huang, Teng-Xiang, Meek Yang, Hannah Giang, Bin Dong, and Ning Fang. "Resolving the Heterogeneous Adsorption of Antibody Fragment on a 2D Layered Molybdenum Disulfide by Super-Resolution Imaging." Langmuir, Vol. 38, No. 24, 7455-7461, 2022.
3. Chen, Fei, Paul W. Tillberg, and Edward S. Boyden. "Expansion Microscopy." Science, Vol. 347, No. 6221, 543-548, 2015.
4. Chozinski, Tyler J., Aaron R. Halpern, Haruhisa Okawa, Hyeon-Jin Kim, Grant J. Tremel, Rachel O. L. Wong, and Joshua C. Vaughan. "Expansion Microscopy with Conventional Antibodies and Fluorescent Proteins." Nature Methods, Vol. 13, No. 6, 485-488, 2016.
5. Van de Linde, Sebastian, Anna Löschberger, Teresa Klein, Meike Heidbreder, Steve Wolter, Mike Heilemann, and Markus Sauer. "Direct Stochastic Optical Reconstruction Microscopy with Standard Fluorescent Probes.", Nature Protocols, Vol. 6, No. 7, 991-1009, 2011.

Exciton-polaritons in van der Waals heterostructures coupled to optical bound state in the continuum

Dong-Jin Shin[1], HyunHee Cho[1], Woo Hun Choi[1], Ho Seung Lee[1], and Su-Hyun Gong[1*]

[1]Department of Physics, Korea University, Seoul, Republic of Korea
[*]corresponding author: shgong@korea.ac.kr

Abstract: We realized the subwavelength-thick exciton-polariton platform exclusively consists of van der Waals two-dimensional (2D) materials. By leveraging their exceptional optical properties and van der Waals nature, we achieve successful integration between bound state in the continuum (BIC) modes and excitonic resonances of atomically thin 2D semiconductors.

Bound states in the continuum (BICs) are peculiar states that, despite being embedded in the continuum spectrum of modes, remain localized without any coupling to far-field radiation. This counterintuitive phenomenon, first theorized in quantum mechanics, has found a fertile ground in photonics, offering unprecedented opportunities for enhancing light-matter interactions without the inherent loss mechanisms typical in resonant systems.

Exciton-polaritons are hybrid light-matter quasiparticles that arise from the strong coupling between excitons (bound electron-hole pairs) and photons. These quasiparticles embody the dual nature of light and matter, showing unique properties that originate from both their photonic and excitonic components. Recently, exciton-polaritons derived from strong light-matter interaction between an excitonic resonance and an optical BICs become promising candidate for polariton condensation because of their topologically protected states with theoretically infinite lifetime. Unlike previous platforms that take advantage of the local minimum at the energy-momentum dispersion[1], polariton platforms based on BICs utilizes the topologically protected meta-stable state with supposedly infinite lifetime[2,3]. This could provide achievement of extremely low threshold density of condensation of exciton-polaritons.

Here, we successfully realized exciton-polaritons in van der Waals heterostructures coupled to optical bound state in the continuum. The integration between atomically thin 2D semiconductors and optical BICs is considered challenging due to atomically thin size and their vulnerability to external environments during fabrication. By manipulating the van der Waals nature of 2D materials, we successfully realized the integration of excitonic resonances of atomically thin 2D semiconductors with optical BIC modes. Under reflectance measurement, we found our system show anti-crossing behavior with Rabi splitting of ~20 meV. Also, we found the BIC polariton show nonlinear behavior, as increasing the non-resonant pump fluence. To confirm the topological properties of the BICs polariton, we measured the degree of linear polarization of emission. We believe our system provide a robust platform for investigating exciton-polaritons in van der Waals heterostructures coupled to optical BICs.

References

1. Zhang, L., Gogna, R., Burg, W. et al. Photonic-crystal exciton-polaritons in monolayer semiconductors. Nat Commun 9, 713 (2018).
2. Ardizzone, V., Riminucci, F., Zanotti, S. et al. Polariton Bose–Einstein condensate from a bound state in the continuum.

Nature 605, 447–452 (2022).

3. Maggiolini, E., Polimeno, L., Todisco, F. et al. Strongly enhanced light–matter coupling of monolayer WS_2 from a bound state in the continuum. Nat. Mater. 22, 964–969 (2023).

All-Optical Excitation and Control of Ultrafast Lattice Dynamics in WSSe

S. I. Rey*, M. J. Cross, M. L. Welsch, F. Schröder, B. Zhou, N. Stenger, P. U. Jepsen and E. J. R. Kelleher

DTU Electro, Department of Electrical and Photonics Engineering, Technical University of Denmark, Ørsteds Plads, 343, Kongens Lyngby, DK-2800, Denmark

*sirpu@dtu.dk

Abstract: A coherent acoustic phonon in the alloy WSSe is revealed using double-pump-probe spectroscopy. The proposed mechanism involves a cascaded process of exciton formation, phonon recycling, thermoelastic deformation and a potential piezoelectric enhancement of the coherent oscillation. The coherent phonon response is optically controlled using a tailored pump pulse sequence.

Control of the structural properties of materials on ultrafast timescales is relevant for future high-speed logic devices. Coherent acoustic phonons (CAPs) can alter the symmetry of a material and give access to topologically protected phases [1]. Such coherent oscillations exist in several TMDs [2]. Here, we show for the first time the coherent acoustic mode in the tungsten based TMD alloy WSSe.

Approximately 100 fs long pulses at 800 nm are used for single- and double-pump-probe spectroscopy on commercially available crystals of WSSe (HQ Graphene and grown using chemical vapor transport), with lateral size of ~1 cm. The alloy's atomic species ratio is S/Se, 29.8/37.0. A controllable two-pump-pulse sequence was generated by frequency doubling to 400 nm and delaying one pump pulse with respect to the other.

Fig. 1(a) shows a schematic of the proposed activation mechanism for CAPs in WSSe. The transient dynamics are shown in Fig. 1(b), compared against its symmetric counterparts (WS_2 and WSe_2). Initially, a single pump pulse drives the material out of equilibrium. Excitons rapidly form under 400 nm (3.1 eV) excitation [3]. The decay constant, τ=369 fs, agrees with previously reported data on TMDs [4]. At high pump fluence (~5 mJ/cm^2) not all photoexcited carriers can form excitons, instead carriers thermalize to the bottom of the conduction band emitting phonons in the process. The phonon recycling effect [5] can re-excite trapped carriers into the conduction band, thus repopulating available states and increasing the transient reflection signal, as highlighted in Fig. 1(b). Additionally, the generated phonons increase the lattice temperature, subsequently causing a deformation of the material via the thermoelastic effect that initiates a CAP. The CAP is seen as a modulation of transient reflection at a frequency of 26.98 GHz.

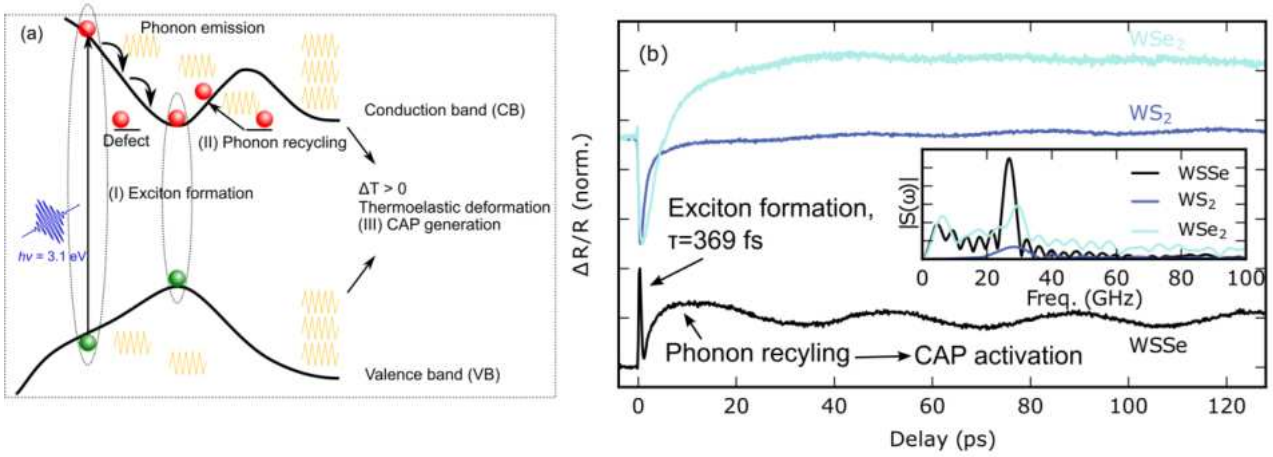


Figure 1. (a) CAP generation mechanism in WSSe. (b) Transient reflection of tungsten-based TMDs. Inset: spectrum.

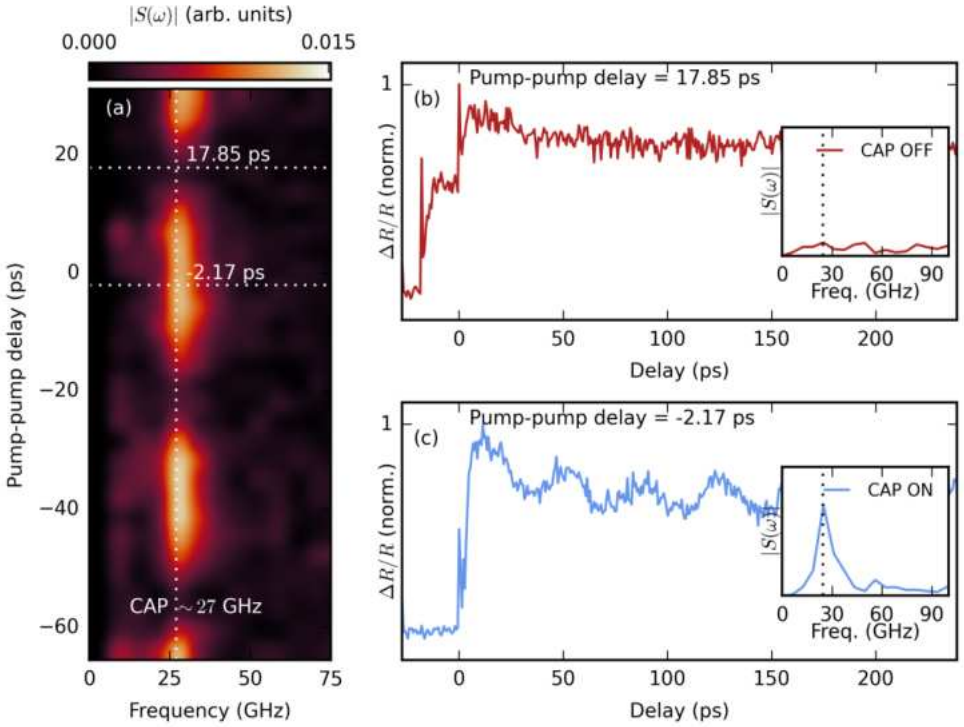


Figure 2. (a) Spectrum vs. pump-pump delay. All-optical suppression (b) and enhancement (c) of CAP oscillations.

Comparison with WS_2 and WSe_2 shows CAPs are also activated, but with much smaller amplitude. We propose that the asymmetric composition of the alloy breaks the inversion symmetry of the crystal and induces a piezoelectric field that enhances the change of the refractive index of the strained layer via the Franz-Keldysh effect [6].

A second 400 nm pump pulse of a similar fluence, but variably adjusted in time with respect to the arrival of the first, can optically control the amplitude of the coherent oscillation by careful tuning of the temporal separation between the respective pump pulses. In Fig. 2(a), we plot the two-dimensional (2D) frequency-delay dynamics over a relative pump-pump delay time of 90 ps. The magnitude of the CAP at 27 GHz shows a sinusoidal variation as a function of the delay, with an extinction of 10 dB. Corresponding minima and maxima in the 2D map represent constructive and destructive interference of the excited acoustic phonon wave-packets. In Fig. 2(b) and 2(c), we plot horizontal cuts of the time-domain (inset spectral) dynamics at 17.85 ps and -2.17 ps, which correspond to a suppression and enhancement of the coherent oscillation, respectively.

Our results highlight the potential of asymmetric alloys as a platform for high-Q acoustic resonators with a broad range of potential applications in quantum nanoacoustics and nanophononics. Using a tailored sequence of carefully timed pump pulses, we can optically control the amplitude of the coherent oscillation, with implications for the future development of ultrafast logic devices.

This work was supported by the Danish Independent Research Fund project ULTRA-LOWD.

References

1. T.G. Park, *et al.*, Nanoscale **13**, 19264, (2021)
2. S. Ge, *et al.*, Sci. Rep. **4**, (2014).
3. T. Zheng, *et al.*, Nano Lett. **21**, 931 (2021).
4. P. Valencia-Acuna, *et al.*, Phys. Rev. B **102**, 035414 (2020).
5. X. Wang, *et al.*, J. Phys. Chem. Lett. **13**, 10395 (2022).
6. R. Liu, *et al.,* Phys. Rev. B. **72**, 195335, (2005).

Metal-Insulator Transition in Vanadium Dioxide Inspected by Analytical Electron Microscopy

J. Krpenský[1,2], M. Horák[1], J. Planer[1], P. Kepič[1], J. Kabát[1], A. Konečná[1], and V. Křápek[1*]

[1]Brno University of Technology, Technická 2, 616 69 Brno, Czechia
[2]CIC nanoGUNE, Tolosa Hiribidea 76, 20018, Donostia-San Sebastián, Spain
[*]corresponding author: krapek@vutbr.cz

Abstract: Vanadium dioxide is an emerging plasmonic material with metal-insulator transition, relevant for active plasmonics and switchable optical metasurfaces. We study the metal-insulator transition with analytical electron microscopy, locally correlating signatures of the transition in chemical, crystallographic, and optical properties.

Vanadium dioxide (VO_2) stands out among materials exhibiting metal-insulator phase transition (MIT) due to the proximity of its transition temperature (about 68 °C) to the room temperature, which makes it a promising candidate for applications in photonics including fast optical switching or tunable optical metasurfaces [1]. Here we probed the MIT in a scanning transmission electron microscope (STEM) with in-situ heating. A combination of imaging, diffraction, and spectroscopy with nanometer spatial resolution allowed us to locally correlate the optical properties of VO2 with applied temperature and local variations in stoichiometry.

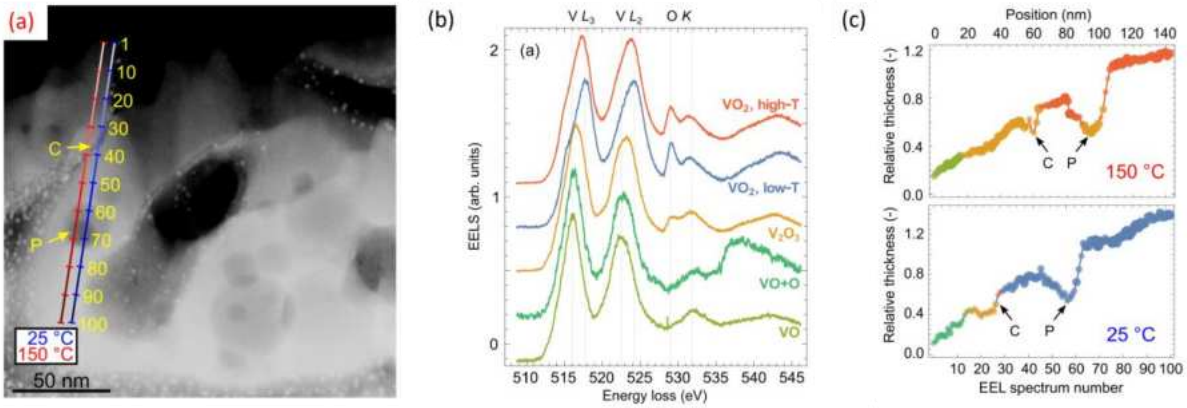


Figure 1: (a) HA ADF of the lamella with a crack (c) and a pore (P). The lines denote the positions where EEL spectra were recorded. (b) Characteristic EEL spectra determined by cluster analysis were attributed to distinct stoichiometries (VO, V_2O_3, VO_2). (c) Distribution of the stoichiometry across the sample. EEL spectrum number corresponds to the position indicated in panel a, the color of the symbols corresponds to the color of the spectra in panel b (green – VO, yellow – V_2O_3, red or blue – VO_2), and vertical position of the symbols indicates the local thickness.

We fabricated a thin layer of VO_2 by evaporation and verified the presence of MIT by ellipsometric characterization of the dielectric function. Next, we fabricated V-shaped lamellas for STEM from the thin layer by focused ion beam milling with Ga ions. The high-resolution and high-angle annular dark field (HA ADF) STEM imaging revealed pronounced structural inhomogeneity – a porous and polycrystalline character of the examined lamella (Fig. 1a). Energy-dispersive X-ray spectroscopy (EDX) revealed a rather homogeneous elemental

composition with only discernible contamination by Ga ions implanted during the milling. Core-loss electron energy loss spectra (Fig. 1b) were processed by cluster analysis and interpreted with ab-initio simulations and by comparison with recent literature [2, 3]. They revealed the presence of the oxides with reduced oxidation number (VO, V_2O_3). Interestingly, the local thickness of the lamella was found as the only parameter determining the local stoichiometry (Fig. 1c).

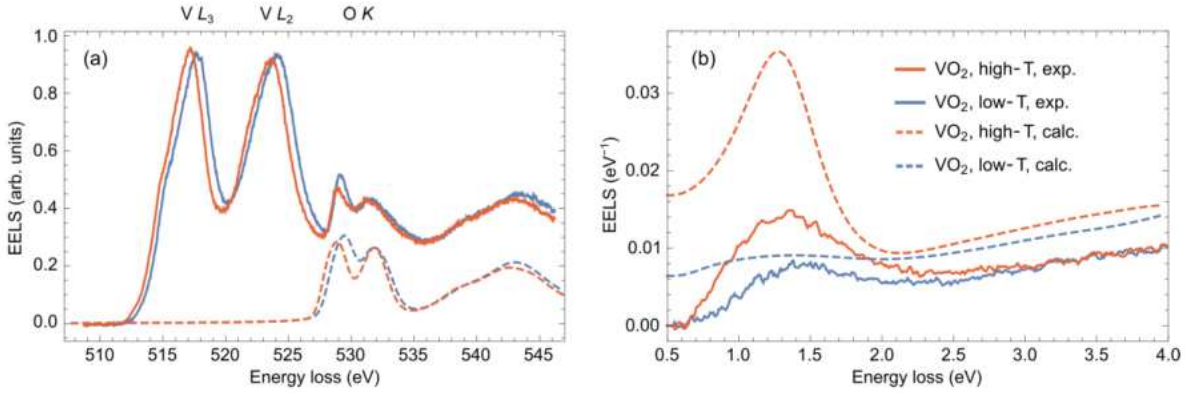


Figure 2: (a) Core-loss EEL spectra of VO_2 obtained at 25 °C (solid blue line), and 150 °C (solid red line) are compared with ab-initio-calculated O K peaks corresponding to the monoclinic phase (dashed blue line) and rutile phase (dashed red line). (b) Comparison of the experimentally acquired low-loss EELS at 25 °C (solid blue line), and 150 °C (solid red line) compared with calculations using a classical dielectric formalism (dashed blue and red lines).

Figure 2 shows the signatures of MIT in the part of the lamella attributed to VO_2. In core-loss EELS [Fig. 2(a)] we observe an increase in the relative intensity of the 1st to 2nd oxygen K peak upon heating. Ab-initio simulations explain this increase by the change of the crystal lattice from monoclinic to rutile phase, as expected for the MIT. In low-loss EELS [Fig. 2(b)] the emergence of the plasmon peak around the energy of 1.4 eV upon heating clearly manifests the change of the phase from dielectric to metallic.

During the conference, we will discuss further details, including a comparison of a porous VO_2 lamella to VO_2 nanocrystals, a manifestation of the MIT in electron diffraction, and a hysteresis curve of the transition. Additional information is also available in Ref. [4]. We acknowledge the support of the Czech Science Foundation (project No. 22-04859S), and the Ministry of Education of the Czech Republic (project CzechNanoLab Research Infrastructure, No. LM2018110).

References

1. Tripathi, A. John, J., Kruk, S., Zhang, Z., Nguyen, H. S., Berguiga, L., Romeo, P. R., Orobtchouk, R., Ramanathan, S., Kivshar, Y., and Cueff, S., "Tunable Mie-Resonant Dielectric Metasurfaces Based on VO2 Phase-Transition Materials," ACS Photonics, Vol. 8, 1206–1213, 2021.
2. Gloter, A., Serin, V., Turquat, Ch., Cesari, C., Leroux, Ch., and Nihoul, G., "Vanadium valency and hybridization in V-doped hafnia investigated by electron energy loss spectroscopy," Eur. Phys. J. B, Vol. 22, 179–186, 2001.
3. Hébert, C., Willinger, M., Su, D. S., Pongratz, P., Schattschneider, P., and Schlögl, R., "Oxygen K-edge in vanadium oxides: simulations and experiments," Eur. Phys. J. B, Vol. 28, 407–414, 2002.
4. Krpenský, J., Horák, M., Kabát, J., Planer, J., Kepič, P., Křápek, V., and Konečná, A., "Analytical electron microscopy analysis of insulating and metallic phases in nanostructured vanadium dioxide", arXiv:2309.11980v2, 2024.

TDBC microstructures made by local photo-bleaching in J-aggregate thin organic layers for photonics applications

Komlan S. Gadedjisso-Tossou[1], A. Bard[2], K Chevrier[2], C. Symonds[2], J-M Benoit[2], J. Bellessa[2], A. Gassenq*[2]

[1]Laboratoire de Physique des Matériaux et Composants à Semi-conducteurs (LPMCS), Université de Lomé, Togo;

[2]Institut Lumière Matière, UMR5260 CNRS-UCBL, Lyon, France;

*corresponding author: alban.gassenq@univ-lyon1.fr

Abstract: We have study the local photobleaching in TDBC layers for grating and strong coupling applications. With this method, the refractive index can be both locally and spectrally modulated. In this work, fundamental properties and fabricated micro-devices have been investigated highlighting the high potential of this interesting materials for photonics applications.

Tetrachlorodiethyl Benzimidazo Carbocyanine (TDBC) layers are very interesting for photonics applications due to their huge oscillator strength, narrow absorption, local photo bleaching, and low-cost fabrication. They are mainly used in strong coupling studies [1], but also for light concentration [2], absorption enhancement [3]… However, these intrinsic properties are still not very well understood and need to be investigated to fully exploit the high potential of this material, especially regarding the bleaching properties (i.e photochemical alteration of a molecule that become unable to fluoresce).

During the recent past years, we have studied different TDBC micro-devices showing that micro-structures with resolutions down to 1 µm can be successfully fabricated using a laser writer for strong coupling applications [4] and grating fabrication [5]. Furthermore, material intrinsic properties studies have been also investigated. Using Raman spectroscopy, we have shown that a slight change in the molecule give a huge oscillator strength modification [6,7].

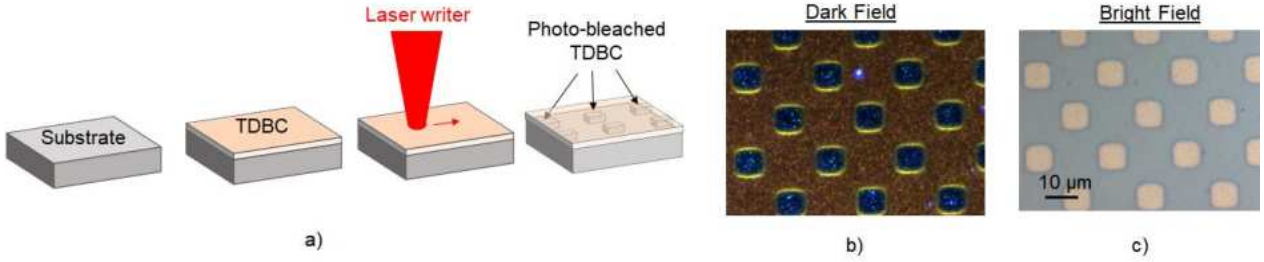


Figure 1 : a) process flow of the local photo-bleaching using a laser writer; fabricated sample observed with an optical microscope in b) dark field and c) bright field

Figure 1-a presents the process flow used to locally bleached TDBC layers. 17 nm thick TDBC layers are spin-coated [8] on SiO_2 or Ag on SiO_2 substrates [9] and then insolated with a laser writer (µPG Heidenberg). The Figure 1-b and c presents examples of a fabricated structures with insolated periodic squares on 50 nm Ag layer on a SiO_2 substrate. Images were measured with an optical microscope in both dark field (DF) and bright field (BF) modes. In the BF image, we clearly see that the refractive index is modulate at the microscale since the TDBC become transparent in the bleached region. For the DF image, the outline are detected indicating that the interface are abrupt between the bleached and active regions.

Furthermore, we also investigated the refractive index change as a function of the bleaching. The Drude-Laurentz model [6] is the most used in the literature with 5 constant material parameters: f_{osc} the oscillator strength, Eg the energy of the HUMO-LUMO (Highest Occupied Molecular Orbital and Lowest Unoccupied Molecular Orbital) transition, ΔE the absorption spectral width and ε_0 the constant part of the dielectric function. After bleaching, only the fundamental transition at around 590 nm wavelength range is modified in the refractive index. Furthermore, since many values are reported in the literature, we have studied the potential origins of these differences. Several parameters can lead to an undervaluation of the oscillator strength such as the layer thickness evaluation, the roughness, the use of polyvinyl alcohol as hang layer and the layer bleaching. Therefore, we highlight here the need of a better investigation of these layers for further applications of this promising materials.

The authors would like to thank M. Boutsady and S. Karkache from IUT Lyon 1, the master Nanoscale in Lyon and the CNRS Africa fellowship for funding.

References

[1] A. Bard, S. Minot, J-M. C. Symonds, Alban Gassenq, F. Bessueille, C. de la Vega, K. Chevrier, Y. De Wilde, V. Krachmalnicoff, Extended hybridization and energy transfer in multimaterial polaritonic metasurfaces, Adv. Opt. Mater. 10 (2022) 2200349 https://doi.org/10.1002/adom.202200349

[2] A. Cacciola, C. Triolo, O. Di Stefano, A. Genco, M. Mazzeo, R. Saija, S. Patanè, S. Savasta, Subdiffraction Light Concentration by J-Aggregate Nanostructures, ACS Photonics. (2015) https://doi.org/10.1021/acsphotonics.5b00197

[3] M.A. Castillo, C. Estévez-Varela, W.P. Wardley, R. Serna, I. Pastoriza-Santos, S. Núñez-Sánchez, M. Lopez-Garcia, Enhanced Light Absorption in All-Polymer Biomimetic Photonic Structures by Near-Zero-Index Organic Matter, Adv. Funct. Mater. 32 (2022) 1–26 https://doi.org/10.1002/adfm.202113039

[4] C. de la Vega, E. Bailly, K. Chevrier, J-P. Hugonin, A; Gassenq, J-M. Benoit, J. Bellessa, J-J. Greffet, Y. De Wilde, and V. Krachmalnicoff, Plasmon-Mediated Energy Transfer between Two Systems out of Equilibrium, ACS Photonics. 10 (2023) 1169–1176 https://doi.org/10.1021/acsphotonics.2c01931

[5] A. Gassenq, K. Chevrier, A. Bard, J. Benoit, C. Symonds, J. Bellessa, Selective grating obtained by dye micro-structuration based on local photo- bleaching using laser writer, Appl. Opt. 59 (2020) 5697–5701 https://doi.org/10.1364/AO.393103

[6] A. Gassenq, K. Chevrier, A. Bard, J. Benoit, C. Symonds, Study of dye local photo-bleaching obtained by UV lithography for photonics applications, CLEO IEEE. 59 (2021) 2482524 https://doi.org/10.1109/CLEO/Europe-EQEC52157.2021.9542441

[7] A. Gassenq, Y. Pipon, G. Montagnac, O. Boisron, V. Martinez, A. Bard, J. Benoit, J. Bellessa, Raman investigation of local photo-bleaching in TDBC dye layer for photonics applications, J. Raman Spectrosc. (2022) 6–9 https://doi.org/10.1002/jrs.6303

[8] A. Sorokin, I. Ropakova, S. Wolter, R. Lange, I. Barke, S. Speller, S. Yefimova, Y. Malyukin, S. Lochbrunner, Exciton Dynamics and Self-Trapping of Carbocyanine J-Aggregates in Polymer Films, J. Phys. Chem. C. 123 (2019) 9428–9444 https://doi.org/10.1021/acs.jpcc.8b09338

[9] K. Chevrier, J-M. Benoit, C. Symonds, J. Paparone, J. Laverdant, J. Bellessa, Organic Exciton in Strong Coupling with Long-Range Surface Plasmons and Waveguided Modes, ACS Photonics. 5 (2018) 80–84 https://doi.org/10.1021/acsphotonics.7b00556

Ultrathin bismuth and antimony films as alternative materials towards versatile and sustainable metastructures

F. Chacon-Sanchez, C. Ruiz de Galarreta, R. Serna
Instituto de Óptica (IO-CSIC), Serrano 121, 28006 Madrid, Spain
*corresponding author: fernando.chacon@csic.es

Abstract: Semimetals are versatile, unconventional materials with great potential for their application on metasurfaces. We will study the tailoring potential of their dielectric function via ultra-thin film morphology control and apply this tailoring for structural coloration, combining them with industrial materials like silicon or steel to achieve vivid, sustainable structural colors.

When designing an optical device, like plasmonic metasurfaces, interference-based cavities or perfect absorbers, the choice of material is crucial due to its refractive index (or dielectric function). Because of their near-ideal refractive index, the more extended materials used for the above-mentioned photonic applications are either transparent dielectrics or very conductive metals. Lossy materials were frequently not even taken into consideration since optical losses have been traditionally considered suboptimal. However, in the last ten years the scientific community has started to look for alternative, usually lossy materials to try to overcome some material limitations and to look forward to new developments such as active or switchable devices [1,2]. Among all these alternative materials, the semimetals bismuth (Bi) and antimony (Sb) have proven to be very attractive, showing a rich optical behavior arising from their strong interband transitions in the NIR [3]. As a result, Bi and Sb -based nanostructures can display epsilon-near-zero and interband plasmonic behavior as a lossy metal in the VIS-UV and act as a lossy dielectric with ultra-high refractive index (n~10) that can support Mie resonances. Another very interesting feature is their potential as a phase-change material (PCM), exploiting the low-temperature (270ºC) solid-liquid transition for Bi and the metastable amorphous-crystalline transition for Sb. Towards their potential day-to-day application, they can prove advantageous since they are inexpensive, abundant materials, that show low toxicity and good biocompatibility, making them ideal candidates for sustainable photonics.

The scientific relevance of Bi and Sb is undoubtedly on the rise, with an increasing number or reports in the last few years studying different fundamental phenomena [4, 5] and designing devices for their application, addressing different regions of the UV-NIR spectra [6, 7]. We have recently reported the design and fabrication of Bi-based gap-surface plasmon metasurfaces (GSP) and Fabry-Perot cavities (FPC) for non-diffractive structural color generation [8].

In this contribution, we move forward to the study of Bi and Sb within the ultrathin film regime (t~10nm) with the aim to further investigate the potential tailoring of their optical response. The films are prepared via pulsed laser deposition (PLD). We will show how with the fine tuning of the deposition parameters we are able to successfully modify the morphology and/or structure of our films in a robust and consistent way. This unprecedented control of the morphology and structure allows us to access to new optical properties with a well-defined dielectric function while using the same building blocks. An example of the achieved tailoring of the optical properties is displayed on Fig. 1 in which we have plotted the dielectric functions (ε) for different films as a function of thickness and approaching the near percolation regime, or achieving the amorphous phase for the case of Sb. The unique optical properties of Bi allow us to modulate the spectral regions of the spectra where high losses or epsilon-near-zero are displayed, therefore enabling am effective control of the dielectric function that has

not been possible for the archetypical noble metals (Au and Ag) although this approach through the modification of their morphology was atempted [9]

Once the tailoring potential of the Bi and Sb ultrathin films has been established, we have studied their application to structural color generation via FPC. Moreover, we will show the possibilities to generate vivid, robust structural colors directly using the substrate as a back-mirror, focusing on industrially ubiquitous substrates like silicon or steel. This opens the possibility of the use of structural color generation for consumer products, as well as in specific high-tech applications.

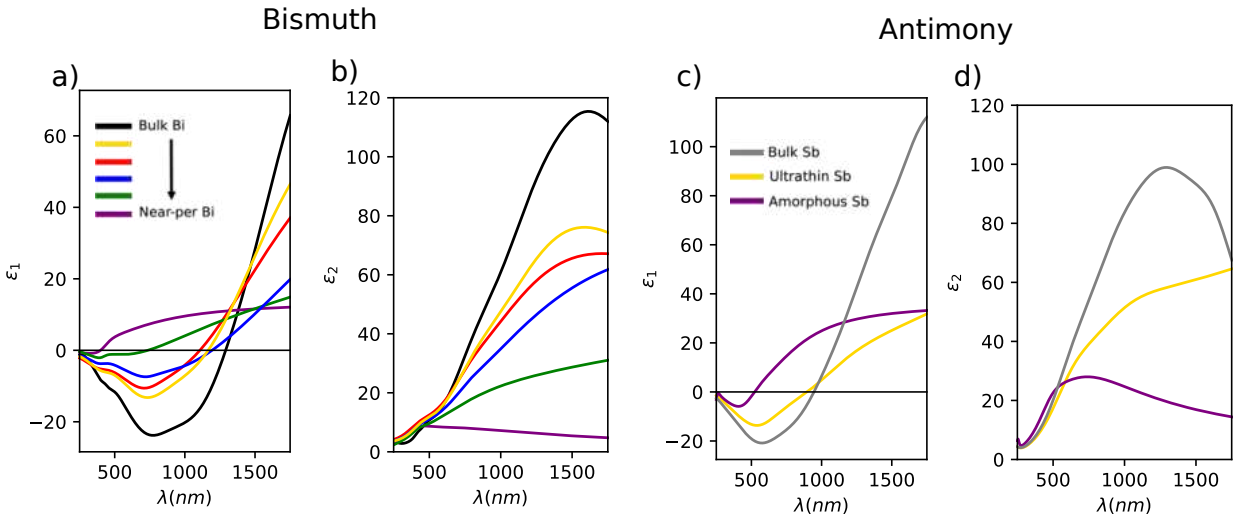


Fig.1 Real (ε_1) and imaginary (ε_2) part of the dielectric function for several deposited Bi (a,b) and Sb (c,d) films. As can be seen in the legend, Bi dielectric functions range from bulk Bi to near-percolation films (i.e. almost nanoparticles), whereas for Sb we have bulk Sb, an ultrathin crystalline film and an amorphous film.

References

1. Kats MA, Blanchard R, Genevet P, Capasso F. “Nanometre optical coatings based on strong interference effects in highly absorbing media.” Nat Mater. 2013 Jan;12(1):20-4.
2. G. Naik et al.“Alternative plasmonic materials: beyond gold and silver” Advanced Materials, **25**, 24, 3264-3294 (2013).
3. J. Toudert and R. Serna, “Interband transitions in semi-metal, semiconductors, and topological insulators: a new driving force for plasmonics and nanophotonics,” Opt. Mater. Express **7**(7), 2299–2325 (2017).
4. J. Toudert, R. Serna, C. Deeb, and E. Rebollar, "Optical properties of bismuth nanostructures towards the ultrathin film regime," Opt. Mater. Express 9, 2924-2936 (2019)
5. M. Alvarez-Alegria et al., “Nanosecond Laser Switching of Phase-Change Random Metasurfaces with Tunable ON-State”,*Adv. Opt. Mater*. 2101405, (2022).
6. J. Toudert et al. “Mid-to-far infrared tunable perfect absorption by a sub - λ/100 nanofilm in a fractal phasor resonant cavity”, Optics Express, (2018), 34043, 26(26)
7. Z. Cheng et al. “Antimony thin films demonstrate programmable optical nonlinearity”, Science Advances, (2021), 7(1)
8. F. Chacon-Sanchez, C. Ruiz de Galarreta et al. “Building Conventional Metasurfaces with Unconventional Interband Plasmonics: A Versatile Route for Sustainable Structural Color Generation Based on Bismuth”, Adv. Opt. Mater., (2023), 2302130
9. J. Kim et al. “Generation of Reflection Colors from Metal-Insulator-Metal Cavity Structure Enabled by Thickness-Dependent Refractive Indices of Metal Thin Film”, ACS Photonics, (2019), 2342-2349, 6(9)

Harmonic enhancement via a time-varying Fabry-Perot resonator

T. D. Karamanos[1,*], S. Amanatiadis[2], N. Kantartzis[2] and F. Lemoult[1]

[1] Institut Langevin, ESPCI Paris, Université PSL, CNRS, Paris, France
[2] Aristotle Univ. of Thessaloniki, Dept. of Electrical & Comp. Eng., Thessaloniki, Greece
*theodosios.karamanos@espci.fr

Abstract: Time-varying surfaces are a promising emerging means for the generation of higher frequencies in future THz communication systems. In this work, we present a novel time-varying Fabry-Perot setup to enhance generated higher-order harmonics. The design is aided by a rigorous semi-analytic technique that aims to empower optimization efforts.

Recently, the THz regime has been approached due to the continuous progress of the telecommunication systems beyond the 5G limits. Therefore, efficient excitation setups are required to generate these frequencies and recently emerging time-varying media applications are increasingly considered suitable for this task [1–3]. Nevertheless, early cavity antenna solutions with a time-varying graphene generated only minimally enhanced harmonics [3]. In this work, we propose a time-varying Fabry-Perot configuration for the improvement of the produced higher-order harmonics, based on a rigorous semi-analytic methodology that enables rapid optimization processes.

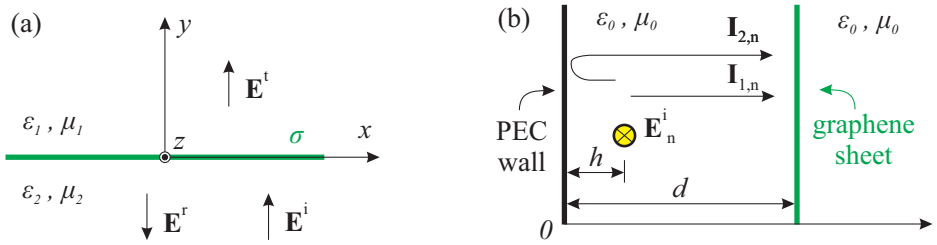


Figure 1: Setup (a) for normal incidence on a single graphene sheet on the xz-plane and (b) of the time-varying 1D Fabry-Perot resonator with an E-field source in its interior, generating the initial waves $\mathbf{I}_{i,n}$.

Let us assume a graphene sheet on the xz-plane and an incident wave $\mathbf{E}^{\mathrm{i}} = E^{\mathrm{i}} \cos(\omega t - k_2 y)\, \hat{\mathbf{z}}$, with $k_2 = \omega\sqrt{\varepsilon_2 \mu_2}$ (Fig. 1a). For the sake of simplicity, also, we assume for the graphene that $\bar{\bar{\sigma}} = \sigma\, \hat{\mathbf{z}}\hat{\mathbf{z}}$. In this context, the boundary conditions can be written, after some manipulation, as

$$E^{\mathrm{t}} - E^{\mathrm{i}} = E^{\mathrm{r}} \qquad \text{and} \qquad (\eta_1 + \eta_2)\, E^{\mathrm{t}} + (\eta_1 \eta_2)\, \sigma * E^{\mathrm{t}} = (2\eta_1) E^{\mathrm{i}}, \qquad \eta_i = \sqrt{\varepsilon_i \mu_i} \tag{1}$$

Next, we perform the convolution in the second formula of (1), considering that for non-time-varying media, $\sigma(t - t', t') = \sigma(t')$, i.e. invariant with respect to t. Additionally, for media with an instantaneous response, it holds that $\sigma(t - t', t') = \sigma'(t)\delta(t - t')$. In the general case of dispersive media, the Fourier transform of the convolution in (1) turns to [4],

$$(\eta_1 + \eta_2)\, E^{\mathrm{t}}(\omega) + (\eta_1 \eta_2) \int_{-\infty}^{\infty} \sigma(\omega - \omega', \omega')\, E^{\mathrm{t}}(\omega')\, d\omega' = (2\eta_1) E^{\mathrm{i}}(\omega). \tag{2}$$

In order to work further with (2), we need to discretize it for a specific number of n frequencies, or $\omega_n = \omega_0 + n\omega_{\mathrm{s}}$, where s is the sampling frequency. As a result, in (2) the convolution can be calculated in a discrete form for a given value n, as

$$\frac{\eta_1 + \eta_2}{2\eta_1}\, E^{\mathrm{t}}[n] + \frac{\eta_2}{2} \sum_{m=-N}^{N} \sigma[n - m] E^{\mathrm{t}}[m] = E^{\mathrm{i}}[n] \Rightarrow \left\{ \frac{\eta_1 + \eta_2}{2\eta_1}[I] + \frac{\eta_2}{2}[S] \right\} \mathbf{E}_n^{\mathrm{t}} = \mathbf{E}_n^{\mathrm{i}}, \tag{3}$$

where for all sampled frequencies ω_n, (3) receives the matrix form $[A]\mathbf{E}_n^{\mathrm{t}} = \mathbf{E}_n^{\mathrm{i}}$, with $\mathbf{E}_n^{\mathrm{t}}$ and $\mathbf{E}_n^{\mathrm{i}}$ the vectors containing the harmonics of the transmitted and incident/source waves, respectively. The $\mathbf{E}_n^{\mathrm{i}}$ vector is known and with the assumption of a monochromatic incidence at ω_0, only its E_0^{i} element is

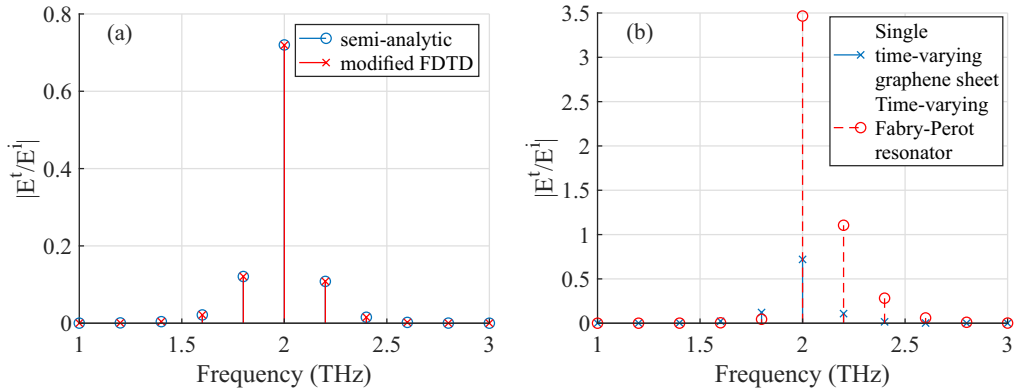


Figure 2: (a) Semi-analytic results validated with a modified FDTD algorithm for a $\delta(f - f_0)$ incidence on a single time-varying graphene sheet. (b) 1st harmonic ($f_1 = 2.2$ THz) enhancement via the optimized time-varying Fabry-Perot resonator, calculated with the proposed semi-analytic technique.

non-zero. Therefore, the computation of matrix $[S]$ and the solution of the system in (3) leads to the response of the time-varying graphene sheet. Note that the surface conductivity of graphene follows a Drude type dispersion [1]. Hence, if the surface conductivity is controlled (modulated) along a sinusoidal way via the chemical potential, $\mu_c(t) = \mu_{c,0}\,(1 + M\cos(\omega_{\rm mod}t))$, we arrive at

$$\sigma(t) = \frac{e^2\mu_c(t)}{\pi\hbar^2}\,e^{-2\Gamma t}\,u(t) \Rightarrow \sigma(\omega) = \frac{e^2\mu_{c,0}}{\pi\hbar^2}\,\frac{1}{\mathrm{j}\omega + 2\Gamma}\left[\frac{M}{2}\delta(\omega-\omega_{\rm mod})+\delta(\omega)+\frac{M}{2}\delta(\omega+\omega_{\rm mod})\right]. \quad (4)$$

for M the modulation strength and $\omega_{\rm mod}$, the modulation frequency. In that way, the $[S]$ matrix in (3) can be filled and, thus, $\mathbf{E}_n^{\rm t}$ and $\mathbf{E}_n^{\rm r}$ can be acquired. Let us, now, try to enhance the generated harmonics by the time-varying graphene via the 1D Fabry-Perot resonator of Fig. 1b. After some algebra, and if $[T] = [A]^{-1}$ and $[R] = [T] - [I]$, the total transmitted field after the multiple reflections is evluated as

$$\mathbf{E}_{n,\rm tot}^{\rm t} = [T]\left([I] + \mathrm{diag}\{e^{-\mathrm{j}2k_nd}\}\,[R]\right)^{-1}\,\mathrm{diag}\{e^{-\mathrm{j}k_nd}\}\,\mathrm{diag}\{\mathrm{j}2\sin(k_nh)\}\,\mathbf{E}_n^{\rm i}. \quad (5)$$

For the validation of the proposed semi-analytic scheme and the featured resonator, the extracted results of our method are compared with a properly modified FDTD algorithm that treats graphene as an equivalent surface current $\vec{J}_{\rm gr} = \sigma\vec{E}$ in the frequency domain. The latter is introduced in the FDTD update equations via Ampère's law, while the Drude frequency dispersion model is straightforwardly resolved through an auxiliary differential equation (ADE) scheme [5]. In our investigation, we assume a monochromatic source in the Fabry-Perot resonator of Fig. 1b with $f_0 = \omega_0/2\pi = 2$ THz. Moreover, $h = \pi c_0/2\omega_0$, $\eta_1 = \eta_2 = \eta_0 = \sqrt{\mu_0/\varepsilon_0}$, $M = 0.5$, $\mu_c = 0.5$ eV, and $\omega_{\rm s} = \omega_{\rm mod} = \omega_0/10$, whereas $2N$ harmonics of f_0 are examined in (3), with $N = 5$, or $f_n = f_0 \pm nf_{\rm mod}$. The verification results of (5) via the modified FDTD algorithm is presented in Fig. 2a, which reveals a perfect match. Subsequently, we proceed to our initial goal of enhancing one of the generated harmonics with the time-varying Fabry-Perot resonator of Fig. 1b, setting $f_1 = 2.2$ THz. After performing a very rapid sweep for the thickness d, using (5), we find that the maximum transmitted E-field for f_1 is achieved for $d = 4.4\lambda_0$. In particular, as shown in Fig. 2b, the amplitude of the first harmonic is enhanced more than ten times, when compared with the one generated by a single sheet of a time-varying graphene.

As future work, a more optimized structure to suppress other harmonics is envisioned as well as the implementation of the proposed setup on a novel THz antenna.

REFERENCES

[1] M. Salary et al., *Phys. Rev. B*, 97(11), 115421, 2018.
[2] E. Galiffi et al., *Advanced Photonics*, 4(1), 014002-014002, 2022.
[3] S. Amanatiadis et al., *17th Metamaterials Congress 2023*, IEEE, X–007, 2023.
[4] G. Ptitcyn, et al., *Laser & Phot. Rev.* 17(3): 2100683, 2023.
[5] S. Amanatiadis et al., *16th Metamaterials Congress 2022*, IEEE, X–016, 2022.

Identify Defect and Strain of Monolayer WSe_2 through Exciton Anisotropy

Shu-Hsien Chen[1], Sih-Wei Chang[1], and Hsuen-Li Chen[1,2*]

[1]Department of Materials Science and Engineering, National Taiwan University, Taipei, 10617, Taiwan
[2]Center of Atomic Initiative for New Materials, National Taiwan University, Taipei, Taiwan
E-mail: hsuenlichen@ntu.edu.tw

Abstract: Identify the quality through variations of anisotropic exciton resonances. The optical power requirement through exciton anisotropy is 10^{10} times smaller than Raman measurements while obtaining an optical signal with a standard deviation of 10 times smaller. Therefore, we believe that exciton anisotropy is much more sensitive to characterize TMDCs films.

Two-dimensional (2D) materials have emerged as promising for next-generation devices, owing to their unique properties. Fundamental research and emerging applications in various fields rely on the availability of high-quality 2D materials. Nevertheless, defects and strain significantly affect the various properties of 2D materials; hence, developing rapid and non-destructive inspection technology is essential.

Polyethylene terephthalate (PET) substrate performs low thermal conductivity.[1] Strong laser irradiation increases the local temperature of the PET substrates, resulting in surface damage on the WSe_2 films, as shown in **Figure 1**. We adjusted the intense laser irradiation (8.79 mW) time from 0 to 20s to create different defect densities. To avoid damaging the surface, we used a laser excitation intensity of 2.82 mW for Raman measurements. The wavenumber of E^1_{2g} mode upshifted from 256.18 to 257.44 cm^{-1}, indicating that defects increased, as shown in **Figure 2(a)**. Moreover, we analyze the exciton anisotropy of WSe_2 films through the wavelength-dependent spectroscopic ellipsometer (SE). We can obtain ellipsometric parameters Ψ where the absolute amplitude ratios (tan Ψ) of the reflection coefficient of TE- and TM- polarized light from the film surface. In addition, exciton anisotropy would perform different absorption and reflection coefficients of TE and TM-polarized lights.[2] Therefore, Ψ and exciton anisotropy are highly correlated. As defect densities increase, the value of Ψ spectra at the D-exciton resonance in WSe_2 film decreases from ca. 9.53° to 8.94°, which means the exciton anisotropy diminishes, as shown in **Figure 2(b)**. Due to the lower signal-to-noise ratio through Raman spectra than Ψ spectra, we obtain the E^1_{2g} mode with relatively larger error bars than the Ψ value of D-exciton anisotropy, as shown in **Figure 2(c)**.

Furthermore, we explore the effect of uniaxial tensile strains on the exciton anisotropy and phonon vibrations of a monolayer WSe_2 film on the polydimethylsiloxane (PDMS) substrate. Since the E^1_{2g} mode is an in-plane lattice vibration mode along the direction parallel to the applied strain, the downward shift in wavenumber is caused by an increase in the lattice constant with increasing tensile strain, as shown in **Figure 3(a)**. In addition, the wavenumber of the E^1_{2g} mode in the Raman spectra with a slope of approximately 2.63 cm^{-1}/% strain. Due to the low signal-to-noise ratio, we obtain the E^1_{2g} mode with relatively large error bars and an average SD of about 0.437, as shown in **Figure 3(b)**.

Furthermore, exciton anisotropy is affected by applied strain due to lattice distortion. We propose that the in-plane exciton resonance is disturbed in WSe_2 films. The tensile strain changes from 0.0% to 1.0%, and the D exciton in the Ψ spectrum significantly decreases, as shown in **Figure 3(c)**. We estimate the relationship between the Ψ value of the D exciton and the strain by a linear fit with a slope of approximately ca. 1.693°/% strain, as shown in **Figure 3(d)**. The SD of the Ψ value in the exciton anisotropy signal is about 0.030, which is much smaller than the SD of the Raman spectra. Moreover, the optical power requirement for WSe_2 through exciton anisotropy in Ψ is 10^{10} times smaller than in

Raman spectroscopy. The exciton anisotropy signal fluctuates less than the Raman scattering signal. Here, we consider that changes in exciton anisotropy are more sensitive than Raman scattering signals.

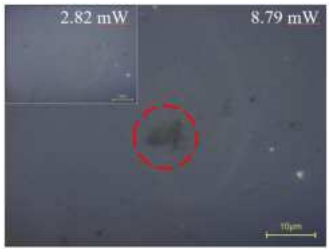


Figure 1. WSe_2 surface imaged by optical microscopy under laser irradiation of 4.13 mW. (Inset: 2.82 mW.) The scale bar is 10 μm.

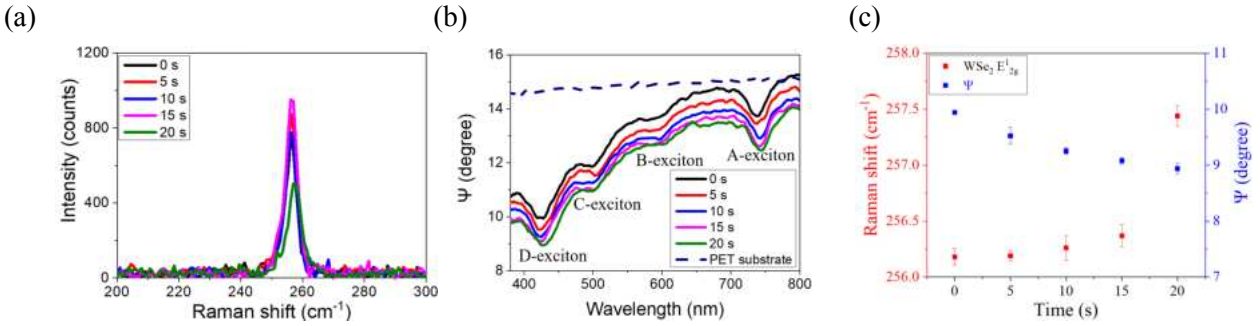


Figure 2. (a) Raman (b) Ψ spectra of WSe_2 films with different laser irradiation. (c) Correlation between the Ψ values of D-exciton and Raman shift E^1_{2g} mode at different laser irradiation times.

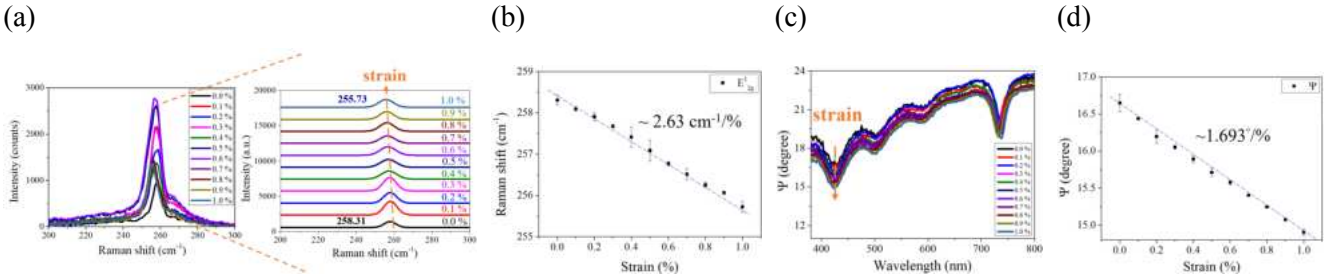


Figure 3. (a) Raman (c) Ψ spectra of WSe_2 films with strain. Correlation between the (b) Raman shift E^1_{2g} mode and (d) Ψ values of D-exciton and the strain applied.

Acknowledgments

The authors thank the National Science and Technology Council, Taiwan, for supporting this study under contracts 112-2221-E-002-211-MY3 and 112-2221-E-002-087-MY3.

References

[1] P. K. Chow, R. B. Jacobs-Gedrim, J. Gao, T.-M. Lu, B. Yu, H. Terrones, N. Koratkar, *ACS nano* **2015**, 9, 1520.

[2] Y.-L. Liu, C.-C. Yu, K.-T. Lin, E.-Y. Wang, T.-C. Yang, H.-L. Chen, C.-W. Chen, C.-K. Chang, L.-C. Chen, K.-H. Chen, *Analytical chemistry* **2014**, 86, 7192.

Second optical harmonic generation in high-Q dielectric metasurfaces integrated with transition metal dichalcogenide films

A. A. Nazarenko[12], A. M. Chernyak[12], A. I. Musorin[12], A. S. Shorokhov[1] and A. A. Fedyanin[1*]

[1]Lomonosov Moscow State University, Russia
[2]MSU-BIT University, P.R.C.
[*]corresponding author: fedyanin@nanolab.phys.msu.ru

Abstract: Atomically thin transition metal dichalcogenides are a promising class of novel materials, that provide new approaches in photonics, for instance, in nonlinear optics. Coupling two-dimensional semiconductors with dielectric resonant metasurfaces provides an opportunity to achieve higher efficiencies of nonlinear optical processes.

Metamaterials appear to be one of the most promising materials for numerous applications in photonics. They can be used to control various properties of light, such as direction, polarization or phase, as well as to enhance light-matter interaction due to their resonant interaction [1]. If a high-quality resonance is excited, then the interaction occurs more effectively [2].

However, such three-dimensional structures are difficult to manufacture at the nanoscale, which is required for operation in the optical range. Therefore, planar metamaterials, or metasurfaces, are used for optical range applications, as they can be easily fabricated by means of existing technologies such as lithography and nanoprinting methods.

Our research is focused on dielectric metasurfaces. They have low ohmic losses and their resonant features are associated with Mie resonances [3], that can be decomposed into a multipole series. These modes depend on the particle size and other structural properties [4]. They are widely used to enhance optical [5] and magneto-optical effects [6]. Due to the high localization of the field nonlinear effects, such as third harmonic generation, are enhanced in the vicinity of Mie resonances [7].

As a noncentrosymmetric material, a transition metal dichalcogenide monolayer possesses a large second-order nonlinear susceptibility [8], thus second-harmonic generation is greatly enhanced due to excitonic states [9]. These resonances are significantly increased at cryogenic temperatures [10] and when coupled with metasurface due to the spectral overlap with its high-quality resonance [11, 12].

In this work, a high-quality resonant dielectric metasurface is used to enhance non-linear effects, that occur in a transition metal dichalcogenide monolayer placed on top of the array and coupled with metasurface. We observe the amplification of the second-harmonic signal in the presence of the mentioned above spectral overlap of material and structural resonances. A metasurface consisting of titanium dioxide nanodiscs on a silicon dioxide substrate provides a high-quality structural resonance in the optical range. The spectral position of this resonance can be adjusted by tuning the angle of incidence of the incoming radiation. A monolayer of molybdenum diselenide is chosen as a source of non-linear optics, since it has exciton resonances in the studied spectral range [13]. When the two resonances overlap, the signal is significantly amplified. The second-harmonic signal is amplified compared to the exciton resonance of a two-dimensional film and compared to the metasurface resonance as well.

This work is supported by the Russian Science Foundation (No. 20-12-00371, calculations of transmittance and non-linear spectra). The study is carried out within the framework of the Development Program of MSU, an interdisciplinary scientific and educational school "Photonic and Quantum Technologies. Digital Medicine".

This work is supported by a grant from the Foundation for the Development of Theoretical Physics and Mathematics "BASIS" (No. 22-1-3-5-1, multipole decompositon).

References

1. Zhang J. et al. “Strong field enhancement and light-matter interactions with all-dielectric metamaterials based on split bar resonators”, Optics express, Vol. 22, No. 25, 30889-30898, 2014.
2. Y. Yang, I. I. Kravchenko, D. P. Briggs, J. Valentine, “All-dielectric metasurface analogue of electromagnetically induced transparency”, Nat. Commun., Vol. 5, No. 1, 5753, 2014.
3. Staude I., Schilling J. “Metamaterial-inspired silicon nanophotonics”, Nature Photonics, Vol. 11, No. 5, 274-284, 2017.
4. Kuznetsov A.I., Miroshnichenko A.E., Fu Y.H et al. “Magnetic light”, Sci. Rep., Vol. 2., 492, 2012.
5. Staude I. et al. “Tailoring directional scattering through magnetic and electric resonances in subwavelength silicon nanodisks”, ACS nano., Vol. 7, No. 9, 7824-7832, 2013.
6. Barsukova M. G. et al. “Enhanced magneto-optical effects in hybrid Ni-Si metasurfaces”, Apl Photonics., Vol. 4, No. 1, 2019.
7. Shcherbakov M. R. et al. “Enhanced third-harmonic generation in silicon nanoparticles driven by magnetic response”, Nano letters., Vol. 14, No.11, 6488-6492, 2014.
8. Wang C. Y., Guo G. Y. “Nonlinear optical properties of transition-metal dichalcogenide MX2 (M= Mo, W; X= S, Se) monolayers and trilayers from first-principles calculations”, The Journal of Physical Chemistry C., Vol. 119, No. 23, 13268-13276, 2015.
9. Splendiani A. et al. “Emerging photoluminescence in monolayer MoS2”, Nano letters., Vol. 10, No. 4, 1271-1275, 2010.
10. Wang G. et al. “Giant enhancement of the optical second-harmonic emission of WSe 2 monolayers by laser excitation at exciton resonances”, Physical review letters., Vol. 114, No. 9, 097403, 2015.
11. Bernhardt N. et al. “Quasi-BIC resonant enhancement of second-harmonic generation in WS2 monolayers”, Nano Letters., Vol, 20, No. 7, 5309-5314, 2020.
12. Yuan L. et al. “Manipulation of exciton dynamics in single-layer WSe2 using a toroidal dielectric metasurface”, Nano Letters., Vol. 21, No. 23, 9930-9938, 2021.
13. Palummo M., Bernardi M., Grossman J. C. “Exciton radiative lifetimes in two-dimensional transition metal dichalcogenides”, Nano Lett., Vol. 15, No. 5, 2794, 2015.

Structured Light Generation Using Spherulite in Linear and Nonlinear Realm

Yuanfeng Liu[1], Le Zhou[1], Youcheng Xu[1], Yongzheng Wen[1], Natalia M. Litchinitser[2], Yang Shen[1*], Jingbo Sun[1*], and Ji Zhou[1*]

[1] School of Materials Science and Engineering, Tsinghua University; Beijing 100084, China.
[2] Department of Electrical and Computer Engineering, Duke University; Durham, North Carolina 27708, USA.
[*]Corresponding author: zhouji@tsinghua.edu.cn; jingbosun@tsinghua.edu.cn; shyang_mse@mail.tsinghua.edu.cn

Abstract: Structured light exhibits spatially varying phase or polarization, implying intriguing physical properties for advanced optical applications. Here, we introduce naturally-crystalized spherulites as the structured light generator. The cylindrical anisotropy of the spherulite can be engineered through molecular design, offering a flexible toolbox for structured light generation.

Structured light is characterized by its spatially varying phase or polarization, setting it apart from classical light fields. This structured phase or polarization leads to intriguing physical phenomena such as optical orbital angular momentum (OAM), optical inseparable states, vector diffraction, infinite number of modes, and et al[1-4]. Those remarkable optical properties of structured light have inspired advanced applications particularly in optical communication, quantum technology, and optical manipulation[1]. Significant progress has been made in generating structured light over the past several decades, hastening the process towards practical applications.

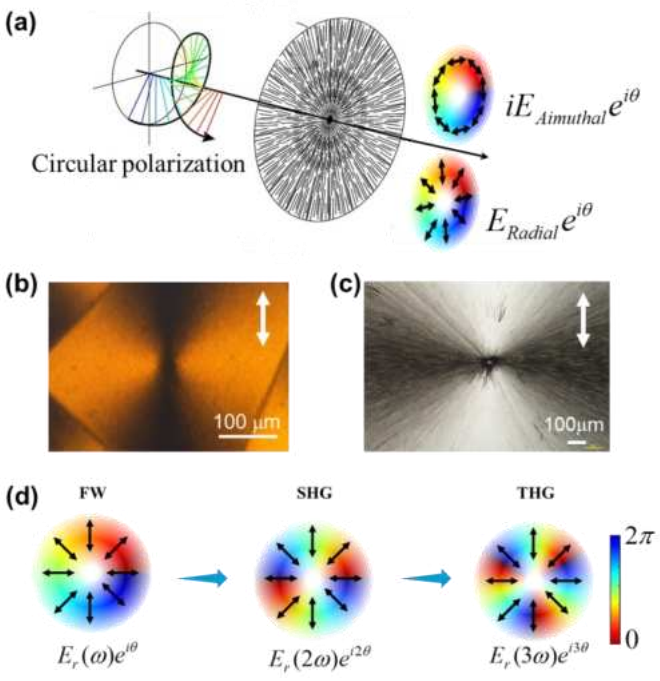


Fig. 1. Generating structured light using spherulites. (a) The schematic of generating a vector vortex beam using a circularly polarized beam as the incidence. (b) The optical image of a spherulite under transmissive mode. The incidence light is vertically polarized. (c) The optical image of a 7OCB spherulite under transmissive mode. The incidence light is vertically polarized. (d) The phase and polarization evolution from fundamental wave (FW) to SHG and THG for a radial polarization vortex beam.

Metasurfaces play a significant role in structuring the polarization and phase of light due to their flexible design capabilities, ultra-thin thickness, and ease of on-chip integration. Nevertheless, metasurfaces encounter some challenges related to fabrication costs, lithography limits, and scattering losses of meta-atoms. Here, we propose spherulite material as a new avenue for structured light generation. The spherulite material is prepared using a self-assembly method to induce cylindrical molecular orientation and optical anisotropy. It should be noted that the cylindrical symmetry of spherulite perfectly matches the symmetry of cylindrical-type structured light such as the radial polarization beam, the azimuthal polarization beam, and the OAM beam. Therefore, the spherulite material can potentially serve as the structured light generator, which is unique compared to conventional crystals with symmetry under Cartesian coordinate.

To illustrate the working principle of spherulite in generating structured light, a circularly polarized beam can be decomposed into radial polarization and azimuthal polarization components:

$$E_L = \frac{P(r)\left(\boldsymbol{e}_r + i\boldsymbol{e}_\theta\right)e^{i\theta}}{\sqrt{2}}, \quad E_R = \frac{P(r)\left(\boldsymbol{e}_r - i\boldsymbol{e}_\theta\right)e^{-i\theta}}{\sqrt{2}} \tag{1}$$

The $P(r)$ is the amplitude. $\boldsymbol{e}_r$ and $\boldsymbol{e}_\theta$ are the unit vectors along radial direction and azimuthal direction[5]. Because of the optical cylindrical anisotropy of the spherulite material, one can easily tune the electrical field of light in the radial and azimuthal directions (Fig. 1a). Specifically, extinguishing the radial polarization component results in the generation of an azimuthal polarization beam. Similarly, extinguishing the azimuthal polarization component results in the generation of a radial polarization beam. Herein, we prepared two types of spherulites for generating azimuthal (see Fig. 1b) and radial polarization beams (see Fig. 1c)[5]. Moreover, one can extend the linear optical behavior into nonlinear realm. For example, if a cylindrical anisotropy spherulite exhibits a prominent nonlinear optical coefficient in the radial direction, one can generate second-harmonic (SH) and third-harmonic (TH) vortex beams with radial polarization (Fig. 1d).

In summary, we introduce spherulite materials as a novel approach for structured light generation. The spherulite is easily fabricated through self-assembly, exhibiting uniformity at the molecular level, and is versatile through molecular engineering, thus holding great promise for structuring light in both linear and nonlinear realms.

This work was supported by the National Key R&D Program of China (Grant No. 2022YFB3806000). The Basic Science Center Project of NSFC (Grant No. 52388201).

References

1 Shen, Y. *et al.* "Optical vortices 30 years on: OAM manipulation from topological charge to multiple singularities," Light Sci Appl, Vol. 8, No. 90, 2019.

2 Nape, I. *et al.* "Revealing the invariance of vectorial structured light in complex media," *Nature Photonics* Vol. 16, 538-546, 2022.

3 Rosales-Guzmán, C., B. Ndagano and A. Forbes, "A review of complex vector light fields and their applications," Journal of Optics, Vol. 20, No.12, 123001, 2018.

4 Shen, Y. and C. Rosales-Guzmán, "Nonseparable states of light: from quantum to classical," Laser & Photonics Reviews, Vol. 16, 2100533, 2022.

5 Liu, Y. *et al.* "Optical vector vortex generation by spherulites with cylindrical anisotropy," Nano Lett, Vol. 22, No. 6, 2444-2449, 2022.

Cost-Efficient Deterministic Engineering of Quantum Light Emission in Two-Dimensional Semiconductors

S. Lazić[1,2*], S. Djurdjić Mijin[1,3], and I. de Pedro Embid[1]

[1]Dpt. de Física de Materiales, Facultad de Ciencias, Universidad Autónoma de Madrid (UAM), 28049 Madrid, Spain

[2]Instituto Universitario de Ciencia de Materiales "Nicolás Cabrera" (INC) and Condensed Matter Physics Center (IFIMAC), UAM, 28049 Madrid, Spain

[3]Institute of Physics Belgrade, University of Belgrade, Pregrevica 118, 11080 Belgrade, Serbia

[*]corresponding author: lazic.snezana@uam.es

Abstract: Various techniques, including strain engineering and surface treatments, have been tested for spatially deterministic generation of quantum light emitters in 2D layered semiconductors. Here, we develop a more cost-efficient and simpler method by placing mechanically exfoliated GaSe flakes onto a substrate carrying dispersed radiative microparticles with a distinctive bipyramidal shape.

Localized defect states in two-dimensional (2D) van der Waals (vdW) materials, including semiconducting transition metal dichalcogenides (TMDs), GaSe and insulating h-BN, have emerged as a promising physical system for scalable quantum technologies. Addressing the challenge of achieving scalability and reliable deterministic generation of quantum light emitters (QLEs) at precise locations, various strategies have been explored. The most comment state-of-the-art technique includes ***(i)*** strain engineering achieved by placing the active material (in the form of exfoliated 2D sheets) onto micro- or nano-scale structures obtained via lithographic substrate patterning, as well as ***(ii)*** different local surface treatments of the active medium. The former technique, in particular, has shown to be quite useful for the production of large-scale arrays of QLEs at predetermined sites in (few)monolayer thin vdW systems. The produced QLEs originate from optically active electronic states associated with extrinsically induced structural imperfections within the crystal lattice forming either ***(i)*** localized exciton trapping sites (e.g. excitons bind to impurity atoms or trapped in a potential dip created by structural defects or local strain) as in the case of TMDs and GaSe or ***(ii)*** deep-level atom-like defects as in the case of h-BN, both acting as recombination centers, resulting in non-classical light emission. While these methods have demonstrated considerable success, their high cost renders them less accessible, highlighting the need for a more economical approach to deterministically generate strain-induced QLEs in these materials. In this work, we demonstrate scalable and lithography free approach toward creating large areas of spatially localized non-classical emitters in 2D semiconductors flakes. The proof of concept was achieved by placing the WSe_2 and GaSe flakes, which were previously mechanically exfoliated from commercially available bulk crystals, over luminescent rare earth ion doped micro particles dispersed onto a Si substrate coated with 300 nm-thick SiO_2 layer. Once the location of the dispersed particle on the Si/SiO_2 surface was identified by an optical microscope, the precise placement of the flake was achieved using all-dry viscoelastic polydimethylsiloxane stamp method.[1] Because of the strong intra-layer bonding and weak van der Waals forces between the layers in 2D materials, the flake accommodates around the underlying microparticle inducing microscopic strain deformation at fixed spatial position. This, in turn, creates site-controlled 3D confinement potential for charge carriers with quantized energy levels, yielding optically allowed excitonic transitions which are necessary to produce quantum light. The advantage of using luminescent microparticles is that their optical activity enables the precise determination of their position, hence, revealing the location of the exciton traps instigated in the 2D sheet by the underlying microparticles. In addition, their bipyramidal shape containing

several sharp corners, which are inherent to this geometry, allows to create nanoscale sites for exciton confinement. Low temperature micro-photoluminescence (μ-PL) measurements performed on the flake at different spatial locations around and on top of the microparticle reveal significant spectral changes determined by the unique strain condition at each location. At some positions, we observed the appearance of narrow emission peaks associated with quantum confinement of excitons. The excitation power dependent measurements reveal linear and sub-linear power dependencies of different PL lines, thus enabling their assignment to the specific excitonic radiative transitions (i.e., exciton, X and biexciton, XX). The X-XX assignment was also corroborated by the polarization-resolved μ-PL measurements which show collinear elliptical polarization of the specific excitonic transitions with the same polarization degree, therefore confirming their origin from the same microscopic trap. Photon correlation measurements evidenced the quantum nature of the detected X and XX PL peaks. Moreover, employing conventional μ-PL spectroscopy eliminates the need for the use of scanning electron microscopy (SEM) or atomic force microscopy (AFM) imaging for precise (sub)micrometer scale QLEs site identification within the flake.

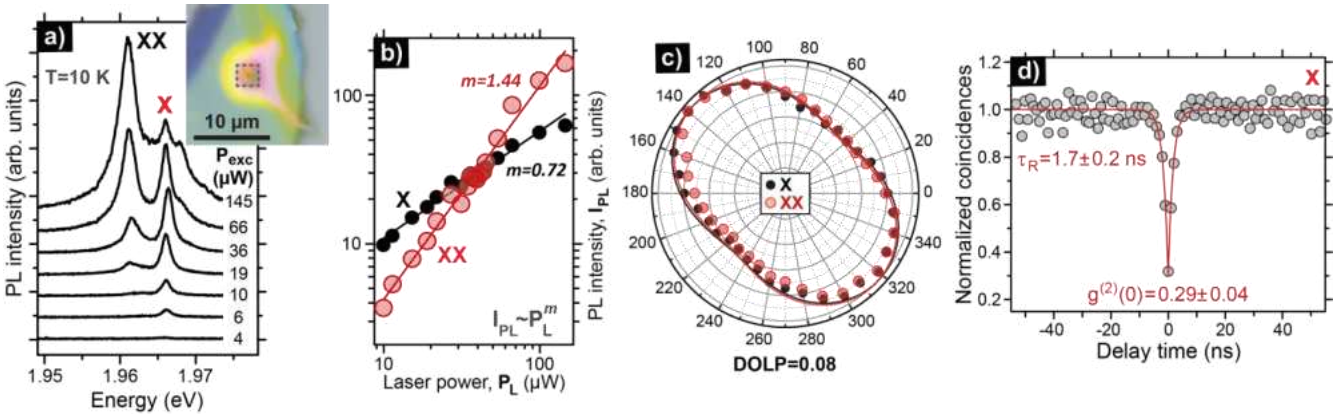


Figure 1. **(a)** Low-temperature μ-PL spectra for different laser excitation powers on exciton trap induced within the GaSe flake by strain deformation localized in the region above the luminescent $LiYF_4:Nd^{3+}$ microparticle. Inset: Optical microscopy images of GaSe flake deposited on top of the $LiYF_4:Nd^{3+}$ microparticle. **(b)** Excitation power dependent and **(c)** normalized polar plots of the integrated peak intensities of exciton (X, black circles) and biexciton (XX, red circles) in (a). **(d)** Normalized coincidence counts for the exciton emission peak X in (a).

The observed excitonic complexes originating from strain engineered localized traps in GaSe sheets suggest that this system is suitable for entangled photon pairs production via XX-X radiative cascade. This is especially relevant given that the polarization state of the emitted X-XX cascade could also be controlled by e.g. strain, as seen for WSe_2 in Ref. 2. The excellent agreement between our results and the previous reports on strain-induced emission of antibunched photons in GaSe[3] unequivocally confirms the suitability of our approach for the deterministic generation of highly localized QLE. The introduction of such cost-effective and practical platform for quantum light generation expands the accessibility of 2D QLEs, fostering advancements in both research and practical applications in nanophotonics and the related quantum technologies.

References

1. Castellanos-Gomez, A. et al., "Deterministic transfer of two-dimensional materials by all-dry viscoelastic stamping", 2D Materials 1, 011002, 2014.
2. Kern, J. et al., "Nanoscale positioning of single-photon emitters in atomically thin WSe_2", Adv. Mater. 28, 7101, 2016.
3. Luo, W. et al., "Deterministic localization of strain-induced single-photon emitters in multilayer GaSe", ACS Photonics 10, 2530, 2023.

Investigating the Optical Properties of Thin Films Coated with MWCNTs

S.Islam[1*], H.Furuta[1*]

[1]Kochi University of Technology, Japan
[2]Kochi University of Technology, Japan
[*]Corresponding author: 256003q@gs.kochi-tech.ac.jp, furuta.hiroshi@kochi-tech.ac.jp

Abstract: The study aimed to investigate the relationship between the density and alignment of randomly aligned multi-walled carbon nanotube (MWCNT) coatings and their optical properties in the visible region. The results showed that 0.0002 gm of MWCNT exhibited low reflectance and high absorption, making it suitable for optical applications.

Carbon nanotubes (CNTs) have attracted significant attention in optoelectronics applications due to their unique light absorption properties[1]. Ghai et al. [2] reported that structurally modified flower-like CNTs (FCNTs) exhibited an impressive absorption capacity of 99.97% within the wavelength range of 300-2000 nm. Wood et al.[3] explained that CNT forest density, surface roughness, and forest height are crucial factors influencing optical reflectance and attenuation, which are important for meeting the optical requirements of CNT-based devices. However, the impact of CNT density and alignment on optical absorption in the visible region remains unexplored. In this study, we have varied the amount of CNTs on a fixed substrate surface area and investigated the effects of CNT density, alignment, and inter-tube distance to determine the optimal CNT density for achieving low reflectance in the visible region.

Thermally oxidized mid-resistive silicon substrates measuring precisely 1 cm x 1 cm were used. Prior to deposition, the mass of each individual substrate was measured using an analytical microbalance and recorded. A dispersed multi-walled carbon nanotube (MWCNT) ink obtained from Meijo Nanocarbon was used, with MWCNT loadings ranging from 0.00005 gm to 0.008 gm studied. The deposition was carried out via a simple drop-casting technique, where using a micropipette, precise volumes of the MWCNT ink were deposited drop-wise onto the center of each silicon substrate and then allowed to dry naturally at ambient conditions. The mass of MWCNTs was calculated by subtracting the substrate's mass before deposition.

Samples with varying MWCNT coating weights were analyzed using an integrating sphere spectrometer to measure the total reflectance over 400-800 nm wavelengths. For total reflectance measurements, samples were tilted 10° from the incident light direction. This configuration approach using an integrating sphere enabled the characterization of optical properties as a function of MWCNT coating weight under controlled experimental conditions.

A scanning electron microscopy (SEM) analysis was performed on three different multi-walled carbon nanotube (MWCNT) films, as shown in Figure 1. The first film, weighing 0.0002 gm and characterized by low weight, exhibited a thickness of 1.67 um. The second film, weighing 0.0014 gm and considered moderate weight, displayed an average thickness of 3.11 um. Finally, the third film, weighing 0.008 gm and characterized by heavy weight, showed an average thickness of 77.197 um. Furthermore, a top surface analysis revealed that the intertube distance between carbon nanotubes (CNTs) in the 0.0002 gm MWCNT film was greater than that in the 0.008 gm MWCNT film.

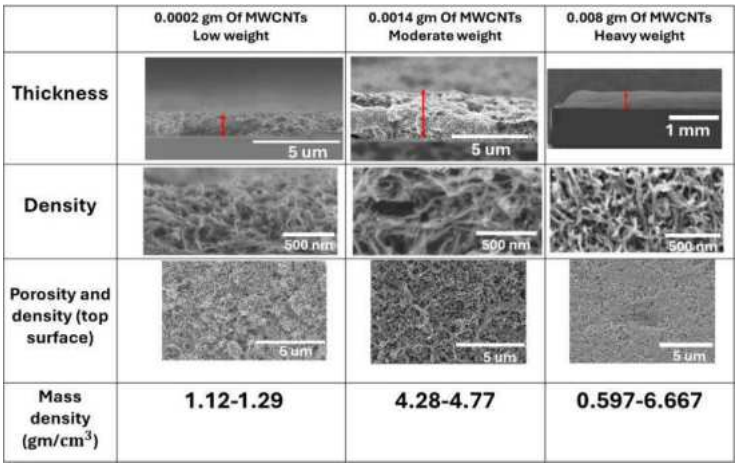


Figure 1: Morphological analysis of low, moderate, and heavy weight of MWCNTs coating.

The coated samples were classified based on the weight of multi-walled carbon nanotubes (MWCNTs) into three categories: low (0 gm to 0.0002 gm), moderate (0.001 gm to 0.005 gm), and high (0.007 gm to 0.008 gm). In Figure 2, it can be observed that the MWCNT coating with a weight of 0.008 gm (with a mass density ranging from 0.597 gm/cm3 to 6.667 gm/cm3) exhibits a total reflectance of 5.55% at 400 nm. Similarly, the MWCNT coating weighing 0.0014 gm (with a mass density ranging from 4.28 gm/cm3 to 4.77 gm/cm3) shows a total reflectance of 3.3% at 400 nm. Notably, the 0.0002 gm (mass density range 1.12 gm/cm3-1.29 gm/cm3) MWCNT coating shows an extremely low reflectance of 2.7% at 400 nm.

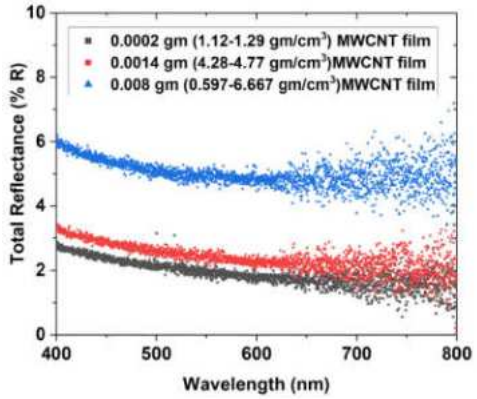


Figure 2: Reflectance analysis of low, moderate, and high densified MWCNT coated samples.

The above analysis revealed that MWCNT coatings with lower density exhibited reduced reflectance, with the 0.0002 gm (mass density range 1.12 gm/cm3-1.29 gm/cm3) MWCNT coating demonstrating the lowest reflectance of 2.7% at 400 nm. These findings emphasize that the optimized density of MWCNT-based coatings plays a significant role in governing their optical properties and enhancing light absorption for optoelectronic applications.

References

[1] H. Miyaji et al., "Optical reflectance of patterned frost column-like CNT forest for metamaterial applications," Diam Relat Mater, vol. 83, pp. 196–203, Mar. 2018, DOI: 10.1016/j.diamond.2018.02.004.

[2] V. Ghai, H. Singh, and P. K. Agnihotri, "Structure Dependent Broadband Optical Absorption in Carbon Nanotubes," ACS Applied Optical Materials, vol. 1, no. 1, pp. 252–260, Jan. 2023, DOI: 10.1021/acsaom.2c00047.

[3] B. D. Wood, J. S. Dyer, V. A. Thurgood, N. A. Tomlin, J. H. Lehman, and T. C. Shen, "Optical reflection and absorption of carbon nanotube forest films on substrates," J Appl Phys, vol. 118, no. 1, Jul. 2015, DOI: 10.1063/1.4923390.

Optical antennas and plasmonics-based devices

Versatile Flexible Plasmonic Chip for Non-Invasive Dual Modal Glucose Detection

A. Campu [1,2*], **S. Astilean**[1,3], **and M. Focsan** [1,3]

[1] Nanobiophotonics and Laser Microspectroscopy Center, Interdisciplinary Research Institute in Bio-Nano-Sciences, Babes-Bolyai University, Treboniu Laurian No. 42, 400271 Cluj-Napoca, Romania.
[2] Environmental Science, Physics, Physical Education and Sport Department, Faculty of Sciences, Lucian Blaga University, Doctor Ion Rațiu No. 5-7, 550012 Sibiu, Romania.
[3] Biomolecular Physics Department, Faculty of Physics, Babes-Bolyai University, Mihail Kogalniceanu No. 1, 400084 Cluj-Napoca, Romania.
[*]corresponding author: andreea.campu@ubbcluj.ro

Abstract: Glucose is a key metabolite and primary nutrient in the metabolism; thus, its monitoring is imperative for the prevention, early diagnosis, and treatment of diabetes. Great efforts are invested in the development of highly efficient non-invasive sensors able to detect glucose from body fluids such as sweat or tears.

In this scientific context, this work aims to develop a versatile flexible hybrid plasmonic sensor for the non-invasive reliable real-time dual SERS – electrochemical (Surface Enhanced Raman Spectroscopy) glucose detection in artificial sweat. Concretely, the approach proposes an innovative fabrication process which relies on the use of a flexible and biocompatible polydimethylsiloxane polymer substrate whose surface roughness was modified during the thermal curing process by the imprinting of the 3D matrix of Whatman No 1. filter paper. A self-designed filter paper electrode mould was attached to its surface for the deposition of a 20 nm gold thin film via a physical vapor deposition technique to obtain the counter electrode (CE) and working electrode (WE). The Ag/AgCl reference electrode (RE) was fabricated using a similar mould through a screen-printing method. Thus, the dual SERS – electrochemical sensor is obtained. Further, WE was functionalized with Thiol-Polyethylene glycol-Amine in order to immobilize gold nanobipyramids for the enhancement of the sensors detection capabilities. Next, an enzymatic biosensing protocol was developed by successively grafting onto WE a well-known Raman reporter for SERS detection and the biorecognition molecule - glucose oxidase enzyme. The as-developed sensor was then exposed to several different glucose concentrations to assess its dual detection performance. Finally, to validate the flexible hybrid plasmonic sensor was exposed to artificial sweat spiked with glucose to demonstrate its potential as a lab-on-the-skin sensing devices for efficient glucose monitoring and, implicitly, diabetes management.

Acknowledgements: This work was supported by CNCS-UEFISCDI Romania, under the project number PN-III-P1-1.1-PD-2021-0175.

Developing Spatiotemporal Modulated Graphene-Based Waveguide to Integrate the whole Terahertz Transceiver Front-End in one Device

Mahsa Valizadeh[1], Leila Yousefi[1,2*] and MirFaez Miri[3]

[1]School of Electrical and Computer Engineering, College of Engineering, University of Tehran, Tehran, 1417614411, Iran.
[2]School of Engineering and Informatics, University of Sussex, Falmer, UK, BN1 9RH
[3] Department of Physics, University of Tehran, Tehran, 14395547, Iran
[*]Corresponding Author: l.yousefi@sussex.ac.uk

Abstract: Here, attractive features of spatiotemporally modulated graphene-based waveguides are utilized to integrate all functionalities of a THz transceiver front-end in one device. We have implemented the leaky wave antenna, isolator, and mixer all in one device using spatiotemporal modulated structures.

Spatiotemporal modulation, defined as the periodic modulation of a structure's constitutive parameters in both time and space, leads to unique properties such as nonreciprocal response, frequency mixing and mode conversion [1-4]. At microwave frequencies, these features are realized using varactors as the modulating part [3,4]. Here, in the realm of THz frequencies, we have used graphene as an appropriate material to implement time and space modulation utilizing its exceptional tunable surface conductivity [5-7].

In this study, we introduce an integrated device that encapsulates the entire front-end of a THz transceiver within a single unit, employing a spatiotemporally modulated graphene-based waveguide. This innovative approach leverages spatial modulation, frequency mixing capabilities, and a nonreciprocal response to simultaneously realize a leaky-wave antenna, mixer, and isolator, all within one cohesive structure.

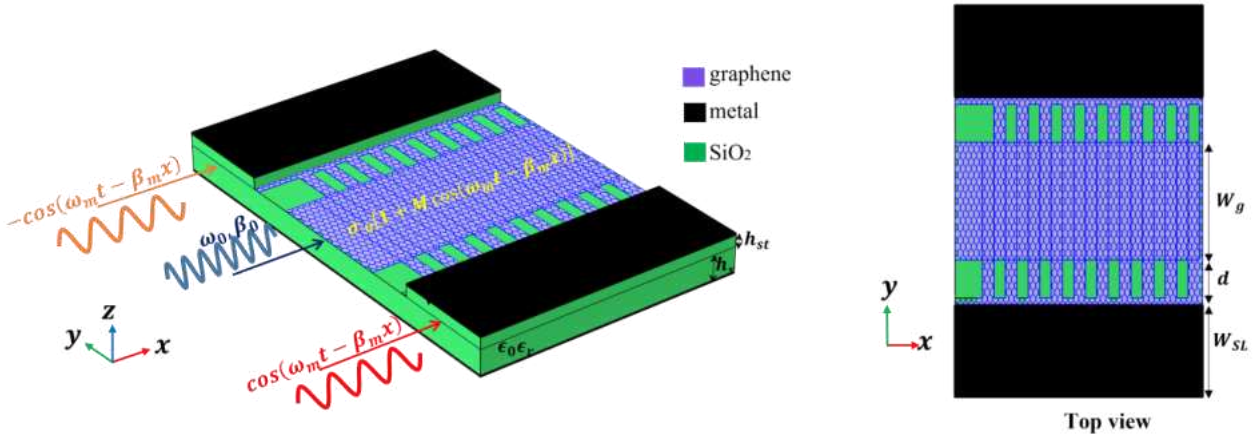


Figure 1. The structure of the proposed integrated THz transceiver front-end. $\boldsymbol{h_s = 20\ \mu m, h_{st} = 5\ \mu m, , \epsilon_r = 3.8,}$ $\boldsymbol{W_g = 200\mu m, W_{SL} = 100\mu m, d = 10\mu m}$

The proposed structure of THz transceiver is shown in Figure 1. It consists of a main plasmonic waveguide, constructed from a graphene layer on top of a back-metalized SiO_2 substrate, in the middle of the structure which is guiding the main signal with the frequency of $f_0 = 2\ THz$. This waveguide is accompanied by two quasi-TEM side waveguides, carrying the modulating waves. These waveguides are strip line waveguides with the graphene layer as the middle strip. The graphene of the main waveguide is modulated by frequency of $f_m = 200\ GHz$. The middle graphene layer is divided into two ribbon groups with periodicity of $\lambda_r = 20\ \mu m$ biased by two out of phase side modulating waveguides to increase the modulating propagation constant and make it big enough to generate leaky waves.

The proposed integrated THz transceiver is numerically investigated using full wave numerical simulation performed by COMSOL Multiphysics software. In this simulation, the effect of the modulating waveguides is modeled through the modulated surface conductivity of graphene sheet, and three different physics for three harmonic frequencies of f_0, $f_0 \pm f_m$ are introduced and studied. The results are shown in Figs. 2, 3.

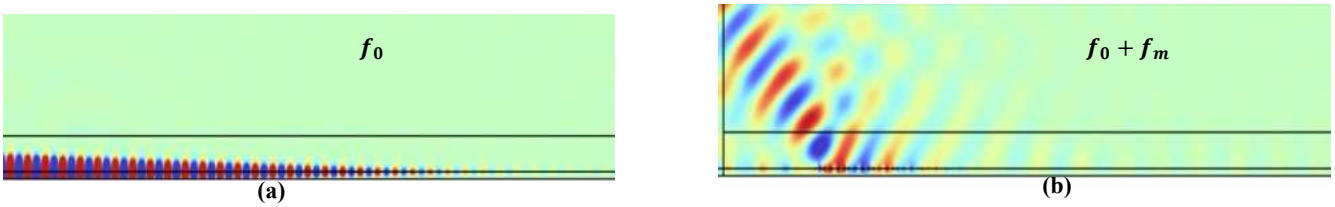


Figure 2. Numerical full wave simulation results a) The structure is excited by a plasmonic wave at the frequency of f_0 b) the wave is converted to the frequency of $f_0 + f_m$ and radiates away from the structure.

As shown in Fig. 2, when the structure is excited at the frequency of f_0 (see Fig. 2a), the modulation happens and the frequency is shifted to the $f_0 + f_m$ and interestingly it radiates away from the structure (see Fig. 2b). Therefore, the proposed spatiotemporal modulated device works simultaneously as a leaky wave antenna and as a mixer. The device also is able to do beam steering as shown in Fig. 3. Figure 3 shows the radiation pattern of the device when the modulation frequency f_{m} varies from 100 GHz to 400GHz. As clearly shown in this figure, the beam steers as the modulation frequency changes proofing the ability of the proposed structure for providing beams at different directions.

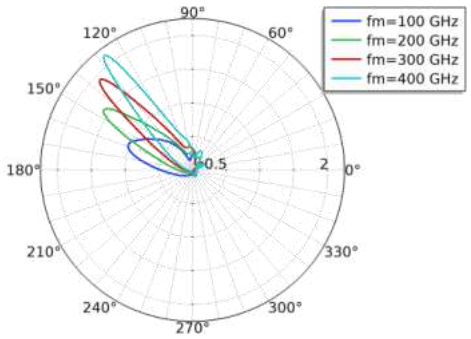


Figure 3. The radiation pattern of the proposed device for different modulation frequencies.

References

1. Taravati, S., N. Chamanara, and C. Caloz, *Nonreciprocal electromagnetic scattering from a periodically space-time modulated slab and application to a quasisonic isolator.* Physical Review B, 2017. **96**(16): p. 165144.
2. Ramaccia, D., et al., *Nonreciprocity in antenna radiation induced by space-time varying metamaterial cloaks.* IEEE Antennas and Wireless Propagation Letters, 2018. **17**(11): p. 1968-1972.
3. Taravati, S. and C. Caloz, *Mixer-duplexer-antenna leaky-wave system based on periodic space-time modulation.* IEEE Transactions on Antennas and Propagation, 2016. **65**(2): p. 442-452.
4. Guo, X., et al., *Nonreciprocal metasurface with space–time phase modulation.* Light: Science & Applications, 2019. **8**(1): p. 1-9.
5. Bao, Q. and K.P. Loh, *Graphene photonics, plasmonics, and broadband optoelectronic devices.* ACS nano, 2012. **6**(5): p. 3677-3694.
6. Kumar, S., et al., *Femtosecond carrier dynamics and saturable absorption in graphene suspensions.* Applied physics letters, 2009. **95**(19): p. 191911.
7. Ghaffari, V. and L. Yousefi, *Integrated optical beam steering device using switchable nanoantennas and a reflective metalens.* Scientific Reports, 2023. **13**(1): p. 7099.

Vanadium dioxide for compensation of angle-dependent shifts in structural color filters

K. Rovenská[1,2*], F. Ligmajer[1,2], P. Kepič[1,2], B. Idesová[1,2], J. Chochol[3], J. Liška[1,2] and T. Šikola[1,2]

[1]Central European Institute of Technology, Brno University of Technology, Czech Republic

[2]Institute of Physical Engineering, Faculty of Mechanical Engineering, Brno University of Technology, Czech Republic

[3]onsemi, Czech Republic

[*]corresponding author: katarina.rovenska@ceitec.vutbr.cz

Abstract: Structural color filters propose an advanced alternative to conventional color filters. However, their optical response shifts with angle variations of the incident light. We address this problem by introducing a conformal tunable VO_2 layer onto bare aluminum structural color filters. This approach is adaptable and suits any existing structural filters.

Structural color filters are maintaining a trending status in the discussions of the future imaging and spectroscopic techniques. Compared to their traditional counterparts based on pigments and dyes, structural color filters offer less complicated and thus cheaper fabrication, minimal environmental impact and little to no degradation in performance over time. One of the remaining challenges that keeps structural color filters from overtaking the market is the dependence of their spectral response on the angle of incident illumination. So far, researchers have addressed this problem by fixating the geometry of color filters, either by using ultrathin metallic structures [1] or often restricting the allowed polarization states of incoming light [2] and thus limiting their overall efficiency.

In our work, we demonstrate a versatile solution for angle-dependent spectral shifts by introducing a thin conformal vanadium dioxide (VO_2) layer onto holey aluminum structural color filters illustrated in Fig 1. [3] Using the optical response of a bare holey aluminum color filters as a reference, a spectral redshift occurs as the angle of light incidence increases. As VO_2 undergoes its insulator-to-metal transition, a contrary effect can be observed; upon heating, the spectral response of VO_2 shifts towards small wavelengths. [4] The insulator-to-metal transition (IMT) in VO_2 occurs relatively close to room temperature, at ca. 67°C, and is easily reversed by cooling the material below the transition temperature. Other commonly used phase-changing materials, including GeSbTe, Sb_2S_3 or other chalcogenide glasses necessitate more extreme conditions for their phase transitions; temperatures ranging from 100-200° C or higher are required to initiate the phase transition or its reversal. [5] Such a comparison highlights VO_2 as a material with easily accessible IMT that can be well-incorporated into complex devices. The IMT of VO2 can be induced by thermal, optical or electrical excitation, is fully and easily reversible, and resists material degradation at both its phase states. [6]

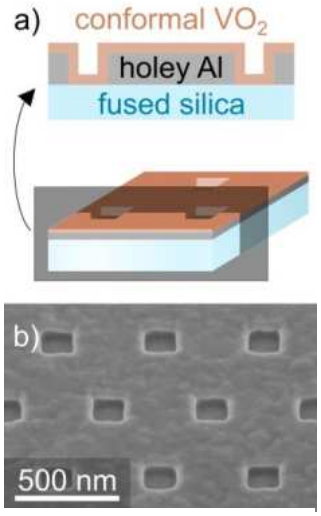


Fig. 1: VO_2-filled holey Al structural color filters. a) Sample layout. b) SEM micrograph of the structural color filter shown in a), imaged under 40° tilt.

The presented research inspects the shifts in the spectral response of such systems upon varying angles of light incidence both below and above the IMT temperature of VO_2. We show that by driving the VO_2 through its easily repeatable

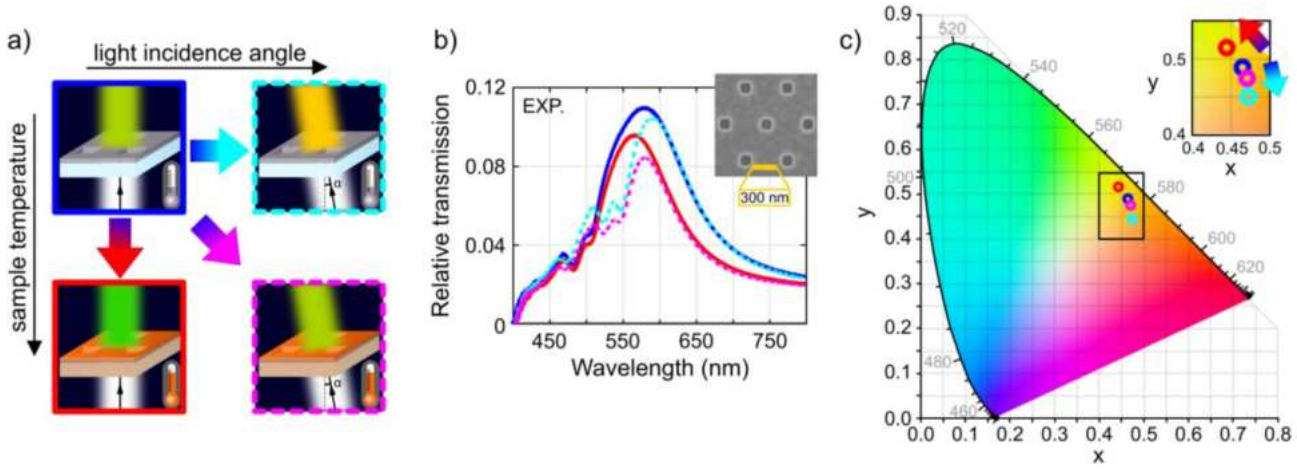


Fig. 2: VO_2-filled structural color filter can be used for compensation of spectral red-shifts caused by non-normal sample illumination. (a) A schematic of the experimental concept. (b) Relative transmission of the VO_2-filled color filter corresponding to the four settings shown in (a) – curve colors correspond to the frame colors in (a). The VO_2-filled color filter illuminated at a non-zero angle of incidence regains its original transmission peak position when heated. A SEM micrograph of the measured VO_2-filled color filter is shown in the inset. (c) A CIE diagram showing the color compensation illustrated in (b).

IMT, the original spectral position of the color filter's transmission maximum can be efficiently retrieved, i.e. that VO_2 can be used to mitigate angle-dependent shifts in structural color filters. This is enabled by the compensation of the angle-related redshift using a blueshift that accompanies the IMT in the conformal VO_2 layer deposited on the color filters, as displayed in Fig. 2.

Available through the atomic layer deposition method, a conformal VO_2 layer can be seamlessly integrated into the fabrication of virtually any structural color filter regardless of its design and preceding fabrication steps, rendering the color filter less prone to angle-dependent shifts by easily achievable thermal control.

We acknowledge CzechNanoLab project LM2023051 funded by MEYS CR and the Czech Grant Agency project 21-29468S.

References

1. Yang., C. et al. "Angle robust reflection/transmission plasmonic filters using ultrathin metal patch array," Adv. Opt. Mater., Vol. 4, No. 12, 1981–1986, 2016
2. Sun, S., et al "Wide-incident-angle chromatic polarized transmission on trilayer silver/dilectric nanowire gratings" J. Opt. Soc. Am. B, Vol. 31, No. 5, 1981–1986, 2014
3. Rovenská, K. "Structural color filters with compensated angle-dependent shifts," Opt. Express, Vol. 31, No. 26, 43048, 2023.
4. Kepič, P. "Optically tunable Mie resonance VO2 nanoantennas for metasurfaces in the visible," ACS Photonics, Vol. 8, No. 4, 1048–1057, 2021
5. Tripathi, D. et al. "Recent development in Chalcogenide phase change material-based nanophotonics," Nanotechnology, 34, 502001, 2023.
6. Cueff, S. et al. "VO2 nanophotonics," APL Photonics, 5, 110901, 2020.

Chiral spin-preserving reflection in helicoid-based plasmonic metamaterials

Eunji Im[1], Hyeohn Kim[4], Ji-hyeok Huh[2], Ki Tae Nam[4*] and Seungwoo Lee[1, 2, 3*]

[1]Department of Biomicrosystem Technology, Korea University, Seoul 02841, Republic of Korea
[2]KU-KIST Graduate School of Converging Science and Technology, Korea University, Seoul 02841, Republic of Korea
[3]Department of Integrative Energy Engineering and KU Photonics Center, Korea University, Seoul 02841, Republic of Korea
[4]Department of Materials Science and Engineering, Seoul National University, Seoul 08826, Republic of Korea

[*]corresponding author: *seungwoo@korea.ac.kr*
[*]corresponding author: *nkitae@snu.ac.kr*

Abstract: We figured out that induced magnetic dipole of chiral meta-atom is critical to CD like a chiral molecule. And we suggest the simple method to enhancing magnetic dipole by MIM (Metal-Insulator-Metal) motif with chiral geometry.

Bio-chemical responses in nature depend on chiral recognition. Organisms are sensitive to chirality and specialized in tailoring chirality of biomolecules to achieve specific function. Therefore, the modern drugs are generally chiral. People use light interaction with chiral molecule to recognize chirality of molecules. Especially circular dichroism (CD) is generally used for measuring the chirality of molecule in the medical world. But CD signal of molecule which density is low is very weak and have resonance in UV band, not visible range. For this reason, people need to enhance the CD signal of molecule and lengthen the resonance wavelength by coupling with artificial chiral nanostructure.

The interaction between the chirality of molecules and light conveniently tested by measuring circular dichroism (CD) and optical rotational dispersion. Especially CD is generally used for measuring the chirality of molecule in the medical world. According to the Rosenfeld's calculation, the strength of the CD signal of a chiral molecule is given by.

$$\mathrm{CD}_0 \sim \mathrm{Im}(\boldsymbol{\mu}_{12} \cdot \boldsymbol{m}_{21}) \qquad (1)$$

Where $\boldsymbol{\mu}_{12}$ and $\boldsymbol{m}_{21}$ is electric and magnetic transition dipole of molecule, respectively. And the indices 1 and 2 is the ground and excited states of the molecule. This equation means that a CD signal in molecular system occurs by the coupling between the electric and magnetic dipole of the molecule which induced by incident light.

On the other hand, the plasmonic chiral optical interaction corresponds to classical electromagnetism that follows Maxwell's equations. But the classical results can also be understood in terms of the quantum equation. Therefore, the non-zero CD signals in chiral complex originate from dynamic magnetic moments which are induced by incident light in nanostructure. Therefore, to the large chiral optical response, it is important to strengthen the dynamic magnetic dipole moment and break the orthogonality with the electric dipole moment.

We would like to introduce a novel strategy to modulate circular dichroism (CD) using isotropic, 432-symmetric chiral gold nanoparticles (helicoids) which are plasmonic nanoparticles with biomolecule-encoded chiral nanostructures. Interestingly, through a versatile metal layer deposition on helicoids, the reflected CD can be reversed, which can make both reflection and transmission exhibit unnatural CD of the same sign.

As the hat-shaped structure is on the helicoid particles, the strengths of electric and magnetic dipole of helicoid particles become boosted through capacitive plasmonic coupling which is confirmed through the redshifts of the resonance mode.

In this study, we showed that it is possible to control the CD by increasing the overall chirality of the nanostructure through metal deposition on plasmonic chiral particles.

Acknowledgement

This work was supported by national Research Foundation of Korea under Project Number NRF-RS-2023-00272363, Samsung Research Funding & Incubation Center for Future Technology grant (SRFC-MA2301-02).

References

1. Rosenfeld, L. “Quantenmechanische Theorie der natürlichen optischen Aktivität von Flüssigkeiten und Gasen,” Zeitschrift Für Physik, 52, 161–174, 1929.
2. Kuzyk, A. et al., “DNA-based self-assembly of chiral plasmonic nanostructures with tailored optical response” Nature, 483, 311–314, 2012.

Plasmon-enhanced photovoltaics, photocatalysis, and solar fuels

Noble Metal – Chalcopyrite Hybrid Nanostructures for Enhanced Plasmonic Photocatalysis

B.M. Reinhard[1,*]

[1]Department of Chemistry and The Photonics Center, Boston University, Boston, MA 02215, United States

[*]corresponding author: bmr@bu.edu

Abstract: Chalcopyrite ($CuFeS_2$) nanocrystals, which support quasistatic resonances in the visible, and noble metal nanoparticles are combined into one nanostructure to provide a bi-resonant hybrid material. The interplay of metal and $CuFeS_2$ resonances on the photoreactivity of the hybrid material is characterized for different nanoarchitectures and reactions.

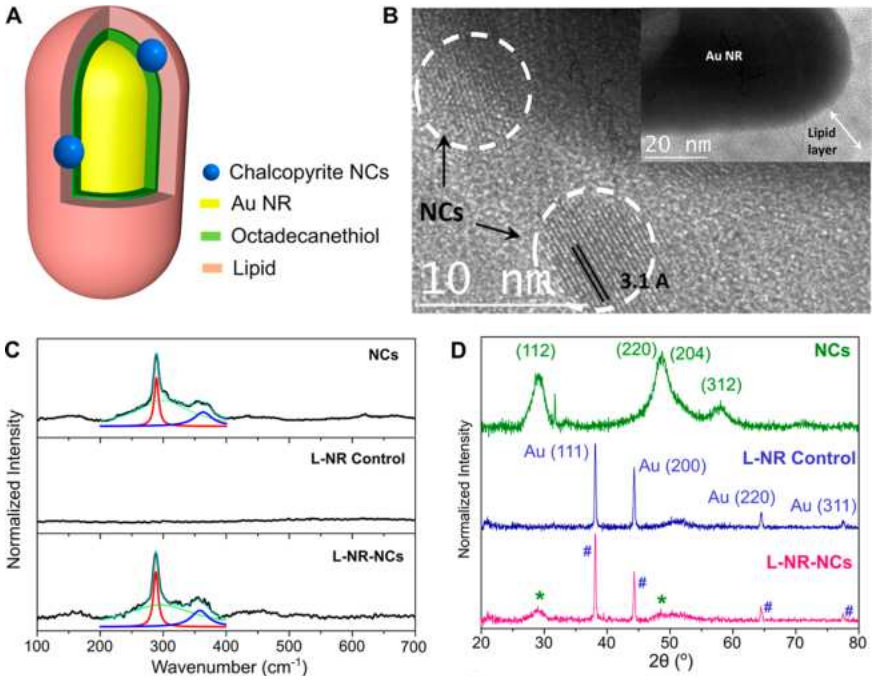


Figure 1: A) Schematic drawing and B) TEM image of hybrid $CuFeS_2$ NC – Au NR hybrid nanocatalyst. C) Raman spectra of (top to bottom): NCs, NRs, and hybrid structure. D) XRD spectra of (top to bottom): NCs, NR, and hybrid structure. Reprinted with permission from An et al, ACS Nano 16, 6813 (2022). Copyright American Chemical Society.

Chalcopyrite ($CuFeS_2$) nanocrystals (NCs) provide quasistatic resonances in the visible,[1,2] which provides unique opportunities for implementing noble-metal – semiconductor hybrid structures with plasmonic resonances supported by both building blocks. These resonances are of high interest for facilitating charge and energy transfer in the hybrid nanostructures.

We have integrated $CuFeS_2$ NCs in a lipid coating self-assembled around gold and silver nanorods (NRs) and nanoparticles (NPs).[3] Figure 1 provides characterization data for a representative hybrid structure. Importantly, in

the case of the gold NRs as central core, the hybrid structures were observed to support enhanced oxygen and hydrogen evolution reactivity when excited at 530 nm or 730 nm, respectively.[3] The wavelength-dependent reactivity suggests the existence of different light-driven charge transfer processes between NR and NCs that can generate different reactive centers under excitation with green or red light. A model for the light-dependent reactivity is presented and discussed.

The mechanism of the reactions and, in particular, the role of the chalcopyrite NC as catalytic site was independently evaluated through Raman spectroscopy. These spectroscopic studies indicate the existence of a Cu(I)/Cu(II) redox pair coupled catalysis on the chalcopyrite NC surface that synergistically cooperates with plasmonic effects.[3]

To obtain further quantitative insight into the effect that the coupling of the resonances in NCs and NPs has on light-driven reactivity of the hybrid structures, hybrid materials assembled from $CuFeS_2$ NCs and noble metal NRs and NPs with different overlap between the resonances of the two building blocks were implemented and the resulting performance characterized. The evidence for synergistic interactions between noble metal nanostructures and $CuFeS_2$ NC components in facilitating light driven reactivity collected in these studies will be presented.

In the last part of this presentation we will review strategies to further enhance the performance of plasmonic photoreactors containing both noble metal and chalcopyrite building blocks in the future.

References

(1) Gaspari, R.; Della Valle, G.; Ghosh, S.; Kriegel, I.; Scotognella, F.; Cavalli, A.; Manna, L. Quasi-Static Resonances in the Visible Spectrum from All-Dielectric Intermediate Band Semiconductor Nanocrystals. *Nano Lett.* **2017**, *17* (12), 7691–7695. https://doi.org/10.1021/acs.nanolett.7b03787.

(2) Ghosh, S.; Avellini, T.; Petrelli, A.; Kriegel, I.; Gaspari, R.; Almeida, G.; Bertoni, G.; Cavalli, A.; Scotognella, F.; Pellegrino, T.; Manna, L. Colloidal $CuFeS_2$ Nanocrystals: Intermediate Fe d-Band Leads to High Photothermal Conversion Efficiency. *Chem. Mater.* **2016**, *28* (13), 4848–4858. https://doi.org/10.1021/acs.chemmater.6b02192.

(3) An, X.; Kays, J. C.; Lightcap, I. V.; Ouyang, T.; Dennis, A.; Reinhard, B. M. Wavelength-Dependent Bifunctional Plasmonic Photocatalysis in Au/Chalcopyrite Hybrid Nanostructures. *ACS Nano* **2022**, *16*, 6813–6824.

Light-accelerated NiFe oxyhydroxides-alloy photoanode metasurfaces for efficient and stable solar water splitting

Fei Xiang[1], Ning Li[1], Arturo Burguete-Lopez[1], Zhao He[1], Maxim Elizarov[1], Andrea Fratalocchi[1*]

[1]PRIMALIGHT, King Abdullah University of Science and Technology (KAUST), Thuwal 23955-6900, Saudi Arabia
[*]corresponding author: andrea.fratalocchi@kaust.edu.sa

Abstract: We report a light-accelerated NiFe oxyhydroxides-alloy metamaterial as a catalytic-protective layer on Si photoanodes for efficient and durable solar water splitting. This technique enables a record applied bias photon-to-current efficiency (ABPE) efficiency of 4.24% in homojunction-free photoanodes. It extends the device's lifetime to beyond 250 hours.

Green hydrogen production through photoelectrochemical (PEC) water-splitting with solar energy attracts significant research interests in contributing to a clean energy economy and sustainable development [1–3]. Currently, the efficiency of the hydrogen evolution reaction at the photocathode side is relatively high (ABPE above 12%) [4, 5], while the bottleneck for the entire device is at the photoanode side due to the sluggish kinetics, with a bestreported ABPE of 3.91% for buried homojunction-free photoanodes [5]. Thus, current research efforts on PEC devices aim to develop new photoanodes with enhanced efficiency [6, 7].

Besides the efficiency performance, the stability of the photoanodes is another aspect that needs improvement. For the buried homojunction-free photoanodes with ABPE above 3%, the reported device lifetime is below 100 hours [5, 8]. The poor stability of the photoanodes originates from the photo-corrosion of the co-catalyst and the chemical instability of the semiconductor absorber in the strong alkaline medium (pH ∼14) [7]. While many protective layers, such as the Al_2O_3 and SiO_x, were proposed to prolong the Si photoanodes lifetime to above 200 hours, the efficiency of the photoanodes drops to below 1%, which is impractical for the large-scale implementation of the PEC devices [9, 10].

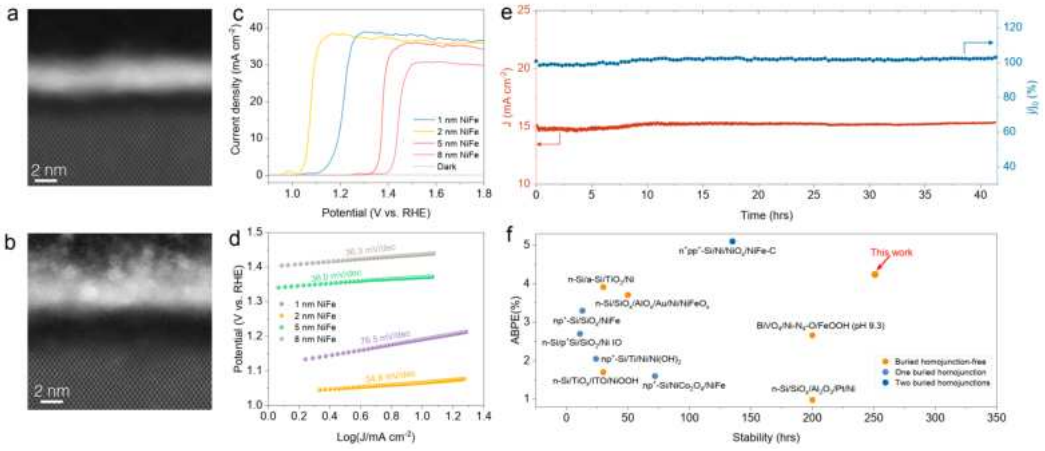


Fig. 1 (a) Cross-sectional STEM image of the as-fabricated photoanodes. (b) Cross-sectional STEM image of the photoanodes after 20 hours working under 1.09 V vs. RHE. (c) J-E curve of photoanodes with varied NiFe alloy thickness. (d) Tafel slope calculated from the J-E curves in (c). (e) Long-term stability test of the device with an optimized thickness of NiFe nanolayer at the initial current density of 15 mA cm^{-2}. (f) Applied bias photon-to-current efficiency and stability of the device compared with the state-of-the-art.

Ni-based oxyhydroxides were reported as highly efficient and stable catalysts in electrochemical water splitting [11, 12]. However, this type of material is not directly available. The traditional generation of state-of-the-art Ni-based oxyhydroxides requires a bias above 1.4 V for at least 24 hours in electrochemical

conversion or a multistep hydrothermal treatment with a high temperature above 70°C for at least 6 hours [12–14]. These approaches require vast energy powers and are impractical for fabricating PEC photoanodes.

In this work, we report a light-accelerated atomic reconfiguration in the NiFe alloy film to self-generate a NiFe oxyhydroxides-alloy metamaterial as a catalytic-protective layer for the Si photoanodes. This dynamic evolution process of NiFe oxyhydroxides involves surface amorphization and chemical state changes in Ni/Fe-containing species, reporting an ABPE efficiency of 4.24% in the optimized photoanodes with a 2 nm NiFe alloy layer. Figure 1a reports the scanning transmission electron microscope (STEM) image of the as-fabricated photoanodes, demonstrating the layered structure from the top NiFe alloy layer to the Si substrate. After continuous working under 1.09 V *vs.* reversible hydrogen electrode (RHE) for 20 hours, the surface region of the NiFe alloy expands above 137% in volume. It forms a porous NiFe oxyhydroxides layer hybridized with the NiFe alloy film (Fig. 1b). Figure 1c reports the J-E responses of the photoanodes with different NiFe alloy thicknesses. The optimized photoanodes with 2 nm NiFe alloy layer show a low onset potential of 1.06 V *vs.* RHE to reach a current density of 10 mA cm^{-2} and a high saturated current density of 38.4 mA cm^{-2}. Besides, the optimized photoanodes with 2 nm NiFe alloy layer show the fastest reaction kinetics in water oxidation, reporting the lowest Tafel slope of 36.0 mV/dec (Fig. 1d). During the continuous working process under constant bias conditions (Fig. 1e), the engineered photoanodes maintain nearly 100% retention of the initial current density over 40 hours, demonstrating the high stability of the evolved NiFe oxyhydroxides-alloy photoanodes. Figure 1f compares the ABPE efficiency and the stability performances of the engineered photoanodes against the state-of-the-art. This technique paves the way for designing and implementing highly efficient, stable, and large-scalable PEC devices beyond hydrogen production.

References

1. Reece, S. Y. et al. Wireless solar water splitting using silicon-based semiconductors and earth-abundant catalysts. Science 334, 645–648 (2011).
2. Tian, Y. et al. Enhanced Solar-to-Hydrogen Generation with Broadband Epsilon-Near-Zero Nanostructured Photocatalysts. Advanced Materials 29, 1701165 (2017).
3. Andrei, V. et al. Floating perovskite-BiVO4 devices for scalable solar fuel production. Nature 608, 518–522 (2022).
4. Shen, J. et al. Oxygen-vacancy-rich nickel hydroxide nanosheet: a multifunctional layer between Ir and Si toward enhanced solar hydrogen production in alkaline media. Energy & Environmental Science 15, 3051–3061 (2022).
5. Liu, B. et al. Bifacial passivation of n-silicon metal–insulator–semiconductor photoelectrodes for efficient oxygen and hydrogen evolution reactions. Energy & Environmental Science 13, 221–228 (2020).
6. Yang, J. et al. A multifunctional biphasic water splitting catalyst tailored for integration with high-performance semiconductor photoanodes. Nature materials 16, 335–341 (2017).
7. Chen, Y. W. et al. Atomic layer-deposited tunnel oxide stabilizes silicon photoanodes for water oxidation. Nature Materials 10, 539–544 (2011).
8. Ma, J. et al. Identifying and Removing the Interfacial States in Metal-Oxide–Semiconductor Schottky Si Photoanodes for the Highest Fill Factor. Journal of the American Chemical Society 144, 17540–17548 (2022).
9. Digdaya, I. A., Adhyaksa, G. W., Trzesniewski, B. J., Garnett, E. C. & Smith, W. A. Interfacial engineering of metal-insulator-semiconductor junctions for efficient and stable photoelectrochemical water oxidation. Nature communications 8, 15968 (2017).
10. Vanka, S. et al. InGaN/Si double-junction photocathode for unassisted solar water splitting. ACS Energy Letters 5, 3741–3751 (2020).
11. Liang, C. et al. Exceptional performance of hierarchical Ni–Fe oxyhydroxide@ NiFe alloy nanowire array electrocatalysts for large current density water splitting. Energy & Environmental Science 13, 86–95 (2020).
12. Wang, X. et al. Pivotal role of reversible NiO6 geometric conversion in oxygen evolution. Nature 611, 702–708 (2022).
13. Wang, T. et al. NiFe (Oxy) hydroxides derived from NiFe disulfides as an efficient oxygen evolution catalyst for rechargeable Zn–air batteries: the effect of surface S residues. Advanced Materials 30, 1800757 (2018).
14. Yu, L. et al. Non-noble metal-nitride based electrocatalysts for high-performance alkaline seawater electrolysis. Nature communications 10, 5106 (2019).
15. Lastname, F. M., F. M. Lastname and F. M. Lastname, “Title of the journal paper,” Journal Title Abbreviation, Vol. 34, No. 10, 1064–1076, 1986.

Plasmonic-enhanced Fabry-Pérot cavity for photocatalysis application

Ning Lyu[1,2*], Anjalie Edirisooriya[2], Zelio Fusco[2], Fiona Beck[2], Christin David[1,3]

[1] Institut für Festkörpertheorie und Optik, Friedrich-Schiller-Universität Jena, 07743 Jena, Germany
[2] School of Engineering, Australian National University, Canberra ACT2600, Australia
[3]Abbe Centre of Photonics, 07745 Jena, Germany
[*]corresponding author: ning.lyu@uni-jena.de

Abstract: Photocatalysis holds immense potential for harnessing clean energy through chemical processes, such as water splitting and CO2 reduction [1]. This typically encompasses multistep electron transfer processes that culminate in the simultaneous generation of diverse products [2,3]. However, achieving a highly efficient and selective conversion of a specific product remains a challenge. Thus, we first concentrated on a single-step reaction: the N-demethylation of Methylene blue (MB) driven by light with an effective wavelength range between 530 to 710nm [5]. Here, gold nanoparticles (Au NPs) exhibit a strong resonance and significant efficiency at this wavelength range, and provide active control when coupled with other resonances, such as in a Fabry-Pérot cavity [4].

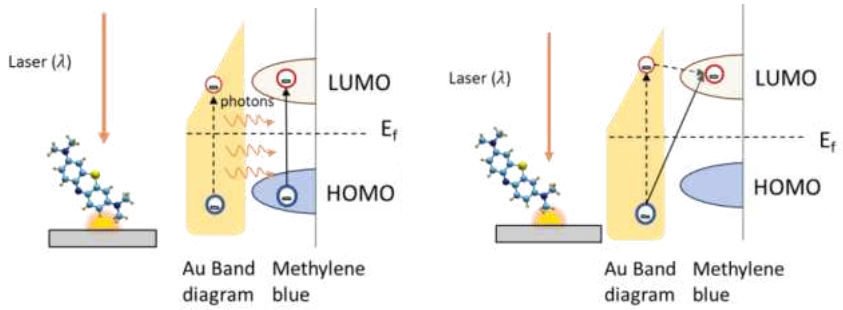


Figure 1: Localized Surface Plasmon Resonance (LSPR) band diagram for MB and gold nanoparticles showing the radiative decay (left) and non-radiative decay (right).

A thin layer of titanium dioxide (TiO2) was sputtered onto the surface of a metal mirror film. This interface displays a high reflectance, facilitating the occurrence of Fabry-Pérot (FP) resonances with a peak position determined by the TiO2 thickness. Additionally, Au nanoparticles were synthesized using an annealing process deposited onto the TiO2 layer. Coupling the Localized Surface Plasmon Resonance (LSPR, Fig. 1) with the constructive peak ('switch on') and destructive valley ('switch off') of the Fabry-Pérot resonance allows tailored designs for enhancing and suppressing photocatalysis, respectively, enabling selectivity of the reaction pathway.

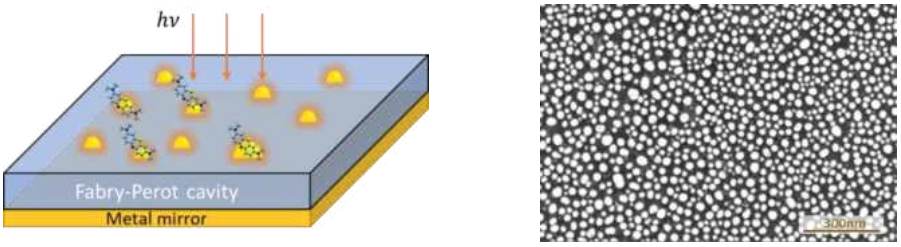


Figure 2: Configuration of plasmonic FP cavity showing random Au NPs on the TiO2 cavity with MB attached (left) and an SEM image of the gold nanoparticles with average radius r_{ave}=13nm and gap size g_{ave}=8nm (right).

Analysis of scanning electron microscope (SEM) images revealed that the interparticle gap of Au NPs is smaller than its size, indicating a non-negligible coupling between the Au nanoparticles (Fig.2). In simulations, utilizing a periodic model with averaged parameters proves inaccurate for describing this specific design. Consequently, we imported a 200×200nm^2 Atomic Force Microscopy (AFM) image into the model to describe the location and shape of nanoparticles and employed the Finite Element Method (FEM) to assess its optical performance.

The coupling of LSPR and FP resonances were characterized with a spectrophotometer, resulting in an absorption peak and dip in the absorption spectra of 'switch on/off' samples, respectively. With Ti metal mirror, the absorption doubles for the 'switch the resonance on' sample. Furthermore, to assess catalysis capability, surface-enhanced Raman spectroscopy was employed to monitor the progression of the MB N-demethylation reaction. The yield of the reaction is analyzed with the integration of the Raman peak of the reaction product. It was observed that the active design with enhanced absorption maintained a 7-fold enhancement in comparison to the low absorption 'switch off' sample over a 30s period (Fig. 3).

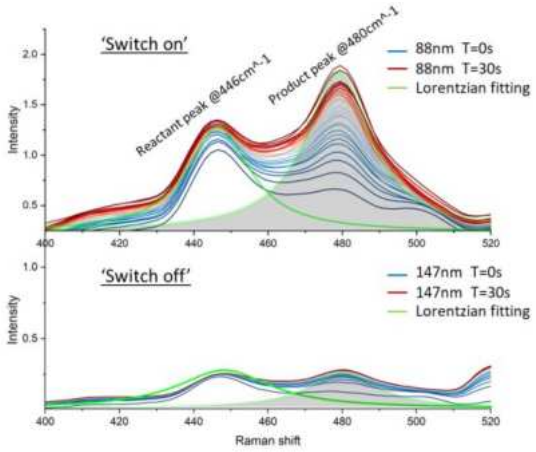


Figure 3: Temporal SERS results of 'switch on/off' samples in 30s; the product peak fits with Lorentzian curve.

In conclusion, nanoparticle-cavity designs based on the coupling of LSPR and FP resonances achieved an active control on photocatalysis with tailored configurations. However, the Ti substrate exhibits instability during the annealing process at 500°C. Thus, the absorption peak is not only attributed to the resonance. To improve selectivity behavior, it is proposed to substitute Ti with a high-temperature-resistant material, such as Au.

Acknowledgements: The authors thank the German Research Foundation DFG (Deutsche Forschungsgemeinschaft) for financial support through the International Research Training Group IRTG 2675 and, additionally, the Australian National Fabrication Facility and TMOS for the support of experiments.

References

1. Y. Ma et al, Chemical Reviews, 114(19), 9987, (2014).
2. S. N. Habisreutinger et al, Angewandte Chemie International Edition, 52(29), 737, (2013).
3. J. L White, M. F. Baruch, J. E. Pander III, et al. Chemical Reviews, 115(23), 12888, (2015).
4. S. Zhao, Z. Fusco and F. J. Beck. Optica, 9(9), 1084-1039, (2022).
5. Z. Fusco., et al (2022). Journal of Materials Chemistry C, 10(19), 7511-7524.

Hot electron induced photoreduction of Fullerene C60 using coupled plasmonic - Fabry-Perot systems

Anjalie Edirisooriya[1*], Ning Lyu[1,2], Zelio Fusco[1], Fiona Beck[1]
[1] School of Engineering, Australian National University, Canberra ACT2600, Australia
[2] Institut für Fetkörpertheorie und Optik, Friedrich-Schiller-Universität Jena, 07743 Jena, Germany
[*]corresponding author: anjalie.edirisooriya@anu.edu.au

Abstract: This research establishes that fullerene can be efficiently reduced by hot electrons in a Plasmonic-Fabry-Perot coupled system, emphasizing the pivotal role of hot electrons generated by localized surface plasmons. The study highlights the intricate dynamics among nanoparticle size, hot electron generation, and photoreduction efficiency in plasmon-driven processes. The findings offer a promising avenue for controlling chemical reduction processes and optimizing plasmonic catalysts, with implications for diverse applications like photocatalysis.

Summary: Disordered plasmonic arrays of Au nanoparticles (NP) were fabricated on Si-SiO2 substrates using thermal evaporation and annealing. The particle size distribution was evaluated by analysis of SEM images, which revealed average radii of 4nm, 6 nm, 8 nm, 10 nm and 15 nm, respectively, obtained by changing the initial thickness of the Au film (Figure 1(a)). UV-Visible spectroscopy was used to characterize the fabricated Au NP arrays for their absorption properties (Figure 1(b)). The reference Si-SiO2 substrate reveals a strong peak in the absorption spectra associated with the SiO2 layer present in the substrate that acts as an anti-reflection coating supporting Fabry-Perot (FP) modes. In Au NP arrays, a strong absorption in the visible region occurs due to surface plasmonic resonances of the Au NPs. As gold particle size increases, the absorption peak undergoes broadening and shift towards longer wavelengths, indicating changes in plasmonic resonance conditions. Fullerene C60 was deposited through thermal evaporation onto Au NP arrays and onto a Si/SiO2 substrate, serving as a control sample for measurement comparison. The introduction of the C60 layer caused a redshift and broadening of the absorption peak in the reference Si/SiO2 substrate due to the changes in the dielectric environment (Figure 1(c)). The absorption peaks of the NP arrays showed significant splitting when the C60 layer was present. The observed peak separation resulted from the strong coupling between LSPR and FP modes in the altered dielectric environment produced by the C60 layer. Theoretical studies reveal that Fullerene C60 can undergo a reduction process of up to six electrons due to its triply degenerated LUMO[1]. To monitor this multi-electron reduction using the Au–C60 systems, in-situ real-time Raman measurements were performed. Temporal evolutions of the control and AU NP arrays with different radii were taken for 300s upon irradiation with an excitation wavelength lext = 633 nm and 0.66 mW of power. The measurements were performed at -100^{o}C to reduce the intrinsic C60 photopolymerization process. No indications of photo-polymerization or electron reduction were observed in the control as evidenced by the absence of newly emerging peaks. In contrast, in the samples containing Au NP arrays under the same conditions, distinct new peaks emerge. These new peaks can be confidently associated with 1, 3, and 6 electron reductions of C60 (Figure 1(d)). The clear emergence of these peaks strongly suggests that C60 molecules undergo multiple electron reductions, a process facilitated by the presence of plasmons associated with the Au NP arrays. Quantitative analysis of the photoreduction yield at each NP radii clearly demonstrate a strong dependence of yield on NP size(Figure 1(e)). Specifically, the 6 nm NP array exhibits the maximum yield for total electrons reduced, while conversely, the 15 nm array demonstrates the lowest yield. This observation underscores the significant influence of nanoparticle size on the efficiency of C60 photoreduction. The wavelength dependence study further highlighted higher overall yields and proportionally more multiple electron transfers at shorter wavelengths, particularly for radii in the middle range of the investigated radii. To gain insights into the observed trends in the

results, comprehensive full-field three-dimensional optical simulations were conducted for the nanoparticle (NP) arrays, incorporating experimentally obtained parameters. The optical simulations were employed to calculate average near-field enhancements and hot electron generation rates for each nanoparticle radius. This analysis aimed to discern the specific plasmonic effects responsible for the observed photoreductions. A comparative analysis of these calculations clearly demonstrates the substantial role played by hot electrons in the reduction of C60, overshadowing the impact of near fields. The discerned trend in yields for each nanoparticle radius can definitively be associated with the quantity of generated hot electrons. In conclusion, this study employing a Plasmonic-Fabry-Perot (Plasmonic-FP) coupled system clearly demonstrates that the multi-electron reduction of C60 can be effectively facilitated through the leveraging of hot electrons. Furthermore, it underscores the intricate interplay among nanoparticle size, hot electron generation, and photoreduction efficiency in plasmon-driven processes. This emphasizes the significance of experimental validation in understanding these complex dynamics. By harnessing the plasmonic effects induced by the interaction between light and metallic nanoparticles, the study unveils a promising avenue for precisely controlling and enhancing chemical reduction processes. This insight not only deepens our understanding of plasmon-driven reactions but also opens up new possibilities for the design and optimization of plasmonic catalysts with implications for various applications in fields such as photocatalysis.

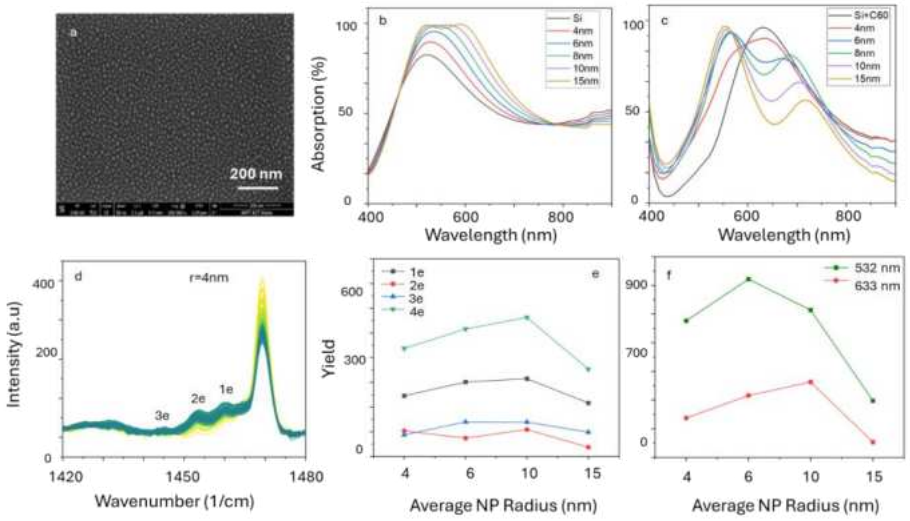


Figure 1: a) Top view SEM of AU NP array with aberage radius of 4nm b) Absorption spectra of the NP arrays c) Absorption profiles of AU NP arrays with C60 d) Temporal Raman spectra for r=4nm sample taken at 633nm excitationElectron reduction yields calculated for 633nm excitation e) Yield for each electron reduction at 633nm excitation f)Wavelength dependence of total yields

References

[1] G. Klupp, S. Margadonna, K. Prassides, Fullerenes, Ref Mod in Materials Sci and Materials Engineering, 2016

[2] S. Zhao, Z. Fusco, F.J. Beck, Strong and tunable absorption in coupled nanoparticle cavity systems for plasmonically enhanced hot electron devices, Optica, 2022

[3] A. Edirisooriya, Z. Fusco, F.J. Beck, In preparation

[4] Z. Fusco, K. Catchpole, F.J. Beck, Investigation of the mechanisms of plasmon-mediated photocatalysis: synergistic contributin of near-field and charge transfer effects, J. Material Chemistry C, 2022

MAPLE simulation for multilayer-layers solar cell based in ZnS- CZTSSe

H. J. El-Khozondar[1], A. N. Sahmoud[2], R. J. El-Khozondar[2], Y. F. Nassar[1]

[1] Electrical Engineering and Smart Systems Departments, Islamic University of Gaza, Gaza, Palestine.

[2]Physics Department, Al-Aqsa University, Gaza, Palestine

[*]Corresponding author: hkhozondar@iugaza.edu.ps

Abstract: The model is implemented using Maple to assess open-circuit voltage, short-circuit current density, conversion efficiency, and fill factor for a ZnO(window)/CdS(buffe)/ CZTSSe(absorber) solar cell. The varying thicknesses of Buffer layer (w_n) is considered in the calculations. The outcomes reveal that w_n leads to a significant enhancement in all performance indicators.

Keywords: CZTSSe, solar cell, MAPLE, high performance

The advancement of thin-film solar cells has prompted researchers to explore various materials to enhance conversion efficiency, reduce the use of hazardous raw materials, or lower manufacturing costs. One approach involves the utilization of simulation tools, which permit the manipulation of solar cell materials, parameters, dimensions, and other variables to assess the cell's performance metrics without material wastage. This article introduces a mathematical model designed for thin-film solar cells based on Copper zinc tin sulfo-selenide (CZTSSe). Solar cells based on CZTSSe is intensively studied as all components are abundant in nature [1-3]. In this work we want to understand the efficiency of the cell using Maple program. The proposed structure is shown in figure 1.

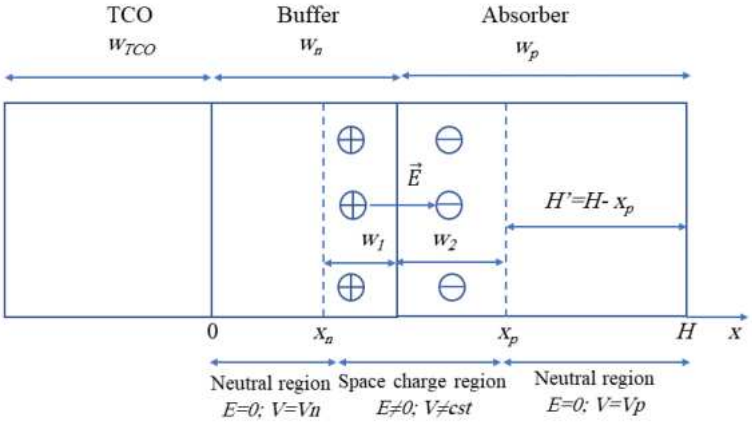


Fig 1: the proposed solar cell structure

The total photo current density is defined as follows:

$$J_{ph} = \int_{\lambda_1}^{\lambda_2} J_{ph}(\lambda);\ \ where\ Jph(\lambda) = Jp(\lambda) + Jn(\lambda) + Jzce(\lambda) \qquad (1)$$

Photocurrent $Jph(\lambda)$ is defined as the sum of the current density due to the holes in N region ($Jn(\lambda)$), the current density due to the electrons in the P region ($Jp(\lambda)$), and the current density in the space charge zone ($Jzce(\lambda)$).

The three Solar cell characteristics that describes its performance are: the open-circuit voltage (*Voc*), the fill factor (*FF*) and the power conversion efficiency (η) as defined in equation (2)

$$V_{oc} = \frac{kT}{q}\ln\left(\frac{J_{ph}}{J_0}+1\right); FF = \frac{P_m}{V_{oc}I_{sc}};\ \eta = \frac{P_m}{P_i} \qquad (2)$$

where *Jo* is the dark current density, I_{sc} is the cell short-circuit current, P_m is the maximum power and P_i is the incident power. The simulations are performed as function of the width w_n. Results are given in figures 2.

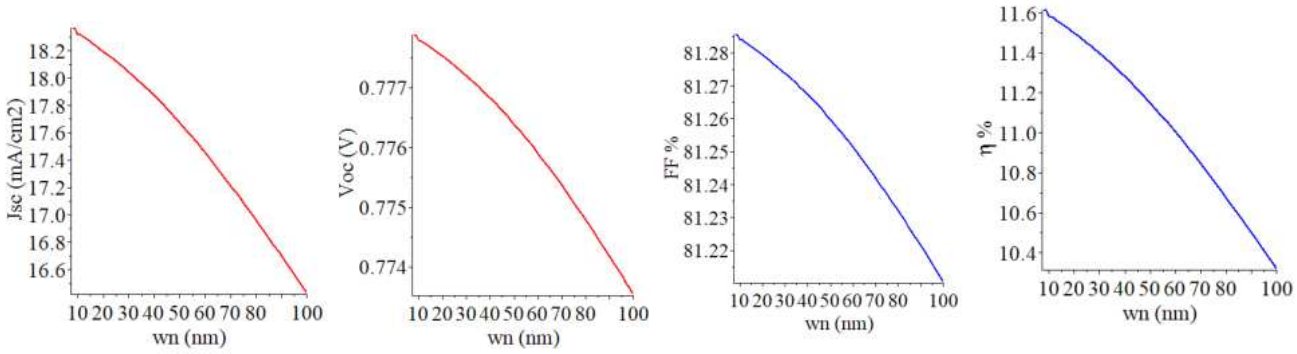


Fig 2: effect of w_n on solar characteristics

Fig. 2 shows the effect of the thickness *wn* of the CdS buffer layer on the cell performance for: *EgCdS* = 2.42 eV, *EgCZTSSe* = 1.13 eV, *wZnO* = 200 nm and *wp* =3µm. The breadth of the space charge area, known as w1, is 12.6 nm. Given that the buffer layer's maximum width, wnmax, is 100 nm, which exceeds w1, the buffer layer comprises not only the space charge area with a width of w_1 for $w_n < w_1$ (where x_n equals 0), but also a secondary neutral zone with a width of $x_n = w_n - w_1$ for $w_n > w_1$. Fig. 2 shows that if $w_n < w_1$, the cell's performance is unaffected. However, after wn surpasses w_1, the neutral zone effect kicks in, marginally reducing the current and, as a result, efficiency. This effect is caused by the minority carriers (holes) in the N layer (CdS) having a shorter diffusion length than minority carriers (electrons) in the P layer (CZTS). As a result, increasing the thickness of w_n causes more photon absorption in the N layer before it reaches the P layer, lowering absorption there. As a result, it is preferred that w_n stay equal to or smaller than w_1. Furthermore, it is important to note that the thickness of the buffer layer, w_n, has no major effect on the cell's performance. While this may appear insignificant at first, it confirms the previous finding. However, this does not indicate that the buffer layer should be removed, as its role in creating the electric field within the space charge zone is critical to junction formation.

References

[1] H.T. Ali, Jamil, M., Mahmood, K., Yusuf, M., Ikramb, S., Ali, A., Amin, N., K. Javaidb, M.Y Alib, M.R. Nawaz, "A simulation study of perovskite based solar cells using CZTS as HTM with different electron transporting materials," Journal of Ovonic Research, Vol. 17, 437 - 445, 2021.

[2] J.H. C. Yan, K. Sun, S. Johnston, Y. Zhang, H. Sun, A. Pu, M. He, F. Liu, K. Eder, L. Yang, J.M. Cairney, N.J. Ekins-Daukes, Z. Hameiri, J.A. Stride, S. Chen, M.A. Green, X. Hao, "Cu2ZnSnS4 solar cells with over 10% power conversion efficiency enabled by heterojunction heat treatment," Nat. Energy, Vol. 3, 764–772, 2018.

[3] O.K. Simya, Mahaboobbatcha, A., Balachander, K. , "A comparative study on the performance of Kesterite based thin film solar cells using SCAPS simulation program," Superlattices and Microstructures, Vol. 82, 248-261, 2015.

Research on the enhancement of photocatalytic activity of bismuth-based materials by plasma effect

Derek Hao*

School of Science, STEM College, RMIT University, Melbourne, 3000 Australia
*Corresponding author: derek.hao@rmit.edu.au

Abstract: The study investigates the enhancement of photocatalytic activity in bismuth oxide material through plasma effect. The research explores the preparation of C/Bi/Bi_2O_3 composite photocatalyst. The reduced particle size and plasma effect of bismuth increase the photocatalytic efficiency, offering promising applications in environmental remediation and energy conversion.

In recent years, bismuth-based materials have made significant advances in the field of photocatalysis, which is the acceleration of photoreaction in the presence of a catalyst.[1] These materials are particularly interesting due to their unique properties including the adjustable band structure and light absorption, good stability and non-toxicity, good photocatalytic activity, etc.[2] More importantly, bismuth nanoparticles can exhibit surface plasmon resonance, which can be employed to improve the photocatalytic activity of materials.[3]

Compared with other Bi-based photocatalysts, α-Bi_2O_3 is the most common Bi-based photocatalyst with a lot of advantages. For instance, it has a narrow band gap which can be excited by visible light, moreover, α-Bi_2O_3 is nontoxic and easy-prepared. However, the band gap around 2.7 eV indicates that α-Bi_2O_3 can only utilize a small amount of solar energy.[4,5] Meanwhile, the grain size of α-Bi_2O_3 obtained by calcination method is often too large for interface reactions. Herein, as shown in Figure 1, a new C/Bi/Bi_2O_3 composite photocatalyst was synthesized through an uncomplicated, single-step process utilizing EDTA-Bi as the starting material. This composite catalyst demonstrated superior performance in photodegradation of 2,4-dichlorophenol compared to pure Bi_2O_3, under both simulated sunlight and visible light. The presence of metallic Bi and residual organic carbon in the composite not only boosts light absorption but also promotes the swift separation of photo-induced charge carriers, leading to enhanced photocatalytic efficiency. Additionally, this research introduces an easy-to-implement technique for crafting C/Bi/Bi_2O_3 composites, offering a practical approach for enhancing the photocatalytic activity of composite materials.

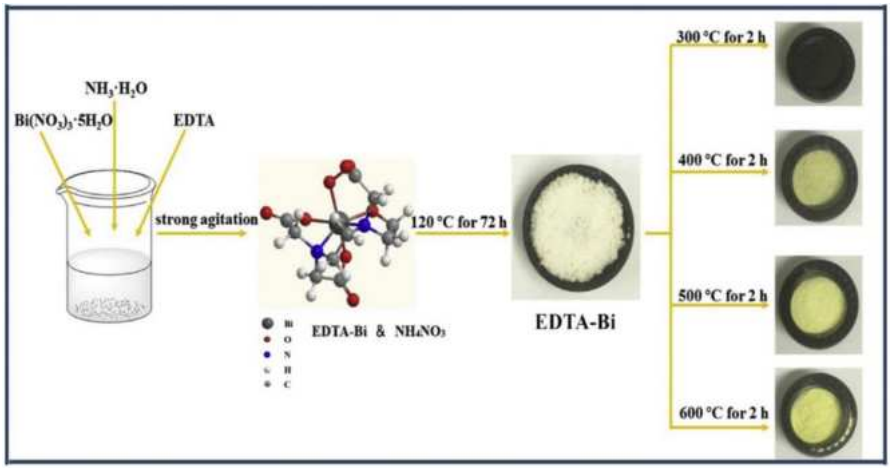


Figure 1. A flow diagram of the f C/Bi/Bi_2O_3 preparation method.

Acknowledgements: Dr. Derek Hao acknowledges the kind support from the Australian Research Council, Humboldt Research Foundation, the European Union, and the Polish National Agency for Academic Exchange.

References

1. Sood, S. et al. "α-Bi_2O_3 nanorods: An efficient sunlight active photocatalyst for degradation of Rhodamine B and 2,4,6-trichlorophenol," Ceram. Int., Vol. 41, Issue 3, 3355-3364, 2015.
2. Ayekoe, P. Y., D. Robert and D. L. Droh, "TiO_2/Bi_2O_3 photocatalysts for elimination of water contaminants. Part 1: synthesis of α- and β-Bi_2O_3 nanoparticles," Environ. Chem. Lett., Vol. 13, 327-332, 2015.
3. Li, F. M., et al. "Highly sensitive detection of chromium (VI) by photoelectrochemical sensor under visible light based on Bi SPR-promoted $BiPO_4$/BiOI heterojunction," Sensor. Actuat. B-Chem., Vol. 305, 127449, 2020.
4. Riente, P. et al. "Light-Driven Organocatalysis Using Inexpensive, Nontoxic Bi_2O_3 as the Photocatalyst," Angew. Chem. In. Edit. Vol. 53, Issue 36, 9613-9616, 2014.
5. Balachandran, S and M. Swaminathan, "Facile Fabrication of Heterostructured Bi_2O_3–ZnO Photocatalyst and Its Enhanced Photocatalytic Activity" J. Phys. Chem. C, Vol. 116, Issue 50, 26306-26312, 2012.

Large-area self-organized plasmonic gold nanowire matrix for advanced photochemical applications

G. Ferrando[1*], M. Gardella[1], L.D. Pham[2], H. S. Nguyen[2], C.H. Le[2], T.H. Mai[2], G. Zambito[1], M.Barelli[1], M.C. Giordano[1], F. Buatier de Mongeot[1]

[1]Dipartimento di Fisica, Università di Genova, Via Dodecaneso 33, I-16146 Genova, Italy
[2]Institute of Materials Science, Vietnam Academy of Science and Technology (VAST), 18 Hoang Quoc Viet, Cau Giay, Hanoi, Vietnam
[*]giulio.ferrando@edu.unige.it

Abstract: Renewable energy and waste water treatment require advanced nanoscale platforms. Localized Surface Plasmon Resonances (LSPR) show promise. Here is proposed a self-organized method creates glass nanorippled templates for gold nanowire growth, enhancing photocatalysis and electrode performance. Plasmonic NWs extend absorption, offering potential for scalable solar energy conversion and large-area photonics.

Photochemical reactions, such as photocatalysis and water splitting, are of great since they can promote molecular degradation of organic pollutants[1,2], or energy storage via hydrogen production in view of renewable energy conversion[3]. While large band gap semiconductor oxides like TiO_2 exhibit robust photocatalytic activity and chemical stability, their limited absorption of solar light, primarily confined to the ultraviolet (UV) spectrum (5% absorption), poses a challenge for efficient light utilization. A promising approach to improve the functionalities of such electrodes in the visible range is based on the excitation of Localized Surface Plasmon Resonances (LSPR) in nanoparticles. Specifically, LSPR facilitates the strong confinement of incident light within a subwavelength volume, thereby enhancing light scattering and absorption cross sections. These properties have garnered increasing interest for their potential application in photochemical processes, particularly in waste water treatment and energy storage through the water splitting process. Notably, LSPR can directly influence photochemical reactions through its local field enhancement and the injection of "hot electrons." Moreover, it can be coupled with another photocatalyst such as TiO_2 to further enhance its efficacy.
However, for this kind of applications is crucial to develop fabrication techniques that are usable over large-areas. To address these challenges, we have developed a self-organized method[4,5] capable of producing glass nanorippled templates spanning centimeters squared, with scalability up to meters squared. These templates serve as a substrate for the growth of laterally separated gold nanowires. This unique system holds promise as both a standalone photocatalyst and a functionalized electrode.
In the former application, we utilized this sample in a photochemical reaction involving the photobleaching of Methylene Blue (MB)[2]. Specifically, using a monochromatized and polarized illumination, we observed an higher MB's photodissociation rate at the wavelength at which the LSPR is tuned in resonance with the MB's maximum optical absorption. This observation is pivotal in demonstrating the active role of plasmonic resonance in the photodissociation process and optimizing the fabrication of plasmonic substrates for the photodissociation of colored dye molecules. Therefore, these findings underline the potential of nanophotonics solutions in environmental applications such as waste water treatment.
Regarding the use of this system as electrode we deposit an ultra-thin film of TiO_2 on the top of the NW matrix and we use this kind of system as electrode for an Oxygen Evolution Reaction (OER)[3]. In this setup, the Au NW arrays serve dual purposes: as a transparent conductive layer and as a plasmonic medium, resonantly enhancing

the photoconversion efficiency of a reference photoelectrochemical OER at visible photon energies significantly lower than the TiO_2 band gap. A spectrally selective and polarization-dependent detection of the photocurrent demonstrates the key role played by the plasmonic NWs that promote both polarization-sensitive optical absorption, via resonant near-field enhancement, and hot-carrier injection over a broader visible spectral range. This extension surpasses the band gap of the TiO_2 layer, yielding a notable gain of approximately 3.8 within the visible spectrum. These results qualify the hybrid Au NWs-TiO_2 as a promising and scalable self-organized platform for solar energy conversion via photochemical reactions and pave the way for large-area photonics and energy storage applications.

References

1. Ferrando, G. *et al.* "Flat-optics hybrid MoS_2 /polymer films for photochemical conversion." *Nanoscale* **15**, 1953–1961 (2023).
2. Barelli, M., Ferrando, G., Giordano, M. C. & Buatier de Mongeot, F. "Wavelength-Dependent Plasmonic Photobleaching of Dye Molecules by Large-Area Au Nanostripe Arrays." *ACS Appl. Nano Mater.* **5**, 3470–3479 (2022).
3. Giordano, M. C. *et al.* "Self-Organized Plasmonic Nanowire Arrays Coated with Ultrathin TiO_2 Films for Photoelectrochemical Energy Storage." *ACS Appl. Nano Mater.* **6**, 21579–21586 (2023).
4. Giordano, M. C., Sacco, F. Di, Barelli, M., Portale, G. & Buatier De Mongeot, F. "Self-Organized Tailoring of Faceted Glass Nanowrinkles for Organic Nanoelectronics." *ACS Appl. Nano Mater.* **4**, 1940–1950 (2021).
5. Giordano, M. C. & de Mongeot, F. B. "Anisotropic Nanoscale Wrinkling in Solid-State Substrates." *Adv. Mater.* **30**, 1–8 (2018).

Templated Self-Assembled Plasmonic Metasurfaces. From Lasing and Sensing to Photocatalysis

T. Tamulevičius[1,2,3,*], K. Midveris[1], G. Klyvis[1], T. Klinavičius[1], M. Haris[2], N. Khinevic[2], A. Tamulevičienė[1,3], M. Juodėnas[1], D. Peckus[1,2], J. Henzie[4], S. Tamulevičius[1,2]

[1]Institute of Materials Science, Kaunas University of Technology, Kaunas 51423, Lithuania
[2]Physics Department, Kaunas University of Technology, Kaunas 51368, Lithuania
[3]UAB Nanoversa, Kaunas 51423, Lithuania
[4]International Center for Materials Nanoarchitectonics, National Institute for Materials Science, Tsukuba 305-0044, Japan
[*]corresponding author: tomas.tamulevicius@ktu.lt

Abstract: Chemically synthesized plasmonic nanoparticle colloid templated self-assembly onto soft lithography replicated elastomer templates is a well-established method for originating 1 cm^2 scale metasurfaces. Regular noble metal nanoparticle arrays couple the scattered localized plasmon light into high-Q surface lattice resonances serving in nanolasing, Raman enhancing, and photocatalysis.

Precise average size control, high monodispersity, and reproducibility of chemically synthesized plasmonic nanoparticles enable their applications for photonic devices which are originally made employing top-down methods [1-2]. Templated nanoparticle self-assembly from concentrated nanoparticle colloids is an established method for the manipulation and deposition of nanoparticles into well-defined positions originating desired photonic coupling and controlled local field enhancements [2-4]. Regular sub-wavelength spaced noble metal nanoparticles arrays can diffractively couple the scattered light from broad localized surface plasmons (LSPs) into narrow and high-Q resonances termed plasmonic lattices or surface lattice resonances (SLRs) [2-4]. The wavelength taylorability of SLR positions rises from the size-dependent LSPR coupling with the pitch-determined Rayleigh's anomaly [2-4]. The laterally confined light can act as an optical resonator for a dye nanolaser [5,6], can confine the electromagnetic radiation for desired wavelength Raman enhancement [4], and can contribute to efficient solar water splitting by metasurface photoelectrodes [7]. Electron beam lithography defined master replication with soft lithography into elastomer deposition templates act as plasmonic metasurface carrier for direct application or as a transfer carried for integration into more complex photonic structures.

The work was supported by the European Economic Recovery and Resilience Plan "New Generation Lithuania" and the budget of the Republic of Lithuania, Project No. 02-002-P-0001.

References

1. Khinevich N., *et al.* "Size and Crystallinity Effect on the Ultrafast Optical Response of Chemically Synthesized Silver Nanoparticles" J. Materiomics, 2023, 10.1016/j.jmat.2023.08.009.
2. Juodėnas M., *et al.* "Surface Lattice Resonances in Self-Assembled Arrays of Monodisperse Ag Cuboctahedra," ACS Nano, Vol., 13, No. 8, 9038–9047, 2019.
3. Juodėnas M., *et al.* "Effect of Ag Nanocube Optomechanical Modes on Plasmonic Surface Lattice Resonances," ACS Photonics, Vol. 7, No. 11, 3130–3140, 2020.
4. Khinevich N., *et al.* "Wavelength-tailored Enhancement of Raman Scattering on a Resonant Plasmonic Lattice," Sens. Actuator B-Chem., Vol. 394, 134418, 2023.
5. Hakala T. K., *et al.* "Lasing in dark and bright modes of a finite-sized plasmonic lattice," Nat. Commun.,Vol. 8,

13687, 2017.
6. A. Yang, *et al.* “Real-time tunable lasing from plasmonic nanocavity arrays,” Nat. Commun., Vol. 6, 6939, 2015.
7. Hüttenhofer L., *et al.* “Metasurface Photoelectrodes for Enhanced Solar Fuel Generation,” Adv. Energy Mater., Vol. 11, No. 46, 2102877, 2021.

Near-unity Index Meta-surfaces for Effective CO_2 Reduction to Methanol

Joel Y. Y. Loh[1],

[1]University of Manchester, Electrical and Electronic Department, Photon Science Institute, University of Manchester, Oxford Road, United Kingdom
*corresponding author: joel.loh@manchester.ac.uk

Abstract: Metal-based photo-absorbing metamaterials can achieve electromagnetic field amplification and broadband absorption throughout the visible spectrum by reaching an effective refractive index similar to that of air. For instance, a ZnO/Cu metamaterial surface comprising periodically arranged nano-cubes demonstrates near-perfect 97% absorption from 350 to 650 nm. By having an index below 1, the plasmonic electric field expands to the entire visible spectrum, which enhances light-to-dark adsorption of CO_2 gas and with angular invariance. Fourier Transform Infrared Spectroscopy reveals additional intermediate species, suggesting new adsorption and reaction pathways.

Summary: Figure 1 shows the cross-sectional microscopy of 90nm copper / 10 nm ZnO nano-cubes on a gold layer [1]. The optical absorption spectrum of the meta-surface is wider and higher than that of a nanoparticle film. For randomly distributed nanoparticles, most absorption is via internal scattering of incident light, with a copper plasmonic absorption edge at 600nm. For the meta-surface, the edge is extended to 650nm (**Figure 1**). To show the difference in the underlying EM mechanism, we show the results associated with the conventional effective medium theory and the boundary sheet theory. **Figure 2** shows the real and imaginary component of the index, and the calculated absorption spectrum of the meta-surface nano-cube array and periodicity, using the MG effective medium theory. The absorption spectrum is similar to that of the nanoparticle film but not the meta-surface, and while the refractive index is close to 1, it is still high enough to induce reflection. A different refractive index theory is needed.

Using the boundary sheet theory we calculated that the meta-surface has an index real component below 1 and imaginary component near or below zero (**Figure 3**). This means that the metamaterial scatters or reflects minimal light because light effectively does not see any scattering medium. This is also effective at various incident angles of light- showing the metamaterial is a perfect absorber at all angles (**Figure 4**).

When a CO_2 gas is passed over the meta-surface, its chemisorption profile under light and dark is different than that of a copper nanoparticle film. The in-situ FTIR spectroscopy showed a large increase in absorption in the 1050−1220 cm^{-1} band under 1 sun illumination (**Figure 4**), which is associated with adsorbed methoxy (*CH_3O) or gaseous CH_3OH species. By contrast, the particle film showed relatively small absorption changes in the same band. This separate hydrogenation pathway suggests an additional indirect charge transfer that is present in the meta-surface, even though the nanoparticle film should also exhibit plasmonic effects. This is revealed by the electric field intensity spectrum (**Figure 5**), which showed that while a nanoparticle film only shows strong plasmonic fields at the resonance wavelength of ~600nm, the plasmonic field in the meta-surface covers 350nm to 650nm. Such a range of plasmonic energies can likely enhance the adsorption of gas molecules through an energy ladder of charge injection.

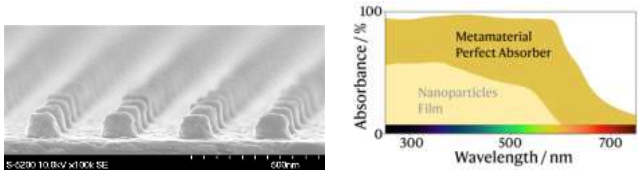


Figure 1. The cross-sectional microscopy image of the meta-surface (left). The optical absorption spectra of the fabricated meta-surface and uniform ZnO / Cu film (right).

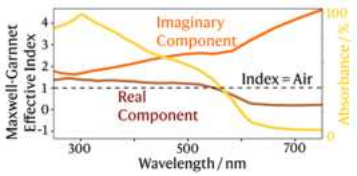


Figure 2. Effective medium theory shows the real and imaginary components of the refractive index of a Cu layer with a low volumetric filling ratio. Also shown is the simulated absorption spectrum of the Cu layer, which does not match the experimental absorption spectrum.

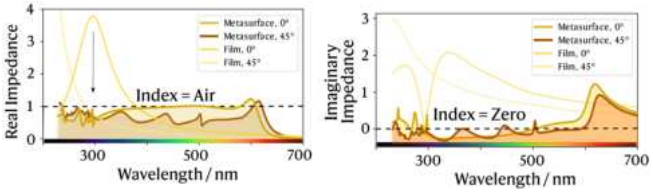


Figure 3. The Boundary Sheet theory shows the real and imaginary components of impedances of the meta-surface and ZnO / Cu film. The meta-surface impedance shows minor changes in profile whereas the film shows significant changes both across the spectrum and incident angle.

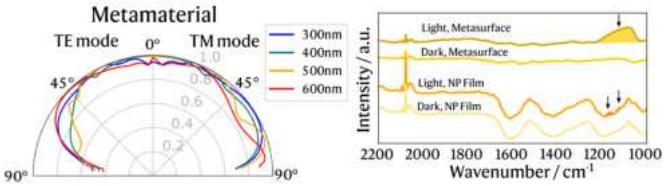


Figure 4. Polar plots of the meta-surface under a range of incident angles at selected wavelengths of 300, 400, 500, 600 nm. Fourier transform infrared spectra of the meta-surface and quartz fiber surface coating under 250 °C temperature and CO_2 and H_2 flow, compared between under dark and light conditions.

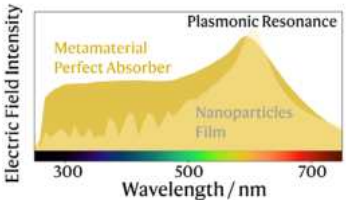


Figure 5. Average electric field intensities between the nano-cubes at the optimal periodicity, and nano-cubes with random periodicities, such that it is considered a nanoparticle film

References

1. J.Y.Y. Loh, M. Safari, C.L. Mao, C.J. Viasus, G.V. Eleftheriades, G.A. Ozin, N.P. Kherani, “Near-perfect absorbing copper metamaterial for solar fuel generation”, *ACS Nanoletters*, 21, 9130, (2021)
2. V. Asadchy, M. Albooyeh, S. Tcvetkova, A. Díaz-Rubio, Y. Ra'di, Y. Ra'di, S. Tretyakov, Perfect control of reflection and refraction using spatially dispersive metasurfaces, *Ann. Phys*. 2016
3. T. V. Teperik, F. J. García de Abajo, A. G. Borisov, M. Abdelsalam, P. N. Bartlett, Y. Sugawara & J. J. Baumberg, “Omnidirectional absorption in nanostructured metal surfaces”, *Nature Photonics*, 2, 299–301 (2008)
4. Z. Wang, H. Song, H. Pang, Y. Ning, T. D. Dao, Z. Wang, J. Ye, Photo-assisted methanol synthesis via CO2 reduction under ambient pressure over plasmonic Cu/ZnO catalys, *Appl. Catalysis* B., 250, 10-16, 2019

Plasmonics and nano-optics

A Direct Approach towards Nanoscale Mapping of Plasmonic Heat Generation in Nanostructures

Serene Pauly[1*], and Dr. Amit Kumar[1]

[1]Queen's University, Belfast, UK
[*]Email: spauly01@qub.ac.uk

Abstract: This work focuses on direct visualization and optimization of nanoscale plasmonic heating in metallic nanostructures. Through integration of scanning thermal microscopy with laser-enabled plasmonic excitation, our methodology allows for precise measurement and analysis of localized heating effects. Additionally, the study examines wavelength, and morphological effects on influencing the thermal response.

Data demands have been predicted to grow 40% annually and one of the key players to make an impact is heat assisted magnetic recording (HAMR) with increased storage density up to 1 Tb/in^2, surpassing today's hard disk drives (HDD) [1]. One of its main components is a near field transducer (NFT) whose design is based on excitation of surface plasmons nanostructure to produce sub-diffraction limited thermal spot. A major bottleneck associated with nanoscale light confinement is the significant joule heating produced [1][2]. As a result, the performance and dependability of NFTs will decline, and plasmonic nanostructures will steadily deteriorate. Therefore, it is essential to directly measure the elevation of nanoscale temperature as a function of light intensity since this will lead to a comprehensive understanding of thermal distribution. While the topic has been explored from different perspectives for plasmonic response and arising thermal effects, most of this work focuses on macroscopic measurement of heat whereas plasmonic mediated heating is a nanoscale phenomenon. Our work combines different strands of the problem together and develop a holistic approach that allows direct visualisation of plasmonic-mediated thermal transport at nanoscale resolution. One of the major challenges in the field of thermal plasmonics, as mentioned in several publications [4] [6] is the need to directly quantify light-induced heat with nanoscale resolution, however much of the present literature has macroscopic temperature measurement utilising far field methods such as fluorescence microscopy, Raman spectroscopy, and others [6] [4]. Hence, our work aims to fill this gap in literature by investigating thermal distribution in nanometric plasmonic structures at high spatial resolution. The work consists of a novel method to visualize plasmonic-mediated thermal transport at a nanoscale resolution using scanning thermal microscopy. SThM is a variant of an Atomic Force Microscopy (AFM) which consists of a nano-thermocouple probe operating on passive mode. In passive mode, the probe functions as a temperature sensor and senses sample surface temperature distribution with 10 nm spatial resolution [3] and thermal sensitivity of 10 mK. Within this context the key objective we have achieved are 1) optimised plasmonic coupling to achieve wave vector matching by tilting the direction of illumination 2) direct measurement of temperature changes using SThM 3) replicate HAMR conditions in terms of plasmonic nanostructures. The SThM setup for thermal mapping is shown in broad strokes in Fig. 1, together with the related temperature map.

In pursuit of a comprehensive approach, the present study employs COMSOL simulations as a predictive framework to elucidate temperature distribution patterns as a function of structural morphology. This computational methodology facilitates an in-depth exploration of thermal dynamics within the structure, enabling the identification and characterization of hotspots. The utilization of COMSOL simulations affords a robust and quantitative means to analyze the thermal behavior of the system, providing valuable insights into the intricate interplay between morphology and temperature distribution. This study is a good starting point for significant advancements in the study of fundamental

physics related to thermal signatures that are produced by plasmonic responses.

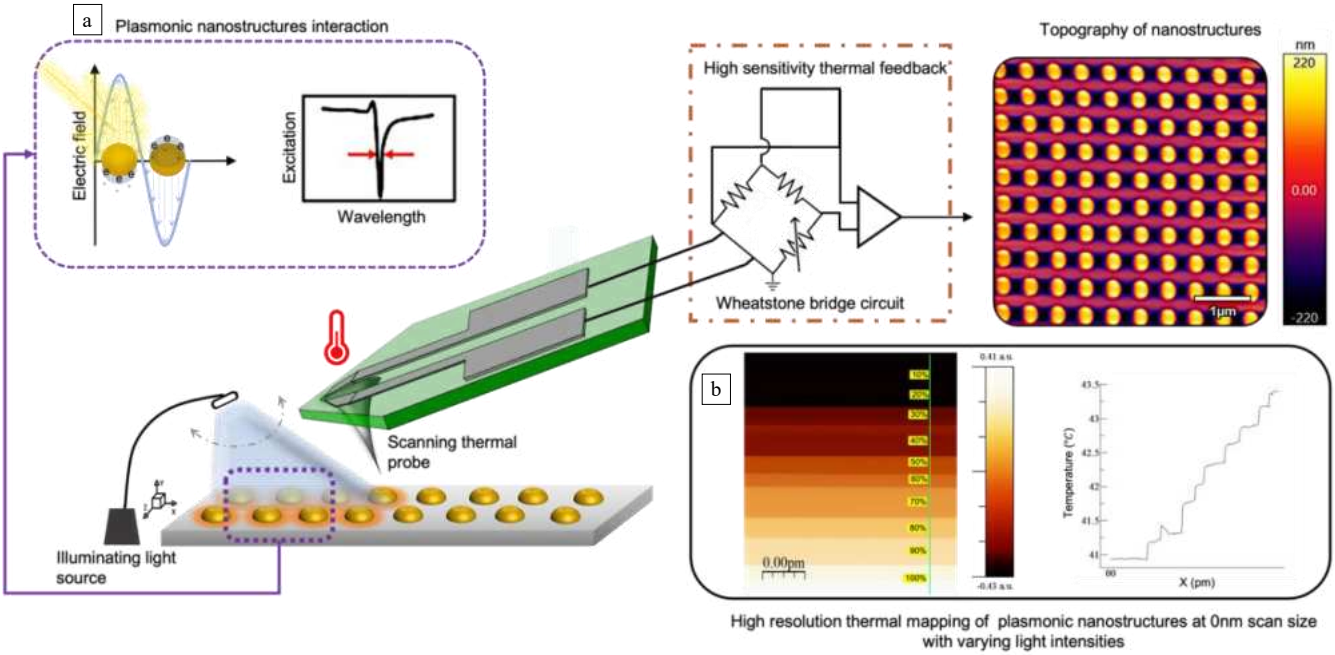


Figure 1: *Thermal mapping of plasmonic nanostructures with localized illumination. a) depicting LSPR on plasmonic nanostructure upon illumination b) SThM image at 0 nm scan size and varying light intensity and its corresponding line profile.*

This research was supported by PIADS (Photonics Integration and Data Storage), an EPSRC initiative, and Queen's University.

References

1. L. Steinmetz et al., "Experimental and theoretical validation of Plasmonic Nanoparticle Heat Generation by using lock-in Thermography," The Journal of Physical Chemistry C, vol. 125, no. 10, pp. 5890–5896, 2021. doi:10.1021/acs.jpcc.0c11419
2. M. Kuttge et al., "Local density of states, spectrum, and far-field interference of surface plasmon polaritons probed by cathodoluminescence," Physical Review B, vol. 79, no. 11, 2009. doi:10.1103/physrevb.79.113405
3. B. Desiatov, I. Goykhman, and U. Levy, "Direct temperature mapping of nanoscale plasmonic devices," Nano Letters, vol. 14, no. 2, pp. 648–652, 2014. doi:10.1021/nl403872d
4. Y. Zhang et al., "A review on principles and applications of Scanning Thermal Microscopy (sthm)," Advanced Functional Materials, vol. 30, no. 18, 2019. doi:10.1002/adfm.201900892
5. N. Zhou et al., "Plasmonic near-field transducer for heat-assisted magnetic recording," Nanophotonics, vol. 3, no. 3, pp. 141–155, 2014. doi:10.1515/nanoph-2014-0001
6. L. Steinmetz et al., "Experimental and theoretical validation of Plasmonic Nanoparticle Heat Generation by using lock-in Thermography," The Journal of Physical Chemistry C, vol. 125, no. 10, pp. 5890–5896, 2021. doi:10.1021/acs.jpcc.0c11419

Optimized Near-infrared Absorption of Reflective Aluminum Gratings: Theoretical and Experimental Investigation

R. Avrahamy,[1*] D. Cohen,[2] B. Milgrom,[3] B. Amir,[2] D. Belker,[1] A. Solodar,[4] E. Golan,[4] O. Sadot,[2] and A. A. Ishaaya[1]

[1]School of Electrical & Computer Engineering, Ben-Gurion University of the Negev, P.O.B 653, Beer-Sheva 8410501, Israel
[2] Department of Mechanical Engineering, Ben-Gurion University of the Negev, P.O.B 653, Beer-Sheva 8410501, Israel
[3] School of Electrical Engineering, Jerusalem College of Technology, P.O.B 16031, Jerusalem 9372115, Israel
[4] Nano-fabrication center Ilse Katz Institute for Nanoscale Science and Technology, Ben-Gurion University of the Negev, P.O.B 653, Beer-Sheva 8410501, Israel

[*]corresponding author: roiav@post.bgu.ac.il

Abstract: We inversely design reflective Aluminum gratings for narrow-/wide-linewidth TE/TM/unpolarized perfect absorption around 1.06μm. Expanding the widely studied P-polarization plasmonic case, we highlight the achievability of perfect S-polarization absorption in the simplest 1D geometry without extra materials. Optical and thermal measurements of the absorption of a large-area fabricated design match simulations.

The physical mechanisms behind enhanced photo-absorption in metallic reflection gratings, initially linked solely to excitations of surface plasmon polaritons (SPP), have been extensively studied and proven complex [1]. Under P-polarized incidence, in addition to SPPs, the modal mixture can comprise standing waves and cavity modes commonly referred to as localized SPP (LSP modes) and geometrically induced surface modes labeled spoof surface plasmons. Simple 1D metallic grating geometry does not offer versatile coupling and confinement mechanisms for S-polarized incidence, and thus, such reports are uncommon. Relevant studies mainly include designs with additional dielectric layers, smooth or periodic, to offer more physical complexity. Aluminium (Al) is the most prevalent metal, and due to its many benefits, Al and its alloys are essential for almost every industry, e.g., transportation, packaging, construction, electricity, machinery, etc. In the past decade, high-power fiber lasers with superior beam quality have become accessible and affordable. They are used in many applications, such as material processing, wireless power transfer, laser guidance and designation, satellite optical communication, and defense-related laser systems. Owing to their superior performance, Ytterbium (Yb)-doped fiber lasers, centered around 1.06 μm, dominate the high-power market nowadays. With such applications in mind, here we investigate the absorption enhancement of bulk Al around λ_0=1.065μm. Also, we achieve perfect S-polarized absorption in the simplest 1D geometry without adding material complexity. Such geometry can potentially be patterned remotely on large scales, e.g., with femtosecond pulsed lasers, and has the benefit of possible single-step fabrication.

The general design and its dimensions, i.e., period Λ, grooves width a, depth h, and the polar incidence angle θ, are shown in Fig. 1(a). The S- and P-polarization correspond to an incident electrical field, $\mathbf{E}_i$ perpendicular and parallel to the incident plane (xz), respectively. Using an in-house numerical EM simulation and optimization tool [2], we optimize the dimensions of several designs to maximize $A(\lambda_0)$ in TE, TM, and unpolarized irradiations. Here, we detail the properties of a design optimized for S-polarized operation. Unlike the P-polarization case, there is no transverse (along $\hat{z}$) confinement mechanism under S-polarization incidence. Thus, the groove should be high enough to fully encompass the mode distribution to achieve perfect absorption. This notion is demonstrated in Fig. 1(b), in which we plot a scan of the TE-polarized $A(\lambda)$ of an optimized design, with dimensions Λ_o=0.68 μm, a_o=0.517 μm, and h_o=1.836 μm, for a span of h. Note that this design, optimized while limiting Λ_o to inhibit reflective diffraction orders for θ<35º, shows low $A(\lambda)$ in the simulated spectrum $\forall h$<1 μm.

It is apparent that coupling to confined longitudinal modes (along $\hat{x}$) of the symmetrical MDM Fabry–Pérot resonant cavity propels the absorption enhancement. Considering perfect mirrors, such modes resonate according

to $2n_dk_0a=2\pi m$ with n_d- refractive index of the dielectric, k_0- wavenumber, and m- longitudinal mode order. Assuming that the additional optical phase accumulations due to the non-ideal metal are negligible, the resonant condition, for $n_d=1$, m=1, will be satisfied close to $a_{FP}\approx\lambda_0/2=0.5325$ μm that matches $a_o=0.517$ μm. Fig. 1(c) shows a comparison of $A(\lambda)$ for h_o and $h_1=2.6$ μm, marked with a dashed blue line in Fig. 1(b). The former shows a global $A(\lambda_0)>99.98\%$ maximum and additional local maxima at $\lambda_1=0.966$ μm. For h_1, the absorption peaks shifts $\lambda_0\rightarrow\lambda_{0d}=1.083$ μm with $A(\lambda_{0d})=83.46\%$, and $\lambda_1\rightarrow\lambda_{1d}=1.026$ μm with $A(\lambda_{1d})=98.48\%$. In Figs. 1(d)-1(f), we plot the color map distribution of $|\mathbf{E}|$ for h_o- Fig. 1(d) and h_1- Figs. 1(e)-1(f) under TE-polarized incidence at wavelengths λ_0, λ_{0d}, and λ_{1d}, respectively. The distributions in Figs. 1(d)-1(f) implies that the absorption peaks correspond to the laterally confined modes with m=1. Specifically, Figs. 1(d) and 1(e) depict optimal and non-optimal, due to h, coupling to TE_{10}, respectively, and Figs. 1(f) corresponds to close to optimal coupling to TE_{11}.

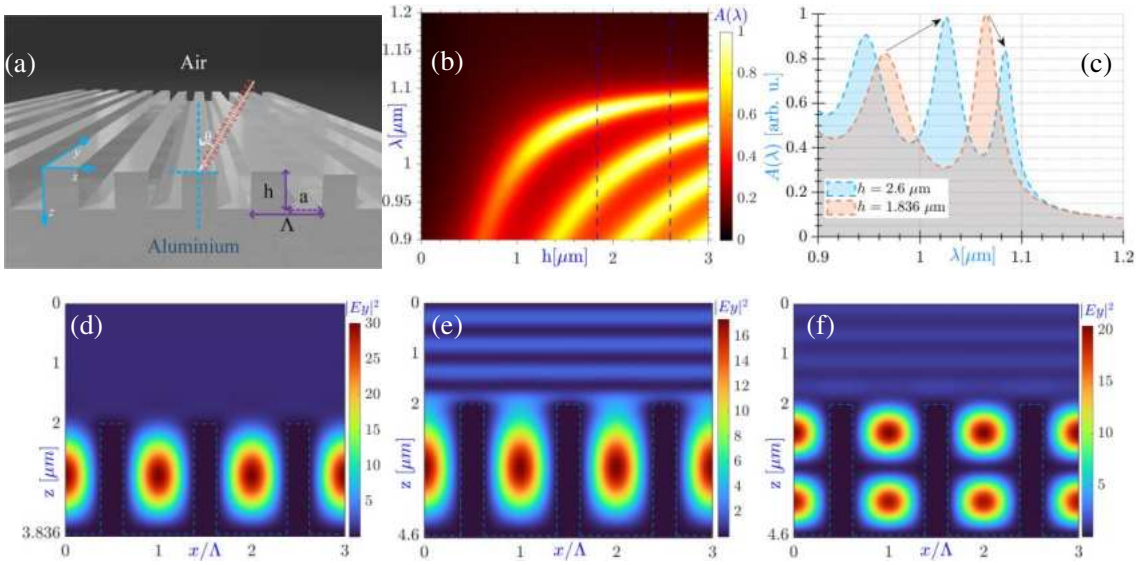


Fig. 1. (a) 3D illustration of the design schematic and reference frame as described in the text; TE polarized $A(\lambda)$ for $\Lambda_o=0.68$ μm, $a_o=0.517$ μm, and (b) a span of h and (c) $h_o=1.836$ μm, $h_1=2.6$ μm marked with a dashed blue line in (b); (d)-(e) TE-polarized $|\mathbf{E}|$ distribution inside and near the design for (d) h_o at λ_0 and (e)-(f) h_1 at λ_{0d}, and λ_{1d}, respectively.

We fabricated a 1 cm^2 sample of another design, optimized for unpolarized incidence, and comprehensively measured its $A(\lambda)$ at near-to-normal Gaussian-beam incidence. The spectral absorption, derived from reflection, was measured using a super continuous laser source and a spectrum analyzer. The single-frequency absorption was measured both optically and thermally using an in-house linearly polarized Yb-doped photonic crystal fiber laser source with ~0.2 nm linewidth at $\lambda_0=1065$ nm. In the thermal experiments, the absorption was numerically derived from the EM-induced heating of the sample, measured using thermocouples. Taking into account a scattered reflection pattern that was carefully investigated, the optical and thermal measurements agreed well with the simulations of the fabricated design, which experimentally showed more than 9.5- and 6-fold absorption enhancement over bulk Al in S- and P-polarization, respectively. The Al prevalence and progress of fiber-based optical sources, around 1.06 μm, promote the proposed designs as promising candidates for many applications.

References

1. Y. Cui, Y. He, Y. Jin, F. Ding, L. Yang, Y. Ye, S. Zhong, Y. Lin, and S. He, "Plasmonic and metamaterial structures as electromagnetic absorbers," Laser & Photonics Rev. 8, 495–520 (2014).
2. R. Avrahamy, B. Milgrom, M. Zohar, and M. Auslender, "Chalcogenide-based, all-dielectric, ultrathin metamaterials with perfect, incidence-angle sensitive, mid-infrared absorption: inverse design, analysis, and applications," Nanoscale 13, 11455–11469 (2021).

Analyzing Absorption Mechanisms of Plasmonic and Dielectric Surface Lattice Resonance Embedded in Absorptive Medium

Joshua T. Y. Tse[1*], Shunsuke Murai[1], and Katsuhisa Tanaka[1]

[1]Department of Material Chemistry, Graduate School of Engineering, Kyoto University, Japan
[*]corresponding author: tse@dipole7.kuic.kyoto-u.ac.jp

Abstract: In this work, we present an analytical model based on the temporal coupled-mode theory that describes different absorption pathways of surface lattice resonance with absorptive nanoparticle array and index-matching layer. Each component of absorption is further analyzed to reveal general guidelines on optimizing nanoparticle arrays for photoluminescence enhancement.

Plasmonic nanoparticles which support localized surface plasmon resonance (LSPR) were known to possess extraordinarily strong light localization and EM field enhancement near the vicinity of the nanoparticles. When the nanoparticles are arranged in a periodic structure, it gives rise to a new type of plasmonic-photonic hybrid mode called surface lattice resonance (SLR). SLR retains the strong light confinement and field enhancement properties of LSPR, while greatly improving the low Q-factor of LSPR. We utilize such properties of SLR and explore the potential of SLR in enhancing the absorption efficiency in photoluminescence processes [1,2].

In our previous work, we have established a modified coupled-mode theory (CMT) that describes the SLR supported on TiO_2 nanoparticle arrays embedded in an absorptive index-matching layer [3]. We generalized the well-established lossless CMT by introducing a non-resonant absorption factor for the index-matching layer to modify the excitation and decay of the SLR. Yet, this modified CMT is incompatible with plasmonic nanoparticle arrays which exhibit intrinsic ohmic absorption. Therefore, we generalize the modified CMT to utilize the strong light-matter interaction enhancement provided by plasmonic nanoparticles. We generalize the modified CMT by separating the absorptive decay rate Γ_{abs} and the non-resonant absorption A_0 into components contributed by the fluorescent dye (*dye*) and the nanoparticle (*NP*) respectively, denoted as $\Gamma_{abs} = \Gamma_{abs,dye} + \Gamma_{abs,NP}$ and $A_0 = A_{0,dye} + A_{0,NP}$. Under this formulation, we can divide the total absorption of the system into the contributions between the fluorescent dye and the nanoparticle, that is $A = A_{dye} + A_{NP}$, where the two components are

$$A_{dye} = A_{0,dye} + (1 - A_0)\frac{2\Gamma_{rad}\Gamma_{abs,dye}}{\Gamma_{tot}^2}\frac{|\langle \kappa^* | s_+ \rangle|^2}{\langle s_+ | s_+ \rangle} \quad (1)$$

$$A_{NP} = A_{0,NP} + (1 - A_0)\frac{2\Gamma_{rad}\Gamma_{abs,NP}}{\Gamma_{tot}^2}\frac{|\langle \kappa^* | s_+ \rangle|^2}{\langle s_+ | s_+ \rangle} \quad (2)$$

at the resonant wavelength of the SLR, where Γ_{tot} is the total decay rate and Γ_{rad} is the radiative decay rate of the SLR, $|s_+\rangle$ is the incident wave and $|\kappa\rangle$ are the in-coupling constants.

The modified CMT is verified by FDTD simulations with nanoparticle arrays with the geometry illustrated in Fig. 1(a), where Al nanocylinders are placed on a transparent substrate (n = 1.46) and are covered by an absorptive index-matching layer (also n = 1.46) of thickness t = 280 nm. The nanoparticles have diameter D = 90 nm, height H = 100 nm and the period P of the square lattice is 380 nm. The extinction coefficient κ of the index-matching layer is modulated to simulate the absorption introduced by absorbers randomly distributed inside the index-

matching layer at various concentrations. The total absorption is calculated by $A = 1 - T - R$, where T is the transmissivity and R is reflectivity of the nanoparticle array. The divergence of the Poynting vector inside the nanoparticle is integrated to obtain A_{NP}, and A_{dye} is calculated by $A_{dye} = A - A_{NP}$. As shown in Fig. 1(b), the modified CMT accurately predicts the total absorption as well as by dye and by nanoparticle using the parameters from spectral fitting.

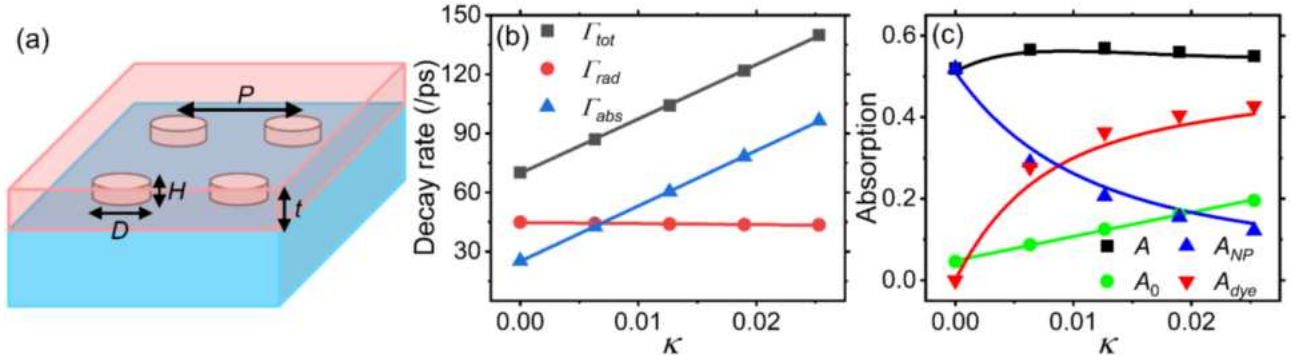


Figure 1. (a) The illustration of the nanoparticle array used in simulations. (b) Γ_{tot}, Γ_{rad} and Γ_{abs} are plotted as a function of κ. (c) The simulated A, A_0, A_{dye} and A_{NP} are plotted as a function of κ. The symbols represent simulated results and the solid lines are the CMT predictions.

We further analyze the origin of Γ_{abs} and A_0 by comparing nanoparticle arrays with different geometrical parameters. We discovered that $A_{0,dye}$ originates from the absorption of the index-matching layer without nanoparticles and $A_{0,NP}$ originates from the absorption cross section of LSPR of the individual nanoparticles. More importantly, we found that $\Gamma_{abs,dye}$ correlates with the nearfield intensity confined within the fluorescent index-matching layer normalized to the total nearfield intensity, while both the material choice and skin depth of the nanoparticle contributes significantly to $\Gamma_{abs,NP}$. These insights provide guidance on optimizing SLR for photoluminescence enhancement applications. In particular, lossless dielectric nanoparticle arrays have a distinct advantage in enhancing efficient energy transfer towards fluorescent dye molecules due to the near-zero $A_{0,NP}$ and $\Gamma_{abs,NP}$. We can also infer from $\Gamma_{abs,dye}$ the spontaneous emission enhancement efficiency, using the Lorentz reciprocity theorem and the relation of $\Gamma_{abs,dye}$ with the nearfield intensity. The significantly larger $\Gamma_{abs,dye}$ on plasmonic nanoparticle arrays would induce a much stronger Purcell effect for directional emission enhancement with SLR, therefore making them a superior choice over purely dielectric nanoparticle arrays.

This work was partly supported by the Nanotechnology Hub, Kyoto University. This work was financially supported by the Grant-in-Aid (Grant Nos. 22H01776 and 21H04619) from MEXT, Japan, the Asahi Glass Foundation and Futaba Foundation.

References

1. Murai, S., Agata, K. and Tanaka, K., "Photoluminescence from an Emitter Layer Sandwiched between the Stack of Metasurfaces," J. Appl. Phys., Vol. 129, No. 18, 183101, 2021.
2. Pirruccio, G., Ramezani, M., Rodriguez, S. R.-K. and Rivas, J. G., "Coherent Control of the Optical Absorption in a Plasmonic Lattice Coupled to a Luminescent Layer," Phys. Rev. Lett., Vol. 116, No. 10, 103002, 2016.
3. Tse, J. T. Y., Murai, S., and Tanaka, K., "Resonant Critical Coupling of Surface Lattice Resonances with a Fluorescent Absorptive Thin Film," J. Phys. Chem. C, Vol. 127, No. 45, 22212–22221, 2023.

Spin angular momentum of enhanced electric fields around a plasmonic nanostructures excited by circularly polarized light.

N. Ichiji[1*], T. Ishida[1], I. Morichika[1], T. Tatsuma[1], and S. Ashihara[1]

[1]Institute of Industrial Science, The University of Tokyo, Japan
[*]ichiji@iis.u-tokyo.ac.jp

Abstract: We evaluated the spin angular momentum (SAM) in the electromagnetic field around plasmonic nanostructures excited by circularly polarized light. We revealed that the enhanced electromagnetic field can possess unidirectional SAM and their direction can be reversed depending on the resonance mode.

Circular dichroism (CD) spectroscopy, a technique that detects differences in the absorption coefficients of left- and right-handed circularly polarized (CP) light, is a powerful tool in materials science for structural analysis. A major challenge in CD spectroscopy is the inherent weakness of the CD signal resulting from chirality. Therefore, improving the detection accuracy of these signals is an important and ongoing challenge [1].

In chemical reactions with low signal-to-noise ratios of the observables, localized surface plasmon (LSP) is often used to enhance the electromagnetic field intensity. In particular, lattice resonance with periodically arranged nanoscale metal structures can increase the electric field intensity in the vicinity of the structure by several orders of magnitude and is widely used for signal enhancement in absorption measurements [2]. However, plasmonic structures, such as nanorods, do not always maintain circular polarization in the enhanced electromagnetic field. Therefore, it is not appropriate to directly apply plasmonic structures optimized for electric field enhancement to observation techniques that require the circular polarization of light, such as CD spectroscopy. In this study, we have analyzed the enhanced electromagnetic field of plasmonic structures excited by CP light using finite-difference time-domain (FDTD) simulations (Ansys Lumerical).

Figure 1 (a) shows a schematic of the FDTD simulation model used in this study. A plasmonic structure made of Au with a thickness of 50 nm was placed in a vacuum and circularly polarized light is normally injected from a plane wave source. Circular disk and square structures were targeted, and both antenna-type and aperture-type structures were evaluated. From the electromagnetic field, a physical quantity corresponding to circular polarization, the spin angular momentum (SAM), $\boldsymbol{S}$, is calculated using $\boldsymbol{S} = (1/4\omega)\mathrm{Im}(\epsilon \boldsymbol{E}^* \times \boldsymbol{E} + \mu \boldsymbol{H} \times \boldsymbol{H})$ [3]. Here, $\boldsymbol{E}$, $\boldsymbol{H}$, ϵ, μ, and ω are electric field, magnetic field, permittivity, permeability, and angular frequency, respectively. The asterisks signify their complex conjugates. Figure 1 (b,c) show the S_z components at $\lambda = 1200$ nm in a circular disc/aperture structure with a radius of $r = 250$ nm. Each value is normalized by the S_z of the incident CP light, calculated with the model without the plasmonic structure.

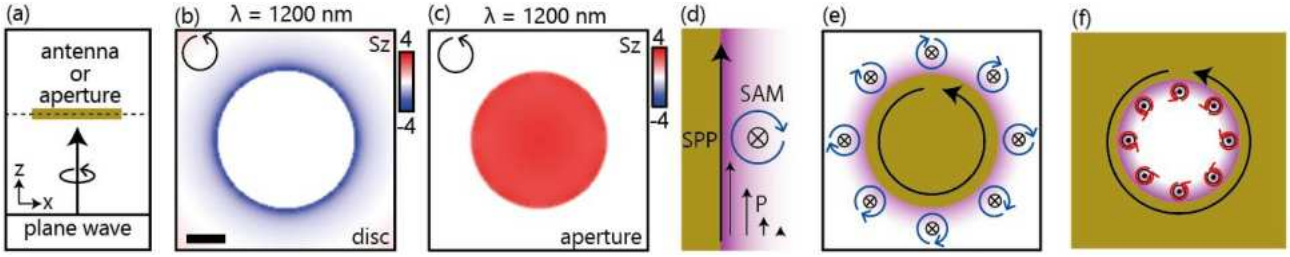


Figure 1 (a) Schematic of the FDTD simulation model. (b,c) Spatial distributions of Sz components near the plasmonic structures, normalized by the Sz components of the incident light. (d) Schematic of the SAM of the SPP on the (d) planer metal surface, (e) nano disc excited by CP light, and (f) nano aperture excited by CP light.

The sign reversal of the S_z outside the nanoantenna and inside the aperture can be explained as follows. The SAM of an electromagnetic field is proportional to the rotation of the Poynting vector, expressed as $\boldsymbol{P} = (1/2\omega^2)\nabla \times \boldsymbol{S}$ [3]. Surface waves, such as surface plasmon polaritons (SPPs), which decay exponentially from the interface, have a SAM oriented perpendicular to their propagation direction, as shown in Fig. 1 (d) [3]. In a circular structure excited by CP light, a plasmon mode is formed in which the direction of rotation is defined by the handedness of the CP light. Therefore, for nanodiscs where the evanescent field decays outwards and for apertures where the evanescent field decays inwards, the direction of the associated SAM is opposite, as schematically illustrated in Fig. 1 (e,f).

We then calculated the S_z for the square nano apertures. At a long wavelength ($\lambda = 1600$ nm), the associated S_z is positive, similar to that of the circular aperture. From the H_z distribution obtained at the same observation plane (top panel of Fig. 2 (b)), we can confirm that the dipole mode is excited at the aperture. Additionally, by calculating the Poynting vector, which represents the energy flow of the electromagnetic wave, we can confirm that the energy flow of the plasmon mode at the inner wall surface is in the same direction as the handedness of the incident CP light, i.e., counterclockwise (bottom panel of Fig. 2 (b)). The path of the charge movement for one oscillation period of the dipole mode is schematically illustrated in Fig. 2 (c).

On the other hand, in the short wavelength region ($\lambda = 750$ nm), the sign reversal of S_z near the inner wall surface is observed (Fig. 2. (d)). This non-intuitive sign reversal is because the one higher-order bright mode excited in the square structure by CP light is a negative hexapole mode [4]. The H_z distribution and Poynting vector plotted in Fig. 2 (e) corroborate that the excited mode is the hexapole mode, and the direction of energy flow is clockwise, opposite to the handedness of the incident CP light. The charge movement in the negative hexapole mode is schematically shown in Fig. 2 (f).

From these calculations, we have concluded that exciting the plasmonic structure with CP light produces a near-field with SAM in the vicinity of the plasmonic structure. Furthermore, our results reveal that the direction of the SAM can be controlled by selecting either a nano-antenna or an aperture, and by choosing which mode to excite, through appropriate design of the plasmonic structure.

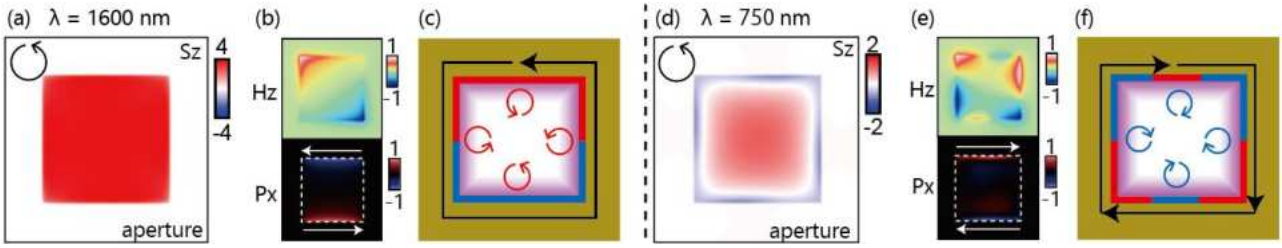


Figure 2 (a) Spatial distributions of S_z components near the square aperture normalized by the S_z components of the incident light. (b) H_z component. (c) P_x component. (d) Schematic of the charge movement during one oscillation period. (e-h) Same as (a-d), but for $\lambda = 750$ nm.

References

1. Mohammadi, M. "Nanophotonic platforms for enhanced chiral sensing" ACS Photonics, Vol. 5, 2669-2675, 2018.
2. Kravets, V. G. et al., "Plasmonic surface lattice resonance: A review of properties and applications", Chem. Rev., Vol. 118, No. 12, 2018
3. Shi, P. et al., Transverse spin dynamics in structured electromagnetic guided waves, Proc. Natl. Acad. Sci. USA Vol. 118, e2018816118 (2021).
4. Yoonkyung, E. L. et al., "Optical torque from enhanced scattering by multipolar plasmonic resonance", Nanophotonics, Vol. 3, No. 6, 343-350, 2014

On the quantization of non-Hermitian nanophotonic systems

L. Hands[1], **A. Demetriadou**[1] **and B. Yuen**[1*]

[1]Metamaterials and Nanophotonics Group, School of Physics and Astronomy, University of Birmingham, United Kingdom
[*]Corresponding author: b.yuen@bham.ac.uk

Abstract:. *We present a new method that gives an exact and complete description for the quantum emitters coupled to non-Hermitian photonic devices, via the pseudomode transformation. Using this method, we obtain the non-Markovian quantum dynamics for a quantum emitters coupled with a silicon spherical particle.*

In recent years, quantum emitters have been coupled to increasingly more complex photonic systems, such as photonic crystals, for optical switching and photon generation, and nanoplasmonic devices for molecular sensing. These systems are usually non-Hermitian due to radiative and material losses, presenting a significant challenge for their quantized description, with issues arising for decomposing and normalizing the photonic modes, mode divergence, creating canonical field operators and mode mixing [1, 2].

Here, we present an exact and complete method that gives a quantized description of open, non-Hermitian photonic systems, that efficiently radiate energy to the far-field [3]. The complete electromagnetic field with its continuous spectrum is first quantized by a suitable mode expansion. The quantized continuum is then transformed into a discrete set of pseudomodes [4] which give a non-Hermitian description of the system, and correspond one-to-one with the classical photonic solutions. The discreet pseudomodes, $\boldsymbol{v}_{\xi n}(\boldsymbol{r})$, are obtained from the continuum modes $\boldsymbol{u}_{\boldsymbol{\xi}}(k, \boldsymbol{r})$ (which are solutions to the Helmholtz Equations), via the transformation:

$$\int_0^\infty k dk\, \rho(k) \boldsymbol{u}_\xi(\boldsymbol{k}, \boldsymbol{r}) \boldsymbol{u}_\xi(\boldsymbol{k}, \boldsymbol{r}') e^{-ick\tau} = \sum_n z_{\xi n} \boldsymbol{v}_{\xi n}(\boldsymbol{r}) \boldsymbol{v}_{\xi n}(\boldsymbol{r}') \Theta(\tau - \Delta_t(\boldsymbol{r}, \boldsymbol{r}')) e^{-icz_{\xi n}\tau}$$

where $z_{\xi n}$ are the poles of the radial equation $\rho(k)$ and (ξ, n) their corresponding quantum number, and Θ is a step-wise function [3]. This transformation arises naturally from the fundamental quantum equations of motion. We then employ this method for an example of a quantum emitter (QE) coupled to a spherical silicon particle of radius $1\mu m$. Classically, the spherical particle can be described in a continuum frequency space using vector

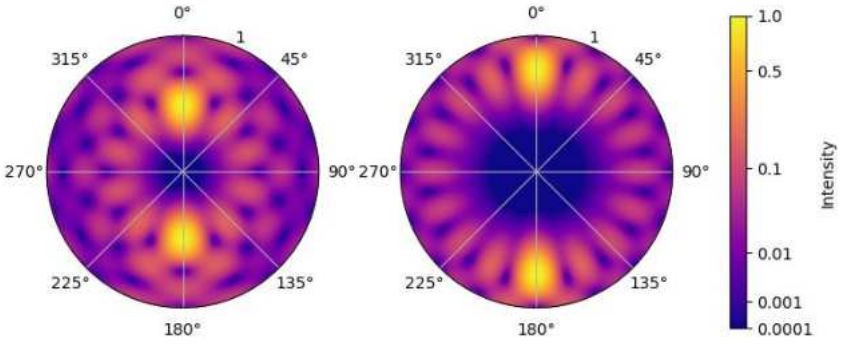


Figure 1: The intensity distribution of the Pseudomodes of the two most dominant modes of a silicon sphere of r=1um at 1550μm: left is the (l = 5,n = 4) mode and right the (l = 8, n = 3) mode.

spherical harmonics, which are readily quantized. From this we show that there is a one-to-one correspondence between the Mie modes and our derived pseudomodes, with identical angular components but a differing radial component. In Figure 1 we plot two such pseudomodes that are almost degenerate for this system: (l = 8, n = 3) and (l = 5, n = 4) (where l and n are the angular and radial mode indices).

Significantly, the pseudomode transformation method does not require the Markovian approximation, and thus allows us to also obtain non-Markovian dynamics for radiative non-Hermitian system. We do so using more than 1000 pseudomodes and demonstrate the results (in Figure 2) for dipole moments of $d = 100$ and $10000\,D$. We note that the (8,3) mode strongly couples to the quantum emitter displaying clear Rabi oscillations. However,

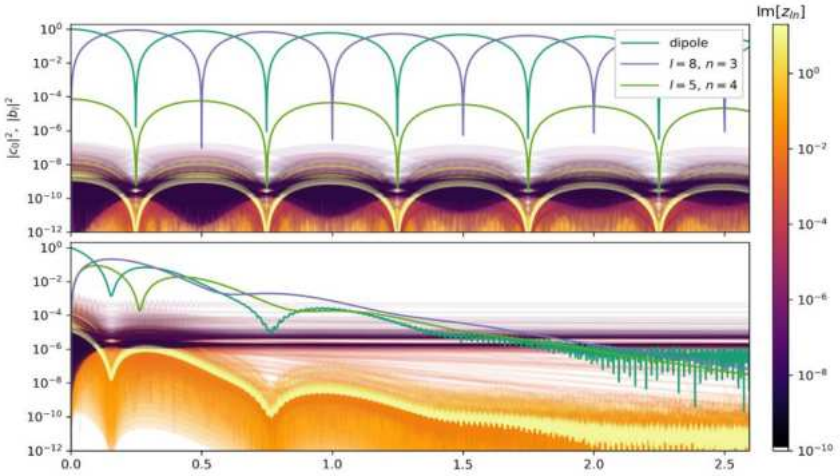


Figure 2: The Quantum Dynamics of a quantum emitter coupled to a dielectric silicon sphere. The dominant modes are (8,3) and (5,4) and dipole moments of 100 D (top) and 10000 D (bottom) were chosen for the quantum emitter. Note that the strongly coupled (8,3) mode is out phase with the dipole forming rabi oscillations, but the radiating (5,4) mode remains in phase. Also note the Markovian nature of the weakly coupled modes in the shaded purple regions which retain knowledge of their initial states.

the more radiative (5,4) mode is comparatively less strongly coupled but is in phase with the quantum emitter. The remaining modes, (demonstrated through the shaded regions on the plot) cause a lamb shift (δw_0) on the quantum emitter and an additional decay rate given by $-Re(\delta\omega 0)$. Therefore, our method reveals that non-Markovian dynamics arise for all weakly radiating modes, regardless of coupling strength and frequency. This is explicitly clear in the $d = 10000D$ case as the purple shaded pseudomodes do not oscillate in phase with the quantum emitter and continue to exchange energy with the mode even at times far from the initial decay of the emitter.

In conclusion, we present a method for the exact and complete second quantization of non-Hermitian photonic systems, through the pseudomode transformation. We use the method to demonstrate non-Markovian dynamics for a QE coupled to a spherical Silicon sphere, which are often ignored.

References

1. Richter,M., et al., "Quantization of Quasinormal Modes for Open Cavities and Plasmonic Cavity Quantum Electrodynamics," Phys. Rev. Lett. 122, 213901, 2019
2. Medina A., García-Vidal F. J., Fernández-Domínguez, A. I., and Feist J., "Few-Mode Field Quantization of Arbitrary Electromagnetic Spectral Densities" Phys. Rev. Lett. 126, 093601, 2021.
3. Yuen B., And Demetriadou A., "Exact and Complete quantization of open nanophotonic devices," arXiv.
4. Garraway, B. M, "Decay of an atom coupled strongly to a reservoir," Phys. Rev. A 55, 4636, 1997.

Lattice resonances in multipartite periodic arrays with electric and magnetic response

J. R. Deop-Ruano[1*], J. J. Alvarez-Serrano[1], L. Cerdán[2], V. Aglieri[3], A. Toma[3], and A. Manjavacas[1*]

[1]Instituto de Óptica "Daza de Valdés" (IO-CSIC), Spain
[2]Instituto de Química Física "Blas Cabrera" (IQF-CSIC), Spain
[3]Istituto Italiano di Tecnologia, Italy
[*]corresponding author: juan.deop@csic.es
[*]corresponding author: a.manjavacas@csic.es

Abstract: Arrays with multipartite unit cells can be engineered to support lattice resonances with exceptional properties. Here, we show the excitation of out-of-plane lattice resonances at normal incidence in a bipartite array of metallic nanostructures. Furthermore, we analyze a metallo-dielectric array exhibiting a lattice resonance with perfect absorption.

Periodic arrays of nanostructures can present **collective modes commonly known as lattice resonances**. These modes emerge from the coherent interaction between the constituents of the array, resulting in strong responses with narrow spectral profiles. Motivated by their unique properties, periodic arrays are being exploited in a wide range of applications, including nanoscale light-emitting devices, ultrasensitive biosensors, and light-to-heat transducers [1].

The properties of lattice resonances are strongly dependent on the geometry of the unit cell. In particular, **multipartite arrays** with more than one particle per unit cell result in the **hybridization of lattice resonances** [2], which give rise to exceptional properties such as super- and subradiant behaviors [3]. Most of past theoretical works on lattice resonances in multipartite arrays have focused in the interaction between the electric dipoles, thus neglecting the magnetic response of the system. However, arrays with complex unit cells supporting both an electric and a magnetic response present a rich behavior that is yet to be explored.

Here, we extend the hybridization model to **account for the magnetic response** of the array and study two different arrays with complex unit cells in which the magnetic response plays a crucial role. First, we explore the **excitation of out-of-plane lattice resonances at normal incidence** in periodic arrays of metallic nanostructures [4]. These modes are characterized by a dominant component of the dipole perpendicular to the plane of the array. Due to the transversality condition of the electromagnetic field, it was assumed that out-of-plane modes can only be accessed at oblique incidence. Nevertheless, we show that, by exploiting the **interaction between the electric and magnetic dipoles** of the array, it is possible to excite an out-of-plane lattice resonance at normal incidence with an extremely high quality factor (see Figure 1).

Furthermore, we also study the emergence of lattice resonances with perfect absorption in metallo-dielectric arrays [5]. It is well-known that two dimensional arrays of electric dipoles can only absorb up to half of the incident light. This poses a strong limitation on their usage for certain fields such as thermoplasmonics. Here, **by spectrally overlapping two electric and magnetic lattice resonances, we achieve a lattice resonance with perfect absorption (>0.99)**. Unlike other approaches to achieve perfect absorption, our method achieves an

extremely narrow resonance with a high dependence on the incident polarization, which can be employed as a polarization selective filter, among other applications. This work sheds light on the excitation of lattice resonances in arrays with complex unit cells presenting both an electric and a magnetic response.

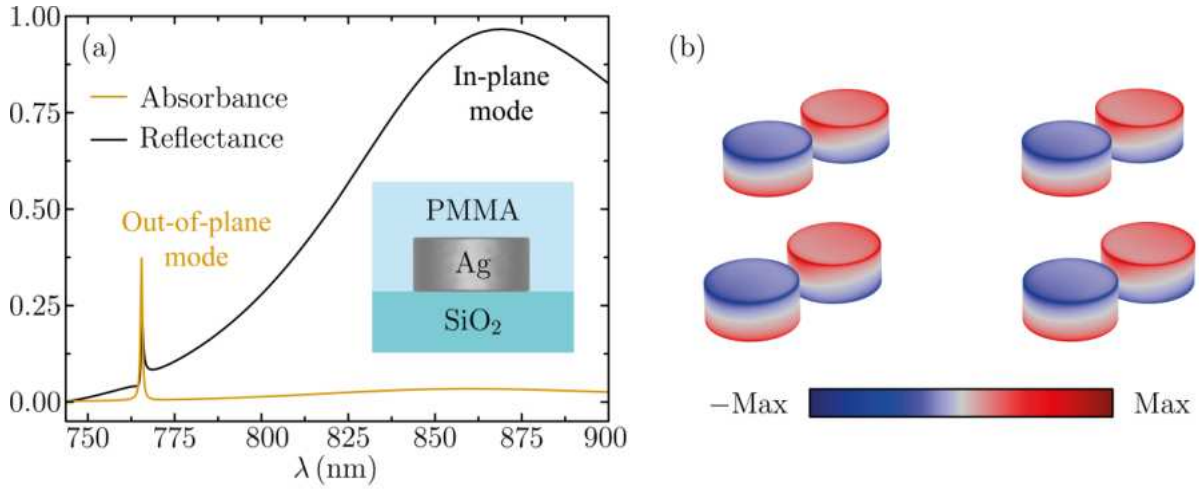


Figure 1. Optical response of a bipartite array of silver nanodisks sitting on silica and coated with PMMA for illumination at normal incidence. (a) Reflectance and absorbance spectra. (b) Induced charge density of the out-of-plane lattice resonance

References

1. Kravets, V. G.; Kabashin, A. V.; Barnes, W. L.; and Grigorenko, A. N., "Plasmonic Surface Lattice Resonances: A Review of Properties and Applications", Chem. Rev., Vol. 118, No. 12, 5912−5951, 2018.
2. Baur, S.; Sanders, S.; and Manjavacas, A., "Hybridization of Lattice Resonances", ACS Nano 2018, Vol. 12, No. 2, 1618, 2018.
3. Cuartero-González, A.; Sanders, S.; Zundel, L., Fernández-Domínguez, A. I.; and A. Manjavacas, "Super- and Subradiant Lattice Resonances in Bipartite Nanoparticle Arrays", ACS Nano, Vol. 14, No. 9, 11876−11887, 2020.
4. Alvarez-Serrano, J. J.; Deop-Ruano, J. R.; Aglieri, V.; Toma, A.; and Manjavacas, A., "Normal Incidence Excitation of Out-of-Plane Lattice Resonances in Bipartite Arrays of Metallic Nanostructures," ACS Photonics, Vol. 11, No. 1, 301−309, 2024.
5. Cerdán, L.; Deop-Ruano, J. R.; Alvarez-Serrano, J. J.; and Manjavacas, A., "Perfect Absorption with Independent Electric and Magnetic Lattice Resonances in Metallo-Dielectric Arrays," Adv. Optical Mater., 2302737, 2024.

Plasmonic anisotropy of metallic nanoparticles induced by uniaxially-stretched graphene substrates

C. Yamano[1], S. Ozeki[1], R. Kato[1, 2], T. Tanaka[1, 2], and T. Yano[1, 2*]

[1]Institute of Post-LED Photonics, Tokushima University, Tokushima, Japan
[2]RIKEN, Saitama, Japan
[*]corresponding author: yano.takaaki@tokushima-u.ac.jp

Abstract: Precise control of localized surface plasmon resonance (LSPR) wavelengths has been highly demanded for the practical use of metallic nanostructures in various nanophotonic devices. In this study, we demonstrated anisotropic control of the LSPR wavelengths of gold nanoparticles on a graphene substrate, achieved by uniaxially stretching the graphene.

In this study, we demonstrated active control of localized surface plasmon resonances (LSPR) of gold nanoparticles on stretched graphene by inducing a change in the dielectric constant (refractive index) of graphene through the application of uniaxial stress to graphene. As shown in Figure 1(a), gold nanoparticles (100 nm in diameter) were monodispersed and adsorbed on graphene placed on a stretchable polymer (PET: Polyethyleneterephthalate) film. Figures 1(b) show dark-field optical images of gold nanoparticles before and after uniaxial stretching of the graphene substrate, respectively. The gold nanoparticles moved in the stretching direction, and the scattering color changed from orange to green. The dark-field scattering spectra of the nanoparticles show that the LSPR wavelength blue-shifts from 585 nm to 550 nm before and after stretching (Fig. 1c). This is attributed to the uniaxial stress on the graphene underlying the gold nanoparticles, which changed the dielectric constant of the graphene. Furthermore, the LSPR wavelength of the gold nanoparticles on the stretched graphene was found to be dependent on the incident polarization direction. This is attributed to the anisotropy of the dielectric constant in the graphene plane between the stretching direction and its perpendicular direction.

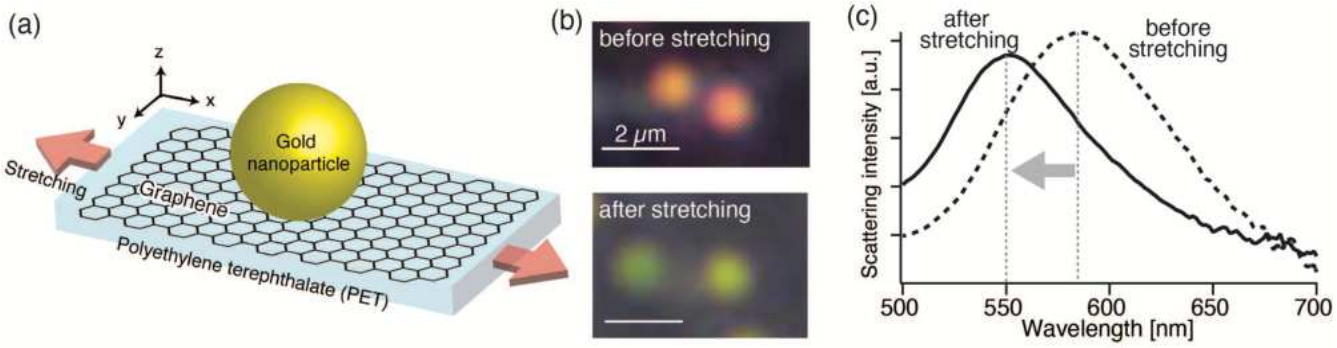


Figure 1 (a) Schematic of gold nanoparticles adsorbed on a stretched graphene substrate. Uniaxial stretching of graphene changes the dielectric constant in the graphene plane and modulates the plasmon resonance properties of the gold nanoparticles. (b) Dark-field optical images of the gold nanoparticles before and after stretching. (c) Dark-field scattering spectra of the gold nanoparticles before and after stretching.

High-Q and Small Size Cavity with Mie Scattering Mirror

Bokyung Kim [1], Seokhyeon Hong [1], Youngsoo Kim [1], Seung Hyeon Hong [1], Juhan Lee [1] and Soon-Hong Kwon [1*]

[1] Chung-Ang University, Korea
[*] shkwon@cau.ac.kr

Abstract: We propose a new Mie scattering based two-dimensional resonator. Using strong backscattering based on Kerker condition, resonators have a physical size on the order of a wavelength and can achieve quality factor(Q) values up to 120,000.

Photon localization technology is actively researched in the development of optical waveguides, metasurface s, resonators, and light sources, and is related to future industries such as 3D imaging, VR and AR, and holograp hic displays. Notably, resonators, which are structures capable of trapping photons at or below the wavelength of light, are core in light localization research. Photonic crystal resonators, microdisk resonators, surface plasmon resonators, and BIC(bounded states in the continuum) resonators are studied for light localization, and each physical principle captures light based on photonic-bandgap, total reflection, surface plasmon, and BIC. The surface plasmon resonators have the advantage of small physical size, but inevitably suffer from metallic absorption loss. Photonic crystal, microdisk, and BIC resonators have the advantages of small mode sizes and high order Q-factors, but the considerably large physical size are required to build up large enough photonic bandgap, TIR, or quasi-infinitely periodic structure. The large physical size would be the critical limitation to develop highly integrated photonic circuits.

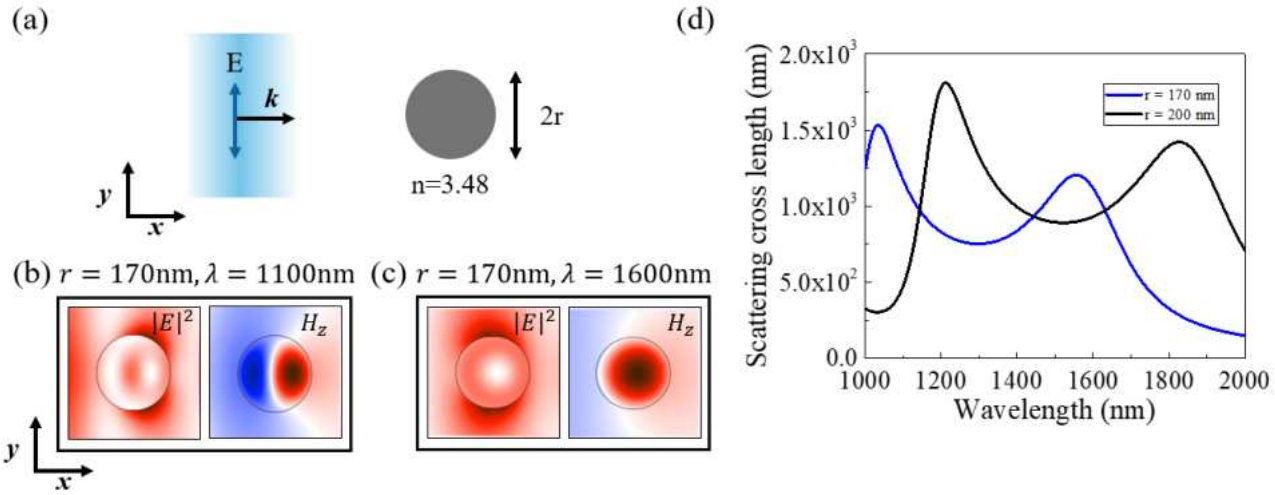


Figure 1 (a) Linearly polarized light is scattered by an infinitely long cylinder. **(b-c)** Mode profiles of an electric dipole (ED) and magnetic dipole (MD) modes. **(d)** Scattering crossing lengths of the infinitely long cylinders for different radii.

We propose a high-Q resonator with a wavelength-sized cavity based on Mie scattering. Mie scattering is a type of interaction between light and matter, occurring when the size of matter is comparable to the wavelength of light. It is analyzed through multipole analysis, and strong resonances occur in structures where electromagnetic dipoles are formed[1]. By examining the scattering pattern, we can identify points corresponding to the Kerker condition, where the electric and magnetic dipoles overlap, leading to strong backscattering due to the interference of two dipoles[2].

Using Mie scattering based conditions, we design a two-dimensional resonator consisting of a center cylinder and surrounding larger cylinders, as shown in Figure 2. The center cylinder has a radius of 170 nm and exhibits the magnetic dipole at a wavelength of 1580 nm. And the surrounding cylinders with a radius of 200 nm has the optical property of strong backscattering at 1580 nm due to the overlap of ED and MD modes. As results, the lights of the magnetic dipole mode excited at the center cylinder can be confined by the strong backscattering from the surrounding larger cylinders. The number of the surrounding cylinders was varied from 4 to 10 while the distance from the center is kept to be equal. The center of each structure was fixed, and the distance from the center to the outer structure was also investigated to determine the wavelength of light trapped inside and the Q-factor. When the number of outer cylinders was 8, lights with a wavelength of 1580 nm was trapped, showing a high Q-factor of 120,000.

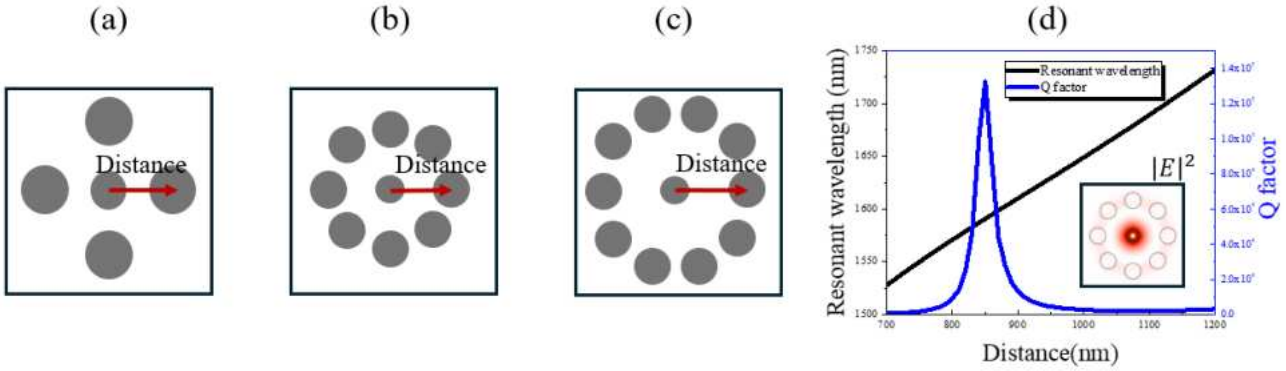


Figure 2 (a-c) Mie scattering resonators when the number of the outlying cylinders are 4, 8, and 10, respectively. **(d)**Q factor and resonant wavelengths as functions of the distance between the cavity center and the surround cylinders when the number of surrounding cylinders is 8.

To verify the feasibility of the design, the resonant wavelength and the Q-factor were calculated as the radius of the center cylinder changes. The strong drop in Q factor values as the radius of the center changes indicates that the formation of a magnetic dipole in the center is critical to performance.

Due to its compact physical size and straightforward dielectric-based design, it finds applications in nanolasers, optical switching devices, optical sensors, and optical waveguides. Particularly, it enables the realization of high-density photonic integrated circuits with remarkably low power consumption. The advancement of these photon-based devices is intricately linked to ultra-low power, small size, and ultra-fine photonic device technology, positioning them as pivotal technologies for the information society.

References

1. Arseniy I. Kuznetsov et al., “Optically resonant dielectric nanostructure”, Science, Vol 354, No. 6314, aag2472, 2016.
2. Fu, Y., Kuznetsov, A., Miroshnichenko, A. et al., “Directional visible light scattering by silicon nanoparticles”, Nature Communications, Vol 4, No.1527, 2013.

Mie-assisted photonic memories based on the phase change of silicon nanoparticles

Jhih-Jia Chen[1], Te-Hsin Yen[1], Kentaro Nishida[1], Junichi Takahara[2], Mihail Petrov[3], and Shi-Wei Chu[1,4,5]*

[1]Department of Physics, National Taiwan University, 1, Sec 4, Roosevelt Rd., Taipei 10617, Taiwan
[2]Graduate School of Engineering, Osaka University, 2-1 Yamadaoka, Suita, Osaka, 565-0871, Japan
[3]School of Physics and Engineering, ITMO University, St. Petersburg 197101, Russia
[4]Molecular Imaging Center, National Taiwan University, 1, Sec 4, Roosevelt Rd., Taipei 10617, Taiwan
[5]Brain Research Center, National Tsing Hua University, 101, Sec 2, Guangfu Road, Hsinchu 30013, Taiwan
*Corresponding author: swchu@phys.ntu.edu.tw, r12222001@ntu.edu.tw

Abstract:
Photonic memories based on phase change materials have recently attracted much attention, but mostly require rare materials. Here, we demonstrate that silicon nanostructures exhibit laser-induced phase change, through a confocal micro-spectroscopy setup, leading to clearly bistable states with 80% scattering modulation The results are promising for silicon-based all-photonic memories.

1. Introduction:

Current computing technology based on the von Neumann architecture faces its physical limitation, known as the von Neumann bottleneck. The performance of computers is nowadays restricted by the speed of the information transfer between the central processing unit (CPU) and memories instead of the CPU computational capacity. Besides, as electrons move faster along circuits, a larger amount of energy is dissipated in the form of heat[1]. To further increase the speed of the information transfer and avoid energy loss, all-photonic computing is one of the best options due to its high speed[2], low energy loss[3,4,5], and wavelength-division multiplexing[5,6].

For all-photonic computing, photonic memories are one of the most critical elements. To achieve binary/multi-level memories, phase-change materials (PCMs) are usually considered because of the distinct difference in the refractive index between the two phases and their non-volatile nature. Among the PCMs, germanium-antimony-tellurium (GeSbTe or GST) is commonly used owing to its high repeatability[6] and large contrast[7] between amorphous and crystalline states. However, the scarcity of the material escalates the fabrication costs. Besides, most GST-based photonic memories require additional resonator design[6,7,8,9], which increases complexity and costs in the fabrication process. Maintaining a consistent composition of GST throughout the entire domain also proved challenging.

Here, we demonstrate that silicon-based nanostructures have the potential to achieve photonic memories based on laser-induced phase change. The nanoparticles can be reversibly amorphized and crystallized by sub-nanosecond laser irradiation. The advantages of using silicon include its abundance on Earth, mature nano-fabrication with mass production, as well as nanoscale Mie resonance that strongly confines the electromagnetic field, thus mitigating the need for additional resonators.

2. Photonic memories based on silicon nanoparticles

The experimental setup is based on a confocal laser scanning microscope, as shown in Figure 1(a). We used a pulsed laser with 0.1ns pulse width to induce the phase change of crystalline silicon nanoblocks (SiNBs). The corresponding scattering intensity variation was detected by a photomultiplier tube (PMT). In the same setup, an LED white light and

a spectrometer are employed to measure the back-scattering spectrum of the SiNB before and after phase change.

Figure 1(b) is an experimentally acquired scattering intensities from an isolated SiNB, whose size is 210x210 nm^2, with a height of 150 nm. When the input intensity increases from zero (solid line), the scattering intensity initially increases linearly. Intriguingly, at ~0.1mW/μm^2 excitation, a sudden drop of scattering appears, with 80% intensity modulation. This represents the transition from "ON" to "OFF" state. On the other hand, by decreasing input intensity from the "OFF" state (dashed line), the scattering intensity keeps reducing until ~0.04mW/μm^2, where an 80% sudden increase is observed. The steep variation between the "ON" and "OFF" states clearly forms a hysteresis curve, manifesting the potential for photonic memories.

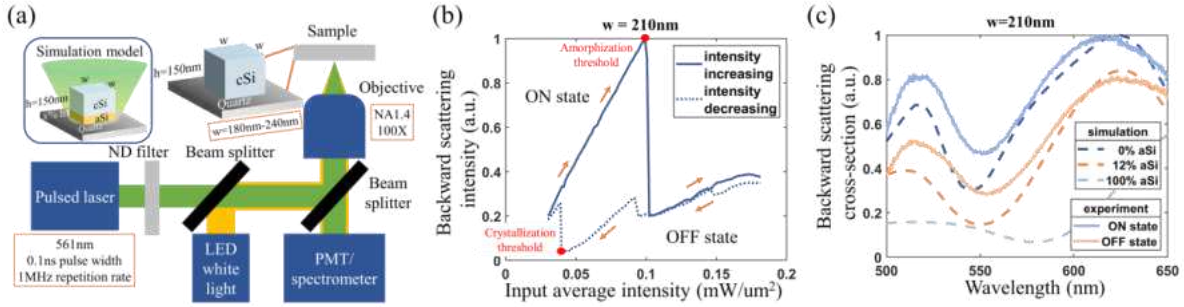


Figure 1. (a) Experimental setup for scattering detection from a SiNB. The width of SiNBs ranges from 180nm to 240nm, and the height is 150nm. The simulation model with different amounts of amorphous silicon is shown in the inset; x is from 0 (fully crystalline) to 100 (fully amorphous). (Abbreviation: cSi: crystalline silicon, aSi: amorphous silicon). (b) Experimentally measured relationships between input and scattering intensities from a SiNB of 210nm width. The solid and dashed lines are obtained by increasing and decreasing the input intensity. (c) Comparison of the experimental (solid lines) and simulated (dashed lines) spectrum.

To investigate the mechanism behind the unexpected scattering state transition, we measure the spectrum at "ON" and "OFF" states respectively, as shown in the solid lines of Fig. 1(c). Two Mie resonant peaks are found, at 520 nm and 620 nm respectively. Comparing the "OFF" spectra over the "ON" one, the 520-nm peak exhibits a blue shift, while the 620-nm peak shows a red shift. We assume the underlying mechanism is due to the phase change of silicon via pulse excitation[10], so we built a model to simulate partial amorphization on a SiNB, as shown in the inset of Fig. 1(a), where a thin layer becomes amorphous (x% aSi thickness) and the rest remains crystalline. The dashed lines in Fig. 1(c) present the simulation results. When there is no amorphous silicon (0% aSi), the blue dashed curve has two peaks that agree well with the "ON" state experimental results. Notably, when we increase the percentage of layered aSi in simulation, the spectrum displays similar blue and red shifts for the two peaks, and the best fit versus the "OFF" state measurement is found at 12% amorphous layer thickness. That is, the crystalline SiNB is partially amorphized at ~0.1mW/μm^2 (amorphization threshold) when input intensity is increasing at the "ON" state; on the other hand, it is "re-crystallized" at ~0.04mW/μm^2 when input intensity is decreasing at the "OFF" state. The controllable and reversible phase change of silicon nanostructures, as well as the clear bistable transition, lay a solid foundation for future photonic memory applications.

References

1. Waldrop, M. M., "The chips are down for Moore's law", Nature, 530, 4, 2016.
2. Rickman, A., "The commercialization of silicon photonics", Nature Photon 8, 579–582, 2014.
3. Caulfield, H. J. and S. Dolev, "Why future supercomputing requires optics", Nature Photonics 4(5): 261-263, 2010.
4. Thomson, D., et al., "Roadmap on silicon photonics", Journal of Optics, 18(7), 073003, 2016.
5. Biberman, A., & Bergman, K., "Optical interconnection networks for high-performance computing systems", Reports on Progress in Physics, 75(4), 046402, 2012.
6. Ríos, C., et al., "Integrated all-photonic non-volatile multi-level memory", Nature photonics, 9(11), 725-732, 2015.
7. Rios, C., et al., "On-chip photonic memory elements employing phase-change materials", 2013.
8. Cheng, Z., et al, "Device-level photonic memories and logic applications using phase-change materials", Advanced Materials, 30(32), 1802435, 2018.
9. Feldmann, J., et al, "Calculating with light using a chip-scale all-optical abacus", Nature communications, 8(1), 1256, 2017.
10. Wang, L., et al, "Fast reversible phase change silicon for visible active photonics", Advanced Functional Materials, 30(17), 1910784, 2020.

Hybrid full-space metalens for ultraviolet light

B. Idesová[1,2*], F. Ligmajer[1,2], O. Červinka[1,2] and T. Šikola[1,2]

[1]Central European Institute of Technology, Brno University of Technology, Czech Republic
[2]Faculty of Mechanical Engineering, Brno University of Technology, Czech Republic
[*]corresponding author: beata.idesova@ceitec.vutbr.cz

Abstract: Conventional optical elements used nowadays are bulky and heavy, while metasurfaces offer a promising solution allowing for miniaturization and multifunctionality. In this work, we use hybrid nanostructures made of hafnium dioxide and aluminium to fabricate a metalens operating both in reflection and transmission simultaneously for a wavelength of 325 nm.

Great attention has been drawn to the manipulation of ultraviolet (UV) light because of its application in the telecommunication and consumer electronics industry, where extreme-UV lithography is a primary workhorse. However, absorption and tight precision constraints set limits on the fabrication of optical components, such as lenses, suitable for this part of the spectra. Nanophotonics offers a solution in the form of metasurfaces which can manipulate the amplitude, phase and polarization of the incident light by engineering its building blocks [1]. Moreover, metasurfaces are lightweight, compact and multifunctional [2], following the nowadays popular trend of miniaturization in not only the electronics industry.

With optical applications in mind, where low absorption is a key requirement, dielectric metasurfaces are mainly used because of their significantly lower losses compared to metallic metasurfaces based on plasmonic resonances [3]. In literature, UV metasurfaces are mostly explored or proposed on material platforms composed of oxides (HfO_2, Nb_2O_5, Ta_2O_5, ZnO) and nitrides (AlN, Si_3N_4) [4]. These materials are not mouldable like, e.g., the traditional fused silica, but they still offer large bandgaps which prevent UV light absorption. All of these materials were so far used for metasurfaces operating in transmission, meaning they were able to manipulate the transmitted light only. Recently, Jiang et al. [5] theoretically explored and proposed a metasurface which could project two distinct holograms simultaneously yet independently, both in reflection and transmission, a so-called full-space metahologram. Their main thought was to use two materials – Nb_2O_5 and MgF_2. MgF_2 is usually used for antireflective coatings in the optical industry. However, nanostructuring such a material presents a great challenge since it

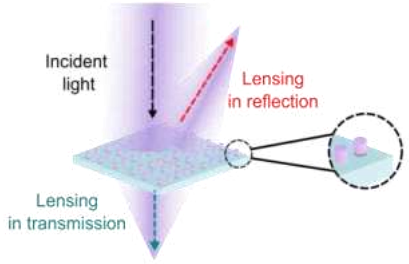


Figure 1: Schematics of a full-space metalens.

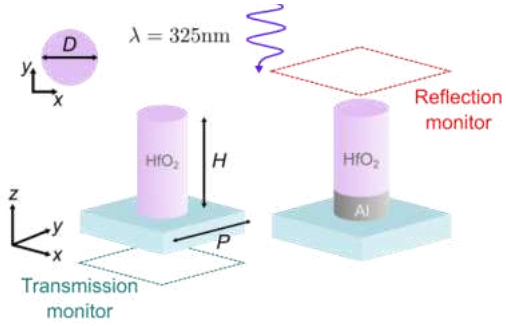


Figure 2: Two types of building blocks: pure HfO_2 operating in transmission and hybrid Al+HfO_2 operating in reflection.

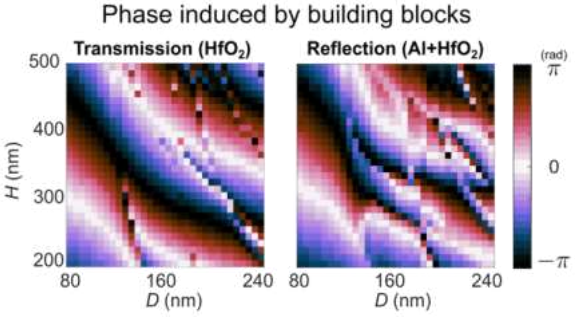


Figure 3: Phase induced by respective building blocks calculated using RCWA simulations for varying height *H* and diameter *D*.

is very hard and non-reactive, preventing the possibility of reactive etching.

In our work, we demonstrate a metasurface capable of lensing both in transmission and reflection simultaneously yet independently as is schematically shown in Figure 1 using CMOS-compatible materials. Such a metasurface could find an application as a controlling device for laser stability, in on-chip UV photodetectors and UV LiDAR systems. To achieve simultaneous operation in reflection and transmission, we utilize two types of nanostructures. The first one is composed of pure HfO_2 for its large bandgap of 5.7 eV and the second one is composed of HfO_2 and Al, forming a hybrid nanostructure (See Figure 2). In this hybrid nanostructure, Al serves as a backside mirror to ensure high reflectivity of the incident light.

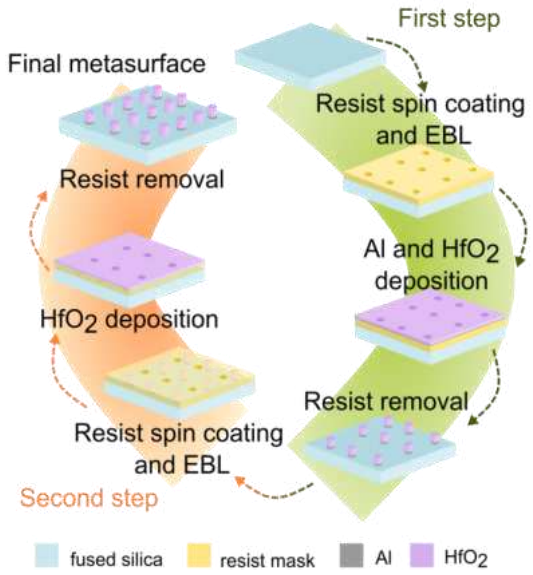


Figure 4: Schematics of two-step lithography fabrication of hybrid metasurfaces from two types of building blocks – pure HfO_2 and hybrid Al+HfO_2.

In the first step, we used rigorous coupled-wave analysis (RCWA) simulations to estimate the amplitude and phase change induced by each type of building block for varying heights H and diameters D and constant Al thickness 30 nm (See Figure 3). In these simulations, we set periodicity P = 250 nm while illuminating nanostructures with a plane wave of a wavelength of 325 nm. The transmissivity for pure HfO_2 nanostructures was close to unity, while the reflectivity of the Al+HfO_2 nanostructures was sustained above 0.8 for nanostructures with diameters greater than 150 nm. The final metasurface was composed of interposed arrays of pure and hybrid nanostructures mimicking the lens profile. Such a full-space metalens was fabricated using two-step electron beam lithography whose workflow is schematically shown in Figure 4. This approach allows for the deposition of HfO_2 and Al directly into the precisely patterned resist mask, using atomic layer deposition and electron beam evaporation, respectively. Finally, the full-space metalens characterization was done by measuring the intensity profile of the focused spots, quantifying its focusing efficiency in our custom-built optical setup.

This work was supported by the Specific research project ID CEITEC VUT-J-24-8581. We also acknowledge the CzechNanoLab Research Infrastructure supported by MEYS CR (LM2023051).

References

1. Neshev, D., I. Aharonovich, “Optical metasurfaces: new generation building blocks for multi-functional optics,” Light Sci Appl, Vol 7, 58, 2018.
2. Ding, F., B. Chang, Q. Wei, et al., “Versatile polarization generation and manipulation using dielectric metasurfaces,” Laser & Photonics Reviews, Vol 14, 2000116, 2020.
3. Genevet, P., F. Capasso, F. Aieta, et al., “Recent advances in planar optics: from plasmonic to dielectric metasurfaces,“ Optica, Vol 4, 139, 2017.
4. Zhao, D., Z. Lin, Z. Zhu, et al., “Recent advances in ultraviolet nanophotonics: from plasmonics and metamaterials to metasurfaces”, Nanophotonics, vol 10, 2283-2308, 2021.
5. Jiang, B., Q. Liu, M. Chao, et al., “The full-space metasurface holography of ultraviolet range”, Optics and Lasers in Engineering, vol. m167, 107595, 2023.

High NA multifocal array metalens

Hyemi Park[1,2#], Yongjae Jo[2#], and Inki Kim[1,2,3*]

[1]Department of intelligent precision Healthcare Convergence, Sungkyunkwan University, Republic of Korea
[2]Department of Biophysics, Institudeof Quantum Biophysics, Sungkyunkwan University, Republic of Korea
[3]Department of MetaBioHealth, Sungkyunkwan University, Korea, Republic of Korea
[*]corresponding author: inki.kim@skku.edu

Abstract: We introduce a novel metalens capable of generating a 10x10 multifocus array with high NA, unlike conventional low-NA microlens arrays. This method enhances imaging speed and quality, promising advancements in various imaging applications with superior resolution and efficiency.

As imaging technologies employing microlens arrays advance in the field, there is an increasing demand for optical components capable of generating multifocus. However, augmenting the number of focal points while maintaining a high numerical aperture (NA) presents a significant challenge. And also previous multifocal research had increased the number of focal points up to 50, but faced limitations on uniformity, resolution, positioning, and short focal distances [1,2]. In this study, we propose a novel approach for creating a multifocus array using a single metalens. Metalens are composed of meta-atoms with subwavelength dimensions. By manipulating the arrangement of these meta-atoms, we can freely modulate phase, an advantage we harnessed to achieve multifocus. In contrast to conventional microlens arrays, which typically have a low NA of around 0.3, our designed metalens maintains a high NA while accommodating an array of up to 10x10 focal points.

We designed the metalens phase profile and conducted simulations for multifocus generation using Rayleigh-Sommerfeld optical propagation.

$$\psi(x,y) = -\frac{2\pi}{\lambda}\sqrt{\left(x + x_{shift}\right)^2 + \left(y + y_{shift}\right)^2 + f^2\Big)} - f \qquad (1)$$

In this phase profile equation (1), x and y represent the spatial coordinates. λ is the wavelength of the incident light, f is focal length, and x_shift, y_shift indicate the desired shift in the coordinate focal position.

Additionally, Rigorous Coupled-Wave Analysis (RCWA) electromagnetic wave simulations were performed to develop a comprehensive meta-atom library. Silicon Nitride (SiN) was chosen for lens fabrication to function effectively in the visible light spectrum, with circular-shaped meta-atoms used to ensure polarization independence. We focused on optimizing the metalens for the specific wavelength of 532 nm.

To optimize its performance, we conducted simulations varying the NA, focal distance, and the lens size. To assess the lens's effectiveness, we measured resolution, Signal-to-Noise Ratio (SNR), and the uniformity of brightness. Our simulation results demonstrated that each focal point maintained uniform intensity and consistent size. The resolution achieved met the diffraction limit, and ensuring uniformity and high-quality imaging across the entire lens. Additionally, our multifocus metalens has achieved a variety of beam shapes array through a flexible design approach.

This technique significantly improves imaging applications without compromising image quality, offering a substantial advantage over other imaging method. With its high-resolution maintenance and multifocus capabilities, we expect that our research will be applicable in a diverse range of imaging fields, leading to advancements across various domains.

References

1. Zhang, Qiuyu, et al. "Inverse design of polarization-insensitive C-band Dammann grating based on dielectric metasurface." Results in Physics 45 (2023): 106238.
2. Wen, Jing, et al. "All-dielectric synthetic-phase metasurfaces generating practical airy beams." ACS nano 15.1 (2021): 1030-1038.

Lensless localized surface plasmon resonance sensor using porous anodic alumina based nanostructured metal-insulator-metal multilayers

A. Dutovs[1], A. Reķe[1], U. Malinovskis[1], R. Poplausks[1], D. Erts[1,2], J. Prikulis[1,3]*

[1]Institute of Chemical Physics, University of Latvia, 19 Raina Blvd., Riga LV-1586, Latvia,
[2]Faculty of Chemistry, University of Latvia, 1 Jelgavas Str., Riga LV-1004, Latvia,
[3]Faculty of Physics, Mathematics and Optometry, University of Latvia, 3 Jelgavas Str., Riga LV-1004, Latvia
*corresponding author: juris.prikulis@lu.lv

Abstract: We demonstrate a proof-of-concept localized surface plasmon resonance (LSPR) sensor device using high-density gold nanoparticle (AuNP) arrays on porous anodic aluminum oxide (PAAO) substrates. Refractometric sensitivity of approximately 100% relative intensity change per refractive index unit (RIU) was achieved in measurements of optical scattering in an off-resonance wavelength band.

Capillary force assisted convective deposition of colloidal nanoparticles on PAAO has enabled low-cost production of high density (≈100 μm^{-2}) non-close-packed (NCP) arrays of gold nanoparticles (AuNP) (fig. 1 inset). The considered metal-insulator-metal (MIM) structure consists of bulk Al substrate, PAAO membrane and AuNP array. Tuning the PAAO layer thickness in the optical subwavelength range can enhance the LSPR signal amplitude by constructive interference of the scattered light by AuNP and their reflection at the PAAO-Al interface [1]. Specifically, for 60 nm diameter AuNP, PAAO thickness ≈300 nm the scattering is maximized at ≈575 nm wavelength. While LSPR sensors commonly function by detecting resonance wavelength shift in response to changes in refractive index (RI), an alternative approach to detection involves measuring signal intensity in an off-resonance band. Specifically, this can be done at longer wavelengths where the intensity decreases to approximately half of its maximum value.

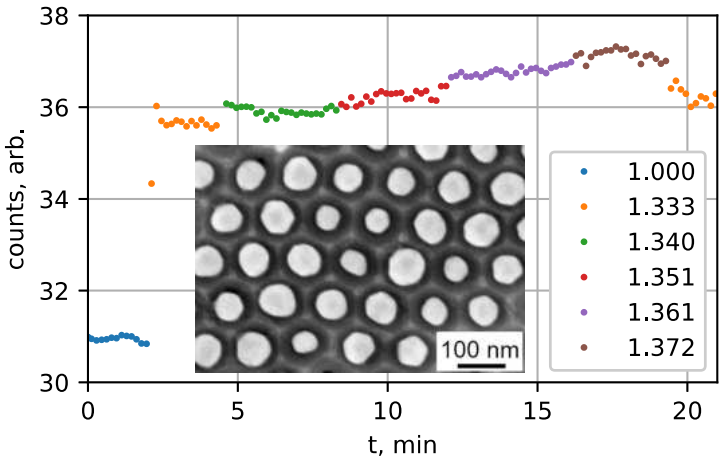


Figure 1. Integrated scattering intensity in the orange-red spectral range (≈610-630 nm) in media with different refractive indices, air n=1.000, water n=1.333 and 4%, 10%, 16%, 22% solutions of NaCl with RI values listed data point labels. Inset: 60 nm diameter AuNP on PAAO template.

PAAO was produced through a two-step anodization process of bulk aluminum substrates in a 0.3 M oxalic acid electrolyte at a 40 V potential [2]. The electrochemical cell was equipped with an optical window, enabling

real-time monitoring of PAAO layer thickness via reflective interference spectroscopy [3]. AuNP with a nominal diameter 60 nm (Sigma-Aldrich 753653) were deposited on PAAO by immersing the anodized substrate into the colloidal suspension and gradually withdrawing it at a rate of 0.1 μm/s. When subjected to angled illumination by a broadband visible light source (white light emitting diode, 3 W, 2700 K, 150 lm, PHILIPS), the Al-PAAO-AuNP MIM structure exhibited bright green-yellow colors visible to the naked eye. The sample was placed within a fluidic cell, enabling the measurement of scattered light by the MIM system in various RI media (NaCl solutions). The scattered light was collected without any lenses from an area with $\approx$5mm diameter by a multimode optical fiber, 200 μm core diameter, 0.22 numerical aperture at a $\approx$1cm distance from the sample surface. The collected light was analyzed using a miniature spectrometer (Ocean Optics USB4000). Instead of measuring the peak wavelength shift, we integrated the intensity in a narrow off-resonance band where scattering intensity is reduced by approximately one half of the maximum value.

The integrated scattering intensity is shown as a function of time in figure 1. The liquid cell was initially filled with air, then water, followed by increasing NaCl concentrations every $\approx$4 minutes, and finally with water again. Although the steps of intensity levels between measurements in different concentrations are somewhat fuzzy, most likely due to solution mixing and incomplete replacement, it is still possible to evaluate the sensitivity of such a sensor. Considering that the RI change $\Delta n=0.04$ between water and maximum concentration leads to intensity change from $\approx$35.5 to $\approx$37.0 counts in arbitrary units, the sensitivity exceeds 100 %/RIU by a good margin.

This study demonstrates the potential of PAAO based MIM structures for high-brightness LSPR sensing. Due to the large number of AuNP per surface area in NCP array without aggregation, the system has large total scattering cross-section while preserving LSPR resonances. This enables significant simplification of optical components in practical LSPR sensor systems.

Acknowledgements: the work was performed within the Latvian Council of Science fundamental and applied research project LZP-2020/1-0200 “Nanostructured multilayer hybrid coatings for interferometric and optoelectronic sensors”.

References

1. Malinovskis, U., R. Popļausks, A. Jurkevičiūtė, A. Dutovs, K. Berzins, V. Perkanuks, W. Simka, I. Muiznieks, D. Erts, and J. Prikulis, “Optimization of Colloidal Gold Nanoparticles on Porous Anodic Aluminum Oxide Substrates for Refractometric Sensing,” ACS Omega, Vol. 7, No. 44, 40324–40332, 2022.
2. Masuda, H. and K. Fukuda, “Ordered Metal Nanohole Arrays Made by a Two-Step Replication of Honeycomb Structures of Anodic Alumina,” Science, Vol. 268, No. 5216, 1466–1468, 1995.
3. Dutovs, A., R. Popļausks, O. Putāns, V. Perkanuks, A. Jurkevičiūtė, T. Tamulevičius, U. Malinovskis, I. Olyshevets, D. Erts, and J. Prikulis. “In Situ Optical Sub-Wavelength Thickness Control of Porous Anodic Aluminum Oxide,” Beilstein J. Nanotechnol., Vol. 15, 126–133, 2024.

Integrated Plasmo-Photonic Bimodal Interferometer for Temperature Sensing

L. Damakoudi[1*], S. Simos[1], K. Fotiadis[1], D. Spasopoulos[1], E. Chatzianagnostou[1], O. Bhalerao[2,3], S. Suckow[2], M. C. Lemme[2,3], E. Lidorikis[4], N. Pleros[1], and K. Vyrsokinos[5]

[1]Department of Informatics - CIRI, Aristotle University of Thessaloniki, Greece

[2] AMO GmbH, Advanced Microelectronic Center Aachen (AMICA), Otto-Blumenthal-Strasse, Aachen, Germany

[3] RWTH Aachen University, Chair of Electronic Devices, Otto-Blumenthal-Straße 25, 52074 Aachen

[4]Department of Materials Science and Engineering, University of Ioannina, Ioannina, 45110, Greece

[5]Department of Physics - CIRI, Aristotle University of Thessaloniki, Greece

[*]corresponding author: damakoudi@csd.auth.gr

Abstract: This work reports on an integrated plasmo-photonic bimodal interferometer with 1.233 nm/℃ sensitivity.

Photonic temperature sensors compared to other techniques relying on different physical mechanisms, exhibit superior performance demonstrating high sensitivity to temperature variations, wide temperature range, stability, and immunity to electromagnetic interference [1-3]. While early prototypes were based on fiber solutions [4], photonic integration enabled the miniaturization of these sensors without compromising their performance. Meanwhile, the field of plasmonics has attracted attention for its ability to offer compactness and extreme light confinement, enabling a diverse range of applications [5]. In this work, we propose an integrated plasmo-photonic bimodal interferometric sensing platform that leverages the advantages of both technologies, achieving an experimental temperature sensitivity of 0.563 nm/℃ with an air-cladded sensing area. This value increases to 1.233 nm/℃ by utilizing water instead of air, taking advantage of the higher thermo-optic coefficient (TOC). In principle, the proposed sensor can operate at different temperature ranges by using materials with different thermal properties on top of the sensing area.

Figure 1(a) shows a 3D conceptual schematic of the plasmo-photonic bimodal interferometric device that serves as a temperature measurement platform. The photonic part consists of cladded polymeric SU8 waveguides with dimensions of 1.8 (H) x 1.5 (W) μm^2. The SU8 waveguide is thinned to 0.9 μm for a 75 μm long distance, and an Aluminum (Al) metal stripe with dimensions of 80 nm (H) x 7 μm (W) is deposited to form a cavity that can be left empty or host thermo-optically sensitive materials in gas or liquid state. Two metal/insulator interfaces are formed at the top and bottom surfaces of the metal stripe, capable to support surface plasmon polariton (SPP) modes. These modes propagate along the two metal surfaces and interfere at the output photonic waveguide,

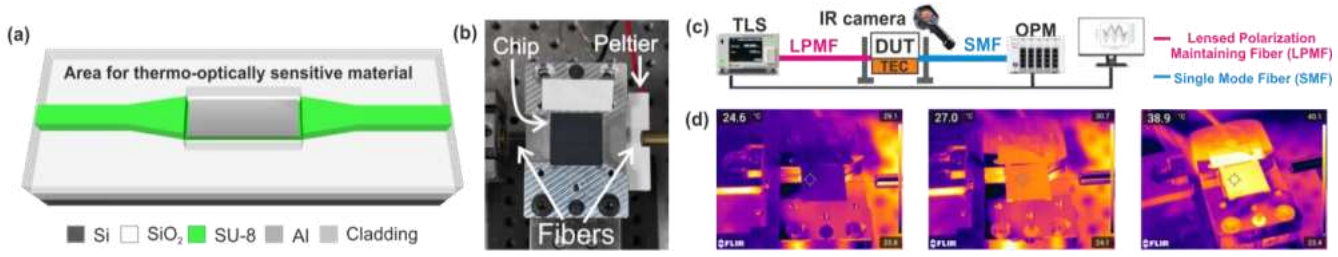


Figure 1: (a) 3D conceptual design of the plasmo-photonic bimodal interferometric temperature sensing platform. (b) Image of the DUT and TEC configuration. (c) Schematic of the experimental setup. (d) Thermal images at three different temperatures, 24.6 ℃, 27℃, 38.9 ℃, demonstrating the thermal change during this heating scheme.

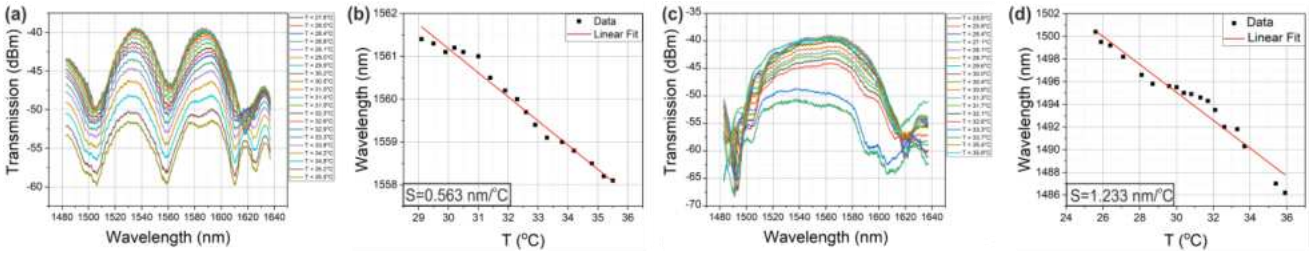


Figure 2: (a) Experimental spectral response of the temperature sensing platform under air conditions. (b) Least squares linear fit of the wavelength dip shift vs. temperature change, revealing an experimental sensitivity of 0.563 nm/℃. (c) Experimental spectral response of the temperature sensing platform filled with water. (d) Least squares linear fit of the wavelength dip shift with the temperature change, in the presence of water, showing an experimental sensitivity of 1.233 nm/℃.

realizing a single-arm interferometer. A more detailed description of the sensor and its operation as a refractive index sensor is given in [6,7]. Any temperature variation on the sensor chip will lead to changes of the refractive indices of the materials, that will alter the effective indices of both SPP modes. Therefore, an intense wavelength shift of the interference dips at the sensor output will be recorded.

The sensor chip was heated by a Peltier module located directly under the chip holder as shown in Figure 1(b), while the temperature was measured at the chip surface with an IR thermal camera. Figure 1(c) shows the experimental setup employed to perform the measurements consisted of a tunable laser source (TLS) and an optical power meter (OPM). The response of the sensor was first investigated with air acting as the medium on top of the plasmonic waveguide, in a temperature range from 27.6°C to 35.5°C. By analyzing the recorded spectral response of Figure 2(a), an experimental sensitivity of 0.563 nm/°C was calculated, as can be seen in Figure 2(b). Subsequently, a drop of water was injected into the thermo-optically sensitive material region exploiting the relatively higher TOC of water compared to air and the experiment was repeated for a temperature range from 25.6°C to 35.9°C, as presented in Figure 2(c). The linear fitting of the data in Figure 2(d), revealed an experimental sensitivity of 1.233 nm/°C confirming the sensitivity improvement of the sensor versus the TOC.

In summary, an integrated plasmo-photonic interferometer is experimentally evaluated for temperature sensing with high precision. The sensitivity of the device is directly related to the TOC of the material on the sensing area as confirmed by air and water measurements. The proposed temperature sensor is capable to support operation at different temperature ranges by placing liquids with diverse thermal properties on the plasmonic surface.

This work was supported by European H2020 projects ICT GRACED (no. 101007448) and AMBROSIA (no. 101093166).

References

1. R. K. Gangwar, A. K. Pathak, and S. Kumar, Photonics, vol. 10, no. 6, p. 1199, 2023.
2. Z. Ding and Y. Shi, IEEE Photonics Journal, vol. 13, no. 4, pp. 1-5, Aug. 2021, Art. no. 6800505
3. G. Syriopoulos et al., Sensors, vol. 23, no. 13, pp. 7765, 2023.
4. S. Lin, et al., *Measurement*, vol. 221, p. 113456, 2023.
5. A. N. Koya et al., Appl. Phys. Rev., vol. 10, no. 2, p. 021318, 2023.
6. K. Fotiadis, et al., ACS Photonics, vol. 10, no. 8, pp. 2580-2588, 2023.
7. K. Fotiadis et al., "Single-arm Interferometric Plasmonic Sensor integrated on a cladded polymeric photonic platform" CLEO 2024 (accepted)

Self-referenced integrated plasmo-photonic sensor for temperature compensated refractive index sensing measurements

S. Simos[1*], L. Damakoudi [1], E. Chatzianagnostou[1], K. Fotiadis[1], D. Spasopoulos[1], D. V. Bellas[1,2], O. Bhalerao[3,4], S. Suckow[3], M. C. Lemme[3,4] and N. Pleros[1]

[1]*Department of Informatics - CIRI, Aristotle University of Thessaloniki, Greece*

[2]*Department of Materials Science and Engineering, University of Ioannina, Ioannina, 45110, Greece*

[3]*AMO GmbH, Advanced Microelectronic Center Aachen (AMICA), Otto-Blumenthal-Strasse, Aachen, Germany*

[4]*RWTH Aachen University, Chair of Electronic Devices, Otto-Blumenthal-Straße 25, 52074 Aachen*

[*]corresponding author: simostyl@csd.auth.gr

Abstract: In this work we propose a self-referenced plasmo-photonic refractive index sensor configuration, integrated on a polymer platform, to compensate for the effect of temperature.

Integrated plasmo-photonic sensors leverage the enhanced sensing credentials of plasmonics with the low-loss characteristics of photonics paving the way for powerful sensing devices with small footprint. On top of that, when integrated in polymer-based photonic platforms, they can offer lower-cost and faster fabrication [1,2]. However, due to the high thermo-optic coefficient of polymeric materials, temperature-induced variations become more prominent and limit the sensor performance. To date, several works have reported methods to compensate the effect of temperature on optical refractive index (RI) sensing. However, most of them consider fiber-based sensors while the respective works on integrated photonic circuits are limited to Si-based platforms [3,4], leaving room for further investigation on polymeric integrated devices.

In this work, we propose an integrated self-referenced scheme to compensate for the effect of temperature variations and improve the performance of the Aluminum-on-SU-8 bimodal plasmo-photonic sensor reported in [1]. The proposed self-referenced sensor is realized by cascading an SU-8 Bragg grating after the bimodal interferometer, as illustrated in the 3D schematic representation of Fig. 1(a). The bimodal sensor consists of an Aluminum stripe with 75 μm length located between two access SU-8 waveguides and on top of a thinner SU-8 layer. The working principle and the experimental evaluation of the sensor have been shown in detail in [1,5]. The Bragg grating has been placed at the bimodal sensor output to serve as a reference by tracking temperature variations. Opting for a narrow Bragg grating resonance at the edge of the sensor spectral response, a period of 520 nm and waveguide widths of $W_1 = 7$ μm and $W_2 = 6.1$ μm have been selected after numerical simulations.

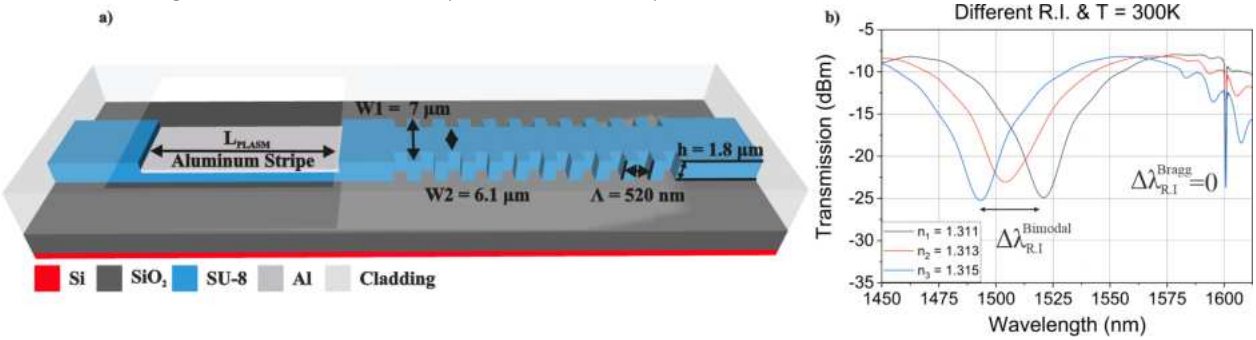


Fig. 1. (a) 3D schematic layout of the self-referenced bimodal plasmo-photonic sensor. (b) Spectral responses at constant temperature when mediums with different RIs are applied on the sensor surface.

The spectral response of the proposed configuration consists of two parts: (i) the sensor spectral response

comprising wavelength dips due to the bimodal interference and (ii) a sharp wavelength dip due to the Bragg grating resonance, as can be seen in Fig. 1(b). The simulated spectral responses of the proposed configuration when mediums with different RIs are applied on the sensor surface at a constant temperature are illustrated in Fig. 1(b). As can be observed, the RI changes cause a wavelength shift to the bimodal dips ($\Delta\lambda_{RI}^{Bimodal}$) revealing a sensitivity of 6078 nm/RIU, which is close to the experimentally reported values of [5], while the Bragg grating resonance remains unaffected by these changes due to being covered with cladding ($\Delta\lambda_{RI}^{Bragg} = 0$) making it ideal for a reference structure. Fig. 2(a) shows the respective simulated spectral response when the configuration is exposed to different temperatures and considering that a material with the same RI is applied on top of its surface. As can be observed, both parts of the transfer function are affected by variations in temperature with the bimodal sensor and the Bragg exhibiting a temperature sensitivity of 687 pm/K and 111pm/K, respectively. From these results, we can extract the calibration curve of the proposed self-referenced sensor shown in Fig. 2(b) which correlates the thermal shift of the bimodal dip ($\Delta\lambda_{\Delta T}^{Bimodal}$) with the thermal shift of the Bragg resonance ($\Delta\lambda_{\Delta T}^{Bragg}$) cancelling the factor of temperature.

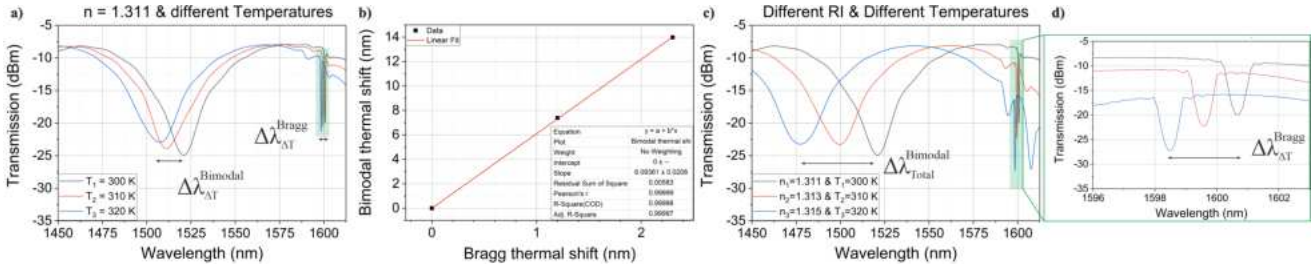


Fig. 2. (a) Spectral responses and resonances shifting for different temperatures. (b) Calibration curve. (c) Spectral responses and resonances drifting for different RIs and different temperatures. (d) Magnified view of the Bragg resonance drift.

Figure 2(c) shows a practical example of how the bimodal dips are shifted when both RI and temperature changes occur, while Fig. 2(d) presents a zoomed in view of the Bragg resonance shifts that are affected only by temperature. Measuring this $\Delta\lambda_{\Delta T}^{Bragg}$ and using the calibration curve of Fig. 2(b), we can define the shift of the bimodal dip due to the temperature change and subtract it from the total shift. For example, the $\Delta\lambda_{Total}^{Bimodal}$ corresponding to the black and blue curves of Fig. 2(c) is 40.21 nm, while the $\Delta\lambda_{\Delta T}^{Bragg}$ equals to 2.3 nm corresponding to the $\Delta\lambda_{\Delta T}^{Bimodal}$ value of 13.98 nm according to the calibration curve. By subtracting this value from the $\Delta\lambda_{Total}^{Bimodal}$, we find that the pure $\Delta\lambda_{RI}^{Bimodal}$ equals to 26.23 nm which is in good agreement with the value of 26.7 nm calculated from Fig. 1(b).

Therefore, the proposed polymer-based self-referenced sensor can effectively compensate for the temperature-induced wavelength drift hence eliminating a major flaw of polymer sensing platforms enhancing their resolution.

This work was supported by European H2020 projects ICT GRACED (no. 101007448) and AMBROSIA (no. 101093166).

References

1. K. Fotiadis et al., ACS Photonics (2023), doi:10.1021/acsphotonics.3c00290
2. L. Ji et al., Photonic Sensors (2020), doi:10.1007/s13320-020-0589-y
3. J. Li et al., Optik (2021), doi:10.1016/j.ijleo.2021.166838
4. K. B. Gylfason et al., Optics Express (2010), doi:10.1364/oe.18.003226
5. K. Fotiadis et al., "Single-arm Interferometric Plasmonic Sensor integrated on a cladded polymeric photonic platform" CLEO 2024 (accepted)

Self-Assembled Plasmonic Nanoparticles for Photocatalysis

A. Tamulevičienė[1,2,3*], K. Midveris[1], T. Klinavičius[1], M. Haris[2], M. Juodėnas[1], D. Peckus[1,2], S. Tamulevičius[1,2], T. Tamulevičius[1,2,3]

[1]Institute of Materials Science, Kaunas University of Technology, Kaunas 51423, Lithuania
[2]Physics Department, Kaunas University of Technology, Kaunas 51368, Lithuania
[3]UAB Nanoversa, Kaunas 51423, Lithuania
[*]corresponding author: asta.tamuleviciene@ktu.lt

Abstract: Chemically synthesized gold nanoparticles were self-assembled on a template and transferred onto TiO_2 layer. The photoelectrochemical performance and spectral response of high-Q surface lattice resonance demonstrating electrode was compared with the counterpart containing random particles originated by dewetting of thin film and having broader localized surface plasmon resonance.

Recently plasmonic photocatalysis utilizing solar power for fuel generation has become an intensely growing field. The possibility to synthesize a variety of noble metal nanoparticles, *i.e.* gold, silver, platinum, etc. having different morphologies opened new paths for investigation. The most common approach is to use metal nanoparticles together with TiO_2-based materials to enable effective charge carrier separation and tune the optical response of the structure from UV to the longer wavelength regions (visible and IR) [1-2].

One of the needs for effective catalysis is to have controllable nanoparticle distribution on the surface. Colloidal nanoparticles can be deposited on solid TiO_2 surface creating active catalytic sheets [2]. The problem here is that nanoparticles tend to agglomerate on the surface if nanoparticle surface is not functionalized. Templated nanoparticle self-assembly [3] or deposition of monolayer from liquid-liquid interface can solve this problem without additional functionalization of particle surface. Ordered array of noble metal nanoparticles has additional advantage – surface lattice resonance that was shown to increase the electromagnetic field enhancement in a controlled way [3] and such photoelectrodes could also contribute to higher efficiency in solar water splitting at certain wavelength bands [1]. The water splitting performance and spectral response of regular gold nanoparticle array photoelectrodes carrying photonic modes were compared with TiO_2 nanoparticles formed by dewetting gold films.

This project has received funding from the Research Council of Lithuania (LMTLT), agreement No. S-MIP-23-93.

References

1. Hüttenhofer L., *et al.* “Metasurface Photoelectrodes for Enhanced Solar Fuel Generation,” Adv. Energy Mater., Vol. 11, No. 46, 2102877, 2021.
2. Kumar, A., *et al.* “Recent Advances in Plasmonic Photocatalysis Based on TiO_2 and Noble Metal Nanoparticles for Energy Conversion, Environmental Remediation, and Organic Synthesis”, Small, Vol. 18, 2101638, 2022.
3. Khinevich N., *et al.* “Wavelength-tailored Enhancement of Raman Scattering on a Resonant Plasmonic Lattice,” Sens. Actuator B-Chem., Vol. 394, 134418, 2023.

Fluorescence enhancement of novel azulene-tetrazoles using metasurface structures

V. Anastasoaie[1*], I. Mihalache[1], R. Tomescu[1], A. Dinescu[1], E.-M. Ungureanu[2], O. Brincoveanu[1] and D. Cristea[1]

[1] National Institute for Research and Development in Microtechnologies (IMT-Bucharest), Bucharest, Romania
[2] National University of Science and Technology POLITEHNICA Bucharest, Faculty of Chemical Engineering and Biotechnology
*corresponding author: veronica.anastasoaie@imt.ro

Abstract: This study aims to enhance the fluorescence of novel azulene-tetrazole derivatives using a platform based on plasmonic metasurfaces with the aim of developing new biosensors. We focus on two important azulene-tetrazole derivatives. We investigate the effect on fluorescence of gold, silver or aluminum nanostructures on silicon or glass substrates.

Azulenes are non-alternating aromatic compounds that possess unique properties due to the presence of an electron-rich five-membered ring and an electron-deficient seven-membered ring. They are well known for their distinctive color and fluorescence properties, which have been used to develop chemical sensors and dosimeters with distinct colorimetric and fluorescent responses [1]. Also, azulene-derivatives have applications in engineering, optoelectronics [2] and medicine, for anti-inflammatory, antibacterial, anti-diabetic and anti-retroviral therapy [3]. An interesting class of azulene derivatives are the tetrazole-substituted azulenes, which combines the properties of azulenes with those of tetrazoles [4]. The tetrazole class has applications in biochemistry and medicinal chemistry. They are used as biologically active compounds and drugs, and have potential for developing new biologically active substances [5]. Due to the relatively low quantum yield of azulene fluorophores [6], it is necessary to increase their emission efficiency in order to develop more efficient sensors. Therefore, it is crucial to investigate the potential for fluorescence enhancement (FLEN) in azulenes. One promising method for increasing fluorescence is to use a metasurface platform. Metasurfaces are arrays of nanostructures smaller than the wavelength, which can manipulate electromagnetic waves and allow precise control of the properties of light and other forms of electromagnetic radiation [7]. Metasurfaces have been used in advanced sensing and medical diagnostics, with the potential to overcome the technical drawbacks of traditional sensor technologies [8]. Here, we investigated the FLEN of new azulene-tetrazole (**Az-Ta**) derivatives using a low-cost metasurface-based platform consisting of randomly distributed metal aggregates. Our aim is to develop new and selective fluorescence biosensors based on metasurface structures.

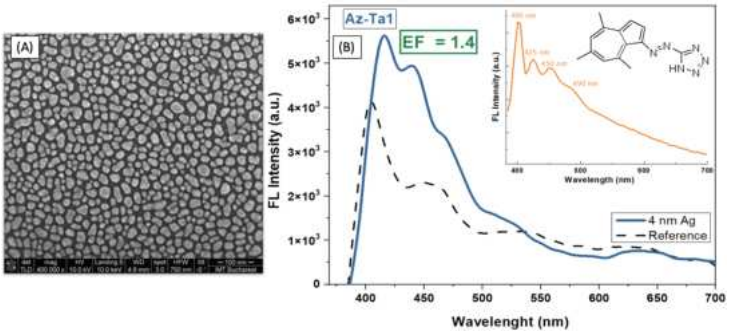


Figure 1. SEM micrograph of Ag metasurface and **Az-Ta1** fluorescence intensity in the presence of Ag metasurfaces compared to reference (bare silicon); inset shows the chemical structure of **Az-Ta1** and the fluorescence emission spectrum of **Az-Ta1** solution in ACN.

We analyzed the fluorescence emission of two azulene-tetrazole derivatives: (E)-5-((4,6,8-trimethylazulen-1-yl)diazenyl)-1H-tetrazole (**Az-Ta1**) and (E)-5-(azulen-1-yldiazenyl)-1H- tetrazole (**Az-Ta4**) dispersed in acetonitrile (ACN). For this study we used gold (Au), silver (Ag) and aluminium (Al) nanostructures patterned on a silicon or glass substrate. The metallic nanoaggregates were fabricated by electron beam evaporation of discontinuous layers 4 nm thick (mass equivalent) (Fig. 1A and Fig. 2A) and Az-Ta has been coated on top of the metasurface.

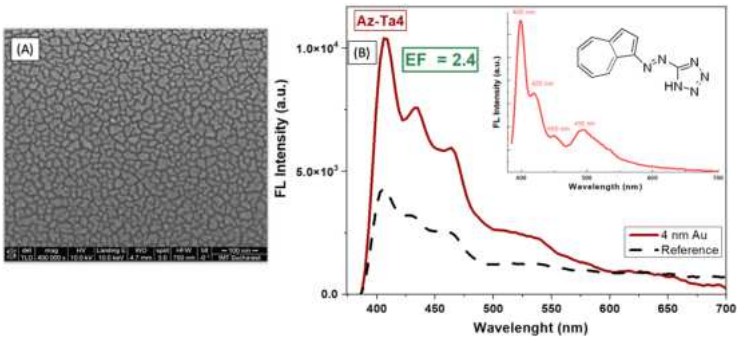


Figure 2. SEM micrograph of Au and **Az-Ta4** fluorescence intensity in the presence of Au metasurfaces compared to reference (bare silicon); the inset shows the chemical structure of **Az-Ta4** and the fluorescence emission spectrum of **Az-Ta4** solution in ACN.

As the studies are still in their beginning stages, in this summary we present the best preliminary results obtained. We observed that the random metasurfaces provide a significant enhancement of the fluorescence of the azulene-tetrazole derivatives. The best result for of FLEN **Az-Ta1** was obtained on Ag/silicon metasurfaces with an enhancement factor (EF) of 1.4, as shown in Fig. 1. **Az-Ta4** exhibited the highest fluorescence enhancement on Au/silicon metasurfaces, with an enhancement factor of 2.4, as can be seen in Fig. 2.

Acknowledgements: This work is funded by the Core Program of IMT-Bucharest within the National Research Development and Innovation Plan 2022-2026, carried out with the support of Romanian Ministry of Research, Innovation and Digitization, project no. 2307.

References

1. Murfin, L. C. and Lewis, S. E. “Azulene-A Bright Core for Sensing and Imaging,” Molecules, Vol. 12, No. 26, 353, 2021.
2. Xin, H. and Gao, X. “Application of Azulene in Constructing Organic Optoelectronic Materials: New Tricks for an Old Dog,” Chempluschem., Vol. 82, No. 7, 945-956, 2017.
3. Bakun, P., Czarczynska-Goslinska, B., Goslinski, T. and Lijewski. S. “In vitro and in vivo biological activities of azulene derivatives with potential applications in medicine,” Med Chem Res., Vol. 30, No. 4, 834-846, 2021.
4. Păun, A.-M., Matica, O.-T., Anăstăsoaie, V., Enache, L.-B., Diacu, E. and Ungureanu, E.-M. “Recognition of Heavy Metal Ions by Using E-5-((5-Isopropyl-3,8-Dimethylazulen-1-yl) Dyazenyl)-1H-Tetrazole Modified Electrodes.” Symmetry, Vol. 13, No. 4, 644, 2021.
5. Ostrovskii, V., Popova, E. and Trifonov, R. “Tetrazoles,” Comprehensive Heterocyclic Chemistry IV, Vol. 6, 182-232, 2022.
6. Steer, R. P. “Photophysics of molecules containing multiples of the azulene carbon framework,” JPPC, Vol. 40, 68-80, 2019.
7. Wang, L. and Karaaslan, M. “Advanced Metamaterials for Engineers,” IOP Publishing Limited, 2023.
8. Taibi, A., Durant, A., Lacoste, C., Binnie, D. T. and Spada, L. L. "Metasurfaces for sensing and medical diagnostics," 2019 IEEE International Conference on RFID Technology and Applications (RFID-TA), 151-156, 2019.

Manipulation of 2-Dimensional layers of plasmonic nanoparticles using a SAW device

Chandresh Sindal, Julien Reboud, Narayana M. S. Sirimuthu, Alasdair W. Clark, Jonathan M. Cooper*

Biomedical Engineering Division, University of Glasgow, Glasgow, United Kingdom

*corresponding author, E-mail: jon.cooper@glasgow.ac.uk

Abstract

We present the acoustic manipulation of 2D structures of metallic nanoparticles and their use for localized surface plasmon resonance (LSPR) sensing, creating a unique LSPR scanning system. The movable nanoparticle monolayers were patterned using standing surface acoustic wave (SSAW) tweezers. We validated their functionality for refractive index sensing.

1. Introduction

Optically active nanoparticles (NPs) have been used extensively to generate plasmonic-enhanced optical components (e.g. in LSPR or Raman applications) [1], although in such cases the particles most often remain static, requiring the sensed moieties and material structures to be built up on or bound to the particles themselves, so limiting the applicability of the techniques on native, unmodified structures (such as those in imaging applications). The ability to manipulate and pattern these particles in real-time, and in an arbitrary fashion, may open up research avenues for new sensors and devices. Surface acoustic waves (SAW) may be an answer to this problem. SAW devices have previously been used for contactless microparticle manipulation and alignment [2] in applications for patterning, separation, and mixing of particles and biomaterials. Z. Mao *et al.* reported the focusing and enrichment of nanometer scale particles by using travelling SAW [3] whilst H. Sazan et al [4] were able to form microstructures of silver NPs using standing SAW. R. Habibi et al [5] demonstrated NP collection using a microparticle bed in a microfluidic chamber, utilizing acoustic resonances and scattering forces to attract NPs in a specific location. Here we use SAW to manipulate 2D plasmonic AuNP monolayers in a contactless manner and demonstrate their use for label-free localized LSPR sensing.

2. Monolayer preparation

AuNPs were washed in DI water by centrifugation at 16,000 and 7,500 rpm for 25 and 10 minutes for 15 and 30 nm, respectively. Following previous reports [6], 1 ml of Hexane was then added to create an oil-water interface. 2 ml of Ethanol was subsequently added, which acts to form a monolayer of NPs at the oil-water interface. The Hexane was completely evaporated over 10 hours, resulting leaving the monolayer of NPs at the air-water interface (Figure 1).

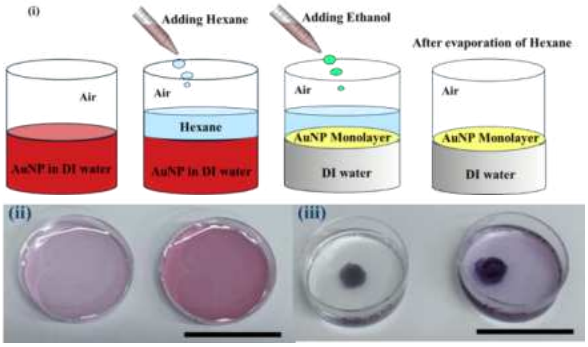


Figure 1: (i) Steps to form a monolayer of AuNPs, illustrated in pictures (ii-iii) of 30 (left) and 15 nm (right), before (ii) and after (iii) adding hexane and ethanol. Monolayer size is ~1cm., (scale bar: 3 cm)

2.1. Characterization

Glass cover slips (18x18 mm) were coated with 10 nm of Ti-Au (using a plasma coater) before being observed in scanning electron microscopy (SEM). Figure 2 shows closed packing of a 2-dimensional monolayer of gold nanoparticles. Two different approaches were explored to transfer the monolayer for characterization with SEM: top lift up and glass capillary method [7]. The results confirm the monolayer remains intact after transfer.

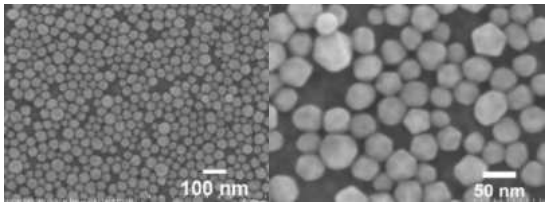


Figure 2: SEM images of AuNP monolayers at two magnifications.

3. SAW manipulation of AuNP monolayer

A pair of interdigitated transducers (IDTs) was used to generate SSAW, comprising 30 pairs of electrode "fingers" of 130 µm, leading to a resonant frequency at 30 MHz, with a 1 mm aperture. IDTs were fabricated as described previously [8] on 128^0 Y-cut 4-inch lithium niobate ($LiNbO_3$) wafer using photolithography. PDMS chambers were prepared by mixing monomers with curing agents in 10:1 ratio and polymerized at 70ºC for 2 h. The 1 mm square PDMS chamber was plasma bonded over the SAW device.

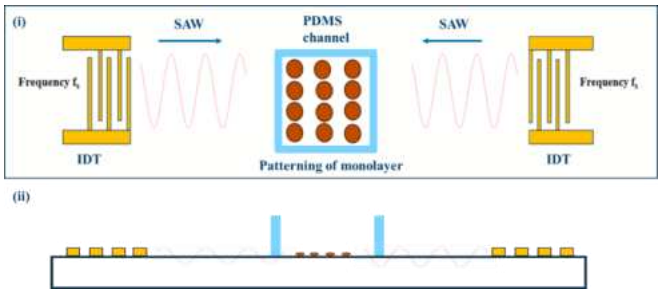


Figure 3: Schematic diagram to ilustrate the SSAW manipulation of 2D monolayers in a PDMS chamber (i) top and (ii) side view. Surface deformation are in the order of nm.

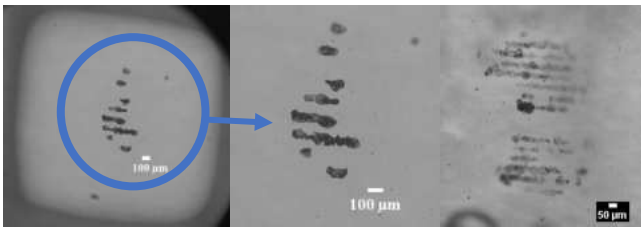


Figure 4: SAW manipulation of AuNP monolayer in a PDMS chamber: (i) and (ii) 15 nm AuNPs, and (iii) 30 nm AuNP. The monolayer fragments align on the SAW nodes due to the radiation force [8], spaced by 65µm, half wavelength of the acoustic waves. By changing the phase or frequency, the monolayers can be moved along the surface to scan it.

One pair of IDTs was connected to an RF signal generator to generate standing-SAW (S-SAW) at a resonant frequency of 30 MHz with an applied power of -20 dBm. The AuNP monolayers from the air-liquid interface was transferred by into a PDMS chamber. Initially, when the SAW was OFF, the monolayers were freely floating in DI water. Upon actuating the S-SAW, NPs moved towards the pressure nodes forming structured lines (due to the gold particles acoustic properties, leading to a positive acoustic contrast factor) – Figure 4. The spacings between lines are 65 µm which is equivalent to half of the propagating wavelength.

3.1 LSPR sensing with gold monolayer

The plasmonic effect of arrays of metallic nanoparticles is sensitive to the surrounding medium optical properties. If the interparticle distance is reduced, then a red shift with broadening in the spectra is visible. The monolayer represents a perfect example for aggregated NPs which leads to broadening of the spectra and red shift at the same time [9, 10]. We used different refractive indices in the solution to illustrate the functionality of the monolayers as LSPR sensors. Figure 4 shows that with increasing refractive index (RI, created with 1%, 2%, 3% and 4% concentration of NaCl), a red shift in the spectra is observed. Results show that the absorbance peak was red shifted as the RIs increased (figure 5). All experiments were performed in triplicate. Smoothing of data and normalization was performed to reduce noise.

4. Conclusions

We successfully demonstrated the manipulation of 2D AuNPs monolayers using SSAW, and used them for RI sensing using LSPR. Future work will focus in implementing a robust scanning control and explore RI sensitivity for different SSAW actuation.

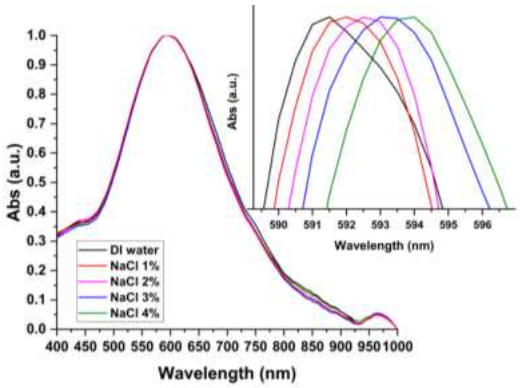


Figure 5: (i) Spectra of 15 nm AuNP monolayer in NaCl (1-4% in DI water).

Acknowledgements

The authors thank the staff of the James Watt Nanofabrication Centre (JWNC) at the University of Glasgow and Dr Christian Witte for devices and MSJE, Govt of India for providing funding for studies of Chandresh Sindal.

References

[1] Trung-Dung Luong and Nam-Trung Nguyen," Surface Acoustic Wave Driven Microfluidics – A Review", Micro and Nano systems, 2010.

[2] Li, Z., Wang, W., & Yin, Y. (2020). Colloidal Assembly and Active Tuning of Coupled Plasmonic Nanospheres. Trends in Chemistry, 2(7), 593–608. https://doi.org/10.1016/j.trechm.2020.03.008

[3] Mao, Z., Li, P., Wu, M., Bachman, H., Mesyngier, N., Guo, X., Liu, S., Costanzo, F., & Huang, T. J. (2017). Enriching Nanoparticles via Acoustofluidics. ACS Nano,11(1),603–612. https://doi.org/10.1021/acsnano.6b06784

[4] Sazan, H., Piperno, S., Layani, M., Magdassi, S., & Shpaisman, H. (2019). Directed assembly of nanoparticles into continuous microstructures by standing surface acoustic waves. Journal of Colloid and Interface Science, 536, 701–709. https://doi.org/https://doi.org/10.1016/j.jcis.2018.10.100

[5] Habibi, R., & Neild, A. (2019). Sound wave activated nano-sieve (SWANS) for enrichment of nanoparticles. Lab on a Chip, 19(18), 3032–3044. https://doi.org/10.1039/C9LC00369J

[6] Song, L., Xu, B. bin, Cheng, Q., Wang, X., Luo, X., Chen, X., Chen, T., & Huang, Y. (2021). Instant interfacial self-assembly for homogeneous nanoparticle monolayer enabled conformal "lift-on" thin film technology. Science Advances, 7(52). https://doi.org/10.1126/sciadv.abk2852

[7] Chang, J., Lee, J., Georgescu, A., Huh, D., & Kang, T. (2019). Generalized On-Demand Production of Nanoparticle Monolayers on Arbitrary Solid Surfaces via Capillarity-Mediated Inverse Transfer. Nano Letters, 19(3), 2074–2083. https://doi.org/10.1021/acs.nanolett.9b00248

[8] Witte, Christian (2015) Micromanipulation in microfluidics using optoelectronic and acoustic tweezing. PhD thesis. http://theses.gla.ac.uk/6391/

[9] Borah, R., Ninakanti, R., Bals, S., & Verbruggen, S. W. (2022). Plasmon resonance of gold and silver nanoparticle arrays in the Kretschmann (attenuated total reflectance) vs. direct incidence configuration. Scientific Reports, 12(1), 15738. https://doi.org/10.1038/s41598-022-20117-7

[10] Ja'afar, P. N. S. S., Razali, N. M., Ambran, S., & Ahmad, F. (2021). Sodium Chloride Concentration Measurement via Optical Fiber Tip Sensor. IOP Conference Series: Materials Science and Engineering, 1051(1), 012030. https://doi.org/10.1088/1757-899X/1051/1/012030

Optical response of Smooth and rough Mono and bilayers of plasmonic materials

J. A. Polito-Lucas[1] and Ana L. González[1*]

[1]Institute of Physics, Benemérita Universidad Autónoma de Puebla, México

[*]corresponding author: ana.gonzalezron@.correo.buap.mx

Abstract: Rough thin films were modeled using DDA and patterns composed by hemispheres and hemi ellipsoids. The reflected, transmitted and absorbed light of these rough films are compared with that of a real roughness pattern obtained by AFM. Smooth and rough mono- and bilayers of plasmonic materials and nitrides are presented.

Summary

Au and Ag are superb nanoscale plasmonic materials due to their surface plasmon properties in the visible region. However, they have a disadvantage, their optical efficiency spectra are strongly reduced and broadened in intensity due to the dispersion phenomenon caused by electron confinement, this has been observed in thin films with thickness less than 12 nm [1], above this thickness the bulk response is recovered. On the other hand, plasmonic thin films of Nb have shown that size quantum effects are relevant for films with thickness less than 20 nm. The latter may favor Nb over Ag and Au for both plasmonic and photonic applications [2,3].

In this work we have investigated the effect of thickness and roughness on the optical response of thin films. Thin film surfaces with uniform roughness were modeled using the Discrete Dipole Approximation (DDA). The theoretical basis of the DDA are explained in detail in [4]. Briefly, a unit cell of N dipoles (TUC) is periodically repeated along the *yz* plane to create an infinite film, see Figure 1. The polarizability of each dipole is calculated using the Lattice Dispersion Relation [5], which requires the dielectric function of the material, the polarization state of the incident wave plane and the dipole-dipole separation distance, d. DDA calculates the scattered electric field, the Mueller matrix and the reflection and transmission coefficients of the films mimicked by the array of dipoles.

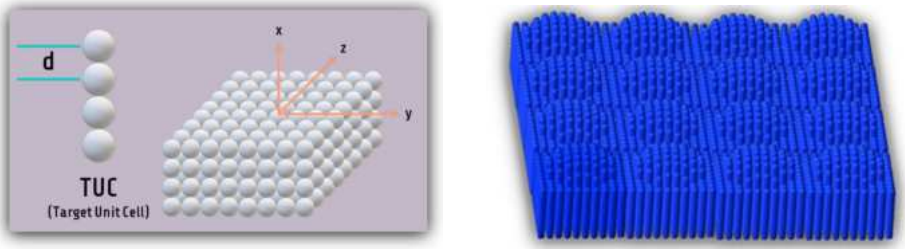


Figure 1. *Left.* Scheme of a column of N dipoles (each one represented by a small sphere) which is repeated along the *yz* plane to mimick a thin film with a smooth surface. d is the separation distance between adjacent dipoles. *Right*. TUC of dipoles repeated periodically to represent a film with a rough surface of hemispherical patterns.

The optical response of films with rough patterns composed by hemispheres (SS) and hemiellipsoids (SE) is compared with that of a real roughness pattern obtained from AFM topography images. In Figure 2 the reflected light of an Ag thin film with a thickness of 50 nm is shown. There, the roughness (h) has been varied from 0 to 25

nm. In the calculations, h is the length of the axis of the hemisphere or hemi-ellipsoid perpendicular to the film surface. The right panel of Figure 2 shows the calculated reflectance of an Ag film with a rough surface that replicates the topography observed in a niobium thin film deposited by magnetron sputtering. For this film, the reflectance was calculated using three TUCs whose size is represented by Zone A, Zone B and Zone C. As we can see, the reflectance is very similar due to the uniform roughness along the sample.

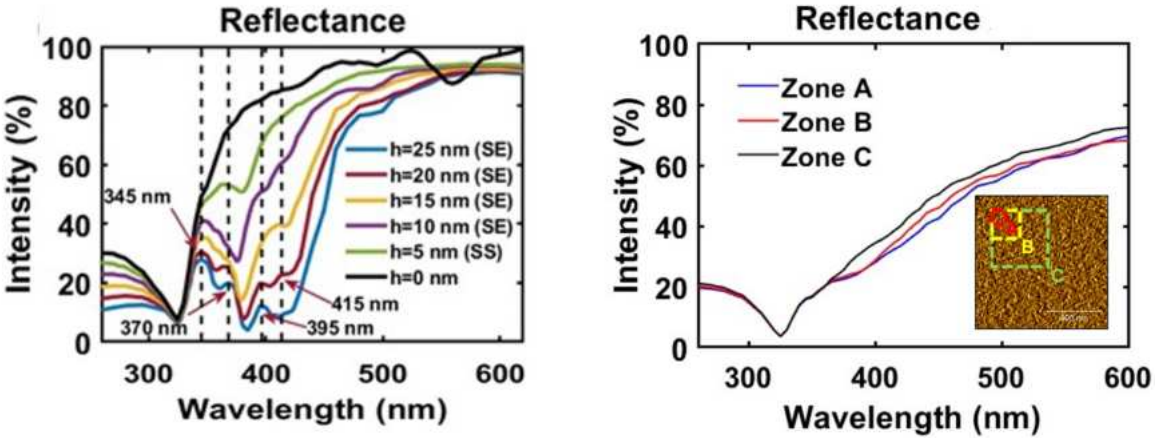


Figure 2. Light reflection of an Ag film with different roughness. *Left.* The roughness was obtained from hemispherical and hemi-ellipsoidal patterns. *Right*. The roughness was created from a real pattern observed from an AFM image of a thin film of niobium.

Reflected, transmitted and absorbed light of smooth and rough mono- and bilayers of Ag, Au, Nb, Ti and other materials were calculated.

Acknowledgement

Authors thank VIEP-BUAP 2024 for the financial support. J. A. Polito-Lucas thanks CONAHCYT for the scholarship No. 861219

References

1. Gong, J., R Dai, Z. Wang and Z Zhang, “Thickness Dispersion of Surface Plasmon of Ag Nano-thin Films: Determination by Ellipsometry Iterated with Transmittance Method”, Sci. Rep., Vol. 5, 9279, 2015.
2. Naik, G. V., V. M. Shalaev and A. Boltasseva, “Alternative Plasmonic Materials: Beyond Gold and Silver”, Adv. Mater., Vol. 25, No. 24, 3264–3294, 2013.
3. Polito-Lucas J. A., F. J. Flores-Ruiz, V. Garcia-Vazquez and A. L. González, “Tailoring optical response in nanostructured bilayers: Effects of surface roughness and layer thickness on NbN/Nb and TiN/Ti”,Superficies y vacío, Vol. 37, 240201, 2024.
4. Draine, B. T. and P. J. Flatau, “Discrete-dipole approximation for periodic targets: theory and tests”, J. Opt. Soc. Am. A, Vol. 25, No. 11, 2693–2703, 2008.
5. Draine, B. T. and J. Goodman, ”Beyond Clausius-Mossoti: Wave propagation on a polarizable point lattice and the discrete dipole approximation”, The Astrop. J., Vol. 405, No. 2, 685–697, 1993.

Infrared Surface Lattice Resonances using Plasmonic Transition Metal Nitrides

Hsing-Yu Kuo[1,2*], Tzu-Yu Peng [1,2], Jia-Wern Chen[1], Yu-Jung Lu [1,2]

[1]Research Center for Applied Sciences, Academia Sinica, Taipei, Taiwan
[2] Department of Physics, National Taiwan University, Taipei 10617, Taiwan
[*]E-mail: vuivui1205@gmail.com

Abstract: We report high Q surface lattice resonances using plasmonic transition metal nitride nanoparticle arrays, which possess a high-quality factor (Q-factor) that is sensitive to the surrounding environment of the nanoparticle structure. We intend to utilize this plasmonic nanostructures for future design of high temperature enable optical sensing systems.

Surface lattice resonances (SLRs) as an alternative optical cavity are widely investigated owing to their high Q-factor, which is indicative of strong light confinement [1]. SLRs also exhibit pronounced field enhancement, supporting strong light-matter interactions [1]. Notably, most of the SLR's designs are based on noble metals such as gold or silver [1,2,3]. However, those noble metals are unstable at high temperatures, which gave rise to the idea of designing an SLR cavity that can be tailored to high-temperature surroundings. Here, we demonstrate high Q SLR using plasmonic transition metal nitrides, renowned for their high melting temperatures as refractory plasmonic materials [4]. Employing Finite-Difference Time-Domain (FDTD) simulations, we design SLRs using titanium nitride (TiN) and hafnium nitride (HfN), and ascertain their SLRs modes within the infrared spectrum. By combining the inherent advantages of SLRs, particularly their sensitivity to the refractive index of the environment and the refractory properties of transition metal nitrides, we could pave the way to high-temperature functional sensing devices that operate in the infrared.

Figure 1(a) depicts the scheme of the system we designed, which is composed of TiN (HfN) nanoparticle arrays with a periodicity of 1045 nm (1070 nm), a diameter of 230 nm (220 nm), and a height of 250 nm (230 nm) on SiO_2 substrate. Figures 1(b) and 1(c) show the calculated transmission spectra *via* FDTD simulations. The result reveals the SLR mode of TiN (HfN) occurs at 1470 nm (1568 nm), with a Q-factor of 81 (148). The results indicate that SLR modes exhibit sharp dips within the infrared range. In addition, Figures 2(a) and 2(b) demonstrate how we can tune the SLR mode by varying the refractive index of the surrounding medium. This wavelength-tunable property inspires the design of sensors tailored for the infrared range. Due to the refractory properties of transition metal nitrides [4], We intend to utilize this plasmonic nanostructure for the future design of high-temperature optical sensing systems.

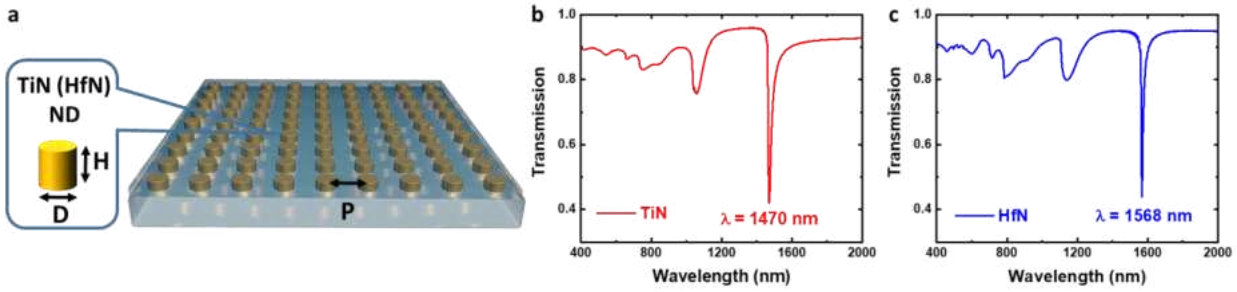


Figure 1. TMN-based SLR nanostructure and their optical properties. (a) Schematics of TiN (HfN) nanoparticle arrays to form surface lattice resonances. (b) calculated transmission spectrum of SLR mode from TiN nanoparticle arrays. (c) calculated transmission spectrum of SLR mode from HfN nanoparticle arrays.

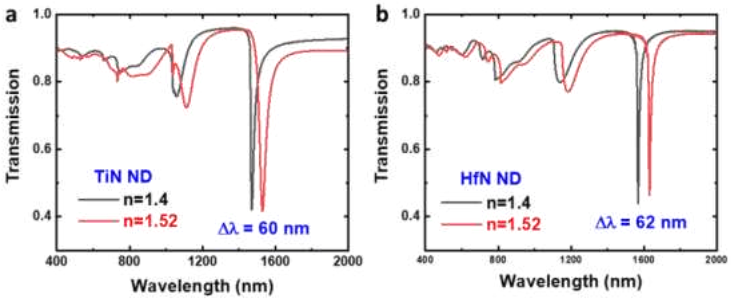


Figure 2. FDTD simulation results of tuning the SLR mode by varying refractive index of environment from 1.4 to 1.52 for (a) TiN nanoparticle arrays and (b) HfN nanoparticle arrays.

References

1. Bin-Alam, M.S., Reshef, O., Mamchur, Y. *et al.* Ultra-high-Q resonances in plasmonic metasurfaces. Nat Commun 12, 974 (2021).
2. Zhou, W., Dridi, M., Suh, J. *et al.* Lasing action in strongly coupled plasmonic nanocavity arrays. Nature Nanotech 8, 506–511 (2013).
3. Wang, D., Yang, A., Wang, W. *et al.* Band-edge engineering for controlled multi-modal nanolasing in plasmonic superlattices. Nature Nanotech 12, 889–894 (2017).
4. Chiao, Zong-Yi, Chen, Yu-Chia, Chen, Jia-Wern, Chu, Yu-Cheng, Yang, Jing-Wei, Peng, Tzu-Yu, Syong, Wei-Ren, Lee, Ho Wai Howard, Chu, Shi-Wei and Lu, Yu-Jung*. "Full-color generation enabled by refractory plasmonic crystals" Nanophotonics, 11, 2891-2899 (2022).

Highly-Sensitive Broadband Gap-Plasmon-Enhanced NbN Superconducting Single Photon Detectors

Feng-Yang Tsai[*1,2], Jing-Wei Yang [1], Jia-Wern Chen[1], Li-Min Wang[3] and Yu-Jung Lu[1,2,3]

[1]Research Center for Applied Sciences, Academia Sinica, Taipei 11529, Taiwan
[2]Graduate Institute of Applied Physics, National Taiwan University, Taipei 10617, Taiwan
[3]Department of Physics, National Taiwan University, Taipei 10617, Taiwan
*corresponding author: Johnny881119@gmail.com

Abstract: We report a broadband gap-plasmon-enhanced superconducting single-photon-detector using NbN superconducting microstrip integrated with silver nanocubes to form gap plasmon resonances from 440 nm to 640 nm. The nonlinear photoresponse is attributed to the gap-plasmon-induced heating that breaks the superconducting state to normal, an impressive detection efficiency of 98% was achieved.

Superconducting single photon detectors (SSPDs) [1,2,3] have many advantages, such as low dark noise, low time jitter, and a wide detection range. However, achieving high detection efficiency with traditional SSPDs for visible light detection is not easy. To overcome this difficulty, we designed a superconducting NbN microstrip photon detector integrated with plasmonic nanostructures to enhance detection efficiency. Here, we demonstrate a superconducting single-photon detector by coupling an NbN-based superconducting microstrip with different sizes of silver nanocubes plasmonic resonators. To achieve high detection efficiency, we designed different Ag nanocube arrays and excited the gap plasmon resonances at wavelengths of 640 nm (red), 510 nm (green), and 440 nm (blue), using the Finite-difference time-domain (FDTD) method to simulate gap plasmon resonances at these wavelengths. In our previous results, the gap-plasmon-enhanced SMSPD enhanced detection efficiency from 62% to 98% at 532 nm [4]. We will discuss the working mechanisms and potential applications of broadband gap-plasmon-enhanced SSPD in the entire visible region.

Fig. 1 displays the properties of the NbN film. Fig. 1(a) presents the NbN film sample. The ellipsometry results plotted in Fig. 1(b) reveal that the wavelength region above the epsilon near zero (ENZ) covers the visible range. Therefore, we can use the plasmonic property of NbN in the visible range to design a metal/insulator/metal structure as gap-plasmon. Fig. 1(c) depicts an AFM image indicating that our NbN films have an atomically smooth surface with a root-mean-square (RMS) roughness of approximately 0.3 nm. Fig.1(d) illustrates that the metal-superconductor transition temperature (Tc) of NbN films is about 12 K, which was measured by superconducting quantum interference devices (SQUIDs). Fig. 2 showcases that the designed plasmonic nanostructure on an NbN superconducting microwire (4 μm). Fig. 3 presents Finite-Difference Time-Domain simulations of the electric field intensity at wavelengths of 510 nm and 640 nm.

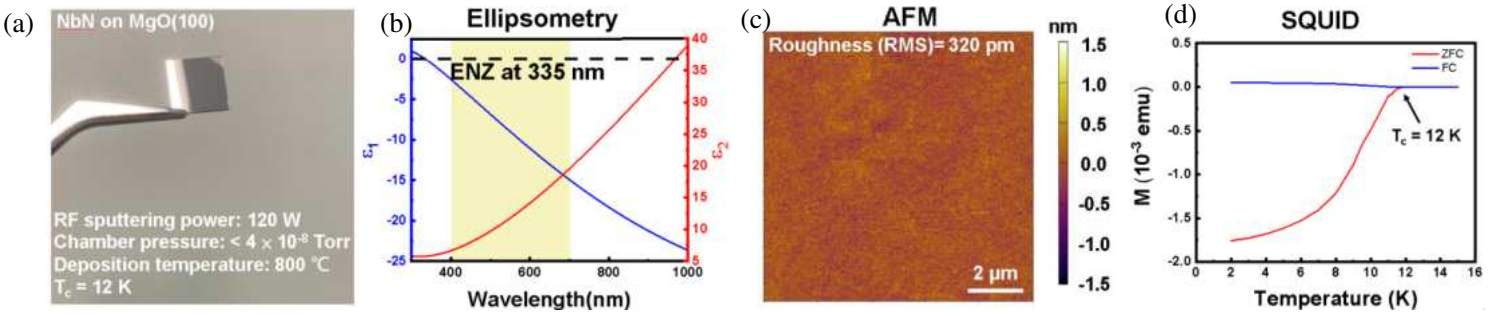


Figure 1. Characterization of NbN film. The measurement of (a)Sample of NbN film, (b)Ellipsometry, (c)AFM, (d)SQUIDs.

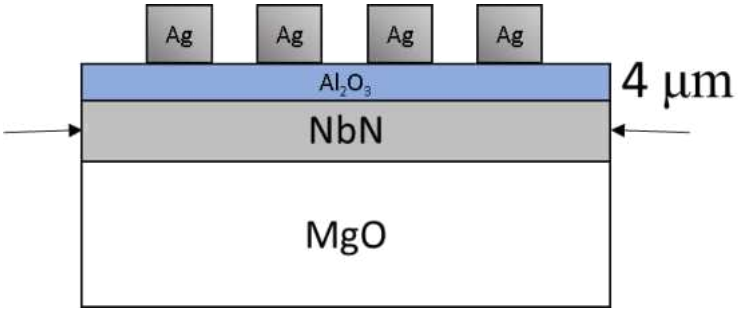


Figure 2. Schematic of the gap-plasmon-enhenced SMPD, featuring Ag nanocubes on NbN microstrip photodetectors capped with 5-nm Al_2O_3. Highly-Sensitive Broadband SMPD can be achieved by tailoring the size of silver nanocubes.

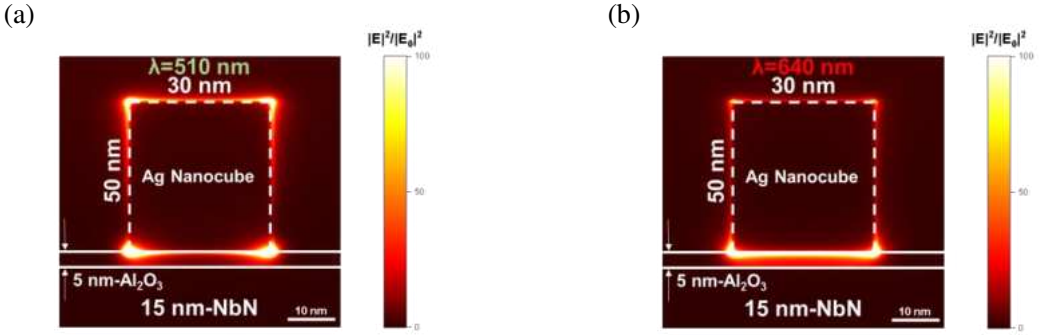


Figure 3. Calculated electric-field enhancement for the plasmonic nanostructures at a different wavelengths. (a) at 510 nm. (b) at 640 nm.

References

1. G. Gol'Tsman et al., "Picosecond superconducting single-photon optical detector." Applied physics letters 79, 705 (2001).
2. Karl, P., Ubl, M., Flad, P., Giessen, H., Mennle, S., Yang, J.W., Lu, Y.-J. & Peng, T.-Y. Niobium nitride plasmonic perfect absorbers for tunable infrared superconducting nanowire photodetection. Opt. Express (2021).
3. Karl, P., Mennle, S., Ubl, M., Hentschel, M., Flad, P., Yang, J.-W., Peng, T.-Y., Lu, Y.-J. & Giessen, H. Tunable infrared high absorbing polarization independent niobium nitride plasmonic perfect absorber nanowire photodetectors. Opt. Mater. Express 12, 2453-2461 (2022).
4. Jing-Wei Yang, Tzu-Yu Peng, Daniel D. A. Clarke, Frank Daniel Bello, Jia-Wern Chen, Hao-Chen Yeh, Wei-Ren Syong, Chi-Te Liang, Ortwin Hess,* and Yu-Jung Lu*. Nanoscale Gap-Plasmon-Enhanced Superconducting Photon Detectors at Single-Photon Level. Nano Letters 23, 11387–11394 (2023)

Revisable Tuning of Tamm Plasmon Polaritons

Ming-Jyun Ye [1], and Kuo-Ping Chen [2 *]

[1] College of Photonics, National Yang Ming Chiao Tung University, Tainan 711, Taiwan
[2] Institute of Photonics Technologies, National Tsing Hua University, Taiwan
**kpchen@ee.nthu.edu.tw*

Abstract: Phase-change materials (PCMs) provide a specific combination of properties. The binary semiconducting chalcogenide Sb_2S_3 is consider one of the promising candidates, especially its intrinsic high refractive index, low loss and wide bandgap properties, in near infrared (NIR). Here, the Sb_2S_3 transformation from amorphous to crystal state embedded between the distribute Bragg reflector (DBR) and metal layer. At the interface between DBR and metal layer in specific parameter, Phase-change Tamm plasmon–polariton (PC-TPP) resonance could be produce. The PC-TPP resonance has a 70 nm modulation wavelength. Also, the resonance achieves around 100 nm-shifted in NIR at the proper incident angle.

Key Words-- *Sb_2S_3, distribute Bragg reflector (DBR), Phase-change materials (PCMs), Tamm Plasmon Polaritons metasurface (TPP), High Refractive Index (HRI)*

1. Introduction

Phase-change materials (PCMs) has been widely applied in switchable electronic and photonics [1-5]. The crystal phase of vanadium dioxide (VO_2) was changed from monoclinic state near 340 K. Also, the working system of germanium-antimony-tellurium (GST) was above 380 K at communication wavelength. However, these two PCMs have a high extinction coefficient around 0.5 and 2.0 in visible, respectively [6]. Here, the binary semiconducting chalcogenide Sb_2S_3 has bandgap 1.8 to 2.1 eV to move the absorption band-edge in visible. Meanwhile, the high refractive index of Sb_2S_3 could be tuned from 3 to 4 at around 650 nm. And, its extinction coefficient was below 0.5 after 600 nm in both states.

One of the plasmon resonance was theoretically demonstrated at the surface photonic crystal and metals, called Tamm state. Between distributed Bragg reflector and metal layer, it has the strong confinement at the interface, known as Tamm plasmon polariton (TPP) [7, 8].

In this research, Sb_2S_3 was used as function layer in the TPP structure. After annealing process, the modulable wavelength was demonstrate around 70 nm. The analysis of angle-dependence resonance also was proved close to 100 nm in proper incidence light. In the future, the optical signal would be encoded to electrical signal, called photocurrent. It was shown that our design would be added in LiDAR [9], sensor [10].

2. Results and discussion

The finite-difference time-domain (FDTD) method has been used to calculate the Phase change Tamm plasmon–polariton (PC-TPP) resonance with normal light incidence in NIR. In this modeling setup, the DBR unit cell consist of two layers 145 nm silica and 95 nm TiO_2 with several pairs, as shown in Figure 1 (a). With the specific Sb_2S_3 and gold thickness, the PC-TPP resonance could be achieved 70 nm modulation after Sb_2S_3 annealing from amorphous to crystal state, as shown in Figure 1 (b). The optical constants of Sb_2S_3 were taken in the visible spectra range from, as shown in Figure 1 (c). It was shown phase change material Sb_2S_3 has the HRI and low extinction coefficient property, compared to commercial material, silicon, in NIR.

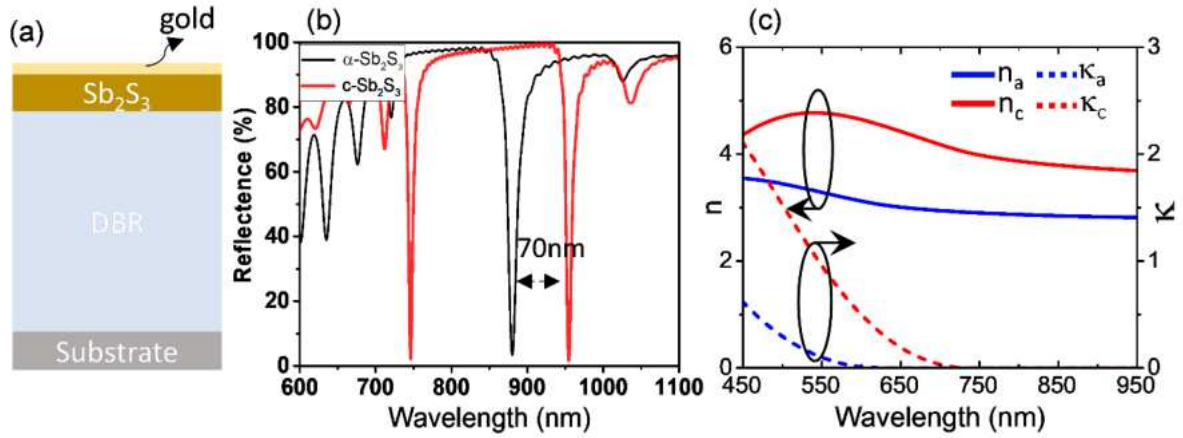


Figure 1 (a) The structure of Sb_2S_3 TPP device. (b) The TPP resonance shifted from 870 nm to 960 after transformation state. (c) The real optical constant of the α–and c- Sb_2S_3 after annealing.

Further, the simulated PC-TPP reflectance spectrums were calculated with different Sb_2S_3 thickness in NIR, depicted in Figure 2. In Figure 2 (a, b), the dashed line was illustrated that design was with 30 nm gold and 130 nm Sb_2S_3 and applied at 870 nm. After annealing process, the resonance was tuned to 960 nm. This design could be easily used in NIR spectrum from 750 nm to 950.

In addition, the angle-dependent TPP resonance was theoretically investigated in Figure 2 (c, d). In amorphous state, the TPP resonance was tuned from 960 nm decreases to 780 nm at the normal and tilt 60 degrees incident light, respectively.

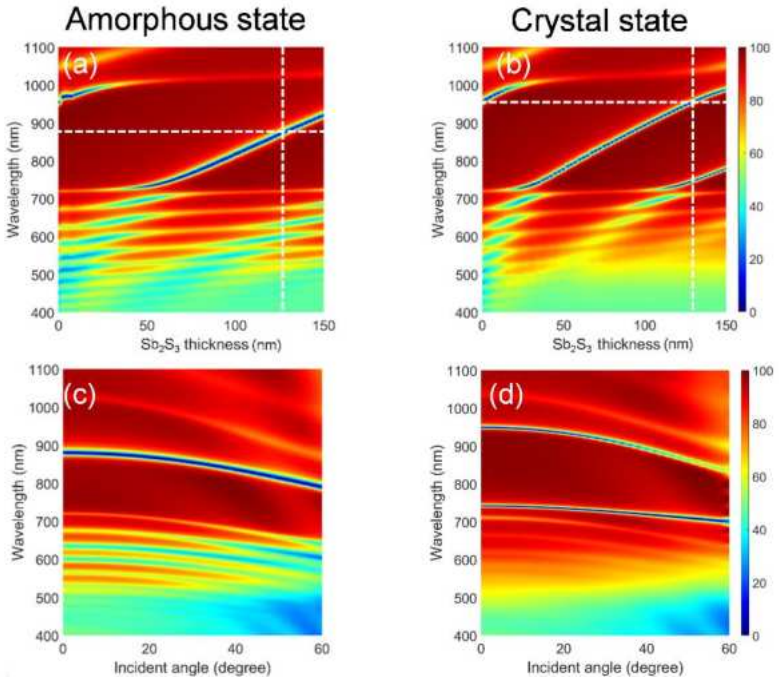


Figure 2 Reflectance spectrum of simulated parameter tuning of PS-TPP of Sb_2S_3 thickness(a) α–and (b) c- state. 130 nm Sb_2S_3 at the proper incident angle in PC-TPP structure (c) α–and (d) c- state.

3. Conclusions

In summary, the PC-TPP resonance has a 70 nm modulation wavelength. The angle-dependent resonance was demonstrated around 100 nm-shifted in NIR spectrum.

4. References

[1] Y. Zhang *et al.*, "Electrically reconfigurable non-volatile metasurface using low-loss optical phase-change material," *Nature Nanotechnology,* vol. 16, no. 6, pp. 661-666, 2021.

[2] L. Lu *et al.*, "Reversible tuning of Mie resonances in the visible spectrum," *ACS nano,* vol. 15, no. 12, pp. 19722-19732, 2021.

[3] H. Liu *et al.*, "Rewritable color nanoprints in antimony trisulfide films," *Science advances,* vol. 6, no. 51, p. eabb7171, 2020.

[4] H. Yoon *et al.*, "Reversible phase modulation and hydrogen storage in multivalent VO2 epitaxial thin films," *Nature materials,* vol. 15, no. 10, pp. 1113-1119, 2016.

[5] A. Howes *et al.*, "Optical limiting based on Huygens' metasurfaces," *Nano Letters,* vol. 20, no. 6, pp. 4638-4644, 2020.

[6] W. Dong *et al.*, "Wide bandgap phase change material tuned visible photonics," *Advanced Functional Materials,* vol. 29, no. 6, p. 1806181, 2019.

[7] M. Kaliteevski *et al.*, "Tamm plasmon-polaritons: Possible electromagnetic states at the interface of a metal and a dielectric Bragg mirror," *Physical Review B,* vol. 76, no. 16, p. 165415, 2007.

[8] B. R. Wu *et al.*, "Quasi-Bound States in the Continuum with Temperature-Tunable Q Factors and Critical Coupling Point at Brewster's Angle," *Laser & Photonics Reviews,* vol. 15, no. 5, p. 2000290, 2021.

[9] M. Wurdack *et al.*, "Observation of hybrid Tamm-plasmon exciton-polaritons with GaAs quantum wells and a MoSe2 monolayer," *Nature communications,* vol. 8, no. 1, pp. 1-6, 2017.

[10] J. Leuthold and A. Dorodnyy, "On-demand emission from Tamm plasmons," *Nature Materials,* vol. 20, no. 12, pp. 1595-1596, 2021.

Large-area, two-dimensional single-crystal gold for low-loss nanoplasmonics

Chenxinyu Pan[1], Yuanbiao Tong[1], Anatoly V. Zayats[2], Limin Tong[1], Pan Wang[1]

1. State Key Laboratory of Extreme Photonics and Instrumentation, College of Optical Science and Engineering, Zhejiang University, Hangzhou 310027, China

2. Department of Physics and London Centre for Nanotechnology, King's College London, Strand, London WC2R 2LS, UK

Abstract: Two-dimensional gold with a single-crystal structure is highly desired for upcoming technologies. In this work, we demonstrate the fabrication of large-area (>10^4 μm^2), two-dimensional single-crystal gold using a chemical etching approach with an atomic-level precision, and its use for the realization of ultrathin plasmonic structures with low loss.

Two-dimensional (2D) single-crystal gold (<5 nm) is an attractive material due to its capability of extreme optical confinement via the excitation of surface plasmons[1], which is of great interest for the study of light-matter interactions at nanoscale and the development of ultrathin nanophotonic devices including ultrafast optical modulators and high-sensitivity optical sensors. However, unlike materials with layered crystal structures, gold cannot be directly exfoliated into 2D layers from its bulk crystal. Wet-chemical approaches have been extensively utilized to fabricate low-dimensional metals, but the synthesis of 2D gold (usually less than 1 μm in lateral size) with a large area remains extremely challenging due to the concurrent increase in the thickness and lateral size[2,3]. Here, we introduce an atomic-level-precision etching approach to fabricate 2D gold flakes (2DGFs) with large size (100s of μm) and thickness down to 2 nm, and demonstrated the fabrication of ultrathin plasmonic structures with low-loss[4].

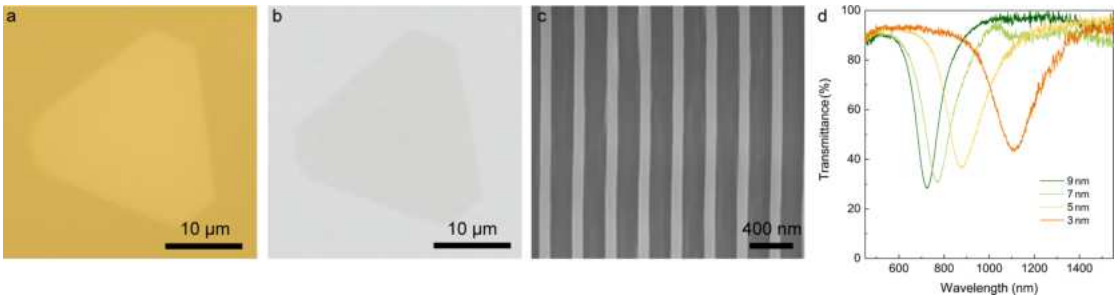


Fig. 1 a,b, Optical micrographs of a 2DGF with a thickness of 2.5 nm, taken in reflection (a) and transmission (b). **c**, Scanning electron microscopy image of a nanoribbon array fabricated with a 2DGF with a thickness of 3 nm. **d,** Transmission spectra of nanoribbon arrays fabricated with 2DGFs for various nanoribbon thicknesses (w = 100 nm).

2DGFs were fabricated by chemical etching of chemically-synthesized large-area single-crystal gold flakes[5] with a large thickness (~20 nm). During the etching, the thickness of the gold flakes can be controlled with an atomic-level precision while keeping the lateral dimensions essentially unchanged. Figure 1a and 1b show optical micrographs of an as-fabricated 2DGF with a thickness of 2.1 nm, which is almost transparent due to its thin thickness (Fig. 1b). By using electron-beam lithography and reactive ion etching, 2DGFs can be patterned into ultrathin nanoribbon arrays, as shown in Fig. 1c. A strong resonance dip (Fig. 1d, orange line) can be observed in its transmittance due to the excitation of a dipolar localized surface plasmon mode, which is difficult to be realized with sputtered gold. The resonance dip is blue shifted dramatically from 1115 to 724 nm with the increase of the nanoribbon thickness from 3 to 9 nm.

In conclusion, we have demonstrated the fabrication of 2D single-crystal gold and its use for low-loss nanoplasmonics. The results hold great potential of nanoscale light-matter interactions for fundamental studies, and also provide an attractive platform for the development of ultrathin optoelectronic, plasmonic and quantum devices.

References

[1] Rivera, N., Kaminer, I., Zhen, B., Joannopoulos, J. D. & Soljacic, M. Shrinking light to allow forbidden transitions on the atomic scale. *Science* **353**, 263-269 (2016).
[2] Huang, X. *et al.* Synthesis of hexagonal close-packed gold nanostructures. *Nat. Commun.* **2**, 292 (2011).
[3] Ye, S. J. *et al.* Sub-Nanometer Thick Gold Nanosheets as Highly Efficient Catalysts. *Adv. Sci.* **6**, 1900911 (2019).
[4] Pan, C. X. Y. *et al.* Large-area single-crystal gold of single nanometer thickness for nanophotonics. *Nat. Commun.* (2024) *accepted*.
[5] Krauss, E. *et al.* Controlled Growth of High-Aspect-Ratio Single-Crystalline Gold Platelets. *Cryst. Growth Des.* **18**, 1297-1302 (2018).

Chirality switchable molecular traps based on plasmonic metastructures with intertwined Fibonacci spirals

Chung-Kai Tseng, Tang-Chun Liu, Diksha Thakur, and Chao-Yi Tai
Department of Optics and Photonics, National Central University, 300, Jhongda Rd., Jhongli, Taoyuan 32001, Taiwan
email: cytai@dop.ncu.edu.tw

Abstract: High density molecular traps are realized by metastructures with intertwined Fibonacci spirals. Depending on the chirality of incident light, traps are switchable following either clockwise or counterclockwise spirals. The associated trapping potential is larger than $10k_BT$ with incident intensity I=15 mW/μm^2 showing capability to stably trap molecules at room temperatures.

Mother nature has been teaching us in a variety of aspects. For instance, phyllotaxis adapted in some plants makes the most efficient capture of light. Inspired by this, in this work, a sunflower seed like pattern [1] is adopted which enables the construction of dense molecular traps on a chip. Essentially, Vogel's model is utilized to construct clockwise (CW) and counterclockwise (CCW) intertwined spirals [2], forming spatially separated molecular traps switchable by right/left circularly polarized (R/L CP) incident light. In order to produce resonance in the visible wavelength range, here we use Au nanorod (NR) as the building block with the geometric parameters as follows: height h=10 nm and diameter D=40 nm sitting atop SiO_2 substrate. The center-of-mass of each NR is specified by the polar coordinates (r_n, ϕ_n) where $r_n=kn^{1/2}$ and $\phi_n=n\phi$. The scaling factor k characterizes the distance between neighbouring NRs, and n stands for the sequence number of a NR, counting from the central NR (n=1). Setting the divergence angle $\phi=137.508°$ (the golden angle) with k=32, and a total number of NRs to n=141, the metastructure with two intertwined spirals with opposite chirality is mathematically generated, which gives the highest packing efficiency. Essentially, CW/CCW spirals consist of collections of the nearest/next nearest NRs, corresponding to NRs with sequence number coincident to the Fibonacci sequences with Δn=13/21.

The scattering spectrum is modelled by a finite difference time domain simulator, Lumerical. The material parameters are extracted from literatures [3-4]. Perfect matched layers (PML) are deployed outside as boundaries and a spatial grid size of 1 nm is used so as to obtain results with high accuracy. Fig. 1(a) indicates that the primary resonant wavelength is located at λ=675 nm, regardless of the incident polarizations. Slightly detune the wavelength to the shoulder peak, i.e., λ=700 nm, enables one to observe mode splitting. As shown in Fig. 1(b-c), the hot spots of the electric field distribute predominantly in the gaps between NRs of the CCW/CW spirals subject to L/R CP polarized light incidence, respectively.

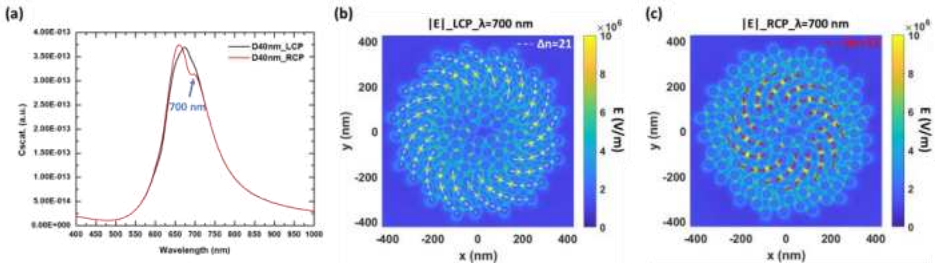


Fig. 1. (a) Scattering spectrum of the designed metastructure. (b/c) Near field electric field distributions excited by L/R CP light at λ=700 nm, respectively. The simulation is conducted at an incident intensity of I=1 mW/μm^2.

Next, to assess the trapping capability, the optical chirality and the associated trapping potentials are calculated, according to equations (1-2). We consider a hybrid configuration, i.e., a 10 nm Ag nanosphere decorated with a molecule

with R/L handedness, designated as Ag-R/L enantiomer here. The resultant electric-/magnetic-/chiral- polarizabilities (α/β/χ) are calculated following [5] with chiral parameters κ=±1. Fig. 2(a-d), depict the calculated optical chirality C, their mutual difference ΔC, and the relative trapping potentials (at z=15 nm above the structure) under L/R CP incidence at λ=700 nm with I=15 mW/μm^2. It is clear in evidence that switchable molecular traps are successfully created for Ag-R/L enantiomers along CW/CCW Fibonacci spirals. Besides, as the trapping potentials are higher than 10 k_BT (k_B: Boltzmann constant) and the averaged separation between opposite traps is only 12 nm, high-density stable-trapping of molecules can be achieved.

$$C = \frac{\omega}{2c^2}\,\mathrm{Im}[\dot{E}\cdot\dot{H}^*] \tag{1}$$

$$U_{xy} = -\frac{\mathrm{Re}[\alpha]|E|^2}{4} - \frac{\mathrm{Re}[\beta]|H|^2}{4} - \frac{\mathrm{Re}[\chi]\,\mathrm{Im}[\dot{E}\cdot\dot{H}^*]}{2} \tag{2}$$

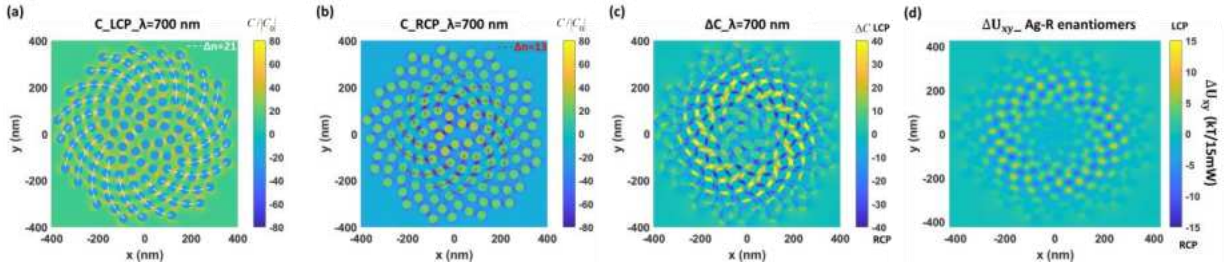


Fig. 2. Optical chirality distributions under (a) LCP, (b) RCP illuminations. (c) Differential optical chirality and (d) trapping potentials.

Regarding to signal readout, the scattered intensities evolved at successive monitoring distances are calculated. Fig. 3 (a) and (b) illustrate this, where the difference between LCP/RCP at z=50 nm is already distinguishable, as marked by the arrows. Fig. 3 (c-d) depict the differential intensities, respectively at z=20 nm, 50 nm, which once again verifies this observation. Further increase the monitoring distance only results in a minimal change of distribution with weakened intensity. This property makes the designed metastructure an efficient platform for molecular trapping and chirality discrimination with fast-readout capability.

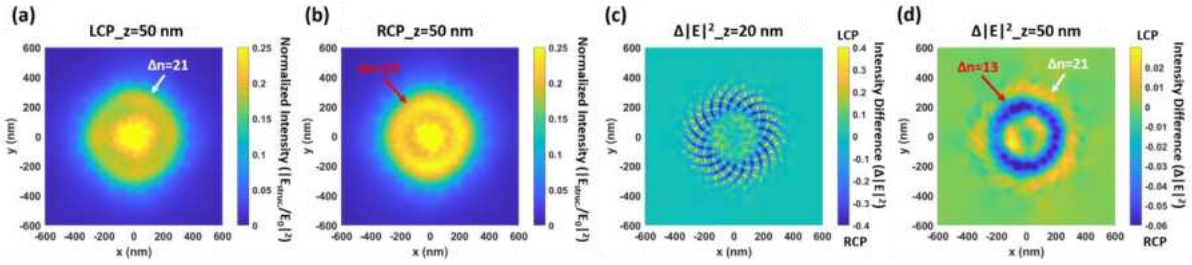


Fig. 3. Scattering patterns of (a) LCP and (b) RCP incidence at z=50nm. (c-d) Differential scattering patterns at z=20, 50 nm, respectively.

References

1. Strauss, S., Lempe, J., Prusinkiewicz, P., Tsiantis, M. and Smith, R.S., "Phyllotaxis: is the golden angle optimal for light capture?," New Phytol, **225**, 499-510 (2020).
2. Helmut Vogel, "A better way to construct the sunflower head," Math. Biosci. **44,** 179-189 (1979).
3. P. B. Johnson and R. W. Christy, "Optical Constants of the Noble Metals," Phys. Rev. B **6,** 4370-4379 (1972).
4. H. R. Philipp, "Silicon Dioxide (SiO_2) (Glass)" in *Handbook of optical constants of solids,* E.D. Palik, ed. (Academic, Orlando, Fla. 1985).
5. A. Canaguier-Durand and C. Genet, "Chiral route to pulling optical forces and left-handed optical torques," Phys. Rev. A **92,** 043823 (2015).

Metal-dielectric gratings with broad geometric range for angle interrogation of surface plasmons

Shafeek A. Samad[1*], Nityanand Kumawat[1], Priyamavada Venugopalan[1] and Sunil Kumar[1,2]

[1]Division of Engineering, New York University Abu Dhabi, PO Box 129188, Abu Dhabi, UAE
[2]Department of Mechanical Engineering, New York University, Brooklyn, NY 11201, USA
[*]corresponding author: sa7490@nyu.edu

Abstract: We report the comprehensive analysis of metal-dielectric gratings with broad opto-geometric parameter range, for the angular interrogation of surface plasmonic excitation. The multi-parameter optimization of sinusoidal and rectangular grating structures yields the design coordinates for sharp resonance features in the angular reflection response of surface plasmons.

Surface plasmons (SP) are collective oscillations of the free electron plasma propagating along the metal-dielectric interface [1]. Grating coupling provides a planar, robust and scalable configuration necessary for the on-chip excitation and control of surface plasmons [2]. The grating coupled surface plasmon resonance (GCSPR) is convenient to study the plasmonic responses in either transmission or reflection mode [3], as well as for zeroth or higher order diffractions [4]. GCSPR devices for sensing and switching have been demonstrated, leveraging on the angle or wavelength interrogation of SP using shallow grooves etched on thin metal films [5], and differential measurements at fixed, small incident angles [6]. In this work, we report the comprehensive parametric analysis of angle interrogation of SP excited at the interface of a metal-dielectric grating. SP responses at steep incident angles (θ_i) for large grating modulation depths (d $\geqslant$100 nm), and varying duty cycles for sinusoidal and rectangular gratings are studied. The results show that the angular spectral features of the SPs can be precisely tuned with the control of grating geometry and the excitation wavelength.

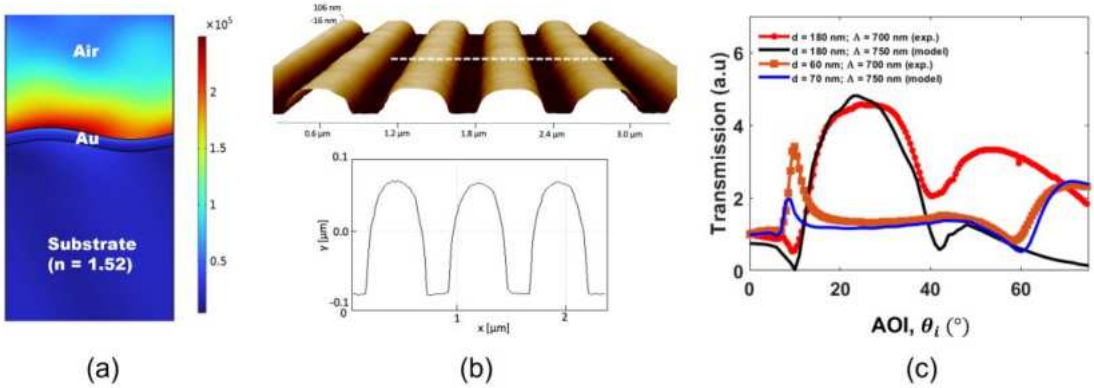


Figure 1: (a) Simulated electric field at θ_i = 11.5°, for a sinusoidal grating with Λ = 750 nm and d = 60 nm, (b) AFM image showing the 3D topography and depth profile of the optical disc-based gratings with Λ = 750 nm and d = 180 nm, and (c) Comparison of the numerical and experimental transmission response of the gratings.

To numerically evaluate the angular response, a Finite Element Method (FEM) solver in COMSOL® Multiphysics 6.0 is used. The model consists of a unit cell of a dielectric grating (n_g = 1.52) coated with continuous film (t = 50 nm) of gold, as plotted in Fig. 1(a). A periodic port placed on top of the unit cell is used to excite TM-polarized light at a fixed wavelength, $\lambda = 633$ nm. To validate this model, transmission measurements of gold-

coated gratings prepared using off-the-shelf commercial optical discs (Λ = 750 nm ; d = 180 nm) are carried out. The topography of these gratings, obtained using AFM, is shown in Fig. 1 (b). The numerical results are found to be in good agreement with the experimental transmission response of gratings, Fig. 1 (c).

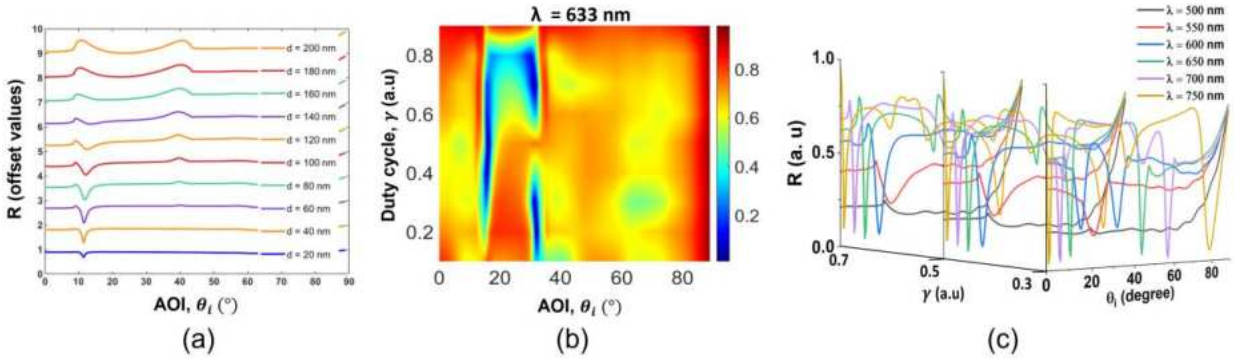


Figure 2: (a) Evolution of the SPR reflection dip with variation in grating depth, (b) 2D reflection map of the rectangular gratings for broad range of angles and duty cycle for a fixed excitation wavelength $\lambda = 633$ nm, and (c) Angular response of rectangular grating-based plasmonic excitation for wavelengths (legends) in the visible domain and for duty cycle varying from 0.3 to 0.7.

Fig. 2(a) shows that, for shallow sinusoidal gratings (d < 120 nm), the plasmonic excitation is manifested by a single narrow reflection dip. The SP response widens and includes multiple low reflection zones for deep gratings. For a fixed grating period, the FWHM of the dip is reduced from 20° to 0.75° by optimizing the grating depth from 180 nm to 60 nm. Further, the performances of metal-dielectric gratings with sinusoidal and rectangular modulation profiles are compared, for varying duty cycles (γ) and for differing excitation wavelengths in the visible and NIR regime, Fig 2 (c-d). Rectangular gratings provide extra artifacts in the angular response than their complementary sinusoidal geometries. It is evident from Fig. 2 (c) that even under weak modulation, rectangular gratings preserve the single SP reflection dip only for $0.4 \leqslant \gamma \leqslant 0.6$, but shows split reflection dips else. The dual dips are observed to be shifting contra-directionally with increase in excitation wavelength. The multi-parameter optimization of gratings in a broad geometric range yields the design coordinates wherein well-defined, narrow resonance are obtained in the angular response of SP, which is desirable for bio-sensing applications.

References

1. Guo, X., "Surface plasmon resonance based biosensor technique: A review," J. Biophoton., 5, 483-50, 2012.
2. Byun, K. M., Kim, S., J., and Kim, D., "Grating-coupled transmission-type surface plasmon resonance sensors based on dielectric and metallic gratings," Appl. Opt. 46, 5703-5708, 2007.
3. Chakraborty, K., Kumawat, N., Sultana, S., and Varma, M.M., "Enhancing the quality factor of grating coupled plasmon resonance in optical recording media," Sens. Actuator A Phys., 244, 50-55, 2016.
4. Sauvage-Vincent, J., Jourlin, Y., Petiton, V., Tishchenko, A. V., Verrier, I., and Parriaux, O., "Low-loss plasmon-triggered switching between reflected free-space diffraction orders," Opt. Express 22, 13314-13321, 2014.
5. Lin, K., Lu, Y., Chen, J., Zheng, R., Wang, P., and Ming, H., "Surface plasmon resonance hydrogen sensor based on metallic grating with high sensitivity," Opt. Express 16, 18599-18604, 2008.
6. Abutoama, M. and Abdulhalim, I., "Angular and intensity modes self-referenced refractive index sensor based on thin dielectric grating combined with thin metal film," IEEE J. Sel. Top. Quantum Electron, vol. 23, no. 2, pp. 72-80, 2017.

Modulable Chiral Plasmonic Activates via Stimulus Triggered Shape-Morphing

Yisheng He, Chunhong Ye*

School of Physical Science and Technology, Shanghai Tech University, Shanghai 201210, China

*corresponding author: yechh@sahnghaitech.edu.cn

Abstract: A unique approach to fabricate chiral plasmonic materials based on helically arranged AuNSs was presented by utilizing polymeric micro-origami. The shape-morphing of the micro-origami from 2D sheets to 3D tubules induced the pre-assembled AuNS chains into 3D helices, which exhibited tunable circular dichroism signals over frequency, magnitude and handedness.

Chiral assembly of plasmonic nanoparitcles have attracted broad interest due to its unique circularly polarized light-dependent optical response, presenting great potentials for photonic and biomedical applications.[1,2] However, it still remains challenging to have a simple strategy to modulate chiroptical properties.[3] In this work, we demonstrate a facile approach to fabricate chiral plasmonic micro-structures composed of 3D helically assembled gold nanoparticles (AuNSs), which is facilitated by the shape-morphing of polymer-based micro-origami.

Gold nanospheres (AuNSs) with an average diameter of 75 ± 2 nm were utilized here. To create helical assemblies of the nanoparticles, AuNSs were aligned onto the responsive polymer-based micro-sheets through template-assisted colloidal assembly by employing unidirectional polydimethylsiloxane wrinkles as templates.[4] Closely packed AuNS linear chains with well-controlled positions and gaps were yielded on the substrate over centimeter area (Figure 1). The polymeric micro-sheets were prepared by photo-crosslinking using a 254 nm UV-light through a photomask with pre-designed rectangle-shaped openings. The chemical components of the micro-sheets are composed of temperature-responsive poly(N-isopropylacrylamide) (PNIPAM) as active layer and non-responsive poly(methyl methacrylate) (PMMA) as passive layer, respectively.

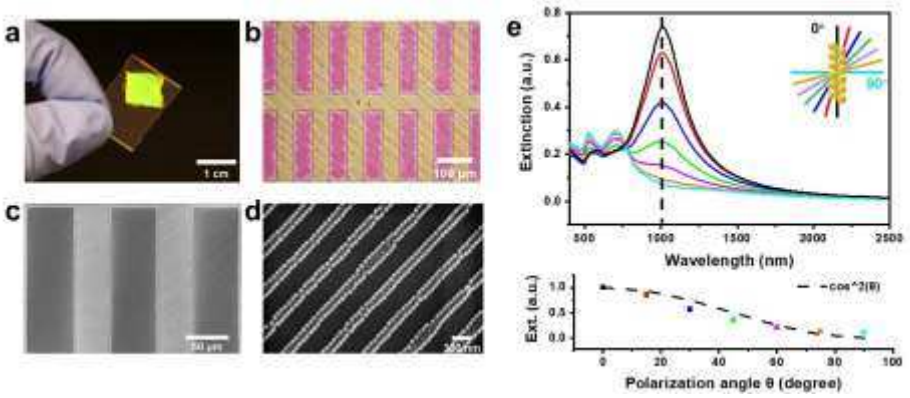


Figure 1. 2D linearly aligned gold nanospheres (AuNSs) structure and optical property. (a-d) Photography, and optical microscope, SEM micro-sheet arrays with homogeneous coverage of linearly AuNS chains. (e) Measured extinction spectra of the entire macroscopic samples within UV-vis-NIR range under varied polarization angles with respect to the axis of chains.

Upon exposure to aqueous solution with a temperature (used 0 °C) below the lower critical solution temperature (LCST, 28 °C) of PNIPAM, the 2D micro-sheets spontaneously rolled up to 3D hollow micro-tubulars. Accompanied with the shape-morphing of micro-sheets, the pre-assembled linearly AuNS chains transformed to

3D helical geometry along the internal wall of micro-tubulars (Figure 2a-c). The AuNS helices with geometrical asymmetry contributed to plasmon-based chiral material.

To quantitatively characterize the chiroptical property, 4x4 Müller matrix data were collected from spectroscopic ellipsometry in transmission mode to evaluate the circular dichroism (CD) and optical asymmetry factor (g-factor). A characteristic CD spectrum was detected with two distinct peaks and dips, as for the typical AuNS helices rolled from 30° aligned AuNSs chains with respect to the long axis of the rectangular micro-sheets (bottom of Figure 2d), whereas the AuNS chains in 2D array as control sample did not show any CD signal (top of Figure 2d). The observed different chiral response supported that chiroptical signal stemmed from the helical arrangements of the closely packed gold nanoparticles with nanometer-sized gaps. To identify the origin of the observed chiral response, the electromagnetic simulations were further carried out for double helical chains with a nanoparticle gap of 2 nm. The calculated CD spectra for left- and right-handed helical structures agreed qualitatively with the measured results with four distinctive features (Figure 2e, f).

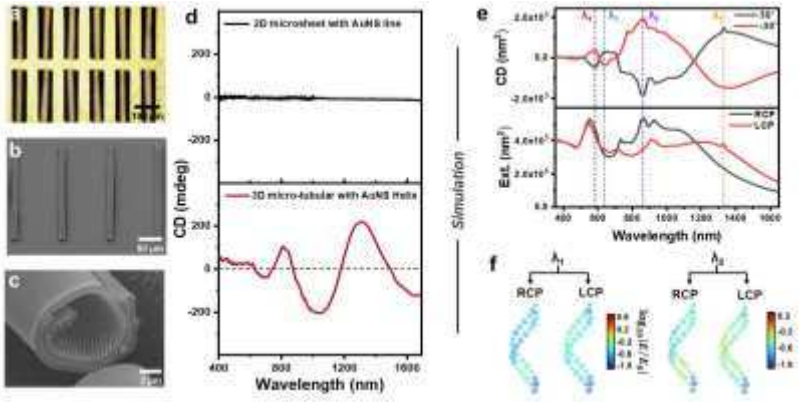


Figure 2. 3D helically aligned AuNSs and chiral optical properties. (a-c) Optical microscope and SEM imageS of the micro-tubes rolled-up from rectangular sheets covered with AuNS chains. (d) Measured CD response at different morphologies. (e) Simulated CD response and extinction cross-sections of left- and right-handed gold nanospheres chains. (f) Simulated electric field enhancement of the corresponding structures.

The micro-origami based approach for constructing 3D AuNS helix enables facile tuning and switch of the handedness. By controlling the assembly angle of AuNSs chains, the CD response frequency, magnitude and handedness can be readily tuned. CD spectra with mirrored symmetry were observed for two rolled-up AuNS helices with opposite handedness, formed by the AuNS chains with tilted angles of different signs, and all the CD spectra showed features with two distinctive dips and peaks, which was also confirmed by FDTD simulation.

References

1. Zhang, Q. and Link, S. et al. "Unraveling the origin of chirality from plasmonic nanoparticle-protein complexes," *Science, 365*, 1475–1478, **2019**.

2. Ma, W. and. Kotov, N. A. et al. "Chiral inorganic nanostructures," *Chem. Rev. 117*, 8041-8093, **2017**.

3. Probst, P. T. and Fery, A. et al. "Mechano-tunable chiral metasurfaces via colloidal assembly." Nat. Mater. 20, 1024-1028, 2021.

4. Hanske, C. and Fery, A. et al "Strongly coupled plasmonic modes on macroscopic areas via template-assisted colloidal self-assembly," *Nano Lett. 14*, 6863-6871, **2014**.

Utilizing a microcone array to control the distance between a microsphere and a SERS substrate for photonic nanojet-mediated SERS

Chen-Ting Hung[1], Yan-Ru Liu[1], Yih-Fan Chen[1*]

[1]Institute of Biophotonics, National Yang Ming Chiao Tung University, Taipei 112, Taiwan, R.O.C.

*corresponding author: chenyf@nycu.edu.tw

Abstract: A photonic nanojet (PNJ) is a narrow and intense electromagnetic beam on the shadow side of a microsphere when illuminated by light. We fabricated a microcone array to control the distance between microspheres and surface-enhanced Raman spectroscopy (SERS) substrates, effectively utilizing the PNJ effect to enhance signals by 15 times.

The photonic nanojet (PNJ) is a subwavelength focusing phenomenon observed on the shadow side of a light-illuminated microsphere. Due to its ability to generate a sub-diffraction-limited focusing spot and an intense electric field, PNJs have found applications in enhancing surface-enhanced Raman spectroscopy (SERS) [1], increasing the intensity of fluorescent dyes, and providing super-resolution imaging. However, since the focusing spot of a PNJ is elongated and typically located a few microns away from the surface of the microsphere, to ensure effective excitation of the electromagnetic hot spots of a SERS substrate by a PNJ, we fabricated microcone arrays with different spacing and used the arrays to control the distance between microspheres and SERS substrates (Figure 1(a)). When the focus of a PNJ was on the surface of a SERS substrate, SERS signals could be significantly enhanced by the PNJ effect.

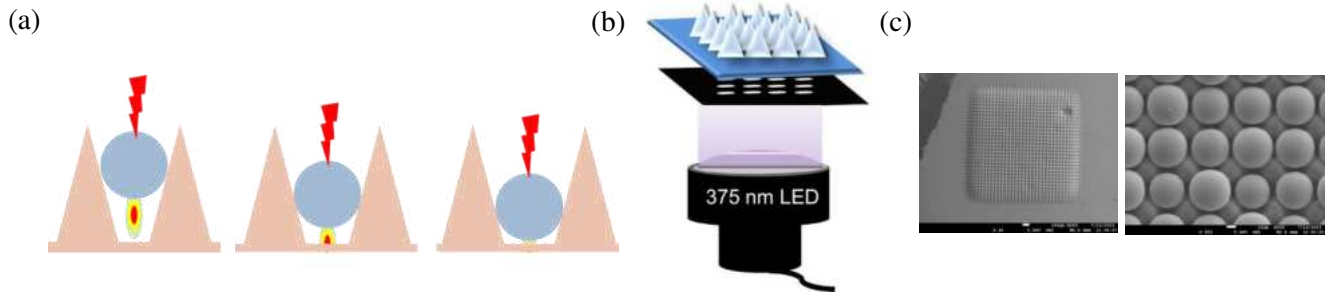


Figure 1. (a) Schematic representation of controlling the distance between microspheres and SERS substrates using microcone arrays with different spacing. (b) Schematic illustration of the fabrication of the microcone arrays. (c) SEM images showing 55 μm silica microspheres on the microcone array.

To fabricate microcone arrays, photopolymerization solution was prepared by mixing poly(ethylene glycol) diacrylate (PEGDA) and 2,2-Dimethoxy-2-phenylacetophenone (DMPA). We then used a 375 nm LED light source and a photomask with a circular hole array to cure the PEGDA solution on a glass slide [2] (Figure 1(b)). After the curing process, a microcone array was formed (Figure 1c). We utilized different photomasks with varying hole arrays to create microcone arrays with different spacing. Next, we modified the microcone arrays with (3-Aminopropyl)triethoxysilane (APTES) and 28 nm silver nanoparticles (AgNPs). Finally, we injected a

mixture of adenine and silica microspheres onto the microcone array, and SERS signals were measured using a Raman spectrometer with a 633 nm laser excitation.

We evaluated the PNJ effects of 55-μm silica microspheres on SERS by measuring 10 μM adenine using AgNP-decorated microcone substrates (Figure 2(a)). SERS spectra were obtained using microcone arrays with different spacings, as shown in Figure 2(b, c). Measurements were taken at locations where microspheres were present and absent, with each SERS spectrum in the figure representing the average of data from 5 locations. By comparing the intensities of the Raman peak at 733 cm^{-1} with and without the 55-μm microspheres, we calculated the additional Raman enhancements, as illustrated in Figure 2(d). Our results indicate a maximum enhancement of ~15 from the PNJ effect when using the 55-μm silica microsphere."

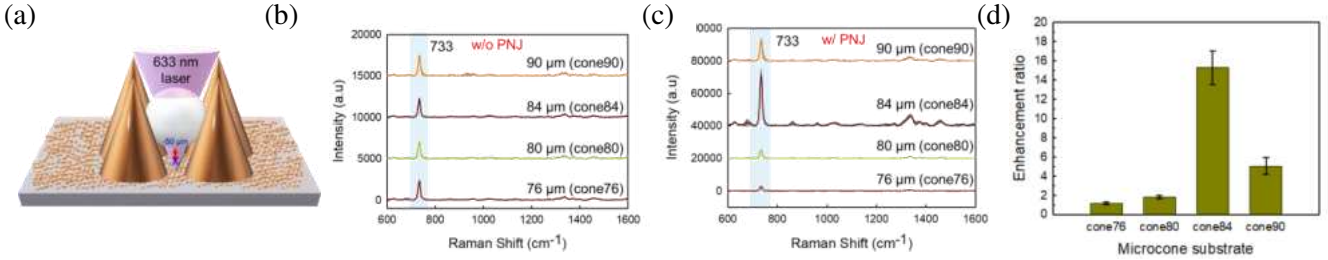


Figure 2. (a) Schematic representation of PNJ-enhanced SERS. (b, c) SERS spectra obtained using AgNP-decorated microcone arrays with different spacings. The circular hole arrays in the masks used for fabricating the microcone substrates had a diagonal distance between adjacent holes ranging from 76 to 90 μm. In the circular hole arrays of the masks used to fabricate the microcone substrates, the distance between adjacent holes diagonally was between 76 and 90 μm. Measurements were conducted (b) without and (c) with the 55 μm silica microspheres. (d) Additional Raman enhancements from the microsphere.

Acknowledgement

We thank the financial support from the Ministry of Science and Technology, Taiwan (MOST 111-2221-E-A49-006-MY3).

References

1. Xie, C.Z., C.H. Li, Y.C. Chang and Y.F. Chen, “Optofluidic accumulation of silica beads on gel-based three-dimensional SERS substrate to enhance sensitivity using multiple photonic nanojets,” ACS Appl. Mater. Interfaces, 15, 31703–31710, 2023.
2. Takahashi, H., T. Kan, G. Lee, N. Dönmez, J. Km, J. Park, D. Kim and Y.J. Heo, “Self-focusing 3D lithography with varying refractive index polyethylene glycol diacrylate,” Appl. Phys. Express, Vol. 13, 076503, 2020.

Investigating the charge carrier dynamics in an array of Split-H ladder (SHL) of Au on amorphous SiO_2

N. Vashistha[1*], R. Sharma[2], T. N. Narayanan[2], R.S. Singh[3], and M. Sharma[4*]

[1] Institute of Physical Chemistry, Friedrich Schiller University Jena, Helmholtzweg 4, 07743 Jena, Germany

[2]Tata Institute of Fundamental Research-Hyderabad, Serilingampally Mandal, Hyderabad 500046, India

[2]Tata Institute of Fundamental Research, Hyderabad 500062, India

[3]*CSIR-National Physical Laboratory, Dr K.S. Krishnan Road, New Delhi, 110012, India*

[4]*Innovation Management Directorate, Council of Scientific & Industrial Research (CSIR), Anusandhan Bhawan, 2, Rafi Marg New Delhi - 110 001, INDIA*

[*]corresponding author: nikita.vashistha@uni-jena.de, mkumar@csir.res.in

Abstract: In this work we investigated carrier dynamics in SHL-array on gold deposited on amorphous SiO_2. Each 140nmx220nm unit cell has a slit width of 260nm. The sample shows multiple resonance bands extending from visible to NIR region and long-lived excited carriers due to structuring induced changes in electron phonon interaction.

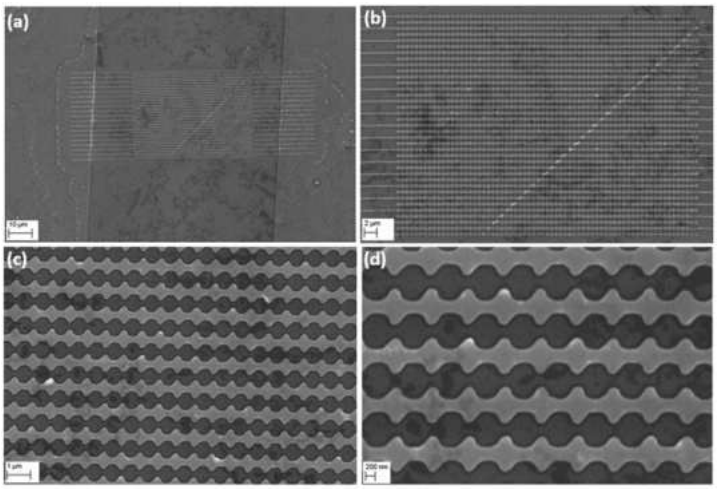


Figure 1: A SEM image of EBL fabricated structures on SiO_2 at varying magnifications.

Figure 1 shows SEM image of the SHL array at different magnifications. From figure 1(d) we can see that the edges of the H shape were over etched during fabrication which gives them a round shape. The sample was then characterized under transient absorption spectroscopy to measure the transient optical response. The sample was exited by a 410 nm pump and analysed with both visible and NIR probe. Figure 2 (a) shows a broad negative dip at 460 nm that decays in 5- 10 ps time (figure 2 (b)). This behavior is attributed to bleaching of SP resonance of 10 nm gold thin film[1]. At later delay times we see appearance of another behavior around 636 nm which stays for a longer time (100s of ps). This behavior is because of the resonant SHL. Positive ΔA signal due to excited state absorption (ESA) of carriers generated through interband transition and SPR dephasing[2]. The decay kinetics of these carriers indicate that they do not decay within the 5 ns measurement window. This suggests either a prolongation of decay induced by the structure itself or the transfer of hot carriers to the SiO_2 substrate.

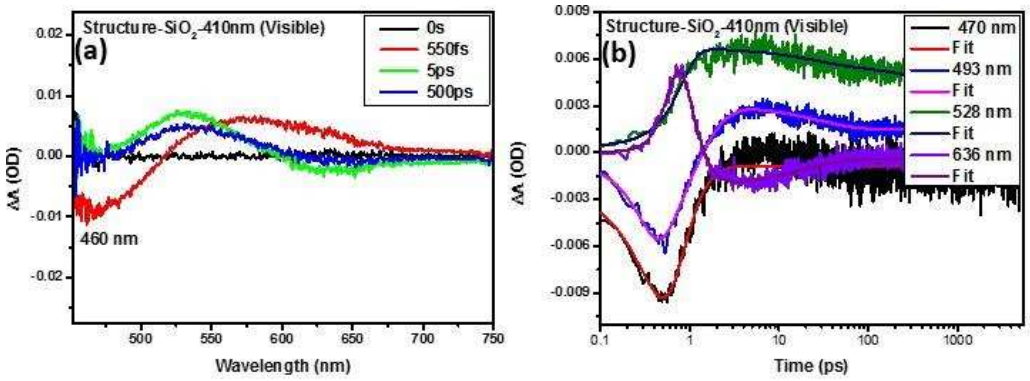


Figure 2: Transient absorption a) spectra b) kinetics of structures fabricated on SiO_2 excited by 410 nm pump and visible probe.

The transient behavior in NIR region (figure 3) show a broad negative signal extending 1150 nm to 1600 nm. The initial behavior at 750 fs is of an Au film over SiO_2. It red shifts to give a GSB at 1450 nm and ESA at 1200 nm. This behavior decays within 5 ps and a broad ESA covers the whole NIR spectra. The ESA in this wavelength region decays completely within 50 ps.

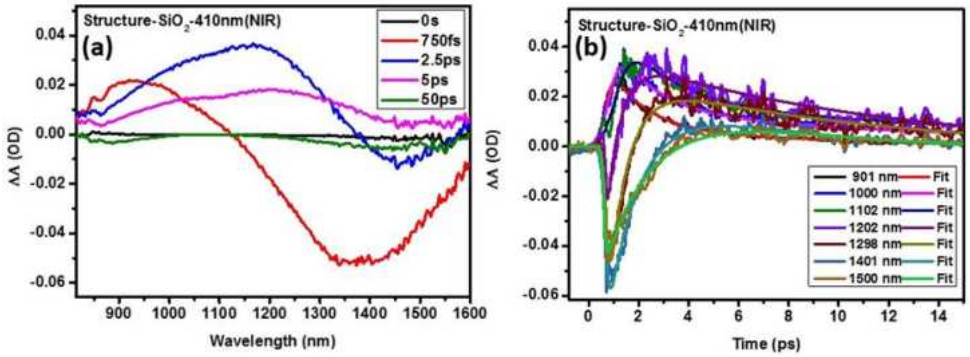


Figure 3: Transient absorption a) spectra b) kinetics of structures fabricated on SiO_2 excited by 410 nm pump and NIR probe.

The fabricated SHL structure has three resonance band centered at 460 nm, 636 nm and 1450 nm. The exited charge carrier in visible shows a prolonged decay time which is one of the crucial criteria in high efficiency solar cells and photocatalytic systems. The extended decay rate arises from unavoidable alterations in phonon interactions, induced by dimensional confinement impacting phonon modes within nanostructures [3].

The authors are thankful to the CSIR-National Physical Laboratory and TIFR, India for providing the measurement facility for this study.

References

1. Z. Xinping, C. Huang, M. Wang, P. Huang, X. He & Z. Wei "Transient localized surface plasmon induced by femtosecond interband excitation in gold nanoparticles," Scientific Reports, Vol. 604, No. 1, 10499, 2021.
2. N. Vashistha, A. Kumar, M. Vij, R. K. Singh, M. Kumar, "Detection and analysis of structural changes in MoO3/Ag heterostructure by ultrafast transient absorption spectroscopy," Journal Title Abbreviation, Vol. 8, 412697, 1986.
3. A. Alizadeh, A. Rostami, H. Baghban, H.B. Bahar, "Tailoring electron–phonon interaction in nanostructures," Photonics Nanostructures: Fundam. Appl., Vol. 12, No. 2, 164–172, 2014.

Investigating Nonlinear Optical Switching via Nanosecond Z-scan: Coupling Saturable Absorption in Gold with Reverse Saturable Absorption in Strontium Titanate

Nikita Vashistha[1], Hitheshwar Prasad[2], N. Sri Ram Gopal[2], Rajiv K. Singh[3], Sandeep Singh[3], S.P. Singh[3], Mahesh Kumar[4*]

[1] Institute of Physical Chemistry, Friedrich Schiller University Jena, Helmholtzweg 4, 07743 Jena, Germany

[2] School of Physics, University of Hyderabad, Prof CR Rao Road, Gachibowli, Ranga Reddy, Telangana,500046, India

[3] *CSIR-National Physical Laboratory, Dr K.S. Krishnan Road, New Delhi, 110012, India*

[4] *Innovation Management Directorate, Council of Scientific & Industrial Research (CSIR), Anusandhan Bhawan, 2, Rafi Marg New Delhi - 110 001, INDIA*

[*]corresponding author: : nikita.vashistha@uni-jena.de, mkumar@csir.res.in

Abstract: This study demonstrates visible region nonlinear optical switching by coupling reverse saturable absorption(RSA) in STO with saturable absorption(SA) in a Gold film. SA in Gold comes from SPR bleaching, while RSA in STO from 2PA. Using a nanosecond pulsed laser(532nm), we achieved optical switching at irradiances from 2.12 to 3.0GW/cm².

Summary:

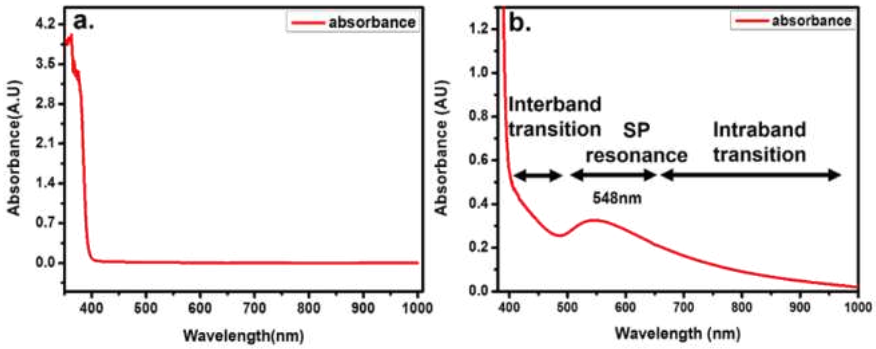
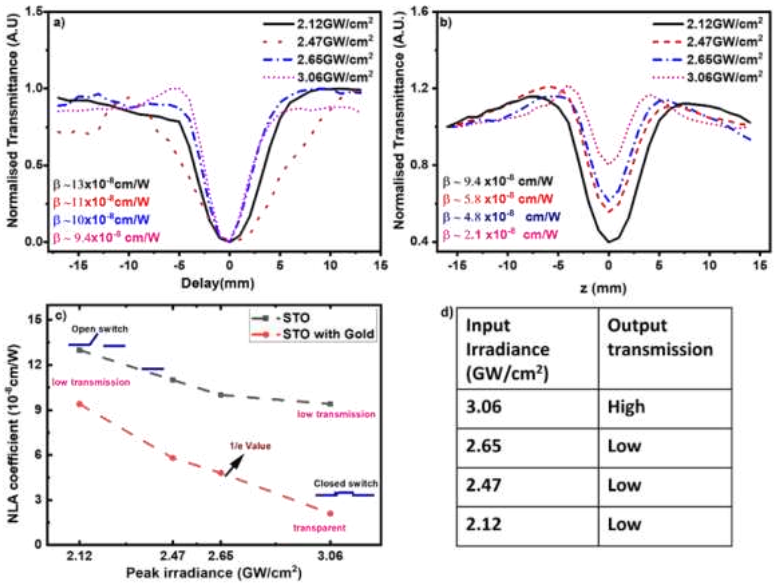


Fig. 1. *Linear absorption spectra of a) STO substrate (100) b) 11 nm Gold thin film deposited on STO through thermal vapour deposition.*

As seen from fig. 1 (a), STO shows high absorption in the UV region (below 400 nm) with the maximum transmission in the Visible and NIR range (400 nm -1000 nm). On deposition of gold film (11 nm) over STO (fig. 1(b)) we see an appearance of interband absorption from 400 nm to 500 nm, a broad SP resonance band at 548 nm and an intraband absorption tail above 650 nm [1]. The interband transitions is from filled d band to empty sp band while the intraband transitions is within the filled and unfilled orbitals of the sp-band in Au [2,3]. Through AFM the RMS (Rq) roughness of the film came out to be around 2.46 nm.

Fig. 2 represent non-linear absorption in STO and gold film deposited on STO, respectively obtained through Z-scan using 532 nm, 6 ns pulses of varying energy (2.12 GW/cm^2, 2.47 GW/cm^2, 2.65 GW/cm^2 and 3.0 GW/cm^2).



Input Irradiance (GW/cm²)	Output transmission
3.06	High
2.65	Low
2.47	Low
2.12	Low

Fig. 2. *Laser irradiance dependent variation in a) normalized transmittance of STO, b) normalized transmittance of 11 nm thick gold film deposited on STO, c) non-linear absorption coefficient (NLA) of STO and Gold over STO. The change in NLA coefficient indicates a shift in switching threshold due to introduction of gold film. d) Truth table of the optical switch thus obtained.*

The value of the non-linear absorption coefficient 'β' (listed in fig 2 (a) and (b)) corresponding to laser energy variation is calculated using following relation [17]

$$\beta = \frac{((m+1)^{1.5} * \Delta T)}{(I_o * L_{eff})} \qquad (1)$$

Where 'm' is a constant, which depends on the order of nonlinearity. For 3rd order nonlinearity, 'm' is taken as 1, ΔT = difference in peak transmittance and the least transmittance (normalized), Leff= effective sample width (cm).

As seen from fig 2 (a) STO dominantly shows RSA which is attributed to 2PA thus making it a good candidate for optical limiter or saturable absorber. For Au-STO heterostructure, we observe a competition between saturable absorption (SA) and reverse saturable absorption (RSA) as the input irradiance varies. For the value of peak irradiance > 2.65 GW/cm^2 or $\beta < 1/e^{th}$ of the initial value, the sample shows high transmission or behaves like a closed switch (low transmission). This result is summarized by the truth table shown in Fig. 2(d). For Gold film deposited on STO (Fig.2 (b)), the SA or decrease in 'β' is due to local field enhancement by SP wave of Au clusters in thin Au film.

The authors would like to thank CSIR-NPL and HCU for providing the instrumental facilities required for this work. One of the authors, Nikita Vashistha, would like to thank UGC for providing a student research fellowship.

References

1. Derrien, T.J., Kruger, J., Bonse, J., "Properties of Surface Plasmon Polaritons on lossy materials: Lifetimes, periods and excitation conditions", J. Opt. (United Kingdom) 18,115007,2016.
2. Wang, W., Fang, J., Huang, X., "Different behaviors between interband and intraband transitions generated hot carriers on g-C_3N_4/Au for photocatalytic H_2 production", Appl. Surf. Sci. 513,145830,2020.
3. Kolwas, K., "Impact of the Interband Transitions in Gold and Silver on the Dynamics of Propagating and Localized Surface Plasmons", Nanomaterials, 10,1411,2020.

META 2024, TOYAMA - JAPAN, JULY 16 - 19, 2024

Hybrid Plasmonic Waveguide NFT for HAMR Heads

W. Lee[1,*], A. B. Neira[2], B. R. McConnell[2], and R. M. Bowman[1,2]

[1]EPSRC and SFI Center of Doctoral Training in Photonic Integration & Advanced Data Storage, School of Mathematics & Physics, Queen's University Belfast, Belfast BT7 1NN
[2]Seagate Technology, 1 Disc Drive, Londonderry BT48 0LY
[*]Corresponding author: wlee16@qub.ac.uk

Abstract

In this study, a novel hybrid plasmonic waveguide as near field transducer is proposed, consisting of high refractive index nanorod separated from metal by low primitivity region. The design aims to enhance mode confinement at the metal-dielectric interface by combining the benefit of both the nanorod and the plasmonic waveguide.

Keywords— HAMR, HPW, NFT, ...

Heat-assisted Magnetic Recording (HAMR) is a technology that has been developed to address the need for higher data storage capacities in hard disk drives (HDDs). The technology enables greater write densities, allowing more data or grains to be stored onto each area of the disk platter by using a laser to heat a small portion of the recording surface.[1] This reduces the coercivity below of that of the applied magnetic field from the recording head, allowing for more stable bits to be written on the disk.

HAMR technology necessitates the utilization of materials that have resistance to high temperature. One of the primary challenges in utilizing these materials to improve thermal stability; is their compatibility with the current HAMR system design. The reliability and long-term stability of refractory materials under repeated thermal cycling is a significant concern. HAMR involves the repeated heating and cooling of the recording media during the read-write process, which can lead to material fatigue and degradation over time. Ensuring that refractory materials can withstand these thermal stresses without compromising their structural integrity or performance is vital for the durability and reliability of HAMR systems.

To achieve this, the laser heat needs to be efficiently transferred to the recording media without causing excessive heating in other components of the HAMR system. The integration and deposition of refractory materials to the recording transducer and their subsequent patterning and alignment with the laser may require new fabrication techniques and equipment. These materials are known for their excellent thermal stability and high reliability, however they diminish the plasmonic performance due to their poor optical properties therefore leading to the need to explore different design avenues.[2]

Here we explore the possibility of doing HAMR using dielectric loaded plasmonic waveguides (DLPW).[3] These nano-waveguides use the dielectric (typically a non-absorptive high refractive index material) to carry the plasmons, therefore enabling low absorption losses while also guaranteeing heat spot confinement through the waveguide size. The effective refractive index that determines the propagation characteristics of the guided mode in the HPW can be calculated using:[4]

$$n_{eff} = n_r\left(1 - \frac{d_g}{d_r}[(n_r^2 - n_m^2)/(n_r^2 - n_d^2)]^{(1/2)}\right) \tag{1}$$

where n_r is the refractive index of the high index nanowire, d_g presents the separation between metal and nanorod,

d_r gives the diameter of the high index nanowire, n_m and n_c donate the refractive indices of the metal and dielectric gap respectively. A schematic of the geometry is shown in Fig (1)

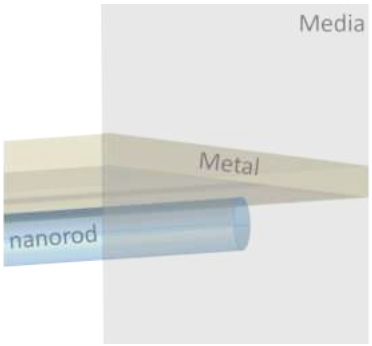


Figure 1: HPW consists of high index nanowire embedded in low permittivity dielectric, separated from the metal (ϵ_m) by a gap of SiO_2 ($\epsilon_d = 2.25$).

We will examine the heatspot confinement generated by the DLPW as well as different methods for coupling light to it and integrated to a typical HAMR head.

Acknowledgment: We acknowledge the support of the Engineering and Physical Sciences Research Council (EPSRC) under grant number EP/S023321/1, Seagate Technology (Ireland) under SOW #00077300.0 and the Royal Academy of Engineering under the Research Chairs and Senior Research Fellowships Scheme.

References

[1] D. Weller, G. Parker, O. Mosendz, E. Champion, B. Stipe, X. Wang, T. Klemmer, G. Ju, and A. Ajan, "A hamr media technology roadmap to an areal density of $4tb/in^2$," *IEEE Trans on Magn*, vol. 50, no. 1, pp. 1–8, 2013.

[2] D. K. Gramotnev and S. I. Bozhevolnyi, "Plasmonics beyond the diffraction limit," *Nature photonics*, vol. 4, no. 2, pp. 83–91, 2010.

[3] H.-S. Chu, Y. A. Akimov, P. Bai, and E.-P. Li, "Hybrid dielectric-loaded plasmonic waveguide and wavelength selective components for efficiently controlling light at subwavelength scale," *JOSA B*, vol. 28, no. 12, pp. 2895–2901, 2011.

[4] R. F. Oulton, V. J. Sorger, D. Genov, D. Pile, and X. Zhang, "A hybrid plasmonic waveguide for subwavelength confinement and long-range propagation," *nature photonics*, vol. 2, no. 8, pp. 496–500, 2008.

Titanium nitride (TiN) nano and microstructures as novel highly efficient SERS platform.

J. Krajczewski[1], A. Michałowska[1], L. Nozka[2,3]

[1] Faculty of Chemistry, University of Warsaw, 1 Pasteur Str, 02-093 Warsaw, Poland
[2] Institute of Physics of the Czech Academy of Sciences, Joint Laboratory of Optics of Palacky University and Institute of Physics AS CR, 17. Listopadu 50a, 772 07 Olomouc, Czech Republic
[3] Palacký University in Olomouc, Faculty of Science, Joint Laboratory of Optics of Palacký University and Institute of Physics AS CR, 17. listopadu 12, 771 46 Olomouc, Czech Republic

*corresponding author: jkrajczewski@chem.uw.edu.pl

Abstract: In this work, we report on a high-efficiency SERS platform based on Titanium Nitride (TiN) nano and microstructures. TiN films were deposited by magnetron sputtering. The structural, and optical properties were carefully studied. SERS measurements confirmed the high SERS activity of TiN samples with good stability and repeatability.

So far, most of the SERS platforms are based on noble metals, especially gold and silver. However, the last research showed very promising optical properties of titanium nitride (TiN) nano and microstructures[1]. Such materials are mainly used in photocatalysis[2], but our last research proved excellent SERS activity in novel, non-metallic materials based on TiN[3]. In this work, we study for the first time samples having the same morphology coated by TiN and Au layers with the same thicknesses.

The Si pyramids were formed by the chemical etching of Si wafers. TiN thin films were prepared by a magnetron sputtering method. The structural properties were done by SEM microscopy. Data analysis showed that deposited Au and TiN layers are continuous and do not change the morphology of the formed Si pyramids. The optical properties were studied by UV–Vis DRS and spectral ellipsometry measurements proved the plasmonic properties of both types of materials. It was found that the SERS efficiency increased as the thickness of the deposited films increased and reached a maximum of 160 nm of film thickness. The minimal detectable amount of Raman reporter molecules (tartazine) was the same for both sample types of the SERS platform and equal to 10^{-9}M concentration. It was also proved that due to their hydrophobic properties, TiN-Si samples can be used as SERS platforms that are reversible after simple rinsing in water even in 20 cycles.

Acknowledgments: J. K. thanks the University of Warsaw, Faculty of Chemistry for its financial support, L. N. thanks the Palacky University (IGA_Prf_2024_04) and MSMT of the Czech Republic (OP JAC CZ.02.01.01/00/22_ 008/0004631) for its financial support.

References

1. Cortie M. B., Gidding J., Dowd A., “Optical properties and plasmon resonances of titanium nitride nanostructures,” Nanotechnology, Vol. 21, No. 11, 1-8, 2010
2. Nguyen D.-T., Do T.-O., “Plasmonic Titanium Nitride/g-C3N4 with Inherent Interface Facilitates Photocatalytic CO2 Reduction,“ACS Appl. Energy Mater, Vol. 6, No. 1, 89–98, 2023
3. Krajczewski J., Michałowska A., Ctvrtlik R., Nozka L., Tomastik J., Vaclavek L., Turczyniak-Surdacka S., Bieńkowski

K., Solarska R., “The battle for the future of SERS – TiN vs Au thin films with the same morphology, “Appl. Surf. Sci., Vol. 618, 156703, 2023

Self-assembled silicon photonic cavities with atomic-scale confinement and self-aligned integration with photonic circuits

Ali Nawaz Babar[1,2] Thor August Schimmell Weis[1], Konstantinos Tsoukalas[1], Shima Kadkhodazadeh[2,3], Guillermo Arregui[1], Babak Vosoughi Lahijani[1], and Søren Stobbe[1,2,*]

[1]DTU Electro, Department of Electrical and Photonics Engineering,
Technical University of Denmark, Ørsteds Plads 343, DK-2800 Kgs. Lyngby, Denmark
[2]NanoPhoton - Center for Nanophotonics, Technical University of Denmark,
Ørsteds Plads 345A, DK-2800 Kgs. Lyngby, Denmark
[3]DTU Nanolab, Technical University of Denmark, B. 347, DK-2800 Kgs. Lyngby, Denmark
[*]corresponding author: ssto@dtu.dk

Abstract: We use surface forces to self-assemble all-silicon photonic nanocavities that confine light to air gaps at the scale of a few atoms. This relies on a new fabrication method that uses self-assembly to bypass the resolution limit of conventional fabrication and results in cavities with unprecedented figures of merit.

Enhancement of the light-matter interaction strength is a central goal in nanophotonics as it is required for building better and more compact devices or even realizing entirely new functionalities within areas such as nanolasers, optical interconnects, and quantum light sources [1]. The strongest enhancements are obtained in cavities, and while research on photonic-crystal cavities has led to very high quality factors, a common assumption in the field has been that dielectric cavities are bound to mode volumes larger than the diffraction limit. Recent developments have disproved this assumption: the diffraction limit does not apply to cavities, and dielectric bowties can confine light to arbitrarily small mode volumes limited only by the capability of the nanofabrication [2]. Interestingly, these insights are not new [3], but the experimental progress in the research on dielectric bowtie devices was for many years impeded by the extreme requirements posed on the nanofabrication.

Further miniaturization of the mode volume and thus the enhancement of the light-matter interaction requires unconventional fabrication concepts as previous demonstrations already go well below the smallest lithography features in the semiconductor industry [2]. We present a new method that combines the atomic-scale resolution of self-assembly with the scalability and circuitry of planar photonic circuits [4]. The method bypasses the resolution limit of lithography and results in dielectric cavities with unprecedented dimensions, confining light in air gaps with widths of about a few silicon atoms, as shown in Fig. 1. The new cavities feature mode volumes 100x below the diffraction limit while at the same time exhibiting quality factors 100x above the theoretical limit of plasmonics, while also being self-aligned to and efficiently coupled to a waveguide. The smallest dimension of devices obtainable with the new method is only limited by structural disorder [5].

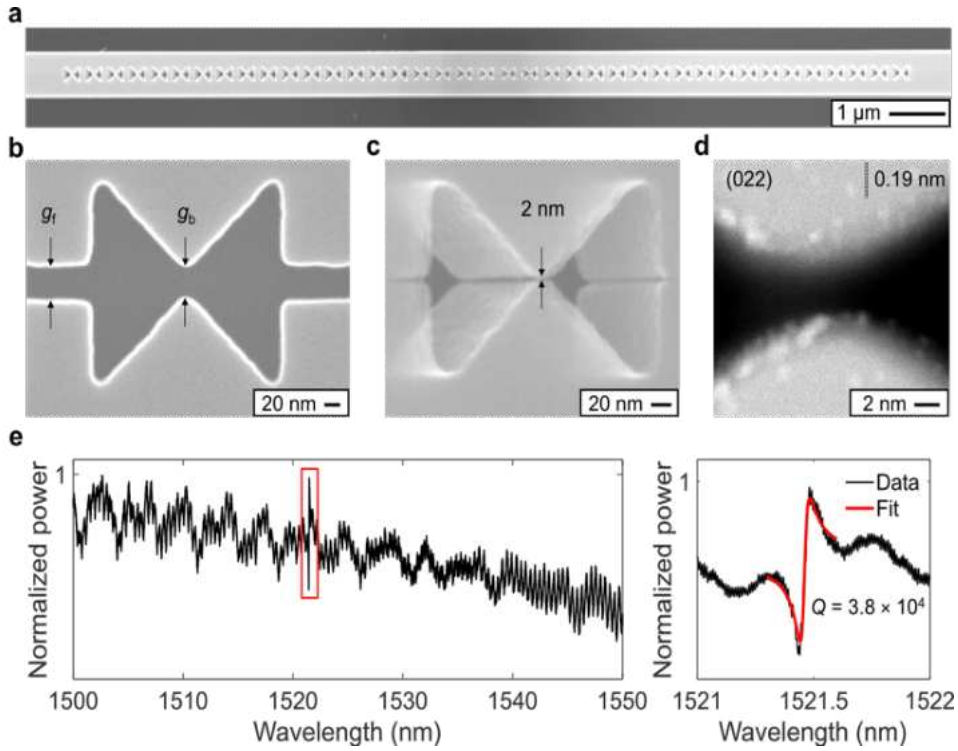


Figure 1. Fabrication and optical characterization of self-assembled atomic-scale photonic cavities. (a) Scanning electron microscope (SEM) image of a self-assembled nanobeam cavity. (b) Top-view SEM image of a single bowtie unit cell before self-assembly, with a fabricated gap, g_f, and a bowtie gap, g_b. (c) A bowtie unit cell after self-assembly with an approximate bowtie width of 2 nm. (d) Top-view high-resolution transmission electron microscope image of the central region of the bowtie with an approximate 2 nm gap. The interplanar distance between the (022) silicon crystal planes is 0.19 nm. (e) Scattered far-field spectrum of a self-assembled nanobeam cavity measured using cross-polarized optical microscopy. The inset shows the resonance of the fundamental mode at the wavelength of 1521.5 nm, and a quality factor of 3.8×10^4, extracted by fitting a Fano lineshape to the resonance.

References

1. Lodahl, P., S. Mahmoodian and S. Stobbe, "Interfacing single photons and single quantum dots with photonic nanostructures," Reviews of Modern Physics Vol. 87, 347-400, 2015.
2. Albrechtsen, M., B. Vosoughi Lahijani, R. E. Christiansen, V. T. H. Nguyen, L. N. Casses, S. E. Hansen, N. Stenger, O. Sigmund, H. Jansen, J. Mørk and S. Stobbe, "Nanometer-scale photon confinement in topology-optimized dielectric cavities," Nature Communications Vol. 13, 6281:1-8, 2022.
3. Gondarenko, A., S. Preble, J. Robinson, L. Chen, H. Lipson and M. Lipson, "Spontaneous Emergence of Periodic Patterns in a Biologically Inspired Simulation of Photonic Structures," Physical Review Letters Vol. 96, 143904:1-4, 2006.
4. Babar, A. N., T. A. S. Weis, K. Tsoukalas, S. Kadkhodazadeh, G. Arregui, B. Vosoughi Lahijani and S. Stobbe, "Self-assembled photonic cavities with atomic-scale confinement," Nature Vol. 624, 57-63, 2023.
5. Rosiek, C. A., G. Arregui, A. Vladimirova, M. Albrechtsen, B. Vosoughi Lahijani, R. E. Christiansen and S. Stobbe, "Observation of strong backscattering in valley-Hall photonic topological interface modes," Nature Photonics Vol. 17, 386–392, 2023.

Tamm Assisted Metasurfaces for classical and quantum photonics applications

Edmund Harbord[1,2], Huili Hou[1,2,3],Talal Alshammari[2] Mengxun Bai[2], David Dlaka[1,2], Angela Stephens[1,2,3], Jon Pugh[1,2], Ruth Oulton[1,2], and Martin Cryan[2]

[1]Quantum Engineering Technology Labs, H. H. Wills Physics Laboratory and School of Electrical, Electronic and Mechanical Engineering, University of Bristol, BS8 1FD, UK

[2]Photonics and Quantum Group, School of Electrical, Electronic and Mechanical Engineering, University of Bristol, BS8 1FD, UK

[3]Quantum Engineering Centre for Doctoral Training, University of Bristol, Tyndall Avenue, BS8 1FD, UK
*corresponding author: edmund.harbord@bristol.ac.uk

Abstract: Tamm optical states are formed at the interface between a distributed Bragg reflector and a thin (~10 nm) layer of metal. We combine these with metasurfaces to form readily manufacturable devices for controlling light at the nanoscale with applications in lasers, single photon sources, and photodetectors.

Tamm optical states – sometimes called Tamm plasmons – are formed at the interface between a distributed Bragg reflectors and a nanoscale layer of metal (see figure 1). Unlike conventional surface plasmons, the majority of the mode is located in the lossless dielectric layer; they have a parabolic dispersion within the light cone, so can be coupled to without momentum matching; and can be excited with both TE- and TM- polarized light[1]. By laterally sculpting the metal layer, it is possible to form confined Tamm plasmons, spatially localized underneath the metal layer. These structures are highly manufacturable, using only metal deposition and a lift-off process, avoiding etching into the surface of the semiconductor and the resulting electronic defect states which cause problems with charging and non-radiative recombination in active photonics.

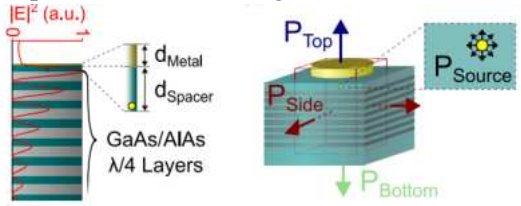


Figure 1 Illustration of a Tamm plasmon and a confined Tamm structure

In order to obtain Tamm Optical States with single mode emission, it is necessary to make very small metal structures, with implications for both classical and quantum photonics: the gain of nanolasers is limited by the small physical volume, and single photon sources face losses due to the

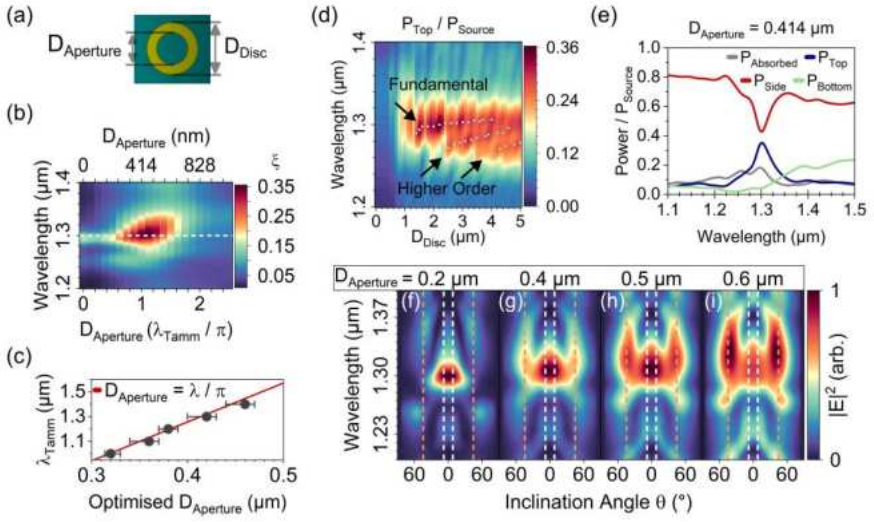


Figure 2 FDTD results for an example metasurface Tamm nanoring

metal layer as well as a deleterious effect of the lack of control of the far field, which is linked to the physical dimensions of the structure.

In this work, we combine the Tamm Optical State with the metasurface, using the readily manufacturability of the metal layer together with the ability of modern nanofabrication to sculpt the surface, decoupling the mode from the far field, and opening the door to photodetectors[2], single photon sources and lasers using the Tamm Assisted Metasurface.

As an illustrative simple example of a metasurface[3], we consider a nanoscale ring (see figure 2), using a Tamm plasmon as a stating point which is optimized for the telecommunications O band. We find that the advantage of using such a nanoring over a conventional confined Tamm plasmon is that it doubles the emission efficiency from 18% to 35%, by the mechanism of reducing the absorption.

This work is funded by Engineering and Physical Sciences Research Council under grant META TAMM (EP/X029360/1). TA acknowledges funding from the Saudi Arabian Cultural Bureau in the UK, and AS and HH acknowledge funding from the Quantum Engineering Centre for Doctoral Training.

References

1. Matthew Parker *et al.*, “Telecommunication wavelength confined Tamm plasmon structures containing InAs/GaAs quantum dot emitters at room temperature,” Phys. Rev. B 100, 165306 (2019)
2. Edmund Harbord *et al.*, “Confined Tamm optical states coupled to quantum dots in a photoconductive detector”, Appl. Phys. Lett. 115, 171101 (2019)
3. Huili Hou *et al.*, arXiv:2402.10734v1

Cd(Zn)O nanostructures for SEIRA sensing in de Mid-IR

P. Ibañez-Romero[1], E. Martinez Castellano[1], J. Yeste[2], F. Gonzalez-Posada[3], T. Taliercio[3], V. Muñoz-Sanjosé [2] , M. Montes Bajo*[1], and A. Hierro[1]

[1] ISOM, Universidad Politécnica de Madrid, Madrid, Spain
[2] Departament de Física Aplicada i Electromagnetisme, Universitat de València, Burjassot, Spain
[3] Univ. Montpellier, IES. UMR 5214, F-34000, Montpellier, France
*corresponding author: miguel.montes@upm.es

Surface Enhanced Infrared Absorption (SEIRA) allows the resonant coupling between a plasmonic mode and a narrow resonance of an analyte. We demonstrate two different approaches for sensing PMMA and vanillin, using Cd(Zn)O nanostructures reporting enhancement factors of up to 220%.

SEIRA enables the resonant coupling between a wideband plasmonic mode upheld by a nanostructure and a narrow resonance of an analyte for detection purposes. Noble metals have been traditionally used for SEIRA, reaching absorption enhancements factors as high as 7-fold [1]. However, such materials suffer great losses in the mid infrared (Mid-IR) [2] which fuels the need to explore other material platforms suited for said part of the spectrum. Cd(Zn)O has sparked great interest lately [3] owing to its great performance in the mid-IR given by its high plasma frequency (3100–4200 cm^{-1}) and its very low losses (500–600 cm^{-1}). In this study we report two different approaches for sensing two different organic molecules, PMMA and vanillin, using Cd(Zn)O nanostructures reaching enhancement factors of up to 220%.

The first approach to be discussed is the use of self-assembled semispherical nanoparticles (NPs) made of $Cd_{0.9}Zn_{0.1}O$ grown by metal organic chemical vapor deposition (MOCVD) on a semi-insulating GaAs substrate. A series of these samples were grown at slightly different conditions yielding a varying surface coverage of NPs with an average diameter of 60 nm. Owing to their geometry and the high refractive index of the substrate, the NPs host a broad localized surface plasmon (LSP) centered at around 1750 cm^{-1} (below the plasma frequency of the $Cd_{0.9}Zn_{0.1}O$) [3] which matches the energy of absorption of the C=O bond of the PMMA molecule.

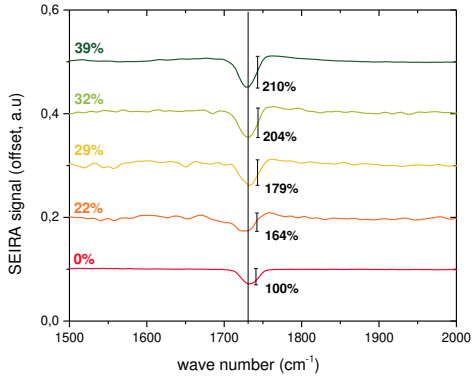


Figure 1. Enhancement of SEIRA signal with the $Cd_{0.9}Zn_{0.1}O$ NP surface coverage compared to the reference. The vertical black line indicates the absorption of the C=O bond of PMMA.

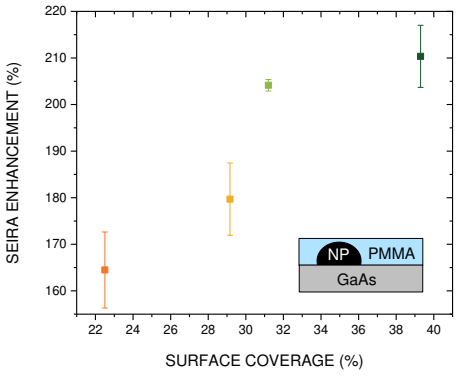


Figure 2. Vibrational signals normalized by the baseline extracted from Eiler´s algorithm. Error bars account for multiple measurements on the same sample.

A 70 nm layer of PMMA was deposited on top of the surface through spin coating and the plasmonic response of the NPs was characterized by transmittance spectroscopy using a Fourier transform infrared (FTIR) spectrometer at an angle of incidence of 45º. The interaction between the broad resonance of the NPs and the narrow vibrational absorption of PMMA are characterized by asymmetric Fano-like profiles, which are analyzed using Eiler's least square smoothing algorithm [4]. The results of the study are shown in Figure 1, where four samples with different surface coverages ranging from 22% to 39% along with a bare GaAs substrate for reference were measured. We report a SEIRA enhancement of up to 210% on the signal compared to that of the reference. Furthermore, we have observed a linear increase of the enhancement with the surface coverage (Figure 2).

For the second approach, 2 µm-pitch, 0.7 fill factor gratings were processed on $Cd_{0.9}Zn_{0.1}O$ thin films deposited on sapphire (Figure 3) featuring LSPs tailored to a frequency of 1550 cm^{-1}. This was done through a novel approach using nanolithography and dry etching never reported before on CdO/sapphire films. Owing to the geometry of the surface, when incoming light is polarized parallel to the stripes the response will assimilate that of a thin film, whereas when the light is perpendicular to stripes an LSP will appear. Two microliters of a 2 mg/ml solution of vanillin in isopropyl alcohol were drop casted on the surface of the samples and the plasmonic response was characterized using a Hyperion 3000 microscope coupled to the FTIR spectrometer. Figure 4 shows how SEIRA enhances the vanillin absorption peaks in perpendicular polarization compared to parallel polarization, where no SEIRA is acting. For vanillin's vibration at 1589 cm^{-1}, this enhancement reaches 175%.

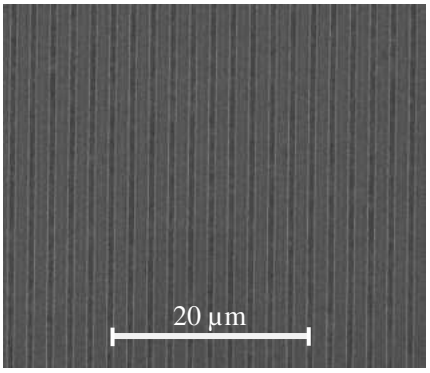


Figure 3. Scanning electron micrograph of the surface of a $Cd_{0.9}Zn_{0.1}O$ grating.

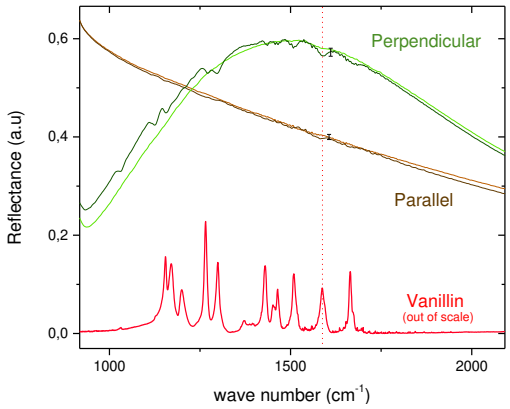


Figure 4. Reflectance spectra from a grating with light polarized parallel (brown) and perpendicular to the stripes (green). Light colored lines were measured before addition of vanillin and darker ones after. Vanillin reference in red magnified for clarity.

This work was funded by the Spanish Ministry of Economy, Industry and Competitiveness (MINECO) under Projects TEC2017-85912-C2, PDC2023-145827-C2, and the Generalitat Valenciana under project Prometeo II 2015/004.

References

1. L. V. Brown, X. Yang, K. Zhao, et al. 'Fan-Shaped Gold Nanoantennas above Reflective Substrates for Surface-Enhanced Infrared Absorption (SEIRA)', *Nano Lett*, vol. 15, no. 2, pp. 1272–1280, Feb. 2015..
2. G. V. Naik, V. M. Shalaev, and A. Boltasseva, 'Alternative Plasmonic Materials: Beyond Gold and Silver', *Advanced Materials*, vol. 25, no. 24, pp. 3264–3294, Jun. 2013..
3. E. M. Castellano, J. Tamayo-Arriola, M. Montes Bajo, et al. Nanophotonics, vol. 10, no. 9, pp. 2509–2518, 2021.
4. P. H. C. Eilers, "A perfect smoother," Anal. Chem.,vol.75,no.14, pp. 3631−3636, 2003.

Plasmonic hydrogen sensor at the ppm level based on the plasmon-triggered switching

P. Giraud[1], H. Bruhier[1], I. Verrier[1], S. Rajab Pacha[2], C. Varenne[2], J. Brunet[2], Amadou Ndiaye[2], and Y. Jourlin[1*]

[1]Université Jean Monnet Saint-Etienne, CNRS, Institut d'Optique Graduate School, Laboratoire Hubert Curien UMR 5516, F-42023, SAINT-ETIENNE, France

[2]Université Clermont Auvergne, CNRS, Sigma Clermont, Institut Pascal, F-63000 Clermont-Ferrand, France

[*]corresponding author: yves.jourlin@univ-st-etienne.fr

Abstract: Plasmonic sensors have garnered significant interest due to their ability to exhibit high sensitivities. In this work, we present the proof of concept for a plasmonic hydrogen sensor with a low detection limit at the ppm level (1.91 ppm).

The plasmon-triggered switching effect is a plasmonic phenomenon that involves two propagative orders, the 0^{th} and the -1^{st}, diffracted in reflection by a relatively deep grating [1]. The evanescent $+1^{st}$ and -2^{nd} orders respectively excite co-propagative and contra-propagative modes, where the resulting interaction between them allows for a low-loss plasmonic interaction between the two propagative orders. As depicted in Fig. 1, order oscillations yield two crossing points, WP1 and WP2, where a local angular translation is observed when the ambient medium undergoes any modification. The transducer response is then evaluated by applying a normalized differential measurement between the orders' diffraction efficiency at a fixed angle, WP1 or WP2, allowing the estimation of an angular shift with a simple light intensity measurement.

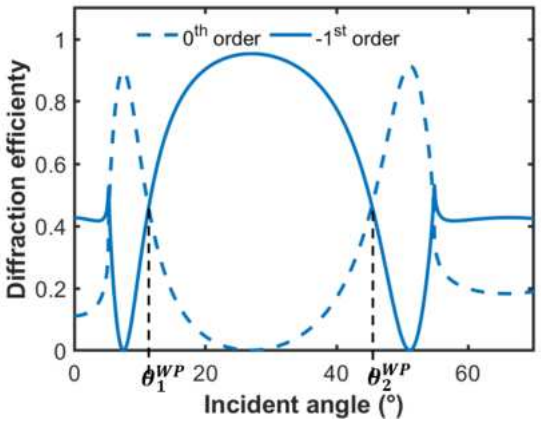


Figure 1: Computed angular responses for an ideal sinusoidal gold grating with a depth of 280 nm and a period of 935 nm in air without sensing layer

The plasmon-triggered switching effect has already shown promise in the security domain [2], biosensing [3], and the control of air quality [4]. The experimental transducer, made of a replica of a printed photoresist layer under a UV laser interference lithographic setup, was coated with a 120 nm gold layer through thermal evaporation. The measured sinusoidal grating period with a Littrow setup was 935 nm, while the depth measured through Atomic Force Microscopy was 303 nm. To adapt the transducer for hydrogen detection, a palladium sensitive layer of 10 nm was also deposited via thermal evaporation.

After an initial angular characterization of the transducer (Fig. 1), it is placed in a chamber where a controlled flow of filtered air with a defined hydrogen concentration is established. The transducer is illuminated with an 850 nm laser diode in TM polarization at WP2, where the 0^{th} and -1^{st} diffracted orders are collected simultaneously over time with two photodiodes. The ambient refractive index is also computed over time using Edlén's formula [5], through the measurement of pressure, temperature, and humidity, to differentiate the response of the hydrogen interaction from the response of the ambient refractive index of air.

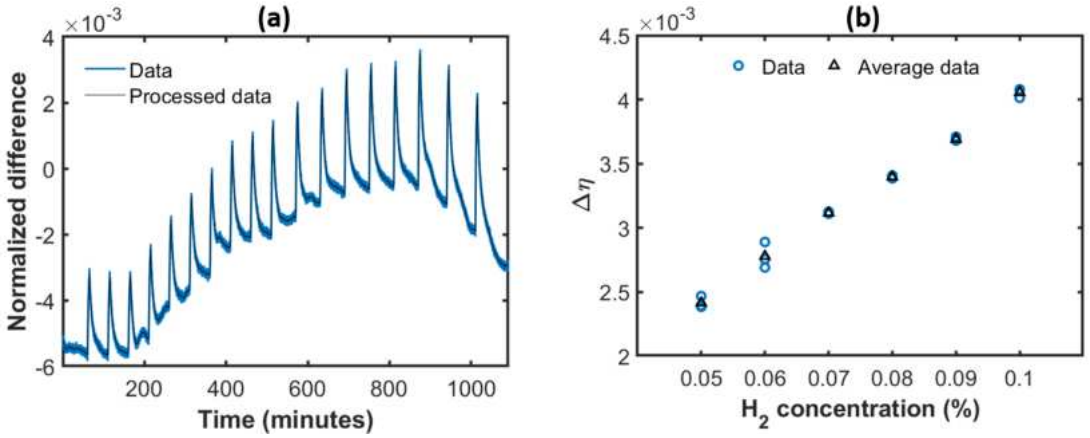


Figure 2: (a) Response to stepwise increasing H2 concentration (0.05-0.1%) composed of 3 cycle for each H2 concentration in filtered Air at room temperature with the corresponding moving average of 100 points plotted in black. (b) Measured Δη as a function of H2 concentration derived from (a) where the plotted black triangles are the average of different Δη for each H2 concentration

From Fig. 2a), the responses under hydrogen concentrations ranging from 500 to 1000 ppm show that the transducer is sensitive to hydrogen. Fig. 2b) displays the difference in the normalized difference before and after each hydrogen cycle. Responses are linear and can distinguish between different hydrogen concentrations, resulting in a detection limit of 1.91 ppm with a white noise measured at $\sigma = 2.10^{-6}$.

The authors thank the NanoSaint-Etienne platform (CNRS RENATECH+) for providing the fabrication means and NAPA company for providing the replica. Funding is provided by the French Région Auvergne-Rhône-Alpes within the framework of the CAPTHY project.

References

1. Sauvage-Vincent J, Jourlin Y, Petiton V, Tishchenko AV, Verrier I, Parriaux O. Low-loss plasmon-triggered switching between reflected free-space diffraction orders. Opt Express. 2 juin 2014;22(11):13314.

2. Parriaux O, Jourlin Y. Lossless 0th and- 1st order switching by dual-excitation of grating waveguide mode. J Opt. 2019;21(7):075603.

3. Laffont E, Crespo-Monteiro NN, Berini P, Jourlin Y. Development of a new plasmonic transducer for the detection of biological species. In: Optical Sensing and Detection VII. SPIE; 2022. p. 97-105.

4. Bruhier H, Dutems J, Laffont E, crespo-monteiro nicolas, Verrier I, Parriaux O, et al. Quasi-lossless common-mode plasmon sensing scheme as a high sensitivity compact SPR sensor. Opt Lett [Internet]. 7 juin 2023 [cité 12 juin 2023]; Disponible sur: https://opg.optica.org/ol/abstract.cfm?doi=10.1364/OL.483692

5. Jones FE. The Refractivity of Air. J Res Natl Bur Stand 1977. févr 1981;86(1):27-32.

Industrial WorkShop: From Design to Manufacture - Complete Inverse Design Flow for MetaOptics

Chenglin Xu[1*], Bryan Stone[2], and JiSoo Park[3]
[1]Synopsys, Inc. Ossining NY, USA
[2]Synopsys, Inc. Marlborough MA, USA
[3]Synopsys, Inc. Seoul, Korea
[*]corresponding author: chenglin@synopsys.com

Abstract: Synopsys offers solutions to metalens design and manufacturing challenges, including tools for hybrid refractive metalens systems that consider manufacturing tolerances. This workshop is presented in two parts:

1. July 16: Introduction to MetaOptic Designer
2. July 18: Demo of hybrid metalens system design and virtual fab simulation

Magnetically Controllable Multimode Interference in Topological Photonic Crystals

Weiyuan Tang[1], Mudi Wang[2], Shaojie Ma[1,3], C.T. Chan[2], Shuang Zhang[1*]

[1]Department of Physics, The University of Hong Kong, Hong Kong, China
[2]Department of Physics, The Hong Kong University of Science and Technology, Hong Kong, China
[3]Department of Optical Science and Engineering, Fudan University, 200433, Shanghai, China
[*]corresponding author: shuzhang@hku.hk

Abstract: We demonstrate magnetically controllable multimode interference based on gyromagnetic topological photonic insulators that support two unidirectional edge modes with different dispersions. Herein, we successfully achieve tunable power splitting in experiments by controlling multimode interference with the magnetic field intensity or the frequency of wave.

To date, most proposed solutions for manipulating multimode interference in topological systems involve modifying the structural dimensions of channels[1-3], such as, by changing the incident channel length to change the propagation phase of the incident waves[1] or controlling the coupling strength between the incident and outgoing channels with bending angles[3]. However, the requirement for varying the geometry of the system severely restricts these techniques' practical utility. In this work, we achieve controllable multimode interference in a topological photonic heterostructure waveguide. The power splitting ratio originating from multimode interference is controlled by the propagating phase difference between two CEMs (Fig.1a), which depends on the incident frequency (Fig.1b) or magnetic field intensity (Fig.1c).

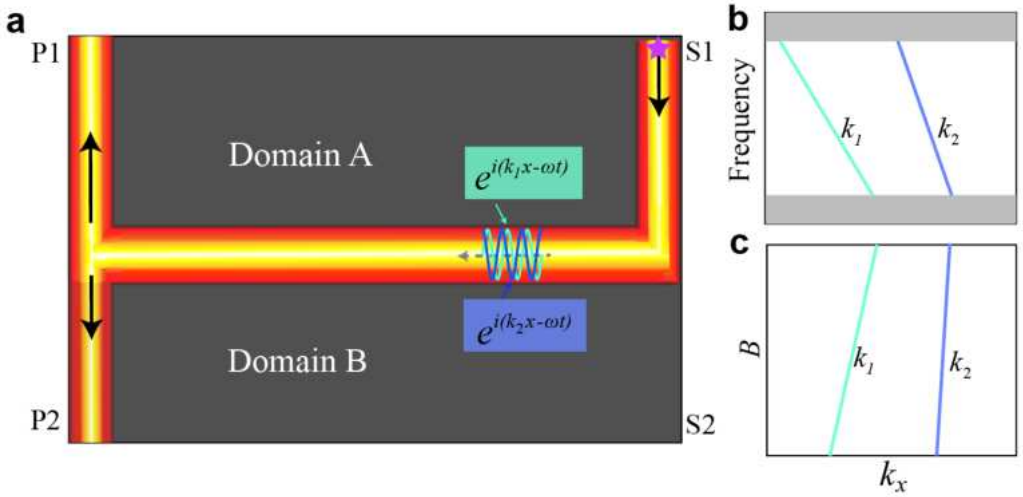


Figure 1 The proposed scheme for controllable power splitting through manipulating multimode interference. a The schematic of a H-shaped heterostructure waveguide. **b-c** The differences between the wave number of two CEMs depend on incident frequency (**b**) and the magnetic field intensity (**c**).

Based on transfer-matrix method, we develop a theoretical model to reveal the fundamental mechanisms underlying the whole course of tunable multimode interference. Then the power splitting ratios for the source being placed in channel S1 and S2 as:

$$R_{S1} = \frac{|e^{i\Delta\varphi}+1|^2}{|e^{i\Delta\varphi}+1|^2+|e^{i\Delta\varphi}-1|^2}, \quad (1)$$

$$R_{S2} = \frac{|e^{i\Delta\varphi}-1|^2}{|e^{i\Delta\varphi}+1|^2+|e^{i\Delta\varphi}-1|^2}, \quad (2)$$

where $\Delta\varphi = (k_2 - k_1)l$ is the phase difference between the mode 1 and mode 2 propagating in the same direction.

Experimentally, our waveguide system is composed of two domains, each of which is constructed by a triangular lattice of yttrium iron garnet (YIG) rods. The magnetic field is applied in positive (negative) directions to the Domain A (B). Note that Domian A and domain B possess opposite gap Chern number for the second bandgap, the interface of the two domains can support two topologically edge modes. By adjusting the distance from the magnet to the YIG rod, the magnetic field intensity can be tuned, and then the interference of the two edge modes is quantitively manipulated, leading to magnetically controllable power splitting ratios. As shown in Fig.2b, the experimental results are consistent with the simulation results. Likewise, tuning power splitting ratios of our waveguide system with the frequency of incident wave is also experimentally verified in Fig. 2c.

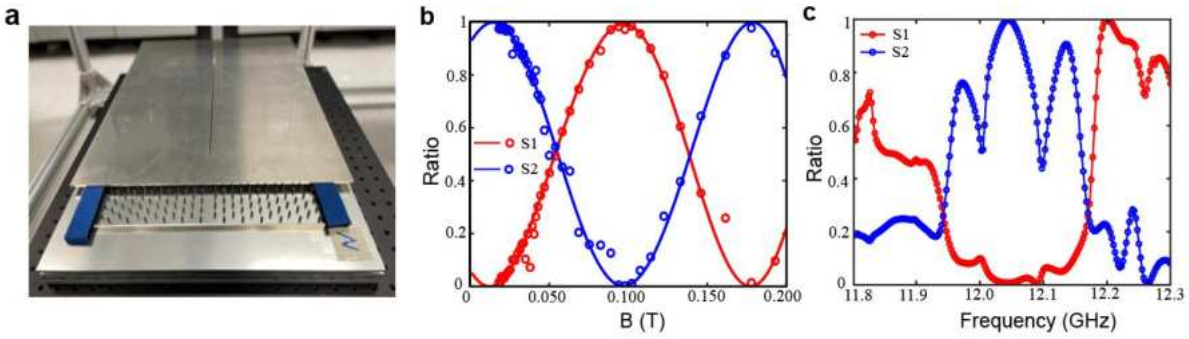


Figure 2 The experimental setup and results. a The experimental setup. **b** The measured (circle) and simulated (solid lines) power splitting ratios tuned by magnetic field intensity. **c** The measured power splitting ratios controlled by wave frequency.

Our method reveals the physical mechanism of the whole process of multimode interference in topological photonic crystal waveguides, which paves a new way for the study of multimode interference. Bedsides, the proposed topological waveguide system can provide a new technical platform for the related applications of microwave devices such as switches, signal processors, and isolation devices.

References

1. Skirlo, S. A., Lu, L. & Soljačić, M. "Multimode one-way waveguides of large Chern numbers," Phys. Rev. Lett. 113, 11, 113904, 2014.
2. He, C. *et al.* "Tunable one-way cross-waveguide splitter based on gyromagnetic photonic crystal," Appl. Phys. Lett. 96, 11, 111111, 2010.
3. Qiao, Z. *et al.* "Current partition at topological channel intersections," Phys. Rev. Lett. 112.20 206601, 2014.

Coupled thermal and mechanical phenomena induced by the fluctuations of the electromagnetic field

J. R. Deop-Ruano[1*], and A. Manjavacas[1*]

[1]Instituto de Óptica "Daza de Valdés" (IO-CSIC), Spain
[*]corresponding author: juan.deop@csic.es
[*]corresponding author: a.manjavacas@csic.es

Abstract: Radiative heat transfer and Casimir interactions arise from the fluctuations of the electromagnetic field. Here, we analyze the simultaneous transfer of momentum and energy in different nanoscopic systems. In doing so, we find that the motion of the nanostructures allows us to modulate the heat transfer, and vice versa.

The **fluctuations of the electromagnetic field** are responsible for the **radiative heat transfer** between material structures [1, 2]. Another phenomenon emerging from the fluctuations of the electromagnetic fields is the **Casimir forces and torques** between neutral nanostructures, which can serve as a means to transfer linear and angular momentum in the nanoscale [3, 4]. Despite their shared physical origin, radiative heat transfer and Casimir interactions are traditionally studied independently. In the former, nanostructures are typically considered steady, while in the latter, thermalized conditions are assumed. However, as we demonstrate in our study**, Casimir interactions can exert a notable influence on radiative heat transfer, and vice versa**.

Here [5], we explore the **simultaneous transfer of energy and angular momentum** in a pair of nanostructures with different temperatures, rotating around a common axis (See Figure 1). We show that, due to the rotation of the nanostructures, **radiative heat transfer between them can be increased, decreased, or even reversed** compared to the transfer in the absence of rotation, determined solely by the temperature difference of the nanostructures. These findings unravel the **possibility of modulating radiative heat transfer between nanostructures through their motion**.

Furthermore, we study the **propulsion of Janus-like nanostructures** placed in an environment at a different temperature [6]. This type of nanostructures are characterized by having two different sides with different optical properties. Due to the unbalance in the thermal radiation produced by the two sides, the structure spontaneously accelerates as it thermalizes with the environment. We completely characterize the force and the associated motion of the structure as a function of its temperature and thickness, for different combinations of materials. In doing so, we prove the possibility **of manipulating material structures using thermal radiation**.

Our calculations rely on the fluctuational electrodynamics framework, which allows us to obtain analytical expressions for the force, torque, and power transferred between the nanostructures. This work unveils nontrivial phenomena resulting from the interplay between Casimir interactions and radiative heat transfer, paving the way for **utilizing moving nanostructures to gain control over radiative heat transfer, as well as to employ thermal radiation to accelerate and manipulate nanostructures**.

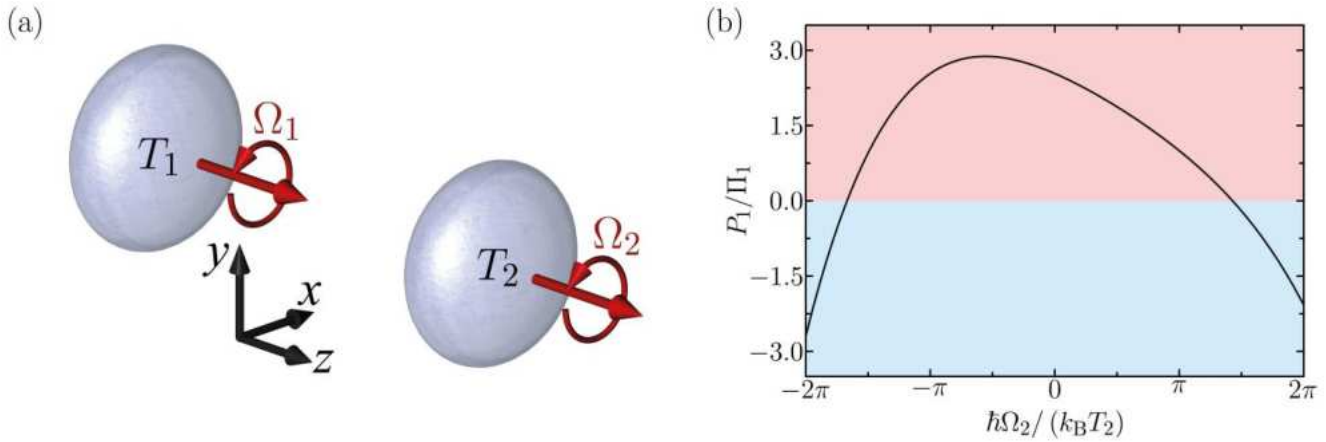


Figure 1. (a) Schematics of the system under consideration. (b) Power transferred between the nanostructures P1, normalized to the power transferred in the absence of rotation Π1, as a function of Ω2 for T1 = 1.5T2, Ω1 = πkBT2/ħ. The red (blue) background indicates positive (negative) values of the normalized power transferred.

References

1. Biehs, S.-A.; Messina, R.; Venkataram, P. S.; Rodriguez, A. W.; Cuevas, J. C.; and Ben-Abdallah, P., "Near-field radiative heat transfer in many-body systems", Rev. Mod. Phys., Vol. 93, 025009, 2021.
2. Manjavacas, A.; and García de Abajo, F. J., "Radiative heat transfer between neighboring particles", Phys. Rev. B, Vol. 86, 075466, 2012.
3. Pendry, J. B., J. Phys. Condens. Matter, "Shearing the vacuum-quantum friction", Vol. 9, 10301, 1997.
4. Sanders, S.; Kort-Kamp, W. J. M.; Dalvit, D. A. R.; and Manjavacas, A., "Nanoscale transfer of angular momentum mediated by the Casimir torque", Commun. Phys., Vol. 2, 1-7, 2019.
5. Deop-Ruano, J. R.; and Manjavacas, A., "Control of the radiative heat transfer in a pair of rotating nanostructures", Phys. Rev. Lett. Vol. 130, 133605, 2023.
6. Deop-Ruano, J. R.; García de Abajo, F. J.; and Manjavacas, A., "Thermal radiation forces on planar structures with asymmetric optical response", Submitted, 2024.

Super-resolution elasticity imaging with nanobells

R. Fuentes-Dominguez[1], M. Paris-Ogayar[2], K. Setchfield[1], R. J. Smith[1], D. Jaque[2] and M. Clark[1]

[1]Optics and Photonics Group, University of Nottingham, Nottingham, UK
[2]Nanomaterials for Bioimaging Group (nanoBIG), Departamento de Fisica de Materiales, Facultad de Ciencias, Autonomous University of Madrid, Spain
*corresponding author: ezzrf1@nottingham.ac.uk

Abstract: We present a new scheme of super-resolution imaging that can reconstruct the size, shape, position and orientation of metallic nanostructures with a precision of 5 nm, using a pump-probe method technique. This also opens a way to extract the elasticity or stiffness of the surrounding environment at the nanoscale.

Super-resolution optical microscopy has a tremendous impact in life sciences over the last decade for its ability to reveal the insights of biological processes at the nanoscale dimensions [1,2]. These methods usually rely on the optical properties of either fluorophores or nanostructures to provide super-resolution.

An alternative to light (photons) is sound (phonons) which offers sub-optical resolution as well as enabling the elasticity quantification on biological cells [3]. This is key to understand changes at sub-cellular level due to diseases (e.g. cancer).

In this talk, a new scheme of super-resolution acoustic imaging [4] will be shown by reconstructing the size, shape, position and orientation of metallic nanostructures ("nanobells) with a precision of 5 nm, using a pump-probe method technique (see Figure 1). This also opens a way to extract, for the first time, the elasticity or stiffness of the surrounding environment at the nanoscale.

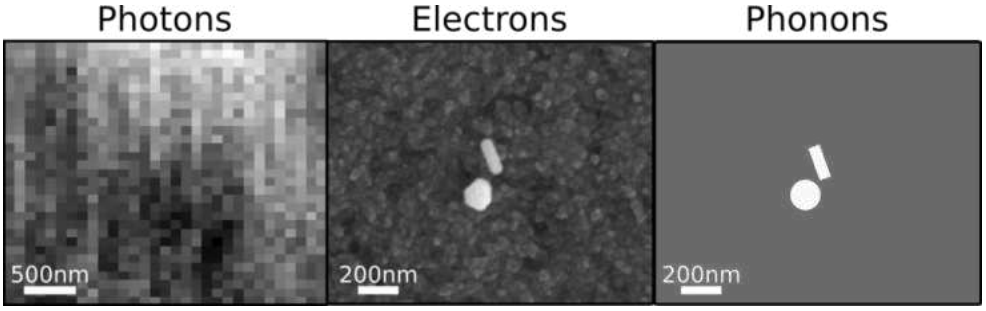


Figure 1: Comparison between different imaging modalities of the same region using: (left) photons or optics, (middle) electrons or scanning electron microscopy, and (right) phonons or the presented work.

Acknowledgements

This work was supported by the Engineering and Physical Sciences Research Council (grant numbers EP/K021877/1, EP/G061661/1) and the NanoPrime EPSRC grant EP/R025282/1. The authors would like to acknowledge the Nanoscale and Microscale Research Centre (nmRC) for providing access to instrumentation and SEM imaging.

References

1. Huang, B., et al. “Super-resolution fluorescence microscopy”. Annual Review of Biochemistry 78, 993-1016, 2009.
2. Parmyd, I. and Eggeling, C. “Super-resolution optical microscopy of lipid plasma membrane dynamics”. Essays in biochemistry 57, 69-80, 2015.
3. Perez-Cota, F., et al. “Picosecond ultrasonics for elasticity-based imaging and characterization of biological cells”. Journal of Applied Physics 128.16, 160902, 2020.
4. Fuentes-Dominguez, R., et al. “Polarization-sensitive super-resolution phononic reconstruction of nanostructures”. ACS Photonics 9.6, 1919-1925, 2022.

Super Resolution Imaging of Resonance Mode Inside Silicon Nitride Nanowire Based on Photothermal Nonlinearity

Yu-An Chen[1], Te-Hsin Yen[1], Kentaro Nishida[1], Chih-Wei Chang[2*], Shi-Wei Chu[1,3,4]

[1]Department of Physics, National Taiwan University, Taiwan
[2]Center for Condensed Matter Sciences, National Taiwan University, Taiwan
[3]Molecular Imaging Center, National Taiwan University, Taiwan
[4]Brain Research Center, National Tsing Hua University, Taiwan
[*]corresponding author: r09222085@ntu.edu.tw

Abstract: As Si_3N_4-based photonic integrated circuits emerge as a promising platform, it is important to diagnose their spatial configuration with resolution beyond diffraction limit. Here, we demonstrate a resolution enhancement of hundred-nanometer-diameter Si_3N_4 nanowires based on photothermal nonlinearity and higher order saturated excitation subtraction and detect the resonance mode inside it.

Introduction

Recently, Si_3N_4-based photonic integrated circuits (PICs) have shown a great potential in the industry[1,2]. To characterize the relationship between nanoscale structure and functional output performance, it is important to develop diagnostic tools that are able to inspect the spatial configuration of Si_3N_4-based PICs with nanometer resolution and high-speed observation, as the diameter of Si_3N_4 is getting smaller and smaller, some are even only tens of nanometers[3-6]. One of the fastest ways for such diagnosis is optical imaging. However, the resolution of an optical microscope is limited by diffraction limit.

The purpose of this study is to achieve optical resolution of Si_3N_4 nanostructures beyond the diffraction limit. Since the Si_3N_4 serve as waveguide in PICs, we start with Si_3N_4 nanowires (NWs) that resemble waveguide geometry. Previously, our group reported the resolution improvement of Si nano cubes through photothermal nonlinearity[7]. In this work, we pursue super-resolution imaging of Si_3N_4 NW with a similar strategy, whose mechanism is explained as follows: the applied laser will cause the temperature increase of the nanoparticle, which result in refractive index changes[8], leading to Mie-resonance spectrum red-shift and nonlinear scattering-excitation dependency. It is possible for Si_3N_4 NWs to exhibit strong photothermal nonlinearity around 561-nm wavelength according to the analytical solution of the Mie resonance of an infinite Si_3N_4 cylinder in vacuum. With strong nonlinear responses, enhanced resolution is achieved by adopting image post-processing methods that depend on the type of nonlinearities. Here we expect that Si_3N_4 NWs show sub-nonlinearity, so we selected the saturated excitation (SAX) subtraction method[9], achieving at least 1.36-fold resolution enhancement at an incident power of 13 mW.

Result

The sample was inhomogeneous Si_3N_4 NWs with diameter ranging from 300 to 800 nm. These NWs were randomly sprayed by acetone on a copper grid. The laser wavelength was 561 nm and its polarization was perpendicular to the NW longitudinal axis. The NA of the objective was 0.6.Fig. 1 (a) & (b) shows the scattering power dependency at the valley and peak position of wire shown in Fig. 1(d) respectively. From Fig. 1(b), sub-linear behavior starts above 17 mW, gradually toward full saturation at ~60 mW. The result of subtraction SAX for Fig. 1(b) is shown in Fig. 1(c), which shows 2-nd order nonlinearity.Fig. 1(d) is the linear backscattering image of a single NW, acquired with ~5-mW excitation power, and Fig. 1(e) is the image subtracting Fig. 1(d) from an image taken at ~17-mW. The average full width half maximum enhancement is ~1.36-fold. The theoretical value of the resolution enhancement of one SAX subtraction is $\sqrt{2}$, which is close to our result. Better resolution enhancement is anticipated by higher excitation power and higher order SAX subtraction.

Discussion

One interesting observation is that the wire image shows clear periodic peaks and all the peak positions show nonlinearity, while all the valley positions show linearity. In order to check the peaks aren't caused by the minor periodic shape change

along the wire, we first simulated the scatter intensity of wire as Fig. 2(a) shown, which shows similar periodic peaks as Fig. 1(d). One guess is the peaks are the result of the standing wave inside wire which is caused by the Mie resonance. As we all know, peak of standing wave should exist higher electric field, which leads to higher absorption. Thus, we simulated the absorption along the wire as Fig. 2(b) shows. The periodic peaks in Fig. 2(b) agrees with our guess again. Moreover, higher nonlinearity region should show higher resolution enhancement. Thus, we compared the resolution enhancement and the scattering intensity as Fig. 2(c) shows. In Fig. 2(c), we can two lines show the same peak region, which fits the guess again. Thus, we concluded that the periodic peaks are the result of the standing wave inside wire which is caused by the Mie resonance and the further checking will be done by the EELS.

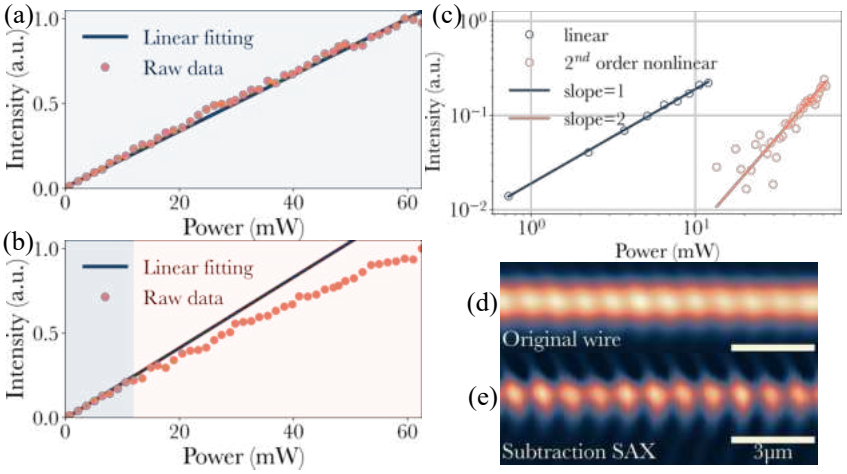


Figure 1. Experiment result, (a) linear result, (b) nonlinear result, (c) SAX analysis result, (d) original wire image, (e) subtraction SAX result.

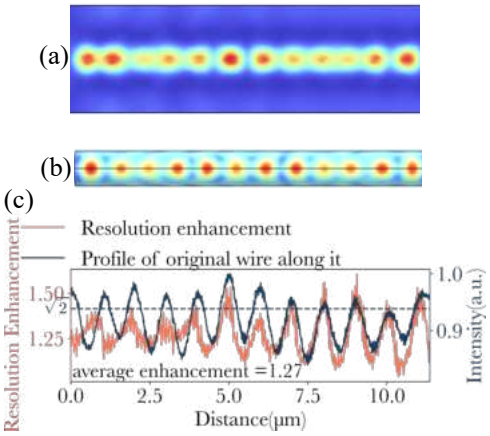


Figure 2. Simulation result (a) enegy flow, (b) absorption, (c) comparison of resolution enhancement and scattering intensity of wire.

Contributions

All the experiment and simulation are done by Yu-An Chen. The topic is generated by Prof. Chih-Wei Chang and Prof. Shi-Wei Chu. Further discussion of the possibility of this topic is from Te-Hsin Yen and Kentaro Nishida. The idea of standing waves is generated by Chun-Yu Yang.

References

1. Sharma, T., J. Q. Wang, B. K. Kaushik, Z. Z. Cheng, R. Kumar, Z. Wei and X. J. Li, “Review of Recent Progress on Silicon Nitride-Based Photonic Integrated Circuits,” IEEE Access, Vol. 8, 195436–195446, 2020.
2. Blumenthal, D. J. and R. Heideman, D. Geuzebroek, A. Leinse, C. Roeloffzen, “Silicon nitride in silicon photonics,” Proc. IEEE, Vol. 106, No. 12, 2209–2231, 2018.
3. Jiang, Y. H., X. Han, H. J. Huang, P. Zhang, A. Dubey, H. F. Xiao, M. R. Yuan, A. Frigg, T. G. Nguyen and A. Boes, “Monolithic photonic integrated circuit based on silicon nitride and lithium niobate on insulator hybrid platform,” Adv. Photonics Research, Vol. 3, No. 10, 2200121, 2022.
4. Buzaverov, K. A., A. S. Baburin, E. V. Sergeev, S. S. Avdeev, E. S. Lotkov, M. Andronik, V. E. Stukalova, D. A. Baklykov, I. V. Dyakonov and N. N. Skryabin, “Low-loss silicon nitride photonic ICs for single-photon applications,” arXiv preprint, 2022.
5. Vogelbacher, F., M. Sagmeister, J. Kraft, X. Zhou, J. H. Huang, M. Z. Li, K. J. Jiang, Y. L. Song, K, Unterrainer and R. Hainberger, “Slot-waveguide silicon nitride organic hybrid distributed feedback laser,” Sci. Rep., Vol. 9, No. 1, 18438, 2019.
6. Bauters J. F., M. J. R. Heck, D. John, D. Dai, M. C. Tien, J. S. Barton, A. Leinse, R. G. Heideman, D. J. Blumenthal and J. E. Bowers, “Ultra-low-loss high-aspect-ratio Si 3 N 4 waveguides,” Opt. Express, Vol. 19, No. 4, 3163–3174, 2011.
7. Duh, Y. S., Y. Nagasaki, Y. L. Tang, P. H. Wu, H. Y. Cheng, T. H. Yen, H. X. Ding, K. Nishida, I. Hotta and J. H. Yang, “Giant photothermal nonlinearity in a single silicon nanostructure,” Nat. Commun., Vol. 11, No. 1, 4101, 2020.
8. Bertolotti, M., V. Bogdanov, A. Ferrari, A. Jascow, N. Nazorova, A. Pikhtin, and L. Schirone, "Temperature dependence of the refractive index in semiconductors," J. Opt. Soc. Am. B, Vol. 7, No. 6, 918–922, 1990.
9. Nawa, Y., Y. Yonemaru, A. Kasai, R. Oketani, H. Hashimoto, N. I. Smith and K. Fujita, “Saturated excitation microscopy using differential excitation for efficient detection of nonlinear fluorescence signals,” APL Photonics, Vol. 3, No. 8, 2018.s

Acoustic and seismic metamaterials

Design of composite mufflers based on dissipative and reactive units

Yuzhen Yang[1*], Han Jia[1], Quanquan Shi[1] and Jun Yang[1]

[1]Key Laboratory of Noise and Vibration Research, Institute of Acoustics, Chinese Academy of Sciences, China
[*]corresponding author: yangyuzhen@mail.ioa.ac.cn

Abstract: We have proposed and validated a design of a composite muffler. This design combines both dissipative and reactive units with different operating mechanisms to take advantage of the benefits offered by each structure. The result achieved a high transmission loss across a wide frequency range in a ventilation duct system.

Noise reduction in duct systems is a major issue in engineering applications, such as tunnel ventilation systems and engine exhaust systems. Acoustic mufflers have long served as the most effective devices to reduce noise in duct systems, while also allowing airflow to pass freely[1].

As the most common component of mufflers, porous sound absorbing materials (PSAM) can achieve efficient noise reduction in the middle and high-frequency range, as they can fully convert the sound energy entering the micropores into thermal energy for energy consumption[2, 3]. In this work, a common melamine porous acoustic material was used to construct the dissipative unit, which is shown as the blue part in FIG.1.

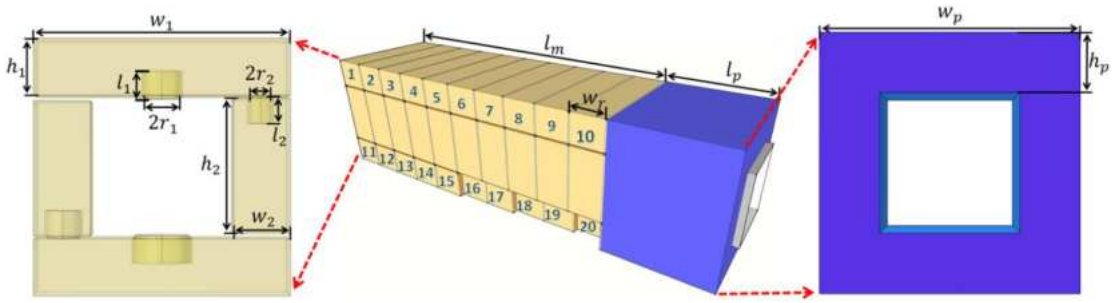


FIG.1. Schematic diagram of the composite muffler

In order to study the performance of the dissipative unit, a finite element model was built by the commercial simulation software COMSOL Multiphysics™ and the Johnson-Champoux-Allard model of porous media acoustics was chosen to characterize the PSAM in the pressure acoustics module. The thickness of PSAM h_{p} was fixed at 43 mm and the TL was calculated when the PSAM length was increased from 40 mm to 1000 mm. The cross-sectional area of the noise ventilation duct was set to 100 mm*100 mm. The TL is plotted in FIG.2.(a) as a function of length and frequency, with the black dashed line in the figure indicating the TL=20 dB contour. The results in the graph show that as the PSAM length increases, the lower frequency limit of TL greater than 20 dB gradually shifts towards low frequency. However, the lower frequency limit moves slowly in the frequency range below 1000 Hz. Based on the data in FIG.2.(a), a PSAM with a length of 220 mm was selected to construct the dissipative muffler to obtain high-efficiency noise reduction above 1000 Hz. We built a sample of dissipative muffler with a 3D printed expanded cavity and PSAM mounted inside.

The next step is to design a low-frequency noise reduction structure. Considering Helmholtz resonators are favorable for broadband noise reduction[4, 5], two order Helmholtz resonators (THR) are used for designing the reactive muffler in this work. As shown in FIG.2.(b), we extended the second cavity of the THR to the side, and this improvement not only reduces the thickness of the structure, but also makes full use of the space around the ventilation duct.

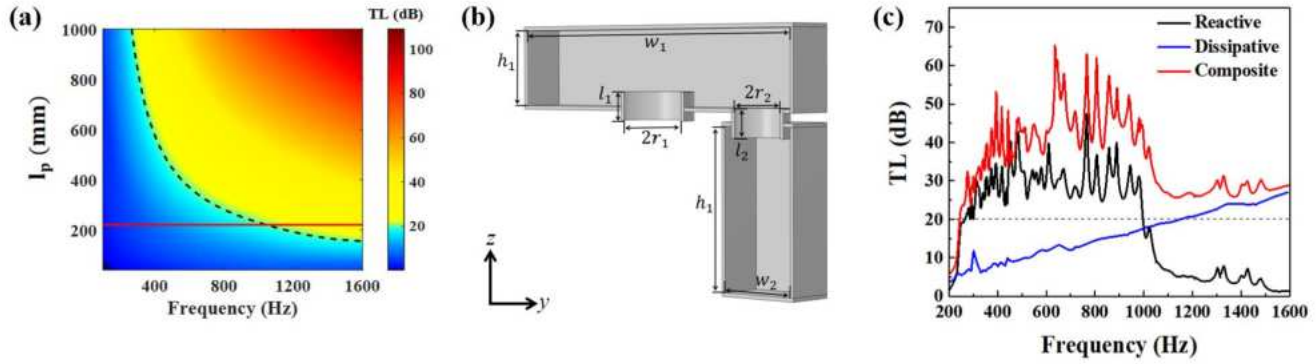


FIG.2. (a) Transmission loss of dissipative muffler constructed by PSAM. (b) Cross-section of a THR. (c) Tested TL curves for different mufflers.

After studying the sound insulation performance of THR units and the analysis of the coupling effect between units in the same cross-section, we designed a low-frequency reactive muffler consisting of 20 THR units with a total length of 522 mm. The arrangement of the 20 units was shown as the yellow part in FIG.1, where 10 units were placed on the upper and lower sides of the ventilation duct, and the annotated numbers in the figure, from 1 to 20, indicate the order in which the units were arranged from low to high resonance frequencies. The arrangment ensures that there is a significant difference between the resonance frequencies of two THRs in the same cross-section, thus eliminating the mutual coupling between the two THRs.

Finally, we attempt to combine these two types of mufflers to design a broadband and high-efficiency composite muffler, as shown in the middle part of FIG.1. Although the working mechanisms and effective frequency bands of the two are different, it is entirely possible to reduce the transmitted sound energy in a wider frequency range and to achieve broadband and higher TL by combining the two kinds of mufflers.

The measured TL curves for different mufflers are shown in FIG.2.(c), with black line, blue line and red line representing TL curves of reactive, dissipative and composite mufflers, respectively. As a reference, the 20 dB contour is marked as gray dashed line in the figure. It can be seen that, on two sides of the cut-off point around 1000 Hz, both the dissipative and the reactive mufflers alone have excellent noise reduction in the target frequency range. The TL curve of the composite muffler is above 20 dB from 244 Hz and overwhelmingly exceeds 30 dB below 1000 Hz. Therefore, the composite muffler surpasses the original effect of individual dissipative muffler and reactive muffler, which plays a positive role in the noise reduction of ventilation ducts.

References

1. M Munjal, Acoustics of ducts and mufflers with application to exhaust and ventilation system, *THEORY OF ACOUSTIC FILTERS*, (1987)..
2. R R Glav, The transfer matrix for a dissipative silencer of arbitrary cross-section, *Journal of Sound and Vibration*, Vol. 236, 575-594 (2000).
3. L Cao, Q Fu, Y Si, B Ding, and J Yu, Porous materials for sound absorption Composites, *Communications*, Vol. 10, 25-35 (2018).
4. Y Gao, Z Li, B Liang, J Yang, and J Cheng, Improving sound absorption via coupling modulation of resonance energy leakage and loss in ventilated metamaterials, *Applied Physics Letters*, Vol. 120, 261701 (2022).
5. D Wu, N Zhang, C Mak, and C Cai, Hybrid noise control using multiple Helmholtz resonator arrays, *Applied Acoustics*, Vol. 143, 31-37 (2019)

Frequency-selective valley edge waveguiding in topological phononic-crystal plates

Jin-Chen Hsu[1*], Chun-Hao Wei[1], and Che-Ting Huang[1]

[1]Deaprtment of Mechanical Engineering, National Yunlin University of Science and Technology, Taiwan
[*]corresponding author: hsujc@yuntech.edu.tw

Abstract: We designed four elastic valley Hall materials composed of pillared phononic-crystal plates with two different topological modulations. By constructing distinct phase domain walls, the valley edge states emerge at different frequencies in the complete band gap. Accordingly, we can demonstrate robust zigzag waveguiding and frequency-selective channeling for elastic Lamb waves.

In the past decade, the discovery of quantum Hall, quantum spin Hall, and quantum valley Hall effects of condensed matters has inspired fascinating research direction of classical wave systems. These effects enable the creation of topological insulators (TIs) with extraordinary wave transport properties, such as defect immunity, backscattering immunity, and topologically protected edge states. However, frequency-dependent transport using topological materials has been still difficult. In this study, we demonstrate waveguiding and frequency-selective channeling for Lamb waves. We tailor a pillared phononic-crystal (PnC) plate with a honeycomb lattice to obtain the frequency band structure with a two-fold Dirac degeneracy at *K* valley. By modulating the relative height or radius of pillars to break the inversion symmetry, the Dirac degeneracy are lifted, giving rise to complete band gaps. Meanwhile, the valley Hall phase transition is induced. Consequently, two groups of distinct topological phases of the material based on radius and height modulations are obtained, respectively. Then by constructing distinct phase domain walls, the topological bands of valley edge states emerge, which could cover different frequency ranges in the complete band gaps. Finally, we are able to design frequency-selective waveguides that is immune to backscattering at sharp corners.

The designed PnC plate consists of a honeycomb array of tungsten pillars deposited on a thin lithium-niobate plate. Figure 1 shows the calculated frequency band structure for the PnC plate. the result shows that the fifth and sixth bands form a deterministic two-fold Dirac degeneracy at *K* point at 429 kHz. Then we modulate the relative height and radius (termed Δh and Δr), respectively, of the adjacent pillars of the unit cell to break the spatial inversion symmetry, the Dirac cone is lifted up, and complete band gaps are opened. Therefore, the A_h ($\Delta h < 0$) and B_h ($\Delta h > 0$) structures (and A_r ($\Delta r > 0$) and B_r ($\Delta r < 0$) structures) respectively belonging to topologically opposite valley Hall phases are obtained.

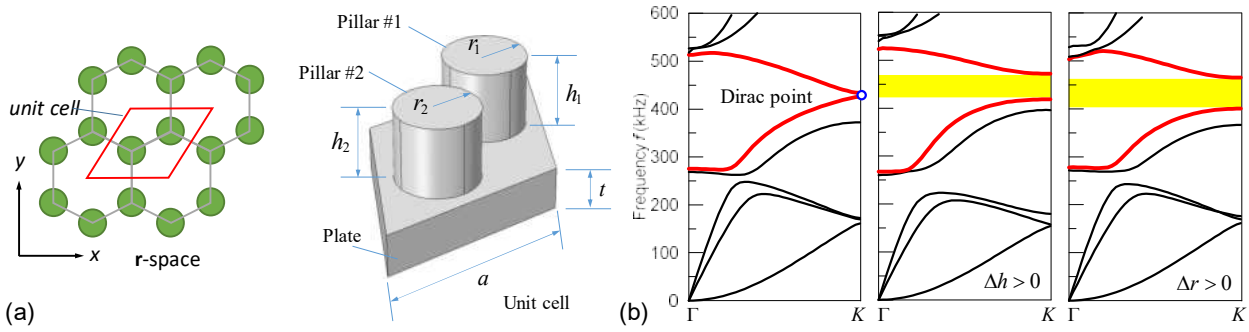


Figure 1 (a) Honeycomb lattice and unit cell. (b) Band structures of original and modulated PnC plates.

The valley Hall phase transition ensures the existence of edge state within the topological band gap and localized at the domain wall between two PnCs of different phases. Here, we combine two different PnC plates to construct the domain wall: negative phase with the A_h (or A_r) structure and positive phase with the B_h (or B_r) structure. Four combinations that yield eight different domain walls can be used, i.e., A_hB_h, A_rB_r, A_hB_r, A_rB_h and their exchange. Consequently, we can show that the projected band structures at the domain walls for the four combinations all exhibit valley edge bands covering different frequency ranges in the complete band gaps.

The most prominent feature of the valley edge state lies in the backscattering immunity to path bending. To illustrate this effect, we build zigzag domain walls and preform full-wave simulations. Three combinations, A_hB_h, A_rB_r, and A_rB_h, are illustrated. The point wave sources are excited at the chosen frequencies 446, 436, 440 kHz, respectively, at the left-end entrance. As shown in Fig. 2, valley edge states are excited and propagate along the domain walls, and the intensity of the displacement field for each combination is nearly uniform along the entire zigzag domain wall path, which indicates that no observable reflection occurs at the two sharp corners.

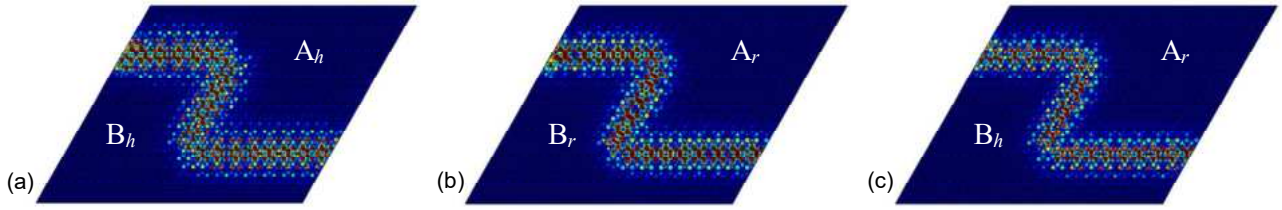


Figure 2 Transmission of valley edge states along zigzag domain wall paths composed of different phases.

Based on the four valley Hall materials, we are able to design frequency-selective topological waveguides. The design utilizes the topological edge bands of different domain walls that extend over different frequency ranges and empty topological band gaps. The waveguide consists of three sections along the horizontal direction using B_rA_r, B_hA_r and, B_rA_r combinations. Figure 3 shows the results of frequency-selective waveguiding, where a source at left entrance are excited using three different frequencies, 430, 436, and 448 kHz, respectively. When the frequency is 436 kHz, waves can freely transmit through the entire waveguide by means of the edge states supported simultaneously by the B_rA_r and B_hA_r combinations, while the other two frequencies are forbidden.

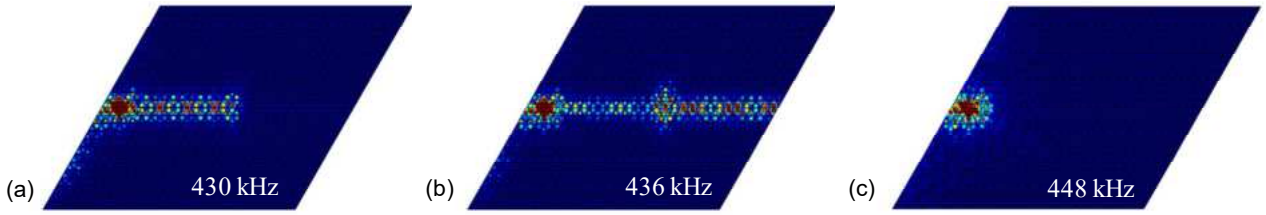


Figure 3 Result of frequency-selective waveguiding in the designed topological PnC plate.

This work was supported by the National Science and Technology Council, Taiwan (111-2221-E-224-038).

References

1. R. K. Pal, M. Ruzzene, “Edge waves in plates with resonators: an elastic analogue of the quantum valley Hall effect,” New Journal of Physics, Vol. 19, 025001, 2017.
2. J. J. Chen, S. Y. Huo, Z. G. Geng, H. B. Huang, X. F. Zhu, “Topological valley transport of plate-mode waves in a homogenous thin plate with periodic stubbed surface,” AIP Advances, Vol. **7**, 115215, 2017.

From Air to Water: Expanding Inverse-Design Applications in Ultrasonic OAM

Chuanxin Zhang [1], Xue Jiang [1*], and Dean Ta[1]

[1] Center for Biomedical Engineering, School of Information Science and Technology, Fudan University, Shanghai, 200433, China
*corresponding author: xuejiang@fudan.edu.cn

Abstract: This study presents an inverse-design methodology for optimizing Orbital Angular Momentum (OAM) beams, enhancing ultrasonic motor performance. Utilizing an airborne 16x16 phased array and holographic lenses, we achieved significant improvements in beam uniformity and signal-to-noise ratio, demonstrating superior particle control in a constructed twisted ultrasonic motor.

Introduction and Background

Recent advancements in the field of acoustic Orbital Angular Momentum (OAM) have opened new avenues in precision acoustic applications, particularly in the development of advanced particle manipulation. Our study presents a breakthrough in this realm, employing an inverse-design methodology that optimizes OAM beams for enhanced performance.

Optimization of Phased Array in Air

Our initial focus was on air-based applications, where we used phased arrays as ideal radiating planes. Phased arrays are crucial due to their ability to control the pattern of emitted acoustic beams. This capability stems from the precise timing (phase) control of each array element. However, these arrays typically encounter limitations when employed in undersampled or sparse configurations, leading to suboptimal OAM beam performance.

Through our methodology, these phased arrays were optimized for air propagation. We incorporated a global optimization strategy, significantly improving the amplitude uniformity and Signal-to-Noise Ratio (SNR) of OAM beams. This was a crucial step towards achieving our goal of constructing a high-performance twisted ultrasonic motor.

Development of Underwater Holographic Lens for OAM

Transitioning to underwater scenarios, we employed thickness-modulated holographic lenses to manipulate acoustic fields. As reported in previous studies, under the assumption of a one-dimensional transmission line model, a critical relationship has been established between the relative phase change at any pixel position and the thickness variation of the lens. This relationship is encapsulated in the formula [1]:

$$\Delta\varphi(x,y)=(k_m-k_h)\Delta T(x,y) \quad (1)$$

However, the design and optimization of these lenses presented a unique challenge due to the three-dimensional nature of the structures and the complex physical mechanisms involved, such as diffraction within the lens material. To address these challenges, we introduced more sophisticated elements into our inverse-design methodology, allowing for a nuanced control of the acoustic field in underwater environments. The distributions of the OAM acoustic field underwater emphasize the efficacy of our approach in this more complex medium.

Ultrasonic Motor Application

The culmination of our study is the development of a twisted ultrasonic motor using inverse-designed OAM beams. This motor operates on the principle of transferring angular momentum from OAM beams to a trapped

particle, inducing rotation [2]. Our approach significantly enhanced the stability and uniformity of the particle's rotational trajectory, a critical improvement over traditional method.

We demonstrate the practical application of our methodology. The OAM beam's interaction with particles in free space is shown, highlighting the advancements in particle control. This capability is pivotal in applications requiring precise manipulation, such as targeted drug delivery or micro-assembly processes.

Conclusion

In conclusion, our study represents a significant leap in the optimization of OAM beams for acoustic applications. By employing an inverse-design methodology, we have successfully navigated the complexities of phased array optimization in air and the nuanced challenges presented by underwater environments. The resulting advancements in ultrasonic motor technology not only demonstrate the practical applications of our research but also pave the way for further exploration and innovation in the field of acoustic manipulation.

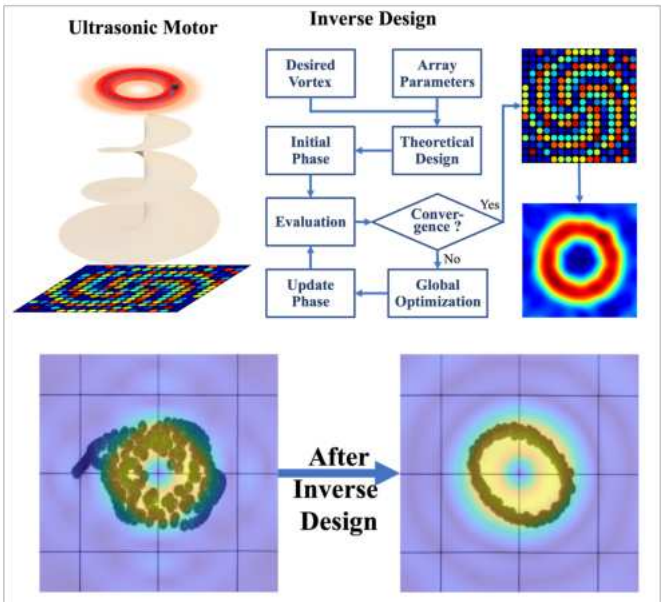


Figure 1. Schematic representation of the inverse-design process used to enhance the performance of an ultrasonic motor through OAM beam optimization.

References

1. Melde, Kai, Andrew G. Mark, Tian Qiu, and Peer Fischer. "Holograms for acoustics." Nature, Vol. 537, No. 7621, 518-522, 2016.
2. Liu, Jingjing, Zhengwei Li, Yujiang Ding, An Chen, Bin Liang, Jing Yang, Jian-Chun Cheng, and Johan Christensen. "Twisting Linear to Orbital Angular Momentum in an Ultrasonic Motor." Advanced Materials, Vol. 34, No. 28, 2201575, 2022.

Water-Air Acoustic Communication Based on Broadband Impedance Matching

Han Jia[1*], Yuzhen Yang[1], and Jun Yang[1]

[1] Key Laboratory of Noise and Vibration Research, Institute of Acoustics, Chinese Academy of Sciences, Beijing 100190, People's Republic of China

[*]corresponding author: hjia@mail.ioa.ac.cn

Abstract: Efficient acoustic communication across the water-air interface has always been expected in ocean explorations. However, the existing researches are mainly concentrated on the narrow-band transmission based on resonance. Here, we combined the air-based and water-based metafluids to realize an exponential gradient impedance matching layer for broadband water-air sound transmission.

The water-air GIML is shown schematically in the right panel of Fig. 1(a). The air-based metafluid is made of square solid inclusions arranged periodically in air and the water-based metafluid is made of square hollow inclusions arranged periodically in water. The corresponding impedance distribution is marked as red squares in Fig. 1(b). The red solid line and black dashed line in Fig. 1(c) show the energy transmission coefficients of equal-thickness and variable-thickness layering method, which are completely consistent. The four-layer GIML can achieve energy transmission above 0.9 in the range of 730 Hz to 1470 Hz. We further calculated the energy transmission coefficients of the impedance matching layers containing 1 layer and 2 layers, as are plotted in Fig. 1(c). The corresponding impedance distributions are shown as different symbols in Fig. 1(b). It can be seen that the transmission bandwidth is expanding with the number of layers. Therefore, we can achieve broadband transmission in a specified bandwidth by choosing an appropriate number of layers. The proposed design method can flexibly adjust the acoustic parameters in each layer of the GIML by changing their geometric parameters, which makes it possible to realize the water-air impedance matching using artificial structures.

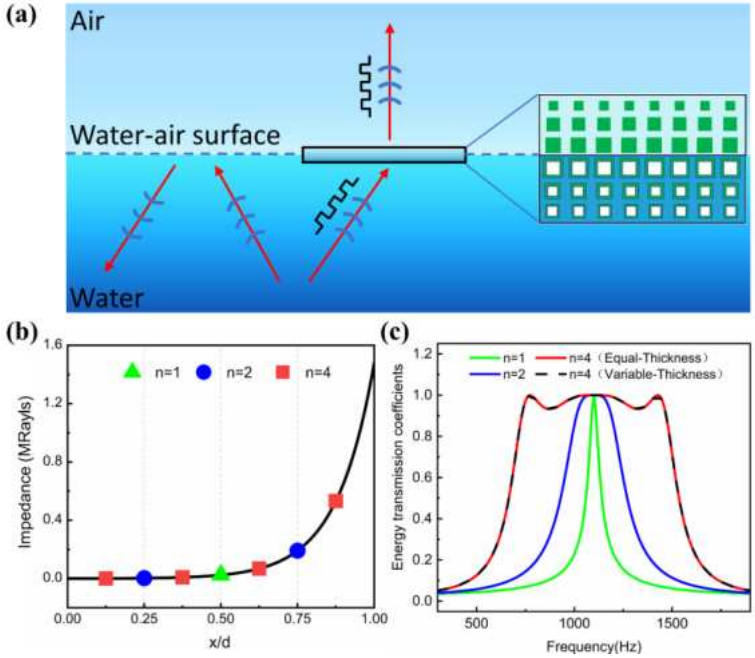


FIG. 1. (a) Schematic of water-air acoustic communication enabled by the proposed GIML. (b) The air-to-water exponential impedance distribution and the discrete impedance value including 1layer, 2layers and 4 layers. (c)

The energy transmission of the water-air GIML containing 1 layer, 2 layers and 4 layers based on equal-thickness and variable-thickness layering method.

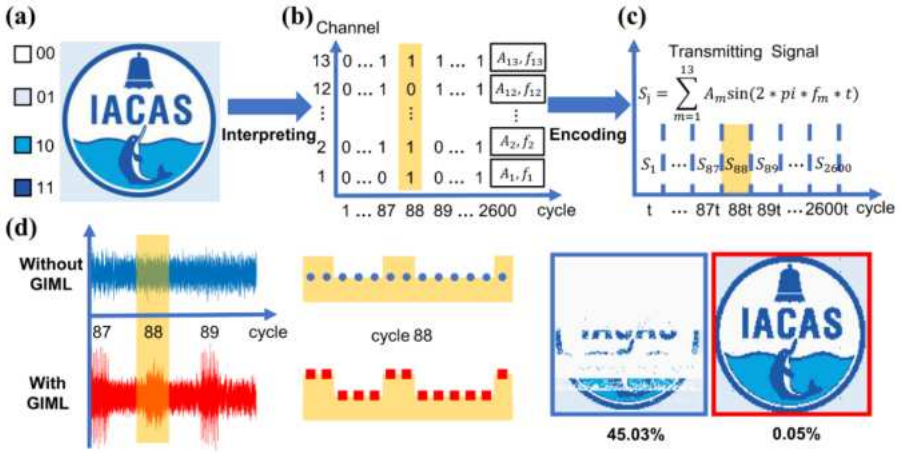


FIG. 2. (a) The transmitted picture including four different colors and 130*130 pixels. (b) The transmitted bit stream allocated to 2600 cycles and 13 channels. (c) The time-domain signal encoded by the bit stream. (d) Left panel: the received time-domain signals in 87th-89th cycle without and with the GIML. Middle panel: comparison between the target code (orange ladder) and the decoded results (circular and square) of the 88th cycle. Right panel: the received complete pictures without (blue frame) and with (red frame) the GIML. The percentages represent the bit error ratio in two cases.

With the broadband transmission enhancement ability between air and water, the proposed GIML is promising for applications in water-air acoustic transmission. Here, we use the designed GIML to realize the air-to-water acoustic communication. In this part, we aim to transmit the picture in Fig. 2(a) from air to water by frequency division multiplexing. The target picture has a size of 130*130 pixels and contains 4 different colors. The schematics of bitstream allocation and encoding are shown in Fig. 2(b) and 2(c), respectively. The bitstream is allocated to 2600 cycles. Each cycle contains 13 channels and is encoded to a time-domain signal. A time-domain sequence containing 2600 coded signals is emitted from the air and received in the water. The received signals were decoded by marking the target signal with a signal-to-noise ratio (SNR) over 20dB as "1" otherwise marking it as "0". The received transmission signals of the 87th-89th cycle are extracted and shown in the left panel of Fig. 2(d). It is obvious that the received picture through the bare interface can hardly be recognized with a bit error rate up to 45.03%, while the received picture through GIML is almost the same as the target picture with a negligible bit error rate of 0.05%. Thus, the broadband impedance matching between air and water can promote the applications in water-air acoustic communication.

References

1. Zhou, P., H. Jia, Y. F. Bi, Y. H. Yang, Y. Z. Yang, P. Zhang and J. Yang. "Water-air acoustic communication based on broadband impedance matching", Applied Physics Letter, Vol. 123, No. 191701, 2023.
2. Bi. Y. F., P. Zhou, H. Jia, F. Lu, Y. Z. Yang, Y. M. Zhang, P. Zhang and J. Yang. "Acoustic metafluid for independent manipulation of the mass density and bulk modulus", Materials & Design, Vol.233, No. 112248, 2023.

optimization, as shown in Fig. 1(a), the transmission matrix takes on an anti-diagonal form, and the reflection matrix becomes nearly zero matrix, which indicates reflectionless transmission. To verify the mode conversion effect, we separately input three modes from the left side and observe the output modes. As shown in Fig. 1(c), the output modes align with our design objectives, confirming the successful mode conversion.

In summary, this study successfully achieves control over three waveguide modes under the same configuration of the complex medium. This work may have potential applications in advanced acoustic devices.

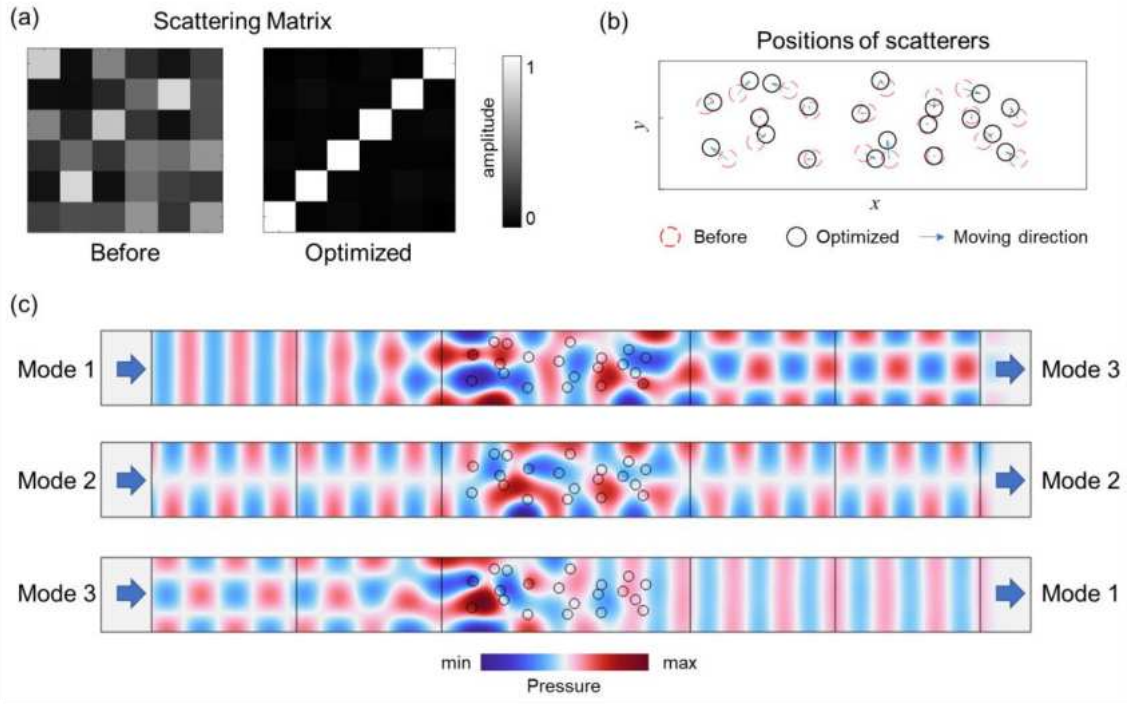


Fig. 1. (a) Amplitude of the scattering matrix before (left) and after optimization (right). (b) Positions of the scatterers before and after optimization. (c) Mode conversion effect after optimization.

Acknowledgements

This work is supported by the National Key R&D Program of China No. 2022YFA1404400.

References

1. Chen, X.; Liu, P.; Hou, Z.; Pei, Y. Magnetic Control Multifunctional Acoustic Metasurface for Reflected Wave Manipulation at Deep Subwavelength Scale. Sci Rep 2017, 7 (1), 9050.
2. Liu, D.; Peng, P. Complete Mode Conversion of Elastic Waves by Utilizing Hexapole Resonances in a Scatterers Structure. Europhys Lett 2024.
3. Rotter, S.; Gigan, S. Light Fields in Complex Media: Mesoscopic Scattering Meets Wave Control. Rev Modern Phys 2017, 89 (1), 015005.
4. Ambichl, P.; Brandsttter, A.; Bhm, J.; Khmayer, M.; Kuhl, U.; Rotter, S. Focusing inside Disordered Media with the Generalized Wigner-Smith Operator. Phys Rev Lett 2017, 119 (3), 033903.
5. Horodynski, M.; Khmayer, M.; Ferise, C.; Rotter, S.; Davy, M. Anti-Reflection Structure for Perfect Transmission through Complex Media. Nature 2022, 607 (7918), 281–286.

Optimally designed ultra-thin underwater metamaterial absorber

Nan GAO[1,2,†], Sichao Qu[1,5,†], Alain Tinel[3], Bruno Morvan[3], Vicente Romero-García[2], Jean-Phillippe Groby[4], Ping Sheng[1]

[1] Department of Physics, The Hong Kong University of Science and Technology, Hong Kong, China
[2] Instituto Universitario de Matemática Pura y Aplicada, Departamento de Matemática Aplicada, Universitat Politècnica de València, Camino de Vera, València, Spain
[3] Laboratoire Ondes et Milieux Complexes UMR CNRS 6294, UNILEHAVRE, Normandie University, Le Havre, France
[4] Laboratoire d'Acoustique de l'Université du Mans (LAUM), UMR 6613, Institutd'Acoustique—Graduate School (IA-GS), CNRS, Le Mans Université, Le Mans, France
[5] Department of Mechanical Engineering, The University of Hong Kong, Hong Kong, China
(†These authors contributed equally to this work.)
Presenting author: ngao@upvnet.upv.es

Abstract:
In this talk, I present an ultra-thin broadband acoustic metamaterial absorber for underwater acoustics. It comprises an optimal combination of Fabry-Perot resonators (FP) made of a low longitudinal sound speed tungsten-polyurethane composite that matches the water impedance.[1]

Contrary to electromagnetic waves, acoustic waves propagate in water with small attenuation.[2] Therefore, they have been exploited as an effective information carrier for underwater communications, positioning, searching, and other operations. In recent years, the emergence of acoustic metamaterials has led to new ways for manipulating sound waves. [3] However, underwater acoustics metamaterials have still not been actively pursued compared to airborne audible sound or ultrasound. The longer wavelength of underwater acoustic waves also usually implies thicker or larger devices for their manipulation. Moreover, underwater acoustic wave absorption is constrained by the causality law, which means that it requires very thick material to achieve high values of absorption.

The response of any passive materials backed by a rigid wall to an external wave must satisfy the causality constraint that relates the thickness of the sample d and its corresponding absorption spectrum $A(\lambda)$ [4]

$$d \geq \frac{1}{4\pi^2}\frac{B_{eff}}{B_w}\left|\int_0^\infty \ln[1-A(\lambda)d\lambda]\right| = d_{min}, \tag{1}$$

where B_{eff} represents the low frequency limit of composite's effective bulk modulus in the static regime and B_w denotes the bulk modulus of host medium. From Eq. (1), it can be seen that if we want to obtain thinner absorbers (i.e. smaller d_{min}) under the constraint of causality, we need to reduce the ratio of effective bulk modulus B_{eff}/B_w. For air, this is very difficult. However, for water, due to its particularly large B_w, it results convenient, and we can design as well as manufacture a composite material to achieve this goal.

In this work, we present a novel underwater metamaterial absorber made of a structured impedance-matched composite that can match the impedance of water. This absorber combines the features of being ultrathin (λ/42 at 4 kHz) as well as 'low-frequency' broadband absorption (from 4kHz to 20 kHz). Our composite is made of high-density tungsten powder dispersed in a low-modulus polyurethane (PU) polymer matrix. The resulting composite is structured into slender solid rods (**Fig. 1a**). With the pressure release boundary condition on its sidewalls, we can regard Young's modulus as its longitudinal wave modulus. This

composite material can significantly slow down the wave velocity, thereby realizing the goal of effective sound energy dissipation in the subwavelength regime. Simultaneously, reducing the composite's Young's modulus and increasing its density also ensures its impedance matching with water (**Fig. 1a**); and we can effectively increase its B_{eff}, to obtain a smaller d_{min} , while simultaneously achieving ultra-thin absorption samples. By combining the FP resonators in accordance to the integration scheme, 9 composite rods with different lengths have been combined into a unit (**Fig. 1a**), which exhibits periodical arrangement and placed on a rigid base to achieve the goal of broadband sound absorption.

Based on the above design strategy, we have successfully obtained our underwater sample (**Fig. 1b**) with ultra-thin thickness (averaged thickness only 8.9mm), realizing high sound absorption (>0.9) in the frequency range of 4-20 kHz (**Fig. 1d**), where the wavelength is much larger than its dimension. The result is demonstrated by both simulations, as well as experiments carried out in a large water pool (**Fig. 1c**). Results obtained from this work provide a novel direction for the design of underwater sound absorbers. Also, due to its ultra-thin design and broadband absorption, it has great significance in practical applications, not only in underwater sound but also in other acoustics fields.

P.S. acknowledges the support of RGC grant A-HKUST601/18 and AoE/P-502/20-3 for this work. J.-P.G. and V.R.-G. acknowledge the support of the ANR-RGC METARoom project (ANR-18-CE08-0021) for this work. This project has received funding from the European Union's Horizon 2020 research and innovation program under the Marie Skłodowska-Curie grant agreement No. 101106904 - MDS-APP-UAF.

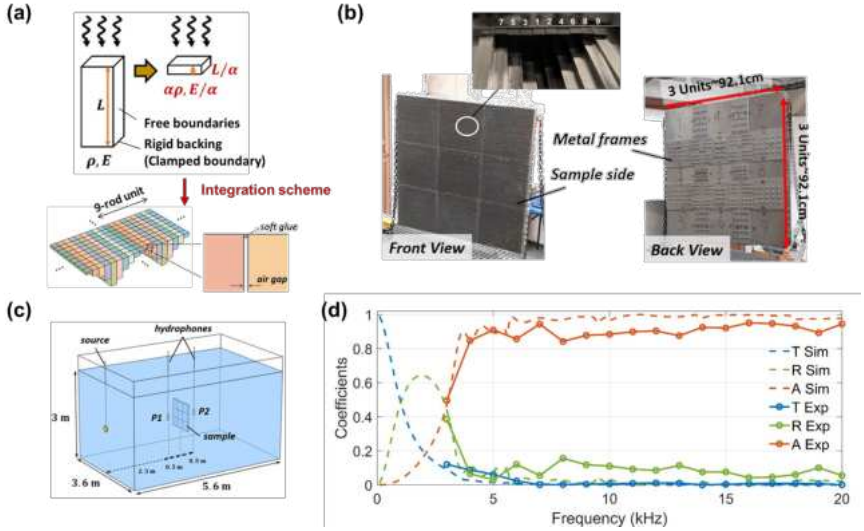


Fig. 1 (a) Design strategy for ultra-thin underwater absorber; (b) Final sample ($\sim 1m \times 1m$) for the experiment; (c) the schematic of the water pool measurement configuration; (d) The experiment (dotted line) and simulation (dashed line) results with the transmittance T (blue), the reflectance R (green), and the absorption A (red).

References

1. Qu, S., *et al*., Underwater metamaterial absorber with impedance-matched composite, *Sci. Adv.* **8**, eabm4206 (2022)
2. Yang. T. C., "Properties of underwater acoustic communication channels in shallow water." The Journal of the Acoustical Society of America 131, 129, 2012.
3. Li, J., Wen, X. H. and Sheng, P., "Acoustic metamaterials." Journal of Applied Physics 129, 17, 2021.
4. Yang, M., Chen, S. Y,, Fu, C. X. and Sheng, P., "Optimal sound-absorbing structures." Materials Horizons, 4(4), 673-680, 2017.

Fast-speed Ultrasonic Imaging Using a Single Sensor by Combining Disordered Metasurface and Artificial Intelligence

W. Wang[1*], J. Hu[2], J. J. Liu[1], B. Liang[1], and J. C. Cheng[1]

[1]Key Laboratory of Modern Acoustics, MOE, Institute of Acoustics, Department of Physics, Collaborative Innovation Center of Advanced Microstructures, Nanjing University, Nanjing 210093, People's Republic of China
[2] Department of Information Science and Technology, Nanjing Forest University, Nanjing, 210037, China
[*]corresponding author: weiwang@smail.nju.edu.cn

Abstract: We propose a mechanism that can realize real-time and single-sensor ultrasonic imaging with ultra-low-cost using a disordered metasurface combined with a neural network. A single fixed sensor and a handcrafted metasurface with costs of much less than one dollar are proved sufficient to yield a high imaging quality.

Imaging using ultrasound is a frontier technique in modern science owing to its high penetration and biocompatibility, with pivotal significance in many applications ranging from crack detection to biological tissue imaging[1,2]. However, existing ultrasonic imaging technologies either allow real-time imaging but lack single-sensor imaging capability[3], or enable single-sensor imaging but do not support real-time imaging[4]. Consequently, real-time single-sensor imaging with low cost, whether in the realm of optics or acoustics, represents a formidable challenge that remains largely unresolved to this day. To overcome the above fundamental limitations, we propose and experimentally demonstrate a mechanism for real-time ultrasonic single-sensor imaging based on the coalescence of artificial structure and artificial intelligence (AI), which features fast imaging speed, low-cost fabrication, compact system size, and high imaging quality. In our proposed mechanism, a single fixed transducer emits a broadband ultrasonic signal, which passes through the object and the disordered metasurface in succession before being received by a single fixed sensor. Utilizing the rich complexity arising from the random parameter distribution and strong dispersion characteristics, a disordered metasurface can effectively encode the information of the objects' scattered field by changing the amplitude of the spectral components at every spatial point and then transmit it to a single fixed sensor. By harnessing the remarkable learning and feature extraction abilities of neural networks, the encoded signal captured by the sensor can be utilized to quickly reconstruct the geometry of the original object even in the absence of prior knowledge regarding the metasurface's internal structure and material parameters, which greatly facilitates the fabrication of the whole system. Therefore, our mechanism achieves the effects of a structurally complex and expensive phased array and multi-sensor imaging system, using only a single sensor and a piece of cheap metasurface.

References

1. Wang, C. H, X. Y. Chen, L. Wang, M. Makihata, H. C. Liu, T. Zhou and X. H. Zhao. "Bioadhesive ultrasound for long-term continuous imaging of diverse organs," Science, Vol. 377, No. 6605, 517–523, 2022.
2. Yun, H. G., R. Rayhana, S. Pant, M. Genest and Z. Liu, "Nonlinear ultrasonic testing and data analytics for damage characterization: A review," Measurement, Vol. 186, 110155, 2021.

3. Krause, M., F. Mielentz, W Müller, V. Schmitz and H. Wiggenhauser, “Ultrasonic imaging of concrete members using an array system,” NDT & E International, Vol. 34, No. 6, 403-408, 2001.
4. Kruizinga, P., P. Meulen, A. Fedjajevs, F. Mastik, G, Springeling, N. Jong, J. G. Bosch and G. Leus, “Compressive 3D ultrasound imaging using a single sensor,” Science Advances, Vol. 3, No. 12, e1701423, 2017.

Chiral and hyperbolic metamaterials

Dielectric metasurface for wave-vector variant and circular polarization dependent transmission

H. Wetter[1*], W. Gao[2], F. Rehberg[1], J. Wingenbach[1], S. Schumacher[1,3] and T. Zentgraf[1,3]

[1]Department of Physics, Paderborn University, Germany
[2]EIT Institute for Advanced Study, Ningbo, China
[3]Institute for Photonic Quantum Systems, Paderborn University, Germany
[*]corresponding author: helene.wetter@uni-paderborn.de

Abstract: We study a silicon metasurface consisting of sinusoidal sidewall waveguides where near-field coupling of local resonances causes negative coupling. This gives rise to fully circularly polarized radiational eigenstates that form a line in k-space. The corresponding metasurface provides wave-vector variant and spin-selective transmission.

Chiral metasurfaces exhibit unique optical properties towards circularly polarized light. Among the various metasurfaces investigated previously [1], some possess points with circular polarization in momentum space. Here, we present a metasurface in which the eigenstates of circular polarization not only occur at one point, but form a line in momentum space.

The corresponding metasurface consist of silicon waveguides on a glass substrate that are embedded in PMMA to approximately create a homogenous environment. The unit cell (see Fig. 1(a)) contains a single waveguide (SW) and double waveguide (DW) depicted in gray and blue, respectively. The sinusoidal modulation of the width enables coupling to the continuum photon states in the ambient environment thus radiation. Since the waveguides are placed in close proximity, the localized mode in the SW and the spatially odd mode in the DW couple. When these modes are degenerate, their near-field coupling results in alternating positive and negative coupling. From the real-space tight-binding Hamiltonian one can derive that this coupling pattern allows a $\pi/2$ phase delay that is crucial for circular polarization. [2]

Based on this concept, the parameters of the metasurface are tailored such that circularly polarized eigenstates emerge forming a line in momentum space (C-line). This C-line emanates from the Dirac point and possesses opposite helicity for the two energy levels (see Fig. 1(b)). The Dirac point itself presents a polarization singularity and the point at which the helicity of the C-line switches. As a result, the helicity can be switched by changing either the energy level or the sign of k_x (wave vector component along x).

This is demonstrated in figure 1(c) which shows the simulated transmission spectra for incident right- and left-polarized light (dashed and solid line, respectively) as well as for two different values of k_x (blue and black). A dip to approximately zero occurs when the incident light matches the polarization and frequency of an eigenstate. If the sign of k_x is changed, the helicity of the lower/higher frequency resonance switches. Additionally, a higher absolute value of k_x corresponds to a larger frequency difference. Both effects are consistent with the eigenstates in figure 1(b).

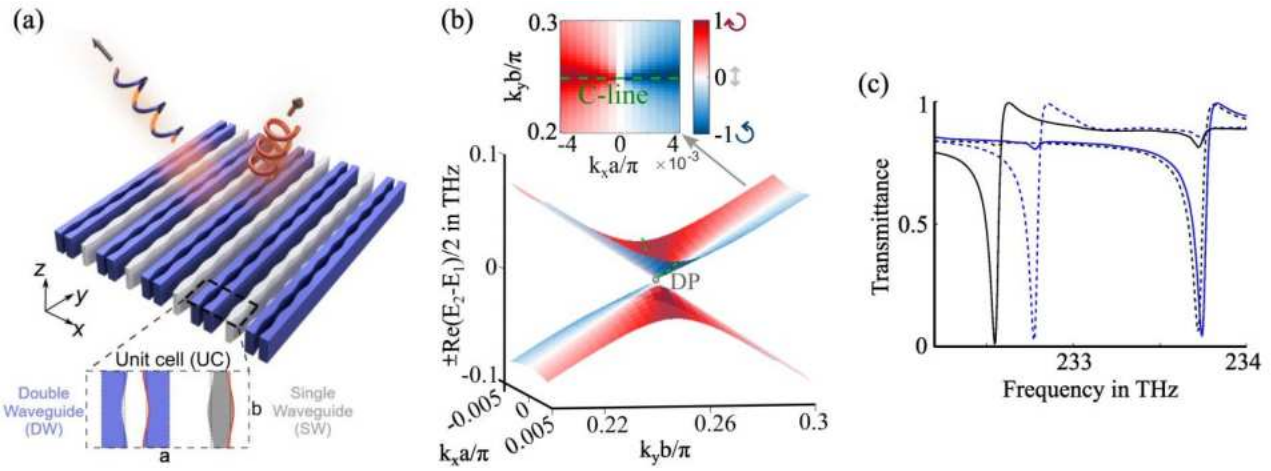


Figure 1: (a) Metasurface consisting of silicon waveguides with sinusoidal modulation and corresponding unit cell from [2]. (b) Eigenfrequencies around the Dirac point (DP). The color corresponds to the eigenpolarization of the corresponding state. Dark blue and red corresponds to left and right circular polarization, respectively, white to linear polarization and the lighter colors cover all degrees of elliptical polarization. The inset shows the eigenpolarization of the upper energy level in momentum space where the C-line is apparent. (c) Simulated transmission spectra for incident right (dashed line) and left circularly polarized light (solid line) and for $k_x a/\pi=0.08$ (blue) and -0.1 (black). For all spectra $k_y b/\pi=0.25$ holds according to the C-line.

References

1. Khaliq, H.S., A. Nauman, J.W. Lee and H.R. Kim, "Recent Progress on Plasmonic and Dielectric Chiral Metasurfaces: Fundamentals, Design Strategies, and Implementation," Advanced Optical Materials, 2300644
2. Gao, W., B. Sain and T. Zentgraf, "Spin-Orbit Interaction of Light Enabled by Negative Coupling in High-Quality-Factor Optical Metasurfaces," Physical Review Applied, Vol. 17, No. 4, 044022, 2022.

META 2024, TOYAMA - JAPAN, JULY 16 – 19, 2024

Photonic Modes in Gyrotropic-Hyperbolic Heterostructures

D. B. Provenzano[1,*] and G. C. la Rocca[1,2]

[1]Scuola Normale Superiore, I-56126 Pisa, Italy
[2]NEST, Scuola Normale Superiore, 56126 Pisa, Italy
[*]daniele.provenzano@sns.it

Abstract: We present an analysis of electromagnetic surface waves localized at the interface of a one-dimensional semi-infinite photonic crystal with gyroelectric and hyperbolic layers. Starting with a single interface, we explore the influence of gyrotropy and other media parameters on the behavior of the surface modes, demonstrating non-reciprocal dispersion characteristics. In the case of multilayered structures, the investigation reveals also the existence of modes with negative group velocity and instances of high values of Goos–Hänchen Shift.

Electromagnetic Surface Waves (ESWs) have gathered attention since the work of Jonathan Zenneck in 1907. Surface modes can exist under certain conditions on a surface bounded by air, or at the interface separating two semi-infinite half-spaces. Among the most remarkable examples of ESWs there are Surface Plasmon-Polaritons (SPPs) and Zenneck Waves (ZWs). The latter can propagate along the interface between a lossless dielectric and a lossy one and, like SPPs, have a TM nature. Their most peculiar features are the attenuation in the in-plane direction – caused by absorption in the lossy medium – and a tilt of the field distribution with respect to the normal to the interface. ESWs can indeed propagate in multilayered systems, and within photonic crystals (PhC), Tamm Waves and Bloch Surface Waves[1] emerge as particularly notable examples.

When the system is subjected to an external magnetic field, thereby breaking time-reversal symmetry, certain types of media may demonstrate non-reciprocal features that significantly influence the propagation of Electromagnetic Surface Waves (ESWs). In the presence of gyrotropy, the dispersion relation of ESWs typically becomes asymmetric with respect to the reversal of the in-plane wavevector.

In this work, we present a theory describing ESWs localized at the interface of a one-dimensional PhC comprising gyroelectric and hyperbolic layers. We start by analyzing Electromagnetic Surface Waves (ESWs) localized at the interface between a Gyroelectric Material (GM) and a Hyperbolic Medium (HM)[2]. We explore the conditions for the existence of this surface mode, which are determined by the media parameters, the operating frequency, and the orientation of the principal axes of the HM (refer to Figure 1, panel A). Our findings reveal that the anisotropy of the HM leads to a tilted behavior in the field lines of the mode, reminiscent of the Zenneck Wave observed in lossy metals (as illustrated in Figure 1, panel B). Additionally, we demonstrate that gyrotropy imparts non-reciprocal dispersion characteristics to these waves. Furthermore, we numerically simulate a specific gyroelectric-hyperbolic interface, consisting of InSb and a stack of graphene layers, which is amenable to the observation of such novel modes. In this scenario, the dispersion relation along the surface is not reciprocal when the in-plane wave vector is reversed, as evidenced by the reflectivity spectra (as depicted in Figure 1, panel C). Remarkably, the propagation length of these waves can extend to several millimeters in such configurations, rendering them suitable for various applications in photonic devices.

We subsequently analyze what happens to such ESWs when the structure becomes a semi-infinite 1D PhC, composed of gyrotropic and hyperbolic layers. Our investigation reveals that, among these waves, some exhibit either forward or backward propagation characteristics, as shown in Figure 2 panel A, depending on the specific type of hyperbolic medium involved. Importantly, we demonstrate that the surface waves under scrutiny inherit key properties from both bulk plasmons and Tamm Waves, underscoring their unique potential in the realm of photonics. When gyrotropy is introduced into the system, the photonic bands are quantitatively and qualitatively

modified (as shown in Figure 2, panel B). We also provide a numerical analysis of a finite system, composed of a few dozen periods, where such effects can be found by looking at the reflection spectra. In this configuration, we show that near-zero values of the reflection coefficient correspond to non-trivial values of the Goos–Hänchen Shift (as illustrated in Figure 2, panel C).

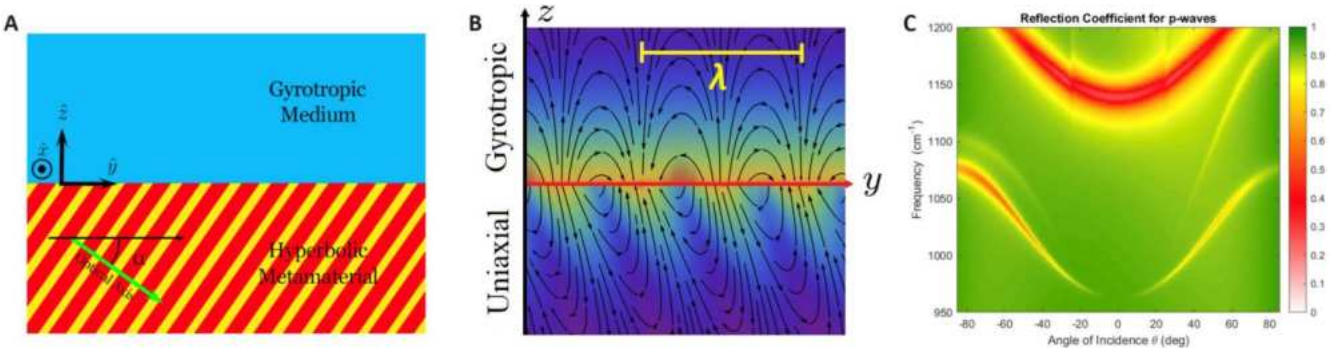


Figure 1: (A) Scheme of the GM-HM interface; (B) Typical electric field lines of a TM mode that propagates along the interface: the lines in the HM have a tilted behavior, which recalls the characteristic profile of ZWs, even though no lossy dielectric functions were involved in our theoretical calculations; (C) Simulated reflectivity spectra in the Otto configuration as a function of the angle of incidence for a realistic case including absorption: notice the non-reciprocal behavior manifested by the asymmetry between opposite angles.

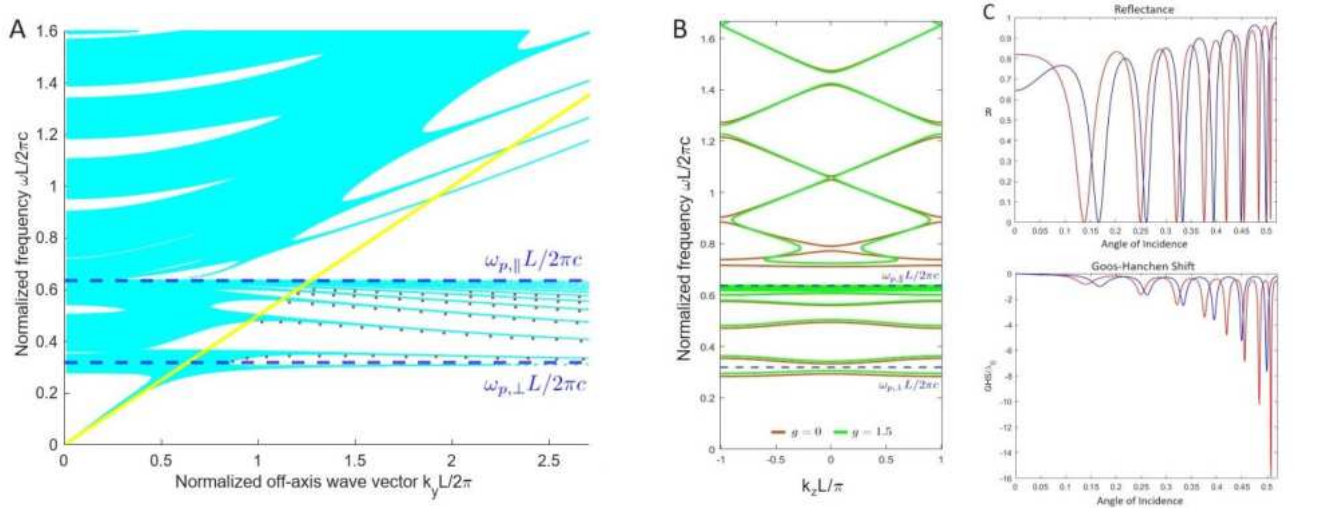


Figure 2: (A) Typical reduced band diagram for TM waves in a Gyrotropic-Hyperbolic PhC. The blue regions represent the bulk bands, the red dots represent the surface modes (propagating with negative group velocity) and the yellow line is the light line characterizing the isotropic half-space. (B) Band diagram relative to the k_y L / 2π = 1 slice in (A), where the red/green lines represent the bands without/with gyrotropy. (C) Reflectance and Goos–Hänchen Shift for a finite multilayered structure for two different values of the frequency, as functions of the incidence angle.

References

1. Polo, J., Mackay, T., & Lakhtakia, A. (2013). Electromagnetic Surface Waves: A Modern Perspective. Elsevier
2. D. B. Provenzano and G. C. la Rocca, "Interface mode between gyroelectric and hyperbolic media," J. Opt. Soc. Am. B 40, 172-177 (2023).

Understanding The Reflective Footprint of Ghost and Leaky Hyperbolic Polaritons in Crystal Quartz

Mark C. Cunningham[1*], Adam L. Lafferty[1], Mario González-Jiménez[2] and Rair Macêdo[1]

[1]James Watt School of Engineering, Electronics and Nanoscale Engineering Division, University of Glasgow, Glasgow, G12 8QQ United Kingdom

[2]School of Chemistry, University of Glasgow, Glasgow, G12 8QQ, United Kingdom

[*]Corresponding author: m.cunningham.2@research.gla.ac.uk

Abstract: We demonstrate the impact of anisotropy orientation on hyperbolic polaritons in quartz using attenuated total reflection. We reveal new insights into leaky and ghost hyperbolic polaritons, including their directional dependency and associated cross-polarization conversion. This highlights their potential to transform direction-dependent optical device development for next-generation sensing and communication technologies.

In natural crystals such as quartz, anisotropic phonon resonances in the infrared can lead to principal elements of the diagonal permittivity tensor possessing opposite signs. This, in turn, leads to hyperbolic dispersion [1]. Hyperbolic materials are great candidates for controlling light at the nanoscale, owing to their strong electromagnetic field confinement and reconfigurable anisotropy orientation. They have been shown to support surface polaritons with long-range and low-loss propagation of subwavelength information, guided waves, and negative refraction [1,2,3,4].

Hyperbolic dispersion is commonly referred to as type I when a single extraordinary component of the dielectric tensor is negative while the two ordinaries are positive, creating a two-sheet hyperboloid isofrequency contour. Conversely, when the extraordinary component is positive while the two ordinary components are negative, an open-sheet hyperbolic isofrequency contour forms, known as type II dispersion [1]. Quartz possesses two hyperbolic regions between $400\text{-}600\ \mathrm{cm}^{-1}$; a type II region between $450\text{-}480\ \mathrm{cm}^{-1}$ and a type I region between $510\text{-}550\ \mathrm{cm}^{-1}$.

Close to these frequencies, there are three wave phenomena that have recently gained significant attention: surface, leaky, and ghost hyperbolic polaritons. Surface polaritons are perhaps the simplest of these effects; being waves that travel at the surface of materials [1]. On the other hand, leaky hyperbolic polaritons (LHPs) have been classified as the hybridization between a propagating bulk mode and a surface wave, noted for their radiation leakage as well as long-range directional and sub-diffractive propagation at interfaces and ghost hyperbolic polaritons (GHPs) possess slanted phase wavefronts into the bulk of the crystal, parallel Poynting vectors to the surface, and exponential decay away from the surface. Unlike surface polaritons, which emerge when the dielectric constant is negative, LHPs [4] are typically associated with type I hyperbolic dispersion and GHPs [3] with type II hyperbolic dispersion.

Between the two hyperbolic regions in crystal quartz ($480\text{-}510\ \mathrm{cm}^{-1}$), all elements of the dielectric tensor are negative, meaning that surface polaritons are supported. To probe these experimentally, we employ attenuated total reflection (ATR) in the Otto configuration [1], where a prism is placed close to the sample surface, separated by a thin air gap. Total internal reflection occurs at the prism-air interface, allowing for the excitation of surface polaritons on the sample surface. We find that the frequencies supporting these surface polaritons between the hyperbolic regions vary significantly depending on the orientation of the anisotropy axis with respect to the crystal surface. When the anisotropy is aligned parallel with both the crystal surface and incidence plane, surface

polaritons are excited at a frequency around $505\ \mathrm{cm}^{-1}$. When rotated so that the anisotropy is perpendicular to the incidence plane (but still parallel to the crystal surface), this excitation frequency is shifted to lower frequencies around $475\ \mathrm{cm}^{-1}$.

Furthermore, we find that LHP manifests with the characteristic lenticular dispersion [4] emerging in ATR spectra, as the high-k_x modes intersect with the free-space light cone (FSLC). Close to the Epsilon-near-zero region at frequencies higher than the type-I hyperbolic region, the existence of the LHP is highly dependent on azimuthal orientation of the crystal anisotropy axis. In addition, we find that the cross-polarization conversion [2] associated with LHPs becomes significantly asymmetric if the anisotropy axis is no longer parallel to the crystal surface).

Finally, we find that for the GHPs a sharp drop in reflectivity is observed for a wide range of incident angles and azimuthal orientations, mirroring the original s-SNOM observations of this phenomenon [3]. We find that cross-polarization conversion associated with GHPs is broadly symmetric and less extreme than that due to the LHPs. When the anisotropy is tilted so that is no longer parallel to the crystal surface, the GHP excitation diminishes significantly as the reflectivity increases.

This new understanding of the anisotropy orientation's impact on quartz's reflective properties, including surface polaritons, LHPs, and GHPs at infrared frequencies, opens avenues for application in sensing and communications. Additionally, employing crystal quartz's reflective properties in the far-field simplifies access to these phenomena, offering a more accessible alternative to the complex and costly near-field methods like s-SNOM. We demonstrate the potential of utilizing these phenomena across a broad spectral range, highlighting their significance for innovative optical device development.

MCC acknowledges funding from the Engineering and Physical Sciences Research Council (EPSRC) under grant number EP/S023321/1.

References

1. Macêdo, R., Dumelow, T., Camley, R. E. & Stamps, R. L. Oriented Asymmetric Wave Propagation and Refraction Bending in Hyperbolic Media. ACS Photonics 5, 5086–5094 (2018).
2. Wu, X., McEleney, C. A., Shi, Z., González-Jiménez, M. & Macêdo, R. Asymmetric Reflection Induced in Reciprocal Hyperbolic Materials. ACS Photonics 9, 2774–2782 (2022).
3. Ma, W. et al. Ghost hyperbolic surface polaritons in bulk anisotropic crystals. Nature 596, 362–366 (2021).
4. Ni, X. et al. Observation of directional leaky polaritons at anisotropic crystal interfaces. Nat Commun 14, 2845 (2023).
5. Passler, N. C. et al. Layer-resolved resonance intensity of evanescent polariton modes in anisotropic multilayers. Phys. Rev. B 107, 235426 (2023).

Enhanced chirality with Mie resonance-based multi-cylinder chiral metasurfaces

S. H. Hong[1], SH. Hong[1], YS. Kim[1], B.K. Kim[1], JH. Lee[1] and SH. Kwon[*]

[1]Department of physics, Chung-Ang University, Korea
[*]corresponding author: shkwon@cau.ac.kr

Abstract: Our proposed single-layer metasurface structure, integrating three dielectric cylinders based on a Mie resonator with a strong electric dipole mode. This design achieves a circular dichroism enhancement of 0.67 and an optical activity enhancement of 1.16×10^6 °/mm, confirmed through simulation to validate its tailored chiral optical effects.

Chiral structures lacking inversion symmetry (cannot be superimposed) exhibit optical properties such as circular dichroism and optical activity. Consequently, chiral structures are being studied to produce thin waveplates, circular polarizers, and chiral sensors [1].

Mie scattering occurs when the size of the structure is comparable to the wavelength of light, leading to strong Mie resonance, such as electric dipole (ED) and magnetic dipole (MD) modes. Dielectric-based Mie resonators have good responsivity with negligible absorption losses. Therefore, recent research has focused on metasurfaces to control the spectral, wavefront and polarizations [2-3]. Mie resonance-based dielectric chiral metasurfaces typically feature multi-layered or complex shapes to achieve high reactivity [4-5]. In contrast, we propose a metasurface consisting of three dielectric cylinders with ED modes, demonstrating high chirality despite its simple and single-layered structure.

As shown in Figure 1. (a), our chiral metasurface consists of three cylinders of different radii, which we refer to as C1, C2, and C3 in order of increasing radius. These cylinders (n=3.48) are arranged in an equilateral triangle configuration on a substrate (n=1.45) in a counterclockwise direction, with the cylinders organized by increasing radius. All cylinders exhibit ED modes at distinct wavelengths. When considering C1, C2, and C3 in order of increasing radius, cylinders C1 and C3 demonstrate ED resonant wavelength at 1400 nm and 1600 nm, respectively, relative to the target wavelength of 1500 nm C2, as depicted in Figure 1. (b). As indicated in Figure 3. (c), the ED phase of each cylinder increases with the radius, leading to varying responses to LCP and RCP light.

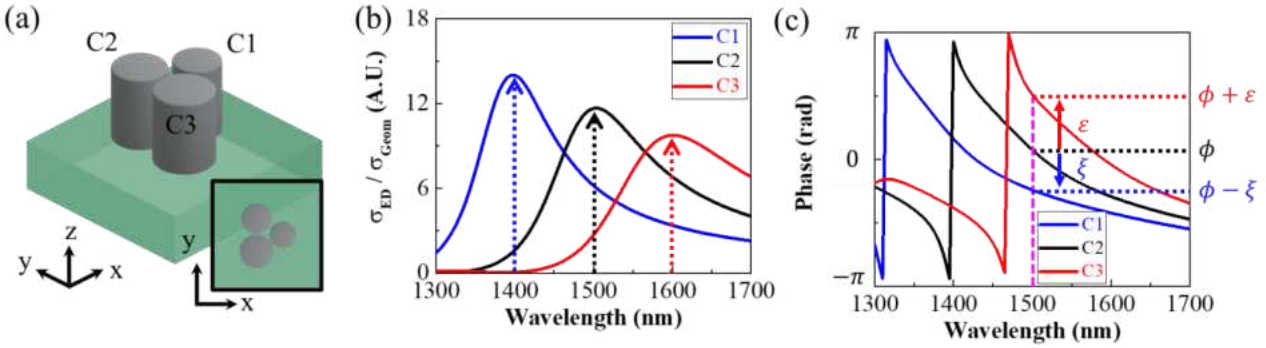


Figure 1. (a) Schematic diagrams of a chiral unitcell, each featuring three dielectric cylinders (C1, C2 and C3) with different radii above the substrate. (b) Normalized electric dipole (ED) scattering cross-section and (c) ED phase of each cylinder as function of incident wavelength.

The optical chirality of our chiral metasurface can be observed in Figure 2. Panels (a) and (b) illustrate the transmittance when LCP and RCP light are incident on the cylinder from the substrate (+z direction) and show the difference between them. Transmittance differences are observed between 1400 nm and 1600 nm, corresponding to the resonance wavelength of each cylinder, with a maximum variance (Circular dichroism) of about 0.67 at 1520 nm, near the target wavelength. Figure 2. (c) shows the variation in polarization angle and ellipticity of the transmitted wave when a linearly polarized (Ex) field is incident in the +z direction. Similar to the previous result, we can observe that the value varies between 1400 nm and 1600 nm, and we confirm that the maximum optical activity of our chiral metasurface is equal to 1.16×10^6 °/mm.

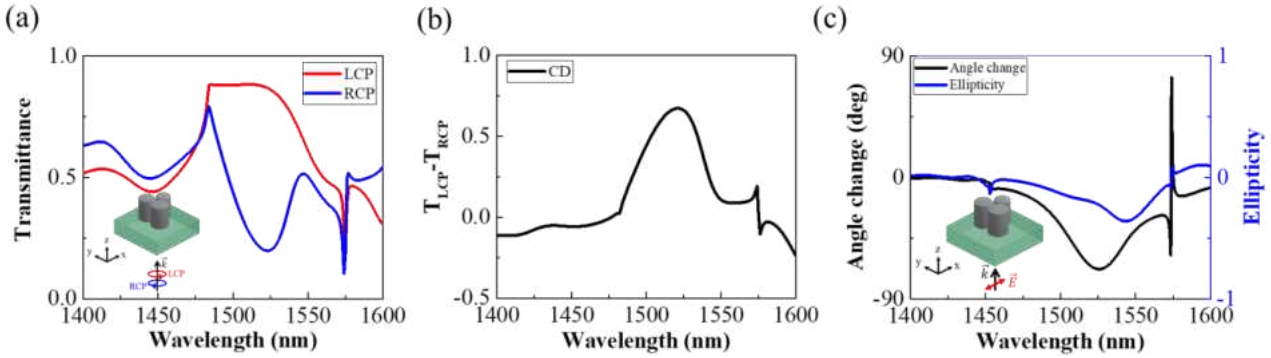


Figure 2. (a) The transmittance, (b) its difference (circular dichroism; CD) and when the left and right polarized light are incident on a chiral metasurface in the +z direction. (c) The change in polarization angle and ellipticity of the transmitted wave when linear polarized (Ex) planewave is incident.

We enhanced the chirality by arranging three dielectric cylinders in a counterclockwise direction, each with sequentially increasing resonance wavelengths of the ED, consequently altering the effective index of the structure effective index of the structure along with the direction of circular polarization. Despite being a single-layered dielectric structure, our chiral metasurface exhibits strong chirality, and we anticipate its potential applications as an ultrathin circular polarizer filter, chiral censor, and waveplate. Additionally, it is expected that adjusting the direction, shape, number, and spacing of the multi-cylinder structure within the unit cell can provide further flexibility.

References

1. S. Oh, O. Hess, “Chiral metamaterials: enhancement and control of optical activity and circular dichroism,” Nano Convergence, Vol. 2, No. 1, 1-14, 2015
2. A. Kuznetsov et.al., “Optical resonant dielectric nanostructures,” Science, Vol. 354, No. 6314, 2472, 2016
3. D. Neshev, A. Miroshnichenko, “Enabling smart vision with metasurfaces,” Nature Photonics, Vol. 17, No. 1, 26-35 2023
4. K. Tanaka et.al., “Chiral Bilayer All-Dielectric Metasurfaces,” ACS Nano, Vol. 14, No. 11, 15926-15935, 2020
5. M. Gorkunov et.al., “Chiral visible light metasurface patterned in monocrystalline silicon by focused ion beam,” Scientific Reports, Vol. 8, No. 1, 1-10, 2018

Unidirectional mode excitation due to magnetochiral effects

Hiroyuki Kurosawa[1*], Keisuke Itoh[2], and Tetsuya Ueda[1]

[1]Kyoto Institute of Technology, Japan
[2]Industorial Technology Institute, Miyagi Prefectural Government, Japan
[*]corresponding author: kurosawa-hiroyuki@kit.ac.jp

Abstract: A numerical study shows that a single metamolecule with magnetism and chirality exhibits unidirectional mode excitation in a waveguide at microwave frequencies. The directionality has a linear response to the magnetization and the chirality, indicating that the anisotropy of the mode excitation originates from the magnetochiral effects.

Broken symmetry plays a crucial role in physics. Broken time and space inversion symmetries are given by magnetism and chirality, and coupling between them brings about magnetochiral (MCh) effects known as directional dichroism for unpolarized waves [1, 2]. The MCh effects in natural materials are generally very weak but metamaterials strongly enhance the effects [3, 4]. In previous studies, the MCh effects in metamaterials are characterized by the difference in transmittance due to the directional dichroism for unpolarized waves. Due to reciprocity, the absorption is equal to the emittance, indicating that it is possible to control the radiation direction of an emitter by the MCh metamolecule. However, the directional radiation due to the MCh effects has not been demonstrated up to now. In this work, we demonstrate that an MCh metamolecule incorporated with a microwave source exhibits directional waveguide mode excitation.

Figure 1(a) shows the schematic of the metamolecule comprising of three dielectric cubes and a ferrite rod. The cubes are spirally arranged and give chirality, whereas the rod is under an external magnetic field along the z-axis and gives magnetization. This metamolecule is placed at the center of a WR-187 waveguide and its transmission characteristics are calculated by numerical simulations. Figure 1(b) shows the calculated transmittance under the external magnetic field of +390 mT. There are dip structures corresponding to the cavity modes of the cubes. We focus on the lowest mode around 3.97 GHz. The depth of the dip depends on the propagation direction of the waveguide mode, which originates from the directional dichroism. A magnetic

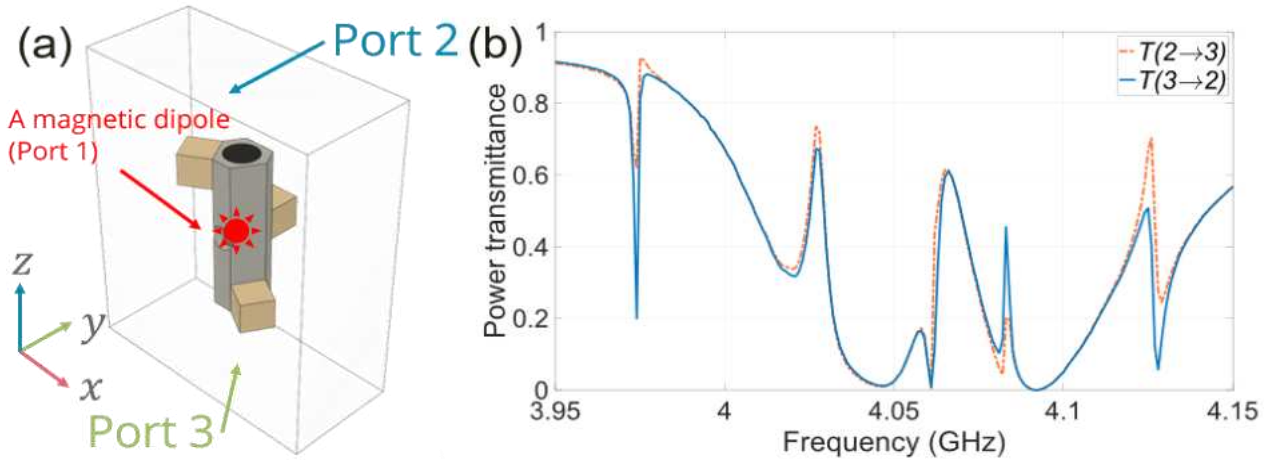


Fig.1: (a) A schematic of the metamolecule. (b) Power transmittance of the metamolecule in the waveguide.

dipole oscillating along the *x*-axis is placed at the center of the metamolecule. We evaluate the anisotropy of the waveguide mode excitation by integrating the absolute value of the z component of the Poynting vector over Ports 2 and 3. Figure 2(a) shows the radiation power spectra. Around the frequency of 3.94 GHz, the power spectra have a peak that corresponds to the sharp dip in the transmittance. There is a significant difference in the radiation power.

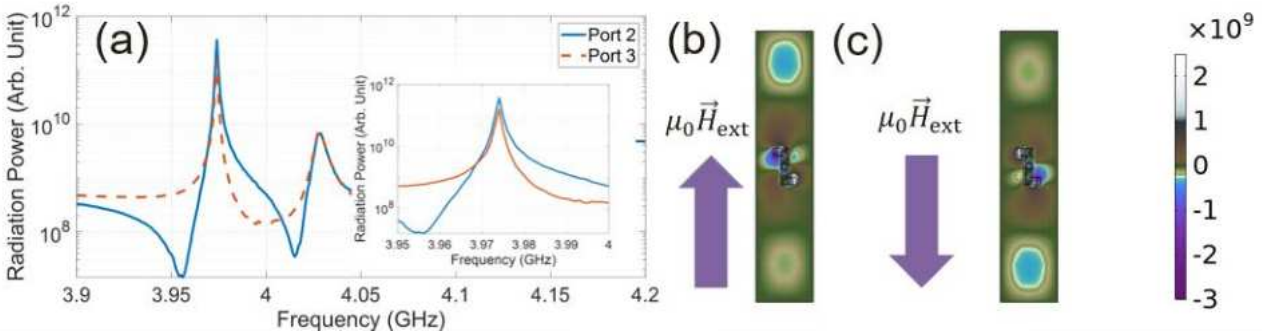


Fig 2: (a) Radiation power spectra of the metamolecule. Electric field distributions at 3.974 GHz under positive (b) and negative (c) external magnetic bias field.

To confirm that the mode excitation is directional, we show the field distributions in the waveguide. Figure 2(b) shows the electric field distributions at 3.97 GHz, where the difference in the radiation intensity is maximum. The metamolecule excites the waveguide mode of TE_{10} and there is a large difference in the excitation intensity between the propagating and counter-propagating modes. The field distribution pattern is reversed following the reversal of the direction of the external dc magnetic field (Fig. 2(c)). We also confirm the reversal of the pattern following the switch of the chirality of the metamolecule from right to left (not shown). These features indicate that the anisotropy of the mode excitation has a linear response to the magnetization and the chirality, and the directional mode excitation originates from the MCh effects.

In summary, we have demonstrated unidirectional mode excitation by a single MCh metamolecule in a waveguide. The metamolecule comprises spirally arranged dielectric cubes giving chirality and a ferrite rod giving magnetization, exhibiting the MCh effects. Due to reciprocity between absorption and emittance, the radiation power from the magnetic dipole in the metamolecule depends on the propagation direction. The field distribution of the waveguide mode has a linear response the magnetization and the chirality, indicating that the directional excitation of the waveguide mode originates from the MCh effects. This study paves the way for the control of directional excitation of a waveguide mode by a single MCh metamolecule.

We acknowledge JSPS KAKENHI 23K04567. This work is based on results obtained from a project, JPNP20004, subsidized by New Energy and Industrial Technology Development Organization (NEDO).

References

1. G. L. J. A. Rikken and E. Raupach, "Observation of magnetochiral dichroism," Nature, **390**, 493 (1997).
2. K. Taniguchi *et al*., "Strong magnetochiral dichroism for visible light emission in a rationally designed paramagnetic enantiopure molecule," Phys. Rev. Materials **3**, 045202 (2019).
3. S. Tomita *et al*., "Metamaterials with magnetism and chirality," J. Phys. D: Applied Physics, **51**, 083001 (2016).
4. H. Kurosawa *et al*. "Unity-order magnetochiral effects by a single metamolecule at microwave frequencies," Opt. Express **30**, 37066 (2022).

Machine learning for metamaterial design

End-to-End Framework for Designing Broadband Achromatic Metalens in High-quality Long-infrared Imaging

Qizhou Wang[1*], Daniele Veraldi[1], Arturo Burguete Lopez[1], Maksim Makarenko[2], and Andrea Fratalocchi[1]

[1]Computer, Electrical and Mathematical Science & Engineering, King Abdullah University of Science and Technology, Saudi Arabia

[2]EXPEC ARC, Saudi Aramco, Dhahran

[*]corresponding author: qihzou.wang@kaust.edu.sa

Abstract: This paper introduces an end-to-end design framework for constructing a broadband achromatic metalens, corrected across 5 equispaced frequencies within the long-wavelength infrared (LWIR) spectrum (8 μm to 12 μm). We combined nanophotonic hardware with computer-vision reconstruction networks, realizing a mean absolute error (MAE) of 0.035 over test dataset.

Flat-optic metalenses offer advantages over conventional lenses, including reduced physical dimensions, minimal optical absorption, and highly customizable amplitude, phase, and polarization [1,2]. In designing achromatic metalenses, traditional approaches predominantly optimize the structure guided by numerical objectives such as focusing efficiency, modulation transfer function (MTF), field of view, and depth of field [3,4]. However, these methods fall short of considering the critical aspect of an imaging device, that is, the image quality. In response to this issue, recent studies have adopted end-to-end methodology to include image post-processing techniques in the design cycle [5]. As the optimization objective is set as the pixel loss of the scene and processed image, these systems are able to retire non-intuitive metalens building blocks and improve the imaging performance.

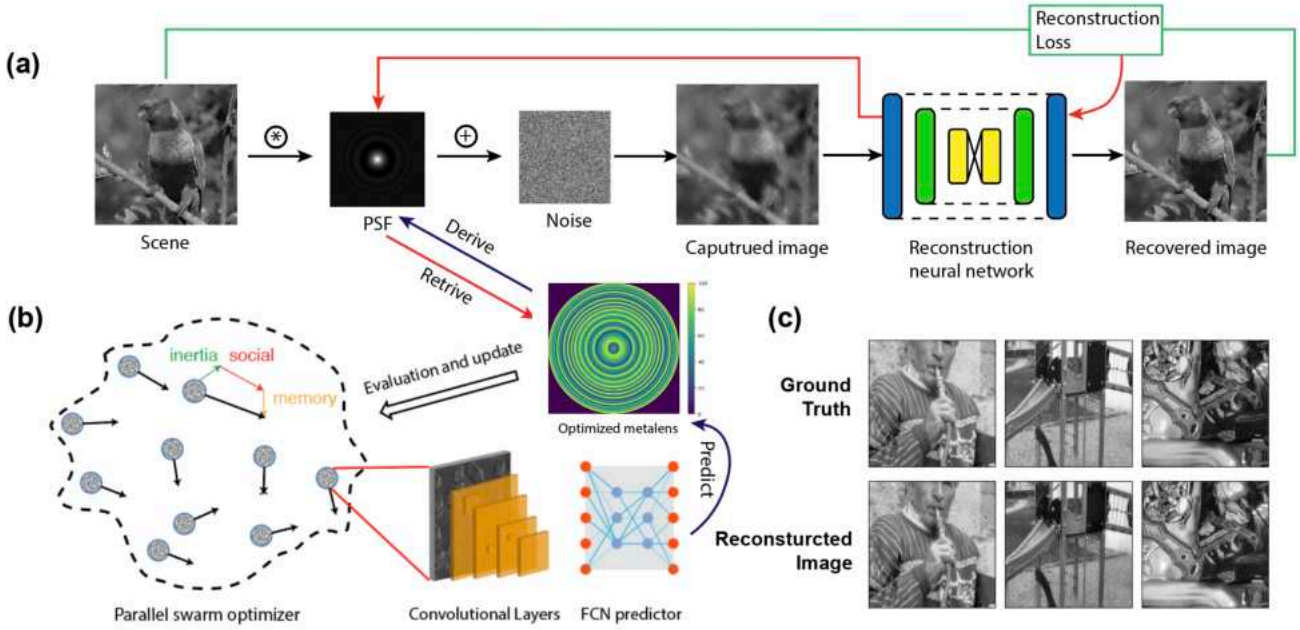


Fig.1. (a) The proposed end-to-end metalens optimization framework. (b) Parallel swarm optimized for the design of nanophotonic structure. (c) Examples of the input test image and the reconstructed output.

One challenge of current end-to-end metalenses is the trade-off on computational efficiency over simulation precision. Simplified models such as the P-B phase [6] or polynomial fitting [7] are frequently used in current metalens studies, and that often causes a drop between the design and the physical world. This work addresses the challenge by building a first-principle end-to-end design framework. Figure 1a shows the workflow of the proposed framework. We employ a unique combination of universal light encoders and finite-difference time-domain (FDTD) simulations to inversely design complex metasurfaces. During each step of optimization, we simulate the light propagation via convolving the point spread function (MTF) calculated from the metalens phase response. A sensor then captures the intensity patterns and transfers them into digital data. We train a reconstruction network based on the U-net backbone that first extracts essential features of the sensor image and reconstructs the scene image. The model defines MAE reconstruction loss indicating the similarity between the network output and the original scene. The loss is propagated through the reconstruction network, the PSF, and the metalens phase profile at the end of each step.

Illustrated in Fig.1b, we employ a parallel swarm-based open-source inverse design software ALFRED [8]. To accelerate the parallel swam search, we trained a phase prediction network on 60000 FDTD simulation results to generate phase delay data on the evolved nanostructures. The model is optimized on 5 equispaced wavelengths from 8 µm to 12 µm. Figure 1c visualizes the imaging performance after 1500 steps of training. The framework achieved an MAE = 0.035 over the test dataset.

Acknowledgments: For computer time, this research used the resources of the Supercomputing Laboratory at King Abdullah University of Science & Technology (KAUST) in Thuwal, Saudi Arabia

References

1. M. Pan *et al.*, “Dielectric metalens for miniaturized imaging systems: progress and challenges,” *Light Sci Appl*, vol. 11, no. 1, Art. no. 1, Jun. 2022.
2. W. T. Chen, A. Y. Zhu, and F. Capasso, “Flat optics with dispersion-engineered metasurfaces,” *Nat Rev Mater*, vol. 5, no. 8, pp. 604–620, Aug. 2020.
3. T. Ryu, M. Kim, Y. Hwang, M.-K. Kim, and J.-K. Yang, “High-efficiency SOI-based metalenses at telecommunication wavelengths,” *Nanophotonics*, vol. 0, no. 0, Oct. 2022, doi: 10.1515/nanoph-2022-0480.
4. K. Ou *et al.*, “Broadband Achromatic Metalens in Mid-Wavelength Infrared,” *Laser & Photonics Reviews*, vol. 15, no. 9, p. 2100020, 2021, doi: 10.1002/lpor.202100020.
5. Z. Lin *et al.*, “End-to-end metasurface inverse design for single-shot multi-channel imaging,” *Opt. Express, OE*, vol. 30, no. 16, pp. 28358–28370, Aug. 2022, doi: 10.1364/OE.449985.
6. M. Zhao *et al.*, “Phase characterisation of metalenses,” *Light Sci Appl*, vol. 10, no. 1, p. 52, Dec. 2021, doi: 10.1038/s41377-021-00492-y.
7. Q. Sun, C. Wang, Q. Fu, X. Dun, and W. Heidrich, “End-to-end complex lens design with differentiate ray tracing,” *ACM Trans. Graph.*, vol. 40, no. 4, pp. 1–13, Aug. 2021, doi: 10.1145/3450626.3459674.
8. M. Makarenko, Q. Wang, A. Burguete-Lopez, F. Getman, and A. Fratalocchi, “Robust and scalable flat-optics on flexible substrates via evolutionary neural networks,” *Advanced Intelligent Systems*, vol. 3, no. 11, p. 2100105, 2021.

Free-form inverse design of dynamically tunable metamaterial absorber for Mid-Infrared applications

Ram Prakash S[1*], Aastha Jain[1], Rajesh Kumar[1] and Anirban Mitra[1]

[1]Depratment of Physics, Indian Institute of Technology Roorkee, Uttarakhand, India
[*]Corresponding author: rprakashs@ph.iitr.ac.in

Abstract: This work presents a free-from inverse design of a dynamically tunable metamaterial absorber using a phase change material. The proposed inverse design is based on a neural-adjoint optimization method using a Wasserstein generative adversarial neural network (WGAN) to predict tunable metamaterial design for the desired absorption spectrum in the mid-infrared region.

Introduction

Designing a tunable metamaterial absorber in the mid-infrared region is crucial due to its application in molecular detection, chemical sensing, thermal imaging, and heat scavenging [1]. Chalcogenide phase change materials (PCM) are very attractive for use in MIR photonic applications due to their non-lossy nature in this regime. Furthermore, PCMs such as $Ge_2Sb_2Te_5$ (GST) show very refractive index contrast with phase change [2]. Thus, the absorption spectra can be dynamically tunable by incorporating GST in the metamaterial absorber structure. The inverse design of the nanophotonic structures is a much-needed technique for fast and accurate prediction of the design parameters for a desired spectral response. Recently, deep learning techniques have shown great promise for the inverse design of metamaterials for various photonic applications [3]. In this work, we present a deep learning-assisted free-form inverse design of a tunable metamaterial absorber operating in the MIR region.

Results and Discussion

The metamaterial absorber structure comprises a top gold periodic nanostructure and a bottom Au mirror. GST is used as the spacer layer. The phase change of GST is used to achieve the dynamically tunable MIR absorber. The period of the unit cell is fixed at 3 um, and the thickness of GST is 140 nm. The top nanostructure layer is divided into an 8X8 symmetrical grid, with each cell taking a random value of 0 or 1. Here, 0 means the presence of Au, and 1 means vacuum. The thickness of the top Au nanostructures is taken to be 200 nm. The finite difference time domain method (FDTD) is used to get the reflection spectrum of the metamaterial absorber [4]. Overall, we simulated 13,000 random nanostructure designs and their corresponding reflection spectrum for the training of the deep neural network. The dataset consists of absorption spectra of a given random design when GST is in the amorphous and crystalline phase.

The full inverse neural network (INN) encompasses two networks: 1) The forward network maps the design to the optical response, i.e. the absorption spectrum and 2) The generative network, which trains on the design parameters of the metamaterials alone. The latent vector of such generative networks represents a learned parameterization of the design. In this work, we use the Wasserstein generative adversarial neural network (WGAN) as the generator network to re-parameterize the image-based geometries into a regularized latent space. The WGAN network consists of two parts. The first part is the generator, which takes the latent variables as the input and the design as the output. The second part is the discriminator, which generates fake designs and

predicts whether the geometry is fake or true. Here, the discriminator output will be trained with a Wasserstein distance loss function as it offers a stable and more robust convergence. Finally, the geometry for a desired spectrum when GST is in the amorphous phase can be obtained by using gradient descent – neural adjoint method. The use of the WGAN as the generator ensures that during the gradient-based optimization method, the design predicted remains in the forward model's interpolation region, thus avoiding the risk of converging toward a non-physical solution.

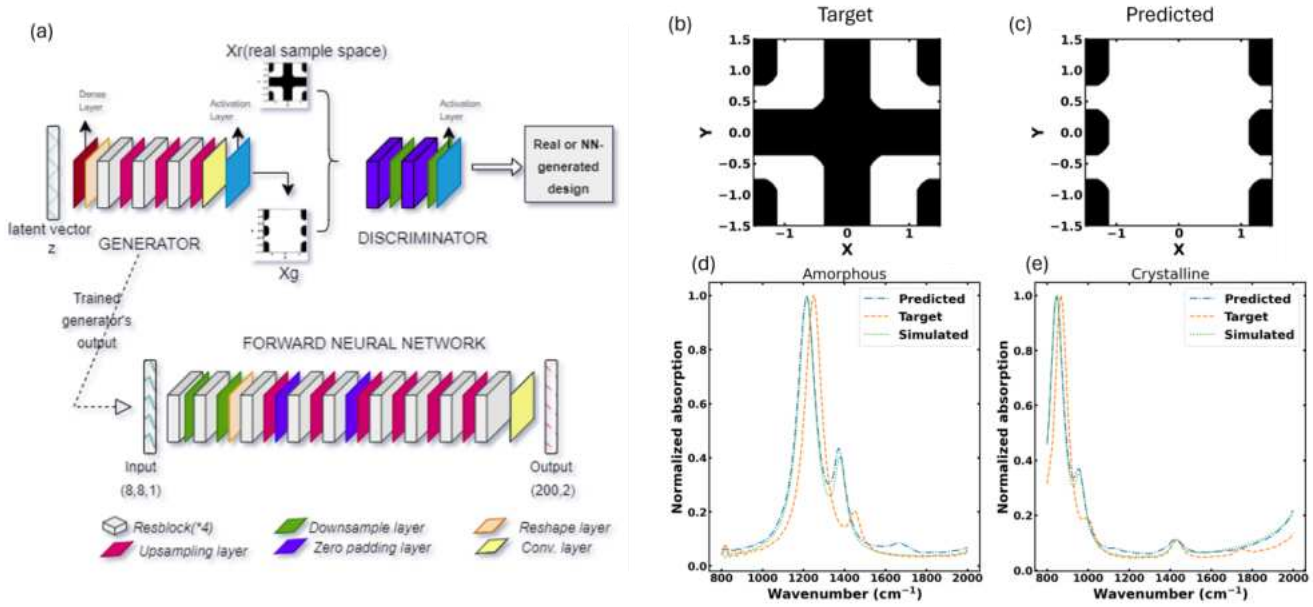


Figure 1: a) Schematic representation of the Inverse neural network. Comparison between (b) target and (c) predicted design by the INN. The predicted, target and the FDTD simulated absorption spectrum when GST is in d) Amorphous and e) crystalline phase.

The design and the corresponding spectrum predicted by the proposed INN are shown in Figure 2. It is seen that a given target spectrum produces a design which is different from the target design. Furthermore, it is noted that the spectrum predicted by the INN matches well with the FDTD-simulated spectrum in both phases of GST. Thus, the above results show that the proposed INN can predict the geometry for any desired absorption spectrum in the MIR region. Furthermore, the use of GST in the structure allows for the tunability of the absorption spectrum thus, we can achieve a dynamically tunable absorber in a wide MIR spectral region.

References

1. Griffiths, P. R, "Fourier transform infrared spectrometry. Science, 222, 297–302, 1983.
2. Shportko, K. et al., "Resonant bonding in crystalline phase-change materials. Nature materials, 7, 653–658, 2008.
3. R Prakash et al., "Inverse design of dynamically tunable phase-change material-based metamaterial absorber induced structural color," Photonics Nanostructures: Fundam. Appl, Vol. 54, pp. 101135 (2023).
4. A. Oskooi et al., "MEEP: A flexible free-software package for electromagnetic simulations by the FDTD method," Computer Physics Communications, Vol. 181, pp. 687-702 (2010)

Broadband large-scale photonics inverse design enabled by experimental machine learning

Maksim Makarenko[1*], Sergei Rodionov[2], Q. Wang[2], Fedor Getman[2], Arturo Burguete-Lopez[2], Andrea Fratalocchi[2]

[1] EXPEC Advanced Research Center, Aramco, Dhahran, Saudi Arabia
[2] PRIMALIGHT, Faculty of Electrical Engineering; Applied Mathematics and Computational Science, King Abdullah University of Science and Technology, Thuwal, Saudi Arabia
*corresponding author, E-mail: maksim.makarenko@aramco.com

Abstract. In this work we propose a new methodology to inverse design for the development of high-efficient wafer-scale wavefront engineering structures using direct experimental fabrications without a need of costly first-principle simulations. We illustrate the efficiency of this approach by training the model to accurately predict flat-optics transmission and reflection responses, resulting in a nearly ten-fold reduction in the validation root-mean-square error compared to the model trained with first-principle simulations.

Summary. Experimental Machine Learning (EML) is a recent development of Machine Learning (ML) that leverages scientific experimentation to design, train, and evaluate ML models [1], [2]. This approach gathers substantial interest as it provides a universal platform to train ML models as close to experimental outcomes, delivering human-level predictions in real-time. Experimental ML generates comprehensive training datasets for adaptive ML systems that dynamically adjust to changing environments and automatically update. These adaptive models combine traditional ML with dynamic optimization algorithms, such as Reinforcement Learning (RL) and population methods, which allows agents to learn from their interactions with the environment and improve their performance over time.

Experimental ML impacts major disciplines such as chemistry [3] and robotics [4]. In chemistry, experimental ML accelerates the discovery of new materials, drugs, and catalysts, keeping track of and optimizing their performance dynamically as the reaction progresses. In robotics, EML trains intelligent systems to perform complex tasks by learning from their interactions with the environment. It allows these systems to adapt to changing conditions, such as the appearance of new objects in their environment or changes in the terrain.

Nanophotonics leverages ML for the inverse design of photonic circuitry supporting broad functionalities depending on many constraints, including working bandwidth, fabrication tolerances, and complete vectorial control on the output material response [5]–[8]. These approaches focus on ML software models, including neural networks[7], [9], decision trees, Gaussian processes[10] and Bayesian inference [11]. ML models leverage approximate solvers trained on pre-defined structures datasets to predict spatial and spectral material responses, including transmission and reflection.

To deal with constraints imposed by available computing resources, current inverse design models employ periodic boundary conditions, devising smaller unit cell structures replicating on larger areas [12]. While this approach reported advances in the implementation of devices that do not possess sharp differences among neighboring units, it does not scale up unit cell design beyond hundreds of micron squares. Enhancing these performances is a significant opportunity to leverage advances in experimental nanophotonics circuitry, which permit aperiodic nanostructuring with nanoscale control over single wafers. Current nanolithography techniques support dense photonic integration with features as small as 20 nm, corresponding in one-millimeter square to over 2 billions light processing units, surpassing current electronics of one order of magnitude [13]. A large-scale universal aperiodic inverse design platform that leverages the nanophotonics density available could open classes of photonics circuitry with considerable complexity for light control [5], for operations including matrix-vector product [14], spectral encoding [5] and privacy-preserving imaging [15].

This study addresses the challenge of large-scale aperiodic inverse design in nanophotonics by developing a photonics platform for experimental machine learning. We composed a 10 million distinct experimental photonic structures dataset, producing the largest publicly available dataset for flat-optics design that outperforms the closest competition by a factor of 20 [7]. It is worth noting that acquiring a similar dataset with first-principle simulations would require an estimated 200 million core hours at a rate of 20 core hours per structure. However, by producing the dataset experimentally, we obtained the required data in just 4 electron beam lithography sessions, with a speed of 1 million samples per 12 hours. We estimate an upper bound of 7.2 ms per single structure for the total rate of both sample production and characterization, which is 15000 times faster than parallel 3-dimensional FDTD simulations obtained with 512 cores of KAUST's Shaheen supercomputer. The characterization is done by using a tunable filter to illuminate a portion of the chip with the geometries with a single wavelength and, through a monochrome camera, acquire the response of more than 100 thousand different geometries in a single frame.

Since we obtained the dataset experimentally, it inherently accounted for any differences in responses between simulated and actual structures caused by variations in refractive index, nonlinear optical effects, or fabrication biases. Using this dataset, we train the model to accurately predict flat-optics transmission and reflection responses, resulting in a nearly ten-fold reduction in the validation root-mean-square error compared to the model trained with first-principle simulations, from 0.012 to 0.0018 root-mean-square error (RMSE).

In addition, we allocate a subset of 4 million samples from the dataset to the design of aperiodic structures. With this subset, we develop a fast and efficient inverse design framework called i-ALFRED, which is capable of designing aperiodic structures on a point-to-point basis while taking into account the information about their closest neighbors. We illustrate the framework's performance by designing a 3x3 mm aperiodic structure with pre-defined random responses, achieving an experimental RMSE of 0.0032.

Acknowledgment. This research received funding from KAUST (Award OSR-2016-CRG5-2995). Parallel simulations are performed on KAUST's Shaheen supercomputer.

References

[1] Yann LeCun, Yoshua Bengio, and Geoffrey Hinton, "Deep learning," *Nature*, vol. 521, no. 7553, pp. 436–444, 2015.

[2] P. Leinen, M. Esders, K. T. Schütt, C. Wagner, K.-R. Müller, and F. S. Tautz, "Autonomous robotic nanofabrication with reinforcement learning," *Science Advances*, vol. 6, no. 36, eabb6987, 2020. eprint: https://www.science.org/doi/pdf/10.1126/sciadv.abb6987.

[3] L.-C. Xu, J. Frey, X. Hou, S.-Q. Zhang, Y.-Y. Li, J. C. A. Oliveira, S.-W. Li, L. Ackermann, and X. Hong, "Enantioselectivity prediction of pallada-electrocatalysed c–h activation using transition state knowledge in machine learning," *Nature Synthesis*, 2023.

[4] X. Yin and R. Müller, "Integration of deep learning and soft robotics for a biomimetic approach to nonlinear sensing," *Nature Machine Intelligence*, vol. 3, no. 6, pp. 507–512, 2021.

[5] M. Makarenko, Q. Wang, A. Burguete-Lopez, and A. Fratalocchi, "Photonic optical accelerators: The future engine for the era of modern AI?" *APL Photonics*, vol. 8, no. 11, p. 110 902, Nov. 2023. eprint: https://pubs.aip.org/aip/app/article-pdf/doi/10.1063/5.0174044/18205576/110902_1_5.0174044.pdf.

[6] Q. Wang, M. Makarenko, A. B. Lopez, F. Getman, and A. Fratalocchi, "Advancing statistical learning and artificial intelligence in nanophotonics inverse design," *Nanophotonics*, 2021.

[7] M. Makarenko, Q. Wang, A. Burguete-Lopez, F. Getman, and A. Fratalocchi, "Robust and scalable flat-optics on flexible substrates via evolutionary neural networks," *Advanced Intelligent Systems*, p. 2 100 105, Aug. 2021.

[8] M. Makarenko, A. Burguete-Lopez, F. Getman, and A. Fratalocchi, "Robust and scalable flat-optics on flexible substrates via evolutionary neural networks," 2021, [Currently under a second round of review in Advanced Intelligent Systems].

[9] M. Makarenko, Q. Wang, A. Burguete-Lopez, S. Giancola, B. Ghanem, L. Passone, and A. Fratalocchi, *Artificial intelligence optical hardware empowers high-resolution hyperspectral video understanding at 1.2 tb/s*, 2023. arXiv: 2312.10639 [cs.CV].

[10] Z. Liu, D. Zhu, L. Raju, and W. Cai, "Tackling photonic inverse design with machine learning," *Advanced Science*, vol. 8, no. 5, p. 2 002 923, 2021. eprint: https://onlinelibrary.wiley.com/doi/pdf/10.1002/advs.202002923.

[11] G. M. Nascimento, E. Ogoshi, A. Fazzio, C. M. Acosta, and G. M. Dalpian, "High-throughput inverse design and bayesian optimization of functionalities: Spin splitting in two-dimensional compounds," *Scientific Data*, vol. 9, no. 1, p. 195, 2022.

[12] S. Molesky, Z. Lin, A. Y. Piggott, W. Jin, J. Vucković, and A. W. Rodriguez, "Inverse design in nanophotonics," *Nature Photonics*, vol. 12, no. 11, pp. 659–670, 2018.

[13] *Skywater technology foundry*, https://www.skywatertechnology.com/darpa-3dsoc-initiative-completes-first-year-update-provided-at-eri-summit-on-key-steps-achieved-to-transfer-technology-into-skywaters-200mm-u-s-foundry/, Accessed: July 25, 2019.

[14] X. Xu, M. Tan, B. Corcoran, J. Wu, A. Boes, T. G. Nguyen, S. T. Chu, B. E. Little, D. G. Hicks, R. Morandotti, A. Mitchell, and D. J. Moss, "11 tops photonic convolutional accelerator for optical neural networks," *Nature*, vol. 589, no. 7840, pp. 44–51, Jan. 2021.

[15] Z. W. Wang, V. Vineet, F. Pittaluga, S. N. Sinha, O. Cossairt, and S. Bing Kang, "Privacy-preserving action recognition using coded aperture videos," in *Proceedings of the IEEE/CVF Conference on Computer Vision and Pattern Recognition (CVPR) Workshops*, Jun. 2019.

Artificial intelligence optical hardware empowers real-time ultra-sensitive detection of dopamine at 10^{-11} mol/L

Ning Li[1], **Qizhou Wang**[1], **Zhao He**[1], **Arturo Burguete-Lopez**[1], **Fei Xiang**[1], **Andrea Fratalocchi**[1]

1. PRIMALIGHT, King Abdullah University of Science and Technology (KAUST), Thuwal 23955-6900, Saudi Arabia

Abstract We discuss integrated platform for ultrasensitive detection comprising artificial intelligence hardware embedded in a monochrome camera. By utilizing the interference media, it reports detection ranges from 10^{-11} mol/L to 10^{-4} mol/L, which improves one to two orders of magnitude of the current state-of-the-art sensitivity requiring electrochemical workstations or mass spectrometers.

Ultra-sensitive detection plays great roles in the field of explosive detection [1], food safety [2], and disease diagnostic [3]. In medical applications, ultrasensitive trace detection of dopamine is critical for the early diagnosis of Alzheimer [4], Parkinson [5], and schizophrenia [6]. The current state-of-the-art for ultrasensitive detection of dopamine relies on expensive equipment, including electrochemical workstation [7], and mass spectrometry [8]. Since 2015, the state-of-the-art the detection limit is 0.5×10^{-10} mol/L when measuring dopamine with phosphate-buffered saline (PBS) as solvent [9].

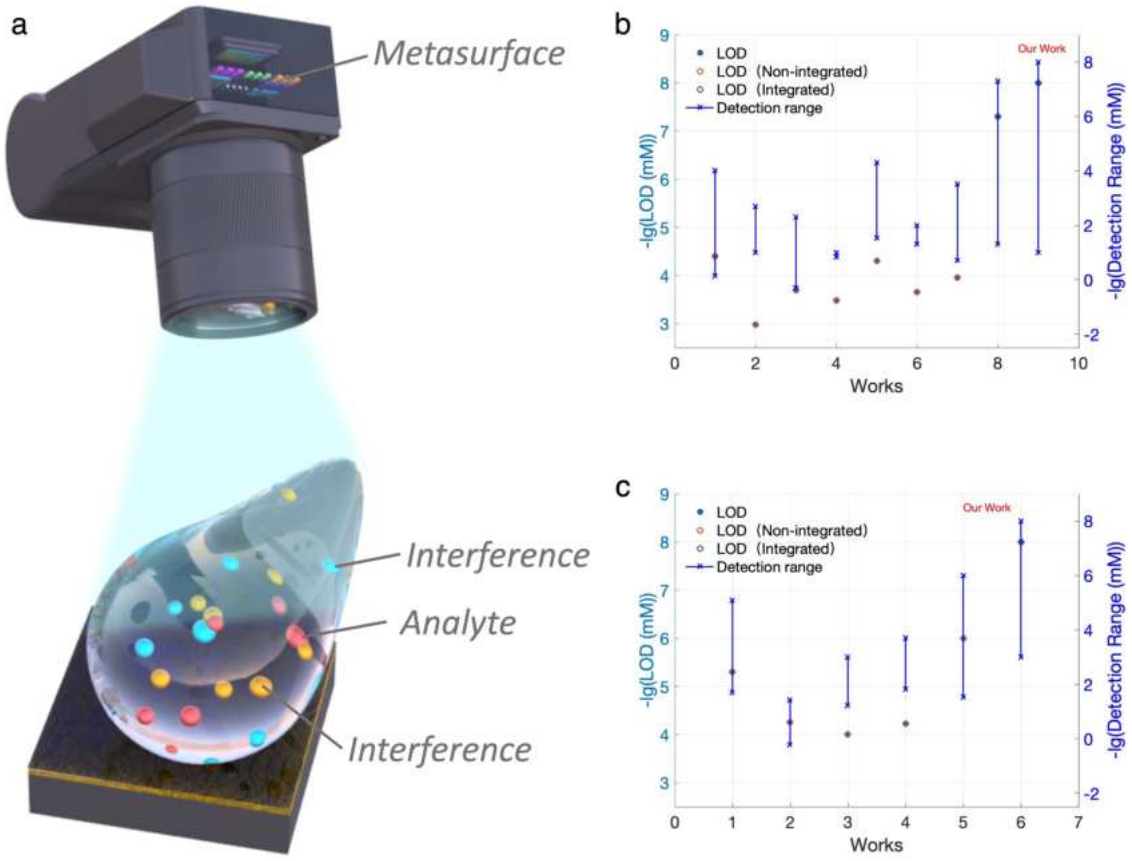


Fig. 1 (a) Integrated platform schematics for ultrasensitive detection. (b-c) State-of-the-art limits of detection and detection range for dopamine are interfered with by (b) PBS solution and (c) uric acid and ascorbic acid.

In this work, we implement an universal platform for ultrasensitive detection employing artificial intelligence (AI) optical hardware, which integrates with a sensor device of a consumer camera. The core of this hardware is inverse-designed metasurface encoders [10–12] (Fig. 1a), trained to provide hardware features extraction to predict the analyte concentration in real-time. In the example of dopamine, this technology reports detection limits as low as 10^{-11} mol/L either with PBS or uric acid and ascorbic acid as interference (Fig. 1b and c). This universal detection platform generalizes to other analytes, providing an inexpensive, scalable platform for rapid, informed detection of diseases at the point of care.

References

1. He, X. *et al.* Ultrasensitive detection of explosives via hydrophobic condensation effect on biomimetic SERS platforms. *Journal of Materials Chemistry C* **5,** 12384–12392 (2017).
2. Zhang, D. *et al.* Hydrophobic slippery surface-based surface-enhanced Raman spectroscopy platform for ultrasensitive detection in food safety applications. *Analytical chemistry* **91,** 4687–4695 (2019).
3. Pollock, N. R. Ultrasensitive detection and quantification of toxins for optimized diagnosis of Clostridium difficile infection. *Journal of clinical microbiology* **54,** 259–264 (2016).
4. Nobili, A. *et al.* Dopamine neuronal loss contributes to memory and reward dysfunction in a model of Alzheimer's disease. *Nature communications* **8,** 14727 (2017).
5. Ahlskog, J. E. Beating a dead horse: dopamine and Parkinson disease. *Neurology* **69,** 1701–1711 (2007).
6. Howes, O. D. & Kapur, S. The dopamine hypothesis of schizophrenia: version III—the final common pathway. *Schizophrenia bulletin* **35,** 549–562 (2009).
7. Kim, Y.-R. *et al.* Electrochemical detection of dopamine in the presence of ascorbic acid using graphene modified electrodes. *Biosensors and Bioelectronics* **25,** 2366–2369 (2010).
8. Syslová, K. *et al.* Monitoring of dopamine and its metabolites in brain microdialysates: Method combining freeze-drying with liquid chromatography–tandem mass spectrometry. *Journal of Chromatography A* **1218,** 3382–3391 (2011).
9. Lei, Y. *et al.* Single-atom doping of MoS2 with manganese enables ultrasensitive detection of dopamine: Experimental and computational approach. *Science advances* **6,** eabc4250 (2020).
10. Getman, F., Makarenko, M., Burguete-Lopez, A. & Fratalocchi, A. Broadband vectorial ultrathin optics with experimental efficiency up to 99% in the visible region via universal approximators. *Light: Science & Applications* **10,** 47 (2021).
11. Makarenko, M., Wang, Q., Burguete-Lopez, A., Getman, F. & Fratalocchi, A. Robust and Scalable Flat-Optics on Flexible Substrates via Evolutionary Neural Networks. *Advanced Intelligent Systems* **3,** 2100105 (2021).
12. Makarenko, M. *et al. Real-time hyperspectral imaging in hardware via trained metasurface encoders* in *Proceedings of the IEEE/CVF Conference on Computer Vision and Pattern Recognition* (2022), 12692–12702.

Space-time metasurfaces for photonics

[1*] [1] [1]

[1]Imperial College London, United Kingdom
[*]corresponding author: svezzoli@imperial.ac.uk

Abstract: Metamaterials control light by acting on its momentum, yet they are static devices and bounded by energy conservation. Here we discuss spatial and temporal diffraction in a film of Indium Tin Oxide, as a first step towards a space-time metasurface for photonic applications.

Metamaterials have revolutionised the way we control light waves. By engineering light scattering on sub-wavelength scales, one can design exotic new materials and applications, like invisibility cloaks and negative refraction. Yet, static metamaterials only act on the momentum of light and thus are still bounded by Lorentz reciprocity and energy conservation. A dynamical metasurface, whose optical response can be arbitrarily modulated at the speed of light through a time-varying complex refractive index n(t), would offer access to the manipulation of the frequency spectrum and a whole new range of functionalities. Yet, despite the abundance of theoretical proposals [1], experimental realisations remain elusive, due to the challenge of finding a material platform that can support large and ultrafast modulations without incurring damage.

Here I will discuss our first steps towards optically driven metasurfaces for photonics, based on Indium Tin Oxide, an epsilon-near-zero material with strong nonlinearities and ultrafast time response [2]. I will report on our recent demonstration of double-slit time diffraction from a deeply sub-wavelength and resonant film of Indium Tin Oxide in the near-infrared [3], the first step towards the creation of more complex time modulations. I will then discuss one possible extension of this experiment to the visible range, which employs the non-perturbative modulation of second harmonic generation at the time-varying interface. Finally, I will present our most recent results, aimed at coupling space and time modulations in a time-varying medium: the observation of slits that diffract light both in time and space. These results represent the basic building blocks for the generation of complex spatiotemporal modulations and one of the first evidences of synthetic motion at optical frequencies.

References

1. Galiffi, E. et al., Advanced Photonics, Vol. 4, Issue 1, 014002 (2022)
2. Alam, M.Z. et al., Science 10.1126/science.aae0330 (2016)
3. Tirole, R. et al, Nat Phys, Vol. 19, 999 (2023)

Fabrication of visible metalenses by thermal oxidation of silicon nanopillars

T. Okatani[1*], R. Ando[1], N. Inomata[1] and Y. Kanamori[1†]

[1]Department of Robotics, Graduate School of Engineering, Tohoku University, Japan
[*]taiyu.okatani.a3@tohoku.ac.jp, [†]ykanamori@tohoku.ac.jp

Abstract: We propose a fabrication method of visible metalens composed of SiO_2 formed by thermal oxidation of Si nanopillars. A prototype transmissive metalens was fabricated by performing electron beam lithography, deep reactive ion etching, and wet thermal oxidation on a 2 μm thick monocrystalline Si layer on a quartz glass substrate.

Metalens is an extremely thin lens realized by controlling the effective refractive index distribution using a subwavelength structure [1]. Various materials have been proposed for subwavelength structures, but in the case of visible metalenses, the highest transmittance can be expected by using SiO_2, which is often used for the substrate. We previously reported that reflective metalenses could be realized by forming Si nanopillars on a silicon-on-insulator substrate and thermally oxidizing them into SiO_2 nanopillars [2]. This method allows the formation of SiO_2 nanopillars with a higher aspect ratio than those fabricated by directly etching SiO_2 [3]. However, since the reflective metalens has limitations in its use in actual applications, a transmissive metalens is also required.

In this study, we prototyped a transmissive metalens using approximately 2 μm thick Si layer transferred onto a quartz glass substrate. The substrate was made of SiO_2, and the Si nanopillars also eventually transformed to SiO_2 nanopillars. Therefore, it was expected that a highly transparent metalens made entirely of SiO_2 would be realized. Figure 1(a) and 1(b) shows microscopic images of the metalens surface before and after thermal oxidation, respectively, observed using transmitted illumination. The brightness of the image increases due to thermal oxidation, suggesting that the transformation from Si to SiO_2 increases transmittance. Figure 1(c) is an image obtained by shifting the observation position 70 μm above the metalens surface, which is the designed focal length. It was confirmed that the transmitted light was focused by the prototyped metalens. Details of the fabrication results and transmittance evaluation will be discussed in the presentation.

Acknowledgements

Part of this work was supported by JSPS KAKENHI Grant Number JP22K14211 and performed in Micro/Nano-Machining Research and Education Center, Tohoku University.

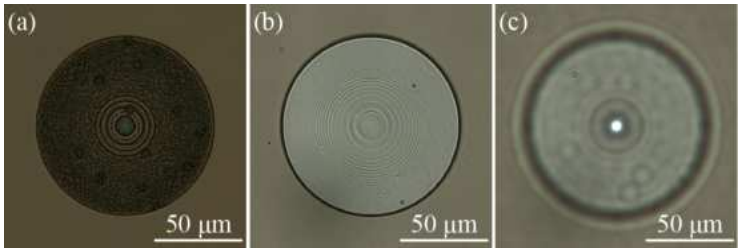


Fig. 1. (a), (b) Microscopic images of the metalens surface before and after thermal oxidation. (c) Image at 70 μm (the focal length) above.

References

1. M. Khorasaninejad M. and F. Capasso, “Metalenses: versatile multifunctional photonic components,” *Science*, Vol. 358, eaam8100, 2017.
2. T. Okatani, Y. Naito and Y. Kanamori, “Fabrication of high-aspect-ratio SiO2 nanopillars by Si thermal oxidation for metalenses in the visible region,” *Jpn. J. Appl. Phys.*, Vol. 62, SG1034, 2023.
3. J.-S. Park, S. Zhang, A. She, W. T. Chen, P. Lin, K. M. A. Yousef, J.-X. Cheng, and F. Capasso, “All-glass, large metalens at visible wavelength using deep-ultraviolet projection lithography,” *Nano Lett.*, Vol. 19, 8673–8682, 2019.

Water sensors using soft films with metamaterials

C. Y. Huang* and Harry Miyosi Silalahi

Department of Applied Physics, Tunghai University, Taichung 40704, Taiwan
*corresponding author: chiayihuang@thu.edu.tw

Abstract: Metamaterials are artificial materials that comprise split ring resonators, and have strong resonance with incident electromagnetic waves [1–4]. The resonance frequency and transmittance of a metamaterial are determined by the refractive index of the medium that surrounds the metamaterial and its geometrical dimensions. Therefore, metamaterials have been used to develop invisible cloaks [1], signal filters [2], image processors [3] and biosensors [4]. This study involves the creation of a metamaterial sandwiched between two soft films using techniques such as photolithography, sputtering, lift-off process, and imprinting. When exposed to water, the soft films cause cracks in the split ring resonators of the metamaterial due to swelling. These cracks disrupt the electromagnetic resonance, leading to an increase in the transmittance of the metamaterial at its resonance frequency. This heightened transmittance serves as an indicator of the presence of water in the soft films, suggesting potential applications for the metamaterial in humidity sensors and water harvesters.

Acknowledgements

This work was financially supported by the National Science and Technology Council (NSTC) of Taiwan under Contract No. NSTC 112-2112-M-029-004.

References

1. Z. Zhen, C. Qian, Y. Jia, Z. Fan, R. Hao, T. Cai, B. Zheng, H. Chen and E. Li, “Realizing transmitted metasurface cloak by a tandem neural network,” Photonics Research, Vol. 9, No. 5, B229–B235, 2021.
2. H. M. Silalahi, Y. H. Shih, S. H. Lin, Y. T. Chen, W. Y. Wei, P. L. Chao and C. Y. Huang, “Electrically controllable terahertz metamaterials with large tunabilities and low operating electric fields using electrowetting-on-dielectric cells,” Optics Letters, Vol. 46, No. 23, 5962–5965, 2021.
3. S. Baek, J. Kim, Y. Kim, W. S. Cho, T. Badloe, S. W. Moon, J. Rho and Jong-Lam Lee, “High numerical aperture RGB achromatic metalens in the visible,” Photonics Research, Vol. 10, No. 12, B30–B39, 2022.
4. H. M. Silalahi, Y. P. Chen, Y. H. Shih, Y. S. Chen, X. Y. Lin, J. H. Liu and C. Y. Huang, “Floating terahertz metamaterials with extremely large refractive index sensitivities,” Photonics Research, Vol. 9, No. 10, 1970–1978, 2021.

Polarization-Insensitive Ultra-Broadband Terahertz Metamaterials for 6G Applications

Bhagwat Singh Chouhan, Partha Pratim Barman, and Bhumidhar Barman and Gagan Kumar

Department of Physics, Indian Institute of Technology Guwahati, Assam, India, 781039
bhagwatsingh@iitg.ac.in

Abstract: Our study presents a novel metamaterial design that enables ultra-wideband terahertz transmission while being insensitive to polarization. This is achieved by stacking a cross-shaped resonator on top of a square ring resonator separated by an optimized polyimide spacer. Our results indicate that stacking the resonators provides wideband terahertz transmission.

Introduction: Exploring the electromagnetic spectrum, the terahertz (THz) domain, spanning 0.1 to 10 THz, lies between the microwave and infrared regions and is largely untapped. This "terahertz gap" offers the potential for revolutionizing high-speed wireless communication, promising data transfer rates up to 1 Tbps. To harness this potential, the development of broadband THz devices like wave plates, switches, and filters is crucial for advancing THz photonics and communication systems [1]. Metamaterials (MMs), with their sub-wavelength structures, stand out for their ability to manipulate THz waves beyond conventional material capabilities. Despite progress, broadening the bandwidth of metamaterials, such as through planar metamaterial, remains challenging. In addressing this, we introduce a two-layer multi-stacked metamaterial configuration that comprises a cross-shaped resonator on the top of square ring structure spacing with a loss-free polyimide. We conduct rigorous simulations to investigate the broadband transmission response, focusing on the thickness of the spacer and positioning of resonators and the near-field coupling between them. Additionally, we employ a transmission line model to elucidate the broadband resonance mechanism of our proposed metamaterial. The finding of broadband enhancement can be useful in the THz photonics and next-generation wireless communications [2].

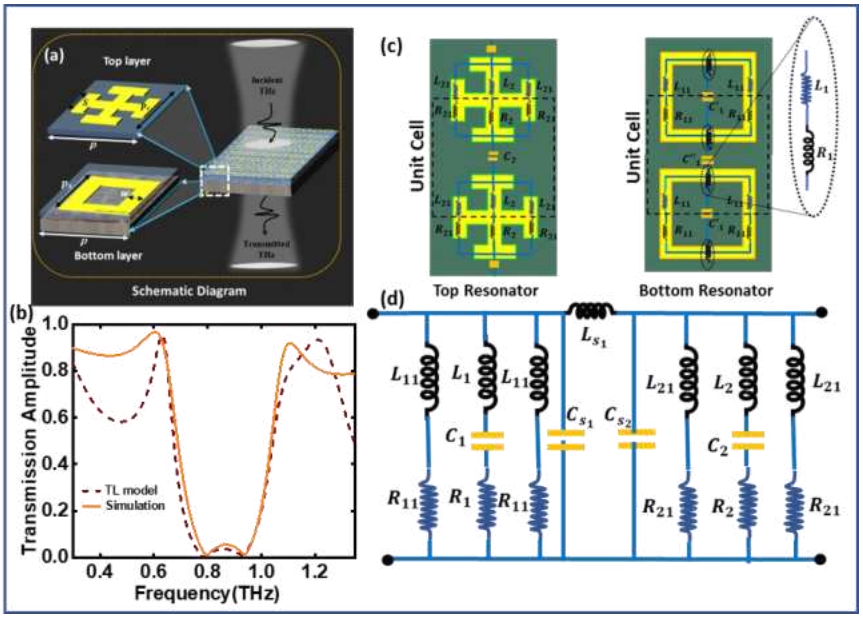


Figure 1: (a) Represents the unit cell of the metamaterial with different resonators. (b) Represents the transmission amplitude calculated from CST and TL line model. (c) Circuital representation of the unit cells. (d) Represents the coupled circuital model of the multistacked MM.

Ultra-broadband transmission of designed MM: The proposed metamaterial configuration, designed using CST software, features a multi-stacked structure with a cross-shaped resonator placed on top of a square ring resonator, separated by a *50 μm* thick loss-free polyimide film. The square ring resonator, with a periodicity of *P=100* µm, lengths of P_c*=63 μm*, and a width of *w=7 μm*, is designed on a *30 μm* thick silicon substrate with *0.2 μm* thick aluminum resonators to prevent THz wave penetration. The cross resonator, with a length of P_s*=81 μm* and *S=20 μm,* is then placed on the ring resonator with the polyimide spacer. The permittivity of quartz and polyimide is chosen to be 4.4 and 3.5, respectively. Simulations utilized a frequency domain solver with tetrahedral meshing and a normally incident plane wave, accommodating both TE and TM polarizations (see Figure 1(a)).

Table 1: Circuit parameters for calculating the electromagnetic response of the TL models.

Parameter	Value	Parameter	Value	Parameter	Value	Parameter	Value	Parameter	Value
$R_1(\Omega)$	05.0	$R_2(\Omega)$	1	C_{S1} (fF)	1.70	$R_{11}(\Omega)$	6.54	L_{21}(pH)	182
L_1(pH)	39.4	L_2(pH)	56.52	C_{S2} (fF)	1.19	$R_{21}(\Omega)$	1.46	-	-
C_1(fF)	0.74	C_2(fF)	0.71	L_{S1} (pH)	41.36	L_{11}(pH)	140	-	-

Analyzing the transmission response of the metamaterial's resonators and their combined effect, we observed a substantial enhancement in transmission bandwidth. The square ring resonator alone showed a bandwidth (FWHM) of 0.22 THz, which enhanced to 0.35 THz upon integrating a cross resonator, marking a bandwidth increase of over 150% in the multilayered setup compared to a single layer. The design's orthogonal symmetry ensures uniform transmission for both TE and TM polarizations, enhancing its applicability. The broadband transmission is due to the superposition of individual resonances (positioned closely), with their convergence boosting the overall bandwidth, demonstrating the synergistic benefit of the multi-stacked approach.

To elucidate the broadband resonance mechanism of our multilayered metamaterial, we formulated a circuital model with coupled resonators [3]. This model employs a series combination of inductance (L), capacitance (C), and resistance (R) to mirror the CST simulation's transmission response, showcased in Figure 1(c) and (d). Table 1 outlines the parameters for L, C, and R. The transmission line (TL) circuit models for this dual-layered structure perfectly matches well validating the model's effectiveness in capturing interactions between the stacked resonators.

Conclusions: We designed polarization-insensitive broadband modulators using stacking of resonators. A FWHM of 350 GHz has been achieved for the multistacked MM, enhancing the bandwidth by over 150% compared to a single resonator. The transmission line model was employed to explain the coupling between the stacked resonators. The designed broadband metamaterial can be used as broad stopband filters and for functional broadband THz device applications.

Acknowledgements

Author G K would like to acknowledge the financial support from MeitY, India, (GG-11/22/2020-R&D-E).

References

1. Ma, Z. T., et al. "Modulators for terahertz communication: The current state of the art." Research (2019).
2. Degl'Innocenti,,et al. "Recent progress in terahertz metamaterial modulators." Nanophotonics 11.8 (2022): 1485-1514.
3. Zhou, Shaolin, et al. "Intercoupling of Cascaded Metasurfaces for Broadband Spectral Scalability." Materials 16.5 (2023): 2013.

Bismuth-based color generation devices : from traditional optical cavities to gap-surface plasmon metastructures

F. Chacon-Sanchez, C. Ruiz de Galarreta, and R. Serna

Instituto de Óptica (IO-CSIC), Spain
*corresponding author: fernando.chacon@csic.es

Abstract: We report the successful use of bismuth nanostructures for generating vivid structural colors through two distinct routes: traditional Fabry-Perot cavities and gap-surface plasmon **metasurfaces**. By exhaustively comparing computational and experimental results from each approach, we assess their suitability for both micro- and macro-coloring sustainable **devices** and its tunability potential.

In this work we explore the potential of a non-conventional plasmonic material (bismuth) for metastructures on the visible (VIS) spectrum, while providing a comparative study for the use of metastructures for structural coloring. [1] The choice of material is based on the excellent plasmonic response demonstrated by Bi-based nanostructures in the ultraviolet and visible [4], as well as the similarity of its dielectric constant with aluminum [fig. 1(a)], widely use on VIS. In addition, Bi exhibits a relatively low melting temperature (~270 ºC), with its solid-to-liquid phase transition being accompanied by significant changes in its optical response. This behaviour, as studied in previous works [6-7], creates the opportunity for optical switching of Bi-nanocomposite films by hot-plate annealing (phase light switching) or under ns-laser irradiation (ultrafast response), with future potential applications on reconfigurable plasmonic metastructures.

In addition, we study from a computational and experimental point of view two different approaches for Bi-based structural coloring: a traditional Fabry-Perot cavity (FPC) and a gap-surface plasmon metastructure (GSP), with apparently similar structures, as seen in Fig.1, but with different physical working mechanisms underneath. Using different computational methods (Transfer Matrix Method for FPC and Finite Element Differences for GSP) we have simulated and optimized both structures,

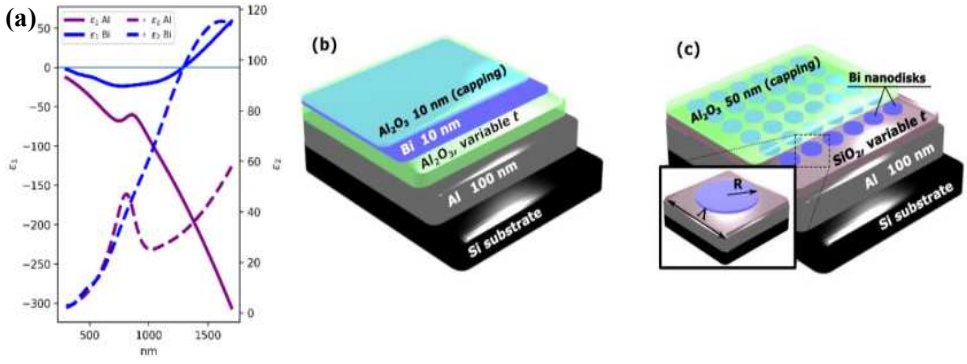


Figure 1. (a) Complex dielectric constant of Bi, compared to Al. (b) General structure of F-P cavity. (c) General structure and variables of gap plasmon metastructures

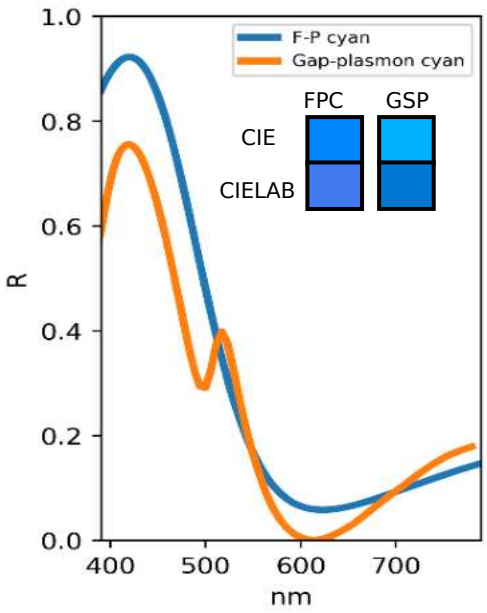


Figure 2. Simulated reflectivity for FPC and GSP tuned for cyan color generation

obtaining crisp, intense colors (Figure 2) for both structures, adding to that the exploration of their angular robustness. We have employed pulsed laser deposition (PLD) for the fabrication of the FPC and PLD and e-beam lithography for the GSP. For the experimental characterization we have performed angular-resolved measurements of their reflectivity and ellipsometry to show their angular robustness. We will discuss the pros and cons of each different type of structure for structural color generation in micro- and macro-structures, the need of a CMY colorbase to obtain a full color palette, and the tunability potential of each structure taking into account Bi's solid-liquid phase change to activate the device.

References

1. F. Chacon-Sanchez, C. Ruiz de Galarreta et al. *"Building Conventional Metasurfaces with Unconventional Interband Plasmonics: A Versatile Route for Sustainable Structural Color Generation Based on Bismuth*", Adv. Opt. Mater. 2302130, (2023).
2. Gururaj V. Naik, Vladimir M. Shalaev, Alexandra Boltasseva. *"Alternative plasmonic materials: beyond gold and silver"*,Advanced Materials, **25**, 24, 3264-3294 (2013).
3. J. Toudert R. Serna and M. Jimenez de Castro, *"Exploring the Optical Potential of Nano-Bismuth: Tunable Surface Plasmon Resonances in the Near Ultraviolet-to-Near Infrared Range",J. Phys. Chem.* C 116, 20530–9 (2012)
4. J. Toudert, R. Serna, *"Interband transitions in semi-metal, semiconductors, and topological insulators: a new driving force for plasmonics and nanophotonics," Opt. Mater. Express*. **7**, 2299 (2017)
5. Y.-P. Chen, C.-C. Lai, W.-S. Tsai, "*Full-color based on bismuth core-shell nanoparticles in one-step fabrication"*,Opt. Express. 28, 24511 (2020)
6. M. Jiménez De Castro, F. Cabello, J. Toudert, R. Serna, E. Haro-Poniatowski, *"Potential of bismuth nanoparticles embedded in a glass matrix for spectral-selective thermo-optical devices*, Appl. Phys. Lett. 105 (2014).
7. M. Garcia-Pardo, E. Nieto-Pinero, A. K. Petford-Long, R. Serna, J. Toudert, *"Active analog tuning of the phase of light in the visible regime by bismuth-based metamaterials"*, Nanophotonics. 9, 885–896 (2020)

Metasurface-Driven Hyperspectral Video Camera and Real-Time Spectral Analysis applications

A. Burguete-Lopez[1*], Q. Wang[1], M. Makarenko[1,2], A. Fratalocchi[1]

[1]PRIMALIGHT, Faculty of Electrical Engineering; Applied Mathematics and Computational Science, King Abdullah University of Science and Technology, Thuwal 23955-6900, Saudi Arabia
[2] EXPEC ARC, Saudi Aramco, Dhahran
*corresponding author: arturo.burguetelopez@kaust.edu.sa

Abstract: We present a hardware-accelerated hyperspectral video camera that employs a metasurface for real-time spectral analysis. The metasurface implements artificial intelligence algorithms, enabling video-rate assessment of object properties inaccessible to traditional cameras. We show experimental results on the system's performance on spectrally enhanced segmentation and fruit ripeness level sensing.

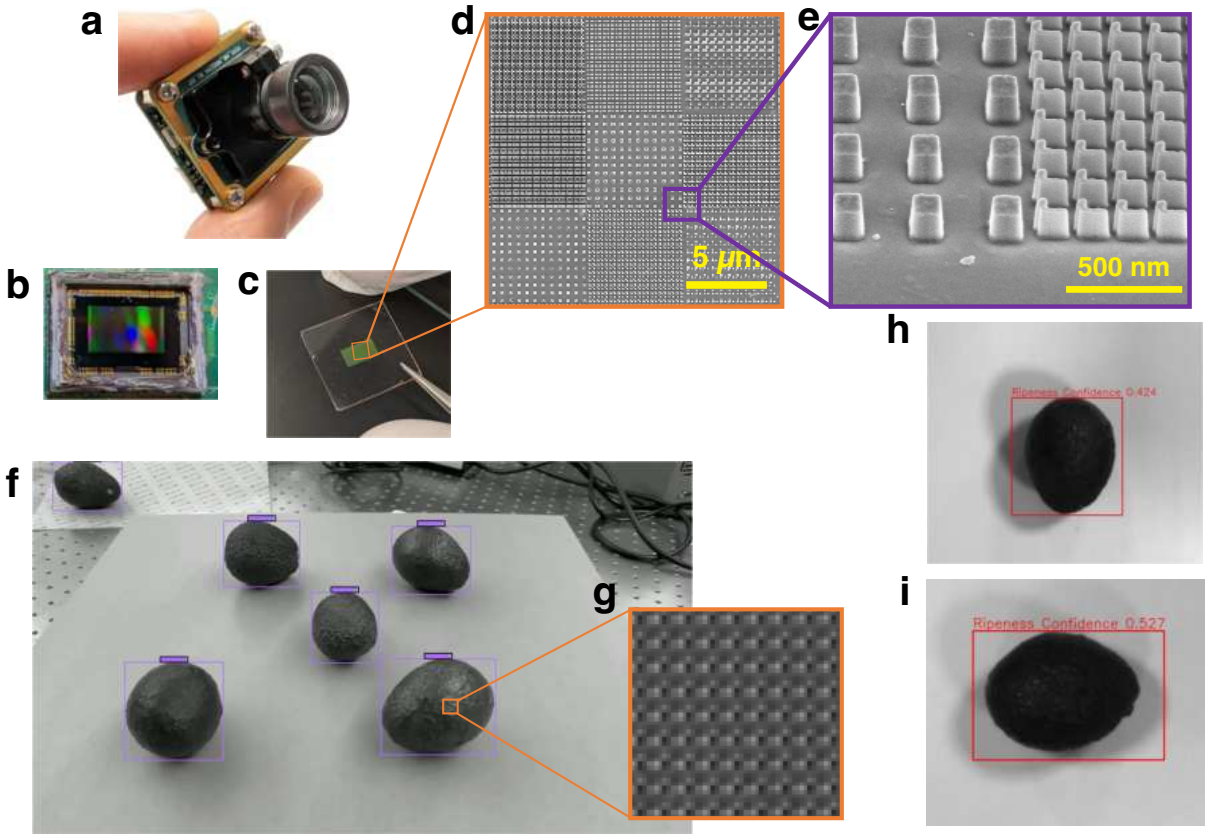


Figure 1: **Metasurface-based AI hyperspectral video camera and demonstration of fruit quality control**. **a** Hyperspectral video camera composed of a modified imaging sensor (**b**) on which a metasurface (**c**) is placed. **d**, **e** Scanning electron microscope images of the nanoresonators comprising the metasurface. **f** Still frame from video footage of a set of avocados on a rotating stage. The panel shows bounding boxes generated in real time around each fruit. **g** closeup of the pixels of the still frame showing the encoding of spectral information by the metasurface. **g,h** Predictions on ripeness using the spectral information of the fruits.

Hyperspectral imaging has emerged as a powerful remote sensing technique spanning diverse disciplines such as astronomy, medicine, environmental monitoring, agricultural science, and archaeology [1]–[4]. This method captures images across hundreds of frequency bands within and beyond the visible light spectrum, assigning a unique spectrum to every pixel, and

facilitating material identification and characterization based on their spectral signatures [5].

Despite notable technological development, state-of-the-art devices face challenges such as low spatial resolution (typically below one megapixel), prolonged acquisition times (up to several minutes per frame), and high cost (ranging from tens to hundreds of thousands of dollars) [6]. Metasurfaces present a promising avenue to address these issues, with the proven realization of components such as frequency filters, spectrometers, and lenses in a highly integrated form factor [7]–[9].

In this work, we introduce a hyperspectral video camera that effectively mitigates the aforementioned challenges. We manufacture the device by integrating metasurface technology with an off-the-shelf camera, resulting in a compact apparatus capable of capturing hyperspectral video at a spatial resolution of over two megapixels and a speed of 120 frames per second. The metasurface is designed to optically execute artificial intelligence operations, encoding the scene's spectral information into a format readable by a conventional camera [10].

Figure 1a displays a photo of the hyperspectral video camera. We enhance the commercial camera sensor (fig. 1b) by adding a suitably engineered transmissive metasurface (fig. 1c) on top. The metasurface comprises nine repeating patterns, illustrated in fig. 1d. The closeup presented in fig. 1e shows that each pattern has distinct nanoresonator structures designed for specific spectral responses. Figure 1f shows a still frame from a video sequence depicting a set of avocados on a moving stage. The bounding boxes around the fruits are generated in real-time, based on spatial and spectral information of the scene. Figure 1g depicts a pixel-level closeup of the frame, illustrating the metasurface's sub-pixel pattern encoding of spectral information. In Figure 1h-i spectral information from the sub-pixel pattern is fed to a neural network classifier, which performs real-time estimation of the fruit's ripeness.

Acknowledgements: Parallel simulations are performed on KAUST's Shaheen supercomputer. Metasurface fabrication is conducted in the KAUST Core Labs nanofabrication cleanroom.

References

[1] M. Vasile, L. Walker, A. Campbell, *et al.*, "Space object identification and classification from hyperspectral material analysis," *Scientific Reports*, vol. 14, no. 1, p. 1570, 1 Jan. 18, 2024.

[2] W. Jahr, B. Schmid, C. Schmied, F. O. Fahrbach, and J. Huisken, "Hyperspectral light sheet microscopy," *Nature Communications*, vol. 6, no. 1, p. 7990, 1 Sep. 2, 2015.

[3] B. Lu, P. D. Dao, J. Liu, Y. He, and J. Shang, "Recent Advances of Hyperspectral Imaging Technology and Applications in Agriculture," *Remote Sensing*, vol. 12, no. 16, p. 2659, 16 Jan. 2020.

[4] A. Tournié, K. Fleischer, I. Bukreeva, *et al.*, "Ancient Greek text concealed on the back of unrolled papyrus revealed through shortwave-infrared hyperspectral imaging," *Science Advances*, vol. 5, no. 10, eaav8936, Oct. 4, 2019.

[5] M. J. Khan, H. S. Khan, A. Yousaf, K. Khurshid, and A. Abbas, "Modern Trends in Hyperspectral Image Analysis: A Review," *IEEE Access*, vol. 6, pp. 14 118–14 129, 2018.

[6] A. Mukundan, Y.-M. Tsao, F.-C. Lin, and H.-C. Wang, "Portable and low-cost hologram verification module using a snapshot-based hyperspectral imaging algorithm," *Scientific Reports*, vol. 12, no. 1, p. 18 475, 1 Nov. 2, 2022.

[7] L. Gao, Y. Qu, L. Wang, and Z. Yu, "Computational spectrometers enabled by nanophotonics and deep learning," *Nanophotonics*, vol. 11, no. 11, pp. 2507–2529, Jun. 1, 2022.

[8] F. Getman, M. Makarenko, A. Burguete-Lopez, and A. Fratalocchi, "Broadband vectorial ultrathin optics with experimental efficiency up to 99% in the visible region via universal approximators," *Light: Science & Applications*, vol. 10, no. 1, pp. 1–14, 1 Mar. 4, 2021.

[9] Z. Li, P. Lin, Y.-W. Huang, *et al.*, "Meta-optics achieves RGB-achromatic focusing for virtual reality," *Science Advances*, vol. 7, no. 5, eabe4458, Jan. 27, 2021.

[10] M. Makarenko, A. Burguete-Lopez, Q. Wang, *et al.*, "Real-time Hyperspectral Imaging in Hardware via Trained Metasurface Encoders," in *2022 IEEE/CVF Conference on Computer Vision and Pattern Recognition (CVPR)*, Jun. 2022, pp. 12 682–12 692.

MEMS-based double filter configuration for air gap sensing in tunable Fabry–Pérot filter

P. Sahani[1], S. Nabana[1], T. Okatani[1], N. Inomata[1], and Y. Kanamori[1*]

[1]Department of Robotics, Graduate School of Engineering, Tohoku University, Japan
[*]Corresponding author: ykanamori@tohoku.ac.jp

Abstract: We fabricate a device that configures the tunable air gap Fabry–Pérot filter with a static gradient thickness filter to estimate air gap dimension in tunable filter. The chip-level microelectromechanical integration of gradient thickness filter can serve the purpose of device miniaturization while performing air gap sensing in visible wavelength range.

1. Introduction

Microelectromechanical systems (MEMS)-based Fabry–Pérot filters (FPFs) have paved the way to realize miniature, lightweight, and cost-effective spectrometers against their bench-top counterparts [1]. Achieving a wide range of tunability with MEMS-based tunable FPF by controlling the air gap dimension subjected to various actuation mechanisms can enable several novel applications through miniaturization and scalability. However, the conventional tunable FPFs with existing technology[2, 3] have limitations in detecting the exact air gap dimension which ultimately affects the target spectral information in applications such as hyperspectral imaging, for example. In this study, we propose an epoch-making concept MEMS device that combines the tunable air gap FPF with a static gradient thickness filter to enable the accurate estimation of the cavity gap dimension in the tunable FPF.

2. Device concept and fabrication

The concept of the proposed device is depicted in Fig. 1. When a broadband light is incident on the double filter region from the top, then a selective spectral component is transmitted through the air gap FPF which further is transmitted through a selective spatial position of the static gradient thickness filter. Knowing the gradient thickness filter position through which light is transmitted from the CMOS pixel output can provide an accurate estimation of the air gap dimension in the air gap FPF. The fabrication of top mirror involves photolithography patterning and Ag sputtering to form a concavity (Fig. 2) for reducing the area of contact with the bottom mirror to minimize the effect of non-parallelism of mirrors on the transmission of FPF. The fabrication of bottom mirror involves Ag sputtering followed by shadow mask SiO_2 sputtering and Ag sputtering to create a static gradient thickness filter and then, Ag sputtering on the opposite side (Fig. 3).

3. Results and Discussion

The top and bottom mirrors are assembled by a PZT using glue as shown in Fig. 4. The transmittance of the tunable air gap FPF is measured by a microscope spectrometer by applying voltage (V_{app}) to the PZT. Figure 5 shows the transmission spectrum undergoes a spectral shift from 552.9 nm to 587.8 nm ($\Delta\lambda$ = 34.9 nm) when V_{app} increases from 0.0 V to 5.0 V. The measured transmission spectra of the double filter region at different spatial positions are shown in Fig. 6. At V_{app} = 0.0 V, the peak occurs at 549.6 nm with maximum transmittance at X = 0.0 mm (black curve in Fig. 6(a)) whereas that occurs at 580.6 nm with maximum value at X = 0.2 mm (red curve in Fig. 6(b)) for V_{app} = 5.0 V. This means the spatially-resolved spectral position of the transmitted light from the double filter region under different V_{app} values (almost) match the spectral position of transmitted light in tunable air gap FPF.

4. Conclusions

In conclusion, we fabricate a device that combines the tunable air gap FPF with a static gradient thickness filter

on the same platform. The fabricated device provides an easy way for accurate estimation of the air gap dimension in the tunable air gap FPF even in the visible wavelength range. The concept technology satisfies the requirement of device miniaturization for many applications and hence, possesses advantages over the conventional way of air gap sensing by capacitive displacement measurement.

Acknowledgements: This work was performed at the Micro/Nano-machining Research and Education Center (MNC), Tohoku University, Japan.

References

1. Snyder, D. T., Pulliam, C. J., Ouyang, Z., et al., "Miniature and fieldable mass spectrometers: recent advances", Analytical Chemistry, Vol. 88, No. 1, 2-29, 2016.
2. Hirokubo, N., Komatsu, H., Hashimoto, N., et al., "Wideband visible wavelength range MEMS Fabry–Perot tunable filter with highly accurate calibration system", IEEE Sensors Journal, Vol. 13, No. 8, 2930-2936, 2013.
3. Kääriäinen, T. and Dönsberg, T., "Active hyperspectral imager using a tunable supercontinuum light source based on a MEMS Fabry–Perot interferometer", Optics Letters, Vol. 46, No. 22, 5533-5536, 2021.

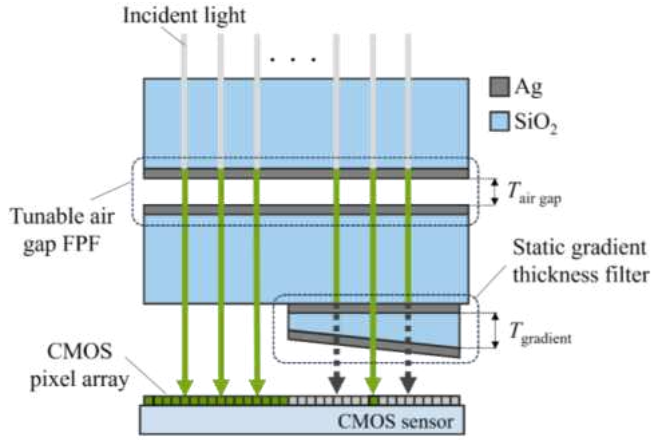


Fig. 1. Schematic of the device concept.

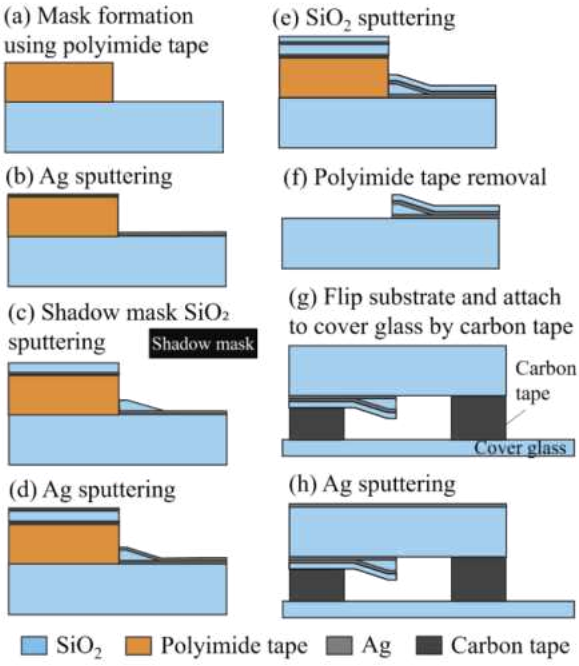


Fig. 3. Fabrication process flow of bottom mirror.

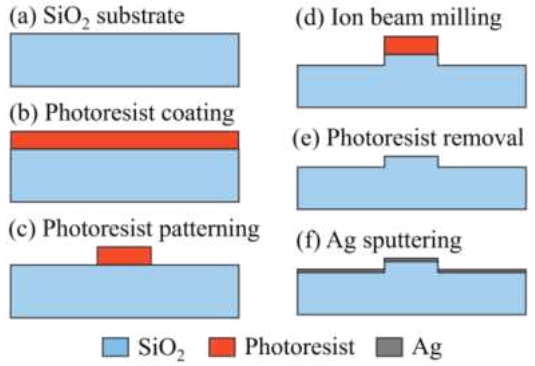


Fig. 2. Fabrication process flow of top mirror.

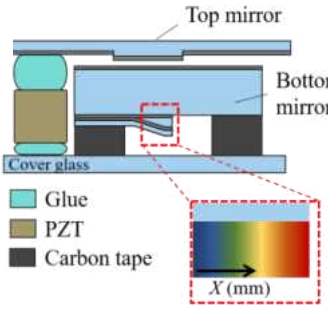


Fig. 4. Assembly of top and bottom mirrors by means of PZT.

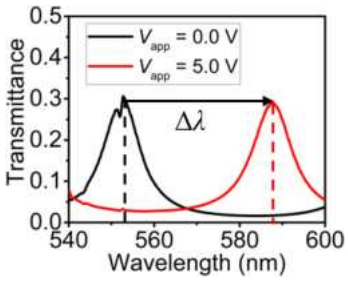


Fig. 5. Transmission spectra of tunable air gap FPF under applied voltage to PZT of 0.0 V and 5.0 V.

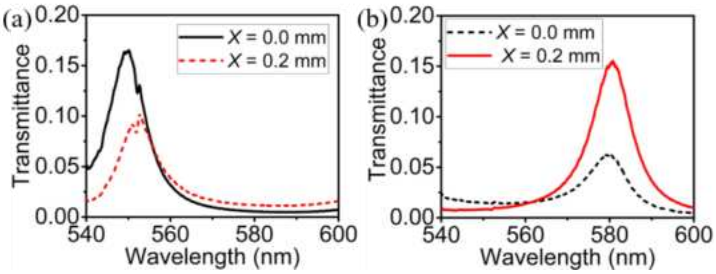


Fig. 6. Transmission spectra of double filter region at positions of X = 0.0 mm, and X = 0.2 mm on the static gradient thickness filter under the PZT actuation voltages of (a) 0.0 V and (b) 5.0 V.

Metamaterial range extended and field localized Parity-Time symmetrical wireless power transfer system.

Abdulrahman Alsaadi[1,2], Inki Kim[1,2*]

[1]Department of Biophysics, Institute of Quantum Biophysics, Sungkyunkwan University, Suwon, Republic of Korea
[2] Department of Intelligent Precision Healthcare Convergence, Sungkyunkwan University, Suwon, Republic of Korea
[*]Corresponding author: inki.kim@skku.edu

Abstract: Conventional wireless power systems are limited in range, efficiency, and robustness. Our system provides, extended-range power transfer using the physics of parity-time symmetry and metamaterials, increasing transfer efficiency stability against distance fluctuations with the ability to localize the power from a larger transmitter to smaller size receiver.

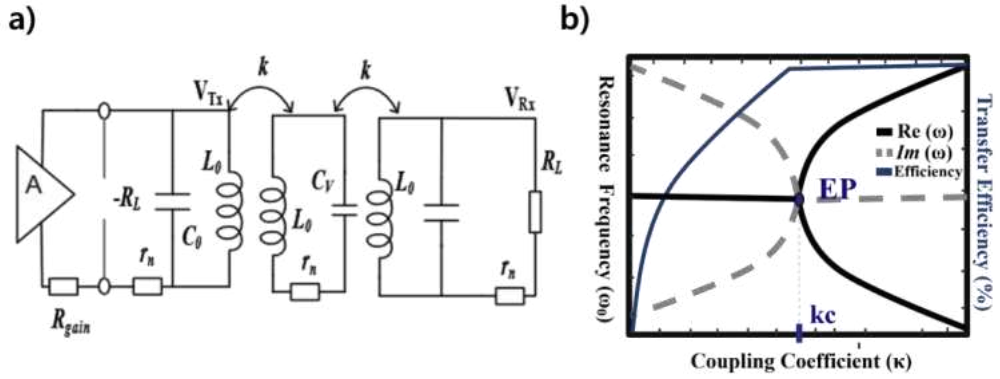


FIG.1 a) PT-WPT circuit schematic b) Resonance frequency and power transfer efficiency against coupling coefficient.

The demand for wireless power transfer (WPT) in medical implants has increased due to its potential to eliminate frequent battery replacements, improving patient well-being and safety. However, conventional wireless power transfer systems have limitations in range efficiency of transmission and Transmitter (Tx) to receiver (Rx) size ratio. This work proposes a stable and extended range wireless power transfer system utilizing parity-time symmetry (PT-symmetry) and electromagnetic metamaterials (MTM) to address these limitations. Previously, Parity-time symmetry was introduced from Quantum physics as a solution to WPT systems instability towards fluctuation in operating frequency and coupling coefficients [1]. PT-symmetry can be implemented in WPT systems by introducing a gain element into the circuit equivalent to the loss element. As shown in Fig.1(a), it is denoted as (-R), which is equivalent to load resistance (RL) [2].

$$\frac{d}{dt}\begin{bmatrix}a_1\\a_2\\a_3\end{bmatrix}=\begin{bmatrix}j\omega_0+g & -j\kappa & 0\\ -j\kappa & j\omega_0 & -j\kappa\\ 0 & -j\kappa & j\omega_0-\gamma\end{bmatrix}\begin{bmatrix}a_1\\a_2\\a_3\end{bmatrix} \quad (1)$$

$$\omega=\omega_0\pm\sqrt{\kappa-\gamma} \quad (2)$$

By utilizing coupled-mode theory for characterizing WPT systems, the operating frequency (ω) can be obtained by solving for the eigenvalues of equation (1). Here ω_0 is the resonance frequency of MTM ($\omega_0=1/\sqrt{(L_0C_0)}$), κ is the coupling rate (ω_0 K/2), g and γ are the gain loss rates, respectively. As shown in equation (2), the system obtains two real fundamental modes if $\kappa\geq\gamma$ which makes it robust against fluctuations in coupling coefficient. Transmission efficiency remains unaffected by the coupling coefficient, as depicted in Fig. 1(b). The inclusion of an electromagnetic metamaterial slab enables the system to transfer power effectively from a larger Transmitter (Tx) to smaller receiver (Rx). Our metamaterial (MTM) is made of

Megahertz spiral resonators that each act as a unit cell, when arranged periodically the structure will behave as a metamaterial with the unique negative refractive index and by making a defect in the structure by tuning one of the unit cells to operate at a lower resonance frequency will make the structure to act as meta lens with hotspot that confines the field into one spot [3]. Electromagnetic wave simulations show that the metamaterial effectively confines the magnetic field (h-field), as shown in Fig. 2(b), surpassing the capabilities of the PT system without Metasurface Fig. 2(a).

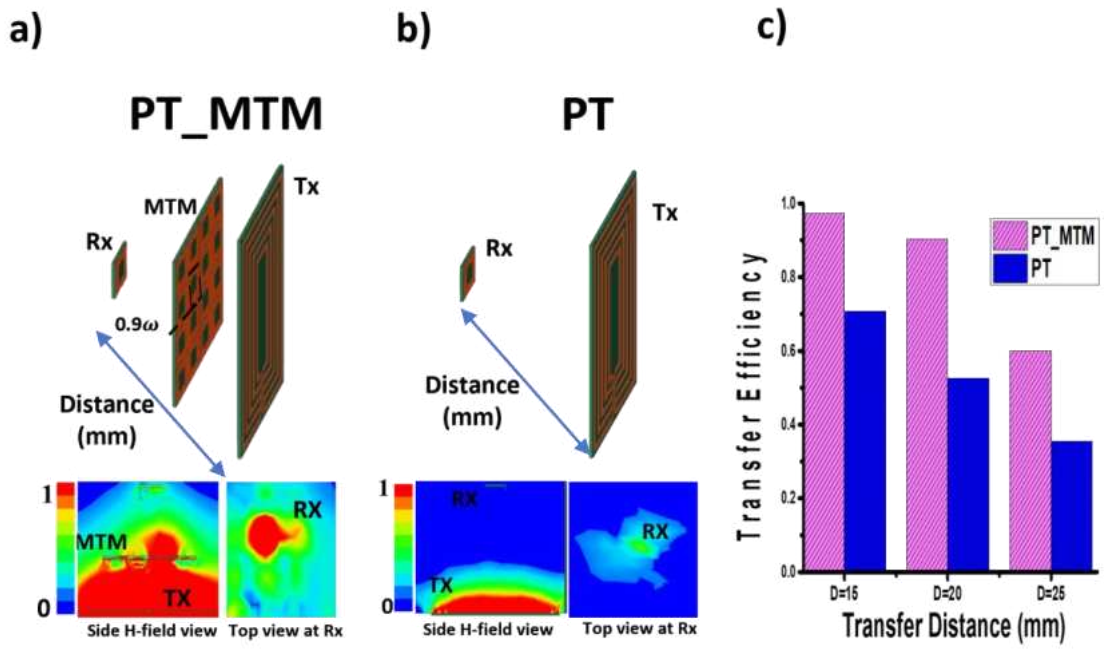


FIG.2 a) and b) shows the H_ Field distribution for PT-WPT system without Metasurface and with PT_MTM respectively. c) Shows the measured transfer efficiency of both configurations at various transfer distances.

Experimental results in FIG. 2 (c) show that the efficiency has increased significantly in the presence of MTM compared to no MTM providing a potential for improving the functionality of wireless power transfer systems to applications where the receiver is not moving continuously and smaller in size than the transmitter such as in medical implants.

References

1. Assawaworrarit, S., Yu, X., & Fan, S. (2017). Robust wireless power transfer using a nonlinear. Nature, 546(7658), 387-390.
2. Sakhdari, M., Hajizadegan, M., & Chen, P. Y. (2020). "Robust extended-range WPT PT-symmetric platform." Physical Review Research, 2(1), 013152. vol. 68, no. 3, pp. 1569-1582 (2020).
3. H. N. Bui, J. -S. Kim and J. -W. Lee, "Design of Tunable Metasurface Using Deep Neural Networks for Field Localized WPT," IEEE Access, vol. 8, pp. 194868-194878 (2020).

Technology of auxetic-structured substrate for skin attachable conformal sensor

Jae-Hwan Lee[1], Tae-Gyong Kim[1], Jun-Sang Lee[2], and Seung-Kyun Kang[1*]

[1]Seoul National University, Republic of Korea
[2]Purdue University, United States
[*]corresponding author: kskg7227@snu.ac.kr

Abstract: This study introduces a novel method to design a substrate with customizable Poisson's ratio using hybrid re-entrant structures and finite element analysis for evaluation and analysis of the strain-dependent Poisson's ratio of substrates. The substrate matches skin's Poisson's ratio across different strains, enabling tailored sensor substrates for various skin areas.

The mismatch in the Poisson's ratios between skin and the substrates of wearable patch sensors leads to mismatched stress, impacting sensor performance and user comfort. Previous solutions have not fully addressed the strain-dependent variability of the skin's Poisson's ratio. This study proposes a solution through the design of a substrate with a tunable Poisson's ratio, capable of matching the skin's properties across a range of strains.

The study employed finite element analysis to evaluate the strain-dependent Poisson's ratio of substrates incorporating a single design of re-entrant structures. By adjusting the design parameters of these structures, the research aimed to tune the substrate's Poisson's ratio to match that of human skin. The hybridization approach of re-entrant structures was explored to achieve a uniform Poisson's ratio across varying strains.

The experimental results are pivotal in validating the effectiveness of re-entrant structure hybridization in controlling the Poisson's ratio of substrates. Through comprehensive finite element analysis (FEA), this study meticulously evaluated the Poisson's ratio of substrates integrated with re-entrant structures under varying strain conditions. The results significantly highlight the capability of these structures to fine-tune the substrate's Poisson's ratio across a broad strain spectrum, showcasing a remarkable alignment with the strain-dependent properties of human skin.

Finite Element Analysis Validation: Initial experiments involved validating the FEA method against traditional tensile testing techniques. By measuring the Poisson's ratio of re-entrant structure-enhanced substrates under controlled conditions, the study confirmed the high accuracy of FEA predictions, underscoring its reliability in simulating biomechanical interactions between the substrate and skin.

Strain-dependent Poisson's Ratio Control: The core achievement of the research was the successful demonstration of strain-dependent control over the substrate's Poisson's ratio. The study illustrated how varying the design parameters of the re-entrant structures—such as their angle, size, and distribution—enabled precise tuning of the substrate's mechanical properties. This adaptability ensured a seamless match with the skin's Poisson's ratio over a wide range of strains, effectively eliminating mismatch stress.

Hybridization of Re-entrant Structures: A novel hybridization strategy involving different re-entrant structure designs was employed to achieve uniform Poisson's ratio control across the entire strain spectrum. This approach led to the development of a substrate that dynamically adjusts its Poisson's ratio in response to changes in applied strain, mirroring the skin's natural biomechanical behavior. The experimental data vividly demonstrate the hybridized substrate's capability to maintain optimal biomechanical compatibility with the skin, ensuring

enhanced performance and comfort of wearable sensors.

Practical Implications and Applications: The practical application of these findings was underscored by the fabrication of a prototype substrate that successfully matched the Poisson's ratio of human skin across various strains. This breakthrough paves the way for the next generation of wearable sensors that can provide high-fidelity data while minimizing discomfort and potential skin irritation, thereby significantly improving user compliance and the overall effectiveness of wearable health monitoring devices.

The research successfully designed and fabricated a substrate with a controlled Poisson's ratio, matching that of the skin across all strains, through the hybridization of re-entrant structures. This achievement opens pathways for developing customized patch sensors capable of adhering to any part of the body without the issue of mismatched stress, enhancing both sensor functionality and wearer comfort.

References

1. Jang, K. I., et al., “Soft network composite materials with deterministic and bio-inspired designs”, Nat. Commun., Vol. 6, No. 1, 6566, 2015.
2. Lee, Y. J., et al., “Auxetic elastomers: Mechanically programmable meta-elastomers with an unusual Poisson’s ratio overcome the gauge limit of a capacitive type strain sensor”, Extreme Mech. Lett., Vol. 31, 100516, 2019.
3. Jiang, Y., et al., “Auxetic mechanical metamaterials to enhance sensitivity of stretchable strain sensors”, Adv. Mat., Vol. 30, No. 12, 1706589, 2018.

Flexible Metasurface as an Efficient Resonator for 7T MRI

Santosh K Maurya[1], Eiska Tegareh[2], and Rita Schmidt[1*]

[1]Department of Brain Sciences, Weizmann Institute of Science, Israel,
[2]Life Sciences Core facilities, Weizmann Institute of Science
[*]corresponding author: rita.schmidt@weizmann.ac.il

Abstract: We proposed a flexible and cost-effective metasurface design based on maze-like geometry of concentric split ring resonators (SRRs) for ultra-high field 7T human MRI. This design not only lowered the resonant frequency but also increased the RF field efficiency by x1.5-2 folds. This have been demonstrated both numerically and experimentally.

The ability of the metamaterial structures to offer unique properties and new solutions opened new avenues in a wide range of applications. In recent years, metamaterial designs have also been explored in the field of MRI to increase SNR and efficiency of the RF coils[1-6]. Previously explored structures were based on either high dielectric substrate or structure with many lumped elements. Both approaches not only increase the complexity of the design but also may result in reduced efficiency. The constraints in MRI include a tight coil-patient setup, the requirement for deep penetration of the magnetic field outside the structure and potential power deposition in the body. The most relevant resonant mode of interest for MRI is the lowest transverse-electric (TE) mode since it provides H-field components that are perpendicular to the main static magnetic field and have large penetration depth. In this study, we aimed to design a flexible and compact metasurface that provides high efficiency for MRI applications.

Instead of using a split-ring as a small sub-unit, here the structure was constructed from a set of concentric split-rings (each having two gaps) with alternating split-rings rotated by 90° - generating a maze-like configuration. This design offers two key advantages – i) a configuration based on set of concentric split-rings (in this case six) provides more homogenous RF magnetic field and increases the RF field efficiency (defined as $B_1/\sqrt{SAR}$ in MRI), ii) a configuration based on alternatingly rotated by 90° split-rings compared to aligned set lowered significantly the resonant frequency of the resonant modes. The designed configuration provided a resonant structure tuned at 298 MHz for 7T human MRI without a need for lumped elements. Fig.1 show the advantages of the design.

To characterize and examine the proposed structure EM simulations, including eigen mode solver and time domain, were done followed by measurements in 7T MRI. All the simulations were carried out using CST Microwave Studio, Darmstadt, Germany. A rectangular sucrose phantom with relative permittivity of 53 and conductivity of 0.3S/m was used to mimic brain tissue properties. Simulations with virtual human model "Duke" were performed in a setup for brain imaging with the metasurface structure bended adjacent to the head. B_1 field map was measured in a setup that included a small surface loop, an added metasurface and a sucrose-based phantom.

In time-domain simulations, a comparison of the simulated B_1 distributions between a setup driven by a surface-coil and one with a proposed here metasurface (of the same dimensions) was performed. The maximal increase in RF field with the metasurface was 1.9-fold higher compared to the surface coil with the same size. An experimental result showed an increase of ~1.7 in B_1 (see Fig.2).

In this study, we demonstrated a new metasurface geometry that provided an efficient resonator at 298 MHz for 7T MRI. This design didn't require high dielectric or lumped elements, which offered a simple implementation, a flexible setup and a high efficiency resonator.

Acknowledgements: This project was partially supported by the Israel Science Foundation.

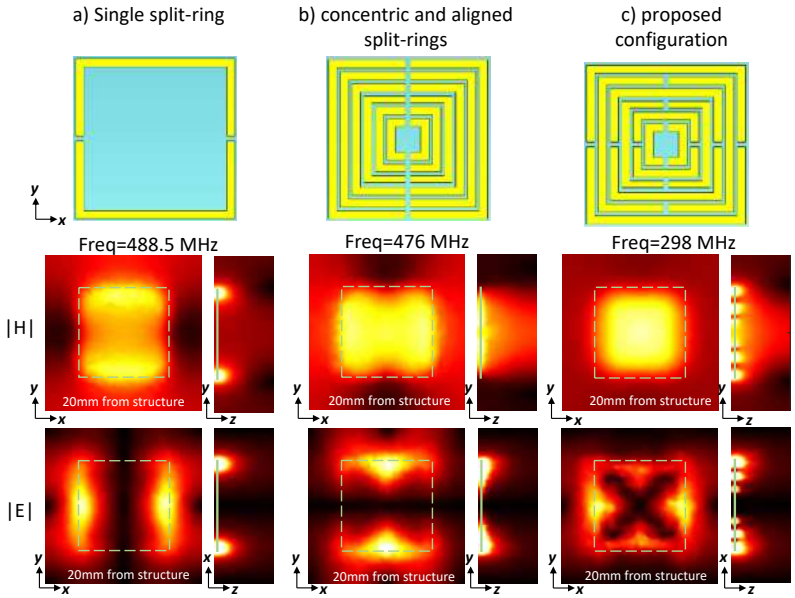


Fig.1 Eigen-mode H- and E-fields for different steps towards the proposed configuration. a) RF fields for a single split-ring, which has peak intensities close to the copper strips. b) RF fields for concentric and aligned split-rings. c) RF fields for the final maze-like configuration. The final setup shows symmetric and "dense" RF field distributions and significantly reduces the RF frequency. The scaling was chosen to optimally visualize the distribution. The dimension of the structure was set to 14x14x0.08 cm^3, the dielectric layer of thickness 0.4 mm and permittivity of 2.6 was used.

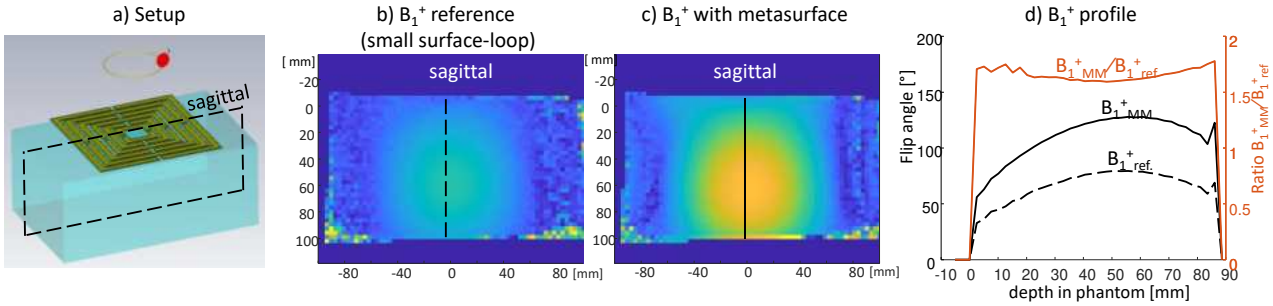


Fig.2 Measured B_1 maps with the proposed metasurface. a) Setup. b) B_1^+ without the metasurface, c) B_1^+ with the metasurface, d) 1D B_1^+ profiles and the ratio between the B1 with and without the structure as function of the depth in phantom. The maps show the B_1^+ ($B_1^+ = (B_{1x}+B_{1y})/2$) measured using vendor's sequence.

References

1. Algarín, J. M., Freire, M. J., Breuer, F., & Behr, V. C. " Metamaterial magnetoinductive lens performance as a function of field strength", *J Magn Reson*, Vol. No.247, 9-14, 2014.
2. Lippke, M., Stoja, E., Philipp, D., Konstandin, S., Jenne, J., Bertuch, T., & Günther, M. "Investigation of a Digitally-Reconfigurable Metasurface for Magnetic Resonance Imaging", IEEE, 668-671, 2022.
3. Slobozhanyuk, A. P., Poddubny, A. N., Raaijmakers, A. J., van den Berg, C. A., Kozachenko, A. V., Dubrovina, I. A., ... & Belov, P. A. "Metasurfaces: Enhancement of Magnetic Resonance Imaging with Metasurfaces", *Adv Mater*, Vol.28, No.9, 1831-1831, 2016.
4. Schmidt, R., Slobozhanyuk, A., Belov, P., & Webb, A. "Flexible and compact hybrid metasurfaces for enhanced ultra high field in vivo", magnetic resonance imaging. *Sci Rep*, Vol.7, No. 1, 1-7, 2017.
5. Schmidt, R., & Webb, A. "Metamaterial combining electric-and magnetic-dipole-based configurations for unique dual-band signal enhancement in ultrahigh-field magnetic resonance imaging.", ACS Appl Mater Interfaces , Vol. 9, No. 40, 34618-34624, 2017.
6. Webb, A., Shchelokova, A., Slobozhanyuk, A., Zivkovic, I., & Schmidt, R. "Novel materials in magnetic resonance imaging: high permittivity ceramics, metamaterials, metasurfaces and artificial dielectrics.", Magn Reson Mater Phy , Vol. 36, No. 6, 875-894, 2022.

Fabrication of delay lines using spoof-surface-plasmon-polariton waveguides coupled with split-ring resonators for microwave integrated circuits

M.V Nguyen, N. Kikuchi, T. Kodama, T. Okatani, N. Inomata, and Y. Kanamori*

Tohoku University, Japan
*Corresponding authors: ykanamori@tohoku.ac.jp

Abstract. We proposed and fabricated three delay lines based on spoof-surface-plasmon-polariton (sSPP) waveguides and split-ring resonators (SRR) with different gap sizes varied at sub-micrometer which results in a phase difference up to 50 degrees and the notch-band central frequency shift of 0.085 GHz for application in phase shifters and modulators.

Introduction

The 5G communication systems require sub-millimeter waves integrated on-chip with microwave-integrated circuit applications in phase shifter and phase/amplitude modulation. Conventional technologies based on radio Frequency (RF) – printed circuits board (PCB) could not be engineered at the sub-micrometer scale, which is not suitable for microwave-integrated circuits [1,2]. Furthermore, to change the time delay, conventional technology takes advantage of the physical length of the transmission line which leads to a large insertion loss [3]. In this work, the propagation constant of the microwaves is engineered to tune the transmission phase.

Design and Fabrication

Three delay lines were designed and fabricated. Each device is constituted by an sSPP waveguide and eight SRRs, which can be divided into five sections: a delay section (I); two transition sections (II), and two co-planar waveguide (CPW) sections (III) as shown in Fig. 1(a). In the delay section, four periodic corrugated rectangular metallic structures, the so-called stubs, are coupled with eight metallic SRRs on both sides; two nearby stubs are connected by a central line as illustrated in Fig. 1(b). Dimensions of the SRRs are depicted in Fig. 1(c). The CPW sections are designed for the input and output of microwaves, which are compatible with an impedance of 50 Ohm for connection with the measurement circuit. Sections (II) are designed for high-efficiency coupling of the microwaves from CPW to the delay line. The designed dimensions of the SRRs are as follows: t = 1.1 μm; w = 500 μm; w_1 = 2.5 mm. g is varied between the three devices for the capacitance difference resulting in phase difference and S_{21} parameter difference at the resonance of the SRRs in the interaction with the incident microwaves.

The structural design and optimization were performed using numerical calculations based on a commercial finite element solver. The devices were micromachined by ion beam milling etching and wet etching of the Cr/Au thin film on a silicon substrate deposited with a 10 μm SiO_2 film on top. The three delay lines were bonded with two SMA connectors (RS PRO SMA board end launch connector) by lead-free solder paste (Sn42Bi58 micro-beads) for optical characterization with a vector network analyzer system (E8363C, Agilent Technologies, Ltd.).

Results and Discussion

The sub-micrometer scale difference in the gap size of the SRRs creates a large phase and transmission contrast between the three delay lines. The optical characterization of the three delay lines varies with different gap sizes of the fabricated SRRs of 2.5, 3, and 4.5 μm are shown in Figs. 1(d) and 1(e). As g increases from 2.5 to 4.5 μm, a large phase difference ($\Delta\varphi$) was achieved at the notch-band between devices with different values of g as shown

in Fig. 1(d): $\Delta\varphi$ = 58.9° with g = 2.5 µm versus g = 3.0 µm (the yellow dotted line), $\Delta\varphi$ = 82.2° with and g = 3.0 µm versus g = 4.5 µm (the blue dotted line); the notch-band central frequency blue shifts as shown in Fig. 1(e): f_1 = 7.031 Ghz, f_2 = 7.073 and f_3 =7.158 GHz, respectively. The frequency difference is 0.042 GHz with g = 2.5 µm versus g = 3 µm, and *0.085* GHz with g = 3.0 µm versus g = 4.5 µm, respectively. The experimental results (the solid lines) are confirmed by numerical calculation (the dotted lines) as presented in Fig. 1(e). Active microwave modulation could be a promising application for delay lines integrating high-speed capacitive switches.

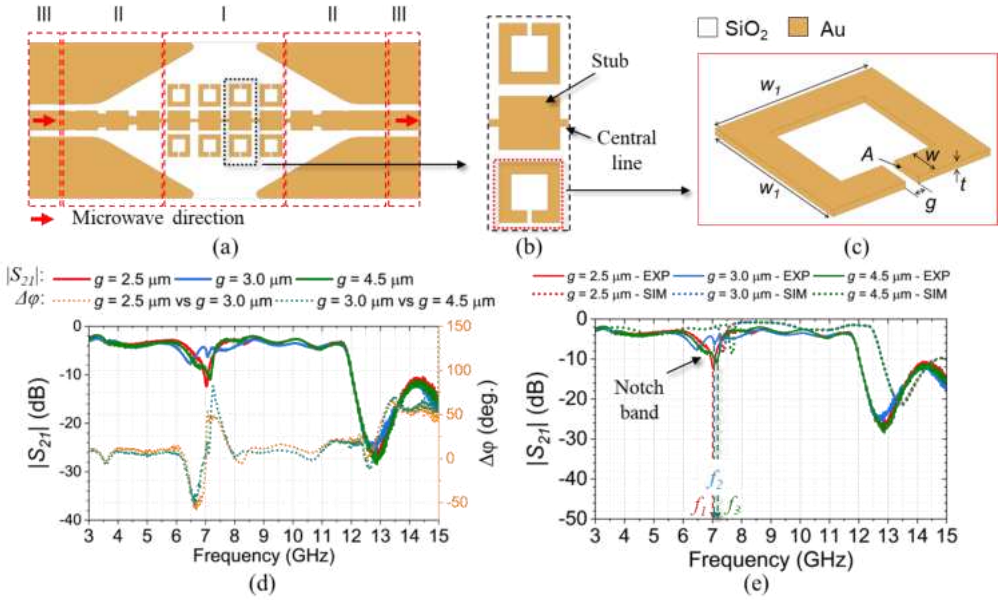


Figure 1. (a) A schematic structure of the delay lines: delay section (I); transition section (II), and CPW section (III). (b) One unit cell of the delay section. (c) Dimensions of SRR. t: the thickness of metal, g: gap, w: width, A: cross-section area, and w_1: width of SRR. (d) The measured $|S_{21}|$ magnitude with g of 2.5, 3, and 4.5 µm and phase difference ($\Delta\varphi$) between devices with g = 2.5 µm versus g = 3 µm; and g = 3 µm versus g = 4.5 µm. (e) Comparison between the measured and simulated $|S_{21}|$ magnitude of the three delay lines with g of 2.5 µm, 3 µm, and 4.5 µm. f_1, f_2, and f_3 are the notch band center frequencies of the notch band, respectively.

References

1. X. Gao, W. Y. Cui, Z. Gu, J. Zhang, Y. Ren, Q. Ma, and T. J. Cui, "Multimode and Reconfigurable Phase Shifter of Spoof Surface Plasmons," IEEE Trans. Antennas. Propag. vol. 71, No. 6, 5361–5369, 2023.
2. C. Ding, F.-Y. Meng, J.-Q. Han, H.-L. Mu, Q.-Y. Fang, and Q. Wu, "Design of Filtering Tunable Liquid Crystal Phase Shifter Based on Spoof Surface Plasmon Polaritons in PCB Technology," IEEE Trans Compon Packaging Manuf Technol, vol. 9, No. 12, 2418–2426, 2019.
3. W. R. Eisenstadt, and Y. Eo, "S-parameter-based IC interconnect transmission line characterization," IEEE Trans. Compon. Packag. Manuf. Technol., Vol. 15, No. 4, 483–490, 1992.

Acknowledgments

The authors thank Dr. Satoshi Tomita and Dr. Seigo Ohno for their useful discussion. This work was supported by JST, CREST Grant Number JPMJCR2102, Japan; and was performed at the Micro/Nano-machining Research and Education Center (MNC), Tohoku University, Japan.

Numerical investigation of dielectric metasurfaces for refractive index-based sensing applications

R. Tomescu*, C. Kusko, V. Anăstăsoaie, and D. Cristea*

National Institute for Research and Development in Microtehnologies—IMT-Bucharest,
126A, Erou Iancu Nicolae Street, 077190 Bucharest, Romania
*corresponding authors: roxana.tomescu@imt.ro; dana.cristea@imt.ro

Abstract: This paper presents a numerical investigation of dielectric metasurfaces tailored for sensing applications. The structures will be used in the development of biosensors that detect changes in the environment's refractive index. The proposed metasurface is a transmission mode array of amorphous silicon disks patterned on a fused silica substrate.

Optical biosensors are well-suited for detecting analytes in a variety of media, including air, water, blood, and food, due to their high sensitivity, compact size, and affordability [1]. An efficient method for detecting the desired analyte using an optical sensor is by analyzing the refractive index (RI) changes of the surrounding medium [2]. RI detection offers real-time, label-free, and non-invasive optical remote readouts, making it a promising solution for the development biosensors. To increase the sensitivity and quality factor of a biosensor, the design must consider the incident wavelength, near-field enhancement, resonant bandwidth, and the quality of the resonances. Various diseases can be detected using RI sensors, including blood components, biological molecules, DNA, cancerous cells, viruses, and bacteria. Also, protein and glucose concentrations in human urine can be detected using these biosensors [3, 4].

This study will explore the potential of metasurfaces for RI-based biosensing applications in visible and near infrared domains. Metasurfaces can control light propagation and emission at the nanoscale, making them suitable for biosensing applications [5] and are the most efficient option for achieving a miniaturized device [6]. They consist of periodic arrays of resonators, also known as meta-atoms, which come in a variety of shapes and sizes. Meta-atoms can sustain resonances that concentrate electromagnetic fields in small volumes by exciting localized surface plasmons, well below the diffraction limit [7]. Metasurfaces have been used to create flat and lightweight optical components, including gratings, lenses, beam shapers, color filters, and absorbers [8].

This paper presents the initial numerical investigations of metasurface structures designed to achieve high sensitivity to changes in the refractive index of the surrounding medium. The aim is to develop highly selective biosensors based on plasmonic and/or dielectric metasurfaces for the detection of specific harmful pathogens. These sensors can operate in either transmission or reflection mode. We designed and numerically analyzed a dielectric metasurface working in transmission mode composed of amorphous silicon disks patterned on a fused silica substrate. In order to investigate the behavior of the resonant structures to the RI changes we varied the diameters (from 400 to 700 nm), height (from 100 to 300 nm) and period (from 700 nm to 1μm) of the disks. The refractive index of the environment was varied between 1 and 1.35 with a 0.5 step. To assess whether the suggested structures can enhance sensitivity to RI changes, we performed a numerical analysis of the proposed metasurface using the 3D finite-difference time-domain (FDTD) method (with OptiFDTD software). We applied periodic boundary conditions to an elemental unit cell to obtain a periodic metasurface. Perfectly matched layers (PML) conditions were used to minimize reflections that may occur when incident radiation touches the boundary on the propagation direction (Z). The incident light was modelled as a Gaussian wave centered at a

wavelength of 800 nm. The investigation covered a wavelength spectrum ranging from 600 nm to 1200 nm. Figure 1 shows the schematic diagram of the proposed dielectric metasurface when the environment refractive index is 1.

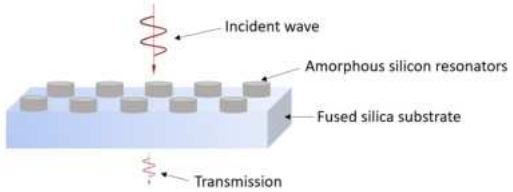


Fig 1 Schematic diagram of the proposed dielectric metasurface place in air

To determine whether this type of dielectric metasurface offers the possibility of developing RI-based biosensors, we calculated the wavelength sensitivity by $S_\lambda\,(\mathrm{nm/RIU}) = \Delta\lambda_{peak} / \Delta n_a$, where $\Delta\lambda_{peak}$ is the shift of the resonance wavelength peak, and Δn_a is the variation of the environment's refractive index. The results from this initial study show a wavelength sensitivity of 160 $\mathrm{nmRIU^{-1}}$ for a metasurface with a periodicity of 900 nm, resonators diameter of 500 nm and 200 nm height. Although the S_λ is small, the results obtained with this dielectric metasurface are comparable to those achieved with more complex structures that are sensitive to light polarization and require expensive and complicated technological processes.

The numerical analysis results, despite the relatively low values for S_λ, demonstrate that the design is a suitable candidate for developing low-cost sensors based on refractive index variation. Our next step is to optimize the design for much bigger wavelength sensitivity. Also, we will fabricate the proposed structures, functionalize the surfaces for pathogen binding, and investigate the sensor performances regarding pathogen detection.

Acknowledgement:

This work was supported by the Core Program of IMT-Bucharest within the National Research Development and Innovation Plan 2022-2026, carried out with the support of Romanian Ministry of Research, Innovation and Digitization, project no. 2307.

References

1. S.A.Rodionov, et.al., "Refractive index sensor based on all-dielectric gradient metasurface," Sensing and Bio-Sensing Research Vol. 22, 100263, 2019;
2. E.Gheroghiu, "Detection of pathogenic bacteria by magneto-immunoassays: a review,", J Biomed; Vol. 35(4): 277–283, 2021;
3. W.Chen, et.al., "Dual-resonance sensing for environmental refractive index based on quasi-BIC states in all-dielectric metasurface," Nanophotonics; Vol. 12(6): 1147–1157, 2023;
4. ML. Tseng, "Dielectric Metasurfaces Enabling Advanced Optical Biosensors," ACS Photonics, Vol. 8, 47−60, 2021;
5. R. H.Siddique, et.al, "Aluminum Metasurface with Hybrid Multipolar Plasmons for 1000-Fold Broadband Visible Fluorescence Enhancement and Multiplexed Biosensing," ACS Nano, Vol 13 (12):13775-1378, 2019;
6. V.Bello, et.al., "Spectral Phase Shift Interferometry for Refractive Index Monitoring in Micro-Capillaries," Sensors, 20(4), 1043, 2020;
7. J.Hu, et.al., "A Review on Metasurface: From Principle to Smart Metadevices," Front. Phys. Vol. 8, 586087, 2021;
8. Y.Yu, et.al., "Metallic planar lens formed by coupled width-variable nanoslits for superfocusing," Optics Express Vol. 19, 9434-9444, 2011;

Advancements in polarization-sensitive metasurfaces

O. Červinka[1*], M. Hrtoň[2], J. Lelek[3], F. Ligmajer[1,2], Š. Venos[3], L. Úlehla[3] and T. Šikola[1,2]

[1] Central European Institute of Technology, Brno University of Technology, Czech Republic

[2] Faculty of Mechanical Engineering, Brno University of Technology, Czech Republic

[3] Meopta - optika, s.r.o., Czech Republic

[*]corresponding author: ondrej.cervinka1@ceitec.vutbr.cz

Abstract: We present two metasurfaces capable of full-Stokes polarization analysis in the visible spectrum. One includes a highly sensitive Shack-Hartmann detector for wavefront sensing, while the other incorporates a holographic approach for enhanced human readability and interpretability. Both metasurfaces include polarization-multiplexing for increased efficiency.

Polarization analysis is an important tool in many areas of science and industry, from advanced imaging [1,2] and communication technologies [3,4] to chiral spectroscopy and optical defects mapping. Metasurfaces allow for spatial resolution of the polarization distribution without the need for a complex optical setup involving several branches or rotating components [5,6,7]. While polarization analysis alone is a powerful instrument, combining it with other functionalities provides an even deeper range of applications. For instance, integrating a Shack-Hartmann sensor into the metasurface can allow for simultaneous measurement of polarization state and local wavefront tilt. Determining these two quantities simultaneously, as opposed to with two separate instruments, enables real-time observation of wavefront deformation when, for example, assembling or anchoring a system of lenses. The described metasurface is pictured in Figure 1A, showing the three zones, each responsible for separating and focusing two orthogonal polarization states of different polarization bases into discrete focal points through polarization multiplexing. The total of six focal points responsible for polarization analysis lie in a hexagonal grid, with the orthogonal states at opposite sides of the hexagon. In our design, an extra, polarization-insensitive zone, focusing all light into a central focal point, was added to aid a computer algorithm in computing the local wavefront tilt via the focal point shift from a reference position. Since, at any point, any of the polarization-sensitive focal points can have zero intensity if the corresponding polarization state is not present in the analyzed light, the central polarization-insensitive focal point ensures the robustness of the automated computation. To facilitate a precise measurement of the wavefront tilt, the geometry of the metasurface has been adjusted by greatly increasing the focal length of all the focusing zones. However, there is a tradeoff between the wavefront tilt resolution and spatial sampling resolution. Since the numerical aperture of the lenses is also greatly decreased when increasing the focal distance, the focal points would overlap if the size of the metasurface zones was not also increased. The final parameters of our device are a focal length of 5 mm and a sampling period of 300 μm. The metasurface is composed of TiO_2 high-aspect-ratio nanostructures fabricated using a proven combination of electron beam lithography and atomic layer deposition. Optical characterization measurements, plotted in Figure 1C and Figure 1D, show great polarization analysis and wavefront tilt detection capabilities. Even though the targeted range of wavefront tilt angles was 0-2°, the linearity of the focal point shift is preserved even for angles larger than 15°.

The second presented metasurface focuses on a visual representation of the polarization state for improved human readability. This was achieved by replacing the polarization-multiplexed lenses in the previously described metasurface with polarization-multiplexed holograms, as shown in Figure 1B. The implementation of holograms

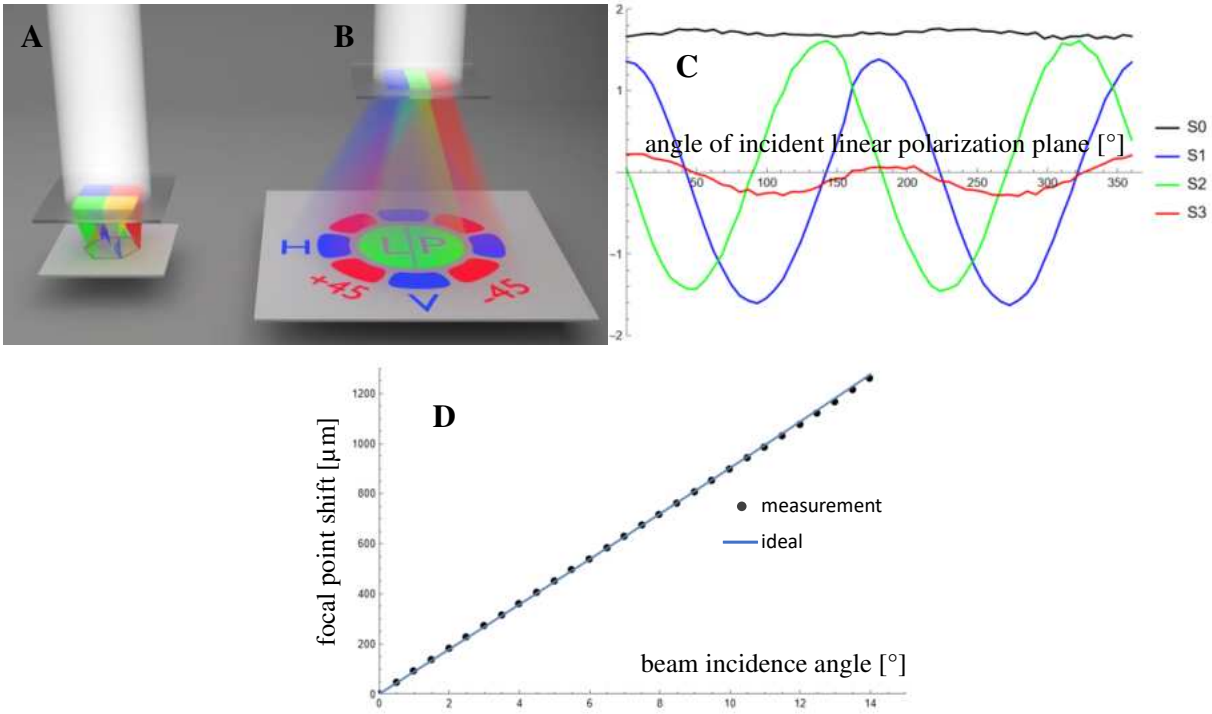


Figure 1: Design of metasurfaces and select optical measurements. (A) Metasurface polarization analyzer with Shack-Hartmann detector, (B) holographic polarization analyzer, (C) full-Stokes polarization measurement for different analyzed polarization states and (D) plot of focal point shift as a function of incoming beam angle.

opens up a great potential for various design options. For example, the focal spots of respective polarizations can now be arbitrarily shaped, allowing for easier comparison of intensities. Moreover, the polarization spots can be equipped with holographic labels designating the given polarization state, greatly improving the interpretability of the polarization measurement to humans. Finally, thanks to a small period of metasurface holograms, their field of view is very large, and the projected polarization-dependent image is easily observable by the eyes. Such a device can then become a handy tool in the assembly of optical setups, where it can be quickly used to assess a polarization state at any given point of an optical setup on optical benches.

We acknowledge CzechNanoLab Research Infrastructure supported by MEYS CR (LM2023051). This work was also supported by the Specific research project CEITEC VUT-J-24-8583.

References

[1]. N. M. Garcia, I. Erausquin, C. Edmiston and V. Gruev, "Surface normal reconstruction using circularly polarized light," *Optics Express, Vol. 23, No. 11, 14391-14406*, 2015.

[2] F. Meriaudeau, M. Ferraton and C. Stolz, "Shape from polarization: a method for solving zenithal angle ambiguity," *Optics Letters, Vol. 37, No. 20, 4218-4220,* 2012.

[3] J. De Bruycker, W. Raes, S. Zvánovec, and N. Stevens, "Polarization Differential Visible Light Communication: Theory and Experimental Evaluation," *Sensors, Vol. 20, No. 19, 5661*, 2020.

[4] K. Takei and H. Yamada, "Highly reliable wireless communication system using polarization rotating wave for M2M application," *Electronics and Communications in Japan*, Vol. 102, No. 3, 29–35, 2019.

[5] Rubin NA, D'Aversa G, Chevalier P, Shi Z, Chen WT, Capasso F. "Matrix Fourier optics enables a compact full-Stokes polarization camera," *Science, Vol. 365, No. 6448,* 2019

[6] E. Arbabi, S. M. Kamali, A. Arbabi and A. Faraon "Full-Stokes Imaging Polarimetry Using Dielectric Metasurfaces," *ACS Photonics Vol. 5, No. 8, 3132-3140,* 2018

[7] Y. Ren, S. Guo, W. Zhu, et al., "Full-Stokes Polarimetry for Visible Light Enabled by an All-Dielectric Metasurface," *Adv. Photonics Res., Vol. 3, No. 7, 2100373,* 2022

Conductivity responsive effective permittivity control in GaAs tunable metamaterials

Minyeul Lee[1], Sungyoung Yoon[2], Meehyun Lim[2], Sungyeol Kim[2], and Jonghwa Shin[1*]

[1]Department of Materials Science and Engineering, KAIST, Daejeon, 34141 Korea
[2]Samsung Electronics, Suwon 16677, Republic of Korea
[*]corresponding author: qubit@kaist.ac.kr

Abstract: In this study, we propose a novel metamaterial configuration utilizing semiconductor conductivity to achieve notable tunability in relative permittivity. Theoretical analysis and simulations confirm the efficacy of this approach. Experimental measurement employing GaAs, including capacitance analysis under LED illumination, reveals this metamaterial's tunability.

Precisely managing the electromagnetic fields is crucial in diverse fields like laser techniques and plasma chambers. Traditional methods of manipulating adjacent materials to control electromagnetic fields had limitations of precise and local adjustment, prompting a shift to metamaterials for more accurate and localized field control. While prior research has left progress in electromagnetic modulation [(1)], obstacles persist, notably in achieving substantial changes and simplifying tuning mechanisms.

Here, we introduce a novel metamaterial concept leveraging the tunable conductivity of semiconductors. The proposed design's functionality is validated through theoretical analysis and electrostatic simulations. Furthermore, experimental validation employing capacitance measurement with a GaAs-based sample confirms this metamaterial's tunable behavior.

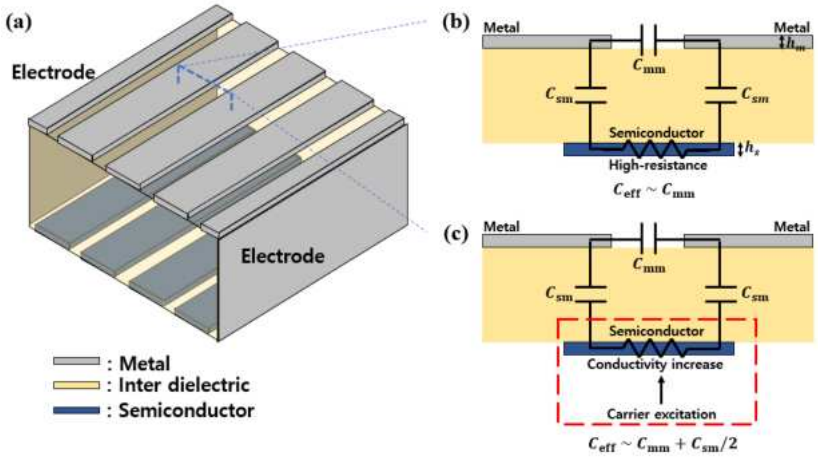
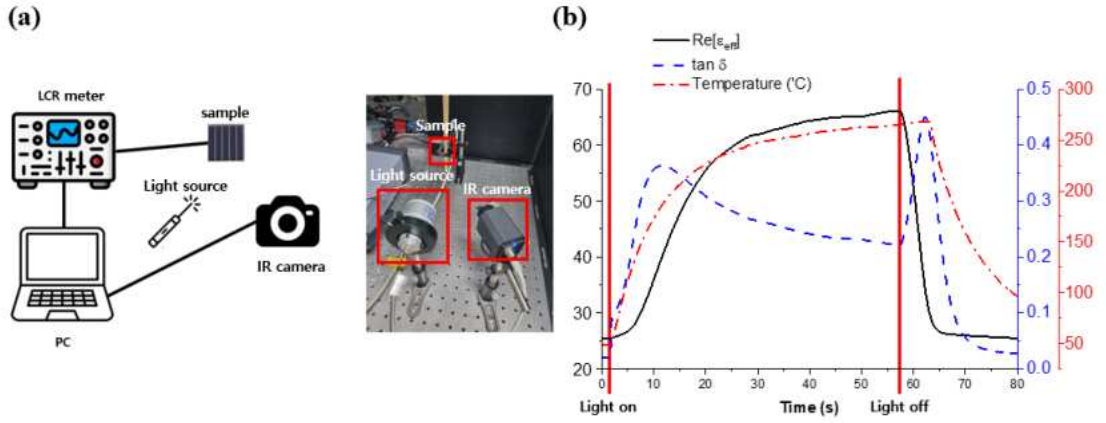


Figure 1. Proposed metamaterial design and working principle analysis from quasi-electrostatic circuit model in the unit cell structure. (a) Schematic of the structure, (b) circuit model and effective capacitance with high-resistance semiconductor and (c) low-resistance semiconductor.

Fig. 1(a) depicts the schematic representation of our metamaterial design, comprising periodic semiconductor

and metal strip-shaped patches arranged in layers, with two layers staggered by half a period. Given the sub-wavelength dimensions of the metamaterial, its operation was elucidated within the quasi-electrostatic regime. Thus, based on the electric circuit analysis, the effective capacitance of one unit cell is determined through the internal capacitor components with a variable resistor that represents the conductivity-variable semiconductor. As demonstrated in Fig. 1(b), when the semiconductor conductivity is low, total capacitance is solely determined by internal capacitance from two metal plates. However, if the semiconductor conductivity becomes sufficiently large, total capacitance increases as an amount of internal capacitance between metal and semiconductor. Detailed value of enhancement can be calculated by using analytical formula derived from quasi-electrostatic assumption:

$$\varepsilon_{\mathrm{eff}} = \frac{a(a-g_{\mathrm{m}}-g_{\mathrm{s}})}{2h_{\mathrm{d}}h_{\mathrm{total}}}\varepsilon_{\mathrm{d}} \tag{1}$$



[Fig.2] (a) experimental setup and (b) measured effective relative permittivity of GaAs-based fabricated sample.

Fig. 2 illustrates the experimental configuration and outcomes of the fabricated GaAs-based metamaterial. The setup utilizes an LED light source to induce conductivity changes in the GaAs semiconductor, and sample temperature is monitored via an IR camera. As depicted in Fig. 2(b), the fabricated metamaterial exhibits a remarkable 2.6 times increase in effective permittivity, closely aligning with the theoretical predictions shown in Fig. 1(b). This newly developed metamaterial holds promise for localized and precise electromagnetic field control.

Acknowledgements

This work was supported by Samsung Electronics Co., Ltd (IO230320-05543-01) and National Research Foundation of Korea (NRF) grants (NRF-2021R1A2C2008687, NRF-2018M3D1A1058998) funded by the Ministry of Science and ICT (MSIT), Republic of Korea.

References

1. Kim, Ju Young, et al. "Highly tunable refractive index visible-light metasurface from block copolymer self-assembly." *Nature communications* 7.1 (2016): 1-9.
2. Chang, Taeyong, et al. "Broadband giant-refractive-index material based on mesoscopic space-filling curves." *Nature communications* 7.1 (2016): 12661.

Real-time terahertz modulation with gold-MoS_2 metasurface

Jianhong Zhang[1], Fangfang Ren[1*], Jiandong Ye[1], Xiaoli Ji[1], and Hai Lu[1]

[1] the School of Electronic Science and Engineering, Nanjing University, Nanjing, China
[*]corresponding author: ffren@nju.edu.cn

Abstract: The authors introduce a method for precise control of terahertz (THz) radiation using a gold split-ring metasurface and MoS_2 layers. Through optical pumping, a high-quality THz signal transmission with 81% modulation depth can be achieved at 0.61 THz, promising advancements in sensing, switching, and filtering for THz applications.

The use of terahertz (THz) radiation, ranging from 0.1 to 10 THz, has gained attention for applications like space exploration, wireless communication, and security checks. Traditional THz devices using natural materials struggle with high modulation depth due to limited interaction with THz signals. Metamaterials, with properties like negative refractive index and perfect lensing, offer potential solutions. This study focuses on metasurface devices with narrowband resonances for advanced THz modulation, aiming for electromagnetically induced transparency-like (EIT-like) resonances with higher quality factors (Q).

The authors demonstrate the modulation of resonance peak intensity by incorporating MoS_2 layers into an asymmetric split-ring metasurface, creating an EIT-like resonance as THz signals traverse the engineered structure. Optical pumps with varying pump fluences are applied to enable real-time manipulation of the EIT-like resonance intensity by adjusting the conductivity in the MoS_2 layers.

The simulation setups using CST studio are employed to analyze the transmission spectra of the proposed hybrid asymmetric split-ring (HASR) metasurface structure. The results demonstrate the emergence of EIT-like resonance profiles under specific structural configurations, particularly when an asymmetric configuration is achieved. To clarify the underlying physical mechanism behind the EIT-like resonance observed in the HASR metasurface structure, the authors conducted calculations to analyze the distribution of surface currents at the transmission resonance peaks or dips, revealing a dipole or quadrupole nature. By systematically varying the structural parameters, the authors delve into the influence of these parameters on the excitation of EIT-like resonances and identifies optimal values for achieving high Q factors and maximizing the modulation depth.

The modulation of the transmission property is investigated under optical excitation with varying pump fluences from 0 to 20.4 $\mu J/cm^2$. In the absence of photoexcitation, an EIT peak emerges amidst two resonance dips, featuring a transmission amplitude of 0.84 at 0.61 THz. As the pump fluence of the pump beam gradually escalates to 20.4 μJ/cm (corresponding to MoS_2 conductivity = 4020 S/m), the EIT transmission decreases in magnitude and undergoes a strong modulation. Consequently, the transmission spectra accomplish a distinctive on-to-off modulation at 0.61 THz characterized by an impressive modulation depth of 81%.

In this modulation process, the recovery time of excited carriers in MoS_2 is approximately in picosecond (ps) range, estimated according to the carrier lifetime of MoS_2.

In summary, the research showcases the potential of metasurface devices for advanced THz modulation through the manipulation of EIT-like resonances. By optimizing structural parameters and conductivity levels within MoS_2 layers, significant modulation depths and precise control over THz signals can be achieved. These findings pave the way for the development of high-speed communication systems and other applications reliant

on THz technology.

The authors acknowledge the National Key Research and Development Program of China (2021YFB3600101) the National Natural Science Foundation of China (62234007, 62293521, U21A20503, U21A2071) for financial support.

References

1. H. T. Chen, W. J. Padilla, J. M. O. Zide, A. C. Gossard, A. J. Taylor and R. D. Averitt, “Active terahertz metamaterial devices, ” Nature, Vol. 444, No. 7119, 597– 600, 2006.
2. M. Liu, E. Plum, H. Li, S. Duan, S. Li, Q. Xu, X. Zhang, C. Zhang, C. Zou, B. Jin, J. Han and W. Zhang, “Switchable chiral mirrors, ”Adv. Opt. Mater., Vol. 8, No. 15, 2000247, 2020.
3. S. E. Harris, J. E. Field and A. Imamoglu, “Nonlinear optical processes using electromagnetically induced transparency, ” Phys. Rev. Lett., Vol. 64, No. 10, 1107–1110, 1990.

Realizing an acoustic T-shaped superscatterer with inverse design

Di Wang[1], Zhongming Gu[1] and Jie Zhu[1]

[1] Institute of Acoustics, School of Physics Science and Engineering, Tongji University, Shanghai 200092, People's Republic of China

Abstract: We present an inverse design approach aimed at realizing efficient and straightforward structures capable of achieving superscattering of ultrasound in water. Through a combination of numerical simulations and experimental investigations, we demonstrate the effectiveness of the proposed super scatterer in significantly enhancing ultrasound backscattering when compared to a rigid cylinder.

Summary

In this work, we propose an effective approach for designing an acoustic super scatterer adorned with T-shaped structures to significantly enhance the sound scattering performance in water. The T-shaped structures are strategically employed to enrich resonant modes and surpass the single-channel limit [1,2]. In order to optimize the structural parameters of the decorations and achieve maximum scattering cross section, we employ the genetic algorithm for global optimization. As a result, the super scatterer exhibits a considerably larger ultrasound shadow region [Fig. 1(b)] in comparison to a cylindrical scatterer with the same diameter [Fig. 1(a)].

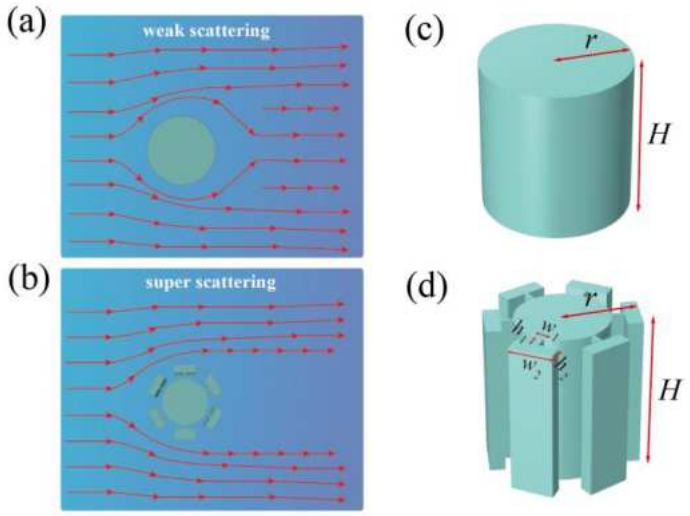


Figure.1 Conceptual schematic of the superscattering effect. (a) and (b) The power flow distribution with the plane ultrasound wave incident from the left. (c) and (d) Models of the cylindrical scatterer and super scatterer.

The T-shaped structures are periodically decorated around the super scatterer, as depicted in Fig. 1(d), which possess four adjustable variables: the length h_1, h_2 and the width w_1, w_2, as well as keep the same radius r with the rigid cylinder in Fig. 1(c). The genetic algorithm is combined with the finite element method to optimize the appropriate geometric parameters, which are all considered as degrees of freedom in the optimization process. It aims to identify the best fit values for the target variables. Subsequently, simulations and calculations are conducted to assess the efficacy

of the proposed methodology. The results obtained through these analyses unequivocally demonstrate that the scattering phenomenon induced by the super scatterer significantly exceeds that of the cylinder scatterer at the target frequency as shown in Figs. 2(a) and (b).

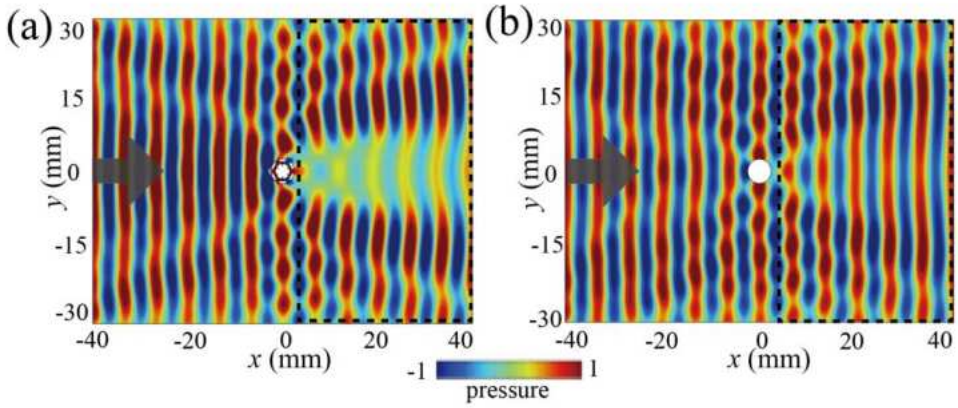


Figure. 2 Numerical simulations of acoustic fields. (a) and (b) Simulated acoustic fields for the super scatterer and cylindrical scatterer, respectively.

Furthermore, we conduct the experimental verifications to validate the superscattering phenomenon. The stainless-steel samples are fabricated using 3D metal printing technology. Besides, all experiments are performed in a dedicated scanning tank and measurements are obtained using an automated scanning system. Notably, the experimental results obtained in water exhibit agreement with the corresponding simulations. The measured data provide compelling evidence of the strong backscattering exhibited by the superscatterer unit. Importantly, it should be emphasized that the working frequency can be arbitrarily tuned by adjusting the structural parameters.

In conclusion, this study successfully achieves ultrasound superscattering in water through the incorporation of T-shaped decorations, which introduces additional resonance modes. By employing an inverse design approach that includes the genetic algorithm and finite element method, we are able to optimize the acoustic super scatterer while considering the complex fluid-structure interaction without relying on complex analytic calculations. The simulation results and experimental measurements exhibit well agreement, validating our proposed model and its superscattering capabilities. The implications of this work extend to various fields where enhanced scattering is demanded, including applications such as acoustic radiation force and medical ultrasound imaging.

ACKNOWLEDGEMENTS

This work was supported by the National Key R&D Program of China (No. 2022YFA1404400), Research Grants Council of Hong Kong SAR (Grant AoE/P-502/20), National Natural Science Foundation of China (No. 92263208 and 12304494).

References

[1] Z. Ruan and S. Fan, *Superscattering of Light from Subwavelength Nanostructures*, Phys. Rev. Lett. **105** (1), 013901 (2010).

[2] Z. Ruan and S. Fan, *Design of subwavelength superscattering nanospheres*, Appl. Phys. Lett. **98** (4), 043101 (2011).

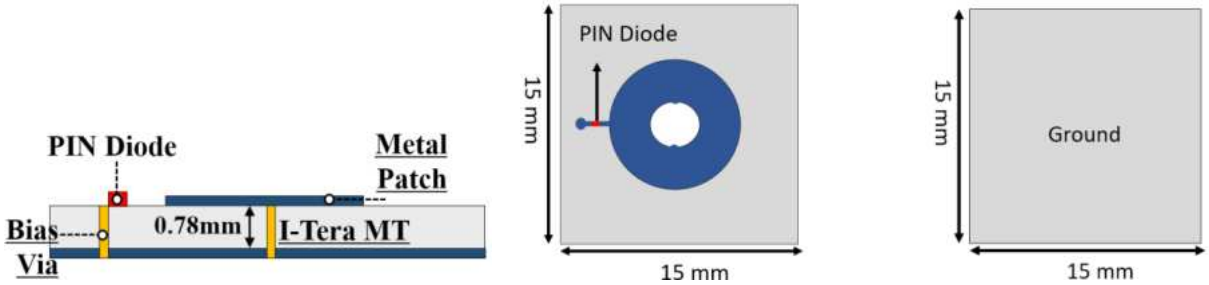
Design of a 3D Reconfigurable Intelligence Surface

B. Rana[1], S.-S. Cho[2], and I.-P. Hong[2*]

[1]Smart Natural Space Research Center, Kongju National University, Cheonan 31080, South Korea
[2] Department of Smart Information Technology Engineering, Kongju National University, Cheonan 31080, South Korea
[*]corresponding author: iphong@kongju.ac.kr

Abstract: In this work, a novel type of reconfigurable intelligent surface (RIS) has been proposed. We have designated these RIS types as '3D RIS.' One advantage that these types of RIS have over traditional RIS is their ability to steer the beam in full space.

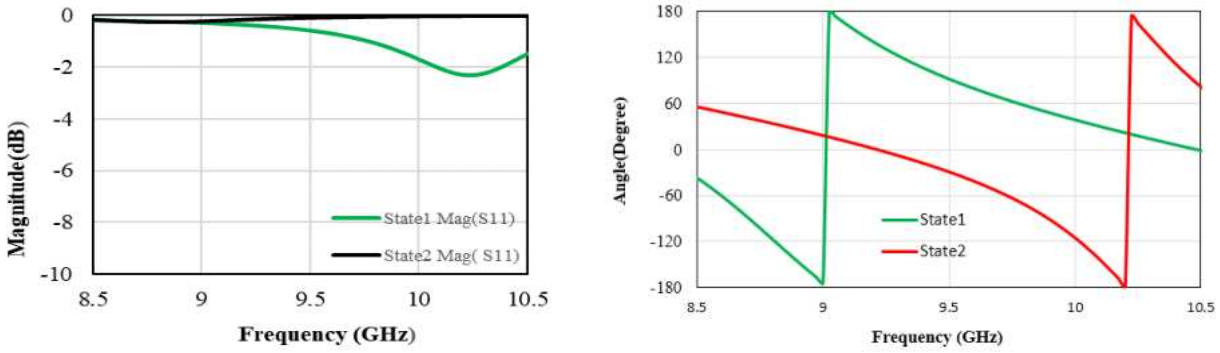
Recent research [1-2] suggests that RIS will be the technology of choice for wireless communications applications. The literature describes various types of RIS, including transmissive and reflective [4-5] types, as well as combinations of both reflective and transmissive types, etc. RIS can be categorized into different groups based on various criteria [3]. In this work, we initially designed a 1-bit reflective type of RIS, as illustrated in Figure 1. Figure 1(a) shows a side view of the unit cell, while Figure 1(b) depicts the top view, and Figure 1(c) shows its bottom view.



(a) (b) (c)

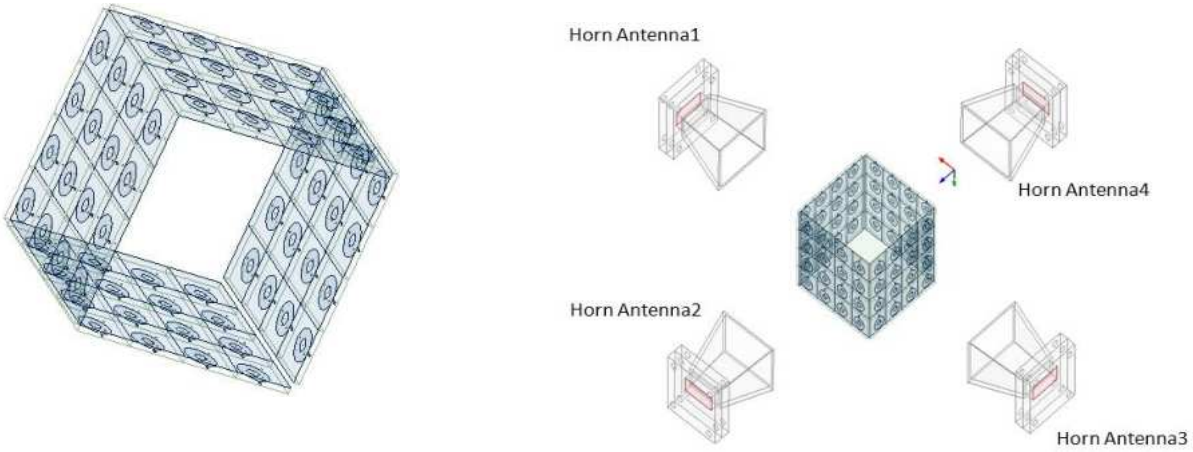
Figure 1: (a) Side view of unit cell (b) top view of the unit cell (c) bottom view of the unit cell

The performance of the unit cell is shown in Figure 2. Figure 2(a) illustrates the magnitude of S_{11} for two different states, indicating magnitudes of -0.31 dB and -0.24 dB observed at 9 GHz. Figure 2(b) displays the



(a) (b)

Figure 2: (a) Magnitude of S_{11} for State1 and State2 (b) Phase of S_{11} for State1 and State2



(a) (b)

Figure 3: (a) Proposed 3D RIS (b) Four horn antenna with proposed 3D RIS

phase of the reflection coefficients at 9 GHz. It is noted here that the unit cell was optimized at 9 GHz for this design. After evaluating the performance of the unit cell, a 3D RIS structure, as shown in Figure 3(a), was proposed. Four planes of the 4×4-unit cell were combined, as depicted in Figure 3(a), to form the 3D RIS structure. To assess the performance of the 3D RIS, four X-band horn antennas, illustrated in Figure 3(b), were designed and positioned in front of the 3D RIS. While similar theoretical concepts have been proposed in the literature, to the best of the authors' knowledge, hardware implementations for this specific type of 3D RIS have not yet been documented. The advantages of this 3D RIS type include its capability to accept incoming signals from various directions and steer the beam as desired. It is noteworthy that in our proposed design, two additional planes can be added, enabling the reflected beam to be steered in all possible directions.

This work was supported in part by the Basic Science Research Program under grant 2020R1I1A3057142, in part by the Priority Research Center Program through the National Research Foundation under Grant 2019R1A6A1A03032988, and in part by the research grant of Kongju National University in 2024.

References

1. Rana, B., Cho, S-S, and Hong, I.-P. "Review paper on hardware of reconfigurable intelligent surfaces," IEEE Access, Vol. 11, 29614 - 29634, 2023.
2. E. Basar, M. Di Renzo, J. De Rosny, M. Debbah, M.-S. Alouini, and R. Zhang, "Wireless communications through reconfigurable intelligent surfaces" IEEE Access, Vol. 7, No. 116753–116773, 2019.
3. H. Li, S. Shen, M. Nerini and B. Clerckx, "Reconfigurable intelligent surfaces 2.0: Beyond diagonal phase shift matrices," EEE Comm. Magazine, Vol. 62, No. 3, 102–108, 2024.

Flexible metamaterial absorber on custom-engineered polymer nanocomposites as substrates

Kumaran, R.[1], Siva Bhagavathi, L. G[2], Rahul Manohar O[1], Anjali M[1], Vijayashri V[2], Chitti Venkata Krishnamurthy[1] and Subramanian, V[1,*]

[1]Microwave Laboratory, Department of Physics, Indian Institute of Technology Madras, Chennai - 600036, India.

[2]Department of Physics, Meenakshi College for Women (Autonomous), Kodambakkam, Chennai – 600024, India.

[*]Corresponding Author: manianvs@iitm.ac.in

Abstract: A thin, flexible metamaterial-based transmission-type absorber is designed and fabricated on a custom-engineered substrate prepared using silver nanoparticles decorated MWCNT embedded in an epoxy resin polymer. This absorber gives a maximum absorption of 97% at 11.6 GHz with a bandwidth of 0.75 GHz. Fabrication, simulation, and experimental details are presented.

Microwave absorbers are very useful for the defense industry, anechoic chambers, consumer electronics, bolometers etc. Conventional absorbers are generally bulky and do not have frequency frequency-selective nature. In this aspect, metamaterial structures help fabricate thin absorbers for selected frequency ranges. These MMAs are generally designed and fabricated with FR4 as substrates that are not flexible and require more than one resonating element to enhance the bandwidth. Moreover, one cannot modify the property of the substrates to have more loss to improve the bandwidth of absorption. To find the solution for both these problems, one has to fabricate custom-engineered substrates that would have optimum dielectric and magnetic properties for reducing the footprint, introducing flexibility, and enhancing the bandwidth with a simple single-resonating element [1]. To achieve these requirements, one should use polymer nanocomposites that give flexibility in manipulating the properties. It is well known that the properties of the insulating polymers can be tailor-made using different morphologies like spherical particles, 1-D nanotubes, and sheets. Among various electrically conducting fillers, silver nanoparticles, carbon nanotubes, and graphene sheets play a vital role in manipulating the dielectric properties of the composite at microwave frequencies [2].

In this paper, we report the preparation of silver nanoparticles decorated acid-functionalized multiwalled carbon nanotubes embedded in an epoxy resin polymer as a substrate to fabricate a flexible, good bandwidth, and miniaturized metamaterial absorber having a simple resonating structure. The conducting fillers (Ag-MWCNT) were synthesized through chemical methods and reinforced with epoxy (by varying the wt%) through step-wise curing at 90°C for 18 hrs to get polymer nanocomposites of 1.45 mm thickness. The XRD and IR measurements confirmed the presence of Ag-MWCNT and epoxy polymers. The decorations of Ag on MWCNT were confirmed using SEM and HRTEM images. The sample was cut into a sheet of 22 mm × 11 mm such that it fits into the WR-90 waveguide to measure the dielectric permittivity at the X-band (8 to 12 GHz) frequency range. The real part of the relative dielectric permittivity (ε_r') of the substrate varies between 6 and 7 and the loss tangent ($tan\delta$) was around 0.15-0.18. Using this dispersion data, a full wave simulation software CST Microwave Studio® was used to design a simple metamaterial structure on both sides of the sample. Figure 1 shows the front and back sides of the MM structure. The simulated structure had an absorption of over 90% between 10.85 and 12.04 GHz with a

maximum absorption of 97.6% at 11.4 GHz. The structure was fabricated on the polymer substrate and the experiment was performed by keeping the sample in the WR-90 waveguide to obtain the scattering parameters. The obtained absorption indicates a maximum value of 97.3% at 11.26 GHz. Figure 2 provides the comparison between the simulated and fabricated MMA devices showing an excellent match. With a sub-wavelength thickness of only 1.45 mm (0.048λ), this metamaterial absorber is a promising candidate for developing frequency selective, transmission type thin flexible absorber.

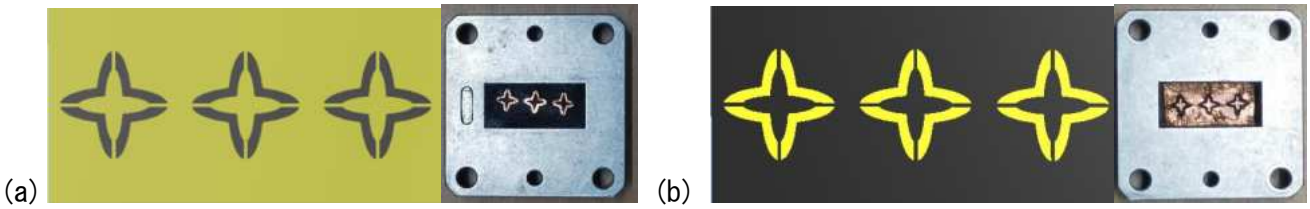


Figure 1. a) Top and (b) bottom views of the proposed metamaterial absorber along with their photographs.

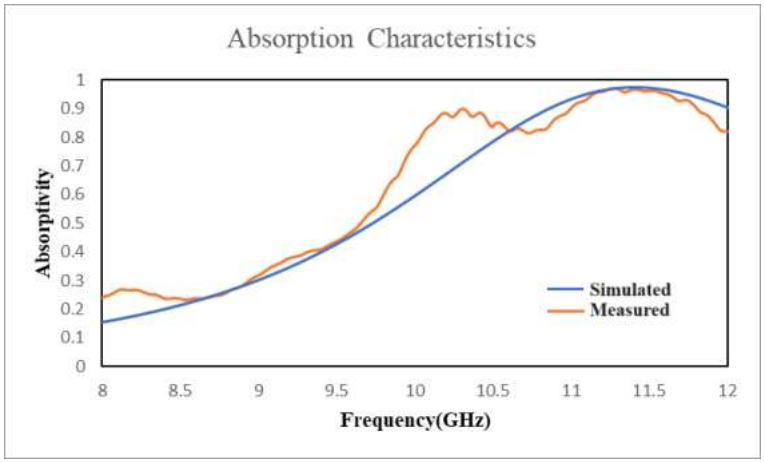


Figure 2: The simulated and experimentally measured absorption data for the developed MMA.

The authors acknowledge the partial financial support through the Institute of Excellence, IIT Madras funding for Microwave and Millimeter Wave Studies (SB/22-23/1265/PHETWO/008421).

References

1. Anjali M, Kumaran Rengaswamy, Abhishek Ukey, Lincy Stephen, C V Krishnamurthy, V Subramanian. “Flexible metamaterial based microwave absorber with epoxy/graphene nanoplatelets composite as substrate,” Journal of Applied Physics, Vol. 133, 063105, 2023.
2. R. Kumaran, A. Vinaya Kumar, S. Ramaprabhu, V. Subramanian, “Absorption enhanced EMI shielding using silver decorated three-dimensional porous architected reduced graphene oxide in polybenzoxazine matrix,” New Journal of Chemistry, Vo. 42, 12945, 2021.

Dynamic medium based on tunable transmissive metasurfaces

Zhedong Wang [1, 2, 3], Chao Qian [1, 2, 3], and Hongsheng Chen [1, 2, 3]

(1) ZJU-UIUC Institute, Interdisciplinary Center for Quantum Information, State Key Laboratory of Extreme Photonics and Instrumentation, Zhejiang University, Hangzhou 310027, China.

(2) ZJU-Hangzhou Global Science and Technology Innovation Center, Key Lab. of Advanced Micro/Nano Electronic Devices & Smart Systems of Zhejiang, Zhejiang University, Hangzhou 310027, China.

(3) Jinhua Institute of Zhejiang University, Zhejiang University, Jinhua 321099, China.

wangzhedong@zju.edu.cn, chaoq@intl.zju.edu.cn and hansomchen@zju.edu.cn

***Abstract*—Here, we introduce dynamic dielectrics medium driven by transmissive tunable metasurfaces. Through the variations of structure or incorporating varactor diode, the metasurfaces exhibits the equivalent electromagnetic features similar to true medium based on the effective medium theory. We validate the viability of dynamic dielectrics and arbitrary permittivity medium.**

I. Introduction

Recent advancements in computational inverse-design approaches have begun to reshape the landscape of structures available in domains of photonics such as nanophotonics and metasurfaces [1], [2]. The methods used to perform structural optimization involve machine learning model, heuristic method (genetic method) or gradient-based approaches (topology optimization) [3], [4]. In the process, the distribution of dielectric medium is gradually optimized to perform ideal optical response. Yet, once the design is complete, the function of the device is fixed, lacking the broad applicability of diverse targets and cannot fulfill the grow demand of real-time and multi-functions for intelligent photonic devices.

In this contribution, we introduce a design strategy that render the transmissive metasurfaces serves as an alternative of dielectric medium in optimization and operation, and give the ability of real-time manipulation of the permittivity based on the equivalent medium theory. The basic thrust of the tunable metasurfaces design stems from the prior knowledge that the incorporated varactor diode or variation of surface structure dimension changes the S parameters of metasurfaces, thus allowing the metasurfaces to serve as a medium whose permittivity depends on the imposed bias voltages. This fine control can achieve arbitrary continuous dielectric constant values, thus reducing the strict requirements for multiphase dielectric medium distribution and improving the convergence speed of optimization. Treating the meta-atom as a tunable dielectric unit, a reconfigurable dynamic focus and the design flowchart are demonstrated. Such on-site regulation features exhibit a promising potential of intelligent photonics devices with multiple functionalities, meanwhile improving the applicability and robustness.

II. Theory And Methodology

According to the effective medium theory, tunable metasurfaces can be equivalent to the corresponding medium with relative permittivity ε and permeability μ [5], [6]. Assuming that a plane wave impinges vertically onto the metasurface slab with thickness d, to retrieve the constitutive parameters, we characterize it as a homogeneous material when d is far less than the incident wavelength λ_0. The S parameters can be formulated as,

$$S_{11} = \frac{R_{01}(1 - e^{i2nk_0d})}{1 - R_{01}^2 e^{i2nk_0d}} \tag{1}$$

$$S_{21} = \frac{(1 - R_{01}^2)e^{i2nk_0d}}{1 - R_{01}^2 e^{i2nk_0d}} \tag{2}$$

where $R_{01} = \frac{z-1}{z+1}$, z is the impedance, and n is the refractive index. Inverting Eq. 1 and Eq. 2, z and n can be derived as,

$$z = \pm\sqrt{\frac{(1 + S_{11})^2 - S_{21}^2}{(1 - S_{21})^2 - S_{11}^2}} \tag{3}$$

$$n = \frac{1}{k_0 d}\{[\ln(e^{ink_0d})]'' + 2m\pi] - i[\ln e^{ink_0d}]'\} \tag{4}$$

Here m is an integer related to the branch index of n'. n' can be obtained by a Taylor expansion approach. Here, ε and μ, as frequency-dependent complex functions, can be extracted as $\varepsilon = n/z$ and $\mu = nz$.

III. Validation

A. Arbitrary permittivity dielectric medium

To be specific, assuming a plane wave impinges onto the metasurfaces vertically where the wave vector is along the negative z-axis. The top layer is rectangular metal patch with the width W. The bottom layer is dielectric substrate with the relative permittivity ε_r = 3.5 (Fig. 1) and the length L = 6 mm. Because the E-field vector is along the y-axis and H-field vector is along the x-axis, the ε_y and μ_x need to be considered as the permittivity and permeability of the effective medium. We set W ranging from 1 mm to 2 mm with the step size of 0.2 mm and the measured permittivity is from 2.83 to 4.45. The retrieved real part of permeability is around 0.995 to 0.998.

And the imaginary part of ε_y and u_x is very close to 0. Thus, the property of the metasurface can be treated as a varying dielectric medium. With the L continuously changing, the effective permittivity of metasurface apparently continuously changes.

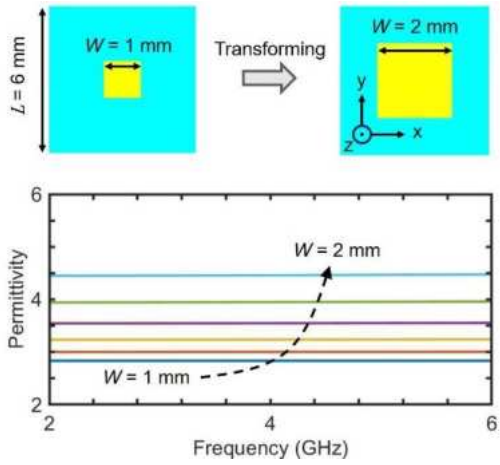


Fig. 1. The front view of metasurface and the retrieved permittivity curves for different metal patches' widths.

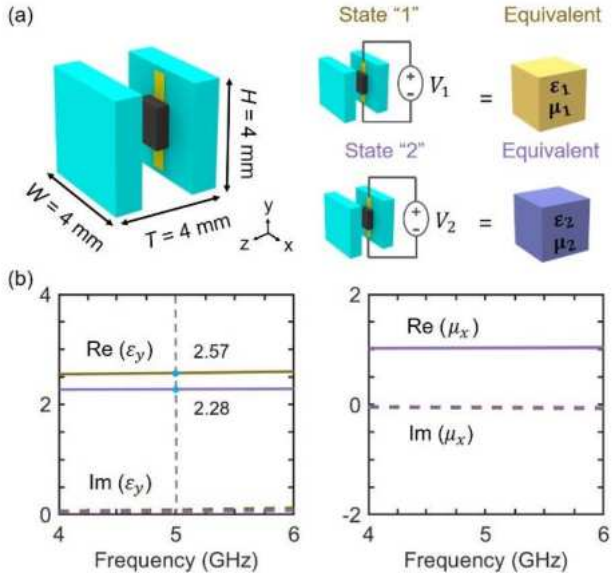


Fig. 2. a, The geometry of tunable metasurface and the corresponding equivalent dielectric under different bias voltages. b, the permittivity and permeability of metasurface when the capacitance of diodes are 0.06 pF and 0.6 pF in 4 – 6 GHz.

B. Dynamic medium based on varactor diodes

The metasurface integrated with varactor diodes can also serve as the dynamic dielectric medium. Tuning the bias voltage on the varactor diodes will change the S parameters of metasurfaces (S_{11} and S_{21}), thus, based on the theory in section 2, it also affects the equivalent constitutive parameters. As a demonstration, the geometry of the designed transmissive metasurface is shown in Fig. 2(a). The meta-atom has three layers; the top and bottom layers (blue blocks) are 1 mm thick F4B substrate with the relative permittivity of 2.55 and the loss tangent of 0.001, and the middle layer is air. The length of cube meta-atom is 4 mm (W, T, H). Two metallic arm-like resonators are etched upon the bottom layer, between which a varactor diode is welded (Aeroflex MGV 125-08). The arm's width b is 0.6 mm and the length h is 1 mm. Without loss of generality, we pick up two states of diode's capacitance (0.6 pF and 0.06 pF) as example, which means that each meta-atom can freely toggle between the two states. Fig. 2(b) shows the retrieved parameters. The retrieved ε_y are 2.28 and 2.57 when the meta-atom works at state "1" and state "2" respectively. For u_x, its real part approaches 1. Both the imaginary part of ε_y and u_x is close to 0.

C. Conclusions

In summary, equivalent dynamic dielectric medium constructed by transmissive metasurfaces have been demonstrated in this work. Based on the effective medium theory, we utilize the change of dimension of metasurface structure to realize the variation of permittivity continuously. Moreover, through biased voltage controlling, the metasurfaces loaded with varactor diodes can be treated as on-site tunable dielectrics. The diodes can respond in microsecond, providing a promising approach to real-time material optimization. Our strategy also can be extended to other multi-functional optical devices with wide band, large scale, and high efficiency, paving the way for the next generation of intelligent photonics devices.

ACKNOWLEDGMENT

The work at Zhejiang University was sponsored by the Key Research and Development Program of the Ministry of Science and Technology under Grants No. 2022YFA1404704, 2022YFA1405200, and 2022YFA1404902, the Key Research and Development Program of Zhejiang Province under Grant No.2022C01036, and the Fundamental Research Funds for the Central Universities.

REFERENCES

[1] S. Molesky et al, "Inverse design in nanophotonics.", *Nature*, vol. 12, pp. 659–670, October 2018.

[2] P. Naseri and S. V. Hum, "A generative machine learning-based approach for inverse design of multilayer metasurfaces," *IEEE Trans. Antennas Propag.*, vol. 69, pp. 5725–5739, September 2021.

[3] X. Liu et al., "Ultrabroadband all-dielectric transmitarray designing based on genetic algorithm optimization and 3-D print technology," *IEEE Trans. Antennas Propag.*, vol. 69, pp. 2003–2012, April 2021.

[4] E. Hassan et al., "Multilayer topology optimization of wideband SIWto-waveguide transitions," *IEEE Trans Microw Theory Tech*, vol. 68, pp. 1326–1339, April 2020.

[5] D. R. Smith et al., "Determination of effective permittivity and permeability of metamaterials from reflection and transmission coefficients," *Phys. Rev. B*, vol. 65, April 2002.

[6] X. Chen et al., "Robust method to retrieve the constitutive effective parameters of metamaterials," *Phys. Rev. E*, vol. 70, July 2004.

An active Fabry–Pérot interferometer operated at terahertz frequencies based on pitch-variable subwavelength gratings

Y. Huang[1], Y. X. Liu[1], T. Okatani[1], N. Inomata[1], and Y. Kanamori[1*]

[1]Department of Robotics, Tohoku University, Japan
[*]Corresponding author: ykanamori@tohoku.ac.jp

Abstract: We constructed, for the first time, an active Fabry–Pérot interferometer (FPI) operated in the terahertz range by properly integrating a pitch-variable subwavelength-grating (PV-SWG) into an FP cavity. The period of PV-SWG can be varied to change the effective refractive index and shift the optical resonant frequency of the FPI.

1. INTRODUCTION

The waveband of 0.318–0.333 Terahertz (THz) is potential to develop high-speed (~Tb/s) wireless communications[1]. The Fabry–Pérot interferometer (FPI) is a candidate to spectrally filter the waves in this band. Conventional active FPIs tune the resonant frequency by moving the mirror[2] or filling the cavity with the liquid crystal[3], which lead to a lower quality factor (Q-factor) and peak transmittance. In this work, we constructed an active FPI based on subwavelength gratings (SWGs) that exhibits controllable effective refractive indices[4]. The proposed FPI achieves a high Q-factor and peak transmittance.

2. DESIGN

The proposed FPI is schematically shown in Fig. 1. The FPI consists of a pair of Si mirrors separated by an air cavity and an individually adjustable PV-SWG (Fig. 1(a)). As the PV-SWG horizontally deforms, the lattice period p varies and contributes to a change in the effective refractive index n_{SWG} (Fig. 1(b)); the resonance of the FPI then shifts correspondingly (Fig. 1(c)). The geometry of the FPI was designed to obtain an optimal transmittance by performing parameter-sweep calculations using the rigorous coupled-wave analysis method via DiffractMOD. A p of 100 μm, a of 85 μm, t of 200 μm, and d of 1620 μm were determined.

3. EXPERIMENTS

The PV-SWG was fabricated with standard surface micromachining technologies (Fig. 2). The cleaned Si wafer underwent photolithography patterning and ICP-RIE etching followed by resist removal to form the PV-SWG, and then was inserted into a pair of Si mirrors on a holder with a fixed anchor and a movable handle (Fig. 3). The optical performances were measured via a THz time-domain spectrometer (THz-TDS). A sharp peak was found at 0.303 THz in the transmittance spectrum of the FPI with an initial p of 100 μm, the measured Q-factor was 34, and the peak transmittance was 0.87 (Fig. 4). By stretching the movable handle, the pitch of the PV-SWG was varied from the initial p of 100 μm to 150 μm, as a result, the n_{SWG} of the PV-SWG decreased from 2.08 to 1.50, and the measured optical resonant frequency (f_{or}) increased from 0.303 THz to 0.320 THz (Fig. 5).

4. CONCLUSIONS

In conclusion, an active FPI based on effective refractive index control of a PV-SWG was numerically and experimentally proposed. A tunable transmittance peak of a maximum of 0.87 and a Q-factor of 34 for waves around 0.303 THz in frequency was achieved by the PV-SWG-based FPI. The proposed FPI contributes to the development of THz communications.

Acknowledgements: JST, CREST Grant Number JPMJCR2102, Japan.

References

1. Kumar, A., Gupta, M., Pitchappa, P., et al., "Terahertz topological photonic integrated circuits for 6G and beyond: A Perspective", J. Appl. Phys., Vol. 132, No. 14, 140901 (2022).
2. Cai, L., Wang, J., Pan, J. Y., et al., "A tunable fiber-optic Fabry–Pérot cavity formed between a silica microsphere and a target", Opt. Commun., Vol. 459, 124996 (2020).
3. Park, H., Parrott, E. P. J., Fan, F., et al., "Evaluating liquid crystal properties for use in terahertz devices", Opt. Express Vol. 20, No. 11, 11899-11905 (2012).
4. Kanamori, Y., Sasaki, M., and Hane, K., "Broadband antireflection gratings fabricated upon silicon substrates", Opt. Lett., Vol. 24, No. 20, 1422-1424 (1999).

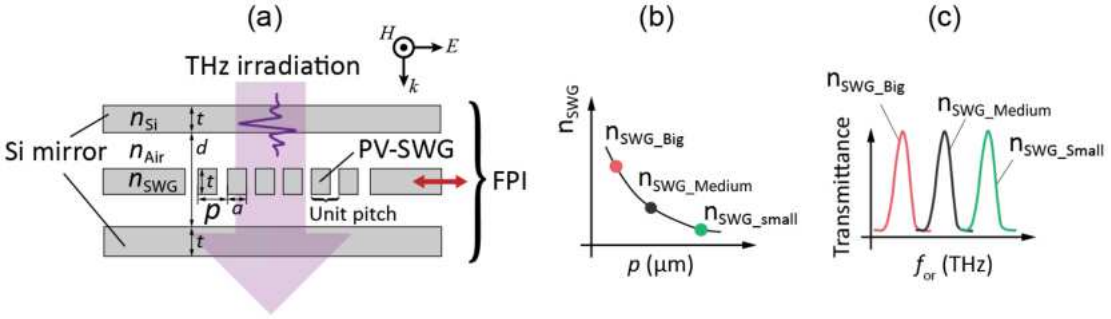


Fig. 1. Schematic of the (a) proposed FPI, (b) n_{SWG} versus p of the PV-SWG, and (c) transmittance of the FPI.

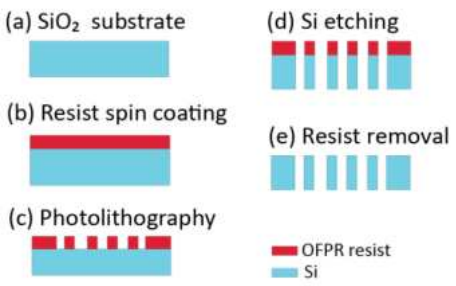


Fig. 2. Fabrication processes of the PV-SWG.

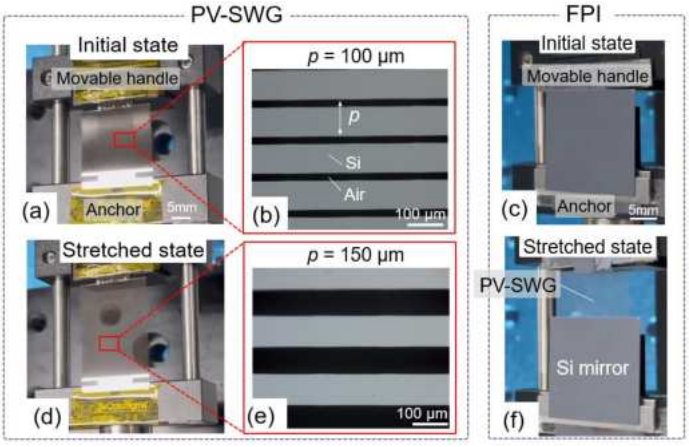


Fig. 3. Fabricated PV-SWG and FPI.

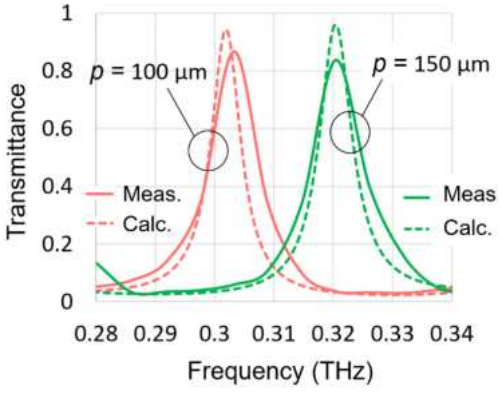


Fig. 4. Transmittance of the FPI.

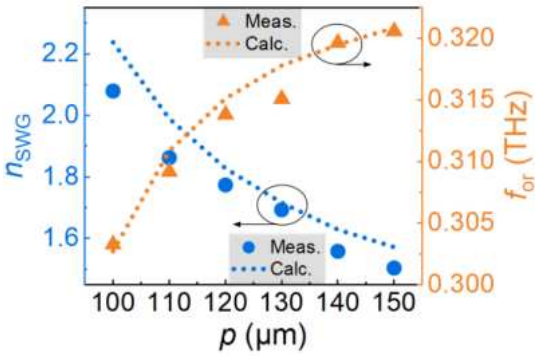


Fig. 5. n_{SWG} and f_{or} versus p of the FPI.

300-GHz-band transmission-type beamforming metasurface for an outdoor-to-indoor signal coverage extension for future wireless networks

A. Pander*, H. Kagami, D. Kitayama, and H. Takahashi

[1]NTT Device Technology Labs., NTT Corporation, 3-1 Morinosato-Wakamiya, Atsugi, Kanagawa, 243-0198, Japan

*Corresponding author: adam.pander@ntt.com

Abstract: 300-GHz-band transmission-type metasurface beamformers were designed, fabricated, and evaluated. Beamforming angles in the range of 18° to 38° with a transmission loss of about 4 dB were achieved. Flexibility, good transparency, and broadband operation of the fabricated self-standing devices make them perfect candidates for future outdoor-to-indoor signal coverage extension applications.

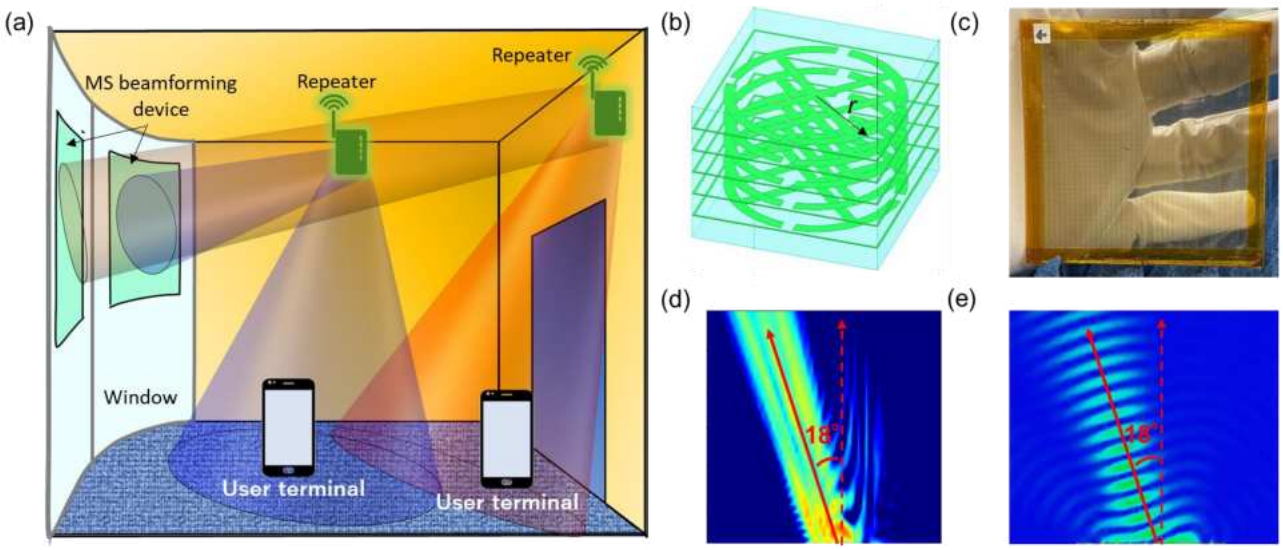


Fig. 1. (a) Schematic representation of the application of passive beamforming metasurfaces in the outdoor-to-indoor signal coverage extension at 300-GHz-band. (b) Schematic of a multilayer metamaterial cell with continuous 2π phase designability. (c) Image of fabricated self-standing beamforming device. (d) The experimental and (e) simulation results of 18° angle beamforming at 300-GHz-band.

In recent years, to meet the constantly increasing demand for larger bandwidth and higher data rates in wireless communication, millimeter-wave frequencies from 30 GHz to 500 GHz became a major development direction to realize high data transmission and high-capacity networks that can support simultaneous users. Despite the promising properties of the high-frequency waves, large space path losses, atmospheric attenuation in gases and rainfall, and non-line-of-sight (NLOS) propagation became the main challenges to overcome [1, 2]. To solve these issues highly-directive millimeter-wave antennas that can configure their radiation pattern to avoid obstacles are required. For this reason, the development of various beamforming techniques, including metamaterial-based designs at millimeter-wave bands, is carried out.

One of the major development directions for passive metasurface (MS) devices at 300-GHz-band wireless communication is the extension of signal coverage. By placing metasurface on various flat and curved surfaces,

such as windows, (Fig.1(a)) is possible to steer the incident beam in the desired direction, for example from the outdoor to the indoor and the other way around [3, 4]. Generally, 300-GHz-band beam steering is difficult to obtain with single-layer binary metasurfaces due to limited phase control and low design efficiency; thus, multilayer metamaterial structures with continuous 2π phase designability are necessary.

In this study, we present a multilayer cell design composed of five layers that can control the transmission phase in over 2π range throughout the change of the radius, *r*, of the structure, as shown in Fig. 1(b). Based on the designed cells, transmission-type devices with different predesigned beamforming angles were fabricated and evaluated. The devices were fabricated using an in-house developed process. An epoxy film was laminated onto the precleaned glass substrates, and the fabrication of metallic patterns was carried out using the conventional photolithography method and electron beam evaporation. The lamination process was repeated five times to form a multilayer structure. As the last step, the device was separated from the bare substrate. An example of a fabricated device is shown in Fig 1(c).

With the successful fabrication of transmission-type metasurfaces, the basic characteristics of the beamforming devices were evaluated. The set of beamforming metasurfaces showed the beam steering angles between 18° and 38° at 300-GHz-band (Fig. 1(d)). The obtained results were in good agreement with the results obtained in the simulation (Fig. 1(e)). The frequency dependency of the fabricated samples was also investigated in the frequency range between 285 and 315 GHz. Only a minor change in the beamforming angle was observed at higher frequencies above 310 GHz. Furthermore, since the devices were stripped from the carrier substrate, the transmission loss was easily evaluated and was within the range of 4-5 dB.

In addition to the evaluated beamforming characteristics, investigated devices exhibited good flexibility and optical transparency of about 60% which makes them very good candidates for low-profile devices that are mounted on buildings, vehicles, and so on.

To the extent of our knowledge, this is the world-first transmission-type metasurface device that combines good flexibility, optical transparency and self-standing design with very good beamforming characteristics, such as low loss, high beam steering angles, good transmission efficiency and broadband operation at 300-GHz-band. The presented device can be successfully applied in the outdoor-to-indoor signal coverage extension in future 6G wireless networks.

References

[1] M. Inomata, W. Yamada, N. Kuno, M. Sasaki, K. Kitao, M. Nakamura, T. Tomie, and Y. Oda, “Sub-terahertz propagation characteristics up to 150 GHz for 6G mobile communication systems,” Int. J. Microw. Wirel. Technol. 15(1), 51–58, 2023.

[2] International Telecommunication Union Recommendation ITU-R P.676-12, Attenuation by Atmospheric Gases and Related Effects, 2019.

[3] D. Kitayama, Y. Hama, K. Goto, K. Miyachi, T. Motegi, and O. Kagaya, “Transparent dynamic metasurface for a visually unaffected reconfigurable intelligent surface: controlling transmission/reflection and making a window into an RF lens,” Opt. Express 29(18), 29292–29307, 2021.

[4] NTT DOCOMO (January 30, 2023), “DOCOMO Conducts World's First Trial of Transmissive Metasurface on Window to Deliver Indoor Radio Waves to Outdoor Foot of Building—Millimeter-wave connection improved at foot of building” [Press Release], https://www.docomo.ne.jp/english/info/media_center/pr/2023/0130_02.html

Giant Optical Anisotropy in van der Waals Materials:Perspectives and Challenges

V. S. Volkov[1*], G. A. Ermolaev[1], D. V. Grudinin[1] , K. V. Voronin[2] , A. A. Vyshnevyy[1] , A. B. Mazitov[3], G. I. Tselikov[1] , I. A. Kruglov[1] , D. A. Ghazaryan[4] , L. Martin-Moreno[5] , A. V. Arsenin[1], and K. S. Novoselov[6]

[1]XPANCEO Emerging Technologies Research Center, UAE
[2]Donostia International Physics Center (DIPC), Spain
[3]Institute of Materials, École Polytechnique Fédérale de Lausanne,Switzerland
[4]Laboratory of Advanced Functional Materials, Yerevan State University, Armenia
[5]Instituto de Nanociencia y Materiales de Aragón (INMA), CSIC-Universidad de Zaragoza, Spain
[6]Department of Materials Science and Engineering, National University of Singapore, Singapore

[*]corresponding author: vsv@xpanceo.com

Abstract: Van der Waals materials are at the core of modern optoelectronics and nanophotonics. However, relatively litlle research attention is devoted to their giant optical anisotropy. Here, we demonstrate that the use of giant anisotropy leads to the next-generation integrated circuits and optical elements.

Materials with high optical anisotropy are of great importance in technology and science [1]. Recently, one of the largest birefringence in the visible and near-infrared intervals up to 0.8 was reported in quasi-one-dimensional crystal BaTiS3 [2]. However, anisotropic nanophotonics requires optical anisotropy of about 1.5 to fully exploit advantages of anisotropic properties [3, 4]. Inspired by this challenge, we focused on two-dimensional materials and their bulk counterpart – van der Waals (vdW) materials. Our findings showed that their fundamental difference between interlayer strong covalent bonding and interlayer weak van der Waals interaction leads to unprecedented high birefringence with values exceeding 1.5 in the infrared and 3.0 in the visible spectral intervals (for example, see optical constants of MoS2 in Figure 1). Thus, our studies enable a new field of vdW anisotropic nanophotonics.

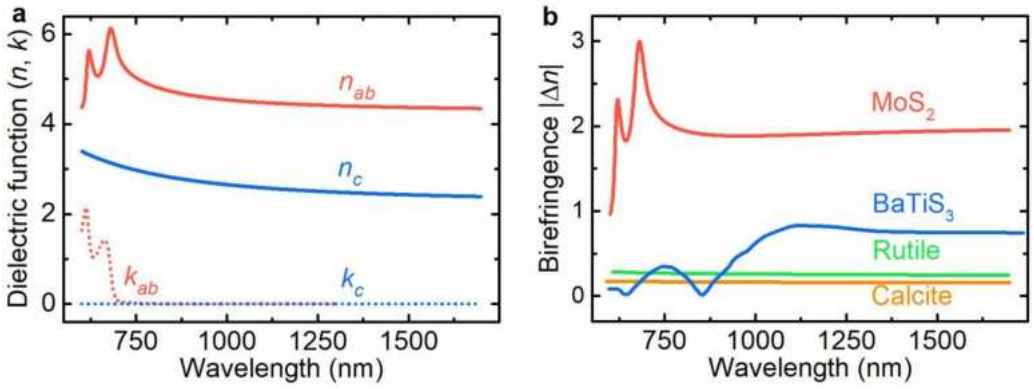


Figure 1: a. Optical constants of MoS2. b. Birefringence of MoS2 in comparison with other anisotropic materials.

In detal, we managed to achieve unmatched lateral dimensions for van der Waals-based waveguides with only several tens of nanometers footprint. In other words, it gives a unique opportunity to place around 10000 waveguides on an mm-scale photonic chip. These characteristics make us a step closer to electronic integrated circuits. Hence, vdW-based photonic integrated circuits can become a decisive platform for an electronic-to-photonic replacement to increase computer data processing. The idea behind the use of vdW materials has four advantages. First, vdW materials have larger optical bandgap in comparison with conventional high refractive index materials (TiO_2, GaP, Si, Ge, and many others) and, therefore, smaller operation wavelength without dissipative losses. Secondly, vdW materials have one of the largest refractive indices among known materials. Thirdly, the record-breaking optical anisotropy of vdW gives an additional degree of freedom for the design optimization of integrated photonic elements. Finally, vdW materials have dangling bonds-free surfaces and atomically sharp edges after the lithography process, which results in minimum scattering losses in photonic waveguides and high intensity nonlinear properties in addition to superior linear response. From a broader perspective, we would like to note that these vdW features are also beneficial for countless optical devices (resonators, dielectric mirrors, waveplates, and many others) beyond on-chip integration.

References

1. Ermolaev G. *et al.*, Nature Communications, 12, 854, 2021.
2. Niu S. *et al.*, Nature Photonics, 12, 392-396, 2018.
3. Ermolaev G. *et al.*, Photonics, 9, 744, 2022.
4. Jahani S. *et al.*, Nature Communications, 9, 1893, 2018.

A Broadband Metamaterial-Based Electromagnetic Absorber with the Capability of being Fabricated by 3-D Printers

M. Javadi[1], L. Yousefi[1,2*]

[1] School of Electrical and Computer Engineering, College of Engineering University of Tehran, Tehran, Iran

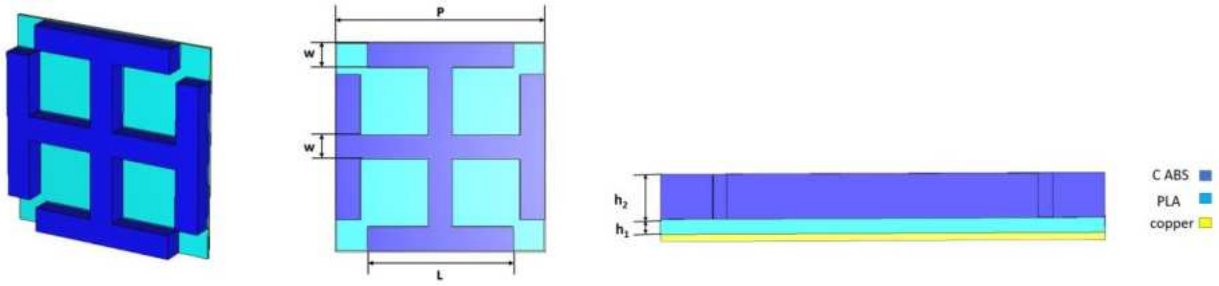
[2] School of Engineering and Informatics, University of Sussex, Falmer, UK, BN1 9RH,

*corresponding Author: l.yousefi@sussex.ac.uk

Abstract: In this paper, a broadband metamaterial-based electromagnetic absorber is proposed which can be fabricated by 3-D printing techniques. The proposed structure provides an absorption of more than 90% in the whole frequency band of 8-12 GHz, for all incident angles in the range of 0 to 30 degrees, and for both TE and TM polarizations.

Electromagnetic (EM) wave absorbers can efficiently absorb the incident waves at their operating frequencies. With the rapid development of Electromagnetic technology, EM wave absorbers have found a variety of practical applications, in sensors [1], imaging systems [2], stealth technology [3], and energy harvesting [4]. Metamaterial-based absorbers are much thinner and lighter than the traditional bulky EM absorbers. However, their absorption bandwidth is inherently narrow due to the resonance nature of metamaterials [5], [6]. Here, a broadband metamaterial-based absorber is proposed that can be fabricated using PLA (Polylactic acid) and conductive ABS (Acrylonitrile Butadiene Styrene), common filaments used in 3-D printing technology. To make the absorber broadband, we have designed the metamaterial to resonate at different frequencies and by using conductive ABS which is a lossy material, we have combined these resonances together resulting in a broadband response for the designed absorber.

The proposed unit cell is shown in Fig. 1. As shown in this figure, the absorber unit cell consists of a PLA substrate, cross-shaped metamaterials made from conductive ABS, and a thin copper layer. The metamaterial shape and dimensions are optimized to achieve a broadband response.

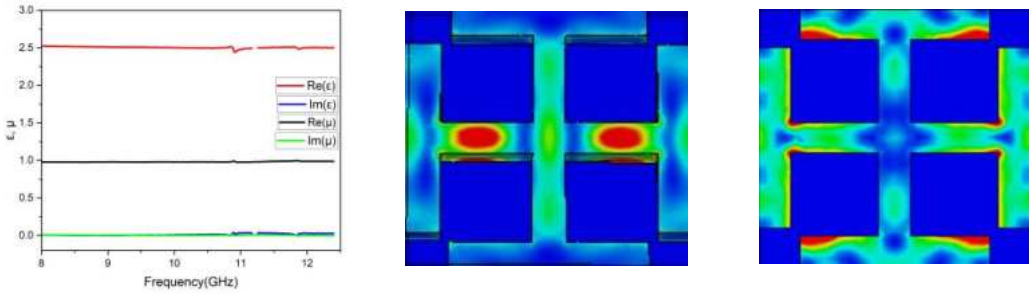


(a) (b) (c)

Fig. 1. Schematic of the unit cell of the proposed metamaterial-based absorber a) perspective view b) top view c) side view. The dimensions are as P=60 mm, L=42 mm, w=7 mm, h1=0.8mm, h2=5mm.

To illustrate the performance of the proposed structure, here, we perform full wave numerical simulation using CST software. The structure is excited using an incident electromagnetic plane wave, and the copper layer is modeled with the conductivity of 5.96×10^7 S/m. For the electromagnetic properties of the conductive ABS, we have used the data reported in [3]. For the PLA layer, we have measured its electromagnetic properties using the waveguide method [7] and the measured data is shown in Fig. 2a. Figures 2b, c show the field distribution inside the cell at two different resonance

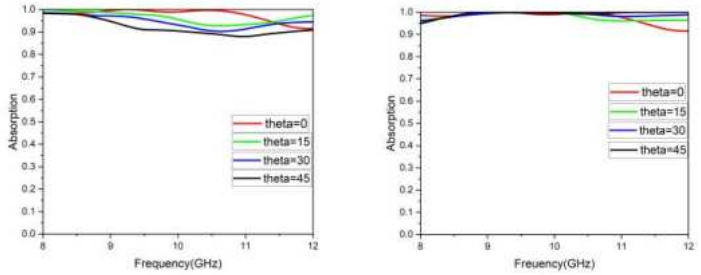
frequencies. As shown in this figure, at different resonance frequencies, field is concentrated in different parts of the metamaterial resulting in a broadband response.



(a) (b) (c)

Fig. 2. a) The measured electromagnetic properties of the PLA. b, c) Numerically calculated power loss density inside the metamaterial absorber at the frequency of b) 9.13 GHz c) 10.44 GHz.

Figure 3 illustrates the absorption of the proposed structure, for different incident angles. As shown in this figure, the absorption exceeds 90% across the whole frequency band of 8-12 GHz , for incident angles in the range of 0 to 30 degrees, and for both TE and TM polarizations of the incident wave, illustrating a polarization-independent broadband response.



(a) (b)

Fig. 3. Absorption of the proposed structure for different incident angles. (a) TE mode (b) TM mode.

References

1. N. Liu, M. Mesch, T. Weiss, M. Hentschel, and H. Giessen, “Infrared perfect absorber and its application as plasmonic sensor,” *Nano Lett,* vol. 10, no. 7, pp. 2342-2348, Jul 14, 2010.
2. C. M. Watts *et al*., “Terahertz compressive imaging with metamaterial spatial light modulators,” *Nature Photonics,* vol. 8, no. 8, pp. 605-609, 2014.
3. S. Zhong, L. Wu, T. Liu, J. Huang, W. Jiang, and Y. Ma, “Transparent transmission-selective radar-infrared bi-stealth structure,” *Opt Express,* vol. 26, no. 13, pp. 16466-16476, Jun 25, 2018.
4. M. Nowak, "Metamaterial-Based Sub-Microwave Electromagnetic Field," *Energies,* vol. 14, April 2021.
5. Chen, X., X. Chen, Z. Wu, Z. Zhang Z. Wang, L. Heng, Sh. Wang, Y. Zou and Z. Tang, "An ultra-broadband and lightweight fishnet-like absorber in the microwave region," *Journal of Physics D: Applied Physics,* vol. 51, no. 28, 2018.
6. Kronberger, R. and P. Soboll, "New 3D printed microwave metamaterial absorbers with conductive printing materials," *Eur.Microw.Conf,* pp. 596-599, 2016.
7. Evseev, V. I., E. A. Lupanova, S. M. Nikulin and V. V. Petrov, " Measurement of Electromagnetic Characteristics Materials in a Rectangular Waveguide”, Photonics & Electromagnetics Research Symposium, Rome, Italy, 2019.

Metamaterials and negative index materials

An Effective Medium Description for Cylinder- and Coated-cylinder-Multifunctional Metamaterials

A. C. Tasolamprou[1], Ch. Mavidis[2,3], M. Kafesaki[2,3]

[1]Department of Physics, National and Kapodistrian University of Athens, Athens 15784, Greece

[2]Institute of Electronic Structure and Laser, Foundation for Research and Technology Hellas, N. Plastira 100, 71110, Heraklion, Crete, Greece

[3]Department of Materials Science and Technology, University of Crete, Heraklion, 70013, Greece

[*]corresponding author: atasolam@phys.uoa.gr

Abstract: We present an effective medium approach for the study of metamaterials made of cylindrical scatterers/meta-atoms based on the Coherent Potential Approximation. We demonstrate the power of this approach and a rich metamaterial behaviour, including frequency regions of engineerable negative permittivity, negative permeability, negative refractive index and hyperbolic response.

The emergence of dielectric metamaterials, supporting resonances and thus interesting metamaterial effects beyond the quasitatic regime (where the wavelength inside the scatterer/meta-atom is comparable to the meta-atom size), made extremely valuable the development of effective medium approaches able to accurately describe the metamaterial response in such frequency regimes, i.e. to go beyond the well-established Maxwell-Garnett effective medium approach. Such approaches are more valuable in the case of meta-atoms made of a polaritonic material, where the dielectric function experiences strong positive and strong negative values. To be able to accurately describe the wave propagation in polaritonic systems of *spherical* scatterers (as well as of high-index dielectric scatterers) different extension of the Maxwell-Garnett approaches have been developed [1]. No such approach though is available (to our knowledge) for systems of cylindrical scatterers.

Here we present an effective medium approach able to accurately describe the wave propagation in metamaterials made of cylindrical scatterers well-beyond the quasi-static regime. Our approach is based on the well-known in the Solid State Physics community Coherent Potential Approximation (CPA) method. In the case of metamaterials made of simple cylinders it was first derived by Yu et. al. [2]. In our work we further developed the approach of Yu et. al., and we extend it the case of coated- and multi-coated cylinders with a potential to incorporate a metasurface at each interface. The cylinders material can be either dielectric, or metals, or polaritonic material or any other resonant isotropic material. The covering metasurfaces can have both magnetic and electric surface impedance, representing for example graphene sheets, patterned or unpatented.

Application of our approach in different realistic cylinder-based systems has revealed in almost all cases an interesting and rich metamaterial response [3,4]. The main idea of the CPA approach for the determination of the homogeneous effective medium parameters describing an inhomogeneous system/metamaterial is the vanishing of the average scattering between the actual system/metamaterial and the effective medium under determination as described in Fig. 1. In Fig. 2 we demonstrate the application of our CPA-based approach for a metamaterial made of SiC cylinders in air. Specifically, we show the effective permittivity and permeability for the two possible incident wave polarizations. Observing the resonant response of the effective parameters, one can identify frequency regions of negative permeability, of combined negative permittivity and permeability resulting to negative refractive index, as well as of hyperbolic response (resulting from mixed positive and

negative permittivity or permeability values).

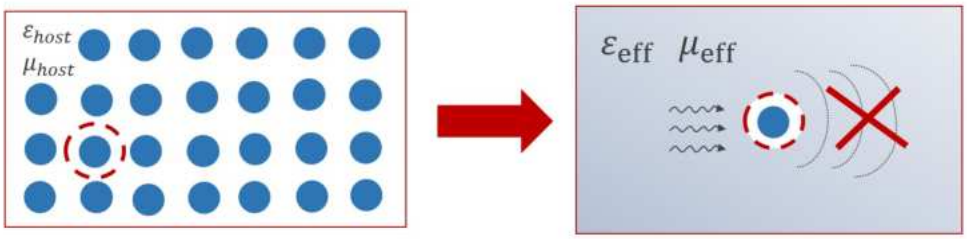


Fig. 1. The application of CPA effective medium approach for the homogenization of a system (left panel) comprising of simple cylinders (blue color) in a host material (white color). The effective medium (uniaxial in this case) is determined by the requirement of vanishing of the average scattering between it (the effective medium) and the actual medium.

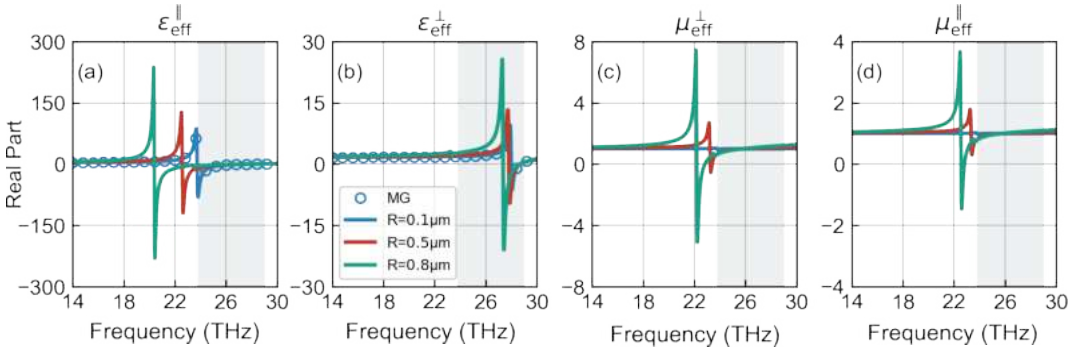


Fig. 2. Real part of the effective permittivity ($\varepsilon_{\mathrm{eff}}$) and permeability ($\mu_{\mathrm{eff}}$) for a system of SiC cylinders in air, in filling ratio 30%. The gray region indicates the frequency regime where the SiC (bulk) permittivity is negative. The superscripts in $\varepsilon_{\mathrm{eff}}$ and μ_{eff} indicate the polarization of the corresponding field in respect to the cylinders axes. The different curves show results for different cylinder radius (R) and the circles present (for comparison) the corresponding results given by the well-established Maxwell-Garnett approach.

We developed an effective medium approach for the description of metamaterials made of cylindrical scatterers. The scatterers can be simple cylinders, coated or multicoated cylinders, and can have a metasurface at each interface. Moreover, almost any material is allowed as constituent of the cylindrical scatters (including resonant materials). Application of the method for systems/metamaterials made of polaritonic cylinders in a host revealed a rich metamaterial response in such systems, including engineerable negative permittivity, negative permeability values, negative refractive index and hyperbolic response.

We acknowledge funding by the Hellenic Foundation for Research and Innovation (H.F.R.I.) under the “Basic Research Financing”, National Recovery and Resilience Plan (Greece 2.0), (Project Number: 14830, PhoToCon

References

1. R. Ruppin, “Evaluation of extended Maxwell-Garnett theories,” Optics Commun., vol. 182, p. 273, 2000.
2. Y. Wu, J. Li, Z.-Q. Zhang, and C. T. Chan, “Effective medium theory for magnetodielectric composites: Beyond the long-wavelength limit”, Phys. Rev. B, vol. 74, p. 08511, 2015.
3. Ch. P. Mavidis, A. C. Tasolamprou, E. N. Economou, C M. Soukoulis, and M Kafesaki, “Polaritonic cylinders as multifunctional metamaterials: Single scattering and effective medium description”, Phys. Rev. B, vol. 102, p. 155310, 2020.
4. Ch.P. Mavidis, A.C. Tasolamprou, E. N. Economou, C. M. Soukoulis, and M. Kafesaki, “Single scattering and effective medium description of multilayer cylinder metamaterials: Application to graphene- and to metasurface-coated cylinders”, Phys. Rev. B, vol 107, p. 134120, 2023.

Enhancing Bandwidth in GHz Metamaterials through Superposed Lorentzian Resonances

Y. Hyeong[1], H. Park[1], and J. Shin[1*]

[1]Korea Institute of Science and Technology, Republic of Korea
[*]corresponding author: qubit@kaist.ac.kr

Abstract: In this study, we propose a GHz-metamaterial with an extended μ bandwidth. Initially, we theoretically investigate the trade-off relationship between magnetic permeability and bandwidth. Based on these results, we introduce a magnetic metamaterial comprising superposed Lorentzian resonances at adjacent frequencies.

Magnetic permeability is one of the fundamental properties that determine the electromagnetic response of a material. However, unlike its counterpart, electric permittivity, magnetic permeability has a fundamental limit on bandwidth. This limitation in the case of a system that can be expressed with a single resonance has been well described analytically by Kabiri et al. [1]. However, the calculations only apply to systems consisting of a single magnetic resonance. In order to extend the problem, the magnetic permeability model for multiple resonance systems is introduced:

$$\mu_{\text{eff}} = 1 + \sum_{i=1}^{m} \frac{a_i \omega^2}{\omega_i^2 - \omega^2 - i\omega\Gamma_i} \tag{1}$$

where a_i is the i[th] resonance amplitude, ω_i is the i[th] resonance frequency, and Γ_i is the i[th] damping frequency, respectively.

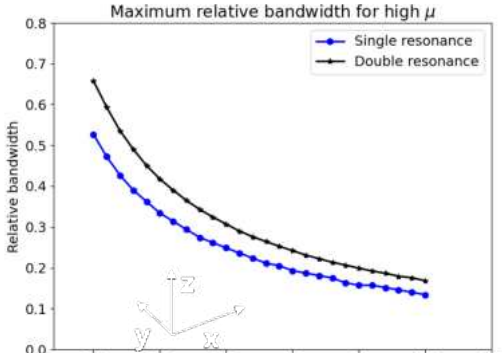


Figure 1 Maximum relative permeability of double resonance system

Based on this model, we investigated the trade-off relation of magnetic permeability and the continuous high permeability bandwidth of a double Lorentzian system using a Brute force method. Figure 1 shows the maximally achievable continuous high-permeability bandwidth depending on the cut-off criteria in single and double Lorentzian resonance systems. For example, the maximally achievable relative bandwidth of $\mu \geq 2$ of single and double Lorentzian resonance systems are 0.343 and 0.4179, respectively. From this result, it is shown that superposing multiple magnetic resonances at adjacent frequencies can extend the high-permeability bandwidth of permeability.

Figure 3 (a) Unit cell of multi-Lorentzian metamaterial (b) Schematic drawing of the multi-Lorentzian metamaterial array

Here, we propose a GHz metamaterial comprising superposed Lorentzian resonances. The metamaterial consists of 2 conductive loops with different loop areas and linewidths as shown in the unit cell in Figure 2 (a). Due to this asymmetry, the magnetic resonances occurring in the structure have slightly different resonance and damping frequencies, thus, resulting in superposition of Lorentzian resonances with similar frequencies. The schematic drawing of the metamaterial array is shown in Figure 2 (b). The structure is periodic in the xy-plane, and 1mm thick (1 layer) in z direction.

Figure 2 Effective permeability extracted from optimized metamaterial structure

We calculated the reflectance and transmittance of the structure using Finite-Difference Time-Domain simulations, and retrieved the effective permeability using the method illustrated by Chen et al. [2]. The optimized result in Figure 3 shows $\mu \geq 2$ bandwidth in $9.55 - 11.9$ GHz, which is 21.9% in relative bandwidth.

This work was funded by the National Research Foundation of Korea. (2019M3A6B3031046)

References

1. Kabiri, A. “On the Fundamental Limitations of Artificial Magnetic Materials,” IEEE Trans. Antennas Propag., Vol. 58, No. 7, 2345-2353, 2010.
2. Chen X. “Robust method to retrieve the constitutive effective parameters of metamaterials,” Physical review E, Vol. 70, No. 1, 2004.

The Bandgap Characteristics of Wave Dispersion in Monocoupled Metamaterial

A.Bhatt[1*], and A.Banerjee[2]

[1] Department of Civil Engineering, Indian Institute of Technology Delhi, India
[*]corresponding author: Abhigna.Sandipkumar.Bhatt@civil.iitd.ac.in

Abstract: Previously, wider bandgap and band merging in metamaterial with simultaneous negative mass and stiffness were noted [1,2]. This article identifies double attenuation peaks in such metamaterial, attributed to
resonance coupling of longitudinal and transverse resonators, ensuring significant spatial attenuation throughout the band.

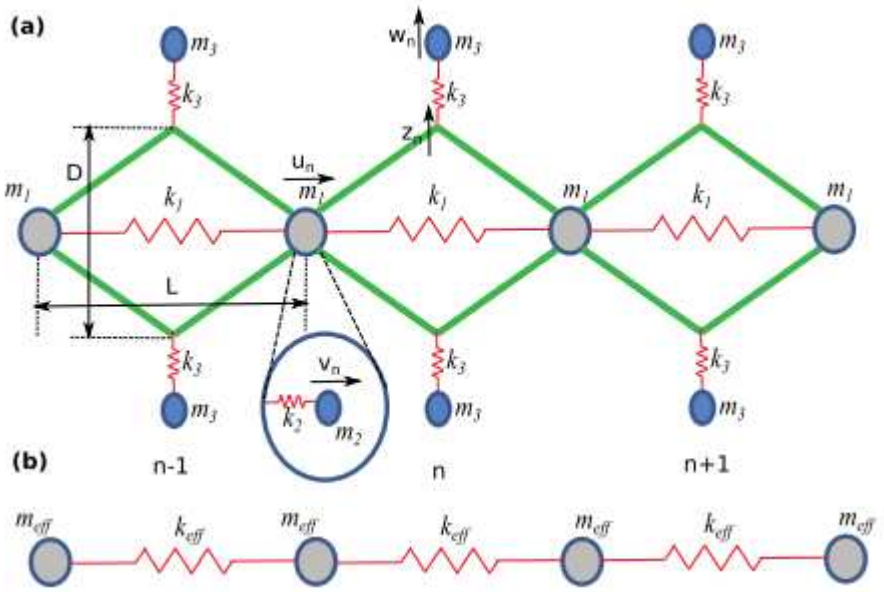


Fig.1 (a) Concurrent negative metamaterial model, (b) Phononic crystals chain

In this research, the focus is on examining the attenuation characteristics, effective mass, and stiffness of acoustic metamaterial that exhibits both negative mass and stiffness simultaneously [3]. By delving into these properties, the study aims to understand how sound waves are affected within this unique material structure. Furthermore, the study investigates the rate at which attenuation occurs across space, which is determined by considering the imaginary component of the propagation constant. This analysis provides insight into how effectively the metamaterial can dampen waves across different spatial dimensions. A crucial aspect explored in the research is the coupling phenomenon between resonators within the metamaterial structure [4]. When the natural frequencies of these resonators are close to each other, they interact and influence each other's behavior. This interaction leads to a distinctive double peak phenomenon within a single attenuation band. This double peak phenomenon is significant because it enhances the material's ability to attenuate sound waves across a wide frequency range. It ensures that the attenuation rate remains substantial throughout the entire bandgap, contributing to the effectiveness of the metamaterial in controlling and manipulating wave propagation.

Wave Dispersion Equation,

$$\xi = \cos^{-1}\left(1 - \frac{\omega^2 M_{eff}}{2 K_{eff}}\right) \tag{1}$$

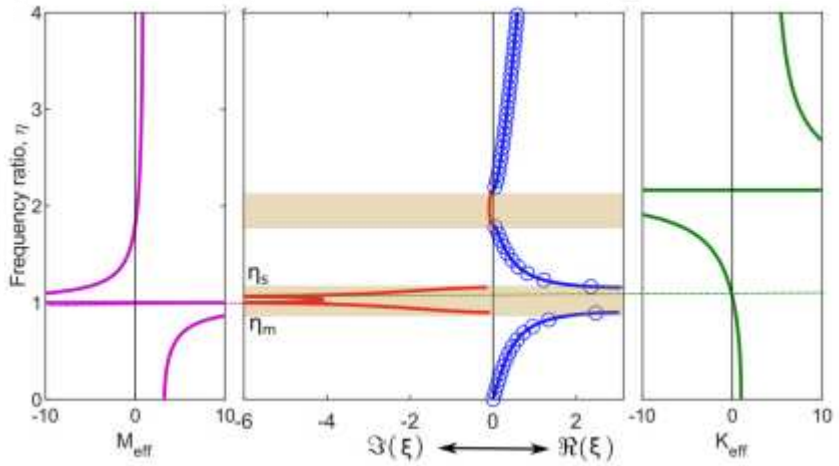


Fig.2 Graphs illustrating Effective Mass, Dispersion Curves, and Effective Stiffness are presented. The dashed purple line represents the peak in attenuation, while the dashed green line indicates the peak within the attenuation band.

This results in coupling between the two resonators, leading to a double peak within a single band. As a consequence, a high level of attenuation is noticeable across the majority of the attenuation band, unlike in other bands. Hence, a substantial decrease in wave amplitude is anticipated in the spatial domain.

Abhigna Bhatt and Arnab Banerjee acknowledge Inspire faculty award, Department of Science and Technology of India , grant number: DST/INSPIRE/04/2018/000052, for partial supporting the research.

References

1. Huang, H. H., C. T. Sun, and G. L. Huang. "On the negative effective mass density in acoustic metamaterials." International Journal of Engineering Science 47.4 (2009): 610-617.
2. Adhikari, Sondipon, et al. "Apparent negative values of Young's moduli of lattice materials under dynamic conditions." International Journal of Engineering Science 150 (2020): 103231.
3. Huang, Hsin-Haou, and Chin-Teh Sun. "Anomalous wave propagation in a one-dimensional acoustic metamaterial having simultaneously negative mass density and Young's modulus." The Journal of the Acoustical Society of America 132.4 (2012): 2887-2895.
4. Li, Jensen, and Che Ting Chan. "Double-negative acoustic metamaterial." Physical Review E 70.5 (2004): 055602.

Dissipative Triatomic Metamaterial for Broadband Asymmetric Elastic-wave Transmission

Sagr Alamri[a], Bing Li[b,*]

[a]Department of Mechanical Engineering, College of Engineering King Khalid University, P.O.Box 394, Abha 61421, Saudi Arabia

[b,*]School of Aeronautics, Northwestern Polytechnical University, Xi'an, Shaanxi, 710072, China

[*]Corresponding author: bingli@nwpu.edu.com

Abstract: An innovative design is proposed for a dissipative triatomic elastic metamaterial to obtain asymmetric wave transmission to realize asymmetric wave transmission in two low-frequency bands. These frequency bands can be analytically and experimentally predicted to realize two paths of wave propagation and wave attenuation along two different directions of transmission.

Based on the transmission equations of the inner and end unit cells derivations, the transmission equations of the entire system for both opposite directions, T^L and T^R, can be calculated respectively as:

$$\left.\begin{aligned} T^L &= \left|\frac{\hat{v}_Q}{\hat{v}_0}\right| = \left|\prod_{\eta=1}^{Q} T_\eta^L\right| \\ T^R &= \left|\frac{\hat{z}_Q}{\hat{z}_0}\right| = \left|\prod_{\eta=1}^{Q} T_\eta^R\right| \end{aligned}\right\} \tag{1}$$

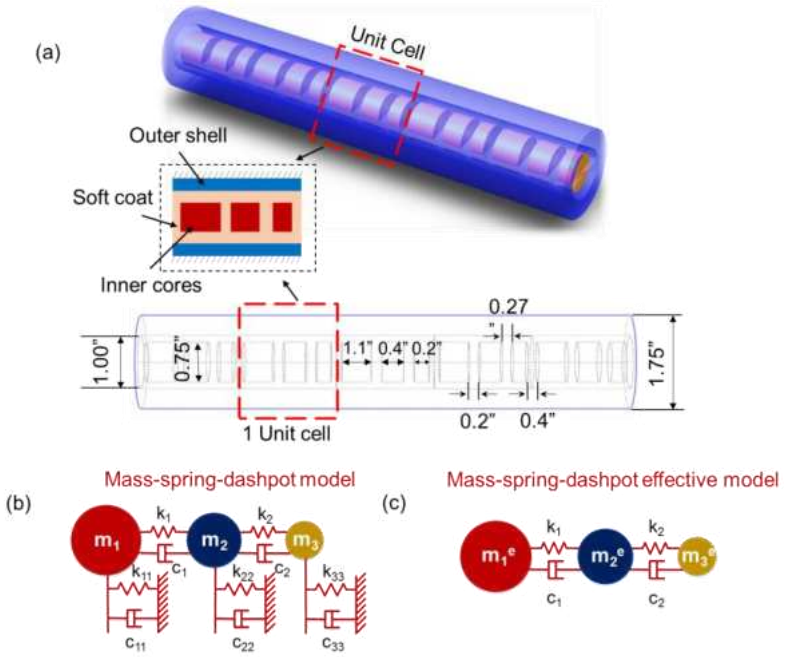


Fig. 1. (a) Schematic of the continuum model for the proposed dissipative diatomic elastic metamaterial. (b) Schematic of a linear triatomic mass-spring-damper model. (c) Transmission along direction *L* and *R* in a dissipative system consisting of *Q* effective unit cells.

Acknowledgments

The authors gratefully acknowledge the support from The University of Akron Faculty Start-up Grant. S. Alamri wants to acknowledge the support provided by the Deanship of Scientific research at King Khalid University (Grant no. R.G.P.2/127/42).

References

1. R. Fleury, D.L. Sounas, C.F. Sieck, M.R. Haberman, A. Alu, Sound isolation and giant linear nonreciprocity in a compact acoustic circulator, *Science*, 343 (2014) 516-519.
2. B. Li, K.T. Tan, Asymmetric wave transmission in a diatomic acoustic/elastic metamaterial, *J. Appl. Phys.*, 120 (2016) 075103.
3. H.H. Huang, C.T. Sun, G.L. Huang, On the negative effective mass density in acoustic metamaterials, *Int. J. Eng. Sci.*, 47 (2009) 610-617.

The critical size of hybrid metal-dielectric nanoslits guide mode resonance optical filters by the spatial Fourier transform analysis

R. He[1*], C. Chen[2], Y. X. Zheng[2], L. Y. Chen[2], and J. P. Guo[3*]

[1]Yiwu Research Institute, Fudan University, China
[2]Department of Optical Science and Engineering, Fudan University, China
[3]Department of Electrical and Computer Engineering, University of Alabama in Huntsville, USA
[*]corresponding author: rheshu@163.com, guoj@uah.edu

Abstract: In this work, we analyze the performance of hybrid metal-dielectric nanoslits guide mode resonance optical filters using finite-difference time-domain simulations and spatial Fourier transform analysis. We propose the empirical values of the critical sizes in both lateral dimensions for maintaining the filter performance.

Surface plasmon resonance optical filter, all-dielectric guide mode resonance optical filter, and hybrid guide mode resonance optical filter are three subwavelength nanosurface optical filters. The periodic surface nanostructures function as a light wave coupler to couple the free-space optical wave into the guided mode. Previous works have reported that the finite sizes in both lateral dimensions affect the spectral linewidth and transmittance of the filter[1-2].

In this work, we simulate the performance of hybrid metal-dielectric nanoslits guide mode resonance optical filters using finite-difference time-domain numerical simulations and spatial Fourier transform analysis. Figure 1(a) shows the structure of hybrid metal-dielectric nanoslits guide mode resonance optical filters. The hybrid GMR filter consists of a thin gold nanoslit grating, a low refractive index magnesium fluoride (MgF_2) layer, a high refractive index silicon layer, and an MgF_2 substrate. A finite-difference time-domain (FDTD) software (Lumerical Solutions, Inc.) is used to calculate the transmittance spectra.

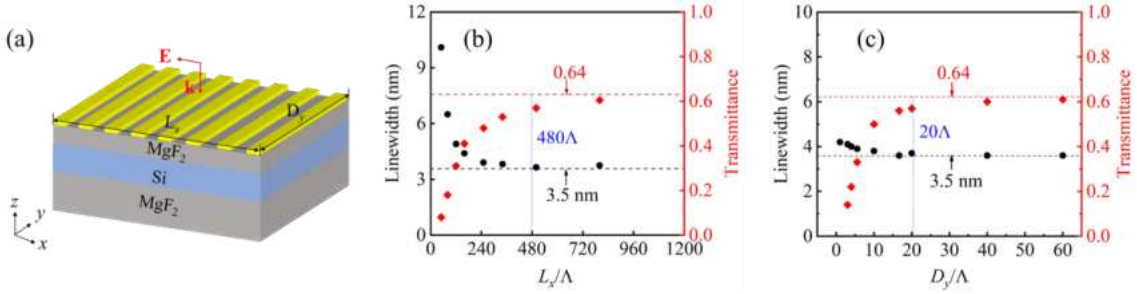


Fig. 1. (a) The structure of the hybrid metal-dielectric nanoslits grating guided-mode resonance metasurface optical filter with a finite size. (b)-(c) The spectral linewidth and transmittance versus the filter sizes in the x and y directions.

Figure. 1(b) shows the transmittance peak linewidth and transmittance versus the filter size L_x. The black dots show that, when the filter size is less than 250Λ, the peak linewidth increases from 3.5 nm corresponding to the peak linewidth of the infinite filter structure. The red diamonds show that the peak transmittance drops dramatically when L_x is less than 480Λ. So, in the x direction, the critical size is 480Λ and the value of 480 is close to the quality factor of the infinite-size filter. Fig. 1(c) plotted the spectral linewidth and the peak transmittance versus the finite size D_y. It is seen that the critical size in the y direction is 20Λ which is much less than the minimum size in the x direction.

Next, the Fourier transform is used to explain the critical size of the hybrid metasurface optical filter in the two lateral directions. When the filter sizes (L_x and D_y) are less than the critical sizes, the device consists equivalently of an aperture window and an infinite-size hybrid optical filter, as shown in Fig. 2(a). After the 1D

aperture window, the diffracted waves with different amplitudes and propagation directions, indicated by θ or α, immediately pass through the infinite-size filter. The transmittance of the finite-size filter is,

$$T(\lambda)=\frac{\iint\left|\iint_{\infty}F(k_x,k_y)\cdot t(k_x,k_y,\lambda)\exp\left[-\mathrm{j}(k_x\cdot x+k_y\cdot y)\right]\mathrm{d}k_x\mathrm{d}k_y\right|^2\mathrm{d}x\mathrm{d}y}{\iint\left|\iint_{\infty}F(k_x,k_y)\exp\left[-\mathrm{j}(k_x\cdot x+k_y\cdot y)\right]\mathrm{d}k_x\mathrm{d}k_y\right|^2\mathrm{d}x\mathrm{d}y}, \qquad (1)$$

where F(k_x, k_y) is the Fourier transform of the aperture function. t (k_x, k_y, λ) is the transmission coefficient of the infinite size filter. According to the spatial Fourier transform of the 1D aperture window function, there exists a critical size to make the most energy focus on the diffracted waves of the incident angle less than the critical angle. Only the diffracted wave of the incident angle less than the critical angle of the infinite-size filter contributes to the transmittance of the filter.

Fig. 2 (b) shows the transmittance versus incident angle (θ and α) of the infinite-size filter in the x-y plane (red) and y-z plane(black). It is seen that the critical angles in the x and y directions of the infinite-size filter are 0.66° and 10°. Figs. 2 (c)-(d) show the calculated transmittance versus filter size L_x or D_y by using the FDTD simulation and Fourier transform analysis. The transmittance curves obtained by the Fourier transform analysis agree well with the transmittance curves calculated by the FDTD numerical simulations. Compared with the minimum size for maintaining the performance of the infinite filter in the x-direction, the size in the y-direction is much less. The different minimum sizes in two lateral directions are due to the difference in critical angles.

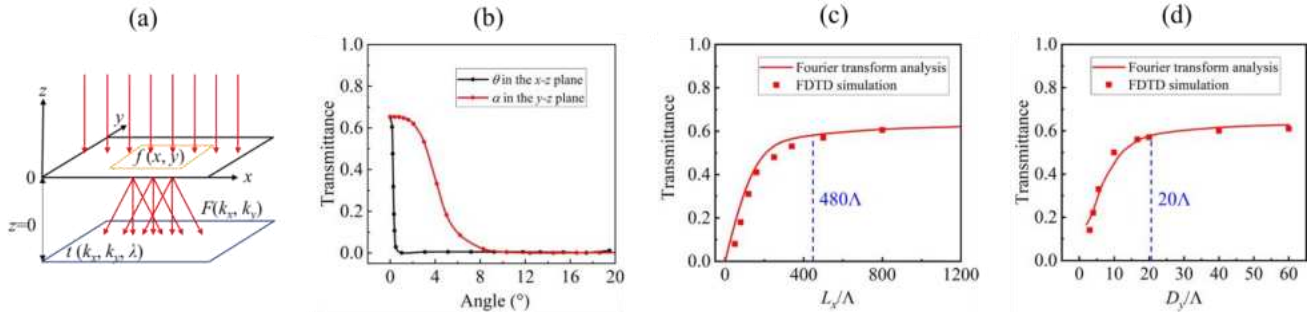


Fig. 2 (a) A schematic of finite size hybrid nanoslits grating GMR optical filter. (b)The transmittance versus incident angle of the infinite-size filter in the x-y plane (red) and y-z plane(black). (c)-(d) The calculated transmittance versus filter size L_x and D_y.

In this work, we show that, in the nanoslits periodic array direction, the critical dimension size for maintaining the performance of the hybrid GMR optical filter is the product of the period and the quality factor of the infinite-size filter. In the grating strip direction, the minimum size is 20 times the slit period which is much less than that of the other direction because of the slow change of the transmittance of the infinite-size device on the angle of incidence in the grating strip direction

References

1. R. R. Boye and R. K. Kostuk, "Investigation of the effect of finite grating size on the performance of guided-mode resonance filters," Appl. Opt., Vol. 39, No. 21, 3649-3653, 2000.
2. S. T. Thurman and G. M. Morris, "Controlling the spectral response in guided-mode resonance filter design," Appl. Opt., Vol. 42, No. 16, 3225-33, 2003.

Bias-free optical metamaterial with nonreciprocal magnetoelectric response

S. Safaei Jazi,[1,*] I. Faniayeu,[2] R. Cichelero,[2] D. C. Tzarouchis,[3,4] M. M. Asgari,[1] A. Dmitriev,[2] S. Fan,[5] and V. Asadchy[1,5]

[1]Department of Electronics and Nanoengineering, Aalto University, P.O. Box 15500, FI-00076 Aalto, Finland

[2]Department of Physics, University of Gothenburg, Gothenburg 41296, Sweden

[3]Department of Electrical and Systems Engineering, University of Pennsylvania, Philadelphia, Pennsylvania 19104, USA

[4]Meta Materials Europe, Marousi 15123, Athens, Greece

[5]Ginzton Laboratory and Department of Electrical Engineering, Stanford University, Stanford, California 94305, USA

[*]Corresponding author: shadi.safaeijazi@aalto.fi

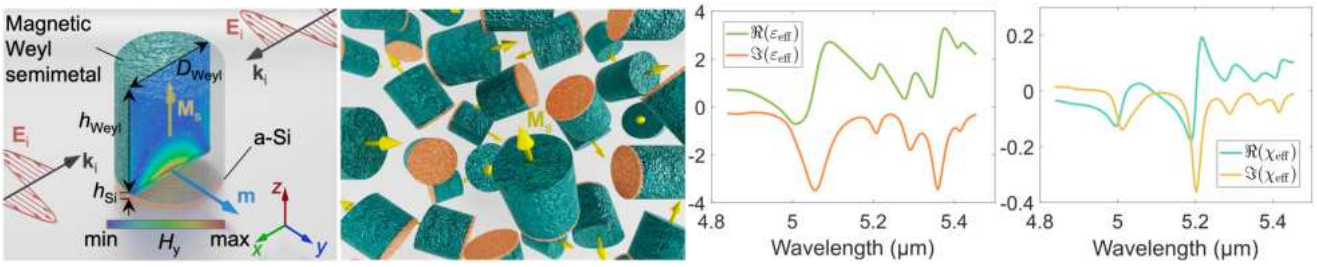
Abstract: We propose the first nonreciprocal magnetoelectric metamaterials with resonant responses at visible and mid-infrared frequencies and without the requirement of external magnetic bias. The designed metamaterial consists of randomly oriented nanocylinder meta-atoms comprising a ferromagnet in a single-domain magnetic state and a high-permittivity dielectric operating near the magnetic Mie-type resonance.

The nonreciprocal magnetoelectric (NME) effect refers to bianisotropic phenomena within which a magnetic field leads to the induction of electric polarization, while reciprocally, an electric field results in the production of magnetization [1]. This effect that happens in materials with both broken parity symmetry and reciprocity is negligible in conventional materials, however, it is expected to have a pioneering impact on applied physics, such as magnetless isolators [2]. As the NME effect can be enhanced using the metamaterial paradigm, several attempts have been made based on the metamaterials technique to achieve a remarkable NME effect (surpassing that in some natural materials), however, most of them were restricted to the microwave spectrum rather than the optical spectrum. In addition, the execution of a three-dimensional isotropic NME metamaterial based on the prior proposals at microwave frequencies and more recent advancements at optical frequencies is unattainable with current technology. Here, we propose the first isotropic optical NME metamaterial that operates without the requirement for an external magnetic field, utilizing common materials and nanofabrication methods [3].

In the proposed isotropic NME metamaterial, a bottom-up approach is employed for the design and analysis of an NME meta-atom and subsequently, the electromagnetic response analysis of a bulk metamaterial consisting of randomly oriented meta-atoms in a host medium, which is considered to be air for simplicity. The meta-atom design features a nanocylinder consisting of two components as shown in Fig. 1(a): a ferromagnet or ferrimagnet (ferrite) in a single-domain magnetic state, paired with a high-permittivity semiconductor or dielectric that functions near the magnetic Mie-type resonance. The ferromagnetic Weyl semimetal $EuCd_2As_2$ and amorphous silicon are considered for the upper and bottom parts, respectively. The Weyl semimetal has an anomalously strong magneto-optical response within the mid to far-infrared frequency range. To prevent the requirement of an external magnetic field, the ferromagnetic component of the nanocylinder is selected to maintain a single magnetic domain, which results in its spontaneous magnetization. In addition, the high-permittivity semiconductor nanocylinder considerably increases the NME effect of the meta-atom because its operation is at the magnetic Mie-type resonance. The single-domain state of the ferromagnetic component restricts its dimensions. The dimensions of the meta-atom are mentioned in the caption of Fig. 1(a).

Figure 1(a) presents a qualitative illustration of the NME effect in a meta-atom when it is stimulated by a

standing wave characterized by a *y*-polarized electric field, with the node of the magnetic field located at the center of the meta-atom. To clarify, only the moments that contribute to the NME effect are depicted here. As demonstrated in Fig. 1(a), the *y*-polarized optical electric field generates a *y*-aligned optical magnetic moment within the meta-atom that is the essence of the optical NME effect. As an alternative, an incident optical magnetic field would induce an electric dipole moment.



(a) (b) (c) (d)

Fig. 1. (a) NME meta-atom comprises Weyl (upper) and amorphous silicon (lower) parts. The dimensions of the meta-atom are h_{Si} = 26 nm, h_{Weyl} = 530 nm, and D_{Weyl} = 530 nm. The field map illustrates the distribution of the magnetic field within the meta-atom when it is in resonance (λ = 5 μm). (b) The isotropic mid-infrared NME metamaterial where yellow arrows indicate the directions of the local spontaneous magnetizations ($\mathbf{M}_s$) within the single-domain ferromagnetic nanocylinders. (c, d) Effective permittivity and Tellegen parameters of the metamaterial (effective permeability of metamaterial is approximately one in this spectrum) [3].

The constitutive relations of isotropic NME metamaterial where the designed meta-atoms are distributed and oriented randomly read

$$\mathbf{D} = \varepsilon_0 \varepsilon_{\text{eff}} \mathbf{E} + \chi_{\text{eff}} / c \, \mathbf{H}, \qquad \mathbf{B} = \mu_0 \mu_{\text{eff}} \mathbf{H} + \chi_{\text{eff}} / c \, \mathbf{E}. \tag{1}$$

Here, c stands for the speed of light, and ε_{eff}, μ_{eff}, and χ_{eff} are the effective permittivity, permeability, and NME parameters. As meta-atoms are arranged randomly, only isotropic effects such as the NME effect can remain. The effective parameters of the metamaterial (Fig. 1(c, d)) show that the NME parameter χ_{eff} at 5.2 μm reaches the value of 0.36 where the volume fraction of metamaterial is N_V = 0.12. This value exceeds four orders of magnitude compared to known natural material at optical frequencies. At the same wavelength, the magnitude of effective permittivity is comparable to the NME parameter (Fig. 1(c)).

In this work, we theoretically proposed the first realistic attempt to attain bias-free optical metamaterial with a nonreciprocal magnetoelectric response. We developed the mentioned procedure to design an NME metamaterial based on conventional materials, such as cobalt and silicon. In the cobalt-based metamaterial, the magnitude of the NME effect surpasses that of natural materials at room temperature by a minimum of two orders of magnitude [3].

References

1. Serdyukov, A., I. Semchenko, S. Tretyakov, and A. Sihvola, "Electromagnetics of Bi-Anisotropic Materials-Theory and Application,", Gordon and Breach Science Publishers, 2001.
2. Asadchy, V., A. Diaz-Rubio, and S. A. Tretyakov, "Bianisotropic metasurfaces: physics and applications," Nanophotonics, Vol. 7, No. 6, 1069 – 1094, 2018.
3. Jazi, S. S., I. Faniayeu, R. Cichelero, D. C. Tzarouchis, M. M. Asgari, A. Dmitriev, S. Fan, and V. Asadchy "Optical Tellegen metamaterial with spontaneous magnetization", Nat. Commun., 2024 (accepted).

First-principles prediction of nonlinear optical response in silicon nanostructures

Gosuke Matsuura[1], Shunsuke Yamda[2], and Mitsuharu Uemoto[1]

[1] Graduate School of Engineering, Kobe University, Japan.

[2] National Institutes for Quantum Science and Technology (QST), Japan.

Abstract: We use multiscale method combining electromagnetics and quantum mechanical simulations to make first-principles predictions of harmonic generation by semiconductor nanostructures. The enhancement of harmonic generation in silicon nanocylinder array is investigated, and its dependency on geometric parameters is analyzed; e.g. the optimum radius representing resonant condition R=25nm is found.

The optical response of nanoscale artificial structures gets attention. In particular, nano-optical devices utilizing nonlinear optical effects under intense laser pulses are expected to enable highly efficient optical wavelength conversion and waveform shaping. Second harmonic generations (SHGs) and high harmonic generations (HHGs) by semiconductor nanoparticles and meta-surfaces have been experimentally confirmed. Simulation of optical response by electromagnetic field analysis is widely used for device analysis and design in fields such as nano-optics. However, conventional electromagnetic field analysis has weaknesses, including difficulty in nonlinear responses in strong light fields and the need for empirical parameters such as dielectric constant. To overcome such weakness, we develop the multiscale method, which combines finite-difference time-domain (FDTD) electromagnetic calculations and first-principles electron dynamics calculations [1-2]. In quantum mechanical calculations, the time-dependent density functional theory (TDDFT) has been used for analyzing laser-matter interactions ("Maxwell+TDDFT") [3]. However, it requires a lot of computational cost. We also develop the semiconductor Bloch equation (SBE)-based multiscale calculation ("Maxwell+SBE"). The governing equation of the electron dynamics is expressed as:

$$\mathrm{i}\frac{\partial}{\partial t}\rho_{ij}^{(\mathbf{k})}(t) = \frac{1}{c}\mathbf{A}(t)\cdot\left[\sum_{l}\mathbf{p}_{il}^{(\mathbf{k})}(t)\,\rho_{lj}^{(\mathbf{k})}(t) - \sum_{l}\rho_{il}^{(\mathbf{k})}(t)\,\mathbf{p}_{lj}^{(\mathbf{k})}(t)\right], \tag{1}$$

where ρ is the density matrix, **p** is the transition dipole moment, and **A** is the vector potential. We couple with Maxwell's wave equation involving the current density J in this electron system and calculate the time evolution.

$$\nabla\times\nabla\times\mathbf{A}(\mathbf{r},t) + \frac{1}{c^2}\frac{\partial^2}{\partial t^2}\mathbf{A}(\mathbf{r},t) = \frac{4\pi}{c}\mathbf{J}(\mathbf{r},t). \tag{2}$$

Incidentally, the coefficients in our SBE [Eq. (1)], such as dipole moment **p**, are calculated from the ground state's wavefunctions, also used as the initial state of TDDFT calculations; our SBE results qualitatively agree with those of TDDFT [see Fig.(a)]. Owing to SBE's less computational cost than TDDFT, the Maxwell+SBE is capable of large scale device models.

In this study, we utilize the Maxwell+SBE method to simulate light excitation and scattering properties in a silicon nanocylinder array under the high-intensity laser pulses. An enhancement of electric field due to Mie resonance caused by the cylinder and light focusing by lensing effect [see Fig. (b)]. This behavior significantly differs that observed from the previously studied nanofilm structure [3]. The power spectrum analysis of the electric field indicated the presence of higher-order harmonic components [see Fig. (c)]. We analyze the effect of varying the size and spacing of the nanocylinder on the intensity of the electric field. The results show that there is a dependence on the size of the cylinders, with a maximum around 25 nm in radius, coinciding with Mie resonance condition [see Fig.(d)]. We also calculate the frequency-resolved electric field profile of propagating light and investigate the characteristics of profiles representing each harmonic order [see Fig. (e)]. We will consider not only cylinders, but also geometries with cylinders attached to a base that approximates a practical meta-surface.

In conclusion, we utilize multiscale Maxwell+TDDFT and Maxwell+SBE methods to simulate the harmonic generation from silicon nanostructures. Our results provide insights into the design and optimization of nonlinear optical devices utilizing nanostructures and meta-surfaces.

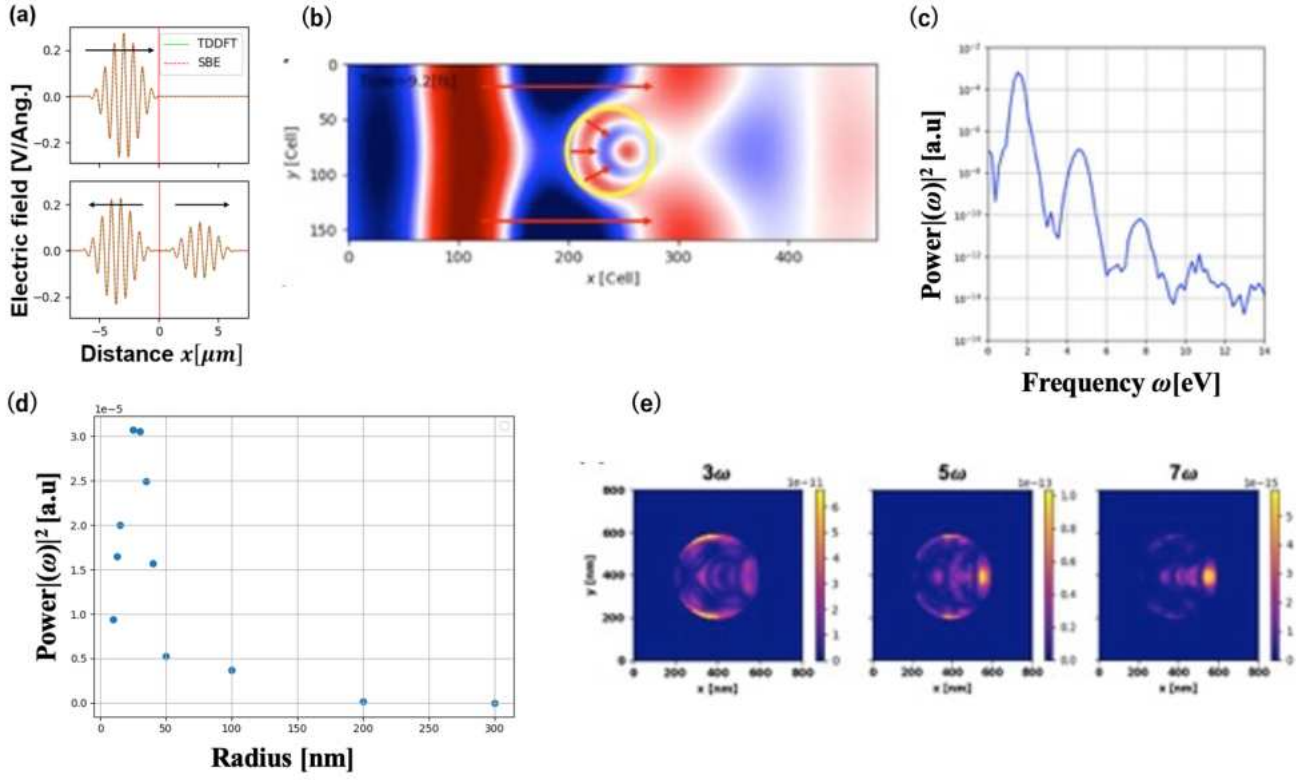


Figure: Calculation results: (a) electric field profile of nanothin film. (b) electric field profile of nanocylinder. (c) power spectra. (d) power spectra.
(e) frequency-resolved current density profiles.

References

1. K. Yabana *et al.,* Phys. Rev. B **85**, 045134 (2012)
2. M. Uemoto *et al.*, Opt. Exp. **30**, 23664-23677 (2022)
3. S. Yamada *et al.*, Phys. Rev. B **107**, 035132 (2023)

Electro-Optical Switching in Nonlinear Metasurfaces

M. D. Feinstein[1,2], **A. Andronikides**[1], **and E. Almeida**[1,2*]

[1]Deparment of Physics, Queens College of City University of New York, United States of America
[2]The Graduate Center of the City University of New York, United States of America
[*]corresponding author: euclides.almeida@qc.cuny.edu

Abstract: We demonstrate a nonlinear metasurface that combines electrical and optical switching in a single device. Broadband mid-infrared to visible light conversion is attained in a metasurface that couples mid-infrared radiation to electrically tunable hybrid graphene-gold plasmons. All-optical switching measurements suggest that the device can be operated at Terahertz rates.

Nonlinear metasurfaces are versatile multifunctional photonic elements that allow for simultaneous generation and manipulation of light in subwavelength scales[1]. Such minute control of optical nonlinearities has enabled novel applications such as nonlinear holography[2], beam shaping[3,] and the generation of quantum-correlated photon pairs in nanoresonators[4]. Active tuning of nonlinear metasurfaces may greatly expand their viability for integration with photonic devices. However, the metasurfaces' building blocks, usually dielectric or metallic nanostructures, have limited dynamic tuning, and an external voltage barely affects their plasmonic or dielectric resonances.

Here we demonstrate a multifunctional nonlinear metasurface that combines electrical and optical switching in a single device. Figures 1(a) and (b) illustrate the electro-optical tunable metadevice and the optical scheme to convert mid-infrared pulses into visible light. The metasurface consists of an array of gold nanorods on top of graphene – a material with exceptional nonlinear optical properties for its thinness[5]. The device is arranged in a back-gated field-effect transistor configuration, and an SEM image of a section of the metasurface is shown in Fig. 1(c). In this metasurface, mid-infrared radiation couples to hybrid graphene-gold plasmons[6], which can be switched on and off by the back-gate voltage, as shown in the transmittance spectrum in Fig. 1(d). A pulsed mid-infrared beam is converted into visible light using a gating femtosecond (150 fs) near-infrared pulse centered at λ = 800 nm. Through interaction with the third-order nonlinearity of graphene, a four-wave mixing (FWM) signal is generated at the frequency $\omega_{FWM} = 2\omega_{MIR} + \omega_{800nm}$, where ω_{MIR} is the frequency of the mid-infrared beam. The energy diagram of this interaction is shown in Fig. 1(b).

Figure 1(e) shows the spectra of the measured FWM signal for different mid-infrared input frequencies. The FWM signal falls in the visible, between 570 and 710 nm, for the range of mid-infrared input frequencies between 4 and 10.5 μm accessible to our experimental system. In Fig. 1(f) we show the "switching ratio" of the four-wave mixing signal, which is defined as the ratio of the nonlinear signal at high doping (0.45 eV) to the signal at low doping (0.15 eV) for both the metasurface (the rods on graphene) and bare graphene. Bare graphene attains a switching ratio of nearly 3x for 9 μm mid-infrared input and around 2x for most of the input range. The metasurface, however, has a higher switching ratio than bare graphene over the entire range, reaching a maximum switching ratio of approximately 8x. Notably, the metasurface switching ratio increases sharply as the wavelength is increased toward the graphene plasmon resonance centered at 7.5 μm.

To characterize the optical switching dynamics of the device, we conducted a cross-correlation experiment, as shown in Fig. 1(g), where we changed the delay between the mid-infrared beam and the 800 nm gate pulse. The cross-correlation experiment for the metasurface at 7.5 μm was taken for two voltage states: 40 V - near the charge

neutral point -, and -10 V. The temporal dynamics of the metasurface is sensitive to the voltage, showing a tunable FWHM (between 180 and 210 fs) and a 44 fs shift in the maximum FWM signal. At 40V, near the charge neutrality point, the gold nanorod resonance dominates. At -10 V, however, the mid-infrared pulse couples to graphene plasmons, changing the dynamics of the FWM process. The signal remains for longer delays between the beams since the sample contains near-fields even after the mid-infrared beam has passed.

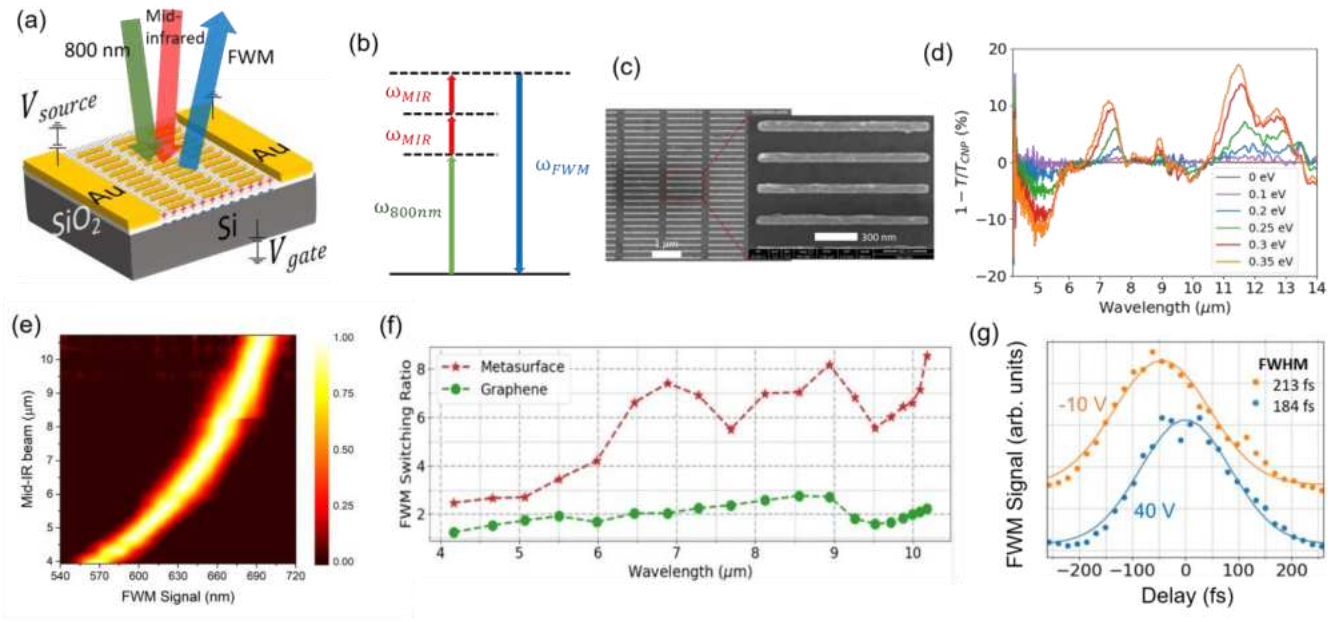


Figure 1. Electro-optical tuning in a nonlinear metasurface. (a) Illustration of the device and the pulse scheme. (b) Energy level diagram for the FWM process. (c) SEM image of the device. (d) Differential transmission spectra of the metasurface as a function of the Fermi level of graphene. (e) FWM signal of the metasurface for several mid-infrared input frequencies. (f) Switching ratio of the FWM signal. (g) Optical switching dynamics of the metasurface.

We demonstrated a novel scheme for simultaneous electrical and optical switching in metasurfaces. Our work represents a significant step for developing electro-optical metasurfaces that convert light from contrasting regions of the electromagnetic spectrum, with potential applications in optical information processing and quantum transduction.

References

1. Li, G., S. Zhang and T. Zentgraf, "Nonlinear Photonic Metasurface," Nature Reviews Materials 2, 17010 (2017).
2. Almeida, E., O. Bitton and Y. Prior, "Nonlinear Metamaterials for Holography," Nature Communications 7, 12533 (2016)
3. Keren-Zur, S., O. Avayu, L. Michaeli and T. Ellenbogen, "Nonlinear Beam Shaping with Plasmonic Metasurfaces," ACS Photonics 3, 117 (2016).
4. Santiago-Cruz, T. et al., "Resonant Metasurfaces for Generating Complex Quantum States," Science 377, 991 (2022).
5. Cox, J. D. and F. J. García de Abajo, "Nonlinear Graphene Nanoplasmonics," Accounts of chemical research 52, 2536-2547 (2019).
6. Feinstein, M. D. and E. Almeida "Hybridization of Graphene-Gold Plasmons for Active Control of Mid-Infrared Radiation," arXiv:2305.05884 (2023).

Metasurfaces and flat optics

Tunable filter based on the Brewster effect in metafilms: From all-pass filter to narrowband perfect absorber

Tomohiro Hoshino[1] **and Yasuhiro Tamayama**[1*]

[1] Department of Electrical, Electronics and Information Engineering, Nagaoka University of Technology, Japan
[*]corresponding author: tamayama@vos.nagaokaut.ac.jp

Abstract: We show that the ratio of the non-radiative loss to the radiative loss of a broadband reflectionless single-layer metamaterial designed so that the Brewster effect occurs can be controlled by varying the arrangement of the constituent meta-atoms without changing the structure of the meta-atoms.

Control of the complex transmission (reflection) spectrum is one of the most important topics in applications of electromagnetic waves. To realize an arbitrary complex transmittance (reflectance) in a single-layer metamaterial, the reflectance (transmittance) needs to be zero. As a broadband reflectionless single-layer metamaterial, we developed Brewster metafilms in our previous study.[1] The Brewster metafilm is realized by two-dimensionally arranging the meta-atoms so that the oscillation direction of the induced electric dipole $\boldsymbol{p}$ in the meta-atoms coincides with the propagation direction of the reflected wave as shown in Fig. 1(a). The complex transmittance of the Brewster metafilm is written as

$$t = \frac{-\mathrm{i}(f - f_0) - \gamma_\mathrm{r} + \gamma_\mathrm{nr}}{-\mathrm{i}(f - f_0) + \gamma_\mathrm{r} + \gamma_\mathrm{nr}}, \qquad (1)$$

where f is the incident frequency, f_0 is the resonance frequency of the Brewster metafilm, and γ_r (γ_nr) is the radiative (non-radiative) loss of the Brewster metafilm. It is found from this equation that the Brewster metafilm behaves as an all-pass filter for $\gamma_\mathrm{nr}/\gamma_\mathrm{r} = 0$ and a narrowband perfect absorber for $\gamma_\mathrm{nr}/\gamma_\mathrm{r} = 1$.[2] In this study, we show that $\gamma_\mathrm{nr}/\gamma_\mathrm{r}$ can be controlled by varying θ in Fig. 1(a) without changing the structure of the meta-atoms.

First, we describe the theory for controlling $\gamma_\mathrm{nr}/\gamma_\mathrm{r}$ without changing the structure of the constituent meta-atoms. The non-radiative loss is determined by materials that compose the meta-atoms. In contrast, the radiative loss is determined by the relationship between the incident electromagnetic fields and the arrangement of the meta-atoms as well as by the structure of the meta-atoms.[3] When the electromagnetic wave propagates along the direction for which the radiation pattern of the meta-atom is large, the electromagnetic wave strongly interact with the meta-atom, which implies the large radiative loss. Therefore, when the meta-atoms are arranged as shown in Fig. 1(a), the radiative loss becomes maximum for θ=45˚ and vanishes for θ=0. If the non-radiative loss is independent of θ, $\gamma_\mathrm{nr}/\gamma_\mathrm{r}$ may be controlled by varying θ without changing the structure of the meta-atoms.

To verify the above theory, we design a Brewster metafilm composed of meta-atoms made of only aluminum. In this case, the non-radiative loss is caused by the Joule loss in aluminum. Figure 1(b) schematically shows the structure of the Brewster metafilm. The unit structure is composed of an electric inductor-capacitor (ELC) resonator combined with two vertical lines, which are used

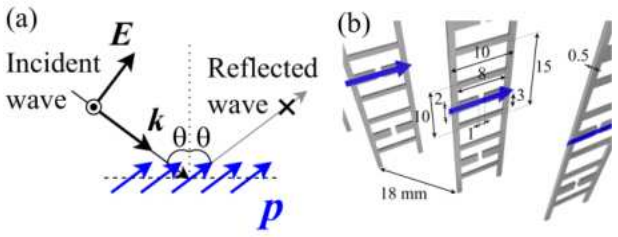


Figure 1: (a) Relationship between the electromagnetic fields and the induced electric dipole in the meta-atoms for realizing the Brewster effect in a single-layer metamaterial. (b) Geometry of the designed Brewster metafilm.

solely for fixing ELC resonators without substrates and do not respond to the incident electric field.

Figure 2 shows the measured and simulated transmission spectra of the Brewster metafilm for several values of θ. As θ decreases, the absolute value of the complex transmittance at the resonance frequency first decreases and then increases. For θ=9˚, the transmittance at the resonance frequency almost vanishes. The variation range of the transmission phase is 2π (smaller than π) when θ is larger (smaller) than 9˚. The theoretical fit of the experimental data to Eq. (1) is also shown in Fig. 2. The fitted curves agree with the experimental data.

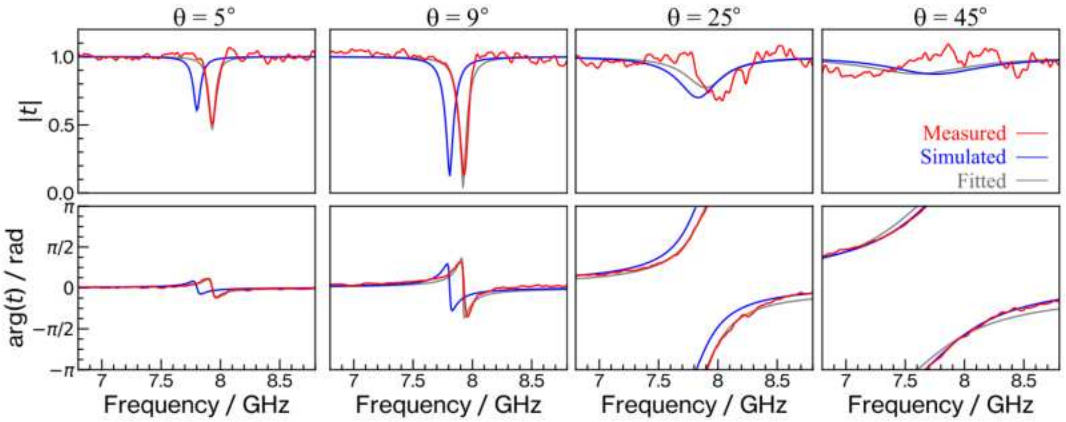


Figure 2: Frequency dependences of the absolute value and the argument of the complex transmittance for several values of θ.

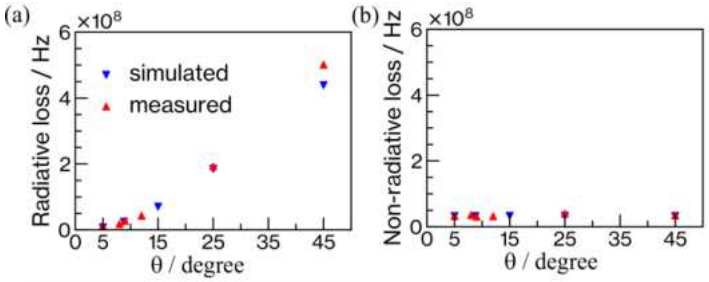


Figure 3: Dependences of (a) the radiative and (b) non-radiative losses on θ.

The radiative and non-radiative losses determined by the fitting are shown in Fig. 3. The radiative loss decreases with decreasing θ, while the non-radiative loss does not show significant dependence on θ. The value of γ_{nr}/γ_r is much smaller than unity for θ=45˚ and becomes unity for about θ=9˚.

In conclusion, we demonstrated the control of γ_{nr}/γ_r in the Brewster metafilm by varying the arrangement of the constituent meta-atoms without changing the structure of the meta-atoms. Because the reflectance of the Brewster metafilms vanishes irrespective of the frequency, the total complex transmittance of the stacked Brewster metafilms agrees with the product of the complex transmittances of the constituent Brewster metafilms. Therefore, the frequency dependence of the complex transmittance may be easily designed in a broad frequency region by stacking the Brewster metafilms with various resonance frequencies, non-radiative losses, and θ.

This research was supported by the Japan Society for the Promotion of Science (JSPS) Grants-in-Aid for Scientific Research (KAKENHI) under Grant No. JP21K04192 and by the Japan Science and Technology Agency (CREST Grant No. JPMJCR2101).

References

1. Tamayama, Y. “Design and analysis of frequency-independent reflectionless single-layer metafilms,” Opt. Lett. Vol. 41, No. 6, 1102–1105, 2016.
2. Tamayama, Y. and Yamamoto, H. “Broadband Control of Group Delay Using the Brewster Effect in Metafilms,” Phys. Rev. Appl. Vol. 18, No. 1, 014029, 2022.
3. Tamayama, Y and Kida, Y. “Tunable group delay in a doubly resonant metasurface composed of two dissimilar split-ring resonators,” J. Opt. Soc. Am. B, Vol. 36, No. 10, 2694–2698, 2019.

Robustness of Active Phase-Change Metasurfaces against High-Power Sources

G. Braid[1], C. Ruiz de Galarreta[1,2], J. Pady[1], A. Comley[3], J. Bertolotti[1] and C. D. Wright[1*]

[1]Centre for Metamaterial Research and Innovation, University of Exeter, Exeter EX4 4QF, UK
[2]Instituto de Òptica, IO-CSIC, Madrid 28006, Spain
[3]AWE Aldermaston, Reading RG7 4PR, UK
[*]corresponding author: David.Wright@exeter.ac.uk

Abstract: Chalcogenide phase-change materials can enable active control of metasurfaces, but the effects of high-power sources on such devices is not yet well-studied. Here, we develop a model for the optical response of metasurfaces subjected to high-power lasers and apply it to previous designs for a beam steerer and a lens.

Metasurfaces allow precise control of optical wavefronts, and have found applications in perfect absorbers, beam steerers, holograms, polarisers, lenses and more [1,2]. Their possible applications are further expanded if they can be actively controlled. Among possible active control mechanisms, one of the most promising is the incorporation of chalcogenide phase-change materials (PCMs) into the metasurface design.

PCMs have two solid phases, amorphous and crystalline, with substantially different optical and electrical properties. Each phase is stable at room temperature, yet can be converted to the other with a suitable thermal stimulus [1]. This allows the optical response of a metasurface to be switched between at least two states, with the further possibility of harnessing intermediate, partially crystallized states for further increased functionality. However, the device will be heated by the light it manipulates, and if the source is high-power, this creates the risk of unwanted switching of the PCM, which could adversely impact on the desired optical response of the device. In this work, we explore the response of PCM metasurfaces to such high-power stimuli, considering in particular, (i) an active beam steerer that switches between anomalous and specular reflection, introduced in reference [2], and (ii) an active lens that controls numerical aperture introduced in reference [1]. These are illustrated schematically in figure 1.

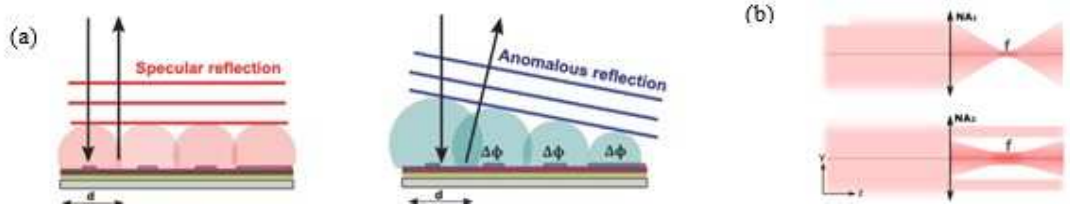
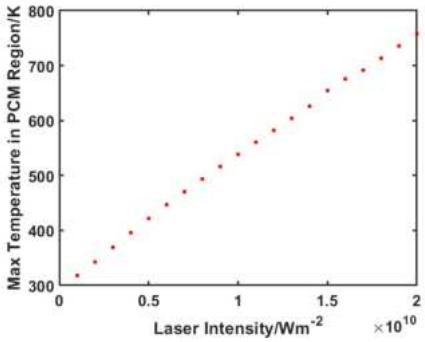


Figure 1. (a) Schematic representation of operation of PCM metasurface beam steerer (adapted with permission from [2]). (b) Schematic representation of operation of NA control lens (adapted with permission from [1]).

We simulate the evolution of the temperature distribution in these metasurfaces under different laser intensities with the commercial finite element analysis package COMSOL Multiphysics. The relationship of maximum temperature to laser intensity for the beam steering metasurface is shown in Figure 2(a). We next combine the thermal model with a Gillespie Cellular Automata (GCA) crystallisation model, based on the work of reference [3], which divides the PCM region into cells to determine stochastically, based on crystal growth and nucleation rate equations, if each cell should experience crystal nucleation, growth or dissociation in each time step. Exemplar growth and nucleation rates, here for the PCM composition $Ge_2Sb_2Se_4Te_1$ (GSST for short) are plotted in figure 2(b), accompanied by simulated crystal distributions for heating at different temperatures.

(a)



(b)

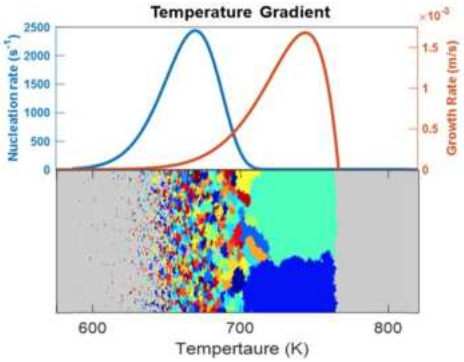
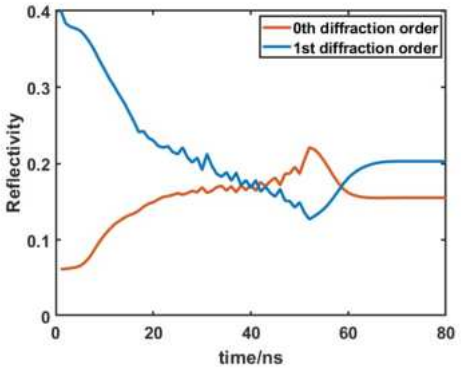


Figure 2. (a) Maximum temperature of PCM layer in the beam steering metasurface of [2] as a function of laser intensity. (b) Nucleation and growth rates for GSST, along with depiction of crystallization at different temperatures. Each colour is a different crystal grain.

Applying our approach to the beam steering metasurface, we find no significant change in optical performance for intensities up to 10^{10} Wm^{-2}, but at higher intensities unwanted crystallization occurs and degrades device performance, as shown in Figure 3(a). We then apply our approach to the active meta-lens. It is computationally demanding to represent the whole lens in one model, so we first explore the responses of individual meta-atoms. High absorption in the crystalline state makes this state the limiting factor. Unwanted amorphisation sets in at around 3×10^{9} Wm^{-2}; the resulting change in optical phase over time is illustrated in figure 3(b).

(a)



(b)

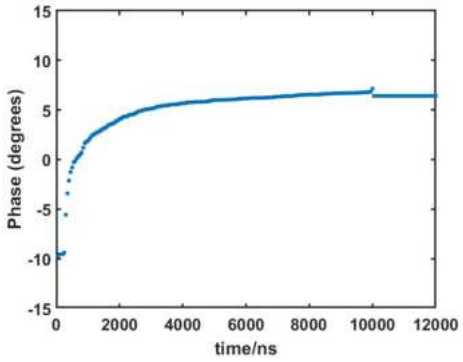


Figure 3. Time evolution of (a) the reflectivity into different diffraction orders when the beam steering metasurface from [2] is subject to a 50 ns pulse of peak intensity 5×10^{10} Wm^{-2}, and (b) the optical phase of crystalline lens unit cell from [1] subject to a 10 μs pulse of peak intensity 3×10^{9} Wm^{-2}.

In summary, we have developed a combined thermal and GCA crystallization model for the response of PCM metasurfaces to high-power laser illumination. Our work highlights the importance of studying the power-handling capabilities of PCM based metasurfaces for high-intensity laser applications.

Funding is acknowledged from the UK EPSRC (EP/L015331/1 and EP/W022931/1) and from AWE Ltd.

References

1. Braid, G., Ruíz de Galaretta, C., Comley, A., Bertolotti, J., Wright, C.D., "Optical and Thermal Design and Analysis of Phase-Change Metalenses for Active Numerical Aperture Control," Nanomaterials **12,** 2689 (2022).
2. Ruíz de Galaretta, C., Alexeev, A., Au, Y.-Y., Lopez-Garcia, M., Klemm, M., Cryan, M., Bertolotti, J., Wright, C. D., "Nonvolatile Reconfigurable Phase-Change Metadevices for Beam Steering in the Near Infrared," Adv. Funct. Mater. **28**, 1704993 (2018).
3. Wang, Y., Ning, J., Lu, L., Bosman, M., Simpson, R., "A scheme for simulating multi-level phase change photonics materials," *npj Comput Mater* **7**, 183 (2021).

Centimeter-scale cylindrical metalens

K. Kim[1] and J. Rho[1,2,3,4*]

[1]Department of Mechanical Engineering, Pohang University of Science and Technology (POSTECH), Pohang 37673, Republic of Korea

[2]Department of Chemical Engineering, Pohang University of Science and Technology (POSTECH), Pohang 37673, Republic of Korea

[3]POSCO-POSTECH-RIST Convergence Research Center for Flat Optics and Metaphotonics, Pohang 37673, Republic of Korea

[4]National Institute of Nanomaterials Technology (NINT), Pohang 37673, Republic of Korea

[*]corresponding author: jsrho@postech.ac.kr

Abstract-

Metalens is a two-dimensional wave manipulator that enables modulating properties of the light with remarkable versatility. In this work, we investigate centimeter-scale cylindrical metalens which operates at a wavelength of 1064 nm with a focal length of 20 mm.

Conventional optical components such as lenses, beam splitters, and prisms play a crucial role in the functionality of telescopes, microscopes, cameras, and displays. However, intricate manufacturing processes and material constraints restrict implementing finely surface curvature and achieving optimized quality, leading to bulky and complex optical system and aberrations. A metasurface, a two-dimensional (2D) wave manipulator capable of modulating the amplitude, phase, and polarization of waves via tailor-made arrangements of meta-atoms. It has been successfully demonstrated in the role of conventional optical components such as focusing, clocking, absorbing, and steering [1-3].

In this work, we demonstrate centimeter-scale cylindrical metalens. We design and fabricate a size of $14\times17\ mm^2$ metalens which has a focal length of $200\ mm$ and operates at $1064\ \mu m$. It has a thickness of $500\ \mu m$, which is much thinner than the conventional refractive lens. We characterize the metalens with an experimental setup and it shows focusing performance comparable to conventional counterparts. We believe that our work paves the way for practical metalens applications.

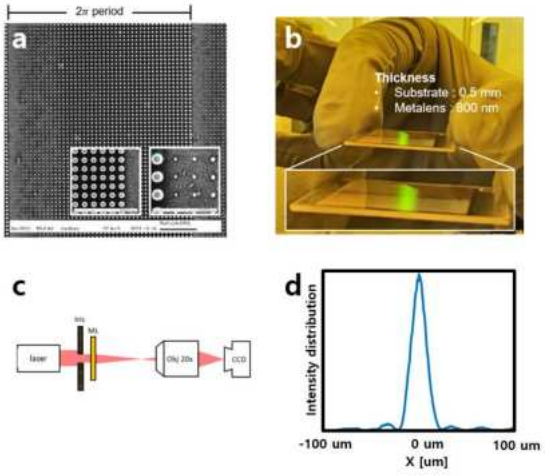


Figure 1. (a) SEM image of metalens's constituent meta-atoms. (b) A photograph of the cylindrical metalens. (c) A schematic of experimental setup for characterizing focusing performance of metalens. (d) Measured intensity distribution of the metalens.

REFERENCES

1. Moon, Seong-Won, et al., "Recent progress on ultrathin metalenses for flat optics.", Iscience, Vol. 23, No. 12, 2020.
2. Ahmed, Rajib, and Haider Butt., "Strain-multiplex metalens array for tunable focusing and imaging.", Advanced Science, Vol. 8, No.4, 2003394, 2021.
3. Chen, Hou-Tong, Antoinette J. Taylor, and Nanfang Yu., "A review of metasurfaces: physics and applications.", Reports on progress in physics, Vol. 79, No. 7, 076401, 2016.

Diverse reconfigurability in far- and mid-infrared few-layer metasurfaces capable of polarization manipulation: case of phase-change materials

A. E. Serebryannikov[1,*] and A. Lakhtakia[2]

[1]ISQI, Faculty of Physics, Adam Mickiewicz University, 61-614 Poznan, Poland
[2]Department of Engineering Science and Mechanics, The Pennsylvania State University, University Park, Pennsylvania 16802, USA
[*]corresponding author: andser@amu.edu.pl

Abstract: Numerical studies on few-layer metasurfaces have clarified how functionality and its possible switching depend on the way in which tunable components are incorporated in the meta-atoms. Two thermally tunable materials, VO_2 and InSb, were used in the few-layer metasurfaces with and without resonant components that are capable of polarization manipulation and related asymmetric transmission.

The use of electrically, magnetically, and thermally tunable materials opens diverse avenues for designing reconfigurable and programmable metasurfaces. Metasurfaces containing thermally tunable phase-change materials (PCM) are widely studied, since their electromagnetic properties change at environmentally feasible conditions. The shapes, volume, properties, and locations of components made of tunable materials determine achievable functionalities and reconfigurablity scenarios which can be controlled by just one parameter—the temperature (T). We compared few-layer metasurfaces comprising either subwavelength resonators or grids, or both, which are fully or partially made of a PCM existing in the metallic (M) phase at higher T and the insulator (I) phase at lower T. The purpose was to compare the functional capability in two cases, i.e., when (i) a PCM fully replaces metals, and (ii) a PCM is used as a material for one layer, while a metal is used in the others, assuming that asymmetric transmission (AT) is obtainable for one of the phases. Functionality switching scenarios typically differ for the cases (i) and (ii). Fig. 1 presents normal-incidence transmission-coefficient magnitude (in terms of S-parameters) vs. frequency for three few-layer metasurfaces comprising split rings [1], calculated using VO_2 parameters from Ref. 2.

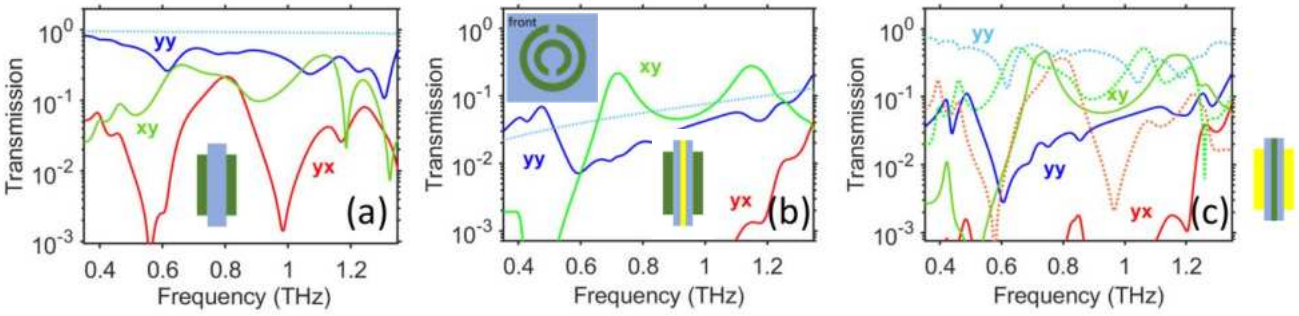


Figure 1. Simulated co-polarized (*xx* and *yy*) and cross-polarized (*yx* and *xy*) transmission-coefficient magnitude for normal incidence on the front (left) face of (a) coupled layers (oriented at 0 deg and 90 deg in the front and back layers) of double split rings made of VO_2; (b) same as (a) but with a Cu-hole layer in the middle; (c) complementary to (b), i.e., with double split rings made of Cu and a VO_2-hole layer. Solid lines – M-phase of VO_2. Dotted (lighter) lines – I-phase of VO_2. Distance between front and back layers is 19.7 μm, period along the *x* and *y* axes is 210 μm, thickness of VO_2 components is 8.75 μm; and interlayer spacer's relative permittivity is 2.1. One of the cross-polarized components must be at least moderately larger than the other cross-polarized and the co-polarized components to achieve AT.

Moderately strong cross-polarized transmittances can appear in the M-phase of VO_2 even in metal-free structure, see Fig. 1(a). However, co-polarized transmission remains strong so that efficient AT cannot be obtained. In the I-phase of VO_2, this regime is changed for co-polarized transmission (passing). Placing a layer of holes in a Cu sheet in the middle results in the weakening of the co-polarized transmittance and of one of the two cross-polarized transmittances, so that AT is possible for M-phase, but the efficiency is not high enough; see Fig. 1(b). Reflection is dominant for I-phase in this case. That is why the resonant and tunable structural components should be *separated*, as in Fig. 1(c). High-contrast AT is achieved in M-phase (at 0.75 and 1.18 THz). In I-phase, it is switchable for the spectral regimes with both co- and cross-polarized transmittances being strong or moderate. Selectivity occurs so that the spectral regimes with strong effect of the phase change do not coincide for *yx* and *xy* transmittances. Moderate-contrast AT is achieved also in I-phase (at 1.06 THz) and replaced by weak transmission in M-phase. Use of only non-resonant components may yield better performance [3].

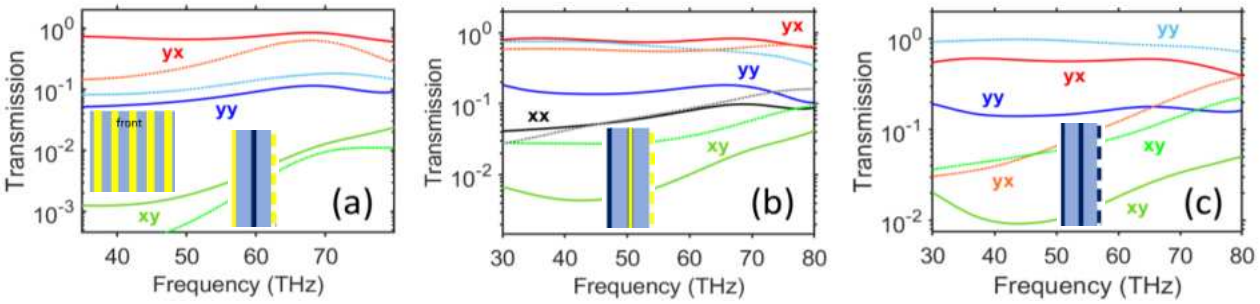


Figure 2. Simulated co- (*xx* and *yy*) and cross-polarized (*yx* and *xy*) transmission-coefficient magnitude (normal incidence) on the front face of three-layer metasurface (oriented at 0 deg, 45 deg, and 90 deg) with strip grids: (a) middle layer is made of VO_2, the other two of Cu; (b) front layer is made of VO_2, the other two of Cu; (c) all layers are made of VO_2. Solid lines – M-phase, dotted lines – I-phase. Distance between front and back layers is 1.75 μm; period in the front/back layers is 1.05 μm and 1.856 μm in the middle layer; thickness of VO_2 components is 87.5 nm; and spacer's relative permittivity is 2.1.

Wideband AT is achieved in M-phase for the only-grid structure in Fig. 2(a). It is switched for dominant reflection, say, at 35-45 THz in I-phase. At 67 THz, the phase change leads rather to variations of contrast and efficiency of AT. Wideband AT is achieved at 30-70 THz in M-phase, also in Fig. 2(b). In I-phase, it is switched for the regime with both *yx* and *yy* transmittances significant but the *xy* transmittance very weak. Generally, the *yy* transmittance is more sensitive to the phase change than the *yx* transmittance. Interestingly, the *yx* transmittance is not sensitive to the phase change at 77 THz. Switching between the moderately efficient AT and co-polarized passing is achieved in Fig. 2(c), at least for 30-60 THz. For I-phase, the cross-polarized transmittance increases with frequency. The structures in Fig. 2 can be *rescaled* for rather arbitrary lower-frequency ranges, including that in Fig. 1. To compare, we examined the same configurations when VO_2 is substituted with InSb and rescaling is applied by decreasing all sizes by factor of 2.5 for Fig. 1 and increasing it by factor of 22 for Fig. 2, so that the aforementioned switching scenarios can be obtained at 1-2.5 THz.

Acknowledgements. Contribution of A.E.S. has been supported by Narodowe Centrum Nauki, project UMO-2020/39/I/ST3/02413. A.L. thanks the Binder Endowment at Penn State. Thanks are also due to Prof. E. Ozbay.

References

[1] Serebryannikov, A. E.; Lakhtakia, A.; Vandenbosch, G. A. E.; Ozbay, E. Sci. Rep., Vol. 12, 3518, 2022.

[2] Wang, D., Zhang, L., Gu, Y. et al., Sci. Rep., Vol. 5, 15020, 2015.

[3] Serebryannikov, A. E.; Lakhtakia, A.; Ozbay, E. Opt. Mater. Express, Vol. 12, No. 12, 4594, 2022.

Polarization- and direction-multiplexed vector holography based on asymmetric transmission of bi-layer metasurfaces and its application

Joonkyo Jung[1], Hyeonhee Kim[1], and Jonghwa Shin[1,*]

[1]Department of Materials Science and Engineering, KAIST, Daejeon 34141, Republic of Korea
[*]corresponding author: qubit@kaist.ac.kr

Abstract: We investigate the potential of bi-layer metasurfaces for achieving full control of asymmetric transmission in optical systems. We demonstrate that the polarization- and direction-multiplexed vector holography can be achieved using bi-layer metasurfaces. With this approach, we also suggest a novel optical encryption algorithm.

An optical system can exhibit distinctive transmission responses depending on the direction of light illumination, i.e., the front- and back-side illuminations, also known as asymmetric transmission. The asymmetric transmission has been actively studied because of its wide applicability to a variety of scientific and engineering fields such as optical communications, imaging or optical encryption. Metasurfaces, arrays of nanostructures with subwavelength scales, have revolutionized the study of asymmetric transmission based on their high degrees of freedom in manipulating light. However, most existing literature have been confined to partial control of asymmetric transmission; only the cross-polarized transmission has been used for achieving asymmetric transmission and, as a result, control of polarization has been ignored. In this study, we demonstrate the polarization- and direction-multiplexed vector holography based on bi-layer metasurfaces, fully utilizing the vector nature of light.

To achieve full control of asymmetric transmission, both co- and cross-polarized transmissions, relative to two orthogonal polarizations as a basis, should be manipulated at will. Recently, we have demonstrated that bi-layer dielectric metasurfaces can generate arbitrary Jones matrices [1]. Based on this extended controllability, we showed that arbitrary control of co- and cross-polarized transmission is achievable. In general, the reciprocity hinders from achieving direction-multiplexed vector holography. To circumvent this problem, we used the spatial partitioning strategy where arbitrary polarization- and direction-multiplexed vector functionalities can be inscribed in a half of transmission space. With this strategy, we experimentally demonstrated the polarization- and direction-multiplexed vector holography and its application to optical encryption as in Figure 1.

In summary, we have proposed that bi-layer metasurfaces can achieve full control of asymmetric transmission. As a proof of concept, we have demonstrated the polarization- and direction-multiplexed vector holography and its application to optical encryption. We believe this extension of achievable functionalities can directly translate to the extension of applications.

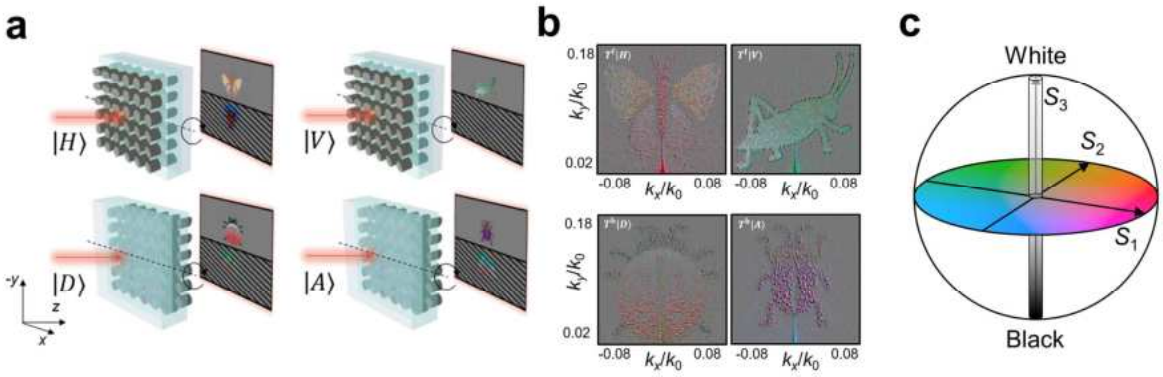


Figure 1. Polarization- and direction-multiplexed vector holography. (a) Schematics of vector holography. (b) Experimental demonstration of the polarization- and direction-multiplexed vector holography. (c) Color mapping of CIELAB color space onto the Stokes parameter space.

References

[1] T. Chang, et al., "Universal Metasurfaces for Complete Linear Control of Coherent Light Transmission", *Adv. Mater.*, **34**, 2204085 (2022).

Unified Metasurfaces for Dynamic Beam Steering

Hsiu-Ping Su[1*], Po-Sheng Huang [1], and Pin Chieh Wu[1]

[1] Department of Photonics, National Cheng Kung University, Tainan 70101, Taiwan
[*]corresponding author: samwii888@gmail.com

Abstract: Research has demonstrated active control of beam deflection, yet it relies on multiple deflectors or complex integration with intricate circuitry. In this work, we introduce a metasurface to adjust the deflection angle by simply altering the position of incident light. This breakthrough holds promise for applications in LiDAR and AR/VR.

As the development of LiDAR and AR/VR technology progresses, the requirements for smaller and more compatible optoelectronic devices have dramatically increased in demand. Metasurfaces are one of the solutions because they possess unprecedented capabilities to manipulate the properties of light at subwavelength scales. Studies have demonstrated dynamical control the direction of deflection light by combining active materials and meticulously designed circuit[1]. However, this design principle needs careful consideration of the interaction between active material and metasurfaces, which presents a significant challenge in achieving the desired design.

In this work, we introduce a novel metasurface characterized by simple design that facilitates multiple deflection angles within a single chip. Our approach begins with the application of the generalized Snell's law[2], assuming the incident light to be normal to the device, which leads to the optical response described by Eq. (1). We subsequently allow the deflection angle to linearly vary along the *x*-direction from 2° to 30°, originating from the origin and extending to *x* equal to the size of the metasurface (*L*), as presented in Eq. (2). By combining Eqs. (1) and (2), we can obtain the required phase profile of the metasurface, as shown in Eq. (3). Notably, Eq. (3) reveals that the deflection angle can be modulated by adjusting the incident light position along the *x*-direction. Here, n_t and θ_t represent the refractive index and deflected angle, respectively. k_0 is the wavenumber. $\theta(x)$ denotes the deflected angle at *x* position across the metasurface.

To ensure a polarization-independent response in our proposed amorphous silicon (a-Si) based metasurface, we opted for a square shape with a variable width (*w*) ranging from 50 nm to 350 nm, while keeping a constant height (*h*) and period (*p*) at 480 nm and 400 nm, respectively, during simulation process (refer to Fig. 1a). The transmittance and phase responses at a wavelength of 940 nm are illustrated in Figs. 1a and 1b. Subsequently, after obtaining the meta-atoms data library, we commence metasurface design using proposed methodology, and the optimized phase distribution profile is represented in Fig. 1c.

$$n_t \sin(\theta_t) = -\frac{1}{k_0}\frac{\partial \Phi(x)}{\partial x} \tag{1}$$

$$\theta(x) = \frac{(\theta(L)-\theta(0))}{L}x + \theta(0) \tag{2}$$

$$\Phi(x) = -k_0 * \frac{L}{(\theta(L)-\theta(0))}\cos\left(\frac{(\theta(L)-\theta(0))}{L}x + \theta(0)\right) \tag{3}$$

To validate the concept, we confirmed in simulations that the direction of deflected light can indeed be modulated by changing the position of incident light. Figure 2a illustrates the operational mechanism of the proposed metasurface. The device has a total size of 1 mm by 1 mm, and the left side of the metasurface is defined as the origin of the *x*-axis.

We have chosen to input light at x equal to 0.1 mm, 0.5 mm, and 0.9 mm, which results in deflection angles of 4.8°, 16°, and 27.2° respectively.

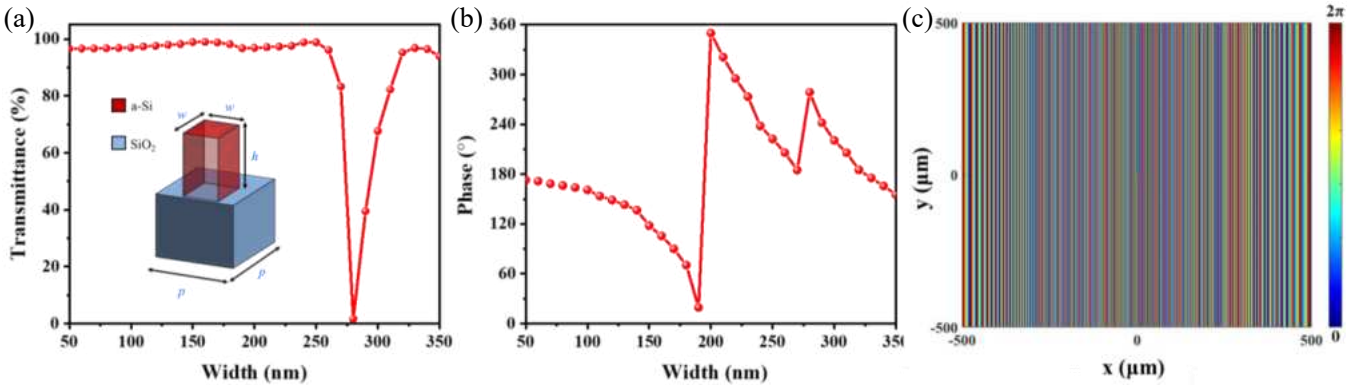


Fig. 1 (a, b) Simulated transmittance and phase spectra versus width of nanostructure at a wavelength of 940 nm. The inset illustrates the unit structure, where the height h and period p are set at 480 nm and 400 nm. (c) Calculated phase distribution of the proposed metasurface. The deflected angle varies along the x-direction from 2° to 30°

Subsequently, we have set the distance of observation 1 mm apart from the device, and the resulting far-field patterns are shown in Figs. 2b, 2c, and 2d. The positions of the patterns in the far-field are in great agreement with predictions from theory. This demonstration suggests that we can achieve any deflection angle within the range of 2° to 30°, depending solely on the position of the incident light.

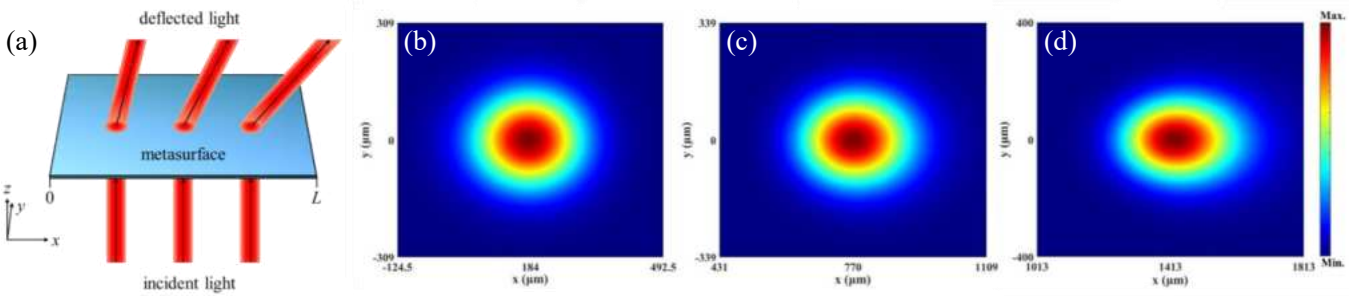


Fig 2. (a) Operational mechanism of the proposed metasurface. (b, c, d) Simulated far-field intensity distribution of light incoming at x = 100 μm, 500 μm, 900 μm. The output beam angle corresponds to 4.8°, 16°, and 27.2°.

In conclusion, our numerical simulations have successfully demonstrated the capability of achieving beam steering within a single metasurface. Based on the design principle, the realized metasurface is able to steering the incoming light along one specific direction without complex design processes. Notably, the deflection angle is not limited to 30°, and can be adjusted as needed. The proposed metasurface holds exciting opportunities for applications in LiDAR, AR/VR systems.

References

1. Ghazaleh Kafaie Shirmanesh, Ruzan Sokhoyan, Pin Chieh Wu, and Harry A. Atwater. “Electro-optically Tunable Multifunctional Metasurfaces”, Vol. 14, No. 6, 6912-6920, 2020.
2. Nanfang Yu, Patrice Genevet, Mikhail A. Kats, Francesco Aieta, Jean-Philippe Tetienne, Federico Capasso, and Zeno Gaburro. “Light Propagation with PhaseDiscontinuities: Generalized Laws of Reflection and Refraction”, Vol. 334, No. 6054, 333-337, 2011.

Large Field-of-View Near-Infrared Imaging based on Telecentric Metaoptics

W. -L. Hsu[1], Q. -C. Zeng[1], C. -Y. Yu[1], Y. -C. Chen[1], Y. -F. Chen[1], C. -C. Chen[2], and C. -M. Wang[1*]

[1] Department of Optics and Photonics, National Central University, Taoyuan, 32001, Taiwan

[2] Taiwan Instrument Research Institute, National Applied Research Laboratories, Hsinchu, 30076, Taiwan
[*]corresponding author: cmwang@cc.ncu.edu.tw

Abstract: In this work, we demonstrate a telecentric-based metalens operating at a wavelength of 940 nm, providing a high-quality focal spot at viewing angles from 0° to 60°. Due to the maximum aspect ratio of the meta-atom being only 4, this metalens is relatively easy to be fabricated.

Near-infrared light at 940 nm is commonly used in facial recognition systems for mobile phones, employing diffractive optical elements [1] and corresponding lenses. The trend toward thinner mobile devices underscores the potential for metalenses, with their thin and lightweight characteristics [2-5], to replace traditional lenses in such systems. Here, we present a telecentric-based metalens designed for operation at 940 nm. With a maximum aspect ratio of only 4 for the meta-atom, this metalens is relatively easy to fabricate. Furthermore, it provides a high-quality focal spot over viewing angles ranging from 0° to 60°.

As shown in the inset of Figure 1(a), the fundamental unit of the metalens is an amorphous silicon (a-Si) nano-cylinder on a silica substrate. The nano-cylinder maintains fixed basic dimensions (thickness: 600 nm and period: 400 nm), while its diameter (D) is varied to analyze corresponding optical properties. Figure 1(a) illustrates the phase shift and transmittance of the nano-cylinder with various D values. These simulations were conducted using the Rigorous Coupled-Wave Analysis method under normal illumination with a wavelength of 940 nm. The refractive index of the a-Si film is 659nm at 940 nm measured by using Spectro ellipsometer. The results indicate that the phase shift reaches 2π as D varies from 150 to 300 nm. Additionally, the majority of the nano-cylinder transmittances up to 0.8, indicating improved performance of the metalens. Notably, the maximum aspect ratio of the nano-cylinder is only 4, making the circular pattern relatively easy for production [6]. Therefore, this metalens is beneficial for mass production. To achieve high-quality images at various viewing angles, this metalens is designed within a telecentric system. Figure 1(b) illustrates the ray tracing diagrams of the metalens' imaging system, including an aperture and the metalens. It is evident that the metalens provides excellent focusing quality at viewing angles ranging from 0 to 60°. Fabrication of the metalens involves E-beam lithography, followed by inductively coupled plasma reactive ion etching (ICP-RIE) processing. Figure 1(c) displays scanning electron microscope (SEM) images of the fabricated metalens. With a diameter of 3 mm, the optical microscope image is shown in the inset of Figure 1(c).

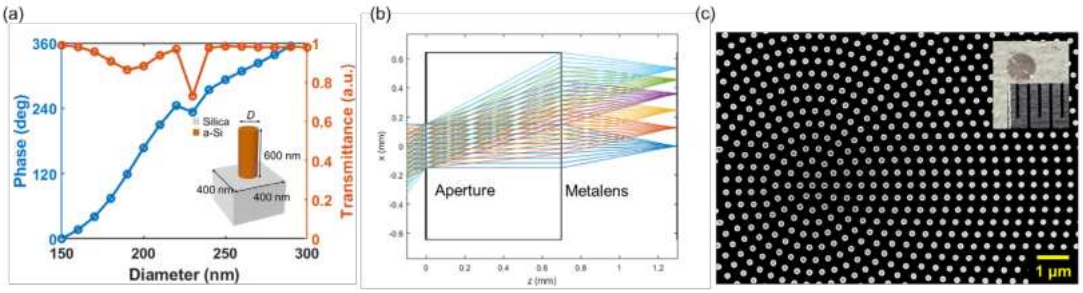


Figure 1. (a) Geometric diagram and optical property of an a-Si nano-cylinder. (b) Ray tracing diagrams of the metalens' imaging system under incident light with various angle from 0° to 60°. (c) SEM images of the fabricated metalens.

Figure 2(a) presents the simulated focus point of the metalens under normal illumination, serving as a reference. A clear theoretical focal spot is evident, along with a weak aperture around the focus point, representing the first-order sidelobe of the Airy disc. For measurement, as shown in Figure 2(b), the measured focus point is comparable to the simulation result. Notably, the first-order sidelobe is too weak to be detected by the sensor, hence it is not observed in the measured focus point. Figure 2(c) displays the modulation transfer function (MTF) curves obtained from the corresponding simulation and measured focus points in Figure 2(a) and 2(b). The measured MTF curve is comparable to the simulation curve. Even when the incident angle is 45°, the metalens still provides a high-quality focal point without obvious deformation, as demonstrated in Figure 2(d) and 2(e). Finally, Figure 2(f) illustrates that the simulation and measurement MTF curves are comparable. It is worth noting that the measurement focus point does not exhibit the first-order sidelobe of the Airy disc. Therefore, the measurement MTF has higher resolution in the spatial low-frequency region.

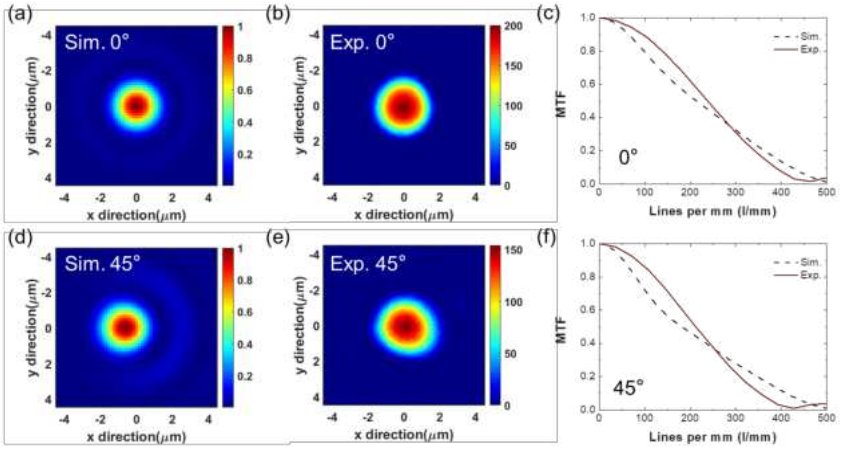


Figure 2. The (a) simulated and (b) measurement focus point under normal illumination. (c) MTF curves corresponding simulation and measured focus points in Figure 2(a) and 2(b). The (d) simulated and (e) measurement focus point when the incident light angle is 45°. (c) MTF curves corresponding simulation and measured focus points in Figure 2(d) and 2(e).

References

1. Mor Z. US9825425B2. "Integrated structured: light projector comprising light - emitting elements on a substrate," 2017.
2. Yu, N. and F. Capasso, "Flat optics with designer metasurfaces," Nature Mater, Vol. 13, 139–150, 2014.
3. Hsiao, H. H., C. H. Chu and D. P. Tsai, "Fundamentals and Applications of Metasurfaces," Small Methods, Vol. 1, No. 4, 1600064, 2017
4. Engelberg, J. and U. Levy, "The Advantages of Metalenses over Diffractive Lenses," Nat. Commun, Vol. 11, No. 1, 1991, 2020
5. Jiang, Q., G. Jin and L. Cao, "When Metasurface Meets Hologram: Principle and Advances," Adv. Opt. Photonics, Vol. 11, No. 3, 518−576, 2019.
6. Hsu, W. L., Y. C. Chen., S. P. Yeh, Q. C. Zeng, Y. W. Huang and C. M. Wang, "Review of Metasurfaces and Metadevices: Advantages of Different Materials and Fabrications," Nanomaterials, Vol. 12, No. 12, 1973, 2022.

Flat optics light harvesting in large-area TMDs films for photoconversion and photochemical applications

G. Ferrando[1*], M. Gardella[1], G. Zambito[1], F. Bisio[1], M. Barelli[1], M.C. Giordano[1], F. Buatier de Mongeot[1]

[1]Dipartimento di Fisica, Università di Genova, Via Dodecaneso 33, I-16146 Genova, Italy

[*]giulio.ferrando@edu.unige.it

Abstract: Two-dimensional Transition Metal Dichalcogenide semiconductors (2D-TMDs) show potential for optoelectronics and photon-to-energy conversion. Moreover, by combining different TMDs layers into van der Waals heterostructures, their optoelectronic response can be engineered further. This work introduces large-area flat optics light harvesting and growth methods to maximize their potential.

Two-dimensional Transition Metal Dichalcogenides semiconductors (2D-TMDs) have recently collected a strong scientific and technological interest over a broad community due to their peculiar optoelectronic response within a broadband spectrum, and to their tunable bandgap that enables promising optoelectronic and photonic functionalities. Additionally, the superior optical absorption coefficients in the Visible spectrum, enhanced by about two orders of magnitude with respect to conventional bulk semiconductors, qualify TMDs as optimal candidates for photodetection and photoconversion applications[1,2]. However, to fully leverage their potential in extreme thickness regimes, effective photon harvesting strategies and large-area growth techniques are essential.

Here, we present an homogeneous growth of large area 2D-TMDs films by means of a physical deposition process based on Ion Beam Sputtering, followed by high temperature recrystallization in a sulfur enriched atmosphere[3]. Furthermore, through periodic modulation of TMDs layers (MoS_2) on a large area nanostructured template, we efficiently steer light parallel to the 2D material, exploiting photonic anomalies in the flat-optics regime[1,4] As a case study, we demonstrate that flat-optics light harvesting in periodically corrugated MoS_2 layers employed as photocatalysts boosts photodissociation of Methylene Blue (MB), a polluting dye molecule commonly used in the textile industry[5]. Additionally, the atomically smooth surfaces and fully saturated in-plane chemical bonds of 2D-TMDs offer an opportunity to engineer the optoelectronic response further by combining different TMDs layers to form van der Waals heterostructures[6].

The fabrication process has been subsequently optimized for the sequential synthesis of vertically stacked large area MoS_2-WS_2 van der Waals heterostructures, which can be supported on a large area graphene layer, which acts as a transparent conductive window. This vertical stacking ensures a type-II staggered band alignment which in turn allows to split excitons across the junction, thus increasing the lifetime of the photogenerated carriers compared to the individual TMD components. Charge separation can be exploited for energy conversion and photocatalytic applications, reflected in the superior photodissociation rate of molecular dye probes in solution near the heterostructure sample, and in the photovoltage and photocurrent measured upon illumination of the large area device.

These results demonstrate that TMDs van der Waals heterostructures represent optimal building blocks for the fabrication of self-powered photodetectors, exploiting charge separation of photogenerated carriers at the 2D interface without any external bias.

References

1. Bhatnagar, M. *et al.* "Broadband and Tunable Light Harvesting in Nanorippled MoS_2 Ultrathin Films." *ACS Appl. Mater. Interfaces* **13**, 13508–13516 (2021).
2. Martella, C. *et al.* "Designer Shape Anisotropy on Transition-Metal-Dichalcogenide Nanosheets." *Adv. Mater.* **30**, 1–9 (2018).
3. Giordano, M. C., Zambito, G., Gardella, M. & Buatier de Mongeot, F. "Deterministic Thermal Sculpting of Large-Scale 2D Semiconductor Nanocircuits." *Adv. Mater. Interfaces* **10**, (2023).
4. Bhatnagar, M. *et al.* "Ultra-broadband photon harvesting in large-area few-layer MoS_2 nanostripe gratings." *Nanoscale* **12**, 24385–24393 (2020).
5. Ferrando, G. *et al.* "Flat-optics hybrid MoS_2 /polymer films for photochemical conversion." *Nanoscale* **15**, 1953–1961 (2023).
6. Jariwala, D., Davoyan, A. R., Wong, J. & Atwater, H. A. "Van der Waals Materials for Atomically-Thin Photovoltaics: Promise and Outlook." *ACS Photonics* **4**, 2962–2970 (2017).

Jones matrix holography with liquid crystal-integrated active metasurface

Hyeyoung Yoon[1,2,4#], Hyounghan Kwon[4], and Inki Kim[1,2,3*]

[1]Department of Biophysics, Institute of Quantum Biophysics, Sungkyunkwan University, Republic of Korea
[2]Department of Intelligent Precision Healthcare Convergence, Sungkyunkwan University, Republic of Korea
[3]Center of Quantum Information, Korea Institute of Science and Technology, Republic of Korea
[4]Department of Meta Bio Health, Sungkyunkwan University, Korea, Republic of Korea
[*]Corresponding author: inki.kim@skku.edu

Abstract: This research integrates a liquid crystal cell with a holographic metasurface for dynamic polarization control, utilizing the Gerchberg-Saxton algorithm and Jones matrix. Devices based on this technology can operate in arbitrary polarization, thereby enhancing the flexibility of optical systems.

Metasurface-based holography is gaining attention in the field of metasurface research due to its flexibility and high precision. In particular, polarization control using metasurfaces can be applied in various areas such as information storage, imaging, and communications. However, existing technologies have primarily focused on fixed polarization states, and there were limitations in changing polarization states in real-time.

We aim to overcome these limitations by combining a liquid crystal cell (LC cell) with a holographic metasurface, presenting a new method that can electrically control any polarization state [1,2]. Such structures can convert linear polarization to circular polarization or vice versa. Meanwhile, the LC cell contains a liquid crystal material that changes its properties in response to electrical signals, allowing for real-time optical property adjustments of the metasurface. The design of this device involves the following process:

Typically, the Gerchberg-Saxton (GS) algorithm is used when designing holography. The GS algorithm plays a pivotal role in the structural design optimization of holography, going through a repetitive optimization process to minimize the difference between the intended and actual optical outputs. For the production of metasurface-based holography, we applied the Jones matrix mathematical model to this GS algorithm [3]. The adoption of the Jones matrix allows for the mathematical representation of arbitrary polarization states and the prediction and control of light behavior. In this process, the optical field and pattern of the metasurface that are necessary to generate the desired optical output are determined, making it possible to predict the metasurface's response to specific polarization conditions. The GS algorithm's repetitive optimization process is carried out to update the optical field data of the metasurface in a direction that makes the desired optical output and the actual optical output nearly identical.

The structure of the metasurface determined through this design and optimization process then moves on to the integration stage with the liquid crystal cell (LC cell). Through the electrical control of the LC cell, the optical properties of the metasurface can be adjusted in real-time. This provides the metasurface with the flexibility to manipulate light in any polarization state. Through this process, metasurface-based holography can realize various optical functions, including polarization control.

In conclusion, the design of LC cell-based metasurface holography involves optimization through the Jones matrix-based GS algorithm, followed by integration with the LC cell. This continuous process lays the

foundation for precisely controlling the optical properties of the metasurface and providing flexibility for a wide range of applications. The development of this technology can contribute to various fields such as high-resolution holographic displays, high-performance optical filters, and real-time information processing. It also enables applications in security, data storage, and optical encryption. Moreover, the ability to electrically control any polarization state significantly enhances the flexibility of optical systems, enabling new forms of optical interfaces and interaction methods.

References

1. Kim, Inki, et al. "Pixelated bifunctional metasurface-driven dynamic vectorial holographic color prints for photonic security platform." Nature Communications 12.1 (2021): 3614.
2. Kim, Inki, et al. "Holographic metasurface gas sensors for instantaneous visual alarms." Science Advances 7.15 (2021): eabe9943.
3. Rubin, Noah A., et al. "Jones matrix holography with metasurfaces." Science Advances 7.33 (2021): eabg7488.

Photocurrent Enhancement induced by Fabry-Pérot quasi-Bound States in the Continuum in Silicon Nanodisk Hexagonal Array beyond 1400 nm in Wavelength

K. Moriasa[1], H. Hasebe[1], H. Sugimoto[1] M. Fujii[1*]

[1]Electrical and Electronic Engineering, Kobe university
[*]fujii@eedept.kobe-u.ac.jp

Abstract: A nanodisk array of polycrystalline silicon with the toroidal dipole resonances in the sub-bandgap region is produced on a metal mirror via a spacer. The structure possesses the Fabry-Pérot bound states in the continuum, and strongly enhances the photocurrent in the eye-safe wavelength.

1. Introduction

Near infrared light in the wavelength longer than 1400 nm is called "eye safe" due to its relatively low hazards to retinas. Eye safe lasers have been used as a light source for LiDARs in atmospheric physics, autonomous driving, etc. However, since the sensitivity of conventional silicon (Si)-based photodetectors is limited to ~1100 nm, several novel photodetection mechanisms have been proposed to extend the detection range[1]. An example is utilizing internal photoemission at the Schottky interface between Si and noble metal nanoantennas. Another approach uses an optical resonator to enhance defect-mediated absorption of polycrystalline Si in the sub-band gap region. In previous work, we demonstrated that sub-radiant toroidal dipole (TD) resonances in a hexagonal array of Si nanodisks can effectively enhance the light absorption in the low extinction coefficient range, and thus can be used for the photocurrent enhancement in the eye safe wavelength range[2].

In this work, we propose a new structure that can achieve perfect absorption in the low extinction coefficient range. The structure is schematically shown in Figure 1(a). A metal mirror is formed below a hexagonal array of Si nanodisks via a silica spacer. The key concept to achieve the perfect absorption is as follows. At a proper spacer thickness, radiation from the nanodisk array is fully suppressed due to the interference with the mirror image in the metal mirror. This state is the Fabry-Pérot bound states in the continuum (FP-BICs). By slightly detuning the interference condition, i.e., by changing the TD radiation phase from the image dipole one via spacer thickness, the nanodisk array comes to partially couple with light. When the radiation loss of the system matches with the material loss, i.e., the critical coupling condition, incident light is perfectly absorbed[3]. In this work, we first discuss the validity of the concept by numerical simulation, and then demonstrate that this approach is useful for photocurrent enhancement of polycrystalline Si in the sub-band gap range.

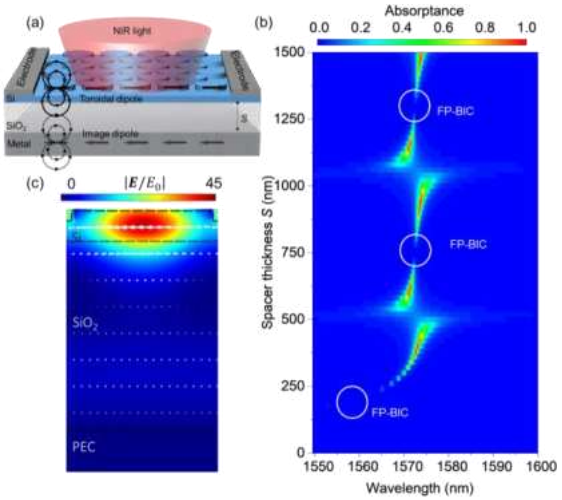


Figure 1. (a) Schematic of Si nanodisk hexagonal array on mirror structure. Interference between a toroidal dipole in a nanodisk and its image creates FP-BIC. (b) Calculated absorption spectra of the structure shown in (a) as a function of spacer thickness (*S*). (c) Electric field map in the cross section in (a) at 1573.7 nm (*S* = 940 nm).

2. Results and discussion

Figure 1(b) shows the calculated absorption spectra of the structure shown in Figure 1(a) as a function of the silica spacer thickness (*S*). A hexagonal array of polycrystalline Si nanodisks with the diameter and the height of

700 and 50 nm, respectively, is formed on a 100 nm thick polycrystalline Si film. The period is 750 nm. The nanodisk array has the TD resonance around 1570 nm. Below the nanodisk array, a silica spacer and a perfect electric conductor mirror are formed. The silica spacer thickness is changed from 0 to 1500 nm. The absorption peak due to TD resonance is periodically modified by the spacer thickness. The absorption disappears at S = 200, 760, and 1280 nm. This is the FP-BIC. Detuning the spacer thickness from the BIC condition turns the FP-BIC into quasi-BIC. At the spacer thicknesses satisfying the critical coupling condition (S = 400, 620, 940, 1160, and 1480 nm), the absorptance becomes nearly unity. Figure 1(c) shows the cross sectional electric field distribution for S = 940 nm. The incident power is strongly confined in the Si nanodisk array.

We fabricate the nanodisk array on mirror structure by using a nanosphere lithography[2]. Figure 2 shows the measured reflectance and photocurrent spectra. The spacer thickness is changed from 980 to 1120 nm. The reflectance dip around 1450 nm is due to the TD resonance. We can see that the reflectance dip and the photocurrent peak are strongly modified by the spacer thickness. When S = 1120 nm, the reflectance peak almost disappears. This is the appearance of FP-BICs. With decreasing the spacer thickness, i.e., by detuning the BIC condition, the reflectance dip becomes deeper. This is accompanied by the increase of the photocurrent at the TD resonance. Therefore, the FP-quasi-BIC enhances photocurrent of the Si nanodisk array in the sub-bandgap wavelength range.

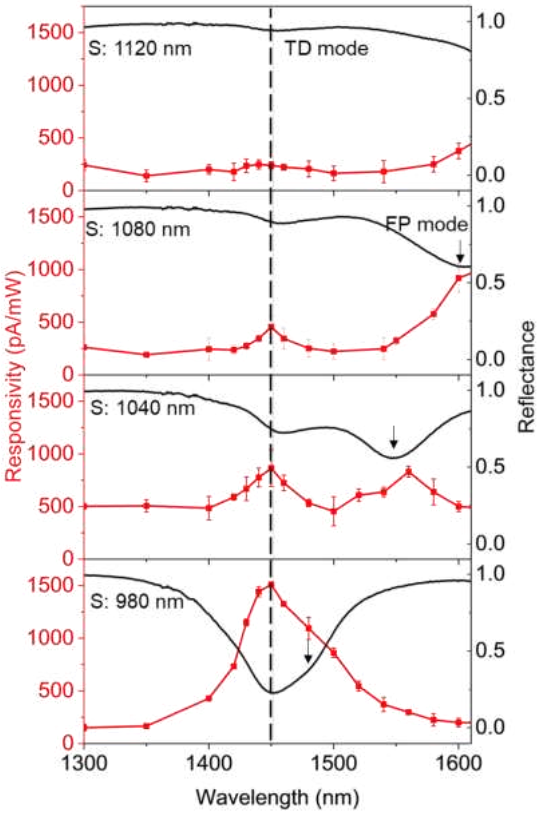


Figure 2. Reflectance (black) and responsivity (red curves) spectra of Si nanodisk array on mirror with different spacer thickness from 980 to 1120 nm. Black arrows and broken line indicate the FP and TD mode wavelength, respectively.

3. Conclusion

We numerically and experimentally investigate absorption property of a Si nanodisk array on a metal mirror structure. Numerical simulations show that the proposed structure possesses FP-BIC in the NIR range and perfect absorption can be achieved at proper spacer thicknesses. In experiments, the reflectance dips at TD resonance are strongly modified by the spacer thickness, and the photocurrent is strongly enhanced in the sub-band gap range. This result indicates that the combination of a TD mode and FP-BIC provides a novel platform for Si-based NIR photodetectors.

References

1. Casalino, M., G. Coppola, R. De La Rue, D. F. Logan. “State-of-the-art all-silicon sub-bandgap photodetectors at telecom and datacom wavelengths”, Laser & Photonics Reviews, Vol. 10, Issue. 6, 895–921, 2016.
2. Hasebe, H., K. Moriasa, K.Yamashita, H. Sugimoto, and M.Fujii,” Toroidal Dipole-Induced Photocurrent Enhancement in Si Nanodisk Hexagonal Array below the Band Gap”, ACS Photonics, Vol. 9, Issue. 10,3302-3309, 2022
3. Moriasa, K., H. Hasebe, H. Sugimoto, and M. Fujii. M, “Bound states in the continuum (BIC) in silicon nanodisk array on mirror structure: Perfect absorption associated with quasi-BIC below the bandgap”, Journal of Applied Physics, Vol. 133, Issue. 17, 173102, 2023.

Enhancement of Circular Dichroism by Engineered Absorption in Chiral Dielectric Metasurface

A. Fitriana[1,2*], K. Tanaka[1,2], and L.R. Jaeger[1,3], M. Hafermann[1], T. Pertsch[2,4], C. Ronning[1], and I. Staude[1,2]

[1] Institute of Solid-State Physics, Friedrich Schiller University Jena, Germany.
[2] Institute of Applied Physics, Abbe Center of Photonics, Friedrich Schiller University Jena, Germany.
[3] Department of Electronic Materials Engineering, Australian National University, Australia
[4] Fraunhofer Institute for Applied Optics and Precision Engineering IOF Jena, Germany
[*]corresponding author: anna.fitriana@uni-jena.de

Abstract: We demonstrate that ion-beam irradiation of chiral dielectric metasurface can enhance optical chirality by carefully tailoring the material absorption. We approach the critical coupling regime associated with maximum circular dichroism by irradiating chiral silicon dimers with energetic Ne^+ ions. This provides potential of tweaking metasurface properties post fabrication using ion-beams.

Chiral dielectric metasurfaces can exhibit strong circular dichroism (CD) while preserving typical properties associated with metasurfaces, such as a flat profile and resonant response [1] based on the excitation of a collective chiral mode in the supercell consisting of four dimers [2]. Importantly, due to the inherent connection between dissipation and CD, chiral dielectrics need to operate in the weak dissipation regime to reach large values of CD. For any given chiral metasurface design, optimal performance in terms of CD is reached for critical coupling, which can be achieved by carefully adjusting the dissipation in the system [3]. Here, we make use of ion-beam irradiation to tune the optical properties of tailored photonic metasurface post fabrication. Specifically, we study periodic three-dimensional dielectric bilayer metasurface with four-fold (C4) rotational symmetry consisting of chiral dimers of silicon nanocuboids embedded in a silica matrix [2]. Figure 1 shows a sketch of the metasurface geometry. We gradually increase the dissipative loss in the chiral silicon metasurfaces via ion-beam induced structural damage. The metasurface was irradiated by Ne^+ ions at energies of 200 keV with carefully adjusted ion fluences ranging from 10^{13} to 10^{15} ions/cm^2 in six irradiation steps. After each step, the polarization-resolved transmission spectra of the metasurface for normal incidence were recorded for the left (LCP) and right-circularly (RCP) polarized light in near-infra-red (NIR) regime. As a reference, we also recorded the spectra for the pristine sample before irradiation. The CD spectra were evaluated based on the relative difference between LCP and RCP transmission and plotted as a function of ion fluence in Fig. 2(a). Fig 2(b) presents the maxima of the CD spectra for different ion fluence. At lower fluences, the results show a substantial increase of the CD signal due to the radiation-induced damage in the nanostructures. We observe a maximum optical chirality with CD of ~0.85 for an ion fluence of 10^{14} ions/cm^2, clearly exceeding that of 0.70 for the pristine metasurface. This indicates that ion-beam irradiation brings the system closer to the critical coupling condition as compared to the pristine fabricated structure. With even higher ion fluences, the overall CD is reduced, which is consistent with an increase of losses beyond the critical coupling condition. As another feature, we also observe a redshift of the CD maxima with increasing ion fluence in Fig. 2(a).

Next, to analyze the effect of ion-beam irradiation on the optical parameters of the silicon, we perform numerical calculations of the transmission spectra for a variation of the silicon's complex refractive index and compare the results with experimental spectra. Good overall agreement is obtained assuming a gradual increase of the

imaginary part of the silicon refractive index with increasing ion fluence. The simulated transmission for optimized geometrical parameters of the metasurface is depicted in Fig. 2(c) alongside corresponding measurement results for a fluence of 10^{14} ion/cm^2. Here, the imaginary part of the silicon refractive index is raised by a factor of 3.8 compared to the pristine material. Furthermore, the observed shift of the CD maxima could be reproduced in the numerical spectra by an increase of the real part of the refractive index, indicating the expected material densification effect due to ion irradiation [4,5].

In summary, we successfully demonstrated a new approach to enhance CD in chiral dielectric metasurface using ion-beam irradiation. Importantly, our approach allows for flexible loss manipulation in the material by controlling the ion fluence. More generally, our results underline the critical importance of carefully tailored dissipation losses for maximizing CD in a given chiral metasurface and establish ion-beam irradiation as a new powerful tool for tweaking metasurface properties post fabrication.

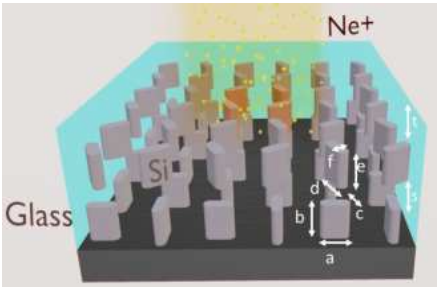


Fig 1 (a) Schematic of the investigated chiral metasurface, here a × b × c = 379 × 391 × 149 nm^3, d × e × f = 423 × 326 × 179 nm^3 and s = 299 nm.

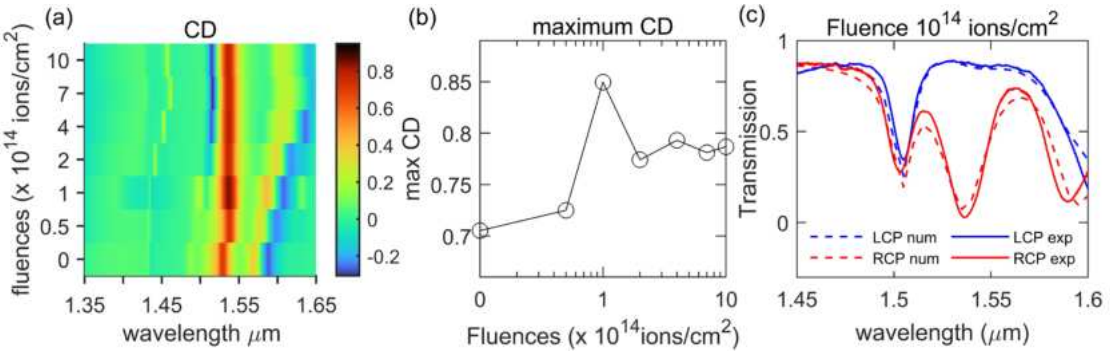


Fig 2 (a) CD spectra with respect to the varying Ne$^+$ ion fluence: 5×10^{13}, 10^{14}, 2×10^{14}, 4×10^{14}, 7×10^{14}, and 10^{15} ions/cm^2. (b) Maxima in CD signals for different fluences. (c) Transmission of LCP and RCP light with 10^{14} ions/cm^2 bombardment: experimental results and simulation of the optimized parameters for refractive indices.

References

1. Wu, C. et al, "Spectrally selective chiral silicon metasurfaces based on infrared Fano resonances." Nature communications Vol. 5, No.1, 3892, 2014.
2. Tanaka, K. et al, “Chiral bilayer all-dielectric metasurfaces,” ACS nano, Vol. 14, No. 11, 15926–15935, 2020.
3. Gorkunov, M. V., A. A. Antonov and Y.S. Kivshar, “Metasurfaces with maximum chirality empowered by bound states in the continuum,” Physical Review Letters, Vol. 125, No. 9, 093903, 2020.
4. Zheng, L. et al, “Densification of silica glass at ambient pressure,” Journal of Chemical Physics, Vol. 125, No.15, 2006.
5. Volkert, C. A. "Stress and plastic flow in silicon during amorphization by ion bombardment." Journal of Applied Physics, Vol. 70, No. 7, 3521-3527, 1991.

Tuneable Optical Edge Detection using Phase-Change Metasurfaces

S. Kendall[1], C. Ruiz de Galarreta[1], J. Shields[1], G. Yang[2], M. Wang[2], J. S. Lee[2], N. Farmakidis[2], A. Moskalenko[2], K. Huang[2], L. Deguzman[3], A. Alù[4], J. Bertolotti[1], H. Bhaskaran[2] and C. D. Wright[1,*]

[1]Department of Engineering, University of Exeter, Exeter, EX4 4QF, UK
[2]Department of Materials, University of Oxford, Parks Road, OX1 3PH, UK
[3]University of North Carolina, Charlotte, NC 28223, USA
[4]Advanced Science Research Center, City College of New York, New York, NY 10031, USA
[*]david.wright@exeter.ac.uk

Abstract: Local and non-local phase-change optical metasurface designs for reconfigurable edge-detection/bright-field imaging are explored. Reconfigurability is achieved via switching phase-change material between crystal and amorphous states. Applications include fast pre-processing for image analysis, optical microscopy and more.

Analog optical computing has seen an increase in attention in recent years due to potential advantages it holds over its digital counterpart, including intrinsic parallelism, low-loss transmission and ultra-high bandwidth [1]. Fast and energy efficient optical computing systems have been demonstrated, for example implementing neural networks [2] and matrix-vector multiplication [3]. Such demonstrations include both free-space and integrated photonic configurations: here we work with free-space arrangements to perform the specific task of edge detection. Edge detection is a key part of image processing and previous metasurface designs have been presented to tackle this (e.g. [4]). Here we introduce the added element of reconfigurability, specifically an ability to switch between edge detection and bright-field imaging modes. This tuneability is achieved through the integration of chalcogenide phase-change materials (PCMs) within the designs. PCMs exhibit vastly different optical properties (n and k) between their amorphous and crystalline states and can be actively switched between states via the use of a thermal stimulus [5]. These differences are exploited in our designs for reconfigurable metasurfaces in the visible through to the mid-infrared wavelength regimes. We demonstrate, in simulation, both simple 1D edge-detection and more complex 2D polarization insensitive operation, whilst also comparing designs based on so-called 'local' metasurfaces operating in the Fourier plane with 'non-local' metasurfaces operating directly in the spatial domain.

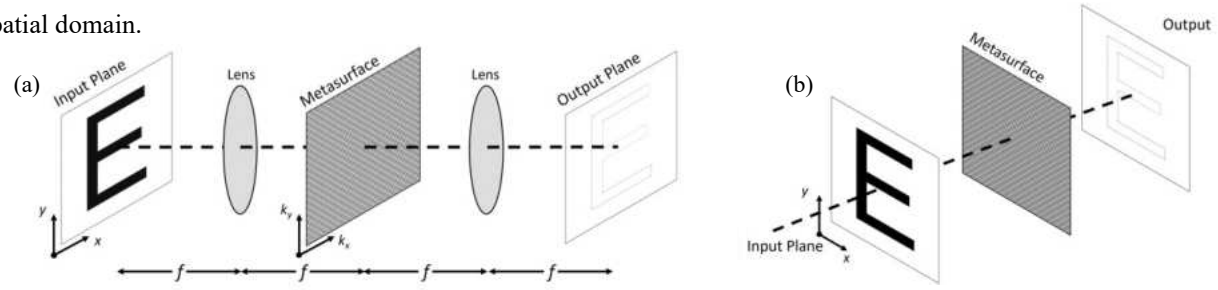


Figure. 1: Schematics of (a) a 4f system designed for edge-detection via the use of a 'local' PCM metasurface placed in the Fourier plane and (b) a system that utilizes a non-local PCM metasurface for edge-detection directly in the spatial domain. The PCM metasurfaces can be reconfigured to switch to and from their amorphous and crystalline states which in turn switches the metasurfaces from an edge-detection mode to a bright-field imaging mode.

Figure 1a demonstrates the concept of edge detection using a metasurface placed in the Fourier plane of a 4f system of the type used in conventional spatial filtering. Here, the 'meta-atoms' vary in size as a function of position on the metasurface. Figure 1b shows a schematic of a system for edge-detection using a non-local metasurface, in which the meta-

atoms are identical across the whole metasurface (in turn simplifying fabrication). Edge-detection functionality can be implemented using optical systems with transfer functions that mimic differentiation, typically second-order differentiation [4]. Hence, the transfer function we aim for is parabolic in transmission amplitude (and constant in optical phase), with the transfer function for bright-field simply being a flat (high) transmission amplitude and again constant optical phase.

In Figure 2a we demonstrate an example of the transmission amplitude and phase response of a $Ge_2Sb_2Te_5$ (GST) local metasurface designed for the mid-infrared regime (specifically at λ=4.5 μm). The radii of the meta-atoms vary in size as a function of position to deliver the desired parabolic transmission amplitude profile, with the response being dominated by localized resonances. The parabolic response shown is for the GST meta-atoms in their amorphous state, the crystalline state shows a flat transmission profile, hence switching to a bright-field imaging mode.

We also created a design for edge-detection via a non-local PCM metasurface, the metasurface meta-atoms are identical such that the whole metasurface can be designed to have a collective parabolic transmission amplitude response as a function of the angle of incident light. Figure 2b shows exemplar results: here we utilize the PCM material Sb_2Se_3 in the near-infrared (λ=1550 nm). The metasurface consists of a hexagonal array of holes in a thin Sb_2Se_3 layer. Edge-detection (up to angles of ±30 °) is obtained with the Sb_2Se_3 layer in its crystalline state, with the amorphous state resulting in bright-field imaging. Usage of a hexagonal array gives access to 2D relatively polarization insensitive edge-detection (particularly at low angles), previously shown for non-reconfigurable Si metasurfaces [6]. The simulated outputs of an example input image into such a non-local metasurface is shown in Figure 2b, displaying its edge-detection and bright-field modes.

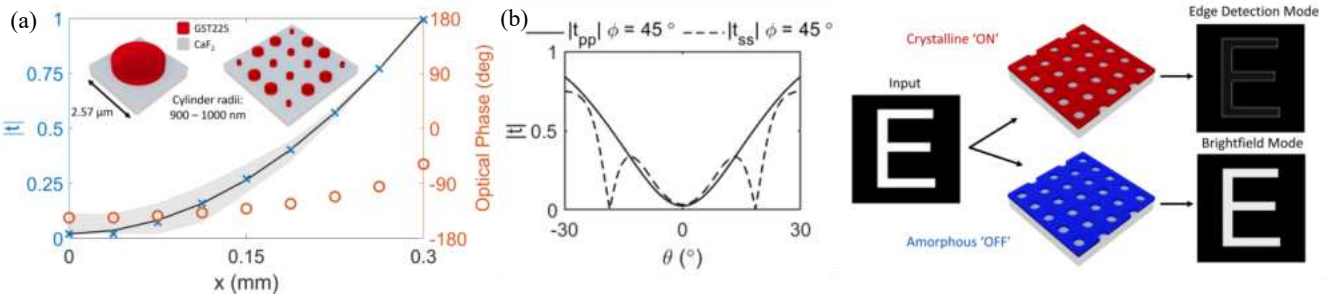


Figure. 2: (a) Optical transmission amplitude and phase response of a local PCM (GST) metasurface designed for edge-detection in the mid-infrared, when the GST is in its amorphous state. Switching the GST to its crystalline state results in bright-field imaging. The grey shaded region around transmission amplitude curve displays upper and lower bounds assuming a fabrication tolerance of 3 nm for meta-atom radii. (b) The transmission amplitude of a non-local Sb_2Se_3 metasurface designed to have a 2D polarization insensitive parabolic response as a function of the elevation and azimuth angle of incident light. This example shows both the s and p polarization responses at an azimuthal angle of 45 °. On the right we show the simulated output of such a metasurface in edge-detection and bright-field imaging modes respectively.

Funding is acknowledged for part of this work from the UK EPSRC (EP/W003341/1, EP/W022931/1, EP/W022931/1).

References

1. McMahon, P. L. The physics of optical computing. Nature Reviews Physics, 1-18, 2023.
2. Lin, X. et al. All-optical machine learning using diffractive deep neural networks. Science 361, 1004-1008, 2018.
3. Feldmann, J. et al. Parallel convolutional processing using an integrated photonic tensor core. Nature 589, 52–58, 2021.
4. Cordaro, A. et al. High-index dielectric metasurfaces performing mathematical operations. Nano letters 19, 8418-8423, 2019.
5. Ruiz de Galarreta C. et al. Tunable optical metasurfaces enabled by chalcogenide phase-change materials: from the visible to the THz. Journal of Optics 22, 114001, 2020.
6. Cotrufo, M. et al. Dispersion engineered metasurfaces for broadband, high-NA, high-efficiency, dual-polarization analog image processing. Nature Communications 14, 7078, 2023.

Inverse design of microwave absorber based on adjoint topological optimization

Hyeonjin Park[1], **Jonghwa Shin**[1*]

[1]Korea Advanced Institute of Science and Technology, Republic of Korea
[*]corresponding author: qubit@kaist.ac.kr

Abstract: Optimization of metal-backed multi-layered slab structure were considered for X-band absorption. The permittivity of each slab was assumed to possess a single Lorentzian resonance. The permittivity value was optimized with a topological adjoint algorithm and achieved an ultra-thin microwave close to the theoretical limit near 89%

It is well known that the minimum thickness of absorber structure cannot be smaller than a certain value confined as integration of reflection coefficient as a function of wavelength as shown below [1] and it is non-trivial to get a structure which approaching the theoretical limit.

$$\left|\int_0^\infty \ln|\rho(\lambda)|d\lambda\right| \leq 2\pi^2 \sum_i \mu_{s,i} d_i \tag{1}$$

In this research, to get a clue about a microwave absorber structure with ultra-thin thickness which approaching the causal limit, we considered topologically freeform multilayered slab structure with N layers where permittivity of each layer considered as single Lorentzian resonance with 4 parameters where $\epsilon_{i,0}, \omega_{i,p}, \omega_{i,o}, \gamma_i$ denotes for contribution of higher frequency resonances, plasma frequency, resonance frequency, and damping frequency, respectively for each i^{th} layer.

$$\epsilon_i(\omega) = \epsilon_{i,0} + \frac{\omega_{i,p}^2}{\omega_{i,0}^2 - \omega^2 - i\omega\gamma_i} \tag{2}$$

Based on this configuration, we conducted inverse design of microwave absorber with 4N in total design parameters based on topological adjoint optimization [2]. In the optimization, the cost function was set as reflectance $f = |E_r|^2$ and the process iterated to the maximum reflectance in X-band frequency range (8–12 GHz) lower than 10 dB.

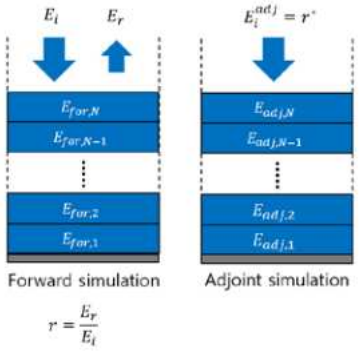


Figure 1. Schematic simulations for adjoint optimization

Figure 1 shows the schematic of adjoint optmization process. In the forward simulation, incident field with unit amplitude exerted on the N layered structure and calculate reflected field and field inside each Lorentzian layer. In the adjoint simulation, nothing but incident field amplitude is now the complex conjugate of reflected

field, and calculate fields inside each layer as a result. The gradient of cost function with respect to each parameter can be defined as this when $\epsilon_{i,j}$ indicates j^{th} parameter of i^{th} layer slab.

$$\frac{\delta f}{\delta \epsilon_{i,j}} = \frac{\delta f}{\delta \epsilon_i}\frac{\delta \epsilon_i}{\delta \epsilon_{i,j}} = 2Re\left[E_{adj} \cdot E_{for} \cdot \frac{\delta \epsilon_i}{\delta \epsilon_{i,j}}\right] \quad (3)$$

Figure 2 shows the target response of optimization and the resultant optimized response of structures with different thicknesses with 20 layers. Right side of figure 2 shows that the total thickness 1 mm thickness is enough to attain 10 dB reflectance in X-band range, and the required permittivity distribution as a function of frequency and layer position in Figure 3 with its real and imaginary values.

The minimum thickness derived with equation (1) for the target response was calculated as 0.89 mm, so with the topological adjoint approach, it was possible to get an absorber structure with 89% performance of the theoretical limit.

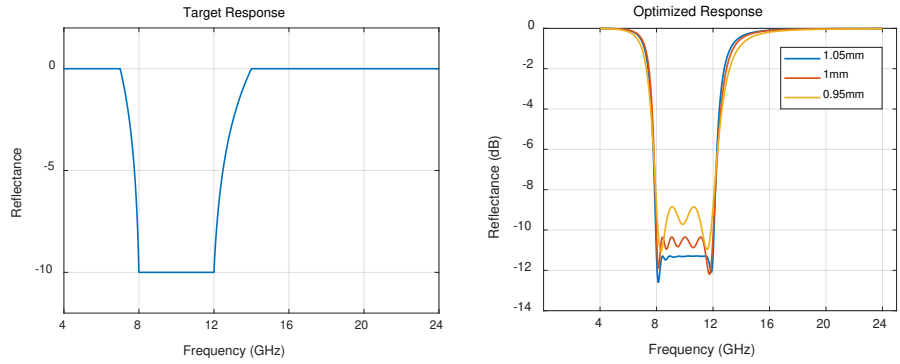


Figure 2. (Left) Target response, (Right) Optimized response of multilayer structure with 20 layers in different total thickness

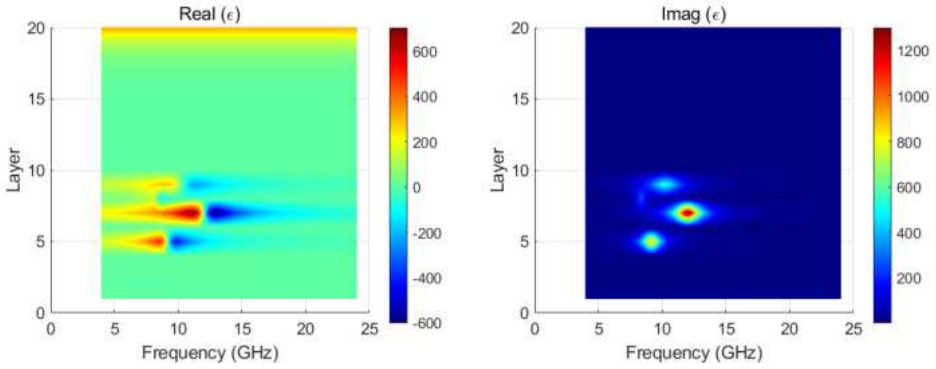


Figure 3 Required permittivity distribution of 1 mm thickness structure case

References

1. Konstantin N. Rozanov, "Ultimate Thickness to Bandwidth Ratio of Radar Absorbers", IEEE Trans. Antennas Propag., Vol. 48, No. 8, 2000.
2. Owen. D. Miller, "Photonic Design: From Fundamental Solar Cell Physics to Computational Inverse Design", Arxiv,1308. 0212, 2013.

Impact of Numerical Simulation Boundary-Domain-Decomposition Errors on Optical Performance of Meta-diffusors

Louis Henri FERNANDEZ-MOURON[1*], Loumi TREMAS[1], Mathys LE GRAND[1], Pascal URARD[1], Habib MOHAMAD[2], Lucie DILHAN[2], Enrico Giuseppe CARNEMOLLA[3], Matteo FISSORE[3], James DOWNING[3], Valérie SERRADEIL[4], Bruce RAE[3] and Denis RIDEAU[1].

STMicroelectronics, [1]850 rue J. Monnet BP16, 38926 Crolles, France. - [2]12 rue J. Horowitz, 38019 Grenoble, France. – [3]1 Tanfield, Inverleigh Row, Edinburgh, UK – [4]190 avenue Célestin Coq ZI, 13106 Rousset, France.

**Corresponding author: louishenri.fernandez-mouron@dauphine.eu*

Performing accurate optical FDTD simulations of large meta-diffusors (~mm) with subwavelength meshing is challenging. A common technique [1-2] involves subdividing the domain and stitching the simulation results, but the resulting error has been rarely studied. We propose a novel approach to emulate this stitching simulation strategy error on meta-diffusors.

Keywords: Meta-diffusor, Metasurface, Boundary-domain-decomposition, stitching, distortion, Optical simulation, Electromagnetics, FDTD, Maxwell Solver.

I- INTRODUCTION

To make possible optical simulations of large meta-surfaces, a commonly used technique consists in boundary domain decomposition [1-2], or stitching, that divides the structure into smaller subdomains with fixed boundary conditions for simulation. This enables efficient optical simulations of large-scale devices but can induce error over the whole optical domain. In this paper, we examined the impact of such error in the Near Fields (NF) and the Far Fields (FF) of a propagating light beam through a metasurface. A metasurface [3] is an engineered material designed to exhibit unique optical properties with subwavelength patterns, formed by scatterers called meta-atoms (MA). Here, the considered metasurfaces have MA grids with regular spacing of size of 256*256.

A systematic study has been conducted using a series of large meta-diffusor designs obtained using a Phase Retrieval (PR) algorithm [4] on a series of random targets (see Figure 1). The targeted phase is mapped using a scalar-to-meta-atom relation, linking a meta-atom parameter to the locally induced phase shift.

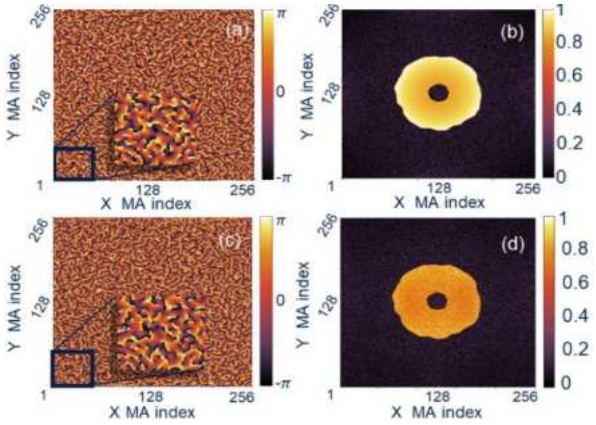


Figure 1 – Metasurface samples from PR. The phase and Far Field moduli (max normalized to unity) respectively in (a,b) come from the PR results and (c,d) from the simulation of the same design.

The designs are simulated with Finite Difference Time Difference (FDTD) and compared to the PR results (Figure 1). The same designs are simulated with and without applying a domain-decomposition (see Figure 2).

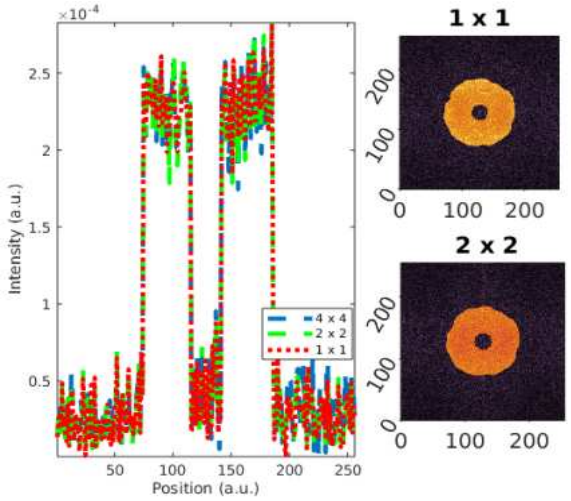


Figure 2 – FF middle cut of the full domain simulation (1 x 1) superposed with stitched example in 2 x 2 and 4 x 4 crops. 2D results (1x1, 2x2) are displayed on the right side.

Despite this seemingly negligeable error in FF (see Figure 2), we develop an error model in NF, and then expand upon this model, in order to approach this error in FF.

The error masks (EM), defined as the difference between the full-domain FDTD NF simulation and the stitched one $|NF - NF_{stitched}|$, are shown in Figure 3, for two sub-domain decomposition sizes (128*128 and 64*64) on non-overlapping regions. The error introduced by this domain-decomposition is clearly visible on both sides of the stitching lines and is roughly of the same amplitude as the maximum of the full NF simulation. Its impact on the FF is obtained using the Fourier Transform of the previous error masks (exact equivalent), with ~0.1 the scale of full NF simulation. In Figure 3, are displayed very clear Dirac combs in FF of the EM. To account for these, we need a model emulating the error induced by the phase and moduli parts.

II- ERROR MODEL FOR STITCHING

In order to perform a systematic study of the impact of stitching errors on the optical zeroth-order (mode in FF) of meta-diffusors, we modeled the error mask using a statistical-based approach. Figure 4 shows the horizontal cutlines of Figure 3-(a) and 3-(b) plots (horizontal crop boundary being removed, thus no perpendicular line overlap), highlighting NF amplitude error profile. The phase difference is also extracted from the same NFs of 6 designs (with 256*256 MA) with their stitched counterparts.

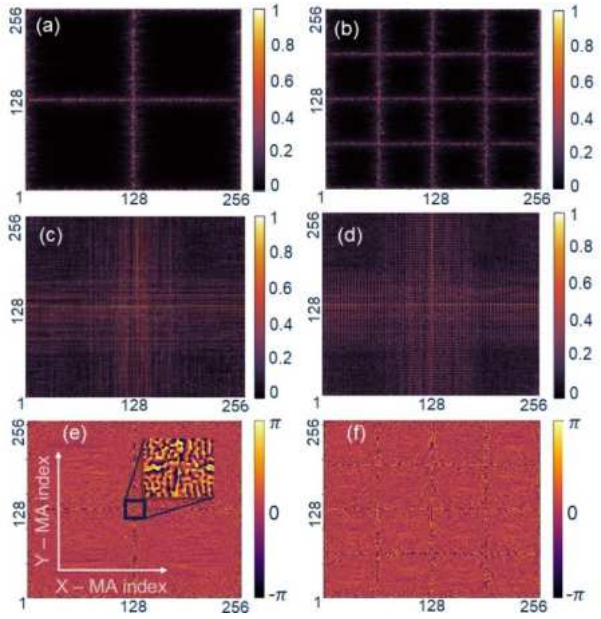


Figure 3– NF moduli of EM for stitching examples cropped in 2x2 (a) and 4x4 (b), (c, d) the respective FF moduli, (e, f) the NF phase.

This error exhibits a maximum at the domain-boundary regions and extends on both sides. We found out that a pseudo-Lorentzian function provides a reasonable fit of the EM (Figure 4 in red) for crop size of 128*128 and 64*64. We verified that this function fits the EM even for smaller crops.

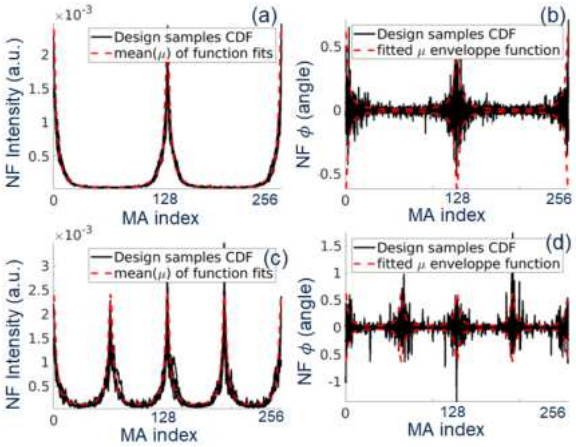


Figure 4– Superposition of 6 different designs EM moduli and phase difference. Also shown are quasi-Lorentzian fit: 2x2 for moduli (a), phase difference (b), 4x4 for moduli (c), phase difference (d).

This fitted model is a sum of pseudo-Lorentzian function: $\mathcal{L}(x,\mu,\gamma) = A/\left(\frac{(x-\mu)^2}{\gamma} + B\gamma\right)$ (1), with μ the center, A a normalization constant and $B{\sim}1/4$ an empirical parameter. For a system size of 256*256 MA, $\gamma{\sim}24.5$ is related to the width of the pseudo-lorentzian, i.e. the typical length of the error range on both sides of the stitching.

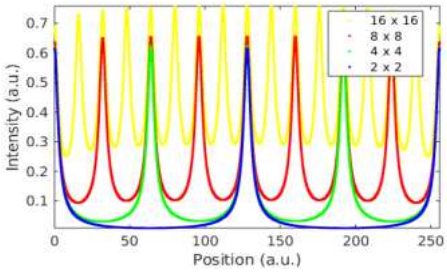


*Figure 5: Prediction of NF EM moduli in 128*128 (2 x 2), 64*64 (4 x 4), 32*32 (8 x 8 crops), and 16*16 crop sizes.*

Figure 5 shows the model predictions for crops as small as 16 x 16 subdomains (i.e. each composed by 16*16 MA). As the crop numbers rise, the minimum error also increases.

To further explain the impact of the stitching error (w.r.t. I), we implemented a stochastic NF error function δ accounting for the white noise or fluctuations in NF error and phase error, using ζ, a gaussian random signal convolved with a pseudo-Gaussian function (accounting for a correlation between MA): $U\left(x, \sigma = \frac{N}{\nu}\right) = \frac{1}{2\sigma} e^{-\frac{|x|}{\sigma}}$ (2), [5] with σ the correlation range, N the size of the system in MA scale and ν the crop factor. ζ maps with various ν are shown in Figure 6. This random fluctuation ζ is combined with the fitted model θ shown in Figure 4, as a filter mask, to produce δ the stochastic error model. We use two embedding models for δ: $\{ U + \delta$ (3), a constant model, $U + \delta U(1-U)$ (4), a quadratic model$\}$. This stochastic approach results are shown in Figure 7 and a clear impact of the random phase and amplitude fluctuation model is pointed out at low ν (sets ζ smoothing range, see Figure 6). This shows that a white noise induced in Near field related to the EM and the phase difference, has also a negligible effect on the Far Field (see Figure 7).

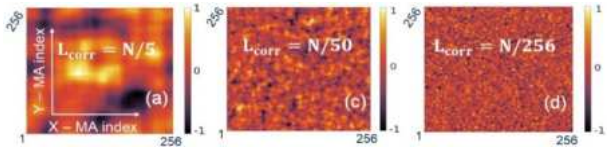


Figure 6 – ζ maps for various correlation $\sigma = N/\nu$ with $N = 256$.

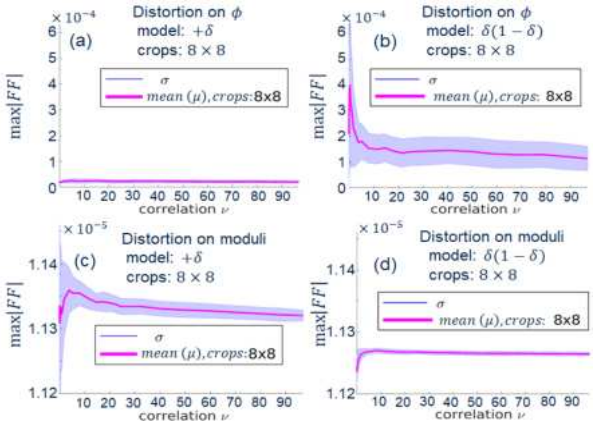


Figure 7– Probability plot of FF maxima with emulated stitched NFs, with distortion on phase, on 128x128 meta-atoms.

Indeed, in Figure 7 we highlight the effect of various distortions on FF zero-order, and the impact of correlation frequency ν, notably the maxima close to the MA scale in (b), or close to the crops number in (c) and (d).With this modelling approach, it is possible to conduct a rigorous analysis and emulate the Z0th error occurring from stitching method in FDTD simulations.

III- CONCLUSION

We propose a statistical error model enabling the predictions of the impact of simulation stitching errors on the optical properties of large metasurfaces. More systematic studies and models will be shown at the conference, in particular the correlation length that is crucial to understand the impact of the stitching error on the optical performances of meta-diffusors.

REFERENCES:

[1] *Bogdanov and Lapointe "Electron-beam lithography for photonic waveguide […]", J. of Vac. Sci. Technol. B: Microelectron. Nanometer Struct. Process, 2012.*

[2] *D. J. Dougherty, et al." Stitching-Error Reduction in Gratings […]", Journal of Ligthwave Technology, vol. 19, no.10, pp. 1527-1531, 2001.*

[3] *P. Lalanne and P. Chavel " Metalenses at visible wavelengths[…]", Laser Photonics Rev., vol.11, no. 3, p. 1600295, 2017.*

[4] *Wang, et al." A hybrid Gerchberg–Saxton-like algorithm for DOE […]", Opt. Lasers in Eng.,89,109-115, 2017.*

[5] *Ding, Li "Autocorrelation and limited sampling […]", Journal of Physics: Conference series, vol. 1544, pp 12009, 2020.*

Time-varying nonlinear effects in Q-boosted metasurfaces

A. Chernyak[1,2*], A. Musorin[1,2], A. Tognazzi[3,4], P. Franceschini[3,5], C. De Angelis[3,5], A. Fedyanin[1]

[1]Lomonosov Moscow State University, Russian Federation,
[2]Shenzhen MSU-BIT University, PRC,
[3]National Institute of Optics – National Research Council (INO-CNR), Via Branze 45, 25123, Brescia, Italy,
[4]Department of Engineering, University of Palermo, Viale delle Scienze ed. 9, 90128, Palermo, Italy,
[5]Department of Information Engineering, University of Brescia, via Branze 38, 25123, Brescia, Italy,
[*]corresponding author: chernyakam@my.msu.ru

Abstract: Metasurfaces provide control of light properties, including enhancement of nonlinear effects, with potential applications through active manipulation of radiation parameters via external refractive index perturbations. In this study, the metasurface we propose is feasible for fabrication and demonstrates an increase in quality factor following photo-excitation from optical pump pulses and dynamically enhanced third harmonic generation.

Dielectric resonant metasurfaces offer significant control over the polarization, phase, amplitude, and frequency of radiation. However, the pursuit of active devices capable of dynamically modulating light parameters remains a focus of current research. Laser pulses represent a particularly compelling external influence, capable of inducing free carrier generation in materials and consequent changes in refractive index (Δn). Leveraging this phenomenon, ultrafast all-optical switching and frequency conversion can be realized through techniques such as pump-probe spectroscopy.

Recent studies have demonstrated the potential for substantial transmission modulation and frequency conversion in various metasurfaces. For instance, experiments utilizing amorphous silicon (a-Si) nanodisks have shown transmission modulation up to 0.5%[1], while metasurfaces composed of germanium (Ge) nanoparticles exhibit frequency conversion and blue shifts of significant magnitude[2].

One avenue towards achieving high-quality resonances lies in breaking the symmetry of metasurface unit cells, leading to the emergence of bound states of the continuum. Such resonances not only amplify optical effects but also enhance magneto-optical ones. Notably, metasurfaces featuring nanodisks with deliberately shifted holes exhibit enhanced magneto-optical effects under external magnetic fields[3].

The concept of Q-boosting metasurfaces has garnered attention for its potential to surpass traditional time-bandwidth limits, enabling efficient interaction between broadband laser pulses and narrowband resonators[4, 5]. By prolonging the interaction time within the resonator system, the quality factor (Q-factor) can be substantially enhanced. In [4], the unit cell design includes two pillars made of different semiconductor materials, e.g., silicon (Si) and Ge. To dynamically control the asymmetry between the pillars, two materials with different bandgaps are chosen, allowing one to excite free carriers in one of the pillars while leaving the other unchanged. With appropriate metasurface dimensions, reducing the refractive index will lower the effective light path in Ge and make the mode more symmetric, lowering the radiative losses and boosting the Q-factor. Along with a blue shift of the resonance, it can be seen a significant Q-factor boost for realistic values of Δn_{Ge} of up to -0.08 experimentally demonstrated earlier[6].

Despite promising theoretical groundwork, the previously proposed structures are extremely challenging under the fabrication point of view [4]. To address these challenges and facilitate experimental exploration, we present a novel approach to studying analogous effects experimentally.

The unit cells of the simulated metasurface are composed by stacked Si and Ge cuboids separated by a silica (SiO2) gap (Fig. 1a). Since in the spectral region of interest Ge has a refractive index of 4.1, such a structure has a resonance at a wavelength of 2285nm with a Q-factor of 550 (Fig 1b). In this case, according to the multipole decomposition, the electric dipole resonance dominates in the particles. Under the influence of laser radiation at a wavelength above the Ge bandgap and below the Si absorption region, for example 1200nm, the refractive index of Ge decreases to 4.02. The resonance of the metasurface undergoes spectral shifts up to 30nm, accompanied by an almost fourfold increase in the Q-factor. In this case, the electric field is relocated from Si to Ge. Now the value of the electrical dipole component in Ge increases by 8 times, while in Si it decreases by 1.5.

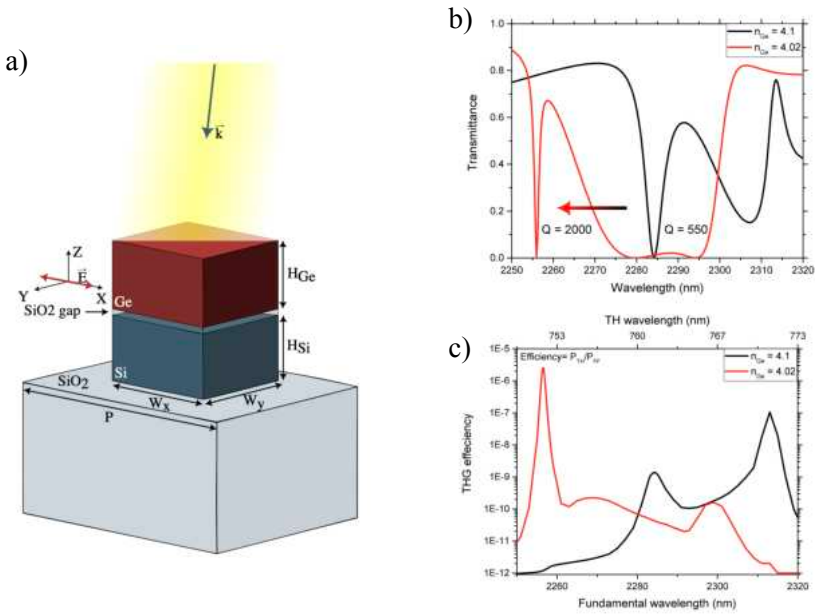


Fig 1: a) Schematic image of simulated metasurface. b) Transmission spectra for static case (black) and new high-Q state (red). c) Third harmonic spectra for unperturbated (black) and perturbed system (red).

Furthermore, we demonstrate nonlinear responses through simulations of third harmonic generation (Fig 1c). The efficiency of third harmonic generation experiences a profound enhancement, surpassing three orders of magnitude, indicative of the metasurface's capacity for nonlinear modulation.

In conclusion, our study underscores the potential of Q-boosting metasurfaces in enabling dynamic control over light-matter interactions, offering insights into both theoretical principles and experimental feasibility in nonlinear optics research.

This work is supported by the Russian Science Foundation (No. 20-12-00371, calculations of transmittance and non-linear spectra). The study is carried out within the framework of the Development Program of MSU, an interdisciplinary scientific and educational school "Photonic and Quantum Technologies. Digital Medicine". This work is supported by a grant from the Foundation for the Development of Theoretical Physics and Mathematics "BASIS" (No. 22-1-3-5-1, multipole decompositon).

References

1. A.I. Kuznetsov, A.E. Miroshnichenko, M.L. Brongersma, Y.S. Kivshar, B. Luk'yanchuk, "Optically resonant dielectric nanostructures", Science, Vol. 354, No. 6314, aag2472, 2016.
2. V.V. Zubyuk, P.A. Shafirin, M.R. Shcherbakov, G. Shvets, A.A. Fedyanin, "Externally driven nonlinear time-variant metasurfaces", ACS Photonics, Vol. 9, No. 2, 493, 2022.
3. A. M. Chernyak, M.G. Barsukova, A.S. Shorokhov, A.I. Musorin, A.A. Fedyanin, "Bound states in the continuum in magnetophotonic metasurfaces", JETP Lett., Vol. 11, No. 1, 46, 2020.
4. P.A. Shafirin, V.V. Zubyuk, A.A. Fedyanin and M.R. Shcherbakov, "Nonlinear response of Q-boosting metasurfaces beyond the time-bandwidth limit", Nanophot., Vol. 11, No. 17, 4053, 2022.
5. P. Franceschini, A. Tognazzi, A. M. Chernyak , A. I. Musorin, A. C. Cino , A. A. Fedyanin, C. De Angelis, "Enhancing second harmonic generation by Q-boosting lossless cavities beyond the time bandwidth limit", Nanophotonics, Vol. 13 No. 1, 1, 2024.
6. T.-T. Yeh, H. Shirai, C.-M. Tu, T. Fuji, T. Kobayashi, C.-W. Luo, "Ultrafast carrier dynamics in Ge by ultra-broadband mid-infrared probe spectroscopy", Sci. Rep., Vol. 7, No. 1, 40492, 2017.

Characterization of metasurface-based optical vortices using quadriwave lateral shearing interferometry

Y. Tahmi[1,2], S.Khadir[1,], M. Ansquer[2], P.Genevet[1,3], B.Wattellier[2]

[1] Université Côte d'Azur, CNRS, CRHEA, 06560 Valbonne, France
[2] PHASICS S.A., Parc Technologique de Saint Aubin, Saint Aubin, France
[3] Physics Department, Colorado School of Mines, Golden, Colorado 80401, USA

Abstract: For more than 30 years, optical vortices (OVs) have been an active research topic with numerous applications. The emergence of metasurfaces has opened up new avenues for the generation of OVs. We propose here a study of optical vortices generated with metasurfaces using a wavefront sensor based on quadriwave lateral shearing interferometer (QLSI).

Ovs show a great interest in the research community during the last years with many applications like optical tweezers[1,2], astrometry[3], supper-diffraction-limit imaging[4] and, quantum states control [5,6]. OVs are mainly characterized by their topological charges (TC), which are normally integers, representing the number of 2π wraps of the phase of optical field around its optical axis (fig1.b). Generation and manipulation of OVs with large TC can be tricky leading to a drop in efficiency for targeted application.

On other hand, metasurfaces offer a way to control wavefront at a subwavelength scale and allows naturally to the generation of OVs (fig1.a). To characterize the phase of metasurfaces, a common way is to use wavefront sensor like QLSI[7]. However, this method is based on the measurement of the spatial derivative of the phase and direct integration of this derivative does not show the presence of OVs on the wavefront. This can be interpreted as the ambiguity of integrate a non-continuous 2D function where the phase singularity at the center of the OV plays the role of the discontinuity.

In this work, we propose a study on the metrology of OVs generated using metasurfaces (MS). The use of metasurfaces allows the generation of several OVs on the same beam with even non-integer TCs. However, taking into account the fabrication errors of the metasurface building blocks, the resulting TC as well as the efficiency can be different from the expected ones. Thus, an accurate and rapid metrology technique is necessary to check the quality of the samples and can significantly help for to optimize the metasurfaces. Here, we use quadriwave lateral shearing interferometery combined with several phase retrieval methods to properly identify and quantify such wavefronts (fig1.c). We used two types of MS (Effective Refractive Index and Pancharatnam-Berry) in this study and compare their performances.

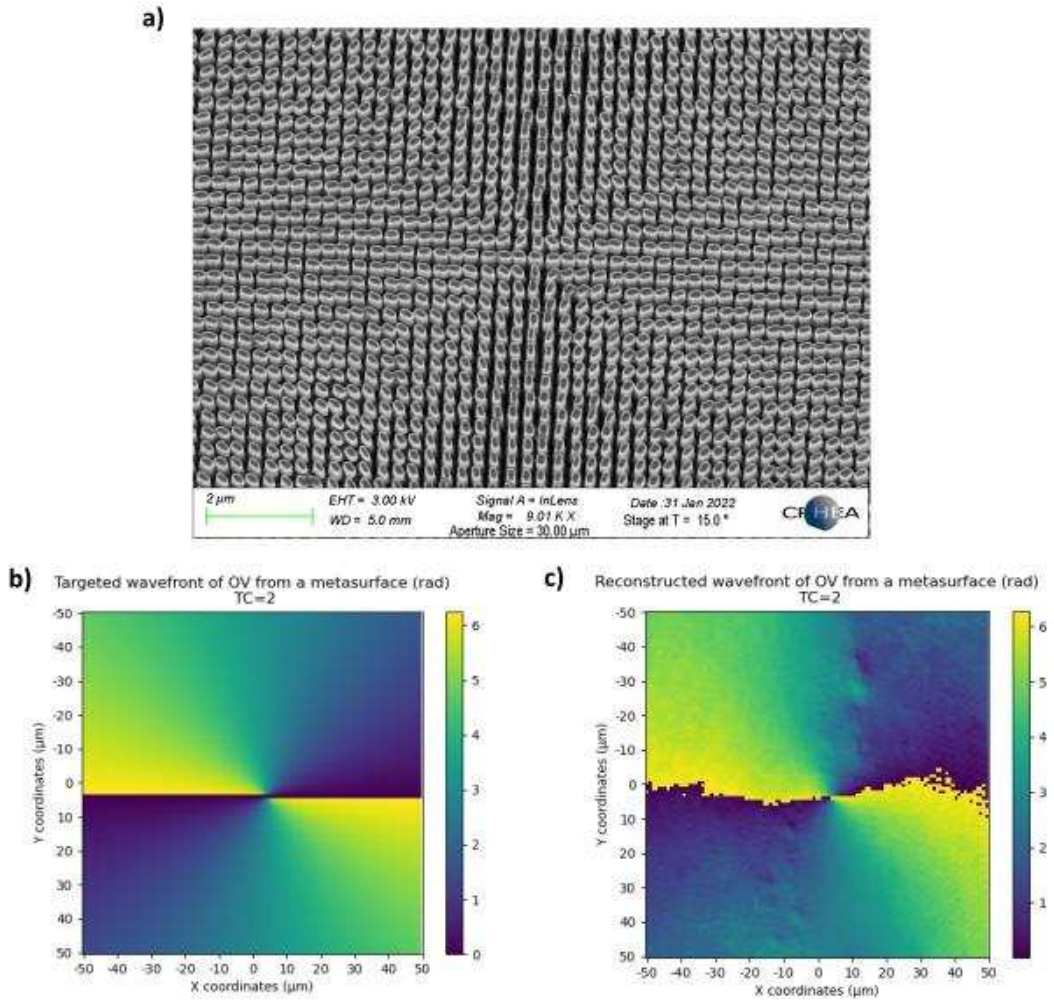


Figure 1 : Pancharatnam Berry metasurface for creating a OV of CT=2, a) Scanning electron microscope image of the metasurface, b)targeted phase modulation of the MS, c) reconstructed wavefront from measurement.

References

1. D.Grier,"A revolution in optical manipulation", *Nature* 424, 810–816 (2003).
2. X. W. Zhuang, "Unraveling DNA condensation with optical tweezers" ,Science 305, 188–190 (2004).
3. M.Harwit," Photon Orbital Angular Momentum in Astrophysics", *ApJ* 597 1266 (2003).
4. F. Tamburini et al. "Overcoming the Rayleigh criterion limit with optical vortices" Phys. Rev. Lett. 97, 163903 (2006).
5. G.Molina-Terriza, et all," Management of the Angular Momentum of Light: Preparation of Photons in Multidimensional Vector States of Angular Momentum", Rev. Lett. 88, 013601 (2001)
6. A. Mair, et all, "Entanglement of the orbital angular momentum states of photons," Nature 412, 313–316 (2001
7. Samira Khadir *et al*, "Metasurface Optical Characterization Using Quadriwave Lateral Shearing Interferometry", *ACS Photonics* 2021 *8* (2), 603-613

Reciprocal Lens: Imaging Based on Lateral Ray Shifting via Non-Local Metasurfaces

Jingguang Chen[1], Wenzhe Liu[1,2*], Lei Shi[1], Jian Zi[1*], and C. T. Chan[2*]

[1]Fudan University, Shanghai, China
[2]The Hong Kong University of Science and Technology, Hong Kong, China
[*]corresponding author: wliubh@connect.ust.hk; jzi@fudan.edu.cn; phchan@ust.hk

Abstract: We report an imaging mechanism via lateral ray shifting from non-local metasurfaces without spatially-varying features and a geometric center, producing upright real images. Experimentally, a C_{6v}-symmetric periodic metasurface at 28.5 GHz demonstrates this "reciprocal lens" behavior following $u+v=\tilde{f}$. Stacking multiple layers additively increases the focal length $\tilde{f}$.

Conventional lenses bend light rays to produce images of an object, which is achieved by space-variant structures, inevitably introducing a geometric center to the lens. These lenses have some fundamental limitations: the rays emitted from an object always get "inverted" when producing a real image, so single lenses cannot produce upright real images. Moreover, precise alignment is needed to produce high-quality images.

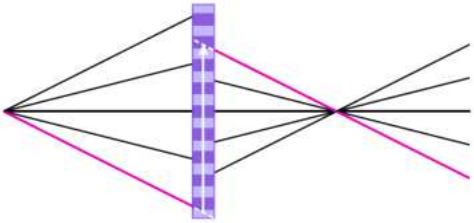


Fig. 1. Imaging based on lateral ray shifting.

We employ a different imaging mechanism based on lateral ray shifting provided by non-local metasurfaces. If a ray emitted from an object with incident angle θ is shifted by a distance proportional to θ in the paraxial limit, an upright real image is formed [Fig .1], following a distinct lens formula

$$u+v=\tilde{f}, \tag{1}$$

Where $\tilde{f}$ is the effective focal length, u and v are the object and image distances, respectively. As this lens formula is of a reciprocal form of the well-known Gaussian lens formula $1/u+1/v=1/f$, we call these ray-shifting imaging element as "reciprocal lenses". A reciprocal lens has a momentum-phase phase modulation that has a positive quadratic dependence on the in-plane wavevector (i.e., incident angle) [1], which is similar to metasurfaces known as "space squeezers" or "space plates" but with a negative squeezing distance [2,3].

We designed and fabricated a C_{6v}-symmetric reciprocal lens [Fig. 2(a)] operating at 28.5 GHz, where the momentum-space phase modulation best fits the quadratic dependence required for the lateral ray displacements [Fig. 2(b)]. Using a metallic mask with an "F"-shaped slot as the object [Fig. 2(c)], we observed an upright, real image with sharp boundaries at 7.5 cm away from the object [Fig. 2(e)], confirming the imaging behavior.

Furthermore, stacking two identical metasurfaces doubled the phase modulation [Fig. 2 (d)], resulting in a focal length of approximately 15-16 cm and producing a high-quality image at this distance [Fig. 2 (f)].

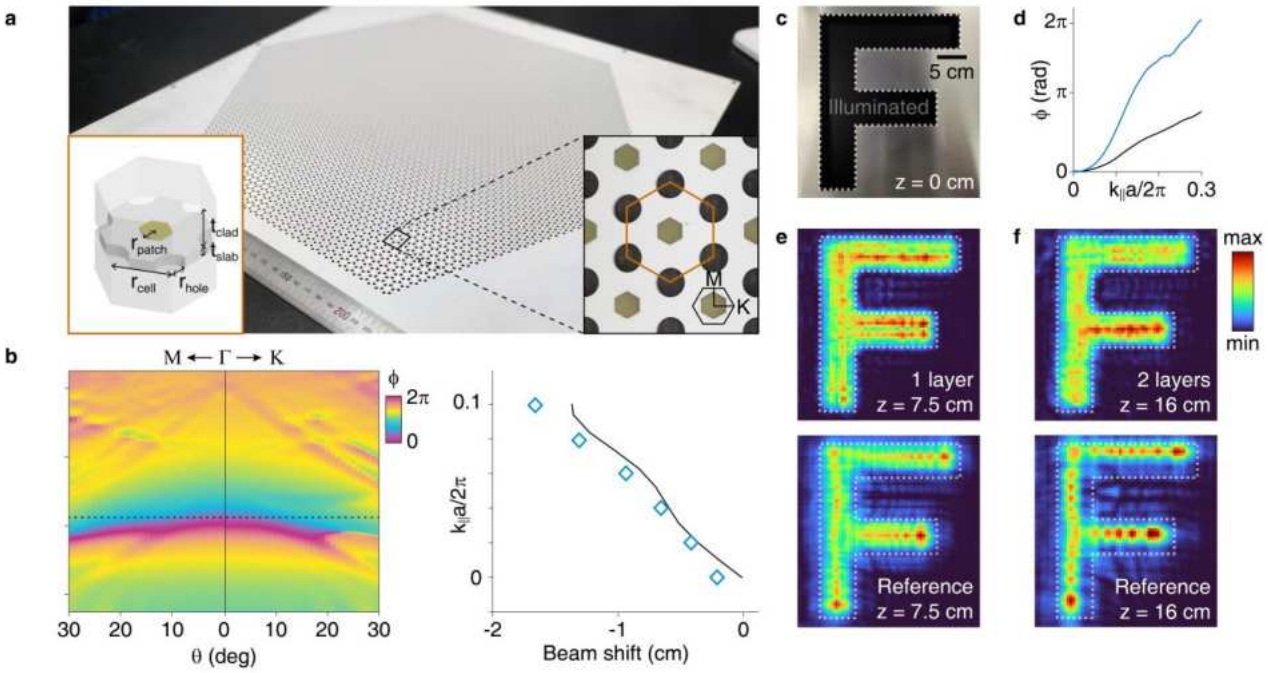


Fig. 2. (a) **Photo of the core layer of the designed reciprocal lens** comprising a honeycomb array of circular holes etched on a PCB. A hexagonal metallic patch is printed at the center of each honeycomb unit cell. The structured PCB acts as a photonic crystal slab and is clad by two background layers. Left inset: schematics of the unit cell. Right inset: zoomed-in photo of the structure. (b) **Angle-resolved transmissive phase-change spectra of the structure (with circularly co-polarized input and output) and the measured beam shifts for different incident angles.** The shifts of the beam centroids for different incident angles (blue diamonds) follow the displacements calculated from the momentum-space phase gradients (black curve). (c) **The "z = 0 cm" photo showing the object**, which is a metallic plate with an "F"-shaped slot cut into it. (d) **Measured transmissive phase distributions** for the one-layered (black curve) and two-layered (blue curve) reciprocal lenses. (e) **The image produced by one layer of reciprocal lens** and its reference. (f) **The image produced by two layers of reciprocal lens** and its reference.

References

1. K. Y. Bliokh and A. Aiello, Goos–Hänchen and Imbert–Fedorov Beam Shifts: An Overview, J. Opt. 15, 014001 (2013).
2. C. Guo, H. Wang, and S. Fan, Squeeze Free Space with Nonlocal Flat Optics, Optica 7, 1133 (2020).
3. O. Y. Long, C. Guo, W. Jin, and S. Fan, Polarization-Independent Isotropic Nonlocal Metasurfaces with Wavelength-Controlled Functionality, Phys. Rev. Appl. 17,024029 (2022).

Fundamental limits to metalens critical dimensions

N. Kossowski[1*], E. Marinov[1], C. Majorel[1], S. Khadir[1] and P. Genevet[2]

[1]Univeristé Côte d'Azur, CNRS-CRHEA, Rue Bernard Gregory, Valbonne, 06650, France
[2]Physics department, Colorado School of Mines, 1523 Illinois Street, Golden, CO, 80401, USA
[*]corresponding author: Nicolas.kossowski@crhea.cnrs.fr

Abstract: Array of micro-metalenses have been proposed to be integrated with pixels matrices of imaging systems to improve the modulation transfer function of imaging systems. Here, we investigate the theoretical limits of the metasurface approach for such applications and identify suitable operating domains.

In the context of the development of more performant imaging systems, arrays of refractive microlenses have been integrated to matrix of pixels in order to improve the spatial resolution and increase signal-to-noise ratio [1]. The role of these microlenses is to focalize at the center of each pixel to decrease the optical and electronic cross-talks between pixels. For practical integration, the size of each of these microlenses is about the size of a single pixel, thus a few microns. Consequently, precisely fabricating refractive microlens is a challenging task[2] compare to the flexibility and semiconductor compatible technology offered by the metasurface approach. However, with a size of few microns only, diffraction by the metasurface itself cannot be neglected and thus the metasurface enters a hybrid diffractive regime affecting its overall performances, and leading to "focal shift" [3].

Here, we theoretically investigated the fundamental limits of micro-metalenses by considering the finite size of the metasurface. To conduct our theoretical study, we based our approach to the Stratton-Chu integral[4] that we adapted to model a metasurface with finite size. We identified two fundamental limits which define the region of operation of metalenses: (i) an upper limit defined by the size of the metasurface itself, and (ii) a lower limit defined by the pitch of the metasurface. The first limit is a hard limit which cannot be overcome. The aperture defines a region of space in which we can achieve control of the phase. Outside of this region, the diffraction by the aperture itself alters the wavefront control. Therefore, to achieve full control of the wavefront, smaller metalens require higher numerical aperture (NA). However, it leads to the emergence of the second limit. High numerical aperture yields to abrupt phase variation which have to be discretized by the meta-atoms. This becomes critical when the size of the metasurface is only few times the wavelength, and thus we dispose of only limited number of meta-atoms to control the wavefront. However, this is a soft limit, meaning it could potentially be alleviate depending on the fabrication processes and physical mechanism used to induce the phase shift.

Consequently, in the domain defined by the upper and lower limits, we can identify two regimes of metalens operation, (i) a regime with full control of the wavefront, characterized by a metalens with high numerical aperture, (ii) a diffractive regime, in which the diffraction of the metalens itself hinder the metasurface optical properties.

In order to test and validate our theory, we fabricated arrays of $10\mu m$ diameter metalenses. The meta-atoms are made of $1\mu m$ height GaN pillars on sapphire substrate and operates at $617nm$ wavelength. Each metalens is designed with different numerical apertures which span the different regime of operation we identified.

Our study highlights the limits of applications of small metasurfaces and clarifies the physical mechanism at works. Moreover, by clearly defining the boundaries of the metasurface approach, our work identifies a path to follow to benefit wavefront control properties of metasurfaces at small scale.

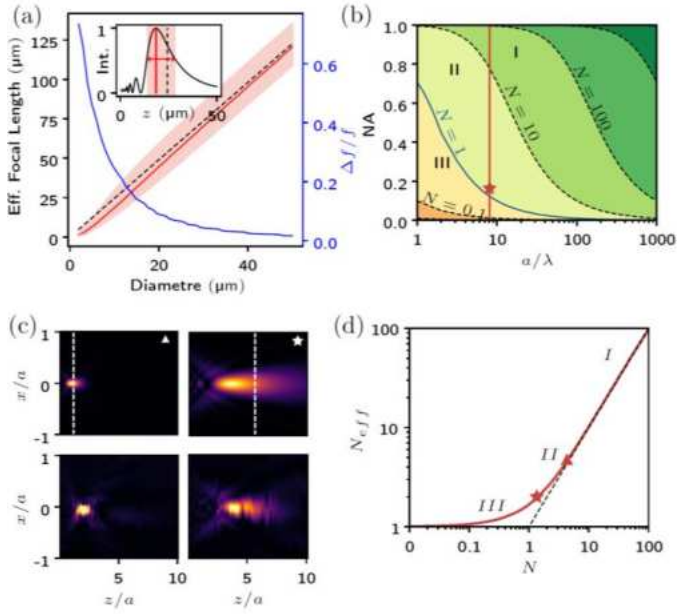


Figure 1: (a) In red, variation of the effective distance focal (maximum of amplitude) in function of the diameter of the metalenses with fix numerical aperture NA = 0.2. In blue (right y-axis), variation of the focal shift with regards to the designed focal length. (b) Mapping of the Fresnel number $N = a^2/\lambda f$, in function of the numerical aperture and the size of the aperture (in wavelength). The green color shows N > 1 and the yellow colors N<1. (c) Comparison between numerical simulations and measurements for GaN metalenses of $2a = 10\mu m$ at $\lambda = 617nm$, with focal length $f = 10\mu m$ and $f = 30\mu m$, represented by the with dashed line. (d) Evolution of the effective Fresnel number in function of the Fresnel number. Red line corresponds to the simulations and the symbols refer to (c).

PG acknowledges financial support from the French National Research Agency ANR Project Millesime 2 (ANR-21-ASTR-0014).

References

1. Rogalski, A., Martyniuk, P. & Kopytko, M. Challenges of small-pixel infrared detectors: a review. *Rep. Prog. Phys.* **79**, 046501 (2016).
2. Cai, S. *et al.* Microlenses arrays: Fabrication, materials, and applications. *Microscopy Research and Technique* **84**, 2784–2806 (2021).
3. Li, Y. Focal shifts in diffracted converging electromagnetic waves. I. Kirchhoff theory. *J. Opt. Soc. Am. A, JOSAA* **22**, 68–76 (2005).
4. Stratton, J. A. & Chu, L. J. Diffraction Theory of Electromagnetic Waves. *Phys. Rev.* **56**, 99–107 (1939).

Mid-infrared achromatic metalens with large field-of-view based on standard i-line stepper

Y.-C. Chen[1], W.-L. Hsu[1], Q.-C. Zeng[1], C.-Y. Yu[1], Y.-H. Lin[2], C.-C. Chen[2], and C.-M. Wang[1*]

[1]Department of Optics and Photonics, National Central University, Taoyuan, 32001, Taiwan
[2]Taiwan Instrument Research Institute, National Applied Research Laboratories, Hsinchu, 30076, Taiwan
[*]cmwang@cc.ncu.edu.tw

Abstract: We proposed an achromatic metalens with a 90° large field of view and a diameter of 5.75 mm for a wavelength range of 8 to 12 μm. This metalens is fabricated by an i-line stepper, which has mass-production advantages and is low-cost. Additionally, it captures great-quality images.

In optical imaging systems, chromatic aberration-free metalenses with large dimensions and a wide field-of-view (FOV) are sought after for delivering high-quality images. However, controlling the group delay of meta-atoms while eliminating chromatic aberration imposes limitations on the maximum diameter [1] of a metalens. Designing a chromatic aberration-free metalens with a substantial diameter presents a significant challenge [2]. In our study, we addressed this challenge by developing a large-area, chromatic aberration-free metalens with a wide FOV for mid-infrared (MIR) wavelength applications.

Figure 1 illustrates the ray tracing diagram, which includes an aperture that limits the range of the marginal ray, forming a telecentric system consisting of an aperture, metalens, and sensor. Typically, a cover layer is used to protect the sensor. Therefore, in this setup, we placed a silicon-based cover layer in front of the sensor. In our design, this metalens provides great focusing quality at viewing angles ranging from 0 to 45°.

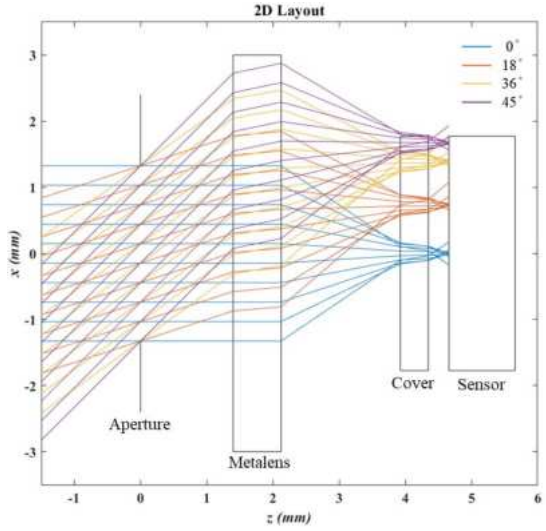


Figure 1. Schematic ray trace of the propose optical system, using an aperture to limit the range of the marginal ray and form a telecentric system.

This metalens features a silicon-based donut-shaped nanorod as its basic building block, situated on a silicon substrate. We utilized the Finite-Difference Time-Domain (FDTD) method to calculate the propagation phase and group delay for the donut-shaped nanorod with various dimensions. Fabrication of the metalens involved i-line stepper lithography, followed by deep reactive ion etching (Deep-RIE) processing [3]. All manufacturing processes comply with the specifications of regular semiconductor factories, enabling mass production of this

metalens. The SEM image in Figure 2(a) presents a tilt view at 45°. The donut-shaped nanorod reaches a height of 11 μm after the Deep-RIE, and the photograph of the 5.75 mm diameter metalens is shown in Figure 2(b).

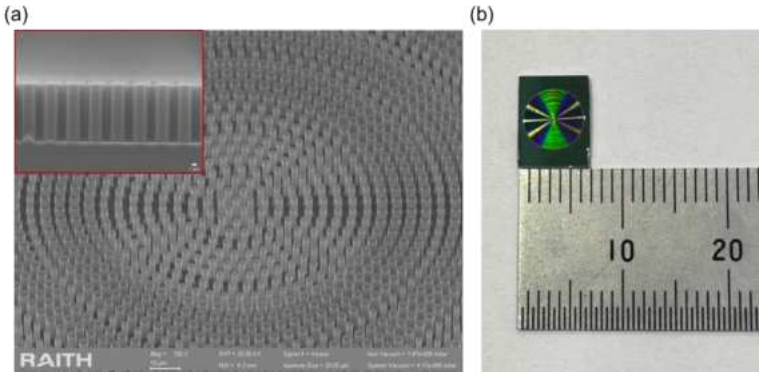


Figure 2(a) The SEM image of proposed MIR metalens, the sub-image show the height of nanorod be approximately 11 μm. (b) The photograph of the 5.75 mm diameter metalens.

In the measurement setup, as depicted in Figure 3(a), a hotplate served as the mid-infrared (MIR) light source, while a chess-type metal frame acted as the object. The proposed metalens was employed to image the object at distance of 9 mm, with the resulting image shown in Figure 3(c). The FOV was measured to be approximately 87°. This metalens demonstrated great image quality, clearly resolving the edges of the metal frame.

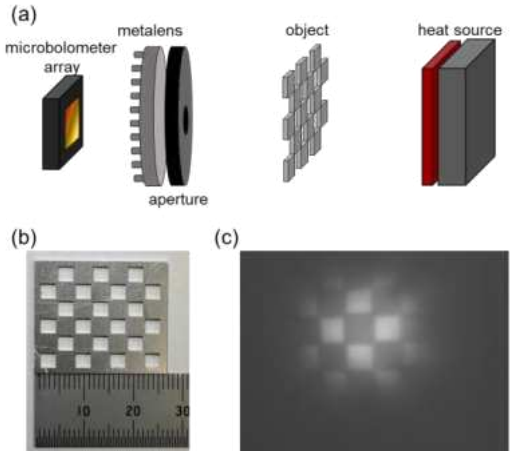


Figure 3 (a)The measurement setup of propose meta-optics system, (b)and the chess-type metal frame acted as the object. (c)The image results of the propose system, the FOV was measured to be approximately 87°.

References

1. Shrestha, S., A.C. Overvig, M. Lu, A. Stein and N. Yu, “Broadband achromatic dielectric metalenses,” Light Sci Appl, Vol. 7, No. 85, 2018.
2. She, A., S. Zhang, S. Shian, D. R. Clarke, and F. Capasso, “Large area metalenses: design, characterization, and mass manufacturing,” Opt. Express, Vol. 26, No. 2, 1573-1585, 2018.
3. Dirdal, C. A., G. U. Jensen, H. Angelskår, P. C. V. Thrane, J. Gjessing, and D. A. Ordnung, “Towards high-throughput large-area metalens fabrication using UV-nanoimprint lithography and Bosch deep reactive ion etching,” Opt. Express, Vol. 28, No. 10, 15542-15561, 2020.

Robust nano-antenna metrology for metasurface design

Cécile LE GALL[a], Bastien ROUZE[a], Cindy BELLANGER[a], Jérôme PRIMOT[a], and Julien JAECK[a]

[a] DOTA, ONERA, Université Paris-Saclay, 91120, Palaiseau, France

[*]corresponding author: julien.jaeck@onera.fr

Abstract: Meta-optics allow the realization of new optical functions that are increasingly complex to realize and characterize locally. We propose an interferometric method to measure both amplitude and phase of an array of meta-elements constituting a metasurface. Tested for MIM (Metal-Isolating-Metal) metasurfaces, this technique can be applied to all metasurfaces.

For more than twenty years, meta-optics have allowed the development of a wide variety of optical functions. Some of them were well known like lenses, wave plates, or prisms. But new or modified functions have also been created such as phase mask coding, color filter, color printing or special holograms. Meta-optics are composed of arrays of dielectric or metallic nano-antennas (or meta-elements).[1, 2] They allow to modify the wavefront of the incident beam and thus to create a particular optical function. By controlling the size, shape, orientation or position of the nano-antennas, it is possible to control the amplitude, phase or polarization of the optical wave.[3–5]

As the optical functions developed become more and more complex, the design step becomes more and more important and must face important modeling problems such as the non-periodization of surfaces, the consideration of non-normal incidences or the multiplicity of different antennas on the same period. On the other hand, the phase of the antennas remain complicated to measure directly, thus the characterization of the metasurfaces is done indirectly through the verification of the designed optical function.[2, 6]

Faced with these two issues, we propose the development of an interferometric technique for the robust metrology of nano-antennas. This technique allows to characterize, experimentally, in amplitude and phase, an array of nano-antennas and thus to build a library of meta-atoms that can then be directly integrated into optical components. It is based on the PISTIL interferometer, a lateral shift interferometer whose use has already been demonstrated in the measurement of coherent laser beams.[7]

PISTIL stands for PISton and TILt. It differs from other lateral shift interferometer such as the Quadri-Wave Lateral Shifting Interferometer (QWLSI)[8] by a mask that split the incident beam and allows to measure the phase shift of two nearby elements. In our configuration, the subsamples are placed on a hexagonal lattice, which allows measuring the phase shift of an element with six of its neighbors directly. As shown in Figure 1, we want to characterize a sample composed of at least two subsamples each inducing a phase shift. At the exit of the sample, the beam is thus locally dephased. It then passes through a mask. We then have several beams each with a different phase shift. All these beams then pass through a diffraction grating that sends the orders -1 and +1 in three directions. These orders will interfere and create an interference pattern, the pistillogram. On this figure, we can observe the 0 orders of each beam, surrounded by interference figures, the petals.

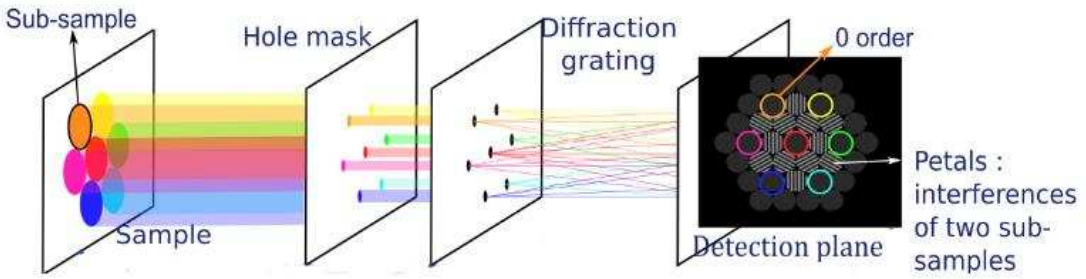


Figure 1: Scheme of PISTIL Interferometer.

Our interferometer can simultaneously measure the phase of nano-structures positioned on the same test sample, and cause them to interfere in pairs. By recovering a global interferogram containing the interference patterns of each sample with its neighbors, and using Fourier processing, we can reconstruct the phase induced by each type of nanostructure at each wavelength. By integrating these results over a wide range of wavelengths, we can then obtain the phase spectrum of each desired structure.

We tested our method on a test sample made up of fifty-two sub-samples containing reflective MIM (Metal-Insulator-Metal) structures in Gold and Zinc Sulfide, for which we varied three geometric parameters (period, length, width) in order to vary phase and amplitude with respect to the wavelength. But this particular case can be generalized to all kinds of nano-antennas, which will allow its user to design its own library of nano-atoms characterized in amplitude and phase.

Acknowledgements :
The PhD of Cecile Le Gall is funded by the Agence Innovation de Defense (AID). The samples were fabricated within the C2N micro nanotechnologies platforms from RENATECH network

References

1. Genevet, P., Capasso, F., Aieta, F., Khorasaninejad, M., and Devlin, R., “Recent advances in planar optics: from plasmonic to dielectric metasurfaces,” Optica 4(1), 139.
2. Boher, M., Jaeck, J., Bouchon, P., Primot, J., and Haidar, R., “Spectrally exclusive phase masks for wavefront coding,” Opt Lett 46(2), 436–439.
3. Bouchon, P., Koechlin, C., Pardo, F., Haidar, R., and Pelouard, J.-L., “Wideband omnidirectional infrared absorber with a patchwork of plasmonic nanoantennas,” Opt. Lett., OL 37(6), 1038–1040.
4. Yuan, Y., Sun, S., Chen, Y., Zhang, K., Ding, X., Ratni, B., Wu, Q., Burokur, S. N., and Qiu, C.-W., “A fully phase-modulated metasurface as an energy-controllable circular polarization router,” Advanced Science 7(18), 2001437.
5. Sun, S., Yang, K.-Y., Wang, C.-M., Juan, T.-K., Chen, W. T., Liao, C. Y., He, Q., Xiao, S., Kung, W.-T., Guo, G.-Y., Zhou, L., and Tsai, D. P., “High-efficiency broadband anomalous reflection by gradient meta-surfaces,” Nano Lett. 12 (12), 6223–6229.
6. Li, Z., Lin, P., Huang, Y.-W., Park, J.-S., Chen, W. T., Shi, Z., Qiu, C.-W., Cheng, J.-X., and Capasso, F., “Meta-optics achieves RGB-achromatic focusing for virtual reality,” Science Advances 7(5), eabe4458.
7. Rouze, B., Primot, J., Lanzoni, P., Zamkotsian, F., Tache, F., and Bellanger, C., “High-dynamic range segmented mirror metrology by two-wavelength PISTIL interferometry: demonstration and performance,” Opt. Express, OE 28(22), 32415–32425.
8. Primot, J. and Sogno, L., “Achromatic three-wave (or more) lateral shearing interferometer,” J. Opt. Soc. Am. A, JOSAA 12(12), 2679–2685.

Meta-lenses for second harmonic generation imaging on the tip of hair-thin optical fiber for advanced endoscopic imaging

R. Fuentes-Dominguez[1*], D. Afuwape[1], F. He[1], R. Cousins[2], and G. S. D. Gordon[1]

[1]Optics and Photonics Group, University of Nottingham, Nottingham, UK
[2]Nanoscale and Microscale Research Centre, University of Nottingham, Nottingham, UK
[*]corresponding author: george.gordon@nottingham.ac.uk

Abstract: We present a method for second harmonic generation (SHG) imaging compatible with hair-thin optical fibres with the use of two meta-lenses for 900 and 450 nm wavelength. These are fabricated using conventional e-beam lithography, polymer encapsulated, and transferred one-by-one to the tip of single-mode optical fibres.

Second-harmonic generation (SHG) has emerged as a powerful nonlinear optical contrast mechanism for biological imaging applications, in particular, imaging fibrillar collagen in a diverse range of tissues [1]. SHG is a coherent process where two lower energy photon are converted to exactly twice the incident frequency or half the wavelength. SHG microscopy has several advantages over conventional fluorescence imaging: the contrast arises from the sample itself, so there is no need for a dye or fluorophore, as well as being free from photobleaching (the signal generated is not limited in time) and occurs instantaneously (no limitation on the laser repetition rate) [2]. However, there are some limitations: SHG is a low efficient process without high numerical aperture objectives and high-power femtosecond pulses, which makes it challenging to translate this technology to in-vivo clinical environment. Previous works have combined SHG imaging with optical fibres, but still with the need of an optical objective to focus light on the sample [3].

Here, we present a method for second harmonic generation imaging compatible with hair-thin optical fibres. The meta-lenses are first fabricated by conventional e-beam lithography on a silicon substrate coated with a thin Cr sacrificial layer, then polymer encapsulated via photolithography, peeled away from the substrate through wet etching the Cr layer, and finally bonded onto fibre facets by optical adhesive. As proof-of-principle, we show two different meta-lenses to focus 900 and 450 nm optical wavelength for generation and detection SHG, respectively, using an array of aluminium dots with the shape of a Fresnel zone-plate lens with a focal length of 250 μm. We also show that by using this method, we can fabricate multi-layer stacks, which are increasingly finding use in advanced imaging systems [4].

Acknowledgements

This work is supported by UKRI Future Leaders Fellowship (MR/T041951/1). The authors would like to acknowledge the Nanoscale and Microscale Research Centre (nmRC) and Faculty of Physics at the University of Nottingham for providing access to cleanroom facilities.

References

1. Chen, X., et al. “Second harmonic generation microscopy for quantitative analysis of collagen fibrillar structure”. Nat Protoc 7, 654-669, 2012.
2. Campagnola, P. J. and Dong, C-Y, “Second harmonic generation microscopy: principles and applications to disease

diagnosis". Laser & Photonics Reviews 5.1, 13-26, 2011.

3. Fu, L., and Gu, M. "Polarization anisotropy in fiber-optic second harmonic generation microscopy". Optics Express 16.7, 5000-5006, 2008.
4. Gordon, G. S. D., et al. "Characterizing Optical Fiber Transmission Matrices Using Metasurface Reflector Stacks for Lensless Imaging without Distal Access". Phys. Rev. X 9, 041050, 2019.

Optimized design strategy of polychromatic metasurfaces considering their fundamental dispersion limits

A. Patoux[1], N. Kossowski[1], C. Majorel[1], S. Khadir[1] and P. Genevet[2*]

[1] Université Cote d'Azur, CNRS-CRHEA, France
[2] Physics department, Colorado School of Mines, USA
[*]corresponding author: patrice.genevet@mines.edu

Abstract: In this work we describe a simple way of quantifying the dispersion limits of a dataset, which can be used to optimize the design of polychromatic metasurfaces. As an example, the design, fabrication and characterization of a highly effective achromatic metalens was performed using this approach.

Metasurface elements, based on fixed nanostructures, are inherently limited in terms of dispersion for the design of achromatic components. To design such components, a very large number of different meta-atoms is required, usually leading to the construction of complex meta-atom designs with high geometric tunability [1].

However, recent studies highlighted some fundamental limits of achromatic diffractive lenses or metalenses performances due to the limited effective refractive index range that such components can achieve [2,3].

Such analysis can be pursue further considering any achromatic metasurface or even polychromatic metasurfaces. Taking the example of an achromatic metasurface, its unwrapped phase function at position (x, y) can be defined as $\boldsymbol{\Phi_{uw}(\lambda, x, y)} = \frac{\boldsymbol{\Phi_{uw}(\lambda_0, x, y)}\,\boldsymbol{\lambda_0}}{\boldsymbol{\lambda}}$ [1,4], where $\boldsymbol{\lambda}$ is the operating wavelength, and $\boldsymbol{\lambda_0}$ is a wavelength of reference within the studied bandwidth.

In that case, the phase equation to solve regarding the meta-atoms optical responses is the following:

$$\boldsymbol{\delta\Phi_{s,i}(\lambda) + C(\lambda) = \Phi_{uw}(\lambda, x_i, y_i) = \frac{\Phi_{uw}(\lambda_0, x_i, y_i)\,\lambda_0}{\lambda}} \quad (1)$$

Where $\delta\Phi_{s,i}(\lambda)$ is the phase shift of the structure #i that is required to get an achromatic response at the position (x_i, y_i), and $\boldsymbol{C(\lambda)}$ represent an arbitrary phase piston varying with λ, spatially constant, thus not impacting the optical response.

To graphically represent how to solve this equation, we consider the ensemble of functions $\Phi(\boldsymbol{\lambda}) = \boldsymbol{A} * \boldsymbol{\lambda_0/\lambda + C_0}$, using the couple of parameters $\boldsymbol{(A, \Phi(\lambda_0))}$. In **Fig. 1b**, we show different phase dispersions obtained for a high number of different structures geometries (illustrated in **Fig. 1a**), obtained through FDTD simulations for the [400-700] nm bandwidth (here, $C(\lambda) = 0$). We also show in orange some target phase shifts, associated to an achromatic metalens whose phase profile at $\boldsymbol{\lambda_0}$ = 400nm is shown in **Fig. 1c**.

We note that with such representation, the target phase shifts are in fact completely represented by the linear function $\boldsymbol{A = \Phi_{uw}(\lambda_0, x_i, y_i)}$. This allows to conclude that the dispersion range, represented by $\boldsymbol{A}$, represents in fact the dispersion limit of the dataset. Hence, here, any optical component having an unwrapped phase shift range greater than 30 radians for $\boldsymbol{\lambda_0} = 400$nm cannot be fully reconstructed using this meta-atom library.

Regarding the influence of $C(\boldsymbol{\lambda})$, this latter can, in this configuration, only take the form $C(\boldsymbol{\lambda}) = \boldsymbol{A' * \lambda_0/\lambda + C'_0}$. Tuning $C(\boldsymbol{\lambda})$ then allows to shift all dataset points cloud identically. As this points cloud representing our dataset does not cover fully the 2D space, this degree of freedom is very interesting to optimize the selection of the geometries to get the best efficiency, i.e. to move the blue points cloud to get the best overlapping with the orange target points.

Based on this approach, we studied the more general case of polychromatic metasurfaces, as well as the influence of several parameters regarding the meta-atom geometries. We also designed, fabricated and characterized a 1mm achromatic metalens that stays within the accessible dispersion range allowed by our dataset in the visible. The results showed very good performances with Strehl ratios remaining overall greater than 80%.

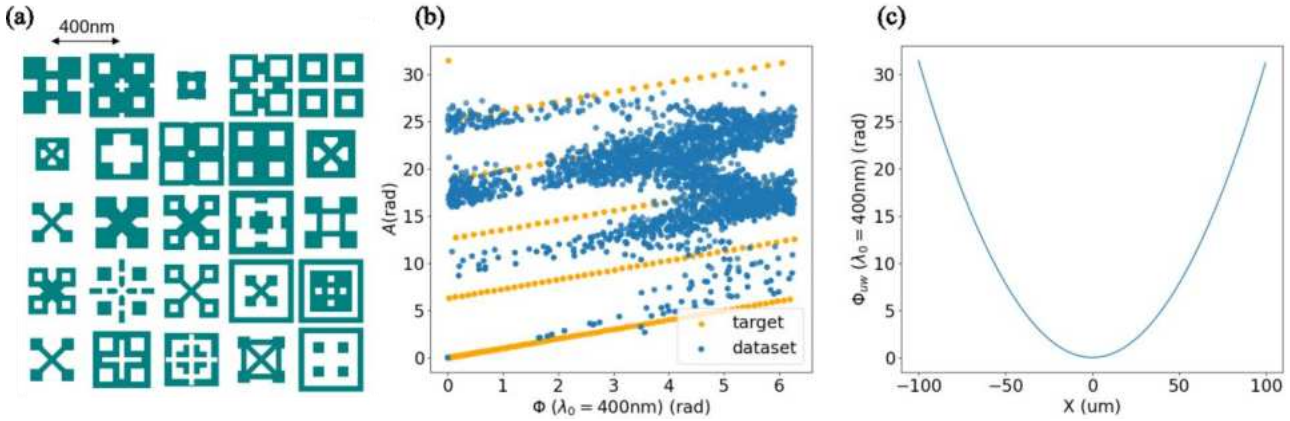


Figure 1: (a) Top view of some of the meta-atoms used for the design of achromatic metasurfaces. (b) Scatter representation of the dispersion properties of the meta-atoms and the target lens phase profile shown in (c).

We acknowledge the support of the IEMN-CNRS for the fabrications of the metasurfaces, as well as Zodiac-Aero-Electric and European Defense Fund (EDF) project Mini-Bot for the funding.

References

1. Shrestha, S., Overvig, A.C., Lu, M. et al. Broadband achromatic dielectric metalenses. Light Sci Appl 7, 85 (2018).
2. Engelberg, J. and Levy, U., Achromatic flat lens performance limits, Optica 8, 834-845 (2021)
3. Presutti, F. and Monticone,F., Focusing on bandwidth: achromatic metalens limits, Optica 7, 624-631 (2020)
4. Wang, S., Wu, P.C., Su, VC. et al. Broadband achromatic optical metasurface devices. Nat Commun 8, 187 (2017).

Toroidal dipole bound states in the continuum in dielectric metasurfaces

Sheng-Wei Kao, Yi-Chi Kao, and Ruey-Lin Chern*

Institute of Applied Mechanics, National Taiwan University, Taiwan
*corresponding author: chernrl@ntu.edu.tw

Abstract: We propose a design of dielectric metasurfaces for investigating the bound states in the continuum (BICs), which are recognized as toroidal dipoles (TDs) characterized by the electric or magnetic fields bent into a torus. Several electric or magnetic TDs are gathered in the unit cell to form multiple TD BICs.

Bound states in the continuum (BICs) are non-leaky localized resonance modes that coexist with a continuous spectrum of radiating waves [1-4]. Since BICs will not radiate to the far field, they are decoupled from the far-field radiation and possess infinite quality factors with zero spectral linewidths. In the presence of the absorption loss, roughness, or finite size of the structure, an idal BIC is turned into a quasi-BIC with a finite quality factor. In 1929, von Neumann and Wigner discovered that one-dimensional (1D) potential can support localized solutions that correspond to isolated discrete eigenvalues embedded in the continuum of positive energy states [5]. In 1985, Friedrich and Wintgen proposed the concept of BIC as a result of complete destructive interference of two resonances undergoing an avoided crossing. When two resonant states approach each other as a function of certain continuous parameter, the resonance width of one of them vanishes and forms the so-called Friedrich-Wintgen (FW) BIC [6]. In recent years, BICs have been found in quantum, photonic, acoustic and water wave, and mathematical systems, which can be applied in a variety of areas, including integrated photonic circuits, filters, lasers, and biosensors.

Toroidal dipoles (TDs) are high order terms of the electric multipole moments, which arise in an electrodynamic multipole expansion as additional terms compared to the electrostatic multipole expansion [7]. For a static TD, the external field of the TD mode is identically zero and the currents create a magnetic field confined within the torus. The static TD, therefore, do not interact directly with electric and magnetic fields [8]. For a dynamic TD, the electric toroidal dipole (ETD) is usually represented as poloidal electric currents flowing on a torus surface and magnetic dipoles arranged in a head-to-tail configuration, which can be excited as BICs in metamaterials [9-10]. On the other hand, magnetic currents flowing in the surface of a torus generates a magnetic toroidal dipole (MTD) [11-12].

In this study, we propose a design of dielectric metasurface consisting of corner or square patches in the unit cell of a square lattice. Symmetric-protected BICs occur at the Brillouin zone center, which are associated with extremely large quality factors and small linewidths. In particular, the BICs are identified as toroidal dipole modes characterized by the electric or magnetic fields bend into a torus, with the magnetic or electric circling around the surface. Several electric or magnetic TDs are gathered in the unit cell to form the multiple TD modes. Multiple electric TDs and magnetic TDs may be oriented normal or parallel to the metasurface, which appear at the polarization singularities in the momentum space and carry integer topological charges.

References

1. Hsu, C. W., Zhen, B., Stone, A. D., Joannopoulos, J. D. & Solja˘ci´c, M. Bound states in the continuum. Nat. Rev. Mater. **1**, 16048 (2016).
2. Peng, C. Trapping light in the continuum—from fantasy to reality. Sci. Bull. **65**, 1527–1532 (2020).
3. Koshelev, K. et al. Subwavelength dielectric resonators for nonlinear nanophotonics. Science **367**, 288–292 (2020).

4. Azzam, S. I. & Kildishev, A. V. Photonic bound states in the continuum: from basics to applications. Adv. Opt. Mater. **9**, 2001469 (2021).
5. von Neuman, J. & Wigner, E. Uber merkwürdige diskrete eigenwerte. Phys. Z. **30**, 465–467 (1929).
6. Friedrich, H. & Wintgen, D. Interfering resonances and bound states in the continuum. Phys. Rev. A **32**, 3231–3242 (1985).
7. Fernandez-Corbaton, I., Nanz, S. & Rockstuhl, C. On the dynamic toroidal multipoles from localized electric current distributions. Sci. Rep. **7**, 7527 (2017).
8. Zel'Dovich, I. B. Electromagnetic interaction with parity violation. Sov. Phys. JETP **6**, 1184–1186 (1958).
9. He, Y., Guo, G., Feng, T., Xu, Y. & Miroshnichenko, A. E. Toroidal dipole bound states in the continuum. Phys. Rev. B **98**, 161112 (2018).
10. Chen, X., Fan, W. & Yan, H. Toroidal dipole bound states in the continuum metasurfaces for terahertz nanofilm sensing. Opt. Express **28**, 17102–17112 (2020).
11. Gurvitz, E. A. et al. The high-order toroidal moments and anapole states in all-dielectric photonics. Laser Photonics Rev. **13**, 1800266 (2019).
12. Yang, Z.-J., Deng, Y., Yu, Y. & He, J. Magnetic toroidal dipole response in individual all-dielectric nanodisk clusters. Nanoscale **12**, 10639 (2020).

Holograms and wide-angle optics with hybrid supercell metasurfaces

Tatiana Contino[1,2*], Harsh Gupta[1,2], Andrea Toma[1] and Michele Tamagnone[1]

[1]Fondazione Istituto Italiano di Tecnologia, via Morego 30, 16163 Genova, Italy

[2]Dipartimento di Chimica e Chimica Industriale, Università di Genova, Genova, Italy

*Corresponding author: tatiana.contino@iit.it

Abstract: In this work, we experimentally demonstrate new types of hybrid supercell metasurfaces which exploit different types of supercells and unit cells in the same design, creating a smooth transition between them. We use this new method to control phase and amplitude of light at the same time designing speckle-free holograms.

Metasurfaces consisting of an array of two-dimensional (2D) subwavelength nanostructures, provide unprecedented control over light at the nanoscale. Metasurfaces are typically created using subwavelength unit cells, which are engineered to impart a local phase profile of light as it propagate through. This technique enables the attainment of various functionalities such as focusing, holograms, polarization functions, and beam shaping. By employing hybrid metasurfaces (comprising multiple cells/supercells optimized collectively) it becomes feasible to simultaneously achieve multiple functions [1,2].

In this work, we propose a new type of hybrid supercell metasurfaces based on smooth transitions between unit-cell-based design and supercells for wide angle and large numerical aperture optics [3]. Figure 1A illustrates an example of a metalens designed in this way, where the center is implemented via traditional unit cell metasurfaces and the edges are implemented with different types of supercells. Each type is identified by the order n_x and n_y it uses to diffract light towards the focus. Previous designs of this type (e.g. [4]) use radial supercells which create a periodic discontinuity on the radius, in order to maintain the same pillar size at different distances from the center. With this design it is possible to smoothly map the full surface to continuous unit cells (e.g. see pillars arrangements in Figure 1B).

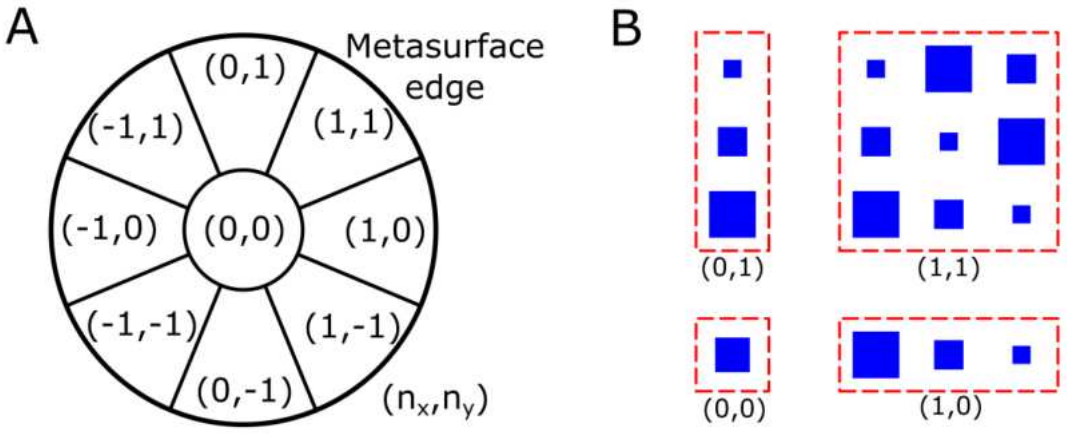


Figure 1. Schematic of the hybrid metasurface. **A**. The design is divided into different regions, each implemented with a different type of unit cell/supercells. **B**. Example of unit cells and supercells.

As a benchmark, we tested experimentally a metasurface composed of (n_x=1, n_y=0) supercells. The selected supercell (Figure 2A) scatters light into the selected order with variable phase and amplitude. Phase is modulated by the position of the pillar (i.e. the detour phase) while amplitude by its length. Thanks to the possibility of modulating both phase and amplitude, we demonstrated a speckle-free hologram design based uniquely on Fresnel diffraction (i.e. without using the Gerchberg-Saxton algorithm or similar methods). Figure 2B shows the designed phase and amplitude. The metasurface operates in reflection, and the pillars (in TiO_2) were fabricated on a silicon substrate coated with aluminum (Figure 2C). A 680 nm laser beam incident at 45° from the normal was used to test the hologram, which was projected normally from the metasurface onto a screen (Figure 2D).

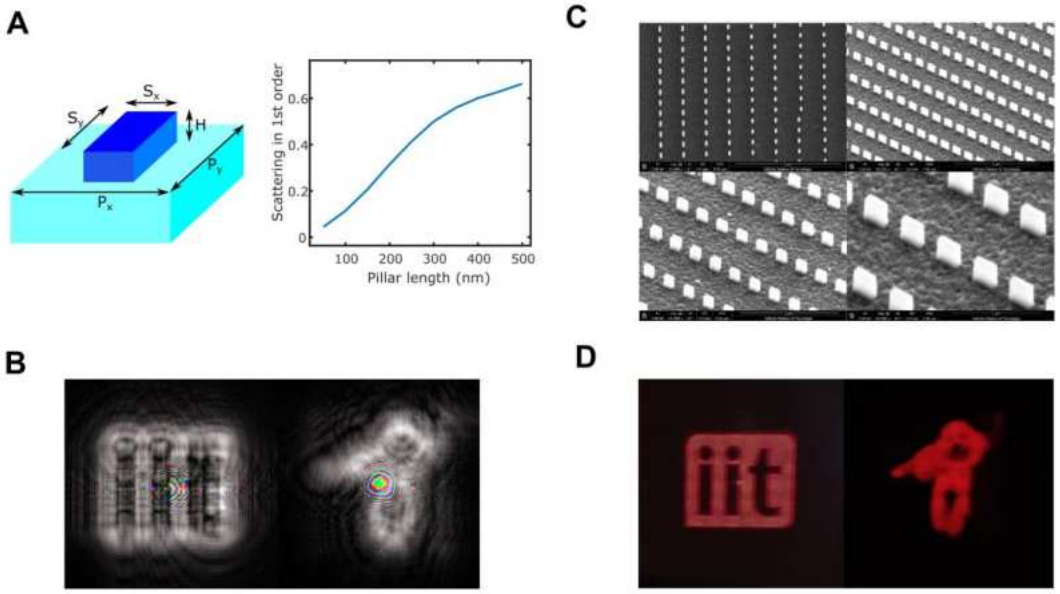


Figure 2. Speckle-free hologram. **A**. Supercell element. P_x = 1000 nm, P_y = 500 nm, H=300 nm, S_x = 100 nm, S_y is variable. The plot represents the simulated scattering amplitude as function of pillar length S_y. **B**. Designed amplitude and phase of the holograms **C**. SEM image of the fabricated metasurface. **D**. Generated hologram projected on a screen.

The presentation will provide additional details on this design, which paves the way to 3D holograms at large viewing angles, which are essential for AR/VR applications.

We acknowledge the financial support of the European Research Council (ERC) under Grant Agreement No. ERC-2020-STG 948250 (SubNanoOptoDevices).

References

1. Spägele, Christina, et al. "Multifunctional wide-angle optics and lasing based on supercell metasurfaces." Nature communications 12.1 (2021): 3787.
2. Huang, Lingling, Shuang Zhang, and Thomas Zentgraf. "Metasurface holography: from fundamentals to applications." Nanophotonics 7.6 (2018): 1169-1190.
3. Arbabi, Amir, et al. "Increasing efficiency of high numerical aperture metasurfaces using the grating averaging technique." Scientific reports 10.1 (2020): 7124.
4. Paniagua-Dominguez, Ramon, et al. "A metalens with a near-unity numerical aperture." Nano letters 18.3 (2018): 2124-2132.

Controlling Diffraction Efficiency Redistribution via Incomplete Phase Metagrating

Qiyao Liu[1†], Zhengtong Liu[2†], Xuezhi Ma[1], Jie Deng[1], Chen Zhang[2], Zhenmin Chen[2], Arash Nemati[1], Sui Kit Ng[1], Sergey Gorelik[3], Siew Lang Teo[1], Rong Ji[1], Zhao Meng[1], Leonard Verano Gonzaga[1], Hong Liu[1], Fuyong Yue[2], Shaohua Yu[2], Yu Luo[4], Qian Wang[1]**

[1] *Institute of Materials Research and Engineering, Agency for Science, Technology and Research (A*STAR), 2 Fusionopolis Way, Innovis 08-03, 138634, Singapore*

[2] *Peng Cheng Laboratory, Shenzhen, 518055, P. R. China*

[3] *Singapore Institute of Food and Biotechnology Innovation, Agency for Science, Technology and Research (A*STAR), 2 Fusionopolis Way, Innovis 08-03, 138634, Singapore*

[4] *Centre for OptoElectronics and Biophotonics School of Electrical and Electronic Engineering, Nanyang Technological University, 639798, Singapore*

[†] *These authors contributed equally to this work.*

Abstract: Our study introduces an unconventional metagrating that surpasses the traditional 2π phase constraint within the supercell of a metasurface, enabling precise control over high-order diffraction with adjustable efficiency redistribution. This work shines light on the design of multifunctional diffraction ultrathin optical components, such as metalens and holograms.

Optical metasurfaces, comprising 2D arrays of subwavelength structures, hold promise for advanced functions in nanophotonics.[1] By optimizing phase discretization of nanoscale meta-atoms, these metasurfaces are able to manipulate wavefronts, polarization, intensity, and spectrum.[2-3] Large period metagratings reveal new wavefront manipulation capabilities, often requiring inverse optimization to enhance diffraction efficiency.[4] Traditionally, metasurfaces aim for a full-range 2π phase change to achieve complete wavefront manipulation akin to conventional optics.[5] However, limiting the phase range to 2π is unnecessary in certain metasurface designs. On the other hand, incomplete phase provides an additional degree of freedom for optical wavefront control. In this study, we present incomplete phase metagratings achieved through intuitive supercell design, deviating from the conventional 2π phase change. Leveraging the flexible phase modulation capability in metagratings, efficiencies of diffracted beams are tailored by incorporating meta-atoms with incomplete phase ranges (e.g., π, 3π, 4π). Under normal incidence of light, the designed metagratings predominantly diffract the light into two adjacent diffraction orders, allowing for adjustable splitting ratios of 0th and 1st order ranging from 0.07 to 24.8.

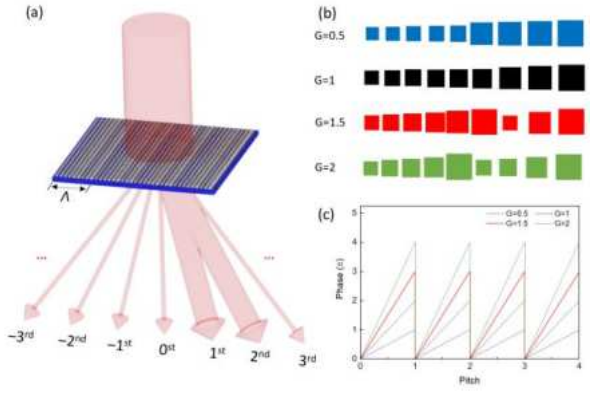


Figure 1. a) Sketch of an incomplete phase metagrating with controlled diffraction efficiency redistribution. b) The design of metagrating unit cells with G factors of 0.5, 1, 1.5 and 2, respectively. The G is the factor of total phase change of each supercell. The pitch of each unit along x- and y-direction is the same (Δ = 270 nm). c) Design phase profile for each metagrating with different G factor.

In contrast to conventional metagratings with fixed 2π phase gradient, incomplete phase metagratings introduce total phase of G*2π per supercell, with G as a scaling factor. As shown in Figure 1 (a) and (b), each grating period contains nine nanobricks. When G = 0.5, nanobrick size gradually increases to cover 0-π phase range per supercell. G = 1 represents conventional metagrating with 2π phase change per supercell, 1st order

being the blazing order. Increasing G from 1.5 to 2 results in non-monotonic nanobrick size increase, yielding wrapped phase of 2πG. Fig. 1c illustrates phase ramp across consecutive unit cells for different G values. The metagratings are fabricated on a quartz substrate, covering a 400×400 μm^2 area. Electron-beam lithography patterns metagratings onto ZEP 520A resist, followed by atomic layer deposition of amorphous TiO_2. Excess TiO_2 atop the resist is removed via controlled reactive ion etching. Remaining resist is stripped, leaving nanobricks.

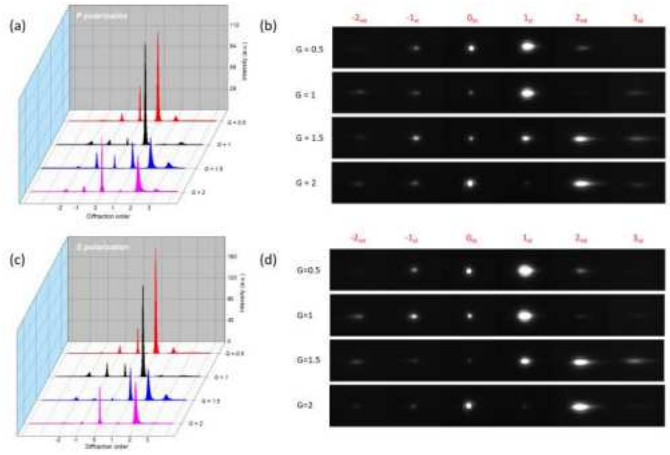


Figure 2. a,b) show the measured diffraction intensity of 0th, ±1st, ±2nd, and +3rd order metagrating with *P* and *S* polarization incidence, respectively; c,d) display the CCD images of diffraction beams of metagratings with G = 0.5, 1, 1.5, 2.

To assess optical performance, a collimated laser source (405 nm central wavelength) is utilized for incidence. A wire-polarizer follows the laser, allowing flexible beam polarization control. Subsequently, the illumination beams is confined to a spot smaller than the area of metagrating. CCD camera (Thorlabs DCC3260M) captures images of diffracted beams, revealing multiple spots with varying brightness, as expected. Corresponding intensity profiles (Fig. 2a, b) are extracted. For G = 1 or 2, the diffraction beam converges into a specified order (1st or 2nd). When G = 0.5 or 1.5, diffraction beam mostly splits into adjacent orders (e.g. 1st and 2nd or 2nd and 3rd). Splitting ratio (I_1/I_0) ranges from 0.07 (G = 2) to 24.8 (G = 1), with polarization independence well demonstrated. Optical images of diffractive spots under *P* and *S* polarized incidences are shown in Fig. 2c, d. Satellite tails appear in high diffraction orders due to oblique incidence on the perpendicular CCD screen. Additionally, introducing oblique incidence angle or wavelength variation adjusts diffraction direction and transmitted beam intensity distribution within a small range due to effective G factor changes.

Our study breaks the 2π phase constraint, designing incomplete phase metagratings for controllable wavefront and intensity reconstruction. Discrete phase distribution offers flexibility to design optical devices with incomplete phases, a feat unattainable with conventional optics. Achieved splitting ratio of I_1/I_0 spans 0.07 to 24.8, with performance unaffected by incidence polarizations.

This work is partially supported by the Agency for Science, Technology and Research (A*STAR) under AME IRG Grant No. M22K2c0080, A20E5c0095, MTC programmatic Grant no M23M2b0056 and the Major Key Project of PCL.

References

1. N. Yu and F. Capasso, “Flat optics with designer metasurfaces,” Nat. Mater., Vol. 13, 139-150, 2014.
2. R. Zhao, G. Geng, et. al. “Controllable Polarization and Diffraction Modulated Multi-Functionality Based on Metasurface,” Adv. Opt. Mater., Vol. 10, 2102596, 2022.
3. W. Zhu, Y. Fan, et. al. “Polarization-Multiplexed Silicon Metasurfaces for Multi-Channel Visible Light Modulation,” Adv. Funct. Mater., Vol. 32, 2200013, 2022.
4. Y. Ra’di, D. L. Sounas, and A. Alù, “Metagratings: Beyond the Limits of Graded Metasurfaces for Wave Front Control,” Phys. Rev. Lett., Vol. 119, No. 6, 067404, 2017.
5. W. T. Chen, A. Y. Zhu, et. al. “Flat optics with dispersion-engineered metasurfaces,” Nat. Rev. Mater., Vol. 5, 604, 2020.

Selective excitation of diverse subwavelength resonances in meta-surfaces comprising volumetric resonators: a brief discussion

A. E. Serebryannikov[1,*]

[1]ISQI, Faculty of Physics, Adam Mickiewicz University, 61-614 Poznan, Poland

[*]corresponding author: andser@amu.edu.pl

Abstract: The approaches to selective excitation of subwavelength resonances in metasurfaces comprising volumetric resonators made of dielectric and phase-change materials are briefly reviewed. The applicability of particular approaches depend on the spectral and spatial features of the incident electromagnetic wave.

While overlaps or coupling of two or more individual resonances may yield a variety of useful physical effects, like Kerker effect or BIC, rarefying the spectrum of resonant modes is the opposite scenario, which is demanded for applications. To this end, selective excitation of the individual resonances is of practical importance, especially when overlaps or coupling effects should be avoided within wide ranges of variation of geometrical parameters and frequency. In particular, resonators made of a dielectric with moderate or high permittivity are widely used, in which diverse resonances can be obtained at subwavelength scale. One of the purposes here is justification of the systematic approach to the selective excitation, based on the recent literature and original theoretico-numerical results.

The approaches to the selective excitation of subwavelength resonances can be assigned to the two big group: (i) the approaches applicable at the *design level* and (ii) the approaches applicable at the *excitation level*. The former includes but is not restricted to:

- proper perturbation and optimization of the resonator geometry;
- the use of higher (nonzero) diffraction orders;
- absorption engineering.

In turn, the latter may include

- excitation by electromagnetic wave with the synthesized spectrum;
- angular selectivity;
- spatial structuring of the incident wave.

The possible choice of a suitable approach depends on the *illumination type*, whose choice, in turn, depends on the targeted frequency range and functionality. We distinguish between (i) monochromatic and (ii) white light illumination types when the selective excitation is considered. It is assumed that the sequences of rectangular pulses could be used to synthesize a desired spectrum. Consideration has been restricted to non-gradient reflective metasurfaces; it was assumed that the unit cells of those metasurfaces can be used to build the gradient ones. The selectively excited resonances may include both volumetric (Mie) and array resonances.

Among the design-level approaches, variations of *geometrical parameters*, e.g., height-to-radius ratio of micro-/nanocylinders is probably the most commonly used technique that may yield a desired number and properties of subwavelength resonances [1]. Moreover, the designed deviation from the canonical shapes can improve the excitation conditions for some resonances and worsen for the others; for example, see ref. [2]. This approach is demanded for the both illumination types. One more but a less common approach is based on such structural design that the spectral locations of the resonances to be suppressed and those remaining in zero-order

reflection are chosen (due to a specific design of unit cell), respectively, at insignificantly larger or smaller frequencies than the *frequency-domain diffraction threshold*. In other words, it works only at the boundary of the diffraction-free range. In this case, redistribution of the incident-wave energy in favor of other transmission/reflection channels than zero-order reflection takes place. Finally, *absorption engineering* exploits the fact that the given imaginary part of permittivity or tan δ may lead to different excitation conditions for the resonances with lower and higher radiation losses, including the case when resonances are closely spaced in the frequency domain. For instance, adding a portion of lossy impurities may weakly or moderately affect the latter, but strongly affect and even suppress the former.

Among the excitation-level approaches, one should mention, first of all, excitation by the incident wave with the *synthesized spectrum*. The strong side of this approach is that it needs no special arrangement at the design level. The selective excitation of resonances is controlled by a waveform whose frequency spectrum is designed so that its maximums correspond to the spectral locations of the desired resonances, whereas the minimums correspond to the undesired resonances. The weak side is that it may be realizable rather at lower, e.g., microwave frequencies, while the possibility of transferring this approach to infrared and visible frequencies is limited. Next, which resonances are efficiently excited and which are not may depend on *incidence angle*. Indeed, the effect of angle variations is known (e.g., see ref. [3]) but has not yet been adequately exploited in metasurfaces. It is probably the simplest approach to reconfiguration, since it needs neither tunable materials nor specially designed waveforms. This approach may use the spectral shift of the diffraction threshold at variable angle of incidence. The preliminary coupling analysis should include examination of wavevector matching and symmetry consistency. *Structuring waves* is a modern approach, which can be applied to the selective excitation; see ref. [4]. In fact, any non-plane wave front yields some extent of freedom for the selective excitation. The Talbot effect can be considered as (one of) the earliest attempts of spatial structuring. Its potential still invokes exploration.

Special attention will be paid to the comparison of two classes of the *reconfiguration* scenarios [5], i.e., the ones achieved (i) without tunable materials but by changing the selectivity conditions within the aforementioned approaches, or (ii) due to the joint effect of tunable materials and those approaches, either at the excitation level or at the design level, or both. For the case (ii), the emphasis will be put on the scenarios which are not achievable without such a joint effect. Some approaches will be discussed in the context of reconfiguration that may involve passive PT-symmetry [6] as one of the states. As a result of the comparative analysis, routes to systematic management of multiple, functionality-enabling subwavelength resonances can be identified.

Acknowledgement: A.E.S. thanks NAWA for support under Polonium program (project DYNAMET, contract number BPN/BFR/2022/1/00023/U/00001).

References

[1] Serebryannikov, A. E., et al., unpublished (2022)

[2] Haddadin, Z., Khan, S., Poulikakos, L. V., *ACS Photon.* 11(1), 187-195 (2023)

[3] Arslan, D., Chong, K. E., Miroshnichenko, A. E., et. al., *J. Phys. D* 50(43), 434002 (2017)

[4] Bliokh, K. Y., Karimi, E., Padgett, M. J., et al., *J. Opt.* 25(10), 103001 (2023)

[5] He, Q., Sun, S., Zhou, L., *Research* 2019, 1849272 (2019)

[6] Liang, Y., Bochkova, E., Burokur, S. N., et al. *Opt. Express* 32(5), 7158-7170 (2024)

Designing a metasurface color router via photonic inverse design

Jeongwoo Son[1*], Rishard Arfin[2], Mohamed H. Bakr[2], and Jens Niegemann[3]

[1]Ansys Korea, Republic of Korea
[2]Department of Electrical and Computer Engineering, McMaster University, Canada
[3]Ansys Canada Ltd., Canada
[*]corresponding author: jeongwoo.son@ansys.com

Abstract

Metasurface color routers have emerged as a promising solution to address the inefficiencies associated with traditional color filters. Here, we present a metasurface color router, designed using an adjoint-based inverse design approach, with optical efficiencies of 57%, 75%, and 54% for red, green, and blue channels, respectively.

1. Introduction

CMOS image sensors (CIS) are ubiquitous in digital cameras and smartphones, providing the foundation for color imaging. These sensors employ color filters to selectively allow specific wavelength ranges to illuminate designated pixels which are composed of red, green, and blue sub-pixels. However, traditional Bayer color filters, which are invented by Bryce E. Bayer in 1976 [1], suffer from a critical limitation: they operate through light absorptions, resulting in significant light loss.

To overcome this challenge, metasurfaces [2], an innovation in the field of nanophotonics, are proposed because of unique properties to manipulate light properties such as amplitude, phase, and polarization. This metasurface selectively guides light of different wavelengths (RGB colors) to specific spatial locations.

Nevertheless, various solutions of metasurfaces, such as metalens [3], and metasurface color router [4], are proposed, designing the new metasurfaces requires a significant amount of computational resources and time.

In here, we leverage an adjoint-based photonic inverse design (PID) approach, which can reduce the computational resources, and design a metasurface color router with a sub-pixel size of 1 μm x 1 μm.

2. Results

2.1. Optimization process of adjoint-based metasurface color router

The adjoint method allows us to efficiently calculate the gradient at all points in space with only two simulations, forward and adjoint, per iteration. Therefore, we can reduce computational resources and time.

To simulate and optimize this metasurface color router, we employed the open-source PID package ‘lumopt’ [5]. This package is based on adjoint method and leverages the Ansys Lumerical FDTD solver for CIS simulations and Silicon photonics. We extended the existing lumopt code by introducing a novel FoM. The FoM is defined as

$$FoM = |\boldsymbol{E}(x_0)|^2, \quad (1)$$

where x_0 describes the positions in the simulation region. This FoM aims to maximize the absorbed energy within a specified volume, thereby enhancing overall performance. To strike a balance between performance and manufacturability, we employed 2D topology optimization. Our design region spans 2 μm x 2 μm x 2 μm**.** The metasurface materials consist of TiO_2 (n=2.4) and Si_3N_4 (n=1.49). The resulting metasurface color router structure, depicted in Fig. 1, achieves optical efficiencies that surpass conventional color filter systems.

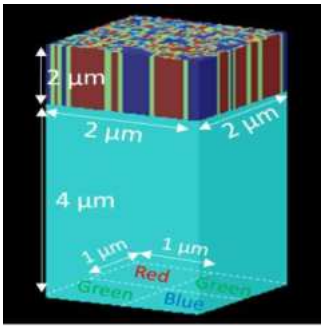


Figure 1: Optimized metasurface color router. Schematic of optimized metasurface color router which is 2 μm x 2 μm x 2 μm in size. The color router is composed of TiO_2 (red) and Si_3N_4 (blue) and has a focal length of 4 μm. The substrate is SiO_2 (cyan)

2.2. FDTD simulation results of the metasurface color router

In Figs 2a-c, we present the electric field distribution on the surface (XY plane) of the color pixels at wavelengths of 650 nm (Red), 550 nm (Green), 450 nm (Blue). The metasurface effectively routes and focuses light to individual sub-pixels while minimizing optical cross talk.

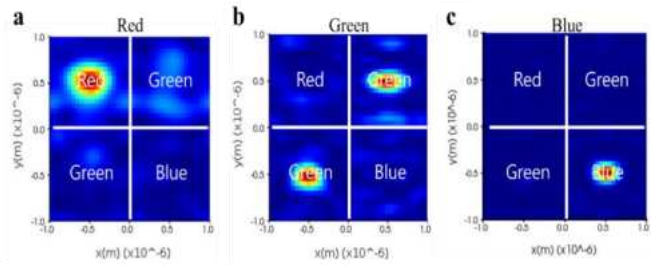


Figure 2 Electric field distribution a-c: The simulated electric field distributions of the transmitted light on the surface of the pixel at 650 nm (Red), 550 nm (Green), and 450 nm (Blue), respectively.

To quantitatively evaluate our metasurface color router, we introduce the concept of optical efficiency (OE) as

$$OE_i = \frac{P_{i-channel}}{P_{inc}}, \quad (2)$$

where i corresponds the color (RGB), $P_{i\text{-channel}}$ denotes the power on the surface of each sub-pixels, and P_{inc} represents the power of the incident light.

Figure 3 illustrates the OE of our optimized metasurface color router across the visible region (400-700 nm). Each color curve corresponds to a specific sub-pixel. Notably, the peak OE values occur at wavelengths of 680 nm (Red), 550 nm (Green), and 540 nm (Blue), with percentages of 57%, 74%, and 54%, respectively. These results significantly outperform the OE of common color filters. Furthermore, the total OE over the visible spectrum reaches an impressive 92%. Our metasurface design demonstrates the potential for enhancing CIS performance while maintaining manufacturability.

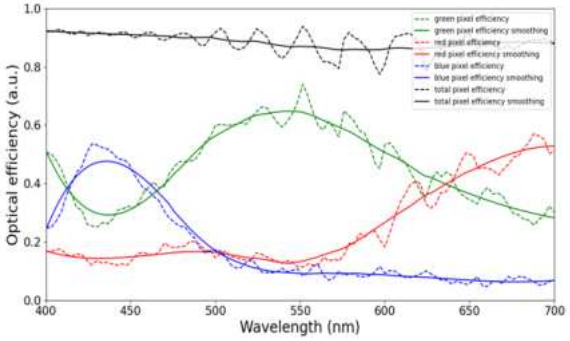


Figure 3 Optical efficiency graph. The optical efficiency of each pixel in the visible region. Each dot line represents the simulated OE results of each pixel. Each solid line is smoothing results of calculated OE.

3. Discussion

We can see the three different colors (RGB), which are primary color, are routed in Bayer pixel (RGGB) by our optimized metasurface color router shown in Fig. 2. Even though there is optical cross talk in the case of red and green, it would be resolved by setting the other FoM to minimize the optical cross talk. In this paper, we used two materials for metasurface color router. It might be a challenge for fabrication. This challenge could be resolved by using only one material such as Si_3N_4. In this case, the only one kind of nanopillars, surrounded with air, compose the metasurface color router.

4. Conclusions

In this work, we designed and optimized the metasurface color router with a high optical efficiency and a commercial pixel size via adjoint-based PID. The total OE is calculated to be 92% over the visible region and it is 57%, 75%, and 54% for red, green, and blue. In comparison with commercial CIS, the OE of our metasurface color router is much higher. We believe that this one will be a new generation of CIS structure and plan next to optimize the color router in different incident angles of light, different polarization of light, and reduce the optical cross talk.

References

[1] Bayer, Bryce. "Color imaging array." *United States Patent, no. 3971065* (1976).

[2] Yu, Nanfang, et al. "Light propagation with phase discontinuities: generalized laws of reflection and refraction." *science* 334.6054 (2011): 333-337.

[3] Chen, Bo Han, et al. "GaN metalens for pixel-level full-color routing at visible light." *Nano letters* 17.10 (2017): 6345-6352.

[4] Zou, Xiujuan, et al. "Pixel-level Bayer-type colour router based on metasurfaces." *Nature Communications* 13.1 (2022): 3288.

[5] Christopher M. Lalau-Keraly, Samarth Bhargava, Owen D. Miller, and Eli Yablonovitch, "Adjoint shape optimization applied to electromagnetic design," *Opt. Express* 21, 21693-21701, 2013.

Laser and cavities

Highly Efficient Stimulated Raman Conversion in SF_6-filled Photonic Crystal Fiber

R. Avrahamy[1], D. Belker[1], A. Halstuch[1], and A. A. Ishaaya[1,*]

[1] School of Electrical and Computer Engineering, Ben-Gurion University of the Negev, Beer-Sheva 8410501, Israel

[*]corresponding author: ishaaya@bgu.ac.il

Abstract: We report a highly efficient stimulated Raman conversion of a nanosecond pulsed Ytterbium-doped laser from 1065 nm to the first Stokes at 1161 nm using a hollow-core photonic crystal fiber pressurized with SF_6. Non-trivially, optimization of the input pump angle of linear polarization facilitates a 100% conversion efficiency increase over previous reports.

In previous work [1], An experimental investigation of stimulated Raman scattering (SRS) conversion with hollow-core photonic bandgap fiber (HC-PCF), filled with Tetrafluoromethane CF4 and Sulphur Hexafluoride SF6 gases, was reported. The conversion process of ns-duration pulses as a function of gas, fiber length, input power, and gas pressure was characterized. For SF_6 pumped at wavelengths of 1030 nm and 1065 nm, the first Stokes was observed at 1119 nm and 1161 nm, respectively. Fiber lengths of 5 m, 6 m, and 15 m generated maximum conversion efficiencies of 11.9%, 34.3%, and 55.7%, respectively, with the 1030 nm pump. The highest conversion efficiency for the 1065 nm pump reached 52.2% with a 15 m fiber, though it required double the peak power of the 1030 nm pump. In this study, we optimize the SRS conversion conditions such that the efficiency reaches up to 70% in a 6 m fiber with a 1065 nm pump. This demonstrates twice as much enhancement over the previous report. The increase is mainly due to a non-trivial correlation between the vibrational Raman conversion efficiency and the input pump beam's angle of linear polarization (AoLP). Also, the pump pulse dynamics (i.e., the rise and fall time relative to the pulse duration) were better adjusted for higher conversion efficiency.

The experimental setup is portrayed in Fig. 1a. The pump source is a high peak power Q-switched Ytterbium-doped PCF laser with a pulse duration of ~25 ns, a wavelength of 1065 nm, and a bandwidth of 0.2 nm. The pump beam is attenuated and linearly polarized via two perpendicularly oriented linear polarizers and a half-wave plate placed in between. These are followed by an additional rotatable half-wave plate to control the AoLP of the beam. The beam is focused using a short focal length aspherical lens into the bare end of the HC-PBG fiber, which is open to the air. The opposite end of the HC-PBG fiber is mounted inside a gas cell, pointing at an antireflection-coated window of the cell. The cell is first vacuum-pumped, except for a minor leakage of the open-aired fiber tip, and then pressurized to 12 bar of SF_6. The fiber is gradually filled with the gas to the state of a steady differential pressure distribution throughout the fiber (with a very slow flow of gas out of the fiber). The output beam, comprising both the pump and the converted Stokes signal, is collimated after the cell window and reflected off two dichroic mirrors to separate the first Stokes signal from the pump. The pump and Stokes beams are measured at the transmission of the first and the reflection of the second dichroic mirrors, respectively. The HC fiber is a commercially available NKT Photonics HC-1060-02 designed for single-mode operation in the transmission range. Fig. 1b displays a scanning electron micrograph of the transverse microstructure of the fiber and its measured attenuation at the relevant spectrum.

In Fig. 2a, we visualize the average powers of the pump and Stokes signal measured at the exit of a 6 m long SF6-filled fiber versus the AoLP of the input pump beam. The Stokes signal power shows significant variations of ~±68.5%, whereas the pump exhibits ~±17.5%. It is noted that we experimentally verified that the input AoLP

does not affect the transmitted pump power for peak powers below the SRS threshold. Consequently, the pump's variations in Fig. 2a are mostly due to corresponding stimulated Raman losses. The conversion efficiency, measured ratio of first Stokes to total coupled power, is plotted in Fig. 2b. The efficiency strongly depends on the AoLP with up to ~±70.6% peak variation, minima are clearly π/2 periodic, and the maxima seem similar though less sharp. Vibrational SRS in a perfectly circular symmetric fiber with a seedless configuration is independent of the AoLP of the pump beam. Thus, we hypothesized that the significant variations of the conversion efficiency stem from the polarization sensitivity of the fiber and that the fiber's imperfection is more significant at the Stokes wavelength as it is out of the fiber's bandgap and has a larger mode field diameter and deeper penetration into the microstructured cladding than the pump. Due to the nonlinear nature of SRS and the long interaction length inside the fiber, slight asymmetries that result in discrepancies in the losses and field distributions can yield significant SRS polarization sensitivity. Consequently, with the optimized AoLP of the input pump beam, we reached ~ 70% conversion efficiency in a 6 m SF_6-filled HC-PBG fiber. This is more than double the efficiency reported in [1] with the same fiber length. To the best of our knowledge, it also displays a record conversion efficiency to a single Stokes order in SF_6-filled HC fibers.

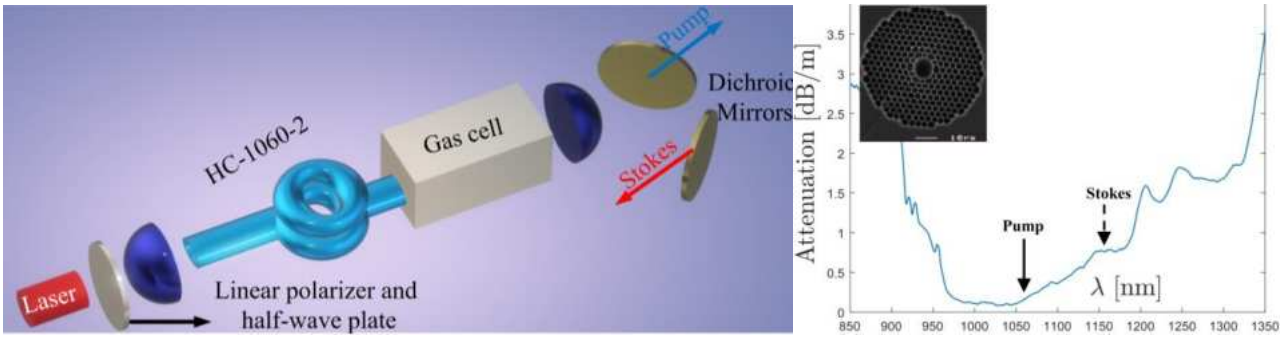


Figure 1. (a) The experimental setup. (b) SEM of the transverse microstructure of the NKT Photonics HC-1060-02 fiber and its measured attenuation in the relevant spectrum.

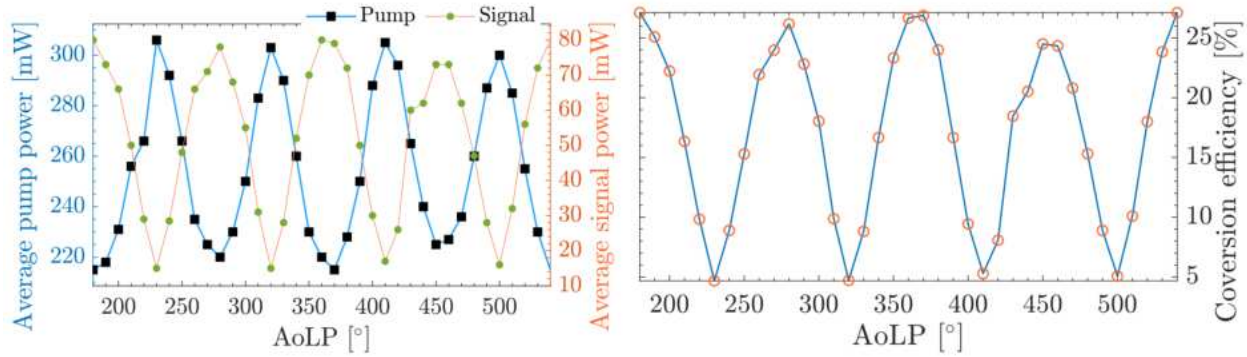


Figure 2. The average powers of the pump and Stokes signal (a) and the conversion efficiency (b), measured at the exit of a 6 m long SF6-filled fiber, versus the AoLP of the input pump beam.

References

1. S. Edelstein and A. A. Ishaaya, "High-efficiency Raman conversion in SF6- and CF4-filled hollow-core photonic bandgap fibers," Opt. Lett. 44, 5856–5859 (2019).

Optical cavity based on reflective metasurfaces

M. W. Ashraf[1*], M. A. Yaqub[1,2], T. Contino[1,2] , and M. Tamagnone[1]

[1]Nanophotonic Devices, Italian Institute of Technology, Via Morego 30, 16163 Genova, Italy

[2]Department of Chemistry and Industrial Chemistry, University of Genova, Via Dodecaneso 31, 16146 Genova, Italy

[*]Corresponding author: muhammad.ashraf@iit.it

Abstract: We present new designs for open optical cavities based on reflecting metasurfaces. Our metasurfaces are a new hybrid of traditional unit cells and supercells. We consider several types of cavities to enhance the Purcell factor of an emitter, including one type that requires only one metasurface to establish a mode.

Metasurfaces are composite structures with two-dimensional arrangements of subwavelength scatterers. By carefully designing the shape, size and position of the scatterers, we can control the propagation of light, its phase, polarization and intensity [1,2,3]. Recently, metasurfaces have been considered to design optical cavities [4-7]. In particular, a wavelength tunable external cavity laser has been demonstrated using a metasurface which can focus light from a laser diode back on itself as feedback [5].

This new approach allows us to design different optical devices with new functionalities based on reflective metasurfaces (using either a metallic or dielectric reflective substrate).

In our contribution, we focus on the potential of metasurfaces for cavity quantum electrodynamics, and we estimate the Purcell factor enhancement for a single photon emitter.

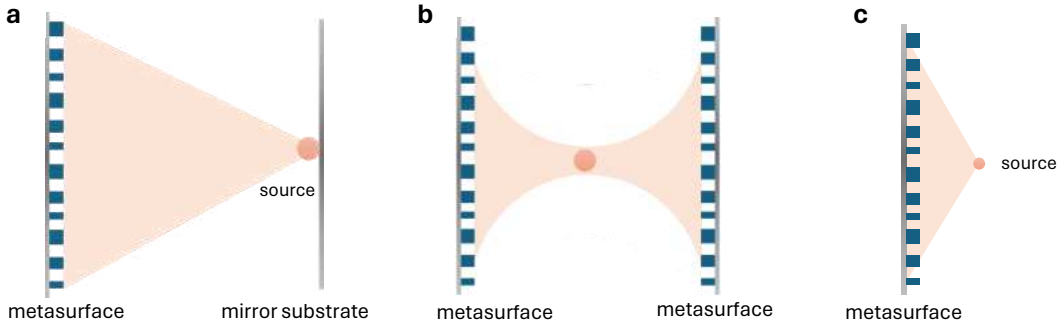


Figure-1: Types of metasurface cavities: (a) metasurface and mirror, (b) two-metasurfaces cavity, (c) evanescent metasurface.

The mathematical framework of implementing an open optical cavity based on one or more reflective metasurfaces and computation of resonant modes was reported in a vision paper [4]. The metasurface cavities considered here are of 3 types (illustrated in Fig. 1): (i) metsurface and mirror, (ii) two reflective metasurfaces, and (iii) a single metasurface which sustains an evanescent field at a significant distance; in all cases, the emitter (source) is coupled inside the field of metasurface. For the first two cases, the metasurfaces are designed to achieve a desired phase profile to retroreflect and focus light emitted by the source back on it. This can be achieved by doubling the wavevector deflection and the phase profile of a traditional metalens:

$$\Phi = 2\varphi(\mathrm{r}) = 2k_0\left(\sqrt{r^2+f^2}-f\right)+\Phi_0$$

The effects that can be achieved are an increase in the Purcell factor, control of polarization and, to some extent, wavelength of emitted light using the chromatic dispersion of the metasurface. We implemented the metasurfaces with hybrid unit cells and supercells design. As an example, in Fig. 2 we show the design of a unit cell (Fig 2a) and a supercell (Fig 2b). Figure 2c also shows the spatial dependence of the Purcell factor of a metasurface designed to target a specific position (circle in the Figure). The Purcell factor is maximized at the design position.

We are using TiO_2 pillars with square cross-sections on a metallic substrate. The simulations have been performed using HFSS and a code developed in our lab.

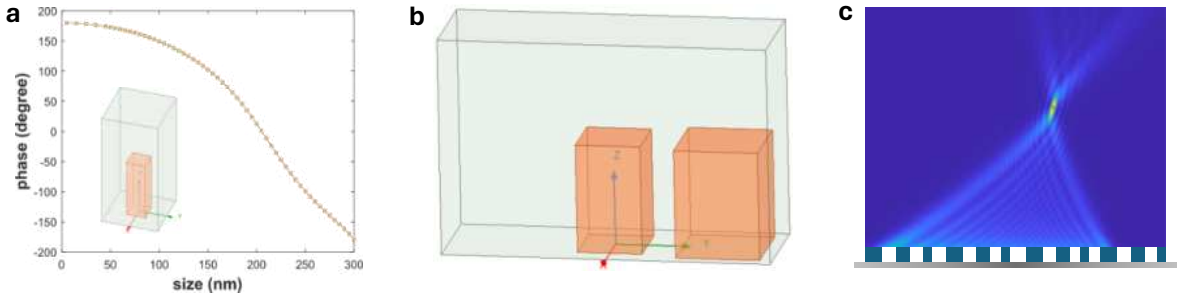


Figure-2: (a) Metasurface phase library: (b) example of designed supercell, (c) plot of the Purcell enhancement for the final design as a function of the position of the emitter.

This idea can also be used to couple different sources and can be applied to photoluminescent materials, quantum dots, nanocrystals, and more.

Acknowledgments

We acknowledge the financial support of the European Research Council (ERC) under Grant Agreement No. ERC-2020-STG 948250 (SubNanoOptoDevices).

References

1. Quevedo-Teruel, O., H. Chen, A. Díaz-Rubio, G. Gok, A. Grbic, G. Minatti, et al, “Roadmap on metasurfaces,” J. Opt., Vol. 21, No. 7, 073002, 2019.
2. Glybovski,, S. B., S. A. Tretyakov, P. A. Belov, Y. S. Kivshar, and C. R. Simovski, “Metasurfaces: From microwaves to visible,” Phys. Rep., Vol. 634, 1-72, 2016.
3. Paniagua-Domínguez, R., Yu, Y. F., Khaidarov, E., et al, “A Metalens with a Near-Unity Numerical Aperture,” Nano Lett., Vol.18, No. 3, 2124−2132, 2018.
4. Spaegale, C., “Open Optical Cavities based on Metasurfaces,” Reviews of Electromagnetics, Vol. 1, 2022.
5. Spagele, C., M. Tamagnone, D. Kazakov, M. Ossiander, M. Piccardo, and F. Capasso, “Multifunctional wide-angle optics and lasing based on supercell metasurfaces,” Nat. Commun., Vol. 12, No. 3787, 2021.
6. Ossiander, M., M. L. Meretska, S. Rourke, C. Spägele, X. Yin, I. B. Chelmus, and F. Capasso, “Metasurface-Stabilized Optical Microcavities,” Nat. Commun. 14, 1114, 2023.
7. Piccardo, M., M. de Oliveira, A. Toma, V. Aglieri, A. Forbes, and A. Ambrosio, “Vortex laser arrays with topological charge control and self-healing of defects,” Nat. Photon., Vol. 16, 359-365, 2022

Reconfigurable Tunable Integrated Optical Filter based on Nested Coupled Dual Ring Resonator

Pragya Mishra[1*], Tushar Gaur[2], Talabattula Srinivas[1]
[1]Indian Institute of Science, Bangalore, India
[2]Synopsys, Hyderabad, India
[*]corresponding author: pragyamishra@iisc.ac.in

Abstract: We present a novel reconfigurable device, Nested Ring Coupled Dual Ring Resonators (NCDRR) for high-speed communication. This device enables the generation of a tunable notch spectrum (through port) and comb spectrum (drop port) through the adjustment of coupling coefficients. Additionally, we have investigated various lineshapes inherent in the nested ring resonator (NRR), rendering it versatile for numerous applications in high-speed communication.

Nested Ring Resonator (NRR) structures, renowned for their double Fano resonance, are favoured in filtering and sensing applications. Like Microring resonators (MRR), NRR output is heavily influenced by resonance linewidth and sharpness. NRR's coupled resonance enables diverse lineshapes, facilitating the production of various filtering responses like Notch, Comb, and Bandpass with an additional cavity. Given the significance of filtering applications, amalgamating these two functionalities into a single reconfigurable Photonic Integrated circuit (PIC) offers substantial advantages. Moreover, We have analyzed different material platforms for tuning the device. The tunability and reconfigurability of the device make it a suitable candidate for general-purpose photonic processors.

This study comprehensively analyses a novel programmable optical device configuration based on nested ring architecture coupled with two racetrack ring resonators. The device can effectively generate notch and comb responses tailored to desired frequencies by optimizing device parameters such as resonator lengths and coupling coefficient.

This research is funded by the Prime Minister's Research Fellowship (PMRF) by the Government of India.

References

1. Darmawan, S., Chin, M.K., "Nested-ring Mach–Zehnder interferometer," Opt Quant Electron 38, 1151–1157 (2006).
2. Xu, Yameng & Li, Jiaxuan & Kong, Mei. (2021). Various resonance lineshapes available in a single microring resonator. Journal of Optics. 23.
3. P. Mishra, T. Gaur and T. Srinivas, "Theoretical Analysis of Integrated Optical Nested Ring Coupled Dual Ring Resonator (NCDRR) For Filtering Applications, " 2023 XXXVth General Assembly and Scientific Symposium of the International Union of Radio Science (URSI GASS), Sapporo, Japan, 2023, pp. 1-3.
4. C. Mosquera, H. Shoman and L. Chrostowski, "A tunable optical notch filter on SOI platform," 2020 IEEE Photonics Conference (IPC), Vancouver, BC, Canada, 2020, pp. 1-2.
5. W. Jiang, Y. Zhang, Y. Guo, F. Zhu and G. Yi, "Switchable and Flexible Comb Filter/Interleaver Based on Ring-Resonators With Tunable Couplers," in IEEE Photonics Technology Letters, vol. 33, no. 12, pp. 607-610, 15 June 15, 2021.
6. T. Gaur, P. Mishra, G. Hegde, and S. Talabattula, "Comparative analysis of lithium niobate and barium titanate material platforms for implementing electro-optically tunable general-purpose photonic processors," Opt. Mater. Express 13, 3217-3231 (2023).

Optical vortex generation using GaN nanopillars and metal nanostructures

◦**Ryuji Kuruma[1], Masato Takiguchi[2,3], Peter Heidt[3], Yuto Moritake[1] ,Taiki Yoda[1] , Adam Mock[4] and Masaya Notomi[1,2,3]**

[1]Tokyo Tech, Tokyo

[2] Nanophotonics Center, NTT Corporation, Kanagawa, Japan,

[3]NTT Basic Research Laboratories, NTT Corporation, Kanagawa, Japan,

[4]ET 100 Central Michigan University, Mount Pleasant, MI 48859, USA

*corresponding author E-mail: kuruma.r.ab@m.titech.ac.jp

Abstract: This study explores generation of Orbital Angular Momenta (OAMs) in sub-wavelength nanowires. We reveal that a hexagonal GaN hollow nanowire exhibits distinctive OAM when Au nanopillars are closely placed, which is due to non-Hermitian perturbation breaking the mirror symmetry. We show a variety of structures optimizing the OAM.

Optical vortices with spiral wavefronts are known to have orbital angular momentum (OAM) and phase singularities near the optical axis. The optical vortices are expected to be used in various fields, such as rotation control of nano-materials and high-capacity information communication. Conventional optical vortex generation methods have involved large device sizes, such as computer holograms and spiral phase plates. Recently, compact optical vortex generation devices are proposed for application to on-chip devices and communication devices, including micro-sized devices using metasurfaces [1] and ring resonators [2]. However, these devices have problems such as few active systems [3] and complex structures. In addition, sub-micron size devices have not yet been realized. We have reported on polarization vortex generation by a hexagonal GaN hollow nanowire laser[4][5] (Fig. 1), but it does not produce OAM. Here, we propose a novel way to generate OAM optical vortex generation device based on hexagonal hollow nanowires.

In this study, we propose a novel structure where Au nanopillars are placed in the vicinity of a hexagonal GaN hollow nanowire, and investigate its eigenmodes of light propagating in the z direction using the finite element method(FEM). We found that when the Au nanopillar is placed in a position that breaks the mirror symmetry of the hexagon, a sufficiently large OAM appears in the eigenmode. The phase rotation direction does not depend on the light propagation direction. First, we optimize the position and size of the Au nanopillar to maximize OAM for infinitely-long nanowires with frequency of 750[THz]. Figure 2(a) shows the electric field profile of the optimized mode having OAM of 3.66. Note that the position of the Au pillar is slightly displaced from the symmetric position. We confirmed that OAM does not appear when we place dielectric nanopillars in a similar manner, which shows that the OAM is generated by non-Hermitian perturbation breaking the mirror symmetry.

Figures 2(b) and 2(d) also show the OAM spectra, which represent the Fourier components of each azimuthal quantum number. Notice that the positive part and negative part of spectrum become asymmetric. This asymmetry generates overall non-zero OAM.

Next, we examine another situation. Here, the Au nanopillar shape is changed to a rectangle and the position and size of the Au nanopillar were optimized under the condition that the pillar always contacts the outer edge of

the hexagonal GaN hollow nanowire. The obtained solution is shown in Fig. 2(c) and has OAM of 4.23.

Note the diameter of hexagonal nanowires is just 0.6λ. Although it has been demonstrated that non-Hermitian perturbation can produce chiral optical properties, our result indicates an interesting possibility of guided modes themselves in the nanowires with sub-wavelength diameters will have orbital angular momentum, the size of this structure can be smaller than conventional OAM devices and different applications can be expected. We will discuss a variety of structures producing OAM by the same method, and discuss the physical mechanism of OAM generation.

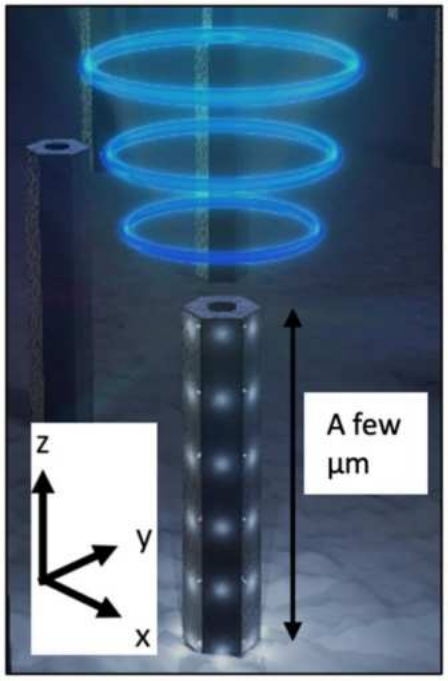


Fig.1 GaN hexagonal hollow nanowire

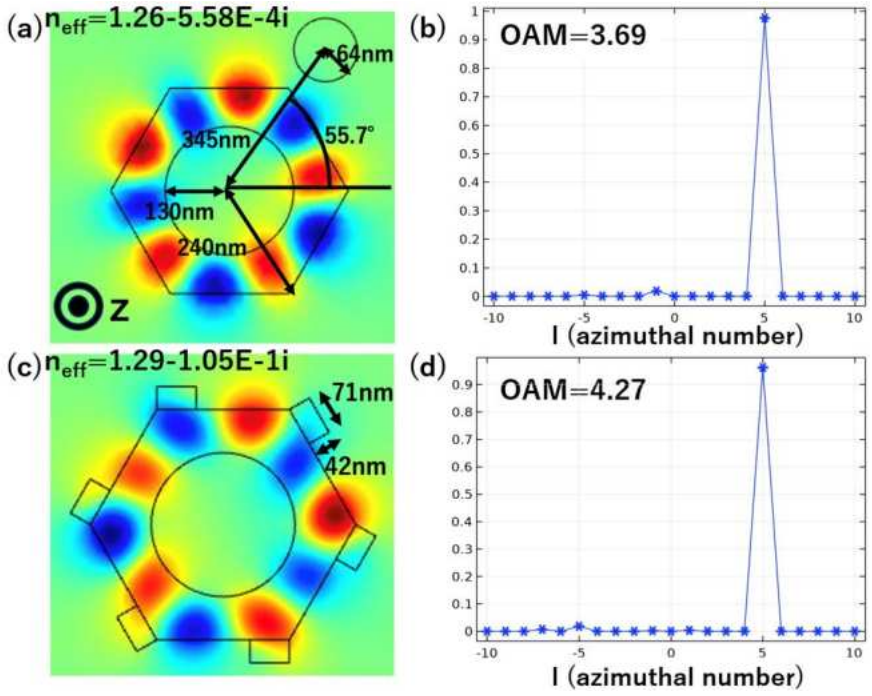


Fig.2(a) Electric field(Ez)(Pillar non-contact) (b)OAM spectrum(Pillar non-contact) (c) Electric field(Ez)(Pillar contact) (d)OAM spectrum (Pillar contact) *n_{eff}:effective mode index

References

1. Nanfang Yu *et al.*,*Science***334**,333-337(2011).
2. Xinlun Cai *et al.*,*Science***338**,363-366(2012).
3. PeiMiao *etal.*, *Science***353**,464-467(2016).
4. M. Takiguchi, et.al., ACS Photonics, 11, 789 (2024)
5. Takiguchi, M.,JSAP spring meeting 15p- PB05-1(2022)
6. Khonina S N et al., Modern Optics 48 1543–57(2001)

Photonic bandgap structures

3D Soft Photonic Crystal Photoswitch between Cubic Lattices

E. Oton[1*], M. Cigl[2], P. Morawiak[1], S. Mironov[2], A. Bubnov[2], W. Piecek[1]

[1]Faculty of New Technologies and Chemistry, Military University of Technology, Warsaw, Poland
[2]Institute of Physics, Czech Academy of Sciences, Prague, Czech Republic
[*]corresponding author: eva.oton@wat.edu.pl

Abstract: An all-optical switchable 3D soft photonic crystal was demonstrated. Two photomodulated systems were prepared: a photoswitch changing from cubic lattice BCC to SC, and shutter from BCC to isotropic medium. Both can switch between states by swapping the illumination source and without loss of monocrystallinity of the photonic crystals.

ABSTRACT

Introducing novel functionalities in 3D photonic crystals has become the focus of study for enhanced ground-breaking photonic applications. Blue Phase (BPs) liquid crystals (LC) are currently being intensively investigated for their unusual optical properties and structure. Unlike other liquid crystals, they self-assemble into highly organized 3D structures [1,2] with lattice periods in the hundreds of nm, which is achieved by the self-assembly of the LC molecules into periodic cubic structures, producing bright selective Bragg reflections – they are 3D photonic crystals.

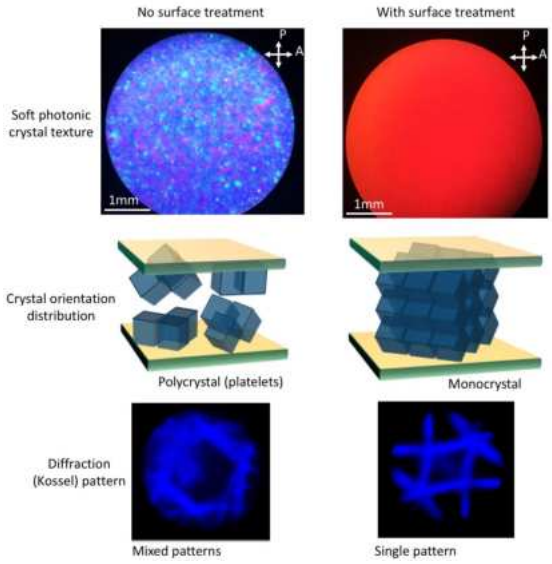


Fig.1 – 3D soft photonic crystal – poly and monocrystalline BPs.

New functionalities can be induced into the BP structures improving their properties [3]. For instance, new properties or improved responses can be designed by adding different kinds of dopants to the crystals structure. A promising research direction involves inducing photoswitching properties in BP crystals solely by light stimuli [4].

However, direct applications for BPs are often limited because crystals notoriously grow as disorganized polycrystals. Polycrystalline (platelet) structure shows a multitude of tiny disorganized 3D photonic crystals that tend to produce scattering thus they show poor optical and electrooptical properties [5]. The efficient control of BP crystal orientation is a problem that must be solved for this advanced material to be used in photonic devices. However, producing large 3D BP monocrystals is a complex problem that becomes even more complicated when involving the control of the lattice orientation.

In our previous work [6], we successfully produced 3D BP photonic crystals (of mm-sized) by designing smart surface anchoring properties and using specific precursor chemical formulations (Fig.1). We proved that large BPs monocrystals can be obtained and specific lattice orientations can be arbitrarily chosen.

This work demonstrates an all-optical switchable 3D photonic crystal obtained by doping monocrystalline BPs with newly synthesized photosensitive derivatives and the same crystal growth tools to produce large monocrystals.

Two systems were produced: a photoswitch between BCC and SC (switch BPI (110) and BPII (100)), and a light shutter, switching between BCC and isotropic state. Both systems can switch stable states back and forth by changing the illumination source only and maintaining the monocrystallinity. Such an all-optical switch provides and accurate control over illumination and material properties. Tailored photoactive dopants work like a molecular switch in the crystal matrix: the cooperative effect of the BP host molecules produces visible macroscopic changes in the crystal structure (Fig.2).

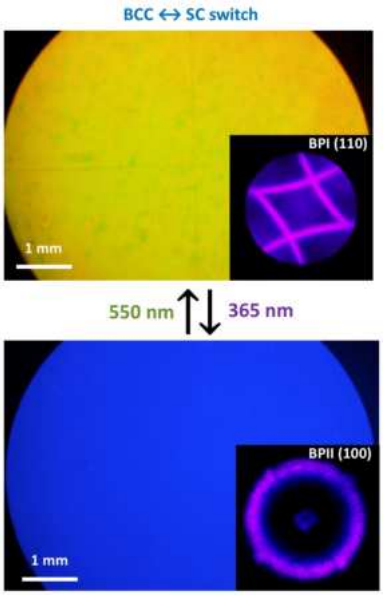


Fig.2 – Photoswitching between BCC and SC.

By illuminating the BP crystals back and forth, the all-optical the BPI ↔ BPII and BPI ↔ ISO switches can be continuously written and erased. The demonstrated effect of reconfigurable BP photonic crystals can be repeatedly recorded and employed in diverse photonics applications like adaptive holographic systems.

These all-optical driven devices demonstrate a rapid and smooth optical transition between two cubic crystal lattices and a cubic crystal lattice and isotropic medium. Newly developed 3D photonic crystal switches promise significant progress in photonic technologies of adaptive optics systems and integrated photonic circuits. Technologies mainly based on all-optical-driven photonic materials show considerable potential for advanced reconfigurable photonic devices such as dynamic optical filters and sensors and optically driven logical elements.

This study offers a valuable insight into driving the use of BPs in practical photonic devices. A deeper understanding of these unique materials will drive the progress of their functionalities for application in innovative photonic technologies.

Acknowledgments: Funded by the National Science Centre, Poland under the OPUS call in the Weave program (UMO-2021/43/I/ST5/02632), and by the Czech Science Foundation (Project No. 23-42944L).

References

1. Belyakov, V.A., “Optics of Chiral Liquid Crystals” in “Diffraction Optics of Complex-Structured Periodic Media”, 80–139, Ed. Springer, Springer-Verlag New York 1992.
2. Hornreich, R.M. and Shtrikman, S. “Theory of structure and properties of cholesteric blue phases”, Phys.Rev. A 24, 635-8, 1981.
3. Zhang, Y., Yoshida, H., Chu, F., Guo, Y.-Q., Yang, Z., Ozaki, M., Wang, Q.-H., “Three-dimensional lattice deformation of blue phase liquid crystals under electrostriction” Soft Matter 18, 3328-3334, 2022.
4. Vijayaraghavan, R. K.; Abraham, S.; Rao, D. S. S.; Prasad, S. K.; Das, S., “Light Induced Generation of Stable Blue Phase in Photoresponsive Diphenylbutadiene Based Mesogen”, Chem. Commun. 46, 2796– 2798, 2010.
5. Oton, E., Netter, E., Nakano, T., Katayama, Y.D., Inoue, F., “Monodomain blue phase liquid crystal layers for phase modulation”, Sci. Rep. 7, 44575, 2017.
6. Oton, E., Yoshida, H., Morawiak, P., Strzeżysz, O., Kula, P., Ozaki, M., Piecek, W., “Orientation control of ideal blue phase photonic crystals”. Sci. Rep. 10, 10148, 2020.

Microlaser with topologically protected light distribution based on a 3D Soft-Matter-Based Photonic Crystal

E. Oton[1], M. Muszyński[2], P. Morawiak[1*], P. Kapuściński[2], P. Oliwa[2], M. Popławska, J. Szczytko[2], W. Piecek[1]

[1]Faculty of New Technologies and Chemistry, Military University of Technology, Warsaw, Poland
[2] Institute of Experimental Physics, Faculty of Physics, University of Warsaw, Warsaw, Poland
[*]corresponding author: przemyslaw.morawiak@wat.edu.pl

Abstract: We report a newly observed lasing from a 3D soft-matter-based photonic crystal with topologically protected distribution of emission. Directional lasing with light of circular polarization is emitted from a custom-made microcavity. It was observed and recorded in real and reciprocal space.

ABSTRACT

Structures of liquid crystals with chiral molecules, producing photonic band structures are promising photonic materials for manipulating of light. Liquid crystal (LC) phases incorporating chiral molecules display 1D, 2D and 3D periodic structures leading to the emergence of a photonic bandgaps, eventually with well defined spatial orienatation and distribution. Blue Phase (BPs) liquid crystals are now in the current focus of exciting research due to their ability to self-assemble into 3D photonic crystals. They show a cubic 3D periodic order, unlike other kinds of LCs, with bright selective Bragg reflection and lattice periods in the order of hundreds of nm [1].

Employing BPs in genuine photonic applications is hindered by the typical tendency of photonic crystals to grow as polycrystalline structures which notoriously exhibit high scattering, so their optical properties are usually worse than those of solid-matter ones [2]. Effectively controlling of mesogenic monocrystal growth is still a problem that needs to be solved. Especially, the control of the monodomain lattice orientation is still not well understood.

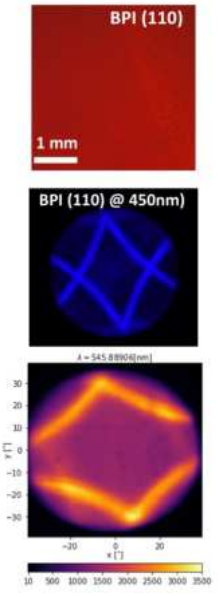


Fig.1 – 3D soft photonic crystal microlaser: texture, diffraction (Kossel) pattern, lasing in reciprocal space.

Through the implementation of specific surface anchoring properties and targeted precursor for chemical formulation of the working mesogen, we successfully grew uniform, millimeters-sized 3D BP photonic crystals. Large monocrystalline BPs (see Kossel patterns) with selected specific crystal lattice orientations were prepared [3]. Custom made large BP photonic crystals were doped with laser dyes and assembled into custom made microcavities. Here we report the successful generation of topologically protected, spatially distributed lasing from such 3D BP photonic crystals. High-intensity, directional topological emission was obtained in the reciprocal space (Fig.1). We show the distinct emission originating from resonant polarization modes that was analyzed, showing strong circular polarizations.

This work shows a significant progress at use of BPs into actual practical photonic applications. Improving the control of these unique materials will surely develop new functionalities to be used in cutting-edge photonic technologies. Notably, the generation of laser light on-demand is an emerging crucial topic in the field of photonic materials.

Acknowledgments: Funded by the National Science Centre, Poland under the OPUS call in the Weave program (UMO-2021/43/I/ST5/02632), and by the Czech Science Foundation (Project No. 23-42944L).

References

1. Belyakov, V.A., “Optics of Chiral Liquid Crystals” in “Diffraction Optics of Complex-Structured Periodic Media”, 80–139, Ed. Springer, Springer-Verlag New York 1992.
2. Oton, E., Netter, E., Nakano, T., Katayama, Y.D., Inoue, F., “Monodomain blue phase liquid crystal layers for phase modulation”, Sci. Rep. 7, 44575, 2017.
3. Oton, E., Yoshida, H., Morawiak, P., Strzeżysz, O., Kula, P., Ozaki, M., Piecek, W., “Orientation control of ideal blue phase photonic crystals”. Sci. Rep. 10, 10148, 2020.

Dirac bound states in the continuum in honeycomb photonic crystal slabs

Yi-Chi Kao, Sheng-Wei Kao, and Ruey-Lin Chern*

Institute of Applied Mechanics, National Taiwan University, Taiwan
*corresponding author: chernrl@ntu.edu.tw

Abstract: We propose a design of photonic crystal slabs for investigating the bound states in the continuum (BICs), which are identified as the Dirac BICs. By changing the geometric parameters of the unit cell without breaking the C_{6v} symmetry, a pair of Friedrich-Wintgen BICs appear near the Dirac point.

Bound states in the continuum (BICs) are non-leaky localized resonance modes that coexist with a continuous spectrum of radiating waves [1–4]. Since BICs will not radiate to the far field, they are decoupled from the far-field radiation. Ideal BICs may have infinite quality factors and zero spectral linewidths. In the presence of the absorption loss, roughness, or finite size of the structure, an ideal BIC is turned into a quasi-BIC with a finite (yet very large) quality factor and nonzero (yet very small) linewidth.

There are in general two categories of BICs. The first one is symmetry-protected (SP) BICs due to symmetry mismatch between resonance modes and incident waves, which usually appear at the center of Brillouin zone for a periodic lattice with perfect symmetry in structure geometry [5,6]. The second one is accidental BICs originating from wave interference between two or more radiation channels, which usually appear at certain wave vector points on isolated dispersion bands (at or off the Brillouin zone center) when the relevant coupling to the radiation continuum completely vanishes [7], which can further be divided into two types: Fabry-Perot (FP) BICs [8,9] and Friedrich-Wintgen (FW) BICs [10]. The former are constructed by two interacting objects with one resonance, while the latter by two interacting resonances in one object1.

Recently, a new type of BICs in the photonic crystal slabs occur at the Dirac point, where two or four dispersion bands meet at a single point. The so-called Dirac BICs can be realized by the generation or annihilation of one or two pairs of *C* points with a Dirac point, resulting in one or two accidental BICs at the *K* point [11]. A Dirac BIC can also obtained by tuning the geometric parameters such that a Dirac point becomes a quasi-BIC, along with a pair of *C* points [12].

In this study, we propose a design of photonic crystal slab consisting of triangular holes arranged as a hexagonal cluster in the unit cell of a honeycomb lattice. When the system holds the C_{6v} symmetry, a SP BIC with an extremely large quality factor occurs at the double Dirac point, where four dispersion bands meet at a single point. By changing the geometric parameters of the unit cell without breaking the C_{6v} symmetry, a band gap is opened near the Dirac point and a pair of FW BIC appear at the anti-crossing points between two upper and two lower dispersion bands.

References

1. Hsu, C. W., Zhen, B., Stone, A. D., Joannopoulos, J. D. & Solja˘ci´c, M. Bound states in the continuum. Nat. Rev. Mater. **1**, 16048 (2016).
2. Peng, C. Trapping light in the continuum—from fantasy to reality. Sci. Bull. **65**, 1527–1532 (2020).
3. Koshelev, K. et al. Subwavelength dielectric resonators for nonlinear nanophotonics. Science **367**, 288–292 (2020).
4. Azzam, S. I. & Kildishev, A. V. Photonic bound states in the continuum: From basics to applications. Adv. Opt. Mater. **9**, 2001469 (2021).
5. Kazarinov, R. & Henry, C. Second-order distributed feedback lasers with mode selection provided by first-order

radiation losses. IEEE J. Quant. Electron. **21**, 144–150 (1985).

6. Li, S., Zhou, C., Liu, T. & Xiao, S. Symmetry-protected bound states in the continuum supported by all-dielectric metasurfaces. Phys. Rev. A **100**, 063803 (2019).
7. Hsu, C. W. et al. Observation of trapped light within the radiation continuum. Nature **499**, 188–191 (2013).
8. Weimann, S. et al. Compact surface fano states embedded in the continuum of waveguide arrays. Phys. Rev. Lett. **111**, 240403 (2013)
9. Huang, L. et al. Topological supercavity resonances in the finite system. Adv. Sci. **9**, 2200257 (2022).
10. Koshelev, K., Favraud, G., Bogdanov, A., Kivshar, Y. & Fratalocchi, A. Nonradiating photonics with resonant dielectric nanostructures. Nanophotonics **8**, 725–745 (2019).
11. Ye, W., Gao, Y. & Liu, J. Singular points of polarizations in the momentum space of photonic crystal slabs. Phys. Rev. Lett. **124**, 153904 (2020).
12. De Tommasi, E. et al. Half-integer topological charge polarization of quasi-Dirac bound states in the continuum. Adv. Opt. Mater. **11**, 2300475 (2023).

Enhancing photodetection and photoluminescence in low dimensional materials with photonic crystals

M. A. Yaqub[1,2,*], H. Gupta[1,2], T. Contino[1,2], M. W. Ashraf[1], M. Tamagnone[1]

[1]*Nano-Photonic Devices, Istituto Italiano di Tecnologia, via Morego 30, 16163 Genova, Italy*

[2]*Dipartimento di Chimica e Chimica Industriale, Università degli Studi di Genova, Via Dodecaneso, 31, 16146 Genova, Italy*

[*]*Corresponding author: muhammad.yaqub@iit.it*

Abstract: We integrate photonic crystals into 2D and vdW materials (in particular GaTe and InSe) aiming to enhance their optical properties such as photoconductivity and photoluminescence. These materials were selected owing to their direct bandgaps. We optimized the design of photonic crystal to maximize the absorption and photoluminescence characteristics.

Keywords: Two-dimensional materials; Photodetectors; Photoluminescence; Photonic crystals

Photodetectors (PDs) are key optoelectronic devices that transform light signals into electrical signals and have received a lot of interest in recent years. The aim is to produce PDs with excellent capabilities including substantial gain, strong detectivity, and significant responsivity with quick response-time and minimal power usage. Due to their remarkable electrical and optoelectronic properties, III-VI group stacked semiconductors, GaSe, GaTe, and InSe, for instance, have just recently gained recognition among 2D materials. In contrast to indirect bandgap multilayer TMDCs like WSe_2 and MoS_2, multilayer InSe and GaTe have direct bandgap values i.e., 1.27 and 1.67 eV, respectively and owing to direct bandwidth they are proved to be promising optoelectronic materials [1, 2].

In this contribution we aim to maximize the efficiency of PDs based on GaTe and InSe using photonic crystal structures. We can achieve that by optimizing the photonic crystal to resonate at the target wavelength. The same approach can be used at the photoluminescence wavelength to maximize it. Ansys HFSS was used to design the structure of GaTe/InSe based photodetectors and for the numerical simulations. We tried different structure (hexagonal and square) photonic crystals, and the results were almost the same for both. The maximum absorption peaks were found at ~500 THz (600 nm) depicting the application of the photodetectors in the visible spectrum, as shown in Figure 1(a) [square photonic crystal not shown]. Some changes were made in design to optimize our structure for the PL characteristics and numerical simulations were carried out for GaTe as shown in Figure 1(b). For GaTe, the dip was observed at ~403 THz (1.67 eV) and for InSe dip was observed at 308 THz (1.27 eV), in consistent with the existing literature [3, 4] (InSe not shown).

We fabricated the devices with electron beam lithography followed by TiO_2 deposition. We developed a new exfoliation method based on UV tape to maximize the yield and to avoid the residues of glue which are commonly found when performing scotch tape exfoliation. The optical pictures of GaTe and InSe flakes

are shown in Figure 2(a) and 2(b), respectively. Figure 2(c) depicts the optimized design to be used in our work to fabricate the photodetector.

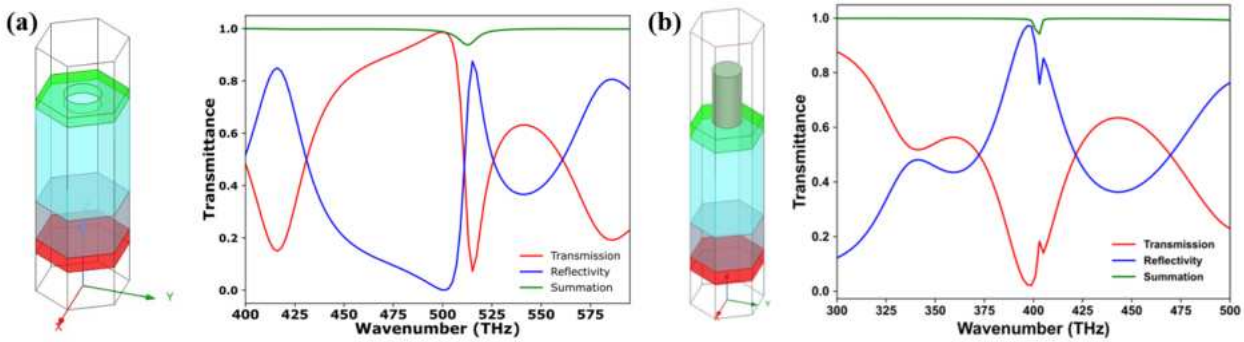


Figure 1 Design and simulation for **(a)** Hexagonal photonic crystal for photodetector for InSe, and **(b)** simulations for PL analysis for GaTe

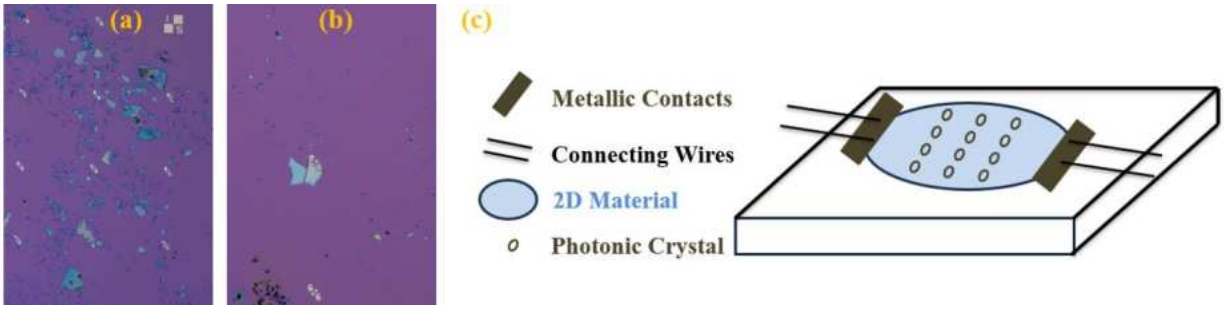


Figure 2 Microscope images of the flakes of **(a)** GaTe, **(b)** InSe, and **(c)** design for our photodetector

We will present more details as well as numerical and experimental results (measurements are currently in progress). In the future we will also explore substrate effects to induce changes in the band structure of the material and to further enhance the performance [5].

Acknowledgement

We acknowledge the financial support of the European Research Council (ERC) under Grant Agreement No. ERC-2020-STG 948250 (SubNanoOptoDevices).

References

1. Wang, Z., Safdar, M., Mirza, M., Xu, K., Wang, Q., Huang, Y., and He, J., "High-performance flexible photodetectors based on GaTe nanosheets", *Nanoscale*, *7*(16), 7252-7258, 2015.
2. Jang, H., Seok, Y., Choi, Y., Cho, S. H., Watanabe, K., Taniguchi, T., and Lee, K., "High-performance near-infrared photodetectors based on surface-doped InSe", Adv. Funct. Mater., 31(3), 2006788, 2021.
3. Zallo, E., Pianetti, A., Prikhodko, A. S., Cecchi, S., Zaytseva, Y. S., Giuliani, A., and Calarco, R., "Two-dimensional single crystal monoclinic gallium telluride on silicon substrate via transformation of epitaxial hexagonal phase" *npj 2D Materials and Applications*, *7*(1), 19, 2023.
4. Brotons-Gisbert, M., Andres-Penares, D., Suh, J., Hidalgo, F., Abargues, R., Rodriguez-Canto, P. J., and Sanchez-Royo, J. F., "Nanotexturing to enhance photoluminescent response of atomically thin indium selenide with highly tunable band gap" *Nano letters*, *16*(5), 3221-3229, 2016.
5. Mao, J., Wu, Z., Guo, F., and Hao, J., "Strain-induced performance enhancement of a monolayer photodetector via patterned substrate engineering" ACS Appl. Mater. Inter., 14(31), 36052-36059, 2022.

High-bandwidth slow-light silicon modulators

[1]Xingjun Wang, and Changhao Han, China
[*]corresponding author: xjwang@pku.edu.cn

Abstract: We realize a modulator with an EO bandwidth of 110 GHz in a length of about 100μm, and enables transmission beyond 224 Gbps PAM-4 per lane.

Silicon modulators are key components in silicon photonics to support the dense integration of electro-optic (EO) functional elements on a compact chip for various applications including high-speed data transmission, signal processing, and photonic computing. Despite numerous advances in promoting the operation speed of silicon modulators, a bandwidth ceiling of 67 GHz emerges in practices and becomes an obstacle to paving silicon photonics toward Tbps level data throughput on a single chip. Here, we theoretically propose and experimentally demonstrate a design strategy for silicon modulators by employing the slow light effect, which shatters the present bandwidth ceiling of silicon modulators and pushes its limit beyond 110 GHz in a small footprint. The proposed silicon modulator is built on a coupled-resonator optical waveguide (CROW) architecture, in which a set of Bragg gratings are appropriately cascaded to give rise to a slow light effect. By comprehensively balancing a series of merits including the group index, photon lifetime, electrical bandwidth, and losses, we found the modulators can benefit from the slow light for better modulation efficiency and compact size while remaining their bandwidth sufficiently high to support ultra-high-speed data transmission. Consequently, we realize a modulator with an EO bandwidth of 110 GHz in a length of about 100μm, and demonstrate a data rate beyond 110 Gbps by applying simple on-off keying modulation for a DSP-free operation. Our work proves that silicon modulators beyond 110 GHz are feasible, thus shedding light on the potentials of silicon photonics in ultra-high-bandwidth applications such as data communication, optical interconnection, and photonic machine learning.

We also have demonstrated the first slow-light-based wavelength-division-multiplexed signal transmitter beyond 1.6 Tbps on SOI platform. By adopting slow-light approach, the bandwidth-efficiency trade-off for pure silicon modulators is reduced greatly, paving the way for beyond 224 Gbps transmission per lane with DNN. Our slow-light modulators with compact footprint and large passband lead to an on-chip data-rate density of greater than 0.8 Tb/s/mm2 is achieved, without any individual resonant wavelength adjusting and temperature control system. This proposed pure-silicon transmitter solution illustrates the great potential of silicon photonics for next-generation optical interconnection in 1.6TE.

.

References

1. Han, C. H, “Slow-light silicon modulator with 110-GHz bandwidth,” Science Advances 9: eadi533, (2023)
2. Han, C. H, “Ultra-compact silicon modulator with 110 GHz bandwidth,” OFC PDP: Postdeadline Paper. Th4C.5, (2022)

Topological valley plasmons in twisted monolayer-double graphene moiré superlattices

Weiwei Luo[1*], Jiang Fan[1], Alexey B. Kuzmenko[2], Wei Cai[1] and Jingjun Xu[1*]

[1]School of Physics, Nankai University, China
[2]Department of Quantum Matter Physics, University of Geneva, Switzerland
*weiwei.luo@nankai.edu.cn; jjxu@nankai.edu.cn

Abstract: We combine the two active fields of topological photonics and moiré superlattices, by demonstrating theoretically that moiré superlattices of small-angle twisted monolayer-bilayer graphene provide a natural platform for valley protected plasmons. Particularly, complete plasmonic bandgap appears and unidirectional transport of plasmonic edge states protected from inter-valley scattering is presented.

Graphene plasmons, hybrids of Dirac quasiparticles and photons, exhibit low-loss, strong electromagnetic confinement and electrical tunability. Graphene plasmons provide excellent opportunities for exploring light-matter interactions at the nanoscale, which is promising for applications in integrated photonics and biosensing[1]. By introducing the concept of topology, unidirectional propagation of graphene plasmons protected against disorder and backscattering can be realized[2]. However, the requirements of complex artificial geometries and configurations obstruct the experimental realizations of topological graphene plasmons. On the other hand, by stacking and twisting different layers of Van der Waals materials, two-dimensional (2D) moiré superlattices are emerging as an important avenue for engineering quantum materials with novel properties[3].

In this work, plasmon properties of small-angle twisted monolayer-bilayer graphene (tMBG) is investigated, whose moiré superlattices consist of triangular domains with the Bernal (ABA) and the rhombohedral (ABC) stacking. The ABA and ABC graphene have different electronic bandstructures where the ABA graphene is a semi-metal with a tunable band overlap, while the ABC one is a semiconductor with a gate-tunable band gap and a flat band [4]. Here we demonstrate theoretically that tMBG moiré superlattice provides a natural platform for GPC, where complete plasmonic bandgap occurs. Furthermore, the effects of nontrivial chiral valley topology of the GPC are emphasized. Finally, robust transport of graphene plasmon waves with suppressed inter-valley scattering is shown at the interfaces separating two GPCs with opposite valley Chern numbers. Our study motivates further explorations of novel photonic phenomena in the rich platform of reconstructed moiré superlattices.

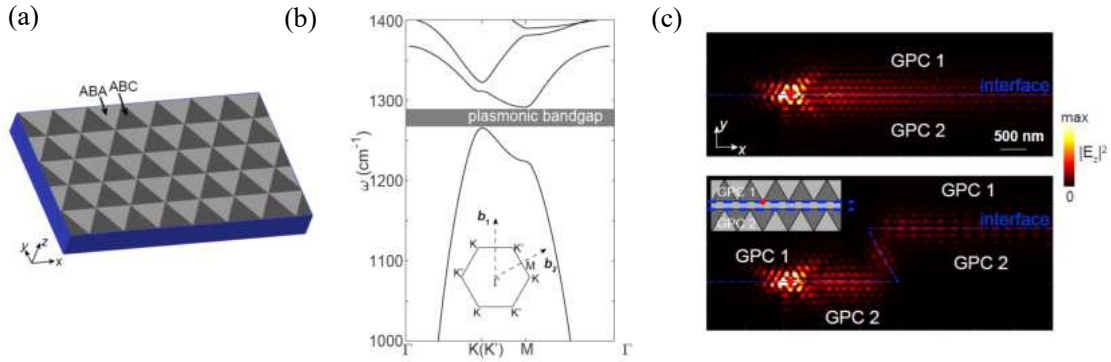


Fig.1 Topological valley plasmons in twisted monolayer-double graphene moiré superlattices. (a) Moiré superlattices of TMBG is consisted of triangular domains of the ABA and ABC stacking graphene. (b) Plasmonic bandgap occurs in the moiré superlattices of TMBG. (c) Backscattering-free propagation of graphene plasmons for the valley topologically protected edge states.

This work has been supported by the National Key Research and Development Program of China (2023YFA1407200, 2022YFA1404800), the National Natural Science Foundation of China (12004196,12127803,12074200), Guangdong Major Project of Basic and Applied Basic Research (2020B0301030009), Changjiang Scholars and Innovative Research Team in University (IRT13 R29) and the 111 Project (B23045). The work of A. B. K. was supportedby the Swiss National Science Foundation.

References

1. Koppens, F. H.; Chang, D. E.; Garcia de Abajo, F. J., Graphene plasmonics: a platform for strong light–matter interactions. *Nano Letters* **2011,** 11 (8), 3370-3377.
2. M. Jung, Z. Fan, G. Shvets, Midinfrared plasmonic valleytronics in metagate-tuned graphene, *Physical Review Letters* **2018**, 121 (8), 086807.
3. Y. Cao, V. Fatemi, S. Fang, K. Watanabe, T. Taniguchi, E. Kaxiras, P. Jarillo-Herrero, Unconventional superconductivity in magic-angle graphene superlattices, *Nature* **2018**, 556 (7699), 43-50.
4. Morpurgo, A. F., The ABC of 2D materials. *Nature Physics* **2015,** *11* (8), 625-626.

Design of inorganic photoelectrodes based on photonic crystals with incorporated Mo_6 clusters.

C. Lebastard[1,2*], A. Renaud[3], S. Cordier[3], T. Uchikoshi[1,2], T. Suzuki[1,2], F. Grasset[1,2]

[1]CNRS-Saint-Gobain-NIMS, IRL 3629, Laboratory for Innovative Key Materials and Structures, National Institute for Materials Science, 1-1 Namiki, Tsukuba, Japan
[2]Research Center for Electronic and Optical Materials, National Institute for Materials Science, 1-1 Namiki, Tsukuba, Japan
3Univ. Rennes-CNRS-Institut des Sciences Chimiques de Rennes, UMR 6226, 35000 Rennes France
[*]corresponding author: lebastard.clementhugo@nims.go.jp/clement.lebastard@cnrs.fr

Abstract: This work describes the elaboration of photoelectrodes based on an inverse opal structure made of semiconductor oxides and hexamolybdenum clusters as light harvesters. Nanostructure fabrication is possible thanks to electrophoretic deposition method, a low-cost and scalable process.

Metal cluster (MC) family gathers a wide range of compounds among them $A_2[Mo_6L^i_8L^a_6]$ are based on a central Mo_6 octahedra, supported by eight inner ligands face-capping the octahedra (L^i = halogen, chalcogen) by six apical ligands at the terminal position (L^a = halogen, hydroxyl, water…) and stabilized by two counter cations (A = alkali, ammonium). They present interesting physicochemical properties such as light absorption which make those compounds attractive for catalysis, optoelectronic, or photovoltaic applications.[1] The association of molybdenum clusters and a photonic crystal (PC) structure have been already thought to increase the emission intensity at the passband's energy,[2] or more recently, to enhance the photo-induced current by a slow photon effect.[3]

This work focuses on the design of photoelectrodes built up from periodic design of PCs with inverse opal (IO) structures. Starting from the silica beads synthesis, their arrangement, the infiltration of the pores by semiconducting metal oxide, the etching of the template and the insertion of MC in the freshly obtain cavities. SiO_2 synthesis has been optimized to modify the size of the beads, so that IO's pore size fits light confinement of MCs. Both SiO_2 opal structure and MC insertion are based on electrophoretic deposition (EPD) to reduce the structure fabrication time, to make possible the scaling and more generally, to promote a low-cost process.

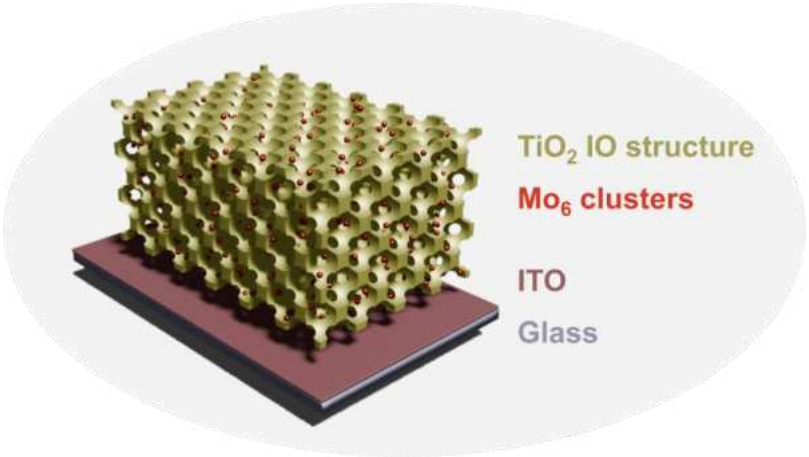


Figure 1: Sketch of the photoelectrode based on an IO structure.

This study is part of the ANR NanoLEtsGOs project (ANR-22-CE09-0015), between the UMR 6226 ISCR and the IRL 3629 LINK, and carried out under the financial project of the Agence National de la Recherche.

References

1. Nguyen N.T.K., Lebastard C., Wilmet M., Dumait N., Renaud A., Cordier S., Ohashi N., Uchikoshi T., Grasset F., "A review on functional nanoarchitectonics nanocomposites based on octahedral metal atom clusters (Nb_6, Mo_6, Ta_6, W_6, Re_6): Inorganic 0D and 2D Powders and Films" Sci. Technol. Adv. Mater., Vol. 23, 547, 2022
2. Dechézelles, J-F. Aubert, T., Grasset, F., Cordier, S., Barthou, C., Schwob, C., Maître, A., Vallée, R. A. L., Cramail, H., Ravaine, S., "Fine tuning of emission through the engineering of colloidal crystals" Phys. Chem. Chem. Phys., Vol. 12, No. 38, 11993, 2010.
3. Nguyen, T. K. N., Grasset, F., Cordier, S., Dumait, N., Ishii, S., Fudouzi, H., Uchikoshi, T., "Light harvesting hexamolybdenum cluster integrated with the 3D ordered semiconductor inverse opals for optoelectronic property" Mater. Today Chem., Vol. 27, 101351, 2023.

Emerging applications

Plasmonic Copper Nanorings for Building Energy Management

X. Baami González[1*], J. D. Tran[2], and D. S. Sutherland[1]

[1] iNANO – Aarhus University, Denmark
[2] Technical University of Denmark, Denmark
[*]: xbaami@inano.au.dk

Abstract: Copper nanorings of a diverse range of sizes (200-800 nm) have been successfully fabricated showing plasmonic behavior. They represent an alternative for future applications such as energy-saving glasses coatings and films to block infrared radiation.

In modern technology and industry, there is a pressing need for energy-saving materials, one of the major examples is advanced materials for windows. Regarding the mentioned application, the major goal is to design new materials capable of blocking infrared (IR) radiation while being optically transparent to visible light [1]. These IR-blocking materials would allow to reduce the transfer of heat radioactivity inside buildings, decreasing the consumption of active cooling systems. This would lead to what we cold smart windows, there are two main types of it: Active smart glass, which necessitates external stimuli for mode switching, and passive smart glass, which alters modes through internal stimuli. In the literature, there can be found several examples of active solutions including low-emissivity materials [2], thermochromic materials [3], and gas-chromic approaches [4]. However, we believe that plasmonic metamaterials represent a feasible alternative and might lead to cost-effective solutions for passive smart windows.

Previously in our group, we have used Sparse Colloidal Lithography (SCL) and Hole Mask Colloidal Lithography (HMCL) to fabricate a diverse number of nanostructures, including gold (Au) nanorings [5-7]. The fabrication method that was described for Au nanorings and crescents in previous publications was not useful when trying to fabricate structures with new metallic materials. To solve this problem, we came up with a solution that combines features of both SCL and HMCL coupled with Physical Vapor Deposition to synthesize new nanorings. This, among others, allowed us to fabricate copper (Cu) structures presenting very similar properties to those made from Au (**Figure 1A**).

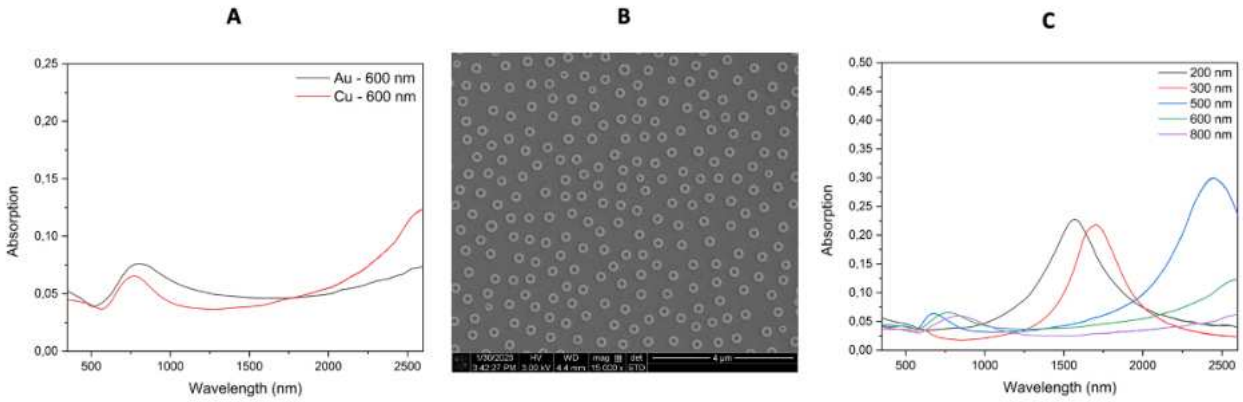


Figure 1: (a) Comparison Au and Cu, **(b)** 300 nm Cu nanorings, **(c)** Absorption results for different sizes Cu nanorings

As presented in **Figure 1B** the Cu nanorings showed a homogeneous structure and distribution. When comparing different ring sizes (**Figure 1C**) there is a clear trend for the displacement of the peak positions. For the low energy peak

as the size of the rings decreases the peak shifts to higher energy, this trend is replicated for the lower intensity high energy peak, but the observed shift is less significant.

Complementary studies have shown that Cu nanorings are stable to oxidation conditions. Consequently, the next efforts within the project are placed on ideally shifting one of the peaks to a region between 750-1150 nm by changing the size of the rings, coupling different sizes, or tunning some of the fabrication parameters.

The resonance peak positions were also shown to be customizable by tuning the size, shape, and material of the nanorings. These results suggest that other parameters such as the temperature or the medium refractive index could be other ways to tune the optical response. Moreover, the results shown by FDTD simulations (**Figure 2**) matched with the experimental ones and allowed us to understand the E-field components, for both, the high- and low-energy resonances. These results suggest that copper, silver, or other metallic materials might be interesting when it comes to applying these nanorings as a new solution for controlling heat dissipation in buildings.

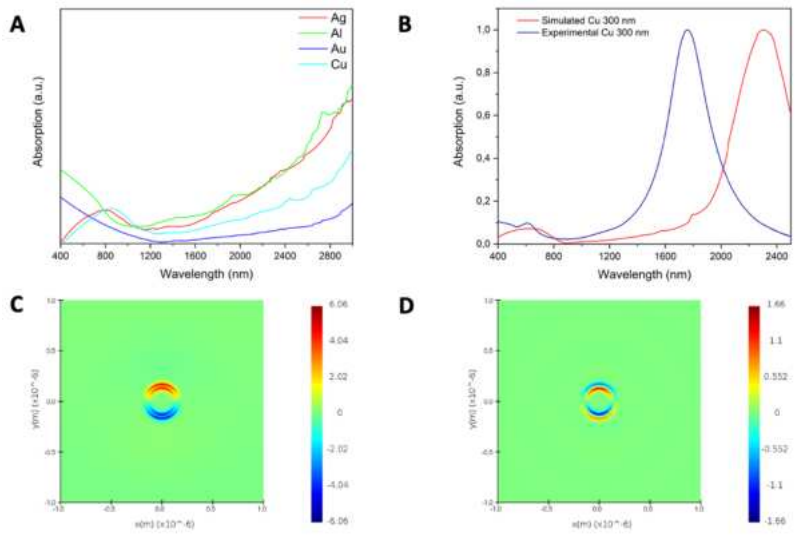


Figure 2: Optical absorption spectra showing; A Simulated 800 nm metallic nanorings, B) Experimental 300 nm Cu nanorings vs Simulated (normalized), C) Z-component of the E-field plot of low energy peak (1977 nm) for a simulated 300 nm Au nanorings, D) Z-component of the E-field plot of high energy peak (594 nm) for a simulated 300 nm Au nanorings.

References

1. [1] L. V. Besteiro, X.T. Kong, Z. Wang, F. Rosei, A.O. Govorov. 2018. Nano Lett., 18, 3147-3156.
2. [2] B.P. Jelle, S.E. Kalnæs, T. Gao. 2015. Energy Build., 96, 329-356.
3. [3] X.H. Li, C. Liu, S.P. Feng, N.X. Fang. 2019. Joule, 3, 290-302.
4. [4] W. Feng, L. Zou, G. Gao, G. Wu, J. Shen, W. Li. 2016. Sol. Energy Mater. Sol. Cells, 2016, 144, 316-323.
5. [5] J. Aizpurua, P. Hanarp, D.S. Sutherland, M. Käll, G.W. Bryant, F.J. García de Abajo. Phys. Rev. Lett., 2003, 90, 057401-057405
6. [6] V.E. Bochenkov, M. Frederiksen, D.S. Sutherland. 2013. Opt. Express, 21, 14763-14770.
7. [7] H. Fredriksson, Y. Alaverdyan, A. Dmitriev, C. Langhammer, D.S. Sutherland, M. Zäch, B. Kasemo. 2007. Adv. Mater. 19, 4297-4302.

Reliability and remaining useful life of flexible silver nanowire-based transparent electrodes

M. Marus[1*], N. Lyapunov[1*], H.T Wong[1], T. L. Chan[1], and H. Hu[2]**

[1]Centre for Advances in Reliability and Safety (CAiRS), Unit 1212-1213, 12/F, Building 19W, Hong Kong Science Park, Pak Shek Kok, New Territories, Hong Kong, China
[2]Department of Electrical and Electronic Engineering, Hong Kong Polytechnic University, Hong Kong, China
[*]contributed equally
[**]corresponding author: haibo.hu@polyu.edu.hk

Abstract: Silver nanowires attract great interest for optoelectronics applications, including highly efficient flexible transparent electrodes. However, knowledge of their reliability remains scarce and lacks systematization. Here, we present a comprehensive reliability study of silver nanowire transparent electrodes and compare them with state-of-the-art indium tin oxide electrodes.

Flexible transparent electrodes enable various emerging devices, such as flexible and bendable organic and quantum dot light emitting diode (OLED & QLED) displays, rollable solar cells, and related photovoltaic (PV) applications [1]. Silver nanowires (AgNW) offer exceptional flexibility, scalability, solution-processability, and additional unique properties, including plasmonic, antibacterial, and more [2]. However, the reliability of AgNW transparent electrodes (TEs) remains scarcely covered in the literature. We propose a comprehensive reliability study on AgNW, indium tin oxide (ITO), and graphene-covered AgNW (AgNW/G) flexible TEs. We conducted temperature-humidity (TH), low-temperature storage (LTS), high-temperature storage (HTS), highly-accelerated stress testing (HAST), and thermal shock testing on TEs studying their electrical and optical degradation over testing periods. Figure 1 shows the preliminary results of TS (left) and TH (right) testing on comparable flexible ITO, AgNW, and AgNW/G TEs on polyethylene terephthalate (PET) substrate.

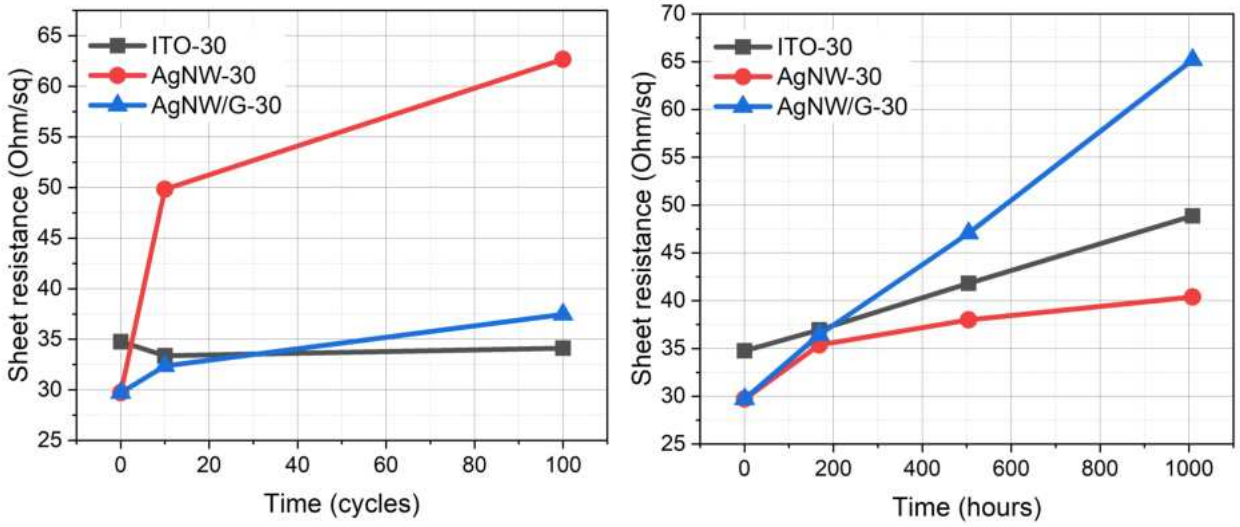


Figure 1 Results of accelerated lifetime testing (ALT) on ITO, AgNW and AgNW/G electrodes with tuned initial sheet resistance of 30 Ohm/s: (left) thermal shock, 0-100 cycles; (right) temperature-humidity testing at 85 °C / 85 R.H.

Initial results indicate advantage of AgNW/G over bare AgNW TEs under TS testing. At the same time, flexible ITO electrode demonstrated advantage at TH testing; while bare AgNW remained more conductive than AgNW/G under same testing.

The work presented in this article is supported by the Centre for Advances in Reliability and Safety (CAiRS) admitted under AIR@InnoHK Research Cluster.

References

1. Marus, M. Hubarevich, A., Wang, H., Smirnov, A., Sun, X. W., Fan, W. J., "Optoelectronic performance optimization for transparent conductive layers based on randomly arranged silver nanorods," Opt. Express, Vol. 23, No. 5, 6209-6214, 2015.
2. Marus, M. Hubarevich, A., Lim, R. J. W., Huang, H., Smirnov, Wang, H., A., Fan, W. J., Sun, X. W., "Effect of silver nanowire length in a broad range on optical and electrical properties as a transparent conductive film" Opt. Mater. Express, Vol. 7, No. 3, 1105-1112, 2017.

Micro/Nano fabrication and characterization techniques

Fabricating High-Performance Metasurfaces via Direct Printing with Polymer Infused Titanium Dioxide Nanoparticles

Dong Kyo Oh[1], Joohoon Kim[1], Hyunjung Kang[1], Yujin Park[1], and Junsuk Rho[1,2,3,4,5*]

[1]Department of Mechanical Engineering, Pohang University of Science and Technology (POSTECH), Pohang 37673, Republic of Korea
[2]Department of Chemical Engineering, Pohang University of Science and Technology (POSTECH), Pohang 37673, Republic of Korea
[3]Department of Electrical Engineering, Pohang University of Science and Technology (POSTECH), Pohang 37673, Republic of Korea
[4]POSCO-POSTECH-RIST Convergence Research Center for Flat Optics and Metaphotonics, Pohang 37673, Republic of Korea
[5]National Institute of Nanomaterials Technology (NINT), Pohang 37673, Republic of Korea
[*]corresponding author: jsrho@postech.ac.kr

Abstract: Investigating high-refractive-index materials for visible metasurfaces, we propose a direct printing method using polymer with titanium dioxide (TiO_2) nanoparticles. This enables precise control of refractive index (up to 1.9), optimized metasurface design, and high-performance fabrication on flexible substrates. This approach offers promise for efficient, multifunctional metasurface applications.

Visible metasurfaces, composed of periodic nanostructures, have garnered significant interest due to their precise manipulation of electromagnetic waves for applications such as holograms, lenses, and optical sensors [1]. Despite their potential, the practical fabrication of these metasurfaces has been hindered by the expensive and time-consuming nature of high-resolution electron-beam lithography (EBL), the conventional method used for their production. Recent efforts have focused on exploring high-refractive-index materials in the visible spectrum to achieve highly efficient metasurfaces. However, these materials typically exist as thin films, requiring additional processes such as etching and lift-off. In our study, we propose a direct printing process using a polymer infused with high-refractive-index nanoparticles for the efficient fabrication of high-performance metasurfaces [2-4].

By incorporating TiO_2 nanoparticles into the polymer matrix, we can finely tune the effective refractive index of the mixture, reaching up to 1.9 depending on the concentration of TiO_2 nanoparticles, as depicted in Fig. 1a. Subsequently, through rigorous analysis based on effective medium theory, we develop optimized designs for metasurfaces (Fig. 1b). Finally, employing the direct printing process with the polymer yields high-performance metasurfaces on flexible substrates, validated through a comparison of diffraction efficiencies (Fig. 1c). Furthermore, we anticipate that various functional materials, beyond TiO_2, can be integrated into this fabrication approach, paving the way for the practical realization of highly efficient and multifunctional metasurfaces [5,6].

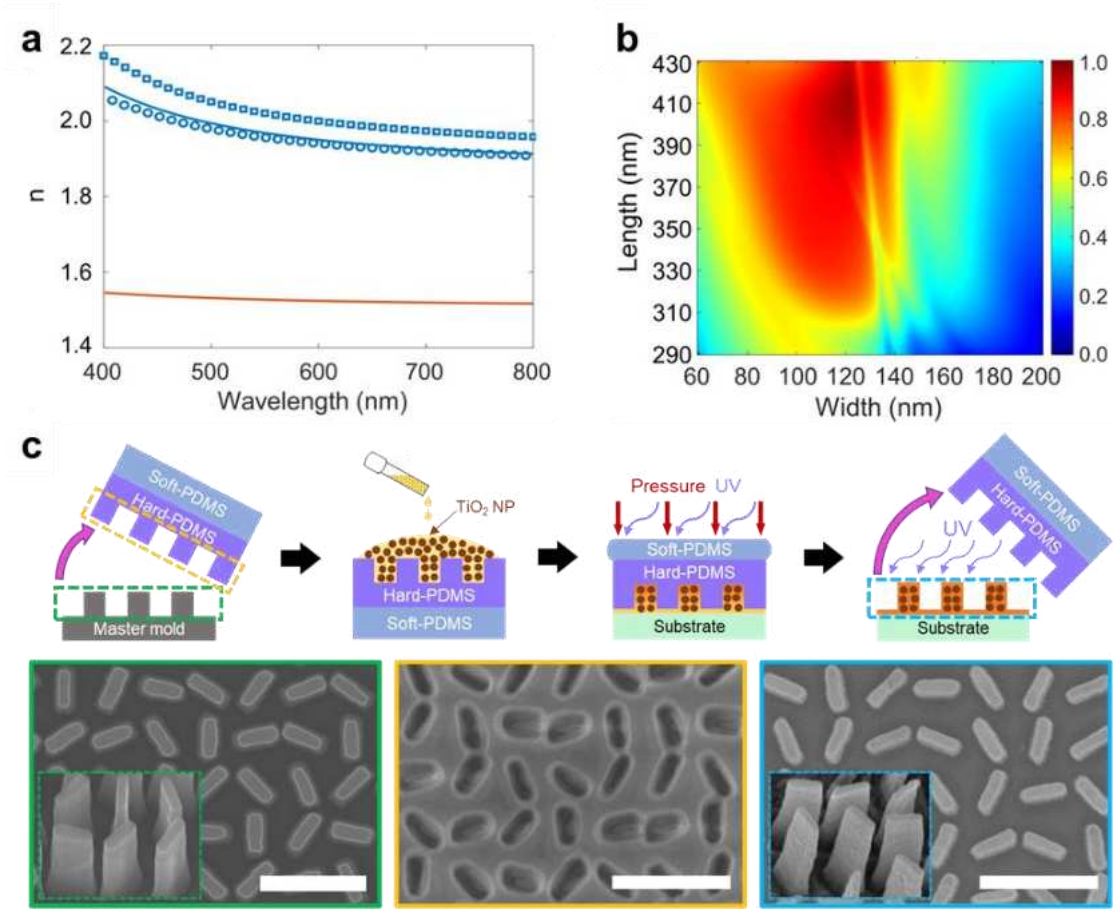


Figure 1. (a) Measured and modeled optical properties of the polymer with TiO_2 nanoparticles and comparison with conventional UV-curable polymer. (b) Rigorous analysis of metaatom dimensions depending on the effective polymer. The height of the metaatom is fixed at 910 nm. (c) the direct printing process of high-refractive-index polymer and SEM images of respective colored surfaces. All scale bars: 1 μm.

References

1. Jung, C. *et al.*, "Metasurface-Driven Optically Variable Devices," *Chem. Rev.*, Vol. 121, No. 21, 13013-13050, 2021.
2. Kim, J. *et al.*, "Metasurface Holography Reaching the Highest Efficiency Limit in the Visible via One-Step Nanoparticle-Embedded-Resin Printing," *Laser Photon. Rev.*, Vol. 16, No. 8, 2200098, 2022.
3. Yoon, G. *et al.*, "Single-step Manufacturing of Hierarchical Dielectric Metalens in the Visible," *Nature Commun.*, Vol. 11, 2268, 2020.
4. Kim, K. *et al.*, "Facile Nanocasting of Dielectric Metasurfaces with Sub-100 nm Resolution," *ACS Appl. Mater. Interfaces*, Vol. 11, No. 29, 26109-26115, 2019.
5. Kim, J. *et al.*, "One-step Printable Platform for High-efficiency Metasurfaces Down to the Deep-ultraviolet Region," *Light-Sci. Appl.*, Vol. 12, 68, 2023.
6. Yoon, G. *et al.*, "Printable Nanocomposite Metalens for High-Contrast Near-Infrared Imaging," *ACS Nano*, Vol. 15, No. 1, 698-706, 2021.

Scanning Reflectance Anisotropy Microscopy: mapping of strained amorphous semiconductors and chiral metasurfaces.

F. Haake[1*], H. Galinski[1], and R. Spoleank[1]

[1]Author: Department of Materials ETH Zurich, Switzerland
[*]corresponding author: fabian.haake@mat.ethz.ch

Abstract: We present a broadband scanning reflectance anisotropy microscope as a platform for measuring ellipsometric properties, particularly sensitive to anisotropies such as strain. Leveraging its inherent phase sensitivity, we can distinguish enantiomorphic states of chiral nano resonators. We show non-destructive mechanical characterization of amorphous semiconductors and chiral metasurfaces.

A common failure mode of flexible electronic devices is catastrophic failure or device degradation due to mechanical strain, making accurate strain control a critical aspect in their design and characterization.

Here, we introduce scanning reflectance microscopy (SRAM) as a broadband multi-material platform for mapping ellipsometric properties on the microscale. This multi-material optical platform serves not only to access microscopic strain distributions but also shows high phase sensitivity.

This technique provides a practical approach to mechanical characterization, yielding valuable insights into the mechanical behavior of diverse materials, including metamaterials, amorphous and crystalline semiconductors, and metals. The microscope's capability to generate diffraction-limited strain and phase maps enables a thorough analysis of materials properties without causing damage. [1]

The capabilities of the technique are discussed on the specific example, strained amorphous semiconductors (aSi & aGe). Recent results include the measurement of chiral nano resonators highlighting the phase sensitivity of SRAM.

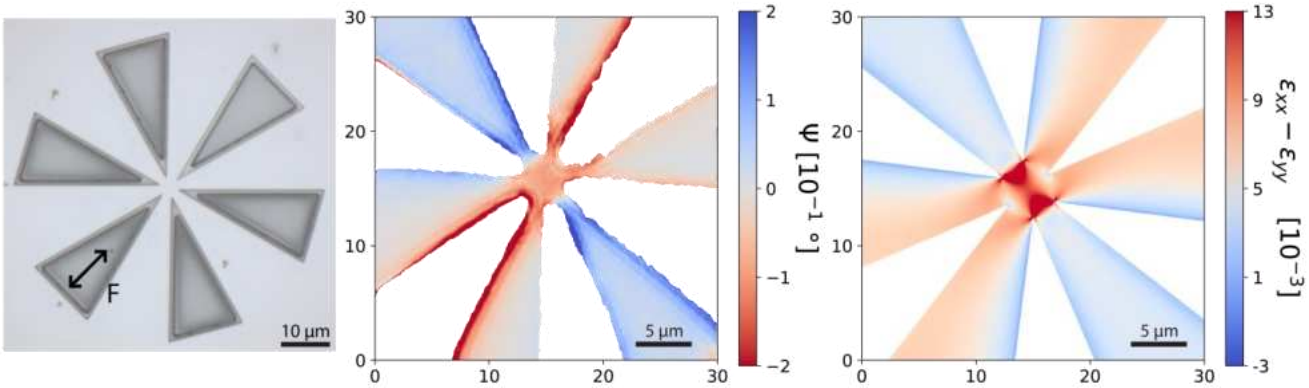


Figure 1: Light microscopy image, SRAM measurement and computed strain distribution ε_{xx}-ε_{yy} and of an uniaxially strained photonic crystal-like structure milled into amorphous silicon.

Figure 1 shows the light microscopy image of a photonic crystal-like structure milled into an amorphous Silicon thin film. The thin film is strained to a total strain of 0.8%. SRAM can resolve the strain distribution of the computed strain state.

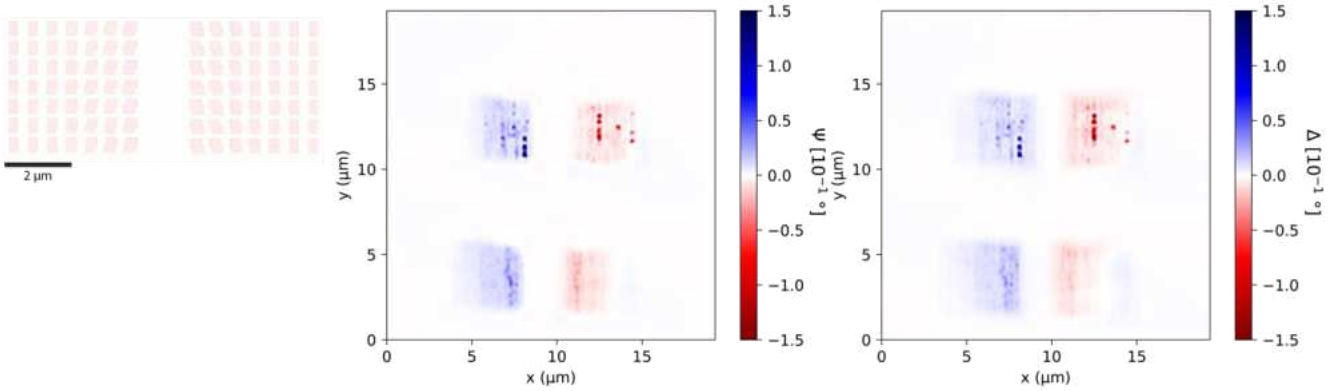


Figure 2: Dimensions of enantiomorphic nano resonators and SRAM maps with ellipsometric amplitude and phase.

Figure 2 shows first results of the amplitude and phase maps of the L/R forms of nano resonator arrays. The arrays are milled with focused ion beam and their chiral feature gets stronger towards the center of the two arrays. The scan is acquired with a probing wavelength of 950 nm.s

References

1. Sendra J., Haake F., Calvo M., Galinski H. and Spolenak R. "Scanning Reflectance Anisotropy Microscopy for Multi-Material Strain Mapping," https://doi.org/10.1002/adfm.202302179, 2023.

High-Index Atomic Layer-Nanoparticle Embedded-Resin Hybrid Metasurfaces for High-Performance Visible Metaphotonics

Dohyun Kang[1], Minseok Choi[1], Hyunjung Kang[1], and Junsuk Rho[1,2,3,4,5*]

[1]Department of Mechanical Engineering, Pohang University of Science and Technology (POSTECH), Pohang 37673, Republic of Korea

[2]Department of Chemical Engineering, Pohang University of Science and Technology (POSTECH), Pohang 37673, Republic of Korea

[3]Department of Electrical Engineering, Pohang University of Science and Technology (POSTECH), Pohang 37673, Republic of Korea

[4]POSCO-POSTECH-RIST Convergence Research Center for Flat Optics and Metaphotonics, Pohang 37673, Republic of Korea

[5]National Institute of Nanomaterials Technology (NINT), Pohang 37673, Republic of Korea
[*]corresponding author: jsrho@postech.ac.kr

Abstract: High-index atomic layer-nanoparticle embedded-resin hybrid metasurfaces are introduced as cost-effective and high-throughput method for high-performance visible metasurfaces. With theoretical 93.7% conversion efficiency at 450 nm, featuring 3 nm titanium dioxide layer, 600 nm height, and 6.6 aspect ratio, these hybrids are poised for commercial adoption, potentially replacing traditional optical components.

Metasurfaces operating in the visible spectrum, composed of subwavelength structures, are gaining attention as viable alternatives to traditional optical components due to their remarkable light modulation capabilities [1]. The conventional electron beam lithography method, traditionally used for their fabrication, is both time-consuming and expensive, impeding the smooth transition of metasurfaces from scientific concepts to practical technology [2]. In response to these challenges, nanoimprint lithography (NIL) has emerged as an efficient and rapid technique for replicating nanostructures from a master mold directly onto a substrate [3]. However, the conventional use of nanoparticle-embedded-resin (nano-PER) is associated with a low refractive index, resulting in a high aspect ratio of nanostructures, thereby posing challenges in fabrication and structural stability. In this study, we introduce a high-index atomic layer-nanoparticle embedded-resin hybrid metasurfaces as a cost-effective and high-throughput method for high-performance visible metasurfaces.

Through the atomic layer coating of titanium dioxide (TiO_2) on the surface of nano-PER, the effective refractive index of the hybrid metasurfaces can be enhanced, with the degree of enhancement depending on the thickness of the TiO2 layer. Using particle swarm optimization method, we determine the optimal parameters for width, length, period, height, and thickness of the TiO2 layer. Ultimately, a mere 3 nm layer of TiO2 allows us to achieve a high theoretical conversion efficiency of 93.7% at a wavelength of 450 nm, coupled with a height of 600 nm and an aspect ratio of 6.6. We hope that these hybrid high-index metasurfaces can be commercially utilized to replace conventional optical components with metasurfaces.

References

1. Jung, C. et al., "Metasurface-Driven Optically Variable Devices," Chem. Rev., Vol. 121, No. 21, 13013-13050, 2021.
2. Oh, D. et al. "Top-down nanofabrication approaches toward single-digit-nanometer scale structures." Journal of Mechanical Science and Technology, 35, 837-85, 2021.
3. Chanda, D. et al. "Large-area flexible 3D optical negative index metamaterial formed by nanotransfer printing." *Nature nanotechnology,* 6.7, 402-407, 2011.

3D Inkjet Printing for the Manufacture of Micron-to-Millimeter-Scale Metamaterial Structures

O. Nelson-Dummett, R. Hague, C. Tuck, and L. Turyanska

University of Nottingham, United Kingdom
*presenting author: oliver.nelson-dummett@nottingham.ac.uk

Abstract: We demonstrate additive manufacturing of complex 3D geometries using inkjet deposition of silver nanoparticles and other materials. We produce 3D lattice structures as well as unsupported overhangs, which can be encapsulated in various materials to enhance the dielectric contrast and create floating elements with a view to create metamaterials.

Inkjet and other drop-on-demand printing is increasingly being adopted for additive manufacturing (AM) of functional materials, including polymers, metals, ceramics, and low-dimensional materials [1]. Being digitally driven and with high geometric degrees of freedom, it has strong potential for the fabrication of metamaterial designs but has mostly been limited to simple 2D designs in the GHz-THz region [2,3]. We developed an Off the Grid strategy for material-jet printing, which allows for higher (sub-droplet) precision of the deposition, and consequently enabled us to create more complex designs with high fidelity [4] (Figure 1a). This strategy was utilized to produce complex 3D architectures. Starting with high solid content inks, we have produced arrays of individual pillars. Inks of silver nanoparticles suspended in a volatile solvent were deposited onto a substrate heated to 70 °C to facilitate fast solvent evaporation. The coffee-ring effect [1] causes the base of the pillar to be flared; the equilibrium diameter of 50 µm is reached after 10-12 drops (Figure 1b-c) with a small depression at the tip (Figure 1d). The pillars were successfully produced in patterned arrays for 2.5D metamaterials, such as photonic cavities (Figure 1e).

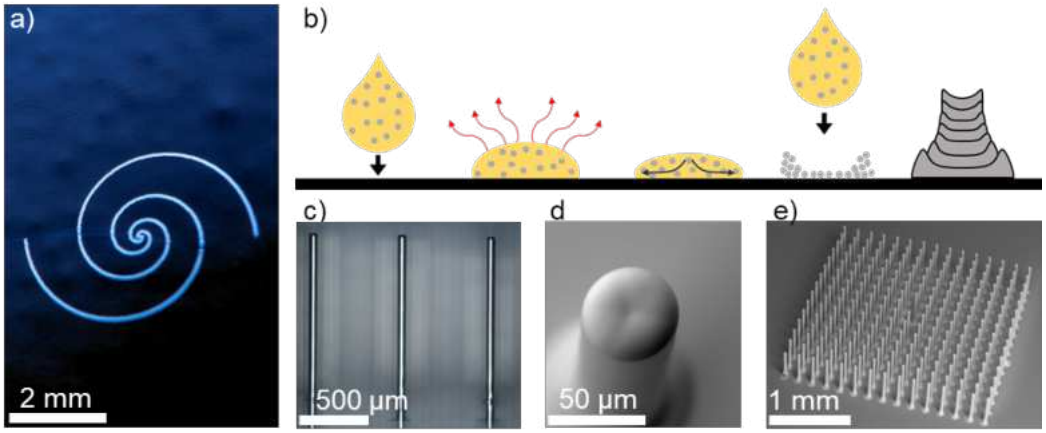


Figure 1. a) Schematic of silver nanoparticle ink (yellow) deposition onto a heated substrate (black) followed by solvent evaporation and drying. Internal flow drives the silver nanoparticles (grey circles) to the edge forming a coffee ring shape, which acts as a template for consecutive droplets. b) A representative optical image of printed pillars with diameter of 50 µm, and SEM images of c) the tip of a pillar with 1500 layers, and d) a 14 x 14 pillar array forming the structure of a photonic cavity metamaterial by leaving out the centermost pillar.

To create overhanging features, we employed the OtG strategy [4], applying a small lateral offset to each layer. Several structures were manufactured, including slanted self-supporting pillars at angles up to 34° from the vertical, as well as tripods and lattices with lateral sizes of 100 mm and heights up to 1.5 mm (Figure 2b-e).

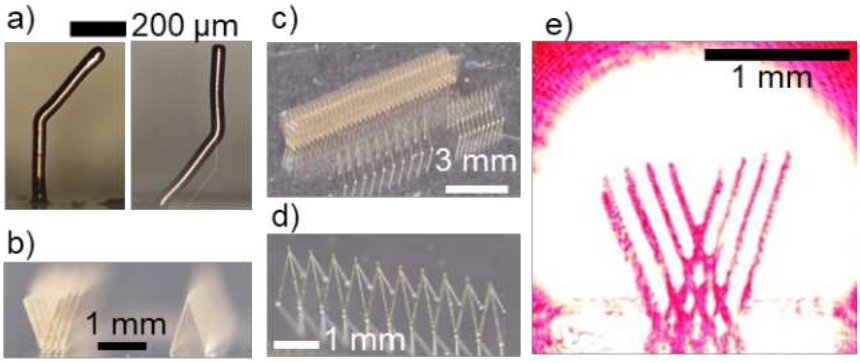


Figure 2. Representative optical images of a) slanted pillars produced using a 1 µm offset per layer, and b-d) various angles of a freestanding lattice and individual tripod structures. The lattice is shown in e) with a laser being shone along its length, demonstrating that the designed gaps in the lattice are continuous throughout.

These pillars, as well as larger silver elements, can be encapsulated in a UV-curable polymer for enhanced dielectric contrast and to support floating elements. When built up in this manner, it unlocks the potential for a range of potential uses, such as anisotropic dielectrics and 3D waveguides.

In conclusion, inkjet printing has the potential to manufacture metamaterials with complex 3D geometry, with accuracy in the micron scale across a range of materials. We demonstrate the ability to print pillar arrays, self-supporting strut-based lattices, and silver embedded in polymer dielectrics for metamaterials such as 2.5D photonic cavities, photonic lattices, and anisotropic dielectrics. The results of this work, opportunities for multi-material inkjet to introduce support materials and higher dielectric contrast materials, could offer promising manufacturing solutions for a wide range of metamaterials.

References

[1] A. Bastola, Y. He, J. Im, G. Rivers, F. Wang, R. Worsley, J.S. Austin, O. Nelson-Dummett, R.D. Wildman, R. Hague, C.J. Tuck, L. Turyanska, Formulation of functional materials for inkjet printing: a pathway towards fully 3D printed electronics, Mater. Today Electron. (2023) 100058.

[2] S.D. Assimonis, V. Fusco, Polarization Insensitive, Wide-Angle, Ultra-wideband, Flexible, Resistively Loaded, Electromagnetic Metamaterial Absorber using Conventional Inkjet-Printing Technology, Sci. Rep. 9 (2019).

[3] K. Chen, T. Bu, Y. Bai, S. Zhuang, Inkjet-printed random coding metal particles for modulation enhancement of an optical-controlled terahertz wave modulator, Opt. Quantum Electron. 48 (2016).

[4] O. Nelson-Dummett, G. Rivers, N. Gilani, M. Simonelli, C.J. Tuck, R.D. Wildman, R.J.M. Hague, L. Turyanska, Off the Grid: A new strategy for material-jet 3D printing with enhanced sub-droplet resolution, Addit. Manuf. Lett. 8 (2024) 100185.

Nanopatterning of Nitride Nanostructures for Optoelectronic Applications

Sudarshana Patra[1,2], Amelia Korveziroska[1], Uttam Manna[1,2], and Mahua Biswas [1,2*]

[1]Department of Physics and [2]Department of Chemistry, Illinois State University, Normal, IL, USA
[*]corresponding author: mbiswas@ilstu.edu

Abstract: In this work, we show the fabrication process of the aluminum nitride (AlN) nanostructure pattern, an attractive material for optoelectronic device research, such as for photodetectors and light-emitting diodes (LEDs) by utilizing a low-temperature, substrate independent and selective deposition method called sequential Infiltration synthesis (SIS).

Optoelectronic devices, such as photodetectors, solar cells, and light-emitting diodes (LEDs), are essentially energy-conversion devices that convert light to electricity or vice versa. In this field of group III-nitride semiconductors such as Gallium Nitride (GaN), Aluminum Nitride (AlN), and compound nitrides such as AlGaN have been pivotal in technology enrichment, [1-3] especially in the light emitting applications whereas bulk and thin films of these nitride materials are used as the active layer for light emitting and light harvesting purposes.[4, 5] Nanostructures of group III nitride materials are attracting significant attention for their advantages over planar structures currently used in commercial devices. In this work, we develop a fabrication process of AlN nanostructure patterns by utilizing a method called Sequential Infiltration Synthesis (SIS). SIS is a localized vapor deposition process using polymers as guiding patterns to achieve large-scale uniformity of organized nanoscale materials at lower temperatures than the conventional process. Conventionally, nitride deposition is

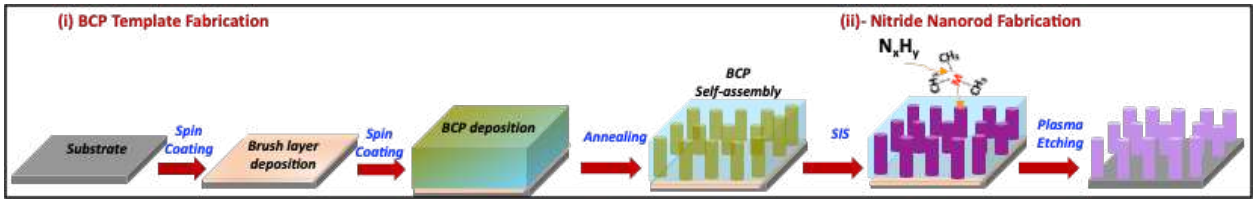


Figure 1: Schematic of the nitride nanopattern growth process using BCP template and SIS method. Step (i) shows a self-assembled vertical cylinder forming BCP nanostructure fabrication process; and step (ii) shows metal nitride nanorod array formation using the template fabricated in step (i), SIS deposition and plasma etching.

performed at high temperature using the established methods such as MBE, MOCVD, and ALD. [6-9] The low-temperature deposition of nitrides is usually challenging because of the unreactivity of the nitride precursors with the starting substrates at temperatures below 500 ºC. SIS has been explored extensively by several research groups and by industry leaders in the last few years including our group for oxide materials. We developed nanopatterns of AlN by SIS technique that can produce scalable, well-ordered, and relatively easy integration of the patterned nanomaterials and investigate their growth mechanism and optical properties. We have characterized the patterns by scanning electron microscope, energy dispersive X-ray spectroscopy (EDS), and Fourier transform infrared (FTIR) spectroscopy. Our approach is expected to produce scalable, well-ordered nanopatterns to be integrated easily into the existing technology.

This material is based upon work supported by the National Science Foundation (NSF), Division of Material Research under Grant No. DMR-2213365.

References

1. Baten, M. Z.; Alam, S.; Sikder, B.; Aziz, A., III-Nitride Light-Emitting Devices. *Photonics* **2021,** *8* (10).
2. Jain, S. C.; Willander, M.; Narayan, J.; Van Overstraeten, R., III-nitrides: Growth, characterization, and properties. *Journal of Applied Physics* **2000,** *87* (3), 965-1006.
3. Monemar, B., Basic III-V nitride research - past, present and future. *Journal of Crystal Growth* **1998,** *189*, 1-7.
4. Zhang, C.; ElAfandy, R.; Han, J., Distributed Bragg Reflectors for GaN-Based Vertical-Cavity Surface-Emitting Lasers. *Applied Sciences-Basel* **2019,** *9* (8), 1593.
5. Kenry; Yong, K. T.; Yu, S. F., AlN nanowires: synthesis, physical properties, and nanoelectronics applications. *Journal of Materials Science* **2012,** *47* (14), 5341-5360.
6. Goto, H.; Shibahara, K.; Yokoyama, S., Atomic layer controlled deposition of silicon nitride with self-limiting mechanism. *Applied Physics Letters* **1996,** *68* (23), 3257-3259.
7. Bae, S. Y.; Min, J. W.; Hwang, H. Y.; Lekhal, K.; Lee, H. J.; Jho, Y. D.; Lee, D. S.; Lee, Y. T.; Ikarashi, N.; Honda, Y.; Amano, H., III-nitride core-shell nanorod array on quartz substrates. *Scientific Reports* **2017,** *7*, 45345.
8. Zhao, S.; Connie, A. T.; Dastjerdi, M. H. T.; Kong, X. H.; Wang, Q.; Djavid, M.; Sadaf, S.; Liu, X. D.; Shih, I.; Guo, H.; Mi, Z., Aluminum nitride nanowire light emitting diodes: Breaking the fundamental bottleneck of deep ultraviolet light sources. *Scientific Reports* **2015,** *5*, 8332.
9. Hersee, S. D.; Sun, X. Y.; Wang, X., The controlled growth of GaN nanowires. *Nano Letters* **2006,** *6* (8), 1808-1811.

Post-synthesis band gap halide anion exchange tuning in $CsPbBr_3$ nanocrystals and issues of light-induced phase segregation

P. Liška[1,2*], T. Musálek[1,2], M. Kratochvíl[3], T. Šamořil[2,4], P. Dvořák[1,2], M. Kolíbal[1,2] and T. Šikola[1,2]

[1]Institute of Physical Engineering, Faculty of Mechanical Engineering, Brno University of Technology, Czech Republic
[2]Central European Institute of Technology, Brno University of Technology, Czech Republic
[3]Institute of Physical and Applied Chemistry, Faculty of Chemistry, Brno University of Technology, Czech Republic
[4]TESCAN ORSAY HOLDING, a.s., Czech Republic
[*]corresponding author: Petr.Liska1@vutbr.cz

Abstract: This study investigates post-synthesis band gap tuning of $CsPbBr_3$ nanocrystals through halide anion exchange (HAE) with CsI. While effective HAE occurs, phase segregation leads to Br-rich core and I-rich shell formations, impacting optical properties. Comprehending these phenomena enhances the development of precise optoelectronic engineering strategies tailored for semiconductor nanocrystals.

The semiconductor industry's reliance on chemical doping for electrical property engineering is paralleled by the effective tuning of optoelectronic properties in LHPs through halide anion exchange (HAE)[1]. Post-synthesis tuning of $CsPbBr_3$ nanocrystals alters their bandgap and optical characteristics, offering replaceable and reversible passive optoelectronic elements, e.g. for photovoltaics[2], high-resolution displays[3], or functional metasurfaces[4]. The photoluminescence response of $CsPbBr_3$ nanocrystals was tuned by employing post-synthesis treatment with CsI in isopropyl alcohol. These nanocrystals were prepared via the hot-injection method and dropcasted onto silicon substrates.

To examine the resulting optical band gap of the HA exchanged $CsPbBr_3$ nanocrystals, scanning electron microscopy (SEM) imaging and photoluminescence (PL) mapping were employed. The overlay of the two images is incorporated in Figure 1a. Here, the nanocrystals are highlighted by white dashed lines, and their PL response is further post-processed. The raw PL spectrum contains two distinguishable peaks, which we assign, in comparison to the literature and our own expertise, to Br-rich (mapped as green) and I-rich (mapped as red) phases. This suggests light-induced segregation of the nanocrystals. However, several sites appear to change their PL response according to the prospect of band gap tuning, as seen in Figure 1d, where several spectra are shown with Br-rich, I-rich, and mixed PL responses. The mixed PL responses exhibit much lower intensities than the rich phases.

To unravel the nature and impact of the phase segregation, time-of-flight secondary ion mass spectrometry (ToF-SIMS) was utilized to image the spatial distribution together with the depth profile of Br and I ions, as seen in Figures 1b and 1c, respectively. Here, the Br ions are detected at the sites of the nanocrystals as expected. However, I ions seem to follow a random pattern across the sample with a preference for occurrence on the edges of the nanocrystals. Moreover, upon examining the depth profile of Br and I ions in Figure 1e and comparing it with the depth PL profile in Figure 1f, we see a strong Br signal present on the surface with I signal rapidly decreasing when reaching certain depth. It is evident that the HAE mainly occurs on the outer shell of the nanocrystal which becomes I-rich. The shell reaches a certain saturation depth and leaves the core of the nanocrystal purely made of the Br-rich phase.

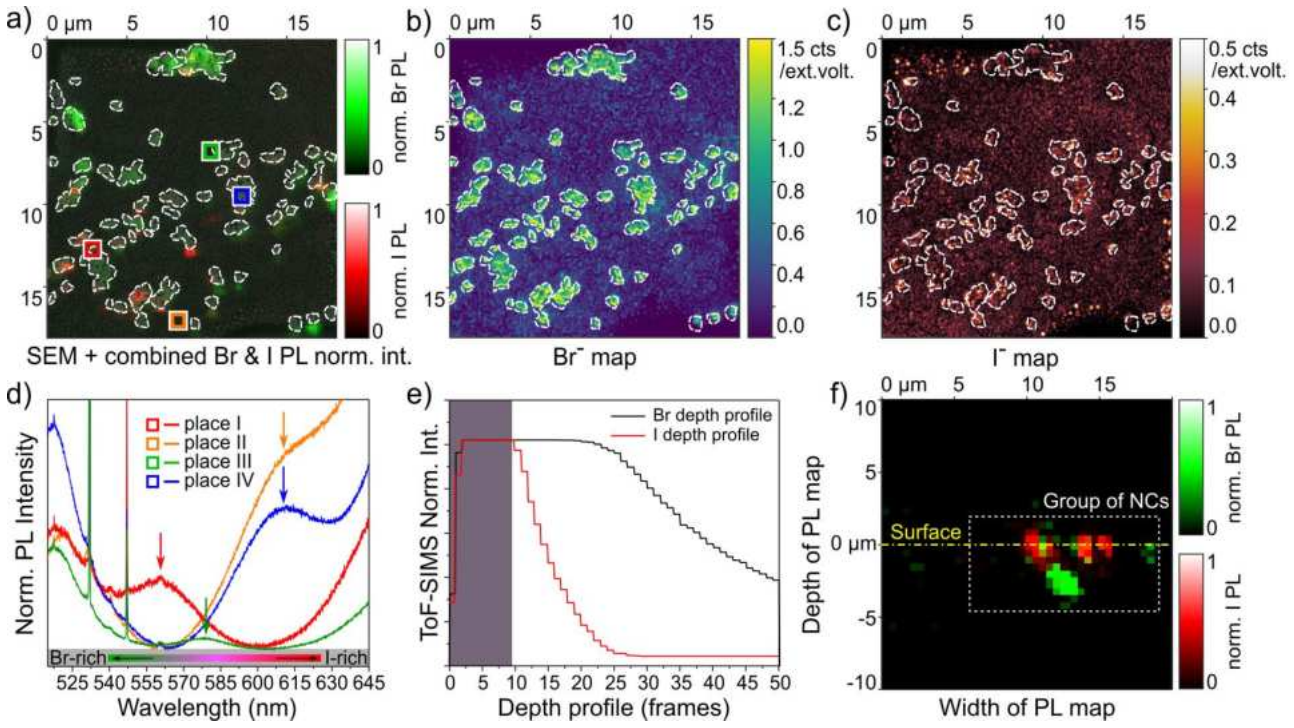


Figure 1 a) SEM and PL map overlay with $CsPbBr_3$ nanocrystals in the white dashed lines regions. b), c) ToF-SIMS chemical maps of Br and I respectively. d) Single spectra obtained from rectangular areas. e) ToF-SIMS depth profile. f) PL depth profile.

To summarize, the correlative optical and chemical imaging of HAE $CsPbBr_3$ nanocrystals revealed that light-induced phase segregation takes place leading to formation of Br-rich and I-rich phases. The band gap tuning of individual HAE $CsPbBr_3$ nanocrystals was found to be existent and prevalent even after light illumination at several sites, however, it was regarded as inefficient and random. Additional sensitive chemical mapping reveals that phase segregation primarily occurs on the outer shell of the $CsPbBr_3$ nanocrystals, saturating at an effective depth. This indicates that, rather than engineering the bandgap and PL response of the $CsPbBr_3$ NCs, non-selective mixing was prevalent due to phase segregation.

The authors acknowledge support by Ministry of Education, Youth, and Sports of the Czech Republic CzechNanoLab project LM2023051, and Specific Research, Brno University of Technology project FCH/FSI-J-24-8514.

References

1. Akkerman, Q. A., V. D'Innocenzo, et al., "Tuning of Optical Properties of Cesium Lead Halide Perovskite Nanocrystals by Anion Exchange Reactions," J. Am. Chem. Soc., Vol. 137, No. 32, 10276–10281, 2015.
2. Duan, J., M. Wang, et al., "Effect of Side-Group-Regulated Dipolar Passivating Molecules on $CsPbBr_3$ Perovskite Solar Cells," ACS Energy Lett., Vol. 6, No. 6, 2336–2342, 2021.
3. Ko, J., K. Ma., J. F. Joung, et al., "Ligand-Assisted Direct Photolithography of Perovskite Nanocrystals Encapsulate with Multifunctional Polymer Ligands for Stable, Full-Colored, High-Resolution Displays," Nano Lett., Vol. 21, No. 5, 2288–2295, 2021.
4. Fan, Y., P. Tonkaev, Y. Wang, et al., "Enhanced Multiphoton Processes in Perovskite Metasurfaces," Nano Lett., Vol. 21, No. 17, 7191-7197, 2021.

All-In-One Etching and Measurements of Silicon Metalens for Near-Infrared Focusing

Bingrui Lu[1,*], Søren Engelberth Hansen[1], Michael Juhl[1], and Søren Stobbe[1,2]

[1]DTU Electro, Department of Electrical and Photonics Engineering,
Technical University of Denmark, Ørsteds Plads 343, DK-2800 Kgs. Lyngby, Denmark
[2]NanoPhoton - Center for Nanophotonics, Technical University of Denmark,
Ørsteds Plads 345A, DK-2800 Kgs. Lyngby, Denmark
[*]corresponding author: binlu@dtu.dk

Abstract: A metalens containing silicon pillars arranged in a triangular lattice for near-infrared wavelengths is fabricated through a high-precision all-in-one etch to avoid wet chemistry processes during fabrication. Measurements demonstrate the focusing property of the metalens. It can be placed on photonic circuits or components to form a 2.5D integrated system.

Metalenses are promising components for micro- and nano-scale optical systems due to their small footprint, planar geometry, and excellent optical performance, and their possible applications include sensing, imaging, communication, astronomy, quantum photonics, and virtual/augmented reality [1]. Silicon offers unique advantages for metalenses but the accurate mapping of device design to fabricated chip remains a challenge. In our work, we apply a recently developed silicon deep-etching process [2] to obtain high-quality fabrication with precise control over the nanostructure geometries. This process replaces the common fluorocarbon inhibitor in the Bosch deep-etching process with oxygen to eliminate passivation build-up, making it a greener process for the environment while keeping a low-power and low-speed etching with fine control. It is also compatible with metal hard masks, which enables very high resolutions [2,3].

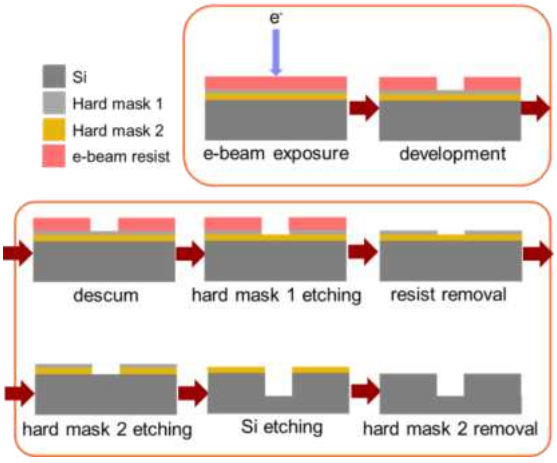


Figure 1. The all-in-one etch fabrication process flow for the silicon metalens.

We consider metalenses consisting of silicon pillars with diameter, D, and height, H, and the pillars are arranged in a triangular lattice. By varying D, an arbitrary phase profile can be realized when the relative phase delay between pillars spans 2π. By exploring the design space for D and H while constraining parameters to realistic values, we find that for a lattice constant of 450 nm and H = 1.5 µm, the required 2π phase span can be achieved for D varying between 140 nm and 356 nm. When using a 110 µm beam waist of collimated Gaussian

input, the designed metalens with a width of 327 µm are simulated to have focal lengths of 884 µm, 806 µm, and 730 µm, respectively, for wavelengths of 1410 nm, 1550 nm, and 1690 nm.

We fabricate our devices using electron-beam lithography (JEOL JBX-9500 FSZ) with proximity effect correction (Beamfox Proximity) and use a metal hard-mask to obtain a high etching selectivity, which is needed for enabling our high-aspect-ratio pillars. Characteristic metalenses fabricated by our method are shown in Fig. 2. We characterize the devices with a collimated light source with a wavelength of 1550 nm and a beam diameter of 2 mm and our experiments confirm the focusing property of the fabricated metalenses. We will present the most recent developments in our labs towards integrating the metalenses with photonic circuits [4,5,6].

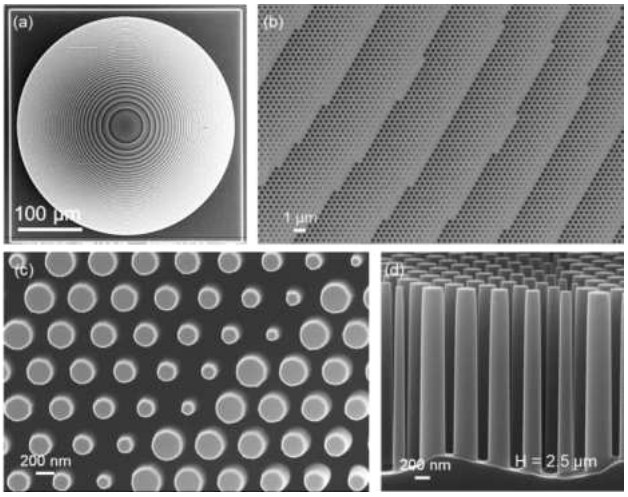


Figure 2. The silicon metalens. (a) The full metalens with a diameter of 324 µm; (b) The outer rings of the metalens with silicon pillars arranged in hexagonal unit cells: (c) and (d) the top and side view of the pillars.

References

1. Chen, W. T., A. Y. Zhu and F. Capasso. “Flat optics with dispersion-engineered metasurfaces,” Nature Reviews Materials, Vol. 5, No. 8, 604–620, 2020.
2. Nguyen, V. T. H., E. Shkondin, F. Jensen, J. Hübner, P. Leussink and H. Jansen, “Ultrahigh aspect ratio etching of silicon in SF6-O2 plasma: The clear-oxidize-remove-etch (CORE) sequence and chromium mask,” J. Vac. Sci. Technol. A, Vol. 38, No. 5, 053002-1–12, 2020.
3. Albrechtsen, M., B. Vosoughi Lahijani, R. E. Christiansen, V. T. H. Nguyen, L. N. Casses, S. E. Hansen, N. Stenger, O. Sigmund, H. Jansen, J. Mørk and S. Stobbe, “Nanometer-scale photon confinement in topology-optimized dielectric cavities,” Nature Communication, Vol. 13, No. 1, 6281–6288, 2022.
4. Hansen, S. E., G. Arregui, A. N. Babar, M. Albrechtsen, B. Vosoughi Lahijani, R. E. Christiansen and S. Stobbe, “Efficient low-reflection fully etched vertical free-space grating couplers for suspended silicon photonics,” Optics Express, Vol. 31, No. 11, 17424–17436, 2023.
5. Vosoughi Lahijani, B., M. Albrechtsen, R. Christiansen, C. Rosiek, K. Tsoukalas, M. Sutherland and S. Stobbe, “Electronic-photonic circuit crossings,” submitted, arXiv:2204.14257 (2022).
6. Babar, A. N., T. A. S. Weis, K. Tsoukalas, S. Kadkhodazadeh, G. Arregui, B. Vosoughi Lahijani and S. Stobbe, “Self-assembled photonic cavities with atomic-scale confinement,” Nature, Vol. 624, 57–63, 2023.
7. Rosiek, C. A., G. Arregui, A. Vladimirova, M. Albrechtsen, B. Vosoughi Lahijani, R. E. Christiansen and S. Stobbe. “Observation of strong backscattering in valley-Hall photonic topological interface modes”, Nature Photonics. Vol. 17, 386–392, 2023.

Evaporative Analysis of Lithium-Ion Battery Electrolytes Using Surface-Enhanced Raman Spectroscopy in a Controlled Microenvironment

M. Moussavi, N. Khinevich, A. Tamulevičienė*, T. Tamulevičius, M. Juodėnas, S. Tamulevičius

Institute of Materials Science, Kaunas University of Technology, K. Baršausko St.59, Kaunas 51423, Lithuania
*corresponding author: Asta.Tamuleviciene@ktu.lt

Abstract: This research aims to develop a novel optical sensor integrated into a battery system for early detection of lithium-ion electrolyte leakage failures. The sensor utilizes surface enhanced Raman scattering measurements and features a graphene-protected substrate comprising a 2D array of silver nanoparticles with a tailored lattice resonance.

Lithium-ion batteries (LIBs) offer the best balance between energy efficiency and performance for high-density energy storage applications. Nevertheless, damage caused by overcharging and heating during LIB operation can lead to major changes in the electrolyte composition and leaks of chemical products outside of the battery. Detecting and monitoring the leakage of trace amounts of electrolyte with high sensitivity is of great significance to improve the safety of LIBs and the devices they power. Traditional analysis techniques often fail to provide in-depth insights into electrolyte dynamics, particularly during operation. This gap underscores the need for innovative approaches to examine the complex interactions within the microenvironment of the battery.

This research aims to develop a novel optical sensor integrated into a battery system for early detection of LIB electrolyte leakage failures. We developed this sensor by leveraging and adapting the localized surface plasmon resonance as well as surface lattice resonance (SLR) (collective response of an ordered plasmonic system) in 2D silver nanoparticle metasurfaces [1, 2]. Recently, we have demonstrated that it is possible to produce surface-enhanced Raman spectroscopy (SERS) substrates that are targeted for the excitation wavelength or a specific Raman peak by tailoring the SLR wavelength [3]. The achieved record quality factor of the tailored SERS substrates was exploited in the current research to detect the specific organic molecules (derivatives of lithium carbonate, organic small molecules such as formaldehyde) emitted by the LIB electrolyte [4].

The fabrication of SERS substrates tuned to match the excitation wavelength (532 nm) comprise several technological steps. Silver nanoparticles with a diameter of 77 nm ± 4.5 nm were chemically synthesized using the seeded growth method. A 20 mm × 20 mm Si mold was fabricated using electron beam lithography (eLine plus, Raith) and reactive ion etching (Apex SLR ICP, Plasma-Therm). The pattern consisted of a square array of 180 nm diameter, 100 nm tall pillars spaced 330 nm center-to-center. The patterned Si mold was used in soft lithography replication cycles to produce polydimethylsiloxane (PDMS) replicas used for the capillarity-assisted deposition of silver nanoparticles. The deposition was performed using a custom-made setup equipped with a motorized linear precision translator and a temperature control system. Long-term stability of the SERS substrates was enhanced by applying a monolayer of graphene onto the plasmonic lattice. Large area graphene layers were deposited from CH_4 and H_2 gas mixture on a metallic catalyst (Cu foil) using a microwave plasma-enhanced chemical vapor deposition technique (IPLAS Innovative Plasma Systems GmbH). Graphene was released from the copper substrate by wet etching and the floating graphene film was subsequently placed on the surface of deionized water for 24 hours for cleaning. Finally, the graphene film was transferred onto the SERS substrate.

SERS mapping was performed using a Raman microscope InVia (Renishaw) equipped with a thermoelectrically cooled CCD detector. The samples were excited and the spectra were collected using the following combination of laser

wavelength and grating: 532 nm (1800 lines/mm). The 30×30 μm^2 surface area was mapped with a step size of 1.5 μm. Long-term stability studies of the SERS substrates were performed by repeatedly measuring the Raman scattering spectrum of the organic molecule 2-Naphthalenethiol (Sigma-Aldrich) within a 3 months' period. The results have proven excellent stability of the elaborated SERS substrate.

A custom-made container made of aluminum oxide ceramic, sealed within an argon atmosphere, was used in the SERS studies of LIB electrolyte lithium hexafluorophosphate ($LiPF_6$) dissolved in a mixture of ethylene carbonate and ethyl methyl carbonate. With an optical window of sapphire for SERS spectroscopy measurements, this chamber served as a reservoir for the LIB electrolyte. The measurements included direct placement of the electrolyte on the SERS substrate (for calibration needs), or measurements, when a few drops of the electrolyte were placed within the chamber, adjacent to a custom SERS substrate, which is not in direct contact with the liquid electrolyte. Periodic SERS measurements were conducted to monitor the presence and concentration of electrolyte analytes adsorbed on the SERS substrate. Preliminary results have demonstrated the ability of the technique to detect time evolution of the signature peaks of the electrolyte components. We have found that the top layer of the SERS substrate – graphene, having a large surface area, possessing superior molecule adsorption ability, can protect the nanoparticles from oxidation or corrosion and improves the uniformity and stability of the SERS signal.

This study leverages a meticulously engineered SERS substrate within a specially designed microenvironment to analyze the evaporative behavior of LIB electrolytes. We believe that this methodology opens new avenues for real-time monitoring of volatile components in LIB, providing insights into electrolyte stability and decomposition pathways.

References

1. Juodėnas M., Peckus D., Tamulevičius T., Yamauchi Y., Tamulevičius S., Henzie J., Effect of Ag nanocube optomechanical modes on plasmonic surface lattice resonances, ACS Photonics, Vol.7, No.11, 3130-3140, 2020.

2. Juodėnas M., Tamulevičius T., Henzie J., Erts D., Tamulevičius S., Surface lattice resonances in self-assembled arrays of monodisperse Ag cuboctahedra, ACS Nano, Vol.13, No. 8, 9038-9047 2019.

3. Khinevich N. et al. Wavelength-tailored enhancement of Raman scattering on a resonant plasmonic lattice, Sensors and actuators B:, Vol. 394, art. No. 134418, 1-8, 2023,

4. Rinkel B. L. D., Hall D.S., Temprano I., Grey C. P., Electrolyte Oxidation Pathways in Lithium-Ion Batteries, Journal of the American Chemical Society Vol.142, No 35, 15058-15074, 2020.

Acknowledgement

The studies were performed within the NANOTRAACES project carried out under the M-ERA.NET 2 scheme. This project has received funding from the Research Council of Lithuania (LMTLT), agreement No MERANET-22-2.

Characterization of small microlens based on metasurface using Quadriwave Lateral Shearing Interferometry

M. Lepers[1,3*], A. Ostrovsky[1], J. Vaillant[2], S. Khadir[3], J.Y. Duboz[3]

[1]STMicroelectronics, 38920, Crolles, France
[2]Univ. Grenoble Alpes, CEA, Leti, 38000, Grenoble
[3]Université Côte d'Azur, CNRS, CRHEA, 06560 Valbonne, France
[*]corresponding author: martin.lepers@st.com

Abstract

In this paper we report the fabrication of metasurfaces-based microlenses on 300 mm glass wafer using 193 nm immersion photolithography and their characterization using Quadriwave Lateral Shearing Interferometry (QLSI). Through this wavefront analysis, we can determine the quality of the fabrication and understand how imperfections affect the metasurface performance.

1. Introduction

In the pursuit of high-resolution CMOS sensors, there is a trend toward reducing pixel size. This miniaturization presents an increasing challenge in gathering sufficient light to maintain the sensor's sensitivity. To increase the light concentration, refractive microlenses are used to focus light on the photosensitive part of the pixel. Metasurfaces provide a planar alternative to refractive microlens and are good candidates to be integrated in a CMOS process [1]. A metalens is a structured surface made of high-refractive index and subwavelength nanopillars (poly-Si) embedded in a low refractive index substrate (SiO2). Local phase-shift manipulation is achieved by varying the pillar diameter and the capacity of a metalens to concentrate light relies on its ability to reproduce a focusing phase function. Most of metalenses use a hyperbolic phase profile [2] as it is allowing for spherical aberration free focusing. However, fabrication errors and the finite size of the metalens disturbs the phase profile actually obtained. Fabrication errors can lead to variability on meta-atoms morphology and positions which create a phase-shift offset between target and fabricated devices. To alleviate these problems, intensive metrology is employed to ensure that the fabrication follows the designs specification with tools such as scanning electron microscopy, ellipsometry or transmission electron microscopy. These measurements only provide morphological information on nanopillar such as the diameter, the height or the side wall angle. To accurately assess the influence of variations in nanopillars morphology on the performance of metasurfaces, it is necessary to perform complementary electromagnetics propagation simulations. Another approach could involve the direct measurement of the phase-shift using a wavefront sensor. To this end, we cannot use the metalens on a CMOS matrix as we have only access to integrated irradiance on pixel. Thus, to observe the wavefront we fabricated similar microlens on a transmissive glass substrate (see figure 1). Wavefront sensors directly provide phase images which holds the complete information on metalens light control performance. It can be used to validate the results of simulations and refine the fidelity of the simulated model. In this paper, we present wavefront characterization of small metalenses with different focal lengths in order to evaluate their fabrication quality. In the first part we present characterization results of metalenses and nanopillars arrays. In the second part we will presents how wavefront analysis can be used to study the impact of fabrication imperfections on metasurface performances.

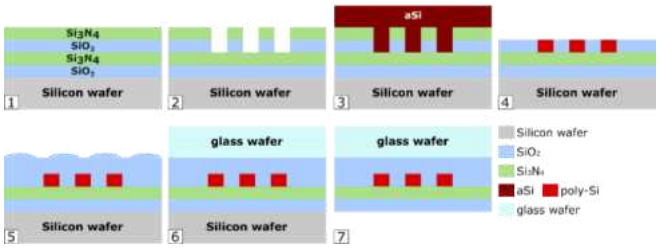


Figure 1: 1. Deposition of SiO2 and Si3N4 on a Silicon wafer using chemical Vapor Deposition 2. Photolithography process (mask alignment, resist deposition, UV exposition, cleaning, etching) to create nanoholes of varying diameters 3. Filling with aSi using Chemical Vapor Deposition 4. Chemical Mechanical Polishing (CMP) of aSi layer and etch down to SiO2 layer to form the nanopillars arrays 5. Deposition of a SiO2 using Chemical Vapor Deposition 6. Direct bonding of glass wafer and grinding 7. Silicon wafer grinding.

2. Fabrication and simulation process

The samples were fabricated using 193 nm DUV immersion photolithography on 300 mm glass wafers [3]. It starts on a silicon wafer on which alternating layers of silicon oxide (SiO_2) and silicon nitride (Si_3N_4) are deposited by PECVD (Plasma Enhanced Chemical Vapor Deposition). The thin Si_3N_4 uniform layer acts as an etch stop layer during the fabrication process and does not alter the relative phase-shift difference between meta-atoms of different sizes. Then nanoholes are etched into the substrate before being filled with amorphous silicon which is then annealed to form poly-silicon. At this stage chemical-mechanical polishing (CMP) is employed to planarize the substrate material until the

targeted height is reached. Finally, silicon oxide is added for passivation and anti-reflecting effect. Other process steps are performed after the passivation but they have no significant effects on metasurface phase-shift function. This process allows for the fabrication of metasurfaces with nanopillars with a diameter (referred as Critical Dimension or CD) ranging from 120 nm to 350 nm, for a height of 700 nm.

Prior to fabrication, simulations based on Rigorous Coupled Wave Analysis (RCWA) using the software Reticolo [4] were conducted in order to calculate the transmission and the local phase-shift variation with nanopillars diameter. The simulation is performed under periodic conditions and with plane wave incidence at 0°. These data are gathered in libraries and used to discretize the phase profile of the metalens to be fabricated.

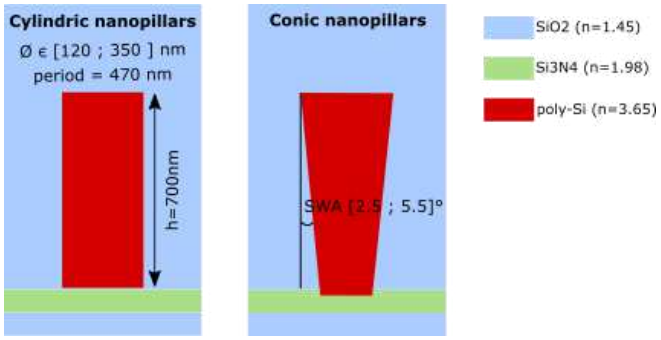


Figure 2: The etching process results in a sidewall angle that produces a top diameter which can be reduced to as low as 80% of the intended diameter. This reduction corresponds to an approximate volume loss of nearly 20%.

To assess the impact of the sidewall angle (see figure 2), the top and bottom critical dimensions of nanopillars with sizes of 120, 218, 290, and 350 nm have been measured using Scanning Electron Microscopy (SEM). The changes in diameter were found to be linearly related to the targeted diameter, thus allowing a linear regression to determine the actual fabricated dimensions for each nanopillar size in the library.

3. Measurement setup

Quadriwave Lateral Shearing Interferometry (QLSI) is a wavefront sensing technology [5]. The system relies on a diffractive grating which may be referred to as a Modified-Hartmann mask to produce an interferogram. The interferogram is made of a dense array of light dots whose displacement can be tracked to retrieve the wavefront gradient information. The measurement setup is precisely described in [6] since it is the same at the exception of the objective and camera used. Two objectives have been used: the Nikon 100X CFI TU Plan Fluor (NA=0.9) and the 10x Nikon CFI planar Fluor (NA = 0.3). The metasurfaces are designed to work at 940 nm and the source is a fiber coupled diode of 10 mW. The camera has a resolution of 1600×1200 which generate a 400×300 pixels phase images. The camera sensor is 11.6×8.7 mm so that the maximal ROI (Region of Interest) that can be defined with $\times 100$ magnification is 116×87 µm with a phase image resolution of 0.290 µm/pixel. In this configuration, the setup is at the diffraction limit which can estimated using Abbe diffraction limit for the microscope at $d = \lambda/2NA = 0.522$ µm.

To construct the phase image, the QLSI measure the phase gradient in the ROI. The interferogram is studied in Fourier space where diffraction spots are identified, cropped and centered before being inverse Fourier transformed. The resulting image contains complex values and the argument of this complex image is proportional to the local wavefront gradient. The resolution is reduced to one-third of its original size due to the cropping steps involved in the gradient retrieval algorithm [5].

4. Wavefront measurement

In this section we discuss the results from the wavefront transmitted through the metasurface analysis. The measurement aimed at three goals: characterizing uniform array of nanopillars referred as a piston, characterizing metalens to retrieve their focal lengths and studying the impact of fabrication.

4.1. Measurement preparation

The nanopillar arrays and metalens are embedded in a silicon oxide ($n = 1.45$) substrate and we must consider the refractive index of the materials to analyze the measured wavefront (see figure 3).

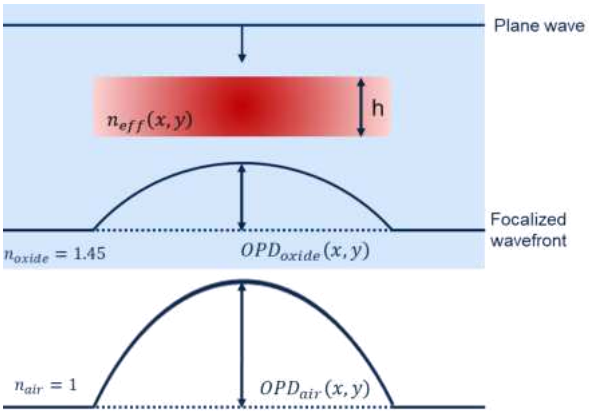


Figure 3: The metasurface we want to characterize is embeded in a silicon oxide substrate. As light propagate through the metasurface the phase accumulated shapes the incident plane wave into a focalized wavefront following a hyperbolic profile.

QLSI is a wavefront sensing technique [5] which returns the Optical Path Difference (OPD) distribution in the object plane. OPD and phase-shift are linked by equation (1):

$$\varphi(x,y) = 2\pi \frac{OPD(x,y)}{\lambda} \qquad (1)$$

where λ is the wavelength of the light in the medium it is observed. The measured OPD originates from the interaction of light with the nanopillars embedded in silicon oxide but

during its propagation it encounter an oxide/air interface which modifies the OPD distribution following equation (2):

$$OPD_{oxide} = \frac{OPD_{air}}{n_{oxyde}} \quad (2)$$

In the scenario examined in this paper, our aim is to validate the phase-shift that has been simulated and measured within the oxide layer. This is to approximate the conditions of a metalens integrated atop a CMOS pixel stack.

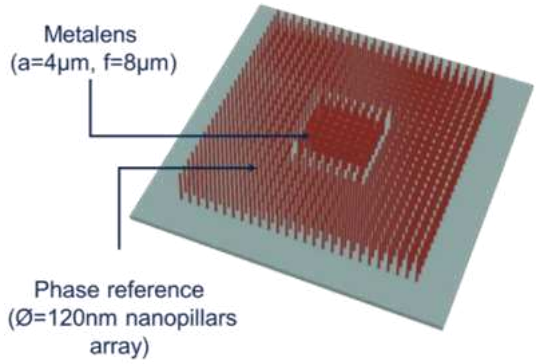


Figure 4: Each design incorporates a surrounding array of nanopillars with a uniform diameter that functions as a phase reference. This reference area is dimensioned to cover at least the same area as the design to be characterized. The sample is arranged in a checkerboard pattern.

QLSI allows to compute a relative phase-shift measurement and therefore requires an area of reference equal to the one that will be characterized. To satisfy this condition, we first designed metasurfaces surrounded by constant phase areas made of a uniform pillar arrays with a diameter of 120 nm (see figure 4). As mentioned in [5] the wavefront gradient retrieved by the QLSI is defined by calculating the argument of a complex number which is defined modulo 2π. In our case we want to characterize a library of nanopillars with phase-shift values ranging from 0 to 2π so local phase step close to π can be found in some places of the samples between reference and the nanopillars arrays.

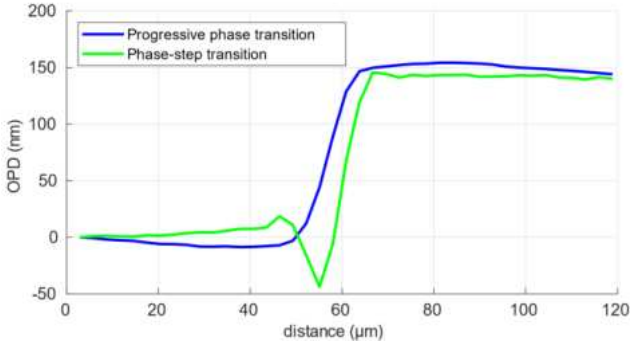


Figure 5: Comparison of the phase variation between the nanopillars arrays of reference and the nanopillars arrays which phase is to be measured. The blue curve describes the phase variation when progressive phase transition is implemented. The green curve describes the same transition with an abrupt separation between the reference and piston.

A phase step of π in the phase image introduces ambiguities during the gradient calculation and should be avoided. Hence, we introduced pillar arrays with increasing diameter, varying from the diameter of reference to the diameter of the array to be measured, in the 20 µm wide region around the target array. By implementing a progressive transition of nanopillars diameter, we create a smooth transition between the arrays of reference and the arrays to be characterized. This design adaptation generates a continuous and linear phase gradient of 3.14 rad/µm, which in turn reduces the risk of errors during the wavefront gradient calculation (see figure 5).

4.2. Nanopillars phase-shift

To validate the phase-shift induced by the nanopillars in periodic conditions, 32 uniforms arrays of nanopillars with diameters ranging from 120 nm to 350 nm (see figure 6) were measured. As previously mentioned, a necessary step for metasurface design is the generation of libraries through simulation. A library may be defined as the variation of the phase-shift with nanopillars diameters at fixed height and period. These simulations are performed considering periodic boundary condition so the phase-shift extracted correspond to the phase-shift of the nanopillars surrounded by morphologically identical nanopillars. This hypothesis is not rigorously verified in a metalens with varying nanopillar diameter. However, as it is customary done with Look-Up Table (LUT) approach, for slow varying phase profile it is still a good approximation.

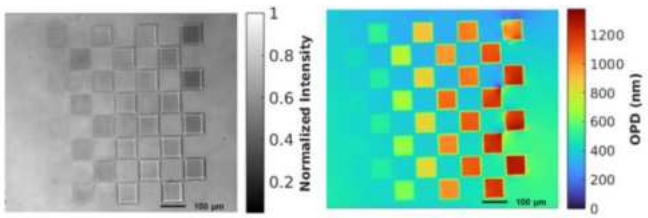


Figure 6: 32 uniforms arrays of nanopillars are disposed on a 800×800 µm square. Each array is 80×80 µm large and is surrounded by 20 µm of phase reference nanopillars. The images have been taken with $\times 10$ magnification inside an ROI of 1.16×0.87 mm. (Left) Intensity Image (Right) Phase Image.

The first objective of our characterization was to validate the library obtained by simulation used for our designs. The comparison between the simulations and the characterization results are displayed on figure 7. The measurements and simulations of cylindric meta-atoms are in good agreement up to 200 nm beyond which the two curves differ significantly. Several factors could explain the discrepancy between the two curves. While the simulations assume perfectly cylindrical nanopillars, the actual pillars exhibit a sidewall angle ranging from 2.5° to 5.5° (see figure 2). Also, significant resonances are observed for larger pillars.

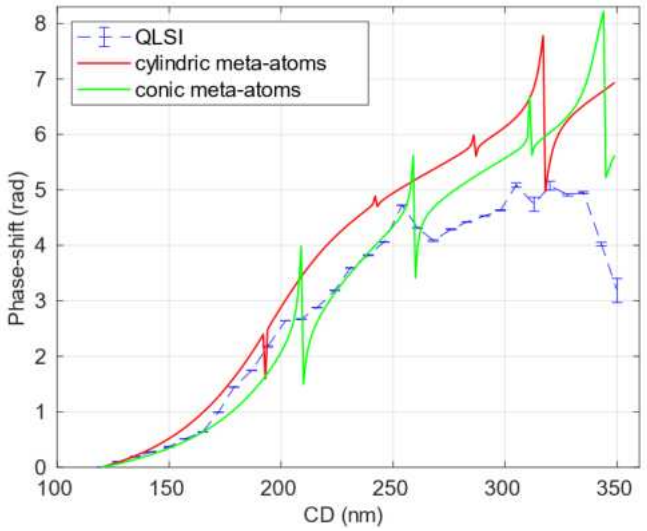


Figure 7: Measured OPD variation with nanopillars diameter (Blue dotted line). The values of OPD are sequentially calculated from the mean OPD of the pixel group located on the targeted area and subtracted from the neighboring nanopillars of reference. The red and green dotted line is extracted from simulation realized with the software Reticolo.

These localized phenomena amplify the impact of fabrication defect, potentially shifting the resonance location and thereby greatly affecting the phase response. In metasurface creation, the phase function is sampled using nanopillars chosen to induce specific phase-shifts. If there is a substantial deviation in the phase-shift, we can expect a degradation of optical performance, including displacement of the focal plane and reduced light concentration. By utilizing SEM data to assess the top and bottom CD, we generate a library of truncated conical nanopillars for comparison with cylindrical nanopillars and measured values.

We note a comparable trend in the phase increment between the experimental data and the conical library up to a 260 nm. Additionally, near the anticipated resonance positions for diameters of 215 nm and 260 nm we measure disturbances in phase variation. Although the two curves do not align perfectly, the discrepancy between the simulated and characterized nanopillars is significantly reduced. This suggests that the meta-atoms sidewall has a non-negligible impact on the phase responses. For pillars with a diameter exceeding 260 nm, there is a higher difference between the experimental data and both simulated libraries. At this stage, the lack of correspondence is presumably due to errors during the acquisition of the phase image despite employing progressive phase transitions. Upon examining the phase image presented in figure 6, it is observed that there is a significant phase gradient at the periphery of the nanopillar arrays with larger diameter. This pronounced gradient disrupts the local comparison between the reference region and the area under investigation, consequently hindering the accurate characterization of this meta-atoms.

4.3. Focal length measurement

The second main objective is to characterize the metalenses to determine focal lengths and analyze their phase profiles. In this study we will specifically examine metalens with an aperture of 8 µm and a focal length of 4 µm and 8 µm. These parameters have been specifically chosen to replicate the metalenses that are being fabricated on CMOS wafers. Smaller metalens have been characterized but the measurement did not have sufficient resolution for a detailed analysis. The metalenses have been designed with a hyperbolic phase [2] profile defined by equation (3):

$$\Phi(x,y) = \frac{2\pi}{\lambda}\left(f - \sqrt{f^2 + r^2}\right) \qquad (3)$$

Where f is the focal length, λ the wavelength in the considered media and r the radial coordinate.

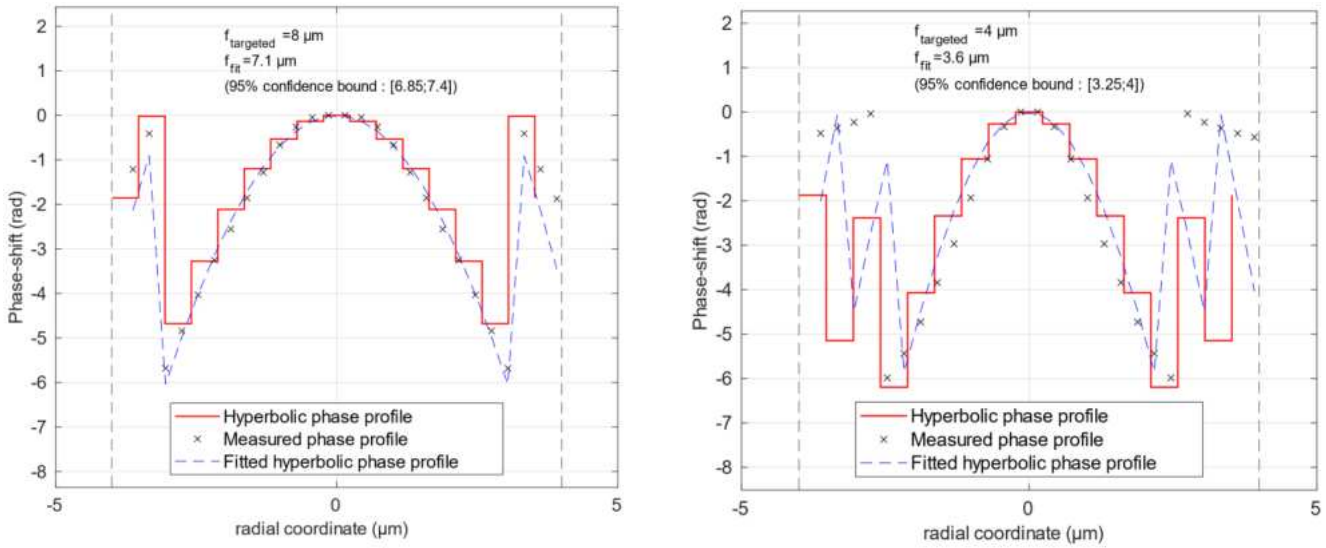


Figure 8: Wrapped measured phase profile (black cross) comparison with the discretized theoric hyperbolic phase profile (red line). The hyperbolic phase profile fitted from experimental point is represented in dashed blue line. The metalens have an 8 µm aperture and 8 and 4 µm focal length. The confidence bound is derived from the variance-covariance matrix of the parameter estimation.

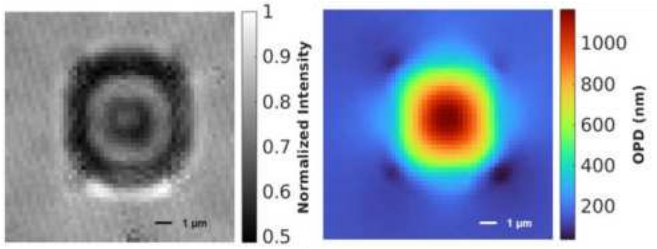


Figure 9: (Left) Intensity image and (Right) phase image of a square metalens with an aperture of 8 µm and focal length of 8 µm.

To retrieve the focal length from the phase profile, we first calculate the radial average of the phase distribution. Then, we fit this data to a hyperbolic phase profile described by equation (3) with f as a fitting parameter. To mitigate the impact of edge effects on the metasurface and limitations in resolution, we fit the function using points only within the first Fresnel zone. The measured phase profile adheres closely to a hyperbolic variation, demonstrating the overall ability to shape the wavefront of the transmitted light. We measure respective focal length of 7.1 µm and 3.6 µm (see figure 8). This slightly lower value may be explained by the shape of the phase profile in the first Fresnel Zones. For the metalens designed with a focal length of 8 µm, the phase-shift appears to decrease more rapidly, resulting in an offset of phase reaching 0.5 radians at (r = 2.5 µm). Such variations in the phase profile can result in a lower fitted focal length and may induce defocus aberrations if not accounted in the pixel stack design. Finally, it is essential to consider uncertainties regarding the position of the object plane when assessing the precision of the methods. In our case, we determined its location based on the sharpness of the intensity image. Increased accuracy in focal length determination maybe achieved adding focusing reticle in the design. Upon examining the metalens, with a targeted focal length of 4 µm, we successfully measured a focal length that aligns with our intended target. Nevertheless, our assessment of the phase profile at the periphery revealed a deviation from the expected phase function. This discrepancy is likely attributable to the fact that peripheral Fresnel zone is sampled by only two nanopillars, which is below the threshold for adequate sampling.

Analyzing the phase function of the metalens through QLSI could enable the measurement of the focal length with sub-micron precision opening up applications related to fabrication quality assessment. Furthermore, the phase profile provides informations on aberrations levels, which could offer additional insights into metalens performance and fabrication quality.

4.4. Discussion of process impact on metalens gradient

The generalized Snell-Descartes equation tells us that light incident on a metasurface is sensitive to phase-shift variation along the direction of interest [7]. For example, the angle of deviation of a plane wave incident on an x-axis gradient follows the equation (4):

$$\sin(\theta_t)\, n_t - \sin(\theta_i)\, n_i = \frac{1}{k_0}\frac{d\phi}{dx} \qquad (4)$$

At the scale of the metasurface, this means we must examine the phase-shift gradient to perceive the change induced by the fabrication process on the wavefront control. We can calculate the gradient of the targeted phase profile from the phase function using the central difference gradient (5):

$$G_x = \frac{d\phi(x,y)}{dx} = \frac{\phi(x+dx,y)-\phi(x-dx,y)}{2dx} \qquad (5.a)$$

$$Gy = \frac{d\phi(x,y)}{dy} = \frac{\phi(x,y+dy)-\phi(x,y-dy)}{2dy} \qquad (5.b)$$

We can then compare the measured gradients along X and Y axis with the gradient extracted from the phase function calculated from equation (3). For instance, we illustrate the comparison between the experimental and theoretical gradients of an 8 µm metalens with an 8 µm focal length.

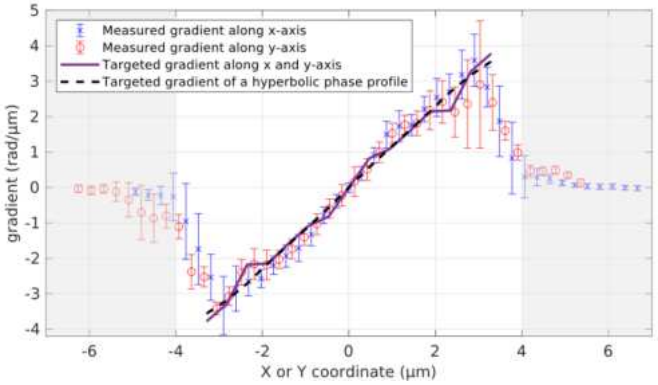


Figure 10: Comparison between measured phase gradient along X and Y axis (blue and red points) with phase gradient expected from conical nanopillars (black dotted line) and phase gradient obtained with cylindrical nanopillars (purple line). The targeted phase gradients are calculated from the theoretical phase distribution following equation (3). The resulting data is presented in the format µ±σ.

The experimental gradient depicted on figure 10, come directly from the gradient measured by the QLSI camera, which is then averaged along the axis normal to the gradient direction. We observe a correspondence between the measured and predicted gradients on both axis of the metalens. We anticipated a minor difference between the phase gradient formed by conical nanopillars and cylindrical nanopillars and we do observe an expected deviation at a distance of 2 µm from the center of the metalens on the y-axis. The validation of the gradient obtained post-fabrication verifies the fidelity of the manufactured structure to generate the intended gradient. We can evaluate the effect of gradient variation on the performance of metalenses obtained from cylindrical and conical libraries. For this aim, we look for the gradient difference between library (6):

$$\Delta G_x = G_{x,cylindric} - G_{x,conic} \qquad (6.a)$$

$$\Delta G_y = G_{y,cylindric} - G_{y,conic} \qquad (6.b)$$

By applying equation (4) and assuming small angle approximations we can compute the difference in the deviation angle between the targeted gradient and the one achieved post-fabrication:

$$\Delta\theta_x = \frac{1}{k_0 n_t}\,\Delta G_x \qquad (7.a)$$

$$\Delta\theta_y = \frac{1}{k_0 n_t}\,\Delta G_Y \qquad (7.b)$$

The difference of deviation angle distribution is represented on figure 11.

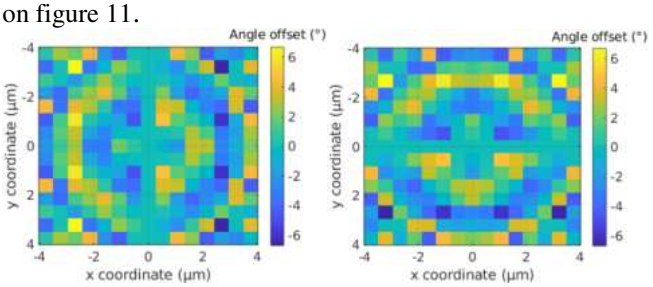


Figure 11: Deviation angle difference distribution between and ideal hyperbolic phase profile and the altered phase profile after fabrication.

The distribution of the deviation angle differences is centered on 0, with values below 2° for 48% on the metalens surface and below 4° on 77% of the metalens surface. At the center of the metalens, the difference in deviation angle is close to 0°, since both cylindric and conic libraries vary theoretically in the same manner for high diameter nanopillars (see figure 7). We have identified two regions where the difference in deviation angle seems to increase. At a radius of 2 µm, a deviation difference of ±4° is attained, which corresponds to an area containing a pillar with a diameter of 260 nm which aligns with a region where a resonance is observed (see figure 11). At the edge of the first Fresnel zone which begins at a radius of 3 µm we observe a deviation difference reaching 6°. In this region, the gradient exhibits more complex behavior due to the inverted distribution of pillar diameters, a consequence of the lens phase profile wrapping. This greater discrepancy may also be attributed to the narrower phase-shift range produced by the library of conical shapes, which does not cover the entire 0 to 2π range. These observations should be considered with caution, given that they are based on comparisons with libraries where each nanopillar is simulated under periodic conditions. There remains uncertainty regarding how these resonances behave within a metalens where such conditions are not strictly met. The resilience of the phase gradient and the contained deviation angle offset could explain the similarities observed in simulation between the two configurations (see figure 12). The simulated focal length is close to 7.3 µm for each configuration and the normalized ensquared energy shows similar concentration capabilities for both designs. The ensquared energy is determined by taking the ratio of the Poynting vector flux through a progressively expanding square aperture up to the limits of the focal plane, to the total Poynting vector flux across the entire focal plane.

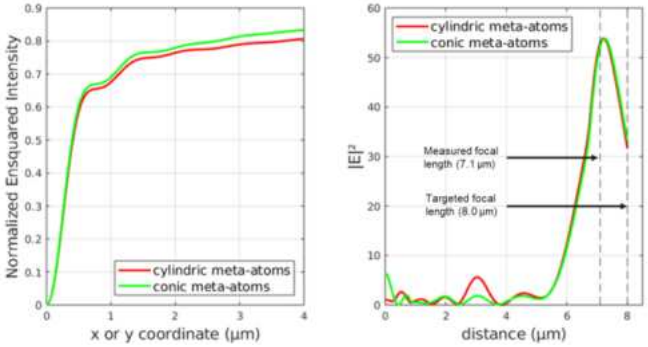


Figure 12: (Left) Normalized Ensquared Energy and (Right) Intensity profile along z-axis comparison between cylindric and conic metalens.

Conclusions

The use of wavefront imaging technology, such as QLSI, enables the analysis of wavefront at a microscopic level, thereby opening new characterization opportunities for micrometer size metasurface. Wavefront sensor allows to validate meta-atoms libraries consistency with simulations, to determine metalens focal length and to assess the impact of fabrication on the original design. In the study presented in this article we acquired valuable experimental data that corroborated our simulations and confirmed our design approach. The sidewall angle created by the process leads to a significant reduction in the volume of the nanopillars, which, in turn, is expected to cause substantial alterations in their performance. The results of the phase characterization confirmed that there was minimal shift in the focal plane and negligible change in focus efficiency. These findings mitigate the importance of process-induced sidewall angle as long as the phase gradient is preserved. This work does not cover the change in transmission resulting from the process modification which could significantly impair the metalens performance. Although characterizing designs with π phase jump poses challenges, QLSI offers a rapid and efficient solution to evaluate metalens performances. The result developed in this paper could be replicated using alternative technique such as ptychography or conventional Shack-Hartmann wavefront sensor, particularly for slow varying phase metasurface. Refinements in the analysis techniques and the experimental apparatus are projected to yield more accurate measurement results. The application of wavefront analyzers for the examination of metasurfaces could be a standard component of most design processes.

Acknowledgements

The authors want to thank Yanel Tahmi for the helpful discussion and his support during the use of QLSI systems.

References

[1] L. Dilhan, J.Vaillant, A.Ostrovsky, L.Masarotto and C. Pichard, "Planar microlenses for near infrared CMOS image sensors" *Electronic Imaging*, 2020, 32 (7), pp.144-1-144-7. 10.2352/ISSN.2470-1173.2020.7.ISS-144, hal-04235049

[2] F.Aieta, P.Genevet, M A. Kats, N.Yu, R.Blanchard, Z.Gaburro and F.Capasso, "Aberration-Free Ultrathin Flat Lenses and Axicons at Telecom Wavelengths Based on Plasmonic Metasurfaces", *Nano Lett.*, vol. 12, nº 9, p. 4932-4936, 2012, doi: 10.1021/nl302516v.

[3] S.Villenave, S.Monfray, H.Benisty, Q.Abadie, S.Audran, S.Guillaumet, B.Vianne, D.Ristoiu, F.Leverd, E.Sungauer and P.Chevalier, "Advanced Optical Filtering Based on Si Nanodisk Integration on 300 mm Glass Wafer", *International Conference on Solid State Devices and Materials*, 2021. doi: 10.7567/SSDM. 2021.E-2-03.

[4] J.-P. Hugonin and P. Lalanne, "Light in complex nanostructures / RETICOLO: V9", 2021. doi: 10.5281/zenodo.5905381.

[5] G. Baffou, "Quantitative phase microscopy using quadriwave lateral shearing interferometry (QLSI): principle, terminology, algorithm and grating shadow description", *J. Phys. D: Appl. Phys.*, vol. 54, nº 29, p. 294002, 2021, doi: 10.1088/1361-6463/abfbf9.

[6] S.Khadir, D.Andrén, R.Verre, Q.Song, S.Monneret, P.Genevet, M.Käll, and G.Baffou, "Metasurface Optical Characterization Using Quadriwave Lateral Shearing Interferometry", *ACS Photonics*, vol. 8, nº 2, p. 603-613, 2021, doi: 10.1021/acsphotonics.0c01707.

[7] Yu.N, P.Genevet, MA.Kats, F.Aieta, JP.Tetienne, Capasso and Z.Gaburro. "Light propagation with phase discontinuities: generalized laws of reflection and refraction", *Science.* 2011 Oct 21;334(6054):333-7. doi: 10.1126/science.1210713.

Single- and multi-layer diffractive lens fabrication on fiber endoscope probes for advanced imaging technologies

F. He[1*], R. Fuentes-Dominguez [1], R. Cousins[2], C. J. Mellor[3], J. K. Barton[4,5] and G. S. D. Gordon[1]

[1]Optics and Photonics Group, University of Nottingham, University Park, Nottingham, NG7 2RD, UK
[2]Nanoscale and Microscale Research Center, University of Nottingham, University Park, Nottingham, NG7 2RD, UK
[3]School of Physics and Astronomy, University of Nottingham, Nottingham, NG7 2RD, UK
[4]Wyant College of Optical Science, University of Arizona, Tucson, Arizona, AZ 85721, US
[5]Biomedical Engineering, University of Arizona, Tucson, Arizona, AZ 85721, US
[*]corresponding author: george.gordon@nottingham.ac.uk

Abstract: We present a novel method to fabricate single- and multi-layer diffractive lenses on optical fibres, which is achieved via transfer bonding pre-fabricated patterns onto fiber facets. As proof-of-principle, we bond Fresnel zone plates, diffractive axicons and double-layer Fresnel zone plates onto optical fiber facets shaping output light with versatile depth-of-fields.

Hair-thin fiber endoscopes are creating new paradigms for biological imaging applications with minimal invasiveness and sub-cellular resolution. To properly perform functionalities desired by various imaging applications, fiber endoscopes may require on-tip light-shaping structures to manipulate the light flow. This can be achieved by fabricating 2D planar optics (i.e. diffractive lenses [1]) with sub-wavelength thickness, which can be designed with nano- and micro-scale structures that enable spatial control of amplitude, phase and polarization with subwavelength resolution [2, 3]. The fabrication methods include FIB milling the designed patterns, directly printing nanostructures and transferring pre-fabricated patterns onto fibers [4, 5]. Despite demonstrating effective light control at fiber facets, they are not all compatible with multi-layer stacking of devices or metasurfaces, which limits their applicability in emerging imaging applications that use multilayered structures to enable advanced imaging modalities [6].

We present a novel method to fabricate single- and multi-layer diffractive light shaping structures on optical fibres. It is achieved via transfer bonding pre-fabricated diffractive lenses onto fiber facets, which means the devices are simple to design, fabricate and transfer. The fabrication process uses a conventional top-down method to define nano- and micro-structures on bulk substrates via electron-beam lithography (EBL) and lift-off processes, but is adapted to facilitate repeated transfer to optical fibers for multi-layer fabrication. Specifically, diffractive lenses are encapsulated in optically transparent polymers, detached from the substrate by etching a sacrificial layer, then finally bonded to fibre tips. As proof-of-principle, we demonstrate Fresnel zone plates, diffractive axicons and double-layer Fresnel zone plates bonded onto optical fiber facets focusing light with versatile depth-of-fields.

Acknowledgements

This work is supported by UKRI Future Leaders Fellowship (MR/T041951/1). The authors would like to acknowledge the Nanoscale and Microscale Research Centre (nmRC) and Faculty of Physics at the University of Nottingham for providing access to cleanroom facilities.

References

1. K. Huang, F. Qin, H. Liu, et al., “Planar diffractive lenses: fundamentals, functionalities, and applications,” Adv. Mater. 30, 1704556 (2018).
2. H.-T. Chen, A. J. Taylor, and N. Yu, “A review of metasurfaces: physics and applications,” Reports on progress physics 79, 076401 (2016).
3. S. M. Kamali, E. Arbabi, A. Arbabi, and A. Faraon, “A review of dielectric optical metasurfaces for wavefront control,” Nanophotonics 7, 1041–1068 (2018).
4. N. Yu and F. Capasso, “Optical metasurfaces and prospect of their applications including fiber optics,” J. Light. Technol. 33, 2344–2358 (2015).
5. Q. Zhao, W. Yuan, J. Qu, et al., “Optical fiber-integrated metasurfaces: An emerging platform for multiple optical applications,” Nanomaterials 12, 793 (2022).
6. G. S. Gordon, M. Gataric, A. G. C. Ramos, et al., “Characterizing optical fiber transmission matrices using metasurface reflector stacks for lensless imaging without distal access,” Phys. Rev. X 9, 041050 (2019).

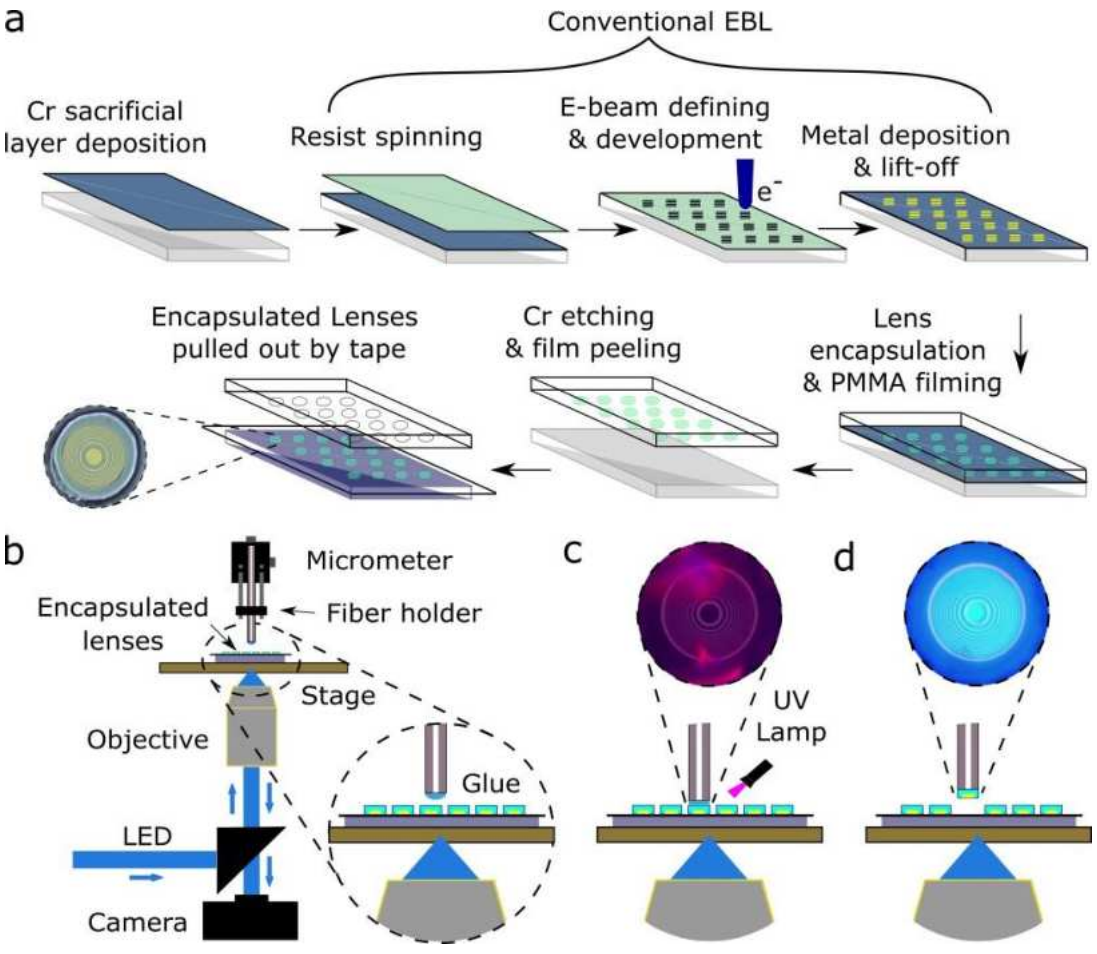


Fig. 1. Fabrication process of single- and multi-layer diffractive lenses onto fibers.

Fabrication of form birefringent 3D metastructures for visible wavelength range using 3D laser printing technique

D. Gailevičius[1], D. Paipulas[1] S. Juodkazis[2], and V. Mizeikis [3*]

[1]Laser Research Center, Vilnius University, Lithuania
[2]Swinburne University of Technology, Australia
[3]Research Institute of Electronics, Shizuoka University, Japan
[*]corresponding author: mizeikis.vygantas@shizuoka.ac.jp

Abstract: We report on the realization of form birefringent phase retarder structures using 3D laser printing technique. The retarders use anisotropic 3D photonic crystal architecture to achieve the high optical birefringence and phase retardation needed in practical applications. In particular, we report on the realization of Q-plate structures having a half-wave retardation and a spatially-variant orientation of the local optical axis, and capable of converting the spin angular momentum (SAM) to orbital angular momentum (OAM) at visible wavelengths.

Form birefringence enables control over the polarization state of light using optically-isotropic, non-birefringent materials, and is highly sought in photonics. The simplest uniaxially form birefringent structures are one-dimensional (1D) sub-wavelength gratings (SWG)[1]. Although such structures can be realized using semiconductor nanofabrication based on planar lithography, this approach requires advanced cleanroom equipment and is time-consuming. Femtosecond 3D laser printing technique, which allows rapid prototyping of 3D nano- and micro-structures[2], may allow simpler and more accessible realization of form birefringent structures. Unfortunately, earlier efforts to use this technique for the fabrication of functional quarter and half-wave retarder elements were successful only partially[3]. In order to increase the retardance, thickness (height) of the laser-printed gratings had to be increased to the degree at which the gratings became unstable mechanically and collapsed after the fabrication. As a solution, the use of anisotropic 3D photonic crystal (PhC) structures was proposed due to the superior mechanical stability and self-supporting nature of 3D structures[4]. This has enabled fabrication of super-compact form birefringent phase retarders exhibiting quarter- and half-wave retardance at optical wavelengths[4]. Here we report on application of these results for the realization of spatially variant Q-plate devices[5]. Schematic image of a Q-plate structure composed of 1D SWGs is shown in Fig. 1(a). Q-plate composed of anisotropic 3D PhC structures is schematically depicted in Fig. 1(b). In both cases orientation of the optic axis exhibits azimuthal variation while the magnitude of retardance is uniform and equal to half-wave. Opto-mechanical setup used for the fabrication is depicted in Fig. 1(c). As a light source, a femtosecond laser (Carbide, Light Conversion) is used. The laser beam is tightly focused into the bulk of photoresist SZ2080™[6], and position of the focal spot is scanned using a 3D nanopositioning system (Aerotech). Figure 1(d) shows Scanning Electron Microscopy (SEM) image of a fabricated Q-plate structure. Experimental characterization of the Q-plate retardance is shown in Fig. 1(e). Here, retardance of the diagonally-oriented sectors appears to be zero, which is an artifact caused by their orientation and the characterization technique used. Retardance of vertically and horizontally-oriented sectors is shown accurately, and is close to the required half-wavelength level. Figure 1(f) shows several experimental and simulated far-field patterns of a Gaussian beam with a central wavelength of 632 nm transmitted through the Q-plate, The incident beam has a vertical linear polarization, whereas the far-field patterns are shown for linearly-polarized vertical, horizontal, as well as right-circular polarization (RCP) components. A satisfactory qualitative agreement

between the experimental and simulated patterns illustrates the SAM-OAM converter functionality.

In conclusion, 3D laser printing of spatially-uniform and spatially-variant form birefringent 3D structures using a modified 3D PhC architecture were realized using 3D laser printing technique, and experimental evidence of their optical functionality was obtained. These results suggest that these and other similar super-compact photonic devices can be realized using the 3D laser printing technique.

This work was supported by the JST CREST Grant Number JPMJCR19I3, Japan.

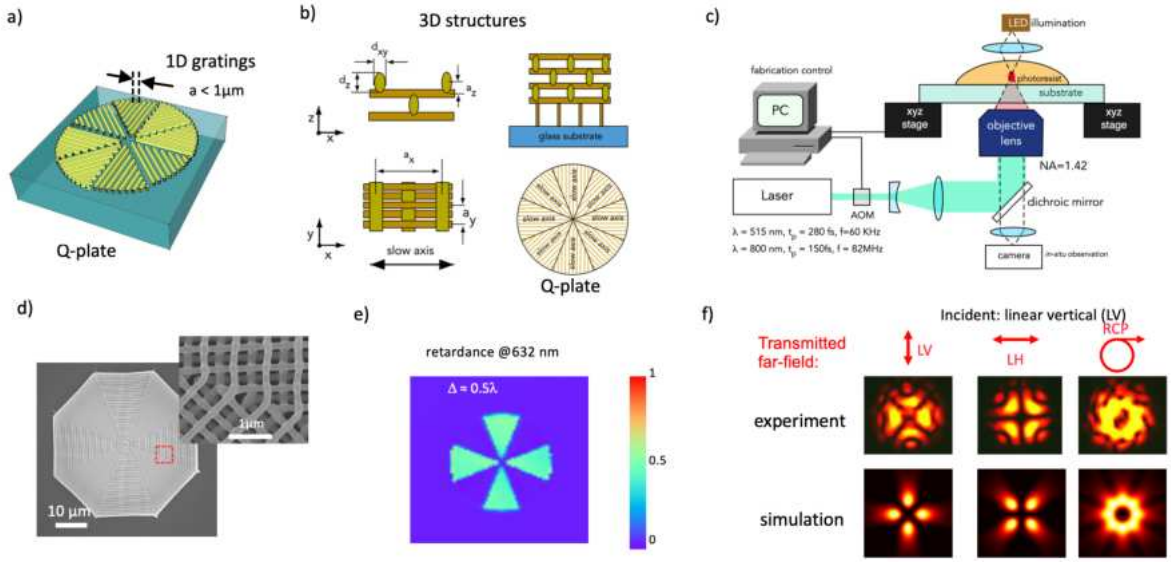


Figure 1. Schematic picture of a Q-plate device consisting of 1D SWGs (a), schematic picture of anisotropic 3D PhC structures exhibiting form birefringence, and a Q-plate device composed of 3D PhCs (b), opto-mechanical setup used for 3D laser printing (c), SEM images of the fabricated Q-plate structure (d), measured spatial map of the retardance (e), measured and simulated far-field transmission patterns for several polarization components, illustrating the SAM-OAM converter functionality (f).

References

1. Emoto, A. *et al.*, "Form birefringence in intrinsic birefringent media possessing a subwavelength structure," Appl. Opt., Vol. 49, 4355-4361, 2010.
2. Malinauskas, M. *et al.*, "Ultrafast laser nanostructuring of photopolymers: A decade of advances," Phys. Rep., Vol. 533, 1–31, 2013.
3. Varapnickas, S. *et al.*, "Birefringent optical retarders from laser 3D-printed dielectric metasurfaces," Appl. Phys. Lett., Vol. 118, 151104, 2021.
4. Gailevičius, D., Paipulas, D., Hada, S., Kretkowski, M., and Mizeikis, V., "Form birefringent polymeric structures realized by 3D laser printing," Opt. Lett., Vol. 48, 5775–5778, 2023.
5. Rubano, A., Cardano, F., Piccirillo, B., and Marrucci, L., "Q-plate technology: a progress review" J. Opt. Soc. Am. B, Vol. 36, D70-D87, 2019.
6. Ovsianikov, A. *et al.*, "Ultra-Low Shrinkage Hybrid Photosensitive Material for Two-Photon Polymerization Microfabrication," ACS Nano, Vol. 2, 2257–2262, 2008.

Zeiss Crossbeam FIB-SEM for nanophotonic materials research and nanofabrication

Olena Vertsanova[1,3*], Benjamin Tordoff[1], Feng Lin Ng[2]
[1] Carl Zeiss Microscopy GmbH, Germany
2 Carl Zeiss Pte. Ltd., Singapore
3 National Technical University of Ukraine "KPI"
* corresponding author: olena.vertsanova@zeiss.com

Abstract: Zeiss Crossbeam FIB-SEM solutions for nanofabrication and nanomaterials research for photonics application are presented. The benefits of Zeiss Gemini optic for high-quality imaging and the long-term current stability of the Ion-sculptor focused ion beam (FIB) column for a very long-running nanostructuring process are demonstrated.

Nanophotonic is currently one of the most promising fields of research in modern optical technologies. The development, study, manipulation, and characterization of optically active nanostructures allow the creation of new materials and devices with unique optical properties for applications in nanoelectronics, biomedicine, energy, telecommunications, etc. The development of materials with advanced optical properties and the creation of nanophotonic devices is one of the main tasks of nanophotonics today.

To increase the efficiency of interaction between light and nanostructures, resonant structures or arrays of structures are used, which leads to the fact that the effective size of the interaction becomes larger than the structure itself. Therefore, producing multiple structural elements with nanometer precision with high productivity is a challenge for nanophotonic research [1,2].

For developing of new nanostructured materials and devices for nanophotonic applications the instruments for nanofabrication and control are needed. Electron microscopy is an indispensable method for studying nanophotonic materials and investigating their fundamental physical phenomena, as well as developing architectures and manufacturing nanostructured devices.

ZEISS Crossbeam FIB-SEM microscope provides a solution for nanofabrication with high precision and high spatial resolution, high stability of processing for array structure fabrication, visualization, and analytics to study their structure, chemistry, and physical properties of nanomaterials. It combines the powerful imaging and analytical performance of a field emission scanning electron microscope (FE-SEM) with superior next-generation focused ion beam (FIB) processing capabilities for the use of nanofabrication of nanophotonic materials [3].

This talk presents the advantages of nanofabrication using a ZEISS Crossbeam FIB-SEM microscope for fundamental research in photonic nanomaterials, such as metamaterials, metasurfaces, nanoantennas, quantum materials, nanoplasmonics.

A combination of high-resolution Zeiss Germini optics for imaging and super stable integrated FIB-column for nanofabrication is an ingenious solution that pushes fabrication approaches in nanodevice fabrication, enabling experiments, and demonstrating new nanophotonic concepts.

ZEISS Crossbeam FIB-SEM microscope allows to production of periodic nanostructures in different materials and visualize the structure with high resolution during the process of nanofabrication for control.

References

1. Scharf, T. "The challenges of nanophononics in modern optical technologies," Open Access Government, 2018.
2. Hentschel, M. and Koshelev K., Sterl F., S. Both S., J. Karst J., L. Shamsafar L., T. Weiss T., Y. Kivshar Y, and H. Giessen "Dielectric Mie voids: confining light in air Light," Science and Applications, Vol.12, No. 3, 2023.
3. Schubert, T. and F. Zhou, R. Pero, N. Randall, T. Bernthaler, G. Schneider "Fast Fabrication of Micropillars

for Micromechanical Testing Using a Combined fs-Laser – FIB/SEM Approach," Microscopy and Microanalysis Vol. 28, 2022.

Modeling and computational techniques

Topology optimization for liquid crystal-based holograms

Peter Ropač[1,2*], Yu-Tung Hsiao[3], Brecht Berteloot[3,+], Miha Ravnik[1,2] and Jeroen Beeckman[3]

[1]Faculty of Mathematics and Physics, University of Ljubljana, Ljubljana, Slovenia
[2]Institute Jožef Stefan, Ljubljana, Slovenia
[3]ELIS Department, Ghent University, Ghent, Belgium
[+]now associated with IMEC, Leuven, Belgium
[*]corresponding author: peter.ropac@fmf.uni-lj.si

Abstract:
We demonstrate a topology optimization-based algorithm to design thin liquid crystal phase-only 2D computer-generated holograms. Our method considers the material properties of liquid crystal, such as elastic energy, by using “gradient limiter” mapping functions. With our method and photopatterning, we can produce high-fidelity and high-contrast liquid crystal-based computer-generated holograms.

We developed a topology optimization-based algorithm which generates phase-only 2D computer-generated holograms based on grayscale or binary target images, named TO-CGH. While there are several similar algorithms, one of the most notable ones is the Gerchberg-Saxton algorithm [1], but with our algorithm, we can enforce design, manufacturing, and material constraints.
Computer-generated holograms (CGHs) are a promising technique to realise direct view 3D holographic displays [2] or holographic displays for virtual (VR) or augmented reality (AR) devices [3], and other applications [4] including data encoding [5], and optical trapping[6]. The CGHs aim to compute a 2D phase or amplitude pattern which when illuminated by a coherent light source is reconstructed into a 2D or 3D image in space.
Topology optimization is a powerful computational inverse design method that has been applied in engineering and scientific research to design and optimize structures with optimal physical or mechanical properties [7]. In the last few years, methods for topology optimization for photonics and optics have emerged enabling the design of improved optical/photonic components and devices [8, 9, 10]. To our best knowledge topology optimization has not yet been used to design a liquid crystal-based optical device.
Optical elements based on liquid crystals (LCs) are widely used for different applications due to their mechanical and electro-optical properties. The average orientation of LC molecules in an enclosed LC material can be tuned via surface anchoring or external stimuli such as electric fields. The emergent optical birefringence is actively exploited in LC-based optical devices [11, 12, 13]. With photoalignment, it is possible to create alignment patterns with very fine features, but the LC will not follow an arbitrarily fine anchoring pattern. The characteristic length scale of the LC is a necessary consideration during the design of LC optical devices.
We use the TO-CGH algorithm, to generate liquid crystal-based computer-generated phase-only holograms, which we manufacture using photoalignment. The algorithm optimizes the values of a 2D phase pattern, based on the value of a cost/objective function which is calculated from the simulated far-field image, using the Fourier transform, and the target far-field image. The algorithm can impose material/design constraints by using "gradient limiter" mapping functions, which are in reality imposed by the elastic energy of the liquid crystal. The algorithm can be modified for different specific applications by using different mapping functions, objective functions or a different optimizer. We compare our algorithm to the standard Gerchberg-Saxton algorithm and discuss the effects of different initial conditions, gradient limiters, target image size, and different target images. Specifically, we apply our algorithm to two binary and four greyscale target images of various sizes and test four different gradient

limiter mappings, with all the numerical simulations supported by experiments. With our TO-CGH algorithm and photoalignment, we can make holograms, which form a far-field image with great accuracy and contrast when reconstructed using a circularly polarized laser. More generally, our liquid crystal-based devices could be used for static augmented reality and indoor lighting applications.

References

[1] R. W. Gerchberg, "A practical algorithm for the determination of phase from image and diffraction plane pictures," *Optik (Stuttg)*, vol. 35, pp. 237–246, 1972, [Online]. Available: https://api.semanticscholar.org/CorpusID:55691159

[2] D. Pi, J. Liu, and Y. Wang, "Review of computer-generated hologram algorithms for color dynamic holographic three-dimensional display," *Light Sci Appl*, vol. 11, no. 1, p. 231, 2022, doi: 10.1038/s41377-022-00916-3.

[3] V. R. Curtis, N. W. Caira, J. Xu, A. G. Sata, and N. C. Pégard, "DCGH: Dynamic Computer Generated Holography for Speckle-Free, High Fidelity 3D Displays," in *2021 IEEE Virtual Reality and 3D User Interfaces (VR)*, 2021, pp. 1–9. doi: 10.1109/VR50410.2021.00097.

[4] C. Jin, C. Liu, R. Shi, and L. Kong, "Precise 3D computer-generated holography based on non-convex optimization with spherical aberration compensation (SAC-NOVO) for two-photon optogenetics," *Opt. Express*, vol. 29, no. 13, pp. 20795–20807, Jun. 2021, doi: 10.1364/OE.426578.

[5] G. S. Spagnolo, L. Cozzella, and M. De Santis, "New 2D barcode solution based on computer generated holograms: Holographic barcode," in *2012 5th International Symposium on Communications, Control and Signal Processing*, 2012, pp. 1–5. doi: 10.1109/ISCCSP.2012.6217831.

[6] R. Di Leonardo, F. Ianni, and G. Ruocco, "Computer generation of optimal holograms for optical trap arrays," *Opt. Express*, vol. 15, no. 4, pp. 1913–1922, Feb. 2007, doi: 10.1364/OE.15.001913.

[7] O. Sigmund and K. Maute, "Topology optimization approaches," *Structural and Multidisciplinary Optimization*, vol. 48, no. 6, pp. 1031–1055, 2013, doi: 10.1007/s00158-013-0978-6.

[8] J. S. Jensen and O. Sigmund, "Systematic design of photonic crystal structures using topology optimization: Low-loss waveguide bends," *Appl Phys Lett*, vol. 84, no. 12, pp. 2022–2024, 2004, doi: 10.1063/1.1688450.

[9] A. M. Hammond, A. Oskooi, M. Chen, Z. Lin, S. G. Johnson, and S. E. Ralph, "High-performance hybrid time/frequency-domain topology optimization for large-scale photonics inverse design," *Opt. Express*, vol. 30, no. 3, pp. 4467–4491, Jan. 2022, doi: 10.1364/OE.442074.

[10] B. S. Lazarov, F. Wang, and O. Sigmund, "Length scale and manufacturability in density-based topology optimization," *Archive of Applied Mechanics*, vol. 86, no. 1, pp. 189–218, 2016, doi: 10.1007/s00419-015-1106-4.

[11] J. Beeckman, K. Neyts, and P. J. M. Vanbrabant, "Liquid-crystal photonic applications," *Optical Engineering*, vol. 50, no. 8, p. 81202, 2011, doi: 10.1117/1.3565046.

[12] I. Nys, B. Berteloot, and K. Neyts, "Photoaligned Chiral Liquid Crystal Grating with Hysteresis Switching," *Adv Opt Mater*, vol. n/a, no. n/a, p. 2201289, 2022, doi: https://doi.org/10.1002/adom.202201289.

[13] C. Yoo *et al.*, "Dual-focal waveguide see-through near-eye display with polarization-dependent lenses," *Opt. Lett.*, vol. 44, no. 8, pp. 1920–1923, Apr. 2019, doi: 10.1364/OL.44.001920.

[14] P. Ropač *et al.*, "Topology optimization for liquid crystal-based holograms", to be published 2024

Finite-difference frequency-domain calculations of chiral material composites

Takamichi Terao

[1]Department of Electrical, Electronic and Computer Engineering, Gifu University, Gifu, Japan
*corresponding author, E-mail: terao.takamichi.x0@f.gifu-u.ac.jp

Abstract

The finite-difference frequency-domain method to investigate electromagnetic wave propagation in chiral material composites was presented. Eigenmode analysis of random chiral material multilayers were demonstrated. These approaches will be useful for the analysis of chiral metamaterials and their composites.

1. Introduction

For the analysis of electromagnetic waves, the finite-difference time-domain (FDTD) method is a calculation method that can be applied regardless of the dimension of the system [1]. The transfer matrix method is also known as a numerical method for multilayer materials, but this method is limited to one-dimensional systems. The finite-difference frequency-domain (FDFD) method, on the other hand, has the advantages of much higher frequency resolution than the FDTD method and, in the case of dispersive media, can be applied to materials with arbitrary frequency dispersion properties. However, because of the numerical computations required to treat very large matrices, in many previous studies it has been applied to problems with small systems. In our previous studies, numerical studies have been performed on metamaterial composites, combining numerical methods suitable for large-scale matrix analysis with the FDFD method [2].

Chiral materials have been manufactured in the microwave range, and the analysis of chiral materials is an important topic [3]. The propagation properties of electromagnetic waves in chiral materials are also related to the topic of the creation of chiral metamaterials, and it is of practical interest to develop a numerical simulation method for this. Related to this issue, it is of interest to verify the effectiveness of the FDFD method by applying it to chiral materials, whose constitutive equations are different from those of normal materials. In a previous study [4], the FDFD method was formulated for the input of a wave source and its response in chiral materials. In this case, the problem is formulated as solving a system of equations numerically. In contrast, the FDFD method for eigenmode analysis and the calculation of photonic band structures requires the solution of large-scale eigenvalue problems. In this study, the application of the FDFD method to chiral materials was presented and its effectiveness was demonstrated.

2. Numerical method

The Maxwell equations in frequency domain are given as

$$\nabla \times \vec{E} = -j\omega\vec{B} \quad (1)$$

$$\nabla \times \vec{H} = j\omega\vec{D} \quad (2)$$

where $e^{j\omega t}$ time harmonic convention is assumed. The constitutive equations of chiral media are given by

$$\vec{D} = \varepsilon\vec{E} + \frac{\chi - j\kappa}{c_0}\vec{H} \quad (3)$$

$$\vec{B} = \mu\vec{H} + \frac{\chi + j\kappa}{c_0}\vec{E} \quad (4)$$

where ε is the permittivity of the medium, μ is the permeability of the medium, c_0 is the speed of light in vacuum, χ is the dimensionless magneto-electric parameter and describes the reciprocity of the material, κ is the dimensionless chirality parameter of the material.

As discussed in the previous section, the FDFD method can be applied irrespective of the dimension of the system. Here, the differential equations of the one-dimensional FDFD method are described. The electric and magnatic field vector components are located as shown in Fig.1.

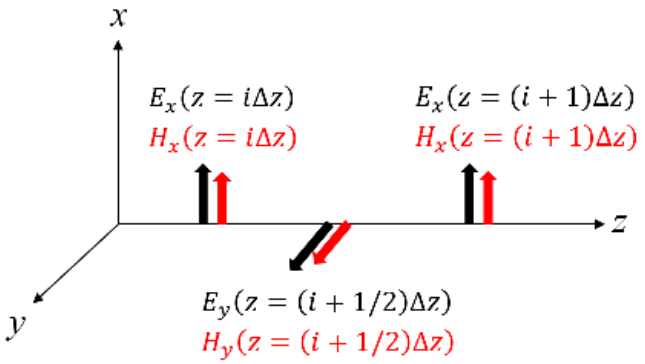


Figure 1: Positions of the field components.

Using these notations, finite-difference expressions for Maxwell's equations are given by

$$\frac{j\mu(z=i\Delta z)}{\alpha(z=i\Delta z)\Delta z}\left[H_y\left(z=\left(i+\frac{1}{2}\right)\Delta z\right) - H_y(z=(i-1/2)\Delta z)\right] + \frac{j\xi(z=i\Delta z)}{\alpha(z=i\Delta z)\Delta z}\left[E_y\left(z=\left(i+\frac{1}{2}\right)\Delta z\right) - E_y(z=(i-1/2)\Delta z)\right] = \omega E_x(z=i\Delta z) \quad (5)$$

$$-\frac{j\zeta(z=i\Delta z)}{\alpha(z=i\Delta z)\Delta z}\left[H_y\left(z=\left(i+\frac{1}{2}\right)\Delta z\right)-H_y\left(z=\left(i-\frac{1}{2}\right)\Delta z\right)\right]-\frac{j\varepsilon(z=i\Delta z)}{\alpha(z=i\Delta z)\Delta z}\left[E_y\left(z=\left(i+\frac{1}{2}\right)\Delta z\right)-E_y(z=(i-1/2)\Delta z)\right]=\omega H_x(z=i\Delta z) \quad (6)$$

$$-\frac{j\mu\left(z=\left(i+\frac{1}{2}\right)\Delta z\right)}{\alpha\left(z=\left(i+\frac{1}{2}\right)\Delta z\right)\Delta z}[H_x(z=(i+1)\Delta z)-H_x(z=i\Delta z)]-\frac{j\xi\left(z=\left(i+\frac{1}{2}\right)\Delta z\right)}{\alpha\left(z=\left(i+\frac{1}{2}\right)\Delta z\right)\Delta z}[E_x(z=(i+1)\Delta z)-E_x(z=i\Delta z)]=\omega E_y\left(z=\left(i+\frac{1}{2}\right)\Delta z\right) \quad (7)$$

$$\frac{j\zeta\left(z=\left(i+\frac{1}{2}\right)\Delta z\right)}{\alpha\left(z=\left(i+\frac{1}{2}\right)\Delta z\right)\Delta z}[H_x(z=(i+1)\Delta z)-H_x(z=i\Delta z)]+\frac{j\varepsilon\left(z=\left(i+\frac{1}{2}\right)\Delta z\right)}{\alpha\left(z=\left(i+\frac{1}{2}\right)\Delta z\right)\Delta z}[E_x(z=(i+1)\Delta z)-E_x(z=i\Delta z)]=\omega H_y\left(z=\left(i+\frac{1}{2}\right)\Delta z\right) \quad , \quad (8)$$

where $\alpha(z)$, $\xi(z)$ and $\zeta(z)$ are defined to be

$$\alpha(z)=\varepsilon(z)\mu(z)-\xi(z)\zeta(z)\,, \quad (9)$$

$$\xi(z)=\frac{\xi(z)-j\kappa(z)}{c_0}\,, \quad (10)$$

$$\zeta(z)=\frac{\xi(z)+j\kappa(z)}{c_0}\,, \quad (11)$$

respectively.

3. Chiral multilayer systems

Multilayers composed of metamaterials with negative refractive index and different materials with positive refractive index have been investigated, and characteristic phenomena such as the zero-*n* gap have been reported in the electromagnetic wave propagation. It has also been pointed out that in random metamaterial multilayers, the nature of wave localization exhibits peculiar properties different from those of ordinary random systems [5]. In view of the above, it is interesting to clarify the wave propagation in chiral (metamaterial) composites with random structures. In this study, a multilayer of chiral material, as shown in Fig. 2, is taken up for eigenmode analysis by applying the FDFD method described above.

Calculated results of eigenmodes calculated by the FDFD method described above was shown in Figure 3. The thickness of each layer d and Δz were given by $d = 1.0$ mm and $\Delta z = 0.1$ mm, respectively. The total number of layers and the ratio of chiral material layers were given as $N = 10^3$ and 0.50, respectively. The parameters are given as $\varepsilon_1 = \varepsilon_0$, $\mu_1 = \mu_0$, $\varepsilon_2 = 4.0\varepsilon_0$, $\mu_2 = \mu_0$, $\chi_2 = 0.0$, and $\kappa_2 = 0.3$. The periodic boundary condition was imposed in z-direction. Using the implicitly restarted Arnoldi method, calculations were also performed for the case $N = 1.5 \times 10^5$. In this case, the dimension of the matrix to be diagonalized was 6×10^6, and the typical CPU time for the calculation was 123 seconds with an Intel Xeon Platinum 8360Y 2.4GHz processor.

4. Conclusions

An eigenmode analysis method based on the FDFD method suitable for bi-isotropic and chiral media was proposed. The method is applied to random chiral multilayers and the localization of electromagnetic waves is investigated numerically. This computational method is also applicable to high-dimensional systems and is expected to be a powerful method for the analysis of chiral metamaterial composites.

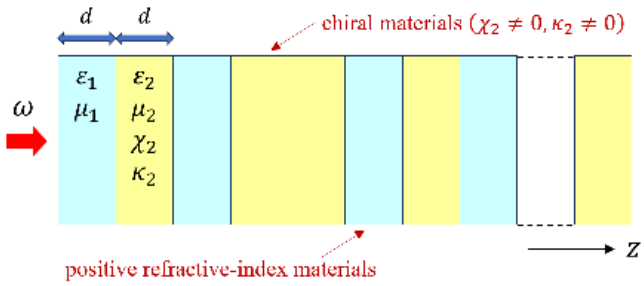


Figure 2: Random chiral material multilayers

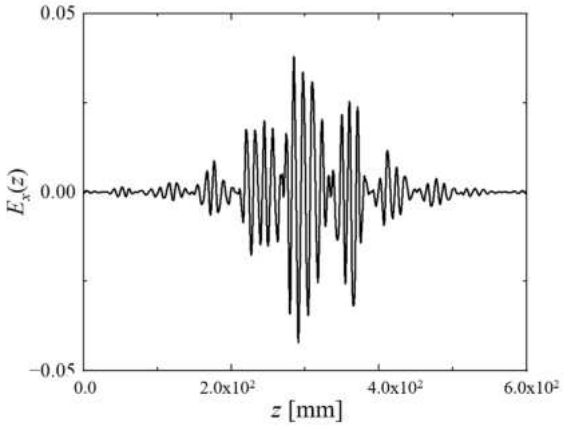


Figure 3: $E_x(z)$ of eigenmode with $\omega d/c_0 = 0.3497$.

Acknowledgements

The author acknowledges the Supercomputer Center at the University of Tokyo for the use of their facilities. This work was supported by JSPS KAKENHI (Grant Number 20K11848).

References

[1] A. Taflove and S. C. Hagness, Computational Electrodynamics: The Finite-Difference Time-Domain Method, 3rd ed. (Artech House, Boston, 2005).

[2] T. Terao, Computing interior eigenvalues of nonsymmetric matrices: Application to three-dimensional metamaterial composites, *Phys. Rev. E* 82: 026702, 2010.

[3] I. V. Lindell, A. H. Sihvola, S. A. Tretyakov, A. J. Viitanen, *Electromagnetic waves in chiral and Bi-isotropic media*, Artech House, Boston, 1994.

[4] E. Alkan, V. Demir, A. Z. Elsherbeni, E. Arvas, Double-Grid Finite-Difference Frequency-Domain (DG-FDFD) Method for scattering from Chiral Objects, Morgan & Claypool Publishers, 2013.

[5] Sergey A. Gredeskul; Yuri S. Kivshar; Ara A. Asatryan; Konstantin Y. Bliokh; Yuri P. Bliokh; Valentin D. Freilikher; Ilya V. Shadrivov, Anderson localization in metamaterials and other complex media (Review Article), Low Temp. Phys. 38, 570-602. 2012.

Applications of a ray-based metalens design tool on freeform metasurfaces

Yijun Ding[1*], Bryan D. Stone[1], and Motoyuki Otake[1]

[1]Synopsys Inc., Pasadena, CA 91101, USA
[*]Corresponding author: joyding@synopsys.com

Abstract: We discuss applications of a ray-based design tool for metalenses. The application examples include (1) reflective metalens on a curved surface for near-eye displays, (2) meta-Alvarez lens, and (3) a metalens for projecting illumination to various angles from an actuated fiber tip in a scanning fiber endoscope.

Summary

In our prior work [1], we developed a ray-based design tool for metalens to reduce the complexity of design workflow. This design tool is especially useful when multiple wavelengths and incident angles need to be considered at the same time or for designing a hybrid imaging system that incorporates both conventional optical elements and metalenses. The ray-based metalens design tool is linked to a meta-atom database that describes the optical properties of the meta-atoms, including transmission and added phase for polarization-insensitive meta-atoms and Jones matrix for polarization-sensitive meta-atoms. These properties are calculated with RCWA or FDTD algorithms using local periodic approximation [2]. Using this link, we can bridge the gap between the length scale of the lenses and that of the meta-atoms, and hence reduce the complexity of the design workflow.

In this paper, we discuss applications of this ray-based design tool. The application examples include (1) reflective metalens on a curved surface for near-eye displays, (2) meta-Alvarez lens, and (3) a metalens for projecting illumination to various angles from an actuated fiber tip in a scanning fiber endoscope.

Metaform elements are formed by combining freeform optic with metasurfaces. They offer greater flexibility for aberration control and form-factor reduction. It may offer solutions to high-resolution optical systems that have volume or weight constraints. In such a system, the metalens is placed on a freeform surface and the meta-atom arrangement on the surface follows a freeform (non-rotational symmetric) function. We followed the example in [3] to design a miniature imager for a near-eye display using a metaform mirror. Note that the metaform mirror tilts the incident beam and corrects the aberrations introduced by the tilt.

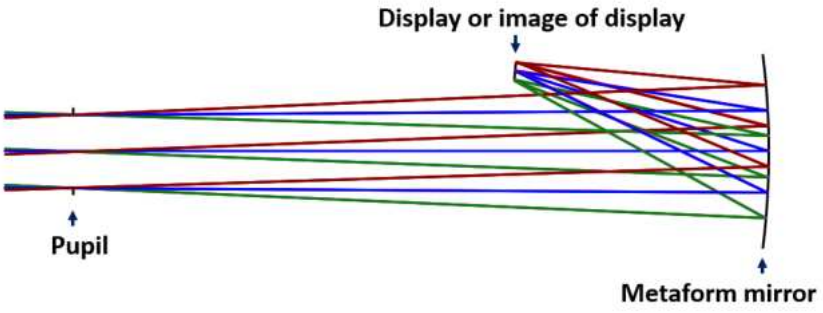


Figure 1: Miniature imager for a near-eye display using a metaform mirror.

The capability of fabricating metalens and MEMS actuation on the same device [4] has generated interests in using meta-Alvarez lens to achieve tunable focus. We started with an Alvarez lens with two cubic metalenses and improved the system performance by adding higher order terms and allowing the two metalenses to be different. Figure 2 shows the modulation transfer function (MTF) plots at the starting point and with the two strategies to improve the system

performance.

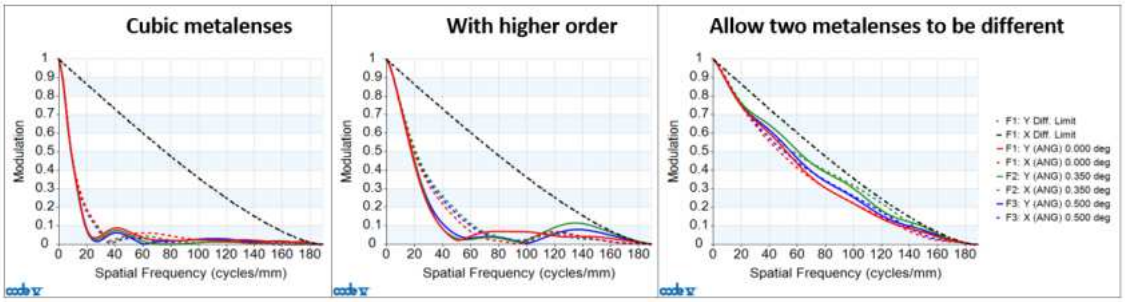


Figure 2: Modulation transfer function (MTF) of meta-Alvarez lens with two identical cubic metalenses (left), two identical metalenses with higher orders (middle), and two freeform metalenses that are allowed to be different (right). MTFs for various focuses are calculated, but not shown here due to space limitations.

Scanning fiber endoscope is one of the smallest forward viewing endoscopes. In a scanning fiber endoscope, the fiber tip can be moved with an actuator in a spiral pattern. The end of the fiber tip is on a spherical surface. A metalens can be used to project light from the fiber tip at a given location to a specific angle to provide illumination. We followed the example of [5] to design such a metalens. The design is shown in Figure 3 (left). The MTF plots in Figure 3 (right) show close to diffraction limited performance for all fields.

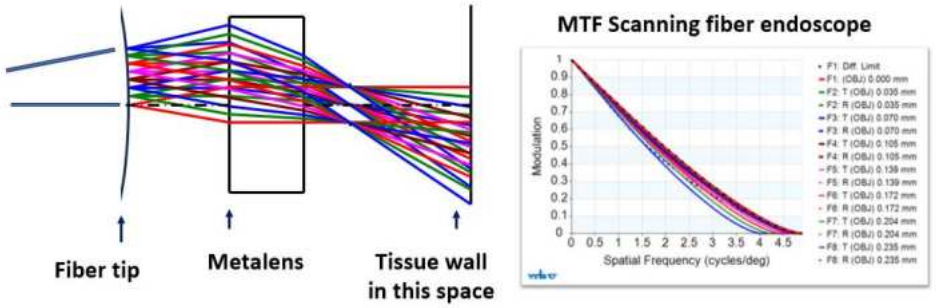


Figure 3: A scanning fiber endoscope illumination system with a metalens as the projector (left). The MTF plots for this system (right).

In conclusion, we find that the design process with the ray-based design tool is simple and intuitive. The design examples have demonstrated that the ray-based design tool offers many flexibilities, including: (1) reflective type metalenses, (2) metalenses on curved surfaces, (3) freeform arrangements (non-rotational symmetric) of the meta-atoms, and (4) designing for an application where the object and/or the image are on curved surfaces.

References

1. Ding, Y., Stone, B. D., Bahl, M., Heller, E., & Scarmozzino, R. (2023, October). Hybrid refractive-metalens design for imaging applications. In *Current Developments in Lens Design and Optical Engineering XXIV* (Vol. 12666, pp. 13-19). SPIE.
2. Bos, J., R. Scarmozzino, M. Bahl, E. Heller, and C. Xu, "A design automation and simulation flow for lens systems containing multiple metasurfaces," in *Proceedings of Meta 2022*, (2022), pp. 1229–1231.
3. Nikolov, D. K., Bauer, A., Cheng, F., Kato, H., Vamivakas, A. N., & Rolland, J. P. (2021). Metaform optics: bridging nanophotonics and freeform optics. *Science Advances*, 7(18), eabe5112.
4. Han,Z., Colburn,S., Majumdar,A., and Böhringer, K.F.(2020). MEMS-actuated metasurface Alvarez lens. *Microsystems & nanoengineering*, *6*(1), 79.
5. Xie, N., Carson, M. D., Fröch, J. E., Majumdar, A., Seibel, E. J., & Böhringer, K. F. (2023). Large field-of-view short-wave infrared metalens for scanning fiber endoscopy. *Journal of Biomedical Optics*, *28*(9), 094802-094802.